Proceeding of the Twenty-Fifth International Conference on Tailings and Mine Waste, 7-10 November 2021, Banff, Alberta, Canada

Tailings and Mine Waste ’21

Edited by

Nicholas A. Beier
G. Ward Wilson
David C. Sego
University of Alberta Geotechnical Center &
Oil Sands Tailing Research Facility (OSTRF)

University of Alberta Geotechnical Center Edmonton, Alberta, Canada

Copyright ©
All rights reserved. No part of this publication or the information contained herein may be reproduced, stored in a retrieval system or transmitted in any form or by any means, electronic, mechanical, by photocopying, recording or otherwise, without written prior permission from the publisher.

Although all care is taken to ensure the integrity and quality of this publication and the information herein, no responsibility is assumed by the publishers nor the author for any damage to property or persons as a result of operation or use of this publication and/or the information contained herein.

Published by: University of Alberta, Department of Civil & Environmental Engineering

ISBN: 978-1-55195-466-0

Printed in Canada

Forward

We are indeed most privileged and honored to host **Tailings and Mine Waste 2021**, marking the 25th conference since its inception. This conference is truly a premier international forum for this critically important topic that has seized global attention with respect to tailings dam safety and sustainability for the mining industry.

Tailings and Mine Waste began 43 years ago in 1978 under the leadership of Dr. John Nelson of Colorado State University. The leadership later turned to Mr. Dan Overton and consultant colleagues who recognized the value of the conference and were steadfast pillars in the continuation of the Tailings and Mine Waste conferences. Through Dr. David Sego of the University of Alberta, Tailings and Mine Waste was hosted in Canada for the first time in 2009, and now the conference is offered as a collaborative partnership between Colorado State University (who will host the conference in 2022), the University of British Columbia, and the University of Alberta.

Tailings and Mine Waste attracts the highest quality of keynote speakers and technical papers and can be considered a key reference for the state-of-practice and its history. This conference continues to provide a premium platform and meeting place for members of the mining industry, engineers, geoscientists, researchers, regulatory groups and key interest groups concerned with environmental issues related to tailings and mine waste management.

This year, Tailings and Mine Waste features over 100 technical papers over three days. Our Keynote Speakers are highly respected practitioners and researchers in dam safety, risk management, advanced mine waste design, mining geoenvironment, hydrogeology, mine reclamation, and public/community engagement and communication. Special to Tailings and Mine Waste 2021 is a Plenary session entitled "Enhancements in Advanced Geotechnique for Tailings Dam Design" which will look at major case studies of recent tailings dam failures.

We want to personally thank the University of Alberta Geotechnical Centre and Dr. Norbert Morgenstern for their encouragement and support for the conference. The conference would not have been possible without the dedication of Vivian Giang, Jen Stogowski and especially Sally Petaske who provided so much assistance and leadership throughout the planning and execution of the conference.

As has been acknowledged many times before, a truly successful conference is only possible through the presentations and the quality of the technical work presented in the proceedings. The manuscripts become a lasting archival record and a snapshot of the state of knowledge in 2021. We want to thank our professional colleagues who willingly shared their experiences and insight with us.

To all the authors, thank you for contributing your technical knowledge and for your efforts in submitting your manuscripts, especially in these unprecedented days when time is our most precious commodity. The proceedings contain information representing hundreds of years of collective experience. We know you will find insight and answers that will assist you in a better understanding of tailings and mine waste management.

G. Ward Wilson, Nicholas A. Beier & David C. Sego
Co-Chairs, Tailings and Mine Waste 2021 Organizing Committee

ORGANIZATION

The Tailings and Mine Waste 2021 Conference was organized by the Department of Civil and Environmental Engineering, University of Alberta, Edmonton, Alberta, Canada in conjunction with Colorado State University, Fort Collins, Colorado, and the University of British Columbia, Vancouver, British Columbia.

ORGANIZING COMMITTEE:

Nicholas A. Beier (Co-Chair)	University of Alberta
G. Ward Wilson (Co-Chair)	University of Alberta
David C. Sego (Co-Chair)	University of Alberta
Vivian Giang	University of Alberta
Sally Petaske	University of Alberta
Jen Stogowski	University of Alberta

Thank you to all our Sponsors and Exhibitors for their continued support of Tailings and Mine Waste Conference.

Thank you to the following sponsors for their support in making the 25th International Conference on Tailings and Mine Waste a success:

Table of Contents

Keynote Abstracts

Tailings and Mine Waste Management

Water Considerations for Tailings Management & Planning

Tailings Properties and Behaviour

Dam Stability

Novel Technologies for Tailings Management

Novel Technologies for Tailings Management (Cont'd)

Data and Tailings Management

Advances in Modelling for Tailings Management

Risk Management & Remote Sensing Tools

Tailings Management Case Studies

Instruments for Tailings Management

Mine Closure Case Studies

Water Considerations for Mine Closure

Mine Closure Design

Oil Sands Tailings

Design and Construction of Oil Sands Tailings Storage Facilities

Design and Construction of Oil Sands Tailings Storage Facilities (Cont'd)

Use of Plants for Oil Sands Tailings Remediation

Oil Sands Tailings: Aging and Treatments

Oil Sands Tailings Modelling

Oil Sands Tailings Filtering and Dewatering

Oil Sands Tailings Properties

Innovative Technologies in Oil Sands Tailings Management

Geosynthetics

Keynote Abstracts

2021 BHP Tailings Storage Facility management update and Miami Avenue TSF Relocation

D. Chad LePoudre
BHP, Calgary, Alberta, Canada

ABSTRACT: This presentation will communicate BHP's journey through tailings management and how our future strategy is pushing the boundaries of current thinking and is underpinned by the Global Industry Standard on Tailings Management (GISTM). Key messages consist of our operating context, BHP's alignment to and implementation of the GISTM, our approach to Tailings Management Systems (TMS), and industry opportunities and challenges we are working to overcome. Risk Reduction project examples are presented, highlighting the tailings relocation project of the Miami Avenue Tailings Storage Facility.

Understanding uncertainty throughout the life of tailings storage facilities – Selected topics

Renato Macciotta
University of Alberta, Edmonton, Alberta, Canada

EXTENDED ABSTRACT:

1 INTRODUCTION

Tailings storage facility (TSF) failures worldwide are not rare. A *Chronology of major tailings dam failures* is published by the WISE Uranium Project (www.wise-uranium.org), and although not comprehensive, provides a clear picture of a consistent trend in the frequency of TSF failures associated with significant consequences (Figure 1) (Macciotta and Lefsrud 2020). The database published by the WISE Uranium Project suggests between one and six high-profile TSF failures since 2000, 2 to 3 failures per year in average. An inspection of the database shows that the failures are associated with substantial damage, environmental impact, loss of life, or a combination of these. Importantly, the database also shows that failure locations are worldwide, regardless of jurisdiction (qualitative observation), although no statistical analysis is presented here on this matter.

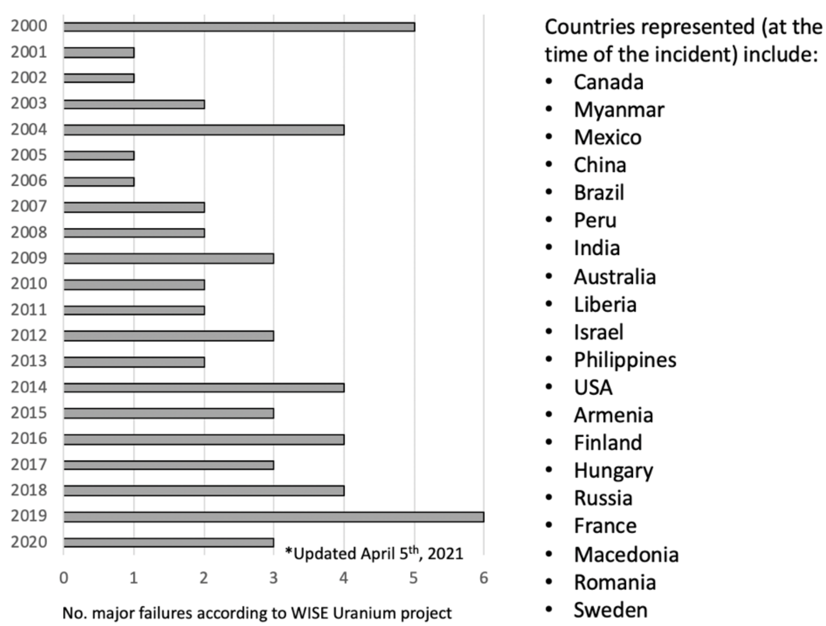

Figure 1 *Major tailings dam failures* since 2000 and up to April 5th, 2021 (after WISE Uranium Project – www.wise-uranium.org/mdaf.html). Countries where major failures occurred are listed in no particular order.

This consistent trend and some very high-consequence events associated with TSF failures over the last decade (including the Mount Polley tailings dam breach in 2014, Morgenstern et al. 2015; the Fundão tailings dam failure in 2015, Morgenstern et al. 2016; and the Feijão Dam I failure north-east of Brumadinho in 2019, Robertson et al. 2019) have led to a number of reviews on TSF failure causes from both technical and organizational perspectives (e.g. Morgenstern 2018, Armstrong et al. 2019, Santamarina et al. 2019, Macciotta and Lefsrud 2020, Franks et al. 2021). Importantly, these failure events have also been followed by revisions to tailings storage regulations and updated guidelines on the design, construction, operation and management of TSF's in different jurisdictions (Cobb 2017, MAC 2017, 2019, and 2021, Morrison et al. 2018, CDA 2019, Zhang and Daly 2019, ANCOLD 2019, AER 2021). Perhaps the most significant initiative towards enhanced safety of TSF's, given it is broadly international and industry-led, is the development of the *Global industry standard on tailings management* (the Global Industry Standard) by an expert panel convened by the International Council on Mining and Metals (ICMM), the United Nations Environment Programme (UNEP) and the Principles for Responsible Investment (PRI) (https://globaltailingsreview.org) (Global Tailings Review Expert Panel 2020). The Global Industry Standard is accompanied by supporting articles on the diversity of topics covered, and by protocols and guidance documents developed by the International Council on Mining and Metals (ICMM) to aid in the adoption of the Global Industry Standard and make it actionable and auditable (ICMM 2020, 2021a, 2021b).

The Global Industry Standard addresses a variety of topics that need to be successfully managed for safe and sustainable TSF design, construction, operation and closure. These include aspects of community engagement, disclosure of information, and risk communication; effective management and allocation of responsibilities and accountabilities within the organizational structure; and decision-making on design, construction, operation and closure that is centred in managing the risks associated with the TSF. This list is not intended to be comprehensive but to highlight the requirement in the standard for a multidisciplinary and multidimensional (organizational, technical, social, etc.) approach.

The common theme in the Global Industry Standard is the technical and organizational identification and management of risk. Although risk is broadly understood as probability of an event and its potential negative consequences (e.g. CDA 2007a, CDA 2013, MAC 2017, Brown 2019, ICMM 2021a), risk is a result of uncertainty in achieving objectives (ISO 2009, captured also on CDA 2007a). In the context of tailings management, the objective is safe, socially acceptable, and economic containment of tailings or other defined TSF performance goals. This keynote presents a discussion on selected topics to understand uncertainty in the life cycle of a TSF. The discussion includes the sources of uncertainty in TSF design, construction, operation and closure; as it impacts our understanding and perception of the risks associated with TSF's and presents an example quantification of uncertainty in risk analyses. Importantly, the keynote discusses the influence of uncertainty and design confidence in the adequate selection of design acceptance criteria, and the role of monitoring for increasing design confidence. The discussion also includes uncertainty associated with human behaviours and the importance of organizational culture and risk communications. The aim of the discussions herein is to contribute to the debate on key topics addressed in the Global Industry Standard, towards actionable and auditable protocols and approaches for enhanced safety of TSF's during operation, closure and post-closure.

2 REFERENCES

Alberta Energy Regulator (AER). 2021. Dams. Content available from https://www.aer.ca/providing-information/by-topic/dams, accessed May 10, 2021

Armstrong, M., Petter, R., Petter, C. 2019. Why have so many tailings dams failed in recent years? Resources Policy 63:101412

Australian National Committee on Large Dams (ANCOLD). 2019. Guidelines on tailings dams – planning, design, construction, operation and closure – revision 1 (July 2019). Available from https://www.ancold.org.au, accessed May 11, 2021

Brown, B.S. 2019. What are the real risks for tailings facilities? In: J. Wesseloo (ed.) Mining geomechanical risk 2019. Australian Centre for Geomechanics. Perth, AU. Pp: 21-30

Canadian Dam Association (CDA). 2007a. Technical Bulletin: Dam safety analysis and assessment. Available at https://www.cda.ca, accessed May 11, 2021

Canadian Dam Association (CDA). 2013. Dam Safety Guidelines 2007. 2013 Edition. Available at https://www.cda.ca, accessed May 11, 2021

Canadian Dam Association (CDA). 2019. Technical Bulletin: Application of dam safety guidelines to mining dams. 2019 Edition. Available at https://www.cda.ca, accessed May 11, 2021

Cobb, C.F. 2017. Update on mine tailings dam regulation in Alaska and North America. Alaska Business Monthly, January 2017. Pg:34-35

Franks, D.M., Stringer, M., Torres-Cruz, L.A., Baker, E., Valenta, R., Thygesen, K., Matthews A., Howchin, J., Barrie, S. 2021. Tailings facility disclosures reveal stability risks. Scientific Reports 11:5353

Global Tailings Review Expert Panel. 2020. Global Industry Standard on Tailings Management. Available at https://globaltailingsreview.org, accessed May 10, 2021

International Council on Mining & Metals (ICMM). 2020. Tailings governance framework: Position statement. Available at https://www.icmm.com, accessed May 11, 2021

International Council on Mining & Metals (ICMM). 2021a. Tailings management good practice guide. Available at https://www.icmm.com, accessed May 11, 2021

International Council on Mining & Metals (ICMM). 2021b. Conformance protocols - Global Industry Standard on Tailings Management. Available at https://www.icmm.com, accessed May 11, 2021

International Organization for Standardization (ISO) 2009. ISO 31000 Risk Management – Principles and Guidelines. ISO, Geneva, Switzerland.

Macciotta, R., Lefsrud, L. 2020. PBRISD, dam safety management systems, and the role of communication and culture for tailings dam failure preventability. CDA Bulletin, 31(4):10–21

Mining Association of Canada (MAC). 2017. A guide to the management of tailings facilities. Third Edition. The Mining Association of Canada. Pp: 86

Mining Association of Canada (MAC). 2019. A guide to the management of tailings facilities. Version 3.1. The Mining Association of Canada. Available at https://mining.ca/our-focus/tailings-management/tailings-guide, accessed May 11, 2021

Mining Association of Canada (MAC). 2021. A guide to the management of tailings facilities. Version 3.2. The Mining Association of Canada. Available at https://mining.ca/our-focus/tailings-management/tailings-guide, accessed May 11, 2021

Morgenstern, N.R. 2018. Geotechnical Risk, Regulation, and Public Policy – 6th de Mello Lecture. Soils and Rocks, Sao Paulo, 41(2):107-129

Morgenstern, N.R., Vick, S.G., van Zyl, D. 2015. Report on Mount Polley Tailings Storage Facility Breach. Independent Expert Engineering Investigation and Review Panel to the Province of British Columbia, January 30, 2015

Morgenstern, N.R., Vick, S.G., Viotti, C.B., Watts, B.D. 2016. Report on the Immediate Causes of the Failure of the Fundão Dam. August 25, 2016

Morrison, K.F., Pedrosa, H.G., dos Santos, G.J.I., Gomide, P.C.R., Ferreira, A.M. 2018. Changes to Tailings Dam Regulation in Brazil in the Aftermath of Failures. Proceedings of the 2018 Tailings & Mine Waste conference. September 30 – October 2, 2018, Keystone, Colorado, USA

Robertson, P.K., de Melo, L., Williams, D.J., Wilson, G.W. 2019. Report of the Expert Panel on the Technical Causes of the Failure of Feijão Dam I. December 12, 2019

Santamarina, C., Torres-Cruz, L.A., Bachus, R.C. 2019. Why coal ash and tailings dam disasters occur. Science 364 (6440):526-528

Zhang, M., Daly, T. 2019. China tightens rules on tailings dam safety. December 19, 2019 news piece available from Reuters at https://www.reuters.com/article/us-china-tailings/china-tightens-rules-on-tailings-dam-safety-idINKBN1YN12S, accessed May 10, 2021

Tailings management: Governance models, lessons from failures, managing uncertainty and building professional capacity

Scott Martens
Canadian Natural Resources, Calgary, Alberta, Canada

EXTENDED ABSTRACT:

1 GOVERNANCE

1.1 *Introduction*

The core of dam safety management is the combination of strong governance and strong engineering practice. Safe dams require high standards of planning, engineering design, construction and operations – and it is governance that provides the framework and the assurance for all of these.

Many leading practices in tailings management and dam safety have been advanced by the oil sands industry, through the work of the companies, researchers, consultants, reviewers, and regulators. The oil sands industry has an excellent track record in the safe management of tailings facilities, with almost 100 tailings dams with more than 1500 dam-years of operations, and no incidents causing a loss of tailings containment.

1.2 *Roles and Accountability*

Governance refers to the organizational structures and processes that a company puts in place to ensure the effective management, oversight, and accountability for tailings. A core aspect of a well-functioning tailings management system is the assignment of accountability, responsibility, and authority. The key roles include the Accountable Executive (AE), the Responsible Person (RP) or Responsible Tailings Facility Engineer (RTFE), the Engineer of Record (EOR), and Independent Review (MAC 2021).

A fundamental principle is that the owner is responsible for dam safety, and must implement a comprehensive tailings management governance system. The EOR is an important component, but only one component of the tailings and dam safety management system. Without an appropriate supporting management structure, the EOR will not be able to ensure safe outcomes for tailings facilities. Because the EOR must be integrated with the overall tailings and dam safety management system, the role of the EOR must be defined together with the other roles (Boswell & Martens 2017).

The owner's organization requires policy and commitment, tailings management systems, and accountability. Accountability starts at the top of the owner's organization – with the Board and the AE, and flows through the RTFE to the EOR. The whole organizational structure is required to provide the required resources, and to support the activities needed to ensure safe design, construction, and operations.

The oil sands operators were early adopters of the Independent Review Board (IRB) concept. The IRB is essential, but just one component of a multi-level review process, that includes peer review, senior internal review, signoff by the responsible professional member, IRB review and the Annual Tailings Management Review with the AE. All those levels of review work together to support safe and effective outcomes.

1.3 *Governance Models*

There isn't a single acceptable governance model for tailings management; companies have successfully used different models for the role of the EOR and the larger governance structure. What is important is that there is a comprehensive understanding and list of responsibilities, and that these are clearly assigned and discharged by the responsible individuals.

A common governance model in the Alberta oil sands includes an internal EOR within the owner's organization, and formal separation of the designer of record (DOR) and EOR roles. The role of the EOR in this model is to implement the design and provide technical direction for the operation. The EOR verifies that the structure is constructed, operated, maintained, and monitored in accordance with the design, the Operations, Maintenance and Surveillance (OMS) manual and regulatory requirements. Where deviations from the design are required or identified, the EOR evaluates these for conformance with the design requirements, and working with the designer, approves the changes or rejects them, and implements any necessary mitigations to maintain the safety of the structure. The EOR reviews the instrumentation and monitoring data to verify the performance of the structure and implement any mitigations necessary to maintain the safe function. The EOR also directs ongoing site investigations and instrumentation installation, subsequent to the initial design, that are required to implement the Observational Method.

Having the EOR internal to the mining company, typically resident at the mine site and close to the work face, provides very direct oversight of the construction and operation, so that any current or anticipated issues can be rapidly identified and mitigated.

Having the EOR role and some of the DOR roles internal to the mining company requires a high level of organizational resources and maturity, including the capacity for internal review by senior engineers, in addition to the independent review.

2 LESSONS FROM FAILURES

2.1 *Root Causes*

Details of failures in the global mining industry have been discussed at length (Morgenstern 2018), with the basic causes being primarily attributed to shortcomings in engineering. However, the terms of reference of recent failure investigation panels were narrowly focused on the immediate technical causes of the failures. The root causes of the failures are the overarching technical and governance reasons that allowed the situation to get to the point of failure (British Columbia Ministry of Energy and Mines 2015, Küpper et al. 2020). Insightful examinations of the root causes have identified an overall governance challenge which has included deficiencies in management systems, poor decision-making processes, breakdowns in communication, and the lack of effective review and monitoring processes (Evans & Davies 2020). It is incumbent on tailings management professionals, whether as an owner, a consultant or a regulator, to critically review their procedures in light of those root causative factors.

2.2 *Observational Method*

The Observational Method (Peck 1969) is a core component of risk management and has been applied successfully in the oil sands. There has been some criticism of the observational method; however, the flaws are not with the method itself, but problems arise when it isn't applied correctly, or when it is abused. The observational method is not applicable for conditions where a failure may develop more rapidly than could be observed or responded to with contingency measures (such as for brittle materials), where failure modes cannot be detected through instrumentation or observation, and where physical, schedule or economic constraints preclude the timely application of contingency measures during construction or operation. In these cases, the initial design must be sufficiently robust to account for these potential circumstances since the design cannot be adapted to manage the risks based on observations.

3 FOCUS AREA FOR IMPROVEMENT: MANAGEMENT OF UNCERTAINTY

3.1 *Uncertainty and Characteristic Parameters*

One common gap that persists in engineering practice is in understanding and addressing uncertainty. "Uncertainty is inherent in the analysis and evaluation of risks related to tailings facilities. Uncertainty may be related to many factors, such as the natural variability of the foundation and construction materials for a proposed tailings facility, design parameters, the accuracy of predictions of future climate conditions, and the challenge of estimating the likelihood of highly improbable events." (ICMM 2021).

One of the most challenging aspects of geotechnical engineering is selecting characteristic parameters from a set of widely distributed data. Whether consciously and deliberately or otherwise, a design engineer is always making a statistical assessment of the input parameters. The variation in the credible values that could be used to characterize design parameters often overwhelms variations in the choice of Factor of Safety.

Regulations in some jurisdictions prescribe a minimum Factor of Safety. Alberta does not, and has taken the approach of requiring the designer to select and justify a Factor of Safety that takes account of the uncertainty in the inputs to the design, the consequences of failure, the level of construction quality control, the ability to implement the Observational Method, and other risk management processes.

3.2 *Modelling: Complexity, Simplicity and Uncertainty*

Another aspect of uncertainty management relates to numerical modelling. There are now very powerful models to analyze and predict soil and rock behaviour. However, ground conditions – either natural or constructed, have a level of complexity that will never be possible to fully model. The ability to model material elements, and the accuracy of constitutive models, vastly exceeds the ability to characterize the heterogeneity of soil and rock. Furthermore, behaviour is often controlled by discontinuities or thin layers in the foundation or tailings, and it is not possible to accurately know the position and orientation of all such features and include them in the models. Complex models therefore always need to be run together with simple models. Theoretical predictions must be compared to empirical relationships. Neither is fully informative, and our judgement will be strongest when we use multiple approaches to provide insight to complex problems. When assessing the engineering analyses for complex issues, it is helpful to look for multiple lines of evidence that converge on the same answer.

Peck (1980) discusses failures that "arose from overlooking or misjudging geological features in the foundation itself. A few had their origin in construction defects in the embankment. They had in common that all were outside the scope of numerical analyses." Peck (1980) further stated "I would venture that 9 out of 10 recent failures occurred not because of inadequacies in the state of the art, but because of oversights that could and should have been avoided, because of lack of communication among parties to the design and construction of the dams, or because of overoptimistic interpretations of geological conditions. The necessary knowledge existed; it was not used." Those words are as true today as they were then.

4 BUILDING PROFESSIONAL CAPACITY

Our profession must continue to build professional capacity and proficiency through training, experience and mentoring. There are a number of excellent continuing education programs on tailings and mine waste run through universities, but they are primarily bringing students to a level of awareness, not mastery of the subjects. They help to identify the knowledge that is needed, but they cannot possibly teach the details and the skills in a broad range of topics over the length of the courses. We need to balance the broad education with opportunities for focused, deep technical education. Universities, professional organizations and industry will need to collaborate to advance opportunities for intensive technical skill development (Jefferies 2021).

Lifelong learning is essential in tailings and geotechnical engineering. Graduate degrees are important for technical professionals. But a master's or Ph.D. degree isn't the finish line of professional education - it is the beginning. It provides a strong enough background in the fundamentals that can be used as a platform to support the ongoing education that is needed to perform at the level commensurate with the responsibility we have as mining professionals.

5 CONCLUSIONS

I believe that our profession has emerged from the tragic events of the past few years much stronger, with the ability to deliver tailings management at the levels of safety that society rightfully demands of us.

- There are strengthened national and international standards for governance and management systems, as well as technical requirements: MAC, CDA, GISTM, ICMM, ICOLD, ANCOLD. We have the tools we need and must consistently apply these.
- We have advanced models for material behaviour. We also need to be aware of the limitations and uncertainties, and take account of these in designs.
- There is uncertainty in all aspects of tailings management – from the foundation conditions, tailings properties to the mine and tailings plans. We must be aware of the uncertainty and manage it appropriately.
- We have established continuing education programs. We need to support and continue to develop these to train the next generation of tailings professionals.
- Most fundamentally, we have a vision for zero fatalities and eliminating catastrophic failures. We know what is needed to achieve the levels of reliability for tailings facilities that the public expects.

6 REFERENCES

Alberta Government. 2018. *Alberta Dam and Canal Safety Directive*.

Boswell, J. and Martens, S. 2017. The Role of the Engineer of Record in an Integrated Dam Safety Management System for Tailings Dams: Recent Perspectives from the Alberta Dam Safety Community. *Proceedings, Canadian Dam Association Conference*, Kelowna.

British Columbia Ministry of Energy and Mines. 2015. *Mount Polley Mine Tailings Storage Facility Breach: Investigation Report of the Chief Inspector of Mines.*

Canadian Dam Association. 2013. *Dam safety guidelines 2007* (2013 edition).

Evans, R. and Davies, M. 2020. Creating and Retaining Knowledge and Expertise. Chapter XI in Oberle, B., Brereton, D., Mihaylova, A. (eds.) (2020) *Towards Zero Harm: A Compendium of Papers Prepared for the Global Tailings Review*. St Gallen, Switzerland: Global Tailings Review. https://globaltailingsreview.org/.

International Council on Mining and Metals (ICMM), United Nations Environment Programme (UNEP) and Principles for Responsible Investment (PRI). 2020. Gl*obal Industry Standard on Tailings Management.* St Gallen, Switzerland: Global Tailings Review. https://globaltailingsreview.org/wp-content/uploads/2020/08/global-industry-standard_EN.pdf

International Council on Mining and Metals (ICMM). 2021. *Tailings Management: Good Practice Guide.* http://www.icmm.com/website/publications/pdfs/environmental-stewardship/2021/guidance_tailings-management.pdf

Jefferies, M. 2021. Improving governance will not be sufficient to avoid dam failures. *Proceedings of the Institution of Civil Engineers - Geotechnical Engineering*. https://doi.org/10.1680/jgeen.21.00105

Küpper, A. van Zyl, D. and Thompson, J. 2020. Mine Tailings – A Systems Approach. Chapter V in Oberle, B., Brereton, D., Mihaylova, A. (eds.) *Towards Zero Harm: A Compendium of*

Papers Prepared for the Global Tailings Review. St Gallen, Switzerland: Global Tailings Review. https://globaltailingsreview.org/.
Lacasse, S., and Höeg, K. 2019. In praise of monitoring and the Observational Method for increased dam safety. *Proceedings, ICOLD 2019*, Ottawa.
Mining Association of Canada (MAC). 2019. *TSM Tailings Management Protocol* (2019 Version).
Mining Association of Canada (MAC). 2021. *A Guide to the Management of Tailings Facilities.* Version 3.2, March.
Morgenstern, N. 2000. Performance in Geotechnical Practice. Inaugural Lumb Lecture. *Transactions of the Hong Kong Institution of Engineers.*
Morgenstern, N. 2010. Improving the safety of mine waste impoundments. *Proceedings, Tailings and Mine Waste 2010*, Vail. 3-10.
Morgenstern, N. 2018. Geotechnical Risk, Regulation, and Public Policy – The Sixth Victor de Mello Lecture. *Soils and Rocks*. 41(2):107-129.
Morgenstern, N. 2020. Tailings Dam Safety - Have We Resolved the Crisis? Keynote Address. *Tailings and Mine Waste 2020*, Ft. Collins.
Peck, R. 1969. Advantages and Limitations of the Observational Method in Applied Soil Mechanics. *Géotechnique*. 19(2): 171-187.
Peck, R. 1980. Where has all the judgement gone? The fifth Laurits Bjerrum memorial lecture. *Canadian Geotechnical Journal*. 17:584-590.

The Tailings Failure of Culture: The meaning of the destruction of the Juukan Gorge Caves in Western Australia

Ginger Gibson
Director, The Firelight Group, Edmonton, Alberta

Ciaran O'Faircheallaigh
Professor of Politics and Public Policy, Griffith University, Brisbane, Australia

ABSTRACT: The extractive industries are often responsible for the large-scale destruction of the cultural heritage of Indigenous peoples. This type of destruction has been foregrounded in the case of the destruction of caves in western Australia. These historic caves were destroyed with the permission of the state government, and with the full knowledge of the mining company, Rio Tinto. These caves were sacred, and their destruction has been devastating to the Indigenous community. This type of destruction is occurring constantly and is state sanctioned. Both international and Indigenous law are now squeezing corporations, forcing senior executives to consider how to address this issue. This paper considers this squeeze that occurred as a result of the destruction of the caves of Juukan Gorge, the outcomes for the industry, and the motivations and values at play that must be reconfigured to address this failure. While the industry has reckoned with tailings failures due to the devastating failures in Canada and Brazil, this destruction of caves presents the industry with the same opportunity to learn through failure. The industry must turn to consider the relationship to cultural heritage specifically, and more broadly to Indigenous peoples and cultural heritage.

Reclamation of hard rock mine sites: current practices and challenges

Bruno Bussière and Marie Guittonny
Université du Québec en Abitibi-Témiscamingue, Research Institute on Mines and the Environment, Rouyn-Noranda, Québec, Canada

ABSTRACT: The mining industry is a significant asset to the Canadian economy, providing a source of exports, employment, and technological development. However, mineral extraction has an environmental cost. One of the most serious environmental issues related to mining is the reclamation of waste disposal areas that generate acid mine drainage (AMD). AMD can occur when meteoric water and atmospheric oxygen react with the sulfide minerals in mine wastes. When acid generation is poorly controlled, it can lead to significant impacts on surrounding ecosystems. This presentation focuses on the reclamation of waste storage facilities from hard rock mines operations that can generate AMD. These facilities constitute the main source of AMD pollution during and after hard rock mine operations.

Reclamation aims to return a mine site to a satisfactory state, which means that the site should not threaten human health or security, should not generate in the long term any contaminant that could significantly affect the surrounding environment, and should be aesthetically acceptable to communities. Moreover, long-term control of the contamination must be done without continuous maintenance, which excludes the collect and treat option to reclaim a mine site. The establishment of vegetation on the site is also favored to control erosion and restore the site's natural appearance. Finally, when possible, reclamation that allows the site a second life after the mine closure is preferred.

Several different types of cover systems can be used to control AMD and return the site to a satisfactory state (Bussière and Guittonny, 2021). The two first reclamation techniques presented aim to control water infiltration. Two types of impervious covers are described: low saturated hydraulic conductivity covers (LSHCC) and store-and-release (SR) covers. Then, oxygen barrier techniques are described, including water covers, covers with capillary barrier effects (CCBE), and elevated water table (EWT) with monolayer covers. Insulation covers, which control mine waste temperature in order to avoid contaminant generation, are then presented. For each method, a historical context is provided followed by a conceptual and technical description of the method, and the factors that influence its design and performance. Different case studies are used to illustrate the real performance of each reclamation method. Finally, the main advantages and limits of the different reclamation techniques are specified to promote comparative analysis.

The practical application of these techniques and advancements in research made over the past ~ 30 years have greatly increased our understanding of how these covers function and interact with the environment. However, many topics, mostly related to their longer-term use, are still not well understood. For example, the influence of climate change and of the ingress of vegetation; the service life of geomembranes and geosynthetic clay liners (GCLs); the accurate evaluation of the different components of the water budget; and the influence of temperature on in situ sulfide oxidation rates. The last part of this presentation will address these challenges related to the long-term performance of reclamation methods by considering that reclaimed sites are integrated in a changing environment.

References

Bussière, B., Guittonny, M. (2020). Hard Rock Mine Reclamation: From Prediction to Management of Acid Mine Drainage. B. Bussière et M. Guittonny (Eds), 14 chapitres, CRC Press, Boca Raton, 408 pages.

Learning to Walk a Reconciliation Journey

Jessica Vandenberghe
University of Alberta, Edmonton, Alberta, Canada

ABSTRACT: This keynote session will emphasize the importance of Equity, Diversity, Inclusion and Decolonization and give a glimpse into the Canadian oppressive history towards Indigenous Peoples. This glimpse is vital so we can begin the discussion around the Indigenous Worldview differences, the impact it has on Indigenous community governance, land ownership, and daily challenges. We need to understand the Truth and the different perspectives so we can begin walking a Reconciliation Journey with Indigenous Peoples and Community as Industry Partners and Canadians.

Tailings and Mine Waste Management

Developing high resolution water balance estimates of tailings storage facilities

Jason Keller
GeoSystems Analysis, Inc., Hood River, OR, USA

Michael Milczarek
GeoSystems Analysis, Inc., Tucson, AZ, USA

Michael Geddis
KGHM International, Tucson, AZ, USA

ABSTRACT: A comprehensive tailings storage facility (TSF) water balance study was conducted to estimate seepage rates during past operations and under proposed future TSF expansion. Multiple methods were used to achieve these objectives: 1) Daily estimates of operational water inflows and outflows were prepared to include high resolution estimates of monthly evaporation rates using Landsat satellite imagery and an energy balance model; 2) A characterization program was conducted to measure tailings *in situ* and laboratory physical and hydraulic properties; 3) These measurements were used to classify the tailings into different material types that correlated to distance from the main cycloned embankment and TSF perimeter; 4) Operational data and satellite imagery were analyzed to estimate the TSF area and supernatant ponded area over time; 5) A TSF hydraulic property model was developed to spatially distribute the different material types within the TSF over time and assign hydraulic properties from the surface to depth. Water balance results indicate that seepage rates are decreasing over time due to operational improvements and reduced tailings permeability due to consolidation at depth. The TSF hydraulic property model indicates that seepage rates are highest along the perimeter of the TSF below ponded areas.

1 INTRODUCTION

Tailings storage facilities (TSFs) are large, often being more than 500 hectares in size, and of variable thickness, ranging from less than one meter near the perimeter to significant depths at the impoundment dam and in the interior. TSF construction methods create multiple and variable layers of distinct tailings textures due to alternating methods and periods of tailings deposition (e.g., slurry in the winter, cyclone in the summer) and movement of tailings deposition sources, both slurry points and moving banks of cyclones. Additionally, tailings consolidation due to settling and over-burden pressure results in long-term physical and hydraulic property changes due to compaction at depth. Consequently, water balance estimates of tailings storage, supernatant evaporation and seepage rates are confounded by the large spatial and temporal depositional variations across a TSF due to construction and operational practices and climatic conditions.

A comprehensive water balance study was conducted to develop hydraulic property and water balance models to quantify past and future (expanded) seepage rates from an unlined TSF and estimate uncertainty. Multiple methods were used to achieve these objectives including detailed estimates of water inflows and outflows, *in situ* and laboratory measurements of the tailings physical and hydraulic properties, analysis of operations data and satellite imagery to estimate the TSF supernatant and tailings depositional spread, and classification and delineation of tailings into different material types. A hydraulic property model was developed based on the field and laboratory data and was then used to predict the spatial distribution of seepage across the TSF. The water balance results were used to guide TSF expansion design and water management to reduce TSF seepage, and as the upper boundary condition for a fate and transport groundwater flow model.

1.1 *Tailings Storage Facility Overview*

The TSF is in a semi-arid, cold desert, climate with an average December temperature (coldest month) of -4 °C and an average July temperature (warmest month) of 20 °C. The tailings embankment is constructed using centerline raise methods with cyclone underflow sand deposition. Cyclone deposition typically occurs during the summer (May to September) with whole tailings deposition via spigotting from various locations on the perimeter of the facility from October to April. The TSF began operating in January 1996. Mining operations were suspended between July 1999 and September 2004. Tailings deposition resumed October 2004 with the restart of mining operation. The TSF was approximately 670 hectares in 2020.

Supernatant is reclaimed from the TSF at the barge operating channel (BOC, Figure 1). The BOC consists of bentonite-amended and compacted alluvium. Recently, the BOC area was enclosed with a ring-road/dyke, and shore-based pumps have been used to maintain the water level at the lowest possible operational depth, all to reduce seepage from the BOC. Future expansion of the BOC includes installation of a HDPE liner under an expansion area, and then intentionally breaching the ring-road to create a lined BOC with minimal seepage. Water is pumped from the BOC to the Repulp building (Figure 1) and either recirculated to bring tailings up to the optimal percent solids required for cyclone operation or sent back to the mill as reclaim water.

1.2 *Conceptual Model of Hydrologic Conditions*

Because tailings emplacement is a fluvial depositional process, the largest tailing particles settle nearest to the cyclone or spigot, whereas finer-grained tailings settle farther away from the deposition source. This process results in tailings segregation into material “types” with different physical and hydraulic properties that determine the amount of water the tailings will retain and lose to seepage. The cycloned main embankment (CME) is constructed from coarse-grained underflow, and the overflow is sent either past the cyclones, or out into the impoundment about 100 feet to form the upstream beach area. The coarse-grained sand in the CME has much higher permeability than the fine-grained overflow of the beach. Moderate permeability tailings represent a transition between coarse-grained tailings to low permeability fine-grained tailings as the slurry moves from the depositional source to the BOC. In addition to the areal distribution of tailings types, the tailing permeability tends to decrease with depth in the TSF as increasing overburden pressure results in tailings compaction.

The tailings surface consists of zones of wet tailings and shallow surficial channels with a large, ponded area between the CME beach and the BOC. Evaporation occurs from these wet areas and to a lesser extent from tailings that are drying between deposition cycles. Evaporation varies significantly between summer and winter, as do depositional practices, both of which control seepage rates. Consequently, seepage from the TSF is expected to be variable through time and space as a function of tailings deposition and growth rates, cyclone sand production, presence of ponded and wet tailings outside of the BOC, evaporative losses and residual pore water that is not lost to evaporation. However, the variability in seepage rates likely reduces with depth through the tailings, primarily because of decreasing permeability with depth, resulting in nearly constant net percolation from the base of the facility. This net percolation is reduced by reclaiming more water and limiting the spatial extent of deposition, both of which have been accomplished over the past several years.

2 METHODS

2.1 *Field Characterization Program*

The field characterization program consisted of:

– Three auger hole transects to log tailings geology and physical attributes (texture and color) and to evaluate layering and segregation;
– *in situ* measurement of seepage within the BOC using a seepage meter;
– *in situ* measurement of tailings saturated hydraulic conductivity (K_{sat});
– *in situ* measurement of K_{sat} of alluvial sediments that represent alluvium under the TSF, and;
– collection of tailings and alluvium samples for laboratory physical and hydraulic testing.

Locations evaluated as part of the field characterization program are shown in Figure 1 and consist of points where auger holes were advanced to collect samples for geologic logging and laboratory testing, and/or *in situ* (field) hydraulic testing.

In situ hydraulic property testing was conducted using a variety of methods to directly measure seepage fluxes within tailings and BOC areas under ponded conditions, or to estimate *in situ* K_{sat} of tailings and alluvium material. Testing was completed using either single-ring cylinder infiltrometer (CI) (Bouwer et al., 1999), air-entry permeameter (Bouwer, 1966), Wooding's infiltrometer (Wooding, 1968), tension infiltrometer (Hussen and Warrick, 1993), or seepage meter (Lee, 1977) measurements. Additionally, CI measurements were made in areas where shallow water conditions prevented the use of the traditional seepage meter method.

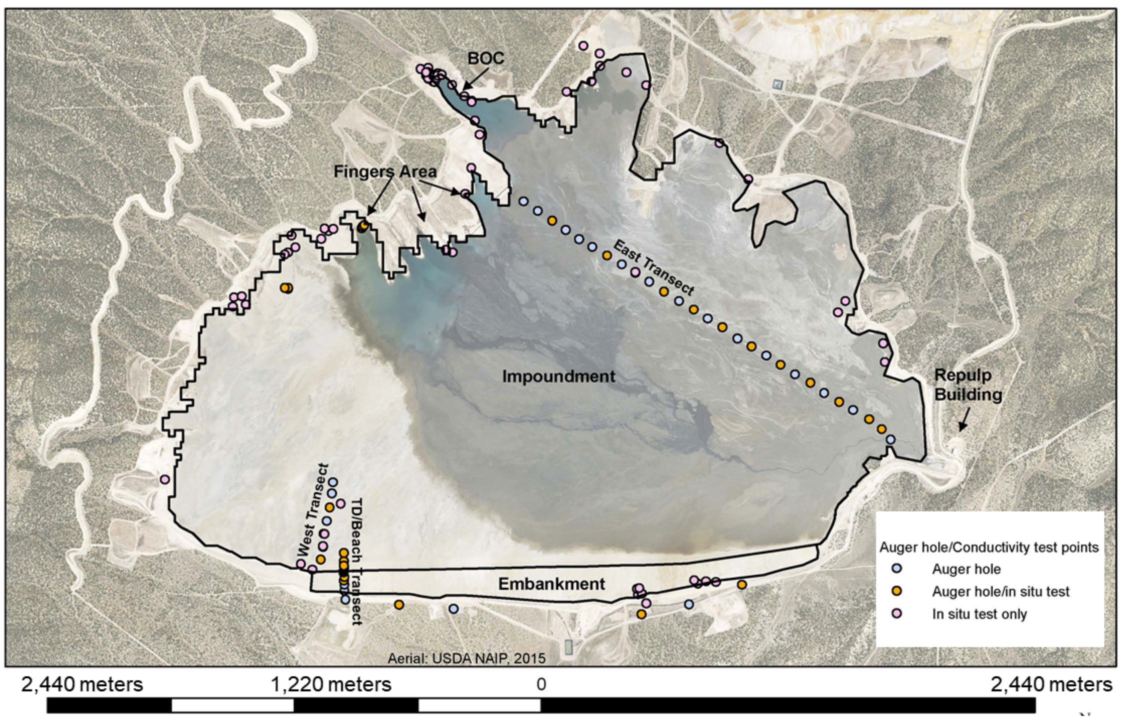

Figure 1. Near surface investigation locations.

2.2 *Laboratory Testing*

A subset of tailings samples collected during the field investigation were selected for laboratory physical and hydraulic property testing, to include particle size distribution (PSD), particle density, 1-D consolidation, K_{sat}, triaxial permeability and moisture retention characteristics (MRC). Twenty (20) samples representing the range of observed tailings field textures were selected and analyzed for PSD and particle density to allow for laboratory calibration of the 221 field texture estimates. Seven composite tailings samples were created for 1-D consolidation, K_{sat} and MRC testing based on the estimated distribution of tailing types from field texture measurements. Three of the seven composite tailings samples were also selected for triaxial permeability testing. Each composite tailings sample was created from two grab samples with similar texture.

Tailings dry bulk densities as a function of depth were estimated from the 1-D consolidation and triaxial permeability testing results, which were used to guide the target remolded dry bulk densities (BD) for the K_{sat} and MRC tests. K_{sat} and MRC tests were conducted in 2-inch diameter columns remolded to high and low dry BDs representative of tailings conditions under greater than 45 m of depth, and between 0 and 45 m of depth respectively.

2.3 *Area and Thickness Estimates*

The boundary of the TSF between 1996 and 2020 was estimated on an approximate six-month time interval using Landsat and Sentinel satellite data and application of a site-specific processing algorithm. The estimated TSF ponded and dry areas were validated against aerial photographs and estimated TSF area reported in mine annual monitoring reports. Linear interpolation of the delineated TSF areas generated a monthly time series of ponded, dry, and partially saturated TSF surface areas. The boundary between the TSF embankment and impoundment area was based on the static location of the cyclone header pipe visible in aerial photographs. TSF material thicknesses were estimated annually (1996 to 2020) as the difference between the pre-mining and TSF surface topography.

2.4 *Water Balance Estimates*

The water balance components of the TSF incorporated into the water balance model are shown in Figure 2. The methods used to calculate or estimate flux rates for the various components are described below.

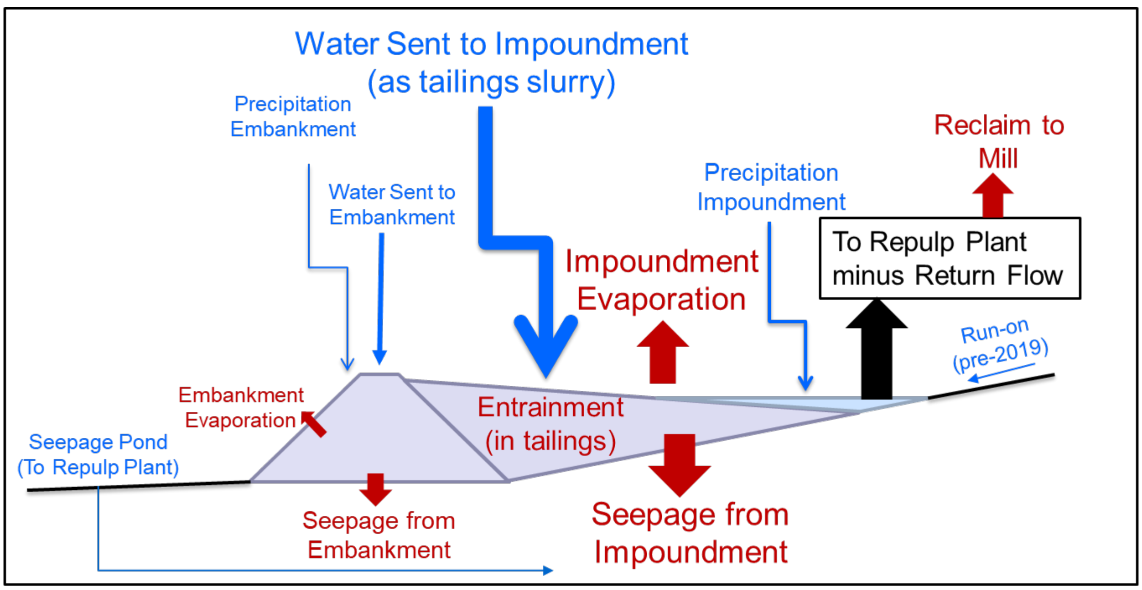

Figure 2. TSF water balance.

2.4.1 *Inflow*

– Tailings Slurry: Two (2) thickeners at the Mill each produce an underflow of condensed tailings slurry that is sent to the TSF. The percentage of solids is estimated using a nuclear transmission style density gauge. By assuming a grain density of 2.7 g/cm^3, the amount of water in the slurry is obtained by difference. Daily estimates of the quantity of water within the tailings slurry was partitioned into water sent to the impoundment and water deposited at the CME. Tailings water flow rates into the CME were dependent on the solids density of the cyclone underflow and the cyclone split between overflow and underflow.
– Precipitation: Daily measured precipitation values from a meteorological station located adjacent to the TSF embankment were applied to the embankment and the impoundment using the TSF area delineations from the satellite imagery.

– Run-on: Daily run-on into the TSF was estimated from the daily precipitation values using the Soil Conservation Service (SCS) curve number (CN) method (USDA, 1986) and the contributing catchment area (which decreased monthly as the TSF area increased). A CN value of 76 was applied, consistent with the value used for the TSF design. Run-on was assumed to be zero due to construction of an alluvium embankment around the west, north, and east perimeter of the TSF in January of 2019.

2.4.2 *Outflow*

– Reclaim water: Daily reclaim water rates were based on measured flow rates from the TSF to the mill. In February 2018 the TSF water reclaim volume increased with the installation of shore-based suction pumps at the BOC. The pump intakes can keep the BOC water level lower than the old barge set-up, thereby decreasing the amount of water left at the BOC, which reduces water available for net percolation.
– Evaporation: Daily evaporation rates were estimated using the three-temperature (3T) energy balance model (Qiu and Zhao, 2010) from local weather data and Landsat 7 and 8 satellite imagery. A summary of the 3T model methodology is provided in Keller et al. (2018).
– Tailing water entrainment: The initial amount of water entrained within the tailings pore space is a function of the slurry flow rate and density of contained solids, the tailings MRCs, and dry BD. The MRC and dry BD for each of the different tailing types were calculated using the conceptual tailings type distribution model, and their estimated distribution over time (Section 3.4). High to moderate permeability tailings associated with the embankment and beach areas were assumed to drain to field capacity after placement, while moderate to low permeability tailings associated with the impoundment were assumed to remain saturated.
– Seepage: Monthly seepage was determined by the difference between total monthly inflow minus outflow from the impoundment and embankment areas separately. Predicted seepage rates calculated from the water balance represent an instantaneous value; in reality, changes in water fluxes are attenuated within the TSF and result in a nearly continuous average TSF seepage with some variability driven by changes along the perimeter during operations.

2.5 *Distributed Seepage*

Estimated seepage from across the TSF was distributed based on the hydraulic property model for the TSF (See also Section 3.4):
– tailings material type and thickness classification and associated K_{sat} values;
– measured seepage fluxes for ponded tailings, and;
– distribution of ponded areas as determined from satellite imagery.

The TSF was divided into 30 m by 30 m rectangular grid cells coincident with the Landsat satellite imagery dataset. Embankment seepage rates were calculated within the water balance model and distributed uniformly across the embankment. The estimated seepage from the unlined BOC was based on the mean seepage flux measured within the BOC side slopes and floor (Section 3.1). Estimated seepage rates from the future HDPE lined BOC areas are assumed to be negligible (< $1x10^{-9}$ cm/s, Giroud and Bonaparte, 1989). Lined and unlined BOC seepage were applied directly and subtracted from the water balance calculated impoundment seepage.

For tailing areas not within the BOC, seepage rates were calculated for each grid cell depending on the tailings type and thickness at each cell. Seepage rates were assumed to be equivalent to the K_{sat}, determined for each tailings type, as modified by the tailing thickness ranges (<15 m, 15 to 45 m, and >45 m) present at each cell. If the tailings thickness was less than 15 m in a cell under surface ponding as determined from the 3T energy balance model, the estimated seepage used the geometric mean of *in situ* measured K_{sat} values from ponded areas outside of the BOC (Section 3.1). For each month, the water balance model calculated seepage was distributed across each grid cell based on the assigned grid cell estimated seepage (i.e., K_{sat}).

Spatially distributed maps of calculated seepage throughout the impoundment and embankment were created semiannually using the average of the six-month period encompassing the months October through March and April through September. The semiannual period approximates months without (October through March) and with (April through September) cycloning.

3 RESULTS

3.1 *TSF Field Characterization*

Tailing materials to depths of 3 m within the TSF East and West transects were composed of alternating layers of sandy and finer-grained tailings caused by the annual change from cycloning to spigotting deposition methods. Tailing percent fines (<0.075 mm) material profiles are shown for the East transect (Figure 3) and the West transect (Figure 4). At the East transect, the predominance of layering and percent fines increased with distance from the spigot and cyclones deposition sources from approximately 30-60% fines within 800 m of the deposition sources to 50-70% fines at distances greater than 800 m. The observed increase in layers with a higher percent fines represents the depositional segregation of tailings from the east side of the TSF towards the BOC. Observed finer over coarser grained layers represents cyclone overflow tailings that were deposited during the summer months on top of slurry tailings. On the West transect, tailings less than 30 m from the CME centerline were consistently sandy (<30% fines) throughout the profile. Immediately downstream of this sandy beach zone, the percentage of fines significantly increased (50 to 70% fines), reflecting the transition from cyclone underflow to cyclone overflow tailings.

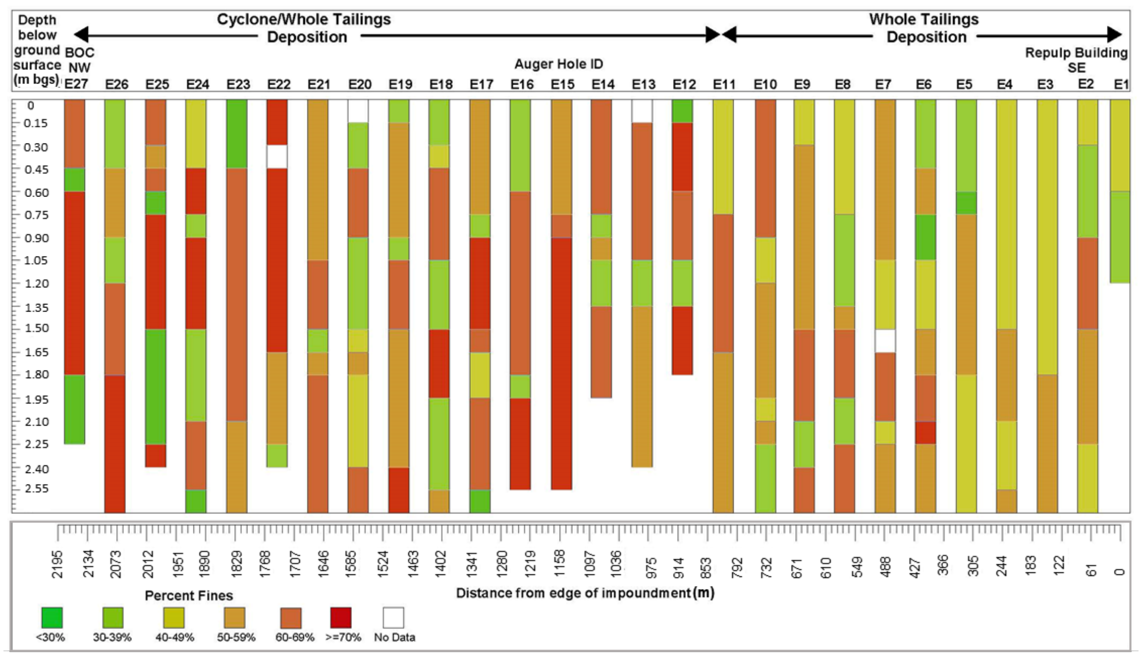

Figure 3. East transect percent fines profile.

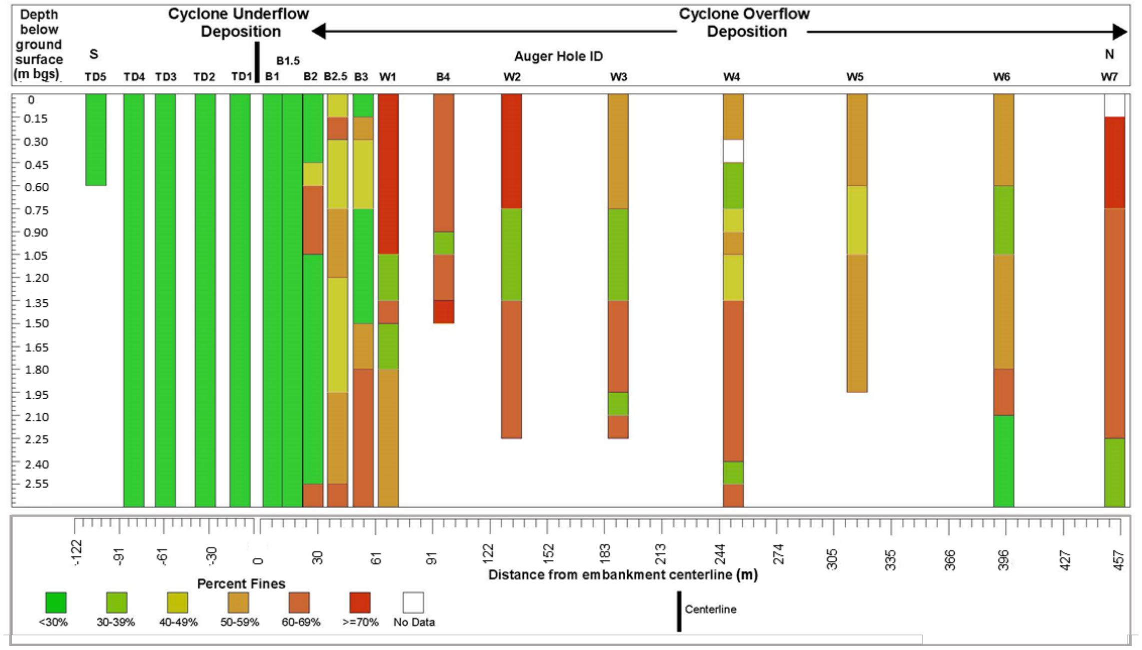

Figure 4. Embankment-beach-west transect percent fines profile.

Results of the tailings *in situ* K_{sat} tests (Woodings (n=21), air entry permeameter (n=7), tension infiltrometer (n=2)) are plotted in Figure 5 as a function of the percent fines. Measured K_{sat} values ranged from between 3.7×10^{-3} centimeters per second (cm/s) to 3.8×10^{-6} cm/s and decreased exponentially as a function of increasing fines content. The geometric mean K_{sat} value ranged from 2.1×10^{-3} cm/s for <30% fines to 1.9×10^{-5} cm/s for >70% fines.

Seepage meter tests completed on the floor of the BOC (constant head and CI, n=4) measured K_{sat} values between 9.3×10^{-6} cm/s to 3.8×10^{-6} cm/s with a geometric mean of 5.7×10^{-6} cm/s. CI tests on the BOC side slopes (n=8) indicated higher flux rates with a range between 8.5×10^{-5} cm/s to 1.5×10^{-5} cm/s and a geometric mean of 3.5×10^{-5} cm/s. Increased seepage along the BOC side slopes may represent variability in bentonite amendment permeability reductions. Arial images were analyzed to estimate the fraction of the BOC between the floor (80%) and side slope (20%). This estimated ratio of side slope to floor was used to calculate a weighted flux rate for the BOC equal to 1.2×10^{-5} cm/s.

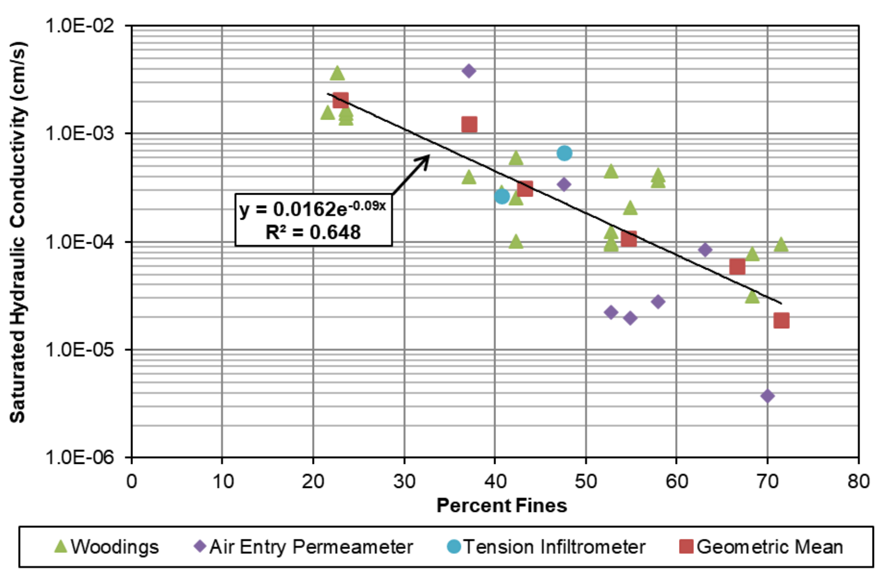

Figure 5. Tailings percent fines as a function of field measured saturated hydraulic conductivity.

3.2 *Laboratory Testing*

Rigid wall and triaxial flex-wall K_{sat} testing was conducted at different bulk densities, equivalent to tailings depths ranging from 23, 45 and 76 m bgs. *In situ* K_{sat} testing results were used to estimate the tailing material types K_{sat} as a function of tailings depth (Figure 6).

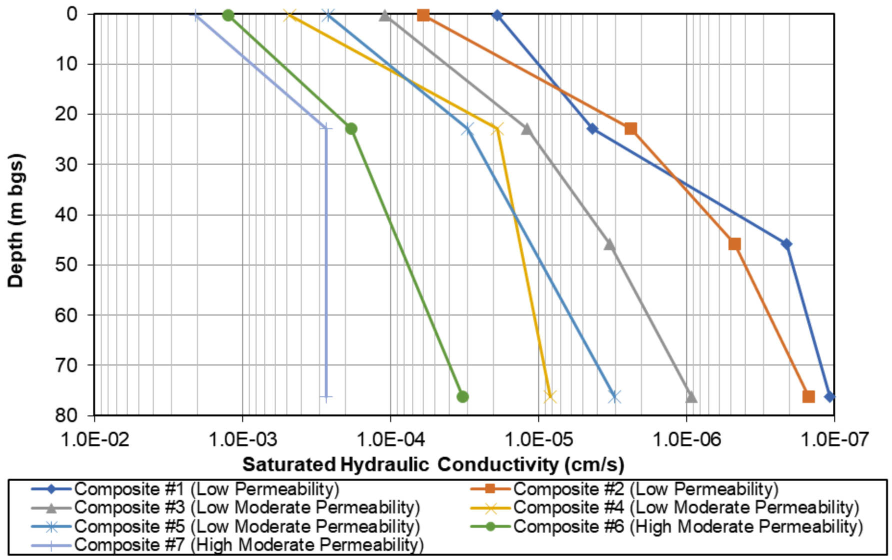

Figure 6. Saturated hydraulic conductivity as a function of tailings depth.

The data indicate that lower percent fine contents correlate with higher K_{sat} values that decrease nonlinearly as tailings depth increases. Comparable K_{sat} values measured between different composite samples allowed representative permeability classifications of Low, Moderate, and High Permeability Tailings to be developed (Figure 6).

3.3 *TSF Boundary and Thickness*

The TSF boundary delineation and thickness evaluation is shown for selected timeframes during operations in Figure 7. The satellite estimated TSF areas were in good agreement with the estimated areas calculated by the mine. The TSF showed a rapid growth progression between 1996 and 1999 during early operations. After the temporary shutdown (1999-2004), tailings growth between 2004 and 2015 primarily occurred along the northern and western edges of the facility. The estimated TSF growth from 2021 through 2028 will occur mainly in the vertical direction. For example, the TSF area in 2018 (approximately 650 hectares) will increase by approximately 50 hectares before closure in 2028 (700 hectares acres total); and the thickness of tailings will increase by approximately 15 m.

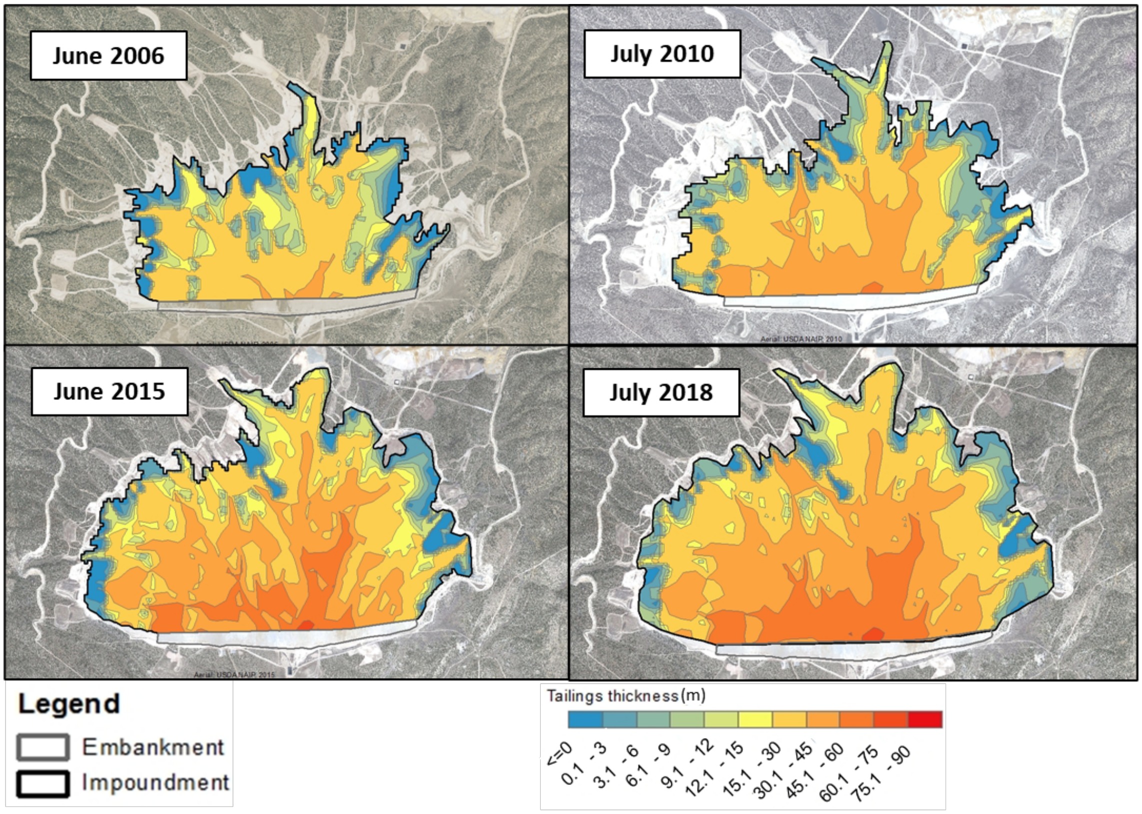

Figure 7. TSF boundary and thickness at select time periods.

3.4 *TSF Hydraulic Property Model*

The measured physical and hydraulic properties can be classified into Low, Moderate, and High Permeability tailings based on their location with respect to distance from the tailings deposition source. K_{sat} assignments for these material types as a function of tailings thickness were estimated from the depth-permeability curves (Figure 6) and are summarized in Table 1.

The tailings permeability type classification, geologic log transect data, and consideration of surface flow paths and fluvial deposition processes were used to estimate the growth and spatial distribution of tailings material types each month. Aerial and vertical representations of the tailings material types for select timeframes during operations are shown in Figure 8.

Table 1. Tailings material type, thickness, and hydraulic conductivity assigned to distribute seepage

Tailings Material Type	Tailings Thickness (m)	Hydraulic Conductivity (cm/s)
Unlined Ponded BOC	-	1.20E-05
Lined Ponded BOC	-	1.00E-09
Ponded Tailings	<3	6.50E-05
High Permeability Tailings	<15	1.80E-05
	15 - 45	7.70E-06
	>45	3.20E-06
Moderate Permeability Tailings	<15	1.20E-05
	15 - 45	3.30E-06
	>45	9.20E-07
Low Permeability Tailings	<15	2.40E-06
	15 - 45	4.70E-07
	>45	1.50E-07

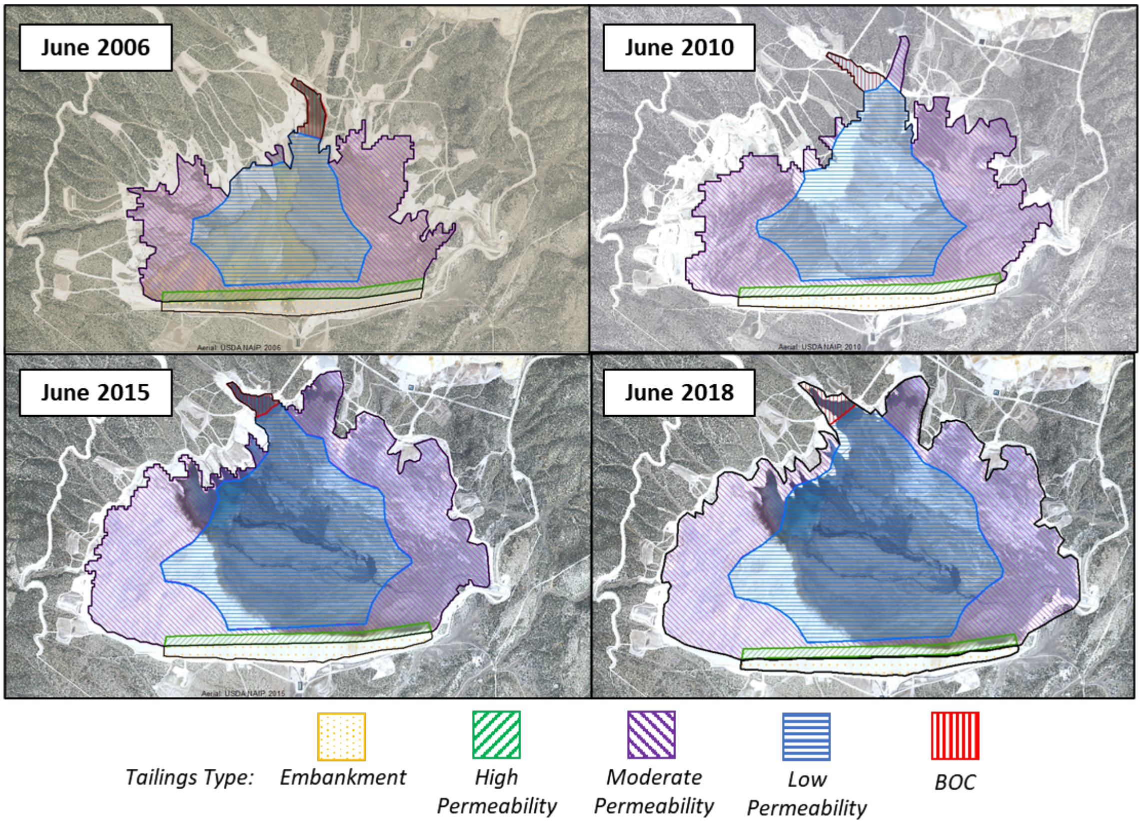

Figure 8. TSF boundary and tailings types at select times.

Coarse-grained cyclone underflow tailings form the embankment and beach area north of the embankment header line and were assigned the High Permeability tailing type to approximately 61 m of the embankment header line, based on the West transect data.

The interior of the impoundment is predominately composed of the finer textured Low Permeability tailings type, whereas near the impoundment perimeter where spigotting occurs, Moderate Permeability tailings types are found. The transition from Moderate Permeability tailings to Low Permeability tailings was defined as 610 m from the edge of the impoundment based on the East transect percent fines observations and K_{sat} relationships. Similarly, the transition from Moderate to Low Permeability was assumed to be 152 m from the embankment header line on the West transect data. The shorter transition distance from the embankment is due to cyclone overflow from the embankment containing finer textured tailings than the slurry (whole) tailings. Exceptions to the 610 m transition exist near the BOC where Low Permeability tailings were based on observed finer textured tailings and the historic existence of ponding in these areas.

3.5 *Estimated Seepage*

The estimated amount of seepage determined by the water balance model was dominated by seepage from the impoundment (Figure 9). Between 2005 and 2020, predicted seepage from the impoundment was variable and ranged from 125 l/s to 309 l/s. Predicted seepage from the impoundment decreased from 2018 through 2020, relative to 2005 through 2017, due to increased water volume reclaimed to the mill. Future seepage from 2025 through 2028 is predicted to decrease due to projected decreased tailings flow to the TSF and continued tailings consolidation.

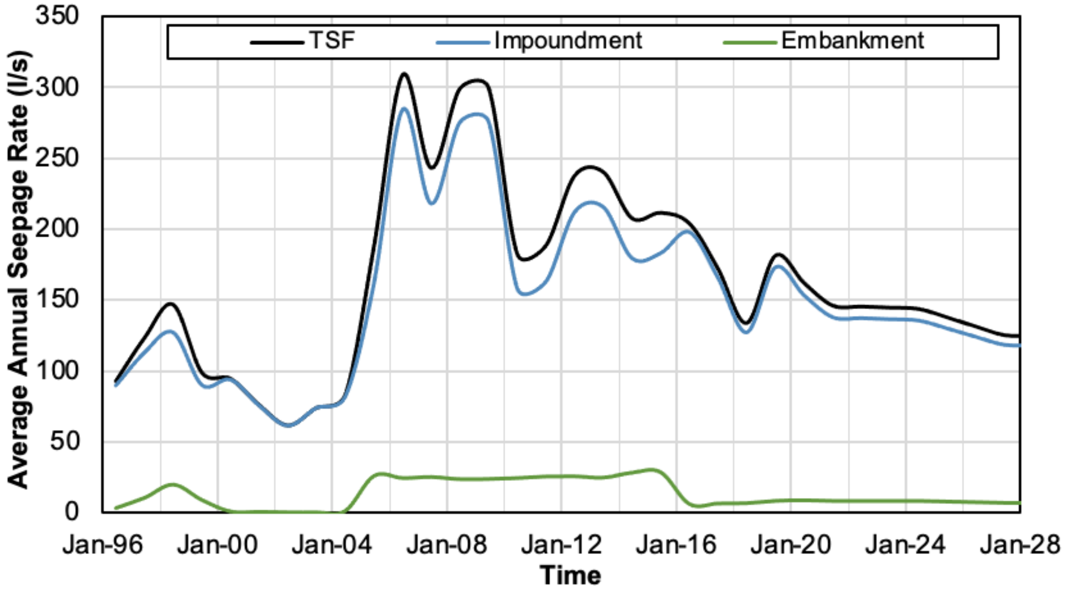

Figure 9. Average annual predicted seepage rate from the TSF, impoundment, and embankment.

Figure 10 shows the predicted distributed seepage from the hydraulic property model during selected timeframes between October-March and April-September. High rates of seepage are predicted to occur from around the perimeter of the impoundment due to the shallow tailings thickness and higher K_{sat} values, low seepage rates are predicted in the center of the impoundment due to the presence of low permeability tailings and consolidation at deeper TSF depths. Over time as the finest particles fill the perimeter areas first and cover the alluvium, and the tailing thickness in these areas become deeper, tailings will continue to consolidate from the overburden pressure causing a reduction in K_{sat} which reduces seepage rates from the interior of the impoundment.

Estimated seepage uncertainty is driven by the largest components of the TSF water balance. The largest inflow component is dominated by water sent to the TSF with the tailings slurry. The largest outflow component, besides seepage, is dominated by impoundment evaporation. Combing these two primary sources of potential uncertainty, the variation in estimated seepage could be 15% lower or 35% higher. Even so, the estimated distributed seepage input into the groundwater model recreated the observed mound growing in groundwater below the TSF.

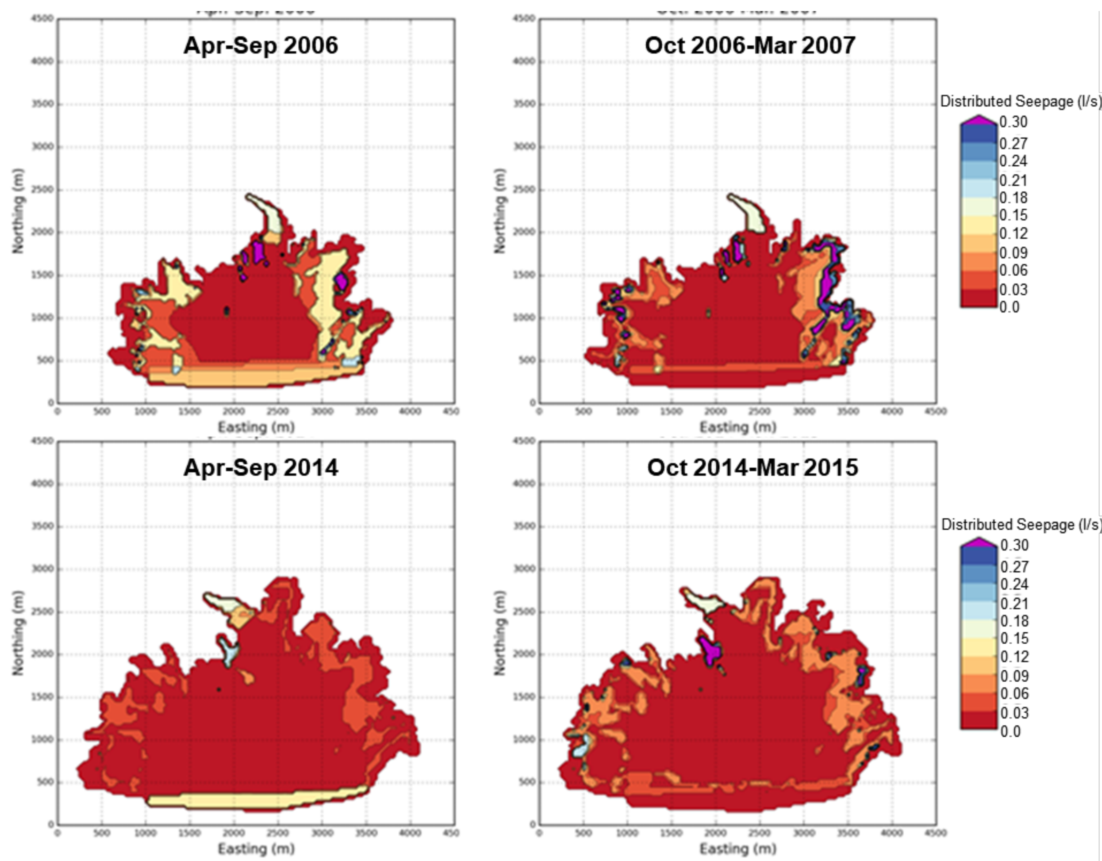

Figure 10. Estimated distributed seepage during selected times.

4 CONCLUSIONS

Conceptual and mathematical water balance models were developed for a large TSF that were constrained by observations and measurement from a combination of field and laboratory characterization data, and desktop analyses. The main objective of this study was to evaluate and quantify the TSF seepage rates that may have occurred during operations, to predict seepage rates that may occur in the future, and the estimated uncertainty. A critical component of the accuracy of past predictions was only allowing infiltration to occur where tailings existed, using the satellite data, and not by making any simplify geometrical assumptions about historical tailings deposition.

A highly detailed water balance model was prepared to estimate all the TSF inflows and outflows with seepage calculated as the difference. A hydraulic property model was also developed to classify tailings material into three different types with specific hydraulic properties. Tailings types were then assigned spatially based the TSF construction over time and distance from the tailings deposition sources. Tailing hydraulic properties were then determined based on the depth of the tailing profile within 30 m by 30 m grids. The hydraulic property model was then used to predict the spatial distribution of seepage across the TSF.

Conclusions regarding the seepage and distributed seepage models are:

– The hydraulic property model was able to distribute seepage to recreate the mound growing in groundwater below the TSF
– Tailing consolidation reduces permeability (seepage) over time as the TSF continues to increase in height, by up to a factor of almost 1,000 times (see Composite #2 in Figure 6), depending on thickness.
– The predicted seepage rates between the water balance and hydraulic property models were in close agreement and indicated that TSF seepage will continue to decrease over time

because the footprint area of the facility will not increase, operational improvements in tailings water management, and increased tailings compaction at depth.

5 REFERENCES

Bouwer, H., J.T. Back, and J.M. Oliver. 1999. Predicting Infiltration and Ground Water Mounds for Artificial Recharge, *J Hydro Eng, ASCE*: 4:350-357.

Bouwer, H. 1966. Rapid Measurement of Air-Entry Value and Hydraulic Conductivity of Soil as Significant Parameters in Flow Systems Analysis, *Water Resour. Res.*: 2:729-738.

Giroud, J.P. and R. Bonaparte. 1989. Leakage through Liners Constructed with Geomembranes – Part I. Geomembrane Liners. *Geotextiles and Geomembranes*: 8:27-67.

Hussen, A.A. and A.W. Warrick. 1993. Alternative analysis of hydraulic data from disc tension infiltrometers. *Water Resour. Res.*: 29:4103–4108.

Keller, J., J. Hendrickx, M. Milczarek, F. Partey, M. Geddis. 2018. High Resolution Estimates of Tailings Facility Evaporation Using Landsat Data. In *Proceedings of Tailings and Mine Waste 2018, Keystone, CO, October 1 - 2, 2018*.

Lee, D.R. 1977. A device for measuring seepage flux in lakes and estuaries. *Limnology and Oceanography*: 22(1):140-147.

Qiu G.Y. and M. Zhao. 2010. Remotely monitoring evaporation rate and soil water status using thermal imaging and "three-temperatures model (3T Model)" under field-scale conditions. *Journal of Environmental Monitoring:* 12(3):716-723.

Wooding, R.A. 1968. Steady infiltration from a shallow circular pond. *Water Resour. Res.*: 4:1259-1273.

United States Department of Agriculture. 1986. Urban hydrology for small watersheds. *Technical Release 55*. Natural Resources Conservation Service.

Flood hazard classification for a hyperconcentrated flow

Gustavo Correa & Gabriel Lopes de Paula & Marco Nascimento & Mariana Brandão
Tetra Tech, Belo Horizonte, Minas Gerais, Brazil

Julia Sa
Newcastle, NSW, Australia

ABSTRACT: Dam failures usually result in social, environmental, and economic damages. In Brazil, these occurrences lead to the tightening of dam safety regulations, regarding Emergency Action Plans. These plans are typically developed based on dam breach simulations, which are used to estimate the characteristics of the inundation. Some hydraulic parameters, calculated in the simulation, can be applied to derive the hazard imposed by the flood in terms of risk to life and damage to infrastructure. One commonly used method to estimate the hazard is the one proposed by Smith et.al. (2014), which considers the hydrodynamic hazard as a function of the flood depth and velocity product.

However, the State-of-The-Art of Dam Breach Analysis is undergoing significant changes. One crucial development is the recent consideration of equations that represent the behavior of the hyper-concentrated flow. These equations take into consideration the rheologic characteristics of the dam discharge. Therefore, it becomes increasingly necessary to derive a hazard classification method that can also represent the hazard imposed by hyper-concentrated fluids, such as the materials stored in tailing dams.

Therefore, this work aims to derive a hazard classification method that also takes into consideration aspects related to the rheologic characteristics of the fluid, based on an adaptation of the method proposed by Smith et al. (2014), which applies, exclusively, to Newtonian flows.

1 INTRODUCTION

Currently, in Brazil, dams are still widely used structures for the disposal of mining tailings, a mineral residue generated during ore processing. Due to the characteristics of the local terrain, building and maintaining these structures is relatively cost effective, when compared to other available techniques. It also offers considerable flexibility, as the dams can be raised to accommodate larger volumes of tailings, as necessary.

However, tailing dams can impose elevated risk on society, as major dam failures can lead to catastrophic and irreversible social-economic and environmental impacts. Therefore, it is crucial to have contingency plans and procedures in place to guarantee an effective response to a potential dam failure and minimize damage and loss of lives. A key step in preparing these plans is understanding the characteristics of the flood resulting from a dam breach, which is usually done through the preparation of hypothetical dam break studies.

Recently there have been several technological advancements that significantly improved the accuracy of dam break modelling, such as an increase in computer power and development of high-resolution digital elevation models (DEMs) for the underlying terrain. Another important innovation is the possibility to model the behavior of non-Newtonian, hyper concentrated fluids, which is usually the nature of the material stored in tailing dams.

In addition to estimating the physical characteristics of the dam break flood, it is equally important to understand the effects this flood might have on the impacted communities i.e., the level of danger individuals in various locations are exposed to. It is important to be able to differentiate the locations where the dam break flood poses an imminent risk to life and has the potential to damage building infrastructures, to the areas where minor impacts are expected.

One of the tools commonly used to assess the risk a dam break events to the population residing downstream are the hazard curves proposed by Smith et al. (2014). These authors proposed a series of hazard threshold curves that relate the quantified physical flood behavior (flood depth and velocity) to the vulnerability of the community exposed to flooding.

Even though the criteria proposed by Smith et al. (2014). was originally derived to be used in floodplain management, the fact that the criteria are based on extensive literature review and are simple to apply lead to it being adopted for dam break studies for tailing dams. However, all the research that went into the development of the curves proposed by Smith et al. (2014). considered water, which has considerably distinctive characteristics to the material stored in tailing dams.

Therefore, this work aims to derive a hazard classification method that also takes into consideration aspects related to the rheologic characteristics of the fluid, based on an adaptation of the method proposed by Smith et al. (2014), which applies, exclusively, to Newtonian flows.

2 LITERATURE REVIEW

According to Cox et al. (2010), during a flood event people are usually at risk while they are on foot, in a vehicle or inside a building. The mechanisms of instability applicable to each of these risk categories are explored in the following sections of this paper.

2.1 *Safety of people on foot*

Based on the existing literature the instability of humans during floods can be characterized by two primary mechanisms: moment instability, (toppling) friction instability (sliding) (Cox et al. ,2010). The moment instability occurs when the moment resulting from the drag force applied by the fluid is greater than the stabilizing moment due to the individual's body weight. The friction instability arises when the magnitude of the drag force surpasses the friction resistance between the person's feet and the surface.

The moment instability seems to be prevalent in higher flood depths and slower velocities, whereas the friction instability is the dominant mechanism in higher velocities and smaller depths. Figure 1 illustrates the two instability mechanisms.

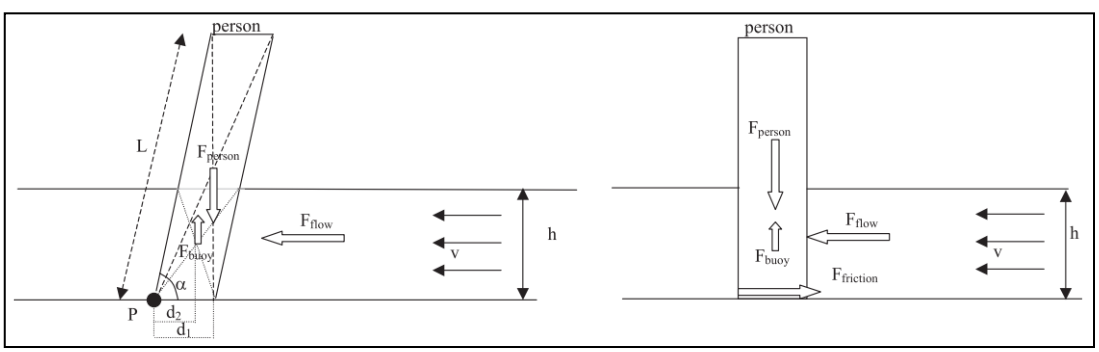

Figure 1. Forces acting on a body exposed to flooding.
Source: Jonkman & Penning-Rowsell (2008)

The moment instability mechanism is based on the assumption that the person will lean forward to resist the flow and simultaneously lock their heal. The individual will become unstable when the moment of the drag force imposed by the fluid in relation to the support point P (the persons' heal) is greater than the resulting moment from the person's weight and uplift force (Jonkman & Penning-Rowsell, 2008). These authors propose the following equations to describe the moment instability mechanism, which consider that the drag force is uniformly applied and disregard the uplift force

$$\sum M_P = 0 \quad (1)$$
$$F_W \times d_1 - 0.5 \times h \times F_d = 0 \quad (2)$$
$$F_W = mg \quad (3)$$
$$F_d = 0.5\rho_f C_D B h v^2 \quad (4)$$

where F_W is the individual's weight, α is the angle as the person leans forward to resist the flow, d_1 is the distance between the persons' centre of mass to the support point P, m is the persons' mass, g is the gravitational acceleration, F_d is the drag force applied by the flow, ρ_f is the density of the flow, C_D is the drag coefficient, B is the height exposed to the flow. Considering the center of mass is at the mi, relative to the x axis, h is the depth of the flow, v is the velocity of the flow.

Considering the center of mass at the center of the body, and combining equations 2, 3 and 4 it is possible to derive the following expressions:

$$m \times g \times cos(\alpha) * L = 0.25 \times \rho_f C_D B h^2 v^2 \quad (5)$$
$$hv = \sqrt{(4\, mgcos(\alpha)L)/(\rho_f\, C_D B))} \quad (6)$$

The drag coefficient is obtained based on dimensional analysis, and it is a function of the Reynolds number and the object subjected to the force (Chanson, 2004). The same author also suggests that for turbulent flow conditions the drag coefficient can be approximated by a constant. In the context of people exposed to floods, the literature recommends values ranging from 1.1 to 2.0 for the drag coefficient (Xia et al., 2014). Chanson (2004) complies a series of studies with empirical relationships for the drag coefficient and sediment transportation. For natural sediments, the author recommends the relationship obtained by Engelung and Hansen (1967).

$$Cd = 24/Re + 1.5 \quad (7)$$

Friction instability occurs when the drag force is greater than the friction resistance generated by the contact of the persons feet with the ground. This mechanism of instability cam be described by the following equations:

$$F_d = F_f \quad (8)$$
$$0.5\rho_f C_D B h v^2 = \mu_f mg \quad (9)$$
$$hv^2 = \frac{\mu_f mg}{0.5\rho_f C_D B} \quad (10)$$

2.2 *Safety of Vehicles and Buildings*

The mechanisms by which vehicles become unstable when exposed to flood waters are discussed in Smith et al. (2019). These authors describes this process as a combination of buoyance, which reduces the downward force on the tires, and consequently their traction, and the lateral hydrodynamic forces acting on the vehicle. The vehicle stability is lost when the horizontal hydrodynamic force applied to the vehicle (F_D) overcomes the traction force of the wheels (F_{Trac}). Equation 11 expresses condition for vehicle instability.

$$F_D > F_{Trac} \quad (11)$$

The traction force can be described as a function of the downward force on the wheels and a coefficient of friction between the tire and the road surface. The downward force is composed by weigh of the vehicle, the buoyancy force, the uplift force due to moving waters impacting on the vehicle. Therefore, the traction force can be expressed as:

$$F_{Trac} = \mu \times (F_W - F_B - F_L) \quad (12)$$

where μ is the friction coefficient between the tires and the road surface, F_W represents the weight of the vehicle, F_B is the buoyance force, which is a faction of the water depth (d) and the depth-averaged flow velocity V. Smith et al. (2019) does not consider the dynamic contribution of the uplift force in his experiments, as the text conducted by the authors were undertaken in stagnant water

Equation 13 provides a formulation for the hydrodynamic force, which can be expressed as a drag force (Smith et al. 2019).

$$F_D = 0.5 \times \rho \times A \times C_D \times V^2 \tag{13}$$

Where ρ is the density of the fluid, A is the area of the vehicle impacted by the fluid, V is the flow velocity and C_D is the dimensionless coefficient of drag.

Combining equations 11, 12 and 13, Smith et al. (2019) proposes an expression that describe the condition for the vehicle stability:

$$V < [(2 \times f_u \times F_{Trac})/(\rho \times A \times C_D)]^{0.5} \tag{14}$$

where f_u is a dimensionless factor obtained as a result of experimental tests.

During a flood event, buildings could be affected by a range of difference forces that could potentially compromise their structural stability. These forces include hydrostatic and hydrodynamic actions as well as the impact of debris, wave action, erosion and scour (ABCB, 2013).

2.3 *Combined Hazard Curves (Smith et al., 2014)*

In order to provide a simplified tool to assess flood hazard in floodplain management and emergency management analysis, Smith et al. (2014) proposed a set of combined hazard curves that consider the vulnerability of people, vehicles and buildings exposed to flooding. Figure 2 illustrates the combined curves, which take into consideration the thresholds proposed by Cox et al. (2010), Shand et al. (2011) and Smith et al. (2014).

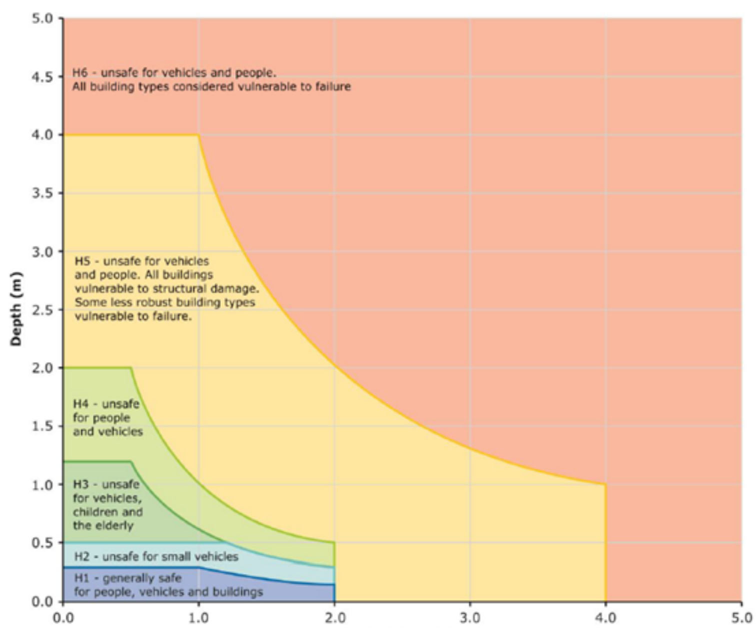

Figure 2. Combined flood hazard curves
Source: Smith et al. (2014)

3 METHODOLOGY

The methodological sequence followed in this work was illustrated in Figure 3.

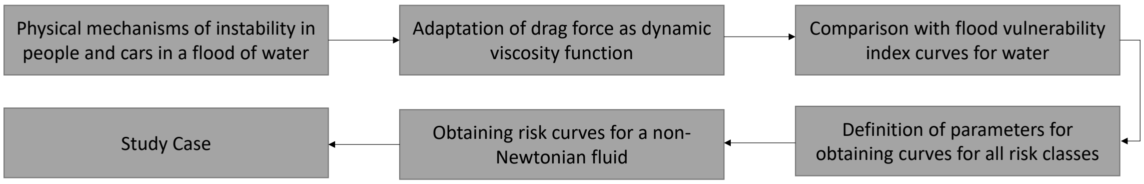

Figure 3. Methodology

Initially, the physical mechanisms of instability in floods with water were researched in the literature. These mechanisms take into account the drag force, and the drag coefficient being a function of the fluid and the object to be dragged. Several authors report that for large Reynolds numbers the drag coefficient is constant. As the flow becomes less turbulent, or laminar, the drag coefficient becomes inversely proportional to Reynolds number. In this work, the simplification, in Equation 15, was adopted:

$$C_d = 24/Re + k \tag{15}$$

Where k is a function of the object's shape, so that $\lim_{Re \to \infty} C_d = k$. Thus, the mathematical treatments performed by Jonkman & Penning-Rowsell (2008) for instability by moment can be written according to Equations 1, 2, 3, 4, 5, 6 and 16:

$$hv = \sqrt{(4\, mgcos(\alpha)L\,)/({}^{24\mu}/_{v} + \rho_f kB)} \tag{16}$$

Replacing the values considering the fluid as water and the lower limits for a person suggested by the Smith et al. (2014), the same risk curve H3 is obtained using the coefficient k = 1.7 in the drag coefficient relation suggested, a value within the range of suggested values in the literature for this case.

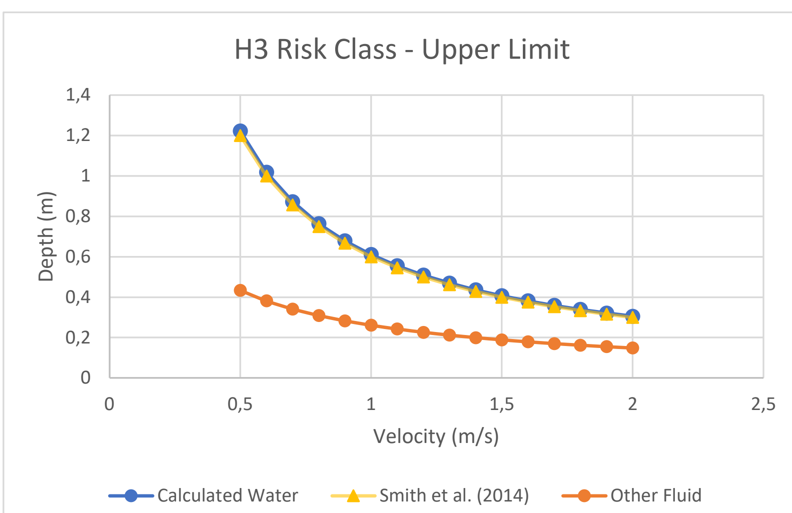

Figure 4. The person moment instability compared with Smith et al. (2014) H3 risk class.

The same was made for friction instability in the Equations 11, 12, 13 and 17:

$$hv^2 = (2\mu_f mg)/({}^{24\mu}/_v + \rho_f kB) \tag{17}$$

Where μ_f is the friction force coefficient.

However, the curve obtained, although similar to the previous one, did not respond well with those proposed by Smith et al. (2014). Therefore, it is possible to conclude that only the instability per moment was considered in this case.

For vehicles, at first, it was based on the studies by Smith et al. (2019), and the vehicle's traction force (F_{tract}) is expressed by Equation 12. In Equation 18 we follow the proposed relationship for the drag coefficient and disregard the lifting force:

$$hv^2 = (\mu_f(mg - \rho_f g\, h))/({}^{24\mu}/_v + \rho_f kB) \tag{18}$$

Although the values calculated by numerical approximation using the values for a vehicle suggested by Smith et al (2018) are similar to those used in Smith et al. (2014), see Figure 5, we selected Equation 16 and adjusted it for water to obtain the same curves proposed by Smith et al. (2014). The same procedure was applied to the other upper limits of risk classes H4, H5 and H6.

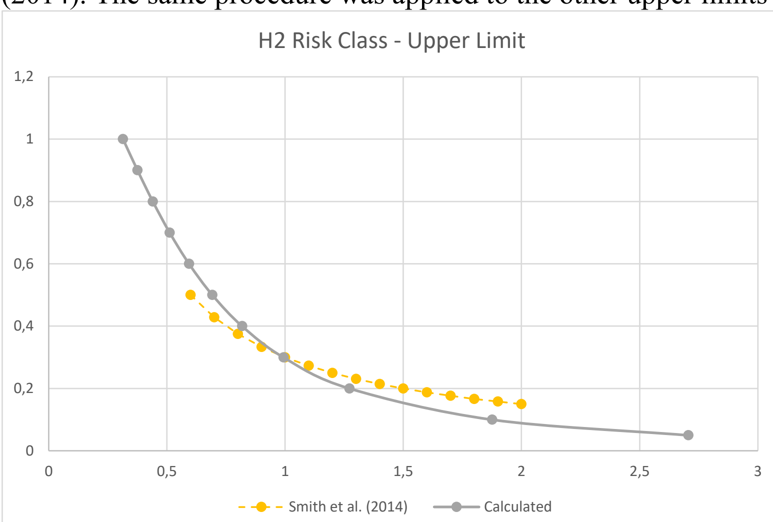

Figure 5. The calculated instability risk compared to Smith et al. (2014)

The curves estimated using moment instability mechanism corresponded well with the thresholds proposed by Smith et al. (2014). Taking this result into consideration, the same equations were used to derive the vulnerability curves for the remaining hazard categories (H4, H5 and H6), replacing the fluid parameters with acceptable values for mining tailings. With the new curves for the risk classes obtained for this new fluid, the depth x velocity (DV) values were calculated for each curve and compared with those used in Smith et al. (2014). The difference relatives to H3 class are shown in Figure 4.

Finally, the new suggested classification for this new fluid was applied to a flood map risk of a hypothetical failure of a tailings dam, and the classifications for the new fluid were compared with the criteria used in Smith et al. (2014).

4 CASE STUDY

A Dam Breach analysis for a hypothetical Tailings Dam was simulated in a two-dimensional hydraulic model, to verify the influence of the parameters (viscosity and density) of the propagated material on the risk curves and, consequently, on the Flood Hazard Map.

To undertake the simulation, a fictional Dam was defined. The structure was positioned near the city of Wollongong (NSW, Australia), Coordinates 6,173,644.5m and 289,679.5m N (Datum GDA94). A location map is shown in the Figure 6 which also provides an illustration of the final Digital Elevation Model (DEM) used in the model, obtained from the ELVIS database (https://elevation.fsdf.org.au/) platform.

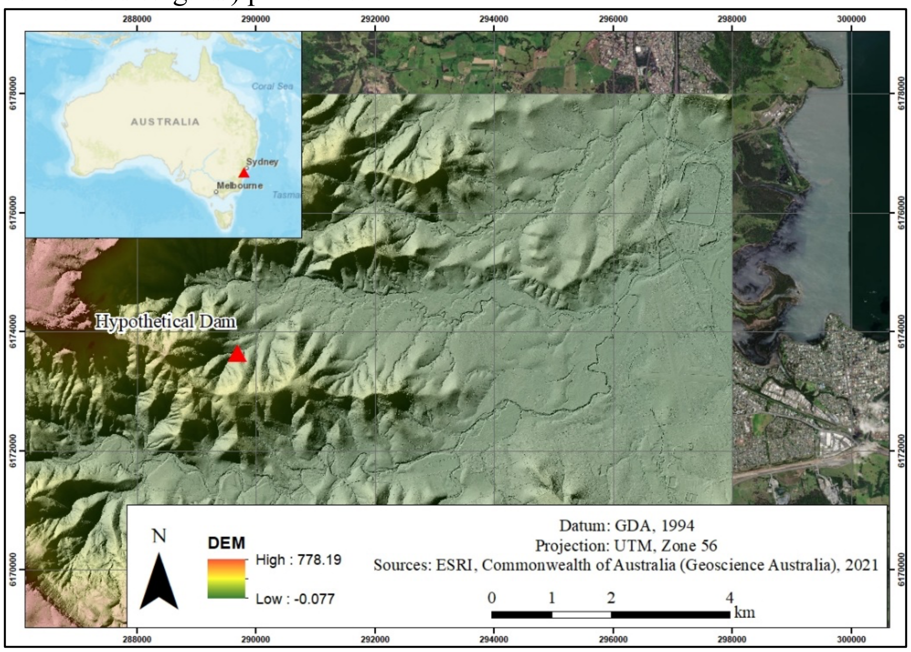

Figure 6. Location map and Digital Elevation Model

The hydraulic software used was the RiverFlow2D™ (Mud and Tailings Flow Model), developed by Hydronia. This software is one of the few that can simulate a wide range of hyperconcentrated flows (non-Newtonian, debris flows, and granular materials.). In addition to being frequently used in Dam Breach Analysis (with Newtonian and non-Newtonian flows). The mathematical model used is based on the publication by Murillo & Garcia-Navarro (2012), in which the internal friction of free surface flows is considered, ranging from pure water to hyperconcentrated flows. In this model, the fluid is assumed to be a homogeneous single-phase mix of water and sediment and has constant properties: e.g., density, yield stress, etc.

The inputs required by RiverFlow2D, regarding the characterization of the propagated material, are Density, Yield Stress, Viscosity, and the Rheological Formulation (Full Bingham, Simplified Bingham, and Quadratic Fluid). With relation to the density of the propagated material, an arbitrary value of 3000 kg/m³ was assumed, which is in line with what is normally obtained for tailings. Additionally, Full Bingham's Rheological formulation was assumed. Viscosity and Yield Stress parameters can be obtained from the literature, knowing the volumetric concentration of the material. A volumetric concentration of 0.50 was assumed for the propagated material, a value also in line with is found for tailings. To define Yield Stress and Viscosity values, the work of Ribeiro (2015) was used, in which results of different rheological tests (for tailings) are presented for different values of volumetric concentrations. From the arbitrated value of the volumetric concentration (0.50), a Yield Stress value of 181.10 Pa and a Viscosity of 0.80 Pa.s were found.

Finally, a breach hydrograph (also fictitious) was attributed to the dam. Figure 7 illustrates two Flood Hazard maps (regarding the Dam Breach Analysis). The first map considers the original curves from Smith et al. (2014), while the second map shows the result that considers the material's properties (density, viscosity). Figure 8 shows a detailed view of the downstream section of the inundation boundaries, in which the discrepancies are more evident.

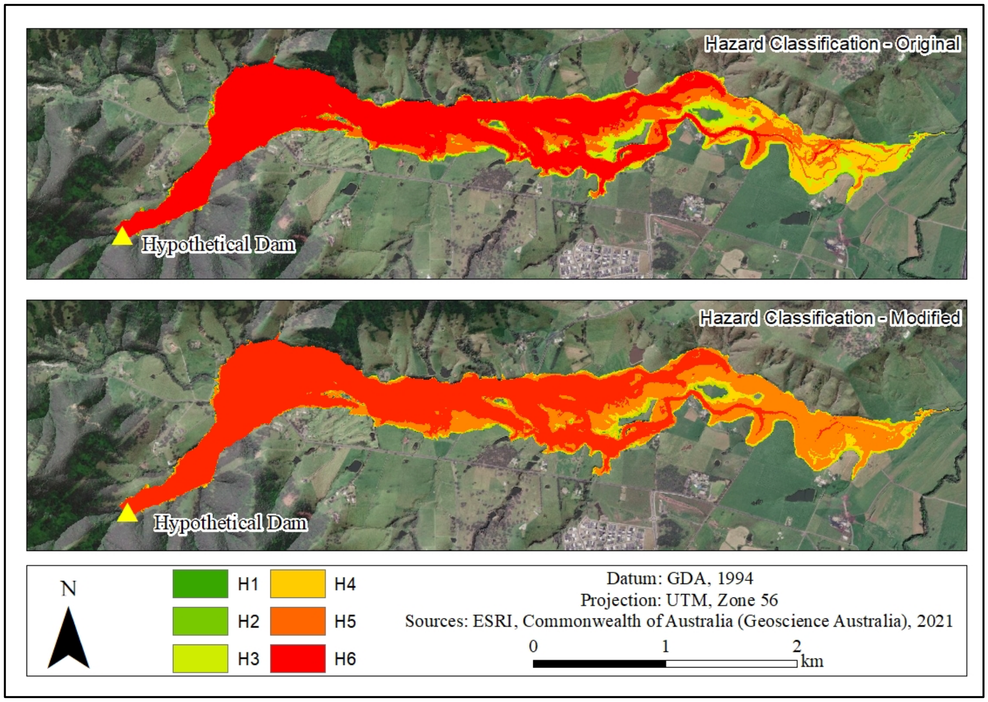

Figure 7. Flood Hazard Maps (Original and Modified)

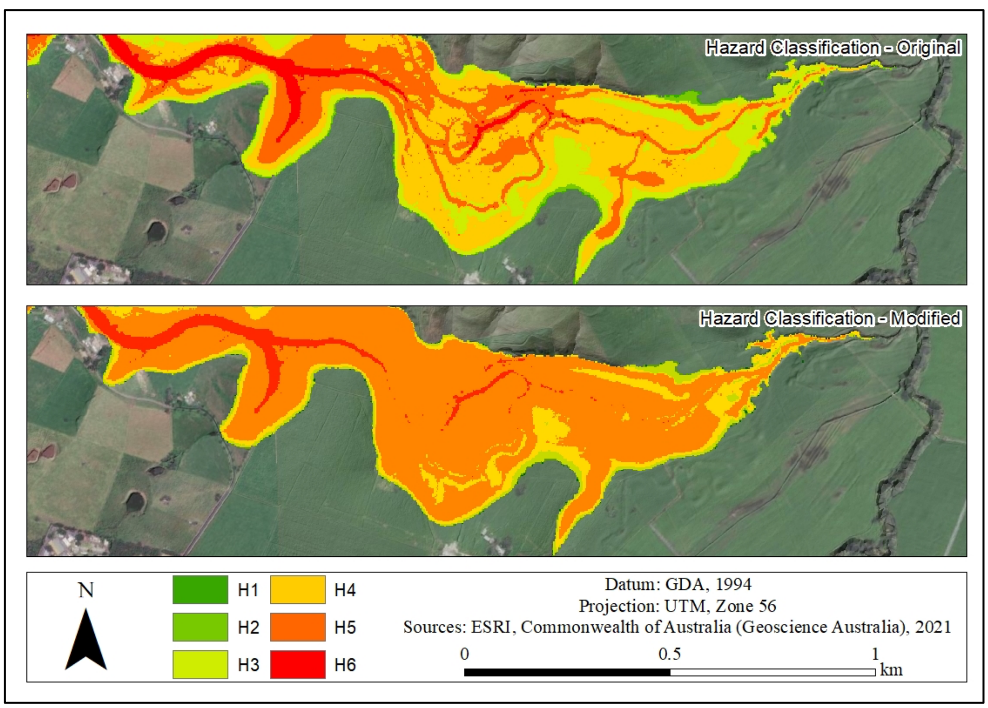

Figure 8. Flood Hazard Maps (Original and Modified) (Zoom)

5 CONCLUSIONS

Through the case study, presented in part 4, it is possible to conclude that the influence of the material parameters (density and viscosity) is significant in the vulnerability curves and, consequently, in the Flood Hazard maps. Especially in Figure 8, it is possible to see that, when the original Smith et al. (2014) curves are used, the hazard levels are lower in comparison to the modified curves. This was expected, since we can assume that denser materials (compared to water) can offer superior hazard conditions in the same flow conditions (depth and speed).

The flood waves caused by the dam´s failure generate flows and velocities significantly higher than the natural floods, which causes great impacts both for the population downstream of the structure and for the environment inserted there. Furthermore, the impact caused by non-Newtonian fluids has greater magnitudes and its effects have only been explored recently.

Therefore, it is not coherent to use same thresholds that consider water when another fluid is simulated. Despite the mathematical simplifications, this work aimed to open the discussion to new classifications of risk for non-Newtonian fluids.

6 REFERENCES

ABCB, Australian Building Codes Board. 2013. Construction of Buildings in Flood Hazard Areas. Version 2012.1.

CHANSON, H. *The Hydraulics of Open Channel Flow: An Introduction: Basic Principles, Sediment Motion, Hydraulic Modelling, Design of Hydraulic Structures: Second Edition*. Elsevier Ltd, 2004.

Cox, R.J., Shand, T.D. and Blacka, M.J. 2010. Appropriate Safety Criteria for People I Floods. WRL Research Report 240. *Report for Institution of Engineers Australia, Australian Rainfall and Runoff Guidelines: Project 10*. 22p.

Jonkman, S.N. and Penning-Rowsell, E. 2008. Human Instability in Flood Flows*. Journal of the American Water Resources Association*, Vol. 44, No. 4, pp 1 – 11.

Minas Gerais, Secretaria de Estado de Desenvolvimento Regional, Política Urbana e Gestão Metropolitana. 2016. Relatório: avaliação dos efeitos e desdobramentos do rompimento da Barragem de Fundão em Mariana-MG. Belo Horizonte: Sedru; 2016. 289 p.

Murillo, J., García-Navarro, P., 2012b. Wave Riemann description of friction terms in unsteady shallow flows: Application to water and mud/debris floods. J. Comput. Phys. 231, 1963–2001.

Pereira, L., Cruz, G., Morato F. G., R. 2019. Impacts from the tailings dam rupture of Brumadinho, Brazil: an analysis based on land cover changes. *Journal of Environmental Analysis and Progress*. 4. 122-129. 10.24221/JEAP.4.2.2019.2373.122-129.

Ribeiro, Vinícius Queiroga Fortes. 2015. Proposta de metodologia para avaliação do efeito de rupturas de estruturas de contenção de rejeitos [manuscrito] / Vinícius Queiroga Fortes Ribeiro.

Shand, T. D., Cox, R. J., Blacka, M. J. and Smith, G. P. 2011. Australian Rainfall and Runoff Revision Project 10: Appropriate Safety Criteria for Vehicles - *Literature Review. Australian Rainfall and Runoff Revision Project 10. Stage 2 Report*. Prepared by the Water Research Laboratory. P10/S2/020.

Smith, G. P., Modra, B. D., & Felder, S. 2019. Full-scale testing of stability curves for vehicles in flood waters. *Journal of Flood Risk Management,* 12(S2), e12527.

Smith, G. P., Davey, E. K., and Cox, R. J. 2014. Flood Hazard. *UNSW Australia Water Research Laboratory Technical Report* 2014/07.

Xia, J., Falconer, R.A., Wang, Y., Xiao, X. New criterion for the stability of a human body in floodwaters. *Journal of Hydraulic Research*, v. 52, n. 1, p. 93–104, 2014.

Rethinking tailings water quality management: smart solutions that fit the problem

Tyler Birkham
Okane Consultants, Cranbrook, BC, Canada

ABSTRACT: Tailings closure planning is a key challenge facing the mining industry, with water quality impact being one of the primary concerns. In an attempt to responsibly manage water quality impacts from tailings facilities, highly engineered solutions to control water and/or oxygen contact with tailings are commonly implemented to reduce metal leaching and acid rock drainage (ML/ARD). While a highly engineered solution such as a geomembrane cover or multi-layered cover system (e.g. capillary break) may be appropriate and effective, simpler cover system solutions that are more cost effective and offer comparable water quality performance should be considered. Case studies are presented that demonstrate site-specific solutions to effectively manage water quality without relying on a highly engineered and costly cover system design. The need for an integrated approach to water quality management is highlighted, including site-specific climate, hydrological and hydrogeological setting, as well as geotechnical and geochemical properties of the tailings and available soils for cover system construction.

1 INTRODUCTION

Tailing storage facilities (TSFs) are a major component of mine closure landscapes, with long-term water quality management being a primary risk. This paper highlights two case studies that demonstrate a site-specific approach to achieve water quality closure objectives. They illustrate how an effective solution for tailings water quality management can also be efficient, if the site is well understood and key mechanisms impacting water quality are controlled appropriately.

In developing strategies to manage water quality risk from TSFs) it is fundamental to ask the question, ‘Where is water quality at risk?’. Management strategies and design objectives can then be focused on the water balance component that is driving the water quality risk. For example, a conceptual water balance in Figure 1 illustrates that precipitation may ultimately partition and report to the receiving environment as either net percolation (NP, water that infiltrates and reports as groundwater recharge), as surficial run-off, and/or near surface interflow. With tailings, water quality risk is typically greater for surface water relative to groundwater as contact with unsaturated and oxidized tailings is greater, and the time for surface water to report to the receiving environment after precipitation events is rapid. Furthermore, oxygen availability is often self-limiting in finer texture tailings with high water content, which is typical for conventional slurry depositions with foundations that are not well drained. The high water content of these tailings (greater than 85% degree of saturation) results in low air permeability and severely limited oxygen resupply by air flow and gas diffusion. In these low oxygen environments, acid generation is low and the full neutralization potential of the saturated zone is available to buffer acid loadings from the overlying oxidized zone. Therefore, metal leaching and acid rock drainage (ML/ARD) risks associated with groundwater flow and seepage are therefore typically lower compared to surface water.

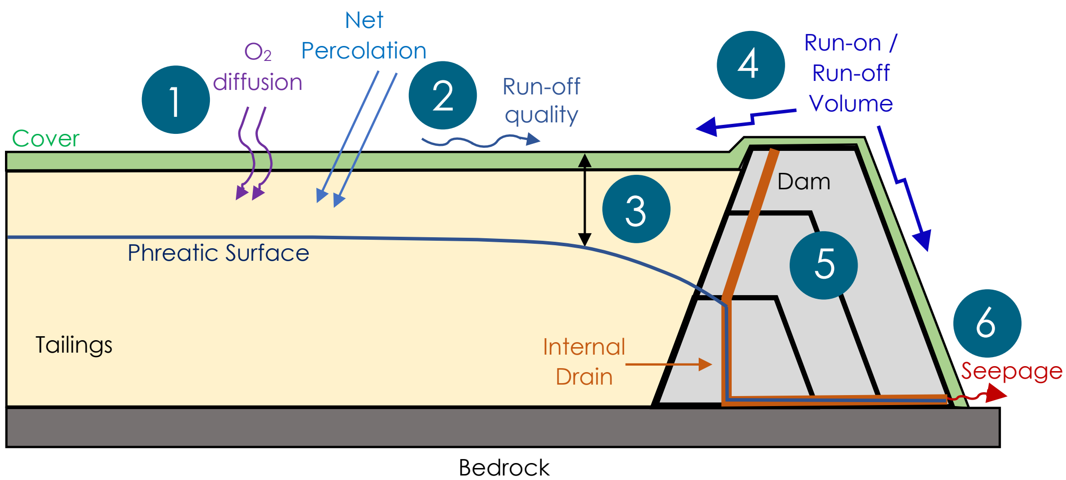

Figure 1. Conceptualization of water balance in a conventional TSF.

This paper focuses on two case studies that demonstrate the management of surface water through simple yet effective control of contact with near-surface oxidization products and associated ML/ARD risk. The case studies highlight the efficacy of simple soil covers to achieve the objectives of the cover system and manage water quality risks to a similar or potentially improved extent relative to a more highly engineered cover system. It is noted that more highly engineered cover systems certainly have widespread benefit and utility; the purpose of this paper is to demonstrate scenarios where a simple soil cover system can work within the hydrogeological, climatic, and geotechnical setting to achieve effective water quality management. Water quality impact from construction materials for TSF dams, dykes or starter walls is another factor that may unexpectedly contribute to ML/ARD risk at a site but is not the focus of this paper.

2 CASE STUDIES

2.1 *Case A - Legacy tailings in cold climate*

Site A is a legacy TSF in eastern Canada that consists of 150 ha footprint area of unsaturated tailings and a ponded area of approximately 50 ha. The water quality in the ponded area is known to have ML/ARD. The ponded water decants to a wetland area before final discharge off the site. Passive treatment by naturally occurring alkalinity in the wetland area has to date managed water quality within compliance limits before final discharge to the receiving environment. The current phreatic surface in the tailings is within 0.5 to 2 m of ground surface and approximately half of the unsaturated surface is vegetated. The closure objective is to achieve long-term geotechnical and geochemical stability, including discharge water quality that meets or exceeds compliance limits and revegetation of the TSF.

The conceptual model of Site A is illustrated in Figure 2. The primary mechanism controlling ML/ARD risk is contact of rainfall and snowmelt with the surficial oxidizing unsaturated zone. Conceptually this risk could be managed by a cover system through control of oxygen to minimize sulphide mineral oxidation. Alternatively, surface water may be managed to reduce contact with the oxidation zone and subsequent ML/ARD. This may be achieved through a relatively simple soil cover system that promotes a high degree of surface run-off but also allows enough water to infiltrate as NP (i.e. groundwater recharge) to maintain the high phreatic surface. Maintaining a high phreatic surface ensures the majority of the tailings volume remains saturated, thereby limiting oxygen exposure and ML/ARD associated with the groundwater system to negligible levels. It is noted that acid generating potential in the unsaturated zone for Site A is significantly less than the overall neutralizing potential over the saturated tailings depth. Therefore, if the phreatic surface can be maintained at current levels, ML/ARD risk through groundwater seepage does not pose a significant water quality risk. It is noted that maintaining a high phreatic surface has geotechnical implications as the tailings will be more flowable and maintenance of containment infrastructure will be a long-term commitment.

The impact of a soil cover system on the hydrology and resultant water quality was investigated using the GeoStudio Flow package (version 11), consisting of SEEP/W (seepage), TEMP/W (thermal) and CTRAN/W (solutes). Climate change was evaluated for precipitation inputs and assumed a representative concentration pathway (RCP) 8.5 scenario, which is the most of the four projected greenhouse gas concentration trajectories. Tailings hydraulic conductivity ranged from $3x10^{-7}$ m/s to $2x10^{-6}$ m/s based on permeameter testing, while input soil cover (clayey silt) hydraulic conductivity ranged from $1x10^{-6}$ m/s to $1x10^{-8}$ m/s with an expected actual value of approximately $5x10^{-8}$ m/s based on material testing. A basal layer of compacted peat was observed in drill cores, with an estimated hydraulic conductivity of $1x10^{-9}$ m/s and a total porosity of 0.5. The Köppen-Geiger climate classification for Site A is cold (D) with no dry season (f) and warm summers (b) (Dfb). Substantial runoff during spring melt is quite common in a Dfb climate, further supporting the focus on surface water management for managing water quality risk. Measured runoff volumes were 50-70% of total rainfall and snowmelt for Site A.

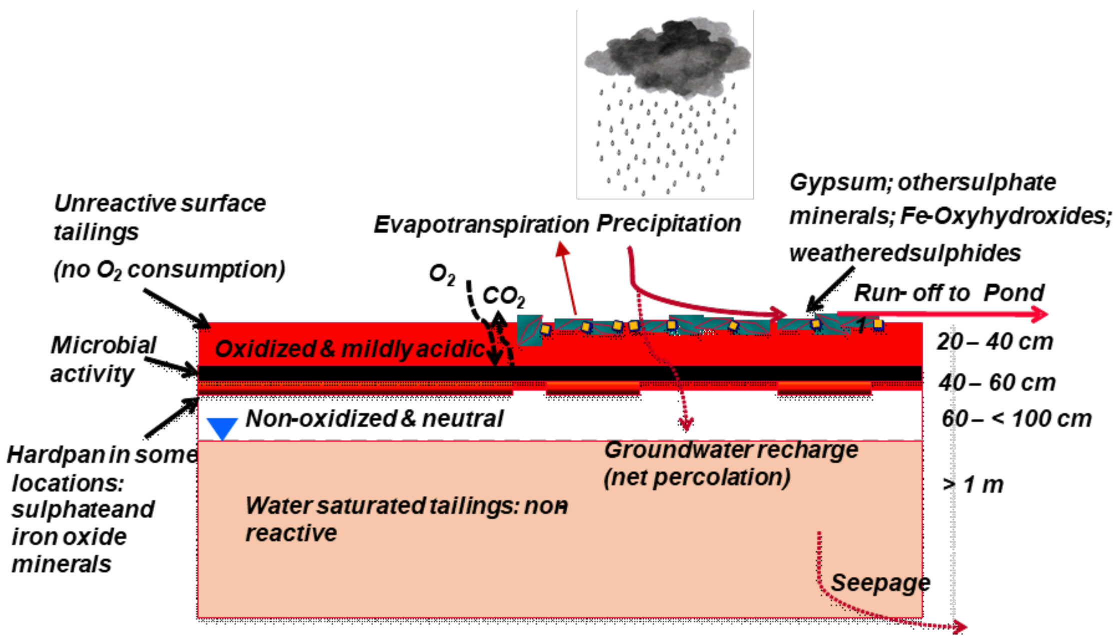

Figure 2. Conceptualization of hydrological and geochemical regime at Site A.

Modelled NP rates and associated depths to the water table are presented in Figures 3 and 4. The TSF contained a north and a south cell, with water flow generally from north towards a polishing pond in the south. One of the key controls resulting in very low net percolation rates and a high water table in the tailings was the underlying compacted peat layer. The low hydraulic conductivity of this peat layer was critical in limiting vertical drainage from the TSF and maintaining a high degree of saturation in the tailings. This highlights the need to evaluate TSF performance within the proper hydrogeological context, as the tailings at Site A would have much higher net percolation rates and be unsaturated without the underlying peat layer holding water in the system. The high water table results in very little storage capacity in the tailings profile and high volumes of runoff.

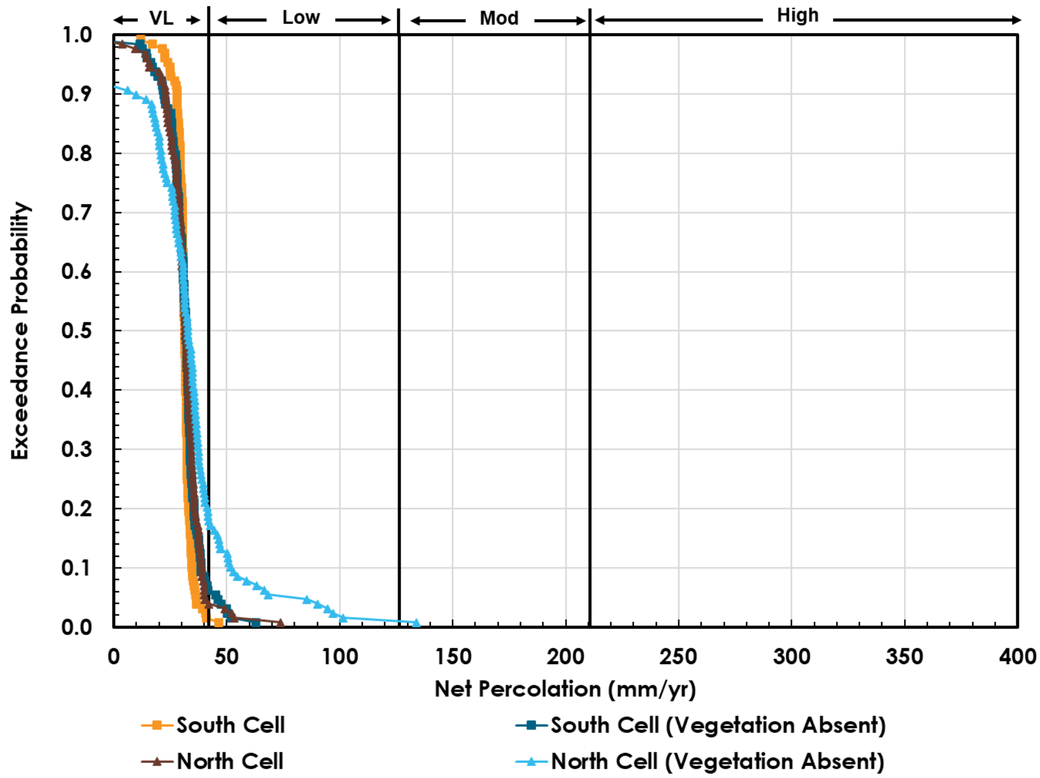

Figure 3. Estimated net percolation rates for uncovered tailings with and without vegetation.

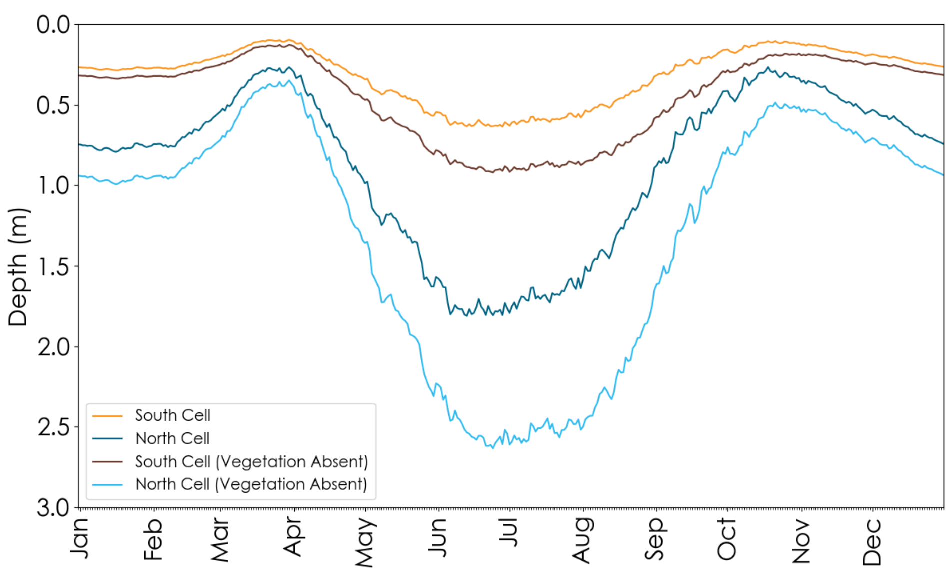

Figure 4. Estimated depth to phreatic surface for uncovered tailings.

An example of the sensitivity of the depth to water table for a nominal soil cover thickness of 50 cm is presented in Figure 5. Similar results were estimated for soil cover thicknesses of 30 cm and 80 cm. The modelling indicated that the soil cover allows enough water to infiltrate as NP to maintain a high water table, with the remaining water resulting in surface runoff (50-70% of total precipitation). The geochemical and water quality implications are that 'clean' water remains 'clean' as high volumes of precipitation do not contact the tailings and are diverted off the site. Additionally, the phreatic surface and exposure of tailings to oxygen is maintained at its current levels resulting in a stable geochemical regime without increased risk of acid generation.

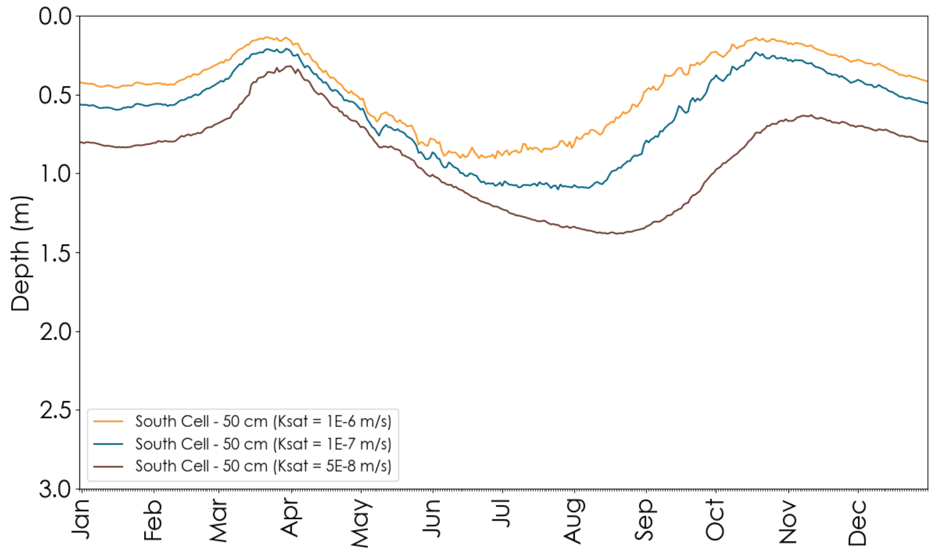

Figure 5. Estimated depth to phreatic surface for uncovered tailings for a soil cover thickness of 50 cm and variable soil cover hydraulic conductivity (isotropy assumed).

It is noteworthy that the estimated water table depth drops with progressively lower soil cover hydraulic conductivity (Figure 5). For a soil cover hydraulic conductivity of 1×10^{-8} m/s (not included in graph), the net percolation rates are decreased to the extent that saturated conditions are not maintained in the tailings and the phreatic surface drops below the TSF base. This is an important result as it demonstrates that a highly engineered cover system that severely limits or shuts off NP (groundwater recharge) could result in desaturation of the tailings and greater risk of oxygen exposure and acid generation. This is demonstrated in Figure 6, where the sensitivity of the phreatic surface to net percolation is presented and water table depths are at or near the base of the tailings (4.5 m depth for this assumed 'average' profile) when net percolation is half or three-quarters of the original or base case scenario.

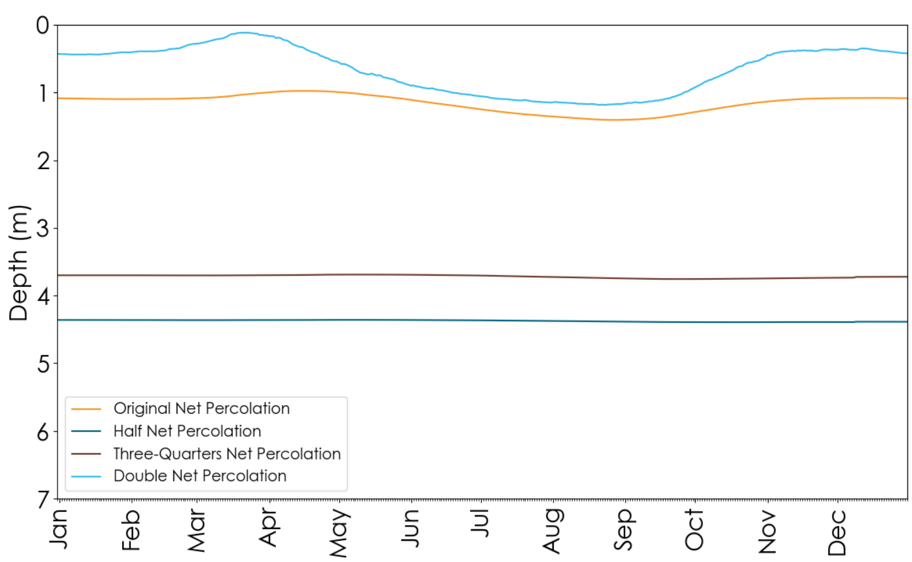

Figure 6. Sensitivity of phreatic surface to changes in net percolation; the base of the tailings is at a depth of 4.5 m with underlying peat layer between 4.5 and 6.5 m depth.

2.2 *Case B - Legacy tailings in warm climate*

Site B is a legacy TSF covering 124 ha located in the eastern United States. The climate is a warm and temperature (Cfa by the Köppen-Geiger system). Annual rainfall is 1,270 mm with annual potential evaporation of 1,020 mm. The tailings are predominantly acid generating (neutralization potential to acid generating potential less than 1:1), with approximately 25% of the tailings oxidized and 75% unoxidized. The TSF is underlain by an high density polyethylene liner and was covered in at least 0.9 m of an alkaline clay material in 2000 with a saturated hydraulic conductivity of approximately $2x10^{-5}$ m/s. The tailings profile is ~20-30 m thick. The primary objectives of the soil cover were to: 1) limit contact of water with tailings; and 2) limit exposure of tailings to oxygen by maintaining high levels of saturation in the near-surface materials.

The measured depth to water table after cover system placement (Figure 7) has remained near or above the tailings interface with the soil cover at various locations across the TSF. Furthermore, a hydrologic model for the site (Geostudio package) indicates that a degree of 85% or greater is consistently maintained in the tailings profile (Figure 8). Therefore, the hydrologic regime for the soil cover systems appears to be providing sufficiently high groundwater recharge to maintain high degrees of saturation and limited oxygen availability. This is further confirmed by observed unoxidized tailings below the soil cover (Figure 9) and non-acidic conditions in the tailings groundwater (Figure 10).

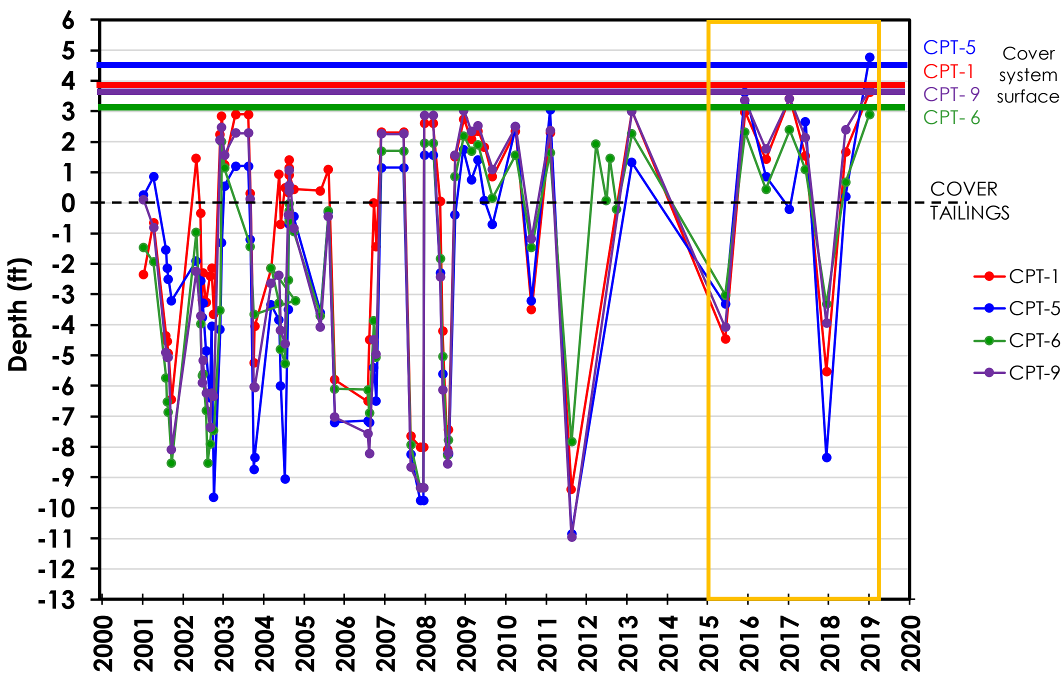

Figure 7. Measured depth to water table after cover placement; yellow box denotes the period for which water quality is presented.

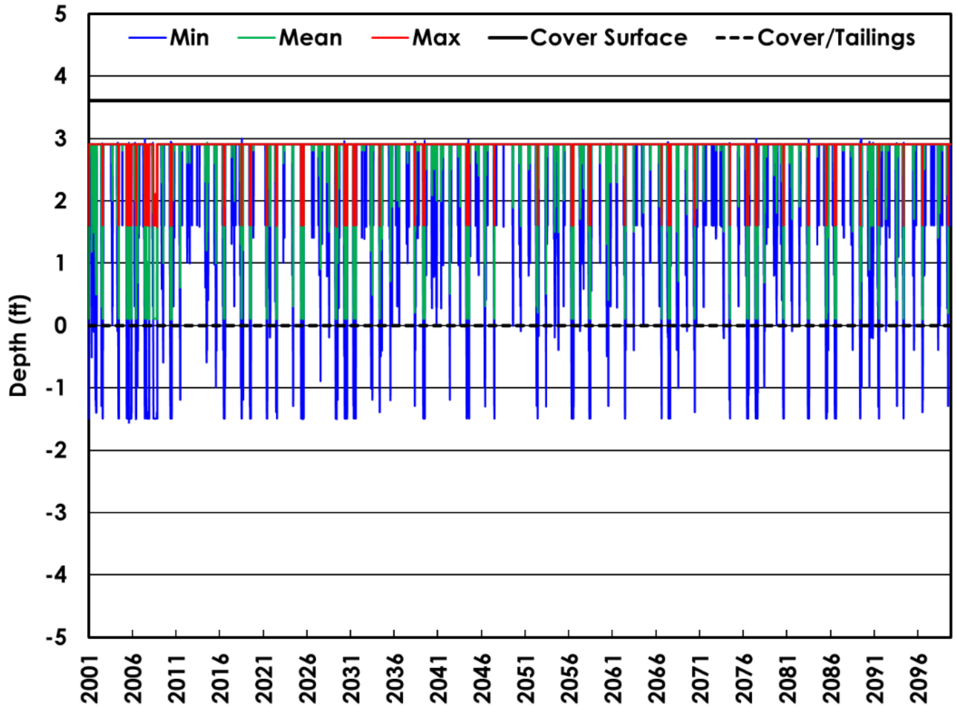

Figure 8. Modelled depth to 85% degree of saturation (accounting for climate change using the RCP 8.5 scenario). The cover surface is indicated by a solid horizontal line and the cover/tailings interface is indicated by a dashed line at a depth of 0 feet.

Figure 9. Test pit showing soil cover profile (brown) and underlying unoxidized tailings (grey).

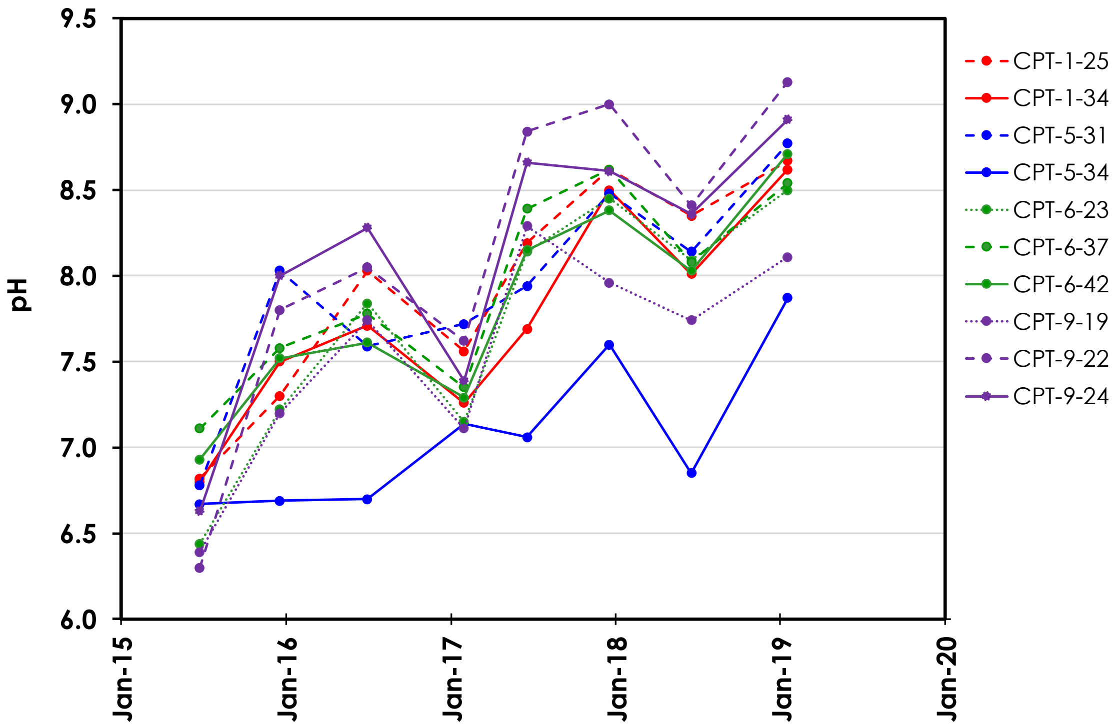

Figure 10. Measured pH of tailings groundwater.

3 CONCLUSIONS

The efficacy of identifying key mechanisms controlling water quality impact at TSFs and developing controls to manage these key mechanisms is demonstrated in two case studies. While highly engineered cover systems certainly have important applications, it is noteworthy that more highly engineered and costly solutions may be avoided while still achieving effective management of water quality. In these case studies, simple cover systems are shown to, in the right conditions, keep clean water from contacting surficial oxidized tailings. The soil cover systems also allow enough groundwater recharge to maintain a sufficiently high phreatic surface for current and climate change scenarios that limit the resupply of oxygen for acid generation. In fact, limiting net percolation (groundwater recharge) too severely for a highly engineered cover system may result in drained conditions and greater potential for oxygen exposure. The case studies discussed herein highlight Okane's pragmatic and objective driven approach to TSF water quality management, summarized by:

1. Identify the mechanisms of ML/ARD generation (e.g. O_2 diffusion), and design cover systems should address the root cause of ML/ARD generation.
2. Identify risks of surface water contamination from run-off.
3. Identify cover system impacts on the phreatic surface, and requirements for the cover system to control the phreatic surface (e.g., mitigation of phreatic surface impacts on surface water and/or root zone).
4. Understand the water balance of the landform and associated stored water effects on geotechnical and geochemical stability.
5. Understand tailings, waste rock, dam and cover system construction material characteristics, their potential for contribution to or mitigation of ML/ARD, and effects on cover system construction and function.
6. Understand process water contribution to seepage quality issues and identify potential water collection and treatment requirements, including passive or semi-passive treatment systems.

An objective driven approach that targets the key mechanisms driving ML/ARD results in cost savings while maintaining effective water quality management. Optimized solutions for TSF water quality management also use less material, either synthetic or natural, resulting in less overall environmental impact such as production and burial of synthetic materials and/or land disturbance for borrow material.

Tailings Water Management: What bathymetric and topographic surveys are telling us

Craig Pezak & Brant Whiting
Freeport-McMoRan, Phoenix, Arizona, U.S.A

ABSTRACT: Tailings reclaim water ponds not only need to be monitored and measured for water balance accounting and supply to ore processing facilities, but their size and location should be managed within defined parameters for meeting design intent and good practices. Reclaim pond geometry is continually changing due to ongoing tailings deposition and reclaim water pumping (among other factors), which causes the surface area-to-volume relationship to change, such that it requires management in the short term and may create future complications. The collection and analysis of bathymetric and topographic data informs reclaim pond management strategies that anticipate changes that could have a negative impact on production goals and dam safety. These data can reveal developing patterns in the pond depth and beach slopes that warrant changes in strategy, which includes the ability to maintain a steady reclaim water supply and be proactive in achieving design intent and good practice.

1 INTRODUCTION

Situated within the tailings storage facility (TSF), the reclaim pond is a key component of the facility that needs to be understood for optimizing water recovery to ore processing facilities while meeting design intent for good practice related to proactive management of facility safety. For example, in an upstream tailings facility, depositional approach is one factor that impacts geometry of the beach and pond that develop and change over time. Collecting consistent, robust data to understand beach and pond formation enables an operator to better anticipate future geometric changes and potentially employ proactive solutions to possible challenges that may spare an operation from reclaim water shortages or unanticipated spikes in water storage that exceed good practice guidelines. Developing a strategy to manage TSF reclaim pond water is critical not only for site goals, but also for safe production.

Many factors may influence the dynamic behavior of the TSF geometry, including depositional practices (e.g. whole tailings spigot, cyclone separation, rotation patterns, distance to water pond, number of depositional points), construction methods and materials, impoundment configuration and footprint, ore characteristics and tailings particle size distribution, reclaim water pumping, temperature and precipitation. Completion and integration of topography and bathymetry survey datasets at regular intervals provide a more complete visualization of the dynamic nature the TSF beach and reclaim pond slopes.

Using 3D modeling software, the integrated dataset is represented to quantify the surface area and volume of the reclaim pond. The TSF surface developed as a result of the integrated dataset is also used to extract cross-sections from desired locations to assess the beach slopes. Frequency of the bathymetric and topographic surveys will be site specific and will depend on the actual pattern of change exhibited by the facility, with quarterly surveys likely being sufficient for most TSFs. This pattern is generally difficult to discern through visual observation alone, but upon collation of sequential surveys a consistent pattern typically emerges and an idealized survey interval can be recommended. Another way to enhance monitoring of the reclaim pond between full surveys is to utilize satellite imagery and remote sensing techniques.

Objectives for reclaim water storage on a TSF for operational production and safe facility management should be purposefully integrated and aligned. Sometimes, the TSF is used to store water for ore processing purposes during water supply shortages, upset conditions, or through dry seasons, and operational rules should always consider safety as the highest priority. Maintaining safe operating criteria, such as minimum beach width and freeboard, may require water storage to be minimized. Furthermore, the TSF must maintain storage volume for excess water that may arrive during seasonal precipitation patterns and extreme events. Site specific guidelines should be established for geotechnical thresholds that include minimum and maximum operational pond sizes and required storage for extreme events, maximum operational pond levels with their associated beach widths and operational water storage objectives adjusted to support the safety of the TSF.

To this end, the tailings team at our site in southern Arizona developed a strategy to maintain their reclaim pond at its minimal practical size. To do this properly, the team considered concepts and questions explored in this paper, generally: what is the optimum reclaim pond volume and area for the TSF considering impoundment geometry, reclaim water supply, precipitation events and geotechnical stability? This paper describes how the monitoring and analysis of TSF geometry at regular intervals provided valuable information and decision support to site operators, engineers and managers. While only one mining operation is highlighted in this paper to illustrate the utility of collecting frequent bathymetry and topography, these methods and analyses are equally applicable and are implemented at several Freeport sites

The site which served as the case study location is the Sierrita Mine, owned and operated by Freeport-McMoRan Inc. Sierrita is located in the arid Southwest United States, near the town of Green Valley. The average high temperatures in the hotter months (May – September) are above 32° C, while the average highs in the cooler months (November – March) are 15-20°C. The average precipitation is 38 cm per year, with most of the rain falling between July and September. The average evaporation is 220 cm per year. The tailings impounded is approximately 4.2 by 3.6 km (15 km^2) and the reclaim pond is generally 1-2 km^2. The ring-dike embankment is constructed using almost exclusively by upstream spigot deposition.

2 METHODS

2.1 *Bathymetric Surveys*

The bathymetry of the tailings reclaim water pond is obtained using a combination of equipment, including a global positioning system (GPS) receiver and single-beam sonar device (hydrographic echo sounder). Measurements from the GPS and echo sounder are synchronized in time to generate a point in three-dimensional space. The sites typically use the CEE Hydro systems™ CEESCOPE™ model with a frequency of 200kHz pulsing at 20 times per second (20 Hertz) and an accuracy of ±0.1% of the depth (CEE HydroSystems, 2021). The CEESCOPE has an integrated Global Navigation Satellite System (GNSS) processor and NovAtel GPS receiver providing preprocessed data accuracy of approximately 1 meter in the X and Y direction. The echo sounder and GPS are attached to a vertical pole on opposite ends, with the pole attached to the side of a manned airboat (Figure 1A). The pole is adjusted, so that the echo sounder emitter is submerged approximately 0.15 meters below the water surface.

Before the survey begins, locations at varying depths should be selected for comparison between measurements from the echo sounder and depths obtained from a manual measurement using a graduated rope and flat, steel plate or other measuring rod. The surveyor takes note of the difference between the soundings that are greater than approximately 0.10 meters and applies a correction to the post-processed soundings. The surveyor uses judgement when determining the depth using the manual measurement (e.g. weighted line) during this process as the tailings are known to have a “soft” bottom of tailings not completely settled, and that is generally 0.02-0.10 meters in thickness. From previous field investigations at Sierrita, it is estimated that a difference of 0.10 meters (when assumed for all points during the survey) causes a net volume difference of approximately 10%, and therefore, no corrections are made. The sonar signal is also dependent on water density and temperature, to which settings within the echo sounder can be customized to match the properties of the water in the TSF. At typical depths for this TSF, the density and temperature do not require adjustments to be made to these settings.

Site surveyors guide the boat's path across all areas of the pond that are greater than approximately 0.16 meters due to difficulty in navigating the airboat in shallow water and slow speeds. During the survey, the boat operator is guided using real-time GPS tracking that records the boat's position, transects and sounding depths, overlain on satellite imagery using the Hydromagic survey software. The boat traverses the pond to form a pattern of perpendicular, longitudinal and transverse lines with approximately 90 meters of spacing as shown in the aerial photo of Figure 1B.

The echo sounder will produce 20 or less depth measurements per second, depending on the return signal captured by the transducer. The Hydromagic software is used to post-process the GPS and sonar data by eliminating incorrect data points, converting depth measurements to elevation, and pairing an elevation point (Z) with each X and Y value. The combined X, Y, Z data points are used to interpolate between transect lines that create a grid spacing of approximately 3 meters. The selection of the optimal interpolated grid spacing is largely controlled by how variable the topography is. Along the survey transect lines, it is observed that TSFs typically have very smooth and slowly changing elevations. This smoothness permits interpolation to smaller pixels relative to the survey spacing. The authors recognize there is a functional limit to how small the pixels of the interpolated surface can get, and interpolating to 3 m seems reasonable for this facility, and while "over-interpolating" never adds information, this spacing and grid size works well for Sierrita.

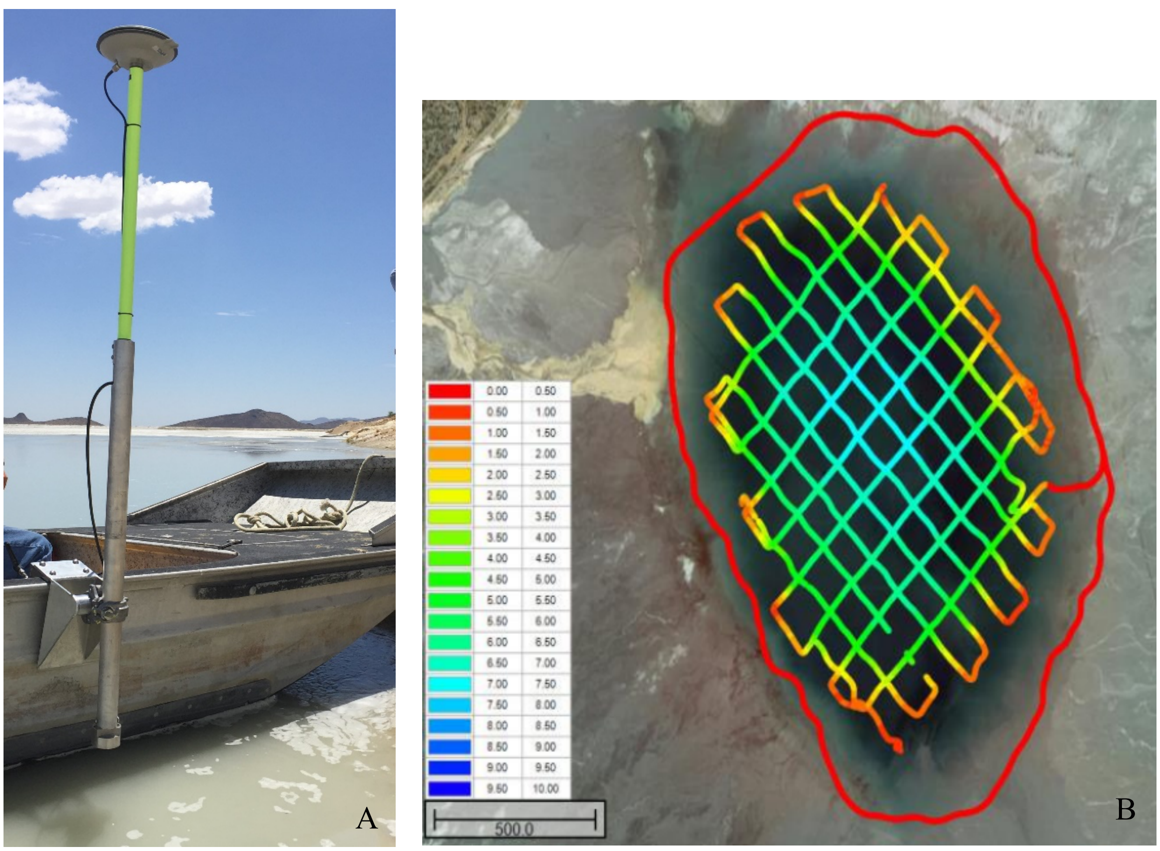

Figure 1. Panel A displays the GPS receiver and echo sounder transducer attached to the boat before the survey begins. Panel B shows the bathymetric survey lines overlain on the aerial photo.

2.2 *Topographic Surveys*

The topography of the tailings impoundment and embankment areas is obtained from a third-party vendor through commercially available satellite images and processed using proprietary algorithms. The vendor (PhotoSat) obtains 50-centimeter pixel resolution stereo photo pairs from the WorldView satellites and uses their proprietary software to produce elevation grids and pond outlines. The satellite tailings survey covers ~212 km^2 and established ground survey monuments are used to tie down the survey horizontally and vertically. The final surface is then compared to 925 check points to allow a statistically valid assessment of the actual accuracy of the survey. The check points are independent of the ground survey monuments. The vertical accuracy is determined by computing the Root Mean Square Error (RMSE) and the 90% confidence level. (FGDC, 1998), which on average are 0.15 and 0.24 meters respectively.

Figure 2. Twenty-eight outlines from the reclaim pond surface area are extracted from satellite imagery using multispectral analysis over a six-month period. The outlines assist site personnel to see how the pond's size and location are impacted by deposition and reclaim pumping.

2.3 *Monitoring*

The location and areal size of the TSF reclaim pond is primarily tracked using satellite imagery from the WorldView and Sentinel satellite systems, as well as the Planet™ satellite, which provides near-daily imagery. Using these sources, the site has access to cloud-free images of the tailings impoundment on average every three-to-five days. These images contain the red, green, blue and near infrared bands needed for multispectral analysis. Using the Normalized Difference Water Index (Xu, 2006), the outline of the reclaim water pond is extracted as a shapefile and its surface area calculated. The pond outlines and areas are cataloged in a Geographical Information System database where they can be conveniently accessed and assessed on a regular time frame.

Figure 2 shows selected pond outlines as an example of how frequent monitoring using satellite technology may be used to demonstrate changes in pond size and location over time. This process provides valuable data that can be used to inform site water management decisions. This image shows 28 different pond outlines produced from multispectral analysis on satellite imagery over six months.

2.4 *Data Integration*

Results from the bathymetric and topographic data processing provide separate point cloud files that are imported into the Muk3D™ software. A third data piece needed for the integration is the water pond outline provided by a third-party vendor (PhotoSat) and verified by measurements from site survey personnel. Because the bathymetric survey boat cannot take measurements adjacent to the edge of the water surface, there is a gap between the edge of the bathymetric survey points and the water's edge (where the tailings beach starts) that requires interpolation. The water surface elevation is input as a polyline with a constant elevation contoured at the water-tailings beach interface to make this delineation.

The bathymetric survey points are first merged with the water elevation polyline so the remaining space can be filled using linearly interpolated values, thus completing a digital surface of the operational pond. The constant slope assumed for the un-surveyed space of the reclaim pond is reasonable, considering that post processing estimates of the un-surveyed volume for this site are less than 5% of the total pond volume and the slopes in the unsurveyed gap of the pond are expected to be smooth and gradual due to the deposition process. Once the operational pond surface has been generated, it is merged into the topographic surface resulting in an integrated surface. The values for volume, surface area and elevation can be computed, and the shape of the water pond observed.

2.5 *Reclaim Pond Capacity Analysis*

A reclaim pond capacity analysis can be carried out to check that the TSF can store the allowable operating pond volume plus the probable maximum flood (PMF) with appropriate residual freeboard. Although the PMF volume does not change frequently, the pond surface area to volume relationship does change due to tailing deposition-induced geometry change, so we estimate residual freeboard and post-PMF beach width to verify that the PMF can be contained. The Sierrita TSF does not have a contributing watershed that adds direct runoff beyond the actual impoundment area, therefore, direct precipitation to the pond and beach area represents the effective area of runoff. As such, the analysis calculates the additional water volume as the Probable Maximum Precipitation (PMP) depth multiplied by the effective TSF footprint and conservatively assumes 100% runoff (i.e. no soil soak-up or infiltration). Using the integrated topographic-bathymetric surface in the Muk3D™ software, the PMF volume is simulated on the digital surface, the resulting freeboard is determined, and the post-event pond extent and its proximity to the embankment crest are evaluated against established criteria.

3 CASE STUDY

In 2019, the site created a reclaim pond management plan to explore strategies to minimize the reclaim pond to the degree practical. A third reclaim barge was commissioned earlier in the year when the pond was relatively deep to draw more water out of the pond and route it into the production circuit. With the third barge functional, part of the pond management plan was to determine the smallest operational pond and how the geometry of the pond was changing with time. The plan identified action items that would help to better anticipate changes to the pond that might impact production rates, reclaim availability and storage. Analyzing the integrated datasets of bathymetry and topography at the Sierrita site over time, allows facility engineers and operators to understand how and when the geometry is changing, which is observed in two primary ways.

First, the integrated tailings surface is used to develop the full surface area to volume relationship from the bottom of the reclaim pond to the lowest point on the embankment. Plotting these area-volume curves together from available surveys reveals the variability that is possible within the relationship over the course of regular operations. To focus solely on the variability of the capacity of the reclaim pond, the full surface area to volume relationship curves were truncated at each date's respective water surface elevation as shown in Figure 3. This does not include the region of the area-volume curve above the water line. This truncation permits the observer to effectively gauge how the pond's volume changes relative to area from survey to survey. In Figure 3, the curve for January 2018 (indicated as 1) displays a relationship where the impoundment has a smaller area-to-volume ratio than the curves dated December 2020 (indicated as 2) and February 2021 (indicated as 3). These last two survey dates represent a changed pond geometry, which contains flatter slopes than compared to the January 2018 survey and contains less water per unit area. Viewing the February 2021 data on Figure 3, the curve has moved in the direction of the January 2018 curve, thus indicating a steepening of the subaqueous slopes compared with the December 2020 survey. This directional transition, not seen since 2019, is a sign the geometry is changing and heading toward a lower area-to-volume ratio. This observation is important because it helps site personnel be aware of changes that can impact reclaim pumping continuity and maintenance activities.

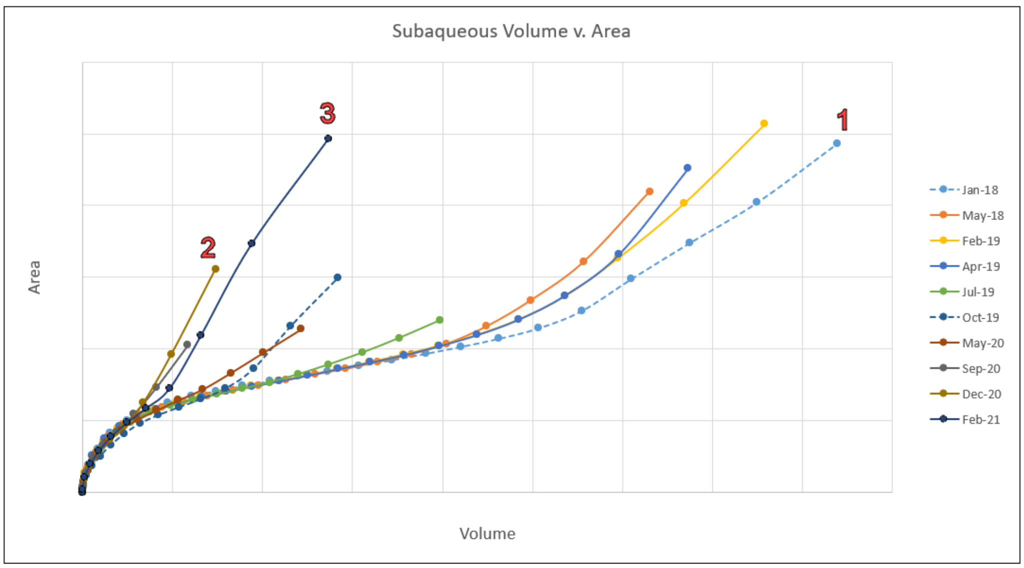

Figure 3. The reclaim pond surface area and volume relationships for each survey. Relationship terminates at the elevation of the water surface elevation, representing the observed pond volume at that time.

The second way the geometry is analyzed is by extracting multiple cross sections from the integrated surface and plotting them by elevation and distance. Figure 4 shows cross sections that transverse the approximate middle area of the pond for all surveys shown. The reclaim pond in cross-sections in Figure 4 clearly demonstrate that the slopes have both shallowed and flattened since January 2018. None of these geometric changes reduces the facilities' ability to handle the design storm, but does have impacts from an operational perspective related to barge maintenance and frequency of relocations.

From January 2018 to October 2019 the surveys were showing a developing pattern that the deeper area of the pond was infilling with tailings and causing the pond slopes to flatten out. This can also be observed in the area-volume curves in Figure 3, but the explicit plotting of cross sections provides clarity on the location of the infilling and how the slopes are changing with time. These surveys show that for a given pond volume, a greater surface area would result compared to historical facility geometries. This information, combined with aforementioned site plan to reclaim more water from the facility and maintain a smaller pond area, led to the installation of an additional barge pump and plan to operate the pond with a smaller area.

By June 2020, the pond volume reached its minimum level and the depth of pond was reduced by approximately 70% compared with historic conditions. Along with the decrease in pond depth, the subaqueous tailings slopes continued to flatten, thus preventing continuous barge pump operation. During this time, operations also noted the reclaim barges were sucking sediment into the water system tanks, effectively limiting the amount of water that could be drawn from the pond. As a result of the pond slopes flattening, the depth of water became too shallow for the barges, to the point where operations had to source water from other areas.

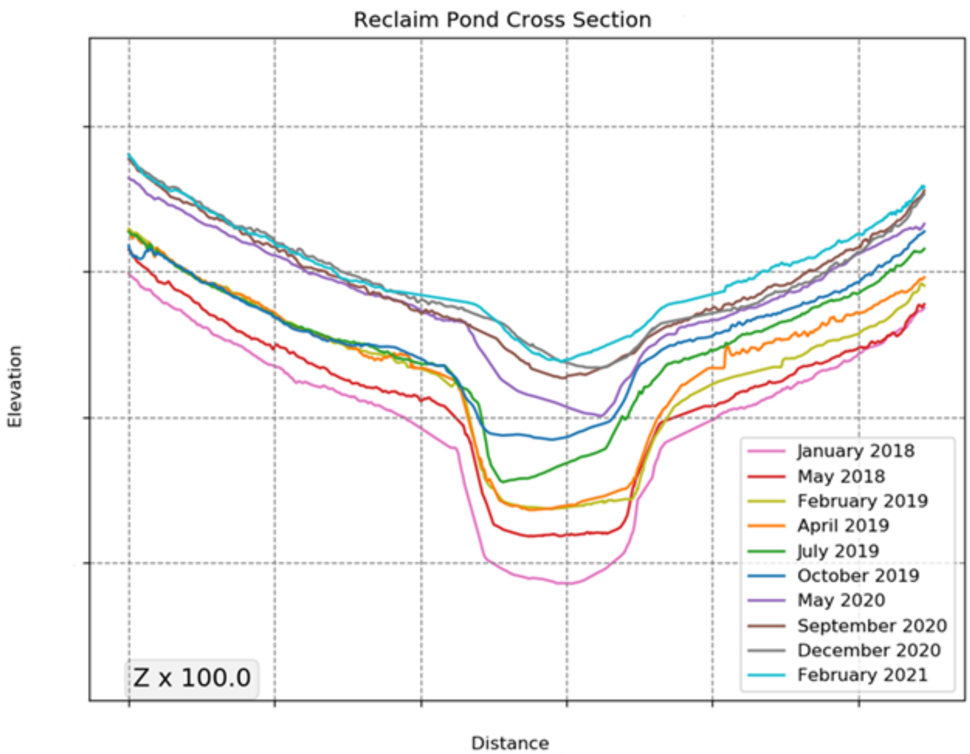

Figure 4. Cross sections of the tailings impoundment through the middle area of the pond.

Following this event, the site and corporate teams developed an action plan that allowed the pond to increase in area and volume until the barge pumps had a specified distance of clear water below the pump intake that would not draw in sediment. Subsequent surveys showed that subaqueous slopes increased, likely in response to operational changes. This allowed operations to have a more favorable pond geometry that reduced barge pump relocation and sediment intake. The second part of the action plan called for the team to develop scenarios in preparation for precipitation events due to the upcoming monsoon and winter seasons when pond volumes typically rise. With the flatter beach slopes, the site wanted to understand how precipitation events and their associated runoff volumes on a surface with flatter slopes would change the pond surface area and elevation.

Since the implementation of the action plan to increase pond area and volume, three additional bathymetric and topographic surveys have been completed. The cross sections for these surveys are shown in Figure 5 (previous surveys removed to make the slope steepening of the green line clearer). The February 2021 cross section gives an indication that the pond slopes are steepening, following the flat and shallow curves from September and December 2020. From Figure 3, the steepening of the slopes is also evident as the area-volume curve of the February 2021 survey has a lower area-volume ratio compared with the September and December 2020 curves. Based on the above analysis of the area-volume curve and integrated tailings surface cross sections, the reclaim pond slopes appear to be improving (steepening) as intended.

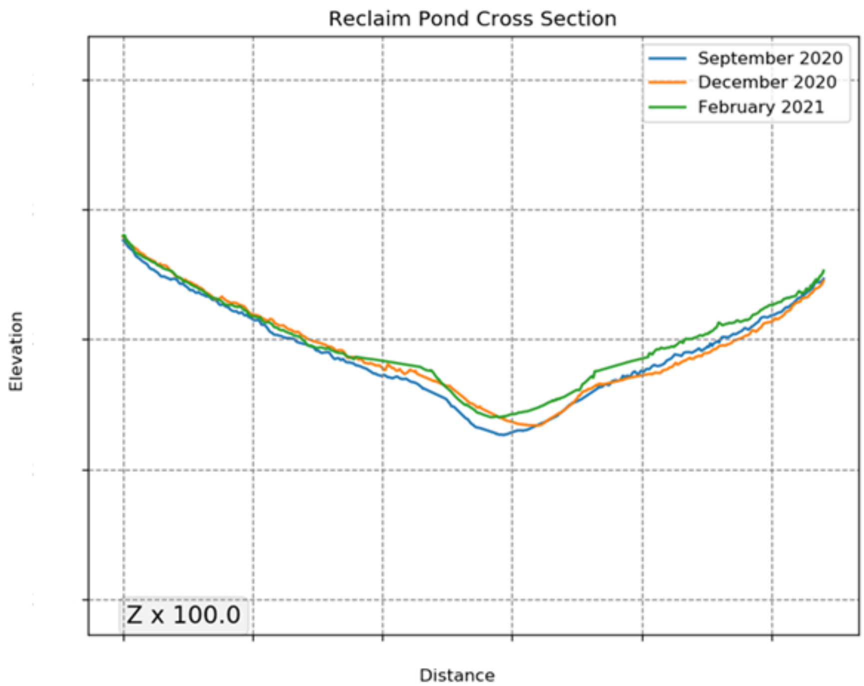

Figure 5. Cross sections of the TSF for the previous three surveys showing change in slope since operational changes were implemented.

As part of the action plan, sensitivity scenarios that adjusted the operational pond water surface elevations (both higher and lower, by a given amount) were evaluated on the most-recent surface. Using Muk3D software, the water level of the operational pond was adjusted upwards and downwards by 0.3 m and 0.6 m and the resultant volume and area were calculated. The pond surface area was observed relative to the embankment and established beach width using GIS tools. The compilation of both the Muk3D results and observations in GIS were used to determine the water surface elevation where the pond's capacity would be too shallow to support the reclaim system and conversely, the elevation where the pond area begins to encroach on operational beach width requirements. These results helped the team understand the balance between adequate reclaim system supply and surplus capacity with relation to operating criteria.

The second part of the analysis was to consider the impact of a PMF event on the operational pond. The operational and PMF volumes were combined and simulated on the impoundment surface to determine the resulting water surface elevation and areal extent. Replicating the first part of the analysis, the same pond water surface elevation intervals were used for the PMF plus operational pond simulations. Following the completion of the scenarios, the results were compared with freeboard, beach width, and water supply benchmarks.

The results of both analyses gave operations and management ideas on how positive and negative fluctuations in reclaim water pond elevations would impact pond geometries. The pond geometry results were important in communicating how much the reclaim pond could rise in water level before encroaching on beach width while also displaying how much the pond could lower in elevation before minimum barge depth is reached. Additionally, when viewing the results along with the cross-sections presented above, operations could view the variability of the deepest part of the pond that ultimately drives planned barge moves. An understanding of the dynamics of the reclaim pond depths, together with updated pond water surface elevation scenario results, informed site personnel and management of current water storage conditions and drove decisions that focused on balancing reclaim pond capacity with defined safety criteria.

The completed analyses spurred operations to further monitor deposition practices and reclaim pumping, with the goal of steepening the reclaim pond's subaqueous slopes and deepening its bowl to effectively gain more capacity within the pond to allow for sustained drafts underneath the barge pumps. These analyses also confirmed that the facility was always able manage the design storm (PMP/PMF).

4 REPORTING AND DOCUMENTATION

To deliver analyses effectively and succinctly, such as those mentioned herein, a comprehensive survey analysis report was developed at Sierrita and other Freeport sites. The report, delivered following the integration and analysis of the topographic and bathymetric surveys, includes pond tracking details such as maximum pond depth locations, weekly pond area measurements, barge depths in relation to pond volume, subaqueous slope measurements, reclaim pond water surface elevation charts, maximum containment information, and determined cross-sections for slope analysis. The report is sent to the site engineers, who review and provide feedback before sending to the respective Engineer of Record of the site for their reference and use. The comprehensive analysis and summary report have been identified by Freeport-McMoRan as good practices and have been implemented at other tailings sites. Various implementations at the other sites have been made, per the request of site engineers, to adequately capture the important pond tracking parameters for each facility. At Morenci, for example, the engineers suggested adding a graph of pond volumes by daily barge depth measurements. Because the facility houses two reclaim ponds, the additional information was a helpful visual when comparing recent pond volume and barge depth trends. The added feedback from the site teams allows each iteration of the report to be concise, yet comprehensive, and tailored to the unique needs of each facility.

5 CONCLUSIONS

The case study presented herein describes how bathymetric and topographic surveys, along with satellite and remote sensing techniques, can provide the relevant data needed to perform analyses and draw conclusions that inform decision makers on questions related to dam safety and water supply. Results of the monitoring and analysis supported site personnel in adapting their water management plan to proactively consider various water storage scenarios and estimate outcomes relative to established geotechnical guidelines. The results from the ongoing work at Sierrita add a layer of confidence that changing pond geometry can be managed in a way that helps keep performance indicators within operational and dam safety limits.

The ongoing collection and assessment of TSF geometry at Sierrita and other sites demonstrates that the selected tools for monitoring and analysis are effective in capturing the dynamic behavior of the TSF reclaim pond and are valuable in their illustration of identifying patterns and assessing outcomes. From an operational perspective, the water depth under the barge pumps remains the key indicator for ensuring continuous pumping and the integrated data sets show that there are many combinations of pond area and volume that can yield desired pond depths. A primary take-away is that monitoring the subaqueous pond slopes through bathymetric surveys is key to anticipating changes in volume and area that can impact water storage and good practice guidelines.

6 ACKNOWLEDGEMENTS

We express appreciation to the Sierrita survey, tailings and engineering groups for providing the necessary data that was used in this case study.

7 REFERENCES

CEE HydroSystems, (2021). Product Information, Technical Specifications (https://ceehydrosystems.com/products/single-beam-echo-sounders/ceescope).

Federal Geographic Data Committee (FGDC), 1998. Part 3: National Standard for Spatial Data Accuracy, FGDC-STD-007.3-1998, (https://www.fgdc.gov/standards/standards_publications/).

Hanqiu, Xu., 2006. Modification of Normalized difference water index (NDWI) to enhance open water features in remotely sensed imagery, International Journal of Remote Sensing, 27:14, 3025-3033, DOI: 10.1080/01431160600589179

Assessing the generation of positive excess pore pressure during undrained compression of unsaturated filtered tailings

Neelufar Aghazamani, Joseph Scalia IV, Christopher A. Bareither
Department of Civil & Environmental Engineering, Colorado State University, Fort Collins, CO

ABSTRACT: Filtered tailings stacks present a geotechnically attractive alternative to conventional slurry-deposited tailings facilities. Stability of filtered tailings stacks requires a dense particle structure to be created either via compaction following placement or from compression due to self-weight. The generation of positive excess pore pressure in unsaturated filtered tailings can prevent sufficiently dense placement and impact achieving desired geotechnical performance. Undrained compression tests were performed on filtered tailings from a precious metal mine, using a modified rigid-wall permeameter with controlled vertical stress. Specimens with different initial dry densities and gravimetric water contents were prepared to assess the impact of the initial conditions on the generation of positive excess pore water pressure. The results illustrate unsaturated filtered tailings, when incrementally loaded, generated excess pore pressure near a specific degree of saturation (≈ 80%). The generated pore pressures did not fully dissipate after 24 h. Results from this study demonstrate the interplay between placement water content and density and illustrate that initial mechanical compaction of placed filtered tailings may not be necessary to ensure construction of a dense stack; an equivalently dense structure may be achieved by self-weight compression.

1 INTRODUCTION

Mining and beneficiation of minerals generate large quantities of mineral byproducts, principally in the form of tailings and waste rock. Conventional tailings facilities use slurry deposition of tailings with solid contents ranging from 15 to 60% (Davies 2018, ICOLD 2018), resulting in loose fabrics after placement, and low strength that has resulted in recent flow-type failures (Córrego do Feijão mine in 2019, Samarco Mariana mine in 2015, and Canada's Mt. Polley mine in 2014). The slurry deposition of tailings also creates long times for consolidation necessitating long-term management of inherently weak materials.

To potentially eliminate flow-type failures from the time of placement, tailings must be sufficiently dewatered prior to placement such that the resultant tailings are sufficiently dense to stay below the critical state line. Filtration has become a widely practiced method of separating solid phase from liquid (generally at smaller scale facilities; Wang et al. 2014), and the resulting filtered tailings, are unsaturated material with high solids content (> 85%) (Lupo and Hall 2010). Filtered tailings are placed via dumping or conveyor to form a tailings stack. Historically termed a "dry stack," this term is incorrect because the tailings are usually placed near or wet of standard Proctor optimum water content, and thus, the placed tailings contain a non-trivial quantity of water. Filtered tailings are envisioned as potential solutions to the potential geotechnical instability of slurry-deposited tailings but are not a perfect solution.

Two major shortcomings of filtered tailings are cost and potential for geochemical instability (e.g., acid rock drainage) if not correctly implemented. In addition, tailings filtration at a large scale has historically not been technically or economically practical. However, this is shifting with increasing technological advancements by filter manufacturers and industry pressures to prevent potential geotechnical failure modes. To minimize costs and maximize throughput, a maximally viable filtered tailings pile will be placed as wet as possible to minimize dewatering. However, the generation of positive excess pore water pressure in unsaturated filtered tailings can potentially prevent sufficiently dense placement and the achievement of geotechnical performance targets. Further investigation is required to enable the optimized construction of filtered tailings stacks.

The purpose of this study is to evaluate the initial behavior of unsaturated tailings under undrained loading and assess the impact of the initial gravimetric water content, initial dry density, and initial degree of saturation on the generation of positive excess pore pressure. Undrained compression tests were performed on initially unsaturated filtered tailings from a precious metal mine using a modified rigid-wall permeameter with controlled vertical stress. Specimens were prepared with different initial dry densities and gravimetric water contents (standard Proctor optimum and wet of optimum). Results from this study can be used to understand the compression behavior of unsaturated tailings, the potential need for initial compaction, and to guide future assessment of filtered tailings placement water contents.

2 MATERIALS

In this study, filtered tailings from a confidential precious metal mine were used for testing. Geotechnical characterization of these filtered tailings are described in Gorakhki et al. (2019) and are summarized in Table 1. Characteristics of the tailings include mechanical sieve and hydrometer (ASTM D422-63; ASTM 2007), Atterberg limits (ASTM D4318-10; ASTM 2014), specific gravity (ASTM D854-14; ASTM 2014), and standard-Proctor-effort compaction (ASTM D698-12; ASTM 2014).

Table 1. Summary of physical characteristics and classification of mine tailings (Gorakhki et al. 2019).

Material	LL[a] (%)	PI[b] (%)	USCS[c]	Gravel (%)	Sand (%)	Fine (<0.075mm) (%)	Clay size (%)	G_s[d]	w_{opt}[e] (%)	$\rho_{d,\,max}$[f] (Mg/m^3)
M-Tailings	30.1	9.2	CL	0	14.3	85.7	23.6	2.715	15.8	1.69

[a] LL: Liquid limit, [b] PI: Plasticity index, [c] USCS: Unified soil classification system, [d] G_s: Specific gravity, [e] w_{opt}: Optimum water content, [f] $\rho_{d,\,max}$: Maximum dry density.

3 METHODS

3.1 *Specimen preparation*

The air-dried filtered tailings were pulverized using a 454 g rubber hammer and then passed through sieve #4 for homogenization. After adding the target amount of water, tailings samples were mixed thoroughly and then sealed for moisture equilibration for 24 h. After 24 h, filtered tailings were mixed, passed again through sieve #4, and then immediately used for test specimen preparation. Filtered tailings with adjusted water contents were compacted within the test cell which had a diameter of 101.6 mm. Specimens were compacted to a height of 25 mm. Compaction was performed on a rigid flat surface and the specimen and cell were subsequently moved to the permeameter base and placed atop the high air entry disk (described in the subsequent section). The initial target dry densities were 80%, 90%, and 95% of the maximum standard Proctor dry unit weight, and +0%, +2%, and +5% of the standard Proctor optimum water content.

3.2 *Undrained Compression Testing*

Undrained compression tests were conducted using a modified rigid-wall permeameter with controlled vertical stress (the unmodified permeameter is described in Daniel 1994), shown schematically in Figure 1. Cell modification involved sealing a saturated 10-mm thick high air-entry ceramic disk (500 kPa air-entry pressure) to the top of the base pedestal, such that the specimen rested atop the high air entry disk. The role of the saturated disk was to measure positive excess pore water pressure within the specimen without contributing water to the specimen. A filter paper was placed atop the high air entry disk before specimen placement to prevent fouling of the disk pores. Another filter paper and an unsaturated 3-mm-thick-porous plastic disk were placed above the specimen and overlain by the top piston. After closing the cell, the space above top piston was filled with water. A pressure transducer was connected via a saturated line connected to the high air entry disk. To control the vertical stress applied to the specimen, water above the top piston was pressurized incrementally using a pressure panel in steps to apply a total vertical stress to the specimen. Specimen volume change was monitored by measuring inflow to the reservoir above the top piston. The total stress applied in the compression tests were 14, 34, 69, 103, 138, 172, 207, 241, 276, 310, 345, 379, 414, 448, 483, 517, 552, and 586 kPa. The upper bound is governed by the capacity of the pressure panel used to apply total vertical stress. One top (air) valve of the cell was kept open for approximately 10-20 min after applying the first load step of 14 kPa (2 psi). The temporary opening of the valve was to let air between the specimen and the piston out and thus assuring the piston cell was in intimate contact with the specimen. After 10-20 min, all outflow valves were closed and remained closed throughout the undrained test (i.e., neither air nor water could leave the cell). Time intervals between each load increment were approximately 24 h. The thickness of the specimen at the end of each load step was back calculated using the final specimen measurements after test termination.

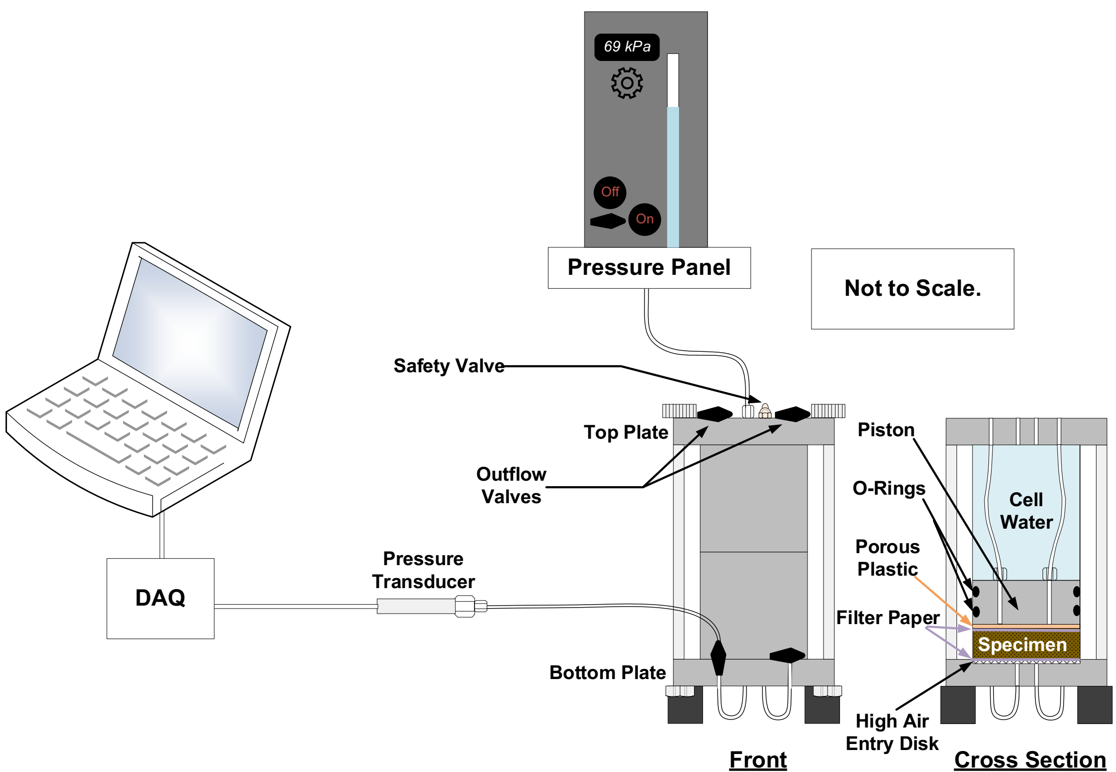

Figure 1. Schematic of the modified rigid-wall permeameter with controlled vertical stress and test setup used to perform an undrained compression test.

4 RESULTS AND DISCUSSION

A list of completed undrained compression tests in this study is in Table 2. The specimens were targeted to have initial degrees of compaction of 80, 90, and 95%, but the length of the test cell impacted the accuracy of compaction and resulted in the values reported in Table 2. A less than 1% loss of moisture during compaction of some of the specimens is also shown in Table 2.

Compression results from eight tests are presented in Figure 2. Compression data were fitted to constitutive models for void ratio versus effective stress. Large-strain void ratio versus effective stress constitutive relationship described by Liu and Znidarčić (1991) was used, i.e., void ratio, $e = A(\sigma + Z)^B$, where A and B are dimensionless fitting parameters, Z is a fitting parameter with units of stress, and σ is applied total stress. Values shown in Figure 2b for positive excess pore pressure are the maximum readings from the pressure transducer during each approximately 24-hour period.

Table 2. List of performed undrained compression tests on M tailings.

Test No.	Gravimetric water content	Initial compaction	Excess pore pressure generated?	Initial degree of saturation (%)	Final degree of saturation (%)	Critical degree of saturation [a] (%)
1	w_{opt} [b]	95% $\gamma_{d,max}$ [c]	No	62	78	NA [d]
2	w_{opt}	90% $\gamma_{d,max}$	No	54	73	NA
3	w_{opt}	80% $\gamma_{d,max}$	No	43	67	NA
4	w_{opt}+1.3%	95% $\gamma_{d,max}$	Yes	68	91	NA
5	w_{opt}+4.3%	98% $\gamma_{d,max}$	Yes	79	100	80
6	w_{opt}+4.4%	97% $\gamma_{d,max}$	Yes	80	100	80
7	w_{opt}+5%	83% $\gamma_{d,max}$	Yes	62	92	78
8	w_{opt}+5%	80% $\gamma_{d,max}$	Yes	56	100	79

(a) At which the ratio of positive excess pore pressure over total vertical stress is ≥ 0.1, (b) w_{opt}: Optimum water content which is 15.8% for M tailings, (c) $\gamma_{d,max}$: Maximum dry unit weight which is 16.6 kN/m^3 for M tailings, (d) NA: Does not apply.

As shown in Figure 2a, specimens initially compacted wet of optimum underwent greater compression compared to specimens with the same degree of compaction but at optimum water content. The higher moisture content (lower capillary suction) of the specimens made tailings clods softer, such that the specimen could be more readily compressed (Fredlund et al. 2012). The generation of appreciable positive excess pore pressure was not observed under the same total vertical stress (Fig. 2b). Appreciable excess pore pressure in this study is defined as when the ratio of positive excess pore pressure over total vertical stress was ≥ 0.1. For example, an specimen initially compacted at to 80% of the maximum dry unit weight at +5% optimum water content generated an appreciable 33 kPa positive excess pore pressure under 103 kPa total stress. Higher initial degree of compaction appears to have shifted the generation of appreciable positive excess pore pressure to greater applied total stress. For example, specimens with initial conditions of 97% maximum dry unit weight with +4.4% optimum water content and 98% maximum dry unit weight with +4.3% optimum water content generated 31 and 36 kPa positive excess pore pressure, respectively, under a 207 kPa total stress. Specimens prepared at optimum water contents did not generate appreciable positive excess pore pressure under vertical stresses as high as 586 kPa.

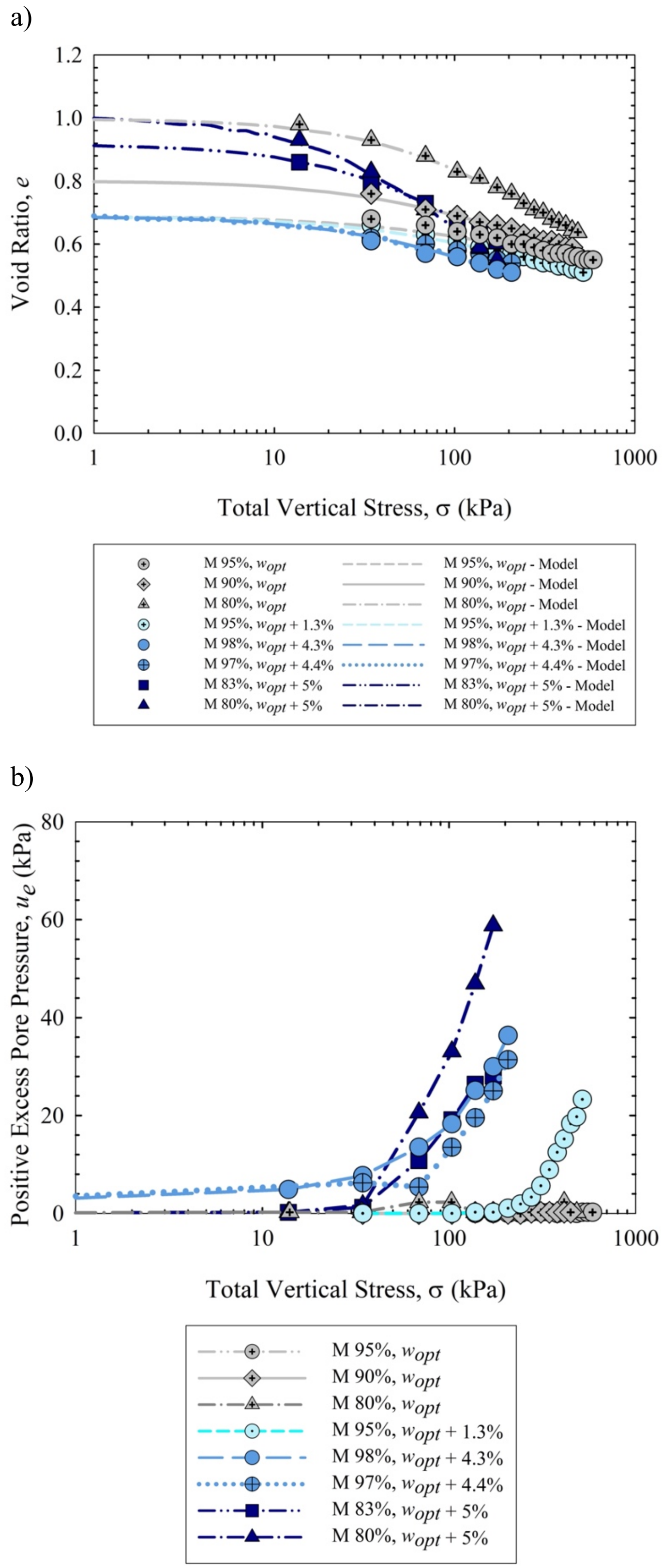

Figure 2. a) Undrained compression test results from the eight tests on filtered tailings; and b) generated positive excess pore pressure for each load step. Tests identified in the legend include the percent of maximum dry unit weight and water content relative to optimum water content (w_{opt}), which is 15.8%. $e = A(\sigma + Z)^B$, a constitutive relationship by Liu and Znidarčić (1991). As-compacted data are plotted at a total vertical stress of 0.01 kPa.

The generation of positive excess pore pressure relative to the degree of saturation is shown in Figure 3. Similar to Figure 2b, the positive excess pore pressures shown in Figure 3 are the maximum readings from the pressure transducer over each 24-hr period. Compression tests demonstrated appreciable generation of positive excess pore pressure at approximately 80% saturation. This degree of saturation, labeled as the critical degree of saturation in Table 2, represents the condition when appreciable positive excess porewater pressure was measured, i.e., the ratio of generated positive excess pore pressure over total vertical stress was equal to or greater than 0.1. The generated positive excess pore pressure did not fully dissipate after 24 h in any of the performed tests. The generated positive excess pore pressure increased under subsequent load steps until 100% saturation of the specimen and continued increasing thereafter. However, higher initial degree of compaction reduced the magnitude of generated positive excess pore pressure if the initial gravimetric water content was not more than +2% optimum water content (i.e., denser specimens compressed less). In Test 4, the specimen did not generate appreciable positive excess pore pressure even until 91% saturation.

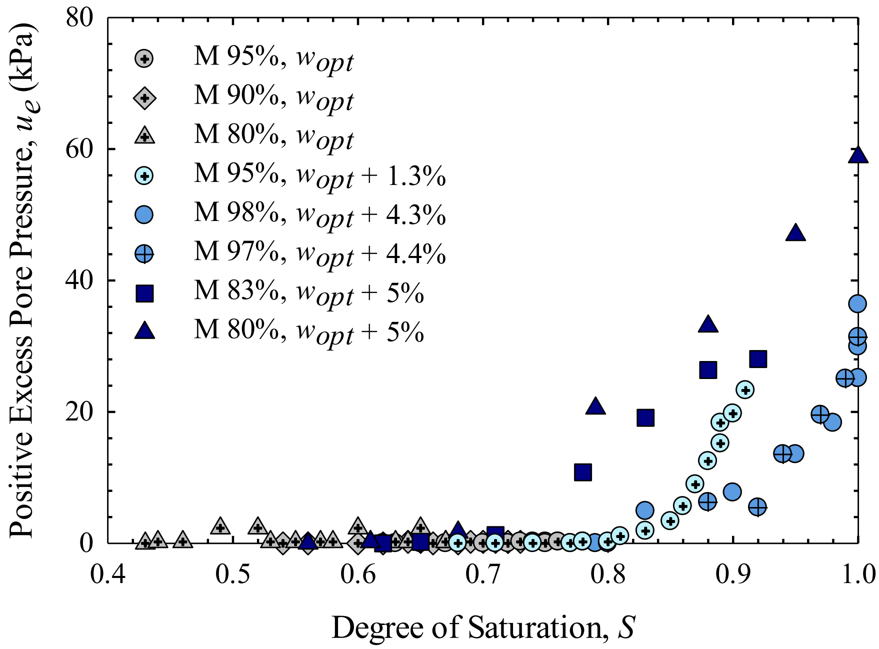

Figure 3. Positive excess porewater pressure generation versus saturation. Tests identified in the legend include the percent of maximum dry unit weight and water content relative to optimum water content (w_{opt}), which is 15.8%.

The results from the compression tests provide a framework to interpret the unsaturated excess porewater pressure generation of the tailings. For degrees of saturation approximately < 70%, zero positive excess pore pressure was recorded via the pressure transducer, despite the specimens compressing noticeably. The volume of air was sufficient to allow for deformation via compression of the continuous air phase. Porewater did not generate an appreciable positive excess pressure because there was sufficient compressibility in the air phase, as well as additional (connected) air in the unsaturated porous plastic top disk and closed tubes. In the field, under drained conditions, air would readily leave the specimen. Low degrees of saturation also result in lower specimen compression (Fredlund et al. 2012), which is illustrated in Figure 2a.

At degrees of saturation greater than approximately 70% but less than approximately 80%, the air phase was no longer continuous. Positive excess porewater pressure is generated under loading, where water phase is continuous, and is measured by the pressure transducer in some conditions (near 80% saturation). However, the generated excess porewater pressure dissipated by the time the next load was applied and did not reach the defined appreciable threshold. The compressibility of air is conversely proportional to absolute air pressure (Fredlund et al. 2012). Therefore, air compressibility decreases as the partial pressure of air inside the specimen increases. When a load is applied, air bubbles become entrapped in the water phase, the partial pressure of air in these bubbles increases (Boyle's law). However, the increased pressure is not appreciable, and the air bubbles are gradually dissolved in the water phase based on Henry's law. As can be found in Table 2, tests in which the specimens did not reach approximately 80% saturation by the termination, did not generate appreciable positive excess porewater pressure.

At degrees of saturation close to or greater than 80% appreciable positive excess porewater pressure was generated. When a load is applied, the air pressure of occluded air bubbles increases, and these air bubbles begin to dissolve. However, there is insufficient air to provide all volume change, and a portion of the load is born by the water phase generating a positive excess porewater pressure. As viewed in Figure 4, the positive excess porewater pressure ratio is much less for specimens with higher initial dry density and lower gravimetric water content. The applied vertical stress on these specimens is mainly born by soil particles rather than water and thus less positive excess porewater pressure is generated comparing to that in tests on looser specimens with higher gravimetric water content. In other words, specimens compacted to 90% or more, with gravimetric water contents less than +2% optimum water content do not generate appreciable positive excess pore pressure even at degrees of saturation above 80%.

In Figure 4, the relationship between the generation of positive excess pore pressure and the dry density of specimens is illustrated. Shaded symbols represent positive excess pore pressure ratios equal to or greater than 0.1. As can be seen in Figure 4a, loose specimens with high moisture contents (+5% wet of optimum) started generating high positive excess pore pressures at lower densities. The test on the initially 95% compacted specimen with +1.3% wet of optimum water content indicated that the positive excess pore pressure ratio remained low if the specimen was sufficiently compacted and dewatered initially (Figs 4a and 4b). Based on Figure 4b, dense specimens with gravimetric water contents less than +2% wet of optimum generated the least amount of positive excess pore pressure. Given that all tests performed were undrained, the increase in the dry density of specimens was due to the reduction of the volume of air (compression and subsequent dissolution into water). There is not a unique dry density at which positive excess pore pressure started being generated.

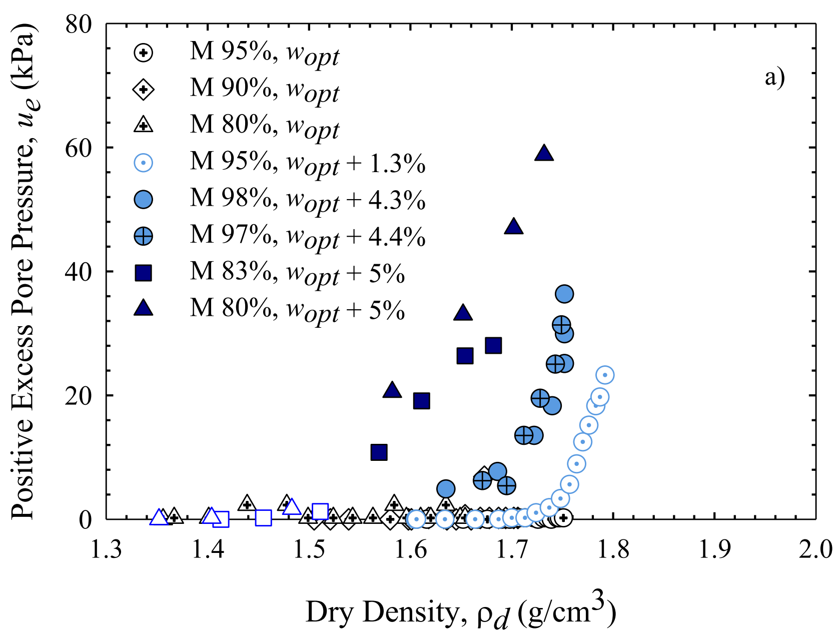

Figure 4. a) The trend of positive excess pore pressure generation as the dry density increases.

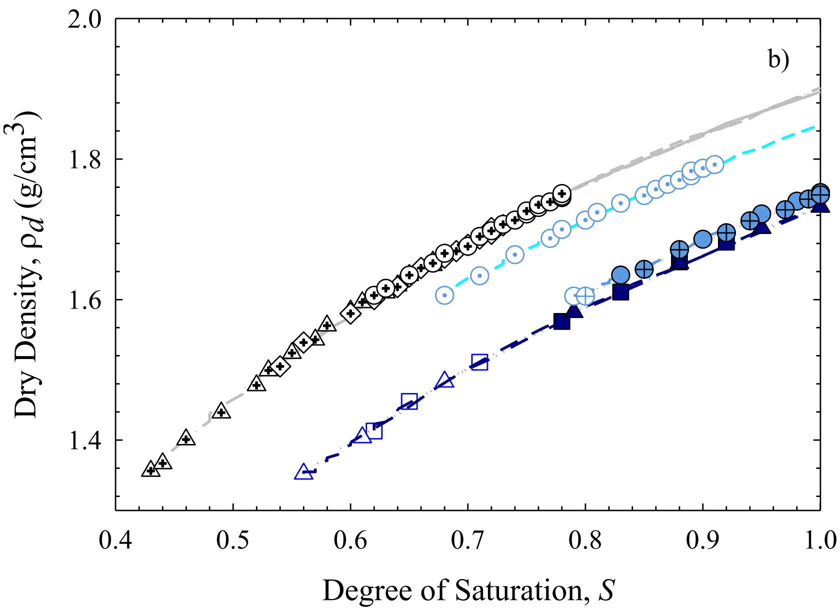

Figure 4. b) The dry density versus degree of saturation S. Tests identified in the legend include the percent of maximum dry unit weight and water content relative to optimum water content (w_{opt}), which is 15.8%. Shaded symbols: The generated u_e had a u_e/σ_v equal to or greater than 1. Open symbols: no significant u_e was measured. Models are derived from $e = A(\sigma + Z)^B$, a constitutive relationship by Liu and Znidarčić (1991).

5 SUMMARY AND CONCLUSIONS

Eight undrained compression tests were performed on filtered tailings from a precious metal mine with various initial dry densities and gravimetric water contents. The gravimetric water contents of these specimens ranged from optimum to +5% wet of optimum. The initial degree of compaction of the specimens ranged from 80 to 98% of the standard Proctor maximum dry density. The goal for these tests was to understand the behavior of filtered tailings under loading, as a filtered tailings stack is constructed. The following conclusions are drawn from this study:

- Greater compression was observed in tests on specimens wet of optimum in comparison to tests on specimens with the same degree of compaction but at optimum water content.
- Appreciable positive excess porewater pressure was not observed under the same total vertical stress for different initial compacted states of the filtered tailings.
- Appreciable positive excess porewater pressure was consistently generated at saturations around 80% for specimens with more than +2% optimum water content. The generated positive excess porewater pressure increased under subsequent loadings. In tests where no appreciable positive excess porewater pressure was observed, the specimens had not reached 78% saturation by the end of the test. In almost all tests, minimum or zero positive excess porewater pressure was generated at degrees of saturation less than 70%. There was not a unique dry density at which positive excess porewater pressure started being generated.
- Tests on specimens with ≥ 90% maximum dry density initial compaction and gravimetric water contents less than +2% wet of optimum resulted in the least amount of generated positive excess porewater pressure, even after reaching 80% saturation.

Generation of positive excess pore water pressure in unsaturated filtered tailings is a factor of the degree of saturation and compressibility of the as placed tailings. Drier tailings are less compressible for a given applied stress but have a lower degree of saturation. Wetter tailings are more compressible for a given applied stress but have a higher degree of saturation. Given that the goal of filtered tailings is to achieve a density sufficiently high (or void ratio sufficiently low) to preclude the possibility of flow, placement must be a balance of factors to achieve success.

Based on the data in this study, which are specific to the tailings studied, compaction of the filtered tailings after placement would only be necessary if the self-weight compression does not achieve a sufficient density to achieve geotechnical stability (although compaction might also be necessary to, for example, to prevent infiltration of precipitation). Additional study, currently in progress, is needed combining the results of this study with a strength analysis of the tailings.

6 REFERENCES

ASTM D422-63, 2007. Standard test method for particle-size analysis of soils. West Conshohocken, PA, www.astm.org, DOI: 10.1520/D0422-63R07E02.

ASTM D2487-11, 2011. Standard practice for classification of soils for engineering purposes (unified soil classification system). West Conshohocken, PA, www.astm.org, DOI: 10.1520/D2487-11.

ASTM D4318-10, 2014. Standard test methods for liquid limit, plastic limit, and plasticity index of soils. West Conshohocken, PA, www.astm.org, DOI: 10.1520/D4318-10.

ASTM D698-12, 2014. Standard test methods for laboratory compaction characteristics of soil using standard effort (12400ft-lbf/ft3 (600 kN-m/m3)). West Conshohocken, PA, www.astm.org.

ASTM D854-14, 2014. Standard test methods for specific gravity of soil solids by water pycnometer. West Conshohocken, PA, www.astm.org, DOI: 10.1520/D0854-14.

Daniel, D. 1994. State-of-the-art: laboratory hydraulic conductivity tests for saturated soils. ASTM STP 1142. American Society for Testing and Materials, Philadelphia, PA, USA.

Davies, M. 2018. Filtered Dry Stacked Tailings-The Fundamentals. Tailings & Mine Waste Conference 2018, Vancouver, BC, Canada, DOI: 10.14288/1.0107683.

Fredlund, D.G., Rahardjo, H., Fredlund, M.D. 2012. *Unsaturated Soil Mechanics in Engineering Practice*. Hoboken, New Jersey: John Wiley & Sons Inc.

Gorakhki, M.R.H., Bareither, C.A., Scalia, J, and Jacobs, M. (2019). Hydraulic conductivity and soil water retention of waste rock and tailings mixtures, *GeoCongress 2019 GSP 312*, ASCE, 41-50. DOI: 10.1061/9780784482148.005.

ICOLD 2018. Tailings Dam Design Technology Update. International Commission on Large Dams Commission Internationale des Grands Barrages, Paris, France.

Liu, J.C., Znidarčić, D. 1991. Modeling One-dimensional Compression Characteristics of Soils. *Journal of Geotechnical Engineering*, 117(1), 162-169, DOI: 10.1061/(ASCE)0733-9410(1991)117:1(162).

Lupo, J., Hall, J. 2010. Dry Stack Tailings – Design Considerations. 14th Tailings & Mine Waste Conference 2010, Vail, Colorado, 327-335, ISBN 978-0-415-61455-9.

Wang, C., Harbottle, D., Liu, Q., Xu, Z. 2014. Current state of fine mineral tailings treatment: A critical review on theory and practice. *Minerals Engineering Journal*, 58: 113-131. DOI: 10.1016/j.mineng.2014.01.018.

A centrifuge investigation on the effect of density and water content on the runout behavior of coal fly ash impoundments

Samuel B. Follett
McMillen Jacobs Associates (formerly at the University of California Davis), Walnut Creek, CA, USA

Srikanth S. C. Madabhushi
University of Colorado Boulder, Boulder, CO, USA

Alejandro Martinez & Daniel W. Wilson
University of California Davis, Davis, CA, USA

Benjamin J. Gallagher
Electric Power Research Institute, Palo Alto, CA, USA

ABSTRACT: Characterizing the behavior of coal fly ash impoundments is critical for assessing the potential consequences of an impoundment failure. As shown by previous failures in the field, saturated ash can undergo flow failure with large runout distances when confinement is lost. The state of impounded ash is affected by the deposition processes and further pond maintenance activities, the former typically involving sluicing of material at water contents greater than 200%. This paper presents the results of an investigation on the effect of the initial slurry water content on the resulting density of the consolidated material and its run-out behavior following a modeled impoundment failure. To accurately model the flow behavior, a centrifuge testing program was conducted at an acceleration equivalent to 60 times Earth's gravity using a novel centrifuge container. This container featured a set of gates that were opened during the centrifuge test to create a rapid loss of confinement of the impounded material. In addition to measuring Cone Penetration Test (CPT) tip resistances prior to inducing the failure, the failure progression was monitored using high frame rate cameras. The results of the two experiments described in this paper show that the looser specimen prepared with a wetter slurry exhibited a flow failure with greater run-out distances, while the denser specimen prepared with a drier slurry exhibited a slope stability failure with limited run-out. This study also shows that the range of behaviors observed in waste containment failures in the field, ranging from flow failure to slope stability, can be modeled in centrifuge experiments.

1 INTRODUCTION

Coal fly ash is a fine particulate material comprised mainly of aluminosilcates and silicates derived from burning of coal. Most fly ash particles are glassy minerals resulting from partial or complete melting during combustion and rapid cooling in the exhaust gas. While roughly 60% of fly ash produced in the USA is utilized in applications such as cement replacement in concrete and soil stabilization (ACAA 2020), an estimated 2B tons are contained in impoundments and landfills (Minkara 2020). The US EPA identified 559 existing ash impoundments during a 2009-2014 assessment of facilities, including impoundments as large as 300 hectares and 100 m deep (US EPA 2014). At the time of assessment completion in 2014, EPA classified 50 impoundments as high hazard dams, meaning a failure could jeopardize human life.

Where impoundments are utilized, fly ash is typically deposited by sluicing the material at water contents in excess of 200%. A similar sluicing process is often used to form tailings and other mine waste impoundments. However, mine tailings can encompass a larger range of material characteristics than fly ash because they can include sand-, silt-, and clay-sized particles. Characterizing the ponded material represents a significant challenge because in many cases the ash and mine wastes are loosely deposited and consist of intermediate and silt-sized particles for which the sampling and in-situ testing methods are less robust (Been 2016). This uncertainty in in-situ properties complicates the assessment of flow liquefaction potential, and therefore the estimation of the consequences of a failure. Flow liquefaction is characterized by significant loss of strength, which can lead to large deformations and ultimately runouts. Soils more prone to flow liquefaction include loose cohesionless sands and silts as well as sensitive clays.

This paper presents the results of two centrifuge runout experiments performed at the UC Davis Center for Geotechnical Modeling (CGM). These experiments have the goal of investigating the effect of initial water content and dry unit weight on the failure behavior and consequences of saturated fly ash impoundments. To achieve this, the deposits were subjected to a sudden loss of confinement in a newly-constructed centrifuge container, which aims to simulate the failure of a containment structure (i.e. dam). The centrifuge tests included CPT soundings and high frame rate cameras to provide information of the deposits' initial properties and behavior and progression of the observed failures.

2 MATERIALS & METHODS

2.1 *Fly ash*

The fly ash material used in this investigation was collected by electrostatic precipitators at a pulverized coal power station with supercritical boilers. A selective catalytic reduction technology operated between the boilers and the electrostatic precipitators. The power station was fueled with eastern bituminous coal resulting in a Class-F ash. EPRI (2014) reported that this ash was not prone to develop diagenesis (i.e. strong cementation) when bought in contact with water; visual evidence obtained during handling of the ash also indicate that the absence of diagenetic reactions. This is further supported by the ash's pH between 7 and 10 and its low calcium content of 1.4% The ash was constituted of about 7% sand-sized particles, 85% silt-sized particles, and 8% particles smaller than 2 μm (Fig. 1a). The 10th percentile particle size, D_{10}, was 3 μm while the 50th percentile particle size, D_{50}, was 210 μm. The fly ash was composed of a large proportion of spherical particles, some of which appeared to be hollow (Fig. 1b).

A list of properties of the tested fly ash is presented in Table 1. The specific gravity of the particles was measured as 2.51 by EPRI (2013). The ash is a non-plastic material with a liquid limit between 21 and 25%. Most laboratory testing did not reveal a plastic limit, indicating the material transitions from "liquid" to semi-solid behavior with a small change in water content. The vertical coefficient of consolidation, C_V, was measured as 0.6 cm^2/s during incremental loading consolidation tests. Based on triaxial compression testing, the ash has a critical state friction angle, ϕ_{cs}, of 25.4°. Additionally, the maximum dry unit weight and the optimum water content are 13.9 kN/m^3 and 20.8% based on the Standard Proctor compaction procedure.

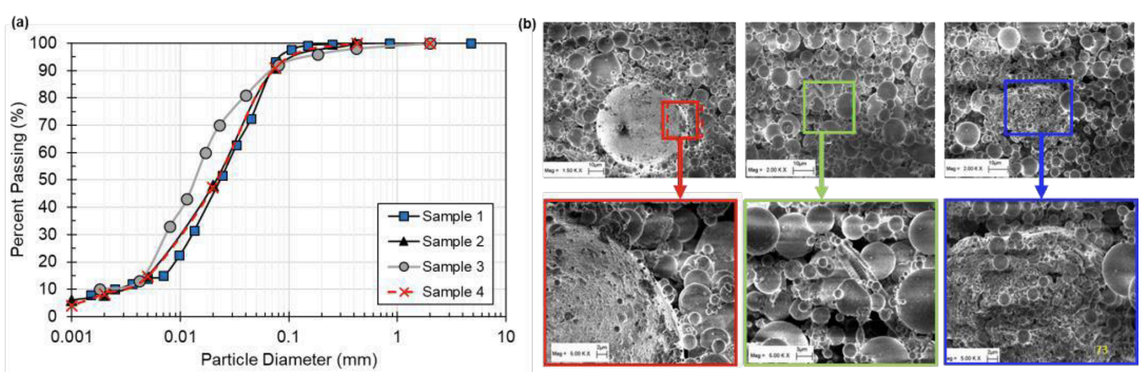

Figure 1: (a) Grain size distribution and (b) SEM images of tested fly ash.

Table 1: Properties of tested fly ash as reported in EPRI (2012, 2013, 2014, 2015, and 2020).

Property	Value	Property	Value
pH	7 to 10	Coefficient of Curvature, Cc	1.1
Calcium Content (%)	1.4	Liquid Limit, L_L (%)	21 to 25
Specific Gravity, G_s	2.51	TX Critical State Friction Angle, ϕ_{cs} (°)	25.4
10th Percentile Particle Size, D_{10} (mm)	0.003	Consolidation Coefficient, C_V (cm^2/s)	0.6
50th Percentile Particle Size, D_{50} (mm)	0.021	Proctor Optimum Water Content (%)	20.8
Coefficient of Uniformity, C_U	8.5	Proctor Maximum Dry Unit Weight (kN/m^3)	13.9

2.2 *Centrifuge modeling of impoundment runout*

Centrifuge modeling is an effective tool for geotechnical engineers to investigate the behavior of soils and of soil-structure interaction problems using reduced scale models. By spinning a reduced scale model in a geotechnical centrifuge, the body forces within the model are increased by the applied centrifugal acceleration. This offers the benefit of matching the magnitude and distribution of soil effective stresses that are relevant for the field application in a scaled model. For example, the effective stress at a depth of 10 m in a soil deposit with a buoyant unit weight of 10 kN/m^3 is 100 kPa (i.e. 10 m × 10 kN/m^3 = 100 kPa). This same stress magnitude can be reached in a centrifuge model subjected to an acceleration of 60 times Earth's gravity (N = 60g) composed of the same soil but with a depth of 0.167 m (i.e. 0.167 m × 10 kN/m^3 × 60 = 100 kPa). Centrifuge modeling has been used to investigate the static and dynamic behavior of slopes and embankments, shallow and deep foundations, dams, and tunnels (e.g. Mason et al. 2013; Nova Roessig & Sitar 2006) as well as debris flows (e.g. Bowman et al. 2010). These investigations have helped further the understanding of the soil behavior and governing processes as well as the possible consequences of failures (i.e. deformations, settlements). Centrifuge modeling has also been used to validate the predictions of numerical models used to make decisions on remediation alternatives for possible failure modes (e.g. Chou et al. 2011).

Scaling laws for centrifuge modeling have been developed for a wide range of physical phenomena (e.g. Garnier et al. 2007). In geotechnical centrifuge modeling, the full-scale structure being modeled is typically referred to as the "prototype" and the actual small-scale model is referred to as the "model"; this nomenclature is adopted throughout this paper. The following are relevant to the fly ash runout experiments presented herein:

$$L_P = NL_M \quad (1)$$

$$Z_P = NZ_M \quad (2)$$

$$t_P = Nt_M \quad (3)$$

$$v_P = v_M \quad (4)$$

$$V_P = N^3V_M \quad (5)$$

where N = centrifuge scaling (applied acceleration/Earth's gravity), L = length dimension, Z = depth, t = time, v = velocity, V = volume, and the subscripts $_P$ and $_M$ refer to the prototype and model scales, respectively. As shown, length, depth, and time scale linearly with N, velocity is independent of N, and volume scales with N^3. It is noted that the scaling law for time considered here is that for inertial processes. Throughout this papers, the dimensions are presented in prototype scale.

To perform the centrifuge experiments, a novel container was designed and constructed at the UC Davis CGM, as shown schematically in Figure 2a. The centrifuge container for runout experiments was designed to simulate a failure due to a sudden loss of lateral confinement, which is an idealization of a rapid failure of a containment facility such as a dam that would lead to a loss of lateral support of the impoundment. The container consists of a rectangular sub-container to hold a soil deposit, two gates that can be opened to induce a runout failure, and a runout basin to collect the runout material. The front face of the deposit consists of the two gates that can be swung open along hinged connections. During the spin-up process (i.e. increase of N), the gates are sealed with rubber o-rings and held shut by a pin. Once the desired g-level is reached and the system reaches equilibrium, the gates can be opened by lifting the pin with two additional pneumatic rotary actuators used to accelerate the door opening. A detailed description of the container is presented in Madabhushi et al. (2022a).

The sub-container has dimensions of 40.0 m in length, 27.6 m in width, and up to 24.0 m in height at 60 g (model dimensions: 0.67 m in length, 0.46 m in width, and up to 0.4 m in height) and the runout basin has dimensions of 73.8 m in length and 58.8 m in width at 60 g (model dimensions: 1.23 m in length and 0.98 m in width). The container also has a dewatering valve located at the bottom of the back wall. This valve was temporarily opened at 60 g to lower the water table to the desired level prior to opening the gates. Pore pressure transducers were used to determine the water table elevation prior to opening the gates. Two blocks of molding clays were added to dampen the impact of the gates against the tray's side walls (Fig. 2b).

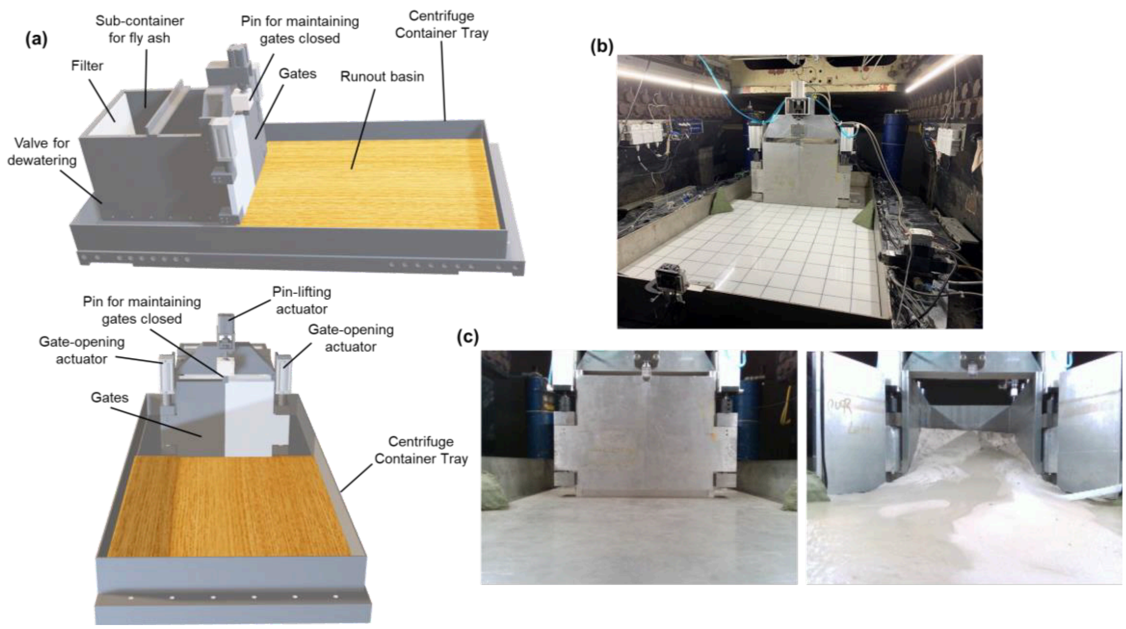

Figure 2: (a) 3D drawing of centrifuge container for runout tests, and photographs of (b) container prior to opening gates and (c) photographs of commissioning tests on loose sand before and after gate opening.

2.3 *Instrumentation and testing sequence*

The centrifuge specimens were instrumented with pore pressure sensors used to monitor the water table location prior to inducing a failure, high frame rate cameras to monitor the progression of the failure, CPT probes, and dielectric constant / electrical conductivity moisture probes. However, it is noted that measurements from the lattermost instrument are not presented in this paper. The testing sequence of the runout centrifuge tests consisted of the following steps: (1) place of sensors into the fly ash sub-container, (2) deposit of fly ash slurry into sub-container (as described in Section 3), (3) load container into centrifuge arm, (4) progressive swing up in four stages, i.e. 10 g, 20 g, 40 g, and 60 g, (5) open drainage valve at the base of the container to bring the water table just below the ash surface, (6) perform two CPT soundings at penetration rates of 100 mm/s and 2 mm/s to obtain undrained and drained penetration resistances, (7) open the gates, (8) observe fly ash runout using high frame rate cameras, and (9) swing down.

3 FLY ASH SEDIMENTATION

To simulate the sluicing process typically employed in the field to fill fly ash and other waste ponds, the specimens for centrifuge testing were prepared by depositing slurry in the sub-container. This procedure is intended to reproduce the depositional processes involved in the formation of a pond which likely influence the microstructure of the deposit. After the slurry is deposited, the model is self-weight consolidated, first at 1 g and then progressively as the acceleration on the model is increased in the centrifuge (step 3 of procedure described in Section

2.3). However, it is noted that this process does not model the heterogeneities at greater scales that result from the sluicing process (i.e. formation of beaches and interlayering) nor does it include any chemical effects associated with specific power station sluice waters or aging effects that might result from decades of operation.

The dry unit weight and water content of a slurry or a consolidated deposit are related to one another by the Zero Air Voids (ZAV) line if the material is saturated. However, a preliminary investigation revealed that the initial water content of the slurry had an important effect on the resulting water content and dry unit weight of a self-weight consolidated specimen. Namely, wetter slurries consolidated to specimens with greater water contents and smaller dry unit weights. The results of this test series are shown in Figures 3a and 3b, which highlights this trend between initial slurry water content and settled water content and dry unit weight.

The centrifuge experiments were performed on two specimens of different initial unit weights. To prepare a specimen with a smaller density, a slurry with an initial water content of 225% was used (Fig. 3a). To fill the fly ash sub-container with the desired height of sedimented ash, five lifts of slurry were required. Each fly ash lift was composed of ash particles mixed with deionized water to the target water content, which were mixed in 5-gallon buckets using a hand-held drill (Fig. 4a). After slurry pouring and settling of all solids at 1g, which took about five days, and subsequent application of 60 g in the centrifuge, the water content and dry unit weight of the loose deposit were 37.2% and 11.6 kN/m^3, respectively (Fig. 3b, Table 2). To prepare a denser specimen, a slurry with an initial water content of 40% was used. The ash particles were mixed with deionized water content in an industrial mixer (Fig. 4c) and deposited through a hose onto the fly ash sub-container (Fig. 4d). At 60 g, the water content and dry unit weight of the dense specimen were 24.7% and 14.2 11.6 kN/m^3, respectively (Fig. 3b, Table 2). The procedures described above used to prepare soil deposits successfully reproduced the range of dry unit weights and water contents obtained from samples from a pond composed of the same ash. The field measurements, reported by EPRI (2020) show a range in dry unit weight between 10 and 16 kN/m^3 and a range in water contents between 45 and 20% (Fig. 3c).

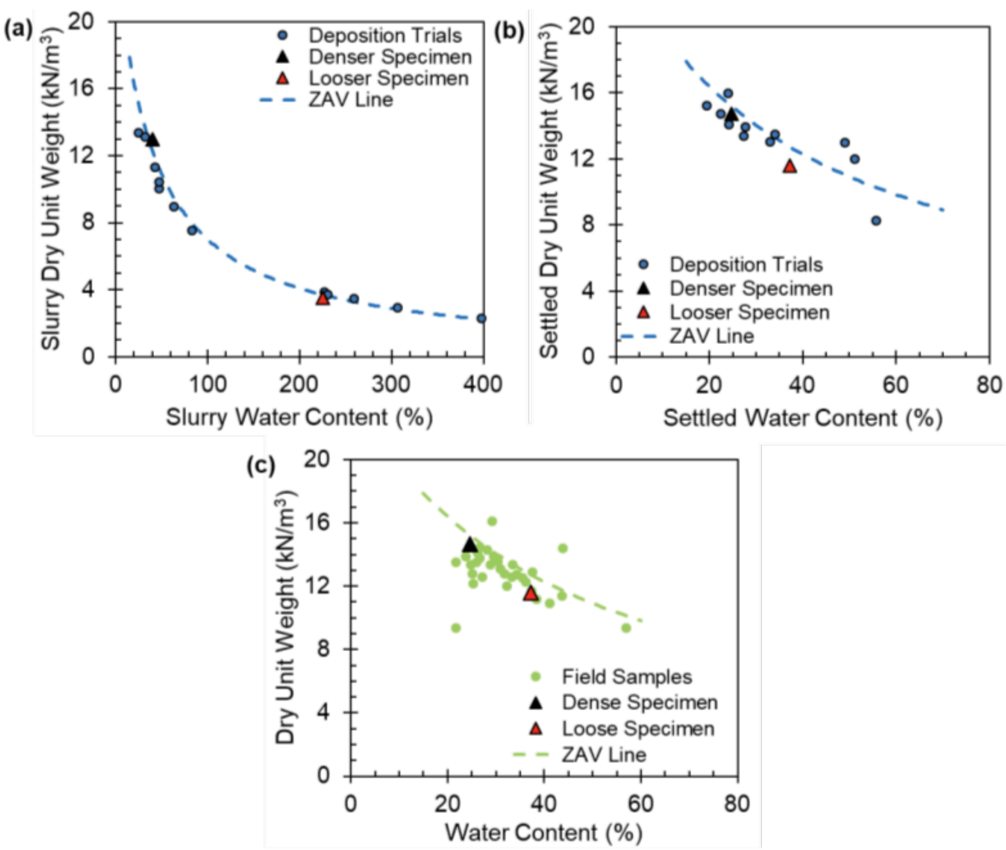

Figure 3: Dry unit weight and water content for (a) slurries and (b) settled specimens. (c) Dry unit weights and water contents of loose and dense specimens compared to in-situ measurements.

Figure 4: (a) Mixing and (b) deposition of slurry for preparation of the loose specimen. (c) Mixing and (d) deposition of a slurry for preparation of the dense specimen.

Table 2: Properties of dense and loose specimens.

Specimen	Water Content at 60g (%)	Dry Unit Weight at 60g (kN/m^3)	Impoundment Height, H_I (m)	Water Table Height, H_{WT} (m)	H_{WT}/H_I	Type of Failure
Dense	24.7	14.7	22.1	21.2	0.96	Slope insta-bility
Loose	37.2	11.6	18.8	18	0.96	Flow failure

4 CENTRIFUGE IMPOUNDMENT RUNOUT TESTS

The results of two centrifuge tests performed at 60 g are presented in this paper. This section first provides a description of the specimens' initial conditions. Then, the results and interpretation of drained and undrained CPT soundings performed before the failure are presented which provide more detailed information of the deposits' properties and expected behavior. Finally, this section provides a description of the observed failures along with measurements of runout distance which highlight the effects of initial density on the failure type and runout behavior.

4.1 *Specimens' initial conditions*

Details of the specimens is presented in Table 2. The dense specimen had an average water content and dry unit weight at 60 g of 24.7% and 14.7 kN/m^3, respectively. The deposit had a prototype height (H_I) of 22.1 m. Once the model had been spun to 60 g, the water table was lowered to a height (H_{WT}) of 21.2 m prior to inducing the failure, leading to a ratio of water table height to impoundment height (H_{WT}/H_I) of 0.96. The loose specimen had an average water content of 37.2% and an average dry unit weight of 11.6 kN/m^3. The H_I, H_{WT}, and H_{WT}/H_I for this specimen were 18.8 m, 18.0 m, and 0.96, respectively. As described in more detail in Section 4.3, the dense specimen exhibited a slope instability failure while the loose specimen showed a flow failure. Based on these initial conditions, distributions of total stress, pore water pressure, and effective stress were calculated, as presented in Figure 5a and 5b. As shown, the effective stress magnitudes in the loose deposit are smaller owing to its smaller total unit weight.

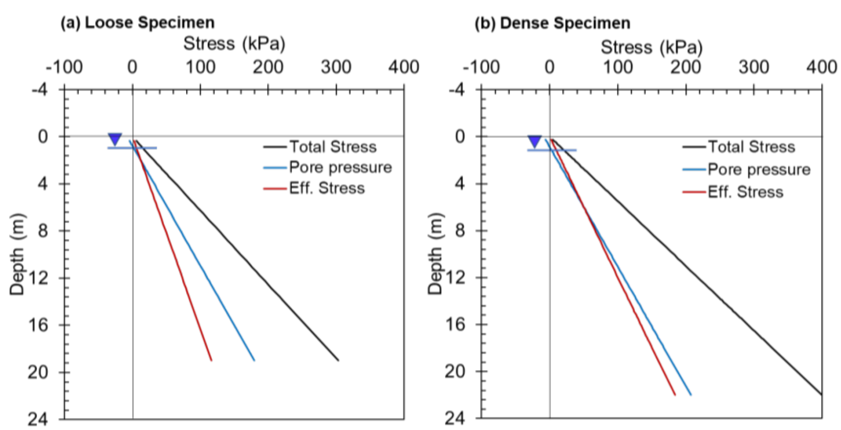

Figure 5: Total and effective stress and pore pressure distributions for (a) loose and (b) dense specimens.

4.2 *Cone Penetration Tests performed prior to containment release*

Cone penetration tests were performed in the centrifuge using a miniature CPT probe at penetration rates of 100 mm/s (i.e. fast) and 2 mm/s (i.e. slow) prior to inducing the failure. These CPT soundings were performed with the goal of obtaining undrained and drained penetration resistances ($q_{c,undrained}$ and $q_{c,drained}$). The penetration rates were determined based on the normalized penetration velocity framework described by DeJong and Randolph (2012), where the normalized velocity $V = vd/C_V$, where v is the penetration rate and d is the diameter of the probe. The authors report that V values greater than about 20 result in undrained penetration while values smaller than 2 result in drained penetration. Considering the penetration rates of 100 mm/s and 2 mm/s, a CPT probe diameter of 10 mm, and a fly ash C_V of 0.6 cm^2/s, the V values are calculated as 16.7 and 0.33 for the fast and slow CPTs, respectively, which are. considered throughout this investigation to correspond to $q_{c,undrained}$ and $q_{c,drained}$ values.

The deposits' density had an important effect on the measured tip resistances, as the values measured in the loose specimen were considerably smaller than those measured in the dense specimen, as shown in Figures 6a and 6b. For the loose specimen, the undrained q_c values were considerably smaller than the drained q_c values. At a depth of 10 m, the undrained q_c was about 0.2 MPa while the drained q_c was about 1.2 MPa. In contrast, the dense specimen exhibited greater undrained q_c than drained q_c, with values of about 4 MPa and 2.8 MPa, respectively.

The $q_{c,undrained}$ values were used to estimate profiles of undrained shear strength (S_u), where $S_u = (q_c-\sigma_v)/N_k$, and N_k is the cone factor which was taken as 20.0 for the interpretation presented here. The S_u values for the loose specimen increased quasi-linearly with depth and ranged between 2 and 16 kPa. The dense specimen exhibited larger S_u values that ranged between 150 and 250 kPa. The S_u values were used to calculate undrained shear strength to consolidation effective stress ratios (S_u/σ'_v). The S_u/σ'_v profiles for both specimens are shown in Figure 7a. The loose specimen shows S_u/σ'_v values of about 0.6 at shallow locations which decrease with depth to a value of about 0.12. The dense deposit shows large S_u/σ'_v at shallow locations, as high as 6.0. At depths greater than 12 m, S_u/σ'_v appears to converge to a value of about 2.0.

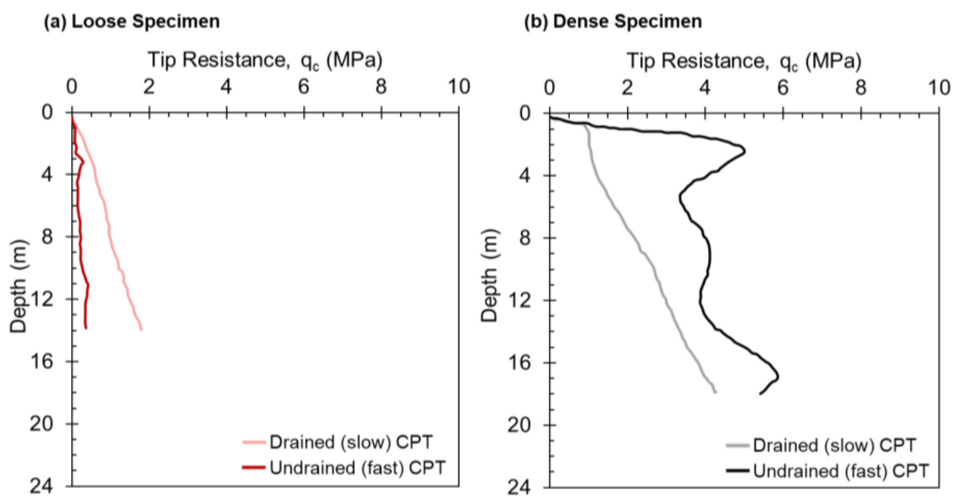

Figure 6: Drained (slow) and undrained (fast) CPT soundings in (a) loose and (b) dense specimens.

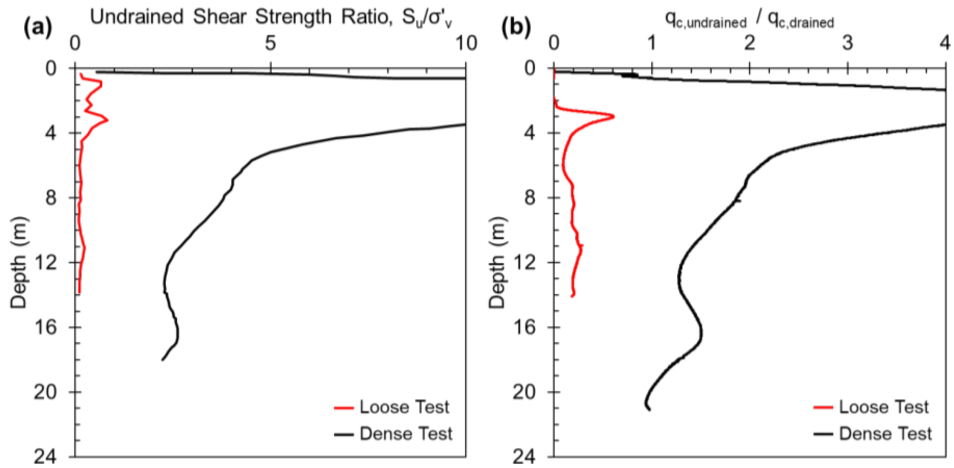

Figure 7: (a) Undrained shear strength ratio (S_u/σ'_v) and (b) ratio of undrained to drain tip resistance ($q_{c,undrained}/q_{c,drained}$) for the loose and dense specimens.

The differences in $q_{c,undrained}$ and $q_{c,drained}$ for a given specimen have been shown by Madabhushi et al. (2022b) to relate to the runout behavior of fly ash impoundments tested in the centrifuge. Using an interpretation based on critical state soil mechanics, it can be deduced that smaller $q_{c,undrained}$ than $q_{c,drained}$ values indicates the generation of positive excess pore pressures during penetration, suggesting a contractive behavior. Conversely, greater $q_{c,undrained}$ than $q_{c,drained}$ values indicates the generation of negative excess pore pressures, suggesting a dilative behavior. As discussed by Robertson (2010) and Been (2016), contractive soil behavior is associated with greater sensitivity, brittleness, and liquefaction potential. Differences in the penetration resistances are captured here using the $q_{c,undrained}/q_{c,drained}$ ratio (Fig. 7b). The loose specimen has values smaller than 1.0 while the dense specimen has values as high as 4.5 at shallow locations and values close to 1.0 at a depth of 20 m. As discussed in the following section, the smaller. ratios measured in the loose specimen are in agreement with the observed flow failure.

4.3 *Runout behavior and failure progression*

The runout behavior of the saturated deposits was greatly influenced by their initial dry unit weight and water content. As previously described, failure of the deposits was induced once the centrifuge was swung up to 60 g and the model reached equilibrium. Upon opening the gates, the loose specimen exhibited a flow failure. The failure progression suggests that static liquefaction within the deposit took place, leading to the rapid flow of material. Figure 8 presents a series of photographs taken during the first 10 seconds of the failure, showing the rapid movement of the material as well as the large volume of soil that exited the sub-container. During the failure, a total volume of 15673 m^3 of fly ash has exited the container, constituting 76% of the deposit's initial volume. The slope of the material along the runout basin was smaller than 0.5°. It is noted that a reliable measurement of the total runout distance was not able to be obtained because the material ran against the container's end tray.

The dense specimen exhibited a slope instability failure. The material runout velocity as well as the volume of material exited and the runout distance were considerably smaller for the dense specimen, as shown in Figure 9. Immediately after opening the gates, the portion of the deposit closest to the gates slid and crumbled. As time progressed, tension cracks were developed behind the scarp, eventually leading to failure and sliding of two additional portions of the deposit. Large blocks of material are visible at locations that were initially shallow which were formed due to suction developed as the material desaturated. Once the material stopped moving, a near-vertical face was formed at a distance of about 20 m behind the original location of the gates. The material that exited the sub-container settled at an average angle of 20.6°. At the end of the test, the runout distance was 37.8 m and a volume of 5939 m^3 had exited the fly ash sub-container, constituting about 25% of the deposit's initial volume.

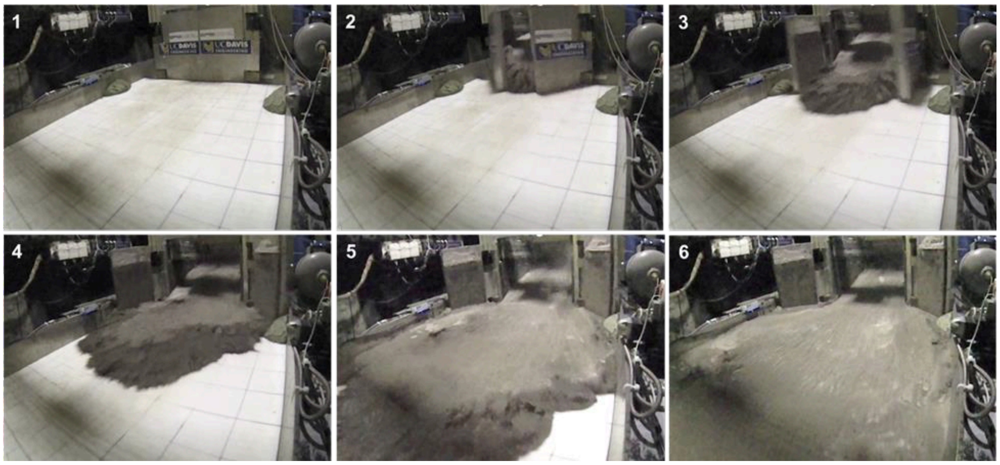
Figure 8: Series of photographs during the first 10 seconds of the failure of the loose specimen.

The footage from the high frame rate cameras was used to obtain measurements of runout distance as a function of time, as shown in Figures 10a and 10b for the loose and dense specimens, respectively. These results highlight the differences in failure type and runout behavior, where the runout front for the loose specimen moved at an average velocity of 11.6 m/s for the first 4.7 seconds then decreasing to a value of 5.8 m/s. In contrast, the runout front for the dense specimen moved at an average velocity of 0.9 m/s for the first 10 seconds, then reducing to a very small value of 0.004 m/s. This continued, slow movement is likely due to water flowing out of the material and its associated seepage forces and loss of suction.

The types of failure observed in the centrifuge tests appear to be representative of those. observed in the field. For example, the failure of the TVA Kingston pond in Tennessee in 2008 resulted in large amounts of material exiting the pond and flowing by large distances. The failing mass came to rest to a slope with an angle of less than 0.5° (Walton & Butler 2009). These observations are in agreement with shown by the loose centrifuge test. Portions of the Kingston pond were also reported to form large blocks of seemingly strong material and a near-vertical face was formed at the back of the failure surface. These types of failure modes are in agreement with those observed in the dense centrifuge test. It is noted that a range of failure modes was observed in the field due to spatial variability in material types and properties; these factors were not considered in the centrifuge testing program described herein.

Figure 9: Photograph of failed dense specimen.

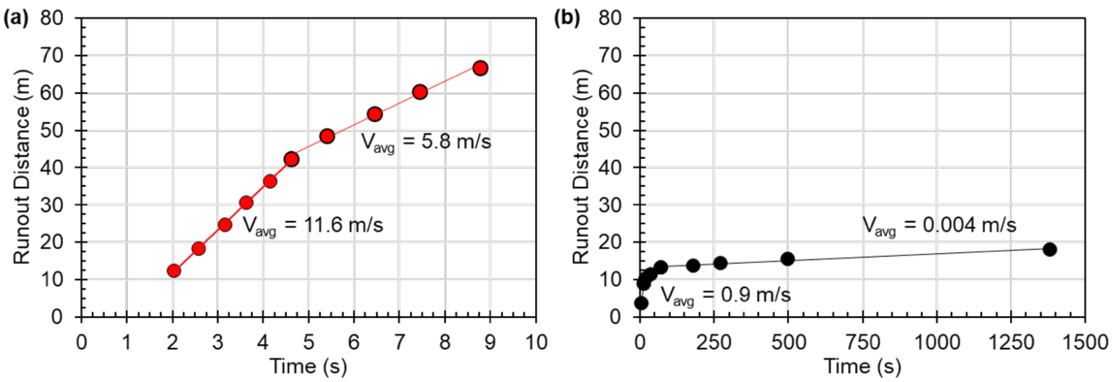

Figure 10: Runout distance as a function of time for the (a) loose specimen and (b) dense specimen (note different x-axis ranges in the figures).

5 CONCLUSIONS

This paper presents the results of two runout centrifuge tests performed on saturated fly ash impoundments with prototype heights between 18.8 and 21.2m (model heights between 0.31 and 0.35 m). The runout experiments were performed with a newly developed container which simulated a rapid failure due to a sudden loss of confinement. The centrifuge tests also included CPT soundings performed prior to inducing the failure.

An investigation on the sedimentation of fly ash revealed a relationship between slurry initial water content and self-weight consolidated water content of fly ash model deposits. Namely, specimens that were deposited with wetter slurries consolidated to greater water contents and smaller dry unit weights. Specifically, to the experiments presented in this paper, a specimen that was prepared with a slurry with a water content of 225% consolidated at 60 g to a water content of 37.2% and a dry unit weight of 11.6 kN/m^3, while a specimen prepared with a slurry of 40% consolidated to a water content of 24.7% and a dry unit weight of 14.2 kN/m^3.

The results of the centrifuge tests indicate that deposits with greater initial water contents and smaller initial dry unit weights are more susceptible to static liquefaction and flow failure in the event of a loss of confinement, leading to greater runout distances and volumes of flowing material. Namely, the 76% of the initial volume of the loose specimen ran out at velocities between 11.6 and 5.8 m/s. In contrast, only 25% of the initial volume of the dense specimen exited at a maximum velocity of 0.9 m/s. These trends are in agreement with expectations based on critical state soil mechanics and general soil behavior and supported by the CPT soundings, indicating that looser deposits have smaller undrained shear strength than dense deposit.

The failure modes observed in the centrifuge experiments appear to be representative of those reported in field failures (e.g. Kingston). These failure modes range from flow failure with large, rapid deformations to the formation of large blocks and near-vertical faces in desaturated zones of ponds. However, there are important aspects that should be considered in future investigations, including the physical and chemical processes involved in ash sedimentation from slurries, quantification of the effects of dewatering and thickening on the properties of ponded ash, and the interactions of a deposit with a failed containment structure such as a dam and downstream terrain features.

6 ACKNOWLEDGEMENTS

This material is based upon work supported in part by the Electric Power Research Institute (EPRI). Any opinions, findings, and conclusions or recommendations expressed in this material are those of the author(s) and do not necessarily reflect those of EPRI.

7 REFERENCES

ACAA. 2020. *2019 CCP Survey Results*. https://acaa-usa.org/wp-content/uploads/coal-combustion-products-use/2019-Survey-Results.pdf

Been, K. 2016. Characterizing mine tailings for geotechnical design. In Lehane et al. (ed.), *Geotechnical and Geophysical Site Charact., Queensland, 5-9 September 2016*, Sydney: Australian Geomech. Soc.

Bowman, E.T., Laue, J., Imre, B., & Springman, S.M. 2010. Experimental modelling of debris flow behaviour using a geotechnical centrifuge." *Canadian Geotechnical Journal* 47(7): 742–762.

Chou, J.C., Kutter, B.L., Travasarou, T., & Chacko, J.M. 2011. Centrifuge modeling of seismically induced uplift in the BART transbay tube. *Journal of Geotechnical and Geoenvironmental Engineering* 137(8): 754-765.

DeJong, J.T. & Randolph, M.F. 2012. Influence of partial consolidation during cone penetration on estimated soil behavior type and pore pressure dissipation measurements. *Journal of Geotechnical and Geoenvironmental Engineering* 138(7): 777–788.

Electric Power Research Institute. 2012. *Geotechnical Properties of Fly Ash and Potential for Static Liquefaction: Volume 1 – Summary and Conclusions*. EPRI, Palo Alto, CA. Report #1023743.

Electric Power Research Institute. 2013. *Embankment Loading on Saturated Coal Ash: Centrifuge Demonstration Test*. Palo Alto, CA. Report #3002001146.

Electric Power Research Institute. 2014. *Engineering Correlations for Geotechnical Parameters for Ponded Fly Ash*. Palo Alto, CA. Report #3002001151.

Electric Power Research Institute. 2015. *Centrifuge Models of Embankment Failures on Saturated Coal Ash.* Palo Alto, CA. Report # 3002006290.

Electric Power Research Institute. 2020. *Evaluation of Fly Ash Diagenesis Potential*. Palo Alto, CA. Report # 3002016517.

Garnier, J., Gaudin, C., Springman, S., Culligan, P. J., Goodings, D., Konig, D., Kutter, B.L., Phillips, R., Randolph, M. F., & Thorel, L. 2007. Catalogue of scaling laws and similitude questions in geotechnical centrifuge modelling. *International Journal of Physical Modelling in Geotechnics* 7(3): 1-23.

Madabhushi, S.S.C., Martinez, A., Wilson, D.W., & Kutter, B.L. 2022a. Design and instrumentation of a novel centrifuge container for fly ash run-out experiments. In review for *International Journal of Physical Modelling in Geotechnics*.

Madabhushi, S.S.C., Follett, S.B., Martinez, A., Wilson, D.W., & Gallagher, B. 2022b. Investigating the use of centrifuge modeling and miniature CPTs to characterize the run-out behavior of fly ash. In press in Athhanasopoulos-Zekkos et al. (ed.) *GeoCongress 2022, Charlotte, 20-23 March 2022,* Reston American Society for Civil Engineers.

Mason, H.B., Trombetta, N.W., Chen, Z., Bray, J.D., Hutchinson, T.C. & Kutter, B. L. 2013. Seismic soil-foundation-structure interaction observed in geotechnical centrifuge experiments. *Soil Dynamics and Earthquake Engineering* 48:162-174.

Minkara, R. 2020. Ten Things You Didn't Know About Fly Ash. *Ash At Work* 2.

Nova Roessig, L. & Sitar, N. 2006. Centrifuge model studies on the seismic response of reinforced soil slopes." *Journal of Geotechnical and Geoenvironmental Engineering* 132(3): 388-400.

Robertson, P.K. 2010. Evaluation of flow liquefaction and liquefied strength using the cone penetration test. *Journal of Geotechnical and Geoenvironmental Engineering* 136(6): 842-853.

US Environmental Protection Agency. 2014. *Coal Combustion Residuals Impoundment Assessment Reports* https://www.epa.gov/sites/default/files/2016-06/documents/ccr_impoundmnt_asesmnt_rprts.pdf

Walton, W.H. & Butler, W. 2009. Root cause analysis of TVA Kingston dredge pond failure on December 22, 2008. *AECOM,* Vernon Hills, IL, June 25.

Characterization and evaluation of the undrained shear strength of a bauxite mine tailings

Guilherme H.S. Pinto & Mauro P. Santos Jr.
Pimenta de Ávila Consultoria, Nova Lima, Minas Gerais, Brazil

Hugo A. Brandão
Pimenta de Ávila Consultoria, Nova Lima, Minas Gerais, Brazil

Hugo M. Resende
Pimenta de Ávila Consultoria, Nova Lima, Minas Gerais, Brazil

ABSTRACT: The correct determination of the geotechnical properties of mine tailings is of fundamental importance in order to accurately determine the safety of a tailings dam. Commonly, the determination of the undrained shear strength will greatly rely on field investigations, such as CPTu and the Field Vane Shear Test, or laboratory test, like the undrained triaxial compression test. The objective of this paper is to compare different methodologies to evaluate the undrained shear strength of a bauxite mine tailings using field assessment (CPTu and Vane Shear Test) and laboratory tests (i.e., Isotropically Consolidated Undrained Triaxial Compression Test - CIUC). Based on CPTu data different methodologies (empirical and analytical) were evaluated in order to determine the undrained shear strength using the bearing capacity factors N_{kt}, N_{ke} and $N_{\Delta u}$. The results obtained were compared with the Vane Shear Test and the CIUC. Furthermore, the site-specific calibration of the bearing factors (N_{kt}, N_{ke} and $N_{\Delta u}$) to the triaxial compression mode was performed.

1 INTRODUCTION

The correct determination of the strength parameters of a soil is highly important in the context of geotechnical engineering since these are crucial aspects for evaluating the stability of a geotechnical structures. If the geotechnical parameters, such as the undrained strength or stiffness, are not correctly determined, there will be a risk of over-dimensioning a geotechnical structure or, which is even of greater concern, one can dimension a structure that will not present enough resilience against the expected load that the structure will face throughout its life cycle. The importance of the physical and chemical characterization of the tailings is also highlighted in the Global Industry Standard on Tailings Management – GISTM (GISTM, 2020).

Case histories of recent failures of tailings storage facilities, like Brumadinho and Mount Polley, demonstrate the importance of a proper understanding of the mechanical behavior of the soils to evaluate the possibility of undrained shear failure (especially where brittle behavior could be expected) and to correctly determine the strength parameters.

To characterize the tailings' geotechnical behavior, one can use different methodologies including field and laboratory tests. Among the field tests commercially available, the Vane Shear Test and the Cone Penetration Test (CPTu) are the ones most often used to determine important properties such as the shear strength and for understanding the in situ of pore pressures profile. As describe by Brown & Gillani (2016), most of the in-situ tests provide only an indirect estimation of shear strength parameters, by using correlations that are predominately developed for natural soils (sedimentary or residual). Since tailings are a by-product of mining with certain unique characteristics, such as geochemistry, angularity, and compressibility, the applicability of the correlations must be evaluated for site specific conditions. Also, the authors, recommend, when possible, to collect high-quality undisturbed samples to perform laboratory tests, such as the isotopically consolidated triaxial test (CIDC/CIUC) or direct simple shear (DSS) to directly measure the shear strength or stiffness parameters.

The CPTu tests are internationally recognized as one of the most important geotechnical in situ tests (Schnaid and Odebrecht, 2012). The test consists of a 60º cone penetrometer pushing equipment and a data acquisition system. The standard test uses a cone with a cross-sectional area of 10 cm² and a 150 cm² friction sleeve located above the cone. The cone penetration is usually carried out with a speed of 2.0±0.5cm/s, with readings being recorded every 1cm to 5cm. This field assessment usually provides three main parameters: i) the cone tip resistance (q_c), which characterizes the soil resistance to cone penetration, ii) the sleeve friction (f_s), which represents the soil adhesion to the friction sleeve and iii) the penetration porewater pressure, commonly measured behind the cone tip (u_2).

In conjunction with the CPTu test, it is also common to perform pore pressure dissipation tests, to determine the in-situ equilibrium pore pressure (u_0). The dissipation test consists of a pause in penetration, followed by the measurement of the pore pressure with time. Using the equilibrium pore pressure relative to its depth is possible to evaluate the in-situ pore pressure regime, allowing the correctly characterize the stress state, which governs the soil's strength and deformability. As described by Martin (1999) in Figure 1, the in-situ pore pressure can be categorized into 6 different regimes.

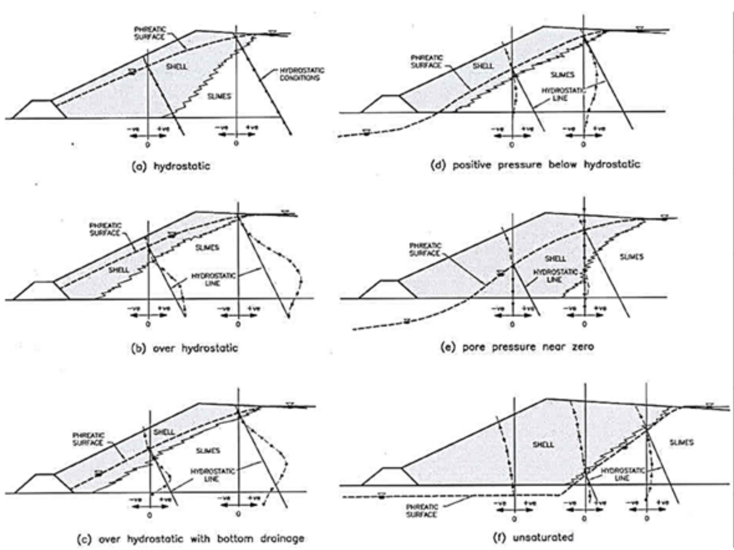

Case	Comments
(a) Hydrostatic	Essentially horizontal seepage flow
(b) Over hydrostatic	Under-consolidated condition
(c) Over hydrostatic with bottom drainage	Under-consolidated condition with double drainage conditions
(d) Positive pressure below hydrostatic	Under-consolidated with vertical seepage or fully consolidated with horizontal and vertical seepage components
(e) Pore pressure near zero	Fully consolidated condition with downward seepage due the bottom drainage
(f) Unsatured	Unsaturated conditions (arid climates)

Figure 1. In situ pore pressure (Martin, 1999).

The undrained shear strength (S_u) can be defined as the soil resistance in a saturated or nearly saturated condition, which is mobilized under a fast loading without allowing time for the soil to change its volume (Lunne et al., 1997). The S_u can be calculated by the CPTu using three independent equations, that rely on the bearing capacity factors: i) for net tip resistance, N_{kt} (Equation 1), ii) for excess porewater pressure, $N_{\Delta u}$ (Equation 2) and iii) for effective cone resistance N_{ke} (Equation 3).

$$S_u = \frac{q_t - \sigma_{v0}}{N_{kt}} \quad (1)$$

q_t – Corrected cone resistance (Equation 4);
σ_{v0} – Total Vertical stress.

$$S_u = \frac{u_2 - u_0}{N_{\Delta u}} \quad (2)$$

u_2 – Penetration porewater pressure (behind the cone tip);
u_0 – Equilibrium porewater pressure obtained from the dissipation test;

$$S_u = \frac{q_t - u_2}{N_{ke}} \quad (3)$$

Different methodologies can be found in the literature to determine the bearing capacity factors, such as Battaglio et al. (1981), Karlsrud et al. (2005), Mayne (2016), Mayne and Peuchen (2018), Agaiby and Mayne (2018), and others. As shown by Herza et al. (2017), the change in the bearing capacity factor, represented by the N_{kt} in Figure 2, as well as the unit weight, will have relevant changes in the factor of safety of the structure.

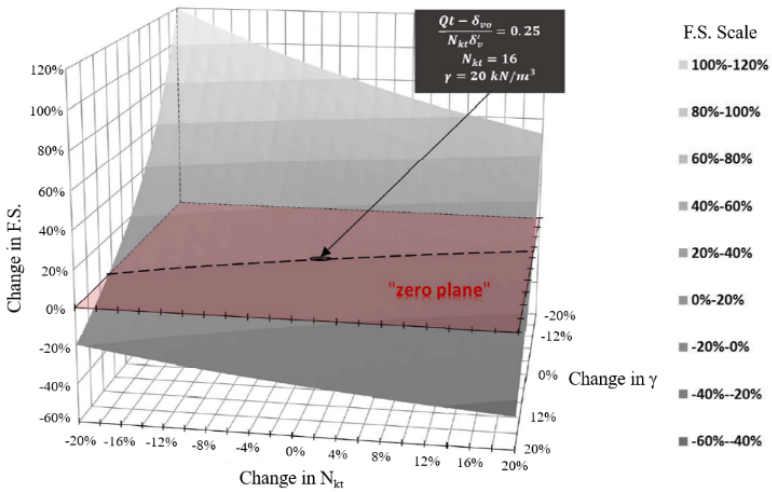

Figure 2. F.S. variations due the Nkt and the unit weight (γ) (Herza et al., 2017).

The Vane Shear Test is the equipment used to determine the undrained shear strength in clay deposits (Schnaid and Odebrecht, 2012). To evaluate the S_u, the Vane Shear Test consists of the rotation of a set of cruciform rectangular blades pushed to pre-defined depths, which can be performed with the blade driven directly into the ground (test type A) or with previous drilling (test type B). The blade's rotation must be controlled, requiring 6±0.6º/min to mobilize an undrained behavior in the tested clay, avoiding the dissipation of the excess porewater pressure generated during the shear as described by the Brazilian standard NBR 10905 (ABNT, 1989).

Finally, in complement of the field assessment, it is understood as best practice to perform laboratory tests, such as the Isotropically Consolidated Undrained Triaxial Compression Test (CIUC), which is standardized by the ASTM D4767:11 (2020). The CIUC test is used to determine the shear strength and stiffness of the soil by axial compression of a soil sample and can be divided into two parts: (i) consolidation phase, usually performed at different stresses that are of interest to the project and; (ii) the shear phase which drives the soil to failure by applying axial loading.

2 METHODOLOGY

To evaluate the bauxite tailings' undrained shear strength (S_u), laboratory and field tests were performed. The field assessment was conducted using the CPTu with dissipation test and the Vane Shear Test. To complement the in-situ characterization, Isotropically Consolidated Undrained Triaxial Compression Tests (CIUC) were performed and considered as the most appropriate mode of shear failure for this material. Also, samples were collected in depth near the CPTu and Vane Shear Test to determine the Solids Content (S.C.) and the unit weight.

The CPTu test was performed following the criteria defined by ASTM D5778 (2020). Following the recommended practice, the porewater pressure measurement was recorded behind the cone, in the u_2 location. The soil behavior-type index was determined using the methodology proposed by Been and Jefferies (1992) and the tailings behavior discussed.

The undrained shear strength determined by the CPTu test was calculated based on the bearing capacity factor, using Equations 1 to 3 presented by Lunne et al. (1997). Such bearing capacity factors were determined by different authors as detailed in the next items. Also, the bauxite tailings' consolidation was evaluated quantitatively using a hybrid formulation of spherical cavity expansion and critical state soil mechanics framework (SCE-CSSM) presented by Agaiby and Mayne (2018) and qualitatively by the methodology proposed by Martin (1999).

The Vane Shear Test was performed following the Brazilian standard NBR 10905 (ABNT, 1989) measuring the yield shear strength and the remolded shear strength (shear strength under large deformations). Using both yield and remolded, it will be calculated the soil sensitivity (S_t), as defined by the ratio of the yield shear strength to the remolded shear strength. Also, the Vane Shear Test was performed next to the CPTu test, making it possible to compare results.

To compare the results of the field assessment, three samples of the bauxite tailings were collected and the CIUC tests were performed, using the confined pressures of 50kPa, 100kPa, and 200kPa. Using the laboratory test, the normally consolidated shear strength ratio based on the maximum deviatoric stress and the slope of the critical state line in the p' x q space (M_{tc}) was calculated.

2.1 *Cone Penetration Test with Pore pressure Measurement*

Using the CPTu data, the corrected cone resistance (q_t) values and the normalized porewater pressure parameter (B_q) were determined by using the Equations 4 and 5 respectively.

$$q_t = q_c + u_2(1 - a) \tag{4}$$

a – Cone area ratio, considered to be equal to 0.80.

$$B_q = \frac{u_2 - u_0}{q_t - \sigma_{v0}} \tag{5}$$

2.1.1 *Battaglio et al. (1981)*

Based on an extensive database, Battaglio et al. (1981) found a relationship between the normalized porewater pressure parameter and the bearing factor for excess porewater pressure as shown by Equation 6.

$$N_{\Delta u} = 4 + 6B_q \tag{6}$$

2.1.2 *Karlsrud et al. (2005)*

Using the B_q values and the soil sensitivity, Karlsrud et al. (2005) develop a methodology to calculate the N_{ke} values, as detailed in Equation 7, valid for sensitivity lower than 15 (S_t < 15), and N_{ke} > 2.0.

$$N_{ke} = 11.5 - 9.05B_q \tag{7}$$

2.1.3 *Mayne (2016)*

Based on the Spherical Cavity Expansion (SCE), Mayne (2016) develop Equation 8 (valid for $Bq \neq 1.0$) Equation 9 to determine $N_{\Delta u}$ and N_{ke}.

$$N_{\Delta u} = \frac{3.90}{\left(1/B_q\right) - 1} \tag{8}$$

$$N_{ke} = 2/M_{tc} + 3.90 \tag{9}$$

M_{tc} – slope of the critical state line in the p' x q space;

2.1.4 *Mayne and Peuchen (2018)*

Based on a database of 407 high-quality triaxial compression tests (CAUC), for a total of 62 different clays categorized into five groups based on their varying degrees of stress-history (ranging from fissured to sensitive clays), as well as for different test conditions (onshore and offshore), the researchers Mayne and Peuchen (2018) developed a relationship between B_q and the bearing factor for net tip resistance N_{kt}, expressed by the Equation 10.

$$N_{kt} = 10.5 - 4.6 \,.\, (B_q + 0.1) \tag{10}$$

2.1.5 *Agaiby and Mayne (2018)*

Agaiby and Mayne (2018) developed analytical equations to determine the overconsolidation ratio (OCR) and N_{kt} using SCE-CSSM. The methodology suggested by the authors proposes that the OCR (Equations 12 to 14) and the N_{kt} (Equation 15) are expressed as a function of the soil rigidity index (I_R), which can be determined using Equation 11.

$$I_R = \exp\left[\frac{1.5 + 2.925 \cdot M_{tc} \cdot a_q}{M_{tc} \cdot (1 - a_q)}\right] \tag{11}$$

I_R – Rigidity Index;

a_q – Slope of the chart made by u_2 - σ_{vo} (y-axis) versus q_t - σ_{vo} (x-axis).

$$OCR = 2\left[\frac{\left(2/M_{tc}\right) \cdot (q_t - \sigma_{vo})/\sigma'_{vo}}{4/3 \cdot (\ln I_R + 1) + \frac{\pi}{2} + 1}\right]^{\frac{1}{\Lambda}} \tag{12}$$

$$OCR = 2\left[\frac{1}{1{,}95 \cdot M_{tc} + 1} \frac{(q_t - u_2)}{\sigma'_{vo}}\right]^{\frac{1}{\Lambda}} \tag{13}$$

$$OCR = 2\left[\frac{(u_2 - u_0/\sigma'_{vo}) - 1}{2/3 \cdot M_{tc} \cdot \ln(I_R) - 1}\right]^{\frac{1}{\Lambda}} \tag{14}$$

σ'_{v0} – Vertical effective stress;

$$N_{kt} = 4/3 \cdot [\ln(I_R) + 1] + \pi/2 + 1 \tag{15}$$

The Λ parameter is the plastic volumetric strain potential ($1-C_s/C_c$). Herein it was adopted the value of 0.80, as recommended by Agaiby and Mayne (2018).

2.1.6 *Been and Jefferies (1992)*

Using a critical state framework, Been and Jefferies (1992) developed a soil behavior classification index (I_C). The I_C is calculated by Equation 16, using the normalized cone tip resistance (Q), Equation 17, the normalized sleeve friction (F), Equation 18 and the normalized porewater pressure parameter (Equation 5). The I_C range is detailed in Table 1.

$$I_c = \sqrt{\left[\left(3 - \log(Q(1 - B_q) + 1\right)^2 + (1.5 + 1.3\log F)^2\right]} \tag{16}$$

$$Q = \frac{q_t - \sigma_{v0}}{\sigma'_{v0}} \tag{17}$$

$$F = \frac{f_s}{q_t - \sigma_{v0}} \tag{18}$$

Table 1. Relationship between Soil Behavior-Type descriptions and I_C - Been and Jefferies (1992).

Zone	CPTu Index I_C	Soil Behavior Classification
6	$I_C < 1.80$	Sands – clean sand dan gravel to silty sand
5	$1.80 < I_C < 2.40$	Sand mixtures – silty sand to sand silty
4	$2.40 < I_C < 2.76$	Silt mixtures – clayey silt to silty clay
3	$2.76 < I_C < 3.22$	Clays
2	$3.22 < I_C$	Organic soils

2.2 *Vane Shear Test*

To calculate the undrained shear strength, using the Vane Shear Test, it was used the Equation 19 suggested in the Brazilian Standard NBR 10905 (ABNT, 1989). Also, the sensitivity can be calculated using the Equation 20, which express the relationship between the yield shear resistance and the remolded shear resistance, providing an idea of the soil brittleness.

$$S_u = 0.86\left(\frac{T}{\pi \cdot D^3}\right) \tag{19}$$

T – Maximum torque measured by the Vane Shear Test, in yield or remolded conditions;

D – Vane diameter (used $6{,}5\text{x}10^{-3}$m as provided by the company that performed the test).

$$S_t = \frac{Su_{yield}}{Su_{remolded}} \tag{20}$$

2.3 *Undrained Consolidated Triaxial Compression Test*

The CIUC tests were performed in undisturbed samples to determine the normally consolidated undrained shear strength ratio using the criteria of the maximum deviatoric stress. Using the results of the triaxial tests the slope of the critical state line in the p' x q space (M_{tc}) was also determined.

3 RESULTS

3.1 *CIUC test*

As shown in Figure 3, the 3 samples generated a high shear-induced excess porewater pressure. Also, it is noted that the bauxite tailings do not lose its resistance during shear showing a very ductile and clay-like behavior, in accordance with what is expected of very plastic tailings. Using the laboratory data, the M_{tc} value was found to be ≅ 1.72 and the normally consolidated undrained shear strength ratio was equal to ≅ 0.32.

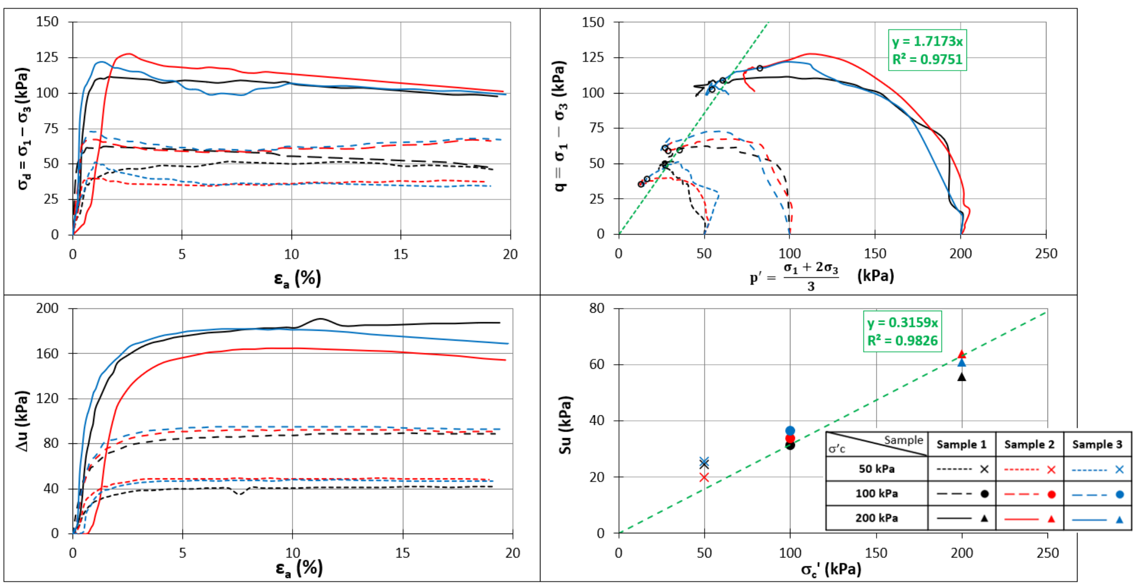

Figure 3. Summary of CIUC test.

3.2 *Field Assessment*

Using the dissipation test, the equilibrium porewater pressure was determined and interpolated over the CPTu test. Figure 4 shows the summary of the main CPTu parameters along with the porewater pressure profile for the tailings. In this figure, the penetration porewater pressure (u_2) is plotted along with the equilibrium pore pressure (u_0) profile and a condition of 100% hydrostatic for comparison. Also, in Figure 4, the results of solids content and unit weight are plotted with depth.

Analyzing Figure 4, three points can be highlighted: (i) the bauxite tailings analyzed generates high porewater pressures during penetration (which is common for saturated and loose clayey soils); ii) the correction of q_c to q_t is relevant, showing a difference around 100kPa (≈33%) at the end of the CPTu profile; and (iii) the seepage conditions measured by the dissipation test indicates an over hydrostatic with bottom drainage condition (case "c" suggested by Martin (1999) and detailed in Figure 1).

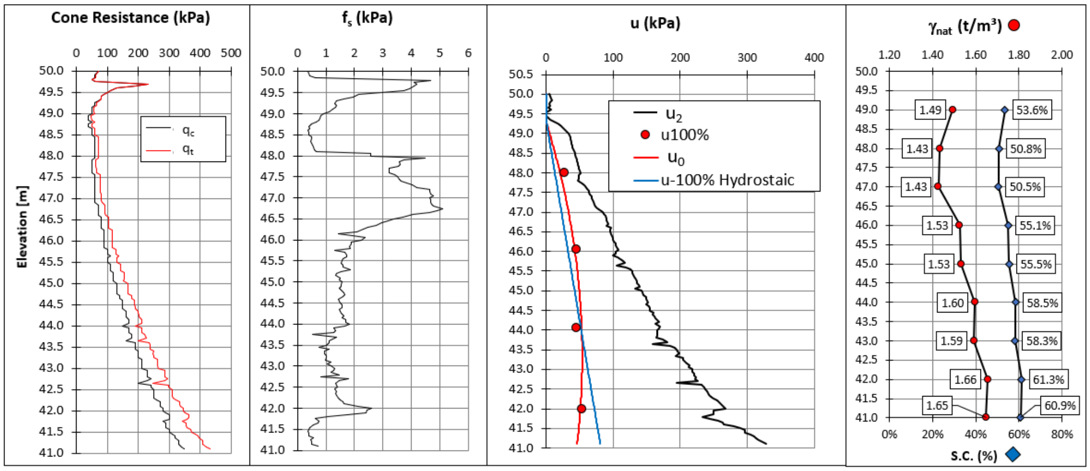

Figure 4. Dissipation test data, Solids Content and Unit Weight.

Using the unit weight and porewater pressure profile, the total and effective vertical stresses were calculated which allows for the calculation of B_q and I_c, as shown in Figure 5.

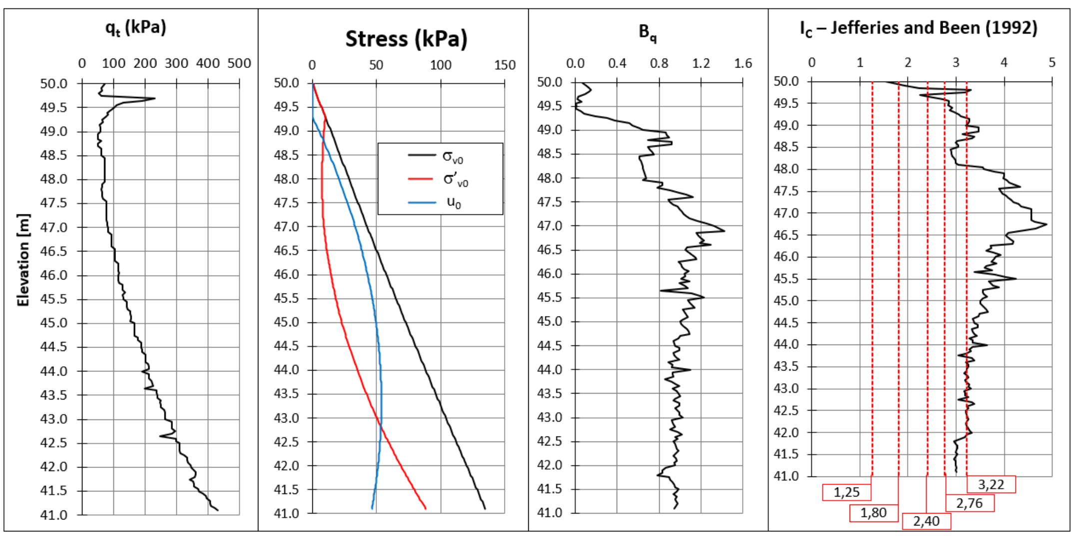

Figure 5. CPTu classification and stress state.

As observed in, the bauxite tailings show a behavior of clayey soil ($2.76<I_C<3.22$) and organic soil ($I_C>3.22$) by using the soil behavior-type classification proposed by Been and Jefferies (1992). The I_C index classifies the soil based on its behavior and not on the composition of the material (grain-size distribution and plasticity). The organic soil classifications highlight the fact that the tailings is highly compressible, contractive and saturated, which is also possible to notice by the low values of cone tip resistance ($q_t<1.0$MPa) and high porewater pressure generated during the test (indicated by the values of B_q).

Using Equation 11, the I_R obtained was 270.7 by using a calculated a_q of 0.65. Using these parameters, and the M_{tc} value of 1.72 (Figure 3), the OCR was calculated (Equations 12 to 14) as proposed by Agaiby and Mayne (2018) and is shown in Figure 6.

The bauxite tailings are predominantly classified as under consolidated (OCR<1) as shown in Figure 6. Also, this result is supported by qualitative analysis proposed by Martin (1999) based on the porewater pressure profile (case “c” suggested by Martin (1999) detailed in Figure 1).

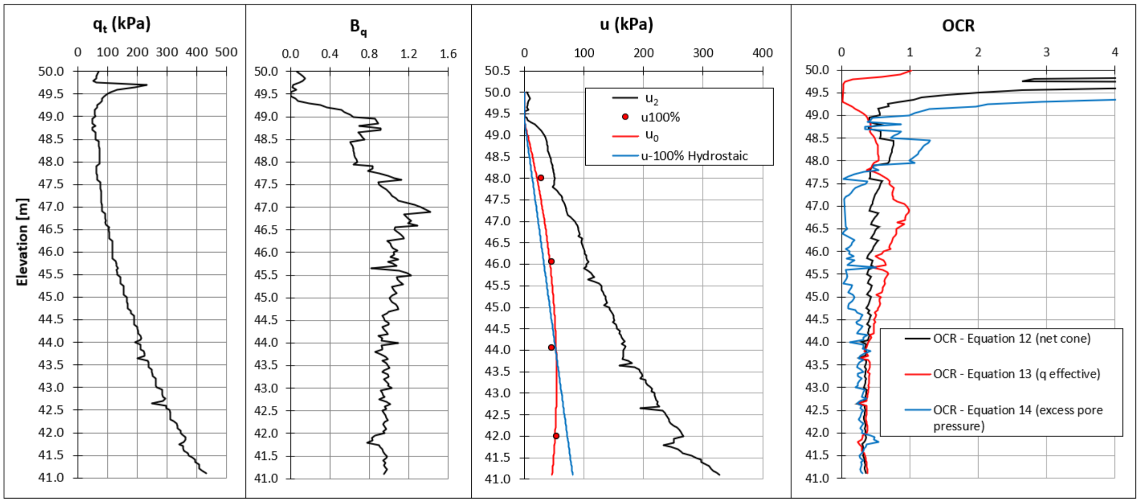

Figure 6. CPTu profile including an OCR evaluation.

After the evaluation of the stress history, the next step is to determine the region of the profile that showed undrained behavior during the CPTu. As described by Schnaid (2009), regions of the investigation where B_q<0.40 is probably responding in a drained or partially drained manner (such as the initial portion of the investigation, between the elevations 50.0m and ≈49.2m on (Figure 5 or Figure 6) and should not be considered as undrained response.

Another way to evaluate the undrained behavior, as shown by Robertson and Cabal (2015), is to compare the results of the undrained shear strength calculated based on the bearing factors N_{kt} and $N_{\Delta u}$. Herein, this comparison was done using the proposed equations by Mayne and Peuchen (2018) and Battaglio et al. (1981), respectively. When the values of undrained shear strength obtained from Equations 1 and 2 are approximate, there is a greater probability that the cone drilling is occurring in an undrained manner. Using these criteria, it was determined that the calculation of the undrained shear strength should be performed below the elevation of 49.2m, as shown in Figure 7.

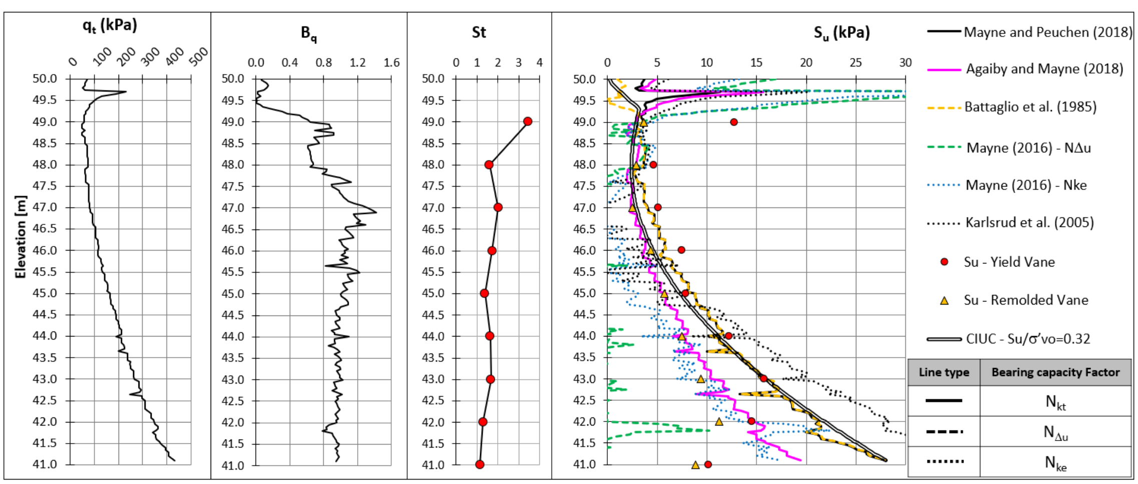

Figure 7. CPTu Undrained Shear Strength evaluation.

Based on the results from the methodologies studied herein the Mayne and Peuchen (2018), the Battaglio et al. (1981) formulations are the ones that more accurately calculated the undrained shear strength based on the compression mode, which is represented by the undrained strength profile calculated from the triaxial compression test.

The results from the Field Vane Test showed, at most of the profile, an upper bound value above that of the triaxial compression mode. Similar results have been reported in the literature, such as those from Bothkennar soft clay showed by Mayne (2016). Under the elevation 42.0m, the shear strength obtained from Vane Test Tests showed decreasing values, which was not observed on the CPTu.

The methodology proposed by Karlsrud et al. (2005), which uses the N_{ke} values, showed S_u values lower than expected from the triaxial compression mode above 45.0m and higher at end of the CPTu profile, in elevations below 45.0m. The methodology proposed by Mayne (2016) to evaluate N_{ke}, on the other hand, showed values lower than expected for the triaxial compression mode over all of the CPTu profile.

The methodology proposed by Agaiby and Mayne (2018) yielded values of undrained shear strength that were very close to the remolded shear strength over the entire profile. In Figure 7 it is noted that Equation 8, proposed by Mayne (2016) for $N_{\Delta u}$ showed very inconsistent results of S_u values. These results happened due to the mathematical limitation imposed by the Equation 8 when $B_q \approx 1.0$.

Furthermore, the current work intended to determine the site-specific calibration of the bearing factors (N_{kt}, N_{ke} and $N_{\Delta u}$) to the triaxial compression mode. As can be seen in Figure 8, the bearing factors of N_{kt}=11, N_{ke}=3 and $N_{\Delta u}$=10. are reasonably good bearing factors to be used to estimate the S_u relative to the triaxial compression mode based on CPTu.

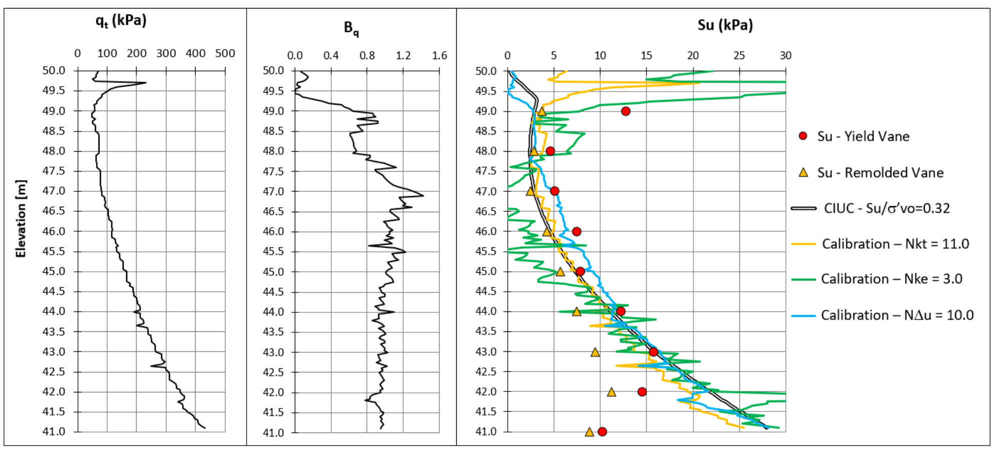

Figure 8. CPTu bearing factors N_{kt}, N_{ke} and $N_{\Delta u}$ for calibration.

4 CONCLUSION

The comparison of different methodologies using field assessment to calculate the undrained shear strength of a bauxite mine tailings was performed to determine which formulations are most appropriate to estimate the undrained shear strength representative of the compression failure mode. Furthermore, the soil behavior-type index using the equations proposed by Been and Jefferies (1992) and the OCR using the suggestion by Agaiby and Mayne (2018) were evaluated.

The undrained shear strength was calculated in the portions of the sounding where B_q>0.4 where the results calculated by Mayne and Peuchen (2018) and Battaglio et al. (1981) yielded similar values, as suggested by Schnaid (2009) and Robertson and Cabal (2015). For the tailings evaluated herein the B_q values indicate that it is very likely that the CPTu was fully undrained below the elevation of 49,0m, as can be seen by the high B_q values (Figure 7).

The undrained shear strength calculated by the bearing factor for net tip resistance (N_{kt}) using Mayne and Peuchen (2018), and the bearing factor for excess porewater pressure ($N_{\Delta u}$) suggested by Battaglio et al. (1981), were the ones to more accurately determine the expected results for the triaxial compression failure mode. The values of the undrained shear strength calculated by the Vane Shear Test yield an upper bound value above that of the triaxial compression failure mode. Similar findings have been reported in the literature such as the example of the Bothkennar soft clay shown by Mayne (2016).

The equation proposed by Karlsrud et al. (2005), based on N_{ke} values, yielded results above that of the triaxial compression mode especially at the end of the CPTu. All the other methods resulted in values below the expected for the triaxial compression mode. The methodology proposed by Agaiby and Mayne (2018) to calculate N_{kt} showed convergence to the remolded shear strength calculated by the Vane shear test, as shown in Figure 7, and the methodology proposed by Mayne (2016) to evaluate $N_{\Delta u}$ did not present reliable results due to its inherent mathematical restriction for $B_q \approx 1.0$ in the Equation 8.

Finally, the site-specific calibration of the bearing factors (N_{kt}, N_{ke} and N_{Δ}) to the triaxial compression mode was presented yielding values of N_{kt}=11, N_{ke}=3 and $N_{\Delta u}$=10.

It is important to highlight that the conclusions obtained in this work were specific to the material being evaluated and the authors do not recommend a direct replication of the results presented herein before a site-specific study of the behavior of the geomaterials involved.

5 ACKNOWLEDGMENTS

The authors thank Pimenta de Ávila Consultoria for all the support in the development of this work.

6 REFERENCES

Agaiby, S.S. & Mayne, P.W. 2018. Evaluating undrained rigidity index of clays from piezocone data. *Proceedings of the 4th International Symposium on Cone Penetration Testing (CPT'18)*. Delft, The Netherlands: CRC Press/Balkema.

Associação Brasileira de Normas Técnicas (ABNT). 1989. NBR 10905: *Solo - Ensaios de palheta in situ - Método de ensaio*. Rio de Janeiro.

American Society for Testing and Materials (ASTM). 2020. D5778: *Standard Test Method for Electronic Friction Cone and Piezocone Penetration Testing of Soils*.

American Society for Testing and Materials (ASTM). 2020. D4767-11: *Standard Test Method for Consolidated Undrained Triaxial Compression Test for Cohesive Soils*.

Battaglio, M.; Jamiolkowski, M; Lancellotta, R. & Maniscalco, R. 1981. Piezometer probe test in cohesive deposits. *In Proceedings of the Session ASCE National Convention*, geotechnical division, Symposium on cone penetration testing and experience. St. Louis, pp 264–302.

Been, K. & Jefferies, M.G. 1992. *Towards systematic CPT interpretation*. In Proceedings of the Wroth Memorial Symposium, Oxford, U.K., pp. 121–134. London, U.K.: Thomas Telford.

Brown, B. & Gillani, I. 2016. Common errors in the slope stability analyses of tailings dams. *In PM Dight (ed.), Proceedings of the First Asia Pacific Slope Stability in Mining Conference*, Australian Centre for Geomechanics, Perth, pp. 545-556.

GISTM 2020, 'Global Industry Standard on Tailings Management', Global Tailings Review, International Council on Mining & Metals (ICMM), UN Environment Programme (UNEP) and Principles for Responsible Investment (PRI), August 2020, https://globaltailingsreview.org/global-industry-standard/

Herza, J, Ashley M and Thorp, J. 2017 Factor of Safety? - Do we use it correctly? *In Proceedings ANCOLD 2017*

Karlsrud, K., Lunne, T., Kort, D.A., Strandvik, S., 2005. CPTU correlations for clays. *In: Proc. 16th International Conference on Soil Mechanics and Geotechnical Engineering*, Osaka, pp. 693–702.

Lunne, T.; Robertson, P.K. & Powell, J.J.M. 1997. *Cone Penetration Testing in Geotechnical Practice*. First Edition. Abingdon: E & FNSpon Press.

Martin, T.E. 1999. Characterization of pore pressure conditions in upstream tailings dams. *In Proceedings of the Tailings & Mine Waste '99*, Fort Collins, Colorado, pp. 303-314.

Mayne, P.W., 2016. Evaluating effective stress parameters and undrained shear strength of soft-firm clays from CPT and DMT. Australian Geomechanics Journal 51 (4): 27-55.

Mayne, P.W. & Peuchen, J. 2018. Evaluation of CPTU Nkt cone factor for undrained strength of clays. *In Proceedings of the 4th International Symposium on Cone Penetration Testing (CPT'18),* Delft, The Netherlands. CRC Press/Balkema.

Robertson, P.K. & Cabal, K.L. 2015. *Guide to Cone Penetration Testing for Geotechnical Engineering*. Sixth Edition. Signal Hill, CA: Gregg Drilling & Testing, Inc.

Schnaid, F. 2009. *In situ testing in geomechanics: the main tests*. Oxon: Taylor & Francis Group.

Schnaid, F. & Odebrecht, E. 2012. *Ensaios de campo e suas aplicações à engenharia de fundações*. São Paulo: Oficina de Textos.

Dynamic behavior of blasted and crushed leached ore and non-plastic tailings

Myzael Valdivia & Denys Parra
Anddes, Lima, Peru

ABSTRACT: Seismic response analysis is of high importance for the design of earth structures located at highly active seismic zones and the material dynamic properties in terms of normalized shear modulus and damping ratio over a wide range of shear strains are inputs for this type of analysis. In the case of heap leach pads and tailings dams, the dynamic properties are estimated based on laboratory testing on drained conditions with RCTS and cyclic-triaxial tests. It is also common in preliminary studies to estimate the dynamic properties based on empirical curves which consider material input parameters such as confining stress, coefficient of uniformity, average size, plasticity, fine content, void ratio, water content, and so on.

This paper presents a summary of laboratory tests performed on ore and tailings samples obtained from different heap leaching and tailings storage facility projects. In case of ore, three samples were analyzed, one blasted leached ore and two crushed leached ore. For the case of tailings, five samples were studied and all of them were non-plastic materials, three coarse-grained tailings, and two fine-grained tailings.

Normalized shear modulus and damping ratio curves obtained by dynamic and cyclic laboratory tests were compared to literature empirical curves. In the case of the ore, the comparisons showed better results with the Wang (2018) empirical relationship compared to Darendeli (2001), Menq (2003), Tapia et al. (2019), and Rollins et al. (2020) to all the blasted and crushed samples, therefore those curves may be used as a preliminary empirical one to consider when laboratory testing is not available. For the case of tailings, Darendeli (2021) curves showed better results compared to Wang (2008), just for normalized shear modulus, but for damping ratio Wang (2018) showed better results compared to Darendeli (2001).

1 INTRODUCTION

The seismic design of mining structures, such as heap leach pads and tailing dams, are very important in highly seismic areas such as South America due to the economic and environmental impact these structures would generate because of a slide. The seismic design of these structures usually involves the site response analysis and calculation of permanent displacements induced by earthquakes in the first stages of the design, and afterwards, dynamic analysis. Furthermore, the dynamic properties of the material that make up these structures (ore and tailings), and that are presented in terms of normalized shear modulus and damping ratio over a wide range of shear deformation, are necessary for this kind of analysis.

In practice, the dynamic characterization of ore from heap leach pad is complicated due to the lack of information in the world scientific literature; however, there are some papers prepared by Parra et al, (2016), Tapia et al. (2019), and Valdivia (2020) on leached ore and mine waste, and another by Rojas et al. (2019) on tailings. We must also consider that there is limited laboratory equipment for dynamic and cyclic testing.

Likewise, most of the seismic designs are performed using normalized shear modulus and damping ratio curves existing in the literature and published by various authors for many decades.

However, most of these curves have been obtained from tests in natural soils resulting in important differences in terms of accelerations compared to the results using curves of representative samples. These uncertainties may underestimate or overestimate the behavior of mine structures when using information from literature and without evaluating its performance with laboratory data in anthropic on-site samples.

2 THEORETICAL BACKGROUND

The dynamic soil properties in different ranges of strains show a linear and nonlinear behavior. This behavior is represented in semi-logarithmic graphs defined as normalized shear modulus reduction curve (G/G_{max}– log γ) and damping ratio curve (D – log γ), showed in Figure 1. The selection of dynamic curves for a soil type depends on many factors such as the physical characteristics. The pioneering studies of Seed and Idriss (1970) and Seed et al. (1986) correspond to the first studies performed to characterize sandy and gravelly soils through dynamic curves. Besides, other subsequently developed studies were those proposed by Rollins et al. (1998) for granular material, and Sun et al. (1988) and Vucetic and Dobry (1991) for fine grain materials with curves based on its plasticity index (PI). Also, Ishibashi y Zhang (1993) unified the studies made on sand and clay to develop prediction equations based on the plasticity index (PI) and mean effective stress (σ'_0).

Three decades after the Seed's studies, empirical prediction formulations were developed by Darendeli (2001) and Menq (2003) to estimate the dynamic curves in more detail. In the case of Darendeli (2001), the parameters considered were the mean effective stress (σ'0), plasticity index (PI), and overconsolidation ratio (OCR) for clean sands, sands with high content of fines, clays, and silts. In the case of Menq (2003), the parameters considered were the mean effective stress (σ'_0), uniformity coefficient (C_u), and medium particle size (D_{50}) for non-plastic sandy and gravelly soils and with low fines content (less than 13%).

Most of the studies were performed with samples obtained from natural deposits; however, sometimes in the selection of borrow materials, blasting and crushing processes are performed changing the internal behavior of the soil. On the other hand, this process is common in open pits when the exploitation of metal-rich ore is performed and then goes through additional process such as heap leaching or milling-flotation with chemical reagents. About anthropogenic materials, Seed et al. (1986) performed tests in crushing material of rockfill used in Venado sandstone of the Pyramid dam that went through a process of blasting and crushing. Furthermore, even though Menq (2003) performed research in granular materials, these were in natural materials. Among recent studies, Senetakis et al. (2012) and Senetakis et al. (2013) performed studies in volcanic-crushed materials obtaining different results compared to quartz materials (which are commonly investigated in the existing literature).

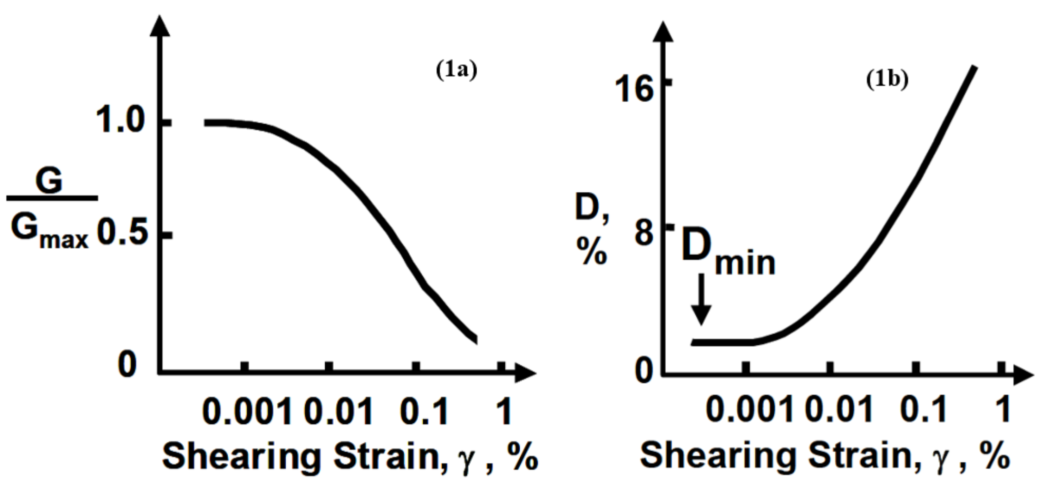

Figure 1. (a) Normalized shear modulus reduction curve and (b) Damping ratio curve, Darendeli (2001)

Parra et al. (2016) and Valdivia (2020) investigated the dynamic behavior of leached ore of two different projects. The results showed that the volcanic material that went through the blasting and crushing process have a similar behavior using the formulations of Senetakis et al. (2013) while the volcanic and quartz materials obtained just by blasting have a similar behavior using the formulations of Menq (2013). Similarly, Rojas et al. (2019) investigated the behavior in tailings of three different projects noting that its behavior was like the obtained by Darendeli (2001). New empirical formulations have been recently published, such as the research of Wang (2018), Tapia et al. (2019), and Rollins et al. (2020). Therefore, this paper aims to review these previous studies with these new prediction curves and provide conclusions and recommendations for the dynamic analysis of mining structures that involve anthropogenic materials such as leached ore and tailings.

3 CASES STUDY – LEACH ORE AND TAILINGS

Research in the dynamic behavior of metal-rich materials was conducted, these materials were obtained from Peruvian mining projects. These materials correspond to the leached ore and tailings. Leached ore was obtained from heap leach pads and tailings were obtained from the tailings dams.

The leached ore is a granular material which was obtained from three different projects named projects 1, 2, and 3. The materials from projects 1 and 2 were reviewed by Parra et al. (2016) and were reconstituted in the laboratory using the parallel or homothetic gradation technique (Dorador, 2010). These materials were tested twice for verification purposes. Likewise, the material of the project 3 was cut to the maximum size allowed in the device of 3/8 inches. In addition, this material had a *in situ* maximum size of 1 inch compared to the materials of the first two projects which were up to 12 inches size. Table 1 summarizes the index properties of these *in situ* materials, the one considered by the homothetic curves and those finally tested in the laboratory. In addition, the table indicates the obtaining method of these samples in the mine site (blasting or crushing).

Table 1. Index properties of leach ore

Material	Sample	Location / type	Gs[1]	Cu[2]	Cc[3]	D_{50}[4]	Fines	WC[5]	γ_t[6]	e[7]	USCS[8]
			-	-	-	(mm)	(%)	(%)	(g/cm^3)	-	-
Project 1	-	Field	2,61	57	1,64	90,0	2,5	2,17-2,23	2,04-2,18	0,150-0,214	GW
Blasted	-	Homothetic		23,48	1,12	3,07	5,0				SW
leached	LO-09	Laboratory		24,3	0,79	2,2	5,0	2,96	2,01	0,296	SW
ore	LO-11	Laboratory		20,1	0,77	2,0	5,0	2,94	1,98	0,312	
Project 2	-	Field	2,25	90	2,77	20,3	4,9	2,60-2,80	1,56-1,68	0,433-0,480	GW
crushed	-	Homothetic		47,04	1,78	2,0	6,0				SW-SM
leached	LO-02	Laboratory		40	1,78	2,0	6,0	3,36	1,60	0,407	SW-SM
ore	LO-03	Laboratory		35	1,78	2,0	6,0	0,7	1,52	0,467	
Project 3		Field	2,68	*	*	6,58	12,8	10	1,68	0,59	GM
crushed leached ore	LO-12	Laboratory		*	*	2,97	21,8**				SM

Notes: 1) Specific gravity, 2) Coefficient of uniformity, 3) Coefficient of curvature, 4) Average diameter by mass, 5) Water content, 6) Total unit weight, 7) Void ratio and 8) Unified Soil Classification System (USCS) Symbol foe Soil Type.
* Not estimated.
** Plastic leached ore with index plasticity (IP) equal to 10.

In project 1, the ore is a material exploited by blasting defined as ROM ore (run of mine). In projects 2 and 3, the ore is a crushed material.

Combined resonant column and torsional shear (RCTS) and cyclic triaxial testing (CTX) were performed in projects 1 and 2, while in project 3 only RCTS testing was performed. The device used in projects 1 and 2 and presented by Parra et al. (2016) has a diameter of 6 inches. All these tests were carried out at the University of Texas at Austin. In project 3, a similar device was used, and the tests were carried out in the Anddes geotechnical laboratory in Lima (Peru). Figure 2 shows all the results of the leached ore testing.

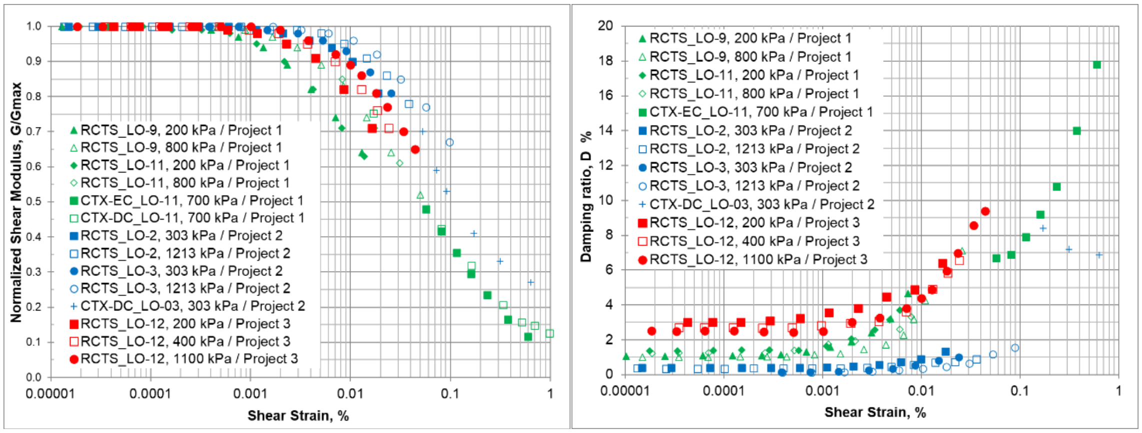

Figure 2. Normalized shear modulus and damping ratio versus shear strain, leached ore (projects 1, 2, and 3)

Similarly, the tailings samples were obtained from three different projects (projects 4, 5, and 6) and correspond to non-plastic materials previously reviewed by Rojas et al. (2019), three of them are coarse-grained (underflow) and two are fine-grained (overflow) tailings. Table 2 summarizes the index properties of these materials. RCTS testing were carried out in the Anddes geotechnical laboratory in Lima (Peru). Figure 3 shows all the results of the tailings testing.

Table 2. Index properties of tailings

Material	Sample	Location / type	Gs[1]	Cu[2]	Cc[3]	D_{50}[4]	Fines	WC[5]	γ_t[6]	e[7]	USCS[8]
			-	-	-	(mm)	(%)	(%)	(g/cm^3)	-	-
Project 4	TL-01	overflow	3,49	*	*	0,12	30,3	5,0	19,13	0,789	SM
Project 5	TL-02	underflow	3,34	*	*	0,10	29,8	5,0	17,56	0,866	SM
	TL-03	underflow	2,64	*	*	0,08	48,6	7,5	15,26	0,700	SM
Project 6	TL-04	underflow	2,84	*	*	0,18	26,0	10,0	14,72	0,890	SM
	TL-05	overflow	2,74	*	*	0,09	43,9	15,0	15,70	0,713	SM

Notes: 1) Specific gravity, 2) Coefficient of uniformity, 3) Coefficient of curvature, 4) Average diameter by mass, 5) Water content, 6) Total unit weight, 7) Void ratio and 8) Unified Soil Classification System (USCS) Symbol foe Soil Type.
* Not estimated.

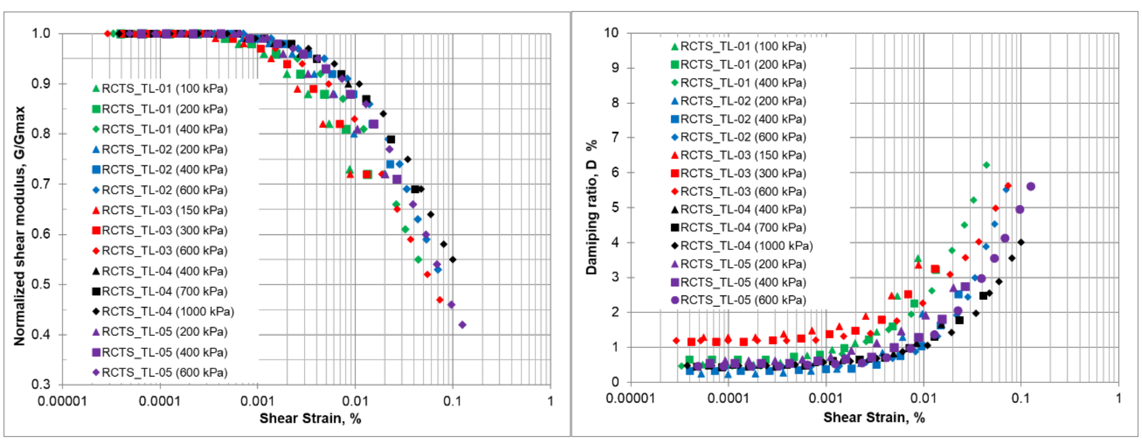

Figure 3. Normalized shear modulus and damping ratio versus shear strain, tailings (projects 4, 5 y 6)

4 COMPARISONS WITH DYNAMIC CURVES FROM LITERATURE

New empirical formulations to estimate dynamic curves in soils have been developed in the last three years, therefore, it is in the interest of the authors to verify the comparisons made in the last five years from the studies of Parra et al. (2016) to Valdivia (2020). The empirical curves of Seed et al. (1986), Darendeli (2001), Menq (2003), Senetakis et al. (2013), Wang (2018), Tapia et al. (2019), and Rollins et al. (2020) were considered to compare it with the dynamic curves obtained in the laboratory for leached ore. On the other hand, the prediction curves of Seed and Idriss (1970), Darendeli (2001), and Wang (2018) were considered to compare it with the dynamic curves obtained in the laboratory for tailings.

4.1 *Leached ore*

Figures 4, 5, and 6 show the comparisons in ore for projects 1, 2, and 3, respectively. For project 1 (Figure 4) and in relation to the normalized shear modulus curve, Menq (2003), Wang (2018), and Tapia et al. (2019) present a good fit for both 200 kPa and 800 kPa confining stresses. However, for the confining stress of 800 kPa and shear strains greater than 0.05%, major differences in the test with the empirical curves used are observed, obtaining a better fit with the curves predicted by Wang (2018). The Rollins et al. (2020) empirical curve presents a greater linearity (or stiffer behavior) compared to those of the laboratory test.

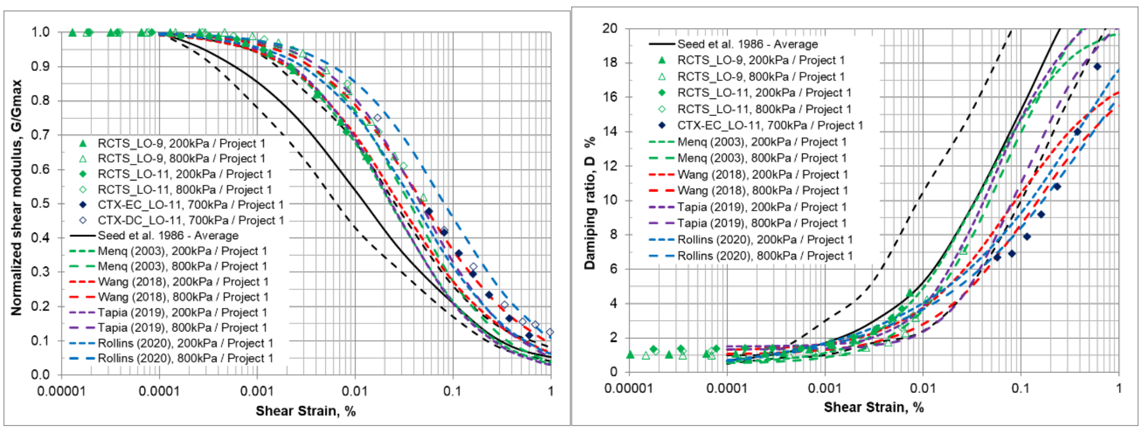

Figure 4. Normalized shear modulus and damping ratio versus shear strain curves of leached ore from project 1 and comparison with dynamic curves from literature

Concerning the damping ratio curve, empirical curves of Menq (2003), Wang (2018), Tapia et al. (2019), and Rollins et al. (2020) show a good fit in low intermediate strains (obtained from the RCTS test); however, at large strains (obtained from the cyclic triaxial test) better similarities with the curves obtained by Wang (2018) and Rollins et al. (2020) are observed, while the curves of Menq (2003) and Tapia et al. (2019) overestimate the damping values compared to the obtained in the laboratory.

For project 2 (Figure 5), there is not a good fit in the normalized shear modulus curve. These differences were commented by Parra et al. (2016) and Valdivia (2020) in relation to its volcanic origin and as a crushed material. An additional comparison with the curve of Senetakis et al. (2013) shows the similarity with the laboratory data, obtaining the linearity in this type of materials.

Concerning the damping ratio curve, the empirical curve of Senetakis et al. (2013) presents a good fit in low intermediate strains (obtained from the RCTS test), followed by the curves of Wang (2018) and Tapia et al. (2019). At large strains (obtained from the cyclic triaxial test) Senetakis et al. (2013) show a good fit as it is close to the low damping values, followed by the curves of Wang (2018) and Rollins et al. (2020), while the curves of Menq (2003) and Tapia et al. (2019), like in the case of project 1, overestimate the damping ratio compared to the obtained in the laboratory.

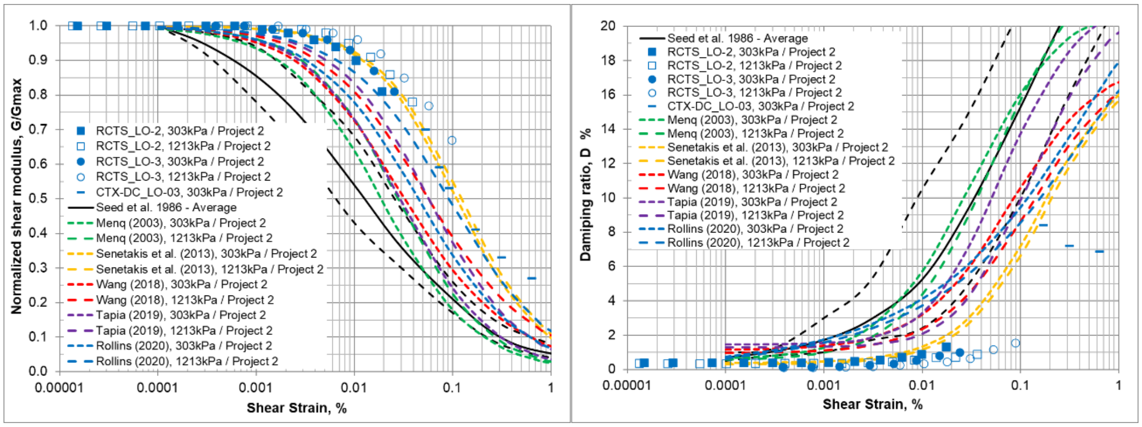

Figure 5. Normalized shear modulus and damping ratio versus shear strain curves of leached ore from project 2 and comparison with dynamic curves from literature

For Project 3 (Figure 6), the Darendeli (2001), Tapia et al. (2019), and Wang (2018) curves were used due to the ore fines content and because it is not possible to estimate the value of Cu, which is an input in Menq (2003) and Rollins et al. (2020) formulations. Darendeli (2001) and Wang (2018) show a good fit in the normalized shear modulus curve for the stresses of 200 kPa and 1100 kPa. The Tapia et al. (2019) empirical curve presents a greater degradation in the curves compared to the ones from the laboratory test.

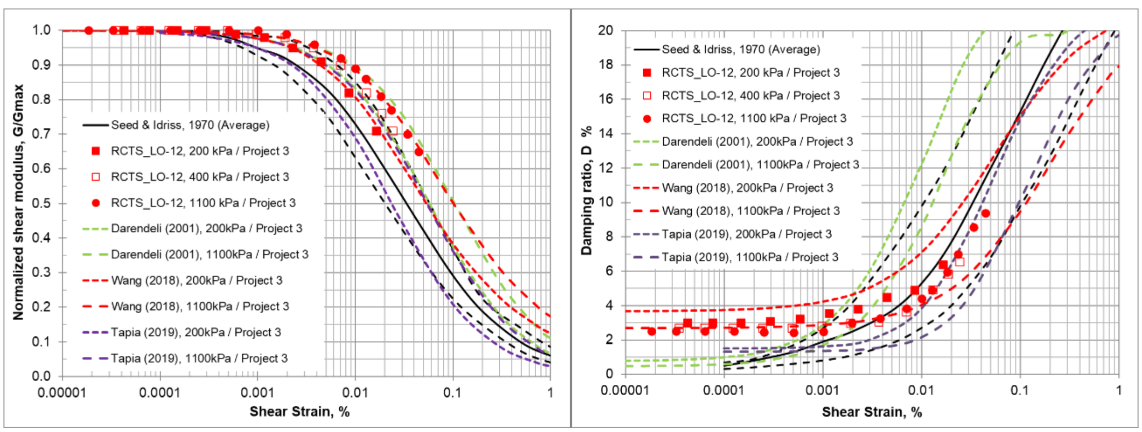

Figure 6. Normalized shear modulus and damping ratio versus shear strain curves of leached ore from project 3 and comparison with dynamic curves from literature

Regarding the damping ratio, the empirical curves of Wang (2018) show again a good fit in low and intermediate strains (obtained from the RCTS test), while the Darendeli (2001) curve underestimates and overestimates the damping values at small and intermediate strains, respectively, compared to the obtained in the laboratory. On the other hand, Tapia et al. (2019) underestimate the damping values at small and intermediate strains.

4.2 *Tailings*

Figures 7, 8, 9, 10, and 11 show comparisons for tailings of projects 4, 5, and 6. Figures 7 and 8 present comparisons of TL-1 and TL-3 tailings samples, respectively, both testing are similar in results. As discussed by Rojas et al. (2019), the empirical curve of Darendeli (2001) presents a good fit with the normalized shear modulus curve from laboratory; however, the empirical curves of Wang (2018) present greater linearity compared to the laboratory data. In the case of damping ratio, both empirical curves present a good fit at small strains; however, at intermediate strains, Wang (2018) presents greater linearity (stiffer behavior) like the laboratory data, while Darendeli (2001) presents overestimated values.

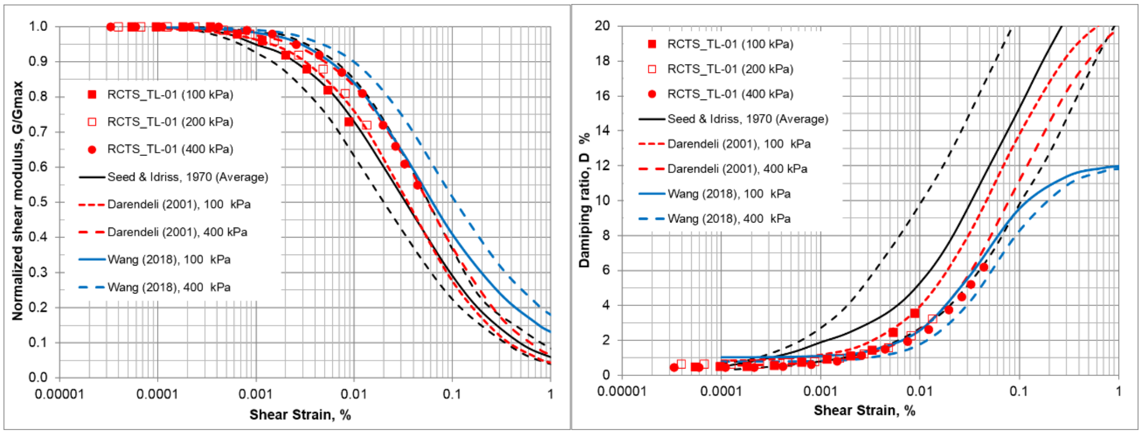

Figure 7. Normalized shear modulus and damping ratio versus shear strain curves of tailings TL-01 from project 1 and comparison with dynamic curves from literature

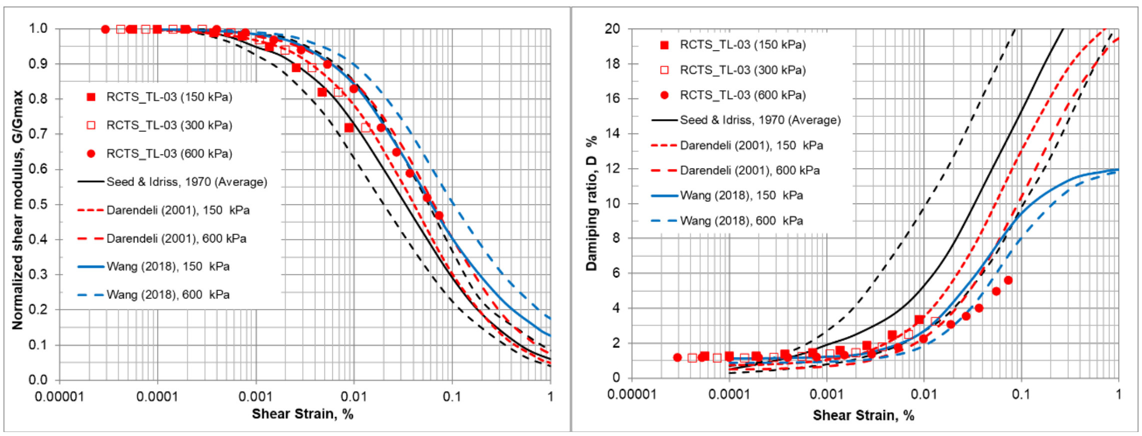

Figure 8. Normalized shear modulus and damping ratio versus shear strain curves of tailings TL-03 from project 3 and comparison with dynamic curves from literature

Figures 9 and 10 present comparisons of TL-2 and TL-4 tailings samples, respectively, both testing are similar in results. The normalized shear modulus curve from laboratory shows a more linear behavior compared to the Darendeli (2001) empirical curve; however, it is below the Wang (2018) curve. In the case of damping ratio, like in the case of TL-1 and TL-3 tailings samples, both prediction curves present a good fit at small strains; however, at higher strains, Wang (2018) presents greater linearity like the laboratory data, while Darendeli (2001) presents overestimated values.

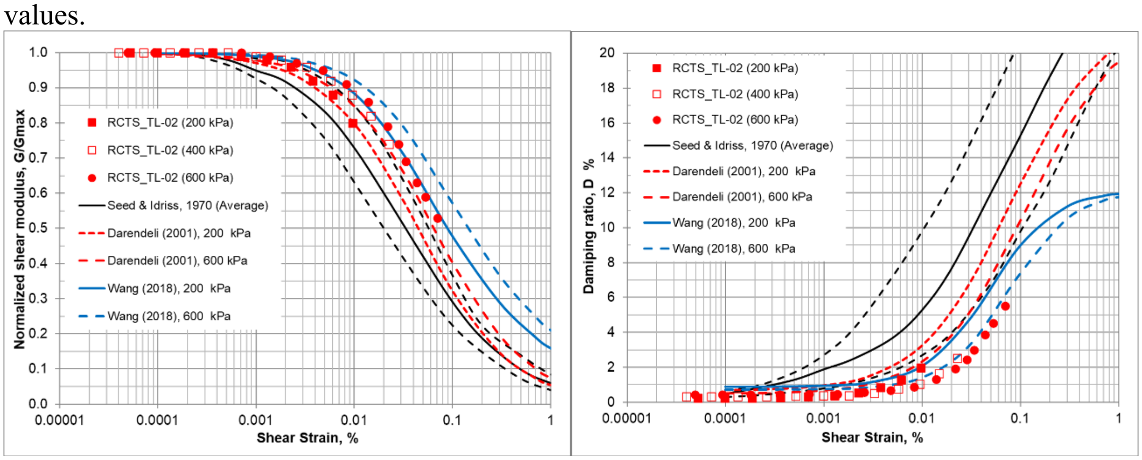

Figure 9. Normalized shear modulus and damping ratio versus shear strain curves of tailings TL-02 from project 2 and comparison with dynamic curves from literature

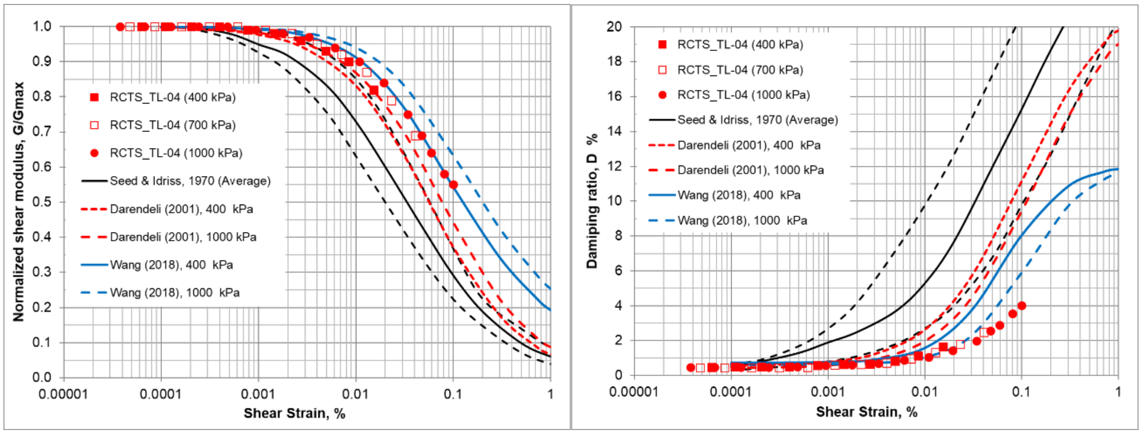

Figure 10. Normalized shear modulus and damping ratio versus shear strain curves of tailings TL-04 from project 3 and comparison with dynamic curves from literature

Figure 11 presents comparisons of the TL-5 tailings sample. The normalized shear modulus curve from laboratory shows a more linear behavior compared to the empirical curve of Darendeli (2001), being closer to the empirical curve of Wang (2018). In the case of the damping ratio, both empirical curves present a good fit at small strains; however, at higher strains, the laboratory data presents a more linear result with lower values; however, Wang (2018) presents values closer to the laboratory data, while Darendeli (2001) presents again overestimated values as in the other observed cases.

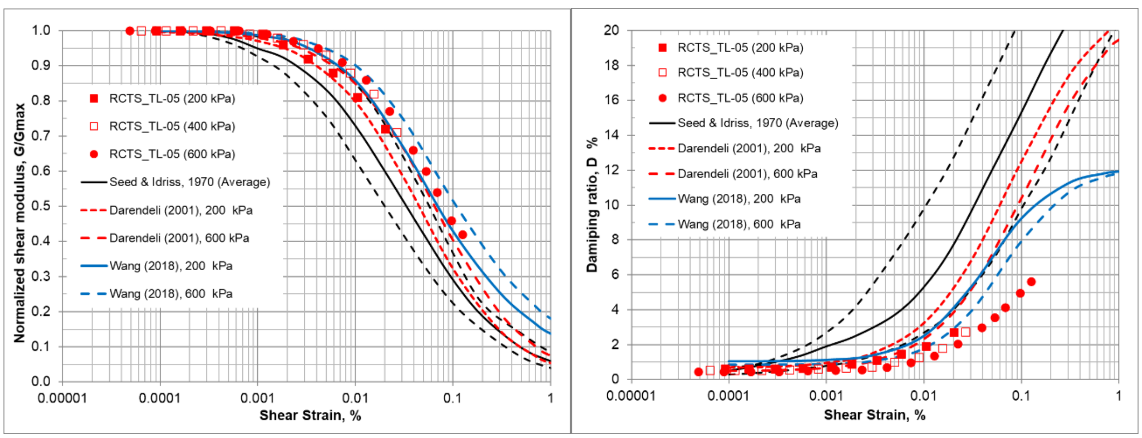

Figure 11. Normalized shear modulus and damping ratio versus shear strain curves of tailings TL-05 from project 3 and comparison with dynamic curves from literature

4.3 *Discussions*

According to the comparisons discussed above, the authors present the following discussions:

4.3.1 *Leached ore*

From the comparisons made with the laboratory testing in leached ore, we conclude that Wang (2018) allows better approaches, except the ore of volcanic origin from project 2, which fits better with Senetakis et al. (2013); however, compared to other curves of literature, Wang (2018) has a better prediction of its dynamic behavior.

It is important to highlight the prediction equations of Wang (2018) compared to other curves of literature. First, it is noted that parameters such as the fines content and plasticity index affect the soil dynamic response such as the case of project 3 which is adequately represented using Wang (2018) prediction curves since these parameters are inputs. Additionally, in higher strains, Wang (2018) predicts in more detail the results obtained in cyclic triaxial, compared to other selected models.

Similarities of the curves compared separately with the Wang (2018) model are observed. For the case of normalized shear modulus, Tapia et al. (2019) presents similar values for the project 1 and 2, while for the case of damping ratio, Rollins (2020) presents similar values in the same projects. Besides, none of these formulations have a good prediction and they are not applicable for the ore of project 3.

4.3.2 *Tailings*

From the comparisons made with the laboratory tests in the tailings, Darendeli (2001) presents better approximations in the normalized shear modulus curve compared to the empirical equations of Wang (2018); however, in certain scenarios such as in the case with high void ratios, the laboratory data is more linear, which Darendeli (2011) does not consider since this parameter is not an input parameter of his formulation. The void ratio parameter is considered by Wang (2018), but its effect is less than the observed in literature. Moreover, is it noted that Wang (2018) has a better estimation of damping ratio values in high strains, such as the one observed for the leached ore, finding that Darendeli (2001) overestimates the damping ratio values in medium and large strains.

5 CONCLUSIONS

This paper presents comparisons of the normalized shear modulus and damping ratio curves in the existing literature with data obtained by RCTS and cyclic triaxial laboratory testing. The tests were carried out on samples of leached ore and non-plastic tailings obtained from three different projects. This is made due to recent publications of Wang (2018) and Rollins et al. (2020) in the international literature and to provide insight from the made comparisons. This will help in future preliminary works on seismic response or dynamic analysis using empirical curves from literature that match best with the behavior in the laboratory.

In the case of leached ore, the comparisons showed better match with Wang (2018) empirical curves compared to other recent curves developed by Tapia et al. (2019) and Rollins (2020). However, there are similarities in Tapia et al. (2019) with Wang (2018) for the case of the normalized shear modulus, while Rollins (2020) and Wang (2018) have the same effect in the case of the damping ratio. In addition, Tapia et al. (2019) and Rollins (2020) curves are not possible to fit the dynamic behavior of leached ore with high fines content and with plasticity as Wang (2018) curves does (such as in the case of the ore in project 3).

In the case of tailings, there is a separated fit. In the normalized shear modulus curve, Darendeli (2001) presents a better approximation compared to Wang (2018), which presents a stiffer behavior due to the sensitivity of the void ratio parameter. This effect of void ratio in the literature is greater than the observed in the tests performed in the tailings. On the other hand, the damping ratio curve from Wang (2018) has a better prediction of the tailings behavior, concluding that Darendeli (2001) overestimates the damping values.

In both materials evaluated, the overestimation of the damping ratio value is highlighted in most of the empirical curves except for the Wang (2018) curves, which will lead to obtain underestimated results in the dynamic response of the structure.

REFERENCES

Darendeli, M. 2001. Developing of a new family of normalized modulus reduction and material damping curves, PhD dissertation, University of Texas at Austin, Austin, Texas.

Dorador, L. “Análisis experimental de las metodologías de curvas homotéticas y corte en la evaluación de propiedades geotécnicas de suelos grueso”, Tesis de Ingeniero Civil y Magister, Universidad de Chile, 2010.

Ishibashi I., and Zhang X. 1993. Unified dynamic shear moduli and damping ratios of sand and clay. Soils and Foundations, 33(1), 182-191.

Menq, F. 2003. Dynamic properties of sandy and gravelly soils. PhD dissertation, University of Texas at Austin.

Parra, D., Reyes, A., Keene, A, Stokoe, K., Jaffal, H. and El Mohtar, C. 2016. On the dynamic properties of leached ore and mine waste. In Proceedings of Heap Leach Mining Solutions 2016, Lima. Peru. Published by InfoMine, Vancouver: 317–332.

Rollins, K., Evans, M., Diehl, N. and Daily, W. 1998. Shear modulus and damping relationship for gravels, Journal of Geotechnical and Environmental Engineering 124(5): 69–81.

Rollins, K., Singh, M. and Roy, J.. 2020. Simplified Equations for Shear-Modulus Degradation and Damping of Gravels. Journal of Geotechnical and Geoenvironmental Engineering. 146. 04020076. 10.1061/(ASCE)GT.1943-5606.0002300.

Seed, H., Wong, R., Idriss, I. and Tokimatsu, K. 1986. Moduli and damping factors for dynamic analyses of cohesionless soil, Journal of Geotechnical Engineering, ASCE: 112:1016–1032.

Seed, H. and Idriss, I. 1970. Soil moduli and damping factors for dynamic response analyses, Report EERC 70-10, Earthquake Engineering Research Center, University of California, Berkley.

Senetakis K., Anastadiadis A. and Pitilakis K. 2012. The small-strain shear modulus and damping ratio of quartz and volcanic sands. Geotech. Testing J. 35 (6), 1-17.

Senetakis, K., Anastasiadis A. and Pitilakis. K. 2013. Normalized shear modulus reduction and damping ratio curves of quartz sand and rhyolitic crushed rock. Soil and Foundations, The Japanese Geotechnical Society: 879–893.

Sun J.I., Golesorkhi R., and Seed H.B. 1988. Dynamic Moduli and Damping Ratios for Cohesive Soils, Report, UCB/EERC-88/15, Univ. of California at Berkeley, 48 pp.

Tapia, E., Ayala, R. and Parra, D. 2019. Normalized Shear Modulus and Reduction and Damping Ratio Curve of Mine Waste and Leached Ore. Proceedings of Tailings and Mine Waste 2019, Vancouver, Canada. Published by University of British Columbia Press, 2019: 1215–1233.

Vucetic, M. and Dobry, R. 1991. Effect of soil plasticity on cyclic response. Journal of Geotechnical Engineering 117(1): 89–107.

Valdivia, M. 2020. Comportamiento dinámico y evaluación de respuesta sísmica 1D de materiales granulares obtenidos por voladura y chancado. Tesis de Ingeniero Civil, Universidad Nacional de Ingeniería, Lima, Perú.

Stability investigation of embankments of a tailings pond with varying embankment raising rate

Surender Singh, Abhishek Kumar & T.G. Sitharam
Department of Civil Engineering, Indian Institute of Technology, Guwahati, Assam, India, 781039.

ABSTRACT: In this article, stability of the embankments of a tailings pond (EoTP), the height of which is to be raised from 51m to 75m, is investigated. The height is provided in four raises by adopting upstream (U/S) and downstream (D/S) construction techniques. The current study is based on the assumption that the tailings are dilative, but this assumption should be confirmed before adopting the recommendations offered in this paper. If the tailings are contractive, then liquefaction needs to be considered and the analyses in this paper would not apply. Information on whether the tailings were dilative or contractive was not available to the authors of this paper. The stability analysis for this project was performed using the finite element based software RS2 by utilizing the transient fully coupled stress- pore pressure analysis with varying embankment-raising rate (ERR). Consequently, the build-up of excess pore water pressure (EPWP) during various phases of construction was analyzed to understand its impact on the overall stability of the EoTPs. Results from the analysis are studied in terms of EPWP and critical strength reduction factor (SRF) observed during various phases of construction. It is observed from the study that the overall stability of EoTPs is considerably influenced by the ERR, particularly for the embankment that will be raised using the U/S type construction technique.

1 INTRODUCTION

This study focuses on assessing the stability of the embankments of a tailings pond (EoTP) while increasing the height of the embankments from 51m to 75m. Both D/S and U/S construction techniques will be utilized to raise the EoTP in four phases. Due to insufficient information regarding the exact nature of tailings, the current study is based on the assumption that they are dilative. A robust two-dimensional transient fully coupled stress-pore pressure was performed in finite element based software RS2 to investigate the hydro-mechanical conditions of the EoTP during various phases of construction. While doing so, development of excess pore water pressures (EPWP) during various phases of construction is determined to understand its impact on the overall stability of the EoTP. In addition, an attempt was made to study the effect of embankment raising rate (ERR) on the build-up of EPWP within the TP and the EoTP (during various phases of construction) for both D/S and U/S case. Further, the variation of factor of safety values with different ERR was calculated and is presented in this paper.

2 TAILINGS POND

The TP selected in the current study is situated near the Rampura Agucha Mine of Bhilwara district in Rajasthan, India. Tailings produced during the extraction of Zinc and Cadmium, is being disposed into the TP constructed near the mine site (Sitharam & Hedge, 2017). The existing height of the EoTP is 51m, which was built in 2 phases with 4 lifts in each phase.

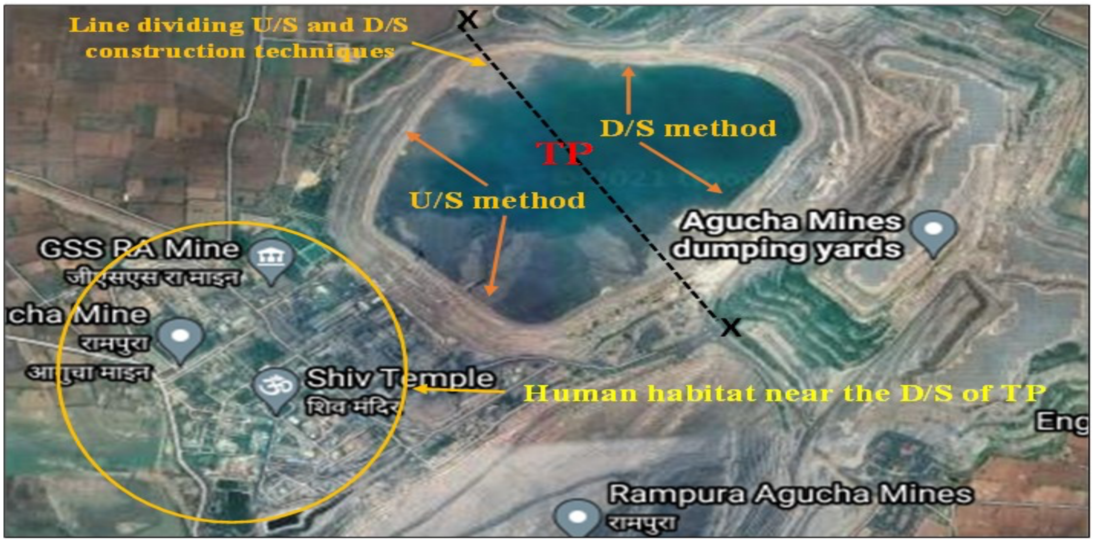

Figure 1. Plan view of TP showing the type of construction method employed at different locations.

In Phase 1, D/S construction technique was utilised to construct the EoTP with a height of 27 m, while in Phase 2, both U/S and D/S building techniques (see Fig. 1) were employed to increase the height of EoTP by 24m (Sitharam and Hedge, 2017). The U/S and D/S building techniques are described by Vick (1990). Further details regarding the geometry of existing EoTP are shown in Figures 2 and 3.

The foundation of the TP consists of a low permeable soil layer, which is underlain by a rocky stratum (Sitharam & Hegde, 2017). The hydraulic conductivity of top foundation soil varies from 0.8×10^{-8} to 1×10^{-8} m/s. The properties of this soil are unknown to the authors and it has been assumed that the Owners have assessed the strength of the low permeable soil layer and have determined that it will not behave in a contractive manner due to the increased loading.

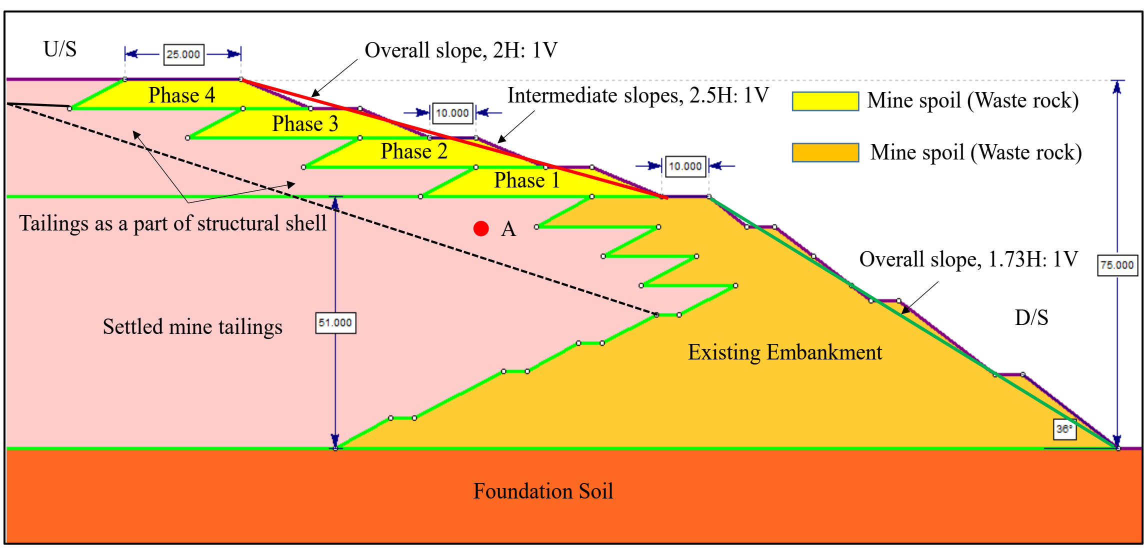

Figure 2. Typical cross-section of TP embankments constructed by U/S method.

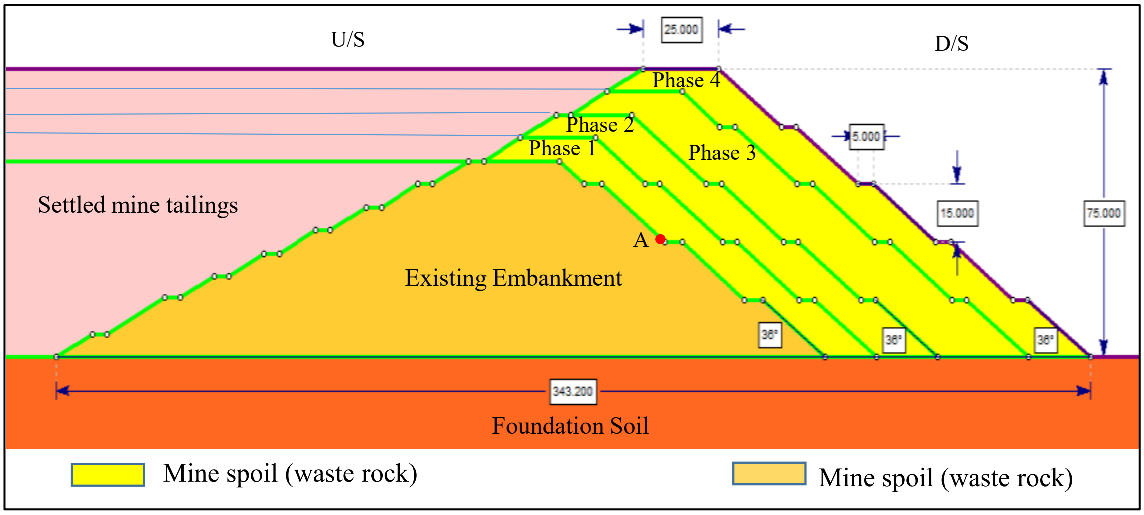

Figure 3. Typical cross-section of TP embankments constructed by D/S method.

The EoTP were constructed with the mine spoils (waste rock) generated from the mining operations, which are cohesionless and contain particle sizes greater than 1000 mm. Little information regarding the tailings was provided to the authors (gradation curve, plasticity, etc.). Given that the shells of the EoTP area built of waste rock, it is possible that there has been drainage of pore water into the waste rock that has desaturated the tailings. But, there are no filter zones between the waste rock and the tailings, the foundation has a low permeability that would prevent under drainage, and there are no instruments in the tailings to demonstrate desaturation. Hence, it is likely that the tailings are contractive and could be liquefiable. But, for the purpose of this study, it has been assumed that the beach tailings will behave in a dilative manner during shearing and thus the stability analysis reported in this paper is based on this assumption. This assumption should be checked before raising in the upstream direction.

3 EMBANKMENT RAISING

The existing TP is expected to surpass its storage capacity within a few years due to the continuous storage of tailings from the Rampura Agucha Mine (Sitharam & Hegde, 2017). As a result, to increase the storage capacity, the concerned authority decided to increase the height of EoTP by another 24m bringing the total height to 75m. The U/S construction technique will be employed in those portions of EoTP where space is not available in the D/S direction. The D/S method will be adopted for the remaining portion of the TP. The total additional height (i.e. 24m) in both D/S and U/S cases will be provided in four lifts (each of 6m height).

3.1 *Construction by U/S method*

In the case of the section to be built using the U/S method, a 10m wide berm (made up of waste rock) will be provided at the end of construction of each phase towards the D/S portion (as shown on Fig. 1). Further details:

- As the stability of EoTP decreases with increase in the overall height of TP (Singh et al. 2020), an intermediate slopes of 2.5H: 1V (1.37H: 1V in existing EoTP) is provided at D/S portion of embankments (refer to Fig. 2). These intermediate slopes results in the overall slope of 2H: 1V which is flatter than the overall slope (1.73H: 1V) of existing TP (see Fig. 2).
- Further, the slope on the U/S slope of each raise is kept similar to that provided in the existing EoTP i.e. 2H: 1V.
- A crest width of 25m will be provided at the end of construction of the embankments in each lift.

3.2 *Construction by D/S method*

To begin with, a 5m wide berm will be provided on the U/S slope at the beginning of the first and third lift (see Fig. 2). Further details:

- Similarly, a berm of 5m at every 15m rise (measured from the foundation level) will be provided on the D/S slope.
- Further, the U/S slope of the embankments (in each lift) is kept at 2H: 1V whereas a slope angle of 1.37H: 1V (similar to that provided in the existing EoTP) is maintained at the D/S slope of embankments (see Fig. 3).
- The top-width of embankments will be maintained at 25m at the end of each lift.

4 CURRENT PRACTICE FOR THE CONSTRUCTION OF U/S TYPE TP

The new embankments in the portion that will use the U/S construction technique may be built over contractive and liquefiable tailings. For EoTP that pose a threat to life if they were to fail, which is the case for this structure, the current practice for the design of U/S type EoTP involves assuming the tailings will liquefy. For such cases, where the beach tailings are contractive, the stability of the EoTP is assessed by considering the post-liquefied shear strength (Saad and Mitri, 2010), calculating the factor of safety and modifying the geometry of the EoTP so that a minimum factor of safety of at least 1.1 is achieved for this condition.

However, drained parameters can be utilized to perform the stability analysis if the embankment material and beached tailings are dilative in nature. Because most of the EoTP failures in the past have been due to contractive tailings and embankment material, it is recommended to utilize the drained analysis with caution only for those TPs that store dilative tailings.

As noted above, there is insufficient information provided by the mine to determine if the tailings are contractive or dilative and this study assumed them to be dilative. However, a thorough investigation should be done to identify the true nature of beach tailings. Hence, the recommendations of this study are only applicable if the beach tailings are proven to be dilative in nature. Accordingly, a modified design should be employed if the tailings are confirmed to be liquefiable.

5 INDIAN STANDARD REGULATIONS FOR TP'S STABILITY

For a full reservoir condition under steady state seepage, IS 7894 (1975) suggests a minimum factor of safety of 1.5. Furthermore, IS 7894 (1975) recommends the use of effective shear strength parameters only for cohesionless soils and where no positive pore water pressure is generated. This is consistent with a drained analysis and, as noted above, is only applicable if the tailings and EoTP are dilative. Accordingly, an ERR with a factor of safety greater than 1.5 is suggested in this study, which can be implemented to raise the height of EoTP.

6 LITERATURE REVIEW

Most of the TP failures that have occurred were built using U/S construction technique (Rico et al. 2008; Dong et al. 2020). Further, liquefaction, which is caused due to the contractive nature of tailings, is found to be the major reason for the failure of these EoTPs. In addition, shear induced failure, caused by the significant build-up of EPWP due to the high ERR, can also lead to the failure of TP (Do et al. 2021; Saad & Mitri, 2011). One of the prime examples of liquefaction-induced failure is the Fundao tailings dam failure, which occurred due to the liquefaction of the contractive tailings triggered during the raising of TP embankment's (Sadrekarimi & Riveros, 2020). As the TP does not provide direct economic benefits to the mining enterprise, in many cases, sufficient attention is not paid to their design and monitoring (Dong et al. 2020). However, failures of TP in recent years have raised a deep concern regarding overall stability of these structures.

Most of the studies in the past (refer to work done by Zhang et al. 2020; Pak & Nabipour, 2017; Coulibalry et al. 2017) had implemented steady state analysis to evaluate the stability of TP, which did not take into account the effect of EPWP developed during various phases of construction. EPWP is developed within the EoTP during the raising of embankment's height. Moreover, the development of EPWP within the EoTP is predominantly influenced by the ERR (defined as the height of embankments raised per year) (Do et al., 2021). The impact of the ERR had been primarily noticed in U/S type TPs where the new embankments are built partially or fully over the tailings (EPA, 1994; Vick, 1990). Such developments in EPWP during the phased construction of TP had been discussed by a few researchers, which took into account the self-weight consolidation of tailings (refer to work done by Orman et al. 2013; Saad & Mitri, 2011). Moreover, the influence of ERR on the building-up of EPWP and therefore on the overall stability of TP has not been explored in the existing literature. Therefore, keeping the above discussion in view, the stability analysis for the current TP is performed using transient analysis, which takes into account the effect of staged construction and ERR.

7 METHODOLOGY ADOPTED

In order to simulate the soil-fluid interaction, Biot's (1941) consolidation theory is utilised in which the soil skeleton is considered as a porous elastic media coupled with a laminar pore fluid using the conditions of compressibility and continuity. The governing equation used in the Biot's (1941) consolidation theory for the two-dimensional analysis is given by Equation 1.

$$\frac{K'}{\gamma_w}\left(K_x \frac{\partial^2 u_w}{\partial x^2} + K_y \frac{\partial^2 u_w}{\partial y^2}\right) = \frac{\partial u_w}{\partial t} - \frac{\partial p}{\partial t} \quad (1)$$

Where, K' = soil bulk modulus, p = mean total stress, u_w = pore water pressure, K_x and K_y are the hydraulic conductivities in x and y directions respectively.

A fully coupled stress-pore pressure analysis is carried out in finite element based software RS2, which utilises Biot's (1941) consolidation theory to simulate the soil-fluid interaction. Furthermore, the stability of EoTP is determined in terms of critical SRF (a parameter commonly employed in FEM-based analysis to quantify the slope stability) using the shear strength reduction (SSR) technique. In SSR technique, shear strength parameters, such as cohesion (c) and angle of internal friction ($\emptyset'$), are reduced by a factor (i.e. SRF) in each step until the slope fails.

8 FINITE ELEMENT MODEL IN RS2

7.1 *Numerical model set-up for stage construction*

The entire TP consists of three components i.e. a) EoTP (including tailings beach as a part of structural shell for U/S case), b) foundation soil and c) tailings deposit (excluding the beach portion). The geometry of the entire TP domain was drawn in RS2 modeller for both the U/S and D/S section as per the details discussed in the previous section. Both side and bottom boundaries were extended sufficiently in horizontal and vertical directions respectively to minimise the edge errors. In order to simulate the construction of the EoTP during various rises, five stages were created in RS2 (i.e. stage 0, 1, 2, 3 and 4). The initial conditions prevailing at the site before the beginning of construction (i.e. at t = 0 year) was defined by stage 0, which is characterised by a TP system (a large portion of which is saturated except the EoTP) with steady state seepage condition. Subsequently, stages 1, 2, 3, and 4 were defined to represent the construction of embankments during four lifts. The construction in each lift includes two phases; a) raising phase (R, which includes the construction of new embankments and filling of pond) and b) consolidation phase (C, representing the consolidation of stored tailings). ERR, which is expressed as the height of embankments raised in m per year, takes into account the time taken (in years) during both raising and consolidation phases. In this study, raising of embankments in each phase was assumed to take 30 days based on the average time taken by various mining industries. Accordingly, the time for the self-weight consolidation in each phase was considered as 153, 211, 335, 700, 2160 days, corresponding to the ERR of 12, 9, 6, 3 and 1 m/year respectively. E.g. to obtain an ERR = 12 m/year, the 6 m height in each lift must be provided in 183 days (i.e. 1/2 year), which can be done by allowing the time in consolidation phase = 153 days along with 30 days of raising phase (30 + 153 = 183 days). Consolidation analysis is carried out in each phase to investigate the transient response of the TP system due to the construction of subsequent phases. Different sets of hydraulic and mechanical boundary conditions are invoked for each phase, which are discussed in the subsequent sections. It is worth noting here that the ERR used in this study was assumed just for the sack of completion of analysis. However, in practical scenario raising an embankment by 12m in 30 days is not possible.

The seepage field within the TP is not only affected by the hydraulic properties of materials (tailings and embankment soil) but also by the beach formed behind the EoTP (Jeong & Kim, 2020; Zhang et al., 2020). The provision of a beach region (which consists of an exposed surface of the dry tailings between the point of discharge and the decant pond) behind the EoTP is a must for the U/S type TP since the foundation of embankments in subsequent phases are built (partially or fully) over the beach tailings (Vick, 1990). In addition, a beach area also aids in maintaining the phreatic line away from the EoTP (Jeong & Kim, 2020). Keeping this in view, a constant beach width (L) to height (H) ratio (L/H = 1.5) (at the end of each phase) is provided in the U/S case during each phase of construction, which is found be sufficient to keep the phreatic line away from the EoTP. It is worth noting here that the beach width is considered as the horizontal distance between the starting point of the embankment's crest (towards the U/S side) and the decant pond (see Fig. 5a).

7.2 *Material properties*

As highlighted earlier, the EoTP was constructed by using the crushed waste rocks (mine spoil) obtained from the mining activities. The foundation system beneath the TP consists of a low permeable soil layer (permeability coefficient, $K_x = 10^{-8}$ m/s) underlain by a rocky strata (Sitharam & Hegde, 2017). Geotechnical properties of mine spoil, tailings and the foundation soil were taken from Sitharam & Hegde (2017) and are listed in Table 1. In addition, hydraulic conductivities of settled tailings and mine spoil were referred from the work by Ormann et al. (2013), and Quille & O'Kelly (2010). To account for the effect of anisotropy, K_y/K_x of 0.3 is assumed for the settled mine tailings whereas a value of K_y/K_x of 0.8 is utilized for the mine spoil (Ormann et al. 2013; Vick, 1990).

Table 1. Geotechnical properties of various materials used in the numerical simulation.

Material type	c' (kPa)	Φ' (Degree)	Bulk unit weight (kPa)	E (kPa)	K_x (m/s)	α (m^{-1})	n
Mine spoil	2	39	20.7	25700	1×10^{-2}	15.10	7.35
Foundation soil	20	38	22.0	51428	1×10^{-8}	0.8	1.80
Settled mine tailings	1	35	20.0	12800	1×10^{-5}	1.6	1.37

7.3 *Constitutive laws used*

Bishop's (1959) effective stress approach, which takes into account the effect of matric suction, was utilised in this study to define the failure of various materials (i.e. embankment material, foundation soil and settled mine tailings). Shear strength of soil in Bishop's (1959) effective stress approach was defined by Equation 2, which is an extension of the Mohr-Coulomb failure criterion.

$$\tau = c' + [(\sigma - u_a) + \chi (u_a - u_w)] \tan\phi' \quad (2)$$

Where, τ = shear strength of soil (kPa), c' = effective cohesion (kPa), σ' = effective normal stress (kPa) and ϕ' = effective internal friction of soil (degree), u_a = air pressure, χ = matric suction coefficient.

Furthermore, the Van Genuchten (1980) - Mualem (1976) model was utilised to define the hydraulic conductivity function (HCF) of settled mine tailings and the mine spoil by using Equation 3 given below.

$$K = K_s(\sqrt{S_e}\left[1-\left(1-S_e{}^{1/m}\right)^m\right]^2 \quad (3)$$

Where, K_s = saturated hydraulic conductivity, h = pressure head, m, n = curve fitting parameters, S_e = Effective degree of saturation

$$S_e = \frac{1}{[1+(\alpha h)^n]^m} \quad (4)$$

The default values provided in RS2 (referred from Vogel et al. 2000) were utilised in this investigation to determine the values of α, n and m, based on the hydraulic conductivities of various materials. For settled mine tailings, α, n and m were selected corresponding to the fine silt (as mine tailings are generally silty in nature) whereas values of α, n and m corresponding to coarse sand are utilised for the mine spoil.

7.4 Mesh convergence study

In order to obtain the optimum meshing parameters for the analysis, a mesh convergence study was performed beforehand for both U/S and D/S case. Trial analyses were run with roughly 940, 1420, 2220, 3120 and 870, 1220, 1940, 2820 number of 6-noded triangular elements respectively for the D/S and U/S type cross-sections. Based on the sensitivity analysis, the D/S type section of TP (at the end of 4th lift) was discretised into 2220 number of 6-noded triangular elements whereas the U/S type section of TP was discretised into 1940 elements. In addition, finer meshing was provided near the zone neighbouring the EoTP as a higher EPWP is expected to develop within this region.

8 RESULTS AND DISCUSSION

8.1 *Build-up of EPWP during various phases of construction for U/S case.*

To study the build-up of EPWP within the TP, a point beneath the embankment built in Phase 1 was selected (see Fig. 1) for the U/S case (as higher EPWPs are expected beneath the embankments). As the EoTP is partially built over the tailings itself, build-up of EPWP within the tailings beneath the embankments plays a critical role in determining the overall stability of the U/S type TP. Figure 4 depicts the build-up of EPWP (at points mentioned earlier) during various phases of construction (i.e. R1, C1, R2, C2, R3, C3, R4 and C4) with different ERR. The EPWP was zero before any construction and rises to 107 kPa during the first raise for every ERR, as shown in Fig. 4. The EPWP remains constant (i.e. 107 kPa) during the first rise, regardless of the ERR, which is owing to the fact that the raising duration for each ERR was maintained the same, i.e. 30 days. Furthermore, it can be observed from Figure 4 that a high EPWP was developed during each phase of raising (i.e. R1, R2, R3 and R4) which gets dissipated (partially or fully depending upon the consolidation time) during the subsequent phases of consolidation (i.e. C1, C2, C3 and C4). Moreover, the increase in EPWP was found to be maximum after second raise (e.g. EPWP increases from 60 kPa to 120 kPa after second raise for an ERR= 6m/year). In addition, the EPWP was observed to increase with increase in ERR, owing to the limited time available for the EPWP dissipation (see Fig. 4).

Figure 5a, b shows the development of EPWP within the TP constructed by U/S technique during the phase 2 construction. It can be seen from Figure 5a, that for U/s case, due to the application of construction load from the newly built embankment, a significantly high EPWP was developed beneath the embankment (at point A) during R2 phase. However, due to the consolidation of mine tailings over a period of time, dissipation of EPWP (developed at R2 phase) takes place during the C2 phase. It must be mentioned here that the maximum EPWP was developed during the second and fourth raise at a point beneath the embankment built in phase 1 (point A) and 3 respectively. However, EPWP developed during the second raise was found to be affecting the failure surface, as it is closer to the slopes of previously built EoTP, which defines the overall stability for the present case.

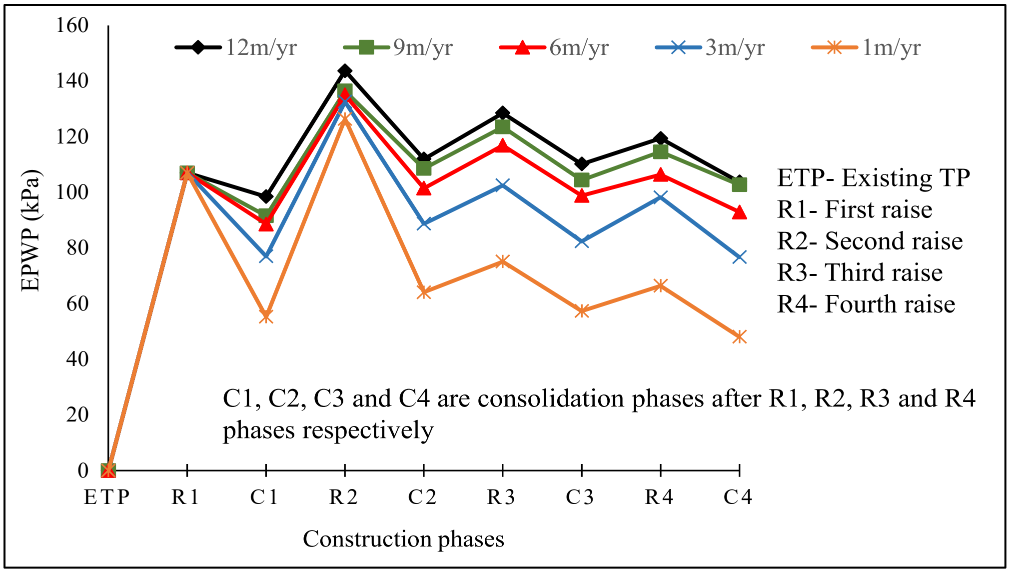

Figure 4. Build-up of EPWP (at point A) during various phases of construction with varying ERR.

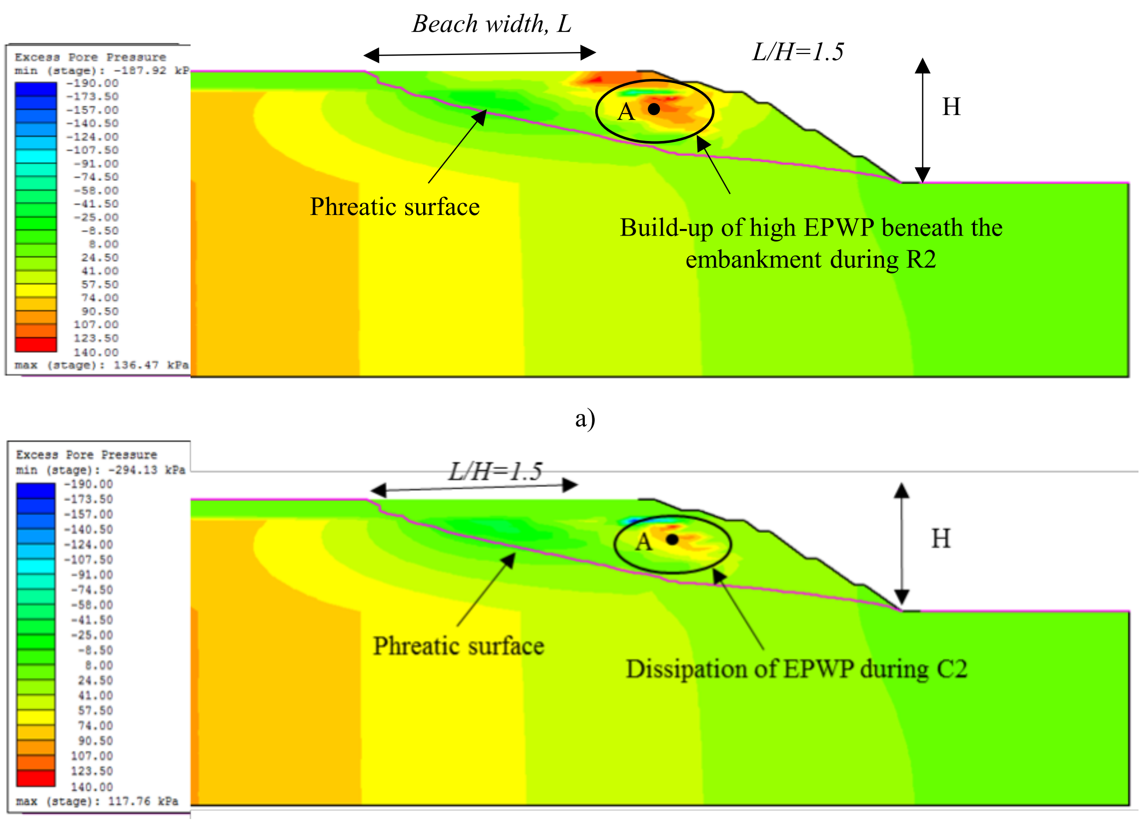

a)

b)

Figure 5. Development of EPWP within the TP for U/S case (with ERR = 6 m/year) during a) R2 and b) C2 phases.

Figure 6 depicts the slip surface pattern observed after the completion of phase 4 construction. It can be seen from Figure 6 that the failure surface passes through the slopes of previously existing EoTP. In addition, the failure surface was observed to be unaffected by subsequent raises due to the steeper (as comparison to the slope provided in newly built embankments) slopes of previously existing EoTP, which make them critical slopes.

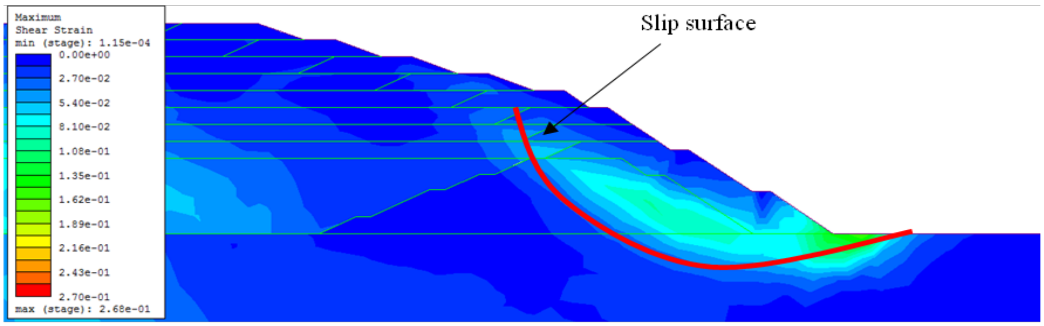

Figure 6. Pattern of slip surface observed at the end of final phase of TP construction (with ERR = 6 m/year) for U/S method.

8.2 *Build-up of EPWP during various phases of construction for D/S case.*

For the D/S case, development of EPWP was studied at a point within the rockfill embankment (see Fig. 3). It can be observed from the Figure 7 that in case of D/S method, ERR have a negligible influence on the development of EPWP in the rockfill embankment or the foundation soil. The EPWP within the rockfill embankment varies from 3 to 15 kPa during various phases of construction (as shown in Fig. 7), which is very minimal and thus do not affect the TP's stability. This is due to the fact that the rockfill embankment, due to its higher hydraulic conductivity (10^{-2} m/s), works as a drainage boundary desaturating the tailings present on its U/S side. Furthermore, because the foundation system has a thin layer of clay that is overlain by weathered rocky stratum (which is normally pervious in nature), EPWP development will not be a worry.

The slip pattern observed at the end of phase 4 construction, as illustrated in Figure 9, corroborates the preceding observations. Because not enough EPWP is produced inside the foundation system, the slip surface does not cross through the foundation soil, as shown in Figure 9 signifying the toe failure.

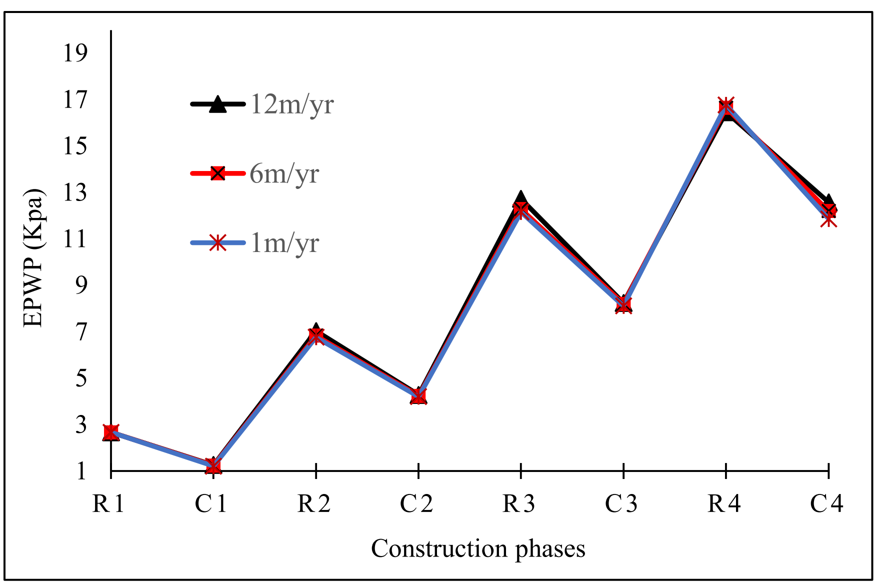

Figure 7. Development of EPWP (at point A) during various phases of construction with varying ERR.

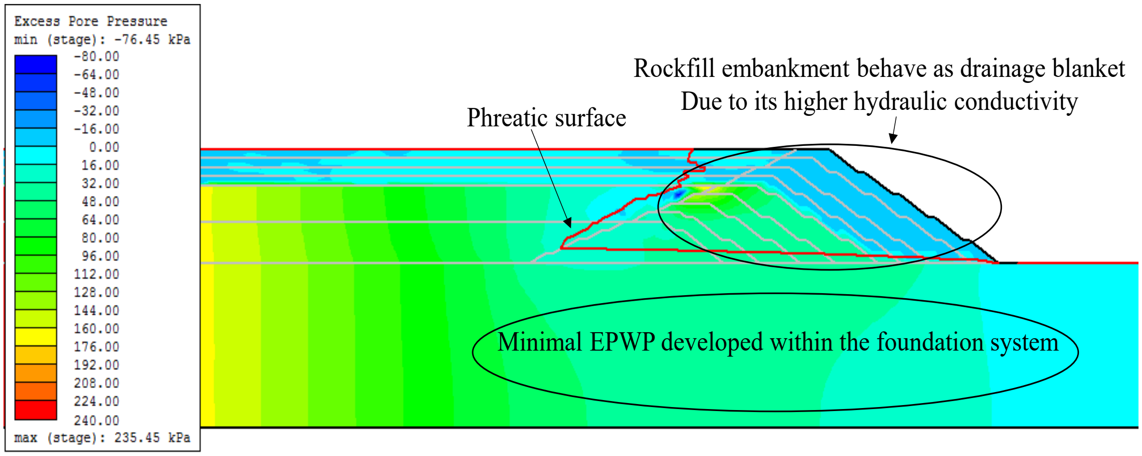

Figure 8. Contours of EPWP for the D/S case (with ERR = 6 m/year) at the end of phase 4 construction.

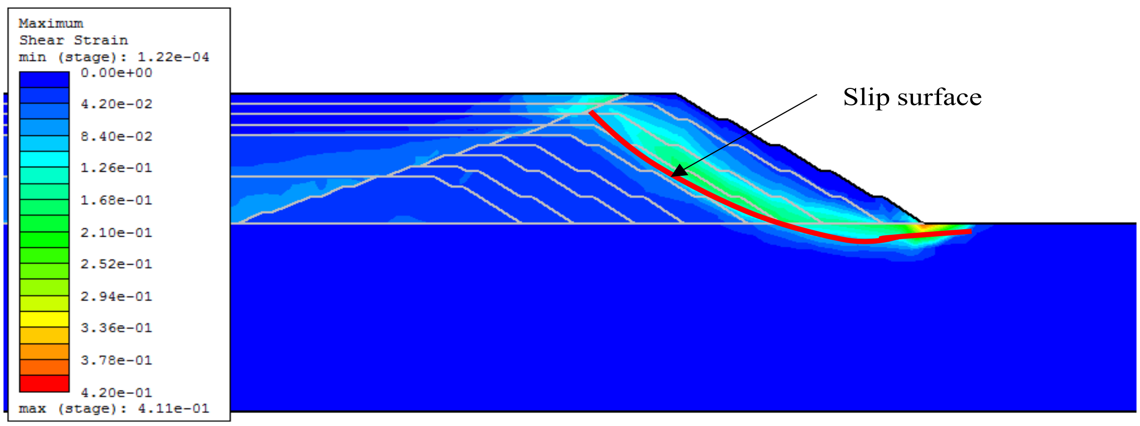

Figure 9. Pattern of slip surface observed at the end of final phase of TP construction (with ERR = 6 m/year) for D/S method.

8.3 Critical SRF obtained for the EoTP

To study the effect of ERR on the overall stability of the U/S type EoTP, the critical SRF obtained at the end of construction of phase 4 was plotted against the ERR in Figure 10. It can be seen from Figure 10 that the critical SRF decreased from 1.73 to 1.54 corresponding to the ERR of 1 and 12 m/year respectively. This is due to the reason that a higher ERR (12, 9 m/year) results in the development of more EPWP as compared to lower ERR (1, 3 m/year), which in turn decreased the effective stresses and ultimately the shear strength of soil.

The TP's stability is not significantly influenced by the ERR in the D/S scenario since not enough EPWP was observed to develop within the rockfill embankment and foundation for various ERR as mentioned in section 8.2.

Figures 6 and 9 present the results of the stability analyses for the U/S and D/S configurations. These are for an ERR of 6m/year and the resulting factor of safety was found to be 1.68 and 2.11, for the U/S and D/S configurations, respectively.

Based on the current analysis, the ERR could be as high as 12 m/year, but given the uncertainty associated with the tailings and the foundation material, an ERR of 6 m/year is recommended as a preliminary value that requires further assessment and study.

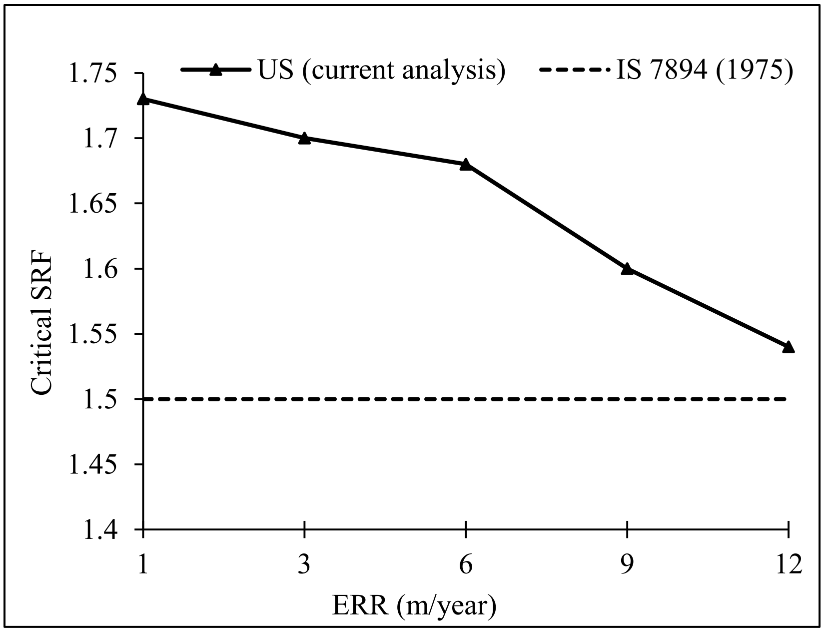

Figure 10. Variation of critical SRF with ERR for the U/S case at the end of phase 4 construction.

9 CONCLUSIONS

The aim of the present study was to examine the stability of a TP, height of which is required to be raised from 51 m to 75 m. The height of EoTP was provided in four phases (6 m lift in each phase) by utilizing both D/S and U/S construction technique. A transient fully coupled stress-pore pressure analysis was performed in the finite element based commercial software RS2 to investigate the hydro-mechanical behaviour of TP during various phases of construction. While doing so, the effect of ERR on the development of EPWP and therefore on the overall stability of TP was investigated. Following four conclusions were drawn from the current analysis:

- EPWP was observed to increase during each phase of raising due to the application of construction loads from the subsequent phases. However, a decrease in EPWP was observed during the subsequent phases of consolidation due to the dissipation of pore water pressure.
- The EPWP was noticed to increase with increase in the ERR for the U/S case. However, in case of D/S method, ERR was found to have a negligible influence on the building up of EPWP within the TP system.
- The overall stability of TP section built by U/S method was found to decrease with an increase in the ERR. The critical SRF obtained at the end of final construction reduced from 1.73 to 1.54 when the ERR was increased from 1 m/year to 12 m/year.
- The resulting factor of safety was found to be 1.68 and 2.11, for the U/S and D/S configurations, respectively for an ERR of 6 m/year.

It is worth noting that the current study was based on the assumptions that the stored tailings are dilative in nature. Further modification in design is required if the tailings are found to be liquefiable (contractive) after a detailed investigation.

10 REFERENCES

Bassam, S. & Han, M. 2010. Staged construction analysis of surface tailings disposal facilities. *International Journal of Mining, Reclamation and Environment,* 24(1): 44-63.

Biot, M. A. 1941. General theory of three-dimensional consolidation. *Journal of applied physics* 12(2):

155-164.
Bishop, A.W., 1959. The principles of effective stress. *Teknisk Ukeblad* 106(39): 859–863.
Coulibaly, Y., Belem T. & Cheng, L. 2017. Numerical analysis and geophysical monitoring for stability assessment of the Northwest tailings dam at Westwood Mine. *International Journal of Mining Science and Technology* 27(4): 701-710.
Do, T. M., Laue, J., Mattsson, H. & Jia, Q. 2021. Numerical Analysis of an Upstream Tailings Dam Subjected to Pond Filling Rates. *Applied Sciences* 11(13): 6044.
Dong, L., Deng, S. & Wang, F. 2020. Some developments and new insights for environmental sustainability and disaster control of tailings dam. *Journal of Cleaner Production* 269: 122270.
EPA 1994. *Design and evaluation of tailings dam*. United State environmental protection agency, office of solid waste, Washington, DC.
IS 7894. 1975. *Code of practice for the stability analysis of the earth dams.* New Del-hi: Indian Standard.
Jeong, Y. & Kim, K. 2020. A Case Study: Determination of the Optimal Tailings Beach Distance as a Guideline for Safe Water Management in an Upstream TSF. *Mining, Metallurgy & Exploration 37*(1): 141-151.
Mualem, Y. 1976. A new model for predicting the hydraulic conductivity of unsaturated porous media. *Water resources research* 12(3): 513-522.
Naeini, M. and Akhtarpour, A. 2018. Numerical analysis of seismic stability of a high centerline tailings dam. *Soil Dynamics and Earthquake Engineering* 107: 179-194.
Ormann, L., Zardari, M. A., Mattsson, H., Bjelkevik, A. & Knutsson, S. 2013. Numerical analysis of strengthening by rockfill embankments on an upstream tailings dam. *Canadian Geotechnical Journal* 50(4): 391-399.
Pak, A. & Nabipour, M. 2017. Numerical study of the effects of drainage systems on saturat-ed/unsaturated seepage and stability of tailings dams. *Mine Water and the Environment* 36(3): 341-355.
Psarropoulos, P. N., & Tsompanakis, Y. (2008). Stability of tailings dams under static and seismic loading. *Canadian Geotechnical Journal* 45(5): 663-675.
Quille, M. E. & O'Kelly, B. C. 2010. Geotechnical properties of zinc/lead mine tailings from Tara Mines, Ireland. In *Proceedings of the 2010 Geo Shanghai International Conference-Geoenvironmental Engineering and Geotechnics: Progress in Modeling and Applications, Shanghai, China, 3–5 June 2010.*
Rico, M., Benito, G., Salgueiro, A. R., Díez-Herrero, A. & Pereira, H. G. 2008. Reported tailings dam failures: a review of the European incidents in the worldwide context. *Journal of Hazardous Materials* 152(2: 846-852.
Saad, B. & Mitri, H. 2011. Hydromechanical analysis of upstream tailings disposal facilities. *Journal of Geotechnical and Geoenvironmental Engineering*, 137(1), 27-42.
Sadrekarimi, A. & Riveros, G. A. 2020. Static Liquefaction Analysis of the Fundão Dam Failure. *Geotechnical and Geological Engineering*, 38(6): 6431-6446.
Singh, S. & Kumar, A. 2021. Methodologies Available for the Determination of Seismic Active Thrust Acting on Retaining Walls: A Critical Review. *Indian Geotechnical Journal*: 1-13.
Singh, S., Kumar, A. & Sitharam, T.G. 2020. Stability Analysis of Tailings Dam Using Finite Element Approach and Conventional Limit Equilibrium Approach. In *Proceedings of Indian Geotechnical Conference, Vishakhapatnam, India, 17-19 December 2020*.
Sitharam, T. G. & Hegde, A. 2017. Stability analysis of rock-fill tailing dam: an Indian case study. *International Journal of Geotechnical Engineering* 11(4): 332-342.
Van Genuchten, M. T. 1980. A closed-form equation for predicting the hydraulic conductivity of unsaturated soils. *Soil science society of America journal* 44(5): 892-898.
Vick, S. G. 1990. *Planning, design, and analysis of tailings dams.* BiTech, Richmond, BC, Canada.
Vogel, T., Van Genuchten, M. T. & Cislerova, M. 2000. Effect of the shape of the soil hydraulic functions near saturation on variably-saturated flow predictions. *Advances in water resources* 24(2): 133-144.
Zhang, C., Chai, J., Cao, J., Xu, Z., Qin, Y. & Lv, Z. 2020. Numerical Simulation of Seepage and Stability of Tailings Dams: A Case Study in Lixi, China. *Water* 12(3): 742.

Evaluation of internal stability of coarse filter materials using large-scale laboratory testing

Christian Armstrong, David Geier, & Matthew Cashimer
Golder Associates Inc., Lakewood, Colorado, United States

Steve Anderson
Golder Associates Inc., Anchorage, Alaska, United States

Aaron Sangha
Teck Alaska Incorporated, Anchorage, Alaska, United States

ABSTRACT: A two-zone filter system, including finer and coarser material zones, was evaluated as part of a tailings storage facility expansion. Large-scale permeameter testing was performed to evaluate the internal stability of proposed coarser filter materials that were identified to be potentially unstable based on empirical methods. Testing consisted of compacting the material in a large-diameter permeameter that can provide a constant hydraulic head. Four hydraulic heads were selected for testing, including the expected hydraulic gradient and gradients above the critical hydraulic gradient. Constant head hydraulic conductivity testing was performed on the specimen between elevated hydraulic gradients to evaluate any potential change in the permeability. Outflow was collected during testing to evaluate the quantity and characteristics of eroded material. Particle-size distribution tests were performed on samples collected before and after testing to evaluate the change in the gradation of the upgradient and downgradient sides of the sample. The large-scale testing indicated that the coarser filter material was internally stable. These results indicate the usefulness of laboratory testing to evaluate the applicability of the applied empirical methods and provide a more direct indication of how filter materials may behave in the field.

1 INTRODUCTION

The design of filters for dams within tailings storage facilities (TSF) dams is critical for both the containment and stability aspects of these facilities. One of the tailings dams at the Red Dog Mine in northwest Alaska includes a downstream raise design. The bulk of the dam fill consists of coarse rockfill (24 inch minus material). On the upstream side of the rockfill there are two progressively finer filter zones. Hydraulic containment is provided by a 100-mil thick HDPE geomembrane, which is covered by tailings (d_{85} nominally 0.17mm).

The filter zones are at an inherent risk for allowing migration of fine-grained material; either from upstream zones due to filter incompatibility between zones, or from within a filter zone due to internal instability of the filter zone itself. Risk is amplified by the wide transition in particle size between finer tailings and the coarser rockfill zones that comprise the dam. Internal instability, also referred to as suffusion, may result in the migration of the finer fraction of the filter materials, which can potentially result in unacceptable seepage, clogging of down gradient drainage systems, settlement or deformation, particle size distribution changes significant enough to cause out-of-specification material (and filter incompatibility with adjacent zones), or downstream stability of the tailings dam. The filter zones must carefully be selected to mitigate this risk, in conjunction with other risk mitigation measures including reducing phreatic levels and gradients and minimizing defects in the geomembrane. As such, numerous methodologies have been developed to evaluate the filter compatibility between zones and also evaluate the internal instability of these materials. For the evaluation of internal stability, the majority of these methods have been developed for sandy gravels without fines, with the exception of the Burenkova and Wan and Fell methodologies (Wan and Fell 2008).

A two-zone filter was necessary for the Red Dog tailings dam due to the large difference in particle size distributions between the fine spigoted tailings and the coarser rockfill. Particle size distributions for the two filter zones were developed following the guidelines outlined by the National Resources Conservation Service (NRCS) Chapter 26 – "Gradation Design of Sand and Gravel Filters" (NRCS 2017). The resulting particle-size distributions were then evaluated for internal stability using three empirical methodologies, which indicated that the coarser of the two filter zones was potentially susceptible to suffusion. An experimental methodology, similar to the one presented by Wan and Fell (2008), was used to evaluate the susceptibility suffusion of the materials using several hydraulic gradients.

2 DEVELOPMENT AND EVALUATION OF TWO-STAGE FILTERS

Criterion for the filter gradations were developed using the NRCS (2017) methodology for both Zone 1 (finer filter) and Zone 2 (coarser filter) materials. These criteria were based on the in-place particle-size distributions of the tailings materials in the beach zone adjacent to the dam and specifications for the rockfill. The resulting specifications for filter zone particle size distributions are presented in Figure 1, along with an average particle-size distribution from the stockpile for the Zone 1 material and the coarsest and finest samples from the Zone 2 stockpile. Both filter materials are considered to be non-plastic based on historic laboratory testing.

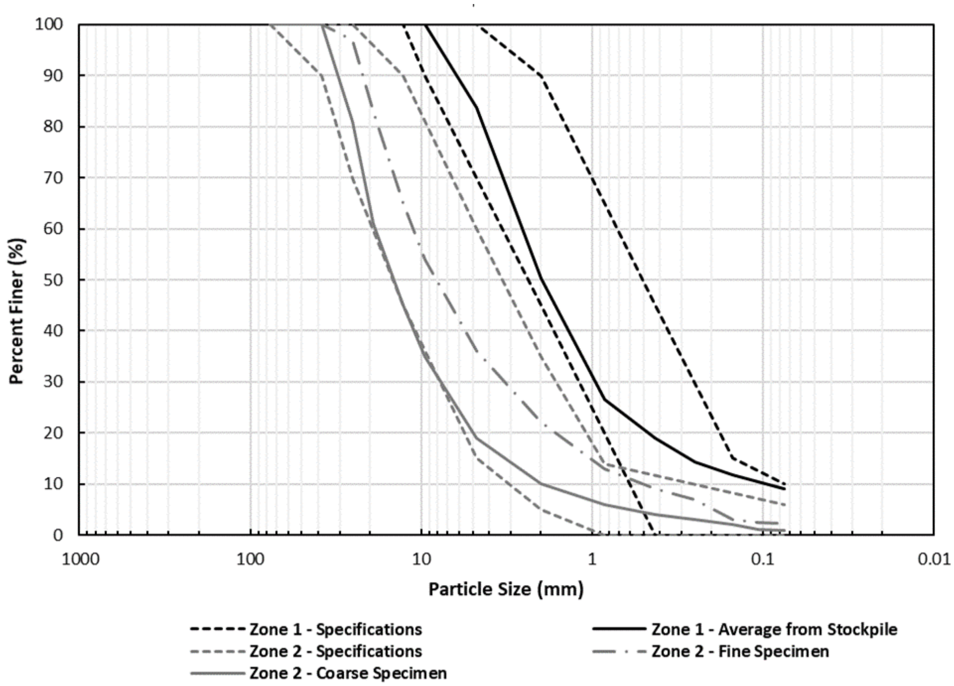

Figure 1. Particle-Size Distributions and Specifications for Two-Zone Filter.

The NRCS method used to develop the filter gradations discusses the risks posed by internal instability and includes criteria intended to produce gradations that are internally stable. However, the susceptibility to suffusion was also evaluated using the following three additional methodologies for verification.

- Kenney and Lau (1985, 1986)
- Wan and Fell (2008)
- Modified Burenkova, developed by Burenkova (1993), modified as presented in Wan and Fell (2008)

These methodologies are all empirical methods that use various characteristics of the particle-size distributions to predict actual performance. The criteria used to predict satisfactory performance have been calibrated against numerous laboratory tests, with testing performed on more coarse specimens for the Kenney and Lau methodology and more fine specimens for the Wan and Fell and Modified Burenkova methodologies. Each of the three methods utilize different criteria, have different rationale for selecting the criteria, and use different delineations between internally stable and unstable materials. As a result, it is not uncommon for different methods to disagree regarding the acceptability of a given soil and for multiple methods to be considered in aggregate. The results for these evaluations are presented in Figure 2 for Kenny and Lau (1985, 1986), Figure 3 for Wan and Fell (2008) and Figure 4 for Modified Burenkova.

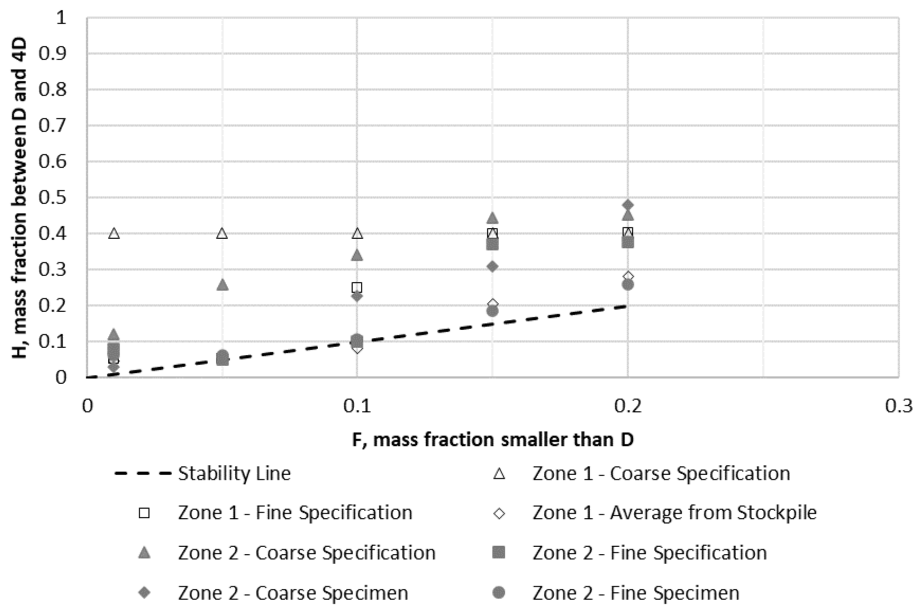

Figure 2. Results from Kenny and Lau (1985, 1986) Evaluation (points above line are stable)

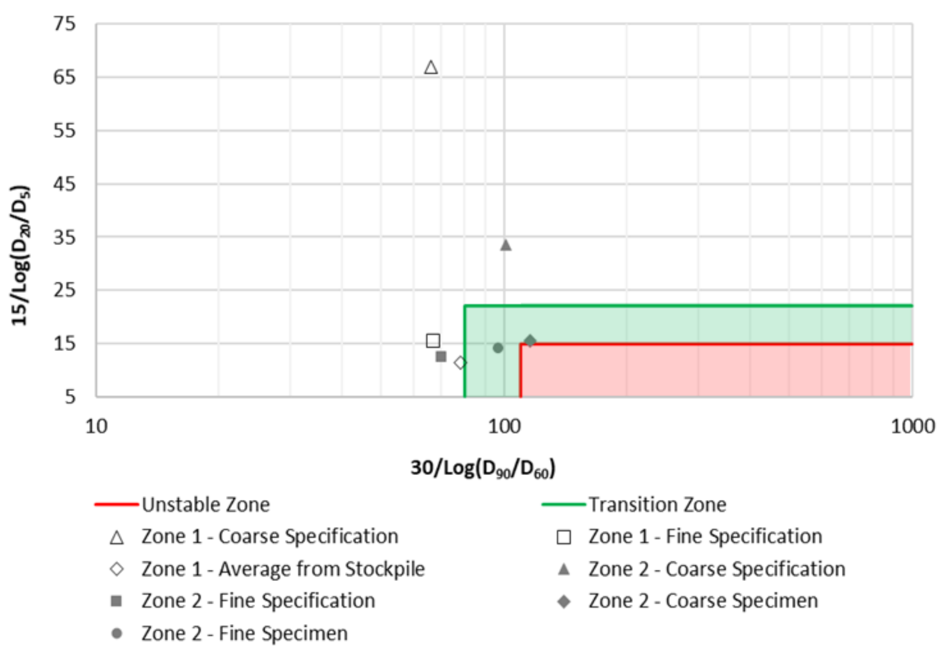

Figure 3. Results from Wan and Fell (2008) Evaluation.

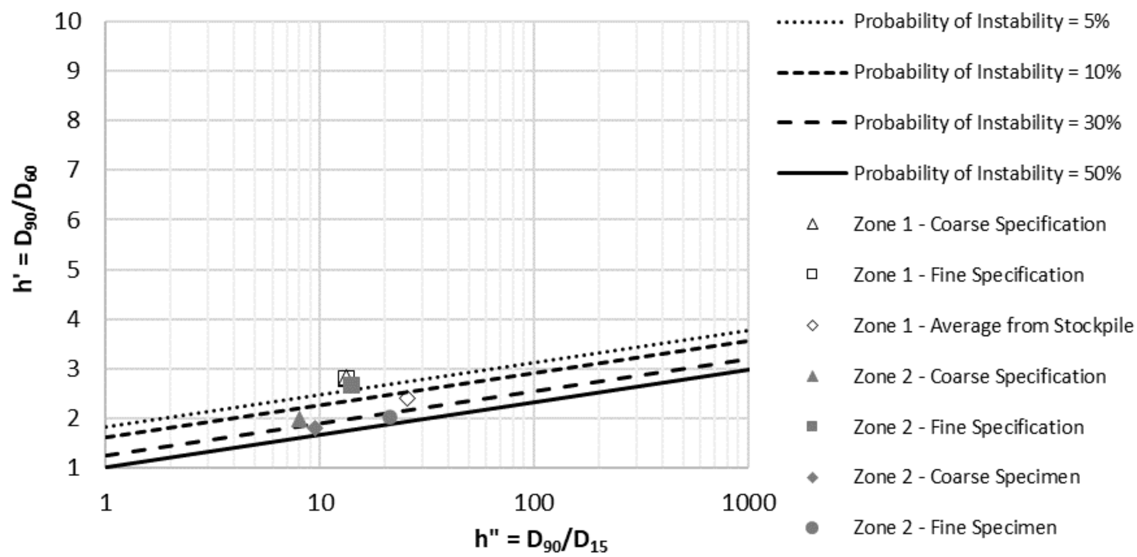

Figure 4. Results from Modified Burenkova Evaluation.

The Kenney and Lau methodology indicated that all specifications are internally stable. Under the Wan and Fell criteria, the fine and coarse sides of the specification for the Zone 2 material are within the stable zone, but grain-size distributions from the coarsest and finest stockpile specimens are in the transition zone. The Modified Burenkova method indicates that the probability of instability ranges from 2 to 36%, with higher values for the Zone 2 materials. The Zone 1 material was generally found to be stable, but there was some uncertainty whether the Zone 2 material would be internally unstable. Additionally, the Wan and Fell (2008) method indicates that filters with less than 20% of material finer than the inflection point in the particle size distribution curve may not be accurately evaluated with the existing methodologies. Therefore, given the potential consequences of poor filter zone performance, Golder performed an experimental laboratory test on the Zone 2 materials to verify that they are internally stable at the expected gradients.

3 EXPERIMENTAL METHOLODGY

3.1 *Laboratory Equipment*

Laboratory testing was performed in Golder's large diameter permeameter modified to perform the suffusion test, as shown in Figure 5. In general, the test set-up is similar to the one used by Wan and Fell (2008), with the exception that flow was upwards rather than downwards and applied hydraulic head was measured using a standpipe and measuring tape rather than pressure transducers. The permeameter consists of a 10-inch diameter cell, top and bottom porous platens, and a filter screen above the bottom platen to prevent clogging of the bottom porous stone. Flow within the permeameter was applied by opening a valve connected to a constant head water source. The valve allowed for application of variable hydraulic head imposed at the base of the specimen. This head was varied to a specified hydraulic gradient based on the length of the specimen. To collect the outflow of water and potentially eroded soil, a PVC collar was attached to the top of the cell and silicon was used to seal the collar to the top of the cell to collect the outflow from the specimen. A 2-inch clear outlet tube was fitted to the collar for the collection of effluent. Five-gallon buckets were used to collect the effluent.

The specimen was reconstituted in 3 (three) nominal 2-inch lifts. The initial height of the specimen was measured prior to the application of water. Clean, coarse gravel, with particle sizes between one to three inches in diameter, was placed on top of the sample to keep the upper porous stone in place during testing, while allowing upwards migration of potentially eroded soil from the specimen. Additionally, the specimen was confined using a spacer and top plate to prevent uplift. Dial gauges were attached to the device to measure any change in height during testing.

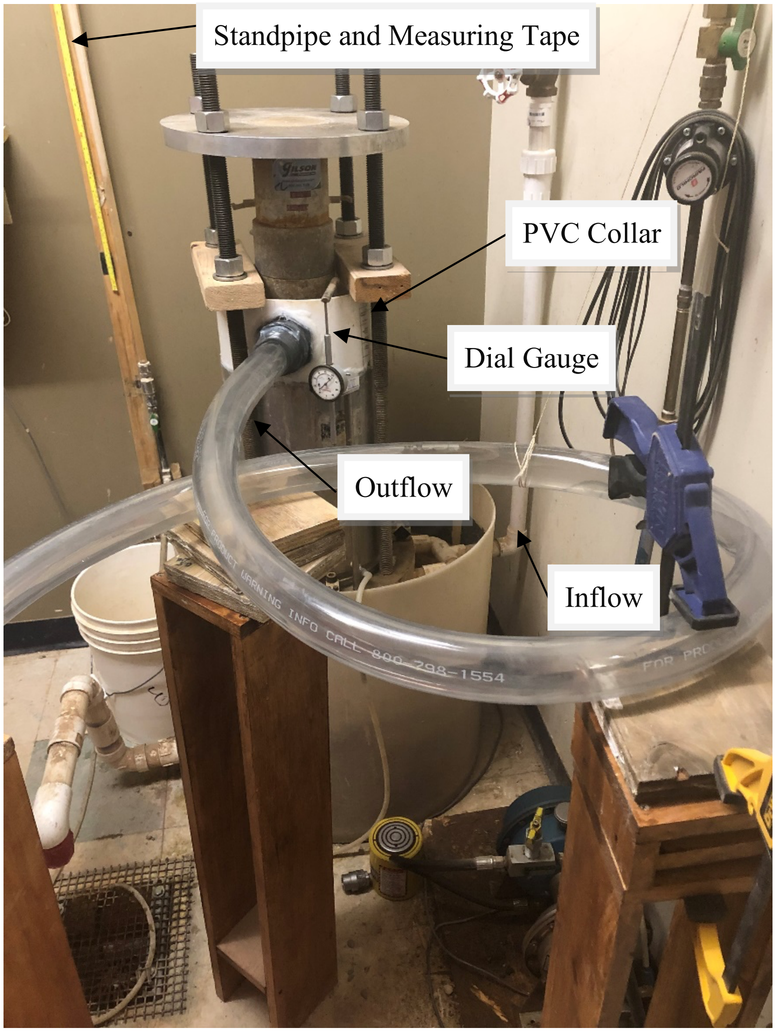

Figure 5. Laboratory Equipment for Suffusion Testing.

3.2 *Experimental Procedure*

Prior to suffusion testing, particle-size distribution testing was performed on the as-received specimen to verify that the material is representative of the Zone 2 material used for construction of the dam. The specimen classified as a well-graded gravel with sand and had approximately 70% gravel, 26% sand, and 4% fines. This gradation was within the Zone 2 specifications, as shown in Figure 7.

The specimen was reconstituted within the permeameter to a dry density of 124 pcf, corresponding to the expected compaction in the field. After compaction, the specimen was saturated from the bottom up. Finally, the hydraulic conductivity was measured by applying a nominal hydraulic gradient of 0.1, equivalent to the expected one in the field assuming an intact geomembrane. This test provided a baseline and was compared to the hydraulic conductivity from latter steps. The hydraulic conductivity was expected to significantly increase by one or more orders of magnitude if the tested material was susceptible to suffusion, resulting in loss of the finer fraction of the specimen.

Three hydraulic gradients (1, 2, and 4) were selected to evaluate the susceptibility to suffusion. These hydraulic gradients range from similar to or higher than the critical hydraulic gradient, 0.8 to 1.2, observed by Wan and Fell (2008) to the hydraulic gradient well above what was predicted from 2-dimensional seepage models using conservative assumptions. As the height of the specimen did not change during testing, and hydraulic head at the top of the specimen was fixed, the hydraulic gradient was increased by increasing the imposed hydraulic head at the base of the specimen as read from the standpipe. Suffusion testing was performed until approximately 50 gallons of effluent, equivalent to approximately 100 pore volumes, was collected. After this volume, the hydraulic head was returned to the nominal hydraulic head (i.e., 0.1), and an additional hydraulic conductivity test was performed.

The collected effluent was allowed to settle for a few days after which water was decanted. The remaining water was poured into bowls and dried out in an oven to measure the amount of soil in the suffusion test effluent.

After completion of testing, the top plate, spacers, and porous platen were removed from the device. The coarse gravel was then removed and visually evaluated to verify that no sediment was located within or on the gravel. The Zone 2 specimen was removed from the cell in two halves, top and bottom, and was placed into two tares and allowed to dry. A final moisture content was taken from the bottom half of the sample to calculate the final wet density. After the moisture content was taken, post-permeability particle-size distribution tests were performed on the top and bottom specimens to evaluate the migration of fines during testing.

4 RESULTS AND DISCUSSION

The susceptibility to suffusion for the Zone 2 material was analyzed by evaluating the consistency of the hydraulic conductivity during testing, collection of effluent during testing, and the change in the particle-size distributions (i.e., before vs after testing, and top vs bottom half of the sample after testing).

The change in the hydraulic conductivity during testing is shown in Figure 6. In general, the range of measured hydraulic conductivities is relatively small and occur within a single order of magnitude. The measured hydraulic conductivity was consistent between the initial reading (taken at nominal gradient of 0.1) and the readings taken at elevated hydraulic gradients. Hydraulic conductivity decreased slightly for the measurements taken at a nominal gradient of 0.1 following each elevated gradient. If the specimen was susceptible to suffusion, this hydraulic conductivity would be expected to increase significantly due to loss of the finer grained fraction of the specimen. However, the Zone 2 material hydraulic properties did not change significantly during testing.

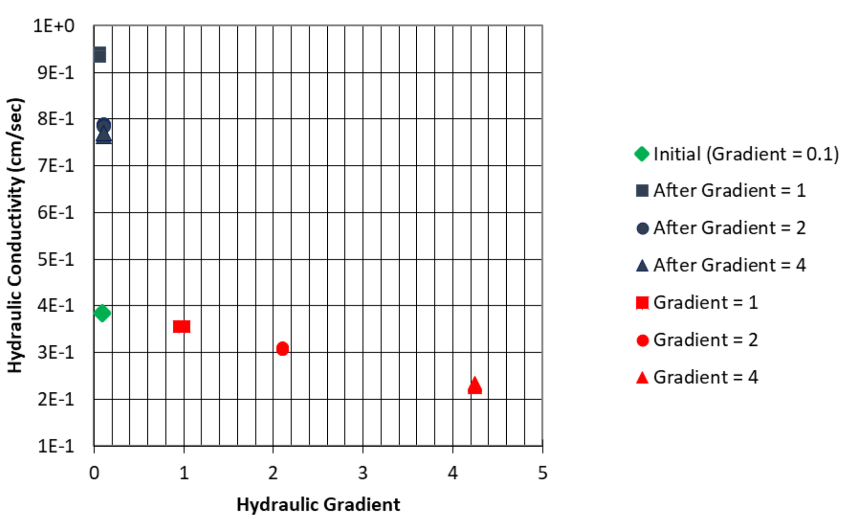

Figure 6. Change in Hydraulic Conductivity during Suffusion Testing.

The masses of migrated fines were measured after each test at elevated hydraulic gradient from the settled soil particles within the buckets. The migrated fines typically were a part of the initial effluent as the water became significantly less turbid after the first 10 gallons of water. The collected soil was a relatively small portion of the total mass of the specimen, being approximately 0.1% of the initial specimen mass. Fines were collected and measured from the effluent collected during application of hydraulic gradients of 2 and 4. Negligible eroded soil was collected during the test at a hydraulic gradient of 1.

To verify that the particle-size distribution had not significantly changed, the pre- and post-permeability particle-size distributions for the Zone 2 materials along with the specifications and field specimens are presented in Figure 7. The as-received Zone 2 was similar to the Zone 2 Fine field specimen, the sample with the highest probability of internal instability, as shown in Figure 4.

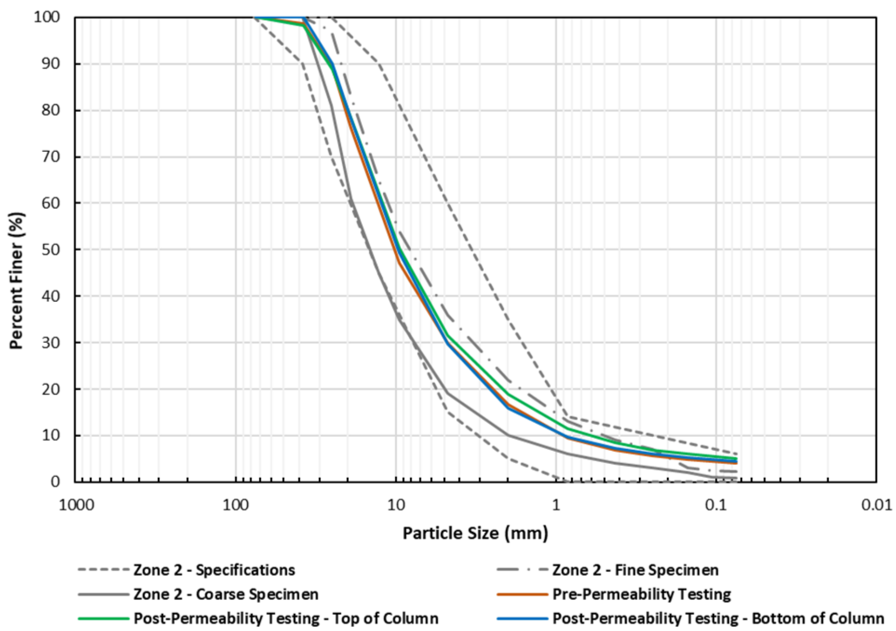

Figure 7. Pre- and Post-Permeability Testing Particle-Size Distributions for Zone 2.

Results from the particle-size distribution indicate that there was not a significant erosion of the Zone 2 material during testing. The grain-size distributions were relatively consistent during testing. There was a negligible difference between the upper and lower portions of the column, indicating that fines did not migrate significantly within the Zone 2 materials during testing. Based upon the laboratory results, the Zone 2 material was not expected to be susceptible to suffusion.

Finally, the upper surface of the compacted specimen did not visually change significantly from the beginning to end of testing. Photos of the specimen prior to saturation and during deconstruction of the specimen are shown in Figure 8.

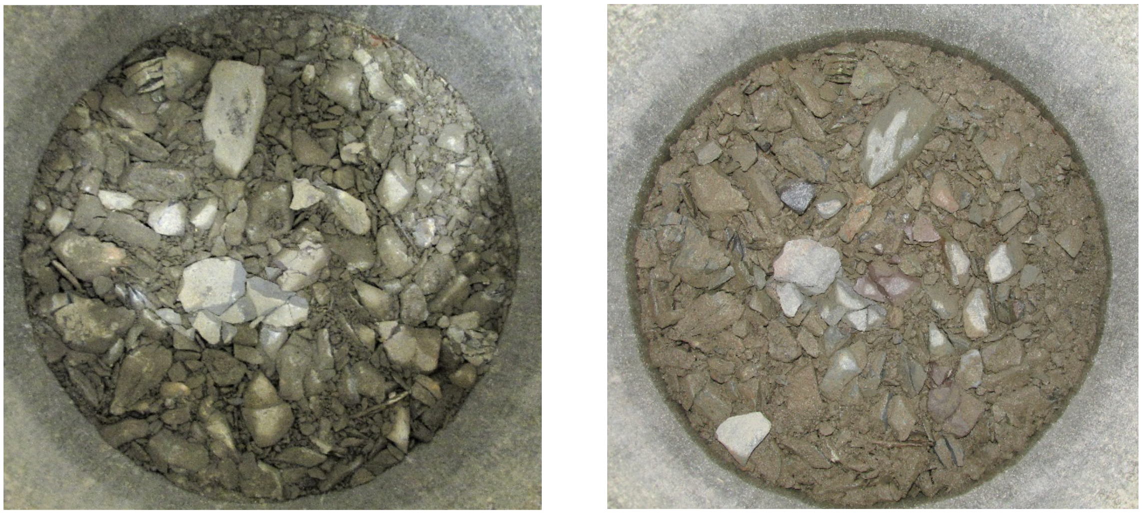

Figure 8. Pre-Permeability (left) and Post-Permeability (right) Upper Surface of Zone 2 material.

5 CONCLUSIONS

The design and evaluation of filter zones for hydraulic dams and tailings dams is a critical component to maintain retention and stability. As part of the planned raise for the Red Dog tailings dam, the susceptibility to suffusion was evaluated for a two-zone filter designed per NRCS (2017) methods. Evaluations were performed using empirical methodologies and laboratory testing. The results given by the empirical methodologies differed as they were developed using different databases of laboratory testing and field observations. To validate that the coarser of the two filter zones was acceptable, a laboratory suffusion test was performed on the material. Three elevated hydraulic gradients were tested. The permeability values, particle size distributions, visual inspection of the materials, and mass of soil in the test effluent all indicate that the material is internally stable.

As the filter zones can significantly affect the containment of waste materials and stability of the facility, it is critical to validate the performance of these materials. As the standard of practice has developed, laboratory testing of project-specific filter materials has become accessible. Similar to other aspects of tailings dam design, the amount of confidence in a given result increases with the level of engineering effort and cost. Increased confidence in the filter performance, particularly for facilities with high hazard potential classification, results in lower risk and also allows optimization of the filter specification and design (e.g., to allow use of less ideal materials that are readily available). These benefits should be weighed against cost and schedule constraints. Laboratory results presented herein indicate suitable performance of filter material that empirical methods indicate may be potentially unstable. Specifically, the Zone 2 material did not show instability in the laboratory testing while plotting within the transition zone for Wan and Fell (2008) and with probability of instability of up to 36 percent for modified Burenkova. For high hazard facilities, in cases where empirical methods indicate internal stability of filter material, laboratory testing can provide an additional level of confidence at a nominal cost.

Future testing could evaluate the effects of changes in the direction of flow, as may occur due to variable water levels within facilities. Additionally, while upward flow yielded gradients that should be able to remove materials, these tests may allow some of the coarser materials to remain in place. Similarly, the scale of the test (specimen height/diameter) could be evaluated to confirm specimen size requirements. Variations of this testing could be performed to evaluate potential migration of material between zones, by placing two material zones adjacent to one another within the apparatus and applying flow in the anticipated orientation. Other variables that may be valuable to investigate, depending on the project, include filter zone density, particle size distribution, and applied gradient. Tests could also be used to evaluate potential for blinding/clogging of filter zones or drainage layers.

6 ACKNOWLEDGEMENTS

Golder Associates Inc. (Golder) would like to thank Teck Alaska Incorporated (Teck) for their contributions. Teck provided access to samples, funding for testing, and input to the process. Golder greatly appreciates Teck's support in advancing the standard of practice and facilitating the sharing of this knowledge to benefit others in the community.

7 REFERENCES

Burenkova, V.V. 1993. Assessment of Suffusion in Noncohesive and Grade Soils. *Proc. 1st Int. Conf. Geo-filters, Karlsruhe, Germany*. Rotterdam: Balkema

Fell, R., MacGregor, P., Stapledon, D., Bell, G., and Foster, M. 2015. *Geotechnical Engineering of Dams, 2nd Edition*. London, UK: Taylor & Francis Group.

Kenney, T.C. and Lau, D. 1985. Internal Stability of Granular Filters. *Canadian Geotechnical Journal* Vol. 22: 215-225.

Kenney, T.C. and Lau, D. 1986. Internal Stability of Granular Filters: Reply. *Canadian Geotechnical Journal* Vol. 23: 420-423.

National Resources Conservation Service (NRCS). 2017. Gradation Design of Sand and Gravel Filters. *National Engineering Handbook* Part 633, Chapter 26.

Wan, C.F. and Fell, R. 2008. Assessing the Potential of Internal Instability and Suffusion in Embankment Dams and Their Foundations. *Journal of Geotechnical and Geoenvironmental Engineering* Vol. 134: 401-407.

Using vibrating wire piezometers to monitor pore pressures during construction of a waste rock buttress – A case study

Louis Geldenhuys, Rynier Shields, Martin Rust
Jones & Wagener Engineering and Environmental Consultants, Johannesburg, South Africa

Florian Hörtkorn
University of Applied Sciences, Karlsuhe, Germany

ABSTRACT: In June 2019 signs of distress were noted along an embankment of an upstream gold Tailings Storage Facility (TSF). Longitudinal cracks were noted along the lowest bench, where localised failures intercepting the phreatic surface would typically occur. The nature of the analysed failures, combined with the high phreatic surface, caused concern for potential progressive failure. Deposition on the facility was halted immediately. Previous CPTu investigations indicated moderate pore pressure conditions in the tailings. After crack formation, another CPTu investigation revealed elevated pore pressures and gradients that posed a risk of localised failures along the toe. Immediate planning of a waste rock buttress was initiated. Vibrating wire piezometers were installed in the embankment to monitor pore pressure reaction and act as critical control during construction. This paper deals with the investigation that led to buttress construction and the monitoring system developed to inform critical stability during construction. Buttress construction was safely completed in December 2019. Due to ongoing stability concerns, the TSF was formally decommissioned in the same period.

1 INTRODUCTION

1.1 *General*

Measures to improve the overall safety of an existing upstream deposited Tailings Storage Facility (TSF) in distress are often limited to construction of a waste rock buttress at the toe of the embankment. This is generally a robust and proven solution and the soil mechanics of such a buttress is well understood. Furthermore, waste rock and appropriate construction machinery to construct this type of buttress is normally readily available in a typical mining environment.

In June 2019 signs of distress, in the form of crack formation, were noted along an embankment of an upstream gold Tailings Storage Facility (TSF). This paper summarises the field investigations and stability analyses before and after observation of the cracks, that led to the design and implementation of a waste rock buttress to address critical stability on the embankment. Part of the investigation revealed high pore pressures near the toe of the TSF, that were frequently monitored using Vibrating Wire Piezometers (VWPs) to ensure loading of the buttress on the saturated tailings proceeded at a rate that would provide safe operations for the contractor.

1.2 *Description of the facility*

The TSF described in this paper is a typical gold TSF constructed in an upstream ring-dyke manner by conventional day wall deposition methods commonly employed in South Africa.

Although no original design records are available, it is estimated that the facility was initially constructed in the 1960's. The original underdrainage system is operational, albeit a limited number of outlets are reporting flow. The overall slope of the facility is 1(V):3.0(H), with an overall height of approximately 39 m. Intermediate slopes are approximately 1(V):2.0(H) with 7 m wide benches typically constructed for every 10 m raise in height. The site is predominantly underlain by a brown clayey sand hillwash layer up to 0.5 m depth, a brown sandy clay layer with very low permeability up to 1.3 m depth, fractured shales up to 3.0 m depth and hard rock siltstone of the Karoo Supergroup formation below that.

Conventional standpipe piezometers are installed at regular intervals along the embankment and measured frequently to monitor any potential rising phreatic level trends that may negatively impact on stability. To compliment standpipe measurements by better defining the pore pressure regime, regular CPTu probing is conducted along the standpipe piezometer lines. Previously, no live monitoring type system existed on the facility, with heavy reliance on visual inspections to identify any immediate signs of distress on the embankment.

Water on the basin is decanted through an elevated penstock, centrally located in the basin. Freeboard is maintained through even deposition in the day wall and formation of beaches when suspended solids are segregated when running to the pool. The operational pool was no deeper than 300 mm, storing minimal water on the TSF. The Rate of Rise (RoR) was marginally above 1 m/year before deposition was halted, which is deemed acceptable for a facility of this nature.

2 INVESTIGATION

2.1 *First observations and steps taken*

A site investigation was conducted the morning after the cracks were observed. The cracks were found to be on the first bench of the facility, and were approximately 120 m long, running along the length of the bench parallel to the outer slope. Seepage and sloughing were also evident at the toe extending up to half of the height of the first bench.

Deposition was immediately halted on the facility. An action plan was implemented in which all operations and construction staff were removed from that flank of the facility and access was closed off. A CPTu contractor was mobilised, monitoring pegs were installed, and an inspection schedule was compiled by appointed operating staff, who were familiar with the risks involved, to allow for regular monitoring of seepage and signs of further instability.

2.2 *Initial CPTu probing*

Cone Penetration Testing with pore pressure measurement (CPTu) was conducted within a week after cracks were observed. This was conducted along three lines (shown relative to the crack position in Figure 1); one north of the cracks (Line 1), another approximately in the middle of the cracks (Line 2) and the third to the south of the cracks (Line 3).

The CPTu data for Line 2 is shown in Figure 2. The pore pressure data indicated that the phreatic level was close to the surface. The high phreatic surface, along with the seepage along the outer slope, indicated the possibility of a low permeability below the tailings with insufficient drainage (Blight 2010). This was an early indicator that there existed pore pressure conditions that could promote instability.

The equilibrium pore pressure gradient is a good indication of the drainage performance of the TSF and could identify any potential seepage problems. If there is a downward flow regime in a tailings dam, especially within the embankment zone, the rate at which pore water pressure increases with depth will be less than hydrostatic for consolidated tailings, i.e. less than 9.81 kPa/m. It is also possible that the rate of pressure build-up with depth exceeds the hydrostatic condition for under-consolidated tailings. This can occur in the following cases:

- If a soil is still undergoing consolidation (excess pore pressures generated during load application or deposition are still dissipating to an equilibrium state).
- If shearing / movement has occurred within the soil body that results in excess pore pressures in the area where movement occurs.
- If the flow / seepage within the soil has an upward vertical component to it.

The rate of pressure increase with depth at 1A, 2A and 3A was higher than hydrostatic (presented in Table 1) and had not been encountered in this facility before. These conditions may be indicative of failure having taken place, or in progress, within the zones where excess pore pressures were observed. Failure in this regard is associated with concentrated shear (shear bands) along a near vertical plane/s below the cracks and possibly along the foundation interface. It could also have been related to artesian conditions below the facility. For probe positions 1B, 2C and 3B (all on the second bench and further from the toe) the rate of pore pressure increase was marginally below hydrostatic. This indicated that little to no downward drainage was taking place. With the rate of pore pressure increase beneath the second bench being lower than that measured beneath the first bench (1A, 2B and 3A), it was an indication that the phenomenon causing the high pore pressures had a greater effect closer to the toe.

The last dissipation test for probe hole 2C, at a depth of 21.4 m below the surface, was conducted in a dilative layer (indicated by lower than zero dynamic pore pressures during probing) with properties different (in terms of cone resistance, sleeve friction and apparent material type) to the rest of the probe depth. It is postulated that this material behaves as a stiff clay, with a very low rate of pore pressure dissipation. This indicates that this is below the tailings. From the dissipation, the pore pressure value was 34 kPa higher than 1 m above in the tailings.

This indicates that there is a higher pore pressure regime within this layer than in the tailings. This is postulated to be one (or a combination of) the following scenarios:

1. There exists a higher pore pressure regime below this layer. This could be due to artesian conditions.
2. There has been loading (either shearing or loading that has caused consolidation) of this clay layer that has generated excess pore pressures that have not yet dissipated.

Table 1. Pore pressure gradients.

	Pressure gradient with depth (kPa/m)	
Line 1	1A	10.0
	1B	8.10
Line 2	2A	10.6
	2B	8.50
Line 3	3A	10.6
	3B	8.80

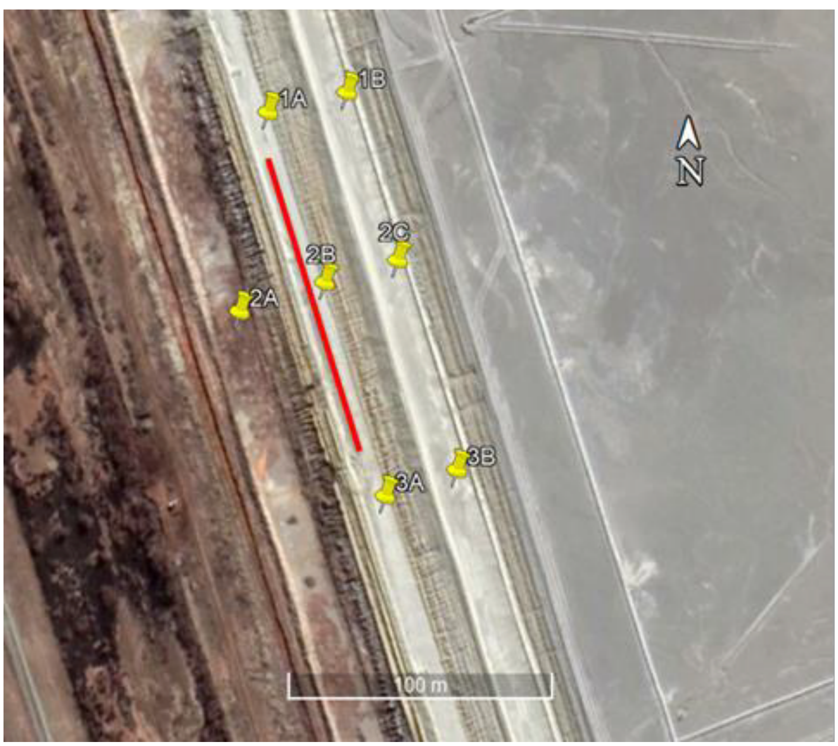

Figure 1. Location of CPTu testing with crack position highlighted.

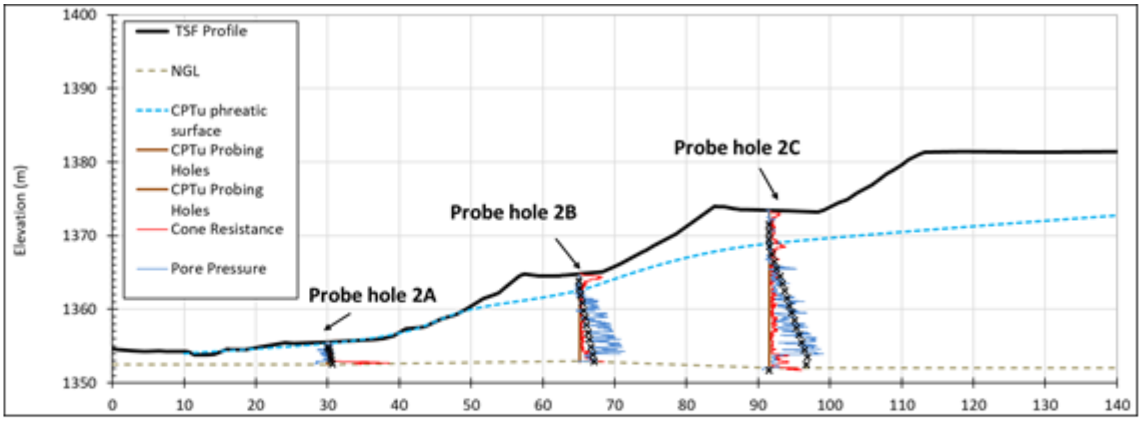

Figure 2. Line 2 CPTu results.

2.3 *Crack observation and movement monitoring*

An example of the cracks is shown in Figure 3. The cracks were measured daily to monitor any progression, whether in length or in width. This was taken as an early precautionary measure to monitor possible further deterioration of the outer slope and to determine whether the mechanism that caused the cracks was still active or not. This was done by installing monitoring pegs either side of the observed cracks at frequent intervals and measuring the distance, both vertical and horizontal, between markers on opposing pegs. A schematic of the peg installation is shown in Figure 4. This method is considered rudimentary and therefore some degree of uncertainty should be accepted and considered in the interpretation of the data. The mechanism behind the cracks is not well understood.

Between 02 July 2019 and 27 August 2019, as much as 10 mm of crack widening was observed between certain pegs.

Figure 3. Initial cracks observed.

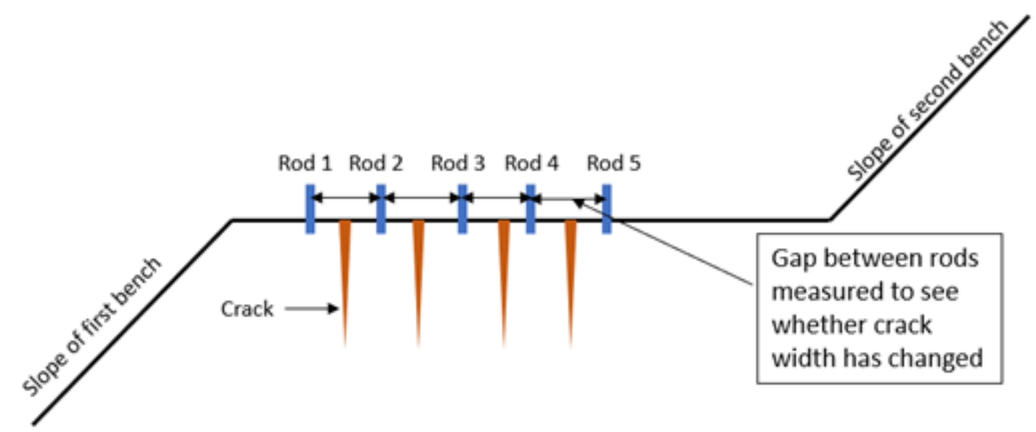

Figure 4. Monitoring peg installation.

2.4 *Test pit profiling and permeability testing*

A test pit was dug in the natural ground outside the solution trench (i.e. outside the TSF footprint) in an area adjacent to where the cracks were observed. This was to determine the possible material layers beneath the tailings. The excavation refused at approximately 1.5 m in a fractured shale. The clay layer immediately above the shale layer was sampled and flexible wall permeability testing revealed that it had a permeability of $2x10^{-10}$ m/s. This confirmed the low permeability noted in the clay beneath the tailings in the CPTu dissipation at probe 2C.

2.5 *Water quality tracing*

During the inspection and following interpretation of CPTu dissipation data, it became apparent that a buried water pipe near the toe of the TSF may be leaking and it was postulated that it could be contributing to the higher than hydrostatic pore pressure build-up observed in the TSF. Water samples were taken from an upstream take-off point on this pipe, the solution trench and a test pit outside the solution trench. Inorganic chemistry, Electrical Conductivity (EC), pH, Oxidation Reduction Potential (ORP) and Total Dissolved Solids (TDS) were tested for each of the samples to confirm whether water from this pipe was seeping into the tailings and natural ground water. Based on the results, the theory of water leaking from a buried pipe into the tailings was discounted.

2.6 *Subsequent CPTu probing*

CPTu testing was repeated along Line 2 on the first bench (2B) and on the second bench (2C) approximately 40 days after the initial probing. This was done to determine whether there had been any reduction in pore pressure and reduction in the elevation of the phreatic level after various mitigation measures had been implemented (halting of deposition, rerouting of pipeline on western flank, draining of solution trench etc.). The probing data showed that no reduction in pore pressures had occurred at both these positions. The elevation of the phreatic surface had also remained the same. This does not necessarily mean that the mitigation measures were unsuccessful. It is likely that the timeframe between testing was too short for any of the effects to become evident yet.

2.7 *Standpipe piezometer monitoring*

Four standpipe piezometers are installed in a line perpendicular to the outer wall in the area where cracking was observed. Piezometers are installed on the benches, in the tailings below the phreatic surface. These piezometers are used for routine measurement of the inferred phreatic surface by the operator. Due to the inherent layering and variance in anisotropy of tailings layers, the value of these piezometer readings is limited. Standpipe water levels were not used as part of this specific assessment.

3 BUTTRESS DESIGN

3.1 *Methodology*

Limit equilibrium, effective stress slope stability analysis, using static drained shear stress parameters (Mohr-Coulomb), was carried out using Geostudio's Slope/W software package. The method of slices as defined by Morgenstern-Price (Morgenstern & Price 1965) was used for the analysis. Slip geometry was optimised for the grid-and-radius slip circle search method.

The pore water pressure in the analysed section was specified in the software by plotting the actual pressures obtained from the CPTu ambient pressure results after dissipation. For the parts of the model where no pore pressure data was available, such as at the toe of the facility or towards the pool, the following assumptions were made:

- The pore pressure on the upstream side was extrapolated to the estimated position of the pool. It was assumed that hydrostatic conditions were present below the pool
- The pore pressures were extrapolated on the downstream side (towards outer slope and toe) to the elevation at which seepage was visible on the outer slope.

The most recent LiDAR survey of the facility was used to determine the cross-section profiles used in the two-dimensional stability analysis.

3.2 *Buttress geometry*

The design of the buttress was aimed at preventing localised slip failures near the toe, at and below the first bench, that may lead to progressive and more catastrophic failure once the phreatic surface was intercepted. Due to the significant liquefiable zones present in the facility, progressive failure could have catastrophic consequences. The immediate prevention of localised failure was therefore addressed through an effective stress model, independent of the risk of larger undrained failures. The risk of these type of failures are addressed separate to this paper.

The buttress is founded in the catchment paddocks, directly outside the toe of the embankment and reaches halfway up the slope toward the first bench. This directly counteracts the anticipated slip failure expected to be initiated from the point of the observed cracks. A nominal layer of waste rock was extended up this slope and onto the first bench to provide cover for the drainage system described in the next section. A typical profile of the buttress is shown in Figure 5. The buttress reaches a total length of 250 m.

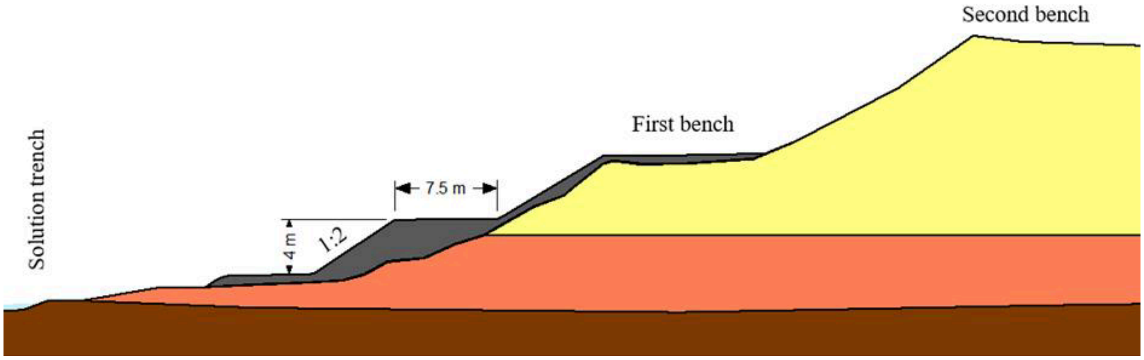

Figure 5. Buttress profile.

3.3 *Drainage design*

To maintain atmospheric pore pressure conditions along the existing outer wall and minimise infiltration from the new overlying buttress, a drainage system was installed between the buttress and embankment. This consisted of a chimney drain at the interface, conveying collected seepage to a collector toe drain. The collector toe drain was purposefully installed away from the TSF toe to prevent further local instability during excavation operations.

3.4 *Positioning of Vibrating Wire Piezometers*

VWPs were selected to monitor pore pressures during construction due to their low time lag response (Duncliff 1988). A total of ten VWPs were installed in two lines, evenly spaced along the buttress length. Each line consists of five piezometers located near the toe of the embankment that measured immediate pore pressure response during loading in the area. For each line, two piezometers were installed next to each other in the catchment paddock and three next to each other on the first bench. Those in the catchment paddock were installed in the impermeable clay layer and the fractured shale layer directly below it. Those on the first bench were installed in the tailings body and in the impermeable clay. This allowed for individual measurement of pore pressure response in the distinctive material layers observed during CPTu probing and test pit profiling. A cross section of installation positions is shown in Figure 6.

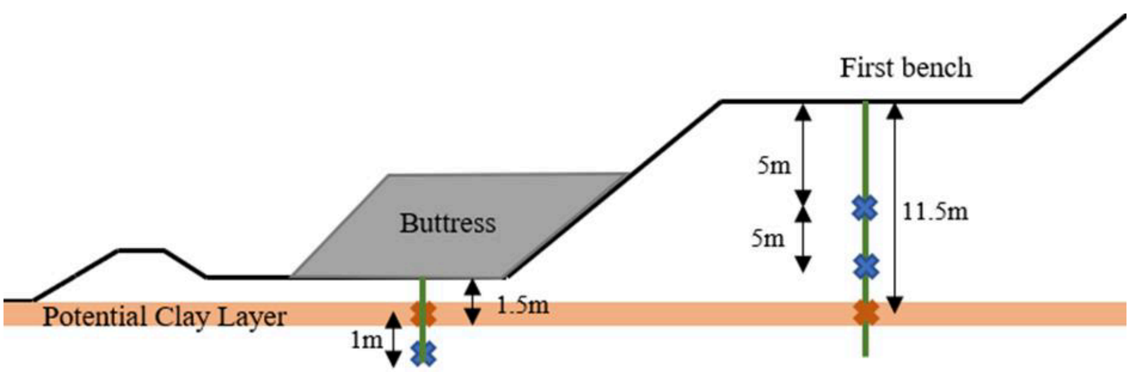

Figure 6. VWP installation positions.

3.5 *Calculating pore pressure trigger levels during construction*

The first buttress lift would therefore have to be as high as possible to prevent putting people and equipment at risk while working at the bottom of the unstable slope. However, there was the concern that loading of the low permeability layer beneath the facility during buttress construction would generate excess pore pressure that would dissipate very slowly. This would result in a loss of effective stress in the material and reduce the FoS. Limit equilibrium stability analysis was conducted for the following:

- FoS at the start of a lift, t=0, where it was assumed there would be no pore pressure dissipation and the excess pore pressure would equal the weight of the buttressing material above. The excess pore pressure was applied to the CPTu-based spatial function in the model.
- FoS at the end of a lift, t=end, where it was assumed that there were no remaining excess pore pressures, and the pressure was the same as prior to buttress placement (i.e. the status quo pore pressures from CPTu testing).

As shown in Figure 7, it was found that that once the buttress lift was higher than 3 m, the FoS dropped lower than having a smaller lift, if the maximum excess pore pressures were generated. Therefore, an initial 2 m lift was selected as a compromise between providing safe working conditions and not reducing the FoS.

With a single lift of 2 m resulting in a FoS of 1.1 if the maximum excess pore pressure would be generated (i.e. 40 kPa if the unit weight of the waste rock is 20 kN/m^3), further analysis was conducted to determine the FoS if fractions of the excess pore pressure were to be generated with the 2 m lift. This was to determine the alert levels for the pore pressures measured in the vibrating wire piezometers during placing of the waste rock. Alert levels are presented in Table 2. Similar alert levels were calculated for the second lift of the buttress.

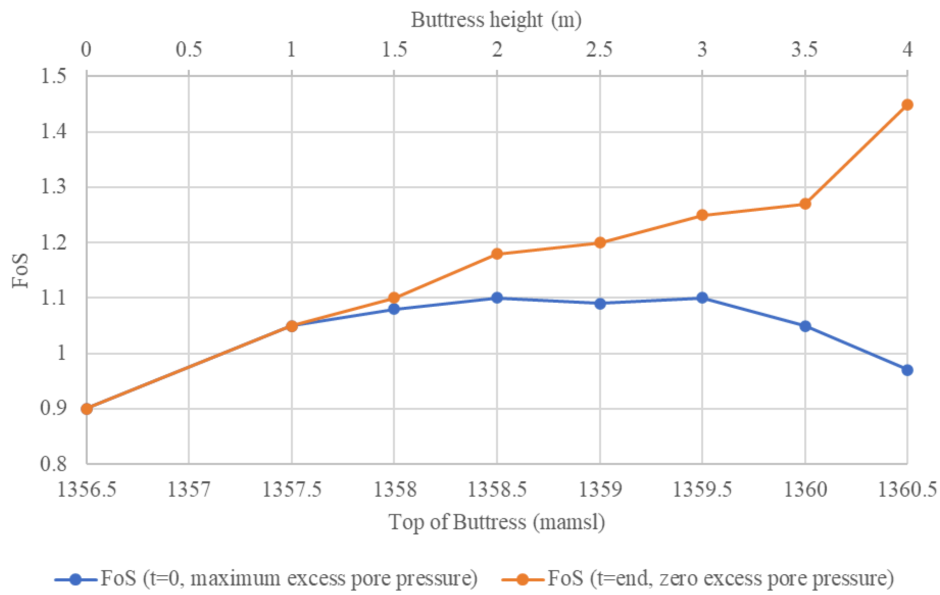

Figure 7. FoS vs height of a single buttress lift.

Table 2. VWP alert levels.

Excess pore pressure (kPa)	FoS	Alert level	Decision
10	1.4	None	Safe
20	1.3	1	Slow down rate of construction
30	1.1	2	Halt construction and monitor
40	1.0	3	Immediately evacuate

4 BUTTRESS CONSTRUCTION AND MONITORING

4.1 *Emergency response planning*

Due to the inherent risk of excess pore pressure response and localised failure during construction, it was pertinent that a clear and concise emergency response plan be developed. This started with daily visual inspections along the entire slope for any new signs of distress. Apart from monitoring rising trends, the engineer used the set of trigger levels described in Section 3.5 to inform the contractor of any potential trigger for failure. This required a direct line of communication between the engineer monitoring pore pressure and the contractor on site. Furthermore, an evacuation plan was developed with emergency assembly points for all personnel on site. Potential outflow along this embankment would have had no further impact on human lives other than the contractor working in the area.

4.2 *Access preparation*

Due to saturation of catchment paddocks at the toe of the embankment, access for heavy machinery was provided through the construction of a waste rock pioneering layer that would act as the initial base of the buttress. The pioneering layer would furthermore displace saturated run-off tailings to provide added weight at the toe.

4.3 *Crack repair*

Cracks were repaired by removing a minimum layer of dry tailings on the first bench in the area concerned. A 400 g/m² separation geotextile was used to line the area and bridge the cracks. The area was then backfilled with the excavated dry tailings again.
This would allow rainwater infiltration to move through the cracks at a reduced rate without mobilising more solids material to erode the cracked area. The backfilled dry tailings was later covered with the buttress drainage layer.

4.4 *Rate of loading*

The buttress was constructed in two stages, each a lift of 2 m. The loading rate was monitored as buttressing progressed over the areas where VWPs were installed. During the first lift, Alert Level 1 was reached. The contractor was instructed to slow down the rate of construction. During the second lift of the buttress, Alert Level 1 was reached and the measured pressures approached Alert Level 2. The contractor was informed to slow down the construction rate and the VWP data was continuously monitored. Had the pore pressures continued to increase to Alert Level 2, construction would have been temporarily halted. This, however, did not happen and pore pressures dissipated sufficiently. Pore pressures measured at the toe during construction are shown in Figure 8.

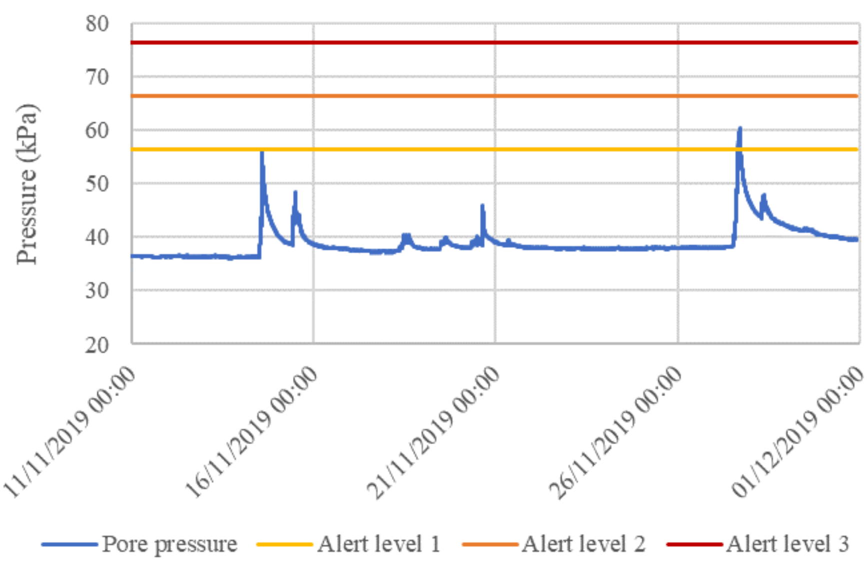

Figure 8. Pore pressures during construction.

5 CONCLUSION

Following cracking that was observed along the first bench of an upstream TSF, deposition was halted and an investigation into the risk of instability ensued. The investigation, mainly comprising of in-situ characterisation of the tailings and pore pressure regime revealed that buttressing was required to prevent localised failure, that may very quickly accelerate to progressive failure. A design for this buttress was done that included the installation of Vibrating Wire Piezometers to monitor pore pressure reaction during loading of the saturated toe with waste rock. Real time monitoring of the data allowed the engineer to inform the contractor of rising pore pressures and risk of instability during construction. Pore pressures in the underlying layers near the toe of the TSF reacted nearly in equal effect to the weight of the waste rock. During certain stages of construction, the rate of loading was reduced and once halted to minimise risk of instability to operating personnel on site. The buttress was successfully constructed, and cracks repaired with no further distress noted to date. Further buttressing is planned to address other credible failure modes and long-term stability during the formal closure stages of the TSF.

6 REFERENCES

Blight, G.E. 2010. Geotechnical engineering for mine waste storage facilities. *Taylor & Francis.*

Dunnicliff, J. 1993. *Geotechnical instrumentation for monitoring field performance*. John Wiley & Sons.

Morgenstern, N.R. & Price, V.E. 1965. The analysis of the stability of general slip surfaces. *Institute of Civil Engineers*, London.

SLOPE/W. 2021. *A software package for slope stability analysis*. GEO-SLOPE International, Canada.

Developing an observation approach for a TSF raise

Raúl Norambuena Mardones & Erik Ketilson
SRK Consulting, Canada

Gerado Garduño
Industrias Peñoles, México

ABSTRACT: Early in 2020, the Velardeña TSF3 developed long, longitudinal cracks along the crest of the starter dam during the construction of the first upstream raise. The construction was paused while the source of the cracking was investigated rendering the future of the facility uncertain. After compiling the construction and operational records, the constructed dam geometry was reviewed against the operational history to develop hypotheses related to the cracking mechanisms. This motivated site investigation and the installation of geotechnical instrumentation installation to confirm potential cracking hypotheses. A modified raise approach was developed, along with critical controls and monitoring thresholds for the construction, the latter adapted to define the operational readiness paraments once resuming the disposition of tailings – forming an approach to which the observational method could be applied during construction and operation. This paper will review the process applied at the outset of the project, the approach to assessing the operational integrity of the TSF and the modifications applied to the design to ensure the facility could continue operation in a safe manner.

1 INTRODUCTION

The tailings management plan for Velardeña Mine involves tailings deposition in Tailings Storage Facility (TSF) 2 and 3, both proposed to be upstream facilities. During the construction of the first raise of TSF3 a set of cracks developed on the crest of the starter dam, extending to the downstream shoulder. The construction of the raise stopped until better understanding of the origin of the cracks and the evaluation of the progression.

However, TSF3 was required for tailings storage within 4 months, and was intended to provide operational continuity to the mine operation with an equivalent capacity of 1 year tailings deposition.

The involvement of the current design engineers was initiated with the realization of the cracking and followed by the compilation and review of the relevant background information of the design, construction and operation, to better understand the underlying mechanisms that could have triggered the cracking.

The process related to how the cracking issue was approached, evaluated to determine if the facility could continue to be used for tailings deposition, and the proposed remediation plan to keep the facility operating are the subject of this paper.

2 VELARDEÑA MINE

The Velardeña Mining District is located in the eastern portion of the state of Durango, in the municipality of Cuencamé. It is approximately 120 km from the city of Torreón, Coahuila.

The mining activity in the Velardeña district dates back to 1606. Since 2003, the Velardeña mine has been fully owned and operated by Peñoles, starting the explorations works on 2007 and the construction of the current mining facilities in 2010 and the operation in 2013.

Velardeña is an underground mine that uses the sublevel stoping method to extract the mineral from two main mineralized bodies Santa Maria and Antares Norte. The plant processes the mineral at a nominal rate of 8,200 tonne per day and produces concentrates of zinc, copper and lead by flotation of the crushed and milled sulfide minerals. The mine has proven reserves of over 20 million tonne and over 105 million tonne of resources which provide a life of mine until 2038.

At Velardeña there are three (3) TSF's, two of them are in active use (TSF2 and TSF3) while TSF 1 is abandoned and is associated to the historical mining activities, before the Peñoles involvement in Velardeña. The management of tailings is expected to continue in these facilities until 2023, when the new facility gets commissioned.

In accordance with Mexican Nom-141 (Semarnat, 2004) code, the site is characterized to be in a humid area with a low seismicity located in an area with mild topographic terrain. There is seasonal influence of hurricanes and tropical storms that provide intense short precipitation events, while the heat and wind provide a high evaporative capacity throughout the year.

Table 1 provide some details on the location and hydrological aspects of Velardeña.

Table 1: Summary of Site Conditions

Parameter	Type	Value
Site Coordinates (UTM WGS 84 - 13)	North	2,774,577.96 m
	South	2,771,674.81 m
	East	628,212.51 m
	West	624,927.56 m
Average Elevation	Meters above sea level	1,400 masl
Temperature	Maximum	45°C
	Minimum	5°C
Precipitation (annual)	1:25 years	530 mm
	1:50 years	590 mm
	1:100 years	620 mm
Evaporation	Maximum Yearly	5,270 mm
	Maximum Monthly (June)	308 mm

Figure 1 shows an aerial photo from the site taken on June 23^{rd,} 2021 part of the periodical drone photogrammetric survey. In the figure, the tailings storage facilities at Velardeña mine, TSF2 at the east of TSF1 while TSF3 on the east of TSF1, separated into two operational cells are identified.

2.1 *TSF Design, Construction and Early Operation*

The original design for TSF2 and TSF3 was completed in 2011 and considered the construction of earthfill starter dams, with a maximum height of 40 and 24 m, respectively, TSF2 with a capacity of 4.2 Mm^3 and TSF3 of 10.6 Mm^3. The original design only developed the starter dams to a detailed level engineering, however, the upstream construction for the futures raises was planned for at a conceptual level.

According to the design, the embankments were built using the available material in the foundation over the impoundment area, this would provide extra capacity in the TSF's life. The material in the area is locally known as "caliche" which is a clayey gravel.

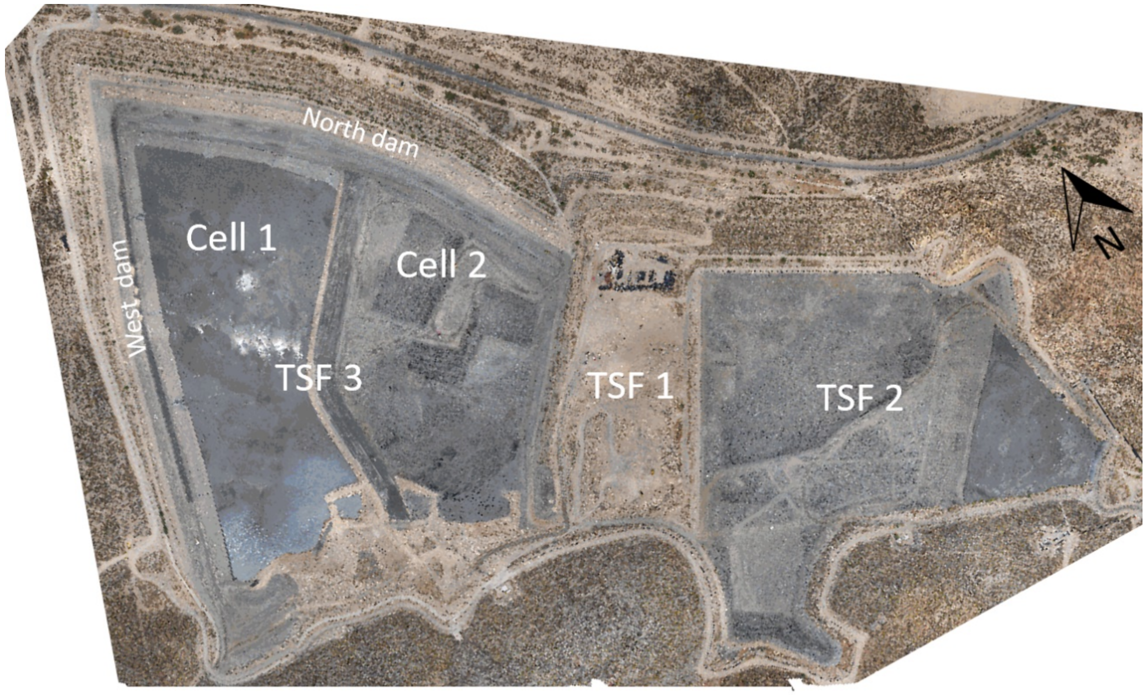

Figure 1: Velardeña tailings storage facilities

The design of the TSF3 starter dam considered a 2.0:1.0 (H:V) downstream slope and an overall upstream slope of 1.8:1.0 (H:V). The upstream face considered a HDPE geomembrane over a GCL as a low permeability barrier for the dam, which extended from the upstream toe up to 2/3 of the overall height. The internal drainage system considered a 0.5 m thick chimney drain which extended throughout the longitudinal extension of the starter dam, this would capture any seepage coming from within the impoundment and would discharge it into discrete finger drains at the foundation level spaced every 60-300 m. The finger drains would discharge into collection boxes located along the downstream toe of the starter dam. The chimney drains and the finger drains consisted of crushed gravel size particles, wrapped in geotextile to provide filtration from the surrounding earthfill material. Along the upstream face above the bench, there was intended to be a lower permeability layer upstream of the drain that would also act as a filter material with a finer PSD comparted to the rest of the starter dam fill.

The design of TSF2 starter dam followed the same concept of slopes, impermeabilization and drainage system.

Figure 2 shows an illustrative cross section of TSF3 picturing the most important elements and aspects from the original design of the starter dam.

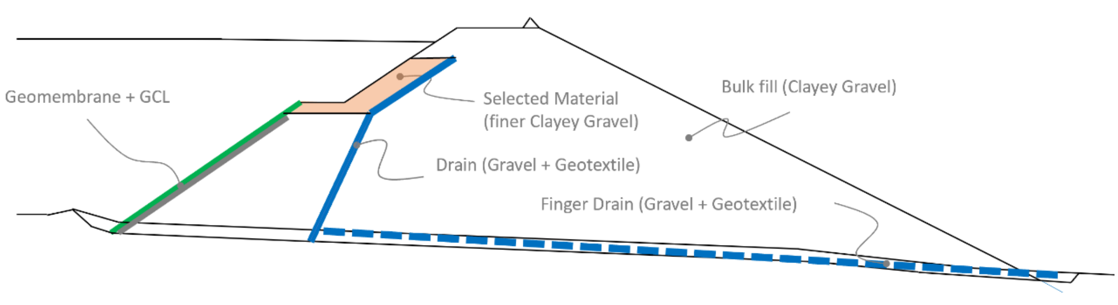

Figure 2: TSF3 general cross section concept.

The construction of the TSF2 starter dam extended from August 2011 to August 2012, while TSF3 construction occurred from October 2013 to May 2014. The construction records of the TSF's included scattered QC/QA data available in weekly reports and compaction reports that were unable to be indexed to specific locations and layers. There were some records from the original designer visiting site during construction but no formal as-built documentation of the construction process indication any deviation from the original design.

By the end of 2012 the mining operation started and with it the TSF's started to receive tailings. The plant originally had a processing capacity of 6000 tpd, of which 5500 tpd were tailings, with plans ramp up the production to 9000 tdp. The capacity of the starter dams of both TSF's was originally estimated to last 10 years, however, with the increase in production the life was significantly shortened. In 2016 another engineering firm was involved to develop the design of the future upstream raises of the facilities.

The engineering for the TSF2 raise considered 2 raises and was soon followed by the construction during the first part of 2017. Each raise considered a 5 m high trapezoidal section with upstream and downstream slopes of 1.5:1.0 (H:V) and a 5 m crest width. The 2016 engineering considered an 80/20 mixture of tailings and borrow material (caliche and ROM material), respectively, as the construction material. The tailings were to be sourced from within the impoundments of the TSFs already dried out after deposition after the end of the active use.

The same concept was followed for TSF3 in terms of the raise engineering, but in this case the design considered 6 raises and the construction started towards the end of 2019. During the construction of the first raise of TSF3, particularly during the construction of the raise associated to Cell 2, cracks started to appear along the starter dam crest and the upper sections of the downstream face (downstream shoulders). The construction activities for the first raise were put on hold until new information became available. Figure 3 shows a timeline associated to the TSFs design, construction and operation until the cracking events observed in early 2020.

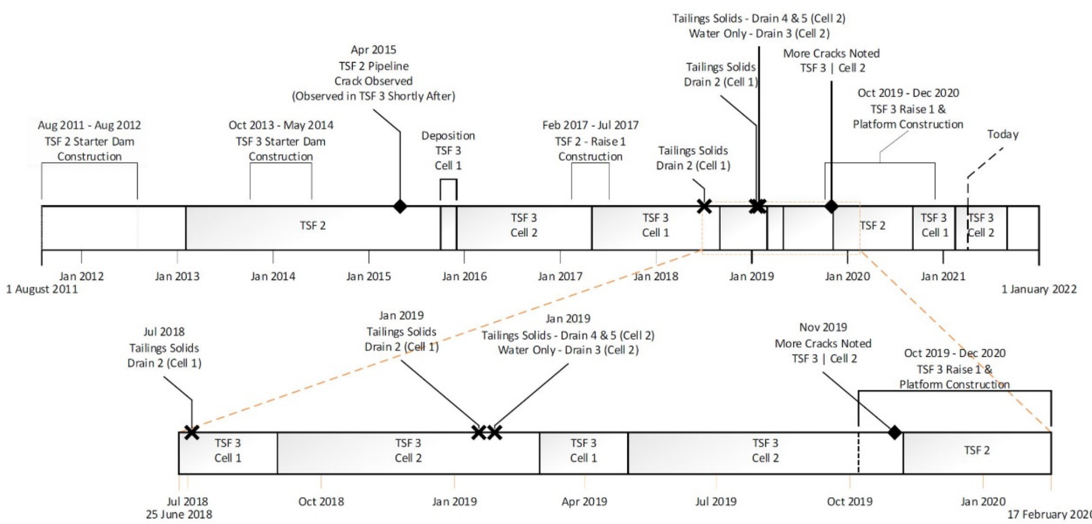

Figure 3: Velardeña Tailings storage facilities timelines design, construction, operation and specific relevant events.

3 THE PROPOSED SOLUTION FOR OPERATIONAL CONTINUITY

The observed cracking in March 2020 created uncertainty on the future use of the facility and in order to ensure operational continuity a mitigation plan was required to be designed and implemented within 4 months.

SRK was able to visit the site in March 2020 immediately prior to the implementation of global travel restrictions. Upon arrival to site the team walked the length of the cracks, to first understand the general alignment, orientation and crack characteristics. After the field activities, site personnel presented general background information related to the TSF3 design and operation, among them the monitoring data of four (4) survey points in TSF3 showing a trend of movement towards the impoundment and down, followed by set of CPT tests results performed in the impoundment late 2019, showing a surficial layer of 15 m of soft tailings in Cell 1.

The recommendation from the visit was to increase the number and the frequency of measurement of the survey points to confirm the trends and direction of the displacements, the installation of strain gauges and gypsum plates to confirm the cracking progression, and to stop all the activities in TSF3 until better understanding of the actual condition of the starter dam and raise.

Early in the review a few deviations and gaps were detected between the design and the construction documentation, most of them minor. However, there were a few findings that might have played some role in the cracking of the starter dam.

- As part of an environmental initiative, the downstream face of the dam was heavily planted with different species of bushes, trees and cactus, these plants had a frequent watering plan by flood irrigation.
- The construction of the raise in TSF3, particularly in Cell 2, started weeks after the maximum capacity was reached, the foundation material of the first raise were soft tailings with high moisture content.
- The drain material was specified to be crushed gravel, however the material in the construction reports was rounded and placed without compaction.
- The geomembrane used as impermeabilization system on the upstream face was not textured and no record of a GCL was found.
- A crack appeared both in TSF2 and TSF3 early in the operation, parallel to the tailing's distribution pipeline located at the crest of the starter dam, close to the upstream shoulder. Site personnel attributed this to the uncompacted filter placed upstream of the drain.
- Normally, the seepage collection system for the TSF does not carry water, however there were three (3) seepage events observed at TSF 3, one occurred in July 2018 and two during January 2019. According to the description of the events, these occurred after the tailings level in the impoundment exceeded the maximum height of the geomembrane, and water and slimes started flowed out from the collection boxes at the downstream toe of the TSF.

With most of the available information compiled and discussed, a few theories were put forward trying to understand potential mechanisms behind the cracking. Several analyses were carried out to prove these mechanisms, most of them making physical sense, but was impossible to uncouple to a unique one, as most of them could have contributed in one way or another. The construction of the raise over soft tailings could have influenced the triggering of the cracks of a system that was already under stresses with a potential weak plane, i.e. the drain.

A failure mode analysis was carried out, and which was supported by limit equilibrium and deformation models using finite elements. The analyses did not flag imminent stability issues that could lead to a downstream failure and potential loss of containment related to the construction of the first raise. Although, the history on the seepage event raised concerns on the performance of the internal drain and its capacity to handle water.

The proposed solution to ensure operational continuity required minimizing any potential flow into the drain that could trigger any kind of internal erosion (e.g., contact erosion, concentrated leaks, backward piping or suffusion). Several options were conceptualized and preliminarily evaluated; deep ground improvement (stone columns), a cut off wall by deep soil mixing or by a slurry wall, the installation of wick drains, construction of relief drains in the impoundment with active sumps to dewater and control the phreatic level low and the partial deconstruction of the starter dam and repair of the drain was considered. None of these options were feasible either because the limited timelines were not sufficient to carry out the design and implement, or, there were permitting constraints that didn't allow to modify the geometry considered within the current permits. Any permit application would require several months to process in addition to typical timelines due to COVID restrictions and corresponding uncertainty and delays.

The proposed solution that met the critical project requirements was the concept of a constructed beach, which consisted of extending the length of the first raise further upstream using compacted tailings. This concept ensured that any deposited tailings would not be placed near the dam crest, increasing the seepage length from freshly deposited tailings to the internal drain of the dam and reducing the potential hydraulic gradients generated in the drain vicinity.

The dimensions of these constructed beaches were driven by the feasibility of fitting a second 5 m raise on top with improved foundation within the available timeline. The minimum constructed beach length achieved was 50 m beyond the upstream crest of the first raise, however as there was initial uncertainty regarding the construction efficiencies, a staged approach was adopted – first targeting a minimum 30 m width upstream of the first raise. Timing allowed for the second stage (additional 20 m) to be added after the first as the site achieved higher construction productivities than initially assumed.

Figure 4 shows a cross section of the constructed beaches concept as the solution to provide operational continuity to TSF3.

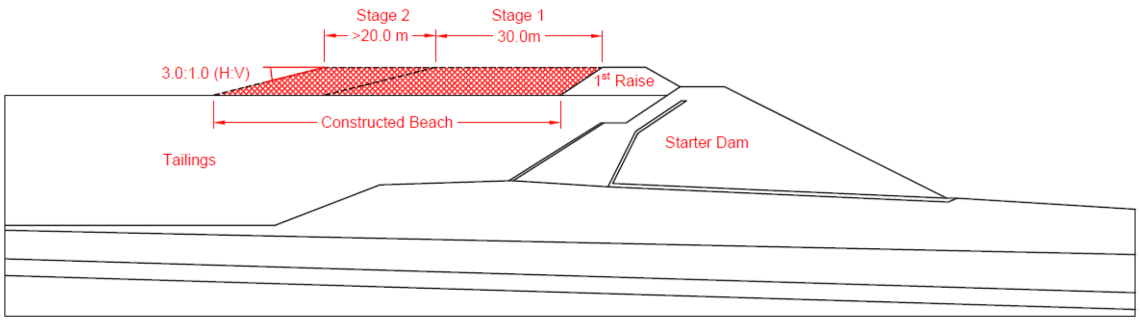

Figure 4: TSF3 representative cross section illustrating the constructed beaches concept.

In parallel to the design of the constructed beach concept, a site investigation campaign was planned and targeted to understand and confirm the internal dam structure, but particularly targeted to install groundwater instrumentation by means of stand pipe and vibrating wire piezometers, this would provide direct measurement of piezometric levels and water levels within the tailings underlying the constructed beaches, providing an early warning to the advancement of the wetting front once tailings were deposited into the facility.

4 OBSERVATIONAL APPROACH FOR THE CONSTRUCTION AND OPERATION

Peck (1969) is recognized as having defined Karl Terzaghi's observational approach for soil mechanics applications, with key concepts including:

"... a third method which could be called the experimental method. The procedure is as follows: Base the design on whatever information can be secured. Make a detailed inventory of all the possible differences between reality and the assumptions. Then compute, on the basis of the original assumptions, various quantities that can be measured in the field. For instance, if assumptions have been made regarding pressure in the water beneath a structure, compute the pressure at various easily accessible points, measure it, and compare the results with the forecast. Or, if assumptions have been made regarding stress-deformation properties, compute displacements, measure them, and make a similar comparison. On the basis of the results of such measurements, gradually close the gaps in knowledge and, if necessary, modify the design during construction..."

Given the above description, there are a few uncertainties on the design and construction process of the constructed beaches that requiring the implementation of an observational approach. The first was the performance of the hydraulically deposited tailings that act as the foundation material for the constructed beaches, and second confirming the hydraulic gradient did not reach the starter dam. The lack of instrumentation (i.e., piezometers), the gaps on the understanding of the design, construction and operation of the facilities, and the availability and suitability of the construction material (i.e., tailings) provided additional degrees of uncertainty that could require to need to modify the design during construction.

The constructed beaches were planned to be built using tailings excavated from TSF 3 Cell 1, the impoundment area was already trafficable as there was over a year since this portion of the TSF was last used for tailings deposition.

The first stage of the constructed beaches required a volume of 157,000 m^3 of compacted tailings, considering a 30 m long section both in the north dam and west dam of TSF3. To reduce the uncertainty as to how much tailings were readily available to excavate, 17 test pits were executed in Cell 1. In each test pits, samples were taken every meter down to the maximum reach of the excavator (5 m) or the maximum depth allowed by the stability of test pit. The laboratory test of the retrieved samples included the determination of the moisture content, Standard Proctor tests, PSDs and specific gravity, the last two to confirm homogeneity. Based on Velardeña's experience in excavating tailings for mine backfill, the objective was to target tailings with a moisture content of 18% to 20%, the handling and placement would allow the tailings to reduce some moisture reaching 14% (+/- 2%) the optimum for compaction. Test pits did not show a sustained phreatic level, Pore Pressure Dissipation (PPD) tests showed full dissipation during the CPTu soundings, but there was some uncertainty on the performance and response of the underlying tailings during construction.

In general, the moisture content showed an increase with depth and interpolating the profiles of the test pits it Cell 1 was possible to generate depth contours at 18% of moisture content. The results showed up to 4 m (depth) near the north dam and 2 m towards the back of the impoundment, this would theoretically support that there was enough material to build the first stage of the constructed beaches.

The excavation for the first stage would provide additional capacity for the future use, the excavation volume was estimated to be 188,000 m^3 considering a bulking factor of 20%, which was later corrected to 15%, with a corrected volume of 181,000 m^3.

In terms of the physical stability of the constructed beaches, laboratory testing samples of the tailings obtained from the site investigation that was being executed in parallel. Triaxial testing on samples compacted to the 95% of the Standard Proctor presented either dilative behavior or the reach of phase transformation under 600 kPa of confining stresses with a peak angle of shear resistance of 35°and 33°at critical state. The hydraulic conductivities were in the order of 10^{-8} to 10^{-7} m/s, which is consistent for materials with fines contents of 95% that have low plasticity and are classified as ML in accordance with the USCS. Stability analyses showed admissible factors of safety to the CDA guidelines both for upstream and downstream conditions.

Some performance pilot tests were developed to understand the behavior of the tailings during the compaction works of the roller compactor, no softening was evident in the foundation even with vibration during compaction applied. However, the resident engineer and the earthwork personnel were warned to shut down the equipment, stop any activities and report back under any signs of softening, cracking or instability, as part of the health and safety protocols.

Settlement plates were installed in the footprint of the proposed constructed beaches, initially a set 18 settlement plates associated to the first stage (6 on Cell 1 north area) were considered. The settlement plates were installed near the foundation level of the constructed beaches, but after construction had begun. This delay resulted in not being able to have recorded the settlement magnitude of the underlying tailings associated to the initial loading of the initial layers.

When the construction began, the settlement plates were the only tool that would provide some insights on the behavior and response of the underlaying tailings. The tailings obtained from the test pits in the impoundment presented moisture contents between 15 and 26%, far from full saturation, but it wasn't clear if the tailings would saturate due to the compression and volume change, becoming more susceptible to triggering undrained behavior. To avoid triggering undrained behavior of the tailings, a rest period of 1 week was implemented after 3 lifts (each layer of 30 cm) were placed.

After the construction advanced and the performance of the settlement plates was analyzed, it was observed that settlements occurred and stabilized immediately after the construction of each layers and there was no consolidation during the rest period. The original rest time was estimate based on the consolidation theory, but after noticing compliant performance of the underlying tailings through the settlement of plates records, the resting time was eliminated.

The earthwork contractor assisted by providing daily measurements of the settlement plates with a precision of 1 mm using total station.

The settlement plates proved to be a good tool for this particular use, but a couple of challenges were identified. First, they are in the same spot where the trucks traffic and dump the material, where the dozers spreading it and where the rollers compact it, there were many interactions that resulted in damage to the of the settlement plates, which resulted in the need to recalibrate and correct the readings. And second, the rods needed to be extended as the construction advanced, this was anticipated, but combined with the damage to the rods resulted in frequent reset of the zero point and required continuous communication between the owner, contractor, and engineer.

Figure 5 presents the settlement plates measurement records during construction of the constructed beach associated to the Cell 2 north.

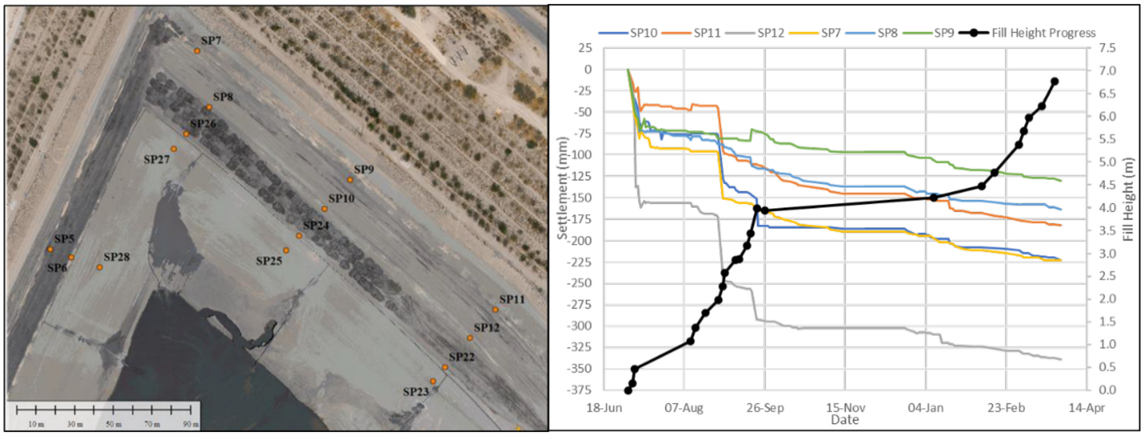

Figure 5: Settlement plates records during the construction of the constructed beaches

4.1 *Construction follow up and additional monitoring*

When the construction started in late May 2020, periodical drone surveys over the Velardeña tailings facilities were arranged, with a frequency between once and twice per month, depending on the drone availability, weather conditions, and availability of the mine surveyors. These drone flights helped to visually assess the construction process with the generated orthophoto and the digital elevation model (DEM) from the photogrammetry provided an additional way to track the construction productivity.

During construction there was a full-time resident engineer, he developed daily reports to keep records of the construction works, list the operators and machinery on duty, summarize the daily activities and achievements, keep track of the excavated and placed volumes of each work front. He also helped to coordinate and optimize the earthwork activities and to manage laboratory in charge of the quality control (QC).

The QC for the constructed beaches considered the compaction control for each layer targeted to 95% of the Standard Proctor Maximum Dry Density (SPMDD). The frequency of testing was inclusive of each 30 cm layer, every 500 m^3 of placed material or a maximum spacing of 50 m between test using the nuclear densimeter. For redundancy and to confirm the nuclear densimeter calibration, sand cone tests (ASTM 2015) were specified every 3000 m^3 of placed material or a minimum of 2 test per layer.

As per recommendation of the Independent Technical Review Board (ITRB) of Peñoles an InSAR monitoring services provider was engaged to provide historical analysis and monthly monitoring of displacements using the Sentinel -1 data (ESA, 2012) on the influence area of the TSFs Velardeña hired the service and received monthly reports including contour plots of vertical, horizontal and total displacements over a plan view of the TSFs, and access to a dashboard with the possibility to enquiry the historical displacements records in any of the SAR pixels.

InSAR has proved to be a good tool to track displacements on a larger scale, but there must be clarity on the limitations of the technology. One of the most applicable to Velardeña is the loss of coherence, areas with active deposition and construction the InSAR, particularly the Sentinel -1 data, was unable to determine displacements. As Velardeña has been working actively in the impoundment and in the raises the InSAR displacement data is not reliable in those areas. Nevertheless, zones such as the downstream face of the starter dam InSAR results to be a good tool to pick displacement patterns.

The piezometric instrumentation was designed to understand the performance of the phreatic levels and piezometric levels in and around the starter dam, particularly, the water levels in the tailings close to the bench in the upstream face where the seepage issues originated in 2018 and 2019. The piezometers were able to be installed towards the end of the construction of the constructed beaches, unable provide information during the construction process as the settlement plates did to feed the observational approach. The piezometers were installed in 6 sections along TSF3 starter dam and raise: two in the north dam of Cell 1, two in the north dam of Cell 2 and two in the west dam of Cell 2. Each section considered six (6) piezometers; one at the toe, two at the centerline of the starter dam at the foundation and at the body, and three in the tailings underneath the constructed beach. The piezometers installed at the toe and centerline were vibrating wire and the ones in the tailings were mix of open pipe and vibrating wire to provide redundancy and readings verification.

Additional survey monuments were installed as part of the site investigation that was running in parallel to the construction. A total of 12 monuments were installed, with the locations distributed on the same sections used for the piezometers, one at the toe of the starter dam and one at the crest of the first raise. But similar to the piezometers the installation of the survey monuments was not immediate at the start of construction, but they were able to be used to confirm the displacements patterns from the monuments on the starter dam with a lower overall magnitude.

After the first few weeks the construction efficiencies were confirmed as the earthworks reached a steady state, considering the time left and the availability of tailings, the decision to proceed with Stage 2 of the constructed beaches was taken. An extension of 20 m for Cell 1, 30 m for Cell 2 North and 10m for Cell 2 west was proposed, requiring an additional 110,000 $m^3$of tailings.

5 OPERATIONAL READINESS AND TARPS

Once the constructed beach associated with Cell 1 was near completion, the activities to ensure operational readiness began. Among the activities developed in this last part previous to the start of operation include: installation of the tailings pipeline with the discharge points and valves, construction of access roads and associated infrastructure, signage around the facility, access restriction gates, level and smoothing of the impoundment base to promote a quick formation of the supernatant pond, reclaim water pond pumps and barges installation, training of the operators, as-built scan of the impoundment and the definition of the TARPs.

An operational checklist was defined and required to be completed by the TSF operators on a daily basis. The requested checklist included the following:

- Perimeter embankments and constructed beaches evaluation,
- Assessment on crack progression and new cracks in the embankments,
- Signs bulging, settlements, signs of seepage and erosion on the embankments,
- Compilation, plot and review of the survey monuments and settlement plates data,
- Drain outlets inspection, verification of sediments transport, and daily rain records,
- Tailings pipelines, valves and connectors examination and tailings solids concentration record,
- Water recovery system check, among other operational items,

These items were linked to TARPs that were designed and defined considering three levels of warning depending on specific findings for each category. Depending on the level of warning predefined actions and reporting where defined. The daily checklist also includes the recording of the piezometer levels, both open pipe and vibrating wire. These levels were linked to specific TARPs based on in parametric stability analyses using limit equilibrium and admissible factors of safety.

Operation of TSF3 Cell 1 started on September 7, 2020 and provided capacity until February 15, 2021.The same approach was applied to Cell 2 of TSF3 in operation since February 2021 and expecting capacity until December 2021.

The following figure presents a photograph of TSF3 of Velardeña, showing Raise 1 with the 30 m Stage 1 and the 20 m Stage 2 of the constructed beach of Cell 1, taken days before the start of operation of Cell 1.

Figure 6: TSF3 Cell 1 constructed beach few days before the initiation of operation.

6 CONCLUSIONS

An observational approach was proposed to provide operational continuity in a safe manner at Velardeña TSF 3 which presented cracks on the starter dam during the construction of the first raise. After the compilation and review of the background information, it was possible to better understand some elements that could have contributed to the cracking of the dam and most important, related to the identification potential failures modes (internal erosion).

The understanding of the dams construction and historical performance helped to select a solution that was feasible and could be implemented under the tight timelines required to ensure operational continuity at Velardeña.

Using Terzaghi's concept of the observational approach (Peck, 1969), Velardeña and the contractors provided the required flexibility to adjust the plans whenever it was required. Once the daily excavation, hauling and placement reached a consistently achievable production rate, it was possible to propose and define the second stage of the constructed beaches, allowing an additional extension to be built. While construction occurred, piezometers and settlements plates were installed and recorded on a daily basis, with the piezometers identifying if increases in pore-water pressure were observed during loading, and the settlement plates were used to monitor the rate of settlement occurring which allowed for the construction rates to be controlled in such a manner that the pore-water pressure was allowed to dissipate. During operation, the piezometers have been used to confirm the design hypothesis and monitor the phreatic and piezometric levels within the constructed beaches, and to provide early warning of an advancing wetting front that could potentially reach the starter dam.

7 ACKNOWLEDGMENTS

The authors are grateful to Minera El Roble and Industrias Peñoles for allowing the material presented on the Velardeña TSFs to be published in this conference paper. The authors would also like to kindly acknowledge their colleagues in SRK Consulting who assisted in the design, supervision, construction, and on-going monitoring on the active TSFs in Velardeña.

8 REFERENCES

Peck R. B. 1969. Ninth Rankine Lecture: Advantages and Limitation of the observational method in applied soil mechanics. *Geotechnique 19*, No 2: 171-187.

SEMARNAT 2004. NOM-141-SEMARNAT-2003: que establece el procedimiento para caracterizar los jales, así como las especificaciones y criterios para la caracterización y preparación del sitio, proyecto,construcción, operación y postoperación de presas de jales". Diario Oficial de la Federación del 13 de septiembre de 2004.

European Space Agency (ESA) 2012. Sentinel-1, ESA's Radar observatory misión for GMES operational services. *ESA SP1233/1. March 2012.* Noordwijk: ESA Communications.

ASTM 2015. D1556 / D1556M-15e1, Standard Test Method for Density and Unit Weight of Soil in Place by Sand-Cone Method, ASTM International, West Conshohocken, PA, 2015, www.astm.org.

Regeneration of filter press fabrics in the mining sector

Bernd Fränkle & Patrick Morsch
Karlsruhe Institute of Technology, Karlsruhe, Baden-Württemberg, Germany

Hermann Nirschl
Karlsruhe Institute of Technology, Karlsruhe, Baden-Württemberg, Germany

ABSTRACT: Filter media of filter presses have a limited operation life. Beside mechanical damage, growing deposition of fine particles (blinding) inside the filter cloth is a problem. Resulting decreasing pore diameters not only affect the efficiency of the filtration process itself, but also make it more difficult to regenerate the filter press between the individual cycles, e.g. leading to an insufficient cake discharge. Therefore, an investigation into media rejuvenation is of interest.

The regeneration of two industrially used cloths from a gold and a silver mine provided by FLSmidth differing in cycle amount, material, weave and fiber type is investigated by using different agents as well as changing exposure times and concentrations. The effectiveness of the cleaning procedures is evaluated by pore size measurements. Regeneration up to the unused state was partly possible by using certain acids for monofilament fabrics. An influence of concentration and exposure time can be stated.

1 INTRODUCTION

Mineral resources are mined all over the planet in an increasing amount. Unfortunately, only a small amount of the crushed ore are valuable minerals so an even higher amount of residues have to be processed and stored, too (Concha 2014). This mine waste which is referred to as tailings is a slurry containing process water and gangue particles. Large tailings ponds were used to store this suspension allowing the particles to sediment. However, evaporation of water, risk of tailings dams, and area limitations demand new solutions. Therefore, filtered tailings meet with increasing attention (Amoah 2018, Amoah 2019). Savings in water costs, save tailings storage and sending a message of intention to create a more sustainable mining are beneficial outcomes.

However, as low residual moisture levels must be achieved filtration of tailings is a complex task. In general, a target residual moisture under 20 wt% is necessary (Gomes et al. 2016). To achieve this moisture level recessed plate filter presses can be used. Referred to their footprint they allow a high throughput at a high filtration pressure especially in parallel operation (Anlauf 2019).

Unfortunately, filter press filter cloths have a limited service life. Mechanical damage and deposition of fine particles inside the filter cloth which is referred to as blinding occur. The latter results in an increased filter media resistance, a non-economical operation, and the necessity of fabric cleaning or replacing, respectively. Frequent replacing of filter cloths is a high financial effort and causes an interest in investigating effective cleaning methods.

2 THEORETICAL BACKGROUND

The description of resistances of porous media, such as filter cloths and filter cakes, is made by the Darcy equation (Darcy 1856) (Eq. 1) (Ripperger 2013). This shows the correlation between the flow rate $\dot{m}$ of a liquid flowing through a porous structure, the fluid density ρ_{Fluid}, the surface area A, the permeability P, the applied pressure difference Δp, and the dynamic viscosity of the fluid η_{Fluid} at assumed laminar flow conditions and neglected friction.

$$\frac{\dot{m}}{\rho_{Fluid} \cdot A} = P \cdot \frac{\Delta p}{\eta_{Fluid}} \qquad \text{(Eq. 1)}$$

The object properties of the object passed by flow can be found in the permeability. It corresponds reciprocally to resistance e.g. for a filter medium or a filter medium blinded by adhering particles. These approaches are also the basis for dealing with more complex filtration tasks with particle size distributions and non-spherical particles. Tailings have broad particle size distributions including a high proportion of fines (Wang et al. 2014, Davies 2011, Mamghaderi et al. 2018, Wennberg et al. 2020). This influences their filtration behavior. Interactions of the particles with the fluid and with each other lead to compressible cakes and higher residual moisture contents (Wakeman 2007). To ensure compaction apparatuses with a higher pressure difference have to be used leading to a structure of small pores with high flow resistance as a side effect (Johns 1991, Kujawa et al. 2019). Therefore, filter presses are used for tailings filtration to allow the necessary filtration pressure (Gomes 2016). In addition, many cloth concerning problems such as filtrate turbidity at the beginning of filtration and cloth blinding are caused by fines (Wakeman 2007). Figure 1 shows schematically a cross-section of a blinded cloth (Fränkle 2021). The free pore diameter d_{Pore} becomes smaller due to blinding ($_{dPore,\ Blinding}$) by adhering particles to the fibers or already deposited particles.

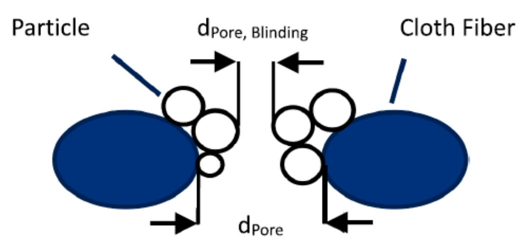

Figure 1. Schematical illustration of cloth blinding (Fränkle 2021).

Filtration efficiency is reduced by blinding by increasing the filter medium resistance and filtration time. This is shown in Figure 2 (Fränkle 2021). Filtrate volume flows over the time of several consecutive, constant pressure filtration cycles for a theoretically optimal regeneration of the filter medium is shown. Furthermore, the filtrate volume flows for an increasing blinding of the filter medium can be seen. To reach the same final moisture the same amount of water must be discharged in each cycle, which results in requiring the same area under each filtrate volume flow versus time curve. Normally, the filtrate flow decreases degressively from a certain initial filtrate flow until a specific time T_{Setup} at which the cake is sufficiently dewatered. For optimal regeneration the same initial resistance could be achieved for each filtration and T_{Setup} would remain constant. However, blinding leads to a deviating behavior in real operation. Original initial filtrate flow cannot be achieved. It increasingly deteriorates in the following cycles. For reaching the same residual cake moisture filtration must be increasingly longer due to lower filtrate flow. At a certain point this leads to the need for timely fabric replacement.

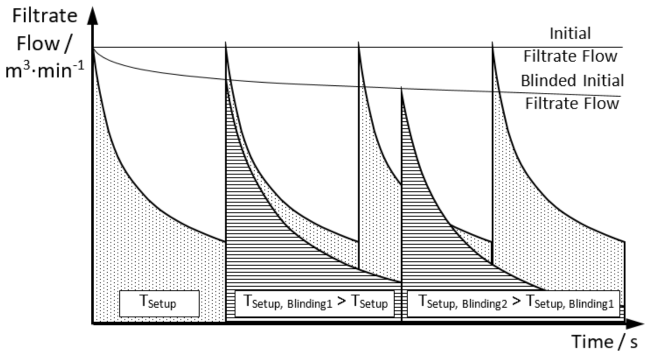

Figure 2: Filtration cycles for tailings filtration for optimal regeneration conditions and cloth blinding (Fränkle 2021).

In General, there are different cleaning options for filter media. The cleaning of surface contamination is a result of incomplete cake dropping (Weigert 2001). Beside manual cleaning of the filter cloth, tilting the plates (Goltermann & Hedlund 1998), vibration (Iwatani 1990), scraper installation (Oelbermann 1991), and jet cleaning (Morsch 2020, Morsch 2021) are common methods. Jet cleaning reduces surface contamination but might also transport particles contaminants deeper into the cloth (Rushton 2000). For cleaning of contamination in the filter medium several mechanisms can be used. Physical cleaning achieved by flow, often induced by backwash in the case of filtration (Cai et al. 2017, Morsch 2020), or by ultrasound (Steenstrup 1988, Ekberg 1988, Busch-Sorensen 1990, Tuori et al. 2001) and chemical cleaning by either their partial or complete dissolution (Smith 2017, DIN 19569-9 2017) or by wetting effects and surfactants, respectively (Rosen 2004).

Filter cloth cleaning in minerals processing, especially tailings processing, has been investigated to a limited extent. Mostly all suppliers of filter presses used in tailings filtration offer jet cleaning systems (Wisdom 2019, Outotec 2020, Aqseptance 2020). Furthermore, acid cleaning is recommended by several companies (Outotec 2020, Universal Filtration & Pumping Solutions 2020, Micronics 2020) and investigated to be successfully for cloths with monofil fibers mainly by permeability measurements (Fränkle 2021).

3 MATERIAL AND METHODS

The industrial used filter cloths including the tailings as well as porometry as used pore size measurement method are shown in the upcoming sections. The methodology is analogous to Fränkle 2021.

3.1 *Tailings filtration filter cloths*

The properties of the filter cloth in unused conditions are listed in Table 1 (Fränkle 2021). They were used in 2x2m recessed plate filter presses on different continents and sent to Germany in dried condition. A nylon cloth from a silver mine (around 5000 filtration cycles) and another from a gold mine (around 6500 cycles) were investigated. Filtration cycle numbers are in the normal range for cloth exchange (Wisdom 2019). The silver mine cloth is woven in satin weave made of mono- and multifil fibers and the gold mine cloth has a plain weave out of monofil fibers. The flow resistances of the cloths measured with a pressurized filter cell and calculated based on the Darcy equation (Eq. 1) is higher for the silver cloth. The diameters of the mean flow pore (MFP) are calculated from porometry tests (Eq. 2). Due to the multifilament fibers used the silver cloth has lower MFPs than the gold cloth.

Table 1. Filter media properties in unused state (Fränkle 2021)

Cloth	Silver Mine Filter Medium	Gold Mine Filter Medium
Material	PA	PA
Weave	Satin	Plain
Fiber type	Mono/Multi	Mono/Mono
Resistance	$5.2 \pm 2.9 \cdot 10^8$ m^{-1}	$6.6 \pm 5.5 \cdot 10^7$ m^{-1}
MFP	35.8 ± 2.2 µm	54.4 ± 1.4 µm

Thickened tailings are dewatered at both sites which have broad particle size distributions, i.e. they have a large fraction of fines below their $x_{50,3}$ value (Fränkle 2021). Table 2 lists an excerpt of the sum distributions measured by laser diffraction. The high fraction of fine particles and the broad distribution are obvious for all tailings. More than ten percent of the solid mass has an equivalent diameter of less than 10 micrometers. $x_{50,3}$ values are below 40 microns.

Table 2. Particle size distribution excerpt (Fränkle 2021)

Particles	Silver mine tailings	Gold mine tailings
$x_{10,3}$	1.3 µm	2.4 µm
$x_{50,3}$	8.9 µm	11.5 µm
$x_{90,3}$	79.0 µm	82.1 µm

3.2 *Pore size measurements*

Blinding is caused by permanent adhering particles inside the filter cloth. This results in a process engineering point of view in a decreasing permeability and an increasing filter medium resistance. To measure the pore size directly porometry measurements can be used where the pore distribution is measured by gas flow. A sample has to be wetted with wetting liquid (e.g. silicone oil) in advance, as shown in Figure 3, and is placed in a permeability cell. Then, pressure is increased continuously, thus, the corresponding volume flow is increasing. The recorded curve in the volume flow over pressure plot is referred to as wet curve.

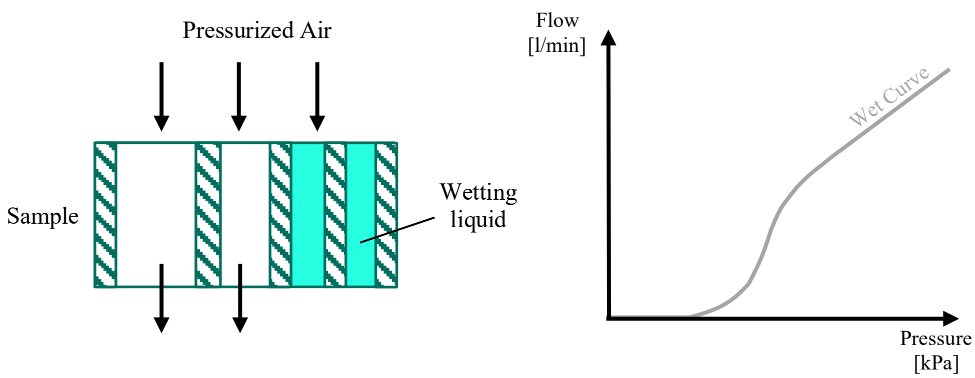

Figure 3. Schematical illustration of pore emptying and corresponding measurement of the wet curve.

According to the Young-Laplace equation (Eq. 2), the pore diameters d_{Pore} of cylindrical pores become emptied with increasing pressure difference Δp. The pressure needed is depending on the fluid surface tension γ and the wetting angle θ. Despite the highly non-cylindrical pore shape, porometer tests are the method of choice for various porous applications even for highly non-cylindrical pores (ASTM E128-99 2019).

$$d_{Pore} = \frac{4 \cdot \gamma \cdot \cos\theta}{\Delta p} \qquad \text{(Eq. 2)}$$

To ensure wetting the linear, non-reactive polydimethylsiloxane silicon oil AK 10 (Wacker Chemie AG) was used. Furthermore, the capillary flow porometer CFP 1500 AFX (Porous Materials Inc.) was used. Wetting is achieved if the surface tension of a fluid is lower than the critical surface tension of the sample. Synthetics are known to be low-energy surfaces. Based on standardized tests checking wetting behavior of different fluids the critical surface tensions of PP and PA are 29 mN/m and 46 mN/m, respectively (ASTM D7541-11 2015, ISO 8296 2008, Ebnesajjad 2014). Therefore, wetting occurs using the silicone oil with an approximate surface tension of 20 mN/m according to its data sheet (Wacker 2020). AK 10 is well tested as wetting agent. Extensive comparative tests of commercially available wetting agents can be found (Kolb 2018). Its low volatility is useful to guarantee that measurement time does not influence the results. Differential pressure of 300 kPa where used, which is corresponding to the ability of emptying capillaries of down to 0.27 µm.

There are several points of interest at the wet curve. The first volume flow detected and its corresponding pressure is referred to as bubble point (see Figure 4). Further increasing the pressure, the flow rate is also increasing. This happens by a higher flow through already emptied capillaries as well as emptying of smaller ones. At a point where the flow rate increase is coming from higher pressure only the pressure starts to decrease. Then, the dry curve is recorded. Afterwards, the half dry curve is calculated the intersect with the wet curve. The corresponding pore size of this pressure is referred to as mean flow pore diameter.

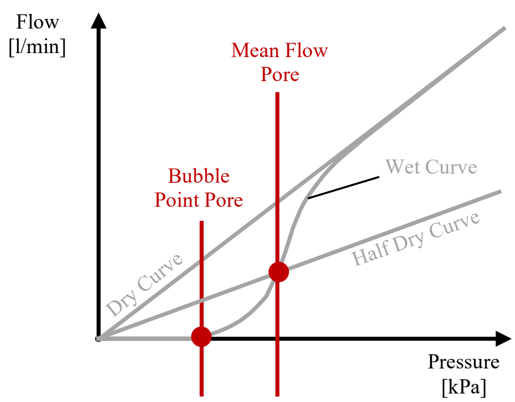

Figure 4. Schematical illustration of porometry results, bubble point determination, and mean flow pore determination.

For sample preparation PP plastic containers were filled with 100 ml cleaning agents. Then, one round permeability sample (44.2 cm² surface area) and a circular porometer sample (3.8 cm² surface area) were placed inside for a specific exposure time. Each test is performed three times permeability samples were used in a previous publication (Fränkle 2021). The area-related cleaning-agent load is 20.83 mol/m².

4 RESULTS & DISCUSSION

Previous investigations on regeneration behavior of tailings filtration cloths enabled the following conclusions (Fränkle 2021):

- Acid cleaning (especially Hydrochloric and sulfamic acid) are effective
- Ultrasonic treatment and bases are not effective
- Ultrasonic and acid treatment at the same time have no further positive influence
- Cloths out of monofil fibers can be nearly completely cleaned
- Elemental composition of the tailings sees not to have an influence on cleaning
- Damaging of the cloths by cleaning cannot be observed

These finding were mainly based on permeability measurements since the flow through the cloth is a direct indicator of filtrate flow behavior. Nevertheless, it is an indirect determination method to check the pore size which results in a certain permeability. To measure the blinding directly a pore size determination would be the direct measurement methodology. To this point, only the pore size changes of cleanings with different solvents were measured (Fränkle 2021). Influences caused by concentration and time variation could be shown using permeability data.

Figure 5 shows the specific mean pore diameter for silver and gold cloths with hydrochloric and acetic acid for different molarities. The hydrochloric and acetic acid cleaned silver cloth as well as the acetic acid cleaned gold cloth pore sizes are lightly increasing with increasing acid availability but regeneration has to be stated ineffective. Contrary to this, once again, hydrochloric acid cleaning is efficient for to monofil fiber gold cloth.

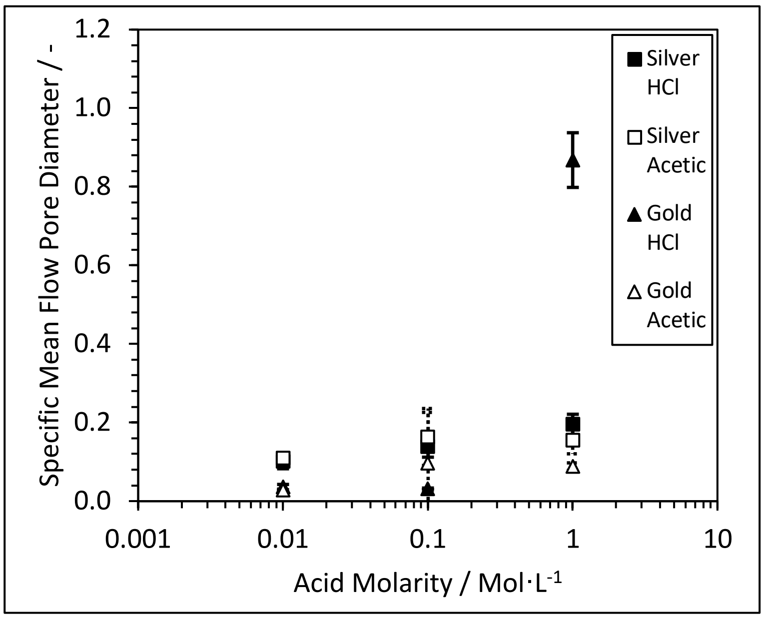

Figure 5. Representation of the mean flow pore results for variable hydrochloric and acetic acid concentrations (0,01, 0,1, and 1-molar 30 min) related to the unused value for the silver and the gold cloths.

For the silver cloths pore low values of related pore sizes are to be stated for both acids and all exposure times. This verifies the permeability results. Due to the multifil fibers, no significant cleaning occurs. The gold cloth samples cleaned with acetic acid also fail to improve increase in pore size for all exposure times. Acetic acid is not able to clean them. In contrast an exposure time dependent cleaning can be seen for the gold cloth cleaned with acetic acid. In the range between 5 to 15 min cleaning the related pore size increases to the range of one.

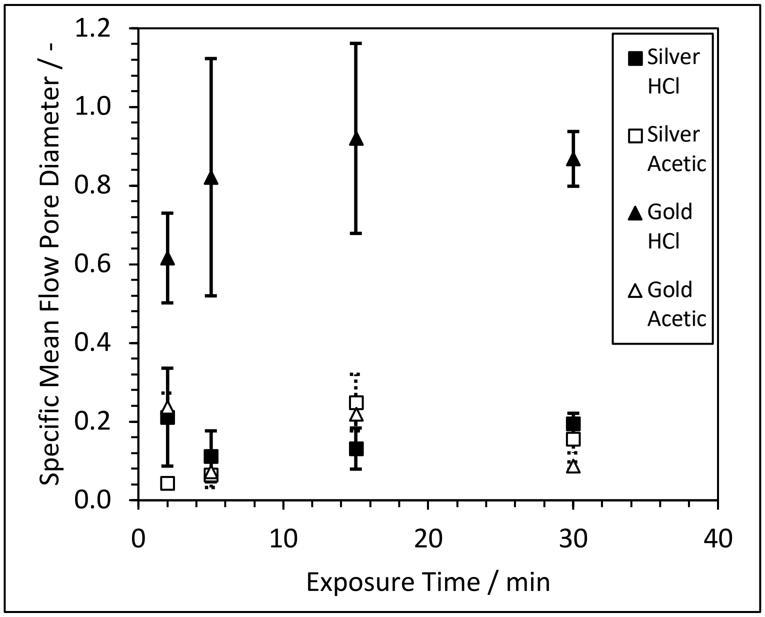

Figure 6. Representation of the mean flow pore results for variable treatment times (2, 5, 15, and 30 min1-molar hydrochloric and acetic acid) related to the unused value for the silver and the gold cloths.

5 CONCLUSION

Pore blinding is a big issue in tailings filtration and effective cleaning is an opportunity to increase cloth life and reducing costs. Therefore, cleaning of industrially used filter cloths using several solvents were investigated. Summarizing, it can be stated that pore size measurements using porometry measurements are able to determine pore blinding and its regeneration. Hydrochloric acid is cleaning effectively cloths out of monofile fibers. Nevertheless, cleaning has a time and concentration dependency.

6 REFERENCES

Amoah, N, Dressel, W., Fourie, A.B., Characterisation of unsaturated geotechnical properties of filtered tailings in dry stack facility, Proceedings of the 22st International Seminar on Paste, Thickened and Filtered Tailings, Perth, 2018. DOI: 10.36487/ACG_rep/1805_31_Amoah.

Amoah, N, Large-Scale Tailings Filtration and Dry Stacking at Karara Magnetite Iron Ore Operation, Proceedings of Tailings and Mine Waste, Vancouver, 2019.

Anlauf, H., Wet Cake Filtration, Wiley-VCH, Weinheim, 2019. DOI: 10.1002/9783527820665.

Aqseptance Group / Diemme Filtration, <https://www.aqseptence.com/app/en/products/diemme-filtration-fast-cycling-filter-press-ght-f/> (accessed 01/05/2020).

ASTM D 7541-11, Standard Practice for Estimating Critical Surface Tensions, 2015.

ASTM E128-99, Standard Test Method for Maximum Pore Diameter and Permeability of Rigid Porous Filters for Laboratory Use, 2019.

Busch-Sorensen, T., Filter for filtration of fluids, 1990, United State Patent 5085772 A.

Cai, J., Hao, W., Zhang, C., Yu, J., Wang, T, Journal of the air & waste management association, 2017 67(12), 1273-1287. DOI: 10.1080/10962247.2017.1311967.

Concha, F.A., Fluid Mechanics and Its Applications Volume 105 Solid-Liquid Separation in the Mining Industry, Springer, Cham 2014. DOI: 10.1007/978-3-319-02484-4.

Darcy, H., Les fontaines publiques de la ville de Dijon, Paris, 1856.

Davies, M.P., Filtered Dry Stacked Tailings – The Fundamentals, Proceedings Tailings and Mine Waste, Vancouver, 2011.

DIN 19569-9, Wastewater treatment plants – Principles for the design of structures and technical equipment – Part 9: Mechanical drainage of sewage sludge, 2017.

DIN ISO 8296, Plastics – Film and Sheeting – Determination of wetting tension, 2008.
Ebnesajjad, S., Surface Treatment of Materials for Adhesive Bonding 2nd Edition, Elsevier, Oxford, 2014. DOI: 10.1016/C2013-0-12914-5.
Ekberg, B., Goran, N., Method of Cleaning Filter Discs in a Suction Dryer Using Ultrasonic Vibration, 1988, United States Patent 4946602 A.
Fränkle, B, Morsch, P, Nirschl, H 2021, 'Regeneration Assessments of Filter Fabrics of Filter Presses in the Mining Sector', *Minerals Engineering*, vol. 168, DOI: 10.1016/j.mineng.2021.106922
Goltermann, J., Hedlund, H.G., Method for Emptying the Press Chambers of a Press Filter and an Apparatus Therefor, 1998, United States Patent 5728307.
Gomes, R.B., De Tomib, G., Assisa, P.S., Journal of Materials Research and Technology 2016; 5(4), 339–344. DOI:10.1016/j.jmrt.2016.03.008.
Iwatani, A., Apparatus for Cake Removal in a Filter Press, 1990, United States Patent 4900436.
Johns, F.E., High Pressure Filtration of Fine Particle Slurries, Filtech, Karlsruhe, 1991.
Kaswalder, F., Cavalli, D., Hawkey, A., Paglianti, A., *Tailings dewatering by pressure filtration: process optimisation and design criteria*, Proceedings of the 22st International Seminar on Paste, Thickened and Filtered Tailings, Perth, 2018. DOI: 10.36487/ACG_rep/1805_35_Kaswalder.
Kolb, H.E., Schmitt, R., Dittler, A., Kasper, G., Separation and Purification Technology, 2018 199, 198–205. DOI: 10.1016/j.seppur.2018.01.024.
Kujawa, C., Winterton, J., Jansen, R., Cooke, R., Innovative process engineering to create better tailings facilities, Proceedings of 6th International Seminar on Tailings Management, Santiago, 2019.
Mamghaderi, H., Gharabaghi, M., Noaparast, M., *Minerals Engineering* 2018 122, *220-226*. DOI: 10.1016/j.mineng.2018.03.041.
Micronics, IS CHEMICAL CLEANING EFFECTIVE FOR CLEANING MY FILTER CLOTH? <https://www.micronicsinc.com/filtration-news/chemical-cleaning-filter-cloth/> (accessed 01/05/2020).
Morsch, P., Chemical Engineering Science 2020 226, 115889. DOI: 10.1016/j.ces.2020.115889.
Morsch, P., Separation and Purification Technology 2020 249, 117073. DOI: 10.1016/j.seppur.2020.117073.
Morsch, P., Separation and Purification Technology 2021 256, 117793. DOI: 10.1016/j.seppur.2020.117793.
Oelbermann, M., Filterpresse, 1991, DE 3933740 A1.
Outotec, J. Palmer, Practical solutions for Mine tailings – Webinar - Part 2, 05/14/2020. <https://www.brighttalk.com/service/player/en-US/theme/default/channel/13517/webcast/404398/play?showChannelList=true> (accessed 01/05/2020), <http://public2.brighttalk.com/resource/core/270553/part-2---practical-solutions-for-mine-tailings_601265.pdf (accessed 01/05/2020).
Ripperger, S., Gösele, W., Alt, C., Loewe, T., Filtration, 1. Fundamentals in Ullmann's Encyclopedia of Industrial Chemistry, Wiley-VCH, Weinheim 2013. DOI: 10.1002/14356007.b02_10.pub3.
Rosen, M.J., Surfactants and interfacial phenomena. Surfactants and Interfacial Phenomena, 3rd Edition, John Wiley & Sons, New Jersey, 2004. DOI: 10.1002/0471670561.
Rushton, A., Ward, A.S., Holdich, R.G., Solid-Liquid Filtration and Separation Technology, Wiley-VCH, Weinheim, 2000.
Smith, J., Sheridan, C., van Dyk, L., Naik, S., Plint, N., Turrer, H.D.G., Minerals Engineering 2018 115, 1-3. DOI: 10.1016/j.mineng.2017.10.011.
Steenstrup, P.R., A Method of Filter-cleaning and an Apparatus for Carrying Out the Method, 1988, WO 1989009646 A1.
Tuori, T., Sekki, H., Ihalainen, J., Pirkonen, P., Mursunen, H., Combined Ultrasonic Cleaning and Washing of Filter Disks, 2001, United States Patent 6217782.
Universal Filtration & Pumping Solutions, Acid Cleaning, <http://automaticfilterpress.com/acid-cleaning/> (accessed 01/05/2020).
Wacker Chemie AG, AK 10 Data Sheet, <https://www.wacker.com/h/de-us/medias/WACKER-AK-10-en-2020.07.01.pdf> (accessed 01/05/2020).
Wakeman, R., Separation and Purification Technology 2007 58, 234–241. DOI: 10.1016/j.seppur.2007.03.018.
Wang, C., Harbottle, D., Liu, Q., Xu, Z., *Minerals Engineering* 2014 58, *113–131.* DOI: 10.1016/j.mineng.2014.01.018.
Weigert, T., Haftung von Filterkuchen bei der Fest/Flüssig-Filtration, VDI-Verlag, Düsseldorf, 2001.

Wennberg, T., Stalnacke, A., Sellgren, A., *Commissioning and Operational Experience of a Thickened Tailing Facility with Two Thickeners,* Proceedings of the 23st International Seminar on Paste, Thickened and Filtered Tailings, Santiago, 2020. DOI: 10.36487/ACG_repo/2052_32.

Wisdom, T., Maintaining high availability and low operational costs for filtered tailings facilities, Proceedings of the 22st International Seminar on Paste, Thickened and Filtered Tailings, Perth, 2019. DOI: 10.36487/ACG_rep/1910_23_Wisdom.

The application of satellite InSAR in calculating tailings consolidation across inactive and closed facilities

Nathan Magnall, Adam Thomas & Hayley Larkin
CGG Satellite Mapping, CGG Services (UK) Ltd., UK

Jon Engels
Tailpro Consulting Ltd, Chile

ABSTRACT: Accurately determining the rate of consolidation across a tailings pond is a vital aspect of tailings performance and management. However, there are various operational and logistical challenges associated with measuring consolidation across a tailings storage facility (TSF). Satellite InSAR is typically used to determine coherent ground displacement along TSF dam walls and beaches, but it is possible to capture tailings consolidation during inactive periods of deposition, or during and after closure. InSAR processing has been applied to images acquired by the Sentinel-1 satellite constellation to determine millimetric levels of consolidation across an inactive region of a tailings pond. Our results show variable compaction across a region associated with the presence or absence of an underlying geomembrane. A by-product of such work is the ability to assess the stability of TSF dam walls, which is of critical importance to the safe operation of such facilities.

1 INTRODUCTION

Historically, Tailings Storage Facilities (TSFs) have been a necessary feature of mining operations across the world. They typically contain conventionally deposited slurries, thickened, paste and filtered tailings waste, contained by a retaining wall (dam) often constructed from the tailings themselves. After construction of the initial starter dyke, the dam is progressively raised in a series of lifts where the crest moves upstream, vertically (centreline) or downstream (Vick 1983). Despite their necessity, TSFs have a long history of failing (WISE Uranium project, 2019), as exemplified by a series of recent failures, not least the Bruhmadinho event which occurred in Brazil on 25th January 2019. The subsequent public call for greater disclosure (Church of England, 2019), has meant that the scrutiny of such structures has never been greater.

Whilst the main focus of this scrutiny is to understand the presence, history and present-day status of all TSFs globally, there remains a need to ensure that operational facilities are performing as expected from a geotechnical, environmental and economic perspective. Satellite imagery is providing a vital source of information within the ongoing disclosure audits, but it has much wider applications. In addition to helping to determine the hazard profile of a TSF, it can also be used to study the performance of the tailings material itself, and therefore the operational performance of the facility.

Some of the key challenges with managing the performance of a TSF is understanding volume, tailings composition, the rate at which tailings can be deposited, where they should be deposited, and the rate at which they consolidate/dewater. These factors play a vital role in ensuring optimal and safe operation whilst maintaining a healthy water balance across the mine. The latter is particularly important in dry and arid regions.

Due to almost continual construction and depositional activities, operational TSFs are notoriously challenging to monitor using conventional surveying techniques. Exposed beaches can be difficult to reliably measure as they are under constant flux and may be highly saturated. Measuring the bathymetry of submerged tailings is also challenging, given potentially hazardous water conditions, and a poor understanding of water depths and underlying tailings morphology can lead to issues with access and safety associated for equipment and personnel.

As deposited tailings dewater, they compact and dry at a specific rate but for the reasons noted above this can be difficult to measure. This study takes steps towards addressing this by using satellite synthetic aperture radar (SAR) imagery to remotely determine rates of tailings consolidation across an active TSF. The approach uses interferometric synthetic aperture radar (InSAR), a remote sensing technique typically used to monitor ground displacement across TSF dams and other mine slopes, to construct a high-precision time series of displacement measurements across exposed tailings beaches. In this study there was a fortuitous 12 month period of inactivity, during which time no new tailings were deposited across a region of a TSF used as a case study in this paper. This presented an ideal window of time to test this approach, simulating a closure style arrangement of a TSF when data was used following the last few days of fresh deposition of tailings. Additionally, the presence of an underlying geomembrane across a section of these tailings meant that rates of consolidation could be compared in areas with and without a geomembrane, which could further improve our understanding of how tailings consolidate with and without an underlying drainage barrier.

The results highlight the effectiveness of InSAR to study tailings compaction, but also how a tailings liner can impact consolidation of tailings material. Furthermore, the results show the importance of considering the effect of a liner on water drainage.

2 METHODOLOGY

Satellite remote sensing covers a range of techniques. This study primarily uses satellite InSAR to determine the consolidation rate within a temporarily closed region of a TSF between September 2017 and September 2018. In addition, this study uses high resolution digital elevation models (DEMs) to determine the thickness of the tailings.

2.1 *InSAR*

InSAR uses satellite SAR imagery to detect ground displacement. In this case we use open-access SAR data from the Sentinel-1 satellite constellation to derive measurements. A SAR image contains two components: 1) the amplitude, which is a measure of the strength of the returned radar signal and can be used to generate an image, and 2) the phase, which is a measure of the final incomplete returned wavelength of the radar signal. By comparing the phase of two radar images it is possible to quantify subtle changes in elevation, and by comparing multiple SAR images acquired over a given time period it is possible to generate a time series of displacement. A more detailed description of SAR interferometry can be found in Bamler & Hart (1998), Rosen et al. (2000) and Hanssen (2001).

InSAR does not provide an absolute measure of ground displacement, instead it provides a relative measurement with respect to a reference point that is either assumed to be stable or constrained using an alternative survey method. Changes to radar phase are not only caused by ground displacement. Topography can also impact phase values; thus a good quality DEM is required to remove the impact of topography. Where a DEM may be inaccurate this can lead to corresponding errors in the InSAR result. Here we use a high resolution DEM derived from Kompsat-3A stereo optical satellite data acquired in 2018.

Subtle inaccuracies in orbital positioning of the satellite can also lead to errors in radar phase, but these can be corrected. Most significantly, atmospheric conditions at the time of SAR image acquisition can impact the measured phase. Atmospheric water vapour can delay the radar signal, leading to a shift in the measured phase and therefore apparent displacement. Atmospheric errors can be correlated with elevation (and therefore modelled and removed), but are often spatially and temporally heterogeneous, which can be more challenging to mitigate.

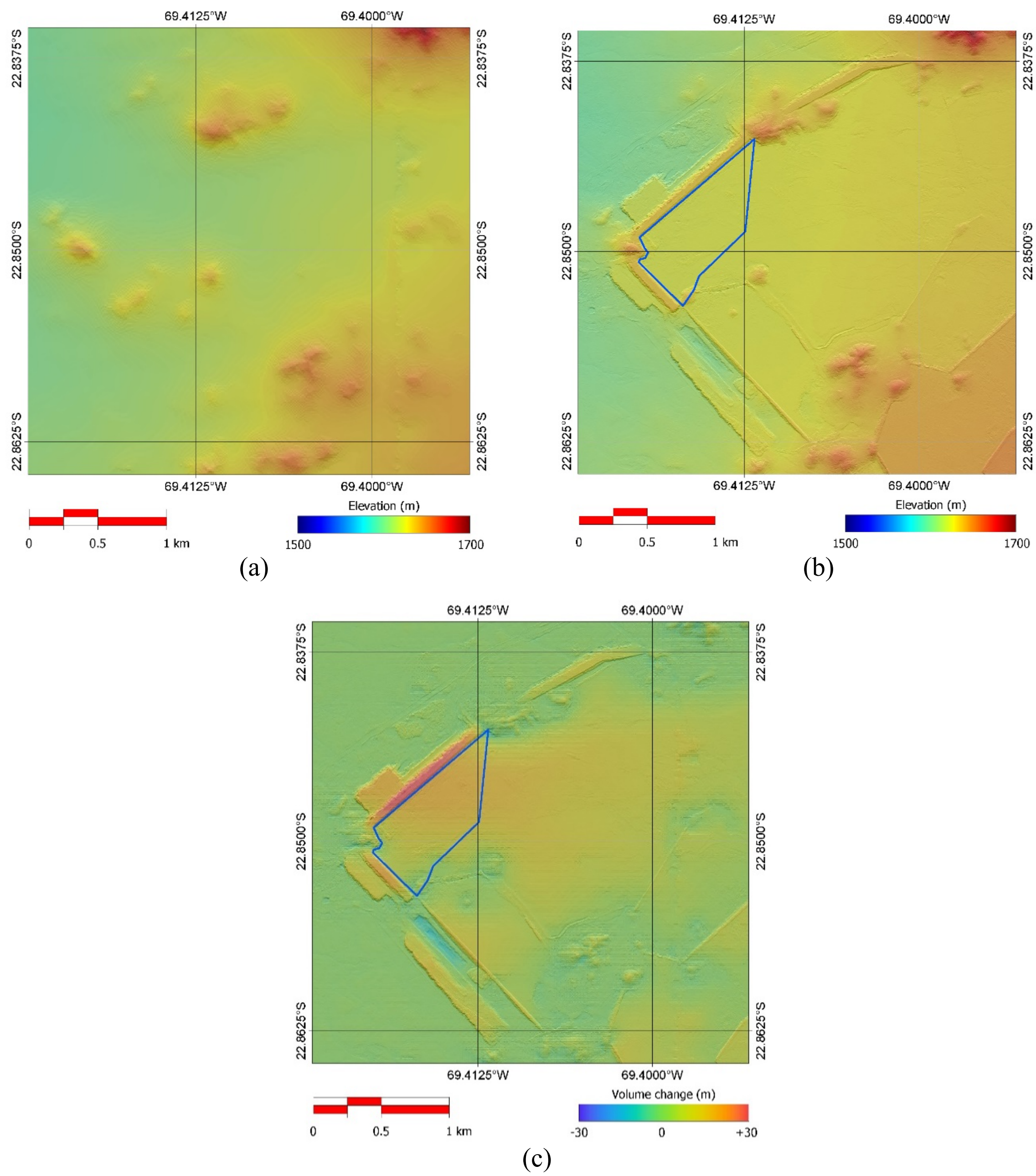

Figure 1. Digital elevation models (DEMs) across the Area Of Interest (AOI). (a) Pre-construction LiDAR DEM. (b) Post-construction DEM from Kompsat-3A optical data, the blue polygon shows the approximate extent of a geomembrane. (c) Volumetric change between the two DEMs. Image © CGG 2020. Data © KARI 2018. Distribution (SI Imaging Services, Republic of Korea), all rights reserved.

Displacement rates of millimetres to metres can be accurately detected using InSAR. However, for InSAR to accurately detect large magnitude displacements, the displacement gradient must not be too high (~2.5 cm of displacement between any two SAR pixels and/or acquisition dates). Adjacent pixels can only move by so much (typically a few centimetres) before the phase values of the pixels become so noisy that it is not possible to determine the amount of ground displacement. InSAR also requires that the ground conditions are similar between two SAR images (termed coherence), and where changes to the ground surface occur measurement points can be lost. Large changes to the ground surface, and therefore a loss of coherence, can occur due to a number of factors, such as excavation works, construction activities, large ground displacements such as a slope failure, and fresh snow fall. Provided the limitations of the technique are properly understood, and errors are mitigated where possible, InSAR can provide precise measurements of ground displacement.

Typically, TSF beaches are difficult to measure using InSAR due to the regular deposition of fresh tailings and/or the presence of water. However, in this case no new tailings were added between September 2017 and September 2018, allowing coherent measurements to be derived across the TSF beaches.

2.2 *Digital Elevation Models (DEMs)*

Using high-resolution optical satellite imagery acquired in stereo mode, it is possible to derive high resolution, high precision topographic models using photogrammetric techniques. Satellites such as Kompsat-3A, Pleiades, WorldView, and SuperView are capable of acquiring stereo data. A post-construction topographic model was derived from two Kompsat-3A optical images, acquired in stereo mode with a 60° separation angle. The spatial resolution of the topographic model is 1 m and the vertical accuracy is +/- 50 cm.

The pre-construction topography was derived from a historic LiDAR survey of the area before the TSF was constructed. By subtracting the pre-construction DEM from the post-construction DEM it was then possible to determine the thickness of the tailings material. The pre-construction DEM, post-construction DEM and difference between the two models, are shown in Figure 1.

3 RESULTS AND DISCUSSION

Measurements of compaction of the tailings surface were generated between September 2017 and September 2018. A geomembrane liner is present in some regions of the TSF (polygon in Figure 1b), allowing for a comparison of the effect of the liner on the tailings consolidation rate.

3.1 *TSF Surface*

The surface of the TSF shows highly heterogeneous rates of compaction, with two distinct compaction zones, which correspond to the presence or absence of a geomembrane liner. Both regions received tailings from the start of deposition in late 2015 up to the start date of the InSAR analysis (following termination of a fresh layer of tailings). Therefore, the measurements made relating to consolidation are measuring the entire mass of tailings deposited since 2015. There are also variable depths of tailings in both regions and this is discussed later in this section.

In areas where the lining is absent the tailings consolidated at an average rate of 156 mm/yr (AOI 1, Figure 2). Where the lining is present the tailings consolidated at an average rate of 105 mm/yr (AOI 2, Figure 2). The rate of consolidation of the tailings was initially higher after the last deposition of fresh tailings with the unlined and lined areas consolidating at an average rate of 343 mm/yr and 217 mm/yr respectively in the 24 days after the deposition of a final fresh layer of tailings (Figure 3 and Table 1). By September 2018 this consolidation rate had slowed to 83 mm/yr and 86 mm/yr for the lined and unlined regions of the tailings respectively, in the 30 days prior to the deposition of a fresh layer of tailings (Figure 3 and Table 1). The slower compaction rate in the lined tailings most likely relates to the slower release of water via lateral movement/drainage and capillary rise via evaporative effects.

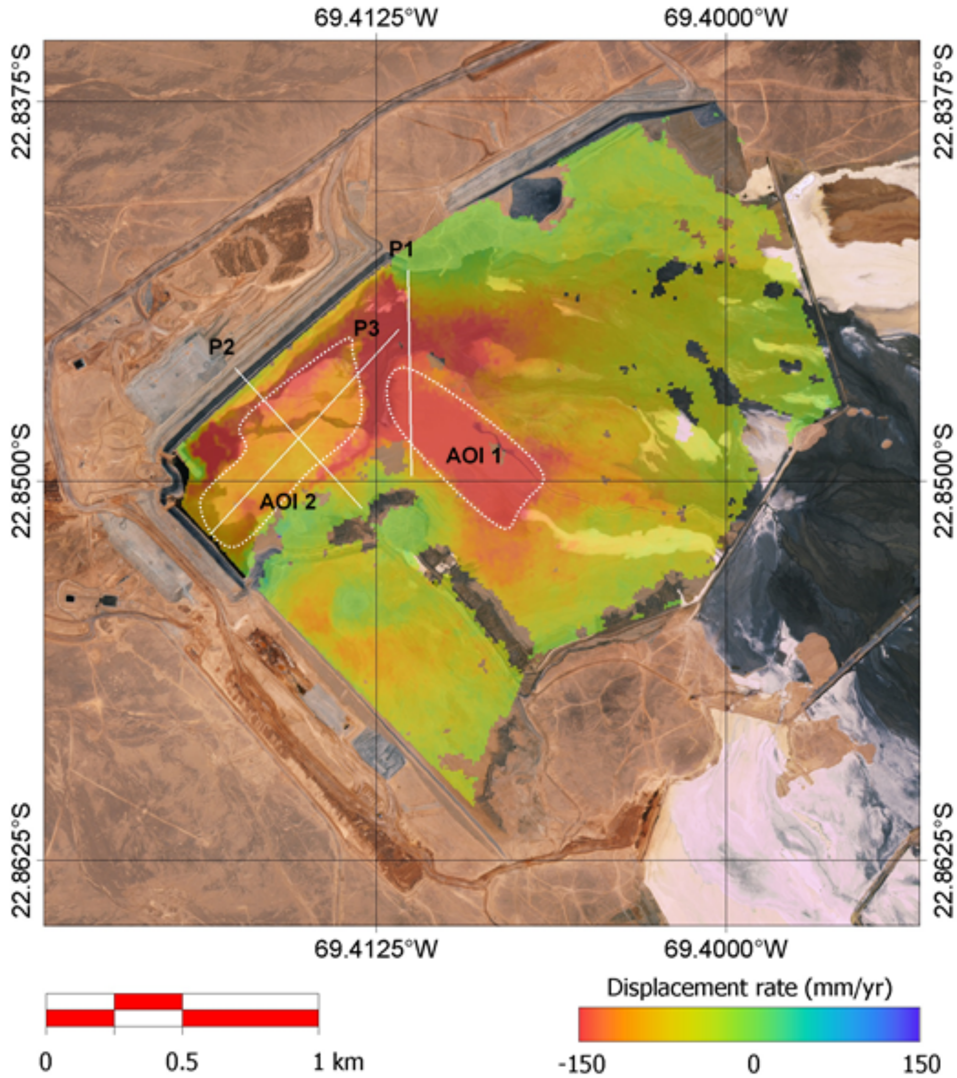

Figure 2. Line-of-sight displacement of the tailings between September 2017 and September 2018. AOI 1 shows the extent of a non-lined region of the tailings. AOI 2 shows the extent of a lined region of the tailings. P1-P3 show the location of profiles in Figure 4. Image © CGG 2020. © Contains modified Copernicus Sentinel data, 2019. Background image © KARI 2018. Distribution (SI Imaging Services, Republic of Korea), all rights reserved.

The consolidation rate across the TSF is strongly correlated with the thickness of the tailings. With thicker regions of tailings consolidating at a faster rate compared to shallower regions (Figure 4). Figure 4a is a profile across an unlined portion of the tailings and shows a clear relationship between tailings thickness and consolidation rate. There is an area of unusually fast consolidation at 200 m along this profile which corresponds to the position of the natural drainage path of the TSF, where lateral water drainage is expected to be at its highest and therefore increasing the consolidation rate of the tailings at this location.

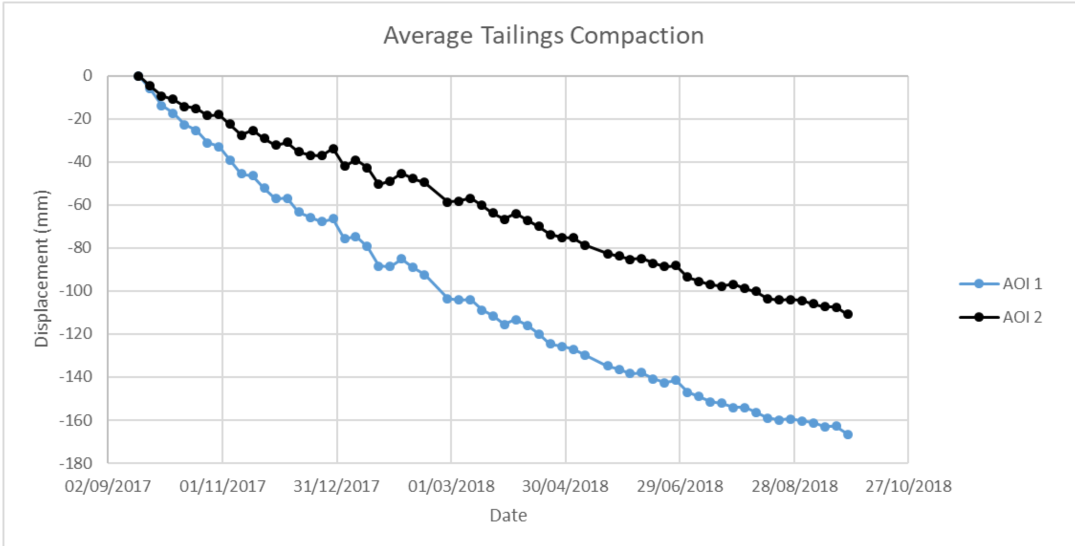

Figure 3. Average cumulative displacement in AOI 1 (unlined) and AOI 2 (lined) between September 2017 and September 2018.

Table 1. Compaction rate of the TSF surface

Lined/Unlined	Initial compaction rate (mm/yr)	Final compaction rate (mm/yr)	Average compaction rate (mm/yr)
Lined (AOI 2)	217	83	105
Unlined (AOI 1)	343	86	156

Figures 4b and 4c show profiles across a mostly lined area of the tailings. Again the rate of consolidation is generally greatest where the tailings are deeper, particularly for the unlined regions. In both profiles there are two faster regions of consolidation which do not correlate to thick tailings - these regions are observed to be on the liner edge where drawdown may be occurring to the unlined region (Figures 4b and 4c). In Figure 4b around 600 m marks the edge of the newly constructed tailings dam, with associated lower consolidation rates.

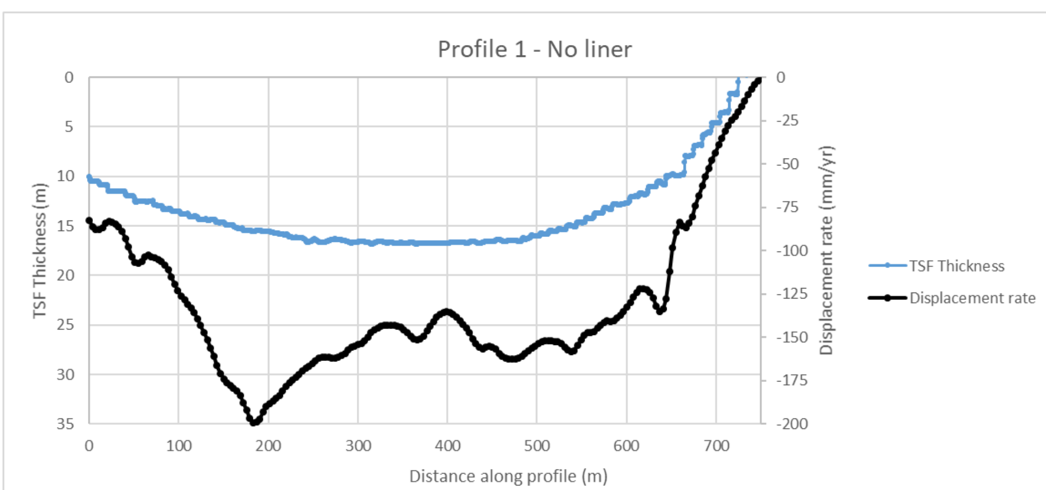

(a)

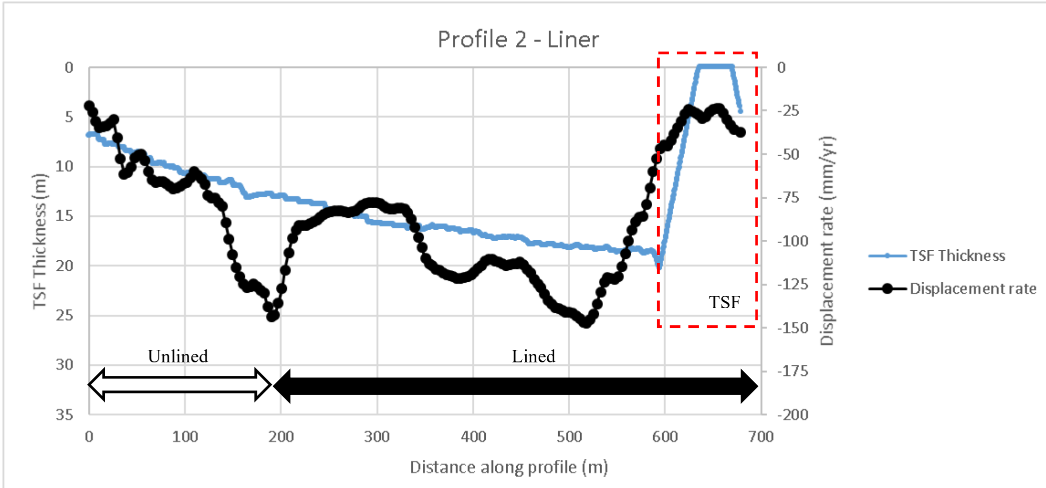

(b)

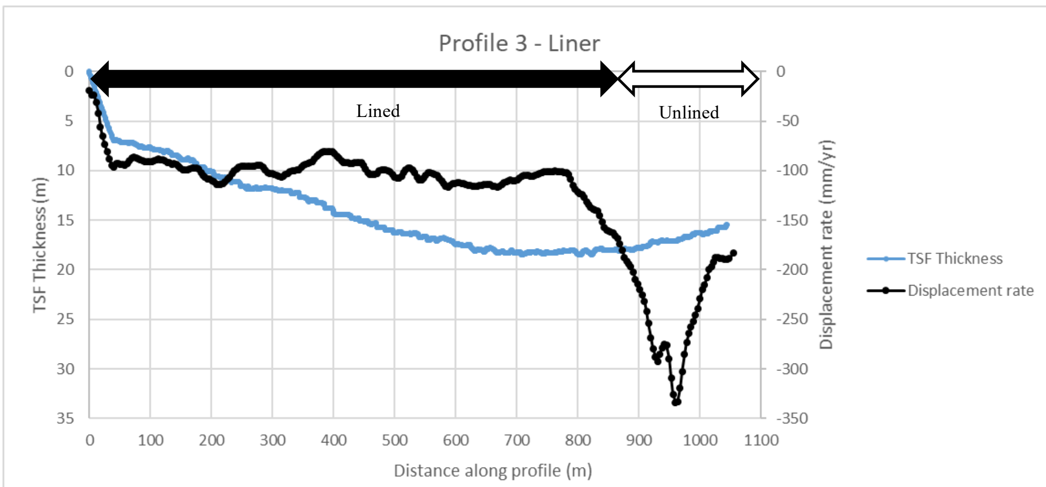

(c)

Figure 4. Profiles along the transects in Figure 2 showing tailings thickness and the measured displacement rate between September 2017 and September 2018.

4 CONSOLIDATION VARIABILITY – LINED VERSUS UNLINED

The following graph shows the correlations between the measured average displacement rate versus the depth of tailings for the three profiles analysed (Figure 5). Profile 2 and 3 are partially unlined, and the data has been separated to show the variability in consolidation behaviour between the two underlying barrier conditions. When reviewing the data, it is important to take into account that along the considered profiles, lateral drainage paths and drawdowns can occur increasing the consolidation rate at localised points.

The blue points represent the unlined areas of Profiles 2 and 3 and the black points show the lined areas. In profile 1 the red crosses represent the unlined region and show a relatively linear relationship (a similar tendency to the unlined section of Profile 2).

It is interesting to observe that the unlined regions have stronger correlations and almost linear relationships between the displacement rate and depth of tailings (neglecting the peak in Profile 3 where a drawdown from the lined to unlined region is observed). The lined regions show weak consolidation rates to depth correlations whereby an upper displacement limit of the tailings is observed. This is likely related to the release rate of water from the tailings mass due to the low permeability barrier conditions and restrictions in the lateral drainage of the tailings mass. Profile 3 shows large displacement rates for very shallow depths which is likely related to the location of the previous decant pond where the tailings were of low density due to predominately sub-aqueous deposition in this area. As a result, the exposed tailings have consolidated at a higher rate following the last discharge of tailings due to the initial lower densities. The deeper lined region of Profile 2 also shows, similar to Profile 3, a steadier and similar consolidation rate regardless of the depth of tailings.

The transition of the lined to unlined region on Profile 3 presents a large jump in the consolidation rate most likely as water from the lined region is moving into the unlined region as a cone of depression (marked as a red oval shape in Figure 5). It is possible the lined region of tailings has a phreatic surface within the tailings mass which is dissipating slowly with time.

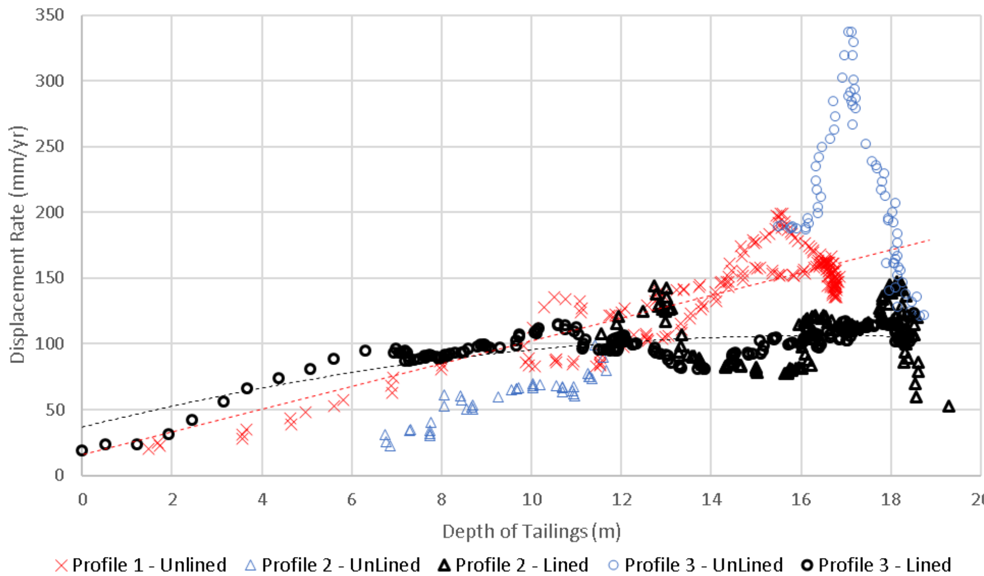

Figure 5. Correlation of displacement rate to tailings depth for the unlined and lined conditions.

5 DENSITY INCREASE

Using the average consolidation rates presented, an estimation of the increase in density can be made for variable depths. This interpreted density increase represents the entire 12 months of InSAR data analysed following deposition of the last fresh layer of tailings. The density profile of the tailings within the mass is naturally variable, and the interpreted density measured represented the total increase for the entire depth analysed. The following graph (Figure 6) shows the increase in density for Profile 1 (unlined) and Profile 3 (for the lined portion) for the period of the InSAR data analysed. It can be seen that the lower depths generate the higher rate of consolidation compared with the increased depths. This also highlights the importance to discharging tailings in relatively thin layers to allow the tailings to bleed and consolidate prior to fresh layer deposition.

It is interesting to observe the higher rates of consolidation for the liner regions for the lower depths of tailings. As mentioned previously, this is likely due to the very low density of the tailings in the region of Profile 3 below the previously active pond. However, more important to note is the reduced potential increase in density with depth for the liner region, indicating, in this particular case, the underlying liner is functioning well and preventing water migration downwards, thus limiting the density gain of the tailings through evaporative capillary rise and lateral movement towards the edge of the liner.

The impact of the liner on consolidation of the tailing material highlights the need to properly account for the reduction in drainage caused by the membrane and the need for effective drainage solutions (Figure 7).

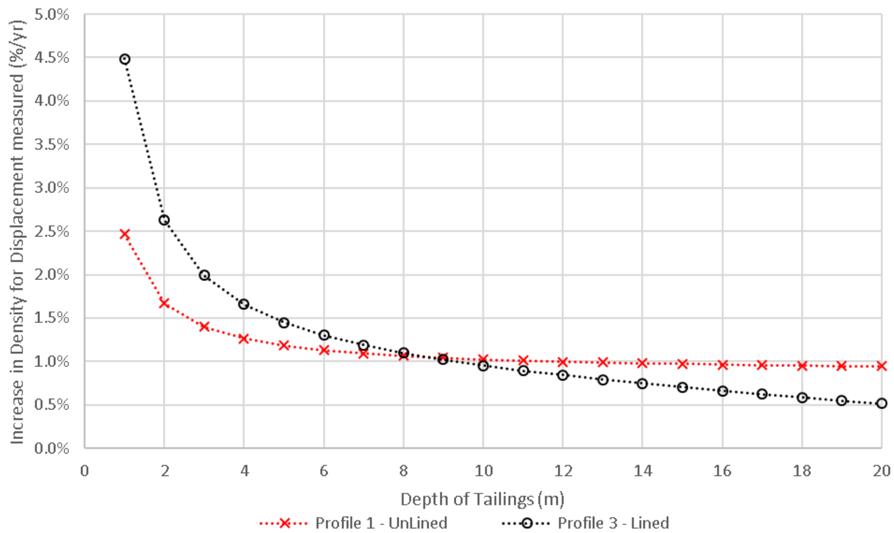

Figure 6. Correlation of displacement rate to tailings depth for the unlined and lined conditions.

6 CONCLUSION

The paper has demonstrated the ability of InSAR to monitor compaction of tailings after deposition. Furthermore, we have been able to identify variations in compaction across the tailings relating to the use of a geomembrane. The tailings consolidate at a faster rate where it is deepest and where the geomembrane is absent, almost on a linear correlation. The use of a liner restricts the movement of water, as intended, but reduces the consolidation rate of the tailings due to the reduced dewatering characteristics of the tailings.

For tailings designers, this paper reiterates the importance of underdrainage systems over geomembrane liners used within a tailings facility basin. These underdrains, usually a combination of finger and spine drains, report to a sump normally on the upstream face of an embankment that can be pumped out and recycled to the decant pond for collection. In this way the tailings mass over the geomembrane can drain, increasing the consolidation rate of the tailings as water is removed from the base of the tailings mass. The following figure presents a lined tailings facility having an underdrainage system over the geomembrane.

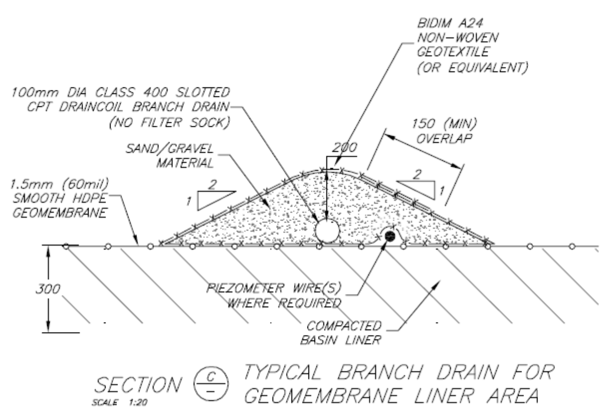

(a)

(b)

(c)

Figure 7. (a) Underdrainage branch and spine drains installed over geomembrane to dewater tailings. (b & c) Photos taken during the commissioning of a fully lined tailings facility.

The application of InSAR for monitoring tailings compaction is by no means simple. In this case, a temporary cessation in the deposition of fresh tailings allowed for regular measurements of tailings beaches simulating a decommissioning stage of a TSF. However, it would be challenging to use InSAR in cases where fresh tailings were being regularly deposited, or in cases where the tailings were covered in water. Despite these challenges, InSAR is an effective tool for monitoring consolidation of tailings where deposition has temporarily ceased or ceased all together. Furthermore, with the ready availability of open-access satellite data, and plans for future missions, such studies are becoming increasingly feasible, timely and cost effective.

7 REFERENCES

Bamler, R., Hart, P., 1998, 'Synthetic aperture radar interferometry', *Inverse Problems*, vol. 14, no. 4, pp. R1–R54.

Hanssen, R.F., 2001, *Radar Interferometry: Data Interpretation and Error Analysis*, Dordrecht, The Netherlands, Kluwer

Rosen, P., Hensley, S., Joughin, I., Li, F., Madsen, S., Rodriguez, E., and Goldstein., R., 2000. 'Synthetic aperture radar interferometry', *Proceedings of IEEE*, vol. 88, no. 3, pp. 333–382.

Vick, S G 1983, *Planning, design, and analysis of tailings dams*, Wiley, New York.

Wise Uranium website., 3rd January 2020, https://www.wise-uranium.org/mdaf.html

Investigating the feasibility of implementing microbially induced calcite precipitation to stabilize gold tailings

Rhonda Hyde, Lita Nolutshungu & Dyllon Randall
The University of Cape Town, Rondebosch, Western Cape, South Africa

ABSTRACT: Microbially Induced Calcite Precipitation (MICP) is an emerging bio-mediated technology which has been successfully applied in soil improvement research as a sustainable method. MICP uses the urease enzyme to breakdown urea into carbonate ions which combine with free calcium ions forming calcium carbonate, acting as a bio-cement. MICP treatment has been proven to increase shear strength and decrease porosity in soils, however its application in soil improvement outside erosion mitigation in granular soils remains limited. This research focused on injecting MICP treatment to increase shear strength and decrease porosity in sand, clay, and gold tailings below surface depth. Results indicated successful cementation in the increase in apparent cohesion in sand and gold tailings and cohesion in clay of 100%, 30% and 8.3% respectively. A general decrease in the angles of internal friction was observed. The porosity of clay and tailings decreased by 20.6% and 7.3%, whilst sand increased by 3%.

1 INTRODUCTION

1.1 *Background*

Tailings are a waste product generated following the extraction of economic materials in mining (Kossoff et al., 2014). These large volumes of tailings produced annually by the mining industry, reaching 14 billion tonnes in 2010, leave a significant environmental footprint spatially in terms of storage and temporally in terms of the design life and management (Adiansyah et al., 2015; Jones & Boger, 2012). Naturally, the immense quantities of material contained within tailings dams result in, upon failure, catastrophic and costly consequences such as the destruction of property and the contamination of water bodies downstream. Therefore, the need for sustainable practices in the mining sector is highlighted by growing research interest as well as rising concerns of the largely irreversible and severe consequences of tailings impoundment failures and other mining operations (Adiansyah et al., 2015; Braun et al., 2017). Existing and widely utilized soil improvement techniques present effective and practical solutions to tackle soil improvement. However, in terms of environmental responsibility, cost, and high energy requirements a gap exists in these traditional methods (Naeimi & Haddad, 2020; Salifu et al., 2016). With these evident shortcomings in the conventional approaches and increasing pressure on the worlds non-renewable resources, there is a growing demand for more sustainable soil improvement techniques (DeJong et al., 2010). Sustainable and effective soil improvement techniques are required in the mining sector for the management and maintenance of tailings facilities.

Bio-mediated soil improvement techniques have grown in their popularity as they seemingly absolve the issues posed by traditional methods (Umar et al., 2016). There are many available alternatives in industry however, a large focus has been placed on bio-mediated approaches and research due to the promising results (Umar et al., 2016). One example is the use of MICP as a soil improvement technique.

1.2 *Microbially induced calcite precipitation process*

Bio-mediated soil improvement utilises biochemical reactions which produce calcite precipitates between soil particles, effectively modifying the engineering properties of the soils (Umar et al., 2016). Microbially induced calcium precipitation (MICP), a prime example, is a microbial geotechnological strategy which alters the soil structure through the formation of calcite crystals (Salifu et al., 2016). The process of MICP entails facultative bacteria with a highly active urease enzyme such as *sporosarcina pasteurii* consuming urea during metabolic processes (DeJong et al., 2010). During this process, urea is decomposed into ammonia (NH_3) and carbon dioxide (CO_2) catalysed by the urease enzyme. The NH_3 and CO_2 diffuse through the cell walls of the bacteria, and into the surrounding calcium rich solution (DeJong et al., 2010). In the presence of water in solution, the NH_3 and CO_2 ionize into ammonium (NH^{4+}) and bicarbonate ions (HCO^{3-}) (Umar et al., 2016). During the ionization of NH_3, hydroxyl ions (OH^-) are formed which increase the local pH and collectively alkalise the bacterial environment to a pH of approximately 9 (DeJong et al., 2006; Van Paassen et al., 2009). Thus, the OH^- and HCO^{3-} ions react, forming carbonate ions (CO_3^{2-}) (Burne & Chen, 2000; Castanier et al., 1999). Calcium ions (Ca^{2+}) from the surrounding calcium rich solution react with the CO_3^{2-} ions forming calcium carbonate ($CaCO_3$) which precipitates as a crystal out of solution (Haouzi & Courcelles, 2018). This overall MICP process is shown in Equation 1 below.

$$\mathrm{CO(NH_2)_2 + 2H_2O + Ca^{2+} \xrightarrow{urease} 2NH_4{}^+ + CaCO_3\downarrow} \tag{1}$$

The calcium carbonate crystals form bridges between the individual soil particles, binding them together and this cementation is responsible for the improved geotechnical properties of a soil treated using MICP (Harkes et al., 2010; Soon et al., 2013). The soil type influences the efficacy of the biologically mediated treatment approach based on the ability of the microorganisms to move freely between the soil particles which is determined by the size of the pore space (DeJong et al., 2010; Mitchell & Santamarina, 2005). Soils with a higher percentage of fines pose a challenge to this migration of microbes, particularly during treatment when there is a continued reduction in pore spaces as treatment proceeds and microbial communities and calcification coat the soil particles (DeJong et al., 2010).

2 METHODOLOGY

2.1 *Overview*

The research objective aimed to interrogate the feasibility of MICP as a soil improvement technique. The experimental approach entailed developing a suitable methodology for administering the MICP technique to the tailings past surface depth. The efficacy and, repeatability of the developed methodology was evaluated to determine its overall technical feasibility as a sustainable soil improvement technique. The rheology of the gold tailings is beyond the scope of this research.

2.2 *Phase 1 – Characterization and preparation*

Three soil types were treated for this study. The clay, sand and gold tailings samples were characterised before treatment to determine the geotechnical characteristics defining the soils behaviour. This included determining the particle size distribution, Atterberg limits, compaction, specific gravity, and porosity of the untreated soils. The tailings were sourced from an active tailings dam north of the Witwatersrand region. The selected culture media, the ammonia-yeast stock solution (ATCC®1376), contained ammonium sulphate ($(NH_4)^2SO_4$), yeast extract and tris buffer. Christensen's Urea Agar (CUA) was used as an indicator agar plate to confirm the availability of viable *sporosarcina pasteurii* cells in the concentrated bacterial culture. The bacteria was then cultivated from a glycerol stock culture following the methodology implemented by various MICP researchers (Lambert & Randall, 2019). The synthetic urine was comprised of 0.3 M of urea, 0.3

M of calcium chloride and nutrient broth at a concentration of 3 g/L to mimic the concentrations found in human urine (Randall & Naidoo, 2018).

2.3 *Phase 2 – Treatment*

Nine stainless steel cylindrical reactors were designed for compatibility with the standard triaxial testing equipment. Each soil type was allocated three reactors for triplicate results and the average for every soil was reported for each experiment. Open inoculation, using the concentrated nutrient culture, was selected as this research aimed to determine the feasibility of the methodology in larger scales (Henze & Randall, 2018). The inoculated soils were compacted into the reactors, rested for 4 hours to allow for bacterial acclimatization, before commencing treatment. The injection was used to steadily dispense the cementation media by hand to the inoculated soil at three distinct points in the soil mass to ensure homogenous distribution of the cementation media.

2.4 *Phase 3 – Testing and analysis*

Daily influent and effluent samples were taken to monitor the variation in pH, urea, dissolved calcium, and ammonium concentrations for the duration of each experiment. The precipitation was quantified by the difference in influent and effluent calcium concentrations (Equation 2).

$$\Delta \text{Calcium} = \text{Ca}_{\text{Influent}} - \text{Ca}_{\text{Effluent}} \quad (2)$$

2.5 *Trial experiment*

The trial experiment was conducted to verify if the proposed methodology was technically sound and determine whether MICP had any meaningful impact on the geotechnical characteristics of each soil type. The specimens were inoculated for 4 hours, 3 treatments were dispensed daily, and 42 treatment cycles were selected, equivalent to 14 treatment days (Henze & Randall, 2018). This varied from the referenced study, as treatment was manual, and did not continue overnight.

2.6 *Primary experiment*

This experiment was the primary focus of the research and was conducted to determine the effect MICP had on the shear strength and porosity of the three soils. The experimental procedure followed that of the trial experiment, excepting the number of treatment cycles. Five treatments daily were administered over a period of nine days equating to 45 treatment cycles. The standard triaxial test was used to determine the shear strength of each column in the consolidated undrained condition.

3 RESULTS AND DISCUSSION

3.1 *Soil characterization*

The results of the particle size distribution tests are plotted on Figure 1. The sand is uniformly graded where most of the soil particles fall within the same grain size boundary and are roughly the same size. The tailings are uniformly gap graded, which falls under a poorly graded description. Therefore, similarly to the sand, most of the tailings soil particles lie within the sand boundary. The clay has the largest fines fraction out of the three soils. The results of the particle density tests are summarized in Figure 2. Sand was observed as the only soil to achieve an increase in particle density and porosity following treatment.

Tailings and clay both achieved decreases in particle density and porosity following treatment. Clay achieved a greater decrease of 6.4% and 20.6% in particle density and porosity than tailings with a decrease of 5.2% and 7.3% respectively. Sand increased in particle density and porosity by 3.6% and 3% respectively. These results indicate that the sand specimens had the greatest success in terms of the deposition of calcium carbonate between the soil particles. The aforementioned impact the particle size of a soil has on the extent of calcite precipitation as well as the migration of the microbial community between particles is highlighted once again. Regarding clay, the particle size likely had a role to play in the deposition of crystals. As shown in Figure 1, there is a substantial fraction of fines in the clay which tend to fill the voids between larger soil particles (Cardoso et al., 2018).

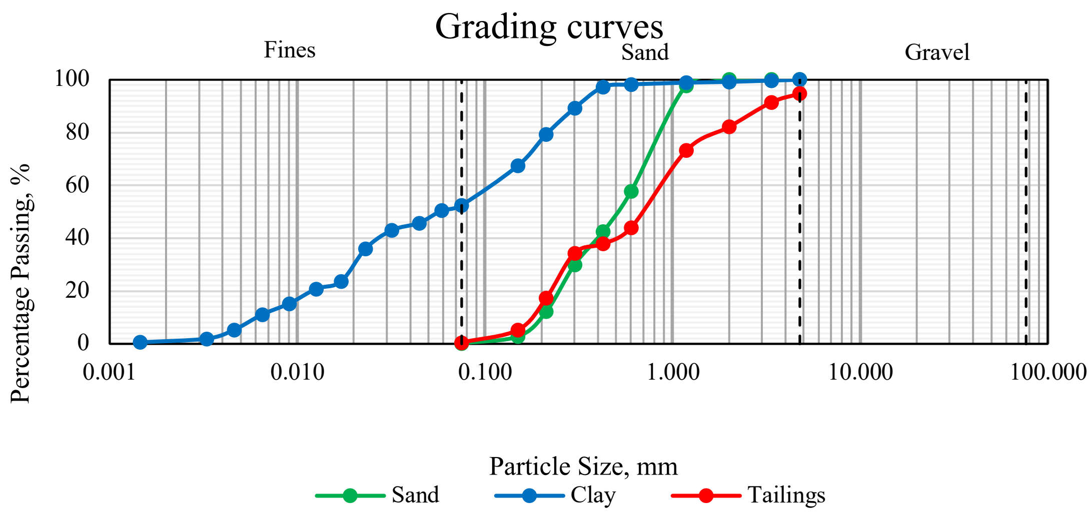

Figure 1. The particle size distribution of the sand, clay and tailings showing the particle size in (mm) plotted against the percentage (%) of the sample by weight that is finer than that sieve size.

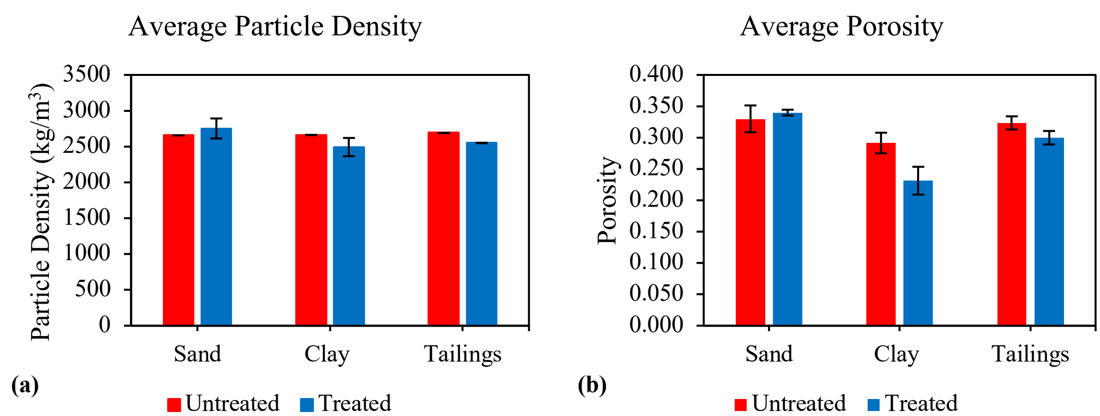

Figure 2. (a) The variation in the average particle density in kg/m^3 of the untreated and MICP treated sand, clay, and tailings soils. (b) The variation in the average porosity of the untreated and MICP treated sand, clay, and tailings soils.

Therefore, the microorganisms were potentially challenged in finding sufficient nucleation sites in the significantly smaller particles and voids to effectively mediate the MICP process (DeJong et al., 2006; Umar et al., 2016). In terms of tailings, the larger, coarser grained particles should be ideal, similarly to sand. Limited success in terms of calcite precipitation should not necessarily result in a decrease in porosity. Therefore, the reduction in porosity is potentially as a result of the treatment dispensation. This is attributed to sand containing a lower fraction of fines which are easier to flush, and thus resulted in the erosion of the tailings and clay specimens which contain higher fractions of fines as shown in Figure 1. This is in line with the magnitude of reduction shown in Figure 2, where clay had the greatest reduction in porosity and the highest fraction of fines in comparison to tailings. In the characterization of gold tailings in the Witwatersrand basin, the porosity of the tailings was found to range between 0.48 to 0.76 across 5 sites (Nengovhela et al., 2006). Therefore, the porosity of 0.32 in this research is slightly lower than expected. This is likely due to samples used being sourced near the embankment wall where the tailings may have mixed with material used for the wall thus affecting the characteristics of the sample. Regarding the particle density, the particle density of 2691kg/m^3 in the untreated gold tailings was consistent with data concerning untreated gold tailings, once again in the Witwatersrand region where the results varied between 2685 and 2754kg/m^3 (Chang et al., 2011).

3.2 *Urea hydrolysis*

The fluctuation in the average urea concentration over the treatment days is shown in Figure 3. The average urea effluent concentrations of sand and clay maintain relatively flat curves that steadily decline throughout treatment to significantly lower concentrations than the influent. The effluent concentration curves steadily approach zero, which indicates that the influent urea is being fully utilized in the system. The flattening curves approach a constant value, where the hydrolysis of urea is no longer rapidly occurring. Here the bacteria have likely acclimatized well to the systems and are steadily continuing to utilize the urea in the influent for continuing metabolic processes.

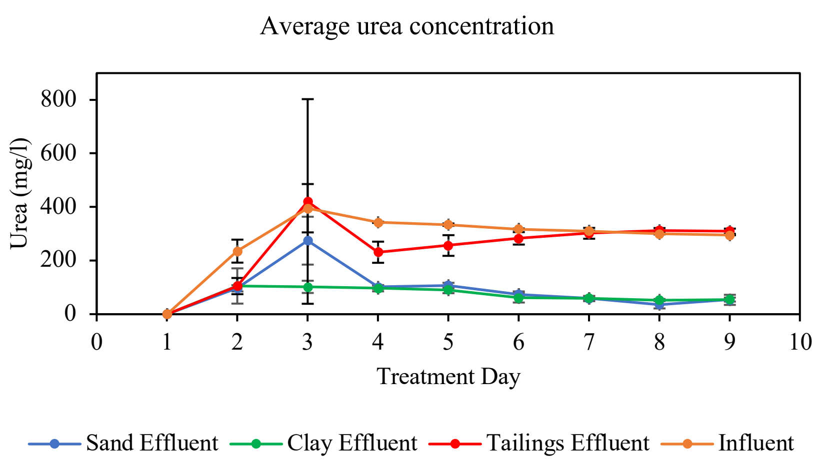

Figure 3. The average urea concentration in mg/L over 9 treatment days for the influent and effluent from the sand, clay and tailings cylinders following the dispensation of the cementation media.

The tailings system on the other hand, has a starkly different reaction. The effluent urea concentration closely follows the influent urea concentration which is diagnostic of the cessation of urea hydrolysis in that system. The influent continues to feed the tailings urea rich synthetic urine, which is initially utilized as evidenced by the drop in urea concentration in day two. Gradually however, the reaction slows to a stop where the concentration coming into the system is the same as the concentration leaving the system. Evidently, the urea in the influent is no longer being broken down and thus the effluent concentration matches that of the influent, where no urea is being hydrolyzed whatsoever. Evidently, the bacteria in this system have not acclimatized well and are no longer performing their metabolic processes and are likely steadily dying.

3.3 *Ammonia production*

Figure 4 displays the fluctuation of the average ammonia concentration over the treatment days. The influent ammonia concentration begins at a starting concentration of 0 mg/L in the influent before the hydrolysis of urea commences. Once the cementation media is fed into the cylinders and $CO(NH_2)^2$ is broken down, the effluent NH_3 concentrations sharply increase after one treatment day, and steadily increase for the remaining treatment days for sand as well as clay. This is indicative of the successful decomposition of urea in the influent resulting in growing concentrations of ammonia in the effluent (Haouzi & Courcelles, 2018).

Tailings, however, exhibit a significantly lower peak in day two in contrast to sand and clay, followed by a gradual decline in NH_3, steadily approaching a concentration of 0 mg/L by day 9. Once again, these results are symptomatic of an issue with the tailings system, as shown by the declining ammonia concentration in the effluent. This could be a result of a number of factors including but not limited to the bacterial species, bacterial concentration, temperature, pH, the chemistry of the cementation solution as well as the soil itself (Sheng et al., 2020). However, based on the apparent success of the hydrolysis of urea and increase in ammonia concentrations in the sand and clay columns, it can be deduced that issue likely lies with the soil itself considering that the other factors remained consistent throughout the experiment.

The presence of particular heavy metals in soils in varying concentrations has been found to result in toxic environments for the exposed bacterial communities, eventually killing the microorganisms (Mugwar & Harbottle, 2016; Ruggiero et al., 2005). This is likely the cause of the negative performance of the tailings system in terms of urea hydrolysis as gold tailings are often contaminated with heavy metals (du Plessis & Curtis, 2021; Mpanza et al., 2020).

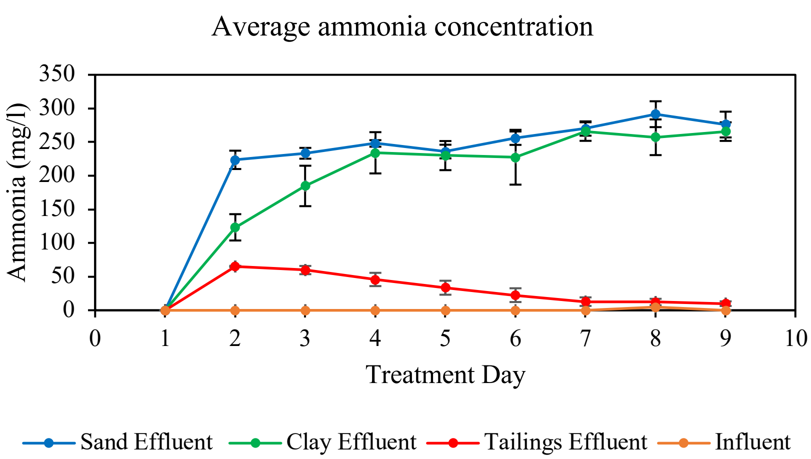

Figure 4. The average ammonia concentration in mg/L over 9 treatment days for the influent and effluent from the sand, clay and tailings cylinders following the dispensation of the cementation media.

3.4 *Calcium carbonate precipitation*

The average calcium concentration in mg/L over the treatment days is shown in Figure 5. The results of the average calcium concentrations confirmed observations made regarding urea hydrolysis and ammonium production. Sand and clay are seen to maintain low flat curves, whilst tailings steadily climb, reaching influent calcium concentrations. Once again, Figure 5 is indicative of the successful completion of the required processes for the eventual precipitation of calcite into the soil structure. For sand and clay, the resulting effluent concentrations are considerably lower than the influent, maintaining concentrations below approximately 100 mg/L for the duration of the treatment days This indicates that the calcium provided to the system by the influent is being utilized resulting in a decline in the effluent concentration. The tailings system appears promising from treatment day 1 to 4, where low effluent concentrations of calcium are maintained similarly to sand and clay. However, from treatment day 5 onwards, the average effluent calcium concentration rapidly rises, reaching the influent concentration on day 8. Evidently, the tailings system begins to increasingly react with fewer and fewer calcium ions until eventually, by day 8, the calcium ions fed into the system are leaving the system in the effluent. Similarly to the urea hydrolysis and ammonia production components of the MICP process, something inhibits the efficacy of the tailings system in carrying out its function. With regards to this component of the MICP process in particular, this phenomenon is not limited to this research. One of the main challenges associated with MICP, is the irregular precipitation of calcium carbonate crystals in the soil of choice (Cheng & Cord-Ruwisch, 2014; Whiffin et al., 2007).

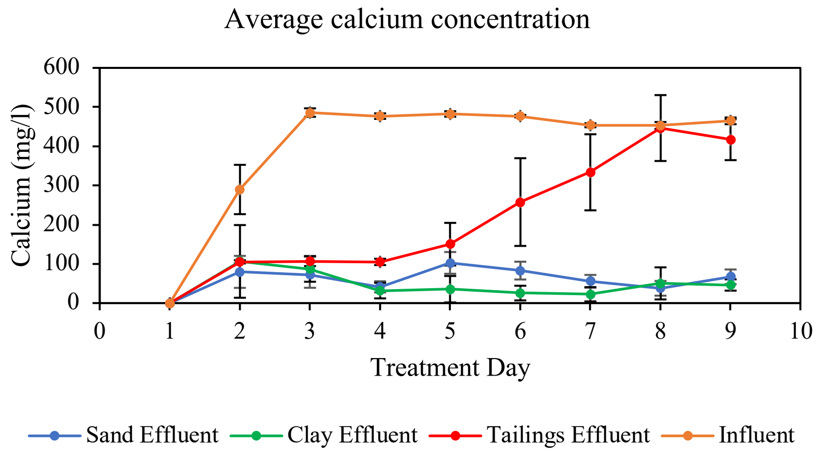

Figure 5. The average calcium concentration in mg/L over 9 treatment days for the influent and effluent from the sand, clay and tailings cylinders following the dispensation of the cementation media.

The inhomogeneous distribution of calcium carbonate crystals results in clogging and the creation of preferential flow paths which further exacerbates the non-uniform cementation (Rowshanbakht et al., 2016; Yasuhara et al., 2012). All three tailings' cylinders displayed no initial external signs of preferential flow paths. However, once the samples were broken apart some significant zones of cementation in the specimen's interior were observed. Sand exhibited the highest level of cementation throughout the soil samples examined. Each sand column displayed unique, inhomogeneous cementation throughout. Despite selective cementation and the evidence of preferential flow paths, sand was able to maintain low effluent calcium concentrations therefore this is likely not the cause of the limited performance of the tailings system in terms of calcium usage. This is similar to the clay specimens, which exhibited no visible changes after treatment and were still able to maintain similarly low effluent concentrations of calcium. This in turn highlights the more likely possibility of the toxicity of the tailings to the microbial community resulting from the presence of heavy metals.

3.5 *Shear strength*

The shear strength parameters for the untreated soils and the treated soils were determined by plotting the Mohr's circles and their corresponding Mohr-Coulomb failure envelope using the deviatoric stress-strain data obtained from the triaxial testing. The shear strength parameters obtained for the untreated and MICP treated soils are summarized in Figure 6. The angle of internal friction as well as the apparent cohesion or cohesion has been found to increase following MICP treatment in some soils (Cheng et al., 2013; Pakbaz et al., 2018).

Remarkably, a decrease in the angle of internal friction was observed in the treated soils. All the untreated soils exhibited uncharacteristically steep failure envelopes, which resulted in high angles of internal friction of 60.6°, 58.3° and 68.7° in sand, clay, and tailings respectively. The treated soils however, exhibited flatter failure envelopes which resulted in lower angles of internal friction, contrary to the expected trend following MICP treatment. The treated sand, tailings and clay achieved angles of 58.4°, 48.1° and 55.8° each. A likely cause of the high angles is the particle morphology of the soils where more angular particles result in higher angles of internal friction. Another likely cause for the high angles of internal friction, is work hardening plasticity which is a phenomenon observed in materials such as soils which deform plastically during failure (Basu, 2020; Nolutshungu, 2017). Evidently, complex behaviour can be observed in terms of the stress-strain behaviour of the soils during triaxial testing therefore the aberration in the angles of internal friction is attributed to this.

On the other hand, the y-intercepts which indicate the apparent cohesion or cohesion for each soil were as expected, where the lowest was observed in the coarser grained sand of 0kPa, and a higher result was seen for tailings specimens at 50kPa and the highest for clay of 60kPa. Following treatment, the sand and tailings soils obtained apparent cohesions of 20kPa and 65kPa respectively and clay obtained a cohesion of 65kPa. Although the tailings had a higher fraction of fines than the sand, the material was largely cohesionless during handling and testing therefore the higher apparent cohesion before treatment was not anticipated. Nonetheless, an increase in the apparent cohesion and cohesion was observed across the board, which is an indication of an improvement in the shear strength of the materials.

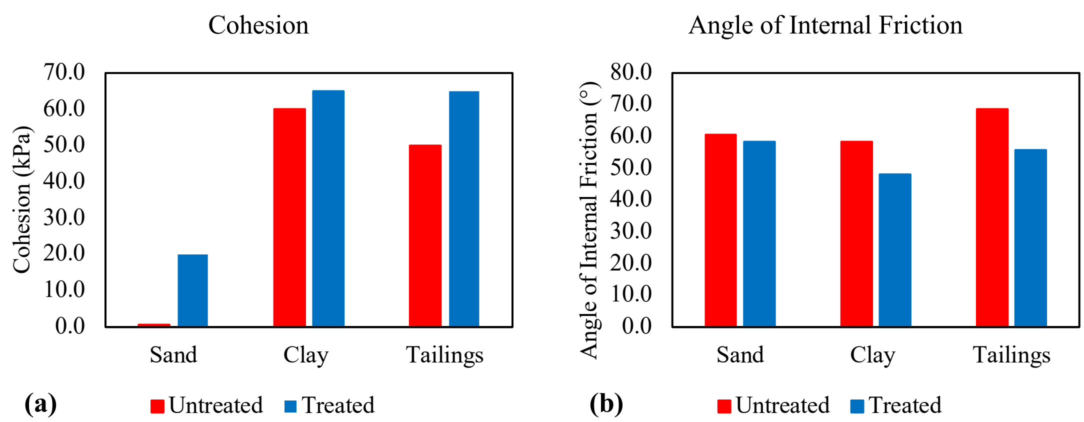

Figure 6. The shear strength parameters of (a) apparent cohesion or cohesion and (b) angle of internal friction, for the untreated and MICP treated sand, clay and tailings soils obtained following consolidated undrained triaxial testing.

The most significant increase in apparent cohesion was seen in the sand, followed by the tailings and lastly in the cohesion of the clay. This alludes to the fact that sand had the highest success with the MICP treatment concerning the objectives of this research, followed by tailings and lastly clay.

Overall, the clay material obtained the lowest change in shear strength parameters, which corresponds with the observations made in the urea, ammonia, and calcium results. An evident positive trend is observed concerning the apparent cohesion and cohesion of the soils, which increased. Overall, the impact calcite precipitation had on the angle of internal friction was inconclusive. Sand, gold tailings and clay achieved a reduction of 3.6%, 17.5% and 18.8% respectively in the friction angles. This was due to the potential interaction a variety of variables such as the particle shape of the soils, the relative density as well as strain hardening which occurred during failure. However, the trend in terms of the apparent cohesion and cohesion is clear, calcite precipitation was able to successfully cement particles of all three soils and thus increase the apparent cohesion or cohesion. Sand obtained the highest increase in apparent cohesion at 100%, whilst tailings obtained an increase of 30%. The cohesion of the clay increased by 8.3%.

4 CONCLUSIONS

Each cylinder exhibited unique behaviour in terms of treatment dosage which potentially had the domino effect of introducing greater variability in the effluent concentrations. Although a noteworthy variation was observed in terms of the urea, ammonia and calcium fluctuations for each cylinder's effluent, the general trends identified were clear. The sand exhibited the greatest calcite precipitation as well as the most significant improvement in the shear strength parameters of specific gravity, porosity, and apparent cohesion. This was followed by the gold tailings, which is similarly coarse grained. However, the prevalence of heavy metals in the gold tailings likely limited the efficacy in terms of calcite precipitation over time. This is investigated further in the authors' ongoing research. Although preferential flow paths and inhomogeneous cementation was observed throughout the sand and gold tailings samples, overall, an improvement in the shear strength parameters was observed except for the angle of internal friction. The injection method was limited in terms of the erosion of soil particles during treatment, particularly in the tailings and the clay which had higher fines contents. This was identified as the likely cause of the reduction in porosity observed following treatment. The injection method did however exhibit promising results in terms of the depth of treatment that can be achieved in sand and tailings.

Overall, the reaction of the sand, clay, and tailings to MICP agreed with the consulted literature whereby the larger the particle size is, the greater the efficacy of the cementation of the soil particles. Therefore, the use of MICP as a soil improvement technique for treatment depths greater than surface level, is feasible for scalable implementation in gold tailings and sands.

5 REFERENCES

Adiansyah, J. S., Rosano, M., Vink, S., & Keir, G. (2015). A framework for a sustainable approach to mine tailings management: Disposal strategies. *Journal of Cleaner Production*, *108*, 1050–1062. https://doi.org/10.1016/j.jclepro.2015.07.139

Basu, D. (2020). Stresses, Strains, Elasticity, and Plasticity. *Advanced Soil Mechanics*.

Braun, T., Hennig, A., & Lottermoser, B. G. (2017). The need for sustainable technology diffusion in mining: Achieving the use of belt conveyor systems in the German hard-rock quarrying industry. *Journal of Sustainable Mining*, *16*(1), 24–30. https://doi.org/10.1016/j.jsm.2017.06.003

Burne, R. A., & Chen, Y. Y. M. (2000). Bacterial ureases in infectious diseases. *Microbes and Infection*, *2*(5), 533–542. https://doi.org/10.1016/S1286-4579(00)00312-9

Castanier, S., Le Métayer-Levrel, G., & Perthuisot, J. P. (1999). Ca-carbonates precipitation and limestone genesis - the microbiogeologist point of view. *Sedimentary Geology*, *126*(1–4), 9–23. https://doi.org/10.1016/S0037-0738(99)00028-7

Chang, N., Heymann, G., & Clayton, C. (2011). The effect of fabric on the behaviour of gold tailings. *Geotechnique*, *61*(3), 187–197. https://doi.org/10.1680/geot.9.P.066

Cheng, L., & Cord-Ruwisch, R. (2014). Upscaling Effects of Soil Improvement by Microbially Induced Calcite Precipitation by Surface Percolation. *Geomicrobiology Journal*, *31*(5), 396–406. https://doi.org/10.1080/01490451.2013.836579

Cheng, L., Cord-Ruwisch, R., & Shahin, M. A. (2013). Cementation of sand soil by microbially induced calcite precipitation at various degrees of saturation. *Canadian Geotechnical Journal*, *50*(1), 81–90. https://doi.org/10.1139/cgj-2012-0023

DeJong, J. T., Fritzges, M. B., & Nüsslein, K. (2006). Microbially Induced Cementation to Control Sand Response to Undrained Shear. *Journal of Geotechnical and Geoenvironmental Engineering*, *132*(5), 591–602. https://doi.org/10.1061/(ASCE)1090-0241(2006)132

DeJong, J. T., Mortensen, B. M., Martinez, B. C., & Nelson, D. C. (2010). Bio-mediated soil improvement. *Ecological Engineering*, *36*(2), 197–210. https://doi.org/10.1016/j.ecoleng.2008.12.029

du Plessis, D. M., & Curtis, C. J. (2021). Trace element contaminants associated with historic gold mining in sediments of dams and pans across Benoni, South Africa. *Environmental Monitoring and Assessment*, *193*(3). https://doi.org/10.1007/s10661-021-08854-0

Haouzi, F.-Z., & Courcelles, B. (2018). Major applications of MICP sand treatment at multi-scale levels: A review. *Geo Edmonton*, *September*.

Harkes, M. P., van Paassen, L. A., Booster, J. L., Whiffin, V. S., & van Loosdrecht, M. C. M. (2010). Fixation and distribution of bacterial activity in sand to induce carbonate precipitation for ground reinforcement. *Ecological Engineering*, *36*(2), 112–117. https://doi.org/10.1016/j.ecoleng.2009.01.004

Henze, J., & Randall, D. G. (2018). Microbial induced calcium carbonate precipitation at elevated pH values (>11) using Sporosarcina pasteurii. *Journal of Environmental Chemical Engineering*, *6*(4), 5008–5013. https://doi.org/10.1016/j.jece.2018.07.046

Jones, H., & Boger, D. V. (2012). Sustainability and waste management in the resource industries. *Industrial and Engineering Chemistry Research*, *51*(30), 10057–10065. https://doi.org/10.1021/ie202963z

Kossoff, D., Dubbin, W. E., Alfredsson, M., Edwards, S. J., Macklin, M. G., & Hudson-Edwards, K. A. (2014). Mine tailings dams: Characteristics, failure, environmental impacts, and remediation. *Applied Geochemistry*, *51*, 229–245. https://doi.org/10.1016/j.apgeochem.2014.09.010

Lambert, S. E., & Randall, D. G. (2019). Manufacturing bio-bricks using microbial induced calcium carbonate precipitation and human urine. *Water Research*, *160*, 158–166. https://doi.org/10.1016/j.watres.2019.05.069

Mitchell, J. K., & Santamarina, J. C. (2005). Biological Considerations in Geotechnical Engineering. *Journal of Geotechnical and Geoenvironmental Engineering*, *131*(10), 1222–1233. https://doi.org/10.1061/(asce)1090-0241(2005)131:10(1222)

Mpanza, M., Adam, E., & Moolla, R. (2020). Dust deposition impacts at a liquidated gold mine village: Gauteng province in South Africa. *International Journal of Environmental Research and Public Health*, *17*(14), 1–26. https://doi.org/10.3390/ijerph17144929

Mugwar, A. J., & Harbottle, M. J. (2016). Toxicity effects on metal sequestration by microbially-induced carbonate precipitation. *Journal of Hazardous Materials*, *314*, 237–248. https://doi.org/10.1016/j.jhazmat.2016.04.039

Naeimi, M., & Haddad, A. (2020). Environmental impacts of chemical and microbial grouting. *Environmental Science and Pollution Research*, *27*(2), 2264–2272. https://doi.org/10.1007/s11356-019-06614-9

Nengovhela, A. C., Yibas, B., & Ogola, J. S. (2006). Characterisation of gold tailings dams of the Witwatersrand Basin with reference to their acid mine drainage potential, Johannesburg, South Africa. *Water SA*, *32*(4), 499–506. https://doi.org/10.4314/wsa.v32i4.5290

Nolutshungu, L. (2017). *Soil Strength*. The University of Cape Town.

Pakbaz, M. S., Behzadipour, H., & Ghezelbash, G. R. (2018). Evaluation of Shear Strength Parameters of Sandy Soils upon Microbial Treatment. *Geomicrobiology Journal*, *35*(8), 721–726. https://doi.org/10.1080/01490451.2018.1455766

Randall, D. G., & Naidoo, V. (2018). Urine: The liquid gold of wastewater. *Journal of Environmental Chemical Engineering*, *6*(2), 2627–2635. https://doi.org/10.1016/j.jece.2018.04.012

Rowshanbakht, K., Khamehchiyan, M., Sajedi, R. H., & Nikudel, M. R. (2016). Effect of injected bacterial suspension volume and relative density on carbonate precipitation resulting from microbial treatment. *Ecological Engineering*, *89*, 49–55. https://doi.org/10.1016/j.ecoleng.2016.01.010

Ruggiero, C. E., Boukhalfa, H., Forsythe, J. H., Lack, J. G., Hersman, L. E., & Neu, M. P. (2005). Actinide and metal toxicity to prospective bioremediation bacteria. *Environmental Microbiology*, *7*(1), 88–97. https://doi.org/10.1111/j.1462-2920.2004.00666.x

Salifu, E., MacLachlan, E., Iyer, K. R., Knapp, C. W., & Tarantino, A. (2016). Application of microbially induced calcite precipitation in erosion mitigation and stabilisation of sandy soil foreshore slopes: A preliminary investigation. *Engineering Geology*, *201*, 96–105. https://doi.org/10.1016/j.enggeo.2015.12.027

Sheng, C., Li, T., Cheng, J., Hao, Z., Hao, Z., & Bin, L. (2020). Factors affecting the performance of microbial - induced carbonate precipitation (MICP) treated soil : a review. *Environmental Earth Sciences*. https://doi.org/10.1007/s12665-020-8840-9

Soon, N. W., Lee, L. M., Khun, T. C., & Ling, H. S. (2013). Improvements in engineering properties of soils through microbial-induced calcite precipitation. *KSCE Journal of Civil Engineering*, *17*(4), 718–728. https://doi.org/10.1007/s12205-013-0149-8

Umar, M., Kassim, K. A., & Ping Chiet, K. T. (2016). Biological process of soil improvement in civil engineering: A review. *Journal of Rock Mechanics and Geotechnical Engineering*, *8*(5), 767–774. https://doi.org/10.1016/j.jrmge.2016.02.004

Van Paassen, L. A., Harkes, M. P., Van Zwieten, G. A., Van Der Zon, W. H., Van Der Star, W. R. L., & Van Loosdrecht, M. C. M. (2009). Scale up of BioGrout: A biological ground reinforcement method. *Proceedings of the 17th International Conference on Soil Mechanics and Geotechnical Engineering: The Academia and Practice of Geotechnical Engineering*, *3*, 2328–2333. https://doi.org/10.3233/978-1-60750-031-5-2328

Whiffin, V. S., van Paassen, L. A., & Harkes, M. P. (2007). Microbial carbonate precipitation as a soil improvement technique. *Geomicrobiology Journal*, *24*(5), 417–423. https://doi.org/10.1080/01490450701436505

Yasuhara, H., Neupane, D., Hayashi, K., & Okamura, M. (2012). Experiments and predictions of physical properties of sand cemented by enzymatically-induced carbonate precipitation. *Soils and Foundations*, *52*(3), 539–549. https://doi.org/10.1016/j.sandf.2012.05.011

Chemically reactive materials in tailing embankments: Lessons from the field

Jim B. Finley
Stantec Consulting Services, Inc., Fort Collins, Colorado, USA

ABSTRACT: With the increase in regulatory and industry concern for tailing facility performance, there is a recognition in the industry that the geochemical reactivity of materials used to construct tailing embankments must also be considered in assessments of long-term gravitational stability. One of the first comprehensive efforts to build a causal relationship between the geochemical reactivity of mine materials and time-dependent changes in geomechanical properties of mine material was undertaken at the Questa Mine, New Mexico, USA. Over time, the industry has recognized the need to include changes in material properties associated with chemical weathering of minerals in the assessment of tailing embankment performance. While there is a formal effort by INAP and MEND to catalogue information (geochemical and geotechnical) for tailing embankments containing geochemical reactive materials, this paper presents results and observations from several facilities where geochemically reactive materials have, or will be, used in tailing embankment construction. The discussion focuses on the interplay between chemical and mechanical weathering processes, how current methods of classifying mine materials are more oriented toward environmental permitting concerns than on time-dependent geomechanical properties, and a probe of the question of time.

1 BACKGROUND

Tailing impoundments are essential elements of all mining operations and are constructed for a variety of purposes to support mining. A major purpose of dams at mines is to generate storage space either for solutions (including water) or mine waste, principally tailing material generated by processing ore. In August 2020, the International Council on Mining and Metals (ICMM) issued the Global Industry Standard on Tailings Management (GISTM), which codified a holistic approach to the creation, operation, and closure of large tailings dams. Much of the focus of guiding principles of the GISTM document rightfully addresses engineering aspects of tailings dams. However, there is also heightened awareness that not only are the engineering properties of materials used to construct the dam important but that because of the constraints for construction materials, there are situations where the geochemical properties of the materials used to construct the dam also important. The time frame of consideration is both short and long term (i.e. closure).

There is an evolving effort by the industry to compile and consolidate available information that addresses the interplay between geochemical reactivity of construction materials and the time-dependent geomechanical properties of construction materials. As the process of gathering information and details proceeds, this paper offers thoughts on key issues needing consideration and resolution related to the degree and extent to which geochemical reactivity of tailing dam construction material influence tailings dam stability. The focus of consideration herein is on the down-stream shell of tailing embankments because materials placed on the upstream side or commonly saturated that limits the geochemical reactivity of embankment material.

2 MATERIAL PROPERTIES

2.1 *Reactive geochemistry*

Simplistically, a plan to place potentially acid generating (PAG) material in the downstream shell of a tailing impoundment begs the response, "you want to do what?" As mining practitioners, we are trained to avoid PAG as much as possible, and if avoidance is not possible, then isolate the PAG and limit consequences from any reaction that does occur. However, a perfectly reasonable reply is, "why not consider using PAG as construction material if contact water for the project is already managed, for example, using water treatment?" As with all mine rock, a spectrum of both rock mechanical properties and rock geochemical properties exists. Current geochemical characterization tools focus on evaluating the potential for development of acid rock drainage (ARD), attempting to determine when ARD onset occurs, and what impact might occur to the receiving environment. Note that none of the evaluations speak to the capability of sulfide-bearing mine rock to serve as construction material. The line between PAG and non-PAG classification for mine rock, again, is primarily based on the potential for development of acid rock drainage. However, a rock that classifies as non-PAG does not mean the sulfide minerals are non-reactive on exposure to surface conditions (i.e. exposure to atmospheric gases and precipitation). Moreover, any amount of reaction could affect the geomechanical properties of the rock. The follow-on, important question is, "how long or how much chemical reaction can occur before the geomechanical properties of the rock are compromised leading to a degradation in the integrity of the engineered structure?"

Investigating the link between geochemical reactivity or extent of geochemical reaction and changes in geomechanical properties of rock was the objective of dual geotechnical and geochemical studies conducted from 2004 through 2009 at the Questa Mine in northern New Mexico (Logsdon 2011). The waste piles at Questa are reasonable analogues for downstream shells of tailings embankments because the angle of repose deposits of waste rock at Questa were originally run-of-mine rock particles excavated from the open pit that were end dumped onto steep hill sides creating a size-segregated vertical profile of material initially with high air and water permeability. While not an engineered structure, as all tailing embankments are, the deposits operate essentially the same in terms of geochemical reactivity in that convective flux of air through the rock occurs and incident precipitation readily infiltrates and percolates through the material. The major findings of the Questa investigation pertinent to the broader question of placing sulfide-bearing rock in the downstream shell of tailing dams are: (1) sulfide minerals actively oxidize and generate low-pH drainage, (2) minerals with a geochemical reactivity comparable to the rate of sulfide oxidation (e.g. calcite, gypsum, iron oxyhydroxide, and ferric iron sulfates) dissolve/precipitate and are visible at the macro-scale, (3) the bulk of the mineralogic mass, composed principally of aluminosilicate minerals, weathers chemically under the low pH conditions created by sulfide oxidation; however, the process is a congruent dissolution with all reaction products transported from the system, rather than result in formation of secondary clay minerals.

While the Questa example is a fair analogue for most tailing embankments, especially rock fill embankments, the similarity depends on the geology, hydroclimatic regime, nature of the sulfide minerals, and hydrology of flows in the system. Differences in the fundamental characteristics of the Questa site suggest that the findings may not apply elsewhere. For example, sites where the tailing embankment is constructed in arid climates where construction materials consist not only of natural soils, but also of accumulated salts, commonly associated with natural caliche layers that develop in the soil profile. In this case, the geochemical-geotechnical question is related to the relative solubility of salt minerals as a function of the form of the salt (e.g. carbonate, sulfate, chloride, nitrate) rather than to oxidation of sulfide minerals. Depending on how water is transferred through the embankment, as percolating precipitation, natural groundwater underflow, and the extent to which tailing decant water flows through embankment material, soluble salts can react in a variety of ways with the worst-case scenario being complete dissolution and transport from the embankment. Because of the potential for complete dissolution, and associated mass loss, the typical approach of including a specification for the maximum concentration of soluble salt in embankment materials is an effective laboratory measure of the potential impact of embankment material geochemical reactivity on geomechanical properties of the embankment.

3 FIELD EXAMPLES

In the following examples of reactive material in the downstream shell of tailing embankments, the facility location and name remain anonymous to focus the discussion on geochemical reactivity and the associated effect on geomechanical properties.

3.1 *Sulfide-bearing rock in embankments*

3.1.1 *Rockfill dam with engineered PAG layers*

A geochemical design for layering PAG and non-PAG rock in the downstream shell of a growing tailing embankment was based on standard geochemical testing for acid base accounting that included interpretation of categories of PAG into moderate and high based on inferred geochemical reactivity. Construction includes a 25 m wide by 3 m thick compacted layer of PAG with a 10 m wide finish of non-PAG at the outer shell to encapsulate PAG in non-PAG. Field bin humidity cells have been implemented under varying configuration of PAG and non-PAG to evaluate at the field bin scale the geochemical reactivity of a well oxygenated system at a larger scale than laboratory humidity cells.

The primary focus to date has been on the reactivity of PAG within the design for placement. Laboratory and field testing provides data on the progression of sulfide oxidation as well as how different configurations of PAG and non-PAG affect the rate of reaction. There is no expectation that sulfide oxidation can be prevented, and the question then is how low of an oxidation rate can be engineered through compaction, manipulating grainsizes, and layering. Sophisticated modeling indicates the potential to slow oxidation rates, disrupt development of convective cells, and predicts seepage chemistry. However, none of these efforts address how sulfide oxidation, regardless of rate, affects the geomechanical properties of the rock fill material.

Often, the focus is solely on the question of acid rock drainage/metal leaching (ARD/ML), which is certainly a concern, without serious effort to understand what the sulfide oxidation reaction means for changes in geomechanical properties. However, if the mine will need to manage ARD/ML from other facilities, such as a waste rock pile, there would likely be limited impact from handling a small increase in water. A laboratory/field testing program is needed that focuses on developing information allowing estimation of the rate of change in geomechanical properties as a function of rate and extent of sulfide oxidation.

3.1.2 *Inadvertent placement of PAG*

Prior to full recognition of both the methods to identify mine rock subject to ARD/ML and the environmental consequences of placing such material in an uncontrolled setting, mine waste rock was used as construction material. Sulfide-bearing rock was used to construct the starter dam. Subsequent construction for full buildout of the embankment did not use PAG rock such that there is a portion of the overall embankment undergoing sulfide oxidation. The embankment is subject to significant freeze-thaw during winter months followed by a large amount of runoff during snowmelt.

Investigation of the effect of sulfide oxidation over multiple decades shows that geochemical reactions have occurred with a measurable increase in finer grained material as well as the presence of secondary weathering products (i.e., metal hydroxides, clay minerals, metal sulfates). While secondary weathering products were observed in borehole samples from the dam crest to the toe, greater residence time of water at the toe likely affects the extent of secondary mineral formation, especially clay minerals. While clay minerals are the ultimate end product of chemical weathering of aluminosilicate minerals, the challenge is to separate clay minerals into categories of primary clays (associated with formation of the ore deposit) and secondary clays (specifically related to sulfuric acid from sulfide oxidation on aluminosilicate minerals). Sulfide oxidation would also create void spaces in the host rock where water may accumulate and freeze as winter sets, which could then contribute to the mechanical breakdown of the rock.

Stability analyses show that there is currently no impact on the geomechanical performance of the embankment, and monitoring has been implemented to track changes that might require more active corrective action, which in this case (and most others) would be adding a buttress.

This example of PAG rock in a tailing embankment demonstrates that the time frame for sulfide oxidation to have an impact on the geomechanial properties of the sulfide-bearing rock can be decades to centuries long.

3.1.3 *Non-PAG, carbon-bearing rockfill*

In this next example, a tailing embankment is constructed using the center-line method with a compacted rock fill downstream embankment. The embankment also has an underdrain that extends from the toe to approximately the center of the facility. Rock routed to the embankment for construction is sorted at the pit based on a PAG/non-PAG classification built from analysis of thousands of samples. The host rocks also contain organic carbon in concentrations of up to several weight percent. Over the course of construction, several instances of surface cracking have occurred, with evidence of venting (gases and water vapor) indicating potential for heating in the subsurface. While heating may not be an immediate issue, there may be mineralogical transformations or overall changes in grain size that could influence the geomechanial properties of the bulk rock fill material.

Drilling and analysis of embankment materials showed a wide range in physical and chemical response to heating. Two of the primary outcomes were a fining of grain size and potential volumetric loss from combustion of organic carbon. Mineralogical changes were also recorded, including the transformation of calcite to gypsum (with attendant change in volume).

A preliminary outcome is that regardless of whether a material classifies as non-PAG, the classification does not imply the rock is non-reactive, only that if sulfide oxidation occurs there is sufficient neutralizing potential to prevent formation of acid rock drainage. Additionally, in this case, there are two forms of potentially reactive materials being used for construction: the sulfide-bearing materials (classified as non-PAG) and the organic carbon content. The investigation is on-going to evaluate the potential effect of the overall reactions on geomechanical properties of the rock fill.

3.1.4 *Cycloned tailing sand dam*

Porphyry copper deposits often have tailing storage facilities built from sand (a defined gradation) that is cycloned from the tailing. Because of the high specific gravity of sulfides, especially pyrite, the sulfides tend to end up in the embankment. Sampling and analysis of the embankment materials show by standard static testing methods that the materials classify as PAG with much of the sulfide minerals liberated (meaning available for oxidation); however, kinetic testing results show limited reactivity even after 40+ weeks of humidity cell cycles.

During operations, there is likely enough water in the embankment to limit ingress of oxygen. However, the formation of red-stained material at the drainpipes indicates that there is some oxidation of sulfide occurring during operations. If sulfide oxidation occurs, the buffering capacity of other minerals in the deposit (mainly aluminosilicates) could be sufficient to neutralize any acidity produced by sulfide oxidation. Over the long term (10s of year), oxidation of sulfides with neutralization could lead to build up of impervious layers due to precipitation of iron hydroxide. The presence of impervious layers might impact the designed hydraulic properties of the embankment.

3.2 *Soluble salts in embankment*

Soluble salts are often found in native soils in arid environments. In certain circumstances, use of material containing soluble salts for construction of tailing embankments cannot be avoided. The potential geochemical reactivity of soluble salts is more straight-forward than for sulfide bearing materials by assuming that the total volume of the salt would dissolve during contact with water and the mass removed from the embankment system. Thus, the issue can be addressed by defining the amount of mass that could be lost without impacting the stability of the embankment. A further consideration is to address the potential for development of relatively impervious layers resulting from dissolution of salts and evaporative concentration of the water such that salt solids reform. If such a process continued long enough, there is potential that the shallow flow of water through the embankment during the rare, high intensity short duration precipitation events could be affected by impervious layers.

4 CONCLUSIONS

Hard rock mines, and in particular open pits, produce an enormous amount of potential construction material, which the mine needs. Not all the material produced is suitable for use in construction for a variety of reasons. In those instances, whether inadvertent or purposefully, for geochemically reactive mine rock, that is used for construction, there are two principal information needs that arise: (1) determining the environmental effect of the reactive rock and (2) understanding the effect on the geomechanical properties of the rock as a result of geochemical reaction. The examples provided in this paper serve to identify different situration where geochemical reactive materials have been used in construction of the downstream shell of tailing impoundments, but, more importantly, that a testing program is needed that addresses the time-dependent change in geomechanical properties as related to the progression of sulfide oxidation when sulfide-bearing rock is used for construction.

Current methods to define the geochemical reactivity of rock materials focus on determining the potential environmental effects from exposing the rock to atmospheric conditions. However, the information generated by standard geochemical characterization does not address the information needs related to the time-dependent changes in geomechanical properties of the geochemically reactive rock. There is a need in the industry to develop laboratory and field testing that would address the important data gap related to rock geochemical properties, rates and consequences of rock reactivity, and time-dependent changes in rock geomechanical properties.

5 REFERENCES

Logsdon, M.J. 2011. Geological, Hydrological, and Geochemical Framework for Questa, in *Proceedings of the 15th International Conference on Tailings and Mine Waste, Keystone, Colorado, 14-17 October*. Vancouver: Information Technology, Creative Media.

Comparison of tailings impoundment filling methods for volume and settlement predictions

Silawat Jeeravipoolvarn
Golder Associates, Calgary, AB, CANADA

Gordan Gjerapic
University of Colorado, Boulder, USA

ABSTRACT: One of the challenges in applying the one-dimensional (1D) finite strain consolidation theory to solve the tailings impoundment filling problem is an accurate representation of the three-dimensional (3D) impoundment geometry when assembling the large strain consolidation model. Due to its complexity, the impoundment filling problem is usually solved by simplifying the general 3D consolidation formulation. While all simplified methods used in the industry utilize the stage-storage curve as a representation of the 3D geometry, they often exhibit considerable differences in the calculated mudline position and the estimated tailings capacity.

This paper examines different impoundment filling methods to predict the consolidation behavior of tailings for a typical 3D impoundment geometry. These filling methods are compared in terms of the domain assembly, calculated mudline position and the mass conservation error. Results from the filling scenarios analyzed in this study indicate that the impoundment capacity predictions are dependent on the adopted geometry representation, and material parameters. For analyzed scenarios, the estimated mass balance error at the end of the filling process was as high as 26 percent for methods using the filling rate adjustment in a 1D column model, i.e., using the tallest column method; and on the order of 1 percent or lower if utilizing quasi-3D implementation of the impoundment geometry. The results demonstrate the importance of enforcing the mass conservation principle for the capacity prediction of a tailings storage facility.

1 INTRODUCTION

Tailings waste materials generated from extraction processes in the mining industry are typically transported via pipelines before being deposited into a tailings storage facility (TSF) for storage and water recovery. As part of the TSF storage and closure designs, it is often required that the tailings volume and settlement are estimated throughout the lifetime of a TSF.

In practice, the tailings volume and settlement predictions are commonly conducted by applying the one-dimensional (1D) finite strain consolidation theory (Gibson et al. 1967) to a three-dimensional (3D) impoundment geometry. Several methods have been developed to address the 3D aspects of a TSF filling problem. One of the methods commonly used in practice is to apply a fill rate adjustment at the deepest area of the impoundment (the tallest column method) effectively assuming that the side of the TSF undergoes the same deformation as the material in the center at the same elevation (see, e.g., Geier et al. 2011). This method is acceptable for a wide-base impoundment where the side slopes have little or no impact to TSF volume predictions. However, in the case of a narrow base TSF design such as a valley fill, this method may result in significant errors regarding both the mass balance and the rate of dewatering (see, e.g., GWP Geo Software Inc. 2007, Gjerapic et al. 2008, Geier et al. 2011, and van Zyl et al. 2020).

Alternatively, the 1D rate of consolidation, as calculated from the tallest column method, may be revised to maintain the mass conservation while accounting for the 3D geometry conditions by using an average dry density from the tallest column method and the total mass of solids in the impoundment (from the production rate and the time of filling) to calculate tailings volume. The average dry density with time may be obtained from either the average dry density at different impoundment elevations or the average dry density for the entire tallest column (as determined from the ultimate void ratio profile). Because the 1D rate of dewatering remains to be evaluated only for the deepest TSF area and the rate of consolidation is associated with the length of the drainage path, it is often desired to consider a more elaborate consolidation model that includes shallower impoundment areas.

One of the methods that accounts for shallower impoundment areas utilizes the approach of converting the 3D impoundment geometry into a 1D effective filling area (Carrier 2021). In this method, the effective filling area is determined by dividing the impoundment volume with the effective filling height. The effective filling height is a weighted average height found by integration of the stage-storage curve. An iterative process is required so that the effective filling height and the simulated height are matched, and the effective area is determined. The method ensures the mass conservation and yields an approximated ultimate capacity requirement for design. This approach is typically used to evaluate the volume of water release vs. time.

To ensure that both the mass balance and the water balance are preserved for an arbitrary TSF 3D geometry, the method with an optimal mass conservative scheme was proposed by Gjerapic et al. (2008). Gjerapic et al. proposed to discretize the TSF into several areas (or columns) with the base of each column located at a different elevation in the impoundment. A separate 1D consolidation model is then created for each column area. The TSF analysis is performed by filling the impoundment from the bottom upwards resulting in a tailings deposition starting with deeper columns and moving to shallower columns in the impoundment. During the filling process, before tailings are deposited into a new column at higher elevation, the deeper column(s) are filled to "catch-up" with the new higher area maintaining a leveled surface filling scheme (this leveled surface may be horizontal or at the constant angle). The "catch-up" is accomplished by filling deeper columns of the impoundment and pausing the consolidation process in shallower areas during the catch-up period. The method results in a filling scheme that enforces mass conservation, i.e., it minimizes the mass balance error, for the impoundment filling problem (Geier et al. 2011, Gjerapic and Znidarcic 2018). Subsequently, FSCA (2019) developed a non-leveled surface filling scheme by using a similar material placement method without allowing for the "catch-up" procedure. A similar approach utilizing a finite number of 1D columns to model the TSF filling process was also reported by Fredlund et al. (2015).

At the present time, the authors are not aware of the commercial software for TSF capacity prediction that uses a fully coupled 3D large strain consolidation approach accounting for both the vertical and lateral drainage paths. The effect of lateral drainage has been shown to be negligible in most cases when considering typical TSF configurations because the vertical drainage paths are significantly shorter than the horizontal extents for the vast majority of tailings impoundments (see e.g., Jeeravipoolvarn et al. 2008, Gjerapic et al. 2008, and van Zyl et al. 2020)

In this paper, five TSF filling methods currently used in practice are investigated. A comprehensive comparison of these methods is expected to provide a practical direction for the TSF capacity design and supply valuable information for the water balance and settlement analyses. The selected methods were compared in terms of the domain assembly, the predicted mudline height (i.e., tailings height), the average void ratio, and the mass conservation error. The mass conservation error was selected as the key performance indicator for ranking of different methods in terms of their validity for the TSF capacity prediction.

2 TAILINGS IMPOUNDMENT FILLING METHODS FOR THE PREDICTION OF TSF CAPACITY

Five methods were evaluated in terms of their ability to provide TSF capacity predictions based on differences in the calculation methodologies (Table 1). Domain assembly strategies for these methods are illustrated in Table 1.

– Method 1 utilizes a stage-storage curve (also known as pond capacity curve and Volume-Elevation curve) to adjust the filling rate at the deepest TSF area and conduct the 1D column simulation. The simulation is conducted only at the deepest area of the impoundment.

– Method 2 uses results from Method 1 to determine the average dry density of tailings with time. The calculated dry density and the total (input) dry mass of tailings are then used to calculate the TSF volume and the mudline position.
– Method 3 converts a 3D stage-storage curve into a 1D effective filling area and uses the area for 1D simulation (i.e., a single 1D cylinder is used to determine the impoundment volume at a specific time of deposition).
– Method 4 utilizes a quasi-3D implementation of the impoundment geometry by discretizing a TSF into several areas, each area representing an individual 1D column with its base at a specific elevation. The impoundment filling proceeds from the bottom towards the top. The filling also allows the mudline at deeper columns to catch-up to columns at higher elevations resulting in a leveled surface filling scheme.
– Method 5 is similar to Method 4 but does not allow for the “catch-up” procedure. The overall TSF dry density is calculated as a function of time by using data from individual columns. The dry density and the total dry mass of tailings is then used to calculate the TSF volume and the mudline position.

Software packages used to perform the consolidation analyses in this paper included FSCA Version 2.2; FILLCON/CONDES and FSConsol Version 3.49.

Table 1 Five impoundment filling methods for the TSF capacity prediction

No.	Method procedure	Calculation methodology	Schematic of impoundment filling domain assembly
1	1D	1D simulation at the deepest area of the impoundment with the fill rate adjustment to account for the 3D geometry.	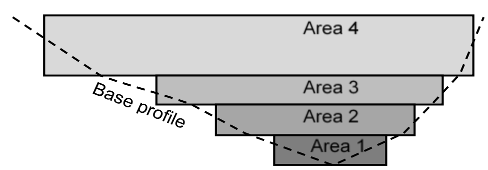
2	1D to 3D volume	Use Method 1 results to determine average TSF density vs. time. Combine the average TSF density and total dry mass to calculate the mudline position at individual times.	
3	1D effective pond area	Convert 3D geometry to a 1D effective area and use 1D simulation (Carrier 2021).	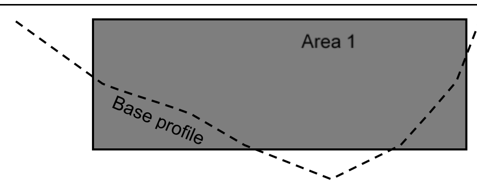
4	Quasi 3D Leveled surface	TSF simulation using multiple columns, start filling from the deepest column and overflow to shallower columns/areas. Allow "catch up" time for each column to create leveled mudline.	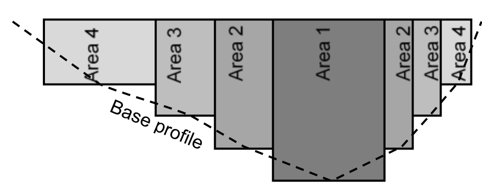
5	Quasi 3D Non-leveled surface	Similar to Method 4 but without the "catch-up" time. Overall TSF dry density is calculated with time by using data from individual columns. The dry density and the total dry mass of tailings is then used to calculate the TSF volume and the mudline position.	

3 COMPARISON OF THE FILLING METHODS USING A NUMERICAL EXAMPLE

To examine differences between the five selected TSF filling methods, a numerical example was evaluated using hypothetical input parameters (impoundment geometry, filling rate and material parameters).

3.1 *Input Parameters*

Material parameters for tailings with the sand to fines ratio (SFR) of 0.1:1 (Case 1 – Finer Tailings), and the SFR of 4:1 (Case 2 – Coarser Tailings) were selected for consolidation analyses. The selected tailing types represent "typical" tailings streams in the oil sands industry. The impoundment was modeled with the impervious bottom boundary. The compressibility relationships for Finer and Coarser Tailings are shown in Figure 1.

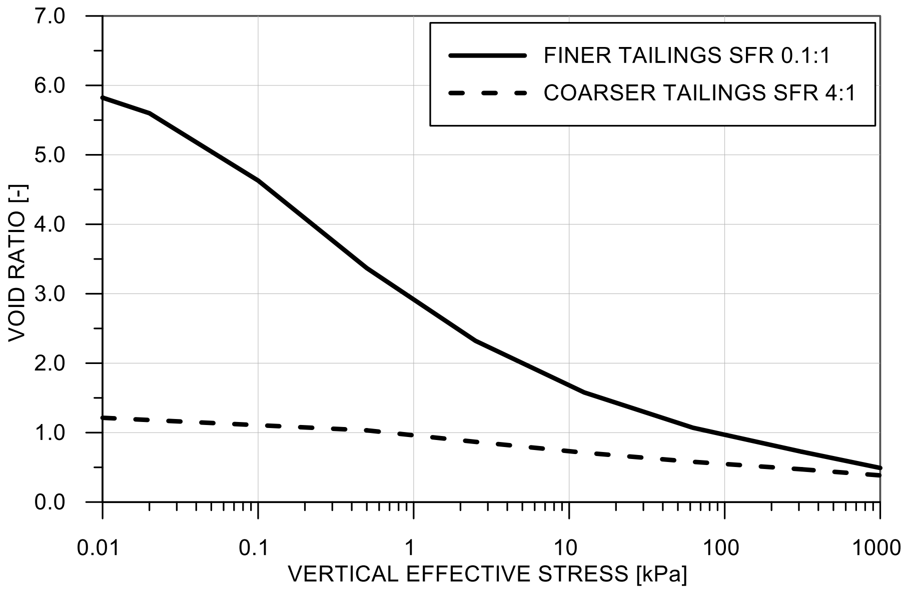

Figure 1. Compressibility functions for Finer Tailings (SFR=0.1:1) and Coarser Tailings (SFR=4:1)

The hydraulic conductivity relationships for Finer and Coarser Tailings are shown in Figure 2.

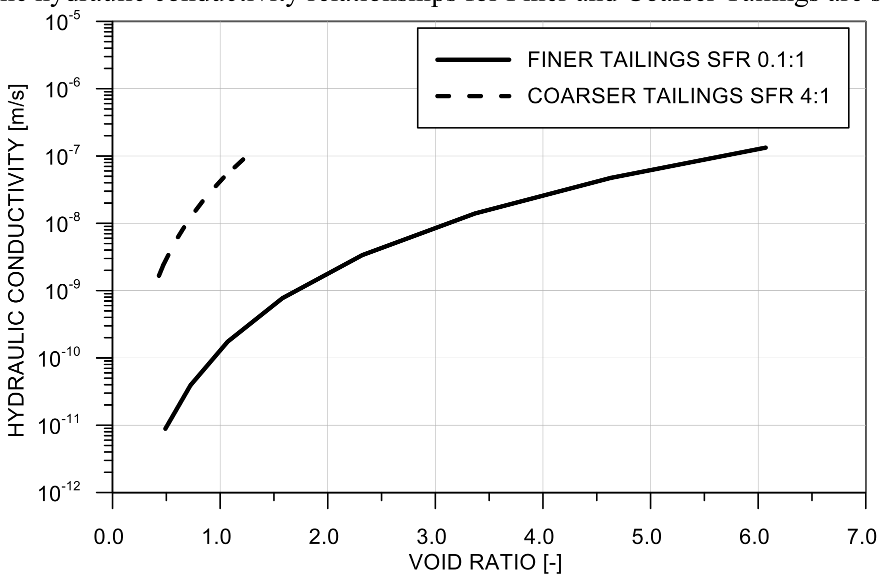

Figure 2. Hydraulic conductivity functions for Finer Tailings (SFR=0.1:1) and Coarser Tailings (SFR=4:1)

The stage-storage curve employed for the analyses is shown in Figure 3. The selected stage-storage curve represents a 3D tailings impoundment geometry for a side-hill or valley-fill deposition scenario.

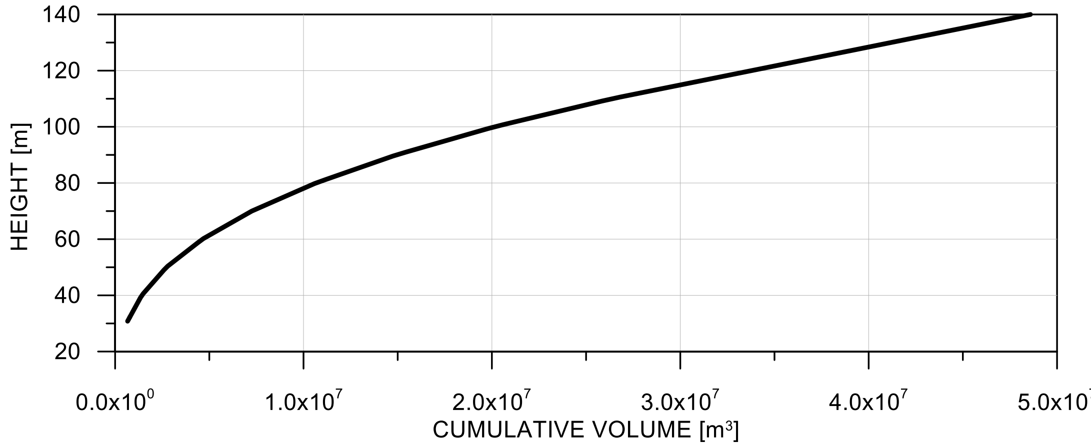

Figure 3. State-storage curve for a hypothetical 3D tailings impoundment

A filling schedule with a constant dry mass production of 700,000 tonne/year was selected for the analyses as shown in Table 2.

Table 2. TSF impoundment filling schedule

Case	Material	Specific gravity	Solids content (%)	Production rate (tonne/year)	Filling period (years)
1	Finer Tailings SFR 0.1:1	2.60	30.0	700,000	10
2	Coarser Tailings SFR 4:1	2.60	68.2	700,000	10

3.2 *Simulation Results*

Results from the two analysis cases were compared in terms of the mudline position with time, the TSF capacity (i.e., the mudline position at the end of filling), average void ratio (by the calculated mass and volume) at the end of filling, and the corresponding mass conservation error.

For the mass conservation error calculations, Equations (1) to (3) were utilized, where ρ_d is the dry density, V is the impoundment volume, i is the layer number, and n is the total number of layers.

$$Mass\ conservation\ error = \frac{Mass\ output - Mass\ input}{Mass\ input} \times 100\% \quad (1)$$

$$Mass\ input = Dry\ mass\ fill\ rate\ \times fill\ period \quad (2)$$

$$Mass\ output = \sum_{i=1}^{n} \rho_{d,i} \times V_i \quad (3)$$

3.2.1 *Case 1: Finer Tailings SFR 0.1:1*

The tailings mudline elevation during the filling period for the Finer Tailings is shown in Figure 4. Methods 1, 2, 4 and 5 demonstrate similar behaviour with a rapid rate of rise at the start of the filling process, followed by a decreasing rate of rise with time. This behaviour is expected as the production rate remains constant throughout the filling process, while the TSF area increases with the increasing impoundment elevation. Method 3, in contrast to other methods, uses a constant rate of rise for a single 1D effective filling area simulation. It must be noted, however, that Method 3 can provide a non-linear filling behavior similar to other methods when additional simulations are performed at different times during the filling period – i.e., we need to use a series of 1D effective filling areas at different elapsed times.

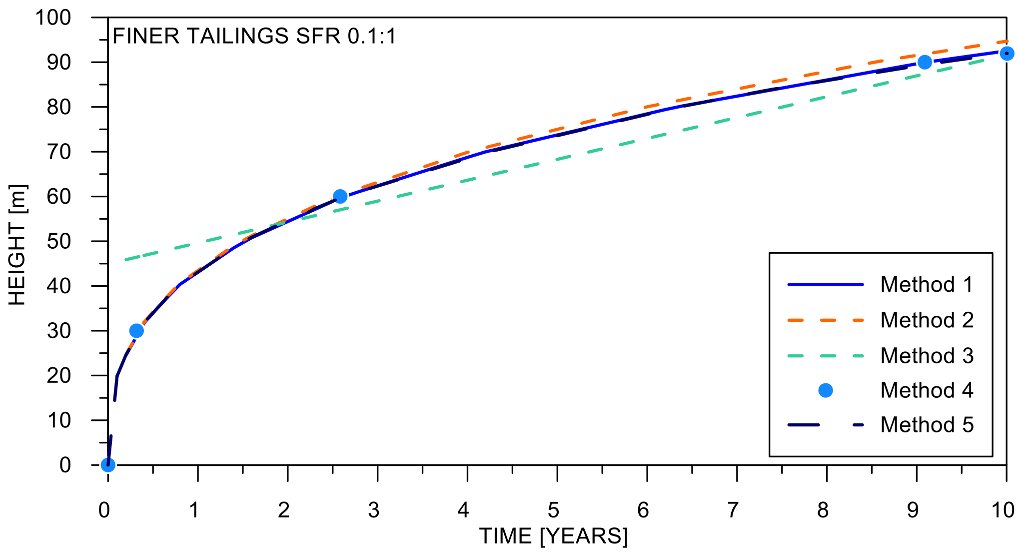

Figure 4. Mudline elevation during filling for Finer Tailings SFR 0.1:1

The ultimate tailings heights shown in Figure 5 illustrate that all considered methods predicted TSF capacity values within a relatively narrow bound at the end of the filling period. The exception was Method 2 for which the height was overestimated as the deepest area was used to predict the overall rate of consolidation for the entire mass and the faster rates of consolidation in shallower areas were not considered.

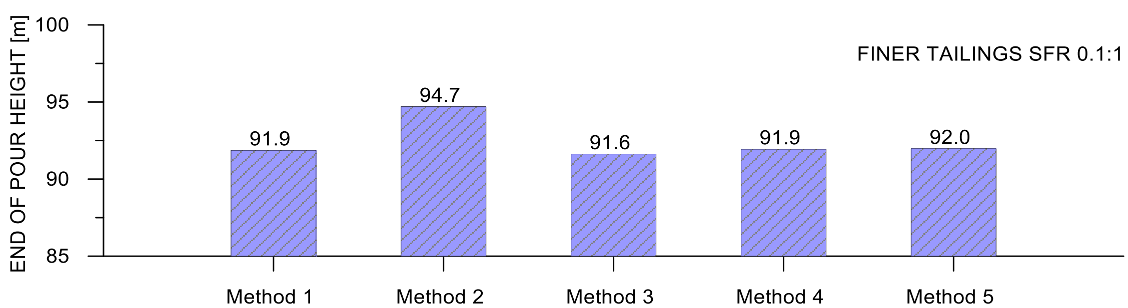

Figure 5. Final height comparison for Finer Tailings SFR 0.1:1

A comparison between different methods displayed in Figure 6 demonstrates the mass balance error on the order of -1% or lower for Methods 2 to 5, and the mass balance error as high as -17% for Method 1. Although Method 2 had a relatively low mass balance error (similar to Methods 3 to 5), the rate of consolidation was underestimated, and the TSF capacity requirement was overestimated.

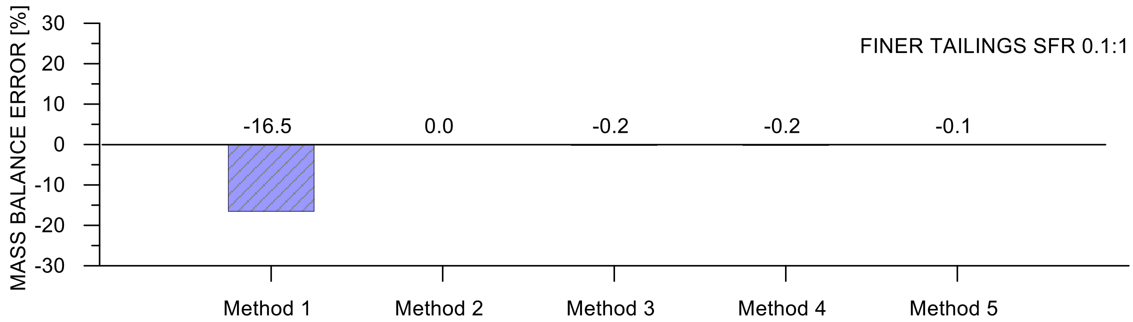

Figure 6. Mass balance error comparison at the end of filling for Finer Tailings SFR 0.1:1

Figure 7 compares the average void ratio at the end of filling indicating that Method 1, i.e., the method with the highest absolute mass balance error, had a significantly higher void ratio (lower dry density) compared to other methods exhibiting smaller absolute mass balance errors.

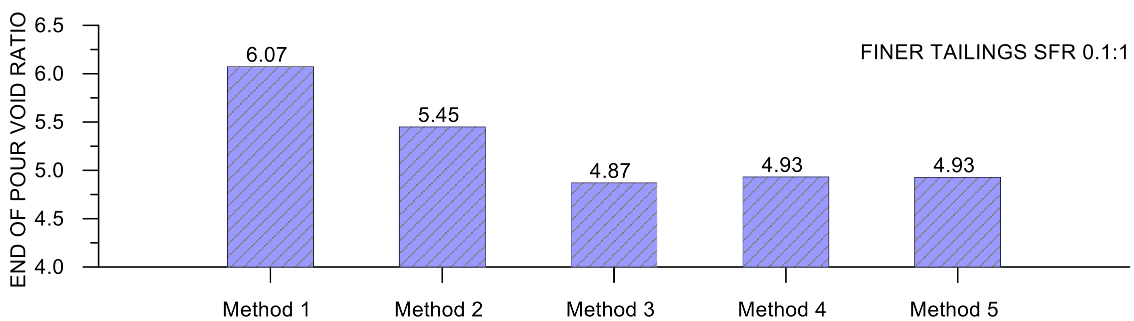

Figure 7. Average void ratio comparison at the end of filling for Finer Tailings SFR 0.1:1

3.2.2 *Case 2: Coarser Tailings SFR 4:1*

The tailings mudline elevation during the filling of Coarser Tailings is shown in Figure 8. The calculated tailings height and the mass balance error comparisons at the end of filling are given in Figures 9 and 10. The average void ratios at the end of filling are compared in Figure 11.

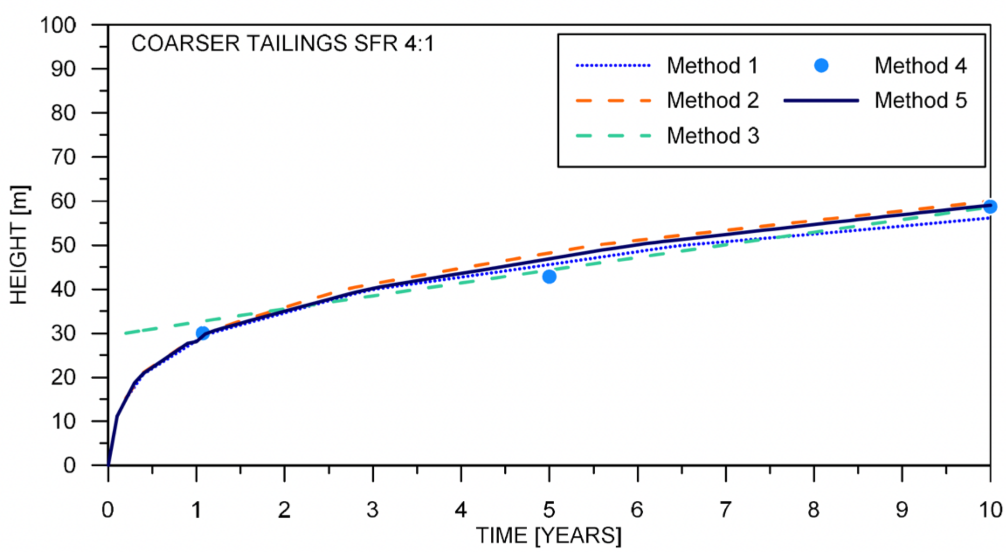

Figure 8. Mudline elevation during filling for Coarser Tailings SFR 4:1

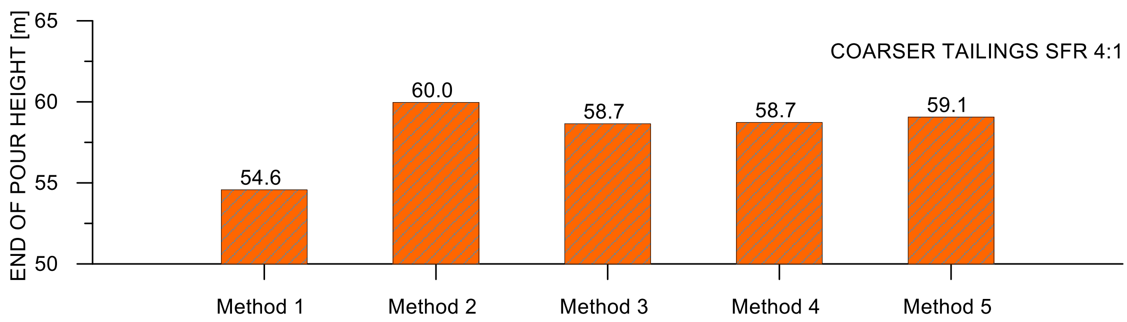

Figure 9. Final height comparison for Coarser Tailings SFR 4:1

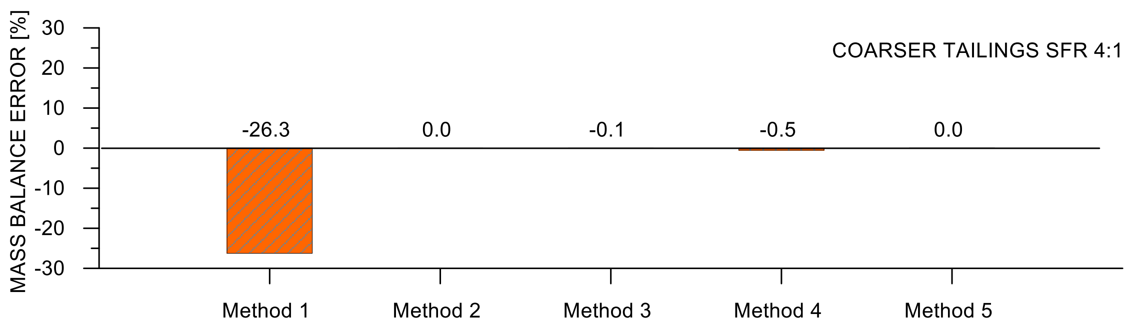

Figure 10. Mass balance error comparison at the end of filling for Coarser Tailings SFR 4:1

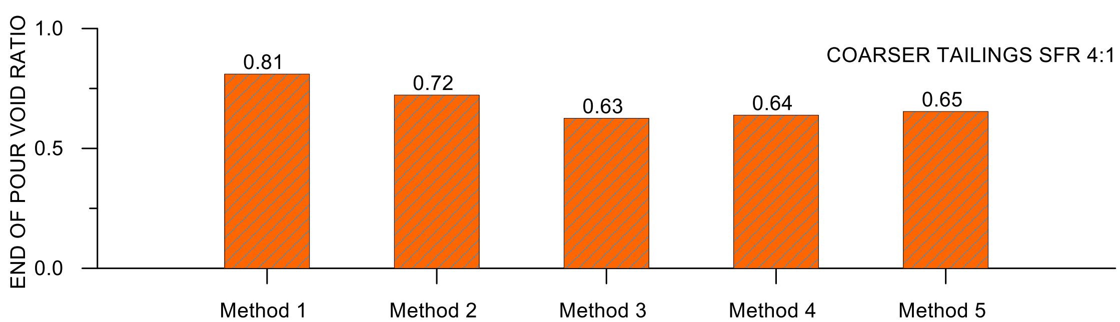

Figure 11. Average void ratio comparison at the end of filling for Coarser Tailings SFR 4:1

The analyses for Coarser Tailings indicate that the ultimate filling height was underestimated by Method 1 (Fig. 9) by as much as 7% (or about 4 m) when compared to values determined from Methods 3 to 5 (mass conservation methods). The mass balance error (Fig. 10) was somewhat larger than previously determined for Finer Tailings. The maximum mass balance error of approximately -26% was determined for Method 1 filling simulation. Similarly to Case 1, Method 1 exhibits the highest mass balance error (Fig. 10), the highest average void ratio (Fig. 11) and the lowest dry density. Considering that Method 1 also predicted the lowest tailings height (see Figure 9), the mass balance error in Method 1 can now be traced to settlements of the impoundment sides, i.e., settlements of tailings areas at shallower depths imposed by the 1D deposition model, as discussed by Gjerapic and Znidarcic (2018).

4 DISCUSSION

The numerical examples on two types of oil sands tailings presented in this paper demonstrate that the use of the tallest column method (Method 1), can result in significant mass balance errors for typical side-hill or valley-fill deposition scenarios (represented in this paper by a 3D tailings impoundment geometry in Figure 3). Consequently, the TSF designers should consider limitations of Method 1 or similar methods when predicting the TSF volume and settlements. Since the mass conservation error is dependent on both the material properties and the impoundment geometry, the use of Method 1 should be restricted to initial TSF assessments for which the impoundment geometry is adequately represented by a 1D column. Such 1D geometry may include an impoundment with a wide base surrounded by a ring dyke or a similar configuration for which the 1D representation is reasonable. The adequacy of a specific consolidation analysis for the assessment of TSF capacity must be evaluated by calculating the mass conservation error.

The observed differences between the methods for the TSF capacity prediction may prove to be within an acceptable range during the simulated filling period. However, these differences are often compounded during closure and post-closure periods. The large strain consolidation method with a significant loss of mass tends to exhibit larger settlement errors (see example in Geier et al. 2011) potentially leading to erroneous predictions of the post-closure TSF geometry. Consequently, the mass balance error should also be evaluated when conducting consolidation analyses for TSF closure designs.

Method 2 results, utilizing the mass balance correction for a 1D column at the deepest TSF area, should be used with caution by scrutinizing impacts of the consolidation properties and geometry to estimated filling rates and densities. For the larger mass balance errors, e.g., on the order of 10 percent or more, the use of Methods 3, 4 or 5 should be considered.

A computational efficiency of Method 3 is convenient for the design work when investigating impacts of different alternatives and multiple design parameters at early stages of the TSF design. A judicious application of Method 3 is expected to result in the TSF capacity predictions that are similar to those of more elaborate 3D material placement methods, i.e., Methods 4 and 5, accounting for the actual 3D impoundment geometry during the calculation process. To produce a non-linear filling curve similar to Methods 4 and 5, Method 3 can be applied to different heights and thus multiple effective filling areas during the impoundment filling process.

Amongst the tested methods, Methods 4 and 5 exhibit a similar 3D domain assembly and provide a consistent mudline prediction while minimizing the mass conservation error. Compared to other methods, however, these two methods require additional computational time. The key difference between Methods 4 and 5 is the catch-up time resulting in a non-leveled surface at the ultimate TSF configuration if using Method 5. Based on the case scenarios investigated in this paper, the difference between Methods 4 and 5 is often negligible. It is recommended that Methods 3, 4 and 5 are considered for the tailings impoundment capacity evaluations with the preference given to Methods 4 and 5 at the feasibility level and later stages of the design.

5 SUMMARY

TSF designers often assume that 3D aspects of a tailings storage facility are adequately addressed in existing software packages by a simple input of a 3D stage-storage curve. As most of the computer programs for TSF capacity evaluations are based on a filling rate adjustment in a 1D column model, this assumption can be incorrect. It is therefore essential for TSF designers to validate the large strain consolidation analysis for the TSF capacity prediction by calculating the error of mass conservation.

Five methods for the TSF capacity prediction were examined in this paper for two types of oil sands tailings and a hypothetical 3D impoundment geometry. The absolute value of the mass balance error at the end of the impoundment filling was on the order of 1 percent or lower for a quasi-3D implementation of the impoundment geometry, and as high as 26 percent for methods using the filling rate adjustment in a 1D column model. For a 3D impoundment simulation, the mass conservation finite strain consolidation method should be considered, and mass conservation checks should be adopted as an integral component of the TSF capacity design and analysis.

6 ACKNOWLEDGEMENT

The authors would like to thank Dr. David Carrier III of Argila Enterprises, Inc. for providing background information for Method 3; Mr. Bill Shaw of WHS Engineering Ltd. and Dr. Samuel Proskin of Thurber Engineering Ltd. for discussion on the practical aspects of pond filling consolidation; and Professor Emeritus Dobroslav Znidarčić and Dr. Ben Wickland for constructive comments and suggestions to improve the manuscript.

7 REFERENCES

Carrier, W.D., III. 2021. Personal communication.

Fredlund M., Donaldson, M., Chaudhary, 2015. Pseudo 3-D deposition and large strain consolidation modeling of tailings deep deposits. Proceedings of Tailings and Mine Waste 2015, Vancouver, BC, October 26 to 28, 2015.

FSCA 2019. User manual, 73p. www.fscasoftware.com.

Geier, D., Gjerapic, G. and Morrison, K. 2011. "Determination of Consolidation Properties, Selection of Computational Methods, and Estimation of Potential Error in Mine Tailings Settlement Calculations", Conf. Proc. From Tailings and Mine Waste 2011, Vancouver, BC, November 6 to 9, pp. 279-291, ISBN: 978-0-88865-815-9.

Gibson, R.E., England, G.L. and Hussey M.J.L. 1967. The Theory of One-dimensional Consolidation of Saturated Clays. I. Finite Non-linear Consolidation of Thin Homogeneous Layers. Géotechnique, 17(3): 261–273.

Gjerapic, G., Johnson, J., Coffin, J. & Znidarcic, D., 2008. Determination of Tailings Impoundment Capacity via Finite-Strain Consolidation Models. In: Alshawabkeh, A.N., Reddy, K.R. & Khire, M.V. eds. GeoCongress 2008: Characterization, Monitoring, and Modeling of GeoSystems (GSP 179) conference proceedings. New Orleans, LA, 798-805.

Gjerapic, G. and Znidarcic, D. 2018. "Improved Methodology for TSF Capacity Prediction", Tailings and Mine Waste '18 conference proceedings, September 30-October 2, Keystone Resort, Keystone, Colorado, USA, Published by UBC Studios, Vancouver BC, pp. 267-276.

GWP Geo Software Inc 2007. FSConsol User manual, 103p. www.fsconsol.com.

Jeeravipoolvarn, S., Scott, J.D., and Chalaturnyk, R.J., 2008, "Multi-Dimensional Finite Strain Consolidation Theory: Modeling Study", Proceedings of the 61st Canadian Geotechnical Conference, September 22-24, Edmonton, AB, pp. 167-175.

Van Zyl., D., Znidarčić, D., and Gjerapić, G. 2020. Modeling Aspects of Tailings Disposal Facility Design – Prediction of Storage Capacity: Short Course. Tailings and Mine Waste 2020, Colorado State University, USA, November 15-18. 2020.

Novel dewatering technology by Extrakt Process Solutions

William Florman, Christian Kujawa
Extrakt Process Solutions LLC, Bowling Green, KY, USA

David Sego
University of Alberta, Edmonton, AB, Canada

ABSTRACT: Extrakt Process Solutions (EPS) has developed a novel and effective high-rate dewatering solution based on ionics, named TNS™. This technology is safe, sustainable, and excels even with high clay content in the tailings. The paper provides a brief introduction to the development path of the technology. Actual test results from a variety of tailings process samples demonstrate the wide applicability of this technology. High-level economic analyses also demonstrate the efficacy of the TNS™ technology as a solution to solids-liquid separation applications to achieve stackable filtered tailings.

1 INTRODUCTION

All existing and planned mine extraction plants use water for tailings transport as well as the processing medium. This is because historically mining operations were an accepted part of life, smaller in size, and water was a widely available resource. Today there is conflict between mine operators and other interest groups regarding access to clean water. At the same time, water retained within the stored tailings has been identified as the main factor in failure of the tailing's storage facilities (ICMM, 2021). The current best available practice to reduce the potential liquefaction of tailings, which leads to dam failures and potentially devastating consequences, is to dewater the tailings via filtration.

Filtration is a well-developed technology with mixed results when filtering tailings. Its effectiveness is adversely impacted by clay in the tailings. The results can be even more pronounced at large scale throughputs, making filtration of the tailings either not possible, too expensive, and/or simply too risky. A path to minimize these risks is outlined in this manuscript.

2 BACKGROUND AND CURRENT INDUSTRY TAILINGS CHALLENGES

The growth in human population and an increase in reliance on metals has resulted in an exponential increase in metals demand. Simultaneously, there has been a reduction in head grade of many metal ore resources. This has resulted in ever larger mining operations.

The historical abundance and utility of water is the reason for water served not only as transport medium but also as process medium. In fact, water together with the advent of dynamite, horizontal centrifugal pumping technology, and thickening has made large scale mining operation possible.

Larger mining operations in turn require ever larger tailings storage facilities. The challenge is that of ensuring tailings storage design for perpetuity.

In practice, as is borne out by the many failures still occurring, tailings storage failure is a result of liquefaction because of water remaining within the tailings or because of water storage on top of the facility. Thus, dewatering of tailings ahead of storage is seen as the single most important criteria for reducing liquefaction events or the severity of such liquefaction events.

Because of growth in population and industry the value of clean water is increasing through demand, resulting in competition for water between interest groups. Interestingly, there is no shortage of water worldwide. However, it costs to desalinate seawater and to pump it to elevations inland. The cost of making seawater available can be as high as 3 to 5 USD/m^3. Minimization and reutilization of water is therefore highly desirable.

2.1 *Other Pressures*

More and more regulatory guidelines are calling for the elimination of tailing ponds. At the same time investors are demanding conformation to environmental and social governance guidelines for the mining industry to gain access to capital. There exists, a nexus, where water recovery from tailings to enhance the stability of tailings storage and minimization of freshwater consumption mesh. Filtration of tailings is seen as the industry objective.

2.2 *Challenges to the Filtration of Tailings*

Growth in operation throughputs has outstripped dewatering equipment development in terms of throughput and technology. Development of equipment has been largely organic. As a result, dewatering plants are currently a significant capital (CapEx) and operating (OpEx) cost.

The cost of dewatering is a new burden to an industry that historically works on low margins and is vulnerable to market cycles.

More so, not all tailings are suitable for dewatering. If the ultra-fine and fine particle presence is high, this can impede dewatering. As well, some minerals, notably the surface-active clays, are refractory to dewatering, and if extensive essentially make tailings filtration either impossible or else cost prohibitive. The challenges are exacerbated often by variability in the ore. It is possible to design a plant for a certain level of clay in the feed, but it is difficult to cater for large swings of clay content in the source ore and resulting tailings.

3 TNS™ DEWATERING TECHNOLOGY

3.1 *Historic Perspective*

Extrakt Process Solutions LLC (EPS) acquired the exclusive license for the original Penn State University patents on the use of ionic liquids for the extraction of oil or bitumen from oil sands.

Further development resulted in the transition of the technology to solids-liquid phase separation. The new chemistry developed is called TNS™. The chemistry is applied in-line similarly to conventional polymer technology. The effectiveness of the new technology is markedly different.

3.2 *Impact on Thickening*

An illustration of the effectiveness of the technology can be seen in Figure 1 showing the impact of the technology for thickening. The phosphate slimes tailings with a top size of 20 µm, containing clays, represent a significant dewatering challenge, resulting in the loss of water to the tailings storage facility.

Figure 1 shows that the TNS™ technology not only improves the thickener underflow solids concentration but also does so at order of magnitude higher solids loading rate than for the available best conventional polymer solution.

The slimes were dewatered with the TNS™ technology at the tailings stream's natural solids concentration. For the conventional polymer technology considerable thickener feed dilution was required to achieve good flocculation. It is possible to use dilution also for the TNS™ technology, thereby improving its efficacy even further. The use of the TNS™ technology therefore will reduce the capital as well as operating costs for the dewatering by thickening.

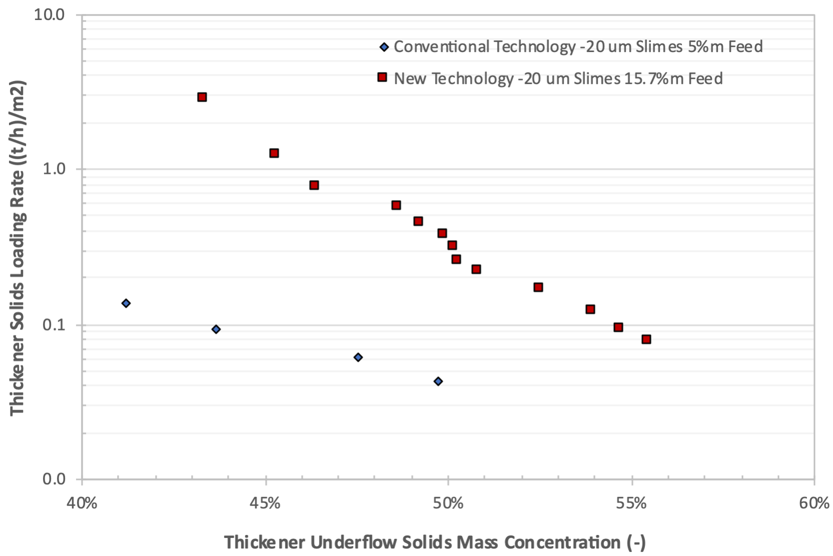

Figure 1: Comparative Thickening of Phosphate Slimes Tailings

3.3 *Impact on Filtration*

Figure 2 provides a comparison of the TNS™ technology to conventional technology in terms of filtration cycle times for phosphate slimes with a top size of 20 µm. The reduced filtration cycle time will result in a considerable decrease in number of filters required to dewater a given volume of these slimes tailings. This means a reduction in CapEx, and because of the high maintenance cost associated with filtration, also a considerable reduction in OpEx.

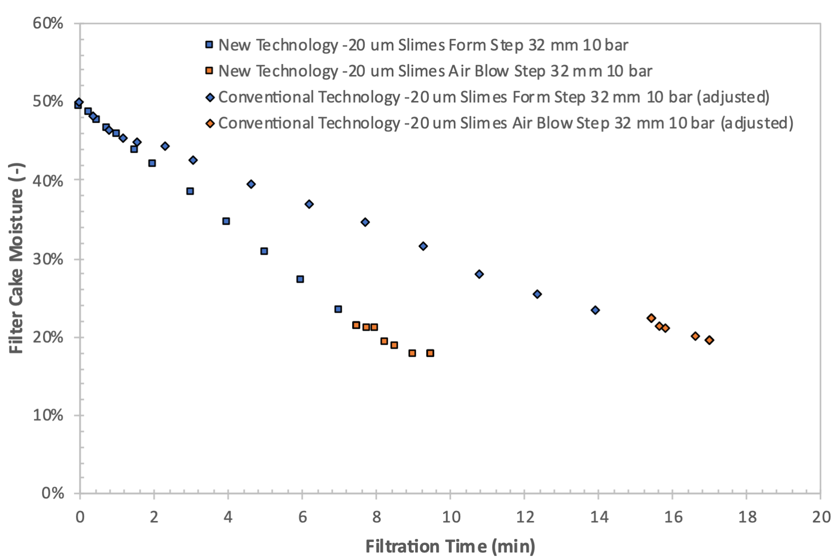

Figure 2: Comparative Filtration of Phosphate Slimes Tailings

3.4 *Impact on Tailings Facility Consolidation*

Large strain consolidation testing was carried out on low-clay porphyry copper tailings in comparison of conventional polymer chemistry to the TNS™ chemistry to demonstrate the continued dewatering achievable on a wet tailing's storage facility using TNS™.

Figure 3 shows that dewatering and consolidation rates higher by two orders of magnitude are achieved with the use of the TNS™ technology compared to conventionally treated tailings.

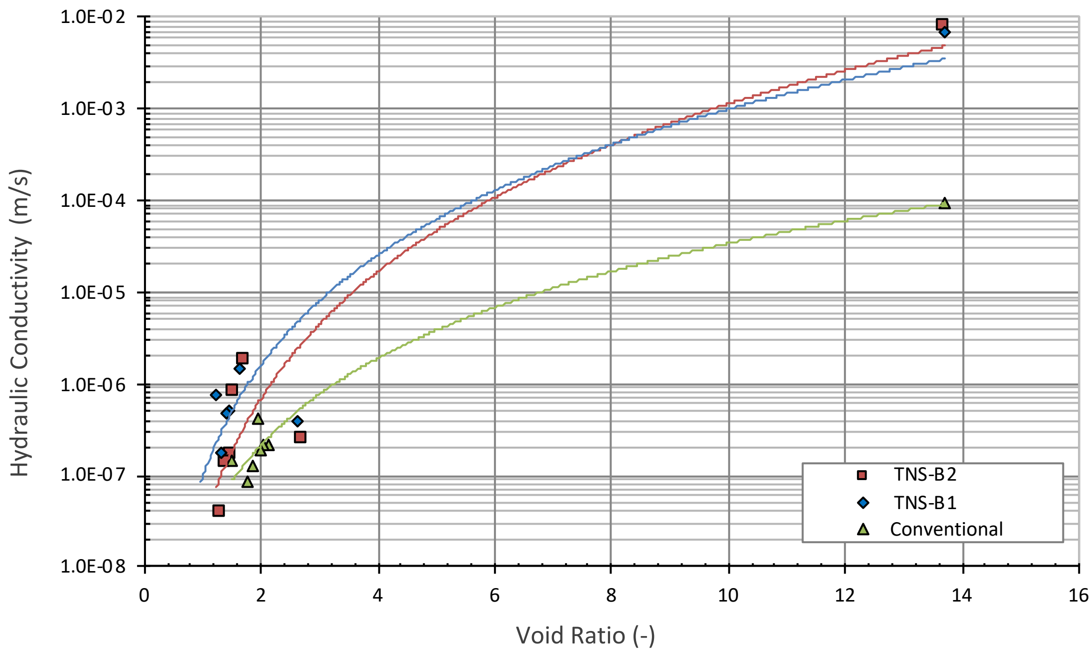

Figure 3: Comparative Large Strain Consolidation of Copper Tailings (Abdulnabi et al. 2019)

3.5 *Advantages of the TNS™ Dewatering Technology*

TNS™ requires minimal mixing and allows flocculation at higher solids concentrations. Up to 70% in solids mass concentration can be flocculated and further dewatered. Dilution of the thickener feed, to achieve meso-type mixing and flocculation is therefore not as critical as with conventional polymer technology.

The ease of flocculation is also evident in the efficient capture of ultra-fines which results in clear supernatant or filtrate, thus making the water available for immediate recycle to extraction.

The floccule network structure that is formed is considerably more resistant to shear than with conventional polymer network structures. Though, if sheared extensively, ultra-fine aggregates will separate from the larger floccules also with TNS™.

Dewatering using TNS™ is characterized via higher settling rates, higher thickener bed consolidation rates, higher filtration rates, and higher wet storage facility consolidation rates. This translates to reduced CapEx, reduced OpEx, along with reduced footprint costs through use of filtration. In virtually all cases, reduced tailing storage cost and reduced fresh-water consumption through higher water utilization is achieved.

Even though the presence of clays does also impact TNS™ flocculation, generally requiring a higher dosage, the flocculation remains robust, and the dewatering rates are still above those achieved with conventional polymer technology when no clays are involved. The possible consistency in dewatering will translate to overall better plant performance, a significant risk reduction associated with plant performance and associated with the storage of filtered tailings

4 ECONOMIC ASSESSMENT EXAMPLE – LARGE PORPHYRY COPPER OPERATION

4.1 *Introduction*

The case study selected for the evaluation of the new technology is a typical large (100,000 MTPD) porphyry copper installation such as is typical in Chile with desalination of seawater at the coast, pumping of water to a concentrator at elevation. Basis of the comparison is the deposition of filtered tailings. Conventional tailings dewatering economics are compared to the TNS™ technology for various clay contents in the plant feed. The dewatering performance values were drawn from EPS' test work database.

4.2 *Scope*

To ensure a true apple-to-apple comparison the scope includes desalination at the coast, pumping of water to site, and filter dewatering of tailings (industry best available technology for safe storage of tailings). As a higher fraction of the process water is recycled this can create a challenge at the mine side, which might require separate attention.

4.3 *Design Criteria*

The general design criteria framing the economic comparisons are presented in Table 1:

Table 1: General Design Criteria

Case	Parameter
Pay-metal	Copper
Ore Clay Content	Variable
Intake Water Type	Sea Water
Plant Location from the Coast (km)	100
Elevation (masl)	3,000
Tailings Storage Method	Filtered
Nominal Plant Throughput (MTPD)	100,000
Head Grade (% Cu)	0.65
Life-Of-Mine (years)	20
Plant Availability (%)	92
Cost of Money (%)	0
Escalation (%)	0
Electricity Price (USD/kWh)	0.100

The variable of interest, as it has the greatest impact on the dewatering of the tailings, is the clay in feed. Two criteria were used as guidelines to classify the clay concentration in feed, a clay content range and the 2 μm particle size fraction which often contains much of the clay. Values for the clay concentration in the feed guidelines are provided in Table 2.

It is important to note that these clay values represent the steady-state average feed condition and thereby provided the upper bound for the basis of design.

Table 2: Clay Category Definitions

Clay Category	Clay Concentration Minimum	Clay Concentration Maximum	Passing 2 μm Maximum
No-Clay	2%	7%	0.3%
Low-Clay	7%	20%	1.7%
Medium-Clay	20%	35%	7%
High-Clay	35%	60%	31%
Extreme-Clay	60%	100%	80%

Table 3 to Table 6 provide a summary of the most salient comparative dewatering design parameters for the best conventional polymer technology as well as TNS™ configuration for each clay content category. In the case of thickening these criteria are based directly on test work results. In the case of filtration, the presented criteria are a mixture of test work results, but also effective average filtration rates computed from the combination of test work results combined with the filter equipment configuration chosen for the assessment.

As expected, the higher the active clay concentration, the worse the dewatering rates and achievable moisture content become. In the case of the extreme clay scenario, no conventional technical solution exists.

Many criteria are not listed for clarity of the paper. Among these are criteria for water treatment, water pumping, reagent dosages, thickener feed solids concentrations, suspended solids in supernatant and filtrates, assumed solids dissolution rates, tailings and storage water recovery, among others.

Table 3: Input Criteria – High-Density Thickener Solids Loading Rate ((t/h)/m²)

No-Clay		Low-Clay		Medium-Clay		High-Clay		Extreme-Clay	
Conventional	TNS™	Conventional	TNS™	Conventional	TNS™	Conventional	TNS™	Conventional	TNS™
0.6	6.0	0.47	4.7	0.35	3.5	0.2	2.0	0.05	0.35

Table 4: Input Criteria - Thickener Underflow Solids Concentration (%m)

No-Clay		Low-Clay		Medium-Clay		High-Clay		Extreme-Clay	
Conventional	TNS™	Conventional	TNS™	Conventional	TNS™	Conventional	TNS™	Conventional	TNS™
64%	68%	61%	65%	55%	59%	40%	50%	16%	35%

Table 5: Input Criteria – Effective Average Filtration Rate ((t/h)/m²)

No-Clay		Low-Clay		Medium-Clay		High-Clay		Extreme-Clay	
Conventional	TNS™	Conventional	TNS™	Conventional	TNS™	Conventional	TNS™	Conventional	TNS™
0.281	0.281	0.200	0.254	0.144	0.217	0.054	0.120	-	0.080

Table 6: Input Criteria – Filter Cake Moisture Concentration (%m)

No-Clay		Low-Clay		Medium-Clay		High-Clay		Extreme-Clay	
Conventional	TNS™	Conventional	TNS™	Conventional	TNS™	Conventional	TNS™	Conventional	TNS™
12%	12%	14%	14%	20%	16%	36%	22%	-	36%

4.4 *Results*

The most important results are summarized in Table 7 and Figure 4. Table 7 provides insight into most significant changes in capacities of streams or equipment.

Table 7: Summary of Major Equipment Differences

Clay Content Case	No-Clay	Low-Clay	Medium-Clay	High-Clay
Fresh Sea Water Desalination	77 m³/h	-183 m³/h	-459 m³/h	-2,464 m³/h
Fresh Water Pumping	37 m³/h	-88 m³/h	-220 m³/h	-1,181 m³/h
Fresh Water Pipeline	12" ⦰ → 12" ⦰	14" ⦰ → 14" ⦰	18" ⦰ → 16" ⦰	26" ⦰ → 18" ⦰
Thickening	2 x 69 m ⦰ → 1x 31 m ⦰	3 x 64 m ⦰ → 1x 35 m ⦰	4 x 64 m ⦰ → 1x 40 m ⦰	5 x 75 m ⦰ → 1x 53 m ⦰
Filtration	12x 2,200 m² → 12x 2,200 m²	17x 2,200 m² → 13x 2,200 m²	22x 2,200 m² → 15x 2,200 m²	59x 2,200 m² → 26x 2,200 m²
Recycle Water Management	+4,290 m³/h	+4,230 m³/h	+4,600 m³/h	+5,900 m³/h

Figure 4 provides a graphical comparison of the costs captured within the scope of this study. Apart from the lack of a technical solution for the conventional extreme-clay case, it should be noted that the conventional high-clay case is not economically feasible and in fact even the conventional medium-clay filtered tailings application is considered too risky currently.

As shown, the implementation of the TNS™ technology becomes more beneficial compared to conventional dewatering technology, the higher the design content of clay in the plant feed.

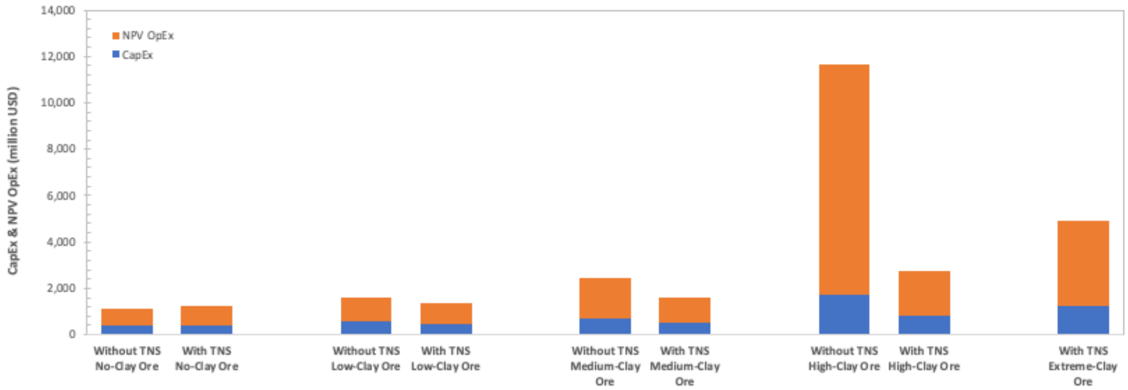

Figure 4: Comparative Capital and Net Present Value Operating Cost Values

4.5 *Risk Reduction*

The results of section 4.4 provide comparative numbers for varying clay in feed at pre-defined values in which the dewatering effort is geared to the pre-defined design level of clay found in tailings. Convention dewatering technology is known to fail when clay in feed exceeds the pre-defined design levels due to variability in feed. TNS™ will provide reliable dewatering performance regardless with minimal loss in performance. This means that geo-stable tailings storage can be achieved at much lower risk by utilizing TNS™.

This robustness of the TNS™ technology regardless of clay variability potentially improves other plant performance indices such as plant availabilities and metal recoveries which are generally a function of consistency in plant operation and by that are coupled to much larger returns for mining operations. TNS™ ensures clean recycle process water, continued and normal thickening and filtration even during high-clay excursions above pre-defined design values. Figure 5 and Figure 6 show the inherent value in consistent plant performance in terms of potential improvement in plant availability and metal recovery which can be unlocked using TNS™.

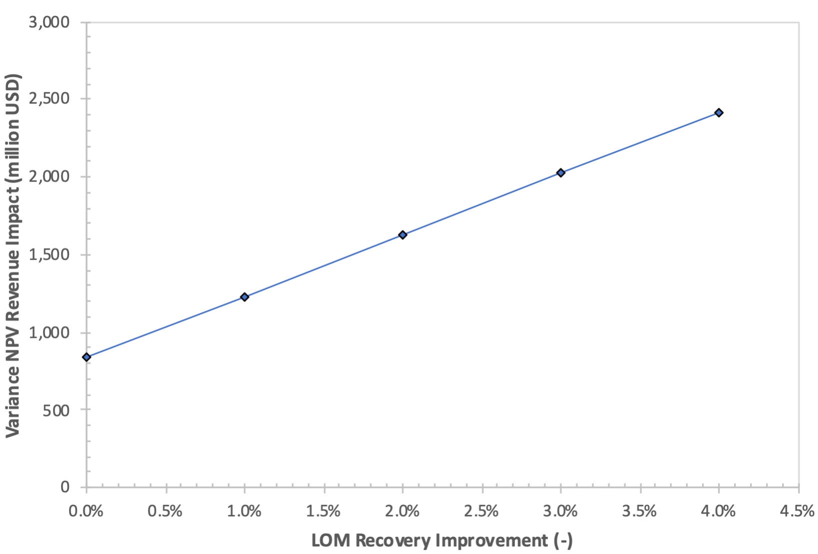

Figure 5: Impact of LOM Recovery Improvement

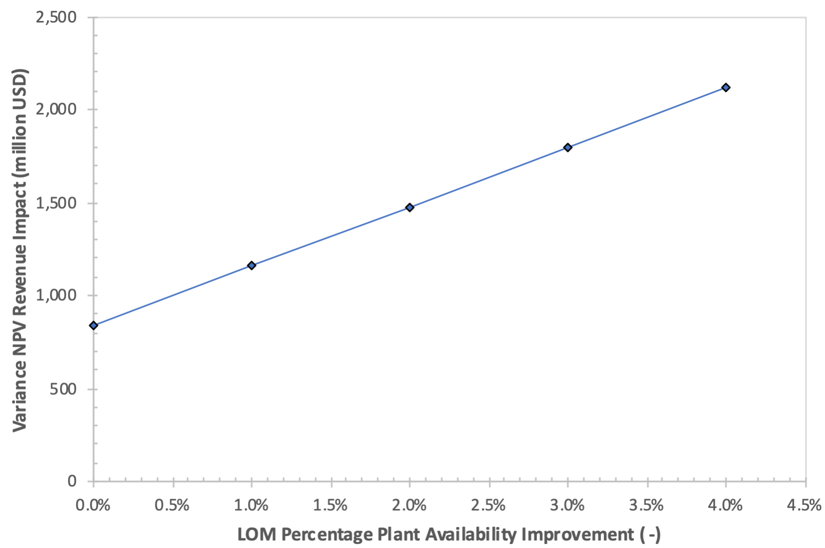

Figure 6: Impact of LOM Plant Availability Improvement

5 CONCLUSION

The benefit nexus of filtered tailings is now achievable regardless of tailings mineralogy. The TNS™ technology makes possible the reduction of fresh-water intake through improved water recovery while also reducing the tailings storage risk through potential liquefaction.

The TNS™ technology not only reduces the capital and operating cost for dewatering of tailings by filtration, but in some cases makes filtration possible where up till now no technical and/or feasible filtration solution has been possible.

The robustness of the TNS™ technology ensures that even with variability in mineralogy, a consistent dewatering performance is achieved. The resulting consistent plant operation will translate to potentially improved metal recoveries and higher plant availabilities, all of which are financially significant to the operator.

A large database of confirmatory test results compiled over the last few years makes a good case for TNS™.

6 REFERENCES

Abdulnabi, A, Sego, D., Beier, N., and Kabwe, L. 2019. Extrakt Copper Tailings Characterization Results Summary. Confidential Report to Extrakt Process Solutions LLC.

International Council on Mining & M (ICMM), 2021. Tailing Management – Good Practice Guide, 128p.

Recent developments in understanding leakage for geomembrane-lined tailings storage facilities

Alan Chou
BGC Engineering, Vancouver, British Columbia, Canada

Prabeen Joshi
Layfield Group, Richmond, British Columbia, Canada

ABSTRACT: Geomembrane liners have been used to line impoundments of Tailings Storage Facilities (TSFs) as a hydraulic barrier to limit outward seepage. Research in landfills has shown that leakage through geomembranes is governed by the presence of defects and wrinkles. It is anticipated that these features would govern leakage of geomembranes in the TSF setting. However, the process of leakage through geomembrane defects when tailings overlie the defects is less well-understood. This paper summarizes recent studies on the topic of leakage through geomembrane liners with a focus on TSF applications. These recent studies suggest that leakage through geomembrane holes that underlie tailings generally follow Darcy's law. However, designers should consider stress and filter-compatibility conditions at the geomembrane contact interfaces. A design example is presented utilizing findings from the recent studies.

1 INTRODUCTION

There are undeniably many applications for geosynthetics in the mining industry. Aside from having the obvious advantage of being a homogeneous engineered material, geosynthetics are versatile, widely available, cost effective, and quickly installed. They are most certainly a useful tool to keep in the mine waste management toolbox.

The use of geomembranes to line impoundments of TSFs, though generally less common than at heap leaches or ponds, has been practiced since the 1980s, possibly earlier. Typically, geomembranes become more economical for TSF lining when there is a lack of volume or ability to produce low permeability earth fill onsite. In these cases, the geomembrane liner may be used to achieve at least one of the following design criteria:

- Limiting seepage to some allowable rate to limit contaminant release into the downstream environment;
- Controlling phreatic surface downstream of the geomembrane to achieve adequate geotechnical stability against failure at impoundments; and
- Keeping tailings submerged.

All of these criteria rely on the geomembrane being fairly intact - that is free of significant defects throughout the service life of the facility. This warrants consideration of the following:

- Construction practices (e.g. handling, placement, seaming, overliner fill placement);
- Built-in stresses (e.g. temperature change from installation to coverage, consolidation, wrinkles, subgrade undulations); and
- Exposure conditions (e.g. time to depletion of antioxidant package and possible mechanical failure).

Mine waste applications can pose harsh environments for geomembrane liners from a loading perspective. Both dead and live loads can be quite large (in the region of MPa's). The practice of preparing a cushioning layer that would be standard at landfills is often cost prohibitive due to the large footprint of mine waste facilities. Moreover, a large portion of the geomembrane may not be covered for an extended period of time.

In Steven G. Vicks' 1990 textbook on Planning, Design, and Analysis of Tailings Dams, he wrote "...some seepage can be expected through membrane liners but that quantity is difficult or impossible to predict. Perhaps it is this lack of predictive methods that lead to the misleading application of such terms as 'impervious' to membrane liners". Since the publication of this textbook, significant strides have been made to better understand leakage through geomembrane liners and more recently specifically for tailings applications. The objective of this paper is to summarize some of these efforts and show how designers can use research findings in TSF design. A design example is also discussed.

2 FIELD OCCURANCE OF DEFECTS

Even in optimal construction and operation conditions, it is widely agreed that installed geomembranes contain physical defects throughout the service life of a containment facility (Giroud & Bonaparte 1989, Rowe 2020). Therefore, it has become general practice to account for some defects in design. The goal is to keep defect numbers as low as reasonably achievable throughout the operational life of the facility.

Based on a review of published Electrical Leak Location (ELL) surveys for landfills (Needham et al., 2004), the majority of defects occur during installation/seaming and placement of overliner fill. In a study of over 300 sites in 16 countries covering more than 3.2 km^2, over 70% of geomembrane damage was caused by overliner fill placement puncture (Nosko & Touze-Foltz, 2000). This is of particular concern if drainage gravels are placed over the geomembrane without adequate protection (Brachman and Gudina, 2008). Summaries of the location, size and causes of the defects are shown in Table 1 and Table 2.

Table 1. Location and causes of geomembrane defects (Adopted from Nosko & Touze-Foltz, 2000).

Location	Frequency of defect by location	Cause of defect				
		Stones	Heavy equipment	Worker	Cuts	Welds
Flat floor	78%	81%	13.2%	4%	1%	0.8%
Corner, edge, etc.	9%	59.2%	18.9%	3.5%	0.9%	17.5%
Underdrainage pipe	4%	30.3%	14.3%	14.5%	13.7%	27.2%
Pipe Penetration	2%	0%	0%	8.5%	0.6%	90.9%
Other	7%	20.6%	19.3%	19.3%	0%	16.7%

Table 2. Size and causes of geomembrane defects (Adopted from Nosko & Touze-Foltz 2000).

Size of Defect	% of Total	Cause of defect				
		Stones	Heavy equipment	Worker	Cuts	Welds
< 0.5 cm^2	10.8%	11.1%	-	-	8.5%	43.4%
0.5-2.0 cm^2	50.0%	57.6%	6.3%	84.4%	61.0%	39.6%
2.0-10 cm^2	24.9%	28.2%	17.9%	15.6%	30.5%	11.3%
> 10 cm^2	14.3%	3.0%	75.8%	-	-	5.7%

The frequency of defects found in the above study is approximately 13/hectare with a median hole size of approximately 1 cm^2. Two other ELL studies performed on sites without overliner fill placement suggest a defect frequency of around 2/hectare (Phanuef & Peggs, 2001, Rollin et al., 1999). Rigorous Construction Quality Assurance (CQA) programs for geomembrane installations is effective at reducing defect frequency (Forget et al., 2005, see Table 3).

Table 3. Number of leaks from ELL surveys (adopted from Forget et al., 2005).

Geomembrane thickness	Leaks/ha in exposed HDPE		Leaks/ha in covered HDPE	
	With CQA	Without CQA	With CQA	Without CQA
2.0 mm	3.2	-	0.2	15.6
1.5 mm	5.1	-	-	24.7
1.0 mm	20.5	31.5	-	-

Note: ha – Hectare; HDPE – High Density Polyethylene

These studies highlight that that holes will likely exist after installation, and the hole frequency can be a factor of geomembrane thickness and whether a CQA program is in place.

An additional consideration is the location of these holes relative to other geometric imperfections in the installed geomembrane. The installed geomembranes (especially HDPE) are also likely to have wrinkles. The wrinkles develop due to a high coefficient of expansion of the material.

As a flatly deployed geomembrane heats up during the day, it expands linearly and "buckles" at areas where the subgrade is in poor contact (typically along seams or creases made during manufacturing or shipping). When the geomembrane contracts at night, it may not return to the exact same state prior to thermal expansion. Multiple expansion and contraction cycles can cause preferential growth of wrinkles in certain areas where geometric irregularity exists. Wrinkles tend to accumulate in places like the toe of slopes (see Figure 1a). These wrinkles have the potential to grow to the point where they can fold over when covered, or simply on their own weight.

Figure 1a (left). Photo of a 16 cm tall wrinkle at the toe of a slope (Photo: Alan Chou). Figure 1b (right). Aerial photo showing connected wrinkles in a smooth HDPE geomembrane (Rowe, 2012).

Wrinkles can develop in continuous patterns (seams and creases on virgin geomembrane tend to be continuous). A drone photo from a field test site of exposed HDPE geomembrane in Ontario is shown in Figure 1b.

In this particular study, the wrinkles were interconnected and covered 30% of the liner surface at the warmest part of the day. In covered applications, smaller wrinkles (< 20 mm in height) go away once they become buried by lower temperature overliner fill (Waud, 2015). However, if larger wrinkles develop, these wrinkles likely remain after coverage. Rowe (2012) postulated that when there is a significant number of wrinkles forming a network as shown in Figure 1b, leakage flowing through geomembrane defects can enter the network of void space created by the wrinkles. This leakage mechanism can explain large leakage rates observed at some landfills.

Despite the fact that wrinkles induce poor contact between the geomembrane and subsoil (therefore facilitate leakage), burial of small wrinkles is commonly accepted practice in North America. It is usually impractical to try to control an installation to the point where near perfect contact can be achieved, though some costly techniques have been practiced at German landfills (Seeger & Muelle, 1996).

The studies referred to above provide an indication of hole size and frequency after coverage depending on the application and quality of installation. Another design question that needs to be answered is how much leakage takes place at these defects when they are progressively covered by tailings.

3 LARGE SCALE PHYSICAL TESTING

To observe the effects of leakage around an idealized defect, a large-scale testing apparatus called Geosynthetic Liner Longevity Simulator (GLLS) was developed by the Geo-Engineering Centre out of Queen's University in Ontario (Figure 2).

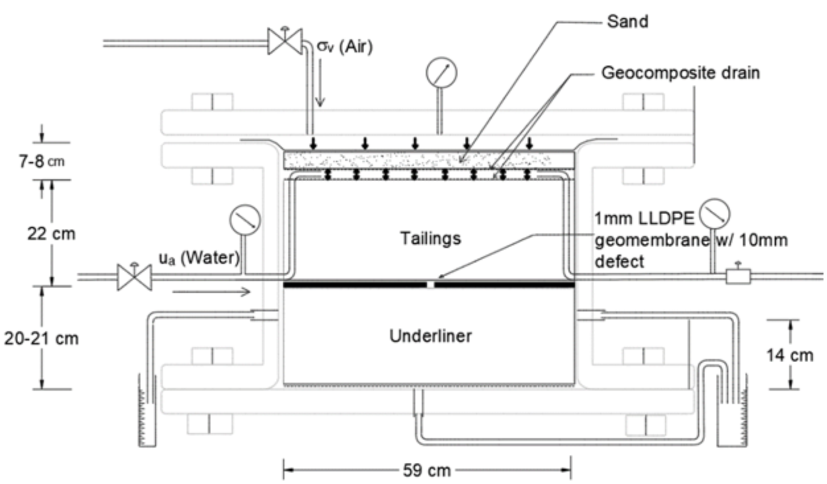

Figure 2. Geosynthetic Liner Longevity Simulator apparatus used by Chou et al. (2018).

The GLLS is essentially a large rigid wall permeameter in which the vertical total stress can be controlled independently from the pore pressure at the top of the permeameter. The permeameter is comprised of a 0.5 m long, 0.6 m dia. section of stainless-steel pipe sealed by blind flanges on both ends. Ports drilled through the flange plates and pipe wall allowed plumbing attachments (gauges, valves, regulators, etc.). These attachments facilitate independent control of boundary conditions which define the steady state conditions in the cell.

Joshi et al. (2016), Rowe et al. (2016), and Chou et al. (2018) all looked at the leakage phenomenon of a silty sand tailings from a copper-molybdenum mine from British Columbia, Canada overlying an HDPE/LLDPE[1] geomembrane with an idealized circular hole. Their results from tests performed with a 1-cm-diameter circular hole are summarized in Table 4.

Table 4. Summary of the tests performed by Joshi et al. (2016), Rowe et al. (2016), and Chou et al. (2018) with a 1 cm diameter circular hole.

Underliner	D_{u15}/D_{t85}	σ_v (kPa)	μ (kPa)	σ_v' (kPa)	Q (L/day)	Reference
Silty Sand	0.06	250-1000	200-500	50-500	3-9	Joshi et al. (2016)
Gravel	18.5	3000	1,500	1500	>2000	Rowe et al. (2016)

[1] LLDPE – Linear Low-Density Polyethylene

Geotextile	N/A	250-3000	250-1500	50-1500	1-7	Rowe et al. (2016)
Silty Sand	0.06	250-3000	250-1500	50-1500	1-7	Rowe et al. (2016)
Gravel	5.6	36-530	30-350	6-180	10-970	Chou et al. (2018)
Gravel	7.6	36-530	30-350	6-180	4-1040	Chou et al. (2018)
Gravel	13.5	36-530	30-350	6-180	10->2000	Chou et al. (2018)

Note: D_{u15} – particle diameter at which 15% of the underliner mass is less than, D_{t85} – particle diameter at which 85% of the tailings mass is less than, σ_v – total vertical stress, μ – pore pressure at top of tailings, σ_v' – vertical effective stress, Q – leakage flow.

Chou et al. (2020) and Fan and Rowe (2021) performed similar tests on a thickened fine-grained (approx. 90% fines) tailings from a copper-zinc mine. Their results are summarized in Table 5 below for tests performed with a 1-cm-diameter circular hole.

Table 5. Summary of the tests performed by Chou et al. (2020) and Fan and Rowe (2021) with a 1 cm diameter circular hole.

Underliner	D_{u15}/D_{t85}	σ_v (kPa)	μ (kPa)	σ_v' (kPa)	Q (L/day)	Reference
Sand	1.5	210-1000	200-800	10-200	1-4	Chou et al. (2020)
Gravel (SP)	14	66-900	60-720	6-180	1-5	Fan and Rowe (2021)
Gravel (GP)	92	66-900	60-720	6-180	2-4	Fan and Rowe (2021)

Note: D_{u15} – particle diameter at which 15% of the underliner mass is less than, D_{t85} – particle diameter at which 85% of the tailings mass is less than, σ_v – total vertical stress, μ – pore pressure at top of tailings, σ_v' – vertical effective stress, Q – leakage flow.

Due to slurry deposition of the tailings, it was observed in the tests that defects and wrinkles generally become infilled with tailings. For the cases where the tailings were filter compatible with the underliner, infilled tailings effectively formed a seal at the defects and fill the voids under the wrinkles (see Figure 3a). The leakage rates observed in the GLLS tests from these defects are typically smaller than those estimated using numerical modeling and established analytical solutions (Rowe et. al, 2016, Badu-Tweneboah & Giroud, 2018; Fan and Rowe, 2021).

The exception appears to be when the underliner is not filter compatible with the tailings, as observed by Chou et al. (2018). This was not observed with fine-grained tailings because the fine-grained tailings appeared to seal off the hole even with filter incompatibility, as observed by Fan and Rowe (2021). Under the conditions observed by Chou et al. (2018), the tailings continued to pipe into the underliner, eroding voids in the deposited mass in the process (Figure 3b). This process appeared to be dependent on the size of void space in the transmissive zone between the geomembrane and underliner materials. The larger the voids in this zone, the more tailings were needed to infill the zone. If the infilled tailings became mobile in the underliner due to filter-incompatibility and a sufficiently large gradient in the underliner, a continually eroding condition resulted in the tests.

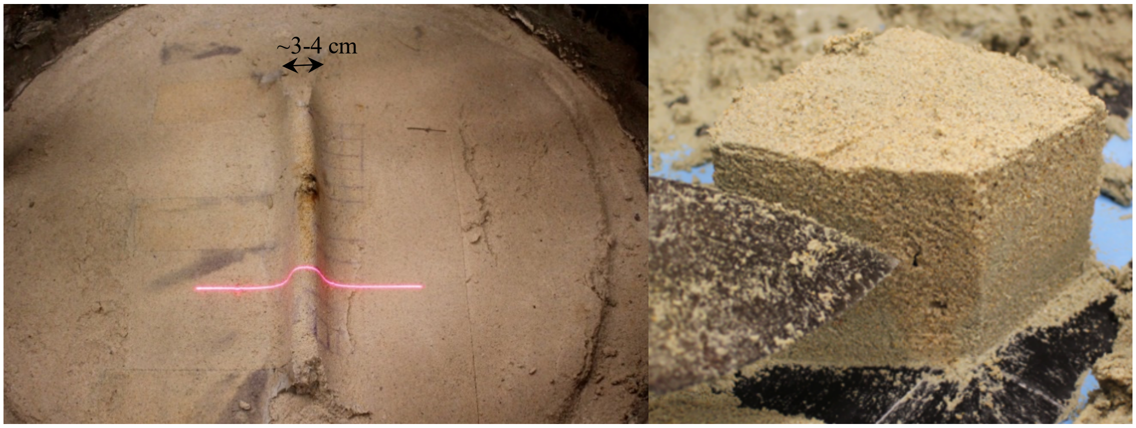

Figure 3a (left). Photograph showing migrated tailings into the underliner beneath a deformed geomembrane wrinkle with a 1 cm diameter hole (Joshi et al., 2016). Figure 3b (right). Example of voids near a geomembrane defect under filter-incompatible testing conditions (Chou et al. 2018).

This piping condition was found to be most severe when combined with low effective vertical stress conditions in the tailings that may take place during initial stages of deposition. From lab observations, it appears that piping eventually ceased (flow rates stabilized) at higher stress levels for less severe filter-incompatible conditions, likely due to reduction of voids space in transmissive zone under higher stresses, but the leakage rates remained much higher than if piping did not take place. It is postulated that the void created in the tailings over the liner during piping remained open due to bridging and resulted in the much large seepage rates (Darcy's Law was no longer valid along the flow path). However, it is possible that once significantly more tailings are deposited over top of this piped layer, the void would collapse and the leakage flow rate will no longer be governed by the piped layer. This remains to be seen in laboratory testing.

4 AN ILLUSTRATIVE DESIGN EXAMPLE

A design example of a 1.5 mm HDPE geomembrane intended to control the phreatic surface within a 500-m long, 50-m tall tailings dam is discussed in this section. A 2-dimentional seepage model was constructed in SEEP W/© to estimate the effects of the liner on the phreatic surface. The following seepage scenarios were analyzed as part of the assessment:

- Scenario 1 - No liner
- Scenario 2 - Liner with fair CQA
- Scenario 3 - Liner with good CQA
- Scenario 4 - Liner is at end of service life

The cross section modelled is shown in Figure 4.

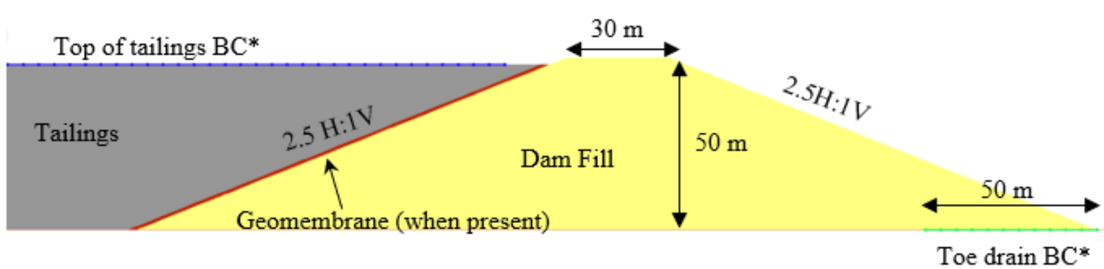

*BC – Boundary Condition

Figure 4. Dam section analyzed for the design example showing materials and the boundary conditions.

The tailings dam has an upstream and downstream slope of 2.5H:1V, a crest width of 30 m, and a toe drain extending 50 m into the dam fill. The geomembrane liner (when present) is on the

upstream slope of the dam. The foundation material was not considered in the model for simplicity (no flow can occur at the bottom of the tailings and dam).
The hydraulic properties of modelled materials are presented Table 6, and the boundary conditions are presented in Table 7.

Table 6. Materials parameters used in SEEP W/ model

Material	Material Type	Saturated Hydraulic Conductivity (k)
Tailings	Saturated	1 x 10^{-7} m/s
Dam Fill	Saturated/Unsaturated*	1 x 10^{-6} m/s
Geomembrane	Saturated	Scenario 1 – same as Tailings (i.e. no liner) Scenario 2 – 2 x 10^{-11} m/s Scenario 3 – 4 x 10^{-12} m/s Scenario 4a – 3 x 10^{-10} m/s Scenario 4b – Scenario 2 with discontinuities

*Unsaturated properties were modelled using SEEP W/ built-in sample volumetric water content function for Silty Sand and hydraulic conductivity function estimated using equations proposed by Fredlund and Xing (1994).

Table 7. Boundary conditions used in SEEP W/ model

Boundary Condition (BC)	BC Type	Value	Representation
Top of tailings BC	Pressure Head	0 m	Active deposition on tailings beach
Toe drain BC	Pressure Head	0 m	Free-draining material relative to Dam Fill

Notes: 1. No recharge is considered in the model
2. No flow is permitted to enter or exit the model except at the zero-pressure boundary condition locations.

For Scenario 1, the geomembrane was not modelled. For Scenarios 2-4b, the geomembrane was modelled using an equivalent hydraulic conductivity (k) for a 1 m-thick layer using calculated leakage rates (similar approaches were adopted by La Touche and Garrick, 2012 and Garrick et al. 2014). In this approach, the leakage rate for a single design circular defect (using median defect area of 1 cm^2 as observed by Nosko & Touze-Foltz, 2000) was first estimated using the simple analytical equation presented by Wissa and Hufeilan (1992), which has shown to overestimate leakage observed in GLLS tests when tailings are in direct contact with the liner (Badu-Tweneboah and Giroud, 2018; Fan and Rowe 2021). Then, the leakage rate was multiplied by the anticipated number of holes expected to be present. This estimate is a judgement dependent on quality of installation and level of CQA. For Scenario 3 (good installation and CQA), 13 holes/hectare were assumed based on findings from Nosko & Touze-Foltz (2000), recognizing this is a conservative assumption because without overliner fill placement, others have recommended 2-5 holes/hectare (Phanuef & Peggs 2001, Rollin et al. 1999; Giroud and Bonaparte, 2001). The estimated total leakage was then used to back-calculate an equivalent k of the geomembrane using the finite element model.

It is noted that the following assumptions are made when this approach is taken:

- Interaction between holes are ignored. In the field, the appearance of holes tends to have some pattern of occurrence and may overlap.
- Some level of CQA is carried out such that holes exceeding 1 cm^2 in size are observed and repaired (heavy equipment damage is prevented).
- Piping of tailings through the geomembrane and underliner does not take place (hole is filled in by tailings and no further movement of tailings takes place).

- For the analytical equation used to estimate leakage, the acting head along the slope is taken to be the same as the head at the base (leakage rates are overestimated).

For Scenario 2 (fair CQA), it is assumed that the number of design defects increase by 5-fold from Scenario 3 (good CQA), based on findings from Forget et al. (2005). The resulting equivalent liner k also increased by a factor of 5, reflecting linearity of Darcy's law under the modelled conditions.

For Scenario 4a and 4b, it was assumed that the service life of the geomembrane is reached during operation, rather than post-closure, which would likely have a different boundary condition on top of the tailings., Presently, there is very little basis on which estimates of defect size and numbers can be made for end of service life of the geomembrane. If the geomembrane is subject to large total and confining stresses at the end of its service life, there is some uncertainty as to how wide the degraded geomembrane would be able to "open up". It is a question requiring more time and research effort. Conceptually, it is understood that cracks may form first around stress concentrations (e.g. wrinkles and crest of benches) and heat-effect areas at the welds. More defects may appear as the antioxidants in the geomembrane are lost over time and polymers breakdown and lose their mechanical properties. However, the timing for this to happen is difficult to predict as it also depends on a number of factors that may be outside of the control of the designer (e.g. performance of antioxidant package with changing tailings chemistry, geomembrane resin, length of exposure of geomembrane prior to coverage by tailings).

The UK Environmental Agency attempted to address the issue of leakage at the end of service life and suggested increasing the number and size of defects as the geomembrane undergoes various stages of degradation (Needham et al., 2004). They proposed (with little basis) crack sizes of 0.1 cm^2 and 10 cm^2 be considered for the end of service life, and that an additional 30-240 defects/hectare be considered for the smaller crack, and 60-110 for the larger crack. Assuming these defects are circular, a similar leakage estimate can be made, and an equivalent k can be back-calculated using the same method as for Scenario 2 and 3. This effectively increases the number of defects to 363-415 per hectare (6 to 32-fold increase from operating conditions). The 415 holes/hectare scenario is modelled in Scenario 4a.

Aside from increasing the total number of defects per area, the mechanism of defects should be considered for the end of service life scenario. Depending on the presence and location of seams that may experience shear stresses due to tailings consolidation and foundation settlement, it may be prudent to conceptualize a scenario in which longitudinal cracks form at these stress-concentrated, continuous locations (e.g. crest of upstream benches). In Scenario 4b, 1 m-wide gaps were included at 3 locations (representing 10-m tall bench locations) in a Scenario 2 equivalent k geomembrane. It is recognized that a scenario with three 1-m gaps is extreme and for illustration only as there are likely more critical issues than seepage if three 1-m movements have taken place.

The model results are shown in Figure 5.

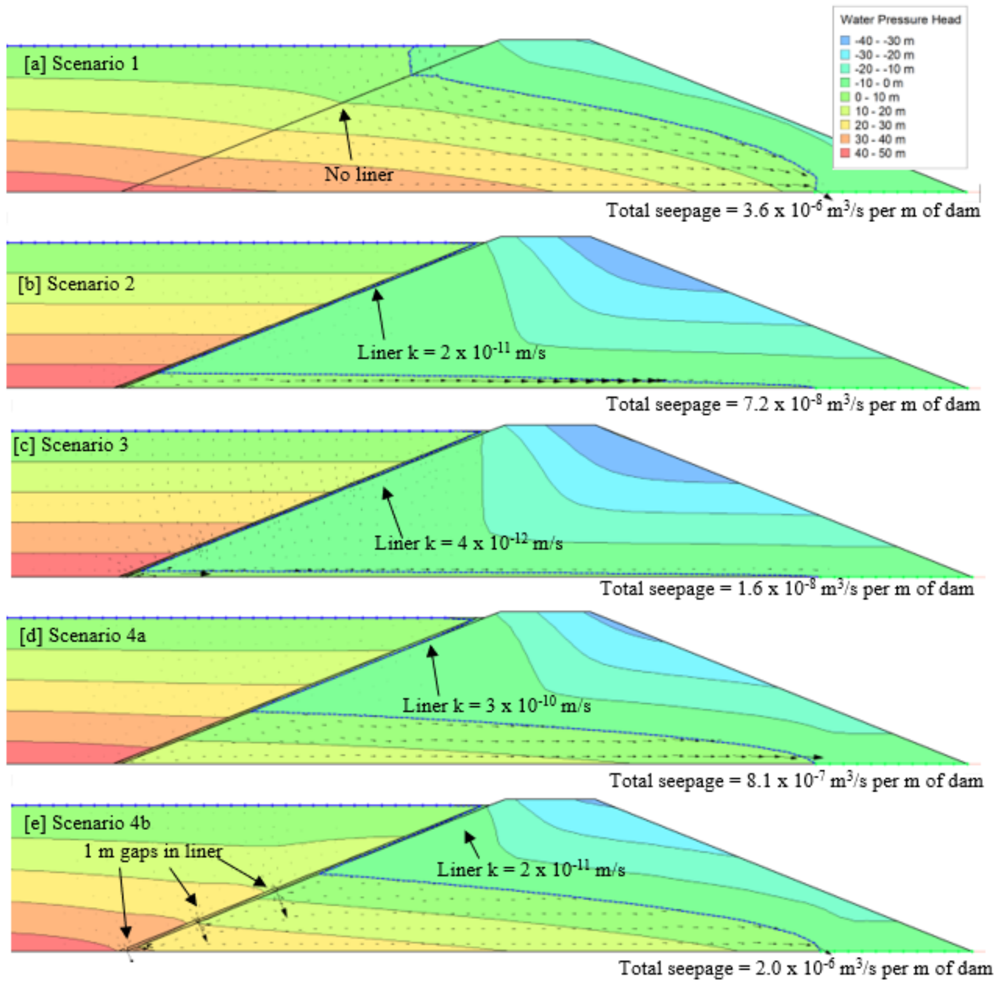

Figure 5. Dam section analyzed for the design example showing materials and the boundary conditions.

The results suggest that with fair to good installation quality and CQA for the 1.5 mm HDPE geomembrane, seepage through the dam for the modelled configuration should result in a significant reduction in the phreatic surface and seepage compared to the case where the dam is not lined. However, the result at the end of geomembrane service life has more uncertainty. Results from Scenarios 4a and 4b arguably illustrate worst case conditions around which a monitoring and action plan could be developed. It takes time for steady-state seepage conditions to develop, and with sufficient monitoring (e.g. pore pressure monitoring and potentially strain monitoring at key geomembrane locations), the effects of potential additional defects at the end of geomembrane service life could be observed well ahead of full development of the higher phreatic surfaces suggested by the seepage model.

5 SUMMARY AND CONCLUSION

A series of field and laboratory studies have expanded our understanding of leakage through geomembranes. The studies suggest that the geomembranes can be effective hydraulic barriers at tailings facilities. However, several design considerations can be drawn from these studies:

- Defects will likely be present during the service life of a geomembrane at a lined tailings facility.
- The number and size of defects will depend on the environment the geomembrane is subjected to during construction and operation and effort of Construction Quality Assurance (CQA).
- The most commonly observed field defect size is between 0.5 ~ 2.0 cm^2.
- Overliner fill placement is likely a large contributing factor to construction defects.

– Defects may interact with wrinkles due to the impracticality of controlling timing of backfilling. However the wrinkles will likely be filled with tailings.
– Slurry deposition of tailings may reduce the void space in a transmissive zone between the geomembrane and underliner material by filling in this void space with tailings. This has the potential to limit leakage.
– If the tailings are filter compatible with the underliner, flow through the defect is generally observed to be governed by defect hole geometry and hydraulic conductivity of the tailings near the hole. Flow rates estimated using numerical modelling and analytical solutions generally provide higher estimates than observed in lab tests.
– Failure to provide filter-compatible conditions may promote piping of tailings through the defect and much higher leakage than predicted using Darcy's law. The potential for piping to develop appears to be stress-dependent. Fine-grained tailings having low plasticity do not appear to experience as much piping as coarser-grained tailing.
– A SEEP W/ design example was presented to demonstrate how geomembrane performance can be considered in design using recent developments.
– There is much uncertainty associated with leakage after the service life of a geomembrane is exceeded. A monitoring and action plan approach should be considered in design.

Though we have come a long way in understanding leakage phenomenon around geomembrane defects for tailings applications, there is still much to be learned about performance of geomembranes at TSFs. Specifically the following topics remain to be explored in more detail:

- long-term performance/leakage of liners at TSFs
- performance of different types of liners (most of the work has been on LLDPE/HDPE)
- effects of cold weather installation
- down-drag effects/stress concentrations due to tailings consolidation on slopes

In addition to laboratory tests, publication of long-term monitoring data at geomembrane-lined facilities is also a key piece of data that can help increase the confidence of designers when considering geomembrane as an economical option as a hydraulic barrier.

Finally, it is iterated that the method presented in this paper should not replace engineering judgement when selecting a method to estimate the hydraulic performance of the geomembrane liner. Depending on the design question and consequence of leakage, the scenarios a designer may look at may be different from those presented in this paper. For example, the designer may adopt higher leakage scenarios for evaluating toe drain size, pumping needs for seepage, or a closure scenario in which boundary conditions are infiltration-based and the liner is at the end of its service life. The estimated performance of a liner also has water balance implications that has been left out of this discussion.

6 ACKNOWLEDGEMENTS

The authors would like to thank the GeoEngineering research team at Queen's University, Kingston Ontario, Klohn Crippen Berger Ltd. , and Golder Associates Ltd. for their ongoing dedication to geomembrane research for TSF application, as well as BGC Engineering Ltd. and Layfield Group for supporting our effort in writing this paper.

7 REFERENCES

Badu-Tweneboah, K., and Giroud, J.P. (2018). Discussion of "Leakage through Holes in Geomembranes below Saturated Tailings" by R.K. Rowe, P. Joshi, R.W.I. Brachman, and H. McLeod. Journal of Geotechnical and Geoenvironmental Engineering, 144(4):07018001-1–2.

Brachman, R. W. I., & Gudina, S. (2008). Gravel contacts and geomembrane strains for a GM/CCL composite liner. Geotextiles and Geomembranes, 26(6), 448-459.

Chou, Y. C., Rowe, R. K., & Brachman, R. W. (2018). Erosion of silty sand tailings through a geomembrane defect under filter incompatible conditions. Canadian Geotechnical Journal, 55(11), 1564-1576.

Chou, A., Brachman, R. W., & Rowe, R. K. (2021). Leakage through a hole in a geomembrane beneath a fine-grained tailings. Canadian Geotechnical Journal, https://doi.org/10.1139/cgj-2020-0289.

Needham, A., Gallagher, E., Peggs, I., Howe, G., & Norris, J. E. (2004). The likely medium to long term generation of defects in geomembrane liners. R&D Technical Report P1-500/1/TR.

Fan, J., & Rowe, R. K. (2021). Seepage through a Circular Geomembrane Hole when covered by Fine-Grained Tailings under Filter Incompatible Conditions. Canadian Geotechnical Journal, https://doi.org/10.1139/cgj-2020-0788.

Fredlund, D. G., & Xing, A. (1994). Equations for the soil-water characteristic curve. Canadian Geotechnical Journal, 31(4), 521-532.

Forget, B. Rollin, A. Jacquelin, T. (2005) Lessons Learned from 10 Years of Leak Detection Surveys on Geomembrane. Sardinia Symposium. Sardinia, Italy

Garrick, H., Digges La Touche, G., Plimmer, B., & Hybert, D. (2014, June). Assessing the hydraulic performance of tailings management facilities. In Proceedings of the 17th Extractive Industry Geology Conference. Extractive Industry Geology Conferences Ltd.

Giroud, J. P., & R. Bonaparte. (1989). Leakage through liners constructed with geomembranes—Part I: Geomembrane liners. Geotextile and Geomembrane 8(1): 27-67.

Giroud, J. P., & R. Bonaparte. (2001). Geosynthetics in liquid-containing structures. In Geotechnical and geoenvironmental engineering handbook. Kluwer Academic Publishing, Norwell, Mass. Pp. 789-824.

Joshi, P., Rowe, R. K., & Brachman, R. W. I. (2016). Physical and hydraulic response of geomembrane wrinkles underlying saturated fine tailings. Geosynthetics International, 24(1), 82-94.

La Touche, G. D., & Garrick, H. (2012, September). Hydraulic performance of liners in tailings management and heap leach facilities. In Proceedings of the International Mine Water Association Symposium, Bunbury, Australia (pp. 371-378).

Needham, A. Gallagher, E. Peggs, I. Howe, G. Norris, J. (2004, January). Likely Medium to Long-Term Generation of Defects in Geomembranes. Environment Agency. Rio House Waterside Drive, Aztec West. Almondsbury, Bristol. ISBN: 1-84432-180-0

Nosko, V. & Touze-Foltz, M (2000), Geomembrane Liner Failure. Proceedings to EuroGeo 2000. Bologna, Italy, pp. 557-560.

Phaneuf, R. & Peggs I. (2001). Landfill Construction Quality: Lessons Learned from Electrical Resistivity Testing of Geomembrane Liners. Geotechnical Fabrics Report, Vol. 19 No.3 pp,28-35.

Rollin, A. Marcotte, M. Jacquelin, T. Chaput, L. (1999). Leak Location in Exposed Geomembrane Liners Using an Electrical Leak Detection Technique. Proceedings to Geosynthetics Conf. 1999. Vol 2, pp.615-636

Rowe, K. (2012). Short- and Long-term Leakage Through Composite Liners. The 7th Arthur Casagrande Lecture. Canadian Geotechnical Journal. Issue 49: pp. 141-169

Rowe, R. K., Joshi, P., Brachman, R. W. I., & McLeod, H. (2016). Leakage through Holes in Geomembranes below Saturated Tailings. Journal of Geotechnical and Geoenvironmental Engineering, 143(2), 04016099.

Rowe, K. (2020). Protecting the Environment with Geosynthetics: 53rd Karl Terzaghi Lecture. Journal of Geotechnical and Geoenvironmental Engineering, 146(9), 04020081.

Rowe, R. K., Abdelaal, F. B., Zafari, M., Morsy, M. S., & Priyanto, D. G. (2020). An approach to high-density polyethylene (HDPE) geomembrane selection for challenging design requirements. Canadian Geotechnical Journal, 57(10), 1550-1565.

SEEP/W (Version 10.0.0.17401) [Computer software]. Calgary, Alberta: GEOSLOPE International, Ltd.

Vick, S. G. (1990). Planning, design, and analysis of tailings dams. BiTech Publishers.

Waud, R. (2015). Field-scale monitoring and laboratory simulation of geosynthetic liners during construction and after placement of waste. M.A.Sc. Thesis. Department of Civil Engineering, Queen's University, Kingston, Ontario.

Wissa, A.E.Z. and Fuleihan, N.F. (1992). Design and reclamation of phosphogypsum disposal sites. AIChE Spring National Meeting, Advances in Phosphate Fertilizer Technology, New Orleans, LA, 20.

Feasibility of bio-mediated carbonate precipitation for dust control at mine tailings facilities

Sean T. O'Donnell & Lucas de Melo
Geosyntec Consultants, Columbia, Maryland, USA

Lucas Carr
Geosyntec Consultants, St. Louis, Missouri, USA

Todd DeJournett
Geosyntec Consultants, Minneapolis, Minnesota, USA

Edward Kavazanjian Jr. & Hamed Khodadadi Tirkolaei
Arizona State University, Tempe, Arizona, USA

ABSTRACT: Microbially induced carbonate precipitation (MICP) and enzyme induced carbonate precipitation (EICP) offer the potential for effective short to long-term mitigation of windblown dust at mine tailings storage facilities (TSFs). Wind erosion of tailings is a significant challenge at many mine sites and must be controlled to comply with fugitive dust emissions requirements. Wind tunnel tests conducted on taconite and copper-molybdenum tailings specimens show that EICP-treated tailings exhibit resistance to wind erosion. Additionally, benchtop experiments with these tailings provide evidence that bacteria capable of catalyzing MICP may be present in some TSFs. A preliminary analysis comparing the cost and environmental impacts of these bio-mediated methods with other dust mitigation strategies, such as the application of polymer emulsions, salt solutions, paper pulping byproducts, and wood chip mulch, was used to identify specific obstacles to the field application of EICP and MICP as well as knowledge gaps where future research into these technologies may be required. Specific obstacles and knowledge gaps identified in this study include byproduct management from MICP and EICP, the availability of low-cost enzyme for EICP, and the longevity of the wind-resistant carbonate crust formed by MICP and EICP as compared with other short to long-term dust mitigation methods.

1 INTRODUCTION

Wind erosion of tailings is a serious issue at many mine sites that must be mitigated to comply with regulatory requirements, reduce potential impacts to human health and the environment, and avoid receiving negative feedback and perception from adjacent landowners and the general public. Wind erosion (and fugitive dust formation) at tailings facilities typically occurs due to desiccation in hot and dry climates or dry freezing in colder climates. Typical methods employed at tailings facilities to mitigate fugitive dust formation include management of the tailings basin water level to keep tailings saturated; application of salt solutions, polymers, or other short-term measures to suppress fugitive dust formation; and establishing vegetation for long-term stabilization of the tailings surface. However, each of these methods have limitations that make them undesirable, inapplicable, or non-cost-effective in some situations and at some tailings facilities. For example, managing the tailings basin water level to keep tailings saturated may work well at facilities in wet, warm climates where water is plentiful and freeze/thaw is not present, but could lead to operational challenges at facilities in dryer and/or cold climates. The water level can also not be kept so high that it destabilizes and/or reduces flood storage volume and the safe operation of the tailings facility. Further, short-term tailings stabilization techniques, such as polymer applications, salts, and mulches, have varying success rates for fugitive dust suppression, may lead to environmental impacts, and/or may be prohibitively expensive. Vegetation, while very effective at minimizing fugitive dust generation, may be difficult to establish in some climates and on some tailings, and may take multiple growing seasons to achieve full effectiveness. As such, new technologies are required to address the need for cost-effective, short-term, environmentally friendly fugitive dust mitigation at tailings facilities.

Two relatively new technologies with the potential for mitigating fugitive dust formation at tailings facilities are microbially induced carbonate precipitation (MICP) and enzyme-induced carbonate precipitation (EICP) (Meyer et al., 2011; Hamdan and Kavazanjian, 2016). MICP and EICP work by altering the geochemistry in an aqueous environment to favor the precipitation of carbonate minerals (e.g., by increasing pH and alkalinity). If formed on the tailings surface, these carbonate minerals could bridge surficial tailings particles to form a thin wind-resistant and potentially water-resistant crust. Although many biological processes can induce carbonate precipitation, the most studied process for MICP and EICP is ureolysis, catalyzed by the urease enzyme. Urease works by hydrolyzing urea ($CO(NH_2)_2$) into carbon dioxide and ammonia; in aqueous environments, the ammonia may speciate to form ammonium (NH_4^+), driving up the pH and facilitating the formation of carbonate minerals when suitable cations (e.g., calcium, Ca^{2+}) are also present. The net urease-catalyzed precipitation reaction for calcium carbonate ($CaCO_3$) is shown below.

$$CO(NH_2)_2 + 2H_2O + Ca^{2+} = CaC0_3 + 2NH_4^+ \quad (1)$$

The urease enzyme required to catalyze the ureolysis reaction may be produced by microbes (MICP) or isolated prior to treatment and added separately as a component of the treatment solution (EICP). MICP may be achieved using either non-native microbes added as part of treatment (Meyer et al., 2011), a technique known as bio-augmentation, or native microbes stimulated in-situ (Gomez et al., 2018), a technique referred to as bio-stimulation. EICP may be achieved using commercially available laboratory grade urease enzyme (Hamdan and Kavazanjian, 2016), or more cost-effective plant-derived urease extracts (Khodadai Tirkolaei et al., 2020).

Preliminary studies indicate that EICP and MICP are effective for mitigating fugitive dust formation from natural soils (Meyer et al., 2011; Hamdan and Kavazanjian, 2016). EICP has also shown promise for mitigating fugitive dust on at least one sample of mine tailings (Hamdan and Kavazanjian, 2016). However, applications of MICP and EICP to mine tailings have been limited, and no studies have shown the ability to stimulate native ureolytic microbes capable of inducing MICP from tailings. Additionally, the costs and environmental impacts associated with EICP and MICP for stabilization of mine tailings have not been thoroughly compared to those of other short-term dust control technologies. This paper presents the results of benchtop stimulation experiments, laboratory wind tunnel experiments, and a comparative analysis of EICP with other dust control technologies to identify specific obstacles to the field application of EICP and MICP as well as knowledge gaps where future research into these technologies may be required.

2 LABORATORY EXPERIMENTS – MICP AND EICP

To characterize the effectiveness of MICP and EICP for dust control at tailings facilities, stimulation experiments and wind tunnel experiments were performed on five tailings specimens obtained from two mine sites in the United States. Stimulation experiments were used to measure the ability to stimulate native ureolytic microbes from tailings, while wind tunnel experiments were used to assess the effectiveness of EICP for fugitive dust control.

2.1 *Tailings*

Five tailings specimens were obtained for this research program. Four were obtained from a taconite tailings facility in Minnesota and one was obtained from a copper-molybdenum ore site in Arizona. The tailings specimens are described further below. Figure 1 shows the grain size distributions for all five tailings specimens.

1. MFN-1: fine, freshly deposited Minnesota taconite tailings;
2. MCN-1: coarse, freshly deposited Minnesota taconite tailings;
3. MFA-1: fine, aged (1-year old) Minnesota taconite tailings;
4. MFA-2: fine, aged (9-years old) Minnesota taconite tailings; and
5. AFN-1: fine, freshly deposited Arizona copper-molybdenum tailings.

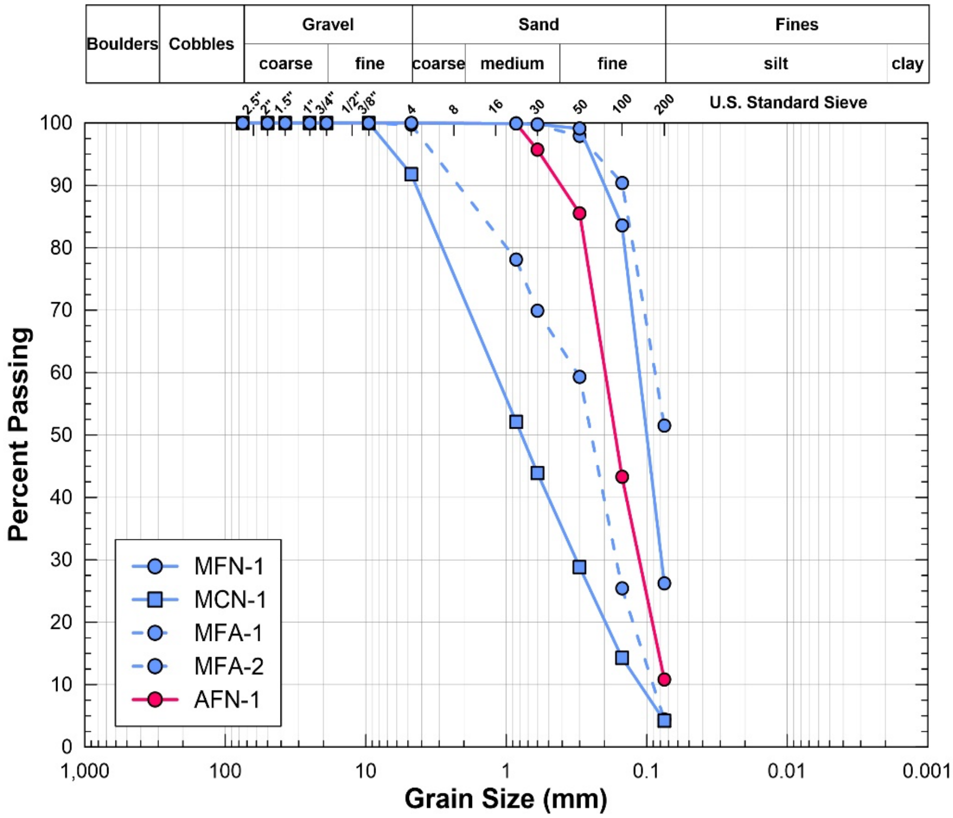

Figure 1. Grain size distributions for tailings specimens.

2.2 *MICP Stimulation Experiments*

Stimulation experiments were performed on each of the tailings specimens to determine the feasibility of stimulating ureolytic microbes in tailings storage facilities. Stimulation experiments were performed using autoclaved 250-mL flasks, 100-mL of autoclaved stimulation solution, and 10-15 grams of tailings. The flasks and stimulation solutions were autoclaved to prevent the growth of exogenous microbes (i.e., microbes that did not originate from the tailings specimens). The stimulation solution used for these experiments was taken from Gomez et al. (2018) and contained 0.1 g/L yeast extract, 12.5 mM ammonium chloride, 42.5 mM sodium acetate, and 350 mM urea. At the beginning of the experiments, the flasks were mixed to suspend the tailings in the stimulation solution and then capped with loose-fitting paraffin caps. 5-mL samples of solution were taken from each flask using sterile pipettes as soon as the tailings had settled to the bottom of the flask (approximately 10 minutes) and every 2-3 days thereafter for fourteen days. pH, conductivity, and ammonia smell were monitored in each of the samples taken from the flasks immediately after removing the samples. These indicators were used to gauge whether ureolysis was occurring (and hence whether ureolytic microbes had been stimulated from the tailings). Stimulation experiments were performed in quintuplicate for each tailings specimen.

The results of the stimulation experiments are shown below in Figure 2. As shown in Figure 2, tailings specimens MFN-1, MFA-1, MCN-1, and MFA-2 show similar trends in pH and conductivity with time. All four specimens show increasing pH and increasing conductivity, which is consistent with ongoing ureolysis (and hence stimulation of ureolytic microbes). An ammonia smell was also observed with these specimens two to five days after beginning the experiments, which is also consistent with ongoing ureolysis. It is noteworthy that the age and grain size of the tailings did not seem to impact the stimulation of native ureolytic bacteria in these specimens; fine, coarse, fresh, and aged tailings all showed evidence of stimulation. As also shown in Figure 2, however, tailings specimen AFN-1 exhibited decreasing pH and relatively stagnant conductivity with time. This implies that ureolysis was not occurring and that ureolytic microbes were not stimulated. Taken together, these results indicate that stimulation of native microbes for MICP may be feasible at some tailings facilities, but not at others. As such, treatability studies may be required to determine the suitability of a given tailings site for dust control via MICP using biostimulation.

Figure 2. Results of stimulation experiments – pH and conductivity with time.

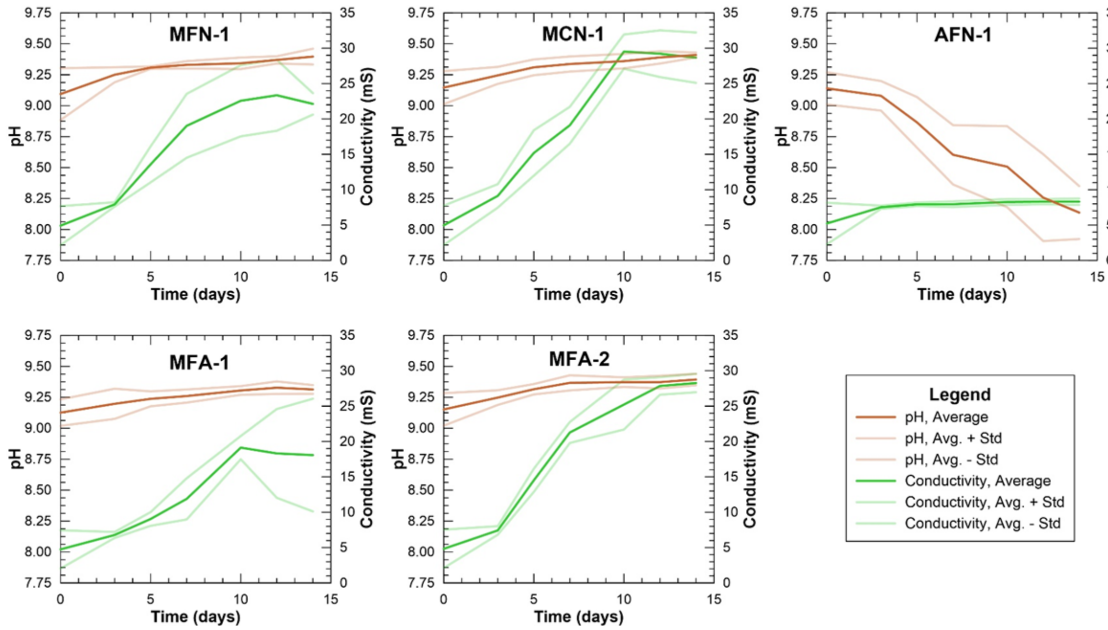

2.3 *EICP Wind Tunnel Tests*

Wind tunnel testing of each of the tailings specimens treated via EICP was conducted to determine the feasibility of EICP for dust control at tailings facilities. Five nine-inch round, two-inch deep cake pans were filled with Ottawa 20-30 sand to one-inch from the top of the pans to reduce the amount of tailings required for each wind tunnel test. The pans were then filled to the top with oven dried tailings from each of the five tailings specimens and leveled using a straight edge. All five pans were sprayed using a spray bottle with 100 mL of a cementation solution containing the following: 0.8 M urea, 1.2 M calcium chloride dihydrate, 2 g/L nonfat powdered milk, and 15 mL of crude enzyme extract. The enzyme extract was obtained from the Center for Bio-Mediated and Bio-Inspired Geotechnics at Arizona State University and was prepared according to the procedures described in Khodadadi Tirkolaei et al. (2020). To prepare the solution, 75 mL of urea and calcium chloride solution were combined with 15 mL of enzyme and nonfat powdered milk solution within the spray bottle immediately prior to application to the tailings. The solutions were mixed directly before application so that the ureolysis reaction and subsequent carbonate precipitation reaction occurred predominantly on the tailings surface rather than in the spray bottle. The smell of ammonia and a white precipitate were observed on all treated tailings surfaces within three minutes of treatment, indicating that ureolysis and carbonate precipitation were occurring. Following treatment, the tailings specimens were air dried for a minimum of two weeks prior to wind tunnel testing.

Each of the EICP-treated tailings specimens was tested along with an untreated control specimen in a wind tunnel constructed at the Johns Hopkins University soil mechanics laboratory. Control specimens were prepared in the same manner as EICP-treated specimens but were not sprayed with the EICP solution. The wind tunnel was constructed using two air compressors to generate air flow, an acrylic test box, and acrylic contraction and diffuser sections. Airflow over the tailings specimens was observed to be turbulent in nature. All tailings specimens were subjected to the same velocity of air flow for five minutes. Air flow velocity was controlled using two sets of valves between the air compressors and the contraction section of the wind tunnel. All tailings specimens were weighed before and after testing to measure mass lost during wind tunnel testing.

Following testing, the carbonate-cemented crust on the EICP-treated specimens was analyzed for the following properties: crust thickness (measured using calipers), crust strength (assessed using a pocket penetrometer), and carbonate content (assessed using acid digestion). The crust on each EICP-treated pan was tested three times with the pocket penetrometer to assess crust strength. Acid digestion was performed according to the following procedure: rinsing all recoverable pieces of carbonate cemented crust from each EICP-treated tailings specimen to remove residual salts, oven drying those pieces of crust to remove moisture, weighing the pieces of crust (weight should reflect tailings and carbonate precipitate), exposing those pieces of crust to 1.0 M hydrochloric acid until no more effervescence was observed and all interparticle bonds were broken, rinsing the resulting tailings with deionized water to remove salts, oven drying the tailings, and weighing them a final time (weigh should reflect only tailings). The difference in mass before and after acid digestion was assumed to be the result of carbonate mineral dissolution during acid digestion.

The results of the EICP wind tunnel tests and cemented crust measurements are shown below in Tables 1 and 2. As shown in Table 1, all EICP-treated specimens showed significantly less mass loss than control specimens. This indicates that EICP-treatment is likely to be effective for dust control at tailings facilities. Further, the composition, age, and gradation of tailings was not observed to impact the effectiveness of EICP-treatment. So, while MICP may require treatability studies to assess its feasibility for use at a given tailings site, it appears that EICP could be more universally effective. This is most likely due to the nature of EICP as a bio-inspired, rather than bio-mediated process. EICP does not rely on in-situ microbes, but rather an exogenous application of enzyme. So, it is not subject to the same constraints as MICP (e.g., presence or absence of microbes, unfavorable chemical conditions for microbial growth, etc.).

Table 1. Mass loss from wind tunnel experiments.

Treatment	Rate of Mass Loss from Tailings Specimens (g/min)				
	MFN-1	MCN-1	MFA-1	MFA-2	AFN-1
Control	388	33.8	61.2	10.2	74.7
EICP	0.114	0.020	0.00	0.0034	0.066

Table 2. Thickness, strength, and carbonate content of cemented crust of EICP-treated tailings.

Parameter	Tailings Specimen				
	MFN-1	MCN-1	MFA-1	MFA-2	AFN-1
Crust thickness (mm)	2.35	3.65	1.06	3.00	5.56
Crust strength (psi)	3.2	6.0	3.5	1.7	5.9
Carbonate content (%)*	3.8%	1.3%	12.5%	5.4%	1.1%

*crust strength represents the puncture strength of the crust from pocket penetrometer testing.

**carbonate content is reported as a percentage of dry mass.

The thickness, strength, and carbonate content of the cemented crust on EICP-treated specimens is reported in Table 2 above. While there was significant variability in thickness, strength, and carbonate content among the tailings specimens, all tailings exhibited a measurable crust that effervesced when exposed to acid (evidence of carbonate precipitation) with a relatively low but measurable strength.

3 COMPARATIVE ANALYSIS

Experimental results presented in Section 2 indicate that EICP and MICP are technically feasible methods for dust control at tailings facilities. However, to be implemented in the field, these technologies must also be cost competitive while not causing adverse environmental impacts when compared with other, existing dust control technologies. This section compares the expected financial and environmental costs of MICP and EICP against those of other common dust control technologies to identify potential knowledge gaps and challenges to successfully implementing MICP and EICP for surficial stabilization of tailings. The other technologies used for comparison with MICP and EICP are salt treatments, polymer emulsions, organic mulch, and paper pulping byproducts.

3.1 *MICP and EICP*

Both MICP and EICP involve spray-applications of nutrients (specifically urea and calcium chloride) to induce ureolysis and carbonate precipitation (Hamdan and Kavazanjian, 2016). Additionally, EICP requires exogenous application of plant-derived urease enzyme, while MICP requires either stimulation of or augmentation with urease-producing microbes. Both EICP and MICP produce ammonium chloride byproduct that could pose environmental risks. However, in surficial application, it is likely that much of the ammonium would volatilize as ammonia gas.

For this analysis, it is assumed that EICP is used for surficial stabilization of tailings as experimental results suggest that EICP may be more widely applicable than MICP. The estimated cost for application of EICP for dust control is $5,500 per acre, including material and application costs (Raymond et al., 2021). It is anticipated that EICP or MICP solutions could be applied using a spray truck.

MICP and EICP have not been applied on a large scale and remain largely in the research phase. However, Raymond et al., 2021 assumed a service life of two weeks for dust suppression at construction sites. For applications on tailings impoundments, where surface traffic is minimal, this is likely a conservative estimate of service life as the carbonate crust is unlikely to be disturbed and cannot be dissolved by rainfall (like some other dust control technologies). However, for the purposes of this analysis, a service life of two weeks is assumed.

3.2 *Salt*

Salts are a chemical method that can be applied to the tailings surface as either a powder or a brine to provide short-term stabilization against wind erosion. Salts work by absorbing small quantities of water from the atmosphere and holding the tailings particles together through matric suction. The most common salts used for stabilization include magnesium chloride and calcium chloride. Salts do not work well in excessively wet or dry climates. In wet regions, precipitation causes salts to dissolve and leach through the treated tailings, rendering them ineffective. Dissolved salts may also cause environmental impacts and additional costs for mitigation. In dry climates, there may not be enough water in the atmosphere for salts to absorb, and an erosion-resistant salt crust may not form (PNNL, 2018).

Salts are typically applied by spraying a concentrated brine solution to the surface of the tailings. It was assumed that brine costs $1.50 per gallon, with application of 2,500 gallons per acre. Unit costs for labor, equipment, and power are assumed to cost $700 per acre (USDA, 2020). Using these assumptions, the unit cost for salt application for tailings stabilization is $4,500 per acre.

The service life of this method is highly dependent on rainfall and relative humidity. In relatively wet or humid climates, salts may provide two to four weeks of stabilization before re-application is required (MIS, 2020). For this analysis, a service life of two weeks is assumed

3.3 *Polymer Emulsion*

Polymers, both natural and synthetic, can be sprayed onto the surface of tailings as an emulsion to produce an erosion-resistant crust. Polymers are large chain molecules composed of smaller repeating units. Anionic polymers, most commonly used for dust suppression, react with cations in the treated tailings to settle out of solution. The large polymer chains then form bridges between tailings particles, resulting in an erosion-resistant crust on the surface of the tailings. Specific polymer formulations are used depending on the physiochemical properties of the tailings upon which they are applied (PNNL, 2018). Most polymers used for dust suppression (specifically polyvinyl acrylics and acetates) are considered non-toxic and environmentally friendly when used according to manufacturer's recommendations (USACE, 2013).

Polymer emulsions are applied topically as a liquid spray to the tailings surface. The unit cost for applying polymer emulsion for dust suppression was reported to be approximately $5,300 per acre (SRI, 2003). However, USACE (2013) found that polymer costs are variable, with application and materials costs ranging from $7 to $10 per gallon and application rates varying from 0.05 gallons per square yard to 1.0 gallons per square yard. For this analysis, an application cost of $5,300 per acre is assumed.

In typical applications, polymer emulsions will provide three months to three years of stabilization, depending on the amount of vehicle and foot traffic in the application area. For application to sluiced tailings, where vehicle and foot traffic is expected to be limited, the effective service life is estimated to be approximately one to three years. For this analysis, a service life of one year is assumed.

3.4 *Organic Mulch*

Mulching involves placing a layer of material on the surface of the tailings to reduce wind and water erosion. In addition to creating a physical barrier to erosion, mulches can also reduce evaporation and maintain moisture in the tailings, further improving erosion resistance. Organic mulches include wood chips, tree bark, and paper products. Mulches can be applied directly with earthmoving equipment or via hydromulching depending on the site requirements. However, many organic mulches, including woodchips, are lightweight and low density, rendering them ineffective in high wind and high surface water flow environments. Further, all organic mulches are susceptible to decomposition, limiting their useful life for tailings stabilization (PNNL, 2018).

For this analysis, it is assumed that wood chip mulch can be obtained for a cost of $15 per cubic yard. To adequately stabilize the tailings surface, it is assumed that the mulch is spread in a one-foot thick layer over the treatment area. Unit costs associated with transportation and placement of the mulch are estimated to be $5 per cubic yard for transportation (it was assumed the mulch would have to be hauled ten miles), and $2 per cubic yard for placement for a total cost of $35,500 per acre.

The service life of this method is dependent on the resistance of the mulch to decomposition and wind erosion. Decomposition of wood chip mulch is expected to take between four and seven years, depending on the rainfall conditions at the site (mulch decomposes faster in wetter locations) (Coleman, 2020). However, high winds may blow the wood chips off of the tailings surface prior to decomposition. For this analysis, a conservative service life of two years is assumed.

3.5 *Paper Pulping Byproducts*

Paper pulp and byproducts of the pulping process may be used for dust suppression and stabilization of the tailings surface. Paper pulp itself may be incorporated into a mulch and applied to the tailings surface in combination with wood chips or other organic material as described in Section 3.4. Additionally, lignosulfonate and tall oil, byproducts of the sulfite pulping process and the Kraft paper process, respectively, may be used to provide short-term stabilization of tailings. These products act as binders, holding tailings particles together and increasing their resistance to erosion. Lignosulfonates and tall oil may be applied topically or mixed into the surficial tailings to bind particles together (Jones, 2017).

While paper pulping byproducts can create relatively strong, erosion resistant crusts on the tailings surface under dry conditions, they also have several limitations. Lignosulfonates tend to be highly soluble and leach during heavy precipitation. Tall oil, while less soluble, is also susceptible to breaking down under heavy rains or prolonged saturated conditions. Further, lignosulfonates tend to be acidic, which may lead to leaching of metals from the tailings or alteration of redox conditions if they leach to groundwater. Leaching of lignosulfonates and tall oil may also lead to high biological oxygen demand in receiving waters, which could result in fish kills (Jones, 2017; PNNL, 2018) and lead to difficulties in performing water treatment and complying with discharge requirements.

For this analysis, it is assumed that lignosulfonate is used for short-term stabilization of tailings. The unit cost for the lignosulfonate solution is estimated to be $3 per gallon. It is further assumed that lignosulfonate can be applied at a rate of 2,000 gallons per acre for a material cost of $6,000 per acre (SRI, 2006). Assuming that a water truck is used to apply the lignosulfonate at a rate of $700 per acre (including equipment operational costs), it is estimated that lignosulfonate can be applied at a cost of $6,700 per acre.

The service life of lignosulfonate is estimated to be two to three months, resulting in the need to reapply once or twice per season. However, intense rain events may dissolve lignosulfonates and reduce the service life, potentially requiring multiple applications during periods of high precipitation and repeat storms. For this analysis, a service life of two months is assumed.

3.6 *Summary and Discussion of Results*

A summary of the costs and environmental impacts associated with the analyzed surficial stabilization technologies is given in Table 3.

Table 3. Comparison of costs and environmental impacts for surficial stabilization technologies

Method	Service Life	Unit Cost* ($/acre/week)	Environmental Impacts
MICP and EICP	2 weeks	$2,750	Ammonium chloride production
Salt	2 weeks	$2,250	Salt dissolution
Polymer Emulsion	1 year	$102	Limited environmental impacts
Organic Mulch	2 years	$341	Limited environmental impacts
Paper Pulping Byproducts	2 months	$770	Metal leaching from tailings; Changes to groundwater redox conditions; Increased BOD in receiving waters

*Unit costs are normalized by expected service life

As shown in Table 3, MICP and EICP may be considerably more expensive than other tailings stabilization options when unit costs are normalized over the expected service life. Additionally, MICP and EICP have potential environmental impacts associated with their ammonium chloride byproduct, which may need to be managed depending on the application rate of the technology. To improve the feasibility of MICP and EICP for surficial stabilization and dust control at tailings facilities, it is thus necessary to reduce the application costs associated with the technology ($/acre) and better estimate service life (to reduce the number of required applications and hence reduce the amount of potential environmental impacts).

According to Raymond et al. (2021), the highest contributor to the overall unit application cost of EICP is the cost of the urease enzyme if commercially available pharmaceutical grade enzyme is used. Therefore, reducing the cost of the urease enzyme is key to successfully implementing EICP for dust control in the field. However, as demonstrated in this study, EICP for dust control may be achieved using a crude urease extract, rather than commercially available pharmaceutical grade enzyme. Khodadadi Tirkolaei et al. (2020) suggest that a simple on-site urease extraction method (involving only a blender, cheese cloth, and jack beans) may be used to generate crude urease extract on-site and vastly improve the cost effectiveness of EICP. Implementation of this cost effective on-site urease extraction method is therefore a key to successfully implementing EICP for dust control at tailings facilities. MICP using stimulated microbes may also prove to be a more cost-effective method for dust control at tailings facilities than EICP, as it does not require exogenous input of urease enzyme or bacteria. However, as shown by the MICP stimulation experiments performed as part of this work, stimulation may not be a viable method for MICP at all tailings sites and more research is required in this area to determine the applicability of MICP for dust control at tailings facilities.

Regarding service life, more research is required to determine the longevity of MICP and EICP crusts for dust control. The service life of MICP and EICP crusts is important for assessing both long-term costs as well as long-term environmental impacts from this technology. While carbonate-cemented crusts will not dissolve with rainwater, they are subject to mechanical breakage induced by wind loading, heavy rains, or other forms of disturbance (i.e. trucks, equipment, foot traffic, etc.). However, in the absence of physical disturbance, MICP and EICP crusts should have a much longer service life than the two weeks assumed herein. Additional research involving in situ, ideally involving side-by-side comparison with other methods, is therefore required to determine how carbonate cemented MICP and EICP crusts respond to environmental stresses, such as wind loading, heavy rains, and UV exposure.

Finally, evaluation of in situ vertical permeability of each dust control methods needs to be performed to provide guidance on the potential development of perched zones and preferable flow paths that may affect operations and performance of the tailings storage facility.

4 CONCLUSIONS

The goal of this paper was to identify specific obstacles to the field application of EICP and MICP for dust control at tailings facilities as well as knowledge gaps where future research into these technologies may be required. To that end, two sets of laboratory experiments (stimulation experiments for MICP and wind tunnel tests for EICP) and a comparative analysis of cost and environmental impacts with other existing technologies were presented herein. The results of the stimulation experiments showed that native ureolytic microbes capable of inducing MICP may be stimulated at some tailings facilities, but not at others. As such, treatability studies may be required to determine the suitability of a given tailings site for dust control via MICP. The results of the wind tunnel experiments showed that EICP is a viable method for dust control at tailings facilities and may be more universally applicable than MICP. This is likely due to fact that EICP does not rely on the growth of microbes, which may be sensitive to tailings chemistry or other environmental conditions. Finally, the results of the comparative analysis showed that EICP is not cost effective when compared with other dust control technologies if off the shelf pharmaceutical grade enzymes are used and a durability of only two weeks is assumed. To improve the applicability of EICP and MICP, implementation of low cost, on-site enzyme extraction methods and additional research to better understand the longevity of EICP and MICP generated crusts subjected to environmental conditions are required.

5 REFERENCES

C. Coleman, (2020). "How Long Does Mulch Last?" Charlestown Landscaping, [Online]. Available: https://www.charlestownlandscaping.com/how-long-does-mulch-last/. [Accessed 25 Sepember 2020].

Gomez, M.G., Graddy, M.R., DeJong, J.T., Nelson, D.C., and Tsesarsky, M. (2018). “Stimulation of Native Microorganisms for Biocementation in Samples Recovered from Field-Scale Treatment Depths.” *J. Geotech Geoenviron. Eng*., 144(1): 04017098.

N. Hamdan and E. Kavazanjian, (2016). "Enzyme-Induced Carbonate Mineral Precipitation for Fugitive Dust Control," *Geotechnique*, 66(7): 546-555.

D. Jones, (2017). "Guidelines for Selection, Specification, and Application of Chemical Dust Control and Stabilization Treatments on Unpaved Roads," University of California Pavement Research Center, Davis, California.

Khodadadi Tirkolaei, H., Javadi, N., Krishnan, V., Hamdan, N., and Kavazanjian, E. (2020). “Crude Urease Extract for Biocementation.” *J. Mater. Civ. Eng*., 32(12): 04020374.

Meyer, F.D., Bang, S., Min, S., Stetler, L.D., and Bang, S.S. (2011). “Microbiologically-Incuded Soil Stabilization: Application of *Sporosarcina pasteurii* for Fugitive Dust Control.” Proceedings, *Geo-Frontiers 2011*, Dallas, TX.

Midwest Industrial Supply, Inc., (2020). "Alternative to Chlorides for Effective Dust Control.” [Online]. Available: https://blog.midwestind.com/alternatives-to-chlorides-for-effective-dust-control/. [Accessed 1 August 2020].

Pacific Northwest National Laboratory, (2018). "Water Application for Dust Control in the Central Plateau: Impacts, Alternatives, and Work Strategies," U.S. Department of Energy, Richland, Washington.

Raymond, A.J., Kendall, A., DeJong, J.T., Kavazanjian, E., Woolley, M., and Martin, K. (2021) “Life Cycle Sustainability Assessment of Fugitive Dust Control Methods,” *Journal of Construction Engineering and Management*, 147(3), https://doi.org/10.1061/(ASCE)CO.1943-7862.0001993

Sierra Research, Inc., (2003). "Final BACM Technological and Economic Feasibility Analysis," San Joaquin Valley Unified Air Pollution Control District, Sacramento, California.

Sierra Research, Inc., (2006). "Alaska Rural Dust Control Alternatives," Alaska Department of Environmental Conservation, Sacramento.

United States Army Corps of Engineers, (2013). "Environmental Considerations for Selecting Cost-Effective Dust Control Technologies," Public Works Technical Bulletin No. 200-1-133, Washington, D.C..

United States Department of Agriculture, (2013). "Cost Scenarios - 373 Dust Control on Unpaved Road and Surfaces,". [Online]. Available: https://efotg.sc.egov.usda.gov/references/public/NM/CostSenarios_373-Dust_Control_on_Unpaved_Roads_and_Surfaces.pdf. [Accessed 19 August 2020].

Review of internet-of-thing enabled geotechnical monitoring hardware for tailings storage facilities

Vincent Le Borgne & Adam Dulmage
GKM Consultants, Sainte-Julie, Quebec, Canada

ABSTRACT: Monitoring has been a part of tailings storage facilities (TSF) for decades. Instruments themselves have proven designs that have become the backbone of monitoring but in recent years, advances in batteries, radio technologies, microprocessors and telecommunications have enabled the Internet-of-things to become an important part of TSF monitoring. The introduction or several new protocols such as LoRa, ZigBee or mesh-based TCP have greatly increased the available connectivity of instruments in TSF. By comparing the technologies offered by several manufacturers, we will show that several parameters have to be optimized concurrently to design robust internet of things (IoT) systems. Typically, a balance has to be found between radio functionalities such as bandwidth and response time, range, power requirements and compatibility with a broad range of instruments. Typical radio ranges are between 1 and 15 km, and can be expanded with mesh networking in some cases. Low power requirements are required in many situations because instruments are remote, isolated and the only available power source is sunshine. Compatibility has to be met with a wide range of instruments signal types such as vibrating wire, thermistors, RS-485, SDi-12, 4-20 mA, time-domain reflectometry and many more.

IoT best practices such as interconnectivity and the possibility to bring disparate technologies are applications into a single framework. Other IoT practices such as self-configuration and intelligent monitoring will be discussed in various contexts. Real-time data puts very different constraints on the hardware when performing background readings that are updated once per month compared to smart sensors that are triggered by external events such as seismic monitors. These new IoT practices also lay the groundwork for future developments such as the use of machine learning and AI for more proactive monitoring of assets.

1 INTRODUCTION

Unfortunate events in recent years have increased the general awareness of the issues posed by tailings and tailings dams. Several major failures, notably in Brazil (Brumhandino), the United States (Florida) and in the Philippines (Benguet province), have shown that deploying remote monitoring techniques could greatly improve long-term safety by providing engineers and mining companies the data they need to make informed decisions. Industry 4.0 practices such the Internet of things (IoT) paradigm have started to make their way into the monitoring of tailings storage facilities (TSF). The IoT is a growing field in which devices are connected to the internet or a local network automatically and with a unique identifier. In many industries, the IoT sees success as a way to collect data from monitoring points, instruments, and the status of machines and data logging systems. We will give an overview of IoT as applied to TSF monitoring. This review will cover the benefits of IoT systems, how the different hardware and software layers are interconnected. It will also compare the features of several manufacturers of IoT hardware for TSF and how to take advantage of the most appropriate products. This will be followed by a short discussion of the functions that TSF monitoring software should have to take full advantage of IoT systems.

1.1 *IoT Characteristics*

Monitoring is an integral part of the culture surrounding TSF. Piezometers, water sampling, surveying and more have been used consistently to ensure the durability and safety of tailings for decades. For some older facilities, instruments such as piezometers have been in the ground for decades and are still in use. Bringing an IoT framework to this field is an evolution prompted by the decreasing costs and increasing power of microprocessors and radio communications (RF) modules. By attaching specific devices to the instruments, an already-existing network of instruments can be converted to an IoT system. In the context of TSF and environmental monitoring at large, an IoT system is a system that monitors and controls sensors over a wide area, whose data are connected remotely and centralized in a server. IoT systems should have several of the following characteristics to varying degrees :

Dynamic and self-adapting
The IoT system should be able to integrate new instruments and deploy redundancies without minimal user intervention. A typical example of this is to take advantage of a centralized server to coordinates the readings of remote instruments of a single site after a seismic event is reported.

Self-configuring
Deploying an instrument should be as simple as turning it on after installation.

Interoperability
In tailings and environmental monitoring, there are different manufacturers of sensors, data loggers and instruments. There are very standards. A well-designed IoT system should be able to accommodate many types of instruments and allow the instruments to interact as needed.

Unique identity
Each instrument can and should have a unique identity built-in into the system. This acts as a stronger redundancy to manually tracking instrument locations, installation parameters, serial numbers and calibration factors.

Integration into larger data networks
An IoT system should be able to allow analysis and comparison of data from many different sources and sites. For instance, working on weather stations, ground-based radar, InSAR and in-ground instruments can lead to insights that were previous unattainable.

Context awareness
In the case of tailings, the context varies very little over time once the instrument is in the ground. While this is a common characteristic of IoT systems, it doesn't apply to well. An example for this is tracking systems on fleet vehicles or safety trackers on workers. These devices should be able to respond accordingly to the location of the worker but also to the locations of surrounding heavy machines.

Intelligent decision-making
Tailings monitoring systems should be able to lead to more intelligent decision-making.

2 IOT ARCHITECTURE

Table 1 summarizes the structure of an IoT project as used in tailings storage facilities. The instrument layer is the instrument itself. An in-depth analysis of instrument types and technologies is beyond the scope of this review insofar as the instruments are largely decoupled from the IoT hardware. Instruments are often installed in the ground and as such cannot have any type of telemetry built-in to them due to the physical constraints of the soil blocking any kind of RF communications. The node layer usually comprises a data logger, an RF module and a power source. The edge device connects the node together, to a local network or to the internet. The management layer is a software layer that assists in the data and inventory management of the instruments and nodes. The application layer is the where all data is aggregated and used for monitoring, modeling and more. While in most systems the layers are well-defined, the exact limit separating them can be blurred. For instance, individual nodes can contain an edge device or contain some level of management tools allowing for data quality control before outputting the data on the network.

Table 1 Table detailing examples of items part of each of the 5 layers of an IoT system for TSF

1. Instrument	*2. Node*	*3. Edge Device*	*4. Management*	*5. Application*
Piezometers	Data logger	Cellular	Instrument inventory	Graphing
Total station	Radio module	Satellite	Data archiving	Automated reports
LIDAR		Gateway	Security	Data analysis
Inclinometers		Distributed gateways	Traceability	Specialized tools

3 INSTRUMENTS AND NODES LAYERS

Nodes are network-enabled devices can transmit readings over RF, collect data from instruments and in most cases locally store the data. They may use a broad variety of standards and protocols to establish communications such as Zigbee, LoRa, Pakbus, and proprietary versions or implementations of each, as well as generic-purpose products such as WiFi and LTE. Using this intermediate step i is usually necessary for TFFs specifically: attaching an internet connection point to to each instrument is not possible in TSFs due to the high costs of wiring and managing power.

Zigbee, LoRa, Pakbus and other associated RF protocols can be sorted in two broad families: Star and mesh networks. Star topology relies on having a transmitter at each instrument/location that transfers directly to an edge device, typically called a gateway (Figure 1 (a)). This link can be unidirectional (the instrument transmits its data on a schedule or when certain conditions are met) or bi-directional, in which polling and other operations can be initiated over the link. Star topology has several advantages over mesh networks: it is simple to use, simple to understand and to manage. While very simple, star networks have a few constraints that have to be carefully considered. There is no way to reroute the data around obstacles should the topology of a site change. It is also not typically possible to extend the range by adding repeaters. However, the most commonly used technology for star networks, LoRa, has a range of up to 15 km, easily covering even the largest TSF.

In mesh networks (Figure 2 (b)), nodes can communicate with each other and transmit relay data between them and all the way up to the gateway or edge device. These networks are often self-healing: if the radio link between two specific nodes is broken, data can be automatically rerouted. The radio technology behind this is more complex than what is required for star networks, but mesh networks tend to more resilient and have fewer points of failures than star networks.

Several manufacturers offer products that work under this principle to enable IoT practices. A comparison of the specifics of each technology can be found in table 2. This list is not exhaustive and is only meant to be representative of the author’s professional experience working in North America.

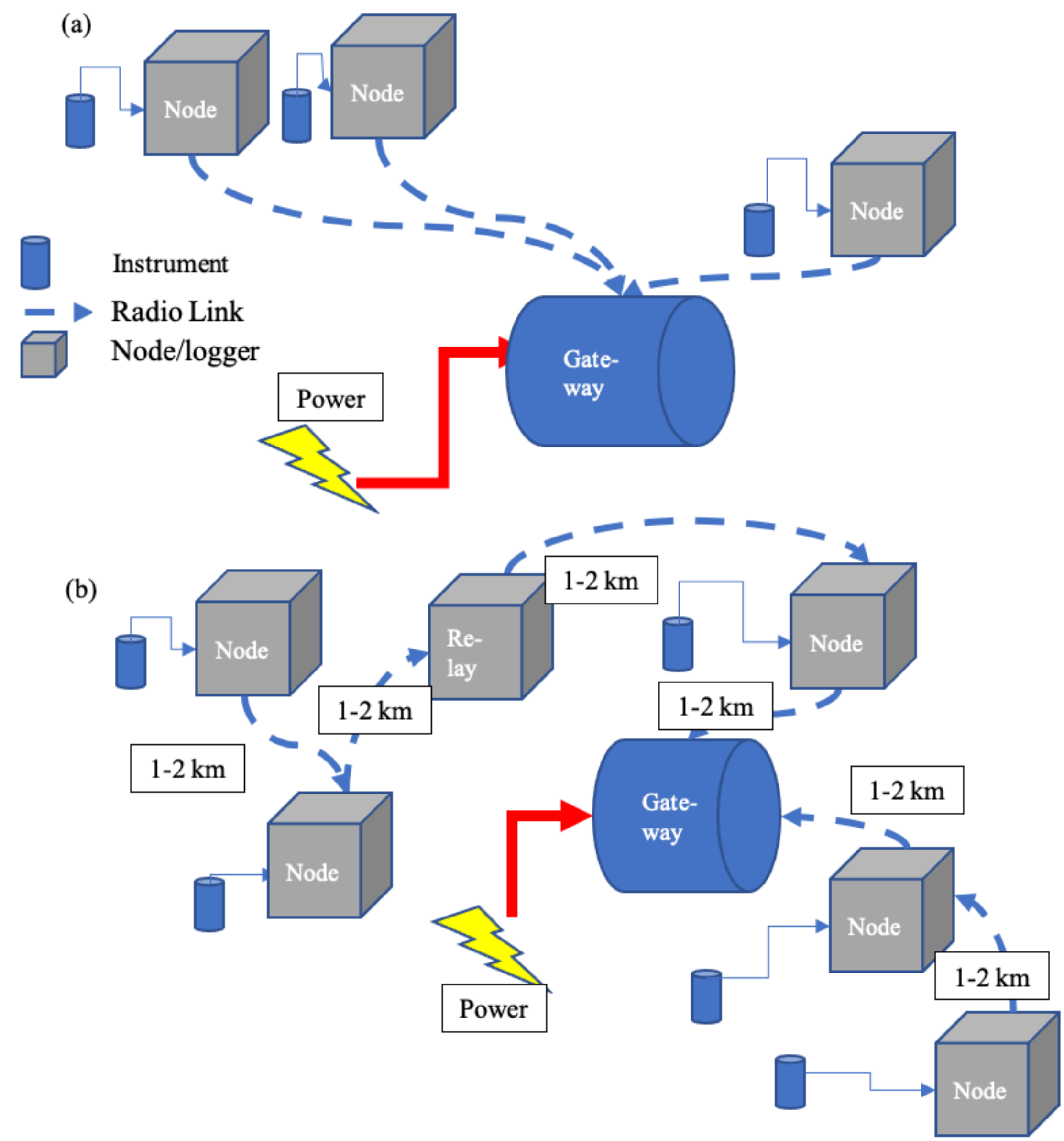

Figure 1 (a) Schematics of a star network. (b) Schematics of a mesh network.

Table 2 Point-by-point comparison of a selection of IoT dataloggers commonly found in TSF applications.

	Protocol	*Net. type*	*Self-healing*	*Nb. of hops*	*Range outdoor*	*Range indoor*	*Edge device*	*Instr. Per node*	*Batt. Life*
Ackcio	Mesh-LoRa	Mesh	Yes	>10	10 km	1 km	Prop. Gateway	1-8	10 yr.
Geokon	Mesh	Mesh	Yes	4	6 km	300 m	Prop. Gateway	1-8	1 yr.
Campbell Scientific	Pakbus	Cust.	N/A	>10*	40 km	1 km	Any	Many	1 yr.
RST	Prop.	Star	N/A	N/A	14 km	1 km	Prop. Gateway	1-40	5 yr.
Senceive	Prop. Mesh	Mesh	Yes	>25	500 m	200 m	Prop. Gateway	1-4	10 yr.
Sensemetrics	Prop.mesh	Mesh	Yes	?	12 km	1 km	Each node	Many	Solar
Worldsensing	LoRa	Star	Yes*	N/A	15 km	1 km	Prop. Gateway	1-5	10 yr.

**Limited by end-user programming.*

Delving in specifics of each technology is beyond the scope of this paper but a few key differences are highlighted in this section. All products are compatible with vibrating wire instruments such as piezometers. All but Geokon's Geonet are compabitle with analog output instrument such as barometers or temperature sensors. Digital instrument (e.g. addressable thermistor strings, addressable in-place inclinometers, digital weather stations, etc synchronizes.) are on a case-by-case for each instrument for every manufacturer as the drivers have to be programmed on request by the manufacturers.

3.1 *Ackcio*

Ackcio products have compatibility with vibrating wire instruments and a large number of digital instruments such as digital in-place inclinometers from leading manufacturers. The nodes deploy a self-healing mesh network that can cover very large areas. The nodes have a large on-board memory. The gateway the network and offers an ethernet connection, a wifi connection and a cellular network connection.

3.2 *Geokon*

Geokon's Geonet product deploys a mesh network with a limited range and a limited number of hops compared to other options such as Ackcio and Senceive. They are compatible with vibrating wire instruments Geokon digital instruments. The gateway synchronizes the network and can be configured to contain a cellular modem with either an LTE-M or 3G connection.

3.3 *Campbell Scientific*

Campbell scientific products have been used for decades and are robust devices that are very flexible in their programming. The manufacturer is however somewhat lagging behind as far as newer IoT practices go. However, the PakBus radio technology (Campbell's proprietary protocol) is flexible if not user friendly. The loggers are completely customizable and programmable, allowing for compatibility with all types of instruments available on the market. While the IoT functionality is not fully realized, these products are often the most cost-effective approach when a large number of instruments to be connected to a single location. Most other systems discussed here can only accommodate a few instruments each whereas Campbell Scientific loggers can be easily expanded to read hundreds of instruments.

3.4 *RST*

RST's R-Star line of products works on a purely star network architecture with a long range using a proprietary protocol. RST offers their own line of loggers that are compatible with all analog and vibrating wire instrument as well as their own digital instrument. There is also a module that allows connection of already-existing Campbell Scientific loggers to an RST network. The gateway offers connection to the internet.

3.5 *Senceive*

Senceive's line of products offers the most robust mesh network in terms of range, number of hops, number of nodes and stability of the products discussed in this review. They offer compatibility with vibrating wire and analog instruments. The nodes have a long battery life but they are the only product that can't be used in standalone (i.e.non-networked data logger) or have an on-board back up memory. If the gateway is out of commission for whatever reason, no data will be acquired until the network is restored.

3.6 *Sensemetrics*

Sensemetrics employ a unique approach. The nodes (THREADS) are all gateways with an ethernet connection that can also communicate with each other with a mesh network architecture. Each THREAD is compatible with most digital instruments but requires external accessories of other manufacturer's data loggers (such as Geokon's Geonet or LC-2) to read vibrating wire instruments. It is also the only system discussed in this review that has a proprietary cloud platform for configuration and management of the loggers and instruments. The battery life of individual THREADs is low and they typically require a solar panel for continuous operations.

3.7 *Worldsensing*

Worldsensing products (Loadsensing) work on a purely star network (LoRa) with a very long radio range. The nodes require very little power and have a battery life of years or more. Nodes are compatible with vibrating wire instruments, analog instruments and a select number of digital instruments.

4 EDGE DEVICES LAYER

Edge devices layer comprises the device that connect the local IoT network to the internet. In other fields, instruments themselves have their own connectivity, but the lack of local networks and power supplies on TSF makes impossible direct connection of each instrument. Many products, such as RST's RSTAR, Senceive, Worldsensing, Ackcio and others use a gateway that acts both as the collection point for the local IoT network and as a connection point for the internet. Some gateways offer different means of connection, typically to a local network over an ethernet cable or to a cellular or satellite mode.

Other products, such as Sensemetrics' THREADS distribute the edge connectivity with each Thread being a data logger, radio transmitter and internet connection point. This gives the most flexibility and redundancy but increases operation costs. It's usually preferable to have fewer edge devices that aggregate data from several nodes due to the extra cost and power requirements incurred by cellular modems, built-in or external.

In a few cases, the instruments themselves connect to the internet or a local server but this is unusual in the tailings monitoring. Cellular modems are commonly built-in into strong motion sensors or seismographs. The typically large amount of data generated by this type of instrument makes it impractical to transmit measurements over local radio links.

5 MANAGEMENT LAYER

The management layer is both a benefit and a core component of an IoT system. In TSF and geotechnical monitoring the standard is to know exactly why an instrument should be at a given location, what is expected to be learned from it and how to handle its data. Even with these widespread precautions, it is not rare for practitioners to lose track of the instrument inventory, of historical data or to ignore data. Large mining companies are showing interest to fully automate their monitoring systems in tailings across the world. This compounds the aforementioned data and instrument management issues as tens or hundreds of sites will be managed concurrently in large companies. In addition to the large number of instruments scattered around the globe, the engineering teams are often located remotely and can oversee several mines, making good management practices that much more important. This section will give an overview of recommended practices and review of existing features in several software to better manage data, users and instruments. Much like for hardware, there are many different platforms available out there. The commercially available platforms discussed here are not an endorsement and reflect the products encountered by the author in various TSF monitoring projects.

5.1 *Data logger management*

Some platforms, such as Vista Data Vision and Multi-Logger Canary are not typically fully integrated with the hardware they pull data from. It makes them more versatile as they are designed to be compatible with text-based data files and other data sources but in return, they typically can't interact with the hardware. This interaction can be beneficial by allowing for manually triggered health checks of the dataloggers. Newer platforms such as Sensemetrics allow not only to have access to all instruments information in a centralized database, but also to have direct access to health and status of the instruments and loggers, making proactive maintenance much easier and cost-effective. This is done at the expense of flexibility and interoperability.

Other features are found in most platforms that facilitate the management of large instrument numbers. Alarms can be set on out of bounds signals, on battery voltage or on logger temperature. Every available platform offers this type of functionality and they make overseeing large number of instruments much more manageable. A properly designed IoT systems has tools to uniquely identify instruments, measurement point, calibration factors, maintenance operations and documentation. Such a centralized system becomes critical as IoT systems grow larger and more complex.

5.2 *Data tracking and archiving*

A common pitfall of large-scale monitoring systems is the traceability of data over years and decades. Modern techniques of integration in databases helps prevent this. Though it is now commonly achieved in an "IoT" framework, this has been an industry 4.0 practice for decades in manufacturing and retail, with dedicated databases for instruments, often included in ERP (enterprise resource planning) packages due to how data from a factory relates in real-time to its financials. TSF need "slower" monitoring and only recently have we started seeing dedicated database systems for this industry.

Mines that have been in operation for decades or that have ambitious monitoring systems can generate more data than is easily manageable by a human team. Progressively moving away from manual tallying, we have seen dataloggers dramatically increase the amount of data collected per instrument without the proper data management tools having been put in place. The author has seen a large gold mine use 500 Mb Excel files to plot their TSF data. This method is unreliable and is prone to human error. This mine has been in operation for only a few years and this situation could have been planned for from the beginning. Having everything catalogued in a searchable database ensures long-term traceability of all data.

5.3 *Data distribution and access rights*

In any given organization, several teams might want to access the data: production, environment, health and safety, and engineering. Every IoT platform should have some form of data sequestering, user management and access rights. Though the details may vary, every platform, offers this in some way or another with varying degrees of autonomy given to individuals to manage their own projects and access rights.

6 APPLICATION

The application ties together the hardware into an actual IoT system. The software should have two main components: hardware control and data management. We have already touched upon some of the hardware control requirements: status updates on the instruments, inventory management, etc. In addition to the aforementioned management features, many features for the front-end should be more common place. Commonly found functions such as graphing of historical data or report generation have been introduced over a decade ago by the software companies such as Vista Data Vision or Geoexplorer. However, with the increasing number of connected instruments and the wider variety of instrument technologies used, more and more features are now recommended to be present. For instance, total stations, ground-based radar and INSAR have now found their place in tailings monitoring. While they are contactless and are not IoT *per se*, their data is complementary to that of in-ground IoT instruments that it should be treated concurrently with these instruments.

Some commonly used instruments require specific tools for plotting and interpreting data. In-place inclinometers and manual inclinometer probes have notoriously tricky data to analyze that can't be displayed accurately on regular time graphs. Distributed monitoring such as ground-based radar and total stations also require specialized tools for plotting. The application layer chosen for an IoT system should include the necessary tools for the instruments of a given TSF monitoring system.

Because industry 4.0 offers a more direct integration of geotechnical data, functions often found in SCADAs (Supervisory control and data acquisition) and other industrial system are now recommended to be added to TSF monitoring system. Real-time alarms, an alarm logging tool, user management are all now becoming standard in this industry.

The application layer encompasses emerging technologies such as machine learning and artificial intelligence. Access to large data sets is necessary to train most machine learning and AI algorithms and the IoT will finally generate the amount of data needed. We will likely see an increase in the application of these methods to TSF in the next five years.

7 CONCLUSION

The IoT and industry 4.0 are major trends in TSF that are going to change the face of the industry. By understanding the properties of the IoT and the different layers of it, modern and efficient IoT systems can be designed and deployed in TSF. They open the door to automated monitoring of the TSF themselves, but also of the instruments, data loggers and data quality. A growing number of providers offer hardware that can read instruments such as piezometers and make their data available online for management and analysis. Each have specific limitations that need to be taken into account when designing a monitoring system: instrument compatibility, radio range, radio network type, battery life, etc. The hardware directly ties in to the various layers of an IoT system sometimes merging several layers into one or leaving them completely independent from each other. As a general rule, the more integrated the layers are, the more the key benefits of an IoT system (Dynamic and self-adapting, Self-configuring, Interoperability, Unique identity Integration into larger data networks, Context awareness and Intelligent decision-making) are developed but at the expense of flexibility and programmability.

Flow liquefaction characteristics of a gold mine tailings

Amir reza Fotovvat & Abouzar Sadrekarimi
Department of Civil and Environmental Engineering, Western University, London, Ontario, Canada

Michael Etezad
Golder Associates Ltd, Mississauga, Ontario, Canada

ABSTRACT: Slurry tailings are generally deposited in a saturated and loose condition within a tailings management facility. Accordingly, flow (static) liquefaction of the tailings is a major concern. In this study, a laboratory experimental program was carried out to evaluate the behavior of a non-plastic gold mine tailings. Monotonic triaxial compression tests were performed on isotropically and anisotropically consolidated samples of the tailings to evaluate their undrained shearing strengths and flow liquefaction behavior. Furthermore, the instability of tailings. specimens subjected to unloading (confining stress relief) stress path was studied. For this case, a constant deviator stress (CDS) was maintained while reducing the mean effective stress in a triaxial test. The results of the monotonically increasing shear tests show that the samples with anisotropic consolidation have higher strengths while experiencing higher strain-softening during liquefaction. The identification of yielding stress ratios of the CDS tests is further explained. Additionally, the agreement between stress ratios at the commencement of instability of the CDS tests with those mobilized following the yielding in undrained shearing is discussed. The outcomes of this study provide a better understanding of instability and flow liquefaction potential of gold mine tailings.

1 INTRODUCTION

Liquefaction flow failure is considered as a triggering factor for a significant number of failure cases of mine tailings dams. Flow liquefaction can take place due to monotonically increasing shear loads as described in several studies (Fourie & Tshabalala 2005, Morgenstern et al. 2016, Robertson et al. 2020). Another mechanics is the reduction of effective confining pressure. Flow liquefaction due to monotonically increasing shearing stress is more commonly investigated than other liquefaction mechanisms in the literature. One of the first reported flow liquefaction failures due to the reduction of effective confining pressure (unloading) is the failure of Wachusett dam in 1907 (Olson et al. 2000).

Unloading can occur as a result of water infiltration (Zhu & Anderson 1998, Leroueil 2001, Dong et al. 2016) or the movement of slimes within two granular layer as observed in Fundão tailings dam failure in Brazil (Morgenstern et al. 2016). A certain stress path, observed in Fundão tailings dam failure, called “constant deviator stress unloading (CDS)” path was employed in the experimental program of the current study to study instability produced by a reduction in effective confining pressure at a constant deviator or shear stress. There are many studies in the literature concentrated on laboratory evaluation of flow liquefaction of tailings using triaxial or direct simple shear testing (Fourie & Papageorgiou 2001, Qiu & Sego 2001, Fourie & Tshabalala 2005, Al-Tarhouni et al. 2011, Chang et al. 2011, Schnaid et al. 2013, Riveros & Sadrekarimi 2020). Observations made in existing experimental studies suggest instability along a CDS unloading path is associated with an abrupt increment of shear strain and eventually a complete failure

(Anderson & Riemer 1995, Gajo et al. 2000, Chu et al. 2003, Dong et al. 2016, Rabbi et al. 2019, Riveros & Sadrekarimi 2020).

This study first investigates the flow liquefaction behavior of a gold mine tailings using monotonically-increasing undrained triaxial compression loading. The second part of this paper reports the drained instability behavior of the tailings studied by constant deviator stress (CDS) path tests.

2 MATERIALS TESTED AND TESTING PROGRAM

The gold mine tailings that was tested in this study contains 84% fines by weight. The grain size distribution curve of the tailings obtained by sieve analysis is shown in Figure 1. Extreme void ratios of 0.62 and 2.08 were obtained as its e_{min} and e_{max}, respectively. The specific gravity of tailings particles (G_s) was determined as 2.72. X-ray diffraction (XRD) analysis revealed the prevalence of quartz, albite, clinochlore, ferroan, and glycolated and Illite minerals in the composition of the tailings. Atterberg limit tests further indicated the non-plastic nature of the tailings. Specimens were prepared using the moist-tamping technique and a triaxial apparatus was used to carry out the testing program. The samples were subsequently first saturated by circulating CO_2, flushing water, and then applying a proper back pressure to reach a *B* parameter of greater than 0.97.

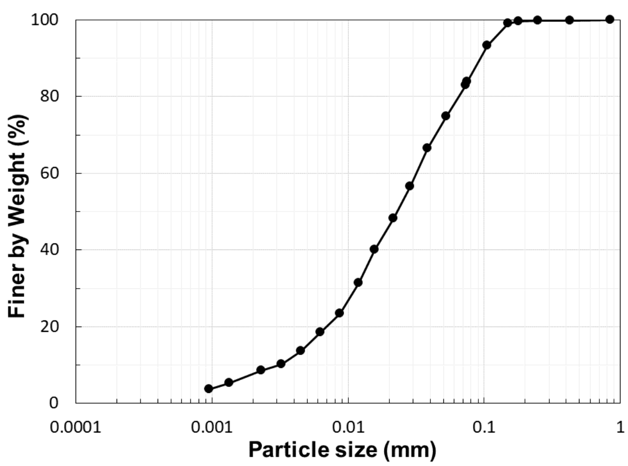

Figure 1. Grain size distribution curve of the tested tailings.

The preliminary tests were carried out to establish the critical state line and find the undrained strength ratios of the tailings. For this series of tests, the specimens were consolidation either isotropically or anisotropically. Isotropic consolidation was achieved by increasing the cell confining pressure to a certain stress. Anisotropic consolidation was then applied following a K_o-consolidation method to produce principal stress ratios similar to an in-situ level-ground condition ($\sigma'_{3c}/\sigma'_{1c} = K_o$). Drainage lines were then closed to impose an undrained shearing condition and the samples were sheared in compression through a strain-controlled mode. Shearing was continued until an axial strain of 25% at a rate of 5% axial strain/hour.

Following the completion of the first series of testing, a second series of testing was carried out which incorporates CDS testing to evaluate instability due to unloading. The specimens were first consolidated isotropically up to a desired stress. They were then sheared through a conventional drained loading to reach a certain deviator stress at the end of consolidation. The specimens were subsequently unloaded by increasing pore pressure, and therefore, decreasing the mean confining pressure applied on the specimen. While unloading, the deviator stress was kept constant by adjusting the required axial force. The undrained shearing responses of isotropically and anisotropically (K_o) consolidated samples of tailings were compared with the instability behavior of the CDS tests. The initiation of unloading in the CDS samples and the end of consolidation of the anisotropically consolidated samples were set to be the same.

Figure 2 demonstrates the triaxial system used in the study, which consists of a uniaxial loading frame, two electromechanical pressure pumps and a distributed data acquisition and control system (DDAC).

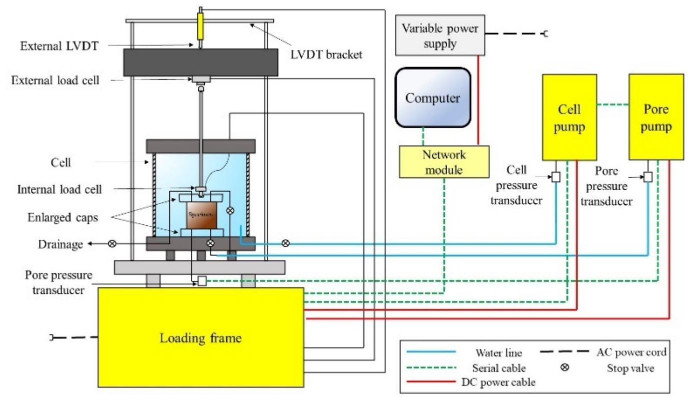

Figure 2. Triaxial setup used in this study.

The preliminary tests are described in Table 1. In this table, K_c is the principal stress ratio ($\sigma'_{3c}/\ \sigma'_{1c}$) at the end of consolidation, which is equal to K_o in case of anisotropic K_oU tests. The first letter in test IDs indicate the consolidation type (I: isotropic, Ko: anisotropic K_o) and the second letter indicates the drainage condition during shearing (U: undrained, D: drained).

Table 1. Summary table of IU, ID and K_oU triaxial tests.

Test ID	Consolidation	Shearing	p'_c (kPa)	e_c	K_c
IU 1			155	1.021	0.00
IU 2		Undrained	200	0.992	0.00
IU 3			300	0.947	0.00
IU 4	Isotropic		600	0.840	0.00
ID 1			150	0.828	0.00
ID 2		Drained	300	0.793	0.00
ID 3			400	0.716	0.00
K_oU 1			80	1.049	0.55
K_oU 2	Anisotropic (K_o)	Undrained	160	1.008	0.55
K_oU 3			300	0.960	0.55

The CDS tests are also summarized in Table 2. The parameter η_c is the after-consolidation stress ratio (q_c/p'_c).

Table 2. The summary table of CDS tests.

Test ID	Rate of unloading (du_e/dt)	p'_c (kPa)	e_c	η_c
CDS 1		147	1.018	0.34
CDS 2	1	156	1.036	0.61
CDS 3		271	1.030	0.31
CDS 4		311	0.975	0.61

3 RESULTS AND DISCUSSIONS

3.1 *Typical results and static liquefaction behavior*

Figure 3 demonstrates the stress paths of the undrained shearing responses of the specimens consolidated both isotropically and anisotropically. The average K_o value was obtained as 0.55. The stress paths indicate contractive behaviors following a peak undrained shear strength, s_u(yield), of the samples. This is followed by a turnover (phase transformation) point (PT) from strain-softening to strain-hardening behavior, which suggests the specimens underwent limited liquefaction. The minimum shear strength is called the post-liquefaction undrained strength, s_u(liq), corresponding to the PT points indicated in Figure 3. The results show a unique projection of the critical state line (CSL) in the plane of q (deviator stress) versus p′ (mean effective stress) for both IU and K_oU tests. However, the undrained shearing strengths of samples with different anisotropy during consolidation were found to show different trends. This is demonstrated in Figure 4 which illustrates the s_u(yield) and s_u(liq) of the tests normalized with respect to their after-consolidation major principal stress (σ'_{1c}) plotted against their consolidation void ratio (e_c).

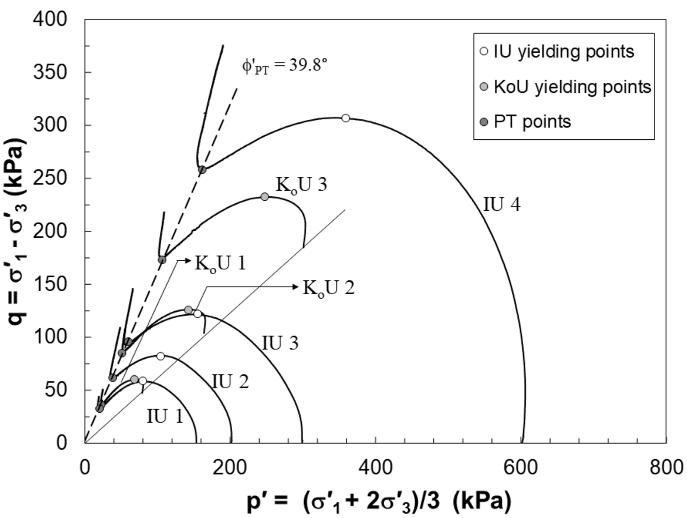

Figure 3. Stress paths of IU and K_oU samples sheared through monotonic compression loading.

As shown in Figure 4, the K_oU samples showed higher resistances for a given void ratio compared to the IU samples for both yielding and post-liquefaction strengths. This is probably due to the interlocking of tailings particles following anisotropic consolidation. Thus, more effort was required to overcome the resultant stiffer fabric, in addition to a reduced potential for pore water pressure generation (Sadrekarimi 2020). The relatively high $s_u(liq)/\sigma'_{1c}$ of these tailings likely results from the absence of complete strain-softening and the use of phase transformation points of the corresponding stress paths to determine s_u(liq) in the specimens of this study.

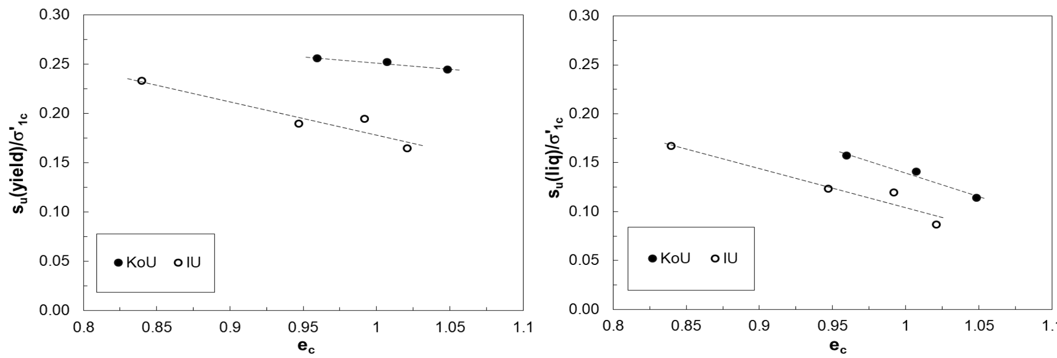

(a) (b)

Figure 4. (a) s_u(yield)/σ′$_{1c}$ and (b) s_u(liq)/σ′$_{1c}$ of both IU and K_oU samples versus e_c.

Figure 5 shows the excess pore pressure generation potential for these two sets of tested samples by plotting their brittleness indices ($I_B = [s_u(liq)-s_u(yield)]/s_u(yield)$) versus maximum excess pore water pressure ratios ($r_{u,max}=\Delta u_{max}/\sigma'_{1c}$), where Δu_{max} is the maximum shear-induced excess pore water pressure developed in the triaxial tests of this study. Brittleness index quantifies the amount of strength loss and strain-softening. This figure also shows an increasing correlation between I_B and $r_{u,max}$, for a given consolidation type, meaning a rising Δu_{max} would induce a more severe undrained strength loss. As a comparison between IU and K_oU samples, Figure 5 further depicts that higher I_B would be obtained at a lower $r_{u,max}$ in anisotropically-consolidated samples than the ones consolidated through isotropic consolidation.

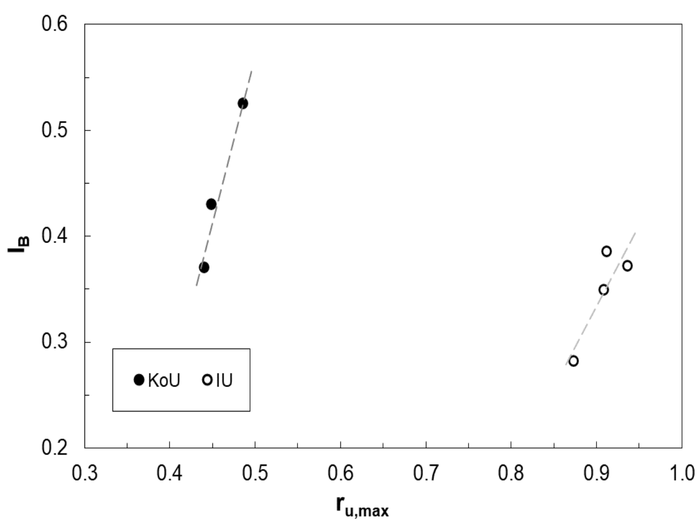

Figure 5. Brittleness index of IU and K_oU tests against their $r_{u,max}$.

Despite the differences in strengths and softening degrees, the projection of the CSL in the plane of mean effective stress and void ratio was found to be unique for both IU and K_oU samples of the tailings in Figure 6. It should be noted that for a better establishment of the CSL, drained-shearing tests carried out on isotropically consolidated samples are also included in. Figure 6.

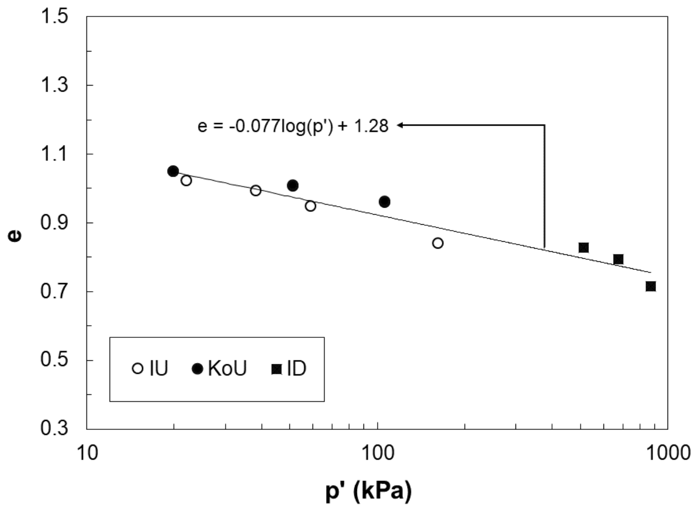

Figure 6. Critical state line of the tested tailings.

3.2 *Constant deviator stress unloading test results*

Figure 7 demonstrates a CDS test (CDS 2), which was first consolidated isotropically and then sheared drained (i.e. anisotropic consolidation) to a certain deviator stress ratio (η_c). Furthermore, K_oU 2 test is shown which was sheared undrained from a η_c same as the CDS 2 test. An IU test, IU1, is also shown, which was consolidated to the same mean effective stress of the unloading point. The figure compares the yielding point of the CDS specimen and those of IU and K_oU samples. It should be noted that all these samples had similar consolidation void ratios. The results suggest a good agreement between the instability stress ratios (η_{IL}) in CDS and undrained tests on anisotropically K_o-consolidated tailings specimens. Therefore, a unique instability line is plotted for both these tests (IL 1) with a slope of $\eta_{IL} = 0.92$. The determination of IL is explained further below. The η_{IL} of the isotropically-consolidated specimen, however, shows a much lower value of $\eta_{IL} = 0.70$.

Another CDS test, CDS 1, was also conducted on a tailings specimen that was consolidated to a lower deviator stress level. A comparison between its instability line, IL 2, with IL 1 reveals a slight difference of 0.03 in their slopes. This suggests that for obtaining an agreement between the η_{IL} of a CDS test and an undrained shear test, in addition to the same void ratios, their η_c should also be the same. It is further observed that specimens subjected to a CDS path failed and experienced a complete collapse when approaching the phase transformation line determined based on the undrained shear tests.

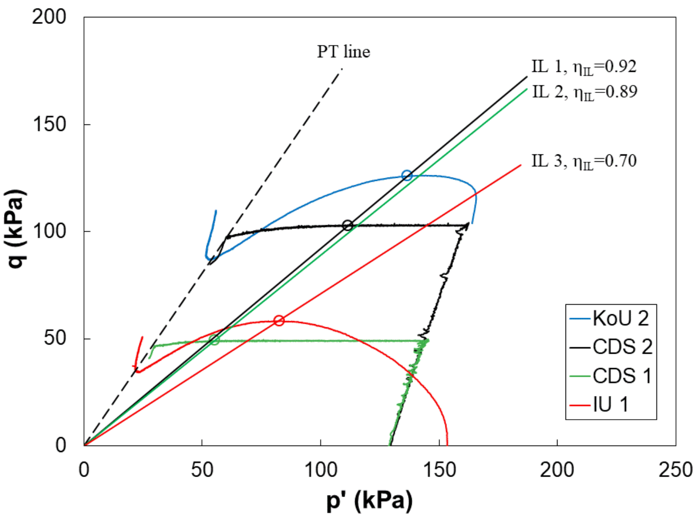

Figure 7. First set of CDS tests and comparison with undrained shear tests on anisotropically- and isotropically-consolidated specimens.

Figure 8 shows the stress path of two additional CDS tests performed on the tailings samples with higher deviator stress levels than CDS1 and CDS2 tests. Furthermore, a K_oU test was carried out, which was sheared undrained at a η_c same as the CDS 3 test. A more noticeable difference (0.06) in η_{IL} of the two CDS tests (loose vs dense) is observed. Again, similar stress ratios at the triggering of instability were measured for CDS3 and its reference K_oU test at similar e_c.

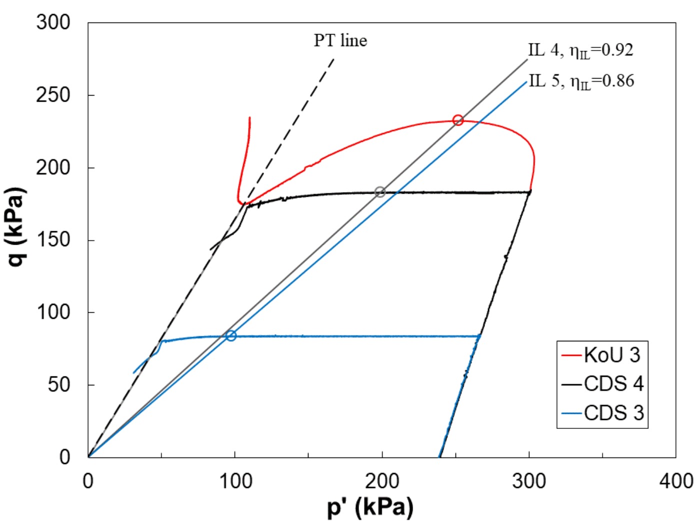

Figure 8. Second set of CDS tests and comparison with an undrained shear test on an anisotropically-consolidated specimen.

The instability points of the tests were obtained by the means of the second-order work increment (∂^2W) method. With regards to the studies of Darve & Laouafa (2000), Sawicki & Świdziński (2010), Monkul et al. (2011), Dong et al. (2016) and Rabbi et al. (2019), the second-order work increment can be formulated for a triaxial test as below:

$$\partial^2 W = \mathrm{d}p'\mathrm{d}\varepsilon_{vol} + \mathrm{d}q\mathrm{d}\varepsilon_a \quad (1)$$

Where ε_{vol} and ε_a are the volumetric and the axial strains, respectively. According to the afore-mentioned studies, a sample is stable as long as $\partial^2W > 0$. Using this method, the instability onset points of tests shown in Figures 7 and 8 were determined. For example, Figure 9 demonstrates ∂^2W for K_oU2, plotted against its increasing stress ratio (η). The instability stress ratio (η_{IL}) was found when $\partial^2W = 0$. The corresponding η_{IL} is comparable to the deviator stress ratio (q/p') at s_u(yield) for the same K_oU2 test in Figure 7.

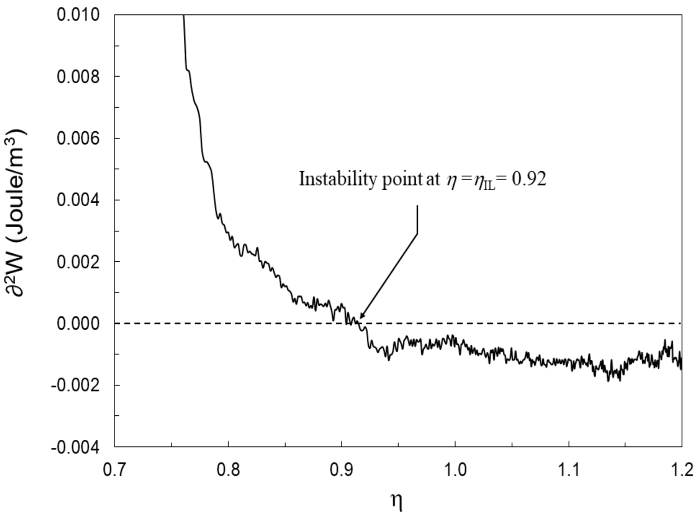

Figure 9. Second-order work increment to identify the instability occurrence in an undrained shear test.

Note that ∂^2W along the unloading path of a constant-deviator stress test can be rewritten as the first term of Equation 1 (i.e. $\partial^2W = dp' d\varepsilon_{vol}$), as the deviator stress is maintained constant ($dq = 0$). Since during unloading $dp' < 0$ (continuously reducing), ∂^2W becomes negative (instability arises) when $d\varepsilon_{vol}$ becomes positive (i.e, contractive volume change). Considering the variation of ε_{vol} during a constant deviator stress unloading path, the inversion of ε_{vol} is interpreted as the instability point. Figure 10a and b show the ε_{vol} of CDSs 1 and 2 plotted against their $\eta = q/p'$, respectively. The figure shows their transformation from a dilative to a contractive volumetric behavior and the identification of instability.

In addition, Figure 10 illustrates the variation of axial strain during unloading. The trend shows a slow increment of ε_a prior to instability. However, as the mean effective stress approaches the instability zone, a progressive acceleration of ε_a is observed, which is followed by a sharp rise as the specimen becomes unstable. Nevertheless, as shown in Figure 10, this rise happens over a range of η, and no precise instance of instability can be recognized by monitoring the change of ε_a.

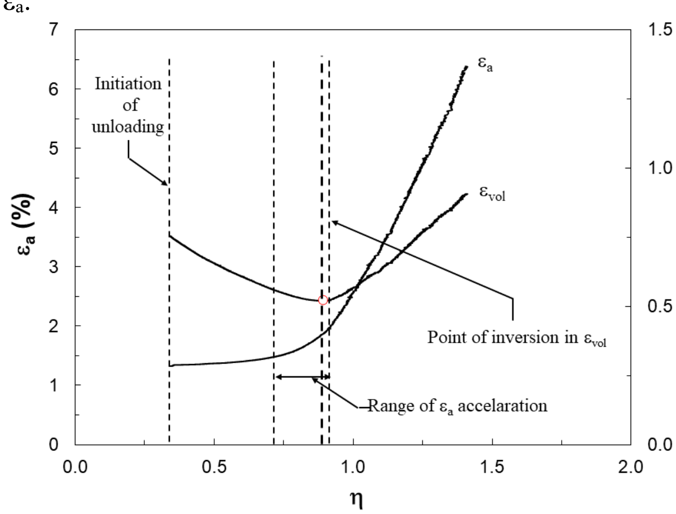

(a)

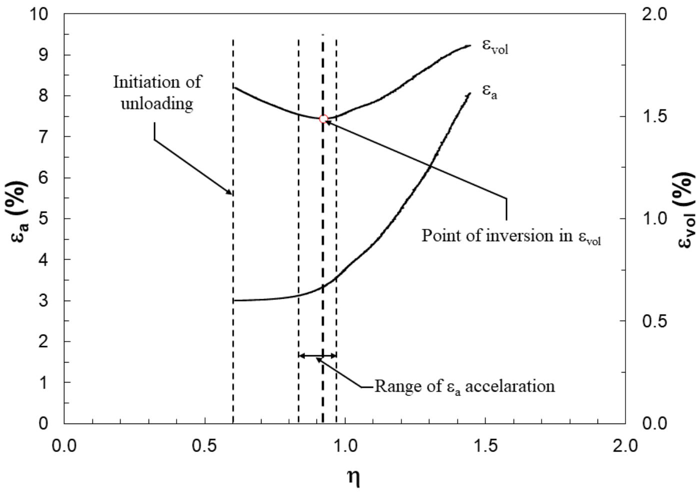

(b)

Figure 10. Volumetric strains in (a) CDS 1 and (b) CDS 2 tests versus deviator stress ratio (η).

4 CONCLUSIONS

The instability of gold tailings specimens due to confining stress relief under a constant deviator stress was studied in this paper through a series of triaxial compression tests. This type of instability is referred to as drained instability in the literature as no shear-induced pore pressure is developed prior to instability. The outcomes of the performed tests suggest an agreement between this type of instability with that exhibited during undrained shearing of an anisotropically consolidated specimen. However, different points of instability triggering were found in specimens subjected to CDS and undrained shearing of isotropically consolidated tests. The second-order work increment method was found to be reliable for identifying the triggering of instability.

5 ACKNOWLEDGEMENTS

Financial support from Golder Associates Innovation Program and Ontario Center of Excellence (OCE) is gratefully acknowledged.

6 REFERENCES

Al-Tarhouni, M., Simms, P., and Sivathayalan, S. 2011. Cyclic behaviour of reconstituted and desiccated–rewet thickened gold tailings in simple shear. *Canadian Geotechnical Journal*, **48**(7): 1044–1060. NRC Research Press.

Anderson, S.A., and Riemer, M.F. 1995. Collapse of saturated soil due to reduction in confinement. *Journal of geotechnical engineering*, **121**(2): 216–220. American Society of Civil Engineers.

Chang, N., Heymann, G., and Clayton, C. 2011. The effect of fabric on the behaviour of gold tailings. *Géotechnique*, **61**(3): 187–197. Thomas Telford Ltd.

Chu, J., Leroueil, S., and Leong, W.K. 2003. Unstable behaviour of sand and its implication for slope instability. *Canadian Geotechnical Journal*, **40**(5): 873–885. NRC Research Press.

Darve, F., and Laouafa, F. 2000. Instabilities in granular materials and application to landslides. Mechanics of Cohesive-frictional Materials: *An International Journal on Experiments*, Modelling and Computation of Materials and Structures, **5**(8): 627–652. Wiley Online Library.

Dong, Q., Xu, C., Cai, Y., Juang, H., Wang, J., Yang, Z., and Gu, C. 2016. Drained instability in loose granular material. *International Journal of Geomechanics*, **16**(2): 4015043. American Society of Civil Engineers.

Fourie, A.B., and Papageorgiou, G. 2001. Defining an appropriate steady state line for Merriespruit gold tailings. *Canadian Geotechnical Journal*, **38**(4): 695–706. NRC Research Press.

Fourie, A.B., and Tshabalala, L. 2005. Initiation of static liquefaction and the role of K0 consolidation. *Canadian geotechnical journal*, **42**(3): 892–906. NRC Research Press.

Gajo, A., Piffer, L., and De Polo, F. 2000. Analysis of certain factors affecting the unstable behaviour of saturated loose sand. Mechanics of Cohesive-frictional Materials: *An International Journal on Experiments*, Modelling and Computation of Materials and Structures, **5**(3): 215–237. Wiley Online Library.

Leroueil, S. 2001. Natural slopes and cuts: movement and failure mechanisms. *Géotechnique*, **51**(3): 197–243. Thomas Telford Ltd.

Monkul, M.M., Yamamuro, J.A., and Lade, P. V. 2011. Failure, instability, and the second work increment in loose silty sand. *Canadian Geotechnical Journal*, **48**(6): 943–955. NRC Research Press.

Morgenstern, N.R., Vick, S.G., Viotti, C.B., and Watts, B.D. 2016. *Fundão tailings dam review panel report on the immediate causes of the failure of the Fundão dam*. Cleary Gottlieb Steen & Hamilton LLP, New York,.

Olson, S.M., Stark, T.D., Walton, W.H., and Castro, G. 2000. 1907 static liquefaction flow failure of the north dike of Wachusett dam. *Journal of Geotechnical and Geoenvironmental engineering*, **126**(12): 1184–1193. American Society of Civil Engineers.

Qiu, Y., and Sego, D.C. 2001. Laboratory properties of mine tailings. *Canadian Geotechnical Journal*, **38**(1): 183–190. NRC Research Press.

Rabbi, A.T.M.Z., Rahman, M.M., and Cameron, D. 2019. Critical state study of natural silty sand instability under undrained and constant shear drained path. *International Journal of Geomechanics*, **19**(8): 4019083. American Society of Civil Engineers.

Riveros, G.A., and Sadrekarimi, A. 2020. Static Liquefaction Behaviour of Gold Mine Tailings. *Canadian Geotechnical Journal*, (ja).

Robertson, P.K., Melo, L., Williams, D.J., and Wilson, G.W. 2020. *Report of the Expert Panel on the Technical Causes of the Failure of Feijão Dam I*.

Sadrekarimi, A. 2020. Forewarning of Static Liquefaction Landslides. *Journal of Geotechnical and Geoenvironmental Engineering*, **146**(9): 4020090. American Society of Civil Engineers.

Sawicki, A., and Świdziński, W. 2010. Modelling the pre-failure instabilities of sand. *Computers and Geotechnics*, **37**(6): 781–788. Elsevier.

Schnaid, F., Bedin, J., Viana da Fonseca, A.J.P., and de Moura Costa Filho, L. 2013. Stiffness and strength governing the static liquefaction of tailings. *Journal of Geotechnical and Geoenvironmental Engineering*, **139**(12): 2136–2144. American Society of Civil Engineers.

Zhu, J.-H., and Anderson, S.A. 1998. Determination of shear strength of Hawaiian residual soil subjected to rainfall-induced landslides. *Géotechnique*, **48**(1): 73–82. Thomas Telford Ltd.

CPTu assessment: investigating how a changing groundwater table may impact data collection and interpretation

Andrew Burgin, Richard Dawson, Mauricio Pinheiro, & Mathieu Wacowich
Stantec Consulting Ltd, Vancouver, British Columbia, Canada

Anelisa Vasconcelos
Belo Horizonte, Minas Gerais, Brasil

ABSTRACT: Piezometric Cone Penetrometer (CPTu) testing is a widely used technique to investigate tailings deposits, including the identification of contractive and potentially liquefiable material below the water table. Twinned CPTu soundings advanced several years apart at Samarco's Germano Complex silty sand tailings facility show that there was a gradual lowering of the water table following active tailings deposition. A comparison of the CPTu profiles for the two data sets show consistent contractant behaviour before and after ground water lowering. Other studies show that unsaturated silty tailings could exhibit a more dilatant response, indicating that re-saturation could render these materials potentially liquefiable. Samarco tailings show low in-situ matric suction values above the SWCC-defined residual water content which minimizes the suction hardening effects and reduces the potential for differing characterization in saturated versus unsaturated deposits.

1 INTRODUCTION

Piezometric Cone Penetrometer (CPTu) testing is a common ground investigation technique, providing a continuous data profile through a deposit. CPTu testing is relatively quick and inexpensive when compared to boreholes. They provide a continuous profile of tip resistance (q_c), sleeve friction (f_s), and dynamic pore pressure (u_2). CPTu soundings have become a preferred investigation method for tailings deposits.

There are a range of CPTu-based semi-empirical relationships and interpretation techniques to characterize sand tailings. The methodology proposed by Robertson & Wride (1998) and Robertson (2010, 2016), which is based on the modified soil behaviour type (Mod SBT_n), has been widely used to assess the behaviour and liquefaction potential of these materials. According to the most recent version of the methodology, contractive/dilative soil behaviour is distinguishable for three (3) different soil types: Sand-like, silt (Transitional) and Clay-like. The method does not differentiate between saturated and unsaturated behavior; assuming that granular soils need to be contractant and sufficiently saturated ($S > 90\%$) to be susceptible to a flow slide.

Russell & Reid (2018) investigated the effects of saturation on the CPTu measurements and data interpretation of sand and silts. They advanced CPTu probes through a clean quartz sand (Sydney sand) and a silty sand gold tailings. The cleaner Sydney sand results show similar behaviour classification between saturated and unsaturated conditions while the silty sand gold tailings results show markedly different interpretations, with a shift from contractive behaviour when saturated to dilative behaviour when unsaturated. They attribute the shift to the effect of "unsaturated" suction hardening with the finer grained siltier material. Similar findings have also been documented by Robertson (2017) and others.

This paper investigates whether silty sand iron ore tailings at the Samarco Germano Complex mine site in Brazil also exhibit different CPTu behavior in the unsaturated versus saturated state, specifically due to conditions before and after a drop in the phreatic surface. Twinned CPTu soundings advanced before and after a lowering of the phreatic surface examine the difference in the data profiles. The work builds on previous findings by Dawson et al (2019) and the Fundão Tailings Dam Review Panel (2016) report.

2 SITE CHARACTERIZATION

Figure 1 shows a satellite image of the Germano tailings complex from 2021. The Germano Complex is predominantly a hydraulically placed iron ore process tailings facility raised using the upstream construction method from 1976 through to 2016. It is situated in a deep valley south of the Fundão valley. There is a large compacted fill starter dam about 70m tall surrounded on downstream and upstream sides by iron ore tailings raised using upstream methods. A foundation drain installed downstream of the starter dam keeps the downstream phreatic surface near the valley bottom. The overall Germano Complex contains ~150Mm^3 of tailings with an ultimate crest-to-toe height of 165m and 3H:1V downstream slopes (Dawson et al, 2019).

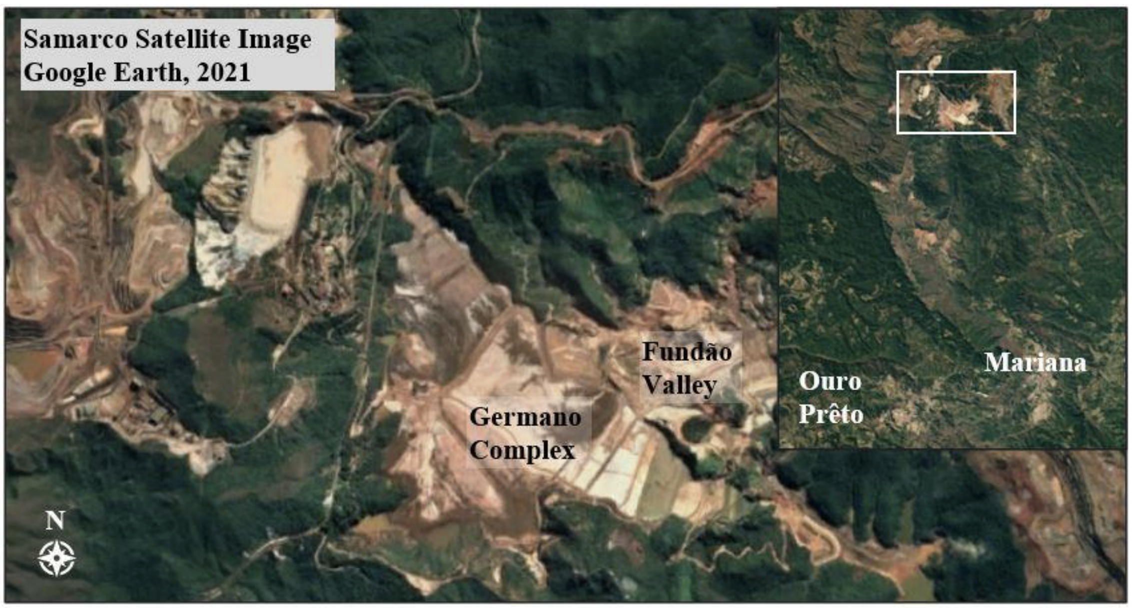

Figure 1. Satellite image of Germano Complex (Google Earth, 2021)

Table 1 summarizes representative index test results for the Samarco sand tailings. The particle size distribution classifies this material as a silty sand/sandy silt, denoted by the United Soil Classification System (USCS) as SM - ML, with ~50% fines (passing sieve No.200) and < 3% clay-size particles (2μm) (Dawson et al, 2019).

Table 1. Sand tailings index test results

Percent Fines (<75μm)	D_{10} (mm)	Specific Gravity, G_s	Atterberg Limits	Typical Deposit Unit Weight (kN/m^3)	Min-Max Void Ratio
ASTM D422	ASTM D422	ASTM D854	ASTM D4318	ASTM D7263	ASTMD4253 / ASTMD4254
45-55%	0.03 – 0.05	2.93	Non-Plastic	20	0.40 – 0.85

Scanning Electron Micrographs (SEM) in Figure 2 show that the individual grains are sub-angular and blocky; both silt- and sand-sized particles have similar grain shapes (Fundão Panel, 2016).

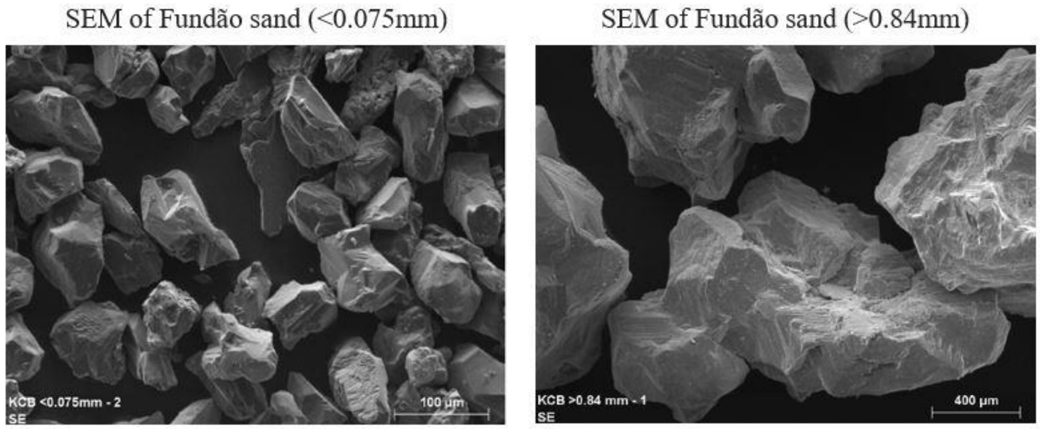

Figure 2. SEM of Samarco sand tailings (adapted from Fundão Panel, 2016)

The soil-water characteristic curve (SWCC) of the sand tailings from Tempe cell testing is shown below in Figure 3 with a saturated volumetric water content of 42% (approximate porosity for the hydraulic fill deposit). The air entry value (AEV) is approximately 5kPa and residual degree of saturation is approximately 5-7%. In situ matric suction values above the water table are estimated to be about 15-30kPa corresponding to saturation values in the range of 30-50% (varying seasonally). Similar in situ values of 6-10kPa have been measured in Vibrating Wire Piezometer (VWP) instruments above the water table.

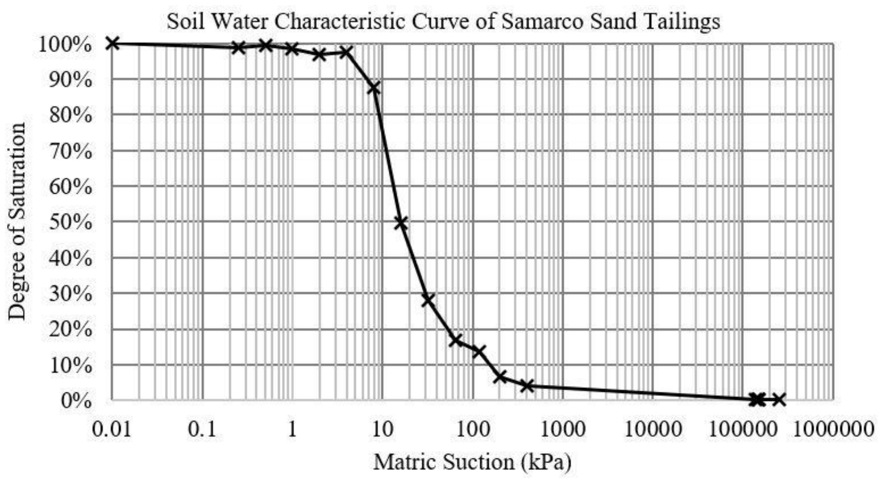

Figure 3. SWCC of Samarco sand tailings

A seismic cone penetrometer test (SCPT) profile was developed in the study area in 2021, extending to 75m depth, collecting shear wave velocity (V_s). The SCPT data below the water table was analyzed using commercially available CPTu interpretation software CPeT-IT© v.3.2.1.7 (CPeT-IT©), distributed by GeoLogismiki. Figure 4 presents the SCPT data on the normalized rigidity index chart, plotting normalized cone resistance (Q_{tn}) taking account of the in-situ vertical stress on the y-axis against small-strain rigidity (G_o/q_n) index on the x-axis. The SCPT data plots with an empirical parameter K*G value < 330, indicating the study area is representative of an ideal soil, that is, young and with no microstructure, and therefore the semi-empirical interpretation Mod SBT_n technique may be applied (Robertson, 2014). In other words the tailings deposit exhibits CPTu response similar to many natural soils used to develop semi-empirical CPTu calibrations.

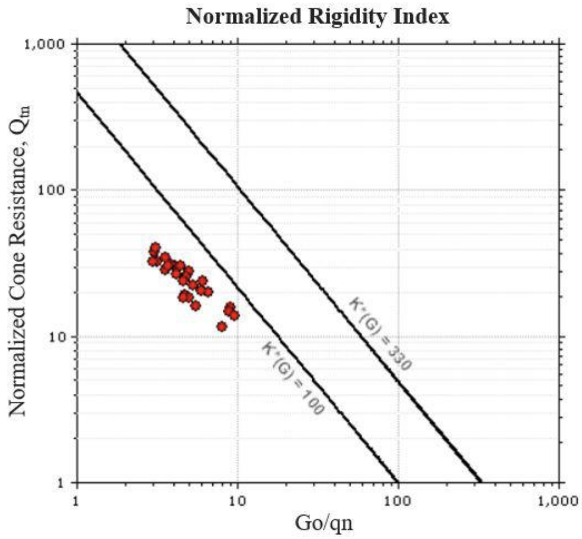

Figure 4. Saturated SCPT data plotted on Normalized Rigidity Index Plot (ref. CPeT-IT)

3 METHODOLOGY

Two (2) twinned CPTu soundings were advanced into the study area at about the same coordinates, with a roughly four (4) year time interval between tests. The first sounding, CPTU-2017, was advanced in 2017 while the second sounding, CPTU-2021, was advanced in 2021 after a lowering of the groundwater level following active tailings deposition. During the time between the two (2) soundings about 5m of additional fill was placed at the CPTu locations. The CPTu soundings were interpreted using CPeT-IT© software.

CPTU-2017 was advanced 83m to terminate at 802m El., and CPTU-2021 was advanced 75m to 816m El. Both soundings terminated at refusal depth near the base of the tailings deposit. Profiles for q_c, f_s, u_2, and normalized clean sand equivalent cone resistance ($Q_{tn,cs}$) were developed for each sounding and then compared to identify data trends and potential variance in data signatures.

Figure 5 presents the basic data interpretation profiles for the twinned soundings:

- The q_c (left) profiles are generally similar below 880m elevation where the data overlaps although it appears the 2021 probe may be more sensitive with higher peaks and troughs. The f_s (centre) profiles appear to shift slightly right in 2021, again with higher peaks and troughs. The high q_c and f_s values within the upper 5m of CPTU-2021 reflect ~5m of the mechanically placed and compacted fill placement that occurred between soundings.
- The u_2 plot (right) profile shows minor excess pore pressure readings above around 860-865m elevation, then a well-developed and generally steady pressure gradient consistent with (near) hydrostatic conditions to depth. The u_2 plot also illustrates the drop in phreatic surface over time, with the hydrostatic gradient of CPTU-2021 shifted down several metres from CPTU-2017. Inferred phreatic surfaces are ~865.0m and ~859.5m for CPTU-2017 and CPTU-2021, respectively; this is the interval where the phreatic surface lowered between the time for the two soundings.

Tailings below 859.5m may be considered as a baseline range for q_c and f_s, where the tailings have remained saturated and therefore results should be repeatable. While the general q_c trend is consistent here, the pronounced peaks and troughs in 2021 with the modest f_s shift suggest a slight shift in this baseline between the two data sets.

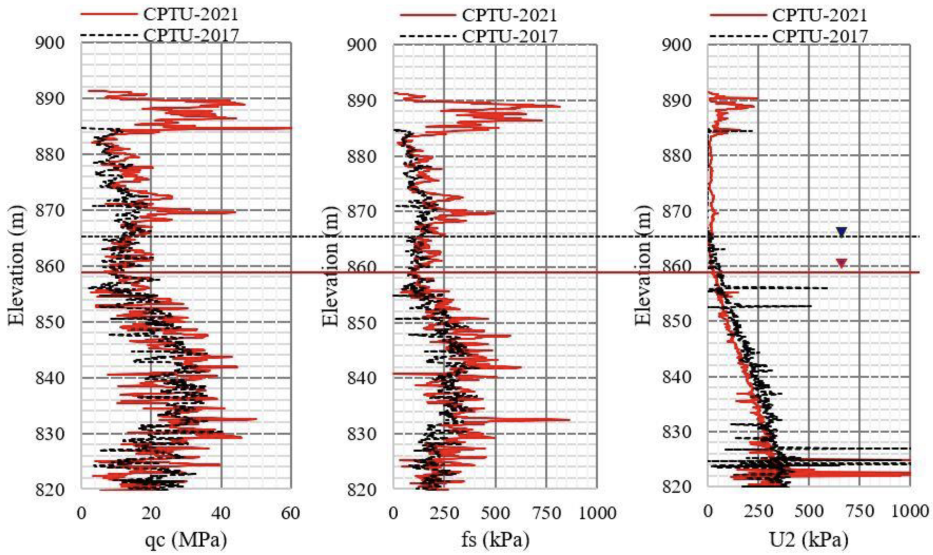

Figure 5. Basic data interpretation profiles for CPTU-2017 and CPTU-2021

4 RESULTS AND DISCUSSION

Interpretation of the u_2 data shows a phreatic surface drop of approximately 5.5m between the two (2) soundings (between 865 and 859.5m elevations), or 1.4m average annual drop. For the purpose of this study the 2017 phreatic surface at 865m is considered the legacy groundwater table representing saturated tailings during the operational period.

Figure 6 presents a more detailed view of the u_2 and $Q_{tn,cs}$ data profiles within this Fringe Zone, bounded as shown. A vertical line at $Q_{tn,cs}$ = 70 has been added to that profile that is generally considered the boundary between dilative and contractive sand-like / transitional materials, therefore potentially susceptible to static liquefaction (Robertson, 2016)

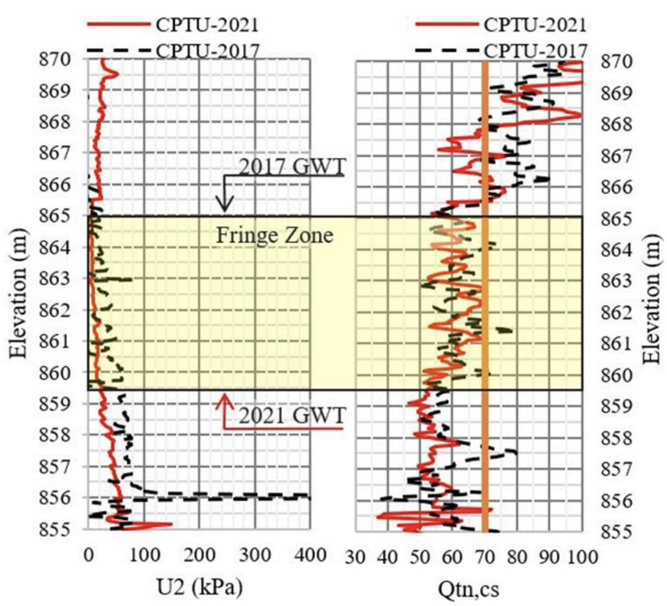

Figure 6. Twinned CPTu profiles with detailed view of Fringe Zone

Figure 6 shows that:

- u_2 profiles clearly illustrate the drop in phreatic surface over time, with development of a (near) hydrostatic gradient in 2021 ~5.5m below the 2017 profile.
- $Q_{tn,cs}$ values generally range from 40 to 80, with a majority of the data < 70 and therefore contractive and potentially susceptible to static liquefaction.
- $Q_{tn,cs}$ profiles appear to be generally consistent with each other, with minor variations that appear to be randomly distributed and there does not appear to be a shift in $Q_{tn,cs}$ profiles towards dilatancy due to de-saturation.
- $Q_{tn,cs}$ values above the legacy water table remain mostly dilative.

Figure 7 presents a statistical distribution of $Q_{tn,cs}$ profiles within the Fringe Zone to further highlight the relative consistency between CPTU-2017 and CPTU-2021 in this region. Both the histograms and cumulative distributions illustrate the statistical similarity between the data sets, with a minor shift towards increasingly contractive behaviour over time as the water table drops and tailings transition from saturated to unsaturated conditions. Both the mean values and standard deviations are essentially the same.

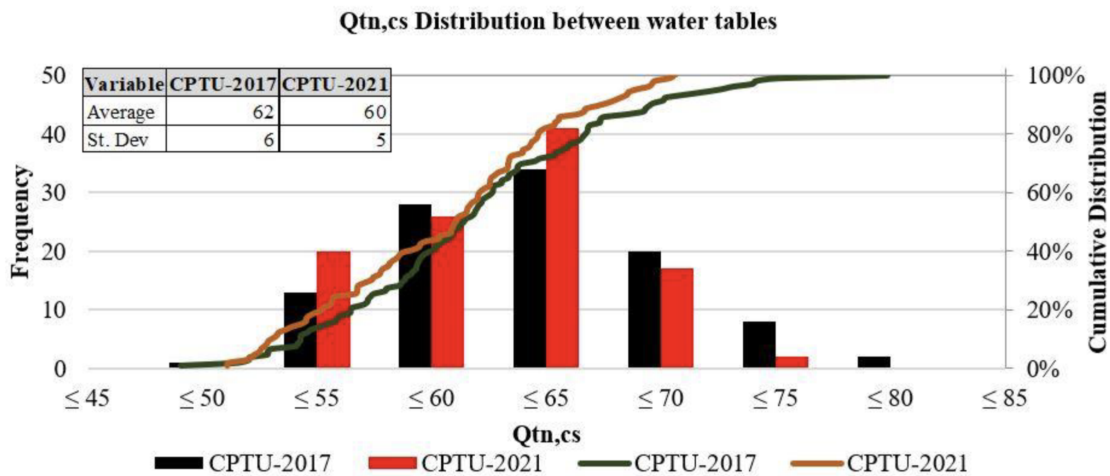

Figure 7. Statistical assessment of $Q_{tn,cs}$ values for CPTU-2017 and CPTU-2021

These results indicate that Robertson's Mod SBT_n behaviour classification system yields generally similar and consistent $Q_{tn,cs}$ profiles before and after a drop in phreatic surface. As such, the Mod SBT_n classification does not appear to be significantly influenced in this Fringe Zone by the effect of "unsaturated" suction hardening, as observed for unsaturated silty sand gold tailings by Russell & Reid (2018).

In this case, low matric suction values appear to be important for understanding the similar behaviour before and after groundwater lowering. Ho and Fredlund (1982) define apparent cohesion due to matric suction as shown in Equation 1:

$$c' = (\mu_a - \mu_w)*\text{Tan}\Phi^b \tag{1}$$

Where:
c' = apparent cohesion due to matric suction, in kPa.
Φ^b = friction angle for changes in matric suction.
$\mu_a - \mu_w$ = matric suction, in kPa.

$\tan\Phi^b$ may further defined by as $\chi\tan\Phi'$ (adapted from Tomboy et al, 2008), where χ is the dimensionless effective stress parameter and Φ' is the effective friction angle. For practical. purposes χ is assumed to vary linearly with degree of saturation and may be approximated as such from 0 - 1 (Robertson, 2017). Assuming $\Phi' = 32$ for Samarco sand (Dawson et al, 2019) Equation (1) may then be used to derive a relationship between degree of saturation above residual values and apparent cohesion, using the SWCC shown above in Figure 3, as shown in Figure 8.

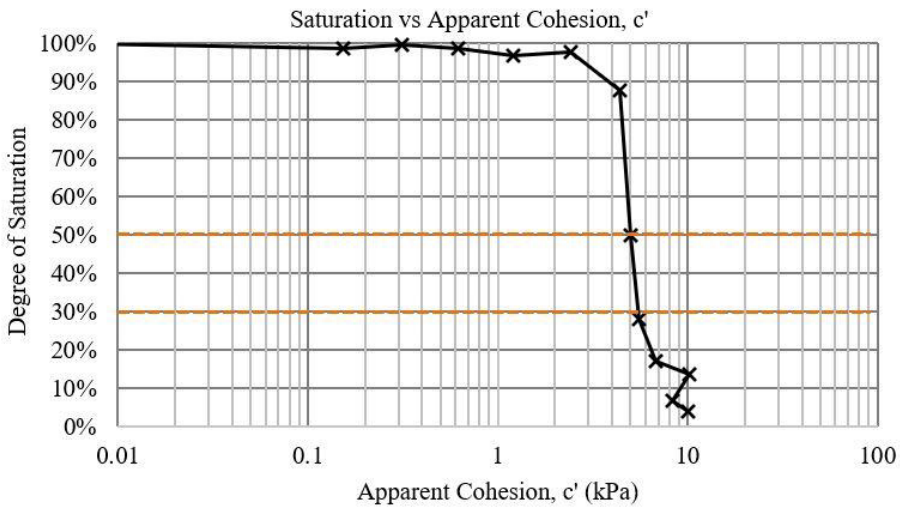

Figure 8. SWCC of Samarco sand tailings converted to saturation-c' in semi-log space

Figure 8 clearly demonstrates that apparent cohesion is about 5-7kPa over the range of saturation values expected above the phreatic surface at the Germano tailings facility, represented by horizontal orange lines. These low values are not expected to significantly change the CPTu soil behaviour response for saturated versus unsaturated sand tailings. Robertson et al (2017) documents a significant change in unsaturated behavior where the matric suctions are in the range of 70 -100kPa for an unsaturated silty sand tailings.

Figure 9 compares the CPTu data within the Fringe Zone (left hand graph) and above the Fringe Zone (right hand graph) using the Robertson Mod SBT_n classification diagram. Both graphs show similar behaviour for the two (2) data sets: contractive behaviour within the Fringe Zone and "mostly" dilative behaviour above this interval. Differences between the two (2) sets of data could be due to instrument calibration, stress normalization (2021 profile has 5m additional fill) and/or deposit variability between the two locations. Notably, there is a higher number of data points showing contractive material above the Fringe Zone (right hand graph in Figure 9) in the more recent 2021 profile, whereas the distribution of contractive tailings within the Fringe Zone remains about the same for the two profiles (right hand graph in Figure 9).

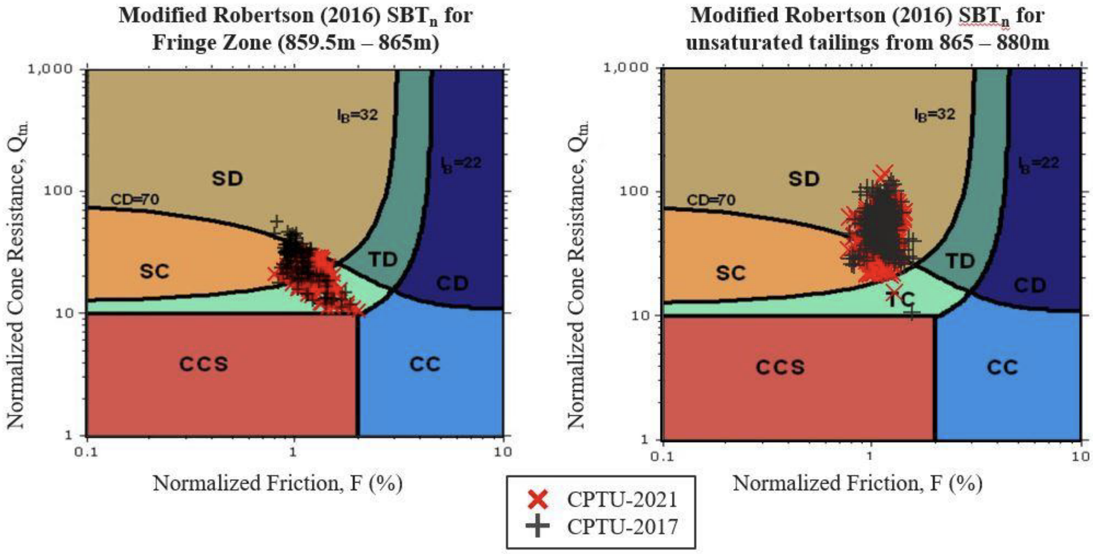

Figure 9. Mod SBT_n plots comparing CPTU-2017 and CPTU-2021 in the Fringe Zone (left) and above the legacy groundwater table (right)

Effective drainage over the starter dam and through the lower structure may help to explain this shift above the legacy groundwater table interface towards dilative behaviour. Subsequent poor drainage behind the impermeable starter dam may have promoted the contractive behaviour in the Fringe Zone, effectively mitigating the density effect described above. Alternatively, the degree of saturation above 865m may be low enough to increase the effect of matric suction and apparent cohesion, similar to what was observed by Russell & Reid (2018) and therefore shifting the data population into the dilative regime. However, it is unlikely that in-situ saturations are low enough (< 5%) at Germano Complex for matric suction to influence the interpretation.

5 CONCLUSIONS

Two (2) twinned CPTus were advanced into silty sand Germano Complex tailings at a similar location but a few years apart, after the groundwater level had dropped 5m. The CPTu data was interpreted using Robertson's (2016) Mod SBT_n classification, and the resulting interpretations compared in terms of normalized clean sand equivalent tip resistance, $Q_{tn,cs}$, for evaluating contractive versus dilative behaviour.

The results show similar and consistent results between the two (2) CPTus in the Fringe Zone (previously saturated tailings); the silty sand tailings remained predominantly contractive and sand-like / transitional. In other words, the effects of suction hardening for the Samarco sand tailings in the Fringe Zone has not impacted the Mod SBT_n classification for contractive versus dilative behavior. This observation can be explained by considering the SWCC for the unsaturated tailings sand showing very low suctions for moisture contents above the residual water content value (about 5%); even though the tailings have high silt contents. Above the Fringe Zone the tailings remain mostly dilatant indicating that the boundary between contractive / dilatant tailings is mostly defined by the legacy water table.

6 ACKNOWLEDGEMENT

The authors which to express our thanks to our clients, our peers in the tailings industry, and our colleagues and project team, in particular Sarah Neuenhagen and Mehdi Qoreishi, at Stantec Consulting for their support and encouragement.

7 REFERENCES

Dawson, R., Burgin, A., Wacowich, W., Bernardo, J., & Vasconcelos, A., 2019. Laboratory and CPT_u Characterization of Samarco Sand Tailings. *Proceedings of Tailings and Mine Waste 2019:* 1421-1433.

Fundão Tailings Dam Review Panel, 2016. Report on the immediate causes of the failure of the Fundão dam.

GeoLogismiki 2014. CPeT-IT User's Manual v.1.4.*www.geologismiki.gr/Documents/CPeT-IT/CPeT-IT%20manual.pdf*.

Google Earth Pro 7.3.4.8248, 2021. Samarco Germano Complex region, Minas Gerais, Brazil. UTM 23K, -20.218° lat, -43.465° lon. Eye alt 8.74km. http://www.google.com/earth/index.html. Accessed August 19, 2021.

Ho, D.F.Y., and Fredlund, D.G., 1982. Increase in strength due to suction for two Hong Kong soils. *Engineering and Construction in Tropical Soils ASCE Speciality Conf.*, *Hawaii,* pp. 263-295.

Robertson, P.K. 2010. Soil Behaviour Type from the CPT: an update. *Gregg Drilling & Testing Inc.*

Robertson,,P.K 2014. Comparing CPT and V_s Liquefaction Triggering Methods. *Journal of Geotechnical Engineering and Geoenvironmental Engineering*: *04015037-6*.

Robertson, P.K 2016. Cone penetration test (CPT)-based soil behaviour type (SBT) classification system – an update. *Canadian Geotechnical Journal,* 53(12): 1910-1927.

Robertson, P.K., & Cabal, K.L. 2014. Cone Penetration Testing for Geotechnical Engineering, 6th Edition. *Gregg Drilling & Testing, Inc.*

Robertson, P.L., Viana da Fonseca, A., Ulrich, B., & Coffin, J 2017. Characterization of unsaturated mine waste: a case history. *Canadian Geotechnical Journal*, 54(12): 1752-1761

Robertson, P.K., & Wride, C.E. 1998. Evaluating cyclic liquefaction potential using a cone penetration test. *Canadian Geotechnical Journal*, 35(3): 442-459.

Russel, A.R., & Reid, D. 2018. Pitfalls in interpretation of cone penetration test data recovered from unsaturated geomaterials, RJ Jewell & AB Fourie (eds). *Proceedings of the 21st International Seminar on Paste and Thickened Tailings,* Australian Centre for Geomechanics, Perth, pp. 483-492.

Schneider, J.A. et al 2012. Comparing CPTU Q-F and Q-$\Delta u_2/\sigma_v'_0$ soil classification charts. *Géotechnique Letters 2,* 209-215.

Tomboy et al, 2008. Shear strength of unsaturated soil and its influence on slope stability. *Unsaturated Soils. Advances in Geo-Engineering: Proceedings of the First European Conference on Unsaturated Soils, E-UNSAT 2008,* pp. 459-464

Tailings state from $SCPT_u$ and laboratory shear wave velocity measurement

Mahmoud N. Hussien, Desheng Deng & Christopher Ong Tone
Wood Resilient Environments, Montréal, QC, Canada

Marie-Pier Breton
ArcelorMittal Exploitation minière Canada s.e.n.c., Port-Cartier, QC, Canada

ABSTRACT: The current comprehension of mechanical soil behavior relates predominantly to sands and clays and engineering of silt in general and tailings in particular is, therefore, challenging. Tailings samples undergo gross densification during extrusion, transfer to testing laboratory and consolidation to the in-situ stresses. In-situ penetration tests (e.g., SPT and CPT) is not even the right/exact answer as they always need a sort of calibration to recover engineering information from the measured data. Calibration in the case of sands implicates controlled chamber testing or references another test method commonly triaxial testing of undisturbed samples or in-situ vane shear in the case of clays. Tailings have, to date, no controlled chamber test studies nor can undisturbed samples be properly tested and the available correlations, in general use today, cannot be straightforwardly utilized. In this paper, shear wave velocity (V_s) measurements were carried out in an Oedometeric cell on tailings samples retrieved from Port-Cartier ArcelorMittal's TSF, Qc. Reconstituted tailings samples were also loaded in shear under constant strain rate triaxial compression either drained or undrained to determine their critical state at large strains. The V_s measurements were used to develop relationships between stress-normalized shear wave velocity (V_{s1}) and void ratio (e), and were combined with the shear results expressed within the framework of Critical State Soil Mechanics (CSSM) to develop a methodology to infer the tailings' state from field measured V_s which is a critical element in evaluating the tailings potential for flow (static) liquefaction.

1 INTRODUCTION

Tailings are the residual wastes of mineral processing that remain after extraction of the desired mineral of value from the ore. Tailings consist of predominantly silt-sized particles and are generally deposited as a slurry into natural valleys closed with dams or by complete peripheral dykes, commonly referred to as tailings storage facilities (TSFs). The lack of post-deposition compaction and the electrical interaction among the finer particles generally entail loose in-situ arrangements whose potential to undergo brittle strain softening, and hence flow, is dominated by their state being characterized by the state parameter ψ (Been and Jefferies 1985). Therefore, quantifying the tailings state and, hence, liquefaction potential is an important economic and safety issue in the mining industry given its catastrophic downstream consequences.

Because of the excessive disturbance associated with sampling and handling procedures, it is not common to test tailings in the laboratory in an undisturbed condition, and engineering of tailings relies largely on in-situ penetration tests (i.e., SPT and CPTu) with the CPTu being the preferred methodology. The CPTu involves hydraulically pushing a probe into the ground at a steady rate and the tailings' response (i.e., tip resistance (q_c), sleeve friction (f_s), and the pore water pressure (u_2)) is continuously measured. A basic issue with the measured data is that it needs a sort of calibration to recover the sought state (ψ) and other engineering information from the measured data.

Methodologies for determining ψ of a soil deposit directly from CPT data were developed first for drained penetration (pore water pressure ratio, $B_q \approx 0$), based on the results of calibration chamber testing, for which Critical State (CS) parameters were known (Been et al 1986, 1987):

$$\psi = \frac{1}{m} ln\left(\frac{Q_p}{k}\right) \tag{1}$$

where Q_p is the tip resistance normalized by the mean effective stress; m, k are two soil specific coefficients. Shuttle and Jefferies (1998), through detailed finite element analyses, linked the coefficients m, k with fundamental mechanical soil properties including the shear rigidity, I_r; the critical void ratio, M; the dilatancy parameter, N; and the plastic hardening modulus, H among others.

Plewes et al (1992) expanded upon the work by Been et al. (1986, 1987) and modified Eq. (1) to allow for the excess pore water pressures around the CPT when undrained conditions prevail:

$$\psi = \frac{1}{m^*} ln\left(\frac{Q_p(1-B_q)}{k^*}\right) \tag{2}$$

the two new coefficients m^*, k^* can be estimated from the slope of the CSL, λ_{10} and the critical state friction ratio, M:

$$k^* = \left(3 + \frac{0.85}{\lambda_{10}}\right) M \tag{3}$$

$$m^* = 11.9 - 13.3\lambda_{10} \tag{4}$$

The Plewes et al. approach is a screening method and it assumed that the value of λ_{10} could be estimated as one-tenth of the normalized CPT friction ratio %F, and $M = 1.2$ for most sands.

Shuttle and Jefferies (2016) used a fundamental approach where spherical cavity expansion theory in a general critical-state soil model is employed to establish a correlation between the tip resistance of CPTu and the two soil specific coefficients m^*, k^*, which can be then used to estimate ψ from Q_p and B_q.

Based on insights from CANLEX results, Robertson (2010) developed an empirical correlation to infer ψ from CPT data as:

$$\psi = 0.56 - 0.33 log Q_{tn,cs} \tag{5}$$

where $Q_{tn,cs}$ is the clean sand equivalent normalized cone resistance that is a proxy for state parameter. Cunning et al (1996) evaluated the in-situ state of cohesionless soils based on shear wave velocity (V_s) measurements. The Cunning's procedure has the advantage that the shear wave velocity measurement is independent of soil compressibility, unlike penetration test results. The relationship involves a normalization for overburden stress that is developed based on laboratory results.

In this paper, laboratory V_s measurements were carried out in an Oedometeric cell using the piezoelectric ring-actuator technique (P-RAT) (Karray et al 2016, Hussien and Karray 2021) on tailings samples retrieved from Port-Cartier ArcelorMittal's TSF, Qc. Reconstituted tailings samples were also loaded in shear under constant strain rate triaxial compression either drained or undrained to determine their critical state at large strains. The V_s measurements were used to develop relationships between stress-normalized shear wave velocity (V_{s1}) and void ratio (e), and were combined with the shear results expressed within the framework of CSSM to develop a methodology to infer the tailings' state from field measured V_s. The obtained state parameter profiles were compared with other classical approaches (e.g., Plewes et al 1992, Cunning et al 1996, Robertson 2010, Shuttle and Jefferies 2016) as will be discussed herein.

2 SITE OVERVIEW AND THE GEOTECHNICAL INVESTIGATION

The facility Port-Cartier (Figure 1) is a sidehill-type TSF with tailings confined by engineered dykes and the natural topography. It comprises four (4) cells: the upper basin, the lower basin, park B, and park C. All the dykes of upper and lower basins were upstream raised on deposited tailings. Tailings are generally deposited hydraulically in the upper basin and excess water is transferred by a spillway to the lower basin and then another spillway to park B. All run-off is collected by a drainage ditch located south of park C and is also transferred to park B. All excess water from park B is then released to the environment after treatment in the TSF basins. The tailings deposited in the upper basin are naturally dried and then trucked to park B for dry disposal.

Figure 1 – Port Cartier TSF, Qc.

A comprehensive geotechnical investigation comprised both in-situ and laboratory testing were carried out in 2019 at Port-Cartier TSF, Qc. The main objective of this investigation is to characterize the Port-Cartier tailings and to assess their physical response to loading with differing effects from confinement (consolidation) to distortional (shear) loading – and whether there was sufficient time for pore water to move or not, and the transition between these two modes.

In this investigation, forty (40) CPTu/SCPTu with dissipation tests were performed in accordance with ASTM D-5778 and ASTM D-7400 standards. Shear wave velocity (V_s) testing was performed in conjunction with the piezocone penetration test (SCPTu) to collect interval velocities. Nine (9) conventional geotechnical boreholes with split-spoon and Shelby-tube sampling were performed. Standard Penetration Tests (SPT) were also performed in conjunction with the boreholes according to ASTM D-1586 standard. The main objective of the conventional subsurface investigation is to obtain representative disturbed and undisturbed samples of tailings for advanced laboratory testing. Fifteen (15) CID and CIU triaxial as well as T_xSS tests were undertaken on tailings samples that had been reconstituted to a range of densities. This testing provides a reference data to define the CSL of the tailings and to determine the tailings' stress-dilatancy (M and N) and state-dilatancy (χ_{tc}) properties as well as tailings' plastic stiffness (H).

Before performing the triaxial testing, the relationship between void ratio (e) and stress-normalized shear wave velocity (V_{s1}) was first established in the laboratory based on a series of laboratory tests using the piezoelectric ring-actuator technique (P-RAT) on tailings samples in loose to dense states. V_{s1} can be estimated as:

$$V_{s1} = V_s \left[\frac{P_a}{\sigma_v'}\right]^{0.25} \tag{6}$$

where σ_v' is the effective vertical stress, P_a is normal atmospheric pressure in the same units as σ_v' (i.e., $P_a \approx 100$ kPa if σ_v' is in kPa). In this study, the P-RAT was incorporated into an oedometer apparatus, and the testing procedure was identical to that of the conventional oedometer test. The V_s measurement was performed at each loading stage before introducing a new load level, and the measurement is based on transmission of a mechanical signal through the tailings' specimens with source and receiver transducers capsulated in the end platens of the oedometer cell.

3 RESULTS AND DISCUSSION

The results for Particle Size Distributions (PSD) on bulk tailings samples are presented in Figure 2. The key observation regarding Figure 2 is that the tailings' samples extracted from different locations within the TSF are greatly similar in grading.

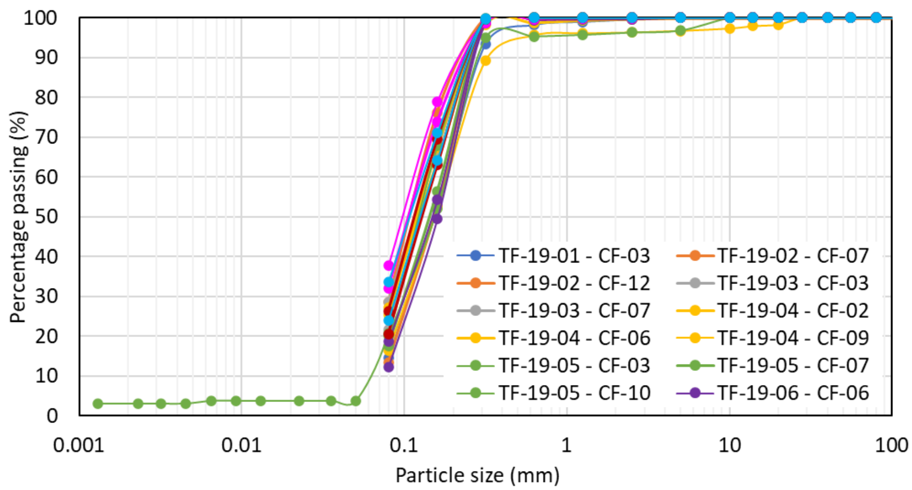

Figure 2 - Particle size distributions for Port-Cartier tailings samples.

The specific gravity of triaxial test samples for critical state locus determination was completed in accordance with ASTM D5550 and it ranged between 2.99 and 3.18.

The CSL for tailings samples was determined using triaxial and T_xSS tests on predominantly loose and dense samples, tested both drained and undrained. The critical state is the point of those tests that reach the condition of continuing deformation at constant deviator stress and constant void ratio. The result of triaxial and T_xSS tests on bulk samples of tailings are presented in Figure 3 as a void ratio versus mean effective stress plot (e versus log p'). The inferred CSL is the green line on this figure. Although a linear semi-log distribution is a reasonable representation of the CSL, close inspection of the test results suggests the curved equation is a better fit:

$$e_c = 1.43 - 0.60 * \left(\frac{\acute{p}}{100}\right)^{0.125} \tag{7}$$

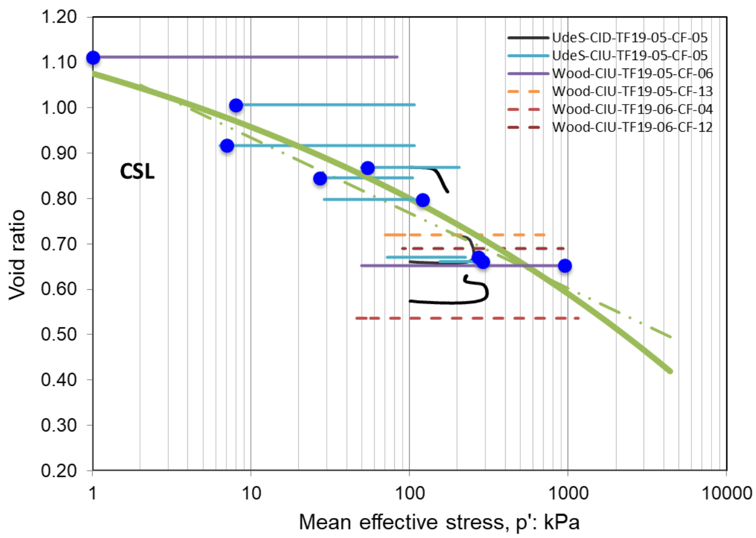

Figure 3 - Laboratory test paths showing critical state locus for the tailings.

Strength and dilatancy parameters inferred from the experimental data are tabulated in Table 1.

Table 1. Strength and dilatancy parameters inferred from experimental data.

M	N	χ_{tc}	ϕ'_c	ν	Γ	λ_{10}
1.52	0.4	7.0	34	0.15	1.10	0.166

Series of tests were carried out on the tailing's samples (TF-19-05 and TF-19-06) in an oedometer cell using the P-RAT that leads to the determination of the relationship between the normalized shear wave velocity (V_{s1}) and the void ratio (e) of the tailings. The results of these tests are shown on Figure 4. The max and the min void ratios of the tailings obtained from standard tests according to ASTM D4253 and ASTM D4254 are plotted on Figure 4 as references. As seen on the figure, both tailings' samples experience similar V_{s1} – e trend.

The results of the V_s, and CSL information (Table 1) were combined with the state parameter concept to develop an equation to use field measured V_s, to estimate the in-situ consolidation state within a soil deposit, thus, the contractive-dilative boundary (ψ=-0.05) with respect to vertical effective stress for large strain loading can be determined from in-situ measurements of V_s. This equation can be written as:

$$V_s = 344.83(0.5424 - 0.0029\psi)\left(\frac{\sigma'_v}{100}\right)^{0.25} \tag{8}$$

Figure 5 shows the contractive-dilative (CD) boundary for Port-Cartier tailings in term of shear wave velocity against effective vertical stress at geostatic stress ratio, K_0 = 0.5. CD boundaries for three different sands are also included in Figure 5 for comparison. These boundaries were plotted using the CSL experimental data and following the procedure proposed by Cunning et al (1996). It is interesting to note that although the CD boundary is very specific to the soil type, the CD of the Port-Cartier tailings is quite similar to the Syncrude tailings sand.

The in-situ measured data at two different SCPTu locations are shown on a plot of V_s, against σ'_v: with the contractive-dilative boundary in Figure 6. All the in-situ V_s, data at relatively shallow depths ($\sigma'_v \approx 80\ kPa$) plots above the proposed boundary and hence the in-situ state is estimated to be on the dilatant side of CSL as the penetration is forced either into the existent dyke constructed from a relatively compacted tailing or into deposited tailings biased towards more granular-soil behavior type. The data plot at deeper depth are close to or under the contractive-dilative boundary, indicating that this part of the deposit (deposited tailings) could be contractant.

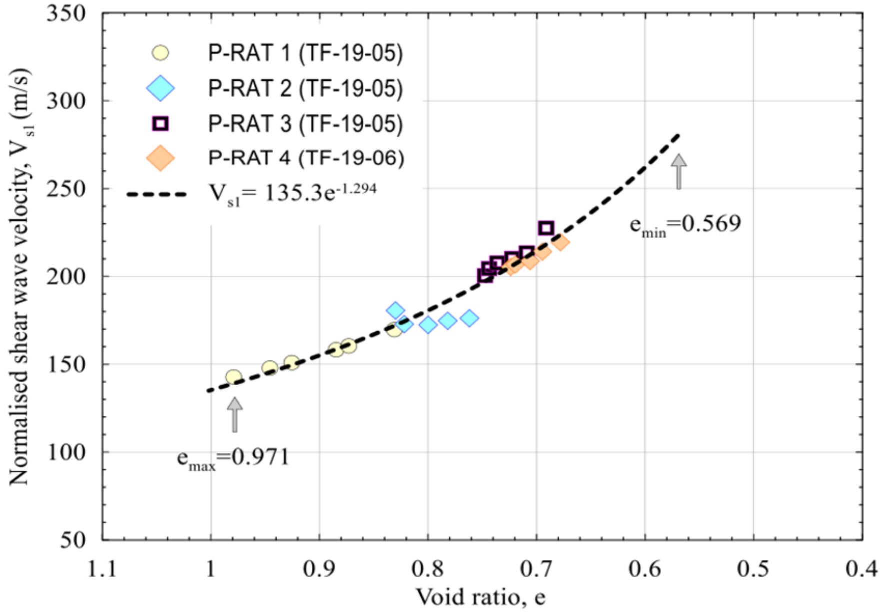

Figure 4 - Relationship between normalized V_{s1} and void ratio for the tailings.

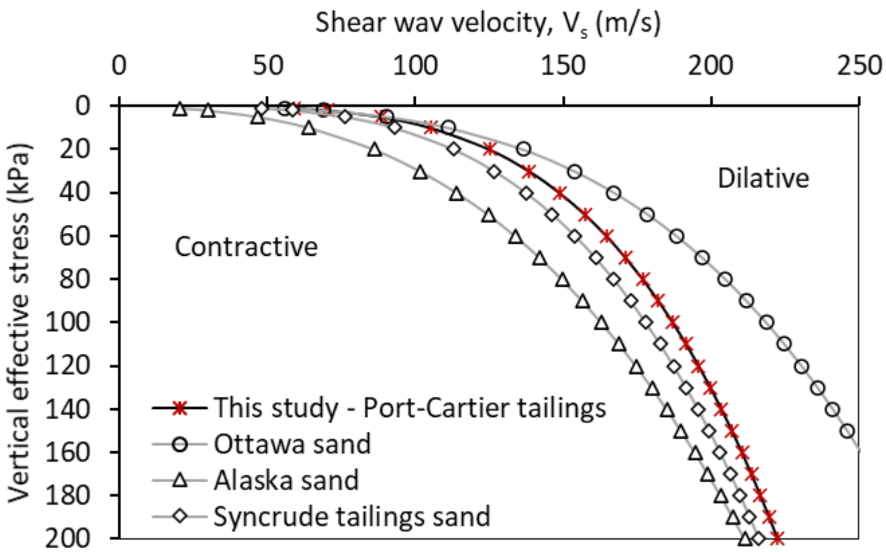

Figure 5 – V_s versus vertical effective stress with contractive-dilative boundary (ψ = -0.05) and K_0=0.5.

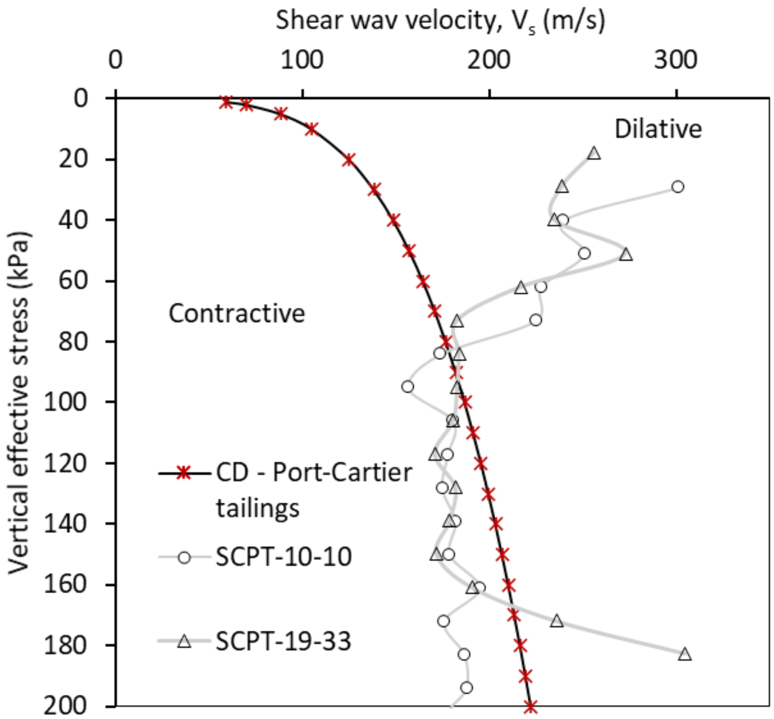

Figure 6 – field data in terms of shear wave velocity compared to proposed contractive-dilative boundary.

The in-situ measured data was processed one step further and plotted in term of state parameter profiles as shown in Figure 7. Figure 7 presents an example of comparisons between the values of the state parameter predicted in this study and those predicted with classical approaches. The vertical red lines on the plots identify the ψ = -0.05 state. Initial estimates were made using the empirical method suggested by Robertson (2010). Shear wave velocities (V_s) profiles from SCPTu and those estimated from Q_{tn}-CPT available data using the correlations proposed by Karray and Hussien (2016, 2017) were used to estimate the ψ. In this figure, the Plewes et al. method was adjusted based on the obtained laboratory data. In general, when applied in this way, the Plewes et al. method gave good predictions of ψ which is quite close to V_s-based estimation.

4 CONCLUSION

Field shear wave velocity (V_s) measurements during an SCPTu campaign were combined with laboratory measurements of V_s in Oedometeric cell and conventional triaxial compression testing on tailings samples retrieved from Port-Cartier ArcelorMittal's TSF, Qc, and this allowed the determination of in-situ state of the tailings from $SCPT_u$ data which is a critical element in evaluating the tailings potential for liquefaction. The obtained state parameter profiles were successfully compared to other classical approaches.

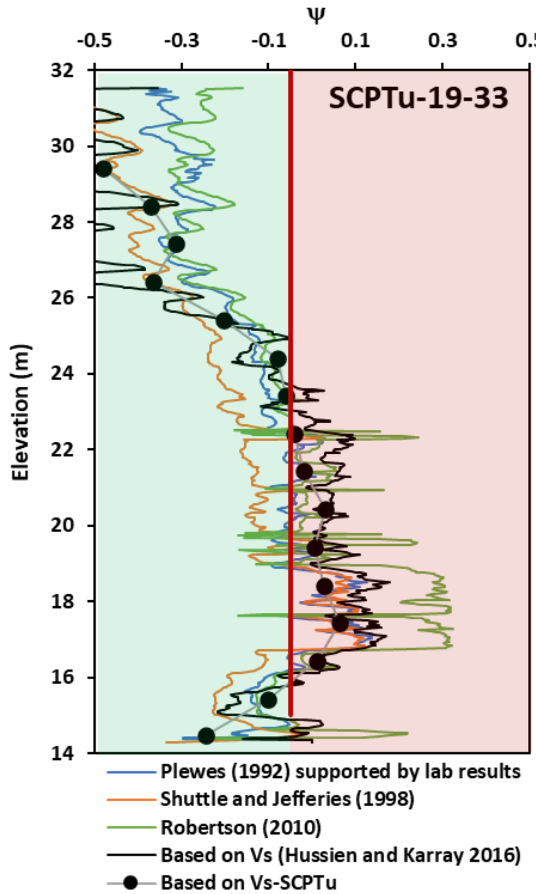

Figure 7 –Comparison of prediction of state parameter, ψ, using the current method with values of ψ predicted with classical approaches.

5 PREFERENCES

ASTM D-1586 — Standard Test Method for Standard Penetration (SPT) and Split-Barrel Sampling of Soils.

ASTM D4253: Standard Test Methods for Maximum Index Density and Unit Weight of Soils Using a Vibratory Table

ASTM D4254: Standard Test Methods for Minimum Index Density and Unit Weight of Soils and Calculation of Relative Density

ASTM D5778-12, 2012, "Standard Test Method for Performing Electronic Friction Piezocone and Piezocone Penetration Testing of Soils", ASTM, West Conshohocken, US.

ASTM D7400-14, 2014, "Standard Test Methods for Downhole Seismic Testing", ASTM, West Conshohocken, US.

Been, K. and Jefferies, M. 1985. A state parameter for sands. *Géotechnique*, 35: 2, 99-112.

Been, K., Crooks, J.H.A., Becker, D.E, and Jefferies, M.G. 1986. The cone penetration test in sands, Part 1: State Parameter interpretation. *Géotechnique*, 36: 239–249.

Been, K., Jefferies, M.G., Crooks, J.H.A., and Rothenburg, L. 1987. The cone penetration test in sands, Part 2: General inference of state. *Géotechnique*, 37(3): 285–299.

Cunning, J.C., Robertson, P.K., and Sego, D.C. 1995. Shear wave velocity to evaluate in situ state of cohesionless soils. *Canadian Geotechnical Journal*, 32: 848–858.

Hussien M. N., Karray M. Shear wave velocity as a geotechnical parameter: an overview. *Canadian Geotechnical Journal*, 2016, 53(2): 252-272, https://doi.org/10.1139/cgj-2014-0524.

Hussien MN and Karray M, "Piezoelectric Ring-Actuator Technique: In-Depth Scrutiny of Interpretation Method," *ASTM, Geotechnical Testing Journal* 44. Published ahead of print, 10 February 2020, https://doi.org/10.1520/GTJ20180205.

Karray M, Hussien MN. 2017. Shear wave velocity as function of cone penetration resistance and grain size

for Holocene-age uncemented soils: a new perspective. *Acta Geotechnica* 12(5): 1129- 1158
Karray, M., M. B. Romdhan, M. N. Hussien, and Y. Éthier. 2015. "Measuring Shear Wave Velocity of Granular Material Using the Piezoelectric Ring Actuator Technique (P-RAT)." *Canadian Geotechnical Journal* 52, no. 9 (September): 1302–1317. https://doi.org/10.1139/cgj-2014-0306.
Plewes, H.D., Davies, M.P, and Jefferies, M.G. 1992. CPT based screening procedure for evaluating liquefaction susceptibility. *In Proceedings of the 45th Canadian Geotechnical Conference*, Toronto, Ont., Vol. 4, pp. 1–9.
Robertson, PK 2010, 'Evaluation of flow liquefaction and liquefied strength using the cone penetration test', *Journal of Geotechnical and Geoenvironmental Engineering*, vol. 136, no. 6, pp. 842–853.
Shuttle DA and Jefferies MG (1998) Dimensionless and unbiased CPT interpretation in sand. *International Journal for Numerical and Analytical Methods in Geomechanics* 22(5): 351–391.
Shuttle, D. & Jefferies, M. 2016. Determining silt state from CPTu. *Geotechnical Research* 3:3.

3D tailings dam breach simulations using the material point method

Xuexin Xia & Paul Simms
Carleton University, Ottawa, Canada

ABSTRACT: 3D simulations of tailings breach, while computationally expensive, may offer insight and guide use of simpler models. Here the authors employ a 3D model using material point method using a thixotropic rheological model (Coussot) to simulate dam breach. This model can describe the transition between the rheology of intact tailings to their fully sheared state. Therefore, as demonstrated in the paper, the state of the tailings in the impoundment bears on the predict runout, which could allow operators to demonstrate implications of tailings technologies or deposition strategies for reducing dam breach consequence. This paper also demonstrates the capacities of these 3D simulations to qualitatively reproduces some key features observed in actual breaches.

1 INTRODUCTION

The flow behaviour of tailings is important to several aspects of tailings management, including controlling deposition and beaching behaviour, understanding segregation behaviour during deposition, and simulating flow out of a breached impoundment. Simulations of these flows have typically used Bingham or similar rheology (Pastor et al. 2014, 2002, Jeyapalan et al. 1983, Gao & Fourie 2019, Mizani et al 2013). However, the behaviour of many non-Newtonian suspensions under dam breach or other sudden failure conditions has been shown to be not well described by Bingham rheology (Coussot et al. 2002, Chanon et al. 2006), and better described by a “thixotropic” or “Viscosity Bifurcation” rheology (VBR). Mizani and Simms (2016) and Mizani et al (2017) showed that the rheology of gold tailings, and oil sands tailings could be better described using VBR, while Parent and Simms (2019) and Parent (2020) showed 3D analysis using VBR of both dam breach and channel formation during deposition. More work, however, needs to be done to convince potential users of the utilities of these somewhat more advanced rheologies. The goal of the present paper is to show potential application of this type rheology to describe the transition of tailings from an intact to a fully flowing state.

While VBR type models are described in these earlier references, the model is briefly reviewed here: as with all Computation fluid dynamics (CFD) models they describe flow: a deformation rate at any point on the material is proportional to the local shear stress. Flow initiation and flow stoppage is imitated in the model by rapid acceleration or deceleration due to a large change in viscosity. In the Bingham model, this is simulated by an arbitrary jump in viscosity at the yield stress, though in reality the variation in viscosity measured in rheometry is smooth In VBR, the viscosity a function of two competing processes, shearing and ageing. Shearing breaks down any network structure or interparticle contacts and reduces viscosity, whereas ageing describes the buildup of structure or the increase in interparticle contacts. There are several such models, one of the first proposed by Coussot et al. (2002), which is described by Equations 1 and 2:

$$\frac{d\lambda}{dt} = \frac{1}{T} - \alpha \dot{\gamma} \lambda \tag{1}$$

$$\mu = \mu_0 (1 + \lambda^n) \tag{2}$$

where α (dimensionless) and T (s) are material constants and $\dot{\gamma}$ is the strain rate (1/s). T is the characteristic time of evolution of the structure. The instantaneous viscosity is dependent on the state or “structure” of the material (λ), where μ_0 is the fully sheared viscosity where structure is minimum (λ=1), and *n* is a parameter describing the rate of viscosity change over time. The model predicts a critical shear rate or shear stress, which depends on the ratio of the ageing and shearing parameters (T and α) in Equation 1, and also the initial structure of the material. Below a critical shear stress or shear rate, the viscosity increases as ageing dominates, and the material comes to a stop. Above the critical shear stress or shear rate, the viscosity degrades the fully sheared value.

The consequence of this model is that the apparent yield stress required to initiate flow at a given density is much higher than the apparent yield stress required to stop flow at the same density, which is common practical observation for many types of tailings. This behaviour is shown in Figures 1 and 2. In Figure 1, different samples tailings are sheared from a rest state but at different constant shear stresses, and the evolution of viscosity is recorded. Here, the intial lambda is chosen such that VBR replicates the initial measured viscosity (~700 PaS). Here, there is a clear threshold yield stress between shearing down and the initiation of flow, versus continuing increase in viscosity (about 400 Pa). In Figure 2, however, one sample is subject to steps of constant decreasing shear stresses, attempting to replicate the stress state tailings are subjected to as they runout from either a deposition point and away from a breach. Here, for identical parameters of the VBR model, the effective yield stress (where the viscosity begins to rapidly increase) is 50 Pa

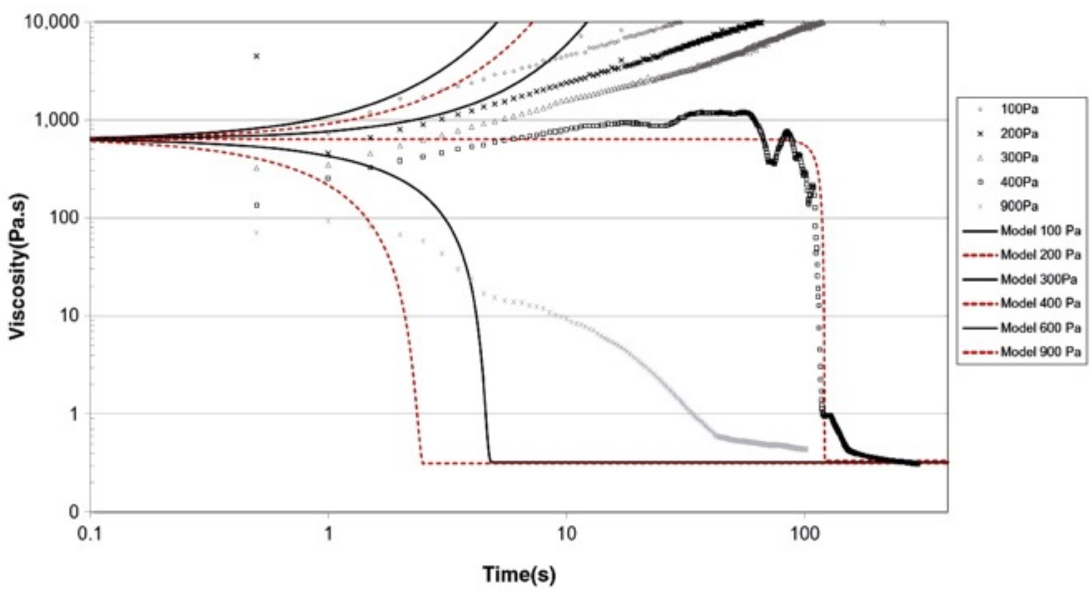

Figure 1. VBR applied to rheometry data from an oil sands tailings, the initial lambda set to mimic the viscosity measured at the start of the test: here the effective yield stress is ~ 400 Pa.

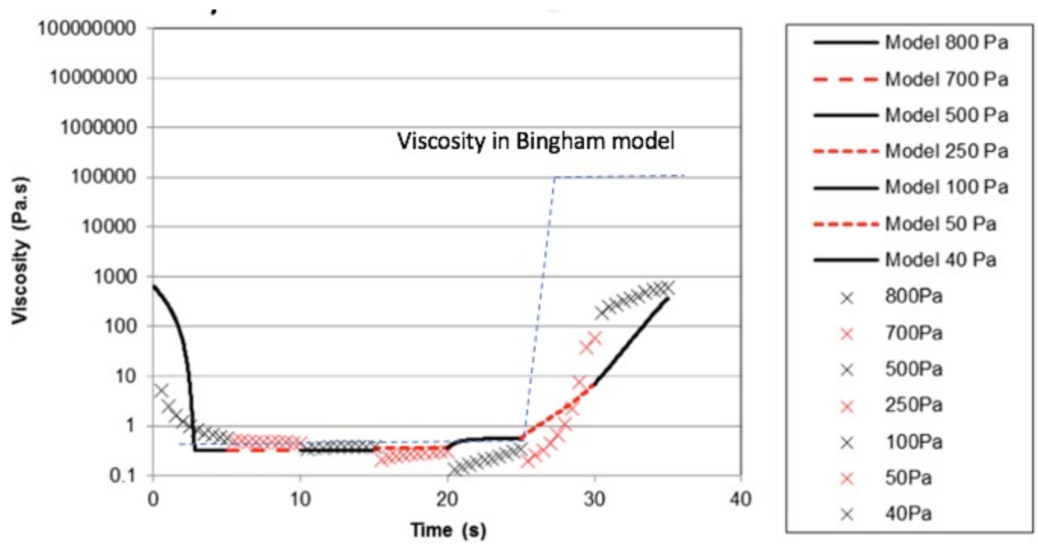

Figure 2. VBR identical parameters to Figure 1, but simulating shear stresses varying from high to low. Here the effective yield stress is 50 Pa.

Though the parameters can be obtained by fitting the type of rheometry data shown in Figures 1 and 2, direct estimation of ageing and shearing parameters (T and α) can be obtained from the effective yield stress derived from the situation in Figure 2. The VBR model only depends on the ratio of these two parameters, not their individual values. Taking $R=\alpha T$, the critical shear stress demarking either a decrease or increase in subsequent viscosity is (Coussot et al. 2002):

$$\tau = 2\, \mu_0 / R\, (1+\lambda_0{}^{n})/ \lambda_0 \qquad (3)$$

using the yield stress determined from the case where the material is completely sheared down, $\lambda_0 = 1$, and then Equation 3 can be rearranged to find R, $R= 2\, \mu_0 / \tau$.

Equation 3 also predicts the critical shear stress required to initiate decrease in viscosity when the material is starting from rest for some value of λ_0. Therefore, the Coussot model and other VBR models can describe the reduction in shear stress from the structured or intact state of the material, to its structureless state. Of course this is less sophisticated than a dynamic or quasi-static deformation analysis using geotechnical constitutive relations, but perhaps provides a practical way to account for the state of the tailings in CFD type flow analysis. Transition from an intact state to the remoulded strength or yield stress make be particularly important for dam breach scenarios where the geometry of the failures is of the type shown in Figure 3. The objective of this paper is to see whether when implemented into a CFD code, the VBR rheology can simulate similar geometries. This type of work is important, as generally a higher peak strength means more money has been invested into the tailings impoundment, as to be able to demonstrate the reward of such activities would be valuable to operators.

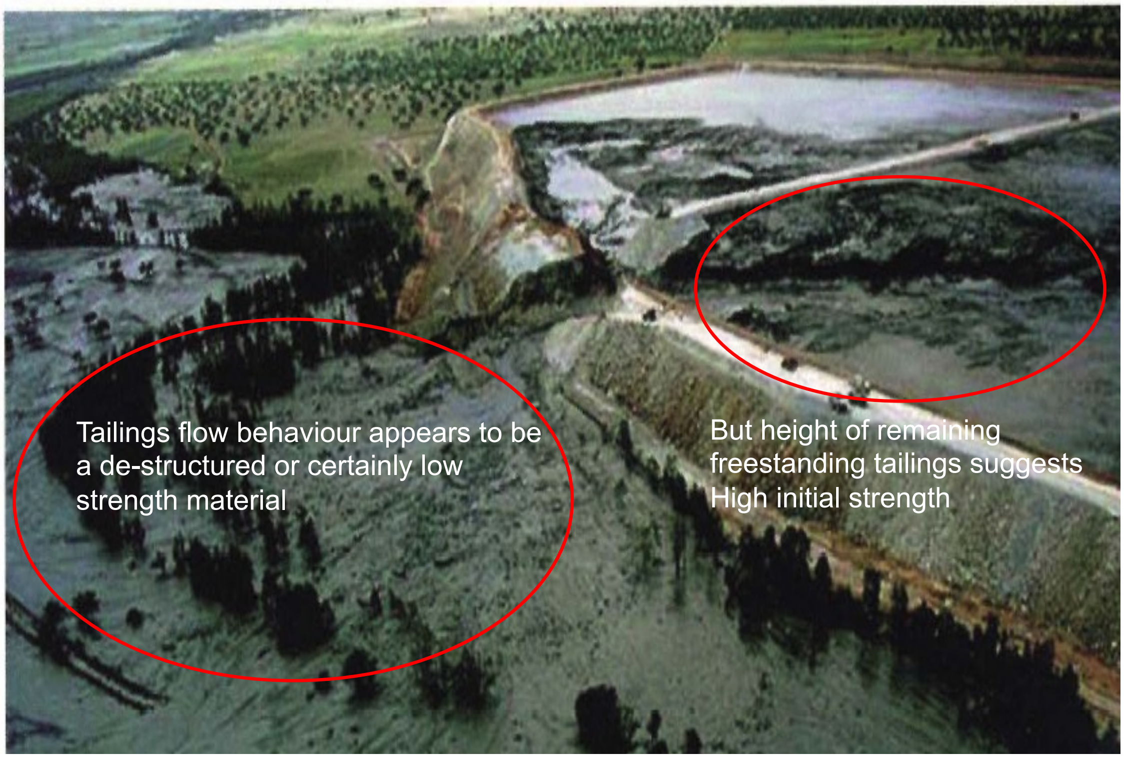

Figure 3. A very common type of tailings impoundment failure, indicating high intact strength, but very low residual strength

2 NUMERICAL IMPLEMENTATION

VBR has been applied to tailings simulations using both smooth particle hydrodynamics (Kazemi & Simms et 2017) and Material Point Method (MPM) (Parent and Simms 2019, Parent 2020). The simulations presented in this paper employ the implementation of the Coussot model (Equations 1 and 2) into the MPM freeware software UNITAH, as described in detail in Parent (2020). MPM combines features of meshfree methods and traditional FEM, by tracking advection of material properties associated with discrete points, called the material points; however, deformation is calculated by mapping information from the points back to a mesh, where momentum equations are solved as per traditional FEM. Thus, MPM combines the advantages of using particles to avoid mesh deformation problems, but retains numerical stability and other advantages of traditional FEM; however, substantial computation cost is associated with transferring information between the mesh and the material points. MPM has been used to describe slope stability failures and other large deformation problems employing conventional geotechnical constitutive models (e.g. Xu et al. 2019), and it is hoped that the CFD-rheology approach can be bridged with those more conventional geotechnical models.

3 SIMULATIONS

All the simulations shown are 3D, though there are several which are symmetric into the page and so are effectively 2D. All simulations employ the same R value, but different values of initial structure. Except for the first case presented, the n value is 2.5. This is a relatively high value, which means the rate of viscosity change is high. The influence of the n value is discussed in the first simulations. The boundary conditions are no-flow for the bottom and the back vertical boundary (the non-failing dam wall), all other boundaries are mirror boundaries to induce symmetry. For all cases shown here, the height of the tailings is 10 m, and the width of the impoundment parallel to the direction of flow is also 10 m. Results are shown with exaggerated scale in the vertical direction.

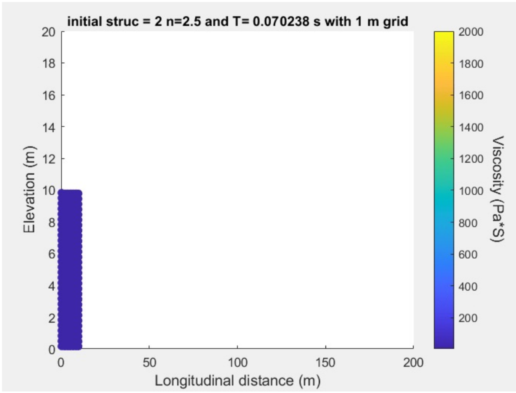

Figure 4. Initial geometry for "2D" simulations

The first simulation compares two simulations identical except for the n value, 1.05 in one and 2.5 in the other. As per Equation 3 the initial state of the material depends on both initial structure and the n value, different initial structure parameters were chosen such that both simulations had the same initial viscosity. The most prominent difference between these two simulations is the rate of viscosity increase moving from left to right. This is considerably faster in the "high n" simulation, which results in longer runouts for the low n simulation. "High n" simulations are closer to what would be predicted to develop in a Bingham fluid, due to the rapid transition in viscosity inherent in that model. The runout versus time is shown in Figure 6. As noted in Parent (2020), the differences in the runout with "n" become more pronounced for higher dams.

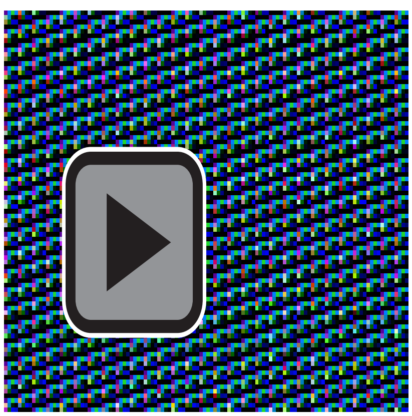

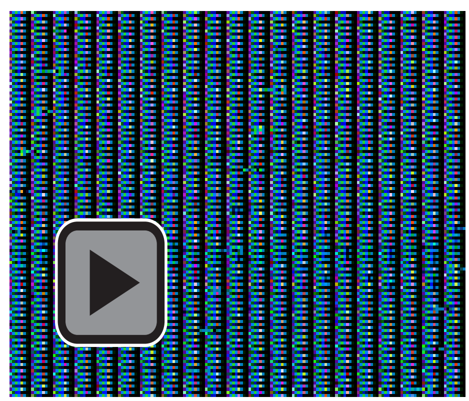

Figure 5. Embedded MOV files of simulations of dam breach with different "n" parameter and the same initial viscosity (only available in electronic version of the paper)

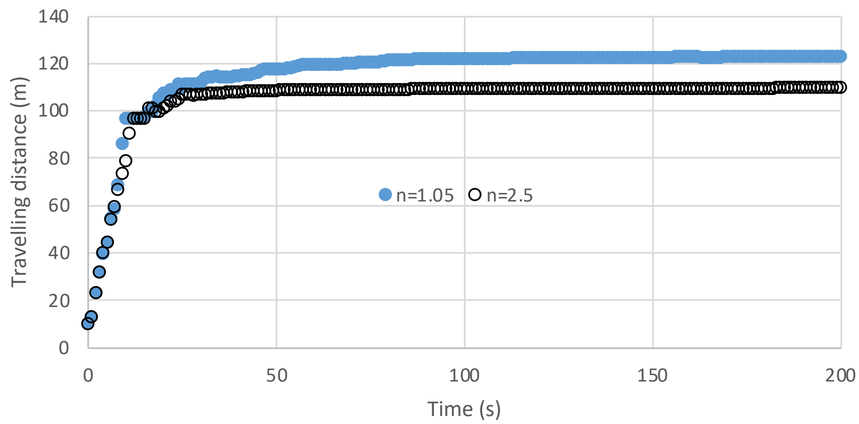

Figure 6 Runout versus time, simulations with different n values, same initial viscosity

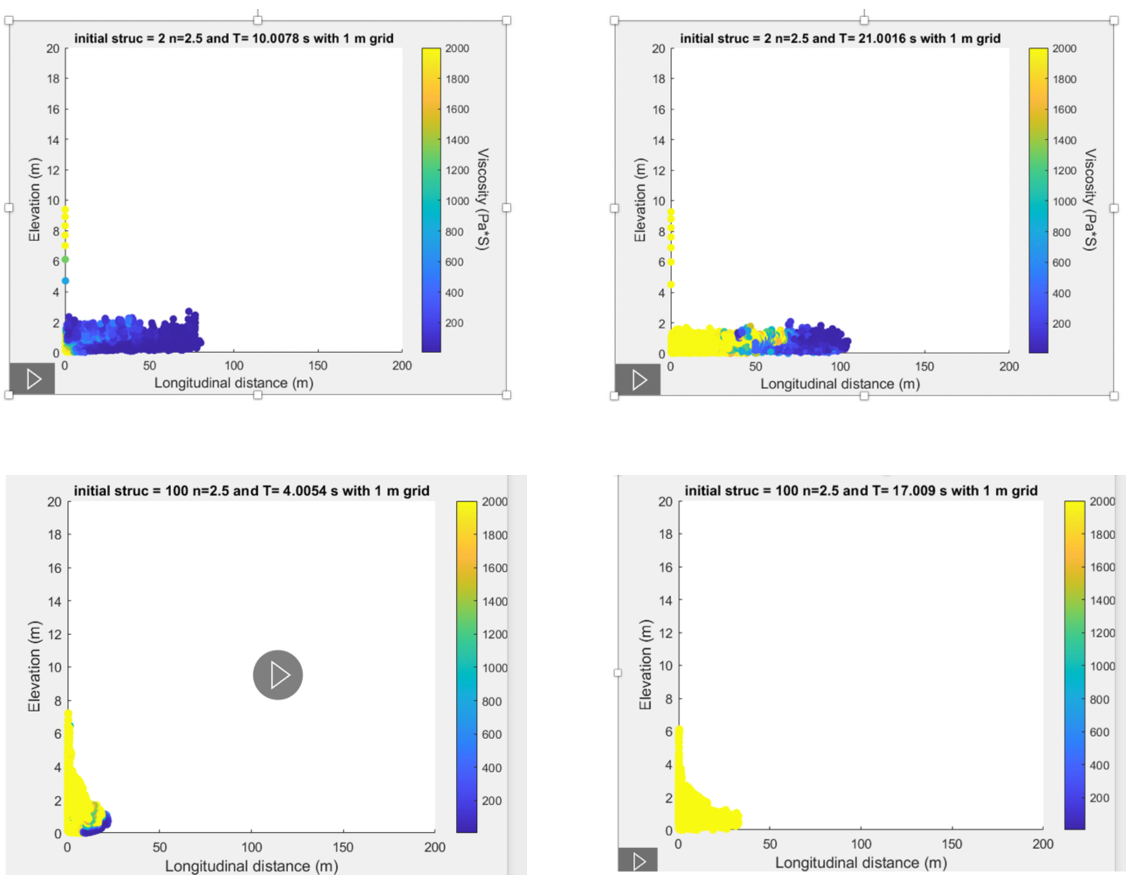

Figure 7. Example simulations for different initial structure values.

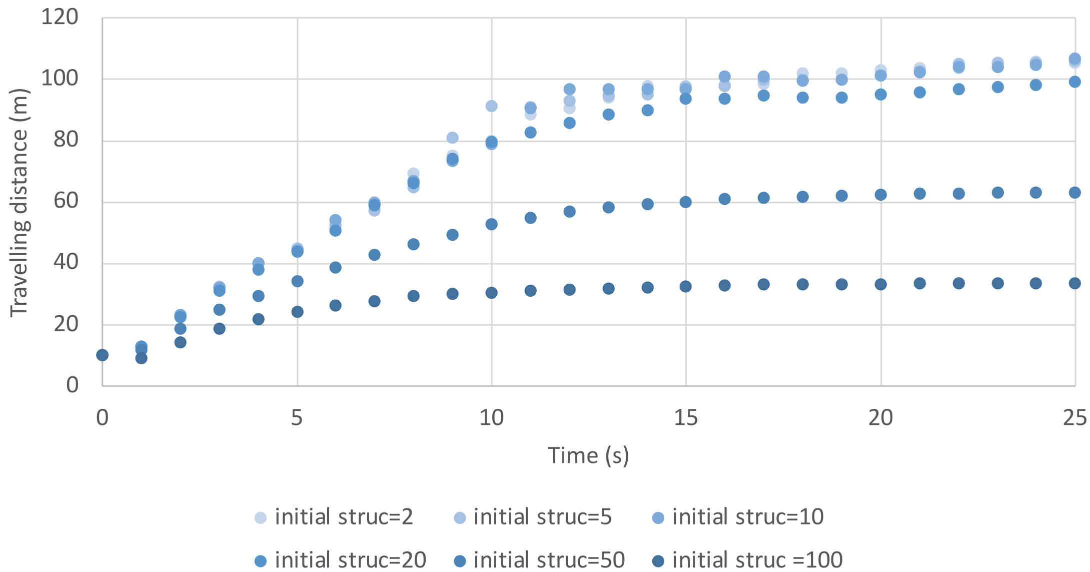

Figure 8. Runout as a function of initial structure

The results in Figure 7 and 8 are for identical parameters excepting the initial structure parameter. As can be seen, up to λ_0=20, there is little influence of the initial structure on the results, as the initial structure is quickly and more or less uniformly degraded throughout the tailings. But for λ_0=50 and 100, the initial viscosity is high enough to resist degradation in most of the tailings, and flow occurs because of localized shearing down to low viscosities. From an energy perspective, the degradation of the higher structure consumes some of the kinetic energy, and reduces the eventual runout. For these simulations, using n=2.5, the difference between the intact strength and the remoulded shear strength/ yield stress is given by the second term in Equation 3, $(1+\lambda_0{}^n)/\ \lambda_0$. For example, for λ_0=50 and 100, the ratio between the two shear strengths is 177 and 500, respectively. For these simulations R=6 Pa, therefore the fully sheared strength / yield stress is 6 Pa, and the strength required to initiate viscosity reduction from the initial structure at 100 is 3 kPa.

The final simulation setup and a few flow visualizations are shown in Figure 9 and 10. Here, the initial impoundment is still 10 m high, but 50 m deep, with a 5 m breach against a line of symmetry. From the front view, the tailings flow out of the breach in the roughly circular expansion seen at several sites, such as in Figure 3. From the top and back views, substantial volume of tailings will remain in the impoundment, as indicated by the high viscosity (yellow) which is at highest elevation behind the dam farthest away from the breach, and at lowest elevation at the breach at 15 s.

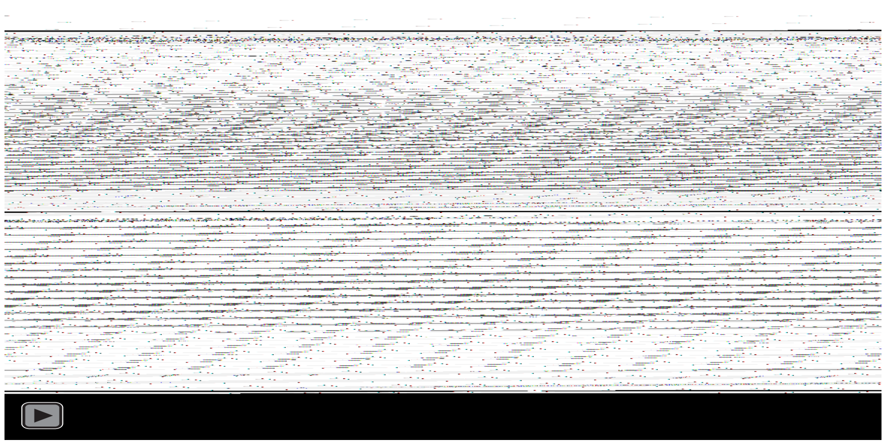

Figure 9. Embedded MOV file of simulation of limited dam breach, front view (only available in electronic version of the paper)

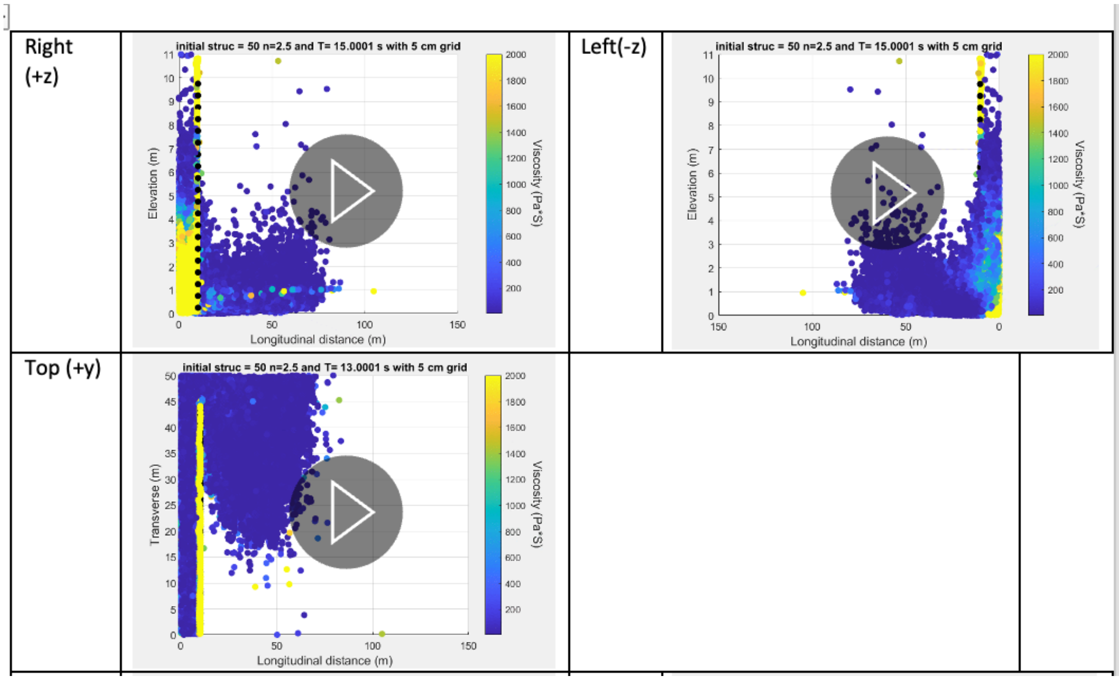

Figure 10. Clockwise from top left, profile of tailings looking along the dam towards the breach, profile of tailings looking along the wall starting at the line of symmetry, top view

4 SUMMARY AND FUTURE WORK

The paper shows how VBR type rheology models can potentially be used to account for the state of the tailings as they are in the impoundment and how that state bears on potential runout lengths. In the paper, this is demonstrated through 2D simulations showing how the initial state of the tailings bears upon the runout. This is useful as such analysis could quantitatively evaluate the positive effects of implementing new tailings technologies or different deposition practices on tailings safety. An example 3D simulation of an impoundment with a restricted dam breach is also shown to give the reader a sense of the capabilities of this kind of modelling.

Future work will include attempting quantitative replication of actual field scenarios, considering both the release geometry, and the geometry of the tailings remaining in the impoundment. Future work will also compare geotechnical models to describe failure initiation (e.g. Zabolotnii et al. 2021) with the failure geometries predicted by the VBR models, as well as comparisons of this advanced true 3D model with the simpler more efficient models conventionally used in practice to model dam breach. Such comparisons should inform parameter selection and improve reliability of the more practical design models.

5 ACKNOWLEDGEMENTS

This work is gratefully support by grants by NSERC, Canada's Oil Sands Innovation Alliance, and Klohn Crippen Burger.

6 REFERENCES

Babaoglu Y, Simms PH. 2017. Simulating deposition of high density tailings using smoothed particle hydrodynamics. *Korea-Australia Rheology Journal,* 29: 229-237.

Coussot T, P., Nguyen, Q. D., Huynh, H. T. & Bonn, D. 2002. Avalanche behaviour in yield stress fluids. *Phys. Rev. Lett*. 88, Article number 175501.

Chanson, H, Jarny, S., Coussot, P. 2006. Dam Break Wave of Thixotropic Fluid. *Journal of Hydraulic Engineering*, *ASCE* (March 2006),132(3):280-285.

Cruchaga, M. A., Celentano, D. J.,, Tezduyar, T. E. 2007. Collapse of a liquid column: numerical simulation and experimental validation. *Computational Mechanics*, *39*(4), 453-476.

Gao J., and Fourie A. 2019. Studies on thickened tailings deposition in flume tests using the computational fluid dynamics (CFD) method. *Canadian Geotechnical Journal*, 56:249-262.

Jeyapalan, J., Duncan, J., Seed, H. 1983. Analyses of Flow Failures of Mine Tailings Dams. *J. Geotech. Engrg.,* 10.1061/(ASCE)0733-9410(1983)109:2(150), 150-171.

Kazemi, K., Simms, P. 2017. Post-failure runout analysis from tailings dams using viscosity bifurcation rheology. *Proceedings of Tailings and Mine Waste 2017*, Banff, Alberta.

Mizani, S., Simms, P., Wilson, W. 2017. Rheology for deposition control of oil sands tailings. *Rheo.l Acta*, 56: 623. doi.org/10.1007/s00397-017-1015-2

Mizani, S. 2017. Experimental Study and Surface Deposition Modelling of Amended Oil Sands Tailings, PhD thesis, Carleton University, Ottawa.

Mizani, S, Simms, P. 2016. Method dependent variation of yield stress in mine tailings explained using a structure based viscosity model. *Minerals Engineering*, 98: 40-48.

Mizani S, He X, Simms P. 2013. Application of lubrication theory to modeling stack geometry of high density mine tailings. *Journal of Non-Newtonian Fluid Mechanics*, 198: 59-70.

Parent, E., Simms, P. 2019. 3D simulations of dam breach and deposition using viscosity bifurcation rheology. *Proceedings of Tailings and Mine Waste 2019,* Vancouver, B.C., Canada.

Parent, E. 2020. Field scale flow modeling of thixotropic mine tailings using the material point method. Master's thesis, Carleton University, Ottawa.

Pastor M, Quecedo M, Fernández-Merodo JA, Herreros MI, González E, Mira P. 2002. Modelling tailings dams and mine waste dumps failures. *Géotechnique* 52(8): 579-591.

Pastor, M., Blanc, T., Haddad, B. 2014. Application of a SPH depth-integrated model to landslide run-out analysis, *Landslides* 11: 793. doi:10.1007/s10346-014-0484-y

Xu, X, Jin, F., Sun, Soga, K., and Zhou, G.D., 2019. Three-dimensional material point method modeling of runout behavior of the Hongshiyan landslide. Can. Geotech. J. 56: 1318–1337 (2019) dx.doi.org/10.1139/cgj-2017-0638

Zabolotnii, E., Morgenstern, N, Wilson, G.W. 2021. Mesh sensitivity in numerical models of strain weakening systems. *Computers and Geotechnics,* doi.org/10.1016/j.compgeo.2021.1042

Critical state based trends for the monotonic response of mine tailings

Luis Vergaray & Jorge Macedo
Georgia Institute of Technology, Atlanta, Georgia, USA

ABSTRACT: Static liquefaction has been associated with numerous recent failures of tailings storage facilities (TSFs) around the world (e.g. the 2019 Brumadhino failure in Brazil). These failures lead to devastating consequences for the environment and civil infrastructure and lead to loss of human lives. Static liquefaction is just another facet of soil behavior under monotonic loadings, and hence it should be explained under a mechanistic framework. In this study, we present trends for the response of mine tailings to monotonic loading considering a) triaxial tests, b) bender element tests, and c) consolidation tests performed on 53 mine tailings materials (including recent case histories). These materials have a broad range of states, a range of particle size distributions (from silty sand to almost pure silt mine tailings), and a broad range of compressibility. The trends are evaluated in the context of static liquefaction using critical state soil mechanics concepts and considering different state definitions. In particular, we present trends for shear strength (residual and peak), state and brittleness soil indexes, excess pore pressure indexes and dilatancy. Finally, static liquefaction screening indexes are proposed based on the observed trends.

1 INTRODUCTION

The static liquefaction of mine tailings has caused numerous recent failures, e.g., the 2014 Mount Polley disaster in Canada (Morgenstern et al., 2015), the 2015 Fundao failure in Brazil (Morgenstern et al., 2016), the 2018 Cadia failure in Australia (Morgenstern et al., 2019), and the 2019 Brumadhino failure in Brazil (Robertson et al., 2019). Such failures of tailings storage facilities (TSFs) have caused unprecedented devastating consequences for the environment, infrastructure damage as well as human losses. These failures have triggered international debates regarding the safety of TSF systems. In particular, the conditions that result in static liquefaction of mine tailings remain a considerable concern affecting the financial viability of mines and the willingness of governments to allow mining.

In the U.S. exist approximately 1200 TSFs, with 60% of them having a significant hazard according to the USACE classification (USACE, 2016). Hence, the safety of TSFs is an important issue. As engineering practice is moving more towards finite element or finite difference-based stress analyses (e.g., the evaluations performed in the forensic studies after recent failures), understanding the mechanical response of mine tailings is also fundamental for the calibration of constitutive models that can later be used in numerical simulations. This is not simple because mine tailings are often characterized as intermediate materials (pure silts or sandy silts), which represents a fundamental challenge for understanding their mechanical response. Tailings are also geologically young materials, with angular grains rather than subrounded and often with lower proportions of quartz than many natural soils; thus, standard geotechnical correlations should not be taken as applicable to tailings without detailed consideration of these factors.

Previous efforts on understanding the trends in the mechanical response of particulate materials under monotonic loadings have been mainly focused on sands with low fine contents (e.g., Sadrekarimi, 2014; Jefferies & Been, 2016, Rabbi et al., 2019). In terms of mine tailings, the experimental studies that have evaluated their mechanical response and the associated mechanical parameters are somewhat limited compared to sand materials (e.g., Jefferies & Been, 2016; Shuttle & Jefferies, 2016; Fourie & Tshabalala, 2005; Carrera et al., 2011). In this study, we present trends for mechanical-based parameters that control the response of mine tailings, in the context of static liquefaction, which have not been previously explored considering a large set of tailings materials. The trends are presented using results from 53 mine tailings materials (including available data from the recent failures previously discussed), which have been processed in a uniform manner.

2 DATABASE

The whole database consists has 53 different mine tailings material, 7 of them were generated as part of this study and the rest were compiled from Shuttle & Cunning (2007), Anderson & Eldridge (2011), Bedin et al. (2012), Schnaid et al. (2013), Been (2016), Li & Coop (2018), Li & Coop (2019), Raposo (2016), Torres (2016), Morgenstern et al. (2016), Riemer et al. (2017), Li (2017), Robertson et al. (2019), Macedo & Petalas (2019), Gill (2019), Reid & Fanni (2020), Reid et al. (2018), Reid et al. (2020), Fourie & Papageorgiou(2001), and Carrera (2011). The mine tailings database corresponds to different ores (i.e., gold, iron, silver, copper, zinc, platinum) covering a broad range of fine contents ($FC = 0 - 100$ %), initial confining stress ($20 - 6000\ kPa$), specific gravity ($Gs = 2.63 - 4.89$), and states (i.e., very loose to dense). The following properties were evaluated for each material: the critical state line (CSL), the stress ratio at critical state (M_{tc}), the state-dilatancy parameter (χ), the stiffness-confinement dependence parameters (A, B) according to $G = A.F(e).(p/p_a)^B$, where $F(e)$ represent the functional form proposed by Hardin & Richart (1963) and Pestana & Whittle (1995). Figure 1 shows the particle size distribution for the materials considered in this study, separating them by fine contents for easier visualization. Additional details are provided in Macedo and Vergaray (2021).

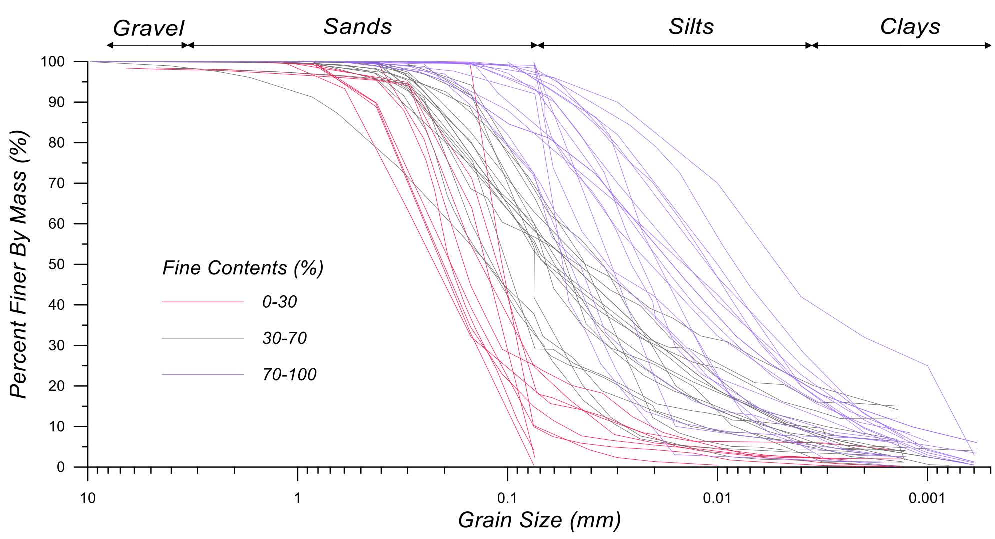

Figure 1. Range of particle size distribution for the materials considered in this study.

It is important to highlight that Γ, λ_e, M_{tc}, N, χ, A, and B are often present as parameters in robust constitutive models, usually formulated for sands (although often named differently or represented by other proxies), and are the basis for the current mechanical-based understanding of static liquefaction. Figure 2 shows an example of the calculation of these parameters for material 12. Figure 2a shows the estimation of the CSL, Figure 2b shows the η_{max} versus D_{min} plot to estimate M_{tc} and N, Figure 2c shows the state-dilatancy relationship to estimate χ, and Figure 2d shows the G versus p plot to estimate A and B, according to equation 3a.

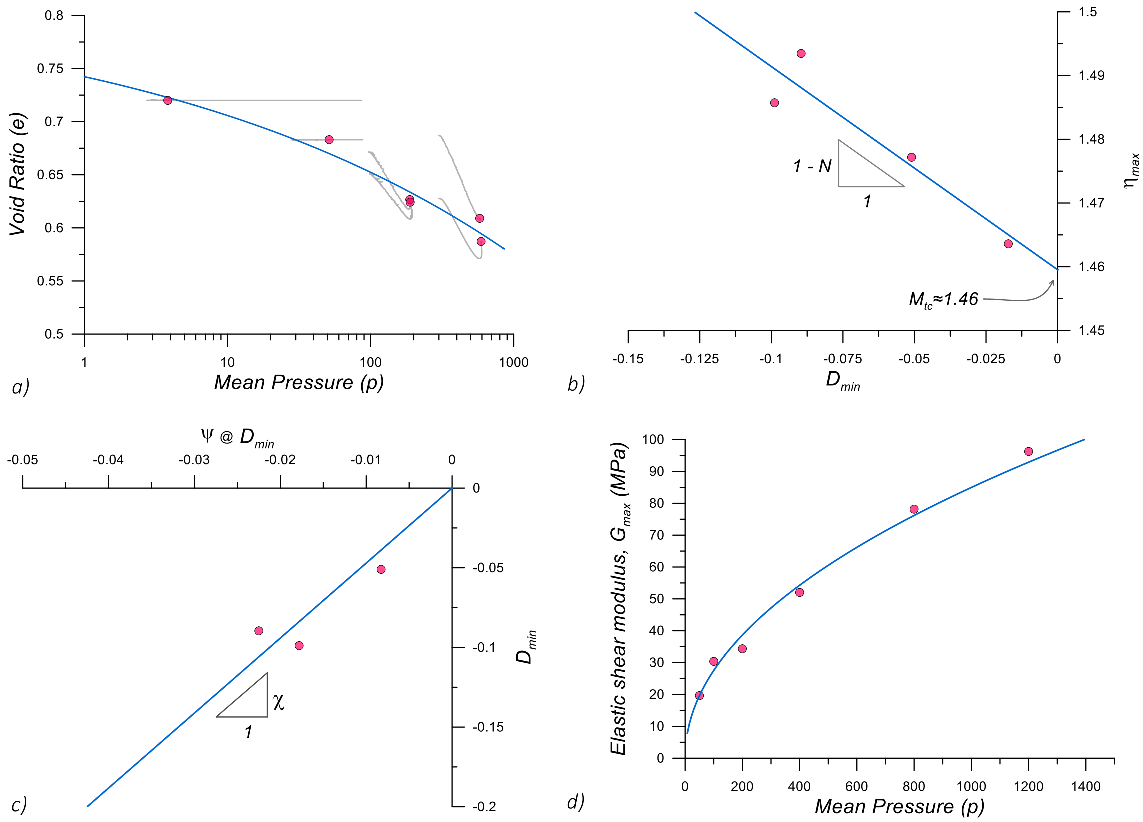

Figure 2. Illustration of the estimation of mechanical-based parameters consistent with the critical state theory for material 12. a) CSL estimation, b) η_{max} versus D_{min} plot to estimate M_{tc} and N, c) state-dilatancy relationship to estimate χ, and d) G versus p plot to estimate A, and B.

3 TRENDS IN THE MECHANICAL RESPONSE OF MINE TAILINGS

3.1 *Critical state parameters and stiffness*

Figure 3a shows the distribution of the CSLs for all the materials considered in this study; it can be observed that the estimated CSLs were, in most cases, followed a linear relationship (in a Semi-Log space). In addition, the estimated CSLs cover a broad spectrum in the e versus p plane (the maximum difference in e for a given p is in the order of 0.55). Figure 3b illustrates the spectrum of the maximum shear modulus (G) variation (i.e., G versus mean pressure) estimated through bender element tests considering a broad range of densities.

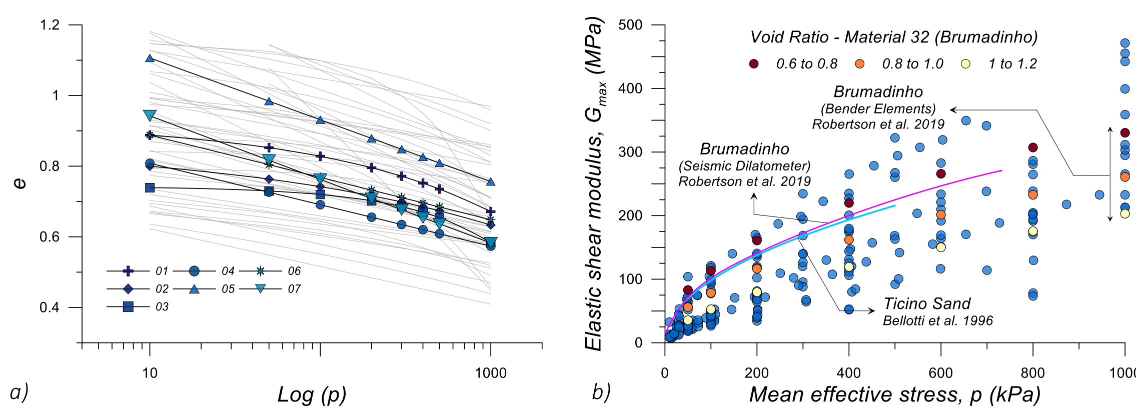

Figure 3. a) Variation of ψ and D_{min} for sands and mine tailings. b) Variation of χ and C_u/D_{50}

3.2 *Stiffness*

Figure 4a shows a histogram of M_{tc} values for tailings materials sand materials. The M_{tc} values for sand materials were obtained from Jefferies & Been (2016). It can be observed that M_{tc} values for mine tailings are generally larger compared to sands, which has also been observed in previous studies (e.g., Reid, 2015). This is due to the angularity associated with mine tailings as a product of the mineral processing. Figure 4b and 4c, show histograms for the A and B coefficients in Equation 2. It can be observed that the A coefficient typically varies from 10 Mpa to 60 Mpa, whereas the variation of B is generally between 0.4 and 0.7. To better understand the variation of the A coefficient, we plotted A versus the initial state parameter in Figure 4d, which suggested a good correlation.

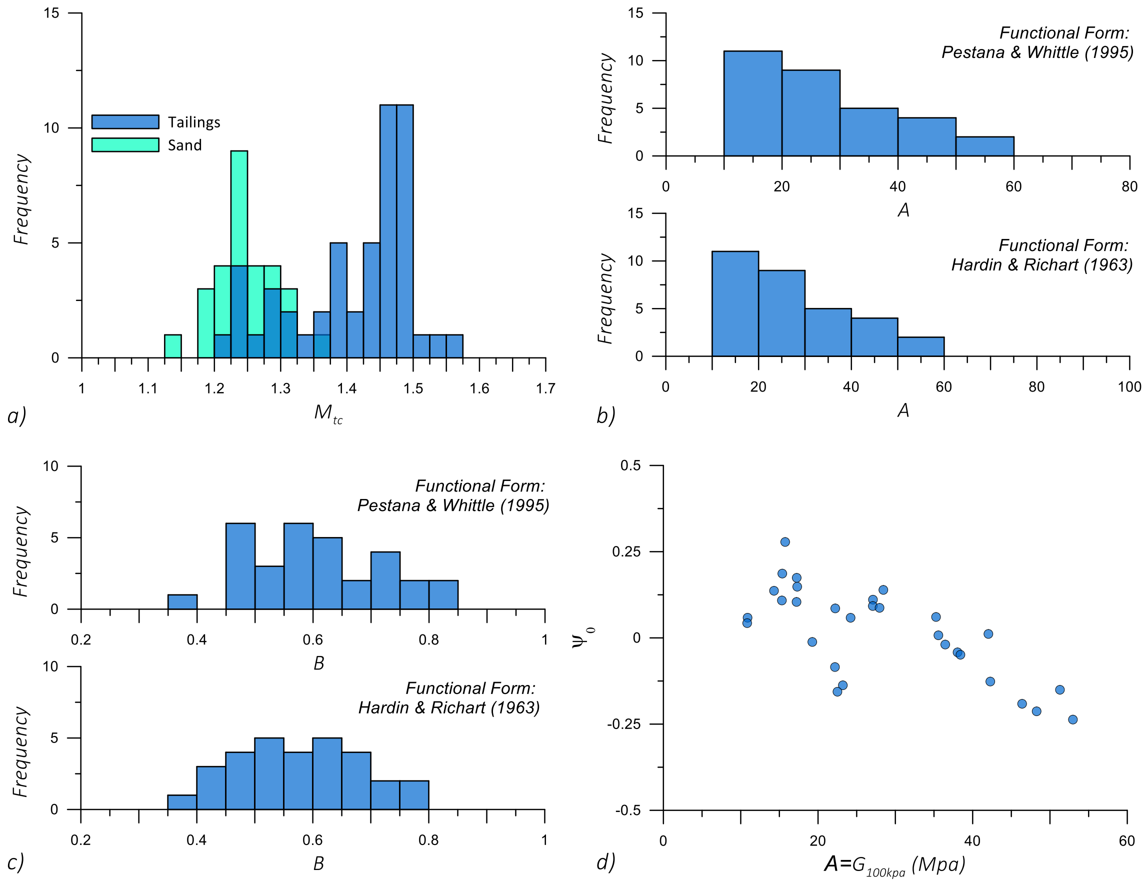

Figure 4. a) Distribution of M_{tc} values for tailing and sand materials, b), c) distribution of the A and B parameters in Equations 3a, and 3b, respectively, and d) A versus state parameter variation.

3.3 *Residual and peak strength*

In the following figures (Fig. 5 to 6) we discuss trends in terms of peak and residual shear strengths. Figure 5a and 5b shows the variations of Su_r/σ'_0 and Su_Y/σ'_0 in terms of I_b, along with upper and lower bound trends for sand materials extracted from Sadrekarimi (2014). It is noticed that, in general, the trends are reasonably consistent. Figure 5c shows the variation of Su_r/σ'_0 in terms of ψ_0 along with similar trends for sands with different compressibility (including the Lagunillas sandy silt) extracted from Sadrekarimi (2013). Figure 5d shows the variation of Su_Y/σ'_0 in terms of and ψ_0 along with upper and lower bound trends for Su_Y/σ'_0 in sands extracted from Jefferies & Been (2016).

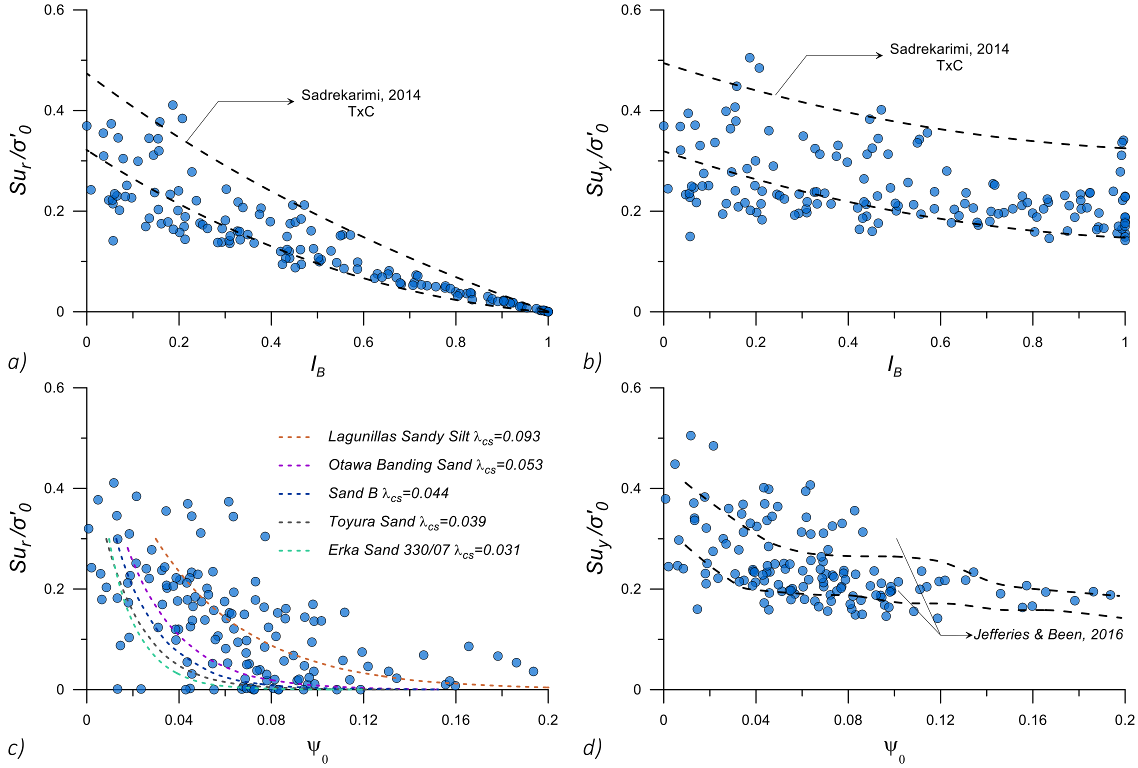

Figure 5. Variation of Su_r/σ'_0 and Su_Y/σ'_0 vs the brittleness index ((a) and (b), respectively); and Su_r/σ'_0 and Su_Y/σ'_0 vs the initial state parameter (ψ_0) ((c) and (d), respectively).

The variation of Su_Y/σ'_0 in Figure 5c suggests that Su_Y/σ'_0 tends to be larger in mine tailings compare to the sands in Jefferies & Been (2016) when ψ is lower than 0.1. To bring the effects of compressibility, we normalized the state parameter by λ_e. This normalization may also cancel out some fabric-related effects as compressibility is expected to be influenced by fabric.

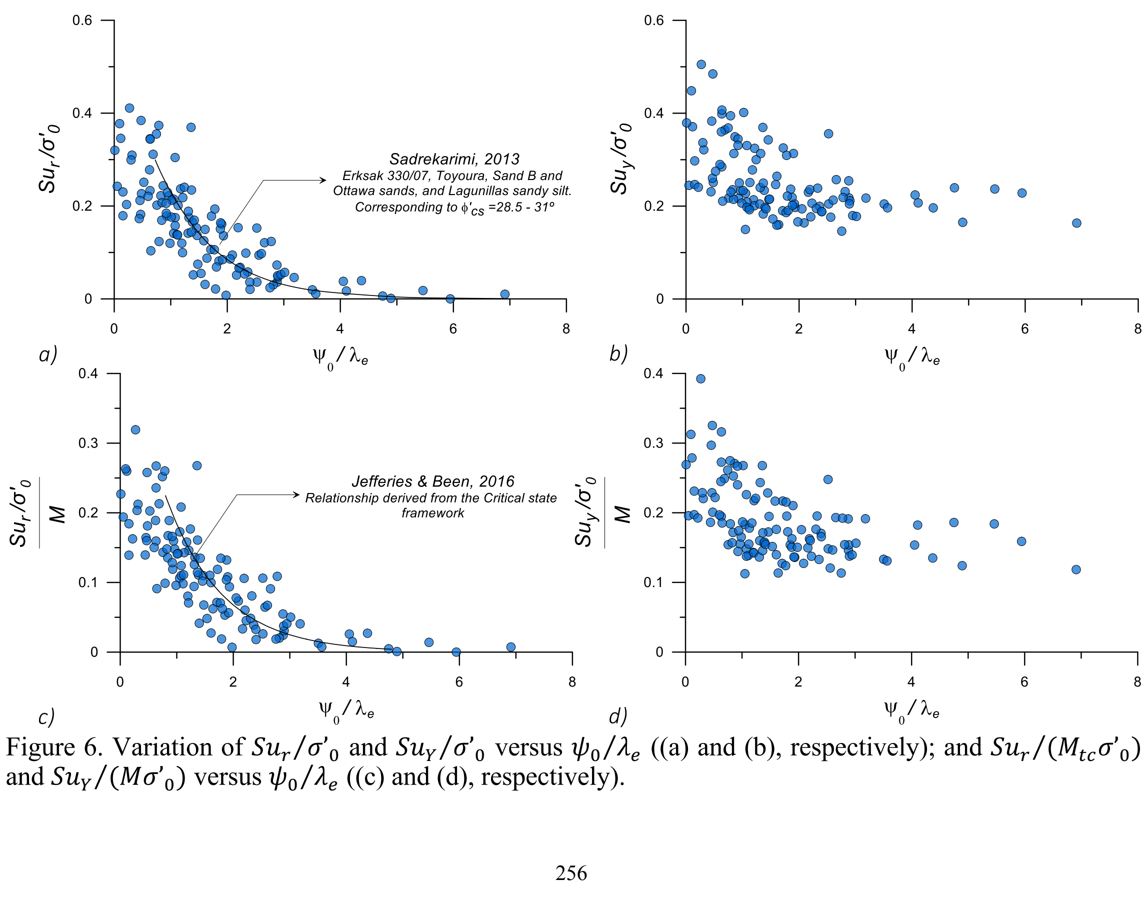

Figure 6. Variation of Su_r/σ'_0 and Su_Y/σ'_0 versus ψ_0/λ_e ((a) and (b), respectively); and $Su_r/(M_{tc}\sigma'_0)$ and $Su_Y/(M\sigma'_0)$ versus ψ_0/λ_e ((c) and (d), respectively).

Figure 6a and 6b shows the variation of Su_r/σ'_0 and Su_Y/σ'_0versus ψ/λ_e, now it can be observed that bringing λ_e decreases the variability in the trends, and the normalized trends for mine tailings are now more consistent with those for sand materials reported by Sadrekarimi (2013). Besides, in Figure 6c and 6d to account for the effects of angularity in strength, we further normalized the Su_r/σ'_0 by M_{tc}, and plotted the results in terms of ψ/λ_e. Recall that from CSSM concepts (e.g., Jefferies & Been, 2016) $Su_r/(M\sigma'_0) = 0.5exp(-\psi/\lambda_e)$, which is also plotted in Figure 6c.

3.4 *State and brittleness soil indexes*

Figure 7a to 7d show the relationship between different parameters to represent the state and brittleness of a soil material. In these figures, the flow liquefaction cases that correspond to full softening and partial softening are presented in red and yellow colors, respectively Figure 7a shows the relationship between I_b and ψ/λ_e, along with the data from Smith et al. (2019), and the upper and lower bounds proposed by them for contractive materials (i.e., $\psi > 0$). It can be observed that our data is consistent with these upper and lower bounds. Of note, the trends suggest that flow liquefaction cases with partial softening may have in general a I_b larger than 0.25 and a ψ/λ_e larger than 0.75, whereas the flow liquefaction cases with full softening may be associated with I_b values higher than 0.6 and ψ/λ_e values larger than 1.5. Figure 7b shows the relationship between I_b and I_P,. As expected I_P increases with the increase of I_b, and I_P values higher than 2.5 seem to be indicative of flow liquefaction with partial softening, whereas values larger than 10 may be indicative of potential flow liquefaction with full softening. Figure 7c shows the variation of ψ/λ_e and I_P , suggesting a good correlation between these parameters until flow liquefaction with full softening occurs in cases with $\psi/\lambda_e > 3$. Finally, Figure 7d shows the variation of ψ_m and ψ/λ_e, again a good correlation is observed until $\psi/\lambda_e > 3$. Interestingly, ψ_m alone brings comparable information as ψ/λ_e because it also includes information on the state pressure index.

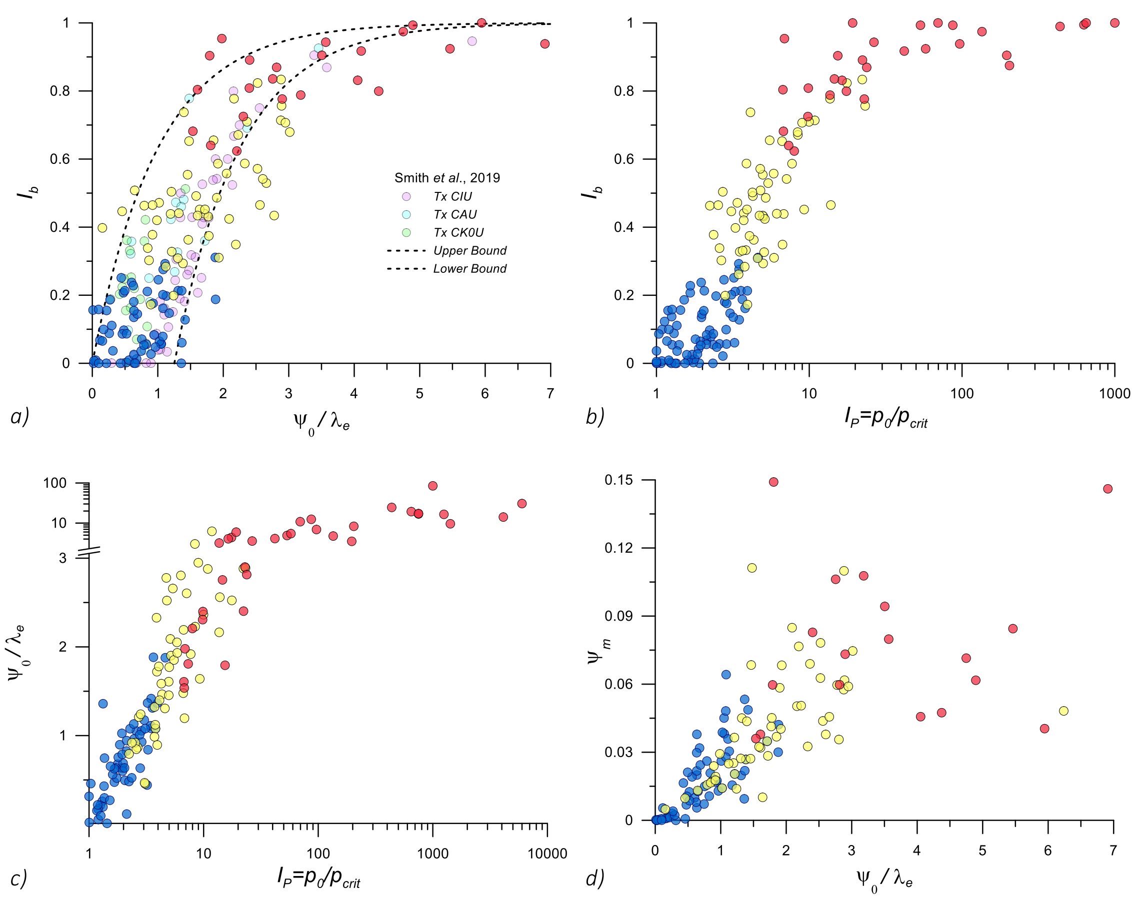

Figure 7. a) Relationship between I_b and ψ/λ_e, b) I_b versus I_p, c) ψ/λ_e versus I_p, and d) ψ_m versus ψ/λ_e.

3.5 *Excess pore pressures*

Figure 8a shows the variation of $r_u = \Delta u/\sigma'_0$ versus I_b along with the trend of r_u relationships for sands considering triaxial extension (TxE), plane strain compression (PSC), and triaxial compression (TxC) conditions. The TxE and PSC trends were extracted from Sadrekarimi (2016), and the TxC trends were extracted from Sadrekarimi (2020). In general, it can be observed that flow liquefaction cases (partial and full softening) show r_u values large than 0.8, and the data is generally consistent with the average trend extracted for sand materials, but it is observed that the r_u values in mine tailings tend to be larger compared to sands in cases with partial softening. Figure 8b shows the r_u variation in terms of ψ. In general, large r_u values were observed with most values higher than 0.6 for $\psi > 0$. As expected r_u increases with the increase in I_b and ψ;and an I_b higher than 0.1 or a ψ higher than 0 are indicative or large excess pore pressure generation (i.e., $r_u >$ 0.6).

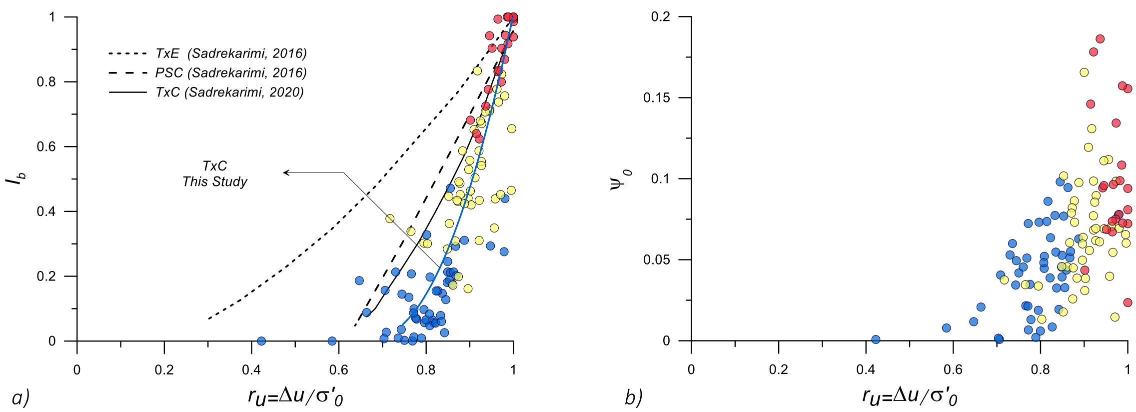

Figure 8. Variation of r_u vs a) the brittleness index, and b) the initial state parameter ψ_0.

3.6 *Dilatancy*

Figure 9a shows the variation of the maximum dilatancy in triaxial CD tests versus ψ_0, considering the mine tailings from this study and data available in Jefferies & Been (2016) for sand materials. If we fit the data to the relationship suggested by Been & Jefferies (1985), given by $D_{min} = \chi\psi$ we obtain representative χ values of 3.0 for sands, and 4.0 for tailings. This suggests that mine tailings have an average stronger scaling of dilatancy compared with sands, given a similar state parameter. This can be explained considering that χ can be though as a kinematic parameter related to the potential of particulate materials to re-accommodate particles. Given the more angularity of mine tailings compared to sands, mine tailings seem to have, on average, a higher potential on re-accommodating particles.

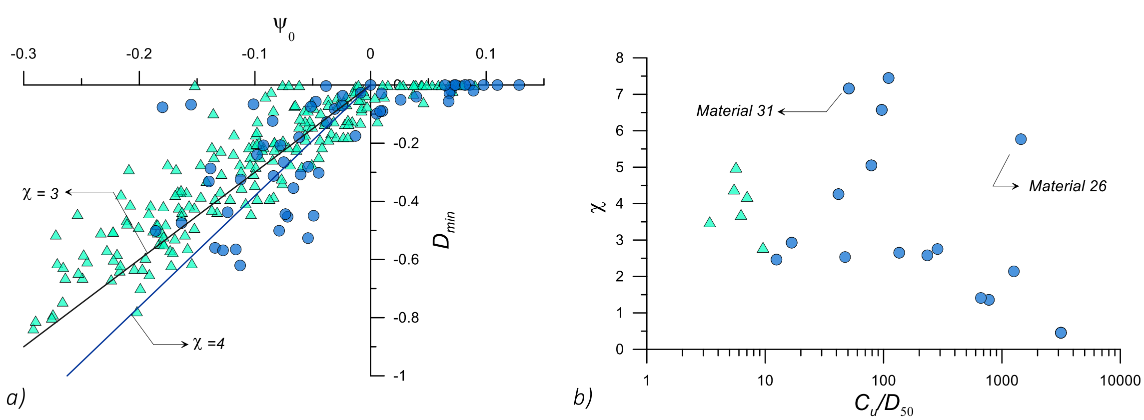

Figure 9. a) Variation of ψ and D_{min} for sands and mine tailings. b) Variation of χ and C_u/D_{50}

Figure 9b shows the variation of χ and C_u/D_{50} for mine tailings and some well-known sand materials (i.e., Erksak, Braster, Changi, Fraser, Nerlek, and Ticino sands). The data for sands was obtained from Jefferies & Been (2016). It can be observed that the χ values in sands vary in a narrow range between 3.5 and 5.0, which correspond to C_u and C_u/D_{50} values that are also in a narrow range (1 to 3, and 3 to 10, respectively). In the case of mine tailings, we observe that χ tends to decrease with the increase of C_u/D_{50}, which is consistent with observations from DEM simulations (Yan & Dong, 2011). We also noticed that the lowest χ values (lower than 1.4) correspond to materials with large FC (larger than 85%) and important clay size fractions. This observation is consistent with the findings from (Cola & Simonini, 2002). The materials 26 and 31 (which correspond to the Cadia and Brumadinho failures previously discussed) showed large χ values (5.8 and 7.2, respectively). These large values may be associated with the large angularity on these materials, and bonding effects, as suggested by Robertson et al. (2019) based on inspections of scanning electron microscope (SEM) images from the Brumadinho tailings.

4 CONCLUSIONS

In this study, we have used critical state soil mechanics (CSSM) concepts to examined salient trends on the mechanical response of mine tailings in the context of static liquefaction, highlighting the role the relative proportions of different particles sizes, and particle properties. Our results suggest that mine tailings fit the same framework as natural sands, with the key difference of showing a much larger M_{tc} and somewhat larger χ, both attributed to underlying particle shape, which then affects standard correlations. Thus, the mechanical response of mine tailings can be reasonably well explained once CSSM-based parameters such as Γ, λ_e, ψ, M_{tc}, χ, N, and G are incorporated.

Additional salient conclusions from this study include:

- The M_{tc} values in mine tailings (in the order of 1.4) are larger, on average, compared to M_{tc} values on natural sands (in the order of 1.2). This is associated to the particle shape of mine tailings, which tend to have more angular particles compared to the subrounded grains found in natural soils.
- Using the functional forms from Hardin & Richart (1963) and Pestana & Whittle (1995) for G (Equation 3), we observed that the parameter A that controls the magnitude of G correlates well with ψ_0. In addition, the parameter B that controls the dependence on p, generally varies from 0.4 to 0.8.
- Compressibility can have an important effect on Su_r/σ'_0, and also controls Su_y/σ'_0. Hence, it should be carefully considered in evaluating appropriate Su_r/σ'_0 and Su_y/σ'_0 design values.
- In general, we observed that the state and brittleness indexes considered in this study such as ψ_0, ψ_{m}, ψ_{v}, I_P, I_b are correlated.
- The trends suggest that flow liquefaction cases with partial softening may have in general I_b, ψ/λ, and I_P values larger than 0.25, 0.75, and 2.5, respectively. Whereas flow liquefaction with full softening is associated with I_b, ψ/λ, and I_P values higher than 0.6, 1.5, and 10, respectively. We recommend using these values as part of screening procedures in engineering practice.

5 ACKNOWLEDGEMENTS

This study has been funded by the National Science Foundation (NSF) under the CMMI 2013947 project and has also received support from the TAilings and IndustriaL waste ENGineering Center (TAILENG). We also thank Mr. Terry Eldridge, Mr. Mike Jefferies, and Dr. Li Wei, who kindly share data on mine tailings and sand materials.

6 REFERENCES

Anderson, C. & Eldridge, T. 2011. Critical state liquefaction assessment of an upstream constructed tailings sand dam. *Tailings and Mine Waste 2010*, 101–112.

Bedin, J. Schnaid, F., Da Fonseca, A.V., & Costa Filho, L.D.M. 2012. Gold tailings liquefaction under critical state soil mechanics. *Géotechnique*, 62(3):263–267.

Been, K. 2016. Characterizing mine tailings for geotechnical design. *Geotechnical and Geophysical Site Characterisation 5*. Australian Geomechanics Society, Sydney, Australia, 41–56.

Been, K. & Jefferies, M.G. 1985. A state parameter for sands. *Géotechnique*, 35(2):99–112.

Carrera, A., Coop, M., & Lancellotta, R. 2011. Influence of grading on the mechanical behaviour of Stava tailings. *Géotechnique*, 61(11):935–946.

Chandler, R. J. & Tosatti, G. 1995. The Stava tailings dams failure, Italy, July 1985. *Proceedings of the Institution of Civil Engineers* , Geotechnical Engineering. 113, No. 2, 67–79.

Cola, S., & Simonini, P. 2002. Mechanical behavior of silty soils of the Venice lagoon as a function of their grading characteristics. *Canadian Geotechnical Journal*, 39(4):879–893.

Fourie, A. B., & Papageorgiou, G. 2001. Defining an appropriate steady state line for Merriespruit gold tailings. *Canadian Geotechnical Journal*, 38(4), 695–706.

Fourie, A.B. & Tshabalala, L. 2005. Initiation of static liquefaction and the role of K0 consolidation. *Canadian Geotechnical Journal*, 42(3):892–906.

Gill, S. S. 2019. Geotechnical properties of tailings: effect of fines content. University of Toronto.

Hardin, B.O., & Richart, F.E. 1963. Elastic wave velocities in granular soils. *Journal of the Soil Mechanics and Foundations Division*, ASCE, 89(SM1):33-65.

Jefferies, M.G., 1993. Nor-Sand: a simple critical state model for sand. *Géotechnique*, 43(1):91–103.

Jefferies, M. G. & Been, K. 2015. Soil liquefaction: a critical state approach, 2nd edn. Boca Raton, FL, USA: *CRC Press*.

Li, W. 2017. The mechanical behaviour of tailings. PhD. Thesis, City University of Hong Kong, Hong Kong.

Li, W. & Coop, M.R. 2019. Mechanical behaviour of Panzhihua iron tailings. *Canadian Geotechnical Journal*, 56(3):420–435.

Li, W., Coop, M. R., Senetakis, K., & Schnaid, F. 2018. The mechanics of a silt-sized gold tailing. *Engineering Geology*, 241, 97–108.

Macedo, J. & Vergaray, L. 2021. Properties of Mine Tailings for Static Liquefaction Assessment. Canadian Geotechnical Journal. https://doi.org/10.1139/cgj-2020-0600.

Macedo, J. & Petalas, A. 2019. Calibration of Two Plasticity Models against the Static and Cyclic Response of Tailings Materials. *Proceedings of Tailings and Mine Waste*. Vancouver.

Morgenstern, N. R., Jefferies, M., Zyl, D., & Wates, J. 2019. Independent Technical Review Board. Report on NTSF Embankment Failure. Ashurst Australia.

Morgenstern, N. R., Vick, S. G., Viotti, C. B., & Watts, B. D. 2016. Fundao tailings dam review panel. Report in the immediate causes of the failure of the Fundao Dam. New York: Cleary Gottlieb Steen and Hamilton LLP. Available at: http://fundaoinvestigation.com/the-panel-report/.

Morgenstern, N. R., Vick, S. G., & Zyl, D. 2015. Independent Expert Engineering Investigation and Review Panel. Report on Mount Polley Tailings Storage Facility Breach. British Columbia. Available at: https://www.mountpolleyreviewpanel.ca/final-report.

Papageorgiou, G. 2004. Liquefaction assessment and flume modelling of the merriespruit gold and bafokeng platinum tailings. PhD. Thesis University of the Witwatersrand

Pestana, J.M. & Whittle, A.J. 1995. Compression model for cohesionless soils. *Géotechnique*, 45(4):611–631.

Rabbi, A.T.M.Z., Rahman, M.M., & Cameron, D.A. 2019. The relation between the state indices and the characteristic features of undrained behaviour of silty sand. *Soils and Foundations*, 59(4):801–813.

Raposo, N. 2016. Deposição de rejeitados espessados. caraterização experimental e modelação numérica. PhD. Thesis, University of Porto.

Reid, D. 2015. Estimating slope of critical state line from cone penetration test — an update. *Canadian Geotechnical Journal*, 52(1), 46–57.

Reid, D. & Fanni, R. 2020. A comparison of intact and reconstituted samples of a silt tailings. *Géotechnique*, 1–13.

Reid, D., Fanni, R., Koh, K., & Orea, I. 2018. Characterisation of a subaqueously deposited silt iron ore tailings. *Géotechnique Letters*, 8(4), 278–283.

Reid, D., Fourie, A., Ayala, J. L., Dickinson, S., Ochoa-Cornejo, F., Fanni, R., Garfias, A., Da Fonseca, A., Ghafghaz, M, Ovalle, C, Riemer, M, Rismanchian, A., & Suazo, G. 2020. Results of a critical state line testing round robin programme. *Géotechnique*, 1–15.

Riemer, M. Macedo, J., Roman, O., & Paihua, S. 2017. Effects of stress state on the cyclic response of mine

tailings and its impact on expanding a tailings impoundment. *3rd International Conference on Performance-based Design in Earthquake Geotechnical Engineering*. Vancouver.
Robertson, P.K., De Melo, L., Williams, D.J., & Wilson, G.W. 2019. Report of the Expert Panel on the Technical Causes of the Failure of Feijão Dam I.
Sadrekarimi, A. 2013. Influence of state and compressibility on liquefied strength of sands. *Canadian Geotechnical Journal*, 50(10):1067–1076.
Sadrekarimi, A. 2014. Effect of the mode of shear on static liquefaction analysis. *Journal of Geotechnical and Geoenvironmental Engineering*, 140(12):04014069.
Sadrekarimi, A. 2016. Static Liquefaction Analysis considering principal stress directions and anisotropy. *Geotechnical and Geological Engineering*, 34(4):1135–1154.
Sadrekarimi, A. 2020. Forewarning of Static Liquefaction Landslides. *Journal of Geotechnical and Geoenvironmental Engineering*, 146(9), 04020090.
Schnaid, F., Bedin, J., Viana da Fonseca, A.J.P., & Costa Filho, L.D. 2013. Stiffness and strength governing the static liquefaction of tailings. *Journal of Geotechnical and Geoenvironmental Engineering*, 139(12):2136–2144.
Shuttle, D.A. & Cunning, J. 2007. Liquefaction potential of silts from CPTu. *Canadian Geotechnical Journal*, 44(1):1–19.
Shuttle, D. & Jefferies, M. 2016. Determining silt state from CPTu. *Geotechnical Research*, 3(3):90–118.
Smith, K., Fanni, R., Capman, P., Reid, D. 2019. Critical State Testing of Tailings: Comparison between Various Tailings and Implications for Design. *Proceedings of Tailings and Mine Waste*. Vancouver.
Soares, M. & Da Fonseca, A.V. 2016. Factors affecting steady state locus in triaxial tests. Geotechnical Testing Journal, 39(6):20150228.
Yan, W. M., & Dong, J. 2011. Effect of Particle Grading on the Response of an Idealized Granular Assemblage. *International Journal of Geomechanics*, 11(4):276–285.
Torres, L.A. 2016. Use of the cone penetration test to assess the liquefaction potential of tailings storage facilities. PhD. Thesis, University of the Witwatersrand, Johannesburg.
USACE. 2016. National inventory of dams. Army Corp of Engineers.

Numerical Simulation of rockfill dams for tailings considering change of design parameters of the conformation material – A case study

Edgar R. Quiroz
Stantec, Lima, Lima, Peru

ABSTRACT: Constitutive models are mathematical expressions of the stress-strain relationship of a material. Analytical models apply physical laws to describe the stress-strain response of the material. These models are based on parameters at microscopic or macroscopic scale. This research work aims to present the main results of rockfill dam for tailings storage facility modeling by the finite element method and fine differences method, considering the calibration of two different constitutive models associated with estimation of material (rockfill) parameters against laboratory results, changes in technical specifications, layer thicknesses of 2, 4 and 8 meters, and rockfill dam elastic parameter and instrumentation monitoring results, based on the experience of a real case study that will be presented. This paper presents the main considerations to be taken into account, approximations made for calibration of the proposed constitutive models, a comparison between the parameters used in the model, and the results of tests conducted in the post-mathematical modeling laboratory. The presenter experiences will be shared and allow to obtain better approximations in this type of designs or verifications of rockfill dam stress and deformation status.

1. INTRODUCTION

1.1 *Rockfill tailings dams*

Many soils and rockfill tailings dams around the world are at the raising stage. Tailings are waste material resulting from mining operations. These are pumped as a slurry to an impoundment and are generally retained by embankments (tailings dams), Barrero et al. (2015). A tailings dam plays a very important role in all stages of the mine especially during the operation. It is a very complex geotechnical structure that need to be stable during operation and closure. There are phenomenons that can cause a dam break or slide, resulting in irreversible damage to the environment; therefore, there are methodologies that assess the safety of these structures over time.

A safety concern is deformation of the dam. The effect of dam's deformation can be estimated using numerical approximations by the finite elements method (FEM) or finite differences method (FDM). The numerical simulations of the stress-strain behavior are an excellent tool to verify with greater precision how safe the dam will be.

1.2 *Constitutive Models*

The Hardening Soil Model (HS model) and Simple Anisotropic Sand Plasticity Models (SANISAND) proposed by Schanz et al. (1999) and Taiebat et al. (2007), respectively, can be used to analyze the behavior of dams comprised of rock and soil materials because of their convenience in the implementation of programs in finite elements and finite differences; through obtaining parameters for each model. Each model uses a specific number of parameters, and the determination of these parameters through testing does not necessarily represent the existing conditions.

For this case study, we are considering the Atacocha tailings dam located in the district of "San Francisco de Asis de Yarusyacan", Province of Cerro de Pasco, with 140 meters of height and a tailings storage capacity of 18.40 Mm3. Development and raising downstream of the dam are planned to take place in 4 phases. During the dam raising process, the structure behavior was evaluated, specifically at two elevations of dam's crest 4110 masl and 4128 masl. See figure 1.

1.3 *Objective*

The objective is to evaluate the structure deformations resulting from waste rock stockpiling in layers of different thicknesses, considering an initial stockpiling in layers of 1 m and a subsequent stockpiling in layers of 2, 4 and 8 meters used for the dam construction. This resulted in changes in the technical specifications and design parameters, which generated considerable deformations in the dam (settlements), and a risk of failure was suspected. As a consequence, it was decided to verify the Atacocha tailings storage facility (TSF) dam stability through a stress-strain analysis by the Finite Differences Method (FDM) at the current stage 4 (elevation of 4110 masl) and by the Finite Elements Method (FEM) for the future planned stage (elevation of 4128 masl) for which the raising construction process, initial parameters of material placement, quality control data, and geotechnical monitoring data obtained from the instrumentation system of the dam were taken into account.

The two-dimensional computational simulation of the stress-strain response of the geotechnical structure was developed within the framework of finite elements and finite differences using PLAXIS 2D and FLAC 2D computational tools.

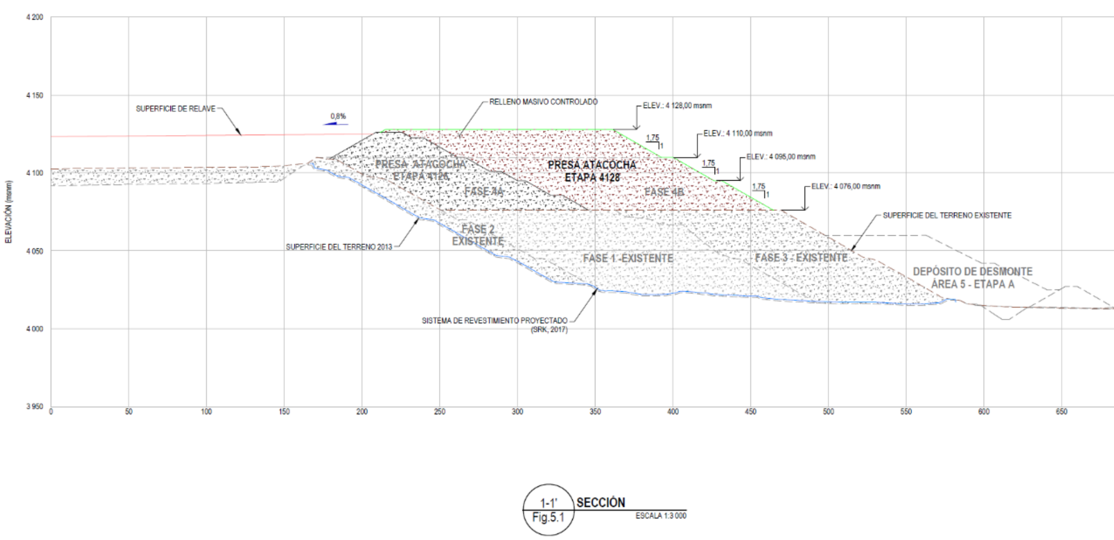

Figure 1. Section with two elevations of dam's crest 4110 masl and 4128 masl.

2. SELECTION OF CONSTITUTIVES MODELS

2.1 *Model selected*

The model to be selected must be capable of reproducing the nonlinear and inelastic stress-strain relation due to nonlinear and inelastic stress, intense dilational behaviors under shearing of dense granular materials, and the dependence of stress on stiffness, Pramthawee et al. (2011).

The Mohr-Coulomb (MC) constitutive model was used to represent the mechanical behavior of most of the materials in the geotechnical units, except for those units identified as "Glory Hole" mine waste rock (Phase 2b and Phase 4).

The Simple ANIsotropic SAND (SANISAND) Plastic Model was selected to represent the mechanical behavior of the geotechnical units of the "Glory Hole" mine waste rock, Phase 2b and

Phase 4 at an elevation of 4110 meters above sea level (masl). SANISAND was developed within the theoretical framework of the critical state theory in soils and the plastic limit surface. The model uses three surfaces:

The first one is the dilation surface that controls the material dilation during the shearing process as a function of the state parameter ψ, defined as $\psi = e - e_c$. When ψ = 0, the dilation surface matches the critical state surface described below.

The second one is the bounding surface that defines the maximum value of the deviatoric stress during a shearing process, and that allows to reproduce the loss of resistance observed in dense samples at the laboratory (strain softening). The bounding surface is defined as a function of ψ, and its position matches the surface of the critical state once ψ = 0.

The third one is the critical state surface that controls the material response at critical state. This surface is defined as a function of the Lode angle and is reached when ψ = 0. In the next section, a brief explanation of the SANISAND model will be provided.

The Hardening Soil (HS) model was selected to represent the mechanical behavior of the geotechnical units of mine waste rock Phase 1, Phase 2, Phase 3, Phase 4, and waste rock at an elevation of 4128 masl. The HS model is based on the concept of isotropic strain hardening. It can sufficiently predict the shear characteristics of embankments (Xu and Song, 2009) and it can be easily implemented in the FEM or FDM software (Schanz et al., 1999). The development and application of the HS model will not be further discussed in this paper.

2.2 *SANISAND Model*

SANISAND is a model that belongs to the family of simple anisotropic sand constitutive models within the framework of critical state soil mechanics and bounding surface plasticity [Manzari and Dafalias (1997), Dafalias and Manzari (2004), Dafalias et al. (2004), Taiebat and Dafalias (2008), Li and Dafalias (2012)].

The formulation of SANISAND model is presented in the triaxial stress–strain space in terms of standard triaxial stress quantities $p = (\sigma_1 + 2\sigma_3)/3$, deviatoric stress $q = (\sigma_1 - \sigma_3)$ and the stress ratio represented by $\eta = q/p$. Additionally, strain quantities are volumetric strain $\varepsilon_v = (\varepsilon_1 + 2\varepsilon_3)$ and deviatoric strain $\varepsilon_q = 2(\varepsilon_1 - \varepsilon_3)/3$, where it should be noted that $\sigma_2 = \sigma_3$ and $\varepsilon_2 = \varepsilon_3$. Note that all stress components in this paper are considered effective and both stress and strain quantities will be assumed to be positive in compression.

Within the range of small deformations and rotations, the basic kinematical assumption of the additive decomposition of total strain rate into elastic and inelastic parts is made, which reads as follows:

$$\dot{\varepsilon} = \dot{\varepsilon}^{e} + \dot{\varepsilon}^{p} \tag{1}$$

Where ε is a generic symbol for the strain tensor, superscripts e and p denote elastic and plastic parts, respectively, and a superposed dot denotes the material time derivative or rate.

It should be noted that the inherent anisotropy (Dafalias et al. (2004)), the plastic strains under constant-stress ratios (Taiebat and Dafalias (2008)), and the anisotropic critical state (Li and Dafalias (2012)) have not been accounted for in the present work.

2.2.1 Critical State

Li and Wang (1998) have proposed the following equation for the location of the critical state line (CSL) in a *e–p* space that has a considerable range of applicability:

$$e_c = e_0 - \lambda(p_c/p_{at})^{\xi} \tag{2}$$

Where e_0, λ and ξ are constants, p_{at} is the atmospheric pressure for normalization, and e_c and p_c refer to the critical void ratio and confining pressure, respectively. The state parameter $\psi = e - e_c$, originally defined by Been and Jefferies (1985), is a measure of how far the material state (void ratio and confining pressure) is from the critical state measured along the e-axis.

2.2.2 Elastic and plastic deformations

The nonlinear elastic response of the SANISAND model is assumed to be hypoelastic. The strain increment is decomposed into elastic and plastic parts, denoted by superscripts e and p, each one having deviatoric and volumetric parts, denoted by subscripts q and v:

$$d\varepsilon_q^e = \frac{dq}{3G}, \quad d\varepsilon_v^e = \frac{dp}{K} \tag{3}$$

$$d\varepsilon_q^p = \frac{d\eta}{H}, \quad d\varepsilon_v^p = d\left|d\varepsilon_q^p\right| \tag{4}$$

Where *K* and *G* are the hypoelastic bulk and shear module, respectively, *H* is the plastic hardening modulus associated with the increment of stress ratio $d\eta$, and *d* is the dilatancy coefficient. Variables *H* and *d* will be defined later in this investigation. The incremental bulk and shear modulus are defined according to Richart et al. (1970) and Li and Dafalias (2000):

$$G = G_0 p_{at} \frac{(2.97 - e)^2}{1 + e} \left(\frac{p}{p_{at}}\right)^{1/2}, K = \frac{2(1 + v)}{3(1 - 2v)} G \tag{5}$$

Where G_0 is a dimensionless material constant, v is the Poisson's ratio, e is the void ratio, and p_{at} is the atmospheric pressure used for normalization.

2.2.3 Yield surfaces

The yield surface can be imagined as a wedge in the *p-q* space and a cone in the multiaxial space. The yield function is expressed by:

$$f = |\eta - \alpha| - m = 0 \tag{6}$$

Where *m* is a material constant representing the opening of the yield surface and α is the deviatoric back stress ratio representing the orientation of the yield surface.

2.2.4 Dilatancy, bounding and critical surfaces

The model uses three concentric and homologous surfaces: the dilatancy, bounding and critical surface. These are considered in the π-plane.

The dilatancy surface is defined by the slope of M^d. This surface enables the model to reproduce contractive volumetric soil response if $\eta < M^d$, and dilative volumetric soil response for $\eta > M^d$. The evolution of the dilatant surface is defined by the state parameter ψ as follows:

$$M^d = M \exp(n^d \psi) \tag{7}$$

Where M and n^d are positive material constants.

The bounding surface is defined by the slope of M^b. This surface enables the model to reproduce softening if $\eta > M^b$, this will result in a peak shear stress in the stress-strain curve. The evolution of the bounding surface is again defined by the state parameter ψ as follows:

$$M^b = M \exp(-n^b \psi) \tag{8}$$

Where n^b is a positive material constant. As the sample reaches the critical state, the distance between the critical void ratio approach 0, the lines representing M^d and M^b converge and collapse with the critical surface line *M*.

2.2.5 Plastic flow

The SANISAND model includes a non-associative flow rule allowing realistic evaluations of plastic strain increments with equation (4). In this equation, *H* controls the increment of the plastic deviatoric strain as a function of distance between M^b and η:

$$H = h(M^b - \eta) \tag{9}$$

Where *h* is a function of current state variables *p* and *e*. The dilatancy coefficient *d* in equation (4) is expressed as follows:

$$d = A_d(M^d - \eta) \tag{10}$$

Where A_d is a function of the fabric-dilatancy tensor.

3. DAM MATERIALS AND MODEL CALIBRATION

3.1 *Dam materials*

Various construction materials were evaluated for inclusion in the analysis model resulting in 18 geotechnical units characterized through specialized tests that were used to estimate the physical resistance parameters. Laboratory tests for the various materials include large-scale shear tests, undrained consolidated triaxial compression tests, one-dimensional consolidation tests, minimum and maximum density tests, and others. Geotechnical units are listed and related to a specific color in Table 1.

3.2 *Calibration model*

The procedure to estimate the parameters of the models is referenced in Schanz et al. (1999) for the HS model and Taiebat et al. (2007) for the SANISAND model.
The parameters obtained from the calibration which were used in the simulation are listed in Table 2 and Table 3 for the SANISAND and HS models respectively.

Table 1. Geotechnical Units

Geotechnical Unit	**Color**	Geotechnical Unit	**Color**
Unit 1: Old rockfill	purple	Unit11: Filter sand	red
Unit 2: Low permeability core	orange	Unit 12: ROM compacted – dike	pink
Unit 3: Existing fill	light peach	Unit 13: ROM “Glory Hole” – phase 1	very light peach
Unit 4: Filter material	grey	Unit 14: ROM “Glory Hole” – phase 2	bright green
Unit 5: Low-permeability soil	green	Unit 15: ROM “Glory Hole” – phase 3	dark blue
Unit 6: Existing rockfill 1	blue	Unit 15A: ROM “Glory Hole” – phase 3	violet
Unit 7: Existing rockfill 2	light blue	Unit 16: ROM “Glory Hole” – phase 4	pale blue
Unit 8: Fine tailings	light grey	Unit 16A: ROM “Glory Hole” – phase 4	very pale blue
Unit 9: Foundation soil	rose	Unit 17: Interface GCL	yellow
Unit 10: Bedrock	sage green	Unit 18: Geomembrane	olive

For location of geological units see figure 7.

Table 2. Material parameters with SANISAND model.

Description	Parameter	Mine Waste Rock – “Glory Hole”
Elasticity	G_O	50
	v	0.33
Critical state	M	1.718
	c	0.5
	λ_c	0.00468
	e_{ref}	0.23
	ξ	0.7
Yield surface	m	0.05
Plastic flow	h_O	5.0
	Ch	0.968
	n^b	3.0
Dilatancy	A_O	0.7
	n^d	2.5
Fabric-dilatancy tensor	z_{max}	4.0
	C_z	600

Table 3. Material parameters with HS model.

Description	Parameter	Waste Rock Stage 1
Specific weight	γ	22
Cohesion	C	0
Internal friction angle	$\emptyset$ (°)	37
Stiffness dependence on the stress state	m	0.3
Secant stiffness in triaxial tests	E_{50}^{ref}	22.0
Tangent stiffness for primary load in tests	E_{edo}^{ref}	22.0
Stiffness in discharge-recharge	E_{u}^{ref}	66.0

3.2.1 Comparison of laboratory and triaxial tests.

The results of the triaxial tests conducted in laboratory were numerically simulated. Figure 2 shows the comparison between the triaxial test results obtained with numerical simulations and the triaxial test results obtained in laboratory.

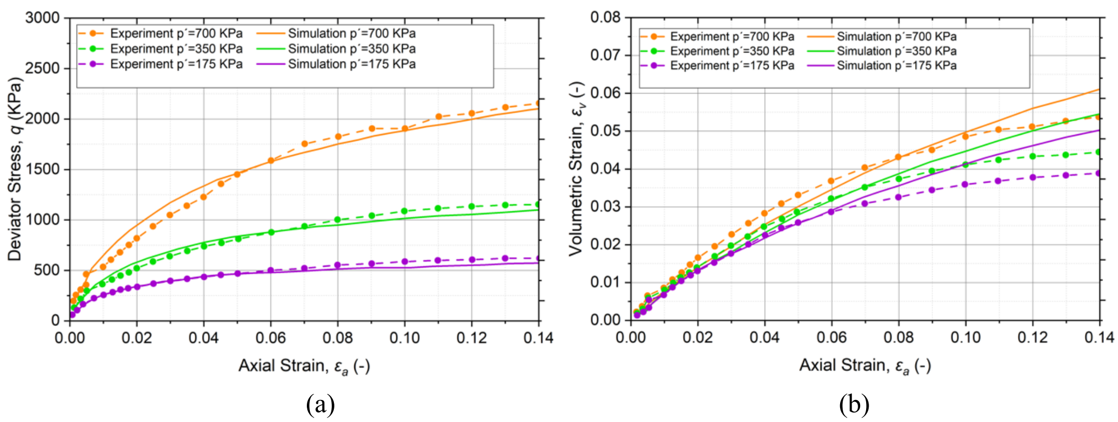

Figure 2. Laboratory drained triaxial tests and numerical simulations (a) stress-strain curves; (b) volumetric strain - axial strain.

3.2.2 Sensitivity simulations of variables G_0 and e_0

To align the response of the model and in-situ conditions, numerical simulations of triaxial tests were performed varying the parameters G0 and e0 for the same confining pressures of the laboratory triaxial tests.

The values used for the sensitivity analysis are presented in Table 4. The parameter G0 was varied within a range G0 / 2– 2G0, where G0 is the calibrated value of the triaxial laboratory tests presented in Table 2. The initial void ratio was varied according to the reported in situ void ratios. The values of G0 = 50 and e0 = 0.175 in Table 4 are the reference values. The values of 100 and 25 for G0, 0.256 and 0.142 for e0 are upper and lower limits, respectively, for DMT materials from Phases 2b and 4.

Table 4. Values for sensitivity analysis.

Description	Parameter	ROM Stage 2b	ROM Stage 4
Elasticity	G_O	10	10
Initial void ratio	e_O	0.256	0.34

Figure 3 through Figure 5 show the response of the model for the case of a triaxial compression under drained conditions.

Figures 3 (a) and Figure 3 (b) illustrate the effect of the parameter ψ on the response of the constitutive model in terms of stress-strain and volumetric strain-axial strain. These figures desmonstrate that, for the same material, the higher the initial void ratio (higher ψ), the lower the maximum mobilized deviating stress and the higher the volumetric strain.

Figures 4 (a) and Figure 4 (b) indicate the effect of the constitutive parameter G_0 on the response of the model under triaxial compression drained conditions. For the same initial void ratio in similar materials, G_0 controls the slope of the stress-strain curve at low strain levels. An implication of this effect is that a material with a low value of G_0 may exhibit a more ductile behavior; that is, the maximum deviator stress is reached at higher values of axial strain.

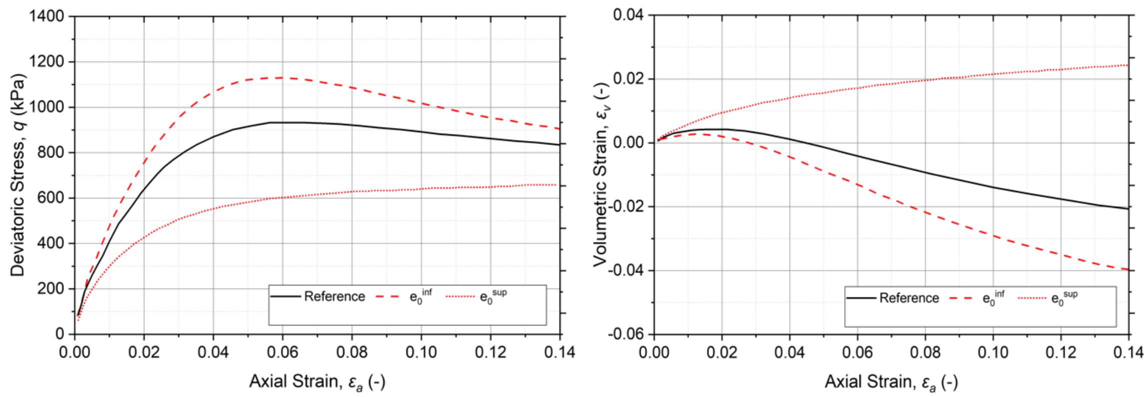

(a) (b)

Figure 3. Results of numerical simulations of drained triaxial compression tests for a confining pressure of 175 kPa, the reference value G0 = 50 and three different void ratios: e0 ^ inf = 0.142 (lower limit), e0 = 0.175 (reference value) and e0 ^ sup = 0.256 (lower limit), e0 = 0.256 (upper limit). Constitutive parameters from Table 2.

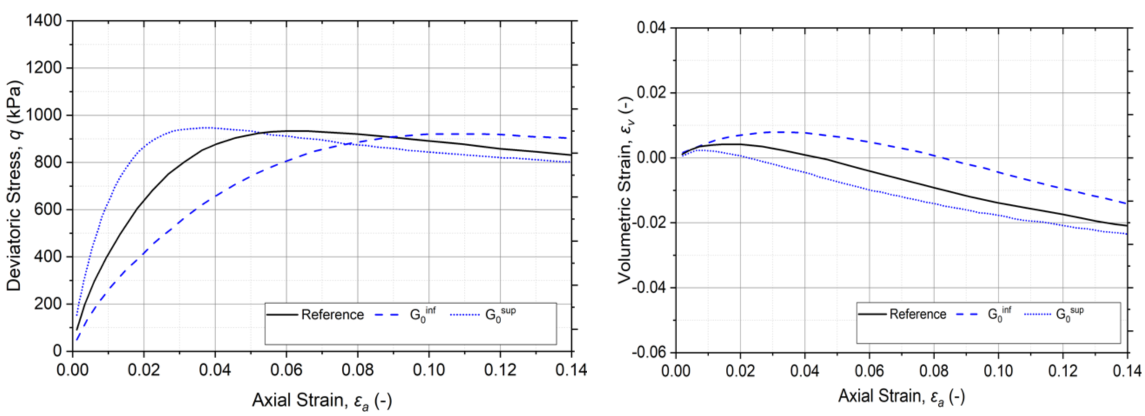

(a) (b)

Figure 4: Results of numerical simulations of drained triaxial compression tests for a confining pressure of 175 kPa, an initial void ratio e_0 = 0.175 and three different elastic parameter values: G_0: G_0^{inf} = 25 (lower limit), G_0 = 50 (reference value) and G_0^{Sup} = 100 (upper limit). Constitutive parameters from Table 2.

Figure 5 (a) shows the response of the model in the p'- e plane to the triaxial compression drained from the materials with different initial void ratios. In this plane, the response of the model is like the behaviors observed in laboratory tests where the trajectories p'- e tend to the Critical State Line (SCL) with a decrease or increase in volume. In Figure 5 (b) it is observed that the response of the model in the p'- e plane before drained triaxial compression is almost identical for materials with different G0 (within the considered sensitivity range) and the same initial void ratio.

Figures 6 (a) and Figure 6 (b) illustrate the response of the model under geometric compression conditions. The response of the model under these compression conditions is sensitive to initial void ratios and does not show sensitivity to variations in G_0 within the range of the sensitivity analysis.

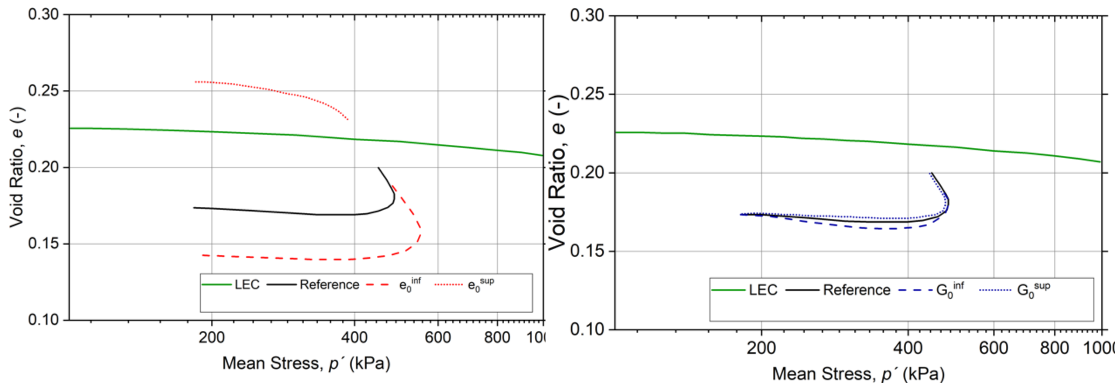

(a) (b)

Figure 5. Results of numerical simulations of drained triaxial compression tests for a confining pressure of 175 kPa. (a) three different void ratios e0 ^ inf = 0.142 (lower limit), e0 = 0.175 (reference value), e0 ^ sup = 0.256 (upper limit) for the reference value $G_0 = 50$ (b) three values of the elastic parameter, G_0^{inf} = 25 (lower limit), $G_0 = 50$ (reference value) and G_0^{Sup} = 100 (upper limit) for the reference void ratio e_0 = 0.175, Critical State Line (CSL) in green color.

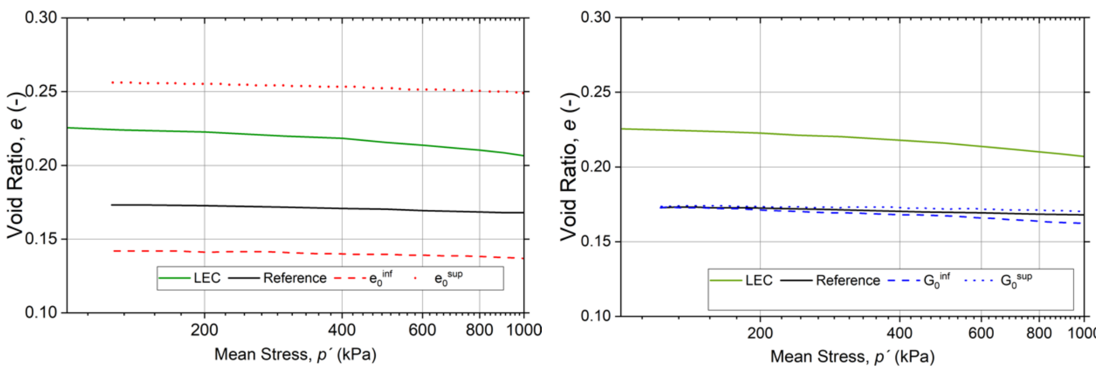

Figure 6. Results of numerical simulations of oedometric compression tests for a confining pressure of 175 kPa. (a) three different void ratios e_0^{inf} = 0.142 (lower limit), e_0 = 0.175 (reference value), e_0^{sup} = 0.256 and the reference value of the elastic parameter G_0 = 50, and (b) three elastic parameter values, G_0^{inf} = 25 (lower limit), $G_0 = 50$ (reference value) and G_0^{Sup} = 100 (upper limit) for the reference void ratio e_0 = 0.175, Critical State Line (CSL) in green color.

4. CHARACTERISTICS OF THE DAM AND DATA FOR THE ANALYSIS CASE

4.1 *Characteristics of Tailings Storage Facility*

The Atacocha dam was built in 4 ascending ascending phases, for which material from the mine waste was used. See figure 1.

The global slopes of the dike dam had a slope of 1.5: 1 (H: V) on the upstream face and 2.5: 1 (H: V) on the downstream face. The raises associated with the 4 phasesbanks that are part of the expansion of the dike in its 4 phases have an inclination slope of 1.75: 1 (H: V). Figure 46 shows the geometry of the current tank conditions, embankment at the which corresponds to the critical cross section. The geotechnical model for the deformation analysis is presented in Figure 7.

The regional stratigraphy comprises rocks with ages ranging from the Permian to the recent Quaternary. To the bottom, continental sedimentary rocks from the Mitu Group (upper Permian) appear, transitioning to a carbonate marine sedimentation from the Triassic - Jurassic represented by the Pucara Group, overlain by the siliciclastic sequence from the Lower Cretaceous Goyllar-isquizga Group. Cholle formation limestones represent a slight marine transgression and subsequent regression, followed by Casapalca red layers (Upper Cretaceous). Subsequent volcanic activity originated the accumulation of the Rumilaca volcanic deposits. Finally, the sequences described are overlain by recent deposits made up of moraine, alluvial and colluvial materials.

4.2 *Instrumentation*

The instrumentation system is focused on the monitoring the physical stability of the dam and includes survey landmarks and vibrating wire piezometers.
The milestones are numbered from 1 through 6, with landmarks 1 and 6 located at the west and east ends of the dam respectively. Landmarks 1 and 6 were installed on natural terrain, landmarks 2 - 5 are located on the crest of Phase 2 and Landmark 4 is close to the analysis sec-tion.

5. ANALYSIS AND EVALUATION

5.1 *Limitations*

The FLAC 2D finite difference and Plaxis 2000 finite element software is used throughout this analysis. The simulation has been developed in a 2D deformation plane along the critical cross section of the Atacocha tailings deposit.
The deformation analysis was carried out using the actual geometry for current conditions of the deposit. The geotechnical model for the deformation analysis is presented in Figure 7 and does not include the units 3, 4, 5, 11, 12, 17 and 18.

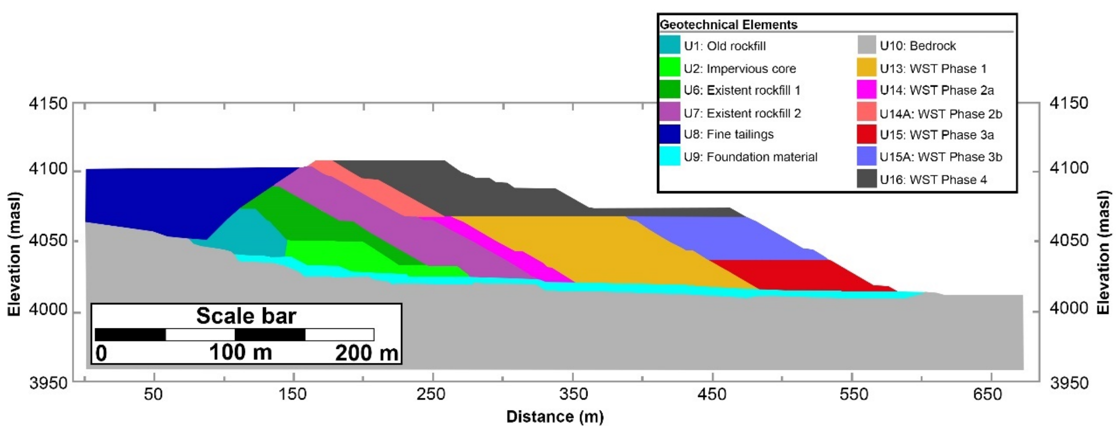

Figure 7. Geotechnical model used for deformation analysis, Stage 4 (elevation 4110 masl).

5.2 *Finite element and finite difference model*

The Atacocha dam is modeled through the discretization of the geotechnical structure by means of quadrilateral elements. The explicit Lagrange´s formulation combined with the mixed discretization technique used by FLAC allows the plastic response of geotechnical materials to be calculated. Each quadrilateral, or zone element, is divided into four subzones, which in turn are represented by triangular elements. In each subzone, plane strain conditions are assumed for the model. The discretization by finite differences for the deformation analysis is shown in Figure 8. The model contains the discretization of the 13 units. Of these units, 11 were modeled with Mohr Coulumb and two with SANISAND. Additionally, Figure 8 includes the control points A, B, C, D, E and F where the vertical and horizontal displacements of the deformation analysis are monitored.

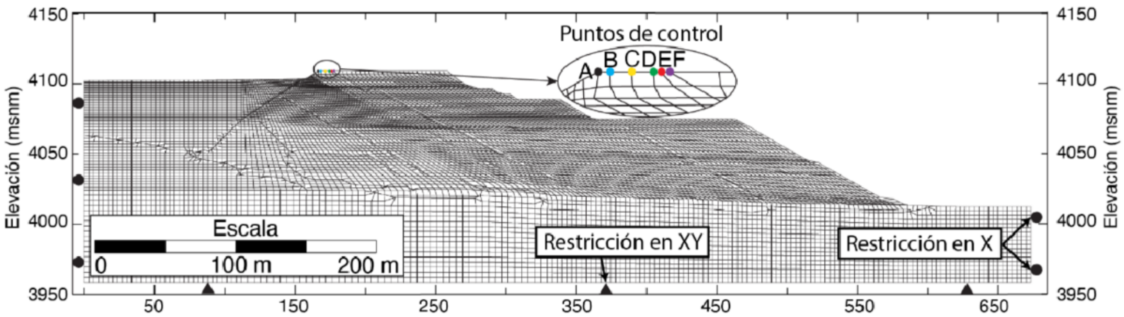

Figure 8. Numerical model with boundary conditions and deformation control points

5.3 *Procedure*

The deformation analysis was carried out by simulating the construction process of the mine cut buttress over time. The numerical simulation begins by activating and bringing to geostatic equilibrium the zones assigned to the fine tailing, bedrock, old rockfill, impermeable core, ex-isting fill, existing rockfill 1 and 2 groups.
The construction of the “Glory Hole” Phase 1 – 4 materials was then completed considering the actual construction sequence. Accordingly, the simulation of the raising of the “Glory Hole” Phases 1 - 4 mine stripping groups was carried out activating the elements of each horizontal row to seek geostatic equilibrium after activation. The construction sequence to simulate the construction of the dam is simulated by six phases: “Glory Hole” Mine Waste Phase 2a, Phase 1, Phase 2b, Phase 3a, Phase 3b and Phase 4.
The “Glory Hole” phase 4 mine waste was constructed assuming 2 lifts per month. The measurements in the numerical model began in December 2019 with the elevation 4,096 masl and end-ed in July 2020 with the elevation 4,110 masl.

5.4 *Numerical modeling cases*

In order to gain a better understanding, three cases of numerical modeling were developed modifying the initial void ratio. For case 1, an initial value $e_o = 0.175$; for case 2, an initial value $e_o = 0.312$; and for case 3, the elastic parameters and void ratios of Stage 2b and Stage 4 materials (SANISAND model) were modified until obtaining displacement values similar to those measured in the survey markers located in the analysis section.

5.5 *Results of the computation at the end of construction*

Although measurements in a reference survey marker 4 may be affected by the quality of measurements, the displacements observed in this mark will be used as a reference to compare the results of the displacement analyzes. This mark, located very close to the analysis section, has shown maximum displacements of approximately 20 mm in the horizontal direction and 40 m in the vertical direction.

5.5.1 Case 1

The maximum displacements obtained for this case are approximately 2.4 and 4.5 mm for horizontal and vertical directions, respectively. These values are well below the observed values. For this case, we have $G_0 = 0.50$ and $e_0 = 0.175$.

5.5.2 Case 2

The maximum displacements obtained for this case are approximately 2.4 and -4.4 mm for horizontal and vertical directions, respectively. These values are also below the observed values. For this case, we have $G_0 = 0.50$ and $e_0 = 0.312$

5.5.3 Case 3

Several numerical simulations were performed modifying the elastic parameters and the initial void ratios of Stage 2b and Stage 4 materials (SANISAND model). The modification took place within ranges deemed suitable until obtaining displacements like those observed in survey marker 4. Table 4 shows the values of G_0 and e_0 adjusted with this procedure for Stage 2b and Stage 4 materials.

Maximum displacements obtained at control point F (Figure 8) are approximately 19 mm in the horizontal direction and -33.2 mm in the vertical direction.

Table 4. State variables and adjusted parameters for deformation analysis.

Descripción	Parámetro	ROM Stage 2b	ROM Stage 4
Elasticidad	G_O	10	10
Relación de vacios inicial	e_O	0.256	0.34

The contours of horizontal (Figure 9) and vertical (Figure 10) displacements in this case show concentration of displacements on the order of 40 and 60 cm, respectively, in zones near the slope face.

The contours of the volumetric (Figure 11) and shear (Figure 12) strains show that maximum volumetric and shear strain occur in the elements near the slope face of Stage 4. These contours also show that the volumetric strain magnitudes are greater than shear strains in all zones.

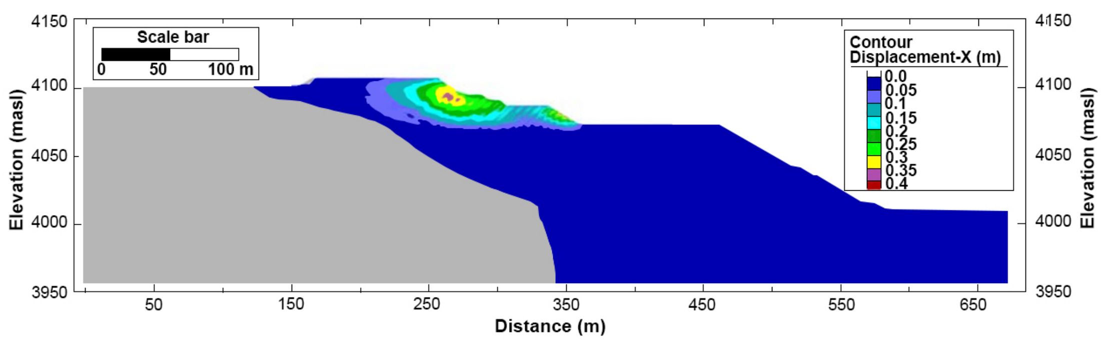

Figure 9. Horizontal displacement contour at the end of Stage 4 construction.

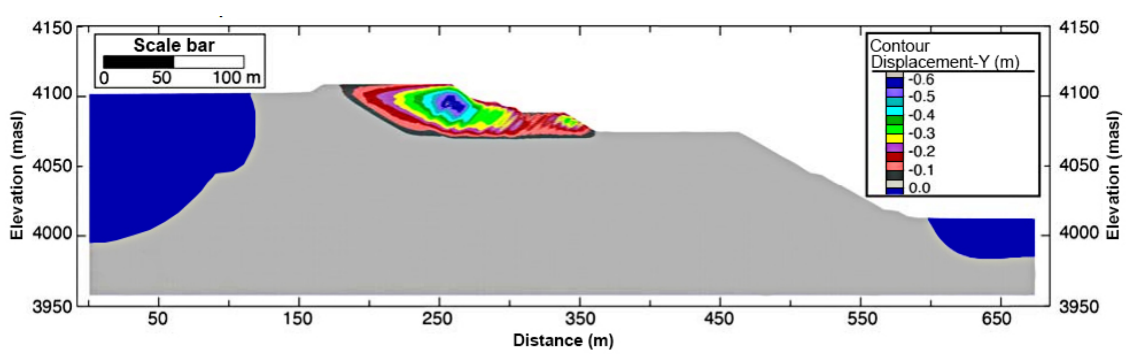

Figure 10. Vertical displacement contour at the end of Stage 4 construction.

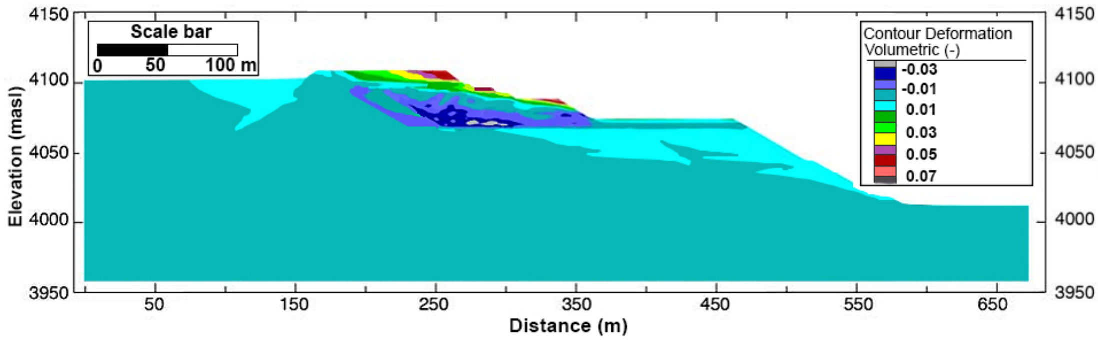

Figure 11. Volumetric strain contour at the end of Stage 4 construction.

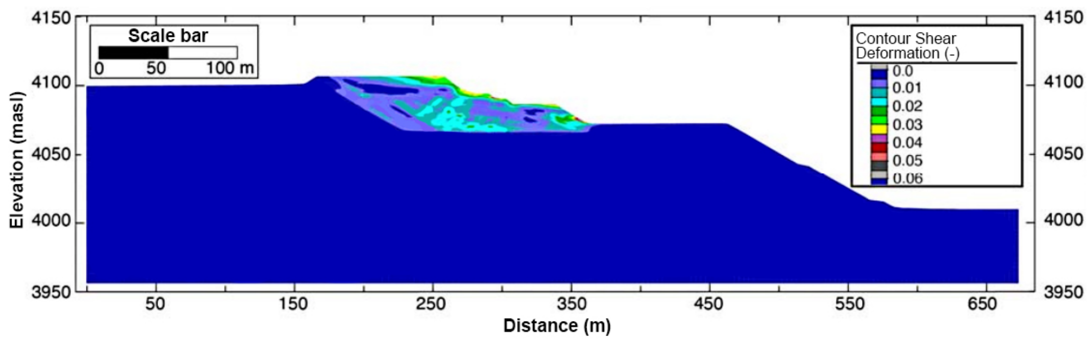

Figure 12. Shear strain contour at the end of Stage 4 construction.

6. CONCLUSIONS

To establish possible hypotheses about the origin of the deformations observed in the dam at level 4,110 masl, a two-dimensional computational simulation of the response of the structure and buttress materials was carried out during the construction process. The simulation was carried out using the finite difference program (FDM), FLAC 2D (SoilModels, 2007) with the goal of establishing whether the change in technical specifications for lift thickness of Phase 2 in February 2020 compromised the stability of the tailings deposit.

The volumetric and shear deformation contours show that the maximum volumetric and shear deformations occur in the elements near the face of the slope of Phase 4. These contours also show that the magnitudes of the volumetric deformations are greater than the shear defor-mations.

The materials from Phases 2b and 4 were considered key for the analysis. For this reason, the mechanical responses of these materials were modeled using SANISAND, an advanced constitutive model based on the critical state theory. The mechanical response of the rest of the materials in the deposit and the buttress, which are not key in the deformation analysis, was modeled with the Mohr-Coulomb constitutive model. The influence of elastic parameters and initial void relationships on the response of the materials was studied.

The displacements obtained with the computational simulations were compared with measurements of displacement at topographic landmarks, especially those between February and June 2020, according to existing monitoring information. The first analyzes yielded very low displacement values compared to those of the measurements with the monitoring milestones. Subsequent analyzes with adjusted values of the elastic parameters and the initial void ratios allowed obtaining higher displacement values, but still lower than those measured.

To establish possible hypotheses about the origin of the deformations observed in the dam at level 4,128 masl, a two-dimensional computational simulation of the response of the storage and buttress materials was carried out during their construction process using the finite element program (FEM) Plaxis 2020 (Bentley, 2020). The model was divided into two stages. The first stage of calibration, d where the displacements at the control point of the topographic land-marks will be found through the Hardening-soil (HS) model; the second stage constitutes a sensitivity analysis due to the variability that the materials could present in the field.

The analysis carried out observes increased settlement in lifts with less control. As such, it is recommended to place lifts of 2m in the area corresponding to the Atacocha Area 5 deposit and in 1m layers in zones above level 4,110 masl.

The continuous monitoring of the topographic control landmarks from February 2019 to January 2020 in Phase 2 detected a uniform trend with vertical displacements likely resulting from the rearrangement of the particles within the structure. In terms of settlements in the period of the indicated readings, there is an average of 10 cm.

Displacements in the body of the dam and shear deformations tend to increase with layer thicknesses of 4m (settlement at el. 4,128≈1.0m) and 8m (settlement at el. 4,128≈1.1m), espe-cially for raises to 4,128 masl, for this reason the layer controls at 2m (settlement at el. 4,128≈0.9m) result in lowest displacements and deformation due to shear.

The comparation of the results of the numerical simulations show that the displacements (horizontal and vertical) reaching the current condition of the reinforcement buttress are con-centrated on the face or near the face of the slope of Phase 4. The analysis also shows that vol-umetric strains are greater than shear strains. This result suggests that the displacements caused by the change in technical specification could be mainly impact to volumetric deformations, which could be associated with the self-weight of the materials of the structure. Volumetric de-formations associated with the observed displacements, and low shear deformations, suggest that the observed displacements do not compromise the stability of the dam structure at level 4,110 masl and 4,128 masl.

7. ACKNOWLEDGEMENTS

The author would like to thank Gerardo Cuba (Nexa Resources, Peru), Arcesio Lizcano (Consultant for Nexa Resources, Canada), Ivan Benites (Consultant for Nexa Resources, Peru), Miguel Isidro (Stantec, Peru) and the anonymous reviewers for their support in this publication.

8. REFERENCES

Barrero A. & Taiebat, M. 2015. Application of an advanced constitutive model in nonlinear dynamic analysis of tailings dam. *GeoQuebec 2015; Department of Civil Engineering - University of British Columbia.* Vancouver, BC, Canada.

Been K. & Jefferies M. state parameter for sands. Geotechnique 1985; 35(2):99–112.

Dafalias, Y.F., and Manzari, M.T. 2004. Simple plasticity sand model accounting for fabric-change effects, Journal of Engineering Mechanics, 36(1): 65 - 78.

Dafalias, Y.F., Papadimitriou, A.G., and Li, X.S. 2004. Sand plasticity model accounting for inherent fabric anisotropy, Journal of Engineering Mechanics, 130(11): 1319-1333.

Pramthawee P., Jongpradist P. & Kongkitkul W. 2011. Evaluation of hardening soil model on numerical simulation of behaviors of high rockfill dams. *Songklanakarin J. Sci. Technol*. 33 (3), 325-334.

Schanz, T. & Vermeer, P.A. 1996. Angles of Friction and Dilatancy of Sand. *Geotechnique*. 46(1), 145-151.

Schanz, T., Vermeer, P.A. and Bonnier, P.G. 1999. The Hardening Soil Model: Formulation and Verific-tion. *Beyond 2000 in Computational Geotechnics-10 years of Plaxis*, Balkema, Rotterdam, pp. 281–96.

Richart, F.E., Jr., Hall, J.R., and Woods, R.D. 1970. Vibration of soils and foundations. International series in theoretical and applied mechanics, Prentice-Hall, Englewood Cliffs, N.J.

Li XS, Wang Y. Linear representation of steady-state line for sand. Journal of Geotechnical and Geoenvironmental Engineering 1998; 124(12):1215–1217

Li, X.S., and Dafalias, Y.F. 2012. Anisotropic critical state theory: role of fabric, Journal of Engineering Mechanics, 138(3): 263-275.

Manzari, M.T., and Dafalias, Y.F. 1997. A two-surface critical plasticity model for sand. Geotecnique, 47(2), 255-272.

Taiebat, M., and Dafalias, Y.F. 2008 SANISAND: simple anisotropic sand plasticity model, International Journal of Numerical and Analytical Methods in Geomechanics, 32(8): 915-948

Xu, M. and Song, E. 2009. Numerical Simulation of the Shear Behavior of Rockfills. Computers and Geotechnics. 36 (8), 1259-1264.

Critical state line from level set discrete element method

Øyvind Torgersrud
Norwegian Geotechnical Institute, Oslo, Norway / Univ. Grenoble Alpes, CNSR, Grenoble INP, 3SR, Grenoble, France

Oda Mohus
Norwegian University of Science and Technology, Trondheim, Norway / Norwegian Geotechnical Institute, Oslo, Norway

Anna Eikebrokk
Norwegian University of Science and Technology, Trondheim, Norway / Norconsult, Oslo, Norway

Gustav Grimstad
Norwegian University of Science and Technology, Trondheim, Norway

Hans Petter Jostad
Norwegian Geotechnical Institute, Oslo, Norway

ABSTRACT: Static liquefaction has been one of the major contributors to the failure of tailings dams worldwide. One of the key material characteristics needed for the assessment of liquefaction susceptibility and/or for numerical modelling of static liquefaction is the Critical State Line (CSL). The CSL is typically determined from advanced laboratory tests such as drained and undrained triaxial tests of loose specimens. However, there are several challenges with this procedure such as selection of a suitable initial void ratio, correct measurement of void ratio after saturation, reaching critical state due to strain limitations and inhomogeneous deformations due to effect of boundary conditions. This paper demonstrates virtual testing using the Level Set Discrete Element Method (LS-DEM) as an alternative method for determination of the critical state line. The advantage of LS-DEM is that it allows for accurate modelling of the shape of individual grains and thus this effect on the CSL. In this study a digital sand specimen with grain geometries obtained from CT scanning of a real sand is used. The virtual testing enables all types of loading and deformation paths and avoids the restrictions and limitations imposed by physical testing methods and apparatuses. The study shows that the simulation results are consistent with critical state theory and can be used to fit a CSL.

1 INTRODUCTION

Static liquefaction has been the cause of several of the most severe tailings dam failures in history, most recently the Fundão and Feijão dam failures in Brazil (Morgenstern et al. (2016) and Robertsson et al. (2019)). Static liquefaction, also referred to as flow liquefaction, is a phenomenon that may occur in loose, saturated soils, such as e.g hydraulically disposed tailings. If a soil subjected to shear deformations shows sufficient contractive behaviour, the material will tend to decrease its volume. This may lead to increased pore pressure and reduced effective stresses if water does not have time to dissipate. The material then becomes unstable and rapidly transform into a liquefied state. The phenomenon will not occur in dense, dilative materials since the soil will tend to increase its volume and strength when sheared.

A key characteristic to assess if a soil will contract or dilate and thus be susceptible to static liquefaction or not, is the critical state line (CSL). The critical state concept in soil mechanics was first introduced by Roscoe et al. (1958) defining the critical state of a granular material as the state where the material keeps deforming in shear without changes in volume, under constant stress. Schofield and Wroth (1968) defined the CSL in terms of void ratio e and triaxial stress variables p' (mean stress) and q (deviatoric stress) as

$$q = M \cdot p' \quad (1)$$

$$e = \Gamma - \lambda \cdot \ln p' \quad (2)$$

where M, Γ and λ are material constants. In triaxial stresses, $q = ½ (\sigma_1 - \sigma_3)$ and $p = 1/3 (\sigma_1' + \sigma_2' + \sigma_3')$. The void ratio e is the ratio between volume of voids, V_v, and the volume of solids, V_s.

Figure 1 illustrates Equation 1 and 2 as curves in p' - q and p' - e space. The critical void ratio of a material is considered independent of the material initial state, e_0, but dependent of the average mean pressure, p. The CSL has become a fundamental concept in soil mechanics and has been adopted in several constitutive frameworks, such as the Norsand model (Jefferies (1993)) and the Sanisand model family (e.g Dafalias and Manzari (2004)).

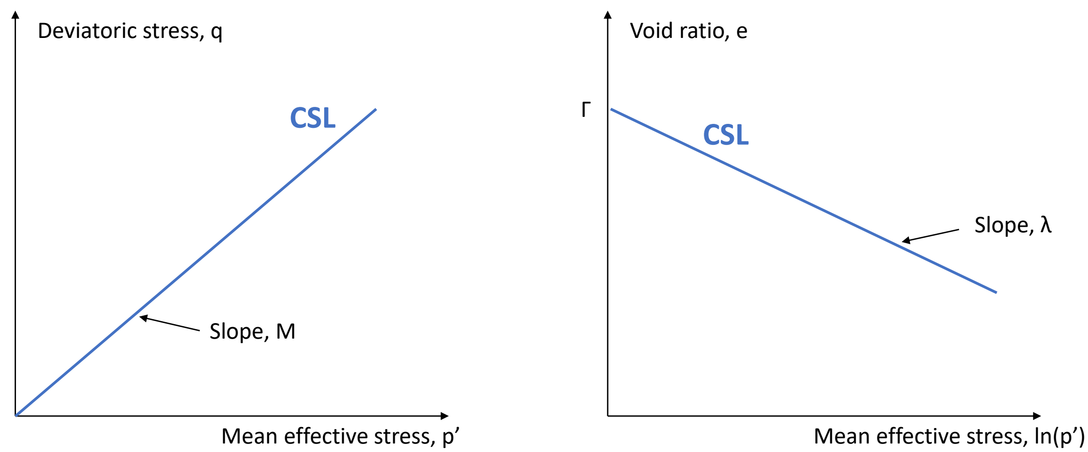

Figure 1. Critical state line (CSL) in p' - q and p' - e space.

The material constants of the CSL are typically inferred from results of a series of advanced laboratory tests such as drained and undrained triaxial compression tests, prepared at different void ratios and consolidation stress levels. Critical state is inferred from the tests when no change in either deviatoric stress ratio, $M = q/p$, nor void ratio, e is measured. Though the techniques to measure the CSL in laboratory has improved with time (Reid et al. (2021)), there are still challenges and uncertainties involved in critical state testing: 1) It takes large shear strains to reach critical state. Due to limitations in the equipment (typically <30% strain in a triaxial cell) it can be questioned whether a true critical state is reached in such tests; 2) Failure in triaxial tests typically develops in localized zones (shear bands). Because of the inhomogeneous deformations in the specimen (especially at large strains) it can be questioned if global measurements of void ratio and stresses/strains are representative for what happens inside the shear band and thus critical state (Salvatore et al. (2017)).

To avoid the challenges and limitations associated with physical critical soil testing, it is natural to ask whether the critical state of a granular soil could be investigated and determined using numerical methods, e.g from computer simulations. The Discrete Element Method (Cundall and Strack (1979)) is a numerical method which can be used to model granular materials as distinct particles interacting with each other. In this way, the model can explicitly represent the discontinuity that is characteristic for a granular material. Several studies, e.g Huang et al. (2014); Li and Dafalias (2012); Wang et al. (2017), have shown that DEM is suited to model the behaviour of granular materials to large strains, providing a well-defined critical state without the issues of inhomogeneous deformations. Most of these studies have considered simplified geometry such as spheres and disks to model the shape of the grains, ignoring the influence of the irregular particle shapes of real soils or tailings. However, more realistic computational modelling of granular soils at the grain scale has become possible through the Level Set Discrete Element Method (LS-DEM) (Kawamoto et al. (2016)) where the real shape of the individual grains, obtained from x-ray computed tomography, are modelled to a high degree of detail by Level-Set (LS) functions (Vlahinić et al. (2014)).

This paper presents LS-DEM simulations on a sand with the objective to evaluate if the method can be used to determine the critical state line.

2 METHODOLOGY

2.1 *LS-DEM*

LS-DEM is a three-dimensional discrete element method which uses level set functions to represent the true shape of the grains. The method is described in Kawamoto et al. (2016) and has proven to give reliable results compared to experimental testing (Kawamoto et al. (2018)). CT images of a sample is used with LS-imaging (Vlahinić et al. (2014)) to create digital avatars of the individual particles. The level set functions are implicit functions whose value at a given point is the distance from the point to the surface of the grains. Following this, the surface of a grain is defined as the points where the level set function is zero.

To calculate contact forces, LS-DEM uses a master-slave approach. The master element is discretized into nodes, and the level set value of the slave is calculated for each node. If the value is negative, there is an overlap, and contact forces exists. In this study, the contact normal forces are modeled by a linear elastic contact model while the tangential forces are modeled by a Coulomb friction model.

Once contact forces are calculated, an explicit time integration scheme is used to update the kinematics of the system. This process is repeated for a given number of time steps. Since the same sample can be tested at different initial states and pressure levels, the issue of sample variation is almost eliminated. Grain scale quantities like interparticle forces, and exact location and rotation of each grain, be easily extracted from the results. As a consequence, the fabric and void ratio is known at all time.

The applied version of LS-DEM uses periodic boundaries (e.g Cundall (1988); O'Sullivan (2011)). Periodic boundaries allow simulation of large assemblies of particles by considering only a selected subdomain. This subdomain is called a periodic cell and is surrounded by identical copies of itself – making the model infinite in extent.

2.2 *Grain morphologies and input parameters*

The simulations were done on Hostun sand, which is characterized by angular and non-spherical grains. The material was chosen mainly because the grain avatars and calibrated input parameters had previously been obtained in Kawamoto et al. (2018). A library of 78 grain avatars with unique morphologies were used to construct a small cubic specimen of 4096 randomly selected grains. Figure *2* shows an illustration of two random grain avatars. The grain size distribution of the specimen is shown in Figure *3*, where d_{eq} is defined as the equivalent diameter of a spherical grain of similar volume. The material classifies as a fine to medium sand.

The input parameters to the LS-DEM model are given in Table 1, being the grain density ρ, the contact normal stiffness k_n, tangential stiffness k_t and friction coefficient μ. These were based on values used in Kawamoto et al. (2018) and were not varied in the simulations presented in this paper.

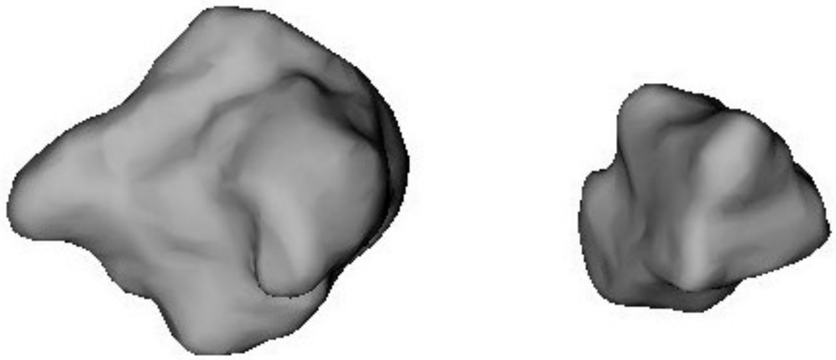

Figure 2. Visualization of two grain avatars.

Table 1. Parameters used in the simulations.

Parameter	Value	Unit
Density (ρ)	2500	kg/m^3
Normal stiffness (k_n)	30000	N/m
Tangential stiffness (k_t)	27000	N/m
Friction coefficient (μ)	0.50	-

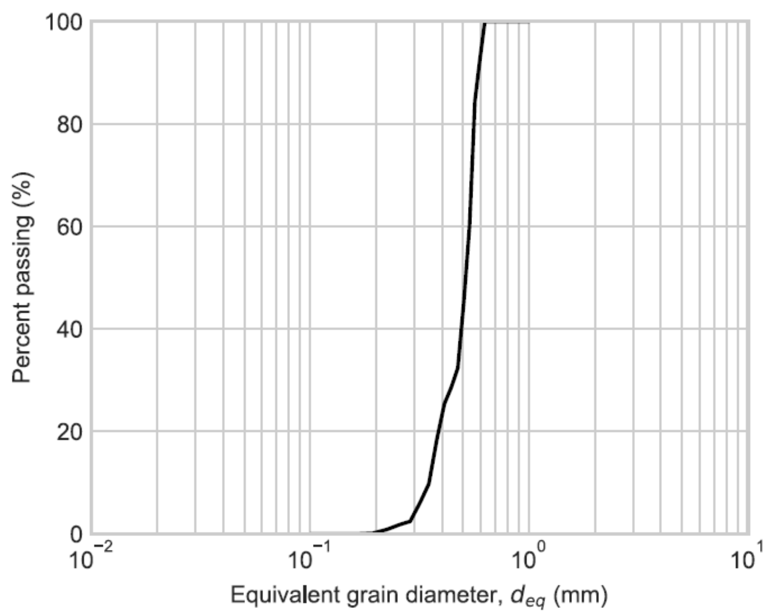

Figure 3. Grain size distribution of the virtual specimen.

2.3 *Specimen preparation and triaxial simulations*

The specimen was created by distributing the grains in a virtual gas-like "cloud" and then applying a negative (compressive) strain rate along the boundary normal directions, until reaching the target void ratio. The collection of grains was packed to initial void ratios (prior to consolidation) ranging from 0.65 to 0.9.

After the initial packing, the specimens were isotropically compressed to pressure levels ranging from 5 kPa to 300 kPa, giving the conditions stated in Table 2. The stress levels were chosen to represent a range of stresses typical for geotechnical engineering. It was observed a significant decrease in the void ratio of the specimen initially packed to $e = 0.9$ during the isotropic compression. This indicates that a specimen with $e = 0.9$ is too loose to be stable and was therefore further compacted to a stable grain configuration during the compression step. The highest void ratio after isotropic compression was $e = 0.79$.

Finally, simulations of drained triaxial compression tests were conducted. A strain rate of 0.05 was imposed in the vertical direction, while the horizontal stresses were kept constant, equal to the stress applied in the isotropic compression phase. All the simulations were run to large strains to reach a well-defined critical state.

Table 2. Overview of the initial conditions of triaxial test simulations.

Analysis	Void ratio after packing (-)	Void ratio after isotropic compression (-)	Isotropic compression pressure (kPa)
triax_VR065_p5	0.65	0.636	5
triax_VR065_p50	0.65	0.638	50
triax_VR065_p100	0.65	0.636	100
triax_VR065_p300	0.65	0.628	300
triax_VR09_p5	0.90	0.747	5
triax_VR09_p50	0.90	0.785	50
triax_VR09_p100	0.90	0.794	100
triax_VR09_p300	0.90	0.791	300

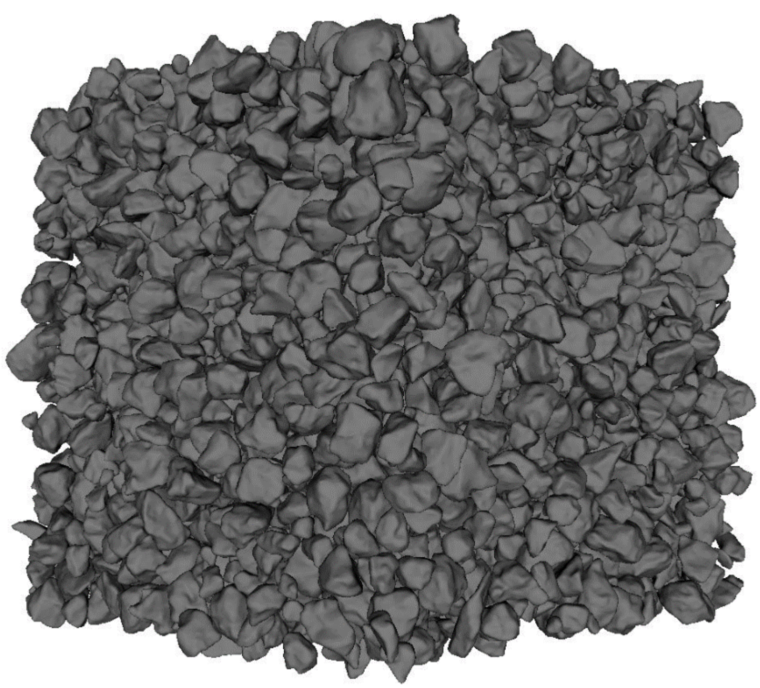

Figure 4. Visualization of the simulated model.

3 SIMULATION RESULTS

The simulated response from each analysis is presented in Figure 5 in terms of the deviatoric stress ratio, $M = q/p'$ versus axial strain, ε_a. Two main observations are made: 1) In the dense samples, the deviatoric stress ratio reaches a peak, before decreasing to a stable value at large strain ($\varepsilon_a >$ 30%). In the looser samples, the deviatoric stress ratio increases to a stable value without showing a peak; 2) The stress ratio converges towards the same value at large strains for the dense and loose samples. Both observations are consistent with the critical state theory and indicates that a critical state stress condition is reached at around 30 % axial strain in all simulations. A critical state stress ratio $M_c = 1.33$ is estimated based on the average of all simulations at axial strain larger than 30%.

Figure 6 plots the void ratio evolution against axial strain for all simulations. It is observed that the void ratio in each simulation seems to approach a constant value at large strain, as postulated by the critical state theory. However, the void ratio requires significantly larger strain to reach the ultimate value, compared to the stress ratio. Further, the ultimate (critical) void ratios appear to be independent of the initial void ratio, which is also in agreement with the critical state theory.

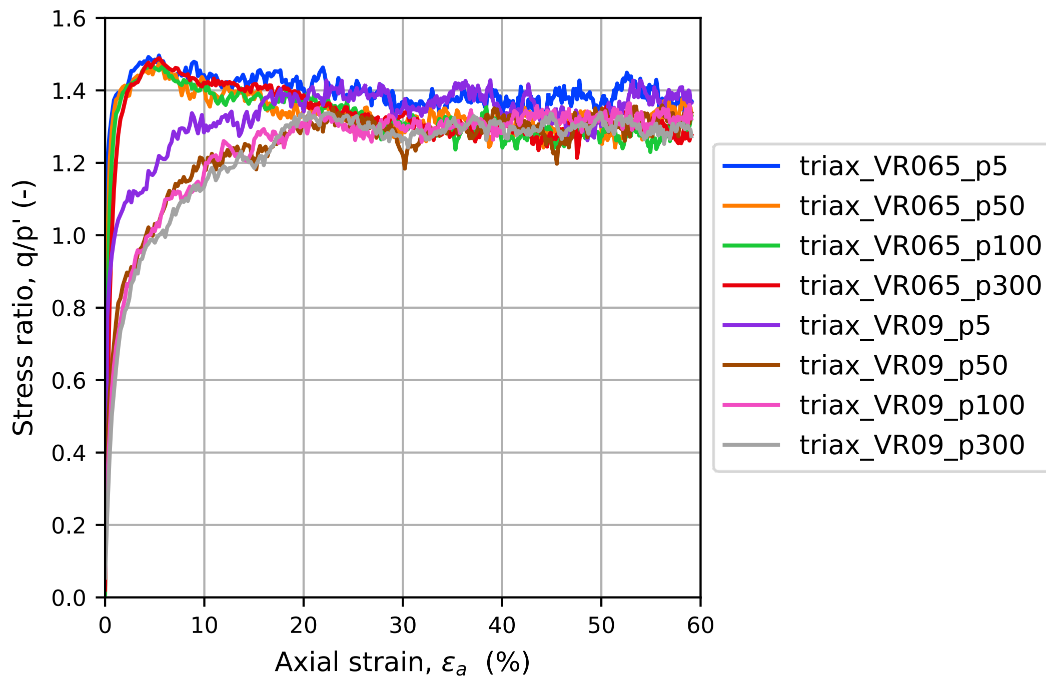

Figure 5. Stress ratio versus axial strain for all simulations.

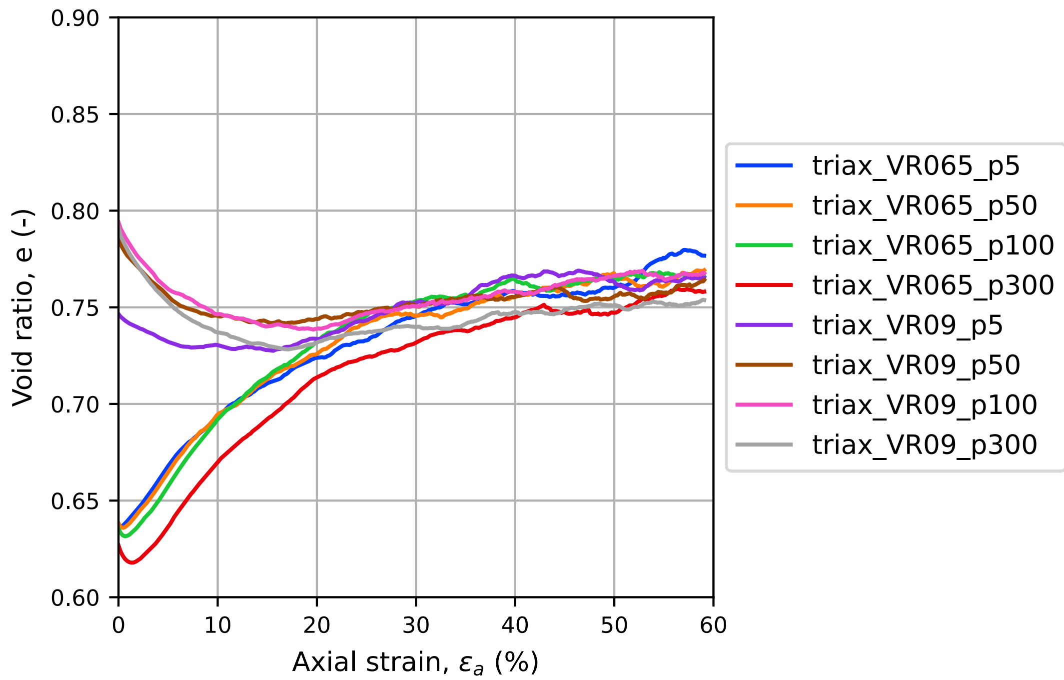

Figure 6. Void ratio versus axial strain for all simulations.

3.1 *Critical state line*

From each of the simulations, the critical void ratio e_c was estimated as the average void ratio between 55% and 60% axial strain. Figure 7 plots the void ratio evolution versus mean stress for all analyses, with the interpreted critical void ratio highlighted with a marker. A best fit of the logarithmic equation proposed in Equation 2 is also included in the plot. The constants Γ and λ were found by regression and are stated in Table 3. It is difficult to spot a clear pressure dependency between the simulations ran at 5, 50, 100 and 300 kPa consolidation pressure, however a slight decrease of e_c with increasing pressure is observed.

Table 3. Best fit CSL parameters for Equation 2.

Parameter	Value
Γ	0.780
λ	0.00352

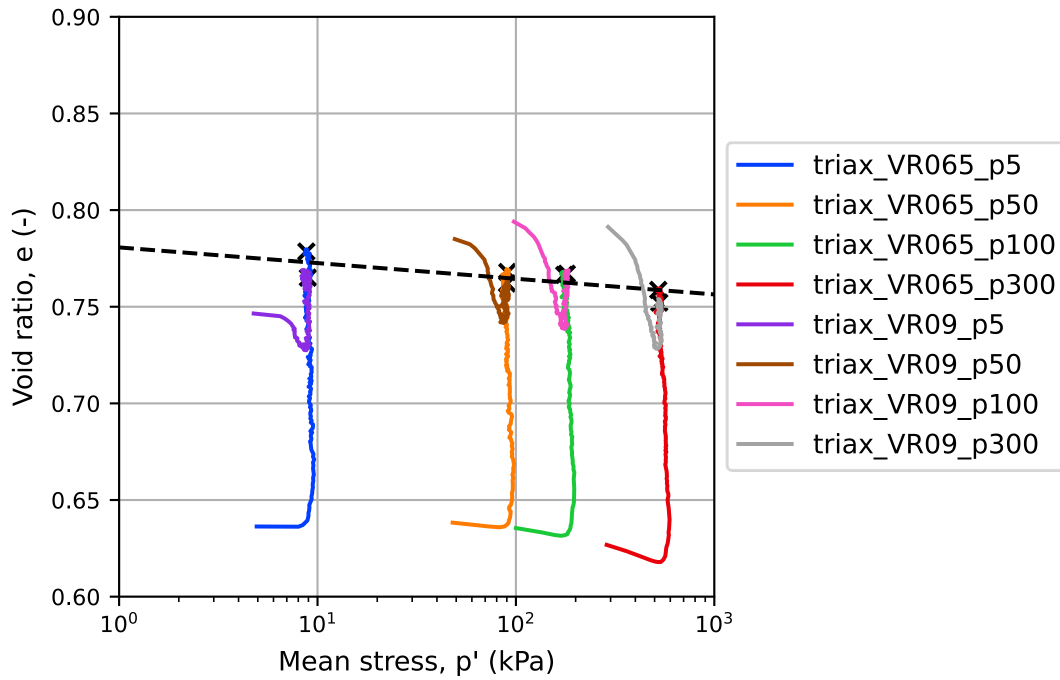

Figure 7. Simulation results in p' - e space, together the best fit critical state line.

4 DISCUSSION

The simulations qualitatively capture the typical mechanical behaviour of sand and agrees well with the critical state theory. This is however a numerical study and no laboratory experiments were executed for comparison and validation of the results.

Results of critical state testing on Hostun sand can be found in literature. As reference, the critical state line of Hostun sand reported by Li (2013) obtained from conventional triaxial testing lies a bit lower than the LS-DEM results presented here. Salvatore et al. (2017) proposed a CSL that is more pressure dependent, based on void ratio measurements from x-ray tomography, however this study involved tests on specimens exposed to larger pressures than in the simulations presented here. At high stresses, crushing of grains could be significant – which is a mechanism that is not captured in the LS-DEM analyses. Another finding in the study by Salvatore et al. (2017) is that the void ratio measured inside and outside the shear band in the triaxial experiment differs significantly. Zhao et al. (2021) also show from tomographic measurements on Hostun sand triaxial tests that the void ratio inside and outside the shear band starts diverging from the onset of localization. The critical void ratio found from the LS-DEM simulations lies in-between the values measured inside and outside the shear band in Zhao et al. (2021). It should be noted that the simulations in this paper were performed on a periodic cell of random grains from a library of 78 different grain morphologies, hence the resulting grain size distribution of the virtual sample is not necessarily comparable with these experiments.

5 CONCLUSION

The paper demonstrates the use of numerical simulations with the discrete element code LS-DEM to infer a critical state line of a sample consisting of virtual Hostun sand grain avatars. The following can be concluded:

- The ultimate void ratio in the simulations is independent of the initial void ratio, i.e it reaches a unique critical state value, which is consistent with the critical state theory.

- All simulations converge towards a constant deviatoric stress ratio (M_c) at critical state, consistent with the critical state theory.
- The ultimate void ratio is reached at significantly larger strain than the ultimate deviatoric stress ratio.
- The critical void ratio, e_c shows a pressure dependency with slightly decreasing e_c with increasing pressure.

The results of this study indicate that LS-DEM may be suited to simulate the critical state behaviour of real sands and other granular materials given their particle shapes. LS-DEM simulations therefore have a potential of becoming a supplement or alternative to standard laboratory testing, overcoming some of the limitations and uncertainties in physical testing. However further experimental validation should be performed. For its relevance to tailings, further work should also consider a tailings material which typically have a less uniform grading, and often contains more fines.

6 ACKNOWLEDGEMENTS

The authors would like to thank California Institute of Technology for providing the LS-DEM code used for the simulations. The research activities have been carried out within the research project SP12 "Towards sustainable mine tailings" (https://www.ngi.no/eng/Projects/Sustainable-mine-tailings/#About-the-project) funded by the Norwegian Geotechnical Institute (NGI).

7 REFERENCES

Cundall, P. A. (1988). Computer Simulations of Dense Sphere Assemblies. *Studies in Applied Mechanics*, Elsevier, 20(C), 113–123.

Cundall, P. A., and Strack, O. D. L. (1979). A discrete numerical model for granular assemblies. *Geotechnique*, 29(1), 47–65.

Dafalias, Y. F., and Manzari, M. T. (2004). Simple Plasticity Sand Model Accounting for Fabric Change Effects. *Journal of Engineering Mechanics*, American Society of Civil Engineers, 130(6), 622–634.

Huang, X., Hanley, K. J., Kwok, C. Y., Wadee, M. A., and Kwok Haking Wong Building, C. Y. (2014). DEM analysis of the influence of the intermediate stress ratio on the critical-state behaviour of granular materials. 16, 641–655.

Jefferies, M. G. (1993). Nor-Sand: A simple critical state model for sand. *Geotechnique*, 43(1), 91–103.

Kawamoto, R., Andò, E., Viggiani, G., and Andrade, J. E. (2016). Level set discrete element method for three-dimensional computations with triaxial case study. *Journal of the Mechanics and Physics of Solids*, Elsevier Ltd, 91, 1–13.

Kawamoto, R., Andò, E., Viggiani, G., and Andrade, J. E. (2018). All you need is shape: Predicting shear banding in sand with LS-DEM. *Journal of the Mechanics and Physics of Solids*, Elsevier Ltd, 111, 375–392.

Li, G. (2013). Etude de l'influence de l'étalement granulométrique sur le comportement mécanique des matériaux granulaires. PhD Thesis. *http://www.theses.fr*, Ecole centrale de Nantes.

Li, X. S., and Dafalias, Y. F. (2012). Anisotropic Critical State Theory: Role of Fabric. *Journal of Engineering Mechanics*, American Society of Civil Engineers (ASCE), 138(3), 263–275.

Morgenstern, N. R., Vick, S. G., Viotti, C. B. and Watts, B. D. (2016). Fundão tailings dam review panel: Report in the immediate causes of the failure of the Fundão Dam. New York: Cleary Gottlieb Steen & Hamilton LLP.

O'Sullivan, C. (2011). *Particulate Discrete Element Modelling: A Geomechanics Perspective - Catherine O'Sullivan.* Spon Press.

Reid, D., Fourie, A., Ayala, J. L., Dickinson, S., Ochoa-Cornejo, F., Fanni, R., Garfias, J., Da Fonseca, A. V., Ghafghazi, M., Ovalle, C., Riemer, M., Rismanchian, A., Olivera, R., and Suazo, G. (2021). Results of a critical state line testing round robin programme. *Geotechnique*, Thomas Telford Ltd, 71(7), 616–630.

Robertson, P.K., de Melo, L., Williams, D. J., and Wilson G.W (2019). Report of the Expert Panel on the Technical Causes of the Failure of Feijão Dam I. http://www.b1technicalinvestigation.com

Roscoe, K. H., Schofield, A. N., and Wroth, C. P. (1958). On the yielding of soils. *Geotechnique*, Thomas Telford Ltd, 8(1), 22–53.

Salvatore, E., Modoni, G., Andò, E., Albano, M., and Viggiani, G. (2017). Determination of the critical state of granular materials with triaxial tests. *Soils and Foundations*, Elsevier, 57(5), 733–744.

Schofield, A. N., and Wroth, C. P. (1968). *Critical state soil mechanics*. Lecturers in Engineering at Cambridge University., New York, McGrav-Hill.
Vlahinić, I., Andò, E., Viggiani, G., and Andrade, J. E. (2014). Towards a more accurate characterization of granular media: Extracting quantitative descriptors from tomographic images. *Granular Matter*, Springer, 16(1), 9–21.
Wang, R., Fu, P., Zhang, J.-M., and Dafalias, Y. F. (2017). Evolution of Various Fabric Tensors for Granular Media toward the Critical State. *Journal of Engineering Mechanics*, American Society of Civil Engineers (ASCE), 143(10), 04017117.
Zhao, C. F., Pinzón, G., Wiebicke, M., Andò, E., Kruyt, N. P., and Viggiani, G. (2021). Evolution of fabric anisotropy of granular soils: x-ray tomography measurements and theoretical modelling. *Computers and Geotechnics*, Elsevier, 133, 104046.

Influence of characterization properties on the critical state of tailings: a parametric study

Guillermo Riveros & Michael Etezad
Golder associates Ltd, Mississauga, Ontario, Canada

ABSTRACT: The Critical state line (CSL) represents a practical means to assess the strength and deformation behavior of tailings. The CSL is commonly used in mine waste geotechnical practice to determine the susceptibility of tailings to static (flow) liquefaction within a tailings storage facility (TSF). Static liquefaction type of failure must be considered for the upstream and centerline tailings dam raise design. Slurry tailings deposition can result in non-homogeneous nature and variation in tailings properties throughout the TSF. Because the location of CSL is highly dependent on the material properties such as the grain size distribution and plasticity, selecting representative tailings samples for testing presents a challenge for tailings practitioners. In this study a large database of tailings from different origins and mineralogy including, gold, iron, copper, and oil sands is used to analyze the effect of different tailings properties on the characteristics of their CSLs. The parameters influencing the vertical intercept (Γ) and the slope (λ) and are studied in detail. It is a common practice to collect two representative samples of high and low fines contents for testing. Findings of this study suggests that this practice may be unconservative in some cases and may result in an unsafe design.

1 INTRODUCTION

Static (flow) liquefaction is one of the main upstream raise and centerline raise tailings dams design concerns, which can result in catastrophic dam failure with little warning. Because liquefaction of loose, saturated, and contractive materials such as tailings could occur rapidly, the conventional approach of dam instrumentation monitoring and visual observation are not normally useful tools to predict and prevent liquefaction failure. The concern regarding static liquefaction of tailings has increased following the failures of Fundão tailings dam in 2015 and Brumadinho tailings dam in 2019, both due to static liquefaction of tailings.

The critical state line provides the means to determine susceptibility of natural soils and tailings to strength loss and static liquefaction (Jefferies and Been 2016). The critical state varies with mean effective stress, resulting in a unique CSL, and provides a base of reference for soil behavior during shearing. At the critical state, soil continues to shear at a constant void ratio (e_{cs}), mean effective stress (p'_{cs}) and deviator stress (q_{cs}). It is understood that the CLS is not related to the soil initial fabric (Been et al. 1991 and Zlatovic and Ishihara 1997). This line is usually inferred by carrying out a series of undrained and drained triaxial tests.

Natural soil and tailings have contractive behavior above the critical state line and dilative behavior below this line. The CSL is typically established following the conventional logarithmic form of Equation 1 below:

$$e_c = \Gamma_1 - \lambda_e \ln p'_{cs} \tag{1}$$

where e_c is the void ratio at critical state, p'_{cs} is the mean effective stress at critical state, Γ_1 is the line's intercept at p'_{cs} = 1 kPa and λ_e is the slope.

The CSL is influenced by particle size gradation (Been and Jefferies 1985, Muir-Wood and Maeda 2008, Carerra et al. 2011), particle angularity and roughness (Cho et al. 2006) plasticity index (Jeffries and Been 2016) and soil mineralogy or crushability (Jefferies and Been 2016).

This study presents the collection and analysis of geotechnical parameters for a variety of mine tailings. The analyses carried out explore the effect of parameters such as the fines content, plasticity index (PI), and gradation parameters like the coefficient of uniformity C_U and the coefficient of curvature C_c on the CSL.

2 LABORATORY TESTING PROGRAM

In this study, the CSL of 29 tailings were evaluated based on the triaxial tests. The tailings include various types of mineralogy (ore type), as well as a range of varying plasticity. The characterization properties for each project's tailings were reviewed and catalogued as shown in Table 1. Except for Tailings 23 and Tailings 24, all the tests were carried out at Golder Associates Ltd. (a member of WSP) laboratories in either Vancouver (Canada) or Perth (Australia).

Table 1. Summary of tailings data analyzed in this study

Name	Ore Type	PI (%)	FC[1] (%)	C_u	C_c	Γ_1	λ_e	Γ_{100}	M_{tc}	φ'_{cs} (°)
Tailings 1	Gold Oxide	8	75.1	23.33	1.54	0.929	0.067	0.62	1.38	34.2
Tailings 2	Gold Porphyry	1	70.4	16.67	2.67	0.744	0.030	0.61	1.52	37.3
Tailings 3	Gold Schist	6	75.8	26.67	1.35	0.807	0.052	0.57	1.34	33.1
Tailings 4	Oil Sands	NP	1.9	2.09	1.14	0.922	0.029	0.79	1.30	32.4
Tailings 5	Oil Sands	NP	1.9	1.91	1.11	0.930	0.023	0.82	1.36	33.6
Tailings 6	Gold Oxide	2	77	--[2]	--	0.762	0.037	0.59	--	--
Tailings 7	Gold Oxide	1	65.6	22.58	4.15	0.724	0.029	0.59	--	--
Tailings 8	Gold	NP	6.6	2.67	0.89	0.871	0.020	0.78	--	--
Tailings 9	Gold	NP	95.6	9.79	1.07	0.827	0.026	0.71	1.50	36.9
Tailings 10	Gold	7	--	--	--	0.851	0.051	0.62	--	--
Tailings 11	Gold	9	--	--	--	0.958	0.051	0.72	--	--
Tailings 12	Gold	8	63.5	--	--	1.014	0.062	0.73	1.32	32.7
Tailings 13	Gold	8	63	--	--	0.736	0.048	0.51	1.31	32.5
Tailings 14	Copper, Gold	2	55	--	--	0.803	0.049	0.58	1.45	35.8
Tailings 15	Copper, Gold	3	56	--	--	0.741	0.042	0.55	1.48	36.3
Tailings 16	Copper, Gold	4	55	--	--	0.772	0.045	0.56	1.48	36.5
Tailings 17	Gold	NP	45	--	--	0.831	0.039	0.65	1.38	34.1
Tailings 18	Gold	NP	68.3	--	--	0.865	0.045	0.66	1.46	35.9
Tailings 19	Gold	NP	59	--	--	0.862	0.044	0.66	1.35	33.5
Tailings 20	Gold	NP	54	--	--	0.784	0.037	0.61	1.51	37.1
Tailings 21	Gold	11	82	--	--	1.014	0.053	0.77	1.31	32.5
Tailings 22	Gold	9	80	--	--	0.930	0.047	0.71	1.22	30.4
Tailings 23	Iron Ore	NP	21	7.33	2.18	0.820	0.031	0.68	1.38	34.1
Tailings 24	Iron Ore	1	88	7.19	1.10	0.860	0.035	0.70	1.38	34.1
Tailings 25	Iron Ore	NP	87	--	--	0.925	0.045	0.72	1.42	35.0
Tailings 26	Iron Ore	14	84	--	--	1.160	0.075	0.81	1.33	33.0
Tailings 27	Iron Ore	19	78	--	--	1.427	0.109	0.93	1.47	36.2
Tailings 28	Iron Ore	4	93	--	--	1.035	0.053	0.79	1.33	33.1

Tailings 29	Iron Ore	5	87	--	--	0.900	0.043	0.70	1.47	36.2

Note:

(1) Fines content

(2) Data not available.

The CLSs were determined using the isotropic triaxial compression (TxC) testing as suggested by Jeffries and Been (2016). Moist tamping using the under-compaction method (Ladd, 1978) was carried out to prepare loose samples. Lubricated oversized end platens were used. The void ratio was determined by freezing the sample following the testing. The methods and procedures employed to determine the CSLs were same as those employed in contributing to the comparative study reported by Reid et al. (2021), where the obtained CSLs were within the range of reasonable CSLs. This provides additional credence to the parameters reported here.

Grain size distribution and Atterberg Limits testing were carried out on the tailings samples to determine the fines content, C_u, C_c, and plasticity of the samples. The testing was carried out by following the relevant ASTM standards.

3 ANALYSIS RESULTS

The CSL for each material was established using Equation 1. The critical state parameters Γ_1 and λ_e, M_{tc} and the mobilized effective friction angles at critical state(ϕ'_{cs}) for each tailings' material are provided in Table 1, and the CSLs of the tailings are presented in Figure 1.

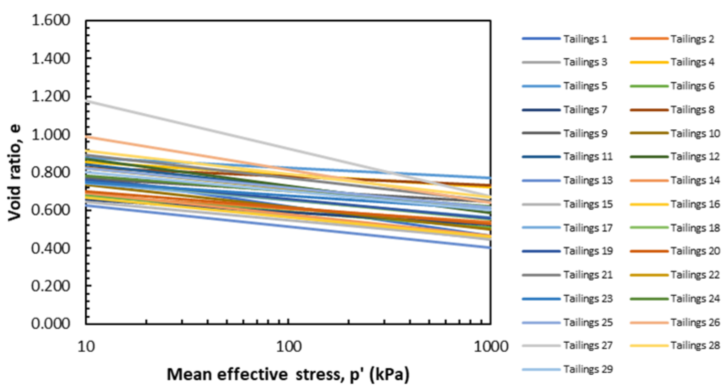

Figure 1. CSLs of the various tailings type analyzed in this study.

Considering that Γ_1 intrinsically requires the extrapolation of the logarithmic regression to a very low mean effective stress of 1 kPa, and such a low mean effective stress is prone to a reduced accuracy in testing, the intercept Γ_{100} (at a mean effective stress of 100 kPa) was used instead. A similar concept was used by Torres-Cruz and Santamarina (2020).

The entire dataset was subsequently analyzed to determine empirical relationships between the multiple characterization properties and the critical state parameters of the tailings. Several regression types were assessed, and those judged to provide the best fit based on the review of the coefficient of determination, R^2 are presented in this study. The results of analyses are separately presented for non-plastic and plastic tailings in order to draw a comparison between the two and identify the effects that plasticity exerts on the tailings.

3.1 *Non-Plastic Tailings*

The change in the critical state parameter Γ_{100} with increase of the fines content is presented in Figure 2. The Γ_{100} of tailings is observed to decrease as the fines content increases from 0% to the range of fines content between 40% to 65%, after which Γ_{100} begins to increase until the tailings entirely consist of silt particles. This can be explained by finer silt particles filling the voids of sand particles and reducing the overall void ratio. A similar observation has been reported by Torres-Cruz (2019).

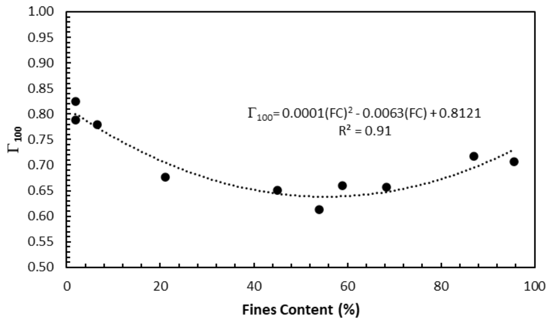

Figure 2. Relationship between Γ_{100} and FC for non-plastic tailings.

Given that the internal "packing" or arrangement of natural soil and tailings particles has been observed to be affected by the materials' gradation (e.g., Omar et al. 2003, Mujtaba et al. 2013), with well-graded soils and tailings achieving higher dry densities than poorly- graded ones, it is of interest to check this effect on the location of the CSL.

The location of the CSL was thus further explored by examining the relationship between Γ_{100} and the grain size distribution parameter C_u, as shown in Figure 3. The plot presents a strong logarithmic relationship for those data which C_u was available. As shown, poorly-graded tailings, i.e., those with $C_u<4$ as per the Unified Soil Classification System (USCS), exhibit higher values of Γ_{100} than well-graded tailings. The respective fines content of each tailings is also included in this figure. However, the inclusion of this parameter does not provide a discernible pattern or sequence.

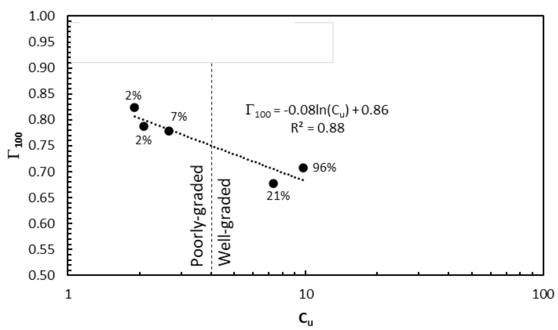

Figure 3. Relationship between Γ_{100} and C_u for non-plastic tailings.

The influence of tailings' gradation curvature, parametrized by C_c, on the magnitude of Γ_{100} was also examined. Figure 4 indicates a gradual decline in Γ_{100} as C_c increases. Based on the data plotted, tailings with smooth gradations exhibit Γ_{100} values ranging from approximately 0.60 to 0.85. The tailings fines content is also included in this figure. Similar to Figure 3, no distinguishable pattern is observed. The steady decrease in Γ_{100} observed is likely due to the tailings' gradations quality (i.e., well-graded vs. poorly-graded).

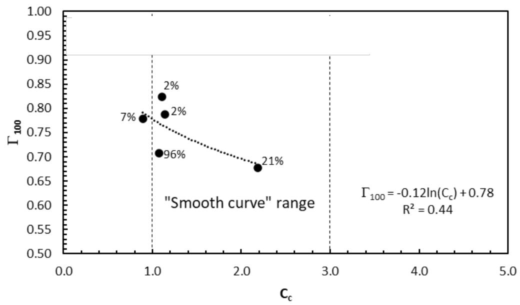

Figure 4. Relationship between Γ_{100} and fines content C_c for non-plastic tailings.

It is known that ϕ'_{cs} is in part affected by particle shape (Koerner 1970). The possible influence of the gradation characteristics (fines content, C_u and C_c) on the ϕ'_{cs} is shown in Figure 5.

Slight increases in ϕ'_{cs} with changes in fines content and C_c are noted as shown in Figures 5A and 5C; however, weak correlations, R^2 values of 0.52 and 0.01, are observed respectively.

In contrast, a stronger relationship between ϕ'_{cs} and C_u (R^2=0.78) is observed in Figure 5B. In this case, ϕ'_{cs} tends to increase slightly as the tailings become more well-graded (i.e., C_u increases). As before, the tailings fines content are included in this plot, which show no distinguishable pattern.

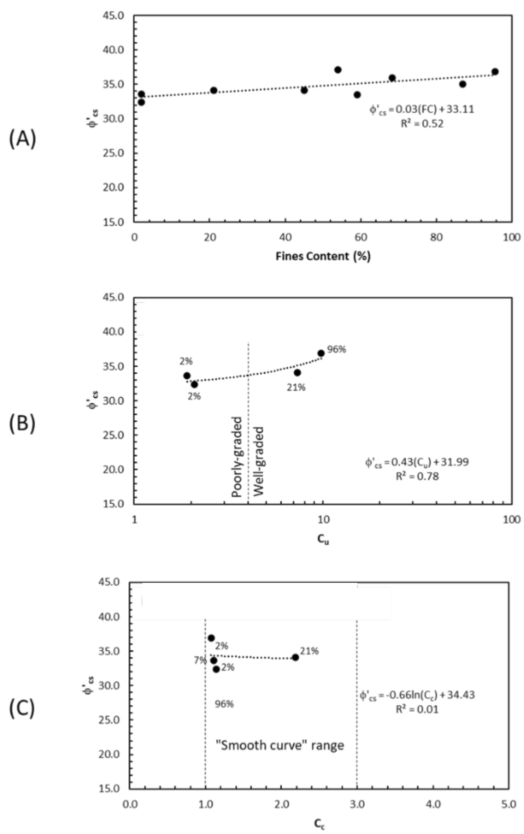

Figure 5. Relationships of ϕ'_{cs} with (A) fines content, (B) C_u, and (C) C_c for non-plastic mine tailings.

Assessing the CSL slope, λ_e, there appears to be no sensible correlation for this parameter with any of the gradation parameters examined.

Figure 6 shows moderate to weak relationships when attempting to correlate λ_e with the tailings' fines content, C_u, and C_c (Figs 6A, 6B, and 6C, respectively). It is understood that λ_e is influenced by the mineralogy, particle shape and grain size distribution of tailings. Accordingly, fine content alone is not likely sufficient to provide a meaningful trend for this parameter. Figures

6B and 6C do not provide a meaningful trend either. For these cases, inclusion of the effect of mineralogy may provide better correlations, but this factor is outside the scope of this study.

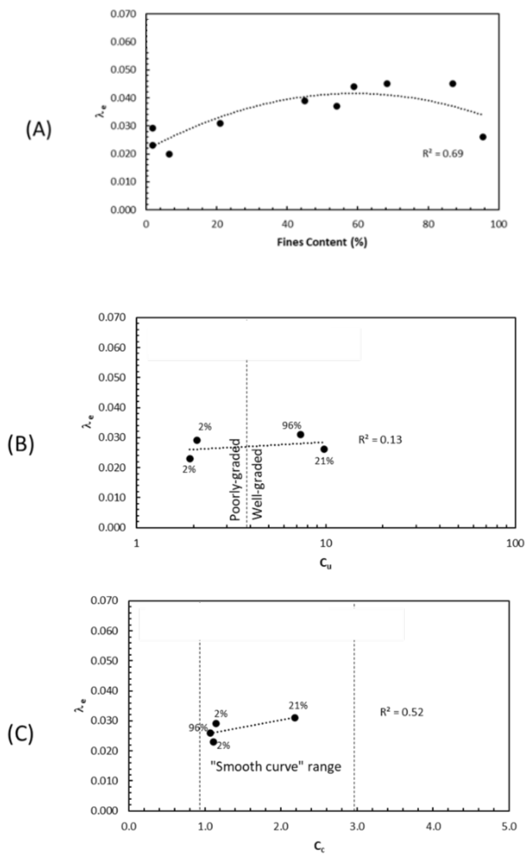

Figure 6. Plots of λ_e with (A) fines content, (B) C_u, and (C) C_c for non-plastic tailings.

An attempt was made to correlate λ_e with ϕ'_{cs}, as both are affected by the particle shape (Sadrekarimi 2013, Nguyen et al. 2020). As shown in Figure 7, no trends or patterns were observed relating λ_e with ϕ'_{cs} and the fines content. As previously noted, inclusion of the effect of mineralogy may provide a better correlation.

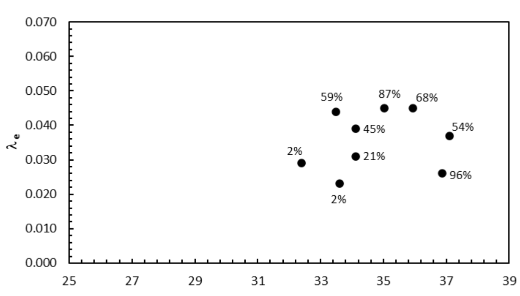

Figure 7. Scatter plot of λ_e vs. ϕ'_{cs} for non-plastic mine tailings.

3.2 *Plastic Tailings*

Figure 8 presents the results obtained by plotting the Γ_{100} with the fines content of plastic tailings (red data points), juxtaposed with those results previously observed for the non-plastic tailings (black data points). In this case, Γ_{100} of plastic tailings tends to be lower than the curve stablished for non-plastic tailings up to fines content of 80% and higher than this curve for fines content more than 80%. Included in the figure are the PI values for each of the plastic data points, generally showing that more highly plastic tailings have higher values of Γ_{100}.

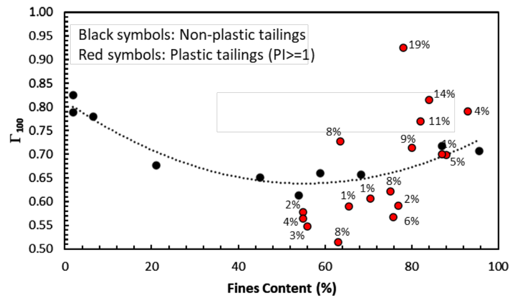

Figure 8. Plot of Γ_{100} vs. fines content for plastic tailings juxtaposed with the relationship established for non-plastic tailings.

The effect of tailings grain size distribution was checked for the next step. As shown in Figure 9, the plastic tailings data shown in red further improve the logarithmic correlation (R^2=0.95) between Γ_{100} and C_u as previously developed for non-plastic tailings.

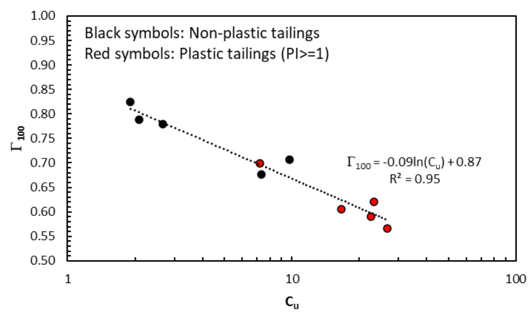

Figure 9. Relationship between Γ_{100} and C_u for plastic and non-plastic tailings.

The relationship of the tailings' plasticity on Γ_{100} is further explored in Figure 10. This figure shows not a strong relationship (R^2=0.48) between the tailings PI and Γ_{100}. Despite the scatter observed, the values of Γ_{100} can be seen to begin meaningfully increase with plasticity after approximately a PI of 9.

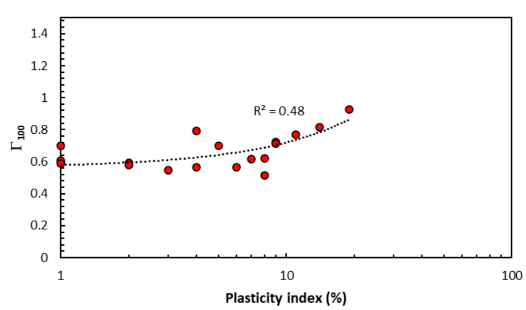

Figure 10. Relationship between Γ_{100} and PI for plastic tailings.

Similar to non-plastic tailings, no discernible correlations are observed between λ_e and either fines content, C_u, or C_c, as shown in Figures 11A through 11C.

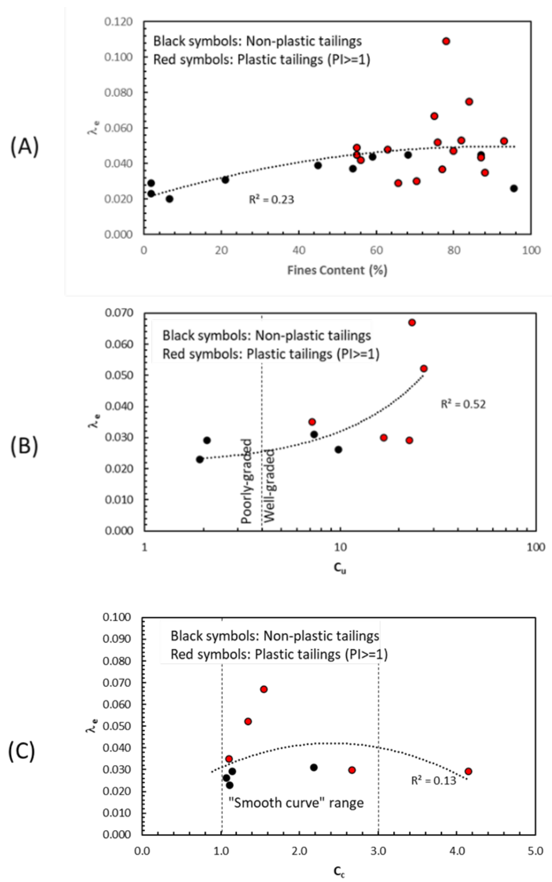

Figure 11. Plots of λ_e with (A) fines content, (B) C_u, and (C) C_c for plastic and non-plastic tailings.

By contrast, Figure 12 shows a strong correlation between PI and the λ_e for plastic tailings. The relationship indicates that the slope λ_e increases as the tailings become more plastic.

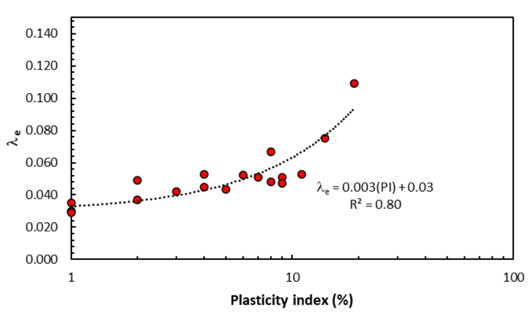

Figure 12. Relationship between λ_e and PI for plastic tailings.

It is of interest to examine a possible relationship between PI and both critical state parameters Γ and λ_e, i.e., the ratio Γ/λ_e, analytically derived by transposing the expression for the critical state line in e-p′ space. As shown in Figure 13, the values of Γ_{100}/λ_e decreases as PI increases. Notwithstanding the relationship observed, deducing from the plots in Figures 12 and 13, the logarithmic decline in Γ/λ_e is reasonably due to the linear increase in λ_e with PI (as shown in Fig. 12), which reduces the ratio in Figure 13.

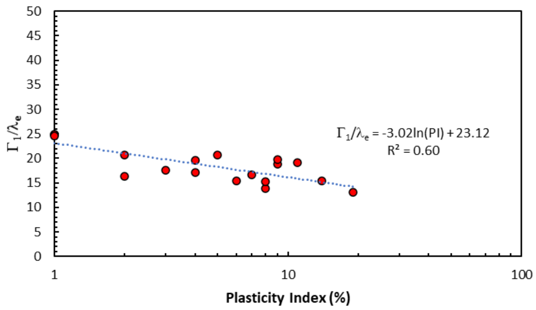

Figure 13. Relationship between Γ_{100}/λ_e and PI for plastic tailings.

4 DISCUSSION

Based on the results presented above, the gradational parameter C_u was observed to exhibit the strongest correlations with the critical state parameter Γ_{100} and the critical state effective friction angle (ϕ'_{cs}) for non-plastic tailings. A strong relationship was also observed between the plasticity index (PI) and λ_e. The fines content was shown to only correlate well with the Γ_{100} of non-plastic tailings, as the data for tailings with higher plasticity was seen to introduce considerable scatter. Although some researchers recommend assuming soil with PI less than 7 as sand-like materials (Idriss and Boulanger 2008), inclusion of these data to non-plastic tailings database considerably reduces the correlation obtained.

In particular, C_u appears to be directly associated with Γ_{100}. Given the well-understood correlation between dry density and grain size distribution (Korfiatis and Manikopoulos 1982, Omar et al. 2003), where well-graded materials are seen to develop a denser intergranular arrangement, this paper's observation appears to be reasonable. Furthermore, previous studies report correlations between the Γ_{100} and the minimum void ratio (e_{min}) for non-plastic soils (Cho et al.2006, Torres-Cruz 2019), and the e_{min} of coarse soils has been correlated through logarithmic regressions with C_u (Kezdi 1979, Al Hussaini 1983, Gesche 2002, De la hoz 2007, Dorador 2010). Therefore, it is understandable to observe a relationship between the C_u and Γ_{100} of non-plastic tailings.

Similarly, a correlation between C_u and ϕ'_{cs} for non-plastic tailings is expected, as gradation quality affects the friction angle values for granular soils (U.S. Navy 1986).

Given the correlations that exist between Γ_{100} and e_{min}, and between the e_{min} and fines content of non-plastic soils (Torres-Cruz and Santamarina 2020), it is comprehensible to observe a connection between the Γ_{100} and fines content of non-plastic tailings. Indeed, the square polynomial relationship in Figure 2 closely resembles the trendlines observed for e_{min} and fines content.

For its part, PI seemed only to correlate well with λ_e, which agrees with observations by Schofield and Wroth (1968). By contrast, no sensible correlation of λ_e with gradation characteristics is observed for non-plastic tailings. This is plausibly due to the stronger influence that other characteristics, such as particle shape and mineralogy could have on this parameter (Sadrekarimi 2013).

In summary, the correlations presented in this study provide guidance to the design engineer to select representative samples to obtain the CSLs, which can be used for the design of TSF.

5 CONCLUSIONS

The critical state lines for tailings from 29 mines of various commodities (gold, iron, copper, oil) were analyzed to understand the effect that plasticity and particle size distribution have on them.

Strong correlations were observed for non-plastic tailings between the fines content and Γ_{100}, between the gradational parameter C_u and Γ_{100}, and between the critical state effective friction angle (ϕ'_{cs}) and C_u. A similarly strong correlation was observed between C_u and Γ_{100} for tailings with plasticity.

The parameter λ_e of non-plastic tailings is believed to be affected by the combination of mineralogy, particle shape and particle size distribution of tailings. A good correlation was observed between the tailings' plasticity and λ_e.

The findings of this paper provide guidance on selecting the representative samples for the CSL testing. It is a common practice in tailings dam design to collect two representative samples of high and low fines contents for testing and develop the CSL for these two conditions. The authors caution against the use of this practice without considering the other parameters affecting the CSL as discussed in this paper and note that this practice may result in an unconservative design. An example of this case is the Merriespruit gold tailings dam, where the critical state lines of tailings with different fines content were observed to be approximately parallel (Fourie and Papageorgiou 2001).

6 ACKNOWLEDGMENTS

Financial support from Golder Associates Innovation Program is gratefully acknowledged.

7 REFERENCES

Al-Hussaini, m. 1983. Effect of particle size and strain conditions on the strength of crushed basalt. *Canadian Geotechnical Journal*, 20(4):706-717

Been, K., and Jefferies, M.G. 1985. A state parameter for sands. *Geotechnique*, 35(2): 99–112.

Been, K., Jefferdcies, M.G., and Hachey, J. 1991. The critical state of sands. *Géotechnique*, 41(3): 365–381.

Carrera, A., Coop, M., and Lancellotta, R. 2011. Influence of grading on the mechanical behavior of stave tailings. *Geotechnique*, 61(11): 935–946.

Cho, G.C., Dodds, J., and Santamarina, J.C. 2006. Particle shape effects on packing density, stiffness, and strength: natural and crushed sands. *Journal of Geotechnical and Geoenvironmental*

De la Hoz, K. 2007. Estimación de los parámetros de resistencia al corte en suelos granulares gruesos, Tesis de Ingeniero Civil y Magister. FCFM. Universidad de Chile. Santiago, Chile.

Dorador, L. 2010. *Análisis experimental de las metodologías de curvas homotéticas y corte en la evaluación de propiedades geotécnicas de suelos gruesos*. Tesis de Ingeniero Civil y Magister. FCFM Universidad de Chile, Santiago, Chile.

Fourie, A.B., and Papageorgiou, G. 2001. Defining an appropriate steady state line for Merriespruit gold tailings. *Canadian Geotechnical Journal*, 38(4): 695–706. NRC Research Press.

Gesche, R. 2002. *Metodología de evaluación de parámetros de resistencia al corte de suelos granulares gruesos*. Tesis de Ingeniero Civil, FCFM. Universidad de Chile. Santiago, Chile.

Idriss, I. M., & Boulanger, R. W. 2008. *Soil liquefaction during earthquakes*. Earthquake Engineering Research Institute.

Jefferies, M., and Been, K. 2016. *Soil liquefaction: A critical state approach (2nd ed.)*. CRC Press.

Kezdi, A. (1979). Soil physics. Amsterdam: Elsevier

Koerner, R. M. 1970. Effect of particle characteristics on soil strength, *J. Soil Mech. Found Div., ASCE*, 96(4): 1221–1234.

Korfiatis, G. P. and Manikopoulos, C. N. 1982. Correlation of maximum dry density and grain size. *J. Geotech. Eng.*, 108, (GT9), 1171–1176.

Ladd, R.S. 1978. Preparing test specimens using undercompaction. *Geotechnical Testing Journal*. 1(1): 16-23.

Muir Wood, D., and Maeda, K. 2008. Changing grading of soil: effect on critical state. *Acta Geotech.* 3, 3-14.

Mujtaba, H., Farooq, K., Sivakugan, N., & Das, B. M. 2013. Correlation between gradational parameters and compaction characteristics of sandy soils. *International Journal of Geotechnical Engineering*, 7(4): 395–401.

Nguyen, H. B. K., Rahman, M. M., & Fourie, A. B. 2020. How particle shape affects the critical state, triggering of instability and dilatancy of granular materials – results from a DEM study. *Géotechnique*, 1–16.

Omar, M., Shanableh, A., Basma, A. and Barakat, S. 2003. Compaction characteristics of granular soils in United Arab Emirates. *Geotech. Geol. Eng.*, 21, 283–295.

Reid, D., Fourie, A., Ayala, J. L. et al. 2021. Results of a critical state line testing round robin program. *Geotechnique*, 71(7): 616-630.

Sadrekarimi, A. 2013. Influence of fines content on liquefied strength of silty sands. *Soil Dynamics and Earthquake Engineering*, 55:108-119.
Schofied, A., and Wroth, C.P. 1968. *Critical state soil mechanics*. London, McGraw Hill.
Torres-Cruz, L.A. 2019. Limit void ratios and steady state line of non-plastic soils. *Geotechnical Engineering*, 172(3): 283-295.
Torres-Cruz, L.A., and Santamarina, J.C. 2020. The critical state line of non-plastic tailings. *Canadian Geotechnical Journal*, 57: 1508–1517.
U.S. Navy 1986. Soil Mechanic-Design Manual 7.1, *Department of the Navy, Naval facilities Engineering Command*, U.S. Government Printing Press, Washington, DC.
Zlatovic, S., and Ishihara, K. 1997. Normalized behavior f very loose non-plastic soils: Effects of fabric. 37(4): 47-56.

Numerical analysis of a downstream dam reinforcement

Guilherme H. S. Pinto & Pedro M. Rocha
Pimenta de Ávila, Nova Lima, Minas Gerais, Brazil

Hugo A. Brandão
Pimenta de Ávila, Nova Lima, Minas Gerais, Brazil

Rodrigo R. V. de Oliveira
Pimenta de Ávila, Nova Lima, Minas Gerais, Brazil

ABSTRACT: After the Brumadinho's incident, many of Brazilian's dams Factor of Safety (F.S.) were reviewed and considered unfit to operate, showing the necessity of reinforcement. The evaluation of the reinforcement construction in large dams is a key aspect to be observed, mainly while the dam is operational when the excess porewater pressure generated during the process and the deformation occurred by the loading could compromise the structure integrity. The present work aiming to evaluate the F.S. of a downstream dam in two conditions: (i) the current condition of the dam, using different failure surfaces, comparing the F.S. obtained with CDA and Brazilian regulators recommendations; and (ii) evaluation of a buttress construction to reinforce the structure, analyzing the excess of porewater pressure generated and the deformation in the foundation soil during and after construction. The results show the necessity of the compare the potential failure surface geometry since the F.S. of the circular surface meets the minimum F.S. established by the regulations in the opposite of the non-circular (more critical). Also, the foundation displacement after the consolidation phase is significant and must be evaluated in the case of liquefaction potential.

1 INTRODUCTION

One way of evaluating a tailings dam stability is the Factor of Safety (F.S.) that can be defined as the relation between resistance shear stress and acting shear stress (Duncan & Wright, 2005). There are different methods to calculate the F.S. as the Shear Strength Reduction (SSR) and, the most used, is the Limit Equilibrium Method (LEM). Commonly, the LEM method is employed with the Morgenstern and Price method which considers the equilibrium of forces and momentums, by assuming an interslice force using a function, for example, a half-sine function (Morgenstern & Price, 1965).

To evaluate dam stability, it is essential to define the minimum F.S.. This value must be defined based on the uncertainties of the structure in hand, the information available, and the dam in situ characteristics such as soil parameters, porewater pressure conditions. Actually, the regulations and recommendations establish a minimum value of factor of safety based on each stage of a dam life cycle (e.g. end of construction, operation and closure).

The Brazilian Standard recommends, in the guideline ABNT NBR 13028 (2017) for dam designs, that the minimum F.S. value for an operating dam is 1.50 (F.S.min≥1.50), and that the designer must define whether to consider drained or undrained parameters. The Brazilian National Mining Agency (ANM) published in 2019 resolution No.13 that defines the minimum F.S. of 1.30 (F.S.min≥1.30) when considering undrained parameters. Finally, the Canadian Dam Association (CDA) published in 2019 a guideline for dam operation, construction, and recommended a minimum F.S. of 1.30 (F.S.min≥1.30) during/after the construction and 1.50 (F.S.min≥1.50) to normal operations conditions. Table 1 summarizes the minimum F.S. recommended by ABNT (2017), ANM (2019) and CDA (2019).

Table 1. F.S. summary.

Reference	Minimum F.S. Required (normal operation)
ABNT NBR 13028 (2017)	1.50
Resolution No. 13 (2019)	1.30
CDA (2019)	1.50

Besides the minimum F.S., none of the indications, be it recommendation or regulation, highlight the importance of the correct evaluation of the probable failure surface. As shown by Brandão et. al (2020), depending on the geometry cross-section analyzed, the F.S. can variate from 1.50 to 1.21 depending on the failure surface choose by the user, being optimized or not using LEM. This can mislead the stability characterization of the structure, being necessary the correct evaluation of the most critical potential failure surface. Also, the authors have shown that the shape and F.S. of the non-circular optimized surface are similar to the evaluated by the SSR method, which does not depend on the user's choice of the failure surface.

The incidents in Brumadinho and Fundao have shown the necessity of reassessing the safety of tailings dams, especially those raised upstream, reviewing soil parameters and also the methodology of the analysis. As described by Brown & Gillani (2016), some wrong assumptions in the evaluation of the soil behavior could mislead the correct evaluation of the structure condition, for example, the Mount Polly (Canada) failure in 2014 occurred due to a consolidated undrained shear failure after the construction. Also, the authors highlight the importance of considering constructive porewater pressures, showing an example in which the F.S. was 2.16, showing an idea that the structure would be stable but using wrong assumptions, to 0.66 using the correct shear strength envelope indicating the failure of the structure.

When these structures did not meet the recommendations, it is necessary to reinforce them. One possible solution can be the construction of a reinforcement buttress. In the case of such types of constructions, one important aspect to be evaluated during the project phase is the generation of porewater pressure excess during the construction period and the displacements, which can compromise the dam safety, as described in detail by Ladd (1991). These evaluations often go unnoticed at the design stage and can lead to catastrophes such as the Cadia failure in 2018.

As reported by Jefferies et al. (2019), the Cadia failure can be described in two phases: (i) Phase 1 incorporates all of the precursors of the failure. The displacement of this phase was slow, and the mass adjusted to changing states of the equilibrium state; (ii) Phase 2 incorporated the sudden losses of resistance of the foundation soil and/or loading increases by the buttress construction, to create conditions to accelerate movements and displacement that lead the structure to fail. As described in the report, the movements accelerated after 2018, and it was possible to correlate with the Stage 1 Buttress construction before Phase 2. The excess of displacement in the downstream triggered a liquefaction mechanism as detailed in the report.

Based on this, the present article has the objective to evaluate the F.S. of a downstream dam using different failure surfaces, optimized and not, and compare the results with the minimum F.S. of different references, as detailed in Table 1. Also, the displacements and the excess of the porewater pressure (generation and dissipation) were evaluated during and after the construction.

2 METHODOLOGY

The objective of the present work is to evaluate the factor of safety of a downstream dam, compare the results with the recommended values by ABNT (2017), ANM (2019) and CDA (2019) (summarized in Table 1) and simulate a reinforcement buttress construction. To evaluate the F.S. it was performed seepage and stability analysis using SEEP/W and SLOPE/W software and the buttress construction was performed with stress-strain analysis using SIGMA/W software developed by Seequent.

Figure 1 shows the geometry model of the downstream dam in the initial condition. The starter dike was designed with a 1H:2V slope and the dam heightening with a 1H:4V slope. The heightening was constructed with tailings underflow. All the overflow was deposited on the tailings' reservoir creating a tailings beach. The structure has a 1m thick drainage system composed of sand and gravel. The material properties used in the LEM analysis and the materials identifications used in the model are presented in Table 2.

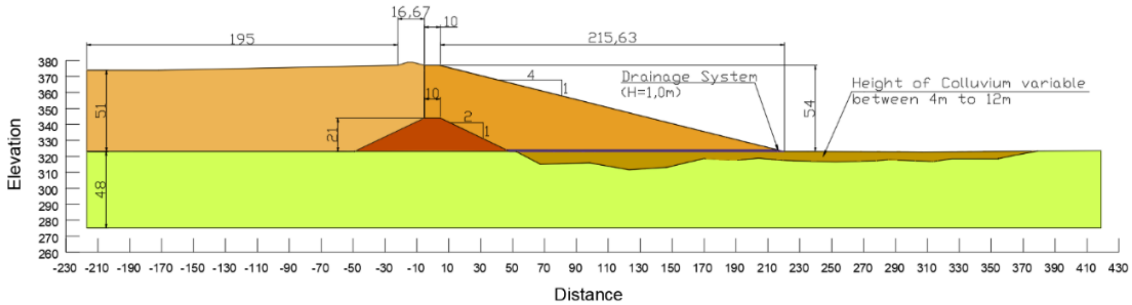

Figure 1. Geometry of the downstream dam analyzed.

Table 2. Resistance parameters adopted in the numerical modelling.

Material	Color	γ kN/m³	Shear Strength Model and Parameter Adopted
Compacted Landfill		20,5	Mohr Coulomb: c'=15 and Φ=30º
Colluvium		16,0	Shear Strength Ratio: Su_{min}=5kPa and Su/s'_{v0}=0,20
Drain		19,0	Mohr Coulomb: Φ=35º
Overflow		18,0	Mohr Coulomb: Φ=28º
Underflow		17,0	Mohr Coulomb: Φ=35º
Residual Soil		21,0	Mohr Coulomb: c'=12 and Φ=28º

To evaluate the F.S. using the LEM in the initial condition (without buttress) a coupled analysis was performed using SLOPE/W and SEEP/W. The Morgenstern – Price / GLE (MP-GLE) method was applied, mainly because it satisfies the force and momentum equations (Morgenstern & Price, 1965), using a function to estimate the interslice force, for example, a function half-sine used in the present work. As described by Duncan & Wright (2005) and Brown & Gillani (2016), this methodology is precise and applicable to almost all types of slope geometries and stratigraphic profiles, in circular and non-circular surfaces.

The initial stability analysis was performed considering four different types of surfaces: (i) circular; (ii) circular optimized; (iii) non-circular; and (iv) non-circular optimized. The optimization process consists in dividing the slip surface into several segments and moving the vertices of each segment randomly, based on the Monte Carlo algorithm, until the lowest safety factor is found (GEP-SLOPE, 2015).

To evaluate the permeability and the volumetric content variation about the matrix suction a saturated/unsaturated behavior was adopted to all materials. Also, the assumption of saturated/unsaturated behavior is close to in situ conditions. Using the material properties available in the SEEP/W library, the volumetric water content and the soil permeability were interpolated defined based on the suction matrix, using the Van Genuchten methodology, as detailed in

Figure 2.

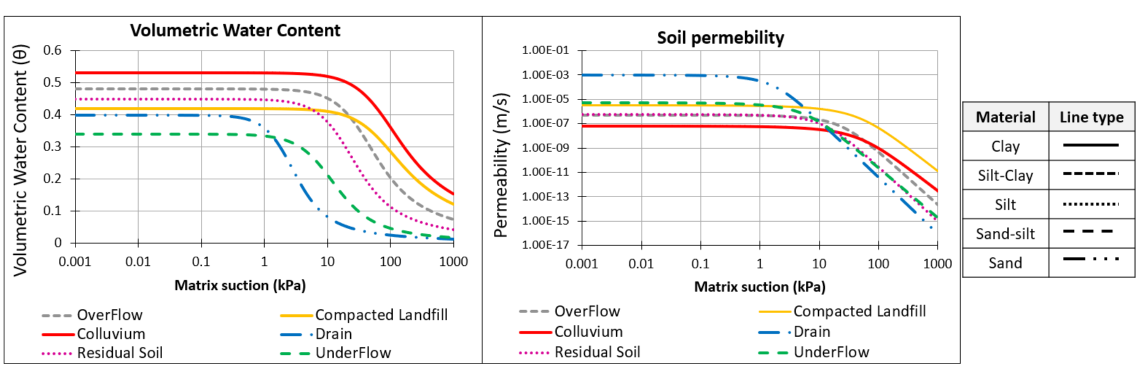

Figure 2. Water volumetric content x matrix suction and permeability x matrix suction.

To simulate the buttress construction, SIGMA/W was used considering linear elastic parameters as detailed in Table 3. The buttress was simulated considering the same strength parameters as the compacted landfill (γ =20 kN/m³, c'=15 and Φ=30º, k_{sat} = 3e10^{-6}m/s).

Table 3. Parameters adopted in the construction modeling.

Material	Color	E' (kPa)	ν
Compacted Landfill		18.000	0.30
Buttress		18.000	0.30
Colluvium		10.000	0.20
Drain		50.000	0.30
Overflow		56.000	0.35
Underflow		80.000	0.35
Residual Soil		27.000	0.30

Based on the stress state and the porewater pressure calculated on SIGMA/W, the F.S. was evaluated without the interactive process to obtain the normal forces between slices, denominated in this paper as Finite Element Method (FEM). The results were compared with the LEM MP-GLE method with the construction porewater pressures coupled analyzes. Both the F.S. were evaluated on time, analyzing the porewater pressure dissipation, considering all construction stages and the period after the construction.

Also, the porewater pressure generated during construction was evaluated using the $\overline{B}$ parameter, calculated with Equation 1, in a specific point in the middle of the Colluvium Soil (loose clayey soils). Finally, the displacements in the colluvium layer were evaluated along the entire length of the buttress, after the dissipation of the porewater pressure and the colluvium consolidation.

$$\overline{B} = \frac{\Delta u}{\sigma_{v0}} \quad (1)$$

3 RESULTS

The first step is to obtain the F.S. is the correct evaluation of the seepage analysis modeled using SEEP/W. Appling a total head boundary condition in the model upstream and downstream, and a drainage boundary condition in the drainage system, the initial phreatic surface was obtained as shown in Figure 3.

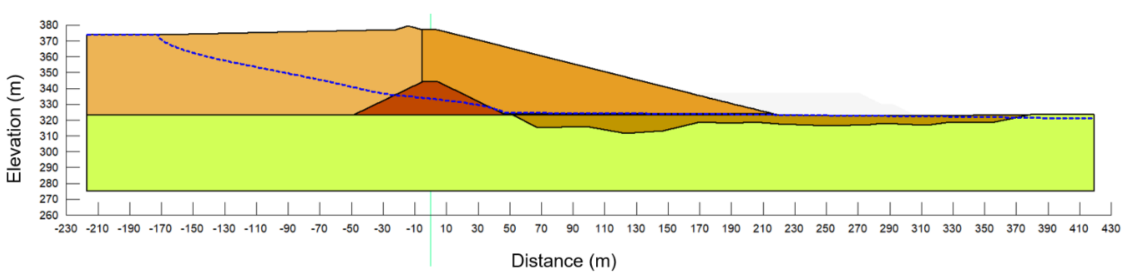

Figure 3. Initial phreatic surface.

As described in item 2, the seepage model was performed using a saturated/unsaturated model, to better simulated the material's behavior. As detailed in Figure 4, the underflow material presented a saturation degree varying from 0,10 up to 0,15 and the overflow presented higher saturation values varying from 0,25 up to 0,45. These values are consistent with the expected behavior of these materials, with overflow being a low permeability material (smaller particles) and underflow a material with higher permeability (larger particles).

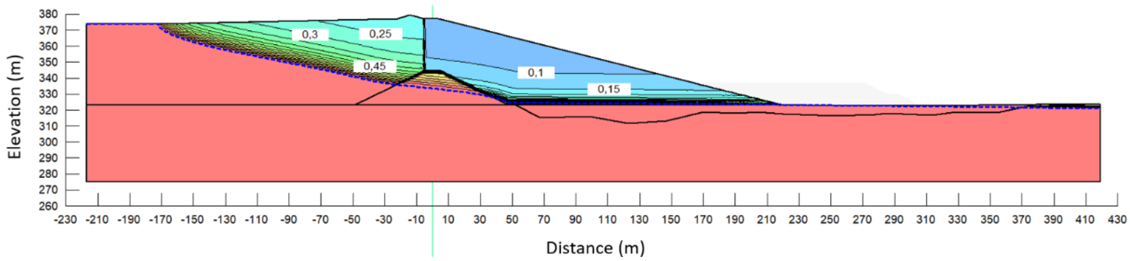

Figure 4. Saturation survey obtained in SEEP/W model.

Considering this model, the initial safety conditions of the structure were evaluated. The summary of the F.S. calculated is shown in Table 4. There are significant differences between the F.S. values obtained for different types of failure surfaces. Figure 5 shows the circular surface with an F.S. of 1.59 which meets the recommended values by ABNT (2017), ANM (2019) and CDA (2019). Sequentially, Figure 6 shows the non-circular surface with an F.S. of 1.44, Figure 7 shows the optimized circular surface with F.S. of 1.39, and Figure 8 shows the optimized non-circular failure surface with an F.S. of 1.35, which meet only the ANM (2019) F.S. criteria.

As described by Brandão et al. (2020), a comparison between the failure surfaces shows the importance of a proper selection of the correct failure surface to assertively assess the dam F.S.. The low resistance colluvium layer under the dam creates a preferential path to develop the failure surface and this condition has a direct influence on the selection of the slip surface type. As shown by the results, Figure 5 to Figure 8 the non-circular optimized failure surface presented the lowest F.S..

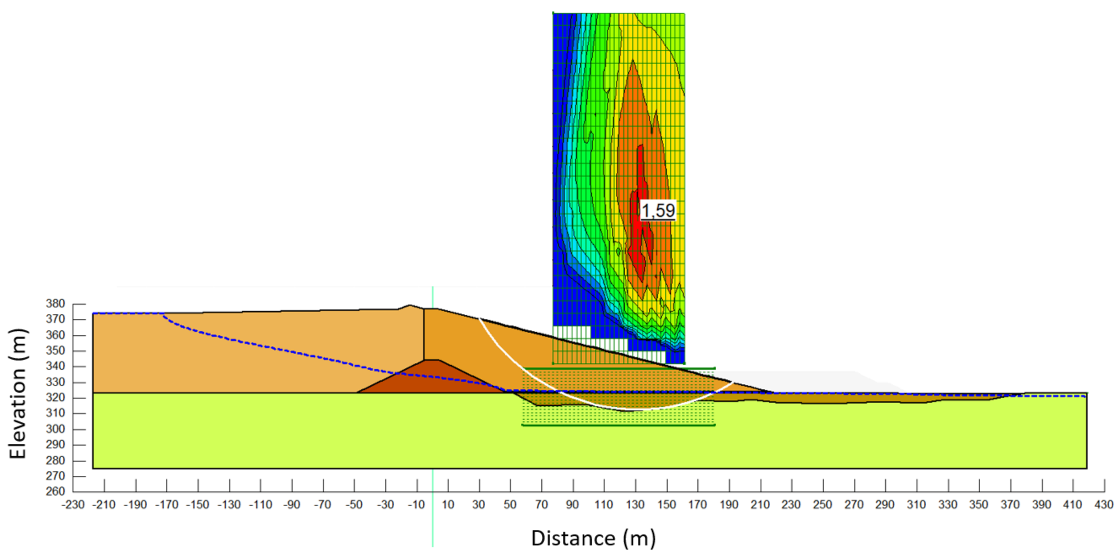

Figure 5. Circular surface.

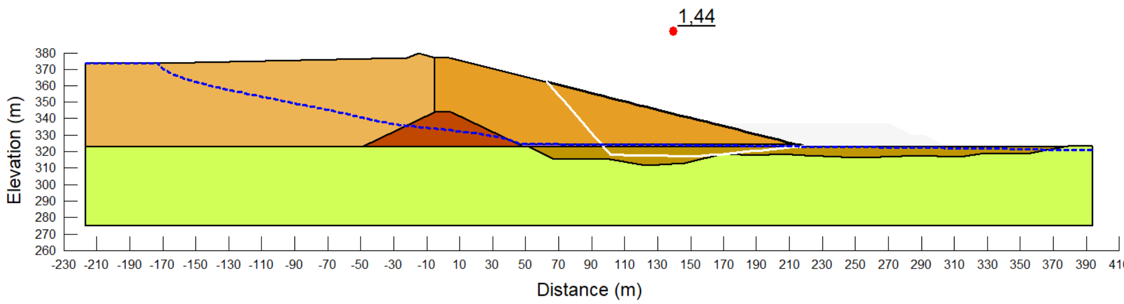

Figure 6. Non-circular surface.

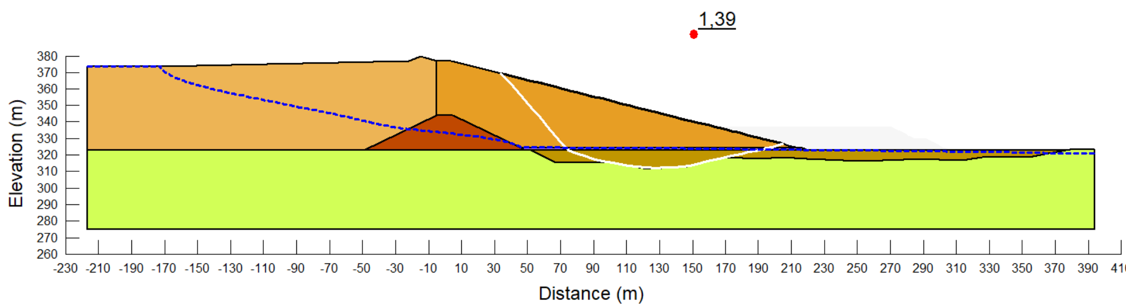

Figure 7. Optimized circular surface.

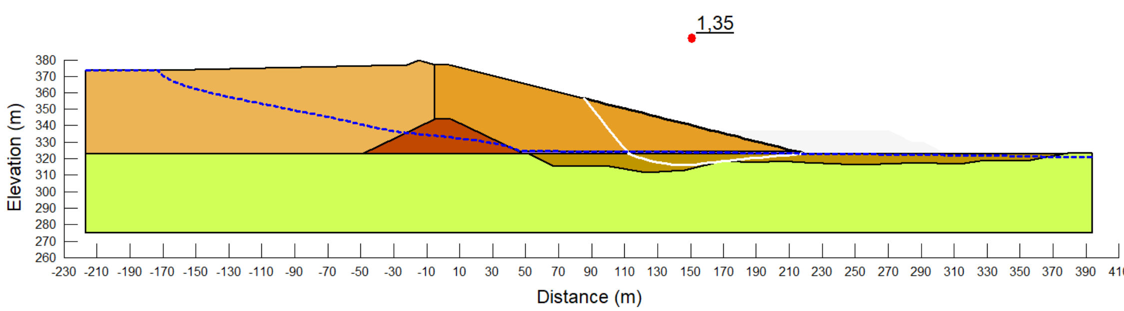

Figure 8. Optimized non-circular surface.

Table 4 shows the F.S. summary and the comparison with the regulations previous cited: ABNT NBR 13028 (2017) with F.S.min≥1.50, Resolution No. 13 (2019) F.S.min≥1.30 and CDA (2019) F.S.min≥1.50 to normal dam operation.

Table 4. F.S. Summary and attendance of the criteria.

Surface	F.S.	ABNT NBR 13028	Res. No. 13	CDA
Circular	1.59	OK	OK	OK
Non-Circular	1.44	Not OK	OK	Not OK
Circular optimized	1.39	Not OK	OK	Not OK
Non-Circular optimized	1.35	Not OK	OK	Not OK

Considering current Brazilian legislation and recommendations, this structure would meet the minimum F.S. established on ABNT NBR 13028 (2017) only if considered a circular failure surface (F.S.≥1.50). When considering non-circular and optimized failure surfaces, circular and non-circular, the structure would meet the minimum F.S. established only by resolution No. 13 by ANM (2019) with F.S.≥1.30, but would not meet the minimum F.S. established by ABNT

NBR 13028 (2017). Considering the CDA (2019) and the F.S.min≥1.50., the structure only meets the minimum F.S. established to the circular failure surface.

Thus, to meet the requirements established by ABNT NBR 13028 (2017) and by CDA (2019), the dam must be reinforced, to achieve an F.S. higher than 1.50, being the criterion adopted in this article. Figure 9 and Figure 10 show the buttress geometry.

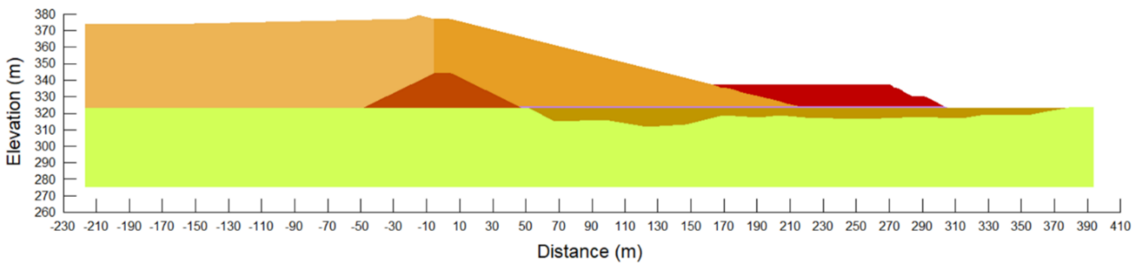

Figure 9. Dam cross-section with the preliminary buttress (in dark-red).

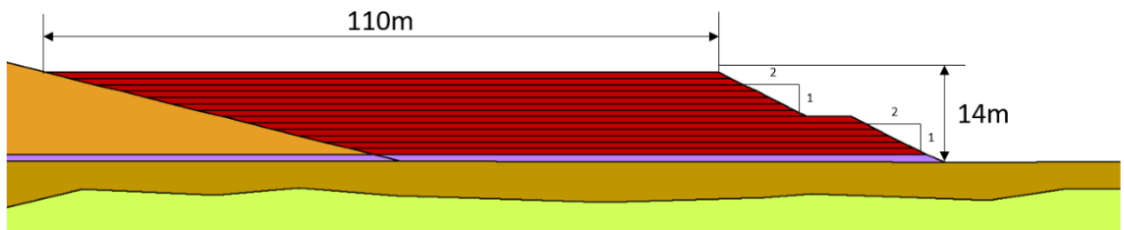

Figure 10. Buttress geometry (in dark-red).

The porewater pressure generation during construction in the low resistance colluvium was simulated considering $\overline{B}$ equal to 1.00 to define the preliminary geometry. This value assumes that the porewater pressure excess is equal to the total stress, being possible to happen in loose saturated soils, in this example the colluvium layer under the phreatic surface. The calculated F.S. LEM considering a non-circular optimized failure surface is equal to 1.44 as detailed in Figure 11.

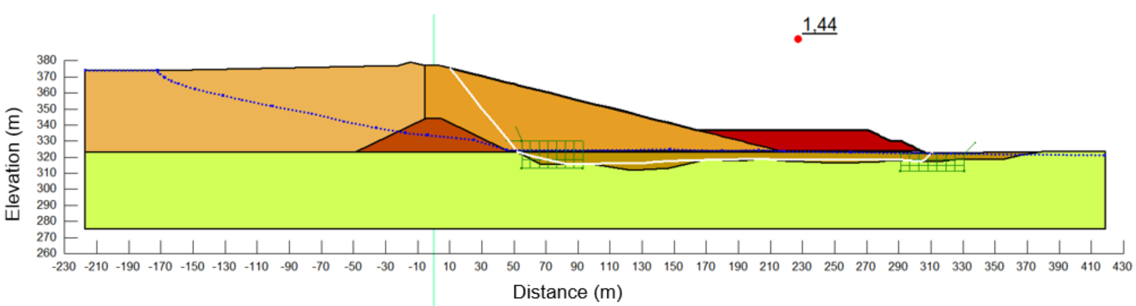

Figure 11. Minimum F.S. obtained in the buttress construction ($\overline{B}$ = 1.00).

Using SIGMA/W to model the buttress construction, the excess porewater pressure generation during and after the construction and the displacements in the colluvium layer were evaluated. The buttress was divided into fourteen layers with 1.0m thickness constructed in 1 day, resulting in two weeks construction period. The consolidation phase, after the construction period, was simulated over 120 days to verify the porewater pressure dissipation and the F.S. variation.

Figure 12 shows the variation of $\overline{B}$ overtime at a single point in the middle of the colluvium layer. The highest $\overline{B}$ found at the beginning of the buttress construction was 0.67 and it is decreasing over time, especially after the end of the construction. Approximately 60 days after the end of construction $\overline{B}$ is equal to 0 indicating the final dissipation of the generated pore pressure.

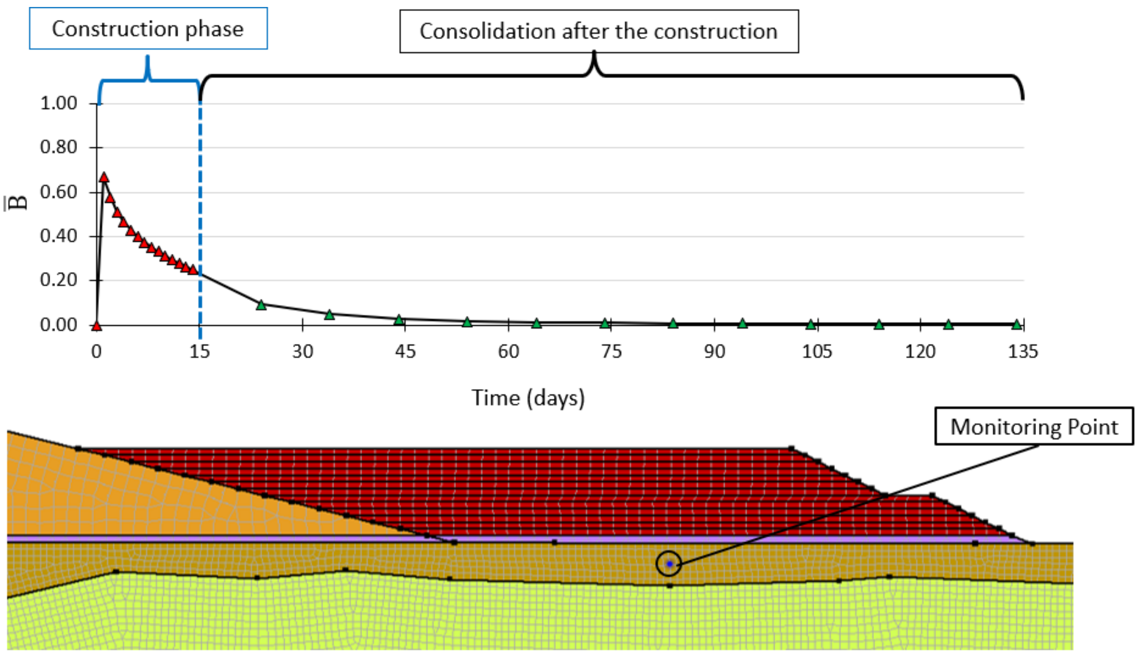

Figure 12. $\overline{B}$ over time.

The F.S. was calculated during and after the construction time as summarized in Figure 13. To evaluate the F.S. it was considered the LEM analyses using the Morgenstern-Price method using a half-sine function to calculate the interslice forces and the FEM method with the SIGMA/W stress state.

Figure 13 shows that at the beginning of the construction, due to the high generation of porewater pressure, the calculated F.S. is lower than 1.50. At the end of the construction, 14th day, the porewater pressure dissipates and the calculated F.S. becomes higher than 1.50 and reached the maximum of around 1.65 after 55 days, approximately, for both methodologies.

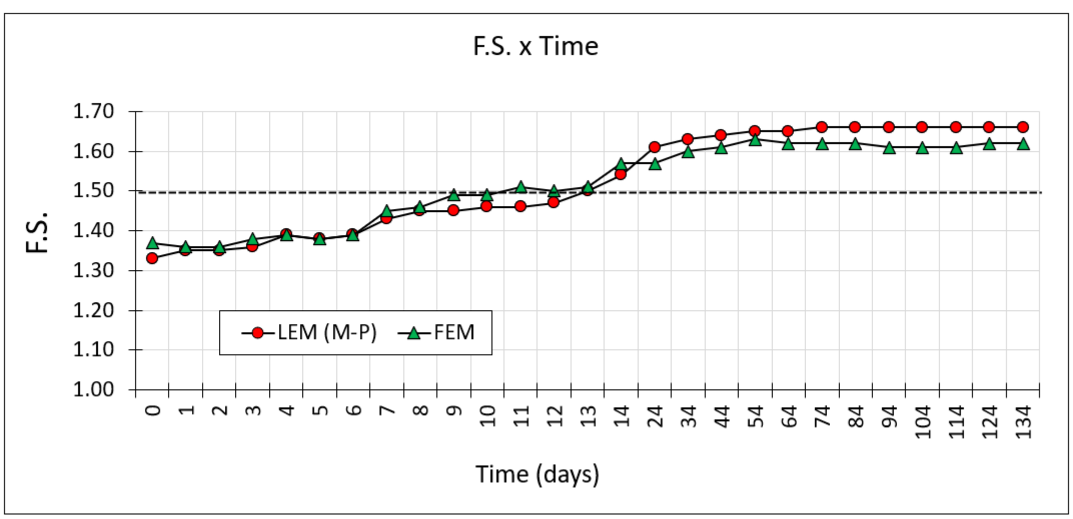

Figure 13. F.S. summary over the time by the LEM and FEM analysis.

Finally, the displacements in the colluvium layer, between the drainage system and the low resistance soil, were evaluated to the end of the consolidation after the construction phase, as the results shown in Figure 14. Around the horizontal distance of 230m to 250m, the vertical displacements found in the colluvium layer after the construction is near 0.50m. In the model analyzed, the displacement of 0.50m did not cause the sectioning of the drainage system, which could lead the structure to fail. Also, the displacement evaluation is extremely necessary for a tailings' storage facility with liquefaction risk, in which little displacements can trigger a liquefaction process, similar to the Cadia failure (Jefferies et al. 2019).

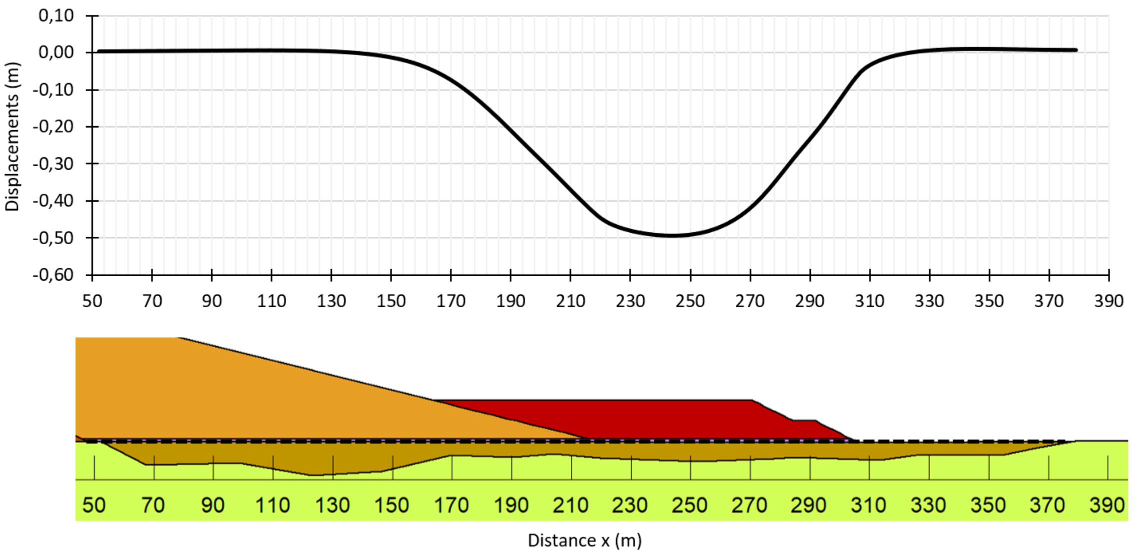

Figure 14. Displacements at the end of the consolidation phase.

4 CONCLUSION

As shown by the results, the selection of the potential failure surface type is essential to evaluate the Factor of Safety. When considering only the circular surfaces, the F.S. can be misleading the structure condition stability and creating a situation where the real F.S. value is lower than the recommended values. In the presented work, the minimum F.S. was met only by the circular surface based on the ABNT (2017) and CDA (2019) values. The optimized non-circular surface presented the lowest F.S. value equal to 1.35, which did not meet ABNT (2017) and CDA (2019) criteria for operating dams.

Based on the results, the simulation of the construction of a reinforcement buttress was performed to stabilize the dam. The F.S. calculated during and after the construction are higher than the initial condition and, after the end of the construction, the calculated F.S. values are higher than 1.50 meeting the F.S. criteria adopted (F.S.min≥1.50). The highest $\overline{B}$ found in the analysis was 0.67, lower than the initial adopted value of 1.00. The displacement observed at the end of construction and the colluvium consolidation would not cause the sectioning of the drainage system, which could lead the structure to fail. Also, is highlighted the importance of the displacement evaluations in structures with liquefaction potential.

5 ACKNOWLEDGMENTS

The authors thank Pimenta de Ávila Consultoria for all the support in the development of this work.

6 REFERENCES

Brandão, H.; Oliveira, R. R. V; Almeida, L. F.; Pinto, G. H. S.; 2020. A comparative study of methods used to determinate the factor of safety. *Tailings and Mine Waste*.

Brown, B. & Gillani, I. 2016. Common errors in the slope stability analyses of tailings dams. *In PM Dight (ed.), Proceedings of the First Asia Pacific Slope Stability in Mining Conference*, Australian Centre for Geomechanics, Perth, pp. 545-556.

Duncan, J. M.; Wright, S. G. (2º ed). 2005 *Soil Strength and Slope Stability*, Hoboken: Wiley.

GEO-SLOPE. 2015. *Stability Modeling with SLOPE/W An Engineering Methodology*. Calgary: Canada.

Jefferies M; Morgenstern, N. R.; Zyl, D.V.; Wates, J.; 2019. *Report on NTSF Embankment Failure Cadia Valley Operations for Ashurst Australia*. H356804-00000-22A-230-0001.

Ladd, C. C. 1991. Stability evaluation during staged construction. 22nd Terzaghi Lecture, *Journal of Geotechnical Engineering.,* ASCE, 117(4),537-615.

Importance of seepage analysis in understanding the Feijao Failure

Murray Fredlund
Bentley Software Inc., Saskatoon, SK, Canada

Krishna Chaudhary & Matt Donaldson
Bentley Software Inc., Saskatoon, SK, Canada

ABSTRACT: The Corrego do Feijao Iron Ore Mine ("Dam I") suffered a sudden failure at approximately 12:28p.m. local time on January 25, 2019. The failure resulted in a catastrophic mudflow that traveled rapidly downstream. This paper presents the seepage analysis of the Vale S.A. ("Vale") Córrego do Feijão Mine Dam I ("Dam I") that was done in connection with the Report of the Expert Panel on the Technical Causes of the Failure of Feijão Dam I, December 2019.[1]

Seepage numerical modeling was considered important for the study in order to establish the saturated and unsaturated flow regime within the tailings prior to failure conditions developing. The tailings structure was subject to climatic influences and subsurface flow from the surrounding groundwater regime. Drainage structures on the downstream face of the dam structure were installed to remove water from the tailings.

The pore-water pressure conditions form a component of the stress-state of the tailings and therefore are considered an input for the related stress/deformation and slope stability numerical modeling. It is the interest of this study to calibrate a groundwater seepage numerical model to the known field measurements in order to gain further understanding of the seepage regime prior to failure.

The seepage regime was able to be calibrated within reasonable variation to known piezometric and CPTu measurements and provided insight into the possible pore-water pressure conditions leading up to failure. Interesting insights were obtained related to mechanisms possibly contributing to ultimate failure conditions.

1 INTRODUCTION / BACKGROUND

It is not always common to perform a seepage analysis as part of a routine stability analysis for a tailings facility. Often the pore-water pressures are represented in stability analysis software as a water table that is interpreted based on standpipe or piezometer measurements. The pore-water pressures below the water table are interpreted as hydrostatic. The difficulty with a simple hydrostatic interpretation of pore-water pressures is that i) CPTu measurements often indicate a non-hydrostatic gradient and ii) piezometer / standpipe readings at a site can exhibit significant variance and need to be interpreted against a seepage model that calibrates unsaturated /saturated flow physics to physical measurements. It was, therefore, considered important by the

[1] This paper is the sole responsibility of its authors and does not reflect the opinions, views, analysis or conclusions of the members of the Expert Panel, none of whom have peer reviewed or approved this submission. The conclusions of the Expert Panel are contained in the Expert Panel Report, which can be accessed at http://www.b1technicalinvestigation.com.

Expert Panel reviewing the Dam I failure to calibrate a 3D groundwater seepage model to the physical measurements of pore-water pressure at the site leading up to the failure event. Such analysis would provide a continuous distribution of pore-water pressures for stress/deformation modeling as well as lead to answering the following questions:
"Was there any significant change in pore-water pressures noted in the days/hours leading up to failure?"

"Are we able to calibrate to field measurements with established material zones and measured hydraulic conductivities?"

"Was there a direct correlation between rainfall events and the piezometric readings?"

"Is it possible that climatic events would have an impact on stability?"

The purpose of the modeling was to provide calibrated pore-water pressures to the stress/deformation model and to also allow insight into the flow regime present in Dam I prior to the failure.

1.1 *Methodology*

The flow regime is complex for Dam I as shown in Figure 1. Seepage numerical modeling was performed to establish the saturated and unsaturated flow regime within the dam prior to failure and allowed an understanding of water flow and pore water pressure conditions in the dam during construction and at the time of failure. The numerical modeling was focused on the tailings impoundment and the upstream-constructed dam.

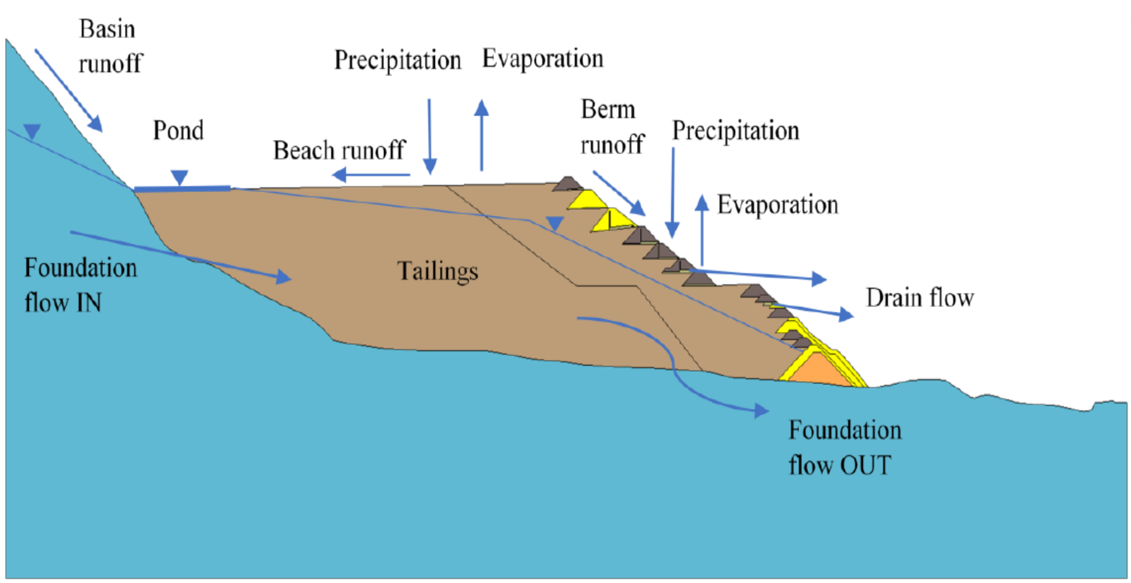

Figure 1 Site conceptual model (Expert Panel Report – Appendix G:Figure 6)

One-dimensional (1D) modeling was used to evaluate the effect of climatic change on near-surface suctions as well as to calculate net rainfall infiltration rates. Two-dimensional (2D) modeling was used for detailed calibration of the seepage model and to calculate pore water pressures during construction and as of the date of failure on January 25, 2019. A three-dimensional (3D) model was created to assess whether the results of the 2D model were consistent with the 2D calibration and to provide a 3D calibration, as well as construction pore water pressures. The 1D, 2D, and 3D seepage modeling and associated calibration utilized the computer softwares SVFLUX, SVDESIGNER, and SVSOILS.

2 CALIBRATION PROCESS

2.1 *Piezometers and CPTu data*

Data was available from 163 piezometers and water level indicators (INAs). The review of the piezometers and INAs resulted in 57 data points (i.e., 41 piezometers and 16 INAs) being considered for calibration. Figure **2** shows the location of the selected piezometers, INAs, and CPTu used in the calibration.

2.2 *Water levels*

The piezometer and INA data were reviewed to determine: (i) any annual trends in the data; and (ii) the trend in 2018 and leading up until the failure.

To determine whether there was a noticeable annual trend in all piezometer readings, the readings were zeroed out at the start of each calendar year. Then, the difference in each reading was plotted. This did not show a discernable annual trend. In addition, there did not appear to be a clear correlation to rainfall data. This was expected due to the buffering influence of the unsaturated zone and the depth at which the piezometers were installed.

The results show that there was a gradual decline in the mean water level since 2016 (Figure **3**). The decline was about 1.4 m for the installations above the setback (900 m msl) and about 0.5 m for the installations on or below the setback. This observation is attributed to a slow net drawdown of water after tailings deposition ceased in 2016. The water appears to be draining from the upper portions of the dam toward the lower portions. The drawdown also creates an increasing unsaturated zone in the upper portions of the dam. The results also show minor short-term increases in water level that appear to be linked to responses during the wet seasons.

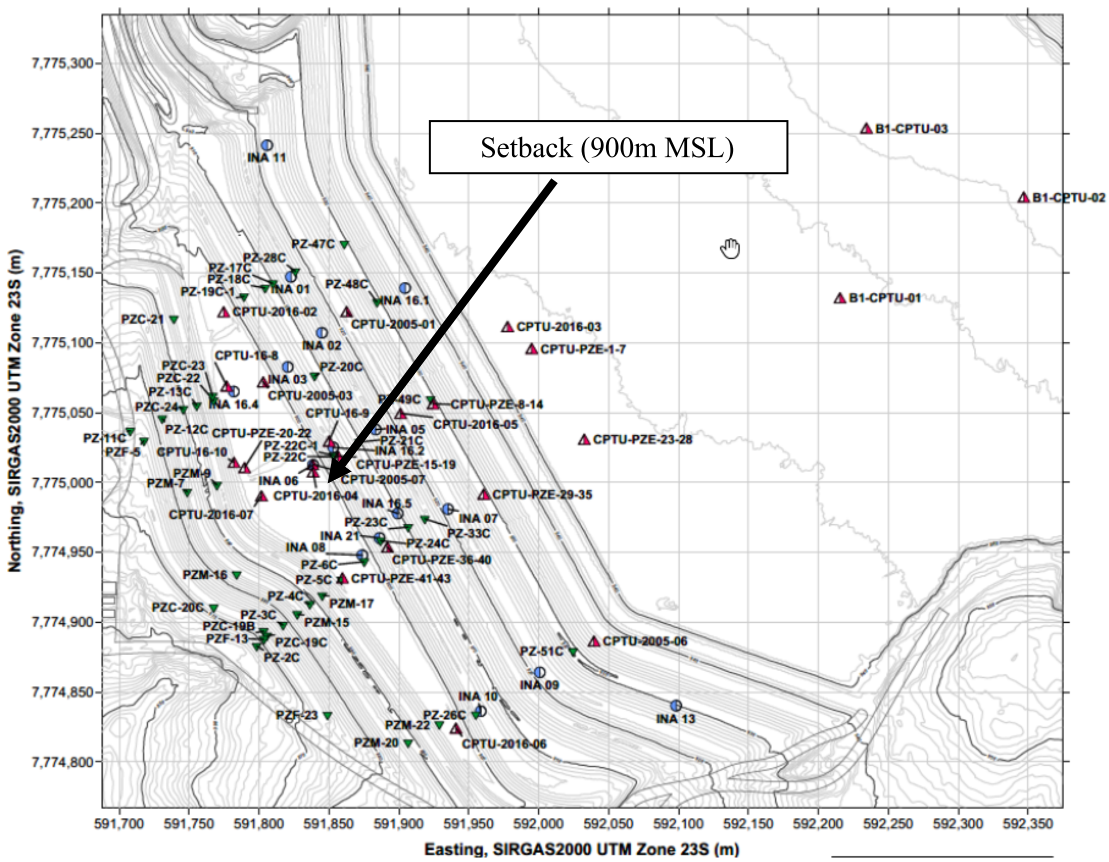

Figure 2 Piezometer, INA, and CPT locations (Expert Panel Report – Appendix G: Figure 23)

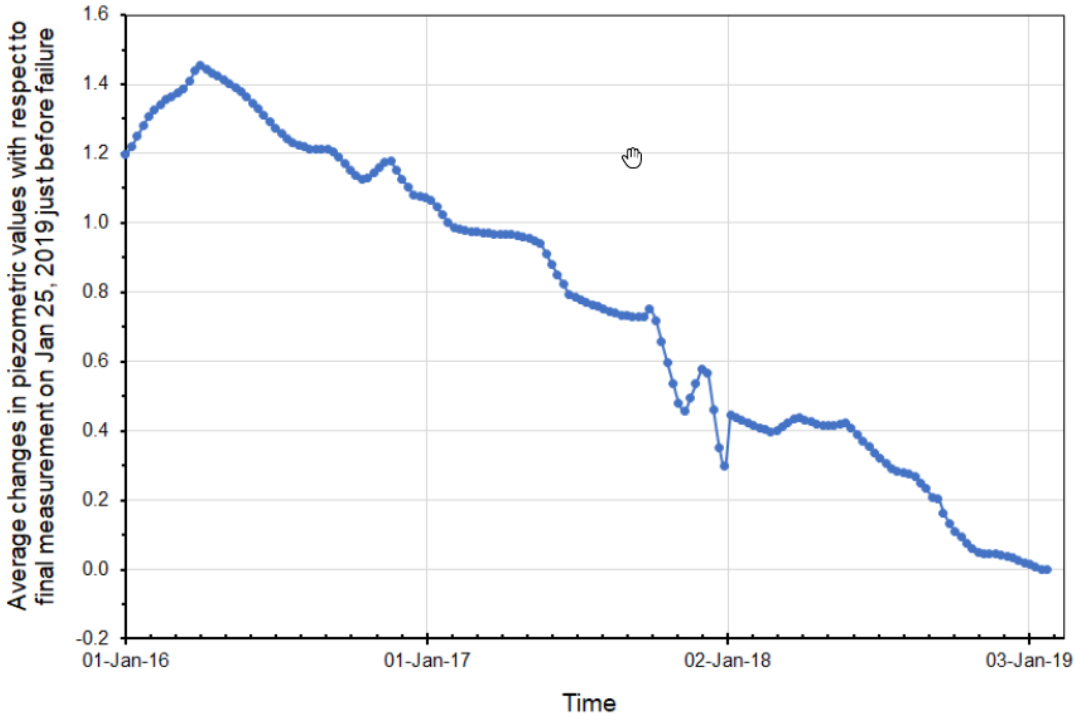

Figure 3 Changes in Piezometer and INA Readings Above Elevation 900 m msl (Expert Panel Report – Appendix G:Figure 24)

2.3 *2D Seepage Calibration (2019)*

Calibration was performed to align the numerical modeling with the observed field conditions and laboratory measured properties. The approach was to calibrate a steady-state model to the pore pressure readings close to January 2019. The calibration included 2D cross-sections 1-1, 2-2, and 3-3. A detailed geometry was utilized for the calibration that included a separation of the tailings into coarse, fine, and slimes zones (Figure 4).

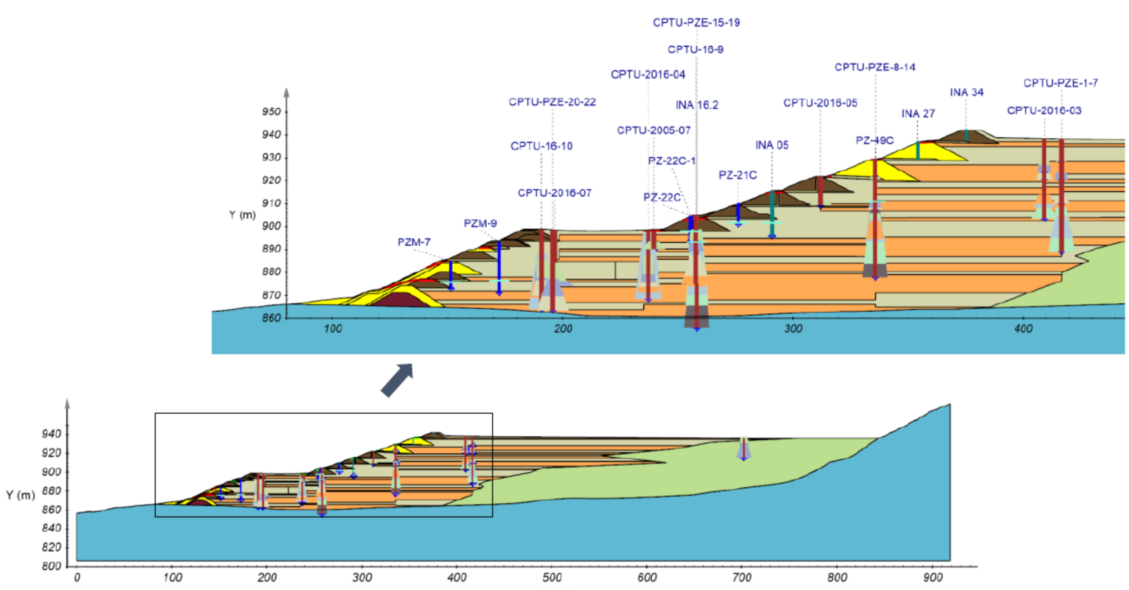

Figure 4 Geometry of Cross-section 2-2 Including Piezometer, INA, and CPTu Data (Expert Panel Report – Appendix G:Figure 32)

The geometry and location of the nearby piezometers, INAs, and CPTu locations for cross-section 2-2 may be seen in Figure 4. The cross-section had more instrumentation installed than cross-section 1-1 and therefore allowed instrumentation comparison in more detail. CPTu pore pressure dissipation testing is plotted as trapezoids with the bottom of the trapezoid indicating the location of the reading and the top of the trapezoid representing a projected zero pore water pressure condition. Each CPTu reading is represented as a separate random color.

The resulting pore pressure distribution can be seen in Figure 5. The results show the potential lateral seepage around Elevation 930 m msl due to the fine tailings layer. The water table is shown to be close to the ground surface at around 900 m msl. The location of the fine tailings layers in the model shows the possibility for the development of perched saturation zones in the model (Elevation ~930 m msl). The pressure readings in the piezometers also show reasonable agreement with the contours of model pressures. Higher water pressures are noted in the Starter Dam where there is no drainage. The water table shows as daylighting on the downstream slope of the Starter Dam.

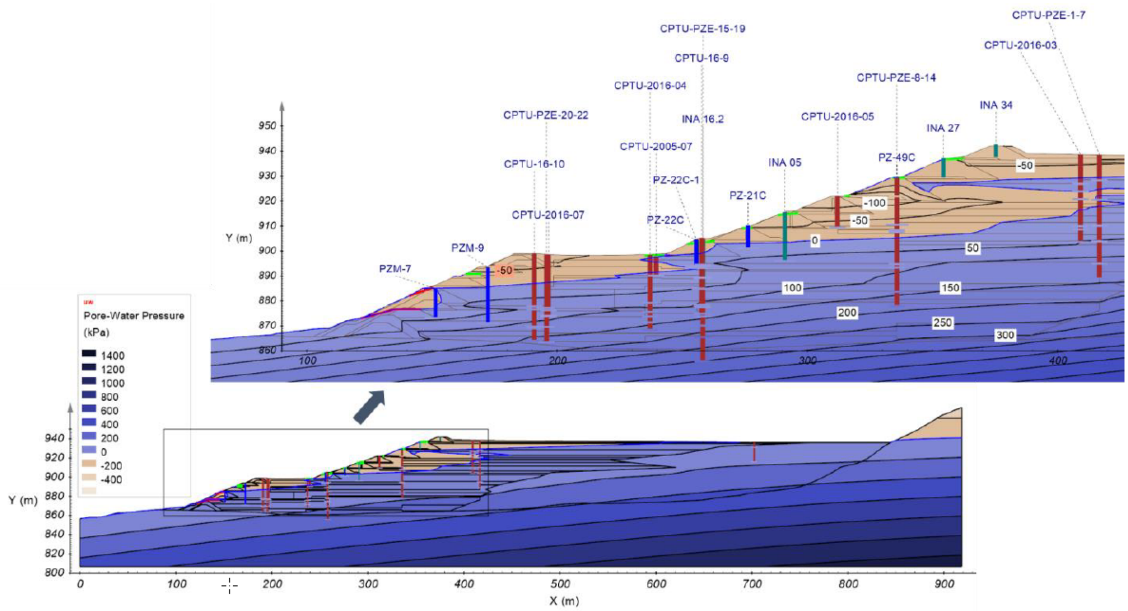

Figure 5 Calibration to Groundwater Flow for Cross-section 2-2 (Expert Panel Report – Appendix G:Figure 33)

The CPTu measurement points are shown in Figure 6. In this cross-section there are 12 CPTu measurement points that are close to the cross-section and were utilized for the calibration. An example calibration can be seen in Figure 6. Some discrepancy with the data was noted that was primarily due to variations between the field and model water table. Overall the alignment of CPTu data with the model results was better when kh/kv = 5 for the coefficient of permeability was utilized.

The correlation coefficient (R^2) value between model results and all CPTu, piezometers, and INA data was 0.965.

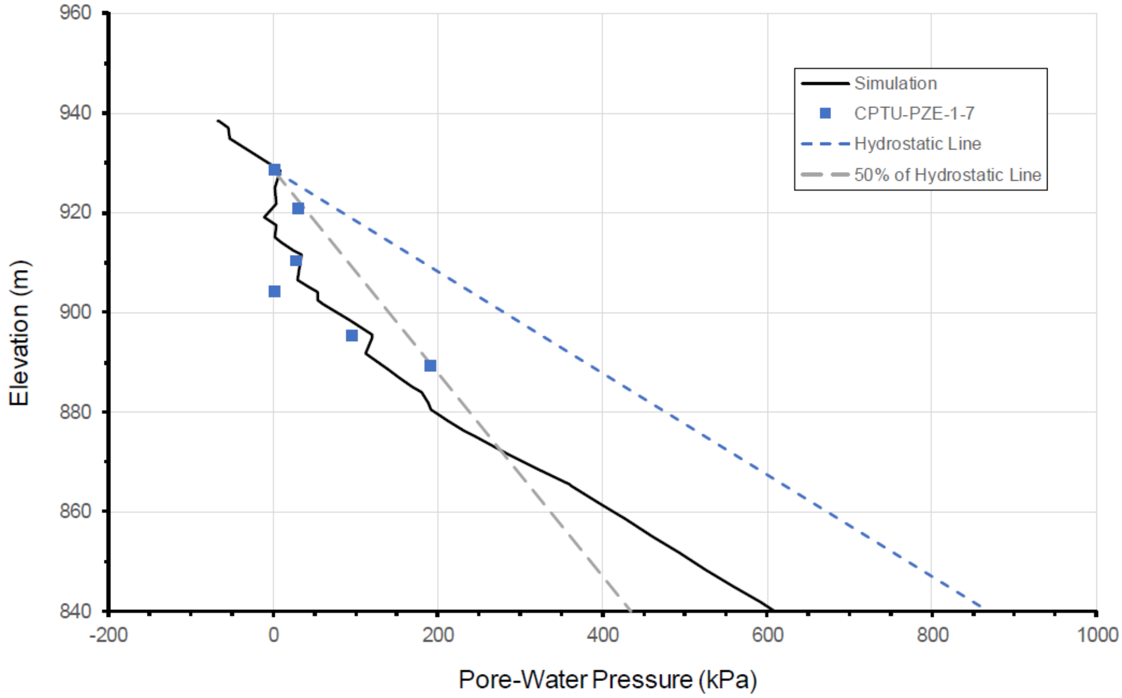

Figure 6 Example CPTu Profile and Comparison to Seepage Pore Water Pressure Results (Expert Panel Report – Appendix G:Figure 35)

2.4 *3D Seepage Calibration (2019)*

A 3D model was also created to evaluate the flow regime that allows a better representation of the curved structure of the dam, the underlying natural ground topography, and the location of drains in the model (Figure 7). Material properties, infiltration rate, and layering utilized for the 3D seepage model were the same as those utilized in the 2D computer model.

The 3D model represented the detailed 3D aspects of the site, including the DHPs and the blanket/chimney drains. A 3D model was created reflecting the heterogenous nature of the tailings. The bulk anisotropy of kh/kv = 5 from the 2D model calibration was used for the three tailings materials in the 3D model.

The model was set up with the following conditions:

- 50% rainfall with the run-off correction method applied;
- Saturated material properties;
- 12 DHPs included (i.e., internal boundary conditions applied).

Calibration was completed to the following data:

- 41 piezometers (September 2018 – January 2019);
- 16 INAs (September 2018 – January 2019); and
- 84 CPTu dissipation test readings (2016 and 2018).

The results of the model are demonstrated in Figure **8**. A large beach length was formed on the tailings surface, and the water table daylights only on the Second and Third Raises. The water table is slightly lower than the 2D counterpart. This was to be expected, given the difference in the location of the pond between the 2D and 3D models. The calibration of the existing model was good as an R^2 value of 0.9524 was calculated which shows excellent agreement with field data.

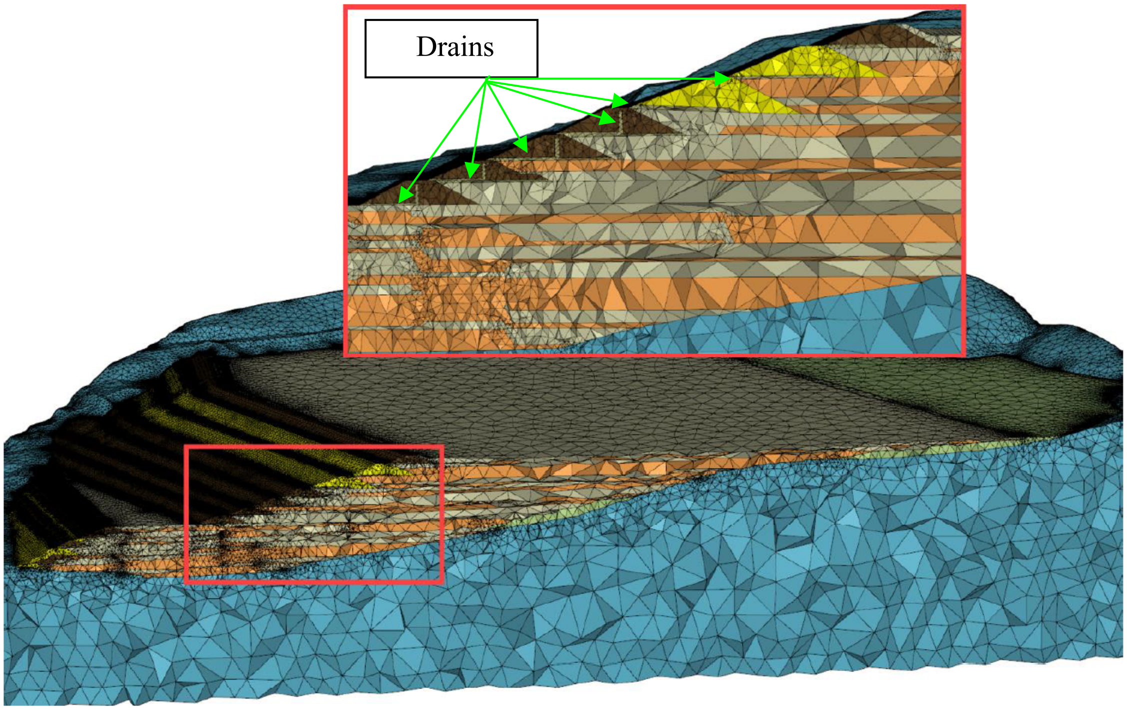

Figure 7 Assumed Location of the Drains and Details (Expert Panel Report – Appendix G:Figure 22)

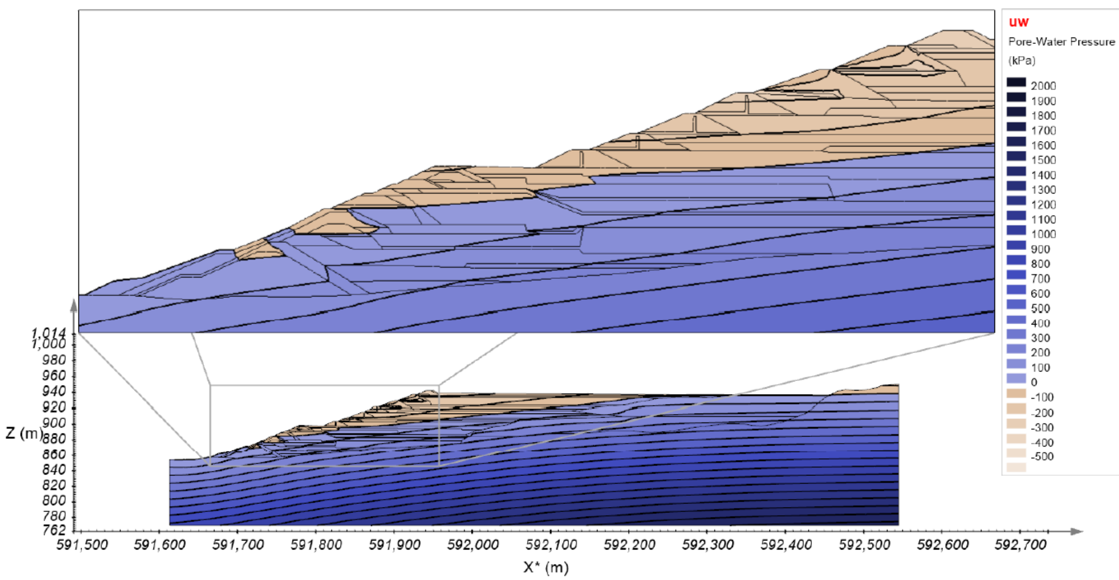

Figure 8 Display of Water Table in 3D Model Along Cross-section 3-3 (Expert Panel Report – Appendix G:Figure 44)

3 CLIMATIC INFILTRATION

More comprehensive modeling of climate flux boundary conditions was performed with SVFLUX^{TM}. The results of this modeling were used to specify the net infiltration rate of rainfall for the seepage models. Calculations were performed to determine both potential evaporation (PE) and actual evaporation (AE) at a partly saturated ground surface. The Fredlund-Wilson-Penman (2000) calculation method of AE was employed, which requires the input of: (i) rain-fall; (ii) temperature; (iii) relative humidity; (iv) windspeed; and (v) net radiation.

The Thornthwaite method was utilized to determine PE, and an annual PE of 945 mm at the site was calculated.

The transient 2D model runs were performed to determine pore water pressure distribution in the three years leading up to the failure. The modeling was set up as follows:

- Unsaturated flow based on SWCCs;
- Soil anisotropy of tailings kv/kh = 0.2;
- Hourly rainfall data was applied with 50% infiltration;
- Cross-sections 1-1, 2-2, and 3-3 were modeled;
- Modeling time was from January 2016 to January 2019;
- Initial conditions were established from a steady-state saturated model using 50% average annual rainfall (1400 mm/year);
- Actual hourly rainfall data from combined F11 (2016) and F18 (2017-2019) automated rain gauges were applied to the top of the entire model;
- Head = 941 m on upstream foundation;
- Head = 856.21 m on downstream foundation; and
- Head = 936 m for pond on tailings.

Pore pressure conditions demonstrate a divide between the saturated and unsaturated zones. The water table was found to slowly decrease by approximately 2 m to 4 m over the three years, which is consistent with an average decrease of 1.6 m in piezometric values recorded by field piezometers and INAs situated above 900 m msl. However, the suctions above the water table decreased due to the rainfall encountered in 2016. The 2017 average rainfall and the 2018 higher than average rainfall furthered the advance of water flow into the system that decreased suctions in a top-down manner shown in Figure 9. Suctions decreased from an average of between 35 kPa and 75 kPa to between 5 kPa and 20 kPa over the three-year period. The vertical downward movement of water is governed by the combined effects of the fine and coarse material vertical permeability. The bottom of the reduced suctions zone reaches approximately 25 m depth after the three years modeled. The decrease in shear strength in the unsaturated zone was calculated using the method described by Fredlund, Xing, Fredlund, and Barbour (1996) over three years leading up to the failure on January 25, 2019.

In summary, the analysis shows:

- The model agrees with the observed decrease in water levels in the three-year period from 2016 to 2019.
- The 50% of hydrostatic pore pressure profile with depth is a reasonable approximation (particularly at the critical elevation of the setback).
- There is a difference in behavior between the unsaturated zone and the saturated zone.
- The unsaturated zone was progressively wetting-up.
- A net average reduction in the shear strength of the unsaturated zone of up to 15 kPa was realized progressing down to a depth of 25 m after three years.

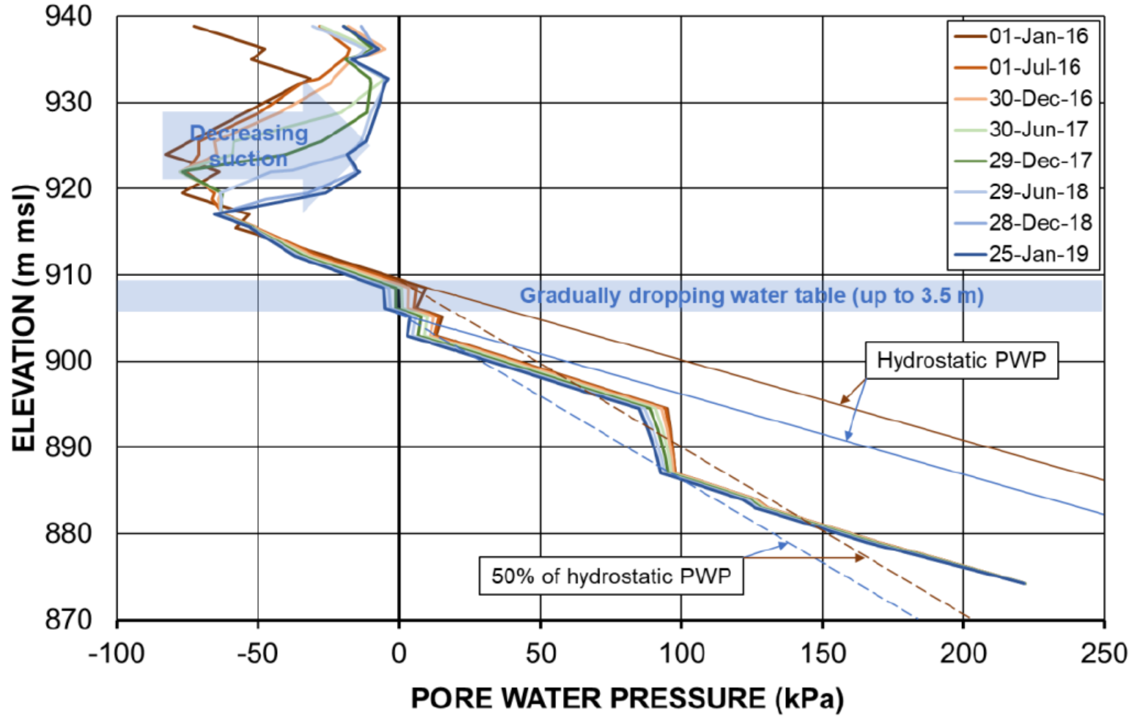

Figure 9 Pore Water Pressure Profile Beside Top Berm on Cross-section 3-3 (Expert Panel Report – Appendix G:Figure 46)

4 SUMMARY & CONCLUSIONS

The seepage analysis effort led to a successful calibration to known piezometer, standpipe, and CPTu data and provided additional insight into the pore-water pressures within the facility. The seepage analysis provided the following conclusions:

1. Net infiltration of rainfall was found to be equal to approximately 50% of total annual rainfall.
2. The piezometers did not register short-term climatic events due to the unsaturated zone acting as a buffer.
3. There was a slow decrease in piezometers and INAs in the three years prior to the failure.
4. There was no significant trend in readings during the week leading up to the failure.
5. CPTu dissipation measurements demonstrated a downward gradient of about 50% of hydrostatic. This was confirmed in the transient 1D and 2D seepage models.
6. Climatic events can change suctions that can result in a net average reduction in the shear strength in the unsaturated zone of up to 15 kPa.

The expert panel states that the reduction in suctions in the unsaturated zone along with creep contributed to failure of the facility.

5 REFERENCES

Fredlund, D.G., Xing, A., Fredlund, M.D., & Barbour, S.L. (1996). The relationship of the unsaturated soil shear strength function to the soil-water characteristic curve. *Canadian Geotechnical Journal*, *33*(3), 440-448.

Report of the Expert Panel on the Technical Causes of the Failure of Feijão Dam I, December, 2019 (http://www.b1technicalinvestigation.com/)

Report of the Expert Panel on the Technical Causes of the Failure of Feijão Dam I – Appendix

G: Seepage Analysis, December, 2019 (http://www.b1technicalinvestigation.com/)
Wilson, G.W., Fredlund, D.G., & Barbour, S.L. (1997). The effect of soil suction on evaporative fluxes from soil surfaces, *The Canadian Geotechnical Journal*, *34*(4), 145-155; Fredlund, M.D., Tran, D., & Fredlund, D.G. (2016). Methodologies for the calculation of actual evaporation in geotechnical engineering, *ASCE International Journal of Geomechanics*, *16*(6).

Dam breach analysis - Topographic and model limitations for 2D finite element numerical modelling

M.G. Walden & N.T. Rocco

NewFields Mining Design and Technical Services LLC, Lone Tree, Colorado, United States.

ABSTRACT: Loss of life and environmental and economic damage can result from tailings dam breaches. As such, preemptive and accurate modelling of the potential tailings breach scenarios is of great significance for the development of appropriate hazard classification, monitoring, mitigation procedures, and emergency preparedness and response plans.

Tailings dam breach simulations are often modelled utilizing 2D (pseudo-3D) numerical models. There are a variety of numerical modelling software available that allow use of site-specific topography. This article presents limitations and requirements for topographic datasets and the influence of the datasets on the numerical stability and results of tailings breach simulations.

General options for topographic data in the public domain, and for purchase, are presented along with lessons learned from merging topographic data of varied resolution. Topographic data used within breach simulations must be overlain by, and interpolated by, subsequent grid element meshing. The requirements for generating a reasonable grid element mesh and subsequent limitations of the mesh size are discussed. The resolution and quality of the topographic data can have a significant impact on the dam breach analysis and subsequent inundation area. Limitations regarding the resolution of the topographic data and finite element mesh size, including model run-time, and numerical convergence are discussed and suggested solutions to maximize the accuracy and efficiency of the dam breach model are provided.

Findings indicate that a number of model sensitivities and limitations should be considered when selecting topography for 2D numerical modelling of tailings dam breaches. A summary of methods to maximize the quality of the topographic data set, and the subsequent dam breach model, are provided.

1 INTRODUCTION

The process of dam breach analyses involves estimation of the volume released during an embankment failure, and routing of the flow, or flood, downstream of the site. Typically, two-dimensional (2D) numerical models are utilized to accurately route the inundation over the downstream topography. This paper reviews common methods used to maximize the quality of the topographic data set, and the subsequent dam breach model.

2 TOPOGRAPHIC DATA

2.1 *General*

The topography downstream of a dam breach can have a significant impact on extents of the resulting flood. For example, a breach into a narrow canyon with a steep grade will propagate further and faster than a breach into a relatively flat floodplain where the flows can dissipate radially. On this same note, accuracy (resolution) of the topography is important to define the true physiography of the landscape. When two topographic data sets of varying resolution are compared, for example one with high 1-meter resolution accuracy and one with low 30-meter resolution accuracy, the volumetric difference can be large enough to significantly impact the model results. Significant topographic changes in the landscape such as a topographic depressions, small canyons, or river channels can be lost when utilizing lower resolution topography. As such, it is important that the most accurate data available is used and that the resolution of the topography be considered in relation to the landscape and topographic features that will be present in the model.

Topography information used dam breach analysis is typically in the form of a digital elevation model (DEM). A digital elevation model is a term used to describe a 3-dimensional computer graphics representation of elevation data to represent terrain. DEM's are commonly found in the form of digital terrain models (DTM) or digital surface models (DSM). A DTM typically represents the bare ground surface without any objects like vegetation and structures while a DSM typically represents the earth's surface and includes objects like vegetation and structures. Water bodies in both DEM and DSM topography are typically represented as flat surfaces unless additional processing has been completed.

DEMs are often constructed from Light Detection and Ranging (LiDAR) data which is a representation of the surface created strictly from the LiDAR point cloud data. This type of DEM can be problematic due to the appearance of water surfaces, as water surfaces do not provide LiDAR return which results in triangulation artifacts. Hydro flattening is a process that can be applied to LiDAR and other DEMs to flatten the water surfaces and remove the triangulation artifacts. It should be noted that hydro flattening is purely a cartographic enhancement; the water body elevation is not representative of the true water surface elevation and should not be used for estimation of water flow or for other hydrologic or hydraulic modelling purposes. Hydro flattened DEMs can be further enhanced to include the delineation of roads, single-line drainages, ridges, bridge crossings, buildings, and other features. However, additional enhancement can significantly increase the time, effort, and cost. Figure 1 a presents an example of raw LiDAR data while Figure 1b presents an example of Hydro-flattened LiDAR.

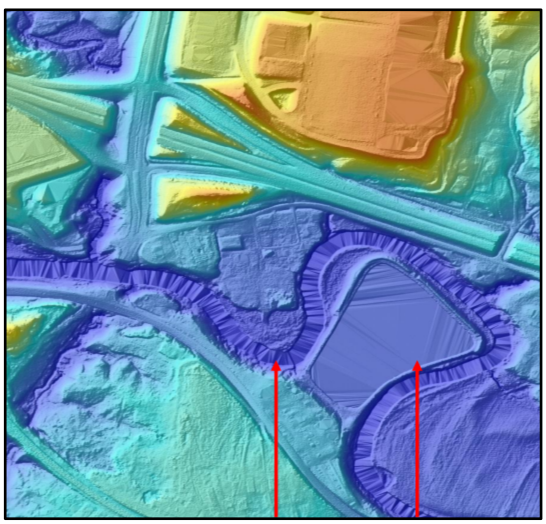

Figure 1a. Raw LiDAR

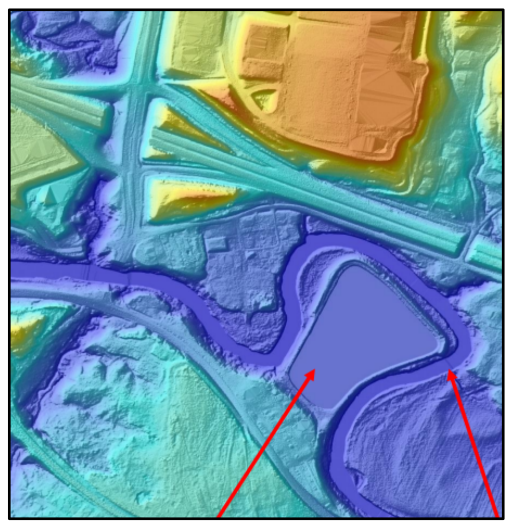

Figure 1b. Hydro-flattened LiDAR (Sanborn, 2019).

Hydro enforcement is another enhancement that can be applied to DEMs. Hydro enforcement is a surface used by engineers for hydraulic and hydrologic modelling. Although it is similar to a hydro flattened DEM, it has additional modification to allow water to flow across the surface as it does in the real world. An example of an additional modification is that the road fills are typically cut through at drainage culverts to allow water to drain as it would in the real world.

DEMs can also be hydro conditioned, which is similar to hydro enforcement, but with additional enhancements. In most DEMs there are natural depressions (sinks) in the topography where water stagnates and collects until filled. When completing hydraulic and hydrologic modelling, sinks can sometimes cause numerical convergence problems in the model. Hydro conditioned DEMs fill the sinks in the topography resulting in a flattened ground area over which modelled water can flow unimpeded across the entire surface.

When obtaining topographic data, it is important to perform relative checks on the condition of the data set. Typical checks include confirmation of the resolution, and confirmation of corrections that have been pre-applied to the topography such as hydro reinforcement of river systems and the removal of vegetation and structures to generate a bare earth model. It is also prudent cross reference the elevations in the data set with control points from the study area.

The selection of which type of DEM and which corrections are appropriate for dam breach modelling depends on the modelling scenario and the intention of the study. If modelling flooding through an urban area, then using a DSM that includes structures may be important to discern flow through urban corridors. However, if modelling flows through densely vegetated forest, it would be more appropriate to use a DTM and apply a representative Manning's coefficients.

The DEM data can be utilized for 2D numerical dam breach modelling once the quality of the topographic data set has been verified and is deemed appropriate for the study area.

2.2 *Sources of Topographic Data*

The publicly available DEM data in the USA can be utilized for accurate dam breach modelling in most states as high-resolution LiDAR data is typically available. If high resolution DEM is not available in the study area lower resolution publicly available topography, such as 1/3 Arc-Second Elevation Data with 10-meter resolution can be considered. The topographic data provided by the United States Geological Survey (USGS) is a typically hydro flattened DTM and does not have additional enhancements.

High resolution LiDAR data is also available in some areas of Canada and can accessed from the Natural Resources Canada (NRCan) website.

DEM data can also be obtained outside of North America through services provided by the National Aeronautics and Space Administration (NASA) but is typically at 30-meter resolution. The USGS also provides 30 Arc-second (30 meter resolution DEM) data globally. Often local sources (country, state, or county specific) can provide better than 30-meter resolution data and should be considered. Depending on the study area and in consideration of the project topography, locality of critical structures, locality of populations, and availability of public data, it may be prudent to purchase a satellite survey, or complete a LiDAR flyover of the study area.

3 COMPUTATIONAL DOMAIN AND GRID ELEMENT SIZE

2D numerical modeling for dam breach analysis requires utilization of a topographic data set and definition of a computational domain around the projected limits of the inundation. Once the computational domain is defined the grid elements are generated. The computational domain should be defined based on the expected inundation area. A larger computational domain will require more grid elements and require a longer run time. However, a computational domain that is too small may not cover the entire inundation area and require adjustment and model revisions. It may be prudent to run a test model with the highest flows expected to ensure that the computational domain that has been defined covers the required area. Figure 2a presents a computational domain that is larger than necessary and Figure 2b presents a smaller computational domain that is more fitting for the expected inundation area.

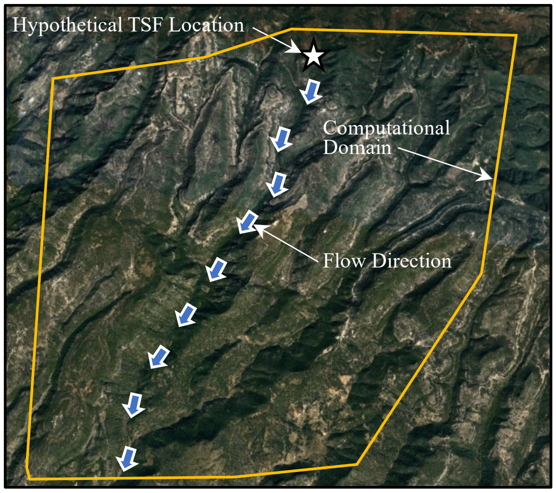

Figure 2a. Poorly Defined Comp. Domain

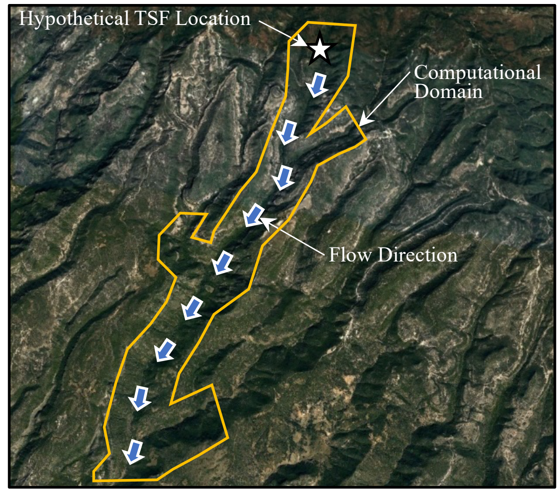

Figure 2b Well Defined Comp. Domain

Most 2D models utilize square grid elements to discretize the project domain. The grid element size can be selected by the user, with finer grid elements typically leading to longer run-times but more accurate results, and coarser grid elements leading to shorter run-times but less accurate results. In general, smaller grid elements will lead to numerical convergence on a more realistic solution.

Studies, such as that by Halliday and Arenas (2019), suggest that low-resolution topography, or low resolution grid elements, will result in overly-conservative runout areas when the natural topography has areas of high relief. The study concludes that the cost of a quality, site specific survey could far outweigh the cost of implementing rapid evacuation response times or designing for high consequence breaches. Horritt and Bates (2001) also demonstrated that increased lateral resolution of a two-dimensional model allows for a better simulation of the water storage in a flood plain.

In general, the grid element size selection should be balanced based on the intent of the study, the potential to impact downstream residences, the relief and complexity of the downstream topography, the resolution of the underlying topography, and the project budget and schedule.

Highly detailed topographic data sets can be capable of generating a relatively accurate grid with 1 meter by 1 meter grid elements. If the study area is 10 kilometers by 10 kilometers, then a 1 meter by 1 meter gridded mesh would result in 100 million grid cells. If the grid cell size is reduced by half the number of grid elements is quadrupled. For reasonable simulation run times, a project with less than 3 million grid elements is typically recommended (FLO-2D, 2018). Large project areas resulting in greater than approximately 3 million grid elements will require more time of pre-processing of data and post-processing of results as well as more computational resources.

4 GRID ELEMENT LIMITATIONS

4.1 *General*

Aside from the simulation run time, there are other limitations that must be recognized to create an efficient flood routing model. There are several numerical limitations confronting the use of small grid elements including Manning's coefficient and the rate of flow into the grid elements. Convergence issues are a common result of numerical limitations and often result from improper modeling procedures. These convergence issues can often be controlled and mitigated by the modelling software but will often result in very long run times. Alternatively, if the model is unable to address the convergence issue by decreasing the time steps and increasing the run time the software can crash or refuse to run.

4.2 *Manning's Coefficient*

2D hydraulic models typically use shallow flow equations of motion for overland flood routing. The basal friction in the model is typically based on Manning's equation which utilizes the friction slope between grid elements (dependent on the grid cell size) and the hydraulic radius (calculated based on the flow depth within the specified cell). If the flow depth to grid element size ratio is too large (the grid cell size is too small) convergence issues can occur. Most models can accommodate this problem by decreasing the timestep, but this can result in very long run times depending on the Manning's coefficients used in the models, the size of the grid cell, and the velocity of the flow. As such, scrutiny is required when considering the selection of Manning's coefficient and the grid element size.

With Manning's roughness coefficient (n) assigned to each land cover classification, there is a high probability that two neighboring cells are assigned very different roughness values (e.g., 0.04 for a main river channel against 0.4 for a heavily vegetated riverbank) which can generate numerical instability during the dam breach simulation. To overcome the associated numerical instabilities buffer zones offset from the center of the main river channels can be defined to gradually increase Manning's coefficient and avoid large disparities between neighboring grid cells, which will improve numerical stability. An example of what a manning n buffer zone might look like along a main channel is presented in Figure 3.

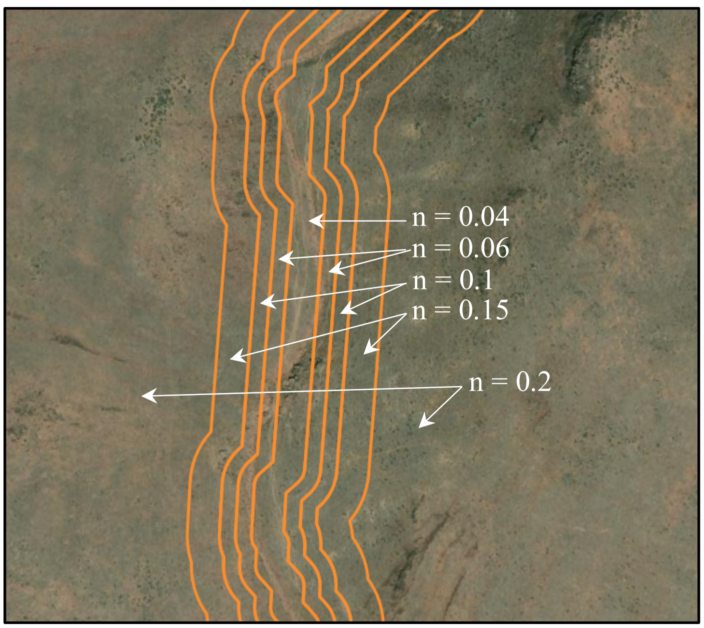

Figure 3. Manning's Coefficient Buffer Zone Along a Main Channel Example

4.3 *Rate of Flow*

Most 2D models calculate an appropriate time step based on the Courant-Friedrich-Lewy condition (Courant number), which relates the flood wave movement to the model discretization in time and space to control how the fluid moves through the computational cells. The concept behind the Courant number is that a particle of fluid should not travel more than one cell per time step, otherwise numerical instabilities will be created. The timestep used for most 2D hydraulic models is determined based on the following equation:

$$\Delta t = C \cdot \Delta X / (V + (g \cdot d)^{0.5} \qquad (1)$$

Where, 'C' represents the Courant number (C<1), 'ΔX' represents the grid element size, 'V' represents the depth averaged velocity, and 'g' is gravitational acceleration and 'd' is the flow depth. The Courant number typically varies from 0.1 to 1.0. A value of 1.0 will enable the model to have the largest possible timestep, which results in a faster runtime. Smaller Courant numbers result in a smaller timesteps and longer run times. However, smaller Courant numbers do generate greater numerical stability.

The rate of outflow from a dam can be represented as a hydrograph that can be input into specific grid elements in a 2D hydraulic model. High velocities near the breach location result in smaller timesteps and longer run times. Steep rising hydrographs, such as those from tailings dam breaches, can result in very slow models with very small timesteps due to the high velocity of outflow. The size of the grid elements are typically adjusted by the user to maintain reasonable timesteps in dam breach models with a high peak flow rates. In general, the peak flow rate divided by the grid cell surface area should be between 1 and 3 cubic meters per second per meter squared ($m^3/s/m^2$) (FLO-2D, 2018).

5 IMPROVING MODEL ACCURACY AND RUN TIME

If a model domain is large and the simulation requires a high degree of accuracy, there are some modelling techniques that can be utilized to improve the simulation speed and accuracy.

One such method involves dividing the project into multiple grid systems (models) and running each "sub-system" in series. The outflows from the earlier grid system/model should be tracked via the use of a floodplain cross section hydrograph or outflow boundary and added into each subsequent grid system/model as an inflow hydrograph. Figure 4 presents a simplified example of what a multiple grid system might look like.

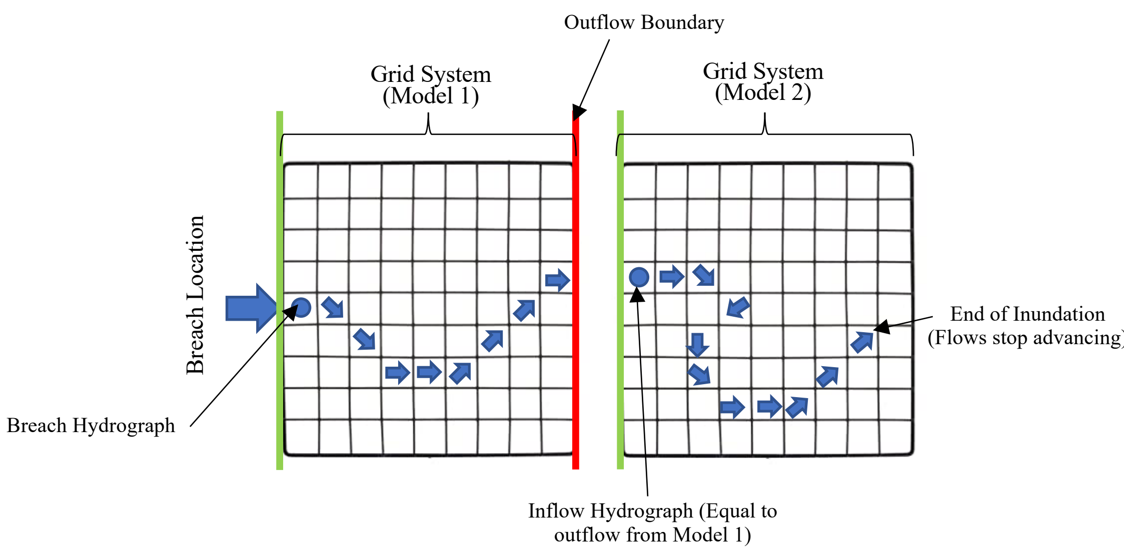

Figure 4. Use of Multiple Grid Systems to Improve Simulation Speed and Accuracy.

Another method that can be used to reduce the model run time when high flow rate hydrographs are utilized in a model is dividing the hydrograph across several grid elements. For example, the inflow hydrograph at the breach location could be divided by 3 and distributed to 3 adjacent grid elements at the breach location. The peak flow rate will then be decreased by the number of grid elements that the hydrograph is distributed among resulting in larger time steps and less run time. The run time can be further improved by assigning the same elevation across the grid elements that the hydrograph is distributed among and assigning the elevation of several of the downstream grid elements slightly lower elevations to create a well-defined slope in the downstream direction and get the flow moving in the correct direction. The adjusted grid elements are considered sacrificial do not significantly influence the results. Figure 5 presents a simplified example of a breach inflow hydrograph distributed across 3 grid elements.

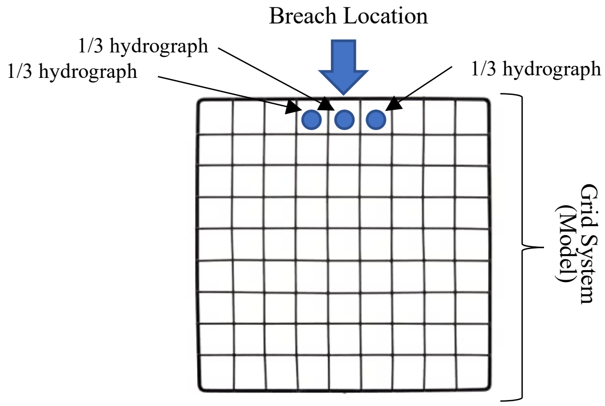

Figure 5. Distributing a Dam Breach Hydrograph Across Several Grid Elements.

A small amount of water flow in the order of 1 to 5 m/s can be added at the start of the model for a set amount of time (often 24 or 48 hours) prior to initiating the breach hydrograph. This helps the model discern relative flow directions and fills in low lying areas (sinks) that can cause convergence issues and improves model run time.

6 RECOMMENDATIONS AND CONCLUSION

Selecting appropriate topography, grid element sizes, and model parameters for a given dam breach analysis project requires consideration of budget, time, and effort necessary to generate a acceptability detailed model.

When selecting topography, it is important that the most accurate data available is used and that the resolution of the topography be considered in relation to the landscape and topographic features that will be present in the model. It is important to perform relative checks on the condition of the topographic data including confirmation of the resolution, and corrections that have been pre-applied to the topography such as hydro reinforcement of river systems and the removal of vegetation and structures. It is also prudent cross reference the elevations in the data set with control points from the study area.

Once appropriate topography is selected the computational domain and grid elements can be defined. The computational domain should be defined based on the expected inundation area and the selection of the grid element size. Selecting a small grid element size less than 5 meters is not typically recommended for large projects. High resolution DEM data does not necessarily justify using small grid elements. Selection of an appropriate grid element size should consider model runtime; model accuracy and detail; the time it takes to prepare and edit the model components; the number of required simulations; and the model peak flow rates.

For large simulations that requires a high degree of accuracy and finer grid-element sizes, modelling techniques can be utilized to improve the simulation speed and accuracy. Some modelling techniques include dividing the project into multiple grid systems, dividing the hydrograph across several grid elements, the use of sacrificial grid elements to promote flow in the downstream direction at the location of the inflow hydrograph, and adding a small initial flow into the model.

Available guidance suggests selecting an appropriate grid cell size based on the peak flow rate used in the model. For reasonable simulation run times, a project with less than 3 million grid elements is typically recommended (FLO-2D, 2018). For larger projects, model run times in the order of 4 to 12 hours can usually produce reasonably detailed results.

Overall, the selection of topography for dam breach analyses using 2D hydraulic modelling software is an important step in dam breach modelling and the setup of the computational domain and grid element resolution can significantly impact model run time and numerical convergence of the model. Specific consideration and understanding of required results, necessary accuracy, and model limitations is required in order to adequately and accurately simulate a dam breach model.

7 REFERENCES

FLO-2D. 2018. FLO-2D Reference Manual, Build No. 18 2018

Halliday, A. and Arenas, A. 2019. Impacts of Topography Quality on Dam Breach Assessments. Tailings and Mine Waste 2019, Vancouver, Canada.

Horritt, M.S., and Bates, P.D., 2001, Effects of spatial resolution on a raster based model of flood flow: Journal of Hydrology, v. 253, p. 239–249

Sanborn Map Company, Inc. 2019. Overview of 3DEP Lidar Specification and Products. Retrieved from: https://drcog.org/sites/default/files/resources/LIDAR2020_Presentation_2019_01_16_Sanborn.pdf.

Advancements in the modelling of tailings dam breaches

Daniel Adria, Negar Ghahramani, Anda Cen, & Scott McDougall
University of British Columbia, Vancouver, British Columbia, Canada

Nahyan Rana & Stephen G Evans
University of Waterloo, Waterloo, Ontario, Canada

W Andy Take
Queen's University, Kingston, Ontario, Canada

ABSTRACT: Tailings dam breach studies are used to understand the risk associated with tailings facilities and to develop emergency response plans. The physical processes of tailings facility breaches and subsequent outflows are not fully understood, which limits the confidence in tailings dam breach studies. The University of British Columbia is assessing case histories with statistical tools and numerical models to address this knowledge gap. We present a back analysis of the 1994 Merriespruit event developed using HEC-RAS 6.0. The sensitivity of the runout model to breach inputs is explored, showing how the interaction of the two is difficult to predict. The continuing aim is to identify trends in analogous breach events to assign a priority of uncertainties in breach modelling to address for forward analysis. Understanding which parameters introduce the most uncertainty in numerical models helps ensure the full range of consequences is addressed in a tailings dam breach study.

1 INTRODUCTION

Risk assessments help inform decisions during the design, construction, operation, and closure phases of extraction projects. Risk is the combination of negative impacts or consequences to the project, the environment, or the public and the associated probabilities of those impacts. A potential adverse outcome of an extraction project is the catastrophic failure of a waste storage facility, as exemplified by recent events at the Mount Polley mine in Canada and the Fundão and Feijão mines in Brazil (Santamarina (2019) and the references therein). While rare, the potential for extreme consequences needs to be appropriately considered. Dam breach studies help assess or predict the consequences of credible failures and therefore form a key element of a risk assessment. These studies include significant uncertainties, and the physical processes and characteristics involved in the failure mechanics of tailings storage facilities and the subsequent outflows are an area of active research.

Models of tailings dam breach simulate complex hydraulic systems, and it cannot be expected that modellers, or even model software developers, have full understanding of model responses to inputs (Hall et al. (2009)). Foundational inputs to tailings dam breach modelling, including breach development time, breach width, and release volume, are highly uncertain, posing additional difficulties on estimating consequences of a tailings dam breach (Wahl (2004); Martin et al. (2015)). Both model sensitivity and input uncertainty need to be assessed to build greater confidence in tailings dam breach studies. Neither are well-quantified, especially for breach inputs.

Carefully investigating each input for every dam breach study is not efficient nor feasible with practical realities of budget and timelines. Without any specific guidance, modellers must rely on their professional judgment or use simple cursory analysis to connect breach inputs to inundation. Neither approach addresses the complete uncertainty of a hypothetical breach runout. Clearly, if a model is sensitive to an uncertain input, then the estimated consequence is of little utility for a risk assessment. Some sensitivity analysis approaches have been suggested (Ferentchak & Jamieson (2008); Froehlich (2008)) but they are limited to addressing the sensitivity of the breach hydrograph to breach inputs. The end goal of a tailings dam breach study is to predict the consequences of failure, and runout characteristics (such as maximum runout distance, inundation area, flow depth, flow velocity, flood wave arrival time, and flood wave intensity) are of more use for consequence assessment (Jakob et al. (2011); Bureau of Reclamation (2015); Canadian Dam Association (Draft, 2020)). Therefore, breach sensitivity analyses should consider the runout.

Ongoing work at the University of British Columbia is addressing these issues. In this paper, we explore them using HEC-RAS 6.0. HEC-RAS is a publicly accessible hydrodynamic model developed by the US Army Corps of Engineers (Brunner (2021)). A systematic rheology calibration method is described, which facilitates more thorough and objective comparisons of modelled and observed inundation areas than single parameter calibration. The interaction of breach hydrographs and runout characteristics is demonstrated by inputting each breach hydrograph sensitivity scenario into the runout model. The numerical modelling, rheology calibration, and preliminary sensitivity analysis are demonstrated with a case study (1994 Merriespruit, South Africa). The complete assessment of model sensitivity and input uncertainty using multiple case studies is the next step in this project but is outside the scope of this paper.

2 MODELLING METHODOLOGY

2.1 *Background*

Ghahramani et al. (2020) and Rana et al. (2021) extensively examined tailings dam breach case studies. Parameters commonly associated with breach-runout impacts were compiled into novel databases and statistically evaluated. These databases form the basis for the cur-rent research and modelling work. The facility, breach, and runout observations reported in these two databases and the references therein allow for the modelling of events. A breach hydrograph is modelled for each case study using direct observations of the breach event or reported breach parameters. The runout is then simulated in HEC-RAS 6.0, with the Zone 1 inundation area (as defined by Ghahramani et al. (2020)) as the main measure of model accuracy.

2.2 *Breach Hydrograph*

Various methods or models have been used to simulate either water-retaining earthfill dam breaches or tailings dam breaches (e.g. Fread & Harbaugh (1973); Rico et al. (2007); Takahashi (2014); Petkovšek et al. (2020)), each with vastly different input requirements. Within these breach analysis methods is a spectrum of complexity, with trade-offs of sophistication for greater input requirements and effort. All methods involve some level of simplification, and their inputs and results need careful consideration. Physical experiments are needed to validate any simplification or suggest improvements for breach modelling, but there is limited work specific to tailings dam breaches. A series of experiments at Queen's University (see Walsh et al. (2019)) is being carried out to address this research gap for tailings dams.

The parametric method (Fread & Harbaugh (1973)) is well utilized in water-retaining earthfill dam breach studies (Wahl (1998); Wahl (2004); Froehlich (2008); Goodell et al. (2018)). With this method, the ultimate breach size, shape, and development time are defined by the user. The discharge from the facility is then dynamically computed using the common weir equation (Francis (1868)) as the breach weir increases and the stored volume decreases each timestep. The parametric approach can be suited for rapid failures such as Feijão. The breach development time is set to a nominally small amount to represent the rapid breach progress in structural or liquefaction failures.

The parametric approach has been adopted for the present modelling work, using the built-in tools in HEC-RAS. The flexibility of this approach lends itself to the many different breach types within the databases. The breach parameters are mostly reported for the case studies, avoiding the primary downside of the parametric method in forward analysis of estimating them through regression equations or other methods (as described in Wahl (2004) for water-retaining dams and

Martin et al. (2015) for tailings dams). Data such as geotechnical characteristics, rheology, or geometry of the depression in the facility post-failure are generally unreported or unavailable for most case studies in the database. This prevents the use of more sophisticated numerical methods. Lastly, when back-analyzing a dozen or more cases, simplicity and repeatability are desirable for practical reasons.

2.3 *Runout Modelling*

The software used for the numerical modelling of the runout is HEC-RAS 6.0. HEC-RAS is widely used in North American jurisdictions for water resource engineering and hydraulic analysis. It has features as robust as most commercially available hydraulic software, including: 1D, 2D (depth averaged flow), or 1D-2D hybrid flow; dam breach modelling; sediment transport and water quality analyses; and mapping, plotting, and animation tools (Brunner (2021)).

HEC-RAS was previously limited to Newtonian flow, which would not be appropriate for flow containing substantial solid volumes, commonly observed in tailings dam breaches. HEC-RAS 6.0 has now implemented common rheological formulations for single fluid flow (Gibson et al. (2021)). These options allow for the improved simulation of non-Newtonian flow characteristics needed for tailings dam breach modelling. In this study, a two-dimensional modelling approach with the quadratic rheological model, also known as the O'Brien formulation, is used (Gibson et al. (2021)).

A key input to any runout model is the representation of the terrain. Public global elevation data is available from various agencies, notably the Shuttle Radar Topography Mission (SRTM) or Advanced Land Observing Satellite (ALOS). The resolution of public data is usually 1 arc-second (roughly 30 m) and may not be an accurate representation of the bare earth (due to random errors or vegetation interference). Terrain data with better resolution and quality can be purchased from specialized suppliers, or local jurisdictions may also have publicly available data. A combination of the latter options has been used for the current modelling, to reduce the impact of erroneous terrain data on the modelled results. The exact source and quality of the terrain data will vary depending on each case. In HEC-RAS, the roughness of the terrain is represented with typical Manning's n values, as described in Chow (1959) and Arcement & Schneider (1989), based on aerial imagery and photographs taken before and after each back analyzed event as available.

The breach hydrograph developed using the observed breach parameters is input at the HEC-RAS model boundary in line with the breached facility, and additional model components are used, as necessary, for individual cases. The most common component is an outflow boundary condition for events where flow continues past the Zone 1 inundation area (as defined in Ghahramani et al. (2020)). Zone 2 tailings flows are much more challenging to model and are outside the scope of this work.

2.4 *Rheology Calibration*

The rheology is defined with the yield stress and viscosity using the quadratic formulation (Gibson et al. (2021)). Both values can vary in orders of magnitude across a range of volumetric solids contents for a given tailings sample, and across a range of tailings samples at a given volumetric solids content, as shown in O'Brien and Julien (1988). While there are direct case study observations or reasonable evidence for many of the breach hydro-graph inputs, there is typically little to no information on the tailings rheology. To address the challenging task of finding a set of rheology inputs that suit each case study, a program was written to explore the full range of rheology parameter combinations.

HEC-RAS can be automated through the RAS Controller, an application programming interface (API). After the model is set up using the conventional HEC-RAS interface and breach hydrograph developed using the observed breach parameters, a Microsoft Excel spreadsheet can control, run, and adjust the HEC-RAS inputs. Over 500 rheology simulations are run, stepping through the range of inputs on a log scale. The Zone 1 inundation area was selected as the primary measurement of model fit. The modelled inundation areas for individual simulations are automatically compared against the observed inundation areas mapped by Ghahramani et al. (2020) or Rana et al. (2021). The error is calculated by removing the overlapping areas between the observed and modelled inundation areas for all the simulations. The error from each simulation is then plotted in the model space of the rheology inputs.

2.5 *Sensitivity Analysis*

In the sensitivity analysis, each breach parameter input is varied by an arbitrary amount (such as a 10% increase) one at a time to produce a set of alternate hydrographs. These are then run in HEC-RAS to generate a set of alternate outputs (e.g., inundation area). The runout for each sensitivity hydrograph is then compared to the runout for the hydrograph developed with the observed breach parameters. All sensitivity simulations use the same rheology inputs, with an appropriate set as determined through the rheology calibration process described above.

3 EXAMPLE CASE STUDY

3.1 *Failure Narrative and Model Inputs*

The Harmony 4A facility was an upstream constructed tailings facility adjacent to the vil-lage of Merriespruit, South Africa. On February 22, 1994, a thunderstorm brought 50 mm of rain in 30 minutes and the sudden influx of water resulted in heavy seepage and some overtopping at the north embankment of the facility. Some time after the pond discharge began, the dam collapsed, releasing a flood wave towards Merriespruit that inundated an area of almost 900,000 m2 and killed 17 people (Wagener (1997); Ghahramani et al. (2020); Rana et al. (2021)). The thin up-stream dam and marginal stability of the Merriespruit dam likely meant that little erosion would need to have occurred before static liquefaction became the dominant breach process. Eyewitness accounts described the breach as a “loud bang” or a “series of explosions” (Wagener, 1997; Blight & Fourie, 2005), which are interpreted as the onset of liquefaction and collapse of the dam.

The dam height was 31 m at the time and location of the failure. The total released volume (including both tailings and free water) was approximately 630,000 m3, and the mean crest width of the breach channel was reportedly ~150 m. No information is publicly available on the rheology of the tailings. The terrain data obtained for the modelling is the WorldDEM™ digital terrain model (DTM), at a 12 m resolution (Airbus Defence and Space (2015)). The terrain resolution is coarse, however the environment is quite flat (at around 1% slope), and it is not uncommon for dam breach studies to use 30 m resolution terrain given their large spatial extent.

Two breach parameters, breach width and release volume, are used for preliminary sensitivity analysis. In individual scenarios, each parameter is increased by 10% from their observed values while all other parameters are held constant. These sensitivity analysis hydrographs are input into HEC-RAS to observe the change in runout characteristics.

3.2 *Results*

Figure 1 shows the breach hydrograph created with the parametric method, as described above, for the failure event. The main breach is the focus, and the preceding overtopping flow is ignored for the purpose of the modelling. Figure 2 shows the hydraulic modelling result completed in HEC-RAS. The rheology values were informed by and iterated using the results of the rheology calibration plot discussed below.

Figure 3 shows an example result of the rheology calibration program for the Merriespruit modelling. Finally, Figure 4 compares inundation areas for the preliminary sensitivity analysis for the event.

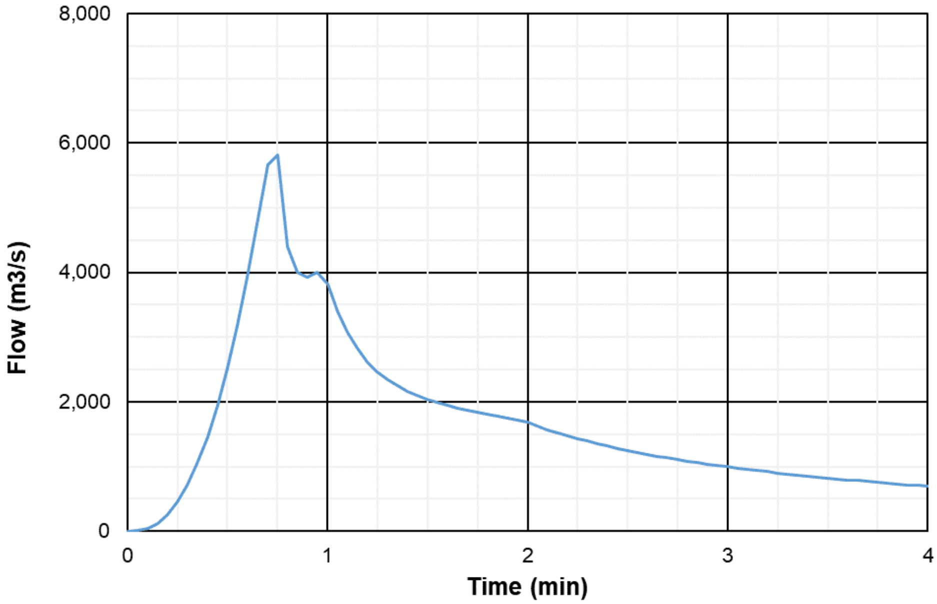

Figure 1. Modelled breach hydrograph for Merriespruit.

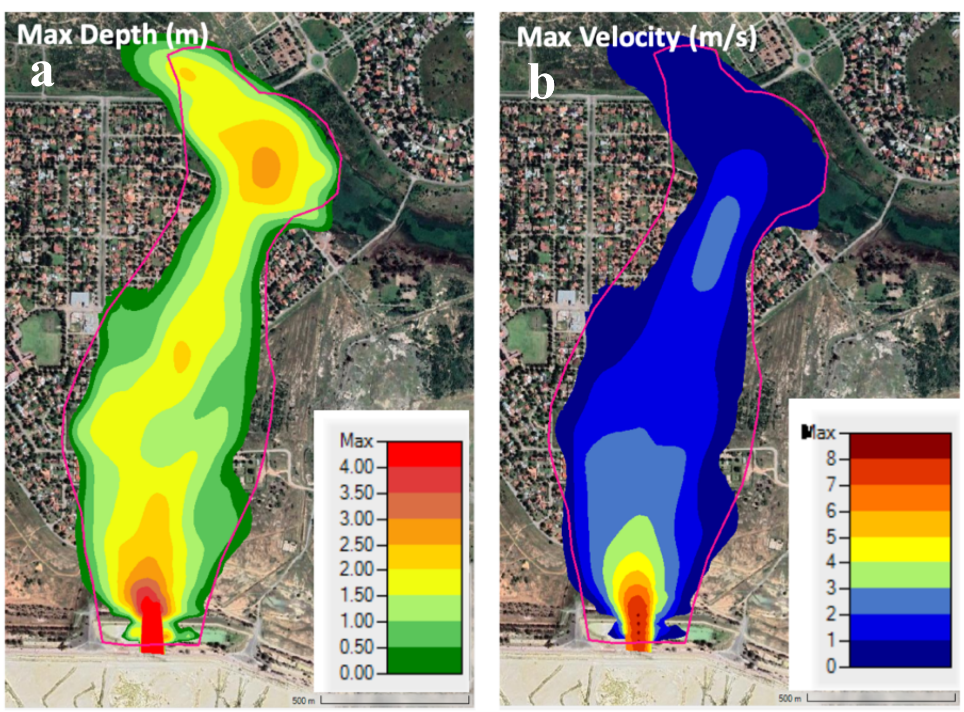

Figure 2. Modelled HEC-RAS runout results for the Merriespruit failure. Figure 2a shows the maximum simulated flow depth while Figure 2b shows the maximum simulated velocity. In both figures, the magenta outline represents the observed inundation area, as mapped by Ghahramani et al. (2020).

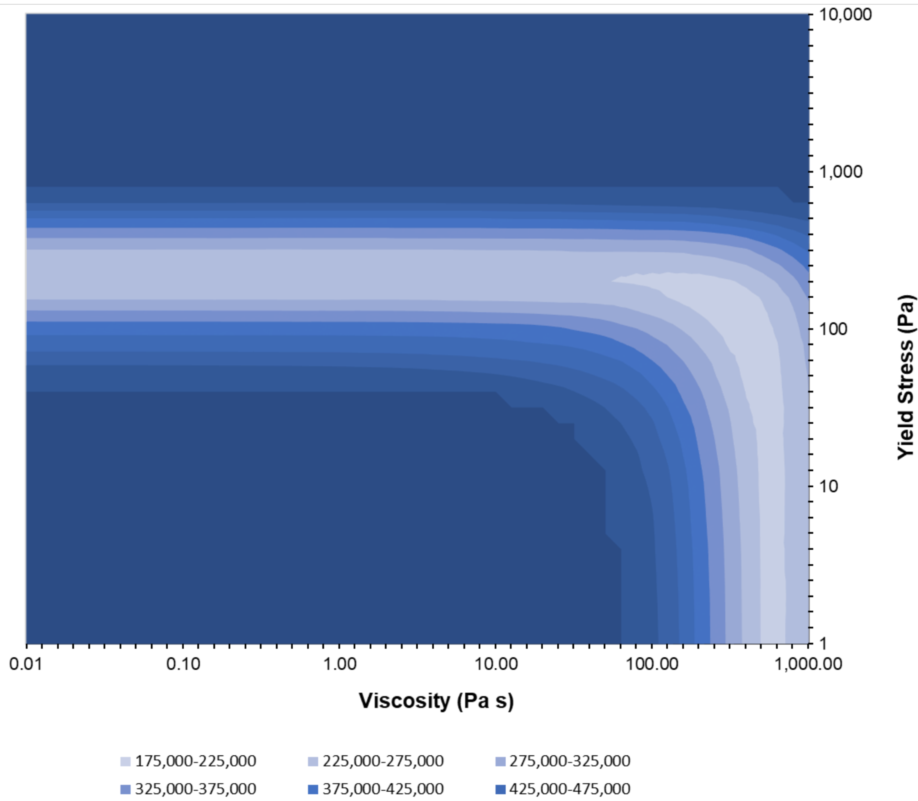

Figure 3. Variation of modelled inundation area error with variation of rheology inputs for the modelled Merriespruit results. Lighter colours are lower area error, with error area in m^2. Tick marks are in log-log scale.

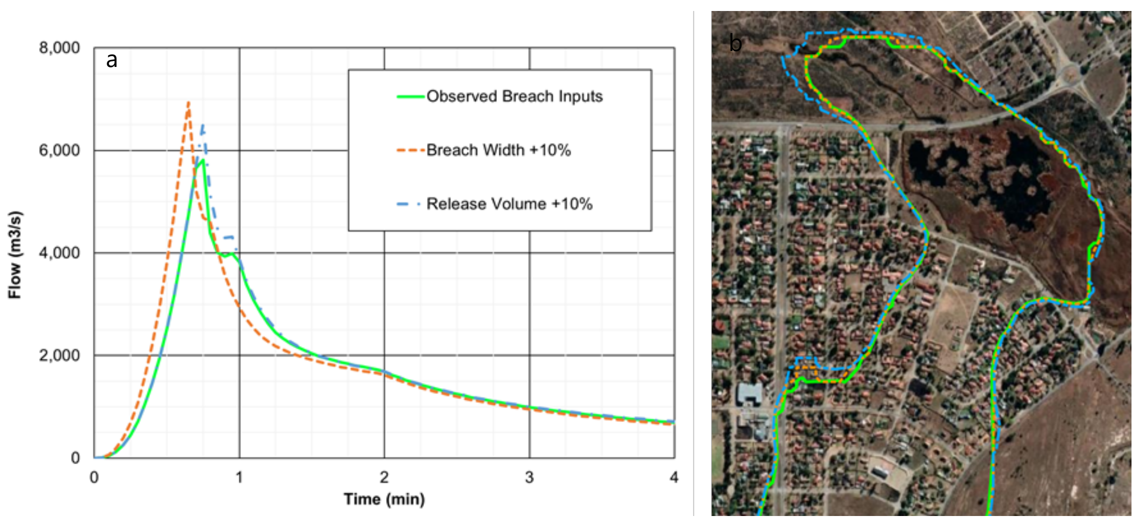

Figure 4. Preliminary sensitivity results. Figure 4a shows the breach hydrographs while Figure 4b shows a closer view of the modelled inundation area near the distal limit. The green elements represent the hydrograph and inundation area with the observed breach parameters. The orange and blue elements represent the same information for the breach width and release volume sensitivity runs, respectively.

4 DISCUSSION

4.1 *Breach and Runout Modelling*

The peak discharge of the modelled hydrograph occurs within a minute, matching the de-scription of rapid erosion and progress to liquefaction. The second local peak represents the switch from the pond and liquefied tailings discharge to liquefied tailings discharge only. Petkovšek et al. (2020) used an erosional breach model to estimate the breach for Merriespruit, and humps can also be observed in their results (see Figure 12 in Petkovšek et al. (2020)).

Overall, the modelled runout results match the observed inundation area, with over 80% of the observed inundation area being correctly modelled. The modelled depths also align with the ob-servations of highwater marks and eyewitness accounts.

4.2 *Rheology Calibration*

Figure 3 illustrates the non-uniqueness of calibrated rheological parameters with respect to inun-dation area as the model constraint. The rheology inputs associated with the lowest area error span more than two orders of magnitude in yield stress and almost an order of magnitude in viscosity. Despite the wide range in values, the actual band of minimum error is narrow.

The rheology calibration should be considered in relation to all the other inputs. Using alternate Manning's n values, terrain data, hydrograph, rheology formulation, or even other software may result in a different contour plot result. Additional rheology formulations such as the Bingham, Herschel-Bulkley, or Voellmey could be considered,

As the plot is only of the model space, further interpretation could provide a narrower range of realistic rheology values. This interpretation could be informed using any available characteriza-tion of the tailings material for each case along comparisons to other similar tailings with meas-ured rheology (such as in O'Brien and Julien (1988)). If there are reliable narratives or descrip-tions of depths (final or maximum), velocities, or arrival times in the runout area, they can be used as a secondary measure of model fit to aid the rheology interpretation. The data for tailings or runout characterization is not available for most of the cases, leading to the reliance on the Zone 1 inundation area as the primary measurement of model fit.

4.3 *Sensitivity Analysis*

The variations in the two breach inputs increased the peak discharge as expected. The re-leased volume variation produced a smaller peak discharge compared to the breach width variation. In-tuition would suggest using the hydrograph with the greater peak is more conservative. By con-trast, the inundation area was markedly larger for the hydrograph with a greater release volume compared to the increased width. This demonstrates the unintuitive interactions between breach and runout modelling that need to be quantified.

Furthermore, a 10% variation in breach parameters is relatively small compared to the uncer-tainty associated with estimating them. Wahl (2004) found breach parameters could span an order of magnitude between breaches of similar dams. This also shows the need to assess both model sensitivity and input uncertainty.

4.4 *Concluding Remarks and Future Work*

The preliminary work presented shows HEC-RAS 6.0 can be used for runout modelling of tailings dam breaches. It also demonstrates that simple sensitivity analysis for only the breach hydrograph does not fully address sensitivity of the consequence of failure to breach inputs.

The University of British Columbia is a member of the CanBreach project, a consortium of three universities and five industrial partners. The physical experiments at Queen's University and forensic and statistical assessments of case studies at the University of Waterloo and UBC support the numerical modelling, demonstrating the importance of multiple avenues of research.

Additional work is planned to include a wider range of breach parameters, beyond breach width and release volume that were the focus of this manuscript. The sensitivity of other runout charac-teristics (e.g., arrival time or flood wave intensity) may not follow the same trend as inundation area nor be as relevant to a given forward analysis. Additional classification of the case studies (such as in Rana et al. (2021)) could improve trends and conclusions for forward analysis as well. There is potential to model up to 36 cases from the database, but the final number may be less due to insufficient data or other practical constraints. To date, 7 cases in total have been modelled or are in progress. Only when a large database of modelled case studies has been completed could trends have sufficient consistency to be relied on, as sensitivity results from a single case study should not be applied to forward analysis. After the numerical modelling is completed, the main assessment of the model sensitivity and input uncertainty can proceed.

5 ACKNOWLEDGEMENTS

This research is part of the CanBreach Project, which is supported by funding through an NSERC Collaborative Research Development Grant and from the following industrial partners: Imperial Oil Resources Inc., Suncor Energy Inc., BGC Engineering Inc., Golder Associates Ltd., and Klohn Crippen Berger. Funding is also provided by Geoscience BC for the primary author.

6 REFERENCES

Airbus Defence and Space. 2015. WorldDEM™. Technical Product Specification. Version 2.0.
Arcement, G.J. & Schneider, V.R. 1989. Guide for Selecting Manning's Roughness Coefficients for Natural Channels and Flood Plains. *US Geological Survey Water-Supply Paper 2339.* U.S. Dept. of the Interior, US Geological Survey. Denver, Colorado.
Blight, G.E., & Fourie, A.B. 2005. Catastrophe revisited – disastrous flow failures of mine and municipal solid waste. *Geotechnical and Geological Engineering* 23:219-248.
Brunner., G.W. 2021. HEC-RAS User's Manual. US Army Corps of Engineers, Institute for Water Resources, Hydrologic Engineering Center. Davis, California.
Bureau of Reclamation. 2015. RCEM – Reclamation Consequence Estimating Methodology Interim Guidelines for Estimating Life Loss for Dam Safety Risk Analysis. U.S. Dept. of the Interior, Bureau of Reclamation. Denver, Colorado.
Canadian Dam Assocation. 2020. Technical Bulletin: Guidelines for Tailings Dam Breach Analyses (Draft)
Chow, V.T., 1959. *Open Channel Hydraulics*. New York: McGraw-Hill.
Ferentchak, J.A. & Jamieson, S.L. 2008. Using Erosion Rate to Refine Earth Dam Breach Paramaeters. *Proceedings of the Association of State Dam Safety Officials Annual Conference.* Indian Wells, California.
Francis, J.B. (2nd ed.) 1868. Lowell Hydraulic Experiments. Lowell: David Van Nostrand.
Froehlich, D.C. 2008, Embankment Dam Brach Parameters and Their Uncertainties. *J. Hydraul. Eng.* 134(12): 1708-1721.
Fread, D. L., & Harbaugh, T. E. 1973. Transient hydraulic simulation of breached earth dams. *J. Hydr. Div*. 99(1), 139–154.
Ghahramani, N., Mitchell, A., Rana, N.M., McDougall, S., Evans, S.G., & Take, W.A. 2020. Tailings-flow runout analysis: examining the applicability of a semi-physical area–volume relationship using a novel database. *Nat. Hazards Earth Syst. Sci.* 20: 3425-3438.
Gibson, S., Floyd, I., Sánchez, A., & Heath, R. 2021. Comparing single-phase, non-Newtonian approaches with experimental results: Validating flume-scale mud and debris flow in HEC-RAS. *Earth Surf. Process Landforms* 46:540-553.
Goodell, C., Johnson, D., Raeburn, R., Monk, S., Karki, A., & Lee, A. 2018. Probabilistic dam breach modelling using HEC-RAS and McBreach. *Proceedings of the United States Society on Dams' 38th Annual Conference & Exhibition*. Miami, Florida.
Hall, J.W., Boyce, S.A., Wang, Y., Dawson, R.J., Tarantola, S., & Saltelli. 2009. A. Sensitivity Analysis for Hydraulic Models. *J. Hydraul. Eng.* 135(11): 959-969.
Jakob, M., Stein, D., & Ulmi, M. 2011. Vulnerability of buildings to debris flow impact. *Nat. Hazards* 60:241–261.
Martin, V., Fontaine, D., & Cathcart, J. 2015. Challenges with conducting tailings dam breach studies. *Proceedings of Tailings and Mine Waste 2015*. Vancouver, British Columbia.
O'Brien, J.S., & Julien, P.Y. 1988. Laboratory Analysis of Mudflow Properities. *J. Hydraul. Eng.* 114 (8):877–887.
Petkovšek, G., Hassan, M.A.A.M., Lumbroso, D., & Collell, M.R. 2020. A Two-Fluid Simulation of Tailings Dam Breaching. *Mine Water and the Environment* 40:151-165.

Rana, N.M., Ghahramani, N., Evans, S.G., McDougall, S., Small, A., & Take, W.A. 2021. Catastrophic mass flows resulting from tailings impoundment failures. *Engineering Geology* 292(2021): 1-20.

Rico, M., Benito, G., Díez-Herrero, A. 2007. Floods from tailings dam failures. *J. Haz. Mat.* 154: pg 79–87.

Takahashi, T. (2nd ed.) 2014. Debris Flow. London: CRC Press.

Santamarina, J.C., Torres-Cruz, L., & Bachus, R.C. 2019. Why coal ash and tailings dam disasters occur. *Sci.* 364 (6440): 526-528.

Wagener, F. 1997. The Merriespruit slimes dam failure: Overview and lessons learnt. *SAICE Journal* 39(3): 11-15.

Wahl, T.L. 1998. 'Prediction of embankment dam breach parameters: A literature review and needs assessment. *Dam Safety Rep. No. DSO-98-004*, U.S. Dept. of the Interior, Bureau of Reclamation. Denver, Colarado.

Wahl, T.L. 2004. Uncertainty of predictions of embankment dam breach parameters. *J. Hydraul. Eng.* 130(5): 389–397.

Walsh, A., Take, W.A., McDougall, S., & Evans, S.G. 2019. Physical Modelling of Tailings Dam Breach. *Proceedings of Tailings and Mine Waste 2019*. Vancouver, British Columbia.

Regional perspectives and trends of land at risk from tailings storage facility failures.

Sally Innis, Jared Lynd & Nadja Kunz
University of British Columbia, Vancouver, Canada

Laurie Reemeyer
Resourceful Paths Consulting, Vancouver, Canada

ABSTRACT: The potential consequences of tailings storage facility (TSF) failures are not well understood from a systems perspective, with most risk analyses focussing on site-by-site analyses at fixed points in time. There is an urgent need to better understand potential TSF consequences that may arise across different spatial and temporal scales so that management and policy interventions can be better designed. This study demonstrates the utility of a novel model developed to map how potential TSF failures may impact environments on a regional scale. By using a recalibrated Geographic Information System-based lahar-inundation model (Laharz), originally presented on at Tailings and Mine Waste 2020, we simulate potential failure scenarios from 110 North American TSFs. We develop an initial methodology for a regional TSF failure consequence analysis by analyzing the extent to which land cover intersects with the modelled inundation zones from potential TSF failures. The methodology garnered from this study can be used as a high-level guide for policymakers to better understand the potential consequences of TSF failures better and may inform the development of policy intervention targeting key land types, such as forests, that may be more at risk and thereby, ultimately build towards more robust tailings management.

1 INTRODUCTION

The Global Tailings Standard and industry bodies have continuously underlined that Tailings Storage Facility (TSF) governance, management and standards must go beyond purely technical deliverables for maintenance (ICMM, 2020). Consequence and risk assessments of TSFs are arguably the most impactful tool in internal and external communication and decision making around monitoring and management. Currently, consequence assessment and risk assessments of potential TSF failures through dam breach inundation studies are conducted at the local and site level. The recent work to publicly disclose location and data on TSFs globally by the Global Tailings Review and Global Tailings Disclosure (GTD), allows for a perspective shift, moving from only a local scale understanding of consequence to also include a regional scale understanding. This shift in perspective has highlighted issues of concern with important implications for overall tailings management and governance. For example, data from the Global Tailings Disclosure revealed that TSFs with a higher reported consequence rating are more likely to have reported stability issues (Franks et al., 2021). It is therefore little wonder that the potential impacts on the surrounding environment, communities, Indigenous rightsholders and broader society are also becoming increasingly important from a range of perspectives.

Outside of the context of TSFs, trends in regional and global pressure on environmental systems from mining and extractives are relatively well studied (Murguía et al., 2016; Sonter et al., 2014; Tost et al., 2020). The regional and global nature of these studies enables mining stakeholders to understand the pressure on environmental systems and can orientate policy discussion on how to best avoid or minimize further environmental degradation. The compilation and analysis of TSFs by Franks et al. (2021) has demonstrated the importance of understanding global distribution of TSF risks. For example, the GTD has revealed that of the 1,743 facilities in the GTD, 29% have not considered the downstream effects of a hypothetical failures. As highlighted through their research, there are consequence trends that need to be further analyzed on regional and global scales. Importantly, a regional, national or global analysis of the potential consequences of TSF failures has not been undertaken. Owen et al.'s (2019) analysis screened 328 TSFs using ESG indicators to identify high-risk facilities and found that 55 projects were located in high risk contexts and 33 of those were additionally located in proximity to communities. The authors highlight the need for a more comprehensive approach to TSF risk disclosure, acknowledging the difficulties with conceptualizing risk with the current TSF disclosure levels.

This paper presents preliminary results aimed to further understand the distribution of risks and consequences of potential TSF failures by making two important academic advances. First, the work applies a recalibrated semi-empirical Laharz model (Innis et al., 2020) to quantify the potential consequence of TSF failures, which addresses the information comprehension disparities laid bare by Owen et al. (2019). Second, a methodology is developed which focuses on the distribution of risk from potential TSF failures to the surrounding environment through Land Cover and Land Cover Change (LCLCC) datasets. LCLCC information, such as Copernicus Global Land Cover 100m, used in this study, presents spatial information of different classes of physical coverage of the Earth including forests, cropland and wetlands. The use of LCLCC data is the basis of much research around the impact of mining on ecosystem services, biome and biodiversity pressure (Kobayashi et al., 2014; Murguía et al., 2016; Tost et al., 2020). LCLCC data allows for an analysis of the direct and cumulative impacts of mining to a broad range of ecosystem classes. Outside of high value land uses such as crop lands and populated areas, land cover and use data are not widely examined during consequence assessments and Tailings Dam Breach Analyses (TDBA; ICMM, 2020; Kheirkhah Gildeh et al., 2020; Martin et al., 2015). Therefore, an analysis of the macro-trends of LCLCC at risk from failure reveals trends of areas most at risk from failures not previously captured at the site level and may encourage broader scopes within failure mitigation measures. Despite the focus on LCLCC, the basis of this research presents a novel methodology to perform high-level, regional or global consequence assessment and will be suitable for applications outside of LCLCC.

1.1 *Regional Tailings Consequence Mapping*

Tailings flow behavior may vary widely based on factors including, but not limited to, the presence of surface water, embankment configuration, failure mechanism, solids content, liquefaction potential and downstream topography (Martin et al., 2019; Small et al., 2017). The variety in tailings compositions between mine sites contributes to the complex nature of modelling tailings flows. The use of modelling to extrapolate the potential areas at risk from TSF failure and in dam breach inundation studies is commonly done through use of numerical models. Numerical models offer representation of the characteristics of flow, however, require site specific data and often data dense, expensive programming (Wang et al., 2018). The use of empirical models for local-scale and site-specific tailings flow inundation assessments is seldom justified due to the level of uncertainty associated with the complexity of the flows (Rana et al., 2021). However, the authors argue that empirical modelling within a probabilistic framework has the potential to be used to aggregate statistics and develop hazard assessments on a regional or even global scale to guide policy or stakeholder/rightsholder engagement.

The results of dam breach inundation studies determine the physical area impacted by a potential failure and are used to inform the consequence classification, emergency preparedness and response planning (Mining Association of Canada (MAC), 2017). The dam failure consequence classification from the Global Industry Tailings Standard includes an analysis of the potential population at risk, potential for loss of life, impact to critical habitats, toxic water release, health, social and cultural impact as well as potential for infrastructure and economic costs (ICMM, 2020). Prospective TSF consequence research at the regional scale has not been explored. Regional understanding of risk can be directed towards investors and policy makers and may allow for better informed decisions on portfolio level ESG risk exposure, compensation for land impacts and required pre-financing for rehabilitation and closures costs, for example.

2 METHDOLOGY

The methodology for the consequence analysis of potential TSF failures at a regional scale is completed in two phases. The first phase is data collection and analysis through the application of the automated and recalibrated Laharz model (Innis et al. 2020). Uncertainty is incorporated in the model through the potential release volume (V_F). The second phase is the geospatial analysis and data aggregation of the LCLCC potential impact analysis. The following subsections detail a short summary of the Laharz model for tailings flows, TSF site selection and data analysis for the regional mapping work.

2.1 *The Laharz model and its application for tailings flows*

To investigate the potential consequences of tailings flows, an inundation model is required. Building off research presented at Tailings and Mine Waste 2020 (Innis et al. 2020), the recalibrated Laharz model was applied to the regional scale across North America. Laharz is an ArcGIS plug-in program originally created to delineate areas of potential lahar inundation based on one or more user-specified volumes (Iverson et al., 1998) and has since been recalibrated to include modelling of debris flows and rock avalanches (Griswold and Iverson, 2008). The program is based on the empirical relationship shown in Equation 1.

$$A \ or \ B = c_{A \ or \ B} V^{2/3} \qquad (1)$$

Where A and B are the total planimetric and maximum cross-sectional inundation areas, respectively, V is the total flow volume and c is an empirical coefficient related to flow mobility (Iverson et al., 1998; Schilling, 2014).

The research done by Ghahramani et al. (2020) and Innis et al. (2021) worked to test and calculate the planimetric and cross-sectional mobility coefficients for tailings flows and subsequently recalibrate and automate the Laharz model for use in tailings flow mapping at the regional scale. Research by Ghahramani et al. (2020) found that c_A for tailings flows is 80 and current research validating the Innis et al. (2020) paper found that c_B for tailings flows is 0.1. Comparatively, lahars have a planimetric and cross-sectional mobility coefficient of 200 and 0.05, respectively, whereas rock avalanches mobility coefficients are 20 and 0.2 (Iverson et al., 1998; Griswold and Iverson, 2008).

The Laharz program requires volume estimates of the modeled flow event, an underlying digital elevation model (DEM), flow path data derived from the DEM and identification of the source areas where the flow may originate to delineate potential areas inundated by a flow as it descends a given drainage (Schilling, 2014). The output of Laharz is a final merged polygon file delineating the downstream area of inundation data for each TSF failure for each given release volume.

2.2 *Spatial Resolution and case filtration*

A benefit of the automated, semi-empirical model, Laharz, lies in its unique ability to run a significant number of hypothetical TSF failures with data available from the GTD without the need for copious time and computing power. In the current paper, an analysis is completed at the regional scale of North America (with the exclusion of non-continental North American countries) to show the potential impacts of TSF failures on wide range of land classifications.

The TSF locations, height and volume information is sourced from GTD data compiled by Franks et al. (2021). The database is estimated to contain approximately 20% of the global distribution of TSFs, however, the countries chosen within this study are well represented within the GTD. Prior to inundation zone modelling, filtration of the GTD is required for use in the Laharz program. To avoid double counting of potential consequences, a single TSF was selected for mine sites with multiple TSFs. TSFs at mines were selected based on a higher consequence rating or the topographic location (the most downstream facility.) Prior to filtration, the GTD contained 220 mines containing at least one TSF in continental North America; the GTD was then filtered given the following criteria and reasoning: (1) TSFs with incomplete data on current and projected storage volumes; (2) TSFs listed as non-conventional storage types such as dry-stack because the recalibrated Laharz model is calibrated based on conventional, saturated tailings flows; and (3) the Laharz program does not perform well with small facilities, therefore TSFs with a height of less than ten (10) meters were not included. Following the filtration method, 173 mines were listed for inclusion in the final analysis. However, more mines were excluded due to DEM or facility visual identification issues leaving 110 for analysis. Therefore, this sample represents half of the facilities across continental North American and 65% of all facilities with applicability to the Laharz program.

2.3 *Laharz input generation*

As discussed in Section 2.1, the recalibrated Laharz program requires several inputs, including sourced and calculated data. The methodology for retrieving the input data for each site is briefly discussed in the following subsections:

2.3.1 *Digital Elevation Model (DEM):*

The most important dataset in required to run the Laharz program is the DEM (Schilling, 2014). Multiple DEM sources cover continental North America. The ALOS PALSAR Global Radar Imagery (JAXA/METI, 2007) and the Shuttle Radar Topography Mission (SRTM; USGS EROS, 2000) were used as the source of DEMs for this project. Both satellite data are freely accessible and provides full and continuous coverage of the North American continent with a 30m spatial resolution.

2.3.2 *Release Volume:*

The final volume of tailings released from a facility is one of the most important input variables to TDBAs (Quelopana, 2019). Historically, the final release volume of TSF failures range significantly from 1% to 100% of the total impounded volume. This variation is due to many factors including the type and volume of the facility, the volume of stored water, dam height or failure mechanism (Martin et al., 2015; Rourke and Luppnow, 2015). Empirical relationships have been developed and tested which estimate the release volume as a factor of the total impounded volume (Concha Larrauri and Lall, 2018; Kheirkhah Gildeh et al., 2020; Quelopana, 2019; Rico et al., 2008). Concha Larrauri & Lall (2018) is the most recent extension of the highly popular Rico et al. (2008) empirical equation, where V_F is the final release volume and V_T is the total impounded volume at the time of failure:

$$V_F = 0.332 \times V_T^{0.95} \qquad r^2 = 0.887 \tag{3}$$

Laharz has the capability of running up to seven release volumes simultaneously. This functionality is exploited to incorporate the uncertainty associated with the release volume of a TSF. Concha Larrauri & Lall's (2018) equation is used to calculate the mean release volume of each facility (MPL). To account for the uncertainty in the volume estimates and show a range of scenarios within prediction intervals, an upper prediction limit (UPL) and lower prediction limit (LPL) is constrained to the upper and lower 50% confidence interval around the V_F regression model, respectively. Given the incorporation of uncertainty around the release volume, the final output of the automated and recalibrated Laharz model comprises of 110 nested hazard maps delineating zones of potential hazard downstream of TSFs across North America. The nested hazard maps were mapped with decreasing degrees of hazard based on the predicted release volumes (LPL, MPL, UPL).

2.3.3 *Slope and Cone Apex:*

The slope and cone apex are selected manually and calculated using the topography data derived from a local DEM. The process of calculation differs based on the orientation and construction type of the TSF and will mirror the outflow patterns from historical TSF failures of similar configurations. For example, for upstream valley filled facilities, the cone apex is selected as the highest point of elevation within the dam structure and the slope is calculated from that point, perpendicular to the embankment. TSFs layout types in flat topography such as ring dykes, have greater degree of uncertainty with the selection of Laharz inputs due to the difficulty in predicting points on the dyke where a failure may occur. For facilities with ring dyke configurations, the slope is calculated from the cone apex, noted as the highest point of elevation on the facility to the lowest point of elevation on the toe of the dam, perpendicular to the embankment.

2.4 *Land cover analysis*

Data for the land cover analysis is obtained from the Copernicus Global Land Cover 100m dataset (Copernicus; Buchhorn et al., 2020). Copernicus is the most recent and extensive land cover dataset available. These data comprise a raster record of 22 land cover classification types, 12 of which are discrete forest type classifications; for this analysis, the discrete forest classification types were further categorized as Open Forest and Closed Forest for comparison. Table 2 summarizes the land cover classifications analyzed.

Table 2. Copernicus land cover classifications and definitions.

Land Cover Class	Definition
Closed Forest	Land covered with dense tree canopy >70% enclosed
Open Forest	Land cover with 15-70% trees and second layer-mixed shrubs and grasslands
Shrubs	Woody perennial plants <5m tall.
Herbaceous Vegetation	Plants without persistent stems of shoots over ground and lacking definite structure (< 10% tree and shrub cover)
Herbaceous Wetland (Wetland)	Land covered with a permanent mixture of water and herbaceous of woody vegetation
Moss and Lichen	Moss and lichen
Bare/sparse vegetation	Lands with exposed soils, sand or rocks. No more than 10% vegetation cover throughout the year.
Cultivated vegetation/agriculture (Cropland)	Land covered by temporary crops followed by a harvest period
Urban/ built up	Land covered by manmade structures
Snow and Ice	Land covered by snow and ice, year-round
Permanent Water bodies	Lakes, reservoirs, and rivers
Open sea	Oceans, seas (fresh or salt water)

To determine the potential impact of TSF failures on land cover types, the Laharz output polygons were overlaid with the Copernicus land cover dataset outputting the aggregate impacted area on each land cover type for the low prediction limit release volume (LPL), the mean prediction limit release volume (MPL) and the high prediction limit release volume (UPL) at each failure. The exercise was carried out separately for each failure.

3 RESULTS AND DISCUSSION

3.1 *Land Cover at Risk from Potential TSF Failures*

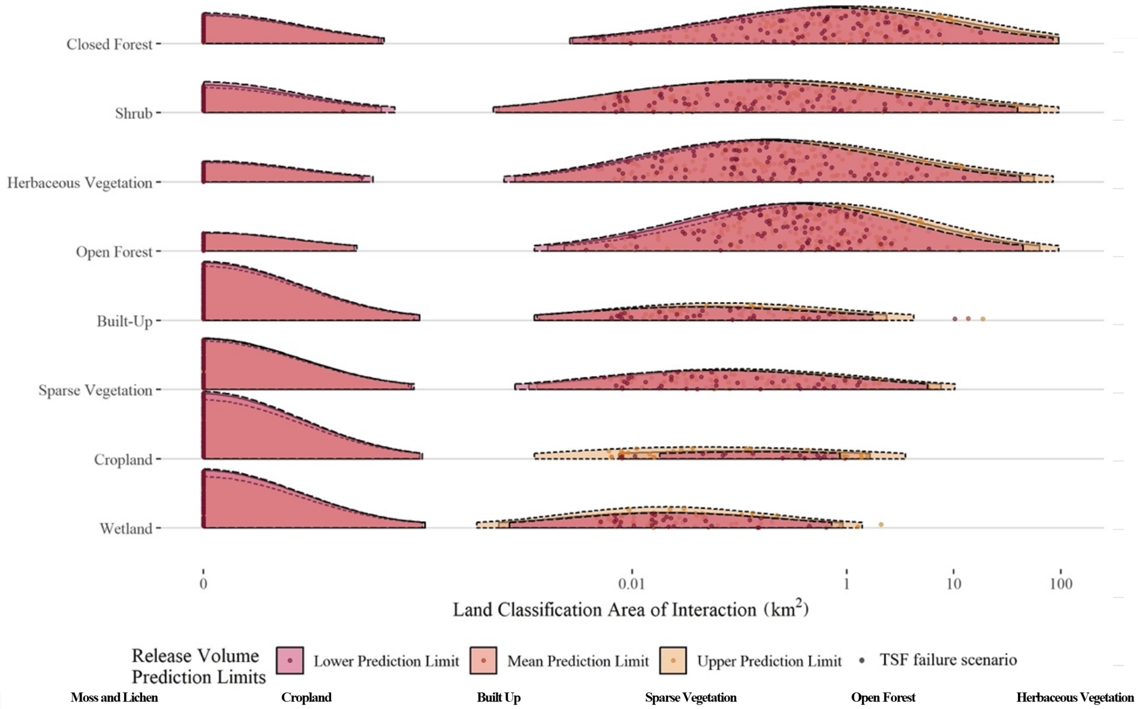

Figure 4. Percentage of failures with interactions with land classification types. The error bars denote the UPL, MPL and LPL of release volume scenarios.

Mining operations with applicable TSF were widely distributed across the continental North America. The interaction and degree of interaction between failures and land classification was measured. An interaction is a defined as cases where a land classification falls within the TSF failure inundation polygon; therefore, an interaction is a binary measure where the failure polygon either interacts with a land classification or does not. Whereas the degree of interaction is the cumulative area of land classification impacted within each failure polygon. All failures interacted with multiple land classifications. Herbaceous vegetation and open forest land classifications interacted with upwards of 70% of the TSF failures (Figure 4). With the open forest classification interacting with approximately 75% of the cases. Closed forests and shrubs demonstrated interactions with potential failures in approximately 65% of total cases. Several land classifications only had a single or no interactions with failures, including open seas, moss and lichen and snow and ice. While the cropland and wetlands land classifications interacted with failures in less than one-third of the cases, the release volume probability spread impacted these classifications the most. Failures interacted with permanent waterbodies in approximately 35% of the cases; given the limitations of the Laharz program for modelling flow within waterbodies, the degree of interaction between waterbodies and failures was not measured.

Figure 5 shows the impact scenarios for all 110 TSF cases run through Laharz for each land classification type. Considering the degree of interaction between the failures and land classification types, the closed forest classification had the highest average area impact for the upper, mean and lower release volumes. The average area of interaction for cases not including non-zero impacts for closed forests ranges between 2.0 and 3.0 km^2. Whereas croplands and wetlands have the lowest area of impact across all cases with small spreads. Approximately 25% of the cases interacted with built -up land with an average impact of less than one square kilometer. It is important to note that a single failure had a significant interaction with built-up land

(>10km^2) which impacted the average area of impact. This facility's hazard classification is marked as extreme.

Figure 5. The degree of interaction of potential TSF failures in North America with land cover classification types in log scale. Each point represents a single TSF failure modelled for three volume scenarios; points at the 0 mark did not interact with the specified land classification.

In evaluating both the interaction and degree of interaction between failures and land cover classifications, the results from the preliminary analysis of land cover impact from potential TSF failures across North America show that there are four land cover classifications (closed forests, open forests, shrubs and herbaceous vegetation) that are more likely to be at risk in terms of interaction and degree of interaction with the modelled failures compared to the other land cover classifications. Regional and global spatial coincidence between mining leases and forests is a growing area of research in conservation science. While much of this body of research focusses on tropical forests and the direct deforestation due to mining activity, particularly in the Amazon, the need improved understanding of potential direct and indirect impacts from mining on forests across spatial and temporal scales is continuously highlighted as necessary (Murguía et al., 2016; Sonter et al., 2020, 2018; Tost et al., 2020). As shown through our analysis, TSF failures present a direct risk to forests across North America as well as a direct risk and indirect risk to biodiversity through habitat loss.

The recent and historical TSF failures underline the necessity of extreme efforts to prevent future failures. Failures represent the conversion of environmentally or economically valued land to land with zero value – destroying the service the land cover paid to humanity at all scales. In the case of historical failures, remediation efforts have been prolonged (Vandeberg et al., 2010), left barren landscapes with no vegetation on land or in aquatic systems (Eriksson and Adamek, 2000) or impacted the growth of native plant species prompting different species types in remedial efforts (Cruz et al., 2020). No remedial efforts return the land to its full pre-failure value. Adopting a systems perspective to navigate mitigative measures for built facilities as well as proposed facilities will work to improve decision making for both the human and natural systems at risk.

3.2 *Laharz performance and limitations*

As demonstrated by an LCLCC analysis across North America, the recalibrated Laharz program is a novel model for regional scale consequence analysis of TSF failures. The model performs efficiently and objectively for over 100 TSFs. The use of a simple, automated semi-empirical model such as Laharz at a regional scale can be used to generate understanding, reframe problems, create opportunities for learning and lead to further exploration. The use of semi-empirical models does not preclude the use of complex numerical models should data be available to support these for specific TSFs.

Given the simplicity of the recalibrated Laharz model, there are known limitations that exist with its application. Traditional inundation area mapping exercises completed at the site-level or local scale are derived using detailed, computation heavy numerical modelling. A model based on semi-empirical equations is less reliable at the local scale. The highly variable nature of tailings contributes to the complexity needed to model tailings flows following failure events. However, a reduction in the complexity of the model allows for an introduction of a consequence analysis on a regional scale. The recalibrated Laharz model should not be used at the site or local scale, particularly when numerical modelling is available. As previously discussed, the recalibrated Laharz program does not adequately model inundation extents in flat waterbodies. The findings related to the interaction of a TSF failure with a waterbody is important and therefore were included in the analysis. However, the degree of interaction (area of the waterbodies potentially impacted) was not further analyzed. As seen in historical failures such as the Samarco failure, where tailings were transported over 600km due to its confluence with the Rio Doce (Burritt and Christ, 2018), the interaction of tailings and waterbodies can leave significant impact on the affected area. Therefore, the model's inability to predict the extent of impact of tailings within waterbodies is a major limitation to understanding a complete picture of potential impact to the downstream area of TSFs.

The actual impacts of a TSF failure pertaining to and beyond LCLCC impacts are context dependent. Therefore, the exclusion of small facilities (heights ≤10m) would then have ancillary impacts on the land cover interactions documented across North America. For the inclusion of smaller facilities in a regional consequence analysis like the one done in this study, further. refinement of the Laharz model would be required.

3.3 *Policy implications and future research directions*

Despite the above limitations, the recalibrated Laharz model provides a step-off point for high-level regional mapping of potential TSF failures. This research has revealed that TSF failures in North America are most likely to pose risks to forests and low-lying vegetation such as shrub and herbaceous vegetation. Laharz can quantify the potential area of forests at risk from failures, however, it is yet to have functionality to quantify the secondary losses of the potential land use and habitat to the ecosystem, local communities and the global community. As demonstrated following historical TSF failures, the indirect impacts from TSF failures can be immense (Kossoff et al., 2014). Furthermore, high valued land for ecosystem service such as forests are already increasingly at risk from the direct impacts of mining (Alvarez-Berríos and Aide, 2015). Mitigating the potential for additional forest and ecosystem destruction through TSF failures is essential. The vast range of TSF disposal methods, local contexts, and the current stage of TSFs significantly impact the ability to create singular, direct policy. The reduction of volume (V_F) within TSFs should be a priority for national policymakers and mine owners, whether this is through reducing water ponding on facilities or through higher density tailings deposition. The application of Laharz on TSFs at a regional scale provides policymakers with a quick and dirty measure for potential cumulative land-impacts and further cause for the requirement for alternative disposal methods such as dry-stacking, especially in areas of high economic and environmental value with already regionally heightened risk.

As discussed, a primary goal of future research directions is to develop the Laharz model as a regional risk tool through further validation and incorporation of uncertainty within the model and its application. The application of the model to different regions and larger spatial scales. allows for this tool to have many potential future research directions. Additionally, as the GTD expands and evolves with the implementation of the Global Tailings Standard, regional and global model application will create a more robust understanding of downstream 'elements at risk' from potential TSF failures. Future research directions are planned to further explore the spatial coincidence between potential inundation areas and protected areas as well as indigenous land. Another direction of interest is further understanding the range of economic and environmental value of the land cover at risk from potential TSF failures. This research would work to integrate the perspective of natural capital into TSF mitigation measures through quantifying the value of natural assets and the benefit these assets bring to the regional or global scale such as carbon sequestration. The cost of losing the land due to TSF failures then extends beyond the. local context. Engaging in an ecosystem services perspective frames mitigation measures to. reflect a broader set of values and aids in bridging silos between differing stakeholders (Deal, 2008).

4 CONCLUSION

TSF failures have wide reaching environmental consequences. The release of the GTD has allowed for an understanding of the potential consequences of TSF failures that explores beyond the local scale. The objective of this research was to provide a methodology for high level analysis of potential TSF failures using the semi-empirical, recalibrated Laharz model at the regional scale and demonstrate the application of this methodology through an analysis of the distribution of risk across North America from potential TSF failures to the surrounding environment through land cover impacts.

The results presented in this study show that the automated, recalibrated Laharz model is an objective, fast model capable of modelling over 100 TSF sites using free, publicly available data. Therefore, the recalibrated Laharz model presents itself as a fit-for-purpose model for regional modelling of inundation area and consequence. The application of the Laharz model methodology for regional consequence analysis ran 110 TSF sites across North America. revealed that the open forest, closed forest, shrub and herbaceous vegetation land classes are most at risk to be impacted by a potential TSF failures. The average area of interaction between TSF failure inundation zones and urban areas and built-up land classifications is approximately 0.5 km^2, however an interaction did occur in 25% of the cases modelled.

This paper provides a methodology to address the current knowledge gap on the regional consequences of TSF failures. Prior to the introduction of the recalibrated Laharz program, an automated semi-empirical method with the ability to run numerous inundation areas was not available. Future research is required to further address uncertainty in the Laharz model and expand its application beyond LCLCC data.

5 REFERENCES

Alvarez-Berríos, N.L., Aide, T.M., 2015. Global demand for gold is another threat for tropical forests. Environ. Res. Lett. 10, 014006. https://doi.org/10.1088/1748-9326/10/1/014006

Buchhorn, M., Lesiv, M., Tsendbazar, N.E., Herold, M., Bertels, L., Smets, B., 2020. Copernicus global land cover layers-collection 2. Remote Sens. 12, 1–14. https://doi.org/10.3390/rs12061044

Burritt, R.L., Christ, K.L., 2018. Water risk in mining: Analysis of the Samarco dam failure. J. Clean. Prod. 178, 196–205. https://doi.org/10.1016/j.jclepro.2018.01.042

Concha Larrauri, P., Lall, U., 2018. Tailings Dams Failures: Updated Statistical Model for Discharge Volume and Runout. Environments 5, 28. https://doi.org/10.3390/environments5020028

Cruz, F.V. da S., Gomes, M.P., Bicalho, E.M., Della Torre, F., Garcia, Q.S., 2020. Does Samarco's spilled mud impair the growth of native trees of the Atlantic Rainforest? Ecotoxicol. Environ. Saf. 189, 110021. https://doi.org/10.1016/J.ECOENV.2019.110021

Deal, R.L., 2008. Integrated restoration of forested ecosystems to achieve multiresource benefits: proceedings of the 2007 national silviculture workshop. Gen. Tech. Rep. PNW-GTR-733. Portland, OR U.S. Dep. Agric. For. Serv. Pacific Northwest Res. Station. 306 p 733. https://doi.org/10.2737/PNW-GTR-733

Eriksson, N., Adamek, P., 2000. The tailings pond failure at the Aznalcóllar mine.

Franks, D.M., Stringer, M., Cruz, L.A.T., Baker, E., Valenta, R., Thygesen, K., Matthews, A., Howchin, J., Barrie, S., 2021. Tailings facility disclosures reveal stability risks. Sci. Rep. 1–7. https://doi.org/10.1038/s41598-021-84897-0

Ghahramani, N., Mitchell, A., Rana, N.M., McDougall, S., Evans, S.G., Take, W.A., 2020. Tailings-flow runout analysis: examining the applicability of a semi-physical area–volume relationship using a novel database. Nat. Hazards Earth Syst. Sci. 20, 3425–3438. https://doi.org/10.5194/nhess-20-3425-2020

Griswold, J., Iverson, R., 2008. Mobility statistics and automated hazard mapping for debris flows and rock avalanches, U.S. Geological Survey Scientific Investigations Report 2007-5276. (ver. 1.1, April 2014).

ICMM, 2020. Global Industry Standard on Tailings Management.

Innis, S., Ghahramani, N., Rana, N.M., McDougall, S., Evans, S.G., Take, W.A., Kunz, N.C., 2020. Automated Hazard Mapping of Tailings Storage Facility Failures. Proc. Tailings Mine Waste 2020 661–670.

Iverson, R.M., Schilling, S.P., Vallance, J.W., 1998. Objective delineation of lahar-inundation hazard zones. Bull. Geol. Soc. Am. 110, 972–984. https://doi.org/10.1130/0016-7606(1998)110<0972:ODOLIH>2.3.CO;2

JAXA/METI, 2007. ALOS PALSAR L 1.0.

Kheirkhah Gildeh, H., Halliday, A., Arenas, A., Zhang, H., 2020. Tailings Dam Breach Analysis: A Review of Methods, Practices, and Uncertainties. Mine Water Environ. https://doi.org/10.1007/s10230-020-00718-2

Kossoff, D., Dubbin, W.E., Alfredsson, M., Edwards, S.J., Macklin, M.G., Hudson-Edwards, K.A., 2014. Mine tailings dams: Characteristics, failure, environmental impacts, and remediation. Appl. Geochemistry 51, 229–245. https://doi.org/10.1016/j.apgeochem.2014.09.010

Martin, V., Al-Mamun, M., Small, A., 2019. CDA technical bulletin on tailings dam breach analyses. Sustain. Safe Dams Around World d, 3484–3498. https://doi.org/10.1201/9780429319778-313

Martin, V., Fontaine, D., Cathcart, J., 2015. Challenges with conducting tailings dam breach assessments. Proc. Tailings Mine Waste 2015 314–328.

Mining Association of Canada (MAC), 2017. A Guide to the Management of Tailings Facilities.

Murguía, D.I., Bringezu, S., Schaldach, R., 2016. Global direct pressures on biodiversity by large-scale metal mining: Spatial distribution and implications for conservation. J. Environ. Manage. 180, 409–420. https://doi.org/10.1016/j.jenvman.2016.05.040

Owen, J.R., Kemp, D., Lèbre, Svobodova, K., Pérez Murillo, G., 2019. Catastrophic tailings dam failures and disaster risk disclosure. Int. J. Disaster Risk Reduct. https://doi.org/10.1016/j.ijdrr.2019.101361
Quelopana, H., 2019. Released Volume Estimation for Dam Break Analysis, in: 6th International Seminar in Tailings Management. Santiago.
Rana, N.M., Ghahramani, N., Evans, S.G., McDougall, S., Small, A., Take, W.A., 2021. Catastrophic mass flows resulting from tailings impoundment failures. Eng. Geol. 292, 106262. https://doi.org/10.1016/J.ENGGEO.2021.106262
Rico, M., Benito, G., Díez-Herrero, A., 2008. Floods from tailings dam failures. J. Hazard. Mater. 154, 79–87. https://doi.org/10.1016/j.jhazmat.2007.09.110
Rourke, H., Luppnow, & D., 2015. The Risks of Excess Water on Tailings Facilities and Its Application to Dam-break Studies.
Schilling, S., 2014. Laharz_py: GIS tools for automated mapping of lahar inundation hazard zones.
Small, A., James, M., Al-mamun, M., 2017. Advancing the state of practice for tailings dam breach assessment using empirical correlations., in: Canadian Dam Association Annual Conference. Kelowna.
Sonter, L.J., Ali, S.H., Watson, J.E.M., 2018. Mining and biodiversity: key issues and research needs in conservation science. Proc. R. Soc. B 285. https://doi.org/10.1098/RSPB.2018.1926
Sonter, L.J., Dade, M.C., Watson, J.E.M., Valenta, R.K., 2020. Renewable energy production will exacerbate mining threats to biodiversity. Nat. Commun. 11, 1–6. https://doi.org/10.1038/s41467-020-17928-5
Sonter, L.J., Moran, C.J., Barrett, D.J., Soares-Filho, B.S., 2014. Processes of land use change in mining regions. J. Clean. Prod. 84, 494–501. https://doi.org/10.1016/j.jclepro.2014.03.084
Tost, M., Murguia, D., Hitch, M., Lutter, S., Luckeneder, S., Feiel, S., Moser, P., 2020. Ecosystem services costs of metal mining and pressures on biomes. Extr. Ind. Soc. 7, 79–86. https://doi.org/10.1016/j.exis.2019.11.013
USGS EROS, 2000. EROS Archive - Digital Elevation - Shuttle Radar Topography Mission (SRTM) 1 Arc-Second Global. https://doi.org/10.5066/F7PR7TFT
Vandeberg, G.S., Martin, C.W., Pierzynski, G.M., 2010. Spatial distribution of trace elements in floodplain alluvium of the upper Blackfoot River, Montana. Environ. Earth Sci. 2010 627 62, 1521–1534. https://doi.org/10.1007/S12665-010-0637-9
Wang, K., Yang, P., Hudson-Edwards, K.A., Lyu, W., Yang, C., Jing, X., 2018. Integration of DSM and SPH to model tailings dam failure run-out slurry routing across 3D real terrain. Water (Switzerland) 10. https://doi.org/10.3390/w10081087

An integrated framework for risk assessment and management of tailings dams

Zhongqiang Liu, Luca Piciullo, Bjørn Kalsnes, Øyvind Torgersrud, Farrokh Nadim & Suzanne Lacasse
Norwegian Geotechnical Institute, Norway

ABSTRACT: In view of recent mine tailings dam failures with devastating consequences, a critical evaluation of the methodologies used for analyzing tailings dam safety and the improvement of the procedures for the risk assessment and management of tailings storage facilities are needed. The paper suggests the adoption of an integrated risk assessment and early warning framework for tailings dams that enables timely implementation of mitigation and warning measures. Recent progress in the characterization of tailings materials, their properties and their uncertainties, remote sensing and monitoring, numerical modelling and reliability-based approaches present the opportunity for an integrated risk management framework. The framework includes consideration of (1) the statistics of reported tailings dam failures; (2) uncertainties in tailings characterization, (3) progress in numerical modelling, and (4) novel technologies available for monitoring and early warning to reduce risk. Reliability-based assessments will enable risk-informed decisions for the safe raising, operation, and closure of tailings dams. The proposed integrated risk framework aims to assist stakeholders making decisions on rehabilitation of tailings dams and safety after closure.

1 INTRODUCTION

Tailings dams are built to store waste tailings from mining activities. Currently, thousands of tailings storage facilities (TSFs) exist around the world. The stored tailings are often highly toxic and the failure of a tailings dam and the uncontrolled release of the impounded waste can have disastrous consequences for the public, the environment and the owner or operator. Keeping the tailings dam safe is one of the biggest challenges of the mining industry as stated by the expert panel analyzing the Mount Polley failure (IEEIR.P, 2015), where more than 25 million m^3 of tailings material were released. Therefore, a correct approach to long-term tailings dam management is crucial to the success, and reputation, of the mining industry as a whole.

Over the past century, catastrophic tailings dam and ash pond failures and the resulting fast-moving mudflows have led to a cumulative loss of almost 3000 lives (Fig. 1). Tailings dams can pose a very high risk to society. Tailings dam failures can occur due to various reasons such as periodic raising of the tailings dam resulting in foundation failure, slope instability or subsidence; anomalous amounts of precipitation; internal erosion within the dams; non-functional drainage systems; soil liquefaction and missing or wrong maintenance. An example from the recent past for a catastrophic event is the failure of the Fundão Tailings Dam in Minas Gerais, Brazil, on 4th November 2015. Approx. 32 mil. m^3 flew out, causing at least 19 deaths, destruction of 158 homes and pollution of three large rivers (663 km length). The very recent catastrophic dam breach of the Córrego do Feijão dam in Minas Gerais in January 2019, with 270 deaths and large sections of agricultural land totally destroyed, has showed in a very dramatic way.

Risk assessment and risk management of tailings dams are urgently needed as the number of tailings dams is expected to increase in the future, and unexpected failures can occur. There is need for a critical evaluation of the methodologies used for analysing tailings dam safety and for improving the procedures for risk assessment, risk mitigation and management. The study proposes an integrated framework for the reliability and risk management associated with tailings dams. The paper is organized as follows: Section 2 is an analysis of reported tailings dam failures; Section 3 discusses novel technologies for monitoring and early warning to help reduce tailings dam risk; Section 4 proposes a generic integrated framework for tailings risk assessment and management; and Section 5 summarizes the discusses and conclusions.

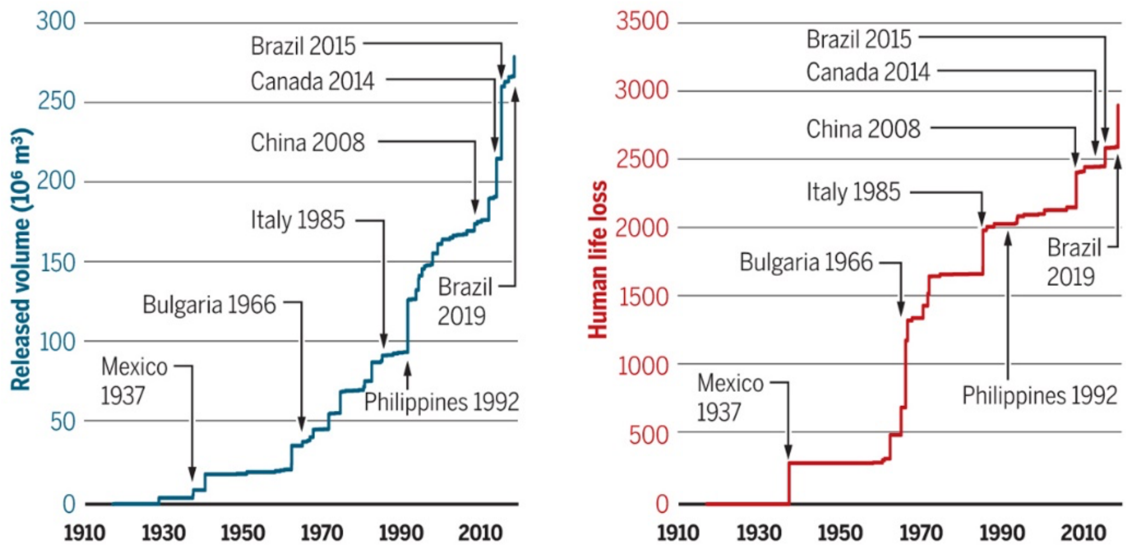

Figure 1. Released volumes and human life losses due to catastrophic tailings and ash-pond dam failures (Santamarina et al. 2019)

2 REPORTED TAILINGS DAM FAILURES

Despite the advances in engineering science and risk management techniques, severe tailings dam accidents continue to occur globally. To date, 257 cases of tailings dam wall failures and 95 accidents among components and other elements have been compiled by CSP^2 worldwide (http://www.csp2.org/tsf-failures-from-1915). Figure 2 demonstrates that the number of tailings dam failures has remained high over the last 60 years. Since 1960 about 4,5 failures have been registered per year.

For each tailings dam failure, information, including released volume, dam construction method, dam height and cause, has been documented in different tailings dam databases (e.g. ICOLD, WISE, World Mine Tailings Failures, CSP^2). However, in the majority of cases, the information available is scarce. The following presents schematically the number of failures as a function of dam type and dam height and the causes of failure.

2.1 *Dam type*

Tailings dam can be divided into four categories according to their construction methods, i.e. upstream, centerline, downstream and water retention. The CSP^2 database contains 116 accidents where the dam type was reported (Fig. 3). The highest number of tailings dam failures (82) refers to the upstream construction method (Piciullo et al., 2021). This TSF raising method, while economical, has proven to be significantly less stable than other construction methods. Downstream and centerline dams have relatively good stability and fewer dam failure events. Anyway, it is important to underline the fact that 127 failures in the database of 257 failures (so nearly 50%), the construction method is not documented. It is probable that a number of the dams with unknown construction method were raised with the upstream method.

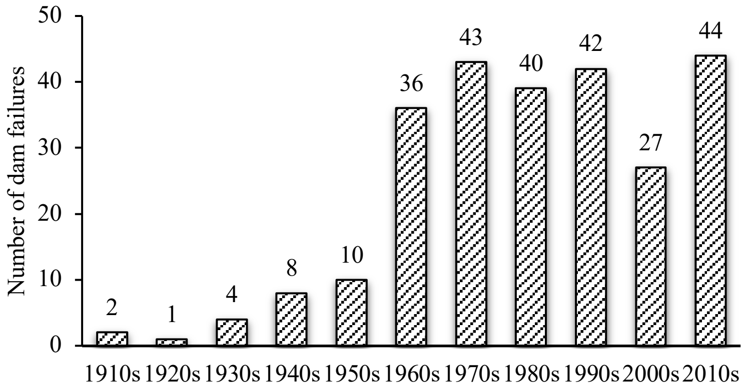

Figure 2. Tailings dam failures over time (data from the CSP[2] database).

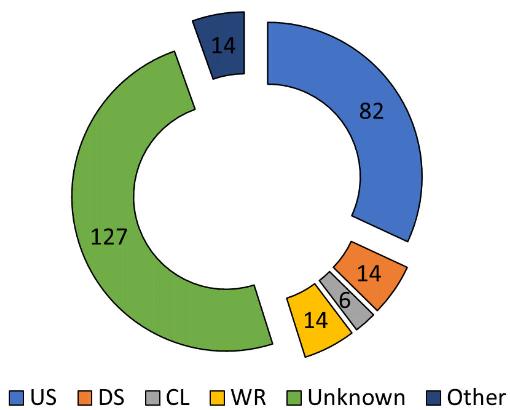

Figure 3. Distribution of number of tailings dam failures by dam type, CSP[2] database.
Legend: US= Upstream; DS=Downstream; CL=Centerline; WR = Water ring.

2.2 *Dam height*

The CSP[2] database reports 132 failures where dam height was at failure was given. The number of tailings dam failures in Figure 4 indicates that the failures occurred mostly with dams less than 30 m. Therefore, more attention should be paid to improving the specification requirements for tailings dams less than 30-m high to ensure their safety.

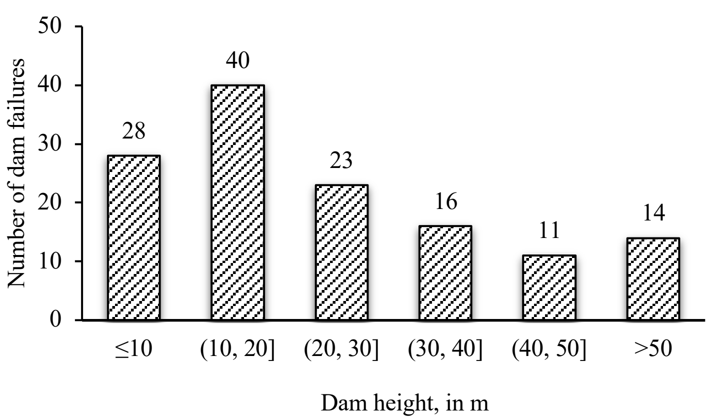

Figure 4. Distribution of number of tailings dam failures by dam height, CSP[2] database.

2.3 *Causes of dam failures*

A preliminary analysis of the CSP^2 database highlights that three causes of dam failure predominate: overtopping (23%), slope instability due to static liquefaction (16%) and dynamic liquefaction under earthquakes (14%) are the most frequent causes of tailings dam failure (Fig. 5; Piciullo et al., 2021). Forty-eight of the 257 tailings dam failures (or 23%) do not have an identified cause. It is possible that even a larger percentage of failures may be attributable to the three main failure modes.

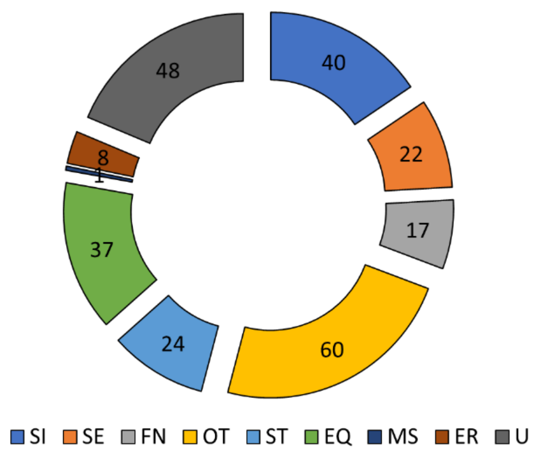

Figure 5: Causes of tailings dam failure, CSP^2 database.
Legend: SI = Slope instability; SE = Seepage; FN = Foundation; OT = Overtopping; ST = Structural; EQ = Earthquake; MS = Mine subsidence; ER = External erosion; U = Unknown.

3 NOVEL TECHNOLOGIES FOR EARLY WARNING TO REDUCE RISK

The considerable number of unknown failure modes in Figure 5 is indicative of a lack of inadequate post-failure investigations. Almost all the known failure modes in Figure 5, other than seismically induced failure, can be monitored and reasonably predicted given an understanding of the expected behavior of the tailings dam system. Although a tailings dam failure is perceived as an isolated event, it is in fact only the final stage of an ongoing deformation process. In many cases, dam deformations in the days and months prior to failure went undetected.

Hui et al. (2018) did a state-of-practice review of tailings dam monitoring using personal experience and consultation with over 40 stakeholders. They identified ineffective manual reading and data processing resulting in delays of up to a few days the identification of behavioral trends. Moreover, conventional monitoring systems can only provide information about surface deformation over a very limited time and space period. Real-time monitoring to foresee deterioration of dams is therefore crucial to mitigate the risk of dam failure.

The techniques for measuring variables can be broadly grouped into two categories: (1) point sensing (measuring one variable in a single location or over a relatively small area) and (2) wide area sensing (measuring parameters over a large area or volume often producing an image), including information gathered from satellites. The earlier trend of few sensors for specific purposes, dedicated monitoring systems with high quality expensive electronics and high accuracy measurements have moved to vast quantity of sensors, ad hoc data sources, very many data, sophisticated processing and interpretation tools based on statistics, including machine learning and artificial intelligence.

Satellite-based radar interferometry (InSAR) constitutes an innovative method for tailings dams monitoring. Figure 6 gives an example of results from time series analyses of InSAR data for three areas on the Feijão Mine tailings dam. Other innovative techniques involve the use of fiber optic sensors and permanent electrical resistivity to give a 2D representation of the soil compared with punctual measurements of standard monitoring techniques.

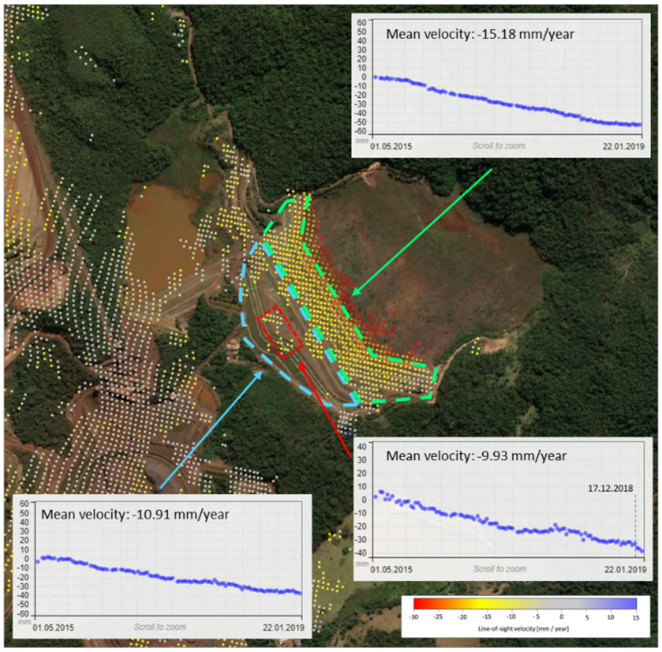

Figure 6: Line-of-sight displacements at the Feijão Mine tailings dam B-I in the period from May 2015 until just before dam failure on January 25, 2019 (displacements averaged over time for all measurement points in the outlined areas (Vöge et al. 2021).

4 PROPOSED RISK-BASED FRAMEWORK FOR TAILINGS DAM SAFETY

Risk assessment, with a quantification of the uncertainties and failure probability, is an essential step in risk management. Combined with the consequences, failure probability provides approximate levels of the risk associated with unsatisfactory dam performance.

The geotechnical aspects of current dam design are rapidly being transformed by advances in numerical analysis, constitutive modelling, instrumentation, real-time monitoring, remote sensing, and interpretation of data including machine learning, all supported by increased ability to model and interpret deformation and seepage regimes. This leads to design procedures that can overcome the limitations associated with the Factor of Safety concept. In addition, history-matching of performance can provide a reliable basis for projecting future performance. This can be described as a "performance-based risk-informed TSF management".

As part of achieving a target of zero failures for tailings dams, Morgenstern (2018) outlined a tailings management system for Performance-Based, Risk-Informed Safe Design Construction Operation and Closure of tailings facilities (PBRISD) and recommended that the "International Council on Mining & Metals" support a tailings management system based on PBRISD, and develop a guidance document that would facilitate its adoption in mining practice. The PBRISD consists of four stages: conceptual, feasibility, construction and operations and closure implementation. The underlying principle for the management system advocated is accountability. This is achieved by multiple layers of review, recurrent risk assessment and performance-based validation from construction through closure. The PBRISD approach requires integrated uncertainty assessment (e.g., geological model, hydrogeological model, geochemical model, geomechanical model, stability model), potential failure mode analysis, and risk assessment, transparent decision-making, and, none the least, appropriate documentation.

4.1 *Proposed integrated risk management framework*

Figure 7 illustrates the proposed integrated risk management framework for TSFs that enables the timely implementation of mitigation and warning measures. The framework includes: (1) hazard and consequence analyses based on (1) a knowledge of the geomechanical and geoenvironmental properties of the tailings material, (2) the statistics of earlier tailings dam failures, (3) slope stability analyses (usually by the finite element analysis with a realistic stress-strain behaviour model), which will also help set the threshold values in the early warning system (EWS) and (4) the analysis of performance data throughout the lifetime of the TSF. Recent progresses in these areas create the opportunity for such integrated framework.

The aim of the risk assessment is to provide operators the tools to make risk-informed decisions on the safety of the TSF and the need for mitigation measures. The analyses also prepare the grounds for risk communication within the company, to the authorities and to the public. As the TSF is raised, or as the facilities pass to new stages of its life cycle, e.g., operation re-start or closure, the premises for the analyses, the assessment and decisions should be updated. Sequential history-matching of performance using the Bayesian updating technique, will be able to provide a more reliable basis for projecting future performance.

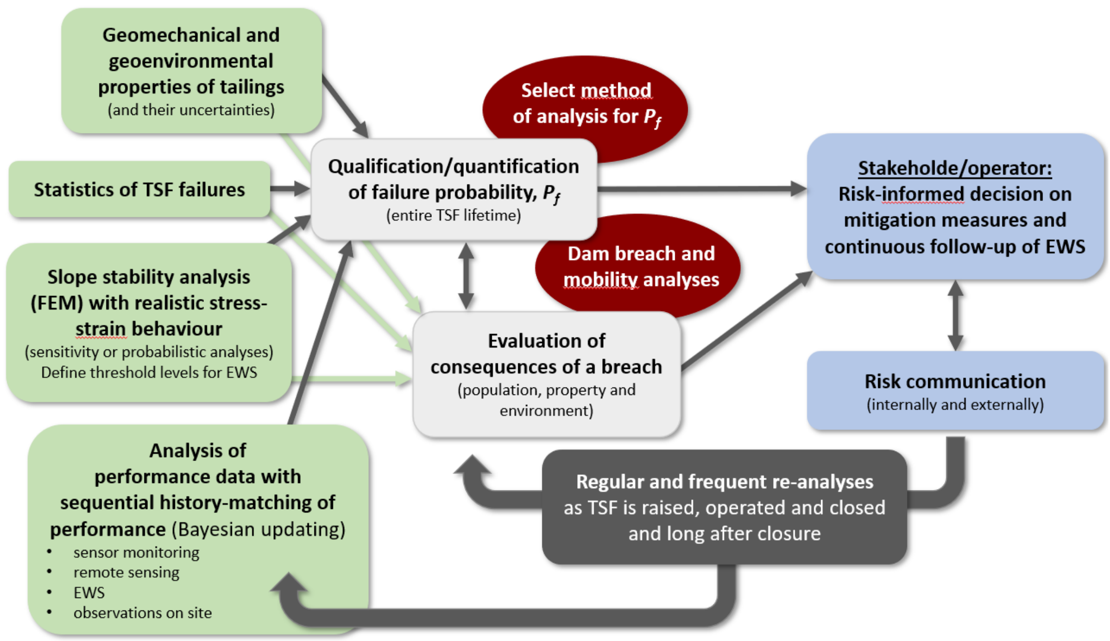

Figure 7. Proposed integrated framework for risk-informed management of tailings dams.

4.2 *Tailings material behaviour*

A good understanding of the chemical and physical properties of tailings materials is essential. Their characteristics are complex due to varying mineral composition, chemical reactions, form and state of tailings materials at deposition and material behaviour. The geomechanical behaviour of tailings is usually described in terms of state parameters and critical state soil mechanics. Series of laboratory triaxial tests need to be carried out to establish the critical state line (CSL). As undisturbed tailings samples are not easily accessible and seldom sampled in situ, it is often necessary to reconstitute test specimens in the laboratory to initial void ratios derived from Cone Penetration Tests (CPT). It is difficult to target the initial void ratio, and there is significant segregation potential. The micromechanics approach can tackle the initial fabric of a test specimen with micro Computed Tomography images and postprocessing. The technique also provides an enhanced understanding of the true initial state of the soil (e.g., Andò, 2013; Viggiani and Tengattini, 2019) in special triaxial cells (Piciullo et al, 2021; Quinteros and Suzuki, 2021).

Schaid (2021) made a careful review of the geocharacterisation of tailings with in situ and laboratory tests. Important advances in modern practice have been reported by Jamiolkowski (2014) describing the geotechnical characterization of the copper tailings at one of the Zelazny Most tailings dam in Poland. For tailings exhibiting strain-weakening, there are currently major uncertainties associated with the residual shear strength and post-seismic reduced shear strength to be used in stability analyses. Therefore, the need for more advanced stability analyses.

4.3 *Numerical modelling*

For a robust design or stability evaluation during the life cycle of a TSF, it is necessary to consider the complete stress-strain behaviour of the soil mass using appropriate constitutive models. Having reliable models for predicting the behaviour of tailings under loading is essential for the evaluation of sustainable and safe mine tailings. Tailings are usually deposited in a loose state: under undrained loading, the material may contract and lose strength. If the tailings are subjected to a shear stress higher than the undrained shear strength, the material becomes unstable and a small change can cause a progressive failure or static liquefaction. This failure mode can easily be overlooked if stability is assessed by conventional limit equilibrium analyses. The preferred approach is to use numerical modelling with the finite element method (FEM) for simulating the initiation of strain-weakening, and the discrete element method (DEM) as an alternative to laboratory testing for the characterization of constitutive model parameters (Piciullo et al. 2021).

Figure 8 presents an example of simulation results of the Fundao Mine tailings dam, from the beginning of undrained phase (Fig. 8(a)) to the softening phase (Fig. 8(b)), as modelled using the Sanisand constitutive model. However, spatially varied geomechanical properties in tailings materials and uncertainties associated with the residual shear strength due to strain-weakening may affect the failure mode of a tailings dam. Numerical simulations enhanced with probabilistic analysis is favourable to evaluate the probabilistic distribution of factors of safety and to describe the evolutions of stresses and strains in spatially varied tailings materials.

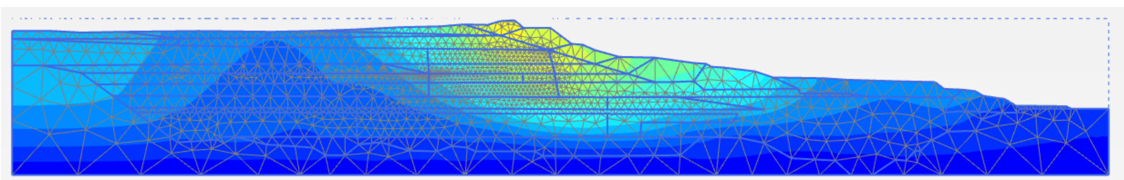

(a) Beginning of undrained phase

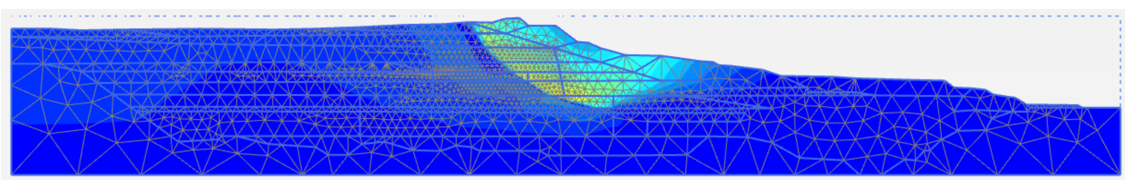

(b) Softening phase

Figure 8. Numerical simulations (incremental displacement), of the Fundao Mine tailings dam.

4.4 *Example of a probabilistic analyses of a tailings dam*

There are several methods to do hazard analysis. The most frequently used quantitative method is the event tree analysis (ETA). Great strides have been made, as ETA and similar methods are used more frequently and results are calibrated against historical records (Davidson 2015). Figure 9 shows an example event tree for one scenario: piping in tailings dam at location of crack during or after construction. At each node, a probability was estimated. The failure probability along one branch of the tree is calculated from the product of the probabilities along the branches leading to failure. The failure probability for one failure mode is the sum of the probabilities on the branches leading to dam failure in one tree. The total failure probability is the sum of the failure probabilities for all failure modes (all event trees).

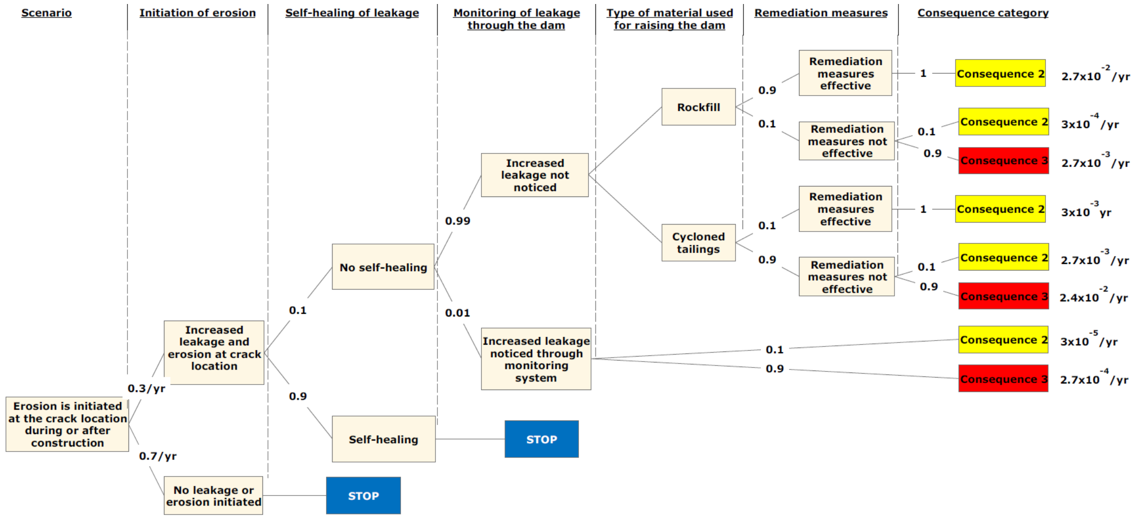

Figure 9: Event tree analysis of one scenario: Piping in tailings dam along existing crack

The Bayesian network analyses were also conducted for the same scenario where the tailings dam is raised by a 4-m high rockfill. The Bayesian network analyses first verified the result of the event tree analyses. Thereafter, the Bayesian network analyses were supplemented with Monte Carlo simulations to obtain the statistics of the probability of non-performance. Figure 10 presents the results of the Monte Carlo simulations with a histogram of the probability of Consequence 2. A mini-table on the figure summarizes the statistics of the annual probability distribution with the Mean ($3 \cdot 10^{-2}$), Standards deviation (SD), Coefficient of Variation (COV)[1], N (number of simulations), and p-value. The best fit of the histogram with a lognormal distribution is also shown. The p-value is obtained from the Kolmogorov-Smirnov goodness-of-fit test. A significance level of 5% is commonly used for this test. The p-values were greater than 5% for all parameters. Thus, the hypothesis of a lognormal marginal distribution for the probability of Consequence Class 2 is not rejected at the 5% significance level.

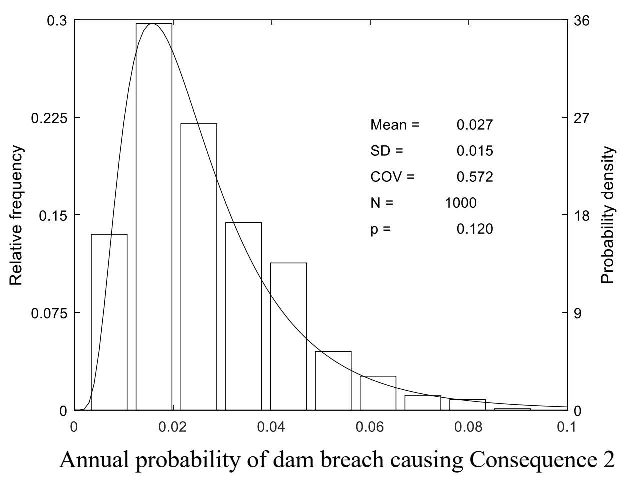

Figure 10: Distribution of probability of non-performance leading to Consequence 2 for the case of "piping in dam along existing crack".

4.5 *Example of tailings runout analysis*

Tailings can travel many km, affecting infrastructure, the local environment, and can even lead to loss of life. Tailings materials mobilized into rivers and lakes can pollute large areas. Modelling of the mobility of liquefied tailings is a challenging and complex task, yet essential for estimating

[1] The coefficient of variation is the ratio of the standard deviation to the mean: COV = SD/mean

the potential elements at risk and consequences. A tailings flow slide following a liquefaction event can be approached by non-Newtonian fluid mechanic models, in particular the Herschel-Bulkley or Bingham model (Oboni and Oboni, 2020). The flow of liquefied tailings has also been shown to depend on the downstream slope and flow velocity, being mainly laminar on flatter slopes and turbulent on steeper slopes with higher velocity (Pirulli et al., 2017). Figure 11 presents an example of simulation results (white areas) of the Feijão Mine tailings dam in terms of runout distance, as modelled using BingClaw (Hofshagen 2021). The volume of the input source area was estimated by interpreting the topography before and post-failure. The figure superposes the extent of the tailings deposit at the end of the sliding based on the interpretation of satellite images (red contour). There is a very good agreement between the simulated runout distance and the observed run-out distance. There is also a general good agreement in the shape of the areal distribution of the final tailings deposit.

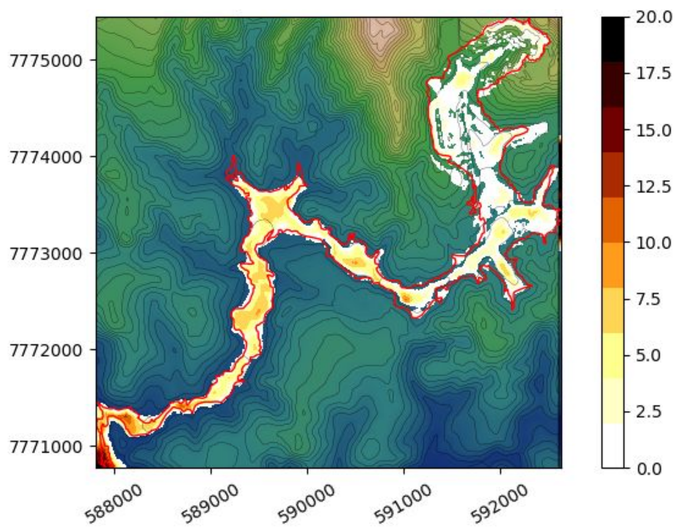

Figure 11. Predicted tailings propagation at 133 min time, plan view of the Feijão Mine tailings dam: red curve is the mapped runout extent: scale on right is debris thickness in m.

4.6 *Risk communication*

Risk is not absolute, nor static, and is not perceived uniformly by all stakeholders. Yet, there is a need for common understanding. Beyond technical decision-making, there are societal values. Risks are perceived as higher when unknown, involuntary, unfamiliar, acute or uncontrollable. The skills required for communication of engineering risk are not a part of the usual engineering education today. Effective communication is two-way communication, it is about people and their frame of mind and it requires gaining trust with consistent and easy-to-understand terminology.

5 CONCLUSION

The purpose of risk assessment is to improve tailings dam safety and risk management. Recent tailings dam failures show that the profession can no longer avoid risk-based decision making as a means of not only identifying critical failure modes but also prioritizing how to address potential dam safety deficiencies in an objective, rational and cost-effective manner.

This paper recommends an integrated risk management framework for TSFs that enables the timely implementation of mitigation and warning measures. The application of such framework will help ensure safe tailings dam design and provide very useful information when the stakeholders need to make decisions regarding rehabilitation and safe closure of a TSF.

6 ACKNOWLEDGEMENT

The research for this paper has been funded by the Norwegian Geotechnical Institute and is part of the project "Towards sustainable mine tailings"(https://www.ngi.no/eng/Projects/Sustainable-mine-tailings/#About-the-project).

7 REFERENCES

Ando, E. 2013. Experimental investigation of microstructural changes in deforming granular media using-ray tomography. Universit´e de Grenoble, 2013. Thesis.

CSP2- Tailings Dam Failures (1915–2016). http://www.csp2.org/tsf-failures-1915-2017 (Accessed on May 2021).

Davidson, R.R. 2015. Misconceptions about Quantitative Risk Assessment of Dams. Dam Safety. Assoc. of State Dam Safety Officials. New Orleans, LA, USA. 19 pp.

Hofshagen G. 2021. Modeling of tailings dam breach using BingClaw and OpenFOAM: Back analysis of the 2019 Córrego do Feijão dam failure. MSc thesis. Norwegian University of Science and Technology.

Hui, S., Charlebois, L., Sun, C. 2018. Real-time monitoring for structural health, public safety, and risk management of mine tailings dams. Can. J. Earth Sci. 55: 221-229.

ICOLD. Tailings Dams-Risk of dangerous occurrences, lessons learnt from practical experiences, Bulletin 121, United Nations Environmental Programme (UNEP), Division of Technology, Industry and Economics (DTIE) and International Commission on Large Dams (ICOLD), Paris, 2001.

Independent Expert Engineering Investigation and Review Panel (IEEIR.P), 2015. Report on Mount Polley Tailings Storage Facility Breach. January 30, 2015

Jamiolkowski, M. 2014. Soil mechanics and the observational method: challenges at the Zelazny Most copper tailings disposal facility. 64(8): 590-618.

Morgenstern, N.R. 2018. Geotechnical Risk, Regulation, and Public Policy. *Soils and Rocks*. **41**(2):107-129. DOI: 10.28927/SR.412107.

Oboni, F., Oboni, C. 2020. Tailings Dam Management for the Twenty-First Century: What Mining Companies Need to Know and Do to Thrive in Our Complex World.

Piciullo, L., Storrøsten, E. B., Liu Z., Nadim F., Lacasse, S. 2021. A new look at the statistics of tailings dam failures. in preparation.

Pirulli, M., Barbero, M., Marchelli, M., Scavia, C. 2017. The failure of the Stava Valley tailings dams (Northern Italy): numerical analysis of the flow dynamics.

Quinteros, S., and Suzuki, Y. 2021. Development of in situ triaxial testing devices for use in CT scanner. in preparation.

Santamarina, J. C., Torres-Cruz, L. A., Bachus, R. C. 2019. Why coal ash and tailings dam disasters occur. Science, 364(6440), 526-528.

Schnaid, F. 2021. On The Geomechanics and Geocharacterization of Tailings. The Ninth James K. Mitchell Lecture.

Viggiani, G., Tengattini, A. 2019. Recent developments in laboratory testing of geomaterials with emphasis on imaging. Proceeding of the XVII ECSMGE-2019 Reykjavik, Iceland, 2019.

Vöge, M., Frauenfelder, R., Salazar, S. Torgersrud, O., Piciullo, L. 2021. Remote Sensing of Tailings Storage Facilities. Tailings and Mine Waste 2021.

WISE Uranium Project. 2019. Chronology of Major Tailings Dam Failures. http://www.wiseuranium.org/mdaf.html (Accessed on May 2021)

World Mine Tailings Failures, https://worldminetailingsfailures.org/ (Accessed on May 2021)

Remote sensing of tailings storage facilities

Malte Vöge, Regula Frauenfelder, Sean Salazar, Øyvind Torgersrud & Luca Piciullo
Norwegian Geotechnical Institute, Norway

ABSTRACT: Failure of a tailings storage facility can have catastrophic consequences. Monitoring tailings infrastructure is therefore a critical part of sustainable mining practices. To assess the applicability of satellite-based radar interferometry (InSAR) for monitoring tailings dams, two case studies were selected for which ground displacements were mapped using InSAR: the Zelazny Most tailings dam in Poland and the recently collapsed Feijão Mine tailings dam in Brazil. In both studies, data from the Sentinel-1 radar satellite were analyzed. Two different processing methods, Persistent Scatterers (PS) and Small Baseline Subset Algorithm (SBAS), were applied and compared. For the Zelazny Most tailings dam, horizontal displacements were of special interest. Therefore, data from different acquisition geometries were analyzed and horizontal and vertical displacements were decomposed from the line-of-sight displacements. In the case of the Feijão Mine tailings dam collapse, we investigated the potential existence of precursors, among others, by using an inverse velocity approach.

1 INTRODUCTION

Tailings dams are generally large-scale geotechnical structures and ensuring their stability is of critical importance for safe and sustainable mine waste management. However, assessing dam stability remains a great challenge, and failures of significant scale keep occurring world-wide (Owen et al., 2020).

The following characteristics make tailings dams particularly vulnerable to failure: (a) embankments constructed of locally sourced fills (soils, coarse waste, overburden from mining operations and tailings); (b) multi-stage raising of the dam; (c) the lack of standardized regulations governing design criteria; and (d) high maintenance costs after mine closure (Rico et al., 2007). Upstream dams, where dam extensions are supported by the tailings themselves, are especially vulnerable to displacements which can trigger failure, e.g., by static liquefaction of the tailings. The consequences of a dam failure can be severe, not only in the direct vicinity of the dams themselves, but also far downstream. Therefore, dam stability requires continuous monitoring and control during emplacement, construction, operation and after decommissioning.

Interferometric synthetic aperture radar (InSAR) has been applied to the study of many natural and anthropogenic phenomena. The availability of near-global coverage of SAR data collected with the current generation of satellite constellations has allowed for an unprecedented amount of data over mining sites, tailings storage facilities, and downstream waterways. Specifically, the European Union's Copernicus Program maintains a network of satellites, including the Sentinel-1 constellation that has provided open access radar data with medium spatial resolution and short repeat pass intervals since 2014.

Here, the applicability of InSAR analyses for monitoring displacements on and around tailings dams was assessed for two selected case studies. The first case study is the Zelazny Most dam in Poland, Europe's largest mine tailings dam. Since 1981, the Zelazny Most dam has experienced significant horizontal displacements due to slickensided layers within the foundation soils

(Jamiolkowski, 2014). The second case study is the recently collapsed Vale S.A. Córrego do Feijão Mine Dam I ("Feijão Mine") tailings dam located in Brazil.

2 METHODOLOGY

Monitoring ground displacements with InSAR is based on the principle that the distance between the satellite and a given point on the ground is a function of the radar signal's phase. Therefore, the phase difference between two acquisitions will provide information about the eventual movement of the ground (e.g., Rosen et al., 2000). Unfortunately, the phase difference caused by displacement is superimposed by various phase components, including the topographic and the atmospheric phase components. While the topographic phase component can be modelled given a sufficiently accurate elevation model, the unknown atmospheric phase component requires filtering techniques. For sufficiently stable filtering of the atmospheric phase, a larger number (20 to 30) of data acquisitions is needed.

Among advanced, multi-temporal InSAR techniques the most common ones are the Persistent Scatterer (PS) and Small Baseline Subset (SBAS) approaches. The PS technique was first proposed by Ferretti et al. (2001) to overcome the limitations of SAR interferometry, often affected by temporal, atmospheric or geometrical decorrelation in surface monitoring related applications. The method is based on identifying stable reflectors in the multi-temporal interferometric SAR scenes. The stable reflectors have been named permanent, or persistent, scatterers and are exploited for obtaining millimeter-scale crust deformations and improved submeter digital elevation models. Ferretti et al. (2000) and Ferretti et al. (2001) proposed an amplitude dispersion index for identifying PS candidates. The persistent scatterers are natural or man-made objects that present a stable signal phase from one acquisition to another, displaying a high coherence over a SAR data stack. Because this index can be applied only for large data stacks, Berardino et al. (2002) proposed the SBAS method, which uses a coherence stability indicator. The SBAS method considers multiple reference images but restricts the image pairs to those with small temporal and spatial baselines. The spatial baseline describes the relative distance between acquisition positions of the satellite. The SBAS technique therefore reduces the effects of temporal and spatial decorrelation. To further reduce the effects of spatial decorrelation, the interferograms are filtered before they are unwrapped. As a result, the SBAS method is better suited for studying natural terrain, where limited strong scatterers are present. Similar to the PS method, only coherent pixels are exploited.

The near-polar, sun-synchronous two-satellite Sentinel-1 constellation acquires data globally with a minimum 12-day repeat cycle. The data are acquired either in ascending or descending orbit geometries, day or night, and in all weather conditions. The Interferometric Wide (IW) swath acquisition mode combines swath width of 250 km with a spatial resolution of approximately 5 m in the across-track dimension by 20 m in the flight direction. While single-orbit InSAR analysis is used to calculate displacements in the vertical directions (up or down), analyses that incorporate data from both ascending and descending orbit geometries can be used to calculate displacements in the horizontal directions (east-west) in addition to the vertical directions. Multi-orbit measurements are generally insensitive to displacements in the north-south horizontal directions and are, thus, limited to the east-west horizontal directions and up-down vertical directions.

3 DISPLACEMENTS AT THE ZELAZNY MOST TAILINGS DAM

The Zelazny Most dam surrounds a tailings storage facility that serves three copper mines, located in southwestern Poland. The mines are operated by KGHM Polska Miedź. Zelazny Most is the largest tailings storage facility in Europe with a ring dam of nearly 15 km in length and a maximum dam height of approximately 75 m at present. The facility's operations began in 1977 and by 2013 a total of 527×10^6 m^3 of tailings had been stored (Jamiolkowski, 2014). The dam is extensively monitored with over 450 surface benchmarks that are surveyed 2 to 4 times a year, 300 vibrating wire piezometers, and 56 inclinometers (Jamiolkowski, 2014).

Figure 1: The Zelazny Most tailings storage facility (aerial image, inset) is located in southwestern Poland (Sources: Google Earth, photo from Jamiolkowski, 2014).

To evaluate the feasibility of SAR interferometry to monitor displacements at Zelazny Most, we first compare results obtained by the SBAS and the PS methods. For this, a total of 141 Sentinel-1 scenes acquired in ascending mode (the satellite orbits going from south to north, tilted slightly towards the west) covering the period from January 2018 to May 2020 were used. While the area covered by a single Sentinel-1 image is about 200 x 250 km, only a smaller area surrounding the dam was processed.

Figure 2 presents the results for both the SBAS and the PS methods. The SBAS method provides a good coverage of the dam with coherent measurements. The PS method also provides coherent measurements along the entire dam; however, the measurements are much sparser, especially along the north-eastern part of the dam, where the line-of-sight vector of the radar beam was almost parallel to the slope of the dam. The area surrounding the dam is dominated by agricultural fields and forests. In such areas most of the radar energy is absorbed or reflections are decorrelated over time due to crop growth or agricultural changes. While the SBAS result covers some of the agricultural areas, the PS method mostly provides measurements where buildings are located. Along the dam, the SBAS method provides measurements on the tailings themselves, close to the crest of the dam, on the so-called beach.

The velocity values provided by the two methods are very consistent. The SBAS results appear smoother than the PS results, which is a result of the spatial filtering that is part of the SBAS processing workflow. The PS method processed data with full spatial resolution and thus retained more detail, which also culminated in a noisier result. The SBAS method shows less details and the smoothness of the results can locally lead to shifted values in areas with high velocity contrasts, e.g., at the crest between the rapidly moving beach and the much more stable dam.

Figure 3 presents a more detailed view of the eastern section of the dam, where the crest of the dam has been extended inward between 2007 and 2009. Here, the SBAS result shows a clear advantage over the PS method, as it provides much better coverage over the extended crest. The SBAS approach was also able to resolve a smaller displacement pattern near the foot of the dam, an area in which the PS analysis did not provide coherent measurement points (see dashed white circle in Figure 3).

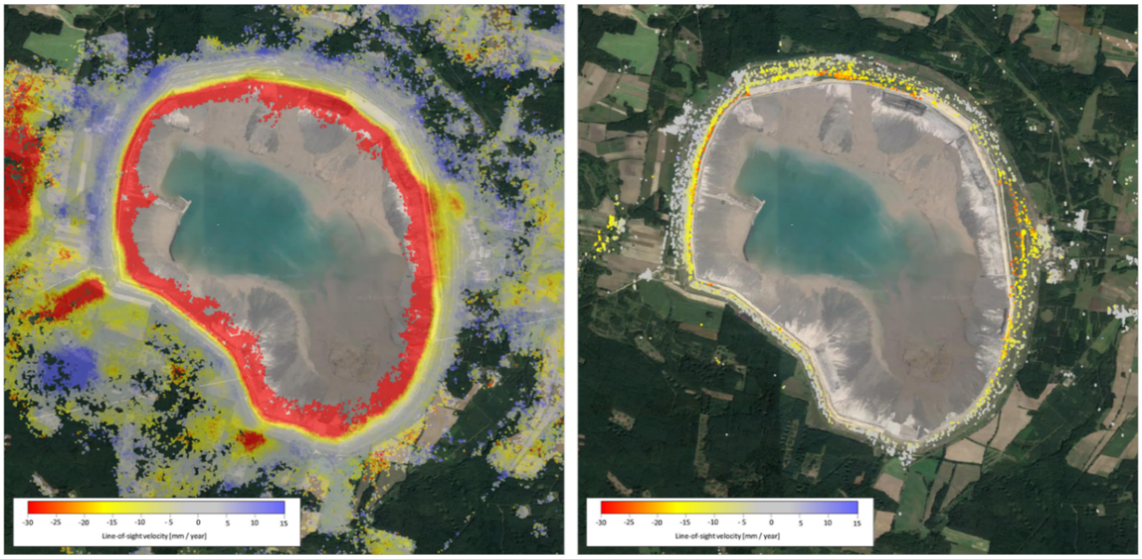

Figure 2: Mean velocity (line-of-sight) obtained by the SBAS method (left panel) and the PS method (right panel). Negative values (yellow/red) represent downward velocity (mm/yr), while positive values (blue) represent upward velocity. Grey colors represent stable areas.

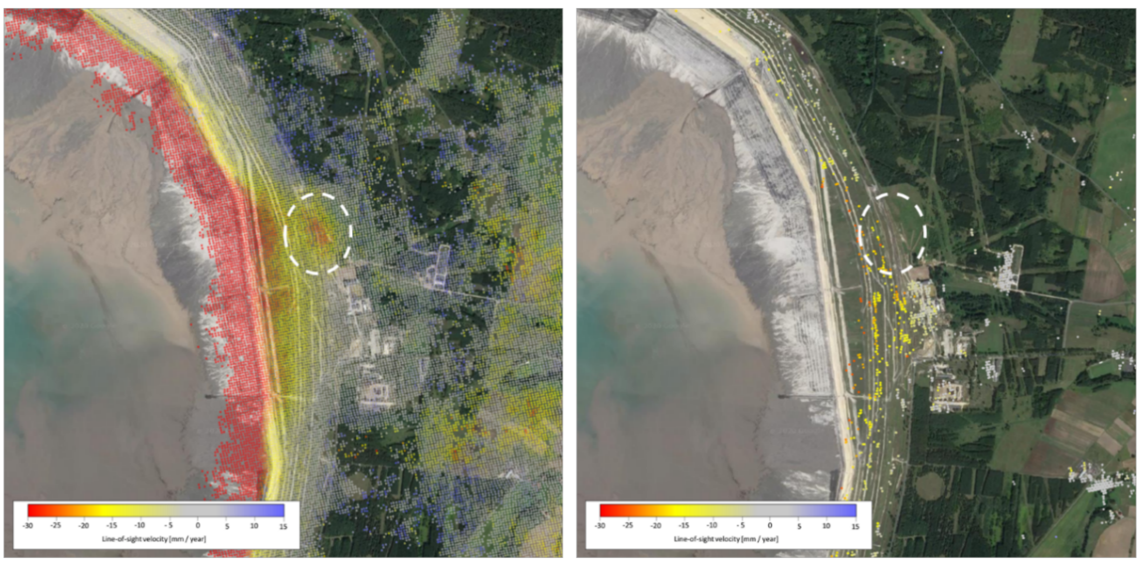

Figure 3: Close-up on the eastern part of the dam. The PS results (right) provide less coverage in the upper part of the dam, where the crest has been extended towards the inside of the dam. The SBAS results (left) indicate a local displacement pattern at the foot of the dam (marked by the dashed white circle), for which the PS results show no coherent measurements points.

To further investigate the direction of the displacements, the aforementioned SBAS results, derived from an ascending orbit, were combined with SBAS results that were derived from a dataset acquired in descending orbit. The descending orbit dataset consisted of a total of 141 scenes covering the same time period as the ascending data stack. The multi-orbit combination allowed for the decomposition of the two line-of-sight velocity maps into the vertical velocity component and the horizontal (east-west) component. More than two orbits would enable the determination of a full three-dimensional velocity vector; however, due to the near-polar orbits and the right-looking setup of the radar instrument, the measurements are generally insensitive to horizontal movements in the north-south direction.

Figure 4 presents the vertical (left panel) and the horizontal east-west (right panel) components of the detected velocity. Areas with negative vertical velocity (yellow to red colors) represent settlements, while positive values (blue) represent heave. For the horizontal east-west component, negative values (purple) represent a movement in the west direction, while positive values (green) represent a movement in the east direction. The vertical velocity map indicates that the beach tailings have a clear vertical component. In contrast, vertical movements on the dam slopes are small, with two very local exceptions on the western and the southern slopes of the dam. Similarly, the horizontal velocity map indicates that there are clear horizontal components. Such horizontal movements are observable within the dam, directed inwards, towards the center of the dam. This trend can be explained by the natural settling of the tailings along the inner slopes of the dam. Horizontal movements are also detectable on the outside slopes of the dam – both on the eastern and western slopes, and directed away from the dam.

The displacement measurements for both vertical and horizontal directions are consistent with those recently published by Mazzanti et al. (2021), who also used a PS processing workflow. The coherent measurement point coverage presented in the Mazzanti et al. (2021) analysis appears to be better than the coverage achieved by the PS results presented in this paper, but it is still more sparse than for the SBAS results presented here, especially for the south-west part of the dam and the beaches. Similar to the PS results presented in this paper, the displacement maps given by Mazzanti et al. (2021) show some more detail than our comparatively smooth SBAS results. Both their study and our analysis show clear vertical and horizontal displacements. The vertical displacement can be related to settlements and/or compaction phenomena, while the horizontal displacements are caused by the weight of the tailings pushing the dam outwards along the slickensided layers within the foundation soils. For a more detailed geotechnical analysis and comparison with ground-based measurements taken from Jamiolkowski (2014) see Mazzanti et al. (2021).

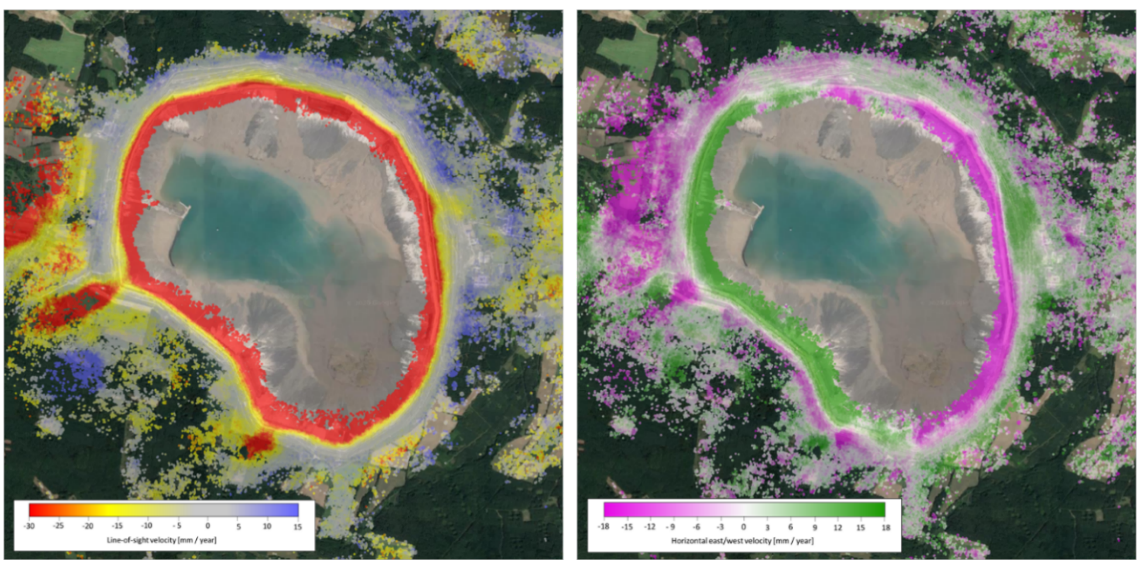

Figure 4: Vertical (left panel) and horizontal east-west (right panel) velocity maps. Left: negative vertical velocity (red) represents settlements, positive vertical velocity (blue) represent heave; Right: negative values (purple) represent westward movement, while positive values (green) represent eastward movement.

4 DISPLACEMENTS PRIOR TO THE FEIJÃO MINE TAILINGS DAM FAILURE

Tailings dam B-I at the Córrego do Feijão Iron Ore Mine I is located south of Belo Horizonte in the state of Minas Gerais, Brazil. The Feijão Mine dam is a horseshoe-shaped dam embedded in the mountain range with the dam face oriented to the south-east (Figure 5). Construction started in 1976 and the dam was raised ten times using the upstream construction method until 2013, to reach its final crest height of 86 m. The dam stopped receiving tailings in July 2016 (Robertson et al., 2019). On January 25, 2019, the dam suffered a sudden and catastrophic failure that extended across almost the entire dam face within 10 seconds (Robertson et al., 2019).

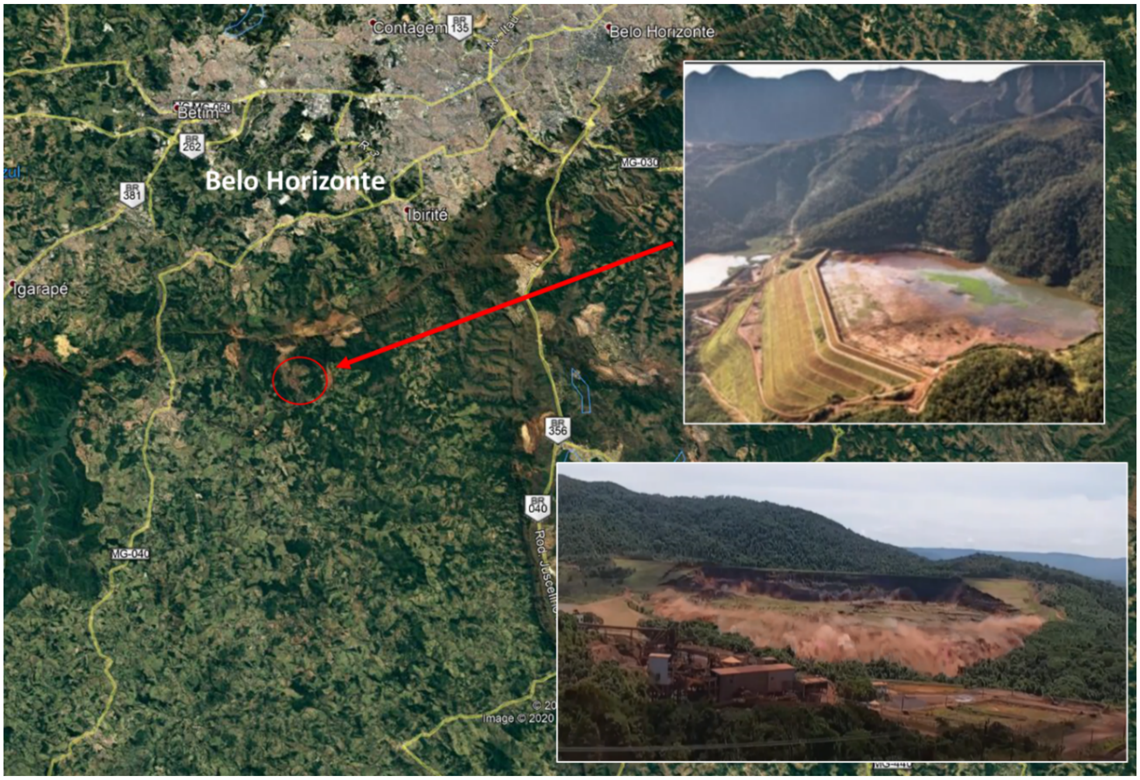

Figure 5: Location of the Feijão Mine tailings dam B-I in the state of Minas Gerais, Brazil. The upper right image (inset) depicts the dam in 2015. The lower right image (inset) depicts the moment of the dam failure, taken from video footage that captured the entire failure. (Sources: Google Earth, photos from https://www.slideshare.net/comcbhvelhas/barragens-de-mineracaovale and https://www.mining.com/video-shows-exact-moment-vales-dam-collapsed/).

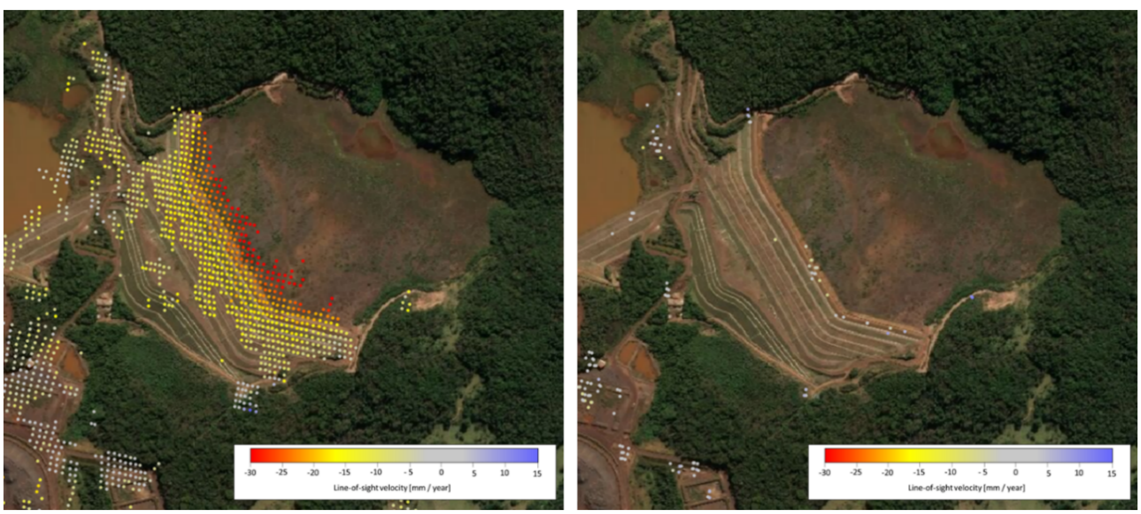

Figure 6: Comparison of the SBAS (left panel) and the PS (right panel) results. The SBAS results cover the entire upper part of the dam face and some patches on the lower part. The PS method yielded only a small number of measurement points along the crest of the dam.

The goal of our study was to determine whether InSAR, using freely available data from the medium-resolution Sentinel-1 constellation, could have shown any considerable deformation prior to the failure. A total of 108 Sentinel-1 scenes from the period between May 2015 until January 22, 2019 (i.e., 3 days before the dam failure) were processed, again using both the SBAS and the PS methods. Unfortunately, the Sentinel-1 constellation only provides descending mode acquisitions over this geographic area, therefore, decomposition of the vertical and the horizontal deformation components was not possible.

Considering the right-looking geometry of the satellite's sensor, the radar line-of-sight is downslope to the dam face at an approximately 45-degree angle to the crest towards the northern edge of the dam. Similar studies using the same satellite dataset have been carried out by Gama et al. (2020) and Grebby et al., (2021), however, both studies were based on shorter observation periods from, respectively, March 2018 and August 2017 to January 2019.

Figure 6 presents a comparison of the SBAS and the PS processing results. While the PS method was only able to detect a small number of coherent measurement points at the crest of the dam, the SBAS results cover almost the entire upper part of the dam, including the beach area. In the lower part of the dam, only patches of measurement points were available; these were mostly located in the center of the dam. It can be hypothesized that the high displacement rates along the beach tailings could have influenced the measurements in the upper part of the dam face, due to the spatial filtering of the SBAS method. This might cause a slight overestimation of the deformation values.

Figure 7 presents a more detailed velocity map for the SBAS results. As for the Zelazny Most dam, the highest displacement rates were observed along the beach, close to crest of the dam, which is likely related to natural settlement of the tailings. Along the crest and the upper part of the dam, the measurement points indicate an average displacement rate of about -15 mm/year in line-of-sight, corresponding to a downslope movement. The lower part of the dam shows less movement at around -10 mm/year. This is expected for a dam constructed with the upstream construction method, as the upper parts of the dam are supported by increasingly thicker layers of soft tailings.

Figure 7 presents results from selected time series analyses for three areas on the dam. Both time series from the lower part of the dam indicate some fluctuations. These fluctuations might be caused by water infiltration during the wet season. A smaller area in the center of the dam face appears to show an increased downward movement following December 17, 2018. A similar observation was also made by Gama et al. (2020) and Grebby et al., (2021) and could indicate a precursor of the pending failure. Yet, this signal is not visible in all the time series and therewith not very conclusive.

Therefore, this apparent increase in velocity was investigated in more detail, using an inverse-velocity approach based on a study by Fukuzono (1985). Figure 8a presents the time series for the center of the dam, from August 2018 until the dam failure (dashed blue line). In order to calculate a stable measure of the inverse velocity, the time series had to be filtered, which was achieved by a simple averaging filter using a width of 7 samples. The resulting filtered time series is also plotted in Figure 8a (orange line). The filtered time series indicates a clear acceleration starting towards the end of October 2018.

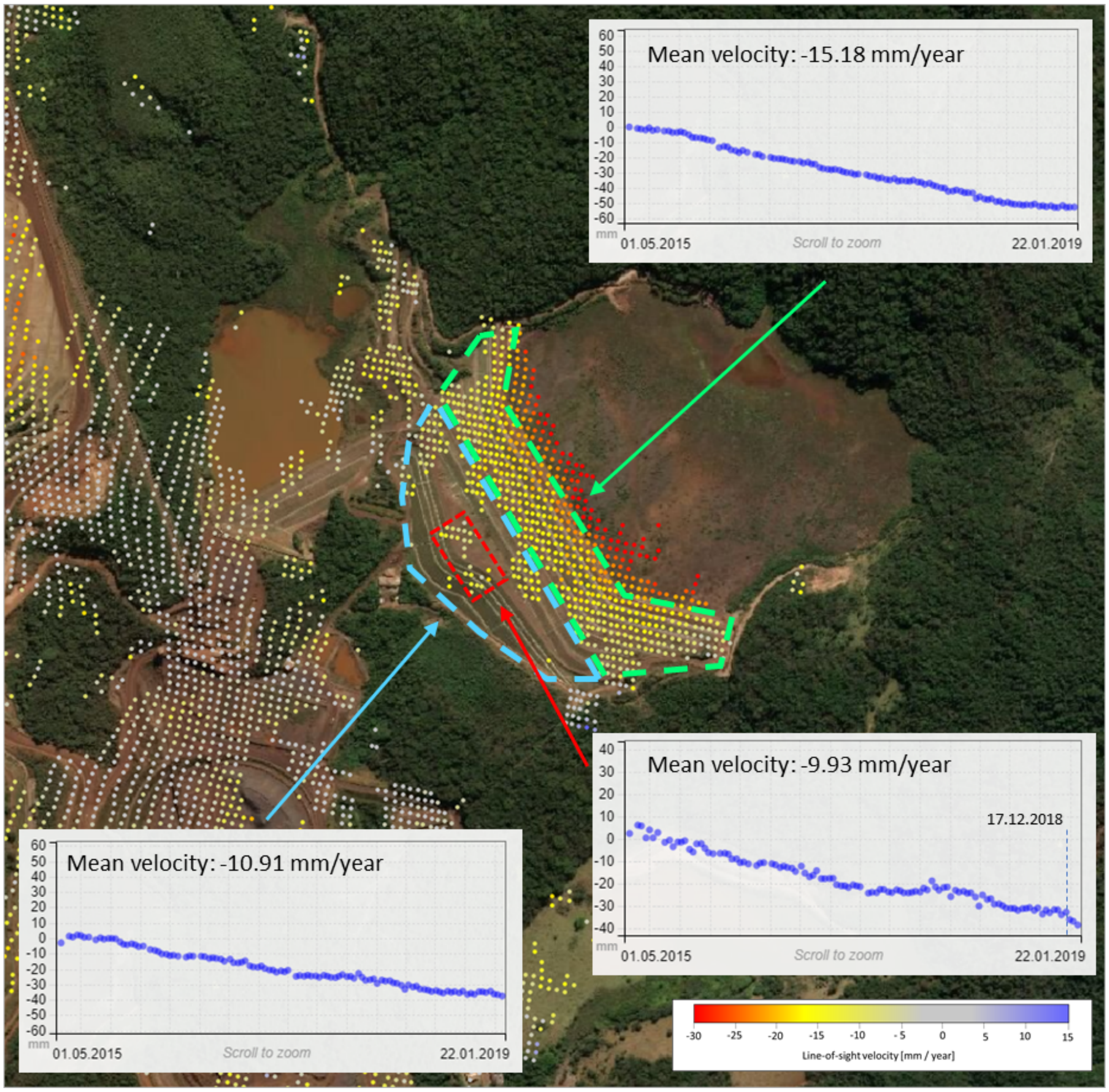

Figure 7: Line-of-sight displacements at the Feijão Mine tailings dam B-I in the period from May 2015 until just before the dam failure on January 25, 2019. The time series plots present the averaged displacement over time for all measurement points in the respective outlined areas.

Figure 8b presents the inverse velocity calculated from the filtered time series for the period from August 2018 until the failure of the dam, plotted as blue and green points. The section of the inverse velocity data points plotted in blue has been selected to fit a linear regression line to the data. The data points plotted in green have not been considered, as they precede the visible onset of the acceleration. The linear regression resulted in a coefficient of determination R^2 of 87%, which can be considered as good. Following the approach by Fukuzono (1985), the intersection of the regression line with the x-axis (inverse velocity = 0), gives a prediction of the time of failure. In our case the predicted time of failure is 22.01.2019, i.e., 3 days before the actual failure. The deviation from the actual time of failure can be explained by the strong filtering that had to be applied to reduce noise and the relatively short period of acceleration, which presents a rather weak statistical basis for the linear regression. The results are in good agreement with those presented by Gama et al. (2020) and Grebby et al. (2021). These two studies also give a detailed discussion of the sources of uncertainty in the inverse velocity method.

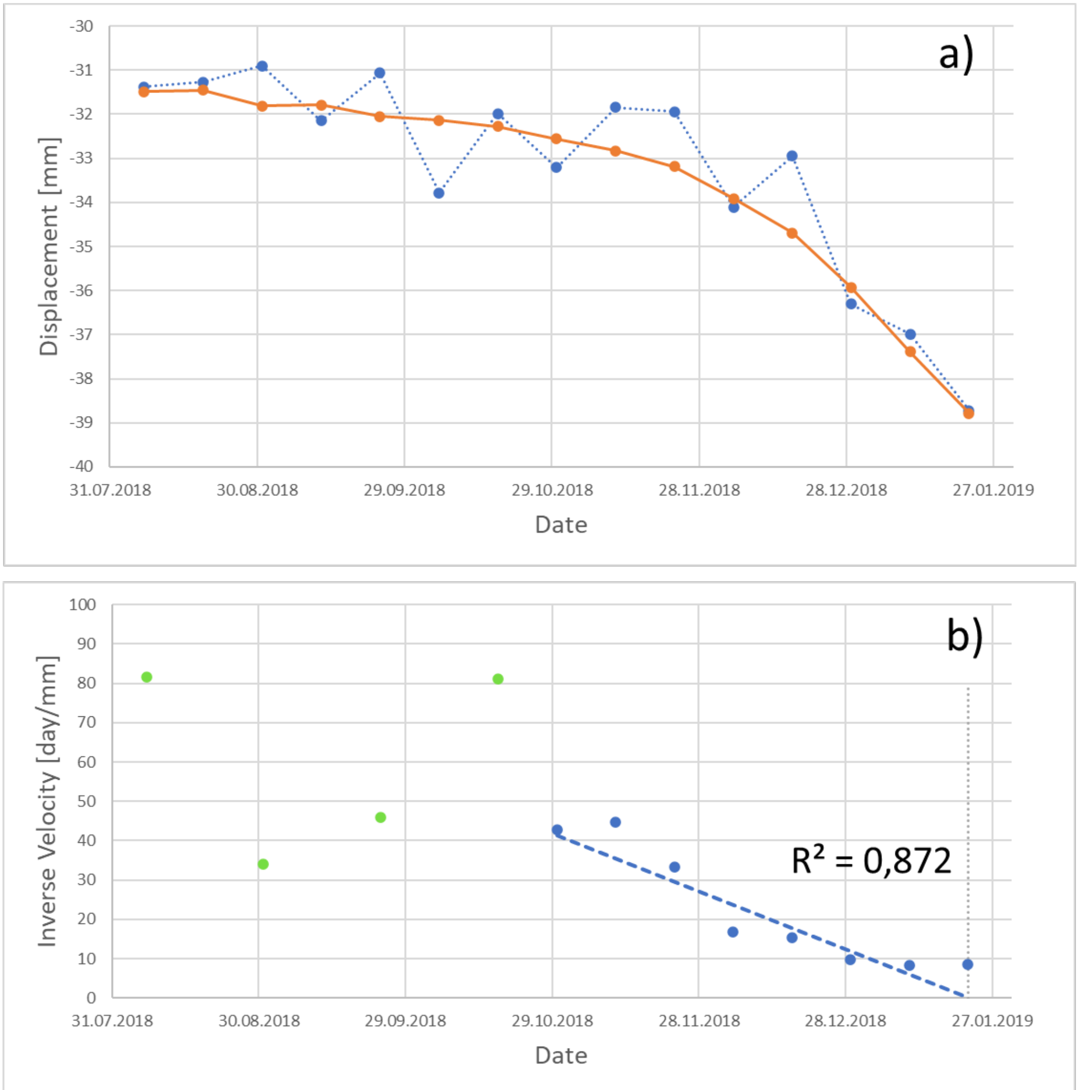

Figure 8: a) Line-of-sight displacement time series for the center part of Feijão Mine tailings dam B-I in the period from August 2018 until just before the dam failure on January 25, 2019 (blue: original time series; orange: filtered time series); b) Inverse velocity calculated for the same period (blue and green points). The blue data points have been used to calculate a linear regression (dashed blue line), resulting in a coefficient of determination R^2 of 87%. The intersection of the regression line with the x-axis, which provides a prediction of the date of failure, is on 22.01.2019.

Although the linear regression provides a good fit to the inverse velocity, the interpretation as a precursor should be considered with care, as the acceleration is only visible for a small number of acquisitions, and other sections of the time series also show hints of short-term acceleration, although with a less good fit to the inverse velocity. In order to conclude whether the InSAR method was able to capture a precursor to the failure, a comparison with auxiliary (ground-based) measurements would be necessary.

5 CONCLUSION

Monitoring of tailings dams is extremely important due to their structural design and often hazardous content. The presented case studies show that satellite based InSAR is a suitable tool for long-term displacement monitoring of tailings dams. We could show that data from the Copernicus Sentinel-1 constellation provide suitable numbers of measurement points also for comparably small dams. As the data from the Copernicus program are freely available, this type of monitoring can be conducted cost-effectively. The temporal resolution of the satellite constellation, of six to twelve days, is well suited for a long-term monitoring strategy. Yet, the Feijão Mine tailings dam case also showed that this resolution still might be too coarse for early warning purposes.

Where multiple orbits are available in ascending and descending orientation, the vertical and horizontal east-west velocity components can be obtained, which not only allows to monitor the magnitude but also the direction or mode of the displacement. This information is particularly important for tailings dams, where certain displacement modes might be tolerable to some degree. In such cases, the decomposed displacement measurements allow to distinguish problematic deformations from expected displacement modes and, therewith, help to better evaluate the safety of the dam.

6 ACKNOWLEDGEMENT

The research for this paper has been funded by two internal projects at the Norwegian Geotechnical Institute, namely the SP12-project "Towards sustainable mine tailings" (https://www.ngi.no/eng/Projects/Sustainable-mine-tailings/#About-the-project), and the GBV-project "Remote sensing and advanced image analysis (GeoSense)".

7 REFERENCES

Owen, J.R., Kemp, D., Lèbrea, É., Svobodovaa, K., Pérez Murillob, G. 2020. Catastrophic tailings dam failures and disaster risk disclosure. International Journal of Disaster Risk Reduction, Volume 42, January 2020, 101361. DOI:10.1016/j.ijdrr.2019.101361

Rosen, P.A., Hensley, S., Joughin, I. R., Li, F. K. 2000. Synthetic Aperture Radar Interferometry. Proceedings of the IEEE 88(3):333 – 382. DOI: 10.1109/5.838084

Rico, M., Benito, G., Díez-Herrero, A. 2007. Floods from tailings dam failures. Journal of Hazardous Materials 154 (2008) ,79–87. DOI:10.1016/j.jhazmat.2007.09.110

Ferretti, A., Prati, C., Rocca, F. 2000. Nonlinear Subsidence Rate Estimation Using Permanent Scatterers in Differential SAR Interferometry IEEE Transactions on Geoscience and Remote Sensing, Vol. 38, No. 5, September 2000

Ferretti, A., Prati, C., Rocca, F. 2001. Permanent Scatterers in SAR Interferometry. IEEE Transactions on Geosciences and Remote Sensing, 39(1), 8–20. doi:10.1109/36.898661.

Fukuzono, T. 1985. A New Method for Predicting the Failure Time of a Slope. Proceedings of the IVth International Conference and Field Workshop on Landslides, Tokyo, Japan

Gama, F.F., Mura, J. C., Paradella, W. R., de Oliveira, C. G. Deformations Prior to the Brumadinho Dam Collapse Revealed by Sentinel-1 InSAR Data Using SBAS and PSI Techniques. Remote Sens. 2020, 12, 3664; doi:10.3390/rs12213664

Grebby, S., Sowter, A., Gluyas, J., Toll, D., Gee1, D., Athab, A., Girindran, R. 2021. Advanced analysis of satellite data reveals ground deformation precursors to the Brumadinho Tailings Dam collapse. Communications Earth & Environment | (2021) 2:2, https://doi.org/10.1038/s43247-020-00079-2

Berardino, P., Fornaro, G., Lanari, R., Sansosti, E. 2002. A new algorithm for surface deformation monitoring based on small baseline differential SAR interferograms. IEEE Transactions on Geoscience and Remote Sensing, 40(11), 2375–2383. doi:10.1109/TGRS.2002.803792

Jamiolkowski, M. 2014. Soil mechanics and the observational method: challenges at the Zelazny Most copper tailings disposal facility. Géotechnique 64(8):590-619. DOI: 10.1680/geot.14.RL.002

Mazzanti, P., Antonielli B., Sciortino, A., Scancella, S., Bozzano, F. 2021. Tracking Deformation Processes at the Legnica Glogow Copper District Poland by Satellite InSAR II: Zelazny Most Tailings Dam. Land 2021, 10, 654

Robertson, P. K., de Melo, L., Williams, D. J., Wilson, G. W. 2019. Report of the Expert Panel on the Technical Causes of the Failure of Feijão Dam I. https://bdrb1investigationstacc.z15.web.core.windows.net

Recent experiences using space observation for quantitative risk assessment of tailings dams

Franco Oboni & Cesar Oboni
Oboni Riskope Associates Inc., Vancouver, BC, Canada

Claudio Angelino
Oboni Riskope Associates Inc., Turin, Italy

ABSTRACT: With the new requirements for tailings dams documentation and management there is a race to use remote monitoring (space, drones), sometimes coupled with machine learning and AI. Remote monitoring is often presented as a solve-all silver bullet. However, our experience is a bit more nuanced and this paper will explain why. We recently performed quantitative risk assessment (QRA) of tailings dams facilities and other geostructures in diverse geographic location. Because of confidentiality we keep the cases anonymous. The knowledge base of any dam is spread over many different documents, many authors and sources produced over time. Sometimes it is extremely poor. Building the knowledge base is a daunting task faced by anyone willing to perform a risk assessment. Space Observation offers the possibility to go back in time, using databases of satellite imagery. Our approach to QRA encompasses 30+ KPIs of which some are observable "from up above". However, a snapshot or the deformation of the last 5, 10, 20 years does not necessarily help predicting a failure. Indeed, several factors complicate the issue: normalization of deviance, human error, as well as design criteria in a divergent world that could make the structure deficient (ditch, etc., deposition patterns, beaches and pond). These can only be identified when analyzing extant reports. The available information discovery path is the file repository of the facilities. A good file repository contains a large quantity of documents allowing to grasp the state of the facilities. The access of documentation related to the construction and operations of the facilities are indeed paramount to understand their factual state and thus the likelihood of failures. Thus they cannot be neglected. With satellite imagery AND the documentation properly analyzed it is possible to understand possible deviance from the design.

1 INTRODUCTION

Dams are all exposed to natural and man-made hazards and they all have, to extents that are sometimes worrisome, gaps in their documented history, past incidents, etc. Experience shows no dam fails because of one single cause. So, beyond the intricacies of engineering analyses, humanity, with the cohort of retiring baby-boomers leaving with their knowledge, is facing an information gap which has stirred specific requirements in the recent Global Industry Standard for Tailings Management (GISTM).

Dam risks informational gap can be addressed using not a single, but a blending of wide-ranging approaches: covering archival documents; space observation (SO); Internet of Things; big data and finally Artificial Intelligence. Each approach brings in some benefits, but if poorly applied, may even be counterproductive. Considering the geographic spread of tailings dams portfolios managed by single mining companies, the cost of travel and classic monitoring, possible travel restrictions and the apparent ease of "seeing" what is happening in a portfolio from a single control room, there is a trend to consider Space Observation as a panacea. This paper examines SO and other approaches from the point of view of a risk assessor.

2 SPECIFIC REQUIREMENTS FOR DAMS RISK ANALYSIS

A risk assessment requires the hazards to be identified. Hazards are events or conditions generating potential losses. Potential hazards may include for example: meteorological conditions; human error, human factors (normalization of deviance); poor management (lack of controls of water balance for example); poor design (inadequate drainage), and finally engineering arrogance (lack of appreciation of mechanisms that trigger failure (Hartford, Baecher, 2004; ICOLD Bulletin 121, 2001)). It is self-evident that some of these are "space observable" and some aren't (Oboni et al., 2018). Affairs are complicated by the number of active and non-active significantly different dams around the world because of age, function, materials, construction style and care, maintenance care, and finally "behavior" or performance. Some information can only be retrieved by examining and understanding archival documents. Many Key Risk Indicators (KRIs aka KPIs) lie deep (pun intended) in the foundations and history of each structure. Dams can fail because of birth defects (e.g., insufficient depth of investigation, geology understanding, etc.), poor management (e.g., normalization of deviance, etc.) among many other causes that will neither be understood by reading only the latest third-party inspection, nor detected by space observation until, unfortunately, too late to allow mitigation.

As we expressed in an ICOLD 2019 paper (Oboni et al., 2019) KRIs generate from choices and historic evolution related for example to: material; berms & erosion; cross section; supervision; maintenance; monitoring; divergence from plans; and finally known errors and omissions. Monitoring is oftentimes considered the panacea, and its latest development, based on Space Observation even a better medicine. But is this true? This is the question we will try to answer in this paper. Furthermore, there are many possible ways to create the necessary knowledge-base for a GISTM conforming risk assessment and we believe that only a blending of these approaches is capable of bringing the answers needed for high quality risk assessments (e.g. benchmarking, causality analyses, etc.). Of course, the proportion of blending and the intensity of the efforts must be scaled as a function of the project size and resources available, and potential consequences.

3 SPACE OBSERVATION

Dam structure can be monitored using traditional instruments such as inclinometers and piezometers; ground-based methods such as ground-based SAR, photogrammetry and global navigation satellite system (GNSS). Remotely based methods include airborne Laser Imaging Detection and Ranging (Li-DAR) and space-borne InSAR. The Canadian company MDA started using InSAR for mining in the early 90s. We started using InSAR data for slope monitoring in 2004, when we used a 6-8 year long observation program for the risk assessment of a deep seated landslide in the Italian Alps. Numerous papers have summarized InSAR (Ulaby et al., 1986; Sousa et al., 2014) and our Tailings Management book includes a chapter on the subject (Oboni, Oboni, 2020). Reproducible measurements of ground movement have been demonstrated to be within 2 millimeters in a month (Henschel, Lehrbass, 2011; Henschel et al, 2015; Mäkitaavola et al, 2016) in optimal conditions.

Recent papers (Scaioni et al. 2018; Maltese et al., 2021) reviewed the available technologies for hydro dam deformation monitoring. Di Martire et al. (2014) compared the displacements estimated via a Differential SAR (DIn-SAR) interferometry technique, the "coherent pixels" technique (Blanco-Sánchez et al. 2008) with those recorded by a network of conventional ground-based sensors to monitor an earth dam.

3.1 *Concepts*

Space Observation offers numerous possibilities to re-create the history of a facility. However it is possible that on specific sites good quality stereo pairs going back many years may be available. Starting in the second half of the seventies, US spy-satellites started bringing back to Earth stereo imagery of various parts of the globe. The US has declassified those images allowing civilians to build, step by step, the history of a tailings facility. We listened to a presentation on this subject by Edumine/Photosat where they showed a real-life example. The precision is reportedly 15cm, acceptable to gain a general understanding of what happened on a site, e.g.: beach lengths, overall slope angle, dam construction phases and finally deposition history, but not enough for evaluating the deformations of a dam.

Radar interferometry and optical observation allow to gain a more in depth understanding of, for example: micro-deformations, humidity, ground temperatures and finally vegetation stress. Analyses can also go back in time using existing databases. We believe there is great value in approaching the study of a site from an historic point of view using both optical and radar imagery to build the history of the site.

3.2 *Some details on Space Observation*

Optical satellite technologies can be used to determine variation of water level by quantifying the extent of the water surface (Yue et al., 2019). Applying a single-channel algorithm to Landsat 4, 5, and 8 thermal images can extend monitoring to the past (from 2018 back to 1984) to perform a pond surface temperature analysis (Sharaf et al., 2019). In our recent studies bearing on a portfolio of inactive dams in Northern Ontario (confidential client) we have shown the effects of freezing thawing cycles, i.e. seasonal effects and long term deformation of the dams, emerging solifluction and erosion patterns, first detected by space observation, and then confirmed by site visits. Sources of inaccuracies are both the baseline of a given interferogram, compared to the critical value (Li et al., 1990; Zebker et al., 1992), and the precision of the ephemeris (Copernicus Sentinels POD Data Hub). The baseline controls the coherence of the interferogram, while the ephemeris accuracy has an influence on the conversion of interferogram phases to absolute height (Reigber et al., 1996). Water levels can be indirectly determined by mapping the reservoir water surface extent using optical images (Yue et al., 2019; Ma et al., 2019; Li et al., 1990).

3.3 *Recent case study*

We recently developed additional experiences on a number of dams in various locations, including semi-Arctic conditions. The satellites used were Sentinel-1B & Radarsat 2 for InSAR deformation and Landsat 5, 7, 8 for Normalized Difference Vegetation Index (NDVI). Below we present a summary of our findings.

NDVI with medium-resolution optical imagery was aimed at analyzing whether a target area contains live green vegetation and to perform a qualitative assessment of the vigor of that vegetation. The process used to perform the analysis consists of: acquiring and processing archive optical satellite image data over each site in order to establish a “history” of the site; processing the imagery to calculate the NDVI and highlight plant vigor and areas of standing water to determine the relative water level; completing an assessment of each considered tailings facility. Note, the calculation of the NDVI value may be sensitive to a number of factors including atmospheric effects, clouds and cloud shadow, soil moisture variation and anisotropic effects. Our comments can be summarized as follows: good vegetation health can be linked to possible drainage on the dams bodies and vicinities; visible changes in vegetation can be linked to changes in relative water levels; whenever possible, space observation results should be checked on the ground with visual inspection and instruments data analysis, especially if there is no observation history of the site.

Deformation monitoring (InSAR) program aimed to identify areas where ground motion patterns are: changing over time; remaining consistent over time; and related to the development of new deformations (i.e. previously unobserved deformations beside seasonal variations). The program initially included one year backward looking analysis and one year forward looking observation. It quickly became obvious that there was significant value in extending the backward analysis as far as possible to understand seasonal effects (freezing-thaw cycles), the effects of meteorology and thus to filter out false positives. At the end the study allowed to identify deformations related to: freeze thaw cycles; areas of potential deformation along dams spillways and the dams themselves; potential subsidence that combined with toe heave could highlight a potential developing instability areas.

Short-Wave InfraRed (SWIR) and near-infrared bands in the Landsat 8, were used to determine the relative water levels during the same periods of time of the NDVI program. Using this band combination makes the water appear darker and the effects of shallow versus deep water and relative water levels for each site were determined from this processing.

Overall, the study showed the great potential of SO on TSF areas, with specific reference to ground movements, vegetation health and water levels within the ponds. The process allowed to drive onsite observations requests including in locations where subsequent site visit confirmed signs of solifluction not previously identified and to draw information allowing to update the a priori ORE2_Tailings™ probability of failure estimates and the NDVI analysis detected anomalies in one of the dams area where some materials were deposited.

The following final comments can then be summarized.

Pros of space observation (SO). SO allows to analyze deformations and movements of wide areas starting from "historic" perspective. This constitutes a significant advantage when undertaking an analysis (risk assessment) of sites with poor archival documentation. SO can easily cover an entire multi-dam area, where a more traditional, costlier ground or drone systems would only make local or fragmentary observations. It can detect deformations and incipient phenomena that would escape a site visit visual observation. It gives clues on potential issues which would not otherwise be visible from the ground via a more traditional "punctual" monitoring system. SO allows to go back in time to detect past behaviors and seasonal effects. It can help to overcome bad weather and difficult or hazardous access conditions. It can reach a higher efficiency if reflectors are installed on the ground in critical spots, to improve the quality of the signal and the reliability of the data. NDVI coupled with meteorological data allow an integrated understanding of the evolution of the site environment.

However, SO also has drawbacks, particularly when related to vegetation cycle interpretation and to measurements taken in nonstandard conditions (water surfaces or very wet areas for example) which may be difficult to interpret. It is sometimes impaired by persistent significant vegetation which makes the measurements interpretation uncertain; can be negatively affected by signal noise disturbances; is negatively affected by the presence of ice and snow.

Thus our experience is that:

1) In difficult ground conditions the use of fixed reflectors should be considered to enhance precision.

2) Any study should start with an extended historic approach, vital to build a solid knowledge basis.

3) The measurements need to be constantly interpreted with great care by expert personnel to address further data requests or more detailed ground interpretation.

4) Analysts should try to correlate unusual behaviors with physical events, as a sudden jump in deformation could for example be linked to a significant meteorological event or to seismic activity, by pursuing attentive visual monitoring and geological survey after unusual readings with cross-checks between ground-based and space-based results.

5) Reading area should be extended to dam slopes and surrounding areas and focus on details near sensitive structures or geological features, thus making the most of the capacity of space monitoring to inspect wide areas which could not be easily and cheaply seen from the ground.

6) Always try to establish cumulative long-term deformations and deformation vectors and avoid as much as possible interruptions in the sequence of the space monitoring.

7) InSAR observation data should not be delivered "as they come" to a wider audience or be used to automate alert systems as attentive expert analysis is required for correct interpretation. Neither should they be used to establish "alert" thresholds without an overall simultaneous understanding of the observation results and the structures' conditions and behavior. Indeed false positive can make the alarm system "cry wolf" and lead to normalization of deviance.

8) If activities are foreseen on a closed site and no in situ observation is performed it is advisable to deliver a schedule of possible work that will be conducted onsite, or any changes foreseen on the ground.

9) Blending techniques is highly effective. Pay attention to any potential changes in the satellite orbital schedule, changes of satellite (over time) to avoid data misinterpretations.

10) InSAR results are displayed at the center of the pixels thus the "colored dot" position is not precise. Beware "over-interpretation" of the results!

11) No analysis should be attempted without climatological and meteorological context pairing, particularly in view of the significant ongoing climate changes.

12) Changes of density in water/tailings, including partially frozen areas, may lead to interferences.

13) Space Observation, like any other monitoring program, cannot shelter its users against fragile failures such as for example those generated by static or dynamic liquefaction, undetected brittle layers, etc.

4 MONITORING RECORDS

Each time we start a new risk assessment we go through monitoring records. It is long and tedious, and generally very frustrating. Even the exact location of boreholes and monitoring instruments is oftentimes not clearly mapped, let alone their elevation. In those conditions it is even difficult to understand if, for example, an inclinometer is indeed anchored in bedrock or not. Thus, we see the benefit in using databases and business intelligence platforms, big data and Internet of things (IoT) but we also see the hazards linked to this practice. They produce beautiful graphics that may be anchored in "alternate reality" rather than in rock, pun intended. And then, of course, instruments break down and may not be replaced as they should. Sometimes their placement follows ease of installation rather than the needs of knowledge-building.

Big data and IoT are indeed becoming common features in all sorts of business activities. They will help define better ranges for reliability and failure of a system's elements, and make it possible to search world-wide occurrences of near-misses, losses, news, etc. At the other end of the spectrum, Thick data are useful to understand deep motivations and can foster SLO, CSR and ESG by fostering proper communication (Oboni, Oboni 2021).

Big data and Thick data are actually two sides of the same coin (Fig. 1). It is essential to understand their differences.

- Big data is a term for large or complex data sets that traditional software has difficulties processing. Processing generally involves, for example, capture, storage, analysis, curation, searching, sharing, transferring, visualizing, querying, updating, etc. However, big data also often refers to the use of predictive analytics, behavior analytics or certain other advanced data analytic methods. Analysis of data sets can find new correlations to spot trends, prevent emerging issues, etc. but focusing solely on Big data can reduce the ability to imagine how a system might be evolving. Big data only is not sufficient for risk assessment, and in particular hazard identification. It can create a distorted view of the risk landscape surrounding an entity. Big data relies on machine learning, isolates variables to identify patterns, reveals insight. Big data gains insight from scale of data points, but loses resolution details. It does not tell you why those patterns exist and is unprepared to cope with new extremes, divergences.
- Thick data requires careful observation of human behavior and its underlying motivations. Thick data is qualitative information that provides insights into the everyday emotional lives of a given population, i.e. how a facility is managed and decisions. taken. Thick data relies on human learning, accepts irreducible complexity, reveals social context of connections between data. Thick data gains insight from anecdotal, small sample stories, but loses scales. It tells you why, but misses identifying complex patterns or future behavior.

To date, big data and thick data have been used and supported by different groups. Organizations grounded in the social sciences tend to use thick data, while corporate IT functions and data scientists tend to favor big data. This constitutes a perfect example of silo culture. Ideally, big data and thick data should "talk to each other", but most of the time do not because of siloed approaches.

If one is seeking a map of an unknown risk territory (risk landscape) and data are scarce, then thick data is the tool of choice. As data availability grows on its way to becoming big data, integrating both types of data becomes important. In the case of innovative companies, that combined insight can be highly inspirational.

When performing risk assessments, we always collect and analyze stories, anecdotes and loss reports to gain insights into pre-existing states of the system. The combined insight may tell us that a system that “looks wonderful” actually has a congenital defect that may raise its probability of failure. Big data would not be capable of highlighting that aspect but could probably reveal a pattern between third-party observations and, say, meteorology. In fact, it could identify patterns among any other groups of variables, which could sound an alarm on shorter-term emergent hazards.

Working successfully with integrated big and thick data certainly enhances any risk assessment. Over the years we have found ways to integrate data from multiple sources and of various natures in our risk assessments. We routinely use incomplete thick data sets in conjunction with expert opinions and literature to generate a first, a priori estimate of the probability of occurrence of hazards and failures. This immensely increases the value of the first-cut risk assessment, which can then be updated using big data and Bayesian techniques.

The combined approach also makes it possible to enhance the value of big data, avoid capital squandering, and reduce the running cost necessary to obtain big data. Recent studies have shown that without that approach data oftentimes remain virtually unused.

Integrating big data and thick data brings value and should be fostered. Thus, it is crucial to explore how big data and thick data can supplement each other. This demands the integration of qualitative evaluation and expert-based judgments with hard quantitative data.

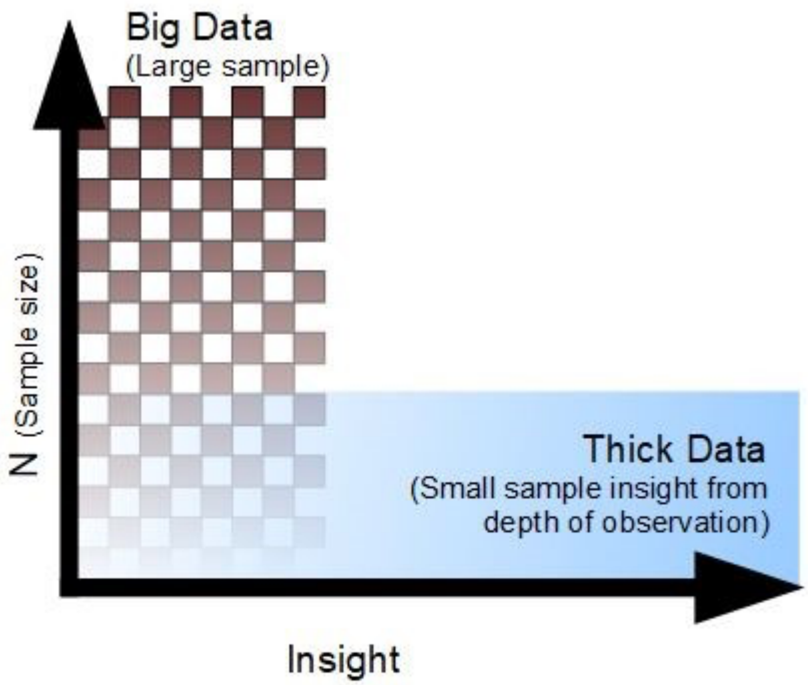

Fig. 1 Big data vs. thick data

Nowadays, measurements, space observation results can be broadcasted to a central record which in turn can deliver them to a “control room” where graphic displays render the global situation in real time. Internet of Things adds wonderful data and Artificial Intelligence may gobble all of this and tell us… what exactly? Let’s remember that AI builds its knowledge on what it feeds on. Indeed, AI is not good, as far as we know, in forecasting something it has never “seen” and is highly unusual.

In that sense it is not better than a human being confronted with a new situation. The key to allowing IoT and AI to deliver a better job lies in blending backward space observation with as long as possible monitoring history. Do not start with today’s data and hope AI can help you tomorrow morning!

5 ADVANCED DOCUMENTS SEARCH FOR KNOWLEDGE BASE CREATION

Once the space observation and monitoring records are gathered we are left with the annoying, and less glamorous, yet paramount part of tailings dams knowledge base creation. That is to ingest, check and understand the mass of reports that may exist to document a tailings dam since inception and cross check it with SO, if possible. When clients tell us to go visit a tailings operation in order to start a risk assessment, we always try to dissuade them from starting the deployment that way. We want to know the dam system before we visit it. As a result, when we go to the site we want to be able to reconnect what we see with what we have learned. Thus, we start by spending days reading and annotating extant reports. That's the only way we know to discover hidden deficiencies, to evaluate uncertainties and to come up with the KPIs we need to feed our quantitative risk assessment platform (Oboni, Oboni, 2020).

As volumes of global data increase exponentially risk analysts have to review larger volumes of information quickly and accurately to increase process efficiencies and avoid paralysis. Fortuitously, the capabilities of technology and machine learning to augment human review have been growing at a rate comparable to that of data (Oboni, Oboni, 2021). Today, we find ourselves with highly developed technological approaches, but it can be difficult to know which technology to utilize and why.

In this section we highlight technologies and tools commonly implemented to drive proactive strategies and work in partnership with reactive tools, in order to aid in risk identification. We also touch on the importance of project management for effective technology implementation in this field.

Please note that the list provided is not exhaustive, as there are many other analytics and machine learning tools that can be deployed to help streamline the ability to identify hazards. However, these are the most common tools used, for instance, in the legal discipline and scientific research and that can be tweaked for risk assessment purposes.

Let's note for a start that there is no one information governance strategy, but professionals in this space commonly refer to it as "getting your data house in order". The process of information governance removes junk data (Fig. 2), reduces the risk of errors in your data and/or alleviates the downstream work of having to sift through stacks of digital hay to find that needle.

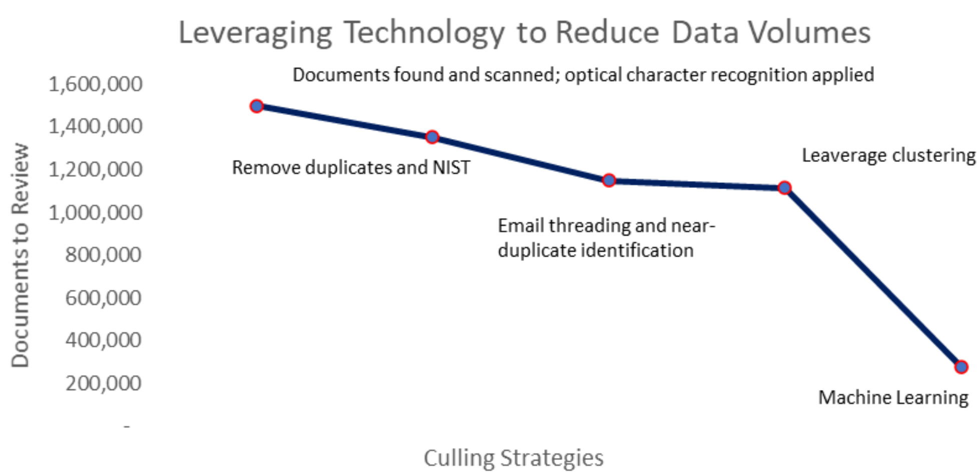

Fig. 2 Leveraging technology to reduce data volumes: stepped approach can reduce documents number five- to six-fold (Oboni, Oboni, 2021)

Due to the age of archival documents, optical character recognition is of course a must. Beyond that, here is a sample of analytic and machine-learning tools, what they do, and why we use them:

- Email threading: identifies and groups together emails that are part of the same conversation/thread: useful to suppress duplicates.

- Near-duplication: groups documents that are highly similar to each other and identifies differences, similar to track-changes. It is useful for identifying documents that have undergone revisions, or for finding 100% text-similar documents of different formats.
- Categorization: allows many documents or paragraphs to be submitted as examples and returns documents that are conceptually similar to those examples: similar to concept searching, but on a larger scale.
- Keyword expansion: identifies different language used to express the same or similar concepts.
- Supervised machine learning and continuous active learning: uses input from reviewers to categorize documents in the database and predict whether they are likely to be relevant. Data volumes can be substantially reduced using this technology.

There are many reasons to incorporate these tools into Quantitative Risk Assessments (QRA) workflows, including providing early access to key information, organizing information faster than ever before, decreasing the time needed for review, reducing costs associated with review, and the ability to handle more work while keeping headcount the same.

Below, we briefly highlight the execution and monitoring/controlling aspects of the implementation of technology in tailings dams risk assessment.

- "Garbage in, garbage out". The phrase skillfully articulates that, in the sense of training continuous active learning tools, the end result directly correlates to user input (human reviewer). The software continues to learn as more documents are coded by human reviewers and uses advanced statistics to determine when reviewers can stop based on the probability and predicted number of documents that directly correlate to human training may remain in the unreviewed set. Therefore, human input remains so far the most essential piece of any machine learning workflow.
- As you embark on your technology implementation journey, it is important to remember that there is not a "magic button" that will completely remove the human element of review. There are tools to help augment human review so identifying hazards/anomalies can be done faster and more accurately. The ultimate goal of incorporating technology into human review is to weed out irrelevant documents and focus on the pertinent issues, while minimizing time spent and concentrating efforts on high value tasks.

Like for monitoring, archival documents search and interpretation is paramount to complete the knowledge base necessary for a rational and sensible risk assessment.

6 CONCLUSIONS

Tailings dams risk assessment must be performed in a rigorous way where systems under scrutiny, their hazards and potential divergence must be clearly and transparently identified to avoid meaningless results. We have first discussed space observation monitoring, a method that, when properly implemented, can bring significant advantages to the analyses, particularly with respect to the past behavior of a structure, which cannot be investigated with any other method. We have of course also stressed the importance of monitoring and archival documents reviews showing how blending these techniques is important to support rational risk assessments. Pros and cons have been highlighted and some recommendations have been suggested: in particular, measurements and results need to be interpreted with great care by expert personnel. Space Observation does not substitute any other monitoring system and the usual on-site visual controls and like any other monitoring program, cannot shelter its users against fragile and sudden failures. In the second part we have concentrated our attention on the need of creating a knowledge-based database of past documentation via modern advanced search techniques by highlighting the new technologies and tools available to us for a proactive strategy in documental review.

7 REFERENCES

Blanco-Sánchez, P.; Mallorquí, J.J.; Duque, S.; Monells, D., 2008. The Coherent Pixels Technique (CPT): An Advanced DInSAR Technique for Nonlinear Deformation Monitoring. Pure Appl. Geophys. 165, 1167–1193.

Di Martire, D.; Iglesias, R.; Monells, D.; Centolanza, G.; Sica, S.; Ramondini, M.; Pagano, L.; Mallorquí, J.J.; Calcaterra, D., 2014. Comparison between Differential SAR Interferometry and Ground Measurements Data in the Displacement Monitoring of the Earth-Dam of Conza Della Campania (Italy). Remote Sens. Environ., 148, 58–69.

Hartford, D. N. and Baecher, G.B., 2004. Risk and uncertainty in dam safety. Thomas Telford.

Henschel, M.D., Lehrbass, B., 2011. Operational Validation of the Accuracy of InSAR Measurements over an Enhanced Oil Recovery Field. Fringe 2011. Frascati, Italy: European Space Agency.

Henschel, M.D., Dudley, J., Lehrbass, B., Shinya S., Stockel, B.-M., 2015. Monitoring Slope Movement from Space with Robust Accuracy Assessment. Slope Stability 2015. Cape Town, South Africa: SAAIM.

International Commission on Large Dams, 2001. Tailings dams: risk of dangerous occurrences: lessons learnt from practical experiences (No. 121). United Nations Publications.

Li, F.K., Goldstein, R.M., 1990. Studies of Multibaseline Spaceborne Interferometric Synthetic Aperture Radars. IEEE Trans. Geosci. Remote Sens. 28, 88–97.

Ma, Y., Xu, N., Sun, J., Wang, X.H., Yang, F., Li, S., 2019. Estimating Water Levels and Volumes of Lakes Dated Back to the 1980s Using Landsat Imagery and Photon-Counting Lidar Datasets. Remote Sens. Environ. 232.

Mäkitaavola, K., Stöckel, B.-M., Sjöberg, J., Hobbs, S., Ekman, J., Henschel, M.D., Wickramanayake, A., 2016. Application of InSAR for monitoring deformations at the Kiirunavaara mine. 3rd International Symposium on Mine Safety Science and Engineering, Montreal.

Maltese, A.; Pipitone, C.; Dardanelli, G.; Capodici, F.; Muller, J.-P., 2021. Toward a Comprehensive Dam Monitoring: On-Site and Remote-Retrieved Forcing Factors and Resulting Displacements (GNSS and PS–InSAR). Remote Sens. 13, 1543. https://doi.org/10.3390/rs13081543)

Oboni, F.; Oboni, C., 2020. Tailings Dam Management for the Twenty-First Century, Springer International Publishing, ISBN 978-3-030-19447-5.

Oboni F., Oboni, C., 2021.Convergent Leadership – Divergent Exposures, Springer International Publishing, ISBN 978-3-030-74930-9.

Oboni, F.; Oboni, C.; Morin, R., 2019. Innovation in Dams Screening Level Risk Assessment, ICOLD 2019, Ottawa, June.

Oboni, F.; Oboni, C.; Morin, R.; Brunke, S.; Dacre. C., 2018. Space Observation, Quantitative Risk Assessment Synergy Deliver Value to Mining Operations & Restoration, Symposium on Mines and the Environment, Rouyn-Noranda, Québec, June 17 to 20.

Reigber, C.; Xia, Y.; Kaufmann, H.; Massmann, F.-H.; Timmen, L.; Bodechtel, J.; Frei, M. Fringe, 1996. 96 Workshop on ERS SAR Interferometry. In Proceedings of the Fringe 96 Workshop, Zurich, Switzerland, 30 September–2 October

Scaioni, M.; Marsella, M.; Crosetto, M.; Tornatore, V.; Wang, J., 2018. Geodetic and Remote-Sensing Sensors for Dam Deformation Monitoring. Sensors 18, 3682.

Sharaf, N.; Fadel, A.; Bresciani, M.; Giardino, C.; Lemaire, B.J.; Slim, K.; Faour, G.; Vinçon-Leite, B., 2019. Lake Surface Temperature Retrieval from Landsat-8 and Retrospective Analysis in Karaoun Reservoir, Lebanon. J. Appl. Rem. Sens. 13, 044505.

Sousa, J.J.; Hlaváˇcová, I.; Bakoˇ n, M.; Lazecký, M.; Patrício, G.; Guimarães, P.; Ruiz,

A.M.; Bastos, L.; Sousa, A.; Bento, R., 2014. Potential of Multi-Temporal InSAR Techniques for Bridges and Dams Monitoring. Procedia Technol. 16, 834–841.

Ulaby, F.T.; Moore, R.K., Fung, A.K., 1986. Microwave Remote Sensing: Active and Passive: Volume 2: Radar Remote Sensing and Surface Scattering and Emission Theory, Artech House, Inc.

Yue, H.; Liu, Y., 2019. Variations in the Lake Area, Water Level, and Water Volume of Hongjiannao Lake during 1986–2018 Based on Landsat and ASTER GDEM Data. Environ. Monit. Assess. 191.

Zebker, H.A.; Villasenor, J., 1992. Decorrelation in Interferometric Radar Echoes. IEEE Trans. Geosci. Remote Sens. 30, 950–959.

Effects of tailings viscosity on liquefaction triggering analyses

Miguel A. Mánica
Institute of Engineering, National Autonomous University of Mexico, Mexico City, Mexico.

Marcos Arroyo & Antonio Gens
CIMNE – Universitat Politècnica de Catalunya – BarcelonaTech, Barcelona, Spain

ABSTRACT: Recent analyses have suggested that creep or rate effects may be present in some tailings and can play a role in triggering liquefaction failure. However, the role of creep in liquefaction triggering analysis of tailing dams is complicated by the effects of drainage and/or consolidation. To gain some understanding of this aspect, we investigate liquefaction triggering using coupled hydromechanical analyses based on CASM-visco, a recently developed visco-plastic extension of CASM. CASM-visco endows the soils with rate-dependent behaviour and enables creep. The model is used to reanalyse the case of the Merriespruit dam failure to illustrate the effect of variable tailings rate-dependence and permeability on liquefaction triggering. It turns out that, if the Merriespruit tailings had been strongly rate-dependent, liquefaction failure will not have been triggered as easily as it happened.

1 INTRODUCTION

Static liquefaction of tailings has caused a series of major industrial disasters in recent years, leading to a substantial re-assessment of tailings management guidelines (e.g. ICMM, 2021). Part of this re-evaluation involves a push towards performance-based design of tailings facilities, particularly, (see ICMM, 2021, 3.4.3.6), for those in which a brittle failure mode -such as static liquefaction- is a credible possibility. Performance-based design involves sequential forecasting of dam behaviour (displacements, deformations, pore pressures…) through all construction phases and systematic validation and updating of the forecasting tools with field data. This kind of intense observational method would require realistic modelling tools, such as stress-deformation analyses. Such analyses have been used for forensic triggering analysis in recent years (Morgenstern et al., 2015; Jefferies et al., 2019; Robertson et al., 2019) and are now becoming common in industrial applications (Sottile et al., 2020; Valdivia et al., 2020; Li et al. 2021).

A key element for this kind of analysis is the hydromechanical constitutive model employed for tailings. Critical state soil mechanics offers a clear framework to understand static liquefaction (Jefferies and Been, 2016) and to formulate constitutive models that reproduce such behaviour. This approach was pioneered by the Nor-Sand model (Jefferies, 1993) but it is by no means restricted to that particular model formulation. For instance, the Clay and Sand Model (CASM), was proposed by Yu (1998) as an extension of classical critical state models, such as the original Cam Clay, to explicitly incorporate the state parameter concept. Slightly evolved versions of CASM are capable of reproducing the undrained softening underlying the flow liquefaction phenomenon as observed in laboratory tests (Gens, 2019), in field tests such as the CPTu (Monforte et al. 2021), or in tailings dam failures (Mánica et al. 2021a).

Critical State models such as Nor-Sand or CASM are formulated for rate-independent elastic-plastic materials, that is, for materials that are non-viscous and do not creep under constant loads. However, it has been recognized since long that most soils show a certain degree of rate-dependency or creep behaviour (Mitchell & Soga, 2005). For the case of tailings dams, creep of fine-grained materials at the foundation was occasionally identified as a relevant design issue, (Wedage et al. 1998). However, the topic has gained more attention recently, after Robertson et al (2019) identified creep of the tailings materials themselves as a major contributing factor to the liquefaction failure observed in the Brumadinho dam.

The role of creep in liquefaction triggering analysis of tailing dams is complicated by the effects of drainage and/or consolidation (Boulanger et al. 2020). To gain some understanding of this aspect, we investigate liquefaction triggering using coupled hydromechanical analyses based on CASM-visco, a viscoplastic extension of CASM. After describing CASM-visco, we use it to reanalyse the case of the Merriespruit dam failure to illustrate the effect of variable tailings rate-dependence and permeability on liquefaction triggering. However, before going into the analysis it is useful to clarify some concepts.

2 LIQUEFACTION TRIGGERING AND UNDRAINED CREEP FAILURE

In the analysis of static liquefaction, it is customary to distinguish two stages: susceptibility and triggering. Susceptibility analyses aim to identify if the conditions in a deposit are potentially liquefiable. The effect of some conditions such as dilatancy or saturation on liquefaction susceptibility is well established. If a soil is contractive, it is more susceptible to liquefaction than if it is dilatant. If it is fully saturated, is more susceptible that if partially saturated. It is unclear, however, how the condition of being more or less viscous (i.e. able to creep) does affect liquefaction susceptibility.

Triggering aims to identify if a potentially liquefiable deposit will indeed liquefy after some loading event. Loading is here understood in a hydromechanical sense, involving a change in drainage conditions, mechanical loading, or both. Evaluation of triggering mechanisms is far more involved than susceptibility analyses. Several authors (Martin & McRoberts, 1999; Boulanger et al. 2020) have identified undrained creep as a potential liquefaction triggering mechanism. However, that identification is problematic, as we shall see.

When discussing creep is useful to distinguish between two limiting cases: drained and undrained creep. Drained creep effects in soils are due to the passage of time without any observed pore pressure or effective stress changes, and are frequently described using the term “aging”. Aging is widely acknowledged as being positive for soil strength and stiffness (Schmertmann, 1991). Aging effects are known to reduce the risk of seismic-induced liquefaction in natural soils and fills (Towhata et al. 2017) and have been used to explain the improved resistance to earthquakes of old tailing dams in Chile (Troncoso et al. 1991). Aging effects are rarely considered in design, because they are difficult to quantify and ignoring them tends to err on the safe side.

Undrained creep involves two different aspects of soil behaviour: limited drainage and creep. The material should remain undrained while creeping under a constant load. Soils subject to constant shear stress under undrained conditions show significant creep strain, and that creep strain is accompanied by increases in pore pressure (e.g. Arulanandan et al. 1971). The constant applied load only guarantees constant total stress, whereas pore pressure and effective stresses are changing. Because of these effective stress changes, undrained creep is not, strictly speaking, a pure creep process, although the terminology is generally accepted (Augustesen et al. 2006).

The stress path observed during triaxial undrained creep follows a q-constant p’-reducing trajectory that is similar to that imposed during constant shear drained tests (CSD). There is ample experimental evidence showing that instability of liquefiable soils may be triggered using CSD (e.g. Skopek et al. 1994). CSD are employed as a laboratory proxy for drained triggering processes, which in the field may correspond to events such as a slowly raising water table.

There are also laboratory experiments (e.g. Leong & Chu, 2002) in which undrained creep has been used to trigger liquefaction instability. In these experiments, the undrained condition is forced by drainage line closure. Strictly speaking, it is that sudden hydraulic change what may be identified as the triggering factor. Creep is not the trigger, but rather one of the conditions that controls how and if the closed drainage line (the actual “trigger”) may lead to failure.

In tailings dams, drainage is controlled by the permeability of the different layers involved and by the presence (or else) of drainage facilities which are typically far more complex than those in a triaxial apparatus. A pure hydraulic trigger to release field undrained creep is thus unlikely. What is instead more likely is a mechanical trigger, that is: a sudden load increase that elicits an undrained response. That undrained response will be modulated by the specific viscous properties of the soil and will thus result in more or less creep. Note that, again, the ability to creep is not the trigger, but rather a material condition that will enable some triggers, but not others. This last observation may be best understood by reference to the experience gained with clays.

Because clays are very impermeable, they offer more possibilities to observe undrained creep in the field, and most experience in this topic has been gained with them. Undrained creep of clays may be also understood as a viscous response that delays the effects of sudden mechanical loading. Loads that, for a material that cannot creep, would have caused immediate failure, would still cause failure, but only sometime after their application. This interpretation is supported by the rate dependency of undrained strength. When undrained failure is forced, fast loading rates result in higher strengths. This added viscous component of undrained resistance has a double-face in design. A delayed undrained failure may be observed under the long-term permanent loads of an embankment, particularly if the design has relied on undrained strengths measured at higher rates than those applied in the field (Bjerrum, 1973). On the other hand, the enhanced short-term strength resulting from viscosity can be usefully exploited when considering short-duration loads, as is the case for railway embankments subject to variable train loads (Lehtonen et al. 2015).

Summarizing: the viscous or creeping properties of a soil do not act as a trigger, but as a conditioning factor, that alongside its permeability, initial state, and effective strength will determine if a particular loading is able to trigger liquefaction. To explore this issue in a quantitative manner we need a suitable constitutive model.

3 CASM-VISCO: A MODEL FOR CREEP ANALYSIS OF LIQUEFIABLE TAILINGS

For reasons of space, the inviscid CASM constitutive model is not described here. The original model can be consulted in Yu (1998), while the slightly modified version employed in this work is described in Mánica et al. (2021a). A viscoplastic extension of CASM is obtained using the overstress theory of Perzyna (1966), where the following strain decomposition is assumed:

$$\dot{\boldsymbol{\varepsilon}} = \dot{\boldsymbol{\varepsilon}}^{\mathrm{e}} + \dot{\boldsymbol{\varepsilon}}^{\mathrm{vp}} \tag{1}$$

where $\dot{\boldsymbol{\varepsilon}}^{\mathrm{e}}$ and $\dot{\boldsymbol{\varepsilon}}^{\mathrm{vp}}$ are the elastic and viscoplastic strain rate tensors respectively. Viscoplastic strains rates are given by

$$\dot{\boldsymbol{\varepsilon}}^{\mathrm{vp}} = \frac{\langle \Phi(f) \rangle}{\eta} \frac{\partial g}{\partial \boldsymbol{\sigma}'} \tag{2}$$

where η is a viscosity parameter, Φ is the overstress function that depends on the rate-independent yield function f, g is the plastic potential function, $\boldsymbol{\sigma}'$ is the effective stress tensor, and $\langle \bullet \rangle$ are the Macaulay brackets accounting only for the positive part of Φ. The following expression was adopted for the overstress function:

$$\Phi(f) = \left(\frac{f}{f_0} \right)^N \tag{3}$$

where f_0 is a reference normalisation stress and N is another viscous parameter, defining the order of the Perzyna's formulation. Because the yield function of CASM is already formulated in a dimensionless form, normalization is not needed and, therefore, $f_0 = 1$ can be assumed. However, the gradient of the plastic potential function $\partial g / \partial \boldsymbol{\sigma}'$ is not dimensionless, resulting in units of $\mathrm{m^2\ s\ kN^{-1}}$ for η. Details on the numerical implementation of Perzyna's viscoplasticity can be found in Mánica et al. (2021b).

4 CASE STUDY

The case study corresponds to the Merriespruit tailings dam failure, which took place on 22 February 1994 in South Africa. A portion of a wall in one of the compartments of the dam failed resulting in some 600,000 $\mathrm{m^3}$ of liquid slime rushing through the town, causing the death of 17 people and a major environmental disaster. The failure occurred a few hours after a heavy thunderstorm that, due to insufficient freeboard, resulted in wall overtopping. The spilling water eroded loose slimes placed on the lower slope resulting ultimately in a massive overall failure. Detailed accounts of the Merriespruit tailing dam construction, operation, and failure are given by Wagener (1997), Strydom and Williams (1999), or Fourie et al. (2001).

The failure was surprising because previous overtopping incidents in similar dams had resulted in erosion gullies, but not in mass failure. Based on a comprehensive post-failure site investigation, Fourie et al. (2001) identified tailings flow liquefaction as the major mechanism leading to the catastrophic slide. The overtopping and subsequent erosion of the impoundment wall were identified as triggering factors. A comprehensive stress-deformation analysis by Mánica et al. (2021a), using CASM, confirmed that, under the conditions of the tailings in Merriespruit, a relatively small erosion at the face was sufficient for the initiation and propagation of liquefaction, leading to a major overall slope failure that would feed the observed flowslide.

The Merriespruit case offers an example of mechanical triggering of liquefaction that allows to examine the influence of different hypothesis about viscosity and permeability on the stability of the dam. This is done subsequently through fully coupled hydromechanical analyses using the finite element code Plaxis (Bentley Systems, 2020).

4.1 *Main features of the analyses*

The geometry, mesh, and mechanical boundary conditions for the analyses are the same as those employed by Mánica et al. (2021a), and they are depicted in Figure 1. The geometry incorporates a portion of the lower slope which, in the triggering analysis stage, is removed to simulate the erosion caused by overtopping. Mánica et al. (2021a), following current practice for tailings dam static liquefaction triggering analysis, assumed a perfect undrained condition during the triggering stage. They also imposed a phreatic surface, following that sketched by Wagener (1997) base on available piezometric information.

The analyses performed here are different, as the triggering phase is analysed using a fully coupled hydromechanical simulation. To do so the permeability of the different materials is input to the problem. The permeability assigned to the tailings corresponds to the mean value of the range reported by Fourie et al. (2001), equal to 3.0 m/year, whereas for the starter dam was assumed as double that of the tailings. The phreatic surface is not directly specified, but computed. A result very close to Wagener (1997) interpretation is obtained using the hydraulic boundary conditions indicated in the figure, also shown in Figure 1. Tailings are assumed saturated even above the phreatic surface, which is a reasonable assumption due to the presence of pool water behind the impoundment wall preceding the failure.

The model includes only two materials: the starter dam and the gold tailings. The first one is characterised with the Mohr-Coulomb model while the second one with CASM-visco. The latter was implemented in Plaxis as a user-defined soil model. Adopted parameters are the same as those used in Mánica et al. (2021a), and they are summarised in Tables 1 and 2. A comprehensive account for their selection is given in Mánica et al. (2021a).

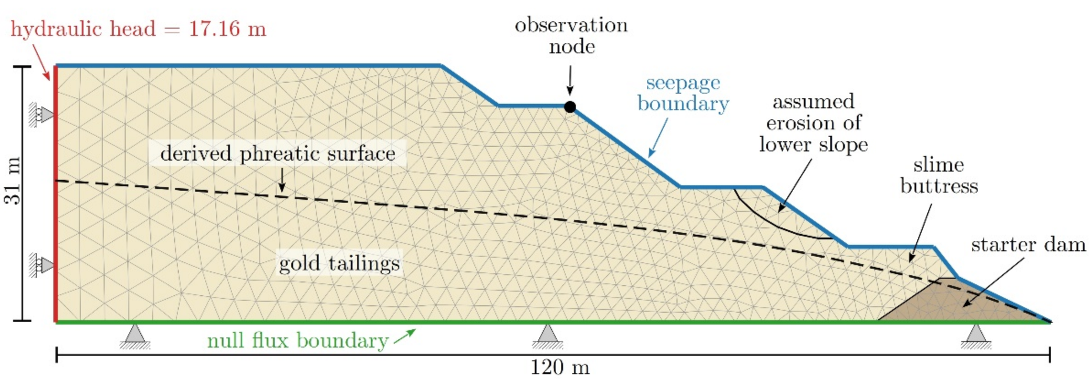

Figure 1. Geometry, boundary conditions, and finite element mesh employed.

Table 1. Employed parameters for tailings

Parameter	Γ	λ	κ	M	S_p	K_0	ν	ψ_{ini}
Units	(-)	(-)	(-)	(-)	(-)	(-)	(-)	(-)
Value	1.89	0.03	0.01	1.56	0.37	0.60	0.30	0.1

Table 2. Employed parameters for the starter dam

Parameter	E	ν	ϕ	c
Units	(kPa)	(-)	(deg)	(kPa)
Value	100E3	0.3	40	20

As for the viscous parameters, a value of N = 5 was employed for all analyses, except for the inviscid analysis. A sensitivity analysis was carried out to explore the effect of η using values of 1.5E-6, 3.0E-6, and 6.0E-6 m^2 day kN^{-1}.

The effect of parameter η on the undrained softening behaviour of the tailing materials is shown in Figure 2. Figure 2a shows the resulting stress paths for anisotropically consolidated undrained triaxial tests for η = 1.5E-6 m^2 day kN^{-1} and different imposed strain rates. As generally observed in the laboratory, undrained peak strengths increase when the loading rate is increased. Figure 2b shows the maximum deviatoric stress vs. the strain rate for the different η values adopted and for the inviscid material. At the same loading rate, a higher undrained peak strength reached is attained when the viscosity parameter η is increased. Independently of the η value selected, the average increase of undrained peak strength is of about 10% per logarithmic cycle of strain rate, which is a ratio typical of plastic clays (Mitchell & Soga, 2005).

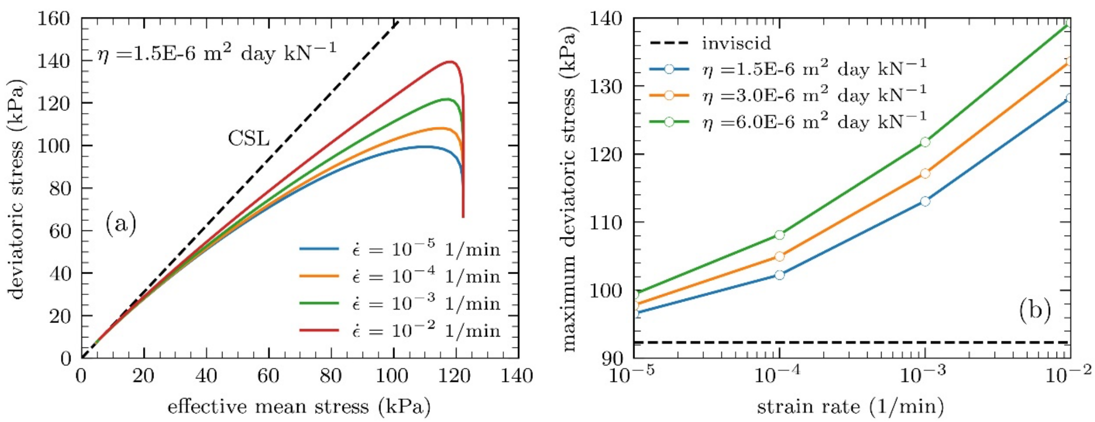

Figure 2. (a) Stress paths and (b) and maximum deviatoric stresses from the simulation of undrained triaxial tests with different strain rates and different viscosity parameters.

4.2 *Simulation results - Erosion phase*

Erosion was simulated by removing the portion of the lower slope indicated in Figure 1. Erosion was assumed to last one hour and 45 minutes. This duration corresponds approximately to eyewitness accounts of the time between the beginning of overtopping and the failure of the dam. Because of the relatively low permeability of the tailings, this loading is very close to a perfectly undrained condition.

Erosion is simulated by linearly reducing throughout the phase the previous equilibrium nodal forces at the erosion boundary. A force reduction factor (FRF) is thus defined as one minus the ratio between the current and initial value of the equilibrium forces at the erosion boundary. Therefore, FRF = 1.0 corresponds to the end of the simulation phase and the complete removal of the eroded material

Figure 3 shows comparative results for different simulations of the erosion phase, expressed as values of FRF vs. horizontal displacement of an observation node located on the slope (Figure 1). From the figure, it is evident that failure was attained during erosion only for the inviscid material and that with a lower viscous effect (η = 1.5e-6 m^2 day kN^{-1}). On the other hand, the more viscous materials -with η values of 3.0E-6 and 6.0E-6 m^2 day kN^{-1}- were able to complete the erosion phase without signs of global instability.

Contours of incremental deviatoric strains are shown in Figures 4. Although the onset of global instability is clear in Figure 3 for the inviscid analysis and the analysis with the lowest η, the failure surface was not completely formed. Those simulations stopped due to numerical convergence problems. These problems were not present in the undrained simulations of the same problem presented in Manica et al (2021a), which is logical, as the coupled hydromechanical solver is more complex than the undrained one. In the case of analyses with η values of 3.0E-6 and 6.0E-6 m^2 day kN^{-1}, although the erosion phase was completed without signs of global instability, the onset of liquefaction can still be identified in the shear bands initiating at the bottom of the dam below the eroded zone (Figures 4c and 4d).

Contours of excess pore pressures at the end of the erosion phase are shown in Figure 5. Positive excess pore-water pressures trace the shear bands, but are far higher in the failed low-viscosity cases (Figures 5a and 5b) than in the more viscous cases (Figures 5a and 5b), where the unloading due to erosion is also visible.

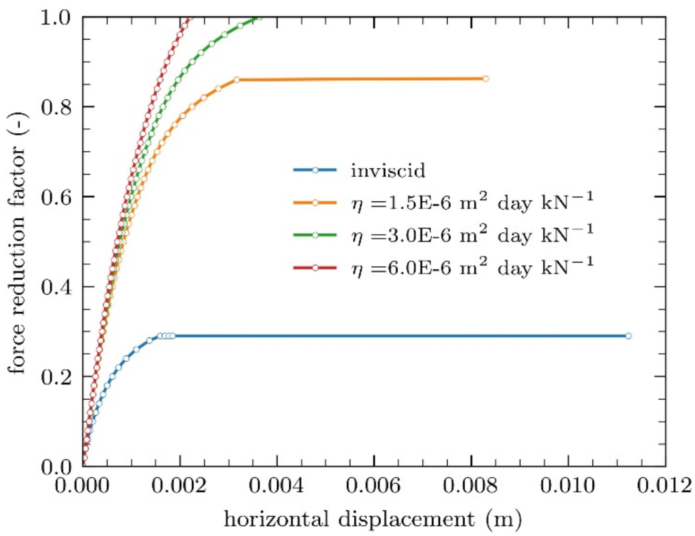

Figure 3. Force reduction factor vs. horizontal displacements at the observation node indicated in Figure 1.

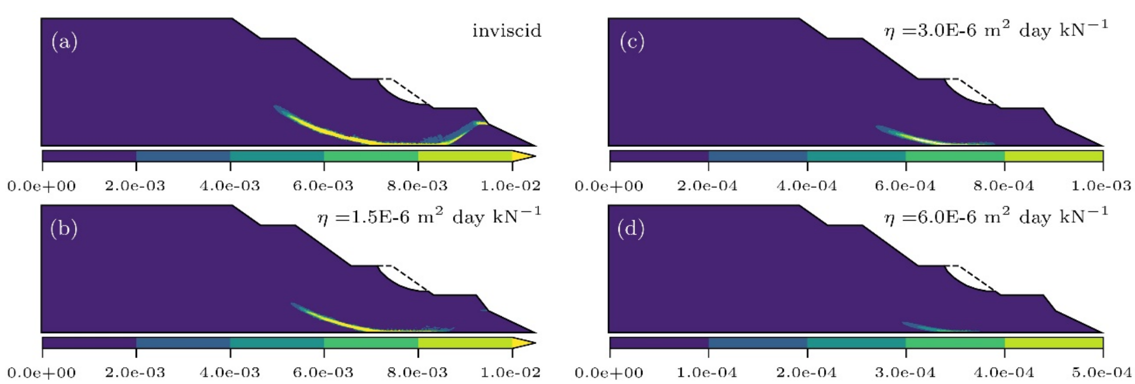

Figure 4. Incremental deviatoric strains at the last converged increment for different values of η. Note that the scale is different for different panels.

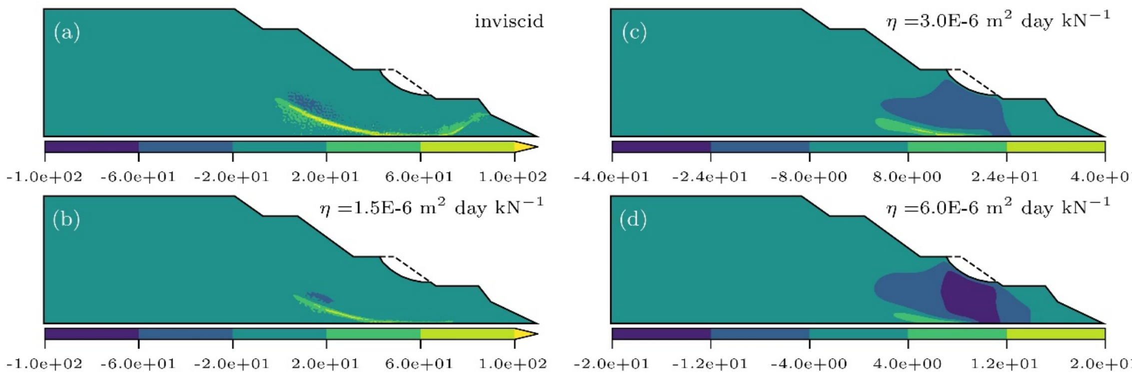

Figure 5. Excess pore-water at the last converged increment for different values of η. Note that the scale is different for different panels.

4.3 *Obtained results - Post-erosion phase*

It is important to notice that, although viscous effects endow the soil with a higher apparent undrained strength for rapid loading, once the loading stops Perzyna's theory predicts viscous drift, by which the rate-dependent yield surface will gradually approximate the inviscid yield surface as plastic deformations accumulate in time. In soils that viscous drift period will be accompanied by water flow and consolidation. If, at the end of the viscous drift, the resulting effective stress state at that stage lies outside the inviscid locus, failure will still occur and will have been only delayed by viscous effects.

The simultaneous effect of viscous drift and consolidation was examined in a new series of simulations. An additional simulation phase, lasting one day, was considered for the material with highest rate effect (η = 6.0E-6 m^2 day kN^{-1}). During this phase, no further modifications were made to the model; the only driving mechanism are the unbalanced forces remaining from the previous phase due to viscous effects. Three cases were examined, with different permeability values for the tailings: the reference value, permeability reduced by a factor of two (1.5 m/year) and a final one with permeability increased by a factor of two (6 m/year).

Figure 6a presents the results in terms of horizontal displacements at the observation node vs. simulation time. The analyses with permeabilities of 3 and 6 m/year showed small displacements after the erosion phase, and eventually reached a stable condition. However, displacements for the analysis with lowest permeability increased monotonically, reaching failure about 10 hours after erosion ceased.

Figure 7 shows incremental deviatoric strains and excess pore-water pressures at the end of each analysis. In the analysis with lowest permeability, a shear band formed during the erosion phase and propagated during undrained creep (Figure 7a) to induce a global instability. The higher permeability values of the other cases made undrained creep impossible through the dissipation of excess pore-water pressure (Figure 7d y 7f). This can also be recognized in Figure 6b, showing the stress paths of the Gauss point indicated in Figure 7b, for the three values of permeability. During the erosion phase, the characteristic undrained softening behaviour that would lead to liquefaction is identified at this location in all cases. However, that softening path is only followed in the more impermeable case after erosion ceases. In the other two cases, the higher dissipation rates increase the mean effective stress and stabilize the stress paths.

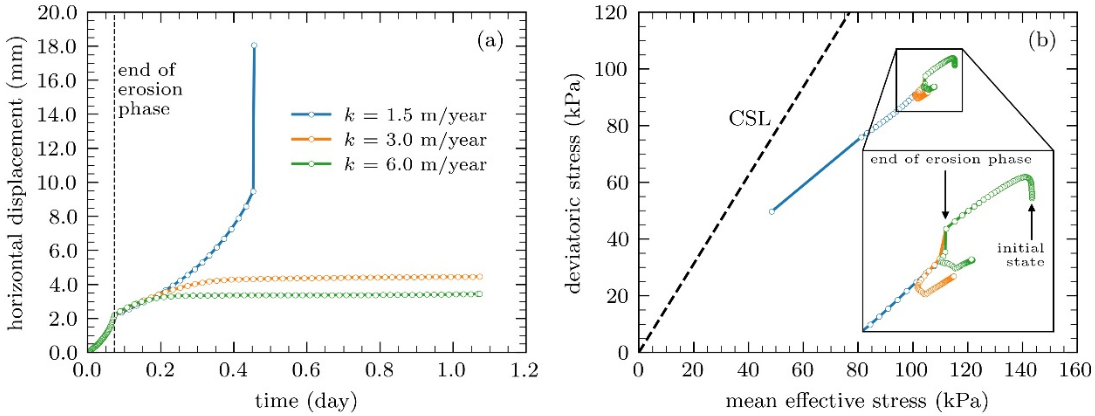

Figure 6. (a) Evolution of horizontal displacements at the node indicated in Figure 1 and (b) stress paths at the Gauss point indicated in Figure 5d for analyses with η = 6.0E-6 m^2 day kN^{-1} and different permeabilities.

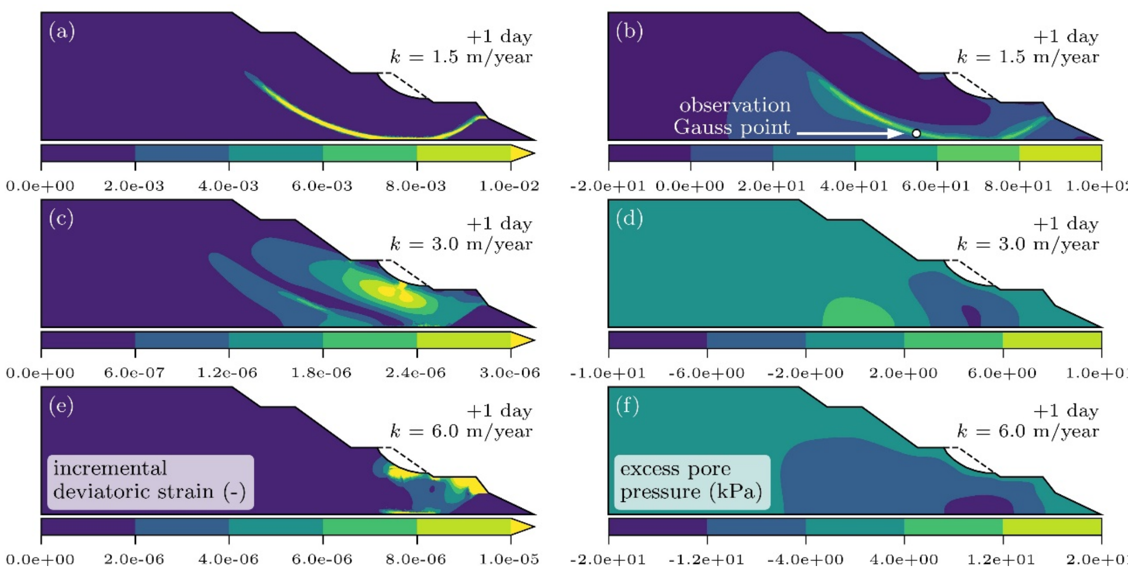

Figure 7. Incremental deviatoric strains (left) and excess pore-water pressure (right) for analyses with η = 6.0E-6 m^2 day kN^{-1} and different permeabilities for the additional phase +1 day after erosion. Note that the scale is different for different panels.

5 CONCLUSIONS

None of the studies of the Merriespruit failure have suggested that creep played a significant role in it, nor there was any observation of significant rate dependence in laboratory testing. The experimental work on creep in tailings is very limited, which is unsurprising, as the magnitude of creep effects usually increases with plasticity, and most tailings are non-plastic. Ongoing and future experimental work will surely establish how much rate-dependency there is in tailings.

In the meantime, it is perhaps preferable to understand the creeping potential (or viscosity) of tailings as another material conditioning factor for liquefaction susceptibility, rather than as a trigger. It is also a conditioning factor whose effect is clearly linked to permeability. Our analysis show that liquefiable tailings of moderate permeability that are able to creep significantly may be less easily triggered into failure.

6 REFERENCES

Arulanandan, K., Shen, C. K., and Young, R. B. (1971). Undrained Creep Behaviour of a Coastal Organic Silty Clay. Géotechnique, 21(4), 359–375.

Augustesen, A., Liingaard, M., & Lade, P. V. (2004). Evaluation of time-dependent behavior of soils. International Journal of Geomechanics, 4(3), 137-156.

Bjerrum, L. (1973). Problems of soil mechanics and construction on soft clays and structurally unstable soils (collapsible, expansive and others). In *Proceedings of the 8th International Conference on Soil Mechanics and Foundation Engineering*, Moscow, pp. 111-159.

Boulanger, R. & Oathes, R. (2020) Modeling Slope Instability Due to Undrained Creep, Proceedings Mining & Tailing Waste Conference, 2020, pp 53-64.

Fourie, A. B., Blight, G. E., and Papageorgiou, G. (2001). Static liquefaction as a possible explanation for the Merriespruit tailings dam failure. Canadian Geotechnical Journal, 38(4), 707–719.

Gens, A. (2019). Hydraulic fills with special focus on liquefaction. In Sigursteinsson, H., Erlingsson, S., and Bessason, B., editors, Proc. XVII European conference on soil mechanics and geotechnical engineering, pages 1–31, Reykjavik. The Icelandic Geotechnical Society.

ICMM, (2021) Tailings management: good practice guide, *International Council for Mining and Metals*

Jefferies, M. G. (1993). Nor-Sand: a simple critical state model for sand. Géotechnique, 43(1), 91-103.

Jefferies, M. and Been, K. (2016). Soil liquefaction: A critical state approach. CRC Press, Taylor & Francis, Boca Raton, FL, USA, 2nd edition.

Jefferies, M., Morgenstern, N. R., Van Zyl, D. V., and Wates, J. (2019). Report on NTSF Embankment Failure. Technical report, Valley Operations for Ashurst Operations., South Orange, NSW, Australia.

Lehtonen, V. J., Meehan, C. L., Länsivaara, T. T., & Mansikkamäki, J. N. (2015). Full-scale embankment failure test under simulated train loading. Géotechnique, 65(12), 961-974.

Leong, W. K., & Chu, J. (2002). Effect of undrained creep on instability behaviour of loose sand. Canadian Geotechnical Journal, 39(6), 1399-1405.

Li, A.L., Fourie, A., Litwinowicz, A. & Laxman, M. (2021) Assessing Static Liquefaction for Upstream Tailings Dams, Proceedings, *Mine Waste and Tailings Conference 2021*, AusiMM-The University of Queensland, pp 389-405

Mánica, M, Arroyo, M, Gens, A & Monforte, L. (2021a) Application of a critical state model to the Merriespruit tailings dam failure, accepted for publication in ICE Journal of Geotechnical Engineering

Mánica, M. A., Gens, A., Ovando-Shelley, E., Botero, E., & Vaunat, J. (2021b). An effective combined framework for modelling the time-dependent behaviour of soft structured clays. Acta Geotechnica, 16(2), 535-550.

Martin, T. E., & McRoberts, E. C. (1999, January). Some considerations in the stability analysis of upstream tailings dams. In Proceedings of the Sixth International Conference on Tailings and Mine Waste (Vol. 99, pp. 287-302). Rotterdam, Netherlands: AA Balkema

Mitchell, J. K., & Soga, K. (2005). Fundamentals of soil behavior (Vol. 3). New York: John Wiley & Sons.

Monforte, L., Gens, A., Arroyo, M., Mánica, M., & Carbonell, J. M. (2021). Analysis of cone penetration in brittle liquefiable soils. Computers and Geotechnics, 134, 104123.

Morgenstern, N. R., Vick, S. G., Viotti, C. B., and Watts, B. D. (2015). Fundão Tailings Dam Review Panel: Report on the immediate causes of the failure of Fundao dam.

Perzyna, P. (1966). Fundamental problems in viscoplasticity. Advances in Applied Mechanics, 9, 243–377.

Robertson, P., de Melo, L., Williams, D. J., and Wilson, G. W. (2019). Report of the expert panel on the technical causes for the failure of Feijão Dam. Published online at http://www.b1technicalinvestigation.com/.

Schmertmann, J. H. (1991). The mechanical aging of soils. Journal of Geotechnical Engineering, 117(9), 1288-1330.

Skopek, P., Morgenstern, N. R., Robertson, P., & Sego, D. C. (1994). Collapse of dry sand. Canadian Geotechnical Journal, 31(6), 1008-1014.

Sottile, M. G., Cueto, I. A., and Sfriso, A. O. (2020). A simplified procedure to numerically evaluate triggering of static liquefaction in upstream-raised tailings storage facilities. arXiv:2010.11705[physics.geo-ph].
Strydom, J. H. and Williams, A. A. B. (1999). A review of important and interesting technical findings regarding the tailings dam failure at Merriespruit. Journal of the South African Institution of Civil Engineering, 41(4):1–9.
Towhata, I., Y. Taguchi, T. Hayashida, S. Goto, Y. Shintaku, Y. Hamada, and S. Aoyama. "Liquefaction perspective of soil ageing." Géotechnique 67, no. 6 (2017): 467-478
Troncoso, J. H.; Vergara, A. and Avendaño, A., "Seismic Failure of Barahona Tailings Dam" (1993). International Conference on Case Histories in Geotechnical Engineering. 34.
Valdivia, M., Quispe, R., Negrón, J., Ayala, R., and Parra, D. (2020). Numerical modelling of a mine waste dump-heap leach pad with different constitutive models. In *Proceedings Tailings and Mine Waste 2020*, pages 91–102.
Yu, H. S. (1998). CASM: a unified state parameter model for clay and sand. International Journal for Numerical and Analytical Methods in Geomechanics, 22(8):621–653.
Wagener, F. (1997). The Merriespruit slimes dam failure: overview and lessons learned. Journal of the South African Institution of Civil Engineering, 39(3), 11–15.
Wedage, A. M. P., Morgenstern, N. R., & Chan, D. H. (1998). Simulation of time-dependent movements in Syncrude tailings dyke foundation. Canadian geotechnical journal, 35(2), 284-298.

Application of the Mine Waste Dump and Stockpile Design Guidelines at Western Canadian Surface Coal Operations

Diego Penate
Stantec Consulting Ltd., Calgary, Alberta, Canada

Andrew Bidwell
Teck Coal Ltd., Calgary, Alberta, Canada

Muhammad Abbas
Stantec Consulting Ltd., Calgary, Alberta, Canada

ABSTRACT: There have been several initiatives to establish guidelines and standards for the investigation, design, construction, operation, and monitoring of waste rock dumps at coal mines dating back to large-scale waste rock dump failures in the late 1960s and early 1970s. The practical reference book titled "Guidelines for Mine Waste Dump and Stockpile Design" (GMWDSD) published in 2017 by the Large Open Pit (LOP) Project represents the current standard of practice. This book is the most recent effort to synthesize past work with more recent research and experience gained since the publication of the widely used Interim Guidelines published in the early to mid-1990s by the British Columbia Mine Waste Rock Pile Research Committee.

This paper presents some commentary and learnings from the application of the 2017 GMWDSD to the design of waste rock dumps at open pit coal mines in western Canada focusing on (i) application of the guidelines under the current regulatory environment; (ii) determination of the waste dump stability rating and hazard classification; (iii) establishment of design acceptance criteria; and (iv) assessment of slope stability and failure runout analysis. It is demonstrated that the 2017 GMWDSD provide an effective and practical framework for the design of waste rock dumps, while noting that each individual site also requires some degree of subjective interpretation, engineering judgment and the application of analytical or empirical methods from other sources. The paper also identifies potential areas of further improvement for the application of the 2017 GMWDSD in the design process.

1 INTRODUCTION AND HISTORICAL CONTEXT

Canada is the world's third largest exporter of metallurgical coal, with exports totaling 11% of the global seaborne metallurgical coal supply in 2019 (World Steel Association, 2020). The exported coal is primarily from open pit mining operations in the province of British Columbia with production totaling approximately 26 million tonnes per year.

Waste rock management is a key component in the design, permitting and operating economics of surface coal operations, with considerations including:

- Environmental factors – focused in reducing the footprint of disturbance for ex-pit waste rock storage along with a preference for backfilling open pits as much as reasonably possible for long-term water quality purposes and to reduce the amount of exposed pit slopes in the closure landscape.
- Economic and mine planning factors – including efficiency and flexibility in waste rock storage to reduce operating costs given the volumes of waste rock generated in modern open pit mining operations, and for optionality in the mine plan when needed in response to coal price fluctuations.
- Safety factors – reflecting increasing standards for safety and decreasing societal and regulatory risk tolerances, and a key aspect of contemporary mine planning.

The above-noted safety considerations have been a strong driver for a conscious effort by the mining industry to improve on the technical knowledge and safety regulations concerning the design and construction of waste dumps, dating back to the tragic failure of a spoils tip in Aberfan, Wales in 1966, killing 116 children and 28 adults.

Driven by numerous waste dump failures at surface coal operations in the Tumbler Ridge and Elk Valley regions of British Columbia during the 1980's and 1990's, the Canadian Centre for Mineral and Energy Technology (CANMET) and the British Columbia Mine Waste Rock Pile Research Committee (BCMWRPRC) published in 1991 a series of interim guidelines for the investigation, design, operation and monitoring of waste dumps. Further work was planned to update and finalize these interim guidelines; however, this was not completed. Nonetheless, these interim guidelines became the de facto standard of practice.

In 2017, the Large Open Pit (LOP) Project initiative sponsored by the mining industry published the Guidelines for Mine Waste Dump and Stockpile Design (GMWDSD) (Hawley and Cunning, 2017), to present the current state of practice, update the knowledge gained since the publication of the 1991 interim guidelines, and provide an updated practical guide for use in the industry.

As the 2017 GMWDSD are utilized by the industry, it is expected that additional practitioners will also provide their comments and learnings from using the guidelines within the specifics of individual projects, to continue pursuing the overall goal of a progressively safer and more efficient mine waste management practice.

2 APPLICATION OF THE 2017 GMWDSD RELATIVE TO CURRENT REGULATORY REQUIREMENTS

The provincial mining regulations in British Columbia and Alberta specify that engineered designs are required for waste rock dumps that exceed certain thresholds for volume, height, footprint area, foundation slope and other factors. However, neither set of provincial regulations are prescriptive with respect to the scope and level of effort for waste dump foundation investigations, analyses or stability acceptance criteria. The current British Columbia regulations require that waste rock dumps be designed "in consideration" of the BCMWRPRC interim guidelines (British Columbia Ministry of Energy and Mines, 2017) but the details of the interim guidelines are not codified in the regulations. Similarly, the current Alberta regulations include a general requirement for an employer to ensure that waste rock dumps are "stable" (Province of Alberta, 2020) and that an application to construct a waste rock dump must be supported by a design report presenting "an overall stability analysis of the dump and foundations, including an outline of the geotechnical parameters used" and "details of testing and instrumentation required to monitor ground water, settlement or lateral movement in the vicinity of the dump and to verify the design parameters described in [the stability analysis]" (Province of Alberta, 2019).

Based on the author's experience, the application of the 2017 GMWDSD is compatible with the above-noted provincial regulatory requirements and meets the current standard of practice. The Waste Dump and Stockpile Stability Rating and Hazard Classification (WSRHC) system in the 2017 GMWDSD was found to be especially useful for guiding and benchmarking the level of effort for site investigation. The 2017 GMWDSD also provide practical guidance on stability acceptance criteria as a function of the assessed consequence of dump failure along with the confidence level of the assessment.

3 STABILITY RATING AND HAZARD CLASSIFICATION SYSTEM

The GMWDSD presents the new WSRHC system, updating the dump stability rating (DSR) proposed in the 1991 BCMWRPRC interim guidelines. The WSRHC system uses a structured approach to assess 22 different factors that are considerations for the stability of waste dumps, from which it calculates their potential for instability using a waste dump and stockpile stability rating (WSR). Based on the WSR, the system categorizes the waste dumps in five hazard classes (WHC), ranging between a relatively very low (WHC I) to very high (WHC V) potential for instability.

Based on the calculated WHC, the 2017 GMWDSD provide recommendations on the level of effort required for the investigation, characterization, analysis, design, construction, and operation of the waste dump.

The GMWDSD provides guidance in selecting the appropriate rating for each of the 22 factors defining the WSR, by providing for each of these factors, detailed tables of "sub-factors" and ratings to guide the selection. However, as is normal within engineering designs the application of the WSRHC system and the selection of the appropriate ratings are guided by the engineering judgment and experience from the designer.

Additionally, the evaluation of some of the design and performance factors might be different during the design, construction and operation, and post-closure stages, resulting in different WSR and corresponding WHC for the same structure over time. Care should be taken to identify variability of the factors between stages and to consequently update the WHC as required, e.g. as part of periodic assessments of a waste dump's condition and performance.

The following observations from the authors present additional considerations in the ratings selection for the foundation slope, stability performance, construction method and loading rate factors of the WSR.

3.1 *Foundation Slope*

For the foundation slope factor, it is important to recognize unique or variable foundation slope configurations and their relation to the potential instability mass to be mobilized.

For example, a steep foundation slope near the toe of the waste dump, followed by a flatter foundation slope towards the heel of the fill will have the same overall foundation slope angle as a flat foundation near the toe of the waste dump, followed by a steep foundation slope towards the heel of the fill. However, it is expected that the steeper foundation slope near the waste dump toe will have a greater influence in the stability as it may be located within the potential failure surface.

In this example, although both of the foundation slope configurations have the same overall foundation slope angle, one of them will likely present a less favorable stability condition based on the potential instability surface, and therefore, the assignment of the WSR foundation slope rating should reflect this additional engineering judgement.

It should also be considered, that as waste dumps are typically constructed in stages, the foundation slope affecting the structure may vary between construction stages. The assessment of the WHC for the structure needs to consider this variability in the evaluation of the WSR, perhaps by assigning different ratings for each stage of construction.

3.2 *Stability Analysis*

As the WSR provides a comprehensive analysis of the factors influencing stability for the structure and the WHC provides an indication of the likelihood for instability, it might be desirable during the design stages to utilize the WHC as input to select the appropriate target stability criteria for the design (Factor of Safety (FoS), Probability of Failure (PoF), etc). A correlation between the stability analysis factors assessed within the WSR and the selection of stability analysis acceptance criteria is presented in Section 4.1.

As the stability analysis acceptance criteria is required as input for the WSR, an iterative process could be conducted to ensure consistency between the stability criteria used as input for the WSR and the selection of stability criteria based on the WHC.

3.3 *Construction Method / Loading Rate*

The importance of the construction methods and loading rates in the stability of the structure generally relates to segregation of the dumped materials, potential development of continuous weak layers within the dump, rate and magnitude of settlement of the dumped waste rock, foundation consolidation, and dissipation of construction-induced pore pressure.

The Construction rating in the WSRHC considers the construction method and loading rate for a dump. Descending sequence construction (commonly referred to "top down dumping") in single, often high, lifts receives a poor stability rating that typically results in a low waste dump and stockpile hazard class (WHC) with a relatively high suggested level of effort for foundation characterization and more conservative design stability acceptance criteria. Conversely, ascending sequence construction (commonly referred to as "bottom up construction") receives a favourable stability rating that results in a relatively lower suggested level of effort for site investigation.

Regardless of whether a dump is initially planned for ascending or descending sequence construction, the authors recommend to conservatively scope the site investigation to meet the GMWDSD suggested level of effort for descending sequence construction and to perform the subsequent analysis and design work for both ascending and descending construction scenarios. This is recommended for two reasons:

- Descending construction is typically favoured for mine planning purposes to decrease haulage distance and thereby improve the short-term costs of dump construction. Therefore, dumps that are initially planned for geotechnically-favourable ascending construction may subsequently be changed to descending construction to improve the short-term economics. If such a change occurs after the completion of a site investigation that was scoped as per the suggested level of effort for an ascending construction design, then the foundation characterization may then not be sufficient to support a design change to descending construction. For this reason, it is also recommended to stage site investigations when possible to provide an opportunity to respond to a change in planned construction methodology.
- Performing the analysis and design work for both ascending and descending construction scenarios will help to proactively quantify the geotechnical aspects of the economic and operational impacts of accommodating a change from ascending to descending construction in terms of: i) increased dump footprint foundation preparation requirements (e.g. sub-excavating and replacing soft soils, construction of foundation shear keys, pre-placement of rock drains along drainage courses), ii) increased monitoring commitments possibly including close monitoring of dump foundation pore pressures during construction which is technically and operationally challenging, iii) establishment and maintenance of relatively larger restricted access zones downslope of the dump due to the potential for runout-style dump failures, and iv) relatively conservative limits on loading rates (typically expressed in terms of bcm/m of dump crest length, or rate of crest advance). Such information can help to provide a basis for reconfirming the value of maintaining an ascending construction plan in the face of short-term project economic considerations.

A construction method rating calculated during the design stage should be revised throughout the life of the project if the assumed construction methodology changed from the time of the assessment.

For post-construction and long-term closure scenarios, the loading rate during construction will have progressively less influence in the stability of the structure, as a considerable portion of the embankment and foundation consolidation should have taken place, and excess pore pressures should have had time to significantly dissipate. However, it is recommended that the beneficial time effects for loading rates and pore pressure dissipation, be captured as part of the performance rating, to maintain an objective evaluation of the construction factors.

3.4 *Performance Rating*

As per the 2017 GMWDSD, "the performance rating is intended to capture the actual, documented stability performance of existing waste dumps and stockpiles" (Hawley and Cunning, 2017). For dumps that are in the design stage, the 2017 GMWDSD recommend to assign a "Fair" rating, i.e. a score of 0 in the WSRHC rating system equivalent to a description of "metastable to stable" for operating dumps. This is a neutral score within the -15 to +15 range of possible Performance Rating scores and it is appropriate to use this during the design stage and in advance of actual performance data.

One challenge with the application of the Performance Rating factor is determining ratings that are representative of current conditions for dormant dumps, which are typically defined as dumps that have had no dumping activity for a minimum of one year but have not yet been reclaimed and transitioned to landform status. Representative performance ratings for dormant dumps are important for the purposes of a mine operator developing a "portfolio" view of dump-related hazards and risks for future, active and dormant dumps and to reduce the potential for the risks associated with dormant dumps to be overlooked or discounted relative to those for active dumps.

Dormant waste dumps generally (but not always) have less significant stability hazards than active dumps and therefore are typically relatively lower risk. Therefore, dormant waste dumps also typically receive less monitoring effort and attention than active dumps. It is important to maintain sufficient monitoring of dormant waste dumps to accurately document their performance on a multi-year basis and to provide sufficient information to update their performance rating. This can be achieved by qualified geotechnical personnel performing periodic visual inspections (e.g. quarterly to annually, under snow-free conditions) to check and document the pattern and extent of visible dump platform tension cracking and settlement over time.

It is preferable to have continuity of monitoring personnel from when the dump was active to improve the repeatability of observations. The visual inspections should be supplemented with suitable long-term displacement monitoring methods for the measurement of slow, ongoing self-weight settlements of large waste rock dumps such as ground-based GPS monitors or survey prisms at selected locations or the application of satellite InSAR monitoring for wide area coverage of dormant dumps. Ground-based radar units may also be suitable for monitoring of long-term waste dump movements; however, the likely slow movement rates (perhaps in the order of a few mm/day or lower over time) could be challenging to track accurately without subsampling of the radar data to remove the standard atmospheric noise corrections. Furthermore, radar units are typically less cost-effective for due diligence monitoring of dormant waste dumps than the other methods noted above and the typical line of sight for ground-based units viewing dormant dump faces would not detect the significant vertical component of long-term dump settlement.

Suitable monitoring can identify situations where dormant dump performance improves over time. For example, a dump that had a Poor to Very Poor performance rating during active dumping may have been metastable to unstable due to construction-induced pore pressures within the foundation or zones of the dump in response to relatively rapid loading rates. The construction-induced excess pore pressures would dissipate over time after active dumping ceases and the dump performance would correspondingly improve over time. In such a case, it would be unnecessarily conservative to maintain a Poor to Very Poor performance rating after the dump had been dormant for some time.

Conversely, there can be situations where the stability performance of a dormant waste dump can worsen over time, such as:

- A dump with a foundation characterized by unfavourable bedrock structure prone to creep and the development of progressive failure mechanisms (e.g. development of flexural toppling).
- Post-operations surface runoff control that inadvertently results in concentrations of drainage onto dumps and potentially into open tension cracks on dump platforms that gradually develop due to typical long-term settlement of the dumped material prior to resloping and regrading for reclamation and closure. Such conditions can be worse than during active dumping operations when dump platforms are frequently graded to maintain trafficability and prevent ponding of surface runoff.

Situations such as these can lead to ongoing and potentially increasing dump movements that would preclude successful reclamation and transition to landform status and it could be non-conservative to carry-forward the performance rating from when the dump was active. Diligent monitoring of dump performance after a dump transitions from active to dormant status is necessary to identify such behaviour and manage the associated risks.

4 STABILITY ANALYSIS ACCEPTANCE CRITERIA

Factors of Safety (FoS) are one of the acceptance criteria most commonly used for stability analysis of waste dumps. They are widely used amongst practitioners as they provide a simplified interpretation of the relationship between driving and resisting forces within a waste dump. They are typically well understood and consistent with the expected performance of the structures.

Stability acceptance criteria has historically been defined by minimum FoS using a deterministic approach. The 2017 GMWDSD expand this traditional acceptance criteria by also incorporating probabilistic elements for static analysis represented by a maximum Probability of Failure (PoF), and a maximum allowable strain for seismic scenarios.

The suggested stability analysis criteria in the 2017 GMWDSD also maintain several of the concepts utilized in previous guidelines. This can be evidenced in the categorization of the waste dumps by consequence level, and the use of a level of confidence concept for selection of the applicable stability acceptance criteria.

However, categorization of acceptable stability criteria based on the time stage (i.e. short-term vs long-term) and the location of the analyzed instability surface (i.e. spoils surface vs deep-seated) as per the BCMWRPRC interim guidelines were not incorporated in the 2017 GMWDSD.

4.1 *Correlation with WHC*

The 2017 GMWDSD recommend the use of the proposed stability rating (WSR) to assign the dump a hazard class (WHC) and based on this, provide recommendations about the level of effort required in the stability analysis. However, a direct recommendation to select target FoS, PoF or allowable strain based on the WSR and WHC is not provided and is to be based on the designer's experience and judgement.

Instead, Table 8.5 of the GMWDSD provide a guideline for the selection of "Consequence" and "Confidence" levels to be used as input to select the applicable acceptance criteria.

Three consequence levels (Low, Moderate, High) are presented based on criteria such as overall slope, height, potential environmental impact, and annual precipitation, among others. It is observed that these criteria are also covered in the calculation of the WSR and WHC, in a more structured way and using 22 factors influencing stability (see Figure 3.1 in the 2017 GMWDSD).

Three confidence levels (Low, Moderate, High) are presented based on the level of knowledge of different parameters influencing the analysis, including amongst others waste material properties and instability mechanisms. Based on the inherent variability of the waste materials and the complexity of the processes influencing stability of typical waste dumps, and given the relatively recent development of the 2017 GMWDSD, there might be some reluctancy from the practitioners to adopt a "high" level of confidence in selecting the stability acceptance criteria.

Due to the comprehensive and structured system used by the WSRHC to assess the different factors affecting stability and assign a hazard class (WHC), it might be desirable to utilize the resulting WHC as input to select an appropriate acceptance criteria for the structure.

Table 1 presents a proposed revision to Table 8.5 in the 2017 GMWDSD to include the calculated WHC for the structure as a base for the selection of acceptance FoS. Additionally, the revision to the table also eliminates the "High" confidence level to better represent the perceived current practice for its application. Recommendations for revised PoF and maximum allowable strain criteria based on the WHC were outside scope of this paper, but these items could be revised in a similar way.

Table 1. Suggested Stability Acceptance Criteria

Consequence/WHC	Confidence	Static Analysis Minimum FoS	Pseudo-Static Minimum FoS
Very Low (WHC I)	Low	1.3	1.05
	Moderate	1.2	1.0
Low (WHC II)	Low	1.3 – 1.4	1.05 – 1.1
	Moderate	1.2 – 1.3	1.0 – 1.05
Moderate (WHC III)	Low	1.4 – 1.5	1.1 – 1.15
	Moderate	1.3 – 1.4	1.05 – 1.1
High (WHC IV)	Low	≥1.5	1.15
	Moderate	1.4 – 1.5	1.1 – 1.15
Very High (WHC V)	Low	≥1.6	1.2
	Moderate	≥1.5	1.15

As recognized in Macciotta et al. (2020), it should be noted that recommendations for FoS and PoF presented in the 2017 GMWDSD consider a more conservative acceptance criteria as the level of confidence in the design decreases and the potential consequence for the structure increases. This includes a consideration of the relationship proposed by Lambe (1985) between design confidence and the engineering practice to characterize the site and materials.

If PoF values are to be developed for the proposed FoS presented in

Table 1, care should be given to the definition of the Coefficient of Variation (COV) to establish the correlation between FoS and PoF. The authors recommend following the relationship between FoS and PoF presented in the 2017 GMWDSD which does not follow constant values of COV.

4.2 *Short Term Applicability*

For the scenarios where the configuration of a proposed dump or stockpile is expected to change within a relative short period of time (e.g. intermediate construction stages, temporary access roads built out of mining waste, etc.) relatively less conservative stability acceptance criteria may be reasonable to reflect the risk reduction due to the shortened exposure time. The concept of a short-term stability acceptance criteria was also previously proposed in the BCMWRPRC 1991 interim guidelines.

The definition of an acceptable "short term" would be influenced by the specifics of the project, considering factors such as the number of wet seasons for high precipitation regions or the number of freshet cycles for colder climates, to which the structures will be exposed.

Table 2 presents the suggested FoS values reduced to account for short term conditions. Target acceptance criteria for pseudo-static conditions should consider the seismicity of the region and the selected short-term period.

Table 2. Suggested Stability Acceptance Criteria – Short Term

Consequence/WHC	Confidence	Static Analysis Minimum FoS
Very Low (WHC I)	Low	1.2
	Moderate	1.1
Low (WHC II)	Low	1.2 – 1.3
	Moderate	1.1 – 1.2
Moderate (WHC III)	Low	1.3 – 1.4
	Moderate	1.2 – 1.3
High (WHC IV)	Low	≥1.4
	Moderate	1.3 – 1.4
Very High (WHC V)	Low	≥1.5
	Moderate	≥1.4

5 SEISMIC STABILITY ANALYSIS

Geotechnical slope stability is generally assessed for different static and dynamic loading conditions that are applicable to the structure. In the case of waste dumps, dynamic loading develops under seismic conditions. The GMWDSD suggest that seismic slope stability assessments for waste dumps belonging to WHC class I, II and III may be completed using pseudostatic analysis and that detailed assessments which may include full dynamic analysis, liquefaction analysis, post-seismic shear behavior analysis may be completed for WHC IV and V waste dumps in areas subject to high seismic hazards. The scope of this paper is limited to only pseudostatic analysis.

5.1 *Pseudostatic analysis*

Based on the limit equilibrium method, this method accounts for seismic forces by assuming a constant destabilizing horizontal acceleration acting on the slices of the failure mass. The accelerations are related to the peak ground acceleration (PGA) through the horizontal seismic coefficient (k_h). The method can effectively analyze slope stability for seismic loading given that the appropriate peak ground acceleration (PGA) and material properties are used.

5.1.1 *Selection of Horizontal Seismic Coefficient & PGA*

It is common industry practice to calculate k_h as half of the peak ground acceleration (PGA) as described by Hynes-Griffin and Franklin (1984). The PGA value is site specific and must be selected for a suitable return period (based on the design life of the structure being analyzed). It is also common to use the PGA values with 975-yr return period for waste dumps that will be constructed over a period of years and potentially not re-sloped, reclaimed and transitioned to landform status until the end of mine life. However, the construction of short-term waste dump structures such as temporary access ramps that are buried by subsequent stages of dump construction within 2 years or less, is often a requirement of mining operations and mine waste management. For such structures, using the PGA values for 975-yr return period can lead to unnecessary conservatism in design and analysis. For example, if the 975-yr return period is used to select the PGA value, the probabilities that an earthquake with PGA equal or greater will occur for structures with design lives of 100 years and 2 years are approximately 10% and 0.2%, respectively. In the authors' experience, a more pragmatic design for such short-term structures can be achieved by selecting smaller return periods based on the design life of the short-term structure.

Furthermore, in a probabilistic seismic analysis, the overall probability of failure over the design life of the structure depends on the probability of exceedance of the selected PGA. Therefore, high risk structures should be designed for lower exceedance probability (or higher return period) PGA values.

To help practitioners avoid unnecessary conservatism while sufficiently managing the geotechnical risk, it is suggested that designers consider the design life and risk profile of each structure when selecting the return period for PGA values to apply in seismic analyses.

5.1.2 *Shear Strength Reduction*

All granular materials undergo some degree of shear strength reduction due to cyclic loading. The strength reduction is caused by liquefaction in sandy/silty materials and cyclic softening in clayey materials. It is important to assess the likelihood of strength loss of the slope materials due to earthquake-induced cyclic shaking. Currently, the 2017 GMWDSD do not provide specific guidance on the determination of the material strength reduction for pseudostatic slope stability analysis. In this regard, guidance from Hynes-Griffin and Franklin (1984) could be included wherein, it is recommended pseudostatic analysis that the materials strengths be reduced by 20% compared to static conditions.

6 RUNOUT ANALYSIS

6.1 *Introduction*

Waste rock dump failures can produce highly mobile flow slides that can travel over large distances beyond the footprint of the dump. Prediction of the potential failure runout distances is critical for mine risk management for establishing infrastructure offsets and restricted access zones downslope of a waste dump. To determine the estimated potential runout extents, the 2017 GMWDSD present empirical and dynamic analysis methods which are briefly discussed below.

6.2 *Determination of Runout Extents*

Empirical methods typically attempt to correlate the potential flow slide runout extents to various quantifiable parameters of the source dump. Due to the broad range of influencing parameters, prediction of the dynamic behavior of waste dump flow slides using purely analytical or laboratory driven constitutive relationships is not possible (Hungr et al, 2002). It is usually more practical to back-analyze actual historical flow slide events and establish empirical correlations.

Dynamic analysis methods are typically used to account for site-specific waste dump geometry and failure mechanisms. The 2017 GMWDSD present in detail the theory and methodology of using 2D and 3D dynamic runout analysis methods. As noted in the guidelines, the methodology for using dynamic runout analysis models is not well established yet. Each case requires model calibration using site specific experience and data from similar historical events. Though the output uncertainty is substantially reduced, dynamic methods require much more computational time and effort compared to empirical methods.

6.2.1 *Limitations and Recommendations on Runout Risk Mitigation*

Based on the experience from the authors, in an operating mine based on safety and economics, empirical runout analysis methods provide a quick and repeatable means of runout assessment in the absence of detailed information and can be suitable to inform the application of engineering judgment to the design and risk management for low risk dumps. The uncertainty can be reduced by utilizing local experience and calibrating the data with failures in the local region and from physical and geomorphological settings comparable to the area of analysis. Dynamic runout analysis methods can also be employed for critical sections and/or relatively higher risk dumps where the uncertainty in the empirical methods may not be tolerable, or if the characteristics of the waste dump in question are largely different from the original dataset used for developing the empirical correlation.

Additionally, it is recommended that the critical zones of risk identified from runout analysis and critical stability sections are discussed with the mine planning and operations team to effectively implement the mitigation measure identified in the 2017 GMWDSD. Good communication between the geotechnical design team and the mining team are highly recommended to avoid or safely manage the placement of potentially sensitive materials in critical sections and to control the direction of placement of the spoils to reduce the probability of formation of potentially collapsible or liquefiable layers parallel to the dump face.

7 CONCLUSIONS AND RECOMMENDATIONS

The 2017 GMWDSD provide an effective and practical framework for the design of waste rock dumps and stockpiles that has advanced the state of practice. The following are the main points of the discussion and the potential areas for further improvement in the design process for waste dumps and stockpiles.

- Site investigations for waste dumps that are planned for geotechnically-favorable ascending sequence construction should be conservatively scoped as per the GMWDSD suggested level of effort for descending sequence construction, and initial analysis and design work should be done for both descending and ascending construction scenarios. This will proactively gather the necessary information to support a design and monitoring plan for descending sequence construction if necessary due to a change in the construction plan, and also serve to proactively quantify the geotechnical aspects of the economic and operational impacts of a change from ascending to descending construction
- Sufficient monitoring performance assessments of dormant waste dumps should be conducted to accurately document their performance on a multi-year basis and to provide a basis to update their performance rating.
- Due to the comprehensive and structured system used by the WSRHC to assess the different factors affecting stability and assign the WHC, it might be desirable to utilize the resulting WHC as input to select an appropriate acceptance criteria for the structure. A traditional risk assessment might also be useful to expand in the evaluation of health and safety, social, cultural, economic, and environmental impacts for the selection of the stability acceptance criteria.

- Relatively less conservative analysis inputs and stability acceptance criteria might be reasonable for short-term waste dump structures (e.g. temporary access ramps with service life of less than approximately 2 years).
- To avoid unnecessary conservatism while managing the geotechnical risk, the return period for PGA in seismic stability analysis should be selected considering the design life and risk profile of each waste dump.
- Potential waste dump and foundation materials liquefaction susceptibility and shear strength reduction due to earthquake shaking should be assessed prior to performing pseudostatic slope stability analysis.
- Empirical and dynamic runout analysis methods provide approximate estimates of potential runout failure extents and should be correlated with local experience and comparable physical and geomorphological settings. Effective communication between the geotechnical engineers and the mining team should be actively pursued to reduce the possibility of runout occurrences by avoiding or appropriately managing the placement of sensitive materials in critical sections or parallel to the dump face.

8 REFERENCES

British Columbia Ministry of Energy and Mines, *Health, Safety and Reclamation Code for Mines in British Columbia*, June 2017, accessed June 28, 2020, https://www2.gov.bc.ca/assets/gov/farming-natural-resources-and-industry/mineral-exploration-mining/documents/health-and-safety/code-review/health_safety_and_reclamation_code_2017_rev.pdf

Bray, J.D. and Travasarou, T. 2009. Pseudostatic Coefficient for Use in Simplified Seismic Slope Stability Evaluation. *Journal of Geotechnical and Geoenvironmental Engineering, ASCE*: 135(9): 1336-1340.

Corominas, J. 1996. The angle of reach as a mobility index for small and large landslides. *Canadian Geotechnical Journal*: 33(2): 260–271.

Hawley, M. and Cunning, J. (eds) 2017. *Guidelines For Mine Waste Dump and Stockpile Design*. Melbourne: CSIRO Publishing and Rotterdam: CRC Press/Balkema.

Hungr, O., Dawson, R., Kent, A., Campbell, D., Morgenstern, N. R 2002. *Geological Society of America Reviews in Engineering Geology*: Volume XV 191-208.

Hynes-Griffin M.E., Franklin A.G.1984. Rationalizing the seismic coefficient method. *U.S. Army Corps of Engineers Waterways Experiment Station, Vicksburg, Mississippi, Miscellaneous Paper GL-84-13:* 21.

Lambe, T. W. (1985). Amuay landslides. *11th International Conference on soil mechanics and foundation engineering (pp. 137–158)*, San Francisco, CA: A.A. Balkema.

Macciota, R., Creighton, A., and Martin, C.D. 2020. Design acceptance criteria for operating open-pit slopes: An update. *CIM Journal:* Vol. 00, No. 00, 2020.

McDougall, S. 2016. 2014 Canadian Geotechnical Colloquium: Landslide runout analysis — current practice and challenges. *Canadian Geotechnical Journal:* 54: 605-620.

Province of Alberta, *Coal Conservation Act, Coal Conservation Rules*, February 1, 2019, accessed June 28, 2020, https://www.qp.alberta.ca/documents/Regs/1981_270.pdf

Province of Alberta, *Occupational Health and Safety Code*, January 31, 2020, accessed June 28, 2020, https://www.qp.alberta.ca/documents/OHS/OHSCode.pdf

Kim, J., Liu, Z., Lacasse, S., Nordal, S., 2018. Runout of Flow Landslides. *Geotechnics for Natural and Engineered Sustainable Technologies:433-445.*

Scheidegger, A.E. 1973. On the prediction of the reach and velocity of catastrophic landslides. *Rock Mechanics 5*: 231–236.

World Steel Association, *Blog: COVID-19 and steelmaking raw materials* [online], April 30, 2020, accessed June 14, 2020, https://www.worldsteel.org/media-centre/blog/2020/COVID-19-and-steelmaking-raw-materials.html

Youd, T.L., Idriss, I.M., Andrus, R.D., Arango, I., Castro, G., Christian, J.T., Dobry, R., Finn, W.D. Liam, Harder, Jr., L.F., Hynes, M.E., Ishihara, K., Koester, J.P., Liao, S.S.C., Marcuson, III, W. F., Martin, G.R., Mitchell, J.K., Moriwaki, Y., Power, M.S., Robertson, P.K., Seed, R.B., and Stokoe, II, K.H. 2001. Liquefaction Resistance of Soils: Summary Report from the 1996 NCEER and 1998 NCEER/NSF Workshops on Evaluation of Liquefaction Resistance of Soils. *Journal of Geotechnical and Geoenvironmental Engineering, ASCE:* 127(10): 817-833.

A case study of construction and operation of a tailings facility at a diamond mine in an arctic climate

Hongwei Xia & Bill Horne
Tetra Tech Canada Inc., Edmonton, Alberta, Canada

Kevin Gostlin & Serge Benoit
De Beers Group, Yellowknife, Northwest Territories, Canada

Xiang (William) Liu
De Beers Group, Calgary, Alberta. Canada

ABSTRACT: The Gahcho Kué Diamond Mine (Gahcho Kué), located in a continuous permafrost region in the Northwest Territories, Canada, began commissioning in Q3 2016 and achieved commercial production in March 2017. The mine consists of three open pits with an average kimberlite process rate of 3.3 Mt/year during the anticipated 14-year life of mine.

The by-products from diamond extraction include fine processed kimberlite (PK) (also called tailings in the mining industry) and coarse PK. The fine PK is currently being deposited in a Fine Processed Kimberlite Containment (Fine PKC) Facility and will later be deposited in one of the mined out open pits. Due to the characterized climate in the Arctic region, the construction and operation of the Fine PKC Facility have various challenges and require special considerations to meet the design performance intent and to reduce the risk to the facility operation and final closure.

This paper presents a case study of the design, construction, and operation of the Fine PKC Facility at Gahcho Kué. The challenges encountered during facility construction and operation are summarized. The strategies and considerations to overcome the challenges and reduce the operation and closure risk are described. The results of a drilling program to investigate the in-situ geotechnical conditions of the deposited fine PK are also summarized in this paper.

1 INTRODUCTION

The Gahcho Kué Diamond Mine (Gahcho Kué) is situated at Kennady Lake, approximately 280 km east northeast of Yellowknife, Northwest Territories, Canada (see Figure 1). Gahcho Kué is a joint venture of the De Beers Group (De Beers) and Mountain Province Diamonds Inc. De Beers is the mine operator. Year-round access to Gahcho Kué is by air using an all-weather gravel airstrip. Winter access is via a 120 km winter road spur off the Tibbitt to Contwoyto Winter Road during February and March each year.

Gahcho Kué is located within an area known of the "Barren Lands", boundary between continuous and widespread discontinuous permafrost with an estimated permafrost thickness range between 120 m to 310 m, and a thermal gradient of 1.7 °C/100 m based on the measured ground temperature from three deep boreholes within the mine area. Seven main geological units were identified within the Gahcho Kué area, including, till veneer (<1 m); till blanket (>1 m); glaciolacustrine deposits; glaciofluvial deposits; organic deposits; esker outwash deposits, and bedrock. The mean annual permafrost temperature at Gahcho Kué ranges from -0.5°C to -3.5°C. The thickness of the active layer is in the range of 0.5 m to 4.0 m depending on the geological unit (typically 0.5 m in organic soil and 4.0 m in exposed bedrock area). The climate of Gahcho Kué is classified as sub-arctic with a mean annual air temperature of approximately -8.6°C with the maximum monthly temperature generally occurring in July and the minimum monthly temperature in January. Average annual precipitation is 347 mm with approximately half of it falling as snow.

Gahcho Kué involves the open pit mining of three diamond-bearing kimberlite pipes in sequence, designated as 5034, Hearne, and Tuzo, which all lie underneath Kennady Lake. For safe access to the kimberlite pipes, a large proportion of Kennady Lake was dewatered with a series of water retention or diversion dykes constructed for water management. Pre-stripping of the on-land portion of the 5034 pit began in 2014 and the full extent of the 5034 pit mining commenced in 2016. Mining of Hearne pit started in December 2017 and is expected to be completed in Q1 2023. Tuzo pit will be mined in phases with the first phase started in 2021 and final phase to be completed in 2030.

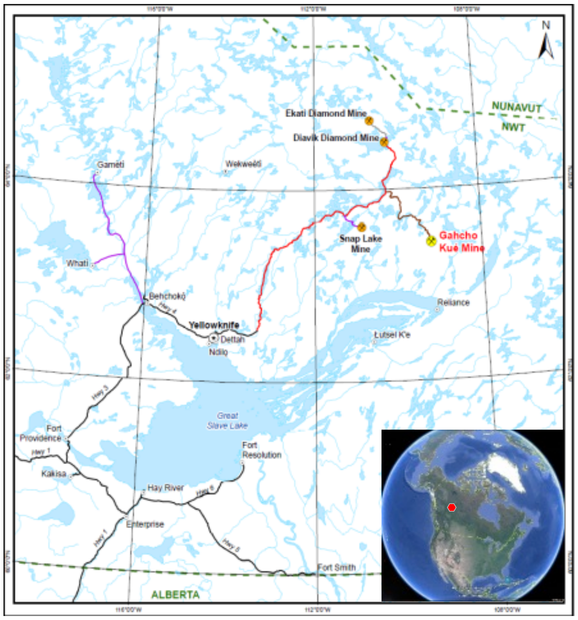

Figure 1. Gahcho Kué Diamond Mine location map

2 PROCESSED KIMBERLITE MANAGEMENT PLAN

Ore processing at Gahcho Kué consists of crushing, screening, dense media separation, and X-ray sorting. The by-products from diamond extraction are split into two waste streams defined by grain size including coarse processed kimberlite (PK) and fine PK (also called tailings in the mining industry, these two terms are used interchangeably in this paper). Coarse PK comprises material with grain size ranging between 0.3 millimeters (mm) and 6.0 mm. Fine PK comprises of material with grain size less than 0.3 mm.

The process plant has an average kimberlite process rate of 3.3 million tonnes (Mt) per annum. The produced coarse PK is conveyed via a belt and piled outside of the plant, from where it is trucked to and stacked in lifts on the coarse PK Facility. The coarse PK Facility is designed to have a full storage capacity of 27 Mt for the life of mine; however, a small percentage of coarse PK will likely be co-disposed with mine rock in the mine rock pile or the mined-out open pit to meet operation requirements.

Fine PK is pumped as a slurry and currently being deposited sub-aerially at a Fine Processed Kimberlite Containment (Fine PKC) Facility. The fine PK will eventually be deposited in the mined-out Hearne pit (in-pit disposal). The Fine PKC Facility is designed to accommodate. approximately 6.5 Mt of fine PK solid which corresponds to about the first five and half years of production. The fine PK will be covered by a layer of coarse PK and a layer of mine rock as surface erosion at closure. The discharge into the mined-out Hearne pit will be managed such that the fine PK will settle to the bottom of the pit without excess mixing with the water stored over the settled fine PK when the water elevation in the pit rises. At closure, the supernatant water in the mined-out Hearne pit will be decanted to the mined-out Tuzo pit, and the settled fine PK in the pit will be capped with freshet water after closure.

3 FINE PKC FACILITY DESIGN

The Fine PKC Facility is in the upstream basin of Kennady Lake, and formed by three dykes (i.e., Dyke A1, Dyke D, and Dyke L), one berm (A2 North Perimeter Berm), and a central discharge causeway. An aerial view of the Fine PKC Facility is presented in Figure 2. Dykes A1 and D are designed as permanent water and fine PK retention structures with a geomembrane liner keyed into competent frozen ground or bedrock to provide containment and storage of Fine PK and to prevent supernatant water in the facility from flowing to the outside receiving environment. The Dyke L which is a filter dyke, is designed to retain fine PK and other suspended solids on the upstream side while allowing water to migrate through the structure into the downstream Water Management Pond (WMP). The generalized design of Dyke L comprises of a run-of-mine core supporting an upstream transition and granular filter system was based on experience gained from similar filter dykes designed by Tetra Tech at the Ekati Diamond Mine and Jericho Diamond Mine. A2 North Perimeter berm is a low waterhead retention structure. The design concept comprises a wide low permeability till core with transition and run-of-mine zones on both sides. Typical design sections of Dykes D and L are shown in Figures 3 and 4 respectively.

The design of the dykes and berm meets or exceeds the requirements of the Canadian Dam Association Dam Safety Guidelines (CDA 2013) and Anglo America (owns 85% of De Beers Group) Technical Standards AA TS 602 102 (Classification, Design Criteria and Surveillance Requirements for Mineral Residual Facilities and Water Management Structures, Specification). The key design parameters are presented in Table 1. The key design features for the dykes are summarized as follows:

- "Downstream" construction.
- Key trench with a geomembrane line system.
- Liner keyed into competent frozen ground or bedrock.
- Bentonite-augmented material to seal the liner.
- Low permeability till core on the upstream of the liner as secondary seepage control.
- Run-of-mine core at downstream with 2.5 Horizontal to 1 Vertical slope.
- Specified filter material to meet the filter combability while attaining the fine PK solid.

Table 1. The key design parameters for the Fine PKC Facility dykes

Dyke/ Berm	Maximum Height (m)	Maximum Width at Base (m)	Total Length of Dyke (m)	Minimum Side Slope (H:V)	Number of Ground Temperature Cable
A1	10.5	84	1,285	2.5:1	5
D	12.5	90	1,050	2.5:1	4
L	19	78	1,300	2.25:1	0
A2	3.8	36	325	2.5:1	2

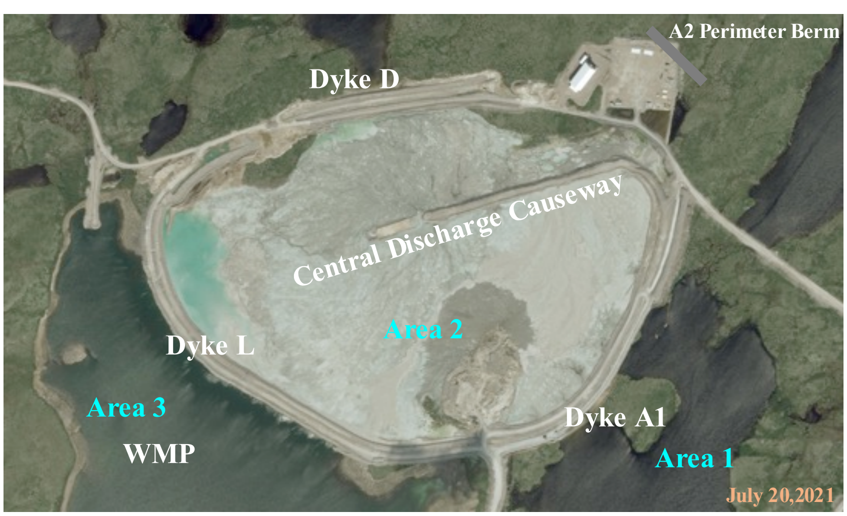

Figure 2. Aerial view of fine PKC Facility

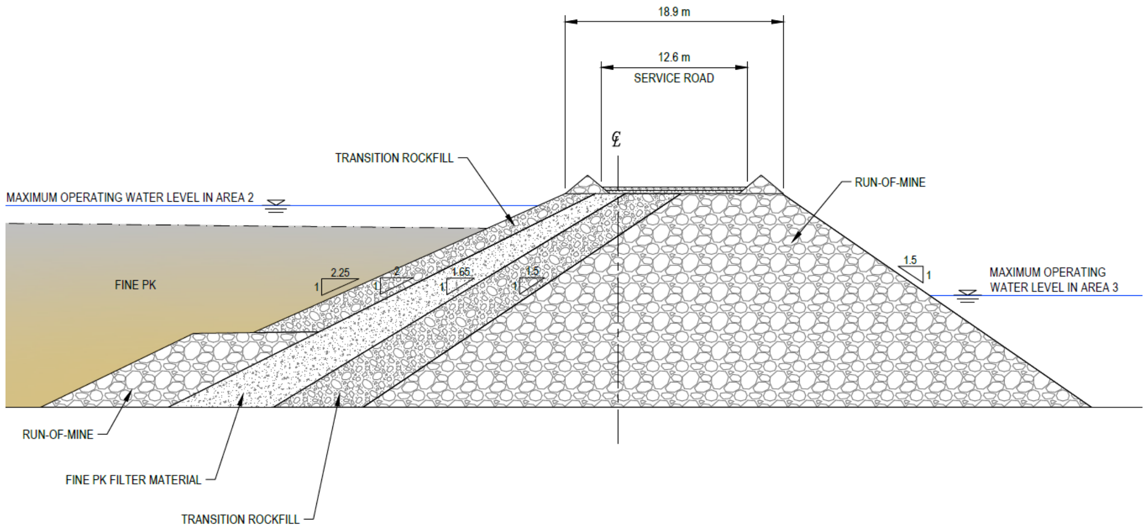

Figure 3. Typical design section of Dyke L

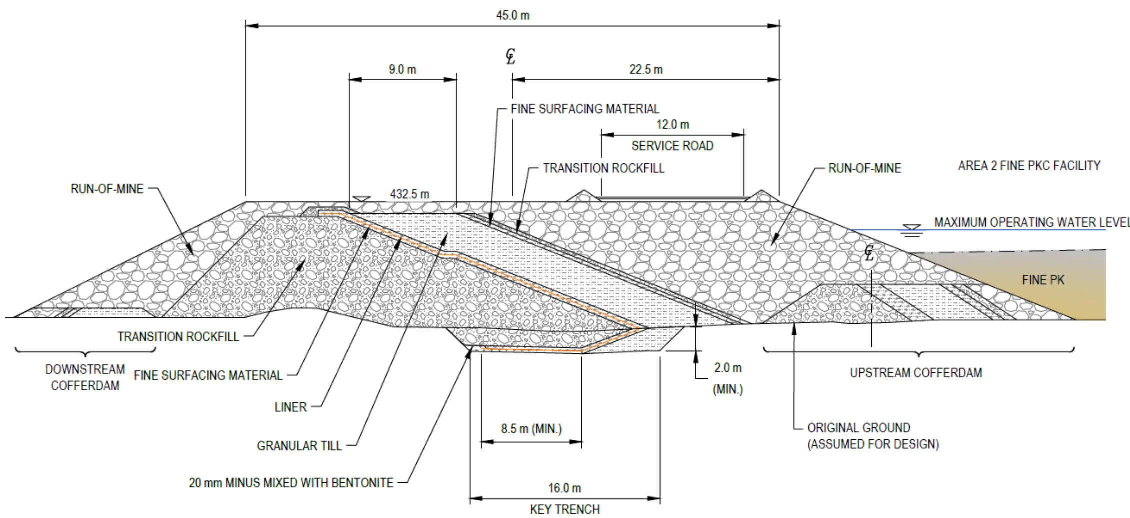

Figure 4. Typical design section of Dyke D

4 FINE PKC FACILITY CONSTRUCTION

Construction of the Fine PKC Facility commenced in June 2016 to facilitate fine PK deposition during the process plant initial commissioning. Construction started from Dyke A1 cofferdam and Dyke L phase 1 (to crest elevation of 419.5 m) to close the connection of Area 2 with other areas. Since the start of commissioning production in September 2016 the dykes have been constructed/raised in stages to complete the perimeter of the fine PK containment. As of to date (August 2021), the crest of the dykes are constructed to 431.0 m, 426.5 m, and 425.7 m for Dykes A1, D, and L, respectively. The raise of the dykes will be continued until the design crest elevation. Construction is expected to be completed in Q4 of 2022.

The construction of the water/fine PK retention dykes (Dykes A1 and D) started with foundation preparation which involved using a Komatsu dozer to remove snow/ice and strip surficial vegetation/organic soil and loose boulders and cobbles. The key trench was developed using drill and blasting techniques followed by excavation to competent frozen till foundation or bedrock. The base and sidewalls of the key trench were cleaned with a Komatsu excavator and compressed air and hand tools. The key trench was inspected and approved by Tetra Tech site engineers prior to the backfill placement and liner installation. A lift of bentonite-augmented material was placed and compacted using the excavator along the key trench bottom to provide a seal with the foundation beneath the liner. The bentonite-augmented material was produced by mixing 20 mm minus material to achieve an average bentonite content of 12% (by weight) with a minimum of 8% (by weight) at any grab sample.

The upper earthwork structure materials were placed using a dozer and excavator in lifts following the maximum lift thicknesses specified in the material placement specifications. Materials lift compaction was carried out with a 10 tons compactor and haul truck traffic prior to the placement of subsequent lifts.

The geomembrane liner system for Dykes A1 and D includes a 1.5 mm double-sided textured high-density polyethylene (HDPE) geomembrane and upstream and downstream 540 g/m^2 nonwoven geotextile for protection. The liner system components were supplied and installed by Layfield Environmental Systems Ltd. with logistical and equipment support provided by the De Beers construction team.

The construction of the filter dyke, Dyke L, occurred in two stages including subaqueous construction and above water construction. During the subaqueous construction phase, the run-of-mine which forms the downstream core was pushed into the water until the design grade elevation of about 1.0 m above the water level was attained. Subaqueous run-of-mine core construction started from the south shoreline and continued to the north shoreline. The lakebed was grubbed using an excavator to about 5 m below the water level to remove boulders and large debris prior to the placement of transition rockfill and filter. The transition rockfill was dumped along the upstream crest of the run-of-mine core and pushed by a bulldozer to the designed crest elevation. The filter zone was constructed in a similar manner to the transition rockfill zone. The placed transition rockfill and filter were compacted using a 10 ton vibratory compactor and subsequent haul truck traffic. The final subaqueous material placement was a zone of run-of-mine armouring, placed upstream of the fine PK filter layer, immediately following its placement to prevent wave erosion on the filter zone. Above water construction was similar to the upper structure construction of Dykes A1 and D, with material placed in lifts and compacted to designed crest elevation.

Major challenges encountered during the construction of the dykes include the following:

- Lakebed foundation preparation prior to material placement. Due to the constraints of the construction equipment, the lakebed was grubbed to the maximum reach limits while maintaining safety. The grubbed underwater foundations were then physically checked using an extendable survey rod from a boat for suitability. Bathymetric survey was also used to determine locations of larger debris. The bathymetric survey was conducted using a specialized drone boat (Seafloor Systems HyDrone-RCV) with a Trimble R8 GNSS receiver connected to an RTK single-frequency depth sounder. Any humps picked up on the surveys were investigated to confirm if boulders were present. Through these exercises plus the observation of exposed shoreline at other fully dewatered areas, it was confirmed that large boulders were removed and the foundation preparation adequate. A dedicated survey team and effective collaboration of all parties involved made this a success.
- Placing material underwater to meet the construction material placement specification. It is challenging to ensure that the transition rockfill and filter zone placed underwater meets the design slopes and width. Extensive bathymetric surveys were conducted along the upstream of each placed material to verify that the material was placed to the design slope and width. Any anomalies along the lakebed were probed by hand to confirm that the material was not slumping.
- Till placement during cold winter. The granular till material was adopted as the secondary seepage control for Dykes A1 and D. Ideally, the granular till should be unfrozen and placed/compacted during the summer to obtain better compaction and reduce the risk of settlement and other potential issues. Due to production and construction requirements, it is impossible to avoid till placement during the winter. The following risk mitigation measures were taken for the till placement during the winter: a) directly used unfrozen till from the open pit stripping if possible to avoid double handling in the winter; b) in case the till is from a stockpile, the frozen layer of the till was removed, and the temperature of the till was tested to ensure that the till is in an unfrozen condition. Frozen till chunks and boulders ware

removed before placement; and c) the thickness of the till placed followed the specified maximum thickness. The compaction of the till was conducted immediately after the placement. Re-compaction was applied if the initial compaction did not meet the minimum specification.

- As expected, the common challenges for the HDPE liner installation in the Arctic region due to the extreme weather condition were encountered. There were delays and slow progress for the liner installation. The logistic constraints due to the remote site and the availability of the equipment and manpower also provided challenges, which slowed the construction process in certain periods.

5 FINE PKC FACILITY OPERATION

Operation of the Fine PKC Facility at Gahcho Kué requires management of fine PK deposition to permanently store in the facility and to manage the water in a safe, economical, and environmentally responsible manner. Fine PK produced in the process plant is conveyed to the Fine PKC Facility as a low-density slurry with solid content at about 30 % by mass via a 3.5 km long HDPE pipeline (12’’ NB, DN300 mm) from a fine PK pump box in the process plant. The flow rate of the fine PK slurry within the pipeline is about 350 m^3/h. To overcome the challenge of the freezing of the pipeline in the Arctic climate, the pipelines are insulated with polyurethane and contain two channels for heat trace if required. An additional pipeline runs in parallel to the mainline to provide contingency in the event of freezing of the pipeline or other pipeline issues.

Subaerial deposition is used to place the fine PK in the facility. The fine PK is deposited in thin layers sloping gently towards the supernatant pond (see Figure 5). The subaerial deposition method is described in detail by Knight and Haile (1983). It involves systematic discharging and deposition of tailings in thin layers from one or more discharge points along the perimeter of the facility or central discharge structure.

The challenges that are faced during the operation of the Fine PKC Facility are summarized as follows:

- Potential ice lenses and wedge formation in the fine PK during the winter;
- Discharge over ice sheets which may trap the ice sheet in the following;
- The formation of uneven beaches which could block the water flow path and cause ponding water locally;
- Water management during freshet; and
- Dyke construction to meet the operation requirements.

Figure 5. A view of fine PK discharge at Gahcho Kué (Photos taken in May 2017).

5.1 *Fine PK deposition planning*

Deposition planning both short-term and long-term is one of the key contributors to the successful operation of the Fine PKC Facility. Short-term deposition planning (i.e. 6 to 12 months) has been used as part of ongoing facility operations to plan the discharge point move, and for scheduling dyke and central discharge causeway raises, and water management. The short-term deposition modelling provides detailed sequenced discharge locations with the required length of deposition time from each spigot. Long-term deposition planning (i.e. to the end of facility service life) is used to size the facility, to verify the planned dyke construction schedule, and to provide details for the long-term strategy for the facility including closure plan and water management plan. The experience gained in short-term deposition operations and planning is being utilized to direct long-term deposition operations towards the preferred closure configurations.

The deposition was modelled using Rift^{TD} software (Version 5), an advanced three-dimensional digital terrain model specifically developed to model tailings deposition. The fine PK properties and input parameters used for the deposition modelling are listed in Table 2.

Table 2. fine PK properties and input parameters used for the deposition modelling

Item	Value
Average daily fine PK dry tonnage	2,850 to 3,600 t/day
Specific gravity	2.7
Dry density of settled fine PK (before July 2020)	0.8 t/m^3
Dry density of settled fine PK (with entrained excess ice) (before July 2020)	0.57 t/m^3
Dry density of settled fine PK (after July 2020)	0.7 t/m^3
Dry density of settled fine PK (with entrained excess ice) (after July 2020)	0.47 t/m^3
Sub-aerial fine PK beach slope	0.8%
Sub-aqueous fine PK beach slope	0.5%
Solid content of Fine PK slurry by mass	30%
Design storage capacity	6.5 Mt
Design service life	5.5 years

A critical element to support the fine PK deposition modelling is the as-built survey of the facility including the bathymetric survey and the aerial fine PK surface. Annual as-built surveys are typically taken in July or August at Gahcho Kué. Additional surveys have been done during the past two winters to facilitate the planning of the discharge point move and water management during the freshet period. The as-built surveys are used to calibrate the deposition model, to back-calculate the average in-situ density of the settled fine PK, and to measure the fine PK beach and underwater slopes which serve as the key inputs for the future fine PK deposition modelling. The as-built survey is also used as the base surface for the next phase deposition modelling.

The key objectives for the operation of the Fine PKC Facility are to effectively utilize the facility by storing the design tonnage of the fine PK without further dyke raises, and to mitigate construction challenges while meeting operation requirements. To achieve these goals, fine PK was discharged below the water level as much as practical in the summer period during the first two years of operation. During the winter period, fine PK was deposited on land in a thin layer to avoid discharge over the ice sheet at the supernatant pond area. If the discharge over the ice sheet cannot be avoided, the discharge duration at that point was limited to keep the thickness of the deposited fine PK over the ice sheet less than 2.5 m which allows the deposited fine PK to thaw in the following summer. The fine PK discharge was started from the Dyke A1 cofferdam in June 2016, and then deposition was shifted south of the central discharge causeway in September 2016. Deposition from the central discharge causeway continued from September 2016 until June 2018. The spigot points were moved to various locations to effectively operate the Fine PKC Facility and deposit the fine PK underwater as much as possible. During the period between July 2018 and May 2019, the fine PK was deposited from the Area 2 Peninsula to facilitate the construction of Dyke D and the raise of Dyke A1. From June 2019 to September 2020, the spigot points were switched back and forth among the central discharge causeway, Area 2 Peninsula, and Dyke A1 perimeter as per deposition planning to facilitate the dyke raise and water management. From October 2020 to the end of service life, the fine PK has been and will be deposited along the central discharge causeway. The discharge point will be moved as per the deposition plan to obtain an appropriate fine PK geometry configuration for closure. The evolution of the Fine PKC Facility from 2018 to 2021 is shown in Figure 6.

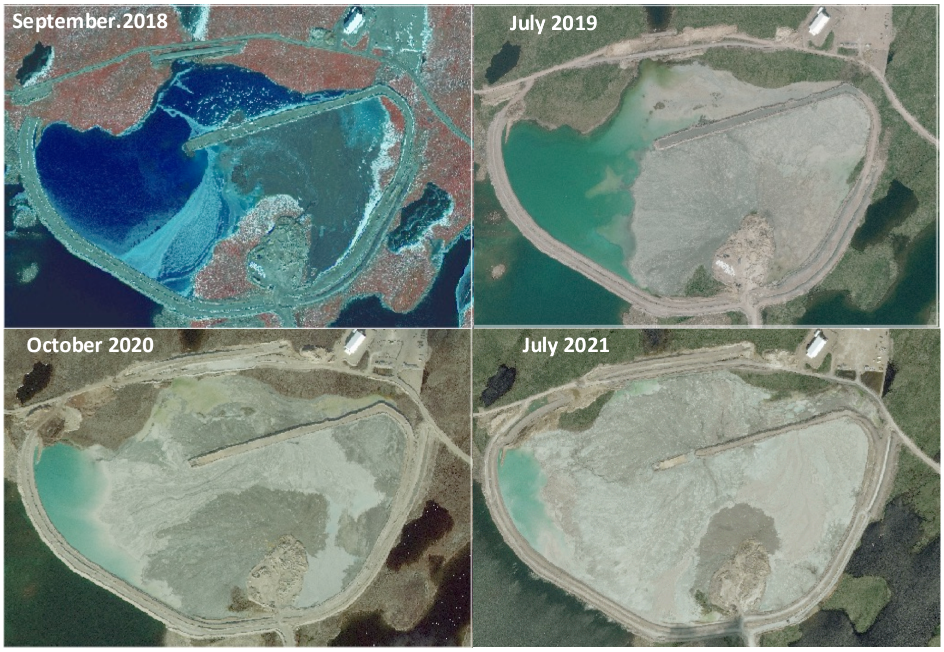

Figure 6. Revolution of the Fine PKC Facility (from 2018 to 2021)

5.2 *Operational surveillance and risk control*

Although the detailed short-term deposition plan is developed and provide a base plan for the Fine PKC Facility operation, the current state of knowledge and modelling technique does not allow accurate prediction due to modelling assumptions adopted and several operational factors such as a delay in the dyke raise and the temporary shutdown of the process plant for maintenance which all could lead to changes in the deposition plan and sequence. A surveillance program is an effective tool to inform decision-making and to verify whether the design intents and performance objectives are being met. A surveillance program has been set up and successfully used for the operation of the Fine PKC Facility.

Operational routine inspections at Gahcho Kué are joint efforts from different disciplines including designated personnel from the process plant, Tetra Tech's on-site Geotechnical Engineers, and the designated personnel from other operating departments, which allow for knowledge sharing and technical exchanges in the areas of fine PK and water management. The frequency of the surveillance activities varies from daily, weekly, monthly, to annually depending on the monitoring aspects and requirements. For example, fine PK discharge and flow direction is observed daily following the fine PK disposal inspection procedure as part of the process plant department's operating procedure. Based on findings from the daily observations, a survey at the fine PK discharge location may be requested if it is deemed necessary to determine the schedule for the next discharge point move. A daily report is distributed to all parties involved to ensure all relevant personnel understand the latest status. If important issues are noted during the inspection, a notification is distributed to the main stakeholders immediately to trigger an investigation of the root cause, perform a risk assessment, and the develop a response and mitigation plan in a timely manner.

The water level in the facility is monitored using a vibrating wire piezometer on a daily basis. Periodically manual water level surveys are performed to verify the performance of the piezometers. Before each spring freshet, a risk assessment is carried out using the monitoring data to evaluate the performance of the facility and identify the potential risk for the water management and develop a mitigation plan accordingly.

To properly manage the risk, a Trigger Action Response Plan (TARP) has been established to ensure that the water and fine PK levels meet the design criteria and safely operate water and fine PKC management system. The trigger levels including Green, Yellow, Orange, and Level Red have been defined for water level, fine PK level, beach slope, seepage, ground temperature readings for each structure associated with the Fine PKC Facility. The trigger levels are maintained up to date to reflect any changes from mine operation and dike construction.

6 IN-SITU GEOTECHNICAL CONDITION OF DEPOSITED FINE PK

6.1 *2021 Site investigation*

The Fine PKC Facility has been receiving fine PK for about four years with an average annual deposition rate of 1.1 Mt. Latest survey data (taken in March 2021) indicates that a maximum of 14 m thick fine PK has been deposited. A geotechnical drilling program in the Fine PKC Facility to examine the characterization of the settled fine PK was conducted in March 2021. A total of three holes (FPK21-01, FPK21-02, and FPK21-03) were drilled at designated locations using a sled-mounted diamond drilling rig with a HQ3 diamond drilling bit (98 mm core diameter). Little to no water was used during drilling to reduce thawing of the frozen core.

Frozen and unfrozen core samples were collected using a HQ3 wireline core barrel for field and laboratory tests. The frozen core recovery ranged from 50% to 90%. The unfrozen core recovery was 0% to 85% due to the difficulty of retaining soft material inside the core barrel. Three multi-bead ground temperature cables (GTCs) were installed to monitor the thermal condition of the deposited fine PK.

6.2 *Subsurface conditions*

Borehole FPK21-01 was drilled to an inferred depth of 9.9 m. It was observed that a 0.9 m thick layer of clear ice overlays frozen fine PK predominately containing excess ice, with sections containing visible ice greater than 50% down to a depth approximately 6.9 m. Below a depth of 6.9 m, unfrozen fine PK material was observed.

Borehole FPK21-02 was drilled to an inferred depth of 12.2 m. It was observed that a 0.3 m thick layer of clear ice overlays frozen fine PK in varying quality containing excess ice, to well-bonded, with some sections containing visible ice greater than 50% down to an inferred depth of approximately 6 m. No sample was recovered between the depth of 6.0 and 11.9 m. Below the inferred depth of 11.9 m, unfrozen silty material was observed.

Borehole FPK21-03 was drilled to an inferred depth of 10.5 m. It was observed that a 0.8 m thick layer of clear ice overlays frozen fine PK predominately containing excess ice, with some sections containing visible ice greater than 50% down to a depth of approximately 6.0 m. Below the inferred depth of 8.3 m, unfrozen fine PK material was observed.

Typical frozen core samples collected during the drilling program are presented in Figure 7.

Figure 7. Frozen core samples collected during the drilling program

6.3 *Properties of deposited fine PK*

Recovered fine PK samples were tested for moisture content, particle size, bulk density, and shear strength. Shear strength tests on unfrozen materials were conducted using RocTest's downhole M-1000 Field Vane Shear Tester. Each run was examined for unfrozen sample to determine if testing was applicable or not. When shear strength testing was applicable, a 5 cm x 11 cm vane was lowered inside the rods using 1-inch steel rods. The vane was lowered a minimum 50 cm beyond the drill bit in attempt to test the undisturbed sample. In addition, a Pilcon Hand Vane Tester and a Soil Penetrometer were used directly on the core sample if the sample appeared relatively undisturbed. For the Pilcon Hand Vane Tester, the 19 mm vane was inserted perpendicularly until the vane was approximately in the centre of the core sample. For the Soil Penetrometer, the adapter foot was used due to the low strength of the core.

Density of the frozen core was determined in two methods. First method was measuring the mass of the sample followed by measuring the core using calipers to determine an estimated volume. Second method was determining the mass of the core sample then using a water displacement method inside a 2 L graduated glass beaker to estimate the volume. Selected frozen and unfrozen samples were shipped off site for moisture content, particle size distribution, and hydrometer testing.

The results from field and lab testing for moisture content and average dry density are presented in Figure 8. Table 3 summarizes the shear strength tested on the unfrozen fine PK samples.

Table 3. Shear strength of the unfrozen fine PK samples

Depth (m)	M-1000 Vane (kPa)	Pilcon Vane (kPa)	Borehole Number
8.9	-	0.5	FPK21-01
9.2	-	1.8	FPK21-01
9.5	-	3.0	FPK21-01
9.6	-	4.0	FPK21-01
9.9	-	4.2	FPK21-01
11.5	2.59	-	FPK21-02
11.5	-	8.0	FPK21-03
11.7	-	6.0	FPK21-03
11.9	-	9.0	FPK21-03
12.0	-	8.0	FPK21-03

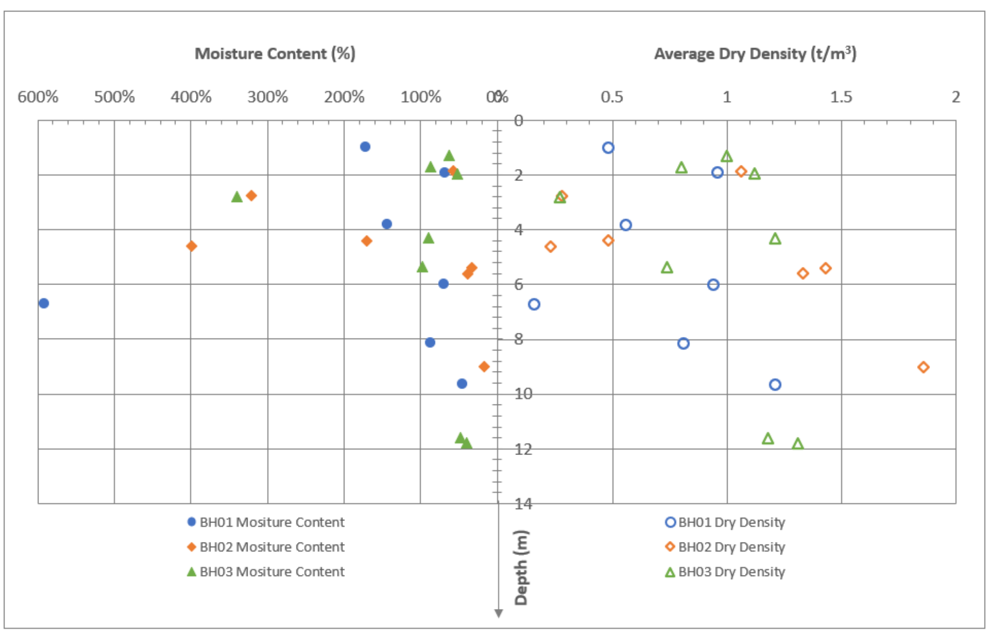

Figure 8. Moisture content and average dry density tested on frozen core samples

6.4 *Thermal condition of deposited fine PK*

The GTCs in FPK21-02 and FPK21-03 were installed to a depth of 9.8 m below the ice surface with the last two beads above the surface to capture future deposition monitoring. The GTC in FPK21-01 was installed to a depth of 1.48 m because of the extended time between grouting the hole and installing the GTC inside the PVC. The unforeseen delay was due to heavy snowfall and high winds preventing access to the borehole. The ground temperature readings suggest the frozen/unfrozen boundary is approximately between 5.3 m to 5.8 m depth for FPK21-02, and 6.4 m to 6.9 m depth for FPK21-03 which implies that the fine PK deposited below the original lake level is in an unfrozen condition. The fine PK deposited above the original lake level is in a frozen condition except for the annual freezing and thawing zone.

7 CONCLUSION

The construction and operation of a tailings facility in the Arctic face various challenges due to the remote site and extreme climate conditions. Appropriate considerations should be taken to effectively construct and operate the facility to meet the design performance intents. This case history presents the construction and operation of the fine PKC Facility at Gahcho Kué and the findings of the in-situ geotechnical conditions of the deposited fine PK through a drilling program leading to the following conclusions:

- The construction and operation of the fine PKC Facility involve coordination between multiple departments and management levels (health and safety, process plant, mining, engineering, environment, contractors, and consultants). Effective collaboration of all parties is one of the keys to success.
- Detailed tailings deposition planning is an integral part of the operation of the fine PKC Facility and provides useful guides to the day-to-day operation and construction planning. Regularly updating the deposition plan is essential.
- Effective operational surveillance and risk control measures are important to achieve success.
- The in-situ geotechnical conditions of the deposited fine PK are as expected. Useful data has been collected through the drilling program and will be used for long-term deposition planning and closure cover design.

8 ACKNOWLEDGMENTS

The authors would like to thank De Beers Group for the opportunity to publish this paper and to share the data contained within.

9 REFERENCES

AngloAmerican. 2019. Mineral Residual Facilities and Water Management Structures Standard and Technical Specifications. Version 5.2. September 2019.

Canadian Dam Association (CDA). 2013. Dam Safety Guidelines. 2013.

Knight, R.B. & Haile. J.P. 1983. Sub-Aerial Tailings Deposition. In Proceedings of 7th Panamerican Conference on Soil Mechanics and Foundation Engineering, Vancouver, pp. 627-639.

Impacts on the National Mining Plan 2030 due to updates in Brazilian regulations

Germano S. Lopes, Pablo C. de C. Gonçalves, Michelle G. Giorgini & Débora P. de C. Costa
Tetra Tech, Belo Horizonte, Minas Gerais, Brazil

ABSTRACT: In 2010, the Brazilian government published two important federal laws, Law No. 12,334/2010, which establishes the National Dam Safety Plan (NDSP), and Law No. 12,305/2010, which establishes the National Solid Waste Policy (NSWP). The set of laws mentioned above is linked to the regularization and adequacy of safety of operations involving the disposal of tailings and mine waste. In the year following the creation of the laws, the Brazilian Ministry of Mines and Energy presented the National Mining Plan 2030 (NMP-2030), where probable scenarios, guidelines and strategic targets for mining were established. That document addressed the Brazilian mineral sector's future context related to environmental, economic, social, market, extraction, and production of ores aspects. However, sustainability stood out among the topics, once the proper disposal of tailings was already a major concern that could impact the future of the sector. Thus, there is a change of perspective in the mineral scenario in order to promote greater safety in the tailings final disposal related to the sustainability of the mineral process. This trend evidences the interconnection among the precepts of federal laws, aimed at the disposal of mining tailings/waste, and the actions foreseen in the NMP-2030. Therefore, this article analyzes the guidelines, strategies of ore production, alternatives for the final disposal of Brazilian tailings and mine waste generated until 2030 and to evaluate the impact of new laws and regulations on what was defined in the NMP-2030 mining plan.

1 THE BRAZILIAN NATIONAL MINING PLAN 2030

The National Mining Plan 2030 (NMP-2030) is a tool developed by the Ministry of Mines and Energy (MME) with the objective of guiding medium to long-term policies that can contribute to making the mineral sector a foundation for the sustainable development of Brazil in the next 20 years (MME, National Mining Plan 2030, 2010).

The scenario defined in the NMP-2030, called "on the Sustainability Trail", articulates economic dynamism with the adoption of more productive practices and more sustainable consumption, due to: a) social and environmental pressures for better use and access to the national territory; and b) against predatory mining practices accentuated by the threat of global climate change. This scenario considers three guidelines, which encompass eleven strategic objectives, presented in the Figure 1 (MME, National Mining Plan 2030, 2010).

The choice for a scenario associated with sustainability is also related to the fact that most countries are articulated around a major alliance aimed at promoting competitiveness in line with sustainability until 2030, as presented in the study Mining & Metals Scenarios to 2030 (World Economic Forum, 2010 *apud* MME, National Mining Plan 2030, 2010). Through this global trend, mining and mineral transformation projects are expected to become more efficient, with a reduction in CO_2 emissions, improvements in water management and waste management, guaranteed, in part, by legislation, more precise and clear information, new consumption patterns and financing lines conditioned to sustainability (MME, National Mining Plan 2030, 2010).

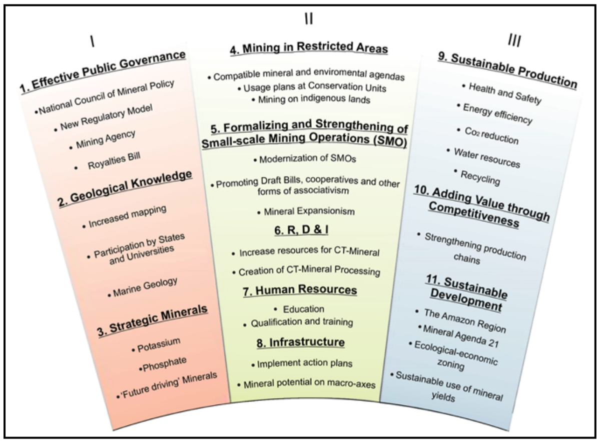

Figure 1. Guidelines and strategic objectives of the NMP-2030 (MME, National Mining Plan 2030, 2010).

In 2016, in the context of the 2016-2019 Multi-Year Plan, a revision of the NMP-2030 was proposed under the justification that, despite the guidelines defined by the Plan being well aligned with the strategic vision that the sector should have (public governance, adding value and densifying knowledge and sustainability), the scenario has changed considerably since 2010 and, given this, the short and medium-term perspectives of the plan should be reviewed (MPDM, 2018). This objective, despite having been proposed, was not achieved by the end of 2019, with the NMP-2030 published in 2010 still in force (ME, 2016-2019 Multi-Year Plan - Annual Evaluation Report 2019 - Annex I: Evolution of Indicators, 2019).

2 CHANGES IN THE MINERAL SECTOR

The scenario associated with sustainability along with the strategic objectives defined in the NMP-2030 drove changes in legislation related to the mineral sector. Therefore, the following sub-items will present the legislation published after 2010 until current days and an analysis of the perception of the Brazilian advance in terms of safety in the disposal of tailings and sustainability in the mineral sector.

2.1 Legislation and regulations created after 2010 and their impacts on the NMP-2030

Since the creation of the NMP-2030 in 2010, legislation and regulations have been drawn up to ensure that the objectives established in the Plan were carried out considering the best aspects of mineral sustainability and safety in disposal procedures. These laws and standards are described in Table 1 and Figure 2 in the form of a timeline.

Table 1. Legislation and standards published in 2010 or after.

Legislation (Publication date)	Topic Description
Law No. 12.334 (2010/07/20)	Law No. 12,334 establishes the National Dam Safety Policy (NDSP) and creates the National Information System on Dam Safety (NISDS). This law applies to dams intended for the accumulation of water for any uses, the final or temporary disposal of tailings and the accumulation of industrial waste (BRASIL, Law No. 12,334, 2010).
Law No. 12.305 (2010/08/02)	Law No. 12,305 establishes the National Solid Waste Policy, providing for its principles, objectives and instruments, as well as guidelines related to the integrated management and management of solid waste, the responsibilities of generators and public authorities and the applicable economic instruments (BRASIL, Law No. 12,305, 2010).

Legislation (Publication date)	Topic Description
Ordinance DNPM[1] No. 70.389 (2017/05/17)	Ordinance DNPM[1] No. 70.389 creates the National Registry of Mining Dams and the Mining Dam Safety Management System (MDSMS), which establishes the minimum content and level of detail of the Dam Safety Plan (DSP), Regular Safety Inspections (RSI) and Special Safety Inspections (SSI), Regular Dam Safety Review (RDSR) and the Emergency Action Plan for Mining Dams (EAPMD). This ordinance also inaugurates the concept of the Self-Rescue Zone (SRZ) (BRASIL, Ordinance DNPM[1] No. 70.389, 2017).
ABNT[2] NBR[3] 13.029 (2017/07/24)	The ABNT[2] NBR[3] 13.029 standard specifies the minimum requirements for the preparation and presentation of a pile project for disposal of waste generated by open pit mine or underground mine, in order to meet the conditions of safety, operability, economy and deactivation, minimizing the impacts on the environment (ABNT[2], NBR[3] 13.029, 2017).
ABNT[2] NBR[3] 13.028 (2017/11/14)	The ABNT[2] NBR[3] 13.028 standard specifies the minimum requirements for the preparation and presentation of mining dam projects, including dams for the disposal of processing tailings, containment of sediments generated by erosion and water reservation in mining, in order to meet the safety conditions, operability, economy and deactivation, minimizing impacts on the environment (ABNT[2], NBR[3] 13.028, 2017).
Law No. 13.540 (2017/12/18)	Law No. 13,540 provides for Financial Compensation for the Exploitation of Mineral Resources (FCEM) (BRASIL, Law No. 13,540, 2017).
Law No. 13.575 (2017/12/26)	Law No. 13,575 creates the National Mining Agency (ANM[4]) and extinguishes the National Department of Mineral Production (DNPM[1]) (BRASIL, Law No. 13,575, 2017).
Decree No. 9.252 (2017/12/28)	Decree No. 9,252 establishes the calculation methodology for the FCEM reference value (BRASIL, Decree No. 9,252, 2017).
Decree No. 9.407 (2018/06/12)	Decree No. 9,407 regulates the distribution of government participation to municipalities affected by mining activity (BRASIL, Decree No. 9,407, 2018).
Resolution ANM[4] No. 13 (2019/08/08)	Resolution ANM[4] No. 13 establishes regulatory measures to ensure the stability of mining dams, notably those built or raised by the "upstream" method or by a method declared to be unknown. It brings national guidelines prohibiting the use of the "upstream" raising method and prohibiting the entrepreneur from designing, building, maintaining and operating in the SRZ. It also brings the need for automated sounder activation systems installed outside the dam break flood. (BRASIL, Resolution ANM[4] No. 13, 2019).
Resolution ANM[4] No. 32 (2020/05/11)	Resolution ANM[4] No. 32 amends Ordinance No. 70,389, creating new requirements for the preparation of the flood map, mandatory automated sirens triggering systems and other mechanisms for alerting in the SRZ, mandatory automated monitoring system of instrumentation with real-time monitoring and full-time and mandatory elaboration of As Is (BRASIL, Resolution ANM[4] No. 32, 2020).
Resolution ANM[4] No. 40 (2020/07/04)	Resolution ANM[4] No. 40 amends Ordinance No. 70,389, where the entrepreneur is required to implement a dam safety monitoring system, such as automated instrumentation monitoring and 24-hour video monitoring for dams with high potential damage (BRASIL, Resolution ANM[4] No. 40, 2020).
Law No. 14.066 (2020/09/30)	Law 14,066 amends Law No. 12,334 (20/09/2010) which establishes the National Dam Safety Policy (NDSP). For this purpose, it prohibits the upstream construction method, and the existing dams built or heightened by the upstream method must be de-characterized. This law also revises the minimum content of the DSP, with the EAPMD being required for all mining tailings dams regardless

[1] DNPM means, in English, Department of Mineral Production.
[2] ABNT means, in English, Brazilian Association of Technical Standards.
[3] NBR means, in English, Brazilian Standard.
[4] ANM means, in English, National Mining Agency.

Legislation (Publication date)	Topic Description
	of classification as to the associated potential damage and risk (BRASIL, Law No. 14,066, 2020).
Resolution ANM[4] No. 51 (2020/12/24)	Resolution ANM[4] No. 51 creates and establishes guidelines for the Assessment of Conformity and Operationality of the EAPMD - ACO, which comprises the Compliance and Operational Report of the EAPMD - COR and the Declaration of Conformity and Operationality of the EAPMD - DCO (BRASIL, Resolution ANM[4] No. 51, 2020).
Resolution ANM[4] No. 56 (2021/01/28)	Resolution ANM[4] No. 56 changes provisions of Resolution No. 51, defining that the technical person responsible for issuing the DCO must be different from the technical person responsible for preparing the EAPMD and the hypothetical failure study in force in the dam (BRASIL, Resolution ANM[4] No. 56, 2021).
Resolution ANM[4] No. 68 (2021/04/30)	Resolution No. 68 establishes the rules regarding the Mine Closure Plan - MCP and revokes the Regulatory Rules for Mining No. 20.4 and No. 20.5, approved by DNPM[1] Ordinance No. 237, of October 18, 2001.

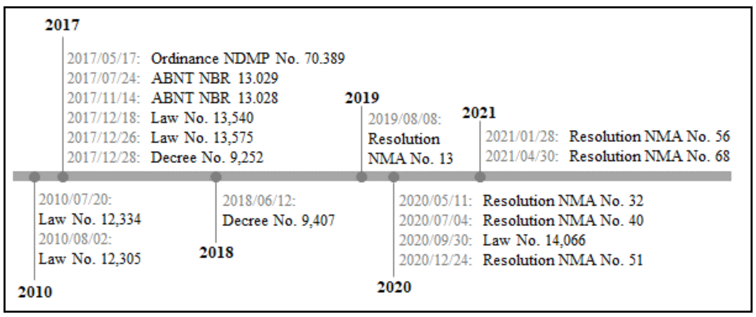

Figure 2. Timeline of the main laws and regulations inherent to mining, published in 2010 and after.

According to publications from the Ministry of Economy (2016-2019 Multi-Year Plan - Annual Evaluation Report 2019, 2019), with the approval of the provisional measures that created the ANM[4] and promoted changes in the legislation on Financial Compensation for the Exploitation of Mineral Resources (FCEM), the activities of the MME were directed towards "Ensuring Efficient Public Governance of the Mineral Sector" through:

- installation of the ANM[4], created by Law No. 13.575/2017, with the modernization of legislation on the safety of dams and the introduction of the electronic protocol for requests;
- updating of FCEM standards, with establishment of the calculation methodology for the reference value of compensation and regulation of the distribution of government participation to municipalities affected by mining activity;
- modernization of the Mining Code regulation, with the updating of obsolete devices, ensuring greater legal certainty and contributing to the reduction of bureaucracy and the operationalization of rules, resulting in gains for the miner;
- end of restrictions on the participation of foreign capital and labor in exploration and mining activities in the frontier strip;
- regulation of article 231 of the Federal Constitution, which deals with the use of water resources, including energy potential, research and mining of mineral wealth in indigenous lands;
- amendment of the legislation on protection of natural underground cavities in order to eliminate eventual conflicts with the mineral extraction activity;
- review of the standards related to mining permit;
- review of the nuclear minerals monopoly.

Current, Brazilian legislation does not yet contemplate new disposal technologies. However, there is a tendency for the mining industries to incorporate alternatives for the disposal of tailings.

2.2 Greater security in the final disposal of the tailings

Brazil is the second largest exporter of iron ore in the world and occupies the same position in the ranking of mineral reserves of this ore with approximately 34 billion tons declared in 2020 (MME, Mineral Sector Bulletin 2020, 2020). With the growing in mineral production, there is also a proportional increase in the generation of tailings and waste.

Robertson (2018) reports the increasing generation of tailings and the consequent increase in the number and size of Tailings Storage Facilities (TSF) in the global mining industry. According to the author, for every 1/3 of a century, the volume of tailings increases approximately 10 times, the area required for their disposal increases around 5 times and the heights of these type of facilities increase approximately 2 times. Consequently, there is an increase in risk linked to tailings and waste disposal operations.

In this context, the search for new technologies and methodologies for the disposal of tailings and mine residues has gained a lot of prestige and attention in the mining sector. This factor is also driven by several negative events associated with dams, the most conventional means of tailings disposal.

According to Davies (2011), Hudson *et. al* (2015) and Amoah *et al.* (2018), the option for a dewatered disposal system in dry stacking type presents itself as a quite advantageous alternative in terms of safety in the final tailings disposal for different reasons, namely: recent technological advances in dewatering and filtering methods, smaller area demand, use of less water in the process, soil-like behavior, and, obviously, a series of restrictions and increased legal requirements on the tailings disposal in dams in Brazil.

In 2011, the methodology is highlighted again with the work of Davies (2011), in which the author presents a graph with tailings disposal trends for different forms of dewatering. The Figure 3 illustrates the graph proposed by Davies (2011). Following up, the Figure 4 presents the contrast between tailings storage facilities in Brazil and in the world based on the Global Tailings Portal.

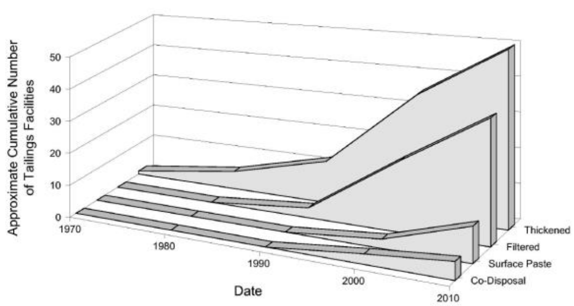

Figure 3. Trends in the use of wastewater in mining by Davies *et. al* (2011).

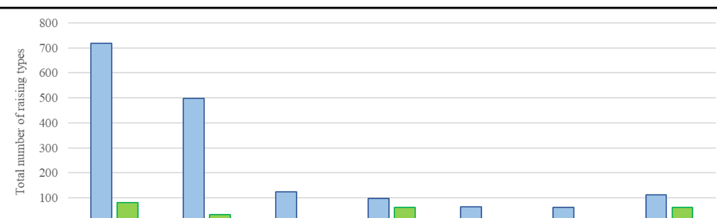

	Upstream	Downstream	Centreline	Single Stage	In-pit	Dry stack	Other
Total number	719	499	124	98	64	63	112
Total number Brazil	82	34	15	62	1	4	62

Figure 4. Contrast between tailings storage facilities in Brazil and in the world (Source of data: Global Tailings Portal, 2021).

2.3 Sustainability in the mining sector

The Sustainable Development Goals (SDGs) defined by the United Nations (UN, 2015), in its plan called "The 2030 Agenda for Sustainable Development", aim to contribute to the viability of better sustainability standards in the world.

One of the points of convergence and of great importance between the Sustainable Development goals, presented in Agenda 2030, and the Sustainability programs in the Mineral Sector, is related to the water resources used. Saving water is a topic of an enormous relevance for the sustainability of mining activities. Many of the mines operated by large companies are in countries where water scarcity is a major risk. Therefore, the conscientious use of water is also one of the main motivations for increasing interest in dewatering tailings. For this reason, there is a very strong trend among mining companies to adopt dewatered disposal and intelligent filtration methods, which provide an efficient solution for dry stacking, help to enhance water recovery and therefore, preserve the entry of water from other sources.

3 ANALYSIS OF THE NATIONAL MINING PLAN 2030

The diagnosis of the content presented in the NMP-2030 was carried out by comparing the Plan's guidelines, objectives and forecasts, considering the focus on iron ore commodities, with what has occurred in Brazil up to the present time. For this, reports published by the MME and by the regulatory agencies of the mining sector were consulted mainly, being the DNPM[1] (until 2017) and the ANM[4] (in force).

The following sub-items will present analyzes involving the NMP-2030 with the consolidated content until 2019. From 2020 through 2023, the planned targets that are in progress will be explained.

3.1 Analysis of guidelines and objectives contemplated in the NMP-2030 with the held until 2019

The guidelines and objectives presented in the NMP-2030 were implemented in public policies through the Multi-Year Plan (MYP), a government budget planning instrument that defines the guidelines, objectives and goals of the federal public administration for the four-year horizon (BRASIL, 1988).

The goals related to the mining sector presented in the MYPs published between 2012 and 2019 were included in the 2041 program - Strategic Management of Geology, Mining and Mineral Transformation - and consisted of nine objectives, totaling 44 goals in the 2012-2015 MYP and 18 goals in the 2016-2019 MYP (MPBM, 2016; ME, 2016-2019 Multi-Year Plan - Annual Evaluation Report 2019, 2019). Of the total of 62 targets expected between 2012 and 2019, 48% were not met.

Some considerations presented in the 2012-2015 MYP and the 2016-2019 MYP for the unmet targets were:

- budgetary difficulties in 2014 and 2015;
- difficulties in the realization of bids for contracting services;
- delays in the execution of services;
- team undersized and relocation of researchers to other projects;
- discontinuity of public policy strategy during the 2016-2019 MYP period, including changes in government priorities;
- incompatibility between budget and financial programming and the dimensioning of the targets;
- absence or insufficiency in the articulation of actors to implement the goal;
- insufficient staff, training and/or training;
- management failures;
- lag in grant systems;
- difficulty in carrying out taskforces;
- amendment or establishment of legal regulations that have impacted the target.

3.2 Analysis of the forecasts presented for iron ore in the NMP-2030 with that carried out until 2019

The NMP-2030 presented forecasts for a number of metallic, non-metallic and energetic mineral goods. These forecasts consisted of projections of values for the production, import, export and apparent consumption (or domestic market) of these mineral goods. According to the Plan, Brazil stands out internally as a producer of niobium, iron ore, bauxite, manganese and several other mineral goods. In the metal segment, iron ore is highlighted by its economic relevance to the Brazilian economy (MME, National Mining Plan 2030, 2010).

According to ANM[4] (Brazilian Mineral Yearbook, 2020), in 2019 the substances of the metal class accounted for about 80% of the total value of Brazilian mineral production, with iron being the substance that showed significant participation in the value of production (Figure 5).

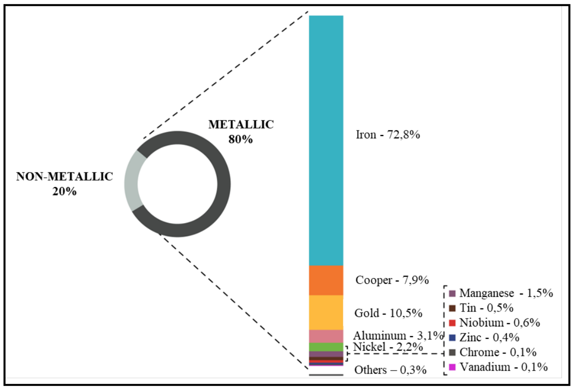

Figure 5: Participation of the main metallic substances in the value of mineral production marketed in 2019 (ANM[4], Brazilian Mineral Yearbook, 2020).

Thus, due to the importance and prominence of iron ore in Brazilian mining, this ore subsidized the analysis of production, export and apparent consumption forecasts presented. It must be highlighted that was not analyzed forecasts for iron ore import because it was considered null in the NMP-2030.

Regarding iron ore production, Figure 6 presents estimated data in the Plan for the years 2015, 2022 and 2030 and actual data for the period 2008 to 2019.

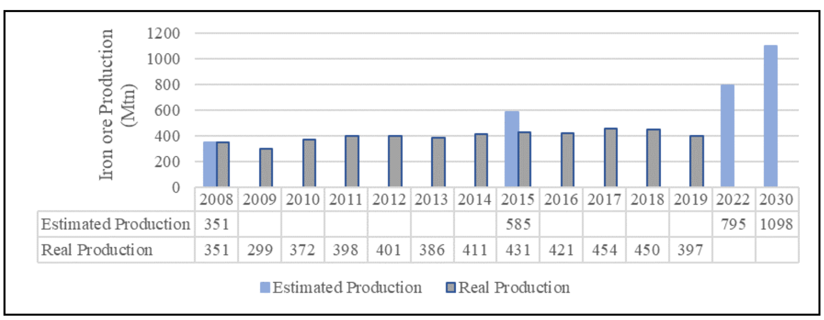

Figure 6. Estimated production versus actual iron ore production in Brazil between 2008 and 2030 (MME, National Mining Plan 2030, 2010; DNPM[1], Mineral Summary - 2010, 2012; DNPM[1], Mineral Summary - 2013, 2013; DNPM[1], Mineral Summary - 2016, 2018; MME, Mineral Sector Bulletin 2020, 2020).

Iron ore production from 2008 to 2019 showed small fluctuations, remaining between 350 Mtn and 450 Mtn. In 2009, production presented the lowest value of the cited period (299 Mtn) because of the fall in production in the states of Minas Gerais and Pará due to the global economic crisis (DNPM[1], Mineral Summary - 2010, 2012). The other production fluctuations that occurred between 2008 and 2019 were due to factors such as:

– difficulties caused by rains in the southeast region in the first quarter of the year, making mining and logistics activities difficult (DNPM[1], Mineral Summary - 2012, 2012; DNPM[1], Mineral Summary - 2013, 2013);
– adverse weather conditions at the end of the year in the North and Southeast regions and the delay in receiving environmental permits for the mining of sections of some mines (DNPM[1], Mineral Summary - 2014, 2014);
– Fundão tailings dam failure in Mariana-MG (ANM[4], Mineral Summary - 2017, 2019).

It is noteworthy that the influence of Barragem 1 tailings dam failure, in Brumadinho-MG, was not considered in the data presented in Figure 6.

Regarding iron ore exports, Figure 7 presents estimated data in the Plan for the years 2015, 2022 and 2030 and actual data for the period 2008 to 2018.

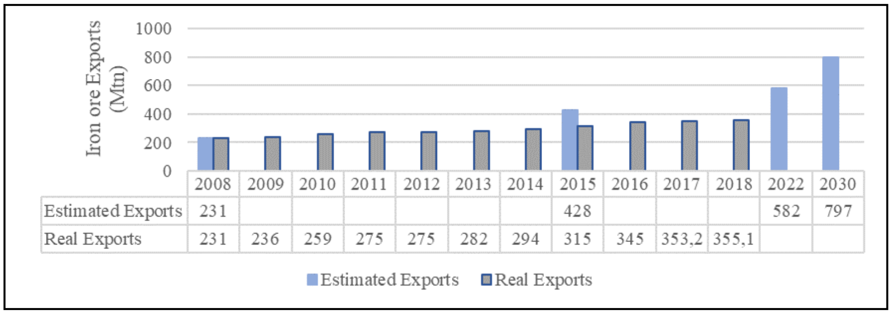

	2008	2009	2010	2011	2012	2013	2014	2015	2016	2017	2018	2022	2030
Estimated Exports	231							428				582	797
Real Exports	231	236	259	275	275	282	294	315	345	353,2	355,1		

Figure 7. Estimated export versus actual export of iron ore in Brazil between 2008 and 2030 (MME, National Mining Plan 2030, 2010; DNPM[1], Mineral Summary - 2009, 2010; DNPM[1], Mineral Summary - 2012, 2012; DNPM[1], Mineral Summary - 2015, 2016; ANM[4], Mineral Summary - 2018, Iron, no date; ANM[4], Synopsis 2019 - Mining and Mineral Transformation (Metallic and Non-Metallic), 2020).

Iron ore exports from 2008 to 2018 increased over the years, but not enough to achieve the NMP-2030 forecast in 2015. As presented in the NMP-2030, China is the main market in Brazil for iron ore exports in the period analyzed. Thus, the growth rates of iron ore exports from Brazil to China were influenced by the situation in which the Chinese economy was in each year.

In the period from 2009 to 2011, there was an expectation that Chinese demand for iron ore would continue to grow in the coming years due to investments in the construction of popular housing, urbanization and infrastructure that were being made in China (DNPM[1], Mineral Summary - 2010, 2012; DNPM[1], Mineral Summary - 2011, 2012; DNPM[1], Mineral Summary - 2012, 2012). However, this prediction has not materialized.

In 2012, average ore export prices decreased compared to 2011, due to China's reduced growth rate, caused by monetary policy measures to reduce inflation, in addition to restructuring the steel sector to reduce excess installed capacity, and the construction sector to avoid a housing bubble (DNPM[1], Mineral Summary - 2013, 2013).

From 2013, despite the slowdown in the Chinese economy, the demand for iron ore in the country was expected to remain warm in the coming years, mainly due to the increase in the rate of urbanization and infrastructure investments in China (DNPM[1], Mineral Summary - 2014, 2014).

However, in 2017, there were greater price differences between high- and low-quality iron ore and it was expected that this price differential would continue to impact the market in the following years (ANM[4], Mineral Summary - 2017, 2019).

Regarding the Brazilian domestic market of iron ore, Figure 8 presents the estimated data in the Plan for the years 2015, 2022 and 2030 and the actual data for the period 2008 to 2017.

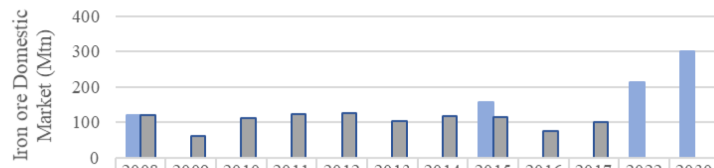

	2008	2009	2010	2011	2012	2013	2014	2015	2016	2017	2022	2030
Estimated Domestic Market	120							157			213	301
Real Domestic Market	120	63	113	123	125	104	117	116	77	100		

Figure 8. Estimated domestic market versus actual domestic market of iron ore in Brazil between 2008 and 2030 (MME, National Mining Plan 2030, 2010; DNPM[1], Mineral Summary - 2009, 2010; DNPM[1], Mineral Summary - 2012, 2012; DNPM[1], Mineral Summary - 2015, 2016; ANM[4], Mineral Summary - 2018, Iron, no date).

The apparent market for iron ore in the period from 2008 to 2017 showed oscillations that accompanied the production of pig iron and the production of pellets, the main products for domestic market in Brazil.

In 2016, the decrease in domestic market of iron ore compared to 2015 was due to the drop in pellet production caused by the stoppage of Samarco's activities due to the collapse of the tailings dam at the Germano Mine in Mariana-MG (ANM[4], Mineral Summary - 2017, 2019).

3.3 Analysis of guidelines and objectives contemplated in the NMP-2030 with the planned until 2023

Mining was included in the Multiannual Plan (MYP) of medium-term planning of the Brazilian federal government from the MYP 1991-1995 to MYP 2020-2023, and from the MYP 2012-2015 there was linking with the guidelines, objectives and goals of the NMP-2030.

Through a historical analysis, it was found that the objectives and targets of both the NMP-2030, the MYP 2012-2015 and the MYP 2016-2019, were not fully met.

Some causes raised by the MYP 2020-2023 that affect the performance of the Brazilian mineral sector in the period from 2012 to 2019 were:

- generation and availability of insufficient knowledge in the mineral sector;
- the public management of mineral resources deficient to meet the demands of the sector;
- insufficient research, development and innovation actions in the mineral sector;
- inadequate legislation and regulation for the mineral sector;
- insufficient action for the internalization of policies in the sustainable and efficient socio-environmental development of mining.

Therefore, the MYP 2020-2023 presents the objectives: develop actions that increase geological knowledge of the territory, improve governance and regulatory stability, favoring greater legal certainty; and incorporate sustainability, innovation and sectoral technological development practices.

In order to consolidate the objectives mentioned, the MYP 2020-2023 aims to reach the value of 5.00 of the Mineral Management Efficiency Index (MMEI), which measures the efforts of the federal administration in the management of the Union's mineral heritage.

For the year 2020, the Intermediate Results presented were: Revitalization of the Brazilian mineral industry; Use of mineral resources in a sustainable way; Demand for Research, License, Extraction and Mining; Expansion of the participation of the mineral sector in territorial management. For the year 2021, the following intermediate results were observed: The analyses of Mining Requirements; The analysis of the Requirement and Research; The public offer of areas in ANM[4] availability; Safety of mining dams; ANM[4] Regulation program; and geological studies.

4 CONCLUSION

The NMP-2030, through the scenario "on the Sustainability Trail", presented guidelines and objectives that provided, among others, for the redefinition of the institutional and regulatory framework. However, only from 2016 on, there were significant changes in the laws and regulations applicable to the theme of disposal of tailings, which may have been influenced by the rupture of the Samarco's dam in November 2015.

Regarding the guidelines and objectives of the NMP-2030, it was observed that in the period from 2012 to 2019 almost 50% of the targets foreseen for the mining sector were not achieved, culminating in the delay on the consolidation of what was proposed. The main factors declared by the Brazilian federal government were budgetary difficulties, delays in the execution of services, undersized of the team and management failures.

On the analysis of production, export and apparent consumption forecasts for iron ore, it was estimated that none of the indicators presented by the NMP-2030 reached the value stipulated in 2015 and this same trend for 2022 is perceived.

Since 2010 the scenario had already changed considerably and in 2016, the NMP-2030 should have been reviewed. However, it wasn't revised and the guidelines, objectives, and targets remain outdated, as they are not aligned with the Brazilian current reality also worldwide reality. In the MYP 2020-2023, it was observed the attempt of the Federal Government to resume the scenario "in the Sustainability Trail" of the NMP-2030. The objectives proposed by 2023 for Brazilian mining involve increasing the geological knowledge of the territory, better air governance and regulatory stability, favoring greater legal certainty, and incorporating practices of sustainability, innovation and sectoral technological development.

5 REFERENCES

ABNT[2], 2017. NBR[3] 13.028. Mining - Preparation and presentation of design of tailings, sediments and/or water dams - Requirements. November 2017, 3° ed, Rio de Janeiro.

ABNT[2]. 2017. NBR[3] 13.029. Mining - Elaboration and presentation of a mining waste disposal design. July 2017, 3° ed, Rio de Janeiro.

AMOAH, N. 2018. Characterization of unsaturated geotechnical properties of filtered magnetite tailings in a dry stack facility. Australian Centre for Geomechanics, Perth, 2018.

ANM[4]. 2019. Mineral Summary - 2017. National Mining Agency, Brasília. Accessed in 2021/08/23. Available in: https://www.gov.br/anm/pt-br/centrais-de-conteudo/publicacoes/serie-estatisticas-e-economia-mineral/sumario-mineral/sumariomineral_2017

ANM[4]. 2020. Brazilian Mineral Yearbook. Main Metallic Commodities 2020. National Mining Agency. Accessed in 2021/08/23. Available in: https://www.gov.br/anm/pt-br/centrais-de-conteudo/publicacoes/serie-estatisticas-e-economia-mineral/anuario-mineral/anuario-mineral-brasileiro/amb_2020_ano_base_2019_revisada2_28_09.pdf

ANM[4]. 2020. Synopsis 2019 - Mining and Mineral Transformation (Metallic and Non-Metallic). National Mining Agency. Accessed in 2021/08/23. Available in: https://www.gov.br/mme/pt-br/assuntos/secretarias/geologia-mineracao-e-transformacao-mineral/publicacoes-1/sinopse-mineracao-e-transformacao-mineral/sinopse-da-mineracao-e-transformacao-mineral-2019-base-2018.pdf/view

ANM[4]. No date. Mineral Summary - 2018, Iron. National Mining Agency, Brasília. Accessed in 2021/08/23. Available in: https://www.gov.br/anm/pt-br/centrais-de-conteudo/publicacoes/serie-estatisticas-e-economia-mineral/sumario-mineral/pasta-sumario-brasileiro-mineral-2018/ferro_sm_2018

BRASIL. 1988. Federal Constitution. Accessed in 2021/08/16. Available in: http://www.planalto.gov.br/ccivil_03/constituicao/constituicao.htm#art65

BRASIL. 2010. Law No. 12,334. Accessed in 2021/08/23. Available in: http://www.planalto.gov.br/ccivil_03/_Ato2007-2010/2010/Lei/L12334.htm

BRASIL. 2010. Law No. 12,305. Accessed in 2021/08/23. Available in: http://www.planalto.gov.br/ccivil_03/_ato2007-2010/2010/lei/l12305.htm

BRASIL. 2017. Decree No. 9,252. Accessed in 2021/08/23. Available in: http://www.planalto.gov.br/ccivil_03/_ato2015-2018/2017/decreto/D9252.htm

BRASIL. 2017. Law No. 13,540. Accessed in 2021/08/03. Available in: http://www.planalto.gov.br/ccivil_03/_ato2015-2018/2017/lei/L13540.htm

BRASIL. 2017. Law No. 13,575. Accessed in 2021/08/23. Available in: http://www.planalto.gov.br/ccivil_03/_ato2015-2018/2017/lei/l13575.htm

BRASIL. 2017. Ordinance DNPM[1] No. 70.389. Accessed in 2021/08/23. Available in: https://www.in.gov.br/materia/-/asset_publisher/Kujrw0TZC2Mb/content/id/20222904/do1-2017-05-19-portaria-n-70-389-de-17-de-maio-de-2017-20222835

BRASIL. 2018. Decree No. 9,407. Accessed in 2021/08/23. Available in: http://www.planalto.gov.br/ccivil_03/_ato2015-2018/2018/decreto/D9407.htm

BRASIL. 2019. Resolution ANM[4] No. 13. Accessed in 2021/08/03. Available in: https://www.in.gov.br/web/dou/-/resolucao-n-13-de-8-de-agosto-de-2019-210037027

BRASIL. 2020. Law No. 14,066. Accessed in 2021/08/23. Available in: http://www.planalto.gov.br/ccivil_03/_ato2019-2022/2020/lei/L14066.htm

BRASIL. 2020. Resolution ANM[4] No. 32. Accessed in 2021/08/23. Available in: https://www.in.gov.br/web/dou/-/resolucao-n-32-de-11-de-maio-de-2020-257201163

BRASIL. 2020. Resolution ANM[4] No. 40. Accessed in 2021/08/23. Available in: https://www.in.gov.br/en/web/dou/-/resolucao-n-40-de-6-de-julho-de-2020-265383714

BRASIL. 2020. Resolution ANM[4] No. 51. Accessed in 2021/08/03. Available in: https://www.in.gov.br/en/web/dou/-/resolucao-n-51-de-24-de-dezembro-de-2020-296821959

BRASIL. 2021. Resolution ANM[4] No. 56. Accessed in 2021/08/23. Available in: https://www.in.gov.br/en/web/dou/-/resolucao-anm-n-56-de-28-de-janeiro-de-2021-301401259

BRASIL. 2021. Resolution ANM[4] No. 68. Accessed in 2021/08/26. Available in: https://www.in.gov.br/en/web/dou/-/resolucao-anm-n-68-de-30-de-abril-de-2021-317640591

DAVIES, M. 2011. Filtered Dry Stacked Tailings – The Fundamentals. Proceeding Tailings and Mine Waste 2011, Vancouver, BC, November 6 to 9, 2011.

DNPM[1]. 2010. Mineral Summary - 2009. Accessed in 2021/08/23. Available in: https://www.gov.br/anm/pt-br/centrais-de-conteudo/publicacoes/serie-estatisticas-e-economia-mineral/sumario-mineral/sumario-mineral-brasileiro-2009/view

DNPM[1]. 2012. Mineral Summary - 2010. National Department of Mineral Production, DNPM[1]/DIPLAM, Brasília. Accessed in 2021/08/23. Available in: https://www.gov.br/anm/pt-br/centrais-de-conteudo/publicacoes/serie-estatisticas-e-economia-mineral/sumario-mineral/sumario-mineral-brasileiro-2010/view

DNPM[1]. 2012. Mineral Summary - 2011. National Department of Mineral Production, DNPM[1]/DIPLAM, Brasília. Accessed in 2021/08/23. Available in: https://www.gov.br/anm/pt-br/centrais-de-conteudo/publicacoes/serie-estatisticas-e-economia-mineral/sumario-mineral/sumario-mineral-brasileiro-2011/view

DNPM[1]. 2012. Mineral Summary - 2012. National Department of Mineral Production, DNPM[1], Brasília. Accessed in 2021/08/23. Available in: https://www.gov.br/anm/pt-br/centrais-de-conteudo/publicacoes/serie-estatisticas-e-economia-mineral/sumario-mineral/sumario-mineral-brasileiro-2012/view

DNPM[1]. 2013. Mineral Summary - 2013. National Department of Mineral Production, DNPM[1], Brasília. Accessed in 2021/08/23. Available in: https://www.gov.br/anm/pt-br/centrais-de-conteudo/publicacoes/serie-estatisticas-e-economia-mineral/sumario-mineral/sumario-mineral-brasileiro-2013/view

DNPM[1]. 2014. Mineral Summary - 2014. National Department of Mineral Production, DNPM[1], Brasília. Accessed in 2021/08/23. Available in: https://www.gov.br/anm/pt-br/centrais-de-conteudo/publicacoes/serie-estatisticas-e-economia-mineral/sumario-mineral/sumario-mineral-brasileiro-2014/view

DNPM[1]. 2016. Mineral Summary - 2015. National Department of Mineral Production, DNPM[1], Brasília. Accessed in 2021/08/23. Available in: https://www.gov.br/anm/pt-br/centrais-de-conteudo/publicacoes/serie-estatisticas-e-economia-mineral/sumario-mineral/sumario-mineral-brasileiro-2015/view

DNPM[1]. 2018. Mineral Summary - 2016. National Department of Mineral Production, DNPM[1], Brasília. Accessed in 2021/08/23. Available in: https://www.gov.br/anm/pt-br/centrais-de-conteudo/publicacoes/serie-estatisticas-e-economia-mineral/sumario-mineral/sumario-mineral-brasileiro-2016/view

Global Tailings Portal. (2021). Tailings storage facilities: raising types. Accessed in 2021/08/24. Available in: https://tailing.grida.no/

HUDSON, A. HUSSEY, A. HARLEY, A. e DYHR, T. M. - Simulating the Performance of a Dry Stack Tailing Design for Water Control Permitting. 10th International Conference on Acid Rock Drainage & IMWA Annual Conference (2015).

ME. 2019. 2016-2019 Multi-Year Plan - Annual Evaluation Report 2019. Ministry of Economy. Accessed in 2021/08/23. Available in: https://www.gov.br/economia/pt-br/assuntos/planejamento-e-orcamento/plano-plurianual-ppa/arquivos/ppas-anteriores/ppa-2016-2019/arquivos/monitormaento-e-

avaliacao-do-ppa/relatorio-de-avalicao-do-ppa-2019-avaliacao_dos_programas_tematicos.pdf
ME. 2019. 2016-2019 Multi-Year Plan - Annual Evaluation Report 2019 - Annex I: Evolution of Indicators. Ministry of Economy. Accessed in 2021/08/23. Available in: https://www.gov.br/economia/pt-br/assuntos/planejamento-e-orcamento/plano-plurianual-ppa/arquivos/ppas-anteriores/ppa-2016-2019/arquivos/monitormaento-e-avaliacao-do-ppa/relatorio-de-avalicao-do-ppa-2019-avaliacao_dos_programas_tematicos-anexos.pdf
ME. no date. Program Mirror of the 2020-2023 Multi-Year Plan. Ministry of Economy. Accessed in 2021/08/23. Available in: https://www.gov.br/economia/pt-br/assuntos/planejamento-e-orcamento/plano-plurianual-ppa/arquivos/espelhos-completos-2021.pdf
MME. 2010. National Mining Plan 2030. Ministry of Mines and Energy. Brasília: MME. Accessed in 2021/08/09. Available in: https://www.gov.br/mme/pt-br/assuntos/secretarias/geologia-mineracao-e-transformacao-mineral/plano-nacional-de-mineracao-2030-1/documentos/book_pnm_2030_2.pdf/@@download/file/Book_PNM_2030_2.pdf
MME. 2020. Mineral Sector Bulletin 2020. Ministry of Mines and Energy, Brasília. Accessed in 2021/08/23. Available in: https://www.gov.br/mme/pt-br/assuntos/secretarias/geologia-mineracao-e-transformacao-mineral/publicacoes-1/boletim-do-setor-mineral/boletim-do-setor-mineral-2013-4o-trim-2020.pdf/view
MPDM. 2018. Catálogo de Metas - MYP 2016-2019. Ministry of Planning, Development and Management. Accessed in 2021/08/21. Available in: https://www.gov.br/economia/pt-br/assuntos/planejamento-e-orcamento/plano-plurianual-ppa/arquivos/ppas-anteriores/ppa-2016-2019/catalogo-de-metas-2018.pdf
MPBM. 2016. Annual Evaluation Report of the 2012-2015 MYP, Base Year 2015, Volume II - Thematic Programs. Ministry of Planning, Budget and Management, Brasília. Accessed in 2021/08/09. Available in: https://www.gov.br/economia/pt-br/assuntos/planejamento-e-orcamento/plano-plurianual-ppa/arquivos/ppas-anteriores/ppa-2012-2015/relatorio-anual-de-avaliacao-do-ppa-2012-2015-ano-base-2015/relatorio-avaliacao-ppa-vol2-programas-tematicos.pdf
UN. 2015. Transforming our world: the 2030 Agenda for Sustainable Development. Accessed in 2021/08/24. Available in: https://www.un.org/ga/search/view_doc.asp?symbol=A/RES/70/1&Lang=E
ROBERTSON, A.M. 2018. Mine Closure for the Sustainability of Mining and Enviroment – Concepts, Challenges and Inovation. Accessed in 2020/06/07. Available in: http://www.mme.gov.br/documents/36108/411072/Mine+Closure+for+Sustainability+Dr+Andrew+Robertson.pdf/4c12bf7d-1694-df0b-5806-f6b3c8351430?version=1.0

One small step forward in enhancing the safety of tailings storage facilities: A case study – Buenavista del Cobre tailings storage facility, Sonora, Mexico.

Vidal Muhech Dip, Alberto Arriaga Ruiz & Rodrigo Chávez Flores
Minera México, Mexico City, México

Óscar Vega-Roldán
CIEPS Consultores, Mexico City, Mexico

Krishna Parameswaran
tfgMM Strategic Consulting, Scottsdale, AZ 85262

ABSTRACT: Buenavista del Cobre S.A. de C.V. mine expanded its capacity from 250,000 to 850,000 mtpd (metric tons per day) copper ore. This expansion required the construction of a new tailings storage facility (TSF)[1]. In the wake of continuing catastrophic tailings dam failures across the globe, improving the safety of tailings storage facility during its entire lifecycle i.e., design, construction, operation to closure and post-closure became our paramount consideration. A down-stream construction method using borrow materials with a pervious embankment design was selected. This design, in our view, is a small step forward that will contribute to enhanced safety of TSFs through the entire mining life cycle.

1 INTRODUCTION

Buenavista del Cobre, owned since 1988 by Grupo México, is a copper mine located next to Cananea City in the state of Sonora, Mexico (see Figure 1). This mine has been operating since the last years of the nineteenth century and was one of the first leach - solvent extraction - electrowinning (SX-EW) operations in the world. There also was a copper smelter that ceased operations in 1999 and remediation of the old smelter site is still in progress.

Ore reserve increases resulting from robust exploration programs with the ever-increasing demand for refined copper justified an increase in the capacity of the mine and the construction of new processing plants.

A long-term plan for implementing the capacity expansion was developed (Muhech Dip V. & Orozco Santoyo R.V. (2012)). Brainstorming sessions and planning activities addressed various topics: processing facilities that were needed, their location and capacities; what new equipment was needed for the increased throughput, infrastructure needs associated with higher requirements for electricity, fuel, water and other utilities due to the expansion; management of additional traffic; and maintenance shops to accommodate the increased fleet of larger trucks and auxiliary drilling equipment.

The expansion called for increasing the ore mined from 250,000 mtpd to 850,000 mtpd copper ore, based on which the size for the new plants and tailings storage facilities– concentrator, leaching and SX-EW – were determined.

Throughout this paper we use tailings storage facility (TSF) instead of tailings dams, because of our view that TSF is a more accurate description. Dams impound water whereas TSF are engineered facilities for perpetual storage of tailings.

2 TAILINGS STORAGE FACILITY-DESIGN AND CONSTRUCTION

The expansion of concentrator capacity (2,500,000 mtpy) required the construction of a new tailings storage facility (TSF). In the wake of the continuing trend of catastrophic failures across the globe, it was clear that we needed to seek an innovative approach to the design and construction of TSFs. Safety of the tailings storage facility during its entire lifecycle i.e., design, construction, operation to closure and post-closure would be our paramount consideration.

2.1 Conceptual depiction of selected TSF design

Constructing an embankment or earth-rock fill dam, which has been successfully used for large water storage dam around the world, would provide a safer structure. Liquefaction of saturated, loose, fine to medium silty sands used to build many tailings storage facilities around the world, mainly by the upstream construction method, has been the cause of failures and severe damage. Some of the failures that occurred in recent times were caused by floods overtopping the crest of the dam. A third reason of failure has been incompetent foundations, incapable of supporting the weight of the dam.

Natural borrow materials used in embankment water dams rarely liquefy. For a TSF built with borrow materials, it is easy to keep a large freeboard to contain, without spilling, the amount of water expected from the design storm.

An earth-rock fill dam with an impervious core of natural materials is the most common type of embankment used to store water, but some large tailings reservoirs have retaining dams constructed in this manner. It includes the No. 7 TSF at the La Caridad mine in Nacozari (Arriaga Ruiz A. G. (2019)), state of Sonora, Mexico. This tailings dam was built between 1981-1984, at 147 m high, and raise to 177 m between 2011-2019. The original downstream slope was 1.6H to 1V and the new downstream slope, due to an update in seismic classification, is 2H to1V.These dams, built to store tailings, keep the water released by tailings within the reservoir, due to their impervious core, so that water must be ponded and pumped away, both to recover it for re-use and to eliminate spills.

Available TSF and water dam construction methods, the causes of catastrophic failures of TSF described in available reports, ICOLD Bulletins (45, 74, 97, 98, 101, 103, 106, 121, 139 & 153) and the Mexican Standard on Tailings Dams (NOM – 141 – SEMARNAT – 2003) were carefully studied. We decided to incorporate the lessons learned from the La Caridad experience in the design of the BVC TSF. However, the new TSF was conceived not as impervious, but as a pervious one, to let water flow through the dam and at the same time prevent the flow of solids, acting both for water recovery and as a water clarifying facility (Figure 1) (Muhech Dip V. & Orozco Santoyo R.V. (2012)).

The downstream construction method using borrow materials for construction and a pervious embankment structure was selected because it would provide the following advantages:

- The crest elevation of the dam would not be dependent to the availability of tailings.
- The material for raising the dam would be subject to strict quality controls.
- A pervious dam would allow water to filter through the body of the dam.
- A pervious dam reduces the contact time between the tailings and the water.
- Collecting filtered water with almost no solids results in reduced pumping system wear.

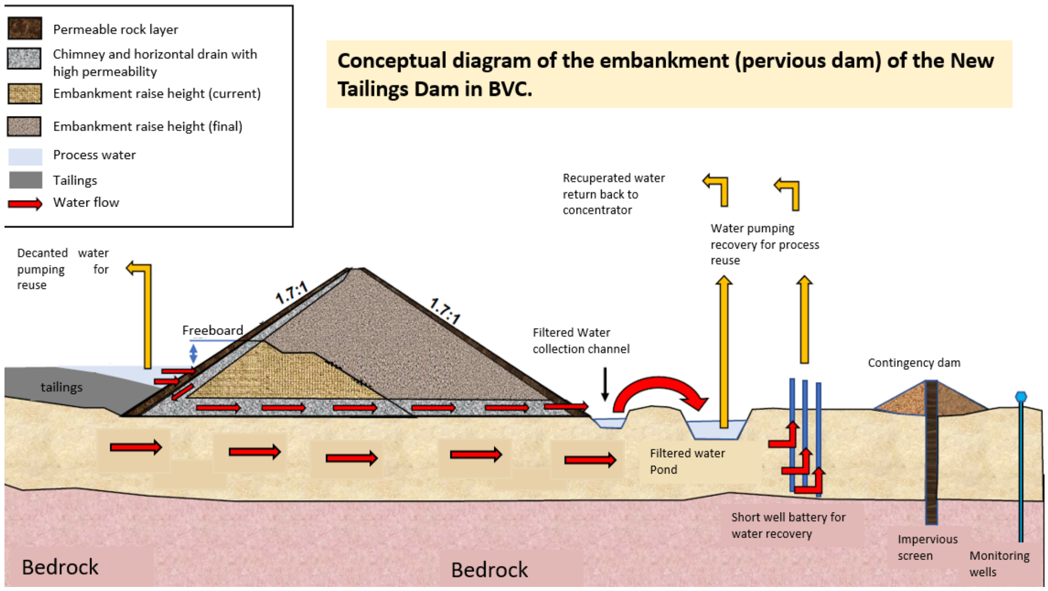

Figure 1. Conceptual design for BVC TSF (Arriaga Ruiz A.G. & Vega-Roldán O. (2016)).

2.2 Design Innovation

The TSF is a large engineered structure, located in a wide valley where site topography can provide the necessary capacity. It will reach a height of 172 m at its main section and 6.5 km along its crest with an embankment base width of 632 m (Figure 2).

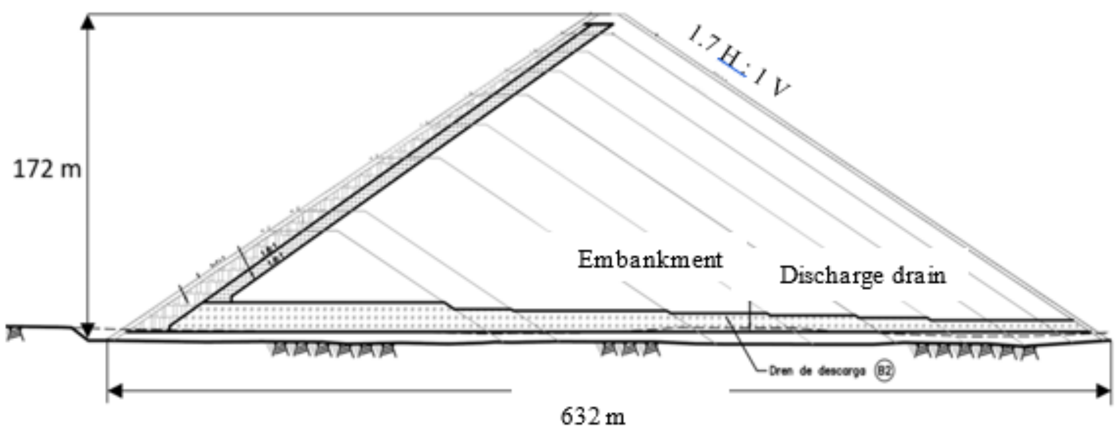

Figure 2. Cross-section of the embankment (considering 8 stage raises).

With safety as the utmost priority, the embankment geometry is a critical consideration. Appropriate upstream and downstream slopes were proposed at 1.7H to 1.0V; confirmed by finite element structural calculations, providing Safety Factors above national regulations for static and pseudo-static conditions (Botero Jaramillo E. & Flores Castrellón O. & Romo Organista M.P. (2014)). Embankment forming materials should be capable of resisting normal structure deformations and develop enough shear strength to provide stability. Materials characterization and stability analysis were key to ensure dam safety within generally accepted norms. Basically, the dam is constructed of borrow materials, obtained from natural competent rock formations close to the dam site (Figure 3), crushed and screened to fit the design parameters. Materials needed are about 158 Mm^3 (Vega-Roldán O. (2018)).

In a water storage earth-rock fill dam with an impervious core, we must assume that some water can flow through it, for it is impossible to achieve total impermeability. Considering that filtrating water will reach the downstream portion of the dam, which is mainly responsible of instability of the dam, it is very important to limit pore pressures in the downstream portion, for they would lower effective compressional stresses and shear strength. The stability of the dam is enhanced if the part of the dam downstream from the core is free from seepage. Usually, this problem is addressed with some internal drainage system within the downstream portion. Moreover, to prevent passage of core material, solids, into the drainage system, this part of the dam is usually provided with a filter zone, that lets water pass into drains but retains solid particles. These essential concepts provided the basic ideas necessary to design the BVC tailings-retention dam.

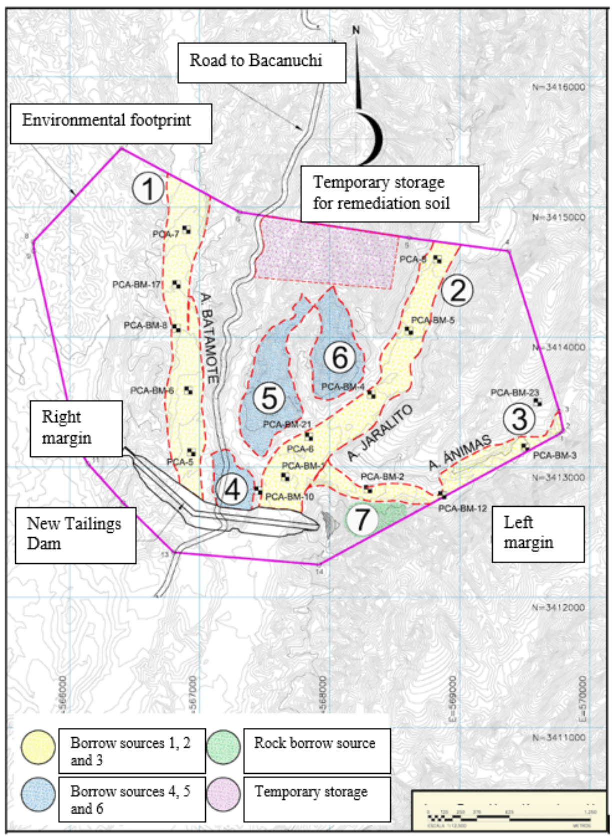

Figure 3. Material borrow sources close to the tailings dam.

First, a semi-pervious core was conceptualized, thought to act in relation to stored tailings the same way a filter does in relation to impervious core material in water storage dams. This semi-pervious core would let water pass but retain tailings solid particles. Water from tailings would not only be recovered, but also clarified. This so-called core was designed inclined, located at the upstream face of dam, and protected with a riprap zone (Figure 4).

The amount of water that could be recovered from tailings was estimated from data on the water sent out from the concentrator, making allowance for water trapped in the tailings and for losses by evaporation and infiltration. The permeability of the semi pervious core should be such as necessary to let the water flow all along the core. Rainwater was also considered.

Downstream of the semi-pervious core, a drainage system was designed. It consists of two kinds of drain. First, inclined chimney drains are located upstream of the core, between it and the main body of the dam, with suitable permeability and width to permit filtrated water to flow down freely, so it would never get pressurized, avoiding any possibility of elevated pore pressure inside the drain.

The second kind of drain are discharge drains, starting inside the dam just at the base of the inclined chimney drains, and going outside the dam to allow drained water to flow towards the downstream face of the dam, to be recirculated back to the process plant. These drains are formed with very pervious material layers located between the foundation material (basically conglomerate rock) and the body of the dam. The vertical dimension of these drains was calculated to assure water flow inside them so as to avoid elevated pore pressure (Figures 4 and 5).

The dam shell is the main part of the embankment from the stability point of view. As previously noted, it is formed of natural materials existing around the dam site, and they are to be compacted to assure both impermeability and shear strength (Vega-Roldán O. (2019)).

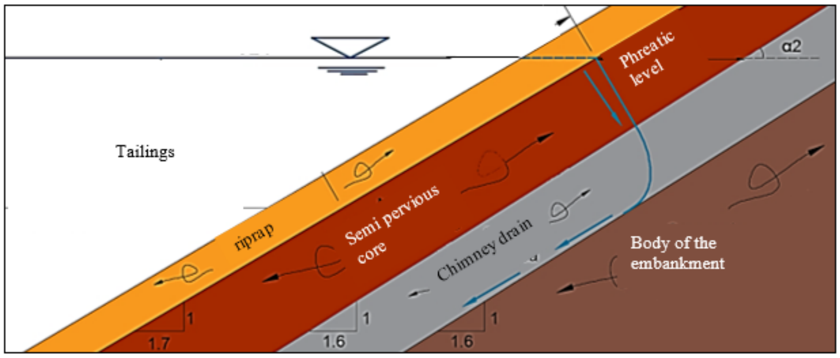

Figure 4. Water flow through the embankment schematic diagram.

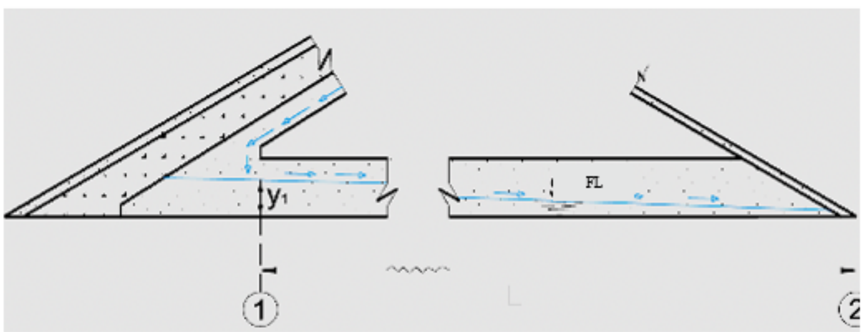

Figure 5. Functionality inside of the chimney and horizontal drains.

2.3 Site condition studies

The following studies provided the basis for designing the TSF:

2.3.1 Hydrological studies

Information from meteorological stations of the National Meteorological Service was used to analyze all four basins to determine surface characteristics, precipitation and evaporation rates (Martínez Guerra R. (2011)). Design hydrographs were calculated for an extraordinary storm to determine the necessary capacity to store its volume. There were several return periods analyzed. ICOLD's recommendation for a tailings dam with BVC's dam's characteristics and dimensions is to design it for a 10,000-year return period event; Grupo México, following the "Safety First Initiative" and exceeding Global Industry Practices, designed it to be capable of withstand an event with a return period of 12,000 years, following CONAGUA (Comisión Nacional del Agua) recommendations (Martínez Guerra R. 2012)).

2.3.2 Geological studies

To determine the mechanical behavior of the site, a geological survey was conducted before the design and construction of the dam to determine the characteristics of the geological structures

(Lara Manriquez E. (2013)). For the definition of the regional geology, the Servicio Geológico Mexicano (Mexican Geological Service) and other previous studies were utilized to determine the characteristics of the geological strata and were taken as a base for the geological study.

2.3.3 Geophysical studies

There were several geophysical studies conducted onsite to determine the physical and mechanical characteristics to properly define the design parameters and the construction method of the embankment.

- Seismic refraction at site.
  To determine the velocity of the elastic waves throughout the terrain and indirectly determine the physical characteristics of the different geological strata (thickness, depth, distribution, etc.), there were 28 geo-seismic refraction spreads performed in the area of the embankment.
- Deep geo-electric prospecting.
  To determine the resistivity characteristics of the area and find the soil lithology and its distribution, there were 18 deep geo-electric soundings (300 meters in depth) performed in the area as part of the geophysical studies.
- Surficial exploration trenches.
  There were 15 surficial exploration trenches (5 meters in depth) made in the area to obtain the surficial stratigraphic sequence of the terrain; this allowed the design engineers to estimate the different stratigraphic layers and the alluvial deposits in the area.
- Mid-deep exploration probes.
  In order to establish the conditions and characteristics of the stratigraphic sequence of the materials of the area, there were 39 mid-deep exploration mixed-continuous probes performed in the area, with depths varying between 25 to 30 meters with unaltered and altered sample recovery.
- Permeability sampling.
  Because of the specific characteristics of the TSF, one of the most important aspects of the study was to determine the hydraulic conductivity of the different formations underneath the site in order to understand their characteristics and to predict the water movement amongst the strata.
- Lab Testing.
  Soil and rock samples were analyzed in the lab to determine their physical and mechanical characteristics.

2.3.4 Hydrogeological studies

The hydrogeological model was determined through an official study made by CONAGUA in 2010 (Estadísticas del Agua en México, CONAGUA, 2010) in which ground water was analyzed in the northern part of the state of Sonora. The type of aquifer on which the TSF is located is defined as a heterogenic and anisotropic aquifer presenting local semi-confined conditions due to the presence of clay deposits. To complete the hydrogeological study, there were several other studies performed onsite to determine ground water quality, static and dynamic water depths, water flow and underground hydraulic behaviors for a better understanding of the site.

2.3.5 Seismic studies

According to ICOLD Bulletins 72 and 141 and the Design Manual of the Comisión Federal de Electricidad (Manual de Diseño de Obras Civiles, Diseño por Sismo CFE, 2014) there are two design earthquakes that need to be considered in the design of a TSF; the Maximum Credible Earthquake and the Operating Basis Earthquake. The former corresponds to the hypothetical earthquake with the most severe intensity.

After analyzing the historical data of past earthquakes, the surface synthetic movements were calculated according to the methodology of the CFE Design Manual for the determination of the acceleration spectrum for rocks.

2.4 Construction Details

2.4.1 Embankment site preparation

Prior to the construction of each stage, site preparation was to be done to achieve structural adherence and proper interaction between the embankment and the underlying ground. Seven meters of excavation works were necessary until sound rock stratum was found for supporting the embankment.

2.4.2 Stormwater Diversion

To divert storm water, it was necessary to build four diversion dams upstream of the TSF. These dams capture storm water coming from the surrounding basins and divert it through a complex series of hydraulic infrastructures, allowing rainwater to flow, unaltered, downstream. The yearly diverted volume of water is 700,000 m^3.

2.4.3 Regulatory approval

In2013, once the engineering and Environmental Impact Assessment (EIA) study were completed, we requested and obtained from, SEMARNAT, the Mexican environmental authority, the required permits to proceed with the construction of the TSF. Long-term monitoring and closure and post-closure activities were considered in the EIA.

2.4.4 Additional considerations

Besides rainwater diversion, there are several other considerations that need to be addressed. Fauna fences were installed along the deposition perimeter to prevent local fauna from entering into the tailings area, local roads were relocated, and water and tailings pipelines and channels were constructed, among many other activities.

2.4.5 Construction materials

As seen in Figure 6, the body of the embankment is composed of five different materials that allow water flow through the body of the embankment while retaining the solids inside the dam (as shown in Table 1). These different materials must follow strict quality control and quality assurance to keep the TSF functioning properly. All materials have different characteristics and are obtained from local borrow sources inside and near the area of the dam. The materials are then hauled to classifying plants alongside the embankment and separated into different types.

Table 1: Design parameters for the TSF. (Vega-Roldán, O. (2013))

Material	Type	Volume (Mm^3)	Percentage (%)	Specifications
A	Semi-pervious Core	11	7	< 2.5” – max. 10% fines
B1	Chimney Drain	8	5	< 4.0” – max. 5% fines
B2	Horizontal Drain	36	23	3/8” < B2 < 6.0”
C	Embankment	98	62	earth and rock fill
D	Riprap	5	3	6.0” < D < 39”
	Total	158	100	

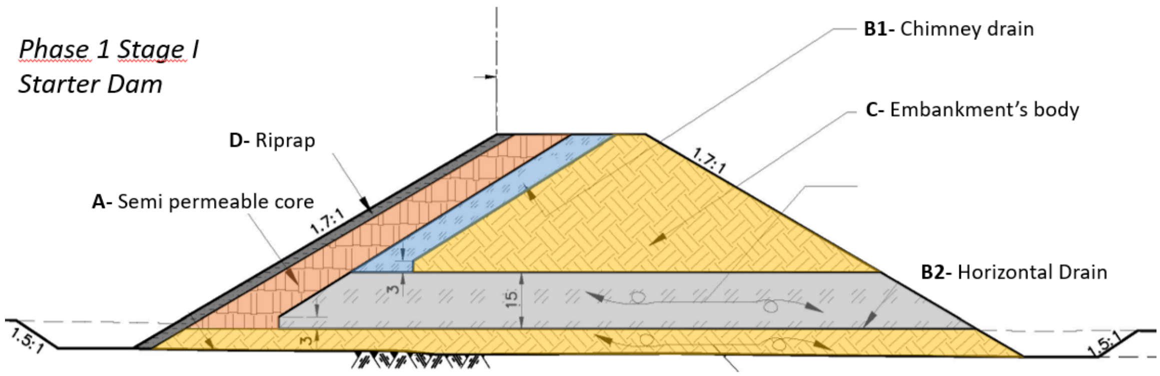

Figure 6. Materials composing the embankment

Figure 7. Materials placed in the embankment

2.4.6 Construction program

The construction of the embankment, and all necessary additional site preparations, was initially programmed in eight downstream raise stages, starting in 2015 and ending in 2055. Because an increase in the rate of deposition of tailings occurred, the raise stages needed to be adjusted (Arriaga Ruiz A. G. (2019)). Given the dynamic nature of the project, the construction program changed to sixteen stages, as shown in Figures 8 and 9 below. These additional stages were made to ensure proper freeboard levels.

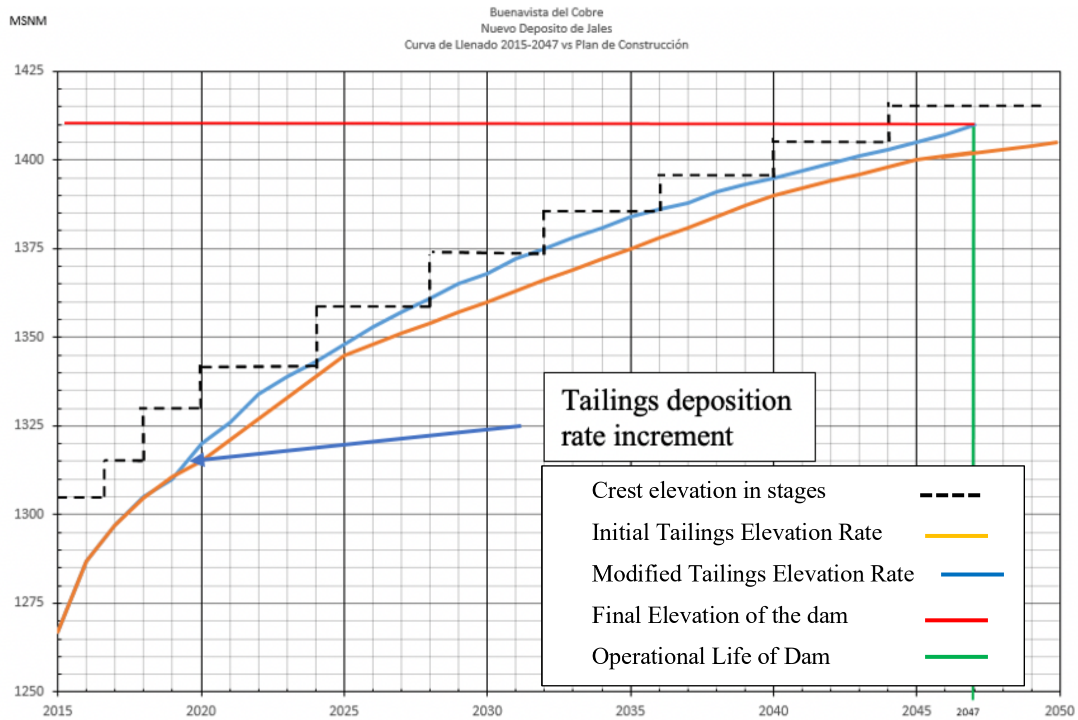

Figure 8. Initial eight stage elevation program.

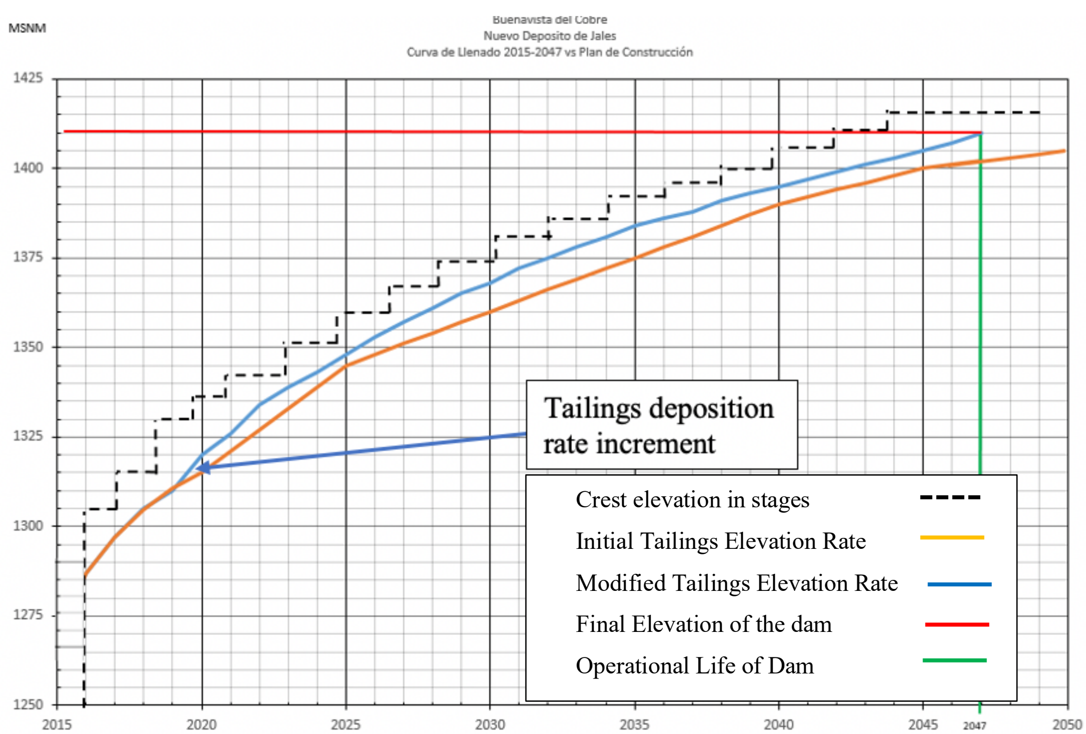

Figure 9. Modified sixteen stage elevation program.

3 ADVANTAGES OF SELECTED TSF DESIGN

The advantages of the selected TSF design are discussed below:

3.1 Construction Pace not dependent on milling rate

Construction of the TSF with borrow materials, using the downstream method, is independent of the rate of deposition of the tailings. This apparently simple fact represents a "quantum leap" advantage over the construction method utilizing the coarse solids in the tailings, because the supply of these sands, material to build the dam, is limited by the milling rate of the concentrator.

The linkage between milling rate - production of sands - and the pace of construction of the TSF is broken. Water overflowing the crest has been the cause of many structural failures in both TSFs and water dams around the world. Having an independent source of construction materials makes it possible to raise the crest of the dam up to the necessary level to reach the freeboard desired. This way, enough "empty" volume is provided to hold the maximum expected storm, eliminating the need for a spillway; nevertheless, a spillway will be constructed at the end of stage 16. This means a substantially safer structure from the hydrological viewpoint.

3.2 Structural resistance

The soundness (quality) of a TSF built with tailings sands is subject to the variable mechanical properties (geology) of the ore being mined at different times in the mine life, to the particle size distribution of the product of the ball mills in the concentrator, and also to the proper separation of the sands from the fines, in the tailings stream, at the TSF site. With at least three variables out of strict quality control, it is very difficult to guarantee the dam's structural stability.

On the contrary, building the body of the TSF with rock from a borrow bank can assure soundness. Producing crushed rock with the required size distribution and mechanical resistance is easy and amenable to quality control.

3.3 Construction of TSF handled as "Construction project"

Handling the construction of the dam as a project, independently of the worries and pressures of production, allows it to be subject to standardized procedures of any project: selecting the proper rock banks, the required aggregate equipment, the haul roads, independent quality control from source to placement, layer by layer checking the proper density, non-conforming layers removed and replaced, continuous reporting, etc. Construction of the dam as a separate construction project eliminates the conflict of interest that arises between the priorities of production (finer grind to increase recovery, meeting the daily production, etc.) and the needs of the dam.

3.4 Water recovery systems

As for every mine, water is an extremely important resource. The design of the TSF took into consideration water recovery as a main requirement. As mentioned, the nature of the embankment permits water flow through the body of the dam while retaining solids in the impoundment; this has proven to be an excellent system because it reduces the maintenance costs of the pumping stations (no solids get pumped) and reduces the amount of water stored in the dam, increasing its structural stability and reducing evaporation losses. As opposed to traditional upstream built dams, where the pond must be as far away from the face of the dam as possible, the proper functioning of this pervious dam allows the ponded water to be in direct contact with the upstream slope of the dam.

Additionally, there are six wells installed downstream of the embankment in order to recover the down-filtered water, as shown in Figure 1.

3.5 Dynamic design

Since the beginning of construction, the TSF has been in continuing design optimization, assuring the expected results are met or exceeded. Throughout the lifespan of the project there has been constant communication between construction and engineering professionals, resulting in a dynamic design. The channel shown in the figure below was not originally considered, but as water approached the right margin it showed the necessity of confining the flow to a channel, to avoid dissipation and erosion.

4 INSTRUMENTATION AND MONITORING

In this section we discuss instrumentation deployed and monitoring parameters needed to guarantee the performance of the TSF during construction and operation.

4.1 Piezometers

Given the importance of monitoring the proper performance of the different materials of the dam, and due to the nature of the filtering dam, water level controls in the horizontal drains are extremely important. Piezometers have been installed in the embankment in order to monitor the water level in the horizontal drains.

4.2 Markers

There is an instrumentation program in place for each stage of the construction of the embankment, in which a series of markers will be installed along the crest of the dam. The geolocation of the markers is continuously monitored.

4.3 Weather stations

Twelve weather stations were installed in order to monitor weather conditions. The weather station grid is solar powered and is interconnected to a central station for remote real time monitoring. The temperature, precipitation and evaporation databases allow for decision making in the water recovery system.

4.4 Deposited tailings volume monitoring

The deposited tailings volume is measured by three different methods; by a constant topographical survey performed onsite that allows for movement detection in the embankment and with a comparison of a 3D model and to an aero-photogrammetric survey performed on a yearly basis. In the past two years, comparing the three methods, the difference is less than 1.00%.

4.5 Quality control

Strict quality assurance procedures have been implemented to maintain placed materials in accordance with specifications. In every layer, an independent quality control specialist checks for relative density and design parameters; noncomplying layers are removed and replaced.

Characteristics that are constantly monitored to ensure quality include: specific gravity, relative density, water content, permeability, dry and humid volumetric weight.

4.6 Future monitoring plans

With the ongoing dynamic design, there is an instrumentation plan ongoing for the TSF that will include 4D control monitoring software, automated total stations, GNSS monitoring receivers, geotechnical sensors, geotechnical sensors, strain gauges, RADAR measurements and seismic sensors deployed in phases.

5 CONCLUSIONS

After five years in operation, the BVC TSF has met our expectations demonstrating enhanced safety:

- The crest of the dam is currently at elevation 1335m and the elevation of the tailings at 1311m. This shows the independence of construction rate vs. rate of production, providing protection against storms.
- The relative density for materials placed has been strictly controlled within the acceptance range, by a third-party quality control company, assuring protection against earthquakes.
- The readings of the piezometers show no water level, indicating no pore pressure.
- The water harvested, both from the drains and under-drains, has yielded above expectancies, reducing the possibilities for generating acid mine drainage.
- Filtered water is clear and free of solids, meaning reduced maintenance for the recovered water systems

Although we have met and exceeded expectations in the five years of operation, with the full deployment of instrumentation and monitoring we hope to demonstrate that the innovative design represents a significant step forward in the safety of TSFs.

6 REFERENCES

Arriaga Ruiz A.G. 2019. Aspectos de Construcción, V Seminario sobre Depósitos de Jales.

Arriaga Ruiz A.G. & Vega-Roldán O. 2016. Diseño y construcción del Depósito de Jales Buenavista del Cobre. XXVIII Reunión Nacional de Ingeniería Geotécnica y XIX Reunión Nacional de Profesores de Ingeniería Geotécnica.

Botero Jaramillo E. & Flores Castrellón O. & Romo Organista M.P. 2014. Análisis de un Depósito de Jales y una Presa de Agua en la Unidad Minera Buenavista del Cobre. Cananea, Son.

Lara Manriquez E. 2013. Estudio Geológico – Geotécnico del Área donde se Construirá El Nuevo Depósito de Jales del Complejo Minero Buenavista del Cobre, en Cananea, Son.

Martínez Guerra R. 2011. Análisis de los Arroyos que Convergen en la Nueva Presa de Jales.

Martínez Guerra R. 2012.Estudio Hidrológico de Ocho Arroyos que Convergen en el Sitio de la Nueva Presa de Jales en Buenavista del Cobre.

Muhech Dip V. & Orozco Santoyo R.V. 2012. Anteproyecto del nuevo depósito para jales "Buenavista del Cobre" en Cananea, Sonora. XXVI Reunión Nacional de Mecánica de Suelos e Ingeniería Geotécnica.

Vega-Roldán O. 2013. Nuevo Depósito de Jales, Clasificación de Materiales.

Vega-Roldán O. 2018. Nuevo Depósito de Jales, Memoria de Cálculo y Análisis de Estabilidad.

Vega-Roldán O. 2019. Aspectos de Diseño. V Seminario sobre Depósitos de Jales.

Design approach for mixed coal refuse (co-managed tailings and coarse refuse) facilities at the Teck Coal Greenhills Operation

Bainbridge, Sophie, Willan, Martyn & Haynes, Andy
Golder Associates Ltd, Vancouver, BC, Canada

Walker, David & Seegar, Courtney
Teck Coal Limited, Elkford, BC, Canada

ABSTRACT: As part of future expansion for the Greenhills Operations steelmaking coal mine, Teck has evaluated the transition from the storage of slurry tailings within the site's tailings storage facility to the use of stacked co-managed facilities. Fine Refuse slurry tailings would be dewatered and combined with coarse coal refuse materials in mixed coal refuse (MCR) facilities, analogous to tailings/waste rock co-mingling.

As part of these studies Golder and Teck have developed a design approach with the intent of preventing potential failure modes that could result in catastrophic flow type failures. This approach includes: characterization of MCR material, including the use of critical state soil mechanics, risk assessment to identify critical failure modes, and the selection of critical components / controls for the design of facilities while also considering the need for redundancy and resilience.

1 INTRODUCTION

1.1 *Site Overview*

The Greenhills Operations (GHO) mine is located in the Kootenay region of BC, approximately 6 km northeast of the town of Elkford and has an annual production capacity of approximately 5.9 million tonnes of marketable steelmaking coal.

The site currently produces Coarse Coal Refuse (CCR) and Fines Refuse (FR) tailings, as by-products of the coal washing process. FR (approximately 500,000 m^3 / year) is fine grained and currently disposed of as a slurry in the GHO Tailings Storage Facility (TSF). CCR (approximately 900,000 m^3/year) is a granular, free-draining material which is currently placed in refuse stockpiles similar to compacted waste rock dumps and/or heap leach piles.

1.2 *Project Context / Overview*

The combined storage of coarse and dewatered fine mine waste materials within single facilities (known as co-management) is a well-established design concept for mine waste management. It has been identified as a potential strategy with a number of advantages including reducing the potential for catastrophic flow-type failures.

As part of future expansion of the GHO mine, Teck has evaluated the use of co-managed facilities for the storage of mine tailings in mixed coal refuse (MCR) facilities. Refuse thickener underflow FR would be dewatered using centrifuges to generate a cake for disposal with the CCR in stacked co-managed facilities. The design methodology was co-developed to address the specific characteristics of mixed mine waste materials and seeks to eliminate failure modes resulting in catastrophic flow type failure. It also adopts design criteria consistent with an 'Extreme' consequence of failure, such as those defined by Canadian Dam Association guidelines (CDA 2013). This eliminates the need to use traditional consequence classification systems which adopt design criteria based on incremental loss of life, e.g. CDA guidelines (2013). This concept is rejected by Teck who run their tailings system on the basis that one potential fatality equates to an extreme consequence.

The approach also aims to identify design components / operational approaches based on the identification of credible failure modes and critical controls while considering the need for redundancy and resilience in facility infrastructure.

2 MATERIAL CHARCTERIZATION

An extensive MCR material characterization program was carried out in four laboratory testing programs between 2014 and 2020.

- 2014: Assessed variations in geotechnical properties, including hydraulic conductivity and shear strength at a range of MCR mix ratios. Results indicated that the peak shear friction angles of tested materials were relatively insensitive to the fines content of the FR material.
- 2018: Assessed variations in geotechnical properties of MCR material, at a 3:1 CCR:FR mix ratio, at a range of FR moisture contents. Results indicated that the peak shear friction angles of tested materials were relatively insensitive to the moisture content of the FR material.
- 2019: Critical state locus (CSL) testing completed on MCR material at the design mix ratio of 1.9:1 CCR:FR, to assess the potential for stress-induced strength loss under static loading conditions.
- 2020: Soil-water characteristic curve (SWCC) testing, to assess transient and long-term saturation of the materials, to inform saturated/unsaturated transient seepage and stability modelling of MCR facilities.

This paper focuses predominantly on testing completed in 2019 and 2020 as these represent the design mix ratio (1.9:1 CCR:FR), based on the mine plan. Comparison and discussion with the results of previous testing programs is also provided.

Individual samples of each waste stream were received as dry tailings, i.e., without process water. Materials were dried and blended in the laboratory to produce MCR samples at the design mix ratio (by dry mass). Samples for hydraulic conductivity and shear strength testing were prepared at 90% of maximum dry density determined by standard proctor effort (SPMDD), at the corresponding moisture content. Properties are summarized in Table 1.

2.1 *Critical State Locus (CSL) Testing*

Stress-induced strength loss under static loading conditions (sometimes referred to as static liquefaction) occurs when soils in a loose (contractive) state are subject to an increase in excess pore pressure during undrained shearing, resulting in a rapid reduction in effective strength. CSL testing was used to determine the required density at which MCR materials would present dilative behaviour during shearing.

The critical state parameters for MCR material were determined based on recommendations in Bishop & Henkel (1969) and Jefferies and Been (2016). Specimens were reconstituted using the moist tamping method to varying densities and consolidated isotropically to confining stresses between 50 and 800 kPa. Once consolidated, specimens were sheared at a constant rate under either drained or undrained conditions until a minimum axial strain of 20% was reached. Sample preparation and test conditions were selected to obtain specimens that were both looser and denser than the expected in situ condition. Due to limitations in the size of commercially available CSL test equipment the MCR material was scalped at 12.7 mm (i.e., the gravel portion of the sample was removed). Particle size distribution curves of the pre and post scalped MCR material were completed to aid interpretation.

Loose MCR materials are compressible and an increase in density due to self-weight consolidation is anticipated. Normal Consolidation Lines (NCL) were determined for the MCR material using isotropic consolidation tests in a triaxial cell for samples compacted to densities of 90 and 95% of SPMDD. These densities were selected to represent potential in situ density states that may occur or be targeted during operations.

The CSL curve fit and NCLs for MCR material are presented in Figure 1. The results indicate that loosely placed MCR material, less than approximately 90% SPMDD, could be susceptible to stress-induced strength loss and would limit the ultimate height of stacked MCR facilities to less than 5 m, if also saturated. Compacted MCR materials with densities above approximately 92% SPMDD, will lead to stacked MCR material remaining in a dilative state, i.e., not susceptible to stress-induced strength loss irrespective of the degree of saturation.

Table 1. Geotechnical Laboratory Testing Results

Property	**Unit**	**Fine Refuse**	**Mixed Coal. Refuse**
Specific Gravity of Solids	-	1.52	1.82
Gravel Content	%	0	31
Sand Content	%	45	52
Fines Content	%	55	18
Optimum Moisture Content by Standard Proctor Effort (OMC)[(a)]	%	19.1	10.2
Maximum Dry Density by Standard Proctor Effort	t/m^3	1.12	1.43
Minimum Density	t/m^3	0.77	1.17
Maximum Void Ratio[(b)]	-	0.97	0.55
Saturated Hydraulic Conductivity	m/s	8.1×10^{-7}	4.1×10^{-6}
Peak Drained Friction Angle	°	-	34
Peak Drained Apparent Cohesion	kPa	-	0
Residual Drained Friction Angle	°	-	29
Residual Drained Apparent Cohesion	kPa	-	0

Moisture content = Mass of water/Mass of solids × 100
Void ratio = Volume of voids/Volume of solids.
- = not tested

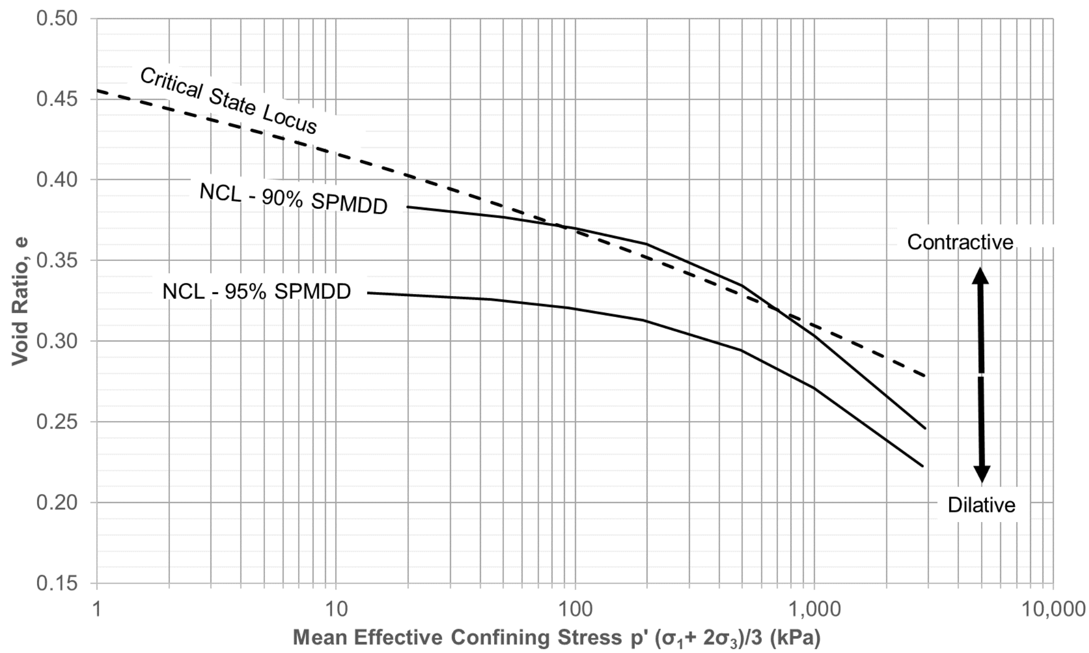

Figure 1. Critical State Locus Curve Fit and Normal Consolidation Lines for MCR Materials

2.2 *Soil Water Characteristic Curve and Unsaturated Hydraulic Conductivity Testing*

The Soil Water Characteristic Curve (SWCC) defines the relationship between moisture content and negative pore-water pressure (suction) within the pore spaces for a tested material. SWCC testing was completed for MCR material at mix ratios of 1.5:1, 2:1 and 2.5:1 CCR:FR, to provide estimates of the expected and upper / lower bounds for sensitivity analyses. An adjusted SWCC for a 2:1 CCR:FR ratio was also developed at 93% SPMDD to reflect a higher initial water content. In addition, a synthetic SWCC was developed for use in sensitivity modelling. Results are presented in Figure 2.

Based on the results of SWCC and saturated hydraulic conductivity testing, unsaturated hydraulic conductivity functions for the measured and initial moisture condition adjusted MCR material, at a 2:1 CCR:FR mix ratio, was estimated using the Fredlund et al (1994) method, incorporated within the SVEnviro software package. The unsaturated hydraulic conductivity was used to carry out saturated/unsaturated transient seepage analysis (Section 4.1).

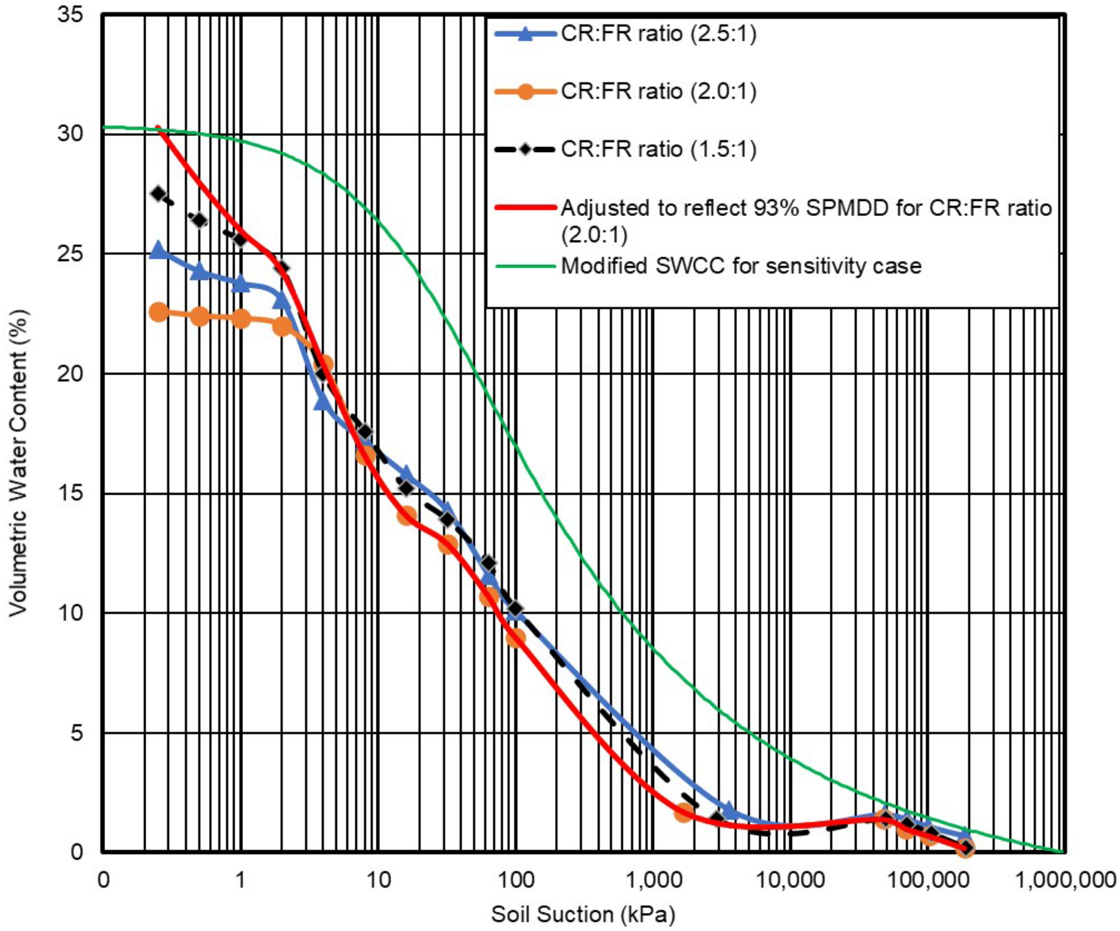

Figure 2. Measured and Synthetic SWCC for MCR Material

3 IDENTIFICATION OF CREDIBLE FAILURE MODES AND CRITICAL CONTROLS

Risk assessment of proposed facilities is a critical component of the design approach and are used to identify potential failure modes with a focus on credible failure modes (as defined by Teck internal guidelines) with the potential to lead to a catastrophic flow type failure, including to any adjacent structures or facilities.

Risk assessments include the assessment of both likelihood and consequences for each potential failure mode and are used to identify critical controls to reduce the likelihood of occurrence or mitigate the consequences of each potential failure mode:

- Controls for which the absence or failure would significantly increase the risk to a facility despite the existence of other controls.
- Controls that reduce the occurrence of more than one unwanted event or mitigate more than one consequence.

A summary of identified potential catastrophic failure modes and associated critical controls, based on site conditions and material characterization are presented in Table 2. Non-catastrophic failure modes and controls should also be identified but are of less importance at the design phase, and therefore beyond the scope of this paper.

Table 2. Summary of Potential Catastrophic Failure Modes and Identified Controls

Failure Mode	Identified Controls
Failure through weak foundation soils and/or bedrock.	Site characterization Stripping of weak foundation material Bottom-up development
Stress-induced strength loss of MCR material under static loading conditions.	Provision of basal drainage system Compaction of placed MCR material Surveillance monitoring program including instrumentation, QPOs and TARPs Operational and construction assurance/verification (SP&Ps) Design using seismic loading associated with Maximum Credible Earthquake
Static failure through MCR material due to increase in phreatic surface or lower than assumed strength parameters.	
Seismic event large enough to cause a run-out type failure of MCR material.	

QPOs = Quantifiable Performance objectives; TARP = Trigger Action Response Plan; SP&Ps = Standard Policies and Procedures

4 SELECTION OF CRITICAL COMPONENTS / CONTROLS FOR MCR FACILITIES

4.1 *Drainage System*

A basal drainage system was identified as a critical design control for potential MCR facilities to reduce phreatic surfaces. This is especially important within the lower sections of the sites, to achieve global stability. It also provides a critical control, alongside compaction (Section 4.2), against shear induced strength loss under static loading conditions.

Basal drainage systems would comprise two components; a blanket toe drain and a series of underdrains within existing drainage features in the natural topographic footprint of a facility. The two components will be connected and function together to manage surface water runoff from the upstream catchment area and water that infiltrates / drains through the facility.

Basal drainage systems will be designed on a facility specific basis based on unsaturated transient flow modelling using representative climate datasets to evaluate potential infiltration rates through the facility. A range of annual time series for precipitation, temperature, and evaporation will be adopted based on the GHO site-wide water balance model. It is also noted that precipitation from longer duration, less intense storms should also be considered as these may provide better estimates for upper bound scenarios for the purposes of assessing infiltration when compared to shorter duration, high intensity events such as the probable maximum precipitation (PMP). The results of transient seepage analysis will be used to inform the exten t and thickness of the blanket toe drain for a specific facility and to demonstrate drain effectiveness in maintaining unsaturated conditions in areas critical for physical stability, under the adopted range of climatic scenarios.

4.2 *Compaction of MCR material*

Based on material characterization, the compaction of the MCR materials was identified as a critical operational control to mitigate the potential risk of stress-induced strength loss under static loading conditions. Based on CSL testing (Section 2.1) it was determined that MCR materials placed at densities above 92% of SPMDD would lead to stacked material remaining in a dilative state under static loading conditions. The combination of compaction and drainage provide redundancy against stress-induced strength loss under static loading conditions.

To support the development of operational requirements for material compaction a field compaction trial was completed to; understand the likely degree of compaction that could be achieved by haul trucks, and whether additional compaction by rollers or similar would be required to achieve the target density. MCR material for the field trial was developed based on field mixing of FR, obtained from the existing TSF, with CCR material from onsite stockpiles.

A total of 12 in situ density tests of compacted MCR material were performed, using a Portable Nuclear Gauge. An additional 10 tests were completed in uncompacted areas of the trial pad for comparison. Results of the compaction trials are presented in terms of air voids / degree of compaction in Figure 3. Air void / compaction lines were calculated based on the average blended specific gravity determined from samples collected as part of the compaction trial.

Results from the compaction trial indicate, with the exception of two values, compaction greater than 92% SPMDD. Results also indicated no discernible difference in the degree of compaction achieved between full laden haul truck and static smooth drum roller, i.e. both compaction methods achieved compaction above the target density.

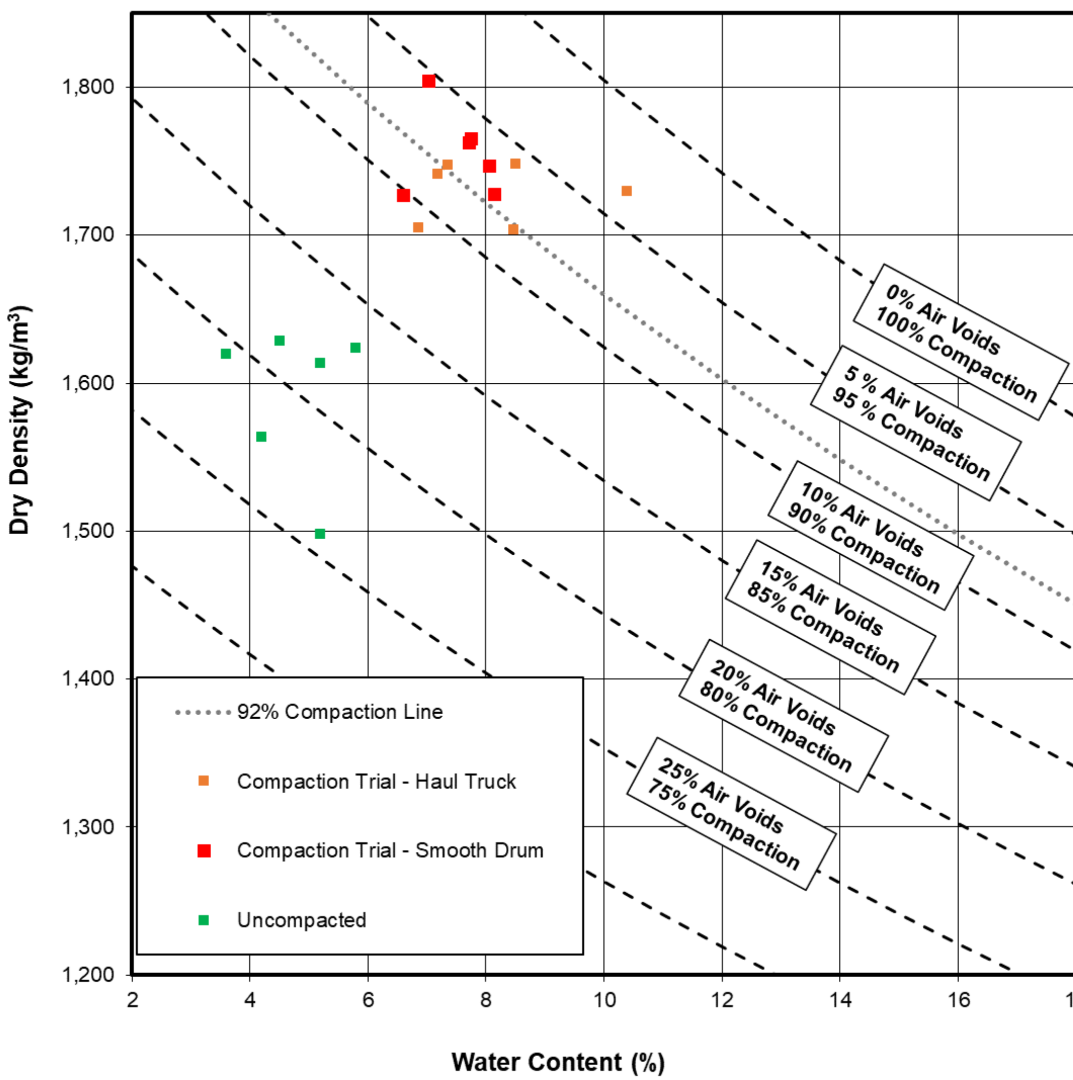

Figure 3. Results of MCR Material Compaction Trial

5 CONCLUSIONS

Golder and Teck have developed an approach to the design of MCR facilities at the GHO mine that, in addition to many operational and closure advantages, allows the ability to eliminate failure modes that could have potentially catastrophic flow type failures. The approach provides robustness and resilience by adopting design criteria consistent with 'Extreme' consequence classification, which sets up the resulting facility for post-closure conditions from the outset.

The approach is based on the results of material characterization programs, including CSL testing which identified the potential for stress-induced strength loss of MCR materials under static loading conditions for a stacked facility greater than 5 m in height.

Based on the results of material characterization a risk assessment is completed to identify potential failure modes and critical controls to inform both the design of facility components as well as operational procedures. Critical controls are developed for credible failure modes to provide redundancy in the design, i.e. critical controls that are complementary but independent of each other in addressing identified credible failure modes.

To address the potential risks associated with stress-induced strength loss of MCR materials under static loading conditions MCR facilities at GHO will incorporate:

- An underdrainage system, designed based on limit equilibrium stability and transient seepage modelling, to maintain critical portions of the MCR material in an unsaturated state.
- An operational requirement to place MCR material as compacted fill, using a bottom-up approach. Results of CSL testing identified a target density of 92% SPMDD which would lead to stacked MCR material remaining in a dilative state, i.e., not susceptible to stress-induced strength loss irrespective of drainage condition.

The results of a field compaction trial for MCR material indicated that the target density could likely be achieved using either haul truck trafficking or smooth drum static compactors.

The material characterization and risk-based design approach discussed in this paper for the design of the GHO MCR co-managed facility, provides a potential framework for the design of similar facilities.

6 REFERENCES

Been, K., Jefferies, M. 2016. Soil Liquefaction: A Critical State Approach, 2nd Edition. CRC Press

Bishop, A., and Henkel, D. 1969. The Measurement of Soil Properties in the Triaxial Test. Edward Arnold Ltd. London.

CDA (Canadian Dam Association). 2013. Dam safety guidelines, 2007. Original 2007, revised 2013.

Fredlund, D., Xing, A., and Huang, S. 1994. Predicting the permeability function for unsaturated soils using the soil-water characteristic curve. Canadian Geotechnical Journal, 31(4):535-546.

LaRonde filtered tailings project – novel design approach

Jason Hamelehle & Rachel Jansen
Paterson & Cooke USA Ltd., Golden, CO, USA

Patrick Laporte
Agnico Eagle Mines Limited, Rouyn-Noranda, QC, Canada

ABSTRACT: As the mining industry, and world at large, takes a closer look at tailings management, filtered tailings has come to the forefront of options for consideration by mine operators. Coinciding with this, filter manufacturers are releasing high-capacity pressure filters at larger sizes and more competitive prices than ever before. Agnico Eagle Mines Ltd.'s LaRonde Complex gold operation in Quebec, Canada is reaching the end of its tailings storage facility capacity. Agnico Eagle decided to transition to a filtered stacked tailings system and included an option for using a phased approach to expedite implementation. This paper, the first in a series following the project progression, details the unique approach and design decisions made during development of the filter plant, including the integration with the existing infrastructure, and the assessment of pressure filter chamber width on dewatering performance.

1 INTRODUCTION

Agnico Eagle Mines Ltd's (AEM) LaRonde Complex gold operation in north-west Quebec includes the LaRonde and the LaRonde Zone 5 (LZ5) underground mines. Tailings produced from both mines are placed in an upstream raise construction tailings storage facility (TSF). Each mine has a corresponding paste backfill plant that periodically sends a portion of tailings underground as mine backfill. The TSF is approaching its full capacity and is expected to cease operation around 2022.

Current mine plans project production through 2030. To continue operation past 2022, AEM requires a new tailings facility. Due to a lack of appetite for a new conventional wet tailings facility, and AEM's experiences at Meliadine (Canada) and Pinos Altos (Mexico) with filtered tailings, AEM decided to transition LaRonde to a filtered stacked tailings system. This system will help limit the new tailings facility footprint and facilitate the closure of the existing TSF.

The tailings production at the LaRonde Complex is double that of Meliadine, and the 10,000 t/d design capacity filtered tailings system needs to accommodate a wide range of operating conditions, such as significantly different ore types from the two mines, and large fluctuations in tailings flowrate when the underground paste backfill plants are running.

A unique design approach was initiated in 2019 that included the integration of the dewatering plant with the existing infrastructure and an independent assessment of commercially available filtration technologies to select the filter type best applied to LaRonde.

1.1 *LaRonde Complex operating description*

The LaRonde Complex has two concentrators in operation treating two different ore bodies; the LaRonde concentrator and the LZ5 concentrator (shown in Figure 1). The LaRonde concentrator produces 6,000 t/d nominal tailings, and the LZ5 concentrator produces 2,000 t/d. Both tailings streams are produced at around 32% solids mass concentration (mass of solids divided by mass of slurry expressed as a percentage) and are blended at the tailings box before being pumped to the TSF for deposition. During normal operation, the blend is around 75% LaRonde tailings and 25% LZ5 tailings at 8,000 t/d.

LZ5 ore may also be sent to the LaRonde concentrator. During these periods, the ratio of LZ5 tailings to LaRonde tailings increases for a fixed total tailings production of 8,000 t/d.
Each mine has a corresponding paste backfill plant. When both backfill plants are running, a portion of combined tailings is used in paste production and the remaining 2,600 t/d are sent to the TSF.

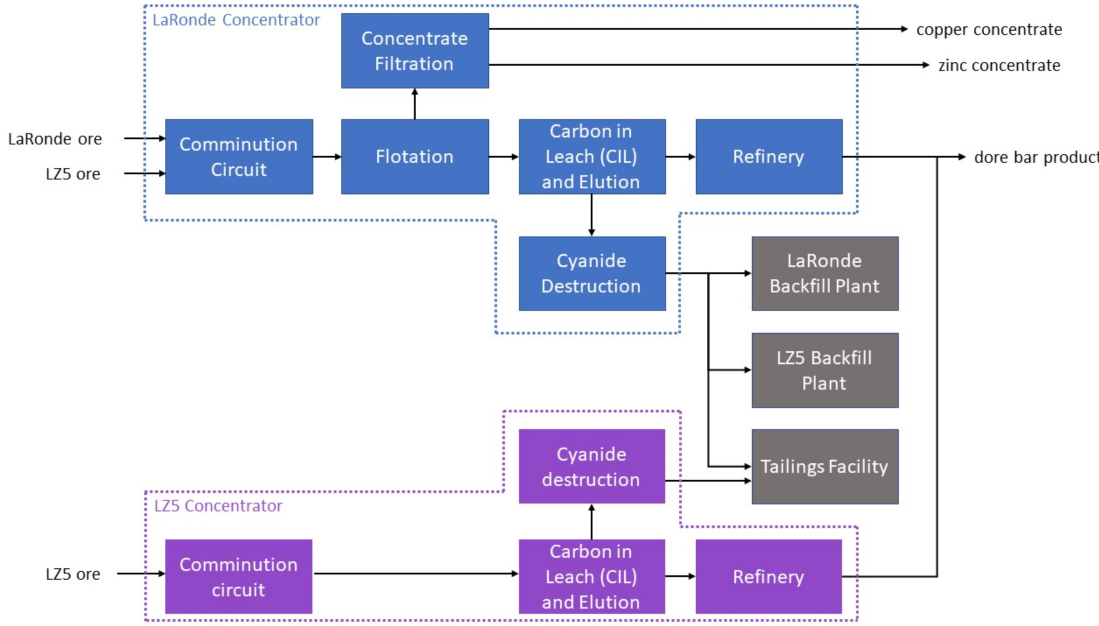

Figure 1. LaRonde Complex process flowsheet

1.2 *Tailings characterization*

Table 1 presents a summary of the tailings characterization, and Figure 2 shows the particle size distributions of LZ5 and LaRonde tailings measured by wet sieving (ASTM D1140-17). Calculated particle size distributions for blends 50/50 and 75/25 are also plotted.

The LZ5 tailings are significantly finer than the LaRonde tailings, indicating that as the ratio of LZ5 tailings increases in the combined tailings blend, the dewatering properties worsen. The tailings mineralogy was assessed using semi-quantitative X-ray diffraction analysis, including clay analysis. Estimates of mineral concentrations are based on relative peak heights and reference intensity ratios (RIR). The tailings do not contain any detectable clays that could be detrimental to dewatering performance. The tailings dewatering behavior is therefore strongly determined by particle size distribution rather than mineralogy in the LaRonde tailings application.

Table 1. Tailings characterization summary

Parameter	LZ5 Tailings		LaRonde Tailings	
Test campaign period	A (2017-2018)	B (2018-2019)	A (2017-2018)	B (2018-2019)
Slurry pH	7.5	9.2	N/A	10.4
Slurry conductivity (mS/cm)	2.3	2.6	N/A	3.2
Solids density (kg/m³)	2,916	2,906	3,134	3,057
Total clay	None detected	None detected	None detected	None detected
Particle size P80 (μm)	32	31	67	84
% mass passing 75 μm	99.4%	99.3%	84.0%	76.3%
% mass passing 20 μm	66.5%	65.8%	38.4%	32.9%

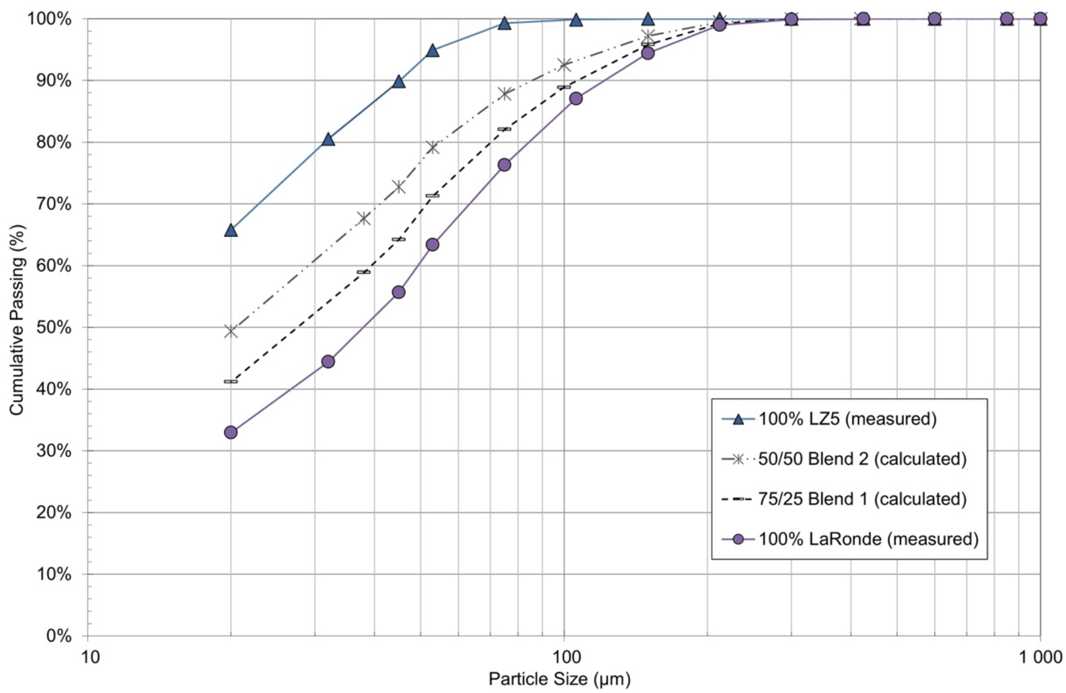

Figure 2. LaRonde and LZ5 tailings particle size distributions from Campaign B

1.3 *Specific challenges*

The new tailings facility needs to be implemented before the existing TSF reaches the end of its operating life. To extend this life and reduce the implementation risk of an 8,000 t/d filtration system, AEM proposed an option for a phased approach where tailings are initially thickened in a new 36 m diameter thickener and deposited in the existing TSF while the filtration plant is constructed in parallel. The intention is to use this phased approach only if needed to keep the project on schedule.

The LZ5 tailings were identified as more problematic for dewatering than the LaRonde tailings, therefore scenarios of 100% LZ5 tailings at 2,000 t/d and 50%/50% LaRonde/LZ5 tailings at 8,000 t/d need to be accommodated. During periods when both backfill plants are running, the tailings dewatering and transport systems will receive around 33% of normal feed flowrate which needs to be handled by the system's design. The environmental conditions at LaRonde Complex can result in periods up to three days when filtered tailings cannot be placed, and the handling of these disruptions were considered.

2 INTEGRATION OF PHASED FILTERED TAILINGS SYSTEM

The initial stage of LaRonde's transition to filtered stacked tailings is thickening blended tailings in a new thickener situated adjacent to the existing TSF and pumping the thickened tailings product onto the main pond TSF as part of its closure plan.

The existing tailings delivery pipeline and distribution system was evaluated using steady state hydraulics to determine whether it could be used during Stage 2 to deliver the higher solids concentration thickened tailings from the new thickener location.

The thickener underflow pumps will ultimately be used to transfer thickened tailings to the filter feed tank for the final stage of transition. The pipeline hydraulics to the filter feed tank were also evaluated to ensure suitable pump selection for both stages.

This evaluation process produces pump operating windows such as shown in Figures 3 and 4 which are used to develop high-level operating philosophies.

2.1 *Existing pipe evaluation*

An initial hydraulics assessment of the 50/50 blend tailings indicated new high-pressure positive displacement pumps and a high-pressure steel pipeline would be required to transport the tailings at the target 60% solids mass concentration thickener underflow with a yield stress of 60 Pa to the furthest point in the TSF. AEM confirmed that diluting the thickener underflow will not negatively impact the deposition plan, therefore the design considered diluting to lower solids concentration to avoid the high costs associated with transporting 60% solids mass concentration tailings.

P&C's evaluation found that tonnages as low as 200 t/h can be accommodated in the existing 16-inch diameter DR11 HDPE pipe, provided the tailings are diluted to lower than 50% solids mass concentration at these lower tonnages. However, the first 50 m of new piping from the thickener to the TSF required 16-inch diameter DR9 HDPE to accommodate the higher pressures downstream of the pump at the design tonnage condition.

When both backfill plants are operating, it is not feasible to transport the minimum 115 t/h tonnage through the 16-inch diameter pipe, and a 10-inch DR11 HDPE pipe is required for this scenario.

2.2 *System operating range*

Figure 3 presents the overall allowable system operating range during the initial stage considering a single operating 8/6 centrifugal pump with 300 kW (400 hp) motor and both the 16-inch diameter DR11 HDPE and 10-inch diameter DR11 HDPE pipelines in parallel. The 50/50 blend tailings are considered as worst-case rheology. Table 2 describes the features of Figure 3.

Table 2. Features of the overall tailings system operation range chart for initial stage

Chart Feature	Description
Dark green area	Recommended operating range for the 16-inch diameter pipe
Light green area	Suitable for intermittent initial stage operations through the 16-inch diameter pipe. The pipeline will operate with a small, settled bed in this region. The laminar to turbulent transition velocity dictates the minimum flowrate with a settled bed. The settled bed depth will be less than the 20% maximum depth in this range
Dark purple area	Recommended operating range for the 10-inch diameter pipe
Light purple area	Suitable for intermittent initial stage operations through the 10-inch diameter pipe. The pipeline will operate with a small, settled bed. The laminar to turbulent transition velocity dictates the minimum flowrate with a settled bed. The settled bed depth will be less than the 20% maximum depth in this range
Pump head limit	60 m discharge head, and 32 m/s impeller tip speed
LZ5 paste backfill plant operating	Scenario where 265 t/h blended tailings report to tailings thickener
LaRonde paste backfill plant operating	Scenario where 205 t/h blended tailings report to tailings thickener
Both paste backfill plants operating	Scenario where 115 t/h blended tailings report to tailings thickener

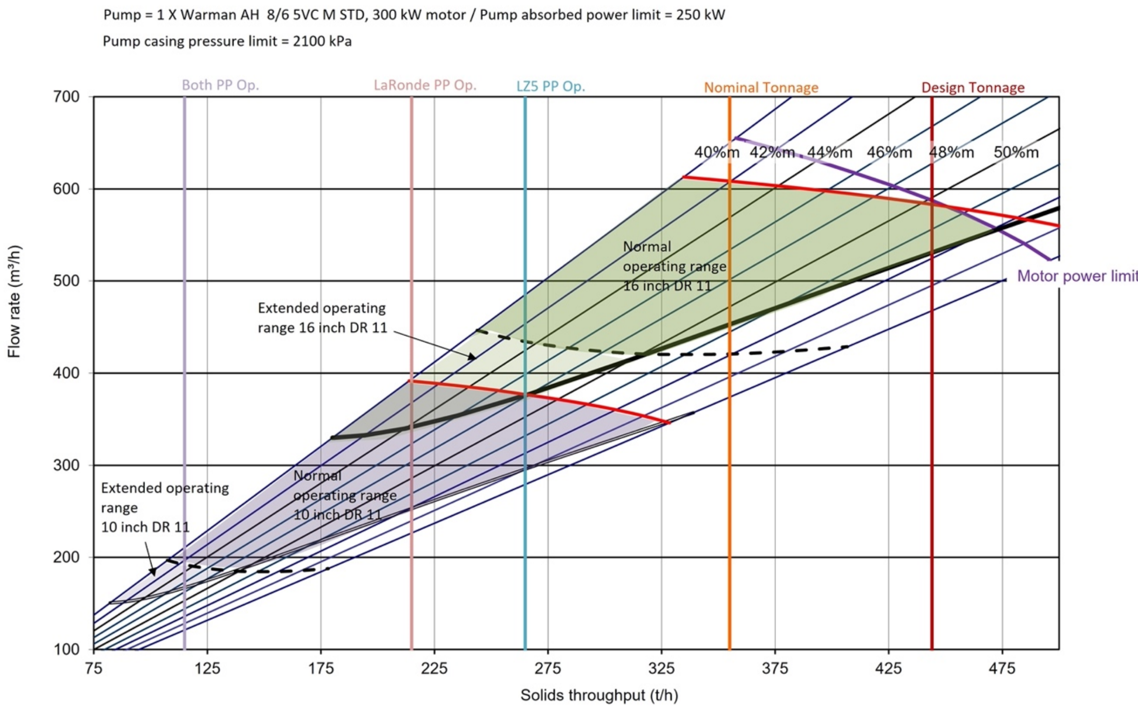

Figure 3. Overall tailings system operation rage – initial stage, 50/50 blend tailings

The dark green area indicates that both the nominal and design tonnages can be transported by the existing 16-inch diameter pipeline when diluted to 50% solids mass concentration. However, when either backfill plant is running, the tailings require dilution to 44% solids mass concentration.

The light purple area shows that a 10-inch pipeline is needed to transport the tailings when both backfill plants are running, and the tailings require dilution to less than 46% solids mass concentration. When either backfill plant is operating, tailings can also be transported using the 10-inch pipeline at 50% to 52% solids mass concentration.

Figure 3 indicates the design tonnage case is above the recommended 8 m/s pump discharge velocity limit. Considering the one-year duration that the tailings are discharged into the TSF, operating above this limit is considered acceptable.

Figure 4 presents the overall allowable system operating range during the final stage to feed the filter feed tank considering a new 8-inch pipeline and the same thickener underflow 8/6 centrifugal pump as for the initial stage. Again the 50/50 blend tailings are considered as worst-case rheology. Table 3 describes the features of Figure 4.

Table 3. Features of the overall tailings system operation range chart for final stage

Chart Feature	Description
Green area	Target thickener underflow concentration range for optimal filter feed. The yellow area is acceptable for the pump and pipeline operation but will impact filter performance
Orange area	Acceptable for intermittent operation to maintain high underflow solids concentrations while the backfill plants are operating

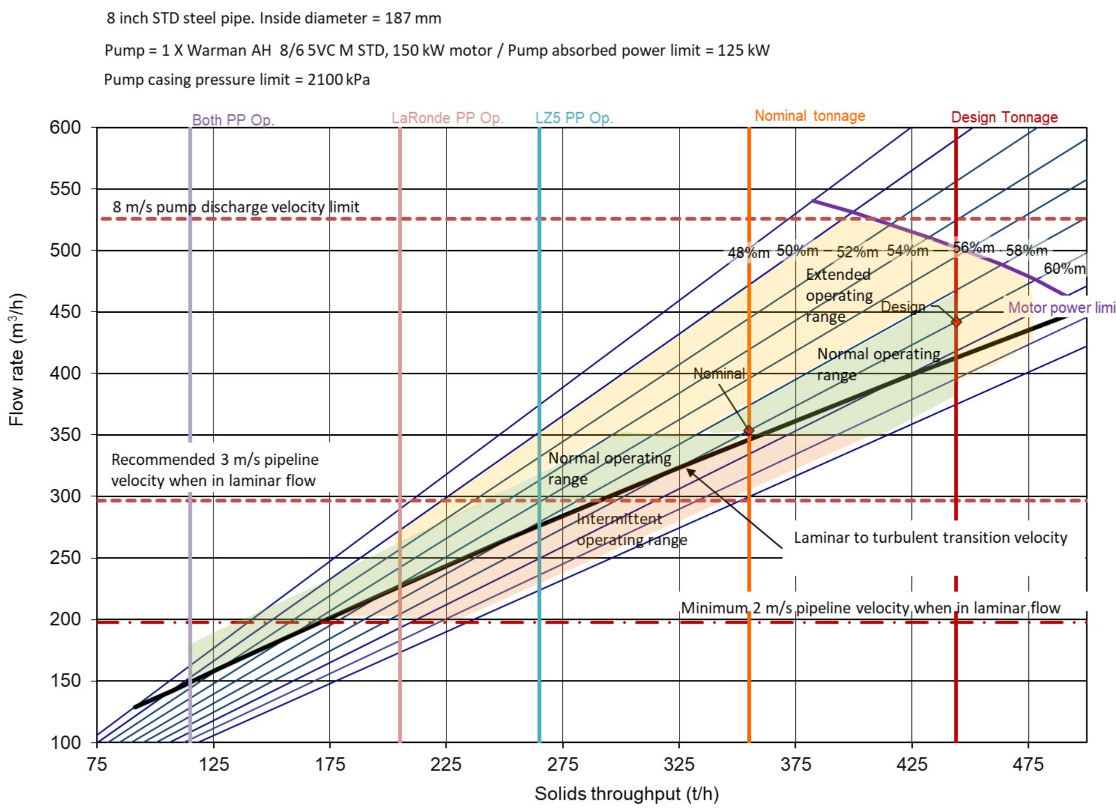

Figure 4. Overall tailings system operation rage – final stage, 50/50 blend tailings

Figure 4 shows the system operating in turbulent flow at the nominal and design tonnages but potentially transitioning to laminar flow at lower tonnages at the target 60% solids mass concentration thickener underflow. The solids concentration must be diluted to less than 50% solids mass concentration when both paste plants are operating, as the filter plant feed tonnage is reduced to 115 t/h. All the operating points are below the 8 m/s pump discharge velocity upper limit.

2.3 *Pump selection*

The final stage pumping duty requires a lower 150 kW (200 hp) installed power compared to the 300 kW (400 hp) minimum motor required for the initial stage. This lower motor power limit is shown by the purple line in Figure 4. At the start of the final stage, the pump drive (sheaves or gear box) should be replaced so the motor operates at a suitable speed to ensure proper motor cooling during the lower pump duty. The 300 kW motor can also be replaced with a smaller 150 kW motor at this time.

Alternatively, it may be feasible to initially install the 450 kW (600 hp) motors from the filter feed pumps (feeding the filters from the filter feed tank) on the underflow pumps for the initial stage, then move those motors to the filter feed pumps in the final stage and install 150 kW motors on the underflow pumps.

3 FILTER ASSESSMENT AND SELECTION

Independent test work was completed in the Paterson & Cooke (P&C) laboratory in Golden, Colorado between 2017 and 2019 to establish the characterization, dewatering properties, transport, and rheological behavior of the tailings.

AEM provided an initial target of 14.5% filter cake moisture content (mass of liquid divided by mass of slurry/cake expressed as a percentage) which was later updated to 16.0% as the filtered tailings stack design developed.

Top-tier original equipment manufacturers (OEM) were approached to provide technical specifications of their filtration equipment. Using these specifications and P&C test work results, each filter type was evaluated. The purpose of this design approach is to assess a wide range of OEM filtration technologies and determine the filter models best suited to this specific application.

3.1 *Filtration test work*

Preliminary vacuum filtration testing was carried out during Campaign A which found that vacuum filtration could not economically achieve a filter cake moisture content of less than 20%, therefore this technology was de-selected for the LaRonde tailings application.

Pressure filtration test work was completed using P&C's Druk 200 laboratory hydraulic pressure filter with 50 cm² filtration area, shown in Figure 5, using form pressures up to 1500 kPa and press pressures up to 1800 kPa. The program tested a range of parameters including feed form pressure, usage of a membrane press, filter chamber width and air blow duration.

Figure 6 shows an example of the impact of filter form pressure on form cake moisture content and form time for the 75/25 blend and the 100% PZ5 tailings. While increasing form pressure did decrease form time, the form times are all one minute or less and the achieved form filter cake moisture contents were similar at around 22% for the 75/25 blend and 27% for 100% LZ5.

As the form times were within one minute of each other, and no other advantages were identified, increasing feed pressure did not show any significant benefit to filtration and a form pressure of 600 kPa was selected. This form pressure was later confirmed by OEM test work and equipment selection. A membrane press of 1500 kPa showed significant improvement in dewatering rates as well as lowering the compressed air consumption during the air blow step.

A major decision point formed around the relationship between the chamber width, air blow time and achievable cake moisture. To achieve the initial filter cake moisture content target of 14.5% for the 75/25 blend, a 45 mm chamber required four minutes of air blow time. Long air blow times above three minutes increases the risk of not uniformly dewatering the cake within a full-size filter chamber, leaving partial wet cake. In addition, longer air blow times will typically result in higher compressed air consumption. To reduce the air blow time, a chamber width of around 32 to 35 mm would be required to achieve 14.5% filter cake moisture content. Figure 7 shows the dewatering rate of the 75/25 blend during the air blow step using various chamber widths. The starting moisture of these curves correspond to the cake moisture content after the form and membrane press steps.

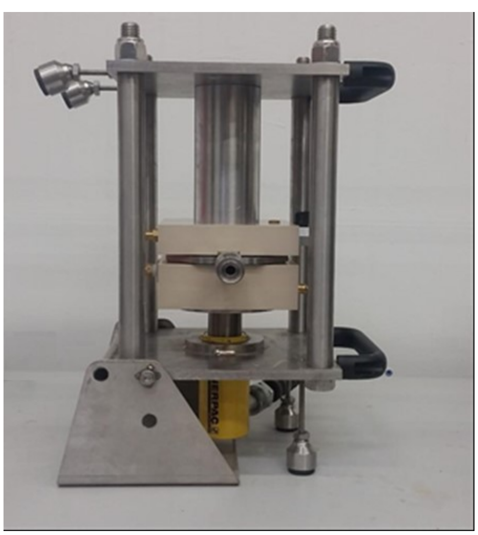

Figure 5. Druk 200 laboratory filter press

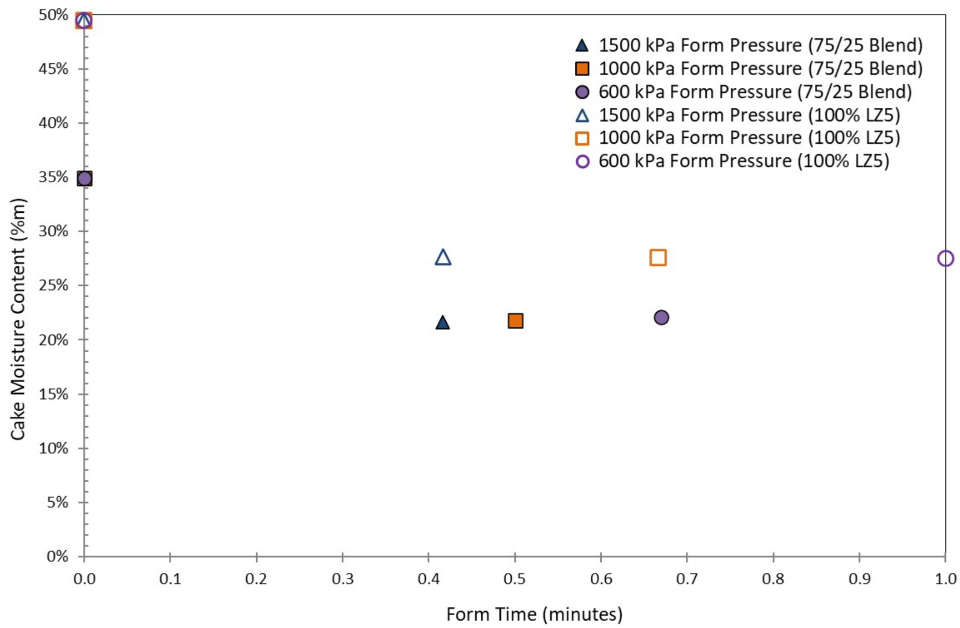

Figure 6. Impact of filter form pressure on form cake moisture content and form time for 75/25 blend and 100% LZ5 tailings

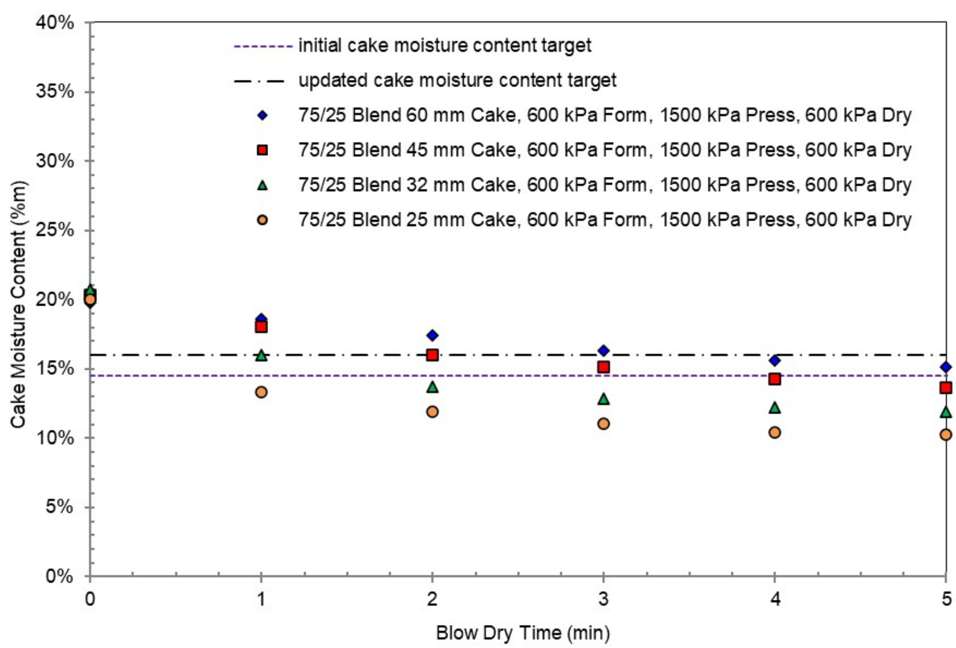

Figure 7. Filter cake air blow dry times with various chamber widths for 75/25 blend

3.2 *Filter selection*

A filter optimization study across six top-tier OEM filter models was completed in June 2019 assuming a filter cake moisture content target of 14.5%. Filter parameters assessed included available pressures, filtration areas, chamber widths and mechanical time specific to each filter. The requirement of using a chamber width of less than 35 mm significantly reduced the number of filter models for consideration.

Expected equipment availability ranged from 79% to 85% and expected air blow times ranged from three to four minutes. To evaluate the sensitivity of filter sizing across these ranges, the number of filters required for each OEM model was determined for the worst-case scenario, 79% availability and four minutes of air blow time, and the best-case scenario, 85% availability and three minutes of air blow time. Figure 8 shows the sizing of these various scenarios.

The study found that three Filter 2 pressure filters from Vendor A, each with 35 mm chamber width, was the optimum selection considering equipment cost.

In July 2019, the target filter cake moisture content was updated to 16% following developments in the tailings stack design. Figure 9 shows that this change allows for 45 mm chamber widths to be used with air blow times less than three minutes. The inclusion of 40 to 45 mm chamber widths expanded the number of filter models that could be considered.

Filter models were re-evaluated using the updated design criteria and other considerations such as local parts and services availability. Vendor A and Vendor B filters were identified as optimum, and the Vendor C Filter 2 was recognized as a suitable third option for meeting the technical, economic and commercial requirements of the LaRonde project.

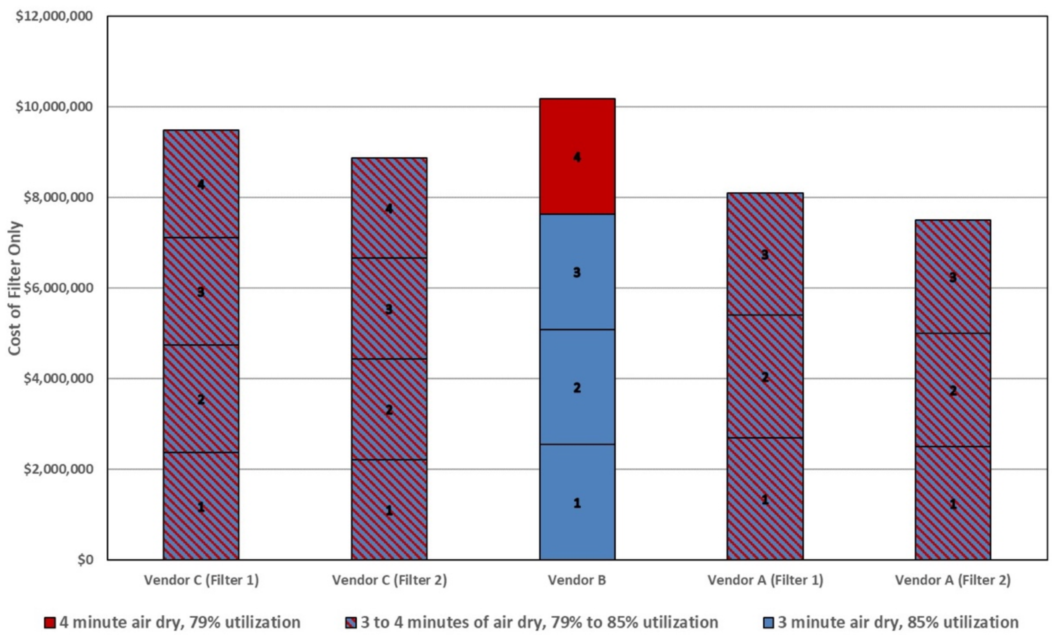

Figure 8. Filter sizing dependance on availability and air dry time for 14.5% filter cake moisture content

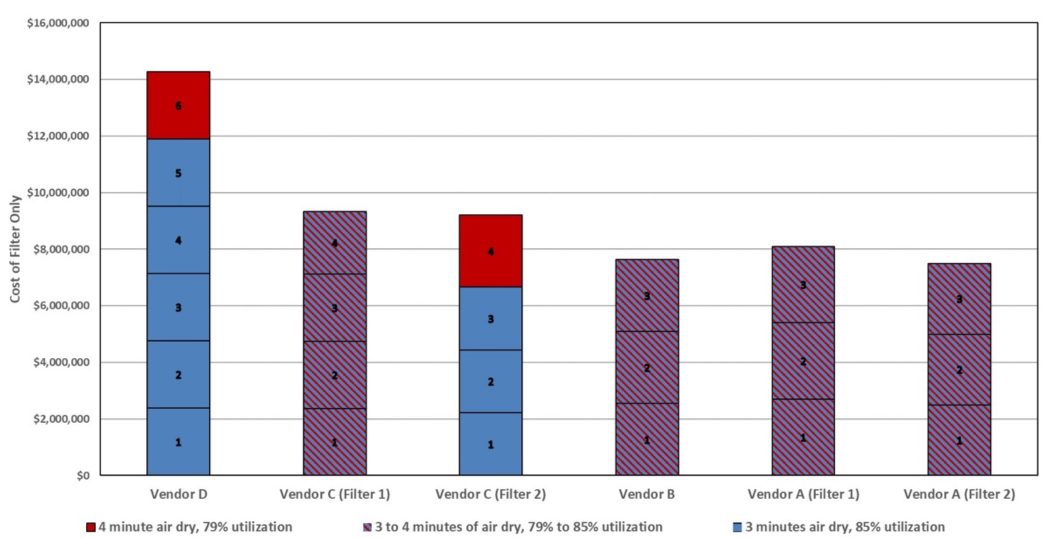

Figure 9. Filter sizing dependance on availability and air dry time for 16.0% filter cake moisture content

Analysis was performed on the number of plates installed in the Vendor A and B filters and its effect on net present value (NPV) of plate replacement, upfront purchase cost and available time for maintenance. Additional plates increase the overall costs, but the additional volume affords increased capacity and allowable downtime. This analysis was performed for the design tonnage of 10,000 t/d. Figure 10 shows the fraction of time available for maintenance for each option. A filter availability of 79% plus one hour per day of cloth washing is recommended, which translates to four hours per day (16.7% fraction of time) of non-operating time per filter. The difference in NPV between these two filter models is roughly CAD 595,000.

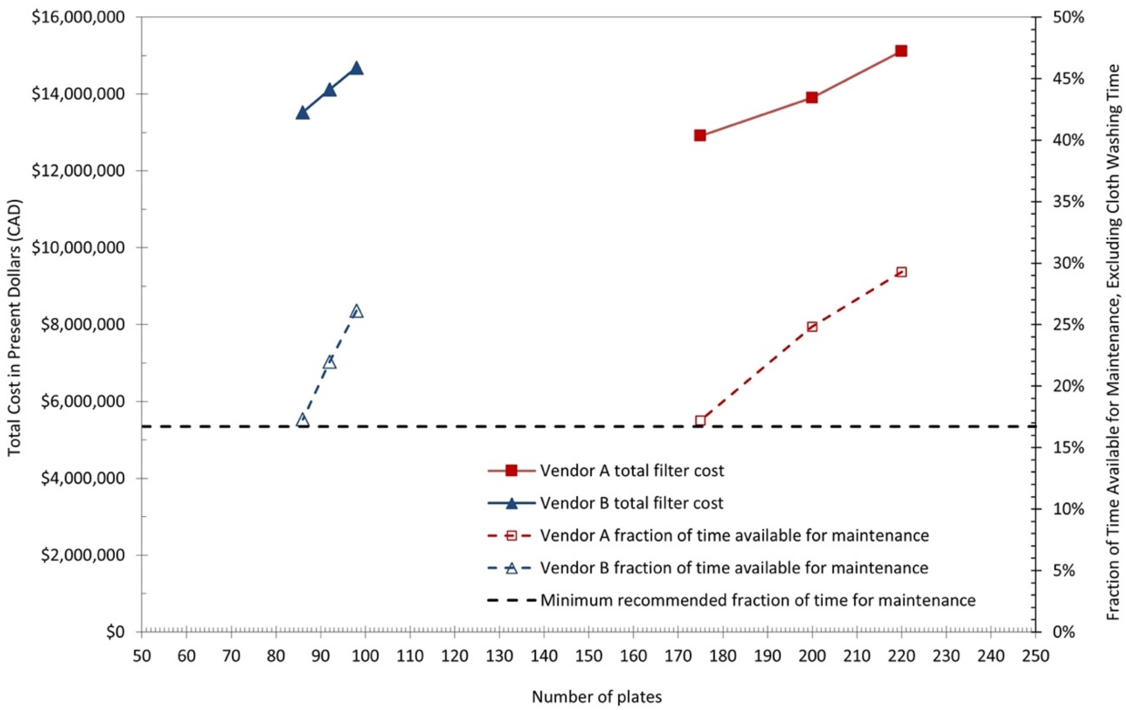

Figure 10. NPV and maintenance time dependance on number of installed plates

4 CONCLUSIONS

There are several top-tier OEMs that offer robust large-scale pressure filter equipment. However, each OEM offers their own unique selection of critical pressure filter features, such as chamber width offerings. P&C and AEM used a novel design approach, including independent test work, hydraulic analysis and OEM equipment specifications to integrate the dewatering plant with the existing infrastructure and to evaluate a wide range of filters and determine the optimum filter for the LaRonde filtered tailings project.

Indirect (non-destructive) measurement of control parameters in tailings dam embankment construction: Challenges and solutions

Hervé Kundulo Wa Kitambo
Golder, Lubumbashi, Haut-Katanga, Democratic Republic of Congo

ABSTRACT: Indirect (non-destructive) measurement methods can be subjected to high cost and multiple regulatory constraints that can be discouraging at times in some countries importing soils laboratory testing equipment. Despite these disadvantages, nuclear moisture-density gauges in particular offer the valuable advantage of obtaining very quickly moisture content and dry density results during tailings dam embankment construction projects. However, benefitting from this valuable advantage offered by the nuclear moisture-density gauge should not be done at the expense of quality construction and the interest of all parties involved on a project. During tailings dam embankment design, analyses such as slope stability, settlement, seepage, etc. are performed. In the process of performing these analyses, certain assumptions are made in terms of engineering properties of construction materials, placement conditions and subsurface conditions. It is very important, in the time of construction, to be cognizant of testing methods limitations while making sure that engineering properties of construction materials, placement conditions as well as subsurface conditions are within design assumptions. It is commonly known that moisture content, a key control parameter throughout embankment construction, should be calibrated on a nuclear gauge with site data to reflect actual moisture content values. But incorporating this requirement efficiently in the quality plan is challenging and project specific. How frequent can nuclear gauge moisture content be checked to eliminate the occurrence of inaccurate results between two calibrations? What factors should be considered in the determination of checking frequency? Presented in this paper is a case study indicating measures that can be inserted in the quality plan; specifically in its Construction Quality Assurance component, to meet the design intent and bring about smooth project execution.

1 INTRODUCTION

Earthworks contractors, just like any contractor in civil engineering, are always concerned with the efficiency of their operations, i.e., getting the maximum production within the allocated time and with the available resources has always been at the forefront of a project manager`s mind. This leads to an attitude of constant solution finding in construction activities. In the case of an embankment construction project, one of the solutions to maximize production is finding testing methods that can yield results within a short period of time and nuclear moisture-density gauges provide that possibility. However, achieving quality construction is usually a team effort and it is very important to look at all perspectives for successful project execution. Because the time factor alone does not make a project successful.

2 ENGINEERING PROPERTIES

During embankment design, from the preliminary phase to the final phase of design, and sometimes during construction, the design is made more detailed as more information related to construction materials and foundation condition is collected from site investigations. Some of the information collected during this process contains the location of sources of construction materials available on site, or within a reasonable hauling distance of the embankment to be built. This is an important aspect of design considering that one of the features of a good embankment design is taking advantage of the engineering properties of the local materials (USSD 2011). Nevertheless, commercial sources can be contacted for filter, drain and riprap materials (USSD 2011).

Construction materials can either be cohesive material (fine-grained) or coarse-grained material. Practically, however, many embankments are built of materials sourced from natural deposits which usually have broadly graded soils which present properties that are intermediate between cohesive and coarse-grained material (USSD 2011). Depending on the engineering property of interest, material of a certain type is selected to achieve a specific goal in the embankment. In embankment engineering, three important properties are considered, namely shear strength, compressibility, and permeability (USSD 2011). The main properties that differentiate cohesive material from coarse-grained material in the embankment design are that cohesive soils have lower shear strength, are less permeable, and are more compressible than coarse-grained material (USSD 2011). Table 2.1 below presents the desirable properties for the different types of material. To obtain input variables of engineering properties to be used in analyses conducted throughout embankment design, laboratory tests are performed on samples compacted consistently with specifications requirements for new construction, and for existing fills and natural materials, laboratory testing are performed on samples retrieved from the fill and on undisturbed samples, respectively (USACE 2003).

Table 2.1. Desirable material properties (Look 2014)

Requirement	Typical	Desirable material property			
	Application	Gravel%	Gravel size	Graduation	Fines
High strength	Pavement	Increase	Increase	Well graded	Reduce
Low Permeability	Liner	Reduce	Reduce	Well graded	Increase
High permeability	Drainage layer	Increase	Increase	Uniformly/ poorly graded	Reduce
Durability	Breakwater	Increase	Increase	-	Reduce

Reproduced by permission of Taylor and Francis Group, LLC, a division of informa plc.

3 CONTROL PARAMETERS

Due to the difficulties posed by the direct measurement of certain engineering properties on site, direct measurement of engineering properties is either limited in terms of frequency or not performed at all. Whether in case of limited use or absence of direct measurement, some control parameters are adopted as alternatives. These parameters can be measured without many difficulties and in a shortest time possible on site and still be correlated to engineering properties (Baecher 1987c). The most used alternatives in embankment construction are compaction moisture content and dry density because these are critical for the satisfactory performance of the embankment (Baecher 1987c).

In-place moisture content and dry density must be related to Optimum Moisture Content (OMC) and Maximum Dry Density (MDD) to determine if a compacted soil is compliant with the design requirements (USACE 1995). Both the lowest acceptable field dry density (most often 95% compaction or higher of the maximum dry density) and the permissible deviation of placement moisture content below and/or above the optimum moisture content of the soil being compacted are provided in the specifications (USACE 1995).

To obtain the maximum dry density and the optimum moisture content of the soil material, standard laboratory compaction testing such as Standard Proctor test and Modified Proctor are performed on the soil material. In the 1940s, the Modified test was introduced as an upgrade of the Standard test (1930s) to take into consideration larger equipment (Look 2014). Thus, the difference between the Modified compaction test and the Standard are not in terms of procedure, sample preparation and apparatus but rather on the rammer weight, free drop height and number of layers placed in the mold resulting in a greater compactive effort which yield higher maximum densities and lower optimum water contents (USACE 1986a).

Below are some statements from various authors on compaction above and below OMC:

- Clays compacted at moisture content above the optimum are characterized by ductile stress-strain behavior and those compacted either at optimum moisture content or below are characterized by brittle stress-strain behavior (USACE 2003)
- Compaction on the wet side of the optimum produces soils with less suction than those compacted on the dry side of the optimum (Look 2014)

Table 3.1 illustrates the variation of control parameters with engineering properties in some typical civil engineering applications. It also correlates the desired control parameters to the weighted plasticity index (WPI) which is the product of the plasticity index (PI) and the percent passing the 0.425mm sieve (VIC ROADS 2016). Considering that PI is determined on the material passing the 0.425mm sieve, PI values are often erroneous in residual soils which are not properly classified by traditional index tests due to the importance of their structure in their engineering behavior (ICOLD 151). The WPI was therefore introduced to compensate for PI limitations in measuring residual soils plasticity properties, hence its susceptibility to volume change with varying moisture content.

Table 3.1 Variation of engineering properties with respect to control parameters (Look 2014)

Desired property	Typical application	Density (with regards to MDD)	Moisture content
Shear strength - High	Pavement	High (Near MDD)	Low (≤ OMC)
Permeability - Low	Dams, canals	MDD, but governed by placement moisture content	High (≥ OMC)
General fill – typical	WPI≤1200	MDD	OMC
Shrinkage – Low	General embankment Fill in dry environment; WPI≥3200	Below MDD but >90% MDD	At Equilibrium Moisture Content – typically 80% OMC
Swelling – Low	General embankment Fill Wet environments; WPI ≥ 3200	Below MDD but >90% MDD	At EMC – typically 120% OMC

Reproduced by permission of Taylor and Francis Group, LLC, a division of informa plc.

To ascertain that construction meets the design intent and leads ultimately to adequate performance of an embankment, control parameters values of moisture content and dry density to be achieved during construction are incorporated in construction specifications.

One of the possibilities to avoid errors in the determination of permeability in the laboratory for seepage analysis is to use samples that are representative of actual field conditions (USACE 1986b). Referring to slope stability, Thiel (2002) recommends that a clear linkage be made between slope stability computations and the ultimate project specifications to ensure that proper materials are provided and placed in a specified manner during construction to meet the slope stability requirements. Angles of internal friction of coarse-grained materials such as sands, gravels and rockfills are heavily impacted by density and consequently, obtaining the fill with the desired strength requires effective monitoring of fill`s density during construction (Duncan et al. 2005). To meet the demand of the design earthquake, the flatness of the side slopes and the perviousness and density of the embankment can be chosen (ICOLD 1995).

Depending on the nature of a project, construction specifications are elaborated to be either performance specifications or compliance specifications (also called method specifications). Holtz et al. (2011) provides good description, specificities as well as applicability of each form of specifications.

4 CONTROL PARAMETER MEASUREMENT

Control parameters for embankment construction can be measured by direct methods or indirect methods. As previously indicated in part 3, measuring moisture content is a requirement to monitor fill placement moisture content and calculating dry density for tests on site (USACE 1995). Moisture content can be measured directly in several ways, such as drying by forced air, hot plate or open flame drying, drying in a microwave and conventional oven drying with the latter consisting in placing the soil sample in the oven at a temperature of 110±5°C and left until it has dried to constant weight (USACE 1995, USACE 1986a).During drying, the time to reach constant weight depends on factors such as soil type, sample size, type of oven and capacity, etc. (USACE 1986a). Of all the methods mentioned above, conventional oven drying is the standard method for accuracy in moisture content measurement (USACE 1995). Having determined the moisture content, dry density is measured directly by determining the weight and volume of a sample, as for example, with a sand cone density test (Baecher 1987c). Direct measurement methods of moisture content and their limitations are presented in Table 4.1. Indirect methods can also be used to measure dry density and moisture content and one of the methods is the use of the Nuclear moisture-density gauge.

Table 4.1. Procedures for determining moisture content of soil material (USACE 1995)

Test Method	Remarks and limitations
Oven drying	The standard for accuracy in moisture content measurement
Hot plate	Inaccuracy in moisture content due to high uncontrolled temperature applied to the soil that can drive off adsorbed water and burn or drive off volatile organic matter, neither of which should be removed in a standard test
Pressure tester method	Most effective and accurate in dry soils (<20% moisture content) Issues of accuracy when used with fine grained clays
Drying by forced air	To be used with caution since the soil may be overdried or underdried
Microwave oven drying	Inaccurate moisture content in soils with high gypsum content

Reproduced with permission from Pearson Education, Inc.

Over the years, the development observed in the design of nuclear moisture-density gauges and a better grasp of the nuclear principles have led to nuclear gauges use gaining ground around the world (USACE 1995). However, despite the advantage of measuring moisture content and dry density in an expedient manner, there have been some reservations in terms of their ability to measure control parameters accurately, i.e. moisture content. Table 4.2. makes a comparison of advantages and disadvantages of sand cone density testing and nuclear moisture-density gauges.

Table 4.2. Comparison between Sand Cone and Nuclear density gauge (Look 2014)

Equipment	Sand Cone	Nuclear density gauges
Equipment cost	Low	High
Advantages	Large sample	Fast
	Direct measurement	Easy to redo
	Conventional approach	More tests can be done
Disadvantages	More procedural steps	No sample
	Slow	Radiation
	Less repeatable	Moisture content results unreliable

Potential problems	Vibration	Presence of trenches and objects within 1m affects results

Reproduced by permission of Taylor and Francis Group, LLC, a division of informa plc.

Nuclear moisture-density gauges come with a set of calibrations to be done for accurate results. Besides factory calibration related to the operation of the device, further calibration specific to the materials being tested needs to be done. Prior to any test, information such as the maximum dry density and the correction factor to be applied for moisture content measurement must be entered into the gauge. While information related to maximum dry density is collected from designated laboratory tests, the correction factor to be applied for moisture content measurement is determined by comparing the moisture content of a laboratory sample with the moisture content determined by a gauge reading performed on the area where the laboratory was taken. Multiple samples and measurements may be taken, and calculation of the correction factor can be done with the average moisture of the samples using the formula below where M represents moisture content (Humboldt Scientific 2012):

$$KVAL = \%M\,(Oven) - \%M\,(Gauge) / [\%M\,(Gauge) + 100] \qquad (1)$$

5 CASE STUDY PRESENTATION

Like many civil engineering projects, there are usually three parties involved on a typical tailings dam embankment construction project, namely the client (owner), engineer (consultant) and contractor. Each party involved in the project has a specific role to play for successful completion of a tailings dam embankment. Considering that satisfactory performance of tailings dam embankment depends on quality construction, the engineer is usually assigned the role of not only providing documentation that contains all the requirements for quality construction but also accompanying the contractor throughout construction. This accompanying process is usually done in the form of Construction Quality Assurance. ICOLD (1986) describes the common models indicating which parties involved on a project can conduct Construction Quality Assurance.

Construction Quality Assurance can be performed in various ways and a detailed description of different Construction Quality Assurance setups is beyond the scope of this paper. In the case study presented herein, the quality plan concept included both Construction Quality Control (CQC) and Construction Quality Assurance (CQA) whose development and implementation was similar to the concept of Quality Control and Quality Assurance defined by Baecher (1987b). Construction Quality Control, under the contractor`s responsibility, was the inspection plan whose objective was that monitoring construction performance to give early warning of variations that adversely influence quality and consequently provided to the contractor a basis for controlling the process (Baecher 1987b). As for Construction Quality Assurance, it was the inspection plan aimed at assuring that soils placed in the tailings dam embankment met specifications (Baecher 1987b) and was the engineer`s responsibility. Both inspections consisted in visual inspections, laboratory and in-situ testing, survey monitoring, etc. The CQA plan also included validation of the suitability of testing standards and quality control procedures.

In developing the Construction Quality Assurance plan, specifically in determining that soils placed in the tailings dam embankment meet construction specifications and considering the scale and complexity of site conditions and borrow areas as well as the potential for latent conditions, Baecher (1987c) recommends that the CQA plan is developed such as the client/engineer`s risk of accepting tests which do not conform to construction specifications is guaranteed and balanced against the contractor`s risk of having tests which conform to construction specifications rejected. To illustrate the challenges encountered in non-destructive measurement of control parameters as well as the importance and implications of decisions made during tailings dam embankment construction in terms of confirming conformance of compaction works to construction specifications as part of Construction Quality Assurance, data collected from a Tailings Storage Facility downstream Stage 4 raise project for a copper/cobalt mine in the Democratic Republic of Congo was used. The main tailings dam embankment is 800m long (Station 0+100 – Station 0+800) and 40 m high. The data presented and analyzed herein are for a 200m stretch of the main tailings dam embankment between Station 0+200 and Station 0+400 (Refer to Figure 5.1).

To keep track of construction activities for field testing purposes, the main tailings dam embankment was divided into height 100m sections which were in turn divided into two sub-sections of approximately 20m each running parallel to the tailings dam embankment axis, namely A and B with section B adjacent to the existing tailings dam embankment. To differentiate the 100m section, indices of 1 and 2 were assigned to A and B with 1 indicating the first 100m, i.e., Station 0+200-Station 0+300 and 2 the following one, Station 0+300 – Station 0+400. Following the minimum testing frequency indicated in the construction specifications, tests were performed in each section and recorded. Figures 5.1-5.2 present respectively the main tailings dam embankment plan view and cross-section.

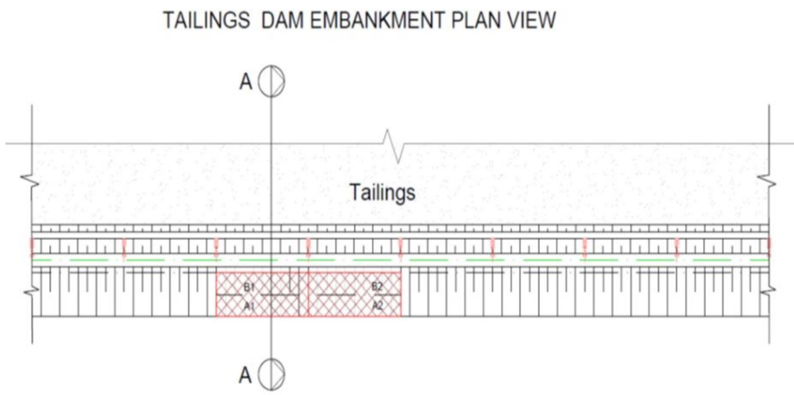

Figure 5.1 Tailings dam embankment plan view (Scale: 1/1000)

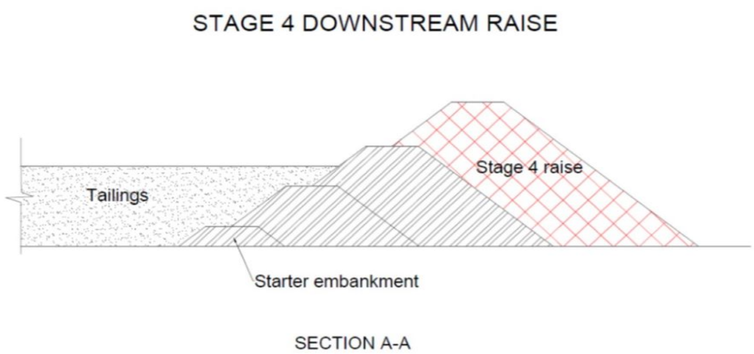

Figure 5.2 Cross-section of the tailings dam embankment (Scale 1/1000)

For control parameter measurement, the Humboldt HS-5001 EZ Serial Number 8041 nuclear moisture-density gauge was used.

Prior to moisture-density testing, all the necessary information required was collected. Maximum dry density from Standard Proctor testing (ASTM D698) following the minimum testing frequency prescribed in the specifications. As for the moisture content correction factor, it was obtained using formula (1).

Two main challenges were encountered in the moisture content correction factor implementation. The first was related to the inability to enter in the gauge a KVAL values greater than 0.02. The gauge was set up for KVAL between -0.10 and +0.02. The other challenge was related to the variability of soil material in the borrow area. Once a KVAL is calculated, it is based on a particular configuration in the borrow area and it is very difficult to predict how long that configuration is going to last before calculation of another one is required. In any real deposit, engineering properties vary somewhat from point to point, even within a soil horizon that otherwise appears uniform (Baecher 1987a). This spatial variation leads inevitably to differences in the way individual elements of a soil deposit behave (Baecher 1987a) and consequently affects KVAL prediction.

Considering the challenges mentioned above and in order to decide on conformance of compacted soil to design requirements, the following measures were implemented as part of the Construction Quality Assurance plan:

- Taking a sample for oven moisture content measurement at each testing location and make the final decision based on the oven moisture content and the corresponding dry density
- To benefit of the advantages provided by the nuclear moisture-density gauge, guidelines for decision making on site were implemented based on the knowledge obtained of the difference between the oven moisture content and the gauge reading with KVAL=0.02

6 FINDINGS

6.1 *Oven moisture content vs Nuclear moisture-density gauge reading*

The goal behind the introduction of the moisture correction factor (KVAL) is the accurate measurement of moisture content by considering elements in the soil material that interfere with the moisture content measuring process and consequently yield erroneous results. These elements are found in materials that high in hydrogenous components (cement, gypsum, coal, or lime) and those high in neutron-absorbing components (boron or cadmium) (Troxler Electronics 2006). Baecher (1987a) defines the correlation coefficient as an expression of the degree to which two parameters vary together and it was used in our case to measure the behavior between the oven moisture content and the gauge reading of moisture content. This was a good indication of the validity of the chosen moisture correction factor. Figures 6.1-6.4 indicate the correlation coefficient for each section tested.

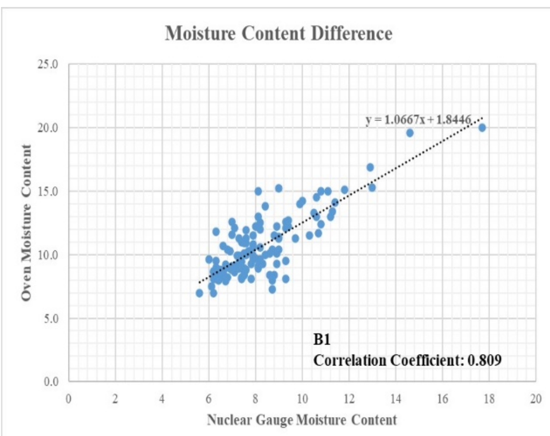

Figure 6.1 Correlation Coefficient Section B1

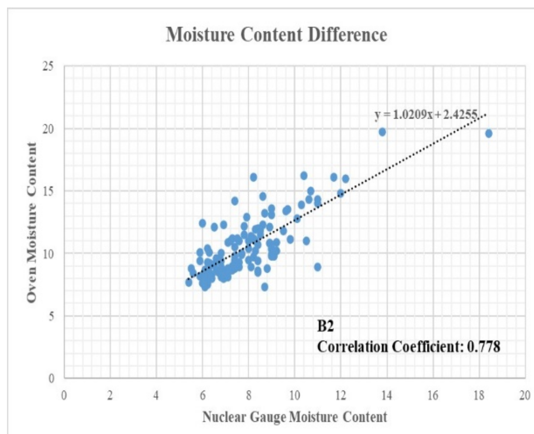

Figure 6.2 Correlation Coefficient Section B2

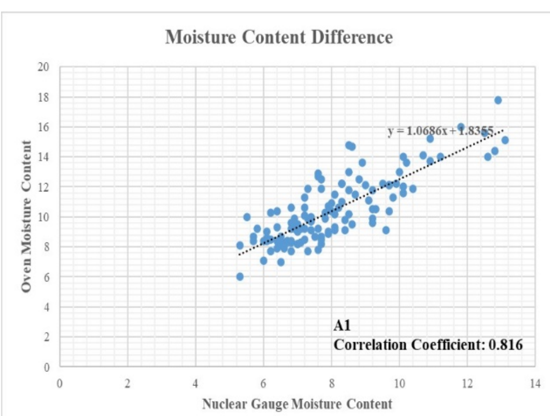

Figure 6.3 Correlation Coefficient Section A1

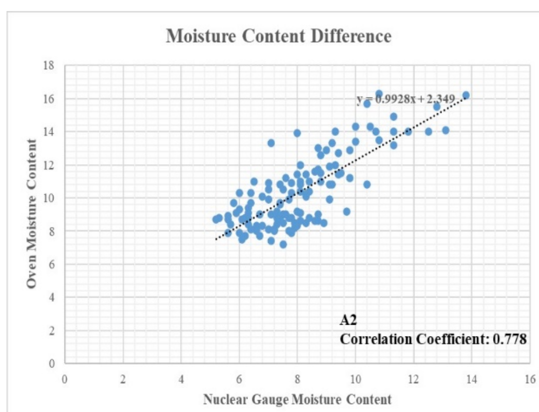

Figure 6.4 Correlation Coefficient Section A2

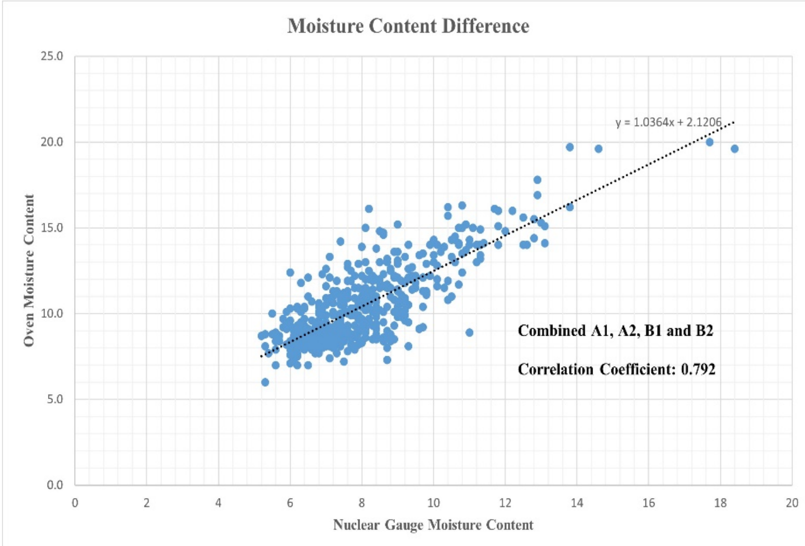

Figure 6.5 Correlation Coefficient Combined A1, A2, B1 and B2

6.2 *Discussion on Correlation Coefficients Results*

As presented by Baecher (1987b), the range of the correlation coefficient is from +1 to -1. A correlation coefficient equal to 1 indicates a perfect linear relation between two parameters having positive slope and a correlation equal to -1 indicates a perfect linear relation between two parameters having a negative slope. A correlation coefficient equal to zero indicates no relation between two parameters and are said to be independent.

Looking at the correlation coefficient values, and the corresponding slopes obtained for each section, it was observed that each section computed a strong linear relation with a positive slope. However strong, it was still lower than 1 which is a perfect correlation. A correlation coefficient equal to 1 would have been an indication that the condition that were in place during the calculation of the moisture correction factor were constant and would have resulted in the gauge reading being almost equal, if not equal to the oven moisture content. However, this was not observed, and resulted in the data scatter observed in Figures 6.1-6.4. Baecher (1987a) presents scatter in geotechnical data to reflect two things, namely real variability in the soil deposit and random measurement. However, random measurement error does not reflect real variations in soil properties, except possibly on a very small scale. The challenging part is how to anticipate the variability in the soil deposit to choose a moisture correction factor that would reflect a perfect correlation, and this is an almost impossible task as no cost-effective investigation, no matter how detailed it can be, can eliminate the possibility of unknown conditions. Look (2014) recommends for nuclear gauge moisture content that every tenth should be calibrated with results of standard oven drying. Depending on the variability in the borrow material, this option still leaves open the possibility of getting inaccurate results on certain occasions in between two calibrations. Considering that ultimately no area of substandard compaction work is accepted in an embankment, it is important to deal with the uncertainty associated with the variability of material coming from the borrow source.

Additionally, USACE (1995) recommends that indirect methods should never be used instead of direct methods or without careful calibration and correlation with results from direct methods. Furthermore, it does recommend having indirect measurement results periodically checked against direct measurements during construction. Specifically, regarding the nuclear gauge, it does not permit it to be used as a primary control but should be used to supplement direct methods. However, taking into consideration the critical value of time in tailings dam embankment construction projects, the shorter the time for making compaction test results available, the greater the benefit to the project. Based on the abovementioned points, combining nuclear gauge reading and collecting soil samples for oven moisture calculation at each testing location turned out to be very practical and important and validated the measures implemented to benefit from the advantages offered by the nuclear moisture-density gauge on one hand and avoiding some of its disadvantages, i.e. no sampling, unreliable moisture content results on the other hand.

6.3 *Guidelines for decision on site*

As indicated in the previous section, it was of great interest to implement guidelines that were going to make it possible to benefit of the advantages of the nuclear moisture-density gauges and preserving quality construction by meeting design requirements as presented in the construction specifications. From the client/engineer and contractor perspective, the guidelines were also a way of protecting the client/engineer from accepting tests which did not conform with construction specifications. Given that moisture content affects dry density, and ultimately percent compaction and based on the knowledge of the difference between the gauge reading of the moisture content and the oven moisture content, the following guidelines for decision on site were adopted and implemented:

- Moisture Content requirement: -6% of OMC to OMC
- Percent Compaction requirement: 100% of the Standard Proctor Maximum Dry Density

The results obtained following the implementation of the guidelines for decision on site during construction are summarized in Figures 6.5-6.8

6.4 *Discussion*

Below are tables making a comparison of what would have happened without the implementation of the guidelines for decision on site, and what was obtained as a result of their implementation.

Table 6.1. Guidelines against no guidelines comparison

Sections	Without Guidelines	
	Tests conforming to specifications rejected	Tests not conforming to specifications accepted
B1	59.6%	Refer to Note below
B2	60.8%	Refer to Note below
A1	64.1%	Refer to Note below
A2	59.1%	Refer to Note below

Table 6.2. Guidelines against no guidelines comparison (Continued)

Sections	With Guidelines implemented	
	Tests conforming to specifications rejected	Tests not conforming to specifications accepted
B1	0%	0%
B2	0%	0.83%
A1	0%	0.83%
A2	0%	1.66%

Note:

- Points within the 98-100% range of Standard Proctor would have ended up below the required minimum percent compaction of 98% Standard Proctor. To ensure that ultimate percent compaction meet construction specifications, the requirement in terms of percent compaction was raised as indicated in the guidelines adopted and implemented for decision on site. Having implemented this requirement several points ended up lower than 100% Standard Proctor percent compaction, but above the required 98% Standard Proctor percent compaction, except in one case. Table 6.3. indicates the percentage of points that fell lower than 100% Standard Proctor, yet higher than the required 98% Standard Proctor. Without this guideline in place, some points could have been considered as meeting the specifications and would have ended up lower than the required percent compaction, resulting in tests not conforming to specifications accepted.

Table 6.3. 100% Standard Proctor > Percentage of points ≥ 98% Standard Proctor

Sections	With Guidelines implemented
B1	29.4%
B2	24.1%
A1	33.3%
A2	32.5%

- Points within the moisture content placement that would have ended up outside specified range

Looking at Figures 6.6-6.9, it was observed that some points, despite being outside of the guidelines for decision on site on moisture content, were considered. These points were considered based on the variability in the material coming from the borrow. Baecher (1987b) points out the fact that it is often the case with geotechnical measurements that one or more data differ strikingly from the bulk of the measurement made and this project was no exception. This situation results from points that are either anomalous or a reflection of real and important variations in soil properties and should therefore be considered. Also, some points lower than 100% Standard Proctor were considered. It should be noted that the implementation of guidelines was not rigid and was supported by knowledge of both the soil material and its behavior at the proper placement condition. USACE (1995) recommends simple control measures consisting of visual observations and rough measurements as the primary means of construction control, which are supplemented by extensive program of control testing.

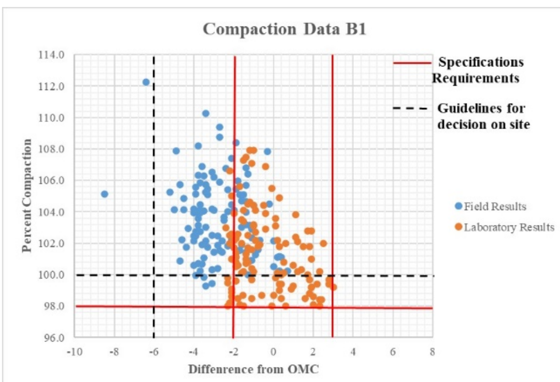

Figure 6.6 Compaction data for Section B1

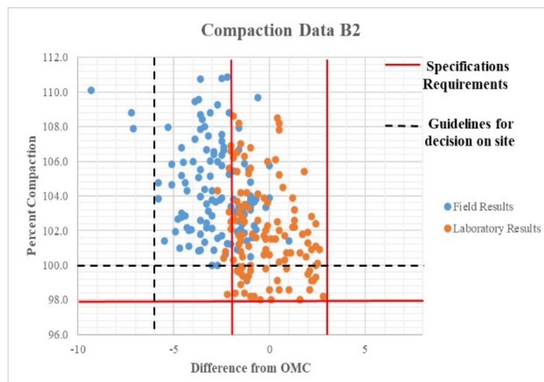

Figure 6.7 Compaction data for Section B2

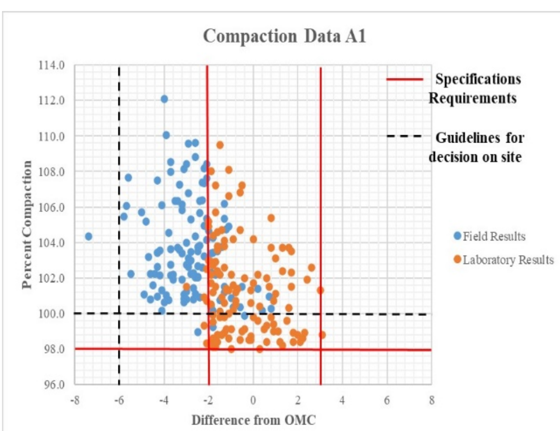

Figure 6.8 Compaction data for Section A1

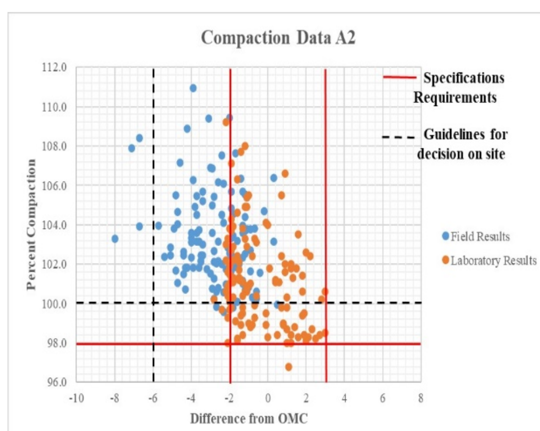

Figure 6.9 Compaction data for Section A2

7 CONCLUSION

Tailings dam embankment design is based on soil materials engineering properties of strength, permeability, and compressibility. Depending on their granulometry, soil materials possess intrinsic properties which influence their selection to play a specific role in a tailings dam embankment. Throughout construction, alignment with engineering properties assumed during design is observed through control parameters of moisture content and density incorporated into construction specifications which, in turn are linked to analyses performed during design. These control parameters can be measured either directly or indirectly. While direct (destructive) methods are more accurate, they are time consuming and can result in significant delays on an tailings dam embankment construction project. Indirect (non-destructive) methods on the other hand, are faster but less reliable in the absence of calibration with site specific data. However, continuous checking of initial data and subsequent update to maintain reliability of results is required. Checking can be spaced out, e.g. 1 per $1000m^3$. However, because of soil deposits variability and the uncertainty associated with how long the conditions measured at the time of calibration would prevail, spacing out of checking initial data can result in inaccurate results between two calibration and therefore affecting negatively decisions made based on them. The negative impact consists in either accepting tests which do not conform to specifications or rejecting those that conform to specifications. When it comes to checking frequency in the quality plan, emphasis should not be on the numbers alone, which should be rather viewed as providing guidance on good practice for satisfactory tailings dam embankment performance. The emphasis should be on the combination of numbers and the close observation of the evolution of site conditions with construction progress and the knowledge of the properties and behavior of the soils at the site. Hence, the provision in the Construction Quality Assurance plan to check moisture content at each testing location to provide the highest possible level of confidence that material has been placed in accordance with construction specifications. Consequently, meeting the design intent.

Besides achieving a quasi-balance of 0% between accepted tests which do not conform to construction specifications and rejected tests which conform to specifications with regards to compaction works, as illustrated in Table 6.2, the Construction Quality Assurance plan, through the guidelines related to nuclear density testing, had the additional advantage of bringing about seamless construction sequencing resulting in efficient project execution.

Quality construction is necessary to transform the design concepts into a successful project (USSD 2011) and this paper is basically stressing on the importance of always looking beyond the numbers on the screen of an indirect measurement device in general, particularly on a nuclear density gauge when deciding about conformity to specifications. Aspects such as soils condition and variability should be considered. One must familiarize with soils behavior and properties under the conditions presented in the specifications and be able to detect during inspection conditions that deviate from them, at least qualitatively. Doing so will be consistent with both the artistic and scientific nature of Geotechnical Engineering.

8 REFERENCES

Baecher, G. 1987a. Error Analysis for Geotechnical Engineering. Department of the Army, US Army Corps of Engineers.

Baecher, G. 1987b. Statistical Analysis of Geotechnical Data. Department of the Army, US Army Corps of Engineers.

Baecher, G. 1987c. Statistical Quality Control of Engineered Embankments. Department of the Army, US Army Corps of Engineers.

Duncan, J. M., Wright, S. T. 2005. Soil Strength and Slope Stability. John Wiley and Sons, Hoboken, NJ, USA.

Humboldt Scientific, 2012. Product Manual Humboldt HS-5001EZ Moisture-Density Gauge. Humboldt Scientific Inc., NC, USA.

Holtz, R.D. and, Kovacs, W.D., Sheahan, T.C. (Second edition) 2011. An introduction to Geotechnical Engineering. Pearson Education Inc., NJ, USA.

International Commission on Large Dams (ICOLD) 1986. Quality Control for Fill Dams Bulletin 56

International Commission on Large Dams (ICOLD) 1995. Tailings Dams and Seismicity Bulletin 98

International Commission on Large Dams (ICOLD) 2017. Tropical Residual Soils as dam foundation and

fill material Bulletin 151
Look, B.G. (Second edition) 2014. Handbook of Geotechnical Investigation and Design Tables. CRC Press, EH Leiden, The Netherlands.
Thiel, R. 2002. Peak vs Residual Shear Strength for Landfill Bottom Liner Stability Analyses. https://www.semanticscholar.org
Troxler Electronic Laboratories 2006. Manual of Operations and Instruction Troxler Model 3430 (and Model 3430-M) Surface Moisture-Density Gauge. Troxler Electronic Laboratories, Inc., NC, USA
United States Army Corps of Engineers (USACE), 1995. Construction Control for Earth and Rock-Fill Dams Engineer Manual. Department of the Army
United States Army Corps of Engineers (USACE), 1986a. Laboratory Soils Testing Engineer Manual. Department of the Army
United States Army Corps of Engineers (USACE), 1986b. Seepage Analysis and Control for Dams Engineer Manual. Department of the Army
United States Army Corps of Engineers (USACE), 2003. Slope Stability. Department of the Army
United States Society on Dams (USSD) Committee on Materials for Embankment Dams, 2011. Materials for Embankment Dams. United States Society on Dams.
VicRoads (VIC ROADS) Test Method RC 326.01, 2016. Weighted Plasticity Index. https://www.vicroads.vic.gov.au/business-and-industry/technical-publications

The Role of the Vane Shear Test in Mine Tailings

Iván Contreras and Jason Harvey
Barr Engineering Co., Minneapolis, MN, USA

ABSTRACT: The vane shear test is a widely used testing technique for determination of the undrained shear strength of soft clays. Its application in mine tailings presents several advantages but also important limitations. As a result, its use in mine tailings requires a good understanding of the principles of the test so that meaningful results can be obtained. The paper presents both the field and laboratory version of the vane shear test along with its advantages and limitations in mine tailings. The necessary modifications of the ASTM standard equipment and procedure are presented, as well as a comparison of the measured undrained shear strength from vane shear testing versus data and correlations from case histories of actual flow liquefaction failures. Finally, the applicability of the field and laboratory vane shear test are outlined with respect to various characterization metrics based on authors' experience.

1 INTRODUCTION

The field vane shear test (FVT) is the most widely used in-situ testing technique for determination of the undrained shear strength of soft clays. Originally introduced in Sweden in 1919, its use has expanded extensively worldwide after the 1940s when the primary work by Carlson (1948), Skempton (1948), and Cading et al. (1948) popularized it in Europe. The FVT is the only in-situ testing technique that allows direct measurement of the undrained shear strength, and it is commonly used as a reference shear strength in combination with the cone penetration test (CPT) to obtain more continuous shear strength profiles in soft clay deposits. Even though it was introduced as a field test, subsequent developments were made with the laboratory vane shear test (LVT), which can be used to test "undisturbed" samples and reconstituted specimens. Over the years, the FVT and LVT equipment and procedures have been standardized (e.g., ASTM D2573 and ASTM D4648, respectively).

FVT and LVT are both particularly useful in mine tailings because when the appropriate procedures are implemented, they allow for determination of the yield and liquefied undrained shear strengths used in slope stability analyses and liquefaction assessments. However, both the FVT and LVT require modifications from the ASTM standard for use in mine tailings. Among the modifications are adjustments to the wait time after vane insertion and the vane rotation rate. Several researchers (Blight (1969); Morris et al. (2000); Castro (2003)) found that the ASTM standard vane rotation rate may not be fast enough to achieve undrained conditions in mine tailings. This is due to the fact that mine tailings generally involve size reduction (e.g., crushing and grinding) and separation of the ore, which often results in drainage and compressibility attributes that differ from those of natural clays that the FVT and LVT were developed.

The paper briefly discusses the ASTM standards for FVT and LVT along with their advantages and limitations for use in mine tailings. Similarly, the applicability of the FVT and LVT in mine tailings and the necessary modifications from the ASTM standards based on the authors' experience testing a particular mine tailings are presented. Finally, the yield and liquefied undrained shear strength ratios measured from FVT and LVT using modified equipment and procedures are compared with literature data, existing correlations, and case histories of actual flow liquefaction failures.

2 STANDARD FVT EQUIPMENT AND PROCEDURE

The FVT standard is described in detail in ASTM D2573. A variety of vane sizes and geometries are available for testing materials of different strengths. The most common vane shape is rectangular; however, the top and bottom ends of the vane can also be tapered. The vane blade thickness is typically about 2 mm, and the area ratio (i.e., the ratio of the volume of soil displaced by the vane blades upon insertion to the cylindrical volume of soil swept by the rotated vane) is less than 10 to 12 percent.

Rod friction against the surround material and/or the use of slip couplings are important factors that must be accounted for or corrected as part of the FVT, especially in very soft soils. To determine the rod friction, a test without the vane attached is performed, and the resistance generated by rod friction is recorded. The rod friction is then subtracted from the actual vane test results with the vane attached.

Per the ASTM standard, the wait time after vane insertion into the undisturbed soil generally should not exceed 5 minutes. The vane is then rotated at a constant rate by applying a measured torque to create a cylindrical failure surface within the in-situ material. The ASTM standard allows for a rotation rate of 0.1 degrees per second (6 degrees per minute) with variations between 0.05 and 0.12 degrees per second (3 and 7 degrees per minute). At this rate, failure (i.e., yield undrained shear strength) is usually reached within 1 to 5 minutes, depending on soil plasticity and coefficient of consolidation.

During the FVT, the torque required to rotate the vane (either manually or motorized) and the cumulative angle of vane rotation are measured to develop a near-continuous shear stress vs. vane rotation relationship. The most common equipment applies and measures the torque at the top of the rods. The yield undrained shear strength (S_u) is then calculated from the maximum measured torque (T_{max}) and the vane diameter (D). For rectangular vanes having a height-to-diameter ratio of 2, Equation (1), is used to calculate the yield undrained shear strength (S_u) from the FVT.

$$(S_u)_{FVT} = \frac{6\,T_{max}}{7\pi D^3} \tag{1}$$

After reaching the yield (i.e., peak) undrained shear strength, the ASTM standard calls for the vane to be rapidly rotated through a minimum of 5 to 10 revolutions. Then, the remolded (i.e., post-peak) undrained shear strength is measured while rotating the vane at the standard rate of 0.1 degrees per second (6 degrees per minute), but nor more than 1 minute after the remolding process. The remolded undrained shear strength is also determined using Equation (1) with the remolded measured torque ($T_{remolded}$) replacing the maximum measured torque (T_{max}). The peak and remolded FVT can be performed at regular intervals between 0.5 to 0.75 m throughout the soil deposit.

2.1 *Advantages and Disadvantages of the FVT in Mine Tailings*

Mine tailings are the waste material from mining operations, meaning that they are recent deposits of a very young geologic age, and therefore have not experienced significant aging or weathering to develop a robust soil structure. Often, mine tailings are hydraulically deposited, where the material comes into equilibrium in a very loose condition with a high in-situ void ratio. Furthermore, mine tailings generally do not experience loading other than continued mine tailings deposition and/or dam construction, resulting in the deposits being nearly normally-consolidated. Finally, mine tailings are commonly composed of non-plastic or low plasticity solids. All of these facts combined create very challenging conditions for the collection of truly "undisturbed" samples for laboratory shear strength testing. This is particularly significant because the yield undrained shear strength is largely controlled by the incipient soil fabric and in-situ void ratio, which can be easily disturbed by conventional methods of sampling, transportation, handling, and preparation (Viana Da Fonseca et al. (2015)).

One of the primary advantages of using FVT combined with the CPT for shear strength determination is that the procedure does not require collection of undisturbed samples for laboratory testing, such that issues related to sample disturbance are eliminated. Additionally, the deposit is more comprehensively and efficiently characterized compared to laboratory testing of discrete samples because CPT produces near-continuous profiles of measurements and multiple FVT can be performed successively with depth. Thus, CPT and FVT provide a better representation of the material variability and may detect particularly strong or weak layers that may go undetected using traditional sampling methods. Finally, CPT and FVT are generally more repeatable and reliable due to the standardization of equipment and procedures.

However, in-situ testing with the FVT also presents some disadvantages or limitations with respect to the control of testing conditions, which are typically afforded a high-level of control within the laboratory environment. For example, the stress state and drainage conditions cannot be controlled or modified as part of in-situ testing, and in many cases, may not even be well known. This is particularly critical because the strain rate (i.e., cone penetration and vane rotation rates) directly affects whether that material behaves in a drained, partially drained, or undrained manner during the in-situ test, as demonstrated by Contreras and Grosser (2019, 2009).

2.2 *Modifications for Using FVT in Mine Tailings*

Mine tailings are comprised of the uneconomical residue left from mineral processing of the ore body, which generally involves size reduction (e.g., crushing and grinding) and separation to achieve liberation and concentration of the desired mineral. The residue then consists of material with particle sizes ranging from coarse (i.e., sand-size) to fine (i.e., silt-size and clay-size). In many instances, the mineral processing can result in a sizable portion of the mine tailings consisting of very fine clay-size materials, which may or not necessarily contain clay minerals. In this way, mine tailings fundamentally differ from natural clays, for which the FVT was originally developed, in terms of compressibility and permeability. Therefore, it can be difficult to achieve and maintain undrained conditions throughout the test if using the standard equipment and procedures in mine tailings. As a result, the authors have found that modifications from the standard, including the vane equipment, the wait time after vane insertion, and the vane rotation rate, are needed to improve data quality when performing FVT in mine tailings.

The ASTM D2573 standard does not provide strict guidelines for the equipment or procedure, but rather broad ranges of acceptable protocol. As a result, it is essential to use the best-available equipment and to develop and maintain material-specific protocol when using the FVT in mine tailings. The authors have developed a practice that uses the best-available equipment and procedures to improve data quality when assessing the undrained shear strength of mine tailings as described subsequently.

2.2.1 *Wait Time After Vane Insertion*

As previously indicated, the ASTM standard allows for up to 5 minutes of wait time after vane insertion until starting the test. While this is acceptable in natural clays, it is preferable in mine tailings with relatively higher permeabilities to reduce the wait time after vane insertion so that shear-induced pore water pressures resulting from vane insertion exhibit little or no dissipation and resulting shear strength gain above what exists in its in-situ condition. The authors have found that better results are obtained when vane rotation starts within one minute of vane insertion (for low plasticity, silt-sized mine tailings). Similar recommendations have been provided by Morris et al. (2000).

2.2.2 *Equipment*

A key component of the FVT equipment is the system applying and measuring the vane torque. Traditional systems require that the torque rods connected to the vane be manually rotated by an operator using a geared drive or directly using a torque wrench with limited control of the vane rotation rate. Torque readings are then manually collected from a calibrated spring torque measurement device, which has limited precision and resolution. Traditional systems also require that rod friction from the surrounding materials be independently measured and subtracted from the measured vane torque.

Alternatively, for measurement of the undrained shear strength of mine tailings, the authors typically use an electronic downhole torque measurement device, whereby the drive motor and torque sensor are positioned inside a downhole equipment housing directly above the vane. The system also provides fully-digital control of the vane rotation rate and near-continuous data acquisition. This has the benefit of eliminating the need for rod friction correction, which can be of the same order of magnitude as the shear strength of mine tailings, and also providing a full shear stress vs. vane rotation relationship.

2.2.3 *Procedure and Vane Rotation Rate*

During FVT soundings in mine tailings, the downhole equipment housing the vane, drive motor, and torque sensor is advanced by hydraulic rams to a depth just shallower than the desired test depth. Test depths are targeted based upon data from adjacent CPT soundings specifically to be within uniform layers of the mine tailings deposit that exhibit undrained behavior during CPT advancement. The vane is then deployed from the housing to the desired test depth, and vane rotation starts within the wait time.

Following a series of field trials, the authors found that the FVT should be run with two stages at different vane rotation rates for determination of yield (i.e., peak) and remolded (i.e., post-peak) undrained shear strengths, as explained subsequently. In the first stage, the vane rotates at a specified constant rate while continuously recording torque measurements and degrees of rotation to determine the maximum torque (i.e., yield undrained shear strength). After determining the maximum torque or approximately 60 degrees of vane rotation, the vane is rapidly rotated at a faster specified constant rate through a total of 3960 degrees of vane rotation to determine the remolded torque (i.e., remolded undrained shear strength). Use of two different rates ensures that undrained conditions are achieved at the maximum shear stress and are maintained throughout the measurement of the remolded shear stresses without drainage and the associated shear strength gain. Upon completion of the test, the vane is retracted into the housing before advancing the downhole equipment housing to the next test depth.

Vane rotation rates for the first stage are determined based on the method developed by Blight (1968), which uses empirical and theoretical approaches to evaluate drainage during the test to ensure that undrained shear is occurring at failure using Equation (2).

$$T = \frac{c_{v-}t_f}{D^2} \tag{2}$$

In Equation (2), the time factor (T) is a function of the coefficient of consolidation (c_v), the time to failure by vane shear (t_f), and the vane diameter (D). The coefficient of consolidation (c_v) values are estimated from pore-water pressure dissipation tests performed concurrent with CPT soundings. Blight (1968) concluded that for time factors less than 0.02, the FVT could be considered fully undrained. However, the authors' field and laboratory trials have found that this time factor criteria may not be universally applicable as it is likely strongly influenced by drainage conditions, and similar observations were noted by Morris et al. (2000). The authors recommend performing multiple FVT at different vane rotation rates to determine the material-specific optimal rate for achieving undrained conditions.

Using these approaches, the authors have found that the vane rate of rotations required to ensure undrained conditions at yield are typically more than an order of magnitude faster than the ASTM standard (for low plasticity, silt-sized tailings). For example, the vane rotation rate for measurement of the yield undrained shear strength was approximately 3.0 degrees per second for a 55 mm diameter vane. Even faster rates of rotation of about 7.0 degrees per second (maximum rate of equipment used) were required for determination of the remolded undrained shear strength.

2.3 *Typical FVT Result in Mine Tailings*

Figure 1 shows a typical FVT result performed in mine tailings (low plasticity, silt-sized tailings) using the equipment and procedures described above in terms of the shear stress vs. vane rotation (blue line). Also included on Figure 1 is the vane rotation rate throughout the duration of the test (red line). As can be seen, the maximum shear stress of 17.6kPa (i.e., yield undrained shear strength) is reached at 10 degrees of vane rotation, and then the shear stress decreases rapidly. Vane rotation then momentarily pauses for less than one second at between 60 and 90 degrees of vane rotation to allow for the drive motor to adjust the vane rotation rate before continuing the test through a total of 3960 degrees. Note in Figure 1 that the momentary pause and abrupt increase in vane rotation rate causes some increase to the measured shear stresses before they continue to decrease. The rapid loss of shear stress moderates after about 360 degrees of vane rotation, although some continued shear stress loss is observed through 3960 degrees of vane rotation.

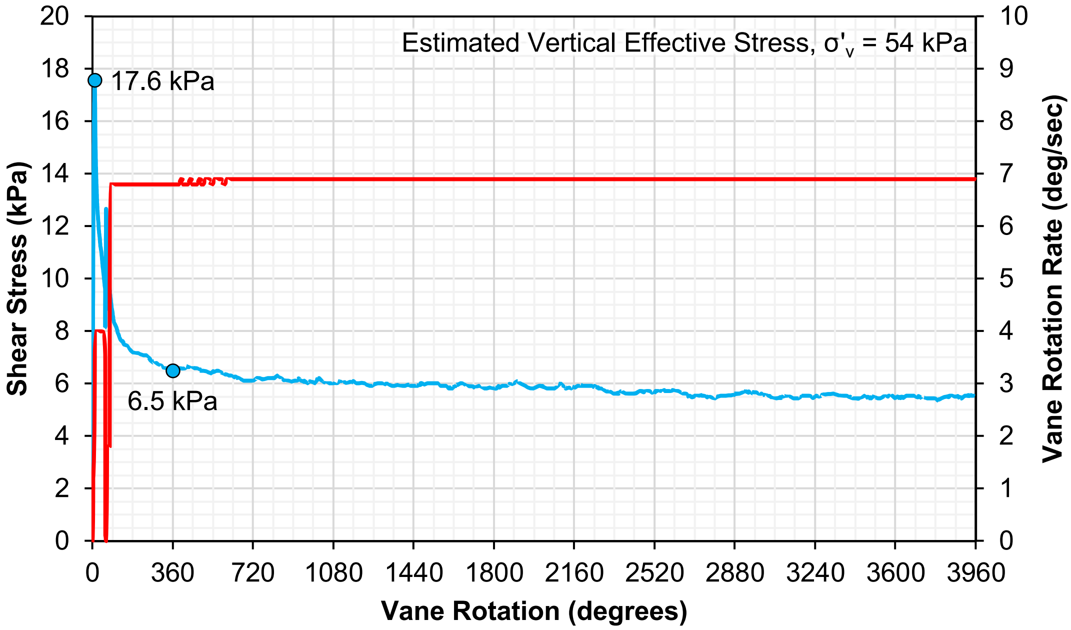

Figure 1. Typical Field Vane Shear Test in Mine Tailings

The selection of the vane rotation to be used for determination of the liquefied undrained shear strength can be contentious and is not trivial because this is the critical parameter for many designs. By thorough evaluation of available site-specific data and comparisons with case histories of actual flow liquefaction failures, as will be illustrated subsequently, the authors are confident that the liquefied undrained shear strength can be defined at 360 degrees of vane rotation for the purpose of slope stability analyses and liquefaction assessments. However, the cause of the continued slow loss of shear stress after 360 degrees is not apparent, and a cursory literature review reveals that there is limited information documenting this phenomenon (Wilson et al. (2016); McConnell (2014)).

One possible explanation is related to the nature of shearing. When the FVT was originally developed for natural clays, it was assumed that a cylindrical soil element between the vane blades rotates as a solid mass and is sheared along the static soil mass outside of the rotating cylinder such that shearing occurs along a well-defined shear band. This expected behavior is reasonable in natural clays with plasticity and developed structure. However, in the case of mine tailings with relatively low plasticity and minimal structure, the shear behavior may be different. It is speculated that as the vane is rotated through very large strains in mine tailings, a wider shear band develops and "turbulent" mixing occurs between the material within the cylindrical soil element and the surrounding soil mass. Olson and Stark (2002) integrated a similar phenomenon of continued slow loss of shear stress after reaching the liquefied undrained shear strength in their back-analysis of flow liquefaction case histories, which they attributed to hydroplaning and mixing that occurs at very large strains.

Alternatively, it has been hypothesized by the authors that through 360 degrees of vane rotation, the shear behavior and liquefied undrained shear strength may be considered from to a geotechnical perspective and applicable to slope stability analyses. However, at very large strain through as much as 3960 degrees of vane rotation, the shear behavior may be more representative of viscous mixing that would be better considered from a rheological perspective and may, for example, be more applicable to the analysis of mine tailings runout in a dam breach scenario.

2.4 *Comparison with Correlations from Actual Flow Liquefaction Failure Case Histories*

Several correlations exist in the literature for estimation of the yield and liquefied undrained shear strength ratios using the CPT, which have been developed based on the back-calculation of actual flow liquefaction failure case histories. The following presents the author's database of yield and liquefied undrained shear strength ratios measured by FVT using the stated equipment and procedures in mine tailings for comparison with common correlations used in geotechnical practice (Olson and Stark 2003; Olson and Stark 2002; and Robertson 2010). The purpose of this comparison is to validate FVT equipment and procedures described herein, as well as the applicability of these correlations to mine tailings.

2.4.1 *Olson and Stark (2002, 2003)*

Figures 2 and 3 illustrate the authors' data representing the yield ($USSR_{YIELD}$) and liquefied ($USSR_{LIQ}$) undrained shear strength ratios, respectively, of the mine tailings computed from direct measurement of the FVT with respect to the normalized corrected tip resistance (q_{t1}) from CPT soundings performed adjacent to the FVT. Data are also compared to the case histories of actual flow liquefaction failures and the correlations proposed by Olson and Stark (2002, 2003) for estimation of yield and liquefied undrained shear strength ratios. Figure 2 shows that the yield undrained shear strength ratio measured by FVT generally ranges between 0.15 and 0.30, and the yield undrained shear strength ratio from back-calculation of actual flow liquefaction case histories generally ranges between 0.16 and 0.32. Figure 3 shows that the liquefied undrained shear strength ratio measured by FVT generally ranges between 0.04 and 0.12, and the liquefied undrained shear strength ratio from back-calculation of actual flow liquefaction case histories generally ranges between 0.03 and 0.12. Therefore, the yield and liquefied undrained shear strength ratios measured by FVT compare well with the range of values from actual flow liquefaction case histories, which provides validity to the procedure and general approach. Furthermore, the yield and liquefied undrained shear strength ratios measured by FVT is generally above the best-estimates from the Olson and Stark (2002, 2003) correlations, suggesting the correlation may be conservative in cases when material-specific data is available.

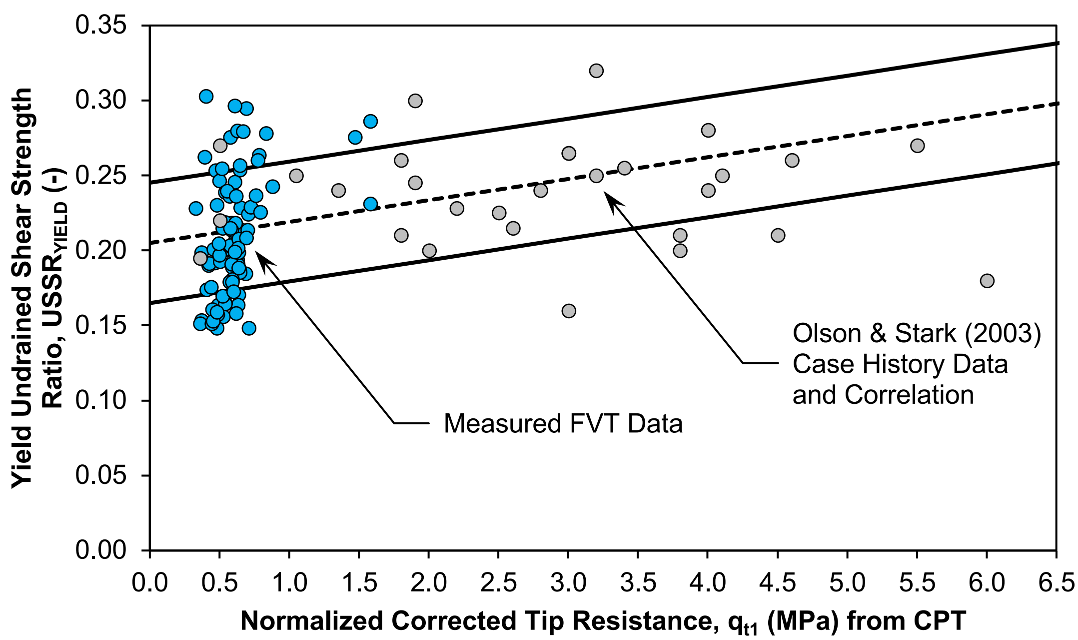

Figure 2. Comparison of Field Vane Shear Test Results to Olson and Stark (2003) Correlation

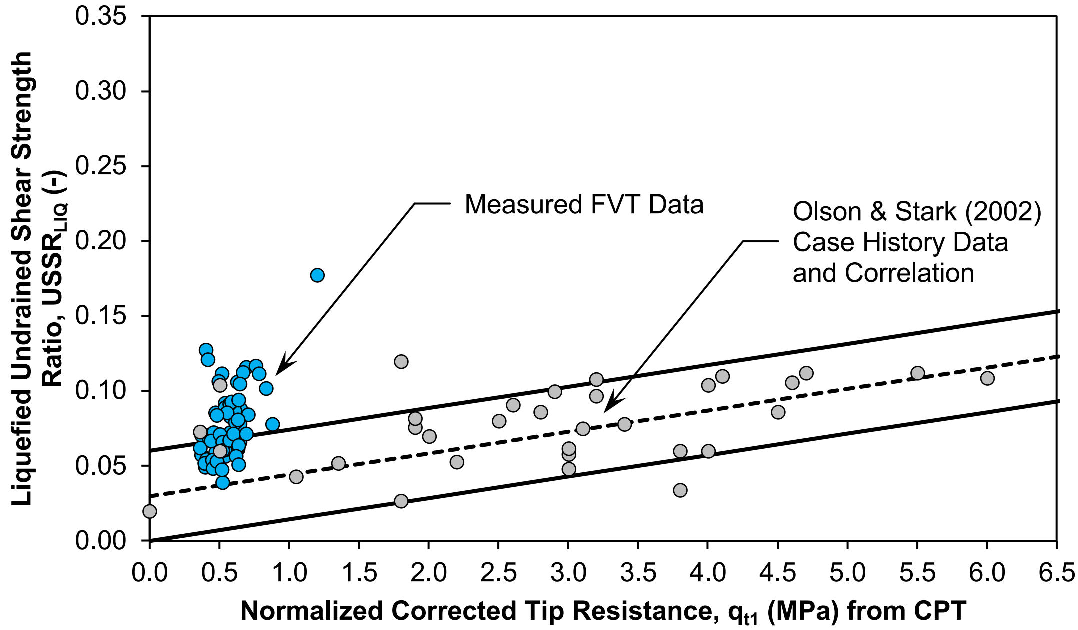

Figure 3. Comparison of Field Vane Shear Test Results to Olson and Stark (2002) Correlation

2.4.2 *Robertson (2010)*

Figure 4 illustrates the author's data representing the liquefied undrained shear strength ratios of the mine tailings computed from direct measurement of the FVT with respect to the equivalent clean sand dimensionless normalized corrected tip resistance ($Q_{tn,cs}$) from CPT soundings performed adjacent to the FVT. Data are also compared to the case histories of actual flow liquefaction failures and the correlation proposed by Robertson (2010) for estimation of liquefied undrained shear strength ratios. Figure 4 shows that the liquefied undrained shear strength ratios measured by FVT generally ranges between 0.04 and 0.12, and the liquefied undrained shear strength ratios from back-calculation of actual flow liquefaction case histories generally ranges between 0.05 and 0.15.

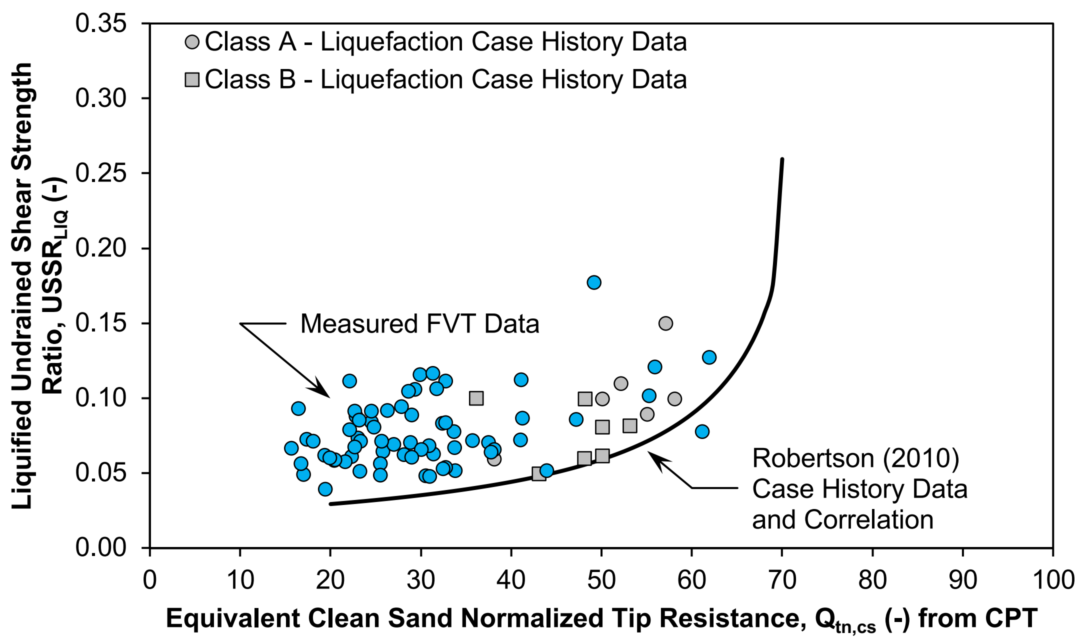

Figure 4. Comparison of Field Vane Shear Test Results to Robertson (2010) Correlation

Therefore, the liquefied undrained shear strength ratios measured by FVT compares well with the range of values from actual flow liquefaction case histories, which again provides validity to the procedure and general approach. Furthermore, the liquefied undrained shear strength ratios measured by FVT is generally above the Robertson (2010) correlation. In general, it can be concluded that the liquefied undrained shear strength ratios estimated by the Robertson (2010) correlation may underestimate the actual values, particularly when applied to fine-grained materials that behave in an undrained manner during CPT penetration. Even in comparison to the back-calculated values from actual flow liquefaction case histories, the Robertson (2010) correlation is objectively a lower-bound estimate.

2.5 *Applicability of FVT in Mine Tailings*

Application of the described FVT equipment and procedures in mine tailings has some limitation since the in-situ drainage conditions cannot be controlled. This is particularly problematic in material zones that exhibit interlayering of materials with high gradation variability, which is common in mine tailings deposits. In that regard, the authors have developed some guidelines to determine whether the FVT is the appropriate tool given the characteristics of the mine tailings to be investigated.

From a broad perspective, the authors found the framework proposed by Idriss and Boulanger (2008) for characterization of the liquefaction behavior of fine-grained soils based on their plasticity to be particularly pertinent – especially given the interest in obtaining the liquefied undrained shear strength from the FVT. Idriss and Boulanger (2008) defined three categories, as follows:

- "Clay-like" material refers to fine-grained materials with plasticity index greater than 7 percent that is expected to exhibit a more ductile shear response.
- "Sand-like" material refers to fine-grained material with plasticity index less than 7 percent that is expected to exhibit a more brittle shear response.
- "Transitional" material refers to fine-grained material with plasticity index between 4 and 7 percent to acknowledge that the boundary at 7 percent is neither precise nor abrupt.

Similarly, Castro (2015) also proposed that plasticity index of 7 percent separates more ductile from more brittle shear responses. The authors have found that the described FVT equipment and procedures can reliably be implemented in the field in mine tailings with "clay-like" material characteristics.

To further refine this characterization, the authors have aggregated data and integrated an understanding of cases in which the FVT was and was not used successfully in order to establish the following guidelines of when the FVT may be applicable in mine tailings.

- Plasticity index is greater than approximately 7 percent.
- Clay-size fraction (2 μm) greater than approximately 20 percent.
- Pore-water pressure dissipation (t_{50}) from CPT is longer than approximately 60 seconds.
- Soil behavior type (I_B) per Robertson (2016) from CPT is less than approximately 18.

Figure 5 illustrates some of these guidelines with respect to the normalized corrected tip resistance (Q_{tn}) and normalized friction ratio (Fr) classification chart by Robertson (2016). Readers should be aware that these guidelines are based on the results from a particular mine tailings deposit and may not be applicable to all sites or materials, although similar approaches maybe used to develop other site-specific or material-specific guidelines.

For mine tailings that do not meet these guidelines, obtaining reliable measurements of undrained shear strength using the FVT can be very challenging, require very specialized equipment, and/or is simply not practical. However, the authors have found that mine tailings within the so called "transitional" material zone may possibly be measured with some reliability using the LVT.

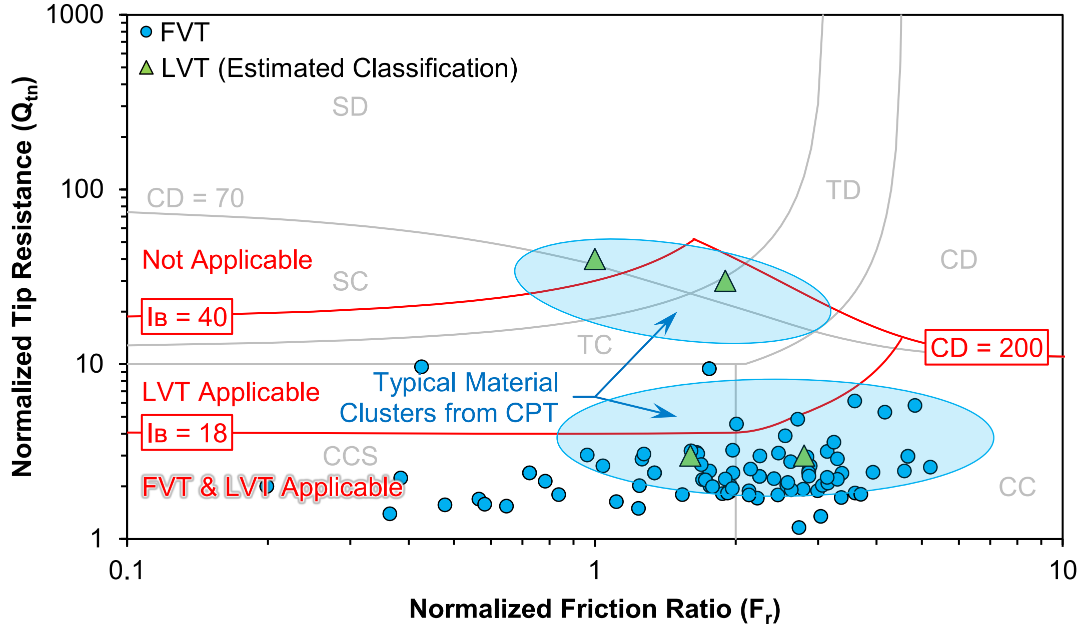

Figure 5. Applicability of Field and Laboratory Vane Shear Test based on CPT Data (Robertson, 2016)

3 STANDARD LVT EQUIPMENT AND PROCEDURE

The LVT standard is described in detail in ASTM D4648. In many ways, the laboratory version of the test is similar to the field version with the key difference being that the LVT is performed on intact samples or reconstituted specimens with more control over the testing environment and variables. A major advantage of the LVT is the testing can be performed on reconstituted specimens, which can be prepared in the laboratory with some consistency to allow for evaluation of other variables. One such variable is the vane rotation rate, which can typically be much faster and adjusted over a wider range with the equipment available in the laboratory. An important disadvantage is that the LVT is often conducted without vertical confinement. To address this issue, the authors developed an apparatus that allows for consolidation and confinement of the specimen throughout the test (a detailed description of the apparatus will be provided in subsequent publications).

3.1 *LVT Program with Mine Tailings*

In principle, the LVT has many of the same issues as the FVT in mine tailings, particularly related to vane rotation rate and maintaining undrained conditions. However, because the laboratory environment is more controlled, some of the variables can be better assessed – particularly by incorporating the modified apparatus allowing for vertical consolidation and confinement of the reconstituted specimen. As such, the LVT can successfully be used for mine tailings classified as either “clay-like” or “transitional” materials, which can be a substantial portion of many mine tailings deposits.

In order to verify that the modifications to the ASTM standard procedures for FVT were appropriate and to further investigate certain aspect of the shear response observed from FVT, the authors developed a testing program using LVT and other laboratory testing data. As part of the laboratory testing program, a series of LVT were performed on multiple reconstituted specimens that were representative of the mine tailings deposit, including both “clay-like” and “transitional” materials. In brief, the representative samples of mine tailings were prepared into a slurry at very high initial void ratios associated with hydraulic deposition in the field, and then poured into the cylindrical container of the LVT apparatus. Although laboratory preparation cannot replicate of the in-situ fabric/structure, the slurry preparation was thought to be suitable for the purposes of this study. After self-weight consolidation, a top platen was placed over the specimen and incremental consolidation loads were applied until reaching the desired consolidation stress for testing. Detailed measurements during the consolidation stage were used to track the specimen void ratio and to determine the coefficient of consolidation (c_v), which was used to determine the vane rotation rate necessary to maintain undrained conditions.

Upon reaching the consolidation stress of interest, the LVT drive motor and torque measurement device were setup, and one of seven small bulkheads was removed from the top platen to allow for vane insertion while maintaining the applied load. Then, the 25 mm diameter by 50 mm high vane was inserted into the specimen. Subsequently, the procedures generally followed those used for FVT in that vane rotation began within 1 minute of vane insertion and two stages at different vane rotation rates were used to measure the yield (i.e., peak) and remolded (i.e., post-peak) undrained shear strengths. Again, one vane rotation rate was used up to 60 degrees of rotation for determining the maximum torque, and a second faster vane rotation rate was used through 3960 degrees of rotation to determine the remolded torque. Unlike the FVT, the LVT drive motor allowed for a wider range of vane rotation rates, which was utilized to rotate the vane much fast for determination of the remolded torque. In doing so, it was observed that for some mine tailings, particularly those classified as "transitional" materials, undrained conditions could be maintained throughout the remolded portion of the LVT. This is in contrast to FVT results suggesting that some drainage and shear stress increase would be observed at larger strains, which was attributed to the limited vane rotation rate in the field.

Upon completion of each LVT, the vane was retracted and the bulkhead was replaced in the top platen. The procedure was then repeated to complete another LVT in a different bulkhead either under the same consolidation stress or after consolidation to a higher load increment. Again, the vertical deformation of the specimen was tracked to estimate the void ratio at the time of the test. A series of reconstituted specimens representative of the mine tailings deposit were tested using this procedure.

3.2 *Results of LVT Program*

In addition to confirming that modifications to the ASTM standard procedures for FVT were appropriate, one of the objectives of the LVT program was to develop a material-specific correlation to estimate the yield and liquefied undrained shear strength ratios with respect to the state parameter. With the void ratio known from each LVT, these values could be compared to the critical state lines measured for the same representative samples of mine tailings to estimate the state parameter of each LVT.

Figure 6 shows the yield and liquefied undrained shear strength ratios measured from each LVT with respect to the associated state parameter (ψ). Note that the liquefied undrained shear strength ratio was determined from the remolded shear stress after 360 degrees of vane rotation. Trendlines drawn through these data points for both the yield and liquefied undrained shear strength ratios can be seen to decrease as the state parameter increases. The result of a consolidated-undrained triaxial compression test performed on the mine tailings that exhibited contractive behavior is also shown on Figure 6 to confirm the liquefied undrained shear strength ratios from the LVT.

For comparison purposes, a large body of triaxial compression test data performed on various natural sands and mine tailings compiled by Jefferies and Been (2016) are plotted on Figure 6 in terms of the yield undrained shear strength ratio and the state parameter. Additionally, the liquefied undrained shear strength ratios from back-calculation of actual flow liquefaction case histories, also compiled by Jefferies and Been (2016), are plotted on Figure 6. Overall, the author's data set from LVT is in good agreement with the literature data validating the results and the LVT as an acceptable tool.

Assuming that the reconstituted specimen preparation used for LVT was sufficiently representative of the in-situ fabric/structure of the mine tailings deposit, the trendlines shown on Figure 6 could be used to estimate the liquefied undrained shear strength ratio by knowing either the in-situ state parameter using the FVRP (Contreras et al. 2020) or the yield undrained shear strength ratio, which may be measured in-situ with the FVT.

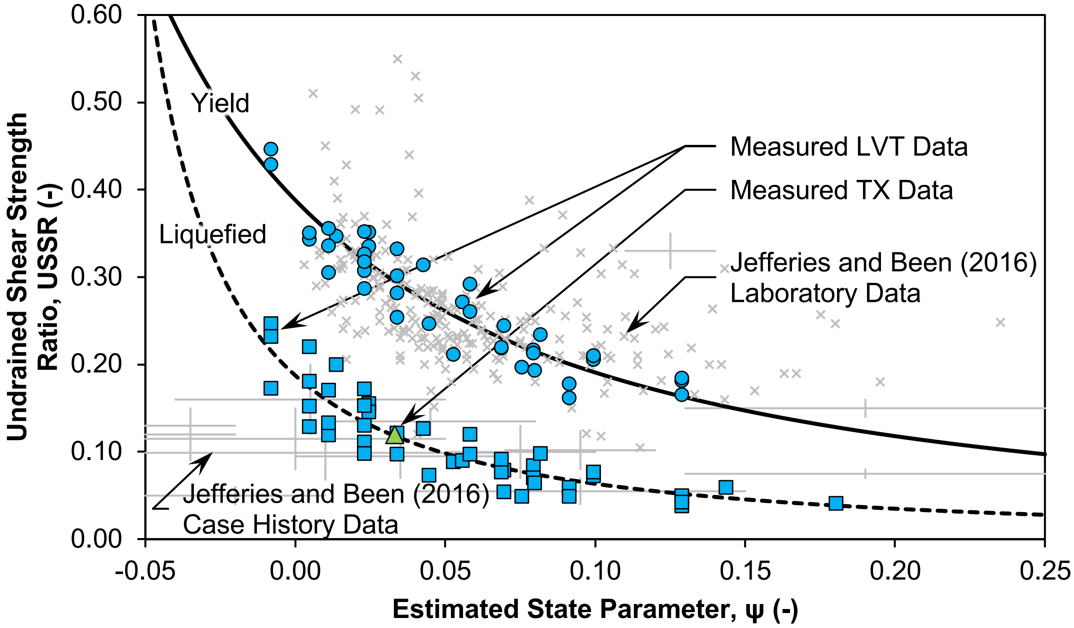

Figure 6. Comparison of Laboratory Vane Shear Test Results with Jefferies and Been (2016) Data

3.2.1 *Applicability of LVT in Mine Tailings*

The laboratory testing program described above has demonstrates that with some modifications the LVT can reliably test both "clay-like" and "transitional" materials. The following guidelines were established to advise when the LVT may be applicable in mine tailings, and these can be directly compared to those for the FVT as outlined previously.

- Plasticity index is greater than 2 percent.
- Clay-size fraction (2 μm) greater than approximately 10 percent.
- Soil behavior type (I_B) per Robertson (2016) from CPT is less than approximately 40.

Some of these guidelines are illustrated on Figure 5 with respect to the normalized corrected tip resistance (Q_{tn}) and normalized friction ratio (Fr) classification chart by Robertson (2016). Also shown on Figure 5 are the approximate classification ranges of similar materials to the representative samples of mine tailings that were used successfully in the LVT program, from which the soil behavior type (I_B) boundary was were derived. Again, readers should be aware that these guidelines are based on the results from a particular mine tailings deposit and may not be applicable to all sites or materials, although similar approaches maybe used to develop other site-specific or material-specific guidelines.

4 CONCLUSIONS

The vane shear test is very useful tool to assess the undrained shear strength of mine tailings. However, its use requires a good understanding of the working principles of the test and modifications in the test procedure and equipment to achieve meaningful results. The following summarizes the main findings of the work presented herein.

The authors found that modifications from the standard, including the vane equipment, the wait time after vane insertion, and the vane rotation rate, are needed to improve data quality when performing FVT in mine tailings. Better and more consistent results are found when the wait time after insertion is less than one minute, the equipment measures the torque downhole above the vane, and the rotation rate is adjusted to yield undrained conditions as described. Additionally, the proposed vane shear test procedure is run in two stages and uses different vane rotation rates in each stage to measure the yield and remolded undrained shear strengths.

Data from authors' FVT database were compared with correlations for the yield and liquefied undrained shear strength ratios and generally a good comparison was found between both data sets which provides validity to the proposed approach. Results of a laboratory testing program using the LVT are also presented and discussed. A correlation between undrained shear strength ratio and state parameter using the LVT is presented and compared with data and case histories from Jefferies and Been (2016).

General guidelines are also provided regarding the materials and limitations where the proposed FVT and LVT procedures provide satisfactory results.

5 REFERENCES

American Society for Testing and Materials. 2015. *Standard Test Method for Field Vane Shear Test in Saturated Fine-Grained Soils, ASTM D2573*.

American Society for Testing and Materials. 2020. *Standard Test Methods For Laboratory Miniature Vane Shear Test For Saturated Fine-Grained Clayey Soil ASTM D4648.*

Blight, G.E. 1968. "A Note on Field Vane Testing of Silty Soils." *Canadian Geotechnical Journal*, 5(3):142-149.

Cadling, L. and Odenstad, S. 1948. *The Vane Borer*, Royal Swedish Geotechnical Institute, Proceedings No. 2.

Carlson, L. 1948. *Determination In Situ of the Shear Strength of Undisturbed Clay by Means of a Rotating Auger*, Proceedings of the 2nd International Conference on Soil Mechanics and Foundation Engineering, Vol. I, pp. 265-270.

Castro G. 2003. "Evaluation of Seismic Stability of Tailings Dams." *12th Pan-American Conference on Soil Mechanics and Geotechnical Engineering. 39th U.S. Rock Mechanics Symposium.* Cambridge, U.K.

Castro G. 2015. "Seismic Analysis and Design of Tailings Dams." SME. Training Class.

Contreras, Iván and Grosser, Aaron. 2009. "Evaluation of CPT Response under Fast Penetration Rate in Silty Soils," Proceeding of the 57th Annual Geotechnical Engineering Conference. University of Minnesota. 107-119.

Contreras, Iván and Grosser, Aaron. 2019. "Liquefaction Susceptibility Evaluation of Mine Tailings Using CPT. Proceeding of Tailings and Mine Waste."

Contreras, Iván, Harvey J. W., Walker, M. D., Sharpe J. D., and Grosser A.T. 2020. "Evaluation of Shear Wave Velocity and Void Ratio in Mine Tailings using the Field Velocity Resistivity Probe" Proceeding of Tailings and Mine Waste."

Idriss, I. M., & Boulanger, R. W. 2008. *Soil liquefaction during earthquakes*. Earthquake Engineering Research Institute.

Jefferies, M., and Been, K. 2016. *Soil Liquefaction: A Critical State Approach*. CRC Press, Taylor & Francis Group, New York, NY, 512 pp.

McConnell, A. 2014. *An Update on Vane Shear Testing by IGS*.

Morris, P.H. and Williams, D.J. 2000. "A Revision of Blight's Model of Field Vane Testing." *Canadian Geotechnical Journal*, 37(5): 1089-1098.

Olson, S.M., and Stark, T.D. 2002. "Liquefied Strength Ratio from Liquefaction Flow Failure Case Histories." *Canadian Geotechnical Journal*, 39(3): 629-647.

Olson, S.M., and Stark, T.D. 2003. "Yield Strength Ratio and Liquefaction Analysis of Slopes and Embankments." *Journal of Geotechnical and Geoenvironmental Engineering*, ASCE, 129(8): 727-737.

Robertson, P.K. 2010. "Evaluation of Flow Liquefaction and Liquefied Strength Using the Cone Penetration Test." *Journal of Geotechnical and Geoenvironmental Engineering*, ASCE, 136(6): 842-853.

Robertson, P.K. 2016. "Cone Penetration Test (CPT)-based Soil Behavior Type (SBT) Classification System - an Update. *Canadian Geotechnical Journal*, 53: 1910-1927.

Skempton, A. W. 1948. *Geotechnique*, Vol. I, pp. 111-124.

Viana Da Fonseca, A., Ferreira, C., Soares, M., Klar, A. 2015. "Improved Laboratory techniques for Advanced Geotechnical Characterization Towards Matching In Situ Properties." *Deformation Characteristics of Geomaterials*, V.A. Rinaldi et al. (Eds.), IOS Press, pp. 231-263.

Wilson, L. J., Kouretzis G. P., and Pineda J. A.; Kelly R. B. 2016. *On the Determination of the Undrained Shear Strength from Vane Shear Testing in Soft Clays*.

Application of distributed acoustic sensing within a tailings dam warning system

Bradley Forbes
BGC Engineering Inc, Kingston, ON, Canada

Susanne Ouellet
Department of Geoscience, University of Calgary, Calgary, AB, Canada

Naia Suszek
BGC Engineering Inc, Calgary, AB, Canada

Matt Lato
BGC Engineering Inc, Ottawa, ON, Canada

Brad Russell
BGC Engineering Inc, Vancouver, BC, Canada

ABSTRACT: Recent tailings dam failures have prompted revisions and enhancements to existing tailings dam monitoring best practices globally. A novel monitoring method is presented to act as a component of an overall tailings dam warning system, capable of providing near real-time detection of a potential dam failure at a North American tailings facility. This method measures vibrations along an optical fiber, using a Distributed Acoustic Sensing system. Several kilometers of a telecommunications-grade fiber optic cable were installed one meter below the crest of multiple tailings dam structures, providing the equivalence of over a thousand discrete measurement points. The sensing system is capable of kilohertz scale, thus providing both high spatial and high temporal resolution assessment along the fiber. This paper details the considerations to install this system at the tailings facility and provides an overview of calibration to detect significant disturbances to the cable, while limiting the number of nuisance alarms.

1 INTRODUCTION

Recent tailings dam failures have prompted increased interest in advanced monitoring methods for tailings dams. Most notably, the 2019 Córrego do Feijão tailings dam failure resulted in 270 deaths, increasing the public scrutiny of tailings dams worldwide and prompting the creation of the first-ever Global Industry Standard on Tailings Management (the Standard) (GTR, 2020). The design, implementation, and operation of monitoring systems to manage risks at all phases of a tailings facility's lifecycle constitutes one of the principles covered within the Standard. It also states that "a comprehensive and integrated engineering monitoring system should be appropriate to verify design assumptions and for monitoring against potential failure modes" (GTR, 2020). This has been discussed within the concept of a proposed risk management framework through recent innovations in cost-effective information and communications technologies (Bartoli et al., 2020). Specifically, internet of things (IoT) based instrumentation is presented as a method to optimize the collection and near real-time availability of measurement data from typical tailings dam instruments, such as piezometers, displacement sensors, and pressure transducers. The full potential of the various instruments is then extracted by automatically feeding heterogeneous data, as it becomes available, into predefined stability analyses (end-to-end architecture).

Such techniques are well suited for monitoring trends in dam performance and for identifying deviations from expected behaviour when dam stability is governed by non-brittle failure modes. However, conventional point-based sensors may be incapable of detecting brittle failure mode in a timely manner. This may be due to inadequate sensor coverage, insufficient data acquisition, or minimal pre-cursory deformation prior to the failure. As discussed by Jefferies and Been (2015), flow liquefaction-type dam failures can occur within seconds to minutes. This is reflected in the executive summary of the official report on the technical causes of the Córrego do Feijão tailings dam failure, which states: “The dam was extensively monitored … None of these methods detected any significant deformations or changes prior to failure” (Robertson et al., 2019). Although the Standard states that brittle modes should be addressed by conservative design criteria, there remains an unmet need for geotechnical instrumentation capable of timely detection and notification to address potential liquefaction-type failures. Suppliers are quickly adapting to meet this need, and new technologies to detect and warn of tailings dam failures are becoming available. As an example, a recently developed ‘dam breach detection system’ uses multiple wire circuits buried below the tailings dam crest connected to a datalogger to issue an alarm if the wire breaks due to a dam failure (Garcia Schmidt et al., 2020).

Within this context, an application optical fiber based distributed acoustic sensing (DAS) is presented as a suitable technology for near real-time detection and notification of a potential dam failure event. This paper describes the installation of a DAS technology at a North American upstream tailings facility in 2019 and reviews considerations involved in the implementation of such an event detection system.

2 BACKGROUND

In 2017 and 2018, geotechnical site investigations at an upstream tailings facility encountered a wide areal extent of potentially liquefiable soils. This prompted a review of potential near real-time monitoring technologies to form a component of a “tailings dam event warning detection and notification system” (Ouellet et al., 2019). The purpose of this system is to provide detection of a potential dam failure at multiple tailings dams at the facility, and to be capable of configuration to an external alarm system to support the owner’s emergency preparedness and response plan (EPRP). Commercially available monitoring solutions (e.g., tiltmeters, geophones, and time domain reflectometry), as well as technologies that are currently less adopted or less established within the tailings dam environment (e.g., doppler radar) were assessed based on four primary technical factors:

1) Sampling rate,
2) Areal extent,
3) Frequency of false alarms, and
4) Maintenance requirements.

Based on the assessment factors list above, DAS was identified as a candidate technology. DAS systems provide a means of using a single fiber optic cable to monitor an array of measurement points (i.e., provide a linear spatial coverage), with selected technologies interrogating the fiber optic cable at kilohertz (kHz) sampling rates. Ultimately, a DAS system was selected to be installed as the dam failure detection system at the given tailings facility.

DAS, the components of the DAS system, and implementation at the facility are discussed further in the following sections. The reader is referred to Ouellet et al. (2019) for additional review of the assessment factors and monitoring systems considered in the selection of the dam breach detection system.

3 DISTRIBUTED ACOUSTIC SENSING

DAS belongs to a wider branch of fiber optic sensing known as distributed fiber optic sensing. A typical system is comprised of a power source, an interrogation unit (i.e., a laser source and receiver) and a fiber optic cable. The latter acts as both transmission medium and the transducer. External perturbations that cause physical changes to the fiber optic cable (e.g., temperature and strain) will also disturb the signal (light) propagating within the cable. Distributed fiber optic sensing technologies specifically utilize the back-reflected component of light scattering phenomenon which occurs continuously along the length of a fiber optic cable (Figure 1). Scattering is a spontaneous, diffuse reflection that is a result of Raman, Brillouin, and Rayleigh mechanisms. A change in local strain or temperature along the fiber will induce a modulation of the scattered signal (amplitude, phase, and frequency). This can be realized spatially along the fiber optic cable through techniques such as optical time domain reflectometry and optical frequency domain reflectometry (e.g., Kingsley & Davis, 1985; Froggatt et al., 2004).

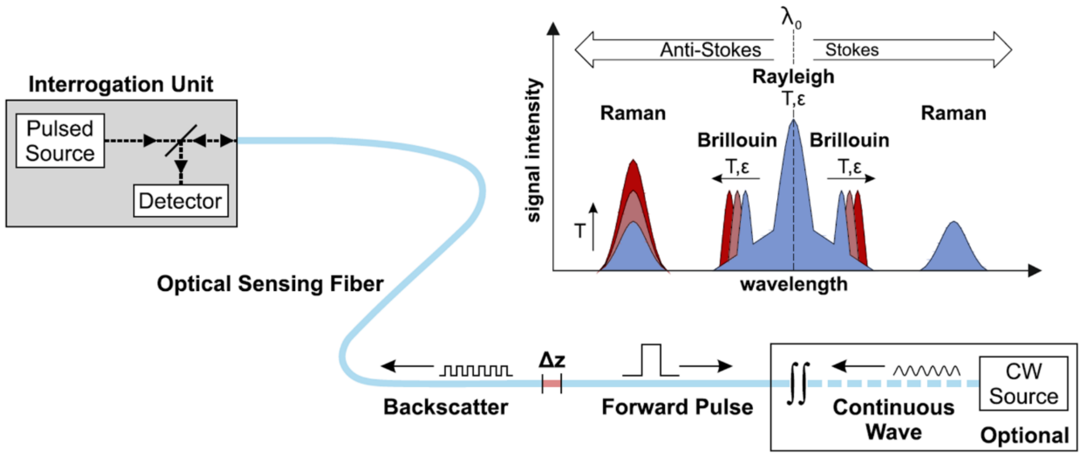

Figure 1. Basic sensing scheme and scattering mechanisms of distributed fiber optic sensing (Courtesy of Monsberger et al., 2020).

DAS is a relatively new distributed sensing technology in comparison to distributed strain sensing and distributed temperature sensing and is primarily associated with monitoring the Rayleigh component of backscattered light (e.g., Owen et al., 2012). Strain acting on the fiber optic cable as a result of seismic (or acoustic) waves will shift the phase and amplitude of the Rayleigh signal, which can be related directly to the strain rate (dynamic strain) acting coaxially along the fiber optic cable (e.g., Lindsey and Martin, 2021).

To date, DAS has primarily been used in applications for oil and gas monitoring and intrusion detection but is rapidly gaining recognition in developing fields such as environmental seismology and for geotechnical engineering applications due to its ability to collect a high number of measurement points along the fiber over distances of tens of kilometers. Recently, the Sweden hydropower firm Energiforsk applied DAS to detect seepage changes as well as identify defects within a test embankment dam by combining DAS with a passive geophysical method known as seismic ambient noise interferometry (Johansson et al., 2021).

4 TAILINGS DAM FAILURE DETECTION AND NOTIFICATION SYSTEM

Implementation of the DAS technology as a component of the dam breach detection system at the site required consideration of the following:

1) Fiber optic cable: A multi-channel telecommunications grade fiber optic cable installed along the crest of multiple dams at the tailings facility. This is a continuous run of single mode fiber optic cable that acts as both the transducer and lead cable. The actively monitored length of cable installed at the facility consist of a 12-channel (12-core) loose tube single jacket armor gel-filled cable manufactured by Superior Essex. One channel of the cable is connected to the interrogation unit via an angled physical contact connector at one end (i.e., not a return loop system).
2) Interrogation unit: An OptaSense OLA-2.1 interrogation unit and related processing equipment was selected for the dam breach detection system. The interrogation unit has a 20 km maximum sensing range, 10 m spatial resolution (i.e., 10 m channel spacing or gauge length), and greater than 1 kHz sampling rate. The OLA-2.1 is considered an intensity-DAS solution as it only measures a relative amplitude change of the strain along the fiber optic cable (i.e., it does not measure the true strain acting on the cable). Signal processing and alarm assessment is performed in real-time by a processing unit and stored

on dedicated rolling recorders. The related graphical user interface is accessed through the control unit.

3) Control unit: A user interface module (PC) running proprietary software. The control unit provides real-time data visualization of the measured signal along the fiber optic cable, system status, alarm notification, and an archive of system performance and activities. User configuration options, including alarm thresholds and notification settings are accessed through the control unit. The control unit can be physical accessed or remotely connected to.

The tailings dam breach detection system also includes infrastructure to deliver and receive alarm notification at the facility (e.g., sirens, radio pagers, etc.). Alarm notification is managed by both the processing unit and control unit.

4.1 *Installation of the Fiber Optic Cable*

Approximately 6 km lateral extent of tailings dams at the facility are monitored with DAS. As discussed above, a 12-channel loose tube single jacket armor gel-filled fiber optic cable was installed in the actively monitored dam sections (Figure 2). This cable construction was selected to provide environmental and physical protection while maintaining sufficient acoustic coupling between the fiber, the cable layers, and the external environment (i.e., the tailings dam). Commercially available tight buffered cables and equivalent engineered cables can provide superior acoustic coupling but have a higher cost and often lower durability and ultimate displacement capacity as a result of the fiber optic cable having a stronger coupling with the surrounding medium (movement). It was also not necessary to have more than one channel; however, the additional channels in the cable assembly were used to create redundant 'loops' and duplicate alignments (not actively monitored) to be used in the event of partial damage to the cable alignment (i.e., cable damage not related to a dam failure event).

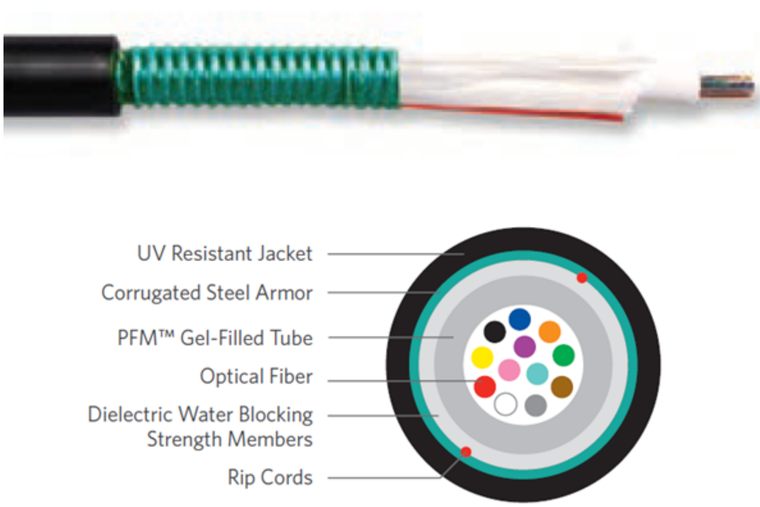

Figure 2. Example side view and section view of a multi-channel single jacket armor gel-filled fiber optic cable (Courtesy of Superior Essex).

The fiber alignment extending across the tailings dams was primarily installed within a 1 m deep trench excavated at a 0.3 m offset from dam crest on the downstream slope. The alignment and depth were selected to mitigate interference and potential damage by trafficking equipment along the dam crest. The typical installation procedure involved placing the fiber optic cable in the center of a 300 mm thick layer of sand in the bottom of the trench, backfilling the trench to approximately 350 mm below the ground surface with the existing dam fill material, placing a continuous roll of identification (caution) tape directly above the fiber optic line parallel to the long axis of the trench, and placing existing dam fill material to approximately 150 mm above ground surface (or equivalent to accommodate expected settlement). The typical installation is shown schematically in Figure 3. The optical fiber was typically placed in a sinuous manner, accommodating approximately 1 m of slack per 10 m of trench length. Permanent sign posts indicating buried fiber optic cable were placed every 100 m and 200 m along the alignment to further mitigate potential damage from trafficking equipment. Modifications to the typical installation were required at road crossings and instances of shallow bedrock along the dams.

The 6 km extent of dam coverage prevented a single (i.e., continuous) installation of cable. Furthermore, it was necessary to install the alignment in sections and connect segments of fiber optic cable to accommodate any conflicts with other dam activities. This was completed by performing arc-fusion splices. Splice locations were placed within protective enclosures, buried or mounted above ground, and clearly identified for future access, as needed. This included a splice from the ‘actively monitored’ dam segment to an overhead lead cable extending from the dam to the facility housing the interrogation unit. A fiber optic cable engineered to self-support overhead spans was used for this length. Although fusion splicing offers a convenient method to install shorter (i.e., more easily managed) cable lengths, splicing also diminishes the signal strength propagating within the fiber. As such, splicing was limited to a minimum to meet the requirements of the system.

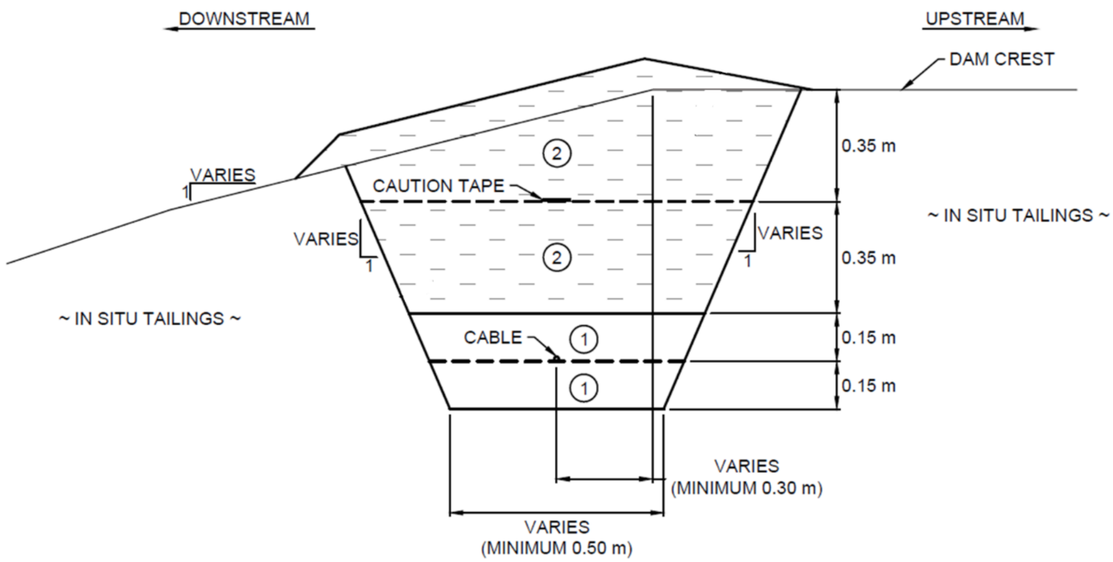

Figure 3. Schematic view of the typical trench installation of the fiber optic cable. Material 1 indicates sand. Material 2 indicates existing dam fill material.

4.2 *Installation of the Interrogation Unit*

The interrogation unit and related processing equipment are rack mountable devices designed for dry indoor environments. These were positioned within an active server room at the given tailings facility in order to have access to clean power (including a backup uninterrupted power supply), environmental control, network accessibility, and security. The control unit was also configured in this room for accessibility.

The server room is located approximately 500 m from the nearest tailings dam of interest, which permitted such an installation at the facility. It is important note that the lead cable between the interrogation unit and the actively monitored cable installed along the tailings dams (or structure of interest) is included in (i.e., the consumes) the sensing range of the system. In a similar application, but without existing infrastructure nearby the tailings facility, it may be necessary to construct a suitable enclosure or control space for the interrogation unit.

4.3 *Alarm Configuration*

As defined in Section 2, the purpose of the tailings failure detection system is to provide near real-time monitoring (i.e., detection) of a dam failure event and be capable of configuration to an external alarm system (to be discussed in Section 4.4). The tailings failure detection system is not intended to provide detection of impending dam failure, given the rapid nature and minimal precursor indicators of a potential flow liquefaction-type failure. Two alarm types were configured to this extent:

1) Fiber Break Alarm: To alert to a break along the fiber optic cable.
2) Near Fiber Break Alarm: To alert to a significant disturbance along the fiber optic cable that does not result in a break.

The Fiber Break Alarm is analogous to a trip-wire system, providing a binary output if a break occurs along the system. The entire fiber alignment of the DAS system has been georeferenced. This enables the system to both detect the break (or severe damage) along the cable and identify the location of the break. The latter feature is advantageous for response time (e.g., visual inspection of the dam).

The Near Fiber Break Alarm consists of a detection algorithm that is triggered by both the acoustic signal propagating within the surrounding medium as well the physical strain acting on the fiber optic cable (e.g., depression or heave along the dam crest). This alarm required a commissioning or 'fine-tuning' period where the background acoustic noise at the facility (e.g., construction activities, traffic, wind, etc.) was assessed in order to define an alarm threshold that would limit false alerts. To maintain a sensitive threshold (i.e., not overly dampen the threshold), the Near Fiber Break Alarm was deactivated along segments of the fiber optic alignment with higher overall noise levels. These segments included the overhead lead cable between the interrogation unit and dam crest, above ground splice locations, and locations expected to be routinely trafficked by equipment (crossing or above the alignment). The Near Fiber Break Alarm was also tested by exposing a section of the cable along approximately 10 meters. A range of physical tests were manually performed on the cable (moving the cable with different intensities, suspending the cable, excavating above the cable). During the tests, the response of the system was observed to allow for additional fine-tuning of the alarms. In comparison, the Fiber Break Alarm did not require site calibration beyond defining the spatial extent of the fiber alignment and the Fiber Break Alarm is active over the entire length of the alignment.

The intent of both the Fiber Break Alarm and Near Fiber Break Alarm is to detect a dam failure event. Nevertheless, potential situations that could cause an alarm to be alerted may include nearby construction activities, vandalism, wildlife damage, and power loss or damage to the interrogation unit. The Near Fiber Break Alarm is inherently more prone to alerting an erroneous alarm; however, it provides a conservative or redundant means of dam failure detection in the event of a potential dam failure event that does not break the fiber optic cable. To the authors' knowledge, this is not a capability available by comparable dam breach detection systems (e.g., electrical-wire circuits).

4.4 *Notifications*

The DAS system is capable of delivering alert notifications for the following items: Fiber Break Alarms, Near Fiber Break Alarms, and system health alarms (e.g., loss in network connectivity, malfunctioning processes, etc.). Configuration options are available for the following:

1) Control unit interface: A graphical user interface on the control unit can indicate alerts in near real-time, providing additional context such as the type of alerts and location, and can be accessed physically and through remote desktop protocol.
2) Email and SMS: Alert notifications can be delivered to specified email addresses and phone numbers via simple mail transfer protocol (SMTP) on the internal network at the facility.
3) Radio pager: A dry contact switch relay can be configured within the facility's distributed control system to notify alerts over a radio pager system. Text and vocal messages can be

configured to describe the type of alert. An alert light can also be indicated at multiple operators' desks.

All the above notification systems can be configured to provide redundant notification measures.

5 DISCUSSION

5.1 *Assessment of the DAS System*

The following section provides an evaluation of the DAS system installed according to the original tailings dam failure and notification assessment factors defined by Ouellet et al. (2019):

1) Sampling rate: The OptaSense OLA-2.1 interrogation unit has sampled the fiber optic alignment at a minimum rate of 1 kHz since installation in 2019. Test alarms (i.e., instances where a Fiber Break or Near Fiber Break Alarm have been physically or digital simulated) generally trigger an alert notification within several seconds of the event.
2) Areal extent: The fiber optic cable alignment provides a linear spatial coverage spanning approximately 6 km across the crest of multiple tailings dam structures. The continuous 10 m spatial resolution of measurements along the fiber alignment is deemed applicable to detect the narrowest width of a dam breach reasonably expected at the facility. It is possible to increase the spatial coverage of the system by adding additional fiber lengths laterally across the upstream and/or downstream regions of the dam; however, the 1-dimensional crest alignment is considered a practical alignment within the scope of detecting a potential near instantaneous liquefaction-type event.
3) Frequency of false alarms: There have been no false Fiber Break Alarms since commissioning the DAS system. However, the threshold limit and zoning of the Near Fiber Break Alarm has required more frequent consideration due to construction activities within proximity of the fiber alignment. A more conservative (i.e., more sensitive) Near Fiber Break Alarm threshold has been selected at the facility. At the current date erroneous Near Fiber Break Alarms (i.e., not pertaining to a dam breach) have been alerted at interval less than once per annual quarter.
4) Maintenance: The DAS system has required minimal maintenance since installation (less than once per year). Maintenance items that have been required since installation have been remotely supported (i.e., a specialist not required to service the system in person). This does not include scheduled alterations and upgrades to the system.

As described, the DAS system is capable of reducing the time delay between a dam failure initiation and dam failure detection. The ability to detect and notify a dam breach scenario within seconds is an important component (however, just one part) of establishing a robust EPRP that enables response actions to occur in a timely manner to be effective.

5.2 *Additional Considerations*

The application of DAS at the tailings facility discussed in this paper is considered a 'retrofitted' fiber optic cable installation, as the dam structures and related infrastructure are well established at the site. As such, installing the cable 1 m below the dam crest provided the most practical and cost-effective installation method for the requirements of the system. Dependent on the monitoring requirements at other sites, alternative cable alignments could consist of multiple fiber runs extending laterally across the dam structure, at various depths and structural components (i.e., filter layer, core material), and at varying offsets from the dam crest (i.e., upstream and downstream) (Figure 4). Such alignments would require operators to consider installing fiber optic cable during the early development stages at their facilities (which may not be used for several years or more). There is strong justification for such early planning when considering that the majority of distributed fiber optic sensing technologies including DAS, distributed temperature sensing, and distributed strain sensing can utilize standard telecommunications grade optical fiber as the transducer (i.e., the same cable will be applicable to many technologies). Furthermore, the installation of multi-channel cables implies that more than one interrogation unit can be used simultaneously. Johansson et al. (2020) have recently demonstrated the benefit of combined distributed temperature sensing and DAS to monitor seepage trends and potential defects within a dam (i.e., using distributed fiber optic temperature sensing to monitor seepage with DAS and seismic noise interferometry to generate 2D and 3D tomographic views of seismic velocity change within the dam structure).

Ouellet et al. (2021) have shown that the application of seismic noise interferometry with geophones as seismic sensors at the tailings dam site can be used to monitor changes in soil behaviour as a result of rainfall and pond level changes. Currently, DAS data is being collected at the site using a separate interrogator unit with plans to apply this method using DAS. As DAS is an emerging technology, advances in interrogation unit technologies and methods (such as seismic noise interferometry) will likely provide additional monitoring capabilities to harness existing in-place fiber optic cable (e.g. unused 'dark' fiber) installed at a site.

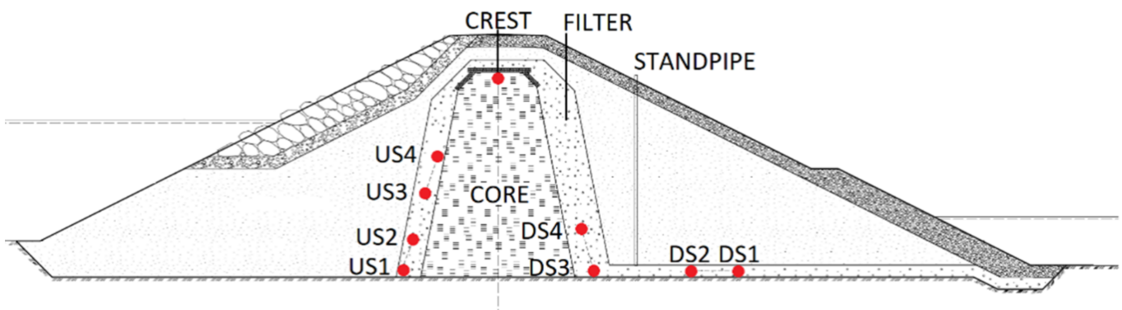

Figure 4. Example cross section of the Näs power plant owned by Vattenfall Vattenkraft AB (Sweden). The fiber optic cable alignment, extending laterally along the facility, is identified by red markers (Courtesy of Johansson et al., 2020).

6 CONCLUSION

This paper has discussed the installation of DAS as part of a dam failure detection system at a tailings facility that was previously identified to have a wide areal extent of potentially liquefiable materials. A continuous fiber optic cable was installed across the crest of approximately 6 km of tailings dam structures at the facility. An interrogation unit, and related processing equipment, monitors the fiber alignment at a sampling rate of at least 1 kHz with a 10 m channel spacing (i.e., a measurement every 10 m along the alignment). Two types of alarms thresholds have been configured to detect potential dam breach scenarios: 1) a Fiber Break Alarm and 2) a Near Fiber Break Alarm. A near real-time notification system has been configured to send alerts in the event of a triggered alarm. Test alarm scenarios indicate that the system can detect an alarm exceedance and notify the location of the alarm along the fiber optic cable (georeferenced location along the tailings dam) typically within seconds of the alarm. Alerts are transmitted and received over multiple device types at the facility and indicate both the type of alarm and approximate position of the alarm along the tailings dam. The near real-time detection and notification of the DAS system is of significance for reducing the time between dam failure initiation and response (e.g., actioning an EPRP), especially within the context of rapid flow liquefaction type failure that may have minimal precursor indicators of failure.

7 REFERENCES

Bartoli, A., Guilhot, D. & Vilajosana, X. 2020. Boosting a more efficient Tailings Dam risk management service through an innovating IoT ecosystem. Proceedings of Tailings and Mine Waste 2020: 649-660.

Froggatt, M., Soller, B., Gifford, D. & Wolfe, M. 2004. Correlation and Keying of Rayleigh Scatter for Loss and Temperature Sensing in Parallel Optical Networks. Proceedings of Optical Fiber Communication Conference: OFC 2004. Los Angeles, CA.

Garcia Schmidt, I., Ketilson, E. & Godley, D. 2020. Last Line of Defense – A Dam Breach Detection System. Accessed online on August 10, 2021: srk.com/en/publications/dam-breach-detection-system.

Global Tailings Review (GTR) 2020. Global Industry Standard on Tailings Management. Coconvened by the ICMM, UN Environment and PRI. Accessed online August 10, 2021: https://globaltailingsreview.org/global-industry-standard.

Jefferies, M. & Been, K (2nd ed.) 2015. *Soil liquefaction: A critical state approach*. Boca Raton, FL: CRC Press.

Johansson, S., Beaupretre, S., Boue, A., Stork, A. 2021. Distributed Acoustic Sensing for Detection of Defects in the Test Dam at Älvkarleby. Energiforsk Report 2021:732, ISBN 978-91-7673-732-3

Johansson, S., Stork, A., David, A., Mondanos, M. & Nygren, C. 2020. Fibre-optic Distributed Acoustic Sensing for detection of seepage and internal erosion, Energiforsk Report 2020:682, ISBN 978-91-7673-682-1.

Kingsley, S.A. & Davies, D.E.N. 1985. OFDR diagnostics for fibre and integrated-optic systems. *Electronics Letters* 21(10): 434-435.

Lindsey, N.J. & Martin, E.R. 2021. Fiber-Optic Seismology. *Annual Review of Earth and Planetary Sciences 2021* 49(1): 309-336.

Monsberger, C.M., Lienhart, W.L. & Hayden, M. 2020. Distributed fiber optic sensing along driven ductile piles: Design, sensor installation and monitoring benefits. *Journal of Civil Structural Health Monitoring* 2020(10): 627-637.

Ouellet, S. et al. 2021. Monitoring Changes in Soil Behaviour with Ambient Noise Interferometry. Manuscript in preparation.

Ouellet, S., Suszek, N., Lato, M., Russell, B., Froese, C. & Carey, E. 2019. Static Liquefaction-Type Tailings Dam Failures: Understanding Options for Detecting Failures. Proceedings of Tailings and Mine Waste 2019: Vancouver, Canada: 415-420.

Owen, A., Duckworth, G. & Worsley, J. 2012. OptaSense: Fibre optic distributed acoustic sensing for border monitoring. Proceedings of the 2012 European Intelligence and Security Informatics Conference: 362-364.

Robertson, P.K., de Melo, L., Williams, D.J., Wilson, G.W. 2019. Report of the Expert Panel on the Technical Causes of the Failure of Feijão Dam I. Commissioned report by Vale S.A.

Actual evaporation from the tailings storage facility using Eddy Covariance instruments

Homin Kim & Brant Whiting
Freeport-McMoRan Inc, Phoenix, Arizona, USA

Mark Schmelter
Freeport-McMoRan Inc, Phoenix, Arizona, USA

ABSTRACT: Pan evaporation has been widely used in mining water balance models to provide evaporation rates in a tailings storage facility (TSF) water balance calculations. Pan evaporation rates represent an unlimited moisture condition such that coefficients are required to convert potential evaporation into estimated evaporation rates of the pond and beach of a TSF. In this paper, we describe efforts to improve evaporation estimates for a large TSF in southern Arizona using eddy covariance instruments. These instruments provide a direct measurement of actual evaporation rate over a given footprint and present an opportunity to reduce uncertainty associated with water balance modeling. Two years of data were collected at the TSF, during which time we obtained actual evaporation rates from dry beach and wet beach areas. We document the initial results of this work, lessons learned and next steps.

1 INTRODUCTION

1.1 *Mine water management context*

Mine water management is a critical consideration of all mining operations throughout the project lifecycle. It is standard practice for engineers responsible for different aspects of the mine to develop water balance models that conceptualize the sources, sinks and storage locations so decisions can be made and risks or opportunities identified. Water balance models are the result of direct observations, mathematical conceptualizations of processes not directly observed, estimates, and assumptions that act as a whole to both explain past behavior and predict ranges of future possibilities. In a general sense, the extent to which these models are based more on direct observations and fewer assumptions and estimates, the more robust the model is. There is, however, a practical limit to the data that can be collected and incorporated into a model due to the effort and resources expended to collect these data and the value to decision-making these additional data provide.

For mines located in arid climates, evaporation from tailings reclaim ponds and beaches constitute a large water outflow of a site water budget and can be convoluted with tailings soak-up and infiltration. Obtaining direct measurements of evaporation from a TSF is problematic, and the general practice is to employ a pan evaporation station and make assumptions regarding calibration coefficients for beach, wet-beach, and pond evaporation using the pan data. Eddy covariance instruments permit direct measurement of actual evaporation rate, but it is more expensive than traditional in-direct methods to measure evaporation. Thus, the focus of this project was to obtain direct measurements of evaporation using eddy covariance instrumentation and analyze the value-proposition associated with the knowledge gained from this effort and determine what is gained from an in-depth data collection campaign targeting actual evaporation rates for a TSF. This paper summarizes our thinking and motivation for this work and, while not yet complete, provides lessons-learned thus far in the process.

1.2 *Sources of uncertainty and the evaporation problem*

It is widely acknowledged that mine water balances are subject to uncertainties, and the practical objective in this process is to eliminate and/or reduce the dominating uncertainties to an achievable level that still supports sound decision making, rather than eliminating all uncertainty; an objective that is not feasible. The most useful water balance models exist in the middle ground between over-monitored (though we are unaware that such a system exists in the industry) and ill-conceived "under-fed" models where too little data drive dubious conceptual representations. In a well-balanced model, variables driving the behavior of the system are measured, where possible, and the others are estimated (i.e., calculated) using appropriate mathematical equations selected to represent the unobserved phenomena that are of interest or are significant drivers of system behavior.

Uncertainties in water balance modeling (as in any other model) derive from structural uncertainty (e.g., have we selected the correct equations to represent the unobservable processes), parameter uncertainty (e.g., how well can we infer parameter values, and are these parameters fixed or random variables?), and measurement error in our observations. Disregarding the first two contributors of uncertainty (done for convenience, rather than validity), even small measurement errors in water balance models can represent very large volumes of water. For example, a 10% error in a bathymetric survey of a TSF reclaim pond represents a volume far larger than a 20% error on operator estimates of flows (i.e., the time when there is not a flow meter on a line, so operating hours of the pump are estimated and a flow rate assumed)—see Figure 1. A 1.5 million m3 pond with 10% error comes out to 150,000 m3 of uncertainty for a given survey—this is potentially larger than all the unmetered flows combined for a month. Similarly, evaporation processes in a large reclaim pond with a large beach can be significant drivers in a water balance model and are a candidate for reduction of uncertainty in process estimates.

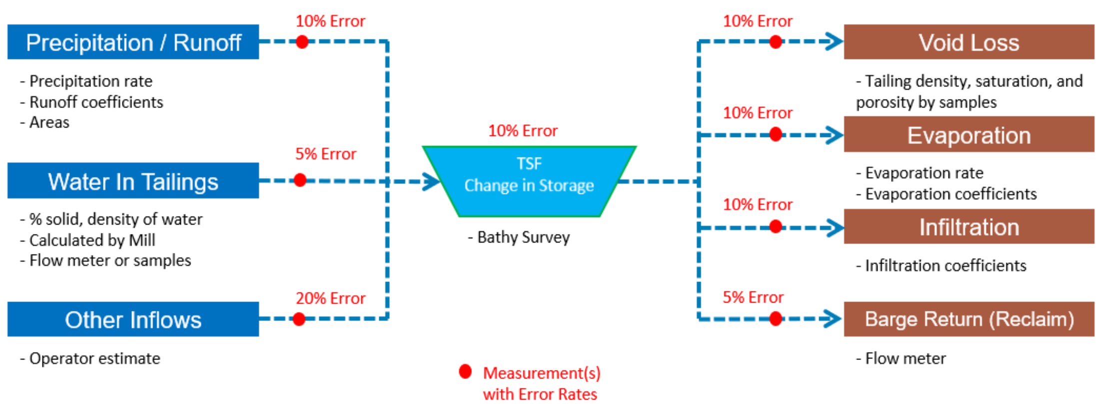

Figure 1. Example TSF Conceptual Water Balance

The reality of calibrating a water balance model requires the engineer to make reasonable assumptions and judgements in order to deal with these uncertainties and not allow the whole exercise to result in an indeterminant system. A notable example of such a situation is the discrimination of deposited tailings void loss (water kept in the tailings voids), evaporation, and infiltration. Each of those water loss mechanisms is generally agreed upon conceptually, not measured directly (at least on a continuous basis like a flow meter on a daily timestep), and have the potential to be major contributors of water consumption/loss to a mining operation. Of the three processes, it is our opinion that evaporation measurement via eddy covariance has the potential to improve estimates of what is actually evaporating on a timestep relevant to a water balance model from a TSF as well as constrain the other two processes (tailings void water and infiltration). Achieving this in a way that can be incorporated into a water balance model has a number of benefits, though the true value added to decision-making is not proven, using pan evaporation rates might be good enough for routine TSF and water management at an operating mine in arid climates.

In what follows, we describe the initial work completed to date at a facility in southern Arizona (the Sierrita Mine) where measurements of actual evaporation rates were collected over a long time period. We discuss the setup of the instrumentation, describe practical considerations to. collecting flux measurements, provide insight on the initial analysis of the data, discuss challenges associated with incorporating these measurements into a water balance model, and generally. describe the next steps in the process that we hope will produce a fair assessment of the knowledge gained and value-add derived from a better understanding of evaporation processes in a TSF.

1.3 *Flux measurement methods*

There are several direct measurement methods to measure fluxes of gases such as H2O, CO2, CH4, including modifications of established techniques and completely new methods (Aubinet et al. 2012, Yamanoi et al. 2012). In addition, there are a number of less direct methods where models are combined with field observations for tuning and verification (Denmead 2008). More information can be found in the literature sources.

In this study, we tested the eddy covariance approach which is one of the most direct and defensible ways to measure fluxes and also allows measurements of sensible heat, latent heat (e.g. evapotranspiration, evaporative water loss, etc.) fluxes integrated over areas of various sizes. As a result, the eddy covariance method has been used in many disciplines, including general research and industry applications, agriculture and environmental monitoring (Baldocchi 2013, Burda 2013). In addition to the eddy covariance method, a Bowen ratio method (Bowen 1926) was also tested as a backup. The Bowen ratio method is a relatively old and well-established technique from the 1920s in which the latent heat flux is computed from a surface energy balance and from a Bowen ratio that is the ratio of sensible and latent heat fluxes. In Rosenberg et al. (1983), the results of the Bowen method heavily rely on soil heat storage data which is difficult to measure correctly over a large footprint area (Rosenberg et al. 1983). Therefore, we mainly focused on the eddy covariance approach in this study, with the main aim of this study to present the usefulness of the eddy covariance method as a direct measurement of actual evaporation rate in a TSF.

2 A CASE STUDY

2.1 *Site overview and climate*

The site where the field campaign was executed is located approximately 40 km south of Tucson in southern Arizona at an elevation of 1068 meters above sea level. The site operates three weather stations around the TSF, including one pan evaporation station at northwest of the TSF. Measurements recorded from the on-site weather station indicate that the annual average precipitation since 2009 is about 305 mm and the annual average pan evaporation rate for the 2009 to 2015 period is 1687 mm. It should be noted that the pan evaporation data includes many anomalous records (zeros, negative values, or excessively high values) caused by instrument malfunctions and poor maintenance. Figure 2 shows the location of the study area, the weather station where pan evaporation is measured and the locations of the eddy covariance tower. Prevailing wind comes from southwest of the TSF as indicated by the wind rose in Figure 3. From an operational perspective, the site operates a typical deposition cycle on north and south of the TSF from a divider berm on the impoundment, both of which have nine sections as shown in Figure 3. There are 12 -14 spigots over a length of about 300 meters on the dam crest and the site gives four to six weeks as a drying period before raising the berm.

2.2 *Eddy covariance tower setting*

Because proper execution of the workflow could pose significant challenges for those new to eddy covariance data collection, we were supported by LI-COR for deciding on instruments and hardware to be used, establishing an appropriate experiment location, and developing a feasible instrument maintenance plan. In addition, the software package from LI-COR provides fully processed and corrected fluxes on site in real time so that we can monitor the tower and download the date remotely. Furthermore, there is a data analysis software that post-processes eddy covariance flux data. By standardizing and automating complex calculations, the analysis is performed correctly and consistently.

We required the typical eddy covariance station to measure actual evaporation rate and added a complement of Biomet instruments on our tower to support the Bowen method as the backup to the eddy covariance. These included instruments to measure air temperature, relative humidity, solar radiation, net radiation, precipitation and soil heat flux. The eddy covariance tower was. located closer to the downwind edge of the site to gain upwind distance, with the system always pointing south to provide sufficient fetch (footprint). Based on the data represented by the wind rose in Figure 3, our setup for the eddy covariance tower was the best setup and acceptable. The additional instruments on the eddy covariance tower required increased power supply, and we installed a double solar panel with four batteries to keep the system running in case solar power was insufficient to keep the system online. We determined that the system could run about two or three days without solar power. Figure 4 shows the initial setting of the eddy covariance tower with the power source.

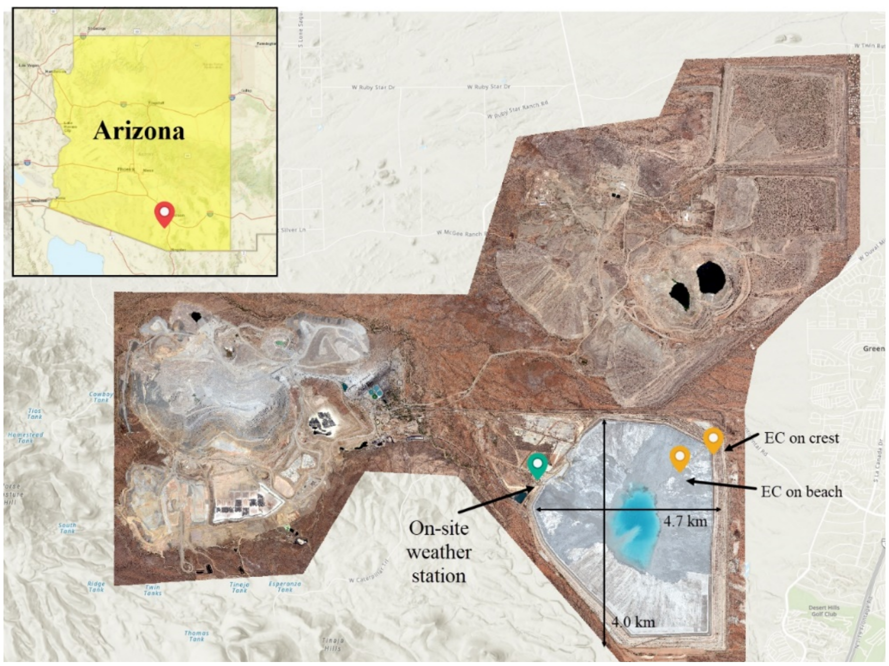

Figure 2. Locations of area of interest (red), one on-site weather station (green), and the eddy covariance tower (yellow).

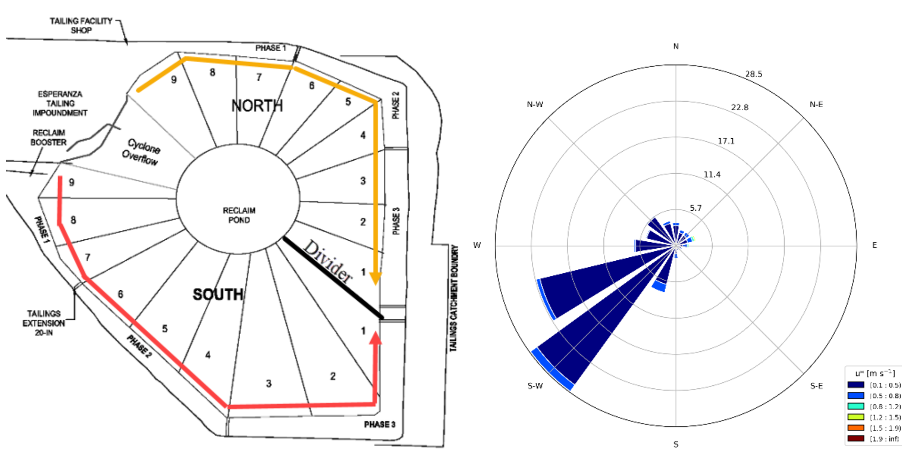

Figure 3. Site deposition sections for North and South (left) and a wind rose (m/s) since Nov 2018 to Jan 2020 (right).

At the beginning of the study, the eddy covariance tower was located on a dry beach area, but the tower was relocated to the dam crest after three months of data collection to avoid the tower being inundated by tailings deposition from the north side of the TSF. The period of record and instrument heights are presented in Table 1. In addition, the approximate locations for before/after moving are shown in Figure 2.

Table 1. Period of record and instrument heights before and after relocation on February/20/2019.

Period of record	Location	Instrument height from the ground
Before: Dec/2018 – Feb/2019	On the beach	4.87 meters (16 feet)
After: Mar/2019 – Jan/2020	On the dam crest	10 meters (33 feet)

Figure 4. Overview of Eddy Covariance system setting.

3 RESULTS

During this experiment, tailings were deposited on the north side of the TSF from N1 to N3 sections one at a time (see the locations in Figure 3), and tailings deposition lasted about 10 days for each section, with no deposition for the next 20 days to give time to dry the beach.

3.1 *Daily evaporation rates*

Both actual evaporation rates measured from the eddy covariance tower and potential evaporation rates measured by pan evaporation from an on-site weather station are presented in Figure 5. We can see that the actual evaporation rates on the TSF have more fluctuations because there was active tailings deposition during the period of measurement. As we described before, pan evaporation provides potential evaporation rates from unlimited water in the pan, and it requires calibration coefficients to estimate the actual evaporation rate. While pan evaporation is valuable information, it does not explicitly represent actual evaporation rates on the TSF, and the discrepancies between actual and pan evaporation rates could play a pivotal role in water balance calculation because of the size of the TSF in this study. In the site water balance, it is observed that evaporation losses are typically greater than either entrainment (void loss) and infiltration. While there are limited management practices that can reduce these losses, obtaining direct information on evaporation will constrain the other unobservable outflow components. It is on this premise that we would like to know whether directly measuring evaporation (in our case via the eddy covariance method) provides value in the form of more representative water balance models.

In Figure 5, the color-coded solid lines are the actual evaporation rates from the eddy covariance tower, and there are gaps in five solid lines from P1 to P5 to inform that the eddy covariance tower stopped working because of power supply issues. The blue solid lines represent the actual evaporation rates while the tower was located on the beach and measured water-limited conditions because there was no tailings deposition during this period. One interesting finding is that the actual evaporation rates from the completely dry condition show similar rates of potential evaporation. On Feb. 20, 2019, the eddy covariance tower was relocated on the dam crest, and the general trend of actual evaporation rates increased as temperatures increased later on. In addition, the site began tailings deposition at the end of March 2019, which is a driving factor that increases actual evaporation rates due to moisture availability from the tailings slurry. In April and May 2019, measured evaporation rates dropped because tailings deposition moved to a different cell during the period. During the summer, we could see large increases in evaporation caused by precipitation as an evaporation source presented in Figure 6.

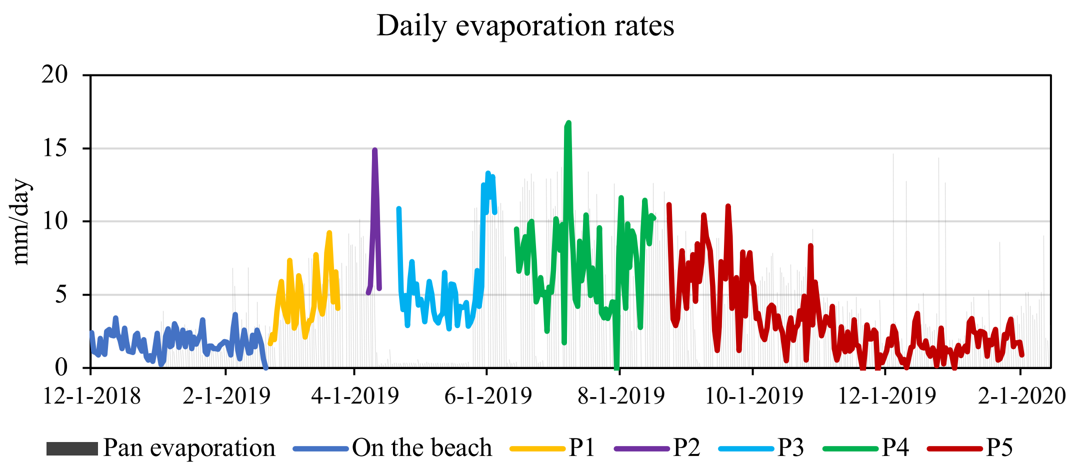

Figure 5. Time series of evaporation rates from both the eddy covariance tower and pan station.

In Figure 6, the eddy covariance tower data from July 2019 to Jan 2020 are presented with precipitation and temperature. During this period, the tower was located on the dam crest—about 3.5 km distance from the on-site weather station. In terms of data quality, the eddy covariance tower stopped reporting data several times because of solar panel power supply issues. Despite these data gaps, actual evaporation rates were observed to increase while tailings deposition occurred upwind of the tower (e.g. a couple of points in July 2019). In addition, a couple of precipitation events in August and September added extra moisture to evaporate, which was captured by the eddy covariance tower. In contrast, rain events during the winter season did not demonstrate large impacts on evaporation increases like in the summer.

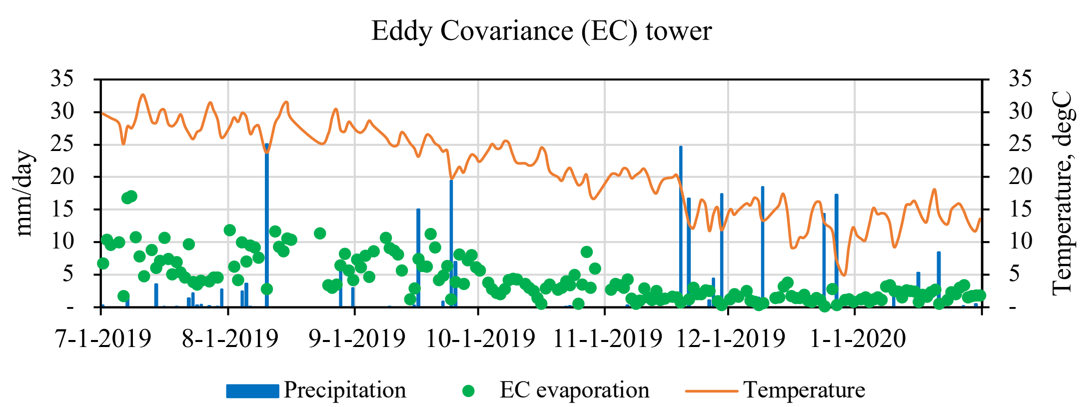

Figure 6. Daily measured data from July 2019 to Jan 2020 at the eddy covariance tower.

Looking more closely in July 2019 with the deposition schedule in Figure 7, there were general patterns in the evaporation rates that correlate with temperature at both locations. According to the deposition schedule and daily actual evaporation rates, we could see rapid change on July 8, 2019 when tailings were deposited upwind of the eddy covariance tower (the tower located near N3 section). These higher evaporation rates went down after a couple of days even though tailings discharge continued in this area. It is difficult to explain this result, but it might be related to the wetting scheme of tailings deposition on the beach. As we can see from the rapid increases on the actual evaporation rate on July 8, 2019, the evaporation from the tailings deposited on a dry surface might concentrate in the area of deposition for a couple of days prior to developing the path for water to travel to the pond, thereby reducing the source of water for evaporation in the immediate area of the spigot.

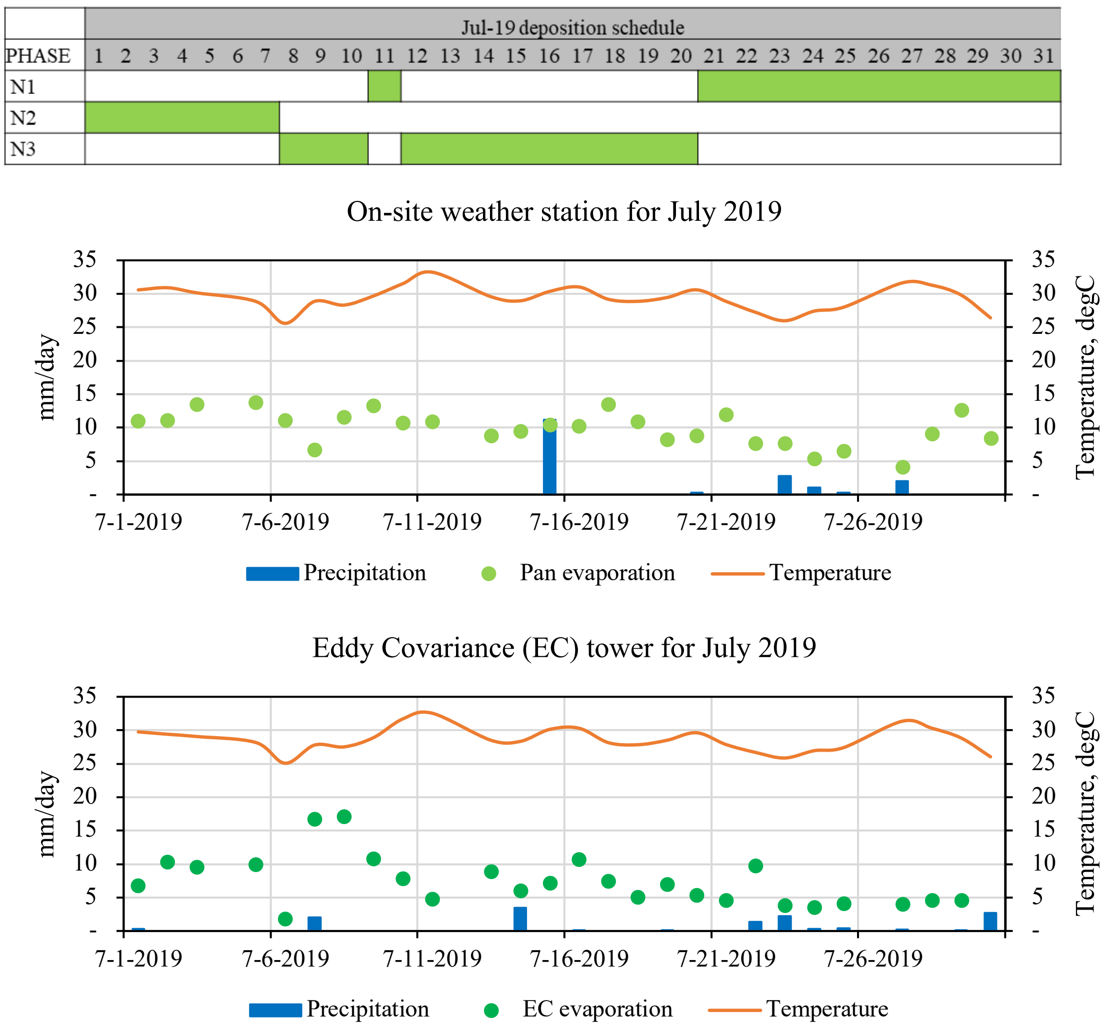

Figure 7. Deposition schedule for July 2019 (top) and data for evaporation, temperature, and precipitation from on-site weather station (middle) and the eddy covariance tower (bottom).

3.2 *Applications of eddy covariance to facility evaporation estimation*

Site operates the deposition cycle as mentioned above and the beach areas around the eddy covariance tower varied between dry to wet conditions commensurate with spigot operations. According to site personnel, deposition lasted about 10 days for one section and no deposition for the next 20 days to let it dry. Considering the deposition cycle, we ran the footprint analysis (Kljun et al. 2015) to explore the spatial behavior of data set. This analysis provides an estimate, in terms of probability, that the eddy covariance evaporation rates came from a particular region. This analysis also provided aggregation of these values for different predefined regions. In Figure 8 (left), we defined three areas as the pond in green, beach in yellow, and embankment in red to see if the eddy covariance tower could capture the evaporation from the pond area. According to the footprint analysis, more than 80% of evaporation rates came from the beach area, and we excluded the portion of evaporation rates from red areas.

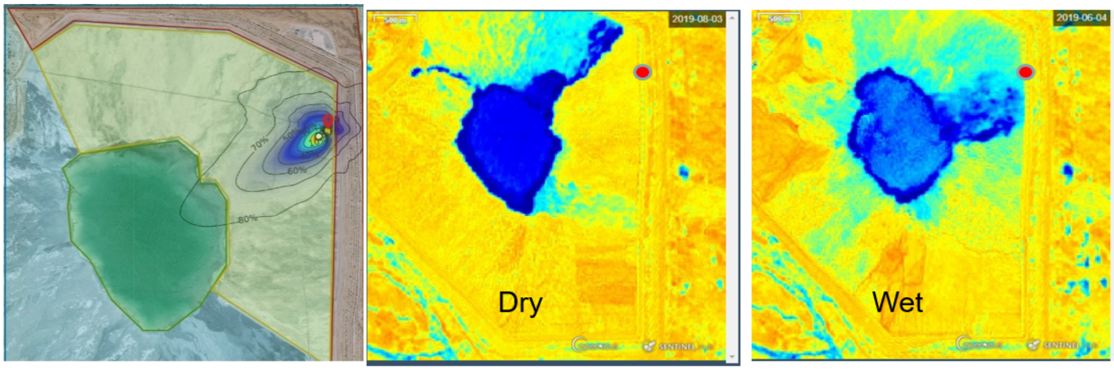

Figure 8. The result of footprint analysis from LI-COR software (left), the Sentinel moisture index as categorized dry beach (middle), and the same index for wet beach (right). The red dots indicate the location of eddy covariance tower.

Using satellite multi-spectral imagery, we retrieved the normalized difference moisture index (NDMI) on the site of interest by using the EO Browser (https://apps.sentinel-hub.com/eo-browser) powered by Sentinel Hub with contributions by ESA (European Space Agency) to discriminate between wet and dry areas. On the middle and right panels of Figure 8, the yellow areas correspond to bare soil that we categorized as dry beach and colors from cyan to dark blue generally correspond to wet beach. Using the moisture index and site-provided deposition schedules, we divided the eddy covariance data into dry and wet conditions and excluded precipitation days to account for only moisture from tailings deposition. As a result, we have 114 days for dry beach and 103 days for wet beach as presented in Table 2.

One objective of the study was to compare the difference between measured evaporation rates of a given footprint with estimates of evaporation based on pan evaporation methods. The intention of this comparison was to explore whether a constant scaling factor existed between actual evaporation of a dry beach (as measured by the eddy covariance instruments) and inferred evaporation rates using a standard coefficient for dry beach and pan evaporation. In addition, we used the AZMET (Arizona Meteorological Network, https://cals.arizona.edu/azmet/) evaporation method for this comparison because of quality issues on pan evaporation rates from the on-site weather station. The AZMET uses a modification of the Penman-Monteith equation (Snyder & Pruitt 1985) with the coefficients based on historical data since 1999 to get an approximate pan evaporation rate from the reference evapotranspiration. Thus, we estimated the reference evapotranspiration using meteorological data from the eddy covariance tower and converted to the pan evaporation with AZMET provided coefficients. This pan evaporation rate derived using the AZMET method is referenced as the Theoretical pan evaporation in Table 2.

Having categorized actual evaporation rates and pan evaporation rates, we compared it to our typical beach coefficients used with pan evaporation (i.e. 0.24 for dry and 0.70 for wet). We found that dry beach evaporation based on pan data was lower than the direct flux measurement. For wet beach, we observed that the pan evaporation method overestimated evaporation relative to the eddy covariance estimate of actual evaporation. The wet period data has a limitation that the actual evaporation from the eddy covariance tower captured the part of a whole cycle of tailings deposition because of the solar panel power supply issues, so the tower measured the first couple of days and missed the rest of period until maintenance could occur on the solar panel. In other words, we could have collected more actual evaporation from tailings deposition, and it will make the wet beach coefficient greater. The potential value of eddy covariance measurements is embodied in this discrepancy.

Table 2. Evaporation rates from 3 methods for dry and wet beach.

Beach category	Total days	Actual evaporation from the eddy covariance, mm	Pan evaporation from on-site, mm	Theoretical pan evaporation, mm
Dry	114	173	450	340
Wet	103	295	640	643

We recognize that there are real trade-offs that must be made in the continuum of collecting enough data to understand something well, versus good enough, versus not good at all. In this study, the site has a dominant wind direction, and due to the size of the TSF, the interpretation of actual evaporation rates needs to take into account the footprint conditions (i.e. the condition of the upwind area). Even if the upwind conditions are known, the relative proportion of the TSF area must be disaggregated into pond, dry beach and wet beach areas because the relationship between measured dry beach evaporation rates to measured wet beach evaporation rates would be needed in an operational water balance model. This problem is the same for pan evaporation-based estimates. Thus, while direct observation of actual evaporation is a sure way to reduce uncertainty of evaporation for a given footprint and time, it introduces other factors and coefficients that require estimation and consideration when applied to an entire TSF water balance model.

4 CONCLUSIONS

This project was initiated to evaluate the usefulness of the eddy covariance methods to provide actual evaporation measurements for an operating TSF—this effort is still on-going, and this paper describes some of the interim results and learnings thus far. Once the eddy covariance system was set up, the instrument requires little maintenance compared to pan station (e.g., no water supply and field visits), but does require maintenance to ensure the power supply. For data availability and analysis, there is a cloud-based platform that displays all data including instruments status and a well-established software package provides the automated and standardized post-data processing calculations, such as the footprint analysis to back-calculate how much evaporation came from defined areas.

With the general conclusion of this study, we also identified a couple of limitations as listed below.

1. With the intention of being able to use the evaporation rates in site water balance models, we discovered that the reality of using the eddy covariance rates at the TSF is not simple. Over a large footprint area, the point measurements are still questionable. Because the study area has rapid tailings depositions over a large impoundment area, the point measurements only have a partial picture of the evaporation regime across the full wet and dry beach areas. The questions raised by this study are
    a. If the upwind area is wet beach and we have good estimates of fluxes from the wet beach, what about the other area of the TSF that comprises dry beach and pond?
    b. How do we scale the wet beach measured evaporation rates down to the dry beach evaporation rates?
2. Readily available satellite imagery can be leveraged to gain snapshots in time that show the dry, wet and pond areas. If we can get concurrent information from satellite imagery to give us the spatial distribution of moisture, we have an opportunity to extrapolate the relative differences in actual evaporation at that moment in time. Furthermore, the continuous measurements from the eddy covariance tower could overcome the discrete nature of satellite imagery and develop time-integrated measures of evaporation for gradually varied spatial conditions (i.e. location of the wet beach caused by rotation of deposition spigots). Overall, further research will be undertaken to explore an opportunity to incorporate satellite imagery and ground measured data for reducing an uncertainty in the evaporation loss and ultimately TSF water balance.

3. The system power was lost for a number of days on separate occasions due to maintenance issues. This issue reminds us that developing a maintenance plan with operations is very important to avoid unnecessary data loss.

While the present study provides the first comprehensive assessment of the eddy covariance methods at one of Freeport-McMoRan facilities, further work is required to define the use case for this method. Our group is continuing to pursue a robust methodology to estimate spatial and temporal actual evaporation rates from the TSF that can be incorporated into a water balance model and ultimately provide improved quantification of water use and future need.

5 REFERENCES

Aubinet, M., Vesala, T., & Papale, D. 2012. *Eddy Covariance: A practical guide to measurement and data analysis*. Dordrecht, Heidelberg, London, New York. Springer, 442 pp.

Baldocchi, D. 2013. A brief history on Eddy Covariance Flux measurements: A personal perspective. *Flux-Letter* 5(2): 1-5.

Bowen, I. 1926. The ratio of heat losses by conduction and by evaporation from any water surface. *Physics Review* 27: 779-787.

Burda, G. 2013. *Eddy Covariance Method for scientific, industrial, agricultural and regulatory applications.* Lincoln, Nebraska: LI-COR Biosciences.

Denmead, O. 2008. Approaches to measuring fluxes of methane and nitrous oxide between landscapes and the atmosphere. *Plant and Soil* 309(1-2): 5 – 24.

Kljun, N., Calanca, P., Rotach, M. W., & Schmid, H. P. 2015. A simple two-dimensional parameterisation for Flux Footprint Prediction (FFP). *Geoscientific Model Development* 8(11): 3695 – 3713. doi:10.5194/gmd-8-3695-2015.

Rosenberg, N., Bald, B., & Verma, S. 1983. *Micro-climate: The Biological Environment*. Wiley-Interscience Publishers: 255-257.

Snyder, R. & Pruitt, W. 1985. Estimating reference evapotranspiration with hourly data. California Irrigation Management Information System Final Report Vol. 1. *Land, Air and Water Resources Paper #10013-A. Univ. of California-Davis. Chpt. VII.*

Yamanoi, K. Hirata, R., Kitamura, K., Maeda, T., Matsuura, S., & editorial board members. 2012. *Practical handbook of tower flux observations*. Sapporo, Japan. Hokkaido Research Center, Forestry and Forest Products Research Institute, 196 pp.

Efemçukuru's mine waste facilities performance under October 2020 Aegean Sea earthquake

Sean Ennis, Ernesto Ruiz & Efrain Rondinel
Stantec Consulting Ltd, Vancouver, British Columbia, Canada

Yavuz Selim Inci, Görkem Uzunçelebi & Halil Ürkmez
Tüprag Metal Madencilik San.Tic.A.Ş, Izmir, Turkey

ABSTRACT: On 30 October 2020, an earthquake of magnitude 7.0 (USGS) originating in the Aegean Sea affected the Turkish western province of Izmir. The epicenter was located at approximately 63 km from the city of Izmir and approximately 50 km from the Efemçukuru gold mine site. Efemçukuru mine waste from the underground mining operation generates tailings and uneconomic mine rock which require surface or underground disposal. A portion of the tailings is stored underground for backfill and the remaining material is stored in a surface waste storage facility. All uneconomic mine rock is stored in a surface storage facility. This paper will present the characteristic of the earthquake, the response of the mine waste structures, and the activation of the emergency response plan. Details of the paper will include a review of the seismic design and associated performance based on visual observations and monitoring instrumentation. A focus will be placed on the existing tailings management system for the site and its implementation pre- and post-earthquake. Emergency response management procedures for dealing with upset conditions and the performance of the structure have also been developed successfully over time through close operator and designer cooperation. The execution of these procedures following the October event are described in this paper.

1 INTRODUCTION

The Samos Island (Aegean Sea) earthquake struck at 13:51/14:51 local time in Greece and Turkey, respectively, on 30th October 2020. It produced wide-ranging effects including tsunami run-up, ground shaking with local zones of high intensity that led to the collapse of structures and 118 fatalities in the two countries. The various geotechnical effects in affected areas included liquefaction, displacement and rockfalls.

1.1 *Site description*

The Efemçukuru Mine is an underground gold mine located approximately 45 km south of the city of Izmir, in western Turkey. The site area is located in a semi-arid, mountainous zone, at altitudes between 550 and 770 m above sea level. General topography in the area is characterized by steep hills and narrow valleys. The average annual precipitation is estimated to be 740 mm spread over distinct wet and dry seasons. Waste from the mining operation includes tailings and uneconomic mine rock. A portion of the tailings is stored underground as backfill material in areas where mining is complete, and the remaining material is stored in a surface waste storage facility. The surface mine waste storage facilities are shown in Figure 1 and include the Central Tailings Storage Facility (C-TSF), the Central Mine Rock Storage Facility (C-MRSF) and the South Tailings Storage Facility (S-TSF). The overall storage design has been integrated such that the placed mine rock piles act to buttress the tailings storage facilities.

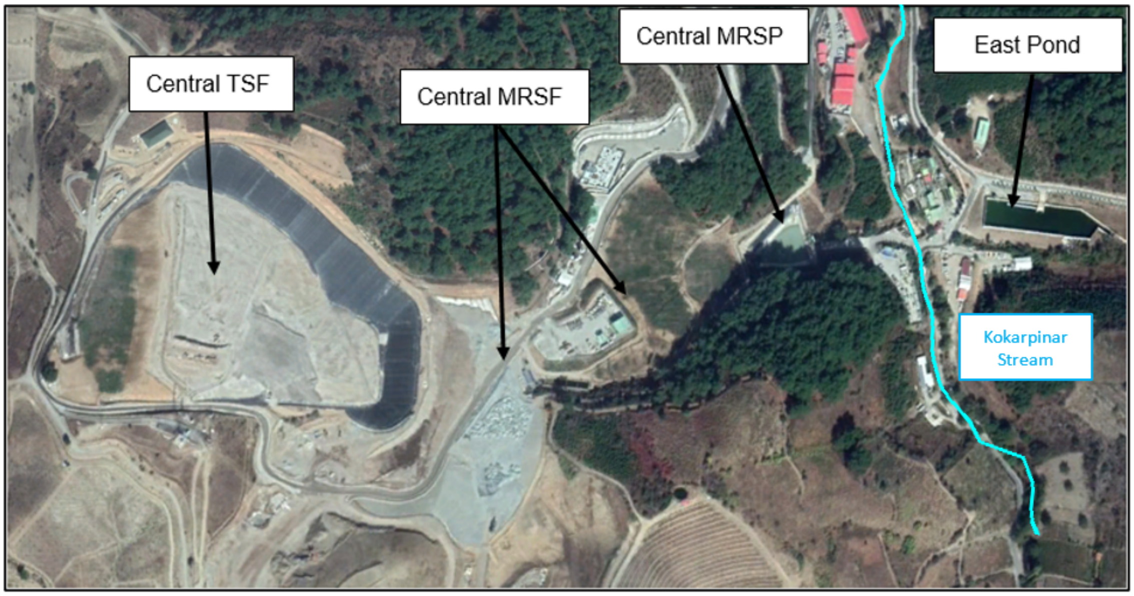

Figure 1. Efemçukuru Surface Waste Storage Facility Layout (November 2020)

The tailings material is dewatered by filtering (approximately 120,000 m^3 per year) at the mine processing plant while the uneconomic mine rock is run-of-mine material hauled to the surface from the underground workings. Both the tailings facility and mine rock storage are designed and constructed to be self-supporting and do not require impoundment structures. Placement and compaction procedures follow stablished technical specifications and Quality Assurance (QA)/Quality Control (QC) practices are executed by the site tailings management team for the placement of tailings and mine rock to meet the site's performance goals. Based on the "Waste Dump and Stockpile Rating and Hazard Classification System (WSRHC-Hawley and Cunning, 2017) and the Canadian Dam Association (CDA) Guidelines for mining dams (CDA, 2014), the TSF and MRSF have been classified as Moderate Risk facilities (Stantec, 2019a and 2019b). This classification is based on a low probability of failure and a high consequence of failure. The high consequence is based on the downstream proximity of the Mine Rock Sedimentation Pond (MRSP), Kokarpinar Stream, and other mine infrastructure.

The TSF and MRSF facilities are placed on low permeability liner systems constructed using different combinations of geosynthetic products and engineered soil fills in order to control seepage from the facilities. The Central and South TSF sites are built with primary and secondary liners (double lined) and a leakage detection system in between. The tailings area double liner system includes geosynthetic clay liner and textured geomembrane. The MRSF sites are built with a single liner system. Contact surface water run-off and seepage flows are collected by a system of ditches and underdrain pipes and discharged in the MRSP before being sent to the water treatment plant. Design storage volumes for the TSF and MRSF are approximately 2.54 Mm^3 of filtered tailings and 1.51 Mm^3 of mine rock, respectively. The site has been in operation since 2011 with portions of the facility already having reclamation cover systems placed (C-MRSF area in Figure 1).

2 SEISMIC TECTONICS

The Aegean Sea region has historically been shaken by moderate to large seismic events with the area experiencing approximately 29 events larger than magnitude (M)6 over the last 100 years within a 250 km radius. The seismotectonic setting around the site is complex, to the south, the Africa plate subducts northwards under the Eurasia plate (Hellenic Trench); towards the east, the Anatolian plate moves westwards driving right lateral faulting in its northern edge. Typically, the seismic events in the region are north-south extensions that are driven by southward migration of the Hellenic Trench. In more recent years, the region was shaken by a M 7.7 earthquake in 1956, which is considered the largest seismic event in Greece for the 20th century (Cetin et al.2020)

2.1 *The October 30, 2020 Aegean Sea Earthquake*

On October 30, 2020, there was an earthquake event (M 7.0) originated in the Aegean Sea, off-shore of Samos Island, Greece. The event was caused due to normal faulting north of Samos Island at shallow crustal depth in the Eurasia plate, and based on the focal mechanism solution, the event happened on a moderately dipping normal fault striking either eastwards or westward, which supports north-south oriented extension. The magnitude slightly exceeds the maximum magnitude estimated for this fault, and historical archives do not indicate an event of this magnitude on this fault in the last 19 centuries (Cetin et al. 2020).

Local strong ground motion stations, 11 in Greece and 66 in Turkey, were able to record the event, within 200 km from the fault rupture. Also, over 200 accelerometers, up to 600 km from the rupture, recorded the event. It was noted that two of the instruments were about 10 km from the rupture plane. These provided the strongest recordings (peak ground acceleration of about 0.23g, and peak ground velocity of about 22 cm/s).

Using on-line tools developed by the United States Geological Society (USGS), contours of peak ground acceleration (PGA) and contours of spectral acceleration at 1 second (Sa-1s) have been developed as shown in Figure 2 and Figure 3.

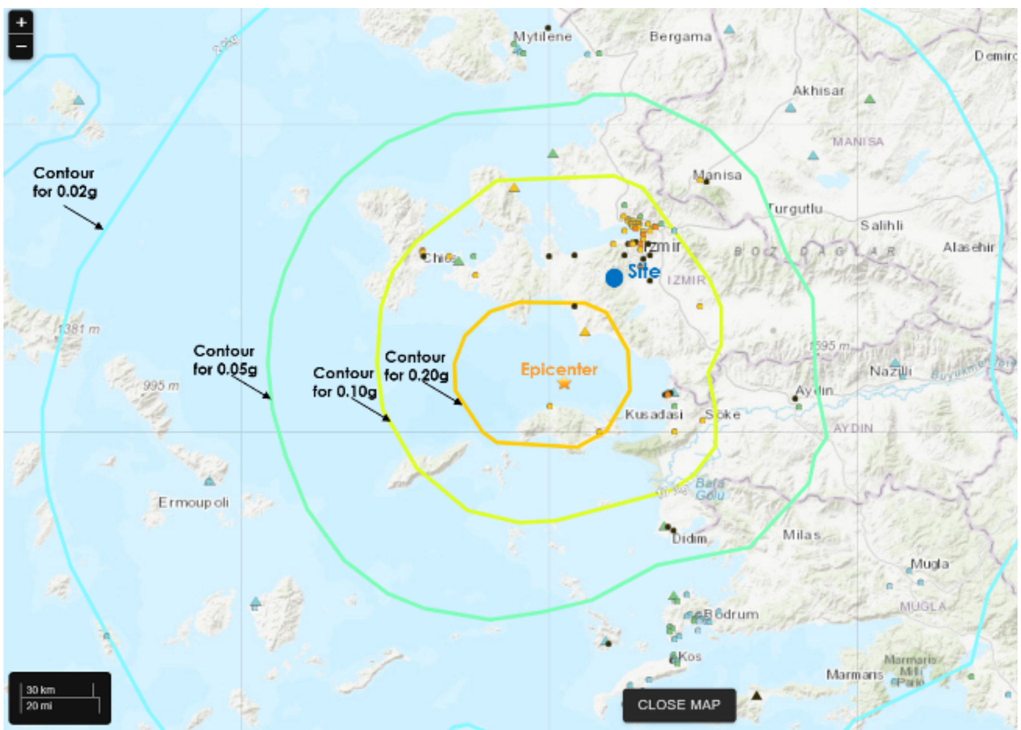

Figure 2 – Earthquake location, and contours of Peak Ground Accelerations. Figures modified from USGS website.

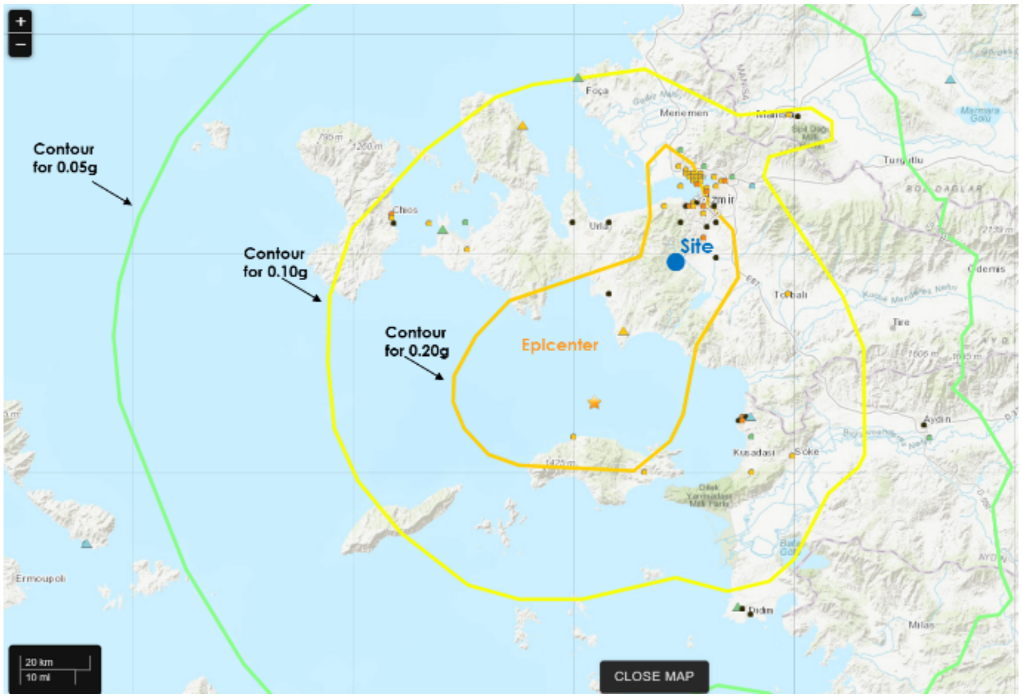

Figure 3 – Earthquake location and contours of Spectral Acceleration at 1 second. Figures modified from USGS website.

Although there was not an accelerometer at the site during the October event, based on these projections, it is estimated that the PGA at the Efemcukuru site was between 0.1g and 0.2g, and the Sa-1s was higher than 0.2g.

2.2 *Efemçukuru's TSF and MRSF Key Seismic Design Features*

In 2016 Stantec (formerly Norwest Corp.) developed the following TSF and MRSF design basis criteria for seismic considerations based on a magnitude earthquake of 7.2 (Tables 1 and 2). Given the potential severity of the area's seismic events, design criteria incorporated an allowable displacement value of ≤20cm for potential slip surfaces intercepting the liner area and ≤ 50cm for slip surfaces that do not intercept the basal liner systems.

Table 1. TSF and MRSF Seismic Design Criteria (Norwest 2014 and 2015)

Return Period	PGA	Sa (02s)	Sa (1.0s)	Design Basis
1-in-475	0.485	1.215	0.485	Operational
1-in-2475	0.972	2.43	0.97	Closure

Table 2. TSF and MRSF Stability Design Criteria (Norwest 2016)

Assessment	Loading Condition	Target Design Criteria
Static	During or at end of construction	Factor of Safety ≥ 1.3
	Long term	Factor of Safety ≥ 1.5
Seismic	Pseudo-static	Factor of Safety ≥ 1.0 Tolerable Displacement ≤ 20cm (lined area) Tolerable Displacement ≤ 50cm (unlined area)
	Post-earthquake (operations)	Factor of Safety ≥ 1.2

The TSF and MRSF structures have an operations, maintenance and surveillance (OMS) manual developed to follow Turkish regulatory requirements (El Dorado 2017), and Mining

Association of Canada (MAC) guidelines. Surveillance measures for the structures related to post-seismic event performance include surface prism stations, vibrating wire piezometers and standpipe wells, seepage flow monitoring and comprehensive visual inspections. Slope inclinometers have not been incorporated into the monitoring system due to concerns over liner integrity (Stantec 2019c). Discussion of the post-event monitoring is included in subsequent sections.

3 EARTHQUAKE RESPONSE AND SITE PERFORMANCE

3.1 *Emergency Preparedness and Response Plan*

The Mine Waste Emergency Response Plan (ERP) at the Efemcukuru mine details a set of procedures to guide and assist Tüprag staff in responding to a geotechnical instability hazardous condition, or a potential or imminent geotechnical emergency condition that may occur at the Central or South Valley TSF and MRSF structures. The ERP document is intended to supplement Tüprag's current management systems such as the OMS Manual and be integrated with the site-wide Emergency and Crisis Management Plan (ECMP).

The Mine Waste ERP document provides the following:

- A plan for responding to unexpected geotechnical-related emergencies at the TSF and MRSF, including procedures to activate the ERP and actions to be taken.
- Responses for different hypothetical hazards that may affect the TSF/MRSF.
- Applicable maps and tables showing the potential failure areas, along with potentially affected areas and infrastructure.
- Listing of required resources to respond to an emergency.
- Listing of roles and responsibilities, and contact information for relevant personnel.
- The overall command structure and internal notification protocol in the event of an emergency.
- Procedures and frequencies for testing the ERP; and
- Procedures for administration and updating of the ERP document.

The ERP document follows the recommendations from the MAC document titled, "A Guide to the Management of Tailings Facilities", Version 3.1.

3.1.1 *Earthquakes*

Earthquakes can impact the physical stability of the TSF and/or MRSF slopes. The Efemçukuru TSF and MRSF have incorporated seismic considerations into the designs, however, damage may depend on the magnitude of the event, distances from the earthquake source, and characteristics of the ground motion. Summary of the adopted earthquake events requiring ERP management or immediate post-event inspection are provided in Tables 3.

Table 3. Summary of Earthquake Events Requiring ERP Management or Immediate Post-Event Inspection

Richter Earthquake Magnitude	Distance to the Structure (Km), From ICOLD, 1998
> 4.0	≤ 25 km
> 5.0	≤ 50 km
> 6.0	≤ 80 km
> 7.0	≤ 125 km
> 8.0	≤ 200 km

3.2 *Earthquake Response*

Immediately following the earthquake event, the site wide ECMP was activated due to the potential for a seismic event to adversely affect a number of structures at the mine including surface and underground infrastructure in addition to the mine waste storage facilities. Procedures laid out in the Mine Waste ERP were activated including immediate inspections of the facilities followed by reading of monitoring instrumentation (See Figure 4). Visual inspections, monitoring results and review of the seepage detection system showed no observable adverse effects on the TSF and MRSF structures.

In conformance with the ERP and OMS procedures, after the earthquake event, the following chain of communication took place between Tüprag and Stantec Engineer of Record (EOR):

– On October 30, 2020 Tuprag informed Stantec of the earthquake event and that no visual damage had been observed and all personnel were safe.
– On November 3, 2020 Tuprag sent Stantec post-earthquake data for processing and review from the following monitoring locations:
  - Observation water wells (Standpipes): C-TSF-GB-01, C-TSF-GB-02, C-TSF-GB-03, C-MRSF-GB-01, C-MRSF-GB-02, C-MRSF-GB-03, C-MRSF-GB-04, C-MRSF-GB-05.
  - Membrane leak detention collection system.
  - Vibrating wire piezometers: VWP-01 and VWP-02 Piezometer located within the base of the main TSF deposit (C-TSF).

Upon initial data review, Stantec did not find any evidence of adverse effects on the facilities caused by the earthquake event. On November 5th, Stantec sent an email to Tuprag supporting the measures taken and emphasizing the importance of following the pertinent components of the OMS manual and ERP.

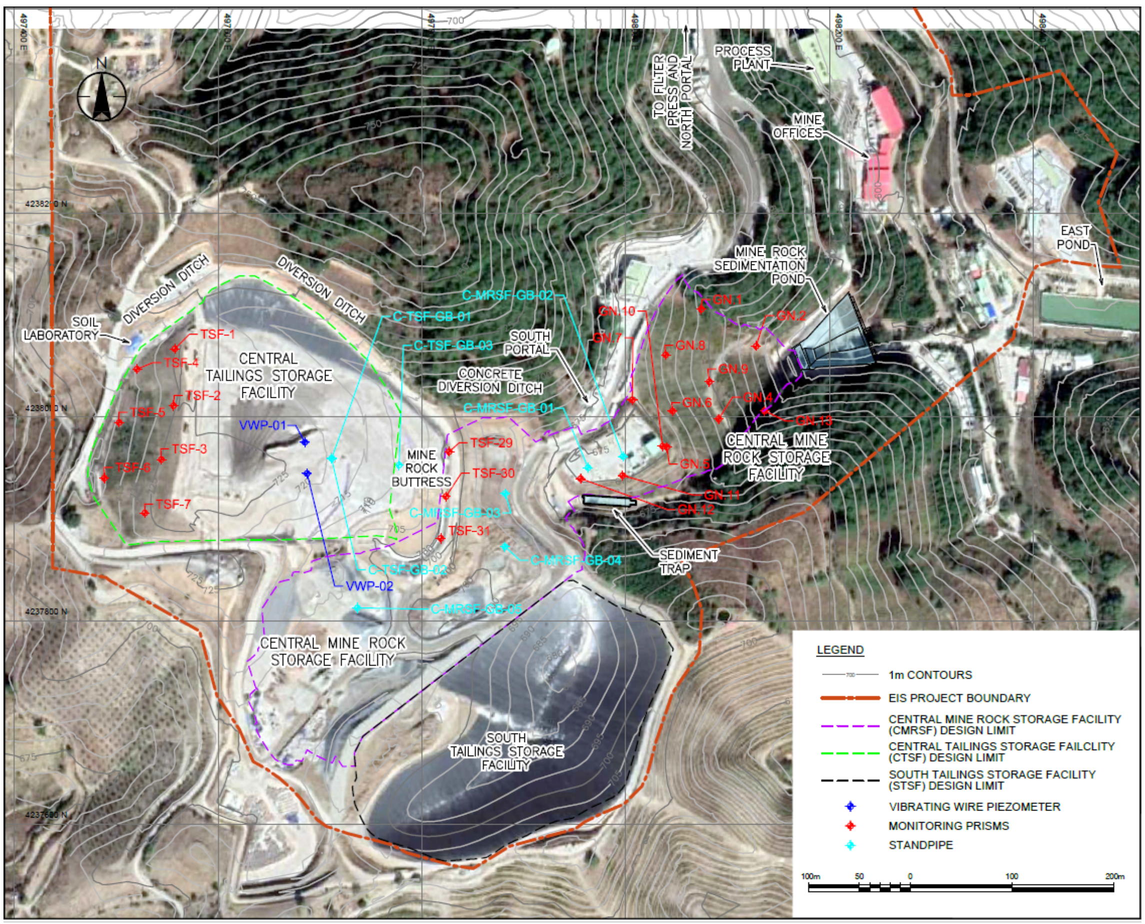

Figure 4. Efemçukuru site mine waste facilities instrumentation location

Tüprag sent Stantec an earthquake event report for review on November 20th, as well as additional site information including:

– October 20, 2020 earthquake technical reports from AFAD and Boğaziçi University Kandilli Observatory Earthquake Research Institute

– C-TSF and C-MRSF deformation observations (survey prisms)
– Continued observation of the leak detection collection system

Review of the follow-up information (Stantec 2020a, 2020b and 2020c) provided greater detail on the scale of the seismic event. The prism data showed no deformations outside of normal ranges and no change in leakage rates or turbidity were observed.

3.3 *Site's performance*

Following the above-mentioned measures, Tuprag's tailings management team produced an earthquake report that summarized the visual inspection findings and a preliminary review of the facilities' instrumentation monitoring data as presented in Table 4 below.

Table 4. Tuprag's Post-earthquake Inspection Summary

Location / Structure	Controls	Inspection	Result
Tailings Storage Facility			
Slope	Crack, settlement, bulging	Visual inspection: no damage detected.	Pass
	Deformation	Deformation Observation	Pass
Membrane Surfaces	Damage	Visual inspection: no damage detected.	Pass
Piezometer Readout	Piezometer Level	Piezometer Readout	Pass
Vertical Water Level Monitoring Pipe	Water Level	Instrumental Measurement	Pass
Drainage Pipes	Seepage Flow	Visual inspection: no damage detected.	Pass
Mine Rock Storage Facility			
Slope	Crack, settlement, bulging	Visual inspection: no damage detected.	Pass
Membrane Surfaces	Damage	Visual inspection: no damage detected.	Pass
Vertical Water Level Monitoring Pipe	Water Level	Instrumental Measurement	Pass
Rehabilitation Areas			
Slope	Deformation	Deformation Observation	Pass
Reinforced Concrete Water Structures			
TSF Sedimentation Pond	Structural Failure	Visual inspection: no damage detected.	Pass
Mine Rock Sed. Pond (WRSP)	Structural Failure	Visual inspection: no damage detected.	Pass
East Pond	Structural Failure	Visual inspection: no damage detected.	Pass
Diversion Ditches	Structural Failure	Visual inspection: no damage detected.	Pass
Other Ditches & structure	Structural Failure	Visual inspection: no damage detected.	Pass
Haul Roads	Crack, settlement	Visual inspection: no damage detected.	Pass
North Portal Temporary Mine Rock Dump Area	Crack, settlement	Visual inspection: no damage detected.	Pass

Specific concerns following the seismic event were related to the potential for slope instability and internal deformation leading to liner damage. Visual inspections, deformation measurements from the prisms and monitoring of the leakage system indicated that slope instability and liner damage did not appear to be issues. Although compaction is closely controlled during construction, the potential generation of excess pore pressures due to localized liquefaction in basal zones of the tailings was also an area of interest. Vibrating wire piezometers installed near the liner in the Central Valley TSF did not show any sharp increases in pore pressures that could be associated with localized liquefaction (see Figures 5 and 6). This supports the effectiveness of the site's construction and QA/QC practices.

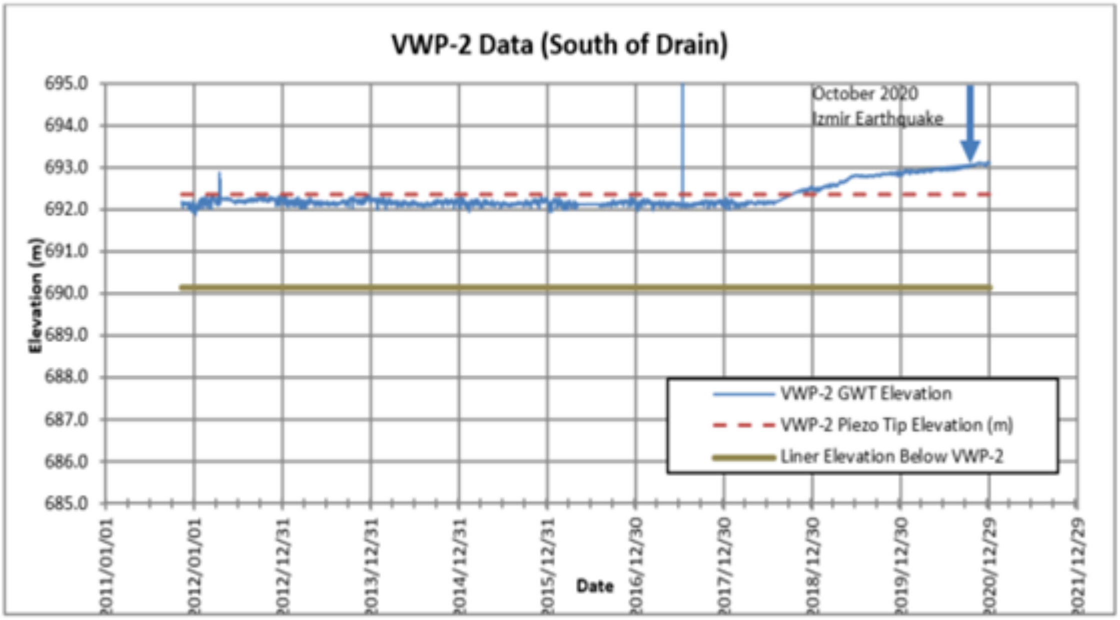

Figure 5. VWP-1 data history including October 2020

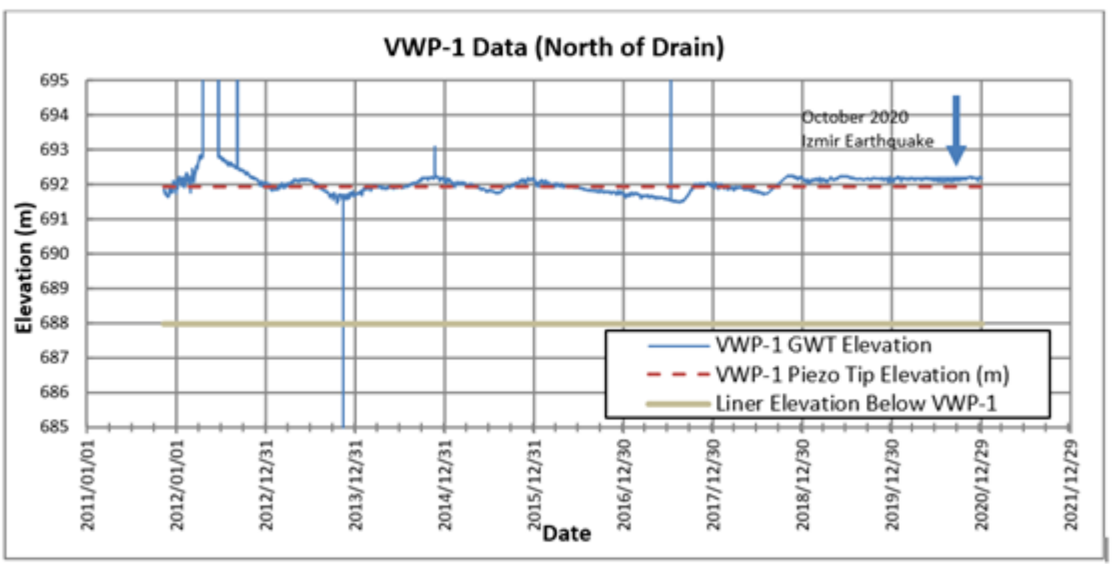

Figure 6. VWP-2 data history including October 2020

4 CONCLUSIONS

The October 20th earthquake was a significant regional seismic event that resulted in flooding, structural damage and fatalities in the Izmir region. Although the event was of significant magnitude (M 7.0), estimates for the seismic acceleration experienced for the Efemcukuru mine site calculated a PGA in the range of 0.2. This is much lower than the operational design event criteria with a PGA equaling 0.485. The performance of the TSF and MRSF structures showed that no adverse effects due to the seismic event were observed either by visual inspection or monitoring instrumentation. This performance validates the design, construction and monitoring practices at the site.

While the magnitude of the seismic event was below the critical design event, the response by the site team demonstrated the value of a robust emergency response plan and the effectiveness of the tailings management team's procedures. The notification of responsible personnel, rapid post-event inspections and monitoring, and communication with the engineer of record were all completed in conformance with the site's overall ECMP. The experience at the Efemcukuru site shows the guidance provided by the MAC standards in developing a tailings management plan and the efforts of a dedicated team are rewarded when disruptive events occur.

5 REFERENCES

Canadian Dam Association (CDA), 2014. Technical Bulletin: Application of Dam Safety Guidelines to Mining Dams.

Cetin, K.O., Mylonakis, G., Sextos, A., Stewart, J., 2020. Seismological and engineering effects of the M 7.0 Samos Island (Aegean Sea) Earthquake. HAEE (Greece), EEA & EF (Turkey), EERI (USA), GEER-069. Dec. 31, 2020.

Eldorado Gold Corporation, 2017. Eldorado Gold Corporation Environmental Policy. October 2017

Hawley, P.M. and Cunning, J., 2017. Guidelines for Mine Waste Dump and Stockpile Design. 2017

Mining Association of Canada (MAC), 2019. Tailings Management Protocol.2019

Norwest Corporation, 2018. Review of Efemçukuru's Gold Mine's Tailings Management System and with MAC's Tailings Management Guidelines. January22, 2018

Norwest Corporation, 2015. Efemçukuru Mine: 2015 Central Valley Tailings Storage Facility Site Investigation and Liquefaction Assessment – Rev 0. December 18, 2015

Norwest Corporation, 2014. 2013 CPT & Drilling Investigation – Summary and Evaluation Rev. 0. May 8, 2014

Developing an Operation, Maintenance, and Surveillance Manual for Tailings and Water Management Facilities, Mining Association of Canada (Second Edition). February 2019.

Stantec Consulting International Ltd., 2019a. Central TSF Classification and Risk Assessment Rev. 1. PowerPoint Presentation. December 2019

Stantec Consulting International Ltd., 2019b. Central MRSF Risk Assessment Rev. 0. PowerPoint presentation. October 2019

Stantec Consulting International Ltd., 2019c. Efemçukuru Central TSF 2019 Site Investigation and Instrumentation Plan – Rev. 0. December 2019

Stantec Consulting International Ltd., 2020a. Assessment of Effectiveness of the Mine's Tailings Management System 2019 Memorandum. February 2020

Stantec Consulting International Ltd., 2020b. July 2020 Preliminary MRSF Capacity Optimization Analysis. PPT document. July 10, 2020

Stantec Consulting International Ltd., 2020c. October 2020 Earthquake Event-EOR Report. December 23, 2020

Tüprag Metal Madencilik, 2014. Crisis & Emergency Management Plan. Document No EFM-5000-Pln-001T. April 2014

Seismic response of Kennecott tailings embankment to the M 5.7 magna earthquake

Masood H. Kafash, Alfonso Cerna-Diaz, JJ Cleason, Richard Davidson, Lisa Yenne
AECOM, Denver, Colorado, USA

Erick Franco
RioTinto, Magna, Utah, USA

ABSTRACT: On March 18, 2020, 7:09AM MDT, a M5.7 earthquake occurred in Magna, Utah, approximately 4 miles east of the existing Tailings Storage Facility (TSF) operated by Rio Tinto Kennecott (RTK) and at a depth of 6.6 miles. Following the earthquake, comprehensive site assessment and analysis were performed to understand the seismic response of the embankment to the mainshock from the Magna earthquake. The assessment consisted of reviewing the physical response after the event occurred and evaluating the implications on design and monitoring. This assessment included reviewing the recorded characteristics of motion and various instrumentation results, including piezometers, InSar data and inclinometers. Advanced numerical analyses were performed with PM4Sand and PM4Silt constitutive models to evaluate and estimate the pore pressure generation in the tailings and foundation, surface movements and deformation response of the tailings embankment and its foundation to the earthquake. The results compared very favorably with the observed behavior. This case history adds valuable precedent to the scarce data base of numerical simulations of actual earthquakes.

1 INTRODUCTION

Kennecott's Tailings Storage Facility (TSF) is located approximately 10 miles west of Salt Lake City, Utah, near the town of Magna. The TSF consists of two adjoining impoundments, the South Impoundment, which has been inactive since 2002, and the currently active North Impoundment. These impoundments cover a combined area of approximately 9,200 acres. The South Impoundment is an upstream facility and the North Impoundment is a centerline facility with the embankment constructed from hydraulically placed and compacted underflow sands.

Photograph 1: Overall View of Kennecott Tailings Impoundment (Google Earth, 2018)

Based on the University of Utah Seismograph Stations (UUSS), 1631 earthquakes were recorded in the Magna, Utah, area from March 18 through April 24, 2020. The largest of these earthquakes was the moment magnitude (M) 5.7 mainshock that occurred at 7:09 am MDT on Wednesday, March 18. The M 5.7 earthquake was measured at a depth of 10.7 km and located in an area of existing faults that have been previously active (Wong and Wu, 2020).

After the earthquake event, and once it was deemed safe to visit the TSF, a group of professionals inspected the tailings storage facility to document disturbances. Along with field inspection, the piezometer data was reviewed and used in the evaluation of the stability of the embankment recognizing the elevated pore pressures. The AECOM team began evaluating the effects of the event on the existing tailings facility, including the Southeast Corner (SE Corner), along the East Slope, and along the North embankment, by reducing the field measurements such as piezometer readings, inclinometer data, surface monitoring, InSAR data, and performing slope stability analyses. Slope stability analyses were completed along 17 sections using effective stress loading conditions considering earthquake induced excess pore pressures to assess the risk of loading from subsequent aftershocks.

A deep-dive geotechnical analyses were performed to take a closer look at the data accumulated from the initial earthquake and the following aftershocks, and to evaluate the impact to the North and South embankment slopes and impoundments. This evaluation included: a) instrumentation evaluation for piezometer, inclinometer, and InSAR data; b) Seismological investigation of contributing faults, aftershocks and characteristics of recorded motions; c) additional field and laboratory testing of the area of observed liquefaction on North Impoundment and Historic South Impoundment Decant Pond Clay area in the South Impoundment; and d) two dimensional numerical analyses to calibrate and validate analyses for use in design.

2 AFTER EVENT RESPONSE

The earthquake occurred at 7:09 AM MDT and the impoundment was immediately evacuated and incident command established. The AECOM Engineer of Record was contacted immediately following the earthquake. The earthquake alarm system functioned as anticipated and State Road 201 (SR201), which is located to the south of the TSF was closed.

After it was deemed safe, initial inspections began on the morning of March 18; however, shortly after, personnel were again required to evacuate the TSF because of potential migration of a nearby chemical gas cloud. This evacuation order would remain in place until later in the afternoon of March 18. Evacuated personnel rendezvoused at a command post at the nearby Saltair facility, which is north and west of the TSF. Because the TSF was included in the gas cloud evacuation zone, the majority of the remaining daylight hours were spent performing remote inspections by observing drone footage of potential areas of concern. Drone footage captured on March 18 included the South Impoundment Southeast Corner, East Slope, and East Abutment areas. Cracking in the Southeast Corner area was not observed during initial review of the drone footage. Drone footage taken near the East Abutment did capture some cracking and movement in the East Abutment area.

RTK has a substantial amount of geotechnical instrumentation throughout the TSF, which includes vibrating wire piezometers (>450) throughout the north and south impoundment areas, in-place inclinometers at the east abutment area, and a shape array at the Southeast Corner. These instruments are connected to dataloggers and a network of local and global telemetry stations which transmit the geotechnical data readings at regular time intervals to a centralized server at the Admin building. Although convenient, the network design turned out to not be robust. If the server fails at the Admin building or if a data transmitting station does not work (e.g. power outage), automatic or remote data acquisition becomes impossible.

Immediately following the earthquake, the server at the Admin building went down, making remote data acquisition infeasible. In the evening on March 18, when personnel were allowed to enter the Admin building, piezometer data acquisition was further complicated because the main network telemetry stations located on the TSF could not transmit the piezometer data due to power outages in the West Cyclone area. Data acquisition on the evening of March 18 had to be performed by manually connecting to the datalogger station which is physically connected to the piezometer cables. This manual method of collecting the data was both time consuming and cumbersome during a critical phase in the post-earthquake response. Although some initial manual readings from some piezometers were obtained during the early morning site inspections, piezometer data was largely unavailable until late in the evening. During manual collection of the data, the Southeast Corner and East Slope areas of the TSF were visually inspected for cracking and deformations. Although some small cracks were observed, there were no indications of continuing movement or compromised stability of the slopes. Personnel collecting data on TSF left the facility at approximately 10:00PM that night.

In addition to the difficulties in obtaining the data, there were some concerns about the frequency at which piezometer data is collected from each data logger. Prior to the earthquake, piezometer readings were collected every 3 to 6 hours, depending on the datalogger. The last piezometer reading that was recorded prior to the earthquake happened at 6:00AM. The first post-earthquake readings were recorded at either 9:00AM or 12:00PM. Because pore pressures had some time to dissipate before the first post-earthquake reading and because of the general logarithmic nature of the dissipation of pore pressure, it will be difficult to estimate the peak excess pore pressure that was induced from the earthquake. On March 19, dataloggers were reprogrammed to record piezometer data hourly. Although hourly data acquisition requires more data storage capacity, it allows for a higher resolution of piezometer data, particularly for an earthquake event.

In the evening of March 18, RTK sent initial piezometer data to AECOM for evaluation and analyses. The objective of the data evaluation and analyses were to review the piezometric response to the earthquake and to evaluate the effective stress slope stability under the new interpreted post-earthquake excess pore pressure conditions. Since there were continuing aftershocks, this analysis was used to judge vulnerability to further earthquake induced rises in pore pressures. The evaluations and analyses that AECOM performed on March 18 were primarily focused on the Southeast Corner of the TSF adjacent to Highway SR201, which remained closed.

At 10:45PM on March 18, a WebEx meeting was held between AECOM and RTK where AECOM presented initial earthquake data evaluations. Although preliminary evaluations suggested that the slopes were stable and excess pore pressures were dissipating, it was determined that Highway SR201 should remain closed while pore pressures were being closely monitored through the night on an hourly basis and into the morning while additional slope stability analyses were being performed. In addition, Highway SR201 was to remain closed until a complete visual inspection could be performed of the Southeast Corner during the daylight hours.

On March 19, engineering personnel were onsite for additional visual inspections. Visual inspections again focused on potential areas of concern, including the Southeast Corner, East Slope, East Abutment, the historic decant pond area of the South Impoundment, and the North Impoundment barge area. Visual inspections were generally performed in teams of 2 or more individuals. In areas where earthquake-induced cracking was observed, the cracks were noted and marked so that they could be monitored over time. Drone footage was also captured in the area of the South Impoundment historic decant pond and the north slope of the South Impoundment. Survey monuments set up for the Southeast Corner Unweighting project were also surveyed.

After further data evaluation, stability analyses, and a mid-day performance review by RTK and AECOM, SR201 was reopened. Daily calls between RTK and AECOM were scheduled to review post-earthquake TSF performance and discuss any potential problems. The piezometer network connection was reestablished for many of the piezometer data collection stations and RTK began sending AECOM piezometer data twice per day.

Inclinometer data was collected from the dataloggers in the field for INC19-NE-1, INC19-NE-2 located at North Impoundment near to east cyclone station, and SAA19-SE2-E located at Southeast (SE) Corner, and it was sent to AECOM for data reduction.

3 RECORDED CHARACTERISTICS OF MOTIONS

Based on the University of Utah Seismograph Stations (UUSS), 1,631 earthquakes have been recorded in the Magna, Utah, area from March 18 through April 24. The largest of these earthquakes was the moment magnitude (M) 5.7 mainshock that occurred at 7:09 am MDT on Wednesday, March 18. The largest aftershocks were two M 4.6 events that occurred at 8:02 AM and 1:12

PM on Wednesday, March 18. M 4.2 aftershocks occurred on April 14 and 17, which were widely felt along the Wasatch Front.

The March 18, 2020 M 5.7 earthquake that occurred north of the town of Magna, west of Salt Lake City as shown on Figure 1, and at a depth of 10.7 km, appears to have occurred on a west-dipping blind normal fault based on UUSS aftershock locations and the mainshock focal mechanism solution. The 2020 Magna sequence occurred in an area that has been previously active. The events occurred in the same area as a small sequence in March 1978 whose largest event was a Richter local magnitude (ML) 3.2 and within a few kilometers of the 1962 ML 5.2 Magna earthquake (Wong and Wu, 2020).

Horizontal peak ground acceleration (PGA) and spectral acceleration (SA) values were obtained by the USGS office in Golden, Colorado who processed the strong motion records. The vast majority of the processed records are from the Utah Urban Strong Motion Network operated by the UUSS. Data was also obtained from a few seismograph stations operated by the USGS as part of the National Strong Motion Program and from three strong motion instruments operated by Rio Tinto Kennecott. The highest recorded horizontal PGA was recorded at station LKC 4.4 km from the epicenter (shown on Figure 1). One horizontal component recorded a PGA of 0.542 g. The geometric mean (RotD50) PGA was 0.428 g. The closest station to the epicenter was the Kennecott East Cyclone station located on top of the South Impoundment at an epicentral distance of 2.1 km. The recorded geometric mean PGA was 0.218 g. The highest vertical acceleration was recorded at the Kennecott East Cyclone with PGA of 0.31g. Table 1 and Figure 1 provide a comparison between Epicentral distance for these sites.

Table 1. Epicentral Distance

Site	Epicentral distance (km)
Dead Man's Cave (Bedrock)	7.10
East Cyclone K2 1161 (Tailings Impoundment)	2.08
ISSR (Free Field, North)	4.55
LKC (Free Field, South)	4.40

Initial analyses completed by Wong and Wu (2020) has shown that in general, the ground motions compare quite favorably with the NGA West2 ground motion models (GMMs) out to distances of 500 km. Most of the data fall within the plus and minus one sigma (16th and 84th percentile) models. However, the data on soft soil within epicentral distances less than 10 km (hypocentral distances 10 to 20 km), including two Kennecott stations are above the median model predictions at all four spectral accelerations and even above the 84th percentile curves for a few stations. This under-prediction by the models is also slightly apparent for the rock sites. If this pattern were just observed for the soft soil sites one might speculate that the under-prediction by the GMMs for soft soil could be due to either an under-estimation of site amplification at short distances or overestimation of soil nonlinearity. However, the fact that the pattern is observed on rock suggests that this is not a site effect. Whether the under-prediction by the GMMs is due to path effects (e.g., geometrical attenuation) or source effects (e.g., rupture directivity) requires further detailed investigation (Wong and Wu, 2020). Recent understanding of faulting orientation and activity based on geologic and seismologic data together suggests that one explanation could be that the Wasatch fault zone being a listric fault (Kleber et al. 2020).

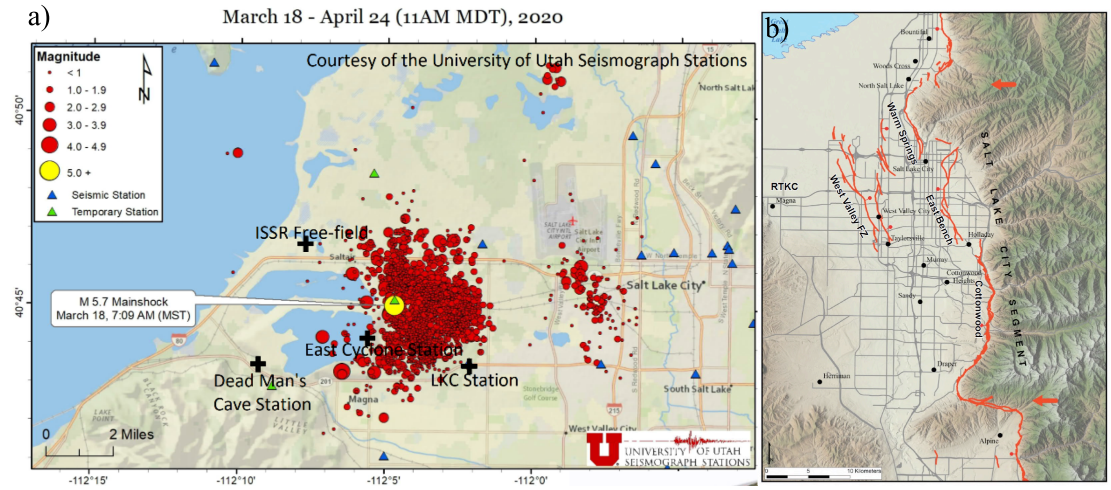

Figure 1. a) March 18 – April 29, 2020 Seismicity near Magna, Utah (after University of Utah Seismograph Stations) annotated with Kennecott stations b) Map of the Salt Lake City segment of the Wasatch fault and the West Valley fault zone (courtesy of the Utah Geological Survey)

4 PIEZOMETER RESPONSE

RTK maintains over 450 vibrating wire piezometers across the North and South Impoundments. Generally, the piezometer readings are collected through an automated data collection system with telemetry on a three to six-hour interval. A pre-earthquake reading was recorded at 6:00AM, approximately 1 hour and 9 minutes prior to the earthquake. In general, the first post-earthquake readings from the dataloggers was recorded at 9AM or 12:00PM, approximately 2 to 5 hours after the event. Readings continued on the 3 or 6-hour schedule until approximately 6:00 PM, approximately 11 hours post-earthquake. RTK then traveled to the telemetry stations to adjust the collection frequency manually due to internet outages. The collection schedule was increased to a 1-hour interval for all instruments. Beginning on the evening of March 18th, piezometer data was sent to AECOM for review twice per day for several weeks until pore pressure returned to normal.

Pore pressures across both the North and South Impoundments responded to the M5.7 earthquake in a similar fashion. An initial spike in direct response to the earthquake was seen followed by immediate dissipation. Dissipation rate, in general, was highest following the earthquake and the piezometer trend flattened over time as pore pressures approached pre-earthquake levels. Figure 2 provides an example of piezometers response at South Impoundment.

A second typical trend was also seen in approximately two percent of piezometers. Immediately following the earthquake, an initial drop in pore pressure was observed followed by a rise in pore pressure. The pore pressure rise was consistent in magnitude with surrounding instruments. The trend began to decrease typically within two weeks after the earthquake. This secondary trend was observed in deep, high clay content areas of the impoundment. A comparison of post-earthquake pore pressures and pre-earthquake pore pressures was performed 23 days following the earthquake. Twenty-three days post-earthquake approximately 68.9% of instruments across the impoundment returned to within 0.50 psi of pre-earthquake values. The largest difference of pre-earthquake to post-earthquake values after 23 days is 4.48 psi. No piezometer showed a response to any of the numerous aftershocks of varying magnitudes.

5 INCLINOMETER RESPONSE

RTK has 3 in-place inclinometer (IPI), as shown on Photograph 1, systems located in the following locations:

- SAA19-SE2-E- Vertical shape array system (Measurand) located on the South Slope of the South Impoundment.
- INC19-NE-1- Addressable in-place inclinometer system (Geokon) located at the east abutment, directly east of the historic decant pond area. Thick uniform deposits of decant pond clay are located within the profile for INC19-NE-1.
- INC19-NE-2- Addressable in-place inclinometer system (Geokon) located at the east abutment area where the North Embankment ties into Impoundment. INC19-NE-2 is located slightly north and east of the historic decant pond area. Thick uniform deposits of decant pond clay are located within the profile of INC19-NE-2.

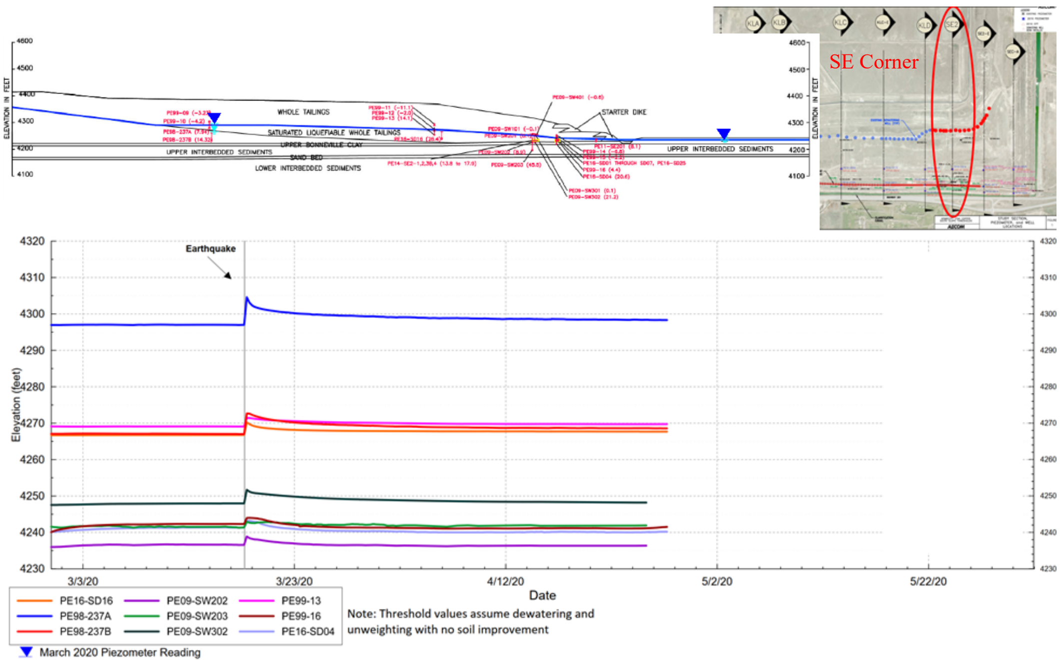

Figure 2. Piezometers response to Magna Earthquake

The 3 IPI systems, shown on Photograph 1, collected displacement data before and after the March 18 earthquake which provide some insight to the earthquake performance of the TSF at the locations of the IPI instruments.

INC19-NE-1 indicates a maximum of approximately 0.7 inches of lateral displacement occurred as a result of the earthquake. This movement appears to have primarily occurred within fine tailings material (Decant Pond Clay). A small amount of lateral deformation appears to have come from saturated whole tailings. Little to no movement has occurred in the underflow sand. The profile of lateral displacement increases in a gradual manner vertically and there are no indications of the development of a shear zone. Because of the direction of the lateral movement (toward the center of the impoundment), most of this movement can likely be attributed to earthquake induced settlement in the area of the inclinometer. There was no further movement after the main shock.

INC19-NE-2 indicates a maximum of approximately 0.6 inches of lateral displacement occurred as a result of the earthquake. This movement appears to have primarily occurred within Decant Pond Clay and saturated whole tailings consistent with the behavior of INC19-NE-1. No indication of the development of a shear zone is observed in the response of the inclinometer.

SAA19-SE2-E as seen in Figure 3 indicates a maximum of approximately 0.4 inches of lateral displacement occurred as a result of the earthquake. This movement appears to have primarily occurred within saturated whole tailings. Minimal movement is observed to have come from the foundation materials and little to no movement occurred in the drier, surficial materials. Some post-earthquake movement can be seen on the inclinometer profile plots as well as the time series plots of Figure 3; however, the rate and direction of the post-earthquake movement is near the rate and in the same direction that inclinometer was moving before the earthquake.

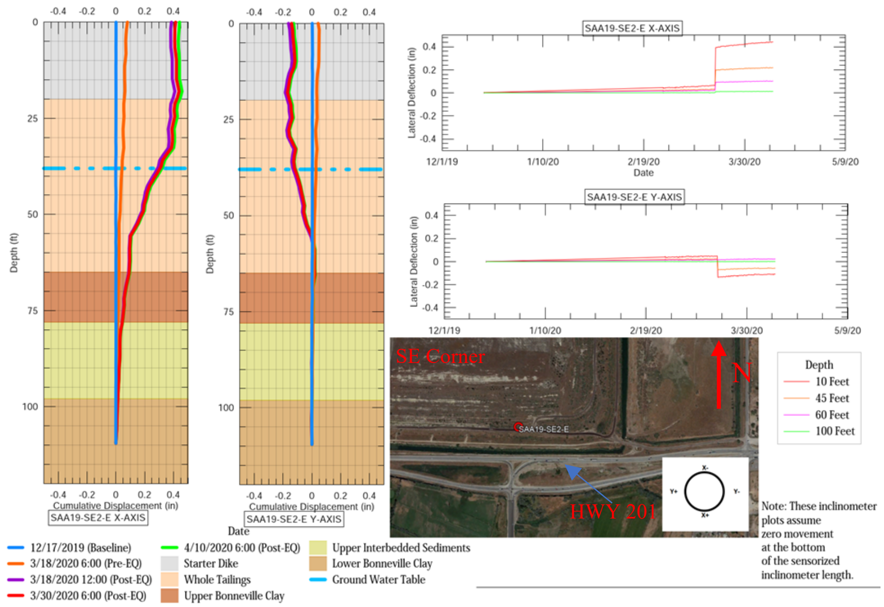

Figure 3. SAA19-SE2-E inclinometer response to Magna Earthquake

6 SURFACE MOVEMENT AND INSAR DATA

InSAR uses satellite remote sensing to estimate ground movements. This is done by comparing data from satellite sensors at two different times and computing an estimated movement from one time to the next. A review of the InSAR report data suggests that minimal ground surface movements were detected in the timeframe leading up to the earthquake. Additional InSAR scans that bracket the time before the earthquake to a few days after the earthquake indicate that earthquake-induced movement occurred. The InSAR satellite scans suggest maximum earthquake-induced movement on the order of 4 inches. The locations of maximum detected movement occurred at the southeastern crest area of the South Impoundment. This is consistent with where the majority of surface cracking was observed during on-site inspections. Movement was also detected in other locations throughout the South Impoundment, but movements were generally less than 1 inch. Movements detected in the North Embankment areas were estimated to be less than 0.5 inches. Subsequent InSAR scans that were performed during bracketed time periods after the earthquake suggest that movement is not progressing within the North or South Impoundments. The reported InSAR movements, unless calibrated to a physical ground surface measurement, should be considered as a qualitative assessment of ground surface displacements.

7 OBSERVED FIELD BEHAVIOR

Cracking was observed on roads and haul roads along the East Slope of the South Impoundment. The cracks were identified on the light vehicle road just below the crest of the East slope and on the haul road on the crest of the east slope. The light vehicle road and haul road both run parallel to the length of the slope. The observed cracks ran parallel to the roads. The cracks were small with a maximum horizontal offset of 0.25 inches. No vertical offset was observed. Three to five parallel groups of cracks were present in each road. The cracks were observed to span the entire length of the east slope. Over time, the offset of the cracks did not increase in the vertical or horizontal direction. A photograph of the cracks is provided in Photograph 2.

Numerous sand boils were observed in the active North Impoundment interior. Sand boils were located predominantly along the North Slope of the South Impoundment. A photograph of the sand boils can be seen in Photograph 3. As shown in this photo the depth of sand boil was identified within 12 inches from the ground surfaces.

Physical evidence of the M5.7 earthquake was observed in various locations around the North and South Impoundments. The North Embankment performed well, and no structural damage was observed. No wide-spread liquefaction was observed apart from the North Impoundment interior (sand boils). Other physical evidence seen on the South Impoundment did not progress over time.

Photograph 2: Crack in East Abutment Extension Access Road, March 18, 2020 3:03 PM

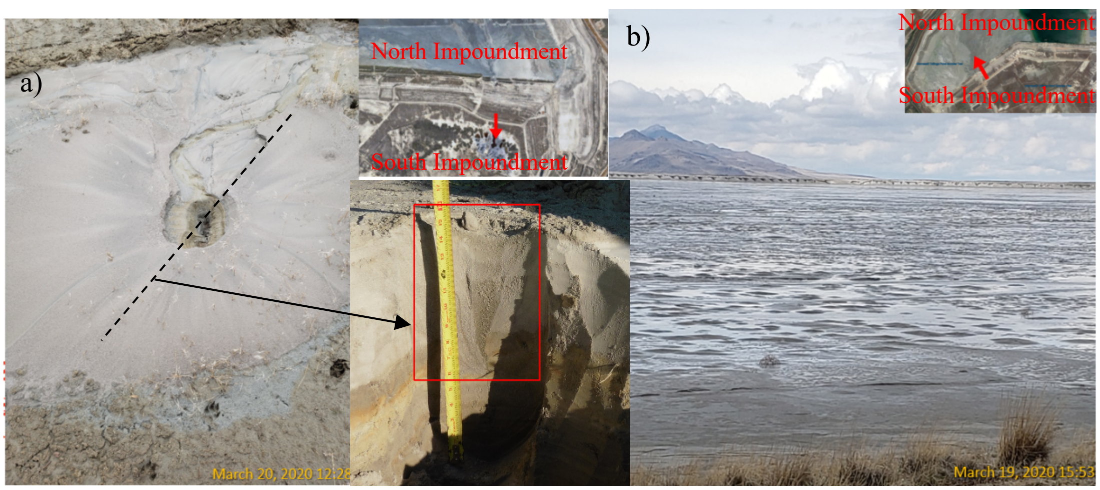

Photograph 3: a) Sand Boil Close-up, March 20, 2020 4:45 PM and b) Sand Boils in North Impoundment Interior, March 19, 2020 3:53 PM

8 NUMERICAL ANALYSIS

Dynamic deformation analyses were performed to simulate the recorded dynamic behavior during the mainshock of the Mw 5.7 Magna earthquake for a section at SE Corner using advanced constitutive modeling techniques. Figure 4 provides the cross section and input mesh of the analyzed section. PM4Silt/Sand model established from the bounding surface plasticity (Boulanger, R. W., and Ziotopoulou, K. 2019) within the FLAC software was used to provide estimates at the SE Corner in terms of:

- Recorded pore water pressure generation and
- Recorded level of deformation during shaking

The recorded motions at the nearest accelerometer to the epicenter, near the East Cyclone station shown on Photograph 1, were deconvoluted and used in analysis. The deconvoluted motion was extracted as an outcrop motion to be used as an input at the base of the 2D FLAC model in conjunction with a compliant base boundary.

The analyses were performed using already developed design parameters prior to the event and no effort on re-calibration of parameters to the observed behavior was performed. The design parameters were obtained using advanced field and laboratory testing results including design curves of cyclic strain accumulation, undrained shear strength and modulus reduction and damping curves. Figure 5 provides an example of calibration process for contractive whole tailings material.

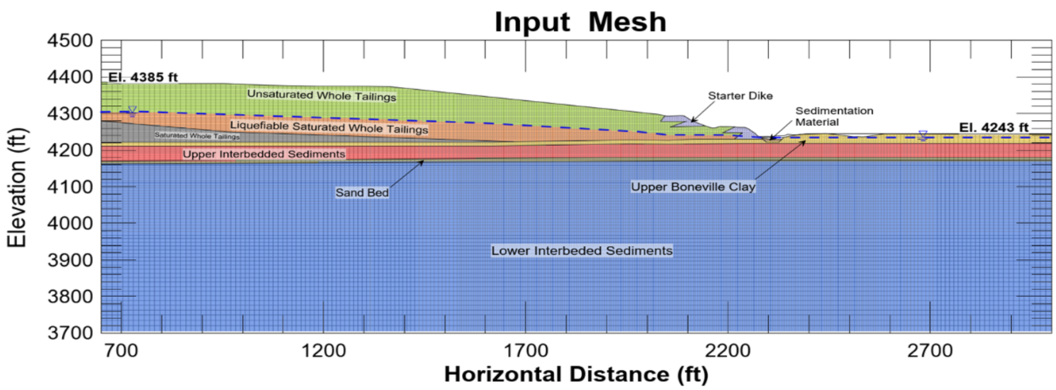

Figure 4. Detailed cross section of SE2 located at SE Corner

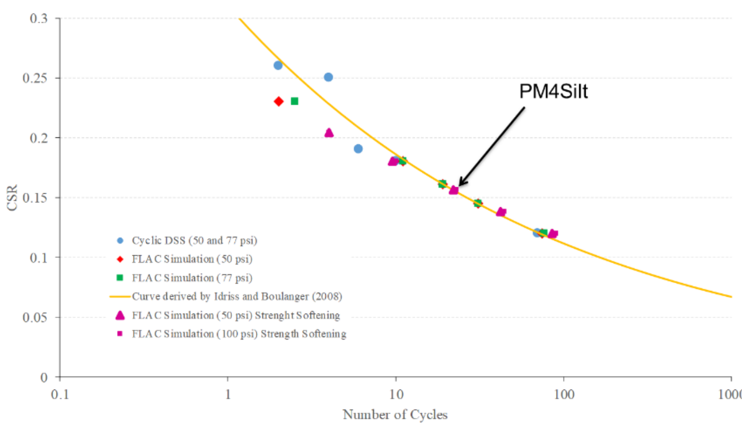

Figure 5. Contractive whole tailings material PM4silt calibration

a) Comparison between cyclic DSS lab testing and PM4silt calibration, Cyclic stress ratio vs number of cycles

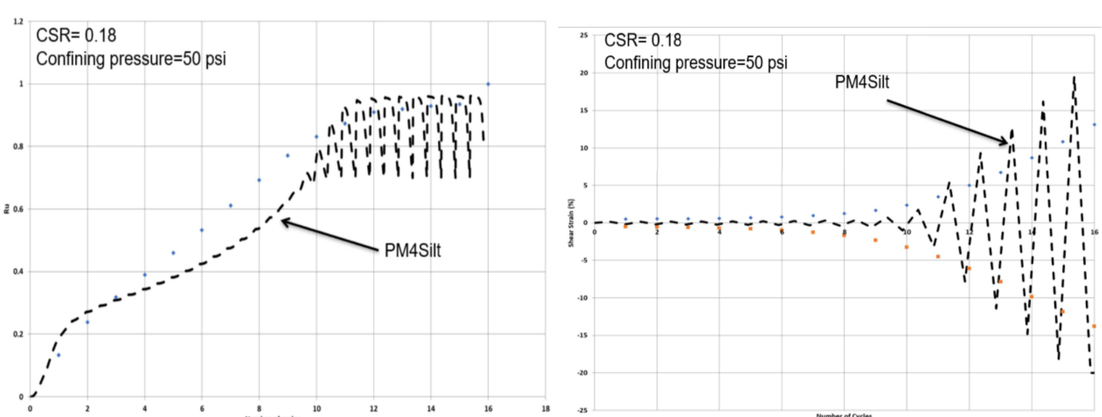

b) Comparison between cyclic DSS lab testing and PM4silt calibration, Ru and strain accumulation vs number of cycles (Dashed lines are PM4silt simulation and symbols are lab data)

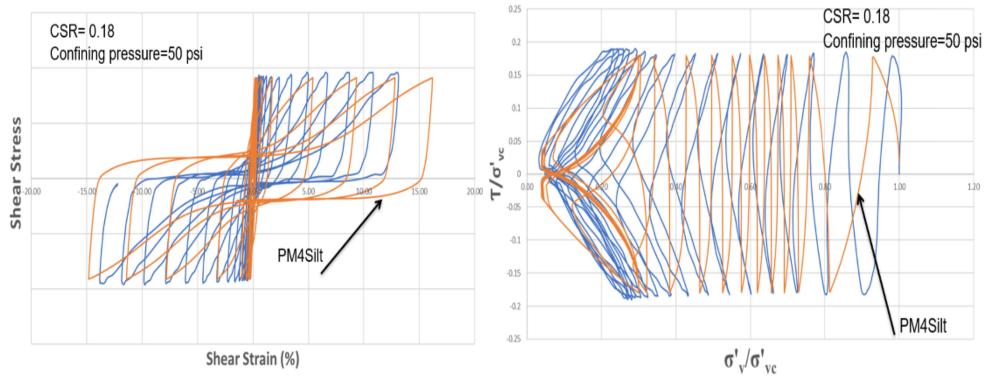

c) Comparison between cyclic DSS lab testing and PM4silt calibration, shear stress versus shear strain and stress paths (Orange color lines are PM4silt simulation and blue color lines are lab data)

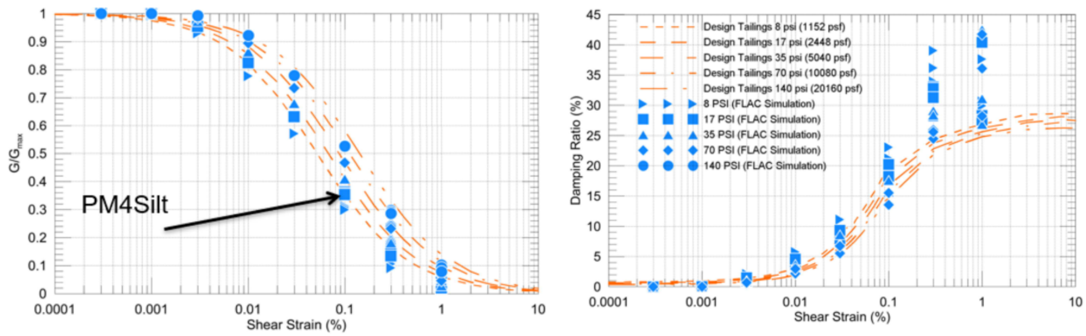

Figure 5 (cont.). Contractive whole tailings material PM4silt calibration

d) Comparison between lab testing and PM4silt calibration, shear modulus degradation and damping curves (blue color symbols are PM4silt simulation and orange color dashed lines are lab data)

Figure 6 provides a comparison between measured and simulated excess pore pressure during and after Magna earthquake for one section. Figure 6 also provides the location of each piezometer along this section in the SE Corner which includes piezometers located in tailings and foundation material. The first piezometer reading was measured approximately 5 hours after the event whereas the numerical simulation depicts the pore pressure generation during the event. Considering the potential pore water dissipation after the event, the PM4 model simulation seems to provide reasonable estimation of pore pressure due to Magna earthquake.

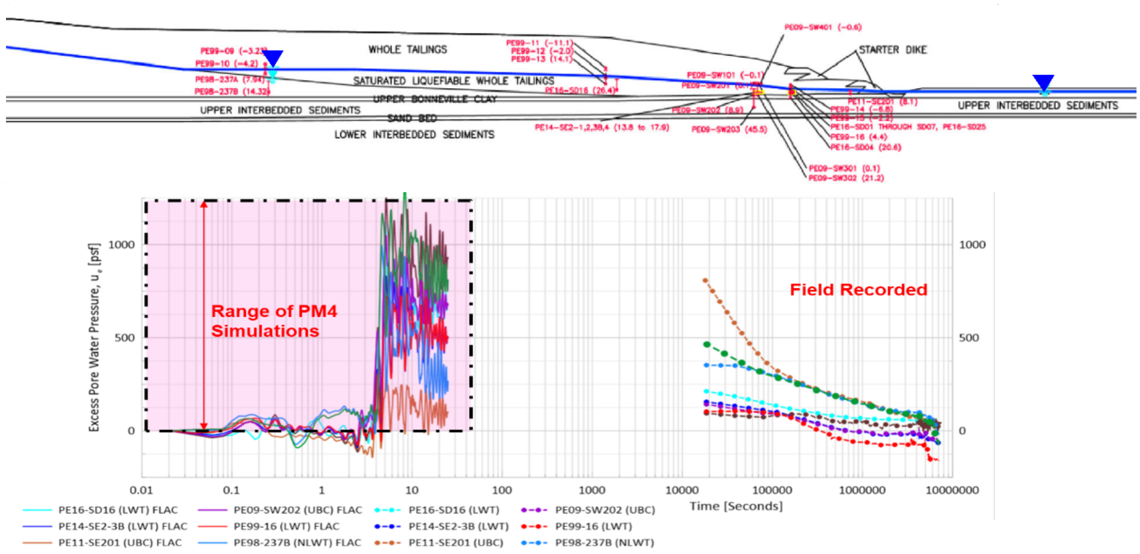

Figure 6. Pore pressure generation comparison between PM4 simulation and field measurements

Figure 7 provides a comparison between measured upstream/downstream displacement values from inclinometer SAA19-SE2_E and PM4 simulation. The measured values are less than half inch whereas the simulated displacements are about 1 inch. There is an overestimation of movements observed from PM4 simulation; however, the shape of the movements has been captured correctly and considering the small magnitude of values, a reasonable match between measured and simulation was obtained.

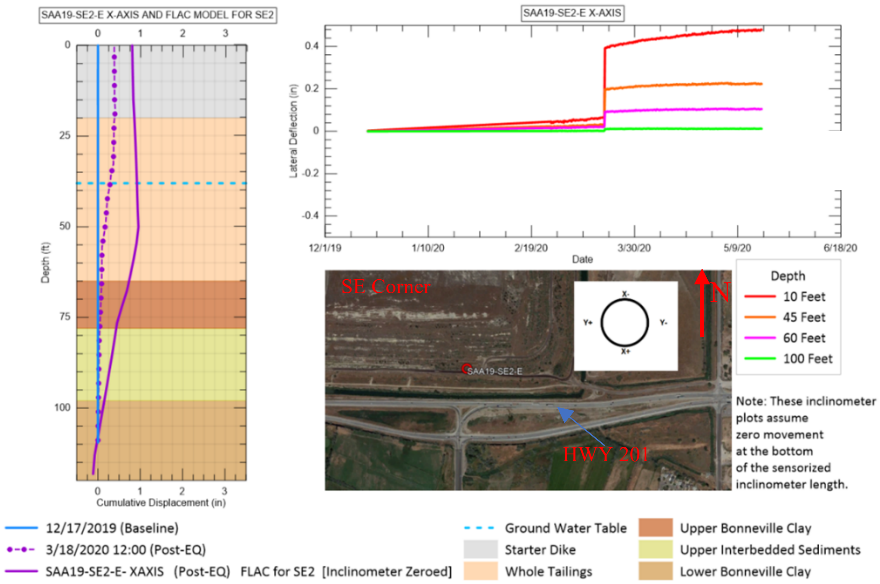

Figure 7. Displacement comparison from inclinometer between PM4 simulation and field measurements

Figure 8 provides InSAR data comparing 4 days before and 3 days after the earthquake. Figure 8 also provides FLAC simulation results at 5-time steps. The maximum measured surface movement at SE Corner is about 4 inches which compares reasonably with measured surface movements of 4 to 5 inch from FLAC simulation at the end of motion. Figure 8 also provides plots of pore pressure ratio (ru) which shows ru less than 0.2, consistent with the good performance of the embankment, in which no widespread liquefaction was observed.

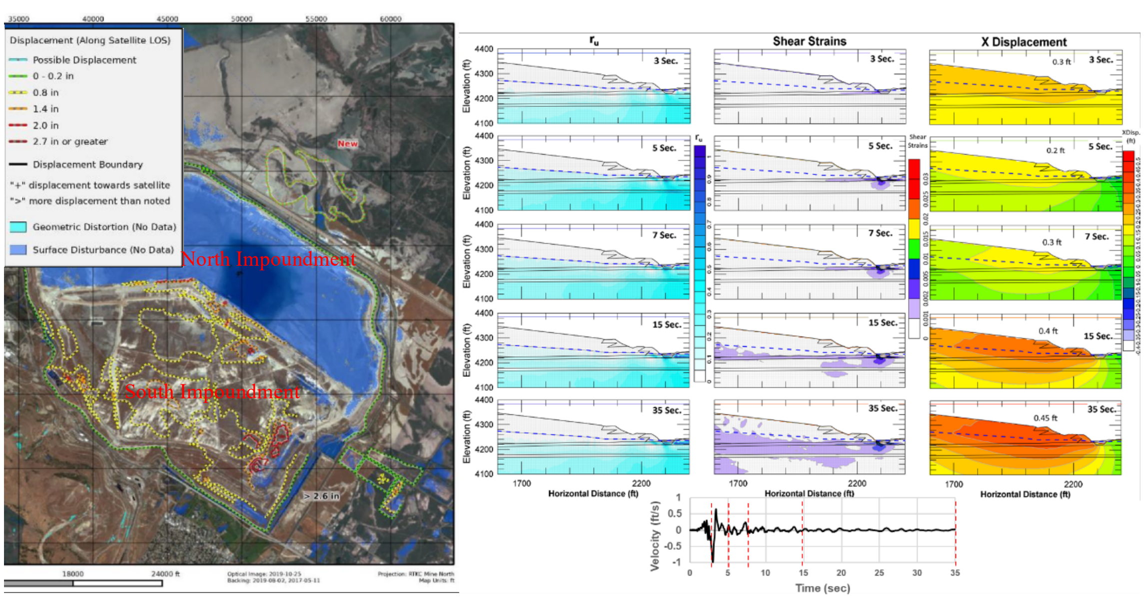

Figure 8. a) InSAR data b) FLAC simulation results

9 CONCLUSION

The North and South Impoundment of the Kennecott TSF performed very well under the significant M5.7 earthquake which occurred on March 18, 2020 and the subsequent aftershocks. This main shock event had a PGA up to 0.54 g horizontally in the free field and a vertical acceleration at the East Cyclone Station of 0.31g. Depending on location and distance from the epicenter (2 to 10 km) significant excess pore pressures were generated in the tailings materials. However, these pore pressures were not sufficient to cause widespread liquefaction or strength reduction, except in the recently deposited North Impoundment interior fine tailings and at one location near the historic South Impoundment decant pond. Movements and cracking were minimal directly after the main shock and they did not progress afterwards despite hundreds of aftershocks. There was no slope instability observed following the earthquake which confirmed the veracity of analyses conducted for slopes throughout the impoundment.

The emergency response of the RTK operations and Engineer of Record teams were very effective. Considering the after-earthquake response, several valuable lessons were learned that can be applied to future emergency events at the RTK TSF. Failure of the piezometer data collection network server resulted in delayed data acquisition and subsequent analyses. This also highlighted the critical need for the data collection network to be more robust with multiple back-ups and availability for real-time remote access.

Dynamic deformation analysis using FLAC2D PM4 models reasonably predict both pore pressure and displacement response and hence, no change to the design parameters was required. The predictions from model simulations are slightly higher than field measurements, but within reasonable range and trend of field measurements. Some of the difference between model simulations and field measurements that could cause these differences are:

- The input motion parameter for the model is a deconvoluted motion from the East cyclone station accelerometer which is located 1200 ft north of SE Corner;
- PM4 model parameters used in analyses are design parameters which have some level of conservatism;
- Recorded piezometer data at SE Corner are from 5 hours after the earthquake, the peak pore water pressure response was most likely missed, although the displacements should be good for comparison;
- The coupled analysis was performed without considering pore pressure dissipation during shaking which may be more important for interbedded whole tailings than foundation material.

10 ACKNOWLEDGMENTS

The authors would like to thank the Independent Technical Review Board (ITRB) members, Professors Norbert R. Morgenstern, I. M. Idriss, Ross W. Boulanger and Dr. Zavis M. Zavodni for their continuous support, encouragement, and input; this work could not have been carried out without their valuable feedback. A special thank you is also extended to RioTinto and AECOM engineers who have supported this project.

11 REFERENCES

Boulanger, R. W., and Ziotopoulou, K. 2019. A constitutive model for clays and plastic silts in plane-strain earthquake engineering applications. Soil Dynamics and Earthquake Engineering, 127(2019): 105832, 10.1016/j.soildyn.2019.105832.

U of U Seismograph Stations. April 24, 2020. Recent Earthquake Map, https://quake.utah.edu/earthquake-center/quake-map.

Wong, I., Wu, Q. 2020. Analyses of The 18 March 2020 M 5.7 Magna, Utah Earthquake Strong Motion Data, LCI. (13 April 2020).

Kleber, E. J., A. P. McKean, A. I. Hiscock, M. D. Hylland, C. L. Hardwick, G. N. McDonald, Z. W. Anderson, S. D. Bowman, G. C. Willis, and B. A. Erickson (2020). Geologic Setting, Ground Effects, and Proposed Structural Model for the 18 March 2020 Mw 5.7 Magna, Utah, Seismol. Res. Lett. XX, 1–15.

The magnitude-frequency of tailings flows resulting from failures of tailings impoundments

Nahyan M. Rana & Stephen G. Evans
University of Waterloo, Waterloo, Ontario, Canada

Negar Ghahramani & Scott McDougall
The University of British Columbia, Vancouver, British Columbia, Canada

W. Andy Take
Queen's University, Kingston, Ontario, Canada

ABSTRACT: Recent tailings flow occurrences have raised questions about their historical magnitude and frequency distribution. Recently published datasets provide a wider knowledge base to facilitate some statistical insights. This paper presents preliminary global statistics on tailings dam failures and tailings flows in comparison to constructed tailings facilities. These preliminary statistics are based on voluntarily reported and lower-bound estimates of the number of constructed tailings facilities worldwide, some necessary presumptions about the historical mine waste failure inventory, and a comprehensive database of tailings flows. This paper forms an initial step of a larger research effort to scrutinize and enhance existing records of tailings and mine waste failures, and induced fatalities, to present annual probabilities of failure/flow incidents, and to contextualize the hazard-risk distribution by comparison to those of analogous human-engineered facilities and mass movement hazards.

1 INTRODUCTION

Tailings are fine-grained, wet to saturated waste rocks produced mainly from mineral extractive operations (Franks et al. (2021); Rana et al. (2021a)). For environmental protection, tailings are conventionally impounded behind a dam that is typically built out of the coarse fraction of tailings, waste rockfill, earthfill and/or foundation materials (Blight (2010)). The dams are commonly raised according to the upstream, downstream and/or centerline methods during the operational phase, allowing the amassment of large volumes of tailings and, in many cases, supernatant ponds. Ensuring the geotechnical stability of tailings facilities is therefore a crucial component of mine waste management, to prevent post-breach geomorphological (and geochemical) consequences that can be rendered by downstream mass movements, or "tailings flows" (e.g. Kossoff et al. (2014); de Lima et al. (2020); ICMM et al. (2020); Rana et al. (2021a)).

Recent tailings dam failures involving life loss and environmental damage have raised concerns about the magnitude and frequency of tailings flow occurrences (e.g. Lyu et al. (2019); Santamarina et al. (2019); Rana et al. (2021a)). The 2014 Mt. Polley (Canada), 2015 Fundao and 2019 Feijao (both Brazil) events produced a combined outflow volume of ~67 million m^3 (M m^3) of materials into the downstream environment (Morgenstern et al. (2015, 2016); Robertson et al. (2019)). Rana et al. (2021a) calculated that this combined volume accounts for over 50% of the total volume of all 34 tailings flows with volumes of ≥ 0.2 M m^3 that occurred worldwide in 1965-2020. Rana et al. (2021a) further estimated that catastrophic tailings flows with volumes of ≥ 1 M m^3 have occurred once every 2-3 years in the period 1965-2020. This magnitude-frequency statistical analysis has helped provide an initial insight into the global hazard of tailings flows. Similar analyses have previously been performed for analogous phenomena such as natural debris flows (e.g. Guthrie & Evans (2004); Hungr et al. (2008)), and the failures of rockslide dams (Evans (2006)) and artificial water dams (Foster et al. (2000); Evans (2006)).

To build on the work of Rana et al. (2021a), this paper previews the next steps in scrutinizing and contextualizing tailings breach-flow occurrence data as follows: (1) evaluating the historical record of mine waste failure incidents with focus on tailings impoundment failures; (2) calculating the annual rates and probabilities of tailings dam failures and tailings flows in comparison to tailings facility construction rates; (3) assessing the human consequences of tailings dam failures and tailings flows over time; and (4) comparing failure and fatality rates to those of water-retention dam breaches and other applicable types of mass movements and anthropogenic operations. Addressing these objectives will ultimately help stakeholders (1) understand the implications for the long-term sustainability and risk of tailings facilities, (2) access up-to-date statistical information on tailings breach-flow incidents, and (3) gather overall context on the hazards and risks posed by engineered impoundments.

2 MODERN DATA SOURCES

Preparing a detailed record of case histories is a first step to generating statistically valid magnitude-frequency results. Of particular importance in this process is to investigate whether the developed record, or a subset of it, is complete – i.e. whether the database includes all cases that meet the specified magnitude and/or temporal criteria for inclusion. Table 1 lists published global datasets on the constructions and failures of tailings and mine waste facilities, with reference to the study authors, dataset focus and purpose, temporal coverage and number of cases.

Table 1: Published global datasets on the constructions and failures of tailings and mine waste facilities.

Dataset reference	Dataset focus	Dataset purpose and application	Number of cases	Temporal coverage
Rico et al. (2008)	Tailings flows	Empirical modelling of outflow-runout	29	1965-2000
Bowker & Chambers (2015)	Mine waste failures	Collection of case histories and basic background data	226	1917-2009
Small et al. (2017)	Mine waste flows	Collection of case histories and outflow-runout data	79	1928-2015
Larrauri & Lall (2018)	Tailings flows	Empirical modelling of outflow-runout	35	1965-2015
Ghahramani et al. (2020)	Tailings flows	Empirical modelling of inundation area	33	1965-2019
Franks et al. (2021)	Tailings impoundments	Comprehensive reporting of data on tailings impoundments constructed over time	1,743	1817-2020
Rana et al. (2021b)	Mine waste failures	Case inventory that was screened to generate tailings flow database	362	1915-2020
Rana et al. (2021a,b)	Tailings flows	Comprehensive collection and analysis of case history data and empirical modelling of outflow-runout	63	1928-2020

Events since 1965 are covered in all the listed datasets, primarily due to two reasons. First, the 1965 Chilean earthquake triggered the simultaneous failures of 10 tailings facilities, including the El Cobre tailings flow that killed over 200 people (Dobry & Alvarez (1967)). This marked the beginning of increased public scrutiny and reporting on mine waste hazards. Second, high-resolution global satellites were commenced in the mid-1960s, with the El Cobre event being the first catastrophic tailings flow captured on remotely sensed imagery (see Rana et al. (2021a,b)). Major tailings flows since then have been comprehensively documented through geographic information systems (GIS) mapping by Ghahramani et al. (2020) and Rana et al. (2021a,b).

Building on preceding research (see references cited in Table 1), Rana et al. (2021a,b) presented a comprehensive global database of 63 tailings flows from 1928-2020. For consistency, the authors defined “tailings flows” to be mass flows originating from the failures of impoundments (i.e. dammed facilities) containing fine-grained, wet to saturated waste rocks mainly produced from mining activity, industrial processing and some power plant operations (e.g. alumina from bauxite and fly ash from coal). Their tailings flow database therefore excludes waste rock piles/dumps, coarse colliery waste (e.g. 1972 Buffalo Creek, USA) and spoil tips (e.g. 1966 Aberfan, Wales). Based on their detailed review of historical documentation and processed satellite/aerial imagery, Rana et al. (2021a,b) concluded that their database can be considered complete for tailings flows with volumes of ≥ 0.2 M m^3 from 1965-2020, amounting to 34 cases. In its current version, the tailings flow database in Rana et al. (2021b) does not explicitly consider the number of lives lost due to tailings flows for fatality rate assessment.

Rana et al. (2021b) also developed an inventory of 362 mine waste failure incidents in 1915-2020. All of these incidents were reported in pre-existing datasets (ICOLD (2001); WISE (2020); and other preceding studies cited in Table 1), with each case being screened by the authors to generate the tailings flow database based on some case selection criteria (see supplementary article in Rana et al. (2021b)). The pre-existing datasets that were consulted by Rana et al. (2021b) were predominantly focused on tailings, including Bowker & Chambers (2015) and Small et al. (2017) who titled their datasets as "tailings storage facility failures" and "tailings dam failures" respectively. However, a cursory review of the mine waste failure inventory reveals the inclusion of some well-publicized incidents involving other categories of mine waste such as coarse colliery waste (e.g. 1972 Buffalo Creek, USA), spoil tips (e.g. 1966 Aberfan, Wales) and even waste rock piles (e.g. 1985 Quintette, Canada). This inconsistency is likely due to (1) the vague definitions of tailings in publications preceding Franks et al. (2021) and Rana et al. (2021a,b) and (2) the sparsity of reported information on low-consequence failure or instability incidents. As such, an important next step in this research – but outside the scope of the present paper – is to isolate the mine waste failure inventory of 362 cases in Rana et al. (2021b) according to the appropriate category of mine waste (i.e. tailings, coarse colliery waste, spoil tips, waste rock dumps, others or unknown).

Franks et al. (2021) developed a comprehensive database of tailings impoundments constructed worldwide over time. Their data is derived from a detailed, but statistically incomplete, record collated through voluntary survey responses from publicly-listed extractive companies. The database generally excludes (or under-represents the number of) facilities that are abandoned, state-owned and privately-owned, tailings that are not stored in a standard impoundment facility (e.g. backfill or heap leach pads) and other forms of mine waste, such as waste rock piles, coarse colliery waste and spoil tips. The survey revealed data on 1743 facilities, 725 of which are active as of early 2021. Upon proportionally extrapolating data in comparison to global mineral commodity production, the authors estimated that the total number of active tailings facilities worldwide is ~3400, and a conservative lower-bound for the total number of active, inactive and closed tailings facilities (excluding abandoned sites) is ~8100. An upper-bound estimate of the total number of tailings facilities worldwide is yet to be determined.

Franks et al. (2021) observed an accelerating rate of tailings production and storage, and that tailings facilities are, on average, increasing in size. Their analysis also revealed that 10% of reported facilities noted stability concerns or failures at some point in their operational history.

3 GRAPHICAL ANALYSIS

Figure 1 illustrates the reported trends (as annual and cumulative numbers) of constructed tailings storage facilities and mine waste failure incidents worldwide since 1915. The data is extracted from incomplete inventories in Franks et al. (2021) and Rana et al. (2021b), and thus the figure reports the minimum-estimates of the true global record. As remarked earlier, the mine waste failure inventory includes some non-tailings incidents, and to present representative magnitude-frequency results, an important next step is to scrutinize the inventory according to corresponding categories of mine waste. The purpose of Figure 1 is therefore to simply provide a general snapshot of the trends of reported mine waste failures and constructed tailings facilities over the same time interval. Figure 1 shows an accelerating trend of tailings storage since the 1950s and a relatively steady rate of mine waste failures since 1965. It is noted that the mid-1960s included the disasters of 1965 El Cobre (Chile), 1966 Sgorigrad (Bulgaria) and 1966

Aberfan (Wales), after which the public reporting of tailings and mine waste failure/flow incidents significantly improved.

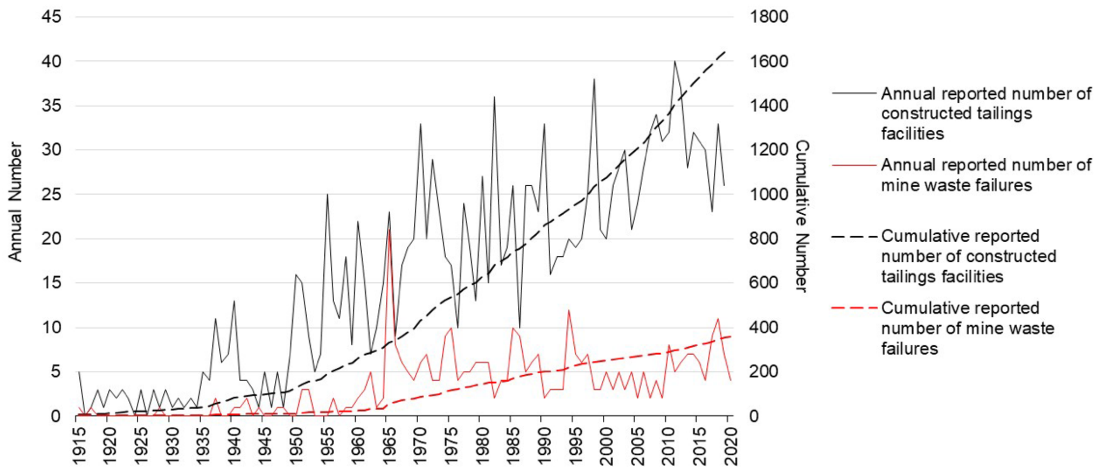

Figure 1. Annual number (left axis; solid lines) and cumulative number (right axis; dashed lines) of reported constructed tailings storage facilities (colored black, based on incomplete inventory in Franks et al. (2021)) and reported mine waste failure incidents (colored red, based on incomplete inventory in Rana et al. (2021b)) worldwide since 1915.

Figure 2 displays the annual frequency of 60 tailings flows in comparison to the cumulative reported volume of 56 tailings flows since 1965 (which amounts to 125.83 M m^3). The data is extracted from Rana et al. (2021b). The plots yield two noteworthy insights: first, there has been at least one tailings flow every year from 2007-2020; and second, the 2014 Mt. Polley (25 M m^3) and 2015 Fundao (32 M m^3) events make up nearly half (45%) of the combined volume of the 56 tailings flows since 1965.

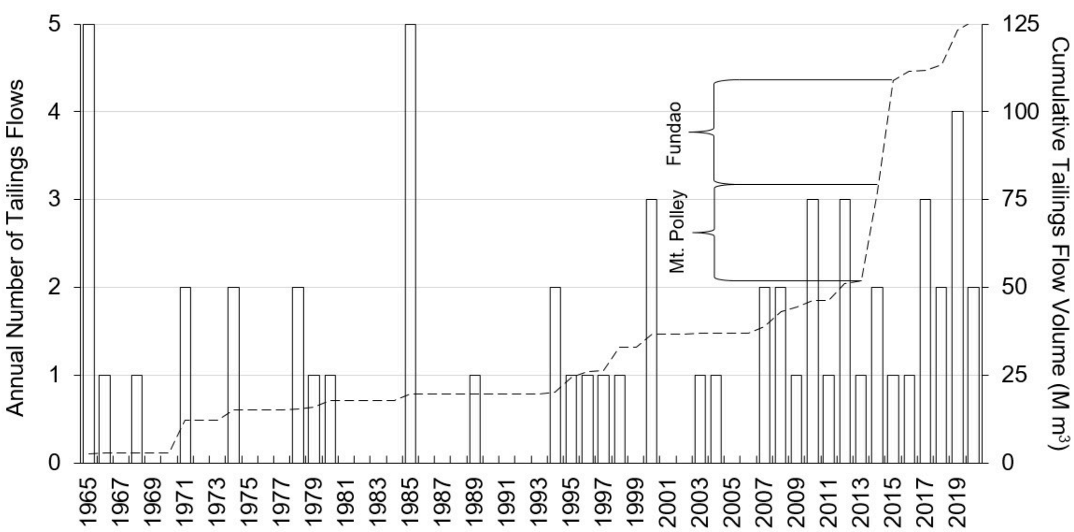

Figure 2. Annual number of 60 tailings flows (left axis; bar graph) and cumulative reported volume of 56 tailings flows (right axis; dashed line) since 1965.

Figure 3 illustrates the post-1965 trends, in semi-log scale, of annual sums of 5-year planned storage volumes in constructed tailings facilities and major tailings flow volumes, using data from Franks et al. (2021) and Rana et al. (2021b). It is noted that “major” tailings flows are defined as those with volumes of over 0.2 M m^3. The figure is intended to present a general overview of the fractions of stored tailings (which, as remarked earlier, is the voluntarily reported minimum-estimate) that have produced tailings flows.

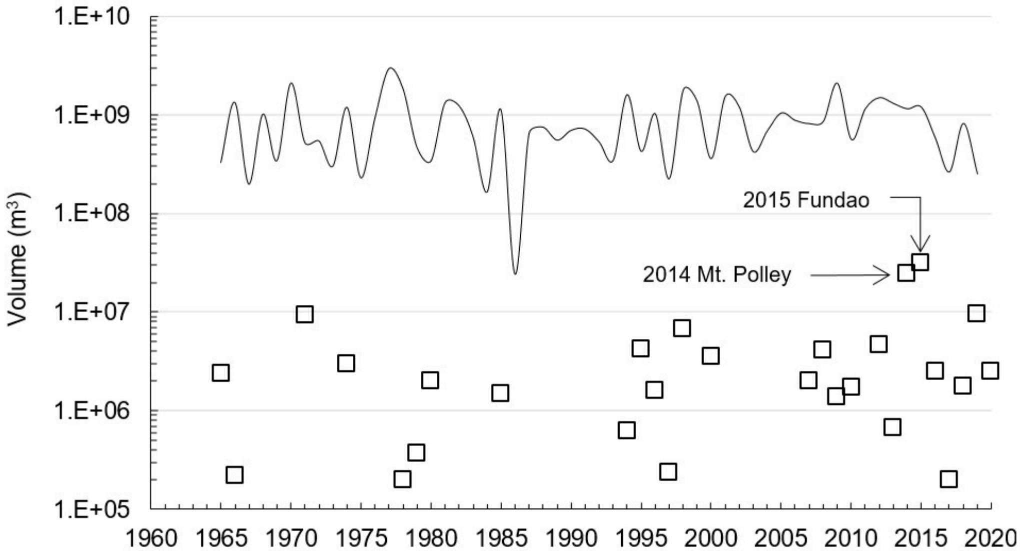

Figure 3. Semi-log trends of annual sums of 5-year planned storage volumes in constructed tailings facilities (solid line; data from Franks et al. (2021)) and major tailings flow volumes (open squares; data from Rana et al. (2021b)) since 1965.

Excluding 1986, the reported annual volume of stored tailings has generally ranged from 200 to 2000 M m^3. The annual volume of tailings flows has typically varied from 0.2 to 10 M m^3, with 2014 and 2015 being anomalously high due to the Mt. Polley (25 M m^3) and Fundao (32 M m^3) disasters. On the years that major tailings flows have occurred, the volumetric percentage of stored tailings that manifested into tailings flows ranged between < 0.01% (in 1978) and < 3.8% (in 2019) with a mean of < 0.66%. It is noted that the "<" symbol is a reminder that the volume of stored tailings is derived from voluntarily reported survey data in Franks et al. (2021).

If a lower-bound estimate for the total number of tailings facilities worldwide is taken to be ~8100 (as per Franks et al. (2021)), and the number of all tailings flows since 1928 is 63 (as per Rana et al. (2021a,b)), then the percentage of facilities that have generated tailings flows is ≤ 0.8%, corresponding to one out of at least 128 facilities. To estimate the percentage of tailings facilities that have failed, the historical number of tailings impoundment failures worldwide is preliminarily estimated to be in the order of ~350 based on the mine waste failure inventory of 362 cases in Rana et al. (2021b) that is predominantly focused on tailings. (Note earlier discussions on this issue and the intended objective of isolating the inventory according to the appropriate categories of mine waste for future analysis.) This indicates that the percentage of tailings facilities that have experienced some form of failure is ≤ 4.3%, equivalent to one out of at least 23 facilities. In comparison, Franks et al. (2021) found that ~10% of reported tailings facilities have experienced at least one stability concern in their operational history. To provide further context, Foster et al. (2000) estimated a mean global failure rate of 1.2% for water-retention embankment dams that were built up to 1986 (this estimate has yet to be modernized).

Figure 4 shows cumulative magnitude-frequency curves for tailings flows with volumes of ≥ 0.2 M m^3 and constructed tailings facilities with 5-year planned storage volumes of ≥ 0.1 M m^3. A power-law relationship is distinctly observed for tailings flows of ≥ 1 M m^3 and for tailings impoundments of ≥ 10 M m^3. The two power-law relationships are parallel (and similar in shape), as indicated by the same slope of -0.88, which suggests that the annual frequency profiles of tailings flow volumes and stored tailings volumes are roughly proportional in log-log scale. The figure indicates a mean recurrence rate (i.e. equivalent to the inverse of annual frequency) of ~17 years for catastrophic tailings flows of ≥ 10 M m^3. For context, at least 12 tailings facilities are reportedly constructed every year with a 5-year planned storage volume of ≥ 10 M m^3, based on the voluntarily reported data in Franks et al. (2021).

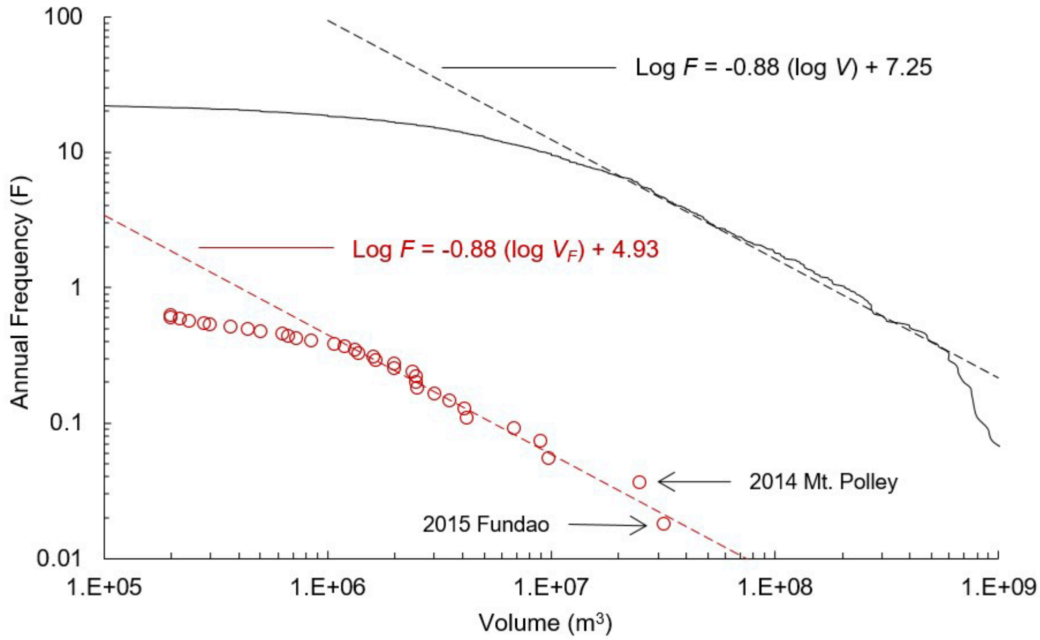

Figure 4. Comparison of cumulative magnitude-frequency curves for major tailings flows (red; complete data from Rana et al. (2021b)) and constructed tailings facilities (black; incomplete data from Franks et al. (2021)). Figure is modified from Rana et al. (2021a).

4 DISCUSSION AND CONCLUDING REMARKS

Tailings flows are significant mass movement phenomena generated in human-modified landscapes. Characterizing their magnitude-frequency distribution helps contextualize the worst-case hazard and risk of mineral extractive activities. This paper forms an initial step in this effort.

The open-access databases recently published by Franks et al. (2021) and Rana et al. (2021a,b) provide a wider knowledge base to facilitate more insightful statistical inferences into tailings and mine waste instability occurrences. Some of the observations of note in this paper are that one out of at least 23 tailings impoundments ($\leq 4.3\%$) has experienced some form of failure, and that one out of at least 128 tailings facilities ($\leq 0.8\%$) have generated tailings flows. However, it should be cautioned that these are preliminary statistics that are based on a lower-bound estimate of the number of constructed tailings facilities worldwide (hence the usage of the term "at least") and some necessary presumptions about the mine waste failure inventory. The quality of these statistics will be improved upon isolating the mine waste failure inventory according to the appropriate categories of mine waste (with specific focus on tailings) and, if feasible, assigning an upper-bound to the total number of tailings facilities worldwide.

Tailings flows have occurred at least once every year from 2007 through 2020. The combined volume of 56 tailings flows since 1965 (with publicly reported volumes) is 125.83 M m^3, 45% of which is contributed by the 2014 Mt. Polley and 2015 Fundao disasters. On the years that major tailings flows have occurred since 1965, the volumetric percentage of stored tailings that manifested into tailings flows ranged between $< 0.01\%$ (in 1978) and $< 3.8\%$ (in 2019) with a mean of $< 0.66\%$. It is worth reiterating that the temporal data on stored tailings volumes is derived from the voluntarily reported survey data in Franks et al. (2021), hence the "<" symbol.

It is recognized that this research effort is limited by the incomplete data on constructed tailings and mine waste facilities and the unconditioned record on the failures of these facilities. To improve and expand on this endeavor, the next steps should ideally involve the following objectives within a larger, more detailed scope: (i) scrutinize and enhance the existing inventory of mine waste failure incidents; (ii) produce a dataset of the number of lives lost due to tailings and mine waste failure incidents for fatality rate risk assessment; (iii) present the annual probabilities of tailings and mine waste failures and flows; and (iv) compare the estimated rates and probabilities to those of analogous human-engineered facilities and mass movement hazards for context. Research to address these objectives is underway.

5 ACKNOWLEDGEMENTS

This research is carried out within the CanBreach tailings project which comprises five industrial partners (Imperial Oil, Suncor Energy, BGC Engineering, Klohn Crippen Berger and Golder Associates) and three Canadian research institutions (University of Waterloo, University of British Columbia and Queen's University). This work is joint-funded by the listed industrial partners, a Collaborative Research and Development (CRD) grant (CRDPJ 533226-18) issued by the Natural Sciences and Engineering Research Council (NSERC) of Canada and a Science Domestic Graduate (PhD) Scholarship from the University of Waterloo.

6 REFERENCES

Blight, G.E. 2010. *Geotechnical Engineering for Mine Waste Storage Facilities*. London: CRC Press.

Bowker, L.N. & Chambers, D.M. 2015. The risks, public liability and economics of tailings storage facility failures. *University of Maine Press*.

Dobry, R. & Alvarez, L. 1967. Seismic failures of Chilean tailings dams. *Journal of Soil Mechanics and Foundations Division* 93: 237–260.

Evans, S.G. 2006. Single-event landslides resulting from massive rock slope failure: characterising their frequency and impact on society. In: Landslides from massive rock slope failure (pp. 53-73). Springer, Dordrecht.

Foster, M., Fell, R. & Spannagle, M. 2000. The statistics of embankment dam failures and accidents. *Canadian Geotechnical Journal* 37(5): 1000-1024.

Franks, D.M., Stringer, M., Torres-Cruz, L.A., Baker, E., Valenta, R., Thygesen, K., Matthews, A., Howchin, J. & Barrie, S. 2021. Tailings facility disclosures reveal stability risks. *Scientific Reports* 11 (1): 1–7.

Ghahramani, N., Mitchell, A., Rana, N.M., McDougall, S., Evans, S.G. & Take, W.A. 2020. Tailings-flow runout analysis: Examining the applicability of a semi-physical area–volume relationship using a novel database. *Natural Hazards and Earth System Science* 20: 3425–3438.

Guthrie, R.H. & Evans, S.G. 2004. Magnitude and frequency of landslides triggered by a storm event, Loughborough Inlet, British Columbia. *Natural Hazards and Earth System Science* 4: 475–483.

Hungr, O., McDougall, S., Wise, M. & Cullen, M. 2008. Magnitude-frequency relationships of debris flows and debris avalanches in relation to slope relief. *Geomorphology* 96(3–4): 355–365.

International Commission on Large Dams (ICOLD). 2001. *Tailings dams – risk of dangerous occurrences, lessons learnt from practical experiences*. Paris: Bulletin 121.

International Council on Mining and Metals (ICMM), United Nations Environment Programme (UNEP) & Principles for Responsible Investment (PRI). 2020. Global Industry Standard on Tailings Management.

Kossoff, D., Dubbin, W.E., Alfredsson, M., Edwards, S.J., Macklin, M.G. & Hudson-Edwards, K.A. 2014. Mine tailings dams: Characteristics, failure, environmental impacts, and remediation. *Applied Geochemistry* 51: 229-245.

Larrauri, P. & Lall, U. 2018. Tailings dams failures: updated statistical model for discharge volume and runout. *Environments* 5(28).

de Lima, R.E., de Lima Picanço, J., da Silva, A.F. & Acordes, F.A. 2020. An anthropogenic flow type gravitational mass movement: the Córrego do Feijão tailings dam disaster, Brumadinho, Brazil. *Landslides* 17: 2895-2906.

Lyu, Z., Chai, J., Xu, Z., Qin, Y. & Cao, J. 2019. A comprehensive review on reasons for tailings dam failures based on case history. *Advances in Civil Engineering*.

Morgenstern, N.R., Vick, S.G. & Van Zyl, D. 2015. Report on Mount Polley tailings storage facility breach. Report of independent expert engineering investigation and review panel for the Government

of British Columbia and the Williams Lake and Soda Creek Indian Bands (Canada).
Morgenstern N.R., Vick, S.G., Viotti, C.B. & Watts, B.D. 2016. Fundão tailings dam review panel: report on the immediate causes of the failure of the Fundão dam.
Rana, N.M., Ghahramani, N., Evans, S.G., McDougall, S., Small, A. & Take, W.A. 2021a. Catastrophic mass flows resulting from tailings impoundment failures. *Engineering Geology* 106262.
Rana, N. M., Ghahramani, N., Evans, S.G., McDougall, S., Small, A. & Take, W.A. 2021b. A comprehensive global database of tailings flows. *Scholars Portal Dataverse* v2.
Rico, M., Benito, G. & Diez-Herrero, A. 2008. Floods from tailings dam failures. *Journal of Hazardous Materials* 154(1–3): 79–87.
Robertson, P.K., de Melo, L., Williams, D.J. & Wilson, G.W. 2019. Report of the expert panel on the technical causes of the failure of Feijão Dam I. Investigation report commissioned by Vale S.A.
Santamarina, J.C., Torres-Cruz, L.A. & Bachus, R.C. 2019. Why coal ash and tailings dam disasters occur. *Science* 364(6440): 526–528.
Small, A., James, M. & Al-Mamun, M. 2017. Advancing the state of practice for tailings dam breach assessment using empirical correlations. In *Proceedings of the Canadian Dam Association Annual Conference*, Kelowna, British Columbia, Canada.
World Information on Service Energy (WISE). 2020. Chronology of major tailings dam failures (online database).

EcoTails® – The comingled tailings solution for variable ore bodies

Kenneth Rahal & Todd Wisdom
FLSmidth, Salt Lake City, Utah, USA

ABSTRACT: As ore body grades decline there is significant pressure on mining companies to find new projects that show clear economic payback. This is made more challenging by pressure from both investors and the public for mining companies to implement more sustainable, safer, practices as water costs and scarcity increase. These lower grade ore bodies also present challenges in regard to finer grain sizes and more mineralization variability than past high-grade ore bodies, both of which can both have significant impact on the dewatering costs.

The EcoTails® solution combines saturated filtered tailings with mine waste in a continuous process to produce a stable deposit. The EcoTails tailings solution is able to economically deal with difficult to dewater tailings by using fast filtration to reduce or elimination of cake blow, to desaturate the cake, to reduce the number of filters required. EcoTails is also able to compensate for the variability found in ore bodies by varying the waste rock to filter cake blend ratio to maintain the required mixed deposition moisture and material strength. Adjusting the blend ratio enables the throughput to be maintained in the dewatering plant by relaxing the moisture target in the filter cake.

Two case studies are presented that highlight the impact of EcoTails on CAPEX and OPEX. The first case study is for a mine that has tailings that are difficult to filter, resulting in significant cake blow. The second case study is for an ore body with significant variability which led to a wide range of dewatering rates.

1 INTRODUCTION

The demand for minerals and metals, especially copper is growing. As the World Bank's 2017 report titled "The Growing Role of Minerals and Metals for a Low-Carbon Future" shows, demand for metals, including copper, could rise tenfold by 2050 if the world moves towards a low-carbon energy future. This growth in demand is coinciding with continued declines in ore body quality. Mudd (2009) showed that ore body grades for copper, lead, zinc and other minerals have been declining globally. This has forced companies to process larger tonnages to achieve economy of scale. These larger throughputs require larger amounts of water and result in larger amounts of tailings that will have to be safely stored into perpetuity.

This increase in water consumption and tailings generation are coinciding with investor pressure for more sustainable mining practices (Global Sustainable Investment Alliance 2018, RBC Global Asset Management 2018). More mining companies are investigating filtered tailings as part of their long-term sustainability plans and to reduce risks associated with tailings storage. Additional benefits of filtered tailings are:

- Water reclamation and makeup water minimisation reduces costs
- Minimised tailings management facility (TMF) area – footprint can be less than 50% of a conventional TSF
- Reduction in closure costs at end of mine life – progressive closure possible

- Reduced tailings risk improves safety
- Suited to areas of high seismic activity

FLSmidth (FLS) recommends that miners conduct tailings solutions technology trade-off studies which includes analyzing different tailings solution options, including different flowsheets and equipment. This analysis includes determining the most economic approach for each solution. Filtered tailings is often included to determine if the increased recycling of process water can be part of the mine's sustainability plan. FLSmidth's own program in support of sustainability, MissionZero, has the goal of offering solutions that support zero water waste by 2030. We already have technology that enables our customers to recover up to 95% of their process water. This dry-stack tailing solution also solves problems associated with waste water management and is economically competitive with alternative water management options such as desalination, even for high tonnages.

However, it can be difficult to justify the extra capital expense associated with filtered tailings during studies due to unquantified or underestimated costs. As discussed by Carneiro and Fourie (2019) studies often underestimate closure costs and less tangible costs are not included. Even if as many costs are known/estimated as possible, the difference in risks and consequence of failure for different tailings solutions are often ignored. Pyle et al (2019) have shown that if past tailings failures are used to assign a value to the risk and cost of failure of a traditional wet impoundment then filtered tailings can become economically competitive for some projects. As each mine site is different, it is important to understand the factors that can help guide the process to determine which solution is best. These factors include:

- Water cost and availability
- Space requirements for waste (tailings and waste rock)
- Regulatory requirements

One of the reasons that these trade-off studies can show filtered tailings to be cost prohibitive at some mines is due to hard to filter material or large variability in ore body leading to a wide range filtration performance. These difficulties can potentially be overcome using the EcoTails solution. EcoTails is an efficient, co-mingled tailings option that combines fully saturated filter cake with waste rock. The materials are blended during conveyance in specially designed transfer chutes using the energy input from the conveyors. This eliminates the need for mechanical mixing which in turn reduces the cost and complexity of the solution. Another cost savings is to produce the fully saturated filter cake using fast filtration.

Fast filtering is designed to achieve quick pressure filter total cycle times of less than 10 minutes. This is achieved through:

- High pressure feeding
    - 15 Bar terminal pressure
        - Low Plate Feed Ports Enable High Pressures without plate damage
        - Reduces Cake Formation Time
- No membranes required
- Fast Opening and Closing
- Reduced/eliminated Cake Blow

The low plate feed ports, as seen below in Figure 1a, are necessary to achieve high terminal pressure without membranes as uniform filling in the chambers. Turbulence in the feed eye and chamber is maintained which allows for the cake to form in layers throughout the entire chamber (Figure 1b). This results in uniform pressure throughout the filter. The formation of the cake in layers against the media results in a homogenous cake (Figure 1c).

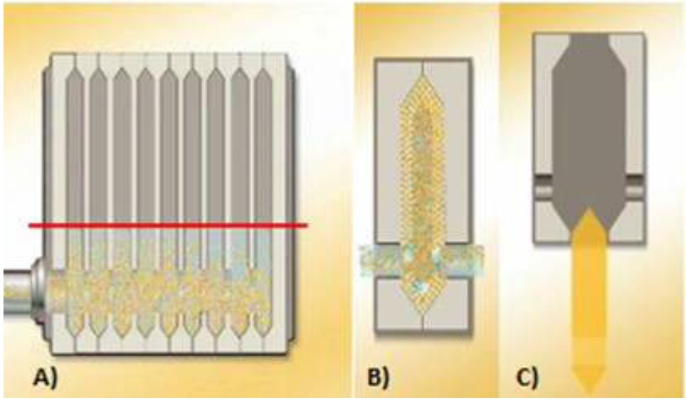

Figure 1: Lower Feed Eye.

If an upper feed port is used, as seen below in Figure 2a, gravity causes the non-uniform filling of the chambers. As the chambers are not evenly filled, a pressure gradient forms, which at high feed pressure can cause damage to the plates. Typically 7 Bar is the highest feed pressure in this type of feeding arrangement to minimize plate damage.

Another side effect of an upper feed port is that turbulence is not maintained so the particles settle in the chamber at different rates as seen in Figure 2b, due to particle size, and can form a non-homogenous cake (Figure 2c).

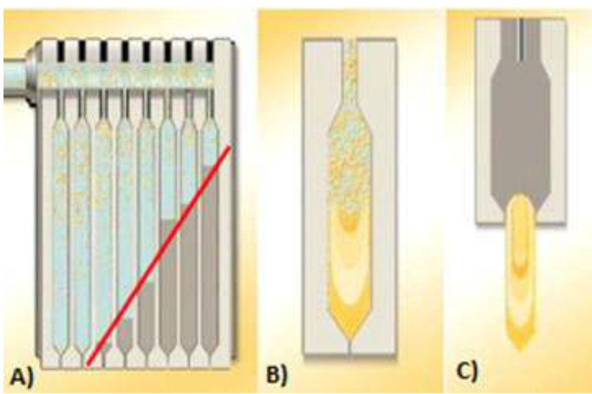

Figure 2: Upper Feed Eye.

Fast filtering can achieve higher density cakes than low pressure feed filters, without the use of membranes, therefore the moisture content of the cake is reduced. This allows for the reduction of air blowing of the cake. This in turn decrease the filtration cycle time and increases throughput. This reduction in air blow also reduces CAPEX and OPEX by reducing the number of compressors needed to achieve the target moisture. Also, filtration rate is proportional to the differential pressure between the feed pressure and atmospheric pressure so feeding at 15 Bar pressure is 2.14 times as fast as at 7 Bar feed pressure. The purpose of fast filtering is to achieve the lowest possible cycle time that can achieve the moisture target. Lower cycle times lead to higher filtration rates and fewer filters to achieve the required throughput. When fast filtering is used as part of the EcoTails solution, the cake blow can be eliminated as the lower strength of the filter cake is compensated for by the waste rock (Wisdom et al. (2018)).

The addition of waste rock to fast-filtered tailings has been shown to improve shear strength and reduce liquefaction potential of the tailings, which promotes geotechnical stability (Bareither et al. (2018)). GeoWaste™ can also reduce ARD potential of waste rock by encapsulating the waste rock in filter cake to inhibit ingress of oxygen which promotes geochemical stability.

The properties of the GeoWaste material depend on the blend ratio between waste rock and the filter cake (Bareither et al. (2018)). This allows the EcoTails solution to be designed to compensate for variation in filtration performance due to feed variation. This is done by holding the cycle time of the filters constant and allowing them to produce a variable wetter cake which is compensated for by increasing the amount of waste rock in the GeoWaste blend.

The underlying question is whether or not the reduced number of filters, filter feed pumps, and air compressors is offset by the crushers and increased size of the conveyors and stackers required for the EcoTails solution. This will be highlighted in the case studies below.

2 CASE STUDIES

These case studies are based on lab testing and are conceptual in nature with an accuracy of ±30%. Throughputs have been rounded to respect customer confidentiality. It should be noted that the FLS sizing methodology requires a minimum of 15% excess capacity on filters to allow for maintenance. While FLS normally recommends a spare filter, no spare filter(s) are included in these studies. Potentially shared equipment (feed pumps, compressors, receivers, etc.) are not optimized at the conceptual stage of these studies.

For these case studies, none of the benefits of the GeoWaste on the stack height, lift height, etc. are included in the sizing of the material handling equipment which would likely only. improve the economic justification for EcoTails and GeoWaste. Therefore, the sizing of the material handling equipment is based solely on throughput and material conveyance properties and the cost estimates for the EcoTails solutions are considered conservative and likely can be improved.

All CAPEX is for equipment only and does not include spares or installation. The OPEX includes labor, power, filter media, and spares/consumables. The costs used for determination of OPEX are shown in Table 1.

Table 1: High Tonnage OPEX Assumptions

Normalized Labor Cost ($/hr))	$50.00
Normalized Power Rate ($/kWhr)	$0.10

2.1 *High Tonnage Copper/Gold Mine*

The first case study is for a high tonnage (HT) mine that has tailings that are difficult to filter, resulting in significant cake blow to reach the target cake solids concentration. This operation produces 6250 tph of tailings at 60 wt% solids from a thickener. The PSD of the tailings is described in Table 2. The waste rock is on average 95 wt% solids.

Table 2: High Tonnage Tailings PSD

P80 (μm)	125
% Passing 10 microns	23

The moisture target of the filtered only solution was 85 wt% solids while the EcoTails solution had two targets of 83.5 and 82 wt% solids. Two targets were used to determine what impact the different material handling sizes would have on the economics.

2.1.1 *HT Filtered Tailings*

The pressure filter testing was conducted using 15 bar feed pressure and required 10 minutes of cake blow to achieve the target moisture.

The lab testing resulted in the following dewatering equipment list to achieve 85 wt% solids in the filter cake:

- Twelve (12) AFP IV M5030 pressure filters with 50 mm chambers and greater than 93 m^3 of total filtration volume each
- Twelve (12) Hybrid Apron Belt Feeders
- Twenty-four (24) 500 hp Air Compressors
- Twenty-four (24) 114 m^3 Air Receivers

- One (1) 100 m Plant takeaway conveyor
- 5 km overland conveyor (6,250 tph capacity)
- 1 Mobile Stacking Conveyor system

The installed power including tanks, pumps, air compressors & receivers, filter discharge feeders, and instrumentation is 54.8 MW. The consumed power is 50% lower due to the batch operation of the pressure filters. The reduction in power does not include pumping efficiencies or the base loading of auxiliary equipment when not in use. Installed, and to a much lesser extent consumed, power can also be reduced by shared resources in a batch operation, which can be evaluated during more detailed engineering studies.

2.1.2 *HT EcoTails*

The pressure filter testing was conducted using 15 bar feed pressure and required 2.25 minutes of cake blow to achieve 83.5 wt% solids in the filter cake and just grid sweep to remove the water between the filter plates and filter media to achieve a saturated, 82 wt%, solids in the filter cake. The Ecotails target was 87.5 wt% solids, which required a blend ratio of 0.6:1 (3750 tph waste rock) for the 83.5 wt% cake and 0.9:1 blend ratio (5625 tph waste rock) for the 82 wt% cake.

The lab testing resulted in the following dewatering equipment list to achieve 83.5 wt% solids in the filter cake and 87.5 wt% solids in the GeoWaste:

- Seven (7) AFP IV M5030 pressure filters with 50 mm chambers and greater than 93 m^3 of total filtration volume each
- Seven (7) Hybrid Apron Belt Feeders
- Seven (7) 500 hp Air Compressors
- Seven (7) 114 m^3 Air Receivers
- One (1) TSU 1400 x 2100 Gyratory Crusher
- One (1) 100 m Plant takeaway conveyor
- 5 km overland conveyor (10,000 tph capacity)
- 1 Mobile Stacking Conveyor system

The installed power including tanks, pumps, air compressors & receivers, filter discharge feeders, and instrumentation is 41.4 MW. The consumed power is 27% lower due to the batch operation of the pressure filters. The reduction in power does not include pumping efficiencies or the base loading of auxiliary equipment when not in use. Installed, and to a much lesser extent consumed, power can also be impacted by shared resources in a batch operation, which can be evaluated during more detailed engineering studies.

The lab testing resulted in the following dewatering equipment list to achieve 83.5 wt% solids in the filter cake and 87.5 wt% solids in the GeoWaste:

- Five (5) AFP IV M5030 pressure filters with 50 mm chambers and greater than 93 m^3 of total filtration volume each
- Five (5) Hybrid Apron Belt Feeders
- Two (2) 500 hp Air Compressors
- Two (2) 114 m^3 Air Receivers
- One (1) TSU 1600 x 2900 Gyratory Crusher
- One (1) 100 m Plant takeaway conveyor
- 5 km overland conveyor (11,875 tph capacity)
- 1 Mobile Stacking Conveyor system

The installed power including tanks, pumps, air compressors & receivers, filter discharge feeders, and instrumentation is 34.7 MW. The consumed power is 18% lower due to the batch operation of the pressure filters. The reduction in power does not include pumping efficiencies or the base loading of auxiliary equipment when not in use. Installed, and to a much lesser extent consumed, power can also be impacted by shared resources in a batch operation, which can be evaluated during more detailed engineering studies.

2.1.3 *HT Comparison*

A comparison of the CAPEX & OPEX for the three options in this case study are shown in Figure 3. The costs are normalized to the 82% solids scenario to highlight the increase in cost to produce dryer cakes.

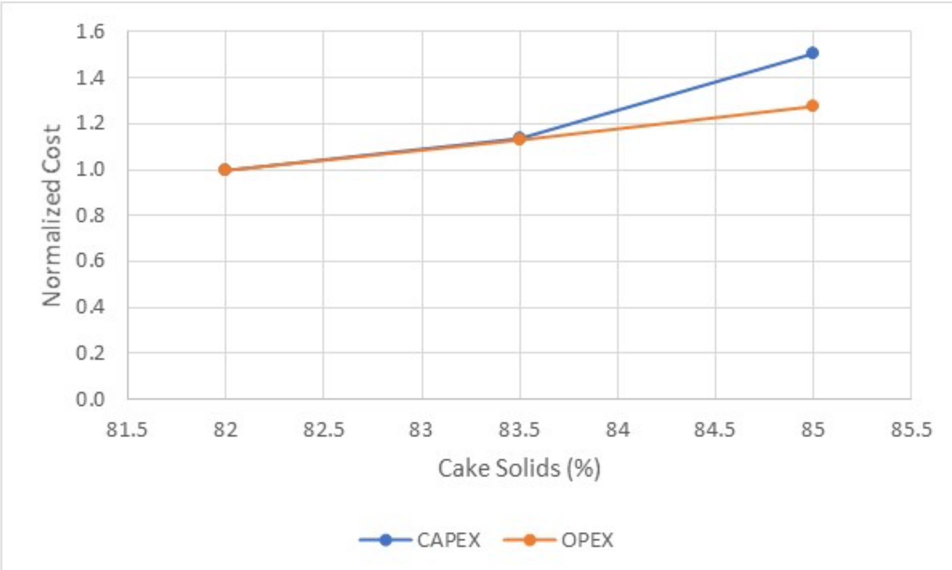

Figure 3: High Tonnage CAPEX & OPEX Comparison.

The increase in cake dryness from 82 wt% to 83.5 wt% to 85 wt% solids increased the number of filters from 5 to 7 to 12. The increase from 82 wt% to 83.5 wt% increased the CAPEX by 14% and the OPEX by 13%. The increase in cake dryness allowed for the reduction in crusher size and conveyor/stacker belt width. However, these costs savings were overshadowed by the increase in filters necessary to achieve the higher wt% solids in the cake. Increasing the cake solids to 85 wt% allows for elimination of the crusher and further reduction in cost of the conveyor/stacking system. However, the increase in the number filters results in a 51% increase in CAPEX and 28% increase in OPEX when compared to the 82 wt% solution.

2.2 *Medium Tonnage Copper/Gold Mine*

The second case study is for an ore body with significant variability which led to a wide range of dewatering rates. This medium tonnage (MT) mine produces 2,083 tph of tailings at 58 to 63 wt% solids from a thickener. The moisture target of the material to be disposed (filtered cake or EcoTails) was 85 wt% solids. The particle size distribution, PSD, of the tailings is described in Table 3. There was significant variability in the orebody and subsequent tailings so the customer sent 12 samples for testing. A composite sample was also generated and tested.

Table 3: Medium Tonnage Tailings PSD

P80 (µm)	95 – 121
P10 (µm)	2.4 – 3.1

The pressure filter testing was conducted using 10 bar feed pressure with sufficient cake blow to achieve the moisture target using the feed density correlating to the thickener underflow density achieved for that sample. It should be noted that this mine is at greater than 4000 masl which affects the sizing of motors and compressors. At this altitude, air compressors must be water cooled and require significantly greater installed and consumed power than at lower altitudes.

2.2.1 *MT Filtered Tailings*

The filtration testing revealed that to achieve 85 wt% solids in the filter cake, the filtration rate varied from 95.4 to 188.8 kg/hr/m^2 for the 13 samples. This was due to the consolidation time varying by up to 325% and the cake blow time varying by up to 225%. The composite sample, an equal mixture of all other samples, achieved a filtration rate of 120.6 kg/hr/m^2.

If the sizing of the equipment is based on the sample with the best dewatering results then the equipment list would include:

- Nine (9) AFP IV M2525 (2.5 m by 2.5 m plate) pressure filters with 50 mm chambers and greater than 32 m^3 of total filtration volume each
- Nine (9) Discharge Feeders
- Fifteen (15) 1860 kw water cooled Air Compressors
- Fifteen (15) 114 m^3 Air Receivers
- 1 Plant takeaway conveyor
- 5 km overland conveyor (2,083 tph capacity)
- 1 Mobile Stacking Conveyor system

If the sizing of the equipment is based on the sample with the worst dewatering results then the equipment list would include:

- Eighteen (18) AFP IV M2525 (2.5 m by 2.5 m plate) pressure filters with 50 mm chambers and greater than 32 m^3 of total filtration volume each
- Eighteen (18) Discharge Feeders
- Thirty (30) 1860 kw water cooled Air Compressors
- Thirty (30) 114 m^3 Air Receivers
- 1 Plant takeaway conveyor
- 5 km overland conveyor (2,083 tph capacity)
- 1 Mobile Stacking Conveyor system

However, if the sizing of the equipment is based on the composite sample, which is often the only sample sent by customers for testing, then the equipment list would include:

- Fourteen (14) AFP IV M2525 (2.5 m by 2.5 m plate) pressure filters with 50 mm chambers and greater than 32 m^3 of total filtration volume each
- Fourteen (14) Discharge Feeders
- Twenty-four (24) 1860 kw water cooled Air Compressors
- Twenty-four (24) 114 m^3 Air Receivers
- 1 Plant takeaway conveyor
- 5 km overland conveyor (2,083 tph capacity)
- 1 Mobile Stacking Conveyor system

The installed power including tanks, pumps, air compressors & receivers, filter discharge feeders, and instrumentation is 78.6 MW, 42.2 MW, and 63.5 MW for the worst case, best case and composite, respectively. The consumed power is 61%, 60%, and 61% lower due to the batch operation of the pressure filters. The reduction in power does not include pumping efficiencies or the base loading of auxiliary equipment when not in use. Installed, and to a much lesser extent consumed, power can also be impacted by shared resources in a batch operation, which can be evaluated during more detailed engineering studies.

This case study highlights the need to perform sufficient variation testing to fully understand your orebody and its impact on the dewatering solution through the life of mine. If filtration system had been designed with 9 filters, based on the best filtering sample, it would have half the number of filters required to filter the worst filtered sample. If mine throughput is maintained at nameplate capacity, this means that the plant would not be able to achieve the target moisture and either costly manual working of the cake to dry it would be required or the filter plant would need to be bypassed all together, requiring a wet impoundment for disposal. If the composite sample was the basis of design, then the dewatering system would still not have enough filters to handle the worst-case material. This might be mitigated by extensive blending in large feed stockpile. However, it would be critical that the mine plan be able to achieve a true composite through the life of mine and that no deviation from the planned occurred.

2.2.2 *MT EcoTails*

The filter cake target was set at 82% solids for the EcoTails solution based on the availability and moisture of waste rock to achieve the blended 85% solids for deposition. The filtration rate ranged from 176.1 to 302.1 kg/hr/m^2. This results in the filters required to range from 8 to 6. These results show the improved stability of operation the results from using the EcoTails solution. It is worth noting that the "worst" case Ecotails still required fewer filters than the "best" Filtered tailings solution.

If the sizing of the equipment is based on the sample with the best dewatering results then the equipment list would include:

- Six (6) AFP IV M2525 (2.5 m by 2.5 m plate) pressure filters with 50 mm chambers and greater than 32 m^3 of total filtration volume each
- Six (6) Discharge Feeders
- Ten (10) 1860 kw water cooled Air Compressors
- Ten (10) 114 m^3 Air Receivers
- One (1) TSU 1100 x 1500 Gyratory Crusher
- 1 Plant takeaway conveyor
- 5 km overland conveyor (3850 tph capacity)
- 1 Mobile Stacking Conveyor system

If the sizing of the equipment is based on the sample with the worst dewatering results then the equipment list would include:

- Eight (8) AFP IV M2525 (2.5 m by 2.5 m plate) pressure filters with 50 mm chambers and greater than 32 m^3 of total filtration volume each
- Eight (8) Discharge Feeders
- Thirteen (13) 1860 kw water cooled Air Compressors
- Thirteen (13) 114 m^3 Air Receivers
- One (1) TSU 1400 x 2100 Gyratory Crusher
- 1 Plant takeaway conveyor (4500 tph capacity)
- 5 km overland conveyor
- 1 Mobile Stacking Conveyor system

However, if the sizing of the equipment is based on the composite sample, which is often the only sample sent by customers for testing, then the equipment list would include:

- Seven (7) AFP IV M2525 (2.5 m by 2.5 m plate) pressure filters with 50 mm chambers and greater than 32 m^3 of total filtration volume each
- Seven (7) Discharge Feeders
- Twelve (12) 1860 kw water cooled Air Compressors
- Twelve (12) 114 m^3 Air Receivers
- One (1) TSU 1100 x 1500 Gyratory Crusher
- 1 Plant takeaway conveyor
- 5 km overland conveyor (4000 tph capacity)
- 1 Mobile Stacking Conveyor system

The installed power including tanks, pumps, air compressors & receivers, filter discharge feeders, and instrumentation is 41.1 MW, 32.6 MW, and 38.2 MW for the worst case, best case and composite, respectively. The consumed power is 65%, 60%, and 62% lower due to the batch operation of the pressure filters. The reduction in power does not include pumping efficiencies or the base loading of auxiliary equipment when not in use. Installed, and to a much lesser extent consumed, power can also be impacted by shared resources in a batch operation, which can be evaluated during more detailed engineering studies.

For this case study, the waste rock required for blending with the worst and best case filter cake to achieve the required disposal moisture and strength varies from 1770 to 2500 tph. The material handling system size is the same for each scenario but the belt speed changes from 3.75 to 4 m/s to accommodate the different tonnages.

2.2.3 *MT Comparison*

A comparison of the CAPEX & OPEX for the options in this case study are shown in Figure 4. The costs are normalized to the best case filtered solution to highlight the cost saving potential of EcoTails.

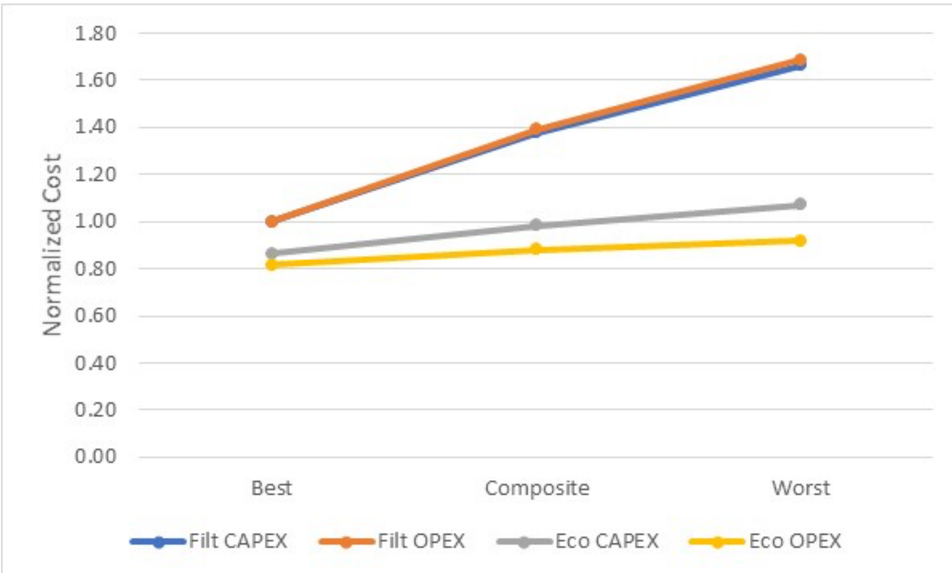

Figure 4: Medium Tonnage CAPEX & OPEX Comparison.

The variability in dewatering performance of the samples leads to serious design issues for the filtered solution. If the composite is used, as often done by companies, the filtration system would have 4 fewer filters, or approximately 30% capacity, than needed to dewater the worst performing sample. If the worst case is used to design the dewatering system then there would be up to 100% excess capacity at times, which leads to CAPEX and OPEX being 66% and 69% higher than the best case, respectively.

EcoTails enables these design issues to be resolved by varying the water rock blend ratio to compensate for the variability in the dewatering performance of the samples. EcoTails requires fewer filters, varying between 6 to 8, than even the best case Filtered Tailings. If the system is designed for the worst case scenario then there would be 2 spare filters during the best performing material with only 1 spare during most of the life of the mine. All of the filters could be operated during the worst performing material and then maintenance can be performed with better filtering material is run through the plant. Figure 4 shows that the worst case Ecotails solution is only 7% higher CAPEX than the best filtered solution, but the OPEX is 8% lower. The CAPEX and OPEX are only 24% and 12% higher, respectively, for the worst case versus the best case on EcoTails. FLSmidth would recommend the EcoTails solution for this case study.

3 CONCLUSIONS

As ore body grades decline there is significant pressure on mining companies to find new projects that show clear economic payback. FLSmidth recommends consideration of EcoTails which combines saturated filtered tailings with mine waste in a continuous process to produce a stable deposit. The EcoTails tailings solution is able to economically deal with difficult to dewater tailings by using fast filtration to reduce or eliminate of cake blow to reduce the number of filters required. EcoTails is also able to compensate for the variability found in ore bodies by varying the waste rock to filter cake blend ratio to maintain the required blended deposition moisture and material strength.

This paper presented two case studies which showed the advantages of EcoTails. The first case study showed that for a mine with difficult to filter tailings:

1. The CAPEX could be reduced by 51% by using EcoTails due to the decrease in the number of filters;
2. The OPEX could also be reduced by 28% due to the reduction in the cake blow and resulting number of air compressors.

The second case study showed that for an ore body with significant variability:

3. Filtered tailing capacity requirements varied by 100% causing CAPEX and OPEX to vary by 66% and 69%;
4. EcoTails reduced variability to 25% which is much more normal and results in CAPEX and OPEX to vary by 24 and 12%;
5. EcoTails system required to handle all variation would have CAPEX and OPEX that are 64 and 54% lower, respectively than the filtered system required to handle all variation.

In all cases, the reduction in the quantity of filters and associated filter feed pumps and compressors for the EcoTails solution results in a more economically attractive solution when compared to traditional filtered tailings even when the added expense of crushers for the waste rock and higher capacity material handling systems are fully considered.

4 REFERENCES

Mudd, G.M. 2009. The Sustainability of Mining in Australia: Key Production Trends and Environmental Implications; Research Report No. RP5; Department of Civil Engineering, Monash University and Mineral Policy Institute: Melbourne, Australia.

Global Sustainable Investment Alliance. 2018. Global Sustainable Investment Review. https://www.gsi-alliance.org/wp-content/uploads/2019/03/GSIR_Review2018.3.28.pdf.

RBC Global Asset Management. 2018. Responsible Investing Survey: Executive Summary. https//us/rbcgam/com/resources/docs/pdf/HTML-files/files/ESF/Responsible_Investing _Executive_Summary_2018.pdf.

Bareither, C.A., Gorakhki, M.H., Scalia, J., Jacobs, M. 2018. Compression behavior of filtered tailings and waste rock mixtures: GeoWaste, Proc. Tailings and Mine Waste 2018, UBC Studios, University of British Columbia, Vancouver, BC, 163-173

Hamade, M.M.P., Bareither, C.A. 2018. Undrained shear behavior of synthetic waste rock and synthetic tailings mixtures, Geotechnical Testing Journal, published online 26 Oct. 2018.

Jehring, M.M., Bareither, C.A. 2016. Tailings composition effects on shear strength behavior of co-mixed mine waste rock and tailings, Acta Geotechnica, 11(5), 1147-1166.

Burden, R., D. J. Williams, G. W. Wilson and M. Jacobs 2018. The Shear Strength of Filtered Tailings and Waste Rock Blends. Tailings and Mine Waste 2018. Keystone, CO.

Wisdom, T., Jacobs, M. and Chaponnel, J. 2018. GeoWaste™ – continuous comingled tailings for large-scale mines. Paste 2018. Perth, Australia. 465-472.

Filtered tailings and waste rock blends: A way to build better dry stacks?

Ralph Burden & G Ward Wilson
University of Alberta, Edmonton, Alberta, Canada

David Williams
University of Queensland, Brisbane, Queensland, Australia

ABSTRACT: Filtered tailings "dry stacks", which typically use pressure filtration to rapidly de-water the tailings before stacking, are becoming an increasingly widely used approach to mine waste management. Another emerging technology is co-disposal; blending of waste rock and tailings to create a new, engineered material with favorable properties. Combining these techniques offers an attractive solution to mine waste management; for example, the addition of waste rock to a filtered tailings stack has the potential to improve stability, reduce overall waste volumes, and enable faster stacking which could make "dry stacked" options economical at the biggest mines.

This paper presents an overview of recent research into the geotechnical properties of filtered tailings and waste rock blends. Results from a series of shear strength and consolidation tests are also presented. It is shown that the addition of waste rock to filtered tailings stacks significantly increases the shear strength and reduces the pore pressure response during placement. This could potentially allow higher and faster lifts to be stacked safely.

1 INTRODUCTION

Waste management and its associated problems is arguably the biggest environmental challenge facing the mining industry. Mining is an inherently waste-producing activity; in open pit mining, large quantities of overburden material are often stripped before ore can be mined. Furthermore, the vast majority of the ore also becomes a waste product; even high grade deposits contain only a few grams per ton of recoverable metal. In typical metal mining operations, ore is recovered in a wet extraction process. The by-product, "tailings", is discharged from the mill in the form of a fluid slurry, typically about 20-40% solids by mass. Conventionally, these are stored behind dams often constructed from the tailings themselves. These structures can present a challenge for reclamation and closure, and are a long-term geotechnical risk and liability. As large, high-profile failures continue to occur, such as the recent Fundão (Morgerstern, Vick et al. 2016) and Córrego do Feijão disasters, tailings dams are increasingly becoming seen as unacceptable by many stakeholders.

A promising new approach is "dry stacking"; deposition of tailings in a self-supporting pile that has the potential to eliminate or reduce the need for a dam. This has now been successfully demonstrated in many commercial-scale metal mining operations (Wickland and Longo 2017). In the vast majority of cases, creating stackable tailings is achieved by using filtration techniques. Another technology that is gaining traction in dry-stacking is waste rock and tailings co-disposal. Combining these techniques offers an attractive solution to mine waste management. Adding co-mingled waste rock to a filtered tailings stack can improve stability, as well as reduce overall waste volumes.

2 BACKGROUND

2.1 *Filtered Tailings*

Densified tailings technologies are broadly divided into 3 categories based on mechanical properties and method of dewatering: Thickened Tailings (TT), typically around 50-65% solids, Paste Tailings (PT), typically 70-80% solids and Filtered Tailings (FT) (>80% solids). Figure 1 summarizes the properties, and pros and cons, of different densified tailings technologies.

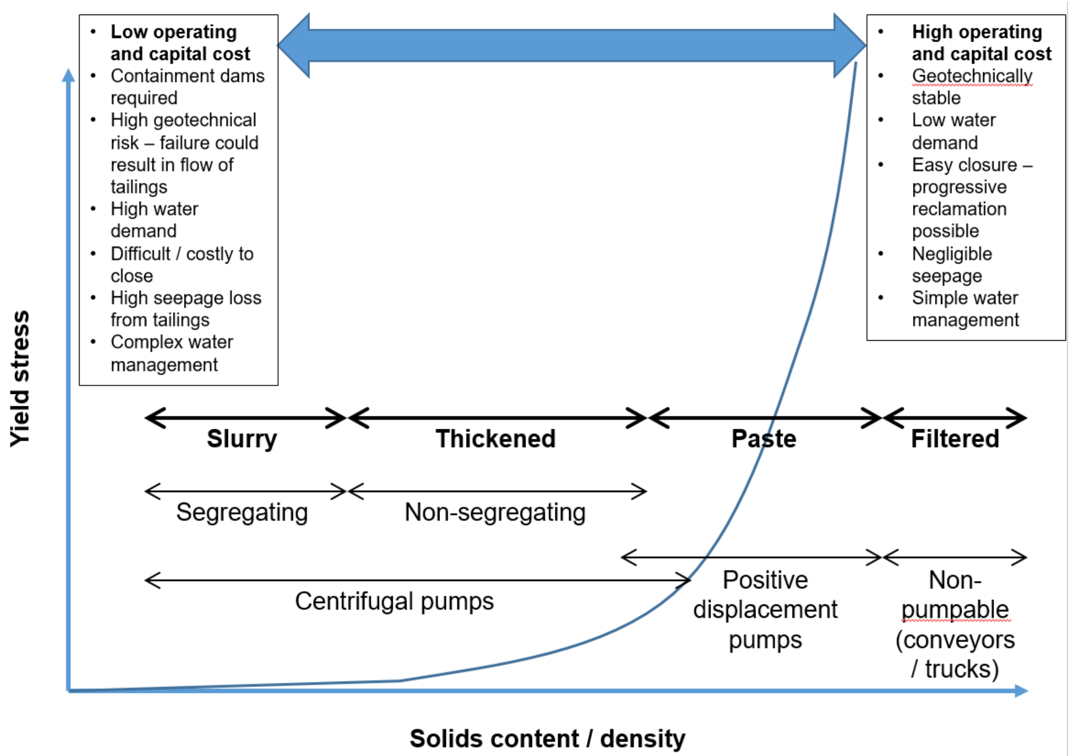

Figure 1. The tailings continuum (after Davies and and Rice (2001) and Jewell and Fourie (2006)).

TT and PT technologies have many potential benefits; namely reduced water consumption, reduced waste volumes and improved geotechnical stability, whilst still maintaining relatively low operating costs and good geochemical performance (Jewell and Fourie 2006, Williams, Seddon et al. 2008). However, some form of containment structure is still required for deposition of TT of PT alone. Construction of a stable, self-supporting deposit requires filtration or co-disposal technologies.

Filtered tailings "dry stacking" is becoming an increasingly popular alternative to traditional methods of tailings disposal and is now widespread in practice (Davies and Rice 2001, Jewell and Fourie 2006, Wickland and Longo 2017). Pressure- or vacuum-filtration is used rapidly dewater the tailings. In a typical operation, filter cakes are dried so they are in the unsaturated condition, transported to the impoundment by truck or conveyor, and then spread and compacted using equipment. This can be a costly and time-consuming process. Perhaps as a result, FT technologies have only been successfully applied at small- to medium-scale operations. The largest mines currently using FT technologies have a throughput around 20,000 tonnes per day.

2.2 *Co-disposal*

In general terms, "Co-disposal" refers to the disposal of waste rock and tailings in the same place. Co-disposal has been applied in many forms with varying degrees of mixing. These include pumped co-disposal, waste rock inclusions in a tailings impoundment, deposition of tailings into waste rock cells, and layered co-disposal. A good overview of these techniques is given by Bussiere (2007); a summary of several co-disposal case histories in given by Habte and Bocking (2017). More recent research has focussed on producing homogenous blends to create an engineered material which has favourable properties, known as "paste rock" (Wilson et al. 2008). Blended co-disposal is the focus of this paper.

The principle behind "paste rock" blends was to create an engineered material which retained the high shear strength and low compressibility of the waste rock skeleton, combined with the low permeability and high water retention properties of the tailings. The focus was more on mitigation of ARD from waste rock dumps, or for use as a cover material, than for dry-stacking. Any non-segregating tailings, typically paste or thickened, could be used. However, the need for a prescriptive "optimum" mix ratio, which is often not compatible with the mine plan, and the high costs compared to traditional methods of tailings disposal, have generally been prohibitive to the commercial application of this technology.

An alternative approach currently under development is co-disposal of filtered tailings and waste rock. Filtered tailings and waste rock blends have the potential to be geotechnically stable at a much wider range of mix ratios, since they do not rely upon a continuous waste rock skeleton. This makes this a more viable and robust technology than thickened or paste tailings and waste rock blends. In practice, mines do not usually produce waste materials in the perfect ratio, and the ratio of waste rock and tailings produced usually varies throughout the life of the mine.

Addition of waste rock has the potential to improve the stability of a filtered tailings deposit by increasing shear strength, and reducing the build-up of pore pressures during stacking. This may enable the material to be stacked rapidly in high lifts without prior drying of the filter cakes, which could make large-scale "dry-stacking" economical at mines with throughputs in excess of 100,000 tons per day. Blending could be achieved using the same system of conveyors that is used to transport the materials.

3 GEOTECHNICAL PROPERTIES

This section gives a brief overview of some of the results of a programme of laboratory tests on filtered tailings and waste rock blends. All mix ratios are given as rock : tailings by dry mass. Samples were blended using a concrete mixer to produce homogenous mixtures. Whilst it is recognized that this is not always representative of field conditions, "perfect" blending is targeted for laboratory trials in order to produce good quality, repeatable results. Due to constraints in equipment size, shear strength tests were scalped to -37 mm and compression tests were scalped to -19 mm. Further details on blending procedure is given by Burden, Wilson et al. (2018).

3.1 *Index properties*

Specific gravity of solids and moisture contents for the waste rock and tailings used in this study are given in Table 1.

Table 1: Index Properties

Material	Specific Gravity G_s	Moisture content w (%)*
Waste Rock	2.76	2.1
Filtered Tailings	2.73	19.3

*Mass of water / Mass of solids

Particle size distributions for the filtered gold tailings and waste rock used in the study are given in Figure 2. Waste rock was scalped in the field to -100 mm.

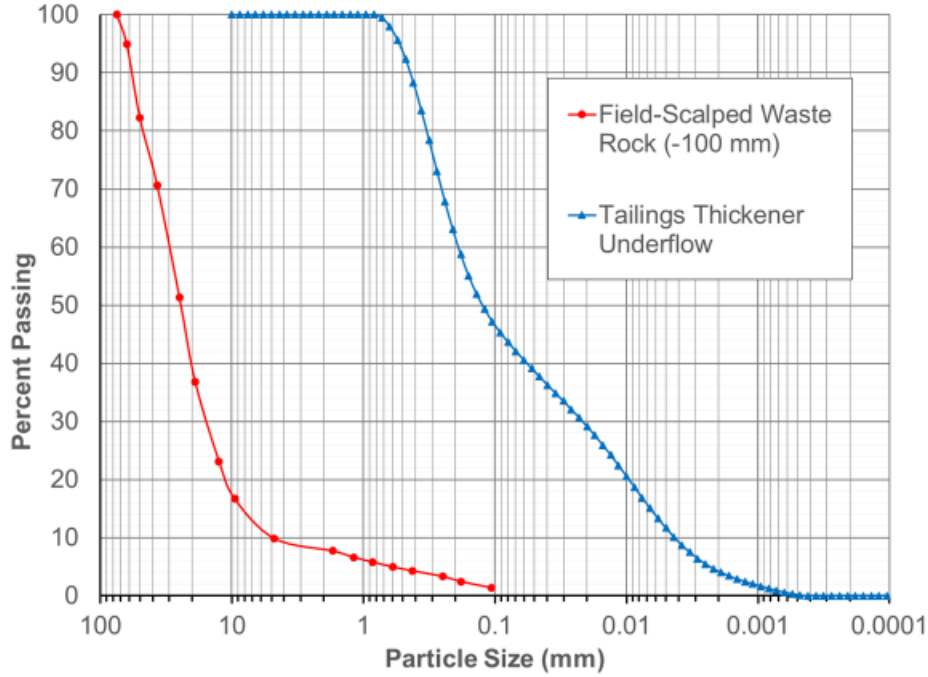

Figure 2. Particle size distributions of waste rock and filtered tailings.

3.2 *Shear strength tests*

Large scale direct shear tests on blends at a range of mix ratios, as well as filtered tailings and waste rock alone. A 300 x 300 mm shear box was used. The blends were tested at their natural moisture contents. A low strain rate of 0.1 mm/min was used to ensure fully drained conditions. Tests were carried out at normal stresses of 250, 500 and 1000 kPa. Results are plotted in Figure 3.

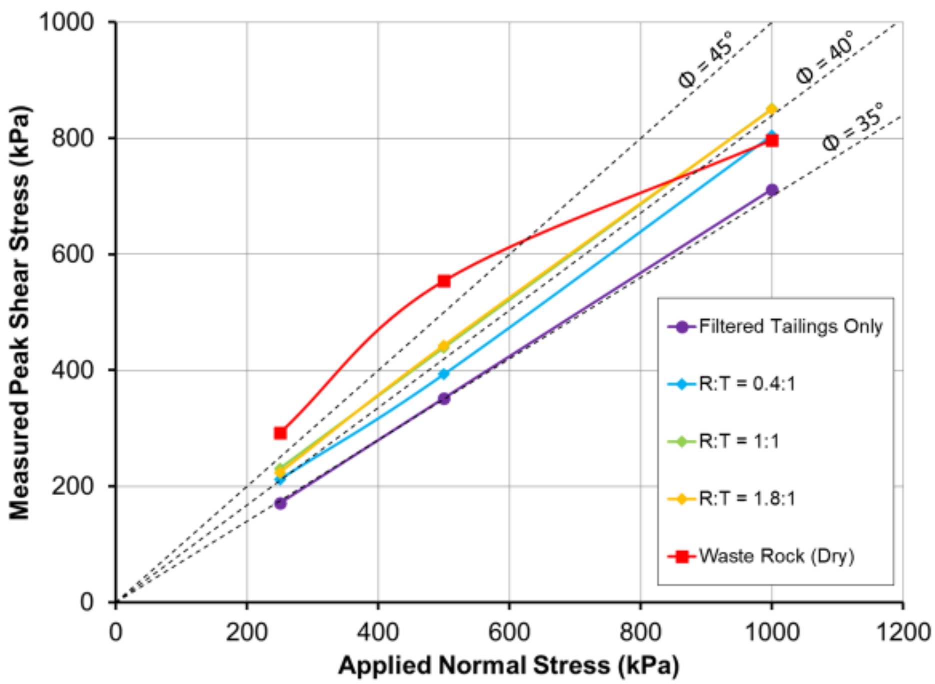

Figure 3. Large Scale direct shear test results for filtered tailings – waste rock blends.

Addition of waste rock to filtered tailings resulted in a significant increase in shear strength. Some rock breakage occurred at 1000 kPa. The results suggest that, at higher stresses where rock breakage may occur, the strength of the blended materials is greater than rock alone. This is probably because the tailings occupy void space between rock particles, reducing the stress at clast-to-clast contacts and resulting in less rock breaking. Significance of this effect would be dependent upon the strength of the waste rock used. It should be noted that for the materials under consideration, the "just filled" point (shown in Figure 2) occurs at a mix ratio of around 1.8. Thus, it can be seen that addition of a relatively small amount rock increases the shear strength significantly, even when the blend is still in the "floating" condition. An increase in strength at the "just filled" point may be expected, however, in the tests here, no improvement in shear strength is evident for mix ratios above 1:1.

3.3 *Compression tests*

The objective of the compression tests was to simulate the stacking of the material at a constant rate of and measure the settlement and pore pressure response. Controlled Rate of Loading (CRL) tests were used, using an incrementally increasing load rate to account for the increasing drainage path length as the stack rises. Preliminary results are presented here, detailed analysis and discussion of the method is beyond the scope of this paper.

The consolidation cell used in this study was a Slurry Consolidometer, custom built to the specifications of the University of Queensland. The cell has an internal diameter of 150mm and is capable of accommodating samples up to 300 mm high. Axial load is applied via a 10 kN high precision electromechanical load frame. It is equipped with top and base load cells, a base pore pressure transducer and further pressure transducers located throughout the height of the cell. Settlement is measured via an LVTD. The device is computer controlled and any combination of load steps and load rates may be applied. Drainage is from the top of the sample only. The Slurry Consolidometer is shown in Figure 4.

Figure 4. Slurry Consolidometer.

Figure 5 shows the base pore pressure response normalized with respect to vertical stress measured at the base. The samples were loaded up to a peak stress of 560 kPa, using an initial seating load of 100 kPa, and thereafter incrementally increasing rate over approximately 2 hours. The load was then maintained and dissipation of excess pore pressure was monitored. Applied stress is plotted on the secondary axis. Actual measured pore pressure is shown on the first plot.

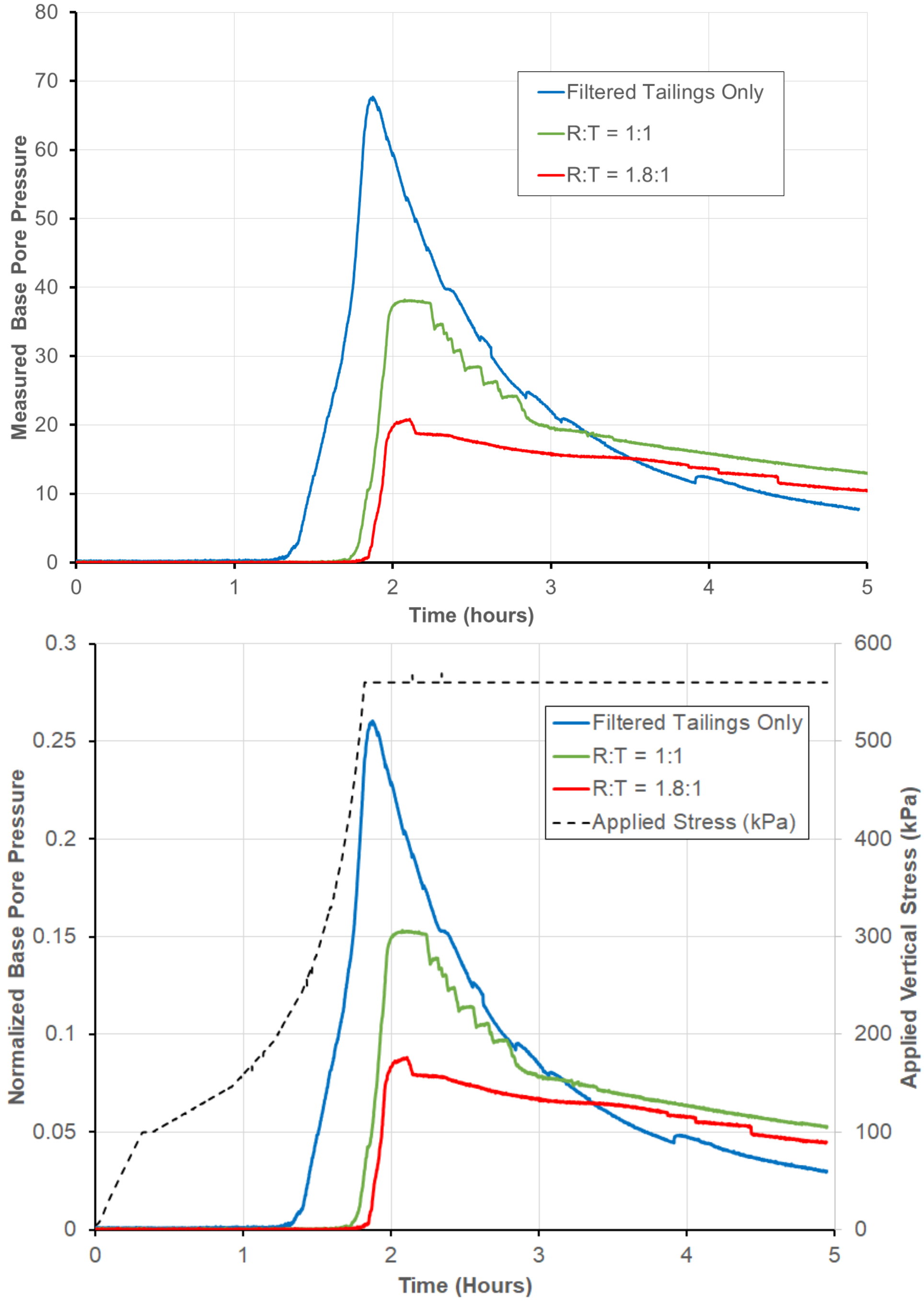

Figure 5. Pore pressure response for filtered tailings and filtered tailings and waste rock blends in CRL test.

The samples are placed loose in the cell at their natural blended moisture content. Initially, the sample undergoes compaction and removal of large air voids. When a continuous water phase forms excess pore pressures develop. The results show that increasing rock content reduces the build-up of excess pore pressures under compressive loading. This suggests that addition of rock to a filtered tailings stack reduced the build-up of pore pressures at the base of the stack, allowing for faster placement in higher lifts.

4 DISCUSSION AND CONCLUSIONS

A dry stack consisting of co-mingled waste rock and filtered tailings has the potential to be more geotechnically stable than filtered tailings alone. It has been shown that increasing rock content increases shear strength, and reduces the build-up of pore pressure during stacking. This may allow dry stacked tailings to be placed rapidly in high lifts. Most mines currently employing filtered tailings technologies operate by spreading and compacting the material in thin lifts, which is equipment-intensive and difficult to scale up, so this new technique may make “dry stacking” more economically viable especially at large mines.

Generally speaking, stacking of waste rock is straightforward because the rock is dry, extremely permeable and pore pressures are not an issue. During “dry stacking” of tailings, pore pressure generation due to compaction is paramount and may result in failure due to undrained loading and liquefaction. Predicting the performance of a dry stacked tailings blend, at a given mix ratio and initial water moisture content, is a critical design question. The slurry consolidometer provides a robust test method to address this need. A range of blends produced by any filtration system or tailings and waste rock types may be quickly and easily evaluated. Once compaction is complete, the system moves to consolidation and drain-down, which can only be evaluated after representative samples have been prepared. These samples could be prepared using the slurry consolidometer. Samples could also be prepared for the tri-axial testing if required.

5 REFERENCES

Burden, R., D. J. Williams, G. W. Wilson and M. Jacobs (2018). The Shear Strength of Filtered Tailings and Waste Rock Blends. Tailings and Mine Waste 2018. Keystone, CO.

Bussiere, B. (2007). "Colloquium 2004: Hydrogeotechnical properties of hard rock tailings from metal mines and emerging geoenvironmental disposal approaches." Canadian Geotechnical Journal 44(9): 1019-1052.

Davies, M. P. and S. Rice (2001). "An alternative to conventional tailings management–“dry stack” filtered tailings." Proceeding of Tailings and Mine Waste’01: 411-420.

Habte, K. and K. Bocking (2017). Co-disposal practice in mind waste management. Tailings and Mine Waste '17. Banff, Alberta, Canada.

Jewell, R. J. and A. B. Fourie (2006). Paste and thickened tailings: A guide, Australian Centre for Geomechanics, The University of Western Australia.

Morgerstern, N., S. Vick and B. Watts (2016). Fundão Tailings Dam Review Panel Report on the Immediate Causes of the Failure of the Fundão Dam.

Wilson, G., B. Wickland and J. Miskolczi (2008). Design and performance of paste rock systems for improved mine waste management. Proceedings of the 1st International Seminar on Management of Rock Dumps, Stockpiles and Heap Leach Pads, Perth, Australia.

Wickland, B. E., G. W. Wilson, D. Wijewickreme and B. Klein (2006). "Design and evaluation of mixtures of mine waste rock and tailings." Canadian Geotechnical Journal 43(9): 928-945.

Wickland, B. and S. Longo (2017). Mine waste case examples of stacked tailings and co-disposal. Tailings and Mine Waste '17. Banff, Alberta, Canada.

Geotechnical characterization of a filtered tailings stack

Daniel Klassen
Klohn Crippen Berger, Vancouver, British Columbia, Canada

Joseph Quinn
Klohn Crippen Berger (UK), York, UK

ABSTRACT: This paper summarizes the geotechnical characterization of a filtered tailings disposal facility at the Hecla Greens Creek polymetallic mine in Alaska. The tailings were placed in the facility during two periods of operations, at first with minimal compaction (old tailings), and later with compaction in lifts (new tailings). Characterization of the tailings is based on the results of site investigation data collected over the course of 25 years, including 8 drilling programs, 3 cone penetration test (CPT) programs, and 7 advanced laboratory testing programs. Laboratory tests performed on the tailings include oedometer tests, direct shear tests, monotonic and cyclic triaxial tests, and monotonic and cyclic direct simple shear tests. A program of triaxial tests on reconstituted samples of tailings was used to define the critical state line and parameters for the NorSand constitutive model, which were then used for inversion of the CPT data to obtain the state parameter. Saturation of the tailings was assessed using P-wave velocities from seismic cone penetration tests, CPT dissipation tests, vibrating wire piezometer readings, tube samples, and field density tests. Monotonic and cyclic strengths from the laboratory tests were interpreted within a critical state framework to link the observed laboratory behaviour to the field via the state parameter.

1 INTRODUCTION

The Greens Creek polymetallic mine is owned and operated by Hecla Mining Company, and is located on northern Admiralty Island, about 29 km southwest of Juneau, Alaska. Filter-pressed tailings from the mill are transported by truck and placed in a filtered tailings stack. Additional details on the operation and design of the tailings disposal facility are described by Erickson et al. (2017) and Butikofer et al. (2017). Until recently, the understanding of the geotechnical behaviour of the tailings has been largely based on laboratory tests, and this has been correlated to field conditions using relative compaction (% Proctor). This approach has limitations since it does not account for the influence of confining stress, and since relative compaction is difficult to measure at depths greater than a few meters. A critical state approach overcomes these limitations because it accounts for the effects of both density and confining stress, and because there are established methods of assessing the in-situ state of soils at depth using the cone penetration test (CPT). This allows the results of the laboratory tests to be linked to the field via the state parameter. The geotechnical characterization of the tailings stack was updated based on this approach, supported by a CPT program. This paper summarizes the results of the characterization.

2 TAILINGS PLACEMENT

Tailings placement in the filtered tailings stack occurred from 1989 to 1993, referred to as "old tailings", and from 1996 to present, referred to as "new tailings". Changes at the mill between these time periods resulted in subtle changes to the tailings, but overall the gradations are quite similar. The primary difference is in the placement methodology. The old tailings were placed in thick lifts (approximately 10 m) with minimal compaction. The new tailings are spread with a bulldozer from the top of a 3H:1V slope, and are track-walked in for compaction, with 0.3 m to 0.5 m lifts on the slope (Erickson et al. 2017). The target density for tailings placement is at least 90% Standard Proctor density, but results of 96% and higher are typical (Erickson et al. 2017).

3 SITE INVESTIGATIONS

Site investigation data on the tailings have been collected in multiple campaigns spanning 25 years, including 8 drilling programs, 3 CPT programs, and 7 advanced laboratory testing programs. In-situ tests on the tailings have included Standard Penetration Tests, seismic CPT, surface geophysics, vane shear, field density, and slug/falling head tests. Advanced laboratory tests have been performed on undisturbed and reconstituted samples and have included oedometer, direct shear, triaxial (drained and undrained, monotonic and cyclic), and direct simple shear tests (DSS; monotonic and cyclic). Vibrating wire piezometers have been installed in the tailings to monitor pore water pressures.

One of the laboratory test programs was performed on high-quality samples obtained by pushing 230 mm long, 75 mm diameter tubes into the tailings surface in an excavated area of the tailings stack, as described by Butikofer et al. (2017). A more recent site investigation program included seismic CPTs and laboratory tests on both standard Shelby tube samples and reconstituted samples at a range of void ratios.

4 TAILINGS DESCRIPTION

The index properties are generally consistent between the new and old tailings. A summary of the index properties is presented in Table 1, which shows that they tend to cluster within a narrow range of low-plasticity fine tailings. The range of tailings gradation is illustrated on Figure 1, which also shows the gradation of a bulk sample used in this study to prepare reconstituted samples to characterize the tailings.

Table 1. Tailings index properties

Parameter	Old / New Tailings	Minimum	16th Percentile	Median	Mean	84th Percentile	Maximum	Number of Tests
Plasticity Index	Old	1	1	4	4	7	9	11
	New	0	1	2	3	5	7	49
	Both	0	1	3	3	6	9	60
Liquid Limit	Old	14	18	20	20	22	27	11
	New	14	16	18	19	21	26	49
	Both	14	16	19	19	21	27	60
Water Content (Gravimetric)	Old	11	14	15	16	19	21	33
	New	3	11	14	14	18	38	594
	Both	3	11	14	15	18	38	627
Fines Content (< 75 mm)	Old	78	83	91	89	95	97	13
	New	65	77	82	82	86	96	116
	Both	65	77	83	83	88	97	129
Clay Content (< 2 mm)	Old	3	4	11	10	16	18	10
	New	0	3	6	6	9	12	114
	Both	0	3	6	7	9	18	124
Specific Gravity	Old	3.13	3.19	3.26	3.31	3.46	3.50	5
	New	3.13	3.32	3.44	3.45	3.59	3.76	89
	Both	3.13	3.29	3.44	3.44	3.59	3.76	94

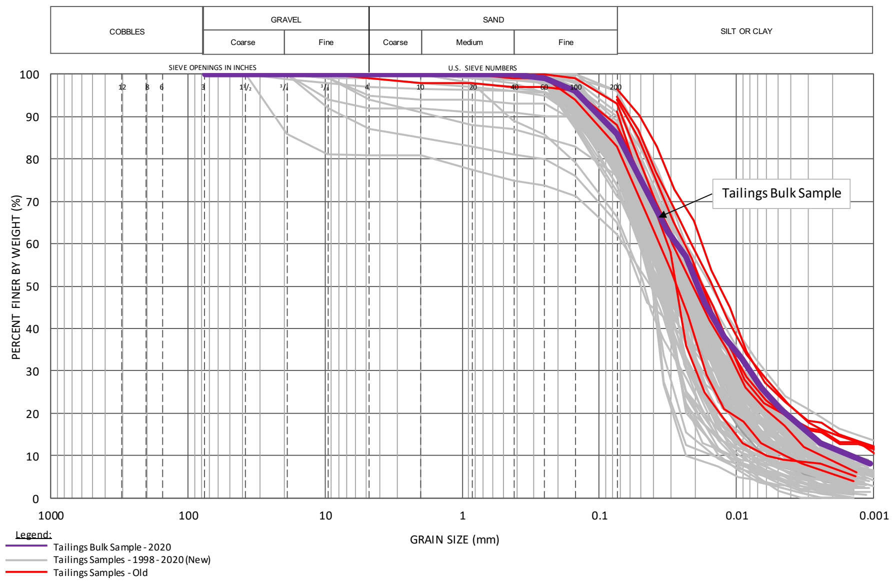

Figure 1. Tailings grain size distribution.

The mineralogy of the tailings was assessed in 2009 using 12 samples from four boreholes (Lindsay et al. 2009). The primary component in the tailings samples was found to be pyrite, which has led to a higher specific gravity than typical in natural soils (see Table 1). A breakdown of the tailings mineralogy is shown in Table 2.

Table 2. Tailings mineralogy.

Mineral Type	Chemical Formula	Percent by Weight (Average)	Standard Deviation
Pyrite	FeS2	34.3	4.3
Dolomite	CaMg(CO3)2	27.2	3.0
Quartz	SiO2	12.1	3.6
Barite	BaSO4	12.0	3.8
Muscovite	KAl2AlSi3O10(OH)2	3.8	2.5
Calcite	CaCO3	3.4	0.8
Sphalerite	(Zn,Fe)S	2.5	1.0
Cymrite	BaAl2Si2(O,OH)8·H20	2.1	0.6
K-feldspar	KAlSi3O8	1.5	0.6
Chlorite	(Mg,Fe)5Al(Si3Al)O10(OH)8	1.5	0.4
Hydroxylapatite	Ca5(PO4)3(OH)	1.2	0.3
Galena	PbS	0.7	0.2

5 STATE PARAMETER

The aim of the work summarized in this paper was to develop a state-based interpretation of the Greens Creek tailings. As such, focus was placed on estimating the in-situ state parameter of the tailings. The first step in this process was to develop a critical state line (CSL), which was developed from a series of isotropically consolidated drained and undrained triaxial compression tests on the bulk sample illustrated in Figure 1 (see Figure 2). These triaxial tests were prepared by moist tamping using material from the bulk sample.

Having identified the CSL, this was used to estimate the in-situ state parameter (ψ). The approach taken to estimate ψ was to use the CPT inversion methodology outlined by Jefferies and Been (2016) and to compare the results with the Plewes et al. (1992) and Robertson (2010) empirical methods. The CPT inversion method involves completing numerical simulations of an expanding spherical cavity, which can be related to CPT penetration and used to infer ψ from CPT tip resistance. These simulations are completed using the constitutive soil model NorSand, which is based on the CSL and other parameters that can be obtained from triaxial testing.

The results (Figure 3) showed that the old tailings, which were placed with minimal compaction, are looser than the new tailings, which are systematically compacted during placement. Figure 3 also shows that the results from the CPT inversion methodology tended to plot between those of the empirical methods.

The distribution of old tailings is bimodal, with the largest peak at ψ = +0.04 and a second smaller peak at ψ = -0.08. The dilative zones of the old tailings likely correspond to the surfaces of compacted lifts, and the contractive zones in between are uncompacted. This observation was used to separate the old tailings into dense and loose subunits, as summarized in Table 3. Table 3 also summarizes various statistics for the ψ distributions for the old and new tailings.

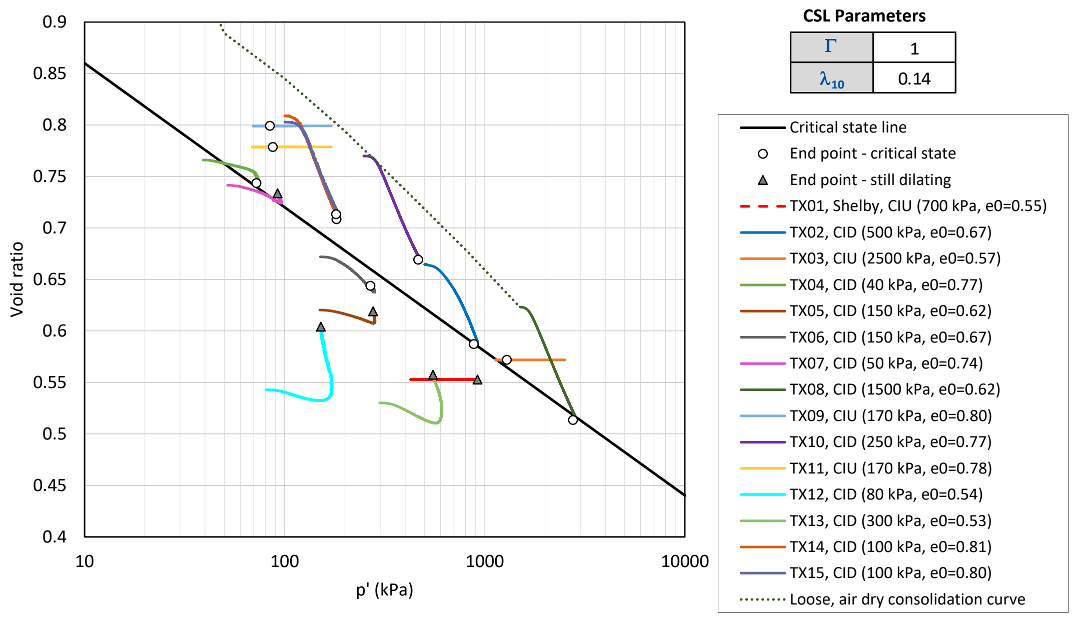

Figure 2. Tailings critical state line.

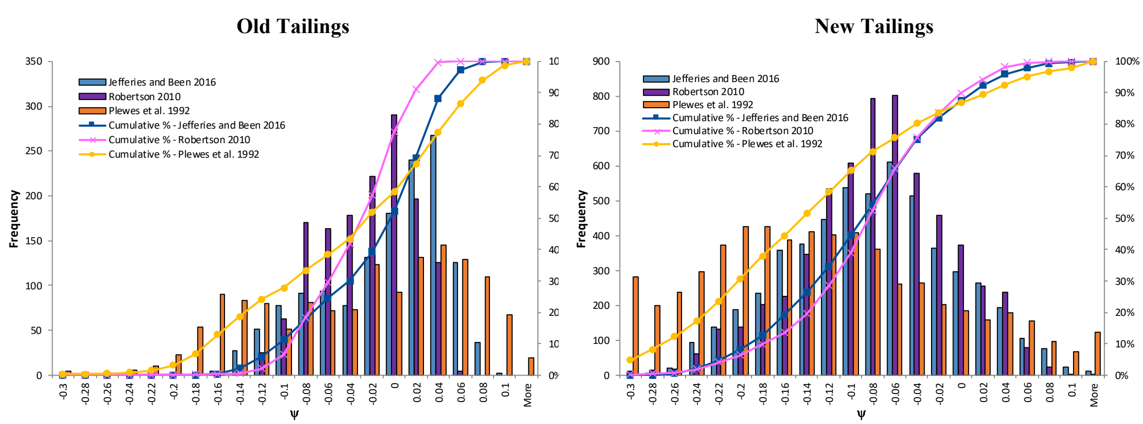

Figure 3. Tailings state parameter.

Table 3. Tailings state parameter statistics.

Old/New Tailings	State Parameter, ψ		
	50th percentile	80th percentile	90th percentile
Old Tailings (All)	0.00	0.03	0.04
Old Tailings (Uncompacted Layers)	0.01	0.04	0.05
New Tailings	-0.09	-0.03	0.01
All Tailings	-0.08	0.00	0.03

6 SATURATION

Saturation of the tailings was assessed by several methods. Compression wave velocity (V_p) from the seismic CPT data ranged from 350 m/s to 1450 m/s, whereas V_p for saturated soils exceeds 1450 m/s to 1500 m/s (Jamiolkowski 2012), suggesting that the tailings may be partially unsaturated. However, many of the piezometers and CPT dissipation tests showed positive pressures consistent with saturated conditions, as shown in the left plot in Figure 4. The CPT data showed both negative and positive excess pore pressure responses, as indicated by the middle plot (B_q) in Figure 4, which shows that layers with significant positive pore pressure response occur at a range of elevations are not limited to the base of the stack. Degree of saturation was also calculated based on various field density test methods, and from trimmed samples extruded from both high-quality samples and standard Shelby tubes, as shown in the right plot of Figure 4. Based on these results, the tailings are predominately unsaturated, but the degree of saturation is typically high, with localized saturated zones (at a smaller scale than is tested by V_p measurements, which were collected at 1 m depth intervals).

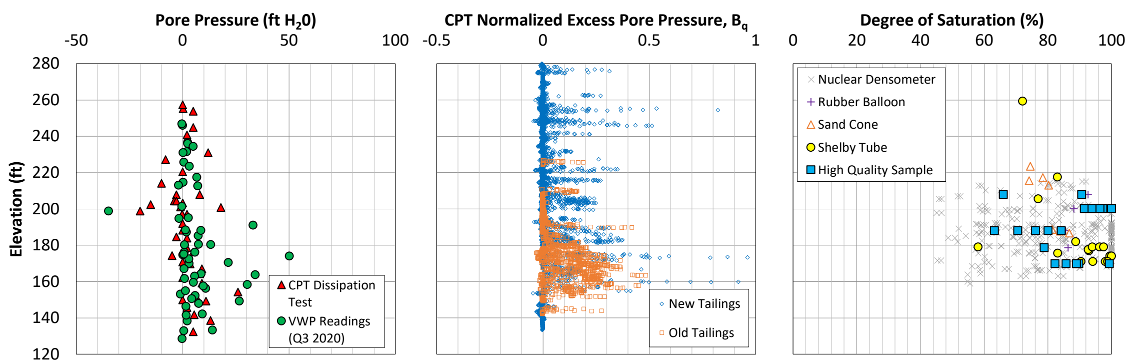

Figure 4. Pore pressure and degree of saturation measurements.

7 STRENGTH

The friction angle of the tailings was assessed from drained and undrained triaxial tests, and the component of friction due to stress dilatancy (peak minus critical state friction angle) is compared to data from Jefferies and Been (2016) in Figure 5. A trendline was plotted through the data as shown, and this was used to relate in-situ state parameter from the CPT inversion to peak friction angle. Critical state friction angles of 34° for old tailings and 35° for new tailings were used based on triaxial and direct shear tests. Representative peak friction angles of 34° and 36° were selected for old tailings and new tailings, respectively.

Undrained strength was assessed from laboratory undrained triaxial and DSS tests, and from CPT data, as shown in Figure 6. The two lowest laboratory peak undrained strength ratio (s_u/σ'_{vo}) results are for the only samples tested that were non-plastic, and the calculated state parameter for these samples may be inaccurate due to variability in the CSL. The calculation of s_u/σ'_{vo} from CPT data used the method of Lunne et al. (1997) with an empirical cone factor of N_{kt}=18, which was based on a comparison of the CPT to vane shear tests (VST) in adjacent drill holes. There was significant scatter in this comparison, so only the VSTs with the lowest corresponding CPT tip resistance values were used, as the higher values likely had a greater influence of partial drainage and are not reliable. The CPT data in Figure 6 are filtered to only show results with significant positive excess pore pressure response ($B_q > 0.1$), where it is expected that conditions were likely close to undrained during the CPT. Both the laboratory and field data show significant scatter in s_u/σ'_{vo}, with the lowest values around 0.2, representing strengths in the loosest saturated zones.

The design strengths account for these low strength zones as well as performance observations of the larger-scale behaviour. An example of this performance data is that of a historical excavation in the tailings, where no movement was observed despite steep slopes (in excess of 45°).

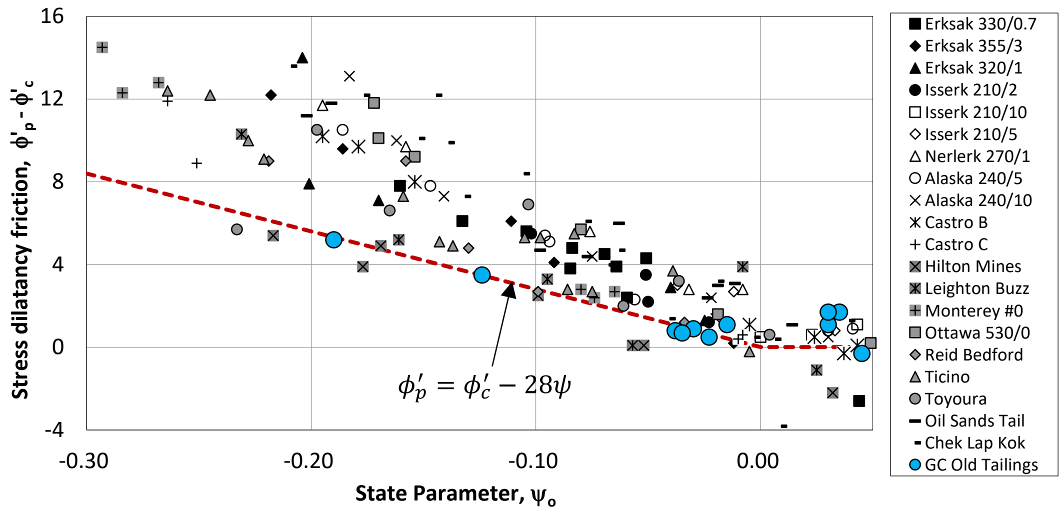

Figure 5. Relationship between friction angle and state parameter from triaxial tests.

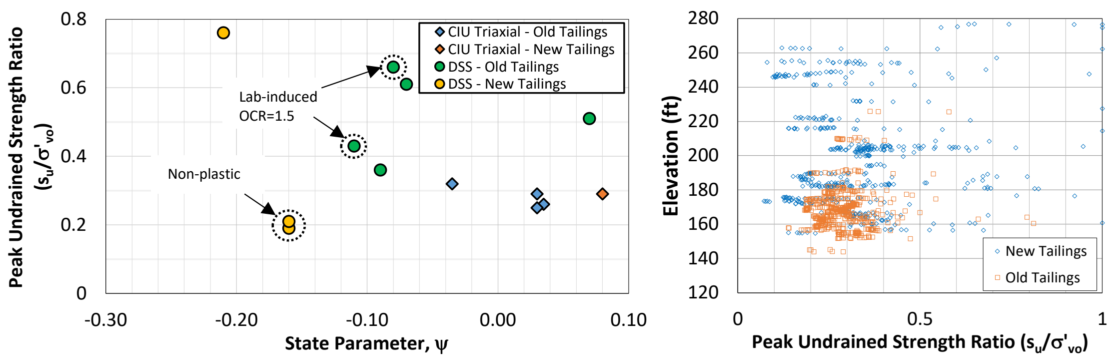

Figure 6. Peak undrained strength ratio from laboratory tests (left) and CPT data (right).

8 CYCLIC BEHAVIOUR

Cyclic laboratory testing of high-quality samples of tailings was described by Butikofer et al. (2017). These tests were compiled with all historical cyclic testing (including a few cyclic triaxial tests on reconstituted samples), plus additional cyclic DSS tests performed on 2019 samples, and results are plotted in terms of cyclic stress ratio (CSR) vs number of cycles to 5% double amplitude strain in Figure 7 (left plot). The results show significant scatter in cyclic resistance, but with a well-defined lower bound. The tests showed gradual accumulation of shear strains, with excess pore pressures reaching less than 100% of the initial vertical effective stress, indicating clay-like behaviour (cyclic softening rather than liquefaction). A curve was plotted through the lower end of the data using the form $CSR=a\times N_{cyc}^{-b}$, with a b value of 0.15 giving a good fit. Cyclic resistance ratio at 30 loading cycles (CRR_{30}) was estimated for each data point by extrapolation using similar curves with a constant b value, and the results are plotted against initial state parameter in the right plot of Figure 7. Plotting in terms of state parameter significantly reduces the scatter, and a trendline is evident that passes close to most of the data, as shown. The trendline is steep at strongly negative state parameters, but relatively flat at contractive or lightly dilative values. These CRR values represent the saturated behaviour, and unsaturated zones in the tailings will likely have greater cyclic resistance.

Post-cyclic undrained strength ratio is plotted against initial state parameter in Figure 8. The lower bound of the data is comparable to the results from a correlation by Jefferies and Been (2016) and represents a relatively modest strength loss compared to the lower bound of peak undrained strength ratio (from approximately 0.20 to 0.15, 25% strength loss), which is reasonable for a clay-like material.

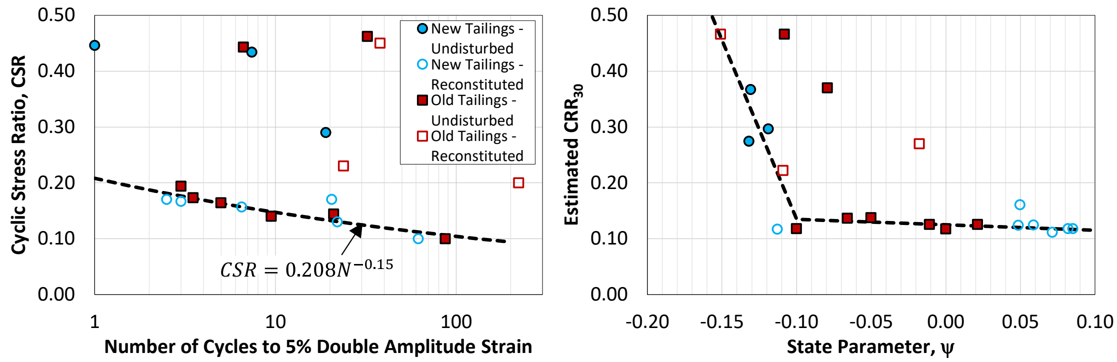

Figure 7. Cyclic test results.

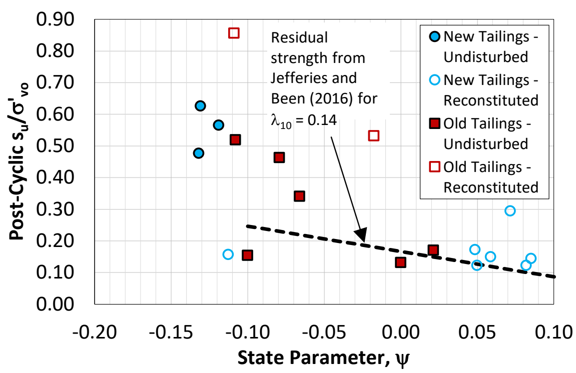

Figure 8. Post-cyclic undrained strength ratio.

9 AGEING

The effect of ageing on the tailings was investigated by comparing CPT data collected in 1997, and 2018 to CPT data collected at approximately the same locations in 2019, and example results are plotted in Figure 9. These results suggest that ageing of the tailings improves the large strain behaviour in the short term (i.e., more dilative, higher minimum undrained strength) but degrades it in the long term (i.e., more contractive, lower minimum undrained strength, greater positive pore pressure response). The causes for these changes are uncertain. Cementation may play a role in the short-term improvement in behaviour. The long-term changes to behaviour are likely caused at least in part by increases in confining stress due to ongoing tailings placement between CPT measurements, but it is not clear whether the estimated stress increase (~250 kPa to 500 kPa) fully accounts for the observed increase in state parameter, so there may be another contributing factor (e.g., chemical processes).

The effect of ageing on the elastic and plastic moduli is of interest for predicting changes in undrained strength over time. Jefferies and Been (2016) presented NorSand simulations of undrained triaxial tests to show that the peak undrained strength and the rate of post-peak softening are affected by the ratio of the plastic hardening modulus (H) and the elastic shear rigidity index (I_r=G/p'). Thus, changes to one of these values without a corresponding change to the other would result in changes to the undrained strength. This was investigated by performing two laboratory triaxial tests on reconstituted specimens that were aged under constant confining stress for 3 days and 31 days. Bender element tests were performed during ageing to track changes in shear wave velocity, and the results are plotted in terms of elastic (small-strain) shear modulus in Figure 10. The results show that elastic stiffness increases linearly with logarithmic time, which is consistent with research on natural soils (e.g., Anderson and Stokoe 1978, Mesri et al. 1990). Schmertmann (1991) presents data to show that this increase in stiffness can occur due to secondary compression effects, such as dispersive particle movements, particle interlocking, and internal stress arching, without the influence of cementation and bonding at the particle contacts.

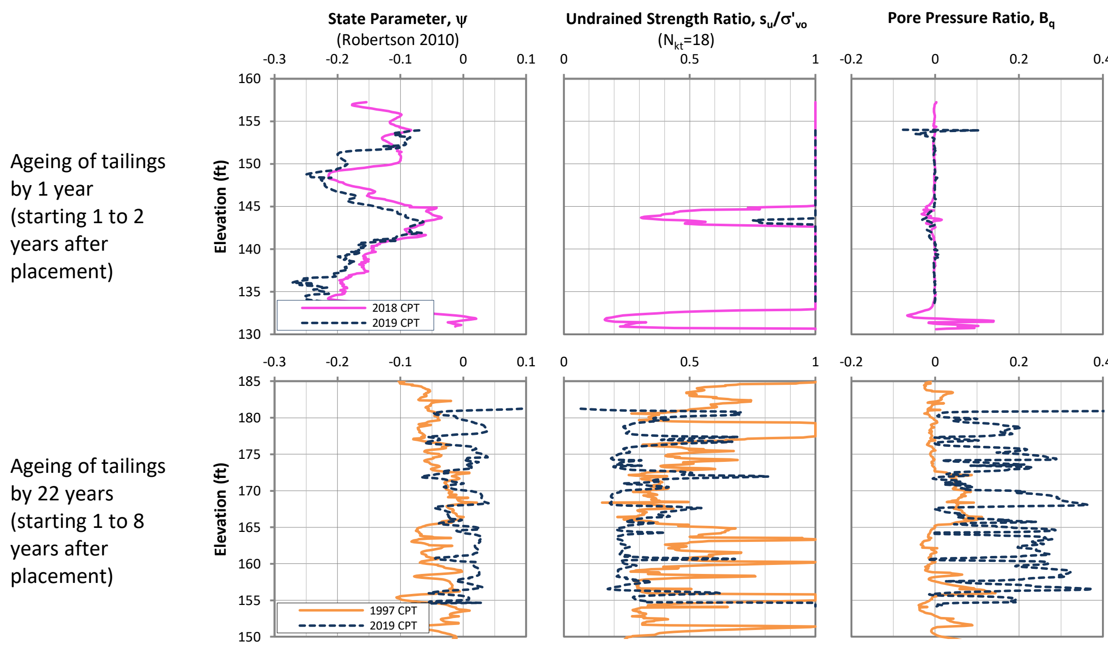

Figure 9. Example CPT comparison for ageing assessment.

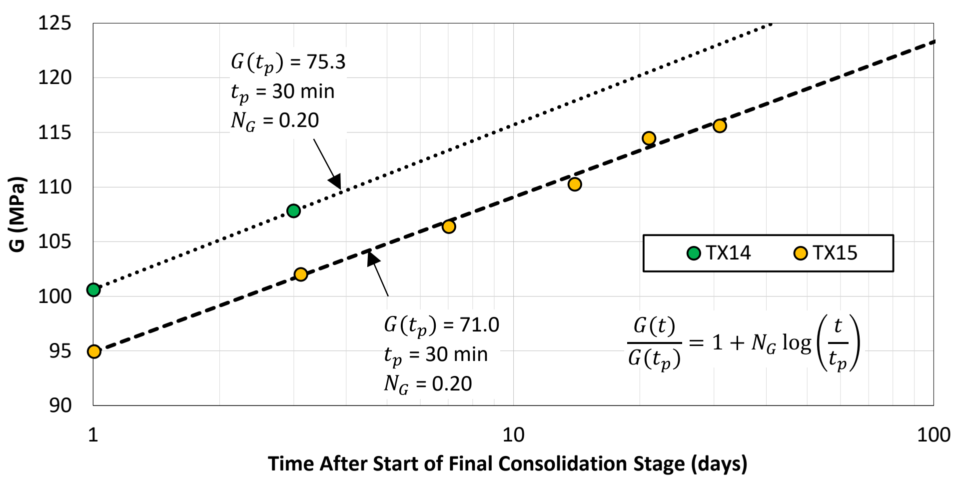

Figure 10. Shear modulus versus time from laboratory bender element tests.

The trendline equation shown in Figure 10 is from Howie et al. (2002), where t_p is the time to end of primary consolidation (30 minutes for these tests), G(t) and G(t_p) represent the shear modulus at times t and t_p, respectively, and N_G represents the % increase (expressed as a fraction) in the shear modulus per log cyclic of ageing time. An N_G value of 20% gives an excellent fit to both tests. Typical N_G values in sands, silts and clays are 1-3%, 3-6%, and 6-19%, respectively (Schmertmann 1991), so the tailings are at the upper end of the range expected for clays. Given the low clay content of the tailings, the secondary compression effects discussed above are likely insufficient to cause this degree of stiffness increase, so there may also be cementation or other processes contributing.

Extrapolating these results to 30 years (the maximum age of the tailings) gives a shear modulus 1.6 times higher than that measured at 1 day of ageing in the laboratory. This increase is consistent with some of the field V_s measurements but does not account for the data showing high stiffness in zones that are significantly younger than 30 years. Thus, additional increases in stiffness are likely occurring in the field, perhaps due to chemical processes.

The triaxial tests on aged samples were also used to investigate changes in plastic hardening modulus (H) over time, where H was interpreted from NorSand simulations of the triaxial tests. Shearing was performed under drained conditions for these tests which makes it easier to interpret H. Since H also varies with state parameter, the values extrapolated to zero state parameter (H_0) were used to compare between samples, and the results are plotted against ageing time in Figure 11. Apart from three tests with unusually high H_0, the tests showed consistent plastic hardening modulus over time.

Therefore, it is expected that the in-situ elastic modulus has increased over time but plastic modulus has not. As shown in Figure 12, this is expected to reduce the peak undrained strength and the quasi-steady state strength compared to unaged specimens in the laboratory.

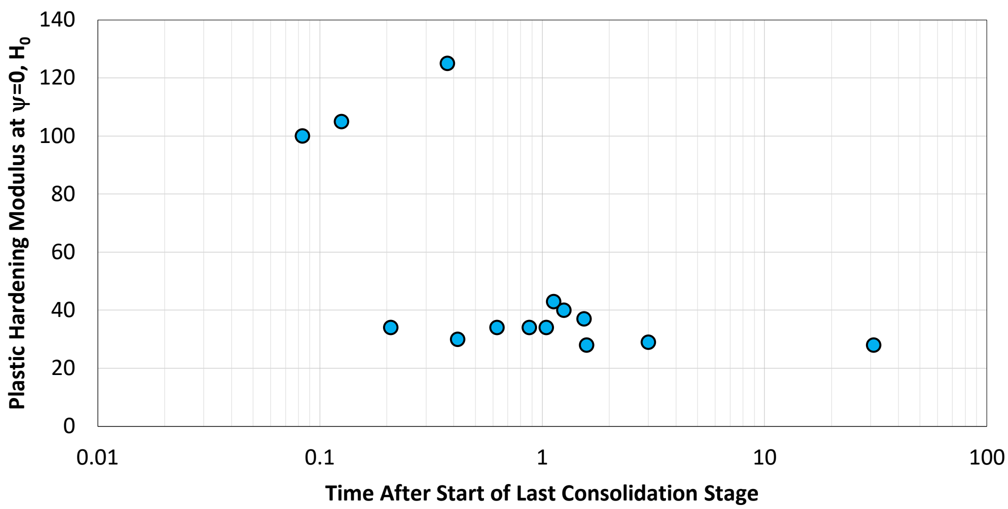

Figure 11. Plastic hardening modulus versus ageing time from triaxial tests.

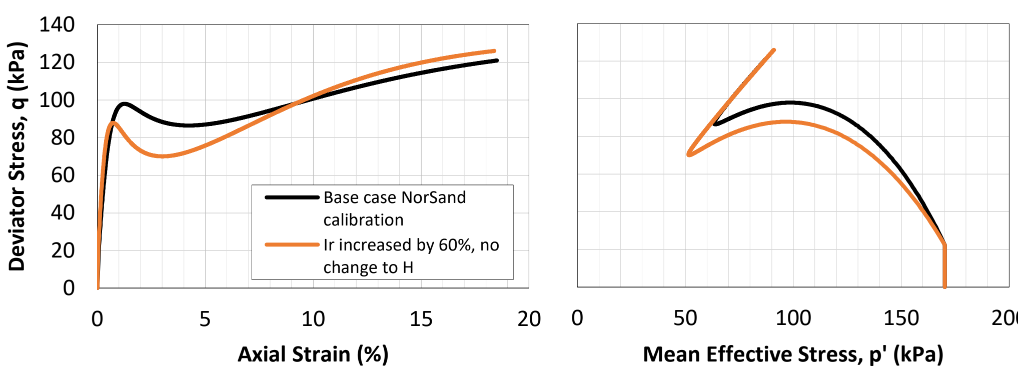

Figure 12. Effect of increasing I_r without increasing H on NorSand undrained triaxial test simulations.

10 CONCLUSIONS

Field and laboratory test data were compiled and interpreted to inform the geotechnical characterization of the Greens Creek filtered tailings stack. The tailings are predominately unsaturated, but with a typically high degree of saturation and local saturated zones. The CPT data show that the tailings are heterogeneous and range from strongly dilative to lightly contractive. Cyclic tests on the contractive tailings show clay-like behaviour with gradual accumulation of shear strains. Post-cyclic tests show that the loosest zones in the tailings may experience a relatively modest strength loss of 25% if they experience significant earthquake shaking. Comparison of CPT data from different site investigation programs shows that the tailings behaviour improves in the short term, but degrades in the long term, and the reasons for these changes are not clear. Laboratory tests on samples that were aged under constant confining stress in the laboratory show that the elastic modulus increases at a faster rate than most natural soils, but no change in the plastic modulus over time was observed, suggesting that a slight decrease in the peak undrained and quasi-steady state strengths may occur over time.

11 REFERENCES

Anderson, D.G. and Stokoe, K.H., 1978. "Shear modulus: A time-dependent soil property." In *Dynamic geotechnical testing*. ASTM International. 66-90.

Butikofer, D., Erickson, B., Marsh, A., Friedel, R., Murray, L. and Piggott, M.J. 2017. "Filtered Tailings Disposal Case History: Operation and Design Considerations Part II." in *Proceedings, International Conference on Tailings and Mine Waste, Banff, Alberta, Canada, November 5-8, 2017*. Edmonton, AB: University of Alberta Geotechnical Centre.

Erickson, B., Butikofer, D., Marsh, A., Friedel, R., Murray, L. and Piggott, M.J. 2017. "Filtered Tailings Disposal Case History: Operation and Design Considerations Part I." in *Proceedings, International Conference on Tailings and Mine Waste, Banff, Alberta, Canada, November 5-8, 2017*. Edmonton, AB: University of Alberta Geotechnical Centre.

Howie, J.A., Shozen, T. and Vaid, Y.P. 2002. "Effect of ageing on stiffness of very loose sand." *Canadian Geotechnical Journal*. 39(1): 149-156.

Jamiolkowski, M. 2012. "Role of geophysical testing in geotechnical site characterization." 3rd De Mello Lecture. Portuguese-Brazilian Geotechnical Congress. *Soils and Rocks*. 35(2): 117-140.

Jefferies, M. and Been, K. 2016. *Soil Liquefaction: A Critical State Approach*. CRC press.

Lindsay, M., Condon, P., Jambor, J., Lear, K., Blowes, D., and Ptacek, C. 2009. "Mineralogical, geochemical, and microbial investigation of a sulfide-rich tailings deposit characterized by neutral drainage." *Applied Geochemistry*. 24: 2212-2221.

Lunne, T., Robertson, P.K., and Powell, J.J.M. 1997. *Cone penetration testing in engineering practice.* Blackie Academic, EF Spon/Routledge Publ., New York.

Mesri, G., Feng, T.W. and Benak, J.M. 1990. "Postdensification penetration resistance of clean sands." *Journal of Geotechnical Engineering*. 116(7): 1095-1115.

Plewes, H.D., Davies, M.P., and Jefferies, M.G. 1992. "CPT Based Screening Procedure for Evaluating Liquefaction Susceptibility," *in Proceedings of the 45th Canadian Geotechnical Conference, October 1992,* Toronto, Ontario. pp. 41-49.

Robertson, P.K. 2010. "Estimating In-Situ State Parameter and Friction Angle in Sandy Soils from CPT," in *Proceedings of the 2nd International Symposium on Cone Penetration Testing (CPT'10), May 2010*, Huntington Beach, California.

Schmertmann, J.H. 1991. "The mechanical aging of soils." *Journal of Geotechnical Engineering*. 117(9): 1288-1330.

Are you considering the potential for human factors to impact your tailings dam safety?

Lucy Philip
Stantec Consulting Ltd., Calgary, Alberta, Canada

ABSTRACT: Traditionally, when tailings dams have safety issues, we think "technical", however, there is increasing evidence that human factors contribute.

What are human factors? They range from: the way we review evidence, make decisions and approach risk; unconscious social pressures; error; work cultures, whether dam safety management systems, company cultures or educational/mentoring; to preventing complacency and. remaining vigilant.

We need to recognise and address human factors and we can learn from other groups where human factors contribute to poor outcomes:

- Medical profession: errors are reported as a leading cause of death, with a variety of human factors implicated.
- Backcountry recreationists: qualified, experienced groups succumb to avalanche hazard, despite advances in equipment, forecasting and technology.
- Maritime industry: human factors cause up to 80% of oil spills and marine accidents.

This paper discusses human factors that impact dam safety and how dam safety systems and cultures can reduce the potential for human factors.

1 BACKGROUND TO HUMAN FACTORS, HEURISTICS AND HEURISTIC TRAPS

Human factors refer to environmental, organisational and job factors, and human and individual characteristics, which influence behaviour that can affect health and safety (HSE 1999).

Heuristics are simple, efficient rules, instilled by evolutionary processes, that explain how people make decisions, come to judgements, and solve problems, typically when facing complex problems or incomplete information. These rules work well under most circumstances, and can ease the cognitive load, but they also can lead to errors or cognitive biases, especially when using heuristic thinking instead of analytical evaluation in unpredictable, high-risk environments.

Heuristics are often referred to as rules of thumb, educated guesses, or mental shortcuts. They usually involve pattern recognition and rely on a subconscious integration of somewhat haphazardly gathered data with prior experience, rather than on a conscious generation of a rigorous analysis that is formally evaluated. Such informal reasoning is fallible and may lead to several types of unconscious bias (Mandell, 2021). Heuristic traps are mental shortcuts that can result in common decision-making flaws, such as cognitive biases (McCammon 2002 and 2004).

1.1 *Expert Halo*

Of the heuristic traps, expert halo is worth explaining further, as we regularly rely on experts for safe management of dams. Experts, like everyone, are subject to heuristic traps, and experts can also be hard to spot. The reason experts are hard to spot relates to confidence, which is not related to skills or experience and should not be used as an indication of expertise. The Dunning-Kruger effect (Kruger & Dunning 1999) presented in Figure 1 demonstrates this.

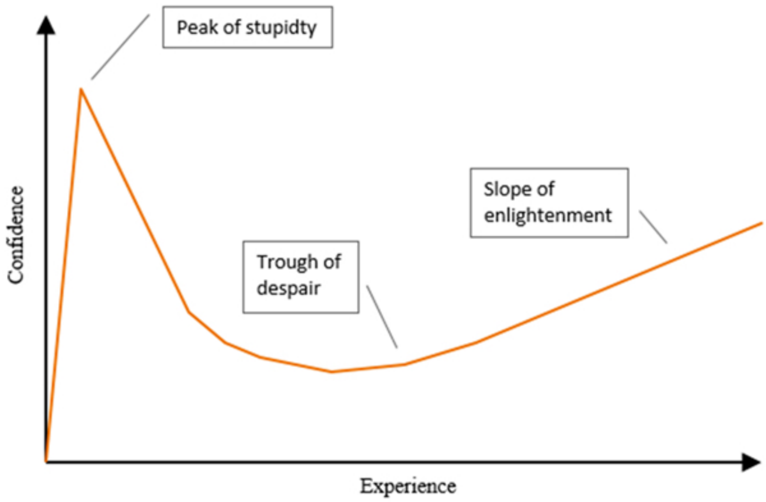

Figure 1. The Dunning-Kruger effect

Kruger and Dunning 1999, found that people have a pattern of overlooking their own weaknesses and, in doing so, tend to overestimate themselves and their abilities. In other words, people really seem to believe they have expertise and value their own contributions in a biased way. Initially, without experience, people are highly confident, they don't know what they don't know, referred to as the "peak of stupidity". As people then realise what they don't know, they progress into a confidence crash, "the trough of despair", and then slowly gain confidence on the "slope of enlightenment", never re-achieving or fully recovering the early confidence level.

2 BACKGROUND TO COGNITIVE BIASES

First proposed by Tversky & Kahneman (1974), cognitive biases are systematic errors in thinking that occur when people process and interpret information, affecting decisions and judgments that people make. These biases can also be thought of as systematic patterns of deviation from rationality, which occur due to the way our cognitive system works. Accordingly, cognitive biases cause us to be irrational in the way we search for, evaluate, interpret, judge, use, and remember information, as well as in the way we make decisions (Vinney 2018). Everyone exhibits cognitive bias, and no-one is exempt (Cherry 2020). Bias can increase mental efficiency, but can also distort thinking, leading to poor decision making and false judgements. Cognitive biases can be caused by emotions, heuristics, motivations and social pressures.

Heuristics and cognitive bias are related terms; a heuristic is a rule, a strategy or mental shortcut whereas a systematic error resulting from the using a heuristic is called cognitive bias.

3 HUMAN FACTORS IN OTHER PROFESSIONS AND INDUSTRIES

Whilst human factors have been extensively applied in other industries, such as aviation, maritime, recreationists, nuclear power, chemical processing and healthcare, for many years, application of human factors to the dam industry is much more recent, and the industry is only just beginning to recognise the importance. There are many parallels that can be applied to dam safety, and it is worthwhile reviewing learnings and experiences from some of those industries.

3.1 *Human Factors in the Medical Profession*

Medical errors are reported as the third leading cause of death in the US, after heart disease and cancer (Makery &Daniel 2016), with recent studies citing around 250,000 deaths per year costing around $20 billion (US) per year caused by errors (Rodziewicz et al 2021).

Medical error has been defined as an unintended act either of omission or commission (the wrong action taken) (Makery & Daniel 2016 and Rodziewicz et al 2021) or one that does not achieve its intended outcome, the failure of a planned action to be completed as intended (an error of execution), the use of a wrong plan to achieve an aim (an error of planning), or a deviation from the process of care. Like dam safety, patient harm from medical error can occur at an individual or system level. Makery & Daniel (2016) report that human error is inevitable and, although it can't be eliminated, we can better measure the problem, to design safer systems, mitigating its frequency, visibility, and consequences. They believe strategies to reduce death from medical care should include:

- Making errors more visible so their effects can be intercepted, i.e., monitoring in dams.
- Having remedies at hand to rescue patients, i.e., emergency planning in dam safety.
- Making errors less frequent by following principles that take human limitations into account, i.e., accounting for human factors such as cognitive biases.
- Safety triggers to alert staff, i.e., Trigger Action Response Plans in dam safety, facilitating a culture of speaking up, fostering a safety culture and engineering hard stops for prevention.

The Word Health Organisation recognises that human factors apply wherever humans work and contends that the traditional approach to medical error is a "perfectibility" model, which assumes that if health-care workers care enough, work hard enough, and are well trained, errors won't occur. WHO reports this attitude as counter-productive and untrue (WHO 2012).

Recent work has looked at the role of cognitive bias in medical errors (Saposnik et al 2016, O'Sullivan & Schofield 2018). O'Sullivan & Schofield (2018) report that significant diagnostic error can result from cognitive bias and that, most likely, all clinical decision-makers are at risk of bias error, which they describe as ubiquitous and not correlating with intelligence or any other measure of cognitive ability. Ironically, a lack of insight into one's own bias is common, demonstrated by doctors who described themselves as "excellent" decision-makers "free from bias" subsequently scoring poorly in formal tests. The causes of bias include learned or innate biases, social and cultural biases, a lack of appreciation for statistics and mathematical rationality, and environmental stimuli competing for attention. Up to 75% of errors in internal medicine are thought to be cognitive, and such errors are identified in all steps of the diagnostic process. Overconfidence, tolerance to risk, anchoring, and information and availability biases have been associated with 37 to 77 % of cases (Saposnik et al 2016). Table 1 presents key biases.

Table 1. Cognitive biases in medicine (O'Sullivan & Schofield, 2018, Mandell, 2021, CMPA unknown)

Bias	Description
Availability bias	More recent and readily available answers and solutions are preferentially favoured because of ease of recall and incorrectly perceived importance.
Base rate neglect	This occurs when the underlying incident rates of conditions or population-based knowledge is ignored as if they do not apply to the patient in question.
Confirmation bias	Diagnosticians tend to interpret the information gained during a consultation to fit their preconceived diagnosis, rather than the converse. This is "cherry-picking" (Mandell 2021) or "search for supportive evidence".
Conjunction rule	The incorrect belief that the probability of multiple events being true is greater than a single event.
Overconfidence	An inflated opinion of diagnostic ability leading to subsequent error. Confidence does not align with the accuracy of these judgements (Expert Halo).
Representativeness	Misinterpreting the likelihood of an event considering both the key similarities to its parent population, and the individual characteristics that define that event.
Search satisfying	Ceasing to look for further information or alternative answers when the first plausible solution is found.
Diagnostic momentum	Continuing a clinical course of action instigated by previous clinicians without considering the information available and changing the plan if required (particularly if the plan is commenced by more senior clinician) (related to Expert Halo).
The framing effect	Reacting differently depending on how information is presented
Premature closure	"Jumping to conclusions". One of the most common errors; clinicians make a quick diagnosis (often based on pattern recognition), fail to consider other possible diagnoses, and prematurely stop collecting further data. A variation, "the bandwagon effect" occurs when subsequent clinicians unquestioningly accept a previous working diagnosis without independently collecting and reviewing relevant data.

Anchoring errors	Steadfastly clinging to an initial impression even as conflicting and contradictory data accumulate, focusing on one particular symptom, sign, or piece of information, at the expense of ignoring or under-emphasising others.
Zebra retreat	Backing away from a rare diagnosis or condition
Authority bias	This is the same as expert halo, declining to disagree with an "expert."
Commission bias	A tendency towards action rather than inaction.

There are several published recommendations and strategies to help solve medical bias issues:

- Gather sufficient information and consider what data is truly relevant (CMPA unknown, O'Sullivan & Schofield 2018)
- "dialectical bootstrapping" which is the act of forcing yourself to assume your first estimate to an answer is incorrect and attempting to answer again (O'Sullivan & Schofield 2018). This involves actively seeking and developing alternative diagnoses (hypotheses in dam safety).
- Diagnostic "time outs" or formal pauses for reflection (CMPA unknown, Mandell 2021)
- Question asking: if it is not the working diagnosis, what else could it be? What are the most dangerous things it could be? Is there any evidence that is at odds with the working diagnosis (hypothesis)? (Mandell 2021, O'Sullivan & Schofield 2018)
- Considering the worst-case scenario diagnoses and then ruling it out (CMPA unknown)
- Giving all team members opportunity to speak up and listening, whilst acknowledging that personal relationships may impact decision making and judgment (CMPA unknown).
- Identify any "red flag" symptoms and investigate appropriately. Reconsider the diagnosis if there are new symptoms or signs, the illness is not following the natural course (i.e., unexpected behavior in dam safety) (CMPA unknown).
- Consider consultation with a colleague or specialist (CMPA unknown).
- Having identified one abnormality, ask is anything more going on? (CMPA unknown).
- Make a conscious decision to arrive at diagnosis or differential diagnosis independent of the labels applied by others (CMPA unknown).
- Remember that you are often wrong and consider the implications of being wrong (O'Sullivan & Schofield 2018).
- A checklist approach, which has been found to be effective (O'Sullivan & Schofield 2018).

Interestingly, O'Sullivan & Schofield (2018) found that whilst focused educational sessions may seem intuitive and practical the evidence to support their use is mixed and there are enough negative studies to suggest it is a low-yield intervention at best, i.e., being aware is not enough.

3.2 *Human Factors in the Backcountry Recreationist Profession*

Year in, year out, experienced and qualified groups succumb to avalanche hazard, despite advances in equipment, technology and avalanche training (Gunn 2010). Two thirds of the annual deaths, have had avalanche training and a higher level of avalanche education is, counter-intuitively, associated with a greater chance of dying (McCammon, 2004). The decisions groups make, and lessons learned post incident have sparked introspection within the avalanche community (Powder Magazine 2018, Backcountry Magazine 2018). What leads to the decisions that these educated groups make, that ultimately turn out to be poor decisions? Are there lessons for dam safety? Can we avoid the same pitfalls impacting risk decisions for our facilities?

Dam failures and safety incidents and avalanches share some technical and planning similarities, such as: strength of materials, presence of weak planes, understanding of beneath surface conditions, emergency preparedness and planning, understanding that "low risk" doesn't mean "no risk". Both avalanche and dam incidents are also impacted by human factors.

McCammon (2002, 2004) changed the thinking on avalanche incidents and introduced the concept of human factors. He analysed 715 recreational accidents and provided insight into the key question "how do people come to believe that a slope is safe, even when they are faced with likely evidence that it isn't?". (We can adapt this question to dam facilities). McCammon introduced the concept of heuristic traps in avalanche risk, which have since been well discussed in research (McClung & Schaerer 2006, Tremper 2018). These are also described as human factors (Bright 2010, Ebert 2015, Furman et al. 2010, Zajchowski et al. 2016). Popular press has also covered human factors as a driver for avalanche safety, replicating findings from the research and discussing specific incidents in more detail (e.g., High Country News 2015).

Dam failures and safety incidents are somewhat like avalanche incidents, in that they are "poor feedback" (High Country News 2015), "wicked learning" (Powder Magazine 2018) environments or "illusions of skill" (Tremper 2018). These have no immediate feedback on the decision-making process and, if nothing bad happens, we tend to evaluate our decisions as the right ones, not because those decisions were good, but because we didn't receive feedback that they were bad. As such, we inadvertently form inaccurate assessments or develop potentially dangerous habits based on poor decision-making (Powder Magazine 2018). We mistake good luck for good decision making, i.e., the dam may not fail but that doesn't mean our design is good. Competence often leads to success but success itself does not indicate competence (Ebert 2015).

Key heuristic traps identified for avalanche incidents are presented in Table 2. Some of these are shared with common medical traps and biases already presented, but not all. Philip (2019) presented further discussion on learnings from the avalanche industry applied to dams.

Table 2. Key heuristic traps commonly identified for avalanche incidents, relevant to dam safety

Heuristic traps	Description
Familiarity (complacency)	Doing what is familiar. People believe a course of action is correct because it has been done before without incident (McClung & Schaerer 2006). More avalanche incidents happen in familiar terrain (around 4 times more likely) where highly trained groups make riskier decisions than in less familiar terrain.
Acceptance (social)	Following what others do to gain acceptance (Tremper, 2018) Feeling uneasy with a situation but not speaking up.
Commitment	People's optimistic preferences for future outcomes affects their forecasts which can limit ability to realize safer options. Parties that are highly committed take more risks than those who are less committed (McCammon 2004). This is also known as "goal blindness".
Expert Halo	Blind trust in a more experienced partner characterizes the "expert halo". People perceived as experts can dominate decision making. Unskilled parties with no leader take less risks than those with an unskilled leader. Leaders make riskier decisions as group size increases. Consensus decision is found to be better (McCammon, 2004).
Tracks (social facilitation and social proof)	Tendency for people to perform differently when in the presence of others than when alone (Tremper, 2018). When some people are doing something, others tend to follow along, also called the "herding instinct" or "safety in numbers". People believe their action is correct because other people are doing it (McClung & Schaerer 2006). People feel safer when following the example of others, regardless of actual hazards present. Larger groups make riskier decisions, McCammon (2004) found groups of 6-10 and solo were at increased risk.
Search for supportive evidence	Willingness to gather facts that lead to certain conclusions and disregard facts that threaten them. Like "confirmation bias" where we accept evidence that supports our belief and discount or rationalize away any contrary evidence (Tremper 2018).
Conservatism	Failure to change one's own mind in the light of new information or evidence (McClung & Schaerer 2006). Similar to "anchoring" where predictions are unduly influenced by initial information. This can result in acquiring information at one location and applying to another. The desire to be consistent overrules critical new information.
Recency	The most recent events or data dominate those in the less recent past which are downgraded or ignored (McClung & Shcaerer 2006). Similar to "availability" where specific events are easily recalled from memory and "anchoring" where the last thing we heard is weighted disproportionality.
Frequency	The most frequent events or data dominate those that are less frequent (McClung & Schaerer 2006).
Illusory correlations	Belief that patterns are evident and/ or variables are causally related when they aren't.
Selective perception	People see problems in terms of own background and experience. Can be counteracted by seeking a diverse team with collective opinions (McClung & Schaerer 2006)
Rules of thumb	Using rules of thumb which oversimplify the problem, also engineering judgment.
Underestimating uncertainty	Caused by optimism, illusory correlation, need to reduce anxiety, and poor understanding of probability. Tendency to overestimate small events and underestimate large events.

Base rate fallacy	Intuitive thinking about probabilities is off target and can lead to serious misjudgments about the risk of certain events (Ebert 2019).

3.3 *Human Factors in the Maritime Industry*

As much as 80% of oil spills and marine accidents have been attributed to human factors (DeCola & Fletcher 2006, Browning 2004) and it has long been recognized that, for significant safety improvements to occur, attention must focus on people and the factors that affect them.

Through the "Prevention through People" program (National Academies Press, 1997) the US coastguard set out a vision to achieve the safest, environmentally sound and cost-effective marine operations by emphasizing the role of people in preventing casualties and pollution. The program was based on the principles that "human factors are the root cause of most marine casualties and therefore should be the target of safety and prevention programs". It set out 5 principles and accompanying goals to tackle the human factors, see Table 3.

Table 3. "Prevention through People" principles and goals

Principles	Goals
Honor the mariner	Know more
Take a quality approach	Train more
Seek nonregulatory solutions	Do more
Share commitment	Offer more
Manage risk	Cooperate more

Pate-Cornell & Murphy (1996) found that people tend to ignore information that is inconsistent with their beliefs, until it becomes irrefutable. This has been cited as a cause for unrealistic optimism where accident risks are characterized by uncertainty. Only when faced with inevitable, catastrophic consequences do people acknowledge the potential for disaster, at which point intervention may not be possible. After the 1988 Piper Alpha oil platform disaster in the North Sea, investigators found a "culture of denial" of the serious risks. Management tended to focus on frequent incidents that could disrupt production rather than focusing on the risk of a catastrophe. Short term production incentives encouraged workers to cut corners. There was a high turnover of staff, indicating employees may not have had the necessary level of understanding of the system, important when a system is being pushed to its limit (Gordon, 1998).

4 HUMAN FACTORS IN THE DAM INDUSTRY

The application of human factors to the dam industry is recent, and the industry is only just beginning to recognise their importance. Much recognition of human factors relates to water dam safety and is the product of Alvi (Alvi, 2013, 2015a, 2015b, 2015c, 2018, Myers et al 2015, Alvi et al 2016), and the results of recent failure investigations (France et al 2018, ASDSO, 2020). There is recognition of the role of human error in tailings dam safety (IEEIRP 2015), and some recognition of human factors in tailings dam safety, described in ICMM, 2021 as the "human element", understanding that "individuals, however professional and qualified, make judgements and decisions based on their own experiences and biases. Embedded ignorance, which we all have, results from a lack of knowledge, or a failure to recognise internal weaknesses or limitations. Complacency, over-confidence, competing priorities and the loss of corporate knowledge over time can be compounding factors". Requirement 11.4 of the Global Tailings Standard requires incident reports "identify and implement lessons…paying particular attention to human and organisational factors" (GTR 2020). Despite some recognition of human factors within the industry, there is little discussion of cognitive bias and heuristic traps (Philip, 2019).

4.1 *Contributions by Irfan Alvi*

Alvi reports "human factors" is a complex interdisciplinary field including application of social sciences, social psychology, cultural anthropology, management, economics and history, that also requires specialist dam knowledge. To prevent future dam failures, Alvi considers it essential that dam safety professionals understand both physical and human factors. Alvi has found within and outside engineering and dams, major failures are usually preceded by a series of steps involving physical and human factors over a relatively long period of time. On its own, each step may not be significant and may go undetected with no single step or factor sufficient to produce failure. However, when enough factors accumulate and "line up", they can produce safety incidents and failures. Given the large number of dams, Alvi considers it inevitable that "unlikely" failures can occur, due to physical and human factors "lining up" in an adverse way.

Alvi reports that, traditionally, dam failure investigations have focused on providing explanations of physical mechanisms. He has found that human factors play a prominent role in failures, and that telling a useful incident "story" of the events leading to failure, requires investigations to include human factors. The interactions between the physical system and human factors can be complex, non-linear and result in incidents having multiple causes, and a lack of distinct "root causes". Alvi has studied numerous dam failures and found that there are usually warning signs which are not recognized, or not sufficiently acted upon, prior to the failure.

Alvi places the human factors contributing to the failure potential, into 3 primary drivers:

- Pressure from non-safety goals, such as delivering water, storing tailings, reducing cost, meeting schedules, protecting the environment, building and maintaining relationships, personal and political goals etc. (referred to in this paper as "commitment" or "goal blindness").
- Human fallibility and limitations associated with misperception, faulty memory, ambiguity and vagueness in language, incompleteness of information, lack of knowledge and/or expertise, unreliability of intuition, inaccuracy of models, cognitive biases operating at the subconscious and group level, use of heuristic shortcuts, emotions, and fatigue.
- Complexity of systems making systems difficult to model predict and control, which can exacerbate human fallibility and limitations.

Best practices for dam safety can counter-balance or mitigate human factors and include:

- Design and construction best practices, including design customization for the site.
- Design conservatism; designs with physical redundancy, robustness and resilience.
- Budget, staffing and schedule contingencies, with people not stretched to their limits. The organization should be adaptable.
- Collaboration within and across organisations.
- Cognitive diversity of teams to avoid or reduce "group think". Cognitively diverse teams can outperform more homogeneous teams of the "best" people.
- Safety culture and safety-oriented personnel selection.
- Peer review and cross-checking.
- Learning from failures and incident. Actively monitoring, reviewing and investigating unusual events to understand their significance, with incidents addressed promptly, with follow-up.
- Recognition of the limitations of individuals and organization's knowledge and skills, rather than simply deferring to authority based on hierarchical position. Decision-making authority should be commensurate with responsibilities and expertise.
- Appropriate system models should be developed, with a full range of potential failure modes identified, and emergency action plans developed accordingly.
- Checklists should be used, especially for recurrent tasks, such as inspections. These should be customized, clear and unambiguous, focused on items which are important but prone to being missed, with an appropriate level of detail for the time available, and regularly updated. Checklists should supplement situation-specific observation and critical thinking.
- Information management should involve thorough documentation, open information sharing within and across organizations. This enables piecing together fragmentary information to help "connect the dots" and better understand system behavior.
- Vigilant regular monitoring to detect warning signs that might indicate impending failure, while there is still ability to recover. To help judge whether a potential warning sign warrants action, "simulated hindsight" can be used: fast-forward into the future, imagine the failure has occurred, and ask whether ignoring the potential warning was justifiable if not.

4.2 *Historic Dam Failures with Human Factor Implications*

Several historic dam failures are now understood to have significant contributing human factors, see examples presented in Table 3.

Table 3. Examples of documented water dam failures with human factor causes or contributions

Dam	Date	Deaths	Contributing Human Factors
Spencer	2019	1 presumed	Unclear roles and responsibilities, complacency regarding failure mode, warning signs ignored, reliance on inspections and maintenance which didn't pick up latent vulnerabilities, anchoring bias, complex emergency procedures (ASDSO 2020)
Oroville Spillway	2017	-	Confirmation bias (perpetuating misunderstanding of the geologic conditions at the spillway), ignorance, complacency and overconfidence in ability to manage risks, conflicting non-dam safety goals, diffusion of responsibility. The PMFAs failed to identify or dismissed the actual failure mode, of the 18 limitations found with the PFMAs, 11 related to human factors and 6 related to "expert halo" (France 2018).
Ka Loko	2006	7	Unclear and conflicting responsibilities, lack of safety culture, failure to adopt best practices, unreliable intuition, risk complacency and ignorance, missed warning signs, lack of resources for inspection. (Alvi 2015, Alvi et al 2016).
Teton	1976	-	Evidence review bias (disregarding conflicting information, assumptions) and financial commitment (Mattox et al, 2014).
Vaiont	1963	~2000	Disregarding conflicting information, expert halo and overconfidence and optimistic misunderstanding of risk (Mattox et al, 2014).
Mulholland	1928	>400	Commitment, warning signs repeatedly ignored, expert halo, lack of collaboration and a non-diverse team (Alvi, 2013).

5 CONCLUSIONS AND RECOMMENDATIONS

Learnings from other professions and groups have shown that people do not always make the right decisions, based on human factors. Engineers are humans, and human factors impact decisions we make during design, construction and operation. Cognitive biases and heuristic traps are present for dam projects and the author has experienced several in action. Dam safety management and governance systems can be vulnerable to commitment, social facilitation and acceptance, complacency/familiarity, expert halo, underestimating uncertainty, selective perception, illusory correlations, evidence review biases (the way we review and weight evidence has a number of linked heuristics: search for supportive evidence, conservatism, recency, frequency, conservatism, use of judgement). Most heuristic traps are applicable across all roles, responsibilities and concepts and, the author senses a system-wide tendency towards complacency/ familiarization, expert halo, evidence review bias and commitment.

The ICMM (2021) states that a "systematic, comprehensive approach to tailings management, with checks and balances, helps to reduce the risk that the human element can ultimately lead to ineffective tailings management, or worse, the failure". Effective governance and good engineering practices are seen as key in mitigating human elements (ICMM 2015) and there is recognition that a framework for decision making, and surveillance may reduce the potential for human error. However, there is little detail and discussion on how to reduce biases or apply those concepts to over the dam life cycle. The author suggests a few ways to defend against human factors, also known as heuristic traps, in tailings dam safety, presented in Table 5.

Table 5. Suggestions to reduce the impact of human factors in tailings dam safety

Suggestion	Description
Recognise cognitive bias and heuristic traps	Be aware of heuristic traps and actively acknowledge and counter them, although, as a strategy this may be low yield (O'Sullivan & Schofield 2018).
Audit systems and process	Audit dam system and dam safety management systems for vulnerabilities rating to human factors including cognitive bias and heuristics. Be aware that cognitive bias is ubiquitous phenomenon, not correlating with intelligence or any other measure of cognitive ability (O'Sullivan and Schofield, 2018).
Emphasise communication	Improve communication. Share questions, opinions, observations and feelings and consider cultural differences.
Encourage curiosity and speaking up	Curious staff will engage more with dam safety and synthesise issues. Growing a speak-up culture, encouraging of challenges to thinking, is important and helps prevent anchoring and expert halo (CMPA unknown date).
Instigate a formal reflective process	Actively seek alternate hypotheses. Assume the initial hypotheses/ interpretation / assumptions are not true, and ask what else could be valid? What are the most dangerous things it could be? Is there any evidence that is at odds with the working hypothesis? (O'Sullivan and Schofield, 2018) (Mandell 2021).
Create cognitively diverse teams	Create diverse teams, that aren't reliant on the decisions of one person, or on very large groups as collective decisions are usually better than those made by an individual (Makriddakis 1990) but may be vulnerable to "social acceptance". Diversity may reduce "selective perception" and prevent "echo chambers" (Syed 2021). Aim for collective brilliance rather than individual brilliance.
Use checklists	Learnings from both the medical profession and water dam industry suggests checklists can be effective.
Use evidence-based decision making	Be wary of using judgement based purely on experience, which may harbor "evidence review biases". Use evidenced-based decision making and be aware that good decision making requires good quality information.
Reduce the commitment pressure	Allow budget and schedule contingencies. Consider and develop Plan Bs. Specialists should advise owners what they need to hear, not what they want to hear, and not react to commitment pressure.
Use cross checks	Make decisions using more than one method as cross-checks. Decisions made using single estimates may be less reliable than those based on more than one (LaChapelle 1980). Consider auditing against rules of thumb as a cross-check.
Consider that you might be wrong/ Dealing with uncertainty	Understand uncertainties and how these may affect behavior if assumptions are wrong. Use sensitivity analyses to understand how changes in assumptions may impact results and use results to optimise investigations targeted at proving or delineating the conditions. Produce robust, resilient and defensive designs.
Share lessons	Share lessons and publish near misses, to help prevent "wicked learning".
Staff dams/projects adequately	If staffing resources are difficult to recruit, consider how to increase efficiency, such as automation, remote monitoring etc. and/or how to simply procedures/roles effectively so that they are executable with less skilled staff.
Avoid complex responsibility matrices	Complex and unclear responsibility has been an issue in several dam failures. Roles should not overlap, and responsibilities should be clear.

6 REFERENCES

Alvi, I., 2013. "Human Factors in Dam Failures," *ASDSO Annual Conference. Providence, RI.*

Alvi, I. 2015a. "Human Factors in Dam Failure & Safety, Case Study: Ka Loko Dam Failure" *ASDSO Northeast Regional Conference. Ocean City, MD: Association of State Dam Safety Officials*.

Alvi, I. 2015b. "Failure of Sella Zerbino Secondary Dam in Molare, Italy," *ASDSO Annual Conference. New Orleans, LA: Association of State Dam Safety Officials.*

Alvi, I., 2015c. "Human Factors in Dam Failure and Safety," *ASDSO Webinar. Lexington, KY: ASDSO.*

Alvi, I., Richards, G., and Baker, M., 2016. "10th Anniversary of Ka Loko Dam Failure, Hawaii," Presentation. *ASDSO Annual Conference. Philadelphia, PA: Association of State Dam Safety Officials*.

Alvi, I., 2018. "Human Factors in the Oroville Dam Spillway Incident," ASDSO Webinar.

Association of State Dam Safety Officials, 2020. "Spencer Dam Failure Investigation Report", April 2020

Backcountry Magazine, 2018. "Illusions of Safety: After a friend's avalanche death, a lesson in intuition", April 12, 2018, "https://backcountrymagazine.com/stories/illusions-safety-friends-avalanche-death-lesson-intuition/

Bright, L. S., 2010. "Group dynamics and decision making: Backcountry recreationists in Avalanche terrain". Doctor of Philosophy, Colorado State University.

Browning, R.M. Jr. 2004. "Ship Ashore: An Overview of Marine Vessel Casualties." Proceedings of the Marine Safety and Security Council of the U.S. Coast Guard. Vol 61, No. 1, Spring 2004.

Canadian Medical Protective Association, undated. "Common Cognitive Biases". Good Practices Guide.

Cherry, K. 2020. "What is Cognitive Bias". Medically reviewed internet article on verywellmind.co. https://www.verywellmind.com/what-is-a-cognitive-bias-2794963

DeCola, E., Fletcher, S. 2006. "An Assessment of the Role of Human Factors in Oil Spills from Vessels". Report to Prince William Sound RCAC. Nuka Research and Planning Group

Ebert, PA. 2015. "Conscious/ Unconscious decision making: Know Your Own Competence". *The Avalanche Review, Vol. 33, No. 4 April 2015*.

Ebert, PA. 2019. "Bayesian reasoning in avalanche terrain: a theoretical investigation". *Journal of Adventure Education and Outdoor Learning, 19 (1), 84–95*.

France, J., Alvi, I., Dickson, P., Falvey, H., Rigbey, S. & Trojanowski, J., 2018. "Independent Forensic Team Report: Oroville Dam Spillway Incident."

Furman N, Schuman S, Shooter W. 2010. "The Roles of Heuristics, Avalanche Forecast, and Risk Propensity in the Decision Making of Backcountry Skiers". *Leisure* Sciences, 32(5):453–469.

Global Tailings Review, 2020. Global Industry Standard on Tailings Management.

Gordon, R.P.E. 1998. The contribution of human factors to accidents in the offshore oil industry. *Reliability Engineering and Systems Safety*. Vol. 61.

Gunn M. 2010. "Out of bounds skiers and avalanche risk: high-risk cohort identification and characterization". Master of Resource Management. Simon Fraser University.

High Country News,2015. "Can human judgement handle avalanches", July 20, 2015. https://www.hcn.org/issues/47.12/can-human-judgment-handle-avalanches

HSE, 1999. Reducing error and influencing behavior. HSG48. 2nd Edition.

ICMM, 2021. Tailings Management, Good Practice Guide

Independent Expert Engineering Investigation and Review Panel, 2015. Report on Mount Polley Tailings Storage Facility Breach.

Kruger, J, Dunning, D. 1999. "Unskilled and unaware of it: how difficulties in recognizing one's own incompetence leads to inflated self-assessments". *J. Personality and Social Psychology, 77 (6)*.

LaChapelle, ER. 1980. "The Fundamental Processes in Conventional Avalanche Forecasting". *Journal of Glaciology, 26 (94), 75-84.*

Makriddakis, SG. 1990. Forecasting, Planning and Strategy for the 21st Century. New York: The Free Press

Makery, M.A. & Daniel, M., 2016. "Medical Error- the third leading cause of death in the US". *British Medical Journal 2016;353.*

Mandell, B.F., 2021. "Cognitive Errors in Clinal Decision Making". An internet article https://www.merckmanuals.com/professional/special-subjects/clinical-decision-making/cognitive-errors-in-clinical-decision-making

Mattox, A., Higman, B., Coil, D., & McKittrick, E., 2014. Big Dams & Bad Choices: Two Case Studies in Human Factors and Dam Failure. http://www.groundtruthtrekking.org/Issues/OtherIssues/dam-fail-ure-human-factors-cases-Teton-Vajont.html

McCammon, I. 2002. "Evidence of Heuristic Traps in Avalanche Accidents". *Proceedings of International Snow Science Workshop, September 29 – October 4, 2002*, Penticton, BC, 244-251.

McCammon, I., 2004. "Heuristic Traps in Recreational Avalanche Accidents: Evidence and Implications". *Avalanche News. No. 68. Spring 2004*

McClung, D. Schaerer, P. 2006. "*The Avalanche Handbook"* 3rd ed. Seattle: The Mountaineers Books.

Myers, D., Ferguson, K., Alvi, I. & Baker, M., 2015. "Reexamination and Lessons Learned from the 2004 Failure of Big Bay Dam, Mississippi," Journal of Dam Safety, 13:2. Lexington, KY: ASDSO.

National Academies Press, 1997. *Advancing the Principles of The Prevention Through People Program*

O' Sullivan, E.D., Schofield, S.J., 2018. "Cognitive Bias in Clinical Medicine" *Journal of the Royal College of Physicians Edinb 2018; 48: 225–232*

Pate-Cornell & Murphy, 1996. Human and management factors in probabilistic risk analysis: the SAM approach and observations from recent applications. *Reliability Engineering & System Safety Volume 53*, 2, p 115-126

Philip, L. 2019. "Human Factors: Can we learn from avalanche incidents and apply the findings to tailings and mine waste?" *Proceedings of Tailings and Mine Waste 2019*

Powder Magazine, 2018. "How We Learn from Avalanche Near Misses", November 26, 2018, https://www.powder.com/stories/learning-from-avalanche-near-misses/

Rodziewicz. T. L, Houseman, B., Hipskind, J. E., 2021. "Medical Error Reduction and Prevention" in: *StatPearls [Internet]. Treasure Island (FL): StatPearls Publishing; 2021 Jan.*

Saposnik, G., Donald Redelmeier, D., Ruff, C. C., Tobler, P.N., 2016. "Cognitive biases associated with medical decisions: a systematic review". *BMC Inform Decision Making. 3;16(1):138.*

Syed, M. 2021. "Euros 2020: What all of us can learn from Gareth Southgate" July 7, *BBC News web article*. https://www.bbc.com/news/world-57698821

Tremper, B. 2018. "Staying Alive in Avalanche Terrain", 3rd edition. Seattle: Mountaineers Books.

Tversky, A., and Kahneman, D., 1974. "Judgment Under Uncertainty: Heuristics and Biases." *Science, vol. 185, no. 4157, pp. 1124-1131*

Vinney, C. 2018. "What is Cognitive bias? Definition and Examples". Internet article https://www.thoughtco.com/cognitive-bias-definition-examples-4177684#:~:text=A%20cognitive%20bias%20is%20a%20systematic%20error%20in,identified%20and%20studied%20numer-ous%20types%20of%20cognitive%20biases.

World Health Organisation, 2012." To Err is Human" *Course handout*. https://www.who.int/patientsafety/education/curriculum/course2_handout.pdf?ua=1

Zajchowski C, Brownlee M, Furman N. 2016. "The Dialectical Utility of Heuristic Processing in Outdoor Adventure Education". *Journal of Outdoor Recreation, Education, and Leadership*, 8(2), 119–135.

Future of tailings management

Priscilla P. Nelson & D. Erik Spiller
Colorado School of Mines, Golden, CO, USA

ABSTRACT: The global mining industry currently anticipates annual production rates of billions of tonnes of mine tailings and waste rock, with increases expected due to increasing utilization of lower-grade ores. There is an increasing concern worldwide for the potential consequences from tailings dam seepage and failure. One way that the mining industry can address and mitigate these risks is by considering the continuity of materials flow and the integrated value chain which includes the ore body itself (characterization and modification of ore and gangue), excavation, transport, mineral processing, and tailings management. The industry has the opportunity to extend the value chain to engage the circular economy through downstream production of value-added products that minimize the need for tailings disposal. This paper reviews the variety of opportunities for tailings management such that the long-term impacts and liability are reduced, and for revenue generation through remining/reprocessing when extraction technology improves.

1 INTRODUCTION

The world's mining industry is rapidly changing and faces challenges that must be addressed with a sociotechnical and environmental approach that integrates across the entire materials flow from the ore body through processing to tailings and beyond, embracing the value chain and engaging the circular economy. If these challenges are managed sustainably, the mining industry will be recognized as an ethical, ecological and diverse industry that can offer long term social and environmental benefits, and attract future generations with jobs that address aspirational goals.

This last point is incredibly important for the mining industry and its workforce of the future. The industry needs more workers, more skills, and more diversity. The incoming generations will need to identify the industry with a noble purpose and meaningful careers, rather than providing jobs that do not engage and generate career alienation. To address the future labor supply needs, the mining industry must change the image of mining work and increase the attractiveness of working in the sector, especially for young women and men – a vision for mining is becoming a high-technology industry that speaks to today's young people.

Many limitations to increasingly sustainable operations of the mining and the workforce environment can be traced back to initial physical planning and design. Since mining is characterized by huge investments and long-term operations, it is very important to have a well-designed physical production system. If the initial plan is falsely or over-constrained, there may be limitations and negative consequences throughout the life of mine and beyond. Retaining options and flexibility in the initial design phases of every major development project is therefore critical to establish the possibilities for mining to incorporate new technologies that may approach multi-dimensional sustainability. The mines of the future need to be designed to promote cooperation and creative problem-solving in multiskilled teams.

There is a need for a new vision for the whole industry based on a social / political / environmental mandate that demands an integrated mining industry. The industry must take opportunities in mining system design to optimize all along the value chain rather than sub-optimizing parts or individual processes. Mining leadership, therefore, has the heavy responsibility to rethink mine planning to generate new conceptual designs that will promote high productivity and a good economy, safety and a healthy work environment, and social and environmental acceptability.

The minerals required to meet the escalating needs for the increasing global population and expectations for quality of life (e.g., more electric vehicles, battery storage, photovoltaic solar and other alternative energy sources) rely on earth resource extraction, processing, concentrating and refining; this means workforce growth, more water for extraction, and more storage for mine tailings. This leads to the focus on minimizing tailings and managing the use of water. Mine water is the single most important environmental issue for the mining sector, and this includes quality and quantity. One opportunity is to develop mining in situ, where production and processing takes place underground. Such technology is not without environmental risks and risks for health and safety.

2 OPPORTUNITIES FOR TAILINGS MANAGEMENT IN THE FUTURE

The estimated worldwide generation of solid wastes from the primary production of mineral and metal commodities is over 100 billion tonnes per year (Tayebi-Khorami et al. 2019), which is expected to increase in the future due to the higher utilization of low-grade ores to meet societal demand/growth. With this unprecedented rate of mining and tailings production and the recent fatal tailings dam failures, there is an increasing concern worldwide about tailings management and the potential consequences from tailings dam seepage and failure. With lower grade ores and the possibility of more extreme weather events associated with global climate change, the industry must address the rising concerns associated with mine tailings management.

Engineered and holistic tailings management involves interventions throughout the value chain. The value chain includes the ore body itself (characterization and modification of ore and gangue), excavation, transport, mineral processing, and tailings management / disposal / storage. This requires a staff that can work through geometallurgical and materials flow considerations, including an integrated selection of physical + geometallurgical + chemical + biological processes to achieve maximum extraction (including remining, reprocessing, and recycling) and minimized tailings volumes, with acceptable social and environmental impacts (minimized negatives, and maximized positives). Intervention can be designed to occur at any step in the value chain.

For the future and as envisioned by the International Council for Mining and Metals (ICMM) (ICMM 2016), the value chain must be extended to engage the circular economy through downstream production of value-added products that minimize the need for tailings disposal, and take advantage of the embodied energy and mining work done in tailings production. As downstream products and markets develop, desired tailings properties (engineered tailings) may drive changes in the upstream value chain to yield enhanced downstream values, with integrated decisions about change being decided considering combinations of economics, social, and environmental drivers and with a whole-life-of-mine perspective that will lead to sustainable outcomes.

Much has been written about the potential use of mine waste for a variety of purposes, as is evidenced by the large number of technical papers published in the past 60 years (Almeida et al. 2020). The uses vary from aggregate and fill material to structural additives for civil engineering applications. Some waste materials also have certain chemical properties or trace elements that make them attractive as a Portland cement additive or that are used in the ceramics industry. As pressures to lower carbon emissions increase and carbon trading schemes develop the emerging technology of using appropriate mine waste for the permanent storage of anthropogenic carbon emissions could offer significant economic opportunities as well as a practical solution to lowering carbon emissions. It can even be argued that there are potentially more applications for the use and reuse of mine waste rock than perhaps for the ore commodity(ies) being mined initially.

2.1 *Main Drivers for Change in Tailings Management*

There is a need for a new vision for the whole mining industry based on. Responsible investment may well be the driving force which will transform the mining industry at a pace never seen before. Concern over liability for failure of a tailings storage facility (TSF) is certainly a driver for change as was discussed previously. However, other driving trends include deeper, higher temperature and more remote mines, lower grades resulting in increased tailings volumes, escalating concern for water quality and quantity, complex ore mineralogy leading to finer grinds, and significant clay mineral contents and complicated surface chemistries with difficult solids and slurry characteristics. All of these challenge reagent and tailings dewatering selections, as well as tailings transport and placement.

In deciding about changes, industry must demonstrate contributions to the United Nations Sustainability Development Goals (SDGs) (United Nations 2015; World Economic Forum 2016; Columbia Center on Sustainable Investment 2020) and be responsive to the evolving Environmental, Social and Governance (ESG) mandate (Barclay 2020). The industry must minimize tailings volumes, facilitate and encourage responsible product design, use, re-use, recycling and disposal, and incentivize innovative methods and technologies for resource recovery and re-use. In addition, TSFs must be designed and monitored in anticipation of the impacts of global climate change including increasing frequency of extreme weather events, and to complete successful closure to accommodate any climate/weather events in perpetuity.

The world's 29,000-35,000 existing active, inactive and abandoned TSFs contain approximately 223 billion tonnes (534 billion cubic meters) of tailings, and an additional 40 to 50 billion tonnes will be generated over the next five years (WMTF 2021). Most exist at legacy sites or are under current construction, and these are designed to previous standards and may not meet current standards. Only a few new TSFs are constructed each year, so that emerging technologies for new facilities are needed to address both new and existing facilities. TSFs are long term liabilities that must be managed as defined in the Global Industry Standard on Tailings Management (GISTM) (Global Tailings Review 2020).

2.2 *Emerging Technologies for Tailings Management*

The mining industry has a great opportunity to incorporate new technologies into tailings management. New capabilities in real-time sensing with unprecedented accuracy means that material characterization can occur continuously along the full material flow from ore body to tailings to ensure that mineralogical knowledge is used to inform mine waste management at all stages of the mining life cycle. The strategic use of digital technologies will allow mine operators to build complex data systems that can provide continuous remote surveillance using mobile, Internet of Things (IoT)-enabled devices, satellite data and video feed from drones or fixed points. Instantaneous access to such data systems and artificial Intelligence (AI) can support improved decision making that can reduce both risks and costs.

In addition, new technologies are available to incorporate into mine operational design, such as mass in situ and preprocessing comminution with pretreatment methods include thermal (via oven, microwave, or radiofrequency), chemical additive, electric, magnetic, ultrasonic, and biomilling. Although not new, there are new applications for electrokinetics to control water and chemistry, and automation and distributed sensing to improve operational safety and reliability. Furthermore, evolving biological processes offer the possibility for selectivity and reaction rate enhancements in many applications.

3 OPPORTUNITIES ALONG THE MATERIALS FLOW

As mining companies begin to contemplate a wider range of technical options for the challenges and opportunities of tailings management, they will inevitably participate in a larger ecosystem of equipment suppliers, service providers, downstream by-product manufacturers and industrial symbiosis partners. They should consider carefully who is best equipped to solve the problem at hand and what the commercial and contractual relationships should be.

Consequences of technical failure in the mining waste field have proven to be very high, so traditional procurement methods (including efforts to maximize risk transfer to partners) may not be appropriate except where accountabilities can be very clearly defined. A further complicating factor is reputational risk. Symbiotic relationships with service providers and by-product companies, particularly if they are local enterprises, can be very beneficial for a mining company's reputation by creating shared value in host communities and boosting ESG scores. On the other hand, if there is a failure (for example in a contracted tailings storage facility) then the mining company may incur a severe reputational penalty even if it believes it has successfully transferred risk ownership in the contract. Given this spread of both positive and negative potential impacts, companies may consider collaborative business relationships (CBRs) and relational contracting methods to build partnerships with companies in waste and by-product value chains. The growth of a circular economy will increase interaction between all industrial sectors, and CBRs will become an increasingly valuable corporate competency.

3.1 *Upstream Opportunities*

As more test data become available, geometallurgical approaches to understanding mineral characteristics and the nature of the ore formation will allow the spatial and temporal distributions of the materials flow to be better predicted. Microwave technologies could be applied to selective and preprocessing comminution and may reduce overall energy consumption and change the character of the mill feed to allow lower-cost extraction (Monti et al. 2016).

Other technologies can be applied to reduce the quantity of tailings that need to be managed. These include in-situ recovery (ISR) extraction operations that avoid the production of tailings, bio-enhanced processing to improve extraction and reduce comminution and transportation costs, and hydro-electrokinetic processes that can operate in situ mining and leaching processes to control the flow of water and increase water recovery. New excavation equipment will allow selective mining that reduces the volume of waste rock and may increase the grade delivered to the processing facilities, and enhanced in situ fracture and fragmentation using microwave and ultrasonic technology applications. In-pit or onsite sorting/classification of ore that can decrease transportation costs and increase ore grade to the processing facilities.

3.2 *Processing Opportunities*

The industry can also consider modification of the mining and processing systems to change the volume and character of the tailings, thereby reducing storage requirements and making for easier placement or reuse. At present, mill operations data are routinely generated but usually underutilized. In the future, data resources can be leveraged to integrate geometallurgy and process mineralogy data, analytics and process simulation for effective plant design and improved performance, and management of materials within the systems. This includes pre-concentration, dry processing and coarser particle flotation integrated with comminution, sortation to yield selected splits (e.g., high silica content that could be used in glass manufacture, or coarse materials that could become sand supply), and separations to remove undesired mineral content to enhance tailings reuse. In addition, multi-physical/chemical/biological beneficiation methods may also eliminate deleterious reagents/chemicals from processing.

Both the management and reuse of tailings materials require knowledge of the temporal and spatial variability of the materials flow. This includes understanding the rheology of tailings slurries, tailings transport and design optimization. The opportunity for real-time characterization of materials flow (including particle size distribution, mineralogy, water content and chemistry) can support waste stream segregation or partitioning by relatively simple gravity and particle size sortation. Consideration should also be given to reuse of heap leach waste materials.

3.3 *Onsite Direct Usage*

Tailings can be modified for easier management and onsite usage that can reduce closure costs and risks. In the process, water resources can be recovered while the physical and chemical properties of the tailings can be improved. 70% of the mines operated by major mining companies are in countries with water scarcity (Sekar et al. 2019). Examples of direct onsite usage opportunities that are coming into use and being developed include dewatering by thickening and/or filtration for a broad range of large-scale (>200,000 tons per day) tailings production, and paste backfill (and advanced observation, instrumentation and sensing to understand long-term behavior (e.g., drainage, self-weight consolidation and cementation), potential for oxidation/ leaching / contamination release into surface or ground waters). Comingled tailings/waste rock and segregation and stockpiling (e.g., carbonate-rich tails to neutralize acid mine drainage (AMD) can be effectively used in engineered applications, and increased use of filtered tailings is expected (including better understanding of filtration requirements, and stack management during high rainfall periods, surface erosion, fugitive dust production, and climate change on long-term behavior).

3.4 *Waste Storage Engineering*

As a result of several recent high-profile failures of tailings storage facilities (TSF), the mining industry has been undergoing a step-change in how TSFs are designed, operated, closed, and managed to comply with the Global Industry Standard on Tailings Management, which was published in August 2020 (Global Tailings Review 2020) as a joint effort by the International Council of Mining and Metals (ICMM), the United Nations Environment Program, and the Principals for Responsible Investment (PRI). The failures and the development of standards have brought focus in the industry on technologies and research that can improve the performance reliability of TSFs and decrease the costs of construction. Regarding TSF design, construction and performance monitoring, the following directions for advancement are receiving attention:

- Real-time assessment and control of tailings feed variability, leading to the assessment of temporal and spatial variability of tailings in the dam (mineralogy, grain size, inferred geotechnical properties). As part of the "data revolution", twin digital TSF models can be constructed that allows companies to analyze near real-time data for trends in TSF functional performance and aggregate the information with other data from sources including production, processing, weather conditions, hydrology, hydrogeology, geotechnical/ structural measurements and seismic events to identify and monitor foreseeable TSF hazards and mitigate potential exposures.
- Data-driven insights: Advanced analytics (e.g., artificial intelligence, machine learning, visualization) enable continuous remote surveillance, access to relevant data and generation of valuable, actionable insights that improve decision-making and reducing risk and cost.
- Soil improvement techniques; e.g., consolidation (surcharge, drainage (wicks), vacuum, electro-osmosis), compaction, vibration and vibro-replacement, chemical or biological stabilization, grout injection (strengthening, and perhaps porous for drainage), reinforcement (geotextiles, geogrids, membranes, fibers) and in situ cementation (chemical and biological).

3.5 *Outsourcing for Off-site Storage*

As a result of several recent high-profile TSF failures, outsourced management of tailings storage could have benefits for both mining companies and the community. At many locations, onsite tailings storage is problematic, and as tailings volumes increase, so will the infrastructure and remediation costs and land requirements. If contracting for offsite storage and management is done well, the costs and risks may be reduced. However, the mining company must ensure the material is delivered in a specified form – and this may mean that dewatering by thickening/clarifying, and filtering, becomes mandatory to prepare the tailings for transport rather than pumping direct to a tailings dam. Outsourced tailings storage and management may work well if the mining company and contracted company are able to work together to define a reasonable specification and consistency for the tailings to be handed over. The outsourced contractor must provide a fit-for-purpose site, designed by staff with the expertise to efficiently deal with specified form of tailings.

3.6 *Downstream Opportunities*

Tailings reuse, remining and recycling represent major opportunities for tailings management in the future. For most potential usages, more knowledge about the tailings materials will be required than is currently and typically being assessed. In this paper, four major areas for downstream opportunities are identified.

3.6.1 *Remining, Reprocessing and Recycling*

Remining of tailings will become increasingly important, including from abandoned or discontinued operations. There have been recent developments in hydraulic re-mining and dredging, particularly pertinent for critical minerals. For example, chemical leaching recovery is of great interest especially for critical minerals including Rare Earth Elements. Bioleaching methods have also been developed for recovery, and phytomining may be used to harvest metals from the living tissue of plant hyperaccumulators. Remining will be increasingly integrated with production. For example, Swedish mining company LKAB is building a 50-ha (hectare) industrial center scheduled for completion in 2021 and at full production in 2027) that will use fossil-free processes to recycle tailings from LKAB's iron ore production into hydrogen, phosphate fertilizer, rare earth elements, and gypsum and fluorine products.

3.6.2 *New "Manufactured" Materials*

The major research focus for tailings reuse has generally been on substitutions for or in conventional construction materials. Traditional construction is commonly cement-based, such as concrete and some mortars. Concrete is the second most-consumed substance on Earth, after water, and the manufacture of concrete involves billions of tons of feedstock, with a use rate of an estimated four tons of concrete per person per year globally. By 2050, concrete production is expected to be four times higher than in 1990.

The manufacture of cement is a major cause of greenhouse gas emissions (Balaji 2017), and about 10% of the global emissions of CO_2 are due to construction materials production (Kappel et al. 2016). Cement could be fully or partially replaced by eco-friendly secondary resources with lower embodied energy. Experience indicates that such substitutions should be taken with caution as mining wastes may contain harmful compounds, such as heavy metals that may leach (Candeis et al. 2013). Strategies to remove or neutralize these elements are also important to optimize the use of mining residues with different compositions.

Silica and alumina are relevant elements for the production of construction products, and pozzolanic activity of the natural pozzolans is closely interrelated with their content of reactive silica. When submitted to a relatively low thermal treatment, silica and alumina state may change to an amorphous form and acquire pozzolanic reactivity, enabling the development of different construction products by partial conventional binder replacement. Some of the produced materials and technologies in use or under development include geopolymers, nano-additives (Brammer 2021), mortars, aggregates, sintering/ceramics, bricks (fired or non-fired), and polymer-based construction materials.

Re-melting of rocks, and subsequent controlled cooling for forming a glass with desired properties, is a relatively recent concept. Activity during the Cold War period occurred in the Soviet Union, with fibers pulled from basalt melts being investigated for aerospace and military purposes, including insulation and textile applications (Acar et al. 2017). Since the dissolution of the Soviet Union, basalt glass fibers are produced and used on a commercial scale. In most cases of metals mining, the minerals that make up tailings are predominantly silicates – plagioclase, biotite, amphibole and pyroxene – similar to the mineralogy of basalt. Nelson et al. (2020) report on a project focused on determining the tailings feedstock compositions and variability that will achieve desired melt temperatures and physical properties (viscosity, interfacial/surface tension, crystallization temperature) to produce glass fiber.

3.6.3 *Direct Use in Industrial Processes*

In some cases, tailings have been used directly as agricultural supplements. Given the global sand shortage, the simple separation of inert sand from a tailings supply can make economic sense. In some cases, direct use of tailings materials in industrial processes has been investigated, including work by Yu et al. (2019 and Tao et al. (2020).

3.6.4 *Environmental Applications Downstream Opportunities*

Tailings and mine waste have been the subject of extensive research related to proactive management of environmental impacts (e.g., AMD, heavy metals, radioactive minerals) including CO_2 sequestration to remediate the effects of climate change. Recent projects include Sun et al. (2020) on bioremediation applications and Outram et al. (2018) on remediation of heavy metals through ion exchange. Current active research will soon yield new AMD active and passive treatments, including biological applications (genomic approaches, phytomining, etc.). Integrated application of subsurface, surface, aerial, and satellite measurements will also be increasingly applied to monitor the biochemical evolution of seepage water through existing TSFs and. legacy mine waste sites. In addition, Harrison et al. (2012) reported on accelerated sequestration of CO_2 by tailings, and McCutcheon et al. (2019) reported later on chemical and biological reactions for CO_2 sequestration.

4 SUMMARY

The release of the industry standard in 2020 by the Global Tailings Review (GTR) represents a major turning point in the regulation of tailings management and transparency, as does the evolving ESG mandate that demands an integrated and responsible mining industry that may well be the driving force for mining industry transformation at a pace not seen before. A majority of publicly listed mining companies have furnished the public with more information than has previously been available, and many CEOs have indicated their strong support for increased transparency, information disclosure, and public accountability (Kemp et al. 2020). The current focus on ESG actually represents a huge opportunity, and the mining industry of the future can contribute much more to economic and social development in communities. The material demands of the world cannot be met without mining, but the industry's success depends on effective community engagement and adaptability, flexibility, and agility so that innovations can be adopted and integrated as they become available.

This will happen through disruptive thinking, innovation, partnerships, and co-creation that will occur within the industry, outside the industry, and together with third parties and universities across the globe. With ore grades declining, more water is needed to process more material just to keep up with production rates. This creates more water and tailings to manage. Contamination of groundwater and tailings dam failures are the biggest environmental risks associated with mining.

4.1 *Minimize Tailings Volumes*

Prominent opportunities for volume minimization include in situ mining and leaching (including biomining and bioprocessing techniques), effective extraction from coarser feed, and ore sorting or pre-concentration to increase mill feed grade. Potential benefits include reduced operating costs, fine tailings volumes, and power consumption at the grinding circuit, and less material sent to the TSF.

4.2 *Processing Advances*

Equipment and circuits are under development that use evolving automation and digital technologies to increase efficiency, reduce energy consumption, decrease manufacturing and operation costs, and extend the lifetime of the equipment. For example, Vale has launched a fines dry magnetic separation pilot plant that performs dry magnetic concentration of low-grade ore using rare earth magnets, reducing the need for potentially dangerous wet tailings dams. Other new processing technologies are in development as well.

4.3 *Tailings Characterization*

For filtration system design and for engineered TSF construction with tailings materials, correct characterization of the current and future tailings and expected variability during the mine life is required. Current practices related to stability evaluations of mine tailings facilities rarely take the tailings heterogeneity into account, and field testing (Engström et al. 2020) has indicated high variabilities of tailings characteristics within very limited distances in a tailings facility. The variabilities cause uncertainties both for tailings beach control and for assessing strength and stability of the complete volume of mine tailings. Tailings characterization needs to become near-real-time, and the demand for critical minerals must also be considered in tailings characterization. Multi-element mining may result in significant changes in the characteristics of the tailings to be managed. Success in this requires advanced geometallurgical models of ore genesis and occurrence/deportment of economic concentrations of secondary and critical minerals.

4.4 *Water and Energy Management*

Reducing the quantity of tailings and improving water recovery by filtration are obvious ways of decreasing water consumption in mining, and the future will see new flotation technologies that reduce the water demand and comminution requirements while improving grade and recovery, and reducing tailings dewatering costs further. Assessing progress in water use efficiency in the mining industry requires the development of benchmark statistics to enable fair and meaningful comparison of water use at different mine sites. Remote monitoring and control with real-time continuous monitoring systems gives mine operators a better understanding of water use and ensures that water can be extracted from multiple sources, transported, and treated at the desired pressure and quantity. The EU project ITERAMS has focused on water management, including investigation of the potential for microbial accumulations in mine water (especially in closed water loops) and their effects on mineral processing (Kinnunen et al. 2020).

4.5 *Transportation and Placement of Tailings*

Experience indicates differences between assumed design parameters (for slurries and tailings) and real data obtained in the field, including variations between the tailings tested during feasibility study and pre-operation level and the tailings effectively processed by the plant (Barrera and Engels 2018). Areas for research focus include consistency in thickening performance, and transport and spatial placement of thickened tailings. An engineered network of instrumentation to measure rheological properties and an expert system to respond are required to facilitate the operational management of the transport and dewatering processes. With near-real-time characterization of tailings, an agile filtration system design can produce engineered tailings materials for TSF construction. Research is also needed to identify leaks and confirm the alignment of buried pipelines. Technology from the underground infrastructure industry can be adopted, including inline inspection acoustic tools that do not disrupt operations.

4.6 *Tailings Storage Facility Design and Operation*

While many new technologies are under development and implementation that will enable improved safety and management of risks associated with TSFs, for at least the next 10 years, TSF construction will continue with only incremental changes. Major foci are the extraction of water, control of water pressures, and accelerated consolidation of tailings materials. Technologies are available and evolving in the civil construction industry that can be seamlessly transferred into tailings management for accelerated consolidation and integrated reinforcement of dam and beach areas during placement, as with geogrids and fibers (Quinterro Olaya et al. 2020). New technologies may well come from other industries or disciplines, so that peripheral vision is needed to identify new opportunities in this fast-moving field of technology development. Distributed sensors, including nanosensors, can be mixed into tailings at placement, and self-organize into a network to provide spatial monitoring of porewater pressures.

Formal design reviews prior to construction and regular inspections and audits during construction and operation will continue to reduce TSF risks. TSF management will need to give more attention to operational changes during the life of a TSF, including business-imposed design changes, or changes in the tailings themselves (e.g., ore grade changes may affect the rate of tailings production, multimetal mining may introduce new processing circuits, or grind size may become finer to increase extraction). The improvements in big sensing and AI systems will be available to manage any change in TSF construction and performance, allowing any change in the TSF risk profile to be managed as well.

4.7 *Digital Tailings Management*

In its tailings governance framework, the ICMM has emphasized the need for better monitoring and management of TSFs for the prevention of future catastrophic failures. Future TSFs will be managed with digital twins, which virtually replicate physical assets and processes. With near-real-time optimization, process efficiency and resource use (such as water and energy) can be improved, and this, in turn, can lead to better regulatory compliance, including the use of digital data reporting on a near-real-time basis. For this to happen, business model changes are needed to drive collaboration regarding issues such as the setting of standards for data collection and sharing. A digital twin effectively provides a baseline from which changes during construction can be measured and recorded. The frequency and resolution of capabilities for aerial and satellite measurements will increase in the future. Digital, physical, and chemical models can be coupled with advanced analytics to validate and predict performance expectations during and after construction.

However, the industry must consider the synergies between data-driven and knowledge-driven models, and companies need to capture expert knowledge from the existing workforce. Analysis of historical data and behaviors will enable insight from trends and patterns that can provide perspective and an opportunity to interject human judgment before decisions are made. When this information is combined with the data-driven approach of AI and ML, the industry will have a much-improved capacity to prevent, predict, and mitigate failures and critical issues on mining sites. Such integrated models will be able to update risk trees in real time, reliably detect anomalies, trigger internal and external alerts, automate compliance and reporting, trigger emergency preparedness plans, as well as constantly update themselves through continuous data assimilation feedback loops.

4.8 *Information Transparency*

There has been resistance from many large mining companies to divulge information related to the properties and behavior of tailings at one site for experience sharing. That there is apprehension regarding potential misuse by third parties is understandable, particularly during the study/permit phase. However, the industry as a whole needs to have a longer-term and collective vision for the possible benefits to gain from shared knowledge and experience, yielding safer and environmentally friendly solutions for all, which is a clear benefit to the industry as a whole.

4.9 *Tailings and Climate Change*

The industry will consider tailings management as a partial solution for meeting zero-carbon goals. For example, FPX Nickel (Canada) plans to launch a carbon-neutral nickel mine and is working with researchers at the University of British Columbia to confirm that tailings from its project could be used for carbon capture. Tesla has approached Giga Metals to use carbonation of tailings to produce *green* nickel. Carbonating mine tailings can have other benefits, such as providing physical stability to tailings (Vanderzee et al. 2018), dust reduction, and immobilization of toxic metals (Hamilton 2016). More ambitious systems intended to reach the scale necessary to remove billions of tons of CO_2 from the air each year, via surficial weathering of alkaline industrial wastes and mined rock material, are under consideration at the laboratory and theoretical level, but they have not yet been implemented at pilot scale (Kelemen et al. 2019, 2020).

5 REFERENCES

Acar, V. et al. 2017. Basalt fibers. In Fiber Technology for Fiber-Reinforced Composites, Elsevier. http://dx.doi.org/10.1016/B978-0-08-101871-2.00008-4

Almeida, J., et al. 2020. Overview of mining residues incorporation in construction materials and barriers for full-scale application. Journal of Building Engineering, 29. DOI: 10.1016/j.jobe.2020.101215

Balaji, M., et al. 2017. Experimental study on the behavior of self-compacting self-cured concrete using chemical admixtures and metakaolin. International Conference on Emerging Trends in Engineering, Science and Sustainable Technology (ICETSST-2017), 2017.

Barclay, D. 2020. Rebooting the Mining ESG Narrative. Published November 30, 2020. https://www.linkedin.com/pulse/rebooting-mining-esg-narrative-dan-barclay/

Barrera, S. and Engels, J. 2018. Filtering, high-density thickening for large production rates: Main challenges. In Paste 2018: Proceedings of the International Seminar on Paste and Thickened Tailings. Edited by R.J. Jewell and A.B. Fourie. Perth: Australian Centre for Geomechanics. doi:10.36487/ACG_rep/1805_02_Barrera. Accessed March 2021.

Brammer, T. J. 2021. Comparison of nano meso inorganic polymers to Portland cement and geopolymers for mine tailings stability and containment of Toxic RCRA 8 Metals and other Leachates. Proceedings of the Annual meeting of the Society for Mining, Metallurgy and Exploration, https://prosealecco.com/

Candeias, C., et al. 2013. Heavy metal pollution in mine-soil-plant system in S. Francisco de Assis - Panasqueira mine (Portugal), Appl. Geochem. 44 (2013) 12–26, https://doi.org/10.1016/j.

Columbia Center on Sustainable Investment (CCSI) 2020. Mining and the SDGs: A 2020 Status Update. CCSI and the Responsible Mining Foundation. https://www.responsibleminingfoundation.org/mining-and-the-sdgs/

Engström, K., et al. 2020. Variability in sand characteristics—a case study at LKAB mine tailings facility in Sweden. In Tailings and Mine Waste 2020: Proceedings of the International Conference on Tailings and Mine Waste. Vancouver, Canada: University of British Columbia. pp. 307–318.

GlobalTailingsReview.org 2020. The Global Industry Standard on Tailings Management. https://globaltailingsreview.org/global-industry-standard/

Hamilton, J.L. 2016. Nesquehonite sequesters transition metals and CO2 during accelerated carbon mineralisation. International Journal of Greenhouse Gas Control 55:73–81.

Harrison, A. L., et al. 2012. Accelerated carbonation of Brucite in mine tailings for carbon sequestration. Environ. Sci. Technol. 2013, 47, 126−134. dx.doi.org/10.1021/es3012854

ICMM (International Council on Mining and Metals) (2016): Mining and metals in the circular economy. https://www.icmm.com/website/publications/pdfs/mining-minerals/2016/research_circulareconomy-2016.pdf.

Kappel, A., et al. 2017. Colour, compressive strength and workability of mortars with an iron rich sewage sludge ash. Construct. Build. Mater. 157 (2017) 1199–1205, https://doi.org/10.1016/j

Kelemen, P., et al. 2019. An overview of the status and challenges of CO2 storage in minerals and geological formations. Frontiers in Climate (November 15). https://doi.org/10.3389/fclim.2019.00009. Accessed March 2021.

Kelemen, P.B., et al. 2020. Engineered carbon mineralization in ultramafic rocks for CO2 removal from air: Review and new insights. Chemical Geology 550 (September 20): 119628–119628.

Kemp, D. 2020. Tailings facility failures in the global mining industry: Will a “transparency turn” drive change? Business Strategy and the Environment 30(1):122–134.

Kinnunen, P., et al. 2020. Review of potential microbial effects on flotation. Minerals 10(6):533.

McCutcheon, J., et al. 2019. Carbon sequestration in biogenic magnesite and other magnesium carbonate minerals. Environ. Sci. Technol. 2019, 53, 3225−3237. DOI: 10.1021/acs.est.8b07055.

Monti, T., et al. 2016. High-resolution dielectric characterization of minerals: a step towards understanding the basic interactions between microwaves and rocks. Int. Journal of Mineral Processing 151(10):8–21. https://doi.org/10.1016/j. apgeochem.2013.07.009

Nelson, P. P., et al. 2020. Glass from tailings. Proceedings of the Tailings and Mine Waste Conference, Colorado State University.

Outram, J. G., et al. 2018. Comparison of powdered and PVC-bound todorokite media for heavy metal removal from acid mine drainage tailings. Ind. Eng. Chem. Res. 57, 14315−14324. DOI: 10.1021/acs.iecr.8b02825

Quinterro Olaya, S., et al. 2020. Use of high performance fibres to enhance tailings. In Tailings and Mine Waste 2020: Proceedings of the International Conference on Tailings and Mine Waste. Vancouver, Canada: University of British Columbia. pp. 327–337.

Sekar, S., et al. 2019. Building Resilience: A Green Growth Framework for Mobilizing Mining Investment. World Bank Group. DOI: 10.1596/978-1-4648-1426-6

Sun, X., et al. 2020. Chemolithoautotropic diazotrophy dominates the nitrogen fixation process in mine tailings. Environ. Sci. Technol. 2020, 54, 6082−6093. https://dx.doi.org/10.1021/acs.est.9b07835

Tao, L., et al. 2020. Efficient removal of sulfur dioxide from flue gas through liquid catalytic oxidation using copper tailing as the in situ iron ion donator. Energy Fuels. 34. 3513−3521. doi.org/10.1021/acs.energyfuels.9b04172

Tayebi-Khorami, M. et al. 2019. Re-Thinking mining waste through an integrative approach led by circular economy aspirations. Minerals 2019, 9, 286; doi:10.3390/min9050286

United Nations 2015. Transforming our world: the 2030 Agenda for Sustainable Development. https://sustainabledevelopment.un.org/post2015/transformingourworld

Vanderzee, S., et al. 2017. Carbon mineralization in ultramafic tailings, central British Columbia: A prospect for stabilizing mine waste and reducing greenhouse gas emissions. In Geoscience BC Summary of Activities 2017: Minerals and Mining, Geoscience BC. Report 2018-1. pp. 109–112.

WMTF 2021. Estimate of world tailings portfolio 2020. https://worldminetailingsfailures.org

World Economic Forum (WEF) 2016. Mapping mining to the sustainable goals: An atlas. https://www.undp.org/content/undp/en/home/librarypage/poverty-reduction/mapping-mining-to-the-sdgs--an-atlas.html

Yu, W., et al. 2019. Preparation of micro-electrolysis material from flotation waste of copper slag and its application for degradation of organic contaminants in water. J. Hazard. Mater. 361. 221−227.

What is a credible tailings dam failure event?

Marc E Orman & Daniel A. Servigna
Wood Environment & Infrastructure Solutions, Inc. Denver, Colorado, US

ABSTRACT: There is a one in 2,000,000 chance that you will die by falling out of bed, a one in 500,000 chance that you will be struck by lightning in a given year, a one in 4,282 chance of being hit by a car, and one in 103 chance of dying in a car crash. What is the chance of an earthquake occurring near a tailings dam that is large enough to cause a catastrophic failure? What is the chance that the thin weak clay layer observed in one borehole is continuous enough to cause a dam failure near the end of the completion of filling? In order to live, we must accept some level of risk. But what is that acceptance level and shouldn't we understand the risk in order to accept it? This is especially true when dealing with tailings storage facilities, which contain materials that will remain hazardous over billions of years. As part of implementing the Global Industry Standard on Tailings Management 2020 (GISTM), tailings storage facility engineers are asked to conduct a credible Failure Modes / Scenarios workshop to evaluate credible failure modes. By definition, the probability of occurrence of a credible failure mode should not be considered. However, return periods are important when considering long term tailings storage. In this paper, the authors describe why geologic time, climate change, and return intervals should be considered in tailings storage facility design when evaluating credible tailings dam failure events. As part of our jobs as tailings impoundment engineers, we should quantify risks of various failure scenarios to ensure the facility remains safe to human health and the environment. The geochemistry of the tailings over time and the geologic processes which have and may affect the site in the future.

1 INTRODUCTION

A Credible Failure Modes / Scenarios workshop is needed to evaluate the risk of the facility as part of implementing the Global Industry Standard on Tailings Management 2020 (GISTM).

A credible failure mode is defined by the GISTM as:

"Refers to technically feasible failure mechanisms given the materials present in the structure and its foundation, the properties of these materials, the configuration of the structure, drainage conditions and surface water control at the facility, throughout its lifecycle. Credible failure modes can and do typically vary during the lifecycle of the facility as the conditions vary. A facility that is appropriately designed and operated considers all of these credible failure modes and includes sufficient resilience against each. Different failure modes will result in different failure scenarios. Credible catastrophic failure modes do not exist for all tailings facilities. The term 'credible failure mode' is not associated with a probability of this event occurring and having credible failure modes is not a reflection of facility safety."

At first approach, this may seem simple, and we should assume the dam is in its current state and credible events would be the maximum credible earthquake and the maximum credible flood. Each of which have associated return periods per most engineering guidelines. However, if geologic time is considered, the GISTM definition is out of context.

Geologists are trained to think in Geologic Time. When considering geologic time, there is no facility that does not have a credible failure mode and an associated probability of occurrence or risk. Engineers mainly focus on velocity and acceleration in the time context of their lives and processes that occur over milliseconds to tens of years. Engineers are not taught about time in the same context as geologists. The last two sentences of the GISTM definition statement are troublesome if you understand Geologic time.

- How can a failure mode not be associated with a probability of occurrence or the consideration of time?
- Should climate change and non-catastrophic failure modes also be considered?

2 A BRIEF SUMMATION OF GEOLOGIC TIME

The Earth is an ever-changing planet, as written in the geologic record. Five thousand years of recorded human history seem like a very long time and the fossil record indicates that humans may have existed 2 million years ago. However, when you consider that the planet formed approximately 4.5 billion years ago, human history is less than 0.1%.

A common way to think of this is to consider the life of planet Earth as one week, and Monday morning as the beginning of the planet. The first life forms found so far are single cell bacteria that date back to 3.5 billion years, which would be on Thursday. Before this time, much of the Earth's record is still obscure. The first recognizable fossil animals have been dated as 600 to 700 million years ago or early Sunday morning in our analogy. Human history would begin at 11:55 on Sunday night. The oldest living trees (bristle cone pines) date at approximately 4 thousand years, would sprout minutes later and the birth of Christ would have been but seconds before the week ends.

Time is to the geologist much as the immensity of space is to the astronomer. Over time, the Earth has been changing continuously since it formed. These processes proceed at very slow rates in human terms. Some examples include; 1.2 centimeters per year (cm/year) of displacement along the San Andres fault system in the last 25 million years, post glacial sea level rise of five millimeters (mm) per year; the rise of Scandinavia of ten mm per year, or the rise of the Himalayas of five mm per year.

From the oil industry, using magnetics over the sea floor, magnetic striping was mapped. From this, scientists learned that the Earth's surface is covered by thirteen tectonic plates, which are essentially floating and moving on the mantle driven by convection currents. The plates vary in thickness, depending on location. Oceanic crust is approximately seven kilometers (km) thick, while the continental crust thickness ranges from 35 to 40 km. These plates are either converging, diverging, or sliding past one another. The contact area locations are the most geologically active areas of the earth and where most of the catastrophic types of changes can occur. Examples includes the Pacific Ring of Fire, the Pontic Mountains in Turkey, and the Zagros Mountains in Iran. The plate boundaries are presented in Figure 1 from NOAA (2020).

Divergent areas are where new crust forms, and the youngest rocks of our planet are found. These areas such as the mid-Atlantic ridge are known for lava flows, hot springs, and earthquakes. The rate of divergence varies for different areas but is in the order of centimeters per year. Divergent examples on earth include the Mid-Atlantic Ridge, The Great Rift Valley, the East African Rift, Red Sea Rift, and the Juan De Fuca Ridge.

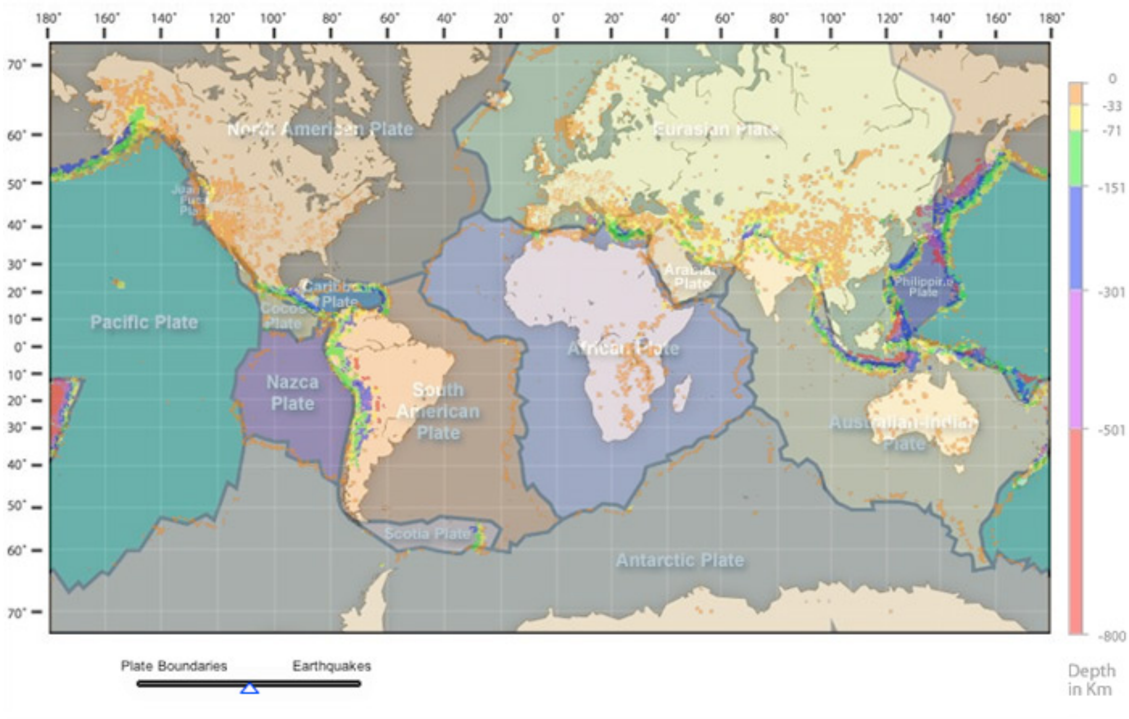

Figure 1. Figure 1. Earth's Plate Boundaries, (NOAA (2020))

Sliding zones, where the plates are grinding against each other along strike slip faults are some the most seismically active areas that have led to some of the most catastrophic disasters. Since the plates do not have smooth boundaries, they can lock up for long periods until the stresses build-up high enough to cause a rupture along the boundary. In most cases, the rupture occurs over a few minutes or hours and displacements of several meters have occurred over many kilometers along the fault. Examples of plate sliding include the San Andreas Fault and the Alpine fault of New Zealand.

Since the Earth is not expanding, if the plates are diverging in one area, they must be converging in another. In the converging areas, the Earth's oceanic crust of one plate is sliding below the thicker continental crust of another plate. These areas contain large volcanoes and are known for generating catastrophic eruptions, earthquakes, and tsunamis. Examples include the Washington -Oregon coastline, the west side of South America, and the Western Pacific ocean.

Figure 2 shows a hypothetical cross section of the plate inter-actions and their relationship to one another. As shown in Figure 2 below, the process is continuous, as new crust is created in one area, given enough time, it will eventually be subjected to convergence, subduction, and death in one discontinuous cycle. While from the figure it appears to be a straight path from spreading to subduction, that is not case. Prior to subduction, the area may change direction and be subjected to stress changes, deformation, decomposition, warping, folding, uplift, weathering, and erosion. The continental crust can be further affected by changes in latitude and climate changes over many cycles as the plates move and change over time.

Layered on top of plate tectonic driven change is climatic change. Through the fossil record, oxygen isotope fractionation of deep sea sediments, and carbon dioxide content of ice cores, geologists have been able to understand changes in climate since life began on the planet. The record clearly shows that hundreds of climate cycles have occurred on the planet as illustrated in Figure 3. These cycles are caused by many things, including plate movement, earth orbital cycles as - proposed by Milankovitch (1998) -, the Earth's magnetic field, and the development of the sun as a star. The cycles are defined by periods of glaciation, development of continental ice sheets, and sea level reduction followed by periods of melting and sea level rise. Currently, it is believed we are in a interglacial part of a cycle with a period of approximately 20,000 years.

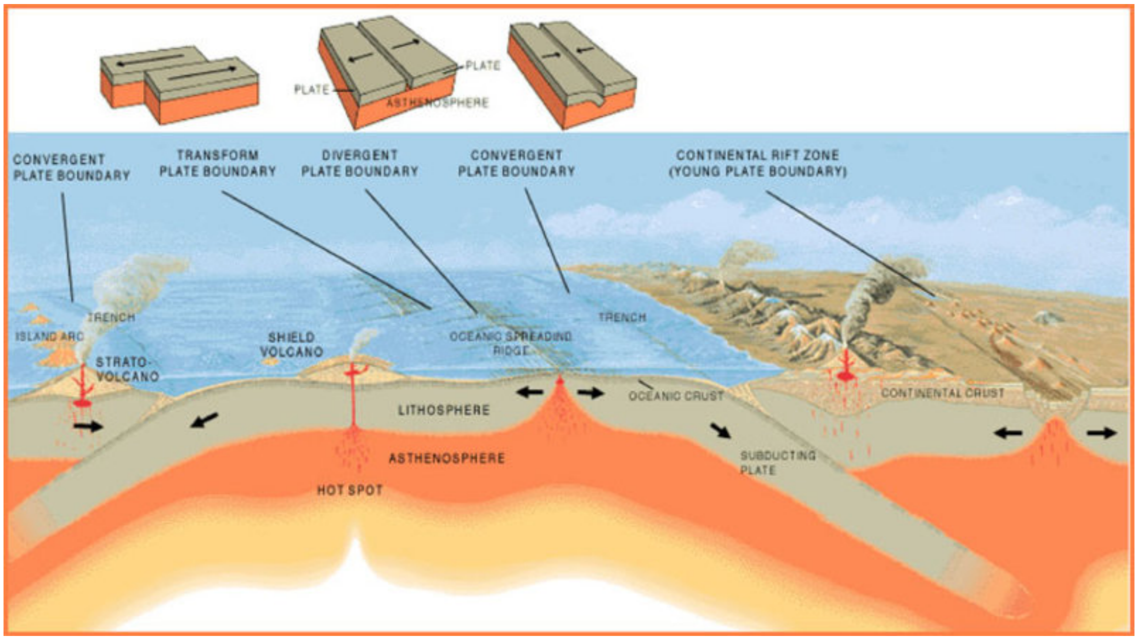

Figure 2. Plate Inter-Actions, NOAA 2020

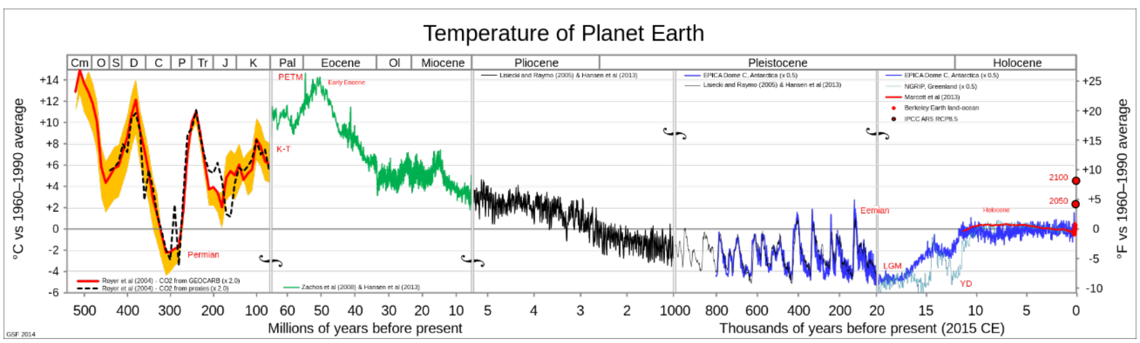

Figure 3. Temperature Changes Over Time (Lisiecki and Raymo (2005) and Petit et. Al., 1999)

3 WHAT IS A CREDIBLE DAM FAILURE?

As you begin to understand geologic time, the definition of what is Credible becomes more complicated. Without a time reference, extreme floods and earthquakes will happen eventually. There will be a catastrophic flood or earthquake in many locations on the planet before the planet comes to an end. Through gravity, erosional processes continue until sediments reach their lowest point. It is all dependent on time.

All facilities have a credible failure mode with an associated probability of occurrence when you consider that the Earth is an ever-changing planet as written in the geologic record. All tailings storage facilities will eventually either erode or be subducted. Prior to these processes, a tailings facility may be breached by a large earthquake formed fault or washed away by a catastrophic flood. However, they may also be breached at a slower pace by erosion, which could lead to the same amount of harm to humans and the environment as a catastrophic event.

The question becomes how much time we should consider in the design of a tailings dam. Based on the dam consequence classification system in the GISTM (2020) an extreme classification should be considered for all new facilities with a flood and earthquake return criteria of 10,000 years. However, the GISTM says time (or probability) should not be considered in the determination of a credible event.

Kevin R. Driscoll of Honeywell (2010) wrote that “Murphy was an optimist” since Murphy’s Law says: “If anything can go wrong, it will go wrong,” but should be revised for Critical Embedded Systems to, “if anything can’t go wrong, it will go wrong anyway.”

NASA’s C. Michael Holloway (after some studies of accidents):“To a first approximation, we can say that accidents are almost always the result of incorrect estimates of the likelihood of one or more things.”

We fatally underestimate the probabilities of what can happen.

Some engineers may say that a failure mode is “not credible”, when it actually can happen with probabilities far greater than requirements allow.

From William Shakespeare’s Hamlet (Act I, Scene 5):“There are more things in Heaven and Earth, Horatio, than are dreamt of in your philosophy.”

The requirements are beyond our experience.

A typical engineer’s total hands-on system experience time is almost non-existent compared to typical system requirements and exposure times. A typical designer engineer (20 years into a 40-year career) has less than 5,000 hours of real hands-on system experience… and, very little of this is in the system’s real environment. He may have no geology education or experience at all.

When an engineer says that the failure can’t happen, it may mean that it hasn’t been seen in less than 5,000 hours of observation. However, 5,000 hours is minuscule compared to the millions of years the facility will be subjected to earth processes before it is subducted.

We should not rely on our experience-based intuition to determine whether a failure can happen within required probability limits.

Regardless of what the GISTM says, some amount of time must be considered when evaluating critical failure modes.

For mine owners and engineers, it is our duty to develop tailings storage facilities that are safe, but does that mean our obligation goes beyond our lifetimes? the lifetimes of our grandchildren? or beyond? For reference, the half-life of uranium 238 is greater than 4 billion years. Although, 1,000 years seems pretty low compared to 4 billion, the time considered should be different for different types of tailings depending on their environmental hazard over time. The engineers who design the facility will be long gone before the facility goes away. However, the closed sites may become resources, abandoned, or traded in packages to other mining companies and these sites continue to live as potential liabilities to human life and the environment. Without the context of time or probability, almost all types of tailings dam failures are credible.

Mining companies are now developing their own internal policies in regard to probability and likelihood of event. Many have adopted policies based on tools similar to Figure 4, which was developed by the New South Wales Dam Safety Committee, 2006 to deal with risks and determine which ones are tolerable and which ones require mitigation. Similar risk evaluation tools have been developed by FEMA (2011), the U.S. Bureau of Reclamation (2012), the Australian Committee on Large Dams (2003), and the Army Corps of Engineers (2011). While the risk tolerance levels proposed in Figure 4 may be adequate for societal and insurance purposes, they would not be the same for mining companies. However, they could be utilized as a starting for mining companies in developing their own internal risk acceptance levels.

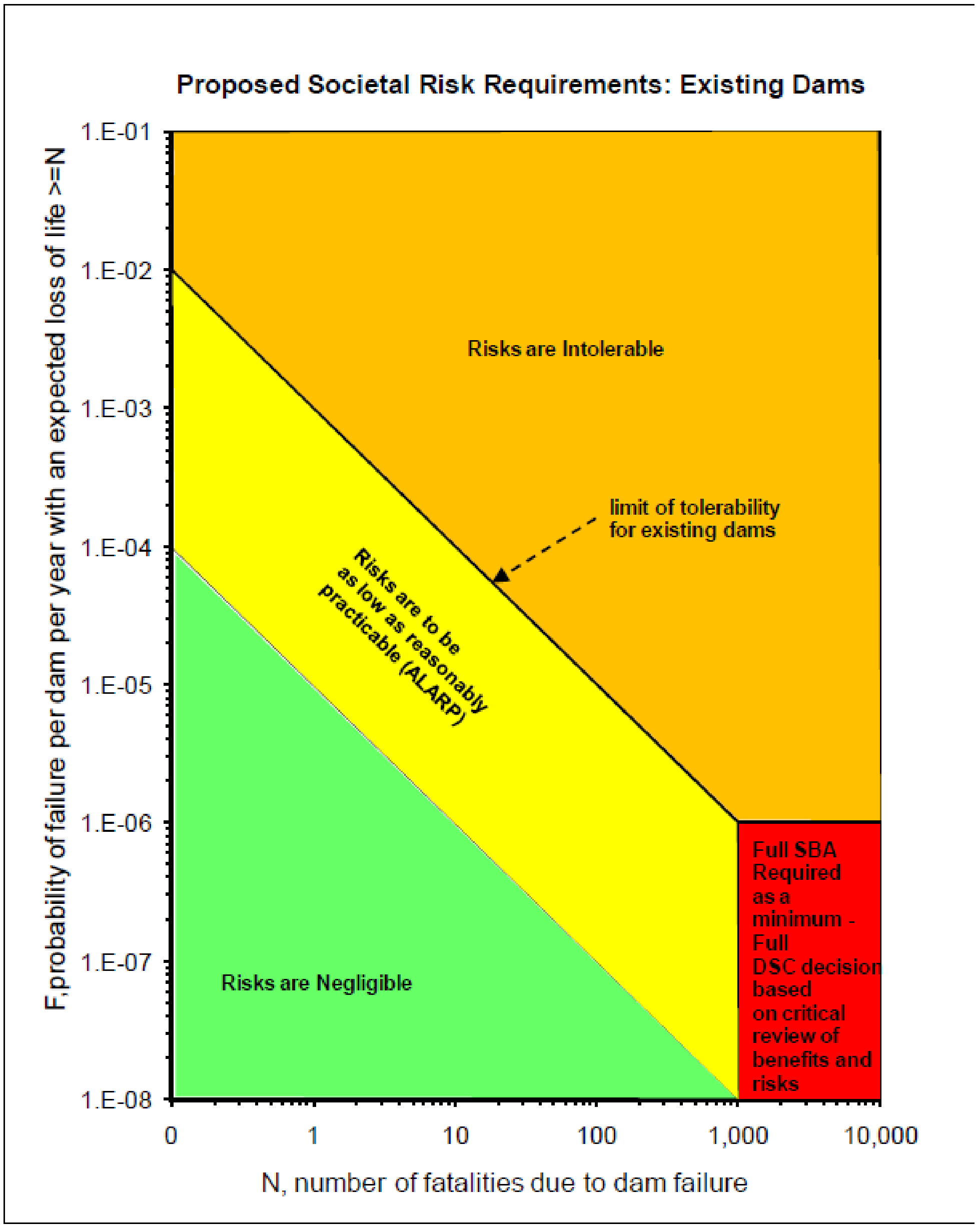

Figure 4. Probability Versus Fatalities (New South Wales, 2006)

In order to determine what a credible failure mode is, we must have a clear understanding of the probability of failure from all possible risks. These risks could involve any aspect of the dam and the site which include:

– The geologic conditions of the site;
– The geotechnical conditions of the site;
– The hydrogeology;
– The hydrology;
– The seismology;
– The mechanical engineering of pumps and pipelines;
– The environmental and geochemical conditions;
– Tailings physical and geochemical properties and how they may change over time (as an example, a CPT study for a site that has been closed for near 50 years was recently completed. The data showed that several zones within the deposit could still liquefy under static and earthquake conditions. However, many areas of the tailings impoundment had consolidated to the point that they would not liquefy due to the design seismic event or even a 10,000 year return event)

– How climate change effect the site over time.

The background of the dam design team should include members who have a clear understanding of all of these aspects.

The Global Industry Standard on Tailings Management was developed by Doctor(s) of Engineering, Industrial Safety, Sociology, Environmental Engineering, Sustainability, Anthropology, and law. There were no geologists on the team and the context of time was probably relatively short when compared to geologic processes but nonetheless, we must select a time frame when determining what defines a credible event.

A time reference for the project, or design risk level, should include considerations of:

– The current stability of the facility;
– The frequency of additional investigations;
– The frequency of the risk reviews and the risk tolerance the owner may have;
– The guidance provided by the selected Standard or Guideline;
– The current rick of the Maximum Credible Earthquake Event;
– The current risk of the Probable Maximum Flood;
– An understanding the geochemistry of the tailings and how long they may remain hazardous in their current environment;
– The current risk of climate change negatively impacting the site; and
– The risk tolerance of the existing regulatory environment.

4 TWO EXTREME EXAMPLES

1. Site A is a closed Gold mine that has 50,000 tons of flotation tailings that were dumped in a small drainage. There are no permanent structures located within 50 miles downstream of the tailings. The gold was mined from a Skarn deposit and Limestone outcrops in the drainage below the tailings. The tailings were generated using only gravity and are slightly acid generating. The terrain is mountainous, and the site receives approximately 50 mm of precipitation per year. The site is currently classified as seismically inactive with no known Holocene faults within 100 miles. Tailings deposition ceased in the 1970s and the site was capped in the 1980s and sloped to drain stormwater through a spillway designed for a 5,000 year return storm event. The tailings dam and tailings were covered by a limestone cobble mulch to inhibit erosion. Recent investigations and testing indicated that the tailings had consolidated and would partially liquify under a 10,000 year return period earthquake. The data also indicated that in approximately 100 years, consolidation would densify the tailings further and the liquefaction potential would be very low. Stability analyses indicate acceptance criteria are met under static and simulated earthquake forces.

   What amount of time should be considered as part of developing credible failure scenarios for a Failure modes risk evaluation?

   Based on the state of the physical and chemical properties of the tailings, and neutralization potential of the country rock this would be a low risk site. The data indicates that within approximately 100 years the tailings will not be liquifiable and the tailings dam will cease to function as a dam, it will have become a landform.

   Even if the site were to be completely abandoned, the risk to the environment or humans would be very low. Based on this information, only risks from credible failure modes that may occur within the next 100 to 200 years should be considered.

2. A closed uranium mine with 10 million tons of tailings are stored in the middle of a large basin located in a dry area which drains into a drinking water source for a major city. The site was closed 30 years ago, and testing indicates that partial consolidation has occurred to the point where approximately half of the tailings have a potential to liquefy due a 10,000-year return period earthquake. The tailings storage facility was constructed using the upstream technique and geotechnical investigation, testing, and analyses indicate that the stability criteria are currently being met. The tailings storage facility was covered with a rock mulch designed to control a 1,000 year return precipitation storm event. The facility cap was graded to drain to a spillway with a capacity for the design storm event.

Given the geochemistry of the tailings and potential to effect human health, this is a much different scenario than Case 1. The tailings will eventually be eroded and flow towards the reservoir in either a slow process over time or catastrophically due to a large earthquake or storm which exceed the design events. This may happen next year, or the facility may remain in its current state until the cap and tailings eventually erode and are carried downstream. Regardless, the tailings will remain a hazard until the planet ceases to exist.

What amount of time should be considered as part of developing credible failure scenarios for a Failure modes risk evaluation? Given the geochemistry of the tailings, the mine owner should consider long term solutions to reducing the risks.

Depending on the final selected time frame, the dam could be buttressed, and the tailings and dam covered by a rock mulch designed for the time interval selected as the design criteria for stability and erosion. The only way to completely remove the any risk would be to relocate the tailings either off site or underground as an inert paste or slurry. However, the addition or a rock buttress and use of larger size rock mulch could reduce the risks to tolerable levels.

5 CONCLUSIONS

The GISTM (2020) provides a good starting point for the site selection, design, operation, and closure of tailings dams. It is important to have a team with a broad experience base involved in all levels of planning. Time is an important part of risk analyses and mitigation planning. Geologic time and climate change should be considered for facilities located in critical areas or ones which hold tailings which will remain hazardous for many thousands of years. Our common goal as engineers and dam owners should be building tailings storage facilities that are not only economical now but ones which will remain safe for generations to come.

6 REFERENCES

Global Industry Standard on Tailings Management (2020). International Council on Mining and Metals, UN environment Program, Principles for Responsible Investment.

Federal Guidelines For Dam Safety Risk Management (2015). Federal Emergency Management Association, U.S. Department of Homeland Security.

Driscoll K.R. (2010). Murphy Was an Optimist. In: Schoitsch E. (eds) Computer Safety, Reliability, and Security. SAFECOMP 2010. Lecture Notes in Computer Science, vol 6351. Springer, Berlin, Heidelberg. https://doi.org/10.1007/978-3-642-15651-9_36.

U.S. Bureau of Reclamation and U.S. Army Corps of Engineers (2012). Best Practise in Dam Safety and Levee Safety Risk Analysis, Denver, Colorado.

U.S. Army Corps of Engineers (2011). Safety of Dams – Policy and Procedures. ER-1110-2-1156.

Petit, J. R.; Jouzel, J.; Raynaud, D.; Barkov, N. I.; Barnola, J. M.; Basile, I.; Bender, M.; Chappellaz, J.; Davis, J.; Delaygue, G.; Delmotte, M.; Kotlyakov, V. M.; Legrand, M.; Lipenkov (2006). New South Wales Government Dams Safety Committee, Risk Management Policy Framework for Dam Safety, New South Wales Australia.

Lisiecki, Lorraine E.; Raymo, Maureen E. (2005). "A Pliocene-Pleistocene stack of 57 globally distributed benthic d18O records" (PDF). Paleoceanography. 20 (1):PA1003. Bibcode:2005PalOc.20.1003L. doi:10.1029/2004PA001071. hdl:2027.42/149224.

Australian Committee on Large Dams (2003), Guidelines on Risk Assessment, Sydney, New South Wales, Australia.

V.; Lorius, C.; Pépin, L.; Ritz, C.; Saltzman, E.; Stievenard, M. (1999). Climate and Atmospheric History of the Past 420,000 years from the Vostok Ice Core, Antarctica. Nature. 399 (6735): 429–436. Bibcode:1999Natur.399.429P. doi:10.1038/20859. S2CID 204993577.

Milankovitch, Milutin (1998). Canon of Insolation and the Ice Age Problem. Belgrade: Zavod za Udžbenike i Nastavna Sredstva. ISBN 978-86-17-06619-0

Mine Closure and Rehabilitation

Modelling surface strengthening for soft tailings capping

Jed Greenwood, Farzaan Abbasy, Phil Solseng, Jim Langseth & Nav Dhadli
Barr Engineering and Environmental Science Canada, Ltd, Calgary, Alberta, Canada

Dirk Luger
Deltares, Delft, The Netherlands

ABSTRACT: Conventional practice limits cap placement to tailings that have achieved trafficable strengths. This research modelled capping of non-trafficable, deep, fine-grained tailings deposits using subaerial hydraulic methods (deltaic capping). Deltaic capping could be a more cost-effective, safer, lower environmental impact technique than mechanical spreading of a cap over geogrid and geotextile. This work explores whether deltaic capping could be successful on soft tailings if the surface of the tailings has been strengthened. Surface strengthening was modelled to represent dried/frozen/treated tailings, geotextiles, and vegetation. This work used FLAC, a deformation-based geotechnical model, in large-strain mode. The model included elements critical for realistic modelling of cap placement: tailings deformation and cap settlement, infill that restores the cap profile as the cap settles, cap advance, and tailings strain softening (loss of strength from large shear deformations). The results are encouraging for surface strengthening combined with deltaic capping.

1 INTRODUCTION

1.1 *Background*

The oil sands industry anticipates that deep fine-grained deposits will comprise an important and ongoing component of a producer's mine, tailings, and long-term reclamation and closure plans. Often the surface of these deposits is too weak to support even low ground-pressure construction equipment. To begin reclamation to a terrestrial closure landform, it is essential that a stable cap be placed on these deposits to provide a working surface.

This research is aimed at developing a better understanding of the potential of deltaic capping as a method to cost-effectively cap non-trafficable, deep tailings deposits (soft, fines-dominated treated tailings). Deltaic capping is sub-aerial placement of a cap using hydraulic transport and deposition of a sand (or other granular) slurry, applying the natural processes that build river deltas. The focus is on tailings weaker than those that could normally be capped using mechanical methods as conventional practice limits mechanical sand cap placement to tailings that have already achieved trafficable strengths, i.e., 25 kPa (McKenna et al., 2016).

The current research explores potential enhancements to the applicability of deltaic capping by including a strengthened surface over the fine tailings deposit. Natural materials as well as artificial materials were evaluated as surface strengthening materials.

1.2 *Objectives*

The primary objectives of the research were to; (1) test the influence of a strengthened tailings surface on cap success compared to no surface strengthening; and (2) identify whether there were critical features of surface strengthening essential to success.

The definition of failure is an important consideration for this modelling effort. In general terms, it is defined as failure (loss of stability) of the cap. Failure was not considered to have occurred if the cap layer remained continuous even if it underwent some degree of deformation.

The type of failure observed in the work reported herein was slope instability (plastic shear deformation) of the cap and underlying fine tailings. In modelling terms, the cap began sinking uncontrollably into the tailings and the model would no longer converge. Other types of failure can occur, such as punching failure or squeezing failure, but those were not observed in this work, primarily due to the geometry of the deposit and cap.

2 METHODOLOGY

This section describes the geometry of the tailings and cap, the input parameters for the tailings including strain softening, and the matrix showing the various simulations that were performed.

2.1 *Tailings and cap geometry and parameters*

The cap was modelled as advancing 300 m into an assumed 400-m-long and 50-m-deep tailings deposit, illustrated conceptually in Figure 1. The modelling assumed there was no water cap and tailings strength was initially held constant with depth to focus on the role of surface strengthening in potential cap failure. Toward the end of the research work, in order to test the effect of a non-uniform undrained shear strength with depth, a linearly increasing undrained shear strength with depth was incorporated.

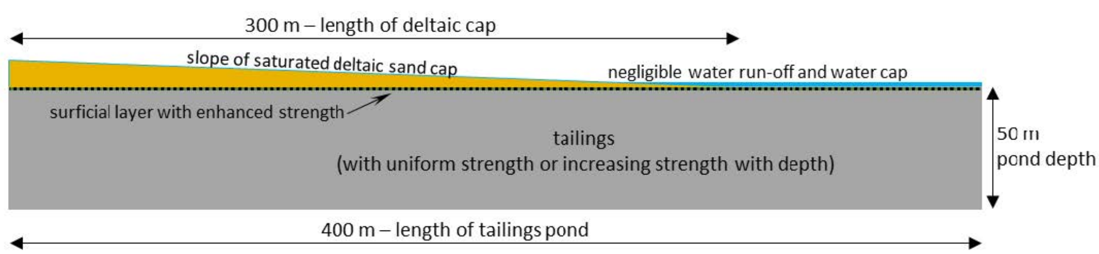

Figure 1. Tailings deposit and cap geometry

Cap slopes and peak undrained shear strengths modelled are shown in Table 1. Most of the modelling used a constant peak undrained shear strength with depth. Other properties of the tailings were computed from the undrained shear strength to initialize the calculation, including the solids content, void ratio, and dry density (Beier et al, 2012; Dunmola et al, 2012; Hockley, 2018). The surface strengthening modelling focused on the scenarios (cap slope and tailings strength) that were just below the limits of success from prior work without surface strengthening.

Table 1. Matrix of capping simulations

Tailings undrained shear strength, s_u [kPa]	Constitutive model	Surface Strengthening, Strength and Thickness	Capping Material	Cap Slope [%]
2 (uniform) 3 (uniform) 4 (uniform) from 2-10 (linear)	Mohr-Coulomb with strain softening	12 kPa at 1 m thick 100 kPa at 1 m thick 150 kPa at 2 m thick	saturated sand	0.25 0.5 1

In order to compare how surface strengthening affected the boundaries between success and failure, a baseline scenario without surface strengthening was also modelled.

The cap was assumed to consist of saturated sand delivered in a sand-water slurry and was modelled with a constant slope. Complications associated with modelling granular material with a very flat wedge shape were removed by treating the cap as a surcharge load. As such, no sand behaviour properties were used to simulate the cap. Thus, the only relevant property of the cap material was its saturated density, 1950 kg/m^3 for sand at 45% porosity. The water transporting the sand was ignored, as was drainage of water from the cap.

An important property of fines-dominated oil sands tailings is strain softening. As the cap advances, the shear strain in the tailings will increase with increasing shear stress under the growing cap load. After the peak shear strength is mobilized, the strength will decrease with increasing shear strain, towards a remoulded (residual) shear strength, as represented in Figure 2. For strains beyond the value where the peak shear strength is reached, increased load and decreased tailings strength can result in cap failure. The shear stiffness of the tailings was related to the peak shear strength and the peak was generally reached at 10-14% shear strain. Beyond the peak, vane rotation was mapped to shear strain using a linear conversion of 2.75 degrees of vane rotation producing 1 percent shear strain.

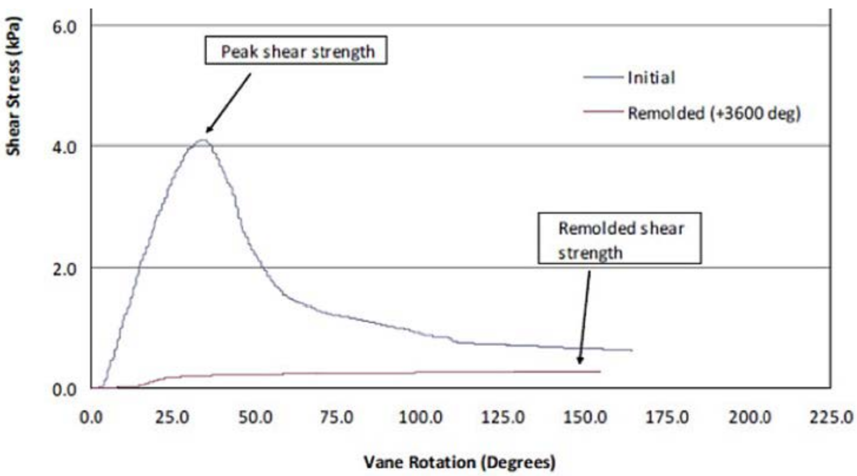

Figure 2. Shear stress as a function of vane rotation for vane shear test on tailings (COSIA, 2012)

2.2 *Model*

2.2.1 *FLAC Model*

Analysis of the cap advance was performed using the engineering mechanics code FLAC (www.itascacg.com/software/FLAC). Notable conclusions from prior modelling were that failure potential is increased as the model incorporates realistic factors: settling due to deformation of the tailings from the cap load, infilling of the resulting depression in the cap, progressive advance of the cap, and strain softening of the underlying tailings. These factors were all included in the modelling for surface strengthening. The modelling was intended to capture key mechanisms in the capping process, which include:

- Large-strain deformation of soft tailings
- Progressive advancement of a granular cap over tailings
- Undrained response of soft tailings material to capping
- Various failure modes

FLAC simulates the behaviour of soil, rock, or other geotechnical materials using a continuum mechanics concept. Materials are represented by zones, which form a grid to fit the shape of the geometry modelled. Each element behaves according to a prescribed linear or nonlinear stress-strain law in response to the applied forces or boundary restraints. The material can yield and deform, and the grid can deform (in large-strain mode) and move with the material within limits. The analyses presented here assumed that cap failure ensued when those limits were exceeded and caused the numerical simulation to stop.

For this application, major advantages of FLAC are its deformation analysis approach and its ability to accept user-defined inputs and functions. In this project, user-defined functions were applied to add cap advance and infill to the model in addition to the strain softening behaviour of the tailings.

The deformation of the fine tailings and strengthened zone in response to the simulated load from the cap was modelled in large strain mode within the two-dimensional version of FLAC. This means that the gridpoints not only track the computed displacements, but the gridpoints actually move by the computed amount. As the cap is infilled, or has its surface profile restored, the load becomes greater in response to the settlement of the fine tailings because the load at any point is calculated based on the height from the top of the cap to the top of the tailings surface. A simplification used in this modelling was that the cap material supply was not limited, so regardless of the volume of displacement, it was assumed that the cap was always fully restored to the design profile at the next step or cycle.

2.2.2 *Surface Strengthening Modelling*

The surface strengthening was applied over the top layer of grid elements, which were modelled at a thickness of 2 m. The mesh in this area of the model domain was not refined to assess thinner layers of strengthened material because changing the zone (grid element) size alters the strain softening relationship. In order to be consistent with the strain softening modelling that had been performed previously, the surface strengthened thickness had to remain at 2 m. Of course, not all surface strengthening techniques would achieve this thickness. However, the undrained shear strength of the strengthened surface could be "prorated" such that the model could account for different, mostly thinner, strengthened zones. For example, a 50-kPa strengthened zone 2 m thick would adequately represent a 100-kPa strengthened layer of 1 m thickness. This approach was tested in the model and found to hold, at least for sufficiently deep potential failure surfaces, which were generally observed in this modelling effort.

2.2.3 *Surface Strengthening Parameters*

The following surface strengthening materials were considered for simulation:

- Vegetation (dewaters the tailings and the roots provide tensile strength)
- Desiccated crust or frozen surface
- Hay or fibres mixed with tailings
- Geogrid/geotextile (thin)
- Polymer-treated tailings or cement-treated tailings
- Clayey or silty layer (assume a uniform layer)

Table 2. Surface strengthening cases modelled

Surface Strengthening Material	Peak Shear Strength	Thickness of Strengthened Zone	Comments	Modelled Strength Based on 2-m-Thick Strengthened Zone
Vegetation	12 kPa	1 m	Based on research presented in Laberge et al. (2019)	6 kPa
Low Case: Frozen Surface / Polymer- or Cement-Treated Tailings	100 kPa	1 m	Consistent with adding a polymer or cement to the tailings	50 kPa
High Case: Frozen Surface / Polymer- or Cement-Treated Tailings	150 kPa	2 m	Consistent with adding a polymer or cement to the tailings	150 kPa
Geogrid / Geotextile	150 kPa	2 m	Modelled in combination with 150-kPa surface strengthening	Tensile strengths of 150 kPa and 15 kPa

Some of the materials considered could be represented by applying an increased undrained shear strength to the uppermost 2 m of the fine tailings, others by including tensile strength. In evaluating these surface strengthening scenarios, it was concluded that several of them could be reasonably combined for modelling, and others were not needed in order to capture the potential successful scenarios. The scenarios modelled to represent the surface strengthening conditions were as shown in Table 2.

The Geogrid/Geotextile case was modelled as a tensile strength and was applied to the 150-kPa surface strengthened tailings deposit with constant 3-kPa tailings and a 0.5% cap slope. Based on the outcome of that modelling, no other tensile strength scenarios were considered. Desiccated crusts and clayey or silty layers were not modelled because much stronger surface strengthening cases were shown to have only marginal benefits, so these lesser treatments had even less merit.

Mixing hay or fibres into the tailings, at a first approximation, can be considered similar to the frozen surface/polymer- or cement-treated tailings cases. However, hay and fibres have additional effects and may be worth exploring in more detail.

3 RESULTS

This section describes the results of the model simulations in which the tailings exhibit uniform undrained shear strength with depth as well as linearly increasing strength with depth. Surface strengthening was applied to each case with various combinations of increased undrained shear strength and tensile strength. The results are shown in tabular form and graphically.

3.1 *Uniform Tailings Strength with Depth*

Table 3 summarizes results of the scenarios with a uniform tailings strength with depth. The body of the table shows the distance the cap advanced at failure, or 300 m if the cap successfully reached the full target distance. The table is organized by cap slope, tailings strength, and surface strength. It includes a 2-kPa base case with no surface strengthening, in order to illuminate the change resulting from surface strengthening. Cases that succeeded are shown with an asterisk. The 1% cap slope scenarios were not modelled for these tailings strengths; most or perhaps all would fail.

Table 3. Cap advance by cap slope, tailings strength and surface strength (successful cases with asterisk)

Cap Slope	0.25%	0.25%	0.5%	0.5%
Tailings Strength, s_u (uniform)	2 kPa	3 kPa	3 kPa	4 kPa
Surface Strength	Cap Advance (m)			
Same as tailings	126	300*	126	294
s_u=6 kPa	128	300*	128	296
s_u=50 kPa	136	300*	140	300*
s_u=150 kPa	220	300*	158	300*
s_u=150 kPa with 15-kPa tensile strength	--	--	168	--
s_u=150 kPa with 150-kPa tensile strength	--	--	222	--

Two tensile strengths were modelled for the 3-kPa scenario with a 0.5% slope: a tensile strength of 15 kPa (0.1*s_u) intended to represent vegetation, and a tensile strength of 150 kPa (equal to s_u) to represent geofabric.

Selected graphics from the model output are shown in Figure 3. This case had a cap slope of 0.5%, a peak tailings undrained shear strength of 3 kPa, and surface strengthening of 150 kPa in the upper 2 m of the deposit; no tensile strength was included. As seen in Table 3, the cap advanced to 158 m and failed. The top profile in Figure 3 is color-coded contours showing tailings total displacement in metres, with 0.5-m contour intervals. Black displacement vectors are superimposed, indicating settlement at the left (origin) end and a mud wave in front of the advancing cap beyond 158 m. A line indicating the cap surface is included on the upper profile and deposit dimensions are on the bottom profile.

The middle profile shows the undrained shear strength of the tailings. Blue is 3 kPa, and the contour interval is 250 Pa. The bright red color is about 500 Pa, approximately the remoulded shear strength of the tailings. The bottom profile is the shear strain in the tailings, with contour intervals of 5%. The red is 5% strain or less; the bright green band is around 50% strain.

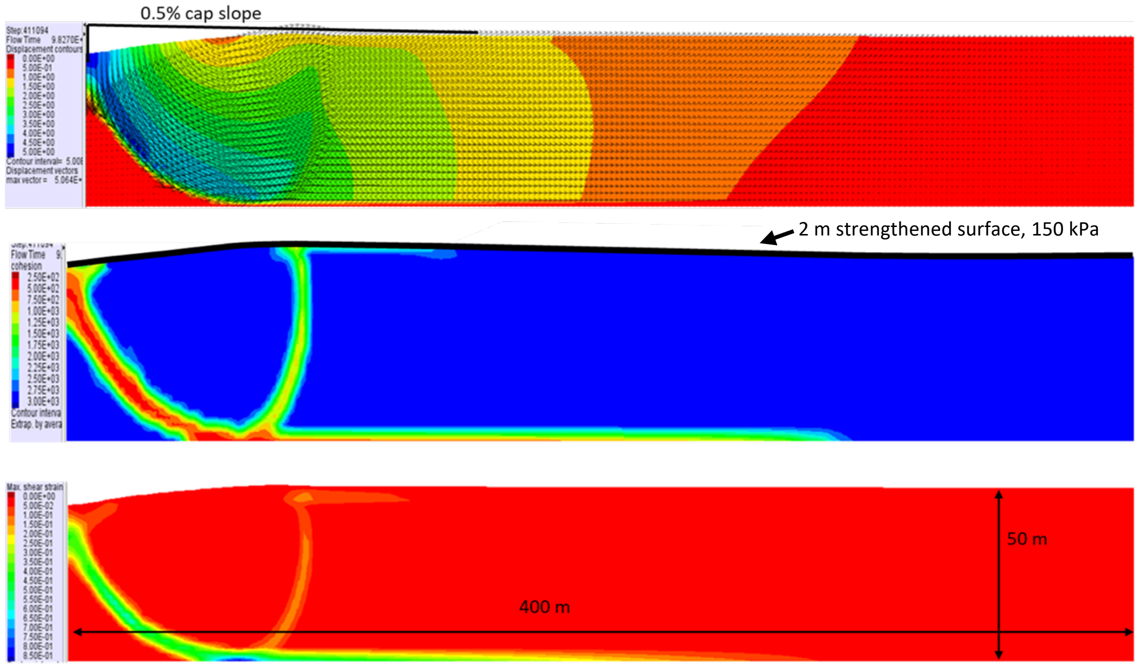

Figure 3. Cap slope 0.5%, tailings strength 3 kPa, surface strengthening 150 kPa, 2 m thick, no tensile strength: displacement vectors and displacement contours (upper profile), undrained shear strength (middle profile), maximum shear strain (lower profile)

3.2 *Increasing tailings strength with depth*

For this modelling, the strength was set at 2 kPa just below the 2-m-thick strengthened surface and increased linearly to 10 kPa at 50 m deep. The 2-m zone at the top for strengthened surfaces meant that the profile of increasing strength was 48 m thick.

Table 4 summarizes results of the scenarios for an increasing tailings strength with depth. It includes a second baseline case, but with a 1% cap slope rather than 0.25%, to provide a point of comparison for these cases. Cases that succeeded are shown with an asterisk.

Table 4. Increasing tailings strength profile results for cap advance (successful cases with asterisk)

Cap Slope	0.25%	1%
Tailings Strength, s_u, increase from 2 to 10 kPa	2 to 10 kPa	2 to10 kPa
Surface Strength	Cap Advance (m)	
Same as tailings	--	133
s_u=6-kPa	--	244
s_u=6 kPa with 6-kPa tensile strength	--	244
s_u=20 kPa with 20-kPa tensile strength	--	300*
s_u=50 kPa	--	300*
s_u=150 kPa	300*	--

Two tensile strengths were modelled for the increasing strength with depth scenario with a 1% slope: a tensile strength of 6 kPa (equal to s_u) intended to represent vegetation roots after a short period of growth (perhaps 2-3 years), and a tensile strength of 20 kPa (again equal to s_u) to represent vegetation roots after a longer period of growth (perhaps 5 years or more).

Selected graphics from the model output are shown in Figures 4 and 5. These cases had a cap slope of 1% and a linearly increasing tailings strength of 2 to 10 kPa. The Figure 4 case has surface strengthening of 6 kPa in the upper 2 m of the deposit; no tensile strength was included. As seen in Table 4, the cap advanced to 244 m, 56 m shy of the 300-m target, and failed. The top, middle, and bottom illustrations in Figure 4 are the same categories as in Figure 3, with the same color-coding and contour intervals, except in the bottom profile where the strain contour interval is 10%. In the bottom profile, the shear strain in the tailings shown in red is 10% strain or less; the blue band is in the range of 100% strain.

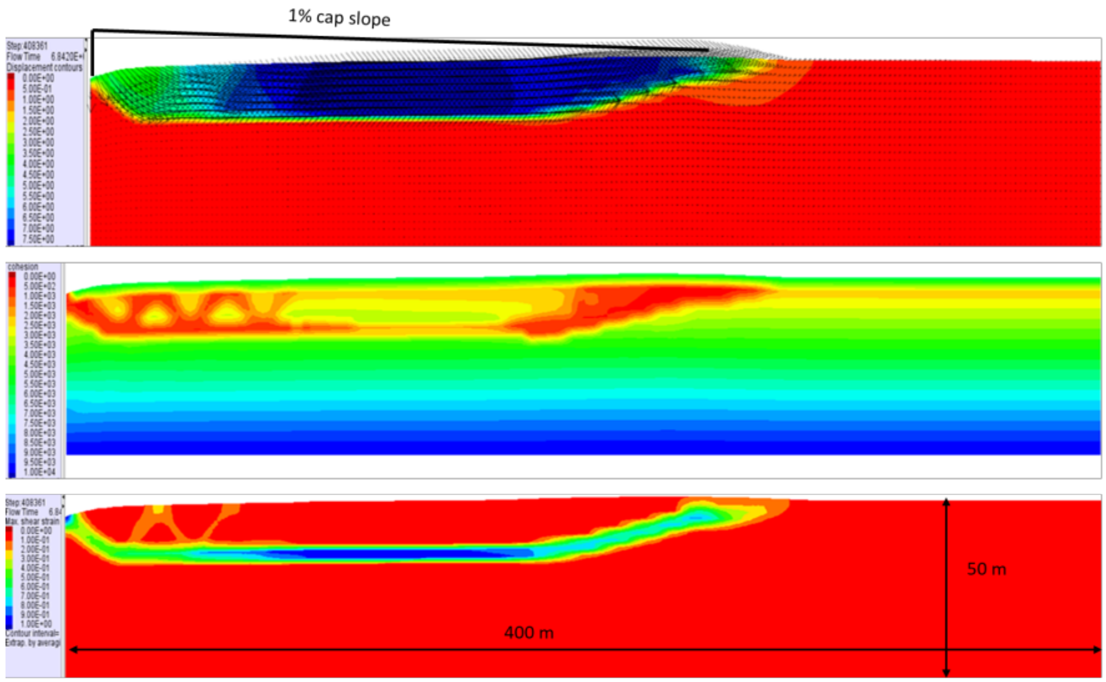

Figure 4. Cap slope 1%, tailings strength linearly increasing from 2-10 kPa, surface strengthening 6 kPa at 2 m thick: displacement vectors and displacement contours (upper profile), undrained shear strength (middle profile), maximum shear strain (lower profile)

The Figure 5 case has surface strengthening of 20 kPa and tensile strength of 20 kPa in the upper 2 m of the deposit. As seen in Table 4, the cap advanced to the 300-m target. The color-coding contour intervals are different than in Figures 3 and 4. The top profile is total displacement in m with contour intervals of 0.05 m, so the dark blue is approximately 0.6 m displacement. The middle profile shows the undrained shear strength of the tailings in kPa with 0.5 kPa contour intervals, so that the blue at the bottom is 10 kPa and the yellow-orange near the top is 2 kPa. The 2-m thick strengthened surface of 20 kPa is a thin dark line at the top. The bottom profile shows strain with a contour interval of 0.2%; the shear strain in the tailings shown in red is 0.2% strain or less; the blue patch at the left side is in the range of 2% strain.

4 DISCUSSION

This section discusses the results of the model simulations in which the tailings exhibited uniform undrained shear strength with depth in addition to linearly increasing strength with depth. It also compares the benefits of the various types and amounts of surface strengthening.

4.1 *Uniform tailings strength with depth*

The results of the modelling for this condition are shown in Table 3. The “Same as tailings” row means no surface strengthening was applied, and so provides a baseline for assessing how much benefit is gained from surface strengthening.

The 0.25% cap slope cases all failed for 2-kPa tailings. Surface strengthening had marginal benefit, increasing the distance the cap could advance from 126 m with no surface strengthening by only 10 m for 50-kPa surface strengthening. The 150-kPa surface strength had a greater effect, adding nearly 100 m to the cap advance, but still far from success.

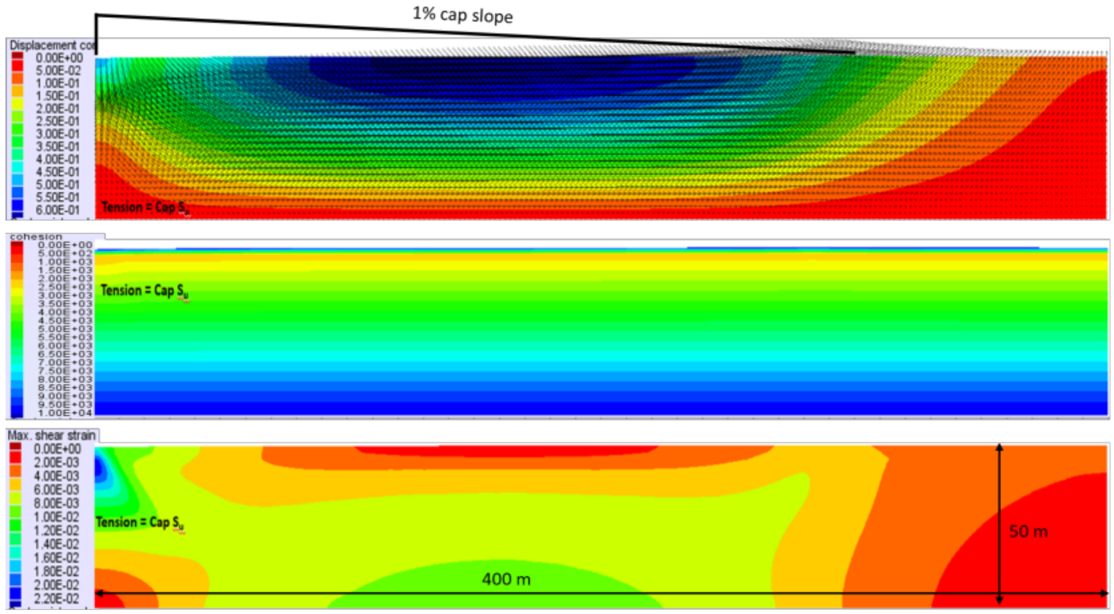

Figure 5. Cap slope 1%, tailings strength linearly increasing from 2-10 kPa, surface strengthening 20 kPa at 2 m thick, tensile strength 20 kPa: displacement vectors and displacement contours (upper profile), undrained shear strength (middle profile), maximum shear strain (lower profile)

The 3-kPa tailings were all successful for the 0.25% cap slope, so there was no advantage to adding surface strength, apart from presumably improving the margin of safety against failure.

The 0.5% cap slope cases all failed for 3-kPa tailings. Surface strengthening had marginal benefit, increasing the distance the cap could advance from 126 m with no surface strengthening to 158 m with the 150-kPa surface strength, about a 30 m improvement.

The 0.5% cap slope for 4-kPa tailings was nearly successful without surface strengthening, advancing 294 m, so the minor benefit from the 50-kPa surface strength was sufficient to reach 300 m, but the 6-kPa surface strength was not sufficient.

Figure 3 illustrates a cap slope of 0.5%, a peak undrained tailings shear strength of 3 kPa, and surface strengthening of 150 kPa. The top profile in Figure 3 shows that near the upstream end of the cap (left end) the tailings deformed 4-5 m downward as the cap failed. The middle and bottom profiles show the failure mode for this capping scenario – the primary failure surface extends to the bottom of the tailings basin and continues along the bottom. This results in a very large and deep failure surface such that the strengthened zone comprises a very small proportion of the overall failure surface. That is why even a very strong strengthened surface of 150 kPa had negligible benefit for resisting cap failure.

This comparison shows that while the caps advanced further over the strengthened surface relative to the base case, significant surface strengthening was not effective at materially increasing the distance a cap would advance when the tailings undrained shear strength was constant with depth, even using very flat cap slopes of 0.25% and 0.5%.

4.1.1 *Surface strengthening with tensile strength on a uniform tailings strength profile*

One of the strengthening methods checked was adding tensile strength at the surface. Many surface strengthening methods will develop some tensile strength in the strengthened zone. The magnitude of tensile strength is dependent on the strengthening technique, and it can range from minimal for silt or clay at the surface to significant for techniques like geosynthetic reinforcement. In order to assess the potential benefit of tensile strength in the strengthened zone, the 3-kPa scenario with a 0.5% slope and a 2-m-thick strengthened zone at 150 kPa was modeled with and without tensile strength. A tensile strength of 15 kPa ($0.1*s_u$) was used to represent vegetation and a tensile strength of 150 kPa (equal to s_u) was used to represent geofabric.

As can be seen for the 150-kPa surface strengthened cases in Table 3, the 0.5% slope cap advanced 158 m on 3-kPa tailings without tensile strength and gained only an additional 10 m using a tensile strength of 15 kPa, advancing to 168 m. More benefit was achieved when the tensile strength was set to 150 kPa, but the cap still advanced only to 222 m, about 60 m further than without tensile strength. Consequently, adding tensile strength is not a decisive factor for tailings with a uniform strength profile.

4.2 *Increasing tailings strength with depth*

Consistent with principles of geotechnical behaviour, the modelling largely showed only marginal benefit from surface strengthening for tailings with a uniform strength with depth, as seen in Table 3. An increasing undrained peak shear strength with depth has often been observed in tailings basins. The results of the modelling for this condition are in Table 4.

A profile of increasing tailings strength with depth, absent surface strengthening, produced better cap advance than constant strength tailings, but was generally not sufficient to achieve success; compare baseline cases from Tables 3 and 4. The linearly increasing strength profile of 2 to 10 kPa with a cap slope of 1% was unsuccessful; the cap advance stopped at 133 m. This was not much further than the 126 m for the base case with a uniform strength of 3 kPa and a 0.5% cap slope. It was much less than the 294-m advance for the 4-kPa base case with a 0.5% cap slope. Of course, the linearly increasing profile had a steeper cap slope than the base cases with uniform undrained shear strength, but even if their advance distances were halved, the increasing strength profile performance does not show a distinct advantage.

Using a profile of increasing strength with depth in combination with surface strengthening had a dramatic effect on cap advance. The base case for a 1% cap slope stopped at 133 m but with a mere 6-kPa surface strengthened zone the cap advanced to 244 m, an increase of more than 100 m. Raising the surface strength to 50 kPa resulted in successful capping to 300 m. These are radically better outcomes than were observed for a uniform strength profile with depth, for instance the 3 kPa tailings with a 0.5% cap slope cases seen in Table 3.

Figure 4 illustrates a cap slope of 1%, an increasing profile of peak undrained tailings shear strength from 2 to 10 kPa, and surface strengthening of 6 kPa. The top profile in Figure 4 shows that near the upstream end of the cap (left end) the tailings deformed 3-4 m as the cap failed. Even greater displacements, 6-7 m, occurred in the center of the failed zone. The middle and bottom profiles show the primary failure surface extended about 15 m deep into the tailings basin where the tailings strength was 4 to 5 kPa, and returned to the surface near the cap front where there is little counterbalancing effect, in the vicinity of 240-250 m along the basin length. While this is a contrast to the very large and deep failure surface in Figure 3, the failure modes are fundamentally similar. The shallower failure surface with a linearly increasing undrained shear strength results in the strengthened surface constituting a larger proportion of the failure surface, such that its beneficial effect is more pronounced. Consequently, when tailings strengths increase with depth, even modest increases in surface strength can significantly improve the distance a cap can advance before failure.

To test the potential benefits of adding tensile strength, a case was run combining 6-kPa tensile strength with 6-kPa shear strength to represent what might be achieved with a few years growth of vegetation that dewaters the surface and adds root tensile strength. These modest strengthening effects in the top 2 m resulted in no change in the cap advance – it remained 244 m. The successful case shown in Figure 5, with 20 kPa tensile strength and 20 kPa surface strength, a potentially credible outcome of a longer period of vegetation growth, suggests the matter of modestly increased shear strength, possibly with tensile strength, for deposit profiles with increasing undrained shear strength merits further exploration.

5 CONCLUSIONS

This work met the original objectives and identified a very important topic for further investigation. The findings related to the objectives are very different for constant versus increasing tailings strength profiles with depth.

Constant undrained shear strength profiles with depth result in very deep potential failure surfaces. For such profiles, the modelling found that (1) surface strengthening provided marginal benefit and (2) tensile strength within the surface strengthened zone was not a significant benefit. Thus, there were no features critical to success for constant tailings strength profiles.

The tailings strength profile is an important factor in the success of a cap with surface strengthening treatments, though an increasing-strength-with-depth profile alone is not sufficient to assure capping success for these weak tailings. A conclusion of this research is that an increasing undrained shear strength profile with depth can have a dramatic beneficial impact when combined with surface strengthening treatments. This research suggested that adding tensile strength in combination with surface strengthening may be of great benefit for such tailings strength profiles. This offers the prospect that modest surface strengthening such as provided by vegetation could be of value. It appears likely that features critical to success for strength profiles that increase with depth are the rate of strength increase and the shear strength and the tensile strength of the surface treatments.

Taken together the modelling reviewed in this paper shows that neither increasing strength with depth alone nor surface strengthening alone is sufficient to assure deltaic capping success for these weak tailings. However, when both increasing strength with depth and surface strengthening are present, the likelihood of success is dramatically improved.

Future work should explore a range of profiles of increasing tailings strength with depth and ranges of values for tensile strength and the surface strength thickness and magnitude.

This research in combination with other related work has demonstrated that capping soft tailings will require integration of the choice of cap materials, the cap geometry, tailings character and behaviour, and the features of surface strengthening for successful cap placement. This work demonstrated that deltaic capping continues to have promise, and merits development to confirm model predictions of behaviours and move toward potential commercial application. The promise of deltaic capping is a more cost-effective, safer, and lower environmental impact technique for capping tailings deposits. Deltaic capping can be applied to a range of tailings, from non-trafficable, weak tailings to much stronger tailings deposits.

The authors wish to thank the Institute for Oil Sands Innovation (IOSI) and Canada's Oil Sands Innovation Alliance (COSIA) for funding this research work. We also wish to thank Nan Wang of Syncrude, the industry representative who provided guidance and support.

6 REFERENCES

Beier, Nicholas, et al., 2012. "Geotechnical Aspects of Flocculation-based Technologies for Dewatering Mature Fine Tailings," Proceedings, 65th Canadian Geotechnical Conference, Winnipeg, Manitoba, September 30 – October 3, 2012.

Canada's Oil Sands Innovation Alliance, 2012. Technical Guide for Fluid Fine Tailings Management, Appendix B, August 30, 2012.

Dunmola, Adedeji, et al., 2013. "Geotechnical Benefits of Flocculation in Dewatering Oil Sands Mature Fine Tailings," Proceedings, 66th Canadian Geotechnical Conference, Montreal, September 29 – October 3, 2013.

Hockley, Daryl, 2018. "Clay Effects on Tailings Geotechnical Properties," Workshop Lecture Series, volume 22, Introduction to Oil Sands Clays, chapter 9, Clay Minerals Society, January 1, 2018.

Laberge, Scott, et al., 2019. "Utilizing Native Plants to Increase the Strength and Solids Content of Treated Oil Sands Tailings," Proceedings, Tailings and Mine Waste 2019, Vancouver, British Columbia, Canada, November 17-20, 2019.

McKenna, Gord, et al., 2016. "Shear Strength and Density of Oil Sands Fine Tailings for Reclamation to a Boreal Forest Landscape," Proceedings, Fifth International Oil Sands Tailings Conference, Lake Louise, Alberta, Canada, December 4-7, 2016.

Integrating multidisciplinary modelling tools to foster scoping surveys and upstream mine waste management

Y. Toubri & I. Demers
Université du Québec en Abitibi Témiscamingue, Rouyn-Noranda, Quebec, Canada

Nicholas Beier
University of Alberta, Edmonton, Alberta, Canada

ABSTRACT: Hard rock mines may induce water quality exceedances stemming from mine drainage. Environmental issues identification at the upstream levels of the development and/or the operation phases steer sustainable solutions design. Nonetheless, this upstream reasoning presents data-limited challenges. To overcome these challenges, the upstream reasoning was amended with a multidisciplinary modelling approach. In this regard, 3D geological modelling, core-logging datasets and stochastic simulation were combined into one modelling approach enabling mine waste classification. This modelling approach overcome issues related to small sample sizes and could be performed along the operation phase. Additionally, incorporating kinetic modelling in the upstream scoping surveys allowed a dynamic geochemical assessment that assists the aforementioned static 3D geomodel. The upstream kinetic modelling and a what-if scenario approach were used to investigate worse case scenarios along the development stage. Finally, merging kinetic and stochastic approaches will produce a holistic screening tool for both development and operation stages.

1 INTRODUCTION

Geochemical assessment and management of mine wastes gave rise to growing endeavor to fulfill the environmental and social commitments requested by stakeholders. Thorough weighing of trade-offs related to ore profitability, mine wastes management costs and remediation liability is indispensable to sustain the mining business. Surface and underground water is the main vulnerable component of the hard rock mines surroundings. Acid mine drainage (AMD) or contaminated neutral drainage (CND) are by far a potential source of water quality deterioration. The United States Environmental Protection Agency (EPA) categorized water pollution within mining facilities as one of the top three ecological-security threats in the world (Dold, 2008). Therefore, water quality exceedances increase management and remediation costs and consequently could shrink the ore profitability. In this regard, several improvements have been suggested to enhance conventional assessment and management practices (e.g. Benzaazoua et al. 2004; Bussière, 2007; Demers et al. 2015; Jouini et al. 2020; Lessard et al. 2018; Parbhakar-Fox et al. 2011). Meanwhile, mining companies and academic researchers realized that proactive solutions should be designed and incorporated in the mine cycle as early as possible to mitigate geo-environmental risks and to anticipate and/or alleviate their costs. In this respect, Aubertin et al. (2016) proposed the “design for closure” thinking, which aims to continuously incorporate environmental issues and their respective solutions in each design effort. Likewise, Benzaazoua *et al.* (2008) suggested the upstream mine waste management as a key reasoning to mitigate environmental risks. The upstream mine waste management implies any proactive practice designed beforehand specifically to eliminate or minimize an environmental footprint.

Although an increasing attention is being given to geochemical assessment and integrated management via novel experimental approaches throughout the upstream stages of mines life, none has explored the capabilities of integrated multidisciplinary modelling approaches to support the upstream reasoning. The present paper focuses on bridging different types of modelling tools to enhance mine waste geochemical assessment and management during both the development and operation stages. Modelling approaches described herein are intended to supply efficient and cost-effective screening tools designed not to replace the experimental protocols but to support them at the upstream levels. Since upstream stages are constrained by the lack of materials and data, suitable modelling approaches are needed for environmental risk identification. The first screening tool presented, merged 3D geological modelling, core-logging data and stochastic simulation to enable mine waste classification before stripping operations. The classification is mainly based on contents of deleterious elements in the ore body and its host rock. This multidisciplinary modelling approach was designed to repurpose the advantages of 3D geological modelling for mine waste classification. However, to fulfill the 3D geological modelling requirements, sufficient datasets are needed to yield good resolution. In this regard, core-logging data and a stochastic approach were combined to address the shortage linked to sample sizes. Although this approach assists in mine waste classification, it yields static 3D geomodels that only describe the total contents of the desired deleterious element throughout the ore body and its host rock as mining operations progress. Therefore, the second screening tool was intended to incorporate kinetic modelling in the geochemical upstream assessment to take into account the temporal dimension. A kinetic model using a water film concept was developed to simulate the likelihood of contaminant release as function of time and to perform a parametric analysis for early risk identification. Since the first modelling toolkit is applicable for mine waste classification during operation and advanced exploration stages, the second modelling approach is devoted to the geochemical assessment during the development stage. Both approaches are based on minimal characterization data and core-logging datasets. The next step will be to upgrade the kinetic model through the stochastic simulation to carry out broader scoping surveys and move beyond the deterministic thinking commonly used in geochemistry. As pointed out, the main objective is to foster the upstream modelling thinking, to overcome interdisciplinary barriers among different modelling disciplines and to move towards integrated multidisciplinary modelling reasoning during upstream geochemical assessment and mine waste management.

2 MATERIALS AND METHODS

2.1 *Spatial modelling for mine waste classification*

3D spatial modelling could be seamlessly performed for economic elements that constitute the ore body as exhaustive sampling and chemical analyses are continuously undertaken for these elements of interest. However, the task is more challenging when 3D spatial modelling is repurposed for classification of mine wastes in terms of their content of deleterious elements. The chemical analyses performed for these elements do not always wrap the entire extent of the ore body and its host rock. Therefore, performing 3D geological modelling only based on the available datasets will produce poor interpolation outcome. The following describes how to overcome this challenge in order to produce high quality 3D geomodel that could be used for mine waste classification before stripping (upstream stage of stripping operation).

2.1.1 *Case study: Éléonore mine site*

The Éléonore mine site is located in the Eeyou Istchee James Bay municipality in northern Quebec (Canada), 540 km northeast of Rouyn-Noranda. The main ore body, the Roberto deposit, consists of gold mineralization hosted in the vicinity of the tectonometamorphic contact between the La Grande and the Opinaca subprovinces. The Roberto deposit displays multiple mineralization textures along a deeply plunging ore body (Fontaine, 2019). The mineralization is closely associated with arsenopyrite. Consequently, arsenic is the main deleterious element in Éléonore setting. Visualizing the 3D spatial distribution of As throughout the ore body and its country rock will provide the opportunity for mine waste classification; only mine waste with low As content will be deposited in the above-ground facilities, the remnant mine waste should be used as paste and/or rockfill.

2.1.2 *Stochastic simulation*

The prerequisite to perform the stochastic approach described herein is to use two continuous variables and one discrete variable at least. In the present study, the first continuous variable is the available chemical analyses of As, the second continuous variable is the length of arsenopyrite intervals described in the core-logging reports of up to 12 000 drill cores. The discrete variable is the qualitative assessment of the arsenopyrite proportions based on a standard scale ranging from 0.01 to 100. Each number on the standard scale is referred herein as a class that qualitatively describes the prevalence of arsenopyrite in a given interval of occurrence. The class number and length were recovered from the core-logging dataset. Sufficient core-logging datasets should be available including exploration and mining drill cores. "Sufficient" refers to the required number of drill cores to portray a 3D geomodel of the ore body. This number varies depending on the geological setting and the mineralization style. This requirement justifies the use of this approach during the advanced exploration stage and/or the operation stage as they involve high number of drill cores. Table 1 summarizes the component of the database of core-logging as well as the number of arsenopyrite intervals that were analyzed for As.

Table 1. Number of arsenopyrite intervals per class and the sample size that was analyzed. Confidence interval: 95%. Adapted from Toubri et al. 2021

Arsenopyrite classes	0.1	0.5	1	2	3
Arsenopyrite intervals	4203	43719	21193	8769	3132
Intervals with As grade	71	666	256	83	59
Margin of error (%)	11.53	3.77	6.09	10.71	12.64

The classes 0.1, 0.5, 1, 2, and 3 were selected from the standard scale (0.01 to 100) because more than 95% of arsenopyrite intervals fell in these classes. The margin of error in table 1 was calculated based on the known sample size (intervals with As grade) and the confidence interval.

Considering two independent continuous variables A and B (Fig. 1a), first we establish a power law between A and B by plotting A/B variable versus B variable. Using the logarithmic scale A/B correlates significantly with B (Fig. 1b). The parameters of the power law (a and b) as well as the correlation coefficient should be mentioned. The second step, we perform an iterative Monte Carlo simulation coupled to correlative sampling (Fig. 1c). Firstly, we set a normal or log-normal probability distribution functions (PDFs) for A/B and B variables based on their initial sample size shown in Figure 1b. The Monte Carlo simulation should sample the PDF of each variable while maintaining the correlation trend among A/B and B variables. The correlation of sampling was not set at deterministic value but it follows a Gaussian distribution centred on the aforementioned correlation coefficient value. The standard deviation of the Gaussian distribution controlled the extent of scattering. The outcome is a linear-shaped scatter that should display comparable power low parameters as the initial sample size; if not the Monte Carlo simulation should be performed again after adjusting the PDFs properties. This is an iterative process to generate a large scatter while abiding by the features of the initial dataset. Afterwards, the desired values of variable B could be selected as well as their respective values of variable A/B (Fig. 1c). Finally, the normalization is cancelled and a larger dataset is obtained (Fig. 1d). This method was used to enlarge the As sample size within each class. Furthermore, ten realizations were produced for each class to underline the effect of ergodic fluctuations. The available As grades were used as values of variable A, and lengths of intervals of occurrence of arsenopyrite represent the variable B.

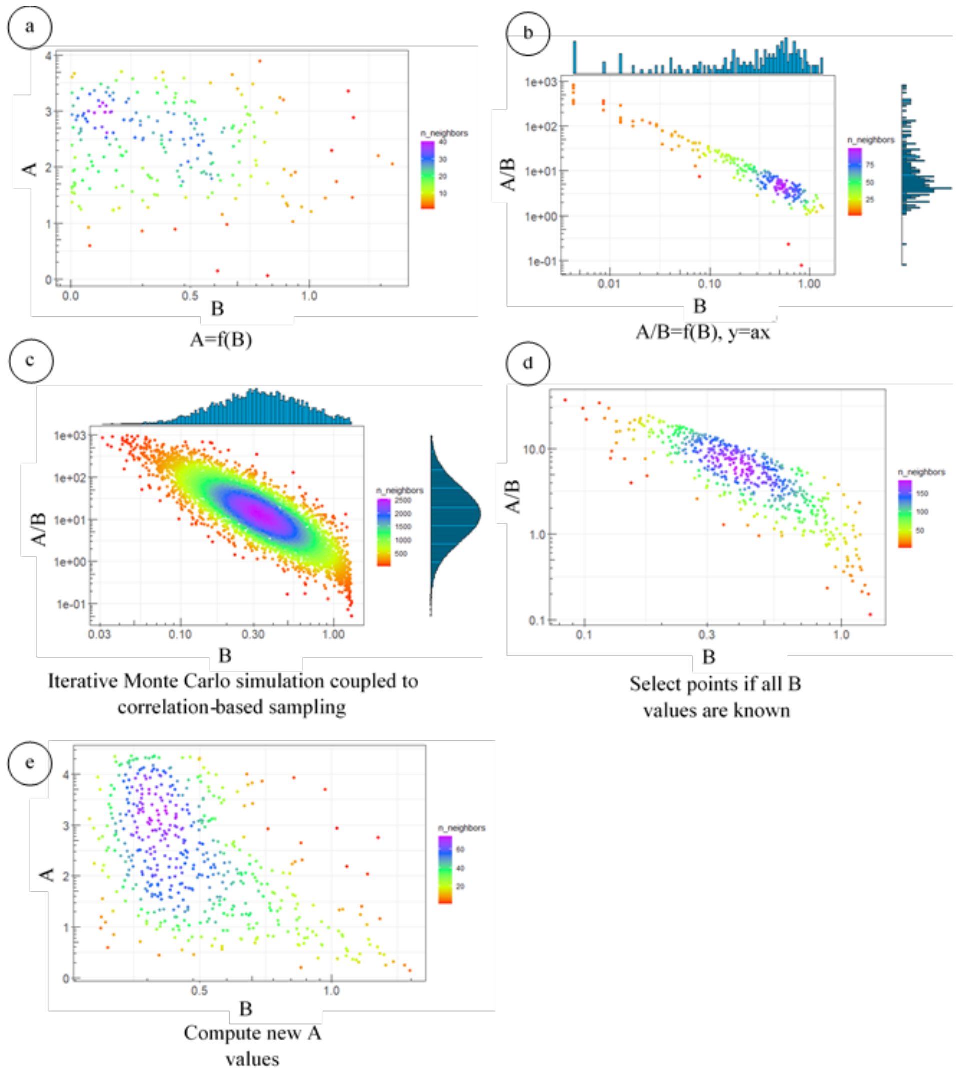

Figure 1. The iterative Monte Carlo simulation and the correlation based sampling. Adapted from Toubri et al. 2021

2.1.3 *Variography and spatial continuity*

Geological logging dataset provides the spatial position of intervals of occurrence of arsenopyrite. Consequently, each simulated As grade obtained from the stochastic process, inherits the coordinates of its interval. A 3D variography analysis was undertaken to highlight the spatial anisotropy, the spatial continuity, and the conformity of the 3D geomodel with the geological features of the deposit. The Stanford Geostatistical Modelling Software (SGeMS) was used to establish 3D directional and omnidirectional variograms. Afterwards, the Leapfrog Geo software to perform interpolation and establish the 3D geomodel based on the variograms and the structural measurements from the surface and underground mapping.

2.2 *Kinetic modelling approach for water quality assessment*

Geochemical transport modelling is extensively utilized during operation and remediation stages (Mayer *et al.*, 2002; Wilson *et al.*, 2018). Few studies used geochemical transport modelling during the development stage because the programs being used are data-extensive. Herein, the kinetic modelling was performed based upon minimal data characterization obtained from the feasibility study of a mine project. Subsequently, a parametric analysis was carried out to enhance the upstream geochemical scoping survey and risk identification.

2.2.1 *Case study: Akasaba West project*

The Akasaba West Au-Cu deposit is located in the Abitibi-Témiscamingue region, 15 km east of Val d'Or in Quebec, Canada. The mineralization style consists of thinly disseminated sulfides hosted in moderately to strongly altered metavolcanic rocks (Vermette, 2018). Geological core-logging of diamond drill cores indicates that the ore is characterized by < 5 % pyrite and < 1% chalcopyrite occurring as disseminations and locally as clusters, veinlets, or thin massive sulfide lenses.

2.2.2 *Laboratory testing*

Four weathering cells were set up to assess the geochemical responses of different lithologies belonging to the Akasaba West ore body and its host rock. Weathering cell kinetic test is a cost-effective method for geochemical assessment when limited amount of materials is available. Prior to testing, samples were characterized to determine their specific surface area, grain size distribution, chemical and mineralogical composition. Special attention has been paid to Mn as it was mentioned that it could be present in the effluent (Vermette, 2018).

2.2.3 *Conceptual model*

Experimental results from weathering cells were simulated by using one weathering cell for calibration and three other weathering cells for benchmarking. Weathering cell setup provides highly oxidizing conditions; atmospheric oxygen and water are not transport-limited throughout the test period. Therefore, the conceptual model considers surface controlled oxidation and dissolution reactions, see Toubri et al. 2021b for details. Based upon mineralogical characterization, the rate law for each mineral was compiled from the literature and integrated in the kinetic keyword block of the model. The kinetics was coupled with equilibrium and transport processes thought relevant for the system. The leaching solution as well as the pore water of the system were considered to be in equilibrium with the partial pressures of atmospheric oxygen and carbon dioxide. These equilibrium reactions allowed no restriction in oxygen supply. The advective transport was included to simulate the advection of the leach solution as a function of the residence time and volumetric flow. The residence time would relate kinetic reactions to advective transport in order to control the time duration of the water-rock interactions. The conceptual model assumed that a thin water film is surrounding the particle surfaces. Hence, kinetic reactions are assumed to occur within the water film - the particle surface boundary. Subsequently, the products of the kinetic reactions were transferred to the bulk solution through a diffusion boundary. An oxygen reservoir was implemented within the water film to trigger and maintain sulfide oxidation. This conceptual model was solved using PHREEQC; a freely available program that can solve 1D geochemical transport problems that do not include a gas transport component.

2.3 *Integration of kinetic modelling and stochastic simulation*

Using parametric analysis to highlight risks of water contamination is an efficient approach to simulate various mineral associations that were not tested in the laboratory because of the lack of materials. However, the parametric analysis is still a deterministic approach that could overlook other leaching scenarios. Furthermore, unlike the operation stage, the development stage has not benefited from the capabilities of Monte Carlo simulation. In this respect, stochastic 2D spatial distribution of the main sulfides and neutralizing minerals in Akasaba West setting will be produced for various realizations. The 2D space will represent the cross section of waste rock piles that do not exceed the critical length in order to maintain kinetically controlled conditions (Nicholson et al., 2003). Variography will be used to establish contour maps of the spatial distribution of minerals. Thereafter, kinetic modelling will be performed along mesh points to produce contour maps of water quality. This method will supply robust risk identification as it overcomes the deterministic approach and copes with a broader range of possible scenarios.

3 RESULTS AND DISCUSSION

3.1 *Spatial modelling for mine waste classification*

3.1.1 *Results of Monte Carlo simulation*

Results from the stochastic process suggested herein are shown in Figure 2. The process was able to propagate the epistemic uncertainty to the simulated sample size (Fig. 2).

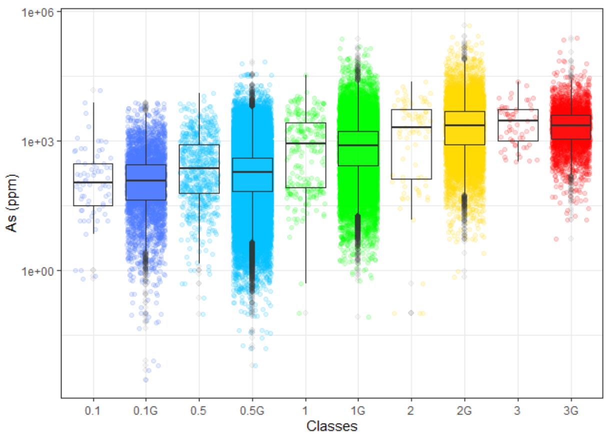

Figure 2. Results of the first realization of the stochastic simulation compared to the initial sample size (G denotes the generated data by the stochastic process for each class). Adapted from Toubri et al. 2021

It is worth mentioning that Figure 2 displays the first realization, nine other realizations were produced to underline the magnitude of the ergodic fluctuations. No substantial differences were noted among the ten realizations. More details are given in Toubri et al. (2021).

3.1.2 *Variography and spatial continuity*

The generated sample size of As grades is now sufficient to carry out 3D geological modelling. Nonetheless, it is worth mentioning that in each realization completely different As grade is attributed to each interval. Therefore, variography analysis was performed to verify if the ten realizations produce substantial differences in terms of 3D spatial continuity. Figure 3 displays the differences among the ten variograms produced from the realizations. The iterative process being used has proven to be reliable in producing coherent variograms that abide by the geological features of the deposit; the highest continuity plane in these realizations complies with the structural trend of the gold-bearing ore deposit (Toubri et al. 2021).

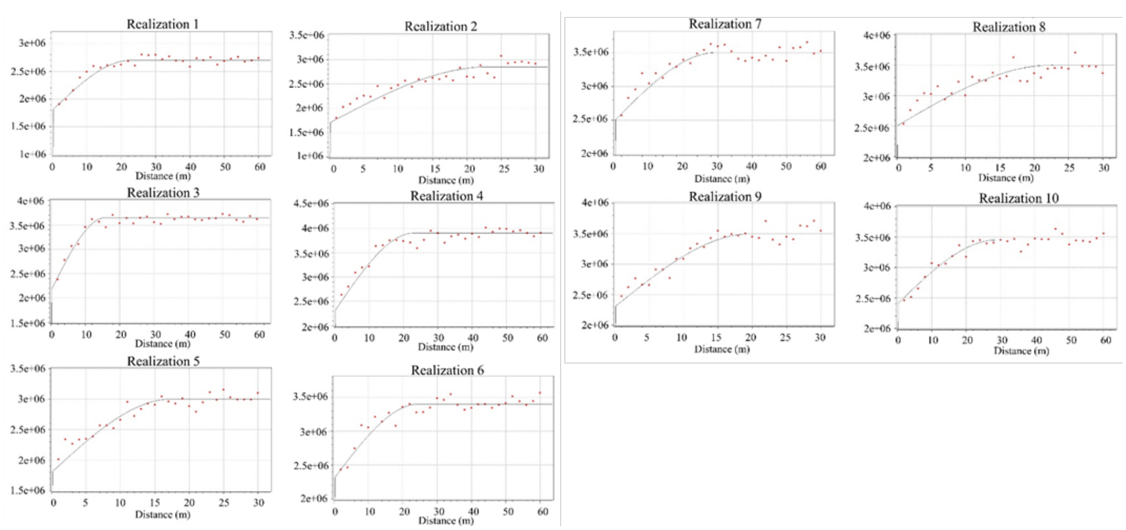

Figure 3. Realizations of directional variograms showing the highest spatial continuity.

3.1.3 *Mine wastes classification*

The 3D geomodel of As spatial distribution was produced for each variogram. Afterwards, the 3D geomodel was projected on underground stopes of Éléonore mine to visualize galleries with high to extreme content of As (Fig. 4). Mine waste from these sectors will be mainly used in backfill to avoid the damage that could affect water quality in case they are stored in the above-ground facilities. To validate the 3D geomodel, measured As grades were projected on it to underline the agreement. Certainly, the 3D geomodel does not display the exact same measured As grade, but values are on the same magnitude. Accordingly, the agreement is good enough to perform mine waste classification based on As content in the ore and its host rock.

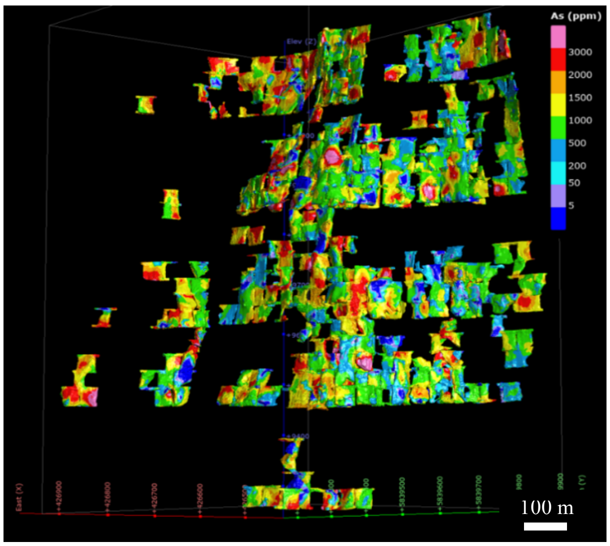

Figure 4. Underground stopes classified in terms of their As grades.

This process was applied during the operation stage of Éléonore mine to explore its reliability using underground drill cores information. Presently, it could be applied during advanced exploration stages using the drill core information utilized to build the 3D model of the ore body. The main requirement to achieve the process is that the deleterious element should be associated to a mineral phase that could be noticed and described during drill core logging. In cases where the bearing mineral phase is imperceptible, geological logging should comprise portable X-ray fluorescence analysis. Therefore, new perspectives for mine waste management could be envisioned to decrease the environmental footprint of the mine waste disposal using drill core logging.

3.2 *Kinetic modelling approach for water quality assessment*

3.2.1 *Calibration and benchmarking*

The kinetic modelling approach was designed to comply with the upstream level of the development stage of Akasaba West project. According to mineralogical characterization, Mn was mainly detected in calcite (Vermette 2018). So it was simulated as trace element in calcite. The stoichiometric coefficient of Mn in calcite was used as a calibration parameter. Other parameters were used in calibration, such as the diffusion coefficient (D_e) of a chemical element from the water film towards the pore water, available surface of reaction of albite was also used in calibration as albite is present in high weight proportions. Besides the pH, the following elements were simulated in each weathering cell: Fe, Al, K, Na, Ca, Mg and Mn. Only the pH, Ca, Mn and sulfate are presented here. A good agreement between the experimental data and the PHREEQC kinetic model was achieved using D_e=8.10^{-11} m^2/s for chemicals diffusing from the water film to the pore water. The obtained value of D_e within the water film was roughly one order of magnitude lower than the diffusion of ions in free water. A stoichiometric coefficient of Mn ranging between 0.00039 and 0.0015 for 1 mole of calcite yielded a good agreement with the experimental leaching trends (Fig. 5). The release of Mn is pH-dependent; at lower pH values the dissolution rate of calcite increases. Therefore, increasing the sulfide content would result in higher concentrations of Mn. Meanwhile, low reactive minerals such as silicates dissolve slowly and could raise the pH after a lag time. Despite their low reactivity, silicates contribute to alleviate Mn lixiviation. To underline the model reliability and limitation, three benchmarking cases were performed (not shown here). The benchmarking cases display a good agreement. However the model presented the following limitation: the model did not properly simulate the Mn leaching when calcite and pyrite contents were as low as 0.4% wt and 0.8% wt, respectively, but the simulated values are closer to laboratory results for calcite and pyrite contents above 1% wt and 4 % wt respectively.

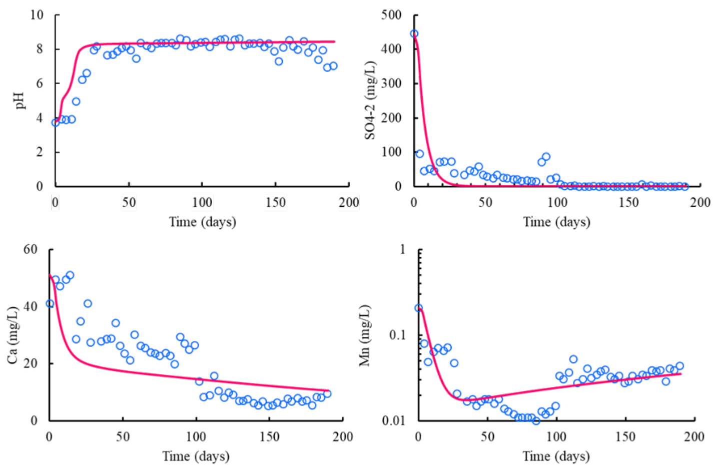

Figure 5. Experimental (empty circles) versus modelling (solid line) results from the calibration case. Adapted from Toubri et al. 2021b

3.2.2 *Parametric analysis*

Based on results of the kinetic model, the parametric analysis was performed to underline the contamination risks under more acidic conditions (Fig. 6). Through testing different mineral assemblages' scenarios, the parametric analysis stresses a considerable contamination potential linked to Cu and Mn lixiviation. In the absence of calcite and the presence of less than 30% wt of albite, acidic conditions would set up and foster chalcopyrite dissolution. On the other hand, in the presence of calcite, the Mn concentrations increase especially when silicates are present at low weight proportions (Fig. 6).

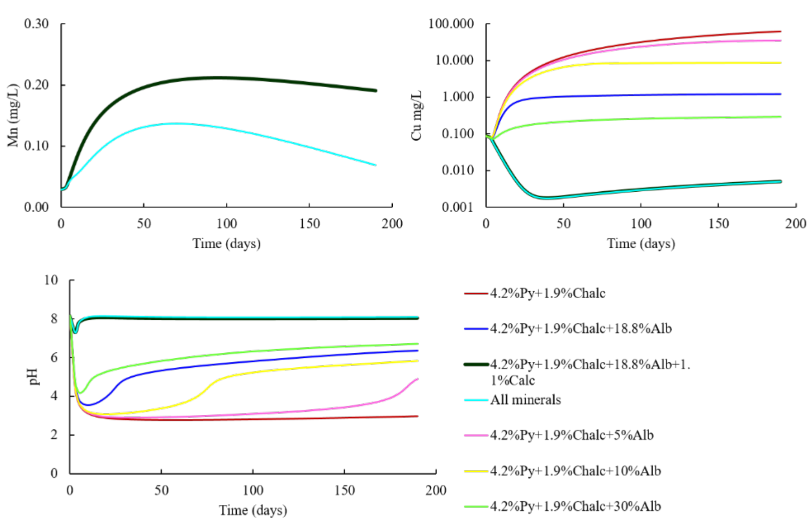

Figure 6. Parametric analysis using various scenarios of mineral assemblages.

4 CONCLUSION

This work is a bridging effort to dissolve interdisciplinary barriers to assist mine manager's decision-making throughout different upstream stages. A 3D geomodel was built using restrained datasets to assist in mine waste classification before extraction. Figure 7 summarizes the approach suggested in this work. Based on core logging data, the approach aimed to cope with two types of variability; the spatial variability and the mineral assemblage variability. The first was assessed to enable mine waste spatial classification and the second was deemed necessary to perform broader scoping surveys of the geochemical behaviour of mine wastes.

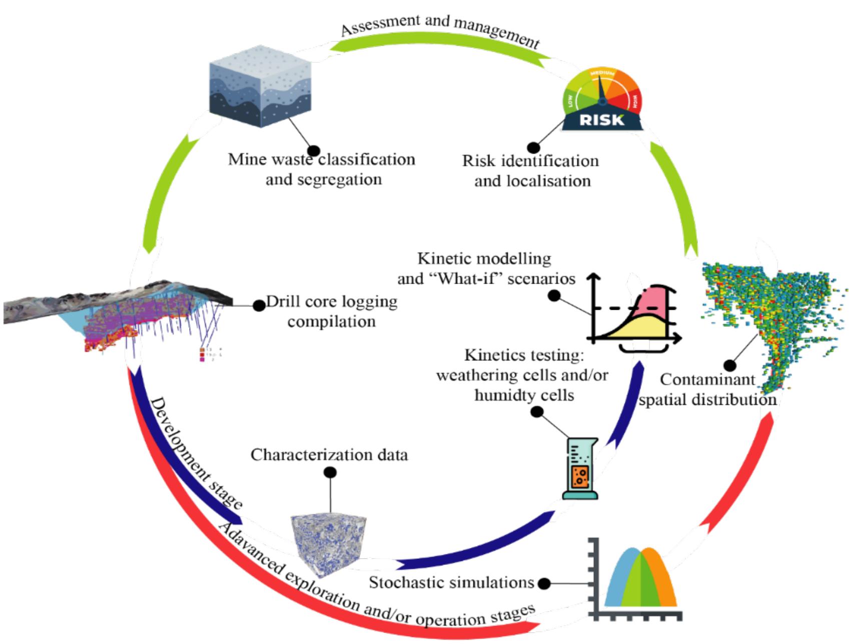

Figure 7. A summary of the integration reasoning suggested in this work.

This approach highlights that core-logging data are of great importance not only for geologists and mining engineers but also for mine waste managers. In this regard, core-logging data should be carefully compiled and upgraded throughout the whole life of a mine. Furthermore, using stochastic simulation to repurpose 3D geological modelling for mine waste classification revealed a promising horizon for mine waste management to be integrated with a broader spectrum of disciplines. The present work also bridged kinetic modelling and parametric analysis to geochemical assessment during the development stage without using data-intensive programs. This approach enables a better risk identification through coupling kinetic testing, kinetic modelling and assessment of a larger spectrum of scenarios that were not evaluated in the lab owing to the lack of material. Both upstream modelling attempts, however, could be further improved through merging kinetic modelling and stochastic simulation capabilities. Future work will be focused on this subject to improve the integration thinking suggested herein.

5 ACKNOWLEDGEMENT

The authors thank the staff of Akasaba West project and Éléonore mine site for their support and the Unité de Recherche et Service en Technologie Minérale (URSTM) staff for their assistance in the laboratory. The authors are grateful for the insights and suggestions from Dr. J. Mahoney, Dr. D. Parkhurst and Dr. D. Kinniburgh during the formulation of the PHREEQC and PHREEPLOT models used in this work. Funding for this study was provided by NSERC TERRE-NET program (NSERC-TERRE-NET 479708-2015), led by Dr. D. Blowes (University of Waterloo).

REFERENCES

Aubertin, M., Bussière, B., Pabst, T., James, M. and Mbonimpa, M. (2016). Review of the reclamation techniques for acid-generating mine wastes upon closure of disposal sites. Dans Geo-Chicago 2016 (p. 343-358).

Benzaazoua, M., Bussière, B., Demers, I., Aubertin, M., Fried, É. and Blier, A. (2008). Integrated mine tailings management by combining environmental desulphurization and cemented paste backfill: Application to mine Doyon, Quebec, Canada. Minerals engineering, 21(4), 330-340.

Benzaazoua, M., Perez, P., Belem, T. and Fall, M. (2004). A laboratory study of the behaviour of surface paste disposal. Proceedings of the 8th International Symposium on Mining with Backfill, The Nonferrous Metals Society of China, Beijing.

Bussière, B. (2007). Colloquium 2004: Hydrogeotechnical properties of hard rock tailings from metal mines and emerging geoenvironmental disposal approaches. Canadian Geotechnical Journal, 44(9), 1019-1052.

Demers, I., Bouda, M., Mbonimpa, M., Benzaazoua, M., Bois, D. and Gagnon, M. (2015). Valorization of acid mine drainage treatment sludge as remediation component to control acid generation from mine wastes, part 2: field experimentation. Minerals Engineering, 76, 117-125.

Dold, B. (2008). Sustainability in metal mining: from exploration, over processing to mine waste management. Reviews in Environmental Science and bio/technology, 7(4), 275.

Fontaine, A. (2019). Géologie des minéralisations aurifères de la mine Éléonore, Eeyou Istchee Baie-James, province du Supérieur, Québec, Canada. Université du Québec, Institut national de la recherche scientifique.

Jouini, M., Benzaazoua, M., Neculita, C.M. and Genty, T. (2020). Performances of stabilization/solidification process of acid mine drainage passive treatment residues: Assessment of the environmental and mechanical behaviors. Journal of Environmental Management, 269, 110764.

Lessard, F., Bussière, B., Côté, J., Benzaazoua, M., Boulanger-Martel, V. and Marcoux, L. (2018). Integrated environmental management of pyrrhotite tailings at Raglan Mine: Part 2 desulphurized tailings as cover material. Journal of cleaner production, 186, 883-893.

Mayer, K.U., Frind, E.O. and Blowes, D.W. (2002). Multicomponent reactive transport modelling in variably saturated porous media using a generalized formulation for kinetically controlled reactions. Water Resources Research, 38(9), 13-11-13-21

Nicholson, R.V., Rinker, Michael J., Acott, Gerry. and Venhuis, M.A. (2003). Integration of field data and a geochemical transport model to assess mitigation strategies for an acid-generating mine rock pile at a uranium mine. Proceedings, Sudbury.

Parbhakar-Fox, A.K., Edraki, M., Walters, S. and Bradshaw, D. (2011). Development of a textural index for the prediction of acid rock drainage. Minerals Engineering, 24(12), 1277-1287.

Toubri, Y., Demers, I., Poirier, A., Pépin, G., Gosselin, M.C. and Beier, N.A. (2021). Merging 3D geological modelling and stochastic simulation to foster the waste rock upstream management. Journal of Geochemical Exploration, 106739.

Toubri, Y., Vermette, D., Demers, I., Beier, N.A. and Benzaazoua, M. (2021b). Incorporating multicomponent kinetic modelling in the upstream geochemical assessment of metallic orebodies. Journal of Contaminant Hydrology (paper under review).

Vermette, D. (2018). Approche de caractérisation géoenvironnementale axée sur l'utilisation des concepts géométallurgiques. http://depositum.uqat.ca/765/1/Memoire_DVermette.pdf.

Wilson, D., Amos, R.T., Blowes, D.W., Langman, J.B., Ptacek, C.J., Smith, L. and Sego, D.C. (2018). Diavik waste rock project: A conceptual model for temperature and sulfide-content dependent geochemical evolution of waste rock–Laboratory scale. Applied geochemistry, 89, 160-172.

Development of future daily precipitation and applications for water management practices

Homin Kim & Geoffrey Niggeler
Freeport-McMoRan Inc, Phoenix, AZ, USA & Climax Molybdenum Co. Henderson Operations, CO, USA

Brant Whiting
Freeport-McMoRan Inc, Phoenix, AZ, USA

Mark Schmelter
Freeport-McMoRan Inc, Phoenix, AZ, USA

ABSTRACT: Precipitation forecasting has long been a question of great interest in Water Management practices, as it informs water storage and supply planning, development of geotechnical guidelines and closure planning. Precipitation projections are a required component of any forward-looking water balance model. Developing reasonable precipitation projections that can be used in probabilistic modeling facilitates risk-informed decision making. This paper presents a methodology that uses regional data and combines them to increase the period-of-record and improve the reliability of annual and multi-year precipitation totals. Further, this paper describes a method to develop data-based precipitation sequences that can be used as the basis for probabilistic modeling of mine water balances. The approach taken in this study generated daily precipitation sequences for a certain duration based on a chosen exceedance probability from the actual historical patterns. Examples of this methodology are used to illustrate the process and benefits of such an approach.

1 INTRODUCTION

1.1 *Water Management Context*

Water management of tailings storage facilities (TSFs) is a fundamental requirement of good TSF stewardship. The term "water management" encompasses a number of aspects that span all phases of the TSF lifecycle, with a significant portion being in the operational and closure phases. During operations, water management signifies the collective effort to help ensure that sufficient water resources are available to support ongoing production of metal, adequate facilities are in place and operating as designed to handle seasonal and discrete precipitation accumulation, and that stability of the facility is not compromised due to inadequate water management practices. For closure, recognizing that every facility has finite capacity to store water and route runoff, developing reliable likelihoods of exceedance for discrete and long-term precipitation accumulations is a primary concern and is typically evaluated through water balance modelling.

The concept of the "design storm" is well-founded in engineering and practice, and it is typically straightforward to evaluate whether or not a given facility has sufficient freeboard to handle discrete design events, such as the 100-year, 24-hour storm. What is generally less understood is how robust a facility may be against non-discrete events—for example, what if the 1 in 100-year annual accumulation occurs? Can we handle the 72-hour probable maximum precipitation (PMP) after a prolonged wet season? What if an El Nino pattern sets up, and we have several wet years in a row? For answers to these types of questions, the engineer must have representative estimates for not only the likelihoods of accumulating different precipitation depths over extended time-frames—such as one-year, five-year, and perhaps longer periods—but also for reasonable sequences of daily precipitation that sum up to the total depth for a given timeframe and probability. Several challenges are recognized to achieve this; the predominant challenge is generally finding precipitation gages with sufficiently long periods-of-record that allow reliable computation of these statistics; developing these estimates in a way that maximizes the value of existing data and minimizes the number of assumptions; and giving specific definition to the ideas of what a "wet season" is. Addressing these challenges is the focus of this paper.

1.2 *Framing Principles of Stochastic Sequence Development*

At the outset of this paper, we wish to highlight several important but sometimes underappreciated aspects (especially by stakeholders) to developing forward-looking stochastic climate sequences that are of particular interest and relevant to the core methodology disclosed in this paper. These aspects are of importance when considering the value added by the described methodology over the alternatives.

First, individual stochastic sequences are always going to be "wrong"—that is, we are confident that any single sequence describing future precipitation is not how the future will evolve exactly. Therefore, good stochastic sequences as an ensemble are representative of the range of possibilities, but no one single trace within that ensemble predicts the future exactly.

Second, to model precipitation accumulation beyond a discrete event we must estimate both the total depth that accumulates over the duration of interest (e.g. one-year, two-year), as well as how precipitation accumulates within that time frame. Just like discrete design storms define a total depth (e.g. 60 mm in six-hour), a critical component of runoff modeling is the selection of the hyetograph to describe the total depth—it is not good practice to assume uniform rainfall distribution from the onset of precipitation to the end of the event. Longer-term precipitation is seasonal and accumulating a depth at the 1 in 100 probability two-year duration comprises many individual storms, most of which will not be beyond the two-year individual event. Developing reasonable accumulation patterns within the duration of interest is as critical to water management modeling as is establishing the total depth.

Last, simplicity is preferred over complexity. Certainly, the practice of statistics and probabilistic modeling can necessarily get complicated, however, increased complexity should not be conflated with increased validity. In the statistical modeling world, "parsimonious models" is an oft-used term to describe the preference for simpler models with fewer parameters and inputs over more complicated models that run the risk of being overfitted. Parsimonious models have minimized user inputs and maximized the information available in the data without necessarily having to tease out and model each sub-process explicitly.

1.3 *General description of methodologies*

Typical approaches to generating stochastic daily precipitation series in the mining subdiscipline of water balance modeling range from recycling past climate sequences at the site from local gages (i.e. use the five-year of daily records repeatedly), using a nearby gage (with and without scaling of data), to assigning independent probability distributions to monthly precipitation totals with an embedded Markov process for the likelihoods of having daily precipitation events during that month. While there are pros and cons to each of these typical methods, we will primarily focus our summary on key issues that the proposed methodology addresses, rather than deficiencies of other methods.

The approach in this paper uses site-specific and regional data to develop likelihoods of ac-cumulating precipitation for annual and longer durations. Regional gages located in a similar climatology can be scaled to the site of interest and aggregated to statistically increase the period-of-record for that location. This increased period-of-record is summarized over one-year, two-year, to five-year durations and frequency statistics are generated and compiled into a depth-duration-frequency (DDF) table. The regional gages are also used to evaluate how precipitation is produced within the interval and provide direct precipitation sequences that intrinsically embed multi-year correlations (i.e. series of wet years). While getting 255 mm of precipitation in a year has an associated likelihood defined by the DDF table, the climate sequences provide estimates of how that accumulation is distributed throughout the duration.

2 DATA AND METHODOLOGY

This section is divided into three parts. The first part deals with the general description of the methodology, the second part addresses the development of the DDF table and daily precipitation sequences with two sites, and the third part addresses how to implement the GoldSim software (ver. 12.1 2020) to run weather scenarios with an event-based risk following a longer-duration sequence.

2.1 *Methodology*

Forward-looking, or predictive models, require forcing assumptions to make the model compute, and these model inputs are typically observable but unknown at the moment of prediction (by definition). For example, mill tonnage, tailings water content, actual precipitation, reclaim pond withdrawal rates, etc. are all observable and are represented by data in a model calibration setting, but assumptions about these data that drive the model must be made when looking to the future. Incorporation of the latest mine plan, future thickener performance, future pumping rates, and the like can be developed with reasonable justifications. Precipitation, however, is not a forcing dataset that the mine has any control over, and yet assumptions still must be made. For a predictive model to be useful in decision making—whether identification of risks or opportunities—assumptions around total precipitation accumulation depths that could occur over an assumed duration, a valid likelihood (probability) associated with that depth, and a decomposition to how that total depth might incrementally accumulate on a daily and seasonal basis within the duration of interest must be developed and defended. This can be simplified into a two-step process:

1. Definition of total precipitation depths for the location of interest and range of durations (e.g. one-year, two-year, three-year, four-year, five-year, monsoon season, etc.) with its associated probability. We summarize this in a depth-duration-frequency table.
2. Development of precipitation sequences of matching durations, that when summed, equal the total depth defined in step 1 (e.g. daily precipitation sequences for 365 days that sums to the one-year median depth).

When the development of the DDF table uses multiple regional gages, care must be taken to ensure that the gages being combined are independent datasets—a common requirement of most statistical methodologies. Obviously, two gages measuring precipitation for 50-years cannot be combined in this analysis to a total of 100 gage-years if they are separated by only meters apart because they are essentially duplicate measurements. Precipitation gages separated 20 km, however, are unlikely to experience the same severity of precipitation in the American southwest due to the spatial decay of convective storm events and are more likely candidates to trade space for time. For an area like Arizona or New Mexico where most of the precipitation received on an annual basis is in the summer monsoon via convective storms, spatial independence of precipitation observation of gages more than 20 km away seems to be a reasonable assumption. This justification is partly based on the observation that convective storms on the one to six-hour duration in Arizona have an areal reduction factor of approximately 0.6 for 250 square km, or approximately a 9 km radius. Thus, the same storm event at two locations 9 km apart are likely to be very different experiences.

The development of a DDF table for a site of interest entails the following steps and a flow diagram is presented in Figure 1.

1. Identify and obtain daily precipitation data for select regional surrogate sites based on criteria such as period of record, similar climatology, data quality, etc.
2. QA/QC of dataset, including data imputation as needed (not the focus of this paper, but certainly a requirement worth noting)
3. Development of a scaling factor between the surrogate sites and the site of interest (several possibilities here, ranging from a comparison of overlapping years between the two sites to regressing quantiles for precipitation depths for durations of interest)
4. For each surrogate gage and duration of interest, temporally accumulate the depths. For a one-year duration, sum all precipitation data by calendar or water year. For a five-year duration, find the five-year in the dataset where the five-year total is maximized, and "lock-in" that position as the reference point from which non-overlapping five-year

aggregations are computed. For example, if your dataset spans from 1950 to 2005, and the largest rolling five-year total is from 1978–1982 , then aggregate data from 1978–1982, 1983–1987, and so on, rather than simply starting the five-year period at 1950–1954, 1955–1959. Doing so ensures the capture of the wettest five-year period that presumably incorporates successive wet years in sequences (e.g. El Nino pattern) thereby naturally building in those effects without having to explicitly model them.

5. For each duration, combine the scaled surrogate site accumulations into a single vector and compute frequency statistics. The fitted distribution uses the accumulation of gage-years and can be used to create quantities of interest, such as the 0.5% prob-ability 5-year accumulation.
6. Create the DDF table for durations and frequencies of interest.

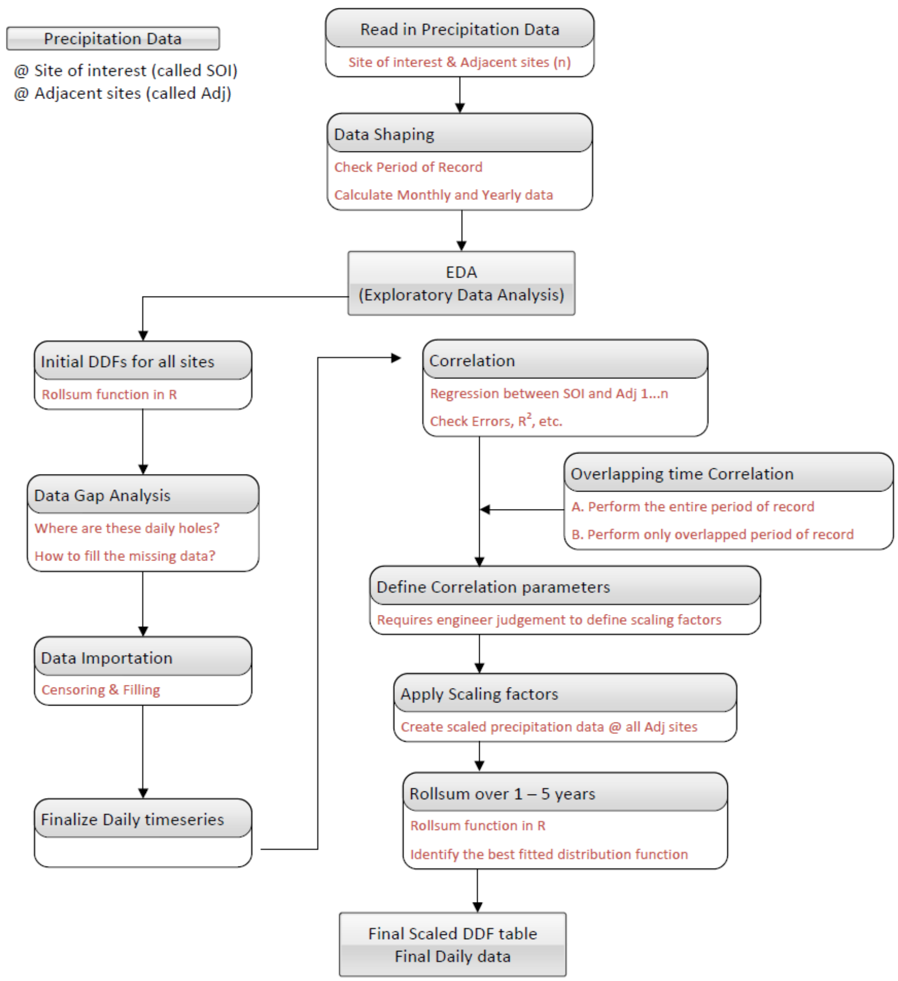

Figure 1. A flow diagram to develop a DDF table.

With the creation of a DDF table, the modeler now has the ability to define in terms of proba-bility different precipitation thresholds for durations of interest. The next step involves develop-ing a time-series of daily precipitation events that sum to that value.

Variability in precipitation patterns is a feature of our climate rather than a deficiency in our understanding, and so an ensemble of daily precipitation values must be developed to account for this. The regional gages provide many years of daily precipitation that sum to a known value. These intervals can be scaled up or down to the value of interest from the DDF table, and thereby used as reasonable surrogates for what could happen in the future. By selecting a target depth, interrogating the regional data for the timespans and locations where that depth was achieved (or something close), and scaling that time series up or down to exactly match the target value from the DDF, any temporal patterns intrinsic in the data will be naturally incorporated into modeling scenarios without having to model them explicitly.

2.2 *Study areas and data*

There are two mine operation sites described in this section–one in Arizona and the other in New Mexico. In Figure 2, the regional weather stations and on-site weather stations are illustrated with 30 km radius boundary for reference. The Arizona site is located approximately 40 km south of Tucson at 1068 meters MSL and the average of annual precipitation is about 305 mm. The New Mexico site is located 20 km southeast of Silver City at 1615 meters MSL. Most precipitation falls for both sites from June to September (monsoon season) when the storms are more intense compared to the winter season.

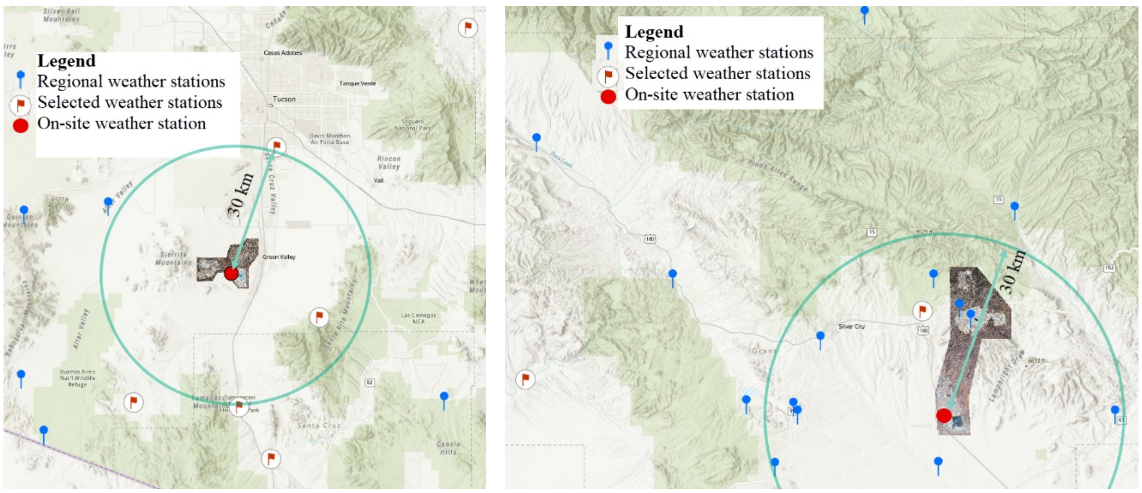

Figure 2. Locations of regional weather stations utilized in this study for the New Mexico (right) and the Arizona (left) sites.

Mine operations in this study have on-site weather stations. While a mine site may have multiple weather stations running at each site, this study is mainly focused on the one closest to a tailings storage facility and which is symbolized by a red dot in Figure 2. The on-site weather station in Arizona has been active since 2009 and the site in New Mexico has precipitation records since 2007. About 10 years of historical data at these two sites limits the data source for use in predicting future precipitation scenarios for multi-year durations. In this study, we were interested in modeling up to five years in the future primarily because this fits with medium-term mine forecasts. The analytical procedures are described in the following section and both data management and statistical analysis were performed using R studio (Version 1.1.456, 2019).

2.3 *Regional precipitation sequences development*

The first step is doing a regional search for precipitation data. Criteria for selecting the regional weather stations were long periods of record, climatologically transposable to site of interest, data quality, and reasonable distances. Regarding the distance of a potential gages, care must be taken that gages are not too close to each other to satisfy statistical data independence requirements, while still being close enough to the site to be climatologically similar and therefore transposable This concept was described in section 2.1.

For the New Mexico site, two weather stations were selected among 16 potential regional stations. For the Arizona site, we selected six stations from 11 stations in the region. Table 1 presents the summary of selected regional stations for each site. All regional precipitation data were retrieved from Global Historical Climatology Network Daily (GHCND). Prior to analyzing the selected data further, a set of quality assurance and quality control checks were performed on the raw dataset to fill holes of missing data either with zero precipitation or censoring the whole year(s). Once QA/QC were completed, an autocorrelation analysis was performed to determine if each year's precipitation at each station is statistically independent of preceding years. Because the results of autocorrelation showed that each year's precipitations are not statistically independent, the exceedance probability for a multi-year event can only be determined through frequency analysis of multi-year precipitation totals, rather than serial combination of independent events. When developing the DDF for multi-year periods, these dependencies must be accounted for and multi-year sequences cannot be generated through combination of single years.

Table 1. Details of selected regional weather stations for sites of interest.

Site of interest	Selected station	Period of records*	Elevation, meter	Distance, km	Averaged annual precipitation, mm/year	Data quality
Sierrita (Arizona site)	On-site	2009 – 2019	1068	-	305	99 %
	Redington	1941 – 2019	896	82	345	95 %
	Airport	1946 – 2019	777	32	284	98 %
	Nogales	1952 – 2019	1055	47	417	97 %
	Tumaca-cori	1946 – 2019	996	32	386	97 %
	Arivoca	1899 – 2019	1112	39	455	50 %
	Santa Rita	1950 – 2010	1311	24	554	92 %
Chino (New Mexico site)	On-site	2007 – 2019	1615	-	300	99 %
	Redrock	1905 – 2019	1236	58	318	95 %
	Fort Bayard	1895 – 2010	1859	18	401	99 %

*The end of records is 2019 since the analysis performed in the middle of 2020.

Following the results of the auto-correlation analysis, the quality-controlled daily precipitation records from all stations, including on-site data were aggregated into non-overlapping n-year duration totals, with n = 1, 2, 3, 4, and 5. The individual aggregated values at each duration for stations were ranked and quantiles were calculated (0.1 % interval between 0 % and 100 %). A regression was performed on quantiles from the on-site weather station and each selected regional station to develop a site scaling factor for each regional station. We combined all selected station data with scaling factors into a single dataset to estimate probability of precipitation accumulation at each duration and exceedance probability (EP) as shown in Figure 3. On the left side of Figure 3, the distribution of one-year accumulative precipitation for each regional station around the Arizona site are shown in solid lines and the black triangles represent on-site, one-year accumulative precipitation data. On the right of Figure 3, all six stations were combined into the one single dataset illustrated by the blue diamond symbols and three probability distributions were selected to be plotted. What stands out in Figure 3 is that the 95th quantile in the combined single dataset for one-year precipitation accumulation is 500 mm (~20") while the short period-of-record gage on-site returned the 82th quantile for the same one-year accumulation. In other words, the probability of exceeding 500 mm in one year is much lower (5% EP) than what was revealed by site data alone (18% EP). Consequently, frequency analysis with a longer period of record provides more accurate information to the site and higher confidence in the precipitation events to be expected. In particular, trading space for time such as is described here improves the reliability of the tails of the distributions, where extreme precipitation depths are estimated for use in risk-informed decision-making.

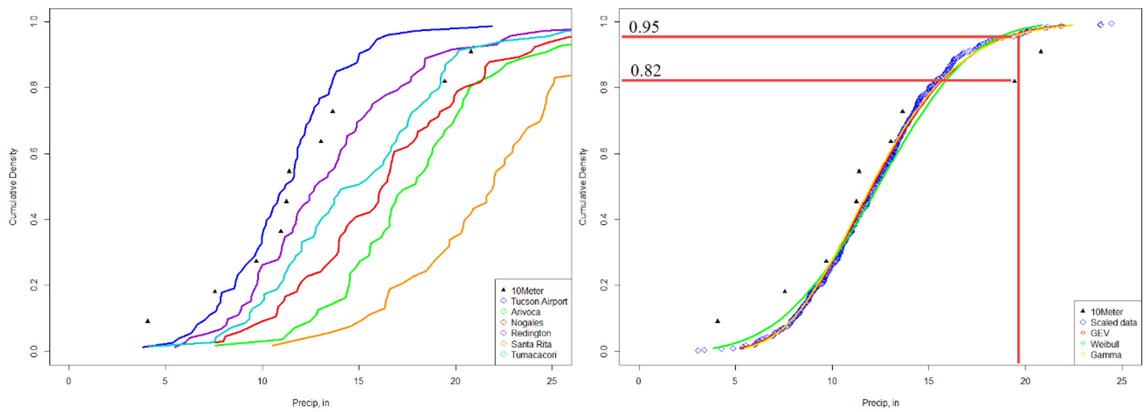

Figure 3. The one-year accumulative precipitation for all stations (left) and the combined dataset with three probability distributions with a particular example of 500 mm/year (~20 inch/year) (right). Black triangles represent on-site data and other lines show selected regional weather station data.

With the combined dataset using scaling factors, a variety of goodness-of-fit statistics were fitted to quantify how well each probability distribution fits the dataset. Once the best probability distribution was identified, it was used to derive a DDF table for the site of interest.

Table 2 shows the variation of total precipitation for the two sites as a function of event duration and exceedance probability. For example, at the site in Arizona, the analysis indicates only a 0.5 % probability of 2663 mm of total precipitation being exceeded in a five-year duration. The values given in Table 2 represent the total depth and likelihood of occurrence of a given amount of precipitation and are the first step in defining probabilistic precipitation sequences for forward-looking models. The following paragraph addresses how total precipitation depths from the DDF table are distributed into daily values and transposed from selected weather stations to the on-site location.

Table 2. Total precipitation depths as a function of duration and EP for Arizona and New Mexico sites.

Depth-duration-frequency at the site in Arizona, mm					
Exceedance probability	1-year	2-year	3-year	4-year	5-year
50 %	310	621	933	1250	1568
20 %	393	751	1102	1458	1810
10 %	445	835	1215	1597	1971
4 %	506	938	1361	1772	2176
2 %	548	1013	1470	1903	2329
1 %	588	1085	1580	2034	2481
0.5 %	625	1156	1692	2164	2633
Depth-duration-frequency at the site in New Mexico, mm					
Exceedance probability	1-year	2-year	3-year	4-year	5-year
50 %	284	569	848	1130	1433
20 %	358	673	983	1316	1618
10 %	396	732	1062	1427	1712
4 %	437	795	1151	1554	1808
2 %	462	836	1207	1641	1864
1 %	485	871	1260	1722	1910
0.5 %	505	902	1306	1798	1948

To generate site-specific precipitation sequences with the variation of total precipitation depths in Table 2, historic measured daily precipitation data from the region are used as follows.

1. Select a target precipitation accumulation from the DDF table based on duration and EP as shown in Table 2.
2. From the database of selected weather stations in Table 1, extract all n-year duration measured daily precipitation time series and compute the total precipitation of each n-year accumulation.
3. Compute the ratios of the total observed precipitation from the target depth from Step 1.
4. Compute the absolute values of the differences between the total overserved precipitation and the target depth.
5. Rank the absolute differences from lowest to highest.
6. Select the top 30 lowest absolute difference and multiply every daily precipitation with selected time series by their associated ratio from Step 3. As a result, 30 different daily precipitation sequences that sum to a prescribed depth with estimated likelihood can be used as probabilistic model precipitation sequences.

The 30 different precipitation sequences of the 0.5 % EP with five-year duration in Figure 4 are based on actual sequences that were historically observed in regional weather stations and serve as a strong statistical foundation for daily precipitation forecasting. In this study, it was decided that the selection of 30 sequences of precipitation was sufficient to capture the general variation of precipitation patterns that all give the same accumulation total. A greater number of sequences could be developed with a longer period of record if desired.

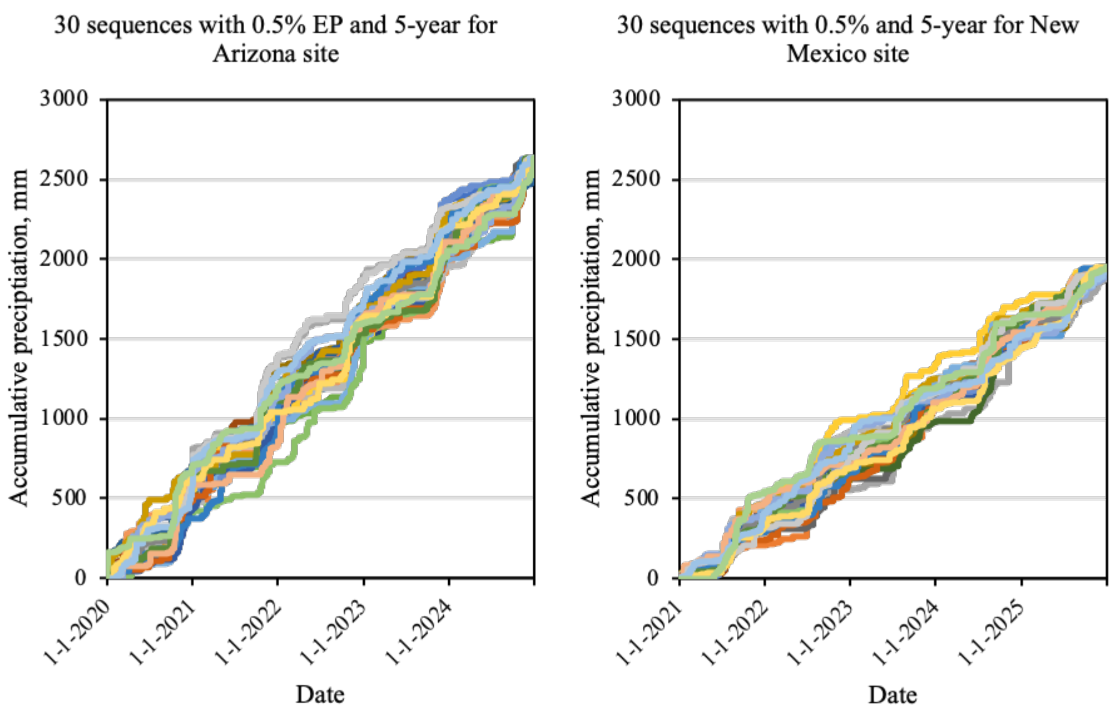

Figure 4. Thirty different precipitation sequences to meet total precipitation of 2633 mm at the Arizona site (left) and 1948 mm at the New Mexico site (right) in five-year duration with 0.5 % EP

2.4 *Water balance model implementation*

The GoldSim software (GoldSim Ver 12.1, 2020) has been widely utilized for water balance model development in particular at mining facilities. The advantage of a dynamic simulation model framework such as GoldSim, is that it can provide understanding of how much run-off needs to be managed based on the likely precipitation scenarios such as one-time event and seasonal variations or a combination of these. In addition, the software can be an interactive tool to evaluate and determine water handling design criteria such as pump stations, pond system, etc. The outcomes from these advantages are presented at the end of this section.

To implement the precipitation sequences in GoldSim, we generated Excel spreadsheet files because GoldSim can import Excel directly. Each file represents one of five durations (n = 1, 2, 3, 4, and 5) of future precipitation and each contains seven worksheets corresponding to the seven EP classes which are 50%, 20%, 10%, 4%, 2%, 1%, and 0.5 %. On each worksheet page, 30 different independent precipitation sequences are given. Once the five Excel files are compiled and connected to the GoldSim water balance model, step-by-step instructions to properly execute is available via a button on the water model's dashboard as shown in Figure 5.

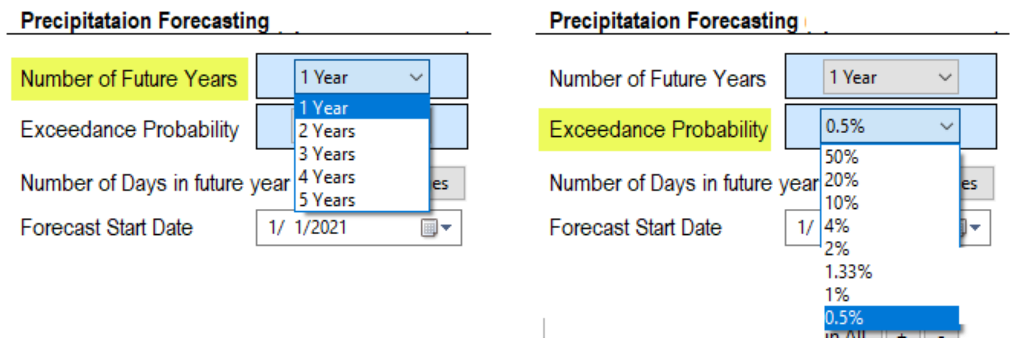

Figure 5. The settings to execute precipitation sequences on GoldSim dashboard.

The New Mexico site took advantage of the GoldSim water model for two primary purposes. One is to evaluate what level of event-based precipitation accumulation would cause run-off volumes to encroach on three established threshold requirements and the other is to better understand how multi-year precipitation sequences with their associated probabilities could create conditions that might impact established operational water management practices and criteria. To address the concern of site management, each of five forecast durations and seven EPs were simulated in the model with a 72-hr PMP event. Each simulation includes 30 realizations of precipitation patterns. Thus, a total of 1050 simulations were run.

For discussion purposes of how such precipitation sequence development can assist in risk-informed decision making, Figure 6 shows the three sample freeboard predictions following a one-year precipitation accumulation with 0.5 % EP (the 1:200 wet-year) followed by the 72-hr PMP. To determine freeboard exceedance, Threshold 1 represents the condition when the average of 30 sequences (black dashed line on Figure 6) is exceeded. Threshold 2 represents the condition when the average is not exceeded, but some precipitation patterns exceed the threshold. Threshold 3 represents the condition where no precipitation patterns are exceeding the threshold. Site management can use the results of these predictions and the likelihoods associated with each threshold to make related water-management decisions in a risk-informed manner.

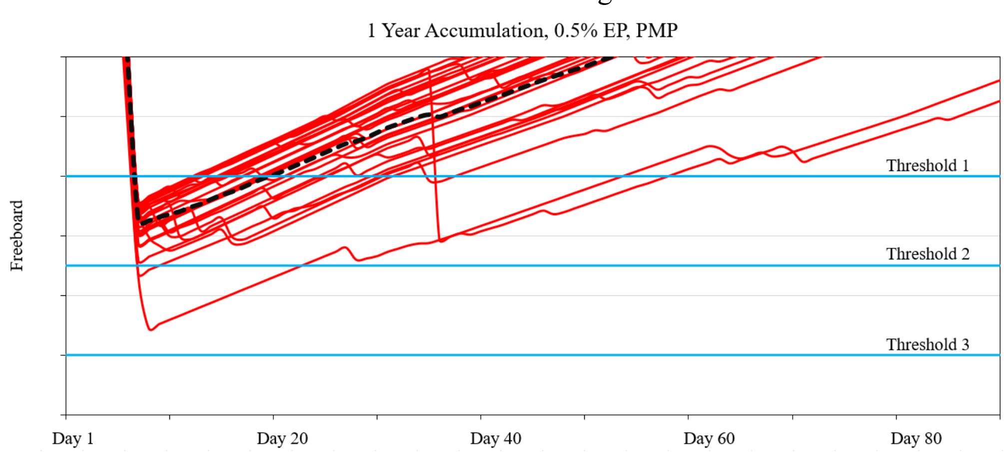

Figure 6. Predicted freeboard of TSF following one-year duration and 0.5 % EP accumulation with 72-hr PMP to evaluate the risk of exceeding three sample thresholds. Red solid lines indicate the 30 precipitation patterns and the black dashed line represents the average of 30 sequences.

3 COMPREHENSIVE IMPLEMENTATION

Prior to efforts to update the water balance model at a Colorado site, the GoldSim water model did not assign probabilities on climate projections and provided multiple projections based on pre-defined conditions such as wet, dry, and average, with wet and dry being qualitatively defined. Therefore, more robust climate pattern forecasting approach was developed and its usage in the storage capacity probability assessment illustrated a greater understanding of the uncertainties leading to a potential site-wide risk assessment. While it is not possible to present all results of this assessment in this paper, the facility overview, summary of GoldSim projections, and major contributions are addressed in the following section.

3.1 *Facility overview and climate*

The Colorado site is located approximately 110 km west of Denver along the west side of the continental divide in the Williams Fork River valley at an elevation of approximately 2770 meters. At this elevation, the summers are relatively short, with daily average temperatures close to 21 °C and UV index reaching 10 most days. The winters are usually long and harsh, with average daily winter temperatures below -7 °C; nighttime lows regularly below -18 °C. Annual average precipitation is 460 mm with 267 mm of that usually in the form of snow. The site operates an on-site weather station and measured daily precipitation are available since 2010. Historically, climate forecasting was performed using data from the Williams Fork Dam station which is located about 24 km north of the site and 450 meters lower in elevation. On the other hand, Dillon Dam weather station is located 24 km south of the site and 30 meters lower in elevation. It has over 105 years of data compared to 34 years of data at Williams Fork Dam. Therefore, Dillon Dam weather station was selected for the proposed precipitation sequences development and Figure 7 shows the two regional weather station locations and site of interest.

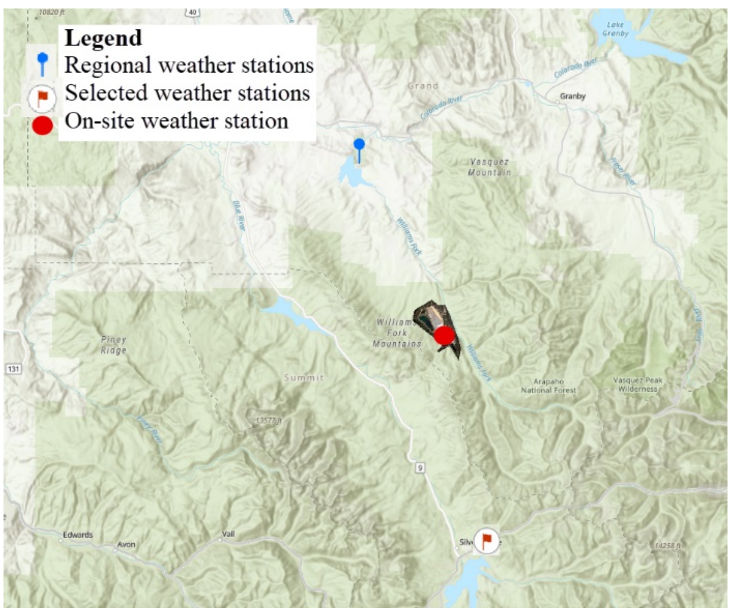

Figure 7. Locations for the Colorado site and regional weather stations

3.2 *Site-specific water strategy*

Water management at the Henderson Mill site is of paramount importance to sustain an operating mill while complying with all environmental, water rights and dam safety criteria. The most significant characteristic of the Henderson Mill process water system is that it is currently a "closed loop" system. That is, only the water necessary for use in the milling process is taken into the system and there is no water treatment or discharge from this system. The water within the system is stored, circulated, and eventually used to extinction. This characteristic elevates the importance of managing and maintaining the water system so that there is neither too much water nor not enough water to support mill operations. Therefore, the water management strategy at the Henderson Mill is to ensure there is enough water to support mill operations, while ensuring safety of the TSF, stewardship of the environment, and compliance with state water rights laws and regulations.

3.3 *Key takeaways*

To confidently execute the site water strategy, a statistical method for predicting site specific climate conditions was necessary. As a closed loop system, climate governs the stored water levels on site and hence also drives the site water risks. A simplified version of the method described in this paper was applied to the site's water balance model, which enabled strategic decisions to be based on regional probability of occurrence rather than discrete, local scenarios or qualitatively-defined "wet" and "dry" conditions (Table 3).

Table 3. Established forecasting parameters used by the site Water Management Team

Climate criteria	1% EP for annual precipitation
Production criteria	Current LOM forecast
Forecast period	5 years
TSF Pond elevation	Established forecasting parameters

Furthermore, the methods could be applied over a range of climate probabilities, mill production scenarios, and forecasting horizons to provide decision makers with an assessment of the system sensitivities as shown in Table 4.

Table 4. High level summary of the site's GoldSim model prediction capabilities and standard scenarios.

Model parameter	Capability range	Typical scenario
Mill production	0 – 365 days/year 0 – 36,288 Tonnes/day (0 – 40,000 Tons/day)	180 days/year 27,215 Tonnes (30,000 Tons/day)
Production variability	Production can change monthly Production is constant for the entire forecast	Custom production based on current LOM forecast
Climate (EP of annual precipitation)	50 %, 20 %, 10 %, 4%, 2%, 1.33 %, 1%, 0.5 %	50 %, 4 %, 1 %
Forecast period	1 day to 5 years	5 years
Water treatment	0 – 0.1 m3 per second (0 – 1500 gallon per minute)	0 m3 per second (0 gallon per minute)

In Figure 8, the water model was calibrated until the early nine-year mark and switched to forecast mode covering five years beyond the date of last measured data. The model projections considering a scenario that included a dramatic change in production amid a relatively wet climate pattern showed stored water levels had the potential to exceed the established management criteria (Figure 8). Through discussion and evaluations of this potential with site leadership, it was determined that additional water management tools would be needed in the future to allow the site to maintain a high level of operational flexibility. Hence, the decision was made to pursue the design and permitting of a water treatment plant capable of maintaining site water balance for a wider range of projected scenarios and criteria.

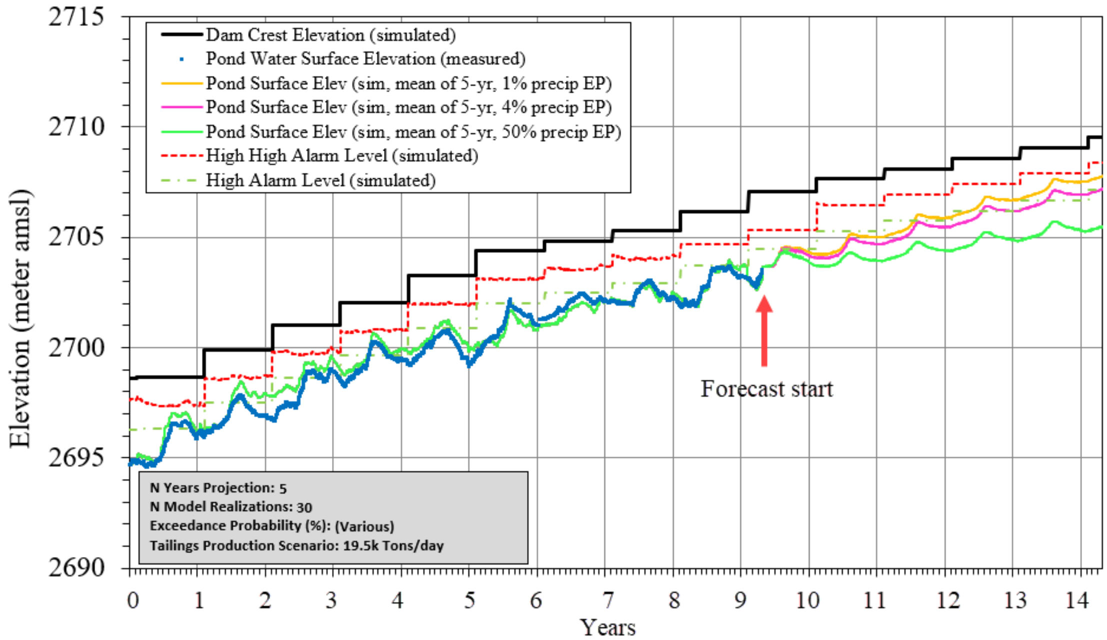

Figure 8. Pond surface elevation results of five-year projection with 50 %, 4 %, and 1 % EPs.

4 CONCLUSIONS

This paper presented a robust data-based methodology to develop future daily precipitation sequences over a range of durations. With long periods-of-record from regional weather stations, the future precipitation sequences use observed historical precipitation patterns and can be used to estimate likelihoods going forward so that mine leadership teams have more confidence in decisions that impact production, safety and the environment.

It is hoped that the methodology described in this paper at a minimum evokes thought about how we can make model forcing data (such as precipitation) more data-based and reliable, with the aspiration that this methodology can be employed by others to improve their probabilistic models. The benefits of the methodology described in this paper are summarized below:

- The proposed method maximizes the use of regional data and utilizes probabilities assessment.
- By trading space for time, the tails of the distributions are better defined and have reduced uncertainties relative to at-a-station statistics and more reliable in risk-informed decision-making.
- Regional precipitation patterns in the long period of record near a site can be used to overcome the limited on-site record and increase the confidence in forecasting. For example, n-year duration precipitation sequences implicitly account for historical El Niño impacts within a n-year time horizon.
- The DDF tables can be easily scaled to account for projected climate change effects.
- Regional precipitation analysis accounts for extreme wet and dry periods and quantifies the probability associated with reaching these periods.
- Improved quantitative definition of “wet” and “dry” years with associated likelihood.
- Probability assessment related to storage capacity and pond surface elevation support a greater understanding of the uncertainties that can support a risk-informed decision-making process.
- From a management perspective, we can evaluate scenarios associated with different durations and their associated EPs. The EP explicitly defines the probability of accumulating a certain amount of precipitation over a given timeframe that is based on many station-years of data. In addition, the EP and corresponding duration can be modeled using various temporal

patterns (i.e. 30 sequences) to test design criteria and develop a site-specific risk profile or tolerance.
- Implementation in a simulation software such as GoldSim provides the framework to incorporate the dynamics of facility production and changes to TSF geometry. When combined this provides a robust tool for assessing risk related to managing excess water and the how production plans may influence that risk.

5 ACKNOWLEDGEMENT

We wish to thank W. W. Wheeler & Associates, Inc., Applied Weather Associates, LLC and Paul Haby of Golder for their support related to the development of this work.

6 REFERENCES

Applied Weather Associates. 2018. *Arizona-New Mexico regional precipitation and meteorological analysis report*. Monument, CO: AWA.
GoldSim Ver 12.1. 2020. *The GoldSim Technology Group*. Seattle, WA.

Coal Tailings Closure Guideline: Targeting a consistent, measurable and sustainable approach

Sally Moodie
BHP, Brisbane, Queensland, Australia

Kim Ferguson
BHP, Adelaide, South Australia, Australia

Chad LePoudre
BHP, Saskatoon, Saskatchewan, Canada

ABSTRACT: When considering closure, BHP seeks outcomes that balance our values, obligations, safety and costs with the expectations of external stakeholders. Within Minerals Australia, BHP manages 25 coal tailings storage facilities in Queensland and New South Wales, many of which are nearing the end of their operational life. These facilities vary in age, size, construction and their integration with the environment.

Identifying and managing risks associate with these facilities is challenging. Development of the Coal Tailings Closure Guideline (the Guideline) will help manage the complexity and longevity of any potential impact these facilities may have on our employees, the environment and communities, and our resultant reputation. The Guideline reflects recent guidance on organizational responsibility and standards developed by the Global Tailings Review (GTR), the International Council on Mining and Metals (ICMM) and internally. The Guideline emphasizes the importance of environmental and social risk management in combination with stability objectives.

The closure design of future coal tailings storage facilities will be assessed against a consistent set of performance targets defined in the Guideline. This will allow measurable assessment of performance during closure phases and enable mitigation or additional assurance when required. The Guideline also provides a framework for ensuring transparency of residual liabilities and risks in instances where performance targets are not met. It will be adopted during the design of any future tailings facilities, ensuring integration of closure risk mitigation from the outset and throughout operations, rather than at the end of operational life.

1 INTRODUCTION

When considering closure, BHP seeks outcomes that balance our values, obligations, safety and costs with the expectations of external stakeholders with alternative land-use, on-going management, relinquishment, or divestment for closed operations. The Coal Tailings Closure Guideline (the Guideline) was developed in response to a business need to provide clear direction and reasoning for the timing and closure methodology of its 25 coal tailings storage facilities in Queensland and New South Wales, Australia.

This paper outlines the opportunity, intent and challenge of the Guideline, and provides an overview of the approaches adopted for its successful implementation.

2 OPPORTUNITY

Many of the 25 facilities are nearing the end of their operational life. Their closure provides an opportunity to:

- Reduce risk to employees, the environment and communities.
- Refine and reduce uncertainty in closure methods
- Decrease the financial liabilities of closure held by government authorities.

- Improve our corporate reputation with government, community and shareholders.

A closure study commenced in late 2019 to investigate establishing "a path to relinquishment for coal tailings facilities with the development of a prioritised plan" (BHP, p1). Any plan to close the facilities needed to clearly weigh the outcomes against the opportunity's benefits, thus resulting in good business decisions. As each of the 25 facilities are unique, a consistent measurement of benefit is needed to ensure prioritisation. Furthermore, a sustainable approach would need to be demonstrated so that business decisions remained relevant and maximised the benefits.

The Guideline was proposed to be developed in parallel with the closure study to help support the business decision. As its design needed to fulfil this role, the Guideline was to be:

1. Consistent.
2. Measurable.
3. Sustainable.

The following sections define how these outcomes were met.

3 CONSISTENT

Early discussions of the Guideline's intent concluded that its structure was to be simple. This meant a set of consistent performance targets arranged in a table, with an overarching document describing the application of the targets. With the varying attributes and subsequent risks of each facility, the Guideline needed to reflect a wide breadth of risks consistently to achieve the risk prioritized plan.

Closure design for facilities has historically been focused on stability objectives. This focus has often lead to environmental and social risks being inadequately represented. The Guideline has been developed to emphasise the importance of non-stability objectives, such as the protection of surface and groundwater environments and indigenous and local community values, to provide a comprehensive oversight that can be consistently applied.

Advocacy undertaken by the GTR (2020) and ICMM (2021), which has broadened tailings management responsibilities beyond structural stability, has significantly progressed these inadequacies. For example, Global Industry Standard on Tailings Management's Principle 3 requires social, environmental, local economic and technical knowledge to be used to inform decisions throughout a facility's lifecycle, including closure (GTR, 2020).

To reflect the above, initial versions of the Guideline proposed that each of the 25 facilities would outline their own social, environmental and local economic values and subsequent closure objectives. However, as this approach developed, it appeared evident that the immature regulatory commitments (largely due to the age of environmental licenses), often broad language in internal standards and dispersive external commitment posed a threat to fulfilling the objectives at a site level. To achieve consistency, the Guideline adopted SMART targets – those that are Specific, Measurable, Achievable, Realistic and Time bound.

The requirement for the SMART targets was significantly challenging for the environmental, local economic and social areas. There were limited references that could be directly applied, and the difficulties in developing risks at a facility level were amplified for a portfolio-level risk definition. To overcome this, more than 20 BHP coal and international subject matter experts were convened for the "Coal Tailings Collaboration Campaign". An external facilitator was engaged to host three agile sprints that identified, developed and aligned the experts on performance targets representing sub-categories within the environment and social sphere.

Consequently, of the 19 SMART targets, eight were defined as stability (technical) and 11 were defined as either environmental or social (including local economic and Indigenous relations). While the Guideline does delineate these targets into categories, it emphasises that they must be holistically connected through the design and management of closure. For example, to manage surface water or seepage for stability, the environmental consequence of oxidation of potentially acid forming materials needs to be equally managed. With the definition of the 19 SMART targets, the assessment of coal tailings facility designs, operational practices and performance of closure utilizing the 19 targets, and associated Guideline, can support consistent and holistic business decisions.

4 MEASURABLE

The Guideline also needed to allow for measurement of closure performance. This was influenced by the uncertainties pertaining to future closure performance, the sometimes slow or progressive nature of closure processes, and that complete risk mitigation may not be feasibility achieved. The following three concepts were integrated into the Guideline for these variances:

1. Risk Assessed Performance.
2. Closure Phases.
3. Completion Levels.

4.1 *Risk Assessed Performance*

The often-limited understanding and information of the complex site-specific environment challenged predicting future closure performance, particularly for environmental targets. Consequently, several environmental targets specified that uncertainty of performance was to be measured against the resilience of receptors.

The Guideline requires a source-pathway-receptor model be developed for risk quantification for groundwater, surface water, air quality, erosion and soil contamination targets. A typical source-pathway-receptor model requires linkage of all three components for impact to occur. The Guideline also states that where insufficient information is available to measure performance, the targets can alternatively consider whether a risk has the potential to be outside the resilience of receptors.

Where this risk-assessed performance is undertaken, the Guideline specifies that studies and monitoring should be defined prior to, and during, operation to reduce risk uncertainty. Early closure phase monitoring programs should also support the reduction of uncertainty in the closure design's performance.

4.2 *Closure Phases*

In an approach to balance assurance and risk, the Guideline proposes different targets aligned to different closure phases. Two phases were defined: Active Care Phase and Passive Case Phase.

Under the Guideline, a facility will enter the Active Care Phase once closure measures are implemented. While the facility is in this phase, risks can be more readily identified and mitigated, as activities such as monitoring, inspection, and water management are conducted.

In the Passive Care Phase, the facility is in a steady state condition. Monitoring will have shown that no further intervention or regular surveillance is required and there is no requirement for active intervention to manage water.

This approach requires the Passive Care Phase to have more stringent targets for the facility, yet less assurance. Conversely, in the Active Care Phase, the targets are less stringent whilst more assurance is provided through regular maintenance and monitoring practices. This approach is aligned with international (GTR, 2020) and local Australian National Committee on Large Dams (ANCOLD) (2012) standards. It is also well aligned with many of BHP's mine site plans, where the tailings facilities may be subject to progressive closure (and subsequently risk reduced), yet the surrounding mine remains operational.

4.3 *Completion Levels*

There can be a misconception that a closed facility poses no risk and that immediately following 'closure works' the risks are eliminated. However, dependent on the embankment and foundation construction, limited seepage pathways can result in the tailings mass remaining saturated for periods beyond 100 years. In this scenario, some level of residual risk remains and facilities are likely to be classified a "Dam" under local regulations and require ongoing monitoring and maintenance expenses. Furthermore, even if the facility is classified as 'stable' − in line with international and local standards − it may still not be accepted by the government for relinquishment.

The Guideline's targets are defined to manage closure risk to an acceptable level. While a key factor, this approach does not consider the risk of not achieving the benefits from the 'opportunity' - as defined in section 2 of this paper. To address this, the Guideline proposes different states for the closed tailings facilities (Completion Levels) in addition to the targets.

Completion Levels are proposed to define the anticipated residual risk, or conversely, residual liability. Of particular focus within the Completion Levels is the facility's presence of non-credible failure modes and the saturation of the tailings material. In the scenario where the tailings remains saturated the Guideline would classify it to have a mid-ranking Completion Level and remain a 'Dam', as material could flow in the event of an embankment failure.

5 SUSTAINABLE

While the term "sustainable" can be broad, this objective considered the futureproofing of the Guideline and its ability to meet the needs of its audience and clients, BHP and external stakeholders respectively. In parallel to the development of the Guideline was the surrounding governance structure, that included:

- Application of use.
- Roles and responsibilities.
- Review process and frequency.

While the driver for developing the Guideline has been the closure of the 25 facilities, a clear mandate is its applicability to the design of new facilities and the review of already closed facilities. To support this mandate, BHP internal standards for closure and tailings management require further developments to be designed in consideration of closure. Annual reviews and revisions of existing disturbances and facilities also supports this mandate. The Guideline (2021, p3) states that it is to be "adopted during the design of a tailings facility and used to address closure risks from the outset of design and throughout the facility's lifecycle".

The roles and responsibilities of both the Guideline and the stakeholders is addressed within the introductory sections. These roles and responsibilities are reflective of those required by corporate level mandatory guidance as well as developed to support both BHP's Projects and Operational functions of the business. The Project and Operational teams were involved in reviewing the document, were requested to access the usability of the Guideline and associated targets in their daily roles.

A continuous improvement cycle will be employed to mature the Guideline over the coming years. This will also allow the Guideline to be updated to reflect the rapidly changing regulatory requirements and community and shareholder expectations for both the management of mine. closure and tailings facilities and evolving available technological solutions.

6 CONCLUSION

To support business decisions relating to closing coal tailings storage facilities, a Guideline was proposed to provide a consistent framework for measurable assessment and reflect the sustainable needs of the business. The development of the Guideline has overcome several challenges to define 19 SMART performance targets for coal tailings facility closure. The Guideline will be subject to review and refinement as it is implemented to ensure its value in providing input to holistic and consistent business decision making in tailings facility closure.

7 REFERENCES

ANCOLD (2012) Guidelines on Tailings Dams.
BHP (2019) Tailings Closure Opportunity Assessment – Opportunity Framing Memorandum
BHP (2021) Coal Tailings Closure Guideline
GTR (2020) Global Industry Standard on Tailings Management
ICMM (2021) Integrated Mine Closure: Good practice guide

Effects of desiccation on shear strength of tailings – comparison of clayey and sandy tailings

David Reid & Andy Fourie
The University of Western Australia, Perth, WA, Australia

Adrian Russell
The University of New South Wales, Sydney, NSW, Australia

ABSTRACT: It is common in arid environments for tailings deposition to be cycled around the tailings storage facility (TSF) in thin lifts to promote desiccation of the tailings. This desiccation process can result in significant increases in the density of the tailings at shallow depths, and may indeed produce unsaturated conditions. Either of these outcomes are beneficial for the storage capacity and stability of a TSF. While implementation of this deposition strategy, and visual observation of its qualitative benefits are common, there is relatively little detailed data supporting the extent to which increased surficial densities may result in altered in situ shear strengths upon later loading and/or resaturation. To investigate this, the current work examines the undrained shear strength of blocks of desiccated bauxite and iron ore tailings when saturated and consolidated to a range of vertical effective stresses in the laboratory. The work builds upon earlier testing of a desiccated block of gold tailings presented at this conference. The results indicate that the clayey bauxite and iron ore tailings achieve much greater increases in undrained shear strength than a previously tested sandy silt gold tailings.

1 INTRODUCTION

It is common practice in arid environments for tailings deposition to be cycled such that desiccation is promoted on the tailings. This desiccation can serve to increase the average stored density of the tailings – an outcome which is easily quantified – and is also likely to result in the tailings being stronger owing to the desiccation process, even if subsequently resaturated at depth. While it seems uncontroversial to suggest that desiccation processes will result in stronger tailings, there is very little data quantifying this effect.

One program of testing to investigate the effects of desiccation was carried out at Carleton University on low plasticity tailings made up predominately of silt (Al-Tarhouni et al. 2011, Daliri et al. 2014). The tailings samples were artificially desiccated in the laboratory from a slurry, and then saturated prior to testing. Another program of testing was carried out at The University of Western Australia as part of the TAILLIQ research project on intact and saturated surficial block samples of a low plasticity sandy silt gold tailings (Reid et al. 2018). The samples had been previously desiccated on the TSF surface. Both programs showed that significant increases in cyclic resistance and/or undrained strength ratios (nearly double) occurred at low vertical effective stresses as a result of desiccation. However, to the authors' knowledge there is little published data on the effects of desiccation on predominately-clay tailings, materials where the benefits of desiccation are likely to be greater. Tailings with a significant clay proportion will generally have smaller pores sizes than sand or silt tailings, thus the desaturation will involve larger suctions than for sand or silt tailings. Suction is, to the first order, inversely proportional to the pore diameter for a given degree of saturation. A larger suction will induce more significant changes to the tailings pore geometries and particle contact networks, and a more significant void ratio reduction, and these alterations are not reversed when the tailings becomes saturated later. Also, the changes may make the tailings overconsolidated when they are later saturated.

This paper outlines testing on block samples of an iron ore and bauxite tailings that were deposited in an arid environment and underwent significant post-deposition desiccation. Both of these tailings included a significant proportion of clay, and thus allowed the extension of previous studies on the effects of desiccation of tailings. The block sampling and testing works were carried out as part of the TAILLIQ project to improve the characterization and testing of tailings with a focus on reducing the occurrence of static liquefaction failures of TSFs.

2 MATERIALS AND METHODS

2.1 *Sampling and sample preparation*

Testing outlined herein was all carried out on small specimens trimmed intact from larger high quality block samples. A number of block samples were obtained from an iron ore and a bauxite TSF as part of the TAILLIQ project sampling works. As both TSFs were located in an arid environment with deposition carried out to promote thin-layer drying, their surface and near-surface comprised a stiff, desiccated tailings amenable to trimming to create block samples for subsequent transport back to the laboratory. At the iron ore TSF, the block samples were obtained from the base of a 4m deep battered excavation that was created to enable linking of the laboratory response of block samples to in situ tests. For the bauxite TSF, samples were obtained in two areas: (a) a "farmed" region near the perimeter, where the material had been reworked and compacted (after drying) as part of TSF operations, and locations further within the beach where farming had not occurred.

Images of the block sampling process for the iron ore and bauxite tailings are presented in Figure 1, Figure 2, and Figure 3. As indicated in Figure 3, for the unfarmed portion of the bauxite TSF, block sampling required little more than selecting an appropriately sized existing block that could be handled and packed owing to the significant cracking present. At the other locations trimming was required to create block-sized samples that could be handled.

Figure 1. Block sampling process – iron ore tailings

Figure 2. Block sampling process – bauxite tailings, farmed area

Figure 3. Block sampling process – bauxite tailings, unfarmed area

After trimming, the blocks were wrapped first in a layer of cling wrap, then aluminum foil, then a final layer of cling wrap prior to being placed into foam-lined boxes for transport. This form of sampling, packing, and transport is commonly adopted for unsaturated tailings block samples (Chang et al. 2011, Reid and Fanni 2020) and is likely to provide the highest quality surficial samples for element testing.

Once in the laboratory, specimens for element testing were created by first trimming portions of the block with a scalpel to the approximate (but slightly larger) diameter than that required for testing – 72mm in this case, for the DSS specimens prepared. Then a sharp cutting ring was slowly advanced into the block, with additional trimming carried out to minimize the disturbance caused by advancing of the ring. This process is shown for the iron ore tailings block in Figure 4.

Figure 4. Trimming samples from the block – iron ore tailings

The trimmings from the block specimens were used to carry out index tests as summarized in Table 1. The blocks from the three sites had varied water contents – those for the iron ore tailings from the base of a 4 m excavation were 25 – 28%, while those for the farmed and unfarmed bauxite tailings were at 17% and 6%, respectively.

Table 1. Index properties of iron ore and bauxite tailings

Property	Iron ore	Bauxite - Farmed	Bauxite - Unfarmed
Specific Gravity, Gs	3.71	2.87	2.87
Liquid limit (LL)	37%	44%	53%
Plastic limit (PL)	21 %	24%	24%
Plasticity Index (PI)	16%	20%	29%
% < 75 µm	99%	62%	87%

2.2 *DSS test methods*

DSS testing in the study was carried out under constant volume shearing conditions, within a membrane and stacked ring arrangement (i.e. SGI-type) apparatus. The bottom and top platens included “dead zones” of approximately 3 mm depth to prevent sliding of the specimen on the platens during shearing.

For the iron ore tailings, specimens within the stainless steel rings (after trimming) were placed onto the bottom platen of the DSS, and slowly extruded from the ring by placing a filter stone above the sample and pulling the stainless steel ring upwards. The samples were self-supporting owing to their initially unsaturated and stiff condition. A membrane and O-ring were then placed around the sample and platen, followed by the stack of Teflon-coated rings. A bedding load of 125 kPa was applied, which was a slightly higher value for the base of the excavation where the blocks were taken. The specimen was then brought into contact with a water reservoir at the base and top platen for three hours to remove suction from the specimen. As noted by Al-Tarhouni et al. (2011), for the purpose of testing using the constant volume approach (e.g. Dyick et al. 1987) it is sufficient to remove suction from the specimen to enable reasonable results, rather than providing a back pressure and high-quality saturation process such as when carrying out undrained triaxial testing.

Owing to the dry and stiff condition of the bauxite tailings, rather than saturating within the DSS device (which has somewhat limited drainage access) the rings were placed on a large filter stone, a bedding load of 10 kPa was applied to the top of the rings through another filter stone using weights, and the entire setup was then flooded in a water bath overnight prior to transferring the specimens to the DSS apparatus and testing as per the iron ore tailings described previously.

Specimens for both tailings were consolidated in stages to a range of vertical effective stresses from 100 up to 1000 kPa, then sheared at an approximate rate of 5% shear strain per hour. The wide range of vertical effective stresses was adopted to investigate at what stress the effects of desiccation would be eliminated.

3 TEST RESULTS

3.1 *General shearing behaviour*

Normalized undrained shear stress vs. shear strain responses for all of the DSS tests carried out are presented in Figure 5 and Figure 6 for the iron ore and bauxite tailings, respectively. For both tailings, a reduction in normalized shear strength with increasing vertical effective stress is seen, consistent with the desiccation process having caused some form of overconsolidation of the tailings. At vertical effective stresses of typically 750 to 1000 kPa most of this desiccation-induced strength increase has been removed and the strength results are approaching typical normally consolidated values for clays in DSS loading, consistent with testing on slurry-prepared samples of the same materials underway in parallel to this study. Peak strengths selected from each test for subsequent synthesis are also annotated in Figure 5 and and Figure 6. No clear trends between vertical effective stress and strain to peak strength can be discerned from the results.

For the bauxite tailings, there may be slightly greater increases in shear strength at low stresses for the farmed samples. This could be a result of the modified fabric induced through compaction. It is noted that owing to the compaction process, the cause of the increases in shear strength seen in the farmed bauxite material cannot be strictly isolated to desiccation effects. Therefore, for the purposes of focusing on desiccation-induced strength gain in this study, the focus is primarily on the iron ore and unfarmed bauxite tailings.

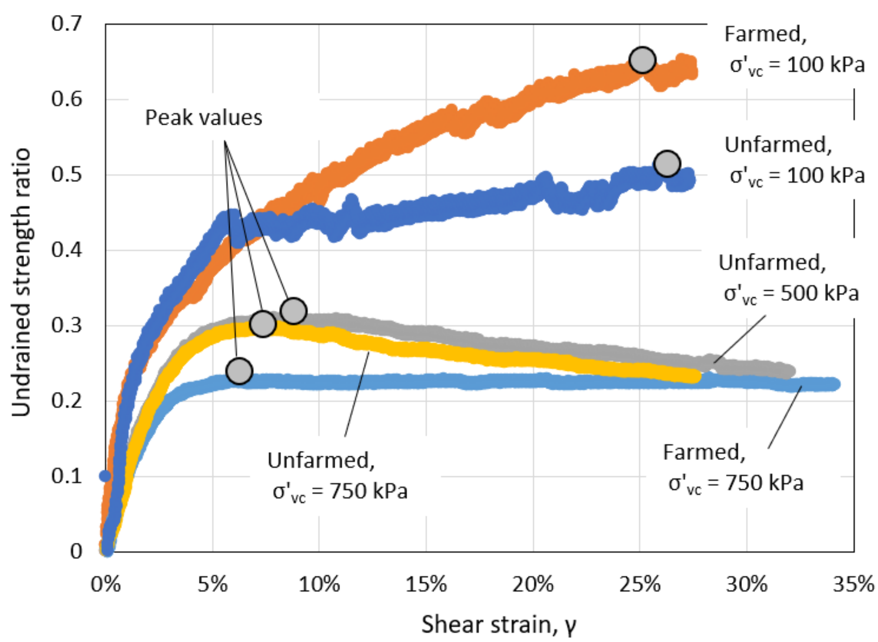

Figure 5. DSS shearing behaviour of iron ore tailings specimens trimmed from block sample

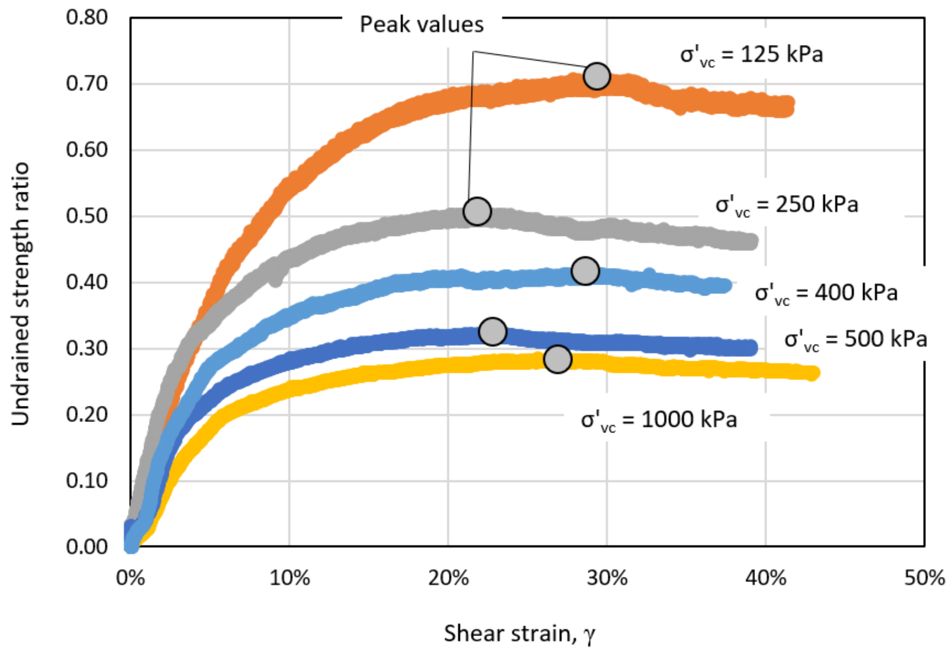

Figure 6. DSS shearing behaviour of bauxite tailings specimens trimmed from block samples

3.2 *Synthesis of data – SHANSEP interpretation*

One means for accounting for the desiccation-induced strengthening of the tailings is through an equivalent preconsolidation stress. To examine the data in this context, the results are synthesized in Figure 7 in a SHANSEP framework (Ladd and Foote 1974). Two trendlines included in the figure are drawn using the SHANSEP equation:

$$\frac{s_u}{\sigma'_{vc}} = s\ OCR^m \tag{1}$$

Where *s* is normally consolidated undrained strength ratio (0.20 to 0.25 typical for these tailings), OCR is the overconsolidation ratio and *m* is the SHANSEP exponent –the higher the value of *m*, the greater the effect of overconsolidation on strength.

Good fits are obtained using assumed preconsolidation pressures of 600 to 900 kPa and *m* exponents of 0.45 and 0.55, and assuming the strength ratios for normally consolidated conditions are 0.25 for each tailings. This interpretation supports, in general, the hypothesis that desiccation, then rewetting, causes the tailings state to retreat to a location to the left of the saturated normal consolidation line and thus become overconsolidated. The applied total stresses were too small for volumetric collapse to occur during the rewetting. This was supported by observations during the sample preparation, where the rewetting caused very slight, if any, volumetric expansions, and definitely no volumetric compressions.

It is noted, however, that the values of *m* required to produce reasonable fits to the data are much lower than typically observed for clays which have been overconsolidated by mechanical/geological loading followed by unloading (Ladd 1991, Ladd and DeGroot 2003).

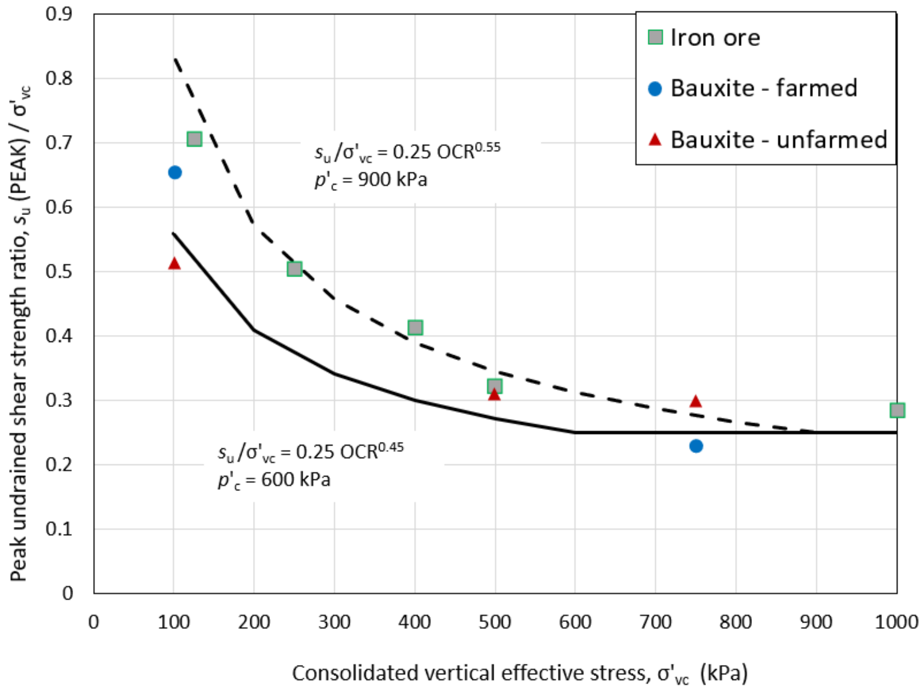

Figure 7. Summary of data for SHANSEP-type interpretation of results

3.3 *Synthesis of data – Comparison to sandy silt gold tailings*

A second synthesis of the data is presented in Figure 8, where the data from this study is compared to similar testing of desiccated block samples of a sandy silt gold tailings as presented by Reid et al. (2018). The comparison suggests that despite the sandy silt gold tailings block having been dried to approximately 10% water content in an arid environment, the subsequent rewetting caused a lesser overconsolidation effect to develop, meaning the rewetted state attained was closer to the normal consolidation line (but still on the left hand side).

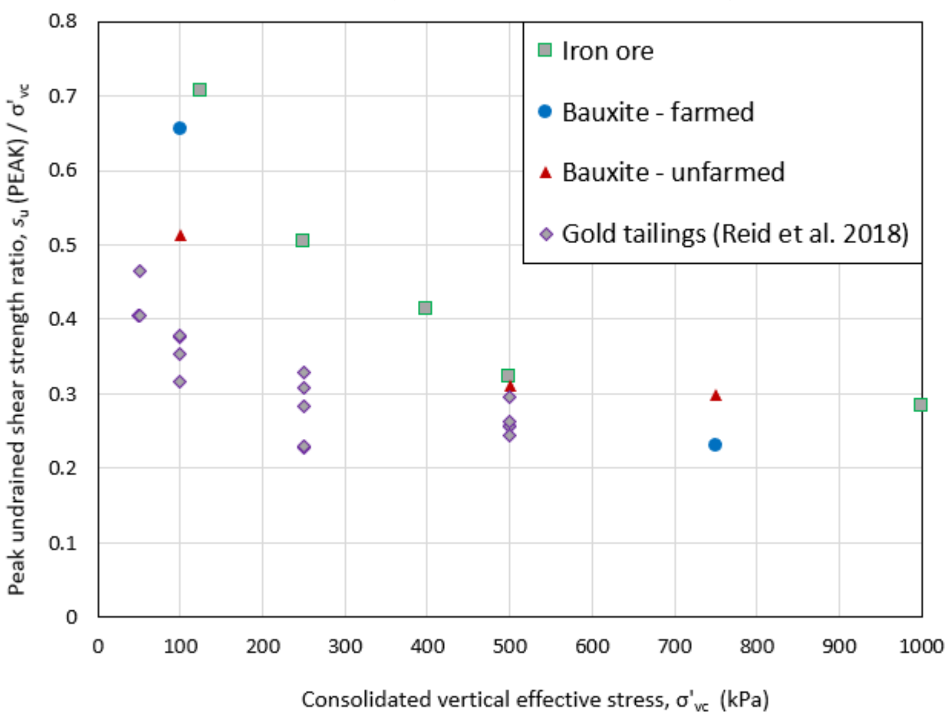

Figure 8. Comparison of current study's data to results from a sandy silt gold tailings (Reid et al. 2018)

4 IMPLICATIONS

For the three tailings considered here the rewetted samples became overconsolidated. The rewetted states retreated to the left side of the saturated normal consolidation line by elastic swelling so follow an unload-reload line as their effective stress is reduced by the suction removal. The preconsoldiation pressures attained likely correspond to intercepts of the elastic unload-reload line with the saturated normal consolidation line. Suction hardening, and suction dependent normal consolidation lines, only have an influence when volumetric collapse occurs during rewetting, but this was not the case here. The applied total stresses were a maximum of 125 kPa during rewetting. If much larger total stresses were applied during rewetting it is possible that volumetric collapse would have occurred, and the required interpretations would be more complex.

The results of this study clearly demonstrate the beneficial outcomes of thin layer deposition and desiccation on the subsequent behaviour of tailings, even when resaturated subsequently in the life of the TSF. While this behaviour is consistent with what the authors would suggest are expectations across industry, there is very little data directly quantifying these effects of which we are aware.

It is first important to note that if such magnitudes of desiccation-rewetting induced overconsolidation can regularly be achieved in a TSF this would seemingly obviate the potential for contractive brittle undrained shearing – particularly as below the lower portions of a slope, an area of significant importance for TSF stability, the vertical effective stresses often remain relatively low compared to locations below the crest or further upstream within the TSF. It is also noted that deposition control and management to achieve such outcomes are within the capabilities of current tailings management practice. This is particularly the case for a new TSF, where there is, or at least should be, a focus on deposition control from commencement of deposition. Alternatively, for many existing facilities, areas of historic deposition where such desiccation was not achieved are likely to control stability.

Another interesting consideration is that within a TSF managed in a way such that desiccation then rewetting regularly occurs, it would be a trivial exercise – in the context of typical tailings wall raise and geotechnical investigation works – to regularly collect high quality block samples for the type of testing carried out in this study. This would provide frequent information as to the magnitude of desiccation-rewetting induced strength gains, and how these results would affect future TSF stability. Such sampling and testing would be far easier to carry out than attempting to obtain high quality specimens within the same desiccated tailings in the future, when covered by potentially 10's of meters of subsequent tailings. We would argue that if a TSF is to be developed in an arid environment with the goal of using desiccation-induced strength gains to promote stability, regular block sampling should be considered to support the deposition strategy and provide useful evidence of the benefits gained.

5 CONCLUSIONS

A laboratory study was carried out to examine the effects of desiccation on the resulting undrained shearing behaviour of two predominately clay tailings for comparison to previous testing on a sandy silt tailings. The study comprised DSS tests on intact specimens trimmed from surface or near-surface block samples. The specimens were resaturated to simulate the behaviour of tailings that may have rewet following desiccation and subsequent loading to greater depths within the TSF. The results on the predominately clay tailings indicated that the desiccation process appears to result in significant increases to undrained shear strength at low vertical effective stresses, then reduces such that undrained strength ratios comparable to a normally consolidated value occur at vertical effective stresses greater than 500 kPa. The benefits of desiccation on undrained strengths were of a greater magnitude for the predominately clay tailings than for previous testing on sandy silt tailings blocks, generally consistent with expectations for the effects of desiccation and suction on soil behaviour. The benefits of desiccation on TSF stability were emphasized.

6 ACKNOWLEDGEMENTS

This work forms part of TAILLIQ (Tailings Liquefaction), which is an Australian Research Council (ARC) Linkage Project supported by financial and in-kind contributions from Anglo American, BHP, Freeport-McMoRan, Newmont, Rio Tinto, and Teck. The TAILLIQ project is being carried out at The University of New South Wales (UNSW), The University of South Australia, The University of Western Australia (lead university), and The University of Wollongong. We acknowledge the support and contributions of project personnel at each of the supporting organisations. We thank the mine site personnel who assisted in the block sampling process. We also thank the personnel who assisted us in collection of the block samples.

7 REFERENCES

Al-Tarhouni, M., Simms, P. & Sivathayalan, S., 2011. Cyclic behaviour of reconstituted and desiccated–rewet thickened gold tailings in simple shear. *Canadian Geotechnical Journal*, 48(7): 1044–1060.

Chang, N., Heymann, G. & Clayton, C., 2011. The effect of fabric on the behaviour of gold tailings. *Géotechnique* 61(3): 187–197.

Daliri, F, Kim, H., Simms, P., and Sivathayalan, S., 2014. Impact of Desiccation on Monotonic and Cyclic Shear Strength of Thickened Gold Tailings. *Journal of Geotechnical and Geoenvironmental Engineering* 140(9).

Dyvick, R, Berre, T, Lacasse, S and Raddim, B. 1987. Comparison of truly undrained and constant volume direct simple shear test. *Géotechnique* 37(1): 3-10.

Ladd, CC. 1991. Stability evaluation during staged construction. Journal of Geotechnical Engineering 117(4)

Ladd, CC, and DeGroot, DJ. 2003. Recommended practice for soft ground site characterization. The Arthur Casagrande Lecture, Proceedings of the 12th Panamericna Conference on Soil Mechanics and Geotechnical Engineering, Boston, MA, Vol. 1, oo. 3-57.

Ladd, CC, and Foot, R. 1974. New design procedure for stability of soft clays. *Journal of Geotechnical Engineering Division, ASCE* 100(7): 763-786.

Reid, D. and Fanni, R. 2020. Comparison of truly undrained and constant volume direct simple shear test. *Géotechnique* Ahead of print.

Reid, D., Fourie, AB, Castro, J, and Lupo, J. 2018. Undrained strength evolution with loading on an undisturbed block samples of desiccated gold tailings. Proceedings of Tailings and Mine Waste 2018, Keystone, CO.

Challenges in characterization of gold tailings for geotechnical design purposes

Doru Bobei & Hashan Subasinghe
Worley Group, Sydney, New South Wales, Australia

ABSTRACT: This paper presents the results and interpretations of gold tailings data collected from four (4) separate tailings storage facilities. The assessment of undrained shear strength using field methods to include fast shear vanes and cone penetration testing was found to present difficulties. These estimates were found to overpredict the shear strength and an alternative methodology is discussed. Typical tailings materials with a 60% to 70% silt content were studied with one group of tailings to contain 5% clay content and the other to have a slightly higher clay content of 15%. Undrained consolidated triaxial tests (CIU) conducted on undisturbed, in-situ samples revealed a contradictory tailings response to vary from non-flow to flow response. Such results were interpreted within the critical state framework to provide a plausible explanation of these results. The predictive capability of a constitutive model, NorSand is demonstrated to allow for development of a number of relationships between the undrained shear strength and the state parameter. An example of the ability of CPT to predict the variation of undrained shear strength with depth on consideration of these relationships is presented.

1 INTRODUCTION

Mine tailings are the fine-grained fraction generated after grinding and processing of mined ore to be considered of low economic value. The tailings stream is re-directed from the processing plant at a low solid content slurry through transportation pipelines towards a purposely built storage facility. The tailings impoundment could be either above ground such as tailings dams or below ground such as open-pits or underground cavities. Given the large quantities of tailings generated over the life of the mine, the most cost-effective way is to store the tailings in large dams built using the upstream construction methodology (i.e. a starter bund constructed first, to then be followed by a number of subsequent raises, partly built over the previous raise and impounded soft tailings). Although the upstream technique appears to offer an attractive financial alternative, these structures are particularly vulnerable to a number of factors that may contribute to the failure of tailings dams as highlighted in previous published case studies to include Sullivan Mine (1991), Stava Mine (1985), Merriespruit (1994), among many others.

To prevent undesirable outcomes, the geotechnical engineer needs to appropriately understand the implications of potential factors to include: (1) seepage and internal erosion due to water seepage field; (2) potential failure of the foundation materials; (2) overtopping impounded water flowing over the dam face; (4) tailings potential for liquefaction under static and seismic conditions; and (5) others external causes such as mine subsidence and blasting. Of particular concern is the geo-mechanical characterization of tailings for use in slope stability assessments, with an important consideration given towards the tailings affinity to develop a flow liquefaction response. The practicing geotechnical engineer may find this an arduous task with a number of difficulties, uncertainties, and conflicting points of view likely to be encountered as discussed in this paper.

2 TAILINGS PROPERTIES

The paper uses the field and laboratory data reported from a number of gold tailings sites to mainly include two (2) sites located in Australia from which one is the tailings dam at Cadia mine in NSW. The second site mainly referred to in this study are tailings collected from another gold mine in Australia. Additional data was gathered from published gold tailings results such as Al Tarhouni et al. (2011) and Riveros and Sadrekarimi (2020). Typical gold tailings were found to contain 60% to 70% silt fraction and this study has placed an emphasis on these predominant tailings fraction. Sieve analyses for the silt tailings were conducted in compliance with the AS 1289.3.6.1. The average particle size distributions (PSDs) obtained for each material is shown in Figure 1. The PSDs for the silt tailings are grouped in two categories namely: (a) silt tailings with clay-size (< 2 μm) content of 5%; and (b) silt tailings with clay-size (< 2 μm) content of 15%. To differentiate between the silt tailings groups the paper has adopted a terminology where the 5% clay content tailings material is considered to contain "non-plastic fines" and the 15% clay content tailings material is considered to include "plastic fines". Specific gravities (G_s) of the silt tailings were also determined in accordance with the AS 1289.3.5.1. The basic soil index properties for both silt tailings groups are summarized in Table 1.

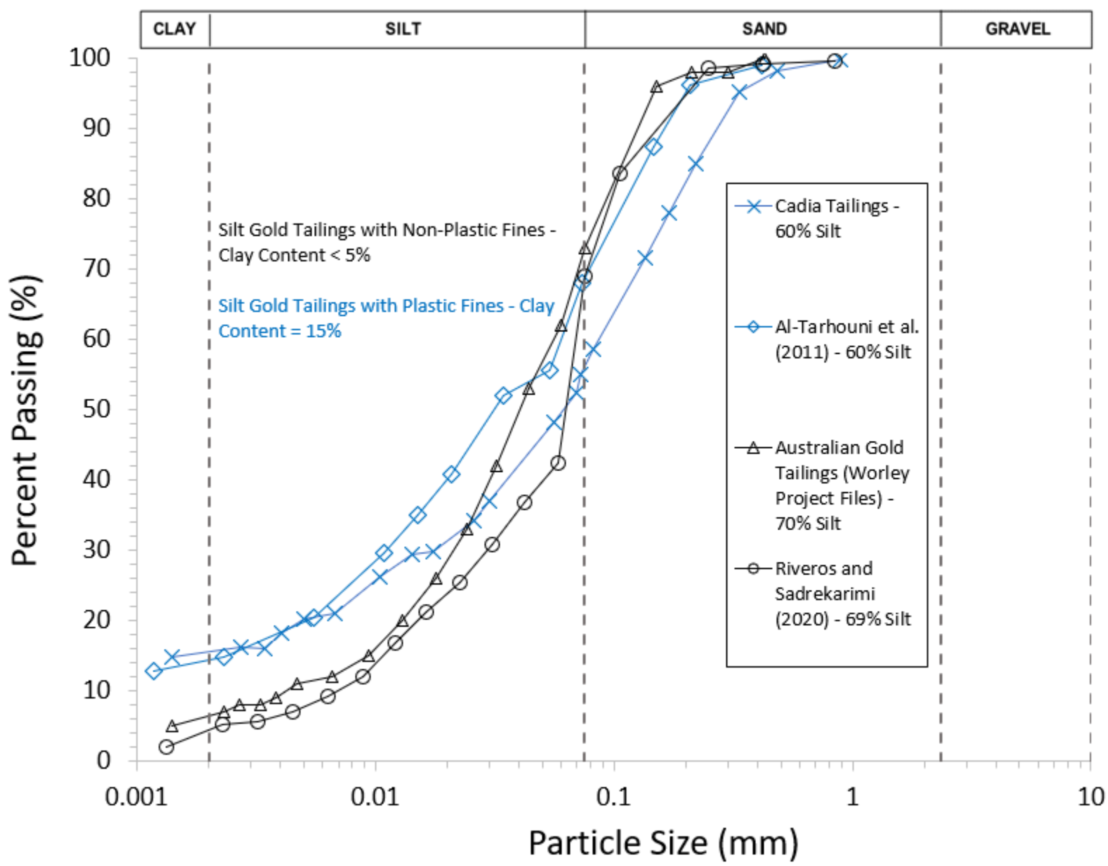

Figure 1. Particle size distribution of studied gold tailings.

Table 1. Basic properties of studied gold tailings.

Tailings	D_{50} (mm)	FC (%)	Clay (%)	G_s	MC (%)	LL (%)	PL (%)	PI (%)
Australian Gold Tailings (Worley Project Files)	0.04	73	5	2.73	0.6 - 0.77	Not Obtainable	Not Obtainable	NP
Cadia Gold Tailings	0.06	55	15	2.69 - 2.74	0.60 - 0.68	18 - 23	15 - 16	2 - 8

3 UNDRAINED SHEAR STRENGTH

The undrained shear strength was assessed by in-situ testing methods such as: (a) field shear vanes; and (b) piezocones (CPTu). The field shear vanes are commonly used as a direct measurement of the undrained shear strength (s_u). In this project, a typical field vane was used with a diameter of 50mm and a height to diameter ratio of 2. The piezocone testing was conducted using a standard cone: cone angle of 60 degrees, a cross-sectional area of 10 cm^2, and a porous element located immediately behind the cone. The cone was advanced during field probing at a standard rate of 20mm/sec. The data was measured electronically to include the tip resistance (q_c), sleeve friction (f_s) and the penetration pore water pressure (u). The CPT interpretations considers the tip resistance values corrected for pore pressure effects (q_t) and a cone factor denoted as N_{kt}, which is mathematically expressed as:

$$s_u = (q_t - \sigma_{v0})/N_{kt}. \tag{1}$$

The N_{kt} values for natural soils normally range between 10 and 20 with an initial value of 16 adopted for the CPT interpretations.

The shear vane and CPT interpretations for tailings with non-plastic fines are presented in Figure 2(a). The plot of s_u values with depth displayed unusually high values of shear-strength ratio $s_u/\sigma'_v > 0.5$. Blight (1966) and Chandler (1988) have previously pointed out the need to conduct the shear vane in a true undrained condition and the need to increase the speed of shear vanes in silty soils to avoid dissipation of pore water pressure to occur during the test. Accordingly, a range of vane speeds were studied from 50deg/min to 200deg/min, with dissipation testing carried out adjacent to each shear vane. The purpose of the dissipation testing is to accurately characterize the horizontal coefficient of consolidation (c_h). The results are plotted in Figure 2(b) against a dimensionless time factor (T). According to Chandler (1988), T=0.05 is to be considered as the limit to separate undrained and drained shearing. All field vane results were found to plot above T > 0.5 to indicate the possibility of a partial drainage condition developing during shear vane testing. The in-situ vane measurement appears to over-estimate the undrained shear strength. The authors have encountered many similar situations where planning for in-situ measurements of tailings undrained shear strength is considered a routine exercise to generally not be given a thorough consideration. As a result, the designer is left in the office without an opportunity to calibrate the CPT cone testing data and to rely on personal preference, published results on similar materials, or previous experience when selecting the design parameters.

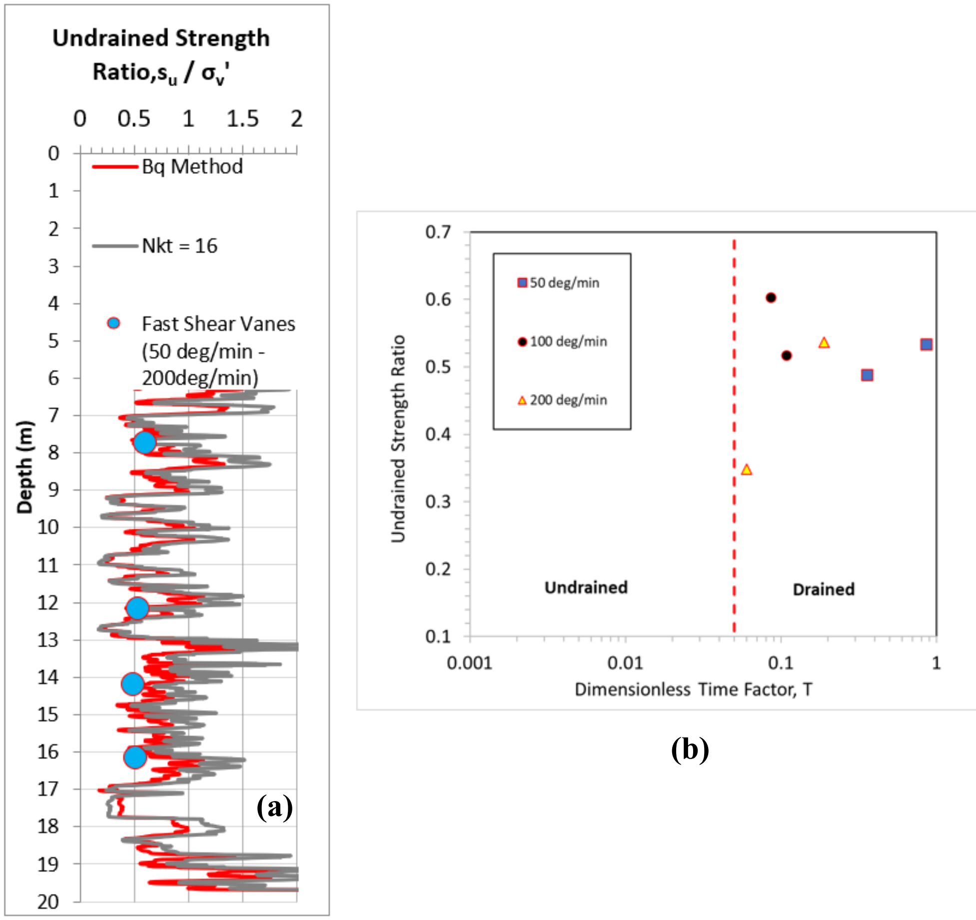

Figure 2. (a) Results of shear strength ratio interpretation with depth; and (b) Fast shear vane assessment of undrained shear strength.

4 TAILINGS LIQUEFACTION

Understanding tailings behavior is one of the most challenging issues for a geotechnical engineer. Traditionally, the undrained soil response and especially the static liquefaction of granular materials has been extensively studied over the years primarily due to its dramatic and devastating effects resulting from quick flow slides as reported in Koppejan et al. (1948), Morgenstern (2000), Sladen (1985), among other cases. Very often, static liquefaction is studied using the triaxial apparatus to obtain a better understanding of the mechanism and parameters controlling the static liquefaction response. Studies by Poulos et al. (1985), Been and Jefferies (1985), Vaid et al. (1990), Lade (1992), Ishihara (1993), Yamamuro and Lade (1997), Bobei and Lo (2001), have consistently reported that the initial state (i.e., expressed in terms of void ratio e_0 and confining pressure p'_0) significantly affects the undrained soil response. Combinations of e_0 and p'_0 will lead to three (3) distinct types of undrained responses termed: flow, limited flow and non-flow as illustrated in Figure 3. In general, the term 'static liquefaction' is used to describe the flow and limited flow responses where the soil loses a large percentage of its shear resistance. Whilst the behavior of clean sands is relatively well understood, the tailings materials are commonly referred to in the technical literature as "transitional materials" meaning the tailings behavior is expected to be somewhere between a sand-like and a clay like soil.

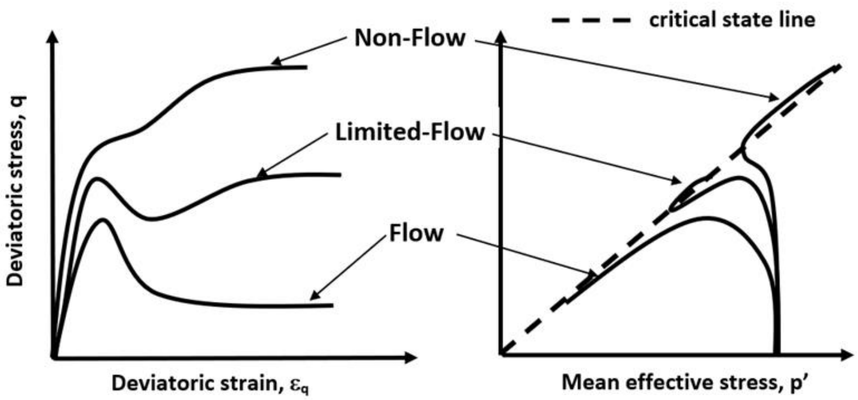

Figure 3. Types of undrained responses for granular materials

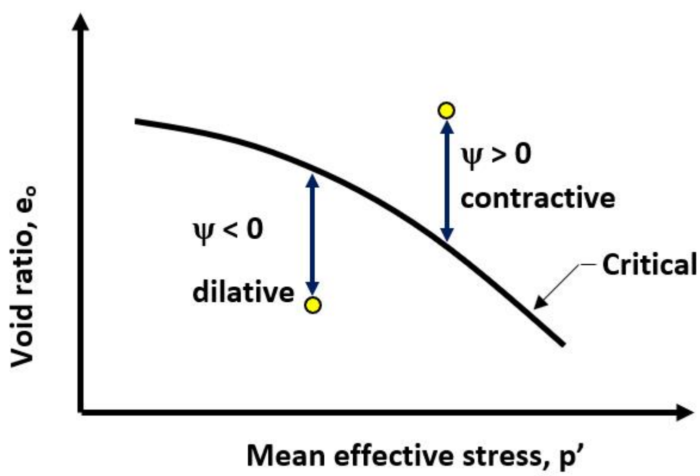

Figure 4. Tailings state expressed within the critical state soil mechanics framework

The liquefaction behavior of sand has often been explained within the critical state framework in terms of a state parameter, ψ, as schematically illustrated in Figure 4. The state parameter is defined by Been and Jefferies (1985) as the difference between the current void ratio and the void ratio at the same mean effective stress on the Critical State (CS) line. Furthermore, a positive ψ value at the commencement of undrained shearing is associated with static liquefaction whereas a negative ψ value is associated with a non-flow behavior.

5 VOID RATIO

The in-situ state of tailings is a fundamental parameter when assessing the liquefaction behavior. While the confining pressure may be estimated with a relative degree of confidence, the void ratio is not so easily measured. The determination of in-situ void ratio is further complicated on consideration of tailings deposition which requires using a number of spigot points at selected locations around the perimeter of the dam to achieve a relatively uniform tailings beach. Once the deposition reaches a specific elevation, the spigot points are moved to a different location to continue filling the tailings basin. Due to the alternating cycles of discharge locations, the tailings deposit is often stratified and non-homogenous with interlayered sandy and silty tailings zones. The tailings deposition should aim to allow for a fresh tailings layer to be deposited on the previous layer that has a sufficient time to undergo sedimentation self-weight consolidation and drying. Under these conditions, the in-situ void ratio may be expected to vary widely with in-situ states where the tailings may be anticipated to manifest a non-flow to a flow response.

For this study, the void ratio was assessed based on moisture content measurements on samples collected from depths below the inferred piezometric water level. Figure 5 plots the void ratio with depth for three (3) tailings dam sites. Contrary to expectations, it is surprising to note the void ratio remains reasonably constant with depth, irrespective of the tailings grading or deposition strategy at each site. The void ratio was found to range between values of $e_0 = 0.6$ to 0.7.

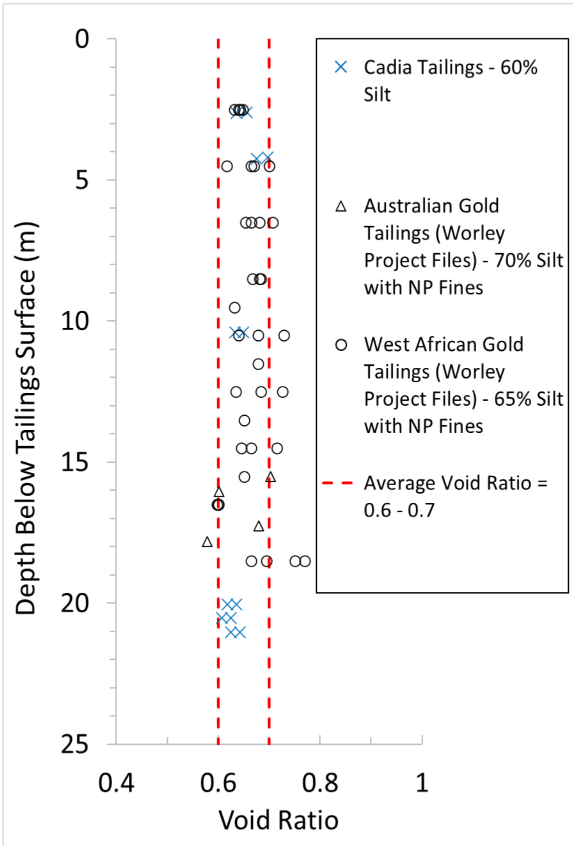

Figure 5. In-situ void ratio of gold tailings at three (3) different sites

6 TRIAXIAL TESTS

Drained and undrained triaxial tests have been conducted on in-situ soil samples as well as a set of laboratory samples prepared using the moist tamping technique. The moist tamped samples had a diameter of 100mm with a height to diameter ratio of 2. Free ends with enlarged platens were used to minimize the end restraints. Such technique has been previously noted to achieve uniform sample deformations to large axial strains of 20% to 25% Bobei et al. (2009). For all the tests, the sample saturation was achieved by raising the back pressure to a maximum of 300kPa. Over the duration of saturation, the stress state was maintained at an effective stress of 20kPa. Full saturation was achieved when Skempton's pore pressure parameter B has achieved a value equal or greater than 95%. On completion of soil saturation, the samples were isotropically consolidated before the start of undrained shearing. Figure 6(a) and 6(b) presents the results of undrained shearing as plots of effective stress paths: deviatoric stress $q = \sigma'_1 - \sigma'_3$ vs. mean effective stress $p' = (\sigma'_1 + 2\sigma'_3)/3$.

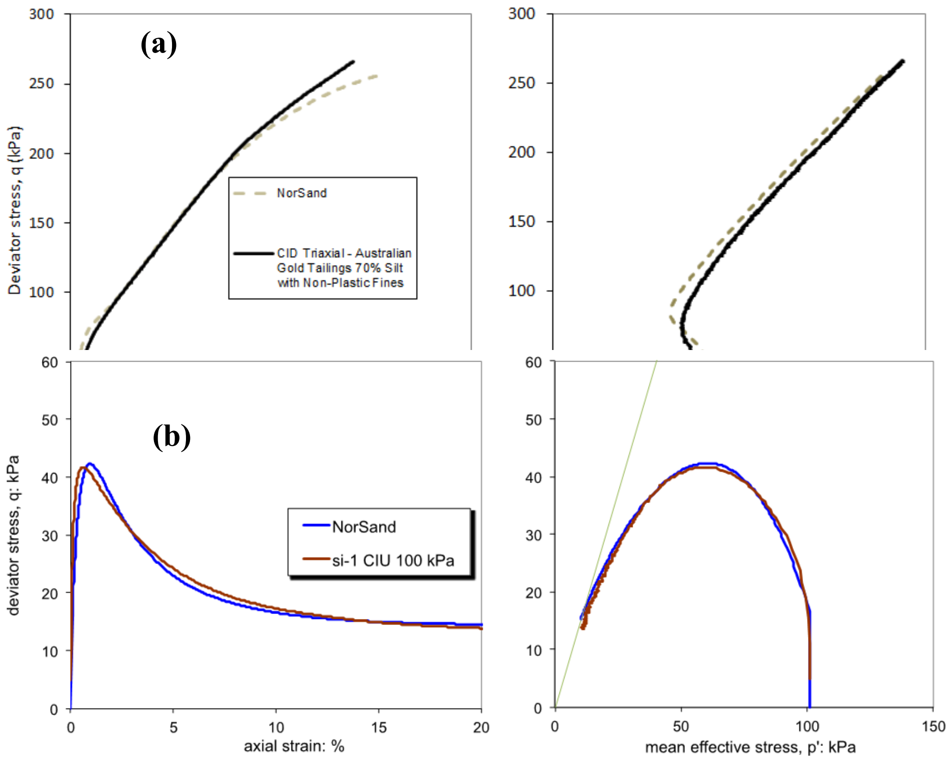

Figure 6. Actual and predicted (NorSand) stress-strain and q-p' responses: (a) Gold tailings with Non-Plastic Fines (b) Gold tailings with Plastic Fines

The response manifested by the two group of tailings was noted to vary significantly with the non-plastic tailings to display a non-flow response in contrast to the plastic tailings to manifest a flow behavior.

7 CRITICAL STATE LINE

The critical state is a fundamental concept in soil mechanics as it represents a reference state to assess the state and behavior of soil under loading. It was firstly introduced by (Roscoe et al. 1958) to describe the behavior of remolded clays, and nowadays the concept was extended to represent a more general framework of soil behavior. All drained and undrained tests were interpreted, and the critical state is reached only when the following conditions are satisfied: dq=0, dp'=0, du =0 while $d\varepsilon q \neq 0$. The critical state inferred for gold tailings is illustrated in Figure 7. The critical state data points were fitted with a non-linear relationship as follows:

$$e_c = a - b*(p'/100)^c \tag{2}$$

Where:

e_c	critical state void ratio
p'	mean effective stress measured in kPa, and
a, b, c	constants defining the CSL (for values, refer to Figure 7)

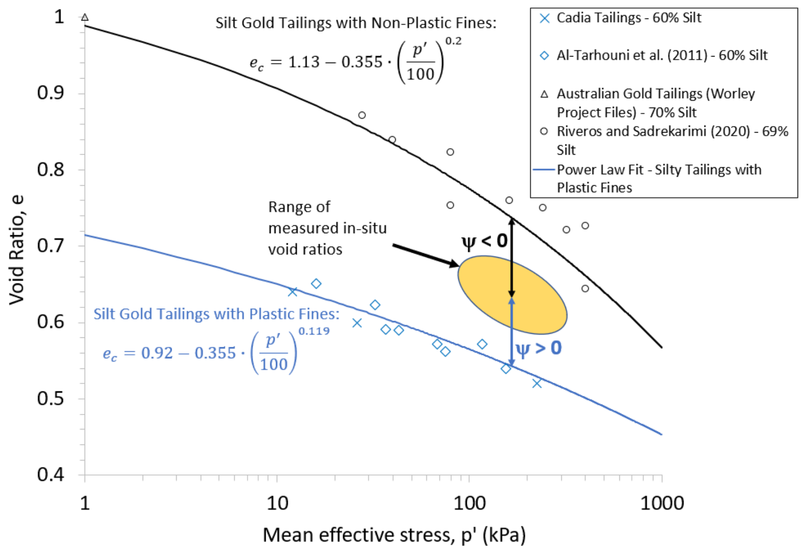

Figure 7. Critical State Lines for Gold Tailings

The CS line plots indicate the non-plastic tailings would retain a location as represented by the black symbols and associated curve fit. A significant downward shift in the CS line was noted to occur for the plastic tailings. The shift in the CS line due to the presence of fines (fraction less than 75μm) has been reported in the past studies primarily for sand with non-plastic fines Bobei (2009). In the case of the gold tailings, it appears that a small clay fraction of 15% is sufficient to cause a dramatic change in the shape and position of the CS line. In this framework, the void ratio range for gold tailings of $e_0 = 0.6$ to 0.7 would suggest: (a) a potential non-flow response for non-plastic tailings ($\psi < 0$) and (b) a flow response for the plastic tailings when a small amount of clay content is present ($\psi > 0$). As such, the framework of critical state appears to explain the behavioral trend of both plastic and non-plastic tailings. The inferred state parameter using the in-situ moisture content is plotted with depth in Figure 8(b).

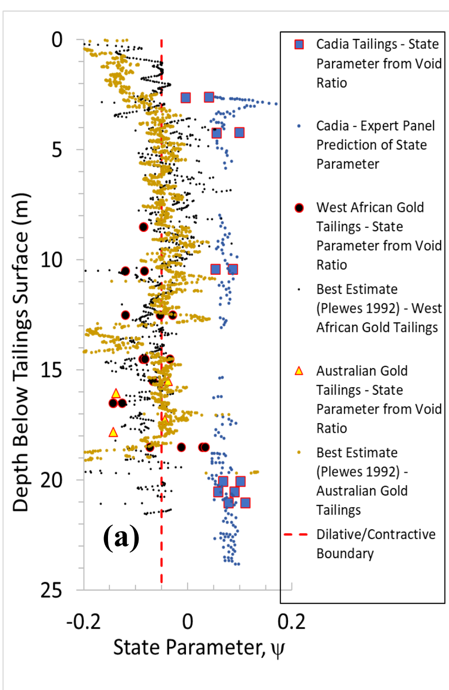

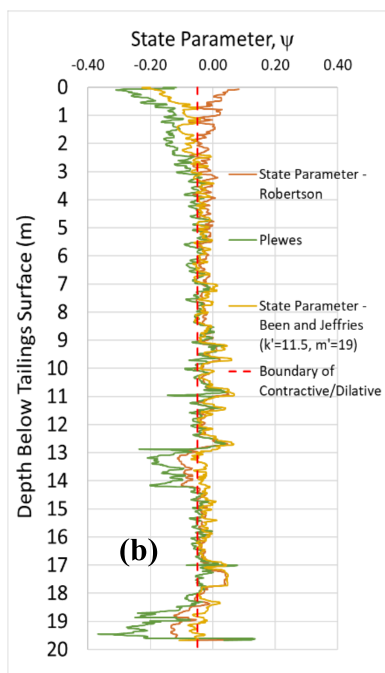

Figure 8. (a) Comparison of state parameter with measured void ratio and (b) Prediction of state parameter using different methods

Circular and triangular symbols represent the non-plastic tailings and square symbols were adopted for the plastic tailings. Interpretations of CPT data to determine the state parameter was also included in Figure 8(a) and 8(b). Methods proposed by Plewes et al.(1992), Robertson (2010) and calibration chamber simulations conducted for the Cadia Expert Panel Review Report appear to capture the patterns of tailings response of ψ vs. depth in good agreement with the moisture derived ψ.

8 CONSTITUTIVE MODELLING

The technical literature abounds with constitutive models developed to predict the response of granular materials in undrained loading. Among these, NorSand has gained popularity in recent years among practicing engineers due to its relative simplicity to replicate the laboratory triaxial test results over a range of initial states (void ratio and confining pressures). The basis for such predictions is eight (8) input parameters to capture the shape of critical state line, state at the start of shearing with respect to the critical state via the state parameter ψ and the stress dilatancy rule using a hardening rule. The model is capable to predict the strain softening characteristic of a flow liquefaction response and the non-flow response by switching the values of state parameter from positive to negative values.

The numerical predictions for gold tailings with non-plastic and plastic fines using NorSand are shown in Figure 6(a) and 6(b). Both stress-strain and q-p' paths are found to be predicted well for both tailings' types. On this premise, the model was also used to estimate the peak undrained shear strength, s_u, and the liquefied undrained shear strength, $s_{u,(liq)}$ normalized with respect to σ'_v for a range of ψ values (-0.05 to 0.2). The results were summarized in Figure 9. As anticipated, the general trend is for both s_u/σ'_v and $s_{u,(liq)}/\sigma'_v$ to reduce with the increase in ψ. Tailings with non-plastic fines do however record higher strength ratios compared to the tailings that contain plastic fines. An interesting observation is the variation of s_u/σ'_v for tailings with non-plastic fines to remain constant with the increase in ψ past a value of 0.07. The tailings with plastic fines show a continuous decrease in s_u/σ'_v without reaching an asymptotic value. The $s_{u,(liq)}/\sigma'_v$ plots show a trend to reduce to zero at $\psi > 0.2$ for tailings with non-plastic fines and $\psi > 0.15$ for tailings with plastic fines. The equivalent strength ratios s_u/σ'_v and $s_{u,(liq)}/\sigma'_v$ for direct simple shear conditions have been developed on the assumption of $s_u(DSS) = 0.8*s_u(Triax)$ (Sadrekarimi, 2014).

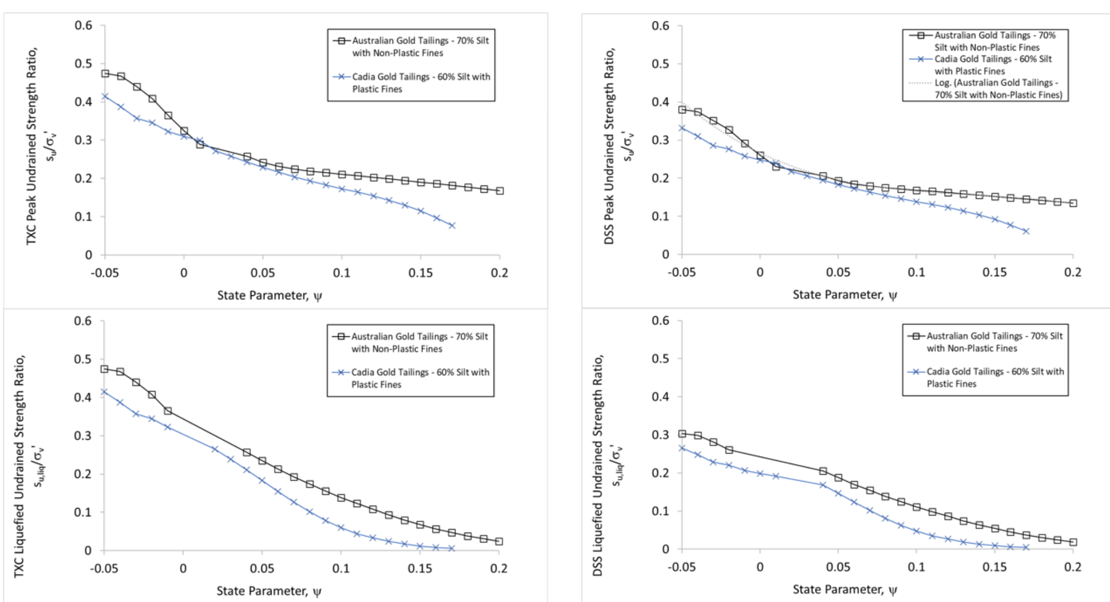

Figure 9. Peak and liquefied shear strength ratios with state parameter

Quantification of the undrained shear strength with state parameter for DSS illustrated above was then implemented for CPT interpretation. The amended CPT trace for non-plastic gold tailings is shown in Figure 10 to illustrate the variation of s_u/σ'_v and $s_{u,(liq)}/\sigma'_v$ with depth. It is noted that to achieve the numerically predicted s_u/σ'_v values, a larger cone factor of N_{kt} =30 would be appropriate. The in-situ fast shear vane data has also been plotted on the CPT trace, and was shown to over-predict the s_u/σ'_v ratio by 30% to 40%.

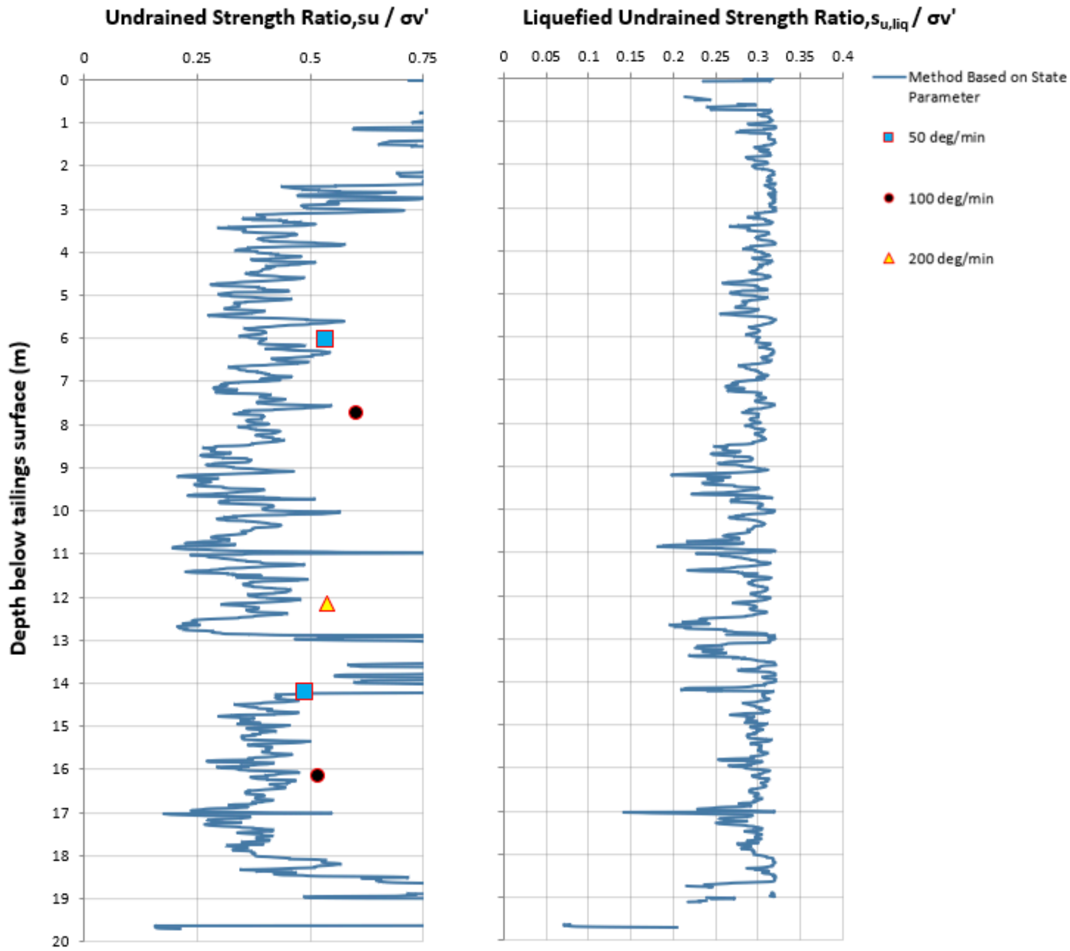

Figure 10. Peak and liquefied shear strength ratio with depth

9 CONCLUSIONS

A geotechnical characterization of gold tailings was presented based on the results collected from two (2) tailings storage facilities (TSFs) located in Australia with additional data collected from published literature. Field testing using cone penetration testing were supplemented by in-situ direct shear strength measurements using fast shear vanes. Laboratory investigations were also conducted to include basic soil index tests, particle size distribution and triaxial (drained and undrained) testing. The tailings contained 60% to 70% silt and 5% to 15% clay to require grouping in two categories, namely tailings with non-plastic fines and tailings with plastic fines.

The results of CPT dissipation testing were interrogated in the context of rapid shear vane measurements of peak undrained shear strength (vane speed between 60 to 200 deg/min). The tailings were found to display high horizontal coefficient of consolidation (c_h) to indicate the shear vanes were unable to measure the peak undrained shear strength without the influence of drainage effects.

Given the challenges in assessing the undrained shear strength using in-situ methods, an alternative method was required to characterize the peak and liquefied undrained shear strength. Best efforts were made to preserve the in-situ moisture content to understand the tailings state. The corresponding void ratio was found to remain constant with depth irrespective of deposition history, drying and self-consolidation conditions and geographical location of tailings facilities.

Tailings in undrained triaxial shearing displayed: (a) non-flow response for tailings with non-plastic fines and (b) flow response for tailings with plastic fines. Both groups of tailings were tested under similar initial states (e_0 and p'_0), yet the response under loading differed significantly. To develop a better understanding, this study focused on characterization of gold tailings materials in the context of the critical state framework. Tailings with a small amount of clay content were found to shift the critical state lower, which explains the measured undrained response.

Given the difficulties in assessing the undrained shear strength using traditional field-testing methods, the paper has turned the attention to calibration of a constitutive model capable of simulating a range of flow and non-flow responses. Predictions of undrained shear strength for a range of state parameters were simulated and a trend was developed to be adopted in CPT interpretations. In this context, the in-situ fast shear vane results were found to over-predict the undrained shear strength by 30% to 40%.

10 REFERENCES

Al-Tarhouni M., Simms P., & Sivathayalan S. 2011. Cyclic behaviour of reconstituted and desiccated–rewet thickened gold tailings in simple shear. *Canadian Geotechnical Journal* 48:1044-1060.

Been K. & Jefferies M.G. 1985. A state parameter for sands, *Géotechnique*, 35 (2), 99-112.

Bjerrum L. 1973. Problems of soil mechanics and construction on soft clays, *Proceedings of 8th International Conference on Soil Mechanics and Foundation Engineering*, Moscow, 3, 111-159.

Blight, G.E. 1968. A note on field vane testing of silty soils. *Canadian Geotechnical Journal* 5: 142-149

Bobei, D.C., & Lo, S-C.R. 2001. Static liquefaction of Sydney sand mixed with both plastic and non-plastic fines. *Proceedings of the 14th Southeast Asian Geotechnical Conference*, Hong Kong, Dec. 9-14, pp. 485-491.

Bobei, D.C. & Lo, S-C.R. 2005. Reverse behaviour and critical state of sand with a small amount of fines. *Proceedings of the 16th International Conference on Soil Mechanics and Foundation Engineering*, Osaka, Nov. 21-25, Vol. 1, pp. 475-478.

Bobei D.C., Lo, S. R., Wanatowski D., Gnanendran C. T. & Rahman, M. M. 2009. A modified state parameter for characterizing static liquefaction of sand with fines, *Canadian Geotechnical Journal* 46(3), 281-295.

Chandler, R. 1988. The in situ measurement of the undrained shear strength of clays using the field vane. In A. Richards (ed) *Vane shear testing in soils: field and laboratory studies*, Tampa, Florida, January 1987 .Baltimore: ASTM.

Independent Technical Review Board. 2019. *Report on NTSF embankment failure. Cadia Valley Operations for Ashurst Australia*.

Ishihara, K. 1993. Liquefaction and flow failure during earthquakes. *Géotechnique*, 43(3): 349–415.

Jefferies, M. G. 1993. Nor-Sand: a simple critical state model for sand. *Géotechnique*, 43(1): 91–103.

Riveros, G.A. & Sadrekarimi, A. 2021. Static Liquefaction Behaviour of Gold Mine Tailings, *Canadian Geotechnical Journal* 58(6), 889-901.

Lade, P.V. 1992. Static instability and liquefaction of loose fine sandy slopes. *Journal of Geotechnical Engineering*, ASCE, 118(1): 51–71.

Poulos, S.J., Castro, G., & France, J.W. 1985. Liquefaction evaluation procedure. *Journal of Geotechnical Engineering*, ASCE, 111(6): 772–791.

Plewes, HD, Davies, MP & Jefferies, MG 1992, 'CPT based screening procedure for evaluation liquefaction susceptibility', Proceedings of the 45th Canadian Geotechnical Conference, *Canadian Geotechnical Society*, pp. 41–49.

Robertson, P.K., 2010. Estimating in-situ state parameter and friction angle in sandy soils from the CPT. *2nd International Symposium on Cone Penetration Testing*, CPT'10, Huntington Beach, CA, USA.

Roscoe K.H Schofield A.N. & Wroth C.P. 1958. On yielding of soils, *Géotechnique*, 8, 22 - 53.

Sadrekarimi, A. 2014. Effect of the Model of Shear on Static Liquefaction Analysis, *Journal of Geotechnical and Geoenvironmental Engineering (ASCE)*, 140(12)

Sladen, J.A., D'Hollander, R.D., & Krahn, J. 1985. The liquefaction of sands, a collapse surface approach. *Canadian Geotechnical Journal*, 22: 564–578.

Vaid, Y.P., Chung, E.K.F., & Kuerbis, R.H. 1990. Stress path and steady state. *Canadian Geotechnical Journal*. 27: 1–7.

Yamamuro, J.A., & Lade, P.V. 1997. Static liquefaction of very loose sands. *Canadian Geotechnical Journal*, 34: 905–917.

A case-study on lime treatment of mine waste tailings containing low concentration of clay minerals

Narain Hariharan, Nikolas Romaniuk, Mike Tate, Jesse Fox
Graymont, Richmond, BC, Canada

Javier Castaneda Garay, Sergio Serment Moreno
Calidra, Monterrey, Mexico

ABSTRACT: Modification of mine waste tailings to improve their strength and stability reduces operational and reclamation risks for mine operators. Lime has been used in soil treatment applications with proven performance for decades to dewater and stabilize expansive soils. Recent research has shown that this technology can also be applied to beneficially modify fine clay fractions in mine waste tailings to improve their geotechnical characteristics and accelerate reclamation timeframes.

The objective of this study was two-fold. First, to investigate the impact of lime treatment on improving the unconfined compressive strength (UCS) of a non-plastic tailings deposit in Mexico. Second, to understand the non-traditional mechanisms governing strength gain through mineralogical evaluation. Despite low clay levels, the lime treated tailings exhibited nearly 25 times higher UCS within 28 days after treatment compared to the untreated deposits. The changes in chemical composition of non-clay minerals in this deposit after lime addition influenced strength development.

1 INTRODUCTION

Lime (CaO) is a versatile material and has been successfully used in infrastructure construction worldwide including soil treatment applications, such as stabilizing pavement base and subgrades, airport runways and rail-road beds (Little et al. (1987)). Lime proves especially effective at providing a workable soil platform in construction operations through its ability to alter the physical properties of clays and specifically reducing the plasticity index and expansion index of soils (Little (1995)). The alteration of physical properties is, in part, a result of lime treatment increasing the soil pH to as high as 12.45 providing hydroxyl ions which solubilize and interact with the silicates and aluminates released from the clay minerals (Lane (1983); Rogers and Glendinning (1996)). This results in long-term strength building pozzolanic reactions forming cementitious calcium bound silicate and aluminate hydrate minerals. Lime is the chemical stabilizer most widely used for treating soils with plasticity indexes greater than 15 by coagulating and permanently modifying the clay minerals present.

Extensive work done by Graymont over the past 5 years has demonstrated benefits of using lime to improve the filterability of mine waste tailings containing high concentrations of clay minerals and significantly increase the long-term strength of the dewatered mine waste tailings (Romaniuk (2016); Tate et al. (2017)). Mine waste tailings stored in containment facilities pose serious liability concerns for both operators and the investors highlighted by the recent dam failures in Brumadinho, Mt Polley, and Fundão (Armstrong et al. (2019)). These recent failures have driven critics, investors, and regulators to pressure operators to transform and reclaim the mine waste tailings as geo-mechanically stable and self-supporting materials capable of supporting landform development. Treatment of the Athabasca oil sands fluid fine tailings (FFT) with lime after dewatering through a filter press or centrifuge consistently achieves the minimum required undrained shear strength of 20 kPa to deploy soft ground reclamation techniques. In fact, the addition of lime increased the shear strength of cakes obtained after pressure filtration of the FFT beyond 100 kPa within 56 days after treatment which serves as a directional indicator to assess the feasibility of hard-ground reclamation techniques as well (McKenna et al. (2016)).

Although significant strides have been made in establishing the benefit of lime in the management of mine tailings containing clays, there has been limited work done to explore the benefits of lime in mine tailings having low concentrations of clay minerals. Consequently, there is also a limited understanding of the mechanism of interactions between lime and non-clay minerals present in mine waste tailings. Non-clay pozzolanic minerals, such as volcanic ash, can be quite reactive with lime. Vitruvius, a famous Roman engineer, developed mortar and cement formulations containing a volcanic pozzolan and lime for the construction of the Roman Empire (Sear (1990)). Despite being non plastic, these minerals reacted with lime to increase the strength of the structures built (Jackson et al. (2005); Jackson and Marra (2006)). This historical example serves as a motivation to explore the improvements in strength characteristics of mine waste tailings via the interaction of naturally occurring non-clay minerals with lime.

The focus of this case study is to investigate the impact of lime treatment to improve the strength of a mine tailings deposit in Mexico where little to no clay minerals were identified in the geological characterization of the facility and characterize the mineralogical evolution of the tailings after lime addition to probe alternate mechanisms that can contribute to strength growth beyond pozzolanic stabilization of clay mineral.

2 OBJECTIVES

The primary objective of this case study was to investigate the impact of lime treatment on changes in engineering and physicochemical properties of a Mexican mine tailing deposit and in doing so understand the effectiveness of treating mineral compositions containing low concentration of clay minerals with lime. The performance of lime treated tailings deposits were evaluated through the following tasks:

1. Procure untreated pond deposit samples from the tailings facility in Mexico and perform basic engineering and chemical characterization of the samples including determining the optimum lime dose for treatment.
2. Assess the impact of lime treatment on the unconfined compressive strength of the tailing deposits by comparing the strengths before treatment and after 7 days and 28 days post lime addition.
3. Understand the mineralogical composition of the untreated deposits and evaluate the transformation in mineralogy after lime treatment using X-ray diffraction (XRD) and attempt to validate the XRD findings by obtaining scanning electron microscope (SEM) images.
4. Summarize the learnings from the study and understand the requirements for effective mineral stabilization using lime through alternate mechanisms not involving interactions between lime and clay minerals.

3 TEST METHODS

This section provides a brief overview of the material characterization process and test methods used for engineering and physicochemical evaluation of the mine tailings deposits.

3.1 *Material Characterization and Determination of Lime Fixation Point*

Engineering characterization of the materials included determining the Atterberg limits by ASTM D4318 (ASTM D4318-17 (2017)) accompanied by soil classification, measurement of methylene blue index (MBI) (Omotoso et al. (2008)) and pH of the tailings deposits (ASTM D4972-19 (2019)) percent passing 74 micron and assessment of the compaction characteristics by determining the optimum moisture content (OMC) following ASTM D1557 (ASTM D1557 (2017)).

The lime fixation point of the tailings deposits was determined by the Eades and Grim test method following ASTM D6276-19 (ASTM D6279-19 (2019), Eades and Grim (1960)). The lime fixation point in soil treatment applications is defined as the optimum lime dose required to elevate the pH of the soils to 12.45 which is seen as the optimal pH required to necessitate pozzolanic reactions with clay minerals. All tests in this study were performed using quicklime (CaO) in dry powder form.

3.2 *Determination of Unconfined Compressive Strength (UCS)*

UCS testing was performed in accordance with ASTM D2166 (ASTM D2166 (2016)) on both the native tailings samples and samples treated with the optimum lime dose using their respective OMC values. 2.4-inch diameter by 5-inch height cylindrical molds were used for preparing samples for UCS testing. UCS was measured after allowing the samples to age under ambient temperature and relative humidity for 7 and 28 days. Three samples were prepared for all test mixes to ensure consistency in results.

3.3 *X-Ray Diffraction (XRD) Analysis*

Powdered samples were used for XRD analysis by grinding the tailings samples using a mortar and pestle followed by sieving to pass 45 μm sieve. The soil minerals present in the powdered native and lime treated samples were determined using a Bruker D-8 X-ray diffractometer using CuKα radiation powered to 40 kV at 40 mA (Deng et al. (2014)). Phase identification was done by matching against the mineral collection data using the Match! Software. Exactly 4.50 g of the samples tested were mixed with 0.5 g of ZnO (internal standard) and 15 mL of ethanol followed by milling for 5 minutes in a micronizer to eliminate preferential orientation of the particles. The suspension was then spray-dried (Hillier (1999)) in a heated chamber to generate spherical aggregates. The spray-dried samples were then side loaded prior to XRD analysis. In addition, the clay fraction of the samples (passing 2 μm) was extracted and analyzed to identify the cations saturating the interlayer of swelling clay minerals. The samples were scanned from 3 to 60 degrees (2θ) for 60 min at 0.02 degrees/sec.

3.4 *Scanning Electron Microscope (SEM) Analysis*

SEM images were obtained on the mine tailing deposit samples to validate the XRD and XRF findings and detect the presence of cementitious products in the lime treated samples. SEM analysis was used along with elemental composition analysis to identify mineral phases present. SEM images were obtained on the native samples and 28-day aged lime treated samples.

4 RESULTS AND DISCUSSION

This section presents the results obtained in this laboratory case-study using the various test methods outlined in the previous section. A discussion of the various findings is also included.

4.1 *Material Characterization and Lime Fixation Point*

The optimum lime dose or the lime fixation point (Hilt et al. (1960)) for the samples was determined to be 3 percent by dry weight of the tailings solids. Table 1 summarizes the results obtained from the physical and chemical characterization tests for both untreated and 3% lime treated samples.

Table 1: Characterization of Mine Tailing Deposits

Sample	Liquid Limit (%)	Plastic Limit (%)	Plasticity Index (%)	% Passing 74 µm	Soil Classification	MBI	OMC (%)	pH
Untreated Deposits	19	19	0	58.3	Non-plastic	2.0	12.4	7.78
Lime Treated Deposits	23	24	-1	43.2	Non-plastic	1.9	12.9	12.45

As observed through the Atterberg limits results presented in Table 1, mine tailing deposits from Mexico investigated in this case-study were non-plastic with very low concentration of clay minerals as indicated by an MBI of 2.0. Both the liquid limit and plastic limit of the deposits increased by a similar proportion in the samples 48 hours after treatment with lime and hence did not result in any significant difference in the plasticity index of the samples contrary to what is normally observed in soil treatment application wherein a significant increase in plastic limit accompanied by a decrease in plasticity index is expected. There was a 0.5% increase in OMC observed in the lime treated samples which is expected due to the lowering of dry density of the soils likely due to some coagulation of the fine particles as indicated by the drop in the fraction of particles passing 74 µm after lime addition. In summary, the characterization data clearly suggests that the mine tailing deposits would be traditionally considered unsuitable for treatment using lime with limited scope for long-term strength improvements due to the absence of clay minerals.

4.2 *UCS Analysis*

The average values of the Day 7 and Day 28 UCS test results obtained on the untreated and 3% lime treated samples remolded at their respective OMC values are presented in Figure 1.

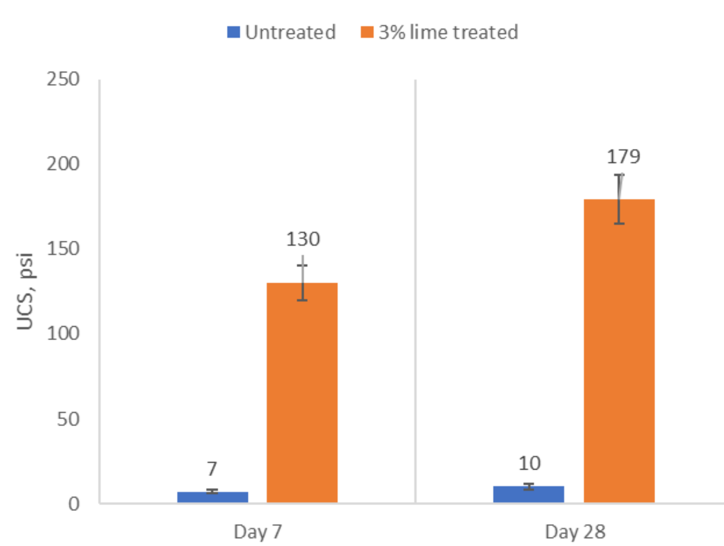

Figure 1. Comparison of the evolution of UCS of the mine tailing deposits over 28 days before and after treatment with lime.

Despite the absence of clay minerals as illustrated previously, there was a rapid and significant increase in UCS of the tailing deposits after treatment with lime, as observed in Figure 1, thereby invoking curiosity regarding the nature of minerals present in these deposits and the chemical interactions between lime and the minerals present. It is also important to recognize that reconstituting the tailings samples could significantly disturb the chemical bonds between calcium ions from lime and the soil minerals present and thereby impact the strength of the samples when compared to in-situ strengths obtained after treatment with lime. In any case, a nearly 20 times increase in UCS within 7 days after treatment with lime and a further sustained increase in UCS between Day 7 and Day 28 clearly indicate the impact of lime towards transformation of a soft mine tailings deposit into a deposit capable of being repurposed and used as backfill material, subgrade for construction of roadways or in other landform applications.

4.3 *X-ray Diffraction (XRD) Analysis*

To understand the reasons for the remarkable increase in UCS values after the addition of lime, XRD patterns were obtained on the coarse fraction (0.6 to 2.0 mm) and fine fraction (passing 0.6 mm) of the as-received samples and 28 days after treatment with lime. The purpose of obtaining the XRD patterns of the as-received samples was to understand the overall mineralogical composition and identify any naturally occurring minerals containing silica and alumina phases which could result in pozzolanic reactions after interactions with lime. The purpose of obtaining the XRD patterns 28 days after lime addition was to allow sufficient time for hydration of the quick lime, complete any cation exchange interactions and release the soluble calcium required to influence the formation of strength building cementitious compounds. The XRD patterns of both the coarse and fine fractions of the native and lime treated samples are presented in Figure 2 and Figure 3 respectively.

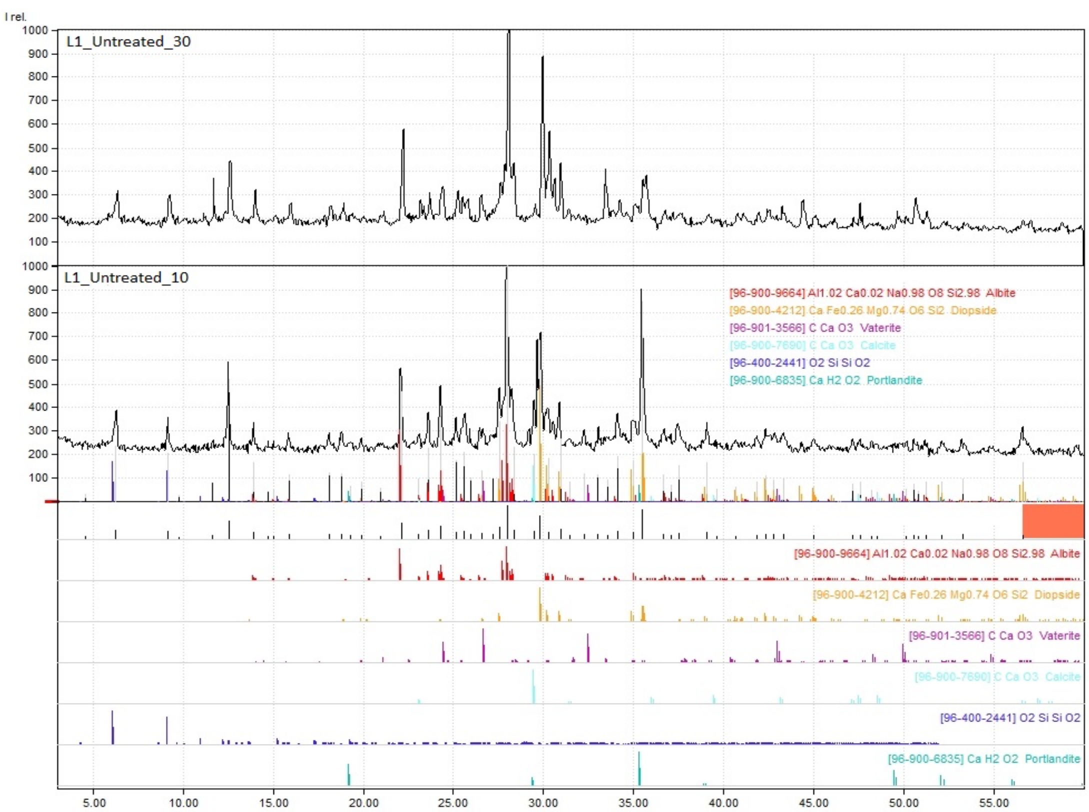

Figure 2. XRD patterns of the coarse and fine fractions of the untreated mine tailings sample.

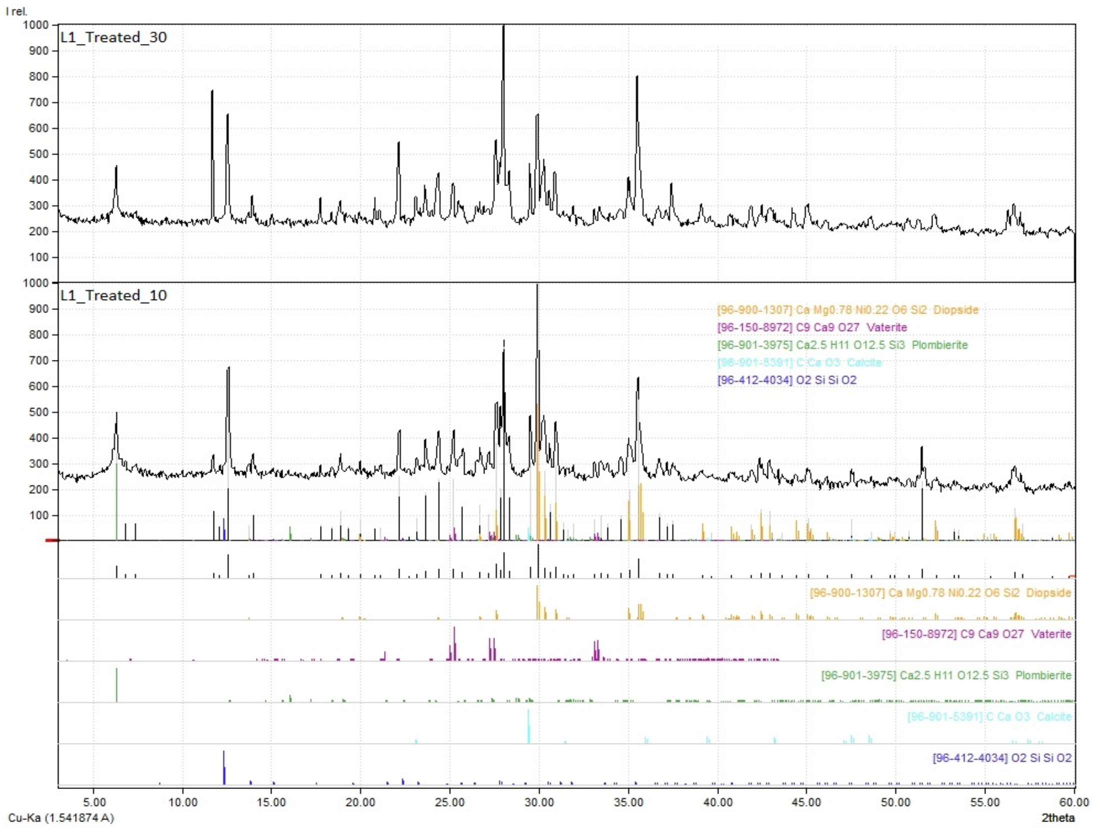

Figure 3. XRD patterns of the coarse and fine fractions of the Day 28 lime treated mine tailings sample.

The coarse and fine fractions of the untreated samples exhibited somewhat different XRD patterns (Figure 2). The primary rock phases in the coarse fraction appear to be albite (a sodic plagioclase feldspar) and abundant quartz, calcium carbonate phases (calcite and metastable vaterite), and portlandite. The primary rock phases in the fine fraction were abundant albite and diopside, very little quartz, calcium carbonate phases, and portlandite. The coarse fraction was found to have more portlandite than the fine fraction.

Both the coarse and fine fractions of the lime treated samples gave somewhat similar XRD patterns despite the different size fractions (Figure 3). These are composed of a primary rock phase (diopside, a clinopyroxene), calcium carbonate phases (calcite and metastable vaterite), a trace of quartz, and plombierite. The coarse fraction was found to have more plombierite than the fine fraction.

Based on the minerals identified above in the untreated and lime treated samples, the formation of plombierite likely in an authigenic phase was most intriguing. Plombierite is an unusual and rare calcium-silicate-hydrate mineral with an interlayer spacing that closely resembles tobermorite, which is a more common and abundant mineral phase found in aluminous tobermorite mineral cements in ancient Roman seawater concretes (Jackson et al. (2011)). The presence of portlandite in the untreated samples is puzzling and hard to explain given the pH of the untreated sample was only 7.78. It is hypothesized that the increase in pH to 12.45 due to addition of lime reactivates the portlandite inherently present in the tailings deposits which, by way of a hydrothermal treatment with a silicate mineral assemblage, resulted in the formation of plombierite. The formation of plombierite after the addition of lime is seen as the primary mechanism supporting the long-term sustained strength improvements seen in the UCS test results presented in Figure 1.

The findings of the XRD analysis demonstrates a unique and novel mechanism of soil mineral stabilization using lime that is non reliant on the presence of clay minerals, such as kaolinite, illites, or smectites, and instead involves direct interactions with naturally occurring pozzolanic minerals present in mine tailing deposits.

4.4 *SEM Analysis*

To validate the XRD findings described above, SEM images were obtained of the mine tailing deposits both before and after treatment with lime. SEM images of the lime treated samples were also obtained 28 days after treatment consistent with the procedure followed for XRD analysis. SEM image of the untreated and lime treated sample are presented in Figure 4 and Figure 5 respectively.

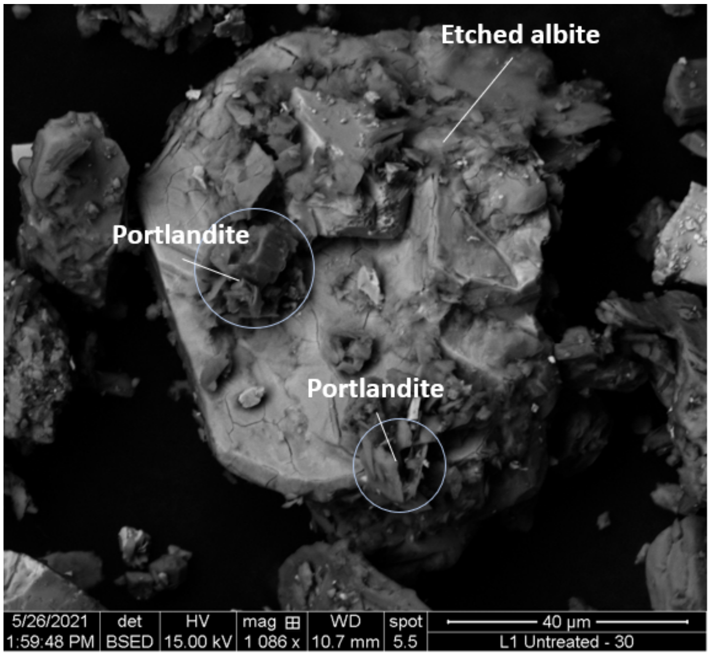

Figure 4. SEM image of the untreated mine tailings sample.

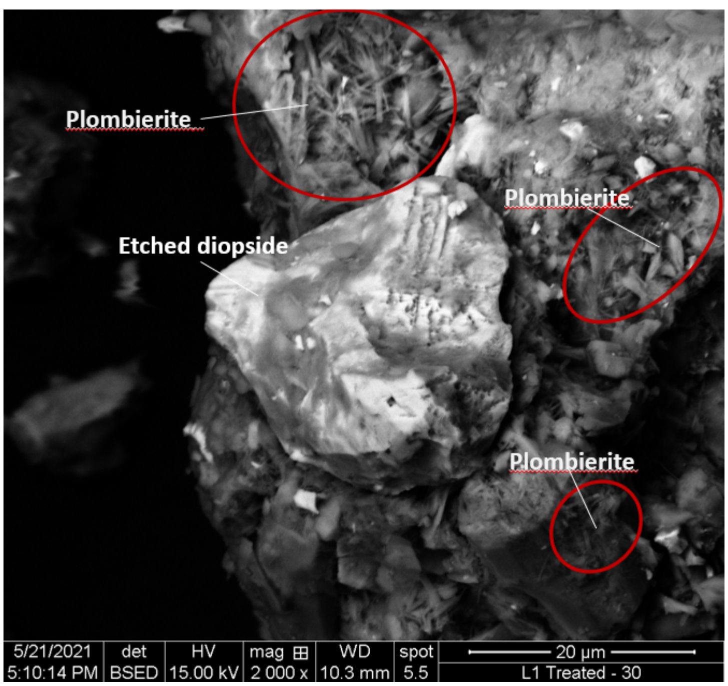

Figure 5. SEM image of the lime treated mine tailings sample.

The following observations can be made based on the SEM images presented in Figure 4 and Figure 5:

- The large crystal fragment in Figure 4 is likely identified as an etched albite while the plate like crystals that adhere to the surface of the larger crystal fragment appear to be portlandite which corresponds to the XRD phase assemblage of the untreated samples presented earlier.
- The radial spherulites of platey and acicular crystals occurring in pore spaces in Figure 5 confirm the presence of plombierite, as authigenic mineral cements as identified in the XRD patterns of the lime treated samples. The large crystal fragment is identified as an etched diopside fragment.

In summary, the SEM analysis appears to validate the findings and observations made through the XRD analysis and strengthen the case for the hypothesized mechanism of strength gain in the lime treated tailing deposits due to the interaction of soluble calcium from lime with the amorphous silica assemblages naturally present in the tailing deposits resulting in the formation of a mineral cement – plombierite.

5 SUMMARY AND CONCLUSIONS

In this case-study, the impacts of lime treatment on the engineering and physicochemical properties of a mine waste tailings source in Mexico having very low concentration of clay minerals were investigated. The findings of the study illustrate alternative mechanisms responsible for long-term strength development in soil-lime systems beyond traditional pozzolanic reactions wherein strength gain is realized at pH levels above 12 through the interaction of soluble calcium released from lime with the soluble silica and alumina phases of the clay minerals. The following major conclusions can be drawn from the various testing conducted in this study:

- Treatment of non-plastic mine waste tailings with 3% quicklime resulted in an increase in UCS from less than 10 psi before treatment to an average of 179 psi within 28 days after lime addition.
- Due to an increase in pH after lime addition, the naturally occurring inert silica phases present in the tailings were able to solubilize and react directly with portlandite inherently present in the tailings and with the additional calcium released by the quicklime added thereby resulting in repurposing dormant minerals into cementitious phases.
- The formation of mineral cement - plombierite through the interaction of lime and silicious phases present in the tailings is perceived as the primary mechanism contributing to the long-term strength improvements observed.
- SEM images of the lime treated samples confirmed the formation of radial spherulites of platey and acicular crystals of plombierite within the pore spaces of the large parent crystal fragments, such as albite and diopside.

The results of this case-study highlight the ability of lime to transform soft mine tailings deposits into strong and self-supporting materials capable of being reclaimed and used as alternatives for mine backfill, roadway stabilization and other landform development applications. The ability of lime to chemically modify dormant naturally occurring silica and alumina phases in geological deposits into cementitious phases offers potential for the use of lime treated tailing waste as a source of natural pozzolans that could be considered as cement alternatives in a variety of construction applications. Most importantly, the study illustrates that lime can be successfully used towards the management of mine waste tailings where clays are absent thereby strengthening the argument for further exploring the benefits of lime specific to the chemical composition of the tailing waste source.

6 ACKNOWLEDGEMENTS

The authors are grateful to Dr. Marie Jackson, University of Utah for her inputs regarding the test methods and for coordinating the XRD and SEM test work and to ENGEO labs, California for performing the UCS testing.

REFERENCES

ASTM D1557. 2007. Standard test methods for laboratory compaction characteristics of soil using stand ard effort (12 400 ft-lbf/ft3 (600 KN-m/m3)). *ASTM International*, West Conshohocken, PA.

ASTM D2166. 2016. Standard test method for unconfined compressive strength of cohesive soil. *ASTM International*, West Conshohocken, PA.

ASTM D4318-17. 2017. Standard test methods for liquid limit, plastic limit, and plasticity index of soils. *ASTM International*, West Conshohocken, PA.

ASTM D4972. 2019. Standard test methods for pH of soils. *ASTM International*, West Conshohocken, PA.

ASTM D6276. 2019. Standard test method for using ph to estimate the soil-lime proportion requirement for soil stabilization. *ASTM International*, West Conshohocken, PA.

Armstrong, M., Petter, R. and Petter, C.J.R.P. 2019. Why have so many tailings dams failed in recent years?. *Resources Policy*, Vol. 63, p. 101412.

Deng, Y., White, N. and Dixon, J.B. 2014. *Soil mineralogy laboratory manual*, 15th ed., Texas A&M University, College Station, Texas.

Eades,J.L. Grim, R.E. 1960. Reaction of Hydrated Lime with Pure Clay Minerals in Soil Stabilization. HRB Bull. 262, pp. 51-63.

Hariharan, N. 2013. Effect of ionic stabilization on vertical movement in expansive subgrade soils in Texas. *Thesis*, Texas A&M University, College Station, Texas.

Hillier, S. 1999. Use of an air brush to spray dry samples for X-ray powder diffraction. *Clay Minerals,* vol. 34(1), pp. 127-135.

Jackson,M. D., Marra, F., Hay, R. L., Cawood, C., and Winkler, E. 2005. The judicious selection and preservation of tuff and travertine building stone in ancient Rome, *Archaeometry*, 47, 485–510.

Jackson, M. D., Marra, F. 2006. Roman stone masonry: volcanic foundations of the ancient city, *American Journal of Archaeology*, 110, 403–36.

Jackson, M.D., Rossetto, P.C., Kosso, C.K., Buonfiglio, M. and Marra.F. 2011. Building Materials of the Theatre of Marcellus, Rome. Archaeometry, 53, pp. 728-742.

Lane, S. 1983. Lime coagulation and stabilization of total oilsands tailings. *Annual Technical Meeting*: *Petroleum Society of Canada*, Banff, Canada.

Little, D.N. 1995. Stabilization of pavement subgrades and base courses with lime.

Little, D.N., Thompson, M.R., Terrell, R.L., Epps, J.A. and Barenberg, E.J. 1987. Soil stabilization for roadways and airfields. LITTLE (DALLAS N) AND ASSOCIATES BRYAN TX.

McKenna, G., Mooder, B., Burton, B. and Jamieson, A. 2016. Shear strength and density of oil sands fine tailings for reclamation to a boreal forest landscape. *Fifth International Oil Sands Tailings Conference (IOSTC)*(DC Sego, W. Wilson, and NA Beier, editors), pp. 130-153.

Rogers, C., and Glendinning, S. 1996. Modification of clay soils using lime. *Lime Stabilization: Proceedings of the Seminar held at Loughborough University Civil & Building Engineering Department,* pp. 99-114.

Romaniuk, N. 2016. Dewatering and altering of MFT characteristics using lime (CaO) additive. *A Report by Apex Engineering*.

Sear, F. 1990. Vitruvius and Roman theater design, *American Journal of Archaeology*, 94, 249–58.

Tate, M. J., Leikam, J., Fox, J. and Romaniuk, N. 2017. Use of calcium hydroxide as a coagulant to improve oil sands tailings treatment. *22nd International Conference on Tailings and Mine Waste*, pp. 720-732, University of Alberta Geotechnical Centre, Denver, Colorado.

Hydraulic performance of a storage cover for closure of a tailing facility

Kelly Greaser
Stantec Consulting Services Inc., Denver, Colorado, USA

Cynthia Gulde
Chevron Environmental Management Company, Denver, Colorado, USA

ABSTRACT: A storage cover lysimeter study was initiated at a tailing facility in New Mexico to evaluate the performance of alluvial cover materials over circumneutral tailing in a semi-arid climate for final closure. Three test plots were installed along with climate monitoring stations. The test plots contain soil monitoring instrumentation in the vadose zone, two of which include constructed lysimeters. The raw data demonstrate the covers perform as designed and significantly reduce or eliminate net infiltration. Further, the raw data demonstrate the depth of wetting increases with increasing cover thickness.

A cover performance assessment was completed using soil-atmosphere modeling and calibrated material properties. The assessment evaluated the effect of cover thickness, climate, and material properties on the covers' hydraulic performance. The predictions demonstrate that all covers performed effectively. The model predictions also show that with increasing cover thickness infiltration reaches greater depths in the tailings (i.e., water penetrates deeper below the surface) and evapotranspires more slowly.

Irrigation tests were performed at the test plots to confirm that the cover and underlying tailing material are effective in storing and releasing moisture. The results confirmed thinner covers performed more effectively compared to the thicker cover.

Raw data collected over 13 years, the cover performance assessment, and the irrigation tests all demonstrate that a thin cover (23 to 30 cm) is more effective at limiting net infiltration and releasing water to the atmosphere via evapotranspiration than a thick cover (61 cm or greater) for this site.

1 INTRODUCTION

Closure of large mining facilities such as tailing facilities can be costly due to the volume of cover material needed to reduce long-term seepage through the tailing. Consequently, the use of thin covers can provide significant cost-savings if thin covers accomplish performance objectives. This paper presents a case study for a tailing facility in New Mexico. where extensive studies were completed to evaluate net infiltration[1] through storage covers for closure of the facility. Ultimately, raw data and analyses demonstrate that a thin cover (23 to 30 cm) is more effective at limiting net infiltration and releasing water to the atmosphere via evapotranspiration than a thick cover (61 cm or greater).

[1]Net infiltration is defined as water that infiltrates into the soil profile that is not subsequently released to the atmosphere through evaporation or transpiration. It is also referred to as deep drainage or percolation.

2 BACKGROUND

In the summer of 2000, a storage cover lysimeter study was initiated at a tailing facility in New Mexico to evaluate the performance of alluvial cover materials considered for final closure of the tailing impoundment. During closure, the design objectives of the cover soil are to prevent erosion of the tailing, minimize erosion of the cover, provide a growth medium for revegetation and, in conjunction with the underlying tailing, provide a water storage (evapotranspiration or store and release) cover system that would reduce net infiltration into the deeper tailing profile. This paper focuses on the store and release and net infiltration objectives of the cover design. The store and release cover system will store precipitation during wet periods and release the moisture back to the atmosphere via evapotranspiration during dry periods. The net effect is a significant reduction, or elimination, of net infiltration into the deeper tailing profile, and ultimately seepage from the tailing impoundment.

Three test plots were installed over the circumneutral tailing in an area that had been previously covered for about 25 years and had developed a mature shrub vegetative cover. The tailing was not compacted prior to cover placement. Details of construction are provided below.

- TP 1: Existing 28-cm thick alluvial cover with mature grass/shrub vegetation overlying undisturbed in situ sandy tailing (very deep tailing profile). TP-1 has no lysimeter.
- TP-2: 23-cm thick alluvial cover with backfilled sandy tailing (2.5-meter deep tailing profile) within a constructed lysimeter.
- TP-3: 61-cm thick alluvial cover with backfilled sandy tailing (2.5-meter deep tailing profile) within a constructed lysimeter.

Each test plot is instrumented with 10 soil moisture sensors and 10 soil temperature/suction sensors at various depths from near the surface to just over 2.7 m below ground surface (bgs). Each lysimeter was constructed with a 1.9-cm thick High Density Polyethylene tank with a diameter of 239 cm and a height of 234 cm, and volume of approximately 10,600 liters. The constructed lysimeters at TP-2 and TP-3 are equipped with a piping system and tipping bucket to measure flow. Following excavation into the tailing, the lysimeter tanks were lowered into the excavation and backfilled with the excavated tailing. A 23-cm cover was placed at TP-2 and a 61-cm cover was placed at TP-3. A primary climate monitoring station was installed near the test plots and three secondary precipitation monitoring stations were installed across the tailing facility.

TP-1 is the most representative of post-closure conditions and has been the focus of the storage cover lysimeter study. The soil monitoring sensors were installed in undisturbed cover and tailing, and the overlying vegetation was not disturbed.

Throughout the program, 13 years of climate, soil, and lysimeter flow data have been collected. In 2004, a cover performance assessment was completed. In 2009, the model constructed for TP-1 for the cover performance assessment was successfully validated. In 2013, irrigation tests were completed at each of the three test plots.

3 DATA COLLECTION AND ANALYSIS

Over the 13 years of the study, the climate was generally wetter compared to long-term averages. Based on data from 1910 to 2013 from a nearby National Weather Service (NWS) station, the long-term annual average precipitation is 32.79 cm for the area. However, the annual average for the period from 2001 to 2013, the period over which the test plots were monitored, is 33.73 cm, nearly a centimeter wetter compared to the long-term average. Annual precipitation in 2005 was the highest over the period of record for the lysimeters. Anomalously high precipitation occurred in December 2007 and November 2013. Based on a Gumbel distribution, the measured monthly precipitation was a 2,000-year and 200-year event, respectively. Climate at the tailing facility is generally semi-arid and average annual potential evapotranspiration is 135.1 cm, calculated using the data from the primary weather station from 2001 to 2013 with the FAO Penman-Monteith method (Allen et al. 1998).

Neither lysimeter at TP-2 or TP-3 has measured naturally-induced drainage over the 13 years of the study. Following the extremely high precipitation event in December 2007 (8.48 cm in 1 month, represented a 2,000-year event based on a Gumbel distribution), at a seasonal time when evapotranspiration is low, each test plot responded to the high precipitation event, although drainage did not occur and the test plots exhibited gradual drying since this high precipitation event. At TP-1, the moisture content of the deepest sensor at 211 cm bgs increased from 5% to 6.7% approximately 8 months following the high precipitation which occurred in December. Prior to the high precipitation event, the moisture content had oscillated between 5.2% and 4.5%. After approximately 3 years, the moisture content of the deepest sensor returned to normal. The deepest moisture content sensor (229 cm bgs) at TP-2 did not appear to respond to the high precipitation event. At TP-3, the deepest moisture content sensor at 211 cm bgs increased sharply from 3% to nearly 10% in less than 4 months in response to the high precipitation in December 2007.

The deepest suction sensors at TP-1 and TP-3 showed a sharp increase in moisture content in March 2008. The deepest suction sensor at TP-1 showed a decrease in suction of less than one order of magnitude while the deepest suction sensor at TP-3 showed a decrease in suction of nearly 2 orders of magnitude. By the end of 2008, soil suction for the deepest sensors had nearly returned to previous levels. At TP-2, similar to the moisture content measurements, soil suction at the deepest sensor did not appear to respond to the high precipitation in December 2007. Figure 1 presents the soil suction measurements for select sensors at TP-1 along with precipitation over the period of record for comparison.

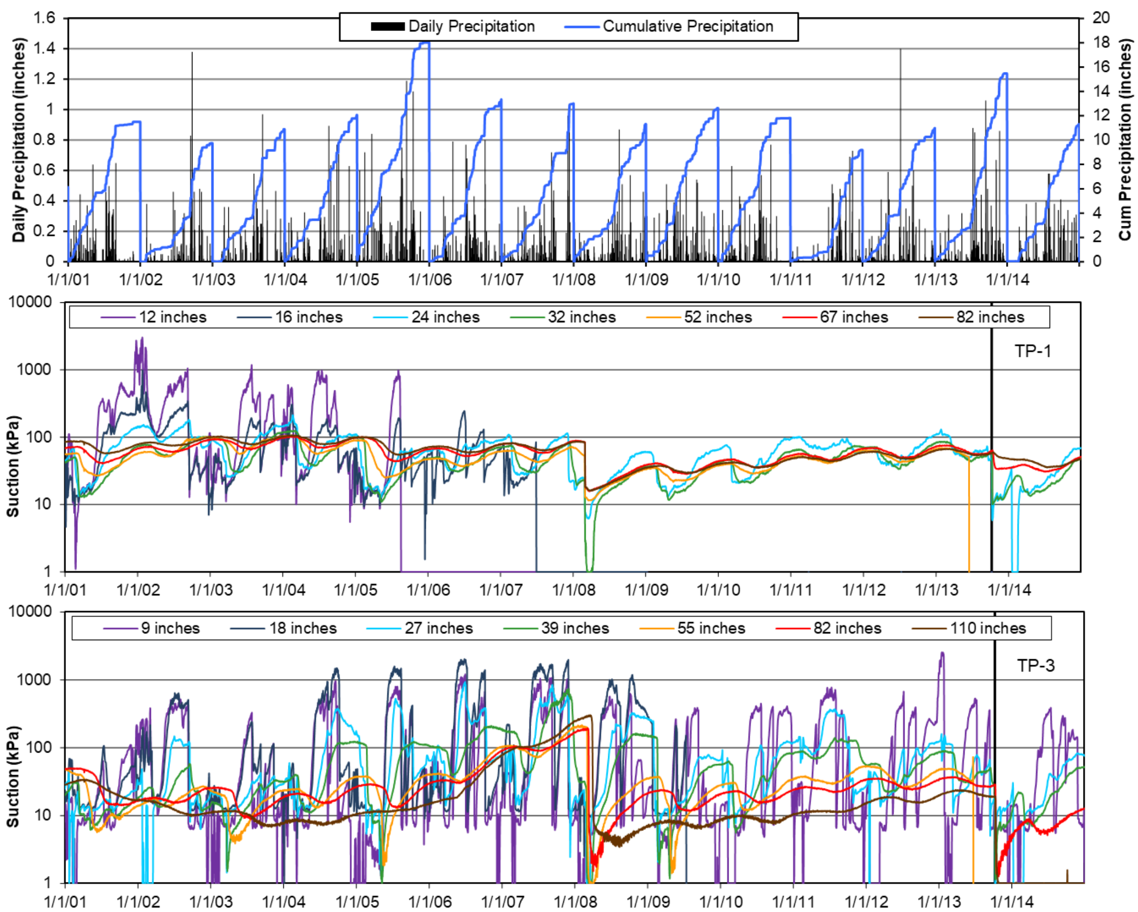

Figure 1. Precipitation and Soil Suction Measured at TP-1 and TP-3

Consequently, even though the precipitation which occurred in December 2007 was extreme (2,000-year event), the cover and tailing stored the water and released it to the atmosphere through evaporation and transpiration, as designed. Further, the increase in moisture content was less at TP-1 with a thinner cover compared to the thicker cover at TP-3. Similarly, the decrease in soil suction was less at TP-1 compared to TP-3. Along with the lack of response at TP-2 with a thin cover, the data from all three test plots confirms less net infiltration with thin (23 to 30 cm) covers compared to thicker covers.

In addition, the measured data demonstrates the depth of wetting in the short-term following precipitation events increases with increasing cover thickness. The short-term depth of wetting at TP-1 and TP-2 with 28-cm and 23-cm covers, respectively, ranges from 76 to 102 cm. The depth of wetting at TP-3 with a 61-cm alluvial cover is approximately 152 cm. Most of the moisture in TP-1, TP-2, and TP-3 is stored in the uppermost tailing just below the alluvial cover. Although no measurable (naturally-induced) net infiltration has occurred over the history of the program, the difference in the depth of wetting indicates the thinner covers perform more effectively as store and release covers over the tailing, which demonstrates the effectiveness of the thinner covers to store precipitation during wet periods and subsequently release via evapotranspiration.

Finally, average storage at various depths within the test plots also confirms the thinner covers perform more effectively hydraulically compared to the thicker cover. Average storage below 61 cm bgs (the thickness of the cover at TP-3) is much higher at TP-3 compared to TP-1 and TP-2 with thinner covers. Over similar intervals, the average storage at TP-3 ranges from 10% to 225% higher compared to TP-1 and TP-2. The average storage below the cover at TP-3 is more than 13 cm while the average storage at TP-1 below 61 cm is 8.9 cm and at TP-2 it is 6.9 cm. This demonstrates water penetrates to greater depths with thicker covers.

4 COVER HYDRAULIC PERFORMANCE ASSESSMENT

Soil-atmosphere models were constructed in HYDRUS-1D (Simunek et. al 1998) to calibrate material properties for each test plot; the discussion herein focuses on TP-1 because this test plot best represents deep, in situ, undisturbed conditions with a well-established vegetated cover. The modeling was completed using data from 2000 through 2004. To define input parameters for material properties, paired measurements of soil moisture and suction were used to estimate soil water characteristic curves for various layers in the cover and tailing. The curves better represent in situ conditions rather than solely relying on laboratory testing. Although the curves were not well constrained at low and high moisture contents due to the limits of the raw data over the four-year monitoring period available. Consequently, the curves were constrained to the porosity of the alluvial cover material and upper tailing measured in the lab. The effective porosity of the tailing was decreased with depth to represent increasing confining stress. Several possible curves were defined for each sensor pair. Initial modeling was used to identify which set of curves best simulated the measured moisture and suction. For calibration, the saturated hydraulic conductivity (Ksat) was varied along with inputs for vegetation.

Climate data from the primary climate station was used and pre-processed to account for snow conditions using the Kustas et al. equation (1994). Input parameters for root distribution were defined using the model for semi-arid steppe vegetation (Schenk and Jackson 2002) and truncated at 57 cm based on observations of root growth behaviour at the facility. The annual distribution of leaf area index (LAI) was estimated based on data from the Moderate Resolution Imaging Spectroradiometer (MODIS) on board the Earth Observation System (EOS) satellite (NASA 2004). The data were used to develop the annual distribution, although LAI in the winter was set to zero to account for the absence of shrubs on the test plots. The upper boundary condition was defined as atmospheric with runoff while the lower boundary condition was defined as free draining. Simulations were completed with an hourly time step in the summer to represent the intensity of summer storms.

Following manual calibration, the objective parameter estimation program UCODE (Poeter and Hill 1998) was used to achieve calibration. Calibration focused on non-winter periods. In situ suction and moisture measurements with depth every 15 days were used for calibration along with constraints on cumulative outflow from the bottom of the model domain. Measurements representing frozen soil conditions were weighted significantly less compared to non-soil freezing conditions in order to emphasize calibration to summer months. Calibration was considered complete when no significant improvement in the match between the predicted and measured soil suction and moisture could be achieved by further reasonable adjustment of input parameters. Figure 2 presents the results of the calibrated model compared to measurements for total water storage across the profile. The calibrated Ksat of the alluvial cover is 2.8×10^{-2} cm/s while the calibrated Ksat of the upper tailing is 4×10^{-3} cm/s. Overall, the calibrated model provides an acceptable match to measured suction and moisture content changes in the alluvium (detailed profile data not shown). The model did not reproduce extremely dry suctions measured in the alluvium. This is conservative in that the model predicts wetter near-surface conditions. As a result, the model slightly overpredicts the moisture content in the upper tailing, which again is considered conservative. The model also predicted slightly wetter conditions than measured for the lower five tailing layers. The model parameters generated from calibration of TP-1 are adequate for predictions of cover hydraulic performance.

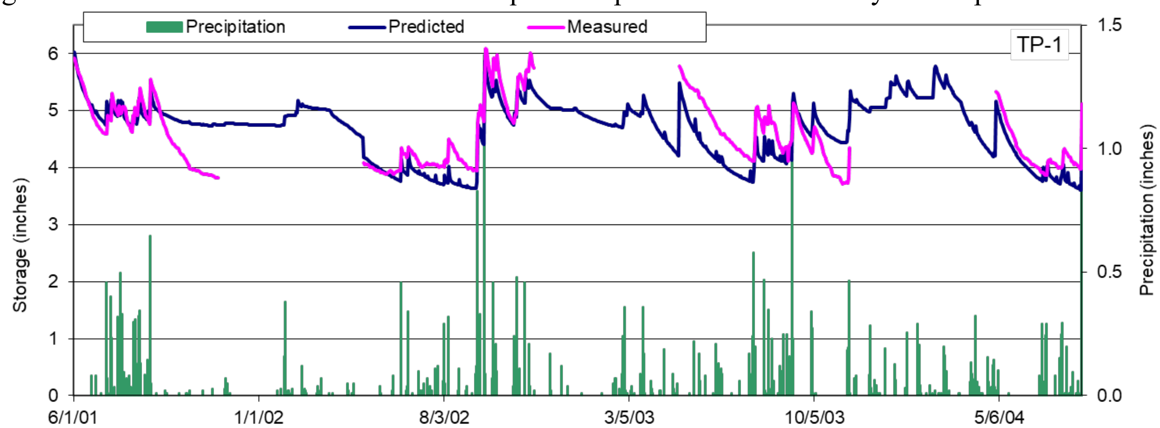

Figure 2. Precipitation, Measured Storage, and Predicted Storage for TP-1 over the Simulation Period

A cover hydraulic performance assessment was completed using soil-atmosphere modeling and calibrated material properties for TP-1. Cover performance predictions were conducted to evaluate the performance of a vegetated alluvial cover for a range of expected conditions, including average and extreme climate conditions and uncertainty or changes in the tailings and alluvial material properties. A range of cover thicknesses were evaluated, from 23 to 91 cm. The analysis also considered cover performance without vegetation, such as in the event of a fire. Long-term climate data from the nearby NWS station was used and adjusted to represent the tailing facility.

Three main parameters for material properties were varied to evaluate their effects on net infiltration: cover thickness, Ksat, and effective porosity. Cover thicknesses simulated included: 23, 46, and 91 cm. The calibrated Ksat values for TP-1 were increased by a factor of 2 and 5 for each layer and the calibrated porosities were also increased by 25% for each layer to evaluate uncertainty and variability in the materials.

The predictions demonstrated that all covers performed effectively as store and release covers for all scenarios simulated. Under natural climatic events, water that infiltrated from rainfall and snowmelt was stored within the uppermost layers of the alluvium and tailings and subsequently lost by evapotranspiration. The simulated performance of the covers was insensitive to a reasonable range of material properties to be expected at the tailing facility and to possible extreme, prolonged wet climatic conditions. Cover performance in simulations without vegetation (such as following a fire) demonstrated slower release of stored moisture, but evaporation alone can effectively release stored water from the cover/tailing system. The model predictions demonstrate that infiltration reaches greater depths in the tailing and evapotranspires more slowly with increasing cover thickness. The predictions with a 23-cm alluvial cover more effectively limited infiltration into the tailing and allowed for faster evapotranspiration of the stored water than covers with a greater alluvial cover thickness. Net infiltration was insignificant for all covers and simulations evaluated.

Finally, the calibrated models were validated in 2009. The validation (not discussed further) was successful and confirmed the results of the cover hydraulic performance assessment.

5 IRRIGATION TESTS

Irrigation tests were performed at the test plots at the tailing facility to confirm that the cover and the underlying tailing material are effective in storing and releasing moisture. A 3-day, constant rate irrigation test was initiated on October 8, 2013 and concluded on October 11, 2013. The surface of the test plots was irrigated using a rotor sprinkler Rain Bird 5000plus. Rotor sprinklers were chosen over spray sprinklers because they are capable of applying more uniform irrigation in high wind conditions and have interchangeable nozzles allowing for flexibility in adjusting the rate.

The optimum irrigation rate and duration resulting in outflow without generating runoff or creating ponded conditions was estimated for each test plot using the soil-atmosphere models discussed above. To limit uncertainties and to enable comparison of responses between the tests, one irrigation rate was targeted for all three test plots. A rate of 1.3×10^{-4} cm/s was selected as a threshold rate expected to create breakthrough (net infiltration). This is equivalent to 11 cm of irrigation applied in a 24-hour period and 33 cm applied in a 72-hour period. For comparison, the 24-hour, 1000-year event corresponds to 11.2 cm while the 72-hour, 1000-year event is 12.1 cm. Therefore, the target application rate exceeds any natural rain event that may be considered for the cover design. The modeling results predicted breakthrough at TP-1 (outflow equivalent) and TP-3 using this application rate. However, all simulated model conditions for TP-2 failed to predict breakthrough. The actual application rate ranged from 1.2×10^{-4} to 2.0×10^{-4} cm/s due to wind, inconsistency over the arc of the sprinkler, water pressure variations, and natural precipitation events. Over the 3-day period of the test, the total precipitation applied to each test plot exceeded or was roughly equivalent to the long-term annual average precipitation for the tailing facility.

Similar to the calibrated model, the discussion of results will focus on TP-1 because this test plot best represents deep, in situ, undisturbed conditions with a well-established vegetated cover. The middle and lower soil profile at TP-1 immediately prior to the irrigation tests were near field capacity. Soil suction and moisture content in the upper 30 cm of the soil profile exhibited drying up to the point of irrigation. These sensors showed an immediate response to irrigation. The sensors installed mid-profile, from 69 to 140 cm, showed a delayed response to the irrigation. Each of the sensors in the middle of the profile reached near-saturated conditions at progressively later times following the start of the test, indicating propagation of the wetting front deeper in the profile. Each of the upper and mid-profile sensors exhibited a drying trend soon after completion of the test and through the end of 2013. Soil suction and moisture content measured at 170 and 168 cm indicated wetting between October 15 and October 17, 2013. Following the initial wetting from the irrigation test, the suction and moisture content sensors measured generally stable soil moisture conditions relatively quickly. The lowest suction and moisture sensors at 208 and 211 cm exhibited a gradual increase in wetting through the end of 2013; however, the lower profile did not approach saturation.

Drainage at the undisturbed profile location and the two lysimeters was calculated using multiple methods. Precision limitations in the sensors and sensor calibration affect this type of analysis, particularly at low suctions. The first method of calculation used Darcy's Law and the lowest two suction sensors to calculate a gradient and unsaturated hydraulic conductivity at the measured suction. These flux calculations were completed once the wetting front reached the bottom of each profile. The second method of calculation summed only downward flux (ignoring times of upward flux). The third method of calculation assumed a uniform downward unit gradient, ignoring the calculated gradient. The fourth method of calculation used the measured change in moisture content and assumed the flux was all drainage (i.e., an increase in moisture content will translate to drainage through time while a decrease in moisture content was assumed to have resulted from drainage) therefore upward flux is ignored. The second, third, and fourth methods of flux calculation are conservative since upward flux is ignored. The fourth method represents the maximum flux to be expected.

The wetting front propagated to the bottom of the undisturbed soil profile at TP-1 approximately a week following termination of the test. Through the end of 2013, a uniform downward gradient was measured at the bottom of the profile by the suction and moisture content sensors. The wetting front reached the bottom sensors at TP-2 and TP-3 in a similar time period.

The drainage calculated using the darcian gradient and unit gradient at TP-1 were negligible and could not have been measured with a lysimeter. The total change in storage of the bottom moisture content sensor represents approximately 0.15 inches 60 days following the test. The results of the modeling completed prior to the tests indicated higher predicted drainage (2.3 inches after 60 days) than the results of the drainage calculation, although the simulated irrigation was less than applied (13.04 inches compared to 17.45 inches, respectively). The modeling completed prior to the tests used calibrated properties from the cover hydraulic performance assessment. In this case, the model predicted more drainage than occurred in reality, which is conservative for the purposes of the cover hydraulic performance assessment.

The Ksat of the deeper tailing layers in the undisturbed profile at TP-1 are generally lower than the conductivities of shallow tailing layers, effectively inhibiting downward flow. The upper profile reached saturation on the second day of irrigation, but the lower profile remained unchanged for nearly 30 days. Data from November 10, 2013, 30 days after the irrigation test was terminated, indicate a slight increase in moisture near the bottom of the profile. A similar pattern is observed in soil suction on December 10, 2013, 60 days after the irrigation test was terminated. In addition, the unsaturated hydraulic conductivity of the tailing near the bottom two sensors did not increase significantly.

At TP-1, even though the soil suction sensors show a response to irrigation, negligible drainage was calculated from the profile because the deep profile remained near field capacity and the calculated unsaturated hydraulic conductivity remained low. The soil suction profiles show that the upper profile approached the maximum retentive capacity; however, because flow in the lower profile is slow, the water infiltrating the soil profile is stored and subsequently released in the upper profile. The soil suction and moisture content data from the irrigation test show the soil cover-tailing system is effective at limiting net drainage at this location. Similarly, the calculated drainage at TP-2 was negligible; no drainage was measured at the lysimeter.

At TP-3, breakthrough was measured on October 13, 2013, two days after the irrigation test was terminated. Approximately 0.51 cm of outflow was recorded at the lysimeter on that day. Cumulative drainage 30 days after irrigation totalled 5.97 cm and cumulative drainage 60 days after the test totalled 8 cm. The cumulative flux calculated assuming a unit gradient was 14.5 cm 30 days following the test and 25 cm 60 days following the test. The total change in moisture of the bottom moisture content sensor represents approximately 13 cm 60 days following the test, which demonstrates the assumption of unit gradient is overly conservative. TP-3 was the only test plot in which drainage occurred as a result of the irrigation testing, even though the least amount of irrigation was applied compared to TP-1 and TP-2. Even though breakthrough was achieved at TP-3, the soil-tailing profile is still considered effective at limiting net infiltration because the amount of water applied during the test was far greater than a 1000-year event and the measured drainage through the end of 2013 is a fraction of the irrigation applied, demonstrating the profile stored and released the majority of the applied water.

The calculated drainage at TP-1 and TP-2 was much lower compared to the measured drainage at TP-3 even though a larger volume of water was applied at TP-1 and TP-2. Along with measured drainage at TP-3 and no drainage at TP-2, this demonstrates the thinner covers at TP-1 and TP-2 perform more effectively as store and release covers.

As indicated in the cover performance assessment, the calibrated model for TP-1 is considered conservative in that it slightly over-predicts the moisture content in the alluvial cover material and tailing. The modeling completed prior to the tests predicted limited drainage at TP-1 following the irrigation tests (2.3 inches after 60 days) with negligible drainage calculated from sensor readings after test completion. The results of the irrigation tests demonstrate the calibrated material properties are conservative while confirming the conclusions of the cover hydraulic performance assessment (discussed above).

6 CONCLUSIONS

The data collected and evaluations completed through the storage cover lysimeter study are sufficient to assess cover hydraulic performance for closure and post-closure of the tailing facility. The raw data collected, as well as model simulations, and the irrigation tests have demonstrated that thinner covers (23 to 30 cm) are more effective at limiting the depth of wetting, promoting evapotranspiration, and thereby reducing net infiltration than thicker covers (61 to 91 cm). Raw data and evaluations completed to date indicate that 30- to 91-cm thick covers are protective of groundwater with thinner covers exhibiting lower net infiltration. In the semi-arid climate at the tailing facility, the primary reason thinner covers perform better is likely due to the prominent vegetation at the tailing facility which is characterized as semi-arid steppe. The vegetation is dominated by grasses, with relatively shallow roots. Consequently, thinner covers, which store water higher in the profile, allow the shallow roots to transpire water more efficiently. In contrast, thicker covers allow deeper penetration of water to depths with lower root density, which leads to less effective transpiration. Similarly, evaporation is more effective at removing water from thinner covers compared to thicker covers.

7 REFERENCES

Allen, R. G., Pereira, L. S., Raes, D., and Smith, M. (1998) *Crop Evapotranspiration – Guidelines for computing crop water requirements*, FAO Irrigation and Drainage Paper No 56, FAO, 300 p.

Kustas, W. P., Rango, A. and Uijlenhoet, R. (1994) 'A Simple Energy Budget Algorithm for the Snowmelt Runoff Model', *Water Resources Research*, v. 30, no. 5, p. 1515-1527.

Poeter, E.P. and Hill, M.C. (1998) *Documentation of UCODE, a computer code for universal inverse modeling*, U.S. Geological Survey Water-Resources Investigations Report 98-4080, 116 p.

Schenk, H. J., and Jackson, R. B. (2002) 'The Global Biogeography of Roots', *Ecological Monographs*, v. 72, p. 311-328.

Simunek, J., Sejna, M., and van Genuchten, M. Th. (1998) *The Hdyrus-1D Software Package for Simulating the One-Dimensional Movement of Water, Heat, and Multiple Solutes in Variably-Saturated Media*, Version 2.0, U.S. Salinity Laboratory Agricultural Research Service, 178 p.

Closure planning under the ECCC high emission scenario

Alvin Tong, & James McKinley
Stantec Consulting Ltd., Calgary, Alberta, Canada

Karyn Lewis
Lupin Mines Incorporated, British Columbia, Canada

ABSTRACT: The Lupin Gold Mine (Lupin) is located approximately 285 km southeast of Kugluktuk, Nunavut and is owned by Lupin Mines Incorporated (LMI). Lupin is a remote high-arctic site that is situated in an area of continuous permafrost. In 2017, LMI decided to end their Care and Maintenance period and enter Active Closure. Intervening parties submitted various requirements for supporting evidence prior to approving the plan, one of which included confirmation of the long-term performance of the tailings containment area (TCA) cover with the consideration of climate change.

More specifically, LMI was required to consider a range of emission scenarios from multiple climate models in their closure planning. The high emission scenario (HES) predicts a 7.8 °C increase in air temperature by the year 2100. Using historical thermistor data from Lupin, thermal modeling was conducted to evaluate the impact of the HES temperature increase on site permafrost. Under the HES scenario, it is modeled that by the year 2075, the annual thaw depth during summer will exceed the frost penetration depth, and long-term progressive degradation of the permafrost to the point where it will not long exist in the project area.

As part of the closure plan approval process, LMI was required to demonstrate that their TCA closure plan would still work in the face of climate change. LMI used a combination of previous work completed as part of the TCA closure plan and additional field work, combined with current monitoring data, and development of post-closure monitoring plan to demonstrate that not only is the TCA cover technology currently working, but that it should continue to work under the most extreme climate change scenarios

1 INTRODUCTION

The Lupin Gold Mine (Lupin) is located approximately 285 km southeast of Kugluktuk, Nunavut and is owned by Lupin Mines Incorporated (LMI), a wholly owned indirect subsidiary of Mandalay Resources Corporation. Lupin is a remote high-arctic site that is situated in an area of continuous permafrost and is only accessible year-round by air.

The original (late 1980s to mid-2000s) tailings closure and management plan at Lupin, as with a number of other mines in the north, was to isolate the potentially acid generating (PAG) tailings within permafrost-core dams in a tailings containment area (TCA) and then cover the tailings with 1 m of esker for encapsulation by permafrost (Figure 1). After decades of monitoring, ground temperature data indicated that the annual thaw zone (active layer) was extending deeper than 1m and that it would require thicker cover to encapsulate the tailings completely within permafrost if the temperature trend continued.

To mitigate the risks to the mine plan, schedule, and costs associated with potentially doubling the esker cover thickness in order to meet the permafrost encapsulation goal, Lupin evaluated the use of a partially saturated (store and release) esker cover to maintain a high degree of saturation in cover material and tailings and to limit acid generation. It should be noted that based on the latest site-specific climate model under high emission scenario, doubling the cover thickness will not achieve permafrost encapsulation. The partially saturated cover concept does not rely on permafrost encapsulation, is significantly less sensitive to climate related annual temperature changes or, and allows natural vegetation, making it ideal for a site such as Lupin. This change in closure concept was approved in 2006 as part of the interim abandonment and reclamation plan (IARP).

In 2017, LMI decided to end their Care and Maintenance period and submitted a Final Closure and Reclamation Plan (FCRP) for Lupin to the Nunavut Water Board (NWB) in 2018. Regulators and stakeholder parties submitted various confirmation requirements and evidence for proof of concept, which included demonstration that the TCA closure plan would continue to work in the face of climate change. The regulators and stakeholders specifically required evidence More specifically, LMI was tasked with evaluating the plan under Environment Canada and Climate Change's (ECCCs) high emission scenario (HES), which predicts a 7.8 °C increase in air temperature by the year 2100. A series of field studies and confirmation evaluations were done to support closure plan and they are outlined in the technical paper, Lupin Mine – A Case Study in Adaptive Tailings Management (Stantec 2020).

The active closure activities started in 2020 as per the approved closure plan. The 2020 closure activities in the TCA included treatment and discharge of the ponded water within the facility and the continued construction of the partially saturated tailings cover. Engineering support and technical supervision were provided during closure activities. Site observation during the 2021 active closure provided further insight and confirmation of the tailings cover performance, as support to the technical documents addended to the approved closure plan.

2 CLOSURE ACTIVITIES

The Lupin Tailings Containment Area (TCA) configuration is shown on Figure 1. The approved closure plan included completing the tailings covers, constructing surface water management structures, treating all water to meet discharge requirement, then initiate the post-closure monitoring. Two major closure activities are being carried out in the TCA:

1. Transfer of water into Pond 1 and Pond 2 for treatment and discharge to the environment.
2. Continuation of the cover construction in Cell 5 and 3.

The initial site condition at the end of 2019 was typical under care and maintenance. Most of the ponds and open areas of the tailing cells contained water from previous freshets and precipitations. The maintenance treatment operation typically would be to treat then discharge to lower Pond 2 as much as practicable. The treatment was done with monitoring to ensure all the water met requirements before discharge. The monitoring was done daily over specific GPS locations as shown in Figure 2. Discharge was stopped prior the start of winter season with sufficient time to allow water transfer from other ponds to maintain freeboard. Based on site experience, the tailings-impacted water is low in pH (~4) and non-contact water would be readily impacted by the introduction of acidity due to its low buffering capacity. Simply put, a small amount of tailings water would cause a significant drop in pH in non-contact water. The natural background runoff is slightly acidic at pH of 5.5-6 so any treated water above pH of 6 is expected to be reduced to around 6 after freshet.

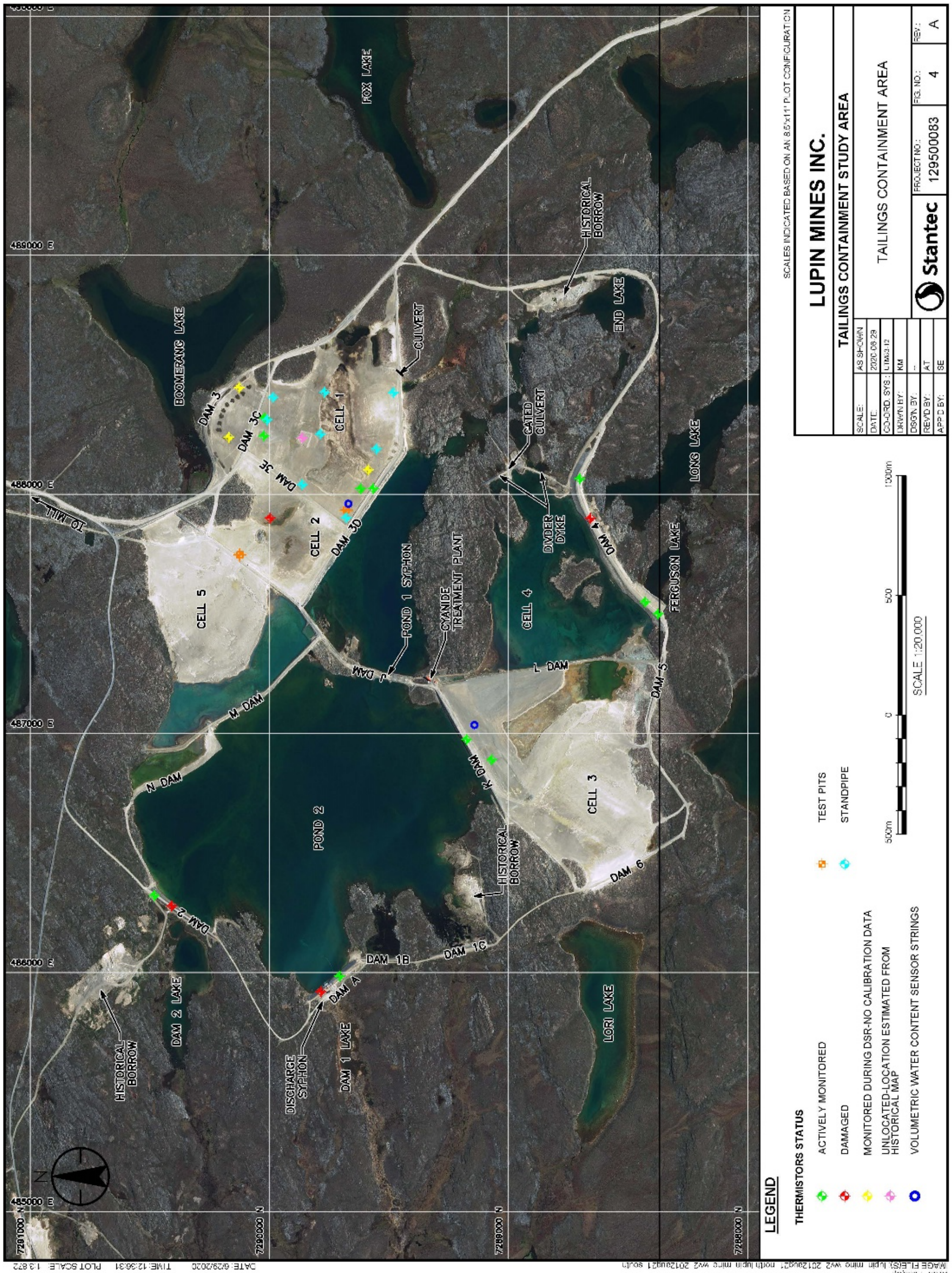

Figure 1. Site Map with Associated Instrumentation

The 2020 discharge activity was done in similar fashion with the significant change of in-line treatment between Pond 1 and Pond 2 started mid-season. The in-line treatment allowed the water transfer to be done earlier and a greater amount of water was transferred to facilitate cover construction. The end result was at the end of 2020, all of the Pond 2 water was treated to meet discharge requirement, and water from other ponds was transferred reaching low points in preparation for continuation of 2021closure construction. Due the significant reduction of water levels in previously flooded area in the tailings cells, old tailings that was deposited during operation is now exposed.

As part of the 2020 closure activities, significant portions of the Cell 3 and 5 tailings cover were constructed. This cover reduced a significant portion of exposed tailings to contact runoff water and reduced the amount of the water to be ponded in the low-lying areas.

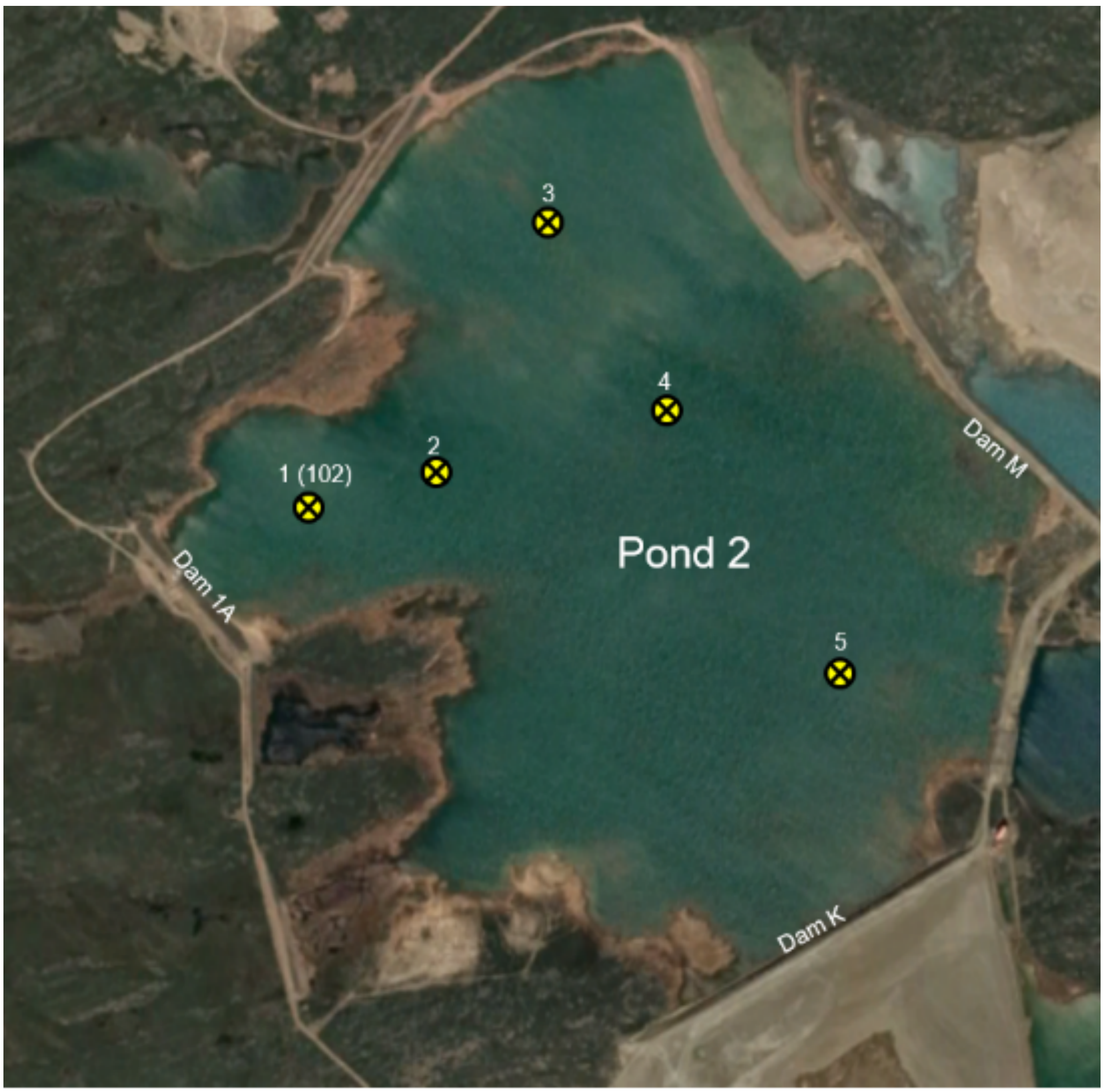

Figure 2. Approximate In-situ pH Monitoring Station Location

3 2021 CLOSURE CONSTRUCTION OBSERVATIONS

At the start of 2021, in-situ monitoring was completed in Pond 2 as soon as open water allowed. The monitoring data indicated the water quality in Pond 2 did not return to untreated pH at beginning of 2020. Table 1 shows the comparison of the pH monitoring data between the start of

2020, end of 2020, and start 2021. The dissimilar water quality results between start of 2020 and start of 2021 suggest there are beneficial changes in TCA water quality that may have been influenced by 2020 closure activities. Preliminary hypotheses suggest if tailings-impacted water is seeping into Pond 2, the pH is expected to drop to levels similar to, or lower than, the measured value in June 2020. The drop to pH ~6 is expected due to slightly acidic background pH levels. This preliminary data set further confirms that the dams, along with the thermistor data and geophysical surveys (Stantec 2020), are performing according to the design and controlling the seepage.

Table 1. In-situ pH Monitoring Data

	June 2020	Sept 2020	June 2021
Averaged Monitored pH in Pond 2	4.9	7.0	6.1

As mentioned above, the water in Cell 3 and 5 was mostly dewatered in 2020 in preparation for the cover construction. The dewatering exposed tailings along the previously flooded cell areas where water levels fluctuated during care and maintenance. Physical inspection was completed safely in 2021 in the dewatered tailings cells. Shallow testpits were dug to investigate the in-situ tailings conditions where deeper tailings were submerged, and shallow tailings were vulnerable to drying at surface. The excavated tailings profile indicated that oxidation is limited to the surface (orange/rust zone) where a high degree of saturation could not be maintained when the water level is low (Figure 3). Tailings at depth, where a high degree of saturation could be maintained, was observed with minimal, if no, oxidization (grey zone).

Figure 3. Shallow Testpit in Exposed In-situ Tailings

Similar observations were collected from the deeper testpits that were dug within the tailings cover in 2019. In support of the closure plan approval, two testpits were dug within the historical covered tailings to confirm the performance of the cover. One of the testpit was excavated within Cell 1, which was covered in 1995. Wet cover material was encountered approximately 0.6m below ground surface (bgs), which generally corresponds with the water level measured in a nearby standpipe. A layer of cold wet tailings was encountered approximately 1.3 m bgs and frozen tailings was encountered approximately 1.5 m bgs. No oxidized tailings were observed in the test pit. Groundwater was observed seeping into the test pit at approximately 1.3 m bgs. The testpit profile is provided in Figure 4.

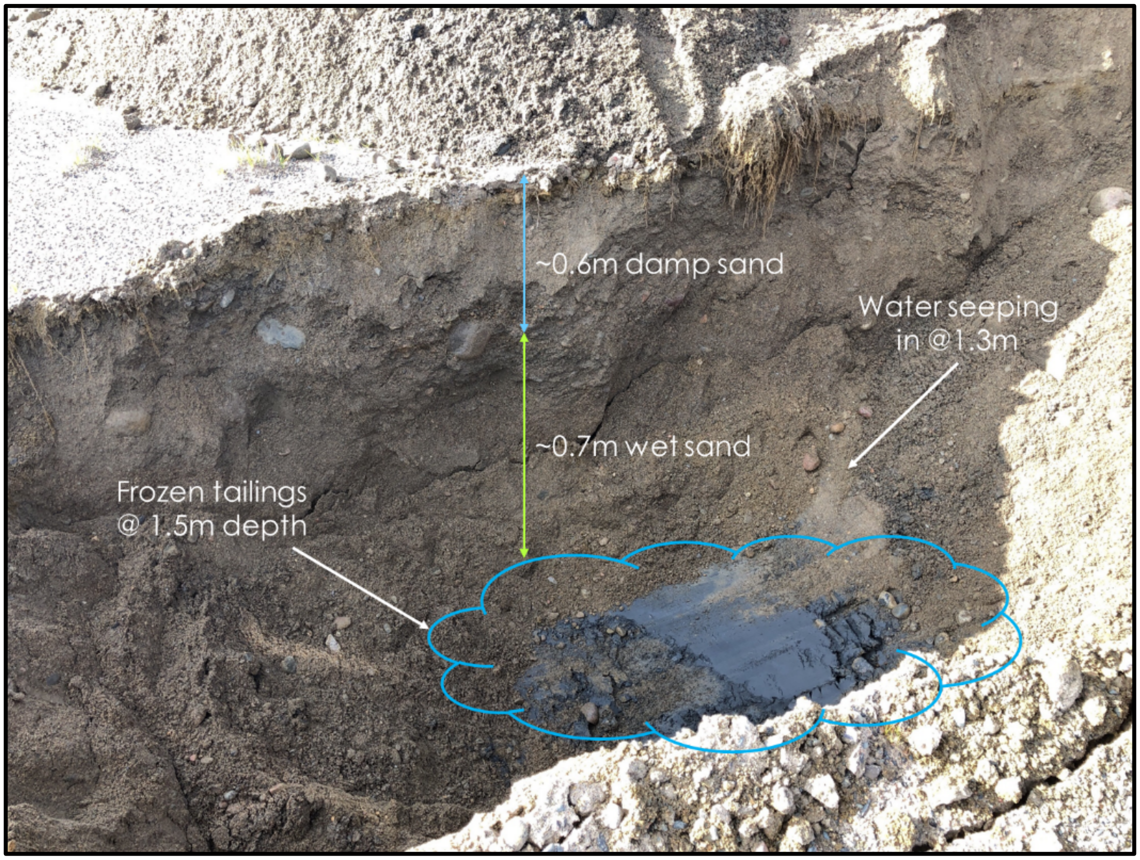

Figure 4. Testpit profile within existing tailings cover

4 CONFIRMATION FROM OBSERVATIONS

Although there is significant uncertainty regarding the extent to which climate change and temperature increases in the north will occur, the TCA closure cover at Lupin Mine should continue to function as designed, regardless of the extent of temperature increases. The 2021 construction observations further provide confidence on the closure plan. The relatively similar water quality measured in Pond 2 at the start of 2021 construction season, after freshet strongly, indicates the dams are currently performing as intended. Separately, shallow testpit results further confirms the previous evaluation results (Stantec 2020) that oxidization is significantly limited in saturated tailings, regardless of its frozen state, as long as it is saturated. To continue support and monitor the performance of the TCA plan, additional instrumentations are planned in 2021, including more thermistors and volumetric moisture content probes. Annual inspection and in-situ water quality monitoring are included the draft post closure monitoring plan which is not yet finalized with ongoing consultation with the stakeholders.

Developing closure plans in the context of climate change is quickly becoming the rule rather than the exception. Historically, closure plans were required to look ahead years if not decades. However, given the timeframe over which climate change is potentially projected to occur, closure plans must now look ahead in terms of centuries. The ability to successfully support the Lupin TCA cover design application while accounting for climate change uncertainty, supported by sound engineering and sufficient site evidence, illustrates an important lesson that can hopefully be used by other mines in the world.

5 REFERENCES

EcoMetrix Incorporated., 2006 (EcoMetrix 2006). Geochemistry and Water Quality, Volume 3 of Seepage and water Quality for Reclaimed Tailings Containment Area, Lupin Operation, report submitted to Kinross Gold Corporation, April, 2006.

Holubec Consulting Inc. 2005. Closure Plan for Tailings Containment Area. Prepared for Kinross Gold Corporation – Lupin Operation.

SRK 2016. Lupin Mine Tailings Management Facility, 2015 Dam Safety Review: Final Draft Report submitted to Lupin Mine Inc., 2016

Stantec 2020, Lupin Mine – A Case Study in Adaptive Tailings Management, proceedings in Tailings and Mine Waste 2020.

Passive treatment of mine influenced water

Rachel James, Silvia Mancini & Andrew Holmes
Geosyntec Consultants International Inc., Toronto, Ontario, Canada

Herwig Goldemund
Geosyntec Consultants Inc., Kennesaw, Georgia, United States

Kevin Dufresne
Geosyntec Consultants International Inc., Guelph, Ontario, Canada

Evan Cox
Geosyntec Consultants International Inc., Waterloo, Ontario, Canada

ABSTRACT: Mining companies are increasingly experiencing water treatment obligations that may endure in-perpetuity. Due to these pressures, mining companies are considering and investigating innovative environmental management solutions; implemented during initial mine planning through source control and water management, to operational and post closure water treatment and reclamation. Passive and semi-passive water treatment and alternative source control technologies are examples of innovative solutions. These technologies treat and manage mine-influenced water (MIW) through stimulation of (bio)geochemical processes, and may minimize compliance issues and operational requirements, and assist in meeting sustainability goals.

This paper provides an overview of passive and semi-passive MIW treatment and management technologies and recent innovations for these technologies. Applications of technologies including constructed wetlands, pit lake in-pit treatment, permeable reactive barriers (PRB), Gravel Bed Reactors™ (GBR), phytotechnologies, and organic cover systems are detailed as case studies. The deployment of mobile treatment systems to mine sites, such as containerized reactors and "wetlands on wheels", will be discussed as an important stage to facilitate treatability studies, regulatory approval, and advancement of technology application to full-scale. Each technology is discussed from a perspective of site-specific considerations and implementation. Further, treatment system configurations and treatment mechanisms are explored to highlight the flexibility of their application in the context of adaptive mine closure.

1 INTRODUCTION

MIW can consist of metal cations (e.g., cadmium, lead, zinc), transition metals (iron, manganese, copper, chromium, mercury), non-metals (sulfur, nitrogen, selenium), metalloids (arsenic, antimony), and actinides (uranium). These constituents can be present in the geological formation of the target resource and become mobilized through disturbance of material and exposure to the atmosphere and/or aerated waters. The leaching of inorganic constituents can occur in neutral or acidic pH water; with acidic pH typically associated with accelerated rates of metal leaching through acid mine drainage that can develop through activities related to ore processing and tailings and waste rock management (INAP, 2009).

Specifically, MIW typically consists of elevated concentrations of sulphate in 1000s of milligrams per liter (mg/L) as a product of iron sulphide oxidation when reduced iron minerals are exposed to oxygen and water at surface. MIW can also consist of nitrogen compounds that form through the degradation of cyanide (a product of gold cyanidation processing), or the dissolution of residual waste from nitrate- and ammonia-based explosives.

Some of the challenges mine sites face in managing environmental and social impacts related to MIW relate to diverse and challenging chemical and physical conditions. Chemical conditions can include complex composition of MIW potentially requiring treatment solutions that can involve the generation of more problematic secondary constituents. Physical conditions can include remote locations with limited access to power, cold or arid climate conditions, and variable flow rates. Many of these challenges are not specific to mining and solutions can be adapted from other sectors such as power and agriculture.

Passive water treatment technologies that treat and manage MIW have the potential to treat MIW effectively and reduce operational requirements while assisting in meeting sustainability goals. Passive treatment systems rely on stimulating and optimizing natural biological and/or geochemical processes to remove inorganic constituents from impacted water. Passive water treatment systems generally require little to no maintenance once installed, whereas active tank-based water treatment systems use mechanical devices under specialized operation and require continual flow control, reagent addition, solids/residual management, and power. Semi-passive treatment systems combine concepts from passive treatment, relying on natural biological and geochemical treatment, and active treatment, such as chemical amendment and flow control. Due to their low maintenance requirements and lower operating costs, the incorporation of passive and semi-passive treatment systems can be ideal for long-term water management for mine sites with predicted long term water treatment requirements.

A wide range of constituents can be treated passively and semi-passively based on a variety of biological and abiotic treatment mechanisms. The biological and abiotic treatment mechanisms are well documented in literature (Simon et al. (2002); Duncan et al. (2004); Sobolewski, (2005); Zhang and Frankenberger (2005); Zagury et al. (2007); Martin et al. (2009); Herbert et al. (2014); USDIBR (2011); USEPA (2014); Higgins et al. (2017); Seervi et al. (2017); Skousen et al. (2017); Rezadehbashi and Baldwin (2018); and Nielsen et al. (2018)).

Both biological and abiotic treatment mechanisms can be leveraged in passive and semi-passive treatment systems. Biological treatment systems typically rely on shifting the biogeochemical conditions of a treatment system to stimulate microbial populations that can either directly or indirectly reduce, adsorb, assimilate and/or precipitate inorganic constituents. Microbial populations are stimulated through supply of a source of carbon and nutrients (e.g., phosphorus) to sustain their growth and activity. The carbon source provides electron donors for the microbial reactions to occur. These microbes are naturally found in geographically diverse, pristine, and contaminated water (Nancharaiah and Lens (2015); Nielsen et al. (2018); and Rezadehbashi and Baldwin (2018)).

Non-biological or abiotic treatment relies on physical-chemical treatment mechanisms such as precipitation, cation exchange, adsorption and reduction. Abiotic adsorption systems utilize a fixed bed or barrier to house an adsorptive media. Abiotic reduction of inorganic constituents can be accomplished using ferrous hydroxide, electrocoagulation, ZVI, ferrous hydroxides and others.

2 PROSPECTIVE TECHNOLOGIES

The following sections provide summaries and case studies of highlighted passive and semi-passive technologies that have been demonstrated to treat MIW including GBR™s, constructed wetlands, in-pit lake treatment, and PRBs; and have the potential to manage MIW including TreeWell® technology and organic cover systems.

2.1 *Gravel Bed Reactors (GBR)*

A GBR is a fixed-film bioreactor, whereby an engineered bed of gravel or crushed rock media is placed in a lined cell or container in which the treatment conditions are controlled to support the growth and activity of microbes and biofilms on the media surface. Fixed-film bioreactors have been heavily applied across numerous industrial water treatment processes to biodegrade or immobilize contaminants that may be present in impacted water streams. GBRs are a unique configuration of fixed-film technology which have been developed to address low porosity and resultant high back pressures of organic bed systems, more controlled reduction rate and increased rates of removal. GBRs can be installed either below ground surface in an excavation, on-surface within a bermed or constructed cell, or as a hybrid of both (some portion below grade surrounded by berms above grade). Figure 1 presents a schematic for a GBR. A backfilled pit in situ water treatment system is another example that has been used to create conditions for biological semi-passive treatment of MIW, whereby an existing backfilled mine pit is dosed with carbon to support biological treatment mechanisms in groundwater (Heffernan, 2019). A GBR can be considered a purpose-built backfilled pit that allows more control and hydraulic isolation within the treatment system.

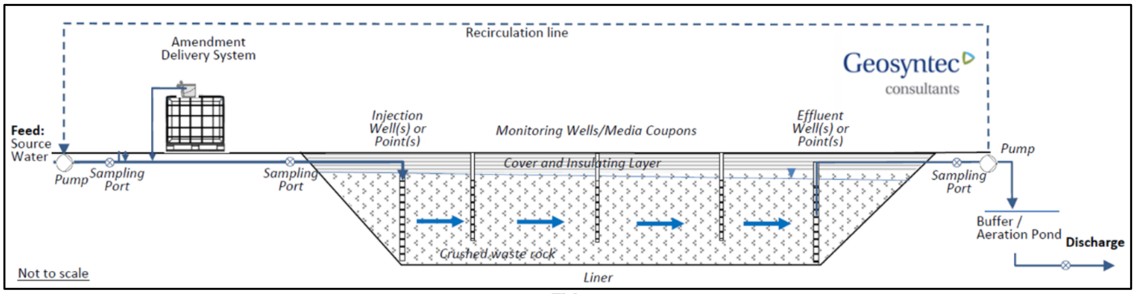

Figure 1. Schematic of a Gravel Bed Reactor (GBR™)

Impacted industrial water, surface water and/or groundwater (the influent) is typically pumped into the GBR, and the treated effluent is discharged to surface water or recharged to the subsurface. In some cases, post-GBR polishing is needed to adjust oxygen levels, pH or other chemistry to match influent conditions or meet specific regulatory criteria. Depending on the constituents to be treated, chemical amendments such as electron donors (typically carbon substrates) or electron acceptors (typically oxygen or anionic substrates such as nitrate or sulphate) are dosed into the influent to promote the desired operating conditions and resulting biological reactions. GBRs are conceptually simple and very flexible reactors that can be engineered in varying ways to treat a wide variety of metals, inorganics and organics. GBRs have successfully treated selenium-impacted water at several sites to concentrations below applicable water quality guidelines.

One example case study is of a water treatment project conducted on behalf of a coal mining company in West Virginia to mitigate selenium impacts to surface water emanating from seeps (Mancini (2019)). The GBR was installed beneath a parking lot at the facility to accommodate limited available space. The field application was designed to be capable of treating flows up to 550 m^3/day, although during operations it averaged a flow rate of approximately 270 m^3/day. The field application ran from March to May 2012 and was intended to continue operating, however the coal company went into bankruptcy and GBR operations, although successful, were suspended.

The seep source water had an aerobic ORP averaging 55 mV, DO averaging 4.8 mg/L, near neutral pH (7.03), a temperature ranging from 13 to 18 ºC, selenium ranging from 15 to 25 µg/L, and nitrate averaging 6 mg/L as N. A field application of the GBR technology was initiated in March 2012. The GBR was designed as a lined excavated trench underneath a parking lot at the facility. The gravel media bed was constructed inside a plastic-lined trench of approximately 28 m length by 8 m width by 1.5 m depth (approximately 360 m^3). The media of the reactor was 2-cm sandstone gravel. The GBR had a treatment capacity varying from 165 to 550 m^3/day. Citric acid and later acetic acid were used as electron donors. Main equipment included: i) the transfer pump to transfer water from the sump to the GBR; ii) an electron donor dosing system to add citric acid or acetic acid to the influent of the GBR; iii) an ORP probe at the outlet of the GBR to monitor effluent ORP to provide feedback to guide the electron donor dosing rate (adjustments to the dosing rate were conducted manually); and iv) associated controls and monitoring equipment for the GBR. The performance of the GBR was assessed from March through May of 2012, after which the GBR operations were suspended as the company entered bankruptcy. During operations, the GBR effectively reduced selenium concentrations in the effluent to levels below the treatment goal of <5 µg/L; nitrate concentrations were treated to below detection (<6.0 mg/L as N). The system operated at a flow rate of approximately 270 m^3/day.

2.2 *Constructed Wetlands*

Constructed (i.e., engineered) wetlands have a long and successful history in treating a variety of MIW. Over 40 years of research and practical full-scale applications of constructed wetlands throughout the world support the technical feasibility of the approach (ITRC, 2003). Research on the use of constructed wetlands for wastewater treatment began in Europe in the 1950's and in the United States in the late 1960's (USEPA, 2000). By the late 1990s, over 650 constructed wetlands sites were reported to have been constructed in North America (ITRC, 2003).

Constructed wetland systems incorporate biological (i.e., plant uptake, microbial activity), physical (i.e., adsorption, settlement and filtration), and chemical (i.e., reduction, precipitation) treatment processes. Constructed wetlands are engineered treatment systems comprised of treatment cells planted with a variety of typically native wetland plants (e.g., cattails, rushes, reeds, etc.). The primary treatment involves microbiological processes mediated by plants (e.g., phytovolatilization, etc.). Plants uptake nutrients such as nitrogen and phosphorus in addition to potential contaminants like metals and metalloids.

In general, there are two main types of constructed wetlands: 1) surface-flow wetlands, which mimic natural wetland systems; and 2) subsurface-flow wetlands, where the water table remains below ground surface (USEPA, 2000, ITRC, 2003). Within the subsurface-flow wetlands, there are two sub-categories: horizontal-flow and vertical-flow wetlands. Vertical-flow wetlands have the advantages of increased contact time, decreased potential for clogging, and increased oxygen delivery to the subsurface as compared to horizontal-flow wetlands and surface-flow wetlands. This results in more efficient treatment on a smaller footprint. The system is operational throughout the year and is able to mitigate problems with odors and mosquitoes (when properly maintained). However, a surface-flow wetland component may still be useful for flow equalization and pre-treatment of higher-strength MIW. Figure 2 presents a schematic of a vertical subsurface flow wetland.

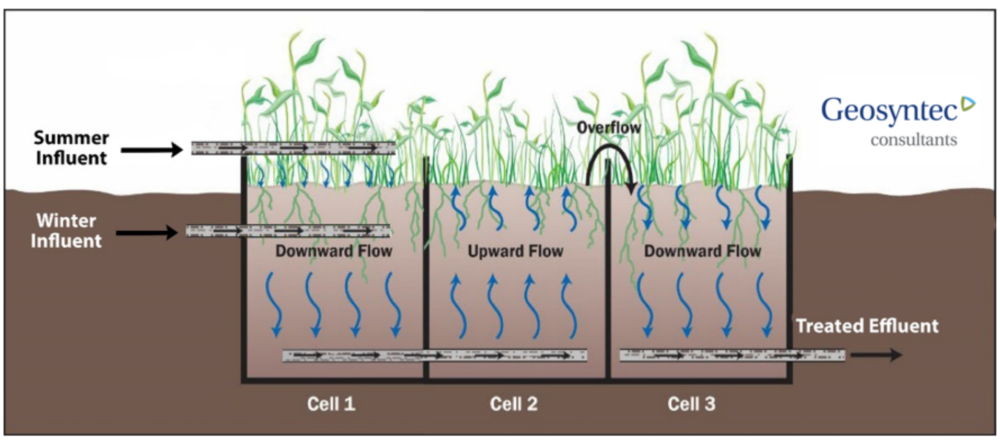

Figure 2. Schematic of a Three-Cell Subsurface Vertical Flow Wetland System

Much of the treatment success of a wetland system is dependent on the ability to affect oxidation and reduction (redox) conditions. Metal and metalloid treatment in wetlands can occur at faster rates when sub-oxic and anoxic conditions are achieved. A subsurface vertical-flow wetland system allows for the manipulation of redox conditions within individual treatment cells (i.e., alteration between aerobic and anaerobic/anoxic cells). This is especially important for the treatment of complex MIW, which may require aerobic treatment of various compounds including ammonia nitrogen, biological oxygen demand, chemical oxygen demand, and volatile organic compounds as well as anaerobic/anoxic conditions to accomplish treatment of metals, metalloids and inorganics. The manipulation of redox conditions is accomplished by adjusting water levels within treatment cells coupled with addition of organic carbon (e.g., mulch, wood chips) as an electron donor source for microorganisms in the anoxic treatment cell(s) to facilitate target treatment mechanisms.

The operation of constructed wetlands in cold weather climates can be a challenge; however, operation of subsurface wetlands extends the zones in which cold-climate operation of these systems can be operated. Depending on the location and climate, these wetlands can be cycled between winter and summer operation to effectively treat impacted water year-round.

Vertical flow wetlands, such as the example hybrid vertical subsurface flow wetland system (Figure 2) have a significant advantage over surface or horizontal-flow wetlands most notably due to the design of isolated treatment cells to combine aerobic with anaerobic processes which can target specific treatment mechanisms as required by site specific conditions. The depth of this type of design also provides advantages for cold climate treatment. Other advantages of this hybrid vertical design wetland system are summarized in Table 1.

Table 1. Summary of Treatment Efficacy Comparing a Hybrid Vertical Subsurface Flow Wetland System and Surface Flow Wetland

Efficacy Category	Hybrid Vertical Subsurface Flow Wetland System	Surface Flow Wetland
Cold Climate / Seasonal Treatment	Yes	Limited
Long Term Stability	Adaptable design; isolated treatment	Limited
Operation and Maintenance	Low; passive	Low; passive
Treatment Flow per Unit of Land Area	High	Low
Footprint	Mid	Large
Cost for Implementation	Mid	Low
Power Demand	Low	Low
Isolated Treatment Cells	Yes	Yes

One example constructed wetland case study is of an ongoing hybrid passive water treatment system that is being operated to support the closure of silver mine in Western USA through water quality management to meet discharge permit limits. Geosyntec conducted bench-scale and pilot-scale treatability testing to design a passive water treatment system to treat approximately 6,500 cubic metre per day (m^3/d) of MIW emanating from a mine portal prior to discharge to the receiving environment. Target treatment constituents included cadmium, copper, iron, lead, manganese, nickel, silver, and zinc. Bench-scale testing included: batch mesocosm testing for coagulation, flocculation and settling; manganese treatment with potassium permanganate; and adsorptive media tests using biochar, zeolite, and granular activated carbon. Pilot-scale testing involved construction of an approximate 130 m^3/d passive treatment system that was operated for 27 weeks. The pilot-scale system demonstrated that an in-mine pilot passive water treatment system could achieve metals removal in a remote, high altitude environment which includes cold temperatures, high flow variability, and variability in metals concentrations. Construction of the ultimate treatment system was a sulfate-reducing Gravel Bed Reactor (GBR™) followed by constructed wetlands as a polishing system. The passive treatment system provided a successful closure option for the mine with an approximate 75% cost reduction compared to active treatment. The hybrid treatment system is currently operating successfully at full-scale.

2.3 *In-Pit Lake Treatment*

In-pit lake treatment strategies are an example of a semi-passive water treatment systems which require little process equipment and minimal operational supervision (with the exception of chemical dosing equipment). Such systems could include adding chemical amendments directly to a MIW collection pond or pit lake and allowing treatment to take place in-situ or installing a passive treatment system as part of a naturally flowing system (e.g., backfilling the collection pond or pit lake, or installing reactive barriers). Either of these options would require occasional monitoring and maintenance to ensure proper operation. Modified in-pit lake treatment through backfilling a collection pond or pit lake with inert substrate is one method to increase surface area and biological film density to achieve sub-oxic conditions more readily in shallow water.

The microbial community within the collection pond or pit lake tend to use alternative electron acceptors if the process is energetically favorable under specific conditions such as redox potential, availability of carbon (organic matter), geochemical parameters (hardness, pH, alkalinity) and temperature. In the absence of DO, nitrate is usually consumed first, passing through a reduction pathway to nitrogen gas, next are selenite and selenate which can be reduced to elemental Se, while the sulphate is reduced to form sulphides.

For in-pit lake treatment systems where naturally occurring organic carbon is low, an external carbon source is provided through either a simple or complex media to serve as a source of electron donor for the microbial reduction of inorganic constituents. The carbon serves two purposes: 1) it increases the oxygen demand of the water and depletes DO resulting in anoxic conditions conducive for constituent reduction; and 2) it supplies carbon, an essential energy source for the growth and sustenance of the microbial community capable of degrading the constituent. Table 2 presents a summary of applications of in-pit lake treatment that have been documented in literature.

Table 2. Summary of Applications of In-Pit Lake Treatment for Mine Water Treatment*

Lake Name	Distribution Method
Berkeley Pit-Lake	Shore-based plant, lime applied using pipeline
Meirama Mine Pit-Lake	Liming of influent stream
Rävlidmyran Pit-Lake	Lime injected through a pipeline from trucks
Lake Senftenberg	Lime applied using hopper barges without mixing
Lake Geierswalde	Resuspension of lime from bottom of pit-lake and applied using sprinklers
Lake Bockwitz	Soda applied into the lake using air/solid mixture injection
Lake Hain	Shore-based plant, slurry applied using sprinklers and distributed via lake convective currents
Lake Bernstein	Limed using a commercial barge and underwater pipeline
Lake Scheibe	Shore-based plant for application of lime slurry and CO_2 for buffering
Lake Nero	Shore-based plant used to create slurry and applied via pipeline

**Gammons, C. H., & Icopini, G. A. (2020). Mine Water and the Environment, 39(3), 427–439*

The effectiveness of in-pit lake treatment systems is contingent upon successful implementation under site-specific conditions. Some of the essential site-specific conditions from an implementation perspective include geographic location and access to the pit lake with suitable geomorphology, resource availability within the area, shape and limnology of the pit lake being treated, seasonal access constraints and climatic conditions. Engineered cover systems and other similar systems to maintain sub-oxic conditions can improve the effectiveness of the treatment technologies.

2.4 *Permeable Reactive Barriers (PRB)*

A PRB is a wall or trench of reactive material that is constructed in the ground, perpendicular to groundwater flow which allows impacted water to contact the reactive zone for treatment. A PRB can utilize biological or physical-chemical treatment mechanisms. In biological PRB systems treatment of dissolved metals requires an initial reduction of sulphate via microbial processes. Bacteria use sulphate (SO_4^{2-}) as the terminal electron acceptor in the oxidation of the labile carbon to carbon dioxide (CO_2). If any aqueous metals (e.g., iron, zinc, cobalt, cadmium, and others) are present, these metal cations will precipitate as metal sulphides. Carbon substrate based PRBs containing a wide range of solid-phase organic carbon (e.g., plant mulch, compost, wood chips, saw dust, etc.) have been successfully implemented for the treatment of dissolved metals in groundwater. A biological treatment zone can also be established (sometime called a permeable reactive zone or biobarrier) through injection of liquid carbon media directly into groundwater, for example emulsified vegetable oil or similar substrate can be injected into permanent wells installed along the remedial alignment. In physical-chemical PRB systems abiotic adsorptive media (e.g., zeolite, phyllosilicate minerals, activated alumina, activated carbon, ZVI, and others) or material that can stimulate chemical fixation (e.g., phosphate-based minerals) or pH adjustment (e.g., calcium carbonate, lime, caustic magnesia, steel slag, and others) is housed within a fixed bed or barrier. In some cases, amendments such as elemental sulfur, phosphate minerals, reductants such as ZVI and others can provide system performance benefits for both biological and abiotic treatment technologies. Table 3 presents an example of the treatment amendments and processes that have been applied by Geosyntec to treat water impacted with zinc, cadmium, cobalt and nickel.

Table 3. Example Amendments and Water Treatment Processes that have been used in a Permeable Reactive Barrier Deployment for Treatment of Metals-Impacted Water

Amendments and Processes	Zinc	Cadmium	Cobalt	Nickel
Biosequestration, microbial reduction and/or precipitation	X	X	X	X
ZVI-based approaches - reductive precipitation of dissolved metals and sorption on surface adsorption sites of ZVI	X	X	X	X
Phosphate based materials, such as Apatite, for chemical fixation as insoluble phosphate mineral phases	X	X	X	X
Zeolite, phyllosilicate minerals or activated alumina	X	X	X	X
Iron mineral sorbents- added as a treatment wall or generated *in situ* via biostimulation or hydrolysis of injected iron salts	X	X	X	X
Activated carbon and other sorptive solid carbon materials	X	X	X	X
Alkaline materials, such as calcium carbonate, lime, caustic magnesia, steel slag for acidic pH buffering and precipitation	X	X	X	X

One example PRB case study is of a ZVI-based PRB that was designed, constructed and operated to treat hexavalent chromium [Cr(VI)] in groundwater at an industrial site. A pre-design laboratory column study was conducted to determine the Cr(VI) removal capacity by a commercial ZVI source, including assessment of the influence of background inorganic chemistry on the removal kinetics and the rate of ZVI passivation under a continuous exposure to site water containing approximately 100 mg/L of Cr(VI). Using the obtained Cr(VI) treatment rate, the anticipated maximum Cr(VI) concentration and the site groundwater velocity, and the PRB design lifetime of 20 yrs, the dimensions of ZVI required for treatment was calculated. Based on the lateral and vertical distribution of the Cr(VI) plume at the PRB location, the design PRB length was 78 m and the PRB depth ranged from 1 m below ground surface (bgs) to approximately 12 m bgs in saturated silty sediments underlain by a heavy clay unit. The laboratory study demonstrated the tested commercial ZVI product was capable of treating Cr(VI) of up to 100 mg/L in site groundwater and the ZVI permeability loss due to precipitate formation was minimal and would not impact PRB performance. The PRB was successfully installed at the site using biopolymer-supported excavation and backfill.

2.5 *Alternative Water Management Technologies*

The implementation of water management at mine sites is crucial to limiting water contact with point sources and is typically implemented via water collection infrastructure to collect mine waste seepage and runoff water; and conveyance and diversion infrastructure to isolate clean water from mine waste solid and liquid storage facilities. Alternative means of water management using phytotechnologies such as TreeWell® technology and innovative source control technologies such as organic cover systems can limit mobilization of MIW at its source thereby minimizing the volume of impacted water that requires management and treatment.

Phytoremediation can be an appropriate treatment strategy for mine sites. Plant-based remediation technologies can be effective as either a sequestration/containment strategy or for accumulation and recovery of metals/metalloids from soil and/or groundwater. Plants can effectively remove inorganic constituents from impacted mine sites via root uptake. Once absorbed by roots, plants have the capacity to (i) sequester the metal in plant tissue and/or (ii) phytovolatilize the contaminant in a volatile and non-toxic form. The TreeWell® technology is an innovative type of phytoremediation that provides hydraulic control and contaminant sequestration from surface water and groundwater. The TreeWell® system uses a patented design to focus groundwater extraction from a targeted depth interval using a specialized planting unit; optimum planting media that promotes downward root growth and focuses groundwater uptake from a targeted depth interval. One example application of a TreeWell® system includes treatment of mercury-impacted groundwater at an industrial site. Approximately 200 TreeWell® planting units were installed over a one-acre area of a former water collection pond to prevent the flux of mercury impacted groundwater from discharging to the receiving environment. The magnitude of an inward hydraulic gradient to the TreeWell® plot grew each growing season for several years. The water treatment objectives for the project were achieved via hydraulic control, plant uptake and transpiration of target groundwater concomitant to metal sequestration in the root zone around each planting.

Innovative source control technologies can provide cost savings to mine waste management and provide improved containment of mine waste in storage areas. One example of source control is the use of organic covers systems to prevent air and water influx to mine waste storage piles. Potential benefits of organic covers include use of site and local materials as substrate for vegetation, waste reuse thereby supporting circular economy, and competitive cost compared to other types of cover systems, such as geosynthetic clay liners and subaqueous disposal. Organic covers are designed utilizing carbon layers from mulch or municipal compost. The organic material can mitigate mobilization of contaminants from mine waste through oxygen consumption through carbon degradation, preventing oxygen ingress and subsequent mineral oxidation; and reduction of water infiltration thereby mitigating seepage water contact. Table 4 provides a summary of mine sites that have implemented organic cover systems using a variety of organic substrates.

Table 4. Summary of Organic Cover Systems that have been Applied at Mine Sites for Source Control of Metals-Impacted Water

Organic Material	Site Name/Location	Commodity Mined
Pulp and paper biosolids	Copper Cliff Tailings[1]	Ni, Cu, Au, Ag
Mixed municipal compost and biosolids fertilizer	Strathcona Tailings[2,5]	Ni, Cu, Au, Ag
	Delnite Tailings[3]	Au
Sawdust and municipal biosolids	East Sullivan Mine[4]	Au

Notes: 1) Beauchemin et al., 2018; 2) *Asemaninejad et al., 2021;* 3) Paktunc, 2013; 4) Germain et al., 2009; 5) McAlary et al., 2019.

3 FROM INNOVATION TO IMPLEMENTATION - STRATEGIES FOR SCALE UP

Successful implementation of an innovative technology requires proof of concept and demonstration to gain buy in from stakeholders, regulators and rightsholders. This is achieved through an assessment of the technology along the scale of technology readiness and can involve laboratory treatability testing to field pilots and demonstrations. Treatability testing conducted in batch mesocosm and flow through vertical and horizontal benchscale columns provides the capability of testing all stages of technology development. To increase level of certainty on performance, costing and design requirements it is important to identify any technical or design uncertainties prior to field demonstration and full-scale design.

Figure 3 presents a summary of the stages of innovative technology scale up, from technology screening and conceptualization to full-scale technology deployment. The Level of certainty of the engineering design, treatment performance, and long-term reliability of the technology increases with through each stage of technology testing.

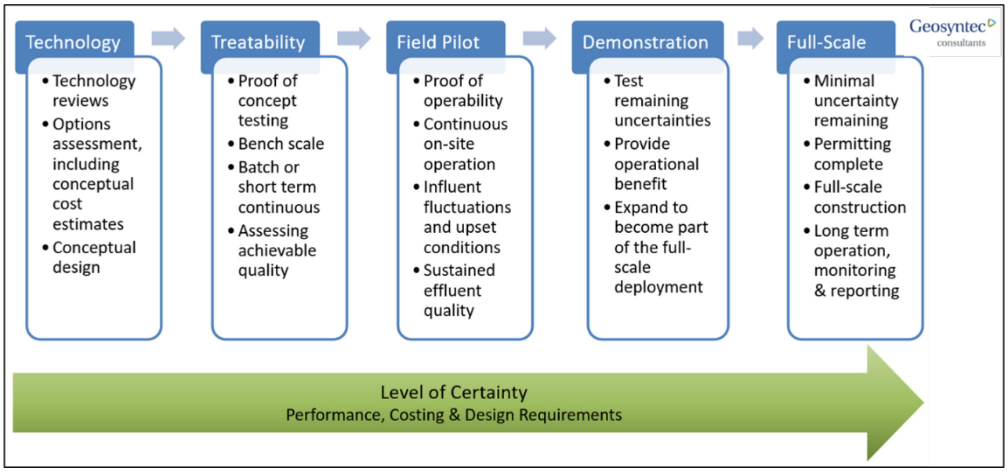

Figure 3. The Stages of Innovative Technology Development to Full-Scale Implementation

Example field-scale mobile treatment pilot systems are presented in Figure 4. In Figure 4A, constructed wetlands approach was piloted to achieve pretreatment of site leachate using Geosyntec's mobile wetlands pilot system termed "Wetlands-on-Wheels" (WOW). In Figure 4B, site water is treated in 5 horizontal large-scale columns within a temperature-controlled container. The system provides a relatively low discharge water volume that allows site specific treatment uncertainties such a low temperature, carbon dose substrate type and mechanism, and other operational variables to be tested to evaluate potential worst case effluent water quality for various operational scenarios. This information is used to inform engineering design for field pilot, demonstration, and full-scale water treatment system, and provides confidence to environmental regulators, stakeholders and rightsholders on the upper and lower bound scenarios that may be anticipated using the technology, thereby allowing development of robust system and water quality monitoring programs and mitigation procedures to manage off specification water should the tested scenarios occur.

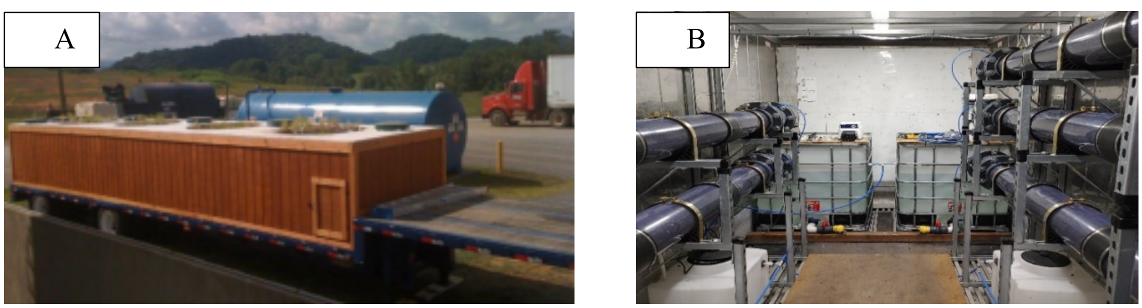

Figure 4. Example Field-Scale Mobile Treatment Pilot Treatment Systems

4 CONCLUSIONS

Passive and semi-passive treatment of inorganic constituents is gaining acceptance at many mine sites. The use of GBR, constructed wetland, pit lake in-pit treatment, and PRB treatment techniques can provide flexible MIW treatment options with lower operational costs when compared to active treatment systems. Passive and semi-passive treatment approaches can be a potential option to treat MIW to meet regulatory requirements for operational and closed mines and should be further investigated to validate potential site-specific risks, challenges, and opportunities. The selection of an appropriate passive and semi-passive treatment system can depend on a number of factors including impacted water flowrate, footprint, climate, available local carbon and gravel materials, etc. Alternative water management technologies including phytotechnologies like TreeWells® and organic covers systems can provide hydraulic and source control to limit deleterious constituents from leaching from waste rock and tailings and thus prevent mobilization of MIW at its source. Passive and semi-passive treatment and management of MIW can lead to many advantages when compared to active treatment; primarily, the ability to operate these systems with lower operating cost and oversite which is a major advantage in longer term water quality management for closure planning of mines.

5 ACKNOWLEDGEMENTS

The authors would like to acknowledge Trevor Carlson, Greg Corcoran, Ron Gestler, Jason Kersteins, Brent Miller, Brian Petty and Andrzej Przepiora at Geosyntec Consultants Inc. for their contributions of technical findings from technology development and pilot programs included herein.

6 REFERENCES

Asemaninejad, A., Langley, S., Mackinnon, T., Spiers, G., Beckett, P., Mykytczuk, N., Basiliko, N. 2021. Blended municipal compost and biosolids materials for mine reclamation: Long-term field studies to explore metal mobility, soil fertility and microbial communities. Science of the Total Environment, 760(15), 143393. https://doi.org/10.1016/j.scitotenv.2020.143393

Beauchemin, S., Clemente, J. S., Thibault, Y., Langley, S., Gregorich, E. G., & Tisch, B. 2018. Geochemical stability of acid-generating pyrrhotite tailings 4 to 5 years after addition of oxygen-consuming organic covers. Science of the Total Environment, 645, 1643–1655. https://doi.org/10.1016/j.scitotenv.2018.07.261

Duncan, W. F. A., Mattes, A. G., Gould, W. D., & Goodazi, F. 2004. Multi-stage biological treatment system for removal of heavy metal contaminants. The Fifth International Symposium on Waste Processing and Recycling in Mineral and Metallurgical Industries (pp. 469–483).

Germain, D., Tassé, N., Cyr, J. 2009. The East-Sullivan Mine Site : Merging Prevention and Treatment of Acid Mine Drainage. In: Proceedings of the 14th British Columbia MEND Metal Leaching/Acid Rock Drainage Workshop. Vancouver, BC, Canada. https://bc-mlard.ca/files/supporting-documents/2009-16a-GERMAIN-ETAL-east-sullivan-mine-prevention-treatment-amd.pdf

Heffernan, V. 2019. Genomics applications to wastewater start proving their worth. Canadian Mining Journal, April 2019, pp. 15-17.

Herbert, R. B., Winbjörk, H., Hellman, M., & Hallin, S. 2014. Nitrogen removal and spatial distribution of denitrifier and anammox communities in a bioreactor for mine drainage treatment. Water Research, 66, 350–360. https://doi.org/10.1016/j.watres.2014.08.038

Higgins, J., Mattes, A., Stiebel, W., & Wootton, B. 2017. Eco-Engineered Bioreactors Advanced Natural Wastewater Treatment. CRC Press. Report prepared for Teck Coal Limited.

[INAP] The International Network for Acid Prevention. 2009. Global Acid Rock Drainage Guide (GARD Guide).

[ITRC] Interstate Technology and Regulatory Council. 2003. Technical and Regulatory Guidance Document for Constructed Treatment Wetlands; Interstate Technology & Regulatory Council, December 2003.

ITRC (2013). Biochemical Reactors for Mining Influenced Waters.

Mancini, S., Cox, E., deVlaming, L., Bechard, K., James, R.E., Przepiora, A., & Risacher, F. (2019). Gravel Bed Reactors: A Water Treatment Technology for Industrial & Mining Applications. Article published in The British Columbia Environment Industry Guide, by Matrix Group Publishing Inc. for the British Columbia Environment Industry Association (BCEIA). May 2019, 19-20.

Martin, A. J., Jones, R. & Buckwalter-Davis, M. (2009). Passive and semi-passive treatment alternatives for the bioremediation of selenium from mine waters. B. C.'s 33rd Annual Miner Reclamation Symposium, Cranbrook, British Columbia.

McAlary M., Ptacek, C., Bain, J., Blowes, D., Fyfe, J., Marshall, S. 2019. Effectiveness of Organic Carbon Cover Systems on Sulfide-rich Tailings. In: Proceedings of the 24th British Columbia MEND Metal Leaching/Acid Rock Drainage Workshop. Vancouver, BC, Canada. https://bc-mlard.ca/files/presentations/2019-8-MCALARY-ETAL-effectiveness-organic-carbon-cover.pdf

Nancharaiah, Y. V. & Lens, P. N. L. (2015). Ecology and Biotechnology of Selenium-Respiring Bacteria. *Microbiology and Molecular Biology Reviews*, 79(1), 61–80.

Nielsen, G., Hatam, I., Abuan, K. A., Janin, A., Coudert, L., Blais, J. F., Mercier, G. & Baldwin, S. A. (2018). Semi-passive in-situ pilot scale bioreactor successfully removed sulfate and metals from mine

impacted water under subarctic climatic conditions. Water Research, 140, 268–279. https://doi.org/10.1016/j.watres.2018.04.035
Paktunc, D. 2013. Mobilization of arsenic from mine tailings through reductive dissolution of goethite influenced by organic cover. Applied Geochemistry, 36, 49–56. https://doi.org/10.1016/j.apgeochem.2013.05.012
Rezadehbashi, M., & Baldwin, S. A. (2018). Core Sulphate-Reducing Microorganisms in Metal-Removing Semi-Passive Biochemical Reactors and the Co-Occurrence of Methanogens. Microorganisms, 6(1), 16. https://doi.org/10.3390/microorganisms6010016
Seervi, V., Yadav, H.L., Srivastav, S.K. & Jamal, A. (2017). Overview of Active and Passive Systems for Treating Acid Mine Drainage. IARJSET, 4(5), 131–137. https://doi.org/10.17148/IARJSET.2017.4525
Simon, F.G., Meggyes, T., & McDonald, C. (2002). Advanced Groundwater Remediation: Active and Passive Technologies. Thomas Telford Publishing.
Skousen, J., Zipper, C. E., Rose, A., Ziemkiewicz, P. F., Nairn, R., McDonald, L. M., & Kleinmann, R. L. (2017). Review of Passive Systems for Acid Mine Drainage Treatment. Mine Water and the Environment. *Springer Berlin Heidelberg*.
Sobolewski, A. (2005). Evaluation of Treatment Options to Reduce Water-Borne Selenium at Coal Mines in West-Central Alberta. Report prepared for Alberta Environment Water Research Users Group, Edmonton. https://open.alberta.ca/dataset/456eee9c-86d5-46e6-bc2e-e605c6599eba/resource/b96ac61e-78db-4b2c-b0d5-40d9c0bf772e/download/3877073-2006-evaluation-treatment-options-reduce-water-borne-selenium.pdf
[USDIBR] US Department of the Interior Bureau of Reclamation. (2011). Reclamation Managing Water in the West: Western Water and Power Solution Bulletin. Research and Development Office – Denver, Colorado. Bioreactors Remove Selenium from Water at Reduced Cost. Bulletin No. 30, September 2011.
[USEPA] US Environmental Protection Agency (2000). Constructed Wetlands Treatment of Municipal Wastewaters Manual. EPA/625/R-99/010.
USEPA (2014). Reference Guide to Treatment Technologies for Mining-Influenced Water.
Vaccari, D.A., Strom, P.F., & Alleman, J.E. (2006). Environmental Biology for Engineers and Scientists. *Wiley-Interscience*. pp. 97
Zagury, G. J., & Neculita, C.M. (2007). Passive treatment of acid mine drainage in bioreactors using sulfate-reducing bacteria: critical review and research needs. Ottawa Geo 2007, 1439–1446. https://doi.org/10.2134/jeq2006.0066
Zhang, Y & Frankenberger, W.T. (2005). Removal of selenium from river water by a microbial community enhanced with Enterobacter taylorae in organic carbon coated sand columns. Science of the Total Environment, 346: 280– 285

Clean water clean: Design and construction of a realigned diversion channel around the main pit and waste dumps at the Faro Mine Site, Yukon Territory, Canada

Geoff Karcher
Northern Contaminated Sites Program, Crown-Indigenous Relations and Northern Affairs Canada, Ottawa, Ontario, Canada

Michael Nahir
Parsons Corporation, Chelsea, Quebec, Canada

ABSTRACT: The Faro Mine Complex is an abandoned open pit lead-zinc mine located in the Yukon Territory, Canada. The mine was a key economic driver in the Yukon while it was in operation. At one point it was one of the largest open pit lead-zinc mines in the world. The mine was abandoned in 1998, after almost 30 years of operation and has been in care and maintenance since. Metal leaching and acid rock drainage (ML/ARD) are major problems at Faro due to the large volumes sulfidic waste rock and tailings near to water courses. An environmental assessment for the final remediation is currently being reviewed by the Yukon Environmental and Socio-economic Assessment Board (YESAB). The mine site is in the traditional territory of the Kaska First Nation and is upstream of the Selkirk First Nation who rely on salmon harvesting as a food source.

Routine monitoring identified increasing zinc concentrations in the receiving water at the site's downstream compliance point. Focused monitoring and hydrogeological assessment were completed to determine the source zone. Following a year of detailed investigation and implementation of an interim mitigation, it was determined that the best course of action was to advance a portion of the final remediation plan as an urgent work. This urgent work includes the diverting the natural watercourse into a new lined channel that is vertically and horizontally separated from the former creek where impacted water discharge is occurring. Integration of this urgent work into these future remediation plans is an important consideration.

This paper will walk through the realignment design and key considerations, discuss the channel construction, which is currently underway, and outline some of the main design and construction challenges.

1 BACKGROUND

1.1 *Site History*

Significant lead-zinc ore deposits were first discovered in the Anvil Range near what would become the Town of Faro in 1953. Mine development began in 1969 and the Faro Mine Site was officially opened on January 27, 1970 by the Anvil Mining Corporation (later Cypress Anvil Mining Corporation) and operated continuously until 1982. In 1979, Cypress Anvil purchased the nearby Grum property which was also developed for lead-zinc extraction. Concentrate production at the Faro mill was suspended in 1982 as a result of poor economic conditions and in 1984 all operations ceased.

Starting in 1985 and until 1998 a series of owners operated discontinuously at the Faro Mine Complex. On April 21, 1998 an interim receiver was appointed to handle the company's assets and conduct care and maintenance operations. This continued until February 28, 2009. The Government of Canada worked with the Yukon Government to manage the site until 2018. Since then the Government of Canada has retained full responsibility for care and maintenance and remediation planning at the site.

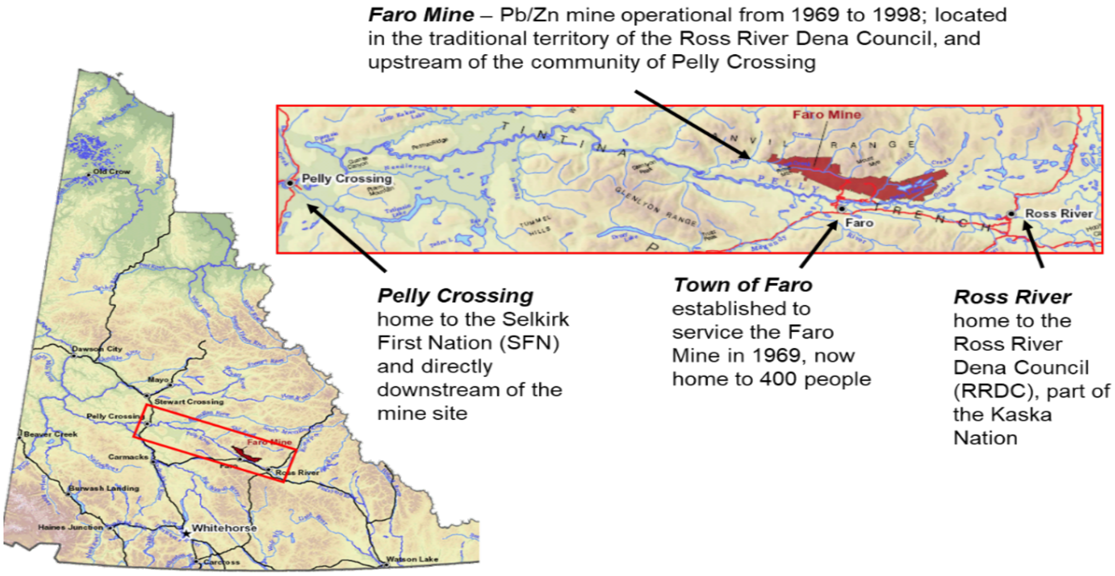

Figure 1. Faro Mine Site Location

The mine site is in the traditional territory of the Kaska First Nation and is upstream of the Selkirk First Nation who rely on salmon harvesting as a food source.

1.2 *Remediation plan*

The site is in care and maintenance pending completion of design, environmental assessment and water licensing prior to implementation of the remediation. Objectives for care and maintenance and the final remediation were developed with stakeholders and are to:

1. Protect human health and safety
2. Protect and, to the extent practicable, restore the environment including land, air, water, fish and wildlife
3. Return the mine site to an acceptable state of use that reflects pre-mining land use where practicable
4. Maximize local and Yukon socio-economic benefits
5. Manage long-term site risk in a cost-effective manner

The mine site is highly contaminated from tailings and waste rock primarily due to the acid leaching of zinc and other metals formed from geologic reactions accelerated by mining. The mass of tailings at the Faro Mine Site is 57 million tonnes behind three dams spanning an area of 205 hectares. The main waste rock pile surrounding the main pit is 260 million tonnes spanning an area of 335 hectares. See Figure 2.

Figure 2. New Diversion Construction Area

The main features of the remediation plan are to:

1. Keep clean water clean by extending and upgrading non-contact water diversion channels to convey the PMF in most cases;
2. Collect and treat all contaminated water by improving and expanding contact water collection systems and building a new water treatment plant;
3. Stabilize and revegetate landforms by re-shaping, covering, revegetating and establishing surface drainage on the waste rock and tailings;
4. Upgrading tailings dams and spillways to withstand the maximum credible earthquake and PMF
5. Demolition of buildings and infrastructure not required post remediation; and
6. Develop a post remediation performance monitoring and adaptive management plan

2 URGENT WORK REQUIREMENT

Water quality at the site continues to degrade which has necessitated the implementation of urgent works. In this context urgent works can be considered as the implementation of select final remediation measures in advance of the full remediation project. The North Fork Rose Creek (NFRC) Realignment Project was identified as an urgent work and has two parts, the non-contact water diversion channel (NCWD) and the contact water collection system (CWS).

2.1 *Adaptive Management*

In October 2013, routine monitoring identified elevated levels of Zinc from an unknown source at the site's downstream monitoring location, X14 (circled in orange, Figure 3). Additional monitoring identified elevated concentrations of zinc at locations NF1 and NF2 (circled in yellow, Figure 3). These stations are located immediately upgradient and downgradient of a rock drain located in the mine site's main haul road. At this location the haul road is constructed of waste rock fill on top of a rock drain to a depth of more than 70 metres bisecting NFRC.

Investigative drilling was completed at NF2 and NF1 in spring and summer 2014 to delineate and intercept what was believed to be a low volume high concentration seep from the immediately adjacent waste rock dumps. This program was not successful. In the Fall of 2014 Environment and Climate Change Canada (ECCC) issued a Letter of Direction to Crown Indigenous Relations Northern Affairs Canada and the Yukon Government requiring that steps be taken to immediately stop the deposit of a deleterious substance into Rose Creek.

In January 2015, an interception system was installed to collect a portion of the water exiting the downstream side of the rock drain. This system was operated during the winter low flow season until 2017 but was dis-continued due to its marginal effectiveness in terms of load capture.

2.2 *Decision to advance to UW*

Based on the inability of investigative drilling to identify a source, the in-effectiveness of the implemented SIS and the requirements stated in the Letter of Direction from ECCC a decision was taken to advance the design and implementation of a 1.9 km section of the NFRC diversion channel, a component of the remediation plan, as an urgent work.

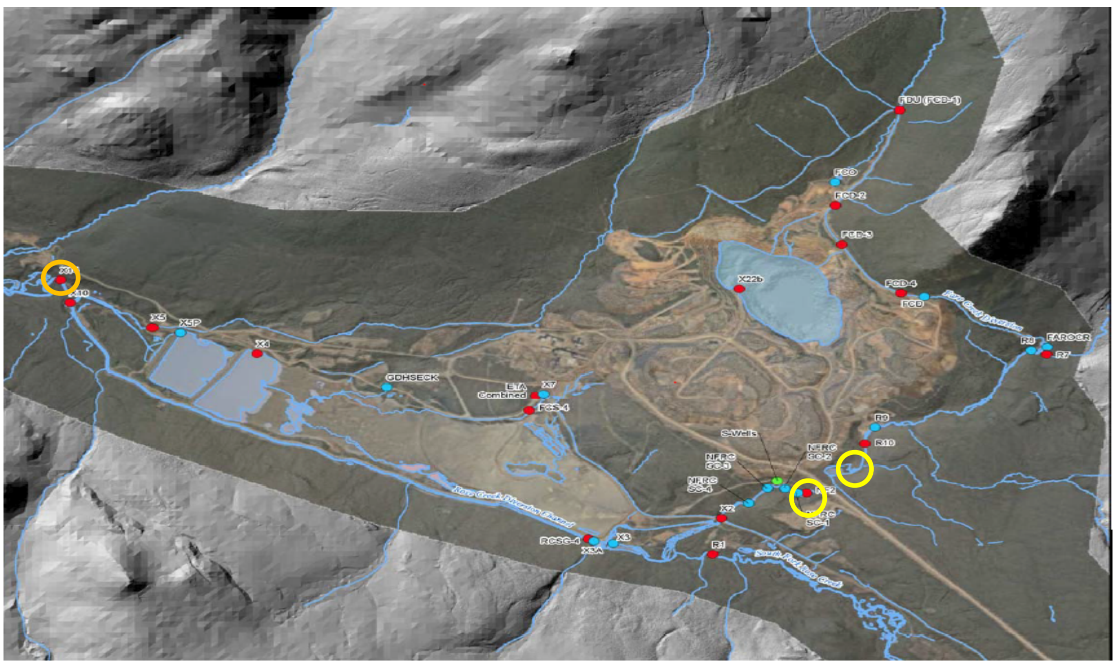

Figure 3. Faro Monitoring Stations

3 PROJECT DESIGN

3.1 *Overview*

The overarching objective of this urgent work, to “keep clean water clean”, will be achieved through hydraulic separation of clean water in a in a new channel. The new diversion is separated horizontally and vertically from the natural channel. Capture and conveyance of remaining contact “contaminated” water for treatment will be completed concurrently as a separate project.

CIRNAC engaged BGC Engineering to provide options, design and specifications. BGC acted as the owner’s engineer.

CIRNAC also contracted Parsons as the construction manager (CM) to oversee the project and hire various subcontractors to execute the different elements of the work. The CM also undertakes responsibilities as the Environmental Manager with sub-contractors undertaking monitoring and providing specific expertise.

3.2 *Climate*

The Faro Mine Site is located within the Central Yukon Basin climate zone (Smith et al. 2004). The climate is characterized as sub-arctic continental. The mean annual air temperature is approximately -2°C. The hottest month is July with a mean of +12ºC and coldest month is January with a mean of -15ºC. The average annual mean precipitation is 443mm. The Faro mine is in a zone of discontinuous permafrost and the NFRC is in a sporadic permafrost area. One other important consideration from a construction perspective is hours of daylight. In Faro, this ranges from a high of 18.8 hours in June to a low of 5.8 hours in December.

3.3 *Non-Contact Water*

Initial discussions between Canada, the Yukon Government and consultants took place in February 2015. A draft Design Basis Report was issued on August 31, 2015 followed by a Preliminary Final Design Basis Report on March 31, 2016. In April 2016, a change in project governance required that new design contracts be established and the lead designers for this work changed.

Through 2016 and the first half of 2017, the new designer assessed the existing conceptual designs. Based on this assessment and outcomes of internal and external reviews 5 alternative layouts were developed and were considered against the 2016 "base case" conceptual design. Field programs were completed and included over 80 boreholes, 200 test pits, a test excavation and down hole geo-physics. Alternatives were assessed against the following:

Alternatives Criteria Assessed:

- Implementation and constructability
- Effectiveness and longevity
- Remediation plan integration
- Contract risks
- Construction water management risks
- Earthwork quantities
- Diversion channel
- Design & construction schedule risks
- Environmental considerations
- Estimated contact water collection and risk

A conceptual design report was issued in July 2017. Further integration between the urgent works designers and the overall remediation plan design team was completed to ensure that the design of the NCWD was consistent with the overall remediation plan for the site. The selected option consists of a 1.9 km long vertically and horizontally separated engineered channel through the NFRC valley. Clean water enters the channel through an inlet dam and is returned to the existing NFRC water course at a location below the mine haul road and upstream of the mine access road. Construction in the dry is achieved through the use of a constructed 1/5-year construction diversion channel.

A detailed design for the new clean water diversion was completed in April 2018 (BGC 2018c) and early works construction was initiated in Fall 2018. Substantial construction was completed fall 2020.

3.4 *Contact water*

Collection of contact water is important in reducing loading of contaminant to Rose Creek. Figure 4 shows that the NCWD re-connects with the natural creek above X2. There is a risk that remaining surface water flow and groundwater could impact the NFRC channel downstream of this confluence.

The project team elected to take a phased approach to the design and implementation of the CWS. This decision was based on a number of factors including:

- The design of the NCWD was further advanced. A phased approach allowed implementation of the NCWD to advance while the CWS concepts were developed.
- The impact of the NCWD on the groundwater flow regime was uncertain. Transient changes in the flow systems will occur following diversion.
- A phased approach allows for better integration with overall remediation design.

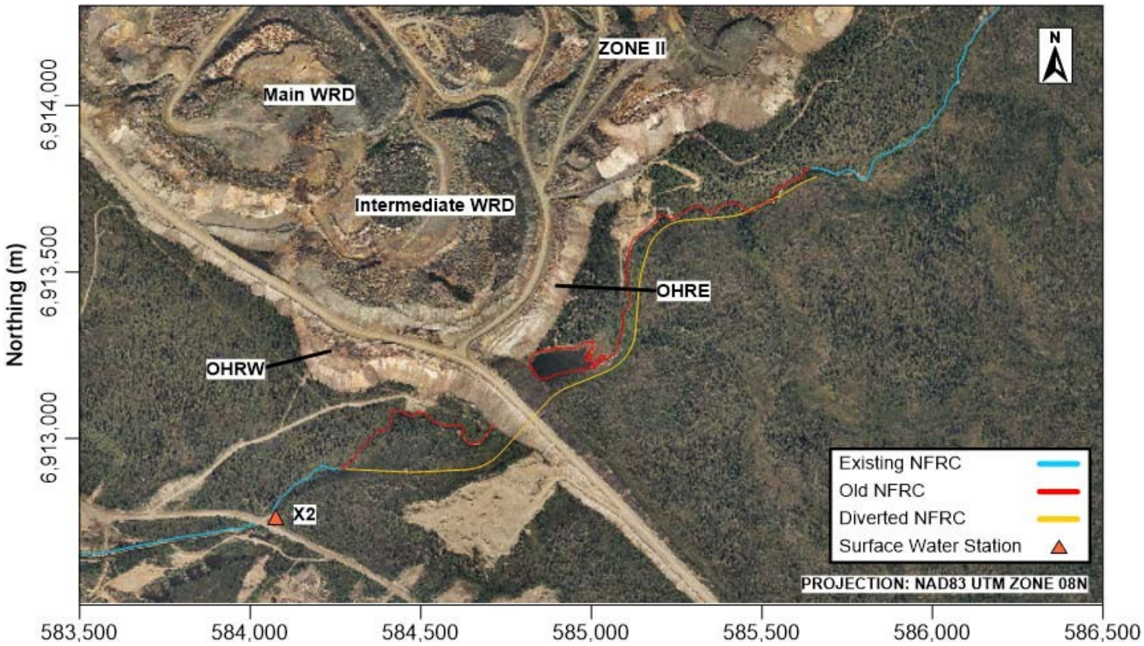

Figure 4. Channel Layout

To support the phased approach the project team undertook a detailed options analysis, implemented a contact water monitoring program and has advanced the design of an interim contact water collection system.

3.4.1 *Detailed Options Analysis (DOA)*

The DOA was completed in August 2018 and evaluated options for the interception, collection and conveyance of shallow groundwater and baseflow in the old NFRC channel. The stated initial objective for the contact water system was to improve water quality at station X2 (see Figure 4).

A total of 14 options were initially considered. Each was a combination of pumping wells, with and without shallow trench collection at one of 3 locations. Locations are shown in Figure 5. These were evaluated against 6 criteria including collection quantity and quality, residual impact, longevity, constructability, maintenance and operability, and cost. From this initial evaluation three were carried forward for detailed evaluation. These were:

Option 1: Location 2 – shallow trench,
Option 2: Location 1 – shallow trench, and
Option 3: Location 2- 10 m well with shallow trench.

Selection of the preferred long-term contact water collection option was deferred until monitoring and data collection, as envisioned through the contact water monitoring program, was completed.

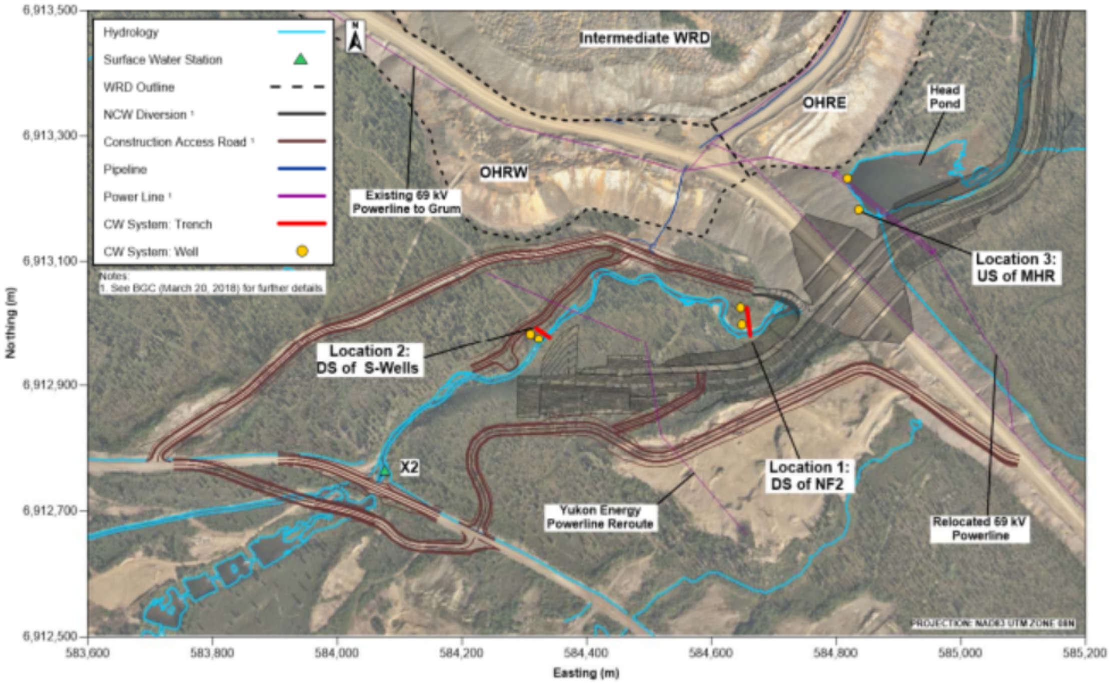

Figure 5. Contact Water Collection Locations

3.4.2 *Contact Water Monitoring Program (CWMP)*

The objective of the CWMP is to observe the pre-diversion geochemical and hydrogeological conditions in the NFRC valley and monitor potential changes to groundwater flow and contact water loading following implementation of the NCWD. This monitoring program was started in Fall 2018 and will extend a minimum of 1 year after the NCWD is commissioned, currently envisioned through Fall 2021.

3.4.3 *Interim contact water collection*

While monitoring will inform and support optimization of long-term contact water capture, the ability to collect contact water at the time of NCWD commissioning is required to mitigate the risk of continued impacts downstream of the confluence of the NCWD and the natural NFRC channel.

Location 2 (see Figure 5) was selected for implementation of the interim solution. This location is preferred because it is located nearer the downstream confluence reducing opportunity for contact water by-pass. It is also a strong candidate location for the permanent collection system potentially allowing for phased expansion and better integration with the remediation plan.

4 PROJECT IMPLEMENTATION CHALLENGES AND OPPORTUNITIES

4.1 *Fisheries Act Requirements*

The NFRC is fish habitat. As such the project required a Fisheries Act Authorization (FAA) from Fisheries and Oceans Canada. The requirements of the FAA created two challenges for the project. First, the project was deemed to result in a net reduction of fish habitat requiring the inclusion of habitat compensation in the design. Options for habitat compensation in the project area are limited and required the evaluation of several options to achieve the required compensation. The FAA also required erection of fish barriers and completion of a fish salvage prior to construction. Barrier design was a challenge due to the need for a temporary barrier that could withstand ice-loading over multiple winter seasons.

4.2 *Integration with Remediation Design*

Design of the final remediation plan for the Faro Mine Site is being completed by other designers. During detailed design for the NCWD the final remediation plan was only developed to a conceptual level. Integration of the urgent works detailed design with conceptual level remediation plans required active project management by CIRNAC and refinements by both designers to meet shared objectives.

4.3 *New Construction Management approach to procurement*

The IFT package for the NCWD was developed as a single contract during design. To meet socio-economic requirements within the interim construction manager's contract work was broken out into 13 smaller packages. This approach helped the project to achieve one of its over-arching objectives to maximize local and Yukon socio-economic benefits but resulted in significant additional work and some delay for the designers to re-package the IFT documents.

4.4 *Construction Challenges*

4.4.1 *Permafrost and frozen conditions*

The construction access roads, CDC, NCW Diversion Channel, and Inlet Dam were constructed within the NFRC floodplain, where permafrost soils were present. Geotechnical investigations in the NFRC valley showed that permafrost, where present, is generally warmer than -1°C and of thickness ranging from approximately 2 m to greater than 20 m. Permafrost excavated to warm ambient temperatures and long summer daylight hours, or backfilling with warm construction fills, resulted in permafrost warming and occasional thaw settlement. Permafrost can also impede surface and shallow ground water from infiltrating and result in a wet and poorly drained ground surface. Where permafrost is absent, the groundwater table within the NFRC floodplain was within a few metres of the existing ground surface. Based on construction experience with the permafrost test cut in the NFRC Valley (BGC March 22, 2016), the surficial frozen material was excavated with an excavator, since the permafrost temperature is generally close to 0°C. A 1.6 m total thickness composite-lined channel layer system was proven to provide thermal insulation to sections in permafrost to mitigate against thawing and differential settlement. On the other hand, stripped areas that had been exposed for extended cold periods and cleared of snow cover during the winter prior to excavation could drive frost into the ground and result in a cold frozen crust made it harder to excavate. In this case, bulldozers equipped with a ripper tooth were used to break up the frozen crust.

4.4.2 *Groundwater*

In some areas, excavation exposed groundwater seeps within the seasonal active layer (above the top of permafrost), from below the base of the permafrost (when penetrating the permafrost), or within the excavation in non-permafrost areas. The groundwater was managed to facilitate channel subgrade preparation, particularly when excavation was below the groundwater table. For these situations, the construction included pumping and treating exposed groundwater and then placement of coarse grained rockfill to improve workability and a woven geotextile fabric to improve the shear resistance of the foundation.

4.4.3 *Borrow Sources Challenges*

The primary planned source of non-acid generating clean fill (NAG) for the new channel was the haul road which needed to be excavated to facilitate the diversion. However, the haul road was found to have insufficient NAG rock requiring development of new sources at greater expense and increased project risk as in some cases the sources were not tested. The Potentially Acid Generating (PAG) and unusable rock ratio were high. Frozen large stones that accounted for 10-15% of the total volume had to be removed. The borrow sorting approach was slow and added to schedule. As a result, the borrow was separated by a block sorting method, four different classes had to move to different areas depending on classification. Class 1 was useable NAG, class 2 was untested boulders, class 3 was PAG, and class 4 was approved oversized NAG but suitable for riprap. Because of borrow delays some of the planned winter work was moved to the spring where the thaw created other challenges such loss of thermal blanket. Also construction restrictions due to conflicts with the bird nesting window (May 3rd – Aug 23rd) and the fish spawning window (April 1-July 1) became a factor.

Figure 6. Geomembrane liner in Construction Diversion Channel (May 2019)

Figure 7. Construction of thermal blanket on main channel (Apr 2020)

Figure 8. Completed yet-to-be-commissioned new channel along-side temporary construction channel on right. (June 2020)

5 LESSONS LEARNED

A number of key lessons were learned from the design and implementation of the NFRC urgent works projects and will be applied to future projects at the Faro Mine Site.

- It was more difficult than anticipated to separate and advance a component of the final remediation plan as an urgent work given that many dependencies and interactions were not fully understood. Additional effort to further integrate the urgent works design into the overall remediation plan at the outset may have saved time overall.
- The decision to separate non-contact and contact water design to expedite the NCWD construction was the right decision. However, delay in confirming a contact water approach led to schedule becoming the driver for the interim CWS. Earlier focus on system design may have allowed for efficiencies.
- In some cases, expected borrow volume estimates fell short of construction requirements and borrow source ML/ARD (PAG) was underestimated. Development of additional sources and storage locations was required during construction. Additional confirmatory investigations or contingency planning ahead of construction would help to manage this risk.
- When using a construction manager, effort should be made to have the construction manager in place with sufficient time for their involvement in design and constructability review.

6 ACKNOWLEDGEMENT

Acknowledgement is expressed to BGC Engineering Ltd for their assistance in the development and review of this paper.

Determining the diffusional flux of radium-226 and its mineralogical hosts in submerged historical uranium mine tailings

Cheryl Wiramanaden, Cynthia Russel, & Tyler Nash
Minnow Aquatic Environmental Services, a Trinity Consulting Company, Guelph, Ontario, Canada

Deborah Berthelot, & Holly Heffner
BHP Canada Inc., Saskatoon, Saskatchewan, Canada

ABSTRACT: Uranium mining was undertaken in the Elliot Lake area of north-eastern Ontario for approximately forty years, until the early 1990's when most mines ceased operations. Some of the decommissioned mines used flooding as the closure option for tailings management areas (TMAs) to control pyrite oxidation and metal leaching, including radium-226, a long-lived radionuclide in the uranium-238 decay chain. Water overlying the TMAs is treated for pH and radium-226 prior to being released to receiving environments. As part of decommissioning approval processes, Environmental Impact Statements included modelling and predictions of how radium-226 in the overlying water and basin pore water would behave over time. While current radium-226 concentrations are within the predicted concentrations, 25 years have passed. Thus, a present-day investigation was conducted to estimate radum-226 diffusional flux from tailings, to characterize radium-226 control mechanisms in the tailings, and to identify the potential risks to compliance associated with changes in environmental conditions.

1 INTRODUCTION

1.1 *Background and Setting*

In the Elliot Lake area of north-eastern Ontario, Canada uranium mining took place for forty years, until the early 1990's. In this area, the uranium ore zone consisted of layers of pebbles, usually quartz, embedded in a sericitic, pyritic matrix. The uranium ore itself occurred as a mixture, predominantly composed of brannerite, uraninite, and monazite (MacLaren 1977). The former mines are generally located in the Serpent River Watershed (SRW), which is located between Sudbury and Sault Ste. Marie, Ontario. The watershed drains a land of 1376 km^2 and flows southward into the Serpent Harbour at the North Channel of Lake Huron. The SRW is a chain-lake system containing more than 70 lakes.

There are eleven decommissioned tailings management areas (TMAs) that are associated with the closed mining operations that were located in the SRW. The TMAs contain waste rock, tailings, and over time, have also received treatment solids in various locations. The tailings included pyrite (5 to 7%; CANMET 1998), some of which was deposited directly into a water body (i.e., a TMA), and in other locations, tailings remained beached and subaerial oxidation of pyrite was allowed to occur, prior to leveling and submergence. Once flooded, overlying water of the TMA was and is still treated with lime, when necessary, to control pH, and with barium chloride to treat for radium-226. Of the eleven TMAs, six were flooded, three were part of the study, and one, the Quirke TMA is presented herein. Decommissioning of the flooded Quirke TMA (Figure 1) was completed in 1997.

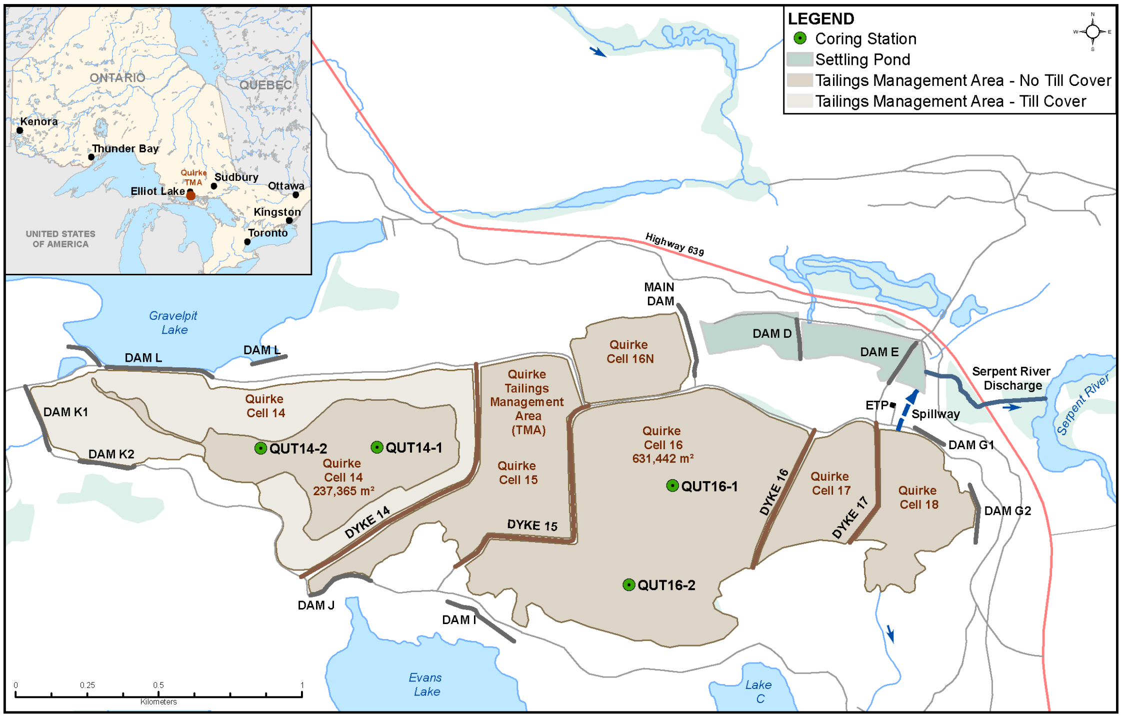

Figure 1: Map of Coring Stations at Quirke TMA, Elliot Lake, March 2017

1.2 *Study Objectives*

The main objective of the study was to determine the mechanisms that control the release of radium-226 from TMA sediments to the overlying water. A secondary objective was to then infer the stability of radium-226 in sediments, and to outline the change in environmental conditions necessary for an increase in radium-226 release to occur.

2 METHODS

2.1 *Approach*

Characterizing the TMA sediment in terms of radium-226 and potential for geochemical change in the future was achieved using various analytical techniques that, in combination, were used to fully characterize surface sediments within the TMA water bodies. To this end a winter field program, in March 2017, was conducted and involved the collection of sediment cores to provide depth profiles (0 to 6 cm) of surface sediment, pore water radium-226 concentrations, and supporting measures. In addition, surface sediment grabs were collected at each coring station for analysis of mineralogy (using X-ray diffraction; XRD), sequential extraction analysis (SEA), and total organic carbon (TOC).

Radium-226 is not a redox active element, it remains in the 2+ oxidation state under all environmental conditions. However, mineral hosts may become soluble based on changes in environmental redox conditions (such as iron oxyhydroxides and pyrite), changes in saturation index of a host (such as barite and gypsum), or changes in pH (such as calcite). Radium is remobilized based on the changing stability of its host, and scavenged based on the availability of a host (i.e., in changing environmental conditions, and in water compared to sediment; Figure 2). If radium-226 were remobilized in sediment, it will be dissolved in pore water, and will diffuse along a concentration gradient. Should radium-226 flux towards the sediment-water-interface (SWI), other mineral hosts may attenuate radium in sediment, lowering its flux. It was on this basis that potential for radium-226 remobilization was evaluated.

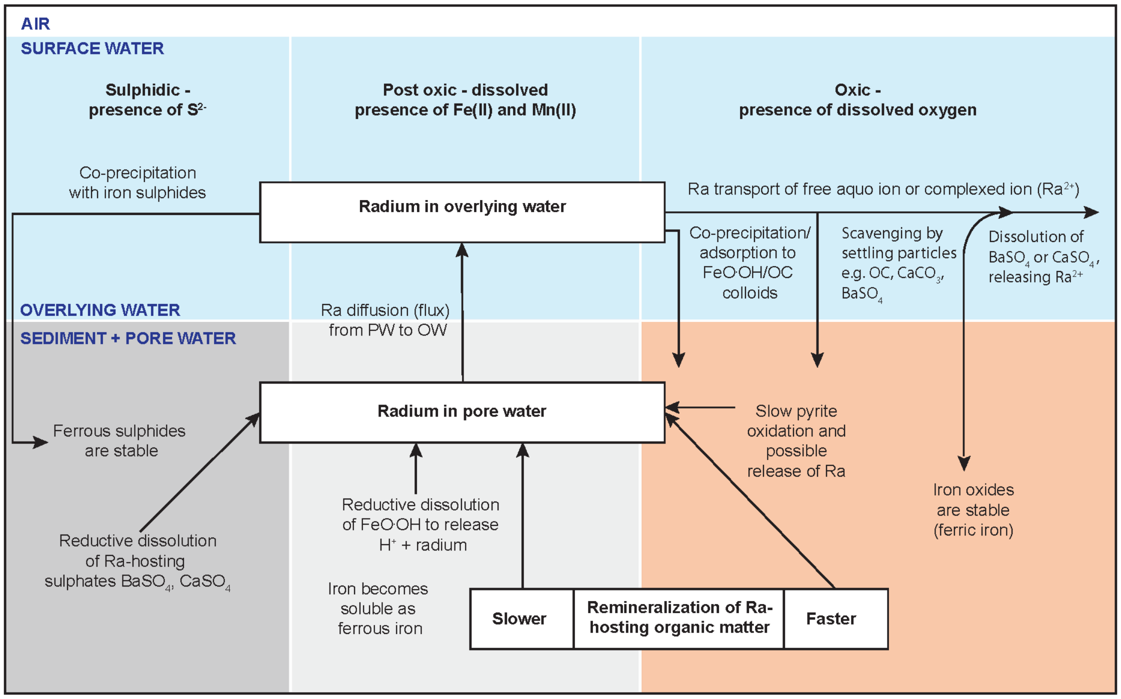

Figure 2: Schematic Outlining Radium Environmental Chemistry

2.2 *Field Sampling*

Three TMAs were sampled, however for the sake of brevity, only the Quirke TMA (two water bodies) are presented (Quirke Cell 14 and Quirke Cell 16), both cells had two sampling stations (Figure 1).

A water column profile of temperature, conductivity, dissolved oxygen, and pH was collected at each coring station using a YSI handheld portable field meter equipped with a sonde. One overlying water sample was collected (30 cm above the SWI) using a peristaltic pump with inline filtration (pore size 0.45 µm) and for analysis of dissolved metals, dissolved radium-226, and dissolved sulphate. All water samples were kept cold (4 to 9ºC) until they were shipped in coolers with ice packs, overnight to ALS Environmental in Burnaby BC for sulphate and metals analysis and to SRC Analytical in Saskatoon, SK for dissolved radium-226 analysis.

All cores (a minimum of three per station) were collected using a Tech Ops gravity corer in accordance with the Federal Technical Guidance Manual for Environmental Effects Monitoring (Environment Canada 2012). The Tech Ops cores were 10.16 cm in diameter, and the core tube was made of clear polycarbonate plastic. On collection, the cores were inspected to ensure the surface sediments were intact, ensuring that the core had been collected exactly perpendicular to the SWI, and then capped minimizing headspace at the top of the core. All cores were sectioned on site within 48 hours of collection and were stored in bags containing nitrogen gas if storage continued overnight. Prior to sectioning, photographs were taken, and observations noted. The cores were extruded into a sealed glove bag, which contained nitrogen gas to prevent unwanted oxidation of redox sensitive analytes during sample collection. The cores were sectioned in 2 cm increments using a polycarbonate core collar (to mark the 2 cm) and a box slicer (made from stainless steel). Three sections from the first core were placed into separate sealed plastic containers and kept in a nitrogen atmosphere, until they could be combined with sections from the same depths of the second core. The combined sediment sections, now considered one sample, were homogenized and a representative sub-sample was collected for porosity and bulk density analysis. The remaining sediment sample was placed in acid-washed centrifuge tubes (85 mL; polycarbonate) and capped securely. The capped centrifuge tubes were removed from the nitrogen atmosphere and placed in a centrifuge (Eppendorf Centrifuge 5804 R) that was refrigerated to 4ºC. The samples were centrifuged for 30 minutes at 10,000 g to separate the pore water from

sediment, according to the US EPA method for pore water extraction (US EPA 2001). Once centrifugation was complete, the tubes were brought back into the nitrogen atmosphere where pore water was extracted, using plastic transfer pipettes that had been purged with nitrogen gas, and samples were preserved (where necessary). For metals and radium-226 analysis, samples were preserved using nitric acid; for sulphide analysis, samples were preserved using zinc acetate followed by sodium hydroxide; and samples for anions analysis were not preserved. All preservative and sample vials for pore water analysis were provided by the analytical laboratories, consistent with the overlying water analysis. The remaining sediment in the centrifuge tubes were collected using disposable plastic spoons and sub-sampled into whirlpak™ bags for analysis of metals and radium-226 (0 to 6 cm), and XRD for the two lower sections only (2 to 6 cm).
Sediment surface grabs (0 to 2 cm) were also collected at the coring stations, using a Petite Ponar. These sediment samples were collected for analysis for XRD and Tessier SEA (Tessier 1979). Sediment samples for metals analysis were sent to ALS Minerals (North Vancouver, BC), sediment sampled for porosity and bulk density were sent to Flett Research (Winnipeg, MB), and sediment samples for XRD, radium-226, and SEA analyses were sent to SRC Analytical (Saskatoon, SK). All samples were sent overnight in coolers with ice packs.

2.3 *Data Analysis*

2.3.1 *Data Quality*

Upon receipt of the chemical data from ALS, SRC, and Flett Research, a data quality assessment was performed. This included assessment of field precision, laboratory precision and laboratory accuracy against the data quality objectives established at the outset of the project, by the laboratory. There was one exceedance of the pore water blank data quality objective for barium, which should be noted. Other than this single incident, the data quality was considered excellent.

2.3.2 *Diffusive Flux*

Pore water diffusive flux is based on the concentration gradient between the pore water metal concentration in the top sediment section (0 to 2 cm) and the metal concentration in the overlying water, provided this makes geochemical sense, particularly in terms of redox conditions of the sediment and overlying water. The flux estimate calculation considers diffusion and the random path-length that an ion diffuses through, given the particles that obstruct it. Other factors, such as attenuation of metals (e.g., by precipitation or co-precipitation, or biological uptake) in sediment, are not considered in the calculation of diffusive flux. Pore water diffusive flux calculations were made according to Ullman and Aller (1982), using literature-based ideal solution diffusion coefficients (Li and Gregory 1974) which were corrected for geometric tortuosity (which is related to porosity; Boudreau 1996) and the solution conditions of pore water to determine the bulk sediment diffusion coefficient, Dsi (of solute, i), according to Equation 1.

$$J_i = \Phi \times Ds_i \times \frac{dc_i}{dz} \qquad (1)$$

Where Ji is the flux of solute, i (mg/cm^2/yr); Φ is sediment porosity; and Dsi is the bulk sediment diffusion coefficient of solute i, and dc_i/dz is the concentration gradient of solute i, from the sediment to the overlying water.
The ideal solution diffusion coefficient (Doi) for a temperature of 4°C was used in all calculations. A literature value diffusion coefficient (Li and Gregory 1974) was corrected to 4°C using the Stokes-Einstein relationship (Li and Gregory 1974). The literature diffusion coefficient varies based on the redox and pH conditions of the pore water. Therefore, the diffusion coefficient from the literature was selected, with an understanding of pH, and particularly of redox, based on the pore water and sediment chemistry profiles. Porosity for each coring station was measured for the top 2 cm of sediment and used in the diffusive flux estimate calculations.

Redox changes will influence diffusion from pore water, in that oxidizing environments will lead to iron and manganese precipitation, and sulphidic environments will lead to iron sulphide precipitation. Both precipitates will scavenge radium, decreasing flux. However, flux calculations have assumed that all radium-226 in pore water will diffuse (i.e., under post-oxic conditions) thus, the most conservative approach has been taken. The diffusive fluxes are also dependent on the concentration gradient between pore water and overlying water radium-226 concentrations. Increased pore water radium-226 concentrations combined with decreased overlying water radium-226 concentrations will create a large concentration gradient, and subsequent increased flux. One risk associated with flux calculations is that the water samples collected represent a snapshot of pore water conditions, as opposed to a true annual flux.

To account for varying water quality in both overlying water and pore water, the radium-226 flux from each station was estimated using the greatest concentration gradient calculable based on known annual variability in surface water quality (at each station). There were insufficient data to determine an adequate range in pore water radium-226 within each TMA. A surface water factor (referred to as the 'annual range factor') was developed for each TMA using 2017 monitoring data of surface water radium-226 concentrations. This factor was calculated by taking the maximum radium-226 concentration for 2017 and dividing by the minimum radium-226 concentration. The pore water concentration was then multiplied by the annual range factor (to achieve a maximum concentration) and the overlying water concentrations was divided by the annual range factor (to achieve a minimum concentration). These combined calculations provided the greatest concentration gradient between pore water and overlying water, which would result in the greatest flux under the reasonable condition that concentrations would only vary by the same degree that is observed in the surface water.

2.3.3 *PHREEQC Modelling of Mineral Solubilities*

The stability of the most abundant radium-226 host phases were assessed using PHREEQC. Goethite and calcite are pH sensitive and were the dominant phases in several of the flooded basin sediments. Solubility curves with varying pH were created for iron and calcium in equilibrium with goethite and calcite, respectively, using the modelling software PHREEQC (Version 3.3.8.11728) and the thermodynamic database MINTEQ V4. Dissolution of goethite and calcite was modelled using water quality from coring stations where these minerals were present. The pH for these calculations ranged from pH 2 to 12 and was adjusted by adding sodium hydroxide (to raise pH) or hydrochloric acid (to lower pH). The water was not allowed to equilibrate with atmospheric gases (CO_2, and O_2) to be representative of the depth of the sampled water and redox conditions.

Several sulphate minerals were identified as significant hosts for radium-226 in the flooded TMA sediments. To assess the stability of anhydrite, barite, and gypsum, saturation indices were calculated using PHREEQC (Version 3.5.0-14000). Saturation indices were calculated using both the overlying water and pore water (0 to 2 cm) chemistry from each coring station. Although sulphate minerals are susceptible to reductive dissolution, the redox conditions of the modelled water were represented by the sulphate and sulphide values of the input data, and additional redox constraints were not necessary to account for the potential for sulphate reduction in the PHREEQC calculations.

3 RESULTS

3.1 *Mineralogy*

Mineralogy in Quirke Cell 14 surface sediment (stations QUT14-1, and -2) consisted of phyllosilicates biotite and muscovite, calcite, pyrite, and quartz (Table 1). Both stations were dominated by quartz (56.8% to 73.8%) and muscovite (16.2% to 36.8%) throughout the entire sampled depth (0 to 6 cm).

Table 1 Surface sediment mineralogy (wt %) in Quirke TMA coring stations, Elliot Lake, March 2017

Station Code	Sediment Section (cm)	Quartz	Phyllosilicates (clinochlore, biotite, muscovite)	Goethite	Pyrite	Calcite	Anhydrite	Gypsum
QUT 14-1	**0-2**	56.8	34.1	-	0.8	8.3	-	-
	2-4	62.3	36.8	-	0.9	-	-	-
	4-6	62.4	35.3	-	2.3	-	-	-
QUT 14-2	**0-2**	61.6	33.9	-	-	4.5	-	-
	2-4	67.6	31.5	-	0.9	-	-	-
	4-6	73.8	25.3	-	0.9	-	-	-
QUT 16-1	**0-2**	6.9	8.5	76.5	-	-	8.2	-
	2-4	8.1	-	33.6	5.6	52.7	-	-
	4-6	9.8	-	-	-	51.2	-	39.0
QUT 16-2	**0-2**	54.9	33	-	3.0	-	9.0	-
	2-4	63.7	29.2	-	1.7	3.7	1.7	-
	4-6	63.9	26.7	-	1.6	5.0	2.9	-

Biotite and muscovite (phyllosilicates) comprised a significant portion of the surface sediments in Quirke Cell 14. Biotite and muscovite adsorb radium-226 (Ames et al. 1983) and thus impede the diffusion of radium-226 to the overlying water, but overall are expected to play a small part in determining the behaviour of radium-226. Based on their abundance in the surface sediments (Table 1), calcite which can adsorb and co-precipitate radium-226 (as in Andrews et al. 1989), and historically pyrite (and associated acid production during oxidation), likely had a much greater effect on the behaviour of radium-226 in Quirke Cell 14 compared to other minerals. In addition, although not detectable in XRD analysis, SEA results suggested that amorphous iron oxyhydroxides were likely present which would also have a control on radium-226 cycling and fluxes (Section 3.2).

Mineralogy in Quirke Cell 16 (stations QUT16-1, and -2) included tailings-associated anhydrite, phyllosilicates (biotite and muscovite), pyrite, and quartz (all documented to be present in tailings waste; Paktunc and Davé 2002), and treatment-associated calcite and gypsum, (Table 1). A high abundance of goethite was present at station QUT16-1, more than could be attributed to pyritic oxidation alone (based on total iron concentrations). Thus, the high abundance of goethite was attributed to the presence of treatment solids, historical subaerial pyrite oxidation, and seepage of historical acidic, iron-rich water through the upstream Dyke 15 (Figure 1).

Sediment mineralogy data showed that the two Cell 16 sampling stations were quite different from each other. Station QUT16-1 was dominated by goethite in the surface sediments (76.5%) with calcite at depth (51.2 to 52.7%) and had a high abundance of pyrite (5.6%) in the mid-sediment section (2 to 4 cm). In contrast, station QUT16-2 sediment consisted primarily of quartz (54.9 to 63.9%) and muscovite (26.7 to 33.0%; Table 1) and contained pyrite and anhydrite throughout the sediment sections (0 to 6 cm). Iron oxyhydroxides (i.e., goethite, and amorphous) adsorb radium-226 (Sajih et al. 2014), and likely anhydrite will also adsorb radium-226 (based on the ability of gypsum to adsorb radium-226; Yoshida et al. 2009, Nirdosh et al. 1984) and can impede the diffusion of radium-226 to the overlying water. Thus, goethite, pyrite, and calcite are likely, directly or indirectly, the strongest influencers of radium-226 remobilization.

Although not detected by XRD at any station (Cell 14 or Cell 16), there were above background concentrations of barium in surface sediments at all stations, suggesting that barite was present, and this would also host radium-226 (Section 3.2).

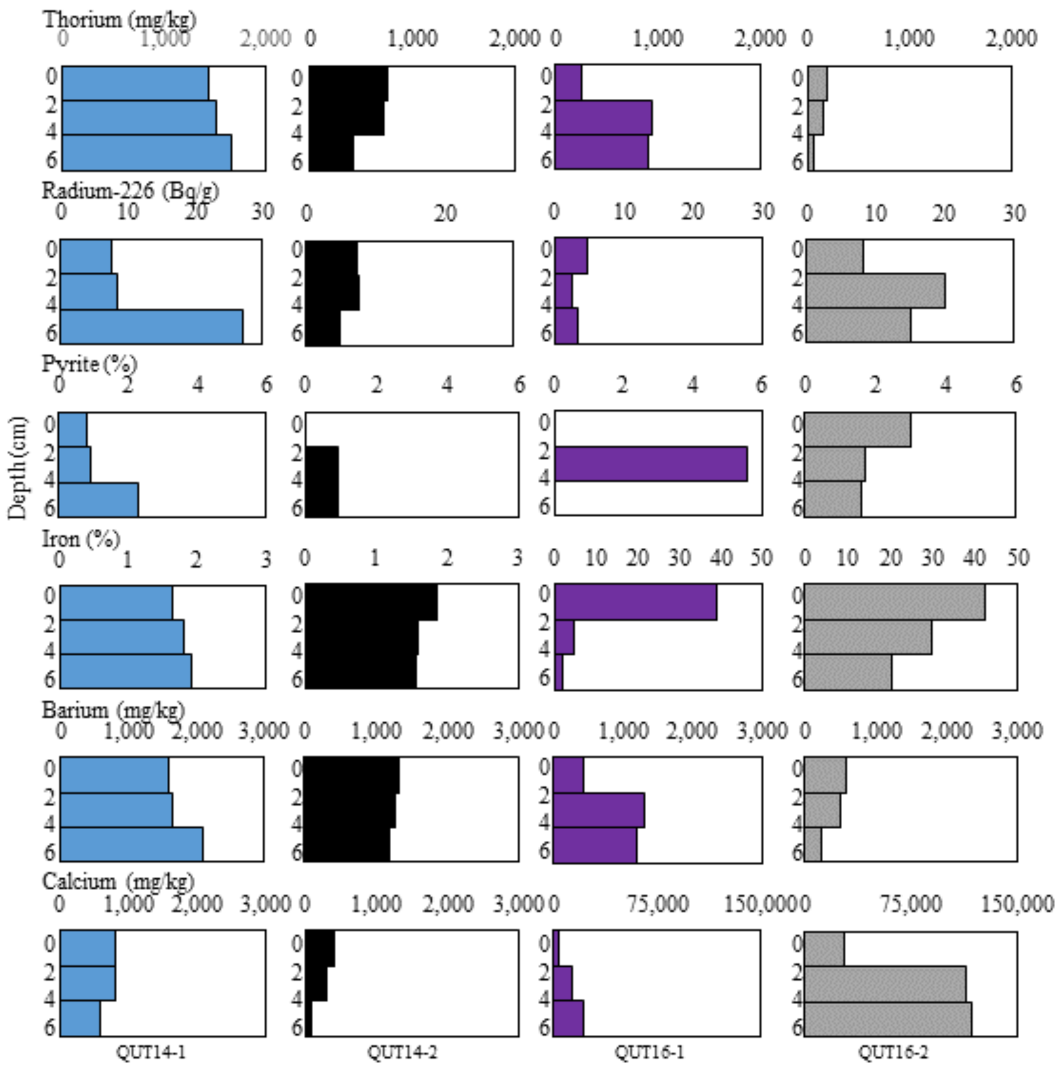

Figure 3: Thorium, radium-26, pyrite, iron, barium, and calcium in sediment cores collected from Quirke TMA, Elliot Lake, March 2017

3.2 *Sediment Chemistry and Sequential Extraction Analysis*

Radium-226 concentration profiles were similar to pyrite at station QUT14-1, while at station QUT14-2, pyrite was absent in surface sediments and did not show similarity to the radium-226 depth profile. This suggested that surface sediment pyrite has been depleted through pyrite oxidation. Further, changes in sediment radium-226 concentration with depth were somewhat similar to thorium at station QUT14-2, compared to station QUT14-1 where there was no pattern between thorium and radium-226. This suggested that at station QUT14-2 radium-226 has undergone a small degree of redistribution, potentially while tailings were beached, allowing subaerial oxidation of pyrite to occur. While at station QUT14-1 little radium-226 redistribution appears to have occurred. Sediment barium concentrations (0 to 6 cm) ranged from 1,195 mg/kg to 2,100 mg/kg at the two stations (Figure 3). These barium concentrations corresponded to 0.11% to 0.21% by weight, which is too low for detection by the XRD mineralogy (Table 1). However, barium concentrations were above the 95th percentile of references sediments in the area (795 mg/kg; Minnow 2021). Barium may be present due to historical treatment of radium-226, as barium chloride additions are commonly used to treat radium-226 and it may be present in the form of trace and possibly amorphous barite which hosts radium-226 through adsorption or co-precipitation (Skeaff 1977, Sebesta et al. 1981).

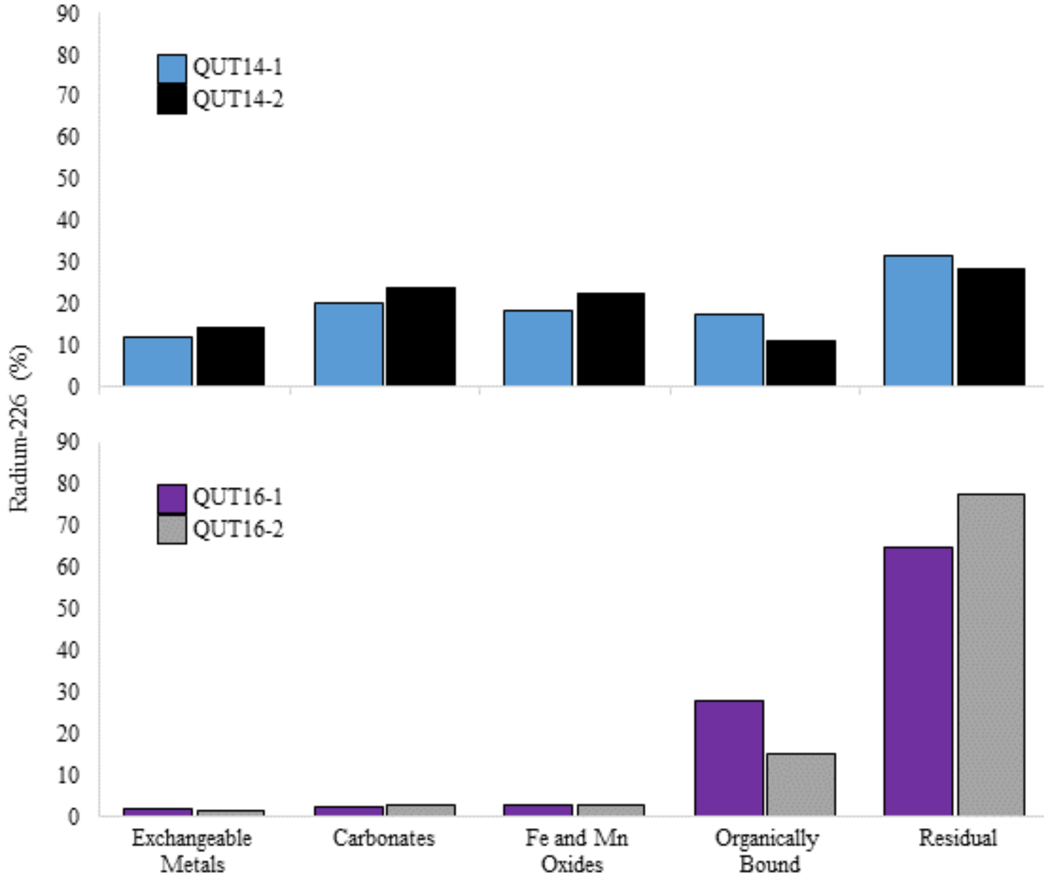

Figure 4: Proportion of radium-226 in sequential extractions of surface sediment from Quirke Cells 14 and 16, Elliot Lake, March 2017

Sequential extraction analysis of Cell 14 surface sediments showed that radium-226 was similarly hosted at both stations (Figure 4). Radium-226 was associated predominantly with the residual phase, this could include mineral hosts such as resistant sulphides (e.g., pyrite) and muscovite. The secondary host of radium-266 was the carbonate extraction. Calcite was detected in surface sediment at both Cell 14 stations likely formed due to added lime as part of the historical and ongoing treatment of Quirke TMA for acid neutralization; where, calcite would have formed as a secondary mineral. Calcite-associated radium-226 is susceptible to remobilization if pH were to decrease, which would be possible due to acid production from (e.g., subaerial) pyrite oxidation. The third most abundant radium-226 extraction, particularly at station QUT14-2, was the iron and manganese oxides phase (Figure 4). Radium-226 extracted in these phases is less strongly sequestered than radium-226 hosted in the residual or carbonate phases. These iron and manganese oxides are susceptible to reductive dissolution (Tessier et al. 1979), which is expected to occur because of the redox status of the sediments at both stations (i.e., post-oxic surface sediments in both stations).

At Quirke Cell 16, sediment depth profiles of radium-226 were not similar to any single analyte that may be expected to correlate to radium-226 solubility (e.g., barium, calcium, iron, thorium, or pyrite; Figure 3). Instead, the radium-226 depth profiles may be influenced by a combination of the presence of calcium (likely calcite) and iron (likely goethite; Table 1 and Figure 3). It was hypothesized radium-226 was not hosted by calcite, but that calcium and radium-226 may be controlled by the same mechanism, where *in situ* liming in Cell 16 (as part of care and maintenance) results in calcite formation, and iron precipitation; iron oxides were present in both crystalline (at station QUT16-1) and amorphous (hypothesized at station QUT16-2) form. It was hypothesized that iron oxides (goethite) at station QUT16-1 have attenuated radium-226 over time (from acidic seepage and pyrite oxidation), and at station QUT16-2 pyrite oxidation in the surface sediment was not complete, and radium-226 was likely hosted by both tailings (i.e., anhydrite and / or muscovite, an aluminosilicate; Table 1), and amorphous iron oxyhydroxides.

The Cell 16 SEA showed that radium-226 was similarly distributed among extractions at both stations, with the majority of radium-226 being in the residual fraction and the secondary host of radium-226 was the organically bound fraction (Figure 4). Very little radium-226 was extracted in the carbonate bound fraction which ruled out the association of radium-226 with calcite, despite the high abundance of calcite in sediment. The majority of radium-226 being hosted in the residual phase suggested that changes in pH and weak changes in redox status are unlikely to remobilize radium-226. It is possible that radium-226 in the residual fraction included radium-226 hosted by anhydrite, which would become unstable under sulphidic conditions, or when the anhydrite saturation index falls below zero (e.g., with decreasing sulphate concentrations).

3.3 *Redox Status in Overlying Water and Sediment*

In Cell 14, the dissolved oxygen concentrations in overlying water at both the deeper station, QUT14-1 (9.89 mg/L, 3.2 m) and the shallower station, QUT14-2 (9.77 mg/L, 1.8 m), were indicative of oxic conditions (Figure 5). Concentrations of the redox active metals (manganese and iron) in the overlying water were trace, which provided further evidence that both stations were oxic in the overlying water (data not shown). Surface sediment pore water (0 to 2 cm) at both stations was inferred to be post-oxic, based on the presence of soluble (reduced) manganese and iron, and at station QUT14-2 the sediment started to become sulphidic at depth (based on very low sulphide concentrations at 4 to 6 cm; data not shown). At station QUT14-2, pore water remained post-oxic throughout the sediments (0 to 6 cm). The oxidant demand necessary to create sulphidic conditions in Cell 14 sediments was predominantly associated with the presence of pyrite (concentrations of total organic carbon were low, ranging 1.1 to 1.4%).

In Cell 16, the dissolved oxygen concentration in overlying water was considerably higher at the shallower station QUT16-2 (3.8 m; 5.20 mg/L) than at the deeper station QUT16-1 (6.0 m; <1.0 mg/L; Figure 6). Station QUT16-2 overlying water was transitioning to post-oxic due to the measurable dissolved oxygen concentrations that were in rapid decline with depth, and the high, typically post-oxic, concentrations of iron and manganese (Figure 6). Station QUT16-1 overlying water was post-oxic, based on non-detectable dissolved oxygen in combination with elevated concentrations of dissolved iron and manganese in the overlying water, indicating that they were present in their reduced, more soluble forms.

Figure 5: Profiles of pore water chemistry and overlying water dissolved oxygen at Coring Stations Quirke Cell 14, Elliot Lake, March 2017

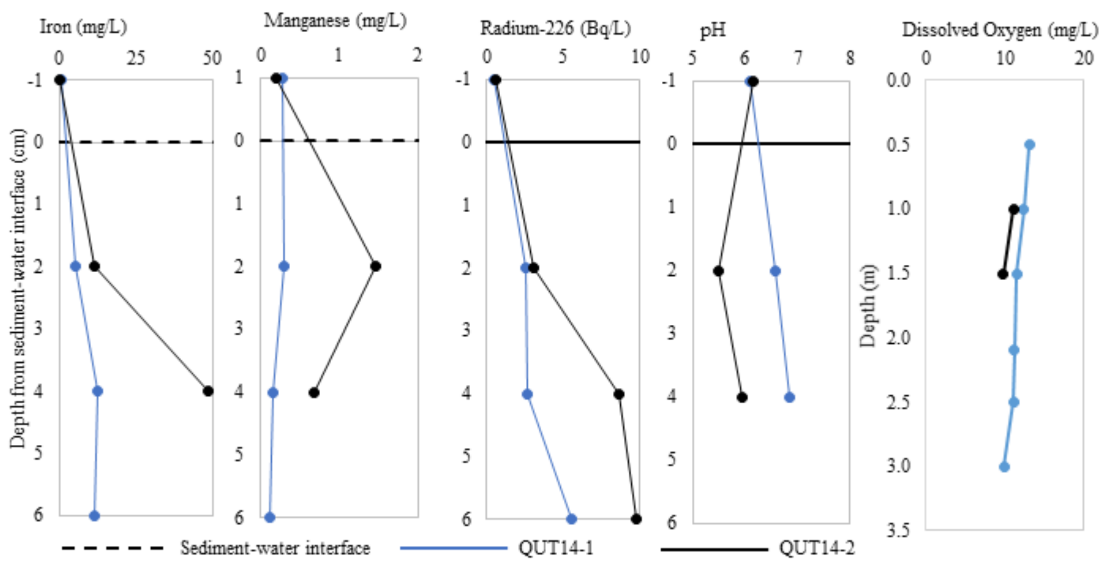

Figure 6: Profiles of pore water chemistry and overlying water dissolved oxygen at Coring Stations Quirke Cell 16, Elliot Lake, March 2017

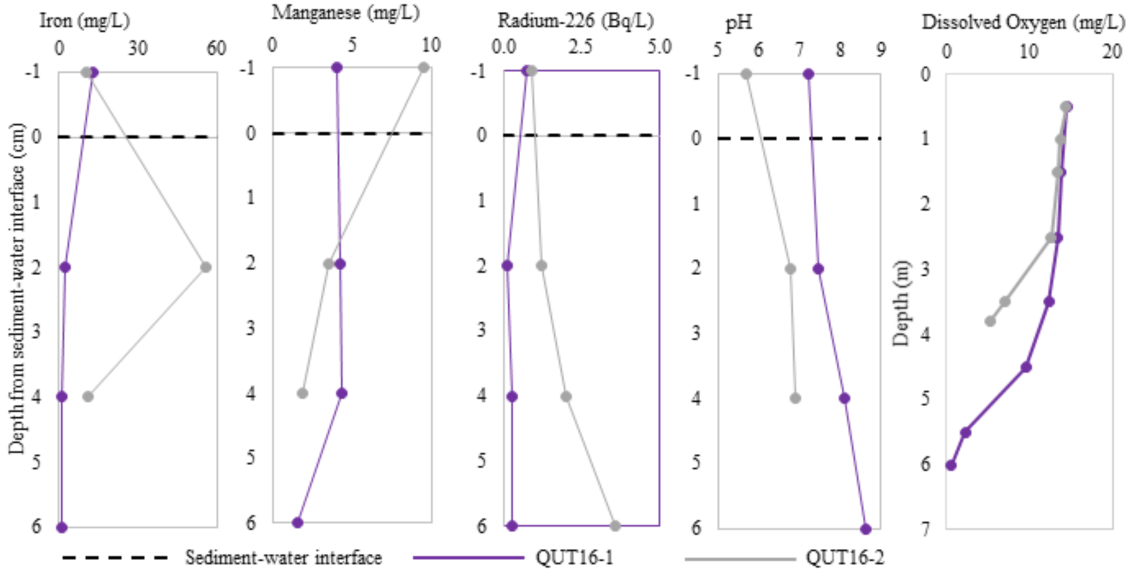

Sediment pore water did not have detectable levels of sulphide at any sediment depth, at either Cell 16 station (data not shown). However dissolved iron concentrations were decreasing at the deepest sediment section (4 to 6 cm) of each profile, possibly indicating the beginning of a sulphidic zone, but the sediments at both stations were considered post-oxic throughout (0 to 6 cm). Organic carbon concentrations in Cell 16 surface sediment ranged 0.4 to 0.9%, thus oxidant demand was assumed to be controlled primarily by pyrite.

3.4 *Radium-226 Diffusive Flux Estimates*

Radium-226 fluxes were very similar among stations QUT14-1 and QUT14-2 (881 $Bq/m^2/yr$ and 846 $Bq/m^2/yr$ respectively). Calculated as a year-round flux based on winter flux estimates (202 MBq/yr) these flux estimates were comparable to year-round flux estimates based on late summer fluxes (ranging 166 MBq/yr to 659 MBq/yr; EcoMetrix 2011). Fluxes were also calculated using an annual range factor, to account for annual variation, and the upper limit (based on observed annual variability) fluxes were calculated to be 2,215 $Bq/m^2/yr$ and 2,108 $Bq/m^2/yr$ respectively for stations QUT14-1 and QUT14-2.

Fluxes were quite different between the two stations (0 $Bq/m^2/yr$ at QUT16-1 and 51.3 $Bq/m^2/yr$ at QUT16-2). To calculate an annual loading to Quirke Cell 16, the two fluxes were applied equally across the cell area. As station QUT16-1 had a zero radium-226 flux, the annual loadings for the whole cell were low compared to Quirke Cell 14. An upper limit for the flux estimate was calculated using the annual range factor which resulted in an increased flux for station QUT16-2, from 51 to 392 $Bq/m^2/yr$ (zero flux for station QUT16-1).

In general, the lower flux estimate from Quirke Cell 16 (compared to Cell 14) was ascribed to the higher abundance of attenuating minerals (i.e., goethite, some anhydrite, and the hypothesized presence of barite due to the deposition of treatment solids) at station QUT16-1, and the hypothesized presence of a higher amount of the more reactive amorphous iron oxyhydroxides at station QUT16-2. Amorphous iron oxyhydroxides are more labile than goethite and will undergo reductive dissolution more readily than goethite, a crystalline mineral.

3.5 *Geochemical Stability of Minerals Hosting Radium-226*

Despite winter ice cover, the overlying water in Quirke Cell 14 was oxygenated (Figure 5). Surface sediments were post-oxic and became sulphidic at depth, suggesting a strong oxidant demand in the sediments, likely due to pyrite. Previous work at nearby stations found that the overlying water was also post-oxic during the summer (June and July; Martin 2003), and flux estimates conducted more recently in September 2009 (EcoMetrix 2011) were comparable to the flux estimates presented in the current study. SEA in Cell 14 showed that radium-226 was associated primarily with the residual extraction (Figure 4) followed by carbonates and then iron and manganese oxides. Therefore, a decrease in pH (in the carbonate component of the sediments) or a decrease in the oxidative potential (in the iron and manganese component of the sediments) would increase the rate of release of radium-226 to the overlying water. However, the majority of radium-226 would not be remobilized by changes in pH or small changes in redox potential, given that the majority of radium-226 was extracted into the residual fraction. Quirke Cell 14 did not have detectable concentrations of sulphate minerals that often control radium-226 remobilization (anhydrite, gypsum, and barite). Calculated site-specific saturation indices were consistent with non-detectable sulphate minerals, as both calcium sulphate (anhydrite and gypsum) and barite were either undersaturated or at equilibrium (Table 2). Likely, the largest risk to remobilization of Quirke Cell 14 radium-226 in sediment would be for sub-aerial (rapid) oxidation of pyrite, particularly at station QUT14-1 which still contained pyrite in the surface sediment. Station QUT14-1 was the deeper station of the two (3.2 m), and thus a large decrease in water level would be necessary for this to happen.

Quirke Cell 16 sediments had generally low radium-226 flux from sediments. Sediment at station QUT16-1 had a high abundance of goethite while at station QUT16-2, the high iron concentrations in sediment were associated with the less stable amorphous iron oxyhydroxide (i.e., not detected by XRD analysis), and this was likely the largest source of radium-226 flux, given that sediments were post-oxic.

Table 2: PHREEQC Calculated Saturated Indices of Sulphate Minerals in Overlying Water and Pore Water in Quirke Cells 14 and 16, Elliot Lake, March 2017

Station Code	Water Type	Input Concentrations (mg/L)			Saturation Index		
		Sulphate	Barium	Calcium	Anhydrite	Barite	Gypsum
QUT 14-1	Overlying	29.8	0.0744	11.9	-2.94	0.36	-2.58
	Pore (0-2 cm)	35.4	0.138	12.7	-2.86	0.68	-2.50
QUT 14-2	Overlying	27.6	0.0814	11.5	-2.99	0.37	-2.63
	Pore (0-2 cm)	48.5	0.354	23.3	-2.53	1.16	-2.17
QUT 16-1	Overlying	1230	0.0110	416	-0.49	0.57	-0.14
	Pore (0-2 cm)	1650	0.00776	460	-0.41	0.48	-0.06
QUT 16-2	Overlying	1260	0.0136	417	-0.49	0.67	-0.13
	Pore (0-2 cm)	1550	0.0196	489	-0.40	0.87	-0.04

Additional potential sources of radium-226 to the overlying water in Quirke Cell 16, were radium-226 hosted by adsorption only on anhydrite. Sequential extraction analysis showed that most radium-226 is hosted by the residual fraction, which would be more resistant to pH and redox changes, but based on the mineralogy of the sediments (assuming that the residual fraction included sulphate-mineral hosts; Liu and Hendry 2011), would be expected to undergo reductive dissolution at QUT16-1, should sediments becoming sulphidic. The saturation indices for the dissolution of anhydrite and barite were modelled using site-specific field measurements and showed that anhydrite and barite were at equilibrium (Table 2). This suggested that these minerals are not yet dissolving, but with the observed decreasing sulphate concentrations (Minnow 2021), they may start to dissolve, releasing radium-226.

At station QUT16-2, it was hypothesized that, other than amorphous iron oxyhydroxides and possibly anhydrite, radium-226 was hosted by stable minerals associated with tailings (i.e., muscovite, an aluminosilicate) and would unlikely be remobilized. Pyrite was present in surface sediment at station QUT16-2, and its exposure to oxidants, and subsequent oxidation and acidification may change the stability of iron associated with iron oxyhydroxides and goethite. Therefore, controlling water levels in Quirke Cell 16 is also important (to help inhibit the deepening of the oxic and post-oxic zones in sediments, which would result in increased pyrite oxidation).

4 SUMMARY

In general radium-226 in sediment with Cells 14 and 16 of the Quirke TMA was hosted by minerals that included iron oxides, which are unstable in post-oxic conditions, by pyrite (controlled by water levels), or by anhydrite (and potentially barite), which are currently stable but may dissolve based on saturation indices, as sulphate concentrations decrease, or if sediments become sulphidic. The potential for sediments to become sulphidic are limited given that the current oxidant demand appears to be controlled by pyrite, as opposed to organic matter. Thus the oxidant demand is unlikely to increase, unless concentrations of organic carbon increase significantly. Likely the main source of radium-226 to the overlying water is through radium-226 dissolution from reducing iron oxides.

Radium-226 diffusive fluxes were calculated at all stations, and within Cell 14 showed good agreement with each other and with previous studies. This suggested that conditions in the cell have not changed in a ten-year period and that controls on the TMA are performing well. There was a zero diffusive flux in QUT16-1 associated with the high abundance of treatment-associated minerals including calcite and attenuating iron oxides, combined with a relatively low diffusive flux at QUT16-2. This cell had relatively higher abundance of pyrite compared to Cell 14, the main control for pyrite oxidation is water cover.

Water levels over the sediment appeared to be the major controller for maintaining current radium-226 fluxes, without increasing them. A second controller may be the beginning of sulphate mineral dissolution, if sulphate concentrations decrease sufficiently to bring saturation indices below zero, particularly for anhydrite in Cell 16, and possibly barite in both cells. In general, the maintenance of radium-226 fluxes at current levels is associated with the continued management of water levels at the two cells (maintaining the current oxygen supply rate to the sediment), and continued monitoring of key indicator parameters including water level, sulphate, pH, and occasional monitoring of surface sediment TOC.

5 REFERENCES

Ames, L.L., McGarrah, J.E. & Walker, B.A. 1983. Sorption of uranium and radium by biotite, muscovite, and phlogopite. *Clays and Clay Minerals* 31: 343-351.

Andrews, J.N., Ford, D.J., Hussain, N., Trivedi, D. & Youngman, M.J. 1989. Natural radioelement solution by circulating ground waters in the Stripa granite. *Geochimica et Cosmochimica Acta* 53: 1791-1802.

Boudreau, B. 1996. The diffusive tortuosity of fine-grained unlithified sediments. *Geochimica et Cosmochimica Acta* 60: 3139-3142.

CANMET 1998. Wet barriers on pyrite uranium tailings laboratory lysimeter studies of oxidation, leaching, and limestone neutralization characteristics of uranium tailings and waste rock. MEND Project 2.13.1a. January.

EcoMetrix Inc. 2011. Cycle III Special Studies – Radium-226 release controls in Cell 14 at Quirke. Prepared for Rio Algom Ltd. February *in* Minnow 2009 Serpent River Watershed State of the Environment. Prepared for Rio Algom Ltd and Denison Mines Inc.

Environment Canada. 2012. Metal Mining Guidance Document for Aquatic Environmental Effects Monitoring. Environment Canada Report EEM/2002/1. June.

Li, Y.-H. & Gregory, S. 1974. Diffusion of ions in seawater and in deep0sea sediments. *Geochimica et Cosmochimica Acta* 38: 703-714.

Liu, D.J. & Hendry, M.J. 2011. Controls on ^{226}Ra during raffinate neutralization at the Key Lake uranium mill, Saskatchewan, Canada. *Applied Geochemistry* 26: 2113-2120.

MacLaren Limited, J.F., (MacLaren). 1977. Environmental Assessment of the proposed Elliot Lake uranium mines expansion. Volume 1. Background Information. March.

Martin, A.J., Crusius, J., McNee, J., & Yanful, E.K.. 2003. The mobility of radium-226 and trace metals in pre-oxidized subaqueous uranium mill tailings. *Applied Geochemistry* 18: 1095-1110.

Minnow (Minnow Environmental Inc.). 2021. Serpent River Watershed State of the Environment. Prepared for Rio Algom Ltd and Denison Mines Inc. *in prep*.

Nirdosh, I., Muthuswami, S.V., & Baird, M.H.I. 1984. Radium in uranium mill tailings – some observations on retention and removal. *Hydrometallurgy* 12: 151-176.

Paktunc, A.D., & Davé, N.K. 2002. Formation of secondary pyrite and carbonate minerals in the Lower Williams Lake tailings basin, Elliot Lake, Ontario, Canada. *American Mineralogist* 87: 593-602.

Sajih, M., Bryan, N.D., Livens, F.R., Vaughan, D.J., Descostes, M., & Phrommavanh, V. 2014. Adsorption of radium and barium on goethite and ferrihydrite: a kinetic and surface complexation modelling study. *Geochimica et Cosmochimica Acta* 146: 150-163.

Sebesta, F., Sedlacek, J., John, J., & Sandrik, R. 1981. Behaviour of radium and barium in a system including uranium mine waste waters and adjacent surface waters. *Environmental Science and Technology* 15: 71-75.

Skeaff, J.M. 1977. Survey of the occurrence of Ra-226 in the Rio Algom Quirke I Uranium Mill, Elliot Lake. CANMET Report No. 77-36. Department of Energy, Mines, and Resources, Canada.

Tessier, A., Campbell, P.G.C. & Bisson, M. 1979. Sequential extraction procedure for the speciation of particulate trace metals. *Analytical Chemistry* 51: 844-851.

Ullman, W.J., & Aller, R.C. 1982. Diffusion co-efficients in nearshore marine sediments. *Limnology and Oceanography* 27: 552-556.

Yoshida, Y., Nakazawa, T., Yoshikawa, H. & Nakanishi, T. 2009. Partition coefficient of radium in gypsum. *Journal of Radioanalytical Nuclear Chemistry* 280: 541-545.

Feasibility of bio-mediated carbonate precipitation for dust control at mine tailings facilities

Sean T. O'Donnell & Lucas de Melo
Geosyntec Consultants, Columbia, Maryland, USA

Lucas Carr
Geosyntec Consultants, St. Louis, Missouri, USA

Todd DeJournett
Geosyntec Consultants, Minneapolis, Minnesota, USA

Edward Kavazanjian Jr. & Hamed Khodadadi Tirkolaei
Arizona State University, Tempe, Arizona, USA

ABSTRACT: Microbially induced carbonate precipitation (MICP) and enzyme induced carbonate precipitation (EICP) offer the potential for effective short to long-term mitigation of windblown dust at mine tailings storage facilities (TSFs). Wind erosion of tailings is a significant challenge at many mine sites and must be controlled to comply with fugitive dust emissions requirements. Wind tunnel tests conducted on taconite and copper-molybdenum tailings specimens show that EICP-treated tailings exhibit resistance to wind erosion. Additionally, benchtop experiments with these tailings provide evidence that bacteria capable of catalyzing MICP may be present in some TSFs. A preliminary analysis comparing the cost and environmental impacts of these bio-mediated methods with other dust mitigation strategies, such as the application of polymer emulsions, salt solutions, paper pulping byproducts, and wood chip mulch, was used to identify specific obstacles to the field application of EICP and MICP as well as knowledge gaps where future research into these technologies may be required. Specific obstacles and knowledge gaps identified in this study include byproduct management from MICP and EICP, the availability of low-cost enzyme for EICP, and the longevity of the wind-resistant carbonate crust formed by MICP and EICP as compared with other short to long-term dust mitigation methods.

1 INTRODUCTION

Wind erosion of tailings is a serious issue at many mine sites that must be mitigated to comply with regulatory requirements, reduce potential impacts to human health and the environment, and avoid receiving negative feedback and perception from adjacent landowners and the general public. Wind erosion (and fugitive dust formation) at tailings facilities typically occurs due to desiccation in hot and dry climates or dry freezing in colder climates. Typical methods employed at tailings facilities to mitigate fugitive dust formation include management of the tailings basin water level to keep tailings saturated; application of salt solutions, polymers, or other short-term measures to suppress fugitive dust formation; and establishing vegetation for long-term stabilization of the tailings surface. However, each of these methods have limitations that make them undesirable, inapplicable, or non-cost-effective in some situations and at some tailings facilities. For example, managing the tailings basin water level to keep tailings saturated may work well at facilities in wet, warm climates where water is plentiful and freeze/thaw is not present, but could lead to operational challenges at facilities in dryer and/or cold climates. The water level can also not be kept so high that it destabilizes and/or reduces flood storage volume and the safe operation of the tailings facility. Further, short-term tailings stabilization techniques, such as polymer applications, salts, and mulches, have varying success rates for fugitive dust suppression, may lead to environmental impacts, and/or may be prohibitively expensive. Vegetation, while very effective at minimizing fugitive dust generation, may be difficult to establish in some climates and on some tailings, and may take multiple growing seasons to achieve full effectiveness. As such, new technologies are required to address the need for cost-effective, short-term, environmentally friendly fugitive dust mitigation at tailings facilities.

Two relatively new technologies with the potential for mitigating fugitive dust formation at tailings facilities are microbially induced carbonate precipitation (MICP) and enzyme-induced carbonate precipitation (EICP) (Meyer et al., 2011; Hamdan and Kavazanjian, 2016). MICP and EICP work by altering the geochemistry in an aqueous environment to favor the precipitation of carbonate minerals (e.g., by increasing pH and alkalinity). If formed on the tailings surface, these carbonate minerals could bridge surficial tailings particles to form a thin wind-resistant and potentially water-resistant crust. Although many biological processes can induce carbonate precipitation, the most studied process for MICP and EICP is ureolysis, catalyzed by the urease enzyme. Urease works by hydrolyzing urea ($CO(NH_2)_2$) into carbon dioxide and ammonia; in aqueous environments, the ammonia may speciate to form ammonium (NH_4^+), driving up the pH and facilitating the formation of carbonate minerals when suitable cations (e.g., calcium, Ca^{2+}) are also present. The net urease-catalyzed precipitation reaction for calcium carbonate ($CaCO_3$) is shown below.

$$CO(NH_2)_2 + 2H_2O + Ca^{2+} = CaC0_3 + 2NH_4^+ \quad (1)$$

The urease enzyme required to catalyze the ureolysis reaction may be produced by microbes (MICP) or isolated prior to treatment and added separately as a component of the treatment solution (EICP). MICP may be achieved using either non-native microbes added as part of treatment (Meyer et al., 2011), a technique known as bio-augmentation, or native microbes stimulated in-situ (Gomez et al., 2018), a technique referred to as bio-stimulation. EICP may be achieved using commercially available laboratory grade urease enzyme (Hamdan and Kavazanjian, 2016), or more cost-effective plant-derived urease extracts (Khodadai Tirkolaei et al., 2020).

Preliminary studies indicate that EICP and MICP are effective for mitigating fugitive dust formation from natural soils (Meyer et al., 2011; Hamdan and Kavazanjian, 2016). EICP has also shown promise for mitigating fugitive dust on at least one sample of mine tailings (Hamdan and Kavazanjian, 2016). However, applications of MICP and EICP to mine tailings have been limited, and no studies have shown the ability to stimulate native ureolytic microbes capable of inducing MICP from tailings. Additionally, the costs and environmental impacts associated with EICP and MICP for stabilization of mine tailings have not been thoroughly compared to those of other short-term dust control technologies. This paper presents the results of benchtop stimulation experiments, laboratory wind tunnel experiments, and a comparative analysis of EICP with other dust control technologies to identify specific obstacles to the field application of EICP and MICP as well as knowledge gaps where future research into these technologies may be required.

2 LABORATORY EXPERIMENTS – MICP AND EICP

To characterize the effectiveness of MICP and EICP for dust control at tailings facilities, stimulation experiments and wind tunnel experiments were performed on five tailings specimens obtained from two mine sites in the United States. Stimulation experiments were used to measure the ability to stimulate native ureolytic microbes from tailings, while wind tunnel experiments were used to assess the effectiveness of EICP for fugitive dust control.

2.1 *Tailings*

Five tailings specimens were obtained for this research program. Four were obtained from a taconite tailings facility in Minnesota and one was obtained from a copper-molybdenum ore site in Arizona. The tailings specimens are described further below. Figure 1 shows the grain size distributions for all five tailings specimens.

1. MFN-1: fine, freshly deposited Minnesota taconite tailings;
2. MCN-1: coarse, freshly deposited Minnesota taconite tailings;
3. MFA-1: fine, aged (1-year old) Minnesota taconite tailings;
4. MFA-2: fine, aged (9-years old) Minnesota taconite tailings; and
5. AFN-1: fine, freshly deposited Arizona copper-molybdenum tailings.

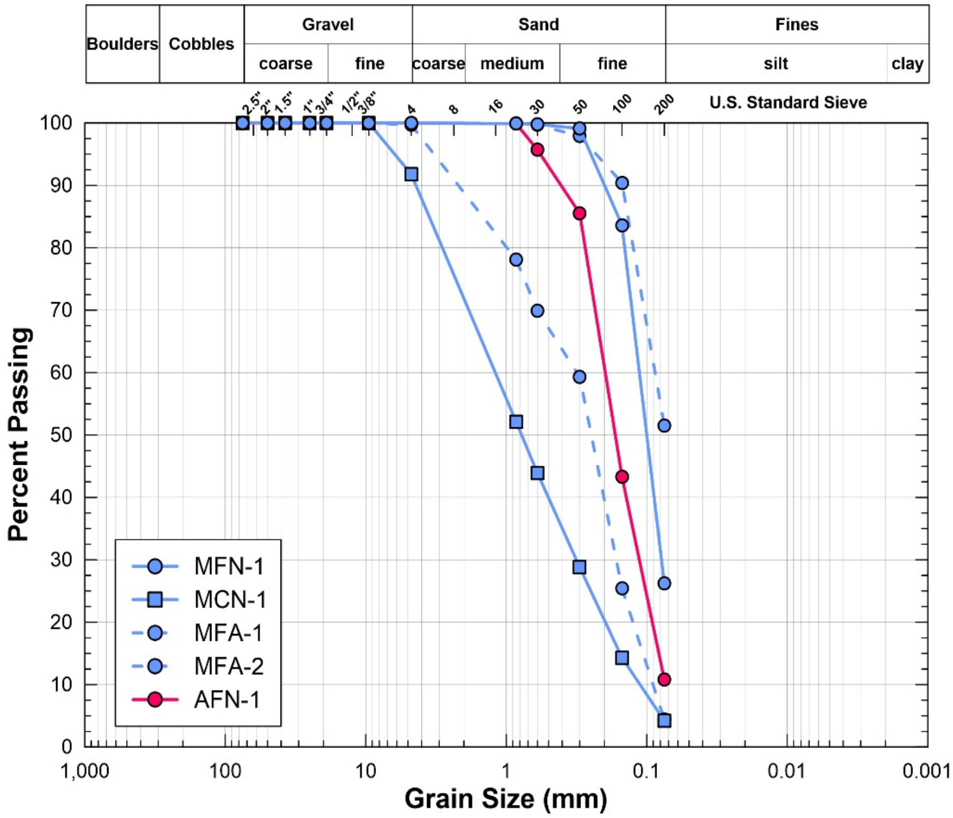

Figure 1. Grain size distributions for tailings specimens.

2.2 *MICP Stimulation Experiments*

Stimulation experiments were performed on each of the tailings specimens to determine the feasibility of stimulating ureolytic microbes in tailings storage facilities. Stimulation experiments were performed using autoclaved 250-mL flasks, 100-mL of autoclaved stimulation solution, and 10-15 grams of tailings. The flasks and stimulation solutions were autoclaved to prevent the growth of exogenous microbes (i.e., microbes that did not originate from the tailings specimens). The stimulation solution used for these experiments was taken from Gomez et al. (2018) and contained 0.1 g/L yeast extract, 12.5 mM ammonium chloride, 42.5 mM sodium acetate, and 350 mM urea. At the beginning of the experiments, the flasks were mixed to suspend the tailings in the stimulation solution and then capped with loose-fitting paraffin caps. 5-mL samples of solution were taken from each flask using sterile pipettes as soon as the tailings had settled to the bottom of the flask (approximately 10 minutes) and every 2-3 days thereafter for fourteen days. pH, conductivity, and ammonia smell were monitored in each of the samples taken from the flasks immediately after removing the samples. These indicators were used to gauge whether ureolysis was occurring (and hence whether ureolytic microbes had been stimulated from the tailings). Stimulation experiments were performed in quintuplicate for each tailings specimen.

The results of the stimulation experiments are shown below in Figure 2. As shown in Figure 2, tailings specimens MFN-1, MFA-1, MCN-1, and MFA-2 show similar trends in pH and conductivity with time. All four specimens show increasing pH and increasing conductivity, which is consistent with ongoing ureolysis (and hence stimulation of ureolytic microbes). An ammonia smell was also observed with these specimens two to five days after beginning the experiments, which is also consistent with ongoing ureolysis. It is noteworthy that the age and grain size of the tailings did not seem to impact the stimulation of native ureolytic bacteria in these specimens; fine, coarse, fresh, and aged tailings all showed evidence of stimulation. As also shown in Figure 2, however, tailings specimen AFN-1 exhibited decreasing pH and relatively stagnant conductivity with time. This implies that ureolysis was not occurring and that ureolytic microbes were not stimulated. Taken together, these results indicate that stimulation of native microbes for MICP may be feasible at some tailings facilities, but not at others. As such, treatability studies may be required to determine the suitability of a given tailings site for dust control via MICP using biostimulation.

Figure 2. Results of stimulation experiments – pH and conductivity with time.

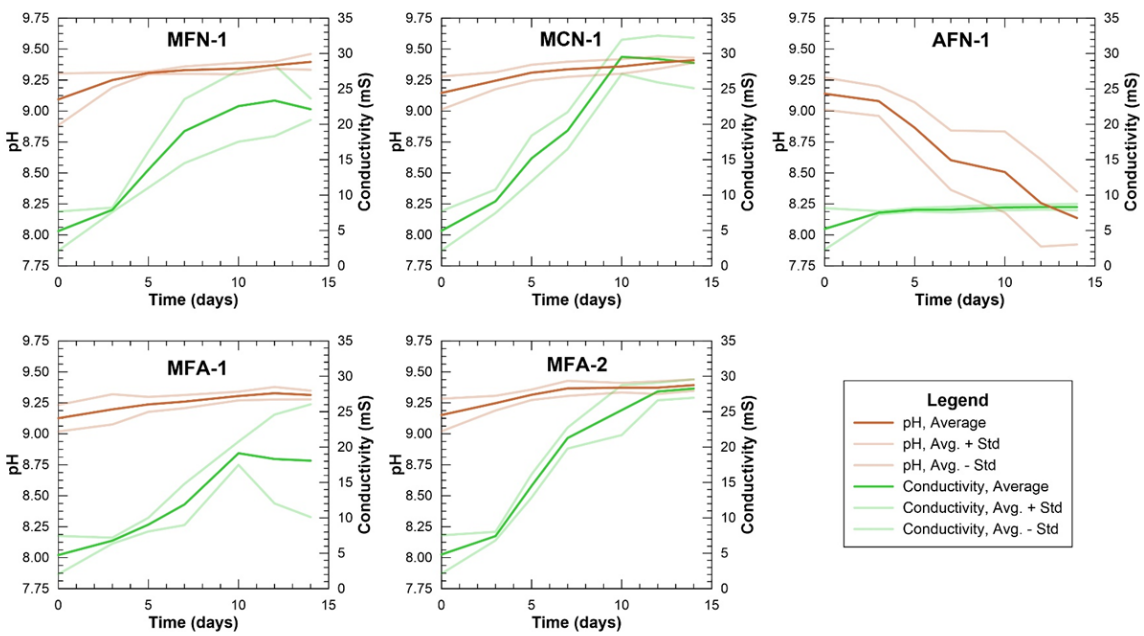

2.3 *EICP Wind Tunnel Tests*

Wind tunnel testing of each of the tailings specimens treated via EICP was conducted to determine the feasibility of EICP for dust control at tailings facilities. Five nine-inch round, two-inch deep cake pans were filled with Ottawa 20-30 sand to one-inch from the top of the pans to reduce the amount of tailings required for each wind tunnel test. The pans were then filled to the top with oven dried tailings from each of the five tailings specimens and leveled using a straight edge. All five pans were sprayed using a spray bottle with 100 mL of a cementation solution containing the following: 0.8 M urea, 1.2 M calcium chloride dihydrate, 2 g/L nonfat powdered milk, and 15 mL of crude enzyme extract. The enzyme extract was obtained from the Center for Bio-Mediated and Bio-Inspired Geotechnics at Arizona State University and was prepared according to the procedures described in Khodadadi Tirkolaei et al. (2020). To prepare the solution, 75 mL of urea and calcium chloride solution were combined with 15 mL of enzyme and nonfat powdered milk solution within the spray bottle immediately prior to application to the tailings. The solutions were mixed directly before application so that the ureolysis reaction and subsequent carbonate precipitation reaction occurred predominantly on the tailings surface rather than in the spray bottle. The smell of ammonia and a white precipitate were observed on all treated tailings surfaces within three minutes of treatment, indicating that ureolysis and carbonate precipitation were occurring. Following treatment, the tailings specimens were air dried for a minimum of two weeks prior to wind tunnel testing.

Each of the EICP-treated tailings specimens was tested along with an untreated control specimen in a wind tunnel constructed at the Johns Hopkins University soil mechanics laboratory. Control specimens were prepared in the same manner as EICP-treated specimens but were not sprayed with the EICP solution. The wind tunnel was constructed using two air compressors to generate air flow, an acrylic test box, and acrylic contraction and diffuser sections. Airflow over the tailings specimens was observed to be turbulent in nature. All tailings specimens were subjected to the same velocity of air flow for five minutes. Air flow velocity was controlled using two sets of valves between the air compressors and the contraction section of the wind tunnel. All tailings specimens were weighed before and after testing to measure mass lost during wind tunnel testing.

Following testing, the carbonate-cemented crust on the EICP-treated specimens was analyzed for the following properties: crust thickness (measured using calipers), crust strength (assessed using a pocket penetrometer), and carbonate content (assessed using acid digestion). The crust on each EICP-treated pan was tested three times with the pocket penetrometer to assess crust strength. Acid digestion was performed according to the following procedure: rinsing all recoverable pieces of carbonate cemented crust from each EICP-treated tailings specimen to remove residual salts, oven drying those pieces of crust to remove moisture, weighing the pieces of crust (weight should reflect tailings and carbonate precipitate), exposing those pieces of crust to 1.0 M hydrochloric acid until no more effervescence was observed and all interparticle bonds were broken, rinsing the resulting tailings with deionized water to remove salts, oven drying the tailings, and weighing them a final time (weigh should reflect only tailings). The difference in mass before and after acid digestion was assumed to be the result of carbonate mineral dissolution during acid digestion.

The results of the EICP wind tunnel tests and cemented crust measurements are shown below in Tables 1 and 2. As shown in Table 1, all EICP-treated specimens showed significantly less mass loss than control specimens. This indicates that EICP-treatment is likely to be effective for dust control at tailings facilities. Further, the composition, age, and gradation of tailings was not observed to impact the effectiveness of EICP-treatment. So, while MICP may require treatability studies to assess its feasibility for use at a given tailings site, it appears that EICP could be more universally effective. This is most likely due to the nature of EICP as a bio-inspired, rather than bio-mediated process. EICP does not rely on in-situ microbes, but rather an exogenous application of enzyme. So, it is not subject to the same constraints as MICP (e.g., presence or absence of microbes, unfavorable chemical conditions for microbial growth, etc.).

Table 1. Mass loss from wind tunnel experiments.

Treatment	Rate of Mass Loss from Tailings Specimens (g/min)				
	MFN-1	MCN-1	MFA-1	MFA-2	AFN-1
Control	388	33.8	61.2	10.2	74.7
EICP	0.114	0.020	0.00	0.0034	0.066

Table 2. Thickness, strength, and carbonate content of cemented crust of EICP-treated tailings.

Parameter	Tailings Specimen				
	MFN-1	MCN-1	MFA-1	MFA-2	AFN-1
Crust thickness (mm)	2.35	3.65	1.06	3.00	5.56
Crust strength (psi)	3.2	6.0	3.5	1.7	5.9
Carbonate content (%)*	3.8%	1.3%	12.5%	5.4%	1.1%

*crust strength represents the puncture strength of the crust from pocket penetrometer testing.
**carbonate content is reported as a percentage of dry mass.

The thickness, strength, and carbonate content of the cemented crust on EICP-treated specimens is reported in Table 2 above. While there was significant variability in thickness, strength, and carbonate content among the tailings specimens, all tailings exhibited a measurable crust that effervesced when exposed to acid (evidence of carbonate precipitation) with a relatively low but measurable strength.

3 COMPARATIVE ANALYSIS

Experimental results presented in Section 2 indicate that EICP and MICP are technically feasible methods for dust control at tailings facilities. However, to be implemented in the field, these technologies must also be cost competitive while not causing adverse environmental impacts when compared with other, existing dust control technologies. This section compares the expected financial and environmental costs of MICP and EICP against those of other common dust control technologies to identify potential knowledge gaps and challenges to successfully implementing MICP and EICP for surficial stabilization of tailings. The other technologies used for comparison with MICP and EICP are salt treatments, polymer emulsions, organic mulch, and paper pulping byproducts.

3.1 *MICP and EICP*

Both MICP and EICP involve spray-applications of nutrients (specifically urea and calcium chloride) to induce ureolysis and carbonate precipitation (Hamdan and Kavazanjian, 2016). Additionally, EICP requires exogenous application of plant-derived urease enzyme, while MICP requires either stimulation of or augmentation with urease-producing microbes. Both EICP and MICP produce ammonium chloride byproduct that could pose environmental risks. However, in surficial application, it is likely that much of the ammonium would volatilize as ammonia gas.

For this analysis, it is assumed that EICP is used for surficial stabilization of tailings as experimental results suggest that EICP may be more widely applicable than MICP. The estimated cost for application of EICP for dust control is $5,500 per acre, including material and application costs (Raymond et al., 2021). It is anticipated that EICP or MICP solutions could be applied using a spray truck.

MICP and EICP have not been applied on a large scale and remain largely in the research phase. However, Raymond et al., 2021 assumed a service life of two weeks for dust suppression at construction sites. For applications on tailings impoundments, where surface traffic is minimal, this is likely a conservative estimate of service life as the carbonate crust is unlikely to be disturbed and cannot be dissolved by rainfall (like some other dust control technologies). However, for the purposes of this analysis, a service life of two weeks is assumed.

3.2 *Salt*

Salts are a chemical method that can be applied to the tailings surface as either a powder or a brine to provide short-term stabilization against wind erosion. Salts work by absorbing small quantities of water from the atmosphere and holding the tailings particles together through matric suction. The most common salts used for stabilization include magnesium chloride and calcium chloride. Salts do not work well in excessively wet or dry climates. In wet regions, precipitation causes salts to dissolve and leach through the treated tailings, rendering them ineffective. Dissolved salts may also cause environmental impacts and additional costs for mitigation. In dry climates, there may not be enough water in the atmosphere for salts to absorb, and an erosion-resistant salt crust may not form (PNNL, 2018).

Salts are typically applied by spraying a concentrated brine solution to the surface of the tailings. It was assumed that brine costs $1.50 per gallon, with application of 2,500 gallons per acre. Unit costs for labor, equipment, and power are assumed to cost $700 per acre (USDA, 2020). Using these assumptions, the unit cost for salt application for tailings stabilization is $4,500 per acre.

The service life of this method is highly dependent on rainfall and relative humidity. In relatively wet or humid climates, salts may provide two to four weeks of stabilization before re-application is required (MIS, 2020). For this analysis, a service life of two weeks is assumed

3.3 *Polymer Emulsion*

Polymers, both natural and synthetic, can be sprayed onto the surface of tailings as an emulsion to produce an erosion-resistant crust. Polymers are large chain molecules composed of smaller repeating units. Anionic polymers, most commonly used for dust suppression, react with cations in the treated tailings to settle out of solution. The large polymer chains then form bridges between tailings particles, resulting in an erosion-resistant crust on the surface of the tailings. Specific polymer formulations are used depending on the physiochemical properties of the tailings upon which they are applied (PNNL, 2018). Most polymers used for dust suppression (specifically polyvinyl acrylics and acetates) are considered non-toxic and environmentally friendly when used according to manufacturer's recommendations (USACE, 2013).

Polymer emulsions are applied topically as a liquid spray to the tailings surface. The unit cost for applying polymer emulsion for dust suppression was reported to be approximately $5,300 per acre (SRI, 2003). However, USACE (2013) found that polymer costs are variable, with application and materials costs ranging from $7 to $10 per gallon and application rates varying from 0.05 gallons per square yard to 1.0 gallons per square yard. For this analysis, an application cost of $5,300 per acre is assumed.

In typical applications, polymer emulsions will provide three months to three years of stabilization, depending on the amount of vehicle and foot traffic in the application area. For application to sluiced tailings, where vehicle and foot traffic is expected to be limited, the effective service life is estimated to be approximately one to three years. For this analysis, a service life of one year is assumed.

3.4 *Organic Mulch*

Mulching involves placing a layer of material on the surface of the tailings to reduce wind and water erosion. In addition to creating a physical barrier to erosion, mulches can also reduce evaporation and maintain moisture in the tailings, further improving erosion resistance. Organic mulches include wood chips, tree bark, and paper products. Mulches can be applied directly with earthmoving equipment or via hydromulching depending on the site requirements. However, many organic mulches, including woodchips, are lightweight and low density, rendering them ineffective in high wind and high surface water flow environments. Further, all organic mulches are susceptible to decomposition, limiting their useful life for tailings stabilization (PNNL, 2018).

For this analysis, it is assumed that wood chip mulch can be obtained for a cost of $15 per cubic yard. To adequately stabilize the tailings surface, it is assumed that the mulch is spread in a one-foot thick layer over the treatment area. Unit costs associated with transportation and placement of the mulch are estimated to be $5 per cubic yard for transportation (it was assumed the mulch would have to be hauled ten miles), and $2 per cubic yard for placement for a total cost of $35,500 per acre.

The service life of this method is dependent on the resistance of the mulch to decomposition and wind erosion. Decomposition of wood chip mulch is expected to take between four and seven years, depending on the rainfall conditions at the site (mulch decomposes faster in wetter locations) (Coleman, 2020). However, high winds may blow the wood chips off of the tailings surface prior to decomposition. For this analysis, a conservative service life of two years is assumed.

3.5 *Paper Pulping Byproducts*

Paper pulp and byproducts of the pulping process may be used for dust suppression and stabilization of the tailings surface. Paper pulp itself may be incorporated into a mulch and applied to the tailings surface in combination with wood chips or other organic material as described in Section 3.4. Additionally, lignosulfonate and tall oil, byproducts of the sulfite pulping process and the Kraft paper process, respectively, may be used to provide short-term stabilization of tailings. These products act as binders, holding tailings particles together and increasing their resistance to erosion. Lignosulfonates and tall oil may be applied topically or mixed into the surficial tailings to bind particles together (Jones, 2017).

While paper pulping byproducts can create relatively strong, erosion resistant crusts on the tailings surface under dry conditions, they also have several limitations. Lignosulfonates tend to be highly soluble and leach during heavy precipitation. Tall oil, while less soluble, is also susceptible to breaking down under heavy rains or prolonged saturated conditions. Further, lignosulfonates tend to be acidic, which may lead to leaching of metals from the tailings or alteration of redox conditions if they leach to groundwater. Leaching of lignosulfonates and tall oil may also lead to high biological oxygen demand in receiving waters, which could result in fish kills (Jones, 2017; PNNL, 2018) and lead to difficulties in performing water treatment and complying with discharge requirements.

For this analysis, it is assumed that lignosulfonate is used for short-term stabilization of tailings. The unit cost for the lignosulfonate solution is estimated to be $3 per gallon. It is further assumed that lignosulfonate can be applied at a rate of 2,000 gallons per acre for a material cost of $6,000 per acre (SRI, 2006). Assuming that a water truck is used to apply the lignosulfonate at a rate of $700 per acre (including equipment operational costs), it is estimated that lignosulfonate can be applied at a cost of $6,700 per acre.

The service life of lignosulfonate is estimated to be two to three months, resulting in the need to reapply once or twice per season. However, intense rain events may dissolve lignosulfonates and reduce the service life, potentially requiring multiple applications during periods of high precipitation and repeat storms. For this analysis, a service life of two months is assumed.

3.6 *Summary and Discussion of Results*

A summary of the costs and environmental impacts associated with the analyzed surficial stabilization technologies is given in Table 3.

Table 3. Comparison of costs and environmental impacts for surficial stabilization technologies

Method	Service Life	Unit Cost* ($/acre/week)	Environmental Impacts
MICP and EICP	2 weeks	$2,750	Ammonium chloride production
Salt	2 weeks	$2,250	Salt dissolution
Polymer Emulsion	1 year	$102	Limited environmental impacts
Organic Mulch	2 years	$341	Limited environmental impacts
Paper Pulping Byproducts	2 months	$770	Metal leaching from tailings; Changes to groundwater redox conditions; Increased BOD in receiving waters

*Unit costs are normalized by expected service life

As shown in Table 3, MICP and EICP may be considerably more expensive than other tailings stabilization options when unit costs are normalized over the expected service life. Additionally, MICP and EICP have potential environmental impacts associated with their ammonium chloride byproduct, which may need to be managed depending on the application rate of the technology. To improve the feasibility of MICP and EICP for surficial stabilization and dust control at tailings facilities, it is thus necessary to reduce the application costs associated with the technology ($/acre) and better estimate service life (to reduce the number of required applications and hence reduce the amount of potential environmental impacts).

According to Raymond et al. (2021), the highest contributor to the overall unit application cost of EICP is the cost of the urease enzyme if commercially available pharmaceutical grade enzyme is used. Therefore, reducing the cost of the urease enzyme is key to successfully implementing EICP for dust control in the field. However, as demonstrated in this study, EICP for dust control may be achieved using a crude urease extract, rather than commercially available pharmaceutical grade enzyme. Khodadadi Tirkolaei et al. (2020) suggest that a simple on-site urease extraction method (involving only a blender, cheese cloth, and jack beans) may be used to generate crude urease extract on-site and vastly improve the cost effectiveness of EICP. Implementation of this cost effective on-site urease extraction method is therefore a key to successfully implementing EICP for dust control at tailings facilities. MICP using stimulated microbes may also prove to be a more cost-effective method for dust control at tailings facilities than EICP, as it does not require exogenous input of urease enzyme or bacteria. However, as shown by the MICP stimulation experiments performed as part of this work, stimulation may not be a viable method for MICP at all tailings sites and more research is required in this area to determine the applicability of MICP for dust control at tailings facilities.

Regarding service life, more research is required to determine the longevity of MICP and EICP crusts for dust control. The service life of MICP and EICP crusts is important for assessing both long-term costs as well as long-term environmental impacts from this technology. While carbonate-cemented crusts will not dissolve with rainwater, they are subject to mechanical breakage induced by wind loading, heavy rains, or other forms of disturbance (i.e. trucks, equipment, foot traffic, etc.). However, in the absence of physical disturbance, MICP and EICP crusts should have a much longer service life than the two weeks assumed herein. Additional research involving in situ, ideally involving side-by-side comparison with other methods, is therefore required to determine how carbonate cemented MICP and EICP crusts respond to environmental stresses, such as wind loading, heavy rains, and UV exposure.

Finally, evaluation of in situ vertical permeability of each dust control methods needs to be performed to provide guidance on the potential development of perched zones and preferable flow paths that may affect operations and performance of the tailings storage facility.

4 CONCLUSIONS

The goal of this paper was to identify specific obstacles to the field application of EICP and MICP for dust control at tailings facilities as well as knowledge gaps where future research into these technologies may be required. To that end, two sets of laboratory experiments (stimulation experiments for MICP and wind tunnel tests for EICP) and a comparative analysis of cost and environmental impacts with other existing technologies were presented herein. The results of the stimulation experiments showed that native ureolytic microbes capable of inducing MICP may be stimulated at some tailings facilities, but not at others. As such, treatability studies may be required to determine the suitability of a given tailings site for dust control via MICP. The results of the wind tunnel experiments showed that EICP is a viable method for dust control at tailings facilities and may be more universally applicable than MICP. This is likely due to fact that EICP does not rely on the growth of microbes, which may be sensitive to tailings chemistry or other environmental conditions. Finally, the results of the comparative analysis showed that EICP is not cost effective when compared with other dust control technologies if off the shelf pharmaceutical grade enzymes are used and a durability of only two weeks is assumed. To improve the applicability of EICP and MICP, implementation of low cost, on-site enzyme extraction methods and additional research to better understand the longevity of EICP and MICP generated crusts subjected to environmental conditions are required.

5 REFERENCES

C. Coleman, (2020). "How Long Does Mulch Last?" Charlestown Landscaping, [Online]. Available: https://www.charlestownlandscaping.com/how-long-does-mulch-last/. [Accessed 25 Sepember 2020].

Gomez, M.G., Graddy, M.R., DeJong, J.T., Nelson, D.C., and Tsesarsky, M. (2018). "Stimulation of Native Microorganisms for Biocementation in Samples Recovered from Field-Scale Treatment Depths." *J. Geotech Geoenviron. Eng*., 144(1): 04017098.

N. Hamdan and E. Kavazanjian, (2016). "Enzyme-Induced Carbonate Mineral Precipitation for Fugitive Dust Control," *Geotechnique*, 66(7): 546-555.

D. Jones, (2017). "Guidelines for Selection, Specification, and Application of Chemical Dust Control and Stabilization Treatments on Unpaved Roads," University of California Pavement Research Center, Davis, California.

Khodadadi Tirkolaei, H., Javadi, N., Krishnan, V., Hamdan, N., and Kavazanjian, E. (2020). "Crude Urease Extract for Biocementation." *J. Mater. Civ. Eng*., 32(12): 04020374.

Meyer, F.D., Bang, S., Min, S., Stetler, L.D., and Bang, S.S. (2011). "Microbiologically-Incuded Soil Stabilization: Application of *Sporosarcina pasteurii* for Fugitive Dust Control." Proceedings, *Geo-Frontiers 2011*, Dallas, TX.

Midwest Industrial Supply, Inc., (2020). "Alternative to Chlorides for Effective Dust Control." [Online]. Available: https://blog.midwestind.com/alternatives-to-chlorides-for-effective-dust-control/. [Accessed 1 August 2020].

Pacific Northwest National Laboratory, (2018). "Water Application for Dust Control in the Central Plateau: Impacts, Alternatives, and Work Strategies," U.S. Department of Energy, Richland, Washington.

Raymond, A.J., Kendall, A., DeJong, J.T., Kavazanjian, E., Woolley, M., and Martin, K. (2021) "Life Cycle Sustainability Assessment of Fugitive Dust Control Methods," *Journal of Construction Engineering and Management*, 147(3), https://doi.org/10.1061/(ASCE)CO.1943-7862.0001993

Sierra Research, Inc., (2003). "Final BACM Technological and Economic Feasibility Analysis," San Joaquin Valley Unified Air Pollution Control District, Sacramento, California.

Sierra Research, Inc., (2006). "Alaska Rural Dust Control Alternatives," Alaska Department of Environmental Conservation, Sacramento.

United States Army Corps of Engineers, (2013). "Environmental Considerations for Selecting Cost-Effective Dust Control Technologies," Public Works Technical Bulletin No. 200-1-133, Washington, D.C..

United States Department of Agriculture, (2013). "Cost Scenarios - 373 Dust Control on Unpaved Road and Surfaces,". [Online]. Available: https://efotg.sc.egov.usda.gov/references/public/NM/CostSenarios_373-Dust_Control_on_Unpaved_Roads_and_Surfaces.pdf. [Accessed 19 August 2020].

3D analysis of traditional and geomorphic tailings dam designs

Neeltje Slingerland
University of Alberta and Golder Associates Ltd., Vancouver, BC, Canada

Feixia Zhang & Nicholas A. Beier
University of Alberta, Edmonton, AB, Canada

ABSTRACT: Geomorphic design of mine waste structures as a concept has existed for decades. The primary driver of this has been to reduce surficial erosion that can lead to breaching of cover systems and extended maintenance timelines; however, few landforms have been designed and constructed as such. While geotechnical engineers and dam designers are sympathetic to this plight, geomorphic design is not yet integrated regularly. Tools are introduced within this paper that will assist engineers and dam designers in achieving their long-term goals.

This project sought to evaluate various traditional and geomorphic tailings dam topographic designs from both a physical stability (short-term) perspective and a geomorphic (long-term) perspective. Two traditional and two geomorphic tailings dam topographic designs were generated with identical substrate and material properties as well as overall dimensions, for a theoretical site based in the Athabasca oil sands; 3D physical stability analyses and 3D landscape evolution modelling analyses were completed on each design. The results of these analyses allowed for an overall ranking of tailings dam designs, and identified one of the geomorphic designs as having both a higher factor of safety and superior geomorphic performance than the other designs. In order to ensure uniform style throughout the volume, all the papers should be prepared strictly according to the instructions set below.

1 INTRODUCTION

Tailings management and tailings dam design has made a dramatic transition over the last 100 years. Tailings deposition in rivers, lakes, and oceans largely ceased in north America by the 1930's due to environmental concerns, particularly where mines were located near agricultural areas. As a result, tailings dams became the new norm in the western world, often constructed in an upstream arrangement. In the 1960's cycloned tailings was initiated for dam construction, as was the use of a centreline construction method for tailings dams. The first centreline cycloned sand dam in the world was the Brenda Mine tailings dam, designed in the late 1960's with a constant downstream dam slope of 4H:1V and constructed from the 1970's into the 1990's. The relatively low downstream dam slope was chosen in consideration of physical stability requirements (Figure 1). With an increasing number of aging sand dams, surficial erosion risks were identified. The platform-bank topography was developed to reduce surficial erosion by reducing slope lengths.

Traditionally, downstream slopes of tailings dams were simply a uniform slope, as illustrated in Figure 1. In some locations, these uniform slopes allowed for concentration of surface water, or overland flow, and erosion became a problem. To inhibit surficial erosion, the Platform-bank topography was developed whereby uniform slopes are broken up into shorter lengths and separated by a bench that can be level, tilting forward, or backward. While this approach can work well when constant monitoring and maintenance are ongoing, eventually surface water flows to a point of least resistance, and large gullies can develop.

In the 1980's geomorphic methods of shaping mine waste structures were developed (Toy & Hadley 1987). The goal of the geomorphic approach is to create a steady-state landscape with respect to erosion and deposition whereby driving forces (Wind, water, gravity) and resisting forces (mass, gravity, friction) are as close to balanced as possible (Toy & Chuse 2005). These approaches have been applied to a limited extent to waste rock and overburden dumps, and to an even lesser degree to tailings dams and tailings storage facilities (TSFs) in general (Hancock & Willgoose 2004, Martin-Duque, Sanz, Bodoque, Lucia, & Martin-Moreno 2010, Sawatsky & Beckstead 1996, DePriest, Hopkinson, Quaranta, Michael, Ziemkiewicz 2015, Toy & Chuse 2005).

While improved aesthetics are one benefit of the geomorphic approach, this (in a strictly engineering context) trivializes the importance of this approach. The purpose of the geomorphic approach is both hydrotechnical and financial in nature; creating a surface with minimal erosion that is capable of being successfully reclaimed to a self-sustaining state. This end result is rarely achieved on TSFs, in part because as an industry we are not yet designing for long-term stability from the initial stages. In other words, true sustainable development (as defined by the United Nations' World Commission on Environment and Development, 1987) remains largely an afterthought.

Two factors have historically inhibited the adoption of geomorphic designs: (1) an unknown factor of safety due to the need to capture the FOS of a range of cross sections or to evaluate in 3D, and (2) their constructability. The now common use of GPS guidance in construction has essentially eliminated the latter: geomorphic designs are regularly constructed in Australia using benches arranged with lateral curves and variable setbacks, such that re-shaping is minimal during progressive reclamation and at closure. The evaluation of physical stability of these geomorphic designs continues to be a sticking point and is the focus of this paper.

Figure 1. Example of Uniform slope topographic design at the Brenda Mine Tailings Dam.

This paper describes the short-term stability and long-term geomorphic assessment of four surficial (topographic) designs for a fictional sand tailings dam in the Athabasca oil sands (AOS). While all dam designs share the same substrate and material characteristics, and overall dimensions, the topography varies. The four dam designs include two traditional (a and b) and two geomorphic (c and d) topographic approaches, named as follows:

a) Uniform slope
b) Platform-bank

c) Catena (or “s-shaped”)
d) Horseshoe (alternating uniform and catena slopes)

Through three-dimensional physical stability assessment (considered short-term stability) and three-dimensional landscape evolution modelling assessment (considered long-term geomorphology), this research seeks to evaluate the sustainability of traditional and geomorphic tailings dam designs.

2 METHODOLOGY

2.1 *Dam design*

2.1.1 *Foundation and dam materials*

The dam materials (predominantly coarse sand tailings) and foundation were chosen to replicate those found in the AOS; the theoretical dams are identical in these respects. The foundation is comprised of the middle (MM) and Lower (LM) subdivisions of the McMurray formation, which is comprised of interbedded bitumen-bearing Cretaceous sands and shales (Bayliss, Philip, Hepp, and Martens, 2013). Four layers of three different materials were included in the foundation: MM cross bedding, peak tidal flat mud (a weak MM layer), and Lower McMurray (LM2), are arranged in simplified form similar to their occurrence on the east side of the Athabasca River (shown in Figure 3). Material properties chosen are listed in Table 1, and are within their respective. documented ranges (Sisson, Chan, & Fear, 2012).

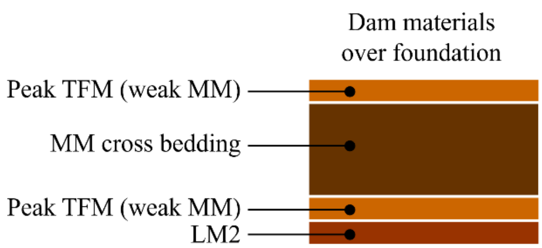

Figure 2. Foundation material arrangement.

Table 1. Properties of dam foundation materials and dam construction materials.

Materials	Unit weight (kN/m^3)	Effective Friction Angle (°)	Cohesion (kPa)	Pore Pressure (B-bar)
Cross bedding	21	45	0	0.3
Peak TFM	21	23	0	0.3
LM2	21	11	0	0.3
Coarse sand tailings	19.5	36	0	0
Overburden starter dyke	19.5	35	0	0

2.1.2 *Topography*

Four distinct surface topographies were designed for the downstream face of the dams: two traditional designs that mimic designs used in the AOS and elsewhere, and two more geomorphic designs. All four dams had the same overall height, length, width, and basal channel dimensions at the bottom of the dam. The traditional designs included a Uniform slope of 7H:1V from top to bottom (base case), and a Platform-bank design with the same overall slope, but with benches punctuating the slope that are tilted backwards; these designs have a constant cross-section for the full width of the dam. The geomorphic designs include an “s-shaped” catena slope with a maximum slope at the inflection point of 3H:1V and an elongated toe, and a Horseshoe design that transitions from Uniform slope at the sides to a Catena slope in the middle. Each of these designs is modelled as though it were a section of a much longer dam, such that the Horseshoe design would alternate from Uniform to Catena cross-sections for the full length. Cross-sections for all four dam surface topographies are illustrated in Figure 3.

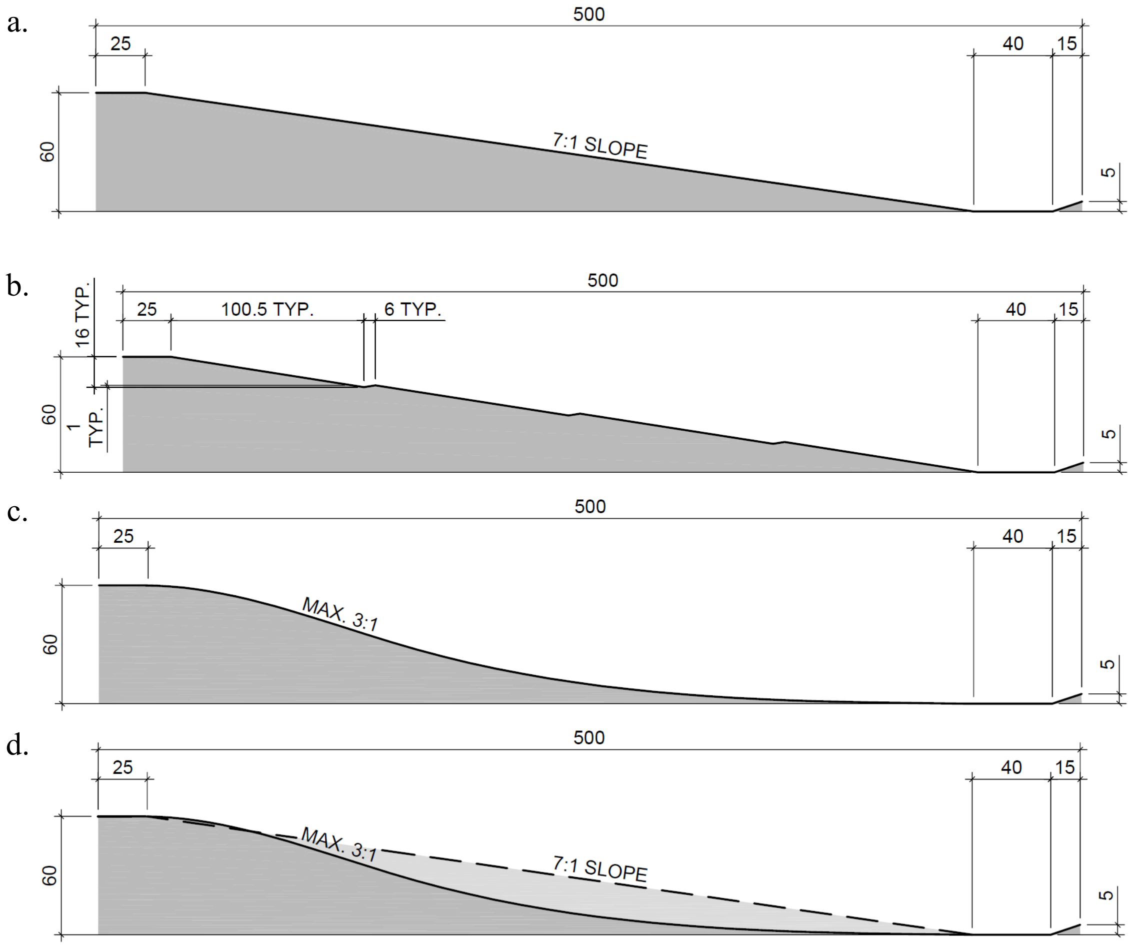

Figure 3. Tailings dam topographies modelled, shown in cross section. (a) uniform slope, (b) platform-bank, (c) catena, and (d) horseshoe (edges dashed). Dimensions are in metres.

2.2 *Geotechnical analyses*

Each of the four tailings dams were subjected to three-dimensional (3D) geotechnical stability modelling using Slide 3, which uses the limit equilibrium method of calculating the factor of safety (FOS) for a failure surface in 3D. Slide 3 evaluates the stability of 3D slip surfaces using vertical column limit equilibrium methods, while the section tool performs 2D analysis of multiple planar surfaces before feeding it back into 3D where a 3D slip surface is generated with global minimum FOS.

Model set-up included importing the surface geometry for foundation materials as well as the dams, defining and applying material properties, identifying slip surface type and search method, applying a groundwater surface, etc. Geometries inputted to Slide 3 are illustrated in Figure 4. Methods chosen for calculations of the FOS included Bishop, Morgenstern-Price, and Spencer. To eliminate edge effects in the models, the cross-sections at the sides of each of the dams were extended horizontally by 500 m, but not evaluated specifically.

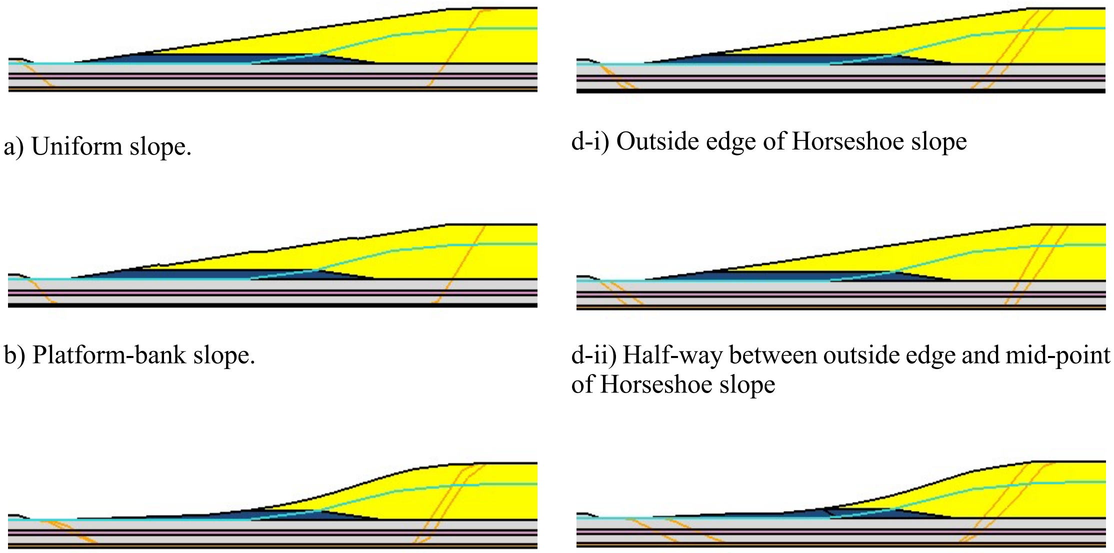

a) Uniform slope.

d-i) Outside edge of Horseshoe slope

b) Platform-bank slope.

d-ii) Half-way between outside edge and mid-point of Horseshoe slope

c) Catena slope.

d-iii) Mid-point of Horseshoe slope

Figure 4. Cross-sections through dams as generated in Slide 3.

2.3 *Geomorphic analyses*

The CAESAR-Lisflood landscape evolution model (LEM) was used to evaluate the long-term geomorphology of the four tailings dam slopes (Coulthard 2017). CAESAR-Lisflood is a reduced complexity LEM, meaning that it simplifies the many actual processes involved in erosion and deposition of soils, and has been evaluated and cross-validated for use with natural and anthropogenic landscapes over more than 20 years. LEMs can be used in a number of different ways; for this study, a series of probable maximum precipitation events for the AOS were simulated to stress-test the dams and learn how each performed relative to one another. CAESAR-Lisflood uses a cellular automata to distribute properties across a grid of cells; properties such as elevation, grain size distribution, moisture content and water depth. Used in catchment mode, CAESAR-Lisflood works by applying hourly precipitation according to user-defined inputs universally across the DEM. The model calculates at what point water begins to pool on the surface, and the velocity of surface flow by gravity according to the elevation of cells. Soil particles are eroded, transported, and deposited according to the flow velocity and their grain size, allowing for fines to be preferentially eroded, for armouring to develop, and for alluvial fans to develop similar to those in nature (i.e., coarser particles dropping out first, followed by fines at the toe).

CAESAR-Lisflood was previously calibrated to an actual AOS sand dam of the same overall dimensions used herein; calibration was completed using three methods: gully size (measured vs. modelled), overall soil loss (measured vs. modelled), and discharge volume (calculated vs. modelled) (Slingerland 2019). The parameters were then applied to simulations completed for the four theoretical dams designed for this research. Model inputs included a particle size distribution for surficial soils (CST in this case), a DEM of the surface topography (the four previously discussed dam topographic designs), an hourly precipitation record of all water landing on the dam surface that could cause erosion (i.e., snow depth was not applied in winter, but snow water equivalent was added during spring snowmelt), and roughly 30 other parameters that can be adjusted to optimize outputs and runtime.

The precipitation record used by CAESAR-Lisflood was generated from a historic 15-year record of hourly rainfall, temperature, and daily snow depth data in the AOS, which was then looped to create a 50-year record before statistical 24-hour storms were added in to ensure a representative record. Calibration took place with this precipitation data, prior to addition of the stress-testing storms that consisted of one PMP event every five years throughout the 50-year simulation. Please refer to Slingerland (2019) and Slingerland, Beier, & Wilson (2019), both publicly available documents, for details on the parameters, input development, and calibration of CAESAR-Lisflood for this work.

3 RESULTS AND DISCUSSION

3.1 *Geotechnical analysis – initial slope designs*

The slope stability analysis was carried out using the software 'Slide 3' (Slide 3 2019, RocScience Inc.). Slide 3 is a 3D limit equilibrium slope stability computer program for evaluating the factor of safety of 3D failure surfaces in soil or rock slopes. Bishop, Janbu, Spensor and GLE/Morgenstern-Price are four choices of limit equilibrium methods in Slide 3. They are based on satisfying force and/or moment equilibrium. Morgenstern-Price (GLE) was used for the calculation of FS, for Morgenstern-Price method is the most general limit equilibrium method with least assumptions among the four limit equilibrium methods mentioned above. Results of the slope stability analyses are summarized in Table 2. Overall, the Uniform slope, Platform-bank, and Horseshoe designs generated similar factors of safety. The Catena design resulted in FOS' just over unity, indicating that it would likely need adjustment to site specific conditions to increase its stability before being constructed. The Horseshoe design resulted in the highest FOS among the options, although there are no examples of its use that the authors know of at time of printing. The integrating a cross-section of Catena shape with lower FOS to portions of the base case of uniform slope leads to an increase in the overall FOS in Horseshoe design than the base case, rather than a decrease in the FOS.

Table 2. Results of three-dimensional geotechnical stability analyses.

Dam Design	GLE FOS
Uniform slope (base case)	1.33
Platform-bank	1.32
Catena	1.04
Horseshoe	1.34

3.2 *Geomorphic analysis*

Geomorphic changes were recorded throughout and following the 50-year stress-testing simulation. The climate conditions integrated into the statistical climate dataset for application to the dams were extreme and more frequent than would occur naturally, therefore the results are purely to be interpreted with respect to relative performance. As all mines in the AOS plan on a walk-away scenario, it was assumed that no maintenance was to be conducted between storm events.

Soil was removed by various erosional processes on the downstream dam slope, and deposited in the basal channel at the toe of the slope. Water in the basal channel then removed some of the deposited sediment in the channel and transported it out of the model geometry. Two main patterns of erosion were noted: one concentrated gully with little impact across the rest of the dam slope, and widely distributed gullies that affect much of the dam slope. In terms of maintenance, one gully is generally less expensive to repair than many, unless it is very deep. Consequences of these erosional patterns are seen in the basal channel: one gully will deposit sediment in one location, while widely distributed gullies will uniformly deposit sediment throughout the basal channel. The larger the gully, the more sediment is deposited, and the need for dredging is increased to prevent overtopping.

Results of the landscape evolution modelling / geomorphic assessment are summarized in Table 3 and Table 4, where soil volume change, erosion and deposition depths, and mean elevation change are provided for the tailings dam slope and basal channel separately. The base case Uniform slope design resulted in the shallowest maximum depth of soil removal, while the Horseshoe design has the lowest total volume of soil loss and lowest mean elevation change (Table 3). For the basal channel, the Catena design accumulated the lowest maximum depth of sediment, due to the elongated toe which leads to deposition of sediment upstream of the channel, while the Horseshoe design yielded the smallest total volume of soil deposited and lowest mean elevation change (

Table 4).

Table 3. Summary of elevation changes on dam slopes. Units are in metres unless otherwise indicated.

	Uniform slope (base case)	Platform-bank	Catena	Horseshoe
Maximum depth of erosion	7.45	23.78	7.64	9.88
Total soil loss (m^3)	71,840	132,030	57,830	29,990
Mean elevation change	-0.17	-0.37	-0.15	-0.05

Table 4. Summary of elevation changes in basal channels. Units are in metres unless otherwise indicated.

	Uniform slope (base case)	Platform-bank	Catena	Horseshoe
Maximum depth of deposition	2.43	3.79	1.13	1.55
Total soil added (m^3)	28,830	39,110	19,350	16,380
Mean elevation change	+0.68	+0.92	+0.46	+0.39

When assessing over the full timeframe of the simulation, the rate of erosion and progress towards a steady state between environment and climate can be viewed (Figure 5). Figure 5 illustrates the soil volume eroded from the downstream tailings dam slope over the full 50-year simulation; a steep slope indicates high erosion rate while a shallow slope indicates a lower erosion rate. Not only is the cumulative total volume of soil eroded less in from the Horseshoe design relative to others, but the rate of erosion is also lower meaning that it is closer to having achieved a steady state by the end of the simulation than the other designs. This graph was used to rank the erosional stability (geomorphic equilibrium) of each of the designs, as shown in Table 5.

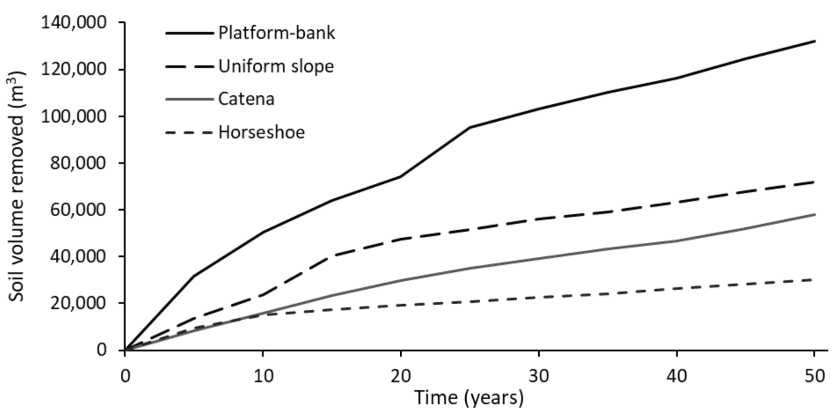

Figure 5. Cumulative soil loss removed from tailings dam slopes over time.

Relative to the base case, and over the full 50-year simulation, the two geomorphic designs performed better, while the Platform-bank design performed worse (i.e., less maintenance required to re-establish the topography). This is evident when viewing the results qualitatively: Uniform slope and catena designs resulted in widely distributed gullies, while the Platform-bank and Horeshoe designs resulted in predominantly single gullies, albeit branching to various degrees (Figure 6).

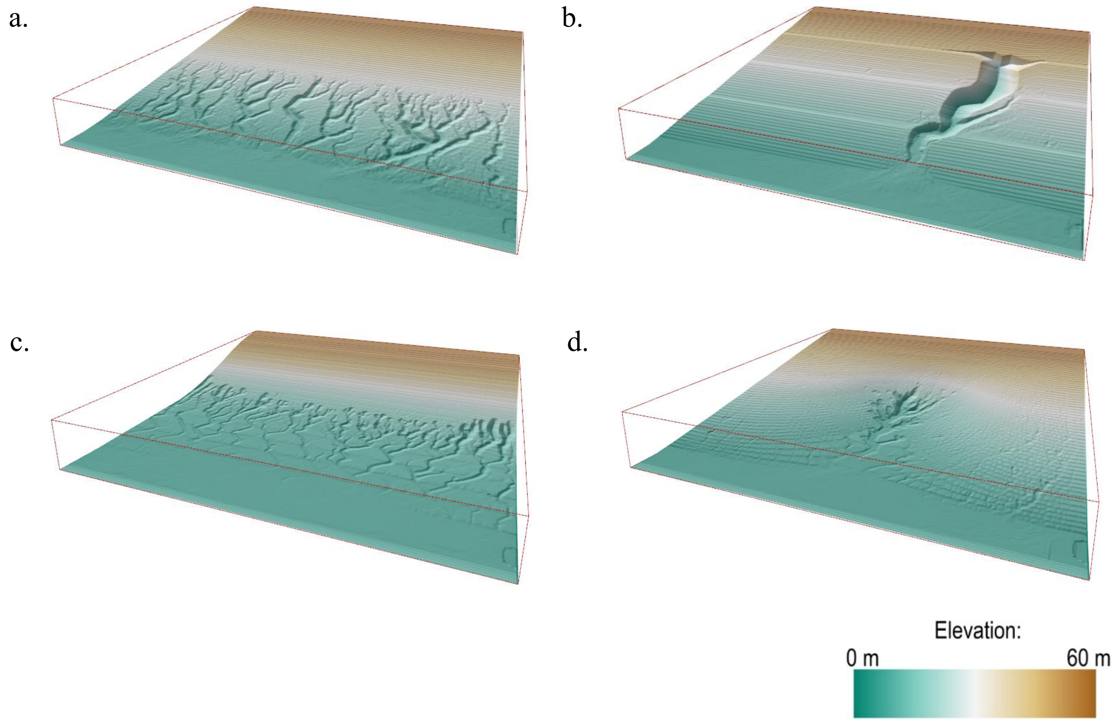

Figure 6. Dam topographies following LEM simulation stress-testing. (a) Uniform slope, (b) Platform-bank, (c) Catena, and (d) Horseshoe.

Additionally, it is likely that the Horseshoe design will develop more densely established vegetation along the central portion of the dam due to increased moisture (given the climate and vegetation of the AOS), such that added erosion resistance is developed: it is possible that this design will develop no gully at all under such circumstances.

These qualitative results have been anecdotally noted in field conditions as well, where Platform-bank designs generally perform well while under constant monitoring and maintenance; however, at some point a weak spot develops and large gullies have developed rapidly. It is arguably more desirable to have a focused erosional feature than widely distributed gullies from a maintenance perspective.

Cumulative results of the geotechnical stability and geomorphic assessments are provided in Table 5. Results of geotechnical stability assessments were ranked from 1 to 4 (worst to best) according to their FOS, and results of landscape evolution modelling were ranked from 1 to 4 (worst to best) according to soil volume eroded from the slope (i.e., maintenance required for repair). As the geotechnical stability assessment demonstrated close results between three of the four top-rated designs, rather than rank them as 4, 3, and 2, all were given a 3. The geomorphic assessment resulted in a clear ranking of performance and therefore no adjustment was needed. This simplistic method of quantification provides a quick evaluation of the degree to which these two objectives are achieved in isolation of other important factors such as economics.

Table 5. Relative performance evaluation of tailings dam designs.

Assessment	Uniform slope	Platform-bank	Catena	Horseshoe
Geotechnical stability (short term)	3	3	1	3
Geomorphic stability (long term)	2	1	3	4
Overall result:	5	4	4	7
Overall performance:	-	Worst (tie)	Worst (tie)	Best

The findings of this study illustrate that this more advanced geomorphic (Horseshoe) form has greater physical stability than either of the traditional forms used for tailings dams. It also sheds light on why geotechnical engineers may have been hesitant to use a geomorphic design in the past: the Catena or “s-curve” slope has been frequently illustrated in cross-section and touted as a mature form with desirable steady-state erosion rates. This is done with reference to centerlines of streams or hillslope drainage pathways, but is without presentation of surrounding topography. When the Catena form is interpreted as a constant cross-section, as illustrated herein, the factor of safety is substantially lower than other designs. Only when adjacent topography is integrated to the design, are the benefits of a geomorphic form realized.

It should be re-iterated that the topographic designs for the downstream dam slopes were not refined to site-specific geomorphic characteristics; the Catena cross-section as well as the distance between alternating cross sections in the Horseshoe design should be refined through additional landscape evolution modelling prior to finalization. Before initiating a geomorphic landform design, characterization of the climate and local landforms is helpful to understand forms that may provide increased stability.

3.3 *Geotechnical analysis of post-erosion conditions*

Based upon site observations, gullies in the AOS are unlikely to progress below a 2.5-m depth during active operation. It is thought that this is due to capillary pressures and water table elevation. Maximum gully depths may change post-closure based on future water table elevations. The CAESAR-Lisflood LEM does not predict water table or capillary pressure, therefore these influences on gully depth are not integrated to the model. While it is of interest whether surficial erosion has the potential to reduce FOS below unity (or potentially lead to a dam failure), the purpose of this LEM work was stress-testing rather than mimicking actual long-term conditions, therefore it would be inappropriate to assess the geomorphic results in terms of resulting physical stability.

4 CONCLUSIONS

This research sought to evaluate a range of traditional and geomorphic downstream dam slope designs in terms of their geotechnical physical stability and their relative geomorphic performance. These can be equated to short- and long-term stability, respectively. Given that the active operational life of a mine tends to be less than 100 years, while the closure landform design life is typically between 1000 years and perpetuity, both short- and long-term stability are essential in tailings dam design.

The Slide3 three-dimensional stability model and CAESAR-Lisflood landscape evolution model were used to assess all four of the designs, which included two traditional designs (Uniform slope and Platform-bank) and two geomorphic designs (Catena and Horseshoe slopes). The 3D geotechnical modelling resulted in factors of safety for each design, while the 3D landscape evolution model resulted in volumes of material removed from the dam slope as well as pattern of erosion, such that they could be ranked. These assessments demonstrated that the Horseshoe geomorphic design performed superior to all others both from a physical stability and a geomorphic performance perspective.

5 ACKNOWLEDGEMENTS

The authors would like to thank Professor Tom Coulthard for making the CAESAR-Lisflood software freely accessible and for his timely feedback during early model parameterisation. The time and efforts of Dr. Ward Wilson and Mr. Scott Martens are also much appreciated, particularly for their input regarding three-dimensional stability modelling and providing an overall external review, respectively.

6 REFERENCES

Bayliss, A.I, Philip, L., Hepp, D., and Martens, S. 2013. “A geotechnical study of glacially-rafted, weak, Clearwater Formation beneath a tailings dam, Fort McMurray region, Alberta”, Canadian Dam Association 2013 Annual Conference Montréal, Québec, October 5-10, 2013.

Coulthard, T. 2017, CAESAR-Lisflood 1.9b [data set] Zenodo, doi:10.5281/zendod.321820

DePriest, N. C., Hopkinson, L. C., Quaranta, J. D., Michael, P. R., & Ziemkiewicz, P. F. (2015). Geomorphic landform design alternatives for an existing valley fill in central Appalachia, USA: Quantifying the key issues. *Ecological Engineering, 81*, 19-29. doi:10.1016/j.ecoleng.2015.04.007

Hancock, G. & Willgoose, G.R. 2004. ‘An experimental and computer simulation study of erosion on a mine tailings dam wall’, Earth Surface Processes and Landforms, vol. 29, pp. 457-475.

Martin-Duque, J.F., Sanz, M.A., Bodoque, J.M., Lucia, A., and C. Martin-Moreno. (2010). Restoring earth surface processes through landform design. A 13-year monitoring of a geomorphic reclamation model for quarries on slopes. *Earth Surface Processes and Landforms, 35*, 531-548.

Sawatsky, L.F. & G.R.E. Beckstead. (1996). Geomorphic approach for design of sustainable drainage systems for mineland reclamation. *International Journal of Surface Mining and Reclamation, 10:3,* 126-129. DOI:10.1080/09208119608964815

Sisson, R., Chan, W.K., and Fear, C. 2012. “Horizon Dyke 10 Geotechnical Design”, CGS GeoManitoba 2012.

Slingerland, N. 2019. ‘Geomorphic landform design and long-term assessment of tailings storage facilities in the Athabasca oil sands’ PhD Dissertation, University of Alberta.

Slingerland, N., Beier, N.A., Wilson, G.W. 2019. Stress testing geomorphic and traditional tailings dam designs for closure using a landscape evolution model. In Fourie & Tibbett (eds.), Mine Closure 2019. P. 1533-1543. ISBN 978-0-9876389-3-9.

Toy, T.J. & Chuse, W.R. 2005. Topographic reconstruction: a geomorphic approach. Ecological Engineering, Vol. 24, pp 29-35. doi:10.1016/j.ecoleng.2004.12.014

Toy, T.J. & Hadley, R.F. 1987. Geomorphology & Reclamation of Disturbed Lands, Academic Press, Orlando, Florida.

World Commission on Environment and Development (UNWCED). 1987. Our common future. Oxford, UK: Oxford University Press.

Case studies of agronomic and ecological design of ET cover systems

Jesse Dillon
Cedar Creek Associates Inc, Fort Collins, Colorado, USA

Terri West
Coeur Mining Inc, Chicago, Illinois, USA

ABSTRACT: An enormous amount of effort is put forth to characterize the cover materials for hydraulic and geotechnical properties to inform analytical modeling of infiltration / percolation on evaporation / transpiration (ET) covers. The agronomic properties of cover materials, along with local climatic conditions, dictate the transpiration potential and sustainability of ecological communities inhabiting the cover. Case studies will be presented to demonstrate how having soil scientists and ecologists collaborating with engineers during the design of cover systems, especially the early feasibility phases, can improve project outcomes. A soil scientist, working in coordination with an ecologist, can evaluate the physical and chemical properties of growth media as they pertain to plant growth to provide realistic predictions of vegetation performance and sustainability, including defining vegetative parameters for more accurate modeling. In addition, performance criteria for cover systems often include both percolation and revegetation components and engaging soil scientists and ecologists during the entire design is often justified, in order to set realistic and achievable success criteria. Case studies will include ET covers on mining facilities in Arizona, Colorado, Nevada, New Mexico, and Utah, where soil scientists and ecologists were and were not involved in the design components to provide contrast of outcomes.

1 INTRODUCTION

Evaporation / transpiration (ET) covers can be a quick, relatively inexpensive way to isolate mining wastes and other materials to keep them in place to prevent potential impacts to people and natural resources. The soil-plant layer of an ET cover slows the downward movement of rainwater and snowmelt and promotes storage of the water. The stored water will either evaporate or transpire. Together, evaporation and transpiration ("evapotranspiration") keep water from seeping into contaminated material and carrying contaminants downward into groundwater. The type of soil is chosen for its ability to store water and promote plant growth. The thickness of the cover depends on how much rainfall and snowmelt is expected in the area. Grass, shrubs, or small trees that form extensive root systems and survive the local climate are usually planted in the soil.

Understanding agronomic and ecological components are vital to the effective operation of the ET covers, as resilient and sustainable vegetation significantly contribute to erosion protection, water removal through transpiration, and meeting mine closure criteria. Therefore, qualified soil scientists and ecologists should be involved in the design of ET covers, even from the most preliminary stages, where often preliminary borrow sources and conceptual designs are considered. Implementation of the following case studies reveal elements of design which require site specific input from a qualified soil scientist or ecologist.

2 CASE STUDIES

Case studies will include ET covers on mining facilities in Arizona, Colorado, Nevada, New Mexico, and Utah, where soil scientists and ecologists were and were not involved in the design components to provide contrast of outcomes. The relevant projects are all located in arid environments where potential evaporation/transpiration outstrips precipitation. These sites include the following:

- Arizona
  - Copper Mine - Heap Leach Pad
  - Copper Mine - Tailings Facility

- Colorado
  - Gold Mine - Cover Test Plots
  - Coal Ash - Disposal Facility

- Nevada
  - Gold Mine - Lysimeter Test Plots
  - Gold Mine - Heap Leach Pad
  - Copper Mine - Tailings Facility

- New Mexico
  - Gold Mine – Waste Rock Dump
  - Uranium Mine – Tailings Facility
  - Uranium Mine – Waste Rock Dump

- Utah
  - Uranium Mine – Lysimeter Test Plots

3 RELEVENT DESIGN ELEMENTS

Based on our experience to date, these are the most important elements to cover design where qualified soil scientists and/or ecologists add value and improve potential outcomes.

3.1 *Agronomic Evaluation of Cover Materials*

It is important to conduct soil testing to understand the physical and chemical parameters of the cover materials. Important agronomic parameters such as soil texture, coarse fragment content, soil pH, Electrical Conductivity (EC), Sodium Absorption Ratio (SAR), organic matter, and available plant nutrients to get an understanding of the potential for cover materials to establish and sustain a resilient plant community. In arid environments physical and chemical parameters which influence plant available water are typically the most important.

Soil samples, for laboratory analysis, should be collected from all the cover materials with the potential to be in the rooting profile. The sampling program should be sufficient to adequately understand the variability of the source materials. The sequencing of the placement of cover materials should also be considered when sampling soil physical and chemical parameters.

In our case studies, we have encountered several constructed covers where borrow materials were sourced from an alluvial area where salt lenses could occur. Source material with elevated salts was placed as the surficial material in on the ET cover. Due to the adverse chemical characteristics of the growth media, no desirable vegetation could be established on the cover (Figure 1 and Figure 2). Therefore, the transpiration and mine closure goals could not be met.

Figure 1. Northern Nevada lysimeter with elevated EC only growing saltlover

Figure 2. Central Nevada cover with elevated EC only growing saltlover

3.2 *Determination of Revegetation Potential*

Based on the agronomic evaluation of cover materials, potential cover layering, and local climatic conditions, a qualified ecologist can determine the revegetation potential. This entails the ecologist predicting plant community assemblages in over the short term and long term. Vegetation sampling of analog or reference sites can help inform the community assemblages and vegetation parameters relevant to cover modeling. However, it is important to understand how cover depth, rooting access to underlying materials, and restrictive layers or capillary breaks can influence revegetation potential, especially if analog or reference sites are used to define performance expectations.

In our case studies, we have encountered designed covers where cover depth is very limited and planting rooting may occur in underlying material. In another case study, the surface 2 feet consisted of 1 foot of fine textured growth media overlaid on 1 foot of competent rock. In both cases, these designs impact the type of vegetation expected to inhabit the cover in both the short and long term. Finally, regulatory agencies in many jurisdictions are requesting more information about ecological sustainability and resiliency, especially regarding climate change. Figure 3 shows how local climate conditions can affect cover vegetation performance on an annual basis.

Figure 3. Utah cover vegetation performance in 2019 and 2021

3.3 *Agronomic Assessment of Rooting Profile*

A common challenge of cover design is limited available suitable materials and cost of sourcing better materials. Therefore, a typical alternative evaluated during ET cover system investigations is use of a thinner cover. As described in the section above, these thinner cover systems can influence the revegetation potential. However, to really understand the potential impact on vegetation establishment and persistence. The physical and chemical characteristics of the entire rooting profile should be understood. This often requires evaluating the geochemistry and physical parameters of tailings or waste materials and can also include an ecological risk assessment which evaluates the potential of plant uptake of contaminants of concern and eventual herbivory by wildlife or livestock.

In our case studies, we have evaluated underlying waste rock, tailings, and other encapsulated materials. In some cases, the physical and chemical properties are found to be suitable for plant rooting and we can predict vegetation potential based on that information. In other cases, the physical and chemical properties are deleterious to plant growth which result in a limited depth of suitable growth media and reduced plant available water. These circumstances create diminutive plants with reduced transpiration which may or may not be sustainable in drought years (Figure 4).

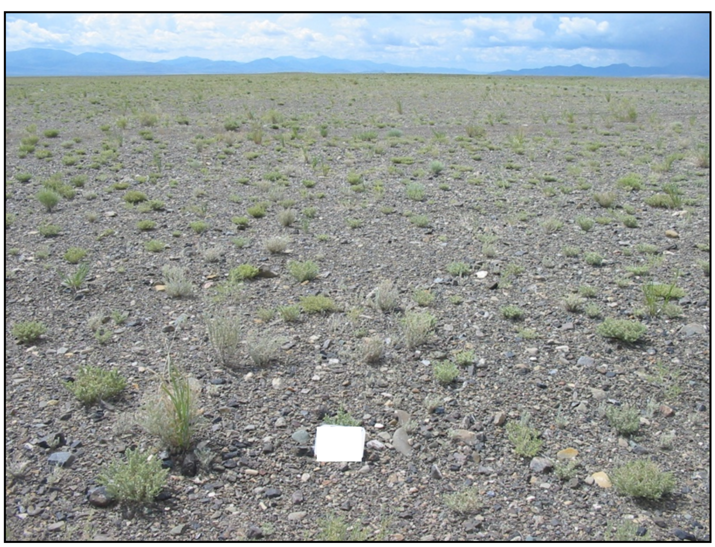

Figure 4. Northern Nevada cover with thin growth media depth

3.4 *Prediction of Potential Transpiration and Root Distribution*

Once the revegetation potential in understood, site-specific model inputs for the vegetation parameters can be developed. These are typically related to transpiration potential and root distribution but can also include root water uptake parameters. These parameters can vary widely based on the anticipated community assemblages. Vegetation components can be perennial, biennial, or annual, and comprised of grasses, forbs, shrubs, and trees. Each of these vegetation types exhibits a different transpiration potential, root distribution, and root water uptake potential.

In our case studies, we have used these parameters to help model the impacts from climate change, succession (either intention or unintentional), and vegetation establishment or persistence failure. We are looking at the lower bound of vegetation contribution to meet our percolation performance criteria. This helps to inform what our vegetation performance criteria should be.

3.5 *Development of Site-Specific Revegetation Plan*

A qualified soil scientist or ecologist should develop a site-specific revegetation plan which aims to optimize the revegetation potential on the cover. It should include information pertaining to reclamation goals, growth media selection, soil amendments, surface preparation techniques, appropriate seed mixes and seeding methods, erosion control measures, and quantifiable success criteria. The revegetation plan should also include operations and maintenance planning for noxious weed control and inter-seeding and other potentially necessary adaptive management actions. The revegetation plan should be developed based on the agronomic assessment of cover materials and determination of revegetation potential.

In our case studies, we have developed special handling for cover materials, recommended necessary amendments, developed optimized seed mixes and revegetation techniques, and implemented monitoring and maintenance action to ensure the ecological components are as effective as possible.

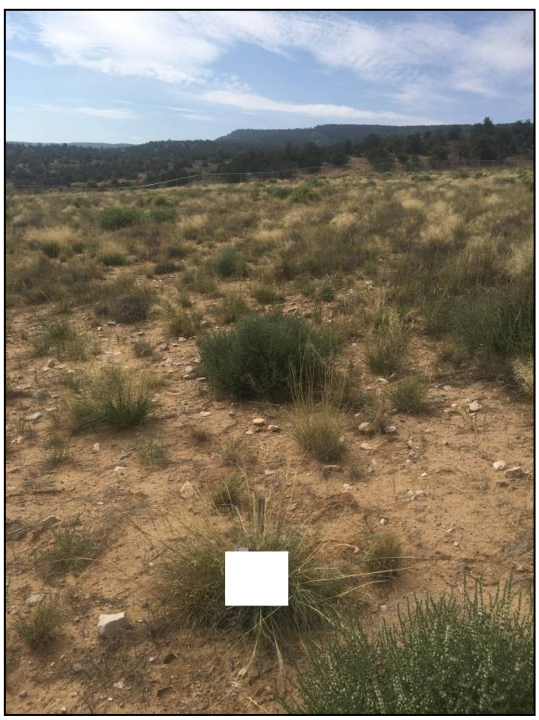

Figure 5. New Mexico cover with proper revegetation design, planning, and implementation

4 CONCLUSION

An enormous amount of effort is put forth to characterize the cover materials for hydraulic and geotechnical properties to inform analytical modeling of infiltration / percolation on evaporation /transpiration (ET) covers. The agronomic properties of cover materials, along with local climatic conditions, dictate the transpiration potential and sustainability of ecological communities inhabiting the cover. Our case studies show that a qualified soil scientist and/or ecologist should be included throughout the design process with the proponent and the engineering teams to ensure the agronomic and ecological components of design are considered, as omission of these elements can cause costly remediation efforts.

Oil Sands Tailings

Closure and abandonment process for an oil sands external tailings facility – Brownfield

Monica Ansah-Sam
Formerly Canadian Natural Resources Limited, Calgary, Alberta, Canada

Derek Etherington
Canadian Natural Resources Limited, Calgary, Alberta, Canada

Joseph Quinn
Klohn Crippen Berger, Calgary, Alberta, Canada

ABSTRACT: Canadian Natural Upgrading Limited's (Canadian Natural) Muskeg River Mine (MRM) is located approximately 70 km north of Fort McMurray, Alberta. The South Expansion Area (SEA), which is an out-of-pit tailings facility at MRM, is the focus of this paper. The SEA has been constructed to its final dyke height and deposition and infilling operations to support closure were completed in 2019. The SEA abuts the south end of the MRM External Tailings Facility (ETF), which is also at its final height, where sand infilling is ongoing.

The closure landform design for the SEA has progressed from a conceptual design stage through to the reclamation soil cover placement stage in recent years. A closure and abandonment plan was submitted to the Alberta Energy Regulator (AER) after infilling of the SEA with Coarse Sand Tailings (CST) was completed. To support the closure design, geotechnical investigations and performance evaluations were completed to confirm the design assumptions prior to and during construction. Ongoing performance monitoring will continue following landform construction completion.

One of the key design goals is to be able to de-register the MRM SEA tailings facility by converting it into a solid earthen structure, with the intent that it will no longer be regulated as a dam. This conversion includes: stabilizing any remaining and potentially mobile material, constructing a landform to avoid excessive ponding of surface water, establishing robust drainage outlets for the plateaus, and minimizing erosion potential of the slopes for the long term.

The MRM SEA tailings facility will continue to be monitored over several years to assess performance of the landform. The resulting surface has received a reclamation soil cover and has been re-vegetated to create an interconnected system of boreal forest uplands for wildlife habitat and future traditional use. This paper provides details of the process followed for this integrated design: the construction, the long term monitoring plan, and Canadian Natural's path towards de-registration, along with recent insights and opportunities for similar landforms.

1 INTRODUCTION

Muskeg River Mine is located west of Canadian Natural's Jackpine and Sharkbite Mines on Mineral Surface Lease 13. The MRM SEA is located north of the convergence of the Athabasca and Muskeg Rivers. The SEA is also situated southwest of the active MRM mine pit and plant, and is bounded by Highway 63 to the west and the MRM access road to the east.

At MRM, to access the ore, overburden and inter-burden waste soils are stripped and placed into out-of-pit and in-pit waste dumps. As a result of processing the ore, tailings are produced and are deposited initially in out-of-pit storage facilities, like the SEA, before transitioning to in-pit storage cells.

In Alberta, each mine is required to submit a Life of Mine Closure Plan (LMCP) to the Regulator every ten years. These plans present the conceptual closure design for the mine and indicate how the mine will meet the overall objective of providing a landscape at closure that supports the development of a locally common boreal forest. Muskeg River Mine's current LMCP (Shell, 2016) lists the goals and objectives for the closure landscape and its component mining landforms and provides a conceptual closure and reclamation design for each landform (Ansah-Sam et.al, 2019).

For the SEA, the detailed closure design involved retrofitting to the facility to meet the closure objectives, while limiting the amount of regrading and material movement.

This paper presents the design processes for integrating a detailed closure landform into the existing tailings facility.

2 BACKGROUND

The SEA consists of a horseshoe shaped dyke extending off the southern portion of the ETF to the southern lease boundary. The SEA abuts the ETF, but each structure is considered a 'separate' landform for design and reporting purposes. The Main South Toe Berm (MSTB) of the ETF is a landform feature that helps reduce the transition slope between the ETF and SEA, given the 35 m vertical differential in final landform elevations. As these structures are closely bounded by mine infrastructure, and the lease boundary, opportunities for closure development outside of the current structure are very limited.

Construction of the SEA was completed using upstream cell construction and beaching techniques to elevation 306 m. After the 306 m dyke elevation was reached in 2017, Canadian Natural continued to remove Fluid Fine Tailings (FFT) through dredging operations and active infilling of the centralized SEA pond with CST. Coarse Sand Tailings infilling was completed in February 2019 and construction of the approved closure and abandonment plan was started in October 2019. The SEA landform construction was completed at the end of August 2020 (up to Phase 3 as represented by red-dashed border on Figure 1). Reclamation soils placement was completed by January 2021. The remainder of the vegetation and tree planting is planned to be completed in 2021.

3 CLOSURE APPROACH AND FRAMEWORK

The intent of the SEA closure approach was to ensure that a strategic process was in-place to progress the design, obtain stakeholder and management buy in, and to accomplish closure in a timely manner. The closure framework for the SEA is summarized below and the various activities and phases to support the closure approach and framework is outlined in Figure 1:

- Formulation of a closure strategy document;
- Review of the Design Basis Memorandum (DBM) for the MRM closure plan;
- Establishment of the SEA Closure Design DBM;
- Development of a planning-level landform design;
- Conduct a Failure Modes and Effects Analysis (FMEA);
- Prepare a detailed SEA closure design;
- Complete technical analyses; and
- Submit a Closure and Abandonment Plan.

4 CLOSURE STRATEGY DOCUMENT

The formulation of a closure strategy is recommended for any closure plan for an entire site. This document should be approved by senior management and used for the planning and design of the individual landforms as well. Contents of a strategy document should include whether the site will be designed for 'zero' maintenance or minimal maintenance at closure. The extent of work involved in a minimal maintenance strategy needs to be defined to allow for senior management to make an informed decision on which option works for the particular site. Since the strategy document usually contains capital/budgetary dependent decision, senior management decisions and endorsement are usually required.

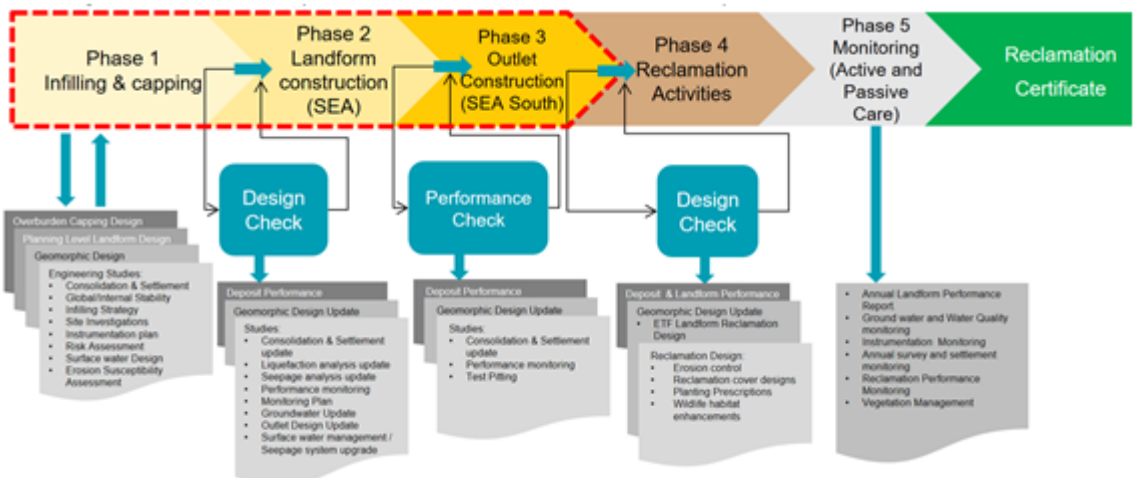

Figure 1. Activities and phases to support SEA closure approach and framework.

5 DESIGN BASIS MEMORANDUM FOR SITE WIDE CLOSURE PLAN

A review of the MRM site wide LMCP and DBM was the first step to progress the SEA closure design. This step ensured integration and alignment of the SEA landform design with the overall MRM site closure design, especially the goals and design objectives, and with the adjacent landforms (as-built or planned). A review of the existing site closure plan is crucial to the structure design since it needs to be consistent with the closure design of the structure or a revision to the site closure plan will need to occur in the next LMCP update to ensure consistency. If there is no site-wide closure plan, the authors recommend a closure plan be completed (at least on a conceptual level) prior to establishing a detailed landform design plan for a containment facility within the site.

6 SEA CLOSURE DESIGN BASIS MEMORANDUM

The establishment of a closure DBM specific to the SEA structure was important. Canadian Natural had to ensure that it was aligned with the overall MRM closure DBM and the authors recommend this practice for all closure designs.

The DBM approach was similar to earlier approaches as detailed in Ansah-Sam et al, 2016. Table 1 provides an example in the DBM for the SEA.

Table 1. Excerpt from SEA design basis.

Design Basis	Design Criteria	Comment
Avoid ponded water near slope crests.	• No permanently ponded water. • No temporary ponding in the critical zone or geotechnical buffer zone.	Ponded water near slope crests can cause gullying and geotechnical instability.
Accommodate beaver dams.	• Design channels to accommodate a 3 m high beaver dam. • Assume beaver dams wash out in 1 in 100 year flood.	It is anticipated some beaver dams will be created in the closure landscape and accommodating for them in design will still allow for channel flow.

7 PLANNING-LEVEL LANDFORM DESIGN DEVELOPMENT

The intent of the planning level stage was to advance a design to close, decommission, and obtain reclamation certification for the SEA. The objective of the design deliverable was to allow Canadian Natural to:

- Identify risks in the planning-level design and upcoming construction, and potential mitigation options for these risks, as well as opportunities associated with the future landform design and construction;
- Establish a work plan for detailed design and subsequent construction. This includes a plan for collecting additional data to support the future design and the steps required to take the future detailed design into construction; and
- Provide a design with enough detail for mine planners to use for any material balances required during an update to the mine plan.

This planning-level design also advanced Canadian Natural's plans to infill the SEA with tailings sand to displace and remove FFT and to cap the facility plateaus with waste or CST material to create a trafficable landform at closure. It incorporated conceptual plans, stability analyses of the SEA dykes, the Closure Landscape Plan (CLP) that was developed in 2016, and Canadian Natural's 2016 LMCP. It also included simplified settlement analyses to estimate the material required to accommodate settlement for planning purposes. The DBM prepared for the SEA design aligned with the Closure Landscape Plan (CLP) design objectives and criteria and included specific objectives and criteria to support the SEA closure and abandonment plan.

8 FAILURE MODES AND EFFECTS ANALYSIS

Two FMEA workshops were conducted for the SEA closure landform design in Q4 2017. The workshops were intended to identify and rank the potential failure modes and business risks associated with transforming this dam containing soft tailings to a landform that can be de-registered and on a potential path toward reclamation certification. Communicating these risks and challenges to mine and tailings planning, operations, geotechnical, and closure design groups was also a key function of the workshops.

The workshop format was designed and facilitated by Canadian Natural and was supported by consultants in preparing background pre-read materials for the workshop participants. Canadian Natural prepared an initial list of potential failure modes and distributed it to participants to individually score the probabilities and consequences; the results were compiled and discussed during the workshop sessions. Existing process controls were considered in the scoring, and mitigation options to further reduce the risks were identified. The workshop results were compiled and synthesized into two categories: a list of ten potential failure modes, and a separate list of eight business risks. The FMEA was revisited and revised in 2019, after infilling, and the detailed design had been completed for the SEA. In addition to the FMEA, an environmental risk assessment was also completed for the SEA in 2020.

9 DETAILED SEA CLOSURE DESIGN

The detailed SEA closure design uses the planning level design as a basis. The design basis details the stability and seepage analyses, settlement analyses, seismic deformation assessment, updated surface water management design, and monitoring plans. The primary goal for the overall SEA landform design is to de-register the dam and to obtain reclamation certification for the landform.

The following are the supporting goals adopted for the design:

- Provide safety for personnel and equipment working on the landform and meet dam safety criteria for all stages of tailings infilling, stabilization, and reclamation;
- Create a safe and geotechnically stable landform (including the plateau, drainage outlet, and slopes) that is designed to require minimal long-term maintenance;

- Control surface water through design of topography, water courses, and wetlands such that water is safely conveyed off-landform to the proposed lease-wide surface water drainage system in a way that minimizes erosion and sedimentation;
- Integrate the landform with the site-wide closure landscape including natural areas and adjacent mining landforms; and
- Allow efficient tailings placement and capping to form a surface that can be reclaimed using typical mine reclamation equipment.

An in depth desktop review of additional information for the SEA, such as construction and design history, is the next step to identify any other key constraints and items that will need to be considered for the detailed landform design.

The landform design process for the SEA involved the following deliverables: geotechnical constraints map development, finalization of the DBM, alignment and collaboration between disciplines, detailed design, opportunities and risks identification, stages of construction and design packages, collaboration and alignment with internal and external stakeholders, and incorporation of any stakeholder commitments.

The geotechnical constraints map is used as a key guide for the overall design process, as design decisions can be easily compared to spatial constraints (Ansah-Sam et al, 2019). Figure 2 provides an example of the geotechnical constraints map utilized for the SEA project.

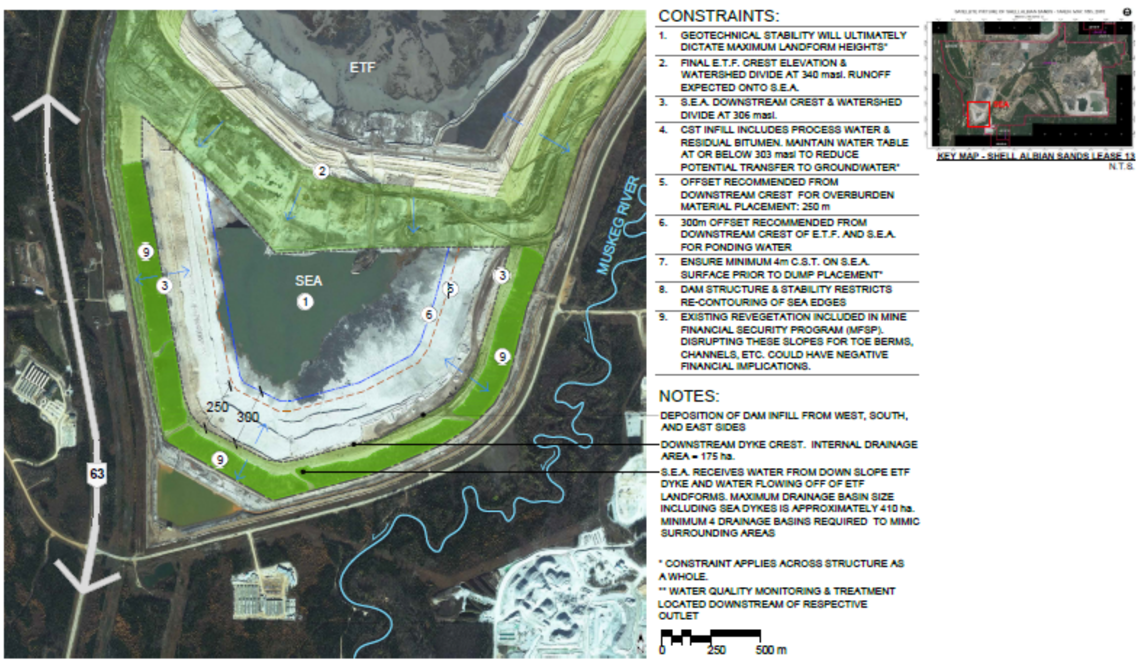

Figure 2. MRM SEA geotechnical area constraints map.

The SEA landform design process involved the following disciplines: Mine and Tailings Planning teams, Geotechnical teams, the Engineer of Record, Environmental teams, Reclamation and Closure teams, Closure designers, and Regulators. Working with these disciplines, the design process identified any gaps in the current performance of the SEA that needed to be addressed for closure. There was a design objective to achieve a cut-and-fill balance to minimize hauling waste material on or off the plateaus. There was one location within the main outlet channel where a decision was made to re-disturb an already reclaimed area to allow for the channel construction. This was a challenging decision given that the reclaimed areas usually have several years of good vegetation growth. For SEA there were limited opportunities to design the plateaus to look more like natural analogues in the region since vegetation re-disturbance would have been required and therefore a balance had to be struck between these competing priorities. The SEA design therefore focused on adjusting the overall geometry and grading to the meet the new design criteria.

Following the completion of the draft design, additional opportunities and risks were identified, under the broad categories of planning, construction, geotechnical, environmental, and cost. The design was then updated to reflect the identified opportunities and risks, and risk mitigation measures were put in place. Residual risks related to long-term landscape performance will be addressed with a long-term monitoring and maintenance plan (Fair et al., 2014) in the closure landscape. A SEA site-wide risk register and FMEA is maintained and updated as risks are addressed or mitigated. The design SEA final landform closure surface, before construction, is shown in Figure 3.

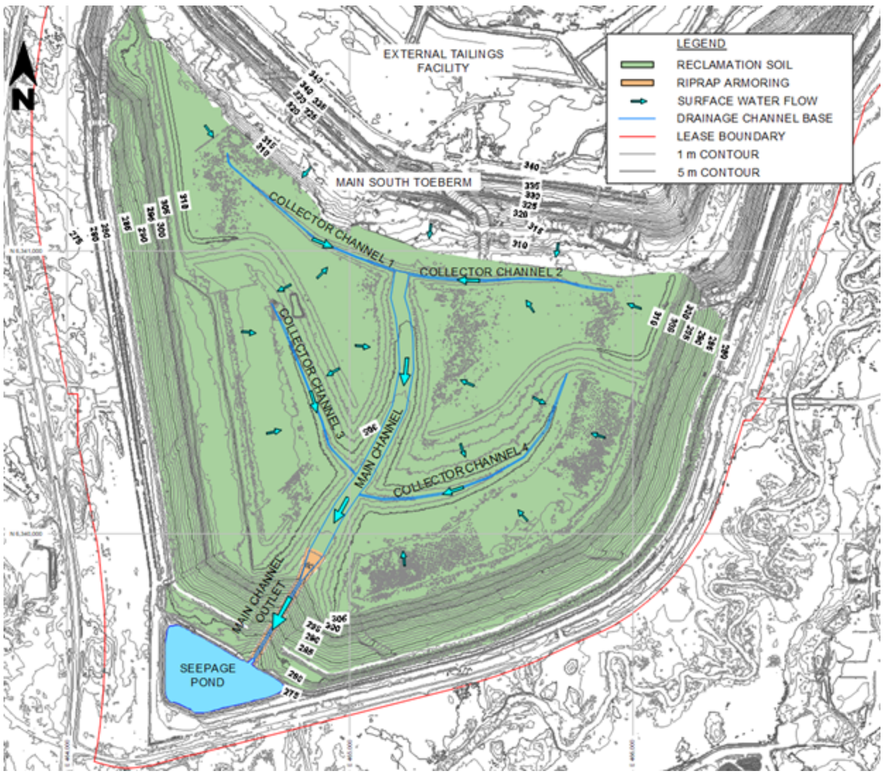

Figure 3. SEA closure design.

10 SUMMARY OF TECHNICAL ANALYSIS

This section summarizes the methodology and results of some key analyses completed by Canadian Natural's retained consultants, such as: stability analysis, seepage analysis, settlement assessment, surface water management, and a run-out assessment. Liquefaction and seismic deformation assessments were also completed, but are not covered in this paper.

10.1 *Stability Analysis*

Slope stability was assessed to verify the target Factor of Safety (FOS) was achieved for all design sections at the SEA with the proposed landform configuration applied. The transition from End of Construction/Operations to Long-term Conditions will be evaluated on an on-going basis using updated performance data with time.

10.2 *Seepage Analysis*

Seepage analyses to estimate the rate of drainage and the resultant phreatic surface were completed for the SEA. For steady state seepage analysis, the as-built landform cross section geometry, vibrating wire piezometer (VWP) monitoring data, and the most recent pore pressure dissipation test results from cone penetration tests (CPT) were used for calibration. For transient seepage conditions, the analysis assessed the potential timelines during which the existing internal drains in the SEA would be required to remain functional. Results showed that the internal drains installed in the SEA should be maintained as long as possible to increase the rate of drain down of the phreatic surface within the dyke over time. According to the analyses, drains in the West, South and East analysis zones of the dyke will receive seepage water until 2050, 2043, and 2066, respectively. Practical measures will be undertaken to maintain drain function for this period, though the drain function is not necessary for the structure stability.

10.3 *Settlement Analysis*

Settlement analyses were completed to obtain a high-level estimate of potential settlements post-infilling. 2017 and 2018 CPTs showed that most of the tailings within the SEA are sand-dominated, and therefore, settlement is expected to be located in localized high fines areas. Any tailings sample in the SEA with less than 15% fines was considered as fully consolidated.

Large strain consolidation tests on fluid fine tailings (FFT) from the MRM ETF were used to derive the hydraulic conductivity and compressibility curves for the SEA. A 1-D consolidation program (FSConsol) based on finite strain consolidation theory (see Gibson et al, 1967) was used to estimate the settlement and consolidation time. Soil and groundwater conditions encountered at the locations of the 2017 and 2018 CPT soundings, later updated with data from 2020, were used to develop FSConsol models at selected locations. Based on this preliminary assessment, settlements were estimated to be < 1.5 m where high fines were encountered within the infilled tailings. 90% of the settlement is expected to occur, at the latest, by 2031. Estimated settlements are considered to be conservative and further testing on samples in the SEA and back analysis, using installed settlement plate data, is ongoing.

10.4 *Surface Water Management*

Table 2 provides the criteria adopted for surface water management at the SEA landform.

Table 2. SEA landform final surface water management criteria.

Item	Criteria
Channel classifications and design events	Critical (major impacts; 1:10,000 year flood). Semi-critical (significant impacts; 1:1000 year flood). Non-critical (minimal impacts; 1:100 year flood). Beaver dams 3 m high wash out in the 1:100 year flood.
Channel evolution	Accept for non-critical channels and critical channels – no erosion.
Time periods	Interim (when at least some surface water must be retained). Closure (after all surface water is acceptable for release).

10.5 *Run-out Assessment*

A run-out flow assessment was completed for the SEA to determine the potential volume and distance traveled by loose tailings material if a liquefaction event occurred behind the main channel. The sequence of events assumed the failure mechanism included: erosion after a significant rainfall event, causing over-steeping of the main channel outlet, leading to instability in the tailings upstream of the channel (a failure mode identified during the FMEA workshop), and a potential flow of tailings material beyond the SEA toe footprint.

There were several approaches used to identify appropriate run-out geometry for this scenario, including:

- Estimation of the geometry from observations of past events (e.g., Martin, Al-Mamun, and Small 2019);

- Empirical relationships between total stored volume (fluid and tailings) and the total released volume (e.g., Rico, Benito, and Diez-Herrero 2008);
- Calculation of the total released volume based on the solids content in the outflow and the amount of water stored in the surface pond (e.g., Fontaine and Martin 2015); and
- Empirical relationships between released volume and the ratio of the surface water pond and the total tailings volume (e.g., Rourke and Luppnow 2015).

After several discussions and reviews between Canadian Natural and the design consultant, it was agreed to use an assumed post-failure slope to identify an outflow volume. That post-failure slope was guided in this case using the post-failure geometry of the failure at Cadia Valley Operations (CVO; Jefferies et al., 2019), which was selected as an analogue based on multiple similarities. Based on the CVO example, a SEA run-out volume was determined by projecting a 10H:1V conical shape (side and back slopes) from the intersection of the upstream toe of the starter dyke and outlet channel centerline. The initial maximum width of the outlet channel was 28 m and the base width was 5 m. The assessment concluded that the likelihood of the run-out event would be low, the volume of tailings mobilized would be low, and the impact to fisheries, wildlife habitats, rare or endangered species, unique landscapes, or sites of cultural significance would be short term and with minimal affects and impacts.

11 CLOSURE AND ABANDONMENT PLAN

Approval of the closure and abandonment plan is a regulatory requirement under the Alberta Dam and Canal Safety Directive (ADCSD). The SEA Closure and Abandonment Plan addressed:

- Canadian Natural's approach to the 2018 ADCSD (AEP 2018);
- A construction and performance summary from historical Annual Construction and Performance Reports (ACPRs);
- Canadian Natural's framework for closure of the SEA. This section also contained a summary of the following:
- The ETF & SEA Overburden Capping Design report;
- The SEA planning-level landform design report;
- The SEA detailed closure design report; and
- The SEA FMEA.

The closure and abandonment plan was approved prior to construction of the final plateaus and drainage channels on the SEA.

12 ALIGNMENT AND COLLABORATION BETWEEN DISCIPLINES

Alignment was aided by presenting the DBM for review comments and sign-off by the teams before proceeding with the design. For the SEA, the DBM considered the balance of economic, reputational, and technical risks. There will always be competing priorities between various disciplines, however there is always a balance that can be struck between those competing priorities to create a fit for purpose design that meets internal and external stakeholder needs.

The closure design package with the supporting design report was submitted to internal stakeholders for sign off on the overall design. This was done by providing an Issued for Review (IFR) package prior to the final submission of Issued for Construction (IFC) packages. This process is progressed more efficiently if stakeholders were involved from the DBM stage right to the landform design stages of the facility. The IFR drawings are rolled out to all stakeholders including those who will be executing the design.

13 LANDFORM CONSTRUCTION EXECUTION

As the SEA was a brownfield site, separated from the active mining activities, a smaller fleet of equipment was required to execute the design. Canadian Natural's Mine Projects group oversaw resourcing the contractors, inclusive of Quality Control (QC) personnel and surveyors, for the duration of the project. Weekly status updates were prepared and reviewed with stakeholders throughout the project to ensure alignment.

An IFC drawing package for the SEA landform bulk earthworks included armoured outlet details that also specified material parameters, testing requirements, and the construction set-out points. Construction staging was executed to ensure the outlet was in-place and available to convey flow off of the SEA plateau before spring rains. The Engineer of Record (EOR) addressed field modifications during execution after an approved design change or revision had been discussed with the design team.

An IFC package for the vegetated channel scope was also completed. This scope was executed (in the same manner as the bulk earthworks) with Canadian Natural's Environment and Closure and Reclamation teams directly involved in the successful deployment of reclamation materials and planting activities. Reclamation soil placement was staged to take advantage of direct placement (hauled direct from another area of the mine being stripped ahead of ore mining) in winter months, while vegetation planting was executed in summer months.

The SEA completion report was prepared and submitted to the Regulator documenting all earthworks activities, testing, and as-built records in December 2020, per ADCSD requirements (AEP, 2018). In addition, all as built records and designs were kept as per Canadian Natural's documentation process. Figure 4 provides an aerial view of the constructed and armoured spillway at the SEA.

Figure 4. Constructed SEA spillway channel.

14 SEA PERFORMANCE MONITORING

During SEA construction, dyke performance was assessed against the design requirements through a combination of visual inspection and the monitoring of geotechnical instruments installed within the dyke slopes and foundation. Geotechnical instruments installed at the SEA to support performance assessments include:

- Slope inclinometers and Shape Array Accelerometers (SAA) to monitor for displacements and/or deformations;
- Vibrating Wire Piezometers (VWP) and Standpipe (SP) water wells to measure construction induced pore pressures and/or to establish the phreatic surface through the dyke; and
- Internal drain pipes to control the phreatic surface and allow seepage flow measurements.

Changes to instrumentation reading frequency were made to reflect construction activity, in response to performance results, or were event driven. The frequencies for monitoring instruments within the SEA dyke were reduced to reflect the transition of the SEA from an active tailings facility to a solid structure based on performance after the SEA reached its ultimate design elevation in 2017.

As the SEA was being infilled, a Cone Penetration Testing (CPT) investigation of the beaches was completed. The CPT investigation was executed to confirm sand density and identify potentially liquefiable zones within the beaches. Vibrating Wire Piezometers were installed to assist in monitoring drainage of the landform with time. Data from these CPTs and VWPs were also utilized to assess where trafficability issues may be encountered during landform construction, specifically within the drainage channel excavations. The Vibrating Wire Piezometers within the infilled deposit have been equipped with radio transmitting data loggers to allow data to be collected monthly to minimize 'disturbance' on the reclaimed surface of the SEA.

Settlement plates were installed in areas targeted from CPT assessments as having potential for settlement over time. Since installation, centimeter scale settlements have been observed. Surveyors will continue to measure these instruments at a frequency set by the EOR until settlement subsides. If settlements beyond tolerances occur, local remediation to establish the design grade is planned.

During SEA landform construction, Quality Control (QC) monitors were present to record and document construction activities, sample soils for laboratory testing, and perform compaction testing.

A visual inspection of the SEA by the EOR is completed and documented nominally on a monthly basis. A summary of all instrumentation performance data is prepared and reviewed monthly by the EOR. In addition, a summary of all performance and inspection findings is prepared and submitted to the Regulator on an annual basis.

15 COLLABORATION AND ALIGNMENT WITH EXTERNAL STAKEHOLDERS

Discussions with the AER started prior to the final design of SEA closure being completed and submitted. Updates were also provided to the regulator throughout the design and construction process. The SEA closure designs was submitted to the regulator under the Closure and Abandonment Plan in 2018.

In addition, the SEA closure design was discussed with First Nations stakeholders and input provided was incorporated into the design as much as practicable.

It is recommended that the details of a landform design be presented to external stakeholders for input. In addition, any processes that the operator may be considering should be discussed with the regulator prior to final submission. This provides an opportunity to obtain feedback prior to submission and potentially allows for a 'smoother' approval process.

16 ADAPTIVE MANAGEMENT

An adaptive management model is used to guide construction, monitoring, and maintenance of the landform (CEMA 2014). As design and construction proceeded, learnings and new information were applied.

As more landforms are constructed and closed within the site, and in industry, additional experience and information will become available that will allow for adaptation of future closure designs. The SEA will be monitored for several years to assess performance.

17 CONCLUSIONS

The design process presented in this paper provides a method for integrating closure designs into an already existing structure and collaborating with internal and external stakeholders to successfully complete the construction of the structure. It also lays out the engineering considerations that needs to be incorporated into the final design. The process also included active participation of all key parties and stakeholders inside and outside of Canadian Natural. Monitoring of the structure will continue and any learnings will be applied to other landform designs within the Canadian Natural site.

18 ACKNOWLEDGEMENTS

The authors would like to acknowledge the following Canadian Natural staff: Mine and Tailings Planning (Michael Bowal, Ali Chamanara, Zeev Cherniawsky, Art Gierach and Ben Roy), Regulatory (Scott Wytrychowski), Environment (Fred Kuzmic, Robert Vassov, Mark Bateman, Ainslie Campbell, Sherri Hanlon), Geotechnical, Hydrogeology and Closure (Scott Martens, Bernard Dzirasah, Kyle Loyer, Evan Davison, Brittany Skinner), Mine Projects (Gary Dolan, Manuel Garbin, Leo Moreno, Curtis Bowal, Uddam Islam, Corey Jacobs and Barton Meadus). The design consultants (BGC Engineering and Klohn Crippen Berger) and the construction crew (Ledcor Group and Little Smoky Forestry Service) are also acknowledged for their support on this project.

19 BIBLIOGRAPHIES

Ansah-Sam M, Hachey L, McKenna G, Mooder B., 2016. The DBM Approach for Setting Engineering Design Criteria for an Oil Sands Mine Closure Plan. Proceedings of the Fifth International Oil Sands Tailings Conference; Lake Louise Alberta, Canada.

Ansah-Sam, M, McGreevy J, McKenna G., 2019. Canada Processes for the Closure Design of Greenfield and Brownfield Overburden Dump Sites.

Canadian Natural, 2018. Muskeg River Mine, South Expansion Area Closure and Abandonment Plan.

Canadian Natural, 2020. Muskeg River Mine South Expansion Area Consequence Classification Re-Assessment.

Cumulative Environmental Management Association (CEMA), 2012. Oil Sands End Pit Lakes Guidance Document. CEMA. Fort McMurray. 494p.

Cumulative Environmental Management Association (CEMA), 2014. Guidelines for Wetlands Establishment on Reclaimed Oil Sands Leases. Third Edition.

Fontaine, D.D., and V. Martin. 2015. "Tailings Mobilization Estimates for Dam Breach Studies''. Proceedings of the 2015 Tailings and Mine Waste Conference. Vancouver, BC, October 26-28, 2015.

Gibson R, England G, Hussey M. 1967. The theory of one-dimensional consolidation of saturated clays. Finite non-linear consolidation of thin homogeneous layers. Geotechnique 17(2):261-273.

Government of Alberta, 2018. Alberta Dam and Canal Safety Directive. Policy: AEP Water Conservation 2018 No. 3.

Jefferies, M., Morgenstern, N., Van Zyl, D., and Wates, J., 2019. "Report on NTSF Embankment Failure Cadia Valley Operations - Final". Issued by the Independent Technical Review Board to Ashurst Australia April 17, 2019.

Martin, V., M. Al-Mamun, and A. Small. 2019. "CDA technical bulletin on tailings dam breach analysis''. Proceedings of the 87th Annual Meeting of the International Commission on Large Dams (ICOLD). Ottawa, ON, June 9-14, 2019.

Rico, M., G. Benito, and A. Diez-Herrero. 2008. "Floods from Tailings Dam Failures". Journal of Hazard Management. pp. 79-87.

Robertson, P.K. 2010. "Evaluation of flow liquefaction and liquefied strength using the cone penetration test". Journal of Geotechnical and Geoenvironmental Engineering. 136 (6): 842-853.

Rourke, H. and D. Luppnow. 2015. "The Risks of Excess Water on Tailings Facilities and its Application to Dam-break Studies". Proceedings of the Tailings and Mine Waste Management for the 21st Century Conference. Sydney, NSW, July 27-28, 2015.

Using a test embankment program to support the design and construction of a tailings closure dam near the crest of an open oilsands mine pit

Logan Hurlbut, Mathieu Boudreau & Lucy Philip
Stantec Consulting Ltd., Calgary, Alberta, Canada

Philip Alsop & Anthony Burnett
Syncrude Canada Ltd., Calgary, Alberta, Canada

ABSTRACT: In 2019 and 2020, Syncrude Canada Ltd. and Stantec Consulting Ltd. developed the design of the South Closure Dam (SCD). The dam has different characteristics from typical oilsands structures because the dam is relatively narrow, low, long, and at the crest of an existing pit. A test embankment program addressed technical uncertainties with the following goals:

– Characterization of weak, laterally unconstrained and gas exsolved, clay layers to understand pore pressure response under small loads.
– Assessment of borrow materials for construction.
– Evaluation of construction techniques in a constrained footprint, to support specification development.

This paper presents background to the SCD, uncertainties addressed by the program, background to successful test embankment design, design, observations, challenges, and adjustments to the program during construction, and post-construction assessment. The findings offer insights to test embankment design and construction, and contributes to the knowledge base for pore-pressure response over shallow McMurray Formation clays.

1 BACKGROUND TO THE SCD

In 2019, Stantec and Syncrude began preliminary design work for a tailings dam approximately 7 km long, up to 10 m tall with an average height of 4.5 m and situated at the crest of an existing oilsands mine pit. The characteristics for the dam were different from typical oilsands tailings dams in that the dam is relatively long, narrow, low in height (compared to typical 40 m to 100 m tall dams and waste dumps) and present at the crest of an existing mine pit. There were technical uncertainties that needed to be overcome to support design and construction.

The dam's foundation soils include weak McMurray formation clay layers, for which behavior (strength and pore pressure response) under large loads and in laterally constrained arrangements is generally understood. However, there are no directly related examples or experience in overcoming the uncertainties for embankment construction over these geological layers with low-height fills, narrow footprint and adjacent to the existing pit wall. The designers hypothesized that the pore pressure response would be favorable compared to the typical industry accepted values due to lower stress application, partial drainage and laterally unloaded clay layers.

The design required retrofitting the existing and planned slopes based on the arrangement of the clay layers near the pit wall to meet Canadian Dam Association (CDA) guidelines for target stability factor of safety (FOS), which are greater than the typical target criteria for pit walls.

The design required development of construction specifications for the relatively small-scale construction, compared with large embankment construction (i.e., >50 m wide lifts) typical in the oilsands industry. Evaluation of proposed borrow materials and construction techniques for use in the low-permeability zone of the embankment was required to confirm design assumptions. The SCD's upstream low-permeability zone is typical of large oilsands tailings dams.

To help resolve the technical uncertainties and support design and construction, the team designed and observed construction of a test embankment program (TEP). This included adjustments to the program during construction, and post-construction assessment.

1.1 *SCD Typical Design Arrangement*

The design of the SCD is a zoned-earthfill embankment constructed using compacted engineered fill materials. The zones of the SCD cross-section include:
- An upstream high specification low permeability mechanically placed zone.
- A base excavation high specification low permeability mechanically placed zone with minimum width of 10 m keyed onto the McMurray Formation
- A downstream mechanically placed tailings sand zone.
- At the end of construction, the dam will have a variable downstream height of up to 10 m and an average height of 4.5 m.

2 BACKGROUND ON SUCCESSFUL TEST EMBANKMENT DESIGN AND EXECUTION

2.1 *Why Use a Test Fill?*

Large-scale, prototype TEPs are generally expensive and complex, requiring an earthworks contractor. Therefore, they are generally not undertaken for design of typical embankment construction projects, rather they are more often included as part of construction bid, if required. Benefits for selecting the use of a test fill program at the design stage for a project may include:
- Confirming design assumptions ahead of construction
- Identifying optimization/cost reduction opportunities
- Proving constructability
- Validating material borrow sources
- Investigating foundation performance

2.2 *Design Guidance*

Several industry documents are available for guidance for the design of a TEP and were used during the development of the TEP design for the SCD:
- USACE EM 1110-1-1804 Geotechnical Investigations Chapter 6 Section I – Test Excavation and Fills
- USACE EM 1110-2-2301 Engineering and Design Test Quarries and Test Fills

2.3 *Design Considerations*

A TEP can provide many benefits, and through proper design, can resolve uncertainties. To realize the benefits of a TEP, there should be careful evaluation and planning. Some design considerations for increasing value of the program include:
- Planning of quality control tests to validate a range of design parameters. The TEP program should be designed to isolate and evaluate as many material parameters as possible.
- Planning construction to evaluate multiple construction techniques and variables. Construction variables may include borrow material sources (isolated into distinct placement panels), lift thicknesses, construction equipment, and methods of moisture conditioning.
- Instrumentation installation should happen ahead of the TEP with a suitable timeframe to establish baseline conditions before loading.
- To confirm requirements for additional scope or variations to scope, the results of the surveys and in-situ testing need to be fed back to the designer expediently.
- Geometric design and location of the TEP may form part of the final embankment construction, assuming the test construction passes quality control and quality assurance specifications. Any

areas or materials that do not meet specifications will require remediation to incorporate the test embankment into the final structure.

Due to the experimental nature of a TEP, there is a need for flexibility and changes in construction and monitoring. The TEP may need to be modified based on: material variability; field observations; initial results; equipment performance; success or not with processing and/or other factors. Additional borrow areas and/or test fills and/or changes to compaction methods may be required if the proposed materials or construction procedures do not result in favorable characteristics or if optimization opportunities are identified. A transparent price structure should be agreed so that the cost implications of changes are readily anticipated and understood.

3 SCD TEST EMBANKMENT PROGRAM DESIGN

3.1 *Test Embankment Program Objectives*

The objectives of the SCD TEP were to:

– Evaluate the suitability of the proposed low-permeability fill material borrow sources.
– Evaluate and provide information on the equipment proposed for the SCD construction.
– Evaluate relevant properties of the compacted fill such as density, hydraulic conductivity, presence of blocky clays after placement and compaction, and homogeneity.
– Evaluate the results of placing the fill material in 0.3 m, 0.5 m and 0.75 m thick lifts to determine compaction requirements can be met for various lift thicknesses.
– Develop guidance for a method specification for fill compaction during construction.
– Increase stress above vibrating wire piezometers (VWP), monitor pore pressure response in the foundation clays and provide data for confirmation/refinement of the SCD design.

3.2 *Characterization of Estuarine Middle McMurray Clays*

The McMurray Formation has historically been informally subdivided into lower (fluvial), middle (estuarine) and upper (coastal plain) (Hein and Fairgrieve (2012)). The Middle McMurray (MM) member generally comprises interbedded bitumen bearing sands and mudstones that were deposited in a shallow, deltaic estuarine environment. Geotechnical borehole drilling for the SCD design during 2019 and 2020 generally encountered sand-dominant facies with layers of clay/silt dominant facies in all areas of the proposed footprint. The geotechnical design of the SCD subdivided the MM into two units: MM Clays and MM Mixed. Where present, the MM Clays frequently governed the upstream stability of the SCD, with potential failures into the existing pit. The MM Clays are the subject of the pore pressure response investigation in the TEP.

The results of geotechnical laboratory testing of samples retrieved during 2019 and 2020 borehole drilling programs indicated that the MM Clays have a range of medium to high plasticity with Atterberg liquid limit values ranging from 23 to 55. The liquidity index values ranged from -0.6 to 0.4, indicating the MM Clays are over-consolidated. The grain-size distribution test results indicated gravel content of 0% to 1% (with one outlier), the sand content ranged between 0% and 35%, the silt content ranged between 50% and 70% and the clay content ranged between 9% and 40%. To design for excess pore pressure response due to relatively rapid loading, the SCD design used the $\bar{B}$ parameter (GEO-SLOPE (2021)) shown in Equation 1 where Δu is the change in pore pressure and $\Delta\sigma_v$ is the change in total vertical stress (which is an approximation for change in major principal stress):

$$\bar{B} = \frac{\Delta u}{\Delta \sigma_v} \quad (1)$$

The original design value for the SCD was $\bar{B} = 0.6$, based on previous experience and design values used at the same mine under much higher dams, without drainage to a free pit face. The design pore pressure parameter was a key variable to be evaluated with data from the TEP.

3.3 *Instrumentation*

Two VWPs were installed during the summer of 2020 in a location within the proposed test embankment footprint. These VWPs were installed within relatively shallow MM Clay and interbedded MM Mixed layers near the pit wall at depths of 11.0 m and 16.6 m. Downhole wireline geophysics were used to aid the installation of the VWP tips. The TEP added approximately 5 m of additional fill above the VWPs during construction in October to November 2020 and the VWPs were further loaded by a 4.2 m material stockpile during March and April 2021. The VWP data was logged on 15-minute intervals during TEP loading and at monthly intervals after.

3.4 *Borrow Materials*

The SCD TEP was constructed using borrow of McMurray Formation inter-burden material generated during mining. Two types of material were used for the test embankment construction and placed in separate panel areas. The nomenclature used for specifying these materials was GR15 and LOS. GR15 generally comprises lean oilsands containing less than 15% blocky clays. LOS is similar to GR15 but with no allowable blocky clays. Fill material was obtained from the same lithological facies anticipated to be used for the SCD construction.

3.4.1 *Design Specification for Low Permeability Materials*

The low-permeability fill material specification for the SCD design includes:

- A mixture of low-grade McMurray Formation oilsands and McMurray Formation clays
- Allowable bitumen content of 4% to 7%
- Maximum blocky clay content of 15% measured as a portion of the mine pit bench height.
- Clay should break down and be well mixed within the matrix of the fill material and no longer blocky once loaded, placed, and compacted.
- Allowable ranges of particle size gradation and plasticity

3.4.2 *Borrow Materials Properties*

Laboratory testing results on the GR15 and LOS materials used to construct the TEP are summarized in Table 1and Table 2.

Table 1. GR15 laboratory testing results

Material Type	Grain Size Analysis (%)				Atterberg Limits			Fluid Content	Bitumen Content
	Gravel	Sand	Silt	Clay	LL	PL	PI		
GR15	0	35	57	8	28	15	13	15.4	N/A
GR15	0	43	55	2	23	10	13	14.4	3.48
GR15	0	28	67	5		Non-Plastic		16.4	4.24
GR15	0	32	62	6		Non-Plastic		16.4	4.46
GR15	0	38	58	4		Non-Plastic		14.4	4.71
GR15	0	38	57	5		Non-Plastic		14.7	3.51
GR15	0	32	58	10	28	12	16	16.1	4.18
GR15	0	32	62	6	27	13	14	13.8	3.68

Table 2. Lean oilsands laboratory testing results

Material Type	Grain Size Analysis (%)				Atterberg Limits			Moisture Content	Bitumen Content
	Gravel	Sand	Silt	Clay	LL	PL	PI		
LOS	0	40	57	3		Non-Plastic		14.6	4.13
LOS	2	37	57	4		Non-Plastic		15.3	3.9
LOS	0	35	60	5		Non-Plastic		16.6	N/A
LOS	4	35	57	4		Non-Plastic		14.4	4.31

3.5 *Geometry and Layout*

The layout of the SCD test embankment is shown in Figure 1. Figure **2** shows a cross section through the test embankment at the VWP location. The configuration of the TEP was selected by considering constraints of existing infrastructure (existing pit wall, construction of an adjacent in-pit dyke, an existing dewatering ditch, access roads and laydown areas), constructable fill widths based on the proposed construction equipment, accessibility, stress distribution of fill loading over the VWPs, available material borrow volumes and construction schedule.

The SCD TEP fill will ultimately be partially incorporated within the SCD structure and partially within an adjacent in-pit dyke structure. The selected location allowed the material placed for the TEP to remain in-place and reduce later construction efforts required for these two structures. Due to this arrangement, minimum requirements for material and construction specifications for these two structures had to be met and verified during TEP construction.

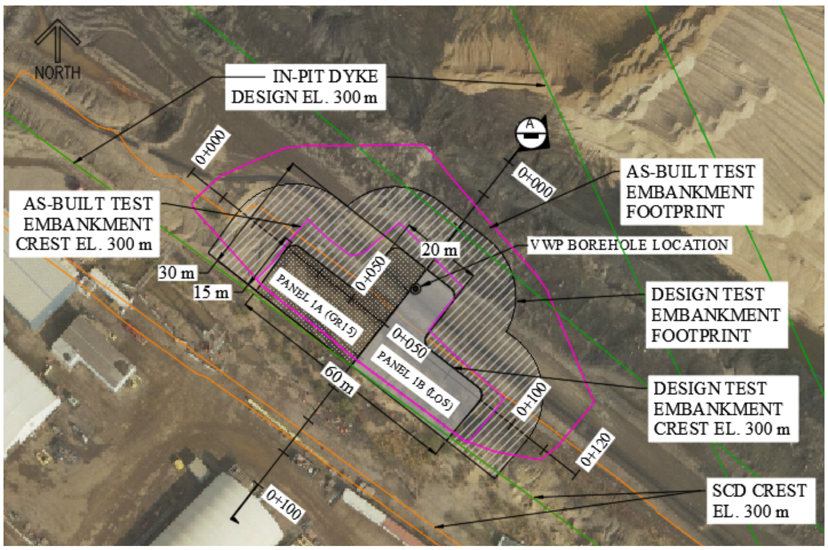

Figure 1. Test embankment layout

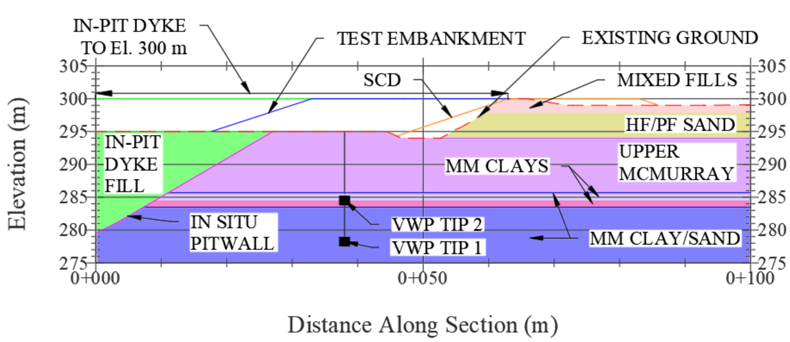

Figure 2. Test embankment cross section A

3.6 *Construction Methodology*

The TEP methodology included foundation preparation (remediation and backfilling of the existing seepage control ditch), subgrade preparation (scarifying, compaction, QC testing, QA inspection and placement approval) and a prescriptive plan for lifts in defined test panels. Two sets of test panels were designed to evaluate variables for the test fill construction including fill material type, lift thickness, placement/spreading and compaction equipment. Details of the test panels are summarized in Table **3**.

Table 3. Test embankment panel characteristics

Panel ID (Material Type)	Panel Length	Test Fill Elevation (m)	Lift Thickness	Number of Lifts	Construction Equipment
1A (GR15)	30 m	295 – 296.5 (1.5 m thick)	0.3 m	5	AT-730, vibrating roller (6.5 t and 16.5 t), D6 or D8 Dozer
		296.5 – 297.5 (1.0 m thick)	0.5 m	2	AT-730 and AT-740, vibrating roller (16.5 t), D6 or D8 Dozer
		297.5 – 299 (1.5 m thick)	0.75 m	2	CAT 777, D8 and D10 Dozer
		299 – 300 (1.0 m thick)	0.5 m	2	CAT 777, D8 dozer
1B (LOS)	30 m	295 – 296.5 (1.5 m thick)	0.3 m	5	AT-730 and AT-740, vibrating roller (16.5 t), D8 Dozer
		296.5 – 297.5 (2.0 m thick)	0.5 m	2	AT-730 and AT-740, vibrating roller (16.5 t), D6 or D8 Dozer
		297.5 – 299 (1.5 m thick)	0.75 m	2	CAT 777, D8 and D10 Dozer
		299 – 300 (1.0 m thick)	0.5 m	2	CAT 777, D8 dozer

3.7 *Survey, Testing and Field Monitoring*

3.7.1 *Survey Control*

An initial base-line survey was undertaken to record the prepared foundation prior to test fill placement. Ground-based survey was also undertaken with the progression of compacted lifts. A final survey of the as constructed test fill recorded the final dimensions of the embankment.

3.7.2 *Geotechnical Testing*

In-situ and laboratory testing was conducted on the test embankment fill as placement progressed. Summaries of the in-situ and laboratory testing are shown in Table 4 and

Table **5**.

Table 4. In-situ tests and testing frequency

Description	Test Method	General Purpose	Test Details	No. of Tests/Measurements
Field Density	ASTM D6938	Compaction performance	Nuclear densometer, sand cone (for validation tests)	Min. 3 per lift
	ASTM D5030		Water replacement Test pit (Larger scale)	Min. 1 per material type/lift thickness set
Field measurement of infiltration rate	Percolation Test	Field-Saturated Hydraulic Conductivity	Falling head and constant head percolation	One per material type and largest acceptable lift thickness, target lift interfaces
Test pit / trench	Material fabric, condition	Visual observation, documentation, grab samples	Notes, photographs by qualified geotechnical personnel	2 per panel per set of lifts.

Table 5. Laboratory tests and testing frequency

Description	Test Method	General Purpose	No. of Tests/Measurements
Standard Proctor	ASTM D698	Compaction benchmark	Min of 1 per each type of material (PG2, GR15 and LOS. Additional tests when material change.
Moisture content	ASTM D2216	Soil characteristic	Min of 1 per proctor and 4 per test pit/trench
Atterberg Limits	ASTM D4318	Soil index test	Min of 1 per proctor and 2 per test pit/trench
Grain-size curve	ASTM D7928	Soil index test	Min of 1 per proctor and 2 per test pit/trench
Flexible-wall permeameter	ASTM D5084	Permeability	Min of 1, select location based on construction performance
Bitumen content	Dean-Stark extraction	Soil characteristic	Min of 1 per proctor and 4 per test pit/trench in GR15 and LOS

3.7.3 *Field monitoring*

Representatives from the design team were present during construction of the test embankment program to provide technical support, take visual observations and document key activities including foundation preparation, lift placement and compaction, quality control testing, and review of test trench excavations.

After each series of lifts, observation trenches, minimum base dimensions 2 m by 5 m, were excavated across the fill, transversely and longitudinally within each test section (four in total). The trenches were excavated to the bottom of the test fill lift, with selected trenches meeting Alberta OH&S regulations so that field QA personnel could enter and make observations. Photographs were taken to document conditions. Particular observations included any visual separation, segregation or low-density zones that might have been present at the interface between lifts. Observations within the test trenches also focused on recording material variability (homogeneity, breaking down of clay lumps during placement and compaction, trends of moisture content and bitumen content, etc.) for relation to construction performance. Excavated trenches were backfilled and compacted in 0.3 m lifts to avoid presence of local defects.

4 CONSTRUCTION

4.1 *Challenges during construction*

The main challenge encountered during the construction of the TEP was the onset of cold weather conditions. The TEP was intended to be undertaken during summer months but experienced delays and the TEP could not be delayed further to the SCD project schedule. The cold weather conditions resulted in slowed progress of construction, and measures were implemented to fulfill testing and quality requirements. These measures included:

- Placing layers of loose sacrificial material to protect installed lifts from precipitation and freezing during construction breaks and overnight periods. This layer was removed prior to placement of the next lift. This resulted in material wastage and decrease in productivity. The placement and removal of material also contributed to some variation within the recorded VWP data.
- Monitoring forecasted weather conditions to plan works during warmer days
- Hoarding, heating and extra equipment was required for undertaking some in-situ water-replacement density tests and field infiltration tests

4.2 *Adjustments to the TEP design during execution*

Adjustments to the TEP were made to reflect site conditions during the construction period. The geometry of the test embankment was extended further towards the pit wall at the VWP location to increase the zone of influence for stress distribution above the VWPs. This was possible because the construction of the adjacent in-pit dyke abutment flare was accelerated which allowed better access and working space for the TEP.

The footprint and volume were reduced for faster construction due to the winter conditions. The final lifts and equipment used was also modified to increase production rates while ensuring the design loading over the VWP instruments was established as planned.

5 PROGRAM FINDINGS

5.1 *Development of Construction Specifications*

The findings of the test embankment program supported the development of construction specifications and a guidance-only method specification for the low permeability zone of the SCD. Table 6 below presents the corresponding maximum lift thickness for a range of anticipated placement and compaction equipment, and guidance on number of passes.

Table 6. Guidance for compaction maximum lift thicknesses by equipment size for Low Permeability Fill

Placement Equipment	Compaction Equipment	Maximum Lift Thicknesses[1]	Min. Compaction Specification (98% SPMDD) and uniform compaction typically achieved with:
D6 or D8 Dozer	Smooth Drum Roller Packer (AMMANN ASC 110D, equivalent or larger) or AT-740 Rock Truck (fully loaded)	0.3 m	8 passes, <5mm rut/roll by dozer
D6 or D8 Dozer	AT-40 Rock Truck (fully loaded) or 777 Haul Truck (fully loaded)	0.5 m	8 passes, <5 mm rut/roll by dozer, <25 mm rut/roll by 777
D8 or D10 Dozer	777 Haul Truck (fully loaded)	0.75 m	8 passes, <25 mm rut/roll by 777

Notes:
[1] For lifts thicker than 0.3 m, full depth testing of each lift is still required, and requires test pits.
[2] Moisture content changes the rut and roll performance, so rut and roll criteria on its own is not sufficient and should be used as an indicator only. Dry-of-optimum materials can show no rutting and still have very low density, leading to potential future collapse when water is introduced.

5.2 *Material performance*

In general, material was uniform and clay lumps in the GR15 material were broken down by the placing and compaction equipment and low-density layers near lift interface locations were not easily identified through visual observations. Figure 3 and Figure 4 show material homogeneity and compaction at lift interfaces from test trench observations. easily identified through visual observations. Figure 3 and Figure 4 show material homogeneity and compaction at lift interfaces from test trench observations.

Figure 5 and Figure 6 show typical material placement and compaction activities during construction.

Figure 3. Test trench in panel 1A (GR15)

Figure 4. Test trench in panel 1B (LOS)

Figure 5. Placing material with D8 dozer and compacting with a 16.5t smooth drum packer

Figure 6. Material placement with D8 dozer and Cat 777 haul truck

Field saturated hydraulic conductivities were calculated using a relationship between percolation time and field saturated hydraulic conductivity for cylindrical test holes (Reynolds et Al. (2015)). The hydraulic conductivity results from field and laboratory testing for the GR15 were consistent with the design parameters used for the low permeability zone. The results on the LOS material were generally about one order of magnitude higher than the GR15 material. This is reflective of the coarser gradation, higher sand content and lower clay content of the LOS versus the GR15. The field-based tests also indicated a range of resulting hydraulic conductivities with the average in general alignment with the one laboratory test on a remolded sample. Hydraulic conductivity field and laboratory testing results are summarized in Figure 7.

Figure 7. Field and laboratory hydraulic conductivity test results

5.3 *Pore pressure response data (MM Clays)*

For consistency with the way limit equilibrium stability models incorporate $\bar{B}$, the $\bar{B}$ values were calculated assuming 100% vertical loading, and evaluated as the test embankment was advanced over the instrument location to the full fill heights. The calculated $\bar{B}$ value of 0.28 in the Tip 2 MM Clay layer during the TEP loading is shown in Figure 8 and seems to be consistent with a lightly overconsolidated clay that is close to or fully saturated. VWP Tip 1 showed lower pore pressure response and faster dissipation than Tip 2 which was expected as it was installed at a lower elevation and subject to less stress increase due to stress distribution at depth. It was also installed in a MM Mixed layer which has higher expected hydraulic conductivity.

In March/April of 2021 the adjacent in-pit dyke south flare was completed to El. 300 m, and a GR15 stockpile was placed above to El. 304.2 m, which allowed further analysis of the pore pressure response. Stockpile unloading and/or excess pore pressure dissipation is ongoing and the resulting pore pressures recorded by the VWPs continuing to decrease (last available reading June 2021). Dissipation of the excess pore pressures may have been impeded or influenced by placement of the adjacent in-pit dyke fills against the pit wall, impeding lateral drainage.

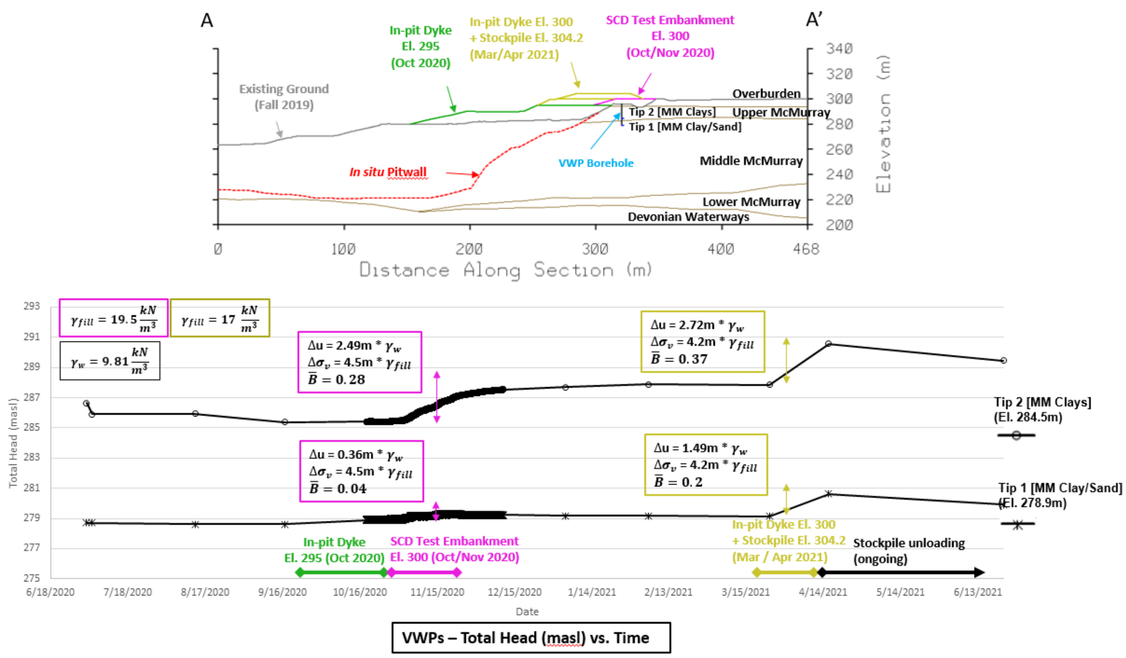

Figure 8. Section across the constructed test embankment and VWP data assessment

The instrumentation data and initial assessment undertaken in 2020 validated the hypothesis that the resulting pore pressure response readings for this low height embankment with shorter drainage paths to the adjacent pit wall were lower than what would typically be expected for large earthworks structures within the oilsands industry. The TEP validated that material parameters assumptions used to design the dam were appropriate (i.e. incorporating the calculated $\bar{B}$ value from the TEP would increase the FOS of the SCD design), and that opportunity exists for further optimization of the design of future similar structures and foundations.

5.4 *Considerations for Future Programs and Future Work*

The experience of designing, undertaking and assessing the results of the TEP has allowed the authors to identify some items for others to consider for development of future TEPs.

Elevation measurements should be taken when the loose lift surface has been placed and after each two-pass increment of compaction roller passes. The survey readings will allow for evaluation of settlement versus roller passes to determine the number of passes acceptable for fill placement. This allows review of material volumes and more accurate review of incremental benefits of additional passes. Follow-up surveys at monthly intervals after the completion of construction would allow monitoring of settlement over time to provide further information.

A large amount of data was generated during the construction of the TEP. Setup of a database or GIS based organization system for managing the data would have been beneficial.

REFERENCES

GEO-SLOPE International Ltd. 2012. Stability Modeling with SLOPE/W. p. 137

Hein, F.J. and Fairgrieve, B. 2012. A regional geologic framework for the Athabasca oil sands, northeastern Alberta, Canada, in F.J. Hein, D. Leckie, S. Larter, and J.R. Suter, eds. *Heavy oil and oil-sand petroleum systems in Alberta and beyond: AAPG Studies in Geology* 64, p. 207-250.

Reynolds, W.D., Galloway, K., and Radcliffe, D.E. (2015). The relationship between perc time and field-saturated hydraulic conductivity for cylindrical test holes., *National Onsite Wastewater Recycling Association (NOWRA) 2015 Onsite Wastewater Mega-Conference, Virginia Beach, VA, USA, November 3-6, 2015.*

USACE EM 1110-1-1804 Geotechnical Investigations Chapter 6 Section I – Test Excavation and Fills

USACE EM 1110-2-2301 Engineering and Design Test Quarries and Test Fills

An update on the construction and performance of the Suncor Tailings Pond 5 Coke Cover

Ayman H. Abusaid, Ying Zhang, & Gordon W. Pollock
Wood Environment & Infrastructure Solutions, Edmonton, Alberta, Canada

Derek Uffen
Suncor Energy Inc., Calgary, Alberta, Canada

ABSTRACT: As part of reclaiming its Pond 5 oil sands tailings pond, Suncor constructed a floating cover on top of the soft tailings deposits between 2010 and 2017. The initial cover consisted of two layers of geosynthetics overlain by 2 m petroleum coke. The coke cover behaves as a buoyant cap that supports limited construction equipment loads. Vertical Strip Drains (VSDs) were installed through the majority of the capped area to facilitate the consolidation of the underlying soft tailings. Papers discussing the initial design and early stages of construction were published in 2010 and 2011. This paper provides an update on the construction activities and performance of the coke cover at Pond 5 since 2011. Additionally, a discussion of the installation and performance of the VSDs will be presented.

1 INTRODUCTION

The Pond 5 Coke Cover project is located within the Suncor Lease 86/17 Tailings Pond 5, west of the Athabasca River and approximately 35 km north of the city of Fort McMurray. The total area of the pond is approximately 500 hectares (ha) with approximately 180 ha to 200 ha consisting of soft tailings. At the start of coke cover placement, the soft tailings ranged in depth from less than 1 m up to as much as 50 m and had initial undrained shear strength as low as 0.5 kPa. The bulk density and undrained shear strength of the soft tailings from 2008 and 2009 were presented by Pollock et al. (2010).

Between 2009 and 2012 and in 2017, Suncor constructed the engineered floating coke cover (generally 2 m thick) over the soft tailings at Pond 5. Coke is a byproduct of the oil sands process and is a light weight, cohesionless material with a high porosity. Given the fluid state of soft tailings, construction was limited to winter months when a minimum thickness of frozen tailings was achieved. One layer of geotextile and one layer of geogrid were placed prior to the coke placement. The cover consisted of a network of coke roads and coke cells, and the coke cover was anchored to the surrounding dykes and beaches. The design, construction and performance of the first 2 m cover were presented in Pollock et al. (2010) and Abusaid et al. (2011).

In 2019 and 2020, Suncor placed an additional 2 m of coke on the engineered cover to facilitate tailings consolidation and improve the stiffness of the engineered cover in support of closure activities. The additional coke placement started in summer months with the soft tailings in an unfrozen state. Aerial photos of Pond 5 are shown in Figure 1, which illustrate the coke placement history.

Between 2011 and 2014, and in 2017, Vertical Strip Drains (VSDs) were installed to facilitate the consolidation of the soft tailings, using the coke cover as a construction platform. The VSDs have approximately 2 m triangular spacing and were installed as deep as 14 m into the soft tailings. The progression and spatial coverage of the VSDs at Pond 5 are shown in Figure 2.

This paper presents an overview of the construction and the associated performance of the coke cover and VSDs at Pond 5 since 2011.

Figure 1. Coke placement history at Pond 5

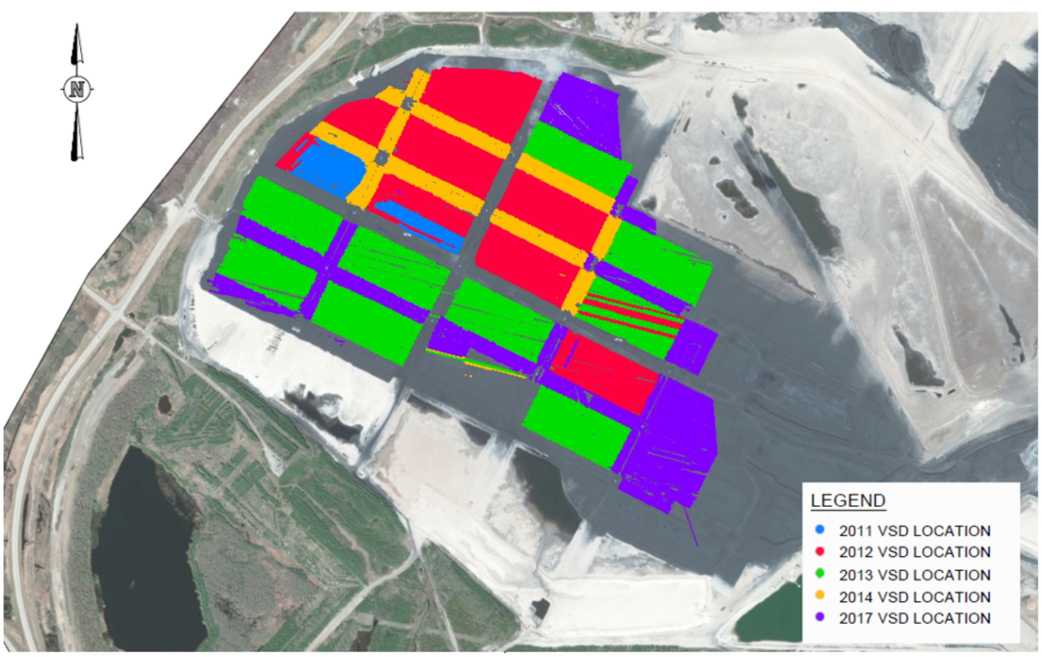

Figure 2. Vertical strip drains at Pond 5

2 COKE COVER

2.1 *Construction*

2.1.1 *Initial 2 m cover*

Pollock et al. (2010) listed the following key elements of the initial 2 m coke cover construction:

- Ice thickening and snow compaction.
- Preparation of High Strength Woven Geotextile (HSWG) anchor areas.
- Installation of HSWG.
- Installation of geogrid.
- Installation of drainage pipework.
- Installation and monitoring of instrumentation.
- Placement of coke material.
- Monitoring trafficability and other performance indicators.

Construction of the coke cover in 2010 adopted winter construction with a minimum thickness of ice (over 0.4 m) to provide a competent platform for CAT 631E scrapers or CAT 740 (40 ton) articulated trucks to transport coke, and for CAT D6 dozers to spread the coke. Some of the pond roads were constructed to 3 m thickness and were used as the main haul roads. The coke roads on tailings sand beaches were constructed in thawed conditions, but with the assistance of geotextile (or geogrid), instrumentation, and field trials. Abusaid et al (2011) presented the details of the above phases and field trials with truck sizes up to CAT 777 (100 ton).

2.1.2 *4 m Cover*

Suncor placed approximately 2 m of additional coke between July 2019 and October 2020 on the engineered cover to facilitate tailings consolidation and improve the stiffness of the engineered cover for closure activities. Prior to the construction, numerical analyses using Fast Lagrangian Analysis of Continua (FLAC) were performed to predict the deformation of the coke cover under different equipment loads and offsets. The development of tension in the geotextile and geogrid were modelled and evaluated. With the guidance of numerical modelling, field trials were conducted to assess the serviceability of the coke cover for the proposed equipment (e.g., CAT 740 and CAT 773 (60 ton)) in terms of the offset of haul trucks from the advancing lift edge and haul truck travel speed. The trials took place in summer 2019 with the underlying tailings in an unfrozen condition. The deformation and cracks were evaluated under different truck operation modes (e.g., braking, dumping, and acceleration) and for multiple truck passes. Table 1 lists the specifications of the equipment for the approximate 4 m coke placement. CAT 740s were selected to transport coke from the coke stockpile to the coke placing front. CAT 773s were not used in the construction due to the limitation on the driving speed for acceptable cover performance based on the field trials. CAT D6 dozers were used to push and compact coke at the advancing face.

Field trials were also completed to evaluate the effectiveness of the compaction within a 2 m lift placed as a single lift. It was observed that the density of the bottom 1 m was less than the top 1 m and was below 90% of Standard Proctor Maximum Dry Density (SPMDD). As a result, during construction the coke was placed in two 1 m lifts with the assistance of grade control markers.

Table 1 Specifications on equipment for the 4 m coke placement

Type of equipment	Maximum speed	Minimum distance between equipment	Minimum distance between equipment and lift edge
CAT 740 truck/ CAT631E scraper	45 km/h on road 15 km/h on cell	15 m	On 1st lift, 15 m On 2nd lift, 5 m
CAT 773 truck	25 km/h on road 15 km/h on cell	15 m	On 1st lift, not allowed On 2nd lift, 15 m

2.2 *Performance – Trafficability*

2.2.1 *Initial 2 m Cover*

As discussed by Abusaid et al. (2011), the initial approximate 2 m coke cover in the pond area was constructed in the winter season. The cover performed well during construction when the underlying ice was over 0.4 m thick, however, surficial cracks were observed on the surface of the coke when the ice was less 0.25 m thick. The summer construction of coke roads on tailings sand beaches was also challenging with cracks extending from the sand to the surface of the road near the construction front due to settlement and sand boils. The observational approach was adopted to establish the proper methods to construct the beach roads. Overall, the methods used during winter construction on the pond and summer construction on the tailings sand beaches were very successful as discussed by Abusaid et al. (2011).

After the coke placement in the winter, the underlying soft tailings thawed in the subsequent summer. As evidenced by thermistor data collected in the subsequent years, the tailings stayed in an unfrozen state due to the insulation of the coke cover. Deflection and surficial cracks in the compacted coke were observed when driving on the coke roads overlying unfrozen tailings. However, the deflection and cracks were less significant in the winter months when the coke itself was frozen to some depth. Also, the trafficability of the roads deteriorated significantly when the water table was near the ground surface in summer months. Several measures were undertaken to successfully improve the performance of the coke roads where serviceability performance was observed to deteriorate:

- Reduced truck speeds
- Placement of additional coke resulting in a thicker and stiffer coke cover
- Dividing the roads into four lanes and switching traffic between different lanes and thus balancing out the number of load cycles for each lane.
- Maintaining a lower water table in the coke cover.

During VSD installation, the coke cover performed well. Generally, only minor surficial cracks and deflection at the coke surface were observed below and around the VSD rigs and these did not affect the installation of the VSDs. At localized locations within some cells, poor cover performance was observed with large deflections and cracks. It is believed the poor cover performance in these areas was a result of less compaction of the coke or a higher water table.

2.2.2 *4 m Cover*

With the addition of 2 m of coke on the cover, the overall performance of the cover improved relative to the original cover:

- The cover was more rigid relative to the original 2 m cover based on visual observation and survey.
- There was less deformation from truck traffic and no obvious "waves" developing in the cover from dynamic equipment loading.
- There was no immediate self-leveling/sinking after coke was placed.

The improved performance is expected to be due to one or a combination of the following factors:

- The thicker coke cover provided both a stiffer overall section to support traffic and increased the thickness of unsaturated coke between the traffic surface and the water table (approximately 3 m of unsaturated coke overlying 1 m of saturated coke versus previously 1 m of unsaturated coke overlying 1 m of saturated coke).
- Improvement in underlying tailings density and strength after the original 2 m cover construction, as discussed in Section 3.2.2.
- The original approximate 2 m coke cover was further compacted under truck traffic and VSD installation equipment over the years.

Figure 3 presents the equipment and site conditions during 4 m coke placement.

a) Placement of the 4th one-meter lift of coke in Cell 5

b) Placement of the 4th one-meter lift of coke in Cell 11

Figure 3. Construction of the 4 m coke cover

3 VERTICAL STRIP DRAINS

3.1 *Construction: Installation and Operation*

VSDs were installed at the majority of the soft tailings of Pond 5 at to accelerate consolidation. Water from VSDs, tailings surface, and precipitation is collected by the drainage system at the base of the coke cover and reported to the sumps at coke road intersections. The water is actively pumped out to other tailings facilities to maintain the low water level within the cover. A VSD consisted of a corrugated plastic center and a non-woven geotextile fabric shell. The VSDs were installed at an approximately 2 m triangular spacing and at an angle from the cross-machine direction of the geotextile. The intent of the angle with the geotextile was to minimize the loss in strength of the geotextile due to punctures caused by the mandrel. The geometry of the perforation in the geotextile caused by VSD installations was examined by excavating the coke around one installed VSD. It was found that the perforation in geotextile and geogrid around the VSD was only slightly larger than the mandrel. The following subsections present some of the issues encountered during installation and how they were overcome.

3.1.1 *Anchorage of VSDs*

Typically, VSDs are installed using a mandrel to push the anchor plate and VSD to the desired depth, whereupon the mandrel is retracted leaving the anchor plate and VSD in place. However, the soft tailings at Pond 5 are in a fluid state and exert an upward pressure on the anchor plate, which pushes it firmly against the end of the mandrel. Therefore, the upward pressure must be overcome so that the anchor plate can separate from the mandrel and stay in place during the withdraw of the mandrel. Field trials were implemented to: (1) establish reliable methods to efficiently and effectively install and anchor the VSDs in the soft tailings or in competent beach sand and (2) develop an approach and utilize equipment that would not adversely affect the performance and integrity of the engineered coke cover.

During the first year of VSD installation, Suncor employed two specialty contractors (Contractors A and B) to undertake the large scale VSD trials independently. Different rigs and VSD spooling methods were adopted by the two contractors, however, the main difference was the techniques used to separate the anchor plate from the mandrel upon extraction (i.e. water versus compressed air). The equipment from both contractors is shown in Figure 4 and details of the two methods are described below.

a) VSD rig of Contractor A b) VSD rig of Contractor B

Figure 4. Equipment for vertical strip drain installation at Pond 5

The method by Contractor A included inserting the mandrel, supplied with VSD material from a conventional top feed spool, through the coke cap and into the soft tailings to the greatest depth capable of the mandrel. Water was then pumped into the top of the mandrel until it was completely full. The mandrel was extracted and the VSD coming out of the top of the mandrel was simultaneously pulled by a ground crew member to remove any slack until the anchor held firm. The ultimate anchor depth was manually recorded. The mandrel was 32 m (105 ft) long and required 95 to 115 liters (25 to 30 gallons) of water to install the VSD to a depth over 12 m below the coke surface. However, water flowed out of the mandrel to the ground during extraction and the mandrel hole in the coke was filled with water. Significant cracking and deformations were observed in coke cover during and after VSD installations, especially with larger and heavier rigs.

The method by Contractor B included inserting the mandrel, supplied with VSD material, then applying a burst of compressed air within the mandrel to overcome the pressure on the anchor plate caused by the soft tailings at the target depth. Surface boils and ejections of soft tailings occurred due to the applied air pressure. Skilled operators were required to refine the timing of the air releases to minimize the soft tailings boils and ejections. Vapor condensation within the air pressure system reduced the pressure during installations and led to difficulties in anchoring some of the drains. A valve along the side of the rig was regularly opened to drain the moisture from the air pressure system. Furthermore, condensation within the air pressure system froze and disabled the VSD equipment during winter months. Contractor B addressed this issue by disconnecting the air hoses from the rigs and placing them in a heated shack overnight.

Based on the success of anchoring and the impact on serviceability of the coke cover, the method by Contractor B and corresponding equipment were deemed safer, more practical and cost effective and therefore it was used in subsequent years for VSD installations at Pond 5.

3.1.2 *VSD Installation at Roads*

In general, VSD installation at coke roads was more difficult than installation at coke cells and sometimes resulted in damaged (overly bent) anchor plates when pushing through the coke. The roads were different than the cells in two ways; coke roads were thicker at most locations but also had undergone significantly more compaction than the cells due to hauling traffic. Predrilling from surface to the bottom of the coke had to be used for VSD installation. Field trials were implemented to determine the required depth of the drilled borehole for VSD installation along the coke road and it was found that the predrill hole had to extend close to the geotextile (bottom of the coke) before the VSD could be installed. This indicated that the degree of compaction of the coke is a factor in the amount of effort required to install the VSDs and it should be taken into consideration when planning and scheduling coke placement and VSD installation.

Another modification to the VSD installation method at coke roads was repositioning the rig location. Typically, at the coke cells several VSDs were installed with one positioning of the rig by adjusting the mast of the rig horizontally from one VSD location to another without relocating the rig. At coke roads where more resistance was encountered, the rig was positioned directly over each VSD location centered between the two tracks to provide more ballast and successfully penetrate the coke.

3.1.3 *VSD Operation*

The VSDs were left with the top unsealed and some slack at the surface. Many VSDs produced water or experienced soft tailings boils at the surface immediately upon completion of the installation, as shown in Figure 5. In localized areas, some VSDs were observed to continue produce water to the ground surface two or more years after installation. However, the majority are expected to expel the water within the porous coke cover where it is removed by the pumping system.

a) VSD upon completion

b) VSD producing water

Figure 5. VSD after installation at Pond 5

3.2 *Performance*

The performance of the VSDs is monitored through a combination of settlement measurements at the pond surface, CPT testing, tailings sampling, laboratory testing, piezometers (vibrating wire and standpipes) and pumping records, as discussed below.

3.2.1 *Settlement*

The amount of settlement due to the consolidation of soft tailings is monitored by settlement plates installed at the base of the coke cover, and annual Light Detection and Ranging (LiDAR) surveys. Figure 6 presents the estimated consolidation settlement between completion of the initial 2 m coke cover and placement of the additional 2 m of coke, by comparing the October 2012 and July 2019 LiDAR surveys. According to Figure 6, the majority of the pond had over 2 m of settlement and the estimated maximum settlement was over 3 m over the seven-year period. Based on LiDAR surveys from adjacent years, the amount of settlement increased due to VSDs.

Figure 7 shows the locations of the settlement plates at Pond 5. Figure 8 presents the measured settlement after the VSD installation using settlement plates in Cell 9. The settlement rate was approximately 0.5 m per year in 2013 then slowly decreased with time to around 0.3 m per year since 2016.

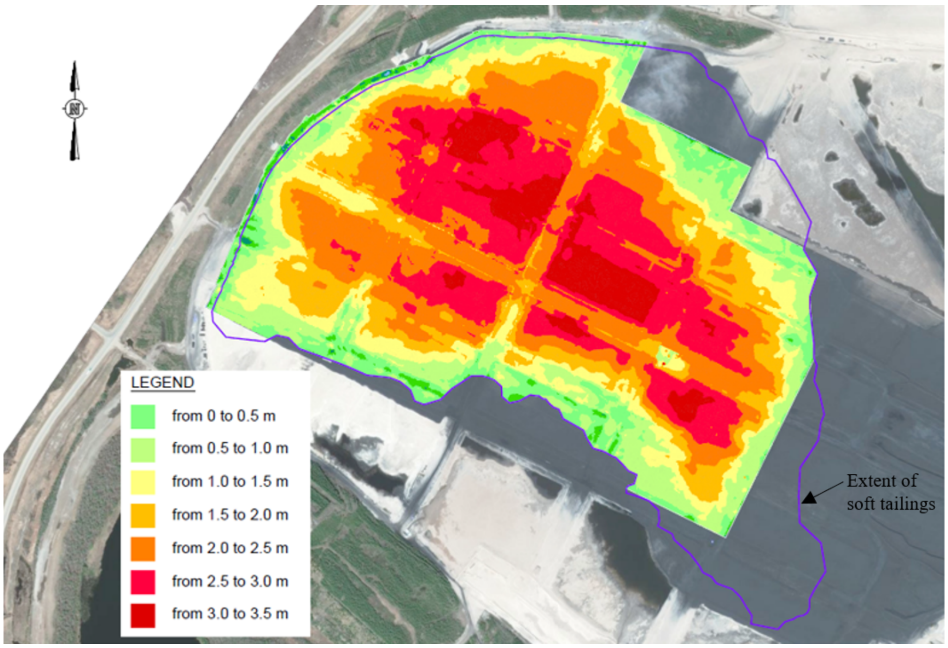

Figure 6. Estimated settlement from 2012 to 2019 using LiDAR surveys

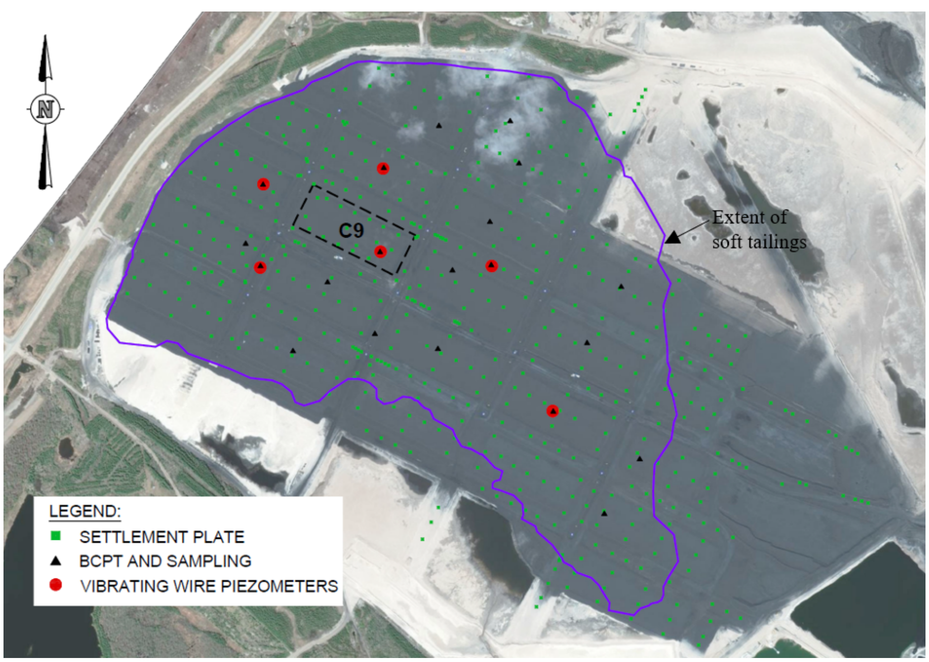

Figure 7. Locations of settlement plates, BCPT and sampling, and vibrating wire piezometers

3.2.2 *BCPT, Sampling, and Laboratory Testing*

Ball Cone Penetrating Tests (BCPT) paired with piston tube sampling and laboratory index tests have been carried out annually to evaluate the solids content, density, and undrained shear strength of the soft tailings at Pond 5. Additional details on sampling and strength characterization of oil sands tailings were addressed in COSIA (2015a) and COSIA (2015b). The BCPT and sampling at Pond 5 are terminated several meters below the VSDs. The locations of the BCPT and sampling are shown in Figure 7. Below is a summary of the general findings:

- BCPT data showed a trend of increase in peak undrained shear strength since the VSD installation. For example, the average peak undrained shear strength at all BCPT locations at the depth of 10 m increased from 2 kPa before VSD installation to 11 kPa in 2019.
- The improvement in the remolded undrained shear strength was less pronounced. The remolded undrained shear strength was less than 0.5 kPa in 2010 according to the cyclic BCPT data at selected depths, and it was in the range of 0.5 kPa to 3 kPa in 2020.
- The laboratory test results demonstrated a trend of increasing solids content and fines/(fines+water) since the VSD installation. The average solids content from all sampling locations increased by 5% to 10% within the VSD depth (14 m below soft tailings-cover interface) from 2012 to 2019. The average solids content increased by less than 2% below the VSDs over the same period.
- The improvement in peak undrained shear strength and solids content appeared to be within the approximate depth of the VSDs, with greater improvement observed in between depths of 6 m and 12 m.

After nine years of sampling and testing since the VSD installation at Pond 5, it was found that the trends within the parameters become clearer over several years, while the change may not always be evident at every test location in a given year.

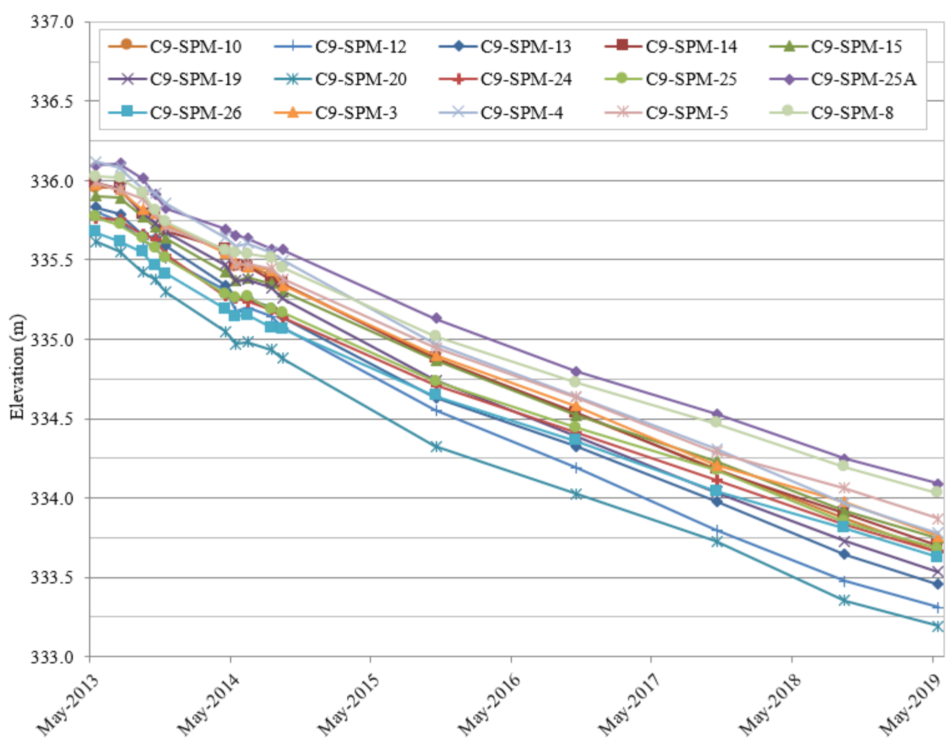

Figure 8. Measured settlement in Cell 9 using settlement plates

3.2.3 *Vibrating Wire Piezometers (VWP)*

Pore pressure in the coke and soft tailings at Pond 5 is monitored by 18 VWPs at six locations since 2016, as shown in Figure 7. There are three piezometer tips at each location: one at the bottom of the coke (above the geotextile), a second tip in the upper tailings towards the middle of the average VSD depth, and a third tip in the lower tailings near the base of the VSDs. To maintain constant tip depths in the soft tailings, the VWPs at each location were attached to a steel rod which was then anchored to a steel plate at ground surface. The total stress above the lower two piezometers were calculated using the unit weight of the tailings and the thickness of the coke determined in the annual sampling and testing programs. The effective stress can be estimated as the difference between the total stress and the measured pore pressure at the piezometer locations in the soft tailings. However, the piezometers are not able to monitor the same "tailings element" with time at constant depths due to the highly compressible nature of the soft tailings. Additionally, the effective stress is also influenced by the accuracy in coke thickness and unit weight of soft tailings. Therefore, it is challenging to determine changes in effective stress in the soft tailings in relatively short time frames. Nevertheless, when evaluating several years of data, the following findings were made from the pore pressures in the soft tailings:

- Excess pore pressures slowly dissipated (i.e., a couple of kPa per year on average) before the most recent 2 m coke placement in 2019 and 2020
- An increase of pore pressure (around B-bar of unity) was observed at all six locations following the most recent 2 m of coke placement.
- Excess pore pressure dissipated at a faster rate (up to 5 kPa per year) after the most recent 2 m coke placement.
- Excess pore pressure at the lower VWPs (base of VSD) appeared to dissipate faster than the upper VWPs (middle of VSD depth).

4 SUMMARY

This paper presented an overview of the construction and performance of the coke cover and VSDs at Pond 5. The coke cover was constructed in two phases: initial 2 m coke cover constructed mostly above a frozen pond, and the second 2 m of coke (4m overall) placed with thawed fluid soft tailings underneath the existing coke. The construction equipment used at Pond 5 included CAT 740 trucks, CAT 631E scrapers, and CAT D6 dozers, although field trials investigated larger equipment (e.g., fully loaded CAT 777). Overall, the trafficability performance of the coke cover was acceptable:

- The initial 2 m cover performed well due to the underlying frozen tailings and the geosynthetics.
- The performance of the 2 m cover would deteriorate when the frozen tailings thawed, or the water table elevation increased. Several measures were adopted to improve the performance of the cover, including reduction in traffic and travel speed, increase of coke thickness, installation of additional geosynthetics, and lowering the water table.
- The 4 m cover is stiffer and performed better during construction even with the underlying soft tailings in a thawed state, when compared to the initial 2 m coke cover.

VSDs were successfully installed in the soft tailings from the coke cover surface using modified equipment and procedures to address the challenges associated with soft tailings and the compacted coke cover. The VSDs performed well after installation as evidenced by accelerated settlement after VSD installation and improvement in the soft tailings properties (peak undrained shear strength and solids content), which is more apparent within the VSD depth than below the VSDs. Slow excess pore pressure dissipation was observed at VWP locations, however, early indications suggest dissipation rates are improving due to coke loading and effective stress is developing in the underlying soft tailings. Continued pore pressure monitoring over a longer time frame will assist in confirming dissipation rates and the development of effective stress in the soft tailings.

The performance of the coke cover and VSDs continues to be monitored and additional effort is underway to understand the mechanisms of Pond 5 soft tailings settlement. Monitoring data results are expected to be discussed in detail in future publications.

5 ACKNOWLEDGEMENTS

The authors would like to recognize E.C. McRoberts of Wood for his technical guidance throughout the project. The authors would also like to recognize Norman Eenkooren of Suncor for his stewardship of the Pond 5 Cover Project.

6 REFERENCES

G. Pollock, X. Liu, E. McRoberts, K. Williams, S. Wells, & J. Fournier, 2010. Suncor Oil Sands Pond Capping Project, *Proceedings from Tailings & Mine Waste' 10.* Vail, Colorado, Oct 2010

A. Abusaid, G. Pollock, C. Fear, E. McRoberts, & S. Wells, 2011. An Update to the Construction of the Suncor Oil Sands Tailings Pond 5 Cover, *Proceedings from Tailings & Mine Waste' 11.* Vancouver, BC, Nov 2011

COSIA (Canada's Oil Sands Innovation Alliance), 2015a. Guidelines for Tailings Deposit Sampling and Measuring Tools, April 27, 2015

COSIA (Canada's Oil Sands Innovation Alliance), 2015b. Measuring Undrained Shear Strength of Oil Sands Tailings Deposit, April 2015

Design of a non-liquefiable sand shear key to improve the stability of an overburden waste dump constructed over a tailings storage facility

Gidley, I.D.C., Boswell, J.E.S., Sobkowicz, J.C
Thurber Engineering Ltd., Calgary, Alberta, Canada

Burnett, A.
Syncrude Canada Ltd., Calgary, Alberta, Canada

ABSTRACT: The Fort Hills Dump (FHD) Stage 3 is an in-pit overburden waste dump under construction at the Syncrude Canada Ltd. (Syncrude) Aurora North Mine. The dump is located on top of a tailings sand and fines deposit, 70 m in thickness, with a footprint of 2.5 km^2. The design height of the dump is 50 metres. To provide a suitable foundation for dump construction, a track-packed sand cap of 10 m thickness was constructed on top of the tailings deposit.

A key concern with the FHD was the performance of the dump as the underlying tailings consolidated. Cracks could develop in the base of the dump, which could be infilled with water from the surrounding topography and the consolidating tailings beneath. This could result in a soft zone at the base of the dump which might threaten overall stability. Hence, a shear key was incorporated in the design to provide additional shear resistance and self-healing against cracking, and to limit the extent of dump base softening towards the dump toe. The shear key was constructed of mechanically placed and compacted tailings sand and was located where the dump was potentially most vulnerable to cracking and softening.

Another concern was that material placed within the shear key could become saturated as the dump settled. As such, the shear key needed to remain dilative over the expected stress ranges. To assess the compaction requirements (i.e. minimum initial dry density) for the shear key to remain dense, laboratory testing was completed to estimate the critical state line (CSL) for the tailings sand and to predict its performance under load.

1 INTRODUCTION

The Aurora Fort Hills Dump (FHD) at the Syncrude Aurora North Mine serves as a primary waste storage area for overburden materials removed during mining. The dump was constructed in multiple stages, with Stage 3 located on top of the Aurora East Pit Northwest (AEPN-W) in-pit tailings storage facility (TSF). While overburden waste dumps are common throughout the oil sands, and several TSFs have been capped, this would be the most significant waste dump to be constructed on an infilled tailings pond. Construction of the dump on top of a TSF posed several challenges for the design team including:

- Total and differential settlement of the dump and underlying tailings
- Slope stability of overburden and potentially liquefiable tailings
- Softening of clays along the base of the dump due to water ingress
- Proximity to active in-pit deposition areas
- Space constraints around the dump footprint.

To mitigate these challenges, several major design defenses were developed, including a track-packed sand cap over the TSF, active drainage during construction of the dump, a higher specification exterior shell zone, a step over into an adjacent area, incorporation of an inverted shear key into the design of the FHD and construction controls and specifications for the initial placement of the dump. The focus of this paper is the design of the shear key and the development of placement and compaction criteria for the material that was selected for construction.

2 BACKGROUND

2.1 *Location*

The FHD is located at the Syncrude Aurora North Mine site, approximately 80 km north of Fort McMurray, Alberta (Figure 1). Stage 1 was completed in 2010 on original ground, north of the in-pit tailings storage facility AEPN-W (existing tailings facilities shown on Figure 2). Stage 2 was also constructed on original ground, west of AEPN-W. Stage 3 is currently being constructed on top of the infilled AEPN-W and will tie into Stage 2 to the west and Stage 1 to the north. AEPN-W was bounded by the old pit high wall to the north and west and hydraulic fill dykes to the east (Dyke 1 North) and south (Dyke 1 West) that separated AEPN-W from the active TSFs AEPN-E and AEPS to the east and south respectively. Stage 3 steps over Dyke 1N in the northeast corner of the footprint onto the upper portion of the beach of the adjacent AEPN-E in-pit tailings storage facility.

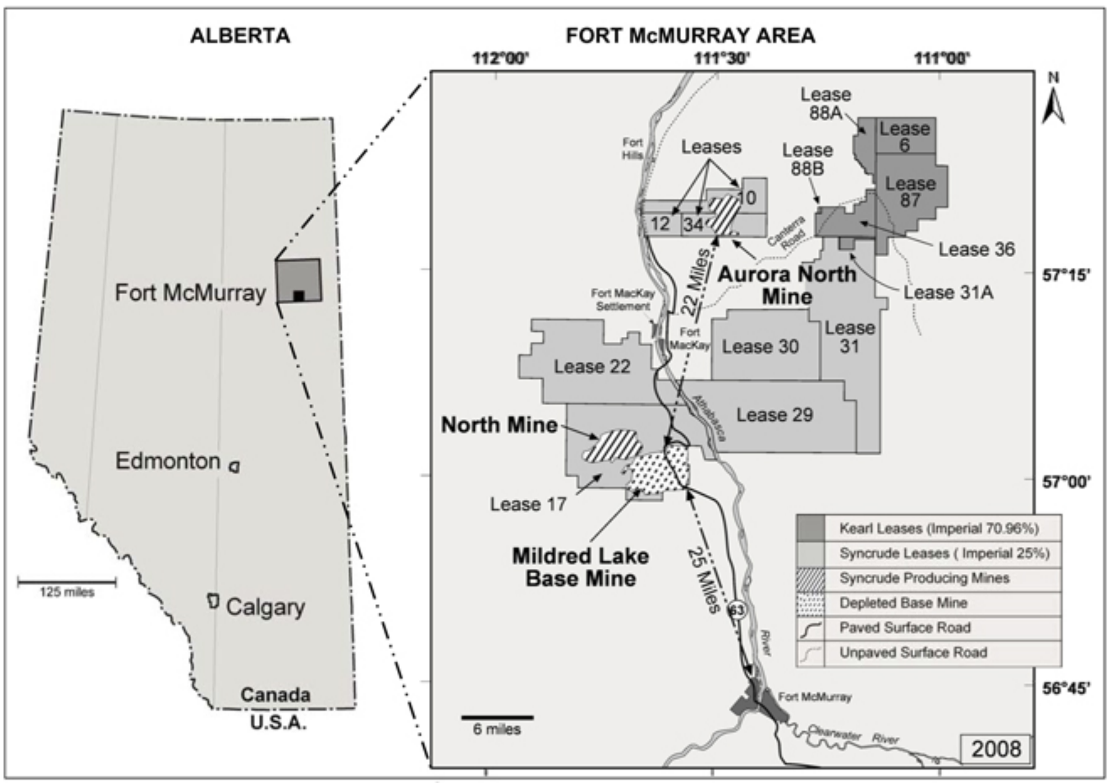

Figure 1. Location of the Syncrude Aurora North Mine Site (United States Securities and Exchange Commission, 2008)

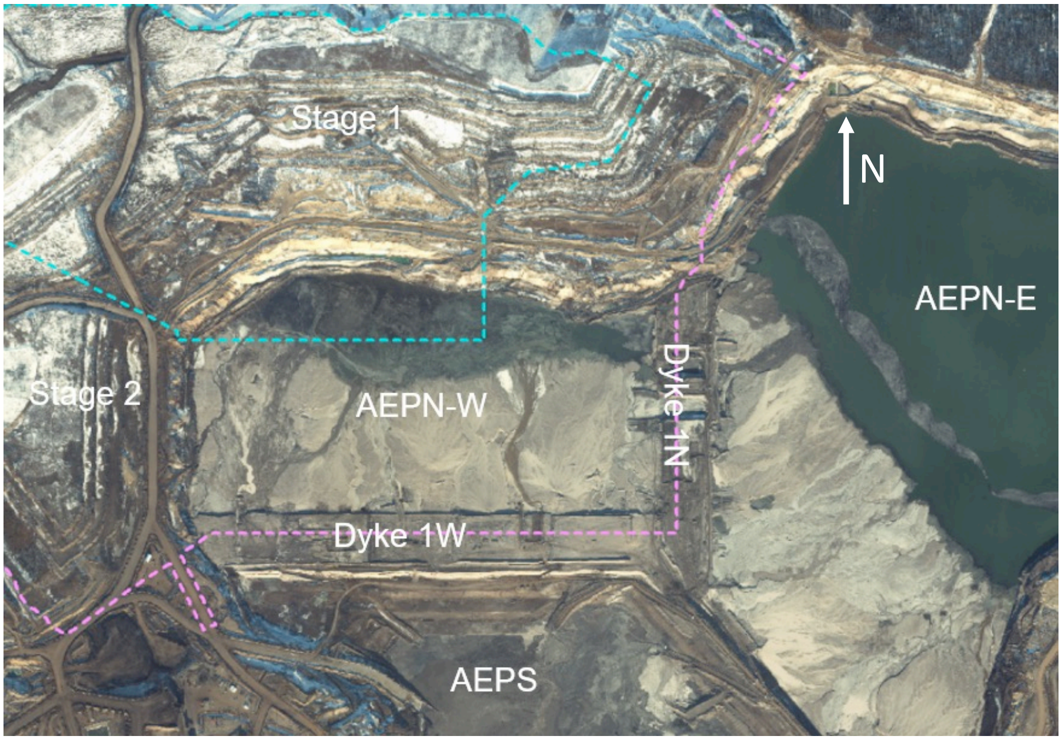

Figure 2. Layout of in-pit storage facilities within the original Aurora East Pit

2.2 *Foundation materials*

Following completion of mining activities, deposition within AEPN-W started in 2012 and followed standard beach construction methods within the oil sands, with tailings sand primarily discharged and deposited from the south dyke. The tailings deposit is a combination of beach above water (BAW) and beach below water (BBW) tailings. The upper beach portions of the BAW nearest to the discharge were track-packed, and the pond was generally located towards the north of AEPN-W, against the old pit high wall. The facility contained zones of coarse and fine tailings, fluid, and bitumen (sometimes in layers). At the end of active deposition, the tailings deposit within AEPN-W was up to 70 m deep.

As part of the dump design, a 10 m thick tracked-packed sand cap was hydraulically placed over the tailings. Placement of the sand cap proceeded simultaneously from the south to north and from east to west, then finally from the northwest to the southeast as soft material and supernatant fluid in the north part of the tailings deposit was channeled through trenches and culverts located through Dyke 1N, flowing into AEPN-E.

Several cone penetration test (CPT) investigation campaigns were conducted across AEPN-W to characterize the contents of the facility. The investigations found that there was significant heterogeneity and layering of fine and coarse material within the deposit, and that a significant portion of the foundation was potentially liquefiable. A general profile of the contents of AEPN-W is shown in Figure 3.

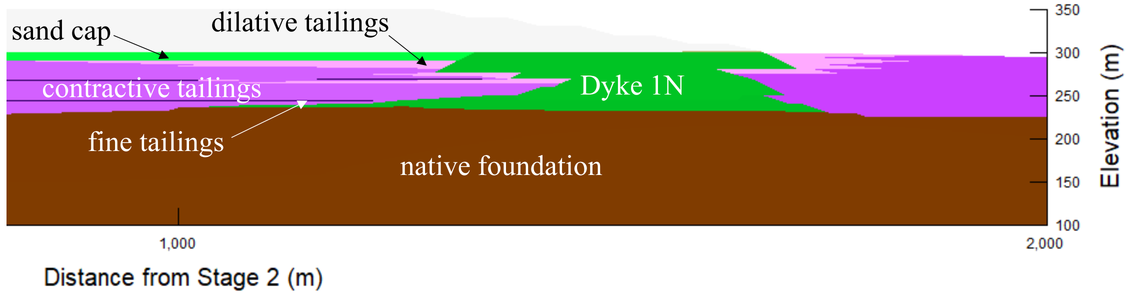

Figure 3. General profile of AEPN-W

2.3 *Waste dump characteristics*

The FHD is an overburden waste dump comprised of two main placement zones, an interior zone and an exterior shell. Typical overburden is made up of a mixture of medium plastic clays and clay tills, and medium to high plastic clay shales from the Clearwater formation. Materials were placed in 2.5 m to 5 m thick lifts and compacted by haul truck traffic. Stage 3 of the FHD was proposed to be 50 m high, with a footprint of 2.5 km east to west and 1 km north to south. The downstream slope was 4 horizontal to 1 vertical (4H:1V), with benches every 10 m in height, resulting in a compound slope of 8H:1V. Included within the profile was a shear key, which is the focus of this paper. A general cross-section of Stage 3 is shown in Figure 4.

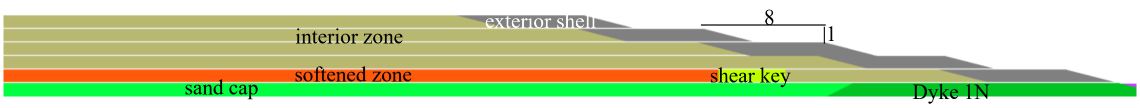

Figure 4. General cross-section of the waste dump (west to east)

3 ANALYSIS AND ASSESSMENT OF OVERBURDEN WASTE DUMP

3.1 *Overview*

As part of the design of Stage 3 of the FHD, assessments were conducted for stability, liquefaction susceptibility, constructability, cracking/softening of construction materials, seepage, fluid management, capping, waste placement methodology, monitoring, and total storage. These assessments identified several issues that needed to be addressed through the design. The following section discusses those issues that are relevant to the development of the design of the shear key.

3.2 *Key issues*

The shear key was meant to address the potential for instability to develop through the base of the waste dump, due to softening of the dump materials. This could happen as the dump settled differentially during construction, resulting in cracks forming along the base and ingress of water from seepage along sand layers in the old high wall, consolidation of the tailings below and proximity to the water table.

Several CPT campaigns were conducted to assess the foundation materials. Consistent with typical beach deposition, the foundation conditions were more favourable towards the south near the discharge locations and less favourable towards the north and east, where the pond had historically been located. CPT soundings revealed that a significant thickness of the foundation was highly compressible, with up to 70 m of normally consolidated clays, silts and sands present in the northern portion of the foundation. The locations with the most compressible foundation material also corresponded to the highest part of the structure. A settlement assessment showed that significant amounts of settlement could be expected to occur over the life of the structure and that differential settlements were expected along Dyke 1N, in areas where the pond had been located, adjacent to the dyke during operation.

A series of 1D settlement assessments for the proposed dump were made and contours of the potential settlement were developed. From the settlement contours, an assessment of the differential settlement and the potential strains along the base of the dump was made, which indicated that cracks were likely to develop along the base of the dump along transitions between the tailings beach (areas of high settlement) and the pit wall and dykes (areas with low settlement). The potential magnitude of settlement was sufficiently large for the base of the dump to be submerged below the phreatic surface.

During the operation of AEPN-W, fluid levels were controlled by a system of pumps and drains within the containment dykes. The system drew down the phreatic surface within the tailings by several metres. This system is intended to remain operational during construction of the dump, but an assessment was made to understand the effects if the system was decommissioned, which, when coupled with local seepage from original ground to the north, would cause fluid levels within the structure to rise significantly.

With the potential for high plastic clays shales, placed relatively dry, to be present at the base of the dump, along with the potential for cracking and ingress of fluid due to seepage and consolidation of the underlying foundation, a key issue for the dump was the potential for the material along the base to soften, resulting in a low strength zone developing along the base of the dump. Stability analyses identified that both large deep-seated failures extending back into the dump and deep-seated failures along the side slopes were possible depending upon the extent of the softened zone.

4 DESIGN OF THE SHEAR KEY

To address the issues described in the previous section, the design of the dump was modified to include a 10 m high, 50 m wide sand shear key, which would serve to increase resistance along the base of the dump to slope failure and to curtail the lateral progression of the softened zone. The key parts of the shear key design, namely, the location, compaction specification and construction methodology, are described in more detail below.

4.1 *Location*

For the shear key to remain effective throughout the life of the dump it had to be optimally located to improve stability for all configurations of the dump. When locating the shear key the following factors were considered:

- Locations of maximum strain in the base of the dump
- Geometry of potential slip surfaces
- Potential locations for fluid ingress
- Construction access and constructability.

The amount of shear strain in the dump was assessed by considering the contour intervals generated from the settlement analyses as well as by using a simplified 2D stress deformation model. The highest tensile strains were present where contour bands were the closest together. These tended to be located near the transition between uncompacted and compacted material such as between uncompacted and tracked packed beaches along the dykes.

The location of the shear key also considered the geometry of the slip surfaces through the dump. If the shear key was too close to the toe, there would be the potential for failure to occur upstream of the shear key through softened material at the base of the dump. Conversely, if the shear key was located too far upstream, failure surfaces could develop which passed through liquefiable tailings or through a softened zone downstream of the shear key (Figure 5).

The shear key also needed to be in an area where it could be constructed with typical mine equipment and with preference to areas closer to material borrow sources. Based on the assessment, the shear key was located 250 m from the dump toe.

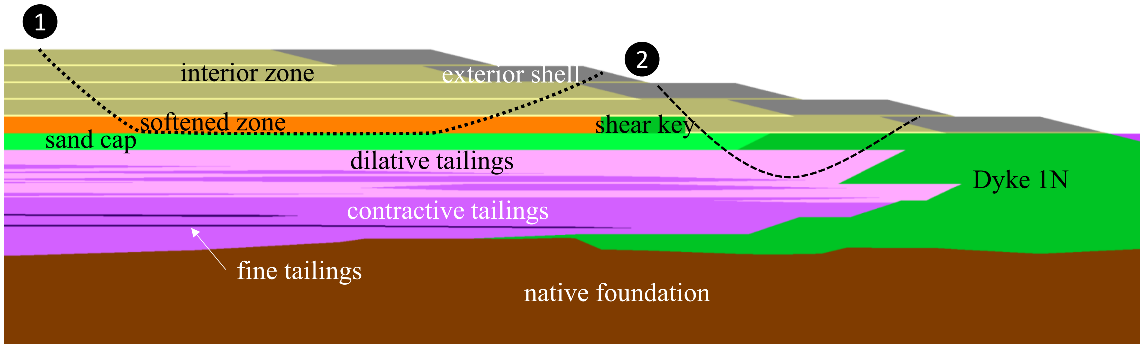

Figure 5. Potential slip surfaces for the dump with a softened base (1) upstream and (2) downstream of the shear key

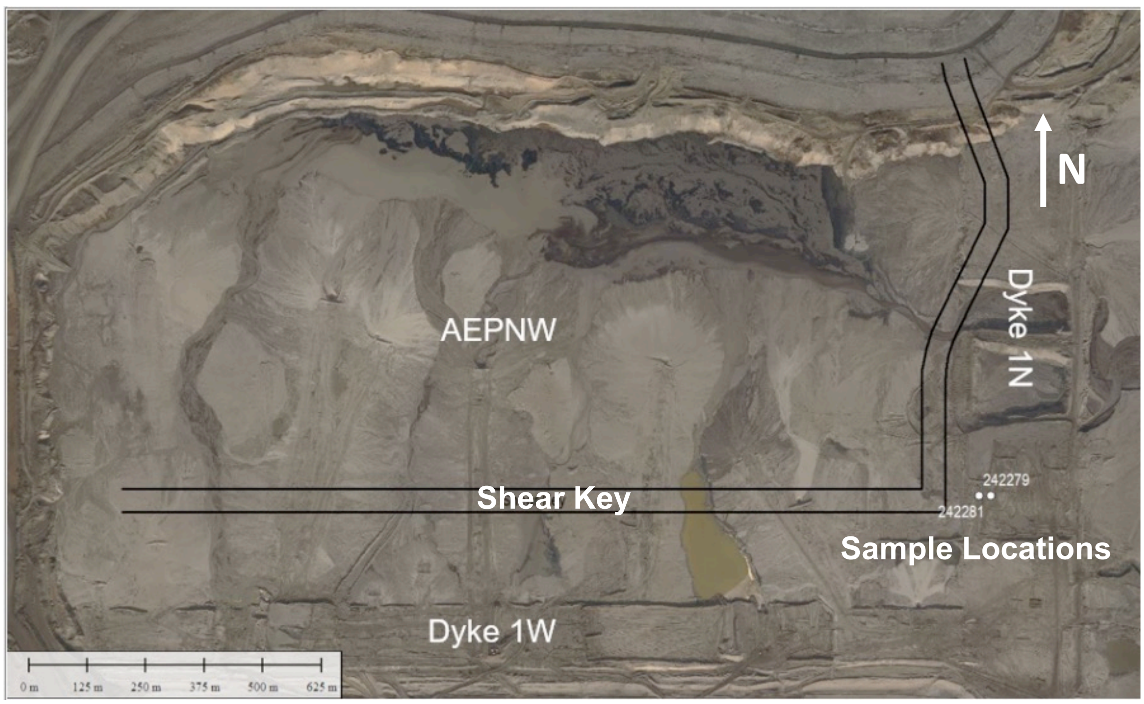

Figure 6. Plan view of shear key location

4.2 *Parameter selection and laboratory testing*

Given the potential magnitude of predicted settlement of the base of the overburden dump, as well as the abundance of water within the foundation and adjacent terrain, it was anticipated that part or all of the shear key would become saturated during the life of the structure. It was important to the stability of the dump that the shear key responded in a dilative manner when subjected to shear, i.e. that it was not at risk of liquefaction for the various loading configurations of the structure.

To address the performance of the shear key, a laboratory program was developed for characterization and selection of the potential borrow sources. The material assessment for the shear key consisted of:

- Consolidated drained (CD) triaxial tests
- Consolidated undrained (CU) triaxial tests
- Oedometer tests
- Direct shear tests
- Particle size distribution (PSD) using sieve and hydrometer
- Minimum and maximum void ratio

- Proctor density
- Critical state line (CSL) assessment.

Several PSDs were determined, to assess the variability of the material. The two samples shown in Figure 7 represented the bounding gradations for the material and were used in most of the assessments. The materials tested were sourced from similar areas and from ore that was processed and deposited similarly. Before conducting the laboratory study, a comprehensive literature review was performed on CSLs for tailings. Two public references were found for Syncrude Base Mine tailings, provided in Sladen and Handford (1987) and Sobkowicz and Handford (1990). The available gradation is also provided in Figure 7. Testing from Sobkowicz and Handford (1990) did not provide a full PSD. However, the samples were described as poorly graded and the D50 was noted as 0.13 mm to 0.17 mm with a geotechnical fines content of 4% to 11%. It was noted that the published PSDs were finer than the materials tested as part of this program.

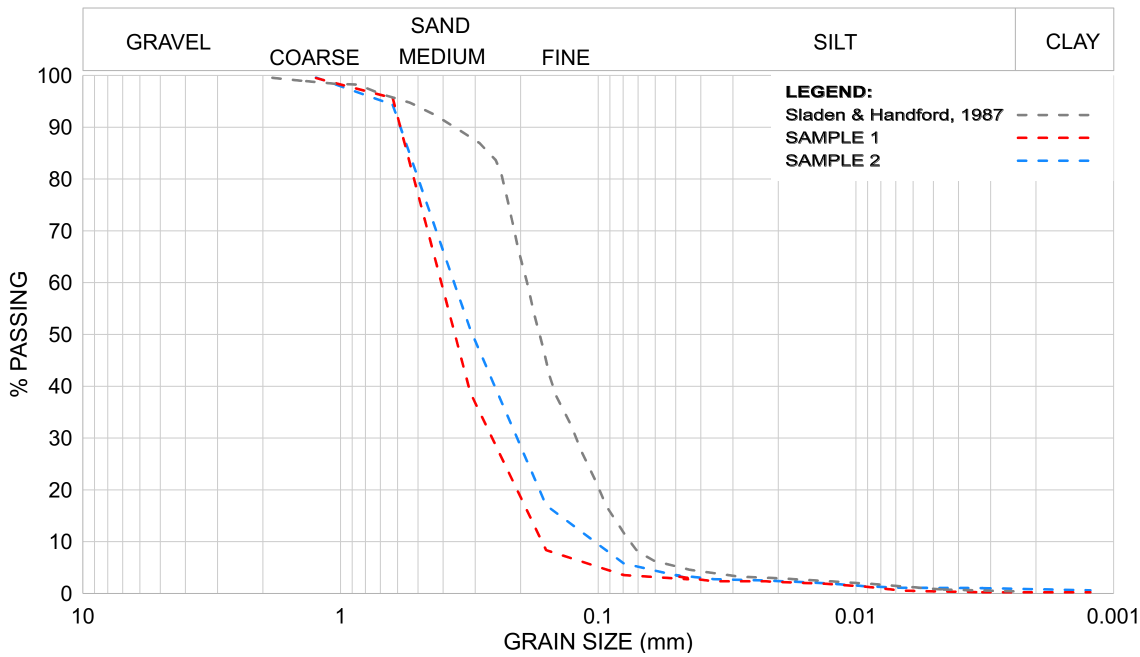

Figure 7. Particle size distribution of the tested samples and from literature

To assess the CSL, a series of CU and CD tests were conducted over the range of fines contents expected for the sands used to construct the shear key. The triaxial test methodology used in the testing was adopted from the recommendations provided by Jefferies and Been (2016), ASTM D4767 and ASTM D7181. Samples were mixed to homogenize the material and were air-dried to 5% moisture content. Air drying was used instead of oven drying due to the presence of bitumen. Reconstituted triaxial test specimens were prepared using the moist tamping method, where the samples were built in seven equal lifts of the same density (Ladd, 1978). Samples were prepared such that they would remain loose of critical state after saturation and consolidation. Samples were sheared in the triaxial apparatus at a constant rate until 25% axial strain (

Figure 8). The resulting CSLs are compared to the CSLs from the literature review in Figure 9. When comparing the CSLs to those available in the literature, it is noted that while the slope of the CSL is similar, there is a substantial difference in the intercept. The similarity in the slope of the CSL is likely due to compressibility and crushability of the sand grains, which is expected since while they are from different sites, they are from the same formation. At the same time, the variation in the intercept is likely due to the differences in PSD, grain shape and mineralogy as discussed in Jefferies and Been (2016). A summary of the results is provided in Table 1.

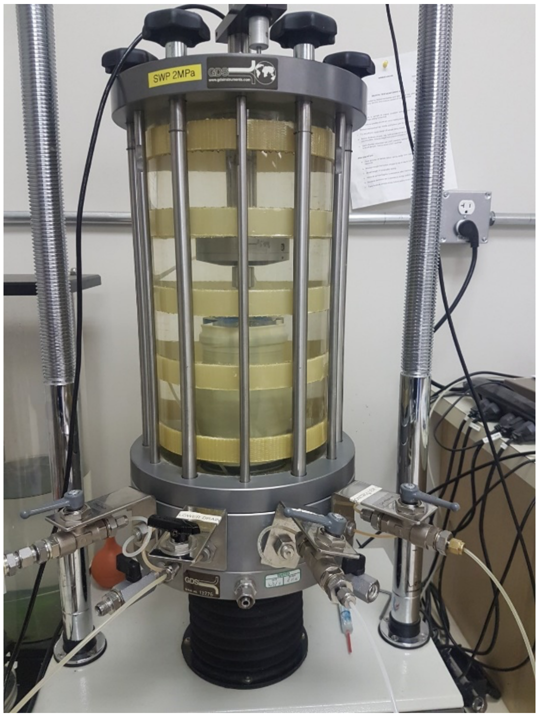

Figure 8. Triaxial apparatus

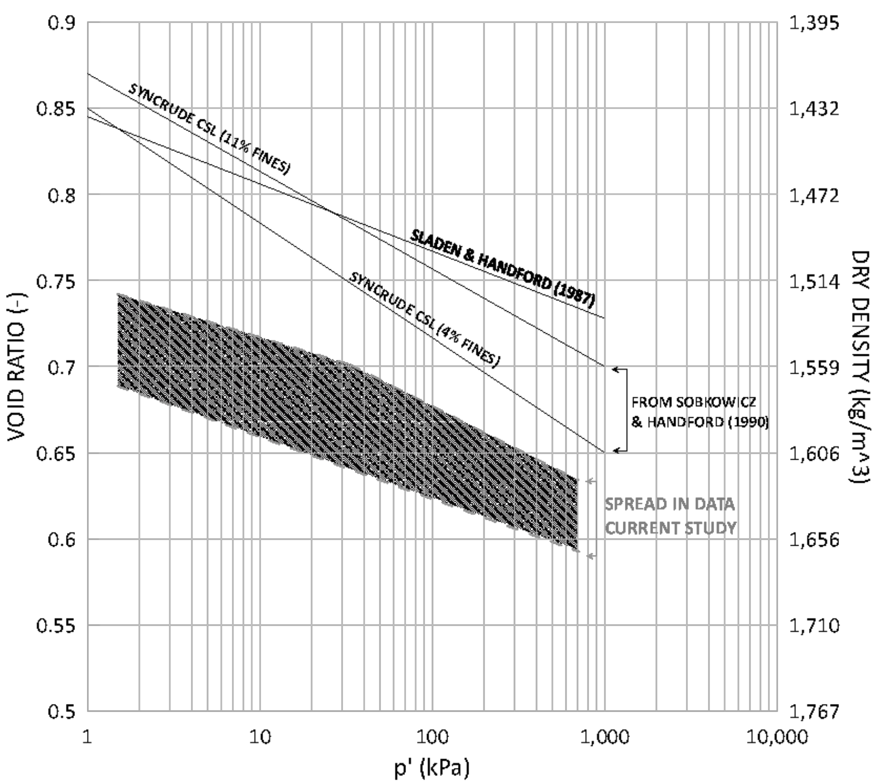

Figure 9. Critical state line assessment

Table 1. Design parameters for the shear key

Parameter	Value
Friction angle	32
Critical state intercept, Γ	0.71 – 0.73
Critical state slope, λ_{10}	0.035 – 0.04
Consolidation index, Cc	0.09
Rebound index, Cr	0.009
Proctor density (kg/m^3)	1730 - 1750
Minimum density (kg/m^3)	1440
Maximum density (kg/m^3)	1875

4.3 *Development of compaction specification*

Given the potential for the shear key to saturate during operation, it needed to be placed dense enough to remain dilative for the expected operational stress ranges. To determine the necessary compaction specification in order to achieve these goals several factors needed to be considered:

- Densities associated with dilative behaviour
- Stress range expected within the shear key
- Expected change in void ratio during operation
- Relationship between relative compaction and relative density
- Ability to achieve the necessary compaction.

Typical construction activities for sand usually specify compaction in the range between 95% and 100% Standard Proctor density. However, some activities require a higher compaction specification to meet the intended purpose. Increasing the placement density also comes with an increased cost, i.e. it could require thinner lifts or different equipment than what is available, so it was important for such a large volume of construction to assess how dense was dense enough?

A series of CSLs were developed for the potential borrow materials to assess over what densities the material would dilate. The CSL defines the border between contractive and dilative behaviour at various confining stresses, where materials loose of the CSL will contract and strain soften in undrained shear and can experience significant strength loss through the process of liquefaction. The issue for the shear key is that material would initially be placed dense, equivalent to the energy imparted by the compaction equipment, and as dump material was built on top of the shear key, the material would continue to densify, however, the overall state of the material, i.e. the distance to the CSL, would decrease (Figure 10). Therefore, the relative compaction (RC) of the material at placement had to be sufficient to maintain a dense state throughout the life of the dump.

To assess the necessary compaction, simulations of several dump cross-sections were analysed using FLAC, a finite difference software used to model stress deformation behaviour, to examine the expected stress change in the shear key during operation.

The stress path that the compacted sand would follow during loading was determined by oedometer tests on samples compacted to different levels. Using the rebound index from oedometer testing with the expected stress change from the modeling, the change in void ratio of the shear key could be estimated during the life of the structure (Figure 10). The compaction specification was selected such that the material would remain dense of the CSL by a state parameter offset of at least -0.05 at a constant mean effective stress, where state is the distance to the CSL in terms of void ratio. An offset of -0.05 was chosen because testing has shown that materials can still experience strain-softening for states between -0.05 and 0 (Jefferies and Been, 2016). An allowance was also made for the accuracy of determining the degree of compaction of the shear key sand during construction.

Based on the analysis and laboratory testing a compaction of 98% Standard Proctor Maximum Dry Density (SPMDD) was selected for the shear key.

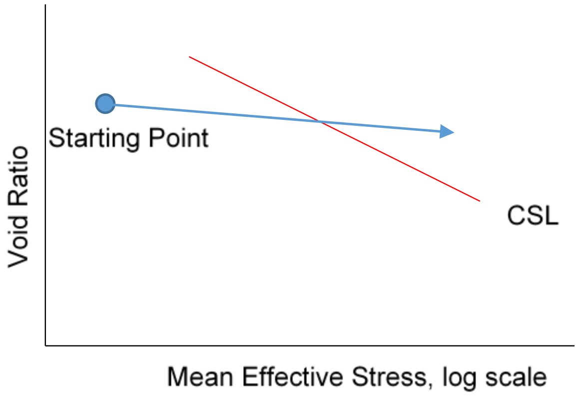

Figure 10. Stress path relative to critical state during dump construction

4.4 *Quality assurance and control methodology*

In standard civil construction, compaction specifications are established and materials are placed in controlled lifts, typically 200 mm to 300 mm thick, using a vibratory roller for compaction (of sand). Compliance with the compaction specification can then be assessed through the use of a nuclear densometer, which has an effective measurement depth of about 300 mm. Construction of the shear key initially planned to use much larger equipment than the standard vibratory rollers used on most construction sites. A test strip was carried out to examine the effectiveness of using mine equipment for compaction. It was found that the equipment was not practical to obtain the necessary compaction level in the shear key and so conventional compaction equipment and lift thicknesses were used instead. Quality control (QC) of the shear key was carried out by establishing a method specification based on the equipment type, number of passes and material placement during the test strip. Nuclear densometer tests along with an assessment of the material gradation and Proctor density were conducted for quality assurance (QA).

5 OBSERVATIONS, LEARNINGS, PERSPECTIVES

It is perhaps useful to reflect on the process of dump assessment and shear key design activities as described in this paper, in order to itemize a few learnings and perspectives which may inform the reader and others contemplating similar designs:

- Recognize the potential for liquefaction of any granular portion or zone of a structure, irrespective of the placement method, and specify a compaction requirement that addresses all stresses and failure modes.
- Consider a range of loading and pore pressures to which the structure will be subjected.
- Bear in mind that a shear key is but one tool in a useful toolbox of design remedies and may be best applied in combination with other design components such as drainage, compaction and buttressing.
- The target compaction density is influenced by many factors, including available material and equipment, risk and cost. In the end, the final compaction specification which was selected was perhaps slightly lower than originally anticipated.
- When selecting compaction requirements to ensure granular materials are placed in a dilative state (for the range of anticipated effective stresses), take account of the accuracy of both the laboratory density/CSL testing and the field compaction testing.
- Team based, collaborative solutions may require more intentional communication, but ultimately serve to deliver a robust, balanced design which is able to cater to a wide range of geotechnical performance demands.

6 CONCLUSIONS

To support the stability of a large waste dump constructed on top of an infilled tailings pond, a 10 m thick, 50 m wide shear key was designed. A typical compaction specification for standard civil construction of structures or embankments is in the range of 95% to 100%, depending upon the application. These specifications are based upon years of construction experience. Given the size and construction methodology of the shear key, the variance between 95% and 100% compaction presented significant cost implications. Based on a series of advanced tests a compaction specification of 98% SPMDD was selected to guard against the potential for liquefaction of the shear key after dump construction was completed. Field trials allowed development of a method specification for QC.

7 ACKNOWLEDGMENTS

The authors would like to thank Syncrude for supporting the publication of this work and specifically Tony Burnett, Raul Sharma, Iqbal Zafar, Victor Fong, Conrad Savoie, Kelsey Lutz and the numerous other Syncrude employees for their leadership, contributions and support during the project. We would also like to acknowledge the contributions of the Syncrude Geotechnical Review Board, as well as the much larger project team within Syncrude and Thurber, beyond the authors named, including Dawit Abraha, Trempess Moore, Mauricio Pinheiro, Amy Rentz, Colin Schmidt, Vincent Gao and Ruslan Amarasinghe.

8 REFERENCES

ASTM D4767-11. Standard test method for consolidated undrained triaxial compression test for cohesive soils, ASTM International, West Conshohocken, PA, 2017, www.astm.org

ASTM D7181-20. Standard Test Method for Consolidated Drained Triaxial Compression Test for Soils, ASTM International, West Conshohocken, PA, 2021, www.astm.org

Jefferies, M. & Been, K. 2016. Soil liquefaction: a critical state approach. Crc Press.

Ladd, R.S. 1978. Preparing test specimens using undercompaction. *Geotechnical testing journal*, ASTM, 1(1): 16-23.

Sladen, J.A. & Handford, G. 1987. A potential systematic error in laboratory testing of very loose sands. *Canadian geotechnical journal,* 24: 462-466.

Sobkowicz, J.C. & Handford, G. 1990. The application of state-of-the-art static liquefaction concepts at Syncrude Canada Ltd. *Proc. 43rd Canadian geotechnical conf., Quebec City, October 11, 1990.*

United States Securities and Exchange Commission. 2008. Form 10-K. Imperial Oil Limited.

Plant growth on oil sands tailings from the bench-scale to a field pilot: Part 1 plant development patterns

Amanda Schoonmaker, Chibuike Chigbo & Kaela Walton-Sather
Northern Alberta Institute of Technology, Peace River, Alberta, Canada

Ahlam Abdulnabi
Thurber Engineering Ltd., Calgary, Alberta, Canada (formerly University of Alberta)

Nicholas Beier
University of Alberta, Edmonton, Alberta, Canada

Scott Laberge
Barr Engineering & Environmental Science Canada Ltd Calgary, Canada

William Smith
BGC Engineering, Calgary, Alberta, Canada

ABSTRACT: The dewatering and eventual reclamation of oil sands tailings deposits are among the greatest challenges facing oil sands operators today. Planting vegetation is a potential method to dewater saturated tailings and increase soil strength through a root bed that acts as a natural reinforcing geotextile. Over two years under greenhouse and outdoor conditions, a series of barrel-sized container trials were executed to quantify rates of water use and changes in geotechnical properties when plants were grown on centrifuged fluid fine tailings. In parallel, we investigated plant establishment and key tailings properties at a field test cell filled with centrifuged fluid fine tailings between 2017 – 2019.

This paper describes key plant growth parameters (survival, leaf and root development) as well as water-use (barrel studies) of the primary species established on both trials, including sandbar willow (*Salix interior*), slender wheatgrass (*Elymus trachycaulus*), water sedge (*Carex aquatilis*) and western dock (*Rumex occidentalis*). These results are described from two viewpoints: (1) in the context of their relative potential to support dewatering and (2) the consistency and repeatability of plant survival and growth as this is an important consideration in future use as a technology.

1 INTRODUCTION

Cost-effective dewatering and consolidation of fluid fine tailings (FFT) continue to be an ongoing challenge in the mineable oil sands. A key tailings management challenge for flocculated and centrifuged material is the rate at which dewatering occurs once placed into a final deposit. For thick lifts, there may be an insufficient surcharge to load the deposit to dewater under self-weight consolidation alone. Also, a common problem with tailings that are treated through centrifugation or flocculant-addition processes is the development of a surficial crust that slows evaporative drying deeper in the deposit. To counteract some of the issues with crusting, wick drains, and other methods to induce a hydraulic gradient are being developed to accelerate dewatering at depth. For densification and consolidation near the surface (less than 2 m depth), vegetation may allow both dewatering and some temporary strength benefit through a fibrous root structure. This phenomenon is well known in the reclamation field and is a primary motivation for grass seeding of sloped ground. It was clearly demonstrated over 20 years ago that plants are capable of dewatering composite tailings (CT) originating from oil sands mining and copper mining (Silva 1999). In this seminal study, plants were shown to dewater large 200 L containers of CT within a single growing season and to provide enhanced bearing capacity throughout the depth of the dewatered CT. Although the species tested in that study were non-native species, and as a result, not desirable for deployment in the northern Boreal zone (due to risk of escape and invasion), the basic concept was demonstrated. Following this work, Wu (2009) tested plant dewatering capability for five native types of grass and found similar results where some of the species (*Agropyron* spp.) were able to uptake water from the high-water content CT tailings resulting in higher solids contents and strength after the 15-week study period.

Renault et al. (2004) and Wu (2009) studied numerous native graminoid species for their capacity for growth on CT, and both found slender wheatgrass (*Elymus trachycaulus*) was one of the strongest candidates in terms of growth and vigor. Yucel et al. (2016) examined seed germination and early establishment of 16 agronomic and native plant species on treated fluid fine tailings (FFT). As observed by Silva (1999) and Wu (2009), most species showed some level of growth and persistence; however, slender wheatgrass had the highest per plant aboveground biomass when grown on centrifuged fluid fine tailings (CFFT). The consistent performance observed in all these studies, despite very distinct differences in texture between CT and FFT for the *Agropyron* genus, and for slender wheatgrass specifically (Renault et al. 2004, Wu 2009, Yucel et al. 2016), aligns with the observation of its strong salinity tolerance in natural systems (Purdy et al. 2005). Although not widely studied on mine tailings to date, another group of species, namely willows (*Salix* spp.), also hold promise for tolerance and vigorous growth on tailings. Willows have been successfully grown in dredged sediments studies (Vervaeke et al. 2001, Smith et al. 2009) and have shown capacity to dewater these similarly soft and chemically challenging deposits (Smith et al. 2009). The species *Salix exigua* and *Salix discolor* have been grown successfully in treated FFT under greenhouse conditions (Yucel et al. 2016).

This paper describes key plant growth parameters (survival, leaf and root development) as well as water-use (barrel and tote trials) in three trials that represented a gradient of scales (~100L, 1000 L and field-scale) and environmental conditions ranging from controlled, indoor greenhouse setting to outdoor trials. All trials were conducted utilizing centrifuged fluid fine tailings (CFFT) though the tailings originated from different mines and in different years of production. The primary species established on all trials, including sandbar willow (*Salix interior*), slender wheatgrass (*Elymus trachycaulus*), water sedge (*Carex aquatilis*) and western dock (*Rumex occidentalis*), are the core focus of this paper. In this paper, we will compare the consistency and repeatability of plant survival and growth in these different trials, as well as their relative potential to support dewatering are described. The reader is encouraged to read the companion paper (Abdulnabi et al. 2021), which focuses on the geotechnical performance of these trials.

2 METHODS

2.1 *Greenhouse and outside trial setup*

Two container-scale trials were conducted between June 2018 and October 2019. The first trial was outdoors (hereafter outside trial), and the second trial was inside a research greenhouse (hereafter GH trial) with capacity for climate control and supplemental lighting (Table 1 provides a summary of core conditions and timelines). For the GH trial, tailings were first homogenized in larger containers (500 L volume) prior to pouring into individual containers to ensure study containers received similar composition of materials. For a detailed description of the geotechnical measurements, the reader is encouraged to read the companion paper (Abdulnabi et al. 2021).

The outside trial experienced two plant installation events in June 2018 and May 2019 due to overwinter mortality of the plants through winter 2018/19 as the totes froze deeply during a period of extreme cold. In nature, the root systems of native plants do not experience deep cold as the soil does not typically freeze deeply. Although the compositional mixtures varied to some degree between the outside and GH trial, the following rooted seedlings were hand planted, including sandbar willow (*Salix interior*), water sedge (*Carex aquatilis*), western dock (*Rumex occidentalis*) and surface seeding of slender wheatgrass (hereafter SWG, *Elymus trachycaulus*, rate of 700 kg ha^{-1}). For the outside trial, 12 rooted seedlings per container were planted, and for the GH trial, 4 rooted seedlings per container were planted (refer to Table 2-3 for detailed compositional description and stock characterization information). The rooted seedling stock was produced in 340 mL cavities (Beaver plastics, Acheson Alberta), and the peat growth substrate mixed with alfalfa pellets resulting in large stock where *S. interior* stem mass averaged 8.6 g, leaf mass 4.6 g and root mass 5.7 g; *C. aquatilis* mean leaf mass was 1.7 g and root mass 1.5 g; *R. occidentalis* leaf mass was 2.6 g and root mass 4.9 g at the time of planting. The first growing season setup and results from the outside trial were presented at a previous conference (Laberge et al. 2019); the results from the second and final growing season are the focus of this discussion.

Table 1. (a) Key trial characteristics of container (outside trial, GH trial) and field deposit trial and (b) chemical properties of tailings in the outside and GH trial. The CFFT for the GH and Field trial originated from the same mine, while the Outside trial was from a different mine.

a.

	Outside trial	GH trial	Field trial
Location	Peace River	Greenhouse	Fort McMurray
Start date	2018-06-16	2019-05-24	2017-06-01
End date	2019-10-04	2019-10-02	2019-09-01
Mean temperature (ºC)[1]	12.93	23.16	14.05
Mean daily temperature was > 10ºC (days)	193	131	337
Mean daily temperature was > 15ºC (days)	85	131	204
Mean daily temperature was > 20ºC (days)	11	131	49
Initial tailings volume (L)	600	82	4,000,000[2]
Container / deposit (width x length x height or diameter x height)	90 x 100 x 100 cm	40 x 75 cm	30 x 60 x 4.5 m
Initial solids content (%)	56	57	47[2]
Water inputs	Local precipitation	Yes, to mimic anticipated precipitation	Local precipitation
Fertilizer addition[3]		Inorganic + Alfalfa	

Notes:

1. Mean daily temperature was calculated from May-September for trials conducted outdoors.
2. From Smith et al. (2018), which represented the initial conditions in the first year after the deposit was poured in 2016.
3. Inorganic fertilization included urea pellets (46-0-0) and Quick-start turf fertilizer (13-26-6, Evergro Canada Inc., Delta BC) each at 150 kg ha^{-1}. Alfalfa pellets (3-0-2, Alfalfa Green Milling Co., Norquay SK) were applied at a rate of 5,000 kg ha^{-1}. Inorganic fertilizer was applied 2x in the GH trial, annually in the outside trial and for the field trial annually in 2018 and twice in 2017 and 2019.

b.

		Outdoor totes		Greenhouse barrels	
		mean	SD	mean	SD
Available Nitrate (N)	mg kg^{-1}	8.3	9.2	<2	-
Available Phosphorus (P)	mg kg^{-1}	4.9	1.2	5.3	0.3
Available Potassium (K)	mg kg^{-1}	144.0	21.9	204.0	23.0
Available Sulphur (S)	mg kg^{-1}	758.0	194.9	220.0	26.5
Soluble Chloride (Cl)	mg L-1	424.0	75.0	234.0	33.6
Electrical Conductivity	dS m^{-1}	6.7	0.7	3.2	0.4
Soluble (CaCl2) pH		6.8	0.2	7.5	0.1
Sodium Adsorption Ratio		10.8	1.7	8.0	0.8

2.1.1 *GH and Outside trials – measurements and sampling*

Destructive harvest of the GH and outside trial followed a similar process where the following was collected: (1) all above-ground vegetation was harvested for determination of leaf biomass and leaf area index (LAI), (2) 1-2 sample cores (where space permitted), collected over the entire depth at 10 cm increments were collected and pooled for assessment of belowground development, (3) one sample core were also collected at the same depth intervals for determination of solids content. A 5 cm diameter soil auger was utilized for all root and solids content sampling activities.

2.2 *Field trial setup*

The field study took place within a self-contained (non-draining) centrifuged fluid fine tailings deposit (30 m width × 60 m length × 4.65 m depth at the time of pouring) within an operating oil sands mine. The deposit was poured in 2016 and initially vegetated with slender wheatgrass (*Elymus trachycaulus*) and sandbar willow (*Salix interior*) in spring 2017 (refer to Smith et al. 2018 for detailed description of initial prescription) with a section of the deposit originally left as an unvegetated control area. Due to differences in surface elevation, the central area (and deepest in terms of deposit thickness) of the deposit was flooded for an extended period until early July 2017. Consequently, higher rates of vegetation mortality occurred, resulting in substantial heterogeneity in vegetation cover across the deposit. The learnings from the 2017 work were utilized to inform experimental planting for 2018-2019 on this deposit.

A larger campaign, including a wider range of species with a subset of those selected for greater tolerance to flooding, was established in early June 2018. The following composition of plants was established throughout the test cell including the area that was previously left as an unvegetated control: slender wheatgrass seed at 300-700 kg ha^{-1} to fill gaps in the seeding work from 2017 and rooted seedlings of *Salix interior*, Bebb's willow (*Salix bebbiana*), water sedge (*Carex aquatilis*), Bebb's sedge (*Carex bebbi*) and western dock (*Rumex occidentalis*) were distributed in 3x3 m plots to ensure a uniform distribution of plants. On July 5, 2018, the deposit was pumped from the surface and additional slender wheatgrass seed was hand-broadcasted at 300 kg ha^{-1} in areas that still showed limited grass establishment and 78 common reed grass plants (*Phragmites australis* subsp. *americanus*) were hand-tossed into the central-most part of the deposit. In 2019, the last iteration of plant establishment occurred at two time periods: May 24 and the second time was on July 3. Except for those areas that already had a large quantity of existing grass development, 700 kg ha^{-1} of slender wheatgrass and 47 kg ha^{-1} of tufted hairgrass (*Deschampsia caespitosa*) were hand broadcasted across the deposit.

2.2.1 *Field study – measurements and sampling*

In September 2017, 2018, and 2019, a comprehensive series of measurements were collected across a spatially explicit sampling grid (a subset of samples from a 3x3 m sampling grid) across the entire deposit. At each measurement point:

1. Vegetation % cover and height, by species.
2. Plant biomass (clipped aboveground vegetation in 0.5 × 0.5 m quadrat) by species. A subsample of leaves was also collected and stored in a plastic bag and refrigerated (while active sampling was ongoing) for determination of leaf area index. These samples were stored at -4ºC upon return to the lab in order to preserve leaf structure.
3. Solids content at 10 cm increments (to 50 cm depth) using a hand-held soil auger. Samples were submitted to an external lab for analysis.
4. Root density sampling at 5cm diameter and 30 cm deep (in 10 cm increments) with a subset of samples (n=10) collected to 60 cm depth and a further subset (n=3) collected to 100 cm depth. These samples were stored frozen at -4ºC upon return to the lab in order to preserve roots until processing could take place.

2.3 *Laboratory methods – all trials*

Due to the large volume of material from the field trial, aboveground biomass was initially air-dried on the bench and then uniformly dried in an oven to weight constancy at 70°C. For all other trials, biomass samples were placed directly into the oven. Total plant dry weight was determined to the nearest 0.1 g but in cases where the sample was very small (< 1 g), a different scale was used, and dry weight was measured to the nearest 0.0001 g. Roots were separated from tailings samples following the procedure outlined in Schoonmaker et al. (2018) and roots were oven-dried to weight constancy at 70°C.

The relationship between leaf mass and surface area was determined on a subset of leaves of individual species that were collected in the field concurrent with vegetation clipping for biomass. Similarly, the relationship between root mass and root length followed a similar process. For leaves, these samples were stored frozen (-4°C) after field collection to preserve the leaf structure and shape. For the determination of leaf area or root length, individual leaves or roots from each species were placed on a flatbed scanner and WinFOLIA™ or WinRHIZO™ software (Regent Instruments Inc., Quebec Canada) was used to estimate the leaf area from the scanned image. The scanned leaves or roots were then oven-dried at 70 °C and weighed to the nearest 0.0001 g. The ratio of leaf area: leaf mass was used to estimate leaf area index (LAI) of all plots where above-ground leaf mass had been harvested and root length density estimated from sampled root cores based on the estimated ratio of root length: root mass.

2.4 *Data presentation and statistics*

Data was presented graphically and, where appropriate, analyzed using R statistical software (R Core Team, 2021). To better understand the variation observed in solids content in the field trial, a logarithmic equation was fit to the individual solids content measurements. The natural log of solids content was examined with depth from the deposit surface (continuous variable), leaf area index (continuous variable) and deposit thickness (as a factor). As individual samples from the same location along the depth from deposit surface would be related (spatially), a random effect for the plot location was also included resulting in a linear mixed effects model (utilizing function *lme*, Bates et al. 2015). For the 2017 regression, the marginal R2 = 0.75 (variance explained by fixed effects) and the conditional R2 = 0.87 (variance explained by fixed effects and random effects). For the 2019 regression, the marginal R2 = 0.74 and conditional R2 = 0.81. Model assumptions were checked with diagnostic plots of fitted and residual values and histogram of residuals to validate equality of variance and normality. As there was observed heteroscedacity, the model was modified to allow for unequal variance by deposit thickness using the *varIdent* function. A global model including individual variables as well as two-way and the three-way interaction were included. The function *stepAIC* was utilized to cross-check for potential simplification of this model, however, the global model was found to be the most parsimonious as indicated by smaller AIC values.

3 RESULTS AND DISCUSSION

3.1 *Patterns of plant development*

3.1.1 *Greenhouse trial*

All planted barrels increased substantially in aboveground biomass over the 6-month trial. The SWG treatment developed more slowly as it had been sown from seed rather than planted as a rooted seedling but ultimately produced more leaf mass than the willow barrel (Table 2). The willow barrel increased its stem wood production from 34 g to 179 g and its leaf mass from 18 g to 64 g (Table 2). Leaf mass production increased from ~8.6 g to 181 g in the *Carex*/*Rumex* barrel and the combined plant species treatment saw an increase from 13.4 g to 133 g in leaf mass and 17.2 g to 100 g in stem wood mass (Table 2).

There were also differences in root morphology of each treatment which may affect the competitive outcome of species. For example, although the grass treatment produced more leaf mass than the willow barrel, the total root mass production was ultimately lower with total root mass of ALL> *Carex*/*Rumex* >*Salix*>SWG (Table 2, Figure 1). However, the specific root length (m root g^{-1} root) of grass treatment was highest, followed by the willow barrel; many fine roots will effectively increase the root surface area available for nutrient uptake and water extraction. These root morphological characteristic differences provide insights as to how effectively these species compete for and take up resources (nutrients and water) for growth and may also influence the capacity of these roots to improve shear strength in tailings. Despite these differences, all planted barrels followed the same overall pattern of root development with depth, with higher quantities at the surface and a non-linear decline with depth (Figure 1).

Table 2. Characteristics of vegetation at the conclusion of individual trials organized by the species or groups of vegetation present.

Parameter	Vegetation type[1]	GH trial	Outside trial	Field trial[2]
Total leaf / stem mass (g)[3]	*Salix; Salix*/SWG	64 /179	5 / 122	
	SWG; SWG/Salix	90	69 / 144	
	Carex/*Rumex*	181	147	
	ALL[4]	133 / 100	142 / 84	274971
Leaf area index (m^2 m^{-2})	*Salix; Salix*/SWG	2.5	0.1	
	SWG; SWG/Salix	2.1	1.1	
	Carex/*Rumex*	5.2	2	
	ALL	5	3.5	4.8
Leaf mass per unit volume of tailings (g L^{-1})[5]	*Salix; Salix*/SWG	0.92	0.01	
	SWG; SWG/Salix	1.28	0.11	
	Carex/*Rumex*	2.58	0.24	
	ALL	1.89	0.24	0.07
Total root mass (g)	*Salix; Salix*/SWG	222.5	59.6	
	SWG; SWG/Salix	26	237.2	
	Carex/*Rumex*	431.9	505.9	
	ALL	555.9	185.6	133600
Total root length (m)	*Salix; Salix*/SWG	5230	1703	
	SWG; SWG/Salix	1798	21563	
	Carex/*Rumex*	5114	6238	
	ALL	6074	11163	3704769
Root length (m) per g of root	*Salix; Salix*/SWG	24	29	
	SWG; SWG/Salix	69	91	
	Carex/*Rumex*	12	12	
	ALL	11	60	28

1. The vegetation types were not identical in some instances between the GH and outside trials. In these instances, the vegetation type for the GH trial is listed first, followed by the Outside trial. For the outside trial, two species are listed in some instances, but it is the first species listed that was the dominant one and were therefore listed with the single species treatments in the GH trial. Specifically for the *Salix*/SWG combination, the slender wheatgrass present was marginal as these were small volunteer plants where the seed blew in from the adjacent tote.
2. For the field trial, the parameters listed were extrapolated estimates based on grid sampling conducted in 2019. These values, therefore, should be taken as approximate.
3. For GH and outside trials, both the leaf and stem mass are shown (leaf / stem).
4. ALL: all plant species grown together and for the field trial all species were present in addition to other species listed in Table 4 caption.
5. The volume of tailings was based on initial volume (Table 1), rather than final consolidated volume.

3.1.2 *Outside trial*

In contrast to the GH trial, the *Salix/*SWG in the outdoor trial developed much more slowly as the starting stem mass was estimated at ~ 100 g (12 seedlings X 8.6 g of stem wood per seedling) and the final stem mass was 122 g (Table 2) and with lower final leaf mass (5 g) compared to starting leaf mass (55 g). The slow development of *Salix* led to decreased LAI, total root mass and total root length compared to other treatments (Table 2, Figure 1). While it is not clear why the *Salix* plants grew much more slowly (relative to the other species in the outside trial or even the *Salix* in the barrel trial), it could be that tailings chemistry contributed to less aggressive growth as both the electrical conductivity and available S were substantially higher in the Outside trial compared with the GH trial as the CFFT in these trials originated from different mines (Table 1b). Additionally, these plants were established when they were already actively growing (non-dormant). For the *Salix*, this may have been a stressful way to be introduced into the container and in an outdoor environment with high evaporative demands.

Herbaceous species tend to be less sensitive to this type of transplanting compared with woody species. In fact, the *Carex*/*Rumex* tote grew a substantial leaf area with an increase from 25.7 g to 147 g (Table 2). The SWG/*Salix* tote also increased in leaf area (though to a lesser degree when compared with the GH trial), with most being attributable to the SWG rather than the *Salix* (Table 2). Root development in the Outside trial shared similarities with the GH trial, though at much lower rooting densities overall with a generally similar non-linear decline with depth (Figure 1).

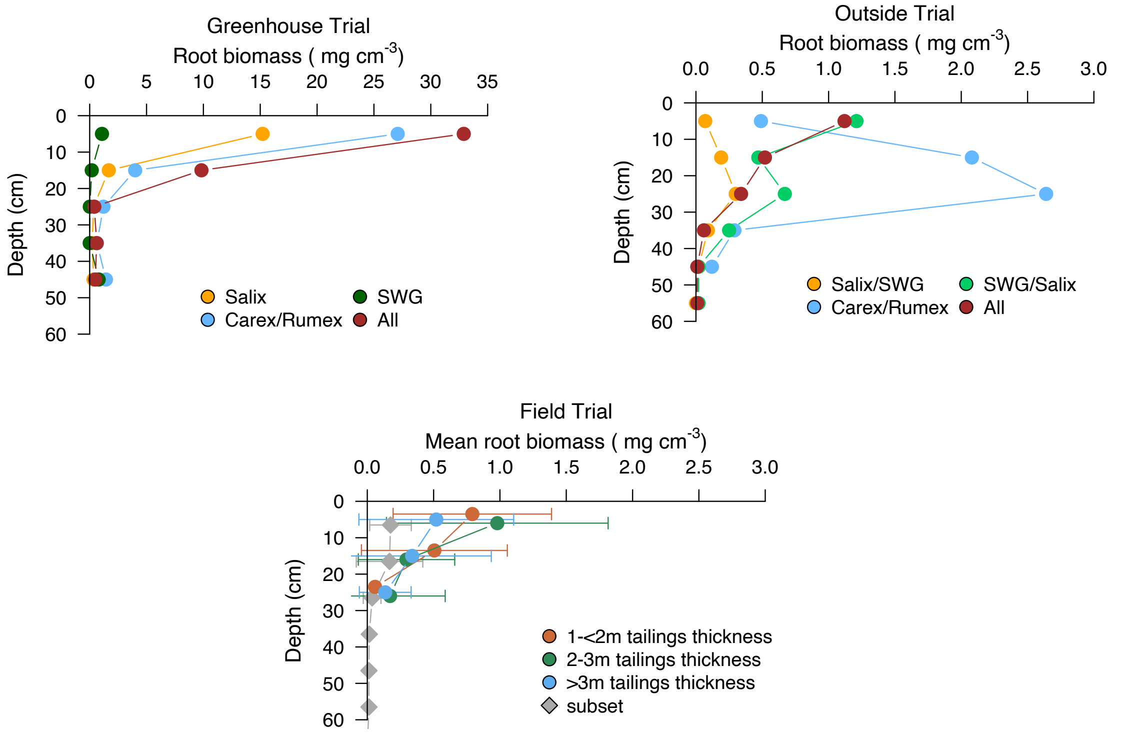

Figure 1. Root biomass density for the greenhouse and outside trials and mean root biomass with depth for the field trial (year 3 results shown). Error bars represent one standard deviation of the mean (n = 60-100).

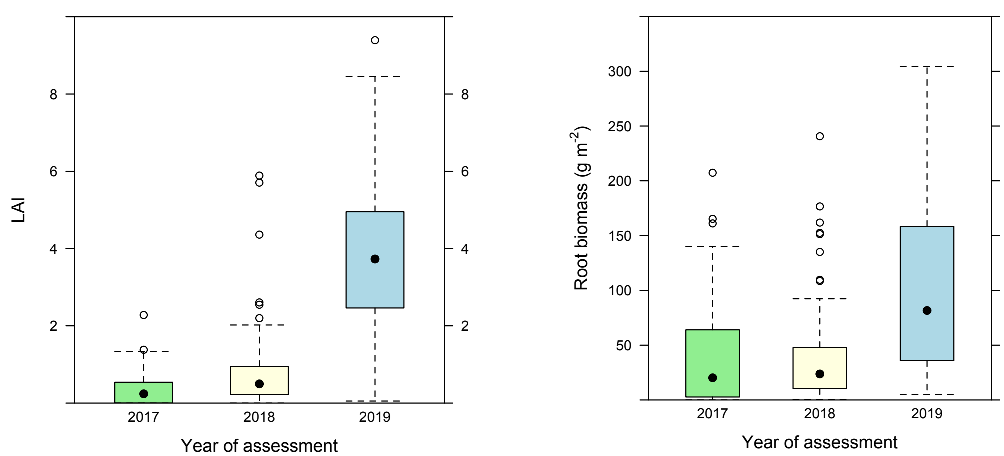

Figure 2. Box and whisker plots illustrating the range of variability and change in leaf area index (LAI) and root biomass at the field trial between 2017 and 2019 (year 1 – 3) (n= 80-100).

3.1.3 *Field trial*

Across the three-year period, since vegetation was first established at the test deposit, key plant parameters have increased steadily where the median LAI in 2019 was near 4.0 compared with a value of ~0.5 in 2017 and median root biomass (expressed on an area basis) tripled (Figure 2). In contrast with 2017 where most vegetation was constrained to the shallower (and drier, sloped) part of the deposit, by 2019, plants were present across the entire deposit though there were notable compositional shifts during this period which reflects the establishment of wetland species which better tolerated the ongoing flooding in the central, wetter part of the deposit (Table 4). LAI throughout much of the deposit showed a similar range in values apart from the shallowest thicknesses of the deposit (<2m) where LAI was > 3 (Figure 3).

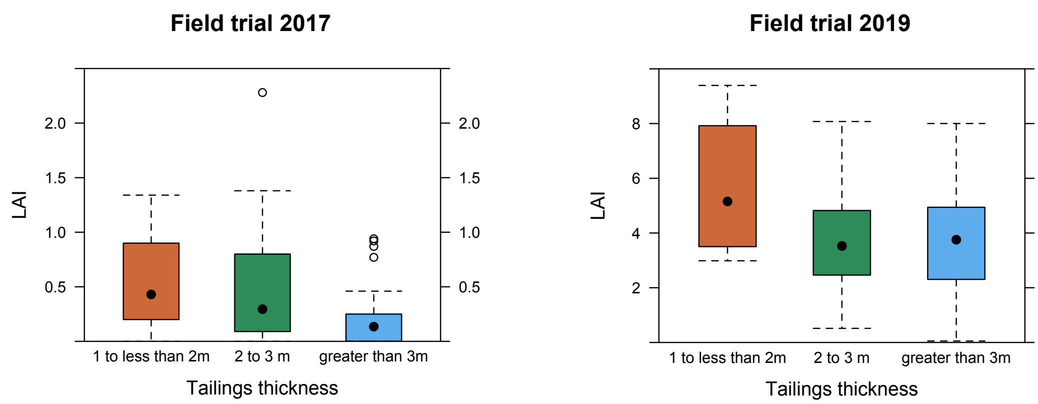

Figure 3. Box and whisker plots from the field trial in Sept 2017 and 2019 illustrating leaf area index (LAI) grouped by tailings thickness (n=100).

Root density with depth follows the non-linear pattern observed in the tote and barrel trials and similar to the LAI results, there was substantial overlap in root biomass density throughout the deposit as expressed by the tailings thickness (Figure 1). A subset of deeper samples taken in 2019 also illustrates that most roots were constrained to the upper 30 cm of the tailings profile. This is likely a function of the species that dominated the test deposit (herbaceous plants, which tend to be shallow rooted) as well as the moisture conditions; if there is plenty of moisture at the surface, there is not a sufficiently good reason for plants to send roots to greater depths to secure water.

3.2 *Plant water use and effect on tailings solids content*

3.2.1 *Greenhouse trial*

Water consumption in the barrels where rooted seedlings were hand-planted utilized more than three times the water relative to the unplanted barrel or the barrel with slender wheatgrass only and the final measured solids content followed a similar pattern, where treatments that utilized more water had higher final solids content (Table 3). The magnitude of this effect varied by species where the greatest increase in solids content was observed in barrels with *Salix* only and when compared to treatments that received a similar amount of water, was 7% and 5% higher than *Carex* /*Rumex* treatment and the combined plant species treatment respectively. Grass treatment received ~70% less water but had the lowest final solids content compared to all planted treatments, which reflects the lowest total root length observed in this study (Table 2)

3.2.2 *Outside trial*

All the totes received water through precipitation inputs, therefore the effect of the planting treatments must be examined through changes in solids content. At the end of the 2019 growing season, only modest improvement was seen in the average solids content with the unplanted tote and willow tote at 73% and the other planted totes at 76-77% (Table 3). Anecdotally, there was a significant degree of surface cracking observed in the unplanted tote but notably not in the planted totes, this would have significantly improved the ability of that tote to lose water via evaporation. The surface of the planted totes, on the other hand, did not show surface cracking and this was most likely a consequence of the plant canopy reducing soil evaporative fluxes (particularly in the totes where LAI was higher and therefore more effectively cover the tailings surface) though the presence of a root network may also have more effectively bound silt, sand and clay particles together thereby making it less prone to fracturing. This may be a beneficial feature to create surficial strength, but it may reduce dewatering from surface evaporation, thereby creating a greater reliance on evapotranspiration. To counterbalance this effect, it is important that high quantities of LAI are present and that the species can effectively tap into moisture at depth within the profile.

Table 3. Mean final solids content (GH and outside trial only) and total water input (presented in L and mm) into individual trials by vegetation type.

Plant treatment where semicolon denotes plant treatments specific to GH or Outside trial	GH trial			Outside trial[1]			Field trial[1,2]	
	Solids content (%)	Water input (L)	Water input (mm)	Solids content (%)	Water input (L)	Water input (mm)	Water input (L)	Water input (mm)
Control (no plant)	59	38	302	73	422	469		
Salix; *Salix/*SWG	75	115	914	73	422	469		
SWG; SWG/Salix	64	38	302	76	422	469		
Carex/*Rumex*	68	115	914	77	422	469		
All	70	115	914	76	422	469	1703 5	946

1. For the outside and field trials, the inputs should be considered approximate as climate data originated from regional weather stations (Environment Canada 2021).
2. Solids content results for the field trial are highly variable and are shown in Figure 4.

Table 4. Proportion of leaf biomass represented by species or genus-level plant groups from sampling conducted between 2017 and 2019 on the field trial.

Vegetation group	**2017**	**2018**	**2019**
Salix[1] spp.	0.32	0.11	0.03
Graminoids[2]	0.66	0.46	0.43
Sedges and rushes[3]	0.00	0.10	0.18
Rumex occidentalis	0.00	0.21	0.17
Typha latifolia	0.00	0.08	0.19
Others[4]	0.00	0.00	0.00

1. *Salix interior* was the predominant species in the *Salix* spp. group.
2. Graminoids were predominately represented by *Elymus trachycaulus* with *Beckmania schyziachne*, *Hordeum jubatum*, *Calamagrostis canadensis* and *Phragmites australis* were also present.
3. Sedges and rushes were dominated by *Carex aquatilis*, *C. bebbii* and *C. atherodes* and *Scirpus microcarpu*s.
4. Others included: *Chamerion angustifolium*, *Polygonum lapathifolium* and *Sonchus arvensis*.

3.2.3 *Field trial*

In the first year of the trial in 2017, the season was drier and did not require pumping off prior to the site investigation. The final year of the field trial was a wet season with above-average precipitation during the growing season. Snowmelt, precipitation and consolidation water collect in the middle of the test cell because downward and lateral drainage is impeded by an HDPE liner and the lack of a cell outlet (Smith et al. 2018); this configuration further enhanced the water storage within the test cell. At the time of measurements in early September 2019, the surface of the deposit was pumped to support sampling efforts. The solids content in 2017, near the surface, was higher despite lower LAI and plant biomass as compared to 2019 though at greater depth

(0.45m), the solids content had increased from 2017 to 2019 and could have been driven by freeze-thaw consolidation (Figure 4).

Despite the waterlogged condition of the deposit, there was still wide variation (~60-75%) in solids content, though, relatively speaking, the variation was less than what was observed in the 2017 season (Figure 4). In addition, due to active revegetation efforts and ongoing flooding that effectively transported seeds and plant propagules across the whole deposit, there was no longer an effective unplanted control to make direct comparisons between planted and unplanted zones. In the absence of a true control in 2019, a log-linear regression was developed in order to relate variation in both years to potential explanatory variables, including the thickness of the tailings (which is also a proxy for location and dryness in the deposit), depth from the surface and the presence of vegetation (as expressed through LAI). In 2017, higher LAI was associated with modest increases in solids content at greater tailings thickness, and this effect was observed to a depth of 0.45 m in some cases (Figure 4). In 2019, this regression illustrated that tailings thickness explained much of this variation but higher LAI (within the >3m and 1-<2m thicknesses) was also associated with marginally higher solids content. This effect dissipated quickly with depth from the surface (Figure 4).

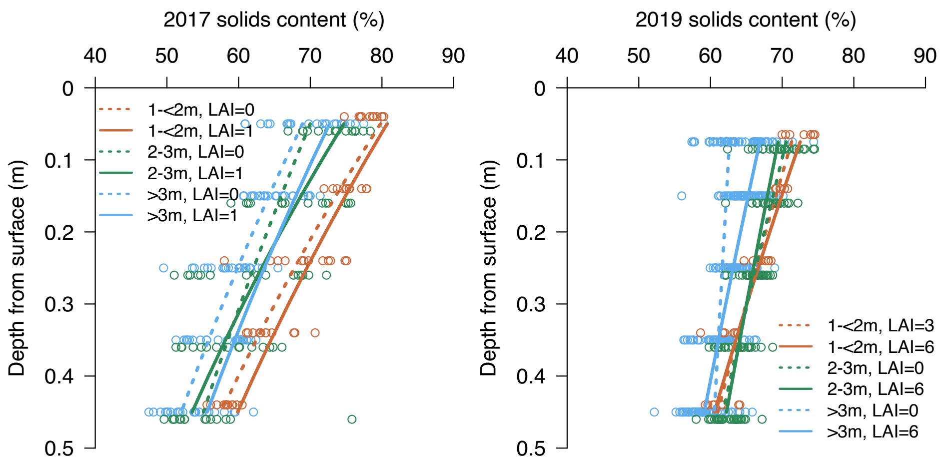

Figure 4. Logarithmic curve fit of solids content (%) as a function of the depth from deposit surface, tailings thickness and contrasting leaf area index (LAI) values from September 2019 at the field trial (n=100 sampling locations).

4 CONCLUSIONS

This collection of trials illustrated that a range of native plant species could be successfully established onto treated fine tailings. Under controlled conditions and with high-quality nursery stock seedlings, rooted seedlings grown in CFFT grew vigorously and consumed three times more water over the 6-month period compared with the unplanted barrel. While the SWG barrel consumed a similar quantity of water compared with the unplanted control, there was some improvement in solids content over that time period. Moving to the outdoors and to a different source of tailings, slower rates of growth and less consistency amongst species was observed. As the outdoor trial was different in multiple ways (larger volume, outdoors and different source of centrifuged fluid fine tailings), it is unclear which factor was behind the lower rates of growth, though the chemistry of these tailings was a likely contributor. Despite slower growth, there were modest improvements in solids content for three out of the four totes that were planted relative to the unplanted tote. In the field, there was consistent increase in plant growth within the deposit over the three-year period, as illustrated by increasing LAI and root density. However, the presence of plants was not sufficient to fully manage precipitation inputs as the deposit was largely saturated (flooded) in the 2019 growing season as compared to the 2017 growing season when the deposit was unsaturated at the time of site investigation. Nevertheless, a slight increase in solids content was seen to be associated with an increase in LAI, and this relationship was more apparent in unsaturated conditions than saturated conditions. Future field investigations should consider surface water management to enhance vegetative growth of woody species and graminoids suited to unsaturated conditions; this approach may be more complementary to other passive evaporative technologies as the root systems of these plants can extract water beyond the surface crust.

5 ACKNOWLEDGMENTS

The authors are grateful for the financial support provided by the Institute for Oil Sands Innovation (IOSI) in conjunction with Imperial Oil and Canadian Natural Resources Limited (CNRL) and the National Sciences and Engineering Research Council. The authors would like to acknowledge the many student research assistants at NAIT that assisted with the execution and maintenance of the container trials and support in the field trial. Thank you to the BGC team for assisting in the field trial data collection and analysis: Charlie Borrell, Jason Abboud, Erin Olauson and Jack Seto.

6 REFERENCES

Bates D., M. Maechler, B. Bolker, S. Walker, R. H. B. Christensen, H. Singmann, B. Dai, G. Grothendieck, P. Green, and M. B. Bolker. 2015. Package lme4. *Convergence* 12:2.

Environment Canada (2021) National climate data and information archive. URL http://www.climate.weatheroffice.ec.gc.ca/Welcome.e.html [last accessed on July 15, 2021].

ESRI (Environmental Systems Research Institute). 2012. ArcGIS 10.1 Help. https://doc.arcgis.com/en/arcgis-online/

Laberge, S. Beier, N.A. Schoonmaker, A. 2019. A study of the impact of evapotranspiration through native plant species on the strength and solids content of treated oil sands tailings. In proceedings of the Tailings And Mine Waste conference Vancouver, BC, November, 2019.

R Core Team. 2021. R: A language and environment for statistical computing. R Foundation for Statistical Computing, Vienna, Austria. URL https://www.R-project.org/

Schoonmaker, A. Degenhardt D, Floreani T. 2018. Evaluating the potential to establish plants to aid in dewatering of an atmospheric fine drying tailings deposit at Muskeg River mine. International Oil sands Tailings Conference, Edmonton, Alberta, Canada

Silva MJ 1999. Plant dewatering and strengthening of mine waste tailings. PhD thesis, Department of Civil and Environmental Engineering, University of Alberta.

Smith, W. Olauson, E. Seto, J. Schoonmaker, A. Nik, R. M. Freeman, G. McKenna, G. 2018. Evaluation of strength enhancement and dewatering technologies for a soft oil sands tailings deposit. International Oil sands Tailings Conference, Edmonton, Alberta, Canada

Wu S 2009. A greenhouse study of selected native plant species for dewatering CT. MSc thesis, Department of Civil and Environmental Engineering, University of Alberta.

Plant growth on oil sands tailings from the bench-scale to a field pilot: Part 2 key geotechnical performance indicators

Ahlam Abdulnabi
Thurber Engineering Ltd., Calgary, Alberta, Canada (formerly University of Alberta)

Abigail Paul, & Nicholas Beier
University of Alberta, Edmonton, Alberta, Canada

Scott Laberge
Barr Engineering & Environmental Science Canada Ltd., Calgary, Alberta, Canada

Amanda Schoonmaker
Northern Alberta Institute of Technology, Peace River, Alberta, Canada

William Smith
BGC Engineering Inc., Calgary, Alberta, Canada

ABSTRACT: Alberta Energy Regulator stipulates volume limitations on the amount of fluid fine tailings that oil sands operators can deposit, and incentivizes producing ready to reclaim deposits. This has led to the expansion of innovative approaches to dewater oil sands deposits. In nature, plants are particularly good at extracting water through the root system and shedding it through the leaves. The growth and development of several plant species native to Alberta on centrifuged fluid fine tailings were investigated on scales ranging from hundred-liter barrels in a controlled greenhouse environment to a thousand-liter totes in an outdoor environment, and eventually a field pilot of nearly a million liters in volume. This paper presents a meta-analysis of key geotechnical performance indicators and their evolution. The study details the undrained shear strength profiles with depth up to 1m below the deposit's surface as they vary over time. The assessment of results shows conflicting outcomes from greenhouse experiments compared to outside experiments in terms of which species contributed to the most dewatering or highest strength. However, in both the greenhouse and the outside trials plants seemed to contribute to strength gain. This was less clear in the field trial due to uncontrollable factors discussed in the paper.

1 INTRODUCTION

1.1 *Oil sands tailings reclamation challenge*

The 2020 state of the oil sands tailings report by the Alberta Energy Regulators (AER) references a 1302 Mm^3 of fluid fine tailings (FFT). To put this number in perspective, this is equivalent to a combined volume of 500 great pyramids of Giza. There is no denying the urgency to develop sustainable technology to reduce FFT volumes industry-wide. A cornerstone in the regulatory agenda is to limit the volume of new fluid tailings that oil sands operators can generate and encourage the reduction of existing legacy tailings. Alberta Energy Regulator. stipulates that all tailings ponds must be 'ready to reclaim' within ten years after the end of a mine's life (AER Directive 085 2017). Over the past few decades, multitudes of technologies evolved to satisfy regulatory requirements not without their respective constraints and limitations. Notably, a few methods aim at leveraging environmental processes such as freeze-thaw and atmospheric evaporation to dewater oil sands tailings. These methods have been quite attractive to the industry as sustainable tools in helping reduce FFT volumes. The expectation of a 'ready to reclaim' deposit often necessitates combining more than one dewatering technology. Evapotranspiration from native plant species was presented as an added tool to further dewater previously treated FFT in the past two decades.

1.2 *Plants as a dewatering tool*

Johnson et al. (1993) show the possibility of increasing solids content of oil sands tailings mixed with sand when using plants as a further dewatering tool. Silva (1999) confirms the potential for dewatering and strength gain when using plants on the same class of material, which became known as composite tailings. In the decade following Silva's work, multiple confirmatory studies emerged (Naeth and Wilkinson 2002, Wu 2009; Wu et al. 2011 Guo 2012). However, the common thread between these studies is that from a geotechnical composition perspective, the tailings were always on the coarse side of the particle size spectrum and were, therefore, easier to dewater, to begin with. Furthermore, most of the emphasis seemed to be centred around the survivorship and establishment of plants and less on plants capability from a geotechnical perspective.

A few recent studies examine the behaviour of plants in fine-dominated oil sands tailings and from a geotechnical perspective; for example, Smith et al. (2018) present some evidence of the strengthening of fine-dominated centrifuged fluid fine tailings (CFFT) field deposit when supplemented with various plants. Laberge et al. (2019) also present evidence of plants' establishment success and contribution to strength after major rainfall rewetting events on fine-dominated tailings. Interestingly, both Smith et al. 2018 and Laberge et al. 2019 examine somewhat similar centrifuged fluid fine tailings, but the reported contribution of plants to strength is quite different in terms of which species yielded the best strength and the overall contrast in strength between vegetated and non-vegetated specimens. Understandably so, since these two studies, despite being conducted on somewhat comparable centrifuged fluid fine tailings, were nearly four orders of magnitude different in terms of scale. Laberge et al. (2019) study was conducted in 1000 L capacity totes, whereas Smith et al. (2018) study was based on a field sale plot of 30 x 60 x 4.65 m (in the order of a million litres). This paper brings the scale issue into sharp focus. It examines the plants' contribution to strength and dewatering from a purely geotechnical perspective. A wealth of data was available from a collaborative research effort between the University of Alberta and Northern Alberta Institute of Technology (NAIT) sponsored by Imperial Oil and Canadian Natural Resources Limited (CNRL) through the Institute for Oil Sands Innovation (IOSI).

The paper presents a meta-analysis of the findings of strength gain and dewatering for centrifuged fluid fine tailings at scales varying from 100 L to about 10^6 L. The ability of plants to achieve higher solids content and strength is assessed compared to un-vegetated control specimens of the same size. The reader is reminded that the analysis presented herein only focuses on the geotechnical parameters. A companion paper in this conference proceeding (Schoonmaker et al. 2021) focuses on growth factors from a plant development and survivorship lens. However, the two papers are quite intertwined as the degree to which the plants were successful in establishing may have implications on the geotechnical data reported here. So to get the full picture, the reader is encouraged to read them both in tandem.

2 MULTI-SCALE AND MULTI-YEAR TRIALS

The Northern Alberta Institute of Technology and the University of Alberta were engaged in a collaborative research effort to delineate the suitability of plants native to Northern Alberta to strengthen and dewater fine oil sands tailings in multi-year multi-scale experiments. Experiments ranged from the bench scale, mesoscale up to a field pilot scale. The studies had multiple goals ranging from assessment of establishment and growth to evaluating strength and dewatering. One of the underlying goals of the many iterations of studies was to investigate the potential of using plants as sacrificial strength gaining agents to get treated oil sands tailings closer to sand capping for reclamation eventuality. Sand capping is a term that describes applying a sand soil cover over previously treated tailings to attain further consolidation and strength gain through the additional surcharge. This paper examines the dichotomy of strength and dewatering behaviour of centrifuged fluid fine tailings from various origins supplemented with different plant species to delineate if they contribute to any strength gain or dewatering. The overarching scheme of the study is the assumption that plants can promote enough strength gain to allow building a soil cover cap over existing deposits, thereby assisting in reclamation efforts.

Reclamation necessitates a sufficient shear strength at the tailings surface to make it trafficable by small trucks/dozers such as those routinely utilized in soft tailings capping at metal mines. McKenna et al. 2016 present a peak undrained shear strength of 25 kPa shear strength as the threshold to allow trafficability of these dozers, which also happens to be the boundary between soft and firm clay. The idea is that once a cap is placed overlaying the soft tailings, it facilitates further consolidation through surcharge enabling eventual reclamation. Therefore, the study's underlying assumption was to utilize the plants as a 'middle man' strengthening tool to bring the tailings up to sufficient shear strength criteria, i.e., trafficable by small machinery for sand capping purposes. As such, we use this number as an anchoring point to review strength data throughout trials.

2.1 *Greenhouse Trial*

This iteration of the study encompasses a set of 5 barrels, each with 100 L capacity in volume each. The greenhouse trial ran from May 24, 2019, to October 2, 2019. Each barrel had a nearly cylindrical shape with a diameter of 400 mm and a height of 750 mm. The tailings were poured after homogenization into each barrel to the thicknesses indicated in Table 1. Volumetric water content and matric suction sensors were embedded at 25 cm and 50 cm from the surface of the tailings in the barrel. These barrels were accommodated in a controlled greenhouse environment where the ambient temperature averaged 23°C during the 6-month trial. During the six months of testing, volumetric water content and matric suction were recorded hourly. Consolidation settlement was measured at the end of the trial. Undrained shear strength was measured intermittently at five elevations within each barrel throughout the study duration using a Geonor H60 hand-held vane.

Table 1. Species planted in the greenhouse barrels trial.

Barrel	Species in the respective barrel	Short name	Initial solids content (%)	Initial tailings thickness (cm)
1	none	Control	57	65
2	sandbar willow (*Salix interior*)	*Salix*	57	66
3	water sedge (*Carex aquatilis*) & western dock (*Rumex occidentalis)*	*Carex/ Rumex*	57	65.5
4	slender wheatgrass (*Elymus trachycaulus*)	SWG	57	62.5
5	all above species combined	All	57	62

Weekly manual watering events took place to reflect the normal precipitation patterns in Fort McMurray, Alberta. The precipitation amount for each event was calculated using climate normals from Weather Canada (May to September data). A total cumulative volume of 37.9 L was added to each of the barrels distributed at several intervals throughout the study. However, the barrels with the *Salix* and the *Carex*/*Rumex* and All had to be watered more to prevent plants from wilting. The amount of water added totalled 114.9 L. To keep the results in perspective, the reader is reminded that those three barrels (*Salix*, *Carex*/*Rumex* and All) experienced nearly threefold water intake compared to the other 2 barrels (control and SWG).

2.2 *Outside Trial*

The second iteration of the study was conducted in 1000 L capacity totes in an outdoor space in Peace River, Alberta. The totes were filled to varying volumes (refer to initial thicknesses seen in Table 2), but overall this was nearly an order of magnitude bigger in volume than the greenhouse iteration. Each tote has a near-cube shape with dimensions of 900 x 1000 x 1000 mm. The totes study was conducted in two growing seasons in an uncontrolled environment experiencing seasonal wetting/drying as well as freezing and thawing with various plant species (Table 2). Due to their size and shape, the totes froze through the entire depth, damaging plant roots, resulting in variable mortality throughout the totes. Consequently, plants were re-established again in the second year of the study. In a large-scale natural system, root systems of plants are not typically exposed to the same degree of freezing observed in these totes.

Table 2. Species planted in the outside trial.

Tote	Species in each respective tote during the 2018 season	Added species in each respective tote during the 2019 season	Short name	Initial solids content (%)	Initial tailings thickness (cm)
A	water sedge (*Carex* aquatilis)	Western dock (*Rumex occidentalis)*	*Carex*/ *Rumex*	40	68
B	None	None	Control	43	80
C	sandbar willow (*Salix interior*)	slender wheatgrass[1] (*Elymus trachycaulus*)	*Salix*/ SWG	44	80
D	slender wheatgrass (*Elymus trachycaulus*)	sandbar willow (*Salix interior*)	SWG/ *Salix*	44	82
E	All above species combined	All above species combined	All	43	80

1. This tote was intended to support only *Salix*; however, the slender wheatgrass present here had spontaneously seeded in at low density.

2.3 *Field Trial*

A field-scale pilot was constructed in 2015 in Fort McMurray, Alberta, Canada, and filled with tailings in 2016. Details on the creation and experimental design of the field pilot can be found in Smith et al. (2018). The test cell was approximately 30 m wide by 60 m long at the crest and was originally filled with tailings to a depth of 4.65 m. The test cell was configured such that the middle of the deposit consists of the full thickness of tailings, whereas the side slopes have a lower tailings thickness overlying them. The volume of material in the plot was nearly four orders of magnitude bigger than the totes (from an overall tailings volume perspective). The pilot was divided into plots with different plants species—Smith et al. (2018) detail plant species and zoning in the 2017 growing season. Similarly, Schoonmaker et al. (2021) delineate plants species distribution in 2019.

3 MATERIALS

A centrifuged fluid fine tailings was used in all of the various scale trials stated above. There were some differences in the origin and geotechnical properties between the trials. ; the tailings in the greenhouse trial the field trial originated from one mine, while the tailings for the outside trial originated from a different mine. However, from a geotechnical perspective, the centrifuged fluid fine tailings can be considered comparable, barring the higher clay content in the outdoor totes trial. Table 3 describes the key geotechnical characteristics of each centrifuged fluid fine tailings used in the trials. The bitumen content is the mass of bitumen divided by the total mass of the tailings.

Table 3. Basic geotechnical characteristics of the centrifuged fluid fine tailings in each trial

Characteristic	Greenhouse trial	Outside trial	Field trial
Fines content[1] (%)	93	89	98
Clay content[2] (%)	7	52	22
Bitumen content (%)	2.1	5.7	1.6
Plastic limit (%)	22	26	24
Liquid Limit	69	57	80

1. Fines content is calculated as geotechnical fines content as the dry mass of fines (finer than 44 µm) divided by the mass of dry solids.
2. The clay content is determined by MBI.

4 RESULTS

The primary results of each of the trials are viewed from a geotechnical lens with two evaluation metrics, namely the undrained shear strength and consolidation settlement. The undrained shear strength is selected as a metric to indicate the strength, whereas the consolidation settlement is a metric to reveal the dewatering performance. To reclaim tailings terrestrially, the shear strength of the tailings ought to be increased to make the surface trafficable, at which point further reclamation work can be carried out on the surface of the ponds. Therefore, the study's underlying assumption was to utilize the plants as a strengthening tool to bring the tailings to sufficient shear strength trafficable by machinery for sand capping purposes. McKenna et al. 2016 present the 25 kPa shear strength as the boundary between soft and firm clay. We use this number as an anchoring point to review strength data. Therefore, the geotechnical behaviour is presented in a dichotomy of strength and dewatering, considering the strength mentioned above limit. The undrained shear strength was measured using a Geonor H60 hand vane in the greenhouse trial, outside trial and the field trial. The consolidation and hence dewatering is assessed from the deformation of the surface of the tailings, and when applicable, from the volumetric water content sensors embedded in the tailings. Results are presented independently for each trial compared to the control specimen first, then the findings from the different scales are contrasted. The reader is reminded that all reported shear strengths are corrected for shaft friction.

4.1 *Consolidation and dewatering*

The assessment of consolidation and dewatering in all trials was conducted based on the settlement or the reduction in deposit thickness and solids content gain. The greenhouse barrels and outdoor trials offer data about the volumetric water content with time at several depths. These are also reviewed to assess water removal efficacy. The following three sections describe the consolidation and dewatering behaviour in each of the trials.

4.1.1 *Greenhouse Trial*

All barrels had an initial homogenous solids content of 57%. Upon decommissioning the barrels, a higher solids content and shear strength were observed at the surface of the tailings, which consistently decreased with depth (including the control barrel). The *Salix* barrel consistently outperformed the other four barrels in extracting water and hence introducing higher solids content. All barrels with vegetation showed evidence of higher water consumption relative to the control (Table 4). Three of the four vegetated barrels (*Salix*, *Carex/Rumex* and All) received three times more water than the control or SWG barrel to prevent the plants from wilting.

The reported average final solids content is presented as a median value with depth. An important note is that higher solids content was evident at the surface than at depth in all barrels. Percent reduction in thickness is calculated as the arithmetic difference between the initial and final thickness divided by the initial tailings thickness.

Table 4 Consolidation and dewatering parameters in the greenhouse barrels trial

Barrel	Initial water content (m^3/m^3)		Final water content (m^3/m^3)		Reduction in thickness (%)	Median final solids content (%)
	25cm	50cm	25cm	50cm		
Control	0.50	0.49	0.44	NA[1]	12	59
Salix	0.49	0.51	0.18	0.24	28	75
Carex/*Rumex*	0.52	0.50	0.32	0.56	19	68
SWG	0.52	0.48	0.23	NA	18	64
All	0.53	0.52	0.25	NA	18	69

1. NA = reading not available either due to sensor malfunction or other external factors

4.1.2 *Outside Trial*

Consolidation was assessed based on the total reduction in thickness of the tailings and the volumetric water content data collected using electronic sensors throughout the trial period. From a consolidation viewpoint, there seems to be little difference between totes with the median solids content varying between 73-77% (Table 5). The most reduction in thickness is evident in the totes with all plants combined, with a close second being the Carex/Rumex combination. Overall, changes in volumetric water contents throughout the tailings in each tote were limited except near the surface. Volumetric water content shows consistent drying with depth in the *Carex/Rumex* combination tote. The control tote only shows dewatering in the top ≈25 cm, likely driven by evaporation with no change in water content at depth. At the end of the trial, the greatest thickness reduction was observed in the *Carex/Rumex* tote and the SWG/*Salix*Tote. The control tote had the least change in thickness compared to the other totes which were vegetated. No meaningful difference in median solids content gain between the vegetated totes and the control was noted.

The depth labels (25, 50, 75cm) refer to the depth below the initial surface, which inevitably change as tailings surface settled. As such, the labels 25, 50, and 75cm should be taken as approximate positions labels used to assess the measured parameters at shallow, middle, and deep locations in each tote, respectively.

Table 5 Consolidation and dewatering parameters in the greenhouse totes trial

Tote	Initial volumetric water content (m^3/m^3)			Final volumetric water content (m^3/m^3)			Reduction in thickness (%)	Median final solids content (%)
	25cm	50cm	75cm	25cm	50cm	75cm		
Carex/ Rumex	0.40	0.39	0.34	0.16	0.17	0.07	26	77
Control	0.37	0.36	0.38	0.04	0.36	0.35	22	73
Salix/SWG[1]	0.40	0.38	0.4	0.22	0.36	0.36	24	73
SWG/Salix	0.38	0.36	NA	0.10	0.31	NA[2]	29	76
All	0.39	0.36	0.39	0.24	0.29	0.19	27	76

1. This tote was intended to support only Salix; however, the slender wheatgrass present here had spontaneously seeded in at low density.
2. NA = reading not available either due to sensor malfunction or other external factors

4.1.3 *Field Trial*

The consolidation behaviour of the filed deposit is mainly assessed from settlement and reduction in thickness. Figure 1 shows the thickness contours in the years 2017 and 2019 throughout the field deposit. Deposit thicknesses shown in Figure 1 were approximated using the geometry of the side slopes and base of the test cell along with known probed depths. The survey data were taken at 1m and 3m spacing for 2017 and 2019, respectively. The consolidation contours seem to follow the geometry of the initial deposit. A 23% reduction in thickness was evident in the centre of the deposit. However, no connection between the settlement and particular plant zones stood out of this geometrical alignment.

Figure 1. Deposit thickness contours from spatial data using QGIS - 2017 data (black solid) vs 2019 data (red dashed).

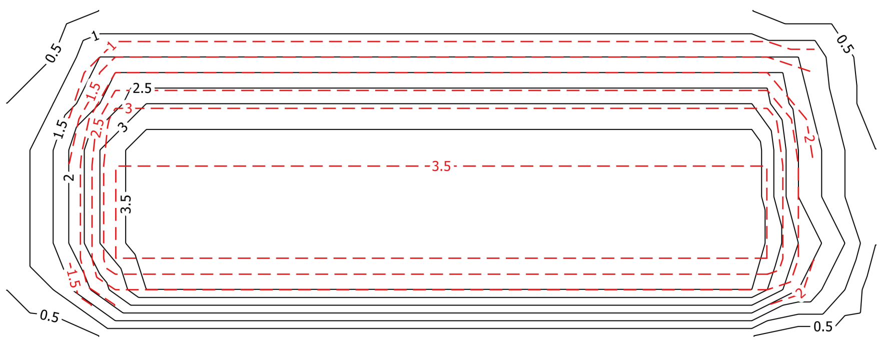

4.2 *Undrained Shear Strength*

The peak undrained shear strength was selected as the metric to assess strength characteristics for all three trials. The one common theme between all trials is that the undrained shear strength seemed to depend highly on the climatic conditions at the time of measurements. The greenhouse barrels and the field trial distinctly show a maximum value closer to the surface of the tailing compared to that at depth. The shape is reminiscent of classic shapes associated with desiccation due to climatic effects. Similarly, plant roots distribution with depth shows a similar shape. Some of the outdoor totes showed the same shape of shear strength profiles. The following sections detail the peak undrained shear strength in each trial. In terms of strength, the undrained shear strength seemed to have a maximum value closer to the surface of the tailing compared to at depth.

4.2.1 *Greenhouse Trial*

The peak undrained strength in the greenhouse barrels increased steadily throughout the six-month duration as the plant became more established. Figure 2 shows the strength evolution with time relative to the depth of the deposit within each barrel. The peak undrained shear strength was observed at a maximum closer to the surface and decreased consistently with depth. The undrained shear strength of the barrel control shows strength of 0 kPa, which is due to a limit of range of the utilized vane. The minimum value that the utilized vane could detect is 1 kPa; hence all the control readings might be a few hundreds of Pascals but certainly below the 1 kPa threshold. The strength gain was most pronounced in the barrel with the *Salix* upon decommissioning the trial with nearly two orders of magnitude higher strength than the control barrel at the conclusion of the trial. There also seems to be an increasing strength trend with time (Figure 2).

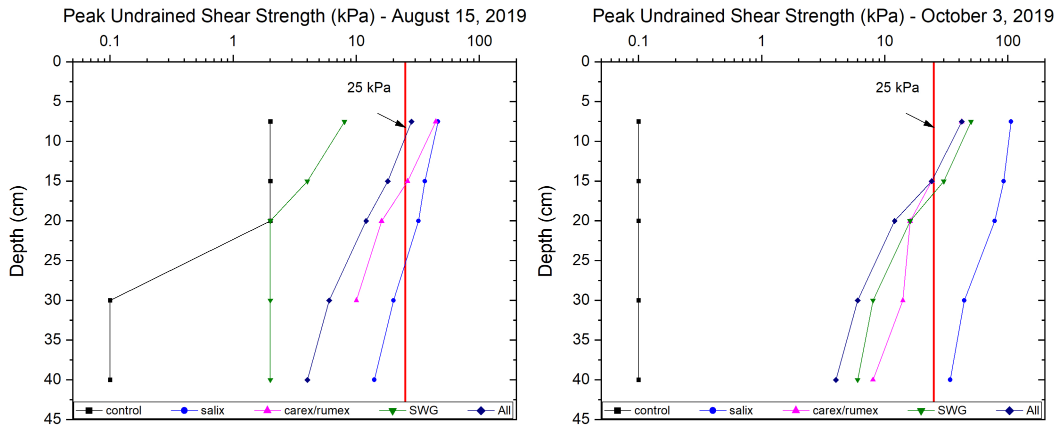

Figure 2. The undrained shear strength profile with depth after 83 days (left) and 132 days (right).

4.2.2 *Outdoor Trial*

The highest strength gain at the end of the trial was attained using the *Carex/Rumex* combination (Figure 3). Strength gain compared to the control tote can be seen in the plants' populated totes, where all except the *Salix* exceed the 25 kPa criteria in a few elevations but not consistently throughout depth.

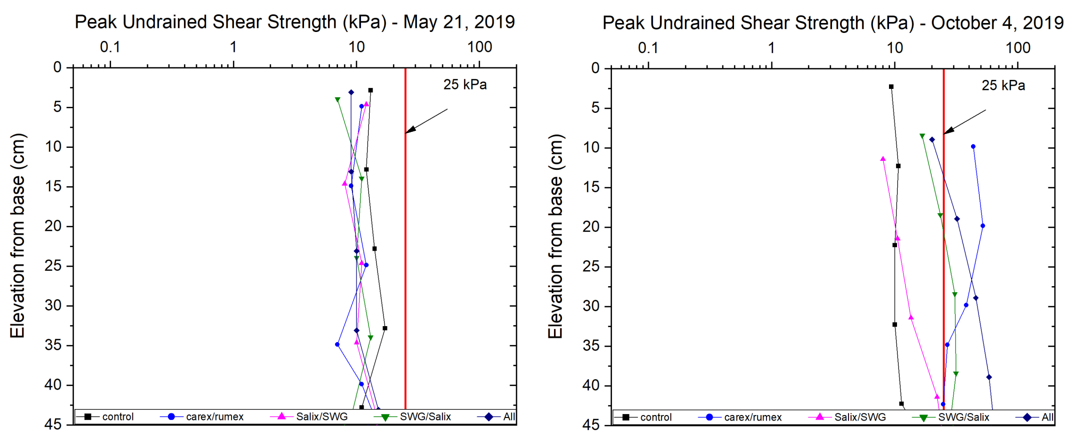

Figure 3. The undrained shear strength in the outdoor tote study 339 days into the study (left) and 475 days into the study (right).

4.2.3 *Field Trial*

The peak undrained shear strength in the field pilot in 2019 was measured with depth at 108 locations across the deposit. All 108 plots were populated with different plants, as discussed at length in Schoonmaker et al. 2021. Data shows that strength in all those locations falls short of the 25 kPa limit we set earlier. The undrained shear strength in 2017 is also plotted to put this finding into perspective.

Figure 4 presents a tricolour grouping of the shear strength data based on the average deposit thickness at the sampling location for ease of assessment. The spatial variability of the deposit at the surface was significant in the 2017 strength data, where the peak undrained shear strength varied within two orders of magnitude at the top 35 cm of the deposit. The variation was more pronounced at the surface and attenuated with depth. The shape of the shear strength profiles with depth consistently shows higher strength at or close to the surface, decreasing nonlinearly with depth. Below 35 cm depth, the shear strength of all plots varied between 2 to 5 kPa regardless of the plant type or lack thereof (Figure 4). Those same trends were observed in 2019 to a lesser degree. The peak undrained shear strength at the surface in 2019 varied within an order of magnitude. Strength and variability are both attenuated with depth. The one stark difference is the absence of plots exceeding 25kPa.

So what caused the peak undrained shear strength in 2019 to regress approximately an order of magnitude compared to the values reported in 2017? When tracing the climatic condition difference between the two years, it became apparent that 2019 was a much wetter season, and the 2017 site investigation was conducted while conditions were dry and the upper 0.20 m of CFFT was unsaturated at the time of inspection (Smith et al. 2018). Figure 5 shows that the deposit was subject to about twice the cumulative precipitation during the peak undrained shear strength testing window. This finding is not surprising to the geotechnical eye—the strength reduction due to wetting events. So wherever the strength at the surface was coming from in 2017, it was precarious and dependent on how well the rainwater was managed on the deposit.

Furthermore, Smith et al. (2018) show that the strength trends were reversed due to light rainfall during testing. The 2017 measurements presented in Figure 4 were conducted after a dry period when the top of the deposit was unsaturated and, therefore, strength was driven by suction. Conversely, in September 2019, the deposit was saturated, and ponded water had to be pumped off prior to testing. The reader is reminded that the peak undrained shear strength decreased nonlinearly with depth, with the highest strength at the surface.

Overall, there was no definitive trend of which plants offered the best dewatering or strength gain when analyzing the shear strength data. In 2017, the common denominator of the plots that exceeded the 25 kPa mark happened to be in thinner areas of the deposits (side slopes). These locations were a combination of the control plots (non-vegetated), the plots with the SWG and *Salix* combined with SWG. In 2019 data, all sample locations were below the 25 kPa threshold regardless of planting zone or geometric position.

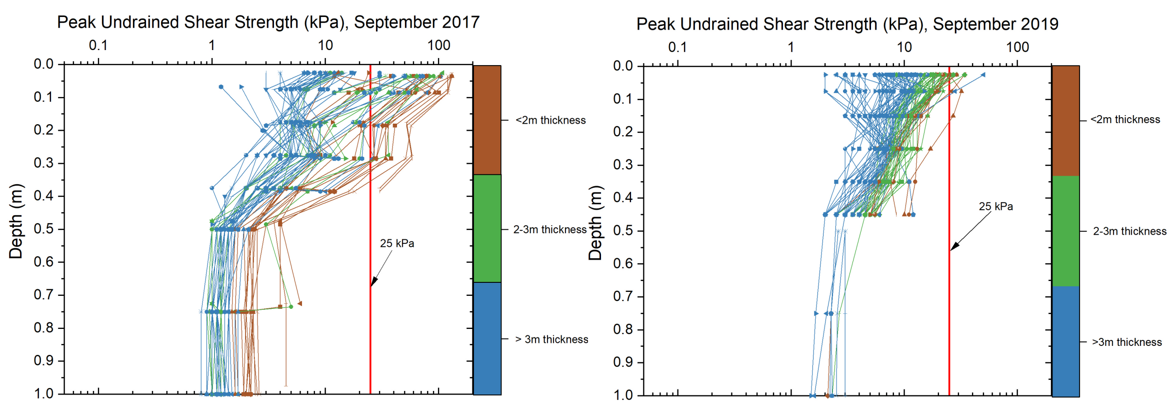

Figure 4. The peak undrained shear strength of the same field deposit in 2017 (left) and 2019 (right).

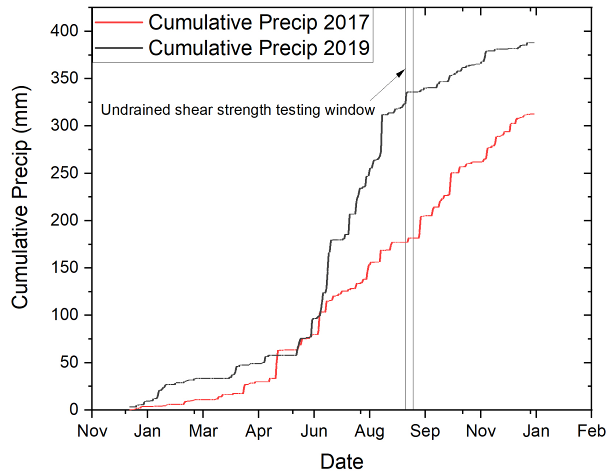

Figure 5. A comparison between the cumulative precipitation between the 2017 and 2019 seasons – Data from Environment Canada at Fort McMurray, Alberta weather station.

Since the entire deposit was vegetated in 2019, a regression approach was employed to observe the relative patterns and relationships amongst key variables within the deposit. The regression presented in Figure 6 visualizes the response of undrained shear vane strength to tailings thickness (as a factor, thickness), depth from the surface of the deposit (continuous) and leaf area index (LAI) (continuous). These variables were analyzed as a multiple linear regression on the natural logarithm of the responding variable. This analysis was conducted using R statistical software (R Core Team, 2021, utilizing a linear mixed-effects model function lme, Bates et al. 2015). A global model including individual variables as well as two-way and three-way interactions were included in each of the 2017 and 2019 datasets.

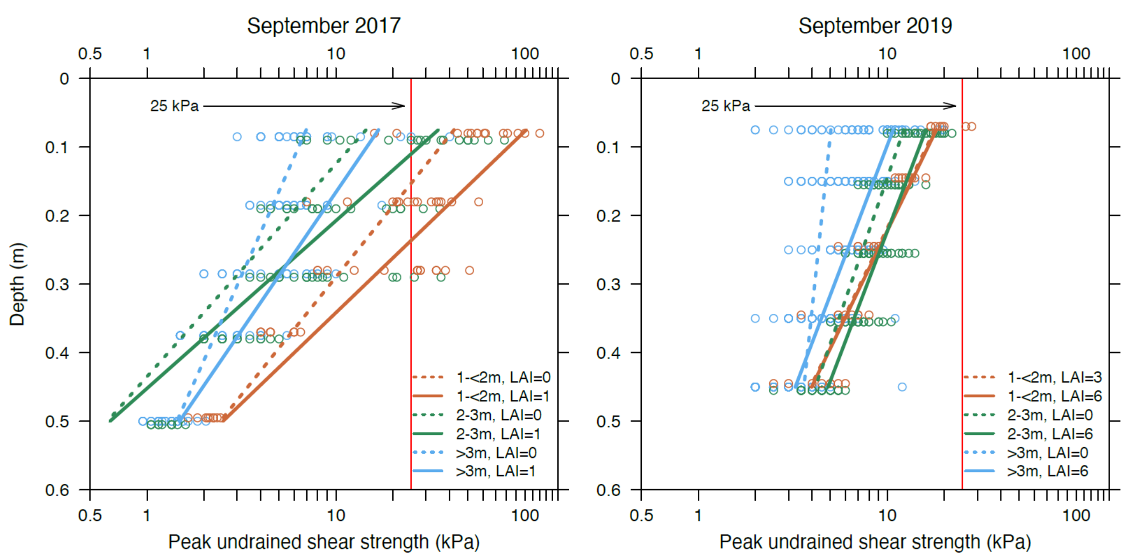

Figure 6. Log-linear regression for the 2017 and 2019 peak undrained shear strength results showing regression line fits by thickness with varying levels of leaf area index (LAI).

There was a substantial shift in the vegetation community across the test cell from 2017 to 2019 and with it leaf area index (LAI) development. Therefore, the reader may notice the difference in LAI limits in the regression analysis (Figure 5). Representative realities in the field constrained the choice of LAI. The deposit in 2017 was wholly represented by graminoids and

Salix to a lesser degree, whereas in 2019, in addition to graminoids and Salix, a large proportion of wetland species were present. Therefore, some caution should be taken when considering the absolute LAI differences between 2017 and 2019, as this LAI may have been differentially impactful or effective. On the whole, in 2017, LAI values were low (maximum of 1 for the 1-<2m and >3m thickness hence the upper bound limit). In 2019, the 1-<2m thickness dataset did not contain LAI values < 3; therefore, an illustration of a regression line fit with lower LAI values would be outside the model's parameterization.

A few observations can be made with these caveats in mind and acknowledging that correlation does not imply causation. In the 2017 dataset, the shallowest tailings thickness (1-<2m, side slopes) resulted in the highest strength near-surface regardless of plants, but the presence of plants at LAI = 1 was associated with greater strength. The same trend was also observed for the other thicknesses in 2017, though to a lesser extent. In both 2017 and 2019, given the same thickness, there was consistent improvement in undrained shear strength with relative increases in LAI with the exception of the 1-<2m thickness in 2019. Interestingly, in 2019, there were no near-zero or zero LAI values in that thickness; therefore, it is difficult to disentangle if the lack of difference between the lowest LAI observed for that thickness (LAI = 3) and a doubling in LAI (= 6) was because the lowest LAI was already impactful or if the presence of plants was unimportant and other factors drove the strength gain.

5 CONCLUSIONS

Utilizing plants as an added tool to further dewater and strengthen previously treated FFT emerged in the past two decades as a potential natural way to leverage environmental processes. The big picture goal of establishing plants in tailings was to aid eventual reclamation efforts. However, the evidence in the literature is limited to composite tailings, i.e., on the coarser side of the geotechnical spectrum. This study assesses the potential of plants to dewater or strengthen tailings at the finer side of the geotechnical spectrum. The investigation encompassed multiple scales and a few years worth of data on centrifuged fluid fine tailings of different origins.

While both the outside trial and greenhouse trial illustrated varying degrees of strength gain in the presence of vegetation, these results were not mirrored in the field trial to the same degree. The greenhouse trial was an idealized state, with growth conditions to support vigorous plant development. The outside trial was less idealized relative to the greenhouse trial but was also a finite tailings volume with limited additional precipitation inputs, allowing for surface drying and forcing the root systems of the plants downward in search of water.

Many confounding factors seemed to hinder any conclusive evidence of plants' efficacy in strengthening or dewatering in the field. What is sure is that any strength gain in the field was limited to the top 35 cm of the tailings and rather dependent on climatic conditions and surface water management. Therefore, climatic processes were driving much of the strength in the field, evidenced by strength reversal due to rainfall events. Further research, controlling the presence of plants in separate, parallel test deposits over multiple years, is needed to ascertain which specific climatic processes contribute or drive strength and to what extent plants are providing a supplemental benefit or conversely may hinder climatic-based dewatering solutions such as evaporation.

6 ACKNOWLEDGMENTS

The authors are grateful for the financial support provided by Natural Sciences and Engineering Research Council (NSERC) and the Institute for Oil Sands Innovation (IOSI) in conjunction with Imperial Oil and Canadian Natural Resources Limited (CNRL). The authors would like to acknowledge Chibuike Chigbo and Kaela Walton-Sather of NAIT for collecting the undrained shear strength and solids content in the greenhouse trials. Thank you to the BGC team for assisting in the field trial data collection and analysis: Charlie Borrell, Jason Abboud, Erin Olauson and Jack Seto. The first author would like to express gratitude to Thurber Calgary Branch for welcoming her as a new team member and supporting her conference attendance.

7 REFERENCES

Alberta Energy Regulator (AER) 2017. Directive 085: Fluid Tailings Management for Oil Sands Mining Projects. Available from: https://www.aer.ca/documents/ directives/Directive085.pdf. [Last accessed on April 10, 2020].

Alberta Energy Regulator (AER) 2020. State of fluid tailings management for mineable oil sands, 2020. Available from: https://www.aer.ca/documents/oilsands/2020-State-Fluid-Tailings-Management-Mineable-OilSands.pdf. [Last accessed on April 11, 2020].

Environment Canada. 2021. National climate data and information archive. URL http://www.climate.weatheroffice.ec.gc.ca/Welcome.e.html [last accessed on April 22, 2021].

Johnson, R. L. Bork, P. Allen, E.A.D. James, W. H. Koverny, L. 1993 Oil Sands Sludge Dewatering by Freeze-thaw and Evapotranspiration. Report to Syncrude Canada Ltd.

Laberge, S. Beier, N.A. Schoonmaker, A. 2019. A study of the impact of evapotranspiration through native plant species on the strength and solids content of treated oil sands tailings. In proceedings of the Tailings And Mine Waste conference Vancouver, BC, November, 2019.

Mckenna, G., Mooder, B., Burton, B., Jamieson, A. 2016. Shear strength and density of oil sands fine tailings for reclamation to a boreal forest landscape. In Fifth International Oil Sands Tailings Conference. December 4-7, 2016, in Lake Louis, Alberta, Canada.

Naeth, M.A. and Wilkinson, S.R. 2002 Plant species suitability for reclamation of oil sands consolidated tailings. In 26th Annual British Columbia Mine Reclamation Symposium in Dawson Creek, BC, 2002. The Technical and Research Committee on Reclamation

R Core Team. 2021. R: A language and environment for statistical computing. R Foundation for Statistical Computing, Vienna, Austria. URL https://www.R-project.org/

Silva MJ 1999. Plant dewatering and strengthening of mine waste tailings. PhD thesis, Department of Civil and Environmental Engineering, University of Alberta.

Smith, W. Olauson, E. Seto, J. Schoonmaker, A. Nik, R. M. Freeman, G. McKenna, G. 2018.Evaluation of strength enhancement and dewatering technologies for a soft oil sands tailings deposit. In international Oil sands Tiligs conference, Edmonton, Alberta, Canada

Wu S 2009. A greenhouse study of selected native plant species for dewatering CT. MSc thesis, Department of Civil and Environmental Engineering, University of Alberta.

Case study assessment examining wholistic effects of deploying worms and plants into oil sands tailings.

Chibuike Chigbo, Amanda Schoonmaker, Bin Xu & Kaela Walton-Sather
Northern Alberta Institute of Technology, Peace River, Alberta, Canada

Heather Kaminsky, Victoria Collins & Simon Sun
Northern Alberta Institute of Technology, Edmonton, Alberta, Canada

Miguel de Lucas Pardo & Floris van Rees
Ecosystem and Sediment Dynamics, Deltares, The Netherlands.

ABSTRACT: Accelerating the dewatering and consolidation process of Fluid Fine Tailings (FFT) to facilitate land reclamation is a major challenge to the oil sands industry in Canada. Significant technology development efforts have focused on engineered solutions, with less attention to biological options. The present study combines and builds upon previous NAIT research on native plants and Deltares research on aquatic and terrestrial worms, which have been independently shown to facilitate the densification of oil sand tailings. This project examines the addition of two worm types (*Lumbriculus variegatus* (LV) or earthworms), an amendment (straw) that was used to enhance worms survival in previous research and/or native plants (*Carex aquatilis* and *Salix interior*) to FFT to provide shear strength gain over a 6-month growth phase focussing on key geotechnical, biological and greenhouse gas findings. Results showed that (a) addition of worms increased the leaf biomass of *C. aquatilis* and triggered a further and relevant increase of strength and solids content relative to what can be achieved with plants solely, although complete worm mortality was observed at the end of the study, (b) planting increased tailings undrained shear strength by 40 to 60 kPa in the presence of worms, solids content by 20% and water use by 98% when compared to unplanted treatments, (c) addition of straw was ineffective in improving plant growth or tailings measured geotechnical properties, (d) planting mitigated greenhouse gas (GHG) emissions, while straw caused high methane (CH_4) production.

1 BACKGROUND

Northern Alberta has the third-largest oil reserve in the world (Alberta Energy 2014) and only about 10% has an overburden depth less than 65 m which could be extracted by surface mining technology using water resulting in oil sands tailings (Jeeravipoolvarn 2010). The latest industry data indicates that there are nearly 1.21 billion m^3 of fluid tailings accumulated in the ponds occupying a total area of about 220 km^2 (Kent 2017). This large volume of tailings constitutes a significant challenge to land reclamation. In this regard, the Energy Resource Conservation Board (ERCB) developed tailings management regulation where a major key requirement is that tailings disposal areas must be trafficable and ready for reclamation (BGC 2010). However, in the absence of human intervention, it will take a significantly long time for land reclamation.

Several chemical, biological, and natural treatment techniques have been tested to accelerate tailings dewatering (Powter et al. 2010; Liang et al. 2015). The use of plants has shown significant promise whereby plants are able to extract tightly bound water and increase surface strength through root development (Silva et al. 1999; Yucel 2016; Schoonmaker et al. 2018). However, tailings can be limited in essential nutrients such as nitrogen (Collins *et al.* 2016), which is a key requirement for plant growth. Other factors such as salinity and hydrocarbons (Allen, 2008) can decrease survival of newly established plants. Conventional inorganic fertilizers or other organic, nutrient and carbon rich amendments have shown the potential to ameliorate some of the adverse effects and encourage plant development. Organic amendments such as peat (Renault *et al.* 2004), biochar (Fellet *et al.* 2014) and alfalfa pellets (Woosaree and Hiltz 2011) have been effectively used to enhance plant development for tailings sand stabilization. These amendments can enhance plant growth by supplying and/or retaining nutrients as well as improving the physical, chemical, and biological properties of the tailing's material.

In addition, a new, eco-friendly method using oligochaete worms has been recently tested for the accelerated treatment of oil sand tailings. For example, *Tubifex tubifex* worms which is indigenous in Western Canada provinces have shown to be effective in accelerating oil sands tailings dewatering by increasing the solids content of fluid fine tailings (FFT) by about 40% and the undrained shear strength by about 60% when compared to benchmark FFT without *T. tubifex* (Yang et al. 2020). However, they can introduce the whirling disease which is harmful to fish (Hallett et al. 2005). An investigation on other worms (terrestrial or aquatic) including *Lumbriculus variegatus* (LV) that share similar characteristics (resistance to toxicity and anoxic conditions (Ellissen, 2007), size, and distribution, feeding modes, etc.) as *T. tubifex*, but without the risk of transmitting whirling disease which is endemic to North Alberta is needed. In previous studies, it was found that 100% *T. tubifex* and *L. variegatus* individuals survive over one month in tailings, but the survival rate drops to 20% after three months (Yang et al. 2020). In current parallel research projects, straw was identified as an additive to ensure a factor 3 worm reproduction after three months.

Although dewatering and densification of soft tailings deposits is a foremost concern by mine operators, the reduction of greenhouse gases represents another interrelated challenge that touches all oil sands mining operations. This is because these types of operations create significant greenhouse gas (GHG) – carbon dioxide (CO_2), methane (CH_4) and nitrous oxide (N_2O) emissions. The growth and development of plants, within a tailings deposit, could have the potential to offset some of the emissions from these ponds. However, plants have complex effects on the production, transport, and oxidation of CH_4 and the overall balance of carbon (Adkinson *et al*. 2011). The complexity of these interactions requires further research to better understand how the mineralogy and chemistry interact with the biological aspects (worms and plants) of fluid tailings ponds in the sequestration or emissions of GHGs, particularly CH_4 and CO_2.

The objective of this study was to evaluate the interacting effects of native plants (*S. interior* [willow] and *C. aquatilis* [Carex]), amendments, and worms (*L. variegatus* [LV] or earthworm (EW)) on tailings dewatering, strength improvement, and GHG gas emissions.

2 MATERIAL AND METHODS

2.1 *Tailings properties*

Centrifuge fluid fine tailings (CFFT) was sourced from an oil sands operation in northern Alberta and characterized using Dean and Stark analysis (Dean & Stark, 1920), Methylene Blue Index (MBI) (Currie et al., 2014; Kaminsky, 2014), particle size distribution analysis (PSD) (Currie et al., 2015), pH, electrical conductivity, and water chemistry. The initial characterization results are presented in Table 1 and 2.

Table 1: Major cations and anions in original CFFT by ion chromatography

Cations [mg/L]						Anions [mg/L]						
Li^+	Na^+	NH_4^+	K^+	Mg^{2+}	Ca^{2+}	F^-	Cl^-	NO_2^-	Br^-	NO_3^-	PO_4^{3-}	SO_4^{2-}
0.14	283.2	4.52	16.8	19.5	45.4	1.9	99.5	2.3	n.a.	4.4	n.a.	228.6

Table 2: CFFT characterization

Characteristic	Value
MBI	9.2
Solid content [wt%]	37%
Water content [wt%]	61%
Bitumen content [wt%]	2%
SFR	0.07
pH	6.5
Conductivity [μS/m]	1002
Sodium Adsorption Ratio (SAR)	8.9
Capillary Suction Time (CST) [s]	1050.3
Atterberg liquid limit (geotech. water wt%)	62.7%
Atterberg plastic limit (geotech. water wt%)	25.0%

2.2 *Plant species*

Native shrub, *S. interior* which inhabits floodplains and dry upland forests, and *C. aquatilis* (Carex) which is a wetland species were chosen as these species are native to Alberta and have demonstrated high level of growth and tolerance to oil sands tailings and represent two distinct plant groups (sedges and woody vegetation). *S. interior* or *C. aquatilis* was propagated from hardwood stem cutting or from root respectively in 77 mL volume styroblock cavities (Beaver Plastics™, Acheson Alberta Canada) filled with commercially available peat, watered as needed and fertilized up to 3 times per week for a three-month period prior to transplanting into the trial barrel.

2.3 *Worm culture*

Standard laboratory cultured *L. variegatus*, a wetland worm which is found throughout North America that occupy the edges of ponds, lakes, or marshes was bought from a local wholesale (Aquatic Research Organisms, Hampton, New Hampshire, USA), and raised in the laboratory using a plastic aquarium with a layer of aquarium gravel substrate, an air pump, and a sinking pellet as a food source. An upland earthworm was harvested in Peace River, Alberta, raised in pails filled with topsoil in the laboratory prior to tailings incorporation. *L. variegatus* and earthworm were applied at 0.012 g m^2 and 100 living worms per barrel, respectively.

2.4 *Amendment materials*

Straw was collected and chopped into pieces (about 2-3 cm in length) and incorporated into the tailings at the rate of 5.8 g L^{-1} of tailings in required barrel prior to planting.

2.5 *Experimental design and setup*

Ten experimental barrels (47.50 cm diameter, 66 cm height and 90 L in volume) were filled with homogenized CFFT with the following factors and levels: (i) presence or absence of plants, (ii) presence or absence of straw, and (iii) worm addition or none. Solids content was subsampled while filling. One organic amendment (straw applied at 5.8g L^{-1}) was incorporated by hand mixing. Urea (46-0-0) and starter fertilizer (0.15 grams per barrel) were sprinkled on the tailings surface of barrels and each barrel received two rooted seedlings *C. aquatilis* and three seedlings of *S. interior*. Finally, the worm culture (LV at 0.012 g m^2 or earthworm at 100 living earthworms per barrel) was added following planting.

2.6 *Plant measurements*

After 25 weeks of growth (October 5, 2020, to March 16, 2021), plants were harvested using hand clippers. Vegetation samples were oven dried at 70ºC for 48 hours or until constant weight. Aboveground plant biomass was determined to the nearest 0.1 g. Tailings root sample core was obtained with a 5 cm diameter soil auger at 0-10 cm, 10-25 cm and 25-40 cm from the tailings surface and stored at -4 Celsius to preserve roots until processing. Root separation from sample cores were soaked in a container of water overnight to allow the tailings to soften, easing separation of the roots from the tailings and reducing root breakage and fragmentation. Following soaking, the whole sample was mixed by hand to break up clods of tailings. Roots were then separated from the sample by washing through a series of soil sieves (#18 [1.0 mm opening], #60 [0.25 mm opening] and #120 [0.12 mm opening]). Root samples were oven dried at 70°C for 24 hrs. and weighed to the nearest 0.0001g.

2.7 *Worm measurements*

Tailings in barrels containing earthworms were manually dispersed and earthworm survival recorded by visual observation. For barrels containing *L. variegatus*, one core at 10 cm increments along the depth of each barrel was sectioned and *L. variegatus* survival recorded by rinsing tailings subsample through two stacked sieves of 350µm opening on top and 100µm opening below.

2.8 *Geotechnical measurements*

After plant harvesting, settlement (distance between the top of the barrel and the surface of the tailings) was measured to the nearest 0.5 cm. Tailings strength was measured using a hand-held shear vane, which was carefully pushed into each barrel to minimize disturbance. The shear strength was analyzed by rotating the hand vane at a uniform rate of approximately 0.5˚/s using the torque application handle until the tailings yielded. The vane was then rotated an additional quarter turn to ensure the tailings material had reached the point of failure before recording the measurement. The maximum torque required to obtain tailings failure was measured and the vane was then rotated 10 complete turns before repeating the procedure above to measure the residual strength of the material. The friction between the rod and the material was negligible compared to the scale of the reading. This measurement was repeated every 10 cm through to a depth of 40 cm (measured from the surface of the tailings). Atterberg limits were measured post dismantling to check for changes. Solids content was measured by taking a representative tailings sample at depths of 0-10 cm (top), 10-25 cm (middle), and 25-40 cm (bottom), weighed, dried at 105 C for 48 hours, and re-weighed to determine dry mass. Solids content (%) was calculated as dry mass divided by wet mass and multiplied by 100.

The liquidity (LI) index and predicted soil strength (Cwr) (Locat and Demers, 1988) for all samples were calculated using the equations:

$$\text{LI (Liquidity Index)} = water\ content\ of\ sample - Plastic\ Limit\ (Liquid\ Limit - Plastic\ Limit) \quad (1)$$

$$Cwr = (19.8/LI)^{2.44} \quad (2)$$

The soil strength prediction was used as an approximation for the expected undrained soil strength based on the solids content measured at the end of the trial. Strength in excess of this value can be attributed to strength from plant roots.

2.9 *Greenhouse gas measurement*

At each barrel, 13 carbon dioxide (CO_2) and 13 methane (CH_4) flux measurements were conducted over the study period (October 5, 2020, to March 16, 2021) using the closed chamber method (Alm *et al*. 2007). For CO_2 flux measurements, a clear chamber (measuring 3730.6 cm^3)

was placed over the barrel. Following each CO_2 or CH_4 flux measurement, the temperature was taken from continuous logging (5 cm and 25 cm from the bottom of the barrel). For the CO_2 flux measurements, a portable infrared gas analyzer (IRGA; EGM–4) was connected to the chamber with clear vinyl tubing, and CO_2 (in ppm) and relative humidity (%) was recorded every 15 seconds over a 120 second flux period. A sensor that logged photosynthetically active radiation (PAR) placed next to the chamber during the CO_2 flux measurements. PAR values, as well as the temperature in the chamber determined from a thermocouple and a temperature reader, were also recorded every 15 seconds over the 120 second flux period. Net ecosystem exchange (NEE) of CO_2 was then calculated from the linear change of the CO_2 concentration over time. At the time of a CO_2 measurement, 2 fluxes were taken, each in full light, as well in dark conditions using a solid-colored tarp. The flux in dark conditions represents ecosystem respiration (ER), and gross ecosystem productivity (GEP) was calculated as the difference between NEE and ER.

CH_4 flux was measured by connecting the chamber tubing to an ultra-portable greenhouse gas analyzer (Los Gatos Research; LGR) and taking real-time measurements at 5, 10, and 15 minutes. Fluxes of CO_2 and CH_4 were calculated based on the linear change in concentration over time. Using the R-squared function in Excel, R^2 values were calculated to evaluate whether concentration change followed a linear trend. The slope function in Excel was applied to CO_2 and CH_4 concentrations, allowing for the NEE and CH_4 flux to be determined.

2.10 *Statistical analysis*

Data was analyzed using R statistical software (R Core Team, 2018). The model was a 2-factor mixed effects model where factor 1 is Presence of plants, and factor 2 is worm incorporation. Analysis of variance (*lme*) was performed to test for differences in: (i) water use, and (ii) solids content, (iii) net ecosystem exchange (NEE), and (iv) methane (CH_4) emission. When significant ($p \leq 0.05$) differences were detected, treatments were separated with a post-hoc (Tukey) adjusted multiple mean comparison using emmeans function (Lenth, 2018). Model assumptions were checked with diagnostic plots of fitted and residual values, as well as histogram of residuals.

3 RESULTS AND DISCUSSION

3.1 *Influence of worm and straw on plant growth*

The observed mortality of worms could be attributed to several factors including tailings or straw properties. Yang *et al.* 2020 concluded that worm survival of 20% after three months may be expected without any additives; however, in the present study, straw was added but 100% mortality was observed. It is possible that the worms could have starved or died by extreme anoxia due to straw degradation. Worms do not generally do well in sandy substrates (Curry 2004), and in this study, the tailings substrate contained a sand to fines ratio of 0.07 (Table 1), representing low sand content, but could still have contributed to the mortality of inoculated worms. Despite the observed mortality, *L. variegatus* substantially increased the leaf mass of *C. aquatilis* (Table 3). We also observed a slight increase in leaf mass of *C. aquatilis* with earthworm but only in the treatment where straw was added. In contrast, the leaf mass of *S. interior* did not differ with or without worms. Worms can modify plant growth by a multitude of mechanisms, both directly and indirectly and a detailed discussion of theses mechanisms is beyond the scope of this article, however it is very difficult to ascribe worm-mediated changes in plant growth to a single mechanism, since worms change several factors that may affect plant growth simultaneously. More importantly, with mortality, worm bodies decompose rapidly, and can further contribute to the nitrogen content of soil. They often leave their nutrient-rich cast in their tunnels, providing a favorable environment for plant root growth. These tunnels also allow roots to penetrate deeper into the soil, where they can reach extra moisture and nutrients. Likewise, the incorporation of straw can also modify the tailings physical, chemical and/or biological properties including soil organic carbon (SOC), thereby providing an improved substrate for plant growth (Larney and Angers 2012).

We did not observe any improvement in total root mass of species with the addition of either type of worm. Previous studies have suggested that worms increase root biomass in soils through their impact on mineralization, the release of phytohormones and soil porosity (Welke and Parkinson 2003). However, we did not observe any clear and visible holes or tunnels burrowed by the worms which could have enhanced root growth overall. Alternatively, plants could have developed smaller roots as the geo-chemically improved sediment environment by the worms could have shifted to an environment that improved nutrient availability, thereby eliminating the need for large root networks. Lastly, it is possible that our sampling method underestimated root mass in some barrels as it the core samples taken were only a subset of the total tailings volume.

Table 3: Leaf and stem mass of *Salix interior*, *Carex aquatilis* and total root mass of *Salix interior* and *Carex aquatilis*, planted in tailings with worm incorporation, straw amendment, or none.

Worm type	Amendment	*Salix interior* Leaf mass (g m^{-2})	*Salix interior* Stem mass (g m^{-2})	*Carex aquatilis* Leaf mass (g m^{-2})	Total root mass (g $barrel^{-1}$)
LV	None	0.01	0.02	0.08	51.32
EW	None	0.01	0.04	0.04	21.27
None	None	0.02	0.03	0.05	87.44
LV	Straw	0.01	0.01	0.06	9.73
EW	Straw	0.01	0.01	0.04	10.64
None	Straw	0.01	0.02	0.04	98.56

3.2 *Influence of plant, worm, and straw on geotechnical properties*

The results of total amount of water added to tailings after 24 weeks of plant growth clearly show that water loss in planted barrels was higher than in unplanted barrels (Figure 1). At least under the controlled environment of the greenhouse, this suggests that plants have the capacity to uptake water from tailings with water loss via plant evapotranspiration at a more accelerated rate compared with surface evaporation.

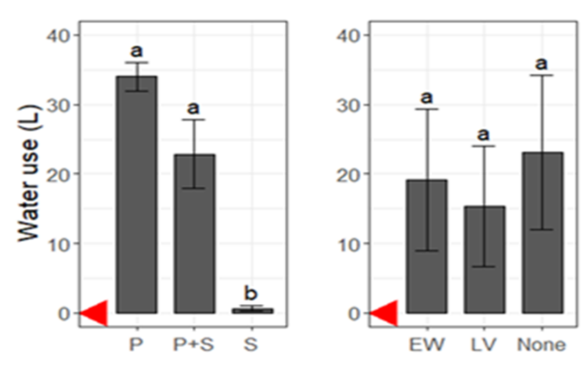

Figure 1; Mean water use (L) for barrel planted with *Salix interior* and *Carex aquatilis*, with worm incorporation (EW= earthworm, LV= *L. variegatus*), straw amendment, or none. Means (± SE, n = 3) followed by different letter(s) are significantly different ($p < 0.05$) from each other among treatments. Red arrow represents control (no plant), P=plants, P+S=plants + straw, S=straw.

This water use result corresponds to the results of undrained shear strength and solids content (Figure 2), which showed a positive strength gain in all vegetated barrels with vegetated plus worm barrels having higher strength. A clear difference in dewatering was observed with the incorporation of both types of worms to plant only barrels, suggesting that the observed corresponding biomass increase (Table 3) was enough to drive significant water use. With plants, there is a relevant effect on undrained shear strength, but with plants and worms, the results were even better reaching up to 60 kPa.

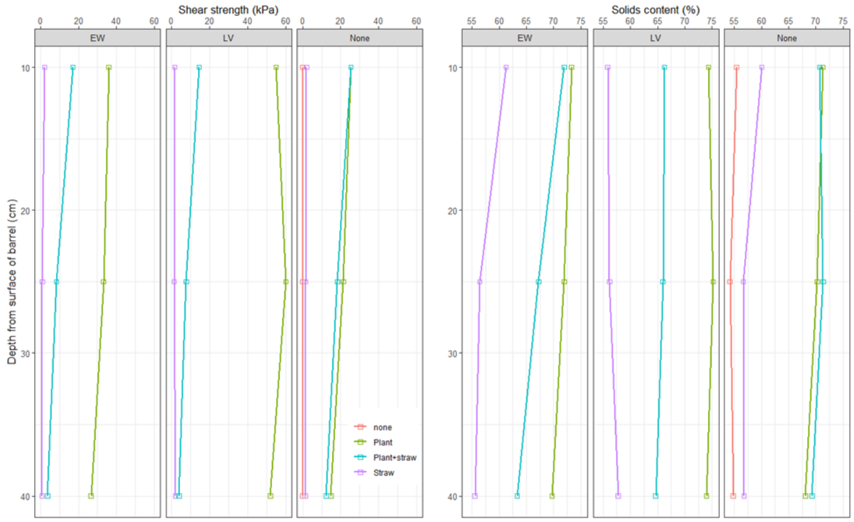

Figure 2: Undrained shear strength and solids content for tailings planted with *Salix interior* and *Carex aquatilis*, with worm incorporation, straw amendment, or none.

In one growing season, *S. interior* and *C. aquatilis* dewatered tailings in barrels to a point where the measured shear strength exceeded the predicted shear strength and was consistently higher than in unplanted barrels, with the highest increase observed in planted barrel inoculated with *L. variegatus* (Figure 3). This observed increase in shear strength may be at least partly attributed to the reinforcement properties of the plant root system. The root mass of plants in this treatment was not the highest which suggests that either our sampling method did not account for all the roots present in that barrel or that the root system in that barrel may have had a different structure (perhaps more finer roots, which would weigh less though potentially provide greater reinforcing strength). An alternative explanation could be that a microbial community shift in the presence of worms could have resulted in sediment strengthening.

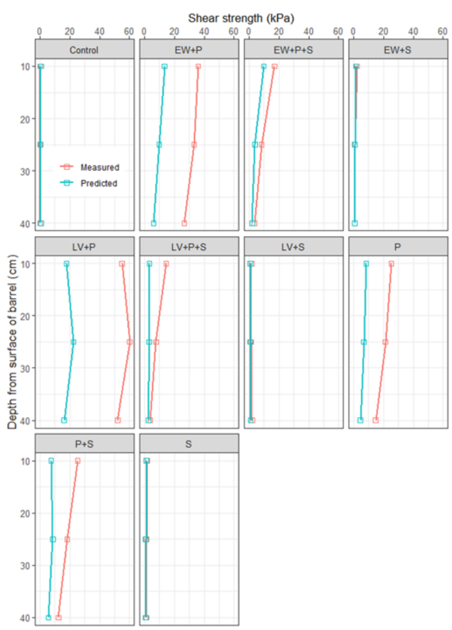

Figure 3: Predicted and measured undrained shear strength for tailings planted with *Salix interior* and *Carex aquatilis*, with worm incorporation, straw amendment, or none.

3.3 *Influence of plant, worm, and straw on Greenhouse Gas Emission*

There were differences in CO_2 fluxes which can be attributed to different combination of plants, worms and/or straw (Figure 4). Without straw or worms, planted barrels had a more negative NEE (sequestered more carbon), when compared to other treatments throughout the sampling period and which is also reflected in the observed biomass differences between these treatments. Organic matter additions can increase soil C content both by virtue of the added C in the amendment itself and through improving of the substrate attributes, but in our case, straw was ineffective in increasing photosynthetic carbon uptake. In fact, plant plus straw sequestered less carbon compared to plant alone barrels, meaning plants in these treatments photosynthesized less due to limited or slow growth as well as the possibility that the CO2 released from the decomposition of straw offset the plant CO2 uptake. Between December 2020 and January 2021, GEP, ER and NEE peaked on December 14th and sharply decreased. The decrease is related to the cutback of leaf biomass due to an aphids' outbreak in greenhouse. Once plants recovered and continued to grow, an increase in GEP, ER and NEE resumed and peaked at the end of the experimental period. The unplanted straw treatment was the least productive and the net uptake of CO_2 was close to 0 (NEE).

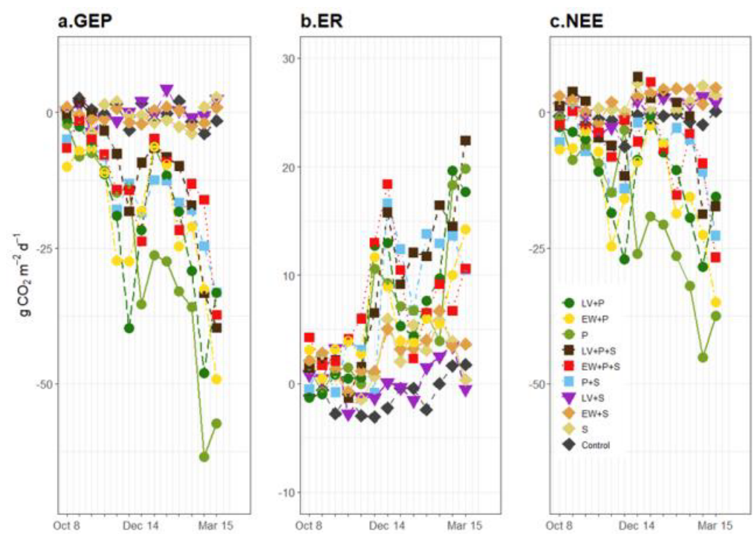

Figure 4: CO_2 flux for barrel planted with *Salix interior* and *Carex aquatilis*, or no plant, with worm incorporation, straw amendment, or none.

CH_4 flux was negligible in plant only treatments and compared to the control treatment, there seems to be a modest decline in CH_4 emission (Figure 5). The incorporation of straw caused high CH_4 production despite the addition of plants and/or worms. Methane emissions are the outcome of the difference between CH_4 production and oxidation (Sander *et al.* 2014). Methanogensis relies on the availability of organic substrate and is controlled by reduced conditions, moisture content and temperature. In the plant only treatment, there is low available carbon source which limits methanogensis. Aerenchyma tissues of C. aqualitis and plant roots are known to transport oxygen internally, which can lead to increased methane oxidation, further reduce the methane emission. The addition of straw, with or without plants, provided a carbon source for methanogenesis and led strictly anaerobic conditions by increasing the moisture content (lower water use) of the tailings (Figure 3). This changed tailings condition stimulates CH_4 production, inhibits CH_4 oxidation, and then increases CH_4 emission (Sander *et al.* 2014).

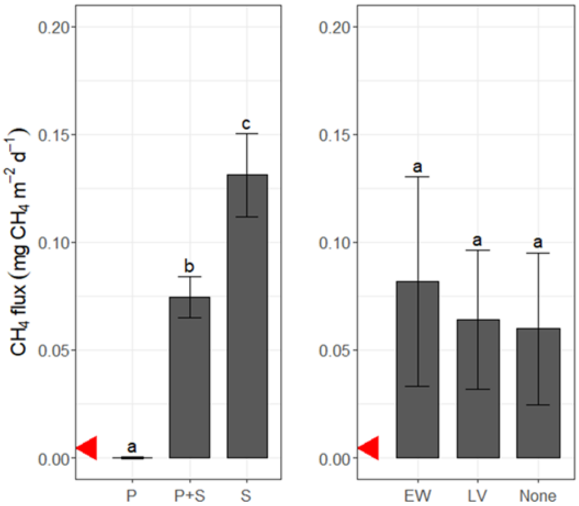

Figure 5: Mean CH_4 flux for barrel planted with *Salix interior* and *Carex aquatilis*, with worm incorporation (EW= earthworm, LV= *L. variegatus*), straw amendment, or none. Means (± SE, n = 3) followed by different letter(s) are significantly different ($p < 0.05$) from each other among treatments. Red arrow represents control.

4 CONCLUSION

This study has provided evidence that the dewatering of oil sands tailings can be accomplished by growing native plant species alone or with incorporation of worms. All barrels planted with *S. interior* and *C. aquatilis* demonstrated increased shear strength, solids content and evapotranspiration. Furthermore, barrels where both plants and worms were incorporated had the largest undrained shear strength and solids content amongst all treatments, and always a relative increase with respect to plant only treatments. Both native species mitigated GHG emissions through primary plant production. The addition of straw caused high CH_4 production, lower or near zero carbon sequestration.

The authors gratefully acknowledge financial support and stewardship for this project from the Canadian Oil Sands Innovation Alliance (COSIA) and the Institute for Oil Sands Innovation (IOSI).

5 REFERENCE LIST

Adkinson A.C., K.H. Syed., and Flanagan, L.B. 2011. Contrasting responses of growing season ecosystem CO_2 exchange to variation in temperature and water table depth in two peatlands in northern Alberta, Canada. *Journal of Geophysical Research* 116: G01004.

Alberta Energy. 2014. Alberta's oil sands: the facts. Government of Alberta, Edmonton, AB.

Allen, E.W. 2008. Process water treatment in Canada's oil sands industry: 1. Target pollutants and treatment objectives. *Journal of Environmental Engineering and Science* 7, 123-138.

Alm, J., Shurpali, N.J., Tuittila, E.S., Laurila, T., Maljanen, M., Saarnio, S., and Minkkinen, K. 2007. Methods for determining emission factors for the use of peat and peatlands flux measurement and modeling. *Boreal Environmental Research* 12, 85–100.

BGC Engineering Inc. 2010. Oil sands tailings technology review. Oil Sands Research and Information Network report TR-1, School of Energy and the Environment, University of Alberta, Edmonton.

Collins, C.E.V., Foght, J.M., Siddique, T. 2016. Co-occurrence of methanogenesis and N_2 fixation in oil sands tailings. *Science of the Total Environment* 565: 306-312.

Currie, R., Bansal, S., Khan, I., Mian, H. 2014. An Investigation of the Methylene Blue Titration Method for Clay Activity of Oil Sands Samples.

Currie, R., Zhao, B., Khan, I. 2015. Design of experiment study in support of development of a standard

for fines measurement in oil sands.
Dean, E.W., Stark, D.D. 1920. A convenient method for the determination of water in petroleum and other organic emulsions. *Industrial and Engineering Chemistry* 12(5), 486–490.
Elissen, H. J. H. 2007. Sludge reduction by aquatic worms in wastewater treatment, with emphasis on the potential application of. *Lumbriculus variegatus*.
Fellet, G., Marmiroli, M., Marchiol, L. 2014. Elements uptake by metal accumulator species grown on mine tailings amended with three types of biochar. *Science of the Total Environment* 468-469: 598-608.
Hallett, S.L., Atkinson, S.D., Erseus, C., and El-Matbouli, M. 2005. Dissemination of triactinomyxons (Myxozoa) via oligochaetes used as live food for aquarium fishes. *Disease of Aquatic Organisms* 65, 137-152.
Jeeravipoolvam, S. 2010. Geotechnical behaviour of in-line thickened oil sands tailings. PhD thesos, Department of Civil and Environmental Engineering, University of Alberta, Edmonton, AB.
Kaminsky, H. (2014). Demystifying the methylene blue index. *4th International Oil Sands Tailings Conference,* Lake Louise: Alberta
Kent, G. 2017. Tailings ponds a critical part of Alberta's oilsands legacy https://calgaryherald.com/business/energy/tailings-ponds-a-critical-part-of-albertas-oilsands-legacy
Larney, F. J., ad Angers, D. 2012. The role of organic amendments in soil reclamation: A review. *Canadian Journal of Soil Science* 92, 19-38.
Lenth, R 2018. Emmeans: Estimated Marginal Means, aka Least-Squares Means. R package version 1.0. https://CRAN.R-project.org/package=emmeans.
Liang, J., Guo, Z., Deng, L., and Liu, Y. 2015. MFT consolidation through microbial induced calcium carbonate precipitation. Canadian Journal of Civil Engineering 42, 975-978.
Powter, C.B., Biggar, K.W., Silva, M.J., McKenna, G.T., and Scordo, E.B. 2011. Review of oil sands tailings technology options. Proceedings of 14th International Conference on *Tailings and Mine Wastes*, Fort Collins, CO. pp 381-391.
R Core Team (2018) R: A language and environment for statistical computing. R Foundation for Statistical Computing, Vienna, Austria. URL https://www.R-project.org/
Renault, S., Szezerki, C., Nakata, C., Sailerova, E., Fedikow, M.A.F. 2004. Phytoremediation of mine tailings and bio-ore production: progress report on seed germination, plant growth and metal accumulation in seedlings planted at Central Manitoba (Au) minesite (NTS 52L13). Report of activities 2003, Manitoba Industry, *Trade and Mines, Manitoba Geological Survey*, p. 200-208.
Sander, B.O., Samson, M., and Buresh, R.J. 2014. Methane and nitrous oxide emission from flooded rice fields as affected by water and straw management between rice crops. *Geoderma* 253, 355-362
Schoonmaker, A., Degenhardt, D., and Floreani, T. 2018. Evaluating the potential to establish plants to aid in dewatering of an atmospheric fine drying tailings deposit at Muskeg River Mine. In, *International Oil Sands Tailings Conference*. Edmonton, AB.
Silva, M.J. 1999. Plant dewatering and strengthening of mine waste tailings. PhD Thesis, University of Alberta, Edmonton.
Welke, S.E., and Parkinson, D. 2003. Effect of Aporrectodea trapezoids activity on seedling growth of Pseudotsuya menziesii, nutrient dynamics and microbial activity in different forest soils. *Forest Ecology and Management* 173, 169-186
Woosaree, J., Hiltz, M. 2011. Cover crop program for tailings sand stabilization, prepared for Suncor Energy. Alberta Innovates Technological Futures, Vegreville, Alberta.
Yang, X., de Lucas Pardo, M., Ibanez, M., Deng, L., Sittoni, L., Ulrich, A., Chen, Q. 2020. Improving engineering properties of mature fine tailings using Tubifex. *Canadian Journal of Civil Engineering*, *47*(7), 812-821.
Yucel, K., Schoonmaker, A., Degenhardt, D., Kaur, J., and Khadka, B. 2016. Evaluating the potential to establish plants to aid in dewatering of an atmospheric fine drying tailings deposit at Muskeg River Mine. In, *International Oil Sands Tailings Conference*. Lake Louise, AB.

Evaluating the biogeochemical and consolidation behavior of oil sands end pit lakes with accelerated aging

Heidi L. Cossey, Petr V. Kuznetsov & Ania C. Ulrich
University of Alberta, Edmonton, Alberta, Canada

ABSTRACT: Over 1 billion m^3 of oil sands tailings have been generated in Alberta, all of which must be reclaimed. End pit lakes (EPLs) are a proposed tailings reclamation method in which treated or untreated tailings are capped with water. Theoretically, EPLs will develop into self-sustaining aquatic ecosystems as the tailings slowly consolidate and organic contaminants undergo bioremediation. However, substantial knowledge gaps exist surrounding the long-term behavior of EPLs. Uncertainties, including EPL water quality due to expressed contaminants from consolidation, must be evaluated to understand the potential for aquatic reclamation of tailings. To address these uncertainties, aging experiments are being conducted in 1 L and 19 L columns containing untreated and coagulant/flocculant treated tailings and a water cap. Aging is accelerated by increasing temperature and hydrocarbons amendments. Preliminary results indicate that treated tailings consolidate at a faster rate than untreated tailings and that column size impacts biogeochemical and geotechnical behavior.

1 INTRODUCTION

Oil sands surface mining in Alberta has generated over 1.3 billion m^3 of waste, known as fluid fine tailings (FFT) (AER 2020). FFT consists of fine-grained solids (silts and clays), water, organic compounds, and chemical constituents. Currently, FFT is being stored in temporary above ground impoundments, known as tailings ponds, however, these tailings must eventually be reclaimed and integrated into mine closure landscapes. Aquatic reclamation of FFT in End Pit Lakes (EPLs) is intriguing because of the small footprint and low cost of EPLs in comparison to terrestrial reclamation. EPLs are proposed to contain 10-80 m of treated or untreated tailings and a 3-10 m water cap in decommissioned mined out pits. A total of 23 EPLs are planned for Alberta's oil sands mines (COSIA 2021). Currently, both Syncrude Canada Ltd. (Syncrude) and Suncor Energy Inc. (Suncor) are evaluating EPLs as a tailings reclamation method. Syncrude has an 800 ha full scale EPL, Base Mine Lake (BML), which was commissioned in December 2012 and currently consists of approximately 45 m of untreated FFT capped with 9 m of water, as well as a demonstration scale EPL, the Syncrude Demonstration Pond (COSIA 2021). Suncor is proposing a unique reclamation method, called a permanent aquatic storage structure (PASS), which involves treating FFT with a coagulant (alum) and flocculant (polyacrylamide, PAM), prior to deposition in an EPL (Suncor 2020; COSIA 2021). Suncor is currently implementing both a commercial scale PASS and an 18 ha demonstration scale PASS, known as Lake Miwasin.

Theoretically, EPLs are a suitable FFT reclamation method because FFT can slowly consolidate (dewater) over time, while the water cap serves as habitat for an aquatic ecosystem. However, substantial knowledge gaps exist surrounding the long-term behavior EPLs. As untreated or treated FFT in EPLs undergo consolidation and as residual hydrocarbons and potentially PAM undergo biodegradation, expressed chemical and organic contaminants will enter the water cap, impacting water quality and the development of an aquatic ecosystem. Further, the environmental fate of aluminum and the extent to which sulfur cycling occurs in PASS tailings is unknown, though extensive sulfur cycling, namely the reduction of sulfate to aqueous and gaseous hydrogen sulfide (H_2S), has been noted in similarly sulfate amended tailings deposits (Reid & Warren 2016; Warren et al. 2016). The objective of this research is to address such knowledge gaps by conducting accelerated aging experiments on laboratory scale EPL columns. This study monitors the evolution of 40 laboratory scale EPL columns over time to elucidate the biogeochemical and consolidation behavior of untreated and PASS treated tailings in EPLs.

2 MATERIALS AND METHODS

2.1 *Sample collection and characterization*

2.1.1 *Sample collection*

Grab samples of untreated FFT were collected in 5 L pails from an oil sands tailings pond in 2019. The 5 L pails were combined and homogenized in a 400 L bin at the Northern Alberta Institute of Technology (NAIT) and re-subsampled into 20 L pails. The 20 L pails were stored at NAIT and then the University of Alberta at 4°C until use. Prior to the experimental set-up in 2021, approximately 130 L of the untreated FFT was treated with a coagulant, alum, and flocculant, PAM, and sheared by means of a conveyance test at NAIT to mimic the PASS treatment process. The alum dose was approximately 875 mg/L of pore water, and the PAM dose was 2.43g/kg of solids. Details on the flocculation procedure can be found in Li et al. (2021a). During PASS treatment at Suncor, the tailings are transported to a disposal area via a 2500 m pipeline. The conveyance testing used in this work simulates the 1500 kJ/m^3 of shear energy input delivered to the PASS treated tailings during pipeline transportation. Full details on the conveyance testing procedure can be found in Li et al. (2021b) and Li et al. (n.d.).

Fresh water from the Beaver Creek Reservoir (BCR) was used as cap water in the columns. BCR water was chosen because it is the fresh water source for Syncrude's BML. Further, the water chemistry of BCR is similar to that of the Athabasca River which runs through the Athabasca oil sands mining area and will likely be hydrologically connected to future EPLs. BCR was collected in 20 L by an oil sands operator in 2015 and stored at the University of Alberta at 4°C until use.

2.1.2 *Sample characterization*

Initial sample characterization of the untreated FFT and PASS-treated FFT (referred to hereinafter as PASS) included measurements of solids and water content, bulk density, peak undrained shear strength, and Methylene Blue Index (MBI). Peak undrained shear strength was measured using a Brookfield rheometer (DV3T, CAN-AM Instruments Ltd., Oakville, ON, CA) and V-71 and V-72 spindles (Brookfield Engineering Labs Ltd., Middleboro, MA, USA). MBI was conducted at NAIT in accordance with the method outlined in Kaminsky (2014).

Initial characterization of the FFT and PASS pore water and BCR water included measurements of pH, electrical conductivity (EC), alkalinity, major cations and anions, and dissolved organic carbon (DOC). pH was measured using a Thermo Scientific Orion Dual Star pH/ISE Benchtop and EC was measured using a Fisher Scientific Accumet AR50 Dual Channel pH/Ion/Conductivity Meter. Alkalinity was examined using a Metrohm Eco Titrator (Herisau, Switzerland) with 0.02 N H_2SO_4 and endpoints were set up a pH of 8.3 and 4.5 for carbonate and total alkalinity, respectively. Major cation analysis was conducted at the Natural Resources Analytical Laboratory (NRAL) at the University of Alberta. Samples were filtered with 0.45 µm nylon filters and analyzed Na^+, K^+, Ca^{2+}, Mg^{2+}, Fe, and Al via Inductively Coupled Plasma –

Optical Emission Spectrometry (ICP-OES) (Thermo iCAP 600 series, Thermo Fisher Scientific, Bremen, Germany). Filtered samples (using 0.2 μm nylon filters) were analyzed for major anions (Cl^-, SO_4^{2-}, NO_3^-, NO_2^-, and PO_4^{3-}) using a Dionex 2100 Ion Chromatography System (Thermo Scientific, Bannockburn, Illinois) in accordance with the procedure outline in Abolfazlzadehdoshanbehbazari et al. (2013). DOC was measured in filtered samples (using 0.45 μm nylon filters) using a Shimadzu TOC-LCPH analyzer (Kyoto, Japan) (sparging time: 6 min; injection volume: 50 μL; injection number: 3 out of 4; acid added: 2.3%).

2.2 *Aging methodology*

Aging is simulated in the EPL columns by accelerating microbially-derived processes that naturally occur in tailings. Two aging methods are investigated in this work: temperature and hydrocarbon amendments. Both of these methods increase microbial activity and enhance microbially-derived consolidation (bioconsolidation) processes. Sulfate reduction and methanogenesis are dominant microbial activities that occur in FFT and contribute to consolidation, contaminant degradation, biogenic gas emissions, and mineral transformations in tailings deposits (Siddique et al. 2006, 2007, 2011, 2014a, 2014b, 2015, 2020; Stasik et al. 2014; Burkus et al. 2014). As such, accelerating these microbially-derived processes will help to elucidate the long-term biogeochemical and consolidation behavior of untreated and PASS treated tailings in EPLs.

2.2.1 *Temperature*

Microbial activity is highly dependent on temperature as higher temperatures (up to an optimum temperature) increase microbial metabolic rates (Pavlostathis & Zhuang 1991). For example, Pavlostathis & Zhuang (1991) found that increasing incubation temperatures from 5 to 20°C increased metabolic rates of sulfate reduction and methanogenesis in samples of subsurface soil from a hazardous waste site. Wong et al. (2015) found that large fractions of methanogens were present in microbial communities in oil sands outcrop samples incubated under anoxic conditions at 23°C and 60°C. However, Wong et al. (2015) noted that while net methane production occurred at 23°C, there was no significant net methane production at 60°C. Further, Siddique et al. (2014a) reported substantial methane production over a period of 140 days in untreated FFT amended with organic carbon and incubated at approximately 20°C. As such, an incubation temperature of 20°C was selected to increase microbial metabolic rates in tailings in this experiment. A control temperature of 10°C was selected based on the work of Dompierre et al. (2016) and Tedford et al. (2019). Dompierre et al. (2016) found that temperatures in BML averaged 19.3 ± 1.0°C in the water cap and 12.9 ± 1.2°C below the FFT-water interface in the summer months. Tedford et al. (2019) found that temperatures in the BML varied seasonally and were between 0 and 20 °C in the water cap and between roughly 3 and 15°C near the FFT-water interface throughout the year. As such, 10°C was selected as a control temperature because it should not substantially accelerate or decelerate tailings microbial activity beyond what is likely to occur in an EPL.

2.2.2 *Hydrocarbon amendments*

Microbial activity in tailings can be accelerated by providing microorganisms with additional carbon sources, such as hydrocarbons. Methanogens are well known hydrocarbon degraders and are capable of degrading residual diluents (naphtha and paraffinic diluents), BTEX (benzene, toluene, ethylbenzene, and xylenes), n-alkanes, iso-alkanes, and cyclo-alkanes (Siddique et al. 2006, 2007, 2011, 2015, 2020; Mohamad Shahimin 2017a, 2017b; Tan et al. 2015). Sulfate reducing bacteria have also been found to degrade light hydrocarbons such as BTEX (Stasik & Wendt-Potthoff 2014). Amending tailings with hydrocarbons will enhance the biogeochemical cycling that has been noted in numerous tailings ponds and deposits, including BML and the Sandhill Fen (which contains sulfate-amended tailings) (Ramos-Padrón et al. 2011; Stasik & Wendt-Potthoff 2014; Dompierre et al. 2016; Reid & Warren 2016). Further, it will also contribute to bioconsolidation of tailings through biogenic gas ebullition, namely carbon dioxide (CO_2) and methane (CH_4), which alters pore water chemistry through CO_2 dissolution and creates transient physical channels in tailings, and through biogeochemical reactions with mineral surfaces (Siddique et al. 2014a, 2014b).

2.3 *Experimental set-up and sampling*

2.3.1 *Column set-up*

16 19 L columns were set up in duplicate and 24 1 L columns were set up in triplicate, as shown in Table 1. 19 L columns were made up of cast acrylic tubes, 4.5" inner diameter (ID), 1/4" thick, approximately 73" tall (Johnston Industrial Plastics Ltd., Edmonton, AB, CA) and a 1/2" thick cast acrylic sheet base (Plastics Plus Ltd., Edmonton, AB, CA). 1 L columns consist of polypropylene 1 L graduated cylinders, approximately 2.4" ID and 16.5" tall (3004001000, Fisherbrand™, Mexico). Each of the 40 columns were set up with a tailings to water ratio of 2.5:1. This resulted in 12.5 L of tailings and 5 L of BCR water in the 19 L columns with 2.5 L of headspace, and 0.75 L of tailings and 0.5 L of BCR water in the 1 L columns with 0.13 L of headspace. The 19 L columns each contain four sampling ports (3/4" stainless steel (316) mini ball valve – FxM NPT, Direct Material, Irving Texas, USA) (one in the water cap, three in the tailings) and the 1 L columns contain a single sampling port (1/2" two way ball valve with 10 mm hose barb) in the tailings. Each column contains a lid made out of 3/16" thick cast acrylic sheet (Plastics Plus Ltd., Edmonton, AB, CA) equipped with a septa (CLS-4209-14, butyl rubber, Chemglass) and tubing (1/8" ID, vinyl, Fisher Scientific, Pittsburgh, PA, USA) to allow for headspace and water cap sampling. After filling each column, each lid was sealed with silicon to prevent biogenic gas from escaping and oxygen from entering the columns. The headspace in each column was then flushed with nitrogen to remove oxygen, creating anaerobic conditions in the columns which promotes sulfate reduction and methanogenesis. The column set-up can be seen in Figure 1 below.

Table 1. Summary of columns set-up for aging experiments. B (for Big) columns refer to 19 L columns set up in duplicate, S (for Small) columns refer to 1 L columns set up in triplicate.

Column	**Temperature**		**Hydrocarbon (HC) Amendment**
	10°C	20°C	
FFT B10	✓		
FFT B20		✓	
FFT B10 + HC	✓		✓
FFT B20 + HC		✓	✓
FFT S10	✓		
FFT S20		✓	
FFT S10 + HC	✓		✓
FFT S20 + HC		✓	✓
PASS B10	✓		
PASS B20		✓	
PASS B10 + HC	✓		✓
PASS B20 + HC		✓	✓
PASS S10	✓		
PASS S20		✓	
PASS S10 + HC	✓		✓
PASS S20 + HC		✓	✓

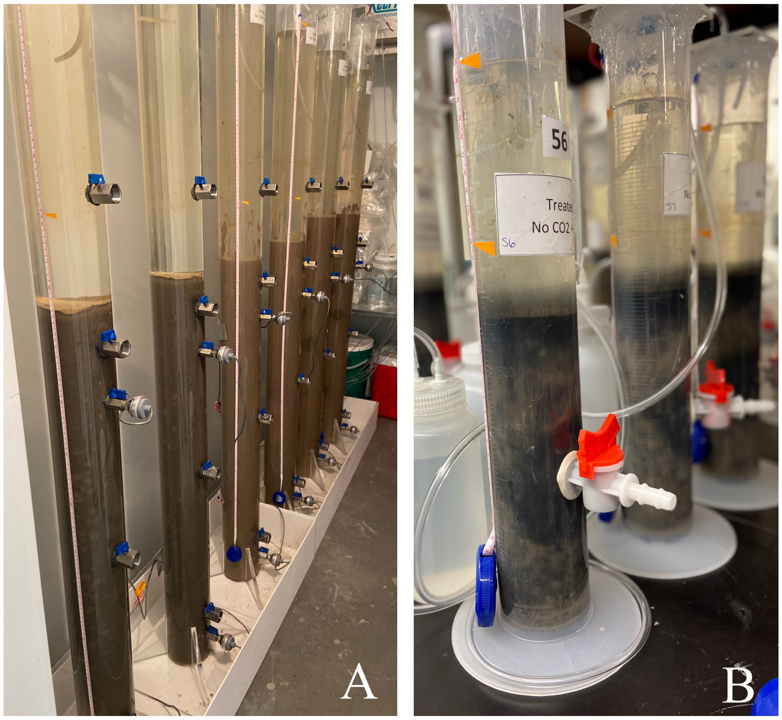

Figure 1. Picture of A: six 19 L columns in a 10°C cooler and B: three 1 L columns stored at 20°C.

As indicated in Table 1, 20 of the columns are being stored at room temperature (20°C) for the duration of the experiment while the other 20 columns are kept in a 10°C cooler (McKinley & Taylor, Edmonton, AB, CA) regulated using a Johnson Controls Inc. electronic temperature control (A419, Milwaukee, WI, USA). 20 of the columns (eight 19L and 12 1L columns) were also amended with hydrocarbons. Based on previous work, hydrocarbon amendments included a mixture of toluene (150 ppm) (≥99.9%, Sigma-Aldrich, St. Louis, Missouri), o-xylene (50 ppm) (99%, Alfa Aesar, Ottawa, Ontario), m-xylene (50 ppm) (>99%, TCI AMERICA, Portland, Oregon), and p-xylenes (50 ppm) (99%, Alfa Aesar, Ottawa, Ontario), n-decane (500 ppm) (99.5%, Fisher Scientific, Fair Lawn, New Jersey), n-octane (500 ppm) (99+%, Thermo Fisher Scientific, Fair Lawn, New Jersey), 3-methylhexane (500 ppm) (99%, ChemSampCo, Dallas, Texas), and 2-methylpentane (500 ppm) (≥99, Sigma Aldrich, St. Louis, Missouri).

2.3.2 *Column sampling and monitoring*

Column sampling and measurements are conducted on the headspace, water cap, and tailings in all 40 columns and will continue for one year. Tailings are continuously monitoring for FFT-water interface settlement and pore water pressure (in the 19 L columns only) to evaluate settlement and consolidation behavior. Pore water pressure is being evaluated using pore pressure transducers (0 to 10 psig, Item # RK-68075-42, Cole Parmer, Montreal, Quebec) connected to the columns using 1/4" stainless steel ball valves ((316) mini ball valve – FxM NPT, Direct Material, Irving Texas, USA) and is continuously monitored using a data logger (Keysight DAQ973A Data Acquisition System and Keysight DAQM901A 20 channel multiplexers, Santa Rosa, CA, USA). The tailings and water cap are being monitored monthly for pH, EC, redox potential, alkalinity, major cations and anions, and DOC. Two different sizes of pH, EC, and redox probes are used. pH is measured in big (19 L) columns using a E-1325M pH probe (Gain Express) and in small (1 L) columns using a Thomas Scientific micro pH electrode (Swedesboro, NJ, USA). EC is measured in big columns using an Atlas Scientific conductivity probe K 0.1 (Long Island City, NY, USA) and in small columns using an MI-915 conductivity electrode (Microelectrodes Inc. Bedford, NH, USA). Redox potential is measured with a Thermo Scientific Orion Dual Star pH/ISE Benchtop and an ORP-1 (Gain Express) probe in the big columns and a Mettler Toledo micro ORP electrode (S7, Greifensee, Switzerland) in the small columns. Gas in the column headspace is being monitoring monthly for concentrations of CO_2 and CH_4. CO_2 and CH_4 are measured using manual injection in a gas chromatography with a flame ionization detector (GC-FID) (Agilent 7890A+/5977B GC-MS, Santa Clara, CA, USA).

3 RESULTS

3.1 *Sample characterization*

Table 3 shows characterization data for the solids and pore water in FFT and PASS and the BCR water. The solids content of the initial PASS (30.1 ± 0.0 wt%) is slightly lower than that of the FFT (33.5 ± 0.7 wt%), likely due to the liquid alum and polymer solutions that were added during PASS treatment. PASS treatment did not improve the shear strength of the FFT, and both the initial PASS and FFT had very low peak undrained shear strengths of 7.93 ± 0.11 Pa and 10.6 ± 0.83 Pa, respectively. This agrees with the findings of Wilson et al. (2018) and Jeeravipoolvarn (2010) who found that flocculation and thickening of FFT had little to no effect on shear strength.

Table 2. Sample characterization for initial FFT, PASS, and BCR samples. Results are presented as average ± one standard deviation of triplicates. N/A indicates that the parameter is not applicable to the sample. BDL indicates Below Detection Limit.

Parameter	**FFT**	**PASS**	**BCR**
Solids content (oven analysis) (wt%)	33.5 ± 0.7	30.1 ± 0.0	N/A
Water content (oven analysis) (wt%)	66.5 ± 0.6	69.9 ± 0.0	N/A
Bulk density (g/mL)	1.23 ± 0.07	1.22 ± 0.03	N/A
Initial void ratio	5.01 ± 0.37	5.68 ± 0.18	N/A
Peak undrained shear strength (Pa)	10.6 ± 0.83	7.93 ± 0.11	N/A
Methylene blue index (MBI) (meq/100 g)	12.2 ± 0.6	12.2 ± 0.6	N/A
Clay content (dry wt% based on MBI)	87.6 ± 4.1	87.6 ± 4.1	N/A
pH	7.33 ± 0.06	7.39 ± 0.16	8.40 ± 0.12
Electrical conductivity (EC) (µS/cm)	761 ± 33	816 ± 8	357 ± 8
Dissolved organic carbon (DOC) (mg/L)	54.8 ± 3.1	53.2 ± 0.2	19.2 ± 0.4
Sodium, Na^+ (mg/L)	232.0 ± 6.0	241.2 ± 2.4	43.0 ± 0.5
Potassium, K^+ (mg/L)	16.4 ± 0.3	17.5 ± 0.2	3.4 ± 0.3
Magnesium, Mg^{2+} (mg/L)	28.9 ± 0.2	39.7 ± 0.7	11.7 ± 0.5
Calcium, Ca^{2+} (mg/L)	37.1 ± 5.6	85.2 ± 2.4	23.6 ± 0.4
Chloride, Cl^- (mg/L)	14.8 ± 2.6	35.7 ± 0.6	7.46 ± 0.3
Phosphate, PO_4^{3-} (mg/L)	2.0 ± 0.9	3.4 ± 1.4	0.3 ± 0.2
Nitrite, NO_2^- (mg/L)	8.2 ± 2.4	2.8 ± 0.1	4.8 ± 1.0
Nitrate, NO_3^- (mg/L)	5.4 ± 1.8	5.8 ± 1.0	5.3 ± 0.6
Sulfate, SO_4^{2-} (mg/L)	317.4 ± 9.6	523.0 ± 4.9	21.7 ± 0.9
Aluminum, Al (mg/L)	BDL	BDL	BDL
Iron, Fe (mg/L)	0.014 ± 0.001	0.017 ± 0.006	0.012 ± 0.004
Total alkalinity (mg $CaCO_3$/L)	415.8 ± 9.0	309.7 ± 4.2	148.8 ± 10.2
Bicarbonate (mg/L)	510.6 ± 10.9	377.8 ± 5.2	181.6 ± 11.6

Compared to FFT pore water, PASS pore water has a higher EC, which is expected given the addition of alum. The higher EC can be attributed to the higher sulfate concentration in PASS (523.0 ± 4.9 mg/L) compared to that of FFT (317.4 ± 9.6 mg/L). In addition, PASS has a higher calcium concentration and lower alkalinity than FFT. Aluminum is below detection in the initial PASS pore water despite the alum addition, but given the pH of the tailings, it is most likely precipitating as $Al(OH)_{3(s)}$. BCR water generally has measurements lower than that of FFT and PASS for all water chemistry parameters listed in Table 2 except pH. The water chemistry of the BCR water is similar to that of the Athabasca River that flows through Alberta's oil sands surface mining region (Government of Alberta 2021).

3.2 *Column monitoring*

Figure 2 shows the FFT-water interface settlement in all 40 columns (big columns in Figure 2A; small columns in Figure 2B) for the first 60 days of the aging experiments. Columns containing PASS are settling and consolidating faster than columns with FFT, which is to be expected given the agglomeration of FFT particles (Li et al. 2021a) and higher hydraulic conductivities (Wilson et al. 2018) associated with treated tailings. However, the interface settlement in six of the small FFT columns is approaching that of the small PASS columns (see FFT S10 and FFT S20 in Figure 2), while differences in interface settlement in FFT columns versus PASS columns appears to be increasing in big columns. The small columns are also settling and undergoing self-weight consolidation at a faster rate than the big columns. For example, on Day 30, the small columns had undergone between 14% and 34% interface settlement relative to the initial height of the tailings in the columns, whereas the big columns had only undergone between 8% and 17% interface settlement relative to the initial height of the tailings. Both sizes of columns have one-way drainage and the same tailings to water ratio and as such, these differences are likely due to scale and/or shape effects. Researchers have noted the impact of cross-sectional area and diameter vs. height ratios (D/H) on settlement and consolidation behavior in cohesive soils and slurries and generally agree that a smaller cross-sectional area hinders interface settlement (Baotian et al. 2013; Gao et al. 2016). However, in this work, sedimentation is occurring at a faster rate in the small columns which have a cross-sectional area 0.3 times that of the big columns. As such, D/H ratios of the big and small columns (0.1 and 0.2, respectively) may be contributing to the different interface settlement rates (Rosine & Sabbagh 2015).

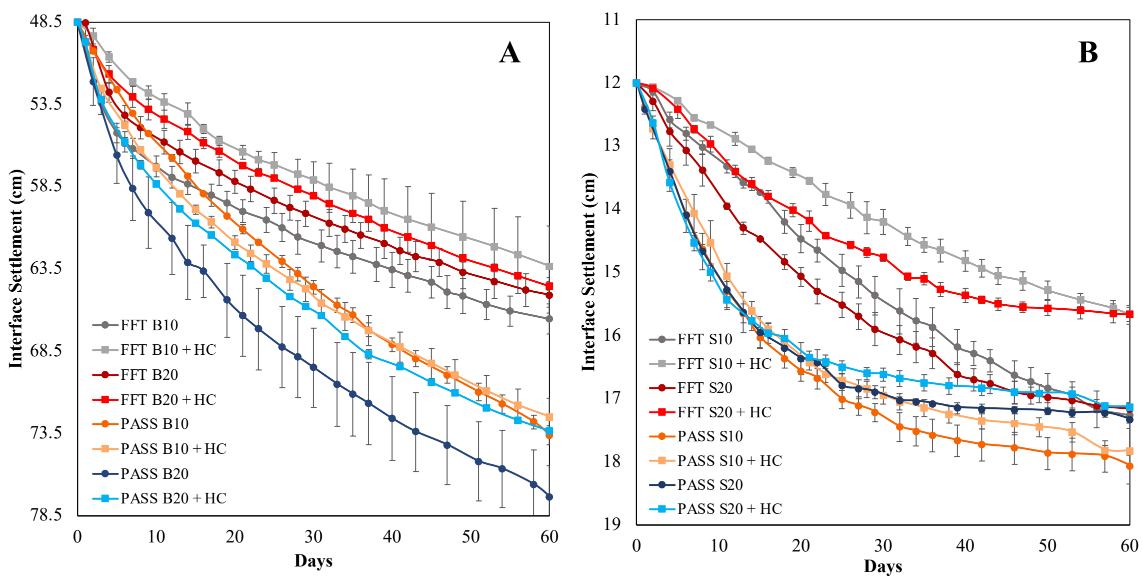

Figure 2. Interface settlement in (A) 16 19 L columns and (B) 24 1 L columns. Results are averaged from duplicate (A) or triplicate (B) columns and deviation bars represent one standard deviation of replicates.

Higher temperatures should theoretically result in a faster settlement and consolidation rate due to increased hydraulic conductivities, and both higher temperatures and hydrocarbon amendments should increase microbial metabolic rates, and thereby bioconsolidation. However, currently there are no clear trends in the effects of temperature and hydrocarbons on interface settlement. This may be because biogenic gases are entrained in the tailings and/or the microorganisms are currently in a lag phase adapting to their new environment before reaching an exponential growth (log) phase (Siddique et al. 2014a). Biogenic gases are visibly trapped in the tailings in all eight of the big columns that were amended with hydrocarbons, which is impeding interface settlement in these columns. However, there are no bubbles visible in the small columns. Redox potentials of the tailings indicate that the big columns quickly became highly reducing environments favourable for sulfate reduction and methanogenesis, particularly those stored at 20℃ and/or amended with hydrocarbons, with redox potentials ranging from -130 to -351 mV on Day 60. Redox potentials in small columns ranged from -6 to -270 mV on Day 60, which still indicates reducing environments, but to a lesser extent than what has developed in the big columns.

Figure 3 presents sodium, Na^+, and sulfate, SO_4^{2-}, concentrations in the water caps of all 40 columns on Day 30 relative to the Day 0 (BCR water only) concentrations. Na^+ and SO_4^{2-} are the ions with the highest concentrations in the initial FFT, PASS, and BCR water, and in all 40 water caps on Day 30. Further, water cap concentrations of Na^+ and SO_4^{2-} are higher on Day 30 than they were on Day 0 in all 40 columns. Concentrations of cations, anions, DOC and alkalinity are generally in agreement with the consolidation trends presented in Figure 1 and can be largely attributed to advective pore water fluxes from the tailings into the overlying water. However, SO_4^{2-} concentrations are lower than Na^+ concentrations in the big columns but higher than Na^+ concentrations in the small columns and in the Day 0 BCR water (with two exceptions, PASS B20 columns and FFT S20 + HC columns). This may indicate SO_4^{2-} reduction is occurring to a greater extent in the big columns, which would be consistent with the redox potentials discussed earlier. Aluminum concentrations were below detection limits in the water caps in all columns on Day 30, except PASS S20, PASS S10 + HC, and PASS 20 + HC columns which had average concentrations of 0.029, 0.015, and 0.044 mg/L, respectively. These aluminum concentrations are below the applicable Alberta Surface Water Quality Guidelines for protection of aquatic life (Government of Alberta, 2018).

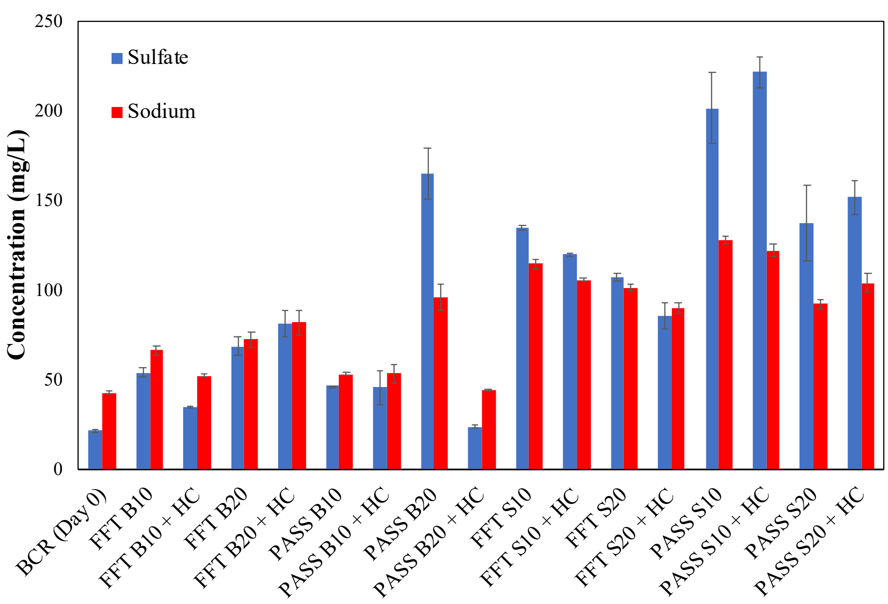

Figure 3. Sodium, Na^+, and sulfate, SO_4^{2-}, water cap concentrations on Day 30 in 19 L and 1 L columns relative to the Day 0 (BCR water) concentrations. Results are averaged from duplicate (in big (B) columns) or triplicate (in small (S) columns) and deviation bars represent one standard deviation of duplicates (B) or triplicates (S).

4 CONCLUSIONS

Monitoring and sampling of the biogeochemical and geotechnical behavior of the tailings and/or water cap in all 40 columns is ongoing. Preliminary results indicate that PASS treated tailings are faster to settle and consolidate, regardless of column size. However, scale and shape effects are likely contributing to the faster rates of interface settlement seen in the smaller (1 L) columns compared to that of the bigger (19 L) columns. Water cap concentrations of Na^+ and SO_4^{2-} are higher on Day 30 than on Day 0 in all 40 columns and are generally consistent with consolidation trends. However, water cap concentrations of SO_4^{2-} were lower than expected in the big columns, which may indicate sulfate reduction is occurring in these columns.

5 FUNDING

The authors gratefully acknowledge research support from the NSERC/COSIA Industrial Research Chair in Oil Sands Tailings Geotechnique (IRCPJ 460863 – 18). H. Cossey received financial support from the Vanier-Banting Secretariat as part of this research.

6 ACKNOWLEDGEMENTS

The authors would like to thank Dr. H. Kaminsky's team at Northern Alberta Institute of Technology (NAIT) for their assistance, support, and expertise throughout this project. H. Cossey is also grateful for financial support from the Vanier-Banting Secretariat in conducting this research.

7 REFERENCES

Abolfazlzadehdoshanbehbazari, M., Birks, S.J., Moncur, M.C., & Ulrich, A.C. 2013. Fate and transport of oil sands process-affected water into the underlying clay till: a field study. *Journal of Contaminant Hydrology* 151: 83-92.

Alberta Energy Regulator (AER), 2020. State of fluid tailings management for mineable oil sands, 2019, Alberta Energy Regulator, Calgary, AB, CA.

Baotian, W., Shuaijie, G., & Funhai, Z. 2013. Research on deposition and consolidation behavior of cohesive sediment with settlement column experiment. *European Journal of Environmental and Civil Engineering* 17: s144-s157.

Burkus, Z., Wheler, J., & Pletcher, S. GHG Emissions from oil sands tailings ponds: overview and modelling based on fermentable substrates. Part I: review of tailings pond facts and practices. Alberta Environment and Sustainable Resource Development, Edmonton, Alberta, Canada, 2014.

Canada's Oil Sands Innovation Alliance (COSIA). Pit Lakes: A Surface Mining Perspective, Canada's Oil Sands Innovation Alliance, Calgary, Alberta, Canada, 2021.

Dompierre, K.A., Lindsay M.B.J., Cruz-Hernández, P., & Halferdahl, G.M. 2016. Initial geochemical characteristics of fluid fine tailings in an oil sands end pit lake. *Science of the Total Environment* 556: 196-206.

Gao, Y.F., Zhang, Y., Zhou, Y., & Li, D. 2016. Effects of column diameter on settling behavior of dredged slurry in sedimentation experiments. *Marine Georesources & Geotechnology* 34: 431-439.

Government of Alberta. 2018. Environmental Quality Guidelines for Alberta Surface Water. Alberta Environment and Parks, Water Branch, Edmonton, AB, CA.

Government of Alberta. 2021. Long Term River Station Data. Available online: http://environment.alberta.ca/apps/EdwReportViewer/LongTermRiverStation.aspx (accessed on 14 May 2021).

Jeeravipoolvarn, S. Geotechnical Behavior of In-Line Thickened Tailings. Ph.D. Thesis, University of Alberta, Edmonton, Alberta, Canada, 2010.

Kaminsky, H. 2014. Demystifying the methylene blue index. Proceedings of the 4th International Oil Sands Tailings Conference, Banff, AB, CA, 7-10 December 2014.

Li, Y., Kaminsky, H., Gong, X.Y., Sun, Y.S., Ghuzi, M., & Sadighian, A. 2021a. What affects dewatering performance of high density slurry? *Minerals* 11: 761.

Li, Y., Kaminsky, H., Romero, C., Gong, X.Y., Ghuzi, M., & Tacas, J. 2021b. Assessing dewatering performance of treated fluid fine tailings with a bench-scale filter press. Proceedings of Tailings and Mine Waste 2021, 7-10 November 2021, Banff, AB, CA.

Li, Y., Kaminsky, H., Sadighian, A., Sun, Y.S., Murphy, F., Gong, X.Y., Ghuzi, M., & Rima, U. n.d. Impact of chemical and physical treatments on freeze-thaw dewatering of fluid fine tailings. *Cold Regions Science and Technology*. Submitted.

Mohamad Shahimin, M.F., & Siddique T. 2017a. Methanogenic biodegradation of paraffinic solvent hydrocarbons in two different oil sands tailings. *Science of the Total Environment* 583: 115–122.

Mohamad Shahimin M.F., & Siddique T. 2017b. Sequential biodegradation of complex naphtha hydrocarbons under methanogenic conditions in two different oil sands tailings. *Environmental Pollution* 221: 398–406.

Pavlostathis, S.G., & Zhuang, P. 1991. Effect of temperature on the development of anaerobic cultures from a contaminated subsurface soil. *Environmental Technology* 12: 679-687.

Ramos-Padrón, E., Bordenave, S., Lin, S., Bhaskar, I.M., Dong, X., Sensen, C.W., Fournier, J., Vourdouw, G., & Gieg, L.M. 2011. Carbon and sulfur cycling by microbial communities in a gypsum-treated oil sands tailings pond. *Environmental Science & Technology* 45: 439–446.

Reid, M.L., & Warren, L.A. 2016. S reactivity of an oil sands composite tailings deposit undergoing reclamation wetland construction. *Journal of Environmental Management* 166: 321-329.

Rosine, T.N., & Sabbagh, T.T. 2015. The impact of the diameter to height ratio on the compressibility parameters of saturated fine-grained soils. *International Journal of Research in Engineering and Technology* 4: 8-19.

Siddique, T., Fedorak, P.M., & Foght, J.M. 2006. Biodegradation of short-chain n-alkanes in oil sands tailings under methanogenic conditions. *Environmental Science & Technology* 40: 5459-5464.

Siddique, T., Fedorak, P.M., Mackinnon, M.D., & Foght, J.M. 2007. Metabolism of BTEX and naphtha compounds to methane in oil sands tailings. *Environmental Science & Technology* 41: 2350-2356.

Siddique, T., Penner, T., Semple, K., & Foght, J.M. 2011. Anaerobic biodegradation of longer-chain n-alkanes coupled to methane production in oil sands tailings. *Environmental Science & Technology* 45: 5892-5899.

Siddique, T., Kuznetsov, P., Kuznetsova, A., Arkell, N., Young, R., Li, C., Guigard, S., Underwood, E., & Foght, J.M. 2014a. Microbially-accelerated consolidation of oil sands tailings. Pathway I: changes in porewater chemistry. *Frontiers in Microbiology* 5: Article 106.

Siddique, T., Kuznetsov, P., Kuznetsova, A., Li, C., Young, R., Arocena, J.M., & Foght, J.M. 2014b. Microbially-accelerated consolidation of oil sands tailings. Pathway II: solid phase biogeochemistry. *Frontiers in Microbiology* 5: Article 107.

Siddique, T., Mohamad Shahimin, M.F., Zamir, S., Semple, K., Li, C., & Foght, J.M. 2015. Long-term incubation reveals methanogenic biodegradation of C5 and C6 iso-alkanes in oil sands tailings. *Environmental Science & Technology* 49: 14732–14739.

Siddique, T., Semple, K., Li, C.,& Foght, J.M. 2020. Methanogenic biodegradation of *iso*-alkanes and cycloalkanes during long-term incubation with oil sands tailings. *Environmental Pollution 258*: 113768.

Stasik, S., & Wendt-Potthoff, K. 2014. Interaction of microbial sulphate reduction and methanogenesis in oil sands tailings ponds. *Chemosphere* 103: 59-66.

Stasik, S., Loick, N., Knöller, K., Weisener, C., & Wendt-Potthoff, K. 2014. Understanding biogeochemical gradients of sulfur, iron and carbon in an oil sands tailings pond. *Chemical Geology* 382: 44–53.

Suncor Energy Operating Inc. (Suncor). 2019 Fort Hills fluid tailings management report. Suncor Energy Operating Inc., Calgary, Alberta, Canada, 2020.

Tan, B.F., Semple, K., & Foght, J. 2015. Anaerobic alkane biodegradation by cultures enriched from oil sands tailings ponds involves multiple species capable of fumarate addition. *FEMS Microbiology Ecology* 91: fiv042

Tedford, E., Halferdahl, G., Pieters, R., & Lawrence, G.A. 2019. Temporal variations in turbidity in an oil sands pit lake. *Environmental Fluid Mechanics* 19:457-473.

Warren, L.A., Kendra, K.E., Brady, A.L., & Slater, G.F. 2016. Sulfur biogeochemistry of an oil sands composite tailings deposit. *Frontiers in Microbiology* 6: 1-14.

Wilson, G.W., Kabwe, L.K., Beier, N.A., & Scott, J.D. 2018. Effect of various treatments on consolidation of oil sands fluid fine tailing. *Canadian Geotechnical Journal* 55: 1059-1066.

Wong, M., An, D., Caffrey, S.M., Soh, J., Dong, X., Sensen, C.W., Oldenburg, T.B.P., Larter, S.R., & Voordouw, G. 2015. Roles of thermophiles and fungi in bitumen degradation in mostly cold oil sands outcrops. *Applied and Environmental Microbiology* 81: 6825-6838.

Stabilization of flocculated fluid fine tailings by lime treatment

Yunhui Li, Heather Kaminsky & Catalina Romero Calducho
Northern Alberta Institute of Technology, Edmonton, AB, Canada

Nikolas Romaniuk, Narain Hariharan & Mike Tate
Graymont, Richmond, BC, Canada

ABSTRACT: Fluid fine tailings (FFT) are a byproduct of oil sands mining with present stockpiles exceeding 1200 Mm^3. Upland reclamation of FFT is not achievable until the surface deposit consolidates and solidifies to provide sufficient strength to support earthmoving equipment. The oil sands industry uses polymers to partially dewater FFT; however, additional post-deposition dewatering mechanisms such as evaporation and freeze-thaw are critical to achieve sufficient strength for eventual reclamation. The development of new tailings strengthening technologies capable of permanently modifying FFT to achieve improved post-deposition dewatering and strength development would be attractive for managing FFT.

Hydrated lime and quicklime are used extensively in soil stabilization to generate long-term strength gain. This study investigated the use of hydrated lime following polymer treatment of FFT to assess strength gain and dewatering with time. The investigation shows lime treatment assisted with further dewatering of flocculated FFT and resulted in superior strength gain with time.

1 INTRODUCTION

Oil sands tailings are a byproduct of oil sands mining with present stockpiles exceeding 1.2 billion m^3 (AER 2019). Tailings are transported and stored in large tailings ponds. The coarse sand particles rapidly settled at the edge of the tailings ponds, leaving the fluid fine tailings (FFT) to accumulate in the center of the ponds. FFT requires decades to centuries to settle into a semi-solid material, resulting in major environmental and fiscal challenges. The clay minerals control the FFT behavoir due to their high surface activities. Upland reclamation to a dry landscape is the main reclamation technology that is targeted by Alberta Energy Regulator (AER). Increased solids concentration through consolidation and/or chemical modification of the clay improves the strength and stability of the deposit. The technologies currently aiming to create dry landforms from the FFT include physical/mechanical methods (filtration, centrifuge), chemical methods (coagulation, flocculation), natural processes (evaporation, freeze-thaw, evapotranspiration), and biochemical methods (BGC 2010). These technologies, however, have not been able to meet the required shear strength (10 kPa) for trafficable surface within a reasonable time period. The development of new tailings strengthening technologies capable of permanently modifying FFT to achieve improved post-deposition dewatering and strength development in a short timeframe would be attractive for managing soft and fluid tailings.

The stabilization of clay-rich materials by incorporation of lime has been widely studied and used throughout the world (Little 1995). There are essentially two methods of improvement by lime treatment of fine clay materials: modification by short-term reactions and stabilization involving long-term reactions. Modification occurs primarily due to the exchange of bivalent calcium cations supplied by hydrated lime $Ca(OH)_2$ and the monovalent cations like sodium (Na^{+1}) adsorbed on the clay surface. The cation exchange destabilizes the inter-colloidal electrostatic repulsions, releases bound water and promotes coagulation (Little 1995; Lane 1983; Rogers & Glendinning 1996; Mosher et al. 2019). At a pH above 12.4, phyllosilicates on the clay surface dissolve into their aluminate and silicate constituents, which can react with soluble calcium and water to form pozzolanic products such as calcium aluminate hydrates (CAH) and calcium silicate hydrates (CSH) (Choquette et al. 1987; Little 1995; Locat et al. 1996; Tran et al. 2014).

Lime stabilization occurs when a significant level of long-term strength gain is developed through a long-term pozzolanic reaction (Bell 1996; Rogers et al. 2006; Khattab, et al. 2007). The pozzolanic reaction can continue for a very long period as long as enough lime is present and the pH remains high. As a result of the long-term pozzolanic reaction, the lime-treated materials can produce very high strength gains. Lime has been reported to increase the plastic limit and decrease the plasticity index in some cases due to the reduction of water affinity of the clay particles caused by the exchange of soluble calcium cations with monovalent cations (Clare & Cruchley 1957; Prakash et al. 1989; Bell 1996). Lime stabilization is a complicated process and affected by many factors such as soil/sample type, temperature, mineralogy, lime content, pH, and curing period (Dash & Hussain 2012).

This study investigated the use of hydrated lime following polymer treatment of FFT to assess the impact of lime treatment on dewatering and strength gain of the flocculated tailings. As shown in Table 1, two types of FFT were treated with three types of treatments: flocculation using an anionic polyacrylamide polymer, lime addition, and the combination of polymer and lime. The treated materials along with untreated FFT samples were filter pressed to characterize the dewatering performance and determining the liquid limit. The filter pressed samples were also assessed for undrained shear strength and then placed in jars to age for either 4 or 10 weeks whereupon the strength was re-evaluated.

Table 1. Experimental design.

Item	Factor	Details
Types of FFT	2	FFT-1 and FFT-2
FFT treatment	4	No treatment
		Flocculation only
		Lime treatment only
		Combination of flocculation and lime addition
Time of curing	2	4 weeks
		10 weeks

2 EXPERIMENTAL

2.1 *Materials*

Two types of FFT used in this project were analyzed for composition, methylene blue index (MBI), fines content, reported weight percent of particles passing 44 micron (COSIA 2015), electrical conductivity (EC), sodium adsorption ratio (SAR), major cations and anions by ion chromatography (IC), and pH (Table 2-3).

Table 2. FFT characterization on composition, MBI, fines%, EC, and SAR.

FFT	Mineral wt%	Bitumen wt%	Water wt%	MBI	Fines wt%	EC (mS/cm)	SAR
FFT-1	44.44	1.79	53.77	7.9	70.4	0.90	6.2
FFT-2	24.68	1.23	73.64	14.1	92.8	1.37	10

Table 3. FFT characterization on water chemistry.

FFT	Li^+	Na^+	K^+	Mg^{2+}	Ca^{2+}	F^-	Cl^-	NO_3^-	SO_4^{2-}	pH

FFT-1	0.01	230.84	14.62	28.60	56.32	2.30	17.50	5.68	365.68	8.46
FFT-2	1.80	381.00	20.50	34.90	52.20	2.48	205.70	2.79		8.20

High calcium hydrated lime, $Ca(OH)_2$, was produced and provided by Graymont. The lime slurry was prepared to 4.8 wt% of slurry using De-ionized (DI) water. The anionic polyacrylamide (PAM) flocculant A3338, produced by SNF Canada, was used in this study. Polymer solution was prepared at a concentration of 0.45 wt% in processed effluent water (PEW). The water chemistry of the PEW is shown in Table 4.

Table 4. PEW characterization on water chemistry.

EC (mS/cm)	Li^+	Na^+	K^+	Mg^{2+}	Ca^{2+}	F^-	Cl^-	NO_3^-	SO_4^{2-}	pH
1.50	0.01	274.66	14.38	13.37	7.15	3.04	176.85	0.00	221.29	9.42

2.2 *FFT flocculation (Li, et al. 2021)*

The setup for flocculation consists of a 6” metal vessel with an inserted baffle, an impeller, a peristaltic pump (coleparmer Drive/DISP MFLX BENCH 115/230) for polymer injection, and an overhead mixer with an online torque sensor and display (Heidolph Hei-Torque 100 Precision Base) used to provide mixing during flocculation (Figure 1).

The desired mass of FFT was subsampled into the flocculation vessel and the baffle inserted. The flocculation vessel with the baffle and the sample was assembled onto the overhead mixer with the impeller. Initially, the FFT was pre-sheared for 1 min at 300 rpm. Once the minute of pre-shearing was completed, the polymer solution was injected into the vessel at a predetermined rate (1200 mL/min) while mixing at 300 rpm. The torque reading on the overhead mixer was monitored during the mixing process. Once the peak or max torque was reached, the mixing speed was reduced immediately to 50 rpm and the mixing was continued at 50 rpm for 15 seconds (flocs conditioning time).

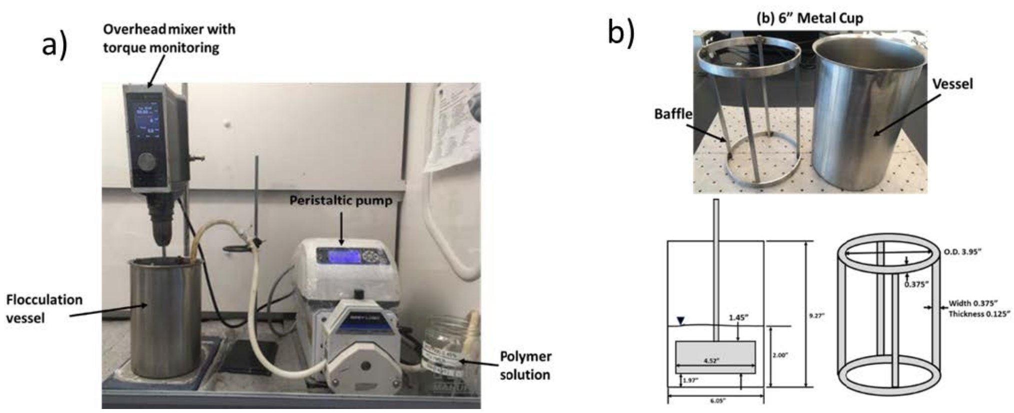

Figure 1. a) Flocculation setup; b) photo and schematic dimensions of flocculation vessels, baffles, and impellers.

2.3 *Determination of lime dosage*

The lime dosage was determined by measuring the pH (potable ExStik®pH100 meter) and EC (Traceable® Conductivity/TDS Pocket Tester) of both the untreated and flocculated FFT samples by titration with the lime slurry. A total of 200 g of untreated FFT was placed in a beaker and mixed at 100 rpm during the titration of lime slurry. Flocculated FFT was dewatered before lime titration with release water draining through a kitchen sieve with 1 cm opening for 30 min. The flocculated FFT was mixed at 20 rpm during the titration with lime slurry to avoid flocs breaking. EC and pH were measured every 2 ml of lime slurry increments after the readings were stable. The point where pH levels and EC readings were stable was considered the optimal lime dosage for the purposes of inducing a pozzolonic reaction.

2.4 *Lime treatment on FFT*

The desired dosage of the lime slurry was introduced into the untreated FFT at 100 rpm of mixing and flocculated FFT at 20 rpm of mixing after water draining for 30 minutes using a graduated pipette. The combined samples were mixed for 1 minute after lime addition.

2.5 *Pressure filtration test*

A modified OFITE's multi-Unit filter press was used for the filter press testing (Figure 2). The filter medium used was Whatman Grade #50 filter paper (particle filtration size of 2.7 μm). The 300 g of samples were fed into the sample cup. Each sample cup was connected to a compressed airline and the pressure was adjusted to the desired pressure (20 psi or 100 psi). An elastic film was placed between the sample and the high pressure gas in each sample cup to avoid sample cracking due to the dewatering. The filtrate was collected and the mass of filtrate was measured automatically with the compressing time by the balance connected to the computer.

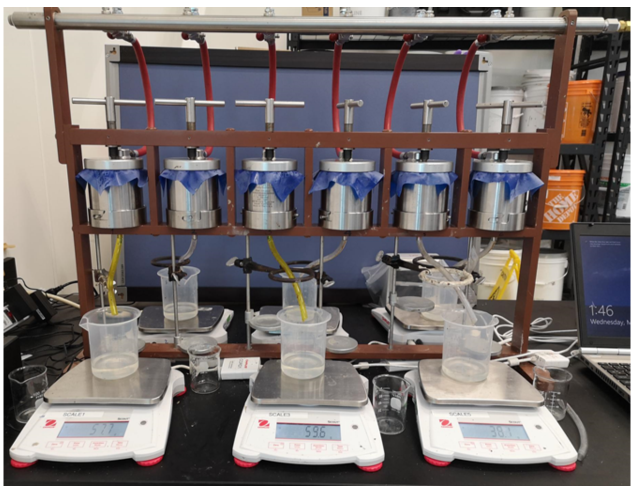

Figure 2. The photo of modified filter press setup with balances.

2.6 *Filter pressed cakes compaction*

The compressed cakes generated in the pressure filter operations were mixed and remolded to saturate the sample jar to undergo curing time (Figure 3). To minimize the effect of air voids, fractions of remolded cake were placed in the jar and compacted using a pestle. The jar was filled up gradually until level to obtain a smooth surface. After compaction, the day 0 undrained shear strength was measured. When the sample completed the curing time (70 days), the shear strength was measured again.

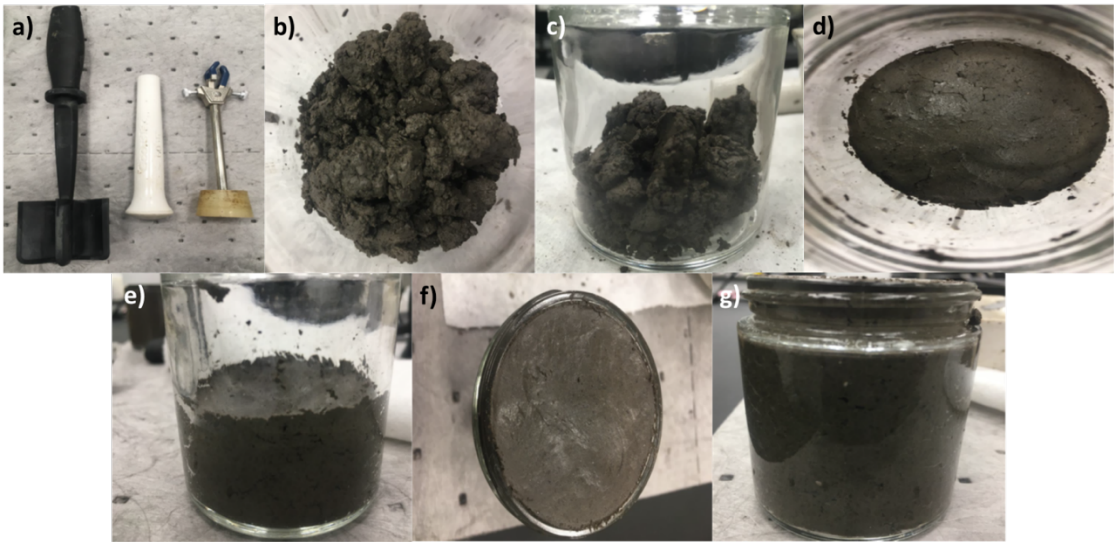

Figure 3. a) Remolding and compacting tools; b) the top view of the remolded sample; c) the side view of the remolded sample; d) top view during compacting the remolded sample; e) side view during compacting the remolded sample; f) top view of the saturated jar with completed compact sample; g) side view of saturated jar with completed compact sample.

2.7 *Strength measurement*

The static yield stress was measured using the Brookfield DVIII Ultra HB and 5HB rheometers with vanes 73 and 74. The maximum yield strength range for HB rheometer is 8 kPa and for 5HB is 40 kPa. The samples were packed in 4 oz. glass jars while measuring the yield stress.

2.8 *Solids content measurement*

The solids contents in this study were measured by placing the samples in an oven for overnight at 105°C. The physically adsorbed water in the samples would be removed but chemically bonded water might be left in the samples.

3 RESULTS AND DISCUSSION

3.1 *Determination of polymer dosage*

The optimal A3338 polymer dosages for two FFT samples were determined by testing the full dosage response curves corresponding to the net water release (NWR) after 24-hour drainage (Sadighian, et al. 2018; Li, et al. 2021). Figure 4 shows that the optimal dosage window for FFT-1 was 1360-1480 g/dry tonne and the optimal dosage window for FFT-2 was 972-1702 g/dry tonne. Throughout this study 1360 g/dry tonne of A3338 was chosen as the optimal dosage for both FFTs.

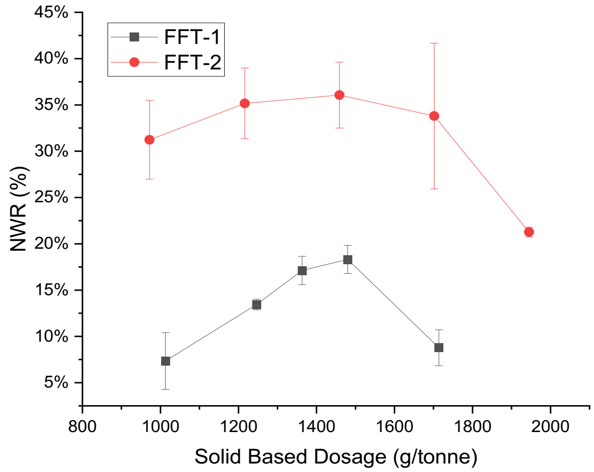

Figure 4. Dosage curves of two FFT treated with polymer A3338. Each dot is the average value of triplicate testing results. The error bars represent the 95% confidence index.

3.2 *Determination of lime dosage*

Previous studies have shown that FFT treatment using lime slurry to a pH of 12.4 and above likely allows for pozzolanic reactions to occur between the soluble calcium ions and the aluminates and silicates released during the partial dissolution of the clay minerals (Mosher et al. 2019). This mechanism helps develop a durable inter-particle matrix resulting in strength gain with time, unlike the anionic flocculant that appears to develop a weak and shear-sensitive structure (Fawell et al. 2015). Therefore, dosing lime to a pH above 12.4 of FFT is necessary to obtain the associated long-term strength and other target geotechnical characteristics. The response of pH and EC to the dosage curves of lime addition to the untreated FFT and flocculated samples are plotted in Figure 5. Lime addition increases the EC of the FFT samples from ~1000 microsiemen/cm (μS/cm) to 6000 – 8000 μS/cm and pH from ~8 to ~13 due to the presence of additional calcium and hydroxyl ions in FFT. The optimum dosage of lime for the FFT treatment was determined where the pH was higher than 12.4 and the EC of the treated FFT was stabilized. The EC stabilized at a higher dosage than required to stabilize the pH. Therefore, the lime dosage was selected to be the 6500 ppm lime by total wet weight of the FFT.

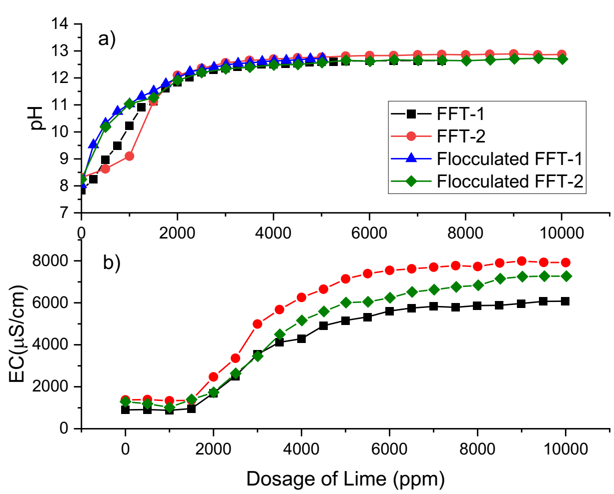

Figure 5. The response of pH and EC to the lime dosage on untreated and flocculated FFT samples.

3.3 *Treated FFT dewatering performance at high pressure level*

Figure 6 shows the photos of the compressed and remolded cakes of FFT-1 both before and after various treatments and after 1-hour pressing at 100 psi. The different pressures applied represented the two application scenarios investigated – high pressure filtration found to require a minimum of 100 psi and a more modest pressure scenario expected from the application of a sand cap (AER, 2021). The lower pressure scenario was ultimately selected for most of the work as pressure filtration is not yet commercial in oil sands. The untreated FFT-1 was still fluid with only a very thin compacted cake, the overall solids content was 52.07 wt%, while FFT-1 treated with A3338 polymer produced a sponge-like compressed cake with the solids content of 57.17 wt%. The lime treatment produced a thin semi-fluid layer on the very top of the cake and left the rest of the compacted cake with a solids content of 61.09 wt%. FFT-1 treated with the combination of A3338 and lime was completely dried by observation after 1 hour of pressing with a solids content of 74.06 wt%. These observations validated the findings in Figure 6 that lime treatment aids in further dewatering the polymer-treated FFT.

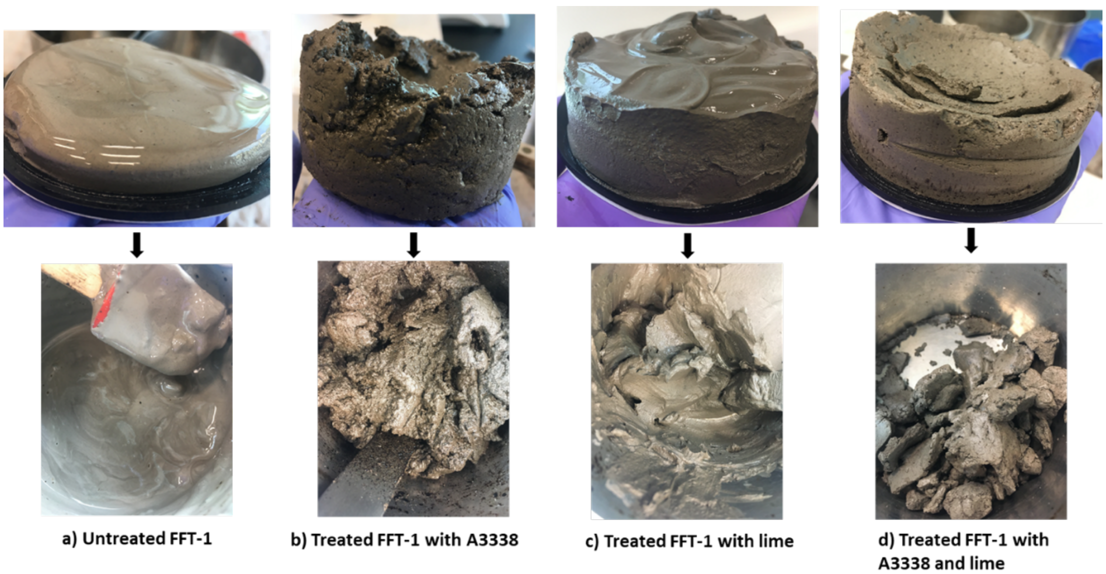

Figure 6 Photos of compressed cakes after pressing for 1 hour at and the corresponding remolded cakes obtained by: a) untreated FFT-1; b) treated FFT-1 with A3338; c) treated FFT-1 with lime; d) treated FFT-1 with A3338 and lime.

3.4 *Filterability to compare FFT dewatering performance with polymer and lime treatments*

Both FFT-1 and FFT-2 were treated with different additives; A3338 polymer at the optimal dosage, lime at the optimal dosage, and the combination of A3338 and lime at the respective optimal dosages. The treated FFT samples were pressed with the modified filter press at 20 psi along with the untreated FFT samples as a control test (Figure 7). The 20 psi of gas pressure was used as it is equivalent to about 5 meters of sand cap. All three types of treatment greatly increased the filtrate flow rate compared with untreated FFT indicating significant improvement in dewatering performance of treated FFT; however, the rate of dewatering vastly different suggesting that floculants, like A3338, and coagualnts, like lime, act in different mechanism to improve filterabiltiy.

The specific resistance to filtration (SRF) values of the treated FFT-1 and FFT-2 with different treatments were calculated and compared in Table 5 (Coulson, et al. 1991; Li, et al. 2018). The linear portions of the filtration flow curves in Figure 7 were chosen for the SRF calculation. The SRF values are consistent with the dewatering performance. The lime treatment dewatered the FFT faster than the A3338 polymer treatment indicating the lime-treated FFT had higher filterability than A3338 treated FFT. The treatment of the combination of A3338 and lime dewatered the FFT most quickly indicating lime assists with further improving the dewatering performance of polymer-treated FFT suggesting that it is possible to harness the dewatering benefits of both polymers and lime.

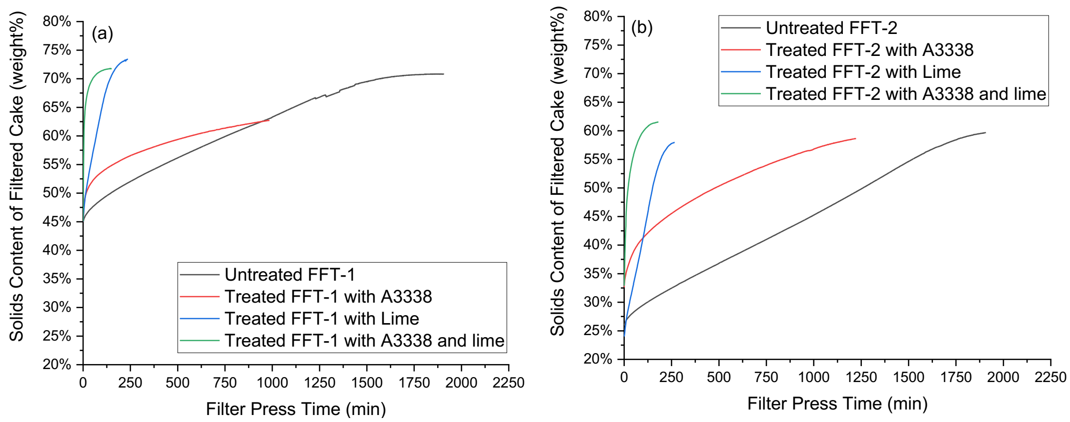

Figure 7. Filter press curves of FFT-1 (a) and FFT-2 (b) with different treatments at 20 psi. Each curve is the average of three sets.

Table 5. Calculated SRF values. The area of filter was 50.27×10^{-4} m^2; viscosity of filtrate was assumed as the same as water (1×10^{-3} Pa·s); concentration of FFT-1 was 614.41 kg/m^3; concentration of FFT-2 was 291.61 kg/m^3.

FFT	Treatment	Average SRF	Standard deviation
FFT-1	no treatment	7.9E+13	2.1E+12
	A3338	1.6E+14	1.8E+13
	Lime	9.6E+12	5.2E+11
	A3338+lime	6.0E+11	1.7E+11
FFT-2	no treatment	7.9E+13	3.0E+12
	A3338	1.3E+14	3.9E+12
	Lime	7.0E+12	4.8E+11
	A3338+lime	1.2E+12	8.9E+11

3.5 *Strength response with treatment and cure time*

The filter pressed cakes dewatered to the plateau of the solids content by the filter press at 20 psi were remolded and tested for peak undrained shear strength before and after curing for 70 days. As seen in Figure 7, the time required for the solids to plateau under 20 psi filtration was much longer for the samples that were not treated with lime. Pozzolanic reactions are time-dependent and thus strength of lime-treated materials develops gradually over a long period. The pozzolanic reactions, producing adequate amounts of cementitious compounds, resulted in visible peak undrained shear strength increases as expected (Dash & Hussain, 2012). As seen in Figures 8 and 9, peak undrained shear strength levels about 20 kPa or significantly higher were obtained with all of the lime treated samples after 70 days of curing compared to after initial dewatering. The untreated and polymer treated FFT samples had peaked undrained shear strengths below 20 kPa after 70 days despite higher solids levels for these samples. The strength difference seen with lime treatment appeared to be related to strength developed through pozzolanic reactions rather than dewatering in this study. There appeared to be a synergistic effect between polymer and lime addition with the lime and polymer samples having the highest strength before and after curing.

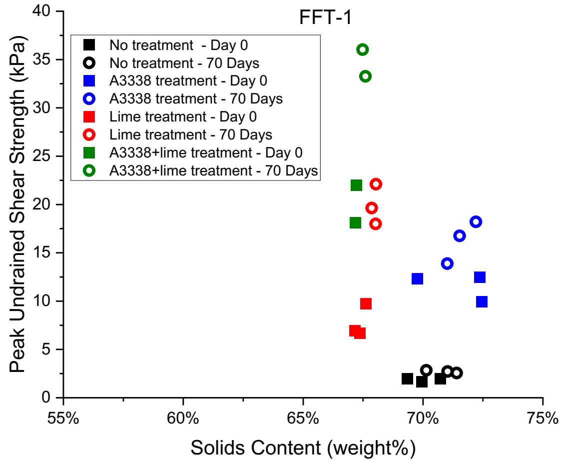

Figure 8. The peak undrained shear strength values and solids contents of filter pressed cakes with different treatments on FFT-1 before and after curing for 70 days.

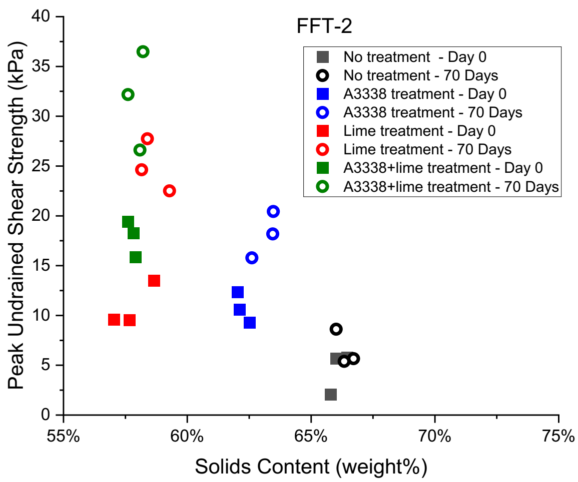

Figure 9. The peak undrained shear strength values and solids contents of filter pressed cakes with different treatments on FFT-2 before and after curing for 70 days.

4 CONCLUSION

The effect of lime stabilization on the untreated FFT and polymer flocculated FFT were investigated in this study through the characterization by pressure filtration dewatering and strength gain during a curing period of 70 days.

High pressure filtration for a fixed period of time suggest that lime treatment alone or in conjunction with polymer improves cake formation resulting in higher solids contents.

Tests run to simulate lower pressure from a sand cap showed that lime-treated samples have significant benefits in material properties. Lime-treated FFT showed peak undrained shear strength gains after curing for 70 days. The strengths obtained were significantly higher than those obtained from untreated and polymer only treated samples over 70 days despite lower solids levels for the lime treated samples. The strength results for FFT-2 were slightly higher than those for FFT-1. This could be related to presence of more reactive clays as indicated by the MBI's of these materials. Pozzolanic reactions rather than solids content appear to be the cause for the strength gain. Further investigation will be focused on the long term strength gain of the lime treated FFT to assist the dry upland reclamation.

The filter press sample preparation showed the lime treatment increased the filtering efficiency of both untreated FFT and flocculated FFT significantly. The lime treatment resulted in further dewatering of polymer treated FFT at a much faster rate. This indicated that lime treatment could be an alternative technology to improve the post-deposition solids and strength levels. This is expected to be particularly relevant for pressure filtration or centrifuge cake deposits.

5 REFERENCES

AER (Alberta Energy Regulator) 2021. Canadian Natural Jackpine mine 2020 fluid tailings management report.

ASTM (2008a) D4318: Test methods for liquid limit, plastic limit, and plasticity index of soils. *ASTM International*, West Conshohocken, PA, USA.

Bell, F.G. 1996. Lime stabilization of clay minerals and soils. *Engineering Geology* 42, 223-237.

Bowles, J.E. 1992. Engineering properties of soils and their measurement. New York: McGraw-Hill.

Choquette, M., Berube, M.A., & Locat, J. 1987. Mineralogical and microtextural changes associated with lime stabilization of marine clays from eastern Canada. *Applied Clay Science* 2(3): 215-232.

Clare, K.E. & Cruchley, A.E. 1957. Laboratory experiments in the stabilization of clays with hydrated lime. *Geotechnique*, 7(2), 97-111.

COSIA 2015. Unified fines method for minus 44 micron material and for particle size distribution. *COSIA Fines Measurement Working Group*.

Coulson, J.M., Richardson, J.F., Backhurst, J.R., Harker, J.H. 1991. Particle technology and separation processes. Chem. Eng. Vol. 2, 4th ed. Pergamon, Chapter 7.

Dash, S.K. & Hussain M. 2012. Lime stabilization of soils: reappraisal. *J. Mater. Civ. Eng.*, 24(6), 707-714.

Fawell, P.D., Costine, A.D., & Grabsch, A.F. 2015. Why small-scale testing of reagents goes wrong. *Proceedings of the 18th International Seminar on Paste and Thickened Tailings*, Australian Centre for Geomachanics, Perth, 153-165.

Kang, X., Bate, B., Chen, R.P., Yang, W., & Wang, F. 2019. Physicochemical and mechanical properties of polymer-amended kaolinite and fly ash-kaolinite mixtures. *J. Mater, Civ. Eng.* 31(6): 04019064.

Khattab, S.A.A., Al-Mukhtar, M., & Fleureau, J.M. 2007. Long term stability characteristics of a lime treated plastic soil. *J. Mater. Civ. Eng.* , 19(4), 358-366.

Lane, S. 1983. Lime coagulation and stabilization of total oil sands tailings. *Petroleum Society of Canada Annual Technical Meeting*, May 10-13, Banff, Alberta, Canada.

Li, Y., Kaminsky, H., Gong, X.Y., Sun, Y.S., Ghuzi, M., & Sadighian, A. 2021. What affects dewatering performance of high density slurry? Minerals, 11, 761.

Little, D.N. 1995. *Handbook for stabilization of pavement subgrades and base courses with lime.* The Lime Association of Texas.

Locat, J., Tremblay, H., & Leroueil, S. 1996. Mechanical and hydraulic behaviour of a soft inorganic clay treated with lime. *Can. Geotech. J.* 33: 654-669.

Mosher, B., Romaniuk, N., Fox, J., Hariharan, N., Leikam, J., & Tate M. 2019. High performance fine tailings dewatering with hydrated lime slurry. *Proceedings of Tailings and Mine Waste*, November 2019, Vancouver, Canada.

Neville, A.M. & Brooks, J.J. 2004. *Concrete technology*. 4th Indian reprint, Person education, Delhi.

Prakash, K., Sridharan, A., & Rao, S.M. 1989. Lime addition and curing effects on the index and compaction characteristics of a montmorillonitic soil. *Geotechnical Eng., AIT*, 20(1), 39-47.

Rogers, C.D.F. & Glendinning, S. 1996. Modification of clay soils using lime. *Lime Stabilization*: 99-114. London: Thomas Telford Publishing.

Rogers, C.D.F., Boardman, D.I., & Papadimitriou, G. 2006. Stress path testing of realistically cured lime and lime/cement stabilized clay. *J. Mater. Civ. Eng.,* 18(2), 259-266.

Sadighian, A., Revington, A., Kaminsky, H., Moyls, B., Li, Y., & Omotoso, O. 2018. A new protocol to assess the quality of tailings flocculation/coagulation: a collaboration to improve tailings treatment at Suncor Energy. *IOSTC 2018*, Edmonton, Canada.

Tran, T.D., Cui, Y.G., Tang, A.M., Audiguier, M., & Cojean, R. 2014. Effects of lime treatment on the microstructure and hydraulic conductivity of Hericourt clay. *Journal of Rock Mechanics and Geotechnical Engineering* 6(5): 399-404.

Ageing in soft soils and clayey tailings

Arazoo Patel, Abdulghader A. Aldaeef & Paul Simms
Carleton University, Ottawa, Canada

ABSTRACT: "Ageing" here refers to increase in strength and pre-consolidation pressure independent of density. This phenomenon can induce significant changes in mechanical properties of reconstituted soft soils, or freshly deposited sediments, or clayey oil sands tailings. Ageing increases the peak strength and post-peak strength, while reducing the compressibility of affected soils due to an increase in apparent pre-consolidation pressure. This may be very important for the settlement and strength development characteristics of deep deposits of tailings or re-deposited soft soils of low hydraulic conductivity where slow consolidation over a long period can be influenced by ageing. This paper reports experimental results on the magnitude and rate of ageing from both tailings (flocculated fluid fine tailings, centrifuge cake) and soils (Leda Clay). Of specific interest to oil sands tailings is the effect of different flocculation protocols on the magnitude of ageing.

1 INTRODUCTION

Consolidation is the dominant mechanism affecting long term dewatering of many types of tailings, and is usually analyzed by large strain consolidation theory, employing constant compressibility (e - σ'_v) and hydraulic conductivity (k-e) functions, the former function defining the stiffness as a function of density, the later the capacity for flow as a function of density. For tailings management, the compressibility function can be used to predict the final distribution of density with depth (e.g. Qi and Simms 2019) and the expected magnitude of settlement, while *k-e* controls the rate of settlement.

Other processes, however, may influence tailings behaviour to a degree that they deserve consideration in tailings impoundment design. Creep and ageing have been found to influence the consolidation performance of tailings deposits (Jeeravipoolvarn, 2005; Jeeravipoolvarn et al., 2009; Miller, 2010, Salam 2020). Creep, the capacity of soil to deform at a constant effective stress, has been long studied in the geotechnical literature and several models for creep-consolidation exist literature (e.g. Yin and Graham, 1994; Vermeer and Neher, 1999; Hinchberger and Rowe, 2005); example application of creep-consolidation models to tailings impoundments can be found in Gheisari et al. (2020, 2019). Some controversary exists over this phenomenon, but a "giveaway" of its role can be clearly seen where stress relaxation occurs – this is where PWP holds or actually increases over time as a soil deforms.

The focus of this paper is ageing, or the increase in pre-consolidation pressure over time. Ageing and destructuration is mostly studied in the soil mechanics literature with reference to differences in compressibility and strength between the intact and reconstituted states of natural clays (Locat and Lefebvre, 1986; Leroueil and Vaughan, 1990; Burland, 1990; Liu and Carter, 1999; Sorensen, 2006), which bears practically on appropriate laboratory procedures to evaluate settlement and strength in those deposits. Rate of ageing is less important to natural clays; however, freshly deposited tailings, dredged sediments, or similar materials are by their very nature "young" materials, and therefore information on their ageing may be required to correctly estimate their long-term consolidation behaviour.

Changes in the compression curve over time have been studied by Zeng et al. (2016) for dredged sediments, and by Salam (2020), Jeeravipoolvarn (2005), Jeeravipoolvarn et al. (2009), and Miller (2010) for different kinds of tailings. Ageing is sometimes correlation with thixotropy (the recovery of strength independent of density changes after remoulding), and we will see the changes in the compression curve are strongly correlated with undrained shear strength.

Generally, the rate of ageing or strength/stiffness development in clays has been observed to be dependent on time (Skempton and Northey, 1952). Interestingly, outside of the soil mechanics literature, ideal suspensions of artificial clays such as Laponite are studied in great depth to understand ageing behaviour in colloidal suspensions (Abou et al., 2001; Ruzicka et al., 2007; Pujala and Bohidar, 2013; Au and Leong, 2015). Ageing is understood to progress from a metastable state, that may be induced either by shearing a colloidal suspension or by rapidly changing its concentration or temperature. Ageing occurs in such systems through either actual movement or rotation of particles, which are influenced by electro-chemical forces, and may form different types of structures, from large flocs to sample spanning networks; or from increases in the strength of existing contacts (Bonacci et al., 2020). Ageing may occur in either repulsion dominated systems (termed glasses), or attraction dominated suspensions (gels). Generally, the rate of ageing, and the increase in strength, increases with the increasing magnitude of net inter-particle electrical chemical forces (Tanaka et al., 2005; Mewis and Wagner, 2012) and with increasing concentration of solids (decreasing void ratio or water content) (Abou et al., 2001; Pujala and Bohidar, 2013; Au and Leong, 2015). In soils, the magnitude of thixotropy is known to increase with decreasing water content in tailings (Banas, 1991; Suthaker, 1995) and in soils (Skempton and Northey, 1952; Seng and Tanaka, 2012), down to the liquid limit, but then subsequently decreases. Evidence of ageing in flocculated fluid fine tailings pilots is seen in terms of increases in sensitivity and shifting of the in-situ compressibility function (Gheisari et al. 2019).

Practically, the potential importance of ageing is the shift in the compressibility function such that tailings will stabilize at a higher void ratio for a given effective stress, meaning that i) the average density of a given deposit at the end of consolidation with be lower, ii) the magnitude of settlement and time to complete settlement will be lower, iii) the average remoulded undrained shear strength will be lower (because of lower density) but the undrained peak strength will be higher. These implications can be negative or positive for a specific deposition scenario. For example, for some aquatic deposition scenarios, less settlement and early completion of settlement would be desirable in order to limit fluxes of water generated by consolidation to the water cover.

This paper will summarize experimental and numerical work on ageing in polymer flocculated fluid fine tailings (fFFT) and in Leda clay – the second material is used as it somewhat similar to FFT (similar mineralogy, Atterberg limits), it does not require application of polymers and so samples can be reused, and it is well-studied in the geotechnical literature for many decades.

2 MATERIALS AND METHODS

2.1 *fFFT*

2.1.1 *Characteristics of the FFT used this study*

Tailings were collected from a pond in Northern Alberta, Canada, and shipped to Carleton University in Ottawa, Canada. The initial solids content was 31% and the liquid limit was 60%. The sands to fine ratio (SFR) was 0.25. The clay content obtained from the Methylene Blue Index (MBI) analysis ranged from 28% to 32%. According to the X-ray diffraction (XRD) results, the composition of the clay fraction was 68-72% Kaolinite and 28-32% Illite. Total Dissolved Solids (TDS) in the pore water collected from the raw fluid fine tailings (rFFT) was 1050 mg/L, electrical conductivity was 1590 microS/cm, while the dominant cations were sodium at 340 mg/L. Typical material characteristics of the tailings used are listed in Table 1.

Table 1. Physical properties of the raw fluid fine tailings parameters

Characteristic	Ave. Value
Initial solids content (%)	31
Initial water content (%)	220
Hydrocarbons content (%)	1.4
Specific gravity	2.12
Liquid limit (%)	60
Plastic limit (%)	27
Plasticity index (%)	33

2.1.2 *Polymer Stock Solution*

Polymer A3338 (SNF), an anionic polyamide based flocculent, was used to prepare the polymer amended oil sands tailings samples. In a plastic weighing dish, 4 g of A3338 polymer (for the preparation of 0.4% polymer stock solution) was weighed using an analytical balance (Fisher Scientific, Sartorius AG Germany, LE225D) and decanted into a 1500 mL glass beaker and completed to 1000 mL with deionized water. The polymer solutions were stirred using a jar tester (Phipps and Bird, USA) at 200 rpm for 5 minutes and at 125 rpm for the following 55 minutes. Then the polymer solution was left for maturation for 1 hour.

2.1.3 *Flocculation protocols*

Four different flocculation protocols were employed, which are described in Table 2. The protocols either employ a four bladed impeller in an open pail, or use a couette rheometer. Additional variables are the rate of polymer solution injection (one shot versus controlled constant flow rate over ~ 6s) and the flocculation control (fixed time or use of torque feedback). The fourth protocol also employs a pipeline transport simulation step after flocculation. More details on specifics of the protocols can be found in Aldaeef et al. (2020), here the purpose is to create differently performing fFFT samples based on the mixing protocol alone.

Table 2. Flocculation protocols

Protocol	**Pro#1**		**Pro#2**	**Pro#3**	**Pro#4**	
	Fixed mixing time		Torque feedback (stopped immediately after peak)		Torque feedback plus pipeline transport simulation step	
Mixing vessel	270 mm Diameter, 5 litre sample		200 mm diameter, 5 litre sample	Couette rheometer, 1 litre sample	Couette rheometer, 1 litre sample	
Impeller fixture	4-bladed vane; Dia. 160 mm and height of 10 mm.			Couette bobbin; Dia. 76 mm and height of 110 mm.		
Gap Ratio	0.80		0.59	0.66	0.66	
Polymer addition	One-shot		Constant flow rate for ~ 6s		Constant flow rate for ~6s	
Rotational Speed (RPM)	320	20	250		250	35
Mixing time (Sec)	10	10	varies		Varies	1560

2.2 *Leda Clay*

The properties of the Leda Clay is given in Table 3. The clay is similar to FFT in terms of Atterberg limits and mineralogy (the same dominant clay minerals), though the clay content is much higher (70% compared to ~30 % in the FFT), and the proportion of the dominant minerals is different.

Table 3. Leda Clay properties

Parameters	Value
Specific gravity	2.7
Liquid limit (%)	51
Plastic limit (%)	28
Plasticity index (%)	23
Clay content (%)	71
D_{90}, D_{60}, D_{50}, D_{10} (μm)	10, 1, <1, <1
Clay mineralogy	Illite (83%), Kaolinite (11%)

The Leda clay samples were all prepared by the same protocol. Samples of Leda clay, which here were initially at water contents near their liquid limit, were placed in a metal dish and disturbed through kneading for 45-50 minutes to obtain a soft plastic remoulded material. Subsequently a pre-determined amount of distilled water was added to reach targeted water content and hand-mixed again for another 50-52 minutes. Samples were then stored in air-tight container for 72 hours to promote homogeneous distribution of water content. The samples were then hand-mixed again for 15 minutes before transferring to PP columns.

2.3 Experimental methods

The flocculated or remoulded samples were placed in sealed in 10 cm diameter 10 cm tall polypropylene (PP) columns. Large batches were created in order to generate many columns for multiple tests, including i) Monitoring of settling using Fall cone tests (Hansbo 1957) ii) G' measurement using an oscillatory rheometer (Mizani et al. 2017) iii) standard oedometer tests using samples obtained by cutting the propylene columns and obtaining sub-samples using a fine wire saw. Destructed sample were also used to determine water and organic content by oven drying. fFFT specimens were also subsampled to perform high powered optical microscopy, within 10 minutes of sample generation.

3 RESULTS

3.1 *fFFT*

The four flocculation protocols produced tailings with substantially different appearance in optical microscopy. Protocol 2 produced the largest flocs. Protocol 1 and 3 produced flocs of comparable size, but the images produced from Protocol 3 samples were consistently darker, perhaps indicating a higher concentration off dispersed finer particles. Protocol 4, the protocol with the transport simulation step, clearly produced the smallest flocs

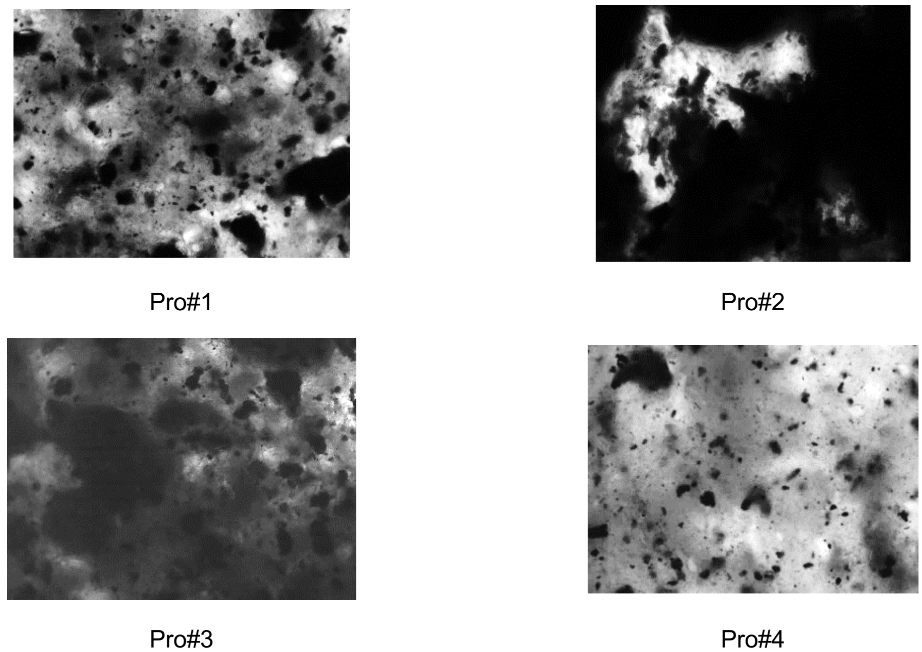

Figure 1. Microscope images for samples of different mixing protocols (image width 650 microns)

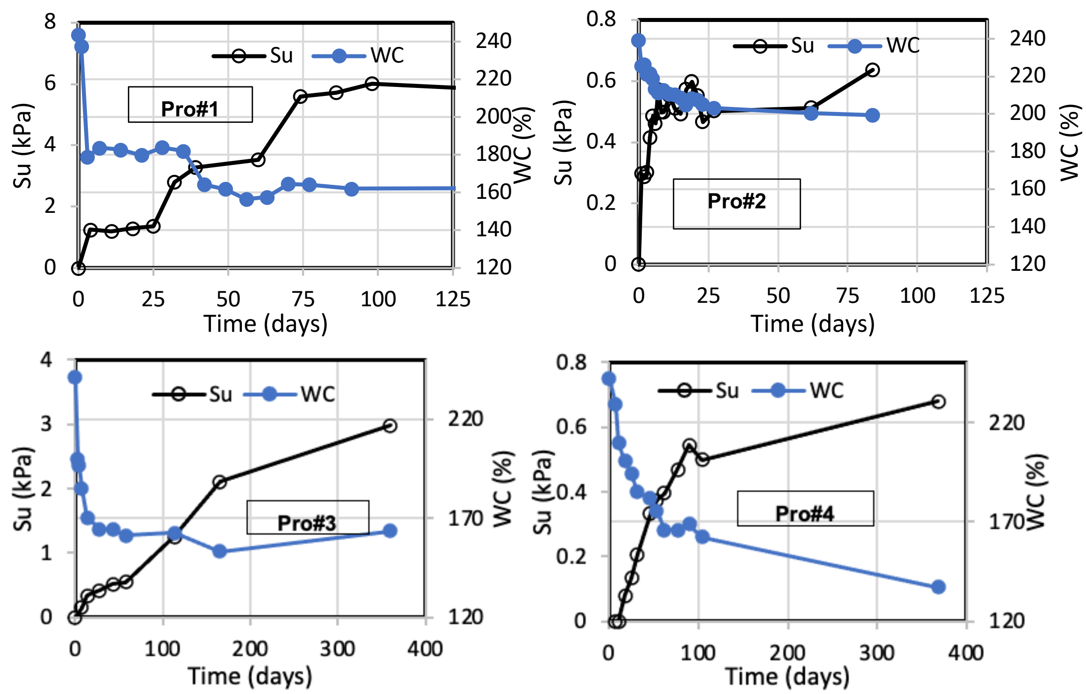

Figure 2. Average water content and shear strength from Fall Cone

Each sample also had different rates of both dewatering and strength gain. The tailings with the largest flocs (Pro#2) had both the slowest initial (over 2 days) and smallest long term dewatering, and along with Pro#4 the lowest shear strengths. Pro#4 had slow initial dewatering but the largest long-term dewatering. Pro#1 gives the fastest short term dewatering, after which the water content stabilizes for about 40 days, and produces the largest strengths. Pro#3 has comparable long term dewatering to Pro#1, but the rate of short term dewatering is slower, and the strength development is slower than for Pro#1.

As shown by Salam (2020), the undrained shear strength measured by fall cone is strongly correlated to the pre-consolidation pressure developed by ageing: Salam (2020) observed a ratio of fall cone shear strength / pre-consolidation pressure of 0.18, which is close to the value determined by Mesri (1975) for clays (0.22). Figure 3 shows that substantially different compressibility curves are generated by the different flocculation protocols. Similarly to the dewatering in the short 10 cm tall column, the compressibility of the Pro # 4 is the softest, while Pro#1 and #3 are much stiffer. How this potentially translates to end of consolidation state is shown in Figure 4, for a hypothetical 50 m deep deposit with an initial void ratio of 5.2, using method of Qi and Simms (2019). Clearly, there is a substantial difference in the magnitude of settlement and the distribution of density. Protocol #4 tailings will also clearly produced the deposit with the highest remoulded shear strength; however the peak strength in the hypothetical deposit for the Pro#1 tailings could be higher.

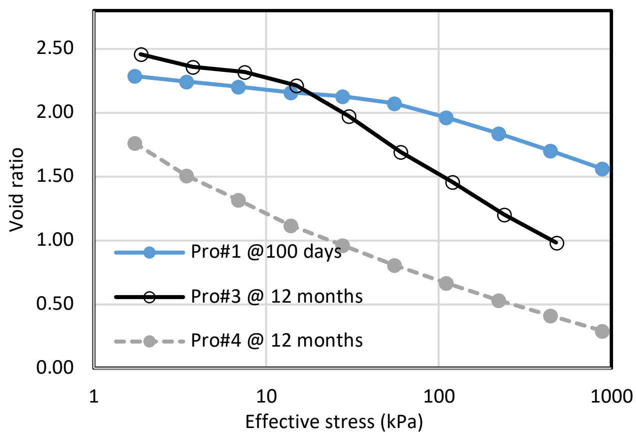

Figure 3. Compressibility from oedometer with 24 hour loading steps

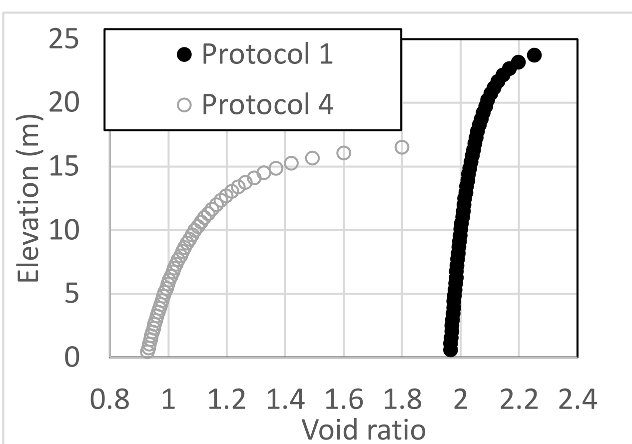

Figure 4. End of consolidation depth profiles, for an initial void ratio of 5.2 and an initial height of 50 m, calculated using compressibility curves measured at 12 months using an oedometer

While the implications of the effect of flocculation protocol are potentially important, however, what controls the magnitude of ageing in these tests? Both protocols that show strong strength generation and high pre-consolidation pressures developed by ageing show a certain degree of initial dewatering, followed by a plateau of relatively stable water content – for Pro#3 the decrease to the plateau takes longer than for Pro#1, and it appears the k-e function for Pro#3 must be somewhat smaller. The difference, at least for this particular dosage and polymer, is that the conditioning step seems to have decreases the residual dispersed fines, allowing for higher k-e and for quicker progress the plateau stage. Interestingly, for ageing there seems to be an optimum in terms of floc size. Pro#2 tailings have the largest flocs, but the tailing stabilize at a much higher water content, while Pro#4 with the smallest flocs is the most compressible and dewaters almost continuously.

3.2 *Leda Clay*

Data from Leda clay samples at water contents starting at twice and 1.5 times the liquid limit are shown. Leda Clay samples generally dewater ~ 5% in the first 3 to 5 days, but then the samples remain stable at the water contents shown in the legend of Figure 5. In Figure 5 the data from Salam (2020) is published previously, while the other two plots are new data found by a new student using a different batch of Leda clay. The figure shows the dependence of ageing on the water content, and provides some support for repeatability. By the time of the conference, the full data set for =85% will be available.

The Leda Clay data shows the same pattern as Pro#1,#2, and #3, where there an initial increase in strength, followed by a plateau, followed by a subsequent increase in strength. Data for the Salam case actually extends for a year, but the strength peaks at the ~100 days data shown in Figure 5 and maintains that value.

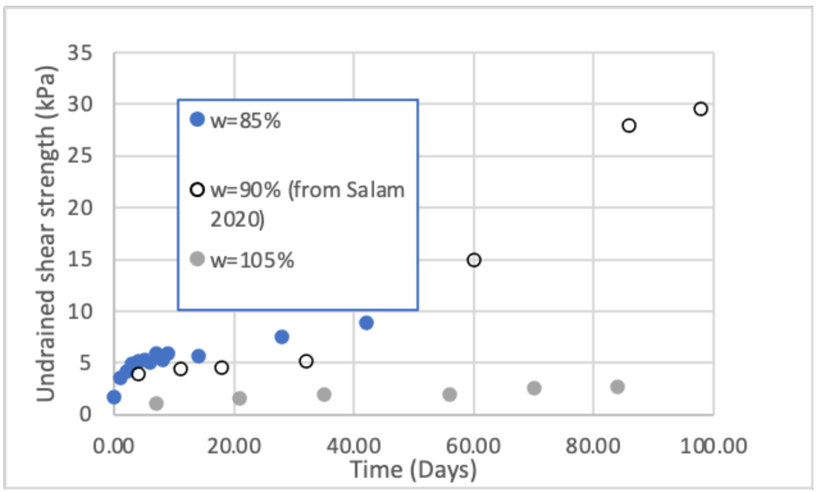

Figure 5. Ageing data for Leda Clay at different water contents

Also included in this paper are two tests on Leda Clay that show both the reversible and recoverable nature of the strength gain by ageing. Figure 6 shows G’ data obtained through oscillatory rheometer, which essentially oscillates the material at a stress range to measure the elastic properties of the materials, G’ being the elastic shear modulus – more details on this method and its application to tailings can be found in Mizani et al. (2017). G’ is also found to correlate linearly with undrained shear strength, though the correlation is different for the samples prepared at different water contents. For example, G’ is about 10 and 20 times the undrained shear strength for the 105% and 85% sample respectively. Figure 6 shows the recovery of G’ for samples remoulded after 14 days of ageing. Though the magnitude of G’ is different, the rate of recovery of both samples is very close, both recovering the original value at about 7 days after remoulding. The change in water content over this time is small (~1.5%). This clearly shows that the nature of the bonding is recoverable and therefore not due to some specific cementation mechanism.

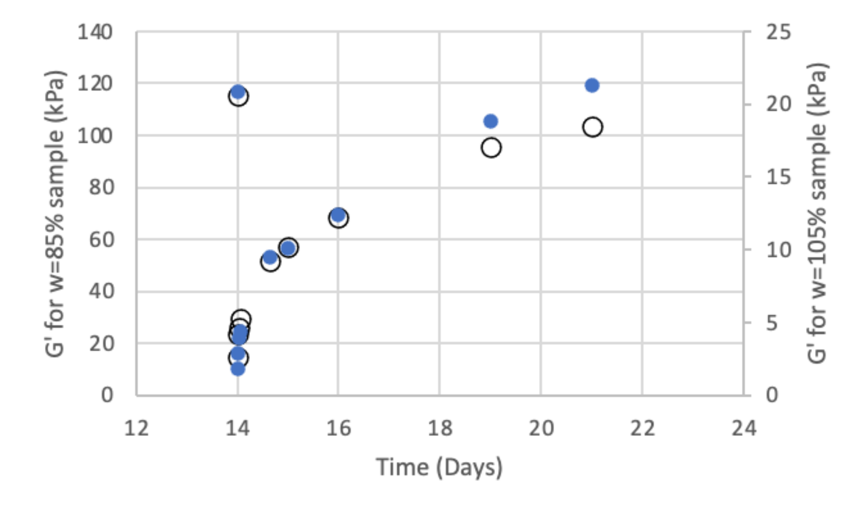

Figure 6. Change in G’ (Elastic shear modulus) after remoulding Leda clay samples at 14 days

4 DISCUSSION

There are some common trends in both the fFFT and Leda Clay samples. For all samples showing significant ageing, there are two distinct phases. The first is characterized by an increase in the shear strength over days to two or three weeks, followed by a period where the shear strength does not increase. This is followed by a second phase of ageing. In general, it appears that the strength at the end of the first phase is a good predictor of the final ageing strength. For Pro#1, Pro#3, and the Leda Clay samples, the final ageing strength appears to be about 5 (6-4) times the strength achieved at the first phase. Therefore, indication of the magnitude (or absence) of ageing can likely be assessed in relatively short tests (less than a month as opposed to the year long tests reported in this paper).

It might be tempting to presume that Pro#4 might be the “best” for many deposition scenarios due to its high dewatering in the 10 cm column, and its high compressibility in the oedometer samples. But k-e should also be considered. For example, using the initial surface fluxes measured in the 10 cm columns, the equivalent surface fluxes can be estimated (Simms 2021) for deposits of any depth. For 25 m of settlement the Pro#4 tailings would require ~140 years of settlement, but the Pro# 3 tailings would require only 35 years. These numbers are rough approximations, but should give a sense of the relative settlement time.

Another question would be how best to determine in a particular tailings, created at full scale, would age. Due to the strong correlation of G’ with shear strength (and therefore preconsolidation pressure as well), and the ability to measure G’ with minimal disturbance, this parameter could be the best index for monitoring tailings as they emerge from the deposit.

5 CONCLUSIONS

1. On the same tailings, differences in flocculation protocol produced substantially different performance in terms of ageing, short and long term dewatering, and shape of the compressibility curve. The differences in the compressibility curve are sufficient to cause substantial changes in the final post-consolidation depth and density profile of a tailings deposit.
2. High shear strength development by ageing and stiffer compressibility curves were associated with i) medium floc size, ii) rapid initial dewatering followed by some time where the rate of dewatering is small. The flocculation protocol with the smallest floc size generated the most long term dewatering and most compressible tailings, but these

tailings likely also had a much lower k-e, as so would take much longer to settle in a real deposit. The tailings with largest flocs had the least dewatering.

3. Tests on Leda Clay show the magnitude of ageing is strongly dependent on water content: samples at 1.5x LL showed much larger increase in shear strength then samples at twice the LL
4. Ageing is both reversible and recoverable. Leda Clay samples at the two different water contents show almost identical rates of recovery in shear strength after remoulding.

6 ACKNOWLEDGEMENTS

This work is supported by an Collaborative Research and Development Grant, jointly funded by COSIA and the Natural Sciences and Engineering Research Council of Canada.

7 REFERENCES

Abou, B., Bonn, D., & Meunier, J. (2001). Aging dynamics in a colloidal glass. *Physical Review E*, *64*(2), 021510.

Aldaeef, A. A., & Simms, P. H. *). Evaluation of Polymer Feed Rate, Polymer Dose, and Mixing Duration for Flocculation Optimization of Clayey Tailings with Various Solid Contents. Geovirtual 2020, Calgary, CA.

Au, P. I., & Leong, Y. K. (2015). Surface chemistry and rheology of Laponite dispersions—Zeta potential, yield stress, ageing, fractal dimension and pyrophosphate. *Applied Clay Science*, *107*, 36-45.

Banas, L. C. (1991). *Thixotropic behaviour of oil sands tailings sludge* (Master's thesis). The University of Alberta, Edmonton, Alberta.

Bonacci, F., Chateau, X., Furst, E. M., Fusier, J., Goyon, J., & Lemaître, A. (2020). Contact and macroscopic ageing in colloidal suspensions. *Nature Materials*, 1-6.

Boone, S. J. (2010). A critical reappraisal of "preconsolidation pressure" interpretations using the oedometer test. *Canadian Geotechnical Journal, 47*(3), 281-296.

Burland, J. B. (1990). On the compressibility and shear strength of natural clays. *Géotechnique, 40*(3), 329-378.

Casagrande, A. (1936). The determination of pre-consolidation load and it's practical significance. In *Proc. Int. Conf. Soil Mech. Found. Eng. Cambridge, Mass., 1936* (Vol. 3, p. 60).

Gheisari, N., Qi, S., & Simms, P., Consolidation–creep modeling of pilot data on deposition of flocculated fluid fine tailings, GeoVirtual 2020.

Gheisari, N., Salam, Muhammad., Qi, S. & Simms, P., Structuration in natural clays, dredged sediments and oil sands tailings, Geo St. John's, 2019.

Graham, J., Crooks, J. H. A., & Bell, A. L. (1983). Time effects on the stress-strain behaviour of natural soft clays. *Géotechnique, 33*(3), 327-340.

Hinchberger, S. D., & Rowe, R. K. (2005). Evaluation of the predictive ability of two elastic-viscoplastic constitutive models. *Canadian Geotechnical Journal, 42*(6), 1675-1694.

Jeeravipoolvarn, S. (2005). *Compression behaviour of thixotropic oil sands tailings* (Master's thesis). The University of Alberta, Edmonton, Alberta.

Jeeravipoolvarn, S., Scott, J. D., & Chalaturnyk, R. J. (2009). 10 m standpipe tests on oil sands tailings: long-term experimental results and prediction. *Canadian Geotechnical Journal, 46*(8), 875-888.

Koumoto, T., & Houlsby, G. T. (2001). Theory and practice of the fall cone test. *Géotechnique*, *51*(8), 701-712.

Leroueil, S., & Vaughan, P. R. (1990). The general and congruent effects of structure in natural soils and weak rocks. *Géotechnique, 40*(3), 467-488.

Liu, M. D., & Carter, J. P. (1999). Virgin compression of structured soils. *Géotechnique, 49*(1), 43-57.

Locat, J., & Lefebvre, G. (1986). The origin of structuration of the Grande-Baleine marine sediments, Québec, Canada. *Quarterly Journal of Engineering Geology and Hydrogeology, 19*(4), 365-374.

Mayne, P. W., Cargill, E., & Miller, B. (2019). Geotechnical characteristics of sensitive Leda clay at Canada test site in Gloucester, Ontario. *AIMS Geosci*, *5*, 390-411.

Mesri, G. (1975). New design procedure for stability of soft clays. *Journal of Geotechnical and Geoenvironmental Engineering*, *101*(Discussion).

Mewis, J., & Wagner, N. J. (2012). *Colloidal suspension rheology*. Cambridge University Press.
Mielenz, R. C., Schieltz, N. C., & King, M. E. (1953). Thermogravimetric analysis of clay and clay-like minerals. *Clays and Clay Minerals*, *2*(1), 285-314.
Miller, W. G. (2010). *Comparison of geoenvironmental properties of caustic and noncaustic oil sand fine tailings*. (Ph.D. Thesis, the University of Alberta).
Mitchell, J. K. (1960). Fundamental aspects of thixotropy in soils. *J. of the Soil Mechanics and Foundations Division, 86*(3), 19-52.
Mizani, S., Simms, P., & Wilson, W. (2017). Rheology for deposition control of polymer-amended oil sands tailings. *Rheologica Acta, 56*(7-8), 623-634.
Pujala, R. K., & Bohidar, H. B. (2013). Slow dynamics, hydration and heterogeneity in Laponite dispersions. *Soft Matter*, *9*(6), 2003-2010.
Qi, S., & Simms, P. (2019). Robust methods to estimate large-strain consolidation parameters from column experiments. *Canadian Geotechnical Journal, 57*(5), 683-705.
Quigley, R. M., & Thompson, C. D. (1966). The fabric of anisotropically consolidated sensitive marine clay. *Canadian Geotechnical Journal, 3*(2), 61-73.
Ruzicka, B., Zulian, L., & Ruocco, G. (2007). Ageing dynamics in Laponite dispersions at various salt concentrations. *Philosophical Magazine*, *87*(3-5), 449-458.
Salam, A. M. (2020). *Effects of Polymers on short-and long-term dewatering of oil sands tailings* (Doctoral dissertation, Carleton University).
Simms, P. (2021). Personnel communication.
Seng, S., & Tanaka, H. (2012). Properties of very soft clays: A study of thixotropic hardening and behavior under low consolidation pressure. *Soils and Foundations*, *52*(2), 335-345.
Skempton, A. W. & Northey, R. D. (1952). The sensitivity of clays. *Geotechnique 3, No. 1*, 30-53.
Sorensen, K. K. (2006). *Influence of viscosity and ageing on the behaviour of clay*s (Doctoral dissertation, University College London).
Suthaker, N. N. (1995). *Geotechnics of oil sand fine tailings* (Doctoral dissertation). The University of Alberta, Edmonton, Canada.
Tanaka, H., Jabbari-Farouji, S., Meunier, J., & Bonn, D. (2005). Kinetics of ergodic-to-nonergodic transitions in charged colloidal suspensions: Aging and gelation. *Physical Review E, 71*(2), 021402.
Theenathayarl, T. (2015). *Behaviour of sensitive Leda clay under simple shear loading* (Doctoral dissertation, Carleton University).
Vermeer, P. A., & Neher, H. P. (1999). A soft soil model that accounts for creep. *Beyond 2000 in computational geotechnics*, 249-261.
Yin, J. H., & Graham, J. (1994). Equivalent times and one-dimensional elastic viscoplastic modelling of time-dependent stress-strain behaviour of clays. *Canadian Geotechnical Journal, 31*(1), 42-52.
Yong, R. N., & Nagaraj, T. S. (1977). Investigation of fabric and compressibility of a sensitive clay. In *Proceedings of the international symposium on soft clay, Asian Institute of Technology* (pp. 327-333).
Zeng, L. L., Hong, Z. S., & Cui, Y. J. (2016). Time-dependent compression behaviour of dredged clays at high water contents in China. *Applied Clay Science, 123*, 320-328.
Zhang, X. W., Kong, L. W., Yang, A. W., & Sayem, H. M. (2017). Thixotropic mechanism of clay: A microstructural investigation. *Soils and Foundations*, *57*(1), 23-35.

On thixotropy of flocculated mature fine tailings: rheometry and lumped structure parameter modelling

Arno Talmon
Deltares & Delft University of Technology, Delft, The Netherlands

Ebi Meshkati & Thijs van Kessel
Deltares, Delft, The Netherlands

Tim Lelieveld & Pavan Goda
Delft University of Technology, Delft, The Netherlands

Milana Trifkovic
University of Calgary, Alberta, Canada

ABSTRACT: Microscopic knowledge of polymer-MFT interaction is important to flocculation and to the modelling of physical properties of flocculated tailings. The rheology, rooted in micro structure, is needed for the modelling of fluid flow in hydraulic transport and for an understanding and quantification of deposition in TSF's. The rheology of flocculated MFT is time- and shear-dependent. Time-dependency consists of irreversible decay (rheomalaxis) and of reversible (thixotropy) properties. The paper describes mixing, rheometry and the capturing of rheology and its time-dependency by the Houska model which uses a lumped structure parameter for time-dependent behavior. Energy dissipation and strength development whilst mixing a flocculant into MFT is quantified to ultimately enable comparisons with prototype conditions in thickener, pipe and deposit. Time-dependency is captured using existing simple non-Newtonian rheological formulations as a basis and a time-dependent, structure dependent, component is added to facilitate a stepwise development in complexity. We show that using lumped structure parameter modelling, the shear and time dependency of both recoverable (thixotropy) and irrecoverable (rheomalaxis) strength in flocculated MFT can successfully be replicated.

1 INTRODUCTION

Polymer flocculated mature fine tailings is created by flocculating mature fine tailings (MFT) with high molecular weight flocculants through a delicate mixing process. This is a common practice used for thickening (strengthening) and accelerating the rate of dewatering in tailings. Reliable quantification of the strength and flow behavior in treated tailings such as flocculated MFT is key to tailings management. Quantification is a rather challenging task because of, first, peculiarity in flow behavior of base material (i.e. MFT), and second, enhanced shear and time-dependency of strength in flocculated MFT originating from polymer amendment. Rheology is often used to quantify flow behavior of tailings. The importance of rheology resides not only in the mixing operation during flocculation process but also in dredging, hydraulic transport and deposition. Previous studies suggest that microscopic alteration of physicochemical properties of clay rich substances affect their macroscopic properties (e.g. Hamza et al. 1996, Mizani et al. 2013, Sasar et al. 2021). Identifying microscopic properties requires dedicated laboratory techniques amongst many such as mercury intrusion porosimetry (MIP), scanning electron microscopy (SEM) and laser scanning confocal microscope (e.g. Govedarica et al. 2020). These techniques, although well established, demand skills, time and can be costly. Moreover, they generally serve to study the material properties and yet do not provide insight into flow behavior. Alternatively, lumped-parameter mathematical models are developed aimed to capture the complex effect and interdependence of microscopic properties into a single parameter, relying on their macroscopic flow behavior. These models predict the structural state in a medium as function of time and shear or in other words dissipated energy in the medium. Such models can be used to predict the flow behavior of treated tailings across different scales, usually indicated by lambda structural parameter (λ). Examples for such models are Moore (1959), Houska (1980) and Toorman (1994). These models are also known as thixotropic models. Thixotropy concerns time dependency of strength in a material under a constant shear and or regeneration of strength at rest (Mewis & Wagner 2009). From an operational perspective using such models one can for instance estimate the strength of flocculated MFT at the end of a mixing operation, a transport pipeline and downstream at the plunge pool. In this paper, the flow behavior of flocculated MFT is examined by means of rheometry, as an attempt to shed light on flocculated MFTs recoverable and irrecoverable (rheo-malaxis) strength characteristics from the viewpoint of dissipated energy per unit volume of flocculated MFT. The conducted rheometry study includes different rheological protocols (sweeps and stepwise) and testing modes: controlled shear rate (CSR) and controlled shear stress (CSS). The Houska (thixotropic) model is used to study the time and shear dependency of flocculated MFT across different structural states (scales). The model is then used to quantify the time scale of strength decay (as a function of shear rate) and strength recovery (as a function of resting time) in flocculated MFT.

2 THEORY

This Section addresses reversible (thixotropic) and irreversible strength properties of MFT in relation to internal flocculated structure. It introduces a concept of lumped parameter modelling for structure, builds on common characterization of rheology, whilst pointing to strong time-dependency effects and concludes with combining this common characterization with lumped structure parameter modelling: the Houska thixotropic rheological model.

2.1 *Time and shear dependent flow behavior*

The time and shear dependency of viscosity, defined as resistance against flow in polymer amended treated tailings such as flocculated MFT are studied in the literature (e.g. Mizani et al. 2017). In this context, shear dependency of such material usually refers to their shear thinning flow behavior: reduction of their viscosity with increasing shear (strain) rate. Time dependency, on one hand, refers to temporal reduction in viscosity under a constant shear (strain) rate and on the other hand, temporal gain in strength at rest. Thus, time dependency consists of two components of destruction (decay of strength/viscosity) and restructuration (recovery of strength/viscosity) of a material's fabric. The term thixotropic behavior is another term for time dependent flow behavior.

2.2 *Lumped parameter modelling and λ structure parameter*

Time dependent flow behavior in a substance is a resultant of various microscopic factors, their interaction and interdependence, amongst many, such as: concentration, shape and size distribution of their constituents. A comprehensive modelling of thixotropy can be a complicated undertaking as it demands detailed knowledge on microscopic physiochemical and mineral properties of the substance (Merckelbach 2000). To overcome extreme complexity of the problem, lumped parameter mathematical modelling is used as a global approach to thixotropic modelling. In this modelling approach, the effect, interaction and interdependence of microscopic details all are simply summarized into a single overarching parameter so called structure parameter (λ). This parameter quantifies the state of structure in the substance: λ equals unity when the fluid is fully built up and intact, λ equals zero when the fluid is fully broken up (Moore 1959). Hence, the parameter λ can be related to the strength in a substance as it specifies the structural connectivity of the substance fabric (Merckelbach 2000).

2.3 *Structuration and internal geometry of flocculated MFT*

For the sake of simplification in understanding and modeling of the mechanical behavior of flocculated FMT, it is assumed that its geometrical internal structure is similar across different scales. The self-similarity of the geometrical structure implies the presence of a power law relationship between size of agglomerates and the number of primary particles in them. The literature shows that in clay rich suspensions the exponent of such power law is generally a fraction (i.e. a numerical quantity that is not a whole number) between 2 and 3. This fractal exponent power law is referred to as the fractal theory. Fractal theory can be combined with lumped parameter modelling described as follows: Kranenburg (1994) stated that the square of equilibrium floc size (R^2) is a function of inverse shear rate (i.e. R^2~1/shear-rate). The author also showed that the yield stress of flocs is directly proportional to R^2. Moore (1959) described the structure parameter λ as a representation for the relative number of internal bonds. Associated mathematical formulation suggests that the structure parameter λ at equilibrium state (when shear destruction is dominant) is inversely related to shear-rate (i.e. λ ~1/shear rate). Bridging these two studies, the structure parameter λ can be related to the square of equilibrium floc size (R^2). The same relationship is found and reported by Sun et al. (2021).

2.4 *Flow curve and equilibrium flow curve*

The flow behavior of a given material is usually illustrated by a flow curve, depicting the relationship between shear stress (on vertical axis) and shear rate (on horizontal axis). If the flow behavior of material under study is time-independent, its flow curve is a unique curve. In thixotropic materials, however, the flow behavior may remarkably vary depending on its shear and resting history, resulting in different flow curves. Toorman (1995), stated that in thixotropic materials the only unique flow curve is the so-called equilibrium flow curve, defined as an equilibrium state at which rate of structural break-down (de-structuration) is equal to the rate of recovery (restructuration) at a given shear rate. This is the point where, under a given shear rate, the measured shear stress in the material does not change with time. By plotting the equilibrium shear stress values against their corresponding shear rates, the equilibrium flow curve can be constructed. In some materials, the equilibrium shear stress values may take a long time to reach or may even not be reached at all, particularly at low shear rates. Different types (shapes) of equilibrium flow curve are known to exist with their well known associated mathematical models such as: Bingham, Hershel-Bulkley, Oswald-DeWaele power law and others. Four typical commonly seen flow curve types are illustrated in Figure 1. All four equilibrium flow curve types (i to iv) can be mathematically described by means of the thixotropic Houska model (1980), which is used in this study. Type iv equilibrium flow curve has been observed in highly thixotropic substances for instance bentonite (Engelund & Wan 1984).

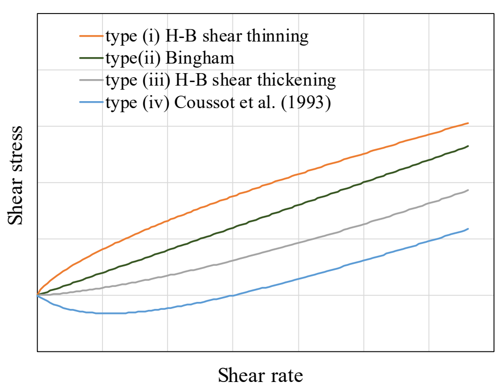

Figure 1. Types of equilibrium flow curves.

2.5 *Lumped parameter-based Houska thixotropic model*

2.5.1 *Equation of state*

The Houska (1980) model consists of a simple non-Newtonian equation of state for base condition (fully destructured) following Herschel-Bulkley plus an additional part that mathematically describes the change in rheology of material relative to its base condition as a function of change in structure parameter λ. The compacted mathematical expression of the Houska equation of state reads:

$$\tau = \tau_\infty + \lambda(\tau_0 - \tau_\infty) + (\mu_\infty + \lambda c)\dot{\gamma}^n \tag{1}$$

where τ_0 = yield stress of fully structured fluid (occurs at $\lambda = 1$), τ_∞ = yield stress of totally destructured fluid (occurs at $\lambda = 0$), n = flow index, μ_∞ = viscosity entirely destructured fluid (=Bingham plastic viscosity if $n = 1$), c = viscosity increment for fully structured fluid, $\dot{\gamma}$= shear rate.

2.5.2 *Kinematic equation*

Growth and decay of structure parameter λ is described by the kinetic equation, Moore (1959):

$$\frac{\partial \lambda}{\partial t} = a\left(\lambda_0 - \lambda\right) - b\lambda\dot{\gamma} \tag{2}$$

where λ = structure parameter [0-λ_0], λ_0 = maximum value of structure [0-1] (Moore assumed λ_0 =1), a and b = respectively coefficients of growth and decay of structure. The first term on the right-hand side of the above equation describes self-recovery of structure. The second term describes the shear down (shear softening) of structure which is related to energy dissipation during the shearing process. The influence of reaggregation (or re-flocculation) in shear (Mietta et al. 2009, Sun 2018) is not explicitly described by this equation. When growth and decay of flocs are in equilibrium, the value of associated equilibrium structure parameter λ_e is given by:

$$\lambda_e = \frac{\lambda_0}{1 + \beta\dot{\gamma}} \tag{3}$$

where $\beta = b/a$ and λ_e = equilibrium structure [0-λ_0]. The quantification of the structure parameter enables us to quantify how flocs size changes in time (grows by accretion of clay platelets and primary particles) or decays (erosion) with dynamic conditions (shear rate, time).

3 MATERIAL AND METHODS

In this section the MFT and its flocculation are described, including quantification of energy dissipation in flocculation. Also, technical details of rheometry are given.

3.1 *MFT and MFT flocculation process*

MFT samples were provided by InnoTech, Canada. These samples had sands to fines ratio (SFR) of 0.1, initial solids content (SC=Ws/Wt) of 31.5% and bitumen content (Wb/Wt) of 4.79% (Dean Stark Analysis). The density of solids and pore water in samples were assumed 2280 kg/m^3 and 1001.4 kg/m^3 respectively. The MFT samples were shipped to Deltares, Delft, the Netherlands. Upon the arrival, the samples were stored in a cold room at a temperature of 10 °C. The flocculation protocol developed by Uni. of Calgary (Nagail 2021) was used to flocculate MFT. This protocol consists of four steps: 1) Ramp up of RPM from 0 to 320 in 1 minute; 2) Pre-shear MFT for 45s at 320 RPM; 3) Polymer addition within 15s at 320 RPM; 4) 30s to 50s at low RPM (conditioning) i.e.30 RPM. SNF-A3338 (from Edmonton, Canada) was used as polymer. Polymer solution consisted of 0.45w% of polymer in model water (0.1wt% $NaHCO_3$ in demi water). Optimal polymer dosage was determined following Nagail (2021) 1000 ppm with respect to solids content in MFT (i.e. 1 gram of dry polymer per 1 kg of dry MFT solids). Two flocculation vessels were used: a small-scale vessel with dimensions according to the 4-inch cup technique developed by Suncor (Sadighian et al. 2016) and a larger vessel which was factor 2.46 larger in size and factor 14.88 larger in volume compared to the 4-inch cup technique. Both rotational velocity of the impeller and torque were measured during the flocculation (mixing) process. The flocculated samples were left for approximately 30 min in the flocculation vessel for any transient effects to subside. After that, the bleed water was removed, and the remaining flocculated MFT of about SC = 32% was used for rheological characterization. Flocculated MFT samples with higher solids content were obtained from a consolidation column. The flocculated MFT samples with lower solids content were obtained by gently diluting a freshly made flocculated MFT with model water, providing a spectrum of flocculated MFT solids concentrations.

3.2 *Cumulative dissipated energy per unit volume of flocculated MFT*

The measured rotational velocity and torque were used to: i) calculate cumulative dissipated energy (D) per unit volume of MFT during the flocculation process by Eq. (4); ii) estimate the wall shear stress within the flocculation vessel. These two values can be used as comparison criteria to evaluate consistency and success of flocculation process (Demoz & Mikula 2012, Yao 2016).

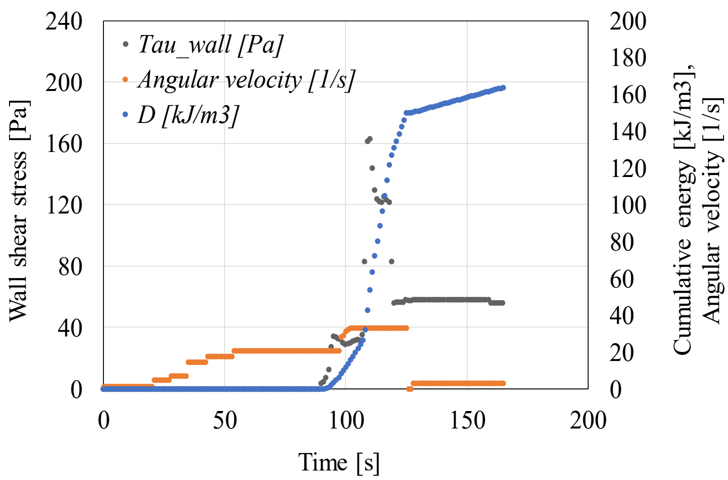

Figure 2. Calculated wall shear stress and cumulative dissipated energy per unit volume of flocculated MFT (D) in polymer mixing.

$$D = \frac{1}{V} \int_{t=0}^{t} T\omega \quad dt \tag{4}$$

where T is torque, ω is rotational velocity(rad/s) and V is volume of MFT in the flocculation vessel). Figure 2 illustrates a typical interpretation of recorded data during the flocculation process. The wall shear stress in the flocculation vessel amounts to 40 to 60 Pa at RPM= 30 which corresponds to 10 to 20 [1/s] fluid shear rate considering the presence of baffles. The cumulative dissipated energy per unit volume in both small- and large-scale flocculation vessels were similar and comparable to previous related studies. For instance, in the experimental study conducted by Mizani (2017) the cumulative energy dissipation per unit volume within a static in-line mixer by which polymer was mixed in MFT was in the order of 100 to 200 kJ/m^3, the same ballpark as in the current study, see in Figure 2. The cumulative dissipated energy per unit volume of our rheometry tests (reported in Section 4), is calculated by the time-integral of shear stress and shear rate:

$$D = \int_{t=0}^{t} \tau\dot{\gamma}dt \tag{5}$$

It can be shown that the unit of cumulative dissipated energy per unit volume [kJ/m^3] is exactly the same as that of pressure [kPa].

3.3 *Rheometry*

A Haake Mars 1 rotoviscometer was used in this study. This is a so-called Searle type rheometer: the inner element is driven, and shear stresses and shear rates are recorded. Testing elements used for this study are bob-cup CC25 Din (Rc/Rb=13.6/12.5=1.08) and vane (FL22)-in-cup (Rc/Rv= 13.6/11=1.24). Controlled Shear Rate (CSR) and Controlled Shear Stress (CSS) testing modes with different protocols are applied. In case of vane-in-cup element, a theoretical conversion factor of 5.8 is used to convert default machine shear rate to a physical shear rate for a virtual gap between the blade tip and cup-wall. After rheological testing, all samples were directed to oven with 110 °C for 24 hr to quantify water content. Reported solid contents are determined from the measured water content, assuming solids density of 2280 kg/m^3 and 4.79% weight percentage of bitumen through all samples.

4 RESULTS AND DISCUSSION

This section shows some key measurement results on how flocculated MFT's rheological properties are shear rate and time dependent. Irreversible and reversible behaviour are clearly distinguishable and their relation with energy dissipation is indicated. The Houska model is applied to describe time dependency in these measurements and results are discussed.

4.1 *Typical flow behavior in flocculated MFT*

Figure 3a shows the flow behavior of flocculated MFT for various solid contents ranging from 24% to 37%. The rheometry tests are conducted with the bob-cup testing element. Each rheometry test includes 180 second linear ramp up of shear rate from 0 to 100 [1/s], followed 60 [s] constant shear rate at 100 [1/s], ended by 180 [s] linear ramp down of shear rate from 100 to 0 [1/s]. Within the range of studied solids content, the flocculated MFT's flow curve is characterized by what is called thixotropic loop with a significant initial peak in the up-ramp (un-remolded) part around 10 [1/s]. A thixotropic loop refers to flow conditions in which the up-ramp and the down-ramp part of the flow curve do not coincide. Figure 3a shows the higher the solids content the larger the peak, the larger the area of thixotropic loop (hereafter is called loop). Note that the magnitude of the peak is highly sensitive to how flocculated MFT samples are handled before being introduced into the rheometer testing element. This may explain why the flocculated MFT sample with 36% solids content in Figure 3a shows a lower peak compared to flocculated MFT sample with 31% solids content. An extreme case in which rheomalaxis (irrecoverable) strength is deliberately destroyed prior to rheometry is provided in Figure 5a. Moreover, for a given solids content in the order of SC 32% and larger, the resting time between flocculation and rheometry showed no to marginal effect on rheology of flocculated MFT (including the magnitude of peak) within the time frame of two weeks. The down-ramp (remolded) part in flocculated MFT flow curve stays lower than the up-ramp (un-remolded) part, indicating de-structuration of flocculated MFT samples during up-ramp.

The amount of cumulative dissipated energy per unit volume of flocculated MFT samples required to shear down the entire peak (up to 50 [1/s]) is found to be in the order of 200 to 550 kJ/m^3. Figure 3b shows a series of sequential tests, with designated resting time in between tests i.e. 5, 15, 30, 60, 120 and 300 minutes, conducted on one sample (with 32.3% solids content) to investigate the eventual strength recovery potential in flocculated MFT. The same testing element and protocol as in Figure 3a is used in Figure 3b. In total 8 rheometry tests were conducted on the sample without extracting the bob. As can be seen, only the up-ramp during of the first test (i.e. T0) was enough to fully destroy the rheomalaxis strength and its peak. It is found that the rheomalaxis strength did not recover within 300 minutes resting time. Additionally, flocculated MFT is somewhat weakened per test with little to no recovery. The thixotropic loops slightly shrunk at each cycle. At a given flocculated MFT solids content, all the ramp-down curves approximately coincide to the same shear stress ballpark value of about 20 Pa for shear rates < 1 [1/s]. This stress value is the so called dynamic yield stress (DYS) defined as the lowest shear stress below which material stops from flowing. In the up-ramps of test T1 to T7 an indentation can be observed (at 5 [1/s]) that maybe an artefact of wall-slip.

It is observed that once the initial peak was sheared down, the measured shear stress at 10 to 20 [1/s] through T1 to T7 (Fig. 3b) is in the same ballpark as the estimated wall shear stress in the flocculation vessel by the end of mixing process (Fig. 1). Additionally, the flow curve loops (T1 to T7) in Figure 3b provide information on strength recovery of flocculated MFT due to thixotropic effect (i.e. gain in strength at rest). It is observed that at shear rate of 10 [1/s] and 300-minutes resting time there is a 65% strength recovery in flocculated MFT. This confirms the time dependency of thixotropy in flocculated MFT.

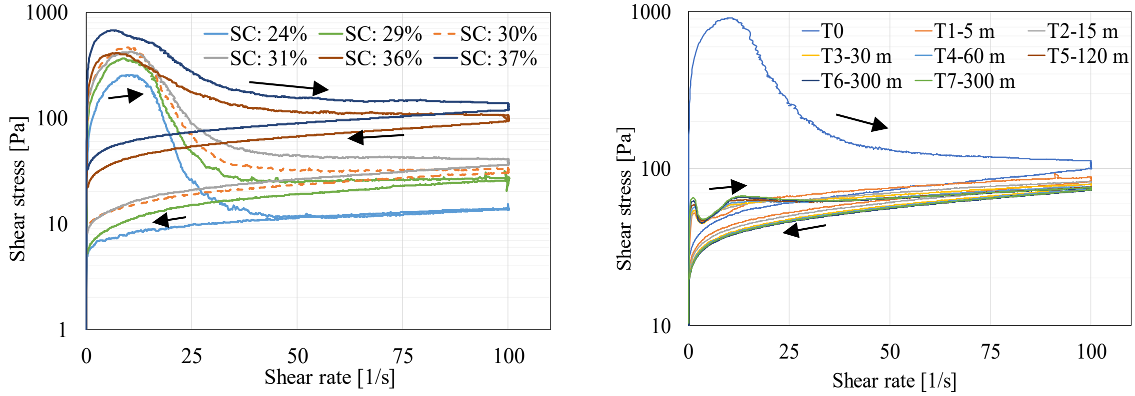

Figure 3. a) flocculated MFT flow curve at different solids content (SC); b) strength recovery in flocculated MFT (with solids content of 32.3%) at different resting time.

4.2 *Shear dependency of strength in flocculated MFT under prolonged shearing*

An endurance test was designed to quantify shear dependency of strength in flocculated MFT under prolonged shearing. This test was conducted on a flocculated MFT sample with 31.1% solids content. This test examines the flow behavior of flocculated MFT against successive alteration between high and low shear rates. The test consisted of 20 times recurrence of the following protocol: 100 [1/s] for 180 [s] followed by 1 [1/s] for 100 [s]. This choice relates to laminar pipeline slurry transport, where shear rates of 100 [1/s] and smaller can be expected. The corresponding shear stress of imposed 1 [1/s] gives an indication for dynamic yield stress (DYS). The bob was not extracted from the cup throughout the test. The cumulative energy per unit volume of the flocculated MFT sample by the end of the test reached to 21000 kJ/m^3, Equation (5). Figure 4a illustrates both the imposed successive shear rate alterations (in blue) and their corresponding measured shear stresses (in orange). As can be seen, the shear stress level in both high (100 [1/s]) and low (1 [1/s]) shear rates gradually decreases as repetition of cycle goes on. This illustrates how from an undisturbed flocculated state the sample losses strength under shearing. In Figure 4b, the measured equilibrium shear stress of imposed shear rates (obtained from Fig. 4a) are plotted against their corresponding cumulative energy per unit volume of the flocculated MFT sample. Within the course of the test, the flocculated MFT sample lost about 55% of its strength at both shear rates. This implies a necessity to keep track of the amount of cumulative dissipated energy when it comes to reporting and/or comparing the rheology of flocculated MFT.

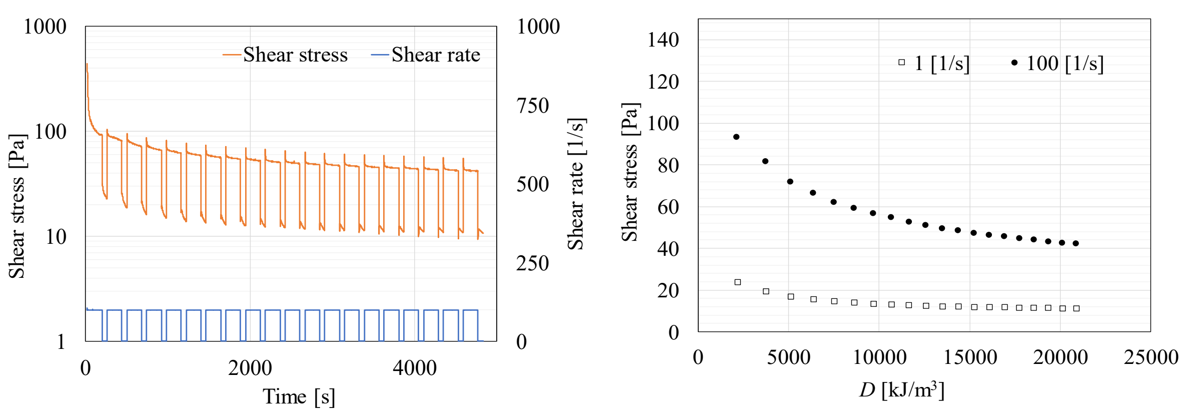

Figure 4. a) endurance test conducted on a flocculated MFT sample with 31.1% solids content applying successive shear rate alteration (in blue) and its corresponding measured shear stresses (in orange); b) strength loss as function of cumulative dissipated energy per unit volume of flocculated MFT.

4.3 *Application of Houska model to flocculated MFT*

An attempt was made to investigate whether the Houska thixotropic model can replicate flocculated MFT's flow behavior. For this, the flow curve of a flocculated MFT sample with 34% solids content (Fig. 5a) was used to calibrate the Houska model parameters of *a* and *b* for flocculated MFT. The sample used for this exercise was homogenised before the rheometry. Hence, its rheomalaxis strength was intentionally destroyed prior to the test. In Figure 5a, the measured flow curves of three consecutive controlled shear rate (CSR) tests using the bob-cup testing element are shown in black and gray shades line. In each cycle, the flocculated MFT sample was first sheared from 0 to100 [1/s] for 180 [s], then a constant shear rate of 100 [1/s] was applied to it for 60 [s], and finally it was sheared from 100 to 0 [1/s] in 180 [s]. This cycle, or in other word loop, was repeated three times (see CSR cycle 1 to 3 in Figure 5a). Additionally, using the vane-in-cup element a shear stress controlled (CSS) test was conducted on an identical flocculated MFT sample which was also pre-mixed prior to the rheometry test (see CSS in Fig. 5a). The result of this test is shown labeled as CSS in Figure 5a. The stress point at which the CSS curve distinctively deviates from the vertical axis is the so-called static yield stress (SYS). This yield point refers to a stress above which material starts to flow.

By trial and error, the Houska model parameters *a* and *b* were varied until the best fit to measured flow curves is obtained. The modeled flow curves (loops) are shown in blue lines in Figure 5a. The model input parameters used to initialize the model are as follows: τ_0 = SYS, τ_∞ = a value slightly smaller than Bingham yield stress of the down-ramp in CSR flow curve of the second cycle, μ_∞ = the slope of the down-ramp in CSR flow curve, $c + \mu_\infty$ = approximately the slope of tangent line fitted to initial part of up-ramp and $n = 1$ assuming a Bingham type of flow curve. In Figure 5a, the three modelled flow curves (shown in blue) can be compared with the three measured flow curves (cycle 1 to 3 shown in black to gray shades). In Figure 5a, the magnitude of structure parameter λ is illustrated by an orange dotted line. In the second and third loop (cycle 2 and 3) the value of the structure parameter λ becomes low and nearly constant. The upper yield stress of the modelled flow curve (in cycle 1) describes the intact reversible structure with flocs at their maximum size and maximum internal connectivity within the flocs. Although cycle 1 and 2 are decently replicated, the model showed difficulties in replicating cycle 3, meaning that the modeled cycle 3 is slightly higher than the measured cycle 3. This is because the structure parameter λ reaches to its lowest value in the model under the imposed cycles of shear rates. Moreover, the measured flow curves are characterized by a downward bend as shear rate decreases (< 7 [1/s]). These bends are not captured by the model. This is because a Bingham type of flow curve was assumed in this modeling exercise ($n = 1$). By choosing smaller values for n the downward bending can be replicated. Such bends at lower shear rates can be an indication for occurrence of wall-slip during rheometry tests.

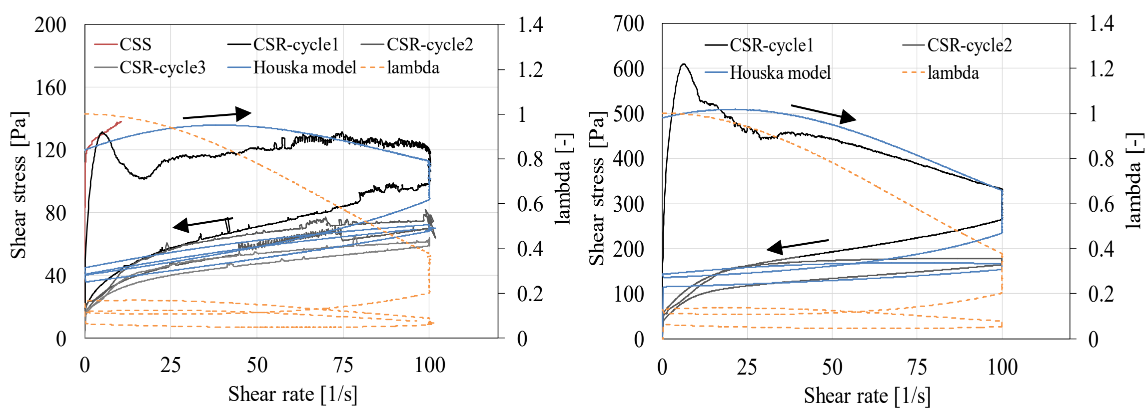

Figure 5. a) Houska model is applied to a flocculated MFT sample with SC 34%. The sample was premixed prior to rheometry. The Houska model parameters are: τ_∞=30 [Pa], μ_∞=0.35 [Pa s], τ_0=90 [Pa], c=0.5 [Pa s], a=0.0003 [1/s], b=0.0001 [-]; b) Houska model is applied to a flocculated MFT sample with SC 40%. The sample was not mixed prior to rheometry. The Houska model parameters were: τ_∞=85 [Pa], μ_∞=0.35 [Pa.s], τ_0=400 [Pa], c=1.4 [Pa s], a=0.0003 [1/s], b=0.0001 [-]. CSS test with vane, CSS test with bob-cup.

To validate the model, the calibrated Houska model was applied to replicate the flow curve of a flocculated MFT sample with 40% solids content. This sample was taken from a flocculated MFT consolidation column under consolidation for about 1.5 month and were not mixed/disturbed before rheometry. Hence, its rheomalaxis strength is preserved (see peak shear stress at 10 [1/s] in Fig. 5b). Only two successive CSR tests were applied to this sample, resulting into two flow curve loops which are shown in black and gray in Figure 5b. No CSS test was applied.

It was found that the calibrated Houska model could well replicate the measured flow curves (loops). The rheomalaxis (irrecoverable) part of the flow curve, however, is not captured by the model. To be able to capture rheomalaxis, an additional relation needs to be implemented in the current Houska model relating the decay of maximum structure λ_0 with dissipated energy. This, although readily developed by Talmon et al. (2019), is not presented in the current manuscript. The values of *a* and *b* provide indicative information on the speed of reconfiguration of the internal structure. For instance, it is found that in flocculated MFT the time scale for reversible structure recovery in shear is ($1/a$) which is about ~1 hour. The time scale for reversible structure decay is $1/(b\dot{\gamma})$, which at a representative shear rate of 50 [1/s] in our tests, is 200 seconds. Such information is relevant to predict thixotropic gain and loss in hydrotransport and deposition flow of flocculated MFT.

5 CONCLUSIONS

This study leads us to conclude:

- By the end of flocculation (mixing) process, the flocculated MFT holds shear stresses of 40 to 60 Pa at a shear rate of 10 to 20 [1/s]. Having said that, only 30 minutes to an hour rest given to flocculated MFT before rheometry allowed resistance buildup of up to 1 kPa at about 10 [1/s]. This peak (resistance), however, is easily sheared away with only 200 to 550 kJ/m^3 cumulative dissipated energy per unit of flocculated MFT. This peak (resistance) is irrecoverable so called as rheomalaxis strength. This is relevant to hydrotransport and deposition flow.
- The magnitude of peak (resistance), sensitive to sample handling, is directly proportional to solids content.
- After rheomalaxis is sheared away, a thixotropic material remains. The thixotropic strength gain in flocculated MFT is found to be up to 65% larger after 300-minutes rest than the flocculated MFT's fully remolded resistance.
- The remolded resistance of flocculated MFT decreases with increasing cumulative dissipated energy per unit of flocculated MFT until it reaches to a base remolded resistance.
- Using smooth bob-cup testing element for rheometry of flocculated MFT appears to have led to occurrence of wall slip at low shear rates in the measured data.
- The Houska thixotropic model could replicate both time and shear dependent strength gain and loss in flocculated MFT. The time dependent strength gain is expected to be important to pattern formation and segregation in deposition flow which can quantitatively be analyzed when the thixotropic effect is embedded in a CFD deposition model.
- We showed that using lumped structure parameter modelling, the shear and time dependency of both recoverable (thixotropy) and irrecoverable (rheomalaxis) strength in flocculated MFT can successfully be replicated. In this model, the collective effect of the governing processes at microscopic level are captured by a single macroscopic parameter. Although this comes with the benefit of simplification of the complex microscopic processes and rather inexpensive pragmatic measurement, we believe that thorough microscopic investigation is necessary to understand the governing physics.
- Similar systematic rheological study on MFT is advised for assessment of tailings dredgeability.

6 ACKNOWLEDGEMENT

The authors would like to express their gratitude to IOSI and COSIA for the technical and financial support of the study.

7 REFERENCES

Coussot, P., Leonov, A.I. & Piau, J.M. 1993. Rheology of concentrated dispersed systems in a low molecular weight matrix. *J. Non-Newtonian Fluid Mechanics* 46: 179-217.

Demoz, A. & Mikula, R. J., 2012. Role of mixing energy in the flocculation of mature fine tailings. *Journal of Environmental Engineering* 138(1): 129-136.

Engelund, F. & Wan, Z. 1984. Instability of hyperconcentrated flow. *Journal of Hydraulic Engineering* 110 (3): 219-233.

Govedarica A., Molina Bacca, E.J. & Trifkovic, M. 2020. Structural Investigation of Tailings Flocculation and Consolidation via Quantitative 3D Dual Fluorescence/Reflectance Confocal Microscopy. *Journal of Colloid and Interface Science*. doi:10.1016/j.jcis.2020.02.098

Hamza, H.A., Stanonik, H.A. & Kessica M.A. 1996. Flocculation of lime treated oil sands tailings. *Fuel* 75(3): 280 – 284.

Houska, M. 1980. Engineering Aspects of the Rheology of Thixotropic Liquids. PhD-thesis (in Czech), Czech Technical University, Prague.

Kranenburg, C. 1994. The fractal structure of cohesive sediments aggregates. *Estuarine Coastal and Shelf Science* 39: 451-460.

Merckelbach, L.M. 2000. Consolidation and strength evolution of soft mud layers, PhD-thesis, Delft University of Technology.

Mietta, F., Chassagne, C. & Winterwerp, J.C. 2009. Shear induced flocculation of a suspension of kaolinite as function of pH and salt concentration. *Journal of Colloid and Interface Science* 336: 134–141.

Mizani, S., Solemani, S., & Simms, P. 2013. Effects of polymer dosage on dewaterability, rheology and spreadability of polymer amended oil sands mature fine tailings. 16th International Seminar on Paste and Thickened Tailings, Belo Horizonte, 17 - 20 June 2013.

Mizani, S., Simms, P. & Wilson,W. 2017. Rheology for deposition control of polymer-amended oil sands tailings. *Rheol Acta*, DOI 10.1007/s00397-017-1015.

Mewis, J. & Wagner, N.J. 2009. Thixotropy. *Advances in Colloid and Interface Science* 147–148: 214–227.

Moore, F. 1959. The rheology of ceramic slips and bodies. *Transactions British Ceramic Society* 58: 470-494.

Nagial, R. 2021. Correlating macroscopic rheological behavior to micro structure of polymer flocculated Mature Fine Tailings (MFT), MSc-thesis, University of Calgary.

Sadighian, A., Revington, A., Kaminsky, H., Moyls, B., Li, Y. & Omotoso, O. 2018. A New Protocol to Assess the Quality of Tailings Flocculation/Coagulation: A Collaboration to Improve Tailings Treatment at Suncor Energy; IOSTC: Edmonton, AB, Canada.

Sasar, M., Johnston, C.T., Kaminsky, H. & Santagata, M. 2021, Oscillatory rheometry to characterize polymer flocculation of fluid fine tailings. *Rheologica Acta* 60: 457–479.

Sun Y. 2018. Recovery of thickened kaolinite suspension properties through shear. MSc-Thesis. University of Alberta.

Sun, M., Jou, D. & Wang, Z. 2021. A Nonlinear Viscoelastic Model for the Yielding of Gelled Waxy Crude Oil. *Energies* 14: 536.

Talmon, A.M., Sittoni, L. & Meshkati Shahmirzadi, E. 2019. A research trajectory towards improving fines capture prediction with Delft3D-slurry – Phase II, Deltares, 11201392-000-ZKS-0004_v0.1, Report for the project IOSI 2017-08.

Toorman, E.A. 1995. The thixotropic behaviour of dense cohesive sediment suspensions. Report HYD149, Hydraulics Laboratory, K.U. Leuven, 69 pp.

Treinen, J.M., Cooke, R. & Salinas, C. 2010. Energy induced rheology reduction of flocculated slurries. Paste 2010.

Yao, Y. 2016. Dewatering Behaviour of Fine Oil Sands Tailings: An Experimental Study. PhD-Thesis Delft University of Technology.

Validation of an engineering model for consolidation and creep in oil sand tailings

F. D. Murphy
Suncor Energy Inc., Calgary, Alberta, CAN

G. Gjerapić & D. Znidarčić
University of Colorado, Boulder, Colorado, USA

A. Sorta
Coanda Research & Development Corporation, Edmonton, CAN

ABSTRACT: A newly developed Consolidation and Creep model (CONCREEP) has been validated against experimental observations on a tall column of treated MFT material over a period of several months. Initial analyses of the column performance indicated that the nonlinear finite strain consolidation theory is incapable of capturing the observed behavior in terms of both the rate and the magnitude of observed settlements. The void ratio profiles recorded over the course of the experiment indicated that the void ratio-effective stress relationship for the material is not a unique function, but changes with time. This observation led to the development of a comprehensive new model for the prediction of consolidation and creep of oil sand tailings and the development of an associated experimental procedure to find the required model parameters. The numerical model and the laboratory testing protocol are described in detail in the companion paper presented at this conference.

This paper compares the results of preliminary consolidation analyses with the experimental data for a 5-meter MFT column collected over several months. Subsequent analyses using the newly developed consolidation and creep model are also compared to the experimental data to highlight the advantages of the new CONCREEP model and the associated experimental procedure.

1 INTRODUCTION

As a part of Suncor's ongoing tailings technology development processes, large columns (0.61 m in diameter x 5 m in height) have been filled with coagulant and flocculant treated Mature Fine Tailings (MFT). Amongst the objectives of these tests was the validation of consolidation models to predict volume changes in controlled conditions, at as large a scale as could be accommodated. Based on earlier testing and analyses (Znidarčić et al. 2016), the Seepage Induced Consolidation (SIC) test and the software for consolidation analyses CONDES were expected to be able to predict the dewatering of these treated MFTs. Several months after the filling of 5-meter column, new samples for SIC testing were created using the same treatment protocols to determine consolidation parameters on the treated MFT on small samples in the laboratory. Subsequent consolidation analyses were then used to make blind predictions of the expected column behavior in terms of the settlement rates and magnitudes and to predict the void ratio profiles (i.e., to assess the variability of void ratio with depth) at various times. A comparison between the analyses (CONDES) predictions and the observed laboratory behavior of 5-meter columns revealed significant discrepancies in terms of the settlement rates and magnitudes and the void ratio profiles. Subsequent parametric studies conducted by varying both the hydraulic conductivity and compressibility parameters were unable to achieve a good match between the predicted and the observed behavior. At that point it was postulated that treated MFTs might exhibit time dependent compressibility relationships and that the creep mechanism should be incorporated in the analyses to achieve a better match between the predicted and the observed behavior. Hence, a new consolidation and creep (CONCREEP) model was developed to improve predictive capabilities of the numerical model and to achieve a better agreement with the behavior of treated MFTs observed in 5-meter column experiments. A detailed description of the CONCREEP model is presented in the companion conference paper (Gjerapic et al 2021) while this paper presents the validation results that include the columns settlement modeling efforts with and without the inclusion of creep.

2 CONSOLIDATION TESTING

A series of Seepage Induced Consolidation (SIC) tests were performed on the treated MFT samples in the laboratory. The treatment protocol for the MFT material used to conduct SIC tests was identical to the treatment of tailings placed in the 5-meter column several months earlier. The SIC testing program followed procedures for testing of MFT materials previously described by Znidarčić et al. (2011) and Estepho et al. (2013). In addition to accurate determination of compressibility and hydraulic conductivity relationships, the correct definition of initial conditions is critical for the successful modeling of the column performance with time. Unless the initial heights, initial void ratio and the total volume of solids in the analyses are consistent with the corresponding quantities in the actual (experimental) column, matching the observed behavior will be impossible. For the 5-meter column in this study, the determination of initial conditions was challenging. Fortunately, several redundant measurements of the initial void ratio (initial solids content) were conducted during filling with the additional density scans available shortly after the completion of the filling operations. The additional measurements included the collection of density samples during filling and several times after filling, the recording of the internal bottom total pressure and the pressure from the external load cells measuring the total weight of the columns. It should be noted that each of these measurements is subject to measurement errors leading to discrepancies when interpreting results. After careful examination of the measurement records, it was concluded that the external load cells measurements provide the most reliable set of data and these were used in subsequent analysis. Once the total height of solids was established, the initial column height, consistent with the measurements of the initial void ratios, could be calculated. It was noted that the maximum observed column height (at the end of the column filling process) is not necessarily equal to the initial column height used for the analyses due to the limited densification of tailings taking place during the filling process, especially at the bottom of the column. For the 5-meter tall column, the filling process lasted approximately 6 hours.

The compressibility and hydraulic conductivity relationships for the MFT sample determined from the SIC test were adjusted to match the initial void ratio corresponding to the initial conditions in the 5-meter column. The compressibility and permeability relationships are defined by the following expressions:

Compressibility $$e=A(\sigma'+Z)^B \qquad (1)$$

Hydraulic Conductivity $$k=Ce^D \qquad (2)$$

Table 1 – Compressibility and hydraulic conductivity parameters for consolidation analysis

A	B	Z	C	D	G_s
(-)	(-)	(kPa)	(m/day)	(-)	(-)
6.93	-0.436	2.0	1.52E-05	6.60	2.42

The compressibility relationship from SIC test is shown in Figure 1.

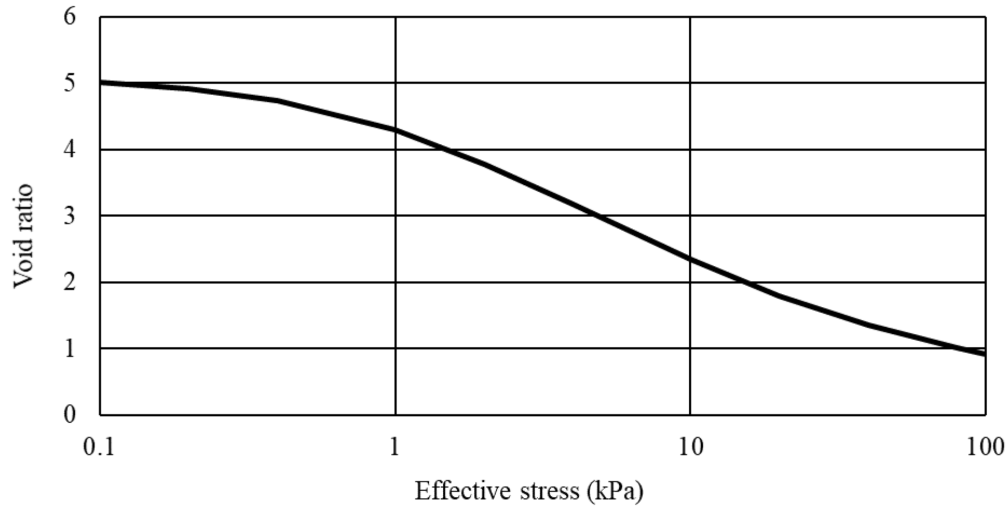

Figure 1. Compressibility relationship for consolidation analysis

The hydraulic conductivity relationship from SIC test is shown in Figure 2.

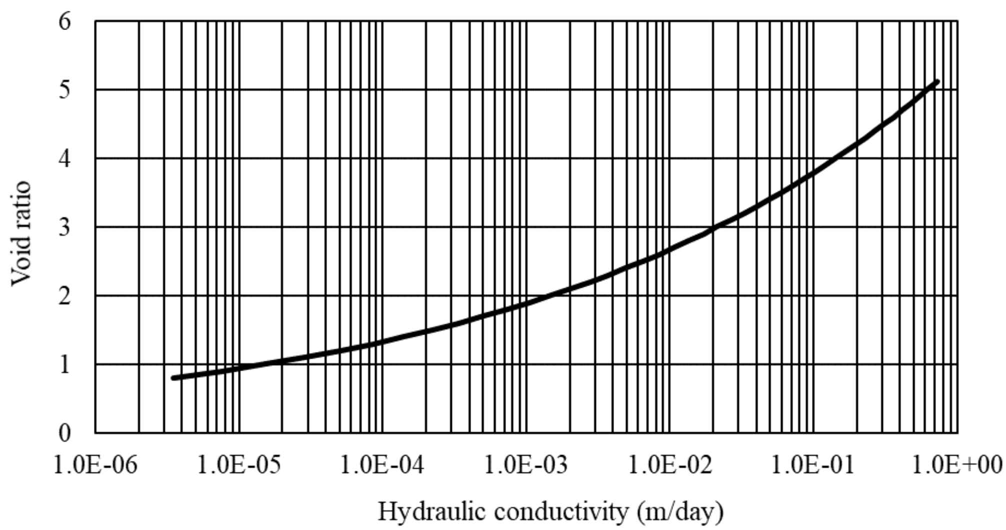

Figure 2. Hydraulic conductivity relationship for consolidation analysis

3 CONSOLIDATION ANALYSIS

Figure 3 presents the consolidation analysis results for a 5-meter column and the corresponding time settlement curve recorded, while Figure 4 shows the void ratio profiles from the consolidation analysis compared to the results of density scans at several times after filling. The settlement analysis indicates that the consolidation in the column is largely completed after 100 days, while the measured data show continuous settlement past that time. In addition, the predicted end-height is higher by 0.63 m than the measured value at 670 days after the cessation of the column filling. The cause of these discrepancies is readily identified when comparing the predicted and measured void ratio profiles in Figure 4. The analysis results indicate that there is practically no void ratio change beyond 90 days, while the scanned values indicate larger void ratio reduction, especially at shallow depths. Several attempts to modify the compressibility and hydraulic conductivity relationships in order to achieve a better agreement between the measured and predicted quantities were unsuccessful and we concluded that the material must be undergoing additional void ratio reduction upon deposition unrelated to the effective stress changes.

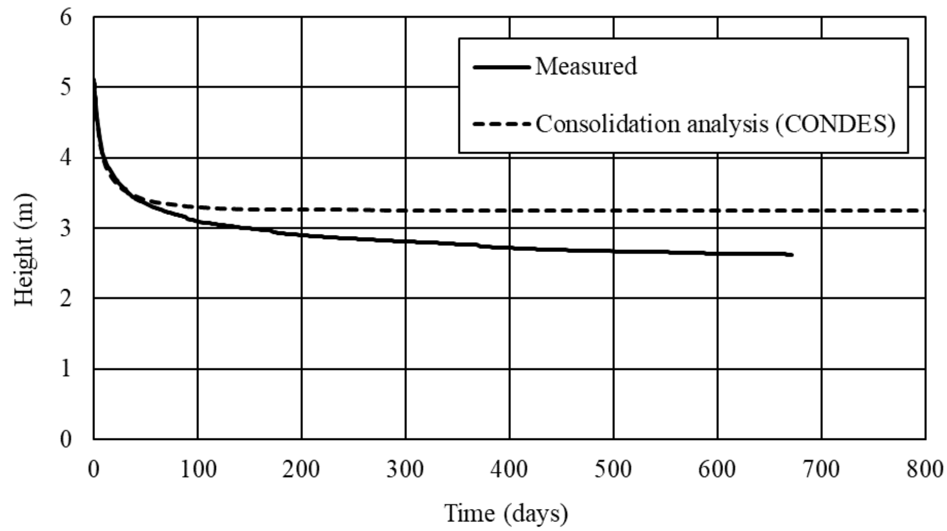

Figure 3. Height vs time comparison between the measured data and consolidation analysis

A comparison between the predicted and measured void ratio profiles illustrating negligible changes in the predicted void ratio profile after 90 days is shown in Figure 4.

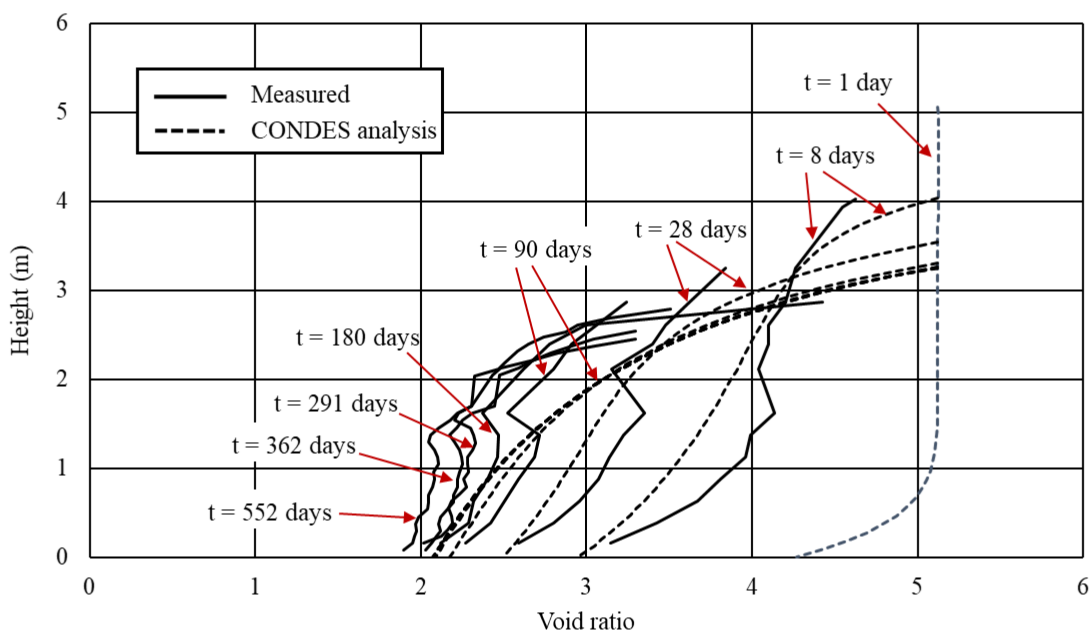

Figure 4. Void ratio distributions comparison between scanned profiles and consolidation analysis

The above observations indicated that the nonlinear finite strain consolidation theory developed by Gibson et al. (1967) needs to be modified in order to achieve a better agreement between the numerical predictions and the observed behavior of the treated MFT material. We postulated that the compressibility behavior of the material exhibits a time dependent compression, i.e. creep, in addition to the compression caused by an increase in effective stresses accounted for in the classical Gibson (*ibid*) theory. In order to test this hypothesis, we developed a new numerical model CONCREEP that accounts for both the consolidation and the creep mechanisms. The proposed model is consistent with the Gibson (*ibid*) theory with the exception that a viscoplastic component is added to the compressibility relationship. The development of the model is described in more detail in the companion paper at this conference (Gjerapić et al. 2021). This paper demonstrates the improvement in the predictive capability of the model, using a comparison against experimental observations, after accounting for the creep mechanism.

4 CONSOLIDATION AND CREEP ANALYSIS

The new model that includes creep, requires a modified testing protocol and additional parameters to describe time dependent compressibility behavior of the material. The new testing protocol and the parameter estimation procedures are described in the companion paper. The modified testing procedure could not be used on the 5-meter column material described in this paper, as all the testing was completed by the time the CONCREEP model and the accompanying testing procedure were developed. However, we used the column scanning data to guide us in developing the creep component of the model. Based on the observation that the creep is most pronounced at shallow depths, or low effective stresses, we took the scanned void ratio values at the top of the column and associated them with the effective stress of 0.1 kPa. We also assumed that the creep effects will diminish with the increased magnitude of effective stresses and will be therefore negligible at the effective stress of about 100 kPa. When these data are combined with the compressibility relationship defined in Table 1 and Figure 1, a set of compressibility curves at different times is obtained as shown in Figure 5.

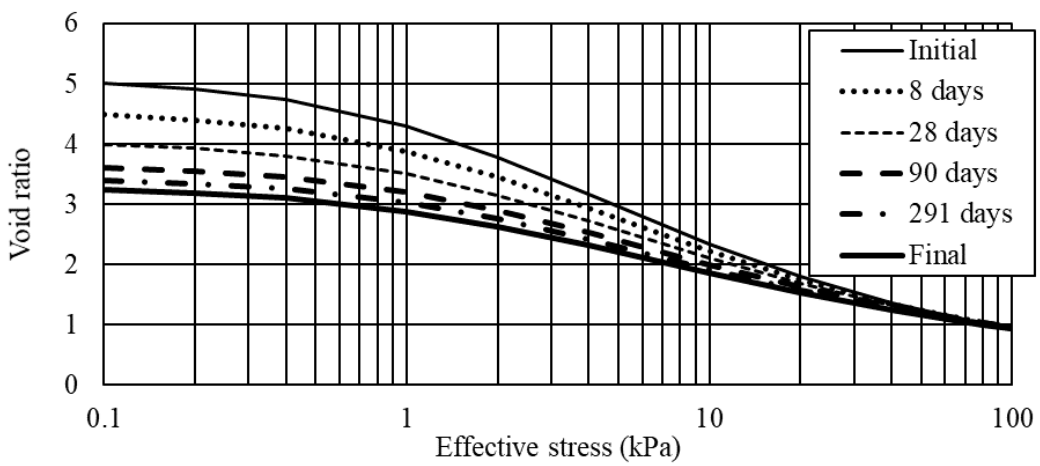

Figure 5. Compressibility curves changes over time due to creep

In order to account for the time dependent compressibility relationship, the compressibility model parameters A, B and Z are expressed as a function of time, see Equations (3), (4) and (5). The number of compressibility parameters has now increased from 3 to 12, though they have clear physical meaning and are easily calibrated with the test data from samples tested in the laboratory following the procedure described in the companion paper (Gjerapić et al. 2021). Parameters A_0, B_0, Z_0 and A_f, B_f and Z_f are the values of the compressibility parameters in Equation (1) at time zero and at infinite time. Parameters a_1, a_2, b_1, b_2, z_1 and z_2 are controlling how the compressibility parameters change with time "t" in between the initial and final values.

$$A = A(t) = A_f + \left(A_0 - A_f\right)\left\{a_1\left[\left(\frac{1}{a_1}\right)^{\frac{1}{a_2}} + t\right]^{a_2}\right\} \tag{3}$$

$$B = B(t) = B_f + (B_0 - B_f)\left\{ b_1 \left[\left(\frac{1}{b_1} \right)^{\frac{1}{b_2}} + t \right]^{b_2} \right\} \tag{4}$$

and,

$$Z = Z(t) = Z_f + (Z_0 - Z_f)\left\{ z_1 \left[\left(\frac{1}{z_1} \right)^{\frac{1}{z_2}} + t \right]^{z_2} \right\} \tag{5}$$

For the MFT material used to conduct the 5-meter column experiment, constitutive parameters defining the initial and the final compressibility relationships are listed in Table 2.

Table 2. Parameters defining initial and final compressibility curves

A_0 (1/kPa)^{B0}	B_0 (-)	Z_0 (kPa)	A_f (1/kPa)^{Bf}	B_f (-)	Z_f (kPa)
6.93	-0.436	2.0	4.10	-0.320	2.0

Parameters defining the change of the compressibility parameters, *A*, *B* and *Z* with time are listed in Table 3.

Table 3. Parameters defining creep evolution of compressibility curves

a_1 (-)	b_1 (-)	z_1 (-)	a_2 (-)	b_2 (-)	z_2 (-)
8.0	20.0	1.0	-0.800	-1.0	-1.0

The hydraulic conductivity parameters, *C* and *D*, do not change due to creep and remain constant. These parameters are presented in Table 1 with the hydraulic conductivity relationship shown in Figure 2.

The settlement analysis for a 5-meter column was then repeated accounting for both deformation mechanisms (consolidation and creep) using the newly developed numerical code CONCREEP. The analysis results are presented in Figures 6 and 7. The analysis results without creep (i.e., consolidation only analysis) are also presented in Figure 6 for the ease of comparison between methods.

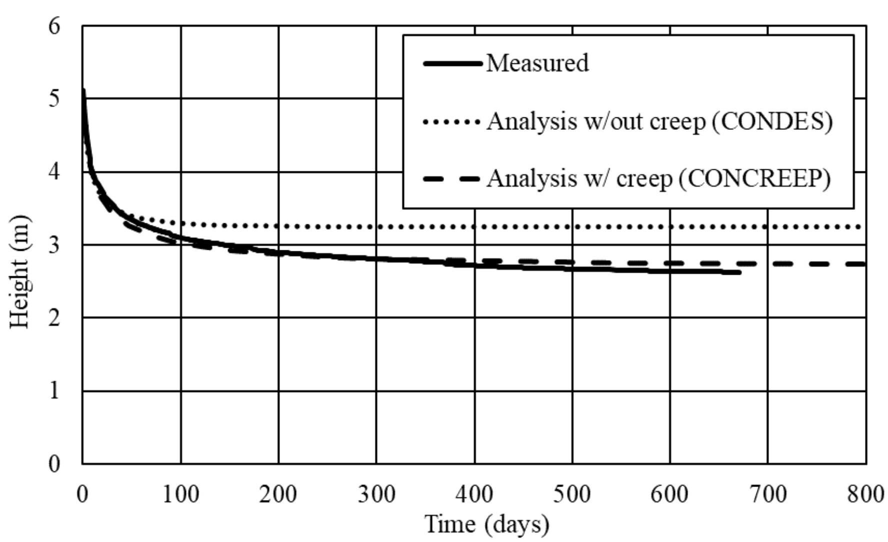

Figure 6. Height vs time comparison between the measured settlements and the analyses with and without creep

The analysis with the effects of creep included shows noticeable improvement in matching the measured values, though the fit is not perfect. Likewise, the calculated void ratio profiles from the CONCREEP model presented in Figure 7 show a markedly better agreement with the scanned (measured) profiles than the profiles obtained from the consolidation only analysis presented in Figure 4. With more experimental data from longer term creep tests on laboratory samples of the treated MFT material, a better fit of creep parameters could be achieved and the match between the observed column behavior and the model prediction would also improve.

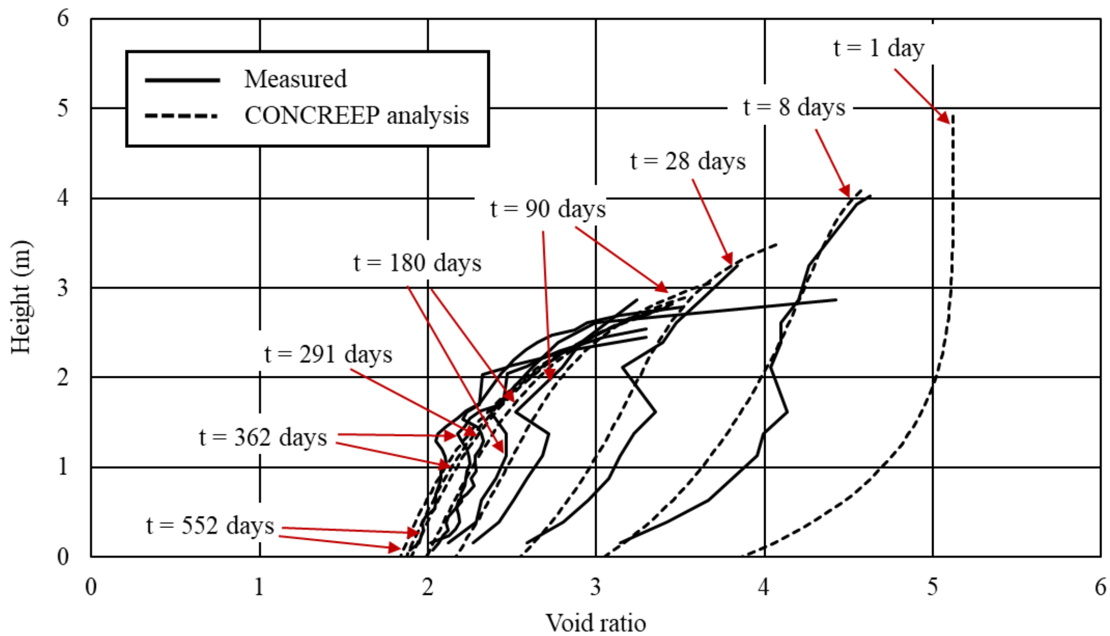

Figure 7. Void ratio distributions comparison between the measured (scanned) profiles, and the analysis accounting for consolidation and creep

5 CONCLUSIONS

The nonlinear finite strain consolidation model as developed by Gibson et al (1967) is not sufficient for predicting behavior of a given coagulated and flocculated MFT treatment material upon deposition. To improve the predictive capability of a numerical model, creep effects observed in the treated MFT behavior must be included in the model and the consolidation testing protocol needs to be modified to include collection of additional data to quantify the effects of creep.

The newly developed numerical code CONCREEP achieved a much better agreement between the observed behavior of the treated MFT material in a 5-meter tall column and the predictions obtained in the analysis than the large strain consolidation model without creep. The model improvements are not achieved only in better predictions of settlement rates and magnitudes, but more importantly in a more realistic prediction of void ratio profiles at various times. The paper demonstrates that the new model is capable of rationally accounting for the creep effects in soft tailings upon deposition.

6 REFERENCES

Estepho, M., van Zyl, D., Znidarčić, D., and Revington, A., 2013, Seepage Induced Consolidation Testing of Mature Fine Tailings, Tailings and Mine Waste ‘13 conference proceedings, November 3-6, Banff, AB, Canada, ISBN: 978-1-55195-326-7, pp.101-109.

Gibson, R.E., England, G.L., and Hussey, M.J.L. 1967. The theory of one-dimensional consolidation of saturated clays. 1. Finite Non-linear Consolidation of Thin Homogeneous Layers. *Géotechnique*, Vol. 17, 261-273.

Gjerapić, G., Murphy, F., Peric, D. and Znidarčić, D., 2021, Development of an Engineering Model for Consolidation and Creep in Tailings, Tailings and Mine Waste '21 conference proceedings, November 7-10, Banff, AB, Canada,

Znidarčić, D., Miller, R., van Zyl, D., Fredlund, M., and Wells, S., 2011, Consolidation Testing of Oil Sand Fine Tailings, Tailings and Mine Waste '11 conference proceedings, November 6-9, Vancouver, BC, Canada, ISBN: 978-0-88865-815-9, pp.251-257.

Znidarčić, D., Van Zyl, D., Ramirez, M., Mittal K., and Kaminsky, H., 2016, Consolidation Characteristics of Flocculated MFT – Experimental Column and SICT data, International Oil Sands Tailings conference proceedings, December 4-7, Lake Louise, AB, Canada, pp. 408-415.

Development of an engineering model for consolidation and creep in tailings

G. Gjerapić & D. Znidarčić
University of Colorado, Boulder, Colorado, USA

D. Perić
Kansas State University, Manhattan, Kansas, USA

F. D. Murphy
Suncor Energy Inc., Calgary, Alberta, Canada

ABSTRACT: Dewatering and reclamation issues associated with oil sands tailings continue to present an environmental liability for the oil sands industry. The settlement process of Mature Fine Tailings (MFT) containing clay minerals is a particular challenge as the MFT treatment involves addition of chemicals as well as the mechanical solid-liquid separation resulting in a material with complex chemical and hydro-geomechanical behavior. Traditionally, the physical behavior of tailings during the settlement process is defined by its consolidation properties, the void ratio – effective stress (compressibility) and the void ratio – hydraulic conductivity (permeability) relationships. The traditional approach, however, fails to capture the behavior of treated MFT if tailings' compressibility changes with time.

This paper presents a consistent approach to define consolidation parameters for treated tailings by allowing the time-dependency of the MFT compressibility curve, i.e. the method accounts for the tailings creep. The time-dependent creep parameters are determined from a series of step-loading consolidation tests using direct measurements of hydraulic conductivity. To capture changes of the tailings compressibility with time, a new constitutive model was implemented in the computer program, CONCREEP.

The proposed methodology to determine constitutive parameters accurately describes the tailings behavior over the range of stresses of interest to the MFT reclamation process. In addition, the proposed methodology allows for the consistent re-calibration of parameters as more data become available either due to longer testing in the laboratory or using the in-situ measurements.

1 INTRODUCTION

1.1 *Background*

The closure of tailings ponds remains a challenge for the oil sands industry in terms of the physical and chemical stability and the post-closure land use. Settlement predictions for the existing impoundments indicate that the consolidation of MFT tailings may require periods of more than 100 years to approach steady-state conditions (Znidarcic et al. 2011). The advent of new technologies to improve initial MFT densities continue to exemplify needs for accurate dewatering and settlement predictions. Consequently, the improvement of existing methods for the MFT settlement prediction and the associated determination of relevant parameters remain of interest to the oil sand industry.

The magnitude and the rate of tailings settlement are typically determined from numerical models based on the large-strain consolidation theory (Gibson et al. 1967), with relevant parameters obtained from specialized laboratory testing (see e.g. Scott et al. 2008). The original formulation of the governing equation for the large strain consolidation by Gibson et al. (1967) does not account for creep. Nevertheless, tailing materials may exhibit significant creep deformations, especially when treated with polymers. This paper describes the development of an engineering model that accounts for both, consolidation and creep of treated tailings and presents a consistent approach for determination of the constitutive model parameters.

1.2 *Existing creep models*

In today's geotechnical practice, the most common creep model assumes linear relationship between the void ratio and the logarithm of time (e-log t) assuming that the excess pore pressures are largely dissipated. The constant of proportionality between the void ratio and the logarithm of time is typically referred to as the secondary compression index, C_α. The C_α concept was introduced by Buisman (1936) at the first International Conference on Soil Mechanics and Foundation Engineering. Buisman (1936) submitted experimental evidence that upon essential dissipation of the excess pore water pressure during "primary consolidation", which was described by the model proposed by Terzaghi (1923), soils exhibit "*saecular*" (from *saeculum*= century) effects where soil compression continuously develops with time under a constant effective stress. Other researchers (e.g. Šuklje 1957, Bjerrum 1967) subsequently studied the concept of creep, but no general acceptance of a particular approach has emerged.

The creep effects received additional attention from various researchers in 1970s and 1980s. By mid 1980s the arguments polarized around two hypotheses A and B (Ladd et al. 1977, Jamiolkowski et al. 1985). The disagreement was related to the question of creep induced compression (if any) during the early stages of compression while the settlement rate is controlled by hydraulic conductivity of soil. To account for a more general relationship between creep deformations and the effective stress, Mesri & Castro (1987) introduced the concept of constant C_α/C_c ratio (where C_c denotes the compression index), and Leroueil et al. (1985) developed a formulation for which the creep magnitude depends on both the preconsolidation pressure and the strain rate. Since 1980s, numerous researchers have studied creep. Today, however, there is no specific method universally accepted by the engineering community to evaluate creep in either natural soils or tailings deposits.

1.3 *Motivation*

The model described in this paper was developed in an effort to model consolidation and creep behavior of an optimized coagulated and polymer treated MFT material, prepared in a manner as described by Sadighian et al. (2018). After completion of the initial testing effort, which included determination of parameters from step-loading, seepage induced consolidation and settling column tests, the time dependency of compressibility curves was observed to dominate the behavior of polymer-treated samples at lower effective stresses. The observed behavior was consistent with the behavior of bauxite tailings previously reported by Sills (1998). After noting that the conventional creep models do not allow sufficient flexibility to fit the observed tailings behavior, the model CONCREEP was developed. The CONCREEP model uses a numerical approach based on Gibson et al. (1967) large strain theory while accounting for the viscoplastic deformations of tailings by using time-dependent constitutive model parameters determined from a series of step-loading consolidation tests and direct measurements of hydraulic conductivity.

2 APPROACH

The approach to solve the problem of consolidation and creep of treated tailings involves: 1) the development of mathematical formulation that captures the physics of consolidation and creep, 2) the development of a constitutive model (including the definition of relevant parameters) with a sufficient flexibility to capture the observed behavior, and 3) the development of laboratory procedure for a reliable determination of constitutive parameters required to describe both the tailings permeability and compressibility relationships governing the tailings deformation and flow behavior.

2.1 *Governing equations for consolidation and creep*

The CONCREEP model uses the large strain formulation introduced by Gibson et al. (1967) to account for a relative movement between fluid and solid particles and describe deformations due to consolidation and creep. The large strain consolidation theory (Gibson et al. 1967) was formulated with the void ratio as a primary variable and the corresponding governing equation is restricted to materials exhibiting a unique relationship between the void ratio and the effective stress. Consequently, the use of the Gibson et al. (1967) equation is restricted to settlement problems without creep. Nevertheless, in porous materials that exhibit creep, the compressibility relationship changes with time and the governing equation and the solution algorithm need to be modified to account for the creep phenomenon. The mass conservation, force equilibrium, effective stress principle and Darcy-Gersevanov law are all accounted for in this derivation, in a similar procedure to the one proposed by Gibson et al. (1967). The process is presented here for completeness and to introduce a consistent notation. For brevity and simplicity, the derivation process in this study implicitly assumes that the solid phase is stationary while noting that the original Gibson et al. (1967) formulation uses material coordinates in which the relative velocity of solids (i.e., the movement of the referent reduced material coordinate system in time) is equal to zero. Consequently, the resulting governing equations describe the large strain consolidation and creep without the loss of generality as long as the calculations are performed in the Lagrangian framework, i.e. using the governing equations in λ-coordinates, see Figure 1.

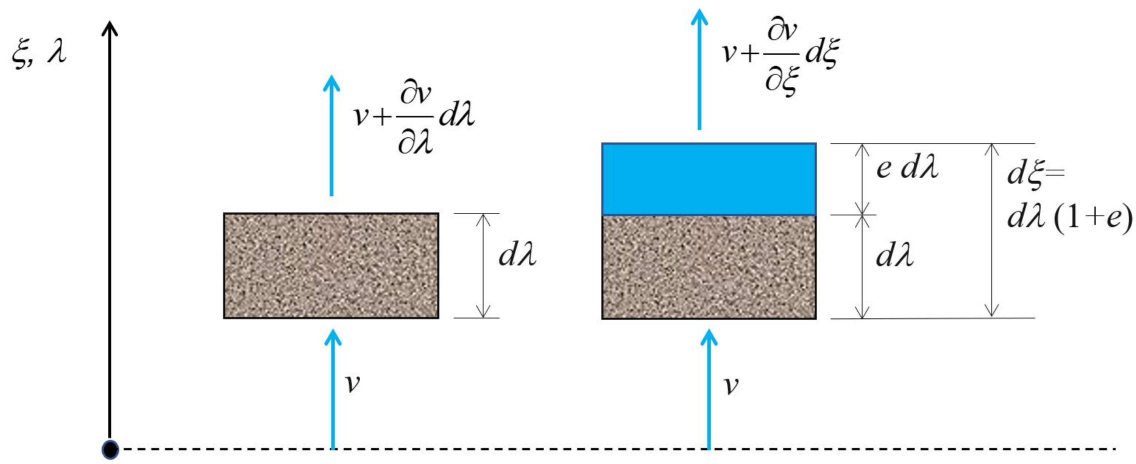

Figure 1. Relations between spatial coordinate ξ and reduced material coordinate λ

The continuity condition, i.e. the mass balance of water for the infinitesimal element in the Eulerian coordinate system depicted in Figure 1, results in

$$-\frac{\partial e}{\partial t} = (1+e)\frac{\partial v}{\partial \xi} \tag{1}$$

In the coordinate system using reduced material coordinates, Equation (1) becomes

$$-\frac{\partial e}{\partial \mathrm{t}} = \frac{\partial v}{\partial \lambda} \tag{2}$$

Darcy's velocity, $v(\xi, t)$, can be written as:

$$v = -k\frac{\partial \mathrm{h}}{\partial \xi} \tag{3}$$

where k is the hydraulic conductivity coefficient and h stands for the total hydraulic head given by

$$h = h_e + h_p = h_e + \frac{u}{\gamma_w} = h_e + \frac{\sigma - \sigma'}{\gamma_w} \tag{4}$$

For the coordinate system in Figure 1, one can impose equilibrium conditions resulting in

$$\frac{\partial \sigma}{\partial \xi} = -\gamma = -\gamma_w \frac{G_s + e}{1 + e} \tag{5}$$

Furthermore, the elevation head and the total head gradients can be expressed as

$$\frac{\partial h_e}{\partial \xi} = 1 \qquad \text{and} \qquad \frac{\partial h}{\partial \xi} = \frac{1}{\gamma_w}\left(-\gamma_w \frac{G_s - 1}{1 + e} - \frac{\partial \sigma'}{\partial \xi}\right) \tag{6}$$

Darcy's velocity, initially defined by Equation (3), can now be written as

$$v = k\left(\frac{G_s - 1}{1 + e} + \frac{1}{\gamma_w}\frac{\partial \sigma'}{\partial \xi}\right) \tag{7}$$

or

$$v = k\left[\frac{G_s - 1}{1 + e} + \frac{1}{\gamma_w(1 + e)}\frac{\partial \sigma'}{\partial e}\frac{\partial e}{\partial \lambda}\right] \tag{8}$$

Equations (2) and (8) must be satisfied in a numerical marching scheme at every time step for a pre-defined set of constitutive properties. Constitutive relationships used for the numerical solution algorithm implemented in the computer program CONCREEP are discussed in Section 2.2.

In soils that exhibit creep, the void ratio changes with time at a constant effective stress. Consequently, the void ratio - effective stress (*e*-*σ*') or the corresponding *σ*'-*e* relationships are non-unique for soils exhibiting creep. This non-uniqueness can be resolved by introducing the void ratio rate or time in the compressibility relationship as follows:

$$\sigma' = \sigma'(e, t) \qquad \text{or} \qquad \sigma' = \sigma'(e, \dot{e}) \tag{9}$$

The relationship defined by Equation (9) is graphically represented by multiple void ratio effective stress curves corresponding to different times or different void ratio rates. The concept of a unique set of compressibility curves describing the *e*-*σ'*relationship for a constant rate of deformation is known as isotache concept, and was initially introduced by Šuklje (1957).

In the present model development, we adopt the first form of Equation (9) although an argument has been made (e.g. Sills 1998) that the second form is more practical as it does not require a t=0 condition to be identified in geologic time. For recently deposited slurries, such an argument is moot as the time of deposition would be known, and any modeling effort would commence with that time. Even if existing deposits are to be analyzed, the modeling effort would start from the present time with the initial conditions determined from the site investigation and model parameters measured on undisturbed samples. Thus, the adoption of a constitutive model that requires definition of the beginning of modeling time (t=0) is appropriate when modeling tailings slurries for engineering purposes.

2.2 *Constitutive model for consolidation and creep*

Rather than adopting the "isotache" approach to evaluate changes in the void ratio based on the pre-defined strain rate relationships, the void ratio changes were herein determined by tracking changes in the compressibility curves in time as determined from laboratory measurements. The adopted "isochrone" approach resulted in a relatively straight forward method to determine creep parameters that define changes in the tailings compressibility curves with time, thus allowing for determination of creep parameters at both small and large times, and for the range of effective stresses of interest.

The form of the compressibility curve is adopted from Liu & Znidarcic (1991) and Abu-Hejleh & Znidarcic (1994) who defined the relationship between the void ratio, *e*, and the effective stress, *σ'*, in the form

$$e = A(\sigma' + Z)^B \tag{10}$$

where A, B and Z are the constitutive model parameters. The hydraulic conductivity, k, was defined as (Somogy 1979):

$$k = Ce^D \tag{11}$$

where C and D are the constitutive model parameters. To account for the creep mechanism, CONCREEP allows the constitutive parameters A, B and Z to change with time. To describe the creep behavior observed in laboratory experiments on tailings samples, A, B and Z are expressed as the algebraic functions of time. The following relationships are adopted in the CONCREEP program:

$$A = A(t) = A_f + (A_0 - A_f)\left\{a_1\left[\left(\frac{1}{a_1}\right)^{\frac{1}{a_2}} + t\right]^{a_2}\right\} \tag{12}$$

$$B = B(t) = B_f + (B_0 - B_f)\left\{b_1\left[\left(\frac{1}{b_1}\right)^{\frac{1}{b_2}} + t\right]^{b_2}\right\} \tag{13}$$

and

$$Z = Z(t) = Z_f + (Z_0 - Z_f)\left\{z_1\left[\left(\frac{1}{z_1}\right)^{\frac{1}{z_2}} + t\right]^{z_2}\right\} \tag{14}$$

Equations (12), (13) and (14) allow for the time-dependency of constitutive properties A, B and Z by introducing additional (creep) parameters. At time equal to zero, parameters A, B and Z are defined by their initial values A_0, B_0 and Z_0. Experimental evidence suggests that there is a limit in the change of parameters A, B and Z. Therefore, parameters A_f, B_f and Z_f are introduced to define the final (limiting values) of parameters A, B and Z at infinite time. Parameters a_1 and a_2 are defined by fitting laboratory data to Equation (12), i.e. by finding the "best-fit" of a_1 and a_2 to match the values of $A = A(t)$ determined at selected (discrete) time increments. Similarly, parameters b_1 and b_2 in Equation (13) are matched to the values of $B = B(t)$ and parameters z_1 and z_2 in Equation (14) are matched to the values of $Z = Z(t)$ based on laboratory compressibility measurements at selected time increments. Selected parameters A_0, B_0, Z_0, A_f, B_f, Z_f, a_1, a_2, b_1, b_2, z_1 and z_2 are used in CONCREEP to account for changes in the material compressibility due to creep.

2.3 *Laboratory procedure for determination of consolidation and creep parameters*

A set of laboratory tests on a sample, or multiple samples, of a slurry are required to collect data for the estimation of constitutive parameters. In order to determine all parameters in the proposed model including A_0, B_0, Z_0, C, D, A_f, B_f, Z_f, a_1, a_2, b_1, b_2, z_1, z_2, a sample must be compressed under several load increments. The hydraulic conductivity should be measured at each load increment and the loads should be sustained for long enough period of time to collect sufficient data for modeling long term compressibility – creep. From our experience with testing soft soils, we determined that for routine testing a set of four load increments is sufficient to properly characterize the compressibility behavior of these materials. At the low end of the stress range, a seating load of 0.1 kPa is considered the lowest value for which reliable data could be collected. The highest stress of interest should correspond to the highest effective stress expected in the project. In between these two extreme values, two additional load increments are desirable in order to better characterize the material in the mid stress range and to provide some data redundancy. Likewise, measuring the hydraulic conductivity at each of these loads provides sufficient data to correctly characterize the void ratio – hydraulic conductivity relationship. When measuring the hydraulic conductivity, the imposed hydraulic gradient should be as low as practical to minimize the void ratio variation within the sample during testing. This is particularly critical at low effective stress range at 0.1 and 1 kPa load increments. A Seepage Induced Consolidation Test Analysis (SICTA) has previously been developed in order to account for the void ratio variation within the sample during hydraulic conductivity measurement (Abu-Hejleh et al. 1996). However, this procedure is only applicable for materials that do not exhibit creep and could not be applied for this model without further development to account for creep in the analysis.

Capturing creep behavior inherently requires prolonged testing times. In addition to being time consuming and expensive, such long duration tests come with a set of challenges that could compromise the quality of data. This includes potential gas generation, bacterial growth or other long term changes that might be taking place in the laboratory. Thus, in each case a compromise will have to be found between the amount of collected data and quality of the data. In ideal circumstances four simultaneous tests would be performed and each test would be targeted for prolonged testing time at one load level. This would provide some redundant data as well as creep data collection at all four load levels. The other extreme would be to test only one sample and collect creep data at each load level. That would require four time longer testing time. Assuming that a minimum of three weeks of creep data collection is desired, the four parallel tests would require about six weeks testing time, while for a single sample test would take six months to complete. It is also noted that any creep model will rely on data extrapolation to times beyond the testing time in laboratory up to the times of interest (centuries or even millennia) or to infinity. The A_f, B_f and Z_f parameters in the proposed model (Eqs. 12 to 14) should be considered as parameters to be used in sensitivity analyses rather than the "true" parameter values at infinite time, as clearly they can never be truly verified. The other six model parameters (a_1, a_2, b_1, b_2, z_1 and z_2) are determined in a best fit process from data collected during the testing period. The longer the period, the more realistic the parameters.

In a soil exhibiting creep, the total void ratio change is an additive decomposition of the void ratio change due to the effective stress change and time evolution of the void ratio. The continuity condition (Eq. 2) requires that this total void ratio change be consistent with the imposed hydraulic gradient and the hydraulic conductivity of the material. The creep induced void ratio change is not associated with an increase in the hydraulic gradient and does not speed up the pore pressure dissipation process. It only causes void ratio change to be larger, but it does not affect the void ratio change rate until the consolidation process ceases. That should not be interpreted as if there are no creep induced void ratio changes during the consolidation process as will be demonstrated later. To better elucidate this peculiarity a thought experiment is helpful. Let us consider a real soil with infinite hydraulic conductivity. Such a soil would under the imposed stress, such as self-weight or externally applied load, undergo instantaneous consolidation followed by creep induced void ratio change proportional to the elapsed time. In that case the two separate void ratio changes would be completely uncoupled and easily distinguishable from each other. In a real soil however, the void ratio change will progress gradually whereby the rate of change is controlled by Darcy's law, and any creep induced void ratio change will be undistinguishable from the effective stress induced change. The creep induced void ratio change will only very slightly affect the initial consolidation rate (Znidarčić 2015). Although the consolidation process theoretically never ends, for all practical purposes the effective stress induced void ratio changes become negligible on a relatively small laboratory specimen after a period of time controlled by the hydraulic conductivity of the material. In the past, 24 hours elapsed time was often considered to be long enough to assume that the consolidation process is completed. However, for slurries, taller samples and very low hydraulic conductivity materials, that time could be substantially longer. Nevertheless, at some point the void ratio change with time could be considered to be caused by creep only and experimental data collected after that time can be used to fit the creep model and determine model parameters. The time after which the creep model is fitted to experimental data should be determined by performing consolidation analysis for each load increment to find at what approximate time the consolidation process is essentially completed. Note that only a rough estimate of this time is sufficient.

Once the creep model parameters are determined from data collected during the creep observation period, the model is used to extrapolate the creep void ratio change to infinite time (A_f, B_f and

Z_f) and to zero time (A_0, B_0 and Z_0). While the parameters at infinite time should be used as variables for parametric studies, the parameters at zero time have a role of separating the creep induced void ratio changes from those caused by the effective stress change during the consolidation process when experimental separation of the two effects is not possible. It is noted that while this might appear to be somewhat undiscriminating process, its effect on any subsequent consolidation/creep analyses will be minimal as only the total void ratio change is relevant for realistic predictions.

3 EXPERIMENTAL AND NUMERICAL RESULTS FOR A TREATED MFT MATERIAL

An MFT sample with the properties listed in Table 1 was treated with 950 ppm of Aluminum Sulfate and 2500 ppm of polyacrylamide. The treated sample was then subjected to the consolidation and creep testing procedure described in Section 2.3. Figure 2 presents the compressibility relationships obtained in the experiments at different elapsed times. The colored markers present the void ratio measurements at different times at four effective stress levels (0.1, 1, 10 and 100 kPa) used to fit compressibility curves, i.e. to determine parameters A, B and Z at discrete times. The times in the legend relate to days elapsed since each load application. Figures 3, 4 and 5 present the change with time of the compressibility parameters A, B and Z obtained by fitting their compressibility values evaluated at discrete times.

Table 1. Properties of source MFT and tailings treatment

Mineral Solids Content	Bitumen Content	Methylene Blue Index, MBI	Clay Content by Sethi correlation	Water based dosage of Aluminum Sulphate dosage	Mineral solids based dosage of Polyacrylamide
(%)	(%)	(meq/100 g)	(%)	(ppm)	(ppm)
21.1%	0.54%	16.55	118.5%	950	2500

Material parameters for the treated MFT sample using the proposed laboratory procedure (Section 2.3) are summarized in Tables 2, 3 and 4.

Table 2. Parameters defining initial and final compressibility curves

A_0	B_0	Z_0	A_f	B_f	Z_f
$(1/\text{kPa})^{B0}$	(-)	(kPa)	$(1/\text{kPa})^{Bf}$	(-)	(kPa)
4.970	-0.260	0.268	4.382	-0.240	0.270

The MFT compressibility relationships at the initial stage (defined by A_0, B_0 and Z_0) and the final (limiting) conditions (defined by A_f, B_f, Z_f) are also displayed in Figure 2.

Material parameters required to define the creep evolution of parameters A, B and Z with time (Eqns. 12, 13 and 14) are summarized in Table 3.

Table 3. Parameters defining creep evolution of compressibility curves

a_1	b_1	z_1	a_2	b_2	z_2
(-)	(-)	(-)	(-)	(-)	(-)
2.000	1.500	5.000	-0.800	-0.950	-0.900

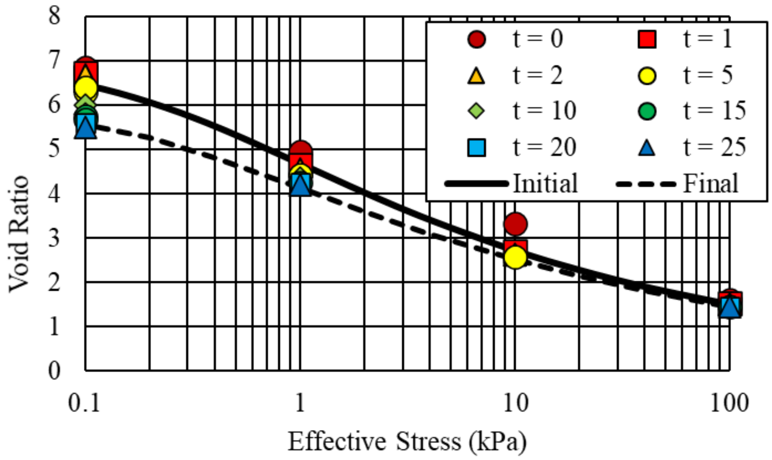

Figure 2. Treated MFT sample – compressibility relationships

The change of the compressibility parameter *A* with time is illustrated in Figure 3.

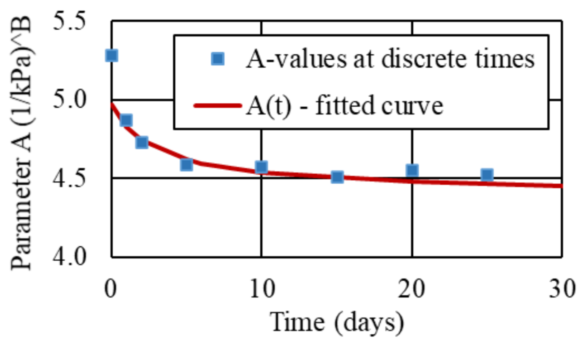

Figure 3. Treated MFT sample – change in the compressibility parameter *A* with time

The change of the compressibility parameter *B* with time is illustrated in Figure 4.

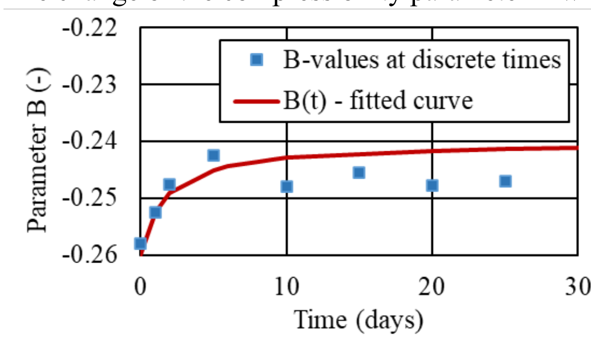

Figure 4. Treated MFT sample – change in the compressibility parameter *B* with time

The change of the compressibility parameter *Z* with time is illustrated in Figure 5.

Material parameters defining density and hydraulic conductivity are summarized in Table 4.

Table 4. Density and hydraulic conductivity parameters

Gs	γ_w	*C*	*D*
(-)	(kN/m^3)	(m/day)	(-)
2.480	9.81	1.02×10^{-6}	4.17

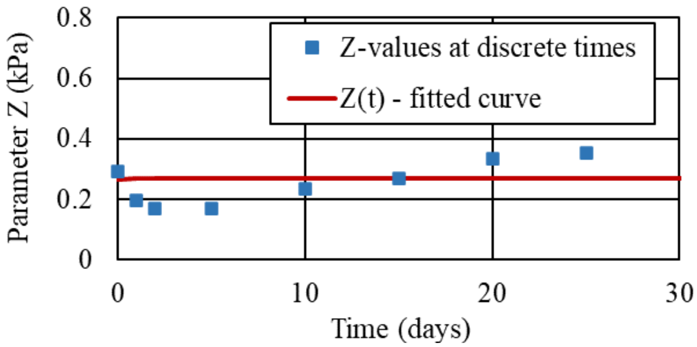

Figure 5. Treated MFT sample – change in the compressibility parameter *Z* with time

Material parameters for the coagulated and flocculated MFT sample (Tables 2 to 4) were used to determine time settlement and void ratio distribution curves for a hypothetical 5-meter high tailings column. The predicted time-settlement curves are displayed in Figure 6.

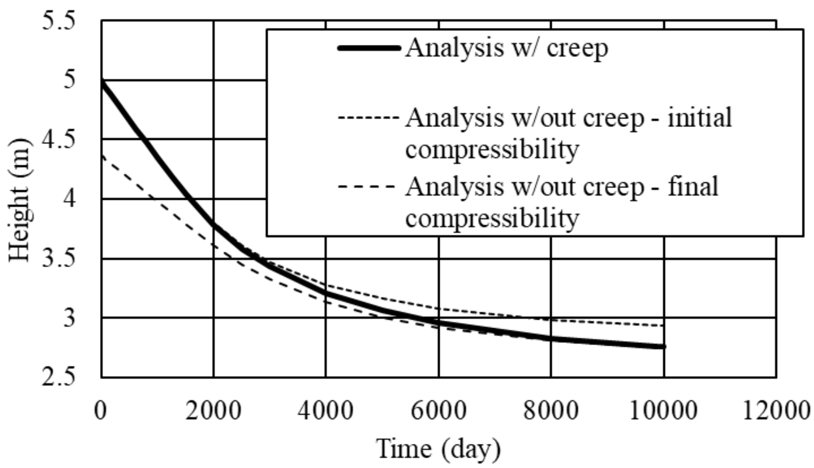

Figure 6. Coagulated & flocculated MFT sample – time settlement curve

The corresponding void ratio profiles are displayed in Figure 7.

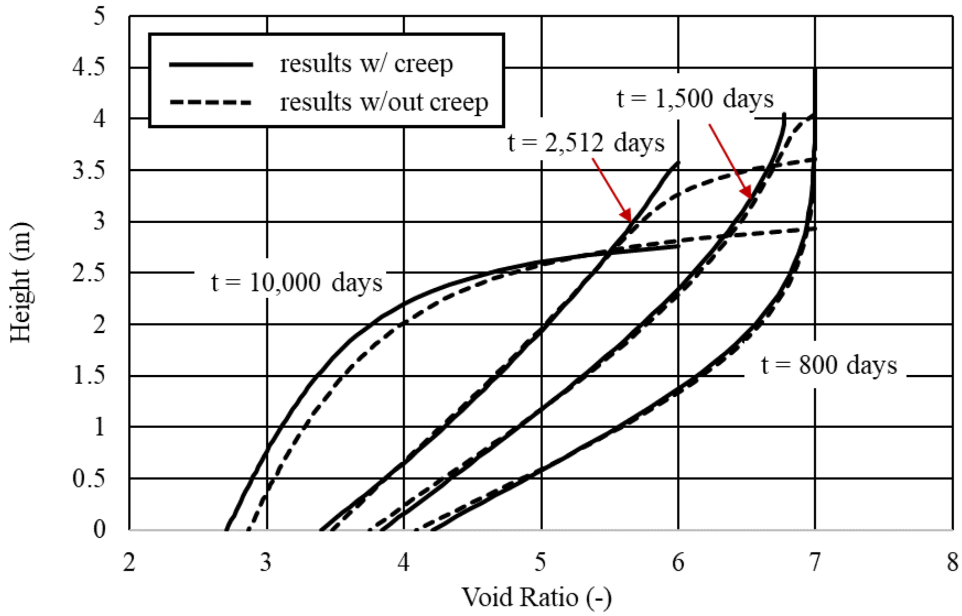

Figure 7. Coagulated & flocculated MFT sample – void ratio profiles.

Figures 2 to 7 demonstrate the importance of creep mechanism at initial stages of the tailings settlement process and the early stages of deposition. Note in Figure 2 that the creep effects are most prominent at low effective stresses while at 100 kPa the creep effects are very small and might be negligible for an engineering application. The same phenomenon is seen in Figure 7 where at shallow depth there are significant differences in void ratio profiles for the consolidation only analyses and the one with creep effect included. These differences diminish with depth as the effective stresses increase. The maximum effective stress at the bottom of the column is 9 kPa for the presented 5-m column example. The creep effects at low effective stresses are caused by the viscoplastic deformation of flocs generated in the MFT treatment process and as the inter-floc volume reduces with time and increase in the effective stress reduces the potential for further volume change. The time settlement curves in Figure 6 show that the settlement rates are unaffected by creep in the early stages (up to 2000 days) because during this period the settlement rate is primarily controlled by the hydraulic conductivity. Only after the settlement rates are reduced in the consolidation process, the creep effects become noticeable. Nevertheless, as void ratio distributions in Figure 7 show, the creep effects are present throughout the consolidation process.

4 CONCLUSIONS

This paper introduces methodology for the consistent evaluation of treated tailings undergoing deformations due to consolidation and creep. The proposed method is applicable to a wide range of materials over the range of stresses of interest to the MFT reclamation process. In addition, the proposed methodology allows for the consistent re-calibration of parameters as more data become available either due to longer testing in the laboratory or by implementing in-situ measurements.

The proposed approach was used to predict the behavior of a treated MFT sample undergoing consolidation and creep in a settling column experiment (see accompanying paper, Murphy et al. 2021).

5 REFERENCES

Abu-Hejleh, A.N. and Znidarcic, D., 1994, Estimation of the Consolidation Constitutive Relations, Computer Methods and Advances in Geomechanics, Siriwardane & Zaman (eds) Balkema, Rotterdam, pp. 499-504.

Bjerrum, L. 1967. Engineering geology of Norwegian normally consolidated marine clays as related to settlements of buildings. *Géotechnique*, Vol. 17, No. 2:81-118.

Gibson, R.E., England, G.L., and Hussey, M.J.L. 1967. The theory of one-dimensional consolidation of saturated clays. 1. Finite Non-linear Consolidation of Thin Homogeneous Layers. *Géotechnique*, Vol. 17, 261-273.

Liu, J.C. and Znidarcic, D. 1991. "Modeling One-Dimensional Compression Characteristics of Soils", Journal of Geotechnical Engineering, ASCE, New-York, Vol. 117, No. 1. pp. 162-169.

Leroueil, S., Kabbaj, M., Tavenas, F. & Bouchard, R. 1985. Stress-strain-strain rate relation for the compressibility of sensitive natural clays. *Géotechnique*, 35(2): 159-180.

Mesri, G., and Castro, A. 1987. The Cα/Cc concept and Ko during secondary compression. *J. Geotech. Engrg., ASCE*, 113(3), 230-247.

Murphy, F., Gjerapic, G., Sorta, A. and Znidarcic, D. 2021. "Validation of an Engineering Model for Consolidation and Creep in Oil Sand Tailings", Tailings and Mine Waste '21 conference proceedings, November 7-10, Banff, AB, Canada.

Sadighian, A., Revington, A., Kaminsky, H., Moyls, B., Li, Y., Omotoso, O., 2018. A New Protocol to Assess the Quality of Tailings Flocculation/Coagulation: A Collaboration to Improve Tailings Treatment at Suncor Energy, International Oil Sands Tailings Conference 2018 proceedings, December 5 – 8, Edmonton, AB, Canada, pp. 81 – 92.

Scott, J.D., Jeeravipoolvarn, S. and Chalaturnyk, R.J. 2008. "Tests for Wide Range of Compressibility and Hydraulic Conductivity of Flocculated Tailings", Proceedings of the 61st Canadian Geotechnical Conference, September 22-24, Edmonton, AB, pp. 738-745.

Sills, G.C. 1998. Development of structure in sedimenting soils. *Philos. T. R. Soc. A,* Vol. 356, 2515-2534

Somogy, F. 1979. "Analysis and Prediction of Phosphatic Clay Consolidation: Implementation Package", Technical Report, Florida Phosphatic Clay Research Project, Lakeland, Florida.

Znidarcic, D., 2015, If it creeps, does it matter? Tailings and Mine Waste '15 conference proceedings, October 25-28, Vancouver, BC, Canada, pp.229-235.

Znidarcic, D., Miller, R., van Zyl, D., Fredlund, M., and Wells, S., 2011, Consolidation Testing of Oil Sand Fine Tailings, Tailings and Mine Waste '11 conference proceedings, November 6-9, Vancouver, BC, Canada, ISBN: 978-0-88865-815-9, pp.251-257.

Influence of bitumen coating on the filterability of clay and non-clay minerals

Dong Wang, Hongbiao Tao, Kaipeng Wang, Xiaoli Tan, Qi Liu
University of Alberta, Edmonton, Alberta, Canada

ABSTRACT: The mining and extraction of the northern Alberta oil sands produce large volumes of a stable tailings stream that contain mainly fine solids, residual bitumen, and process water. Effective dewatering of the oil sands tailings by pressure filtration holds the promise of fast water recycling and land reclamation with stackable filter cakes. Much of the fine solids in the tailings are somewhat associated with bitumen coatings, and the effect of the coated layer on the filtration kinetics of the minerals is still unclear. In this work, we studied the filtration behaviors of bitumen-coated clay and non-clay minerals under different coating conditions, and compared the results with those of the methylated clay and non-clay minerals. It was found that bitumen coating and methylation affected the filterability of the minerals differently. The deviation of the filtration behavior from a monotonic dependence on solid surface hydrophobicity indicated a combined effect of the surface wettability and adsorption layer morphology on the surface of the mineral solids.

1 INTRODUCTION

The Alberta oil sands is an essential unconventional oil resource and a significant economic driver for Canada. Bitumen extraction by warm water is the only commercially used method to recover bitumen from the mined oil sands. During this process, a large volume of tailings stream is produced and directly discharged into the tailings ponds. The coarse solids settle quickly, while the fine solids and residue bitumen form a gel-like suspension known as mature fine tailings (MFT) that contains about 65 wt% process water. Without treatment, the MFT would remain stable for decades. The tailings impoundment area reached about 220 square kilometers by 2017, holding about 1.2 trillion liters of untreated tailings (Natural Resources Defense Council, 2019). These tailings ponds have a significant impact on the environment as the chemicals in the tailings affect the wildlife and pose threats to the region's water resources. The effective treatment of MFT has been one of the most challenging problems faced by oil sands industry.

Several dewatering technologies have been developed to reduce the MFT inventory, such as the consolidated tailings, inline thickened tailings, thin lift drying, centrifuged tailings, etc. (Beier et al. 2013). However, effective and fast warm water recycle and land reclamation is still elusive. The proper treatment of oil sands tailings requires that the tailings be dewatered to below the plasticity limit to develop sufficient long-term strength for reclamation. Recent laboratory and pilot filter press tests showed that the pressure filtration technology could produce filter cakes that were ready for reclamation (Loerke et al. 2017, COSIA Tailings EPA, 2020). However, the required reagent dosages were too high to be economical. At lower dosages, the filter cake would either not form or not amenable for reclamation.

In a previous effort to find the culprit for the difficult dewatering of MFT to improve its pressure filtration, a MFT sample was separated into three layers by high speed centrifugation: a clear process water layer, a "middle layer" (ML), and a "bottom layer" (BL). The ML, containing ultrafine solids and concentrated residual bitumen, showed much lower filterability than the BL in both pressure and vacuum filtration. The ML could also render a model kaolinite slurry unfilterable when it was added amounting to a few wt% of the kaolinite slurry (Wang et al. 2020). Detailed analysis showed that the ML represented 13.5% of the mass of the MFT, and contained 12.0 wt% bitumen, 42.6 wt% fine solids and 45.4 wt% water. Mineralogical analysis of the ML showed that the solids phase contained mainly kaolinite, quartz, and swelling clays such as kaolinite-montmorillonite. Therefore, the detrimental effect of the ML could be attributed to the fine mineral solids, and/or the residual bitumen. To decouple these effects, we studied the filtration behavior of different minerals (without bitumen coating) and the results were reported in an earlier paper (Wang et al. 2020). The role of bitumen on the filtration of MFT was investigated in this study.

Bitumen possesses colloid and gelling propensity in the presence of high asphaltene/resin concentrations (Loeber et al. 1998). Scott et al (1985) proposed that the high gel strength of MFT could be attributed to the presence of the residue bitumen. The high viscosity bitumen droplets could adhere to the edge of the clay surface, aggregate the clay, and eventually block the flowing channels of the interstitial water. The oil sands tailings settling tests conducted by Klein et al. (2013) seemed to support the retardation effects of bitumen on the settling rate of the solids. Removal of residual bitumen by froth flotation was found to improve the settling rate, provided that the bitumen was not completely removed.

Categorically, the residual bitumen in MFT may exist in the forms of bulk bitumen, bitumen emulsion droplets, petroleum "coal" (Jang and Etsell 2005; Zubot et al. 2012) and bitumen adsorbed on mineral surfaces including some solvent-insoluble organics (Majid, et al. 1991). The effect of bitumen emulsions on vacuum filtration had been investigated previously, suggesting that the bitumen emulsions had little effect on filtration (Wang et al. 2020). In this paper, we focus on the roles of bulk bitumen and bitumen coating on mineral surfaces on the filtration behavior of mineral solids. As one of the consequences of bitumen coating is to make the coated surface partially hydrophobic, we also investigated the hydrophobization effect without a bitumen coating, by introducing methyl groups to the tested mineral surfaces and comparing the results with bitumen-coated minerals.

2 EXPERIMENT MATERIALS AND METHODS

2.1 *Materials and sample preparation*

Bitumen froth, obtained from an oil sands operator in northern Alberta, Canada, containing 58 wt% bitumen, 4.0 wt% solids and 38 wt% water, was used as the bulk bitumen sample. A high purity bitumen sample (99.5 wt%) was collected from the same operator and diluted to 60 wt% with toluene as the stock solution for bitumen coating experiment. Kaolinite (BASF ASP 600), montmorillonite (Ward's Sciences), quartz (US Silica), and rutile (TiO_2, US Research Nanomaterials) were used as the model minerals for bitumen coating. 3-chloropropytriethoxy-silane (3CTS), purchased from Sigma-Aldrich, was used as the methylation agent and was prepared as a toluene solution at different concentrations. An anionic polyacrylamide (A3335) from SNF and a cationic polyDADMAC polymer (Alcomer 7115) from BASF were used as the polymer flocculant and coagulant, respectively. Hydrochloric acid (HCl) of analytical grade was purchased from Fisher Scientific and used to treat quartz prior to methylation.

To prepare the bitumen-coated minerals, 20 g dried minerals were mixed with 200 mL bitumen-toluene solutions at 10 wt%, 30 wt%, or 50 wt% bitumen. The suspension was sealed and allowed to stand for one week, with 12-hours of agitation using a magnetic stir bar every other day. After the treatment, the slurry was centrifuged at 12860 rpm (20,000 RCF) for 30 min and the centrifuge cake washed with toluene. The centrifugation and toluene washing were repeated 4-5 times until the supernatant (toluene) was colorless. Afterwards, the bitumen-coated minerals were dried in a fume hood at room temperature overnight and collected for use.

The methylation process of different minerals was slightly different. The quartz methylation process followed Liu and Laskowsk's methods (1989), i.e., the quartz was treated with acid before treatment. The quartz was treated with 0.5 M HCl solution for 12 hours with a magnetic stir bar at 800 rpm. After treatment, the quartz was washed with DI water to remove the remaining HCl and followed by centrifugation at 12860 rpm (20,000 RCF) for 30 mins. The acid-treated quartz was dried at 110°C overnight. Afterwards, 20 g dried acid-treated quartz was mixed with 200 mL 0.005 M, 0.02 M, 0.04 M 3CTS-in-toluene solutions, respectively, and allowed to stand overnight. The obtained samples were named Quartz 1, 2, and 3, respectively. The methylated quartz was washed with toluene followed by centrifugation to remove the remaining 3CTS and dried in a fume hood overnight. As the acid treatment could alter the structure of clays, kaolinite and montmorillonite were not treated with acid before methylation (Bendou and Amrani 2014). Instead, 20 g dried kaolinite or montmorillonite was mixed with 200 mL 0.04 M 3CTS solution and stirred at 800 rpm with a magnetic stir bar for 24 hours. This was followed by toluene washing and centrifugation. The methylated minerals were dried in a fume hood overnight.

2.2 *Contact angle measurement*

The contact angle of bitumen-treated and methylated minerals was measured by the static sessile drop method, which directly measures the water contact angle on the surface of pressed pellets of minerals (Chen et al. 2016; Brookes and Bethell 1984). A solid mass of 150 mg mineral sample was weighed and pressed at 40 MPa for 1 min by an ICL 12 Ton E-Z Press™ pellet presser, and a 1 cm diameter pellet was obtained. The contact angle of the pellet was measured with a FTA2000 contact angle goniometer equipped with an illumination and image analysis system. The images of water droplets on the pellet surface were recorded every 0.1 s, and the first unambiguous image of water droplet shape was used as the contact angle of minerals. Every measurement was repeated three times.

2.3 *Filter press filtration and vacuum filtration*

The procedures of pressure filtration and vacuum filtration were similar to what we reported in the T&MW 2020 conference (Wang et al., 2020). To identify the bulk bitumen effect on filtration, the bitumen froth sample was mixed with a kaolinite slurry at different bitumen contents and prepared in 500 g batches by homogenizing at 300 rpm for 10 mins with a PBT axial-flow impeller. The subsequent dual polymer treatment (A3335 and Alcomer 7115) and filter press tests of the kaolinite slurry followed the procedures of Wang et al. (2020). In the dual-polymer treatment, the torque of the slurry was monitored to control polymer addition points and degree of stirring. The polymer-treated slurry was filtered by a SERFILCO 0.02-7PPHM laboratory filter press at 6.2 bar for 1 hour. The solids content of the filter cake was determined by drying part of the cake in a vacuum oven at 70°C for 24 hours at 0.8 bar. Vacuum filtration was conducted on a laboratory glass filter funnel set up with a filter area of 9.6 cm^2 at 30 to 50 mbar with 20 mL mineral slurries of different solid contents. Filtrate was collected in a graduated tube which allowed the determination of the initial filtration rate (IFR). More details can be found from Wang et al. (2020).

3 RESULTS AND DISCUSSION

3.1 *Effects of bulk bitumen (bitumen froth)*

The effect of bulk bitumen on filtration was evaluated by blending bitumen froth (BF) with MFT and model kaolinite slurry, and then filter the mixture in the laboratory filter press. The results are shown in Figure 1. As can be seen, when the BF was added to the MFT to make a 5 wt% bitumen content, the final solids content of MFT after filtration was decreased from 67.1 wt% to 63.1 wt% with the same polymer treatment (1000 g/t A3335 and 3000 g/t Alcomer 7115) under the same filtration conditions. For the kaolinite slurry, two conditions were tested: (1) Without polymer treatment. In this case, the addition of BF to yield a bitumen content of 3.4 wt% in the kaolinite slurry only caused a slight decrease in the filter cake solids content from 68.5 wt% (without BF) to 66.7 wt% (with 3.4 wt% BF). (2) With polymer treatment (1000 g/t A3335 and 3000 g/t Alcomer 7115). Surprisingly, the use of the high dosage treatment caused the solids content in the filter cake to drop from 66.7 wt% (no polymer treatment) to 65.8 wt% (with 1000 g/t A3335 and

3000 g/t Alcomer 7115). Interestingly, A further increase of bitumen content from 3.4 wt% to 10.2 wt% in the kaolinite slurry did not change the filter cake solids content of kaolinite slurry.

The effect of bulk bitumen on the filtration of MFT and kaolinite slurry was not as drastic as we initially thought. We initially thought that the added bitumen could block the pores of both the filter cake and the filter medium, and stop the filtration altogether like the centrifuged middle layer (ML) did. The filter press results showed that the bulk bitumen only had a slight effect on the kaolinite slurry filtration.

To eliminate the possibility of sample variation, we also tested a different bitumen froth sample, which had a composition of 65.2 wt% bitumen, 12.6 wt% solids, and 22.2 wt% water. When dosed to the kaolinite slurry to 3.4 wt% bitumen, the pressure filter cake was found to contain 66.9 wt% without polymers treatment, and 66.3 wt% solids with 1000 g/t A3335 and 3000 g/t Alcomer 7115. Overall, the bulk bitumen in the form of bitumen froth seems to have little influence on the filtration of MFT and kaolinite slurry. In fact, the bitumen was observed to pass through the filter cake and was visible in the filtrate.

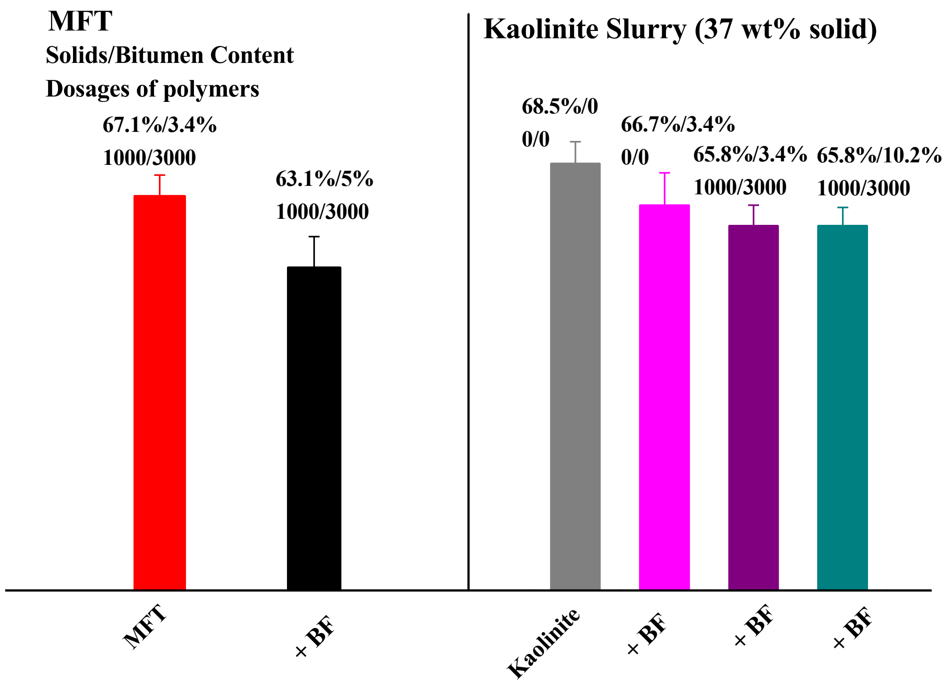

Figure 1. Solids content of the filter cakes of MFT and kaolinite slurry with and without the addition of bitumen froth (BF). Laboratory filter press tests at 6.2 bar for 1 hour.

3.2 *Effects of bitumen coating on minerals*

3.2.1 *The contact angle of bitumen-treated or methylated minerals*

The wetting property of the treated minerals was evaluated by measuring the water contact angle, and the results are shown in Figure 2. As can be seen, after bitumen coating or methylation, the contact angle of quartz increased from 13° to more than 110° (Figure 2A). The significant increase of the contact angle indicated that both the bitumen and 3CTS were coated on the quartz surface and rendered it hydrophobic. The contact angle of rutile increased from 19° to more than 120° after bitumen coating (Figure 2B). Similarly, the contact angle of kaolinite increased from 14° to more than 90° after bitumen treatment, but methylation seemed to have a limited effect on the kaolinite surface as the contact angle was 35° after methylation (Figure 2C). For montmorillonite, neither the bitumen treatment nor methylation procedure used in this work changed the surface hydrophobicity significantly, and the contact angle remained in the range of 20°–28° (Figure 2D).

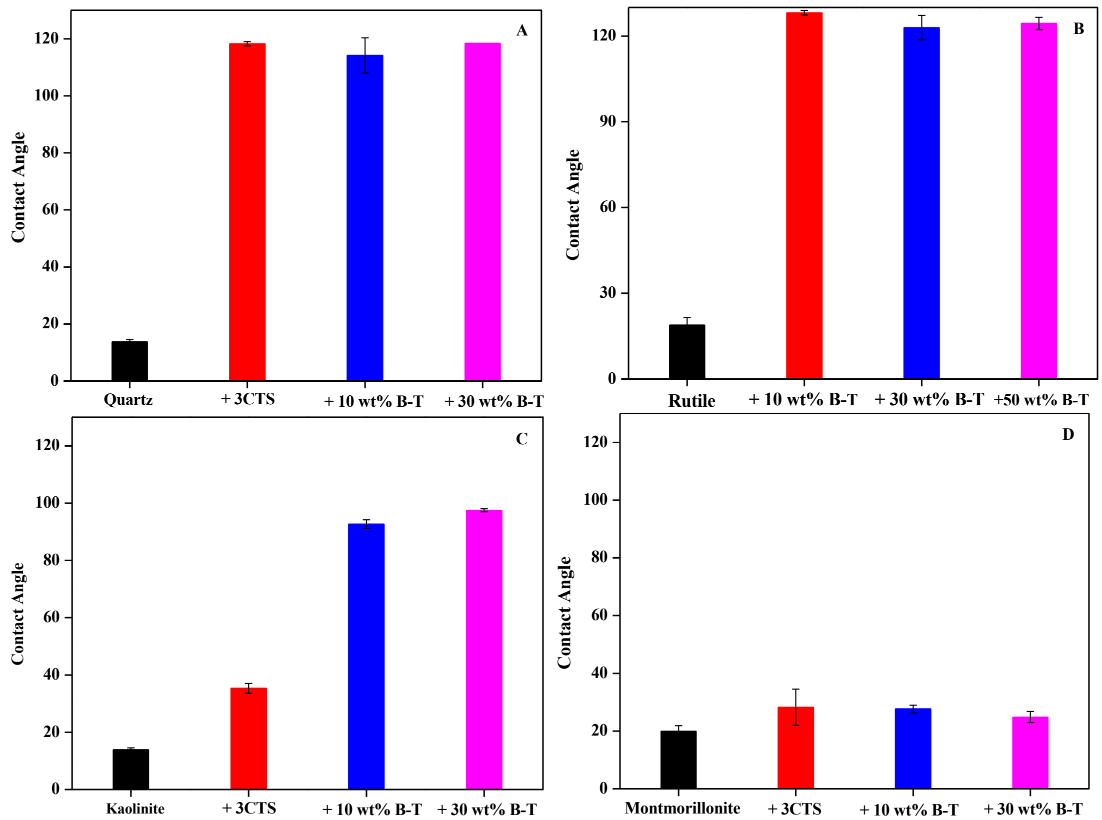

Figure 2. The contact angle of methylated and bitumen-treated minerals.

3.2.2 *Filtration of the bitumen-treated minerals*

Figure 3 shows the filtration results of the four minerals treated at different bitumen concentrations. After treatment with 10 wt% bitumen-toluene (B-T) solution, the filterability of quartz showed a noticeable improvement compared to the untreated quartz, IFR increasing from 0.08 mL/min·cm^2 to 0.18 mL/min·cm^2. However, when the quartz was treated with a higher bitumen concentration (30 wt% bitumen), the filterability of quartz decreased compared to the 10 wt% bitumen concentration (Figure 3A). There seems to be an optimum amount of bitumen coating for quartz to achieve the best filterability.

Rutile showed a similar behavior as quartz, except that the "reversing" of filterability occurred at a higher bitumen concentration of 50 wt% (Figure 3B). The observation seemed to lend support to the postulation that there was an optimum amount of bitumen coating for the coated solids to achieve the best filterability. The reason that a higher bitumen concentration was required to achieve the "optimum" was likely due to the smaller particle size of the rutile sample (d_{50} = 0.66 µm) thus higher specific surface area than quartz (d_{50} = 3.64 µm).

The filtration behavior of bitumen-coated kaolinite (Figure 3C) was similar to quartz, i.e., treatment by 10 wt% bitumen solution improved filtration whereas the 30 wt% bitumen solution reversed the trend. Kaolinite had similar particle size as quartz (d_{50} of kaolinite = 4.1 µm) and since kaolinite is not an expandable clay, its specific surface area was likely similar to that of quartz. Therefore the "optimum" bitumen coating was probably similar to quartz.

Interestingly, the bitumen coating on montmorillonite also slightly improved its filtration behavior, which seems to be consistent with the slight increase in the measured contact angle of the bitumen-treated montmorillonite sample (Figure 2).

As there seemed to be an optimum bitumen concentration to treat the different minerals to achieve the optimum filtration response, we hypothesize that the bitumen-coating layer thickness on the minerals surface dictated the filterability of bitumen-coated minerals in oil sands tailings. There may be a "critical" bitumen thickness value where the minerals achieve the best filterability.

As reported by Chen et al., the organics associated with the fine solids from bitumen, which could not be washed off by toluene, were found to be soft (Chen et al. 2017). The soft bitumen coating on the mineral surface could be mobilized by the pressure differential in filtration if it was sufficiently thick. The mobilized bitumen could block the pores of the filter cake, lowering filtration rate.

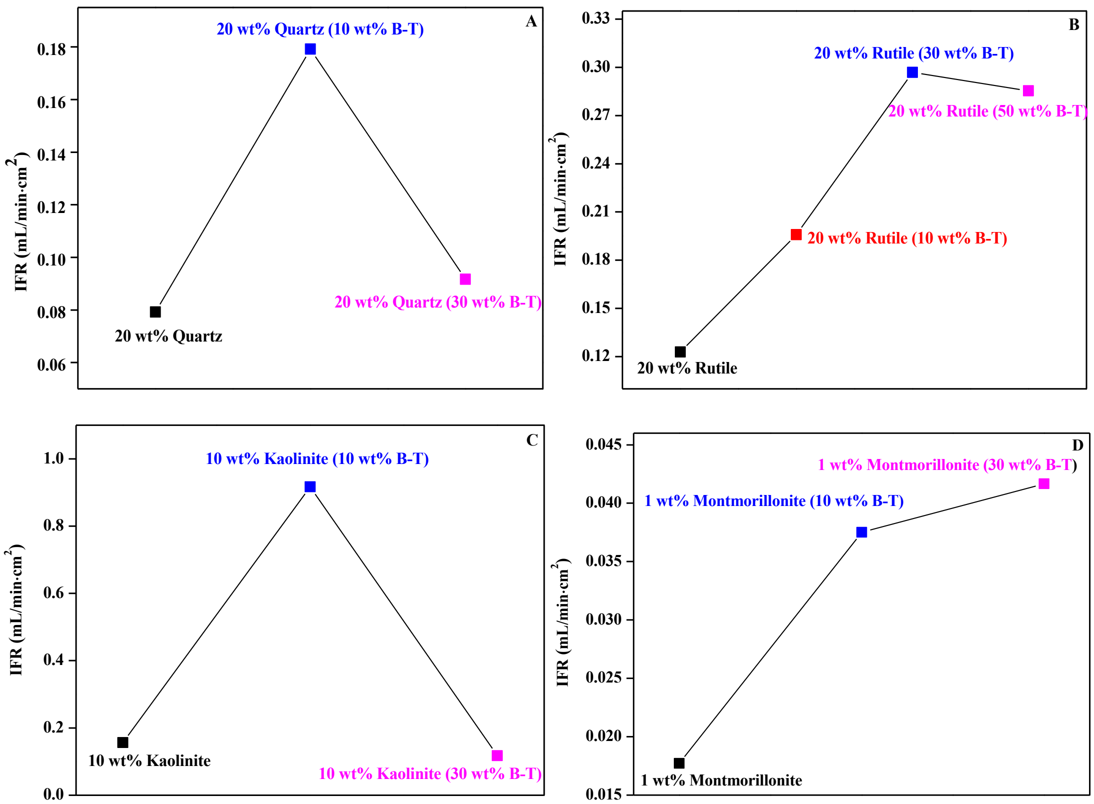

Figure 3. IFR of minerals treated at 10 wt%, 30 wt% or 50 wt% bitumen-toluene concentrations.

It should be noted that the bitumen coating on the mineral surface in this work was obtained by treating the minerals in toluene-diluted bitumen froth. The bitumen in the bitumen froth was likely very different from the bitumen in the tailings. Therefore the bitumen coating on the mineral surface in this work may not be a true representation of the bitumen coating on mineral surface in the oil sands tailings. That is a subject that is worthy further investigation.

3.3 *Bitumen coating versus methylation*

The foregoing description and discussion implied that bitumen coating on the mineral surface had two conflicting roles in filtration: the induced hydrophobicity helped increase filtration rate of the aqueous slurry, but the thickness of the adsorbed bitumen layer may adversely affect filtration due to its mobilization under the pressure gradient. In order to decouple these effects, the minerals were made hydrophobic but without a mobile deformable bitumen coating, i.e., they were treated with a methylation procedure. The resulting hydrophobicity and filtration behavior were compared with bitumen-coated minerals.

Quartz was methylated under different conditions so that the measured contact angles were 14° (Quartz 1), 40° (Quartz 2), 110° (Quartz 3) (Figure 4A). The filtration curves of the three quartz samples are shown in Figure 4B. As can be seen, the more hydrophobic quartz (higher contact angle) had faster filtration rate. In fact, Figure 4 C shows that the initial filtration rate IFR is linearly correlated to contact angle.

However, for bitumen-coated quartz, the initial filtration rate did not monotonically depend on contact angle (Figure 4D). Treatment of quartz with 10 wt% and 30 wt% bitumen-in-toluene solution resulted in similar contact angle, i.e., greater than 110° in both cases. However, the IFR of the quartz treated with 30 wt% bitumen-in-toluene solution had a much lower IFR (0.08 mL/min/cm^2) than the one treated in 10 wt% toluene (0.16 mL/min/cm^2). It can also be seen from Figure 4D that the untreated quartz (contact angle 14°), Quartz 2 (treated with 3CTS, contact angle 40°), and the quartz treated with 30 wt% bitumen-in-toluene solution (contact angle 120°) had similar IFR but with different contact angles. Therefore, surface hydrophobicity was not the only parameter controlling the filtration behavior of the aqueous mineral slurries.

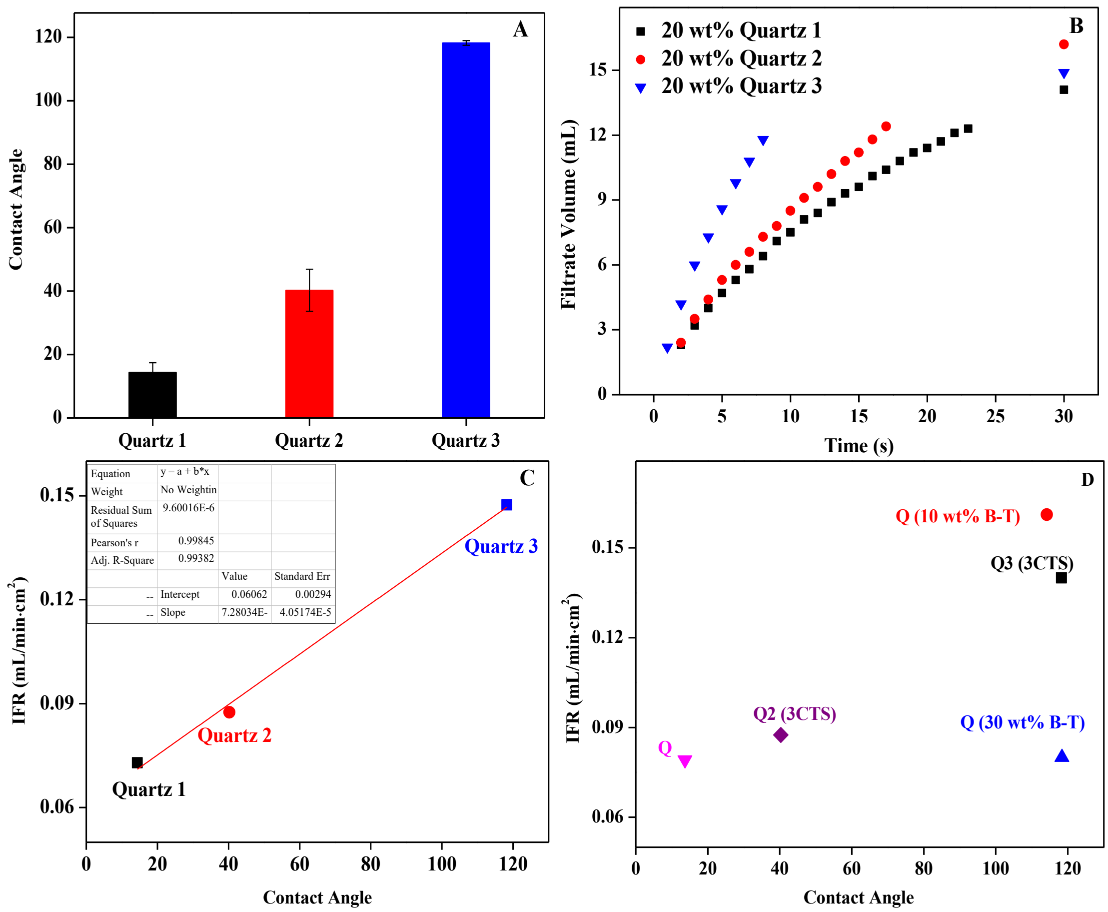

Figure 4. (A) The contact angles of quartz, (B) filtration curves of methylated quartz, (C) correlation between IFR and contact angel of methylated quartz, and (D) correlation between IFR and contact angle for methylated and bitumen-coated quartz.

The methylation agent 3-chloropropytriethoxysilane (3CTS) seemed to interact with the tested kaolinite and montmorillonite samples differently from quartz. Under the methylation procedures used in this work, we were unable to prepare methylated kaolinite and montmorillonite with different hydrophobicity. In fact, the contact angles of methylated kaolinite and montmorillonite had only increased marginally.

On the other hand, bitumen-coating treatment in both 10 wt% and 30 wt% bitumen-in-toluene solutions significantly increased the surface hydrophobicity of the kaolinite, although it only increased the hydrophobicity of montmorillonite marginally. Kaolinite behaved similarly as quartz, i.e., treatment in 10 wt% and 30 wt% bitumen-in-toluene solutions both resulted similar high contact angles, but the 30 wt% bitumen-in-toluene solution treatment showed much lower IFR than the 10 wt%. It can be seen that the results shown in Figure 5A (kaolinite) were very similar to Figure 4D (quartz). Except for the kaolinite that was treated in 10 wt% bitumen-in-toluene, which had a high contact angle and high IFR, the other three kaolinite samples (untreated kaolinite, methylated kaolinite, and 30 wt% bitumen-in-toluene treated kaolinite) all had almost the same IFR despite their totally different contact angles. Therefore, this again clearly shows that surface hydrophobicity was not the only parameter controlling the filtration behavior.

A general relationship between the IFR and contact angle was not observed for montmorillonite, either (Figure 5B). Both the bitumen coating and methylation increased contact angle of the montmorillonite slightly, but bitumen coating could improve filtration while methylation did not.

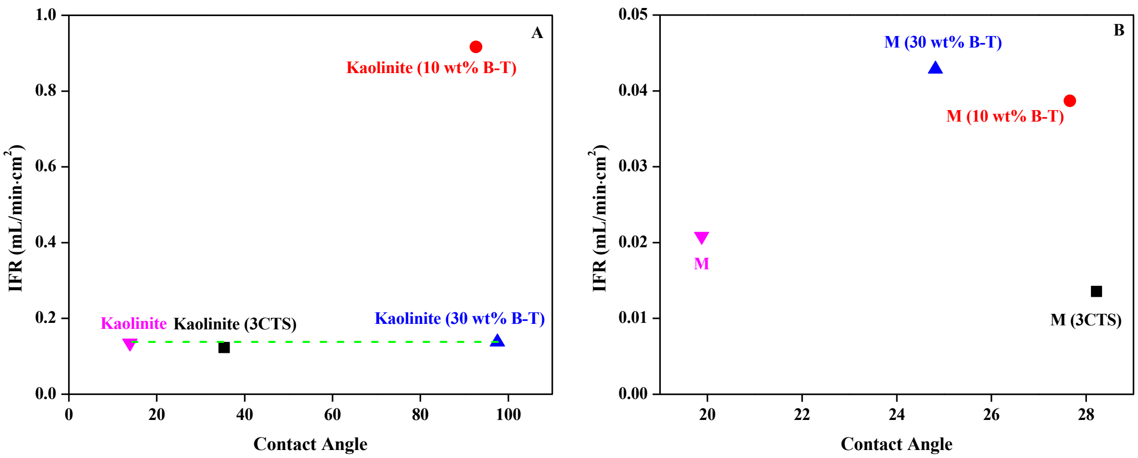

Figure 5. Initial filtration rate (IFR) of (A) kaolinite and (B) montmorillonite as a function of contact angle following methylation or bitumen-coating treatment.

Overall, bitumen coating could render mineral surface hydrophobic, as it significantly increased the contact angle of non-clay minerals and non-swelling clays (quartz, rutile, kaolinite), and marginally increased the contact angle of swelling clay such as montmorillonite. However, the increased hydrophobicity did not monotonically lead to improved filtration of the aqueous slurries of these bitumen-coated minerals. It appears that the filtration also depended on how much bitumen was used to coat the minerals. When a larger amount of bitumen was used, the filtration of the bitumen-coated mineral was adversely affected despite its high surface hydrophobicity. We attributed this observation to the mobility of the surface adsorbed bitumen films, i.e., under the pressure gradient of filtration, the “thick” bitumen layer could be mobilized to block the pores in filter cakes. Further studies are being carried out to investigate this hypothesis.

4 CONCLUSIONS

The role of bitumen in the filtration of oil sands tailings was investigated in this study. The bitumen in the oil sands tailings could be in the form of “bulk free bitumen”, bitumen-in-water emulsion, and bitumen adsorbed on mineral surfaces. The bitumen-in-water emulsion had been reported in our previous work and was found not to significantly affect tailings filtration. The effects of bulk bitumen and surface adsorbed bitumen were studied in this work by pressure filtration using a laboratory filter press, and a laboratory vacuum filtration set up. Four mineral samples were studied: quartz, rutile, kaolinite, and montmorillonite, representing non-clay minerals, non-swelling clay and swelling clay. The minerals were rendered hydrophobic by using either bitumen coating treatment in a toluene solution of bitumen, or methylation treatment in a toluene solution of 3-chloropropytriethoxy-silane (3CTS). The observations were:

(1) Adding a bitumen froth sample to the kaolinite slurry or a mature fine tailings slurry did not significantly affect the filtration. Tests in a laboratory filter press showed that even after adding the bitumen froth amounting to more than 10 wt% bitumen to the kaolinite slurry, the solid content of the pressure filter cake only dropped from 69 wt% to 65 wt%.

(2) Bitumen-coating treatment significantly increased the surface hydrophobicity (judging by contact angles) of non-clay minerals and the non-swelling clays, and marginally increased the hydrophobicity of the swelling clay montmorillonite.

(3) The effects of bitumen coating on the surface of the minerals on their filtration were more varied. When the minerals were treated with 10 wt% bitumen-in-toluene solution, the filtration of all tested minerals was improved, more significantly for the non-clay minerals and non-swelling clay and only marginally for the swelling clay. This correlated to an increase in the measured contact angle, thus mineral surface hydrophobicity. However, at higher concentrations of bitumen in the toluene solution, the filtration of the tested minerals was observed to deteriorate. Interestingly, the "critical" bitumen concentration seemed to depend on the specific surface area of the minerals, i.e, minerals with higher specific surface area had a higher critical bitumen concentration. The observation seemed to hint on the role of the bitumen-coating layer thickness. Although the bitumen-coating thickness had not been studied in this work yet, we hypothesized that the thick adsorbed bitumen layer might be mobilized by the pressure gradient during filtration to block pores in the filter cake while it was formed. More studies are required to further investigate this hypothesis.

(4) To decouple the effects of surface hydrophobicity and adsorbed bitumen layer thickness, methylation of the tested minerals was attempted, with the rationale that such treatment could render the surface hydrophobic but without leaving a deformable and mobile organic coating on the surface. It turned out that only the methylation treatment of quartz was successful, and the quartz filtration rate displayed a clear linear correlation to the contact angle induced by the methylation treatment, lending some support to the hypothesis about the mobile deformable bitumen coating. Methylation attempt on kaolinite and montmorillonite was not successful as the contact angle of these clay minerals did not increase substantially after the methylation treatment.

5 ACKNOWLEDGEMENTS

Financial support was provided by Imperial Oil Ltd., Alberta Innovates and Canada's Oil Sands Innovation Alliance (through the Institute for Oil Sands Innovation), and Natural Sciences and Engineering Research Council of Canada in the form of a Collaborative Research and Development project grant. The authors are also grateful to the technical support and assistance of technical personnel from the Institute for Oil Sands Innovation, Lisa Brandt and Brittany McKinnon.

6 REFERENCES

Adeyinka, OB, Samiei, S, Xu, Z, & Masliyah, JH. 2009. Effect of particle size on the rheology of Athabasca clay suspensions. *The Canadian Journal of Chemical Engineering,* 87(3), 422-434.

Natural Resources Defense Council. 2019. One trillion litres of toxic waste and growing: Alberta's tailings ponds. Retrieved from: https://www.nrdc.org/sites/default/files/media-uploads/edc-and-nrdc-one-trillion-litres-of-toxic-waste-and-growing-albertas-tailings-ponds-june-2017.pdf

Beier, N, Wilson, W, Dunmola, A, Sego, D. 2013. Impact of flocculation-based dewatering on the shear strength of oil sands fine tailings. *Canadian Geotechnical Journal*, 50(9), 1001-1007.

Bendou, S, Amrani, M. 2014. Effect of hydrochloric acid on the structural of sodic-bentonite clay. *Journal of Minerals and Materials Characterization and Engineering*, 2(5), 404-413.

Brookes, GF, & Bethell, PJ. 1984. Zeta potential, contact angle and the use of amines in the chemical dewatering of froth-floated coal. *Powder technology*, 40(1-3), 207-214.

Chen, Q, Liu, J, Thundat, T, Gray, MR, Liu, Q. 2017. Spatially resolved organic coating on clay minerals in bitumen froth revealed by atomic force microscopy adhesion mapping. *Fuel*, 191, 283-289.

Chen, Q, Stricek, I, Cao, M, Gray, MR, Liu, Q. 2016. Influence of hydrothermal treatment on filterability of fine solids in bitumen froth. *Fuel*, 180, 314-323.

COSIA Tailings EPA, 2020. 2019 tailings research report. Retrieved from: https://cosia.ca/sites/default/files/attachments/2019%20Tailings%20Research%20Report_FINAL.pdf

Jang, H. and Etsell, TH, 2005. Morphological and mineralogical characterization of oil sands fly ash. Energy & fuels, 19(5), pp.2121-2128.

Scott, JD, Dusseault, MB, Carrier III, WD.1985. Behaviour of the clay/bitumen/water sludge system from oil sands extraction plants. *Applied clay science*, 1(1-2), 207-218.
Keshmiri, K, Mozaffari, S, Tchoukov, P, Huang, H, Nazemifard, N. 2016. Using microfluidic device to study rheological properties of heavy oil. arXiv preprint arXiv:1611.10163.
Klein, C, Harbottle, D, Alagha, L, Xu, Z. 2013. Impact of fugitive bitumen on polymer-based flocculation of mature fine tailings. *The Canadian Journal of Chemical Engineering*, 91(8), 1427-1432.
Liu, Q, Laskowski, JS. 1989. The role of metal hydroxides at mineral surfaces in dextrin adsorption, I. Studies on modified quartz samples. *International Journal of Mineral Processing,* 26(3-4), 297-316.
Loeber, L, Muller, G, Morel, J, Sutton, O. 1998. Bitumen in colloid science: a chemical, structural and rheological approach. *Fuel*, 77(13), 1443-1450.
Loerke, R, Tan, X, Liu, Q. 2017. Dewatering of oil sands mature fine tailings by dual polymer flocculation and pressure plate filtration. *Energy & Fuels*, 31(7), 6986-6995.
Majid, A., Sparks, BD. Ripmeester, JA, 1991. Characterization of solvent-insoluble organic matter isolated from Alberta oil sands. Fuel, 70(1), pp.78-83.
Wang, D, Tao, H, Wang, K, Tan, X, Liu, Q. 2020. Decoupling the Effects of Ultrafine Solids and Residual Bitumen on the Filterability of Oil Sands Tailings. *In International Conference on Tailings and Mine Waste*. Keystone,Colorado.
Zhu, Y, Tan, X, Liu, Q. 2017. Dual polymer flocculants for mature fine tailings dewatering. *The Canadian Journal of Chemical Engineering*, 95(1), 3-10.
Zubot, W, MacKinnon, MD, Chelme-Ayala, P, Smith, DW, El-Din, MG, 2012. Petroleum coke adsorption as a water management option for oil sands process-affected water. Science of the Total Environment, 427, pp.364-372.

Assessing dewatering performance of treated fluid fine tailings with a modified bench-scale filter press

Yunhui Li, Heather Kaminsky, Catalina Romero, Xue Yuki Gong, Mohammed Ghuzi and Joel Tacas
Northern Alberta Institute of Technology, Edmonton, Canada

ABSTRACT: Filter press is a low-cost and easily operated equipment to assess the filtration performance of tailings. Direct air pressure (20, 30 or 100psi) was applied to a tailings sample and the rate of the filtration was measured either for a fixed time or until the filtered cake dewatered sufficiently but unevenly to crack. The cracking of the filtered cake limits the ability to evaluate the dewaterability of different tailings. In this study, a filter press was modified to use an elastic film or a piston cylinder in between the high-pressure gas and the tailings sample. This applies the same gas pressure to the sample but removes the limitation on dewatering time due to cracking. This permits an assessment of dewatering performance of different tailings treatments at much higher solid contents.

This study showed that the modified filter press produced highly repeatable results. The test can discern differences in different fluid fine tailings (FFT) treatments at a given pressure. The treated FFT can achieve the plastic limit in hours or 1-2 days compared to months or years by settling tests through the column. Furthermore, the release water from pressure filtration can be easily filtered for water chemistry assessment allowing more insight into the behavior of the tailings. We believe that pressure filtration can be an indicator of long-term consolidation trends.

1 INTRODUCTION

Most mining industries produce very large volumes of a by-product called tailings. The tailings slurry is typically discharged into a containment area causing environmental issues. Dewatering the tailings slurry is a typical solution to recycle the release water and reduce the tailings' storage footprint. The most popular dewatering methodology is to separate fine particles in the tailings slurry from water using coagulation and subsequent flocculation. A successful selection of a coagulant and flocculant technology requires a reliable and cost-effective technique to characterize the dewatering performance. Many different methods of evaluating dewatering at lab scale have been studied and used including net water release, capillary suction time, settling, and specific resistance to filtration testing (Sadighian, et al. 2018; Revington, et al. 2010; Alamgir, et al. 2012).

Filtration is one of the most traditional methods for solid-liquid separation and it has been widely used across many industries. Filtration is an example of one consolidation method that can achieve dry tailings through a mechanical driving force process. During the filtration process, shrinkage cracking is frequently encountered resulting in a restriction on further desaturation (Anlauf et al. 1985; Wakeman et al. 1974). Lloyd et al. (1972) suggested that the filter cake cracking may be due to the internal stress development during compression. It was determined in that study that the filter cake cracking could be eliminated through careful control of key input parameters such as initial slurry concentration, fine particle content, surfactant addition, etc. (Barua 2014). It is not desired, however, to change the original properties of the testing materials.

The pressure filter press has been modified by inserting a piston cylinder into the sample cup between the gas and the testing sample (Li, et al. 2018). The modified filter press can effectively press the sample and avoid compressed cake cracking resulting in the premature end of the test (Li, et al. 2018). This permits an assessment of the dewatering performance of different treatments at much higher solid's contents. In this study, further modification was developed to get a repeatable, easily operative, and cost-effective characterization method of dewatering. Fluid fine tailings (FFT) from the oil sands operations in Northern Alberta, Canada were treated with different additives. The impacts of the applied pressure during the filtration and filter media were studied using the modified filter press. The sensitivity of the filtration results to the different types of FFT treatments, different flocculants, different dosages of the tested flocculant, were also investigated to look into whether the filter press was an effective characterizing tool to study FFT dewatering performance.

2 EXPERIMENTAL

2.1 *Materials*

FFT samples from an oil sands tailings pond were characterized by Dean and Stark (D&S) for bitumen, solids, and water content (Dean and Stark, 1920), methylene blue index (MBI) (Omotoso and Morin, 2008), particle size distribution (PSD) by sieving with a 325 mesh sieve (45 microns) (COSIA, 2016), pH, density, and conductivity (Table 1). Pore water extracted by filtration was analyzed with a Thermo Scientific Ion Chromatography system (Table 2). Polymer A3338 and polymer NRG1000 are types of anionic polyacrylamide as the flocculant provided by SNF Canada. Polymer E4964 is also a type of anionic polyacrylamide provided by Kemira Water Solutions Canada, Inc. These polymer solutions were prepared at a concentration of 0.45 wt% in pond effluent water (PEW). DP-OMC-1510 and DP-OMC-1509 were prepared at concentrations of 1% w/v and 0.5% w/v in pond effluent water (PEW), proprietary process additives developed by BASF Corporation used in the sand-mixed FFT treatment (Table 3).

The alum solution used as the coagulant was 48.76 wt% of $Al_2(SO_4)_3 \cdot 14H_2O$ produced by Kemira Water Solutions Canada, Inc. The dosage of alum used in this study was 950 ppm water-based and the desired volume of alum for the test was calculated according to Equation 1.

Table 1. FFT characterization.

FFT	Mineral wt%	Bitumen wt%	Water wt%	MBI meq/100g	Fines wt%	pH	Density kg/m^3	Electric Conductivity µS/cm
ES4400	32.45	2.15	65.40	10.6	89.3	8.7	1240	2484

Table 2. FFT characterization on water chemistry. Unit is ppm.

FFT	Li^+	Na^+	K^+	Mg^{2+}	Ca^{2+}	Cl^-	NO_3^-	SO_4^{2-}
ES4400	0.10	858.21	12.54	7.11	11.66	684.16	8.57	159.89

Table 3. Non-Acid Generating Sand characterization.

Sand	Mineral wt%	Bitumen wt%	Water wt%	Fines wt%	pH	Density kg/m^3
NAGS	96.40	0.20	3.10	3.90	6.69	2650

$$Volume\ of\ Alum\ (ml) = \frac{Alum\ dosage\ (\text{ppm}) \times 10^{-6} \times Alum\ concentration (48.76\%) \times water\ mass\ in\ FFT\ sample (g)}{Alum\ specific\ gravity\ (1.33\ \text{kg}/m^3)} \quad (1)$$

2.2 *FFT treatment by PASS technology*

An overhead mixer with an online torque sensor and display (Heidolph Hei-Torque 100 Precision Base) was used for the flocculation in a 6″ metal baffled cup (Li, et al. 2021). Each flocculation was conducted using a 1 liter of FFT. The FFT sample was mixed for 1 minute at 300 rpm to pre-shear the slurry. The alum solution of 950 ppm water-based dosage was injected within a 1 second interval while mixing at 300 rpm. The alum solution was mixed in for 10 seconds, and the mixing speed was decreased to 80 rpm. Mixing was continued at this speed for 13 minutes. The mixer speed was then increased to 300 rpm and the desired volume of polymer solution was injected using a peristaltic pump (ColeParmer DRIVE/DISP MFLX BENCH 115/230) at a fixed flow rate of 1200 ml/min. Mixing was continued at 300 rpm while monitoring torque response on the overhead mixer screen. When torque reached a peak value and began to decrease, immediately the mixing speed was decreased to 50 rpm. The flocs were then conditioned by mixing at 50 rpm for 15 seconds. Flocculation steps were not applied for the coagulation only samples.

After coagulation and flocculation, the treated FFT was sheared by a custom-built small-scale shearing device (Figure 1). The shearing device was designed with a rotating inner cylindrical bob inside a stationary outer cup, was used to simulate the energy input into treated tailings delivered by shear during pipeline transport to the tailings pond. The size of the bob assembly is 23.2 cm in diameter and 54.7 cm in height. The cup assembly is 24.4 cm in diameter and 55.3 cm in height. The gap between the cup and bob is 6 mm. Eight evenly spaced baffles on the bob and cup surfaces minimize sample wall slip. The conveyance condition was designed based on the field pipeline size (22" in diameter and 1000 meters in length) and treated tailings flow rate (1950 m^3/hour) to simulate the shear energy input (~1500 kJ/m^3) into the treated tailings by transportation in the pipeline to the tailings deposit.

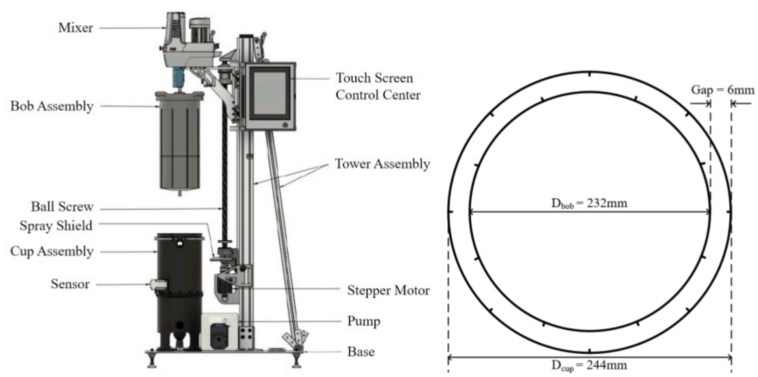

Figure 1. Schematic of the shearing device (left) and overhead view of cup/bob (right) with key measurement.

The dewatering performance of the conveyed FFT was tested on a capillary suction timer (CST) to obtain the full dosage curve for each combination of alum and polymer and to determine the desired dosage for the filter press testing (Sadighian, et al. 2018).

2.3 *Sand-mixed FFT treatment by HFST*

BASF has developed a novel FFT treatment techknology known as high fines sand tailings (HFST) which combines FFT with sand and two regents. The sand-mixed FFT was prepared by combining sand and PEW into a 35wt% slurry, then adding the appropriate FFT ES4400 amount to form a target sand to fines ratio (SFR) of 2. One liter of sand-mixed FFT was prepared for each flocculation.

A Heidolph Hei-Torque 100 Precision Base overhead mixer was used to mix the substrate at a controlled speed during the flocculation process. Flocculation 6″ metal vessel and impeller (Li, et al. 2021) were used except for the metal baffle which was removed to ease mixing of sandy slurry.

The sand-mixed FFT was initially premixed at 200 rpm for 5 min. Completing this time, 50 ppm equivalent to 2.25 mL of 1% w/w DP-OMC-1510 diluted solution was injected at the tip of the mixing blade at 5 mm above the level of the substrate using a micropipette while mixing at 200 rpm. The substrate continued to be mixed for 10 seconds. The 0.5% w/v polymer DP-OMC-1509 solution was injected at the same delivery position using a peristaltic pump at a fixed rate of 1200 mL/min. After polymer injection, 30 seconds of conditioning time at 200 rpm was used.

2.4 *Filter press test*

A modified OFITE's multiple and single unit filter press was used for the filter press testing using a compressed nitrogen line and carbon dioxide bulbs respectively. The sample cup consisted of a stainless-steel test cell with a 250 µm screen and/or a filter medium Whatman Grade #50 filter paper (particle filtration size of 2.7 µm). The samples were fed into the sample cup and the mass of the water released through the filtration process was recorded at one-minute intervals using a top-loading scale. The scale was connected to a laptop computer using WinWedge software to automatically transcribe the data to a spreadsheet. There was a water drain polystyrene tubing at the bottom of each sample cup to collect the filtrate.

NAIT started to use filter press to test the performance of treated FFT in 2017 (Li, et al. 2018). The filter press used as received (Version-1) caused local desaturation of the sample at the point of lowest filtration resistance. As a result, the plastic limit of the desaturated location was reached, and the compressed cake cracked resulting in great internal stress and a locally unsaturated system (Figure 2). Therefore, the filter press test stopped.

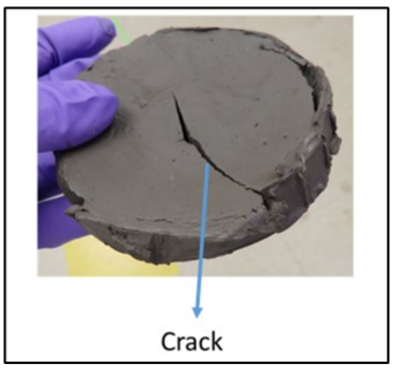

Figure 2. Crack of the compressed cake.

To avoid compressed sample cake cracking resulting in a premature end to the test, NAIT modified the filter press setup in 2018 named Version-2 (Li, et al. 2018). A Teflon piston cylinder was inserted into the SRF sample cup between the sample and the high-pressure gas. The diameter of the piston was designed slightly smaller than the sample cup to reduce friction losses due to binding between the piston and the cylinder. The O-ring on the piston was used to eliminate the gas leak between the sample cup and the piston. Lubricant was applied to the O-rings before each test to reduce friction losses. FFT has a heterogeneous nature resulting in zones that are prone to cracking. The air pressure directly applied before any cracking is likely to be even across the sample surface, and will then only short-circuit when a cracking feature develops. Whereas the piston is insensitive to any cracking feature on the surface as it applies pressure evenly throughout the experiment by design.

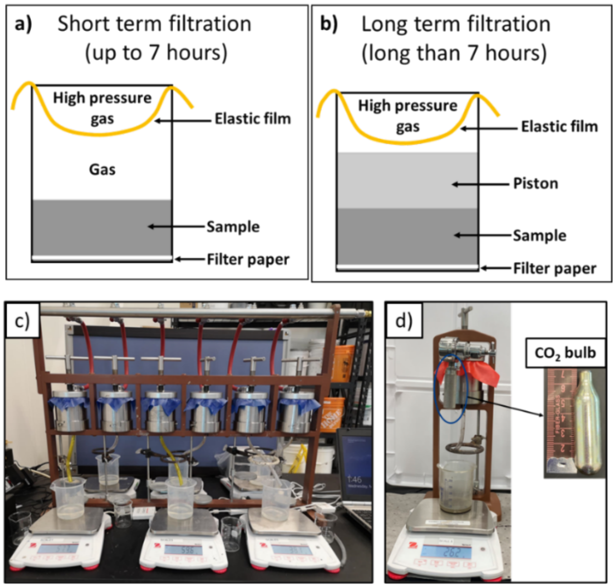

Figure 3. a) Schematic diagram of Version-3 modified filter press setup for short term filtration; b) schematic diagram of Version-3 modified filter press setup for long term filtration; c) the photo of version-3 modified filter press setup with balances; d) individual filter press set up with a balance.

Version-2 allowed the team to perform filtrations until no further dewatering was observed during the filtration (1-4 days). In order to obtain an accurate flow curve, this version-2 setup required an operator to carefully monitor the test and record the volume or mass of the filtrate throughout the long time duration of filtration. The friction between the piston and the cup may lead to lower pressure on the sample. In addition, no individual sample pressure could be monitored or controlled with this version of the filter press.

In Version-3, an elastic film replaced the Teflon piston for the short time duration of filtration (up to 7 hours filtration) as shown in Figure 3a. The elastic film could not only work like a piston to avoid filter press stopping midway due to the cracking as it underwent creep rupture with time leading to leaks for long runs. However the film is readily available and cost-effective without the need for custom machining for a close fit like the piston. For the long duration of filtration (longer than 7 hours), a piston was also recommended to apply between the elastic film and sample to avoid the cracking of the elastic band due to the long time stretching (Figure 3b). Six balances connected to a computer were set up to measure the mass of filtrates automatically and hence labor was freed from babysitting the filtration tests (Figure 3c). The software of "WinWedge" was used to record all the data collected from the balances.

The individual filter press has the advantage of controlling and monitoring gas pressure on each setup (Figure 3d). CO_2 bulb could be used to the individual filter press and therefore lower the risk greatly compared to the gas cylinder. The individual filter press is portable and convenient to be taken to the field for testing.

3 RESULTS AND DISCUSSION

A previous study had shown that the modified filter press could measure the mass/volume of the filtrate with filtration time, the solids content of the filtered cakes, and the solids content of the filtrates (Li, et al. 2018). With the known mass of samples before and after filtration, the real-time solids content of the filtered cakes could be calculated. Therefore, the flow curves with the real-time solids content of the cakes vs. the filtration time could be plotted. It is recommended to measure the evaporation of the filtrate during the filtration, especially for the long term filtration, by placing a jar of water beside the filer press setup.

In this study, the tested FFT ES4400 contains high solids content, high MBI, and high fines content. Two types of treatment along with untreated FFT were used as examples for the filter press test:

- PASS treatment on ES4400 – the combination of alum and anionic polyacrylamide (alum&polymer E4964, alum&polymer NRG1000, and alum&polymer A3338).
- HFST treatment on sand-mixed ES4400 (SFR 2).
- Untreated FFT ES4400

3.1 *Choice of operating pressure*

Choosing appropriate and consistent operating pressure for the filter press tests is critical the compare the filtration rates and the filtration results. Generally, higher operating pressure, higher filtration rate, and solids content of the filtered cake. For untreated FFT the increase of the operating pressure from 20 psi to 30 psi, the filtrate rate did not change (Figure 4), though an increase in filtration rate was noted when the pressure was increased to 100psi.

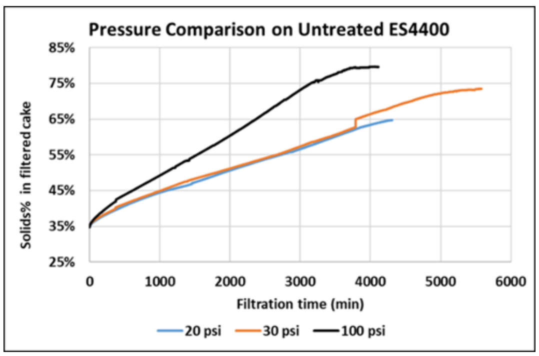

Figure 4. Pressure comparison of filter press curves on untreated FFT ES4400 at 20 psi, 30 psi, and 100 psi.

3.2 *Choice of filter*

A filter is necessary to support the compressed cakes during filtration. Filtering with a large pore size material such as 250 mesh could test the ability of different treatments to capture fines and segregation (Figure 5). The solids% in the filtrate from the untreated FFT was as high as 17% indicating a large number of solids went through the filter to the filtrate. The HFST treatment captured most of the fines using a 250 mesh filter and the solids% in the filtrate was comparable with that using 2.7 µm filter. The filter with a small pore size such as 2.7 µm could yield release water that was ideal for subsequent water analysis such as ion chromatography (IC) without additional filtration steps.

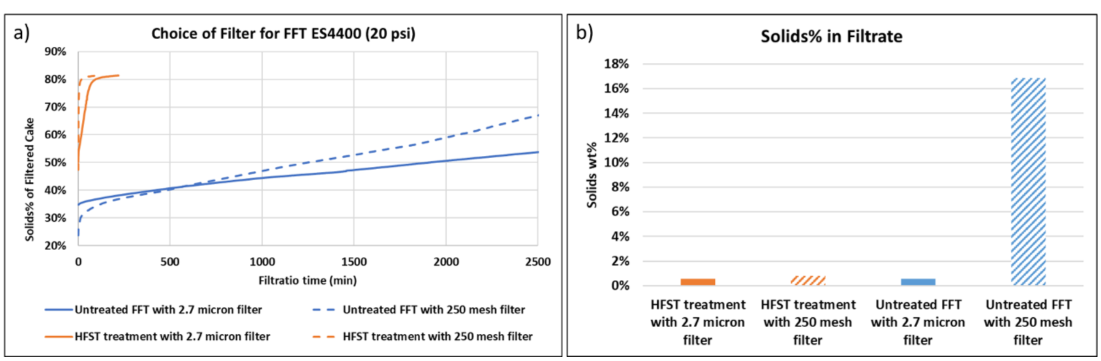

Figure 5. Comparison of different filters: 2.7 µm pore size and 250 mesh pore size on untreated FFT ES4400 and HFST-treated ES4400. a) The solids content of filtered cake with filtration time; b) the solids content in the filtrate. All the filtration tests used 300 g of samples and were performed at 20 psi.

3.3 *Repeatability of filter press tests*

Experimental repeatability of a testing method is paramount to ensuring the reliability of study findings. The repeatability of the modified filter press was tested on samples with 250 mesh filter for a short duration press (10-12 minutes), and samples with 2.7 µm filter for a medium duration (120-150 min) and a long time duration (1000 minutes to achieve a plateau of the flow curve). Figure 6a shows the individual tests performed on 9 medium term and 3 long term tests for a single PASS treatment condition with the 2.7 micron filter. The average time to collect 50 g of filtrate from the PASS treatment (Figure 6a) was 120 minutes with a standard deviation of 5.6 minutes indicating a highly repeatable tests. Figure 6b show the results on 3 individual short term tests on a given HFST treatment using the 250 mesh filter. The range of difference between the highest solid% and lowest solids% in the filtered cake is 5% indicating good repeatability for both filtrations with 2.7 µm filter and 250 mesh filter. All the samples formed compact filtered cakes (Figure 8). As expected in filtration of fluid material, significant shrinkage occurred in the cakes typically cakes went from an input thickness of ~2-3" to a final thickness <1".

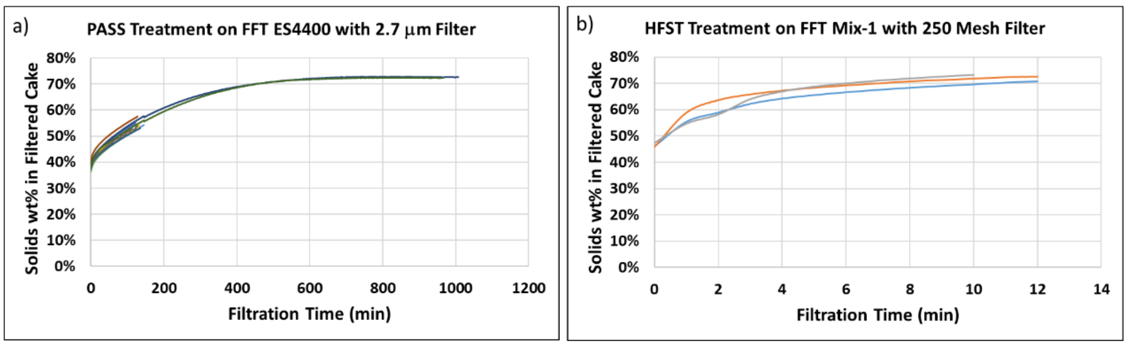

Figure 6. Filter press curves for PASS treatment of alum and polymer E4964 on FFT ES4400 with 2.7 µm filter (a) and HFST treatment on FFT mix-1 with 250 mesh filter.

3.4 *Sensitivity of different treatments*

Filter press tests may differentiate different types of treatment on FFT through the filtration curves. As shown in Figure 7, all the treated FFT ES4400 along with untreated ES4400 were pressed to the plateau of the filtrates and solids content of the filtered cakes at 20 psi with 2.7 µm filter. Untreated FFT ES4400 with 300 g of loaded samples showed the slowest filtration rate indicating the lower dewatering performance. PASS treatment shows much better dewatering performance than no treatment resulting in much higher solids content in the final filtered cake. HFST treatment on the sand-mixed ES4400 shows the highest filtration rate and solids content in the final filtered cakes. Figure 8 shows the photos of the filtered cakes obtained from different treatments and all formed compact cakes.

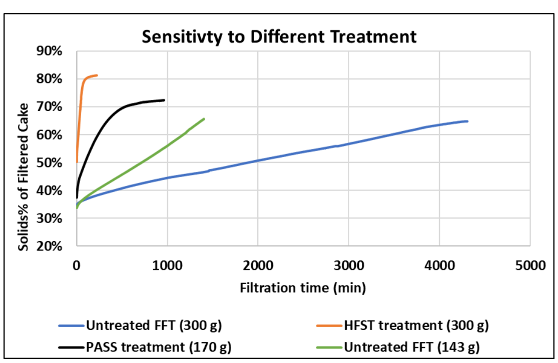

Figure 7. Filter press curves for untreated FFT ES4400, PASS treatment on ES4400, and HFST treatment on sand-mixed ES4400. All the filtrations were done at 20 psi with the 2.7 µm filter. Around 300 g of sample mass was used for the filtration for HFST treatment and nontreatment.

Note that the HFST treatment was conducted on the sand-mixed FFT ES4400 with SFR 2, while other treatments were conducted on FFT. Since the filterability is more affected by the low conductivity materials, which were fines content in this study, the same mass of fines in the filter press testing samples were compared between the HFST treatment and untreated FFT ES4400. That means 143 g of untreated FFT ES4400 and sand-mixed ES4400 with SFR 2 had the same amount of fines (~128 g). The filter press tests confirmed that HFST treatment provided better dewatering performance for the FFT containing the same fines content (Figure 8).

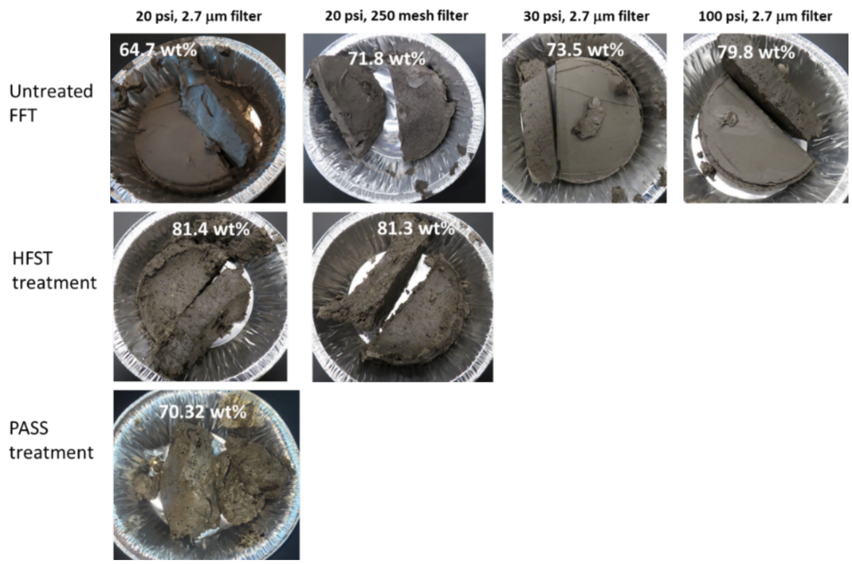

Figure 8. Photos of final filtered cakes from different treatments on FFT ES4400. All filter press tests were performed until no more filtrate was collected.

3.5 *Sensitivity of different polymers*

ES4400 was treated with PASS technology using alum combined with different polymers: A3338, NRG1000, and E4964. Three polymers were all anionic polyacrylamide but had different modifications. The optimal dosage of each polymer was chosen according to the full dosage response curve using CST testing (Li, et al. 2021; Sadighian, et al. 2018). At 20 psi, all three polymers produced comparable initial filtration rates (0-150 minutes of filtration) (Figure 9a). This is consistent with the CST results which represent the initial dewatering performance. Figure 9b shows the CST values of the PASS-treated ES4400 had no significant difference among three polymers by T-Test analysis. The final solids content of the filtered cakes produced by A3338 is higher than the other two polymers at tested dosages.

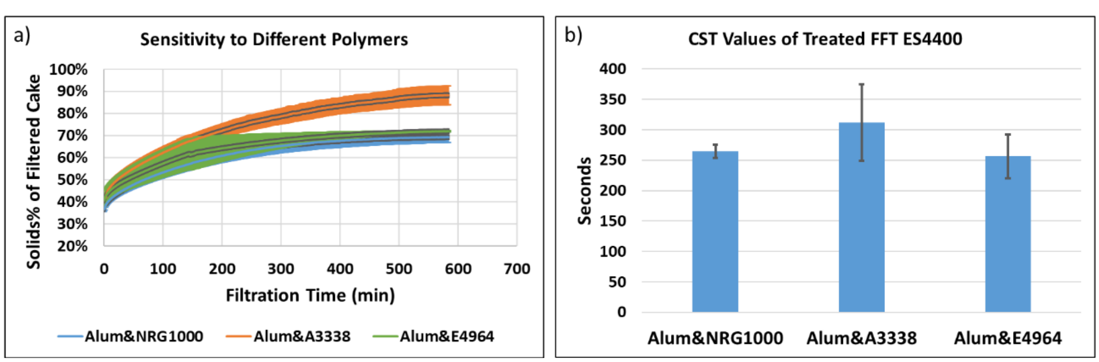

Figure 9. Filter press curves (a) and CST values (b) for the PASS treatment on FFT ES4400 using alum combined with different polymers: NRG1000 (dosage of 2310 g/tonne), E4964 (dosage of 2260 g/tonne solids), and A3338 (dosage of 2130 g/tonne solids). All the filtrations were done at 20 psi with 2.7 μm filter. All the filtration tests used around 170 g of samples.

3.6 *Sensitivity of different dosages*

ES4400 was treated with PASS technology using alum combined with polymer A3338 at different dosages: under dosage (1750 g/tonne solids), optimal dosage (2130 g/tonne solids), and overdosage (2540 g/tonne solids). The optimal dosage produced the highest filtration rate and final solids content of the filtered cake, which is consistent with the lowest CST results (Figure 10). The filter press test might be a good characterization tool for the polymer dosages.

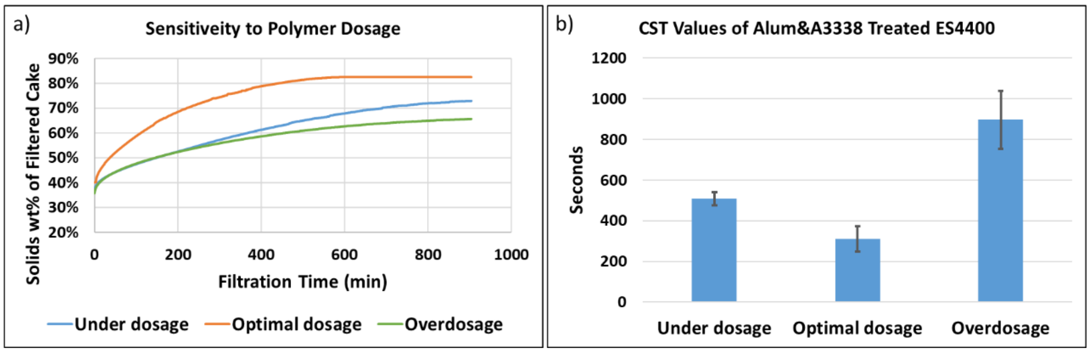

Figure 10. Filter press curves (a) and CST results (b) for PASS treatment on FFT ES4400 using alum and polymers A3338 at different dosages: 1750 g/tonne solids as the under dosage, 2130 g/tonne solids as the optimal dosage, and 2540 g/tonne solids as the overdosage. All the filtration tests were done at 20 psi with 2.7 μm filter. All the filtration tests used around 170 g of samples.

3.7 *Comparison of specific resistance to filtration*

The calculated specific resistance to filtration (SRF) values are determined by the b value according to Eq. 2 (Coulson, et al. 1991; Li, et al. 2018). The linear portion of the filtration flow curves indicates the filterability of the materials and the corresponding linear b portion in the Eq. 2 can be used to calculate the SRF values. The untreated FFT materials with a different loaded mass of samples had comparable SRF values. PASS treatment provided a higher flow rate than untreated FFT and thus a lower SRF value (Figure 11). HFST treatment provided the highest flow rate and therefore, the lowest SRF value. The plateau portions of the flow curves are probably related to the strength/compressibility of the treated materials. This requires further study.

$$SRF = (2 \times P \times A^2) \times b/(\mu \times c) \tag{2}$$

Where p is the pressure drop (Pa), A is the area of filter (50.27×10^{-4} m^2), μ is the viscosity of filtrate and assumed the viscosity of filtrate be the same as water (1×10^{-3} Pa·s), c is the concentration of solids in suspension: 406.67 kg/m^3 for FFT ES4400 and 461.52 kg/m^3 for sand-mixed ES4400 (HFST treatment), b is the slope of time (t) /volume(V) against volume (V) plot (t/V^2).

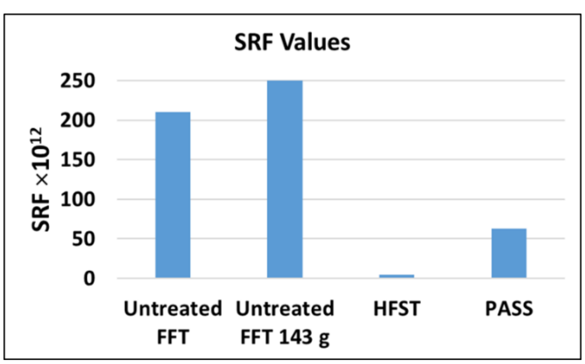

Figure 11. The calculated SRF values or PASS treatment (300 g of samples), HFST treatment (300 g of samples), nontreatment (300 g of samples and 143 g of samples) on FFT ES4400.

4 CONCLUSION AND FUTURE WORK

In this work, a bench-top scale filter press was modified and optimized by using an elastic film between the pressed sample and the high-pressure gas. The modified filter press was cost-effective, easily operative, and could effectively press the sample and avoid compressed cake cracking resulting in the premature end of the test. The mass of filtrate with time was recorded with a balance connected to the computer that no labor is required during the filter press. Individual filter press setup with a CO_2 bulb as the high-pressure gas has lower risk and is convenient to be taken to the field for testing.

The modified filter press provided very repeatable dewatering results. Therefore, the modified filter press is a reliable tool for the characterization of FFT dewatering performance. Pressure applied to the samples affects the filtration flow rates and results. Therefore, comparing the dewatering performance using filter press should use consistent filter press conditions. Choosing different filter media during the filtration could meet different testing needs. The 250 mesh filter provides an indication of fines capture by different treatments on FFT. Other filter papers, such as the 2.7 μm paper used in this study is a useful option to provide filtrate for water chemistry analysis. The modified filter press testing is sensitive to different types of FFT treatment and could be used as a characterizing tool to evaluate the dewatering performance of different types FFT treatment. The dewatering performance obtained by the modified filter press were consistent with the CST results when evaluating different polymers and different dosages on the FFT treatment. Hence, the modified filter press could be a secondary evaluation tool on the dewatering performance of FFT treatment.

Although it is not clear how reliable in the study which is among non equivalent materials (different types of treatment), the filter press test is believed to provide valuable information on filterability and long term consolidation. The linear portions of the filtration flow curves could be used to compare the filterability of the treated FFT. The plateau portions of the filtration curve are probably related to the strength/compressibility of the testing materials. In this study, the treated FFT achieved the plateau of filtration at a very short time compared with untreated FFT. This might indicate that treated FFT required a much shorter time for the consolidation than untreated FFT. The modified filter press could provide an indicator of long-term consolidation information. The future work is to compare the results of pressure filtration with large-strain consolidation (LSC) tests and seepage induced consolidation test (SICT).

5 REFERENCES

Alamgir, A., Harbottle, D., Masliyah, J., Xu, X. 2012. Al-PAM assisted filtration system for abatement of mature fine tailings. *Chemical Engineering Science*, 80, 91-99.

Anlauf, H., Bott, R., Stahl, W., and Krebber, A. (1985). The formation of shrinkage cracks in filter cakes during dewatering of fine sized ores. *Aufbereitungs Technik*, 26(4): 188-196.

Barua, A. (2014). Experimental study of filter cake cracking during deliquoring. Department of Chemical Engineering & Chemical Technology, Imperial College of Science, Technology and Medicine, London.

COSIA Fines Measurement Working Group. 2016. Unified Fines Method for minus 44 micron material and for Particle Size Distribution.

Coulson, J.M., Richardson, J.F., Backhurst, J.R., Harker, J.H. (1991). Particle technology and separation processes. *Chem. Eng*. Vol. 2, 4th ed. Pergamon, Chapter 7.

Dean, E.W. and Stark, D.D. (1920). A convenient method for the determination of water in petroleum and other organic emulsions. *Ind. Eng. Chem.*, 12: 486-490.

Li, Y., Kaminksy, H., Gong, X.Y., Sun, Y.S., Ghuzi, M., and Sadighian, A. (2021). What affects dewatering performance of high density slurry? *Minerals*, 11, 761.

Li, Y., Kaminsky, H., Romaniuk, N. and Tate, M. (2018). Filter press modification to assess dewatering performance of fluid fine tailings. *IOSTC 2018*, Edmonton, AB, 314-323.

Lloyd, P.J. and Dodds, J.A. (1972). Liquid retention in filter cakes. *Filtration & Separation*. Jan/Feb: 91-96.

OSTC. 2012. Technical guide for fluid fine tailings management. Oil Sands Tailings Consortium and COSIA. cosia. ca.

Revington, A.P., Omotoso, O., Wells, P.S., Hann, T.C., Weiss, M.H., Bugg, T., Eastwood, J., Young, S.J., O'neill, H.R., Sanchez, A.C. 2010. Process for flocculating and dewatering oil sands mature fine tailings. Patent CA2701317A1.

Sadighian, A., Revington, A., Kaminsky, H., Moyls, B., Li, Y., and Omotoso, O. (2018). A new protocol to assess the quality of tailings flocculation/coagulation: a collaboration to improve tailings treatment at Suncor Energy. *IOSTC 2018*, Edmonton, AB, 81-92.

Wakeman, R.J. (1974). The role of internal stresses in filter cake cracking. *Filtration & Separation*. Jul/Aug: 357-360.

Field pilot testing of filter press technology for dewatering oil sands fluid fine tailings

Jason Hill, Gavin Freeman, and Cynthia Cote
Canadian Natural Resources Limited; Calgary, Alberta, Canada

Nav Dhadli and Vanessa Warren
Barr Engineering and Environmental Science Canada, Ltd.; Calgary, Alberta, Canada

ABSTRACT: Canadian Natural conducted a field pilot in 2019 to evaluate the use of pressure filtration to dewater fluid fine tailings (FFT). The pilot was successful in establishing routine operation of FFT delivery and pretreatment systems, a large plate and frame filter press, and final placement of the produced filter cake. While acknowledging that the primary objective of the pilot program was to maintain consistent production, the analysis of several process parameters was also done. An overview of the process scheme along with conclusions from the analysis and interpretation of the process and laboratory data is presented. The identification of the most relevant parameters contributing to the plant's performance (i.e., solids throughput and filter cake solids content) is also described. The results contribute to an important step in establishing engineering design parameters and expectations for future commercial-scale operations.

1 INTRODUCTION

The filter press is a well-known technology that delivers rapid water recovery from fluid fine tailings (FFT) by mechanically pressing water out of the fine clay slurry to form a dense cake suitable for immediate transport to a reclamation area (COSIA (2020)). The use of pressure filtration technology in the oil sands had long been dismissed as being impractical due to the clogging of filter materials by fines and residual bitumen. However, within the last decade, improvements in the chemical treatment/amendment of FFT have led to the re-evaluation of filter press technology for FFT treatment. Numerous laboratory studies (e.g., Li et al. (2018); Loerke (2016); Xu et. al (2008); Zhu (2015)) have demonstrated that chemical amendment of FFT through coagulant and/or flocculant addition increases permeability and therefore can improve the filterability of FFT.

From 2012-2014, a small-scale filter press pilot, referred to as the Ledcor Nalco Services (LNS) Pilot, was conducted to test and validate the effectiveness of using flocculation chemicals and pressure filtering using a pilot plant press (COSIA (2021)). It was concluded from this pilot that filter press technology may be a feasible means of dewatering oil sands tailings slurries; however, a larger demonstration trial was recommended to further evaluate and demonstrate this at a commercial scale. In the summer of 2019, Canadian Natural conducted a large-scale field demonstration program referred to as the 2019 Filter Press Pilot Program. This paper focuses on the process performance of the 2019 pilot; the geotechnical performance of the resultant filter cake deposit is discussed in a separate paper (Ansah-Sam et. al. (2021)).

2 PROCESS OVERVIEW

2.1 *Filter Press Pilot Equipment*

Two filter presses were procured from Matec for the pilot: a standard filter press (FP-01), which operated at a maximum pressure of 16 bar and a membrane squeeze filter press (FP-02), which had a maximum feed pressure of 8 bar and membrane squeeze pressure of 18 bar. Both of the filter presses were equipped with a 500 bar hydraulic unit to close, compress, and seal the plates for the high-pressure feed. Filter press FP-01 and FP-02 are shown on Figure 1 and Figure 2, respectively.

Figure 1. FP-01 filter press

Figure 2. FP-02 filter press and membrane water tank

Each filter press contained 101 – 2 m long x 2 m wide filter plates, which created 100 filter chambers to produce 100 filter cakes. Three different filter cake thicknesses were produced by FP-01 (25, 30, and 35 mm). The filter chamber thickness for FP-02 was 25 mm; however, the actual filter cake thickness varied based on the membrane squeeze cycle. Numerous different filter fabrics, which varied by supplier (Matec or Sefar), material (polypropylene or polyamide), construction style, and air permeability were tested.

The process flow diagram of the system is shown on Figure 3, along with primary sample collection points.

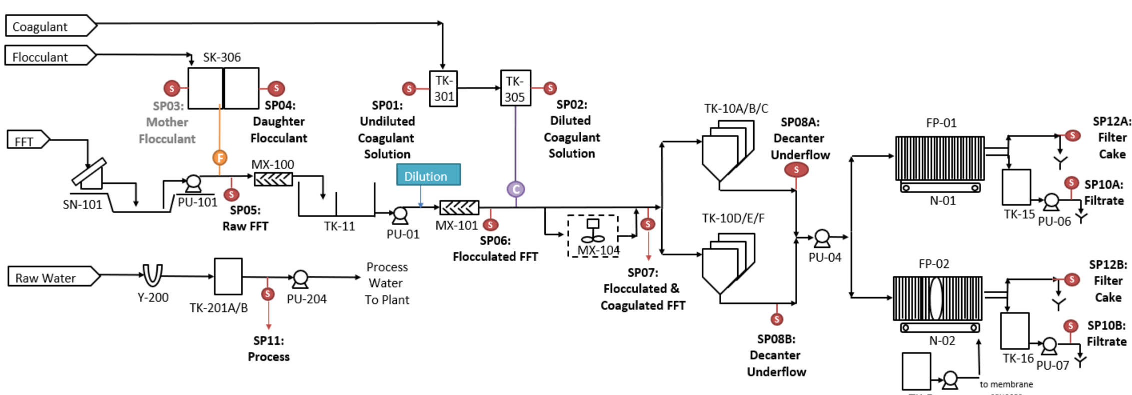

Figure 3. Process flow diagram

The raw FFT was dredged from the MRM ETF Reclaim Pocket and stored in a 10,000 m^3 capacity holding pond after passing through a ¼-inch vibrating screen (SN-101). Following initial filling of the holding pond, raw FFT was periodically supplied as needed. The filling periods are identified on Figure 4, which also displays the Methylene Blue Index (MBI) and D50 particle size of the raw FFT samples. The raw FFT samples were collected from the feed line to the filter press plant and not from the holding pond itself. Note that the average MBI and D50 were noticeably different between the learning and production phases, with higher MBI and lower D50 material in the learning phase. FFT with properties like those observed in the learning phase would generally be considered more difficult to treat and dewater. The focus of the analysis presented in this paper is on the production phase of the pilot operation. This phase was conducted from July 22 to September 5, 2019 and included 214 filter press runs.

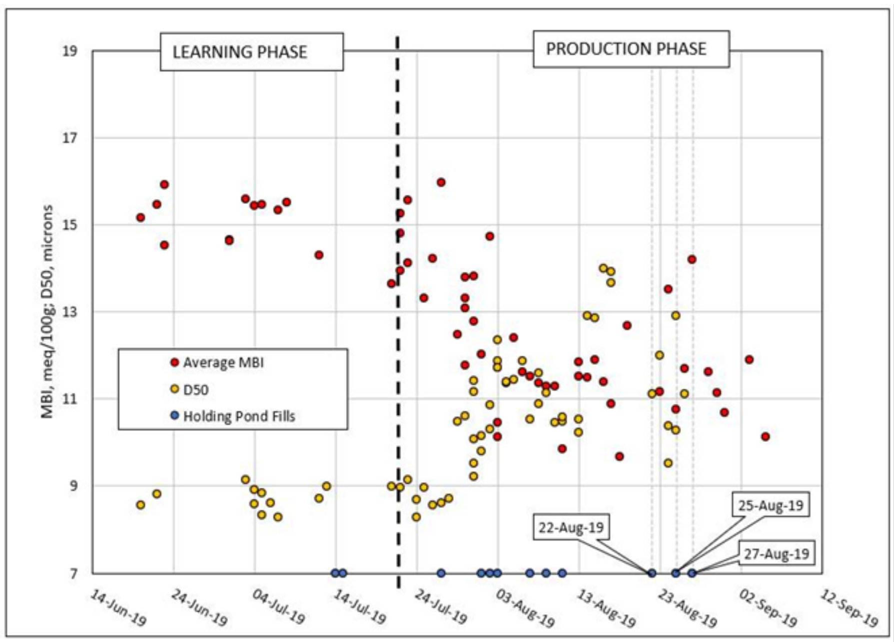

Figure 4. Raw FFT holding pond fills along with MBI and D50

The raw FFT was then pumped to the pilot plant for chemical amendment. The density and flow rate of the raw FFT pumped from the holding pond to the plant was measured using a Coriolis meter (DT-101, FT-101), which was located downstream of the raw FFT feed pump.

Flocculant injection occurred downstream of the Coriolis meter. The flocculant solution was prepared at a daughter concentration of 0.4 wt.%. During the pilot, two different flocculants were used (Table 1).

Table 1. Flocculant types and dosages for 2019 filter press pilot

Flocculant type	Dates	Number of runs[1]	Run ID numbers	Dosage range (g/dry tonne of FFT solids)
SNF-A3338	June 1, 2019 – July 6, 2019	18	1 - 18	1,500 – 1,780
SNF NRG-1320	July 7, 2019 – September 5, 2019	220	19 - 238	500 – 1,500

[1]Excludes commissioning runs.

Following flocculant injection, the flocculated FFT stream passed through static mixer MX-100. Downstream of MX-100, the flocculated FFT stream could be diluted, as needed, using process water. The process water (PW) was supplied from the main raw water (RW) supply, which was then passed through a 1/8-inch basket strainer (Y-200). FFT dilution was only performed on the material used in Runs 1, 182, and 183; consequently, the impact of FFT dilution on filter press performance is not discussed.

The flocculated (and sometimes diluted) FFT stream then passed through a magnetic flow meter (FIT-M1) and nuclear density meter (DT-105). The next step in the FFT treatment process was coagulant injection, which occurred downstream of DT-105. During the pilot, the only coagulant used was alum, which was prepared at target concentrations between 1-10 wt. %. Coagulant dosages ranged from 2,300 – 20,000 g/dry tonne of FFT solids; the higher end of the dosages (>15,000 g/dry tonne of FFT solids) were typically used. Using the higher coagulant dosages improved the filter cake release and overall cake dewatering. The high coagulant dosages are postulated to result in a linked polymer network which facilitates sustained drainage under pressure. It was observed that consistent drainage through the entire cake thickness was jeopardized when the alum addition was lowered substantially. Optimization of the chemical amendment based on FFT feed composition will be further studied in future lab scale experiments.

The treated FFT was then fed to the decanters. The decanters were used as an intermediate tank to ensure sufficient residence time for the chemical treatment to act on the FFT and to provide steady feed to the filter presses. Additionally, the decanters provided FFT storage to allow for batch-style filter press operation. Each of the six decanters were identical with a capacity of 35 m^3. The decanters could be operated individually or as two parallel trains of three decanters (TK-10A/B/C and TK-10D/E/F). Decanters TK-10D/E/F were used for most of the pilot operation (>90% of the runs). A layout of the overall facility is shown on Figure 5. The homogenizers shown on Figure 5 were not used during the pilot.

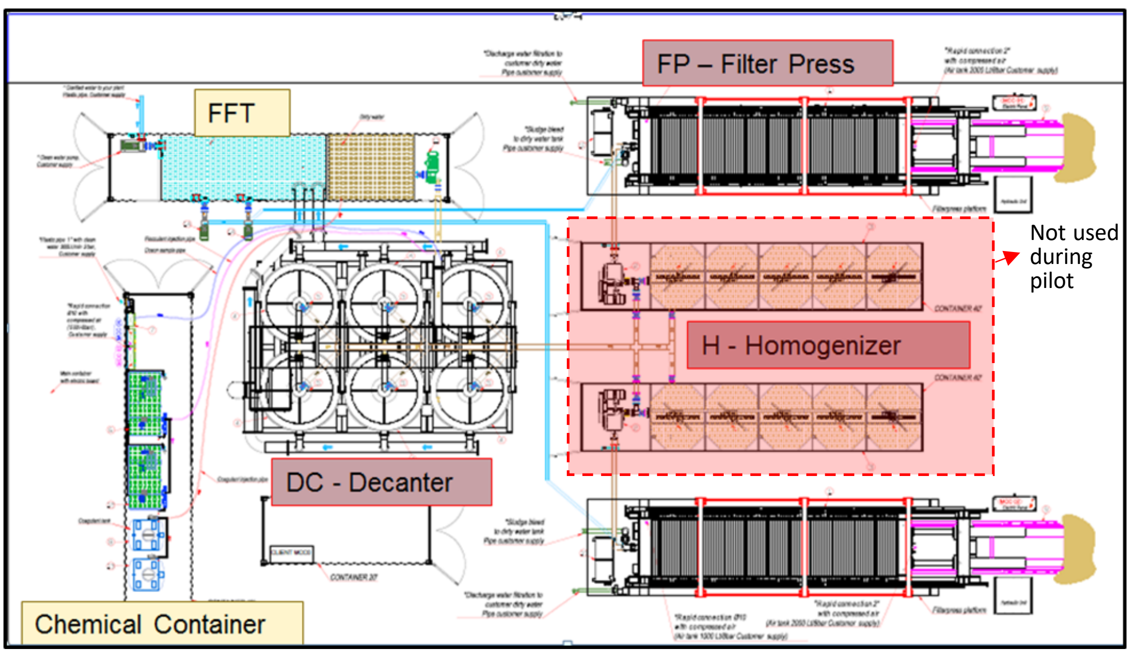

Figure 5. Filter press plant layout

From the decanters, the FFT was fed to the filter press using one of three feed pumps: peristaltic (low shear), diaphragm (medium shear), or centrifugal (high shear). The centrifugal pump was used for all the production phase runs. FP-01 was used for most of the pilot and therefore operation of FP-01 is the focus of the discussion below.

2.2 *Filter Press Operation (FP-01)*

Prior to starting a filter press cycle, the filter press was hydraulically closed to seal each chamber. The treated FFT was then fed to the center of the feed-side of the filter press. To operate the filter press, the operator selected a maximum feed flowrate and high-pressure set point (up to the maximum operational pressure). The filter press then operated using two different process control loops to keep the filter press within the operator-set limits. In the first loop, the speed of the filter press feed pump would increase until the maximum feed flowrate was reached. The treated FFT was then continuously fed into the press until the high-pressure set point was reached. Then, the second loop would take over and the feed flowrate would automatically adjust to hold the press at the high-pressure set point and offset pressure losses due to active dewatering. The filter press cycle was complete when the FFT flowrate decreased to a pre-determined endpoint (e.g., 5 m^3/h), after which the flow was shut off and the pressure released to discharge the cake. An illustration of the various phases of operation and the resultant definition of total cycle time is shown on Figure 6. Note that the cycle times do not include the time associated with cake release since the duration of this activity was dependent on cake quality and was highly variable. For these reasons, the time associated with cake discharge, although ultimately relevant for long-term scale-up, was not factored into determination of filter press throughput (defined as kg of solids/m^2 filtration area/h).

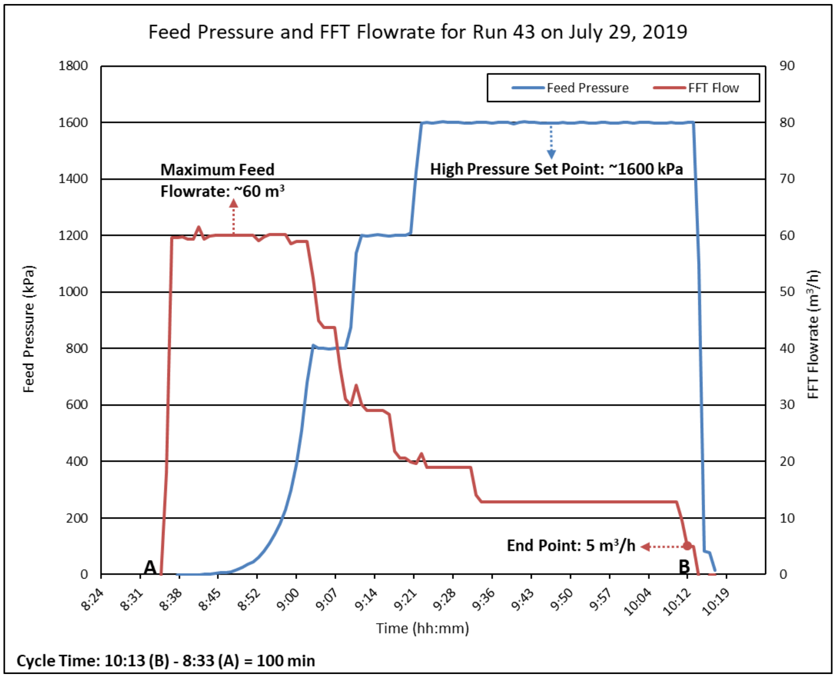

Figure 6. Example of determination of filter press run cycle time

Once a filter press cycle was complete, a core blow was performed to flush out wet material from the feed pipe to the drain. Following the core blow, the dump cycle was executed. During the dump cycle, the FP-01 conveyor (N01) was turned on, ten plates were opened using the built-in traction system, a shaking cycle initiated (and repeated as needed), and the produced filter cake fell onto the conveyor below. Shaking the plates was optional based on filter cake release. This procedure was repeated until all the plates were opened and emptied (ten plates at a time for a total of 100 filter cakes). In instances where the filter cake did not release from the filter fabric, additional shaking or manual removal (scraper) could be performed. The filter cake was discharged from the conveyor and collected by a front-end loader for transport to the depositional test cells for long-term geotechnical monitoring and testing (Figure 7).

Figure 7. Filter cake discharge from FP-01

3 OPERATING SUMMARY

Excluding commissioning runs, a total of 238 filter press runs were performed during the pilot. During the Learning Phase, which extended through July 21, 2019, a total of 24 filter press runs were performed: 21 runs on FP-01 and three runs on FP-02. During the production phase of the pilot, which ran from July 22, 2019 through September 5, 2019, a total of 214 filter press runs were performed: 203 runs on FP01 and 11 runs on FP-02.

In total, approximately 9,100 m^3 of FFT was fed to the filter presses at an average solids content of 27 wt% (Figure 8).

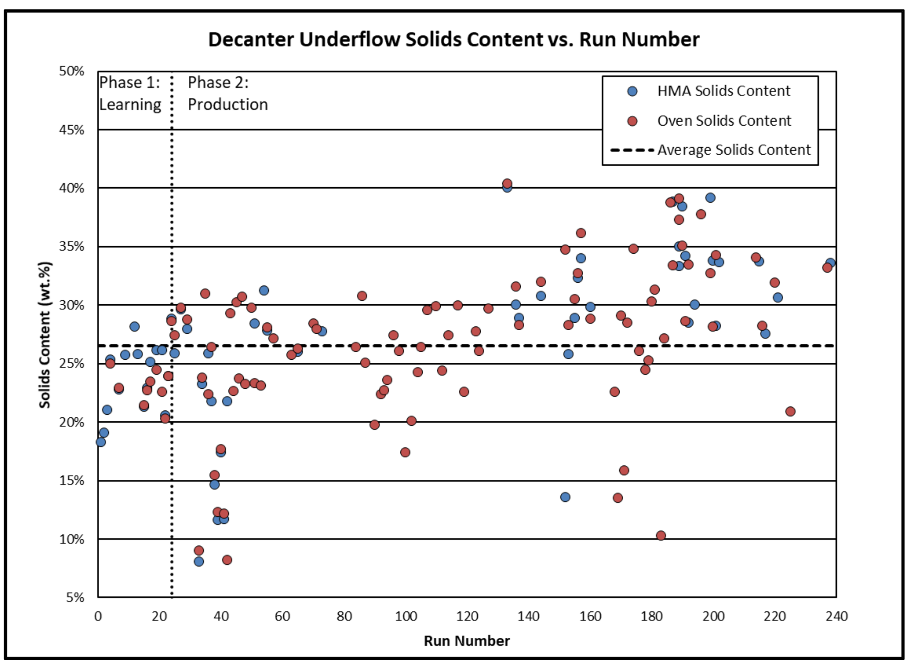

Figure 8. Cumulative FFT feed volume

The average volume of FFT fed per cycle for operation with all 100 plates was 42 m^3. Figure 9 shows the average solids content of the filter cake produced during each run. Most of the filter cake had a solids content between 60 and 70 wt.%, with an average filter cake solids content for the production phase of 63.7 wt.%.

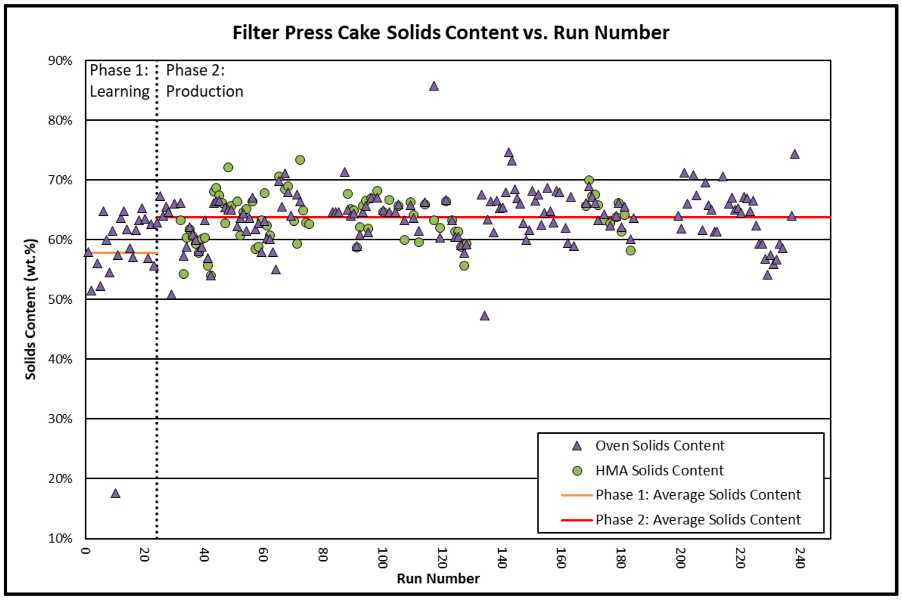

Figure 9. Filter cake solids content

4 PROCESS PERFORMANCE ASSESSMENT

Process and laboratory data collected during the 2019 Filter Press pilot were analyzed to establish correlations with filter press cake quality. High quality being defined as instances where high throughput and/or filter cake solids content were observed). Advanced statistical analyses were used to identify the most relevant variables which were then investigated in greater detail. Mass balances for different operating scenarios were also prepared to establish important engineering design parameters and expectations for commercial-scale operation.

From the advanced statistical analysis, it was determined that the relevant variables from the process and laboratory data correlating with throughput and/or filter cake solids content were:

- Flow rate of the filter press feed (decanter underflow)
- Solids content of the filter press feed (decanter underflow)
- D50 particle size of the filter cake
- Methylene Blue Index (MBI) of the raw FFT feed
- Magnitude of the clay fraction (smaller than 2-micron particle size) of the filter cake

Two of the more compelling correlations are shown on Figure 10. These were between feed solids content and throughput and filter cake D50 particle size and filter cake solids content.

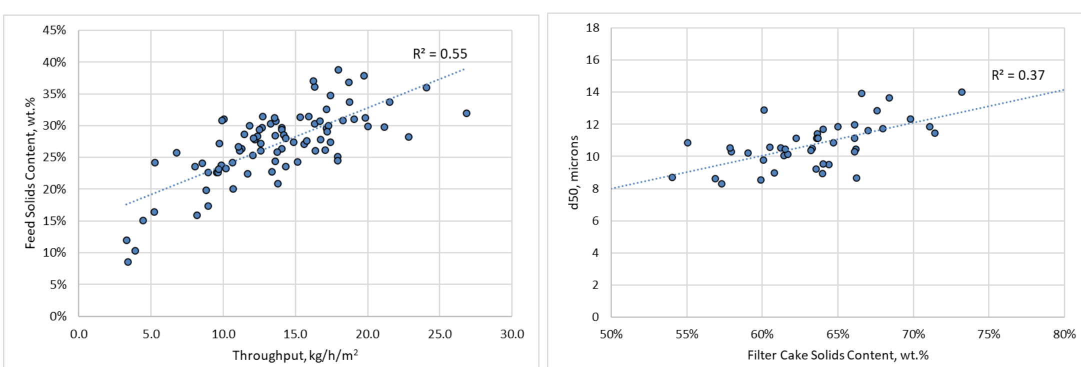

Figure 10. Relationship between filter press feed solids content and throughput and D50 and filter cake solids content

5 SUMMARY OF KEY DESIGN PARAMETERS

Based on collected data and observations from the pilot operation, key process design criteria were established and are summarized in Table 2. This information, along with the requisite assumptions regarding facility operability and reliability, can be used to prepare an approximate scale-up for commercial applications.

Table 2. Key process design criteria

Design Criteria	Range	Units
Filter Press Feed Solids Content	30 – 40	wt.%
Filter Cake Solids Content	60 – 70	wt.%
Throughput (Filtration Rate)*	15 – 20	$kg/h/m^2$

*Excludes time required for cake discharge

Several process parameters were identified that have a relatively strong correlation to filter press performance (defined as high throughput or high filter cake solids content). A relative ranking of these identified parameters is provided in Table 3. Note that chemical amendment is not explicitly addressed since it is assumed that optimal dosage of flocculant and coagulant is a prerequisite to achieving desired performance.

Table 3. Ranking of relevant process parameters

Rank	Process parameter/measurement	Comments
1	Filter Press Feed Solids Content	A strong positive correlation with feed solids content and throughput was observed. High solids content feed to the filter press is recommended for future operation.
2	D50 Particle Size	D50 routinely showed good positive correlation with performance throughout the analysis and appears to be a good indicator of filter press performance. Higher D50 leads to a more permeable filter cake and therefore more rapid and effective filtration.
3	MBI or Clay-Sized Particles Fraction (<2 micron)	MBI (clay activity) or clay-sized particles fraction showed modest negative correlation with performance. This can be considered a secondary contributor since the data was sometimes inconsistent and correlations were not always evident. Lower MBI leads to a more easily treatable and permeable filter cake with associated more rapid and effective filtration.

6 CONCLUSIONS

The analysis of data collected from the 2019 Filter Press Pilot Program showed that pressure filtration is a viable approach to dewatering of FFT and can produce a high solids content product suitable for terrestrial reclamation. In addition to the need for chemical amendments (flocculant and/or coagulant), the most relevant variables related to obtaining high throughput and/or high filter cake solids content are high feed solids content, larger overall particle size distribution (higher D50), and lower MBI or clay-sized fraction. A familiar theme associated with FFT treatment emerged from the filter press performance assessment. That is, those instances where either or both the clay content/activity was low or the particle size distribution was coarser resulted in the best performance due to more effective chemical treatment and the corresponding increased permeability of the filter cake, which facilitated easier water removal.

7 REFERENCES

Ansah-Sam, M., Davison, E. & Skinner, B. 2021. Filter press technology commercial scale pilot – geotechnical deposit performance. *Tailings and Mine Waste 2021*. Banff, AB, Canada.

Canada's Oil Sands Innovation Alliance (COSIA). 2021. *Filter press project*. Accessed on 9/30/2021. https://cosia.ca/initiatives/tailings/projects/filter-press-project.

COSIA. 2020. COSIA Tailings EPA 2019 Tailings Research Report, August 2020.

Li, Y., Kaminsky, H., Romaniuk, N. & Tate, M. 2018. Filter press modification to assess dewatering performance of fluid fine tailings. *IOSTC 2018*. Edmonton, AB, Canada.

Loerke, R.S. 2016. Pressure filtration of oil sands mature fine tailings (MSc Thesis). University of Alberta, Edmonton, AB, Canada.

Xu, Y., Dabros, T. & Kan, J. 2008. Filterability of oil sands tailings. *Process Safety and Environmental Protection* 86 (4): 268-276.

Zhu, Y. 2015. Cationic and anionic dual polymer pairs for mature fine tailings flocculation and dewatering (MSc Thesis). University of Alberta, Edmonton, AB, Canada.

Filter press technology commercial scale pilot – geotechnical deposit performance

Monica Ansah-Sam
Formerly Canadian Natural Resources Limited, Calgary, Alberta, Canada

Evan Davison & Brittany Skinner
Canadian Natural Resources Limited, Calgary, Alberta, Canada

ABSTRACT: Canadian Natural Resources Limited (Canadian Natural) is investigating technologies that will treat fluid fine tailings for closure in a terrestrial application. Geotechnical metrics such as successful capping, strength gain, consolidation timeline, ultimate settlement, deformation, bearing capacity, and increased solids content are being considered as performance indicators for closure designs. These metrics align with Canadian Natural's 'end in mind' tailings strategy, in which closure considerations are integrated into the mine planning process.

Pressure filtration was identified as a potential method to accelerate dewatering, consolidation, and reclamation of fluid fine tailings in oil sands tailings facilities. In 2019, Canadian Natural completed a commercial-scale pilot program which tested the performance of two recessed chamber filter press units at the Muskeg River Mine. The purpose of the Canadian Natural Filter Press Pilot was to evaluate: commercial scale unit operability, impacts of live feed variability on product quality, system reliability, process parameters (such as operating pressure and chemistry), economic metrics (such as throughput and unit costs), and geotechnical components related to deposit performance.

This paper presents the geotechnical performance of the filter press tailings deposit produced during the commercial pilot, and summarizes the geotechnical considerations that were evaluated to support successful commercial deployment of the technology. The paper covers deposit stability, peak and remolded shear strength results, evaporation and re-wetting effects, solids content estimates, dust management, trafficability, and compaction requirements. The paper also comments on the anticipated long-term performance of the deposit including closure considerations and implications.

1 INTRODUCTION AND BACKGROUND

Directive 085, issued under the Oil Sands Conservation Act, sets out requirements for managing fluid tailings volumes for oil sands mining projects in Alberta, Canada, and includes the concept of ready-to-reclaim (RTR) tailings deposits (AER, 2017). Canadian Natural is assessing the economic and technical feasibility of fluid fine tailings (FFT) treatment using commercial scale pressure filtration, with the goal of producing RTR material with high density, strength, and solids content. Three lab-scale pressure filtration programs were undertaken prior to the commercial scale Filter Press Pilot that was executed at Canadian Natural's Muskeg River Mine (MRM) in the summer of 2019.

An initial lab-scale trial was completed in 2012 to confirm that filtration technology and inline polymer mixing would successfully dewater FFT from Canadian Natural's Albian Sands mines. Several uniform thickness filter press cakes were produced using varied press times helping to establish a relationship between press time and cake quality. Both shear strength and solids content increased with longer press times. The observed solids content ranged between 55 and

63% by weight with shear strengths ranging between 19 and 59 kPa. The FFT was successfully dewatered to a soil-type product during the 2012 lab trial.

The second lab-scale program was performed in 2017 with the purpose of determining the effectiveness of various process parameters such as filter cloth type, operating modes (equipment lineup), press times, pressures, and chemical amendments. Geotechnical testing for this program was limited to consolidated undrained triaxial tests to determine strength and hydraulic conductivity characteristics of the filter press cake.

The third lab-scale program, performed in 2019, was used to determine broader geotechnical properties of the filter press cake using two selected chemical amendments. Figure 1 shows equipment and testing from the 2012 and 2019 lab-scale programs conducted by Canadian Natural.

Figure 1. 2012 (left) and 2019 (middle and right) lab-scale filter press programs.

The primary geotechnical objective of the 2019 commercial scale Filter Press Pilot was to further evaluate the geotechnical properties of the material, including, expected solids content range, solids content correlation to peak and remolded shear strengths, moisture content, sand-to-fines ratio (SFR), and consistency of the filter press cake. The pilot was also used to evaluate deposit trafficability, bearing capacity, dust generation, compaction requirements, and the effects of evaporation and re-wetting on filter press cake.

2 FILTER PRESS PILOT OPERATIONS OVERVIEW

The FFT treated during the Filter Press Pilot was dredged from the MRM External Tailings Facility. The FFT treatment process included screening, flocculant and coagulant addition, and pressure filtration. The pressure filtration step was completed using one of two recessed chamber filter press units configured to produce 2 m by 2 m filter press cakes with thicknesses ranging from 25 to 30 mm. The two different filter press units operated at maximum feed pressures of 8 and 16 bar (800 and 1600 kPa), with the lower pressure unit capable of applying a post-feed membrane squeeze pressure of up to 18 bar. The majority of the runs were completed at a feed pressure of 16 bar with no membrane squeeze applied. Total cycle times varied depending on the operating parameters being tested, averaging 80 minutes per cycle during the production phase of the pilot. The dried filter press cakes were dropped from the press onto a conveyer which carried the cakes to a loading pocket where they were collected and placed into deposition cells using a front-end loader.

The Filter Press Pilot was operated in two phases: an initial learning phase in which process variables were tested to determine the optimal set of operating conditions, and a steady-state production phase intended to test the performance of the equipment and produced material under commercial operating conditions. The solids content of the material produced during the learning phase was inconsistent due to variations in operating conditions. The material produced during this stage was segregated into off-spec test cells and was not included in the pilot deposit. Once the pilot entered the production phase, material with consistent solids content was produced and used to build the pilot deposit in a dedicated test cell.

The pilot deposit was conceptually designed to a height of 10 m, however due to operational delays, less cake was produced and the height of the deposit was reduced to 3 m.

3 GEOTECHNICAL SAMPLING AND TESTING

Geotechnical sampling and testing was conducted throughout the pilot to characterize the filter press cake and constructed deposit. Grab samples were collected regularly from the produced material as it was cleared from the base of the filter press conveyor to assess the solids content (via oven drying or halogen moisture analysis), and shear strength (via pocket penetrometer and handheld vane shear testing [hVST]) of the cake prior to placement. Construction of the deposit was monitored and deposit properties were observed and measured during placement of the lifts.

Index testing completed on samples collected from the pilot deposit included oil-water-solids determination using the Dean Stark method, washed sieve and laser diffraction particle size analyses, Atterberg limits, and methylene blue index (MBI) testing. The index testing provided insights on the degree of variability within the filter press deposit, and was used as the basis for selecting representative specimens for advanced testing. Six consolidated undrained triaxial compression tests with pore water pressure measurement were conducted on specimens trimmed from undisturbed Shelby tube samples collected from the pilot deposit. Following saturation, the confining pressure in the triaxial test cells was increased and samples were isotropically consolidated under effective stresses ranging from 100 to 600 kPa. Samples were sheared at a strain rate of 1.5 %/hr to ensure reliable equilibrium pore water pressure measurements (ASTM, 2020). The consolidation testing consisted of one large strain consolidation (LSC) and two oedometer consolidation tests, conducted on samples intended to represent low, mid, and high solids content conditions in the filter press deposit. Maximum consolidation loads of 600 and 1000 kPa were applied in the LSC and oedometer consolidation tests, respectively. Consolidation testing using beam centrifuge was also conducted on batched samples from the pilot deposit. During the beam centrifuge tests, three 25 cm tall specimens were spun for 48 hours under 80 g-force, simulating self-weight consolidation of a 20 m thick deposit over 35 years.

4 GEOTECHNICAL TEST RESULTS

4.1 *Grab Sample Testing*

Throughout the pilot, grab samples were collected from the filter press discharge to measure properties of the material prior to drying or deposition including, initial solids content, vertical penetration resistance, and shear strength. Figure 2 shows a stack of filter press material as well as a representative sample of a single filter press cake prior to placement in the pilot deposit. A single piece of discharged cake was typically observed to be uniformly fine-grained and platy with a firm, dry exterior and a softer, moist interior.

Figure 2. Typical stack (left) and single cake (right) of discharged filter press material.

The measured solids contents of the filter press cake grab samples are shown on Figure 3. The majority of the samples ranged in solids content between 60 and 70% by weight. The average solids contents for the learning and production phases were 59.7 and 63.7% by weight, respectively.

Pocket penetrometer measurements were typically collected from three locations on the filter cake exterior. The appropriate pocket penetrometer tip size (10 mm or 15 mm) was selected based on physical observation of the filter cake: the stiffer the cake, the smaller the tip. The minimum, average, and maximum pocket penetrometer readings from the learning phase were 1.81, 4.07, and 6.75 kg/cm^2, respectively. The minimum, average, and maximum readings for the production phase were 1.36, 1.97, and 2.58 kg/cm^2, respectively.

Hand held vane shear measurements were collected from one to four locations on the filter cake exterior. The appropriate vane blade size (small, standard, or large) was selected based on physical observation of the filter cake: the stiffer the cake, the smaller the blade. The material failed cylindrically during testing, and the peak shear measurement was recorded. Depending on the size of blade used, a conversion was applied to calculate the actual value of the hVST measurement in kg/cm^2. The standard vane blade was used for the majority of the readings

An average of the hVST readings from each sample was converted to an estimated shear strength value using the manufacturer's correlation formula for each blade size. Figure 3 shows the estimated shear strength values with the measured solids contents. The average shear strength readings for the learning phase and production phase were 47.8 and 38.0 kPa, respectively.

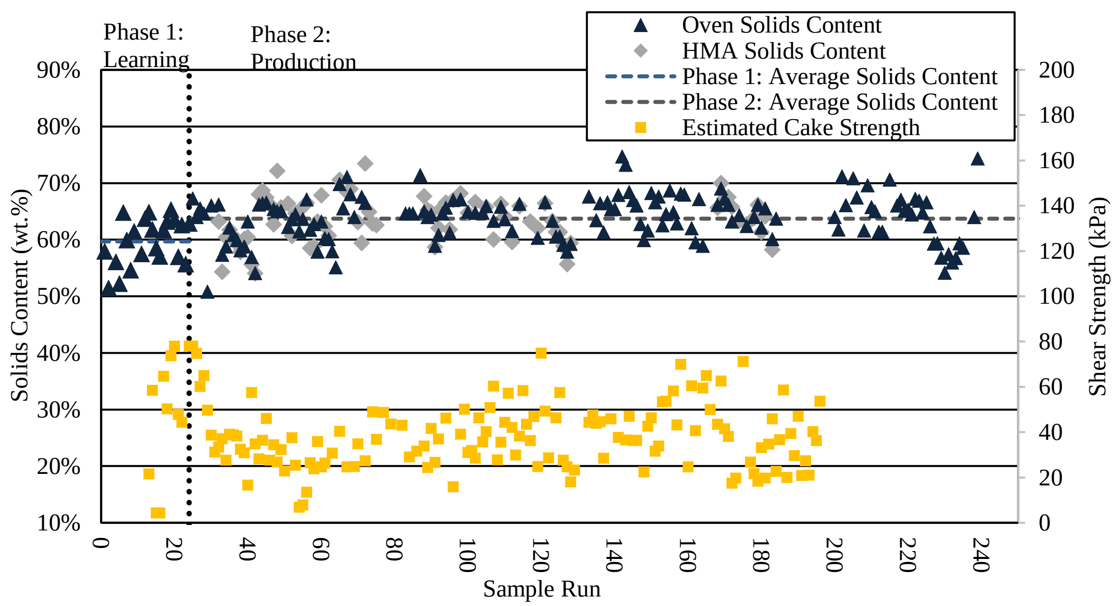

Figure 3. Solids content readings and shear strength for each filter press run.

4.2 *Grab Sample Submersion Test*

Four filter press cake grab samples were submerged in process water, under free-swell and unconfined conditions, for 12 days to test the effects of re-wetting on the cake shear strength over time. The materials with initial solids contents above 50 kPa maintained shear strengths greater than 15 kPa following submersion. Samples with initial solids content less than 50 kPa had a significant reduction in shear strength and structure following submersion. Table 1 lists the initial and final peak shear strengths measured during the submersion test. Figure 4 shows the filter press grab samples at initial submersion and 12 days later.

Table 1. Grab sample submersion test results.

Sample Name	Initial Peak Shear Strength (kPa)	Final Peak Shear Strength (kPa)
A	68	16
B	78	17
C	43	3
D	30	1

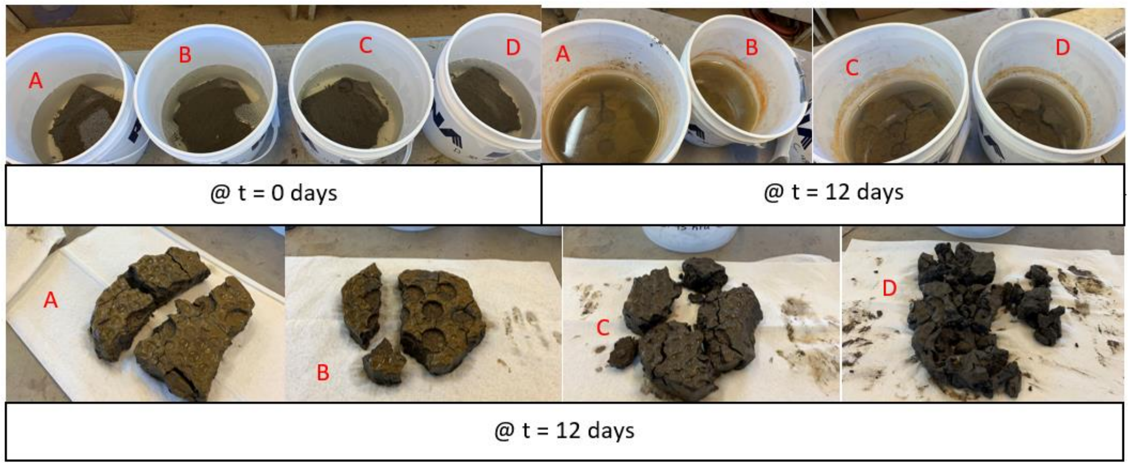

Figure 4. Submerged filter press samples.

4.3 *Deposit Compaction & Density Testing*

Compaction tests were performed on the filter press deposit using a Caterpillar D6 dozer to provide the compactive effort and a nuclear densitometer to measure in-situ density and moisture content. The purpose of this testing was to estimate the field effort required to compact the deposit to typical construction standards. The density and moisture content measurements were performed at four locations throughout the deposit prior to compaction and after 5, 10, 15, 20, and 25 passes. On average for all locations, the optimum field density was achieved after 5 to 10 dozer passes. Figure 5 illustrates the dozer compacting the deposit (left) and the density measurement trend with compactive effort (right).

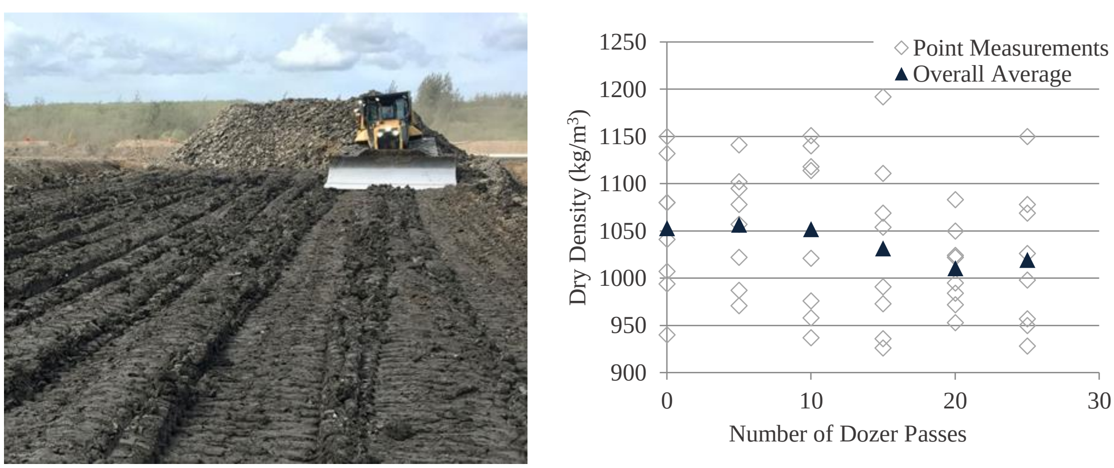

Figure 5. Compaction of filter press deposit with Caterpillar D6 dozer (left) and density measurement after varying degrees of compaction (right).

4.4 *Deposit Survey Data*

Prior to the start of the Filter Press Pilot, a baseline survey was performed in the deposit area. The final survey was performed on October 1, 2019. Single point elevation measurements via sonic ranger, showed a negligible change in the deposit surface elevation between October 2019 and October 2020. Based on the survey data, the estimated volume of filter press cake produced during the pilot was approximately 1,800 m^3. The maximum deposit height was approximately 3 m with variation in thickness throughout the containment cell, as shown on Figure 6.

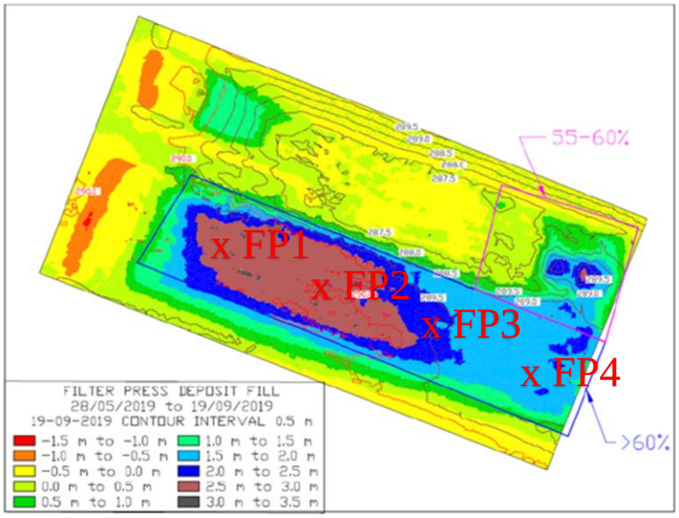

Figure 6. Filter press deposit thickness, final elevations, and in-situ testing locations.

4.5 *In-Situ Deposit Testing*

The undrained shear strength of the compacted pilot deposit was measured using field Vane Shear Testing (fVST), downhole electric Vane Shear Testing (eVST), and Cone Penetrometer Testing (CPTu).

During construction, the fVST instrument was inserted into the soil at depths of 30 and 80 cm to measure the peak and remoulded shear strengths at each location and depth. In September 2019 (one month after deposition), the peak fVST measurements ranged from approximately 18 to 45 kPa. At the same locations and depths, the remoulded shear strengths ranged between 6 and 9 kPa. Shaft friction was not accounted for during the fVST tests due to the shallow testing depths.

In-situ eVST was completed in October 2019 (1-2 months post deposition) at four locations near the fVST locations. The number of eVST performed at each location varied depending on deposit depth, and were typically performed at 0.3 to 0.5 m intervals. All testing was performed using a 150 mm long by 75 mm diameter vane. The eVST peak and remoulded shear strength results ranged from 11 to 58 kPa and 5 to 10 kPa, respectively.

In-situ CPTu testing was also completed in October 2019 at the same deposit locations as the eVST. The final depths for the CPTu testing varied from 0.45 to 3.03 m, depending on the location. The CPTu average peak shear strength at locations 1 through 4 ranged from 23 to 34 kPa. The CPTu with corresponding peak shear strengths, along with the eVST peak and remoulded shear strengths are illustrated on Figure 7.

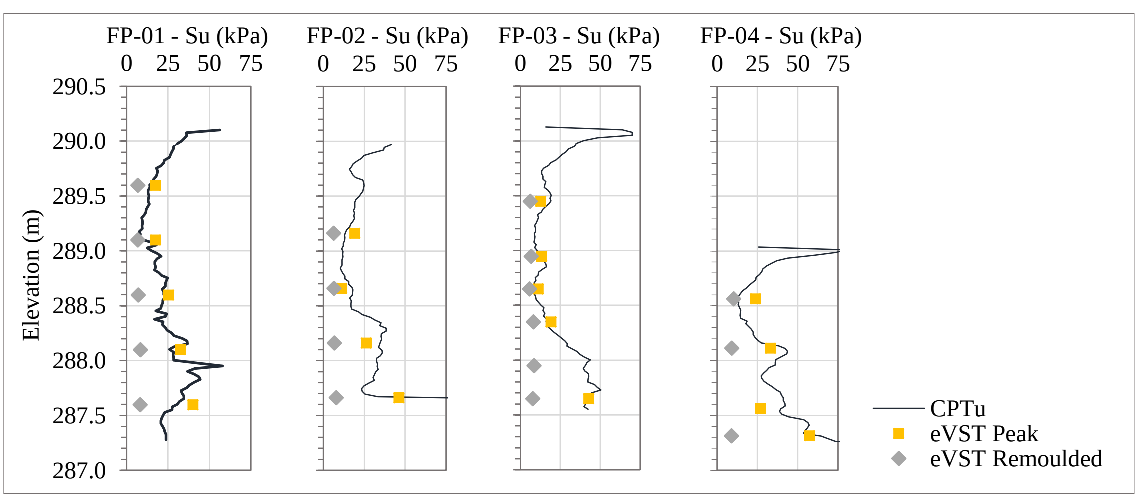

Figure 7. CPTu, eVST peak, and eVST remoulded shear strengths within the pilot deposit.

4.6 *Laboratory Testing*

Oil-water-solids determination using the Dean Stark method and oven-dried water (solids) content testing was performed on all deposit samples. The solids content of the samples tested ranged from 54 to 85% by weight with an average of 67%. Bitumen content ranged from 3.5 to 8% with an average of 4.7%. Specific gravity measurements ranged from 2.0 to 2.4. The remainder of the index testing was conducted only on those samples selected for advanced lab testing. The solids content of the specimens selected for the advanced tests was re-measured immediately prior to the start of the test to establish accurate initial conditions. Results from index testing performed on the samples selected for the advanced tests are listed in Table 2.

Table 2. Index properties of samples from the filter press deposit.

Sample Name	SFR	Fines Content (%)	MBI (meq/ 100g)	Solids Content* (%)	Bitumen Content (%)	Atterberg Limits LL (%)	PL (%)	PI (%)	Test Type
SP12 P9/P208	0.02	98.4	8.6	54.0	4.5	84	36	48	LSC
19-FP1 5105a	0.07	93.6	6.2	69.1	5.4	63	36	48	OED
19-FP1 5102a	0.07	93.5	6.6	73.4	5.5	39	32	7	OED
19-FP1 5102b	0.07	93.5	6.6	69.9	5.5	39	32	7	TRI – G1
19-FP1 5102c	0.07	93.5	6.6	70.8	5.5	39	32	7	TRI – G1
19-FP3 5114	0.05	95.2	7.5	65.6	5.0	67	32	6	TRI – G1
19-FP1 5105b	0.07	93.6	6.2	68.2	5.4	63	36	48	TRI – G2
19-FP2 5109a	0.12	89.4	6.3	66.2	7.3	38	32	6	TRI – G2
19-FP2 5109b	0.12	89.4	6.3	68.5	7.3	38	32	6	TRI – G2

*Oven-dried solids content, including bitumen.

The results from the triaxial tests described in Section 3 were used to produce two Mohr Coulomb failure envelopes to determine the effective shear parameters of the filter press material. The triaxial tests were run on two sample groups, with the Group 1 (G1) and Group 2 (G2) specimens having target dry densities near 1100 and 1070 kg/m^3, respectively. The majority of specimens displayed strain hardening behavior with maximum deviator stress occurring at strains between 10 and 15%. The effective angle of internal friction and effective cohesion for Group 1 specimens were calculated to be 22° and 7 kPa, respectively. The effective angle of internal friction and effective cohesion for Group 2 specimens were calculated to be 17° and 28 kPa, respectively. The B-Parameter values measured during the test ranged from 0.97 to 0.98 for Group 1 specimens and 0.95 to 0.98 for Group 2 specimens.

One large strain and two oedometer consolidation tests were conducted on samples selected to represent low, mid, and high solids content conditions in the pilot deposit. The volume change during loading was highest in the lowest solids content material, with 30% vertical strain measured during the LSC test. The vertical strains measured during the oedometer testing were 18% and 15% on the mid and high solids content samples, respectively. The initial hydraulic conductivities ranged from 1.6×10^{-9} to 1.5×10^{-8} m/s at initial void ratios from 0.8 to 1.72. The final hydraulic conductivities ranged from 6.9×10^{-11} to 2.1×10^{-9} m/s at final void ratios from 0.5 to 0.79.

The consolidation properties of the filter press cake were compared with those of raw FFT, centrifuge fluid fine tailings (CFFT), and atmospheric-dried fluid tailings (AFD) with initial solids contents of 26, 45, and 68%, respectively. The filter press cake was found to be less compressible than raw FFT and CFFT at low effective stresses, given the relatively low initial void ratio achieved through pressure filtration. At effective stresses greater than 100 kPa, the CFFT and filter press cake exhibit similar behavior. The filter press cake was found to be more compressible than AFD tailings, which had an SFR one order of magnitude greater than the filter press cake. At similar void ratios the hydraulic conductivity of the filter press cake was higher than CFFT, and comparable to raw FFT when the FFT LSC results were extrapolated to lower void ratios. The hydraulic conductivity of the filter press cake was lower than AFD tailings at similar void ratios, likely due to the higher SFR of the AFD tailings.

The compressibility and hydraulic conductivity relationships measured during the Oedometer and Large Strain Consolidation testing are shown on Figure 8 and Figure 9, with consolidation test results for raw FFT, CFFT, and AFD tailings included for comparison.

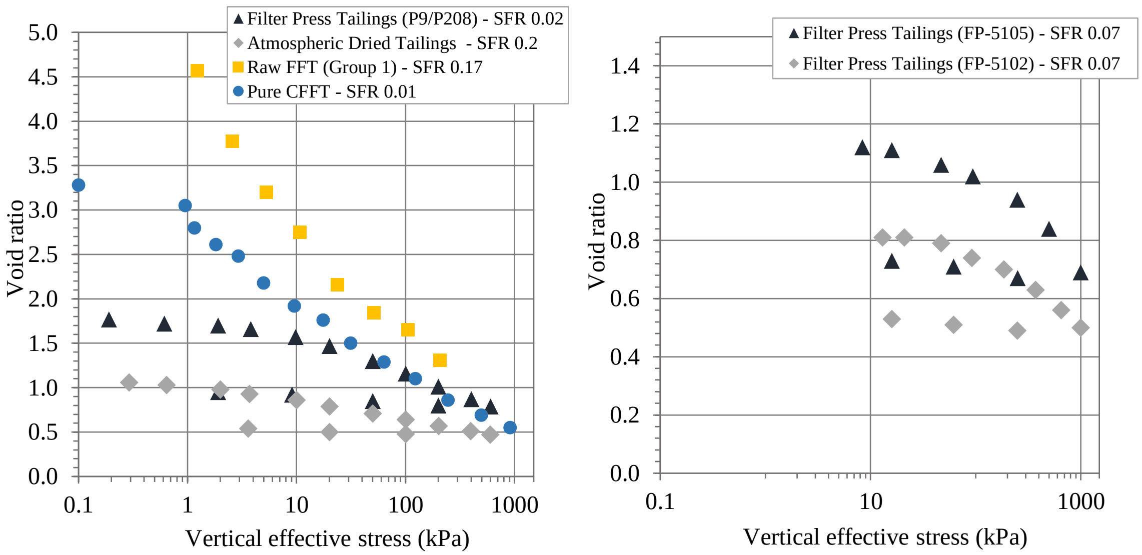

Figure 8. Void ratio vs effective stress measured during large strain (left) and oedometer (right) consolidation testing.

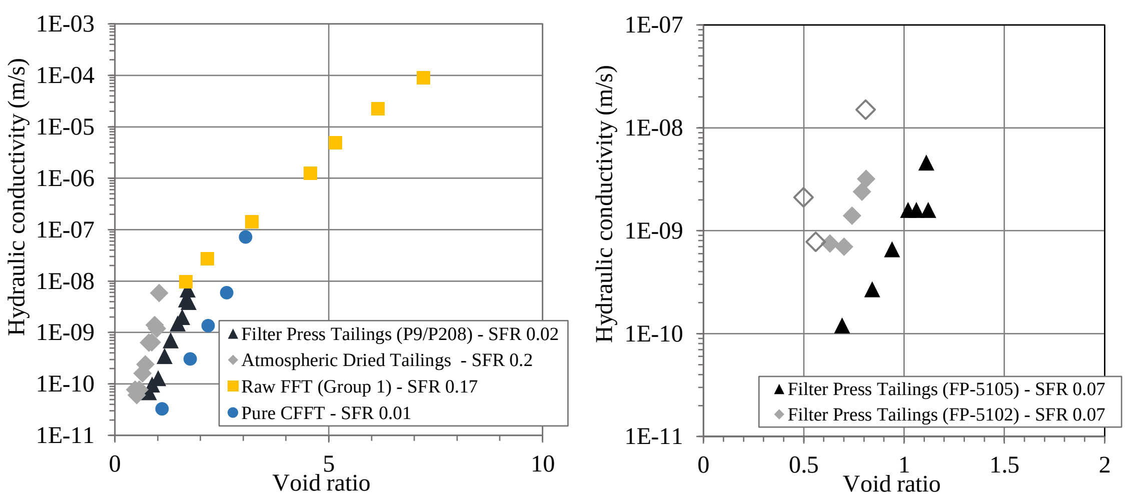

Note: Open symbols indicate data points outside the expected range. These points should be given lower priority in future analyses.

Figure 9. Hydraulic conductivity vs void ratio measured during large strain (left) and oedometer (right) consolidation testing.

Consolidation testing using beam centrifuge was conducted on three batched specimens formed using samples collected from the compacted pilot deposit. Sampling depths ranged from 0 to 2.4 m, generally targeting the 0.6 to 1.2 m interval within the deposit to minimize the impact of surface conditions. Samples were batched to form test specimens with initial solids contents of 58, 65, and 69% for tests 1, 2, and 3, respectively. The test simulated a 20 m thick deposit over a duration of 35 prototype years. Normalized settlement measurements defined, as the measured change in prototype settlement divided by the initial specimen height (Δh/ho), from the three beam centrifuge tests are shown on Figure 10. The three specimens remained in the primary consolidation stage throughout the test. The final normalized settlements for tests 1, 2, and 3 were 6.5, 4.3 and 2.3%, respectively after 35 prototype years.

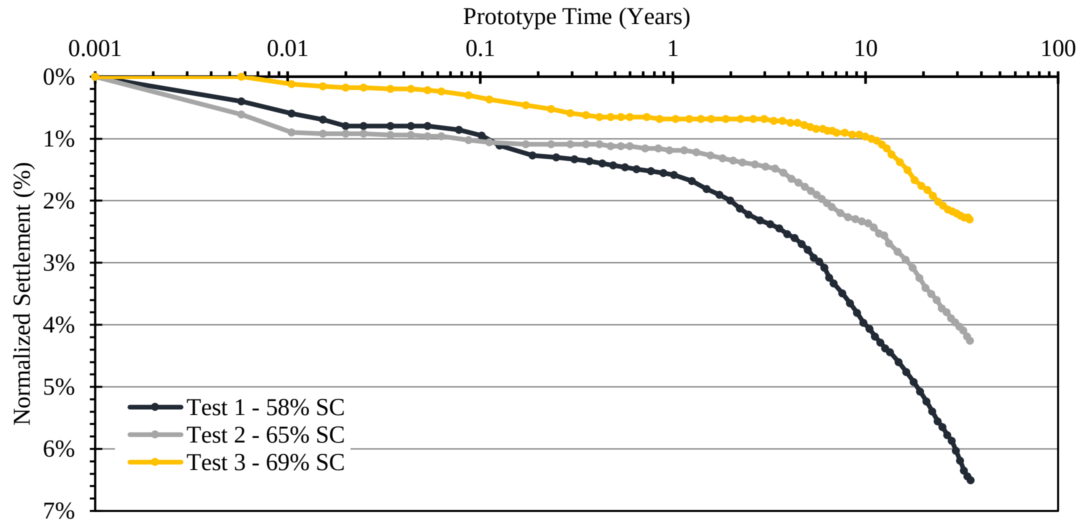

Figure 10. Normalized settlement measurements during beam centrifuge tests.

The test 3 beam centrifuge model, which tested a solids content similar to that of the actual deposit, predicted settlement of 0.7% with one year. Additional monitoring is necessary to confirm the correlation between the modelled and measured settlement results.

5 DISCUSSION

The data collected during the Filter Press Pilot provides insight into future commercial deployment of the technology. The testing completed on the material immediately after filtration demonstrates that a commercial-scale pressure filtration plant is capable of consistently producing dewatered tailings with solids content greater than 65% under optimized process conditions. The feasibility of loading, transporting, and placing the filter press material using standard truck and dozer construction techniques was also demonstrated during the pilot. The compaction testing results show that limited compaction is necessary to remove large voids within the deposit, and that further compaction serves to reduce the strength of the deposit as the material is remoulded. The optimum degree of compaction was found to be between 5 and 10 passes with a D-6 dozer. Dust generation was not observed during pilot operations.

Shear strength loss due to re-wetting was observed in samples of filter press cake that were submerged in water, with the greatest strength loss observed in samples with an initial solids content less than 50%. It is expected that a commercial scale filter press deposit would be designed to shed water and would not experience a reduction in strength due to re-wetting. The deposit will, however, lose the majority of its strength if it is unconfined and submerged in water or if it is deposited into a pond. Stability was demonstrated to a total height of 3.0 m in the pilot deposit with a freestanding slope of at least 50% (2 horizontal to 1 vertical), with steeper side slopes observed in the free-standing production piles, illustrated in Figure 2.

Consolidated undrained triaxial testing on two groups of representative undisturbed samples was completed, yielding calculated effective friction angle and cohesion combinations of 17° and 28 kPa, and 22° and 7 kPa, respectively. These parameters exceeded the values used to design the conceptual 10 m pilot deposit. Updated stability modelling under undrained (Su=32 kPa) conditions confirmed that construction of free standing deposits up to 20 m high with a 5 to 1 horizontal to vertical slope is achievable using filter press cake. Stability modelling under drained conditions (Φ'=17°, c'=10 kPa) indicate that steeper slopes and/or greater deposit heights may be achievable, however undrained conditions are expected to govern in most future design cases.

Electric vane shear testing showed peak and remoulded shear strength within the deposit ranging from 15 to 60 kPa and 5 to 11 kPa, respectively. This result demonstrates that filter press deposits may be capable of supporting a soil cap in excess of 3 m, allowing for reclamation within a year of treatment.

Consolidation test results show that the filter press cake is less compressible than raw FFT and CFFT at low effective stresses, given the void ratio decrease achieved through filtration. The filter press cake was found to be more compressible with lower hydraulic conductivity than AFD tailings that has a higher SFR. The index testing results also show that the material was produced below the liquid limit. Long term settlement results derived from the beam centrifuge testing showed that a 20 m thick deposit may settle up to 6.5% over 35 years, and that further settlement can be expected to occur in subsequent years. The strength of the deposit is expected to facilitate placement of a 3 m soil cap, allowing for accommodation of the settlement over time.

6 CONCLUSION

Ready-to-reclaim targets established for the filter press cake were met or exceeded, with the material reaching the initial solids content target of 60% immediately after production. The Filter Press Pilot demonstrated the technical capabilities of a commercial scale pressure filtration system used to dewater oil sands FFT. The properties of the pilot deposit demonstrate that the technology is capable of successfully dewatering FFT below the liquid limit, producing a material that satisfies the requirements necessary to reclaim treated tailings deposits to a solid landform.

7 ACKNOWLEDGEMENTS

The authors would like to acknowledge the following Canadian Natural staff: Process Innovation (Gavin Freeman, Jason Hill, Cynthia Cote, Michael Ortega, Ian Mountain, Don Macdonald), Geotechnical (Scott Martens), as well as the following external contributors: Teck Resources (Madelaine De Guerre, Madeline Alianto), Golder Associates (Jason Stianson, Josh Sun, Chloe Crossley), and University of Alberta GeoCERF (Gonzalo Zambrano, Rick Chalaturnyk, Yazhao Wang) for their support on this project.

8 BIBLIOGRAPHY

Alberta Energy Regulator (AER). 2017. Directive 085 Fluid Tailings Management for Oil Sands Mining Projects.

ASTM International (ASTM). 2020. D4767-11 Standard Test Method for Consolidated Undrained Triaxial Compression Test for Cohesive Soils.

Geotechnical Centrifuge Experimental Research Facility (GeoCERF). 2019. Centrifuge Modelling of Filter Pressed Oil Sands Tailings.

Golder Associates. 2021. Characterization of the Geotechnical Properties of Muskeg River Mine Tailings.

Effect of sand and flyash on unsaturated soil properties and drying rate of oil sands tailings

Louis Kabwe & G. Ward Wilson
University of Alberta, Edmonton, Alberta, Canada

Nicholas A. Beier
University of Alberta, Edmonton, Alberta, Canada

David Barsi
University of Alberta, Edmonton, Alberta, Canada

ABSTRACT: The effect of sand and flyash addition has significant effect on the unsaturated soil properties of oil sands tailings such as the air entry value (AEV) of the soil water characteristic curve (SWCC) and the drying rate of the oil sands tailings. The AEV decreases exponentially with increasing sand content. In the drying tests, all the drying plots for the tested samples regardless of treatment showed similar curvature at an AE/PE (actual evaporation over potential evaporation) ratio of 0.8. It was concluded that AE/PE of 0.8 and water content of about 20% represent the boundary between the saturated and unsaturated states of all the samples. The thickened tailings (TT) dewater much faster than the untreated fluid fine tailings (FFT). Similarly, the treated TTs with flyash dewater at the same rate, but initially they dewater much faster than the untreated FFTs and TT without flyash. As the drying rate and initial water content were approximately the same for the TTs samples, it is concluded that the inclusion of flyash changes the soil structure, resulting in faster initial evaporation until the saturation boundary is reached. It can be postulated that atmospheric drying is more effective when sand and flyash is added to the thickened tailings. To yield a trafficable surface shear strength the atmospheric drying of the oil sands tailings would have to proceed into the unsaturated state, i.e., AE/PE < 0.8 and shear strength > 60 kPa.

1 INTRODUCTION

The flocculated thickening process is currently a potential technology to convert the oil sands tailings into a material with sufficient strength to support trafficability. The operation of the thickener produces an underflow of FFT with a sand to fine ratio (SFR) of about 1 and a solids content in the range of 40% to 45% (for a "high rate" thickener, or higher for a "paste" thickener) (OSTC and COSIA Report August 2012). The thickened tailings (TT) from the underflow of the thickener is pumped via pipeline to a dedicated disposal area (DDA) that are subsequently allowed to dry under atmospheric condition and freeze-thaw (F/T) and gain strength with time. The TT deposits undergo considerable volume change as soil suction is increased during the drying process. Kearl mine reported that the majority of the TT (approximately 60%) was produced in the second half of 2020 with higher initial TT solids content averaging around 42%, which increased to approximately 57% after seven days (Kearl Annual Tailings Management Report – 2020). To yield a trafficable surface shear strength, the atmospheric drying of the oil sands tailings would have to proceed into the unsaturated state, i.e., AE/PE (actual evaporation/potential evaporation) < 0.8 and shear strength > 60 kPa (Kabwe et al. 2010; Kabwe et al. 2021). Flyash was used in this research study due to the pozzolanic properties of the material and ability to serve as a primary or supplemental cementitious binder (Alhomair, S.A. 2016). Kabwe et al. (2021) has shown that the most important benefit of the flyash addition to flocculent is the increase in shear strength and hydraulic conductivity of the flyash-treated FTT. The rate of drying and the thickness at which the tailings can be deposited are addressed through use of modelling software (Beier et al. 2016), this subject is beyond the topic of this research. The determination of the soil-water characteristic curve (SWCC) has become essential in the analysis of problems associated with unsaturated soils (Fredlund et al. 2011). During the last decade several researchers and practitioners have stressed the importance and the need of adopting unsaturated soil mechanics in the analysis of problems associated with swelling clays and other problematic unsaturated soils (Zapata 1999; Zapata et al. 2000). The objective of the research reported in this paper was to investigate the effects of sand (or SFR) and flyash addition on unsaturated soil properties (i.e., SWCC) and drying rate of the TT treated tailings. The drying rates of the flyash-treated tailings were compared to those of no flyash and untreated FFTs to assess the effects of the treatments.

2 MATERIAL AND METHODS

2.1 *Characterization of the tailings*

Three treated tailings samples have been tested in this research (TT1, TT2 +2%flyash and TT3 +3% flyash) which were all flocculated and thickened (TT). These TTs samples were the same samples tested in Kabwe et al. 2021. Two untreated tailings, FFT2 (Kabwe et al. 2013) and FFT1 (Kabwe et al. 2021) from the same and different origins as the TT samples, respectively were also tested. Table 1 shows the initial properties of the tailings. The properties of the TT samples are after treating by flocculation and thickening. The treatment of TT2 +2%flyash and TT3 +3% flyash was similar to that of TT1 except that flyash was added to the flocculent. The initial solids content of the FFT1 and FFT2 were 30% and 46%, respectively while solids contents of TT1, TT2 +2%flyash and TT2 +3%flyash were 49%, 46%, and 49%, respectively, so the initial solids contents were similar except for the FFT1. The main difference between the FFT and the TT samples was in their sand content. The untreated FFT1 and FFT2 had 8% and 11% sand, respectively while TT 1, TT2 +2%flyash and TT3 +3% flyash had 46%, 45% and 52% sand respectively. The initial water contents of the FFT1 and FFT2 were 227 and 141% while those of the TT1, TT2 +2%flyash and TT3 +3% flyash were 102, 116 and 104, respectively.

Table 1. Initial properties of the tailings

Sample ID	Treatment methods	Solids content (%)	Water content (%)	Fines content (%)	Sand content (%)	SFR	Void ratio	Clay* size (%)	Clay** size (%)
FFT1	none	30.6	227	89	11	0.12	5.17	60	
FFT2	none	46.1	141	92	8	0.1	3.14	52	
TT1	FF + TH	49.0	102	56	44	0.8	2.74	36	38
TT2 +2%FA	FF + TH + 2% FA	46.3	116	73	27	0.4	3.10	38	38
TT3 +3%FA	FF + TH + 3% FA	49.0	104	73	27	0.4	2.71	38	40

FF= Flocculated; TH= thickening; FA= flyash, *by hydrometer; **by methylene blue, SFR = sand to fine ratio.

Geotechnical properties of Atterberg limits, specific gravity and bitumen content are given in Table 2 (Kabwe et al. 2021). The FFT1 and FFT2 had liquid limits of 50% and 47%, respectively typical of most untreated FFT, while those of TT1, TT2 +2%flyash and TT2 +2%flyash were 28%, 41% and 36%, respectively. The lower liquid limits for the TT samples are caused by the sand contents. Generally, for oil sands fine tailings the addition of flocculants raises the liquid limit, but in this case the presence of the large amount of sand dominates the liquid limit. Bitumen content is usually defined as the mass of bitumen divided by the total mass of the tailings. Both calculations (by total mass and by fines mass) of bitumen content are given in Table 2. As the bitumen is generally integrated into the fines, in all analyses of tests on FFTs and TTs the bitumen is considered as part of the fines.

Table 2. Geotechnical properties of the tailings

Sample designation	Liquid limit (%)	Plastic limit (%)	Plasticity (%)	Activity	Specific gravity	Bitumen content by total mass (%)	Bitumen content by fines mass (%)
FFT1	50	21	29	0.58	2.44	1.6	3.6
FFT2	47	20	27	0.57	2.28	3.0	7.1
TT1	28	18	10	0.29	2.63	0.4	1.5
TT2 +2%FA	42	25	17	0.29	2.63	0.5	1.5
TT3 +3%FA	36	17	19	0.29	2.61	0.1	1.5

The particle size distributions (PSD) of the FFT2 and TTs with and without flyash are given in Figure 1. In this research the dispersed hydrometer test was performed to determine the PSD and the degree of fines dispersion for the samples. The tailings underwent hydrometer tests following the procedure outlined in ASTM D 4221-99R05 (ASTM, 2005) to determine the dispersive characteristics of clay soil by hydrometer in conjunction with the ASTM D 0422-63R07 procedure for the standard particle size analysis of soils (ASTM, 2007). The dispersed PSD is used to define the fines content (< 45 µm) and the clay size content (< 2 µm) and the results are shown in Table 1. The Methylene Blue Index (MBI) measurements of the clay size content for the samples are also shown in Table 1 (AGAT Laboratories, Calgary). The MBI test disperses the clay aggregates and flocs (ASTM, 1999). The MBI and the dispersed hydrometer tests yield approximately similar clay-size results Table 1.

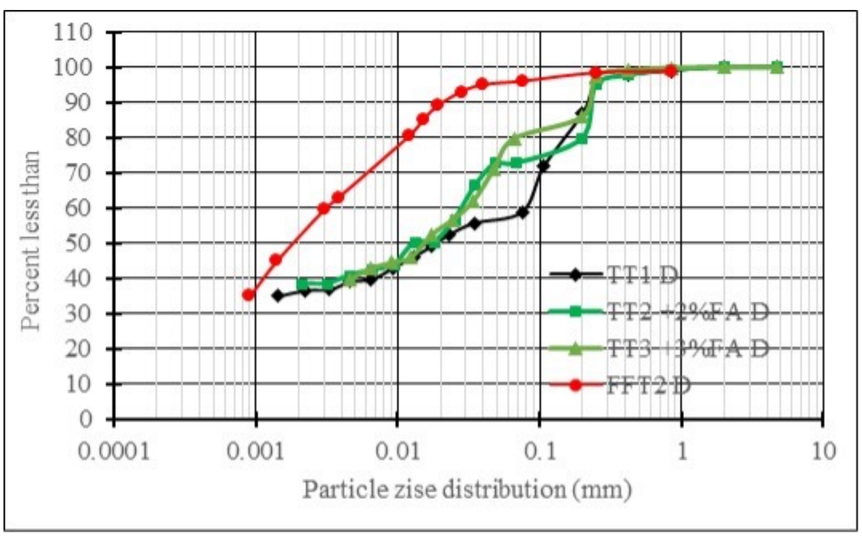

Figure 1. Particle size distribution for oil sands tailings, FFT2, TT1, TT2 and TT3.

2.2 *Soil water characteristic curve SWCC*

The soil water characteristic curve (SWCC) describes the relationship between the water content and soil suction. The SWCC test of the samples was carried out using Tempe cell (ASTM D6838-02 (2008) and WP4 Dewpoint PotentiaMeter. Gravimetric water contents of the samples were measured at values of matric suction up to 400 kPa using the Tempe cell. In the Tempe cell procedure, air pressure is applied over the sample and then the water content is allowed to reach a new equilibrium when the changes in mass of the cell become stable at each suction step. Higher air pressures steps are applied until the maximum suction of 400 kPa is reached. After the final equilibrium is reached, the final moisture content is measured by oven-drying. This water content together with the previous changes in mass are used to back-calculate the water contents corresponding to the other suction values. The matric suctions are then plotted against their corresponding water contents to yield the SWCC. Water contents at high values of suction (i.e., larger than 1500 kPa) were measured using the WP4 Dewpoint PotentiaMeter. Shrinkage curves (void ratio versus gravimetric water content) for the samples were measured following the method described by Fredlund et al. (2011) in order to properly interpret the SWCC results. The curve fits for the gravimetric SWCCs and shrinkage curves for the samples were generated using SVSoils software. The shrinkage curves data with those of the gravimetric SWCCs were integrated using the basic volume-mass relationship (i.e., $Se = wG_s$) to obtain the degree of saturation SWCCs using SVSoils.

2.3 *Drying test*

The drying tests were conducted in identical 180 mm diameter evaporation lysimeters. One lysimeter contained distilled water which provided the reference for the potential evaporation (PE) while the other lysimeters contained the FFT and TT specimens to determine the actual evaporation (AE). The initial thickness and water content of each sample were measured prior to the start of the test. The mass and change in mass of each lysimeter were measured twice a day using a balance to determine the rate of water evaporation from the lysimeter. At the end of the test, the final thickness and diameter of the samples were measured along with the final oven-dry water content of each sample. The water contents of the soil specimens at various times during each test were determined using the final mass of dry soil and water at the end of the test plus the instantaneous masses measured during the test. All tests were conducted at room temperature (22 – 24ºC). The temperature and relative humidity of the air were monitored continuously above the evaporating surfaces.

3 RESULTS AND DISCUSSION

3.1 *Effect of sand to fine ratio SFR on soil water characteristic curve SWCC properties*

Figure 2 shows the shrinkage curves (void ratio versus gravimetric water content) and Figure 3 presents the SWCC plots (degree of saturation versus suction) of untreated (FFT2) and treated oil sands tailings samples (TT1, TT3 +3% flyash and FCT) with various sand to fine ratios (SFR). A flocculated centrifuge tailings (FCT) data set (Kabwe et al. 2021) was also plotted together for comparison purposes. For clarity, the effect of SFR is used in place of the effect of sand. Table 3 presents the SWCCs properties measured from this work and those reported in literature for comparison purposes. The SWCC properties are the air entry value (AEV), residual degree of saturation (θr) and residual suction (Ψr). Fredlund et al. (2011) recommended that the proper AEV for a soil that undergoes substantial volume change as soil suction increases such as oil sands tailings, must be determined from the degree of saturation versus suction plot (Figure 3) (Fredlund et al. 2011). The oil sands samples tested in this work started with water contents well above their liquid limit and underwent large volume changes upon testing. AEV, θr and Ψr were determined graphically from the SWCC plots (Figure 3). Results in Figure 2 and Table 3 indicate that the SWCC for the untreated FFT2 with SFR of 0.1 (8 % sand) was about 1000 kPa. This value is similar to those reported in literature by Fredlund et al. (2011) (SFR ~ 0.1, AEV ~ 1000 kPa), Fredlund et al. (2013) (SFR ~ 0.1, AEV ~ 1000 kPa), and Kabwe et al. (2021) (SFR ~ 0.1, AEV ~ 950 kPa). The AEV of the flyash-treated (TT3 +3% flyash) with SFR of 0.4 (27% sand) was found to be about 400 kPa. The AEV for the TT1 with SFR of 0.8 (44% sands) was found to be about 150 kPa. This AEV value is similar to that reported in literature by Fredlund et al. (2011) (SFR ~ 0.8, AEV ~ 100 kPa). Kabwe et al. (2021) measured an AEV of about 700 kPa for FCT with SFR and sands content of 0.2 and 15% respectively also plotted in Figure 3. The AEV is similar to that found by Schafer & Beier (2019) for the same centrifuge material.

Figure 4 shows the relationship between the AEV and SFR of oil sands tailings data presented in Figure 3 and Table 3. The plot indicates that the AEV decreases exponentially with increasing SFR of oils sands tailings. This confirms that the SFR or sand content affect the AEV of SWCC. This curve [AEV = 1342 EXP(-3.12 x SFR)] can be used to estimate AEV of oil sands tailings material with various SFR.

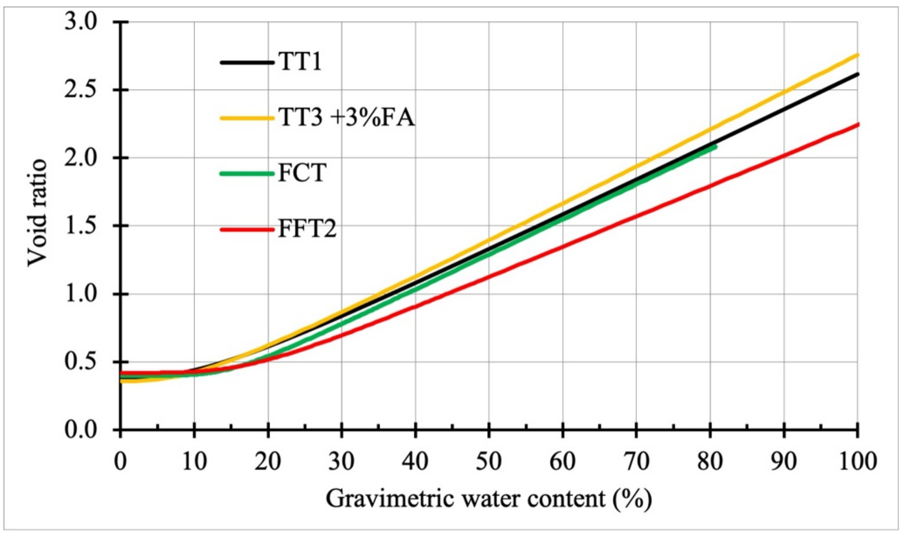

Figure 2. Shrinkage curves for FFT2, TT1, TT3 +3% flyash and FCT samples.

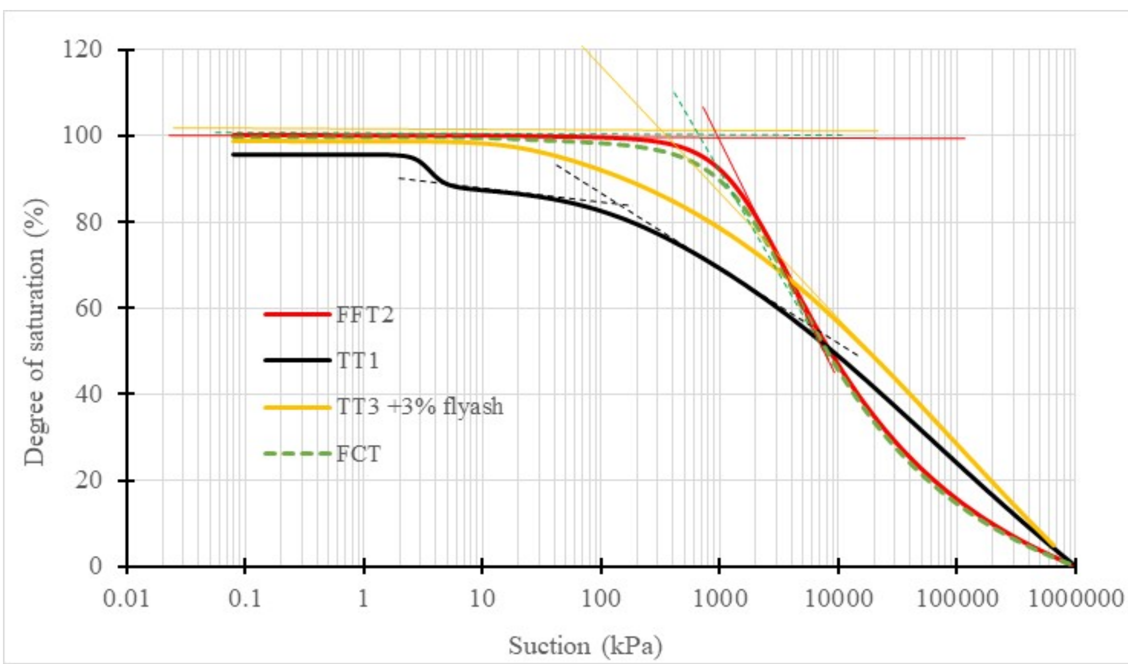

Figure 3. Combined soil water characteristic curves SWCC for FFT2, TT1 and TT3 +3% Flyash and FCT; curve fits generated using SVSoils software.

Table 3. Properties of SWCC of oil sands tailings

Sample designation	Tailings type	Fines content (%)	Sand content (%)	SFR	AEV (kPa)	θr (kPa)	ψr (kPa)
FFT2	FFT	92	8	0.1	1000	25	2000
TT1	TT	56	44	0.8	120	-	-
TT3 +3%FA	TT	73	27	0.4	400	-	-
Fredlund1 et al. 2011	FFT	55	45	0.8	100	20	3000
Fredlund2 et al. 2011	FFT	90	10	0.1	1000	20	15000
Fredlund3 et al. 2013	FFT	90	10	0.1	1000	20	15000
Haley et al. 2020	FCT	85	15	0.2	700	25	3000
Kabwe et al. 2021	FFT	94	6	0.1	965	20	4000
Kabwe et al. 2021	FCT	85	15	0.2	700	25	3000

FCT = Flocculated centrifuged Tailings, θr = residual degree of saturation, ψr = residual suction

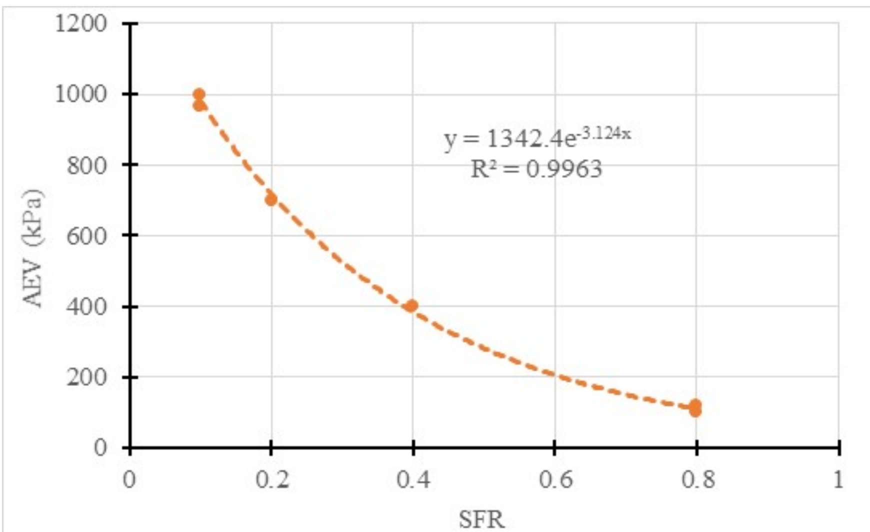

Figure 4. Plot of air entry value (AEV) versus sand to fine ratio (SFR) for oil sands tailings materials.

3.2 *Effect of flocculation and thickening and flyash addition on drying rate of oil sands tailings*

3.2.1 *Effect of flocculation and thickening*

Table 4 and Figure 5 provide the drying test results for the untreated FFT1 and FFT2 and flocculated thickened tailings TT1. The initial void ratio of the untreated FFT1 and FFT2 were 5.17 and 2.85 respectively while that for the TT1 sample was 2.71 (Table 3). The corresponding initial solids and water contents of the FFT1 and FFT2 were 30.6 and 227% and 46.1 and 141%, respectively while the solids and water contents for the TT1 sample was 49 and 102% respectively.

Table 4. Properties of the tailings during evaporation

	AE/PE (Initial) Time (Days)	AE/PE ~0.8 (at Boundary) Time (Days)	AE/PE ~0 (Residual) Time (Days)
FFT1	0	23	28
FFT2	0	19	25
TT1	0	17	22

Figure 5 shows the AE/PE ratio versus time for FFT1, FFT2 and TT1 samples. The surfaces of all the samples were initially wet or near saturation (i.e., AE/PE ~ 1) and were allowed to evaporate to a completely air-dried state under room atmospheric conditions (22 – 24 ºC). All the AE/PE ratios remained closed to unit during the early stage of measurement but the ratio for each sample began to decline as the availability of water decreased. It is interesting to note that the FFT1 with its lower initial solids content and higher water content initially dewatered much slower than FFT2 and TT1. This is attributed to the presence of free bitumen (i.e., 3%) in the FFT pore water, which forms a film on the surface that limits further drying from deeper layers and thus reduces the actual rate of evaporation during the early stages of atmospheric drying. It is also interesting to note in Figure 5 that all the drying plots show similar curvature at an AE/PE ratio of 0.8. The AE/PE ratio for each sample initially slowly decreased with time, and each sample reached an AE/PE value of 0.8 at different times (Table 4 and Figure 5). Results from Figure 5 and Table 4 indicate that FFT1 took longer time (23 days) than FFT2 (19 days) to reach the AE/PE value of 0.8. This is due to the difference in solids content between the two untreated tailings samples. Results also indicate that the treated TT1 sample took less time (16 days) than the two untreated samples to reach the value of 0.8. This is due to the flocculation and thickening treatment on the tailings. Flocculating and thickening, therefore, results in lower initial water contents which increase the drying rate until the saturation boundary (at AE/PE ~ 0.8) is reached. As drying continued in Figure 5 the AE/PE ratio of the samples then started to decline rapidly to reach their lowest values of about zero. It can be concluded that the AE/PE ratio of 0.8 represents the boundary between the saturated and unsaturated states of all the samples.

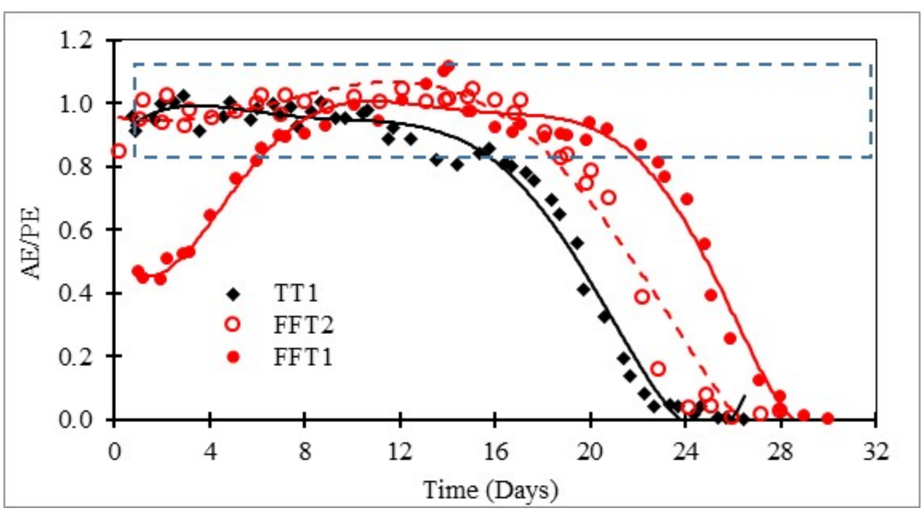

Figure 5. Drying rates as a function of time for FFT1, FFT2 and TT1 tailings samples.

3.2.2 *Effect of flyash addition*

Table 5 and Figures 6, 7 and 8 present the combined drying test results for the flyash-treated thickened tailings TT2 + 2% flyash and TT3 + 3% flyash and no flyash treated FFT1, FFT2 and

TT1. The initial void ratios and solids contents of the TT2 + 2% flyash and TT + 3% flyash before the drying tests were 3.10 and 49% and 2.7 and 46% respectively. The corresponding initial water contents of the TT2 +2% flyash and FTT +3% flyash were 116% and 104% respectively. Results of the drying tests in Table 5 and Figure 6 indicate that the flyash-treated TTs took less time (about 10 days) than the no flyash TT1 to reach the AE/PE value of 0.8, though their initial solids contents were approximately the same. This indicates that the flyash addition increases the drying rate of the oil sands tailings. As drying continued in the unsaturated zone the AE/PE ratio of the flyash-treated samples rapidly reach their lowest values of about zero in less time (17 days) than the no flyash samples (22 – 25 days). It should be noted in Figure 7 that the AE/PE ratios for the flyash-treated tailings became greater than unity in the early process due to deep cracks that appeared on the surfaces of the tailings and that increased the evaporation surface area. It was also noted at the end of the tests that the amount of shrinkages and cracks were not the same for the all samples and these had some impact on the rate of evaporation of the tailings. Results also show that there is little drying difference between the 2% and 3% flyash addition. It can be postulated that atmospheric drying is more effective when flyash is added to the flocculent.

Table 5. Combined properties of the tailings during evaporation

	AE/PE (Initial) Time (Days)	AE/PE ~0.8 (at Boundary) Time (Days)	AE/PE ~0 (Residual) Time (Days)
FFT1	0	23	28
FFT2	0	19	25
TT1	0	17	22
TT2 +2% FA	0	10	17
TT3 +3% FA	0	9	17

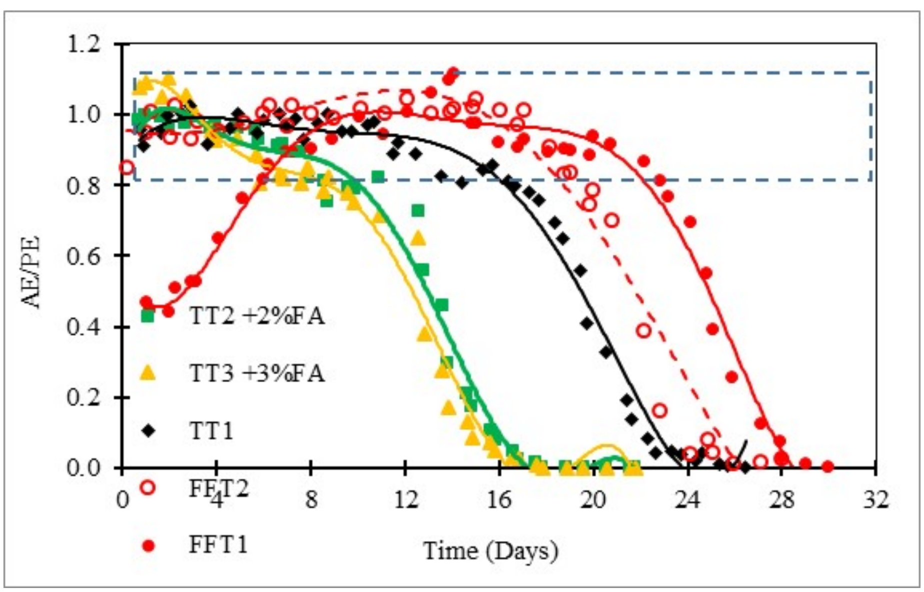

Figure 6. Drying rates as a function of time for FFT1, FFT2, TT1, TT2 +2%flyash and TT3 +3% flyash.

Table 6. Properties of the tailings during evaporation

	AE/PE ~ 1 (Initial)			AE/PE ~ 0.8 (at Boundary)			AE/PE ~ 0 (Residual)		
	Time (Day)	Void ratio (e)	Water content (%)	Time (Day)	Void ratio (e)	Water content (%)	Time (Day)	Void ratio (e)	Water content (%)
FFT	0	3.14	140	22	1.30	30	28	0.90	~0
TT1	0	2.71	102	16	1.37	30	24	1.00	~0
TT2 +2%FA	0	3.10	116	10	1.58	30	16	1.00	~0
TT3 +3%FA	0	2.71	104	10	1.37	30	16	1.00	~0

Figure 6 shows the AE/PE ratio versus water content for the combined samples. The AE/PE ratios of all the samples were initially close to unit (i.e. AE/PE ~ 1) up to the water content of about 70%. As the drying continued all the samples AE/PE ratios initially slowly decreased with decreasing water content to an AE/PE ratio of about 0.8 and water content of about 40%. The AE/PE ratios remained close to 0.8 as the water content further decrease from 40% to about 20%. It is interesting to note that all the drying plots show similar curvature at a water content of about 20%. As drying proceeds into the unsaturated zone the AE/PE ratios of all of the samples then started to decline rapidly to reach their lowest values of about zero. It can be concluded that the AE/PE ratio of 0.8 and the water content of 20% represent the boundary between the saturated and unsaturated states of all the samples tested.

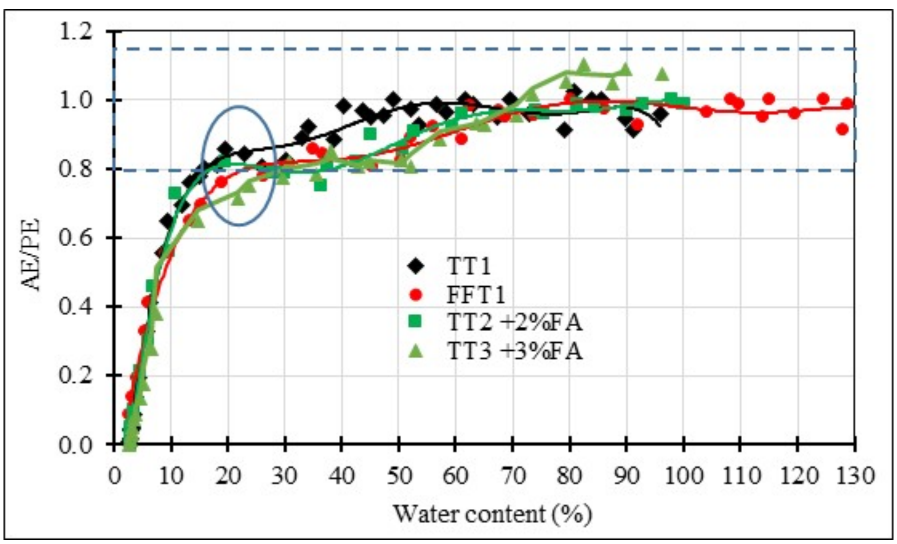

Figure 7. Drying rates as a function of water content for FFT1, TT1, TT2 +2%flyash and TT3 +3% flyash.

In summary, the AE/PE rate is a function of soil texture, water availability and drying rate (Wilson et al., 1997). The TTs treated with flyash dewater at the same rate, but initially they dewater much faster than the treated TT1 without flyash. As the drying rate and initial water content were approximately the same for the TT samples, it can be concluded that the inclusion of flyash changes the soil structure, resulting in faster initial evaporation until the saturation boundary is reached. As the samples desaturate, their evaporation rate is the same. Flocculating and thickening results in lower initial water contents which increase the drying rate until the saturation boundary is reached.

3.2.3 *Effect of atmospheric drying on surface shear strength of oil sands tailings*

Figure 8 illustrates different shear strength boundaries during the atmospheric drying of FCT (Kabwe et al. 2018). The tailings sample was initially wet and saturated (AE/PE ~ 1) and was allowed to evaporate to a completely air-dried state under room conditions (22 – 24 ºC).

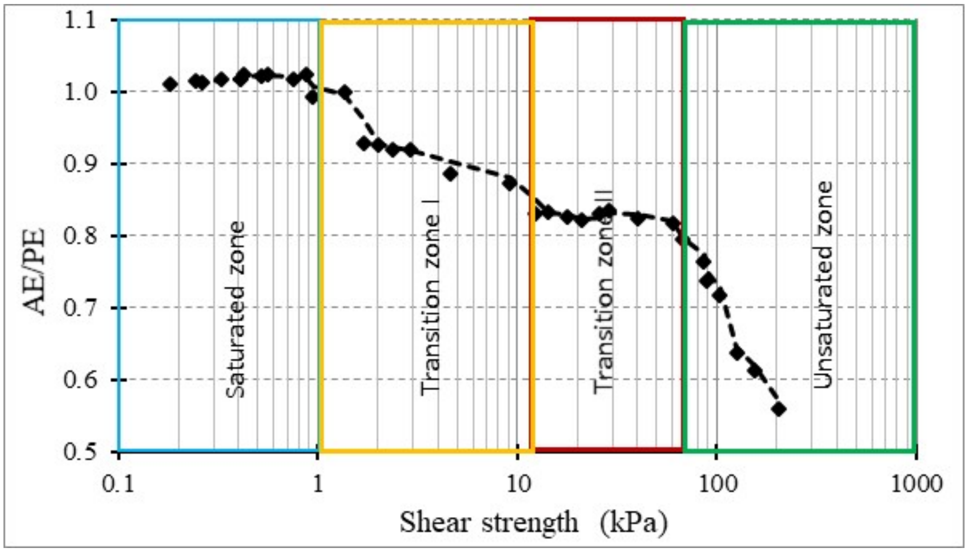

Figure 8. Drying rate as a function of undrained shear strength plot for the oil sands tailings FCT (Kabwe et al. 2018).

The early drying data indicate that the shear strength increased from 0.1 to 1 kPa while the sample was still wet (with excess water on surface) or fully saturated (i.e., AE/PE ~ 1) (saturated zone). At this stage the evaporation rate is controlled by the atmospheric conditions. The increase in shear strength is due to the evaporation shrinkage as shrinkage increases the effective stress and shear strength. Of most importance are the two breaks or the rapidly declines in the AE/PE ratios that occur at shear strengths of about 1 kPa and 60 kPa. The first break at about 1 kPa indicates the onset of desaturation of the tailings. At this stage, the evaporation rate is controlled by the properties of the FCT profile. As the ratio AE/PE decreases progressively from 1 to about 0.8, the volume of the material decreases and there was a slow increase in shear strength from 1 kPa to about 12 kPa (transition zone 1). As the drying continued the AE/PE ratio remains constant at about 0.8 while the shear strength increased from 12 kPa to 60 kPa (transition zone 2). The increase in shear strength is also due to the evaporation shrinkage that increases the effective stress and shear strength. As the AE/PE ratio started to decline rapidly near the plastic limit from 0.8 to about 0.55 there was a substantial increase in shear strength from 60 kPa to about 200 kPa. This second break of the rapidly decline in the AE/PE ratio at about 60 kPa indicates the onset of the unsaturated zone. The unsaturated zone yielded the shear strength necessary to support trafficable surface. In summary, to yield a trafficable surface shear strength the atmospheric drying of the oil sands tailings would have to proceed into the unsaturated state, i.e., AE/PE < 0.8 and shear strength > 60 kPa.

4 SUMMARY AND CONCLUSIONS

SWCCs for oil sands tailings with various SFRs were measured and the AEVs were plotted against the corresponding SFRs. The atmospheric drying tests were conducted on untreated FFTs, TT and flyash-treated TTs to evaluate the effect of flyash addition on atmospheric drying of oil sands tailings. The effect of atmospheric drying on the surface shear strength of FCT was also investigated. The conclusions from these tests are:

1. The plots of AEV versus SFR indicated that the AEV decreases exponentially with increasing SFR of oils sands tailings. This confirms that addition of sand to flocculent significantly affect the SWCC's AEV of oil sands tailings.
2. In the drying tests, the untreated FFT2 with its higher initial water content initially dewatered much slower than the flocculated TT1. Flocculation and thickening, therefore, results in lower initial water contents which increase the drying rate until the saturation boundary is reached.
3. All the drying plots for the samples regardless of treatment showed similar curvature at an AE/PE of 0.8 and water content of about 20%. It was concluded that AE/PE of 0.8 and water content of about 20% represent the boundary between the saturated and unsaturated states of all the samples.
4. The AE/PE rate is a function of soil texture, water availability and drying rate. The TTs treated with flyash dewatered at the same rate, but initially they dewatered much faster than the no flyash TT1. It can be concluded that the inclusion of flyash changes the soil structure, resulting in faster initial evaporation until the saturation boundary is reached.
5. As the flyash-treated TTs reach the unsaturated boundary in less time and all samples materials then dewater at the same rate, it can be postulated that atmospheric drying is more effective when flyash is added to the flocculent. There is little drying difference between the 2% and 3% flyash addition.
6. During the drying process of the FCT tailings there are two breaks of declines in the AE/PE ratio that occur at shear strengths of about 1 kPa and 60 kPa. The first break at about 1 kPa indicates the onset of desaturation of the tailings near the liquid limit. The second break at about 60 kPa occurred as the material begins to desaturated near the plastic limit and there is a substantial increase in shear strength. This second break indicates the onset of the unsaturated state of the tailings material. The unsaturated zone yielded the shear strength necessary to support trafficable surface.

5 ACKNOWLEDGEMENTS

The authors would like to thank Total E&P for funding this research project when it was involved in the oil sands sector and the Saskatchewan Research Council for providing the flocculated and thickened samples. Thanks to Vivian Giang for proofreading and editing the paper.

6 REFERENCES

Alhomair, S.A. 2016. HYDRAULIC CONDUCTIVITY OF FLY ASH-AMENDED MINE TAILINGS, MSc Colorado State University, Colorado, 2016.

ASTM Standard D4221-99, 1999 2005. Standard Test Method for Dispersive Characteristics of Clay Soil by Double Hydrometer. West Conshohocken, PA: ASTM International, DOI: 10.1520/D4221-99R05.

ASTM Standard D422-63, 1963. 2007. Standard Test Method for Particle-Size Analysis of Soils. West Conshohocken, PA: ASTM International, DOI: 10.1520/D0422-63R07.

Fredlund, D,G., Stone J. and Stianson J. (2011). Determination of Water Storage and Permeability Functions for Oil Sands Tailings. Proceedings Tailings and Mine Waste 2011, Vancouver, BC, Canada.

Fredlund, D.G. and Houston, S.L. (2013). Interpretation of soil-water characteristic curves when volume change occurs as soil suction is changed. Advances in Unsaturated Soils – Caicedo et al. (eds) © 2013 Taylor & Francis Group, London, ISBN 978-0-415-62095-6.

Kabwe, L.K., Wilson, G.W., Beier, N.A., and Scott, J.D. (2021). Effect of flyash and freezing and thawing treatment on consolidation of oil sands fluid fine tailings. Canadian Geotechnical Journal 2021 (Accepted).

Kabwe, L.K., Abdulnabi, A., Wilson, G.W., Beier, N.A. (2019). Geotehnical and unsaturated properties of metals mines and oil sands tailings. Proceedings of Tailings and Mie Waste, Vancouver, BC, Canada.

Kabwe, L.K., Wilson, G.W., Beier, N.A., and Scott, J.D (2018). Effects of Atmospheric Drying and Consolidation of Flocculated Thickened Tailings and Centrifuged Cake on Near-Surface Shear Strength. American Society of Civil Engineering, August, 2018.

Kabwe, L.K., Kone, M., Sorta, A., Wilson, G.W., J.D. Scott, and Ulrich, A.C. (2013). Measurements of unsaturated soil properties of old and new mature fine tailings. Proceedings of the Mine Closure, UK — M.

Kearl Oil Sands Mine: Fluid Tailings Management Report for 2020

OSTC and COSIA Report August 2012. Technical guide for fluid fine Tailings Management, August 2012).

Schafer, Haley and Beier, Nicholas 2019. Estimating soil-water characteristic curve from soil-freezing characteristic curve for mine waste tailings using time domain reflectometry. Canadian Geotechnical Journal.

Beier, N.A., Kabwe, L.K., Scott, J.D., Pham, N.H., and Wilson, G.W. (2016). Modeling the effect of flocculation, thickening and desiccation on oil sands tailings. Proceedings of the American Society of Civil Engineers, Chicago, Illinois, USA, August 2016.

Zapata, C.E. 1999. Uncertainty in Soil-Water Characteristic Curve and Impact on Unsaturated Shear Strength Predictions, Ph.D. Dissertation, Arizona State University, Tempe, AZ, USA.

Zapata, C.E., Houston, W.N., Houston, S.L., and Walsh, K.D. 2000. “Soil-Water Characteristic Curve Variability”. Proceedings of Sessions of Geo-Denver 2000, Denver: ASCE Geo-Institute, 84-124.

Wilson, G.W., Fredlund, D.G. and Barbour, S.L. (1997). The effect of soil suction on evaporative fluxes from soil surfaces, Canadian Geotechnical Journal 34, pp. 145-155.

Three methods for rapid estimation of the consolidation properties of mineral slurries

Yagmur Babaoglu
Carleton University, Ottawa, ON, Canada

Shunchao Qi
Sichuan University, Sichuan, China

Paul H. Simms
Carleton University, Ottawa, ON, Canada

ABSTRACT: Relatively rapid estimation of the hydraulic conductivity - void ratio function (*k-e*) is desirable to quickly evaluate the long-term dewatering potential of treated tailings, particularly the finer tailings or tailings with high clay content. Here are summarized three recently developed methods to estimate or measure the *k-e* function. The methods include i) correlations based on a single measured value of *k*, ii) methods that infer consolidation properties using settlement data from sedimentation columns, and iii) methods that directly calculate *k-e* from paired measurements of pore-water pressure and density, also in sedimentation columns. Here the methods are demonstrated using a sedimentation column test on flocculated fluid fine tailings. Additionally, the methods are compared to large strain consolidation data measured using a slurry consolidometer. Each of the new methods has its own strengths, and, as will be demonstrated, complementary use of these methods may lead to useful estimates of *k-e*.

1 INTRODUCTION

The consolidation characteristics of tailings, particularly the hydraulic conductivity – void ratio function (*k-e*), governs the rate of settlement and densification in any tailings impoundment. Well-established methods exist to determine *k-e*, such as the large strain consolidation test or the seepage induced consolidation test, which involve a direct measurement of *k* at fixed void ratio and stresses, or column tests which are analyzed through back-calculation methods to arrive at a *k-e* function. The two first tests may take considerable time, months in the case of clayey tailings, while the latter are subject to various assumptions, such as the form of the *k-e* function, and assumptions as to the uniqueness of the compressibility function. There are well-known procedures to back-calculate *k-e* from column tests (Abu-Hejleh and Znidarcic 1996, Pane and Schiffman 1997), which take advantage of special characteristics, such as the initial slope of the height versus time curve and the hydraulic conductivity at the surface (Been and Sills 1981). The authors' have developed several new techniques over the last 3 or so years, these include techniques for estimating *k-e* using special characteristics of the full settlement curve in sedimentation columns (Qi and Simms 2019, Qi et al. 2020), a one point measurement technique based on statistics of measured *k-e* data from clayey soils and tailings (Babaoglu and Simms 2020a), and calculation of *k-e* in sedimentation columns by high resolution of measurements of water content /density and pore-water pressure that allows direct calculation of k using Darcy's law (called IPM – instantaneous profiling method) (Babaoglu and Simms 2020b).

The purpose of this paper is to briefly review each of these methods and demonstrate their application to a flocculated fine fluid tailings (fFFT). It will be shown that complementary use of these techniques can result in robust estimation of *k-e*, especially for *k-e* at high void ratios. This is a useful contribution as hydraulic conductivity at high void ratios strongly affects the overall rate of settlement in tailings deposits. Users may employ these methods to allow for quicker evaluation of *k-e* to supplement or reduce the number of conventional tests based on their own needs and preferences.

2 METHODS

2.1 *Method 1: Single point estimation of k-e (SPEK)*

This class of methods arises from statistical evaluation of about 80 *k-e* functions for clays, clayey tailings, and dredged sediments, including 36 data sets for oil sands tailings (Babaoglu and Simms 2020a). Originally, this data set was used to evaluate a wide range of previously proposed equations to estimate *k-e* from easily measured predictors, such as the Atterberg limits. However, it was realized that the form of most of these equations is the conventional power form:

$$k = Ae^{B}. \tag{1}$$

In these empirical formulae for *k-e*, all the information on the predictors falls into the modifier, the A parameter. Therefore, if a single point is measured, the rest of the *k-e* function can be expressed as a ratio with the measured point, and this ratio will depend on B, but not A. Following this observation, two Equations were proposed:

$$k = k_{measured\ e_0} \frac{e^5}{e_0^{\ 5}} \tag{2}$$

$$k = k_{measured\ e_0} \frac{e^5}{e_0^{\ 5}} \frac{1+e_0}{1+e} \tag{3}$$

Where a single measured value of k is obtained at a void ratio e_0. Further, it was found that the accuracy of the equations is maximized when the measured point is obtained at a vertical effective stress between 1 and 2 kPa. Applying this rule, Equations 2 and 3 predicted values that are 95% and 92 % within an order of magnitude of all measured data points for oil sands tailings (250 points). Example comparisons of measured and predicted data are shown in Figure 1.

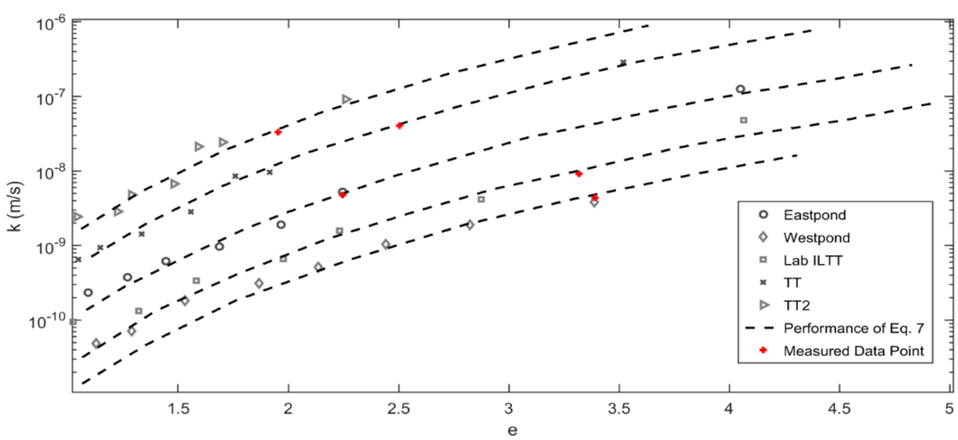

Figure 1. Example applications of Equation 2 to some measured *k-e* functions for oil sands tailings

In general, the experience with this method is that it is most accurate for k values at void ratios close to the measurement point and lower.

2.1.1 *Application of this method to find new k-e data:*

At present, it is recommended that the measured *k-e* data point be found following a conventional step by step large strain consolidation test, up to a vertical effective stress of 1.5 kPa. To comply with conventional practice, it is recommended that at least two steps be used to achieve this load. At the load step for 1.5 kPa, a constant loading test is performed as per ASTM D2434.

2.2 *Instantaneous Profiling Method (IPM)*

This method requires density or water content data and pore-water pressure data collected with depth and over time in a sedimentation column. This data is then employed to determine instantaneous k values using Darcy's law, as per Equation 4:

$$\frac{\left(\frac{e_{t1}}{1+e_{t1}}\right)-\left(\frac{e_{t3}}{1+e_{t3}}\right)}{t_3-t_1}=K\frac{h_1-2h_2+h_3}{\Delta x^2} \tag{4}$$

Where the void ratios (*e*) are measured at elevation x at times t_3 and t_1, where $t_3 = t_2 + \Delta t$ and $t_1 = t_2 - \Delta t$. The heads (*h*) are measured at time t_2, and at elevations X-Δx for h_1 and x+Δx for h_3. The component *x* in Equation 4 should ideally be the height or thickness of solids under large strain conditions and can be determined from the distribution of void ratio with depth over time. However, if Δt is small such that settlement over the time step is also small, Equation 4 can be calculated as per small strain theory, and real heights can be used for values of *h*.

This method is independent of any assumptions with respect to dewatering mechanisms, i.e. sedimentation, consolidation, creep or thixotropy, which is an advantage of this method compared to inverse modelling of column tests. However, for the successful implementation of IPM, the water content and pore water pressure profiles within the column need to be monitored at high resolution. The pore water pressure distributions are generally well-behaved and can be interpolated based on experience of previous tests (e.g. Bartholomeeusen et al. 2002) using an adequate number of pore-water pressure sensors. A much higher resolution, however, is required for water content or density measurements.

2.2.1 *Implementation in a specialized Sedimention Column*

Babaoglu (2021) designed a specialized column to implement IPM for tailings. The column is presented in Figure 2, and it is 23.6 inches tall (approx. 60 cm) and has a diameter of 12 inches. There is a small column located in the centre of the large column (diameter of 2 inches) which accommodates the water content sensors. The column has 10 inlets at various locations to accommodate miniature pore-water pressure sensors (T5 from UMS), which are used to measure pore water pressures during the experiments, though typically 4 sensors are used in a given test.

For the high-resolution measurement profiles of water content, capacitance-based sensors were selected after consideration of a range of ultrasonic and electromagnetic based techniques. These sensors can measure the volumetric water content non-intrusively, as contact of the sensors with the soil or tailings is not required. The sensors move up and down in the inner column as shown in Figure 2. This inner column is connected to the bottom of the large column using a metal connection plate with multiple O-rings to eliminate possible water leakage in the pipe. The diameter and height of the column was selected on the basis of a series of experiments investigating the potential for sidewall effects.

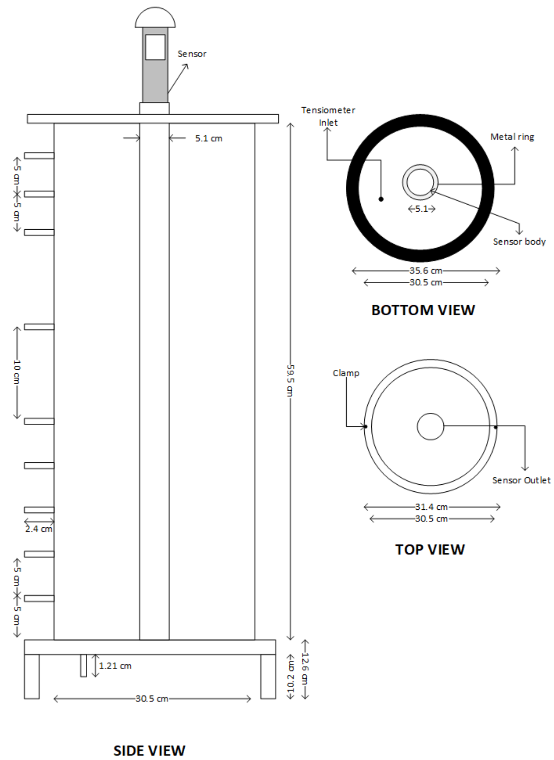

Figure 2. Schematic of instrumented sedimentation column

Each VWC sensors interrogates a region approximately ten centimeter long (vertically); therefore, for more detailed profiling, an automation system vertically moves the sensors within the central column in cm increments. Each sensor requires its own calibration and is sensitive to small changes in the geometry of the inner tube. Therefore, the sensors are calibrated at each depth by collecting samples for oven drying at the beginning and at the end of the experiment. As the sensors cannot directly measure the soil at the mudline, water contents close to the mudline are found algorithmically, through knowledge of how the readings progressively change as the sensor moves from the surface water into the tailings. The settlements during the experiments are observed using high-resolution cameras, to give high resolution data on the tailings water-interface.

2.3 *Method to determine k-e from settlement data only (SCQi2 method)*

Qi and Simms (2019) and Qi et al. (2020) proposed several methods to determine *k-e* from settlement data from sedimentation columns, based on characteristics of such settlement curves when the true *k-e* function can be approximated by the power type function. These methods requires less data than IPM, but requires estimation of the compressibility curve of the test material in the column. The latter can be estimated by measuring water content with depth by oven drying at the end of the sedimentation test, and fitting the data with equations such as Equation 4, where z is the elevation, Gs is the specific gravity, and *a* and *b* are parameters of the compressibility equation $e = a\,\sigma_v'^{\,b}$.

$$z = \frac{1}{Gs - 1}\left[\left(\frac{e}{a}\right)^{\frac{1}{b}}\left(\frac{e}{b+1} + 1\right)\right] \tag{5}$$

One of the methods from Qi et al. (2020) is here described in detail, and henceforth called SCQi2. The method requires a settlement curve from a column test with one way drainage (no bottom drainage), and the compressibility curve. Sufficiently high density settlement data can be obtained using a webcam, if mm elevations are marked on the settlement column. The compressibility function can be evaluated by obtaining depth profiles of density, determined by destructively sampling for oven dried samples with depth at the end of the sedimentation test. It is recommended that the column is sufficiently wide to permit at least 4 samples for oven drying every 2 cm depth. Density can be cross-checked by both the individual oven dried samples, and by constantly recording the weight of the column after each ~ 2 cm layer is removed.

A height of ~ 50 cm and a diameter of 30 cm seems to provide sufficient height to determine k at the high void ratio range (e ~ 2.5 and higher), while minimizing sidewall influence for these relatively low effective stress conditions. Baboaglu (2021) performed experiments to evaluate the sidewall effect using different oil sands tailings type, include centrifuge cake.

The method assumes that the *k-e* function can be adequately described by a power function (Equation 1). Qi and Simms (2019) have shown that for any settlement curve predicted by large strain consolidation theory using the power function for *k-e*, that the modifier, A, only changes the location of the settlement curve. Specifically, for any predicted settlement curve H = f(t), shifting the A value only changes the times associated with each precited H value, such that a change in A value will shift the time for the constant H (Height of tailings-water interface) value by $t_2 / t_1 = A_1 / A_2$. This property allows the A value to be easily determined if the B value, which controls the shape of the settlement curve is already know.

SCQi2 determines B by creating a function relating B to observed variance in predicted values of log T for set number of H values. The column test is simulated using any l-D large strain consolidation software using any reasonable value of A, and three different B values (say 3,5,9). This requires the initial and final heights, the initial void ratio, and the compressibility curve (determined as described previously). To summarize the procedure in point form:

1. Perform sedimentation column test with 1 way drainage, initial height ~ 0.50 m, minimum initial diameter 0.30 m. Test is terminated if settlement is < 1mm over 24 hours. Ensure elevation of the tailings-water interface can be measured with 2 mm accuracy.
2. Remove bleed water. Obtain at least 3 samples for oven drying for every 2 cm of tailings destructively sampled. After every ~ 2 cm is removed, weigh the column. In this way the density profile can be cross -checked using the mass remaining in the column, as well as the water content from oven drying.
3. Estimate the compressibility curve by fitting the void ratio with depth data using Equation 5 or similar. Note this equation assumes hydrostatic conditions have been reached. This can be checked if a pore-pressure sensor is installed at the bottom of the column.
4. Perform 3 LSC numerical analysis using the initial void ratio, initial height, measured compressibility curve, using A=1e-10 and B=3,5, and 9.
5. Choose 5 heights between the initial and final heights. For example, if the sample is 0.50 m tall and consolidated to 0.30 m, the set of H could be 0.3,0.34,0.38,0.42, and 0.46 m.
6. For each of the three simulations, calculate the variation of the log times corresponding to each of these heights. The calculation is done as a sum of each log time at a particular H minus the average log time :

   $$\mathrm{Var} = \Sigma\,(X_n - Y)^2 / n \tag{6}$$

   Where X_n is log t for Height n, Y is the average of all log t, n is the number of heights
7. An equation can now be found relating Var to the power B. A power function with an offset fits this data well:

   $$\mathrm{Var} = cB^d + e \tag{7}$$

8. Evaluate the Var of the measured settlement data, using the same set of heights used in steps 5 through 7, which gives VarM. Then the correct power B, is

   $$B = ((\mathrm{VarM}-e)/c)\hat{}(1/d) \tag{8}$$

9. The parameter *A* can now be found using the translation property.

3 EXAMPLE APPLICATION TO FLOCCULATED FFT

3.1 *Flocculated FFT and column experiment*

A sedimentation column experiment with fFFT that was also instrumented for the IPM method (as shown in Figure 1) is here used to compare the three methods. The initial solids content was 31% and the liquid limit was 60%. The sands to fine ratio (SFR) was 0.25. The clay content obtained from the Methylene Blue Index (MBI) analysis ranged from 28% to 32%. According to the X-ray diffraction (XRD) results, the composition of the clay fraction was 68-72% Kaolinite and 28-32% Illite. Total Dissolved Solids (TDS) in the pore water collected from the raw fluid fine tailings (rFFT) was 1050 mg/L, electrical conductivity was 1590 microS/cm, while the dominant cations were sodium at 340 mg/L. These tailings were also sent to the University of Alberta for testing, flocculated in a similar manner, and then tested using a large strain consolidometer (Abdulnabi et al. 2021). Additional details of the experiment are provided in Table 1.

Table 1. Geotechnical Properties of fFFT and Initial conditions of the experiment

	fFFT
Initial VWC (%)	84
Initial GWC (%)	248
Initial Solids Content (%)	29
Initial e	5.25
Initial height (cm)	46
Final height (cm)	33.7
Specific Gravity	2.12
Miniature pressure sensor positions in the column (from bottom to top)	5-15-20-25-35
Test Duration (days)	25 days

An anionic flocculant was utilized to prepare flocculated FFT at a specific dose using torque feedback to control the flocculation, using the method described by Aldaeef et al. (2019). The samples are generated in 6 batches and deposited into the column one batch after another over less than 15 minutes. Batches were subsampled for CST, rheometry, and optical microscopy to check for consistency: additional results on these specific tests is provided in Babaoglu (2021).

3.2 *Data gathered from the column test*

The VMC and PWP data are shown in Figure 3 and the settlement data in Figure 4. Of interest is that both the height data and the VWC show that the tailings apparently come to an equilibrium state around Day 15 to 17, but thereafter there is another phase in deformation, particularly in the top half of the column. This behaviour is repeated in other sedimentation column tests on fFFT (Babaoglu and Simms 2020b, Babaoglu 2021) and is related to time-dependent changes in the compressibility curve. This is important to note, as the SCQi2 method assumes a constant compressibility curve.

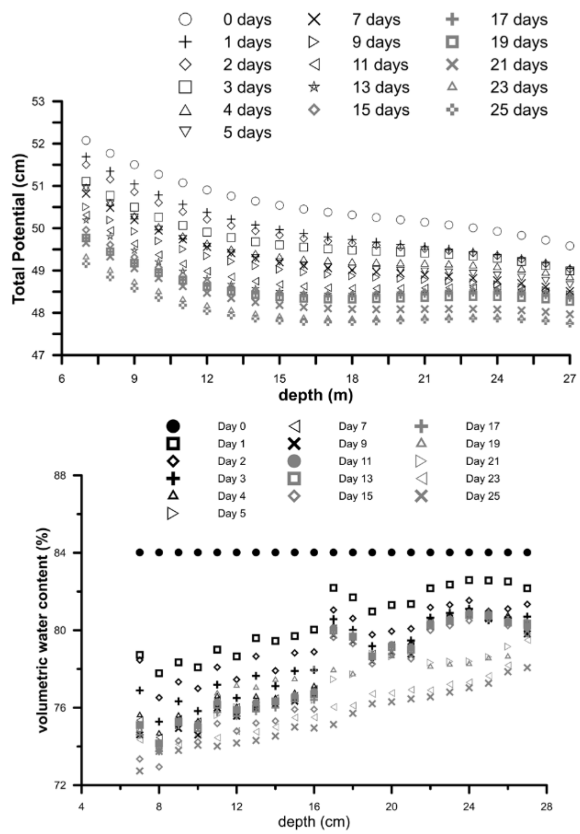

Figure 3. Measured potentials and volumetric water contents for fFFT tailings

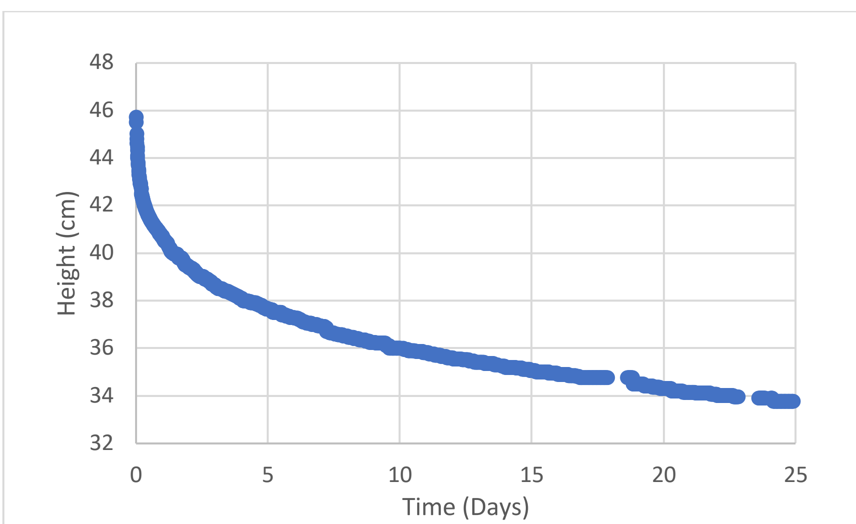

Figure 4. Settlement in fFFT experiment

3.3 *Comparison of k-e from different methods*

The SPEK and the SCQi2 methods give direction predictions of the *k-e* as power functions, but the IPM method gives a "cloud" of data from individual calculations of fluxes and gradients at multiple points. The cloud of measurements for this fFFT is given in Figure 5. This data must then itself be fitted with a *k-e* function, shown in dashed red.

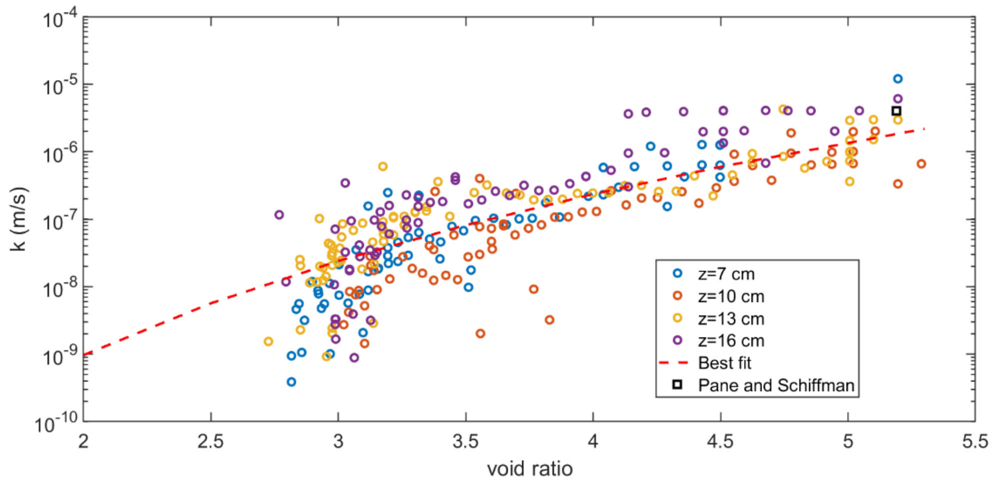

Figure 5. An example of *k-e* data obtained from IPM

The three estimates are compared in Figure 6, along with LSC data measured at the University of Alberta (Abdulnadi et al 2021). Additionally, the Pane and Schiffman (1997) method to calculate *k* at the start of sedimentation is shown as "P&S". To provide more context, the fitted LSC, IPM, and SCQi2 functions are used in a large strain consolidation model to back calculate the settlement curve of the column test, shown in Figure 7. The SPEK method, as expected, shows good agreement with the *k-e* curve at the lower void ratios, but judging by both the LSC data point at e=4.2 and the P&S point, underestimates the *k-e* curve at high void ratios. The IPM method shows good agreement with both the LSC data points, and shows better agreement with the P&S data point, though it can be seen when extrapolated to higher void ratios, it will somewhat underestimate the P&S value. The SCQi2 method shows the best agreement at high void ratios, but will underestimate the true function at lower void ratios. This is because the SCQi2 is the most empirical, in the sense that it is controlled by the settlement curve in the column test, and therefore will predict best in the range of void ratios actually present in the column test. As shown in Figure 7, the SCQi2 method best predicts the initial rapid settlement in the column.

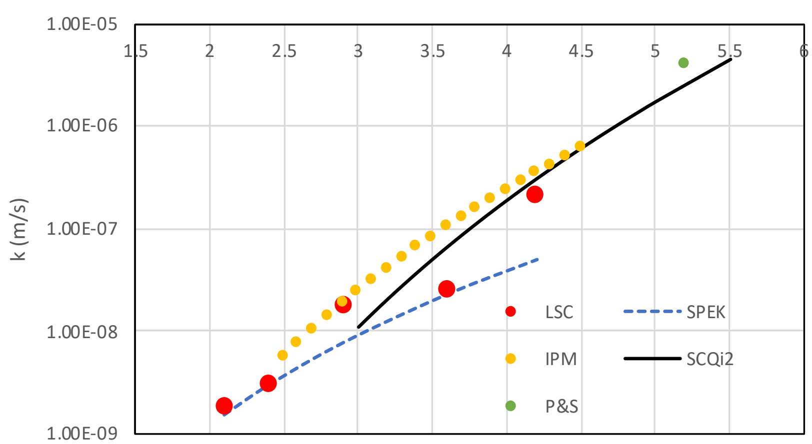

Figure 6. Comparison of all methods to determine *k-e*

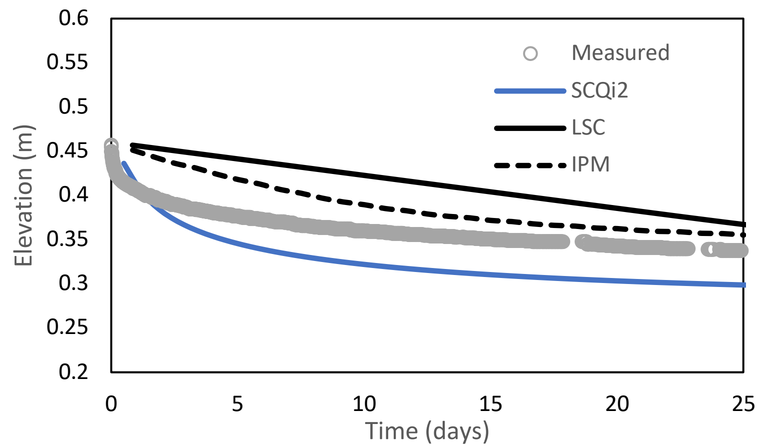

Figure 7. Comparison of LSC predictions of column settlement using estimated *k-e* functions

Finally, the estimated *k-e* functions are used in predictions of settlement for a hypothetical 20 m deposit, shown in Figure 8. In line with the previous observations, considering LSC as the base case, the SPEK method initially underpredicts the rate of settlement, as expected as the k values at high void ratio are lower. The IPM and SCQi2 methods, however, overpredict the rate of settlement at early times. Considering Figures 6 and 7, however, it would seem that the LSC data is actually under-predicting the true k values at the higher void ratios, and that the settlement at early times would likely be better predicted by the IPM and SCQi2 methods.

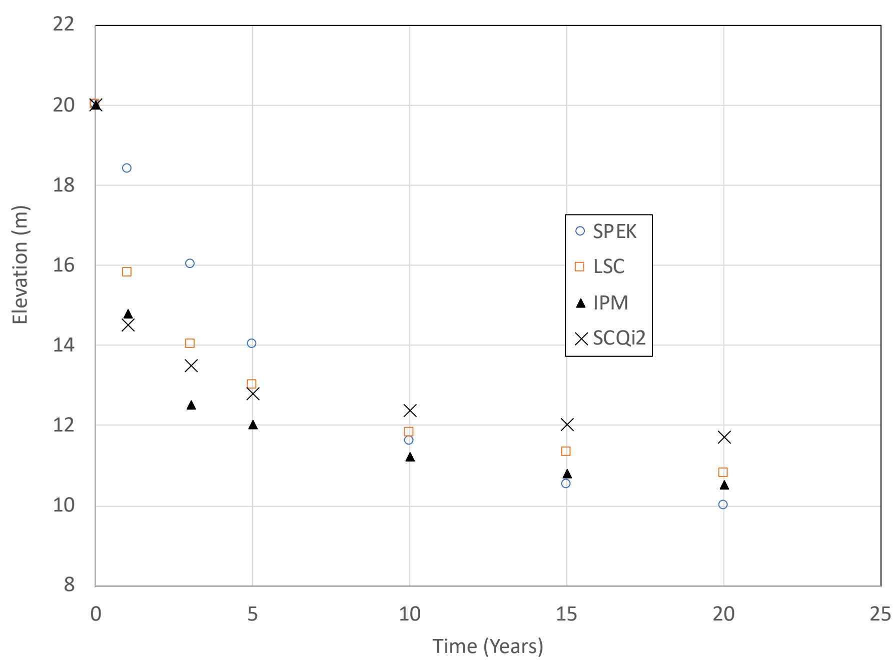

Figure 8. Predictions for a hypothetical 20 m deposit using the estimated *k-e* function

In general, it seems that the IPM method provides a good estimate of *k-e* over its measurement range. As expected, the SPEK method is best at its measurement point and for lower void ratios, but poor for k values at higher void ratios. The SCQi2 method appears the best to quantify the k values at those higher void ratios, but cannot be trusted for lower void ratios beyond those encountered during an individual column test.

The IPM method, though performing the best out of the new rapid methods, is the most demanding, as it requires specialized equipment and programming. However, a composite of the

SPEK and SCQi2 methods, to capture k values at high and low void ratios, could be a credible low cost alternative to IPM.

4 SUMMARY AND CONCLUSIONS

A sedimentation column test of fFFT was used to demonstrate the application of three methods to estimate the *k-e* function: a single measurement point option (SPEK), the use of high resolution density and PWP measurements in a column test to calculate *k-e* (IPM), and a method using known characteristics of the settlement curve (SCQi2). Using independently measured LSC data, and the Pane and Schiffman method, it was shown that the IPM method performs the best. The SPEK method performs well at low void ratios, but is not necessarily accurate for void ratios higher than the measurement point. The SCQi2 method best estimates the k values at the highest void ratios, compares best with the Pane and Schiffman estimate, and when used in a large strain consolidation model best predicts the rapid settlement at early times in the column. This method, however, substantially underpredicts *k-e* at void ratios lower than observed in the column test itself. While IPM appears to the best of these methods, it is the most expensive. An option to explore further is to use a composite *k-e*, using SPEK for lower void ratios and SCQi2 to estimate the higher void ratios. It was observed that fitting LSC data at the standard resolution with a single power function, would tend to underestimate *k-e* at the highest void ratios.

5 ACKNOWLEDGEMENTS

Joint funding from the Natural Science and Engineering Council of Canada (NSERC) and Canada's Oil Sands Innovation Alliance (COSIA) is gratefully acknowledged.

6 REFERENCES

Aldaeef, A. A., and Simms, P. 2019. Influence of pipeline transport on sedimentation and consolidation of flocculated Fluid Fine Tailings (fFFT) Proceedings of the 72nd Canadian Geotechnical Conference, Canadian Geotechnical Society, St. John, Canada.

Abu-Hejleh, A. N. and Znidarcic, D., 1996, Consolidation Characteristics of Phosphatic Clays, *ASCE Journal of Geotechnical Engineering,*122(4): 295-301.

Abdulnabi, A., Amoako, K., Moran, D., Vandara, K., Aldaeef, A.A,, Esmaelizadeh, A.E., Beier, N., Soares, J., Simms, P. 2021. Evaluation of candidate polymers to maximize the geotechnical performance of oil sands tailings. *Canadian Geotechncial Journa*l, doi.org/10.1139/cgj-2020-0714.

Babaoglu, Y. 2021. Rapid Measurement and Estimation of Saturated Hydraulic Conductivity of Mineral Slurries. Doctoral Dissertation, Carleton University.

Babaoglu, Y., and Simms, P. 2020. Improving Hydraulic Conductivity Estimation for Soft Clayey Soils, Sediments, or Tailings Using Predictors Measured at High-Void Ratio. *ASCE Journal of Geotechnical and Geoenvironmental Engineering,* doi/full/10.1061/%28ASCE%29GT.1943-5606.0002344

Babaoglu, Y. and Simms, P. 2020. A rapid measurement method to determine hydraulic conductivity of tailings under self-weight consolidation. Proceedings of Tailings and /Mine Waste 2020.

Bartholomeeusen G, Sills GC, Znidarčić D, Van Kesteren W, Merckelbach LM, Pyke R, et al. 2002. Sidere: numerical prediction of large-strain consolidation. *Géotechnique* 52(9): 639-648 .

Been, K. & Sills, G. C. 1981. Self-weight consolidation of soft soils: an experimental and theoretical study. *Geotechnique* 31(4): 519-535.

Pane, V. & Schiffman, R. L. 1997. The permeability of clay suspensions. *Geotechnique* 47(2): 273-288.

Qi, S, X. Chen, P. Simms, J. Zhou, X. Yang. 2020. Method for determining the permeability function parameters of soft soils considering synchronous sedimentation and consolidation. *Computers and Geotechnics*, 10.1016/j.compgeo.2020.103781.

Qi, S., & Simms, P. 2019. Robust methods to estimate large strain consolidation parameters from column experiments. *Canadian Geotechnical Journal.* Published online ahead of print. https://doi.org/10.1139/cgj-2018-0870

Dynamic properties of oil sand tailings

Grytan Sarkar & Abouzar Sadrekarimi
Western University, Ontario, Canada

ABSTRACT: Canada has the third-largest crude oil reserve in the world, storing an estimated amount of about 171 billion barrels of recoverable oil (10.3% of world proven oil reserve). The remaining slurry after the extraction of bitumen from oil sand consists of sand, fine particles, water, and residual bitumen, which is deposited behind a tailings dam. A tailings dam should be stable against both static and seismic loads. This study presents a detailed laboratory investigation of strain-depended dynamic characteristics (shear modulus and damping ratio) of oil sand tailings from Alberta through a series of dynamic simple shear (DSS) tests. Coarse oil sand tailings (CST) were collected from the Athabasca region of Alberta, Canada. CST comprised of a fines content of 5 to 7%, water content of 5%, D_{50} of 0.22 mm, a bitumen content of 1.5 to 2% and a specific gravity of 2.62. Specimens were reconstituted at different initial void ratios using the moist-tamping technique at three different consolidated relative densities (D_{rc}) corresponding to loose, medium-dense, and dense conditions. Specimens were subsequently subjected to different levels of small strain cyclic shearing at a constant volume (CV). The effect of effective overburden pressure (σ'_{vc}) on the dynamic properties of CST was also studied. Maximum shear modulus (G_{max}) corresponding to very small strains ($\sim10^{-5}$) was determined from shear wave velocity measurements for each effective vertical stress using bender-elements mounted on the DSS apparatus. The obtained shear moduli and damping ratios were further compared with those of other natural sands. Finally, empirical equations were proposed to describe the modulus reduction (G_γ/G_{max}) and damping ratio (ξ) of CST, which can be utilized for seismic response analysis of CST dams.

1 INTRODUCTION

Canada has the third-largest crude oil reserves (about 171 billion barrels in a landmass of over 142,200 km^2) in the world, located mostly in northeastern Alberta and Saskatchewan (Government Alberta 2012, Wang 2017). Of this 171 billion barrels of oil, about 164 billion barrels are stored in the oil sands. Oil sands provide about 35% of Canada's crude oil production, steadily increasing over the last 35 years to around 2.9 million barrels per day. About 47% of the crude oil is currently produced using open-pit mining (Natural Resources Canada 2020). The current mining extraction technology with a recovery yield of about 6% leaves behind a massive volume of toxic waste tailings containing sand, fine particles, process water, organic compounds, and residual bitumen mixtures. Management of mine waste products has been a challenging task for countries, such as Canada, where natural resources drive their economic growth. Often times the accumulated waste slurry is deposited in a tailings pond, typically constructed with a starter dyke of overburden soil or ore deposits, backfilled by coarse sand tailings (CST) using either the upstream or the centerline hydraulic construction method. The fluid-fine-tailings (FFT) are then pumped inside the pond, creating massive tailings dams with heights varying between 60 to 100 m (McRoberts 2008, Sobkowicz and Morgenstern 2009).

Over the last few decades, a number of tailings dams have experienced failures in Canada. For example, the recent coal mine dam failure at Obed mountain, Alberta on October 31, 2013 released about 900,000 tonnes of fine materials and 670,000 m^3 of wastewater to the tributaries of the Athabasca River (Provincial Court of Alberta 2017). Another Opemiska copper mine dam failure was recorded in 2004 in Chapais, Quebec, which spilled about 6,000 m^3 of tailings at Pinchi Lake. Four static liquefaction failures have been also reported between 1972 and 1974 in uncompacted beach oil sands tailings at the upstream face of the Suncor open-pit mine's Tar Island Dyke located in northern Alberta (Plewes et al. 1989). The stability of tailings dams is a great concern to the mining industry for the safe deposition of the waste tailings during construction and post-closure.

Dynamic soil response is critical to loads from earthquakes, machine foundations, wind, waves, and shocks. Shear modulus (G) and damping ratio (ξ) are the two most important factors in dynamic analysis involving soils that depend on shear strain (γ). In general, large strain G and ξ are used in foundation analysis, but seismic problems are governed by small shear strains and fluctuations in G and ξ can occur. The change in shear modulus due to cyclic shear strain is usually represented as modulus reduction by the shear modulus (G_γ) at a certain strain level divided by the maximum shear modulus G_{max} at very small strains (< 10^{-4} %). The modulus reduction and damping ratio curves are essential to perform dynamic analysis of a soil because in many cases it is challenging to obtain these properties through laboratory testing. However, there have been limited studies on the dynamic properties such as modulus reduction and damping ratio of oil sand tailings. In this study, direct simple shear (DSS) testing was conducted to obtain G_γ/G_{max} and ξ curves for reconstituted moist tamped (MT) specimen of coarse oil sand tailings (CST) at three different densities. Dynamic characteristics of CST specimens were subsequently obtained at different levels of small strain cyclic shearing under constant volume (CV) conditions.

2 MATERIALS AND METHODS

2.1 *Soil Tested*

Coarse oil sand tailings (CST), collected from Athabasca, Fort McMurray (AB) were used in this study. As shown in Figure 1, these tailings were coarser than the Athabasca ore sand deposit (Dusseault and Morgenstern 1978) as well as the Syncrude oil sand tailings (Vaid et al. 1995a). Basic index properties of the tailings samples, determined in accordance with the ASTM standard procedures, are summarized in Table 1. Bitumen contents of around 1.5 to 2.0% were also measured in the CST tailings samples following the AASHTO T308 procedure. This is slightly higher than that (≈ 1%) reported by Chalaturnyk et al. (2002) for the Athabasca whole tailings deposit. The mineralogy of the tailings was also examined by X-ray diffraction analysis, which indicated the presence of quartz, chlorite, carbonate, feldspar mineral as well as a small percentage of kaolinite.

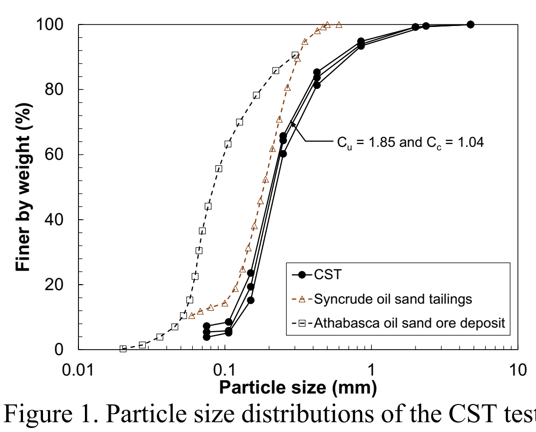

Figure 1. Particle size distributions of the CST tested in this study as well as those of the Syncrude oil sand tailings (Vaid et al. 1995b) and Athabasca oil sand ore deposit (Dusseault and Morgenstern 1978)

Table 1: Physical properties of the Athabasca coarse oil sand tailings (CST) used here

Property	CST
C_U[1]	1.85
C_C[2]	1.04
G_s[3]	2.62
e_{max}[4]	0.771 to 0.777
e_{min}[5]	0.421 to 0.447
Fines content (%)	5.5 to 7.5
Bitumen content (%)	1.5 to 2.0
pH	2.75 to 2.90

[1]*C_U = coefficient of uniformity,* [2]*C_C = coefficient of curvature (ASTM D6913),* [3]*Gs= specific gravity (ASTM D854),* [4]*e_{max} = maximum void ratio (ASTM D4254),* [5]*e_{min}= minimum void ratio (ASTM D4253)*

2.2 *Equipment Used*

A computer-controlled direct simple shear (DSS) testing device equipped with bender elements and manufactured by GDS Instruments (UK) was used in this study. The DSS equipment entails an electro-mechanical actuator to apply vertical stress and a horizontal actuator for applying shear stress. The vertical actuator has a load capacity of 5 kN and a displacement range of 25 mm, while the loading capacity and the displacement range of the horizontal actuator are 2 kN and 25 mm, respectively. Vertical deformation of the specimen is measured not only by the motor's encoder but also with an LVDT with a range of ±2.5 mm. The horizontal deformation of the specimen is measured using another LVDT with a range of ±10 mm. All measurements are converted to digital data and recorded on a local computer. The maximum distance between the top and bottom pedestals is 35.1 mm, allowing for the installation of a specimen with a maximum height of 30 mm.

2.3 *Specimen Preparation*

Oil sand tailings specimens were reconstituted using the moist tamping (MT) technique. MT is often used to simulate field conditions where moist sand is dumped as a fill and subsequently inundated by a rising water table (Olson et al. 2000, Chu et al. 2003). The MT technique also allows the preparation of very loose laboratory specimens with relatively uniform void ratios that would show an entirely strain-softening or contractive behaviour during shearing (Sasitharan et al. 1993, Pitman et al. 1994). In order to prepare MT specimens, a small amount of water (5% of the weight of dry CST) was mixed thoroughly with dry CST. The moist CST was then scooped into the DSS mold and tamped in a single layer to attain the desired specimen height of 26 (±1) mm. The void ratio of the specimen was controlled by varying the weight of dry CST tamped in the specimen mold. All specimens were prepared at a height-to-diameter (H/D) ratio of less than 0.4 to minimize stress-strain non-uniformities during shearing (De Alba et al. 1976, Franke et al. 1979, Vucetic & Lacasse 1982, ASTM 2000).

The specimen mold was formed by a stack of 1.1 mm-thick Teflon-coated stainless steel rings which were held in place by a pair of retainers bolted to the bottom pedestal. These rings provided a rigid radial boundary for the specimen while allowing unrestricted application of horizontal shearing. When assembled, the lower pedestal and the stacked rings served as the specimen preparation mold. A flexible latex membrane, secured by an O-ring to the bottom platen, lines the steel rings' internal circumference. The membrane was folded over the stacked stainless-steel rings for sample preparation and stretched back onto the mold's inside surface area by applying air suction. Given the membrane thickness of 0.82 mm, specimens were prepared with a diameter of 70.4 mm. All specimens were saturated by flushing water through two drainage ports on the top and bottom pedestals, which allowed the ingress of water through sintered stainless-steel porous disks on each pedestal.

2.4 *Testing Method*

After preparation, the specimens were mounted on the DSS device and fastened to the bottom platen by a set of 4 screws. The upper loading platen was subsequently lowered on the sample. A vertical seating stress of 5 kPa was then applied to ensure proper contact between the specimen and the upper platen. The supporting retainers were removed, and the membrane was folded back onto the upper platen and secured by an O-ring. The specimen was then saturated by flushing deaired water through the bottom drainage port until no air bubbles appeared coming out of the sample. The saturated specimen was then consolidated to the target vertical stresses of σ'_{vc}, while the changes in specimen height were measured. The consolidation stress was maintained until the rate of vertical displacement became negligible (< 0.6 μm/min), indicating the end of the primary consolidation.

Dynamic characteristics such as shear modulus and damping ratio were measured based on several strain-controlled cyclic DSS tests in which small shear strain (γ_c) amplitudes were applied in a constant volume (CV) condition. As drainage was allowed no shear-induced pore water pressure was produced in these tests, and the changes in total vertical stress (σ_v) required to maintain a constant specimen height was taken as the equivalent excess pore water pressure that would have generated in a truly undrained test on a saturated sample (ASTM 2007). Throughout this paper, the initial void ratio (e_c) refers to that obtained at the end of the consolidation stage and σ'_{vc} is the vertical stress applied for consolidation.

3 RESULTS AND DISCUSSIONS

3.1 *Shear wave velocity and maximum shear modulus*

In geotechnical engineering, shear wave velocity (V_S) is increasingly used as a non-destructive method for ground characterization, soil parameter prediction, and the determination of maximum shear modulus (G_{max}). In this study, V_S of CST specimens was measured following consolidation using a pair of bender elements. Bender element testing on laboratory samples can produce V_S similar to those observed from mini-hammer tests in centrifuge models and field seismic tests, as reported by Arulnathan et al. (2001). The peak-to-peak method was used to calculate the shear wave arrival time (Δt) because it has been shown to produce accurate V_S measurements (Brignoli et al. 1996). The tip-to-tip distance (L_{tt}) between the bender elements was then divided by Δt to calculate V_S.

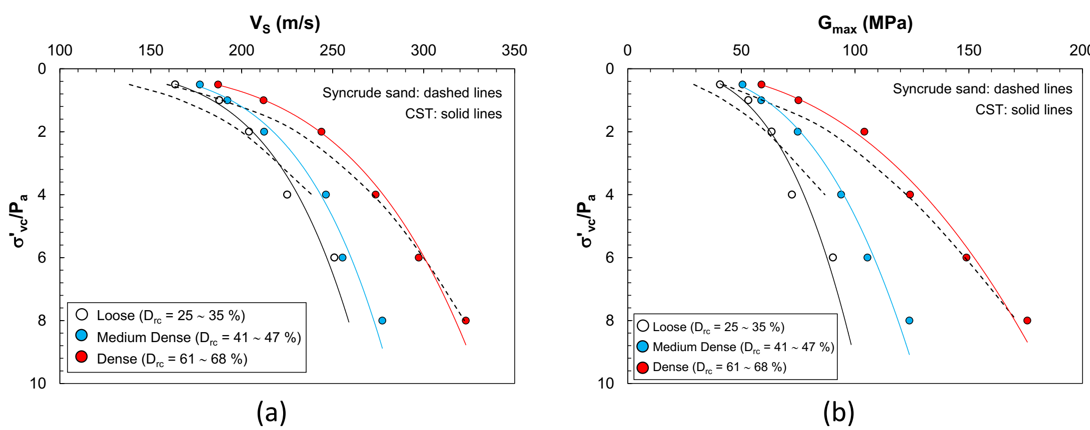

Figure 2. Variations of (a) V_S and (b) G_{max} with σ'_{vc} and comparison with Syncrude oil sand tailings reported by Cunning et al. (1995). P_a = 100 kPa is a reference pressure

Figure 2a depicts the variation of V_S of the CST with σ'_{vc}. V_S increases with increasing σ'_{vc}, and at a given σ'_{vc}, dense specimens have higher V_S values. These results are compared to Cunning et al. (1995) fitted trends for Syncrude oil sand tailings specimens consolidated to a lateral stress coefficient of K_0 = 0.5 and relative densities (D_{rc}) of 25 to 68%. While V_S = 163 – 323 m/s measured here is comparable to those of Syncrude oil sand tailings at σ'_{vc} = 200 to 800 kPa, they exceed V_S of Syncrude oil sand tailings at reduced σ'_{vc} = 50 and 100 kPa. The small differences in V_S of CST and Syncrude oil sand tailings are due to the high fines content of the Syncrude oil sand tailings (FC = 12.4%) compared to FC = 5 - 7% of the CST used in this study. A normalized shear wave velocity, V_{S1}, is used to account for the strong effect of overburden pressure (σ'_{vc}) on V_S as below:

$$V_{S1} = V_S \left(\frac{P_a}{\sigma'_{vc}}\right)^{\beta} \tag{1}$$

Where, P_a is a reference atmospheric pressure (= 100 kPa), and β is a fitting exponent equal to 0.16 to 0.19 for the CST specimens at D_{rc} = 25 to 65%. The relatively lower β compared to that (= 0.25) of silica sands indicates a less significant effect of σ'_{vc} on V_S.

At strain levels of less than 0.001%, soil behavior is commonly assumed to be elastic. A correct assessment of elastic stiffness is required to characterize soil behaviour at small strains (i.e., small-strain shear modulus, G_{max}). As V_S is measured at very small strains ($\approx 10^{-5}$), it is frequently used to calculate G_{max} for analyzing the response of foundations or ground to dynamic/cyclic loads, or in numerical modeling. G_{max} of the CST was calculated from V_S using the following relationship:

$$G_{max}(MPa) = 10^{-6} \rho V_S^2 \tag{2}$$

In which, ρ is the total density of CST in kg/m^3. The variation of G_{max} with σ'_{vc}/P_a is shown in Figure 2b, indicating the significant effect of σ'_{vc} on G_{max}, which is best described by a power function. Maximum shear moduli of Syncrude oil sand tailings (Cunning et al. 1995) are also compared with those of CST in Figure 2b, which shows a general increase of G_{max} with increasing σ'_{vc}.

3.2 *Dynamic Characteristics*

The cyclic behavior of soils is often characterized by a non-linear stress-strain response that becomes more pronounced with increasing γ_c. Therefore, for dynamic soil-structure interaction analysis and determining ground response to a strong earthquake or machine vibration, strain-dependent shear modulus (G_γ) and damping (ξ) characteristics are used. Numerical soil models use changes of G_γ and ξ with γ_c as fundamental input parameters for dynamic analysis. As discussed earlier, G_{max} of the CST was obtained from V_S measurements using bender elements. However, shear strains induced in a soil deposit by a strong earthquake motion can be several orders of magnitude greater (10^4 to 10^2) than those corresponding to G_{max}.

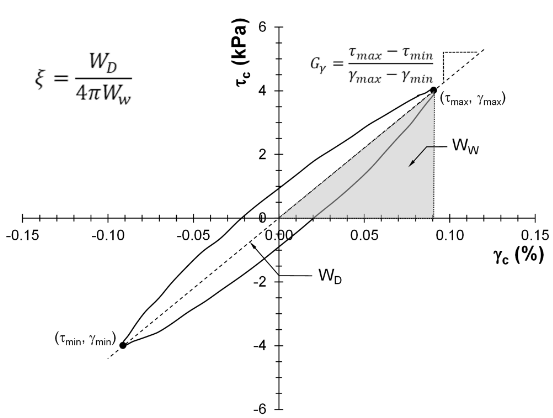

Figure 3. Typical cyclic stress-strain response of a soil (Sarkar and Sadrekarimi 2021)

In this study, a series of strain-controlled cyclic DSS tests were conducted to target low γ_c amplitudes and determine G_γ and ξ of the CST. Reconstituted moist tamped CST specimen were consolidated to σ'_{vc} = 50, 100, 200, 400, 600 and 800 kPa and subsequently sheared in CV conditions. G_γ and ξ of the CST were calculated using the cyclic stress-strain loops from these tests as illustrated in Figure 3. Shear modulus is defined as a secant modulus calculated from the extreme points on each stress-strain loop, while the hysteretic damping ratio (ξ) results from the dissipation of energy by inelastic deformation and non-linear stress-strain behavior of a soil. In Figure 3, W_D is the area of the stress-strain loop corresponding to the amount of energy dissipation, and W_w (= $0.5\tau_{max}\gamma_{max}$) presents the net work done in an elastic system. In order to obtain reasonable stress-strain responses, an initial γ_c of 0.005% was produced and γ_c was then incrementally increased in sequential loading stages for each specimen. Two cycles were applied at a given γ_c, and G_γ and ξ were calculated at the 2nd cycle to minimize modulus degradation and the effect of strain history (Tatsuoka et al. 1991).

3.2.1 *G_γ and ξ of CST*

The shear modulus (G_γ), modulus reduction (G_γ/G_{max}) as well as the rise of damping ratio (ξ) of CST with γ_c are shown in Figures 4, 5, and 6, respectively for loose (D_{rc} = 27 to 27%), medium-dense (D_{rc} = 40 to 48%) and dense (D_{rc} = 53 to 62%) specimens. Because of difficulty with measuring very small displacements in a DSS test, these data are obtained at γ_c > 0.01%. Some scatter is likely the result of sample variability and heterogeneity.

Figure 4 and 5 show that G_γ of CST degrades with rising γ_c as a result of its non-linear stress-strain behavior and the possible increase of pore water pressure. The degradation of G_γ is most noticeable and rapid at γ_c = 0.005 to 1%, after which it reaches the residual modulus of CST. At the residual state, G_γ was found to be nearly constant for specimen onsolidated to loose and medium sate (G_γ =3 to 9 kPa) regardless of e_c and σ'_{vc}. However, for γ_c < 1%, G_γ degradation is more pronounced in specimens subjected to higher σ'_{vc}, and looser void ratios (e_c). As shown in Figure 6, the hysteresis damping ratio (ξ) increases rapidly with rising γ_c from 0.1 to 2%. Specimens consolidated to lower σ'_{vc} exhibit higher ξ for a given γ_c, and decrease as σ'_{vc} increases.

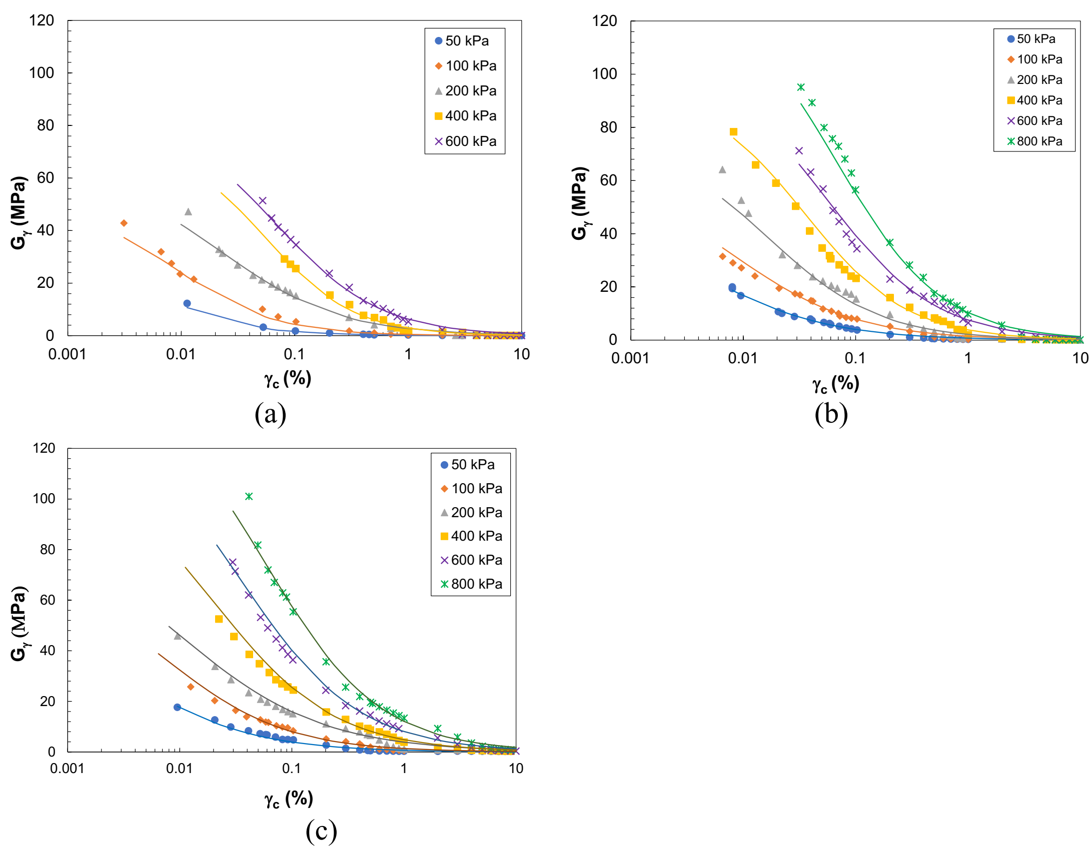

Figure 4. Variation of shear modulus (G_γ) with γ_c for (a) loose (D_{rc} = 27 to 27%), (b) medium-dense (D_{rc} = 40 to 48%), and (c) dense (D_{rc} = 53 to 62%) specimens

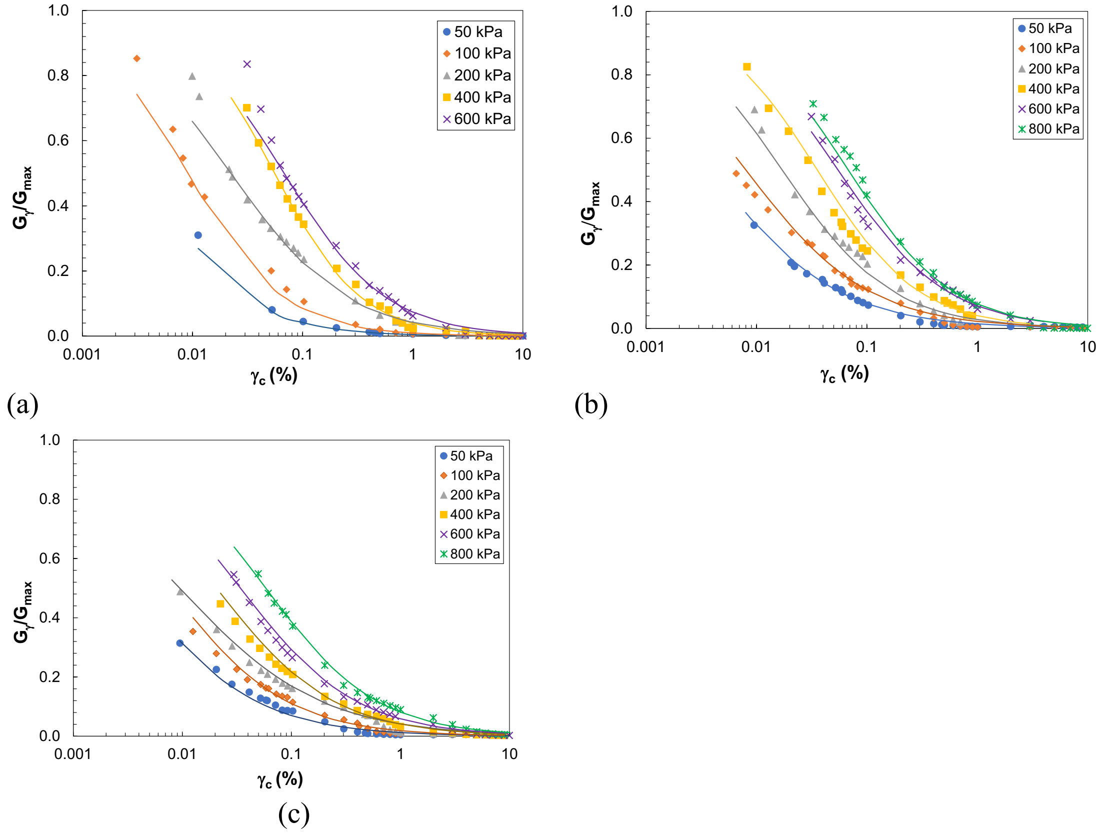

Figure 5. Variation of modulus reduction (G_γ/G_{max}) with γ_c for (a) loose (D_{rc} = 27 to 27%), (b) medium-dense (D_{rc} = 40 to 48%), and (c) dense (D_{rc} = 53 to 62%) specimens

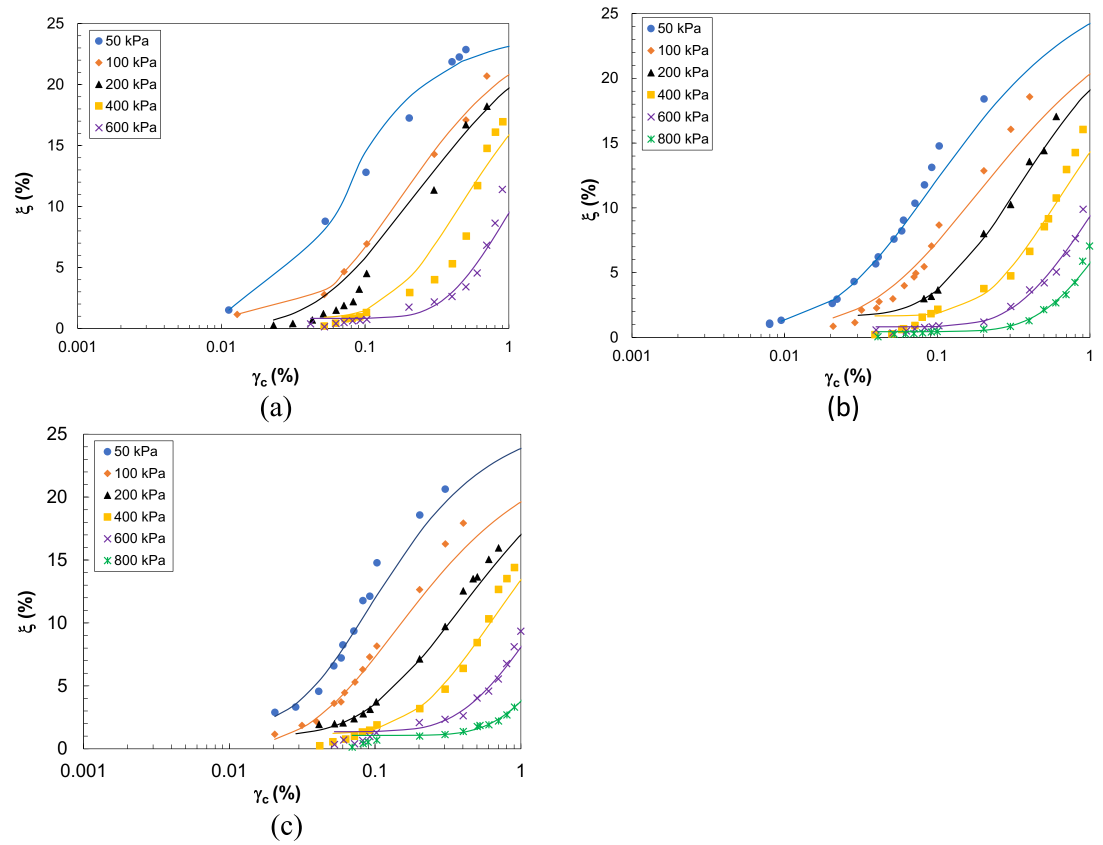

Figure 6. Variation of damping ratio (ξ) with γ_c for (a) loose (D_{rc} = 27 to 27%), (b) medium-dense (D_{rc} = 40 to 48%), and (c) dense (D_{rc} = 53 to 62%) specimens

3.2.2 *Empirical Correlations of G_γ and ξ for CST*

The experimental results on shear modulus reduction and damping ratio of the CST are further fitted with the following series of empirical equations, which account for the effects of e_c, σ'_{vc}, and γ_c. In this study, a modified hyperbolic model introduced by Darendeli (1997) is used to describe the reduction of G_γ/G_{max} with γ_c as below:

$$\frac{G_\gamma}{G_{max}} = \frac{1}{1+\left(\frac{\gamma}{\gamma_{ref}}\right)^{\alpha}} \tag{3}$$

Where, α is the coefficient of curvature and γ_{ref} is a reference strain at which $G_\gamma/G_{max} = 0.5$. The values of γ_{ref} at different σ'_{vc} and e_c were subsequently fitted using the following relationship as a function of σ'_{vc} and e_c:

$$\gamma_{ref}(\%) = [0.049(e_c) - 0.025]\left(\frac{\sigma'_{vc}}{P_a}\right)^{a} \tag{4}$$

In which, the empirical fitting parameter "a" are 1.33, 1.29 and 1.27, respectively for loose (D_{rc} = 27 to 27%), medium-dense (D_{rc} = 40 to 48%), and dense (D_{rc} = 53 to 62%) specimens. The coefficient of curvature (α) of the G_γ/G_{max} –γ_c curves was also fitted at different σ'_{vc} and e_c values by minimizing the normalised error between the actual and the predicted values of the following relationship:

$$\alpha = [1.70(e_c) - 0.20]\left(\frac{\sigma'_{vc}}{P_a}\right)^{b} \tag{5}$$

where, the empirical fitting parameter "b" assumes values of 0.066, 0.065, and 0.035, respectively for loose, medium-dense, and dense specimens. The hysteretic daming ratio is also described by modifying an equation proposed by Michaelides et al. (1998) as below:

$$\xi\ (\%) = c_1 + c_2\left(1 - \frac{G_\gamma}{G_{max}}\right)^{c_3} \tag{6}$$

Where, the fitting parameters c_1, c_2, and c_3 are established by minimizing the normalized error between the actual and the predicted ξ at various σ'_{vc} and e_c values as follows:

$$C_1 = [-3.37(e_c) + 4.23]\left(\frac{\sigma'_{vc}}{P_a}\right)^{f} \tag{7}$$

$$C_2 = [-13.154(e_c) + 41.892]\left(\frac{\sigma'_{vc}}{P_a}\right)^{g} \tag{8}$$

$$C_3 = [30.492(e_c) - 6.623]\left(\frac{\sigma'_{vc}}{P_a}\right)^{h} \tag{9}$$

In which, f = 0.458, 0.282, and 0.188, g = -0.157, -0.051, and -0.010, and h = 0.024, 0.201, and 0.537 for respectively loose, medium-dense, and dense conditions. The predicted trends of Equations (3) and (6) using the above fitting parameters agree quite well with the experimental results of G_γ/G_{max} and ξ as shown in Figures 5 and 6. This validates the use of these equations and calibrated parameters to predict the dynamic properties of the CST. The regression models of G_γ/G_{max}

and ξ developed in this study could be potentially used in local site response analyses to characterize seismic hazard at oil sand tailings dam sites.

3.2.3 *Comparison with other sands*

Figure 7 compares the degradation of G_γ/G_{max} and ξ of CST with those from undrained cyclic simple shear tests on Fraser River sand (Thirugnanasampanther 2016) as well as the upper and lower boundaries of G/G_{max} and ξ proposed by Seed and Idriss (1970) for silica sands at σ'_{vc} = 100 kPa. As demonstrated in Figure 7, the CST of this study present lower G/G_{max} than those of these sands, and their values of ξ are within the lower range of those for silica sands. Figure 7 further shows that, despite the relatively small effect of e_c, the degradation of G_γ and ξ are greater in loose specimens than those of the dense samples.

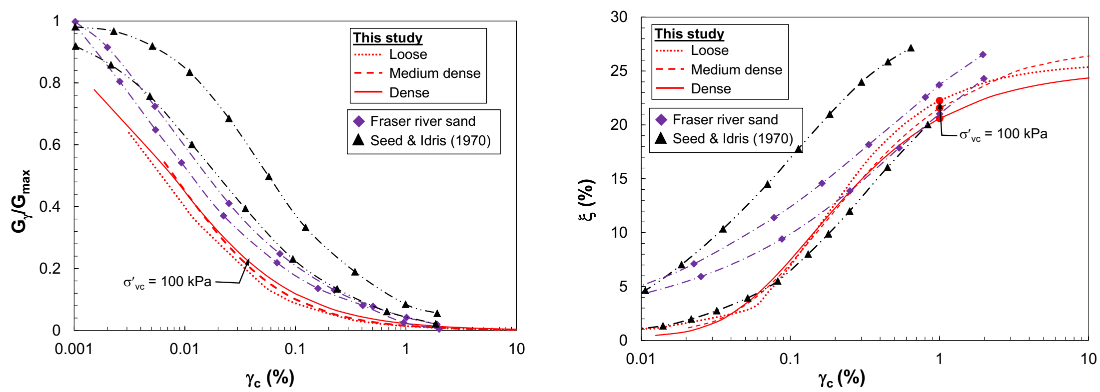

(a) (b)

Figure 7. Comparison of (a) G_γ/G_{max} and (b) ξ of CST with other silica sands reported by Seed and Idriss (1970) and Fraser River sand (Thirugnanasampanther 2016)

4 CONCLUSIONS

In the current study, a series of strain-controlled constant-volume cyclic direct simple shear and bender element tests were carried out on coarse oil sand tailings (CST) to examine their dynamic properties (V_S, G_{max}, G_γ, ξ). Dynamic characteristics (V_S, G_{max}, G_γ, ξ) of the CST were largely affected by the overburden pressure (σ'_{vc}). With increasing σ'_{vc}, V_S, G_{max}, and G_γ increased while ξ decreased. A minor effect of void ratio (e_c) was observed on the G_γ at small shear strains (<1%), which subsequently diminished at larger strains. While specimens consolidated to lower σ'_{vc} exhibited higher ξ, and somewhat lower ξ were developed in dense specimens. Finally, the variations of CST's dynamic properties with shear strain were fitted with empirical relationships as a function of σ'_{vc} and e_c.

5 REFERENCES

De Alba, P., Seed, H.B., & Chan, C.K. 1976. Sand liquefaction in large-scale simple shear tests. Journal of Geotechnical and Geoenvironmental Engineering, 102(ASCE# 12403).

Arulnathan, R., Boulanger, R.W., & Idriss, I.M. 2001. Site response of organic soils. University of Missouri--Rolla.

ASTM. 2007. Standard test method for consolidated undrained direct simple shear testing of cohesive soils. D6528-07,.

ASTM, D. 2000. Standard Test Method for Consolidated Undrained Direct Simple Shear Testing of Cohesive Soils. *In* American Society for Testing and Materials.

Brignoli, E.G.M., Gotti, M., & Stokoe, K.H. 1996. Measurement of shear waves in laboratory specimens by means of piezoelectric transducers. Geotechnical Testing Journal, 19(4): 384–397. ASTM International.

Chalaturnyk, R.J., Don Scott, J., & Özüm, B. 2002. Management of oil sands tailings. Petroleum Science and Technology, 20(9–10): 1025–1046. Taylor & Francis.
Chu, J., Leroueil, S., & Leong, W.K. 2003. Unstable behaviour of sand and its implication for slope instability. Canadian Geotechnical Journal, 40(5): 873–885. NRC Research Press.
Cunning, J.C., Robertson, P.K., & Sego, D.C. 1995. Shear wave velocity to evaluate in situ state of cohesionless soils. Canadian Geotechnical Journal, 32(5): 848–858. NRC Research Press.
Darendeli, M.B. 1997. Dynamic properties of soils subjected to 1994 Northridge earthquake. University of Texas at Austin.
Dusseault, M.B., & Morgenstern, N.R. 1978. Shear strength of Athabasca oil sands. Canadian Geotechnical Journal, 15(2): 216–238. NRC Research Press.
Franke, E., Kiekbusch, M., & Schuppener, B. 1979. A new direct simple shear device. Geotechnical testing journal, 2(4): 190–199. ASTM International.
Government Alberta. 2012. Alberta's Oil Sands.
McRoberts, E. 2008. Considerations in oil sands tailings containment. *In* First International Oil Sands Tailings Conference Proceedings. pp. 7–10.
Michaelides, O., Gazetas, G., Bouckovalas, G., & Chrysikou, E. 1998. Approximate non-linear dynamic axial response of piles. Geotechnique, 48(1): 33–53. Thomas Telford Ltd.
Natural Resources Canada. 2020. Crude oil facts.
Olson, S.M., Stark, T.D., Walton, W.H., & Castro, G. 2000. 1907 static liquefaction flow failure of the north dike of Wachusett dam. Journal of Geotechnical and Geoenvironmental engineering, 126(12): 1184–1193. American Society of Civil Engineers.
Pitman, T.D., Robertson, P.K., & Sego, D.C. 1994. Influence of fines on the collapse of loose sands. Canadian Geotechnical Journal, 31(5): 728–739. NRC Research Press.
Plewes, H.D., O'Neil, G.D., McRoberts, E.C., & Chan, W.K. 1989. Liquefaction considerations for Suncor tailings pond. *In* Proceedings of the Dam Safety Seminar, Edmonton, Alberta, Sept. pp. 61–89.
Provincial Court of Alberta. 2017. Agreed Statement of Facts, Docket No. 151258456P1 & 160061354P1.
Sarkar, G., &Sadrekarimi, A. 2021. Cyclic Shearing Behavior and Dynamic Characteristics of a Fibrous Peat. Canadian Geotechnical Journal, (ja).
Sasitharan, S., Robertson, P.K., Sego, Dc., & Morgenstern, N.R. 1993. Collapse behavior of sand. Canadian Geotechnical Journal, 30(4): 569–577. NRC Research Press.
Seed, H.B., & Idriss, I.M. 1970. Soil moduli and damping factors for dynamic response analysis. *In* Report EERC 70-10.
Sobkowicz, J.C., & Morgenstern, N.R. 2009. A geotechnical perspective on oil sands tailings. *In* Proceedings of the 13th International Conference on Tailings and Mine Waste, Banff, Alta. pp. 1–4.
Tatsuoka, F., Shibuya, S., & Teachavorasinskun, S. 1991. Discussion on "Shear modulus and cyclic undrained behavior of sands." Soils and Foundations, 31: 202–209.
Thirugnanasampanther, S. 2016. Cyclic behaviour and dynamic properties of soils under simple shear loading. Carleton University.
Vaid, Y.P., Sivathayalan, S., Uthayakumar, M., & Eliadorani, A. 1995a. Liquefaction potential of reconstituted Syncrude sand. *In* Proceedings of the 48th Canadian Geotechnical Conference. pp. 319–328.
Vaid, Y.P., Uthayakumar, M., Sivathayalan, S., Robertson, P.K., & Hofmann, B. 1995b. Laboratory testing of Syncrude sand. *In* Proceedings of the 48th Canadian Geotechnical Conference, Vancouver. pp. 223–232.
Vucetic, M., & Lacasse, S. 1982. Specimen size effect in simple shear test. Journal of the Geotechnical Engineering Division, 108(12): 1567–1585. ASCE.
Wang, Y. 2017. A study on chemical stabilization of Oil Sands Mature Fine Tailings.

Coupling between bitumen extraction and tailings management processes

B. Ozum & K. Athar
Apex Engineering Inc., Edmonton, AB, Canada

ABSTRACT: In Alberta, Canada oil sands plants are operating with the Clark Hot Water Extraction process, using *NaOH* as process additive. This process provides acceptable bitumen recovery efficiency; however, it causes serious tailings management, environmental and long-term sustainability challenges. Oil sands plants are operating by zero discharge policy by recycling released water recovered from tailings to extraction plant, which causes coupling between bitumen extraction and tailings management processes. Therefore, solutions to tailings management challenges should also be sought in extraction process too, at where tailings are produced in the first place. This article presents novel bitumen extraction and tailings management processes by utilizing unique advantages of lime (*CaO*) chemistry to reduce-eliminate existing challenges of the oil sands plants.

1 INTRODUCTION

In Alberta, Canada, bitumen is produced at about 1,600,000 bbl/d capacity by surface mining of oil sands ore followed by ore-water slurry-based extraction processes. All of eight oil sands plants are operating by the Clark Hot Water Extraction (CHWE) process developed in 1930s, which operates at 60 – 85 °C temperature, uses caustic *NaOH* as process aid to maintain extraction process slurry *pH* at about 8.2–10.0. (Clark 1939; Clark & Pasternack 1949 & 1932).

Oil sands plants produce about 300,000 t/day tailings for 100,000 barrel/day bitumen production capacity. Most cases, tailings discharged from extraction and froth treatment plants are combined (about 90% of which is the extraction process tailings). A typical CHWE process tailings effluent, composed of about 55 % solids, about 82 % of which are fines (< 45 microns, -325 mesh), and 1-2 % residual bitumen, is discharged to tailings ponds. Upon disposal of tailings into tailings ponds the coarse sand particles segregate quickly and form a beach, the remaining fine tails of 6 to 10 % solids accumulate in the tailing ponds. Fine tails settle quickly to 20 % solids content and over a few years to 30-34 % solids (86-84 % by volume of water) with a stable slurry structure, called the mature fluid fine tailings (FFT). This mature FFT possesses extremely low hydraulic conductivity, in the order of 10^{-7} – 10^{-9} cm/s for void ratio of 9 to 6, and 10^{-10} – 10^{-13} cm/s for void ratio of 3 to 1, which remains in a fluid state for decades (Chalaturnyk et al. 2002; Kasperski 1992; Miller et al. 2010a). Over the years, production rate of mature FFT increased exponentially as capacities of existing plants were increased, new plants were commissioned and process water Na^+ concentration steadily increased. Existing inventory of the legacy mature FFT volume is exceeding 10^9 m^3 and increasing exponentially and remaining as a serious environmental challenge to be addressed.

Increase in extraction process slurry *pH* by *NaOH* additive increases zeta potential on clay surfaces, promotes swelling of clay with water, contributes unduly dispersion of the silt-clay size particles in extraction process slurry and increases production of mature FFT (Liu et al. 2005; Kaya et al. 2003). Also, CHWE process produces surfactant species from water soluble napthenic acids naturally contained in bitumen, reduces water surface tension (γ_W) which promotes unduly dispersion of silt-clay size particles. Surfactant species also reduce bitumen-water interfacial tension ($\gamma_{B/W}$) which promotes bitumen liberation from the oil sands matrix and provides acceptable bitumen recovery efficiency (Masliyah et al. 2004; Kasperski 2001; Speight & Moschopedis, 1980 & 1977/78). However, reduction in $\gamma_{B/W}$ slows down bitumen droplets coalescence and aeration kinetics, suppresses froth formation kinetics and bitumen recovery efficiency, demands large process vessels, and increases capital and operating costs (Ozum et al. 2014a&b; Flury et al. 2014; Pan et al. 2012; Pan & Yoon, 2010). Therefore, it can be concluded that CHWE process operates contradicting the conventional flotation process principles after the liberation of bitumen from oil sands matrix

Suppressed bitumen recovery efficiency increases residual bitumen concentration in the tailings, increases tailings toxicity and causes complications in tailings management processes. Assuming that average bitumen content of the mature FFT is about 2%, over 150×10^6 barrels of bitumen has been discharged into tailings ponds, which also corresponds to a significant revenue loss.

Because regulating authorities enforce zero discharge policy, release water recovered in the tailings ponds is recycled to extraction process, which causes coupling between bitumen extraction and tailings management practices. Recycling release water to extraction plant steadily increases process water sodium (Na^+) concentration and sodium adsorption ratio ($SAR = [Na^+]/\sqrt{\{[Ca^{2+}] + [Mg^{2+}]\}/2}$; concentrations are in milliequivalent/L). When SAR the mature FFT increases beyond 20, it could unduly disperse organic matter and clay particles, reduces hydraulic conductivity and efficiency of tailings management processes (Miller et al. 2010b).

Because construction of oil sands plants demands high capital investments, all oil sands plants were designed by somewhat replicating the original Suncor Energy Inc.'s plant commissioned in 1960s. This policy reduced the risks associated with the large capital investments for new plants; however, advantages and short fallings of the original design were inherited to the newer oil sands plants. Oil sands industry has achieved a remarkable success to produce synthesis crude oil from Alberta's oil sands; however, resulted in sincere tailings management, land reclamation and long-term sustainability challenges, all caused by the use CHWE process.

2 OIL INDUSTRY'S EFFORT TO DEVELOP NOVEL OIL SANDS TECHNOLOGIES

Oil industry and regulating authorities were aware of the challenges associated with CHWE process and adopted strategies for the development of novel bitumen extraction and tailings management processes.

2.1 *Non-Caustic bitumen extraction processes*

Challenges caused by CHWE process were the major reasons for the development of non-caustic extraction processes. Several processes were developed and tested using pilot scale facilities, such as the AOSTRA-Taciuk process based on thermal cracking-retort, Bitmin process based an acidic extraction, cyclone separation process based on diluting ore-water slurry with water and separating bitumen from the sand using cyclones.

Only the low temperature non-additive extraction process was implemented commercially at Albian Sands' Muskeg River Mine and Syncrude Canada Ltd.'s Aurora Mine plants (Mankowski et al. 1999). Booth plants could produce tailings with improved geotechnical characteristics, however, experienced lower than expected bitumen recovery efficiencies and their operations were converted to conventional CHWE process.

In summary, all oil sands plants are continuing to operate with the CHWE process. Development of cost-effective bitumen extraction processes are needed to reduce existing challenges of oil sands plants.

2.2 *Tailings management processes*

The Alberta Energy Regulator (AER, previously Energy Resources Conservation Board) issued Directive 074, February 3, 2009, enforcing oil sands plants to reduce MFT production by 50% by 2011. However, in 2014 it was declared by the industry and AER that tailings disposal practices implemented at the oil sands plants could not comply with the Directive 074 targets.

AER released Directive 085, December 17, 2015, replacing Directive 074 for tailings performance criteria enables the implementation of the Tailings Management Framework (TMF) to reduce volume of the newly produced and legacy fluid tailings (produced by CHWE process) management. Objective of Directive 085 reads: "*The objective of TMF is to minimize fluid tailings accumulation by ensuring that fluid tailings are treated and reclaimed progressively during the life of a project and that all fluid tailings associated with a project are ready to reclaim (RTR) ten years after the end of mine life of that project. The objective will be achieved while balancing environmental, social, and economic needs*". Accomplishment of these objectives probably faces serious challenges.

There are several tailings management processes at different development stages which could be implemented commercially to achieve the objectives of Directive 085 (COSIA 2020 & 2012**)**. Some of these processes were already tested at pilot scale capacity, while Composite Tailings-CT (Caughill et al. 1993), Tailings Reduction Operations-TRO (Pollock et al. 2014), Atmospheric Drying, Coke Capping (Abusaid et al. 2011), Freeze-Thaw (Dawson et al. 1999), Filter Press, Centrifuging (Mikula 2014) and Water Capping-End Pit Lakes (Cossey et al. 2021) processes were tested commercial or semi-commercial operations. Commercial scale operations of the CT production process and TRO are being discontinued while the others are in evaluation stages.

In fact, CT production by treating the blend of cyclone underflow and mature FFT with gypsum ($CaSO_4$) additive has short fallings: (i) does not change mature FFT inventory since additional mature FFT would be produced from the cyclone overflow; (ii) does not save thermal energy by discharging warm cyclone overflow and recycling cold water from the tailings ponds; (iii) emits toxic gaseous H_2S by anaerobic reductio of SO_4^{2-} with residual bitumen; and (iv) causes additional alkaline consumption in the extraction process since addition of $CaSO_4$ reduces *pH* of the process affected water. Steady increase in process water Na^+ concentration and SAR caused by the CHWE process is probably another factor suppressing the performance of CT and TRO processes.

In summary, cost effective tailings management processes are needed to reduce-eliminate production of new mature FFT and dewatering of existing mature FFT inventory all produced by the CHWE process.

3 NOVEL BITUMEN EXTRACTION AND TAILINGS MANAGEMENT PROCESSES

Our process development research for surface mining oil sands plants focuses on: (i) suppressing silt-clay size particles dispersion in extraction process slurry; and (ii) disposing tailings effluent as a nonsegregating tailings material; while satisfying these process objectives, bitumen recovery efficiency, fuel quality of bitumen and process affected water chemistry are considered as constraints to be fulfilled.

Our laboratory investigated bitumen extraction and tailings management processes using lime (CaO) as additives by utilizing the advantages of lime (CaO) chemistry (Fig 1): (i) provides hydroxyl ions (OH^-) which increase *pH*; and (ii) provides calcium cations (Ca^{2+}) which simultaneously reacts with active species in oil sands ore-water slurry systems (Ozum et al. 2014 a&b).

$$CaO + H_2O \rightarrow Ca(OH)_2 \leftrightarrow Ca^{2+} + 2OH^- \qquad \uparrow pH, \quad \downarrow \gamma_W \text{ and } \gamma_{B/W} \tag{1}$$

$$Ca(OH)_2 + Ca(HCO_3)_2 \rightarrow 2\underline{CaCO_3} + 2H_2O \qquad bicarbonate\ softening \tag{2}$$

$$Bitumen^- + Ca^{2+} + Clay^- \rightarrow Bitumen - Ca - Clay \tag{3}$$

$$Clay^- + Ca^{2+} + Clay^- \rightarrow \underline{Clay - Ca - Clay} \qquad coagulates\ clay \tag{4}$$

$$Napth^- + Ca^{2+} + Napth^- \rightarrow \underline{Napth - Ca - Napth} \qquad \uparrow \gamma_W \text{ and } \gamma_{B/W} \tag{5}$$

$$Ca(OH)_2 + CO_2 \rightarrow \underline{CaCO_3} + H_2O \qquad \downarrow pH \tag{6}$$

$$\underline{CaCO_3} + CO_2 + H_2O \rightarrow Ca(HCO_3)_2 \qquad \downarrow pH \tag{7}$$

Figure 1. Lime (*CaO*) chemistry in oil sands ore-water slurry systems.

The first reaction in Figure 1 is the exothermic hydration of lime with water ($\Delta H_f^o = -65.3$ kJ/mol) forming $Ca(OH)_2$, which provides OH^- and Ca^{2+} ions in equilibrium with $Ca(OH)_2$ and increases the *pH* of oil sands ore-water slurry. Increase in temperature shifts the equilibrium towards $Ca(OH)_2$ and reduces OH^- and Ca^{2+} concentrations in the slurry. The second reaction reduces bicarbonates in the slurry, with the same mechanism by any alkaline (such as $NaOH$) additive. The third reaction combines bitumen and clay, which carries clay particles to the extraction froth. The fourth reaction coagulates clay size particles, suppresses clay dispersion, and contributes to reduction of mature FFT production. The fifth reaction suppresses solubility of naphthenates, reduces their surfactant behavior and increases water surface (γ_W) and bitumen-water interfacial ($\gamma_{B/W}$) tensions. The sixth and seventh reactions are the reactions between the excess $Ca(OH)_2$ and atmospheric CO_2 adsorbed and diffused into the slurry, which result in the formation of $CaCO_3$ and $Ca(HCO_3)_2$, stabilizes slurry *pH* at about 8.0 without any cations accumulation in the process affected water.

At the chemical equilibrium, composition of the oil sands ore-water slurry systems treated with CaO are controlled by the initial slurry composition, CaO addition dosage, and temperature (pressure is almost constant); where, adjusting these parameters could provide the most optimal conditions to achieve the objectives of bitumen extraction or tailings management processes, in simple, environmentally friendly, and cost-effective manners.

3.1 *Bitumen extraction using lime (CaO) as process additive*

Our laboratory has been testing performance of lime (CaO) as an extraction process additive replacing *NaOH* of the CHWE process, operating fundamentals of which are depicted in Figure 2 (Arnipally et al. 2019). When CaO is used as additive at dosages maintaining extraction process slurry *pH* at about 8.0 – 8.5, at 50–60 Celsius operating temperature, it reduces $\gamma_{B/W}$ in the water film between bitumen and sand, increases repulsion forces and liberates bitumen from the sand by the same mechanism of CHWE process (Reaction 1, Fig 1).

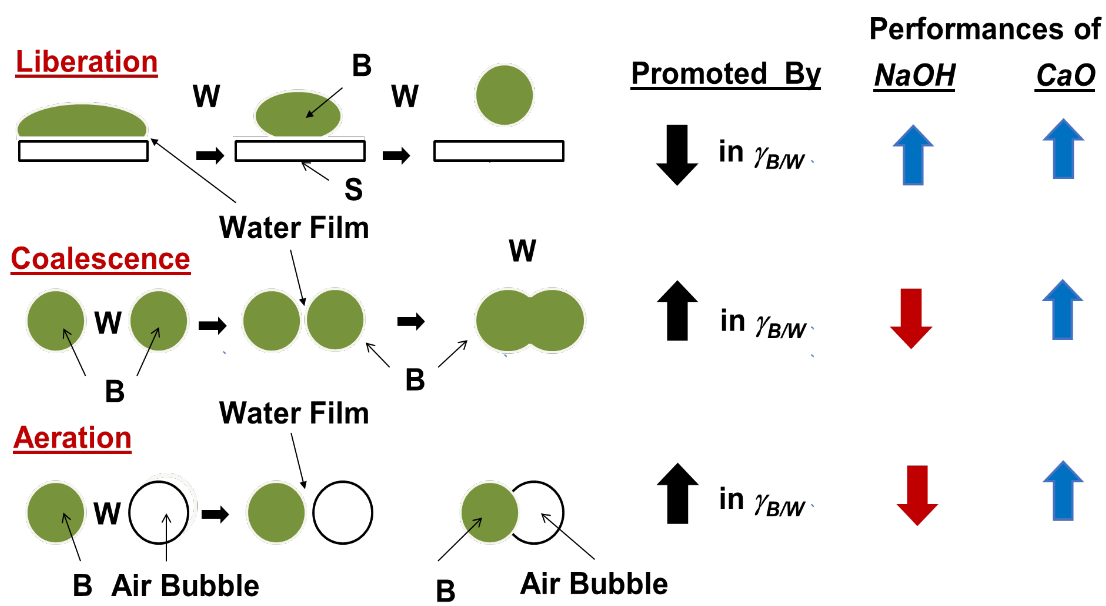

Figure 2. Performance of $\boldsymbol{NaOH}$ and $\boldsymbol{CaO}$ as extraction process additives.

Use of CaO as extraction process additive increases γ_W and $\gamma_{B/W}$ in the extraction process slurry (Reaction 5, Fig 1). Increase in γ_W contributes suppression of silt-clay size particles with coagulation of clay particles by the Reaction 4 (Fig 1). Effect of process additive on dispersion of fines was demonstrated by dispersive and non-dispersive hydrometer tests made on < 45 micron (-325 mesh) size fractions of $NaOH$ and CaO based extraction process tailings (Fig 3).

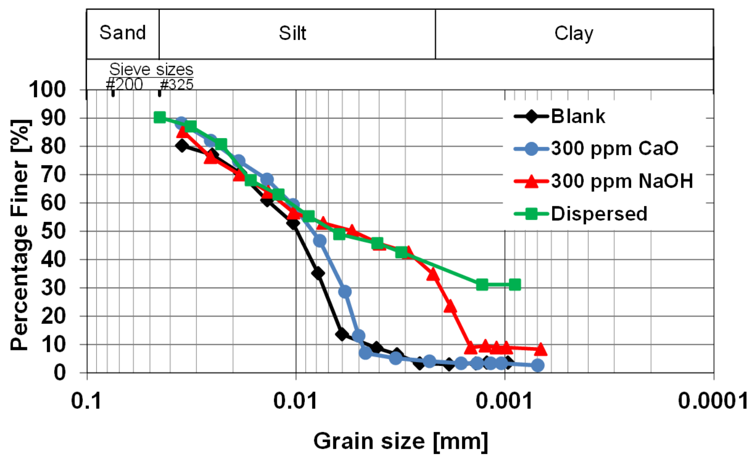

Figure 3. Dispersive and non-dispersive hydrometer tests results (Ozum et al. 2014b).

These tests show that $NaOH$ additive disperses silt and clay size particles >10 microns as good as sodium hexametaphosphate additive of the ASTM D422-63 dispersive hydrometer test. Use of CaO as extraction process additive suppresses dispersion of silt-clay size particles smaller than 10 microns, which would improve thickeners performance and suppress production of mature FFT.

Increase in $\gamma_{B/W}$ promotes bitumen droplets coalescence and aeration kinetics by reducing bitumen wettability with water, increases froth formation kinetics and bitumen extraction efficiency without harming bitumen fuel quality and process affected water chemistry (Arnipally et al. 2018; Flury et al. 2014). Increase in froth formation kinetics reduces volumes of the extraction process vessels, which reduces capital and operating costs of the newly constructed oil sands plants and increases ore-water slurry processing capacity of the existing oil sands plants.

Our experimental studies show that CaO based extraction process could improve bitumen recovery efficiency by a minimum of 5%, which corresponds to about 80,000 barrels/day additional bitumen production by the surface mining bitumen production plants. Increase in bitumen extraction efficiency reduces residual bitumen in the tailings, therefore, reduces the source of the toxicity of the tailings.

Beside our in-house extraction tests using CaO as extraction process additive, our research team was participated in third party verification tests made at Calgary Research Centre, Shell Canada Ltd. in 2005-2006, and NAIT-NARCOSS, as requested by COSIA in 2013 (Ozum & Scott 2010; COSIA 2014). Our in-house and third-party verification tests confirm that CaO performs much superior as extraction process additive compared to $NaOH$ of the CHWE process. Commercial implementation of CaO based extraction process would result remarkable progress to overall performance and to reduce long terms sustainability challenges of the oil sands plants.

Another advantage of CaO based extraction process is that small-scale mobile extraction plants could be commissioned close to mine sites and bitumen rich extraction froth (composed of about 60% bitumen, 30% water, 10% solids) could be transported to main plants by pipelines replacing oil sand ore (composed of about 10 % bitumen and 90% solids) hauling by trucks. Commercial implementation of small-scale mobile extraction plants would reduce operating costs and GHG emissions (Ozum 2019).

3.2 *Tailings management processes using lime (CaO) as additives*

Use of CaO as additive for the management of sands tailings is known for decades. Early studies were focused on increase settling and consolidation characteristics of the tailings produced by the CHWE process and/or recover $NaOH$ by the reaction between CaO and $Na - Clay$, ignoring segregation of sand grains from the fines-water sludge (Hamza et al. 1996; Karr 1984; Kessick 1983&1980).

Our laboratory has been working on nonsegregating tailings (NST) production, whole tailings treatment for direct deposition or before the thickeners, and accelerated dewatering of mature FFT (produced by CHWE process) by using CaO as additive.

3.2.1 *NST production using CaO additive*

NST production process using CaO additive works with the same principles of the CT production process; however, it demands use of high-performance thickeners to thicken cyclone overflow and recycling the warm thickener overflow to extraction plant, which saves thermal energy and reduces GHG emissions. The cyclone underflow and thickener underflow are blended to produce NST material with desired sand-to-fine ratios (SFR) and treated with CaO at dosages to maintain pH of the NST slurry at about 10.0 – 10.5.

Laboratory scale NST production tests were made using tailings material received from Albian Sands' Muskeg River Mine plant when the extraction plant was operating with both non-additive and using sodium citrate ($Na_3C_6H_5O_7$) additive, where NST with SFR of 4 to 5 could be produced using CaO additive at 0.6 to 0.8 kg-CaO/m^3-NST dosages. This study was jointly sponsored by Shell Canada Ltd., Canadian Natural Resources Ltd. and Alberta Energy Research Institute, results of which were summarized in seven reports (AERI 2004-2005). Laboratory scale test results were encouraging, Shell Canada Ltd. initiated a field trial to evaluate performance of NST production using CaO additive; however, the project was terminated without achieving project goals.

NST production from the tailings material produced by using CHWE process for over ten years commonly demands higher dosages of CaO addition, because of the steady change in process affected water chemistry caused the CHWE process. Experimental data to produce NST at 45% solids contents with SFR of 4 and 5 are presented in Tables 1 & 2. In these tests segregation was quantified by "Fines Capture", which was calculated from the Segregation Index (SI) determined by measuring the solids contents of 6 to 8 layers from top to bottom of the settled tailings material (Scott et al. 2007).

Table 1. NST production, tailings material of 45% solids content with SFR of 4.

CaO kg/m^3-NST	*pH* Before Additive	*pH* After Additive	SI$^{(*)}$ (%)	Fines Capture (%)
-	7.2 @ 21.8 C	-	49.3	50.7
0.8	7.7 @ 20.9 C	7.2 @ 20.5 C	43.9	56.1
1.0	7.70@ 20.8 C	10.8 @ 19.9 C	5.3	94.7
1.5	7.6@ 21.9 C	11.0 @ 21.6 C	3.7	96.3
2.0	7.5 @ 21.3 C	11.2 @ 21.1 C	3.7	96.3
2.5	7.7 @ 21.4 C	11.8 @ 21.5 C	4.5	95.5

$^{(*)}$ SI : Segregation Index; Fines Capture = 100 - SI

Table 2. NST production, tailings material of 45% solids content with SFR of 5.

CaO kg/m^3-NST	*pH* Before Additive	*pH* After Additive	SI$^{(*)}$ (%)	Fines Capture (%)
-	7.8 @ 21.4 C	-	48.4	51.6
0.8	7.9 @ 21.1 C	8.3 @ 21.1 C	33.4	66.6
1.0	7.8 @ 21.1 C	8.6 @ 20.4 C	20.3	79.7
1.5	7.9 @ 20.9 C	10.3 @ 20.4 C	4.2	95.8
2.0	7.8 @ 21.1 C	10.0 @ 20.9 C	4.3	95.7
2.5	7.8 @ 21.5 C	11.2 @ 21.2 C	4.5	95.5

$^{(*)}$ SI : Segregation Index; Fines Capture = 100 - SI

Highlights of our observations on NST production are: (i) NST could successfully be produced using CaO additive; (ii) the optimum slurry pH for NST production is about 10.0 to 10.5; (ii) NST production made on recently delivered tailings samples demanded CaO additions at about 1.0 to 1.5 kg- CaO/m^3-NST dosages; (iii) smaller dosages of CaO additions are required for production of NST with lower SFR, however, as SFR gets lower hydraulic conductivity gets lower and suppresses dewatering rate of the NST; (iv) NST production improves process affected water chemistry by reducing released water Na^+ concentration (Donahue et al. 2008; AERI 2004-2005).

Our in-house research findings also indicate that, if CaO based extraction process is implemented, existing mature FFT produced by CHWE process could also be added into the blend of cyclone underflow and thickener underflow, at about 10-15 % of the final NST material.

3.2.2 *Whole tailings treatment for direct deposition or before*

Whole tailings treatment with CaO could be an option for direct deposition of tailings produced by CHWE process as NST materials for most of the tailings produced in extraction process (Ozum et al. 2004).

Our laboratory focused on treatment of cyclone overflow material with CaO followed by recycling thickener overflow to extraction process and blending thickener underflow with cyclone underflow to produce NST material, potentially by using additional CaO for permanent tailings deposition (Fig 4).

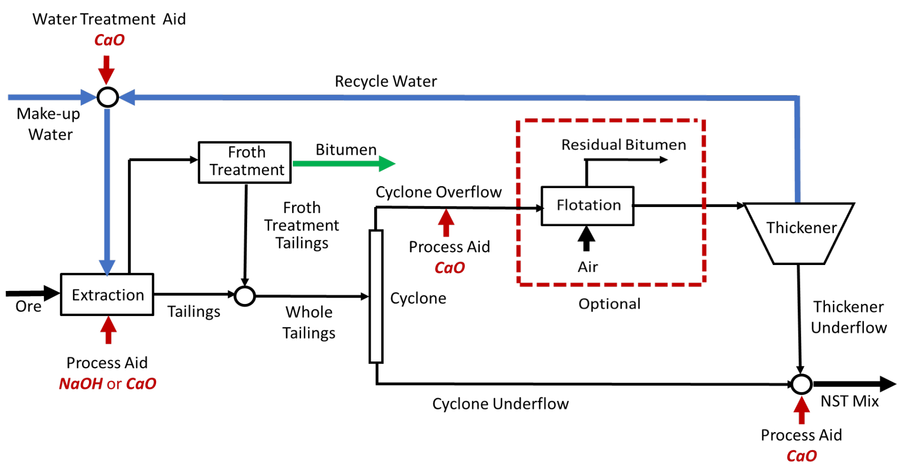

Figure 4. Cyclone overflow treatment with $\boldsymbol{CaO}$.

Laboratory scale tests were made on a simulated cyclone overflow material of 10% solids and 90.3% fines (SFR of 0.1) by diluting a mature FFT sample (40.0% solids with of 90.3% fines, SFR=1, 1.7% bitumen and 58.3% water) with a process water delivered from a commercial plant. Simulated cyclone overflow samples were treated with CaO at 600, 800, 1,000 and 1,200 ppm dosages. About 40% of the total water of simulated cyclone overflow was released as clear water within 24 hours from the samples treated at 1,000 ppm and 1,200 ppm CaO dosages. Treatment of simulated cyclone overflow with CaO reduces activities of surfactant species, reduces wettability of bitumen with water, destabilizes bitumen-in-water emulsion structure and releases bitumen; where the released bitumen could be removed from the slurry by flotation (Fig 5).

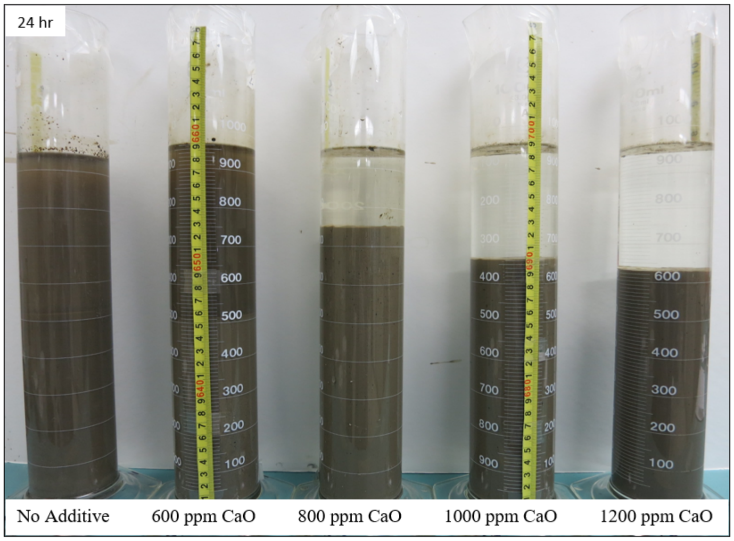

Figure 5. Water recovered from simulated cyclone overflow treated with $\boldsymbol{CaO}$.

Recovered water (RW) samples from simulated cyclone overflow treated with CaO at 800, 1,000 and 1,200 ppm CaO dosages were blended with the process water (PW), at RW/PW volume ratios of 1:1, 1:2 and 1:3. Water chemistry analyses show that, in commercial applications the recovered water by thinning the cyclone overflow treated with CaO at 800, 1,000 and 1,200 ppm CaO dosages could be blended with the process water being used at existing oil sands plants at much higher than 1:3 RW/PW ratios by maintaining the blended water pH at about 8.0 to 8.4 (Table 3). Recycling of the thickener overflow to extraction plant would reduce $NaOH$ addition dosages in extraction process and suppress steady increase in process water Na^+concentration, which would result in a remarkable improvement for overall operations of the oil sands plants.

Table 3. Water chemistry, cyclone overflow treatment with $\boldsymbol{CaO}$.

	RW/PW			Total	Cations				Anions		
CaO	Volume Ratio		Cond.	Alkalinity	Na+	K+	Ca2+	Mg2+	Cl-	SO42-	SAR
(ppm)	(-)	pH	(mS/cm)	(mg-CaCO3/L)	(mg/L)	(mg/L)	(mg/L)	(mg/L)	(mg/L)	(mg/L)	(-)
-	PW	9.0	1.54	382	337	17.7	16.6	15.1	172	61	14
-	RW	8.4	1.85	429	280	18.0	50.0	20.0	186	64	8
600	RW	10.6	1.40	112	298	8.5	7.8	0.8	186	63	27
800	RW	11.6	2.11	115	359	13.0	4.8	0.1	187	66	44
1,000	RW	11.9	2.61	112	382	16.0	13.8	0.1	179	61	28
1,200	RW	12.1	3.41	116	393	18.6	86.1	0.1	182	62	12
800	1:1	10.2	1.55	221	347	15.1	4.8	6.5	178	65	24
800	1:2	10.4	1.52	224	342	15.5	5.6	8.0	178	62	22
800	1:3	9.7	1.50	282	345	18.8	6.7	10.8	179	60	19
1,000	1:1	10.8	1.61	198	373	17.1	3.6	5.6	177	59	29
1,000	1:2	10.3	1.53	246	355	17.1	4.5	9.1	176	57	22
1,000	1:3	9.0	1.51	266	352	17.1	5.6	10.6	174	62	20
1,200	1:1	11.5	1.89	141	365	18.0	1.8	0.5	176	61	62
1,200	1:2	10.8	1.60	216	359	18.0	4.0	8.0	175	60	24
1,200	1:3	10.3	1.56	243	355	17.8	3.6	10.1	175	59	22

RW: Recovered water from mature FFT; PW: Process waterreceived from commercial oil sands plant.

Preliminary tests made to produce NST with SFR of 1, 2 and 3 by adding sand to dewatered simulated cyclone overflow (after one week of settling) treated at 1,000 ppm and 1,200 ppm CaO dosages. Test results were promising, and further NST production test are planned on cyclone overflow, process water and sand samples delivered from oil sands plants.

3.2.3 *Dewatering of existing mature FFT produced by CHWE process*

Treatment of mature FFT with CaO at 1,000 ppm dosages and above (pH >12) achieves the long-term clay stabilization by pozzolanic reactions between silica and alumina within clay minerals and CaO. At our laboratory dewatering of mature FFT using CaO additive is being investigated for two purposes: (i) in-situ treatment of mature FFT followed by sand capping or blending with overburden soils; and (ii) pretreatment of mature FFT before its dewatering by centrifuge, pressure filtration or any commercially proven dewatering technologies (Ozum 2017).

Two mature FFT samples produced at two different oil sands plants were treated with CaO at 1,000 ppm to 100,000 ppm (based on FFT mass) dosages reaching slurry *pH* above 12. Addition of CaO up to 1,000 ppm dosage does not appear to bring about a large change in plasticity of the MFT. It was found that increasing lime dosage over 3,000 ppm results in an increase in the plastic limit and a reduction in the liquid limit, therefore causing a significant reduction in the plasticity of the mature FFT material. Full modifications were achieved after 7 days and 28 days for the two different mature FFT samples (Arnipally et al. 2018). After this dosage, MFT plasticity increase reduces significantly with CaO additions up to around 3,000 – 7,000 ppm dosages; beyond which plasticity continues to reduce with increased CaO but to a lesser degree. It is possible that this region could represent the "lime fixation point".

Our research studies conclude that dewatering of existing mature FFT inventory using CaO additive most likely at about 3,000 ppm to 10,000 ppm dosages has great potential as one of the most cost-effective methods. Our laboratory is committed to perform further tests on mature FFT sample produced at different oil sands pants.

4 CONCLUSIONS

High capital and operating costs, GHG emission, tailings management, land reclamation, water chemistry and long-term sustainability challenges of the oil sands plants are direct results of using CHWE process. Our research findings conclude that reduction or elimination of the use of $NaOH$ in extraction process should be the first step to be taken to improve bitumen extraction efficiency and reduce existing challenges of the oil sands plants. Our laboratory researched bitumen extraction and several tailings management processes, all based on using lime (CaO) as additive and generated a large data pool which could support design and execution of pilot studies needed for their commercial implementations.

5 REFERENCES

Abusaid, A., Pollock, G., Fear, C. McRoberts, E. & Wells, S. 2011, *An Update to the Construction of the Suncor Oil Sands Tailings Pond 5 Cover*, T&MW-2011 Conference Proceedings, November 6-9, Vancouver, BC, Canada.

AERI. 2004-2005. *NST production from Albian Sands Muskeg River Mine tailings material using CaO additive*, seven reports produced for Shell Canada Ltd., Canadian Natural Resources Limited and AERI (Alberta Energy Research Institute), File No. 22456-1959, Edmonton, AB, Canada.

Arnipally, S., Tang, A., Halferdahl, G., Scott, J.D. & Ozum, B. 2019. *CaO in Water-Based Oil Sand Extraction*, COSIA OSIS-2019, June 3-4, Calgary, AB, Canada.

Arnipally, A., Burden, R., Scott, J.D. & Ozum, B. 2018. *Lime as an Additive for Oil Sands Ore-Water Slurry Based Bitumen Extraction, Tailings Disposal and Fluid Fine Tailings Dewatering Processes*, T&MW-2018 Conference, September 30 – October 2, Keystone, CO, USA.

Caughill, D.L., Morgenstern, N.R. & Scott, J.D. 1993. *Geotechnics of Non-Segregating Oil Sand Tailings*. Canadian Geotechnical Journal, 30: 801-811.

Chalaturnyk, R.J., Scott, J.D. & Ozum, B. 2002. *Management of Oil Sands Tailings.* Petroleum Science and Technology, 20: 9-10, 1025-1046.

Clark, K.A. & Pasternack, D.S. 1949. *The Role of Very Fine Mineral in the Hot Water Separation Process as Applied to Bituminous Sand*. Report No. 53, Research Council of Alberta, 24: 1410-1416.

Clark, K.A. 1939. *The Hot Water Method for Recovering Bitumen from Bituminous Sand*, Report on Sullivan Concentrator, Alberta Research Council, Edmonton, Alberta Canada.

Clark, K.A. & Pasternack, D.S. 1932. *Hot Water Separation of Bitumen from Alberta Bituminous Sand*. Industrial Engineering Chemistry, 24: 1410-1416.

COSIA. 2020. *COSIA Tailings EPA-2019 Tailings Research Report*, April 2020, COSIA, Calgary, AB, Canada.

COSIA (2014). *Apex Project Report*, Edited by B. Zhao and H. Mian, January 31, NAIT-NARCOSS, Edmonton, AB, Canada.

COSIA. 2012. *Oil Sands Tailings Technology Development Roadmap Project Report, Vol 1, 2, 3, 4 &5*, Report to Alberta Innovates-Energy and Environment Solutions, June 2012, COSIA, Calgary, AB, Canada.

Cossey, H.L., Batycky, A.E., Kaminsky, H. & Ulrich, A.C. 2021. *Geochemical Stability of Oil Sands Tailings in Mine Closure Landforms*, Minerals 2021, 11, 830, pp. 1-39.

Dawson, R. F., Sego, D.C., and Pollock, G.W. 1999. *Freeze Thaw Dewatering of Oil Sands Fine Tails*, Can. Geotech J. 36: 587–598.

Donahue, R., Jeeravipoolvarn, S., Scott, J.D. & Ozum, B. 2008, *Properties of Nonsegregating Tailings Produced from the Aurora Oil Sands Mine Tailings*, International Oil Sands Tailings Conference, December 8-10, Edmonton, AB, Canada.

Flury, C., Afacan, A., Bakhtiari, M.T., Sjoblom, J. & Xu, Z. 2014. Effect of Caustic Type on Bitumen Extraction from Canadian Oil Sands, *Energy & Fuels, 28; 431−438*.

Hamza, H.A., Stanonik, D.J. & Kessick, M.A. 1996. *Flocculation of Lime-Treated Oil Sands Tailings*, Fuel, Vol. 73(3) 280-284.

Karr, K. 1984. *Dry Tailings Disposal from Oil Sands Mining, Vol 1 & 2,* C-H Synfuels Limited, prepared for Environmental Protection Service, Environment Canada.

Kasperski, K.L. 2001. Review of Research on Aqueous Extraction of Bitumen from Mined Oil Sands, Natural Resources Canada, Western Research Centre, Division Report May 2001, CWRC 01-17.

Kasperski, K.L. 1992 *A Review of Properties and Treatment of Oil Sands Tailings*, AOSTRA Journal of Research, (8): 11-53.

Kaya, A. Oren, A.H. & Yukselen, Y. 2003. *Settling Behavior and Zeta Potential of Kaolinite in Aqueous Media*, Proceedings of The Thirteenth (2003) International Offshore and Polar Engineering Conference, May 25–30, Honolulu, Hawaii, USA.

Kessick, M.A. 1983. *Recovery of water and alkali used in oil sands and heavy oil extraction*, Fuel, 62(11), 296-1298.

Kessick, M.A. 1980. *Ion Exchange and Dewaterability of Clay Sludges*, International Journal of Mineral Processing, 6(4), 277-283.

Liu, J., Xu, Z. & Masliyah, J. 2005. *Interaction forces in bitumen extraction from oil sands*, Journal of Colloid and Interface Science, 287(2); 507-520.

Mankowski, P. Ng, S., Siy, R., Spense, J. & Stapleton, P. 1999. *Syncrude's Low Energy Extraction Process: Commercial Implementation,* Proceedings, 31-st Annual Meeting of the Canadian Mineral Processors, Paper 11, January 19-21, Ottawa, ON, Canada.

Masliyah, J., Zhou, Z., Xu, Z., Czarnecki, J. & Hamza, H. 2004. *Understanding Water-Based Bitumen Extraction from Athabasca Oil Sands*, Canadian Journal of Chemical Engineering, 82: 628-654.

Mikula, R. 2014. *Centrifuge technology setting new standard for advancing tailings solutions*, *New Technology Magazine, April-2014, 26-29*.

Miller, W.G., Scott, J.D., & Sego, D.C. 2010a. *Effect of extraction water chemistry on the consolidation of oil sands fine tailings*, CIM Journal, 1(2); 113-128.

Miller, W.G., Scott, J.D., & Sego, D.C. 2010b. *Influence of the extraction process on the characteristics of oil sands fine tailings*, CIM Journal, 1(2); 93-112.

Ozum, B. 2020. *Treatment of Oil Sands Whole Tailings Lime*, Canadian Patent Application No. 3,101,746, December 5, 2020.

Ozum, B. 2019. *Small Scale Bitumen Extraction Process and Plants*, Canadian Patent Application No. 3,064,756, December 5, 2019.

Ozum, B. 2017. *Process for Improving Dewatering Characteristics of Oil Sands Tailings by Treating with Lime*, Canadian Patent Application No. 2,977,524, August 24, 2017.

Ozum, B., Romaniuk, N., Sorta, A., Feland, B. & Scott, J.D. 2014a. *Integrating oil sands bitumen extraction processes and nonsegregating tailings production*, T&MW Conference, October 6-8, Keystone, CO, USA.

Ozum, B., Romaniuk, N., Sorta, A., Feland, B. & J.D. Scott, J.D. 2014b. *A Paradigm Change Needed in Oil Sands Industry: CaO as Additives for Bitumen Extraction and Nonsegregating Tailings Production Processes*, SPE-170174-MS, June 10-12, SPE Heavy Oil Conference-Canada, Calgary, Alberta, Canada.

Ozum, B. & Scott, J.D. 2010. *Methods to Reduce Production of Oil Sands Fluid Tailings*. 2nd International Oil Sands Tailings Conference, December 5 -8, Edmonton, AB, Canada.

Ozum, B., Chalaturnyk, R.J. & Scott, J.D. 2004. *Production of Nonsegregating Slurry from Whole Tailings,* CIM Edmonton-2004 Conference, May 9-12, Edmonton, AB, Canada

Pan, L., Jung, S. & Yoon, R.H. 2012. *A fundamental study on the role of collector in the kinetics of bubble-particle interaction,* International Journal of Mineral Processing, 106-109, 37-41.

Pan, L. & Yoon, R.H. 2010. *Hydrophobic Forces in Wetting Films*, Faraday Discussion, 146: 325-340.

Pollock, G.W., Changa, D. & Mettananda, A. 2014. *Design of Suncor's fist tailings sand structure under tailings reduction operation – Sand Dump 8*, T&MW Conference Proceeding, 449-462, October 5-8, Keystone, CO, USA.

Scott, J.D., Donahue, R., Blum, J.G., Paradis, T.G., Komishke, B. & Ozum, B. 2007. *Production of Non-segregating Tailings with CaO or CaO and CO_2 for Improved Recycle Water Quality*, CONRAD's Water Usage Workshop, November 21-22, Calgary, Alberta Canada.

Speight, J.G. & Moschopedis, S.E. 1980. *Surface and Interfacial Phenomena Related to the Hot Water Processing of Athabasca Oil Sands*, Information Series 86, Alberta Research Council, Edmonton, Alberta, Canada.

Speight, J.G. & Moschopedis, S.E. 1977/78. *Factors Affecting Bitumen Recovery by the Hot Water Process*, Fuel Processing Technology, 1: 261-268.

Prediction of pipeline shearing of flocculated oil sands tailings

Scott E. Webster, Imran Shah, Tayfun Aydin, & Clara Gomez
Coanda Research & Development Corp., Burnaby, BC, Canada

Babak Derakhshandeh
Suncor Energy Inc., Calgary, AB, Canada

Givemore Sakuhuni
Imperial Oil Ltd., Calgary, AB, Canada

Abu Junaid
Canadian Natural Resources Limited, Calgary, AB, Canada

ABSTRACT: Understanding the effects of pipeline shear on the characteristics of flocculated tailings is important for the development of treatment and deposition technologies. Laboratory prediction of pipeline shear can help design these systems. We explored the relationship between the conditions in a custom laboratory shear device and pipeline loops. Flocculated oil sands fluid fine tailings and reflocculated thickened tailings were sheared at analogous conditions in the shear device and pipeline loops. Samples were collected and characterized, and the pipeline pressure gradient data was compared with the torque data from the shear device after converting both to shear stress values. The shear device produced useful information on the effects of shearing and expected pipeline pressure gradient for homogenous materials despite their non-Newtonian nature. Post-shear characteristics for the device samples were comparable to those from the pipelined tailings. The shear stress data matched for both systems when the material and conditions were appropriate.

1 INTRODUCTION

The primary goal of most oil sands tailings treatment programs is to remove water and gain material strength within a reasonable timeframe for land reclamation. Several technologies have been proposed for dewatering of tailings, including flocculation, filtration, centrifugation, thickening, and natural drying. In many of these treatment methods, tailings are required to be transported to deposition cells using pipeline transport systems.

One of the technologies that has received special attention is the flocculation of fluid fine tailings (FFT) using inline static or dynamic mixers prior to their final deposition in designated deposit areas. The same technique has also been applied to the reflocculation of thickened tailings (TT). Understanding the effects of pipelining on the performance characteristics of these flocculated materials is an important part of the development of these technologies. Flocculated material could potentially be pipelined for several kilometers before being deposited, and there is often a concern that the material characteristics will be adversely affected by the shear it experiences during transport. Therefore, it is important to understand how pipeline transport will affect the properties of the material so that pipelines can be designed to optimize treatment performance. In addition, it would be beneficial to know if certain flocculated material properties provide better pipeline performance characteristics.

There are two factors that are of particular importance. The first is the ability to predict the degradation of material quality such that degradation rates can be minimized during transport. The second is the ability to estimate the pipeline pressure drop for the range of anticipated flocculated material properties with respect to flow rate, pipe diameter, and pipeline length. These are challenging objectives given that flocculated FFT is a complex multiphase system with non-Newtonian fluid properties that can vary considerably along the length of the pipeline.

Coanda previously worked in collaboration with Shell Canada (now Canadian Natural Resources Limited) to address the concerns of material degradation during pipeline transport using a laboratory shear device modelled after a large concentric cylinder geometry. This instrument was designed with the goal of providing a uniform shear distribution while accommodating large flocs. The macroscopic nature of floc structures precludes the use of a traditional concentric cylinder rheometer for this application. Additionally, the greater volume of the shear device provides enough sheared material to perform characterization tests. Derakhshandeh et al. (2016) studied the effects of shear rates from ~10 s^{-1} to ~70 s^{-1} on the dewatering of ~30 wt% FFT suspensions treated with three different flocculants. The study found that shearing did not have a significant impact on dewatering of the samples over a seven-day period. Similar studies have been performed for other oil sands operators under different shear conditions. While these studies showed that the general perception of shearing being detrimental to dewatering of flocculated oil sands tailings may not be true, additional work was required to include the effects of shearing on long-term consolidation behaviour.

A more recent study conducted by Coanda for the Institute for Oil Sands Innovation (IOSI) and Canada's Oil Sands Innovation Alliance (COSIA) investigated the impact of shearing of flocculated FFT and TT on dewatering and compressibility (Webster et al. 2019). Samples of flocculated FFT and TT were sheared using the same shear device and assessed using a variety of performance indicators for dewatering (capillary suction time, CST, and permeability index, PI), rheology (peak yield stress), settling behaviour (settling column mud layer tracking), and consolidation behaviour (large strain consolidometer, LSC, seepage induced consolidation testing, SICT, and beam centrifuge testing). The work resulted in the following conclusions. The immediate dewaterability and yield strength of the flocculated materials suffered when subjected to substantial stress while settling characteristics improved despite sometimes requiring longer times to reach a plateau value. The experimental compressibility and permeability data of the low- and high-shear materials were comparable, with the low-shear material performing marginally better at high void ratios. However, finite strain modeling demonstrated faster consolidation for low-shear materials in most cases, with negligible differences at longer time scales. It was concluded that the optimal amount of shear likely depends on the specific deposition or processing strategy. Certain methods can be less tolerant to shear while deep deposition might benefit from some shear experienced in the pipelines post-flocculation."

1.1 *Objectives for the Current Work*

The overarching objective of this study was to evaluate the use of the benchtop shear device for predicting pipeline shear effects. In particular we compared the material properties for tailings sheared in the device with those for samples sheared in 51 mm and 102 mm pipeline experiments. Based on the work described in the prior studies, we performed experiments where we matched the pipeline wall shear rate for laminar flow and the theoretical shear rate for the shear device, assuming it had a concentric cylinder geometry. By comparing the results, we sought to determine if this approximate shear rate match was sufficient to simulate the pipeline flows in the shear device. Investigation was also carried out to determine if pipeline pressure gradients could be estimated from the torque and speed data from the shear device. The goal was to answer these questions for both flocculated FFT and reflocculated TT.

1.2 *Challenges*

It was recognized from the outset of the project that there were many challenges to overcome and that the assumptions underpinning the theoretical basis for the work would be difficult or impossible to satisfy consistently. A practical approach was adopted and data was generated to try to achieve the objectives despite these issues. While the conditions were not always ideal, it seemed reasonable that it could be possible to achieve some useful simulation of pipeline shear behavior in a type of laboratory device. Identified challenges included:

- Maintaining laminar flow in the pipeline throughout the shearing time.
- Maintaining stable Couette flow in the shear device throughout the shearing time.
- The non-ideal geometry of the shear device, including the use of baffles to prevent wall slip, and the calculation of the nominal uniform shear rate based on the Couette flow assumption.
- The use of the nominal laminar pipeline wall shear rate of 8V/D as representative of the pipeline flow (V is velocity and D is diameter).

– The complex nature of the flow of flocculated tailings materials, including their non-Newtonian nature with yield stress and shear thinning behaviour, lubricated flow, the possibility of settling and stratification, thixotropy, and the shearing effects under examination.

2 APPARATUS AND METHODS

The flocculated tailings samples required for the study were produced in Coanda's Burnaby laboratory, using the 127 mm inline dynamic mixer from the previous study (Webster et al. 2019). The results from a series of preliminary small batch tests at the benchtop scale were used to determine the optimal flocculant dosages. The inline mixer fed material into the pipelines used for the shear testing. Samples were collected downstream of the mixer for shearing in the shear device, ensuring that the same material was tested in both geometries. The 51 mm and 102 mm diameter pipelines were constructed in loops of approximately 40 m in length, and equipped with a progressive cavity recirculation pump, allowing the material to flow around the loop multiple times to experience shear times that were deemed to be commercially relevant. The pipeline flow rates and shear device rotational rates were selected to approximate commercially relevant shear rates, taking the pseudo shear rate in the pipeline to be 8V/D.

The shear device was the same as used in previous work (Derakhshandeh et al. 2016) and was operated at a controlled speed with the torque recorded to provide a measure of shear stress. The laboratory pipeline consisted of two long straight sections connected by large radius (> 1 m) hose bends. The pipeline was instrumented with a series of differential pressure transducers to measure the pressure gradient, allowing the wall shear stress to be determined.

Samples were collected for characterization prior to shearing and again from the pipeline and device at the end of the chosen shear time. Four key performance indicators were chosen to assess the tailings: the capillary suction time (CST, using a Triton type 319 instrument using Whatman #4 filter paper with a 20-25 μm pore size), the peak yield strength (maximum shear achieved using a vane rotated at 0.1 rev/min), a "permeability index" (PI), and a settling column test performed in a 2 L graduated cylinder.

The PI test consisted of allowing the material to settle for 30 minutes, then vacuum filtration of the decanted material at 17 kPa to record the volume of filtrate as a function of time. A linear fit was performed to extract a filtration constant, β, a proportionality constant between the volume squared and time based on standard filtration theory. The filtration constant was converted to an index value as shown in equation (1), which essentially corrects the value for the solids volume fraction, ϕ_s, by considering viscous flow through a porous medium (Kozeny-Carman equation).

$$P.I = \beta \frac{\emptyset_s^2}{(1-\emptyset_s)^3} * 100 \quad (1)$$

The effects of the recirculation pump were assessed by collecting samples from before and after the pump near the start of the experiments and comparing CST and peak yield values. We found that the effects of the pump were generally small in comparison with the overall change in properties recorded throughout the tests. Additionally, commercial pipeline conditions are often far from ideal, and some additional shear from the pump could simulate these effects.

To ensure that the initial materials were as similar as possible for the tests with different shear rates, the flow rate through the mixer was kept the same and a portion of the flow was diverted to a waste tank when filling the pipeline for the lower shear rate condition. The mixer was set to the same speed and the polymer dosage and feed material were also constant for each pair of shear rate comparison tests. The mixer flow rate and speed were different between the 51 mm and 102 mm diameter pipeline experiments as it would have been impractical to use the maximum flow rate required for the 102 mm experiments in the smaller scale tests. Most of the material would have had to be diverted to waste, resulting in excessive material consumption.

The two primary sets of results for the project were obtained by 1) comparing the material properties after shear for samples collected from the shear device and the corresponding pipeline experiment, and 2) by comparing the shear stress as a function of time from the shear device and pipeline data. Testing at more than one pipeline size allowed us to learn about the applicability of these comparisons at multiple scales.

2.1 *Experimental Test Matrix*

For the FFT experiments two polymers of interest were tested. A traditional partially hydrolyzed polyacrylamide (HPAM) flocculant and the XUR polymer from Dow Chemical. For the HPAM polymer, the desired optimum dosage was selected based on the material demonstrating the most reasonable combination of material strength and dewatering in small batch tests, while for the XUR material the dosage was chosen with a focus on maximum dewatering as high strength is typically not achievable with this treatment. The optimal dosage was originally identified as 1000 g/t but was adjusted for the FFT+HPAM tests based on specific tailings material properties and small batch tests performed just before the experiments. Initially the shear rates of 18 s^{-1} and 40 s^{-1} were selected to imitate the conditions in a 508 mm diameter pipe operating at 800 m^3/h and a 406 mm pipeline operating at 1000 m^3/h. Due to settling that was observed for the FFT+HPAM case in the 51 mm pipeline (discussed below), the shear rates were increased to 60 s^{-1} and 75 s^{-1} for the 102 mm tests.

For the TT, only HPAM was used, but at two different dosages. One that produced the optimal combination of material strength and dewatering in small batch experiments, and a lower dosage closer to commercial conditions. These dosages were specified as 300 and 150 g/t on a solids basis. An 80 s^{-1} shear rate was selected to match the commercial scenario of a 356 mm pipe operating at ~1300 m^3/h. For the 102 mm pipeline experiments the shear rate was reduced to 75 s^{-1} to match the maximum capacity of the recirculation pump.

The test matrix based on the above conditions and the tailings properties are presented in Table 1 and Table 2. Reynolds number calculations based on estimated rheology data for the treated tailings materials predicted laminar flow conditions for the pipelines and shear device. The shear times were based on commercially relevant pipeline distances. For runs 1 and 2, the shear times were adjusted during the experiments to explore settling behaviour. Data from these runs is not considered in this paper.

2.2 *Shear Stress Calculations*

The shear stress in the shear device was calculated from the torque data, using the standard equation for a concentric cylinder rheometer, assuming laminar flow of a Newtonian fluid, a narrow gap, and neglecting end effects:

$$\tau = \frac{T}{2\pi R^2 H} \tag{2}$$

where τ is the shear stress, T is the torque, R is the radius, and H is the height. The wall shear stress in the pipeline was calculated as:

$$\tau = \frac{dP}{dL}\frac{D}{4} \tag{3}$$

where dP/dL was the pressure gradient measured by the differential pressure transducers and D was the pipe diameter. For the pipeline pressure gradient data, we used the nominal bulk flow velocity and the pressure transducer locations to calculate the times that a particular unit of fluid would pass by each transducer for each time around the recirculating loop.

3 RESULTS AND DISCUSSION

This section reports the results of the experiments and compare the similarities and differences between the results from the shear device and the pipeline. This will be done in two ways: by comparing the sample characterization results, and by comparing the shear stresses in the two geometries.

Table 1: Experimental test matrix.

Run #	Tailings	Polymer	Dose	Pseudo-Shear Rate	Shear Time	Pipe Diameter
1	FFT	HPAM	800 g/t	18 s^{-1}	8 min	51 mm
2	FFT	HPAM	800 g/t	40 s^{-1}	20 min	51 mm
3	FFT	XUR	1000 g/t	40 s^{-1}	16 min	51 mm
4	FFT	XUR	1000 g/t	18 s^{-1}	16 min	51 mm
5	TT	HPAM	300 g/t	80 s^{-1}	5 min	51 mm
6	TT	HPAM	150 g/t	80 s^{-1}	5 min	51 mm
7	FFT	XUR	1000 g/t	40 s^{-1}	16 min	102 mm
8	FFT	XUR	1000 g/t	18 s^{-1}	16 min	102 mm
9	FFT	HPAM	1100 g/t	75 s^{-1}	8 min	102 mm
10	FFT	HPAM	1100 g/t	60 s^{-1}	8 min	102 mm
11	TT	HPAM	300 g/t	75 s^{-1}	5 min	102 mm
12	TT	HPAM	150 g/t	75 s^{-1}	5 min	102 mm

Table 2: Tailings properties. The clay content was estimated from the MBI value using the method of Sethi described by Kaminsky (2014).

Run #	Type	Solids Content wt%	Density kg/m^3	Bingham Viscosity Pa·s	Bingham Yield Pa	pH	Electrical Conductivity mS/cm	MBI meq/ 100 g	Clay Content %
1	FFT	22.0%	1165	0.0044	0.19	7.9	1.31 @21C	7.5	54
2	FFT	22.0%	1165	0.0045	0.21	7.9	1.45 @19C	7.5	54
3	FFT	23.5%	1183	0.0053	1.17	7.8	1.04 @17C	9.0	65
4	FFT	23.5%	1183	0.0053	1.17	7.8	1.04 @17C	9.0	65
5	TT	40.8%	1345	0.0096	1.00	7.8	0.74 @19C	3.5	25
6	TT	40.8%	1345	0.0096	1.00	7.8	0.74 @19C	3.5	25
7	FFT	24.2%	1166	0.0060	1.72	6.8	1.22 @25C	9.6	69
8	FFT	24.2%	1166	0.0060	1.72	6.8	1.22 @25C	9.6	69
9	FFT	24.8%	1168	0.0064	1.94	7.6	1.18 @25C	9.1	66
10	FFT	24.9%	1170	0.0064	1.94	7.6	1.19 @25C	8.9	64
11	TT	39.6%	1316	0.0091	1.13	7.5	0.85 @24C	3.8	28
12	TT	39.6%	1316	0.0091	1.13	7.5	0.85 @24C	3.8	28

3.1 *FFT+XUR*

The FFT+XUR material came the closest to behaving as expected during the experiments, acting as a homogeneous fluid in laminar flow. Figure 1 shows the sample characterization results. The peak yield values are all relatively low, at less than 10 Pa. Nevertheless, we see that shearing reduced the yield stress as expected for both the 51 and 102 mm experiments, and in both the pipeline and shear device. The initial yield stress was lower for the 102 mm experiments, which we attribute to differences in the FFT or polymer batches, or the higher flow rate through the mixer. The yield stress for the two sheared samples was similar for both the pipeline and shear device samples. It is not clear if the decrease in yield was greater for the higher shear condition (partially due to a missing sample) and the difference in the initial material makes it difficult to compare the 51 and 102 mm data directly.

All the CST results fall in the range of 15-50 s, which are moderate values (especially the results above 20 s). Both sheared samples had lower CST values (better dewatering) in the 51 mm tests, but the pipeline samples had higher (worse) CSTs for the 102 mm tests, while the shear device result was similar to the unsheared value. The difference in behaviour between the 51 and 102 mm tests is somewhat consistent with the differences in initial material observed in the peak yield results. The similarity between the pipeline and shear device samples is not as good for the CST data when compared with the peak yield, but overall the differences were not extreme.

The permeability index results for the sheared samples in the FFT+XUR experiments for the pipeline and shear device for both 2” and 4” scales at both shear rates were similar, which suggests that the shear device is adequately simulating pipeline shear. However, the results also showed evidence of differences between the 51 and 102 mm experiments, with low initial values that increased with shear for the 2” tests, and high initial values that decreased with shear for the 4” results. This difference between scales is not ideal, since the objective was to demonstrate achieving similar results at any scale. However, the potential effects of the scaling problems could not be properly separated from the effects of differences in initial material.

The one month settling column results do not appear to add much new information. Overall, the differences between samples seem modest, which is consistent with conclusions from the previous project where shearing did not dramatically affect longer term dewatering or consolidation properties.

Figure 2 shows the shear stress comparisons for the FFT+XUR experiments. The shear stress values were calculated using equations (2) and (3) above. The pressure gradient data and the times that a particular unit of fluid would pass by each transducer for each time around the recirculating loop were used to calculate the shear stresses shown in the figures. The data from the shear device and pipeline match relatively well for both 51 mm cases, except for the first few minutes of the high shear rate experiment, and for the low shear rate 102 mm test. The shear device torque data for the high-shear rate 102 mm case had an unusual dip at the start of the test, followed by a plateau, which did not align with the pipeline data. This mismatch is attributed to a problem with the shear-device torque measurement. The elevated values for dp06 in the 102 mm, 40 s^{-1} test were likely related to the transducer location, just after the recirculation pump.

Overall, the agreement in the shear stress results is consistent with the agreement in the sample characterization results and suggests that the shear device has provided a reasonable simulation of the pipeline shear for the FFT+XUR material.

3.2 *FFT+HPAM*

The HPAM-treated FFT experiments in the 51 mm pipeline and the corresponding shear device tests experienced significant settling. This obviously violated the homogeneous fluid assumption and prevented the extraction of representative samples from the pipeline. Due to the settling issues, the shear rates were increased for the 102 mm experiments, which successfully resolved the problem. The results from the 51 mm results are omitted from this discussion.

The peak yield results in Figure 3 showed the usual decrease with shearing, to similar very low (< 10 Pa) levels for the pipeline and shear device samples, with slightly lower yields for the higher shear rate samples as expected. The CST values increased slightly with shear, again similarly for both geometries, but remained at very good levels, less than 10 s.

The permeability indices decreased with shear, with similar results for both shear rates and again for both the pipeline and shear device. This decrease was consistent with the increase (worsening) in the CST, though more dramatic. These decreases in the immediate dewatering behaviour do not appear to have negatively impacted the longer-term settling characteristics. The settling column data showed that the sheared samples had settled more than the unsheared samples by around 24 hours after collection and this remained true for the remainder of the monitoring period. The 75 s^{-1} samples had slightly higher solids contents.

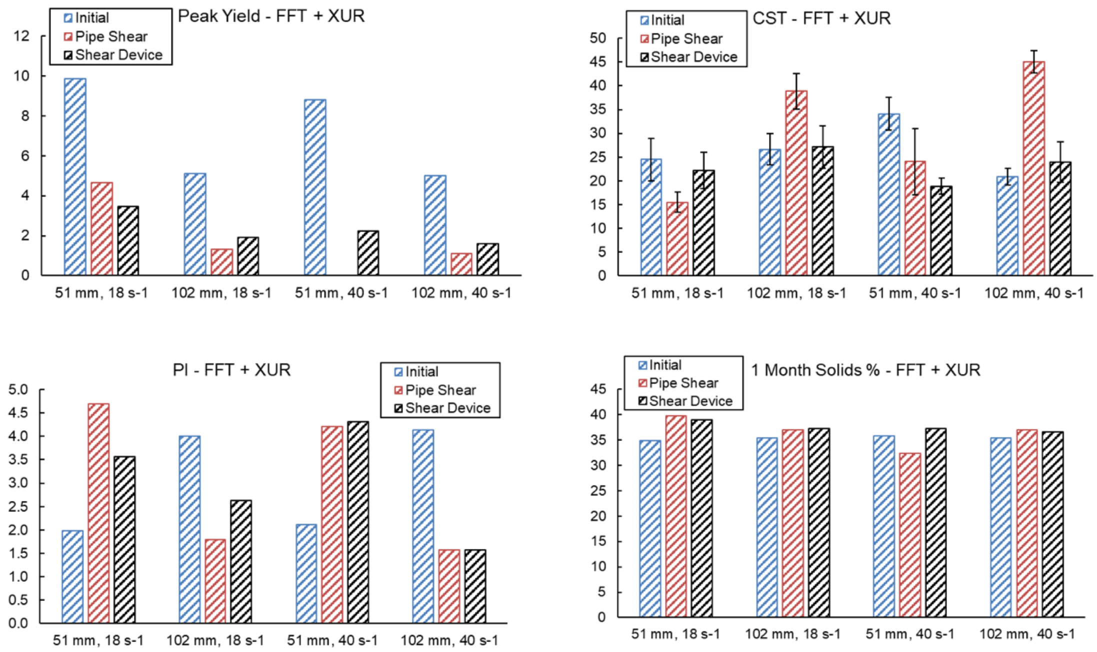

Figure 1: Peak yield, CST, permeability index and one month settling column results for the FFT+XUR experiments. The yield stress of the pipeline sheared sample was not measured for the 51 mm, 40 s^{-1} sample due to an issue with the rheometer.

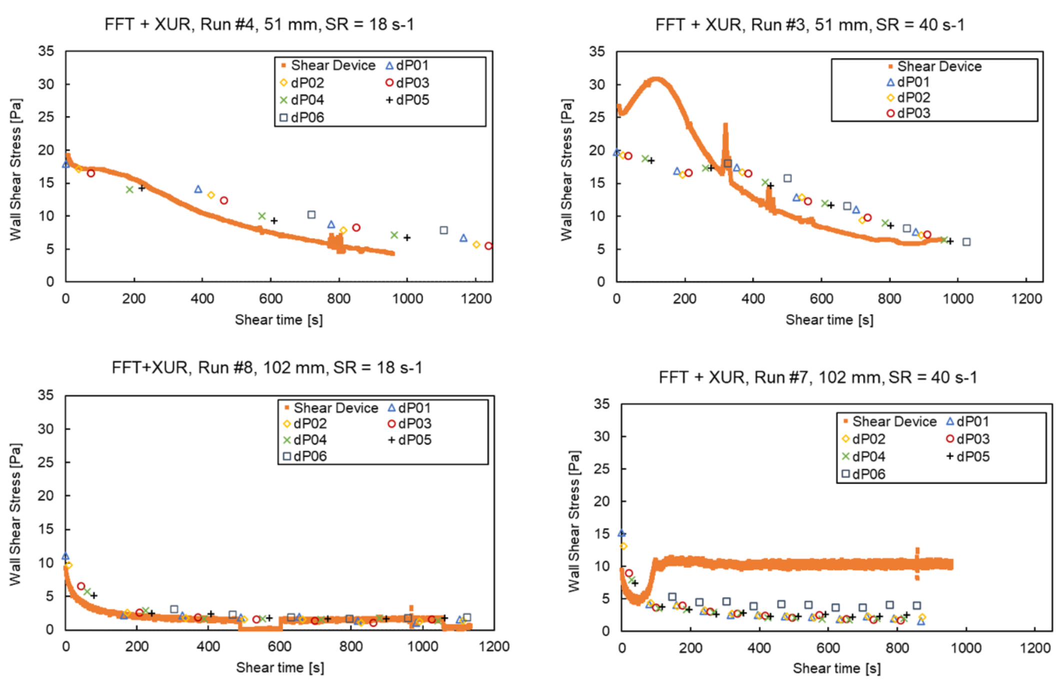

Figure 2: Shear stress comparison for data calculated from the shear device torque and pipeline pressure gradient for the FFT+XUR experiments. The symbols for the pressure gradient data were calculated from pipeline data recorded by each differential pressure transducer at times corresponding to the nominal travel of a fluid element travelling around the pipe at the bulk flow velocity.

The shear stress comparisons for the 102 mm experiments are shown in Figure 4. Agreement was good for the lower shear rate test, with the shear device data dipping lower than the pipeline results before gradually increasing. The higher shear rate result matches well initially in a period where the stress decreases, but then as the pipeline data levels off, the shear device values start gradually increasing and deviating from the pipeline data. This could be due to settled material interfering at the bottom of the bob, but noticeable settling was not observed through the walls of the shear device.

Overall, these results seemed similar to those for the FFT+XUR experiments. Generally, the sample data is comparable for the pipeline and shear device, and the shear stress values are often similar, but there are deviations in certain conditions.

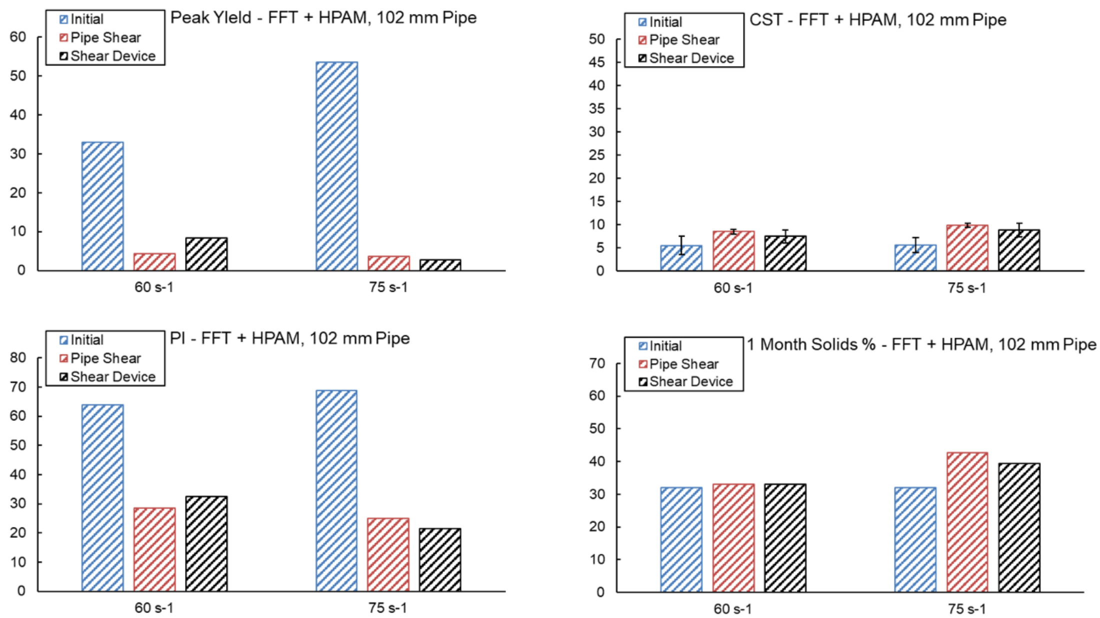

Figure 3: Peak yield, CST, permeability index and one-month settling column results for the 102 mm scale FFT+HPAM experiments.

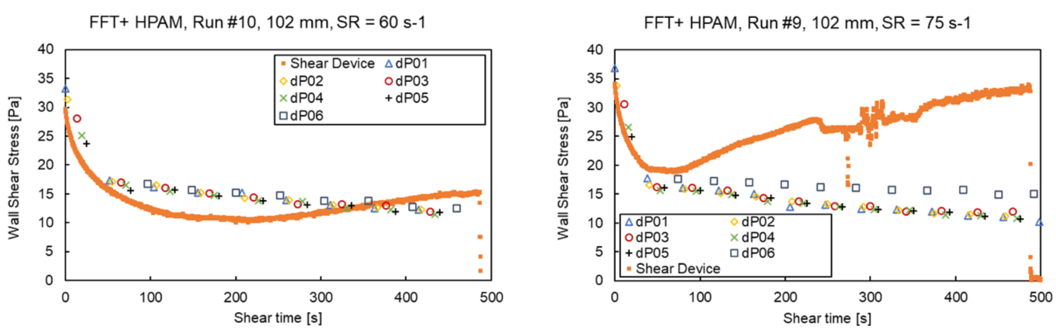

Figure 4: Shear stress comparison for data calculated from the shear device torque and pipeline pressure gradient for the FFT+HPAM experiment in the 102 mm pipeline.

3.3 *TT+HPAM*

Similarly, to the FFT+HPAM case, the discussion of the 51 mm scale results is omitted since they were substantially affected by settling. Unfortunately, even with the increased shear rate selected for the 102 mm pipeline tests, we still observed significant settling in the 300 g/t TT+HPAM test and minor settling in the 150 g/t case. Therefore, we only consider the 150 g/t 4” data in this analysis, though some data from the 300 g/t experiments is included in Figure 5.

As shown in Figure 5, the peak yield started at a very low value around 5 Pa, somewhat expected for the low dosage, and decreased to 2 Pa for both sheard samples. The initial CST was a moderate value of about 22 s and increased slightly to 25 and 28 s for the pipeline and shear device, respectively. The PI results mirrored those for the CST, with the initial value decreasing somewhat for the pipeline, and more so for the shear device, though the difference was not extreme.

The shear stress results did not match in this case for the pipeline and shear device. The values for both geometries stayed relatively similar over time, but the shear device result was 3 to 4 times higher. In this case, since pipeline settling was observed, it seemed plausible that settling is responsible for the elevated shear device stress.

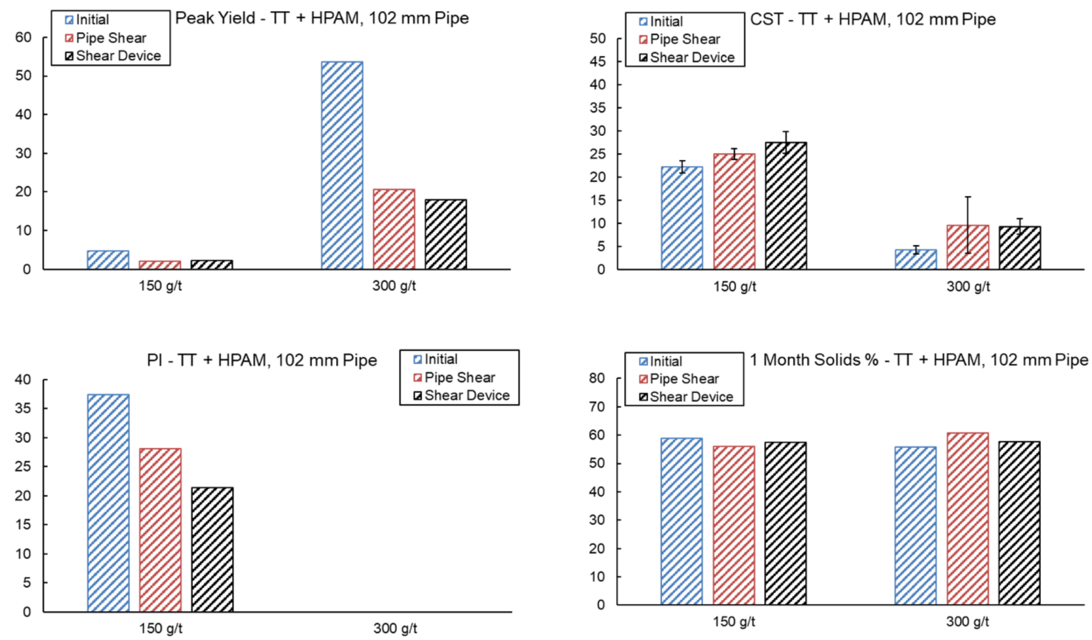

Figure 5: Peak yield, CST, permeability index, and one month settling column results for the 102 mm scale TT+HPAM experiments. PI data for the 300 g/t experiment was not considered reliable and is not shown.

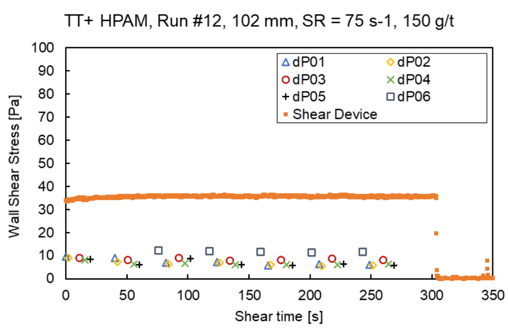

Figure 6: Shear stress comparison for the 75 s^{-1} TT+HPAM experiment with a dosage of 150 g/t in the 102 mm pipeline.

3.4 *Summary*

Overall, the results seemed to indicate that when the material is homogeneous and does not settle, the sample characteristics are relatively similar for the pipeline and shear device. This suggests that under the right conditions the shear device can provide useful information on expected shear effects for material transported in pipelines through a relatively simple laboratory test.

The shear stress results were not always as consistent, but in most cases there was a reasonable match between the shear device and pipeline derived values. In some cases, the shear device torque, and therefore the calculated shear stress, tended to increase at longer shear times. This appeared unphysical and could be detected by individuals reviewing the data. In two cases, the shear device results were not as easy to interpret and could have provided misleading information in absence of the pipeline data, which would be the case when using the shear device alone to predict pipeline pressure gradient.

The positive results appeared to apply to both FFT and TT tailings materials flocculated with either the HPAM or XUR polymer. Shear rate did not seem to influence the applicability of the results, other than the general requirement that the material behaved as a homogeneous fluid without substantial settling. Settling was easy to detect in the pipeline configuration through transparent pipe sections, but somewhat more difficult to observe in the shear device.

We were not able to thoroughly evaluate our ability to match results between pipeline scales because of inconsistent starting material and the problems with the 51 mm tests for the HPAM treated tailings. However, for the XUR treated FFT we found that the shear device and pipeline results were generally similar for both the 51 mm and 102 mm experiments, which is certainly a positive result. Commercial scale data would be useful for validating the applicability of the shear device to such a different environment.

4 CONCLUSIONS

The laboratory shear device provided useful information on the effects of shearing and expected pipeline pressure data for pseudo-homogenous non-Newtonian materials whose rheology cannot be measured using conventional narrow gap rheometers. This conclusion was based on two main observations. First, post-shear sample characterization results were usually very comparable between the shear device and laboratory pipeline, indicating that the batch device is a useful tool to investigate shear effects for FFT and TT. Second, wall shear stress data from the shear device matched the pipeline data when material and conditions were appropriate (no settling, laminar flow).

Therefore, the laboratory shear device was found to be useful for simulating commercial pipeline flows, but with some constraints. The techniques explored in this project should be useful to the oil sands industry for flocculation process and pipeline design. However, care must be taken to perform tests and interpret the data carefully as the flow behaviour of flocculated tailings is very complex. The utility of the shearing device to evaluate pipeline wall shear stress was found to be highly dependent on the nature of the material and shear conditions. Settling of the material at small scales limited the applicability of the experimental observations in laboratory scale pipelines. Existing shear device data sets from experiments performed under suitable conditions (laminar flow and insignificant settling) can now be compared against commercial scale pipeline data.

The authors thank the Institute for Oil Sands Innovation (IOSI) and Canada’s Oil Sands Innovation Alliance (COSIA) for supporting the project.

5 REFERENCES

Webster, S.E., Aydin, T., Gomez, C., Sorta, A., Derakhshandeh, B., Junaid, A. Moussavi Nik, R., & Sakuhuni. G. 2019. Effects of Shear on Dewatering and Compressibility of Treated Oil Sands Tailings. *Proceedings Tailings and Mine Waste 2019.* Vancouver, British Columbia, Canada: 1229-1240.

Derakhshandeh, B., Junaid, A., & Freeman, G. 2016. Effects of shearing and shearing time on dewatering and yield characteristics of oil sands flocculated fine tailings. *Proceedings of the International Oil Sands Tailings Conference*, Lake Louise, Alberta, Canada. 416-421.

Kaminsky, H. 2014. Demystifying the Methylene Blue Index. *Proceedings of the International Oil Sands Tailings Conference*, Lake Louise, Alberta, Canada, 221-229.

Geotextile bags as filtration process to enhance physical stability of oil sands tailings deposits – Concept & lessons learned

Fernando Da Silva
SNC-Lavalin, Calgary, Alberta, Canada

G. Ward Wilson
University of Alberta, Edmonton, Alberta, Canada

Tom Stephens
TenCate Geosynthetics Americas, Bedford, VA, United States

Nathalia Castro
TenCate Geosynthetics Americas, Land O Lakes, FL United States

ABSTRACT: The accumulation of large volumes of Fluid Fine Tailings (FFT) has been a concern in the oil sands mining industry for decades. There are significant challenges involved in the conversion of FFT into deposits capable of facilitating reclamation. Geotextile bags (geobags) accelerate consolidation of FFT and improve stability of closure landforms if the FFT is treated effectively before the geobags are filled. The chemical treatment of the FFT (recipe) needs to assist solids/water separation and ensure fines agglomeration during pipeline transport. The chemically treated FFT dewaters in the geobags and the rate of dewatering is a function of the recipe, the inline mixing process, drainage path, and increased total stress due to loading. This paper describes the geobag concept and some lessons learned from their use as a filtration technology process that is designed to enhance the physical stability of FFT.

1 INTRODUCTION

Mining companies, industry bodies, consulting companies, universities, and regulators have been continually improving best practice guidelines for the construction and management of tailings facilities and mining waste.

Dam safety revised practice does not accept the concept of a tolerable failure rate for tailings dams. This assertion resulted in recommending the implementation of the best available tailings technology based on principals for physical and chemical stability such as eliminating surface water from the impoundment and promoting unsaturated conditions in the tailings with drainage provisions (Wilson, G. W. and Robertson, A. M. 2015).

Geosynthetics technology is a well-established innovative solution available for geotechnical engineering projects that involves their use to combine mechanical and hydraulic properties in a controlled manner (Krystian, W.P., 2007). Geotextile bags (geobags) are made from woven high-strength, high-modulus synthetic fibers and have distinct pore sizes that can be used to dewater the chemically treated oil sands Fluid Fine Tailings (FFT).

The success of oil sands FFT disposal in geobags requires a chemical treatment that combines coagulation and flocculation that is referred to herein as the "recipe". The objective of the recipe is to maximize fines capture, enhance dewatering, accelerate consolidation, and maintain the integrity of the agglomerated fines to ensure that segregation does not occur. The geobags act as a filter pressure system, with most of the water recovery occurring while the bags are being filled.

The filtration properties of the geobags and the short drainage path of the containment are the key contributors for the enhanced dewatering and accelerated consolidation of the FFT. Evaporation and freeze-thaw were also identified as contributors for dewatering with time. This technology also allows for the formation of thick, geotechnically stable, layered deposits by simply stacking the geobags.

2 LESSONS LEARNED FROM OIL SANDS

2.1 *Key testing and processing methods*

The identification and quantification of FFT mineralogy is considered “critical” for the successful manipulation of clay and non-clay mineral behaviour, along with porewater chemistry and pH. Bulk X-Ray Diffraction (XRD) analysis, elemental analysis by X-ray Energy Dispersive Spectrometry (EDS), and Scanning Electron Microscopy (SEM) are performed to characterize the mineralogy of the FFT.

The FFT slurry density, specific gravity, water content, and bulk density are determined to evaluate polymer dosage and concentration as well as release water volumes.

Routine chemical analyses are performed to characterize ion concentrations and pH of the FFT porewater, plant process water, and release water from the treated FFT that can be used as recycle water.

Particle Size Distribution (PSD) is obtained by sieve and hydrometer method, as per ASTM D422-63. Non-clay mineral fines (passing 75 μm) that are pH dependent can significantly influence FFT (solids) mechanical and physical properties. At pH higher than 2, quartz particles possess negative charge, show dispersive behaviour, are more hydrophilic, and therefore behave like clay minerals.

Dilution is used to pre-treat the FFT and achieve efficient flocculation at relatively low dosages and concentrations of flocculant and coagulant. Dilution is optimized to maintain the initial slurry density of the FFT at 20% solids content (wt. %) if initial slurry density is higher than 20%.

Coagulation is applied prior to flocculation to neutralize the electrostatic charges of particles and reduce repulsion between them. Coagulant solution is prepared using Alum and process water. Flocculant solution is prepared using anionic polyacrylamide (PAM) polymer and process water.

Inline mixing of the coagulated FFT with flocculant solution does not require static or dynamic mixing. The residence time is 20 seconds to provide efficient flocculation, fines agglomeration (large floc formation), and solid/water separation.

2.2 *Inherent properties and soil characterization*

Mineralogy is the primary factor controlling the size, shape, and properties of soil particles. These same factors determine the possible ranges of physical and chemical properties of any given soil. A prior knowledge of what minerals are in a soil provides intuitive insight as to its behaviour (Mitchell, 2005).

The mineralogy of the FFT is predominantly non-clay minerals (52.3% quartz <75 μm) and clay minerals (40.1% kaolinite and 4.6% illite <2 μm). The predominance can be reverted to kaolinite and therefore the ratio of clay to massive minerals in the FFT can vary from 0.8 to 1.1, approximately. Quartz, which is a non-clay mineral, is the predominant mineral within the fine particle size fraction of the FFT in this study. Quartz particles have negative charged surfaces at pH >2 (van Lierde, 1980).

The behaviour of kaolinite particles is dependent on the sodium adsorption ratio (SAR), electrolyte concentration, and pH. Kaolinite particles have negative charged surfaces at pH >2 (Goldberg et al., 1991). Illite is non-swelling in nature, has a lower cation exchange capacity than kaolinite, and is also pH and SAR dependent.

The PSD of the treated FFT within the stacked geobags profile referred to in this paper shows that the fines content of 75 μm particles vary from 87 to 100% and that the clay content varies from 31.6 to 50.5%. The sand-to-fines ratio (SFR) varies from 0.02 to 0.16. The measured average solids specific gravity of the treated FFT is 2.28, water content is 86.9%, solids-content is 53.6%, USCS classification is CH, liquid limit is 76.8%, plastic limit is 29.0%, and the liquid index is 47.8%.

Although kaolinite particle sizes could exist in the range of 2 to 11 μm and quartz particles also could exist in the range of 0.2 to 2 μm (Mitchell, 2005), we are assuming that the amount of non-clay minerals in the treated FFT is between 49.5 and 64.2%.

2.3 *Physicochemical treatment of FFT*

The objective of the recipe is to maximize fines capture, enhance dewatering, accelerate consolidation, and maintain the integrity of the aggregate to ensure that fines segregation does not occur.

Quartz particles at pH >2 present negative surface charge. The negative charge of quartz particles increases as the pH increases (van Lierde, 1980). Quartz particles at pH 8 present a highly negative surface charge that leads to a dispersive state by action of electrostatic repulsive forces. These forces are affected by the ionic strength of the soil-water-ionized system, which depends on the pore solution electrolyte concentration and ion types (Verwey and Overbeek, 1948). In the presence of high valence cations, such as Aluminum, the repulsive forces of quartz minerals are reduced, resulting in the coagulation of particles (Da Silva et al., 2014).

The mechanism of coagulation effectively lowers the electrostatic repulsive forces between particles causing charge neutralization and formation of stable micro-flocs (slow-settling flocs). Charge neutralization is equivalent to compressing the diffuse double ionic layer energy barrier (i.e., reducing the double ionic layer charge to near zero).

Kaolinite exhibits a large positive value of zeta potential in the presence of Aluminum (Al^{3+} cations). The zeta potential decreases from +30 mV to –7 mV as the pH increases from 3 to 10 with a point-of-zero charge at pH 9 (Peng and Di, 1994). Kaolinite is the predominant clay mineral within the fine particle size fraction of the FFT in this study. The main source of negative charge in kaolinite clay minerals is the unsatisfied chemical bonds at the broken particle edges. The negative charge may increase through the adsorption of high valence negative ions to positive ions exposed at the broken edges. Since the anion exchange capacity of kaolinite particles is equivalent to the cation exchange capacity, it is logical that dispersed kaolinite could be influenced by cations in the soil-water-ionized system.

All exchangeable cations are adsorbed on the exterior surfaces of illite and kaolinite particles (van Olphen, 1977). Existing data show that illite does not play a dominant role in determining flocculation and dispersion behaviours of kaolinite/illite mixtures (Goldberg, 1991). Therefore, the focus of the physicochemical treatment is on quartz particles since they are predominant and have a significant effect on the flocculation and dispersion behaviour of the FFT.

The initial slurry density of the FFT has a significant influence on the physicochemical treatment performance. Dilution of the FFT to lower solids content is an integral part of the treatment to provide enhanced mixing and energy dissipation. This maximizes flocculant adsorption, reduces fine particle segregation and ensures efficient particles agglomeration when the flocculant is added (Da Silva et al., 2014).

The key to obtain effective coagulation of the FFT is to understand how the individual tailings mineral particles interact with each other within the soil-water-ionized system. Charge neutralization from the existing Ca^{2+} concentration in the FFT pore water is not sufficient to coagulate quartz particles. In addition, the high levels of bicarbonate present in the pore water precipitate Ca^{2+} at pH 8, affecting the ionic strength of the soil-water-ionized system. Therefore, it is necessary to add a coagulant aid to lower the surface charge and reduce the repulsive energy barrier of the quartz mineral particles (Da Silva et al., 2014). Coagulation is the basis of the treatment because it increases the density and shear resistance of the micro-flocs, so they are not destroyed during mixing and settling.

The cations added by the coagulant will also affect the total negative charge of the clay particles in the soil-water ionized system because the remaining anions are attracted to the incompletely neutralized positive ions exposed at the broken edges of clay particles. Furthermore, negative particles can be successfully flocculated with bridging type long chain anionic polymers because regions of the particle with a positive charge serve as points of attachment for the negatively charged polymer. A relatively small amount of an anionic flocculant of medium charge density and very high molecular weight is used to bridge the micro-flocs and form large and fast settling flocs (Da Silva et al., 2014).

Increased calcium cations and pH cause adverse effects on the adsorption of anionic PAM polymer on quartz and kaolinite particles. Poor flocculation of quartz and kaolinite observed between pH 8 and 8.45 is potentially due to adsorption of Ca^{2+} ions on anionic PAM polymer causing steric stabilization at the particle surfaces and inhibiting the formation of hydrogen bonds.

Quartz is the predominant mineral of the FFT in this study, followed by kaolinite and illite. The FFT pore water contains 18 ppm calcium ions and process reclaim water usually contains 19 ppm calcium ions. Efficient fines agglomeration and dewatering of quartz and kaolinite particles are achieved with coagulation of the particles by aluminum ions prior to anionic polymer PAM addition. The FFT has a measured zeta potential - 47 mv at pore water pH 8. The treated FFT with aluminum and anionic PAM polymer has zeta potential - 14 mv at pore water pH 7.

As a result of coagulation of FFT with high valence cations, such as Al^{3+}, there is a risk of increasing calcium concentration in the release water. The consequence is a negative impact on bitumen recovery if the release water exceeds the limits for calcium concentration and is used as reclaim water for bitumen extraction. In summary, the recipe is comprised of inorganic coagulant of high valence cations (Alum) and anionic flocculant of high molecular weight and medium charge density. The anionic flocculant provides excellent flocculation efficiency for treated FFT at zeta potential -14 mv. The recipe is applied inline to promote solids agglomeration and water separation during pipeline transport.

Evaporation tests were conducted on FFT, treated FFT (recipe), and a pumpable centrifuged FFT at 48% solids content by mass (cake) to investigate and compare evaporation rates. Test results (Figure 1) indicate that the actual rate of evaporation of the recipe is close to the potential rate of evaporation of water and is higher than the actual evaporation of the FFT and cake samples at the early portions of the plots. As more water is lost in the early period of the test, the subsequent rate of evaporation of the recipe becomes lower as the sample starts drying faster.

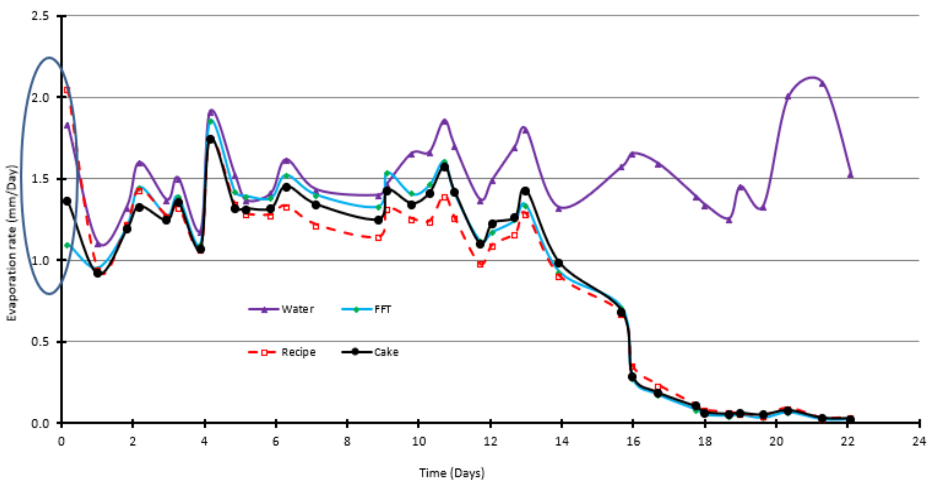

Figure 1 – Rate of potential evaporation (water) and actual evaporation (samples) vs time.

It should be noted in Figure 2, through the ratio of the actual evaporation (AE) and potential evaporation (PE), that the FFT and cake samples dewater much slower (i.e., AE/PE ≤1) than the recipe in the early stage of the drying process when the surfaces are wet. This is possibly attributed to the presence of free bitumen in the FFT and cake that forms a film on the surfaces that limits further drying from deeper layers and thus reduces the actual rate of evaporation (Zang, LL. et al., 2014). Recipe evaporates at a potential rate (i.e., AE/PE ≥1) when the sample is saturated in the early stage of the drying process.

The recipe entraps the bitumen in the tailings and forms an open soil structure. The films on the surfaces of the FFT and cake start to break down as drying continues and the AE/PE ratios continue to gradually increase to reach a value of 0.96 and remain constant until Day 10. Eventually the AE/PE ratios start to decrease to reach a value of 0.8 on Day 12. During this time the AE/PE ratio of the recipe continues to decline gradually and reaches a value of 0.8 on Day 10.

The AE/PE ratio of 0.8 is the boundary between the saturated and unsaturated states of the samples. As drying proceeded in the unsaturated region (i.e., AE/PE <0.8) all the AE/PE ratios started to decline rapidly to reach their lowest values (residual) of close to zero (all the surfaces of the samples become desiccated).

In summary, the recipe loses water much faster and reaches the boundary region (i.e., AE/PE = 0.8) earlier than the FFT and the cake.

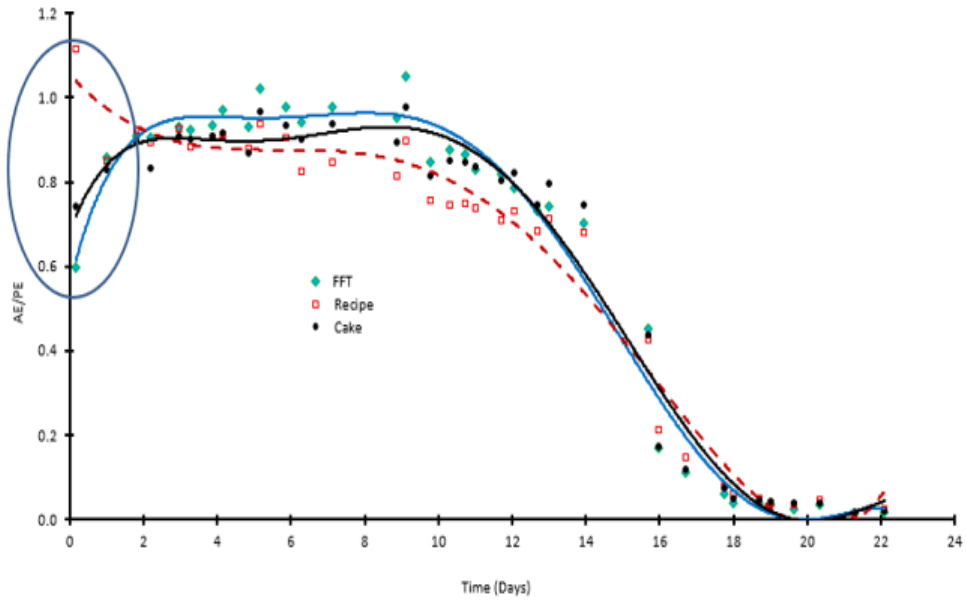

Figure 2 – AE/PE ratios as a function of time for FFT, recipe and cake.

2.4 *Undrained shear strength behaviour*

Under a loading condition, such as stacking 2 layers of geobags (commercial sizes), undrained shear strength and pore water pressures were monitored to evaluate one completed seasonal cycle. Results of the one year completed cycle (Tables 1 and 2) show that the treated FFT still remains contractive inside the geobags, generating and dissipating excess pore water pressure.

Table 1 – Excess pore pressure dissipation

Parameter	Bag filled (initial)	After 1 year	Seasonal cycle completed
Static pore water pressure U_0 (kPa)	19.62	10.79	
Excess pore water pressure Δu (kPa)	9.86	2.35	
Bbar (kPa)	*0.50*	*0.24*	*Excess pore pressure dissipation*

Table 2 shows that the undrained shear strength of the treated FFT increases with time, responding quite well to the relative rapidly loading of 2 layers of geobags. The second layer was stacked immediately following the completion of the first layer (still at 2 kPa undrained shear strength).

Table 2 – Average undrained shear strength (Su) of the stacked geobags.

Parameter	Bag filling completion	After 1 year	Comments
Peak	2.0 kPa	15.0 kPa	Field and lab testing
Peak remolded	0.3 kPa	2.8 kPa	

2.5 *Geobag tensile strength*

Table 3 shows the geobag (commercial size) properties referred to in this paper. The recommended stacked geobags tensile strength is 220 kN/m (Fig.3). This parameter is based on lab analysis cross machine direction (CMD) provided by the manufacturer. The ultimate strength of the geobag is represented by T (ult.) = T (work) x (FS id x FS ss x FS cd x FS bd x FS creep) where: T (work) = 220 kN; FS id (installation damage) = 1.3; FS ss (seam strength) = 2; FS cd (chemical degradation) = 1.0; FS bd (biological degradation) = 1.0; and FS creep = 1.0.

In the context of geobags, the maximum tensile force in the geofabric will be mobilized during pumping. After pumping, as the slurry solidifies, this force relaxes. Therefore, small FS creep can be assigned for geobags such as FS = 1.06. A verification of the FS for circumferential direction can be expressed by: FS = T (work tensile strength) ÷ (T ult.) and therefore, FS = 220 ÷ [24.93 (1.3 x 2.0 x 1.0 x 1.0 x 1.06)] = 3.2.

Table 3 – Geobag properties referred to in this paper.

Input		Output
Geobag height	2.90 m	Max. circumferential tensile force = 24.93 (kN/m)
Geobag circumference	44 m	Max. average axial tensile force = 23.00 (kN/m)
Density of the fill material	1.2 t/m^3	Geobag base contact width = 20.66 m
Seam type	Circumferential	Cross section area = 55.21 m^2
Fill port type	Rigid mech.	Volume/length = 55.21 m^3/m
Fabric type	GT 500	(%) max. fill capacity = 36%
		Pressure at the base = 34.256 kPa
		Circumferential direction FS = 3.2
		Axial direction FS = 3.0
		Fill port rupture FS = 3.2

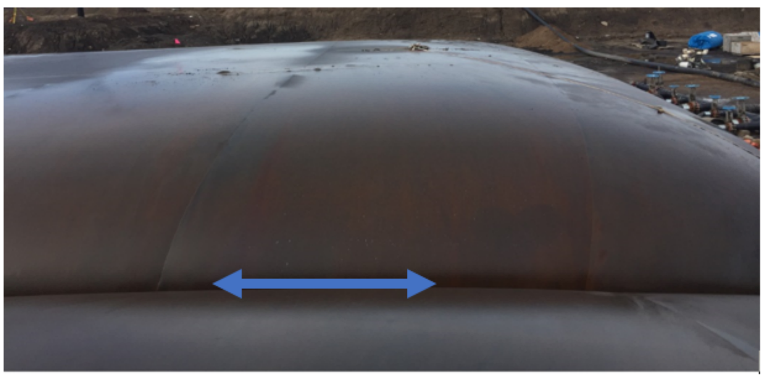

Figure 3 – Stacked geobags tensile strength 220 kN/m.

3 CONCLUSIONS

The primary conclusions for the study presented here are summarized in the points as follows.

(1) Geobags are soil-filled high-strength, high-modulus, woven geotextile made from synthetic fibers with distinct pore sizes, used as dewatering and desludging containment. They are resistant to ultraviolet deterioration and biological degradation, and are inert to most naturally encountered chemicals, alkalis and acids.
(2) Inherent properties of the oil sands constituents and the oil sands extraction process, including water chemistry and pH, collectively dictate the mechanical and physical properties of FFT.
(3) Quartz and kaolinites particles at pH >2, present negative surface charge. The negative surface charge of quartz and kaolinite particles increases as the pH increases.
(4) Increased calcium cations and pH cause adverse effects on the adsorption of anionic PAM polymer on quartz and kaolinite particles.
(5) Efficient fines agglomeration and dewatering of quartz and kaolinite particles are achieved with coagulation of the particles by aluminum ions prior to anionic PAM polymer addition.
(6) FFT solids/water separation is achieved by inline coagulation/flocculation (recipe) addition prior to the discharge in the geobags. Key factors for an efficient inline solids/water

separation are the residence time of the mixing process and minimization of shearing (no static or dynamic mixing are required).

(7) The geobags deposit with treated FFT seems to act more as a filter pressure system, with most of the water recovery happening while the bags are being filled. Fines capture ranges between 97 and 99% (51% silts and 47% clays). The material inside the geobags shows a considerable gain in strength over 10 days period, reaching over 5 kPa at the bottom of the deposit.

(8) Once the treated FFT is discharged in the geobags the filtration properties of the geofabric and the short drainage path of the containment are the key contributors for the enhanced dewatering and accelerated consolidation. Evaporation and freeze-thaw are also identified as contributors for dewatering with time.

(9) Evaporation tests confirmed that FFT treated with the recipe (coagulation + flocculation) loses water faster and reaches the boundary between the saturated and unsaturated state (i.e., AE/PE = 0.8) early than FFT and other recipes with flocculation only.

(10) Filling of the geobags is controlled by the specific strength and hydraulic parameters of the geofabric (seams and intake ports) that limit the intake pressure and the filling height of the geobags.

(11) Field data indicated that during filling the dewatering is due to internal pressure and gravity head, initially, and self-weight consolidation and stacking (loading), subsequently.

(12) Tensile strength with low elongation provided by the geofabric is a key reinforcing parameter of the geobags deposit, allowing stacking at low undrained shear strength (2 kPa), usually achieved when the geobag is completed at the recommended height by the manufacturer.

In order to assess the chemical stability of the stacked geobags, it will be necessary to determine the acid producing minerals (primary and secondary) and acid neutralizing minerals that maybe present along with the metal leaching potential in order to predict future geochemical behaviour. The primary mineralogical composition has a strong influence on the oxidation processes and therefore, the mineralogical and geochemical interactions are essential aspects to understand the parameters controlling acid mine drainage formation and to develop effective prevention methods.

4 ACKNOWLEDGEMENTS

This work is part of the doctoral research program of Mr. Da Silva, supervised by Dr. G. Ward Wilson Professor (Geotechnical & Geoenvironmental) who holds the NSERC/COSIA Industrial Research Chair in Oil Sands Tailings Geotechnique at the University of Alberta. The author also would like to thank members (co-authors) of the Tencate Geosynthetics Americas for the geobags manufacturing data, stability analysis and photos.

5 REFERENCES

Atesok, G., Somasundaran, P., Morgan, L. 1988. Adsorption Properties of Ca2+ on Na-Kaolinite and its Effect on Flocculation Using Polyacrylamides. Colloids and Surfaces, 32: 127-138.

Bernhard Dold. 2010. Basic Concepts in Environmental Geochemistry of Sulfidic Mine-Waste Management, Waste Management, Er Sunil Kumar (Ed.), ISBN: 978-953-7619-84-8, InTech.

Blowes, D.W., Ptacek, C.J. 1994. Acid-neutralization mechanisms in inactive mine-tailings. In: J.L. Jambor and D.W. Blowes (Editors), Short course handbook on environmental geochemistry of sulfide mine-waste. Mineralogical Association of Canada, Nepean, pp.271-291.

Blowes, D.W. et al. 1994. Acid-neutralization Reactions in inactive mine-tailings Impoundments and their Effect on the Transport of dissolved Metals., International Land Reclamation and Mine Drainage Conference and the Third International Conference on the Abatement of Acid Drainage Conference, Pittsburgh, pp. 429-438.

Da Silva, F. 2011. Reducing Risks to Tailings Storage Facilities Through In-Line Flocculant Addition. Geo-Frontiers 2011, Dallas, Texas - Advances in Geotechnical Engineering: pp. 2937-2946.

Da Silva, F. et al. 2014. Evaluation of a New Treatment Technology for Improving Oil Sands Tailings Management. GeoRegina 2014; Proc. Canadian Geotechnical Society, Regina, Saskatchewan, 10/2014.
Da Silva, F. et al. 2014. Geotextile bags for enhanced dewatering and accelerated consolidation of oil sands fluid fine tailings (FFT) Part 1. Tailings & Mine Waste 2014 – Keystone, Colorado, USA.
Gan, W., Liu, Q. 2008. Coagulation of Bitumen with kaolinite in Aqueous Solutions containing Ca, Mg and Fe: Effect of Citric Acid. Journal of Colloid and Interface Science, 324, 85-91.
Goldberg, S., Foster, S., Heick, L. 1991. Flocculation of illite and Kaolinite and illite and Montmorillonite Mixtures as Affected by Sodium Adsorption Ratio and pH. Clays and Clay Minerals, 39(4): 375-380.
Haley L. Schafer, Neeltje Slingerland, Renato Macciotta and Nicholas A. Beier. 2018. IOSTC, Edmonton, AB: pp. 9-12.
Healy. W., La Mer, K. 1964. Flocculation of Mineral Dispersions by Polymers. Int. Miner. Process. Congr. 7th, New York, 1: 359-365.
Hunter, J. 1981. Zeta Potential in Colloid Science: Principles and Applications, Academic Press, London.
Hussain, A., Demirci, S., Ozbayoglu, G. 1996. Zeta Potential Measurements of Three Clays from Turkey and Effects of Clay on Coal Flotation. Journal of Colloid and Interface Science, 184, 535-541.
Jiang, T., Hirasaki, G., Miler, C. 2009. Characterization of Kaolinite Zeta Potential for Interpretation of Wetability Alteration in Diluted Bitumen Emulsion Separation. Rice University, Houston Texas.
Krystian, W. P. 2007. Geosynthetics and geosystems in hydraulic and coastal engineering. New York: Taylor & Francis.
Kuzkin, F., Nebera, P., Zolin, N. 1964. Aspects of the Theory of Suspensions Flocculation by Polyacrylamides. Int. Miner. Process. Congr., 7th New York, 1: 347-357.
Lebedeva, E., Fogden, A., Senden, T., Kanackstedt, M. 2010. Kaolinite Wettability – The effect of Salinity, pH and Calcium. Int. Symp. Society Core Analysis. Halifax, Nova Scotia, Canada.
Zhang, LL., Fredlund, D. G., Fredlund, M. D., Wilson, G. W. 2014. Modeling the unsaturated soil zone in slope stability analysis. Canadian Geotechnical Journal 51 (12), 1384-1398,
Masliyah, J., Czarnecki, J., Xu, Z. 2011. Handbook on Theory and Practice of Bitumen Recovery from Athabasca Oil Sands. Kingsley Knowledge Publishing.
Matijevic, E., Stryker, J., Janauer, E. 1966. Colloid Interface Science. Michalowski, L., Cermak, J. 2003. Triaxial Compression of Sand Reinforced with Fibers. J. Geotechnical and Geo-environmental Eng., 129(2): 125–136.
Mitchell, J.K., Soga, K. 2005. Fundamentals of Soil Behavior, 3rd ed., New York: Wiley.
Pefferkorn, E., Nabzar, L., Varoqui, R. 1987. Colloid Polym. Sci. 265, 889.
Peng, F., Di, P. 1994. Effect of Multivalent Salts – Calcium and Aluminum on the Flocculation of Kaolin Suspension with Anionic Polyacrylamide. Journal of Colloid and Interface Science: 164, 229–237.
Slater, W., Clark, P., Kitchener, A. 1968. Chemical Factors in the Flocculation of Mineral Slurries with Polymeric Flocculants. Int. Miner. Process. Congr., 8th, Leningrad, 1: 316-324.
Scott, J. D., Jeeravipoolvarn, S., Chalaturnyk, R.J., 2008. Tests for Wide Range of Compressibility and Hydraulic Conductivity of Flocculated Tailings, Proceedings of the 61st Canadian Geotechnical Conference, September 22-24, Edmonton, AB, pp. 738-745.
Van, L. A. 1980. Behaviour of Quartz Suspensions in the Presence of Calcium Ions and Acrylate Polymers. Amsterdam: Elsevier Scientific Publishing Company.
Van, O. H. 1977. An Introduction to Clay Colloid Chemistry: 2nd ed., Willey, New York, 318 pp.
Verwey, E., Overbeek, J. 1948. Theory of the Stability of Lyophobics Colloids. Amsterdam: Elsevier.
Wilson, G. W., Robertson, A. M. 2015. The Value of Failure, Invited Plenary Paper for the Mt. Polley Failure presented at Tailings and Mine Waste 2015, Vancouver, Canada, 26-28 October.

Hyperspectral imaging technology for oil sands tailings characterization: An update

Iman Entezari, Dallas McGowan, Joseph Glavina, and David Parkinson
ConeTec Investigations Ltd., Burnaby, British Columbia, Canada

ABSTRACT: This paper presents an update on the use of hyperspectral imaging (HSI) technology for the estimation of oil sands tailings properties. A dataset of paired HSI and laboratory results was compiled and neural networks were employed to develop empirical relationships to estimate tailings properties including the contents of bitumen, solids, water, total fines, FFW (i.e. fines / (fines + water)) as well as methylene blue index (MBI) from HSI data. The development dataset is comprised of paired HSI-laboratory results collected from 2017 to 2020 from multiple tailings storage facilities operated by different mine operators. Results show that using HSI technology, the contents of bitumen, solids, water, total fines, FFW and MBI can be estimated with 0.68, 3, 2.7, 3.1, 2.7 wt%, and 0.93 meq/100g errors, respectively. Mine operators can significantly reduce the cost and turn-around time associated with laboratory analysis by implementing on-site HSI testing of tailings samples.

1 INTRODUCTION

The surface-mining operation to extract bitumen from oil sands produces large volumes of oil sands tailings. Characterization of oil sands tailings is of importance to assess the tailings dewatering and consolidation performance, to monitor their state for reclamation, to control tailings treatment processes, and to meet regulatory reporting requirements. Several in-situ, on-site, and off-site testing methods are employed to characterize oil sands tailings. Laboratory analysis of the tailings samples is widely used for accurate measurement of tailings constituents. This procedure is not only costly and time consuming, but the laboratory results can be variable, a function of the methods used, and subject to human error. In particular, the repeatability and accuracy of some of the laboratory methods depends on how the samples are prepared and how well the agglomerated clays are dispersed.

The preliminary results of our research on the potential of hyperspectral imaging (HSI) technology for tailings characterization were presented in Entezari et al. (2018). Partial least square (PLS) analysis and a dataset of 290 paired HSI-laboratory results from a single oil sands tailings operator were used to develop the HSI models to estimate methylene blue index (MBI), bitumen content, and water content of oil sands tailings samples. Entezari et al. (2019) presented an update on this research as the dataset was expanded to include 790 paired HSI-laboratory results. HSI models were developed to estimate the contents of bitumen, solids, water, total fines as well as MBI and clay to water ratio (CWR). Machine learning modelling, namely neural networks, was used to calibrate the HSI data to the laboratory results and develop the HSI models. All the samples were still from a single mine operator and were mostly fluid and transition tailings samples.

By the end of 2020, our development dataset was expanded to include more than 3000 paired HSI-laboratory results from multiple tailings storage facilities operated by different mine operators. The development dataset includes fluid, transitional and high solids sandy samples. HSI models are re-calibrated using neural networks so that they are applicable on a wider range of tailings materials from various tailings operators, as is the case for the 2020 dataset and model updates presented in this paper. The characteristics of our updated development dataset and the accuracy assessment of the HSI testing to estimate various tailings properties are presented. In addition, the performance of HSI testing on tailings from different tailings operators are analyzed and discussed. The repeatability and reproducibility of HSI testing is also presented.

2 BACKGROUND

2.1 *Hyperspectral imaging (HSI)*

Hyperspectral imaging is a technology based on measuring the reflected light from a target material as a function of wavelength. The spectral response from each target is largely controlled by the chemical composition and crystal structure of the materials within. In this study, the spectra of the samples are measured using two spectrometers with identical resolutions covering visible near-infrared (VNIR), and shortwave infrared (SWIR) portion of the electromagnetic spectrum (350-2500 nm). The instrument is equipped with a contact probe containing an internal light source. Prior to acquiring spectral measurements, samples are homogenized. The contact probe of the spectrometer is pushed into the material so that the window of the probe is in full contact with the sample and the spectrum is acquired. Employing different spectrometers and contact probes result in models robust against variation in instrumentation.

2.2 *Sampling and laboratory analysis*

Tailings samples are collected throughout the oil sands mining region to support tailings planning, research, closure, and regulatory reporting. Samples from fluid, fixed interval, and sonic samplers were studied. The samples are from four mines anonymized as Operators A, B, C, and D in this paper. Typically, a laboratory program is carried out to measure tailings characteristics including the contents of bitumen, solids, water, fines, and clays through MBI testing. Methods such as Dean-Stark analysis are used to measure the bitumen, solids, and water content of tailings, while the fines content is normally measured through a sieve analysis or laser diffraction. Measurements from multiple commercial laboratories, using industry standard practices, were used in this study. For samples from Operators, A, B, and C, Dean Stark analysis is performed to measure the percent of bitumen, solids, and water. The wet sieve method is used to measure percent of fines and MBI is measured through methylene blue titration of samples. Samples from Operator D are solvent washed and oven dried to measure the solids content and laser diffraction is used to measure the particle size distribution. MBI testing is not performed on samples from Operator D and contents of bitumen and water were not reported by the laboratory. Subsampling methods, sample transport and handling, as well as the repeatability of laboratory testing may all impact the consistency, repeatability, and accuracy of the results.

3 DEVELOPMENT DATASET

The development dataset contains paired HSI-laboratory results acquired from 3053 tailings samples from multiple tailings storage facilities and operators collected between 2017 and 2020. The development dataset includes a variety of tailings samples such as fluid tailings, treated tailings, froth treatment tailings, and sandy tailings. Samples with high bitumen concentration (more than 10 wt% bitumen) are also included. From the total of 3053 paired HSI-laboratory results in the development dataset, 2199 are from Operator A, 433 from Operator B, 141 from Operator C, and 280 from Operator D. The data pairs from Operator D are excluded from the development dataset because the laboratory practice used for this operator is different from the other three operators. Figure 1 shows a ternary diagram of the development dataset after excluding data pairs from Operator D. The dataset shows the crescent-shaped property distribution common in oil sands tailings. This figure shows that the tailings range from fluid tailings with high water and high fines along the top-right edge to sandy tailings with high solids, low fines, and low water content in the lower left corner. Table 1 summarizes the range of variation in tailings characteristics for the development dataset.

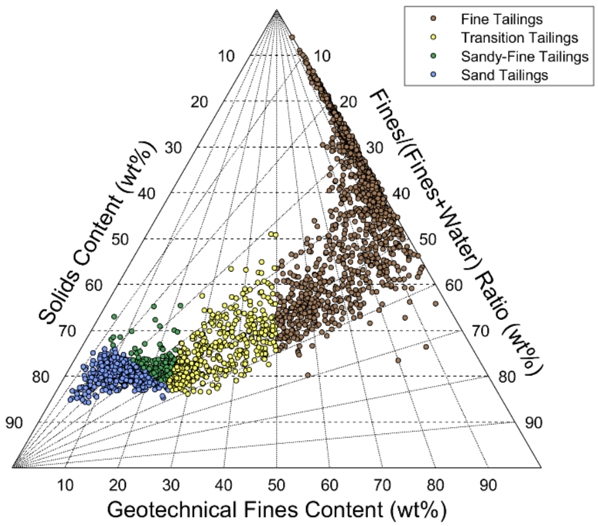

Figure 1. Ternary diagram of the development dataset according to the COSIA's Unified Oil Sands Tailings Classification System.

Table 1. Characteristics of the development Dataset.

Tailings Characteristics	Range	Median
Bitumen (wt%)	0.00 - 16.93	1.53
Solids (wt%)	4.27 – 85.67	57.35
Water (wt%)	13.78 - 95.75	38.17
Total 44 µm fines (wt%)	2.42 - 65.02	28.65
FFW (wt%)	8.77 - 73.48	40.96
Geotech. 44 µm fines (wt%)	3.11 - 101.65	73.60
MBI (meq/100g)	0.12 - 21.48	5.49

4 MODELLING AND ACCURACY ASSESSMENT

4.1 *Neural networks*

Machine learning modelling is used to develop the empirical models and calibrating HSI data to laboratory results. Neural networks and the bootstrap aggregation (Bagging) are used to generate an ensemble-based neural networks model to empirically relate HSI and laboratory results (Entezari et al. 2019).

The development dataset is split into training and test datasets so the performance of the final models could be examined on the test set. Approximately 13% of the development dataset (351 samples) is randomly selected as the test set and is not seen by the neural networks during the training phase. The remaining 87% of the development dataset (2422 samples) is used as the training set. Table 2 lists the number of HSI-laboratory data pairs from different operators used in the training and test sets.

Table 2. Number of HSI-laboratory data pairs used in the training and test sets.

Operator	Training set	Test set
Operator A	1959	240
Operator B	349	84
Operator C	114	27
Total	2422	351

4.2 *Performance assessment*

The performance of the HSI models is evaluated by quantifying properties of the error distribution on the test dataset. The error is defined as: Error = Lab result - HSI estimate. The error for each data point in the test dataset is calculated and the resulting errors are plotted as a cumulative distribution function (CDF). The 50th percentile in the CDF is taken as the bias of the HSI prediction. Positive and negative biases correspond to underestimated and overestimated HSI result, respectively. Assuming the model errors follow a normal distribution, the CDF values at 15.9% and 84.1% correspond to ±1 standard deviation. The model error is the dispersion around the median to the 15.9 and 84.1 percentiles.

Since the development dataset and training set are weighted to Operator A, the performance of the models is also assessed on samples from each operator. In addition, although data pairs from Operator D are excluded from the training and test sets, error assessment is performed on Operator D samples to examine how the HSI models perform on samples tested through a different laboratory procedure.

It is noted that any errors in the laboratory data inherently introduce errors in the models. The performance of the models can only be as good as the laboratory measurements. In other words, the laboratory data is incorrectly assumed to be perfect to determine model errors. Also, any discrepancy between the procedures employed by the commercial laboratories could be a source of error when assessing the performance of the HSI models for any individual operator.

4.3 *Repeatability and reproducibility assessment*

Repeatability and reproducibility statistics for HSI testing are derived using 60 measurements collected of a single fluid fine tailings sample with ~ 70 wt% water content using two HSI systems (30 measurements with each system). The repeatability standard deviation (S_r) and reproducibility standard deviation (S_R) for a given HSI model are calculated using the equations below (ASTM E691 1999):

$$S_r = \sqrt{\textstyle\sum_1^p s^2/p} \tag{1}$$

$$S_R = larger\ of\ S_r\ and \sqrt{S_{\bar{X}}{}^2 + S_r{}^2(n-1)/n} \tag{2}$$

where S is standard deviation of the estimated results from each instrument, $S_{\bar{X}}$ is standard deviation of the averages of the results, p is number of instruments, and n is number of measurements taken by each instrument.

5 RESULTS

5.1 *Overall performance of HSI models*

The relationships between the laboratory measured and HSI predicted tailings properties for the test set are shown in Figure 2. The training set has also been overplotted so that the two datasets can be compared. The CDF of errors on the test set is also shown for each model output. Table 2 summarizes the error values of the model outputs on the test set. There is a strong correlation between the HSI predicted and laboratory results for all tailings characterizations. The bias of the estimated results is also very low and close to zero. It is noted that the FFW model is a model directly calibrated to FFW and is not an indirect estimation of FFW from estimated total fines and water. The geotechnical 44 µm fines can be estimated indirectly using the HSI estimated total 44 µm fines and solids content. The error for estimated geotechnical 44 µm fines is -0.24 ± 5.2 wt% on the test set.

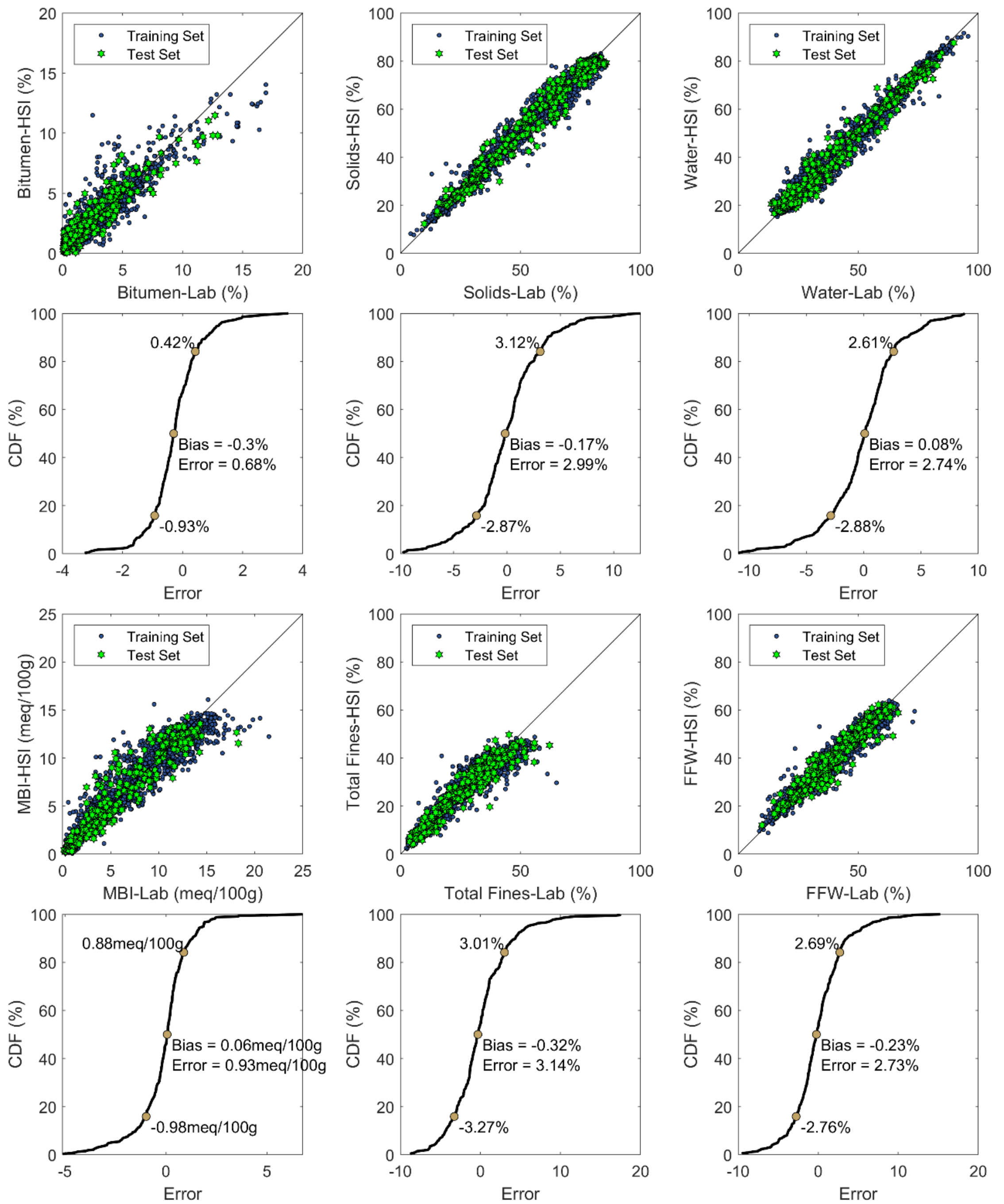

Figure 2. Relationship between HSI estimated vs laboratory measured tailings properties along with CDF of errors.

Table 2. Bias and error of HSI models.

Model	Bias ± Error
Bitumen (wt%)	-0.30 ± 0.68
Solids (wt%)	-0.17 ± 2.99
Water (wt%)	0.08 ± 2.74
MBI (meq/100g)	0.06 ± 0.93
Total 44 µm fines (wt%)	-0.32 ± 3.14
FFW (wt%)	-0.23 ± 2.73

5.2 *Performance on Operator A*

Figure 3 shows the relationships between the laboratory measured and HSI predicted tailings properties for the portion of the test set from Operator A. The error and bias of the models on samples from this operator are listed in Table 3. The performance of the models on the test set from Operator A is similar to the performance observed for the entire test set. This is expected given that much of the training and test sets are from Operator A.

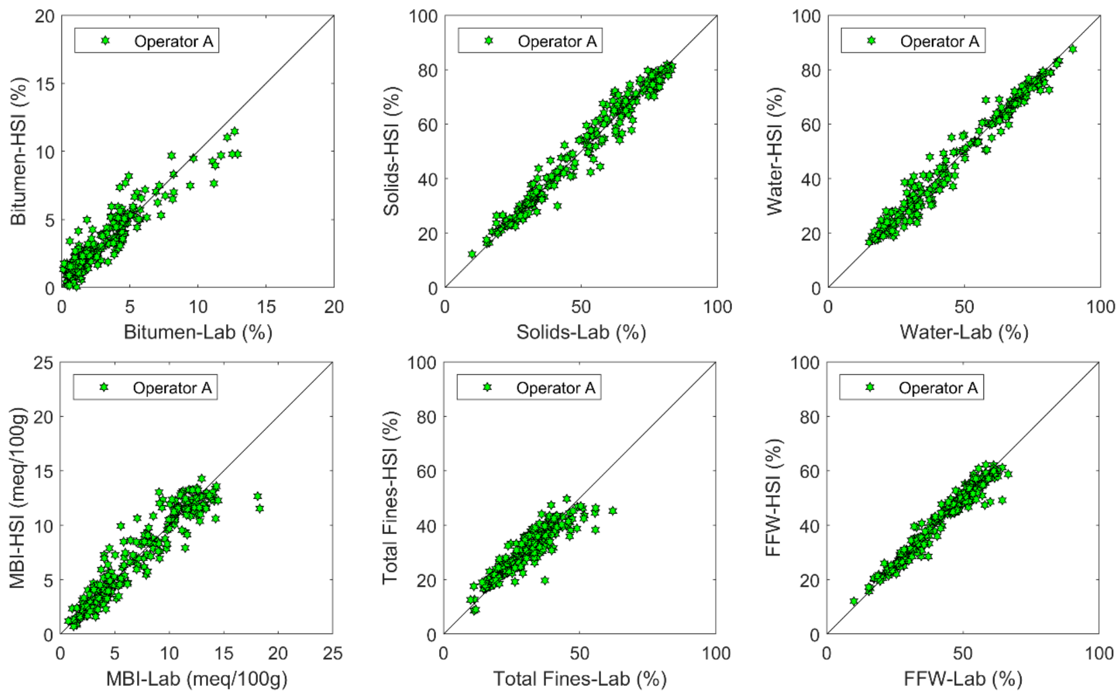

Figure 3. Relationship between HSI estimated vs laboratory measured tailings properties for test samples from Operator A.

5.3 *Performance on Operator B*

The laboratory versus HSI predicted tailings properties for the portion of the test set from Operator B is shown in Figure 4. The samples from this Operator are all high solids samples (median of 79 wt% solids and 11 wt% total fines). There is good agreement between the laboratory measured tailings properties and the HSI predicted results for all the tailings characterization (see Table 3). The error of the FFW model on the samples from Operator B appears to be slightly higher than the overall model performance.

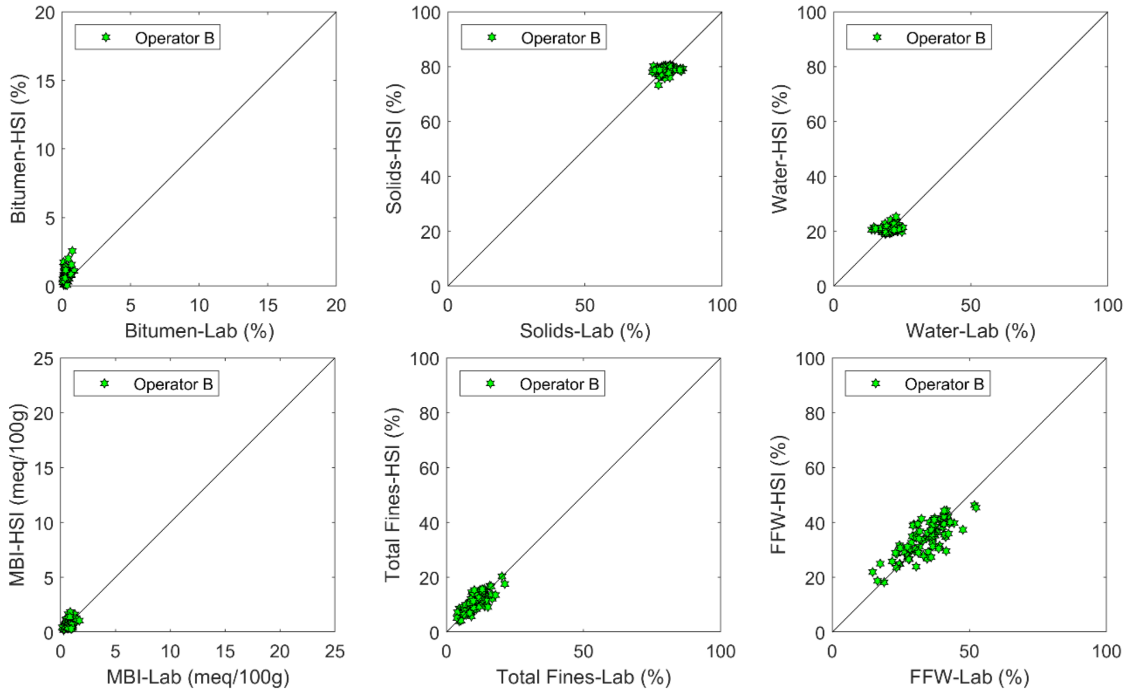

Figure 4. Relationship between HSI estimated vs laboratory measured tailings properties for test samples from Operator B.

5.4 *Performance on Operator C*

The comparison between the laboratory measured and HSI predicted tailings properties for the portion of the test set from Operator C is shown in Figure 5. The number of test samples for this operator is limited to only 27 samples from which only 9 are tested for MBI. The correlation between the laboratory and HSI results is strong for all the tailings properties except for MBI. The estimated bias for HSI estimated MBI is -3.71 meq/100g (Table 3), which means that the model

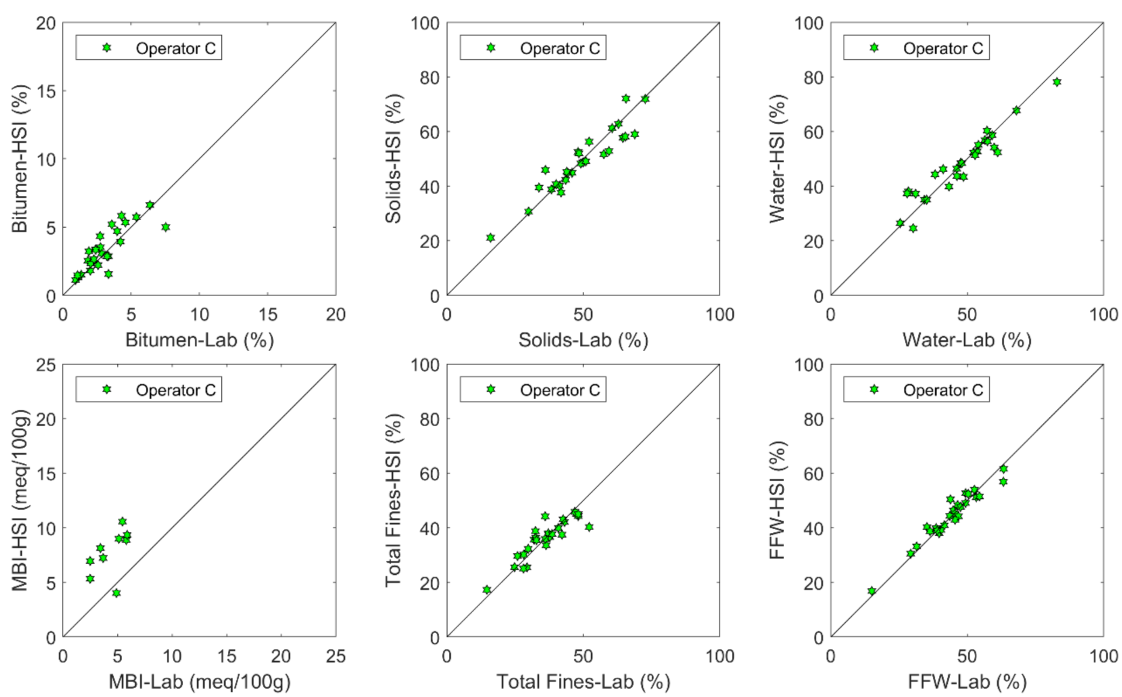

Figure 5. Relationship between HSI estimated vs laboratory measured tailings properties for test samples from Operator C. Note that not all the samples were tested for MBI.

significantly overestimates the MBI relative to the laboratory measurements provided by Operator C. The significant bias could be attributed to procedural differences between the laboratories in the development dataset, laboratory error, or clay mineralogy and activity variation of the tailings from Operator C versus the samples in the training set. Since only 114 data pairs (from which 59 tested for MBI) from Operator C exist in the training set (less than 5% of the training set), the neural networks are generally uninfluenced by the characteristics of the tailings from Operator C. Further investigation is required to determine the source of this bias in MBI estimation. The accuracy and repeatability of the laboratory based MBI testing depends on the sample preparation and personnel expertise. Common sources of error in the MBI testing have been discussed in Kaminsky (2014). The potential errors in laboratory data as well as the procedural differences between the laboratories must be considered when assessing the HSI model error for MBI characterizations.

5.5 *Performance on Operator D*

The relationships between the laboratory measured and HSI predicted tailings properties for the samples from Operator D are shown in Figure 6. Bitumen content, water content, and MBI were not reported by the laboratory for these samples. As can be seen, the HSI models for the prediction of solids, total fines, and FFW does not perform well for the samples from this operator. However, model errors are low for samples with less than ~50 wt% solids. In general, the poor performance of the models on samples from Operator D compared to the other operators could be attributed to the difference between laboratory methods and tailings compositions. Tailings from Operator D are not well represented in the training set as no samples from Operator D exist in the training set. Also, the laboratory procedure for Operator D measures fines through laser diffraction analysis whereas wet sieve is used for fines measurement for the samples in the training set.

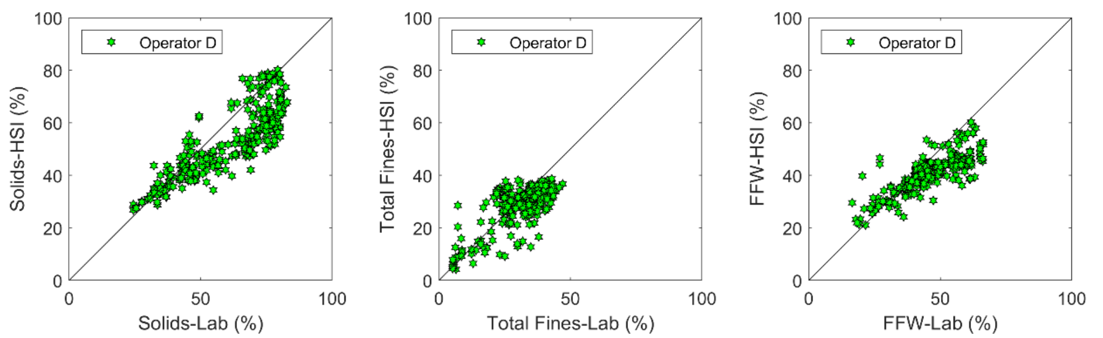

Figure 6. Relationship between HSI estimated vs laboratory measured tailings properties along with CDF of errors for test samples from Operator D. Bitumen content, water content, and MBI were not reported by the laboratory.

Table 3. Bias and error of HSI models on tailings from different operators.

Model	Bias ± Error			
	Operator A	Operator B	Operator C	Operator D
Bitumen (wt%)	-0.31 ± 0.81	-0.24 ± 0.51	-0.33 ± 0.79	NA
Solids (wt%)	-0.26 ± 3.12	0.30 ± 2.00	-0.17 ± 5.12	7.31 ± 9.23
Water (wt%)	0.17 ± 2.84	-0.11 ± 1.99	-0.11 ± 5.11	NA
MBI (meq/100g)	0.03 ± 1.15	0.11 ± 0.31	-3.71 ± 1.00	NA
Total 44 µm fines (wt%)	-0.36 ± 3.52	-0.39 ± 2.26	-0.07 ± 3.43	2.85 ± 5.07
FFW (wt%)	-0.26 ± 2.43	-0.12 ± 5.05	-0.86 ± 2.16	4.4 ± 6.78

5.6 *HSI profile*

Figure 7 illustrates an example profile showing the undrained shear strength (S_u) and gamma measurements from ball gamma cone penetration test (BGCPT) (DeJong et al. 2010, Styler et al. 2018) along with HSI results from samples collected from a paired sample hole. The laboratory results are also overplotted to visually compare the HSI and laboratory results.

The use of HSI for tailings characterization allows tailings samples to be quickly analyzed in a mobile laboratory on site, on a sampling rig, or transported to an offsite facility when turnaround time is not paramount. It is possible to report an HSI profile for a given sample location within minutes of sampling. HSI tailings characterization can provide operators with nearly immediate access to data for modeling, reporting, and process optimization. Relying on HSI technology can reduce costs, logistics, and emissions associated with sample handling, shipping, laboratory testing, and offsite disposal.

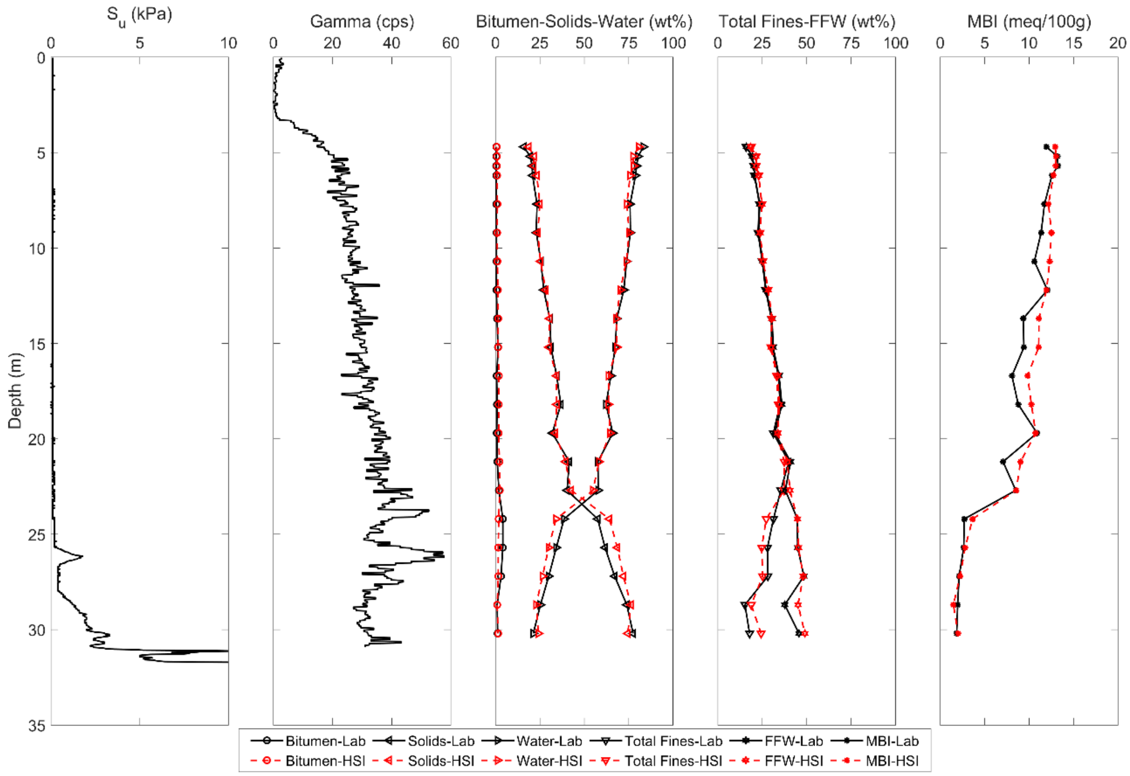

Figure 7. Example profile showing the BGCPT, HSI, and laboratory test results.

5.7 *Repeatability and reproducibility assessment*

Table 4 lists the repeatability and reproducibility standard deviations of the HSI testing on fine tailings. It is evident that the repeatability and reproducibility standard deviations of HSI testing are less than the model's errors. For the HSI estimated geotechnical 44 µm fines (estimated from total 44 µm fines and solids content), the repeatability and reproducibility standard deviations are 2.4 and 5.6 wt%, respectively. The published study by COSIA and InnoTech Alberta (ITA) on the precision of fines measurement (Hiltz & McFarlane 2017) reports that the repeatability and reproducibility standard deviations for measuring the geotechnical 44 µm fines of fine tailings in laboratory are 1.45 and 3.23, respectively, in the interlaboratory study (ILS) Round 2.

The repeatability and reproducibility analysis here was only performed on a fine tailings sample. Further experiments are required to assess the repeatability and reproducibility of HSI testing on sandy tailings (high solids tailings).

Table 4. Repeatability and reproducibility standard deviations of HSI testing.

Model	Repeatability (S_r)	Reproducibility (S_R)
Bitumen (wt%)	0.06	0.12
Solids (wt%)	1.11	1.78
Water (wt%)	1.17	1.94
MBI (meq/100g)	0.29	0.63
Total 44 µm Fines (wt%)	0.71	0.72
FFW (wt%)	0.78	0.79

6 DISCUSSION AND FUTURE WORK

Impact of bitumen: To evaluate the impact of bitumen content of the samples on the prediction results from HSI models, the bitumen content of the samples measured in the laboratory was plotted against the prediction errors for each of the tailings characterizations (Figure 8). Results show that the variation in the bitumen content of the samples does not impact the HSI estimation results (and thus errors) for other tailings characteristics.

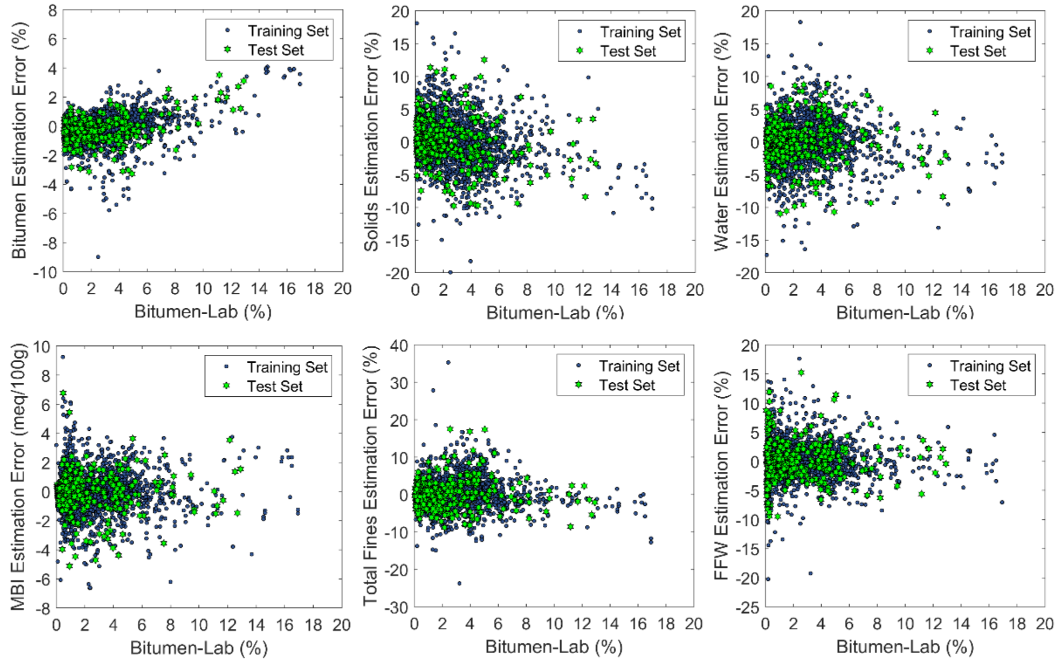

Figure 8. Relationship between bitumen content and estimated errors for various tailings properties.

Sandy segregated samples: There are currently challenges associated with collecting representative HSI data from segregated sandy samples. When collecting HSI data, the tailings that contact the window on the contact probe must be representative of the entire sample. When a sample segregates, the probe may only measure the fluid or solid phase of the sample and the HSI scan is not representative of the entire sample. Although we have been successful in developing a procedure to homogenize the segregated samples by adding a sand suspending polymer, further standardization and experiments are required to ensure this procedure yields consistent results.

Expand the development dataset: Although the development dataset includes samples from multiple oil sands operators, it does not include samples from all operators or tailings storage facilities. In collaboration with several operators, we intend to expand the development dataset. By the end of 2021, the development dataset will approximately include 7700 HSI-laboratory results. This would increase the number of samples for Operators A, B, C, and D to 2700, 500, 1200, 1800, respectively. Also, the development dataset will include approximately 1500 samples from Operator E. Given that mineralogy of tailings varies among sites, including samples from various operators and tailings facilities will allow us to capture the extent of spectral variation and improve the HSI models. When adding new operators and laboratory data to the dataset, the differences between laboratory procedures need to be taken into account and dealt with in modelling. A potential approach to deal with the differences between the laboratory procedures is to use operators name as an input parameter to the models.

7 CONCLUSIONS

This paper presented an update on the use of HSI technology in the estimation of various tailings characteristics. Ensemble-based neural networks were employed to calibrate the spectral features to tailings characteristics. Different HSI systems were used for spectral measurement of tailings samples. This was done to minimize the impact of differences between the instrumentation on the prediction results and develop models that are robust against the variation in the instrumentation.

HSI models were calibrated using the training dataset of paired HSI-laboratory data from 2422 tailings samples from multiple oil sands operators. The performance of the HSI models was evaluated by quantifying properties of the error distribution on a test dataset which was not seen by the neural networks during the training phase. This can be considered a class-A error assessment or a blind test to evaluate the generalization and robustness of the models when applied on data other than the data used for the calibration of the models.

Generally, HSI models were observed to be successful in the estimation of the contents of solids, water, bitumen, and total fines as well as MBI and FFW. Using HSI technology the contents of bitumen, solids, water, total fines, FFW and MBI can be estimated with 0.68, 3, 2.7, 3.1, 2.7 wt%, and 0.93 meq/100g errors, respectively. Overall, the stated errors are attributed to factors including instrument repeatability, laboratory repeatability, laboratory variance, and field sub-sampling to collect samples for HSI testing. The performance assessment on individual operators showed that the HSI models were generally successful in estimation of properties of tailings from Operators A, B, and C except for MBI of tailings from Operator C. They also did not perform well on tailings from Operator D. The variation in tailings composition and laboratory procedures are most likely the reason of this poor performance.

The use of hyperspectral technology for tailings characterization can enable the on-site analysis of the tailings and quick provision of the assessment of the tailings properties. A key advantage of HSI tailings characterizations is that they provide rapid and objective predictions that are less prone to human error, reducing cost, waste, and emissions.

8 REFERENCES

ASTM Standard E691. 1999. Standard practice for conducting an interlaboratory study to determine the precision of a test method. *ASTM International*, West Conshohocken, PA.

Breiman, L. 1996. Bagging predictors. *Machine Learning* 24 (2): 123-140.

DeJong, J., Yafrate, N., DeGroot, D., Low, H. and Randolph, M. 2010. Recommended practice for full-flow penetrometer testing and analysis. *Geotechnical Testing Journal 33(2):* 137-149.

Entezari, I., Rivard, B., Sharp, J., Wells, P.S., Styler, M.A., & McGowan, D. 2018. Real-time prediction of oil sands tailings properties using hyperspectral observations. *Proceedings of 6th International Oil Sands Tailings Conference*, Edmonton, Alberta: 102-106.

Entezari, I., Sharp, J., and McGowan, D., 2019, Characterization of oil sands tailings using hyperspectral technology. *Proceedings of Tailings and Mine Waste 2019*, Vancouver, British Columbia: 519-528.

Hiltz, M. and McFarlane, R. 2017. Precision of particle size measurements for minus 44 micron solids from oil sands; an interlaboratory study. *Prepared by InnoTech Alberta on behalf of COSIA.*

Kaminsky, H. 2014. Demystifying the methylene blue index. *Proceedings of 4th International Oil Sands Tailings Conference,* Banff, Alberta: 221-229.

Styler, M.A., McGowan, D., & Sharp J. 2018. Characterizing soft oil sand tailings by gamma cone penetration testing. *Proceedings of the 6th International Oil Sands Tailings Conference*, Edmonton, Alberta: 112-120.

Automated clay analyzers to measure methylene blue index for oil sands and mining slurries

Jason Ng, Andrea Sedgwick, Heather Kaminsky, Taimur Qureshi, Jewell Gapasin, Laura Ortiz & Bob Battle
Northern Alberta Institute of Technology, Edmonton, Alberta, Canada

Ruijun Sun & Lesley McGilp
Saskatchewan Research Council, Saskatoon, Saskatchewan, Canada

Syed Rizvi
Suncor Energy, Calgary, Alberta, Canada

ABSTRACT: Instrumentation and automation play a critical role in the mining industry to improve process efficiency, reduce costs and to meet stringent environmental commitments. The Northern Alberta Institute of Technology, Saskatchewan Research Council and Suncor Energy have developed two automated clay analyzer prototypes designed for active clay measurement of oil sands and mining tailings. The measurement is based on the modified ASTM methylene blue index (MBI) method, a titration test performed by a technician to measure the amount of methylene blue (MB) dye that can be adsorbed on the clay surfaces in a sample. Prototype A is an at-line instrument based on automation of the lab MBI method with integrated sample preparation, titration, and digital imaging endpoint detection systems. Prototype B is an online instrument which correlates the spectra absorbance of filtrate extracted from the clay samples treated by MB, determining the MB spectroscopic endpoint and MBI value from the correlation.

1 INTRODUCTION

The Athabasca oil sands are a mixture of bitumen, sand, minerals, clays, and water. For surface minable deposits, bitumen is separated from the oil sands using Clark's hot water extraction process, and the bitumen is then upgraded into synthetic crude oil and refined into various fuels and petroleum products. Oil sands tailings (mixture of mineral solids, clays, water, and residual bitumen) are waste by-products produced in surface mining operations, discharging about 3.3 m^3 of tailings into tailings ponds for every barrel of produced bitumen (Masliyah et al. 2011). Large volumes of fluid fine tailings (FFT), a layer of settling fines and clays in the tailings ponds, eventually consolidates to around 30 to 35 wt.% solids after a few years but remains fluid for decades due to slow consolidation rate. The Government of Alberta has issued Directive 085 to ensure timely reclamation of the areas occupied as tailings ponds, which states that all fluid tailings associated with a mining project must be ready to reclaim (RTR) ten years after end of mine life of a project. The clays present in FFT greatly affect consolidation from large volumes of water in which they are dispersed. The tailings problem is also not exclusive to oil sands, as other forms of mining (e.g., potash ores and diamond) also produce potash tailings and kimberlite tailings respectively.

Engineers and decision makers need to be able to monitor clay activity in tailings ponds to make critical decisions. Methylene blue index (MBI) method is an index test developed in oil sands mining, and it has been used extensively to determine clay activity in the oil sands industry (Kaminsky 2014). In MBI titration, a known concentration of cationic methylene blue (MB) dye is added to a dispersed sample. Because MB has a high affinity for clays, it exchanges the ions at the clay surfaces via cation exchange (Hang 1970). When the titration reaches the endpoint, the MB dye is completely saturated on the available surface area. The MBI can be used to understand various properties, such as the amount of water trapped as bound water, surface area available for chemical reactions, exchangeable cation sites available for chemical reactions, and clay activity of tailings. These fundamental properties can further be used to predict the behavior of processes in tailings management processes (Kaminsky 2014). For example, correlations between MBI and yield stress of flocculated slurry, tailings volume, and Atterberg limits have been established (Cerato 2001, Diep et. al. 2014, Omotoso et. al. 2014).

Currently, MBI tests are performed in the lab and require extensive technician involvement to obtain accurate results. There is an increasing need for the MBI test to be automated to improve practicability for in-field measurement. Furthermore, the current endpoint determination in the lab MBI test heavily relies on visual assessment of a light blue halo by a technician, which can vary between different technicians and labs. A more objective endpoint determination method is highly desirable. A digital imaging endpoint detection system with controlled lighting conditions can increase data consistency without any technician color perception bias. Visible spectroscopy has also been utilized to determine cation exchange capacities and surface areas of clay minerals treated by MB, where high speed centrifuges are used to separate the supernatant for spectroscopic analysis (Cenens et al. 1988, Currie et al. 2014). However, the spectroscopic method has not been as widely adopted as the visual halo method in the industry. In this study, two automated clay analyzer prototypes (Prototype A and B) were developed by the Northern Alberta Institute of Technology (NAIT), Saskatchewan Research Council (SRC), and Suncor Energy, where each prototype automates a different lab approach. The prototypes have the potential to collect MBI data in the field, enabling better process monitoring and control in key tailings processes such as sedimentation and flocculation. This can lead to significant savings in operating costs, reduction of the tailings deposit footprints and ultimately faster reclamation. This paper aims to share learnings on the prototype developments and the validation results.

2 MATERIALS AND METHODS

2.1 *Materials*

In this study, 5 well-characterized oil sands FFT (FFT-A to FFT-E) were used during the Prototype A development and validation. Table 1 shows the composition for each FFT from Dean & Stark extraction. In addition, 30 different FFT samples were used in the Prototype A validation.

Table 1. Characterization data of FFT samples.

Sample ID	Bitumen (wt.%)	Water (wt.%)	Solids (wt.%)
FFT-A*	2%	64%	32%
FFT-B	0%	45%	55%
FFT-C	2%	65%	33%
FFT-D	3%	66%	31%
FFT-E	1%	74%	25%

*mass balance is less than 100%.

During Prototype B development, pure kaolinite (Kaolin CAS #1332-58-7, by Kentucky-Tennessee Clay Company), sodium bentonite (CAS #1302-78-9 by Fisher Scientific), silica flour (Sil 325 by Sil Industrial Minerals Inc.) and their mixtures were used to develop and validate the spectroscopic method. Kaolinite and bentonite are known non-active and active clays respectively, and silica flour is a non-clay material finer than 45 µm. Single clay component as well as three-components mixture at controlled active clay fractions were tested. Oil sands FFT, kimberlite, and potash slimes were also used to validate Prototype B.

The MB solution (0.006N) was prepared by dissolving a known amount of MB trihydrate powder (CAS #7220-79-3, by Fisher Scientific) in ultrapure deionized water (18.2 MΩ-cm). As the stability of the MB solution can be negatively impacted by the storage time, lighting conditions and temperature, the MB solution was used up to 5 days before disposal. Each batch of MB solution was tested using a kaolinite standard to ensure representative results. The sodium hydroxide and sulfuric acid solutions were prepared using ultrapure deionized water to a concentration of 10 wt.% w/w and 10 vol.% respectively. Sodium bicarbonate buffer was prepared to a concentration of 0.015M.

2.2 *Methods*

2.2.1 *MBI Determination*

The standard MBI method involves the dispersion of sample, titration of sample and visual halo endpoint determination, which is based on the ASTM C837-09 method (ASTM International 2014). Details of the MBI procedure are described elsewhere (Kaminsky 2014, Omotoso & Morin 2004). The CANMET method is a modified ASTM C837-09 version for oil sands samples (ASTM International 2014, Kaminsky 2014). Sample dispersion is one of the most important steps in the MBI procedure, as titration result becomes incorrect if the sample is not fully dispersed. Full sample dispersion can often be achieved using combinations of sodium hydroxide addition, buffer addition, mixing, heating, and sonication. For samples with significant amount of bitumen (e.g., oil sands ores, froth), an additional cleaning step (e.g., Dean & Stark, solvent wash) may also be required as the organics can impede the interaction of MB dye with the clay surfaces. Prior to titration, the sample must be cooled to between room temperature and 35°C, and the pH must be adjusted to between 2.5 to 3.8 (Currie et. al. 2014, Omotoso & Morin 2004). MB is then added to the sample until the endpoint is visually determined by an experienced technician.

Figure 1 shows the variations of the MB dot and the light blue halo that are commonly seen during MBI titration. The endpoint can be defined as a homogenous halo around the dot before the halo starts to grow much bigger. The buffering capacity (e.g., the difference between the first appearance of the homogenous halo and the fully saturated halo) can be sample dependent, where non-active clay samples typically exhibit minimal buffering capacity and more active clay samples (e.g., bentonitic samples) show a larger buffering capacity. This behavior may be due to longer time required for the MB to completely saturate the interlayers of active clays like bentonite.

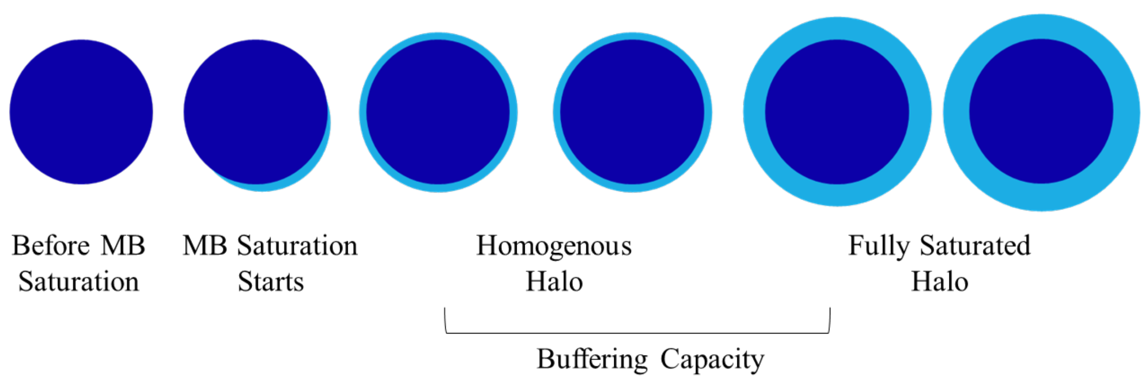

Figure 1. Schematic of methylene blue dot and halo at different stages of titration.

The MBI value can be calculated using Equation 1:

$$MBI = \frac{V_{endpoint} N_{MB}}{m_{solids}} \times 100 \tag{1}$$

Where $V_{endpoint}$ is the endpoint volume in mL, m_{solids} (g) equals the solids fraction multiplied by the slurry mass, and N_{MB} is the normality of the MB solution. The MBI is typically expressed as milliequivalent per 100 grams (meq/100g).

Another MBI determination method is based on a spectroscopic approach. During the titration process of MB on clay mixtures, there are residual MB molecules in the aqueous phase after MB molecules adsorb onto the clay edges, interlayers, external and internal surfaces. The residual MB in the aqueous phase can be correlated to MB adsorption on clay surfaces, where the amount of residual MB molecules increases as the MB molecules approach full coverage on the clay surfaces. A pivot spectroscopic point equivalent to the titration endpoint visible to the human eye exists, as illustrated in Figure 2. During MB titration, a series of aliquots from the clay mixture titrated by MB is extracted, filtered, and measured by a spectrophotometer. The spectra absorbance (ABS) of the filtrate can be plotted against the cumulative MB volume. The ABS increases with increasing MB addition and it passes a transition on the ABS vs. MB volume correlation curve, which is equivalent to the titration endpoint. It is important to filter the supernatant before spectroscopic analysis as some authors have used dilute clay samples without filtration which can yield inaccurate or even erroneous results (Hang 1970, Currie et al. 2014). This work has found that, without filtration, clay particles adsorbed with MB molecules interfere with the spectra ABS as clay particles are not part of the residual MB molecules to be measured.

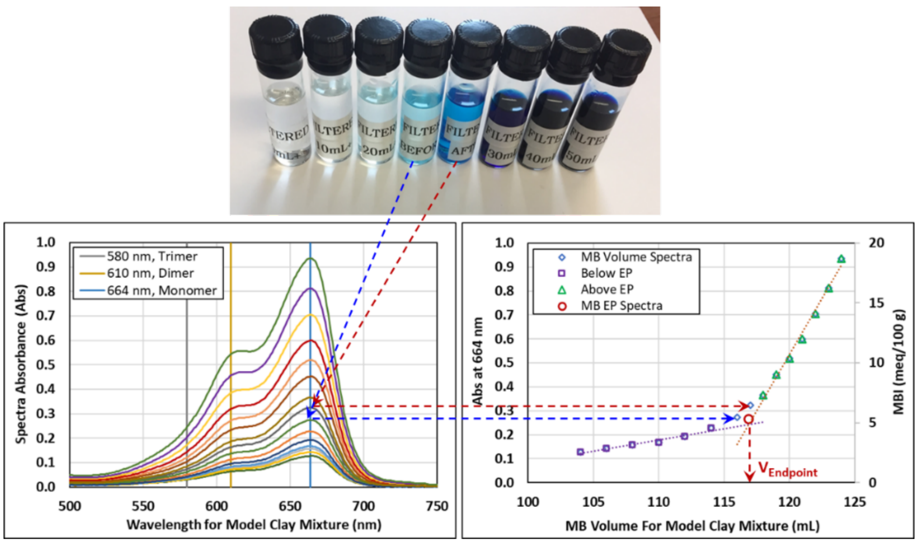

Figure 2. Spectra absorbance of filtrate containing residual MB molecules during MB titration

2.2.2 *Prototype A*

Prototype A active clay analyzer (Figure 3a) was validated against the modified ASTM method. For each MBI test by the Prototype A, a duplicate test on the same sample was performed using the modified ASTM method with manual sample preparation and visual halo endpoint determination by a technician. FFT-A to FFT-E were tested in 6 replicates by both Prototype A and technician, and the order of the tests was randomized. A blind study with 30 different FFT samples were also completed in duplicates on the prototype and a technician, where the sample details were kept blind from the technician. As a quality control, a kaolinite standard was performed each day.

Prototype A is a fully automated at-line instrument capable of testing up to 4 samples in each test set. Once the 250 ml beakers containing the samples are loaded in the prototype ultrasonic bath and the sample details (e.g., sample mass, solids concentration, sample type) are entered in the graphical user interface (GUI), the Prototype A robotic arm (x-y-z axes platform) with attached chemical lines and pH probe adds a user specified volume of buffer to each beaker position. The pH of each sample is measured by the attached pH probe and sodium hydroxide solution is incrementally added to the samples until the pH reaches a setpoint value of 10.5. Once the pHs are adjusted, the samples are heated and mixed for 20 minutes, followed by sonication for 20 minutes to ensure full dispersion of the clays. The samples are then cooled down to room temperature using the built-in chiller, and the pH of the first sample is corrected to a setpoint of pH 3.0 by adding sulfuric acid solution. Prior to MB titration, the robotic arm goes to the glass rod holder station and magnetically attaches a glass rod. An initial volume of MB solution, as specified by the user in the GUI, is added to the first sample through the MB line, and titration is carried out in increments of 0.5 mL of MB solution until the endpoint is reached and the halo becomes prominent. At each titration step, the robotic arm with the attached glass rod transfers an aliquot from the sample mixture onto the nylon filter paper. The sample dots are then imaged sequentially according to MB volume added under a chamber with controlled lighting. As previously mentioned, a halo appears when there is an excess of MB solution that can no longer be adsorbed by the clay surfaces. Using digital image processing and analysis, the Prototype A software determines the endpoint using an in-house developed algorithm. Figure 3b shows an example of the halo calculated by the algorithm with increasing volume of MB added. Before the endpoint, the calculated halo values stay relatively constant. A pivot point occurs near the endpoint, indicating the onset of the halo growth. Further MB additions result in higher halo values, corresponding to more prominent halos around the sample dots. Once the sample is complete, Prototype A moves to titration for the next sample. The glass rod is cleaned with water between samples at a rinsing station.

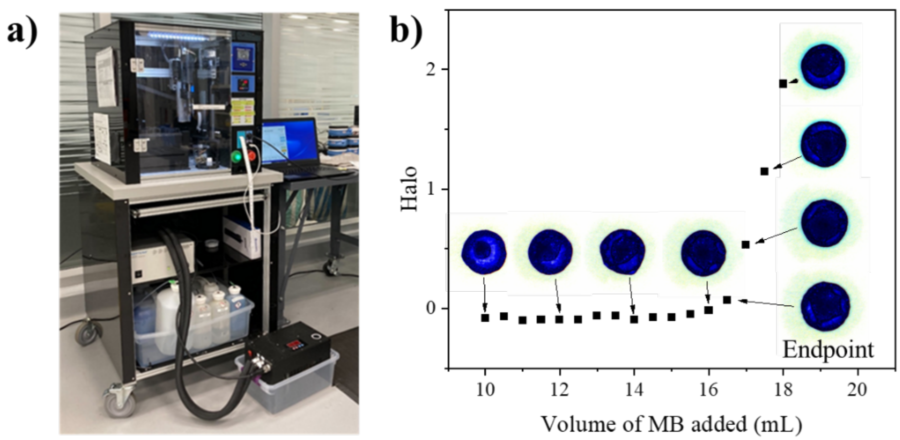

Figure 3. (a) Front view of the automated clay analyzer prototype and (b) Onset of the growth of halo as determined by prototype algorithm

2.2.3 *Prototype B*

Prototype B active clay analyzer incorporates a novel approach to utilize spectroscopy and automated devices to eliminate manual operation. Unlike the conventional method where the halo is determined either visually (ASTM C837-09 or CANMET method) or by a digital imaging processing system (Prototype A), Prototype B measures the spectra ABS of the aqueous phase to determine the spectroscopic endpoint. The prototype architecture is illustrated by Figure 4a, b. An auto sampler can be installed on a process (e.g., slurry pipeline, mixing tank etc.). A controlled volume of slurry sample can be withdrawn and carried by a controlled volume of dilution water injected into the sampler. The diluted mixture is transferred into a mixing chamber where the sample mixture is conditioned by dispersion, pH adjustment and sonication etc.

A controlled volume of MB solution is then injected into the sample mixture in increments. After each MB injection and mixing, an aliquot of the sample mixture is extracted and filtered by an auto sampler equipped with auto filter changer. The filtrate is transferred through an optical flow cell where it is measured by a spectrophotometer. The ABS data of the filtrate are plotted against the cumulative MB volume, and the spectroscopic endpoint can be determined from the correlation. Since the slurry sample volume and MB solution normality are known, and the slurry concentration is provided by other devices (e.g., densitometer) installed on the process, the MBI value can be determined instantaneously. After the MBI value is determined, the spent sample mixture is flushed via an auto drain valve at the bottom of the mixing chamber and the analyzer system is auto cleaned by injecting clean water via auto sampler through the mixing chamber and the auto drain valve. It takes approximately 1 hour to measure one slurry sample with 15 data points in the correlation. The measurement time can be reduced if less data points are required for process control with a set target. The main advantage of Prototype B is that it is online because it can connect to active processes and all procedures are performed automatically. Other advantages include tolerance for trace amounts of residual bitumen in the sample, larger sample sizes (>7 mL) for ease of operation, and capability for very high MBI samples such as kimberlite. It can also be used as an at-line clay analyzer if dry solids or slurry sample information is loaded manually to the mixing chamber. Optimization of the Prototype B active clay analyzer is ongoing, including installation of auto filter changer and completion of full automation and online

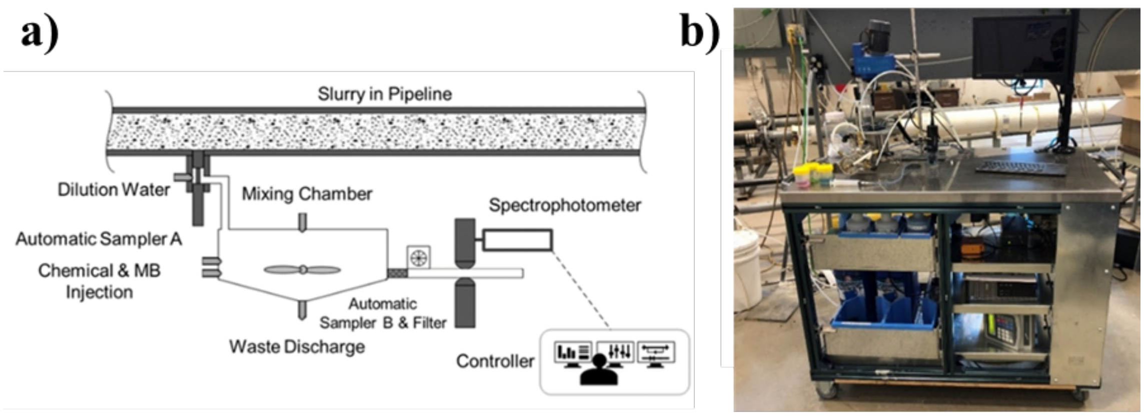

Figure 4. (a) Illustration of prototype B online active clay analyzer architecture and (b) prototype B automated and online active clay analyzer next to a slurry pipeline

capabilities.

3 RESULTS AND DISCUSSION

3.1 *Prototype A Validation*

During the development of Prototype A, numerous MBI tests have been performed using oil sands FFT and clay mixtures. Figure 5 shows the comparison of MBI results for FFT-A to FFT-E from Prototype A and the modified ASTM method. The results are presented as an average of 6 replicates. Prototype A MBI showed good agreement with the lab MBI method, where the p-values ranged from 0.15 for FFT-A to 0.74 for FFT-D. All p-values were above the significance level of 0.05, indicating that there was negligible difference between the Prototype A and technician results. The standard deviation between the replicate tests was mostly higher for the prototype compared to the technician. The lower variability in the technician MBI results may be due to the extensive training and experience of the two technicians who conducted the tests. Higher variability in the technician data is expected if more labs/technicians are involved.

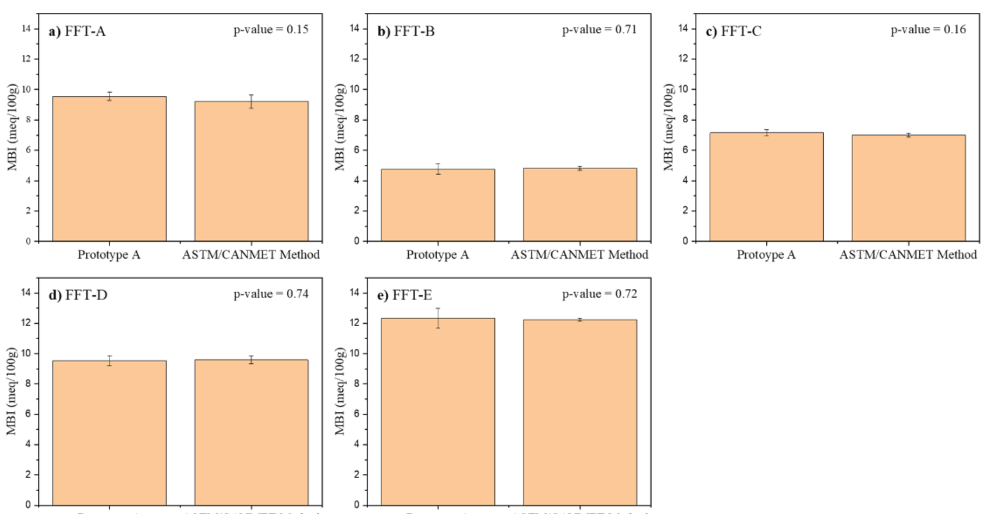

Figure 5. Comparison of Prototype A and ASTM/CANMET MBI for (a) FFT-A to (e) FFT-E

However, both methods showed standard deviations less than 0.5 meq/100g, indicating that the results were repeatable.

To test the robustness of Prototype A, duplicate tests using Prototype A and modified ASTM method were performed on 30 different FFT samples. Figure 6a shows the comparison between the Prototype A MBI and technician MBI for the blind samples. The blind samples covered a wide range of MBI values, from 4 meq/100g to over 15 meq/100g, that are commonly encountered in oil sands tailings ponds. Figure 6a shows that a strong correlation ($R^2 = 0.94$) exists between the Prototype A MBI and technician MBI, indicating that Prototype A measures the changes in the MBI very well. From the Bland Altman plot (Figure 6b), the residual MBI (e.g., technician MBI minus Prototype A MBI) has a slight bias of 0.23 meq/100g, which means that the Prototype A generally determines the endpoint earlier than the technician. This may be due to the digital imaging endpoint detection system being more sensitive to color changes than the human eye.

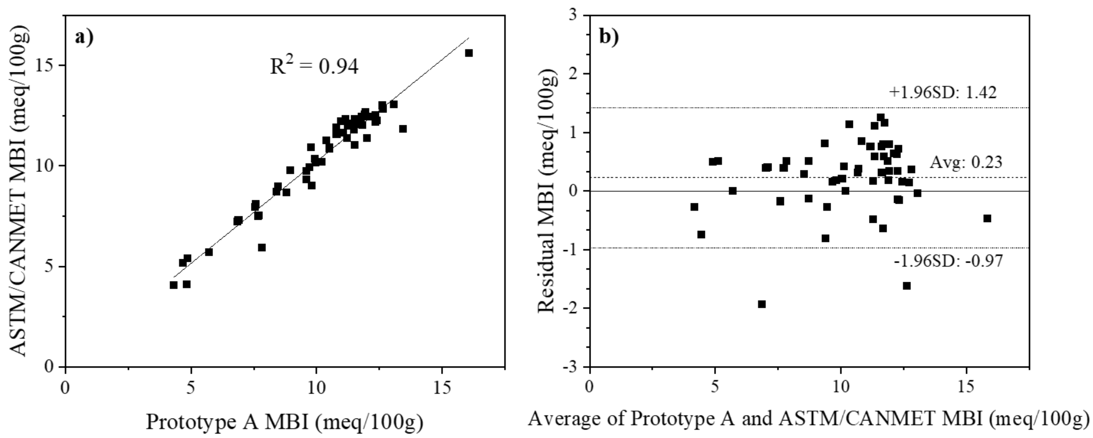

Figure 6. (a) Comparison of Prototype A and ASTM/CANMET MBI for blind FFT samples and (b) Bland Altman plot showing the comparison between the ASTM/CANMET MBI and Prototype A MBI method. The short-dashed line represents the average, and the long-dashed lines represents the ±1.96 standard deviation.

Among the 60 tests performed, only 4 outliers were identified and removed, where Prototype A selected the endpoints very early in the titration process (typically <10 mL of MB added). One of the advantages of Prototype A is that images are captured and stored at each MB increments, allowing users to examine results in detail. From the captured images for the outliers, it was visually obvious that the halo was not yet formed, indicating that the titration was not yet complete. It is hypothesized that the grainy texture of the dot and the presence of bitumen on the dot may have contributed to low endpoints determined by the algorithm. However, it is worth noting that Prototype A still determined endpoints with good agreement with the technician endpoints on the duplicate test for all outlier samples. The outliers may simply be isolated instances.

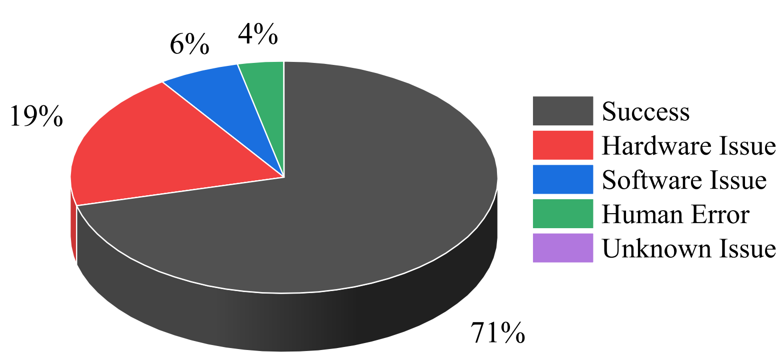

Figure 7. Breakdown of Prototype A reliability

Reliability is a key aspect for any prototype instrument. To estimate the reliability, each test was classified as either a successful or failed test, where a successful test is defined as a fully automated test without issues and a failed test is defined as a test with one or more failures (e.g., hardware, software, or human error) during the test. Figure 7 shows the reliability breakdown during the validation. The success rate was 71%, with the leading cause for a failed test related to hardware (19%), followed by software (6%) and human error (4%). Further work is ongoing to improve the Prototype A reliability for better practicability in real world applications.

3.2 *Prototype B Validation*

Numerous MBI tests have been performed during the development of Prototype B. Results obtained by Prototype B and modified ASTM methods are presented for direct comparison. Figure 8a, b show the MBI values of pure kaolinite and pure bentonite respectively from the two MBI methods. Results from the modified ASTM method were scattered due to manual operation and visual halo endpoint determination, which are known shortcomings of the modified ASTM method. As these results are generated by three technicians from the same lab, the data is expected to be more scattered if more labs/technicians are involved. The MBI results generated by the spectroscopic method are more consistent with narrower scattering. It is more objective than the visual halo endpoint determination in which different technicians may interpret the endpoint differently. The data continued to be consistent as high slurry sample weights were measured, which is a benefit of the spectroscopic method. The larger samples can be withdrawn by the auto sampler from an active process, expanding the capability of this architecture. Figure 8b shows that some MBI data by the spectroscopic method became scattered at very low Bentonite weight range (< 0.1 g), as it becomes more difficult to prepare the sample due to extremely high static charges of the pure and dry Bentonite powder. Industrial samples normally don't have this challenge.

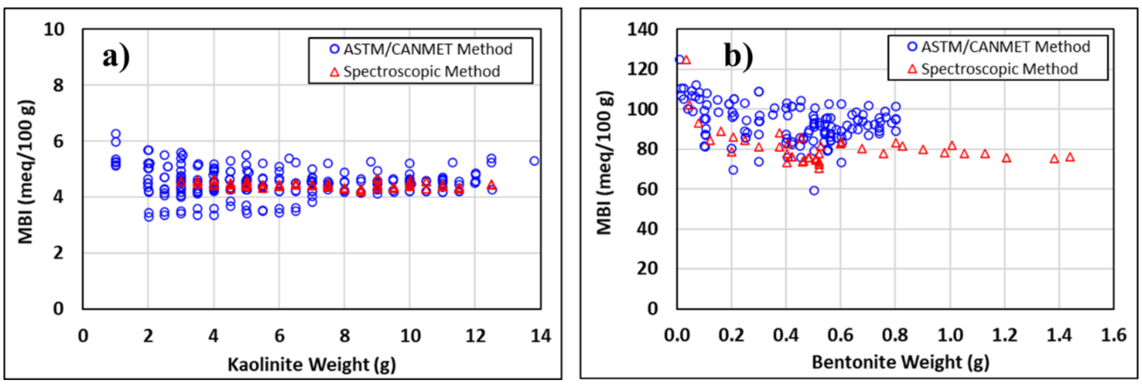

Figure 8. MBI results of (a) pure kaolinite and (b) pure bentonite by CANMET and spectral methods.

Figure 9 shows the MBI value as a function of active clay (e.g., bentonite) fraction in the kaolinite, bentonite and Sil 325 mixture. For method development purposes, the MBI results covered the range of MBI values commonly seen in samples from oil sands, potash, and kimberlite industries.

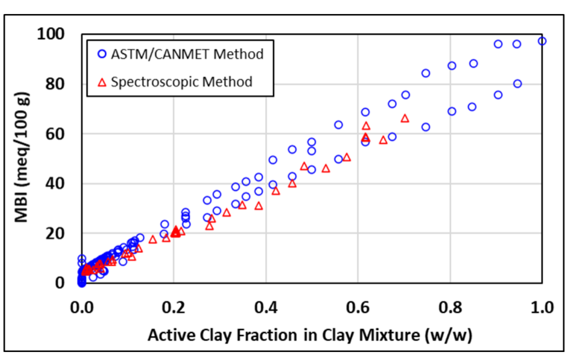

Figure 9. Clay mixture MBI by modified ASTM and spectroscopic methods

The modified ASTM method again generated scattered data, with more scattering at the high active clay fraction. On the other hand, the data by the spectroscopic method was more consistent and more objective as it eliminated the common issues associated with manual operation and visual halo interpretation.

The MBI results of industrial samples generated by the two methods are presented in Table 2. Each set of data was calculated based on an average of 2-8 repeats. For oil sands samples, the MBI difference between the two methods was larger for FFT-C and FFT-D, due to higher bitumen contents in each sample (up to 3 wt.%). Prototype B was also able to handle kimberlite samples with MBI values 5-10 times higher than those of oil sands FFT and the results from the two methods were very close. Prototype B has a capacity of 1500 mL to accommodate samples requiring higher MB volume to titrate (e.g., samples with higher MBI values or larger sample mass). The spectroscopic method for potash samples is under development. as the difference between the two methods is relatively large. This is partly due to the high dissolved salt content in potash samples which interferes with the spectra absorbance. Extra sample conditioning is being investigated to counter the impact of dissolved salt.

Table 2. MBI results of industrial samples by modified ASTM and spectroscopic methods

Sample ID	Average MBI (meq/100g)	
	Modified ASTM Method	Spectroscopic Method
FFT-A	4.5	4.7
FFT-B	4.6	5.2
FFT-C	6.5	7.5
FFT-D	8.6	9.9
FFT-E	11.3	10.9
Kimberlite A	44.0	43.2
Kimberlite B	23.2	23.8
Kimberlite C	25.0	24.0
Kimberlite D	23.4	23.9
Kimberlite E	37.2	36.5
Kimberlite F	33.6	33.7
Potash Slimes	6.8	7.4
Potash Tailings	5.7	8.5

3.3 *Field Validation*

A field validation trial of Prototype A and B was performed at Suncor Energy site in the Regional Municipality of Wood Buffalo in the summer of 2021. The data is still being evaluated and therefore is not included in this paper. Both Prototype A and B offer several advantages over the lab MBI method. The at-line and online instruments enable oil sands and mining operators to access timely MBI data on site, eliminating the need for costly and time-consuming sample transportation and analysis at offsite labs. As the sample dispersion, titration and endpoint determination steps are fully automated, the prototypes require minimal training and experience to operate. Lastly, existing MBI methods have always been subjected to variation between different technicians and labs, as the visual halo method is inherently subjective. Both prototypes offer more objective methods for endpoint determination.

4 CONCLUSIONS

Two automated prototypes (Prototype A and B) for active clay measurement of oil sands and mining tailings were developed based on the methylene blue index (MBI) titration method in this work. Prototype A was developed as an at-line instrument that is fully automated and can test up to 4 samples for each test set. Prototype A was validated using a wide range of oil sands fluid fine tailings (FFT) samples and compared to the modified ASTM method performed by technicians. The results showed that the Prototype A MBI agreed well with the technician MBI results. The digital imaging processing system provided an objective endpoint detection method which may reduce inherent subjectivity of visual halo detection between different technicians and labs. A novel approach to determine the MBI value of clay mixtures was also developed to incorporate a spectroscopic approach. Prototype B correlated the spectra absorbance (ABS) of filtrate after the sample was treated with MB and other chemicals, and it determined the MBI value from the ABS to MB volume correlation. Prototype B is an online instrument, and it can be fully automated to test slurry samples from an active process and generate the MBI value within 1 hour. Both prototypes showed high potential for MBI data collection in the field, which can lead to cost savings and better tailings management performance.

5 ACKNOWLEDGEMENTS

The authors would like to acknowledge and thank Natural Resource Canada (NRCan) for their financial support to this research work through the Clean Growth Program (CGP) funding. Suncor, SRC and NAIT also made contributions to this project. Jason Ng and Ruijun Sun contributed equally to this paper.

6 REFERENCES

Alberta Energy Regulator. 2017. *Directive 085: Fluid Tailings Management for Oil Sands Mining Projects.* Calgary: Alberta Energy Regulator.

ASTM International. 2014. *C837-09(2014): Standard Test Method for Methylene Blue Index of Clay*. West Conshohocken: ASTM International.

Cenens, J. & Schoonheydt, R.A. 1988. Visible Spectroscopy of Methylene Blue on Hectorite, Laponite, B, and Barasym in Aqueous Suspension. *Clays and Clay Minerals* 36(3): 214-224.

Cerato, A. 2001. *Influence of Specific Surface Area on Geotechnical Characteristics of Fine Grained Soils*. Amherst: Department of Civil & Environmental Engineering, University of Massachusetts.

Currie, R., Bansal, S. & MianH. 2014. *An Investigation of the Methylene Blue Titration Method for Clay Activity of Oil Sands Samples*. Edmonton: Oil Sands Research and Information Network.

Diep, J., Weiss, M., Revington, A., Moyls, B., & Mittal, K. 2014. In-line mixing of mature fine tailings and polymers. In Jewell, R., Fourie, A., Wells, P.S. & van Zyl, D. (eds.), *Proceedings of the 17th International Seminar on Paste and Thickened Tailings*. Vancouver: InfoMine Inc.

Kaminsky, H. 2014. Demystifying the Methylene Blue Index, *Proceedings of the 4th International Oil Sands Tailings Conference*. Banff: University of Alberta Geotechnical Centre.

Masliyah, J., Czarnecki J. & Xu, Z. 2011. *Handbook on Theory and Practice of Bitumen Recovery from Athabasca Oil Sands Volume 1: Theoretical Basis*. Edmonton: Kingsley Knowledge Publishing.

Omotoso, O. & Morin, M. 2004. *Standard Operating Procedure 0043-SOP – Methylene Blue Titration: Sludges, Slurries and Dean-Stark Solids*. Devon: Natural Resources Canada.

Omotoso, O. & Melanson, A. 2014. Influence of clay minerals on the storage and treatment of oil sands tailings. In Jewell, R., Fourie, A., Wells, P.S., & van Zyl, D. (eds.), *Proceedings of the 17th International Seminar on Paste and Thickened Tailings*. Vancouver: InfoMine Inc.

Hang, P.T., & Brindley, G.W. 1970. Methylene Blue Absorption by Clay Minerals. Determination of Surface Areas and Cation Exchange Capacities (Clay-Organic Studies XVIII). *Clays and Clay Minerals* 18: 203-212.

Accessing consolidation performance for multi-lift in-pit oil sands tailings with a geotechnical beam centrifuge

Gonzalo Zambrano, Yazhao Wang & Rick Chalaturnyk
University of Alberta, Edmonton, Alberta, Canada

ABSTRACT: The deposition and consolidation of a multi-lift in-pit mine tailings pond was simulated using the geotechnical beam centrifuge in a study conducted at the Geotechnical Centrifuge Experimental Research Facility at the University of Alberta. This study aimed to replicate the multi-lift filling process of the oil sands tailings and the long-term self-weight consolidation behavior of the deep deposit in the geotechnical centrifuge environment. Each modeled lift was created with regards to the centrifuge dimensional and temporal scaling laws and represented a full deposition stages in the field. With spacing markers in between lifts, the evolution of individual lift was simultaneously modelled. After 45 prototype years of deposition and consolidation, index properties and settlement profiles of the tailings pond model were obtained. The data provided by the centrifuge physical modelling, acquired in a matter of days, will help oil sands operators make rapid decisions when developing their field programs. The project demonstrated the capability and flexibility of using the geotechnical beam centrifuge in meeting tailings management challenges and the enormous cost-and time saving advantages when compared to conventional methods.

1 INTRODUCTION

1.1 *Pit lake deposition of oil sands tailings*

Oil sands production in Alberta generates large volumes of fine tailings. The proper disposal and reclamation of tailings is critical in both economic and environmental terms. Pit lakes are used at many mine sites around the world and are a preferable solution for reclamation and closure. In-pit deposition has been part of oil sands mine operation and closure plans since the beginning. Developing a successful pit lake requires advanced planning and iteration of research results. Pit lake designs have changed over time to reflect the state of knowledge of oil sands mine waters and tailings, technological advances, changing regulations, and inputs from local stakeholders and Indigenous communities. (CAPP, 2021). The self-weight consolidation behavior of tailings is crucial to the design of pit lakes and an accurate and timely prediction will greatly facilitate its planning and management.

1.2 *Multi-lift deposition technique*

The multi-lift deposition technique refers to the tailings discharge arrangement that involves multiple subaerial placement of the tailings stream. After each placement, there is an initial water discharge, followed by long-term consolidation of the deposited material under subaqueous conditions. Using the multi-lift deposition technique maximizes the volume of dry tailings in the pit lakes. The multi-lift deposition technique can be applied in more than 30 planned oil sands tailings pit lake sites in northern Alberta (Prakash et al. 2011). The industry is constantly revisiting the pit lake deposition plan and multi-lift deposition technique. With new additions of such as flocculant/coagulant treatment and deposition schedule, the technology needs constant evaluation to reduce risk of uncertainty. It also needs feedback in real time to apply process control to such new additions. Physical modelling using the beam centrifuge is novel technology that can help evaluation and collection accurate and reliable feedback in hours.

1.3 *Centrifuge physical simulation*

A geotechnical beam centrifuge can be used for modeling of large-scale nonlinear problems for which gravity is the primary driving force, including the self-weight consolidation of fine tailings. (Toh, 1992; Sorta et al., 2016; Zambrano-Narvaez et al., 2018a; Zambrano-Narvaez et al., 2018b; Dunmola et al., 2018; Zambrano-Narvaez et al., 2019; Ansah-Sam et al., 2019; Dunmola et al, 2019). The fundamental principle of centrifuge modeling is based on the stress similarity between a prototype and a centrifuge model. Scaling laws for size and time are used to design the appropriate centrifuge operation. Additional description of the scaling relationships for the consolidation process are presented by Croce et al. (1984); Williams (1988); Balay et al. (1988); Taylor (1995); and Garnier et al. (2007). Equations 1 and 2 illustrate the scaling laws for size and time in a geotechnical centrifuge model when modelling the self-weight consolidation of fine tailings.

$$h_p = N * h_m \quad [1]$$

$$t_p = N^2 * t_m \quad [2]$$

In Equation 1, h_p is the height of the prototype being simulated, h_m is the height of the centrifuge model, and N is the multiple of earth gravity that the centrifuge model is subject to in the form of centrifugal force (N times earth gravity). For example, testing a 20 cm thick tailings sample under 100 times of earth gravity can simulate a tailings deposit of 20 m as a prototype. In Equation 2, t_p is the duration of the prototype being simulated and tm is the duration of the centrifuge experiment. For example, a consolidation progress lasting 10 years in the prototype can be reproduced in about a 9 hour centrifuge run under 100 g.

Previous research demonstrated the feasibility of simulating multi-stage consolidation of tailings. A multi-stage filled gold mine tailings pond was physically simulated with a beam centrifuge and compared with numerical simulation work (TOH, 1992, Hall, 2021). In this study, three tests on differently-treated oil sands tailings were experimented, representing a prototype in-pit tailings deposition construction scenario.

2 METHODOLOGY

2.1 *Centrifuge modelling design*

As part of this study a pre-selection assessment of optimum self-weight consolidation performance was conducted on 20 different types of treated oil sands tailings candidates for a multi-lift in-pit lake deposition project. The main properties of these oil sands tailings include different clay-water ratio, flocculent and coagulant dosages, and in-pipe shear conditions. The range of these properties are presented in Table 1. Each assessment includes the self-weight consolidation performance of a 12 m depth prototype deposit during 2.5 prototype years.

Table 1. Oil sand tailings properties of prelection materials for multi-lift study completed at GeoCERF

Description	Range
Clay-water ratio (CWR)	0.244 to 0.400
Coagulant	0 to 950 ppm
Flocculent	0 to 2200 ppm
Treatment condition in pipe	Sheared and non-sheared

After the comprehensive evaluation of a matrix of oil sands tailings samples, three specimens were narrowed down for the multi-lift pit lake model. The specimens were chosen based on consolidation parameters. The only variation within the specimens was flocculant concentration. The selected specimen properties are presented in Table 2.

Table 2. Specimen properties

Specimen ID	CWR	Coagulant	Treatment technique	Flocculent (g/t clay)
A	0.29	No	Non-sheared	2000 (regular)
B				1000 (underdosage)
C				3000 (overdosage)

The lift sequence was determined based on a planned field multi-lift deposition schedule. All three specimens shared the same lift sequence. The first lift had an average thickness value of 21 m and consolidated for one prototype year. The following lifts were each one year apart and had gradually less lift thickness. A total of 15 lifts were planned and prepared. However, not all lifts were deposited as the lifting stage stopped when the consolidation vessel reached full capacity. After the last lift was deposited, the entire deposits consolidated for a total of an average value of 46 prototype years for the three models. The magnitudes of all the lift thickness per specimen are presented in the results section.

The centrifuge operation plan was designed based on the lift schedule. The deposition of each lift required to stop the centrifuge for 10 minutes. All the specimens were spun under 120 G-level, approximately. Table 3 lists the centrifuge test plan for each specimen.

Table 3. Centrifuge test plan

Model ID	G-Level	Thickness		Time	
		Prototype	Model	Prototype	Model
Specimen A Specimen B Specimen C	120	Up to 66 m	Up to 55 cm	Total of 46 yrs average (1 yr per lift)	45 min per lift and a total of 28 hrs

2.2 *Accuracy of centrifuge modelling in large strain consolidation*

The aim of centrifuge modelling is to establish a linear scaling factor so that stress simulation between the model and the equivalent prototype is matched. The acceleration provided by the centrifugal movement was linearly applied to the model through its radial distance. In beam centrifuge modelling, in order to minimize the stress error within the model from the linear acceleration distribution, an effective radius measured from the center of rotation to the 2/3 of the model height should be used (Schofield, 1980). By assigning the target G-level at this effective radius, the under-stress distribution above the effective radius fully compensates the over-stress distribution below the effective radius (Taylor, 1995).

The advantage of a beam centrifuge is that the ratio of the model height and effective radius is near to 0.2 and therefore the maximum error in the stress profile is minor and generally is less than 3% of prototype stress. This is the reason that accurate physical modelling cannot be achieved with a benchtop centrifuge.

The adoption of large-scale consolidation, especially with the addition of multiple lift of tailings, poses an additional challenge to the accuracy of centrifuge modelling. Considering that the specimens will experience multiple stages of large settlements, the choice of a single effective radius will eventually overestimate the stress similarity between the model and the prototype. Therefore, a gradient of effective G force was used as lifts were added. The G assigned at each lift were individually considered given the lift location, ranging from 120 for the first lift to 111 for the last lift.

2.3 *Testing apparatus and instrumentation*

A consolidation cell was constructed to accommodate the sample on the centrifuge platform. The cell was made of a transparent Plexiglass cylinder of 57 cm internal height, 18 cm internal diameter, and a wall thickness of 1.3 cm. The transparent wall allows precise readings of internal tailings interface during the test. The movement of mudline (solids/water interface) is monitored during centrifuge tests through a high-resolution in-flight camera (IDS, 2448x2048 pixel, gigabit ethernet uEye RE model, CINEGON 1·8/4·8 CMPCT RUGGEDZD lenses model).

The cell also supported columns of pore pressure transducers (Model EPRB-1-15B), which can be installed in 2 cm intervals on the side. Multiple pore pressure transducers were attached to the consolidation cell. Porewater pressure was monitored during centrifuge tests. The centrifuge tests were conducted under one-way drainage and subaqueous conditions. The cell top was covered during the test to eliminate the evaporation. Figure 1 shows the on-platform consolidation cell with attached pore pressure transducers.

Figure 1. Consolidation cell with attached pore pressure transducers

Fifteen tailings dispensers were manufactured. The dispensers were used to store tailings sample after treatment and also had an acrylic body and an attached internal ruler for monitoring. The tailings material was prepared in a commercial lab and dispensers were filled according to the prototype lift schedule (Figure 2).

Figure 2. Tailings dispensers with tailings lift

The tailings dispenser was designed to fit the quick transition time expected in the multi-stage testing environment. At the beginning of each lift, the dispenser was installed on top of the consolidation cell and shifted downward to reach the target cumulative lift height. A piston was inserted into the dispenser and pressed to discharge the materials uniformly towards the consolidation cell. The process took less than 10 minutes before reaching the one prototype year of self-weight consolidation. Figure 3a shows the action when a new lift was deposited into the consolidation cell.

Figure 3.Milti-lift setup: a) Depositing a new lift into the consolidation cell with the dispenser; b) 3D-Printed interface markers

A 3D printed interface marker was placed on top of each dispensed layer and could be tracked with the on-board camera (Figure 3b). The marker was thin and light weight and floated between tailings layers. The tracking system allowed for precise measurement of the evolution of each tailings lift throughout the test.

2.4 *Post-flight assessment*

After all lifts were deposited and the deposit was self-weight consolidated for 46 prototype years, the consolidation cell was removed from the centrifuge platform. The entire deposit was excavated from the surface and multiple sub-samples were taken for geotechnical measurements. The sub-samples were corelated with layers and index property profiles were constructed.

3 RESULTS AND ANALYSIS

The centrifuge test plan completed after the self-weight consolidation performance was obtained from three multi-filled tailings specimens. Specimen B with an under-dosage of polymer treatment had 10 lifts deposited into the consolidation cell, the regular treated Specimen A had 14 lifts, and the over-dosage treated Specimen C had 15 lifts deposited. The difference in total lifts deposited was attributed to the different degree of consolidation arising from the flocculant treatment technique. All specimens underwent a total of 46 years of consolidation after multi-filling stage. Deposits thickness evolution over time is summarized and listed in Figure 4, Figure 5, and Figure 6.

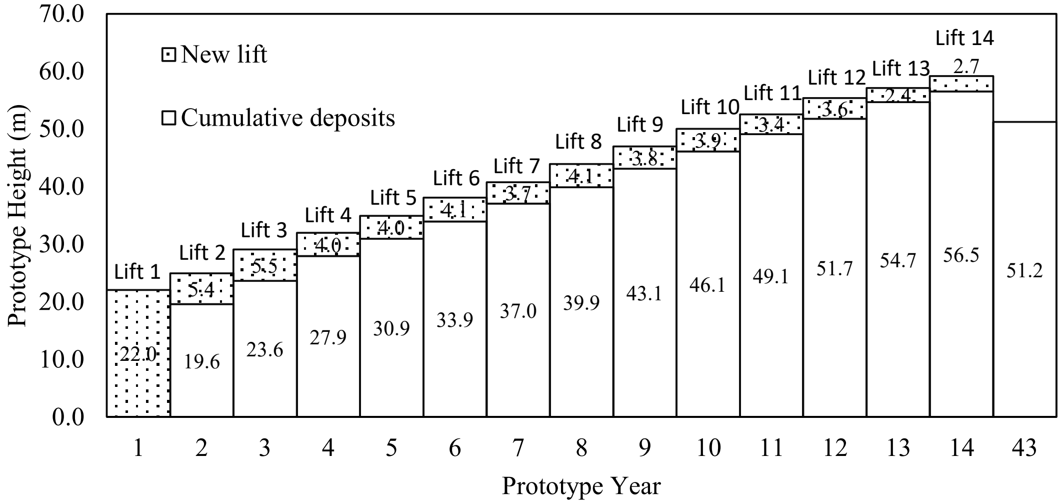

Figure 4. Deposits thickness over time for Specimen A

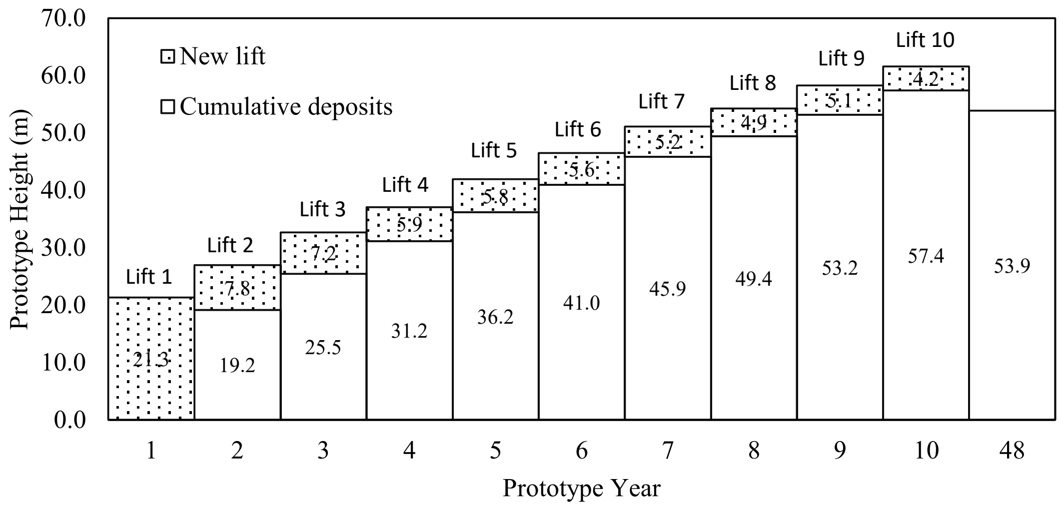

Figure 5. Deposits thickness over time for Specimen B

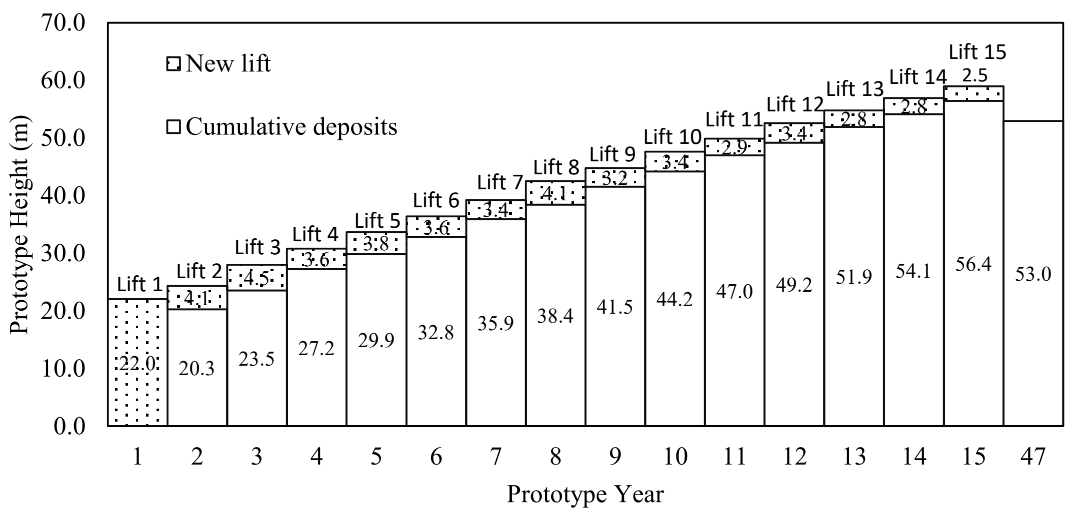

Figure 6. Deposits thickness over time for Specimen C

3.1 *Self-weight consolidation behavior*

Interface settlement curves for all three specimens are summarized in Figure 7. Compared with Specimen A, the over-dosage Specimen C experienced higher degree of consolidation after each lift, and as a result, the entire pit took all 15 lifts. Under-dosage Specimen B experienced lower settlement after each lift and the entire prototype pit filled up quickly in 10 lifts. After 46 prototype years of self-weight consolidation, the pit deposits performed a similar degree of overall consolidation from the same initial thickness of around 60 m. The total number of lifts and the accumulative dry mass stored in these three in-pit scenarios is presented in Table 4. Specimen A & C had similar performance and performed better than Specimen B. This study does not include the economical assessment to quantify the cost of flocculent over-dosage added to Specimen C, but indicates that Specimen A performed similar to C with less operation time to fill the pit.

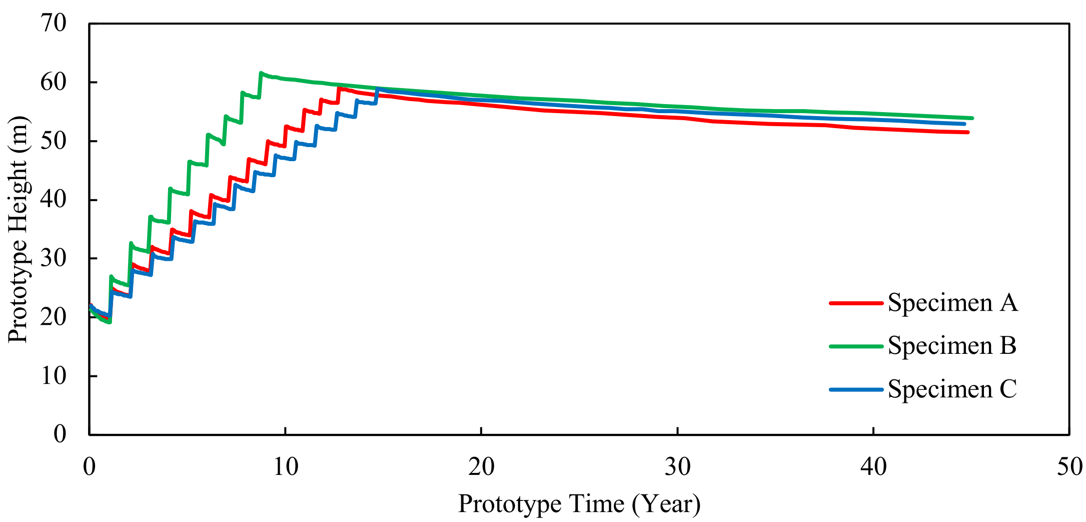

Figure 7. Combined interface settlement curve for all three specimens

Table 4 Maximum number of lifts and total dry mass stored after 46 years of self-weight consolidation

Model ID	Max number of lifts	Total dry mass* (ton)
Specimen A	14	12,286
Specimen B	10	9,942
Specimen C	15	12,192

*scale to prototype with factor of N^3

3.2 *Pore pressure curves*

Pore pressure dissipation curves were a clear indication of the progress of consolidation. The build-up of pore pressure was captured during the in-flight lifting process. The pore pressure dissipation curve for Specimen A is shown in Figure 8. Sensor locations relative to the base of the deposits are also included. Hydrostatic pressure for these sensor locations were determined by spinning the consolidation cell filled with water of the same levels. Excess pore pressure distribution was obtained at the end of the test and was in accordance with the consolidation performance of each model.

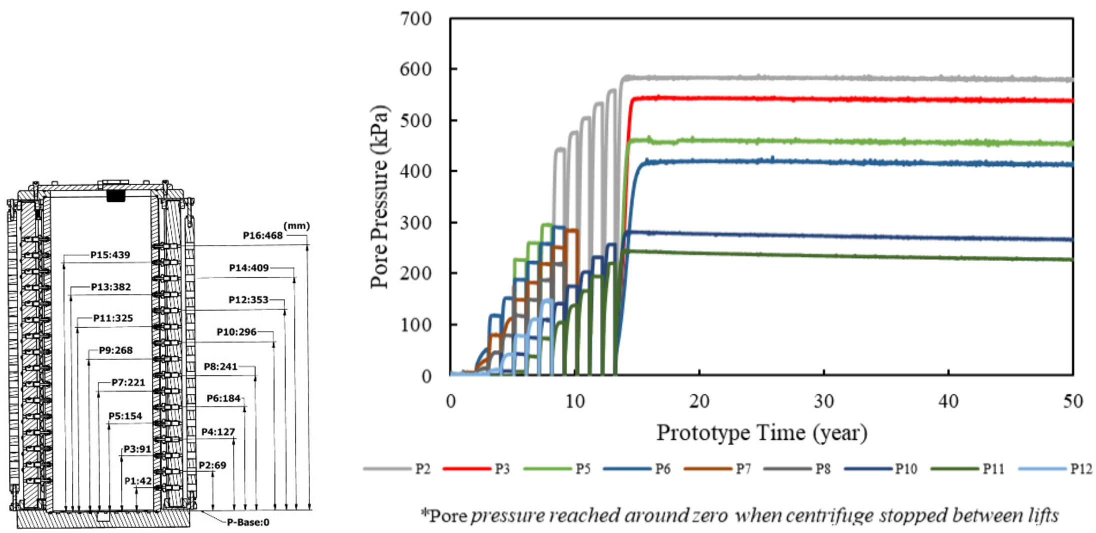

Figure 8. Pore pressure dissipation curve for Specimen A (Sensor locations on the right)

3.3 *Index properties and compressibility*

By conducting post-mortem analysis of consolidated deposits in layers, the solids content profile, void ratio profile, and density profile of the tailings model at the end of the test were obtained. With interface markers, individual layers were marked within the profiles. Figure 9 shows the solids content profiles obtained from all specimens.

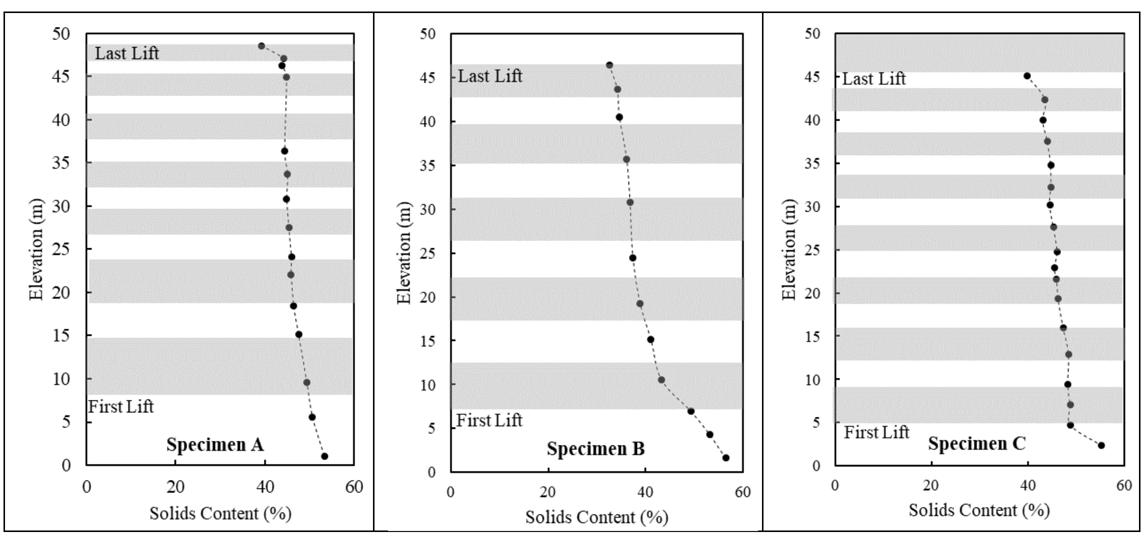

Figure 9. Solids content profiles

Combining the bulk density profile, void ratio profile, and the distribution of excess pore pressure at the end of the centrifuge test, the effective stress (σ') vs void ratio (e) relationship was constructed and represented using the power function shown in Equation 3. Figure 10 shows the void ratio vs effective stress relationship and their fitted power functions. Compressibility parameters A and B can be used for future tailings performance predictions. The hydraulic parameters (k-e) could be estimated through a back analysis, but is not in the scope of this paper. Additional description of the derivation of the compressibility parameters is presented by Zambrano-Narvaez et al. (2019).

Compressibility: $e = A\sigma'^B_v$ [3]

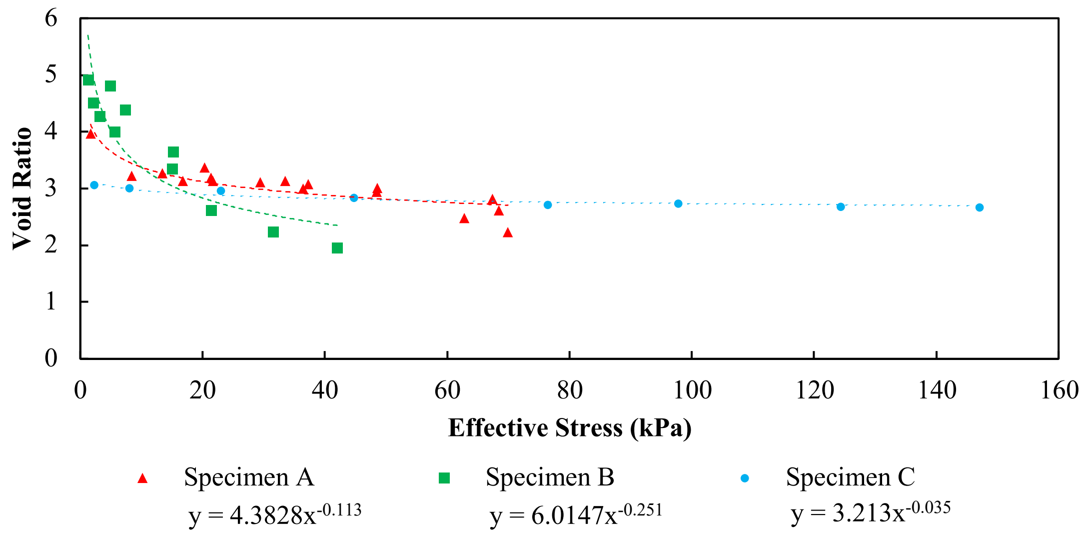

Figure 10. Void ratio vs effective stress relationship and their fitted power functions

4 CONCLUSIONS

The 2-m beam centrifuge in GeoCERF was used to conduct physical simulation on three tailings specimens. The centrifuge model represents a multi-lift in-pit tailings deposit. Twenty types of differently-treated tailings were accessed previously using the same technique for their self-weight consolidation behavior and three specimens were chosen. The selection process took less than one year and demonstrated the efficiency of centrifuge physical modelling.

The testing program took advantage of the scaling laws offered by the beam centrifuge. The stress distribution and long-term consolidation of a large scale protype was achieved with a lab-constructed model and the results were obtained in a matter of days. Considering the large strain settlement and the introduction of multiple new lifts with time, a gradient of G was adopted when scaling and analyzing the model performance.

In-pit deposits and multi-lift technique is one of the preferable ways of storing oil sands tailings by the industry. Improvements and innovations are constantly added requiring quick and effective assessment. This research demonstrated the capability of using the beam centrifuge to evaluate both technologies. Long-term settlement curves, profiles of index properties, and tailings consolidation parameters were obtained efficiently. The building-up of tailings interface during three multi-lift scenarios highlighted how pond capacity was impacted from alteration of tailings treatment techniques. The long-term settlement data predicted the potential closure in-pit lake deposit depth. Also, the quick compressibility parameters deduction with the geotechnical centrifuge would benefit additional tailings pond modelling and verification. These results will help oil sands operator make rapid decisions for developing their field programs. The project demonstrated the capability and flexibility of using the geotechnical beam centrifuge in meeting tailings management challenges and the enormous cost-and time saving advantages compared to conventional methods.

5 REFERENCES

Ansah-Sam, M., Stianson, J., Rudolf, K. and Zambrano Narvaez, G. 2019. Comparison of oil sand tailings consolidation properties derived from beam centrifuge and large-strain consolidometer testing. Proceedings of Tailings and Mine Waste 2019. Vancouver, Canada. November 17–20. pp. 865-878.

Balay, J., R. Berdat and L. Harfouche. 1988. Etude en centrifugeuse de la consolidation sous poids propre desolstrès laches. Proceedings of International Conference Centrifuge 88, Paris, Balkema: Rotterdam: 193–202.

Canadian Oil & Natural Gas Producers (CAPP). 2021. An Introduction to Oil Sands Pit Lakes.

Dunmola, A., Mikula, R., Ali, M., Siman, R., Lorentz, J., Zambrano Narvaez, G., and Chalaturnyk. R.J. 2019. Impact of residual bitumen of the long-term consolidation of FFT. Calgary, Canada. June 3-4.

Dunmola, A., Wang, N., Lorentz, J., Zambrano Narvaez, G., Chalaturnyk. R.J. and Song, J. 2018. Comparison of geotechnical bean centrifuge predictions to field data from 10 m deep FFT centrifuge cake columns. 6th International Oil Sands Tailings Conference. Edmonton, Canada. December 9-12.

Garnier, J., C. Gaudin, S.M. Springman, P.J. Culligan, D. Goddings, D. Konig, B. Kutter, R. Phillips, M.F. Randolph and L. Thorel. 2007. Catalogue of scaling laws and similitude questions in geotechnical centrifuge modelling. *International Journal of Physical Modelling in Geotechnics* 7(3): 1–23.

Hall, T. 2021. Influence of Fill Scheme on Oil Sands Consolidation Modelling in a Geotechnical Centrifuge. MSc theses. University of Alberta. Edmonton.

Prakash, S., Vendenberg, J.A., Buchak, E., 2011. The oil sands pit lake model – sediment diagenesis moule. In: Chan, F., Marinova, D., Anderssen, R.S. (Eds.). Proceedings of 19th International Congress on Modelling and Simulation. Perth, Australia. pp. 3761–3767.

Schofield, A.N. 1980. Cambridge geotechnical centrifuge operations. *Geotechnique*, 30, No. 3. pp.227-268.

Sorta, A.R., D.C. Sego and W. Wilson. 2016. Physical modelling of oil sands tailings consolidation. *International Journal of Physical Modelling in Geotechnics* 16(2): 47–64.

Toh, S.H. 1992. Numerical and centrifuge modelling of mine tailings consolidation. PhD theses. University of Western Australia. Perth.

Williams, D.J. 1988. Consolidation, crusting and loading of a soil slurry at 1 and 100 gravities. Proceedings of 5th Australia – New Zealand Conference on Geomechanics, Sydney, Australia. pp. 202–206.

Zambrano- Narvaez, G., Chalaturnyk, R. and Wang., Y. 2019. Mine tailings consolidation properties derived from beam Centrifuge, Proceedings of Tailings and Mine Waste 2019, Vancouver, Canada. November 17–20. pp 1125- 1135.

Zambrano-Narvaez, G., Wang, Y., Chalaturnyk, R.J., Zahabi, A. and Rennard, D. 2018a. Assessment of self-weight consolidation of co-deposition deposits in the geotechnical bean centrifuge. Sixth International Oil Sands Tailings Conference, Edmonton, Alberta, December 9-12.

Zambrano-Narvaez, G., Wang, Y. and Chalaturnyk, R.J. 2018b. Comparative study of consolidation behavior of differently-treated mature fine tailings specimens through centrifuge modelling. Proceedings of 9th International Conference Physical Modelling Geotechnics, City, University of London, July 17-22, pp. 1271-76.

Zambrano- Narvaez, G. and Chalaturnyk, R. 2014. The New GeoREF Geotechnical Beam Centrifuge at the University of Alberta, Canada, Proceeding of the 8th International conference in Physical Modelling in Geotechnics, Perth, Australia, pp. 163-167.

Geosynthetics

Statistical analysis of error in peel strength measurement for geosynthetics clay liner rolls

Shahin Ghazizadeh & Daniel Servigna
Wood Environment and Infrastructure Solutions, Denver, CO, USA

Christopher A. Bareither
Colorado State University, Fort Collins, CO, USA

ABSTRACT: Peel strength is an index parameter that is corelated to the internal shear strength of needle-punched reinforced geosynthetic clay liners (NP GSLs). In current practice, peel strength of a GCL roll is determined via performing limited number of peel strength tests (e.g. 5 tests) on relatively small specimens (e.g. 100 x 200 m) according to ASTM D6496/6496M. If there are spatial variabilities in peel strength within the GCL roll, the design of liner or cover systems based on limited number of laboratory tests may lead to unconservative or overly conservative designs. The objective of this study was to assess the relationship between measurement errors in peel strength and number of tested specimens. To meet the objectives, first a total of 84 peel strength tests were performed on two different NP GCL. Then a series of statistical analyses were performed using concepts of Students' T-distribution and Confidence Interval to estimate measurement error for various significance level and number of tests. Spatial variability in peel strength of at least 48% of the manufacturer-reported peel strength were observed for both NP GCLs. Achieving a measurement error < 10 % would require performing at least 10 peel strength tests for significance level of 0.05, and at least 15 peel strength tests for significance level of 0.01.

Keywords: geosynthetic clay liner, specimen variability, peel strength, measurement error, confidence interval

1 INTRODUCTION

Geosynthetic clay liners (GCLs) are hydraulic barriers consisting of bentonite encapsulated between two geotextiles, or adhered to a geomembrane. Long-term stability of liner and cover system components, including GCLs, must be withstand applied normal and shear stresses without experiencing substantial internal shear deformation or failure (Bareither et al. 2018; Fox and Stark 2015). Considering hydrated sodium bentonite has a very low internal friction angle (Mesri and Olson 1970), internal shear strength of GCLs are enhanced via stitched bonding or needle-punching. These processes increase the internal shear strength of NP GCLs due to tensile strength of reinforcement fibers and entanglement strength between needle-punched fibers and carrier geotextile of the GCL (Fox and Stark 2015; Ghazizadeh and Bareither 2018).

The internal shear strength of GCLs commonly is related to GCL index parameters such as peel strength and tensile shear strength (Hurst and Rowe 2006; Athanassopoulos and Yuan 2011; Bacas et al. 2013; Von Maubeuge and Ehrenberg 2013). Peel strength is measured as the tensile force per unit width required to peel apart a NP GCL at a constant rate of extension (ASTM D 6496 / 6496M). The maximum or average tensile force per unit width measured during the test is reported as the peel strength. A higher concentration (or density) of reinforcement fibers within the GCL correlates to higher GCL peel strength (von Maubeuge and Ehrenberg

2000, 2013; Athanassopoulos and Yuan 2011; Bacas et al. 2013; Fox and Stark 2015).

Previous studies have identified variability in internal shear strength of NP GCLs (e.g. Zornberg et al. 2005; McCartney et al. 2004, 2009). This variability in GCL internal shear strength can be attributed to variability in reinforcement fibers properties of the NP GCL. Spatial variability in fiber density (i.e., fiber mass per area of the textile) within the non-woven cover geotextile of the GCL and gradual wear of needle-plates during needle-punching can result in spatial variability in reinforcement fibers of NP GCLs (Ghazizadeh and Bareither 2021). Spatial variability of reinforcement fibers can make determination of peel strength for a GCL production roll challenging, in particular, considering that in current practice peel strength is computed from a limited number of tests (e.g., five) on relatively small specimens (100 mm x 200 mm) compared to the size of GCL rolls (ASTM D 6496/6496M). Therefore, current practice of determining peel strength for NP GCLs may lead to unconservative or overly conservative designs.

Considering the aforementioned concerns, two objectives were defined in this study: (i) assess peel strength variability within GCL production rolls; and (ii) determine the relationship between peel strength measurement error and number of peel strength tests. To meet the objectives, peel strength was measured on 84 NP GCL specimens, which were cut from sample rolls of two different NP GCLs that had different manufacturer-reported peel strength. A criterion for measurement error was defined and statistical analyses were performed to determine the probable measurement error.

2 EXPERIMENTAL SETUP

Characteristics of the two NP GCLs used in this study are tabulated in Table 1. Both GCLs were non-heat-treated NP GCLs with granular bentonite and non-woven encapsulating geotextiles. Despite the similarities, GCL-1 has a manufacturer-reported peel strength = 2180 N/m whereas GCL-2 has a manufacturer reported peel strength = 980 N/m.

Peel strength test specimens were cut from two samples of each NP GCL, namely Sample-1 and Sample-2. Schematics of Sample-1 and Sample-2 of GCL-1 and GCL-2 are shown in Figure 1 and Figure 2, respectively. The small rectangles in these figures identify the 100 mm x 200 mm peel strength specimens, which were all cut in machine direction (MD in Figures 1 and 2). The majority of peel strength specimens (i.e., 65 out of 84) were cut from two samples of GCL-1 (Figures 1a and 1b). The location of these two samples within the GCL-1 production roll was not known. Sample-1 and Sample-2 of GCL-2 (Figure 2) consisted of 1-m-wide sections removed along the same needle path at the start and end of the production roll. These samples were smaller than GCL-1 and only 19 specimens were tested from the combined two samples of GCL-2.

All peel strength tests were performed using an automated tensile testing machine with the ASTM-recommended displacement rate of 300 mm/min until displacements of at least 250 mm. Tensile force was measured using an S-type load cell and displacement was monitored via an internal positioning system of the tensile testing machine. At the end of each peel strength test, specimens were inspected visually and in case that there were signs of geotextile elongation, geotextile tearing, or slippage at the geotextile and clamping, test results were discarded.

Table 1. characteristics of geosynthetic clay liners (GCLs) used in this study.

Properties	GCL-1	GCL-2
Manufacturer-reported Peel strength (N/m) [a]	2170	980
Carrier geotextile type	NW	NW
Cover geotextile type	NW	NW
Bentonite Type	Granular	Granular

Note: W = woven; NW = non-woven

[a] Values reported by manufacturers based on [ASTM D6496/6496M (ASTM 2020)]

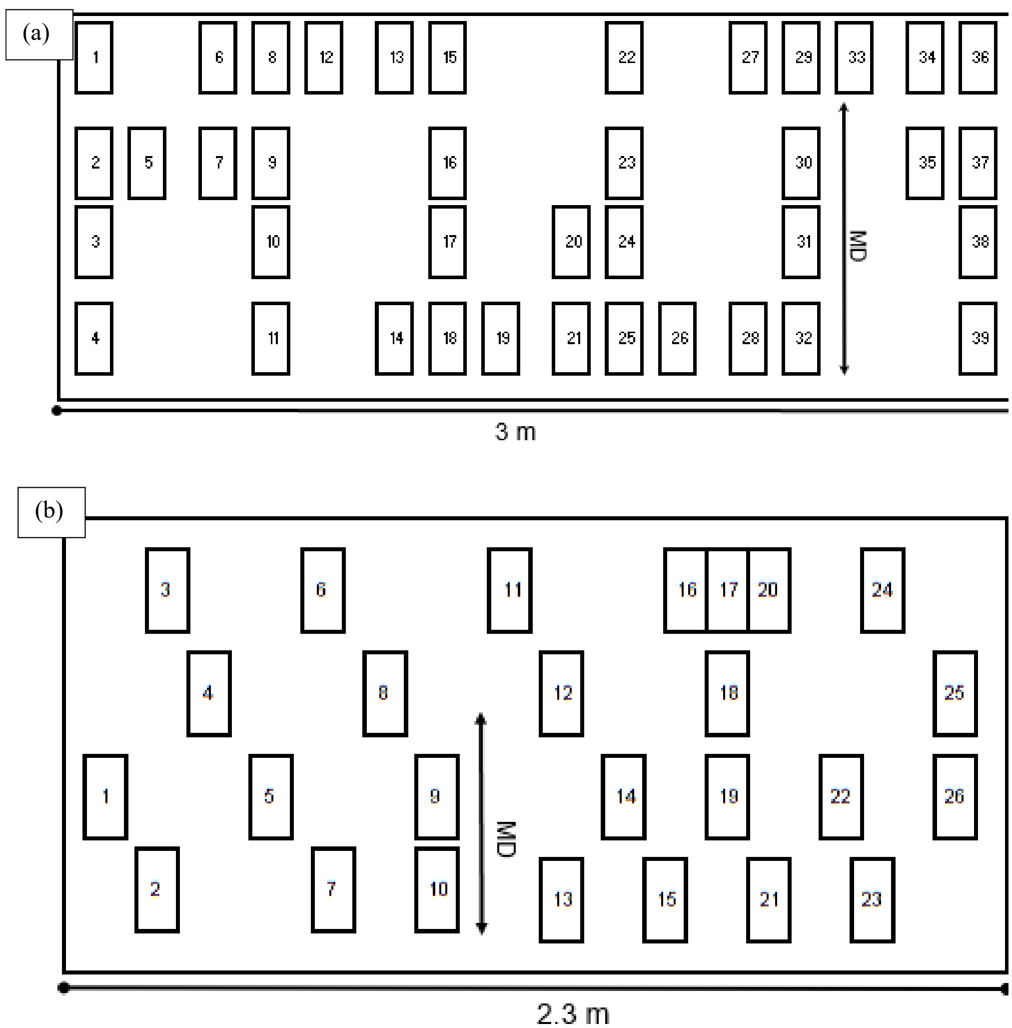

Figure 1. Schematic of (a) sample-1, and (b) sample-2 of GCL-1 with approximate locations of specimens.

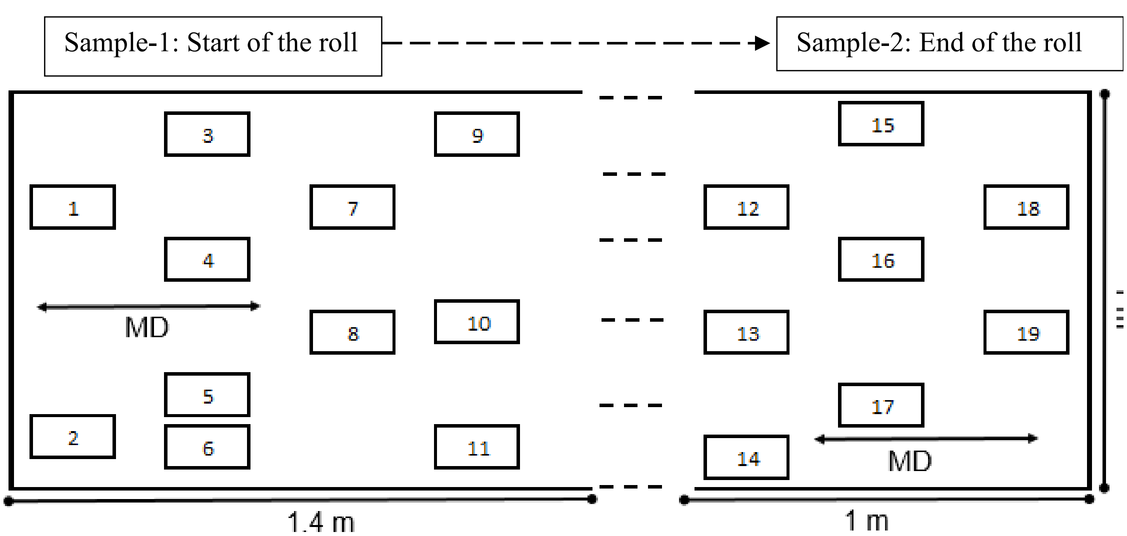

Figure 2. Schematic of Smaple-1 (cut from the start of the production roll) and Sample-2 (cut from the end of production roll) of GCL-2 with approximate locations of specimens.

3 RESULTS

Dot plots of peel strength measured on GCL-1 and GCL-2 are shown in Figure 3. A summary of the number of peel strength tests, minimum and maximum peel strength, standard deviation, coefficient of variation (COV), manufacturer-reported average peel strength, and calculated average peel strength for each GCL Sample is tabulated in Table 2. Combined results from all peel strength tests on a given GCL also are included in Table 2 for comparison.

Table 2. Summary of peel strength tests.

Parameter	GCL-1		GCL-1	GCL-2		GCL-2
	Sample-1	Sample-2	Combined	Sample-1	Sample-2	Combined
Number of tests	39	26	65	11	8	19
Minimum PS (N/m)	1841	2112	1841	1009	663	663
Maximum PS (N/m)	3174	3208	3208	1698	1049	1698
Standard Deviation (N/m)	371	306	357.7	203	131	275
COV (%)	15.5	11.8	14. 4	15.9	15.3	25
Manufacturer-Reported PS (N/m)		2170			980	
Calculated Average PS (N/m)	2389	2591	2470	1279	852	1099

Notes: PS = peel strength; COV = coefficient of variation. All peel strength specimens were obtained from a single GCL-D roll.

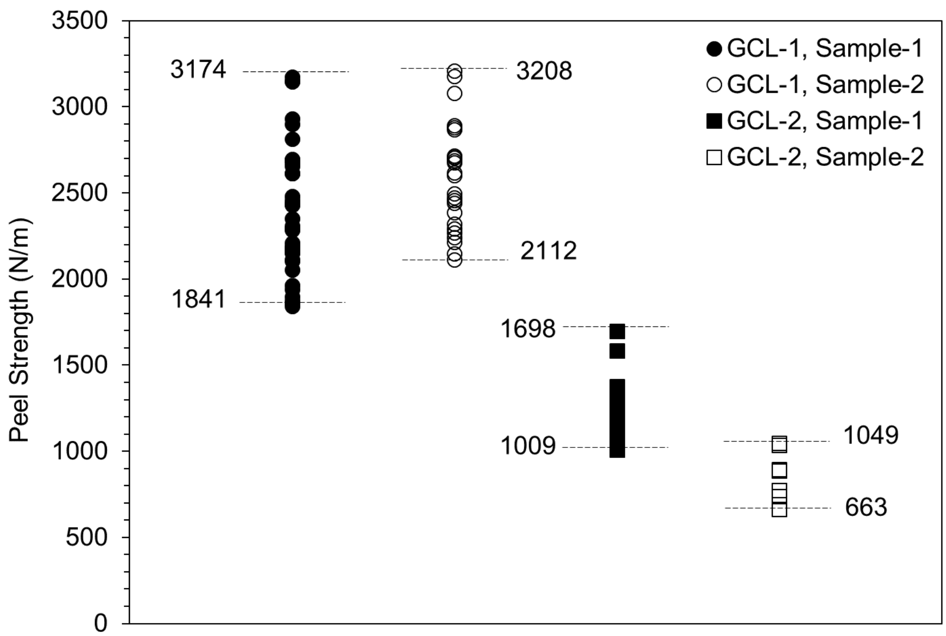

Figure. 3. Dot plot showing variation in peel strength within Sample-1 and Sample-2 of GCL-1 and GCL-2.

Comparable range and coefficient of variation were observed for the peel strength within the two GCL-1 samples (Table 2). Peel strength varied between 1841 N/m to 3174 N/m in Sample-1 of GCL-1 and from 2112 N/m to 3208 N/m in Sample-2 of GCL-1. The average peel strength was 2389 N/m for Sample-1 of GCL-1 and 2591 N/m for Sample-2 of GCL-1. Coefficient of variation was 15.1% for Sample-1 and 11.8% for Sample-2. The combined data from both samples of GCL-1 yielded comparable statistical parameters to both samples. In general, peel strength of individual specimens varied by up to 48% of the manufacturer reported peel strength of GCL-1 (i.e. 2170 N/m).

Variability in peel strength also was observed in Sample-1 and Sample-2 of GCL-2. The two samples of GCL-2 had comparable coefficient of variation (15.3% to 15.9%); however, the range of peel strength in Sample-1 of GCL-2 (1009 N/m to 1698 N/m) was higher than the range in Sample-2 (663 N/m to 1009 N/m) (Table 2).The difference in peel strength range between these two samples was hypothesized to be due to gradual wear of needles during manufacturing of the GCL-2 roll considering that Sample-1 was cut from the start of the production roll whereas Sample-2 was cut from the end of the production roll. The difference in the range of peel strength between the GCL-2 samples resulted in a high coefficient of variation in the combined data set and peel strength variation > 70% of the manufacturer-reported peel strength.

Spatial variation in peel strength within GCL-1 and GCL-2 samples are shown in Figure 4 and Figure 5, respectively, and numbers overlain on the specimens indicate the measured peel strength. In Sample-1 and Sample-2 of GCL-1, no relationship was observed between peel strength and specimen location. However, peel strength for GCL-2 decreased from Sample-1 to Sample-2, which corresponded to progressive movement from the start to the end of the GCL roll. However, no spatial relationship was observed for peel strength and location within each sample. Therefore, peel strength variability in GCL-2 appeared to be random within close spacing, but also exhibit directional variability along the entire GCL roll.

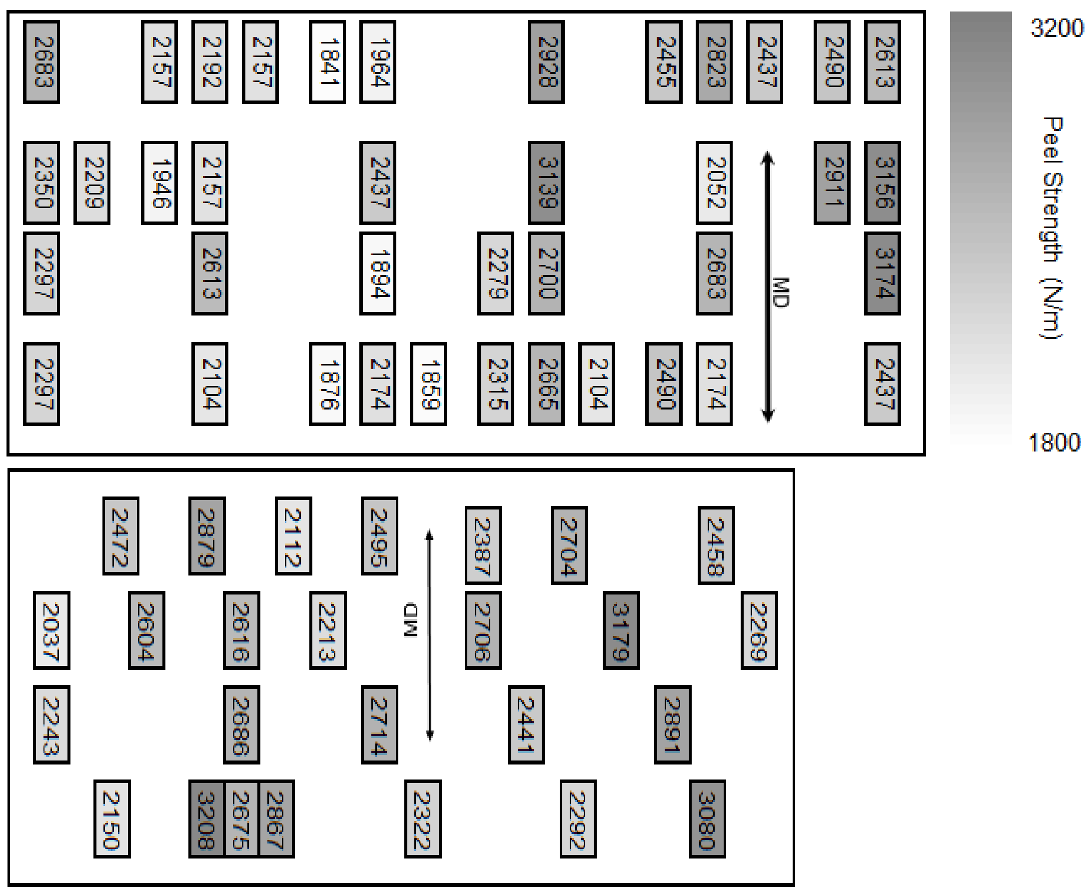

Figure. 4. Distribution of peel strength within (a) sample-1, and (b) sample-2 of GCL-1.

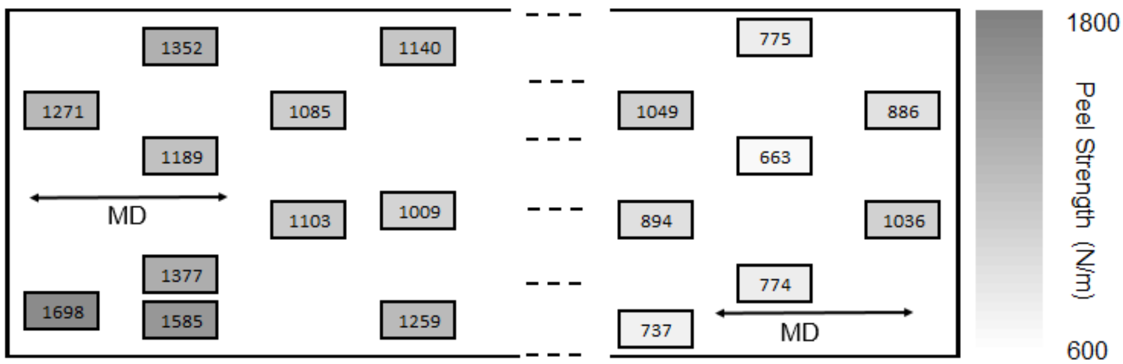

Figure. 5. Distribution of peel strength within Sample-1 and Sample-2 of GCL-2.

Determination of peel strength for a GCL roll is not based on performing a single peel strength test, but rather from the average of specimens from a series of tests. ASTM D6496/6496M requires at least five peel strength tests to determine peel strength of a GCL roll. Theoretically, an increase in the number of peel strength tests would reduce concerns regarding the effect of specimen variability on the calculated average peel strength of a GCL roll. However, performing a high number of peel strength tests may not be practical considering time and resource limitations. Therefore, a fundamental question is “Is there a minimum number of peel strength tests required for a given GCL roll whereupon the average and standard deviation no longer fluctuate?” To answer this question, statistical analyses were performed on the peel strength test results on GCL-1. Analyses were only performed on GCL-1 because (i) peel strength variability was random and (ii) a larger number of tests were conducted.

4 DISCUSSION

The number of peel strength tests conducted on a given GCL roll, n, yields an average peel strength that may or may not represent the average peel strength of the entire production roll deployed in the field. The arithmetic average peel strength of the entire roll is defined PS_roll and the arithmetic average peel strength determined from n peel strength tests is defined as PS_Sample. Therefore, the measurement error, ε, was defined according to Eq. 1.

$$\varepsilon = \frac{|PS_{roll} - PS_{Sample}|}{PS_{roll}} \tag{1}$$

Eq. 1 can also be written as Eq. 2.

$$(1-\varepsilon)\, PS_{roll} \le PS_{Sample} \le (1+\varepsilon)\, PS_{roll} \tag{2}$$

If an entire GCL production roll with dimensions 4.5 m wide x 45 m long (e.g., Agru 2017) was dissected to conducted as many peel strength tests as possible in determination of PS_roll, there would be approximately 10,000 specimens with ASTM-recommend dimensions of 100 mm x 200-mm. Therefore, ε = 0 when n = 10,000 for a given production roll. Peel strength tests on GCL-1 from Sample-1 and Sample-2 were combined (i.e., 65-peel-strength tests) to represent statistical parameters of the population or simply “Population”. Therefore, PS_roll for GCL1 was assumed to be equal to PS_Sample = 2470 N/m (Table 2), such that ε ≈ 0 when n = 65. Rationale for this assumption are: (i) statistical parameters of Sample-1 and Sample-2 of GCL-1 were comparable; (ii) Population data passed the Kolmogorov-Smirnov normality test and can be considered normally distributed; and (iii) peel strength testing on GCL1 specimens were performed by the same operator, following the same procedure, and with the same apparatus.

Considering Eq. 1, the statistical interpretation of the question discussed earlier would be “What is the relationship between n and the probability of having an error = ε in determination of peel strength for a GCL roll?” Answering this question requires implementing the statistical concepts of Confidence Interval and Student's T-distribution (Moore and Kirkland 2007).

Student's T-distribution is a type of continuous probability distribution used to perform statistical analyses, and is used instead of Z-distribution (i.e., normal distribution) when the sample size is relatively small. The concept of Student's T-distribution is visualized in Figure 6., where the Y-axis is the Probability Distribution Function (PDF), and X-axis is a dimensionless parameter, called the T-value. The PDF has a maximum value at $t_\upsilon = 0$, and is symmetrical about $t_{\upsilon,a} = 0$.

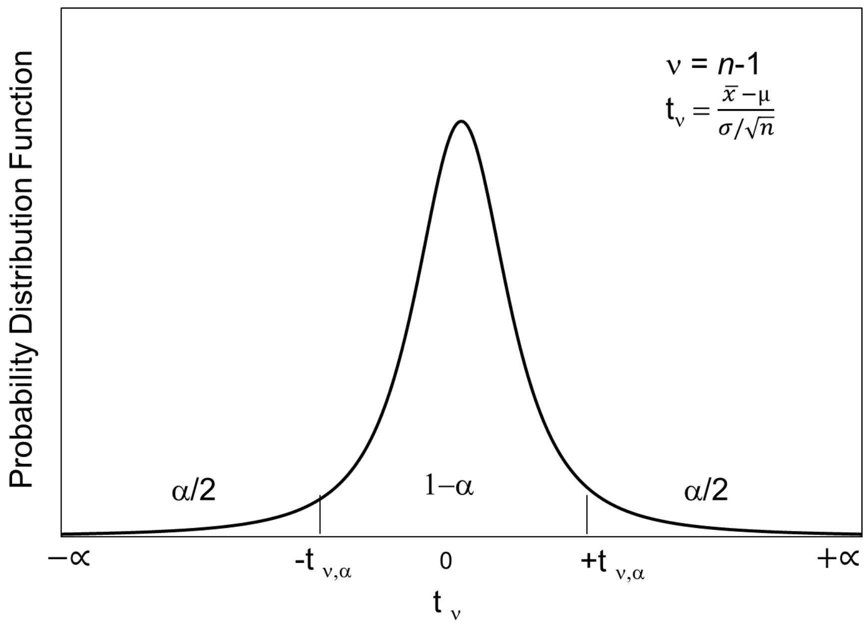

Figure 6. Visualization of the Student's T-distribution.

The T-value ($t_\upsilon \in \,]-\infty, +\infty[\, =$) is defined according to Eq. 3:

$$t_\upsilon = \frac{\bar{x} - \mu}{\sigma/\sqrt{n}} \tag{3}$$

where n = sample size (number of peel strength tests), υ = degrees of freedom, typically equal to n-1, $\bar{x}$ = mean of the Sample (PS_Sample), μ = Population mean (PS_roll), and σ = Population standard deviation. Higher $|t_\upsilon|$ corresponds to larger difference between PS_Sample and PS_roll. Similarly, $t_\upsilon = 0$ indicates that the Sample mean is equal to the Population mean.
Probability Distribution Function is defined in Eq. 4:

$$PDF\ (t_\upsilon) = \frac{\Gamma\left(\frac{\upsilon+1}{2}\right)}{\sqrt{\upsilon\pi}\,\Gamma\left(\frac{\upsilon}{2}\right)} \cdot \left(1 + \frac{{t_\upsilon}^2}{\upsilon}\right)^{\left(-\frac{\upsilon+1}{2}\right)} \tag{4}$$

where Γ = Gamma Function that is defined in Eq. 5.

$$\Gamma(\mathrm{x}) = \int_0^{+\infty} a^{x-1} e^{-a} da \tag{5}$$

Based on the definitions of PDF and t_υ, the area below the PDF is equal to 1 as shown in Eq. 6.

$$\int_{-\infty}^{+\infty} PDF\,(t_\upsilon)\, dt_\upsilon = 1 \tag{6}$$

In Student's T-distribution, a significance level, herein referred to $\alpha \in [0,1]$, and two T-values corresponding to α, namely- $t_{(\upsilon,\alpha)}$ and + $t_{(\upsilon,\alpha)}$ as shown in Figure 6, are defined according to Eq 7.

$$\int_{-\infty}^{-t_{\upsilon,\alpha}} PDF(t_\upsilon)\,dt_\upsilon = \int_{+t_{\upsilon,\alpha}}^{+\infty} PDF(t_\upsilon)\,dt_\upsilon = \frac{\alpha}{2} \tag{7}$$

Or

$$\int_{-t_{\upsilon,\alpha}}^{+t_{\upsilon,\alpha}} PDF(t_\upsilon)\,dt_\upsilon = 1-\alpha \tag{8}$$

This equation states that the area below the PDF for $-t_{\upsilon,\alpha} < t_\upsilon < +t_{\upsilon,\alpha}$ is equal to 1-α. Based on the definition of t_υ in Eq. 3, $\mp t_{\upsilon,\alpha}$ correspond to two values of $\bar{x}$, namely $\overline{x1}$ and $\overline{x2}$ that are from the same distance around μ. Based on Eq. 8, the probability that $\mu - t_{\upsilon,\alpha}\frac{\sigma}{\sqrt{n}} < \bar{x} < \mu + t_{\upsilon,\alpha}\frac{\sigma}{\sqrt{n}}$ is equal to $1-\alpha$, or $P\ (\mu - t_{\upsilon,\alpha}\frac{\sigma}{\sqrt{n}} \le \bar{x} \le \mu + t_{\upsilon,\alpha}\frac{\sigma}{\sqrt{n}}) = 1 - \alpha$. Student's T-distribution parameters (PDF and t_υ) are a function the degrees of freedom, and therefore, depend on *n*. The influence of *n* on Student's T-distribution is visualized in Figure 7. An increase in the Sample size resulted in higher PDF value at $t_\upsilon = 0$, but lower PDF value at $t_\upsilon \rightarrow \mp\infty$. Theoretically, when $n \rightarrow \infty$ (i.e. Sample = Population), Student's T-distribution will be identical to the normal distribution (i.e., Z-distribution). In fact, for $n \ge 50$, the difference between Z-distribution and Student's T-distribution becomes so negligible that Z-distribution is used instead of the Student T-distribution in statistical analyses on high-populations. This was a reason for assuming $PS_{\_Sample} = PS_{\_roll}$ for $n = 65$ in this study.

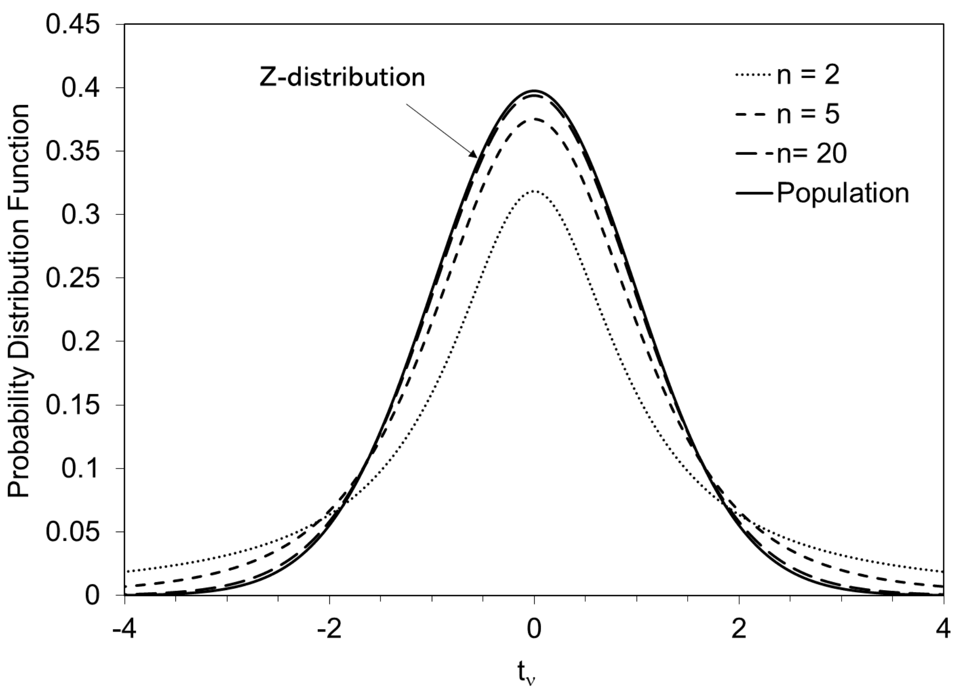

Figure 7. Schematics showing the influence of Sample size on Student's T-distribution.

In Student's T-distribution with a certain degree of freedom, Confidence Interval (CI) is defined as Δt_υ that corresponds to a significance level = α as shown in Eq. 9.

$$\alpha \sim \Delta t_\upsilon = (+t_{\upsilon,\alpha}) - (-t_{\upsilon,\alpha}) = 2t_{\upsilon,\alpha} \tag{9}$$

For a certain Δt_υ, an increase in *n* results in a decrease in α (Figure 7) and an increase in the area bellow PDF (i.e.1- α). For instance, assuming a $|t_{\upsilon,\alpha}| = 1$ (i.e. $\Delta t_\upsilon = 2$), 1 - α = 0.683 for $n \rightarrow \infty$ (Sample = Population), 1 - α = 0.671 for *n* = 20, and 1 - α = 0.626 for *n* = 5. Increase in 1 -α with n for certain CI indicates that there are higher probabilities that the Sample mean lies within a defined range of Population mean when the Sample increased in size.

The statistical analyses of this study, $\bar{x} = PS_{\_Sample}$, $\mu = PS_{\_roll} = 2470$ N/m, and σ = standard deviation of GCL-1 peel strength = 357.7 N/m yield the calculation in Eq. 10.

$$P\left(2470 - t_{v,\alpha}\frac{357.7}{\sqrt{n}} \le PS_{\_Sample} \le 2470 + t_{v,\alpha}\frac{357.7}{\sqrt{n}}\right) = 1-\alpha \tag{10}$$

The measurement error as defined in Eq. 1 can be obtained for different significance levels and n via comparing Eq. 10 and Eq. 2, as shown in Equation 11.

$$\varepsilon = \frac{357.7\ t_{v,\alpha}}{2470\sqrt{n}} \tag{11}$$

The percentage of measurement error calculated from Eq. 11 for significance levels = 0.001, 0.005, 0.01, and 0.05 for $3 \le n \le 50$ are tabulated in Table 3. For a certain n, measurement error decreases with an increase in significance level. For a certain significance level, measurement error decreases with an increase in n. Based on the values in Table 3, estimation of $PS_{\_roll}$ from $PS_{\_Sample}$ based on performing 5 peel strength tests could result in a measurement error of 17% and 28% for significance levels of 0.05 and 0.01, respectively. Therefore, achieving a measurement error < 10 % for the samples of the GCL tested in this study would require at least 10 peel strength tests for $\alpha = 0.05$, and at least 15 peel strength tests for $\alpha = 0.01$.

Table 3. ε (%) as a function of Sample size (n), and significance level (α).

n	α			
	0.05	0.01	0.005	0.001
3	34	78	> 100	> 100
4	22	40	51	88
5	17	28	34	52
6	14	22	26	38
7	13	19	22	31
8	11	17	19	26
9	10	15	17	23
10	10	14	16	21
15	8	10	12	15
20	6	9	10	12
30	6	8	9	11
50	4	5	6	7

Note: α = significance level; n = number of peel strength tests

It is noteworthy to mention that the methodology for statistical analyses of this study is only applicable to NP GCLs such as GCL-1 with random peel strength variability across the roll. This methodology does not apply to GCL rolls with non-random (e.g. directional) peel strength variabilities such as GCL-2 in this study. Additional research is required to quantify the measurement error for the GCL rolls with both random and directional variability in peel strength.

5 CONCLUSIONS

A series of 84 peel strength tests were performed on two different NP GCLs to evaluate the variabilities in peel strength and estimate the peel strength measurement errors. Spatial variabilities in peel strength up to 48% of the manufacturer-reported peel strength were observed in forms of random variabilities as well as directional variabilities. A series of statistical analyses were performed to assess the relationship between the measurement error and number of peel strength tests for the GCL with random spatial variability in peel strength. Results indicated that determination of peel strength based on performing 5 peel strength tests (i.e. ASTM-recommended minimum number of tests) could results in a measurement errors of 17% and 28 % for significance levels of 0.05 and 0.01 respectively.

6 DATA AVAILABILITY

All data, models, and code generated or used during the study appear in the submitted article.

7 REFERENCES

AGRU America (Agru). 2017. Drop-In Specifications, Geosynthetic Clay Liners. 500 Garrison Road, Georgetown, SC 29440, USA.

ASTM. 2016. "Standard test method for determining the internal and interface shear strength of geosynthetic clay liner by the direct shear method". *ASTM D6243/D6243M-16*. West Conshohocken, PA: ASTM.

ASTM. 2020. Standard test method for determining average bonding peel strength between top and bottom layers of needle-punched geosynthetic clay liners. *ASTM D6496/6496M-20*. West Conshohocken, PA: ASTM.

Athanassopoulos, C. and Yuan, Z. 2011. "Correlation between needle punch-reinforced geosynthetic clay liner peel strength and internal shear strength." *Geo-Frontiers 2011: Advances in Geotechnical Engineering*, Han, J. & Alzamora, D. E., (eds.), ASCE, Reston,VA, USA, GSP No. 211, 1922-1930. https://doi.org/10.1061/41165(397)196.

Bacas, B. M., Blanco-Fernandez, E. and Cañizal, J. 2013. "Comparison of the adhesion and shear tensile strength of needle-punched GCLs." *Geotextiles and Geomembranes*, 41(1), 17-25. https://doi.org/10.1016/j.geotexmem.2013.08.007.

Bareither, C. A., Soleimanian, M., and Ghazizadeh, S. 2018. "Direct shear testing of GCLs at elevated temperature and in a non-standard solution." *Geosynthetics International*, 25(3), 350-368. https://doi.org/10.1680/jgein.18.00014.

Ghazizadeh, S. and Bareither, C. A. 2018. "Stress-controlled direct shear testing of geosynthetic clay liners II: assessment of shear behavior." *Geotextiles and Geomembranes*, 46(5), 667-677. https://doi.org/10.1016/j.geotexmem.2018.06.004.

Ghazizadeh, S., & Bareither, C. A. 2021. "Variability of Fiber Reinforcement, Peel Strength, and Internal Shear Strength in Needle Punched GCLs". *Journal of Geotechnical and Geoenvironmental Engineering*. In-print (Manuscript: GTENG-8701).

Hurst, P., & Rowe, R. K. 2006. "Average bonding peel strength of geosynthetic clay liners after short-term exposure to water and jet fuel A-1". *Geotextiles and Geomembranes*, 24(1), 58-63.

McCartney, J. S., Zornberg, J. G., Swan, R. H. Jr. and Gilbert, R. B. 2004. "Reliability-based stability analysis considering GCL shear strength variability." *Geosynthetics International*, 11(3), 212-232. https://doi.org/10.1680/gein.2004.11.3.212.

McCartney, J. S., Zornberg, J. G., and Swan Jr, R. H. 2009. "Analysis of a large database of GCL-geomembrane interface shear strength results." *Journal of Geotechnical and Geoenvironmental Engineering*, 135(2), 209-223. https://doi.org/10.1061/(ASCE)1090-0241(2009)135:2(209).

Mesri, G. and Olson, R. E. 1970. "Shear strength of montmorillonite." *Géotechnique*, 20(3): 261-270. https://doi.org/10.1680/geot.1970.20.3.261.

von Maubeuge, K. P. and Ehrenberg, H. 2000. "Comparison of peel bond and shear tensile test methods for needlepunched geosynthetic clay liners." *Geotextiles and Geomembranes*, 18(2-4), 203-214. https://doi.org/10.1016/S0266-1144(99)00027-8.

von Maubeuge, K. P. and Ehrenberg, H. 2013. "Peel and shear test comparison and geosynthetic clay liner shear strength correlation." Current and Future Practices for the Testing of Multi-Component Geosynthetic Clay Liners, von Maubeuge, K. and Kline, J. (eds.), *ASTM International*, West Conshohocken, PA, 78-90. https://doi.org/10.1520/STP156220120098.

Zornberg, J. G., McCartney, J. S. and Swan, R. H. Jr. 2005. "Analysis of a large database of GCL internal shear strength results." *Journal of Geotechnical and Geoenvironmental Engineering*, 131(3), 367-380. https://doi.org/10.1061/(ASCE)1090-0241(2005)131:3(367).

Dam safety and efficient tailings dewatering through enhanced and adapted drainage solutions

Pascal Saunier & Stephan Fourmont
Afitex-Texel Geosynthetics inc, Ste Marie, QC, Canada

ABSTRACT: Over the past years, dam's breach disasters, fortunately rare, have been investigated revealing that, in many cases, the lack of efficient drainage was one of the main causes of these failures. The accumulation of water into the tailings dam or at the base of them is critical situation engineers and operators want to stay away from to ensure the safety of the work. As with an adequately thick homogeneous layer covering the entire base or at interlifts of the dam, or when being constructed in French drains as finger drains directly placed into the structure during construction, it is not always feasible to set up a granular drainage system. The granular material can be unavailable or expensive on the site and therefore might make its use impossible or financially irrelevant. This is where geosynthetic solutions offer a valuable alternative. However, two problems arise:

- the extreme loads to which these materials are exposed to, which for most of them will lose their drainage properties because of the creep effect,
- the large quantity of very fine particles in the material itself, which can lead to rapid clogging of the geotextile fibers and thus lead to a complete loss of its permeability, and by extension their efficiency.

The particularity of Multi-Linear Drainage Geocomposites (MDLG) is that they resist particularly well to the load, even extreme, once they are confined, and their manufacturing process allows the selection of geotextiles previously tested to be compatible with the materials placed in contact with them. Therefore, creep and clogging are no longer an issue, and those manufactured products offer a stable cost year after year, making easier investment management.
This paper presents, through case studies, the different applications where these materials are particularly efficient, the strategies implemented for their characterization, and the techniques implemented for their efficient installation and use.

1 INCREASED REGULATION OVER THE YEARS

1.1 *History*

Since the 18^{th} century, when we can consider the mining industry started in Canada, the regulation never stopped getting more and more drastic, especially to ensure the security of works and people as high as possible. This tendency is even more important since the beginning of the 21^{st} century were major concerns such as global warming and the protection of the environment is at the center of the political and social concerns. Reducing at a minimum the potential impact of mining operations on the environment led the entire industry to adjust its way of operating and closing their operational sites. Limiting the potential infiltration of processed water into the soil, through a better drainage below a lined pond or a dam, reducing the amount of ore oxidation or leachate generation by building a look proofed cap during a final closure, or reducing the water pressure into the dam for an increased stability and therefore safety during construction and operation.

1.2 *Importance of drainage*

One key factor for safe and environmentally respectful designs is having an efficient drainage. This is true for an increased safety in the works where water can be the most challenging element that needs to be managed, otherwise disasters may occur, but also in ponds or final remediation simply because a liner or low permeability layer is not efficient without a good drainage.

For decades, gravel was used to offer high permeability layers, acting as drainage elements, and located at the Dam's base, below pond, or for the final cover. The two biggest issues granular materials present are:

- They tend to be rare, and therefore more and more expensive to use,
- They generate a heavy quantity of GEG, and especially when the pit is located far away from the construction site.

This is why, since several decades, geosynthetics are more and more used in replacement of those granular materials.

2 MULTILINEAR DRAINAGE GEOCOMPOSITE TECHNOLOGY

2.1 *Description of the technology*

The use of geomembranes in mining applications has been widely documented. However, geocomposite compatibility studies with mined material are scarce and very limited information is available.

The MLDG used in this study is developed by Afitex-Texel and called DRAINTUBE®. It is composed of (Figure 1):

- a nonwoven polyethylene geotextile acting as a filter,
- a series of corrugated polypropylene mini-pipes spaced at regular intervals (from 0.25 m to 2 m on centers). These perforated mini-pipes provide most of the drainage capability of the product; and
- a nonwoven thick polypropylene geotextile acting as the drainage medium and as a cushion to protect the underlying geomembrane.

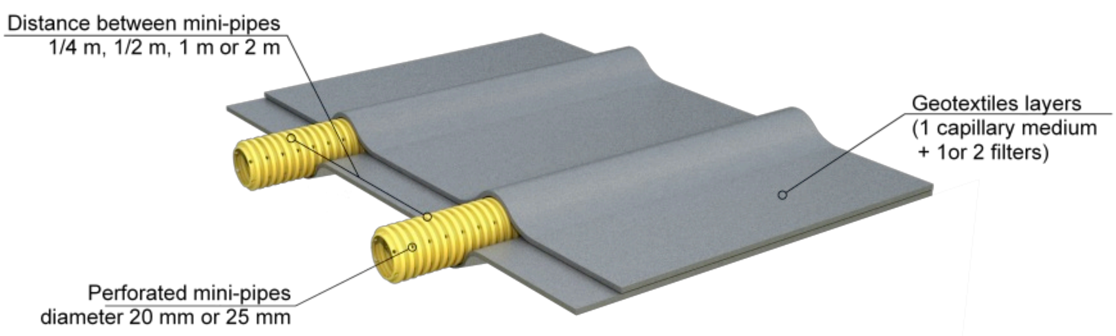

Figure 1. DRAINTUBE® Multi-Linear Drainage Geocomposite.

Filtration applications with mine residues may be among the most challenging filtration applications. First, the high seepage forces and suspended particles that must be filtered can lead to clogging. Second, leachate is typically a highly loaded solution and mineralization can lead to chemical clogging (Faure, 2004; Fourie et al., 2010; Legge et al., 2009). Although it is likely that a clogging problem would also occur with mineral drainage systems (such as gravels, see Giroud, 1996). In order to check if MLDG are able to fulfil the function of a drainage and dewatering layers, long-term hydraulic properties, soil retention, and chemical resistance must be evaluated.

Results of experimental studies aiming at checking these points are presented in the following sections.

2.2 *Behavior under High Compressive Load*

With an ore density between 1.5 and 1.8, the compressive load on the drainage layer can reach 2 MPa (Thiel and Smith, 2004; Castillo, 2005). For traditional planar geocomposites involving a planar drainage core (such as biplanar or triplanar geonet), it has been shown by several authors that the hydraulic properties of these geosynthetics are adversely affected by such high compression stresses.

However, Saunier et al. (2010) have shown that the particular structure of draintube MLDG is favorable to the development of an arching effect around the pipe. As a consequence, the transmissivity (the volumetric flow rate per unit width of specimen per unit gradient in a direction parallel to the plane of the specimen; see ASTM D4716 and GRI GC15 standards) is not affected by the compression stress, nor by time, as no creep can develop in the pipe. Their results are reported in Figure 2.

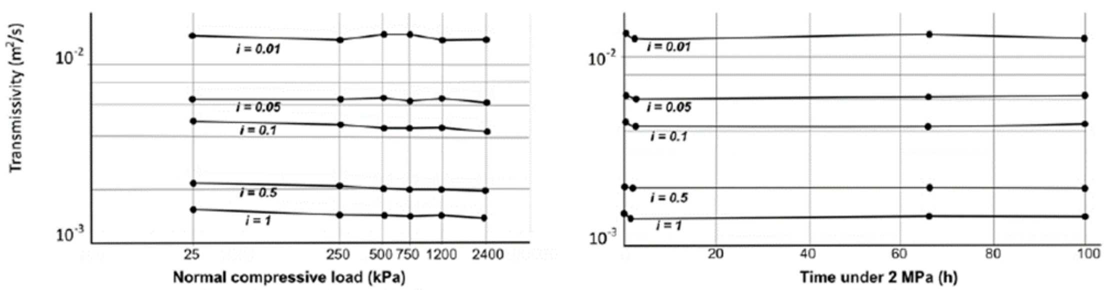

Figure 2: Transmissivity under Different Loads up to 2 Mpa and 100 h (i = hydraulic gradient) (after Saunier et al, 2010).

The lack of sensitivity of the product to compression loads up to 2,400 kPa suggests that these observations are likely to be applicable to the high normal loads which are typically experienced in heap leach pads.

The applied combined reduction factors (intrusion of the geotextile into the drainage core RFIN, creep of the drainage core RFCR, chemical clogging of the drainage core RFCC and biological clogging of the drainage core RFBC) for Draintube MLDG are at least half of those applied to standard geonet geocomposites (Maier, et. al., 2013). In other words, for the same index transmissivity, Draintube MLDG offers at least two times higher long-term flow capacity than a geonet geocomposite. ASTM D7931 provides recommendations to determine the allowable flow rate of drainage geocomposites including MLDG.

3 COMMON APPLICATIONS IN THE MINING INDUSTRY

3.1 *Ponds*

Drainage under single and double lined ponds (figure 3) is crucial to ensure their containment integrity. Indeed, the pressure developed by the high-water table or the accumulation of gas under the geomembrane creates swelling and irreversible degradations of the liner. The use of MLDG allows to protect the geomembrane against puncture (Blond et al., 2003), dissipate such pressures and maintain the performance of the structure over time.

In double lined ponds, Draintube MDLG is also used between the two liners as leak detection layer. In order to control the integrity of the primary liner with geoelectrical methods (such as ARC test, Water Puddle or Dipole), conductive Draintube MLDG, including an electrically. conductive grid, have proven to be effective and are now approved by most inspection agencies (figure 4).

Figure 3. Double lined produced water pond drained with a MLDG below the secondary liner (groundwater) and the primary liner (leak detection layer).

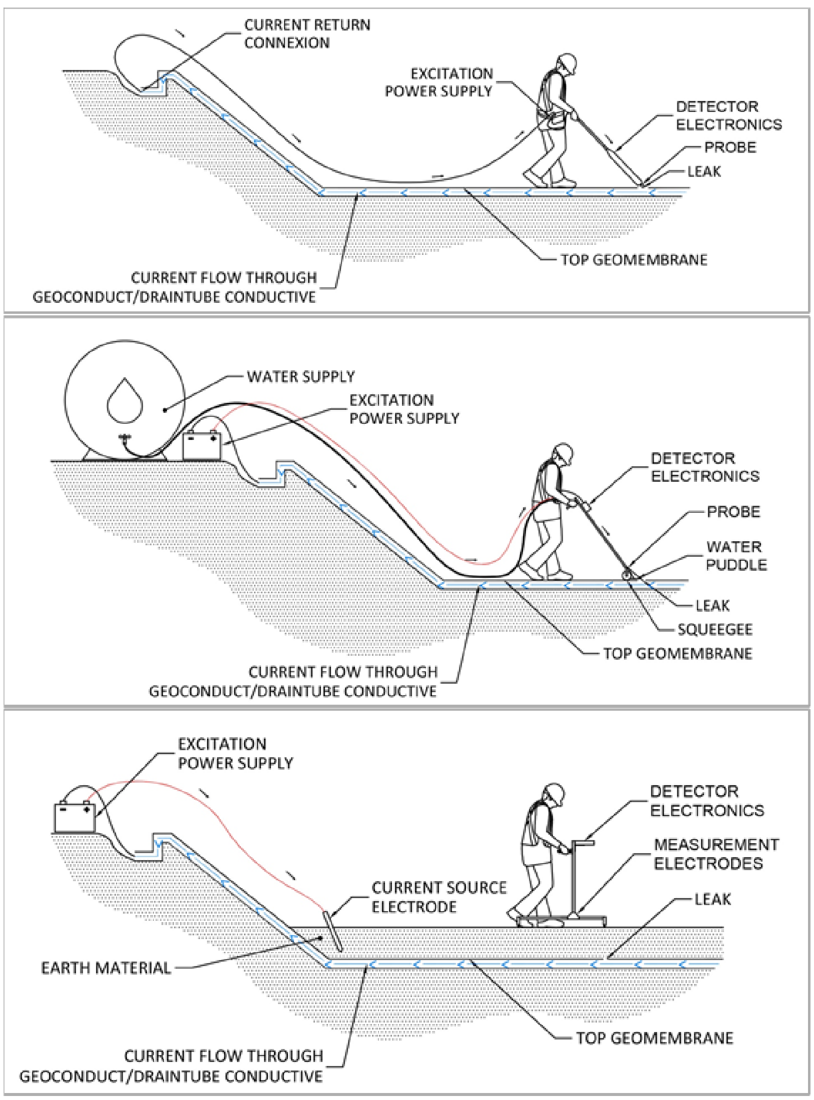

Figure 4. Use of Conductive DRAINTUBE® to run Leak Location Surveys (ARC test, Water Puddle and Dipole).

3.2 *Final cover*

Covers on mine waste disposal sites are required to minimize the infiltration of precipitation. Limiting water infiltration reduces the creation of leachates that can be problematic to manage afterwards, and in some cases, limiting air intrusion into the waste limits the oxidation of the tailings. Finally, the vegetative coverage of these structures allows the mine site to have a more neutral appearance that blends naturally into its environment (figure 5).

Figure 5. Mine Waste disposal site during and after construction of its final cover.

As per Del Greco et al. (2012), Draintube MLDG evacuates the infiltrated water faster and with a higher flow rate than a 500 mm thick gravel drainage layer (coarse clean gravel 1/3 to 1-1/2 in.). Figure 6 shows the typical cross section of the two test pads, 10 m long and 4 m wide.

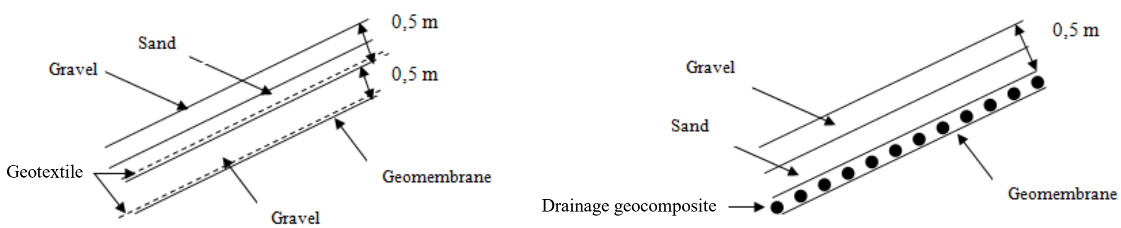

Figure 6. Test pad description.

Flow rate was measured for two initial hydraulic conditions, dry (d) and partially saturated (ps). Regardless of the initial conditions, the Draintube MLDG had a faster response time than the gravel drainage layer, about 30% faster.

Also, the figure 7 shows the flow rate measured for the 4 configurations:

- Draintube MLDG in dry conditions, MLDGd
- Draintube MLDG in partially saturated conditions, MLDGps
- Gravel layer in dry conditions, Gd
- Gravel layer in partially saturated conditions, Gps

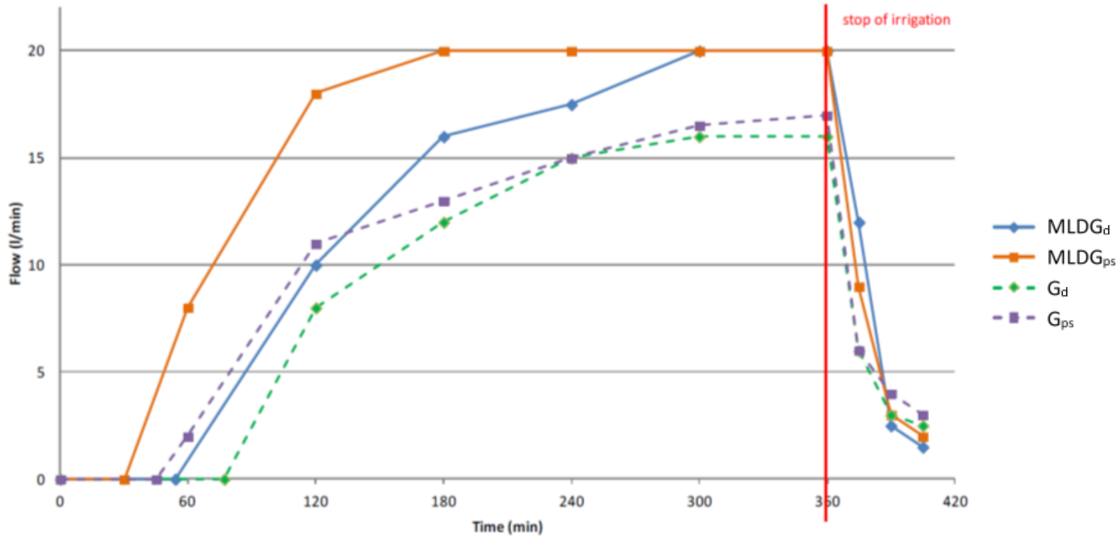

Figure 7. Flow rate comparison over time between MLDG and Gravel layer.

As shown in the Figure 7, the total amount of drained water was greater with Draintube MLDG. Indeed, the gravel drainage layer retained between 20% and 25% more water than the MLDG. The water remaining into the gravel layer may increase the infiltration rate through any defect in the geomembrane or though the low permeability layer.

The mini-pipes of the MLDG collect and evacuate the fluid in one given direction (the direction of the mini-pipes) even if the slope equals to zero. This directional aspect of the MLDG helps to reduce the impact of differential settlements that will occur on a cover and causes reverse slopes. A homogeneous drainage layer will drain in the direction of the reverse slope into the land subsidence whereas the MLDG will drain the water in the direction of its tubes to the collector trenches or ditches.

3.3 *Tailings dewatering*

The tailings deposition in a TSF leads to two major problems when saturated: they are unstable and they occupy a gigantic space, which increases their environmental footprint. It is therefore necessary to reduce their water content as much as possible. Granular drainage layers, if they are efficient, present the problem of increasing cost and reducing the storage capacity of the TSF or the pond. The geosynthetic solution is therefore a promising avenue, both financially and in terms of optimizing the available volume, but only if the management of fine particles is properly addressed. The filtration compatibility of the geotextile filters and the tailings can be confirmed by running a Gradient Ratio test (figure 8).

A complete methodology has been developed and documented (Blond et al. 2018) for MLDG using Texel's F Series filters offering a Filtration Opening Size (FOS) ranged between 60 and 120 microns (as measured per CAN/CGSB 148.1 NO. 10). The objective of the applied methodology is to determine, from the gradient ratio test, that the selected geotextile filter is not blocked/clogged.

The Permittivity values of the system (tailing + geotextile) remain stable over time and similar to the tailing permeability itself (figure 9). The Gradient Ratio curve remains also stable through the duration of the test (figure 10) and can be concluded that the selected filter is compatible with the filtered tailings and will behave in a proper manner against fast clogging or pipping.

Figure 8. Set-up of the filtration test (Gradient Ratio test, ASTM D5101).

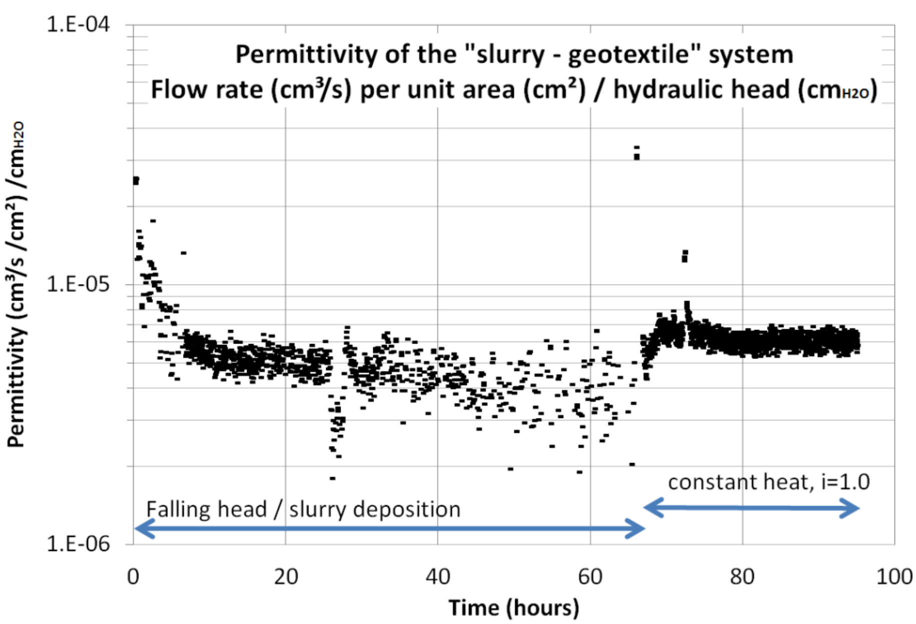

Figure 9. Permittivity versus time.

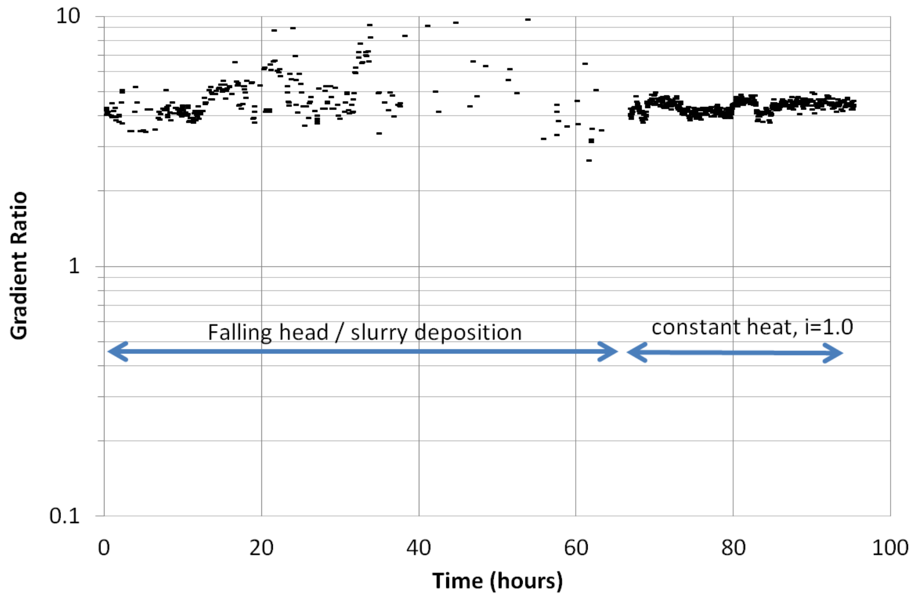

Figure 10. Gradient Ration versus time.

3.4 *Base Dam drainage*

Recently, several dam failures have occurred in Canada and Brazil. After analysis of these disasters, it was found that the lack of drainage was one of the main factors. Downstream expansion is a very popular technique to increase the storage capacity of the dam. However, the risk of water seepage into the structure is high and it is therefore necessary to ensure that effective drainage is carried out at the base of the dam to release the interstitial pressures created.

Draintube MLDG are an advantageous alternative to granular materials because, like them, they are not sensitive to creep when confined and therefore offer a constant flow capacity in time, even under high loads (figure 11).

Figure 11. Drainage at the base of the dam during its downstream expansion using a MLDG.

4 CONCLUSION

Drainage is key for a long-term efficiency in mining works. Granular material is no longer cost effective and increase the environmental footprint of the constructions such as dam expansion, ponds, tailings dewatering and final closures. That is why geosynthetics are use more often to act as thin drainage layers.

Draintube Multi-Linear Drainage Geocomposites are one of the most efficient solutions, especially under high load, because they are not suffering from creep nor intrusion when confined into a soil matrix, because of their core structure. They also offer a great flow capacity, and because some of them are made of components with very well designed filters, they can stay away from fast clogging and therefore keep the works in good condition of use and performance.

5 REFERENCES

Faure, Y.H., Baudoin, A., Pierson, P. and Plé, O. 2006. A Contribution for Predicting Geotextile Clogging during Filtration of Suspended Solids. Geotextiles and Geomembranes, 24: 11-20

Fourie, A.B., Bouazza, A., Lupo, J., and Abrao, P. 2009. Improving the Performance of Mining Infrastructure through the Judicious Use of Geosynthetics. Proceedings of 9th International Conference on Geosynthetics, 2010, Brazil, 1: 193-219

Legge, K.R., Baxter, P., Meyer, P.J., Sander, M.G., and Viljoen, D.T.V. 2009. Keynote Lecture: Geosynthetics for Africa. Proceedings 1st African Regional Geosynthetics Conference, Cape Town, South Africa, pp. 1-40.

Giroud, J.P. 1996. Granular Filters and Geotextile Filters. Geofilters'96, Montréal, Québec, Canada, 1: 565-680.

Thiel, R. and Smith, M.E. 2004. State of the Practice Review of Heap Leach Pad Design Issues, Geotextiles and Geomembranes 22: 555-568.

Castillo, J., Hallman, D., Byrne, P. and Parra, D. 2005. Dynamic Analysis of Heap Leach Pad under High Phreatic Levels. Proceedings of 27th Mining convention, Arequipa, Peru.

Saunier, P., Ragen, W. and Blond, E., 2010. Assessment of the resistance of drain tube planar drainage geocomposites to high compressive loads. 9th International Conference on Geosynthetics. Guarujá, Brazil. Vol. 3

ASTM D4716 / D4716M-14, Standard Test Method for Determining the (In-plane) Flow Rate per Unit Width and Hydraulic Transmissivity of a Geosynthetic Using a Constant Head. ASTM International, West Conshohocken, PA, 2013

Geosynthetic Institute, 2017. GRI GC15, Determining the Flow Rate per Unit Width of Drainage Geocomposites with Discrete High Flow Component. Folsom, PA, 9 pp.

Maier, T.B. and Fourmont, S., 2013. How Tubular Drainage Geocomposite Was Used in Landfill Final Cover. Geosynthetics. Vol. 31, No.3, pp. 48 – 51

ASTM D7931-18, Standard Guide for Specifying Drainage Geocomposites. ASTM International, West Conshohocken, PA, 2018

Blond, E., Bouthot, M., Vermeersch, O.G. and Mlynarek, J. (2003) Selection of protective cushions for geomembrane puncture protection. 56th Annual Canadian Geotechnical Conference, Winnipeg, Manitoba, Canada.

Del Greco O., Fey A., Oggeri C., and Fourmont S. 2012. Behaviour of drainage geosynthetics for landfill capping systems. 5th European Geosynthetics Congress, Valencia, Spain, 2: 114-118

Blond E., Saunier P. and Dolez P. 2018. Filtration of oil sands tailing slurries. Geosynthetics Magazine, October/November 2018. 13-20

CAN/CGSB 148.1 NO. 10, Methods of Testing Geosynthetics - Geotextiles - Filtration Opening Size. Standard by Canadian General Standards Board, Canada.

ASTM D5101, Standard Test Method for Measuring the Filtration Compatibility of Soil-Geotextile Systems. ASTM International, West Conshohocken, PA.

Use of temporary exposed geomembranes to reduce acidic runoff from mine waste storage areas

Michael F. Houlihan & R. David Espinoza
Geosyntec Consultants, Washington D.C., USA

ABSTRACT: Many mine waste storage facilities contain sulfidic minerals that produce acidic runoff or infiltration when exposed to precipitation. Regulations, social governance principles, and good engineering practice require that impacts from such runoff be mitigated. Mitigation can include permanent closure and capping, collection and treatment of the impacted water, or isolation of the waste from precipitation. This paper discusses the use of exposed geomembranes for reducing impacts to surface and groundwater from mine waste storage areas, including a summary of performance challenges and how to address them in design. The illustration of these approaches includes a discussion of an exposed geomembrane used for containment and isolation of acid-forming waste material at a large mine site. The solution substantially reduced the amount of wastewater requiring treatment and prevented a significant capital expenditure to upgrade the existing wastewater treatment system that would have been required to treat the additional impacted water.

1 INTRODUCTION

Many common mineral ores, including copper, zinc, nickel, cobalt, molybdenum, and some coal and iron ores, contain sulfur. After processing to remove the waste material in the ore, the waste material is typically placed in either a waste pile or a tailings surface impoundment. Accordingly, the mine waste may consist of waste rock, spent ore from leaching operations, or tailings from processing of the ore. Water infiltrating through sulfidic mine waste material, when exposed to oxygen, can become sulfidic and highly acidic. Such water represents a significant threat to both surface water and groundwater resources near the waste material management facility through spilling of contaminated waste material or water, seepage of surface water through the containment embankment, or seepage to groundwater or surface water through the foundation below the stored mine waste. Such impacts can substantially impact the viability of water resources for human and environmental communities near the waste storage area and can also adversely impact a mine operations' compliance with applicable regulations and social license to operate the mine. Accordingly, preventing such impacts is of great importance for mine owners.

The key elements that must be present for formation of acidic runoff are oxygen and water. Preventing the contact of processed ores with oxygen and water, therefore, is the basic approach to preventing the formation of acidic runoff. Further, the potential for acidic runoff formation exists for as long as the mine wastes have a net acid-producing potential (i.e., as long as oxidation products formed in the waste material are not buffered by acid-consuming components present in the waste material), which could be in perpetuity. There are numerous examples of the impacts of sulfide-impacted waters from mine sites on the environment (see Espinoza, 2018, and Hojka, 2019). In these and many other cases, the potential for impacts are well known during the mine site design stage and the effort required to remedy the environmental impacts are costly and may take many years (even decades) to complete. For these reasons, prevention is preferable to remediation of such impacts.

Water may accumulate in a mine waste storage facility over its operating life, potentially resulting in a significant quantity of acidified water in the storage facility. This water, if it is acidic or does not otherwise comply with applicable water quality standards, must eventually be treated, so preventing water accumulation during the operating period is key to limiting the amount of water that must be treated. There are a number of strategies for preventing the accumulation of acidic water in runoff from mine waste storage areas, most of which involve covering the waste to prevent infiltration of rainwater. Compared to earth cover systems, exposed geomembrane covers provide a substantially reduced amount of infiltration and, therefore, reduced amount of wastewater that could impact the environment and that needs to be treated.

Exposed geomembrane covers have long been used for isolation of waste materials. When properly designed and constructed, these systems provide the benefits of containment and isolation while temporarily avoiding the cost of a full closure system. They also provide flexibility for operations, opportunities for future use or remediation, and reduced cost for wastewater treatment, as a result of either reduced wastewater volume or the ability to construct a smaller, less costly treatment system. This was the case for the example described in Section 4 of this paper. However, exposed geomembrane covers involve unique design challenges associated with foundation conditions, anchorage, resistance to forces of wind and precipitation, and durability. In this paper, the features, key design considerations, and advantages and disadvantages of temporary exposed geomembrane covers are described.

2 OVERVIEW OF TEMPORARY EXPOSED GEOMEMBRANE COVERS

2.1 *Description*

Temporary exposed geomembrane covers provide a simple and direct barrier layer between waste materials and the environment, preventing contact between the waste and humans or the environment. The components of an exposed geomembrane cover system are shown in Figure 1 and include only a geomembrane barrier layer over waste and, if needed, grading layer(s) between the waste and the geomembrane. In contrast, and for illustrative purposes only, the components of a typical waste disposal facility cover system are identified in Figure 2 and include a topsoil layer, a vegetative support soil layer, and perhaps a geomembrane barrier layer overlain by a geosynthetic drainage layer. Because there is no need to procure, place, and maintain cover soil layers for an exposed geomembrane cover system, it is typically much less costly to construct, easier and less costly to maintain, and easier to repair than a typical cover system. Because of the low permeability of the geomembrane, it is also extremely effective at preventing infiltration of rainfall or surface water that could become contaminated if it were to come into contact with the waste.

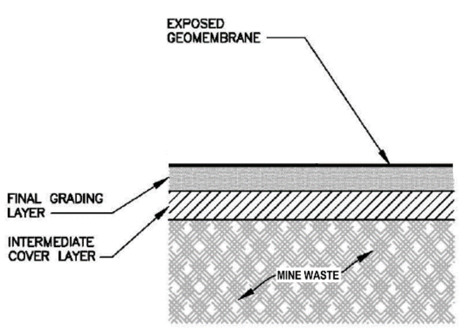

Figure 1. Exposed Geomembrane Cover System

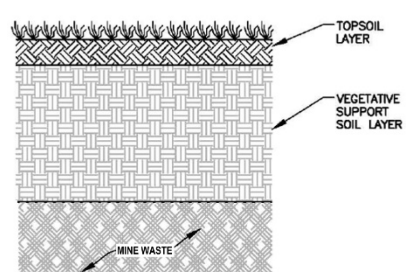

Figure 2. Typical Earth Cover System

2.2 *History of Their Use*

Exposed geomembrane cover systems have been used to cover wastes for decades. Their use as waste facility covers grew out of landfill waste containment practice in the mid- to late 1900's. Covering of temporary waste piles with thin polymer plastic (i.e., geomembrane) sheets was common by the 1980's, and by the late 1990's exposed geomembrane cover use at landfills was relatively common in the United States. Gleason et. al. [2001] describe the successful use of long-term temporary exposed geomembrane cover systems at four municipal waste landfills, and examples of the use of exposed geomembrane covers at mine waste sites are provided by Espinoza et. al. (2019) and Hojka (2018). Development of new materials and products has expanded the range of applicability of exposed geomembranes since 2000 including, for example, a geomembrane integrated with synthetic turf material that provides the benefits of an exposed geomembrane cover and limits the stormwater runoff and wind uplift challenges of exposed geomembranes. Over the past 25 to 30 years, well designed and constructed exposed geomembrane caps have been shown to be durable and require minimal maintenance (see, for example, Geosyntec, 2007), and have even proven to be highly resistant to damage from extreme events including hurricanes.

Photo 1. Exposed geomembrane cap system with synthetic turf (ClosureTurf®, 2020)

2.3 *Regulation*

Exposed geomembrane covers generally meet regulatory requirements for temporary applications (e.g., 1-5 years) but require variances to regulations for longer-term or permanent applications. In the United States, about half of states responding to a 2009 survey allowed exposed geomembrane alternative covers, and regulatory variances allowing exposed geomembrane covers have been allowed in at least 16 states [GRI, 2010]. Variance approvals typically require successful demonstration of the durability and performance of the exposed geomembrane for the duration of the design life under extreme weather conditions that exceed the design condition for more traditional earth cover systems. In addition, integrating waste material cover design with reuse of a site for generating energy from solar resources can meet certain regulatory or social renewables initiatives; for example, the United States Environmental Protection Agency encourages owners to achieve site reuse goals by integrating cover design with alternative energy generation [EPA, 2011].

2.4 *Features and Challenges*

As shown by a comparison of Figures 1 and 2, temporary exposed geomembrane covers are simpler than a comparable earth cover, which offers several advantages. However, the fact that the geomembrane is exposed poses some challenges. Advantageous features of temporary exposed geomembrane covers include the following.

- *Reduced installation cost compared to alternatives*. Elimination of topsoil, cover soil, drainage, and vegetation components of a typical final cover system may reduce construction costs by as much as half, depending on site-specific conditions and the availability of construction materials at the site.
- *Reduced Annual Operation and Maintenance requirements.* Because there are no exposed soils on a temporary exposed geomembrane cover, operation and maintenance costs are

very low if the cover was designed to resist damage as discussed in Section 3 below.

- *Easier access to mine waste materials for future reclamation*. If future reclamation of minerals in the mine waste is a possibility, then a temporary exposed geomembrane cover would allow access to the waste without having to remove the existing cover soils, which would be required for an earth cover system.
- *Very low hydraulic head on the cover system*. Surface water drains rapidly off of temporary exposed geomembrane covers without buildup of water on or within the cover, limiting the hydraulic head on the geomembrane and minimizing infiltration into the waste.
- *Slope stability.* Properly designed exposed geomembrane cover systems are stable and do not experience stability challenges that are common to soil final cover systems. Since there are no soils on the sideslopes of temporary exposed geomembrane covers, stability concerns typical of earth cover systems (e.g., cover system component interface stability associated with slope inclination, water seepage forces, and material interface friction) are not design concerns.
- *Enhanced visual inspection*. Because the geomembrane is exposed, it may be easily inspected for damage, which, if identified, may be easily and inexpensively repaired.

Potential challenges of temporary exposed geomembrane covers should also be considered prior to and during the design, including the following.

- *Vulnerability to environmental damage.* Because the geomembrane is not protected by overlying cover soils, temporary exposed geomembrane covers are susceptible to damage from animals, exposure to sunlight, vandalism, low temperatures, and extreme weather (i.e., wind uplift, hail, lightning strikes, etc.). A general discussion of wind uplift design is presented in Section 3.2 of this paper.
- *Volume and velocity of stormwater runoff.* Stormwater runoff is conveyed quickly off of an exposed geomembrane cover system, resulting in increased stormwater peak flow quantities and increased runoff velocities compared to vegetated surfaces. The increased peak flow quantity requires an increased capacity for stormwater drainage features (i.e., ditches and culverts) and, possibly, a significantly increased peak storage capacity for on-site stormwater management ponds.
- *Limited access.* Access to a cover system is usually required to allow maintenance of stormwater management and other infrastructure features and to make repairs to damaged features on the cover system. However, for an exposed geomembrane cover, vehicular access is either limited to a cover access road or not provided at all in order to protect against puncture or other damage to the exposed geomembrane.
- *Limited Design Life.* Because the geomembrane is not protected from environmental damage (i.e., because it is exposed), its design life is limited and is a function of designed.
- *Limited regulatory approval*. Because temporary exposed geomembrane covers represents a departure from typical engineering practice at mine waste storage facilities, additional analyses or 'performance equivalence' demonstrations could be required to obtain regulatory approval.
- *Aesthetics*. A mine waste storage facility covered with an exposed geomembrane could be perceived as less visually appealing than a fill that has the visual appearance of an earth mound or fill, depending on the location and land use of the surrounding area.
- *Limited Post-Construction Uses.* Because access on a temporary exposed geomembrane cover system must be limited to protect the exposed geomembrane, the potential uses for an area covered with a temporary exposed geomembrane are very limited. For example, it cannot provide the potential wildlife habitat (i.e., animal burrows, nests, and grazing) that a typical soil final cover system could. However, there are some potential uses, such as solar power generation.

2.5 *Applicability Examples*

Temporary exposed geomembrane covers (i.e., a cover system intended for a 1- to 5-year service life) are potentially suitable for the following applications:

- to limit leachate generation before final closure occurs;
- on waste storage areas that will be overfilled or mined in the future;

- to allow foundation soils time to gain strength and allow for additional waste placement and/or construction of a typical final cover system;
- as a means of dust control, or gas or odor control by enhancing gas collection capability; and
- as a partial final cover system to delay future capital costs associated with construction of a typical final cover system in the future.

In contrast, long-term exposed geomembrane covers (i.e., a cover system intended for a 5- to 30-year service life) are potentially suitable for the following applications:

- when the owner is obligated to some degree of maintenance of the site in perpetuity, in which case the owner is avaialble, funded, and present to make repairs or replacements of the cap as components exceed their functional lifespan;
- where the exposed cover system is intended to function as a final cover system as long as feasible; and
- closure where typical final cover is not feasible (i.e., because existing side slopes are too steep to support a typical final cover system, where adequate final cover soils are not available, where environmental conditions do not permit the growth and sustenance of a vegetative erosion control layer, etc.)

3 KEY GEOMEMBRANE DESIGN ISSUES

3.1 *Overview*

Design of an exposed geomembrane involves elements not typical to other geomembrane liner or cover applications, including the following:

- resistance to wind-uplift related damage;
- resistance to environmental factors including ultraviolet radiation (UV) exposure, temperature extremes, and impact loads;
- resistance to down-slope creep caused by excessive thermal elongation and material creep; and
- ability to be properly constructed having high-quality of seams and long-term ease of repair.

The elements of design related to resistance of forces are discussed in Sections 3.2; constructability considerations are addressed in Section 3.3; and performance monitoring is addressed in Section 3.4.

3.2 *Resistance to Wind Uplift, UV Exposure, Temperature, Impact Loads, and Creep*

The geomembrane in an exposed geomembrane cover system must not be adversely affected by repeated exposure to temperature extremes, wet-dry cycles, exposure to UV radiation, and damage from common impact loads. With the exception of impact loads, these factors generally preclude the use of geomembranes with plasticizers.

3.2.1 *Resistance to Wind Uplift:*

Resistance to wind uplift is typically the governing factor in the design of exposed geomembrane cover system. Wind uplift of the geomembrane is a function of the tensile characteristics of the geomembrane, the waste fill geometry, and the design wind velocity. Procedures for the analyses of geomembrane wind uplift are presented by Botelho, et al. (2013). The analyses are for two criteria: (i) resistance of the exposed geomembrane to tensile failure (i.e., rupture) caused by wind uplift; and (ii) resistance of the geomembrane anchor (i.e., ballast or anchor trenches) to the tensile forces caused by wind uplift on the geomembrane. The forces acting on the geomembrane that cause geomembrane uplift, geomembrane tension, and tensile forces at the geomembrane anchors are a function of the wind velocity and the exposed length of the geomembrane, which is based on site-specific characteristics (i.e., waste fill height, side slope inclination, and distance between geomembrane anchors). A key aspect of the analysis is the suction force acting over the exposed length of geomembrane [see Li, Espinoza, and Morris, 2019]. To evaluate the resistance of the geomembrane anchor to wind uplift, the uplift force that is exerted on the geomembrane ballast or anchor trench is calculated. The uplift force on the geomembrane anchor is a function of the tensile force in the uplifted geomembrane, the angle between the uplifted geomembrane and the slope at each geomembrane anchor, and the slope angle. A detailed discussion of anchoring methods for the exposed geomembrane is presented in Giroud et al. (1999).

3.2.2 *UV Radiation:*

Data is generally available for most geomembranes for UV resistance. The service life of the exposed geomembrane must be considered when evaluating the required performance – for example, the design expose life of an exposed temporary cover might only be 5 to 10 years, where an exposed cover used for a regulatory post-closure care period could be 30 years or longer. Interpretation and application of laboratory weathering data over long periods can be very subjective; an approximate prediction method is available from Hsuan and Koerner (1993). It is best to use data obtained for geomembranes that have a demonstrated performance history in the conditions that are anticipated. Based on the performance of exposed geomembrane covers installed in the 1990's, exposed geomembranes can be resistant to UV damage for 30 years or more and continue to cost-effectively perform their function with limited maintenance.

3.2.3 *Temperature Extremes:*

In addition to temperature induced strains, extreme temperatures can significantly impact the strength of many geomembranes. Giroud, et. al (1995) present an excellent discussion of the impact of temperature on the modulus and elongation limits of non-reinforced geomembranes as applicable to wind uplift design and their ability to resist damage due to temperature extremes. The combination of temperature extremes and the high thermal-expansion coefficients of most non-reinforced geomembranes can also produce cyclic tension-relaxation of the geomembrane that can lead to environmental stress cracking.

3.2.4 *Impact Loads:*

Exposed geomembranes will be subject to impact loads from hail and various dropped objects during their service life, including hail, wind-blown debris, and animal traffic. It is likely that there will be many impact events during the life of an exposed geomembrane; the key to limiting damage and repair costs is to monitor for such impacts and repair them promptly before they propagate and threaten the integrity of the remaining geomembrane (which was a cause of the damage discussed in Section 4 of this paper). The ability of a geomembrane to resist puncture, which is related to its impact resistance, has been studied by Koerner et. al (GRI, 2008).

3.2.5 *Downslope Creep and Trampolining:*

The combination of gravity and thermal expansion/contraction acting on a geomembrane placed on a slope can lead to down slope creep movement of the geomembrane. This tendency is reduced with decreased thermal wave action and increasing interface friction and geomembrane tensile modulus. Thermally induced waves can be minimized using a geomembrane having a light surface color or low bending modulus. Note however that lighter colors have lower UV resistance than dark for a given polymer. The combination of high tensile modulus and low bending modulus favors a scrim-reinforced geomembrane. However, such geomembranes may lack adequate seam strength (both shear and peel are important) and interface friction for incorporation into the long-term final closure of many side slopes.

3.3 *Construction Quality Control and Quality Assurance*

The quality of construction is extremely important to the performance of an exposed geomembrane cover. Exposed covers perform well when they are designed and constructed properly, but lack of attention to construction details can produce a cover that cannot resist the forces that it was designed for. Construction quality should be controlled by having an engineer or technician who is experienced in exposed geomembrane installation observe the construction project throughout its entirety, including procurement of materials, surface preparation, deployment of geomembrane, anchor construction, geomembrane seaming, and anchor system installation. Because the forces acting on an exposed geomembrane are concentrated on anchorage points, the construction of anchorage features must be a particular focus of the quality control and assurance program.

3.4 *Performance Monitoring*

Following installation of the geomembrane, a program of monitoring should be implemented to detect and repair problems before they worsen. It is likely that the exposed geomembrane will have minor localized damage during its service life. Such damage may be minor defects caused by hail, etc. or major tears related to excessive wind events. Therefore, the inspection program should include routine monitoring (quarterly or semi-annually, for example) and also monitoring after all significant rainfall and wind events. While some problems are significant and result from a single event, many problems start with small damage and propagate during smaller weather events; therefore, it is important to check the cover for minor damage at regular intervals.

4 CASE STUDY: APPLICATION FOR WASTEWATER MANAGEMENT

4.1 *Site Background*

The valuable mineral at this facility is removed from extracted ore using heap-leaching techniques on geomembrane-lined pads. After the leaching operation has removed the mineral and a pad is closed, the spent ore that remains on the pad continues to produce highly acidic leachate. An exposed geomembrane cover was installed over a portion of one of its closed leach pads to reduce the generation of acidic leachate (see Photo 1). The pad covers an area of is approximately 40 hectares (Ha) (100 ac). The geomembrane cover was fabricated from 1-mm and 1.5-mm thick High Density Polyethylene (HDPE) material and was colored green. The exposed geomembrane cover system installation cost was approximately \$3 million (i.e., about \$7 per m^2 of installed cover). The annual treatment cost for the acidic leachate was reportedly well over one million dollars per year, indicating that the cost of the exposed geomembrane cover would be offset by about two years of acidic leachate treatment costs. Because the geomembrane was designed to have a twenty-year design life, the cost savings over its deign life would be expected to greatly exceed its installation cost.

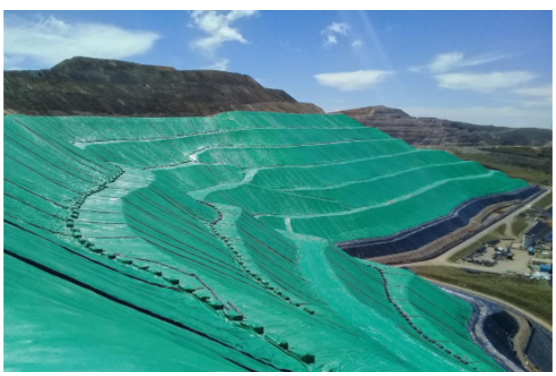

Photo 2 – View of exposed geomembrane after initial installation.

Photo 3 – View of the geomembrane after initial wind damage event.

4.2 *Technical Challenges*

Following installation of the geomembrane, several windstorms occurred over a period of about six months that damaged portions of the exposed geomembrane cover (see Photo 3). Upon performing a visual inspection of the facility it was found that, in general, the anchorage system (i.e., anchor trenches and sandbags) was not sufficient to withstand the forces produced by wind uplift on the geomembrane during the windstorms. The factors contributing to the limited amount of available uplift resistance are described in more detail below.

4.2.1 *Anchor trench and sandbag spacing.*

Anchor trenches were not close enough to adequately limit stresses on the geomembrane, and sandbags were spaced too far apart to prevent geomembrane uplift.

4.2.2 *Anchor trench connection details.*

At some locations, a single anchor trench was used to anchor the geomembrane from both the upper and lower panels on the slope. At these locations the geomembrane was subjected to tensile forces caused by uplift of both the panel above the anchor trench and the panel below it, potentially leading to larger tensile stresses than the anchor trench could resist. The initial damage likely propagated from these locations upward to the next upper bench (where dual anchor trenches were used) inducing geomembrane damage at the anchor trench near the crest of the slope.

4.2.3 *Geomembrane/backfill contact.*

To transfer tensile stresses from the geomembrane to the backfill while avoiding stress concentrations, anchor trench backfill material should be well graded with a maximum particle size less than about 2.5 cm (1 in). The exposed geomembrane at the site was installed directly over the mineral ore which much larger than 2.5 cm (1 in). As a result, the contact between the exposed geomembrane and the anchor trench backfill material could induce tensile strains in the geomembrane up to 2 to 3 times larger those in geomembrane embedded in well-graded backfill.

4.2.4 *Steel-geomembrane interaction.*

Roped sandbags were anchored at the top of each slope using steel bars driven through the exposed geomembrane. These locations represented weak spots where the initial geomembrane damage (tear) could initiate and then propagate as the geomembrane was uplifted during high wind events.

4.2.5 *Horizontal seams at the toe of slope.*

Because exposed geomembranes experience continuous expansion and contraction due to temperature changes, it is not uncommon to see temporary formation of ‘trampolines’ at the toe of a slope due to geomembrane contraction during colder temperatures. Loads on the geomembrane (e.g., snow, hail) at these locations could cause excessive tensile stresses that could lead to geomembrane damage, particularly if seams are near the toe of the slope where a ‘trampoline’ develops.

4.2.6 *Locations of some geomembrane welds.*

The integrity of an exposed geomembrane depends on good fusion and extrusion welding of adjacent geomembrane panels. Some welds were observed that were not well centered over the seam (see ‘Good weld” in Figure 3). To attain a good extrusion weld, the HDPE ribbon must cover both adjacent geomembrane panels approximately equally.

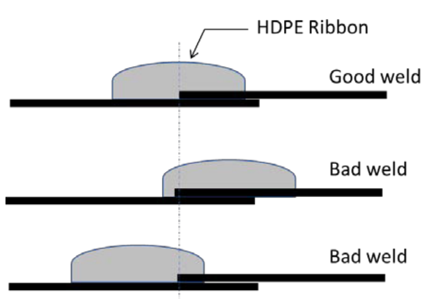

Figure 3 – Seam (weld) quality illustration.

Photo 4 – Repaired exposed geomembrane.

4.3 *Updated Closure System Design and Construction*

To repair the exposed geomembrane, the following guidelines were developed,

- *Reduction in sandbag spacing.* To reduce tensile forces applied to geomembrane, the distance between sandbags was reduced from 21 m to 7 m along the slope.
- *Geomembrane/Backfill contact redesign*. To provide for direct contact between the exposed geomembrane and anchor trench backfill material, backfill material size was revised to require well graded structural fill with a 2.5-cm maximum particle size, which was implemented on damaged portions of geomembrane anchor trench (see discussion of anchor trench backfill material in Brachman and Gudina, 2008).
- *Anchor trench connection details.* To reduce tensile stresses on the geomembrane, the welding details for single anchor trenches was modified to prevent load transfer between panels of the geomembrane.
- *Sandbag steel anchor design.* To avoid tear stresses at sandbag anchorage locations, anchors were relocated away from the slope with the steel bars driven into the underlying mine waste at locations where they would not tear the geomembrane during wind uplift events.
- *Horizontal seams at the toe.* To prevent geomembrane damage due to high tensile stresses resulting from 'trampolining', seams were specified to be oriented parallel to the line of maximum slope, (i.e., oriented down, not across, the slope) and to not locate seams in an area of potential stress concentration.
- *Increased quality control during welding*. To reduce the occurrence of weak geomembrane seams, increased quality control observations and testing of the welds was implemented.
- *Geomembrane performance monitoring***.** Following the implementation of the repairs, a program of visual inspection of the exposed geomembrane after high wind events was recommended to identify conditions which, if unrepaired, could lead to more significant damage.

4.4 *Benefits and Lessons Learned*

The damage that occurred to the cover and the repairs that were made illustrate the importance of proper design (particularly the understanding of anchorage, how wind uplift forces act on the geomembrane and the seams, and the potentially damaging effects of stress concentrations at anchor points) and construction on the performance of the geomembrane. Further, because of the large scale and associated costs of mine waste management operations, there are opportunities for cost savings through application of innovative approaches. At this mine waste site, the use of an exposed geomembrane was a novel approach that required successful assessment of the details of installation and performance as well as overall design. The application demonstrates how exposed geomembrane covers can be used to reduce generation of acidic leachate and, as a result, substantially reduce the cost of wastewater treatment at the mine site for many years.

5 SUMMARY

Based on the discussions in this paper, temporary exposed geomembrane covers offer a number of potential advantages to mine waste facility owners and operators related to leachate management. In particular, exposed geomembrane covers can significantly reduce the amount of leachate to be treated and, in some cases, reduce the size (and therefore capital cost) of wastewater treatment plant needed to treat the leachate. To realize the potential benefits of exposed geomembrane caps, it is critically important that the details of the system be planned out and implemented carefully to prevent service disruptions and potentially costly repairs. The experience described in Section 4, and at many other exposed geomembrane cover sites, demonstrates that these covers can be properly designed and installed in very challenging environments to have reliable and low-maintenance performance over their design lives.

6 REFERENCES

Botelho, K., Heynes, O., and Giroud, J.P., "Evaluating Wind Uplift for Exposed Geomembranes using Computer Modeling", Geosynthetics 2013, April 1-4, Long Beach, California.

Brachman, R.W.I., and Gudina, I. Gravel contacts and geomembrane strains for a GM/CCL composite liner." Geotextiles and Geomembranes 26 (2008), pages E448-459. Elsevier Press, July 2008.

Espinoza, J.C. Gabriel. "Improving Water Management in the Orcopampa Mine." Proceedings of the 22nd International Conference on Tailings and Mine Waste 2018, Keystone, Colorado.

Geosyntec Consultants (2007), "Report on Evaluation of Exposed Geomembrane Cover System at Cells 1 and 2." Geosyntec Consultants, Columbia, MD.

Geosynthetics Research Institute (GRI). "Modification to the "GRI-Method" for the RFCR-Factor Used in the Design of Geotextiles for Puncture Protection of Geomembranes." GSI White Paper #14, 2008.

Geosynthetics Research Institute (GRI). "Regulatory Status of Post-Closure Care of MSW Landfills in the United States." GSI White Paper #17, 2010.

Giroud, J.P., Pelte, T., and Bathurst, R.J., (1995) "Uplift of Geomembranes by Wind", Geosynthetics International, Special Issue on Design of Geomembrane Applications, Industrial Fabrics Association International, Vol. 2, No. 6, pp. 897-952.

Giroud, J.P., Gleason, M.H., and Zornberg, J.G., "Design of Geomembrane Anchorage Against Wind Action", Geosynthetics International, Vol. 6, No. 6, 1999. pp.481-507.

Gleason, M., Houlihan, M.F., and Palutis, J. "Exposed Geomembrane Cover Systems: Technology Summary." Proceedings of Geosynthetics 2001 Conference, Economics, Performance, and Construction Advantages of Geosynthetics, Roseville, MN, 2001. Pages 905-919.

Hojka, Kris. "Encapsulation of Mine Waste with Geomembrane as the Preferred Closure Option for Gordon Lake Sites in NWT." Proceedings of the 23rd International Conference on Tailings and Mine Waste, 2019, Vancouver, British Columbia.

Hsuan, Y.G, and Koerner, R.M. "Can Outdoor degradation be predicted by laboratory accelerated weathering?" Geotechnical Fabrics Report, IFAI, November 1993.

Li, C., Espinoza, R.D., Morris, J.W. F. "Wind-Induced Uplift of Exposed Geomembrane Covers: A Proposed Revision to Conventional Design Approaches." Geotextiles and Geomembranes, Vol. 48, Issue 1, pages 24-31. Elsevier Press, February 2020.

United States Environmental Protection Agency, 2011. "Green Remediation Best Management Practices for Landfill Cover Systems: Energy Production." Office of Solid Waste Management and Emergency Response. EPA 542-F-11-024.

Mine waste covers – interlayer drainage challenges and cost impacts for barrier cover systems

Jay Griffin
Geosyntec Consultants Inc., Walnut Creek, California, USA

Gregory Corcoran
Geosyntec Consultants Inc., San Diego, California, USA

ABSTRACT: Tailings and mine waste cover systems continue to evolve with the inclusion of various hydraulic barrier and interlayer drainage materials, playing a vital role in water management and successful reclamation and restoration at mine sites. With the increasing use of engineered cover systems in the industry, small differences in design, materials, and construction methods can result in significant capital cost savings related to installation. Therefore, it is beneficial for mine owners and operators to recognize the importance of interlayer drainage design and construction, and how the interlayer drainage design and construction can impact mine operations, reclamation, and restoration.

This paper focuses on interlayer drainage system options for barrier-type cover systems (e.g. geomembranes, geosynthetic clay liner, compacted clay, etc.) and the impacts that the interlayer drainage system design can have on the capital costs related to cover system installation and construction schedules. This paper discusses challenges associated with design, material selection, and construction; simplified methods for evaluating costs early in the design process; and examples of innovative solutions and approaches for interlayer drainage.

1 INTRODUCTION

Mine waste cover systems play a vital role in site water management and successful reclamation and restoration at mine and mill sites. With the increasing use of engineered cover systems in the mining industry, small differences in design, construction materials, and construction methods can result in significant capital costs and/or schedule delays related to installation of cover systems.

The International Network for Acid Protection (INAP) Global Cover System Technical Guidance Document (INAP 2017) provides a good summary of the types of cover systems that mine owners can consider for mine wastes. This paper focuses on barrier-type cover systems which INAP (2017) defines as including "one or more low hydraulic conductivity layers to control the ingress of atmospheric water and in some cases, atmospheric oxygen." The types of materials used for the barrier layer in a barrier-type cover system include, but are not limited to, compacted clay, bentonite amended soils, geosynthetic clay liners, and geomembranes.

Barrier-type cover systems typically include soil that is placed above the barrier layer to serve as growth media for vegetation and to protect the barrier layer from damage. For cover system applications on slopes, it is important to provide a drainage layer between the cover soil and barrier layer to remove or drain water that infiltrates through the cover soil and collects on top of the barrier layer. Herein, this drainage layer is referred to as the interlayer. An adequate interlayer drainage system reduces the build-up of hydraulic head on the barrier layer providing two important functions: (1) minimizing the amount of water that could flow through potential defects in the barrier layer, and (2) reducing the seepage forces in the cover soil which improves cover system slope stability. Bonaparte et al. (2002) discusses several cases of inadequate interlayer drainage design leading to excessive cover soil erosion and slope instability, which highlights the importance of interlayer drainage. A generic barrier-type cover system with an interlayer drainage layer is shown on Figure 1.

The materials selected for the interlayer and the layout of the drainage features for the cover system can have a significant effect on the constructability and overall capital costs associated with the construction of a cover system.

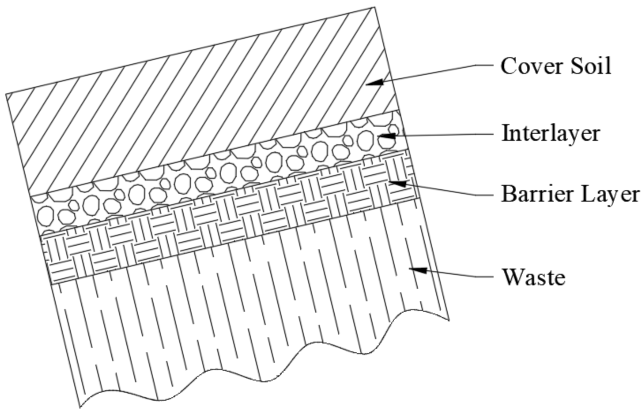

Figure 1. Generic barrier-type cover system with interlayer drainage.

2 INTERLAYER DRAINAGE DESIGN

Design of the interlayer drainage system for a barrier-type cover system on a slope includes specifying the interlayer materials and their required engineering properties related to drainage capacity, potential for clogging, and biotic intrusion (roots or burrowing animals), as well as other drainage features that convey water collected by the interlayer to designated discharge locations. When performing the design of a cover system, the designer also needs to consider the strength of the interlayer materials and the interface shear strength between the interlayer materials and the underlying and overlying layers in the cover system with respect to veneer stability. In addition, designers need to consider material availability on-site and/or the need to import manufactured materials (e.g. geosynthetics) or natural materials (e.g. sand and gravel) from off-site.

2.1 *Materials*

The materials used for the interlayer need to have the ability to convey water without clogging over time. Typically, these are natural granular materials (gravels, sands, and gravel/sand mixtures) designed with an adequate filter layer to prevent migration of fines into the interlayer. The filter layer can be comprised of natural soil or geosynthetic materials (e.g. filter geotextile) placed between the overlying finer-grained cover soil and the underlying granular materials that make up the interlayer. The natural granular materials can be sourced from mine operations, but may require additional processing to achieve required engineering properties such as maximum particle size to limit damage/puncture to the underlying barrier layer or removal of fines to increase the hydraulic conductivity of the granular material.

In addition to natural granular materials, manufactured materials, such as geocomposites, provide an efficient means to install a consistent layer that can provide in-plane drainage for the interlayer. Geocomposites generally consist of a high-density polyethylene (HDPE) geonet core with a nonwoven geotextile heat-bonded to one or both sides (single- or double-sided, see Figure 2). The geonet provides in-plane drainage for water that infiltrates from the overlying material and the nonwoven geotextile reduces clogging of the geonet by retaining overlying soil materials. Manufactured materials come in various configurations and conveyance capacities that the designer can consider.

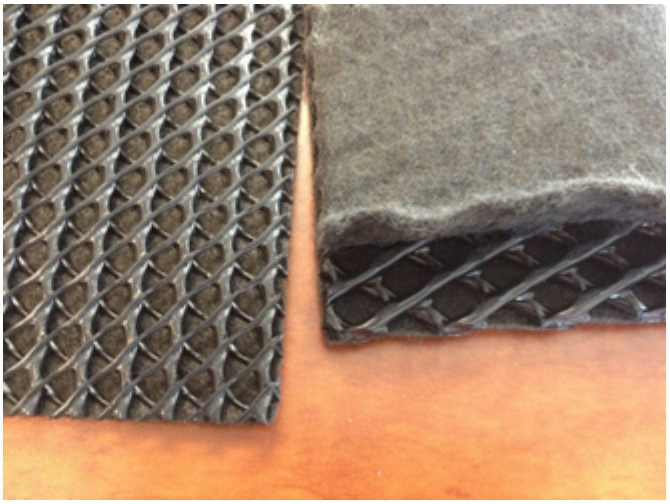

Figure 2. Single-sided (left) and double-sided (right) geocomposites with HDPE geonet cores, tri-axial (left) and bi-axial (right), and nonwoven geotextiles.

Design of an interlayer drainage system requires a good understanding of the engineering properties of the materials that will be used for construction. For granular drainage materials the designer must select a minimum hydraulic conductivity and for geosynthetic materials the designer must select an allowable transmissivity (flow rate). Each of these values may be affected by potential impacts from installation damage, clogging, biological damage, ultraviolet degradation, or underlying material settlement over time. These elements of design should be considered by the designer and can have an effect on the performance of the interlayer drainage system. Typically, reduction factors and safety factors are applied to hydraulic conductivity or transmissivity of the interlayer to develop an allowable value to use in design.

The values selected for design should also be confirmed during construction through conformance testing included as part of an overall construction quality assurance (CQA) program for the cover system.

2.2 *Design Method*

For cover systems constructed on slopes, the interlayer collects water that infiltrates through the overlying cover soil and conveys it downslope by gravity. Several procedures exist for the design of both geosynthetic and granular drainage interlayers for cover systems. Giroud et al. (2000) and Narejo et al. (2007) provide good descriptions of the methods that can be used to design and specify an appropriate interlayer material.

The rate of infiltration, or flow rate, into the interlayer is a key parameter required for design. The authors recommend a simplified approach to establish the infiltration rate called the "unit gradient" method, which is described in Narejo et al. (2007). The "unit gradient" method simply assesses the critical condition where the cover soil is saturated and flow into the interlayer is controlled by the saturated hydraulic conductivity of the cover soil. Because atmospheric water will runoff the surface of the sloped cover soil, the hydraulic head above the cover soil is practically zero and the hydraulic gradient through the cover soil is approximately unity (Narejo, et al. 2007). Using Darcy's law, the flow rate into the interlayer can then be simply estimated by multiplying the cover area of interest and the saturated hydraulic conductivity of the cover soil. This approach reduces the need to understand and estimate storm events and rain-on-snow or freshet events, which can be extreme, because the basis of design is independent of the precipitation and is controlled by the cover soil hydraulic conductivity. Excess precipitation or snow melt will run-off the sloped surface as infiltration through the cover soil and into the interlayer is limited by the saturated hydraulic conductivity of the cover soil. The designer should carefully evaluate the saturated hydraulic conductivity of the cover soil selected for design. The long-term, macro scale hydraulic conductivity for the cover soil should be considered with the understanding that environmental and biological effects on the cover soil will likely increase its hydraulic conductivity over time via pedogenesis (Albright et al. 2010).

On long mine waste slopes, it is impractical to design an interlayer with enough flow capacity to adequately collect and convey interlayer water along the entire length of the slope. As water flows downslope in the interlayer, it continues to accumulate with additional water infiltrating from the cover soil and can eventually exceed the capacity of the interlayer. Therefore, the designer must provide locations along the slope to periodically drain the interlayer. Often this is accomplished using benches on slopes that allow interlayer water to drain to a bench ditch where the water can be conveyed along the bench to down drains and ultimately to the designed discharge points. Figure 3 shows an example of a benched side slope design with a regular spacing of "L" between the benches. Figure 3 also presents an estimated flow profile within the interlayer that shows the thickness of water at the top of each slope length, L, as zero and increasing within the interlayer as the water is conveyed downslope and eventually draining into the bench ditch. Figure 4 shows a photo of a surface water channel on a drainage bench for a cover system that utilized a granular interlayer.

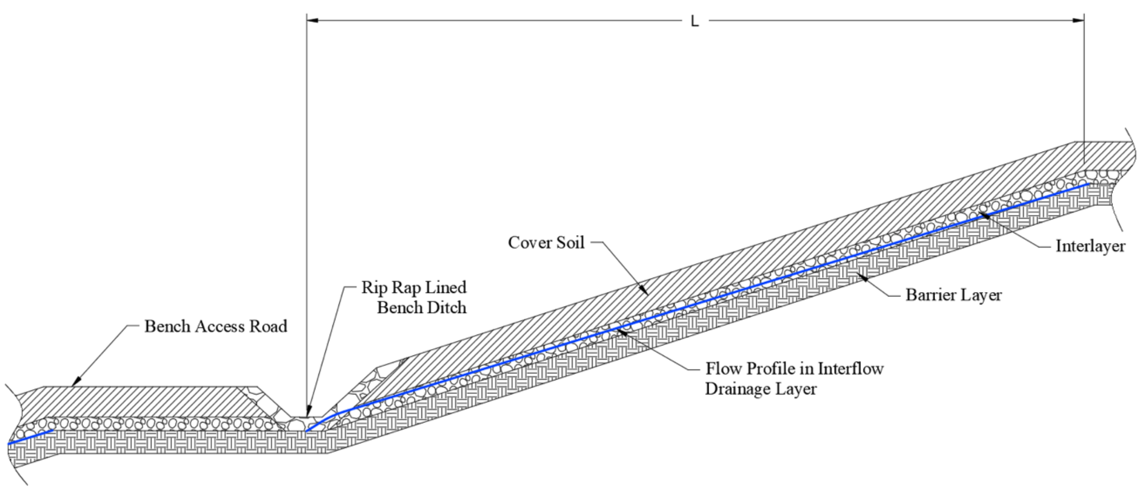

Figure 3. Profile of a generic cover system with slope benches. Not to scale.


Figure 4. Photo of a rip rap-lined surface water channel located on a slope bench.

Alternatively, Figure 5 shows a simplified slope section with in-slope lateral drains instead of benches. The in-slope lateral drains normally consist of a trench filled with a perforated pipe and drainage aggregate to collect the interlayer flow and convey it to designated discharge locations. One benefit of this design is the lack of benches, which significantly reduces grading and material management costs for existing mine waste slopes at angle of repose conditions. However, this design approach also requires significant attention to the design of erosion control features on the slope surface. Figure 6 shows a photo of an in-slope lateral drainage ditch during cover construction.

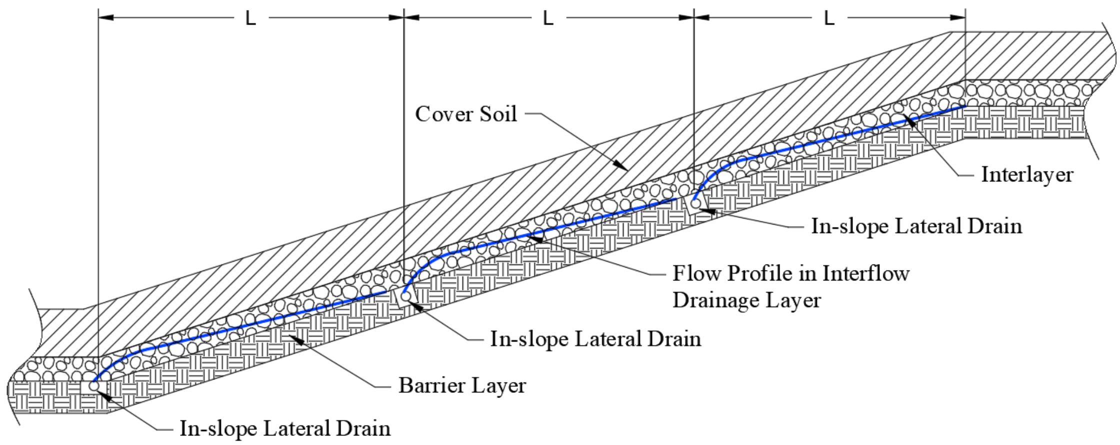

Figure 5. Profile of a generic cover system showing in-slope lateral drains (for illustrative purposes only; not to scale).

Figure 6. Photo of an in-slope lateral drainage ditch and cover soil placement over a geocomposite interlayer.

Determining the spacing between benches or in-slope lateral drains, designated as L in Figures 3 and 5, is the key aspect for design of the interlayer. The designer must balance the drainage capacity of the interlayer material with the spacing of the benches or lateral drains. More frequent spacing (smaller L) allows for an interlayer material with a lower drainage capacity (i.e. smaller geocomposite or thinner section of granular drainage material), and therefore, lower cost. However, more frequent spacing requires grading to construct more benches and requires construction of more in-slope lateral drains. Figure 7 shows an example of a barrier-type cover system under construction where in-slope lateral ditches were designed for a geocomposite interlayer. Section 3 includes a discussion of cost benefits and trade-offs related to the selection of bench or in-slope lateral drain systems.

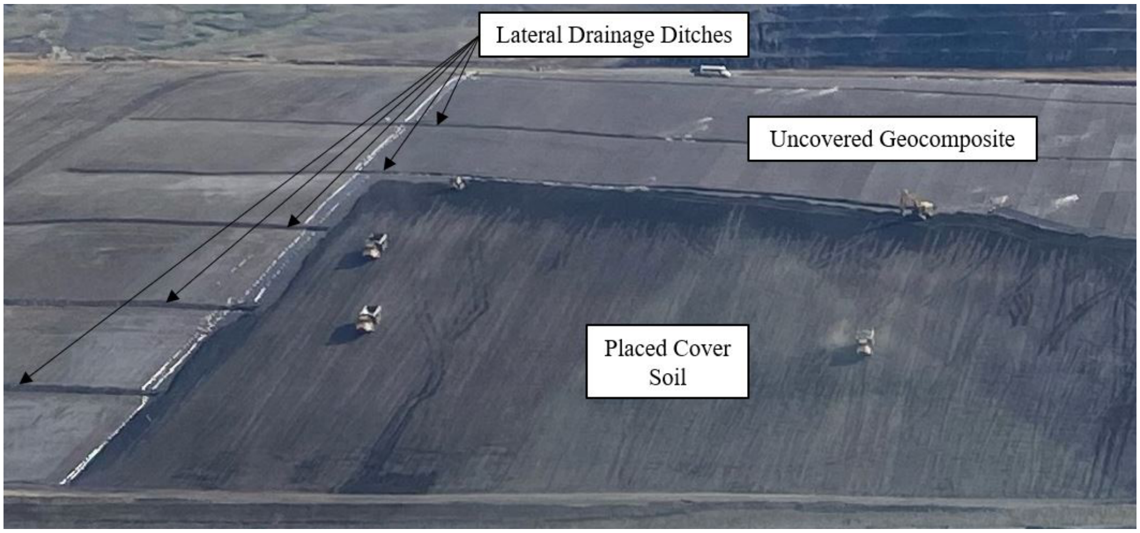

Figure 7. Example mine waste cover project showing lateral drainage ditches, uncovered geocomposite interlayer (upper slope area), and cover soil placed over the geocomposite (lower slope area).

2.3 *Other Design Considerations*

Separate from cost considerations, there are design benefits and drawbacks associated with the selection of benches or in-slope lateral drains as part of the interlayer drainage system. Tables 1 and 2 summarize some of the pros and cons that should be considered by designers and owners.

Table 1. Side slope bench pros and cons

Pros	Cons
Benches are generally beneficial for stability of the cover system. They provide a convenient and relatively flat location to install side slope materials, anchor geosynthetics, and can serve as construction access roads..	Construction of benches can require the toe of the slope to be pushed out (or the top of slope to be pushed inward when the toe of slope is constrained), which can result in a significant increase in the footprint of a mine waste stockpile or dump that may have been constructed with end dumping of the waste materials at angle of repose conditions.
Surface water management features on benches can be accessed for cleaning and maintenance.	Surface bench drains can be susceptible to clogging from sediment build-up, snow, and ice, which can reduce the flow capacity.
Benches can provide a means to manage surface water and limit erosion of cover soils.	Benches may not “blend” into natural topography adjacent to the closure and thus may be less attractive to certain stakeholders.

Table 2. In-slope lateral drain pros and cons

Pros	Cons
Eliminating benches and using in-slope lateral drains minimizes the footprint of the mine waste stockpile or dump.	Requires additional materials for construction of the lateral drains (such as piping and drainage aggregate).
In-slope drains cannot be clogged with sediment from surface erosion or snow.	Cleaning of lateral drains is impractical; therefore, filters and redundant drainage design features, such as perforated piping surrounded by drainage aggregate, should be used.
In-slope drains can be installed below the frost depth to avoid freezing issues.	Without benches, geosynthetics need to be installed on the slope without the benefit of access or a relatively flat area.
Slope contouring can be blended into adjacent topography and be more aesthetically pleasing to certain stakeholders.	

In addition to the interlayer, conveyance systems need to be designed to convey water from the interlayer, and surface water runoff from the cover system, to final discharge locations away from the final cover. Conveyance systems can be comprised of open channels, culvert pipes, lined down chutes, and other stormwater management structures that convey collected interlayer water to appropriate discharge locations.

3 COSTS

Capital costs for construction of the components of a barrier-style cover system can vary widely based on a variety of factors including the mine location, transportation options for off-site material deliveries, size of the cover system, availability and selection of materials, local regulations, and the local labor market. This section provides cost considerations for designers and owners related to the interlayer design and construction.

3.1 *Materials*

The largest cost for construction of the interlayer typically comes from the interlayer materials. Mine sites with granular overburden materials are likely candidates for use of these on-site materials as interlayer materials. However, the materials may require processing to meet the engineering specifications (sizing/crushing, screening, washing to remove fines), which may increase the cost of the material resulting in off-site materials being more cost effective. The potential use of overburden or mine by-product materials also needs to consider the geochemistry of the materials ensure they will not negatively affect water quality, the environment, or the performance of the cover system.

For geosynthetic materials, owners need to consider transportation costs in addition to the costs associated with manufacturing the materials. Materials can be delivered to sites via truck, rail, barge, air, or any combination of these modes of transportation. The location of a mine site tends to dictate the mode of transportation, not only through access to the transportation modes, but also the weather and seasonal conditions. Sites with access to a navigable waterway may be able to benefit from barge or ship delivery, but delivery during seasons when the waterway is not frozen. In other cases, ice roads may be a primary transportation mode and waterways need to be frozen to allow trucks to cross.

Geosynthetics also need to be installed by specialized contractors with knowledge of geosynthetic deployment, seaming, and repair requirements. Specialized equipment may also be required to properly and safely deploy geosynthetic rolls, especially on slopes, and to seam geosynthetic materials in the field.

3.2 *How Interlayer Design Affects Cost*

As mentioned in the design considerations discussion, the spacing, layout, and design of drainage benches or in-slope lateral drains in conjunction with the interlayer material can have a significant effect on the capital cost of the cover system. Simple spreadsheets can be developed to combine design information with cost data to perform a cost-benefit analysis that can assist the owner and designer with selecting the most efficient and economical interlayer design. The spreadsheet can include variables relevant to the design of the interlayer such as slope angle, hydraulic conductivity of the interlayer material (or transmissivity), thickness of the interlayer material (for granular materials), applicable reduction and safety factors related to the design, and spacing of slope outlets/drains. Using the spreadsheet tool, the designer can find the optimal and most cost-effective combination of bench and/or lateral drain spacing and interlayer material flow capacity for the specific slope conditions and geometry. The cost analysis for the interlayer can also be combined with different barrier options to provide a complete estimate of the cover system cost per unit area. For the cost analysis to provide accurate insight to the owner, it is necessary for the designer to work with the mine owner to understand the costs associated with procuring and installing different interlayer materials and constructing slope benches or lateral drains, and conveyance features. Figure 8 presents an example of the outputs for a cover system cost comparison tool that owners can use to inform decision making.

Barrier Layer		Interlayer and Slope Drains					Cover System Cost per Hectare
Material	Cost per Hectare	Material	Interlayer Cost Per Hectare	Slope Drain Spacing, L (m)	Slope Drain Cost per Hectare	Total Cost per Hectare	
Barrier 1	$40,000	Geocomposite 1	$90,000	50	$40,000	$130,000	$170,000
Barrier 1	$40,000	Geocomposite 2	$95,000	55	$38,000	$133,000	$173,000
Barrier 1	$40,000	Geocomposite 3	$120,000	70	$32,000	$152,000	$192,000
Barrier 1	$40,000	Granular Material 1	$130,000	100	$20,000	$150,000	$190,000
Barrier 1	$40,000	Granular Material 2	$170,000	110	$18,000	$188,000	$228,000
Barrier 2	$60,000	Geocomposite 1	$90,000	50	$40,000	$130,000	$190,000
Barrier 2	$60,000	Geocomposite 2	$95,000	55	$38,000	$133,000	$193,000
Barrier 2	$60,000	Geocomposite 3	$120,000	70	$32,000	$152,000	$212,000
Barrier 2	$60,000	Granular Material 1	$130,000	100	$20,000	$150,000	$210,000
Barrier 2	$60,000	Granular Material 2	$170,000	110	$18,000	$188,000	$248,000

Figure 8. Example summary of a simple cost analysis for a barrier-type cover system with the lowest cost option listed first and the cost difference for other options listed (note that costs are for illustrative purposes only and do not reflect actual costs).

4 CONSTRUCTION CHALLENGES

Mine waste stockpiles or dumps can be very large, sometimes hundreds of hectares, with slopes hundreds of meters long that have hundreds of meters of elevation difference between the top and toe. Many mine sites are also located in remote regions, which makes planning and logistics for a barrier-type cover system, and specifically the interlayer drainage system, a critical consideration during the design process. The design process should also take into account construction challenges specific to barrier-type cover systems. Examples of construction challenges include:

- The project size may dictate construction schedules that span several years or construction seasons, resulting in the need to plan material deliveries and storage, labor and equipment availability, material conformance testing, and other site specific logistics.
- Large quantities of materials are required for the interlayer components of a barrier-type cover system, which means that mine owners need to plan for designated laydown and stockpile areas for equipment and materials. These areas may not be readily available near the waste dump or stockpile location.

- If geosynthetic materials are used, they need to be ordered and procured well ahead of construction, as manufacturers often need lead times that can span several months between order placement and manufacturing. In some cases, geosynthetic material availability and manufacturing location can affect the project, and delivery scheduling may need to occur throughout the project to facilitate on-site storage constraints, transportation availability, and the market demand for these materials.
- Transportation of geosynthetic materials to mine sites (which are often remote) can present complicated logistics.
- Geosynthetic materials need to be stored properly to protect the materials from damage.
- Geosynthetics require specialized contractors and equipment for installation.
- Granular materials need to be placed to specific tolerances. If a contractor places an interlayer too thick, significantly more material may be placed than required. If the interlayer is too thin, it may not meet the design intent and may be unable to convey the interlayer water and result in a slope failure.
- Phasing and construction sequencing need to be carefully considered by the mine owner and contractor(s). Other capital projects and mine operations should be considered in the construction scheduling, labor availability and assignments, and housing for non-local personnel.
- If phasing will span multiple construction seasons, temporary terminations for the cover system need to be included in the design and need to account for infiltration and run-off during construction and between construction seasons.
- Haul distances from existing stockpiles or quarry sites for granular materials may dictate the need for additional equipment or acceptance of a reduced production rate for mining operations.
- Placement of natural granular materials and cover soils needs to be accomplished from the toe to maintain stability of the cover system. However, some sites may have limited access at the toe of slope due to wetlands, waterways, restricted areas, mine pits, etc.

As each mine and mill site is different, individualized designs are necessary to develop appropriate solutions to site specific challenges. The creative use of available on-site materials is a key aspect of solving challenges on remote mine and mill sites.

5 CONCLUSIONS

Mine owners and their engineering design teams need to carefully consider the interlayer component of barrier-type cover systems. The interlayer collects infiltrated water within the cover system and is an integral part of maintaining stability of the overlying cover soil on side slopes. The materials selected for the interlayer and their engineering properties define the spacing of benches or in-slope lateral drains along the slope and impact project costs, scheduling, and construction. Construction of the interlayer can also present numerous challenges that can be mitigated when they are properly addressed during design, project planning, material procurement, and project implementation.

6 REFERENCES

Albright, W., Benson, C., Waugh, W. 2010. Water Balance Covers for Waste Containment, Principals and Practice, ASCE Press, IBSN 978-0-7844-1070-7.

Bonaparte, R., Daniel, D.E., & Koerner, R.M. 2002. Assessment and Recommendations for Optimal Performance of Waste Containment Systems, U.S. Environmental Protection Agency, National Risk Management Research Laboratory, Cincinnati, OH.

Giroud, J.P., Zornberg, J.G., & Zhao, A. 2000. Hydraulic Design of Geosynthetic and Granular Liquid Collection Layers, *Geosynthetics International*, Special Issue on Liquid Collection Systems, Vol 7, Nos. 4-6, pp. 285-380.

INAP 2017. Global Cover System Design, Technical Guidance Document. November 2017.

Narejo, D., Bachus, R., Thiel, R., Soong, T., Mengjia, L. 2007. Drainage Design Manual, Second Edition, GSE Environmental.